Bioconjugate Chemistry

Review

pubs.acs.org/bc

Nanoparticles Labeled with Positron Emitting Nuclides: Advantages, Methods, and Applications

Yongjian Liu* and Michael J. Welch

Department of Radiology, Washington University in St. Louis, Missouri 63110, United States

ABSTRACT: Over the past decade, positron emitter labeled nanoparticles have been widely used in and substantially improved for a range of diagnostic biomedical research. However, given growing interest in personalized medicine and translational research, a major challenge in the field will be to develop disease-specific nanoprobes with facile and robust radiolabeling strategies and that provide imaging stability, enhanced sensitivity for disease early stage detection, optimized in vivo pharmacokinetics for reduced nonspecific organ uptake, and improved targeting for elevated efficacy. This review briefly summarizes the major applications of nanoparticles labeled with positron emitters for cardiovascular imaging, lung diagnosis, and tumor theranostics.

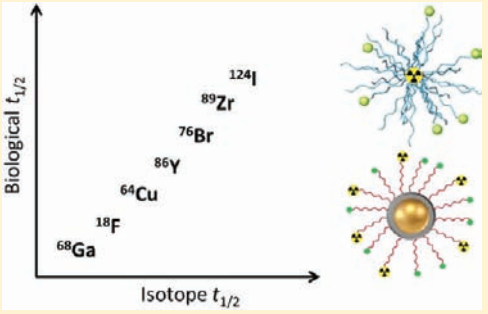

INTRODUCTION

During the past decade, molecular imaging has expanded due to its unique suitability to support personalized medicine by using modified or engineered molecules that can reveal individual biology when coupled with an appropriate imaging approach. Molecular imaging approaches include both single modality, such as positron emission tomography (PET), single photon emission computed tomography (SPECT), magnetic resonance imaging (MRI), magnetic resonance spectroscopy (MRS), computed tomography (CT), ultrasound, bioluminescence, and fluorescence imaging, and also multimodalities, such as PET/CT, SPECT/CT, and PET/MR.[1] Among these approaches, the radionuclide-based imaging methods, especially PET, have been a particular focus in biomedical research due to advantages that include high sensitivity (picomolar level) and limitless tissue penetration.[2]

While many types of molecules have been used in molecular imaging, a growing area of interest is the use of nanoparticles, which have great potential for early detection, accurate diagnosis, and personalized therapy of various diseases, especially cancer.[3] Nanoparticles are structures ranging in size from 1 to 100 nm (Figure 1). Nanoparticles show unique size-dependent physical and chemical properties, which can be optical, magnetic, catalytic, thermodynamic, and electrochemical.[4] Generally, nanoparticles used for biomedical research can be categorized into three groups: (1) inorganic nanoparticles including quantum dots, iron oxide nanoparticles, gold nanostructures, and upconversion nanophosphors; (2) polymer nanoparticles such as core−shell dendrimers and amphiphilic nanoparticles; (3) lipid nanoparticles including liposomes and solid lipid nanoparticles. Additionally, radiolabeled carbon nanotubes and nanodiamonds have also been widely explored for oncological applications.[5−8] Nanoparticle pharmacokinetics and biodistribution have been reviewed in detail elsewhere.[9,10]

Nanoparticle design flexibility enables tunable *in vivo* pharmacokinetics to improve delivery efficacy and to reduce nonspecific organ uptake by varying the size, charge, and surface modification.[11] With a diameter about 100 nm, nanoparticles show prolonged blood circulation and a relatively low rate of mononuclear phagocyte system (MPS) uptake.[10] Their size also fills a critical position between the macroscopic world and molecular-level detail, and they can be designed to provide unique advantages over both macroscopic materials and molecular systems. Because their size is comparable to large biological molecules (antibodies, DNA), nanoparticles can be designed to interact with various biomolecules both on the surface and inside cells, leading to significantly improved diagnosis and treatment efficacy.[3] Another noteworthy physicochemical characteristic is the nanoparticle's high surface area to volume ratio, which enables rich surface chemistry for various targeting components while retaining high loading capacity for detection elements and therapeutic payload, as well as multifunctionality for synergistic applications (Figure 1).[12] Regarding charge, neutral nanoparticles are reported to

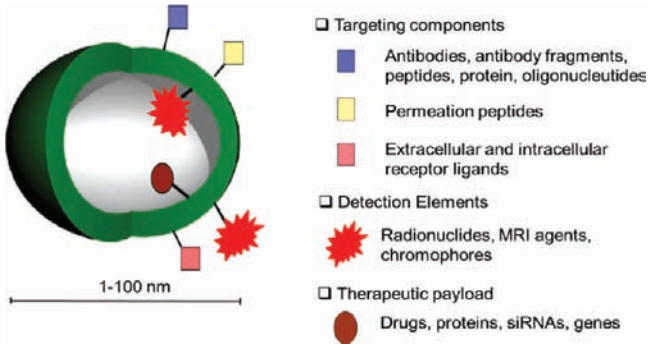

Figure 1. Scheme of multifunctional nanoparticles.

Received: May 24, 2011
Revised: December 31, 2011
Published: January 15, 2012

Table 1. Nuclear Characteristics of Selected PET Radionuclides for Nanoparticles

			β energy (KeV)			
radionuclide	$T_{1/2}$	decay (%)	max.	mean	main photon KeV (%)	production
^{68}Ga	67.7 min	β^+ (89) EC (11)	1899	829	511 (178.3)	^{68}Ge/^{68}Ga generator
^{18}F	109.7 min	β^+ (96.7) EC (0.1)	634	245	511 (193.5)	^{18}O (p, n) ^{18}F
^{64}Cu	12.7 h	β^+ (17) EC (44)	653	278	511 (34.8)	^{64}Ni (p, n) ^{64}Cu
^{76}Br	16.2 h	β^+ (55) EC (45)	3941	1180	511 (109); 559 (74)	^{76}Se (p, n) ^{76}Br
					657 (15.9); 1854	^{76}Se (d, 2n) ^{76}Br
^{86}Y	14.7 h	β^+ (33) EC (66)	3141	664	511 (63.9); 1077 (82.5) (82.5)	^{86}Sr (p, n) ^{86}Y
^{89}Zr	3.3 d	β^+ (23) EC(77)	901	397	909 (100)	^{89}Y(p, n)^{89}Zr
^{124}I	4.18 d	β^+ (23) EC (77)	2138	820	511 (46); 603 (62.9)	^{124}Te (p, n) ^{124}I
					723 (10.3)	^{124}Te (d, 2n) ^{124}I

demonstrate a slow clearance profile and reduced hepatic and splenic accumulations compared to charged nanoparticles,[13] while positively charged nanoparticles administered intravenously often form aggregates due to the presence of negatively charged serum proteins.[14] To reduce opsonization and aggregation caused by protein deposition, hydrophilic polymers such as polyethylene glycol are normally grafted onto the surface of nanoparticles, which also improves blood retention for optimized targeting and delivery.[15]

Over the past decade, growth in the applications of nanoparticles in molecular imaging and drug delivery by utilizing gamma-emitting radioisotopes and positron emitters[16−21] has led to drug discovery and numerous clinical trials.[22−25] Due to broad application of PET isotopes in translational research, we focus on the major biomedical applications of nanoparticles radiolabeled with these positron emitters.[26−30]

APPLICATIONS OF PET RADIONUCLIDE LABELED NANOPARTICLES

PET radionuclide labeled nanoparticles have been extensively used in both preclinical and clinical studies as a tool to explore nanoparticles' *in vivo* pharmacokinetics, imaging capability, and theranostic potential.[19,22,31,32] For nanoparticles with different physicochemical properties and functional groups, the specific PET isotope and radiolabeling strategy need to be carefully considered to generate an optimal imaging outcome. The nuclear characteristics of commonly used PET radionuclides for nanoparticles are summarized in Table 1.

There are two main radiolabeling strategies for nanoparticles. One is to radiolabel the nanoparticle structure itself, either on the surface or in the core. The other approach is to radiolabel the payload encapsulated inside the nanoparticle. These two approaches share much of their chemistry and are both widely used for nanoparticle radiolabeling (Table 2).[33]

In designing a radiolabeled nanoparticle for biomedical applications, some key factors need to be considered. The first of these is radiolabeling integrity. For *in vitro* or *in vivo* applications of radiolabeled nanoparticles, the radionuclide itself is observed or detected rather than the nanoparticle or the payload. Thus the nanoparticle structure and radiolabeling strategy must both be designed to get robust, stable radiolabeling. The second factor to consider is application compatibility—the half-life of the radionuclide needs to be congruent with the binding kinetics of the probe and target, as well as the probe's *in vivo* pharmacokinetics. A third factor is the targeting efficiency and radiolabeling specific activity, since a well-designed nanoparticle that allows increased loading of targeting ligands and high radiolabeling specific activity can provide elevated binding efficiency and reduce the required administration of nanoparticle to just trace amounts. The fourth factor is translational capability, since the U.S. Food and Drug Administration (FDA) approval for human application will be needed to explore the clinical potential of nanoparticles. For example, although there are chelators showing better ^{64}Cu radiolabeling stability for PET imaging,[34] DOTA (1,4,7,10-tetraazacyclododecane-1,4,7,10-tetraacetic acid) is still the most used chelator for translational research owing to its FDA approval and wide applications in clinical trials.[35]

A wide range of nanoparticles have been labeled with a variety of radionuclides. Quantum dots (QDs) are inorganic fluorescent semiconductor nanoparticles with desirable properties for optical imaging applications and have been radiolabeled with various radionuclides to explore their *in vivo* pharmacokinetics in an effort to develop multifunctional imaging probes. However, the hydrophobic nature of QDs leads to short blood circulation and insufficient targeting even after surface pegylation.[13,36] More importantly, their potential toxicity limits the translational application of QDs.[37] Magnetic nanoparticles, especially iron oxide nanoparticles, have also been widely explored for imaging applications because of high T_2 relaxivity for enhanced contrast, lack of radiation burden, biocompatibility, and low clinical toxicity.[38,39] In addition, although most applications of iron nanoparticles have been focused on developing MRI contrast agents, preparation of iron oxide based PET/MR dual functional nanoparticles has been an active research area. So far, various radiolabeling strategies with different positron emitters including ^{64}Cu, ^{68}Ga, and ^{124}I have been used to study the *in vivo* biodistribution profile and targeting efficiency of iron oxide nanoparticles with high radiolabeling yields and specific activities in a variety of animal disease models.[26,40−42] Another target is gold nanostructures, which have tunable optical properties in the near-infrared (NIR) region (650 to 900 nm) and are thus particularly attractive for hyperthermia based on the photothermal effect, leading to increased cancer theranostic applications.[9,43] Of the available imaging modalities, PET is the most widely used technique to monitor the delivery of gold nanostructures due to its high

dx.doi.org/10.1021/bc200264c | Bioconjugate Chem. 2012, 23, 671−682

Table 2. Labeling Strategies and Specific Activities of PET Radionuclides Labeled Nanoparticles

nanoparticle	radionuclide	labeling strategy	specific activity[a]	reference
Quantum dot	^{18}F	nucleophilic substitution	(3.7−7.5) × 10^8 Bq (10−20 mCi)/nmol	122
	^{64}Cu	DOTA	3.7 × 10^7 Bq (1 mCi)/nmol	36
	^{64}Cu	DO3A	6.2 × 10^5 Bq (17 μCi)/mg	123
Iron oxide	^{18}F	Click chemistry	(6.7 ± 0.8) × 10^8 Bq (18 ± 2 mCi)/mg Fe	73
	^{64}Cu	DOTA	(3.7−7.4) × 10^8 Bq (10−20 mCi)/mg Fe	26
	^{68}Ga	Direct labeling	3.6 × 10^8 Bq (10 mCi)/nM Fe	41
	^{68}Ga	NOTA	1.5 × 10^8 Bq (4 mCi)/nmol	124
	^{124}I	Tyrosine	5.1 × 10^7 Bq (1.4 mCi)/mg (Fe+Mn)	42
Aluminum hydroxide	^{18}F	Inorganic interaction	5.4 × 10^6 Bq (146 μCi)/mg	125
Upconversion nanophosphors	^{18}F	Inorganic interaction	7.8 × 10^8 Bq (21 mCi)/mg	126
Gold nanoparticle	^{64}Cu	DOTA	5.9 × 10^{11} Bq (16 Ci)/nmol	44
Latex	^{68}Ga	Direct labeling	2 × 10^5 Bq (5 μCi)/mg	127
	^{64}Cu	DOTA	(13.3 ± 1.0) × 10^5 Bq (36 ± 3 μCi)/nmol	117
	^{64}Cu	TETA, CB-TE2A	(7.7 ± 0.6) × 10^5 Bq (21 ± 2 μCi)/nmol	128
	^{64}Cu	BAT	2.1 × 10^7 Bq (0.6 mCi)/nmol	129
Liposome	^{18}F	Encapsulation	2.8 × 10^7 Bq (0.8 mCi)/nmol	130
Solid lipid nanoparticle	^{18}F	Encapsulation	1.1 × 10^5 Bq (3 μCi)/nmol	131
	^{68}Ga	DTPA	4 × 10^6 Bq (0.1 mCi)/μg	132
	^{64}Cu	BAT	(1.4 ± 0.3) × 10^6 Bq (38 ± 8 μCi)/mg lipid	133
Polymer	^{76}Br	Tyrosine	1.9 × 10^5 Bq (5 μCi)/μg	27
	^{64}Cu	DOTA	1.5 × 10^7 Bq (0.4 mCi)/μg	63
	^{18}F	[^{18}F]FETos	30 Bq (0.8 nCi)/μg	134
Nanotube	^{64}Cu	DOTA	(7.4−11.1) × 10^6 Bq (0.2−0.3 mCi)/μg	5
	^{89}Zr	desferrioxamine B	592 KBq/μg	135
	^{86}Y	DOTA	555 GBq/g	8

[a]The data presented in Table 2 should be reviewed with caution. The values listed in the literature are specific activities quoted during nanoparticle radiolabeling using different units and have also been calculated using different analytical methodologies.

sensitivity and quantitative detection. A recent study of a ^{64}Cu-radiolabeled gold nanoshell showed clear tumor uptake, indicating the potential not only for PET imaging, but also as a theranostic agent.[44]

Polymer nanoparticles have been widely used for biomedical imaging applications using a variety of radiolabeling strategies due to the versatility of synthetic chemistry. The structural design and *in vivo* PET imaging of polymer nanoparticles is reviewed in detail elsewhere.[17] In addition, liposome nanoparticles have been used for drug delivery since their initial discovery 40 years ago and are available with a myriad of possible compositions and modifications.[45] Significant progress has been achieved by utilizing liposomes as nanocarriers for both diagnosis and therapy. A wide variety of radionuclides and labeling strategies have been employed for generating radioactive liposomes, and these are reviewed elsewhere.[46]

Silica nanoparticles, due to the well-known biocompatibility, have also been explored for various biomedical applications with radiolabels.[47,48] With ^{18}F labeling, the thermally hydrocarbonized porous silicon nanoparticle demonstrated that the particles passed intact through the gastrointestinal tract after oral administration and were not absorbed from a subcutaneous deposit. With intravenous injection, a fast MPS clearance profile was confirmed. This silica nanoparticle exhibited excellent *in vivo* stability, low cytotoxicity, and nonimmunogenic profiles, indicating the potential for oral drug delivery.[47] In another study, an organically modified silica nanoparticle also showed no toxicity *in vivo* and full clearance through hepatobiliary excretion, which was confirmed by both ^{124}I and near-infrared dye DY776 labeling.[48] Lately, nanodiamonds have also been proposed as a promising biomaterial for drug delivery owning to the biocompatibility of this form of carbon.[49] With ^{18}F radiolabeling, these nanodiamonds showed high lung, liver, and spleen uptake, and significant excretion through the urinary tract.[7] Another recently emerged nanostructure for oncological applications is known as an upconversion nanoparticle. This nanostructure has very fast radiofluorination kinetics and multimodality imaging properties, but its *in vivo* pharmacokinetics still need improvement to achieve sufficient blood circulation.[50−52]

With increasing support from the National Institute of Health to study and develop nanotechnology,[53] additional applications of nanomedicine research are expected. Here, we describe selected applications of radiolabeled nanoparticles with the focus on core−shell polymeric nanoparticles.

Radiolabeled Nanoparticles for Cardiovascular Imaging. It is well-known that systemically administered nanoparticles tend to be sequestered by the MPS system and accumulate mainly in the liver and spleen. Clearance from the bloodstream depends on particle size, surface configuration, and several other factors, and the first step is opsonization that triggers complement activation and macrophage recognition.[54] To target the low abundance biomarkers in animal cardiovascular disease models, nanoparticles must have high radiolabeling specific activity and binding specificity and be able to circulate for a sufficient period of time in the bloodstream, which requires well-defined structure, composition, and controlled *in vivo* properties. Among various nanostructures (such as iron oxide, silica, and gold nanoparticles),[55−59] amphiphilic core−shell nanostructures have received particular attention because of the tunable *in vivo* pharmacokinetics and versatile conjugation chemistry.[60,61] Shell cross-linked knedel-like

dx.doi.org/10.1021/bc200264c | *Bioconjugate Chem.* 2012, 23, 671−682

nanoparticles (SCKs) are composed of a hydrophobic polystyrene core that can be used to load hydrophobic drug molecules, and a hydrophilic external shell of poly(acrylic acid-*co*-acrylamide) that provides additional sites for other functional units such as imaging moieties. Through various synthetic strategies, especially cross-linking, SCKs can be prepared with controlled size, surface charge, pegylation density, multifunctionality, and tuned *in vivo* pharmacokinetics.[54,62] Additionally, the multivalency of SCKs empowers flexible radiochemistry (^{64}Cu, ^{76}Br, ^{124}I, and ^{18}F) for PET applications. By conducting DOTA conjugation before nanoparticle assembly, the amount of DOTA accessible for ^{64}Cu labeling could be accurately controlled with more than 400 copies per SCK, leading to a specific activity greater than 1.48×10^7 Bq/μg.[63]

Another type of core−shell star-like or comb-like copolymer could be prepared with nitroxide mediated living radical polymerization to create defined sizes and morphologies. In one example, the chelator DOTA was placed in an internal, hydrophilic environment allowing efficient ^{64}Cu radiolabeling to make a protected and high specific activity nanoscopic imaging probe. Biodistribution studies showed a distinct correlation between the length of PEG grafts and the *in vivo* circulation time; with increased PEG chain length, increased blood retention and reduced MPS system uptake were observed.[64] Furthermore, the cargo loading capacity of this type of nanoparticle can be adjusted while retaining similar physicochemical properties. In a recent study, varying amounts of RGD peptide (5−50% RGD) were accurately conjugated to the shell of comb-like nanoparticles for targeting $\alpha_v\beta_3$ integrin, and these RGD-combs all maintained similar sizes and radiolabeling specific activities.[65,66] The *in vitro* studies of the RGD-combs showed positive correlation between RGD peptide loading and uptake in $\alpha_v\beta_3$ integrin-positive U87MG glioblastoma cells, demonstrating the importance of controlled conjugation of targeting groups to achieve optimal targeting performance with multivalent nanoparticle systems.[66] Further, the comb nanoparticles were conjugated with C-type atrial natriuretic factor (CANF) to target the natriuretic peptide clearance receptor (NPRC) in a mouse angiogenesis model. By controlling the number of DOTA conjugation, high specific activity ($5.4 \pm 1.2 \times 10^9$ Bq/nmol) of ^{64}Cu radiolabeling could be achieved, ensuring the trace administration of ^{64}Cu-DOTA-CANF-comb (7 pmol) for imaging studies. PET images showed significantly higher standardized uptake values (SUVs) at angiogenesis sites created by hindlimb ischemia compared to contralateral control sites. More importantly, the SUVs of ^{64}Cu-DOTA-CANF-comb were 3.4 times higher than those obtained with DOTA-CANF peptide tracer and about triple of those from the nontargeted ^{64}Cu-DOTA-comb, demonstrating the superiority of a multivalent nanoprobe over the corresponding monovalent CANF peptide for *in vivo* molecular targeting (Figure 2).[67]

In developing nanoparticles for targeted drug delivery, controlled release kinetics, bioavailability, and reduced toxicity are key considerations, which have made biodegradable nanoparticles an active research area.[68−70] Compared to the inorganic nanoparticles, polymeric nanoparticles can be uniquely prepared with biodegradable core or cross-linker for programmed release of therapeutic payload through enzyme or pH response degradation (Figure 3), which greatly enhances their biocompatibility and makes them better candidates for targeted diagnosis and drug delivery. Thus, a core−shell biodegradable dendritic nanoprobe labeled with ^{76}Br has been prepared for targeting $\alpha_v\beta_3$ integrins expressed in a mouse angiogenesis model. The controlled introduction of targeting CRGDC peptide to the shell offered 50-fold enhancement of *in vitro* binding affinity to $\alpha_v\beta_3$ integrins relative to the monovalent RGD peptide alone. *In vivo*, specific targeting to $\alpha_v\beta_3$ was observed with the targeted nanoprobe demonstrating a 6-fold increase of receptor-mediated endocytosis at the injured site compared to the control nanoprobe (Figure 4).[27] Additionally, the potential

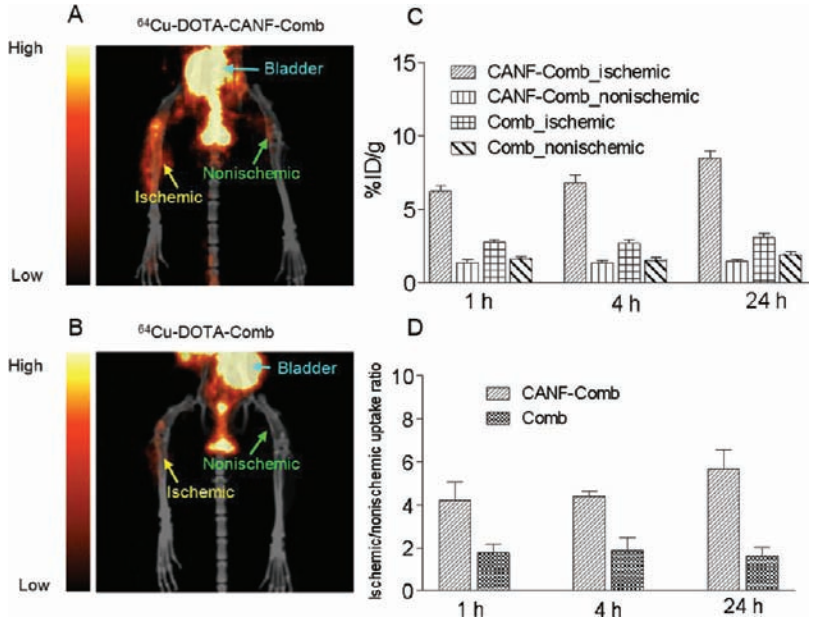

Figure 2. PET/CT images of ^{64}Cu-DOTA-CANF-Comb and ^{64}Cu-DOTA-Comb in the HLI induced angiogenesis model obtained 7 days after ischemia. (A) ^{64}Cu-DOTA-CANF-Comb in HLI model showing the accumulation of activity in the ischemic limb with little observed on the contralateral nonischemic limb. (B) ^{64}Cu-DOTA-Comb in HLI model showing the weak uptake in both ischemic and nonischemic limbs. (C) Uptake of ^{64}Cu-DOTA-CANF-Comb (n = 8) and ^{64}Cu-DOTA-Comb (n = 7). (D) Ischemic/nonischemic uptake ratios of ^{64}Cu-DOTA-CANF-Comb (n = 8) and ^{64}Cu-DOTA-Comb (n = 7). Figure reproduced with permission from reference 67.

dx.doi.org/10.1021/bc200264c | *Bioconjugate Chem.* 2012, 23, 671−682

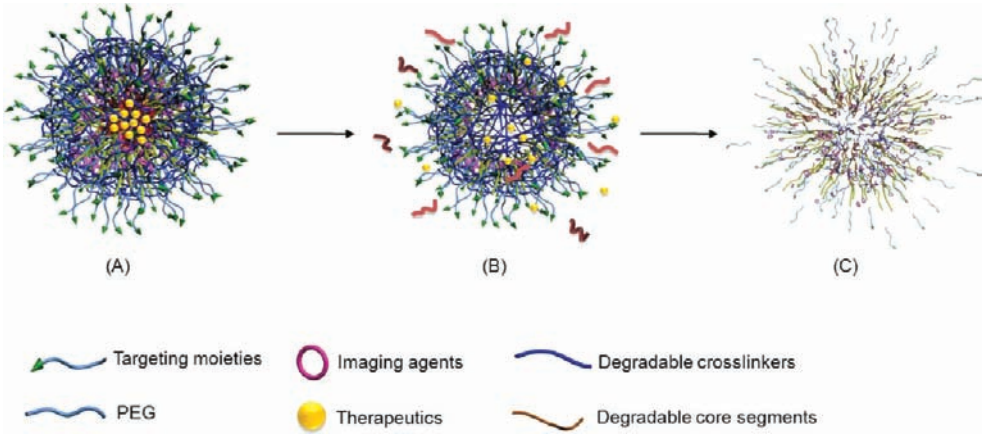

Figure 3. Diagram of the biodegradation process of shell cross-linked knedel-like nanoparticles.

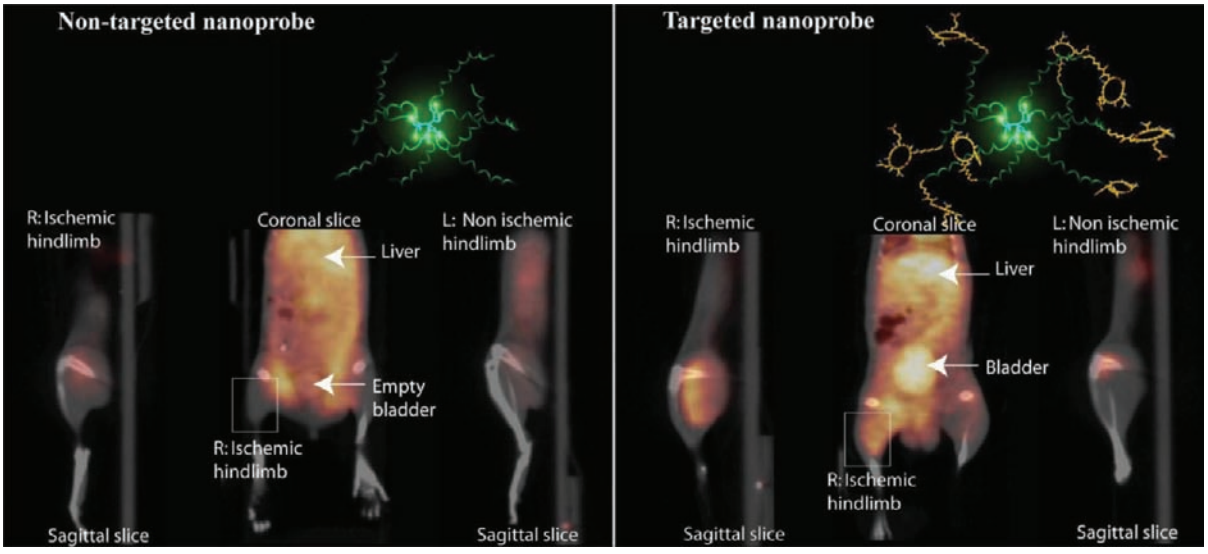

Figure 4. Noninvasive PET/CT images of angiogenesis induced by hindlimb ischemia in a murine model. (A) Nontargeted dendritic nanoprobes (shown bottom center). (B) Uptake of $\alpha\beta_3$-targeted dendritic nanoprobes was higher in ischemic hindlimb (left side of image) as compared with control hindlimb (right side of image). Figure reproduced with permission from reference 27.

of poly(lactide-*co*-glycolide) based biodegradable nanoparticles has also been assessed for PET imaging due to their FDA approval for human use.[71]

Iron oxide nanoparticles have been widely used in cardiovascular imaging with various radiolabels. With carbohydrates such as dextran coating and diethylenetriaminepentaacetic acid (DTPA) conjugation, the ^{64}Cu radiolabeled iron oxide nanoparticle (^{64}Cu-TNP) was used to target macrophage in an apolipoprotein E deficient (apoE$^{-/-}$) mouse model of aneurysms. The high specific activity (3.7×10^8 Bq/mg Fe of nanoparticle) ensured lower dose administration (1.5 mg Fe/kg body weight) than that used in oncology clinical trials (2.6 mg Fe/kg body weight) and sensitive detection of nanoparticle accumulation in various organs. The *in vivo* biodistribution of ^{64}Cu-TNP showed sufficient blood circulation ($t_{1/2} \geq 4$ h) and major accumulation in liver and intestine. PET/CT imaging clearly showed significant localization of ^{64}Cu-TNP in the thoracic aorta with a target-to-background ratio of 5.1 ± 0.9, indicating the clinical translatability of this radiolabeled nanoparticle. Furthermore, an ^{18}F radiolabeled iron oxide nanoparticle (^{18}F-CLIO) has been developed due to the wide availability, sensitivity, and covalent radiolabeling of this radioisotope.[72] With rapid [^{18}F] click fluorination, high radiolabeling efficiency and specific activity were achieved ($(6.8 \pm 0.8) \times 10^8$ Bq/mg Fe of nanoparticle). The *in vivo* pharmacokinetics studies showed comparable blood retention to the ^{64}Cu-TNP. In the apoE$^{-/-}$ aneurysms mouse model, PET imaging showed that the avid internalization by phagocytic cells led to significantly higher tracer accumulation at aneurysms relative to wild-type aorta.[73]

Radiolabeled Nanoparticles for Lung Imaging. The incidence of respiratory disease and infections such as asthma, chronic obstructive pulmonary disease, cystic fibrosis, infectious disease, and tuberculosis is increasing worldwide. The classification of chronic respiratory diseases as a major disease burden by the World Health Organization has led to increased efforts to prevention, diagnosis and treatment of these diseases.[74] The current challenges for respiratory disease treatment include the sustained delivery and controlled release of drugs, reduction of side effects caused by high dose administration, and increasing drug resistance. Nanotechnology-based delivery systems have gained attention for use in pulmonary diagnosis and therapy due to their capacity for targeted

dx.doi.org/10.1021/bc200264c | *Bioconjugate Chem.* 2012, 23, 671–682

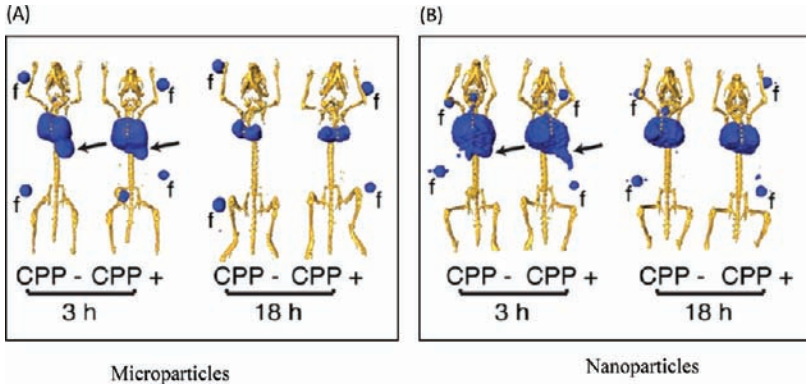

Figure 5. Three-dimensional reconstruction of microPET/CT imaging of ^{76}Br-labeled particles in mice lungs following intratracheal delivery. Arrows indicate gastrointestinal tract activity. Fiduciaries (f) used for coregistration are included. (A) Microparticles; (B) nanoparticles. CPP-: without cell penetration peptide: CPP+: with cell penetration peptide. Figure reproduced with permission from reference 29.

deposition, bioadhesion, bioavailability, and biocompatibility, and their sustained release, which allows reduced dosing frequency and improves convenience for the patient.[75] So far, a variety of nanocarriers have been used for pulmonary applications including liposomes, solid lipid nanoparticles, metal nanoparticles, nanotubes, and polymeric nanoparticles.[76,77] Among these nanostructures, owing to the concern about the toxicity, those with potential clinical pulmonary applications such as polymeric nanoparticles, especially the ones made from biodegradable materials, have been an active area in both lung diagnosis and treatment.[78]

Recently, various materials such as poly(lactide-*co*-glycolide), polyacrylates, and polyacrylamide have been used for formulation of biodegradable nanoparticles.[75,76,79,80] In contrast to the hydrophobic materials, the polyacrylamide based hydrogel offers excellent biocompatibility and hydrophilicity. It also is strongly endosome-disrupting, which makes it a candidate for cytoplasmic delivery/imaging.[81,82] With an acid-degradable cross-linker, the entrapped payload can be released in a pH-dependent manner inside endosomes.[83] In addition, for better cellular delivery, a cell penetration peptide (CPP) can be used on the nanoparticles to get various cargos into the cells without disturbing the stability of the cell membrane and with low cytotoxic effects.[84] In a recent study, it was reported that the optimal size for deposition in the deep lung for systemic delivery is approximately 1−3 μm—microparticles rather than nanoparticles.[85] Therefore, a nona-arginine functionalized polyacrylamide-based microparticle was synthesized to study the delivery efficiency of entrapped protein into nonphagocytic lung epithelial cells (BEAS-2B). *In vitro* results showed effective delivery of encapsulated BSA-Alexa Fluor 488 into the BEAS-2B cells in both CPP- and concentration-dependent manners, as well as a time dependency.[86] As a result, this CPP-modified microparticle was labeled with radiohalogens (^{125}I and ^{76}Br) for animal studies to assess the *in vivo* fate, lung retention, and cellular uptake after intratracheal administration. Furthermore, nanosized CPP particles were also synthesized to compare size-related differences in the clearance profiles. The biodistribution studies revealed that particle retention and extrapulmonary distribution was, in part, size dependent. Microparticles were rapidly cleared by mucociliary routes but, unexpectedly, also through circulation. In contrast, nanoparticles had prolonged lung retention enhanced by the CPP, which was confirmed by the PET imaging analysis with ^{76}Br-radiolabeled nanoparticles (Figure 5). The studies indicate the potential of microparticles for short-term applications and benefits of nanoparticles for serial imaging or therapy of a persistent lung injury.[29] In contrast, a study of acute lung injury used latex nanoparticles coated with anti-intercellular adhesion molecule-1(ICAM-1) antibody and labeled with ^{64}Cu for targeting the pulmonary endothelium. Biodistribution studies showed 3- to 4-fold higher uptake in the lungs of mice injected with ICAM-targeted nanoparticles than those receiving control nanoparticles. PET imaging clearly demonstrated the accumulation of radioactivity in the lungs. However, metabolic studies showed that the *in vivo* stability of this nanoprobe needs further improvement for prolonged pulmonary drug delivery.[28]

Lately, a new type of promising biomaterial-carbon known as a nanodiamond has been explored for biomedical applications due to its biocompatibility, ability to cross the cell membrane, and capability to be functionalized to act as carriers. The initial biodistribution and PET imaging via ^{18}F radiolabeling showed high pulmonary retention, most likely by size exclusion, indicating potential for lung applications.[87] Clinically, ^{68}Ga-labeled carbon nanoparticles have also been used for pulmonary embolism PET/CT ventilation-perfusion imaging, which has shown superiority to conventional V/Q lung scintigraphy.[88]

Radiolabeled Nanoparticles for Tumor Imaging. One hundred years ago, Paul Ehrlich proposed the idea of "magic bullet" for the development of medicine to specifically target the cancer disease.[89] Recently, in development of molecular biology and genetic research, two major antitumor strategies have been revealed: (1) utilization of molecularly targeted therapeutics to block hallmarks of cancer, and (2) development of novel drug delivery systems utilizing tumor-specific nanomedicines to improve the pharmacokinetics and bioavailability of vehicle-carried drugs.[90] Because of the versatile physiochemical properties of the nanostructure, in contrast to conventional anticancer drugs, nanoparticles can provide significant improvements in pharmacokinetics, targeting specificity and efficiency, diagnostic and therapeutic efficacy, and toxicity, which could lead to earlier detection and better control of cancer.[91] In development of nanoparticle-based agents for cancer diagnosis and therapy, important factors are active targeting of biomarkers expressed in the tumor and harnessing the enhanced permeability and retention (EPR) effect due to the leaky neovasculature of the tumor proposed by Matsumura and Maeda[92] that can be used for "passive targeting".[93] Compared with conventional small molecule-based anticancer drugs, macromolecules display superior *in vivo* pharmacokinetics and greater

dx.doi.org/10.1021/bc200264c | *Bioconjugate Chem.* 2012, 23, 671−682

tumor delivery and selectivity.[23,93] Interestingly, a size relationship with the EPR effect was observed that larger and long-circulating macromolecules (>30−45 kDa) are retained in the tumor tissue longer, whereas smaller molecules easily diffuse back out into the bloodstream.[92] Nanoparticle size, surface modification, and vascular mediators all have been studied as approaches to harness the EPR effect for improved tumor diagnosis and therapy using nanoparticles.[93,94]

While the EPR effect is helpful, nanoparticles also offer the ability to specifically target tumors based on an individual patient's biology by targeting various biomarkers on the cancer cells. To date, a range of targeting groups have been developed and used for cancer nanomedicine.[3,95−99] Among them, antisense-based imaging agents such as phosphodiester (PO) oligodeoxynucleotides (ODN) and phosphorothioate (PS)-ODNs, which are designed according to the gene expression profile of human cancerous cells, are promising imaging probes for the early and specific detection of cancer due to the high specificity.[100] However, the rapid degradation by endo- and exonucleases *in vivo* made their PET imaging challenging. Alternatively, with the complete replacement of the sugar−phosphate backbone to amine backbone (peptide nucleic acids or PNA) through chemical modification, the PNAs displayed strong resistance to enzymatic degradation without changing the binding affinity and specificity. Therefore, a specially designed PNA sequence was used to target the elevated expression of upstream of N-ras (unr) mRNA in a mouse MCF-7 breast tumor model with ^{64}Cu radiolabeling. PET imaging clearly showed the tumor accumulation of ^{64}Cu-DOTA-PNA50-K4, indicating the potential of this antisense PNA as a specific molecular probe for cancer diagnosis.[101] Thus, this antisense PNA (PNA50) was conjugated to well-defined SCK nanoparticles for further evaluation. The *in vivo* pharmacokinetic studies demonstrated improved biodistribution profiles relative to PNA alone tracer while maintaining the PNA binding capability to target, indicating the potential of this nanoprobe for sensitive and specific cancer diagnosis.[102]

In another study, SCKs conjugated with folate showed specific interaction with folate receptors overexpressed in KB cells. *In vivo* studies with ^{64}Cu labeling demonstrated improved blood retention and folate receptor-mediated uptake of SCKs in small tumors.[103] To develop sensitive nanoprobes for cancer diagnosis, the click chemistry strategy has also been explored on SCKs to obtain ultrahigh specific activity ^{64}Cu/^{18}F radiolabeled nanoparticles as well as controlled conjugation of targeting ligands by designing click sites both in the core and on the surface.[104,105]

Iron oxide nanoparticles have been widely explored for PET/MR or PET/MR/optical tumor imaging.[106−108] With optimized surface pegylation and DOTA functionalization, a ^{64}Cu radiolabeled iron oxide nanoparticle (specific activity = (3.7−7.4) × 10^8 Bq/mg Fe) showed elevated blood retention of (37.3 ± 12.9)%ID/g at 1 h post injection in mice, confirmed by PET imaging (Figure 6). In another study, a cyclic RGD peptide (c(RGDfC)) was conjugated to a superparamagnetic iron oxide nanoparticle (SPIO) for targeted PET/MR tumor imaging.[109,110] This ^{64}Cu-cRGD-SPIO illustrated low (<15% ID/g) hepatic burden up to 48 h and constant tumor uptake (~5% ID/g) across the study with the highest (11.3 ± 2.5) tumor/muscle ratio observed at 48 h. Furthermore, compared to the control ^{64}Cu-SPIO, ^{64}Cu-cRGD-SPIO had significantly ($p < 0.05$) higher tumor accumulation during the study, indicating $\alpha_v\beta_3$-specific targeting.[40]

Lately, Cerenkov luminescence imaging has become an active topic in biomedical research due to the combination of nuclear tomography with optical techniques generated from the decay of radionuclides, and suitability for rapid, high-throughput screening.[111] Thus, a ^{124}I radiolabeled iron oxide nanoparticle was developed for optical/PET/MR trimodality tumor imaging. The complementary nature of this hybrid nanoprobe facilitated noninvasive differentiation between tumor-metastasized sentinel lymph nodes (SLNs) and tumor-free SLNs.[112]

Silica nanoparticles, which are inherently nontoxic and biocompatible, have been an attractive candidate for theranostics in various patient settings. With cRGDY conjugation, high *in vitro* binding affinity (IC_{50} = 1.2 nM) was achieved. In animal melanoma model, this targeted ^{124}I-cRGDY-PEG-dots nanoprobe showed optimized pharmacokinetics (blood and tumor half-lives = 5.9 and 73.5 h, respectively), $\alpha_v\beta_3$-specific tumor uptake, and high tumor-to-muscle ratio (T/M = 5 at 24 h). Dosimetry studies demonstrated comparable radiation doses to other clinically used PET tracers. Toxicity studies confirmed full clearance in one week and no tissue-specific pathologic effect. Therefore, a human clinical trial has been planned to investigate the potential of this targeted nanoprobe in staging metastatic disease in the clinical setting.[24]

Another effort to develop theranostic agents involves use of various gold nanostructures such as nanoparticles, nanorods, nanoshells, and nanocages due to the well-known biocompatibility. They can serve as optical imaging agents due to the surface plasmon resonance, or PET imaging probe through surface conjugation. More importantly, their photothermal properties empower the conversion of absorbed light into heat through nonradiative electron relaxation dynamics for cancer treatment.[9,43] Thus, gold nanoshell was used for multimodality theranostics with ^{64}Cu radiolabeling and RGD peptide conjugation. PET/CT of this ^{64}Cu-NS-RGDfK showed significant tumor uptake and tumor vascular specificity, indicating active targeting and improved efficacy of photothermal ablation.[113] Additionally, a chelator-free [^{64}Cu]CuS nanoparticle with controlled specific activity was also prepared for tumor theranostic application. The pegylated [^{64}Cu]CuS nanoparticles showed about 15% ID/g blood retention at 4 h in biodistribution studies and high tumor-to-muscle ratio (T/M = 6.55) at 24 h. Interestingly, this PEG-[^{64}Cu]CuS nanoparticle also displayed the photothermal property.[114]

Liposomes, widely used for drug delivery in both clinical and preclinical applications,[115] can also be a good theranostic candidate.[116] Initially, liposomes with ^{64}Cu radiolabeling have been used to probe the EPR effect in tumor-bearing mice. With a remote loading approach for ^{64}Cu encapsulation, improved radiolabeling stability and tumor accumulation ((5.0 ± 2.0)% ID/organ) was obtained, confirmed by PET/CT.[117] This approach was used to study the EPR effect during the transition from premalignant to malignant cancer in a mouse ductal carcinoma model. With disease progression, the vascular volume fraction increased 1.6-fold and the apparent vascular permeability to liposomes increased about 2.5-fold. Thanks to the long *in vivo* half-life ($t_{1/2}$ = 18 h), high tumor/muscle ratio (17.9 ± 8.1) was achieved with ^{64}Cu-liposomes. Interestingly, more heterogeneous intratumoral distribution was observed in the presence of increased vascular permeability.[118] More importantly, by adding encapsulation of EGFR kinase-targeting group SKI212243, this targeted liposome showed significantly higher tumor accumulation at 48 h relative to ^{124}I-SKI212243 alone and greatly improved tumor-to-background contrast ratio

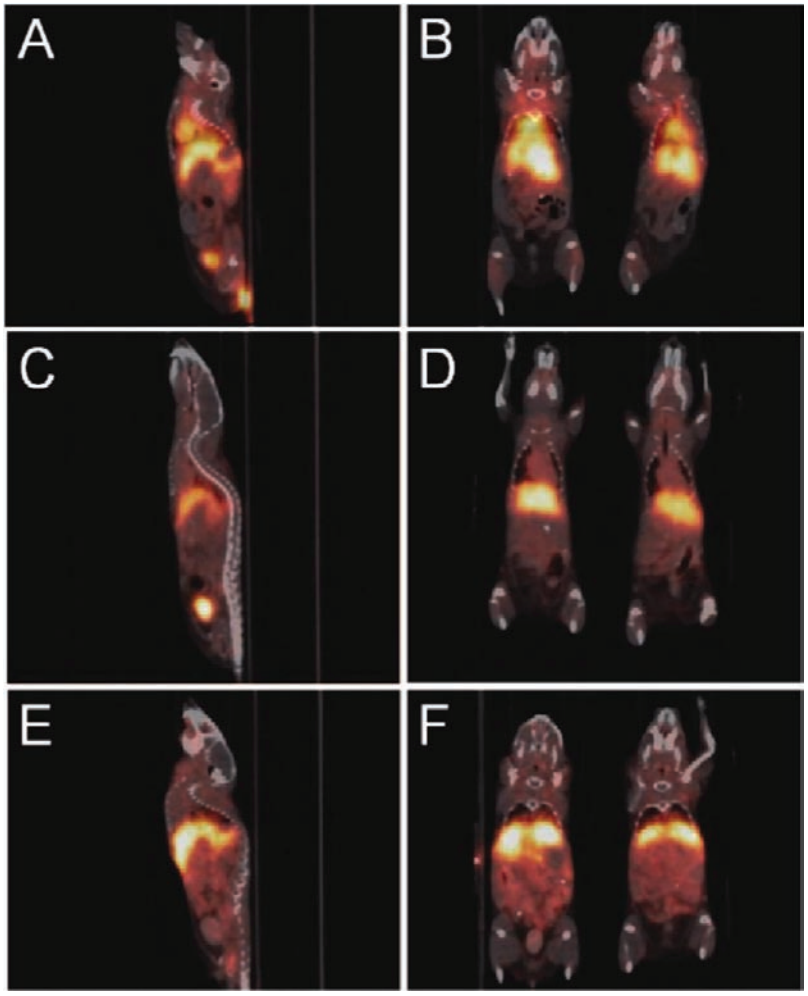

Figure 6. Coregistered microPET/microCT of BALB/c mice administered 100 μCi of ^{64}Cu-mSPIOs (10 mg Fe/kg body weight, 100 μL injection volume). Whole body sagittal (A–E) and coronal (B–F) PET images are decay corrected and scaled by min/max frame: (A, B) 1 h; (C, D) 4 h; and (E, F) 24 h post injection. Figure reproduced with permission from reference 26.

at 48 h, indicating specific targeting (not just the EPR effect due to improved circulation).[119]

Lately, with improvement of nanoparticle *in vivo* pharmacokinetics, use of ^{89}Zr for nanoparticle PET oncological imaging has gained interest owing to its noteworthy physical properties, including long half-life ($t_{1/2}$ = 78.4 h) and high specific activity.[120] In an LS174T colon carcinoma model, the ^{89}Zr-labeled single-walled carbon nanotubes (SWCNT-([^{89}Zr]-DFO)(E4G10) showed rapid tumor accumulation and gradually increased tumor-to-muscle contrast ratio over time (1.61 at 1 h to 5.08 at 96 h). In another colon carcinoma model (CT26), a ^{89}Zr-labeled cross-linked dextran nanoparticle showed primary localization in lymph node (34 ± 16%ID/g). In some tumor bearing mice, PET imaging showed intense tumor uptake (20 ± 5%ID/g), surprisingly higher than other MPS organs, indicating translational potential.[121]

CONCLUSION

A variety of nanoparticles have been engineered and explored for diagnostic and therapeutic potential in various diseases. The examples presented in this review focus on nanoparticles labeled with PET isotopes for cardiovascular, pulmonary, and tumor imaging, as well as for pharmacokinetic evaluation. So far, significant progress has been achieved in nanoparticle structure design, *in vitro* trafficking, and *in vivo* fate mapping by using PET. More effort will be necessary to achieve active targeting and quantification of low-level biomarkers expressed in animal models using customized nanoparticles generated through new chemistry for early disease detection and prevention with PET, and to achieve development of approved biocompatible and biodegradable nanoparticles for personalized medicine and translational research.

AUTHOR INFORMATION

Corresponding Author

*E-mail: liuyo@mir.wustl.edu. Phone: 314-362-8431. Fax: 314-362-9940.

ACKNOWLEDGMENTS

The authors' work presented is supported by the National Heart, Lung and Blood Institute of the National Institutes of Health as a Program of Excellence in Nanotechnology (HHSN268201000046C).

REFERENCES

(1) Schober, O., Rahbar, K., and Riemann, B. (2009) Multimodality molecular imaging--from target description to clinical studies. *Eur. J. Nucl. Med. Mol. Imaging 36*, 302–14.

(2) Hagooly, A., Rossin, R., and Welch, M. J. (2008) Small molecule receptors as imaging targets. *Handb. Exp. Pharmacol.*, 93−129.
(3) Gunasekera, U. A., Pankhurst, Q. A., and Douek, M. (2009) Imaging applications of nanotechnology in cancer. *Target Oncol. 4*, 169−81.
(4) Sanvicens, N., and Marco, M. P. (2008) Multifunctional nanoparticles--properties and prospects for their use in human medicine. *Trends Biotechnol. 26*, 425−33.
(5) Liu, Z., Cai, W., He, L., Nakayama, N., Chen, K., Sun, X., Chen, X., and Dai, H. (2007) In vivo biodistribution and highly efficient tumour targeting of carbon nanotubes in mice. *Nat. Nanotechnol. 2*, 47−52.
(6) Villa, C. H., McDevitt, M. R., Escorcia, F. E., Rey, D. A., Bergkvist, M., Batt, C. A., and Scheinberg, D. A. (2008) Synthesis and biodistribution of oligonucleotide-functionalized, tumor-targetable carbon nanotubes. *Nano Lett. 8*, 4221−8.
(7) Rojas, S., Gispert, J. D., Martin, R., Abad, S., Menchon, C., Pareto, D., Victor, V. M., Alvaro, M., Garcia, H., and Herance, J. R. (2011) Biodistribution of amino-functionalized diamond nanoparticles. in vivo studies based on (18)F radionuclide emission. *ACS Nano 5*, 5552−5559.
(8) McDevitt, M. R., Chattopadhyay, D., Jaggi, J. S., Finn, R. D., Zanzonico, P. B., Villa, C., Rey, D., Mendenhall, J., Batt, C. A., Njardarson, J. T., and Scheinberg, D. A. (2007) PET imaging of soluble yttrium-86-labeled carbon nanotubes in mice. *PLoS One 2*, e907.
(9) Khlebtsov, N., and Dykman, L. (2011) Biodistribution and toxicity of engineered gold nanoparticles: a review of in vitro and in vivo studies. *Chem. Soc. Rev. 40*, 1647−71.
(10) Li, S. D., and Huang, L. (2008) Pharmacokinetics and biodistribution of nanoparticles. *Mol. Pharm. 5*, 496−504.
(11) Owens, D. E. 3rd, and Peppas, N. A. (2006) Opsonization, biodistribution, and pharmacokinetics of polymeric nanoparticles. *Int. J. Pharm. 307*, 93−102.
(12) Cormode, D. P., Skajaa, T., Fayad, Z. A., and Mulder, W. J. (2009) Nanotechnology in medical imaging: probe design and applications. *Arterioscler. Thromb. Vasc. Biol. 29*, 992−1000.
(13) Schipper, M. L., Cheng, Z., Lee, S. W., Bentolila, L. A., Iyer, G., Rao, J., Chen, X., Wu, A. M., Weiss, S., and Gambhir, S. S. (2007) microPET-based biodistribution of quantum dots in living mice. *J. Nucl. Med. 48*, 1511−8.
(14) Zhang, J. S., Liu, F., and Huang, L. (2005) Implications of pharmacokinetic behavior of lipoplex for its inflammatory toxicity. *Adv. Drug Delivery Rev. 57*, 689−98.
(15) Jokerst, J. V., Lobovkina, T., Zare, R. N., and Gambhir, S. S. (2011) Nanoparticle PEGylation for imaging and therapy. *Nanomedicine (Lond.) 6*, 715−28.
(16) Jarzyna, P. A., Gianella, A., Skajaa, T., Knudsen, G., Deddens, L. H., Cormode, D. P., Fayad, Z. A., and Mulder, W. J. (2010) Multifunctional imaging nanoprobes. *Wiley Interdiscip. Rev. Nanomed. Nanobiotechnol. 2*, 138−50.
(17) Welch, M. J., Hawker, C. J., and Wooley, K. L. (2009) The advantages of nanoparticles for PET. *J. Nucl. Med. 50*, 1743−6.
(18) Minchin, R. F., and Martin, D. J. (2010) Nanoparticles for molecular imaging--an overview. *Endocrinology 151*, 474−81.
(19) Loudos, G., Kagadis, G. C., and Psimadas, D. (2010) Current status and future perspectives of in vivo small animal imaging using radiolabeled nanoparticles. *Eur. J. Radiol. 78*, 287−295.
(20) Hong, H., Zhang, Y., Sun, J., and Cai, W. (2009) Molecular imaging and therapy of cancer with radiolabeled nanoparticles. *Nano Today 4*, 399−413.
(21) Gomes, C. M., Abrunhosa, A. J., Ramos, P., and Pauwels, E. K. (2011) Molecular imaging with SPECT as a tool for drug development. *Adv. Drug Delivery Rev. 63*, 547−54.
(22) Heidel, J. D., and Davis, M. E. (2011) Clinical developments in nanotechnology for cancer therapy. *Pharm. Res. 28*, 187−99.
(23) Schluep, T., Hwang, J., Hildebrandt, I. J., Czernin, J., Choi, C. H., Alabi, C. A., Mack, B. C., and Davis, M. E. (2009) Pharmacokinetics and tumor dynamics of the nanoparticle IT-101 from PET imaging and tumor histological measurements. *Proc. Natl. Acad. Sci. U. S. A. 106*, 11394−9.
(24) Benezra, M., Penate-Medina, O., Zanzonico, P. B., Schaer, D., Ow, H., Burns, A., Destanchina, E., Longo, V., Herz, E., Iyer, S., Wolchok, J., Larson, S. M., Wiesner, U., and Bradbury, M. S. (2011) Multimodal silica nanoparticles are effective cancer-targeted probes in a model of human melanoma. *J. Clin. Invest. 121*, 2768−80.
(25) Ray, P. (2011) The pivotal role of multimodality reporter sensors in drug discovery: from cell based assays to real time molecular imaging. *Curr. Pharm. Biotechnol. 12*, 539−46.
(26) Glaus, C., Rossin, R., Welch, M. J., and Bao, G. (2010) In vivo evaluation of (64)Cu-labeled magnetic nanoparticles as a dual-modality PET/MR imaging agent. *Bioconjugate Chem. 21*, 715−22.
(27) Almutairi, A., Rossin, R., Shokeen, M., Hagooly, A., Ananth, A., Capoccia, B., Guillaudeu, S., Abendschein, D., Anderson, C. J., Welch, M. J., and Frechet, J. M. (2009) Biodegradable dendritic positron-emitting nanoprobes for the noninvasive imaging of angiogenesis. *Proc. Natl. Acad. Sci. U. S. A. 106*, 685−90.
(28) Rossin, R., Muro, S., Welch, M. J., Muzykantov, V. R., and Schuster, D. P. (2008) In vivo imaging of 64Cu-labeled polymer nanoparticles targeted to the lung endothelium. *J. Nucl. Med. 49*, 103−11.
(29) Liu, Y., Ibricevic, A., Cohen, J. A., Cohen, J. L., Gunsten, S. P., Frechet, J. M., Walter, M. J., Welch, M. J., and Brody, S. L. (2009) Impact of hydrogel nanoparticle size and functionalization on in vivo behavior for lung imaging and therapeutics. *Mol. Pharm. 6*, 1891−902.
(30) Tang, L. (2008) Radionuclide production and yields at Washington University School of Medicine. *Q. J. Nucl. Med. Mol. Imaging 52*, 121−33.
(31) Hamoudeh, M., Kamleh, M. A., Diab, R., and Fessi, H. (2008) Radionuclides delivery systems for nuclear imaging and radiotherapy of cancer. *Adv. Drug Delivery Rev. 60*, 1329−46.
(32) Shokeen, M., Fettig, N. M., and Rossin, R. (2008) Synthesis, in vitro and in vivo evaluation of radiolabeled nanoparticles. *Q. J. Nucl. Med. Mol. Imaging 52*, 267−77.
(33) Kagadis, G. C., Loudos, G., Katsanos, K., Langer, S. G., and Nikiforidis, G. C. (2010) In vivo small animal imaging: current status and future prospects. *Med. Phys. 37*, 6421−42.
(34) Anderson, C. J., and Ferdani, R. (2009) Copper-64 radiopharmaceuticals for PET imaging of cancer: advances in preclinical and clinical research. *Cancer Biother. Radiopharm. 24*, 379−93.
(35) http://clinicaltrials.gov/ct2/results?term=dota.
(36) Schipper, M. L., Iyer, G., Koh, A. L., Cheng, Z., Ebenstein, Y., Aharoni, A., Keren, S., Bentolila, L. A., Li, J., Rao, J., Chen, X., Banin, U., Wu, A. M., Sinclair, R., Weiss, S., and Gambhir, S. S. (2009) Particle size, surface coating, and PEGylation influence the biodistribution of quantum dots in living mice. *Small 5*, 126−34.
(37) Hardman, R. (2006) A toxicologic review of quantum dots: toxicity depends on physicochemical and environmental factors. *Environ. Health Perspect. 114*, 165−72.
(38) McCarthy, J. R., and Weissleder, R. (2008) Multifunctional magnetic nanoparticles for targeted imaging and therapy. *Adv. Drug Delivery Rev. 60*, 1241−51.
(39) Heesakkers, R. A., Hovels, A. M., Jager, G. J., van den Bosch, H. C., Witjes, J. A., Raat, H. P., Severens, J. L., Adang, E. M., van der Kaa, C. H., Futterer, J. J., and Barentsz, J. (2008) MRI with a lymph-node-specific contrast agent as an alternative to CT scan and lymph-node dissection in patients with prostate cancer: a prospective multicohort study. *Lancet Oncol. 9*, 850−6.
(40) Yang, X., Hong, H., Grailer, J. J., Rowland, I. J., Javadi, A., Hurley, S. A., Xiao, Y., Yang, Y., Zhang, Y., Nickles, R. J., Cai, W., Steeber, D. A., and Gong, S. (2011) cRGD-functionalized, DOX-conjugated, and (64)Cu-labeled superparamagnetic iron oxide nanoparticles for targeted anticancer drug delivery and PET/MR imaging. *Biomaterials 32*, 4151−60.
(41) Stelter, L., Pinkernelle, J. G., Michel, R., Schwartlander, R., Raschzok, N., Morgul, M. H., Koch, M., Denecke, T., Ruf, J., Baumler, H., Jordan, A., Hamm, B., Sauer, I. M., and Teichgraber, U. (2010)

Modification of aminosilanized superparamagnetic nanoparticles: feasibility of multimodal detection using 3T MRI, small animal PET, and fluorescence imaging. *Mol. Imaging Biol. 12*, 25−34.
(42) Choi, J. S., Park, J. C., Nah, H., Woo, S., Oh, J., Kim, K. M., Cheon, G. J., Chang, Y., Yoo, J., and Cheon, J. (2008) A hybrid nanoparticle probe for dual-modality positron emission tomography and magnetic resonance imaging. *Angew. Chem., Int. Ed. Engl. 47*, 6259−62.
(43) Chen, J., Glaus, C., Laforest, R., Zhang, Q., Yang, M., Gidding, M., Welch, M. J., and Xia, Y. (2010) Gold nanocages as photothermal transducers for cancer treatment. *Small 6*, 811−7.
(44) Xie, H., Wang, Z. J., Bao, A., Goins, B., and Phillips, W. T. (2010) In vivo PET imaging and biodistribution of radiolabeled gold nanoshells in rats with tumor xenografts. *Int. J. Pharm. 395*, 324−30.
(45) Gregoriadis, G., and Ryman, B. E. (1971) Liposomes as carriers of enzymes or drugs: a new approach to the treatment of storage diseases. *Biochem. J. 124*, 58P.
(46) Phillips, W. T., Goins, B. A., and Bao, A. (2009) Radioactive liposomes. *Wiley Interdiscip. Rev. Nanomed. Nanobiotechnol. 1*, 69−83.
(47) Bimbo, L. M., Sarparanta, M., Santos, H. A., Airaksinen, A. J., Makila, E., Laaksonen, T., Peltonen, L., Lehto, V. P., Hirvonen, J., and Salonen, J. (2010) Biocompatibility of thermally hydrocarbonized porous silicon nanoparticles and their biodistribution in rats. *ACS Nano 4*, 3023−32.
(48) Kumar, R., Roy, I., Ohulchanskky, T. Y., Vathy, L. A., Bergey, E. J., Sajjad, M., and Prasad, P. N. (2010) In vivo biodistribution and clearance studies using multimodal organically modified silica nanoparticles. *ACS Nano 4*, 699−708.
(49) Martin, R., Menchon, C., Apostolova, N., Victor, V. M., Alvaro, M., Herance, J. R., and Garcia, H. (2010) Nano-jewels in biology. Gold and platinum on diamond nanoparticles as antioxidant systems against cellular oxidative stress. *ACS Nano 4*, 6957−65.
(50) Liu, Q., Sun, Y., Li, C., Zhou, J., Li, C., Yang, T., Zhang, X., Yi, T., Wu, D., and Li, F. (2011) 18F-Labeled magnetic-upconversion nanophosphors via rare-Earth cation-assisted ligand assembly. *ACS Nano 5*, 3146−57.
(51) Zhou, J., Yu, M., Sun, Y., Zhang, X., Zhu, X., Wu, Z., Wu, D., and Li, F. (2011) Fluorine-18-labeled Gd3+/Yb3+/Er3+ co-doped NaYF4 nanophosphors for multimodality PET/MR/UCL imaging. *Biomaterials 32*, 1148−56.
(52) Sun, Y., Yu, M., Liang, S., Zhang, Y., Li, C., Mou, T., Yang, W., Zhang, X., Li, B., Huang, C., and Li, F. (2011) Fluorine-18 labeled rare-earth nanoparticles for positron emission tomography (PET) imaging of sentinel lymph node. *Biomaterials 32*, 2999−3007.
(53) Buxton, D. B. (2011) Nanotechnology research support at the national heart, lung, and blood institute. *Circ. Res. 109*, 250−4.
(54) Sun, G., Hagooly, A., Xu, J., Nystrom, A. M., Li, Z., Rossin, R., Moore, D. A., Wooley, K. L., and Welch, M. J. (2008) Facile, efficient approach to accomplish tunable chemistries and variable biodistributions for shell cross-linked nanoparticles. *Biomacromolecules 9*, 1997−2006.
(55) Nahrendorf, M., Sosnovik, D. E., French, B. A., Swirski, F. K., Bengel, F., Sadeghi, M. M., Lindner, J. R., Wu, J. C., Kraitchman, D. L., Fayad, Z. A., and Sinusas, A. J. (2009) Multimodality cardiovascular molecular imaging, Part II. *Circ. Cardiovasc. Imaging 2*, 56−70.
(56) Sinusas, A. J., Bengel, F., Nahrendorf, M., Epstein, F. H., Wu, J. C., Villanueva, F. S., Fayad, Z. A., and Gropler, R. J. (2008) Multimodality cardiovascular molecular imaging, part I. *Circ. Cardiovasc. Imaging 1*, 244−56.
(57) Nahrendorf, M., Zhang, H., Hembrador, S., Panizzi, P., Sosnovik, D. E., Aikawa, E., Libby, P., Swirski, F. K., and Weissleder, R. (2008) Nanoparticle PET-CT imaging of macrophages in inflammatory atherosclerosis. *Circulation 117*, 379−87.
(58) Buxton, D. B. (2009) Current status of nanotechnology approaches for cardiovascular disease: a personal perspective. *Wiley Interdiscip. Rev. Nanomed. Nanobiotechnol. 1*, 149−55.
(59) Anderson, C. J., Bulte, J. W., Chen, K., Chen, X., Khaw, B. A., Shokeen, M., Wooley, K. L., and VanBrocklin, H. F. (2010) Design of targeted cardiovascular molecular imaging probes. *J. Nucl. Med. 51* (Suppl 1), 3S−17S.
(60) Gaucher, G., Dufresne, M. H., Sant, V. P., Kang, N., Maysinger, D., and Leroux, J. C. (2005) Block copolymer micelles: preparation, characterization and application in drug delivery. *J. Controlled Release 109*, 169−88.
(61) Nishiyama, N., and Kataoka, K. (2006) Current state, achievements, and future prospects of polymeric micelles as nanocarriers for drug and gene delivery. *Pharmacol. Ther. 112*, 630−48.
(62) Xu, J., Sun, G., Rossin, R., Hagooly, A., Li, Z., Fukukawa, K. I., Messmore, B. W., Moore, D. A., Welch, M. J., Hawker, C. J., and Wooley, K. L. (2007) Labeling of polymer nanostructures for medical imaging: importance of crosslinking extent, spacer length, and charge density. *Macromolecules 40*, 2971−2973.
(63) Sun, G., Xu, J., Hagooly, A., Rossin, R., Li, Z., Moore, D. A., Hawker, C. J., Welch, M. J., and Wooley, K. L. (2007) Strategies for optimized radiolabeling of nanoparticles for in vivo PET imaging. *Adv. Mater. 19*, 3157−3162.
(64) Fukukawa, K., Rossin, R., Hagooly, A., Pressly, E. D., Hunt, J. N., Messmore, B. W., Wooley, K. L., Welch, M. J., and Hawker, C. J. (2008) Synthesis and characterization of core-shell star copolymers for in vivo PET imaging applications. *Biomacromolecules 9*, 1329−39.
(65) Pressly, E. D., Rossin, R., Hagooly, A., Fukukawa, K., Messmore, B. W., Welch, M. J., Wooley, K. L., Lamm, M. S., Hule, R. A., Pochan, D. J., and Hawker, C. J. (2007) Structural effects on the biodistribution and positron emission tomography (PET) imaging of well-defined (64)Cu-labeled nanoparticles comprised of amphiphilic block graft copolymers. *Biomacromolecules 8*, 3126−34.
(66) Shokeen, M., Pressly, E. D., Hagooly, A., Zheleznyak, A., Ramos, N., Fiamengo, A. L., Welch, M. J., Hawker, C. J., and Anderson, C. J. (2011) Evaluation of multivalent, functional polymeric nanoparticles for imaging applications. *ACS Nano 5*, 738−47.
(67) Liu, Y., Pressly, E. D., Abendschein, D., Hawker, C. J., Woodard, G. E., Woodard, P. K., and Welch, M. J. (2011) Targeting angiogenesis using a C-type atrial natriuretic factor conjugated nanoprobe and positron emission tomography. *J. Nucl. Med. 52*, 1956−1963.
(68) Kumari, A., Yadav, S. K., and Yadav, S. C. (2010) Biodegradable polymeric nanoparticles based drug delivery systems. *Colloids Surf., B: Biointerfaces 75*, 1−18.
(69) Soppimath, K. S., Aminabhavi, T. M., Kulkarni, A. R., and Rudzinski, W. E. (2001) Biodegradable polymeric nanoparticles as drug delivery devices. *J. Controlled Release 70*, 1−20.
(70) Gan, C. W., Chien, S., and Feng, S. S. (2010) Nanomedicine: enhancement of chemotherapeutical efficacy of docetaxel by using a biodegradable nanoparticle formulation. *Curr. Pharm. Des. 16*, 2308−20.
(71) Courant, T., Roullin, V. G., Cadiou, C., Delavoie, F., Molinari, M., Andry, M. C., and Chuburu, F. (2009) Development and physicochemical characterization of copper complexes-loaded PLGA nanoparticles. *Int. J. Pharm. 379*, 226−34.
(72) Devaraj, N. K., Keliher, E. J., Thurber, G. M., Nahrendorf, M., and Weissleder, R. (2009) 18F labeled nanoparticles for in vivo PET-CT imaging. *Bioconjugate Chem. 20*, 397−401.
(73) Nahrendorf, M., Keliher, E., Marinelli, B., Leuschner, F., Robbins, C. S., Gerszten, R. E., Pittet, M. J., Swirski, F. K., and Weissleder, R. (2011) Detection of macrophages in aortic aneurysms by nanoparticle positron emission tomography-computed tomography. *Arterioscler. Thromb. Vasc. Biol. 31*, 750−7.
(74) Swai, H., Semete, B., Kalombo, L., Chelule, P., Kisich, K., and Sievers, B. (2009) Nanomedicine for respiratory diseases. *Wiley Interdiscip. Rev. Nanomed. Nanobiotechnol. 1*, 255−63.
(75) Rytting, E., Nguyen, J., Wang, X., and Kissel, T. (2008) Biodegradable polymeric nanocarriers for pulmonary drug delivery. *Expert Opin. Drug Delivery 5*, 629−39.
(76) Roy, I., and Vij, N. (2010) Nanodelivery in airway diseases: challenges and therapeutic applications. *Nanomedicine 6*, 237−44.
(77) Roller, J., Laschke, M. W., Tschernig, T., Schramm, R., Veith, N. T., Thorlacius, H., and Menger, M. D. (2011) How to detect a dwarf: in vivo imaging of nanoparticles in the lung. *Nanomedicine 7*, 753−62.

(78) Card, J. W., Zeldin, D. C., Bonner, J. C., and Nestmann, E. R. (2008) Pulmonary applications and toxicity of engineered nanoparticles. *Am. J. Physiol. Lung Cell Mol. Physiol. 295*, L400−11.
(79) Semete, B., Booysen, L. I., Kalombo, L., Venter, J. D., Katata, L., Ramalapa, B., Verschoor, J. A., and Swai, H. (2010) In vivo uptake and acute immune response to orally administered chitosan and PEG coated PLGA nanoparticles. *Toxicol. Appl. Pharmacol. 249*, 158−65.
(80) Semete, B., Booysen, L., Lemmer, Y., Kalombo, L., Katata, L., Verschoor, J., and Swai, H. S. (2010) In vivo evaluation of the biodistribution and safety of PLGA nanoparticles as drug delivery systems. *Nanomedicine 6*, 662−71.
(81) Murthy, N., Xu, M., Schuck, S., Kunisawa, J., Shastri, N., and Frechet, J. M. (2003) A macromolecular delivery vehicle for protein-based vaccines: acid-degradable protein-loaded microgels. *Proc. Natl. Acad. Sci. U. S. A. 100*, 4995−5000.
(82) Murthy, N., Thng, Y. X., Schuck, S., Xu, M. C., and Frechet, J. M. (2002) A novel strategy for encapsulation and release of proteins: hydrogels and microgels with acid-labile acetal cross-linkers. *J. Am. Chem. Soc. 124*, 12398−9.
(83) Standley, S. M., Kwon, Y. J., Murthy, N., Kunisawa, J., Shastri, N., Guillaudeu, S. J., Lau, L., and Frechet, J. M. (2004) Acid-degradable particles for protein-based vaccines: enhanced survival rate for tumor-challenged mice using ovalbumin model. *Bioconjugate Chem. 15*, 1281−8.
(84) Lundberg, P., and Langel, U. (2003) A brief introduction to cell-penetrating peptides. *J. Mol. Recognit. 16*, 227−33.
(85) Shoyele, S. A., and Cawthorne, S. (2006) Particle engineering techniques for inhaled biopharmaceuticals. *Adv. Drug Delivery Rev. 58*, 1009−29.
(86) Cohen, J. L., Almutairi, A., Cohen, J. A., Bernstein, M., Brody, S. L., Schuster, D. P., and Frechet, J. M. (2008) Enhanced cell penetration of acid-degradable particles functionalized with cell-penetrating peptides. *Bioconjugate Chem. 19*, 876−81.
(87) Rojas, S., Gispert, J. D., Martin, R., Abad, S., Menchon, C., Pareto, D., Victor, V. M., Alvaro, M., Garcia, H., and Herance, J. R. (2011) Biodistribution of amino-functionalized diamond nanoparticles. In vivo studies based on 18F radionuclide emission. *ACS Nano 5*, 5552−9.
(88) Hofman, M. S., Beauregard, J. M., Barber, T. W., Neels, O. C., Eu, P., and Hicks, R. J. (2011) 68Ga PET/CT ventilation-perfusion imaging for pulmonary embolism: a pilot study with comparison to conventional scintigraphy. *J. Nucl. Med. 52*, 1513−9.
(89) Strebhardt, K., and Ullrich, A. (2008) Paul Ehrlich's magic bullet concept: 100 years of progress. *Nat. Rev. Cancer 8*, 473−80.
(90) Ting, G., Chang, C. H., and Wang, H. E. (2009) Cancer nanotargeted radiopharmaceuticals for tumor imaging and therapy. *Anticancer Res. 29*, 4107−18.
(91) Ting, G., Chang, C. H., Wang, H. E., and Lee, T. W. (2010) Nanotargeted radionuclides for cancer nuclear imaging and internal radiotherapy. *J. Biomed. Biotechnol.*, 2010.
(92) Pirollo, K. F., and Chang, E. H. (2008) Does a targeting ligand influence nanoparticle tumor localization or uptake? *Trends Biotechnol. 26*, 552−8.
(93) Fang, J., Nakamura, H., and Maeda, H. (2011) The EPR effect: Unique features of tumor blood vessels for drug delivery, factors involved, and limitations and augmentation of the effect. *Adv. Drug Delivery Rev. 63*, 136−51.
(94) Jiang, W., Kim, B. Y., Rutka, J. T., and Chan, W. C. (2008) Nanoparticle-mediated cellular response is size-dependent. *Nat. Nanotechnol. 3*, 145−50.
(95) Adair, J. H., Parette, M. P., Altinoglu, E. I., and Kester, M. (2010) Nanoparticulate alternatives for drug delivery. *ACS Nano 4*, 4967−70.
(96) Minelli, C., Lowe, S. B., and Stevens, M. M. (2010) Engineering nanocomposite materials for cancer therapy. *Small 6*, 2336−57.
(97) Hallaj-Nezhadi, S., Lotfipour, F., and Dass, C. R. (2010) Delivery of nanoparticulate drug delivery systems via the intravenous route for cancer gene therapy. *Pharmazie 65*, 855−9.
(98) Alexis, F., Pridgen, E. M., Langer, R., and Farokhzad, O. C. (2010) Nanoparticle technologies for cancer therapy. *Handb. Exp. Pharmacol.*, 55−86.
(99) Pridgen, E. M., Langer, R., and Farokhzad, O. C. (2007) Biodegradable, polymeric nanoparticle delivery systems for cancer therapy. *Nanomedicine (Lond.) 2*, 669−80.
(100) Younes, C. K., Boisgard, R., and Tavitian, B. (2002) Labelled oligonucleotides as radiopharmaceuticals: pitfalls, problems and perspectives. *Curr. Pharm. Des. 8*, 1451−66.
(101) Sun, X., Fang, H., Li, X., Rossin, R., Welch, M. J., and Taylor, J. S. (2005) MicroPET imaging of MCF-7 tumors in mice via unr mRNA-targeted peptide nucleic acids. *Bioconjugate Chem. 16*, 294−305.
(102) Rossin, R., Sun, X., Fang, H., Turner, J. L., Li, X., Wooley, K. L., Taylor, J. S., Welch, M. J. (2005) in *Journal of Labelled Compounds and Radiopharmaceuticals*, p S35, Wiley, Iowa City.
(103) Rossin, R., Pan, D., Qi, K., Turner, J. L., Sun, X., Wooley, K. L., and Welch, M. J. (2005) 64Cu-labeled folate-conjugated shell cross-linked nanoparticles for tumor imaging and radiotherapy: synthesis, radiolabeling, and biologic evaluation. *J. Nucl. Med. 46*, 1210−8.
(104) Zhou, D., Zeng, D., Lee, N., Dence, C., Wooley, K., Katzenellenbogen, J., and Welch, M. (2011) Fluorine-18 radiolabeling of SCK nanoparticles via copper-free click chemistry. *J. Nucl. Med. Meeting Abstracts 52*, 569.
(105) Zeng, D., Lee, N., Liu, Y., Zhou, D., Dence, C., Wooley, K., Katzenellenbogen, J., and Welch, M. (2011) Novel strategy for preparing Cu-64 nanoparticles with ultrahigh specific activity using metal-free click chemistry. *J. Nucl. Med. Meeting Abstracts 52*, 576.
(106) Xie, J., Chen, K., Huang, J., Lee, S., Wang, J., Gao, J., Li, X., and Chen, X. (2010) PET/NIRF/MRI triple functional iron oxide nanoparticles. *Biomaterials 31*, 3016−22.
(107) Torres Martin de Rosales, R., Tavare, R., Paul, R. L., Jauregui-Osoro, M., Protti, A., Glaria, A., Varma, G., Szanda, I., and Blower, P. J. (2011) Synthesis of 64Cu(II)-bis(dithiocarbamatebisphosphonate) and its conjugation with superparamagnetic iron oxide nanoparticles: in vivo evaluation as dual-modality PET-MRI agent. *Angew. Chem., Int. Ed. Engl. 50*, 5509−13.
(108) Jarrett, B. R., Gustafsson, B., Kukis, D. L., and Louie, A. Y. (2008) Synthesis of 64Cu-labeled magnetic nanoparticles for multimodal imaging. *Bioconjugate Chem. 19*, 1496−504.
(109) Tabatabai, G., Tonn, J. C., Stupp, R., Weller, M. (2011) The role of integrins in glioma biology and anti-glioma therapies. *Curr. Pharm. Des.*
(110) Beer, A. J., Kessler, H., Wester, H. J., and Schwaiger, M. (2011) PET Imaging of Integrin alphaVbeta3 Expression. *Theranostics 1*, 48−57.
(111) Ruggiero, A., Holland, J. P., Lewis, J. S., and Grimm, J. (2010) Cerenkov luminescence imaging of medical isotopes. *J. Nucl. Med. 51*, 1123−30.
(112) Park, J. C., Yu, M. K., An, G. I., Park, S. I., Oh, J., Kim, H. J., Kim, J. H., Wang, E. K., Hong, I. H., Ha, Y. S., Choi, T. H., Jeong, K. S., Chang, Y., Welch, M. J., Jon, S., and Yoo, J. (2010) Facile preparation of a hybrid nanoprobe for triple-modality optical/PET/MR imaging. *Small 6*, 2863−8.
(113) Xie, H., Diagaradjane, P., Deorukhkar, A. A., Goins, B., Bao, A., Phillips, W. T., Wang, Z., Schwartz, J., and Krishnan, S. (2011) Integrin alphavbeta3-targeted gold nanoshells augment tumor vasculature-specific imaging and therapy. *Int. J. Nanomed. 6*, 259−69.
(114) Zhou, M., Zhang, R., Huang, M., Lu, W., Song, S., Melancon, M. P., Tian, M., Liang, D., and Li, C. (2010) A chelator-free multifunctional [64Cu]CuS nanoparticle platform for simultaneous micro-PET/CT imaging and photothermal ablation therapy. *J. Am. Chem. Soc. 132*, 15351−8.
(115) Lammers, T., Kiessling, F., Hennink, W. E., and Storm, G. (2010) Nanotheranostics and image-guided drug delivery: current concepts and future directions. *Mol. Pharm. 7*, 1899−912.
(116) Kelkar, S. S., and Reineke, T. M. (2011) Theranostics: combining imaging and therapy. *Bioconjugate Chem. 22*, 1879−903.

(117) Petersen, A. L., Binderup, T., Rasmussen, P., Henriksen, J. R., Elema, D. R., Kjaer, A., and Andresen, T. L. (2011) 64Cu loaded liposomes as positron emission tomography imaging agents. *Biomaterials 32*, 2334−41.
(118) Rygh, C. B., Qin, S., Seo, J. W., Mahakian, L. M., Zhang, H., Adamson, R., Chen, J. Q., Borowsky, A. D., Cardiff, R. D., Reed, R. K., Curry, F. R., and Ferrara, K. W. (2010) Longitudinal investigation of permeability and distribution of macromolecules in mouse malignant transformation using PET. *Clin. Cancer Res. 17*, 550−9.
(119) Medina, O. P., Pillarsetty, N., Glekas, A., Punzalan, B., Longo, V., Gonen, M., Zanzonico, P., Smith-Jones, P., and Larson, S. M. (2011) Optimizing tumor targeting of the lipophilic EGFR-binding radiotracer SKI 243 using a liposomal nanoparticle delivery system. *J. Controlled Release 149*, 292−8.
(120) Holland, J. P., Sheh, Y., and Lewis, J. S. (2009) Standardized methods for the production of high specific-activity zirconium-89. *Nucl. Med. Biol. 36*, 729−39.
(121) Keliher, E. J., Yoo, J., Nahrendorf, M., Lewis, J. S., Marinelli, B., Newton, A., Pittet, M. J., and Weissleder, R. (2011) (89)Zr-labeled dextran nanoparticles allow in vivo macrophage imaging. *Bioconjugate Chem. 22*, 2383−9.
(122) Duconge, F., Pons, T., Pestourie, C., Herin, L., Theze, B., Gombert, K., Mahler, B., Hinnen, F., Kuhnast, B., Dolle, F., Dubertret, B., and Tavitian, B. (2008) Fluorine-18-labeled phospholipid quantum dot micelles for in vivo multimodal imaging from whole body to cellular scales. *Bioconjugate Chem. 19*, 1921−6.
(123) Tu, C., Ma, X., House, A., Kauzlarich, S. M., and Louie, A. Y. (2011) PET imaging and biodistribution of silicon quantum dots in mice. *ACS Med. Chem. Lett. 2*, 285−288.
(124) Hwang, D., Ko, H., Kim, S.-K., Kim, D., Lee, D., and Kim, S. (2009) Development of a quadruple imaging modality by using nanoparticles. *Chem.—Eur. J. 15*, 9387−9393.
(125) Jauregui-Osoro, M., Williamson, P. A., Glaria, A., Sunassee, K., Charoenphun, P., Green, M. A., Mullen, G. E., and Blower, P. J. (2011) Biocompatible inorganic nanoparticles for [(18)F]-fluoride binding with applications in PET imaging. *Dalton Trans,*.
(126) Liu, Q., Sun, Y., Li, C., Zhou, J., Yang, T., Zhang, X., Yi, T., Wu, D., and Li, F. (2011) (18)F-labeled magnetic-upconversion nanophosphors via rare-earth cation-assisted ligand assembly. *ACS Nano 5*, 3146−57.
(127) Cartier, R., Kaufner, L., Paulke, B. R., Wustneck, R., Pietschmann, S., Michel, R., Bruhn, H., and Pison, U. (2007) Latex nanoparticles for multimodal imaging and detection in vivo. *Nanotechnology 18*, 195102.
(128) Seo, J. W., Mahakian, L. M., Kheirolomoom, A., Zhang, H., Meares, C. F., Ferdani, R., Anderson, C. J., and Ferrara, K. W. (2010) Liposomal Cu-64 labeling method using bifunctional chelators: poly(ethylene glycol) spacer and chelator effects. *Bioconjugate Chem. 21*, 1206−15.
(129) Seo, J. W., Zhang, H., Kukis, D. L., Meares, C. F., and Ferrara, K. W. (2008) A novel method to label preformed liposomes with 64Cu for positron emission tomography (PET) imaging. *Bioconjugate Chem. 19*, 2577−84.
(130) Oku, N., Yamashita, M., Katayama, Y., Urakami, T., Hatanaka, K., Shimizu, K., Asai, T., Tsukada, H., Akai, S., and Kanazawa, H. (2011) PET imaging of brain cancer with positron emitter-labeled liposomes. *Int. J. Pharm. 403*, 170−7.
(131) Marik, J., Tartis, M. S., Zhang, H., Fung, J. Y., Kheirolomoom, A., Sutcliffe, J. L., and Ferrara, K. W. (2007) Long-circulating liposomes radiolabeled with [18F]fluorodipalmitin ([18F]FDP). *Nucl. Med. Biol. 34*, 165−71.
(132) Helbok, A., Decristoforo, C., Dobrozemsky, G., Rangger, C., Diederen, E., Stark, B., Prassl, R., and von Guggenberg, E. (2009) Radiolabeling of lipid-based nanoparticles for diagnostics and therapeutic applications: a comparison using different radiometals. *J. Liposome Res. 20*, 219−27.
(133) Andreozzi, E., Seo, J. W., Ferrara, K., and Louie, A. (2011) Novel method to label solid lipid nanoparticles with (64)cu for positron emission tomography imaging. *Bioconjugate Chem. 22*, 808−18.
(134) Herth, M. M., Barz, M., Moderegger, D., Allmeroth, M., Jahn, M., Thews, O., Zentel, R., and Rosch, F. (2009) Radioactive labeling of defined HPMA-based polymeric structures using [18F]FETos for in vivo imaging by positron emission tomography. *Biomacromolecules 10*, 1697−703.
(135) Ruggiero, A., Villa, C. H., Holland, J. P., Sprinkle, S. R., May, C., Lewis, J. S., Scheinberg, D. A., and McDevitt, M. R. (2010) Imaging and treating tumor vasculature with targeted radiolabeled carbon nanotubes. *Int. J. Nanomed. 5*, 783−802.

Bioconjugate Chemistry

Communication

pubs.acs.org/bc

Evaluation of End-Capped DNA Modules for pRNA Capture and Functionalization

Brian M. Laing and Donald E. Bergstrom*

Department of Medicinal Chemistry and Molecular Pharmacology and Bindley Bioscience Center, Purdue University, West Lafayette, Indiana 47907, United States

Supporting Information

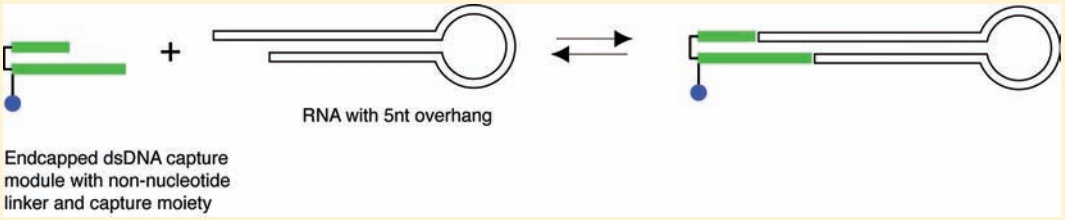

ABSTRACT: The ability of packaging RNA (pRNA) from the phi29 DNA packaging motor to form nanoassemblies and nanostructures has been exploited for the development of the nascent field of RNA nanotechnology and subsequent applications in nanomedicine. For applications in nanomedicine, it is necessary to modify the pRNA structure for the conjugation of active molecules. We have investigated end-capped double-stranded DNA segments as reversible capture reagents for pRNA. These capture agents can be designed to allow the conjugation of any desired molecule for pRNA functionalization. The results of model studies presented in this report show that 5- to 7-nucleotide overhangs on a target RNA can provide efficient handles for the high-affinity association to capped double-stranded DNA.

The emerging field of RNA nanotechnology was ignited by the discovery by Guo and co-workers that packaging RNA (pRNA) from the phi29 bacteriophage DNA packaging nanomotor can be re-engineered and manipulated to form a variety of nanoassemblies and nanostructures.[1−6] Wild-type pRNA spontaneously self-assembles into a hexameric ring via complementary base pairing interactions between loop regions within the pRNA structure.[3,7,8] The pRNA monomer contains two functional domains (Figure 1A): the intermolecular-interacting domain comprising a right-hand and left-hand loop and the 5′/3′ double-stranded helical DNA-translocation domain.[4,5,8] It has been shown that these two domains fold independently of one another, and modification of one domain does not affect the function of the other.[3−5,9,10]

The two interlocking left and right loops of the intermolecular-interacting domain can be engineered for bottom-up nanoparticle assembly and have been modified to produce a variety of nanostructures and shapes including rods, triangles, twins, tetramers, and 3D arrays up to several micrometers in size.[1,4,5] The 3′/5′-paired DNA translocation domain of the pRNA can be re-engineered and modified without affecting the conformation of the intermolecular binding domain and its ability to form multimeric nanostructures.[3,10−12] Guo and co-workers have fabricated pRNA monomers with functional RNA sequences (e.g., ribozymes, aptamers, and siRNA) and small molecules (e.g., folic acid, fluorophores) at the 5′/3′ translocation domain.[2,6,9,10] These properties of pRNA are the basis for the design and fabrication of multifunctional pRNA nanoparticles of the types shown in Figure 1B (dimer model shown), for use in nanomedicine.

In order to take full advantage of the potential of pRNA nanotechnology, it is important to develop methods for the attachment of functional molecules to pRNA. The wild-type pRNA contains a 3′ overhang with the sequence 3′-AAU followed by a double-stranded stem (Figure 1A). We believe that there is a way to rapidly and reversibly add modules to the 3′/5′-pRNA overhang that are small, have high affinity and specificity for the pRNA overhang, are simple to synthesize, and can link virtually any kind of molecule (including small ligands, peptides, lipids, carbohydrates, and fluorophores). Bergstrom and co-workers have utilized a method for stabilizing short segments of double-stranded oligonucleotides by covalently linking the 3′ and 5′ ends of the nucleic acid with a simple spacer.[13−15] The simplest spacer is the C12 hydrocarbon (**S2**) shown in Figure 1D. Nucleic acid duplexes containing just four base pairs and linked by a spacer at one end have melting temperatures (T_m values) in the range 41−62 °C (the same duplexes without the spacers are unstable at room temperature, i.e., T_m < 25 °C). Importantly, we also determined that the end-caps protect double-stranded nucleic acids from degradation by exonucleases.

In the present study, oligodeoxyribonucleotides containing a 5 bp duplex segment capped at one end by a stabilizing spacer and having a 5 nt or 7 nt single-stranded overhang at the other end (Figure 1C, capture modules 5 and 7), would be used as

Received: July 12, 2011
Revised: January 17, 2012
Published: March 26, 2012

dx.doi.org/10.1021/bc200371t | *Bioconjugate Chem.* 2012, 23, 683−687

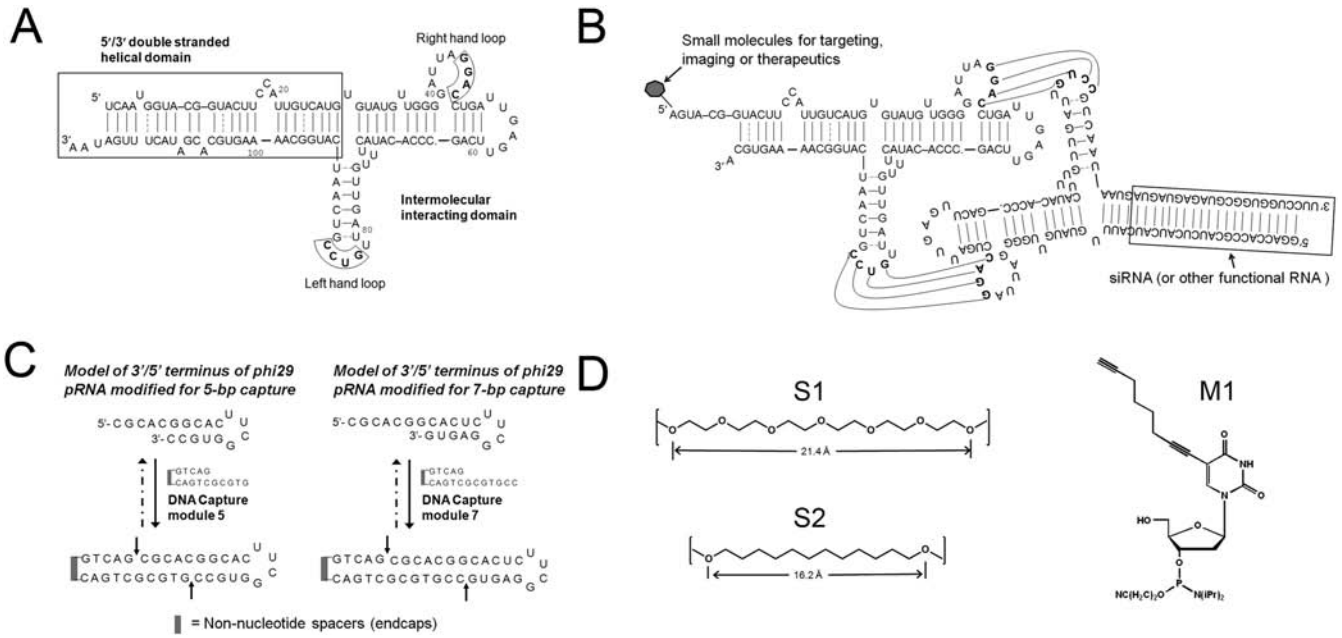

Figure 1. Structures of pRNA and end-capped DNA capture module system. (A) Wild-type pRNA model showing functional domains. (B) Engineered pRNA dimer showing potential modifications for use in nanomedicine applications. (C) Model system for assessing the feasibility of the end-capped DNA capture module strategy. (D) Structures of end-caps (S1 and S2) and modified base (M1) for use in DNA capture modules.

Table 1. Mass Spectrometry (MALDI-TOF-MS) and Melting Temperature (T_m) Analysis of End-Capped DNA Capture Modules[b] and Truncated pRNA Hairpin Models

Name	Sequence/Structure	(M-H)⁻ Calculated	(M-H)⁻ Observed	[a]T_m (°C)
DNA5-S1	GTCAG-3′ / CAGTCGCGTG-5′	4953.21	4953.3	64.6
DNA7-S1	GTCAG-3′ / CAGTCGCGTGCC-5′	5531.7	5531.4	65.8
DNACtrl-S1	G-3′ / CGCGTGCC-5′	3059.1	3059.2	N/A
DNA7-S2	GTCAG-3′ / CAGTCGCGTGCC-5′	5451.57	5454.0	67.2
DNACtrl-dC	3′-CGCGTGCC-5′	2385.6	2385.0	N/A
RNA5	5′-CGCACGGCAC U U / 3′-CCGUG G C	6026.4	6027.1	81.5
RNA7	5′-CGCACGGCACUC U U / 3′-GUGAG G C	6703.0	6702.6	74.4

[a]melting of hairpin. [b]S1 = Hexa(ethylene glycol) spacer; S2 = C12 Hydrocarbon spacer.

reagents for the capture and modification of the 3′/5′ terminal region of a modified pRNA. Modified bases such as the commercially available C5 substituted thymine, bearing an alkyne moiety (Figure 1D, M1), may be incorporated into the capture module. This modification will allow the conjugation of fluorophores, affinity probes, and targeting ligands through a bio-orthogonal 3 + 2 cycloaddition reaction between the alkyne on the modified base and an alkyl azide on the conjugate moiety.

In order to determine the feasibility of our pRNA capture strategy, the model system shown in Figure 1C was developed and tested. The truncated pRNA models are stabilized by a well-established RNA tetraloop (5′-UUCG-3′) known to form RNA hairpins with remarkable stability (T_m values >70 °C).[16,17] The DNA modules were constructed by using a hexa(ethylene glycol) linker (**S1**) or a C12 hydrocarbon (**S2**), which confers significant stability to short sequences.

dx.doi.org/10.1021/bc200371t | *Bioconjugate Chem.* 2012, 23, 683–687

Scheme 1. Anticipated Change in Structure and Hybridization of the End-Capped DNA-Based RNA Capture Model System (A → B → C) with Increasing Temperature

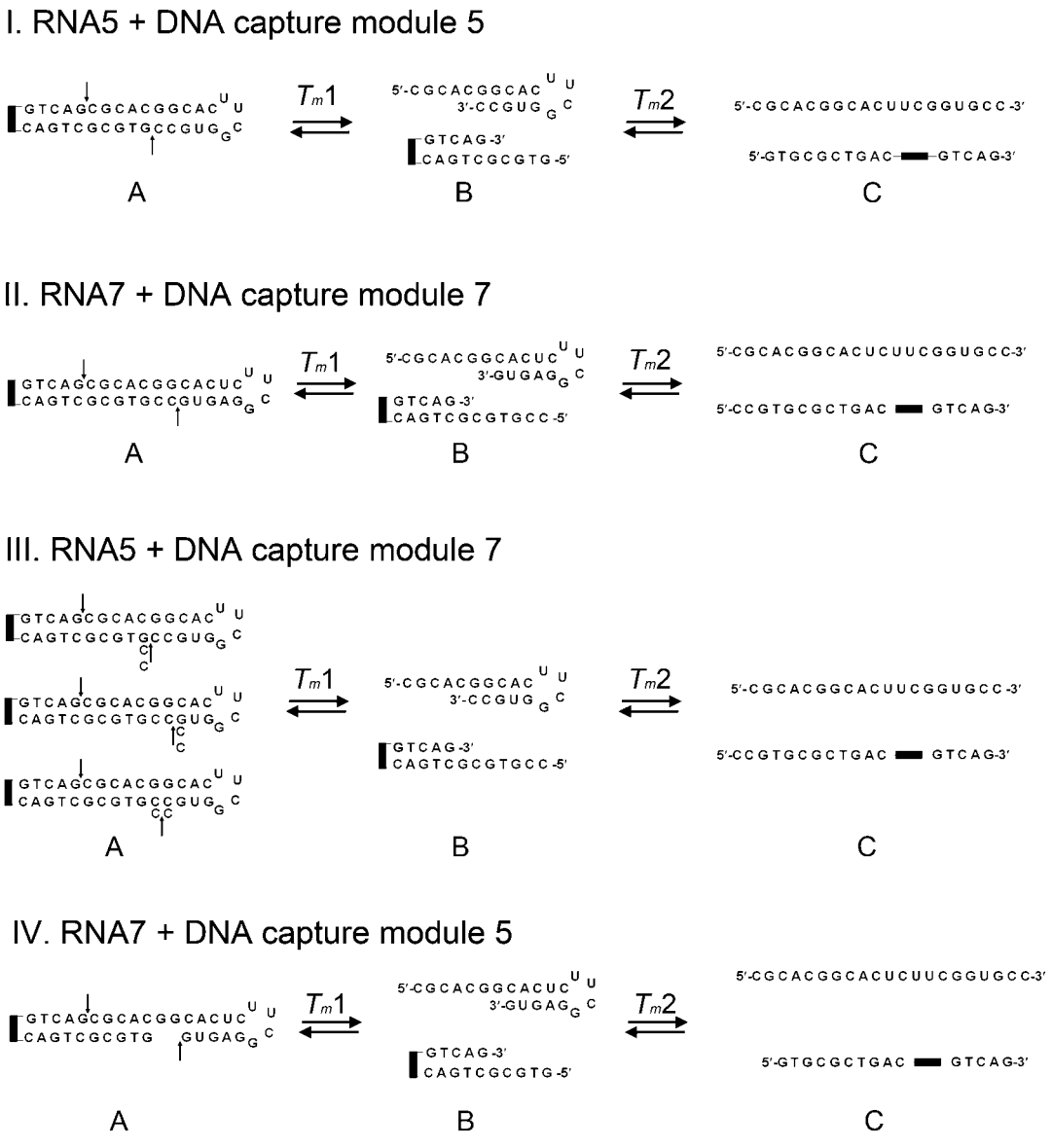

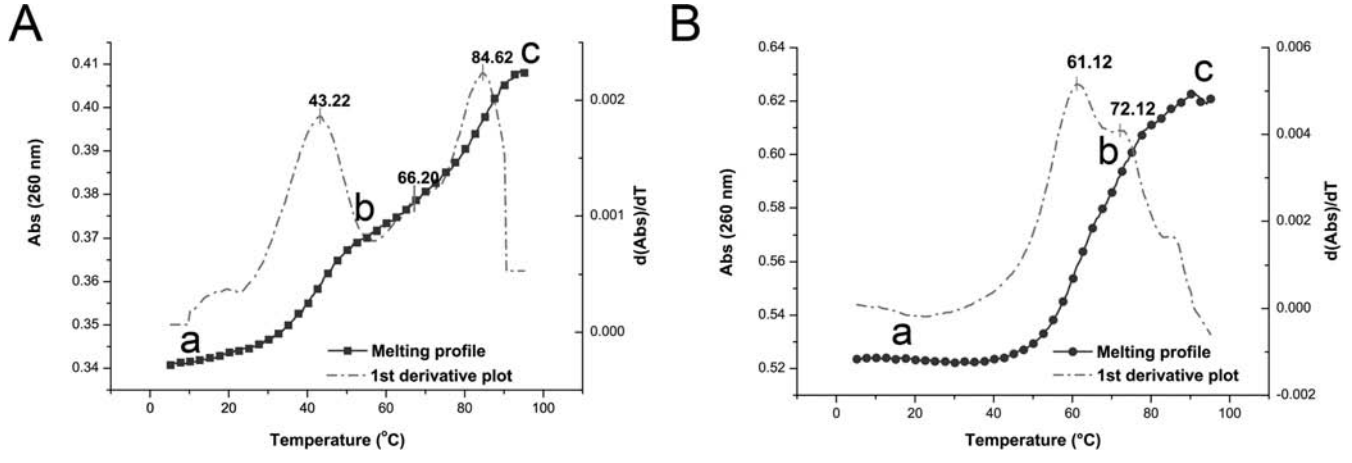

Figure 2. Thermal melting profile and first derivative plots for (A) RNA5 + DNA5-S1 (Table 2, exp 1) and (B) RNA7 + DNA7-S1 (Table 2, exp 2). The states a, b, and c correspond to structures A, B, and C in Scheme 1.

dx.doi.org/10.1021/bc200371t | *Bioconjugate Chem.* 2012, 23, 683–687

The ability of the end-capped DNA capture modules to stably hybridize with the truncated pRNA models were investigated by conducting melting temperature experiments. The RNA hairpin models, RNA5 and RNA7, had T_m values of 81.5 and 74.4 °C, respectively (Table 1). The higher T_m value for RNA5 is most likely due to the higher C•G content in the stem region of RNA5 compared to that of RNA7. The DNA capture modules, DNA5-**S1** and DNA7-**S1**, were determined to have T_m values of 64.6 and 65.8 °C, respectively (Table 1). Spacer **S1** was used in the initial experiments because the hexa(ethylene glycol) linker is well-established as one of the first linkers used to stabilize duplex structure and is commercially available.[18,19]

We anticipated that these structures would be sufficiently stable such that the first dissociation event would be the dissociation of the RNA from DNA when equimolar quantities of complementary RNA and DNA modules are heated (Scheme 1). Hence, at least two transitions (A → B and B → C) should be readily observed in the thermal profile from which approximate T_m values for the first dissociation event (A → B, T_m1) can be determined. The second transition (B → C, T_m2) is expected to involve the melting of the RNA hairpin and the end-capped DNA hairpin. These two events are indistinguishable in the thermal profile in some cases.

Thermal melting profiles were obtained for the hybridization of equimolar (1 μM) concentrations of RNA5 + DNA5-**S1** and RNA7 + DNA7-**S1** (Figure 2). The anticipated transitions were observed in both cases with the T_m values for the first dissociation events determined to be 43.2 and 61.1 °C for capture module 5 and capture module 7, respectively. For biological and therapeutic applications, it is important to have structures that are stable at 37 °C. The T_m values indicate that both capture module 5 and capture module 7 would have sufficient thermal stability under physiological conditions, with capture module 7 exhibiting significantly greater stability.

Control experiments were conducted to assess the level of enhancement provided by the end-capped 5 bp stem used in capture module 7 when compared to modules having a 1 bp stem (DNACtrl-**S1**) or a 1 nt overhang with no end-cap (DNACtrl-dC). The T_m value obtained for the first dissociation event with DNACtrl-S1 was found to be 44.1 °C (Table 2, exp 3, and SI Figure S3), whereas the T_m value for DNACtrl-dC was found to be 41.2 °C (Table 2, exp 4, and SI Figure S4). The observed T_m values indicate that the end-capped 5 bp stem significantly enhances the ability of the DNA capture module to stably hybridize with the RNA target. These results suggest that "preorganization" of the 5 bp duplex stem in the capture module by the end-cap plays a role in augmenting the hybridization stability of the RNA capture system.

Table 2. Melting Temperatures for End-Capped DNA Capture Module Hybridization to Truncated pRNA Models

experiment	oligonucleotides	T_m1[a] (°C)	T_m2[b] (°C)
1	DNA5-S1 + RNA5	43.2	66.2,[c] 84.6
2	DNA7-S1 + RNA7	61.1	72.1[d]
3	DNACtrl-S1 + RNA7	44.1	69.6[d]
4	DNACtrl-dC + RNA7	41.2	68.7[d]
5	DNA7-S2 + RNA7	47.4	62.0,[c] 71.7
6	DNA7-S1 + RNA5	36.2	69.6,[c] 84.1
7	DNA5-S1 + RNA7	32.6	72.2[d]

[a]First dissociation event (melting of DNA-RNA hybrid). [b]Second dissociation event (melting of RNA hairpin). [c]Third dissociation event (melting of end-capped DNA). [d]Second and third dissociation events cannot be differentiated.

Having established the feasibility of the system using spacer **S1** in the DNA capture modules, experiments were conducted using spacer **S2** (C12 spacer), which more closely matches the average distance between the terminal 3′-O and 5′-O of B-DNA duplexes between the terminal base pairs, previously shown to be approximately 16.2 Å.[13] Spacer **S2**, when used as the end-cap in DNA capture module 7, resulted in a T_m value of 67.2 °C for the melting of the 5 bp duplex stem (Table 1), a value slightly higher than spacer **S1**. The first dissociation event when hybridized to RNA7 was determined to be 47.4 °C (Table 2, exp 5, and SI Figure S5). This T_m value, despite being sufficient for physiological conditions, is significantly lower than that obtained with spacer **S1**. This difference in observed hybridization stability may be due to the differences in length, flexibility, and hydrophobicity of the spacers. These are attributes that are important to consider in the future design of end-caps for stabilizing DNA capture modules.

It was of interest to determine the level of tolerance for mismatches or imperfect target sequences. Imperfect sequences and mismatches are potential issues to consider in the proposed strategy, since one of the main methods of preparing full-length (117 nt) pRNA is *in vitro* transcription using T7 RNA polymerase. T7 RNA polymerase lacks proofreading ability and is known to produce aberrant RNA transcripts and extra bases at the 3′ terminus.[20] Another potential application for the use of DNA capture modules is in the capture of microRNA (miRNA) or other small RNA that present short overhanging regions. Mismatch discrimination would be an important concern in these applications. A simple approach was used for these studies in which the previously synthesized RNA models (RNA5 and RNA7) and DNA capture modules (5 and 7) were mismatched such that RNA7 was hybridized with DNA5-S1 and vice versa (Scheme 1-III and IV).

Hybridization of equimolar concentrations of RNA5 and DNA7-**S1** would produce an equilibrium comprising three possible structures shown in Scheme 1-III. The T_m value obtained for the first dissociation event with these structures was found to be 36.2 °C (Table 2, exp 6, and SI Figure S6) indicating that the net result of this interaction is less stable than the exact complement. The combination of RNA7 with DNA5-**S1** produces a structure with two unpaired nucleotides (Scheme 1-IV) and results in a T_m value for the first dissociation event of 32.6 °C (Table 2, exp 7, and SI Figure S7). Both mispaired structures are unstable under physiological conditions and show that the overall system relies on high fidelity of base pairing.

The results presented here indicate that the end-capped DNA capture module system for the functional modification of pRNA is a potentially feasible strategy. The successful application of this strategy would require further optimization in order to create the most versatile and effective capture and functionalization system. The studies of the control modules DNACtrl-**S1** with 1 bp stem and DNACtrl-dC with no end-cap are instructive for the design of an optimized system. These control modules, although less stable than DNA7-**S1**, displayed stability under physiological temperatures. These observations suggest that it may be possible to design even simpler modules with shorter stems or by using stabilizing nucleotides (e.g., LNA) in the single-stranded overhang to enhance hybridization to the pRNA overhang. It would also be necessary to conduct

studies at different concentrations in order to assess the concentration dependence of hybridization. It is evident from the study of the C12 hydrocarbon end-cap that the nature and length of the end-cap are important considerations in the design. This observation is supported by previous work conducted in the Bergstrom lab on the evaluation of spacers for use as dsDNA end-caps.[13−15] The end-capped duplex stem in the capture modules confers high affinity and specificity for hybridization to overhanging sequences at the termini of pRNA overhybridization to the same sequence within the RNA. This specificity is due to the "preorganization" of the duplex stem region by the end-cap. The DNA capture module system can therefore be widely applied to the capture of any nucleic acid structure bearing overhanging sequences at their termini.

■ ASSOCIATED CONTENT

Supporting Information

Experimental procedures and thermal profiles for experiments 3−7. This material is available free of charge via the Internet at http://pubs.acs.org.

■ AUTHOR INFORMATION

Corresponding Author

*Telephone: (503)-360-2331. Fax: (765) 494-1414. E-mail: bergstrom@purdue.edu.

Notes

The authors declare no competing financial interest.

■ ACKNOWLEDGMENTS

This work was supported by the NIH Nanomedicine Development Center on Phi29 DNA-packaging Motor for Nanomedicine, through the NIH Roadmap for Medical Research (PN2 EY 018230). Support from the Walther Cancer Institute and assistance from the National Cancer Institute Grant (P30 CA23168) awarded to Purdue University is also gratefully acknowledged.

■ REFERENCES

(1) Shu, D., Huang, L. P., Hoeprich, S., and Guo, P. (2003) Construction of phi29 DNA-packaging RNA monomers, dimers, and trimers with variable sizes and shapes as potential parts for nanodevices. *J. Nanosci. Nanotechnol. 3*, 295−302.

(2) Guo, P. (2005) RNA nanotechnology: engineering, assembly and applications in detection, gene delivery and therapy. *J. Nanosci. Nanotechnol. 5*, 1964−82.

(3) Hoeprich, S., and Guo, P. (2002) Computer modeling of three-dimensional structure of DNA-packaging RNA (pRNA) monomer, dimer, and hexamer of Phi29 DNA packaging motor. *J. Biol. Chem. 277*, 20794−803.

(4) Shu, D., Moll, W.-D., Deng, Z., Mao, C., and Guo, P. (2004) Bottom-up assembly of RNA arrays and superstructures as potential parts in nanotechnology. *Nano Lett. 4*, 1717−1723.

(5) Khaled, A., Guo, S., Li, F., and Guo, P. (2005) Controllable self-assembly of nanoparticles for specific delivery of multiple therapeutic molecules to cancer cells using RNA nanotechnology. *Nano Lett. 5*, 1797−1808.

(6) Guo, P., Coban, O., Snead, N., Trebley, J., Hoeprich, S., Guo, S., and Shu, Y. (2010) Engineering RNA for targeted siRNA delivery and medical application. *Adv. Drug Delivery Rev. 62*, 650−666.

(7) Guo, P., Bailey, S., Bodley, J. W., and Anderson, D. (1987) Characterization of the small RNA of the bacteriophage phi 29 DNA packaging machine. *Nucleic Acids Res. 15*, 7081−90.

(8) Guo, P., Erickson, S., and Anderson, D. (1987) A small viral RNA is required for in vitro packaging of bacteriophage phi 29 DNA. *Science 236*, 690−4.

(9) Guo, P. (2005) Bacterial virus phi29 DNA-packaging motor and its potential applications in gene therapy and nanotechnology. *Methods Mol. Biol. 300*, 285−324.

(10) Guo, S., Tschammer, N., Mohammed, S, and Guo, P. (2005) Specific delivery of therapeutic RNAs to cancer cells via the dimerization mechanism of phi29 motor pRNA. *Hum. Gene Ther. 16*, 1097−109.

(11) Garver, K., and Guo, P. (1997) Boundary of pRNA functional domains and minimum pRNA sequence requirement for specific connector binding and DNA packaging of phage phi 29. *RNA 3*, 1068−1079.

(12) Garver, K., and Guo, P. (2000) Mapping the inter-RNA interaction of bacterial virus phi29 packaging RNA by site-specific photoaffinity cross-linking. *J. Biol. Chem. 275*, 2817−2824.

(13) Ng, P. S., Laing, B. M., Balasundarum, G., Pingle, M., Friedman, A., and Bergstrom, D. E. (2010) Synthesis and evaluation of new spacers for use as dsDNA end-caps. *Bioconjugate Chem. 21*, 1545−53.

(14) Ng, P. S., Pingle, M. R., Balasundarum, G., Friedman, A., Zu, X., and Bergstrom, D. E. (2003) Endcaps for stabilizing short DNA duplexes. *Nucleosides Nucleotides Nucleic Acids 22*, 1635−7.

(15) Pingle, M. R., Ng, P.-S., Xu, X., and Bergstrom, D. E. (2003) Synthesis of endcap dimethoxytrityl phosphoramidites for endcapped oligonucleotides. *Curr. Protoc. Nucleic Acid Chem.*, 5.6.1−5.6.15.

(16) Hannoush, R. N., and Damha, M. J. (2001) Remarkable stability of hairpins containing 2′,5′-linked RNA loops. *J. Am. Chem. Soc. 123*, 12368−74.

(17) Proctor, D. J., Schaak, J. E., Bevilacqua, J. M., Falzone, C. J., and Bevilacqua, P. C. (2002) Isolation and characterization of a family of stable RNA tetraloops with the motif YNMG that participate in tertiary interactions. *Biochemistry 41*, 12062−75.

(18) Durand, M., Chevrie, K., Chassignol, M., Thuong, N. T., and Maurizot, J. C. (1990) Circular dichroism studies of an oligonucleotide containing a hairpin loop made of a hexaethylene glycol chain: conformation and stability. *Nucleic Acids Res. 18*, 6353−6359.

(19) Gao, H., Chidambaram, N., Chen, B. C., Pelham, D. E., Patel, R., Yang, M., Zhou, L., Cook, A., and Cohen, J. S. (1994) Double-stranded cyclic oligonucleotides with non-nucleotide bridges. *Bioconjugate Chem. 5*, 445−453.

(20) Schenborn, E. T., and Mierendorf, R. C., Jr. (1985) A novel transcription property of SP6 and T7 RNA polymerases: dependence on template structure. *Nucleic Acids Res. 13*, 6223−36.

Bioconjugate Chemistry

Article

pubs.acs.org/bc

^{68}Ga-Complex Lipophilicity and the Targeting Property of a Urea-Based PSMA Inhibitor for PET Imaging

Matthias Eder,*[,†] Martin Schäfer,[†] Ulrike Bauder-Wüst,[†] William-Edmund Hull,[‡] Carmen Wängler,[§] Walter Mier,[∥] Uwe Haberkorn,[∥] and Michael Eisenhut[†]

[†]Radiopharmaceutical Chemistry, [‡]Molecular Structure Analysis, German Cancer Research Center, Heidelberg, Germany

[§]Department of Nuclear Medicine, University Hospital Munich, Munich, Germany

[∥]Department of Nuclear Medicine, University of Heidelberg, Heidelberg, Germany

Supporting Information

ABSTRACT: Urea-based inhibitors of the prostate-specific membrane antigen (PSMA) represent low-molecular-weight pepidomimetics showing the ability to image PSMA-expressing prostate tumors. The highly efficient, acyclic Ga(III) chelator *N,N′*-bis [2-hydroxy-5-(carboxyethyl)benzyl] ethylenediamine-*N,N′*- diacetic acid (HBED-CC) was introduced as a lipophilic side chain into the hydrophilic pharmacophore Glu-NH-CO-NH-Lys which was found favorable to interact with the PSMA "active binding site". This report describes the syntheses, in vitro binding analyses, and biodistribution data of the radiogallium labeled PSMA inhibitor Glu-NH-CO-NH-Lys(Ahx)-HBED-CC in comparison to the corresponding DOTA conjugate. The binding properties were analyzed using competitive cell binding and enzyme-based assays followed by internalization experiments. Compared to the DOTA-conjugate, the HBED-CC derivative showed reduced unspecific binding and considerable higher specific internalization in LNCaP cells. The ^{68}Ga complex of the HBED-CC ligand exhibited higher specificity for PSMA expressing tumor cells resulting in improved in vivo properties. ^{68}Ga labeled Glu-NH-CO-NH-Lys(Ahx)-HBED-CC showed fast blood and organ clearances, low liver accumulation, and high specific uptake in PSMA expressing organs and tumor. It could be demonstrated that the PET-imaging property of a urea-based PSMA inhibitor could significantly be improved with HBED-CC.

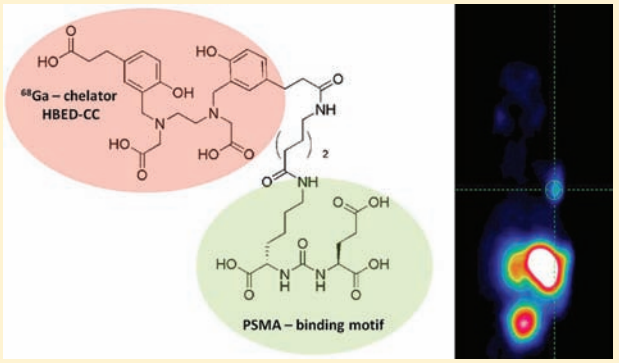

INTRODUCTION

It is still a challenge to select appropriate treatment options for disseminated prostate cancer because of the lack of sensitive imaging agents for diagnosis and therapy monitoring.[1] Prostate-specific membrane antigen (PSMA) is expressed in nearly all prostate cancers with increased expression in poorly differentiated, metastatic, and hormone-refractory carcinomas.[2] Its expression level is about 1000-fold higher compared to the physiologic levels found in other tissues such as kidney, small intestine, or brain.[3] PSMA is primarily restricted to the prostate, it is abundantly expressed at all stages of disease, it is presented on the cell surface, and it is not shed into the circulation.[4] As a consequence, PSMA can be considered a promising target for specific prostate cancer imaging and therapy.[5−7]

The radiohalogenated inhibitors of PSMA exhibiting Glu-NH-CO-NH-Lys as a pharmacophore showed the ability to image PSMA-expressing prostate tumor xenografts.[8,9] More recently, a corresponding DOTA-conjugate was labeled with ^{68}Ga which represents an attractive generator-based alternative to cyclotron-based PET radiopharmaceuticals.[10,11] The readily available ^{68}Ga decays with 89% probability by positron emission allowing high-resolution PET images with the option of accurate quantification. *N,N′*-Bis[2-hydroxy-5-(carboxyethyl)-benzyl]ethylenediamine-*N,N′*- diacetic acid (HBED-CC) was recently proposed as an efficient ^{68}Ga chelator with fast complexing kinetics and a high in vitro as well as in vivo complex stability.[12,13]

Besides the efficient Ga(III) complexing characteristics, HBED-CC was selected because of its lipophilic nature. It was found that the "active binding site" of PSMA is composed of two structural motifs, one representing a lipophilic pocket and the other interacting with urea-based inhibitors.[14] A study comparing a series of linkers located between the urea-based motif and a ^{99m}Tc chelator revealed a clear dependency of binding properties in favor of the more lipophilic compounds.[14] Further studies described the binding site as a pocket interacting with the carboxylic groups and the zinc complexing urea on one hand and with hydrophobic, mostly aromatic groups on the other hand.[15]

Received: June 1, 2011
Revised: February 6, 2012
Published: February 28, 2012

   dx.doi.org/10.1021/bc200279b | *Bioconjugate Chem.* 2012, 23, 688−697

Table 1. Analytical and PSMA-Binding Data

Ga-peptide complexes	m/z[a]	m/z calculated as $[M+H]^+$	analytical HPLC retention[b]	affinity related IC_{50} [nM] determined in enzyme-based assay[c]	affinity related K_i [nM] determined in cell-based assay[c]
[Ga]7	947.4257	947.4250	3.1 min	7.5 ± 2.2	12.0 ± 2.8
[Ga]**8**	819.4104	819.4100	2.4 min	19.4 ± 7.1	37.6 ± 14.3
[Ga]**12**	1284.6368	1284.6364	3.7 min	8.7 ± 3.9	11.1 ± 1.8

[a]High-resolution mass spectrometry data of the free ligands ($[M+H]^+$). [b]Compounds were labeled with ^{68}Ga; runs were performed using a linear A−B gradient (0% B to 100% B in 6 min) at a flow rate of 4 mL/min. Solvent A was 0.1% aqueous TFA and solvent B was MeOH. [c]Compounds were complexed with ^{nat}Ga.

This report describes the syntheses of Glu-NH-CO-NH-Lys(Ahx)-HBED-CC (**7**) and Glu-NH-CO-NH-Lys(Ahx)-DOTA (**8**) together with a reference PSMA inhibitor previously published by Banerjee et al.[10] After ^{68}Ga complexation, these compounds were evaluated in vitro and in vivo to study the influence of these two chelators and side chain variations.

MATERIALS AND METHODS

Reagents. All commercially available chemicals were of analytical grade and were used without further purification. ^{68}Ga was obtained from a $^{68}Ge/^{68}Ga$ generator based on pyrogallol resin support.[12,16] Protected amino acids were obtained from Novabiochem (Merck, Darmstadt, Germany) or IRIS Biotech (Marktredwitz, Germany).

The preparations were analyzed using reversed-phase high-performance liquid chromatography (RP-HPLC; Chromolith RP-18e, 100 × 4.6 mm; Merck, Darmstadt, Germany). Runs were performed using a linear A−B gradient (0% B to 100% B in 6 min) at a flow rate of 4 mL/min. Solvent A consisted of 0.1% aqueous TFA and solvent B was 0.1% TFA in CH_3CN or MeOH (in case of determination of radiochemical yield (RCY) or analysis of serum stability).

For all preparative purifications, a Chromolith RP-18e column (100 × 10 mm; Merck, Darmstadt, Germany) was used with a 6 min gradient starting at 0% raised to 50% and followed by a 1 min increase to 100% B. The flow rate was 6 mL/min. The HPLC system (L6200 A; Merck-Hitachi, Darmstadt, Germany) was equipped with a variable UV and a gamma detector (Bioscan; Washington, USA). UV absorbances were measured at 214 and 254 nm. Mass spectrometry was performed with a MALDI-MS Daltonics Microflex (Bruker Daltonics, Bremen, Germany) system. High-resolution mass spectrometry was performed using a system equipped with a mass spectrometer supporting Orbitrap technology (Exactive, Thermo Fisher Scientific). Full-scan single mass spectra were obtained by scanning m/z = 200−4000. NMR data were obtained with Bruker Avance NMR Spectrometers, AV(I)-600 (600 MHz) and AV(III)-400 (400 MHz). The chemical shifts are referenced to solvent signals (DMSO-d_5 = 2.50/39.757 ppm, DMSO-d_6 = 39.50).

Synthesis of Glu-NH-CO-NH-Lys(Ahx)-HBED-CC (7). In a first step, the isocyanate **2** of the glutamyl moiety was generated in situ by adding a mixture of 3 mmol of bis(*tert*-butyl) L-glutamate hydrochloride (Bachem, Switzerland) (**1**) and 1.5 mL of *N*-ethyldiisopropylamine (DIPEA) in 200 mL of dry CH_2Cl_2 to a solution of 1 mmol triphosgene in 10 mL of dry CH_2Cl_2 at 0 °C over 4 h. After agitation of the reaction mixture for one further hour at 25 °C, 0.5 mmol of a resin-immobilized (2-chloro-tritylresin, Merck, Darmstadt) ε-allyloxycarbonyl protected lysine was added in one portion (in 4 mL DCM) and reacted for 16 h with gentle agitation leading to compound **3**. The resin was filtered off and the allyloxy-protecting group was removed using 100 mg tetrakis-(triphenyl)palladium(0) (Sigma-Aldrich, Germany) and 400 μL morpholine in 4 mL CH_2Cl_2 for 3 h resulting in compound **4**. The following coupling of the aminohexanoic moiety was performed using 2 mmol of the Fmoc-protected 6-amino-hexanoic acid (Sigma-Aldrich, Germany), 1.96 mmol of HBTU (Merck, Darmstadt, Germany), and 2 mmol of *N*-ethyl-diisopropylamine in a final volume of 4 mL DMF. The product **5** was cleaved from the resin by reacting with 4 mL of a 30% 1,1,1,3,3,3-hexafluoroisopropanole (HFIP) in CH_2Cl_2 for two hours at ambient temperature resulting in the *tert*-butyl protected crude product **6** which was purified via RP-HPLC.

To conjugate HBED-CC, the purified product **6** was reacted with an equimolar amount of HBED-CC-TFP-ester synthesized as previously described[12] in the presence of 2 equiv of DIPEA in *N*,*N*-dimethylformamide (DMF; final volume of 1 mL). After HPLC purification, the remaining *tert*-butyl groups were cleaved at room temperature for one hour using 2 mL trifluoroacetic acid to obtain **7** in ∼35% yield after purification by HPLC. High-resolution mass spectrometry was used to confirm the identity (Table 1), and purity was analyzed via analytical HPLC at λ = 206 nm (Supporting Information). Complete and unequivocal NMR ^1H and ^{13}C signal assignments were obtained (Supporting Information).

Synthesis of Glu-NH-CO-NH-Lys(Ahx)-DOTA (8). Precursor **5** was synthesized as mentioned before. After activation with 3.95 equiv of HBTU and DIPEA for 2 h, 4 equiv of tris(*t*-bu)-DOTA (Chematech, Dijon, France) relative to the resin loading were reacted with **5** after removal of the Fmoc-protecting group in a final volume of 3 mL DMF. The product was cleaved from the resin in a 2 mL mixture consisting of trifluoroacetic acid, triisopropylsilane, and water (95:2.5:2.5). The product was purified via semipreparative RP-HPLC resulting in compound **8** (∼30% yield). High-resolution mass spectrometry was used to confirm the identity (Table 1) and purity was analyzed via analytical HPLC at λ = 206 nm (Supporting Information). Complete and unequivocal ^1H and ^{13}C NMR signal assignments were obtained (Supporting Information).

Synthesis of Reference Compound (12). Synthesis of the DOTA conjugate previously published by Banerjee et al.[10] was performed using a modified solid-phase method. Five equivalents of suberic-acid-bis-(*N*-hydroxysuccinimideester) (Sigma-Aldich, Germany) was conjugated to the side chain of the lysine moiety of compound **4** in the presence of 5 equiv of triethylamine in 3 mL DMF. After 2 h, the resin was washed with DMF. In the presence of five equiv of triethylamine, five equiv of Fmoc-Lys-oAll was coupled to the immobilized NHS-ester of intermediate **9** in a final volume of 3 mL DMF for 16 h resulting in **10**. The remaining conjugations of two phenyl-alanine building blocks and tris(*t*-bu)-DOTA were performed

dx.doi.org/10.1021/bc200279b | *Bioconjugate Chem.* 2012, 23, 688−697

according to standard Fmoc-protocols resulting in **11**. Cleavage from resin was performed using a 3 mL mixture of trifluoroacetic acid, triisopropylsilane, and water (95:2.5:2.5). The product was purified via RP-HPLC to obtain **12** in ~8% yield. High-resolution mass spectrometry was used to confirm the identity (Table 1), and purity was analyzed via analytical HPLC at λ = 206 nm (Supporting Information).

^{68}Ga-Labeling. Typically, 0.1−1 nmol of Glu-NH-CO-NH-Lys(Ahx)-HBED-CC (**7**, in 0.1 M HEPES buffer pH 7.5) or 1 nmol of the DOTA conjugates (**8**/**12**, in 0.1 M HEPES buffer pH 7.5) were added in a volume of 100 μL to a mixture of 10 μL 2.1 M HEPES solution and 10 μL [^{68}Ga]Ga^{3+} eluate (50−100 MBq). The pH of the labeling solution was adjusted to 4.2. Depending on the chelator, the reaction mixture was incubated either at ambient temperature or at 80 °C for 2 min. The radiochemical yield (RCY) was determined using RP-HPLC.

^{67}Ga-Labeling. ^{67}Ga was purchased from MDS Nordion (Fleurus, Belgium) as [^{67}Ga]$GaCl_3$ in 0.1 N HCl. Typically, 0.1 nmol of Glu-NH-CO-NH-Lys(Ahx)-HBED-CC (**7**) was added in a volume of 100 μL to a mixture of 10 μL 2.1 M HEPES solution, 2 μL 1 N HCl, and 10 μL [^{67}Ga]$GaCl_3$ (~100 MBq) in 0.1 N HCl resulting in a solution with a pH of 4.2. The reaction mixture was incubated for 2 min at ambient temperature. The RCY was determined using RP-HPLC.

^{nat}Ga-Complexes. A 10× molar excess of Ga(III)-nitrate (Sigma Aldrich, Germany) in 0.1 N HCl (10 μL) was reacted with the compounds **7**, **8**, or **12** (1 mM in 0.1 M HEPES buffer pH 7.5, 40 μL) in a mixture of 10 μL 2.1 M HEPES solution and 2 μL 1 N HCl for 2 min at 80 °C.

Radiochemical Stability. The radiochemical stability of the ^{68}Ga-labeled compounds **7**, **8**, and **12** was determined by incubating in both PBS and human serum for 2 h at 37 °C. An equal volume of MeCN was added to the samples to precipitate serum proteins. Subsequently, the samples were centrifuged for 5 min at 13 000 rpm. An aliquot of the supernatant and the PBS sample was analyzed by RP-HPLC. In addition, serum samples of compound [^{68}Ga]**7** were run on a Superdex 200 GL 5/150 gel filtration column (GE Healthcare, Munich, Germany) to analyze protein binding. To analyze the complex stability against human transferrin, a 400 μL aliquot of [^{68}Ga]**7** was added to 250 μg apo-transferrin in PBS at pH 7 and incubated at 37 °C (water bath) for 2 h. The complex stability was determined using a Superdex 200 GL 5/150 short column with PBS pH 7 as eluent.

Naaladase Assay. Recombinant human PSMA (rhPSMA, R&D systems, Wiesbaden, Germany) was diluted in assay buffer (50 mM HEPES, 0.1 M NaCl, pH 7.5) to 0.4 μg/mL. The substrate Ac-Asp-Glu (Sigma, Taufkirchen, Germany, 40 μM final concentration) was mixed with [^{nat}Ga]**7**, [^{nat}Ga]**8**, or [^{nat}Ga]**12** at concentrations ranging from 0.05 nM to 1000 nM in a final volume of 125 μL assay buffer. The mixtures were combined with 125 μL of the rhPSMA solution (0.4 μg/mL) and incubated for one hour at 37 °C. The reaction was stopped by heating at 95 °C for 5 min. 250 μL of a 15 mM solution of *ortho*-phthaldialdehyde (Sigma, Taufkirchen, Germany) was added to all vials and incubated for 10 min at ambient temperature. Finally, 200 μL aliquots of the reaction solutions were loaded onto a F16 Black Maxisorp Plate (Nunc, Langenselbold, Germany) and read at excitation and emission wavelengths of 330 and 450 nm, respectively, using a microplate reader (DTX-880, Beckman Coulter, Krefeld, Germany). The data were analyzed by a one-site total binding regression algorithm of *GraphPad Prism* (GraphPad Software, California, USA).

Cell Binding Studies. Cell binding studies were performed using PSMA$^+$ LNCaP cells (metastatic lesion of human prostatic adenocarcinoma, ATCC CRL-1740) and PSMA$^-$ PC-3 cells (bone metastasis of a grade IV prostatic adenocarcinoma, ATCC CRL-1435) cultured in DMEM medium supplemented with 10% fetal calf serum and 2 mmol/L L-glutamine (all from Invitrogen). During cell culture, cells were grown at 37 °C in an incubator with humidified air, equilibrated with 5% CO_2. The cells were harvested using trypsin-ethylenediaminetetraacetic acid (trypsin-EDTA; 0.25% trypsin, 0.02% EDTA, all from Invitrogen).

In order to determine the binding affinity, a competitive cell binding assay was performed. LNCaP cells (10^5 per well) were incubated with a 0.2 nM solution of [^{67}Ga]**7** in the presence of 12 different concentrations of [^{nat}Ga]**7**, [^{nat}Ga]**8**, or [^{nat}Ga]**12** (0−5000 nM, 200 μL/well). After incubation at ambient temperature for 1 h with gentle agitation, the binding buffer was removed using a multiscreen vacuum manifold (Millipore, Billerica, MA). After washing twice with 100 μL and once with 200 μL ice-cold binding buffer, the cell-bound radioactivity was measured with a gamma counter (Packard Cobra II, GMI, Minnesota, USA). The 50% inhibitory concentration (IC_{50}) values were calculated by fitting the data using a nonlinear regression algorithm (GraphPad Software). Experiments were performed at least three times including quadruplicate sample measurements.

Determination of Binding Specificity and Internalization. Internalization experiments were performed as previously described.[17] Briefly, 10^5 LNCaP or PC-3 cells were seeded in poly(L-lysine)-coated 24-well cell culture plates 24 h before incubation. After washing with PBS, the cells were incubated with the radiolabeled compounds [^{68}Ga]**7**, [^{68}Ga]**8**, and [^{68}Ga]**12** (25 nM final concentration) for 45 min at 37 °C and at 4 °C, respectively. To determine specific cell uptake, cells were blocked with 2-(phosphonomethyl)-pentanedioic acid (PMPA, Axxora, Loerrach, Germany) to a final concentration of 100 μM. Cellular uptake was terminated by washing 4 times with 1 mL of ice-cold PBS. To remove surface-bound radioactivity, cells were incubated twice with 0.5 mL glycine-HCl in PBS (50 mM, pH 2.8) for 5 min at room temperature. The cells were washed with 1 mL of ice-cold PBS and lysed using 0.5 mL of 0.3 M NaOH. The surface-bound and internalized fractions were measured in a gamma counter.

Specificity of binding was additionally analyzed in a concentration-dependent cell uptake experiment. Solutions of [^{68}Ga]**7**, [^{68}Ga]**8**, or [^{68}Ga]**12** at final concentrations of 2.5, 25, and 250 nM were added to 7 × 10^5 cells suspended in 50 μL OPTIMEM medium (Gibco, Auckland, New Zealand). After 45 min at 37 °C, the samples were briefly vortexed and a 10 μL aliquot was transferred to a 400 μL microcentrifuge tube (Roth, Germany) containing 350 μL of a 75:25 mixture of silicon oil, density 1.05 (Sigma Aldrich, Germany), and mineral oil, density 0.872 (Acros, Nidderau, Germany). Separation of cells from the medium was performed by centrifugation at 12 000 rpm for 2 min. After freezing the tubes using liquid nitrogen, the bottom tips containing the cell pellet were cut off. The cell pellets and the supernatants were separately counted in a gamma counter.

Biodistribution and PET Imaging. Five ×10^6 cells of either LNCaP or PC-3 in 50% Matrigel (Becton Dickinson, Heidelberg, Germany) were subcutaneously inoculated into the right trunk of male 7- to 8-week-old BALB/c nu/nu mice

Scheme 1. Syntheses of Glu-NH-CO-NH-Lys(Ahx)-HBED-CC (7) and Glu-NH-CO-NH-Lys(Ahx)-DOTA (8)

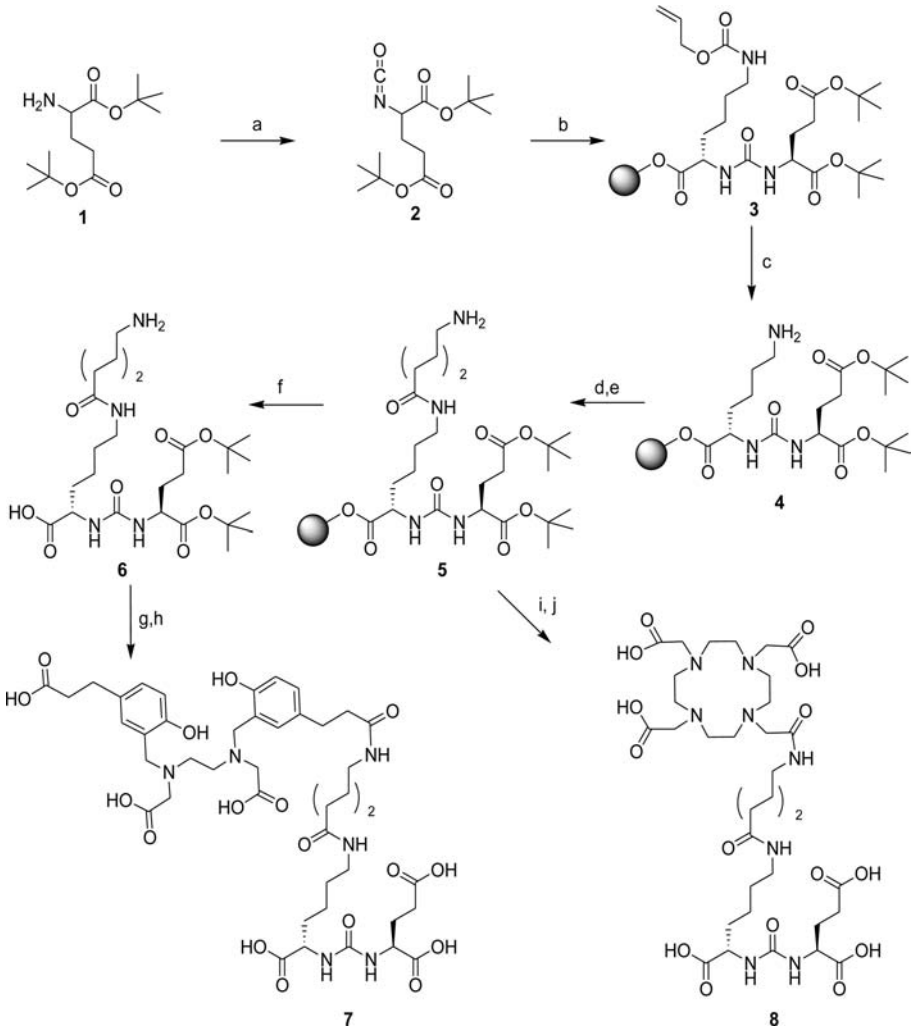

(a) Triphosgene, DIPEA, CH_2Cl_2, 0 °C; (b) H-Lys(Alloc)-2CT-Resin, CH_2Cl_2; (c) $Pd[P(C_6H_5)_3]_4$, morpholine, CH_2Cl_2; (d) Fmoc-6-Ahx-OH, HBTU, DIPEA, DMF; (e) 20% piperidine, DMF; (f) hexafluoroisopropanol/CH_2Cl_2; (g) HBED-CC-TFP ester, DIPEA, DMF; (h) TFA; (i) tris(*t*-bu)DOTA, HBTU, DIPEA; (j) TFA.

(Charles River Laboratories). The tumors were allowed to grow for 3 to 4 weeks until approximately 1 cm^3 in size.

The ^{68}Ga-radiolabeled compounds of **7**, **8**, and **12** were injected via tail vein (1−2 MBq per mouse; 0.1−0.2 nmol). At 1 h after injection, the animals were sacrificed. Organs of interest were dissected, blotted dry, and weighed. The radioactivity was measured with a gamma counter and calculated as % ID/g.

For the microPET studies, 10−25 MBq of compounds [^{68}Ga]**7** and [^{68}Ga]**8** in a volume of 0.15 mL (~0.5 nmol) were injected via a lateral tail vein into mice bearing LNCaP tumor xenografts. The anesthetized animals (2% sevoflurane, Abbott, Wiesbaden, Germany) were placed in prone position into the Inveon small animal PET scanner (Siemens, Knoxville, Tenn, USA) to perform a 50 min dynamic microPET scan starting at 1 min post injection followed by a 20 min static scan.

Statistical Aspects. All experiments were performed at least in triplicate. Quantitative data were expressed as mean ± SD. If applicable, means were compared using Student's *t*-test. *P* values of <0.05 were considered statistically significant.

RESULTS

Chemistry. The synthesis of the resin-bound intermediate **5** was performed using solid-phase chemistry as outlined in Scheme 1. To couple the respective chelators, compound **5** was either cleaved from resin and reacted with an equimolar amount of HBED-CC-TFP-ester resulting in **7** or coupled with HBTU activated tris(t-bu)DOTA resulting in the DOTA-conjugate **8**. The preparation of the reference compound **12** previously published by Banerjee et al.[10] was performed using a modified solid-phase method as outlined in Scheme 2. Briefly, disuccinimidyl suberate was conjugated to the ε-amino group of the lysine group of **4**. After Fmoc-Lys-OAll was coupled to the resulting immobilized NHS-ester, the conjugation of two phenylalanine building blocks and tris(*t*-bu)-DOTA were performed according to standard Fmoc-protocols. Analytical data of compounds **7**, **8**, and **12** are summarized in Table 1.

Radiolabeling and Stability. Radiolabeling with ^{68}Ga was performed at pH 4.2 by incubating the conjugates **7**, **8**, or **12** in a mixture consisting of 50−100 MBq [^{68}Ga]Ga^{3+} and HEPES. Radiochemical yields were determined by RP-HPLC analysis of the reaction mixtures. The retention times obtained for each compound are shown in Table 1. An amount of 0.1 nmol of the

dx.doi.org/10.1021/bc200279b | *Bioconjugate Chem.* 2012, 23, 688−697

Scheme 2. Modified Solid-Phase Synthesis of the DOTA Conjugate Previously Published by Banerjee et al.[10]

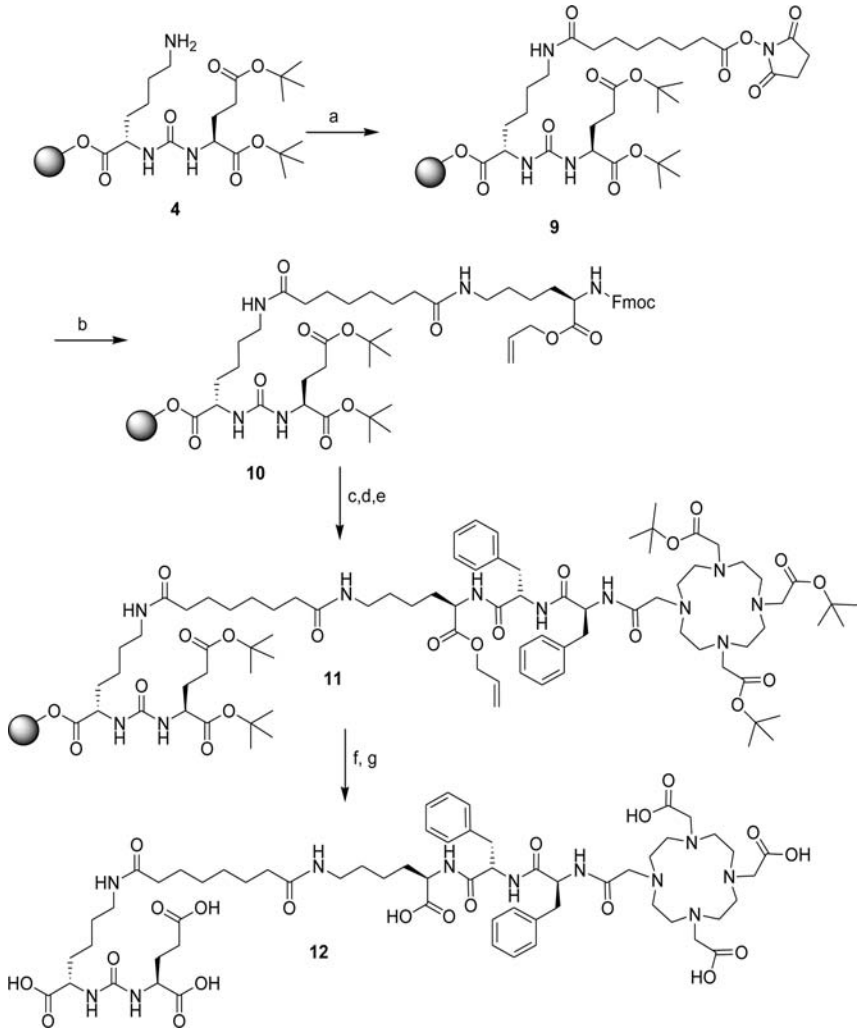

(a) Disuccinimidyl suberate (DSS), TEA, DMF; (b) Fmoc-Lys-oAll, TEA, DMF; (c) 20% piperidine, DMF; (d) Fmoc-Phe-OH, HBTU, DIPEA, DMF; (e) tris(*t*-bu)DOTA, HBTU, DMF; (f) $Pd[P(C_6H_5)_3]_4$, morpholine, CH_2Cl_2; (g) TFA, triisopropylsilane, H_2O (95/2.5/2.5).

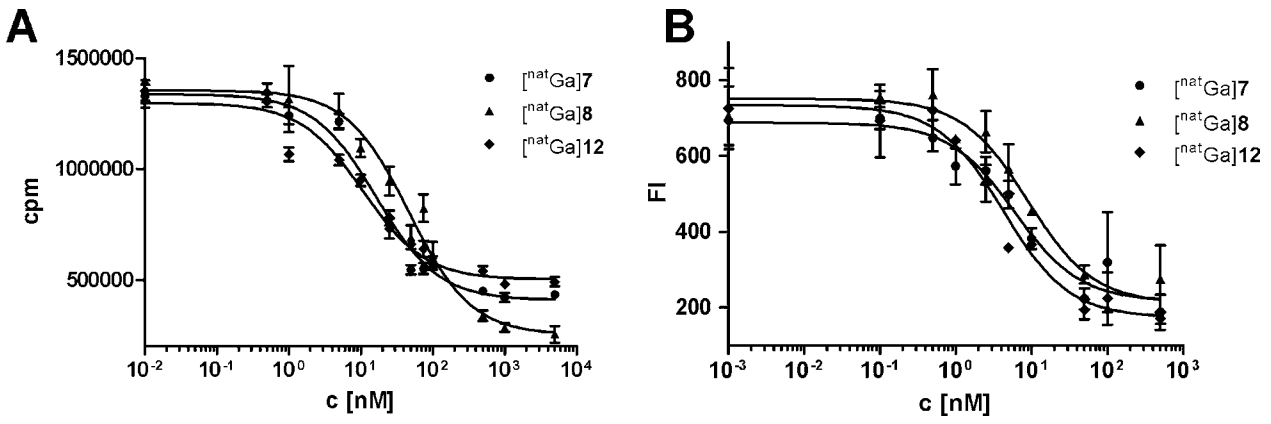

Figure 1. Determination of binding affinity of compounds [^{nat}Ga]**7**, [^{nat}Ga]**8**, and [^{nat}Ga]**12** by competitive titration on LNCaP cells (A) and purified receptor using an enzyme-based assay (B). Data are expressed as mean ± SD (n = 4). cpm = counts per minute; FI = fluorescence intensity.

HBED-CC conjugate **7** in a final concentration of 1.7 μM led to a radiochemical yield of more than 99% in less than 1 min at room temperature. As a consequence, specific activities in the range 500−1000 GBq/μmol were obtained. In order to achieve comparable high radiochemical yields with the DOTA-conjugates **8** and **12**, the compounds were incubated for 2 min at 80 °C using 1 nmol precursor.

Incubation of the ^{68}Ga-labeled compounds **7**, **8**, and **12** in human serum for 2 h at 37 °C resulted in no detectable changes in the radiograms. Stability of the ^{68}Ga-labeled HBED-CC-

dx.doi.org/10.1021/bc200279b | *Bioconjugate Chem.* 2012, 23, 688−697

conjugate 7 could additionally be demonstrated by transferrin challenging and incubation in human serum. No activity was exchanged in presence of 250 μg transferrin or transferred to other serum proteins.

Determination of PSMA Affinity. The variants were competitively analyzed in terms of their binding capacity by performing an enzyme-based assay on rhPSMA (Naaladase-Assay) and a binding assay on LNCaP cells with ^{67}Ga-labeled 7 (RCY > 99%; specific activity ~1000 GBq/μmol) as radioligand. The affinity related IC_{50} and the calculated K_i values of both assays were determined by analyzing the respective binding curves (Figure 1) with *GraphPad Prism*. The data are summarized in Table 1. Compared to the DOTA conjugate [^{nat}Ga]**8**, the HBED-CC conjugate [^{nat}Ga]**7** and the more lipophilic reference compound [^{nat}Ga]**12** showed slightly better affinities to both the purified extracellular receptor rhPSMA and LNCaP cells.

Specific Cell Binding and Internalization. Comparative cell uptake and internalization experiments with LNCaP (PSMA positive) and PC-3 (PSMA negative) cells revealed unspecific cell uptake of [^{68}Ga]**8** and [^{68}Ga]**12** in both cell lines which could not be blocked with excess PMPA (Figure 2A). In contrast, the HBED-CC conjugate ([^{68}Ga]**7**) showed almost no uptake in PSMA-negative PC-3 cells or in LNCaP cells blocked with PMPA. Furthermore, [^{68}Ga]**7** significantly revealed higher specific internalization and cell surface accumulation as compared to the DOTA conjugates (Figure 2B). In another cell uptake experiment, three different concentrations of the radiolabeled compounds (2.5 nM, 25 nM, and 250 nM) were incubated with either LNCaP (Figure 3A) or PC-3 cells (Figure 3B). In accordance with the results received from the internalization experiments, [^{68}Ga]**7** showed a considerably higher uptake in LNCaP cells. Furthermore, the unspecific uptake in PC-3 cells was lower as compared to the DOTA derivatives [^{68}Ga]**8** and [^{68}Ga]**12**.

Biodistribution Studies. The organ and tumor uptake values of the complexes [^{68}Ga]**7**, [^{68}Ga]**8**, and [^{68}Ga]**12** differed in accordance with the aforementioned *in vitro* data (Figure 4). The HBED-CC conjugated compound [^{68}Ga]**7** was cleared rapidly from the circulation and PSMA negative tissue. Remarkably, the liver activity of [^{68}Ga]**7** amounted to only 0.87 ± 0.05% ID/g as early as one hour after injection. The high kidney, spleen, and lung uptake of 139.4 ± 21.4% ID/g, 17.90 ± 2.87% ID/g, and 2.49 ± 0.27% ID/g was nearly completely blocked to 4.02 ± 1.14% ID/g, 1.54 ± 0.33% ID/g, and 0.64 ± 0.32% ID/g, respectively, after the coinjection of 2 mg/kg 2-PMPA (Figure 4B). The tumor uptake amounted to 7.70 ± 1.45% ID/g on LNCaP and 1.30 ± 0.12% ID/g on PC-3.

The DOTA complex [^{68}Ga]**8** showed a completely different uptake pattern. The liver uptake of the DOTA-conjugate was enhanced by a factor of 5.7, the tumor uptake was reduced by factor 2.6, and the kidney uptake was surprisingly lowered to background values. The uptake values of PSMA-negative PC-3 tumors were low for all compounds (1.30 ± 0.13% ID/g ([^{68}Ga]**7**), 0.60 ± 0.06% ID/g ([^{68}Ga]**8**), and 0.58 ± 0.07% ID/g ([^{68}Ga]**12**), respectively) (Figure 4C).

PET-Imaging. The tumor-targeting efficiency of [^{68}Ga]**7** and [^{68}Ga]**8** was evaluated by 50 min dynamic microPET scans followed by a 20 min static scan. The differences observed in biodistribution could have also been visualized by PET imaging. The complexes [^{68}Ga]**7** and [^{68}Ga]**8** were injected intravenously into LNCaP tumor-bearing mice, and microPET scans were carried out for up to 70 min p.i. A coronal PET slice after injection of [^{68}Ga]**7** is shown in Figure 5a. The DOTA complex [^{68}Ga]**8** failed to image the tumor proven by the time activity curves over tumor and muscle (Figure 5B).

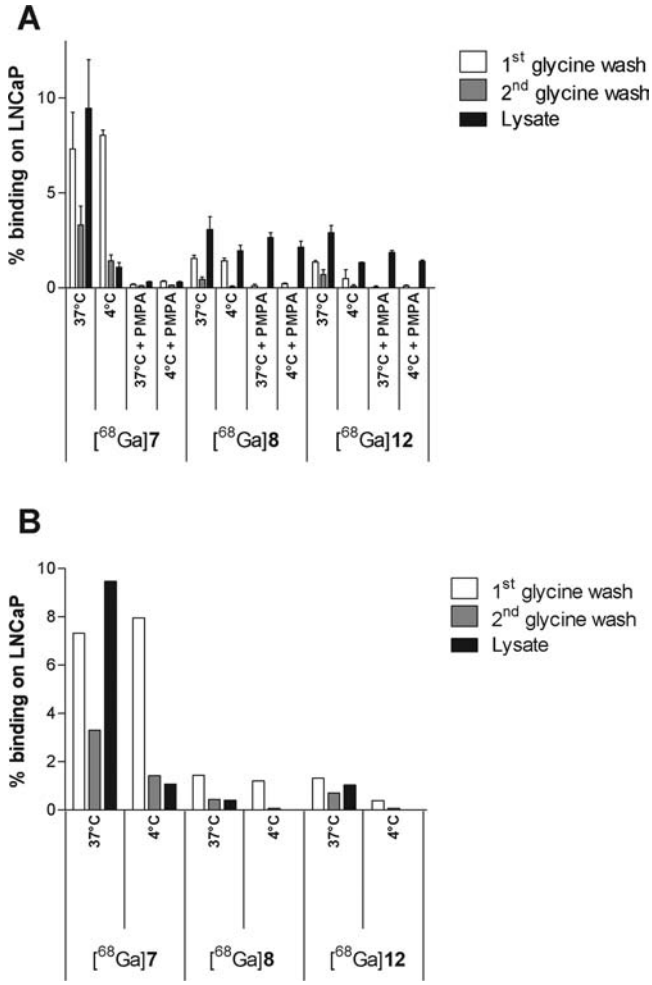

Figure 2. Cell binding and internalization of compounds [^{68}Ga]**7**, [^{68}Ga]**8**, and [^{68}Ga]**12** (A). Specific cell uptake was evaluated by blockade with 100 μM PMPA. Specificity of cell uptake (B) was calculated by subtracting the respective signals resulting from PMPA-blockage. Values are expressed as % of applied radioactivity bound to 10^6 cells. Data are expressed as mean ± SD (n = 3).

Comparison of Biological Properties of L- and D-Forms of [^{68}Ga]7. The ^{68}Ga complex of D-Glu-NH-CO-NH-Lys(Ahx)-HBED-CC was synthesized and compared with the corresponding L-isomer. Time−activity curves obtained from dynamic PET measurements revealed D-[^{68}Ga]**7** to be cleared from the kidneys into the urinary bladder while L-[^{68}Ga]**7** is retained in this organ (Figure 6). This finding is supported by the ~10^3 times lower PSMA affinity of D-[^{68}Ga]**7** (data not shown).

■ DISCUSSION

PSMA is strongly expressed on prostate cancer cells[18] and therefore represents a promising target for the development of imaging agents for tumor staging and followup. Among the currently used radioisotopes, ^{68}Ga exhibits several favorable properties as there are the availability and the facile labeling technology by means of complexation.[11] A series of chelators are available for the complexation of ^{68}Ga which are conjugated to targeting carrier molecules. Besides some reported stabilizing

dx.doi.org/10.1021/bc200279b | *Bioconjugate Chem.* 2012, 23, 688−697

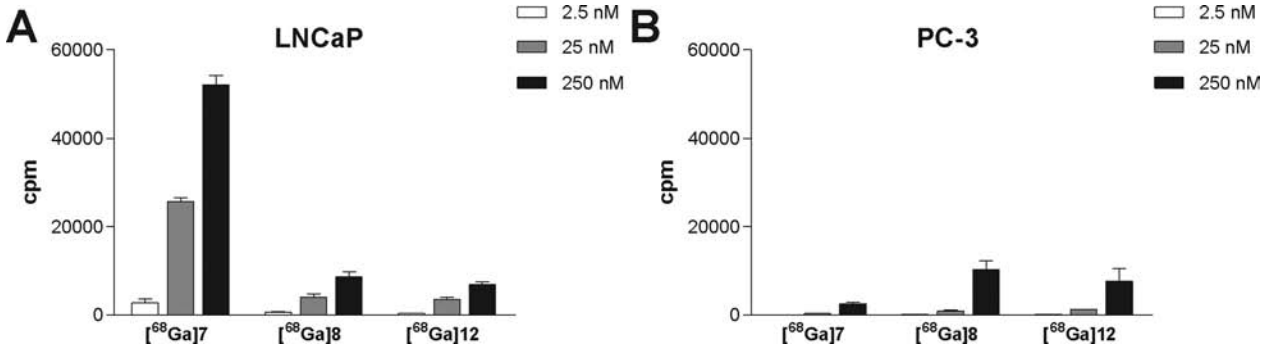

Figure 3. Binding of [^{68}Ga]**7**, [^{68}Ga]**8**, and [^{68}Ga]**12** to LNCaP (PSMA^{+}) cells (A) and PC-3 (PSMA^{-}) cells (B) depending on ^{68}Ga-complex concentration. Values were normalized with respect to added radioactivity of each compound. Data are expressed as mean ± SD (n = 3).

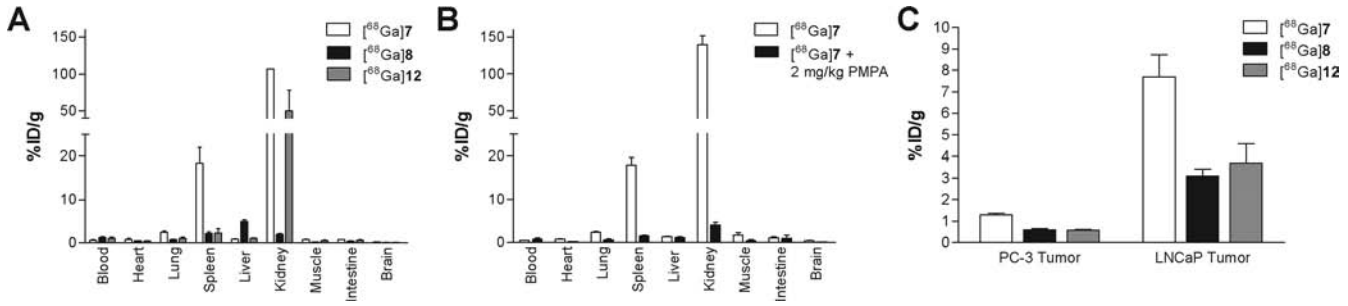

Figure 4. Organ distribution expressed as % ID/g tissue one hour post injection. (A) Comparison of the compounds [^{68}Ga]**7** (PSMA-binding motif coupled to HBED-CC), [^{68}Ga]**8** (PSMA-binding motif coupled to DOTA), and [^{68}Ga]**12**. (B) PSMA-blocking by coadministration of 2 mg/kg body weight PMPA indicating PSMA-specific uptake in kidney and spleen. (C) Uptake in PC-3 tumors and LNCaP tumors 1 h after injection. Data are expressed as mean ± SD (n = 3).

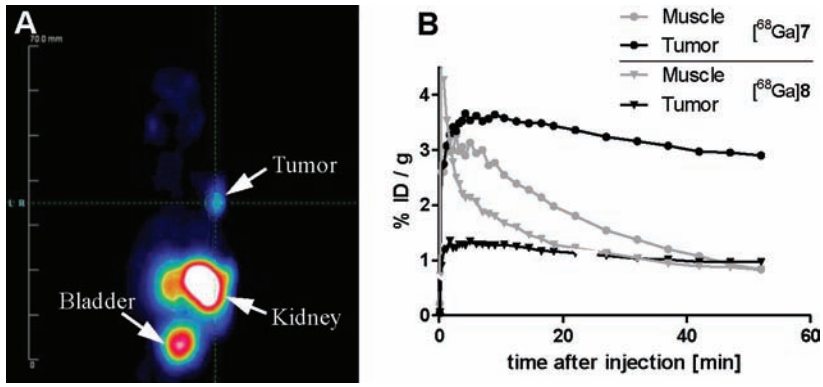

Figure 5. Whole-body coronal microPET image of an athymic male nude mice bearing LNCaP tumor xenografts. The tumor-targeting efficacy of [^{68}Ga]**7** was demonstrated by dynamic microPET scan (B) followed by a static scan (A). The static scan up to 1 h post injection of [^{68}Ga]**7** is shown in (A). Approximately 15 MBq/mouse was injected. Graph B shows the respective time−activity curves in muscle and tumor for [^{68}Ga]**7** and [^{68}Ga]**8**.

effects or pretargeting approaches,[17,19] the function of the chelator in radiopharmaceuticals is usually restricted to serving as a complexing agent without influencing the receptor binding. However, the size-demanding radiometal complexes often exert their influence on the targeting molecule by changing lipophilicity or charge. In particular, the pharmacological property of small molecules can strongly be influenced or abolished with respect to its target binding properties.

An interesting study comparing various linkers located between the PSMA binding group 2-[3-(1,3-dicarboxypropyl)-ureido]pentanedioic acid (DUPA) and a ^{99m}Tc complex showed that the lipophilicity of the linker significantly correlates with improved binding properties.[14] Crystal structure investigations also indicated that, besides the electrostatic interactions of urea and carboxylic groups at the active, Zn(II)-containing center of PSMA, there are lipophilic interactions resulting from a hydrophobic pocket located next to the active site.[8,20] A further study substantiates the PSMA active site as a pocket with multiple interactions as well. The pharmacophore was proposed to present three carboxylic groups able to interact with the respective side chains of PSMA, an oxygen as part of zinc complexation in the active center and an aromatic structure able to interact with a hydrophobic part of the binding pocket composed of tyrosines.[15] This work suggests that these interactions are additive in terms of functional efficiency. Only inhibitors which interact with all parts of the binding site displayed a tight binding mode and a high rate of internal-

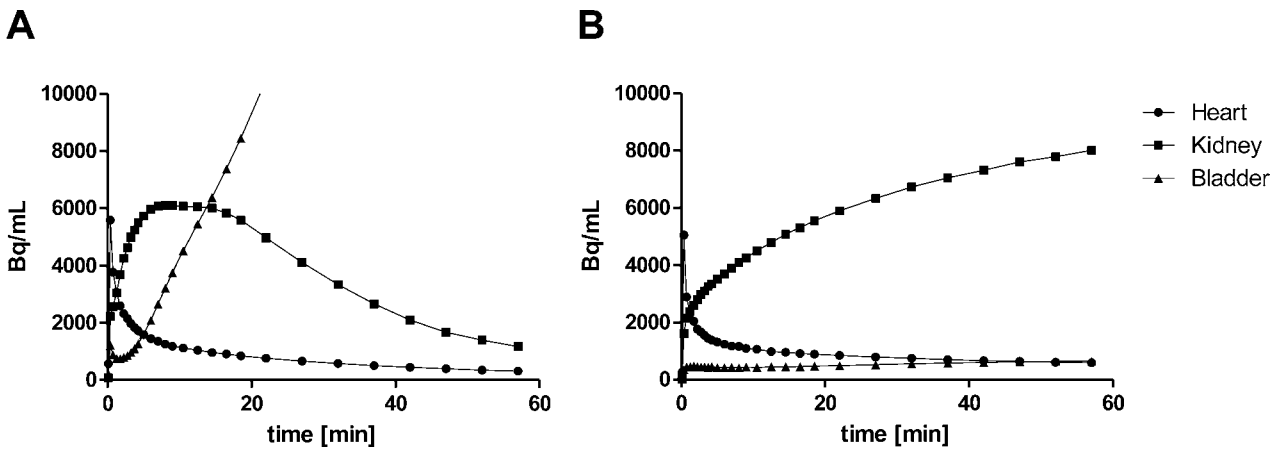

Figure 6. Time−activity curves taken from dynamic PET measurements and expressed as Bq/mL organ normalized to injected dose. The D-form of [^{68}Ga]**7** (A) shows ~10^3 reduced binding capacity to PSMA as compared to the L-form (B). As a consequence, the L-form accumulates in kidneys whereas the D-isomer is rapidly cleared from kidneys into the bladder.

ization. Molecules lacking one of these interactions showed other modes of action and weaker binding.[15]

These results led to the development of the amphiphilic, PSMA-specific tracer [^{68}Ga]**7** consisting of the urea-based pharmacophore and the ^{68}Ga-HBED-CC complex able to interact with the hydrophobic binding pocket. Two ^{68}Ga-DOTA complexes, the hydrophilic [^{68}Ga]**8** and the amphiphilic [^{68}Ga]**12**, were compared with [^{68}Ga]**7** in terms of PSMA-binding characteristics and internalization.

Compared to the DOTA complexes [^{68}Ga]**8** and [^{68}Ga]**12**, the HBED-CC complex [^{68}Ga]**7** showed a significantly enhanced PSMA-specific internalization in LNCaP cells (Figure 2B). In another cell uptake experiment, where three different concentrations of the radiolabeled compounds were given to either LNCaP (Figure 3A) or PC-3 cells (Figure 3B), [^{68}Ga]**7** showed a considerably higher uptake in LNCaP cells, while the unspecific uptake in PC-3 cells was significantly lower as compared to the DOTA derivatives [^{68}Ga]**8** and [^{68}Ga]**12**. The binding data are characteristic for specific and unspecific binding because the values rise in an exponential manner on PSMA$^+$ LNCaP cells (Figure 3A) and linearly on PSMA$^-$ PC-3 cells (Figure 3B).

Despite clear differences regarding unspecific cell uptake, the obtained binding affinity data of all complexes are nearly identical. This might be explained by the fact that, in contrast to the internalized fraction, the cell surface bound radioactivity of the DOTA complexes [^{68}Ga]**8** and [^{68}Ga]**12** could successfully be blocked with PMPA indicating that there is negligible unspecific binding on cell surface proteins. As a consequence, their unspecific cell uptake had only moderate effects on the binding affinity, since competitively determined k_D values were derived from cell surface interactions.

Since it has been reported that the lack of only one interaction or its exact position can have considerable influence on the mode of binding and not obligatory on binding affinity,[15] the obvious effects on internalization and cell uptake, while observing nearly constant K_i values after the replacement with a more hydrophilic chelate, can be considered consistent with such findings. The extent of conformational changes of PSMA induced by inhibitor binding determines the rate of internalization as a motif in the cytoplasmic tail seems to mediate PSMA internalization.[15,21] On the basis of our understanding, these extracellular and intracellular processes depend on the existence of exact interactions and to a lesser extent on binding affinity. As a consequence, hydrophobic interactions of HBED-CC seem to be responsible for the improved binding properties of [^{68}Ga]**7**. However, since the DOTA derivative [^{68}Ga]**12** showed even more lipophilicity (HPLC retention in Table 1), the optimal position of the aromatic structure is probably more important than the lipophilicity of the linker region in general.

Interestingly, the unspecific binding observed in vitro had no particular effect on the tumor uptake in vivo. Since the concentration has a strong influence on unspecific binding, the extent of unspecific uptake in vivo is low, as only small amounts of the tracer reach the tumor cell surfaces. Furthermore, unspecific binding potentially occurs throughout the whole organism, so that the amounts of active substance in the PSMA-positive as well as -negative tumors are reduced, leading to lower tumor uptakes and tumor-to-background ratios. This might explain why unspecific binding of the DOTA-conjugates could not be demonstrated in vivo.

However, clear differences between the HBED-CC complex and the DOTA derivative were observed in organ distribution and tumor uptake. The lower liver value and the higher tumor uptake was in favor of [^{68}Ga]**7**. The extremely low kidney uptake of [^{68}Ga]**8** cannot be explained but is potentially a binding kinetics related effect in the kidney parenchyma. In contrast, the [^{68}Ga]**7** showed high kidney and spleen uptake which was almost completely blocked by coinjection of the PSMA inhibitor PMPA, indicating that the uptake in these organs was mediated by specific binding to PSMA known to be overexpressed in murine kidney and spleen.[18,22−24] With reference to clinical application, PSMA expression is lower in human kidneys.[3]

Both organ distribution and PET imaging indicate improved characteristics of the HBED-CC conjugate. Remarkably, the absolute uptake in dissected tumors was higher as compared to PET imaging. This finding can be attributed to the fact that PET imaging was performed using another batch of mice. The tumor values are generally reduced in the PET images, 7.7 to ~3.5%ID/g for [^{68}Ga]**7** and 3 to ~1%ID/g for [^{68}Ga]**8**, which prevented sufficient tumor-to-background contrast. Explanations might be the batch of mice with a potentially different PSMA expression level or the higher amount of injected compound in PET possibly leading to a competitive effect.

dx.doi.org/10.1021/bc200279b | *Bioconjugate Chem.* 2012, 23, 688−697

However, since the conditions within each experiment were identical for both compounds, we conclude that the tumor-to-background contrast of [^{68}Ga]**7** is higher leading to better image quality even in the case of potentially reduced receptor expression.

To substantiate the notion that the reduced kidney accumulation of [^{68}Ga]**7** after PMPA blockade is PSMA-specific, the D-form of [^{68}Ga]**7** was included in our experiments. The PET study in Figure 6 showed that the D-form is cleared rapidly from the kidney while [^{68}Ga]**7** is accumulating with little bladder excretion. This result adds to the specific interaction of the title complex with PSMA.

The recently summarized[15] structural interactions necessary to form a PSMA binding radiopharmaceutical were obviously met by the HBED-CC complex [^{68}Ga]**7**, which proved to be superior in comparison to the respective ^{68}Ga-DOTA complex [^{68}Ga]**8** in all aspects of the described interactions. Besides the favorable functional properties, this compound can efficiently be obtained with fast Ga(III)-complexing kinetics resulting in high radiochemical yields and excellent specific radioactivities. The possibility of an efficient room-temperature labeling procedure in combination with the advantages of ^{68}Ga as a PET radionuclide may allow the development of a kit-formulated radiopharmaceutical for the targeted imaging of prostate cancer.

■ ASSOCIATED CONTENT

Supporting Information

Analytical HPLC of the purified compounds and NMR data. This material is available free of charge via the Internet at http://pubs.acs.org.

■ AUTHOR INFORMATION

Corresponding Author

*Telephone: 00496221422691. Fax: 00496221422690. E-mail: m.eder@dkfz.de.

Notes

The authors declare no competing financial interest.

■ ACKNOWLEDGMENTS

There is no other financial relationship of the authors than a grant from the BMBF (MoBiTech) for M. Eder, which is gratefully acknowledged. Biodistribution and PET imaging were kindly perfomed by Ursula Schierbaum, Karin Leotta (all German Cancer Research Center, Heidelberg, Germany). High resolution mass spectrometry was kindly performed by Frederic Zoller (Department of Nuclear Medicine, University of Heidelberg, Heidelberg, Germany). All animal experiments complied with the current laws of the Federal Republic of Germany.

■ REFERENCES

(1) Andriole, G. L., Crawford, E. D., Grubb, R. L. 3rd, Buys, S. S., Chia, D., Church, T. R., Fouad, M. N., Gelmann, E. P., Kvale, P. A., Reding, D. J., Weissfeld, J. L., Yokochi, L. A., O'Brien, B., Clapp, J. D., Rathmell, J. M., Riley, T. L., Hayes, R. B., Kramer, B. S., Izmirlian, G., Miller, A. B., Pinsky, P. F., Prorok, P. C., Gohagan, J. K., and Berg, C. D. (2009) Mortality results from a randomized prostate-cancer screening trial. *N. Engl. J. Med. 360*, 1310−1319.

(2) Silver, D. A., Pellicer, I., Fair, W. R., Heston, W. D., and Cordon-Cardo, C. (1997) Prostate-specific membrane antigen expression in normal and malignant human tissues. *Clin. Cancer Res. 3*, 81−85.

(3) Ghosh, A., and Heston, W. D. (2004) Tumor target prostate specific membrane antigen (PSMA) and its regulation in prostate cancer. *J. Cell Biochem. 91*, 528−539.

(4) Schulke, N., Varlamova, O. A., Donovan, G. P., Ma, D., Gardner, J. P., Morrissey, D. M., Arrigale, R. R., Zhan, C., Chodera, A. J., Surowitz, K. G., Maddon, P. J., Heston, W. D., and Olson, W. C. (2003) The homodimer of prostate-specific membrane antigen is a functional target for cancer therapy. *Proc. Natl. Acad. Sci. U. S. A. 100*, 12590−12595.

(5) Henry, M. D., Wen, S., Silva, M. D., Chandra, S., Milton, M., and Worland, P. J. (2004) A prostate-specific membrane antigen-targeted monoclonal antibody-chemotherapeutic conjugate designed for the treatment of prostate cancer. *Cancer Res. 64*, 7995−8001.

(6) Elsasser-Beile, U., Reischl, G., Wiehr, S., Buhler, P., Wolf, P., Alt, K., Shively, J., Judenhofer, M. S., Machulla, H. J., and Pichler, B. J. (2009) PET imaging of prostate cancer xenografts with a highly specific antibody against the prostate-specific membrane antigen. *J. Nucl. Med. 50*, 606−611.

(7) Milowsky, M. I., Nanus, D. M., Kostakoglu, L., Vallabhajosula, S., Goldsmith, S. J., and Bander, N. H. (2004) Phase I trial of yttrium-90-labeled anti-prostate-specific membrane antigen monoclonal antibody J591 for androgen-independent prostate cancer. *J. Clin. Oncol. 22*, 2522−2531.

(8) Hillier, S. M., Maresca, K. P., Femia, F. J., Marquis, J. C., Foss, C. A., Nguyen, N., Zimmerman, C. N., Barrett, J. A., Eckelman, W. C., Pomper, M. G., Joyal, J. L., and Babich, J. W. (2009) Preclinical evaluation of novel glutamate-urea-lysine analogues that target prostate-specific membrane antigen as molecular imaging pharmaceuticals for prostate cancer. *Cancer Res. 69*, 6932−6940.

(9) Chen, Y., Foss, C. A., Byun, Y., Nimmagadda, S., Pullambhatla, M., Fox, J. J., Castanares, M., Lupold, S. E., Babich, J. W., Mease, R. C., and Pomper, M. G. (2008) Radiohalogenated prostate-specific membrane antigen (PSMA)-based ureas as imaging agents for prostate cancer. *J. Med. Chem. 51*, 7933−7943.

(10) Banerjee, S. R., Pullambhatla, M., Byun, Y., Nimmagadda, S., Green, G., Fox, J. J., Horti, A., Mease, R. C., and Pomper, M. G. (2010) 68Ga-labeled inhibitors of prostate-specific membrane antigen (PSMA) for imaging prostate cancer. *J. Med. Chem. 53*, 5333−5341.

(11) Fani, M., Andre, J. P., and Maecke, H. R. (2008) 68Ga-PET: a powerful generator-based alternative to cyclotron-based PET radiopharmaceuticals. *Contrast Media Mol. Imaging 3*, 67−77.

(12) Eder, M., Wangler, B., Knackmuss, S., Legall, F., Little, M., Haberkorn, U., Mier, W., and Eisenhut, M. (2008) Tetrafluorophenolate of HBED-CC: a versatile conjugation agent for (68)Ga-labeled small recombinant antibodies. *Eur. J. Nucl. Med. Mol. Imaging 35*, 1878−1886.

(13) Eder, M., Knackmuss, S., Le Gall, F., Reusch, U., Rybin, V., Little, M., Haberkorn, U., Mier, W., and Eisenhut, M. (2010) 68)Ga-labelled recombinant antibody variants for immuno-PET imaging of solid tumours. *Eur. J. Nucl. Med. Mol. Imaging 37*, 1397−1407.

(14) Kularatne, S. A., Zhou, Z., Yang, J., Post, C. B., and Low, P. S. (2009) Design, synthesis, and preclinical evaluation of prostate-specific membrane antigen targeted (99m)Tc-radioimaging agents. *Mol. Pharm. 6*, 790−800.

(15) Liu, T., Toriyabe, Y., Kazak, M., and Berkman, C. E. (2008) Pseudoirreversible inhibition of prostate-specific membrane antigen by phosphoramidate peptidomimetics. *Biochemistry 47*, 12658−12660.

(16) Schuhmacher, J., and Maier-Borst, W. (1981) A new Ge-68/Ga-68 radioisotope generator system for production of Ga-68 in dilute HCl. *Int. J. Appl. Radiat. Isot. 32*, 31−36.

(17) Mier, W., Zitzmann, S., Kramer, S., Reed, J., Knapp, E. M., Altmann, A., Eisenhut, M., and Haberkorn, U. (2007) Influence of chelate conjugation on a newly identified tumor-targeting peptide. *J. Nucl. Med. 48*, 1545−1552.

(18) Bacich, D. J., Pinto, J. T., Tong, W. P., and Heston, W. D. (2001) Cloning, expression, genomic localization, and enzymatic activities of the mouse homolog of prostate-specific membrane antigen/NAALADase/folate hydrolase. *Mamm. Genome 12*, 117−123.

(19) Schuhmacher, J., Klivenyi, G., Kaul, S., Henze, M., Matys, R., Hauser, H., and Clorius, J. (2001) Pretargeting of human mammary carcinoma xenografts with bispecific anti-MUC1/anti-Ga chelate antibodies and immunoscintigraphy with PET. *Nucl. Med. Biol. 28*, 821−828.
(20) Barinka, C., Byun, Y., Dusich, C. L., Banerjee, S. R., Chen, Y., Castanares, M., Kozikowski, A. P., Mease, R. C., Pomper, M. G., and Lubkowski, J. (2008) Interactions between human glutamate carboxypeptidase II and urea-based inhibitors: structural characterization. *J. Med. Chem. 51*, 7737−7743.
(21) Rajasekaran, S. A., Anilkumar, G., Oshima, E., Bowie, J. U., Liu, H., Heston, W., Bander, N. H., and Rajasekaran, A. K. (2003) A novel cytoplasmic tail MXXXL motif mediates the internalization of prostate-specific membrane antigen. *Mol. Biol. Cell 14*, 4835−4845.
(22) Slusher, B. S., Tsai, G., Yoo, G., and Coyle, J. T. (1992) Immunocytochemical localization of the N-acetyl-aspartyl-glutamate (NAAG) hydrolyzing enzyme N-acetylated alpha-linked acidic dipeptidase (NAALADase). *J. Comp. Neurol. 315*, 217−229.
(23) Foss, C. A., Mease, R. C., Fan, H., Wang, Y., Ravert, H. T., Dannals, R. F., Olszewski, R. T., Heston, W. D., Kozikowski, A. P., and Pomper, M. G. (2005) Radiolabeled small-molecule ligands for prostate-specific membrane antigen: in vivo imaging in experimental models of prostate cancer. *Clin. Cancer Res. 11*, 4022−4028.
(24) Gregor, P. D., Wolchok, J. D., Turaga, V., Latouche, J. B., Sadelain, M., Bacich, D., Heston, W. D., Houghton, A. N., and Scher, H. I. (2005) Induction of autoantibodies to syngeneic prostate-specific membrane antigen by xenogeneic vaccination. *Int. J. Cancer 116*, 415−421.

Bioconjugate Chemistry

Article

pubs.acs.org/bc

Stimulus-Responsive Controlled Release System by Covalent Immobilization of an Enzyme into Mesoporous Silica Nanoparticles

Jessica Méndez, Alina Monteagudo, and Kai Griebenow*

Department of Chemistry, University of Puerto Rico, Río Piedras Campus, P.O. Box 23346, San Juan, PR 00931-3346, United States

Supporting Information

ABSTRACT: Mesoporous silica nanoparticles (MSN) have emerged as an attractive class of drug delivery carriers for therapeutic agents. Herein, we explored the covalent immobilization of proteins into MSN to generate a stimulus-responsive controlled release system. First, MSN were functionalized with thiol groups using (mercaptopropyl)-trimethoxysilane (MPTMS). Functionalization was verified by X-ray photoelectron spectroscopy (XPS), Fourier-transform infrared (FTIR) spectroscopy, and dynamic light scattering. The model enzyme carbonic anhydrase (CA) was coupled to sulfosuccinimidyl 6-[3′(2-pyridyldithio)-propionamido]-hexanoate (Sulfo-LC-SPDP) at a low ratio of 1:1 to prevent enzyme inactivation and subsequently covalently immobilized into MSN via thiol−disulfide interchange. The enzyme could be released from MSN with 10 mM glutathione, which represents intracellular redox conditions, while it remained bound to the MSN at extracellular redox conditions represented by 1 μM glutathione. The activity of the released enzyme was >80% demonstrating that the enzyme was still largely functional and active after immobilization and release. Human cervical cancer (HeLa) cells were incubated with the MSN−CA bioconjugates at various concentrations for 24 h and the data show good biocompatibility. In summary, we demonstrate the potential of MSN as drug delivery systems for proteins.

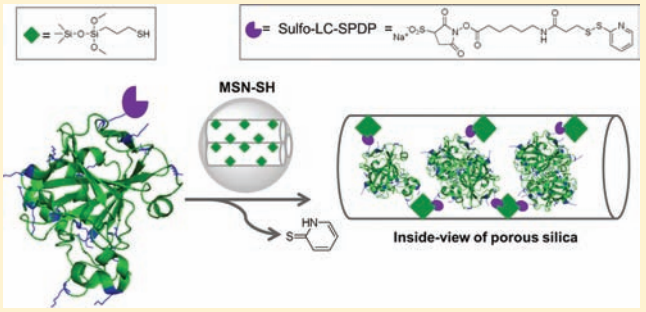

INTRODUCTION

There has been a growing interest in utilizing nanotechnology in the development of drug delivery systems.[1] Nanomaterials, such as polymers, mesoporous silica nanoparticles, and nanotubes, have emerged as potent drug delivery devices.[2−4] Likewise, the employment of proteins including enzymes as therapeutic agents has increased due to their selectivity and catalytic efficiency.[5] Due to recent advances in nanotechnology, the integration of nanosized materials (e.g., nanoparticles) and therapeutic agents (e.g., enzymes) is now conceivable.

Drug delivery systems provide important tools for enhancing the efficacy of therapeutic agents, thus reducing unwanted side effects. For example, locally higher doses of chemotherapeutic agents can be delivered using nanoparticles with 100−300 nm diameter because they accumulate preferentially in tumors.[6,7] However, challenges remain in the design of nanosized delivery systems. For example, it is highly desirable that drug delivery systems show zero premature release until the target is reached and that the release of the drug is controlled by a stimulus-responsive design.[8,9] Stimuli can include pH,[2] electric fields,[10] and photoirradiation[5] and have been utilized for drug release.[2,9,11] In general, stimulus-responsive release systems allow smart release of drugs by responding to endogenous or exogenous activation.[4,12−17] Recently, specific chemical reactions, such as disulfide reduction, have emerged as alternative mechanisms for drug release.[16] The main driving force of the drug release in the cell is by reduced glutathione for such systems.[18]

Herein, we selected silica as the material for the development of a nanosized delivery system. Once injected, MSN degrade into biocompatible monomeric silicic acid ($Si(OH)_4$). Si is an essential human nutrient and has been implicated in protecting against the toxic effects of aluminum and in promoting calcification.[3] In recent years, the use of silica nanoparticles has been extended to biomedical and biotechnological fields, such as biosensors, DNA delivery, drug delivery, and enzyme immobilization.[19] It has been demonstrated that MSN can be endocytosed by cells and thus can serve as carriers for the controlled intracellular release of drugs.[20−23] In addition, MSN are capable of escaping the endosomal entrapment[6,21,24−26] and can potentially protect the delivered protein drug from exposure to proteases. In addition, the large pore volume that MSN possess allow for loading of large protein amounts into the nanoparticles.[21,24−26] Slowing et al. encapsulated cytochrome *c* (Cyt-c) into MSN and realized studies related to the uptake and release of Cyt-c by mammalian cells.[21] They demonstrated that the Cyt-c remained active after its release from MSN. However, as far as we know, there are no reports on conjugating enzymes into MSN via stimulus-responsive

Received: June 8, 2011
Revised: January 31, 2012
Published: February 29, 2012

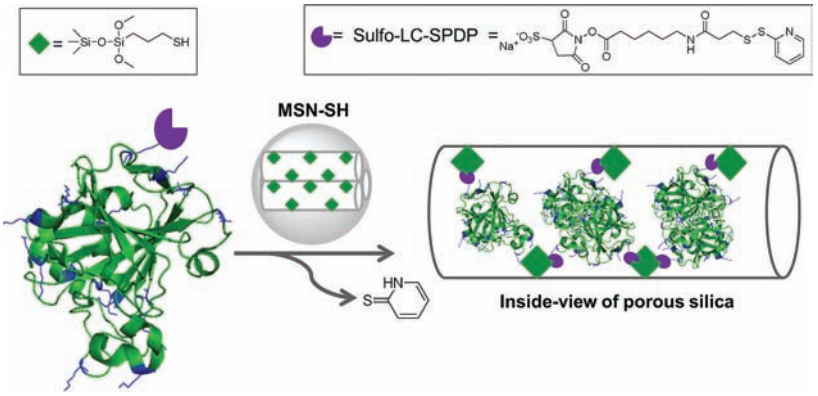

Figure 1. Representation of the immobilization of modified carbonic anhydrase into activated mesoporous silica nanoparticles to generate MSN−CA conjugates and the smart release of CA in the presence of the redox stimulus. The crystal structure of carbonic anhydrase at 1.95 Å atomic resolution was acquired from the protein data bank (access code 1V9E).

bonds, which would allow for the smart release under physiological conditions solely in the presence of a targeted stimulus. This was the goal of our work.

Herein, we report and demonstrate the use of chemically functionalized MSN to form conjugates with an enzyme via formation of stimulus-responsive covalent bonds (Figure 1). Carbonic anhydrase (CA) was selected as the model biological molecule, since it is a well-characterized enzyme with easily measurable bioactivity, which makes it an ideal candidate for the proof-of-concept of our system.[27,28] CA (EC 4.2.1.1) in this study was from bovine erythrocytes and thus belongs to the group of α-CAs, Zn^{2+} containing metalloenzymes. CAs catalyze the conversion of CO_2 and H_2O to H_2CO_3, essential to various biological processes including maintaining the acid−base balance in blood and tissues, enabling efficient transport of carbon dioxide out of tissues, and increasing the CO_2 concentration in chloroplasts.[29] We demonstrate that CA can be released from the silica nanoparticles under conditions emulating intra- but not extracellular redox conditions with more than 80% of residual activity. The system developed is the first step in the direction of a smart protein delivery system, which could be used to treat various diseases.

EXPERIMENTAL PROCEDURES

Mesoporous silica nanoparticles (product number 643637), (3-mercaptopropyl)trimethoxysilane (MPTMS), 4-nitrophenyl acetate (*p*-NPA), L-glutathione, dithiothreitol (DTT), toluene (99.9%), and acetone (99.9%) were from Sigma-Aldrich (St. Louis, MO). Carbonic anhydrase (CA, EC 4.2.1.1) from bovine erythrocytes was from Worthington Biochemical Corporation (Lakewood, NJ). Sulfosuccinimidyl 6-(3′-[2-pyridyldithio]-propionamido)hexanoate (Sulfo-LC-SPDP) was from Proteochem (Denver, CO). The CellTiter 96 AQ_{ueous} nonradioactive cell proliferation assay was from Promega (Madison, WI). HeLa cells were purchased from ATCC (Manassas, VA). Dialysis membranes were obtained from Spectrum Laboratories (Rancho Dominguez, CA). All reagents were used as supplied without further purification.

Thiol-Functionalized Mesoporous Silica Nanoparticles (MSN−SH). MSN were activated by functionalization with thiol groups. The activation was done by the addition of 3.75 mL of (mercaptopropyl)-trimethoxysilane (MPTMS, 95%) to 3.75 mL of a stirred suspension of 125 mg of MSN in refluxing toluene at 110 °C for 1 h. After slow cooling of the mixture, the solid phase was recovered by filtration and washed with 200 mL of toluene and 500 mL of acetone. The product was dried overnight under vacuum.

X-ray Photoelectron Spectroscopy (XPS). XPS was performed using a PHI 5600ci spectrometer with an Al Kα monochromatic source (350 W, 15 kV) and at a takeoff angle of 45°. Survey spectra were obtained at 187.85 eV.

FTIR Spectroscopy. FTIR studies were conducted with a ThermoNicolet Nexus 470 FTIR spectrometer. Silica nanoparticles and the conjugates were measured as KBr pellets (0.5 mg sample per 200 mg of KBr). Each sample was measured at least five times.

Dynamic Light Scattering (DLS). The size of particles was determined by dynamic light scattering (DLS) using a DynaPro Titan.

Carbonic Anhydrase Modification with Sulfo-LC-SDPD. The protein was dissolved in 50 mM phosphate buffered saline (PBS) with 0.15 M NaCl and 10 mM EDTA at pH 7.2 to a final concentration of 2 mg/mL. Sulfosuccinimidyl 6-[3′(2-pyridyldithio)-propionamido]hexanoate (Sulfo-LC-SPDP, 8.5 mg) was added directly to the reaction flask. The mixture was reacted for 30 min at room temperature under gentle stirring and dialyzed thrice against nanopure water at 4 °C using cellulose ester membranes with a 10 kDa cutoff. A volume ratio of 1:100 (sample-to-nanopure water) was used during dialysis. Modified carbonic anhydrase (CA-SPDP) was subsequently lyophilized for 48 h using a 6-L lyophilizer (model 77530, Labconco, Kansas City, MO) at a condenser temperature of −45 °C and a pressure of <60 μm Hg. The lyophilized powder was stored until use at −20 °C.

Degree of Protein Modification. The extent of enzyme modification (i.e., the number of amine groups coupled to the cross-linker) was determined by measurement of the release of pyridine-2-thione and the 2,4,6-trinitrobenzene sulfonic acid (TNBSA) assay. For the pyridine-2-thione release assay, modified carbonic anhydrase was dissolved in 50 mM PBS with 0.15 M NaCl and 10 mM EDTA at pH 7.2 to achieve a protein concentration of 0.5 mg/mL. The absorbance of the samples was measured and recorded at 343 nm. Then, 10 μL of 15 mg/mL dithiothreitol (DTT) solution was added to each sample. After 15 min, the absorbance of the samples was measured and recorded at 343 against a blank treated as above. The molar ratio of SPDP to protein was calculated. For the TNBSA assay, modified carbonic anhydrase was dissolved in 0.1 M sodium bicarbonate buffer, pH 8.5, at a concentration of 0.05−0.2 mg/mL. Then, 0.25 mL of 0.01% (w/v) of a TNBSA

dx.doi.org/10.1021/bc200301a | *Bioconjugate Chem.* 2012, 23, 698−704

solution was added to 0.5 mL of sample solution. The solutions were incubated at 37 °C for 2 h. After incubation, 0.25 mL of 10% SDS solution and 0.125 mL of 1 N HCl were added to each sample. The absorbance of each sample was measured at 335 nm against a blank treated as above. The amount of SPDP bound to the protein was obtained from a calibration curve. For both assays, the samples were prepared in triplicate.

Circular Dichroism (CD) Spectroscopy. CD spectra were acquired with an OLIS DSM-10 UV−vis CD spectrophotometer at 20 °C in the near-UV region (250−320 nm) at 0.5 nm spectral resolution using a 10 mm quartz cell with a protein concentration of 0.6 mg/mL in 15 mM Tris-sulfate buffer at pH 7.6 and 25 °C. Each spectrum was obtained by averaging six scans. Spectra of buffer blanks were measured prior to sampling and were digitally subtracted from the sample CD spectra.

Carbonic Anhydrase Activity. Carbonic anhydrase (1.2 μM) activity was determined at 25 °C by monitoring the hydrolysis of *p*-nitrophenol acetate (*p*-NPA) in 15 mM tris-sulfate buffer, pH 7.6. The hydrolysis was monitored at 400 nm using a Shimadzu 2450 UV−vis spectrophotometer. The assay was performed in a 1 mL cuvette. The reaction was started by mixing 700 μL of 15 mM tris-sulfate buffer, pH 7.6, 100 μL of 16.56 mM *p*-NPA dissolved in acetonitrile, and 200 μL of enzyme solution. The residual activity was calculated with respect to the specific activity of native carbonic anhydrase.[30,31]

Covalent Immobilization of CA into MSN. 2.0 mg of MSN-SH was sonicated for 3 min in 50 mM PBS, 0.15 M NaCl, and 10 mM EDTA, pH 7.2, in Eppendorf vials to create a suspension. Different volumes of a carbonic anhydrase stock solution were added to each MSN−SH suspension. The mixtures were gently stirred overnight at 4 °C. Then, the samples were centrifuged at 14 000 rpm for 20 min. To remove the unreacted enzyme, three cycles of washing/centrifugation were performed. The washing steps were performed with 50 mM PBS containing 0.15 M NaCl and 10 mM EDTA at pH 7.2. The amount of immobilized enzyme was determined by depletion by measuring the protein concentration in the supernatants obtained during washing and comparing it to the total protein amount employed. Protein concentration in the supernatant was determined from the absorbance at 280 nm using a calibration curve generated with native carbonic anhydrase.

Cytotoxicity Assay. Experiments were performed using a human cervical cancer cells line (HeLa). The cells were cultured as recommended by ATCC in minimum essential medium (MEM) with L-glutamine supplemented with 10% fetal bovine serum (FBS) and 1% penicillin. HeLa cells were incubated at 37 °C under 5% CO_2 and used before 25 passages. Mitochondrial function was assessed using the CellTiter 96 aqueous nonradioactive cell proliferation assay (Promega, Madison, WI). About 40 000 cells/well were seeded into 96-well microtiter plates in 100 μL of penicillin free culture medium with 10% FBS. After 24 h, culture medium was replaced with culture medium containing serial dilutions of the MSN−CA bioconjugate suspensions. The cells were incubated with the suspended bioconjugate for 24 h. The MSN suspension settled down over time, and consequently, the cells were in direct contact with the nanoparticles during incubation. Then, 20 μL of 3-(4,5-dimethylthiazol-2-yl)-5-(3-carboxymethoxyphenyl)-2-(4-sulfophenyl)-2*H*-tetrazolium, inner salt, (MTS) was added to each well. After 2 h, the optical intensity of each well was measured spectrophotometrically at 490 nm in a microplate reader (Thermo Electron Corporation, Multiskan Ascent).[32,33] The spectrophotometer baseline was obtained using culture medium without cells. Experiments were performed 8 times.

Controls: HeLa cells treated with 2 μM staurosporin for 6 h were used as positive control, and cells without any treatment were used as negative control.[34] The statistical analysis for the cell viability results indicated that under the tested conditions the cytotoxicity obtained for a CA−SPDP concentration ≥30.87 μg/mL is highly significant from that obtained for the negative control ($p < 0.001$). Consequently the concentration range used for the experiments was 0.3−30.87 μg/mL.

Residual Activity of Released CA from MSN. The MSN−CA bioconjugates were suspended in 1 mL of 50 mM PBS containing 10 mM DTT. The samples were incubated overnight at 37 °C under constant shaking at 125 rpm. Then, the samples were centrifuged at 14 000 rpm for 20 min to precipitate the MSN. DTT was removed from the supernatant using Centricon devices with an exclusion size of 10 kDa and the released enzyme obtained in the supernatant. The specific activity of modified carbonic anhydrase was obtained using these supernatants and the residual activity determined.

Release of Carbonic Anhydrase from MSN in the Presence of Glutathione. The release of CA from MSN was measured by preparing a suspension of 5 mg of MSN−CA conjugates in 1 mL of 50 mM PBS with 1 mM EDTA at pH 7.4 and glutathione (GHS) concentrations of 0, 0.001, and 10 mM. The chemical stability of thiols is affected by parameters such as temperature, pH, and the presence of metal ions. Addition of a chelating agent, i.e., EDTA, greatly improves the chemical stability of thiols.[35] Incubation was performed for 24 h at 37 °C, and the MSN were pelleted by centrifugation at 14 000 rpm for 20 min. The supernatant was removed and used to determine the concentration of released CA and the pelleted MSN were resuspended in fresh GHS−PBS buffer. The solubility of CA is >10 mg/mL according to the manufacturer. The MSN−CA conjugate used in the release experiments contained a total of 1.1 mg of immobilized CA. Therefore, all the release experiments were performed under sink conditions.

Statistical Data Treatment. All data were obtained at least in triplicate, the data averaged, and standard deviations calculated. Statistical significance for comparisons of multiple groups was established using one-way multiple Tukey comparison post-test ANOVA. All statistical analysis were performed with *InStat 3.06* (GraphPad Software Inc., San Diego, CA, USA).

RESULTS AND DISCUSSION

MSN Activation and Characterization. The goal of our investigation was to immobilize CA in MSN by introducing a redox-sensitive covalent SS-bond to accomplish release under intracellular redox conditions. To accomplish this, it was necessary to first chemically decorate MSN with thiol groups. This was accomplished using (3-mercaptopropyl)-trimethoxysilane (MPTMS). MPTMS reacts with the hydroxyl groups of silica forming a covalent bond. Thiol groups are introduced in this way into the material and presented terminal of the propyl groups. XPS was used to investigate the MSN prior to and after modification to confirm the introduction of the thiol groups (Figure 2). The introduction of SH groups into the MSN was evident from photoemission peaks of the 2s and 2p orbitals of S in the MSN−SH spectrum, which were absent in the spectrum of MSN. FTIR spectroscopy was also employed to characterize the product. A broad band centered

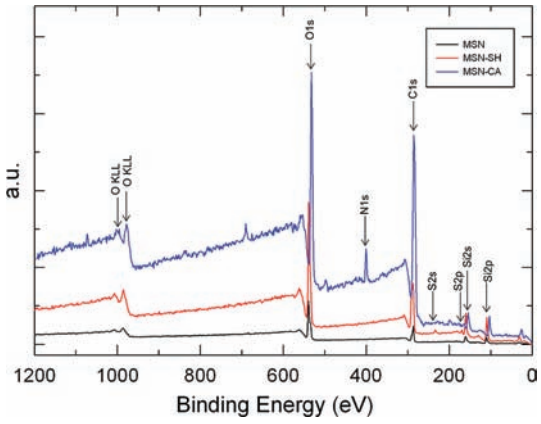

Figure 2. Wide-scan XPS spectra for MSN, MSN−SH, and MSN−CA conjugates.

at 3442 cm^{-1} was observed in the MSN−SH spectrum corresponding to hydroxyl stretching vibrations (Figure 3).

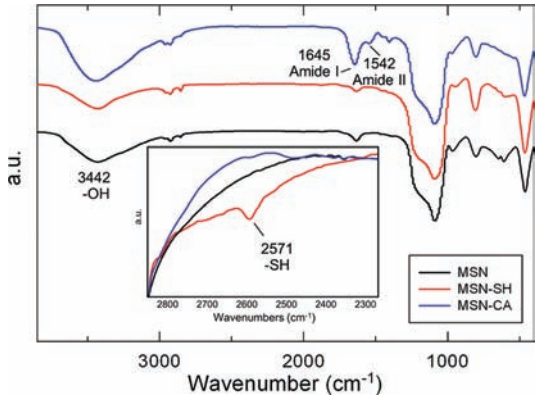

Figure 3. FTIR spectra of MSN, MSN−SH, and MSN−CA conjugates. The inset shows the area corresponding to the SH stretching vibrational mode (2800−2300 nm) expanded (same experiments as main spectra).

Peaks at lower frequencies are due to various vibrational modes of the silicate (Si−OH and Si−O−Si). Bands at 2922 and 2861 cm^{-1} are due to partial hydrolyzation of the material used to synthesize the silica nanoparticles.[36] However, importantly the spectrum of MSN−SH shows a band at 2571 cm^{-1} consistent with SH-stretching vibrations, which is missing in the spectrum of MSN.

Dynamic light scattering (DLS) was employed to determine if the chemical modification process had an effect on the particle size or would cause aggregation of the suspended silica nanoparticles (Table 1). In principle, introduction of SH-groups could cause formation of interparticle disulfide bonds and thus covalent aggregation. DLS data revealed two different hydrodynamic particle size distributions for both samples. Furthermore, somewhat in contrast to our expectations, the data revealed a reduction in the hydrodynamic radius upon chemical modification of the particles (Table 1). SEM micrographs were obtained to evaluate the effect of the modification process on the morphology of the MSN. No substantial morphology changes were detected in the micrographs (for details, see Supporting Information). The characteristics of the particles after modification were still in line with the end application in mind, namely, passive targeted delivery. It should be noted, however, that for clinical applications nanoparticles with a diameter of over 400 nm should be removed from the preparation, because these particles will be effectively cleared by the mononuclear phagocytic system (MPS).

Table 1. Particle Sizes of MSN, MSN−SH, and MSN−CH Determined by Dynamic Light Scattering

sample	diameter (nm)[a]	% intensity
MSN in water	317.2	90.8
	626.0	9.2
MSN−SH in water	184.3	70.6
	687.5	29.4
MSN−CA in water	312.5	100
MSN−CA in 0.9% NaCl	311.5	100

[a]Polydispersity index for all the samples was less than 20%.

CA Activation and CA−SPDP Characterization. We selected carbonic anhydrase (EC **4.2.1.1**, CA) as the model enzyme in our studies because it is a well-studied, accessible, and relatively inexpensive enzyme.[27] First, we introduced an SH-group at the surface of the enzyme in order to immobilize it into the thiol-functionalized MSN. This was accomplished by utilizing the reagent sulfo-LC-SPDP, which reacts with amines through the succinimidyl group. The SPDP molecule also has a disulfide-containing linkage that can be cleaved with reducing agents such as DTT and glutathione.[37] After performing the reaction with the enzyme, the extent of enzyme modification was assessed using two different assays. In the first, the release of pyridine-2-thione was determined, which is the product of the reaction of Sulfo-LC-SPDP with a thiol-containing reagent.[36] The results were corroborated by using the 2,4,6-trinitrobenzene sulfonic acid (TNBSA) assay, which determines the amount of amino groups on the protein surface (largely the ε-amino groups of lysines).[38] Under the conditions employed in this work, both assays demonstrated that the protein was modified with the cross-linker at a linker-to-carbonic anhydrase molar ratio of 1.0 ± 0.5, which represents a ca. 5% modification of the available enzyme surface amino groups. The enzyme activity was reduced to 80.0 ± 0.7% by the chemical modification. [It should be noted that higher levels of modification caused larger enzyme inactivation (for details, see Supporting Information).] Near UV-circular dichroism (CD) spectroscopy was employed to investigate if the enzyme tertiary structure was affected by the modification. The spectra revealed that no significant changes in tertiary structure of SPDP-CA occurred after attaching the cross-linker (Figure 4).

MSN−CA Bioconjugate and Its Characterization. SPDP−CA was covalently immobilized into the thiol-functionalized MSN. The strategy was that the 2-pyridyl disulfide group of the immobilized cross-linker on the enzyme surface would react with the thiol groups introduced into MSN by thiol−disulfide interchange to form aliphatic disulfides.[37] To establish the amount of SPDP−CA that could be immobilized into the MSN−SH, we reacted different amounts of SPDP−CA with 2 mg of MSN−SH. The amount of immobilized enzyme increased proportionally to the amount of enzyme added into the MSN−SH suspension (Figure 5). The maximum immobilization was determined to be 577 ± 65 mg of carbonic anhydrase per 1.0 g of MSN−SH under our conditions.

The bioconjugate was characterized by XPS and FTIR to confirm protein immobilization. The XPS spectrum of MSN−CA presents a new N (1s) signal confirming enzyme

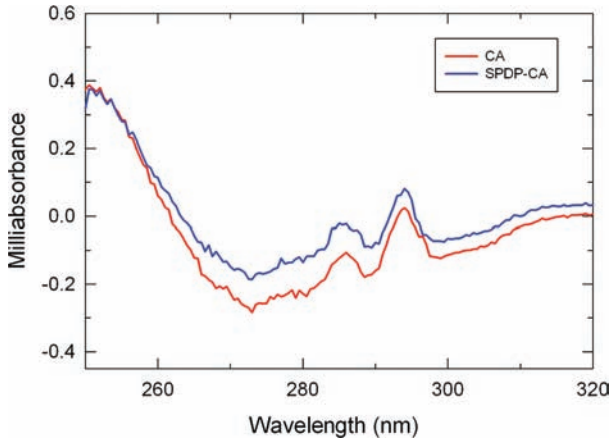

Figure 4. Near-UV CD spectra of nonmodified CA and SPDP-CA. The samples were dissolved in15 mM Tris-sulfate, pH 7.6, at 20 °C.

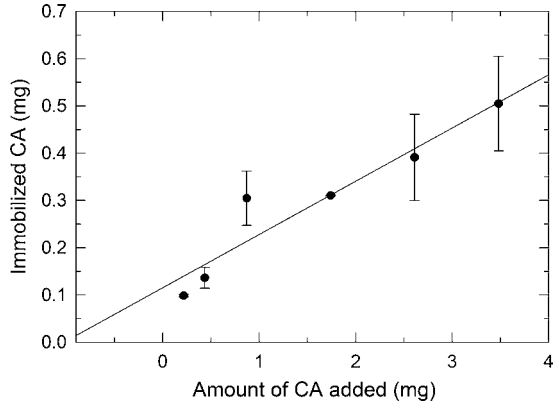

Figure 5. Amount of immobilized CA at various CA concentrations employed during synthesis. The reaction employed 2 mg of MSN–SH.

immobilization (Figure 2). The FTIR spectrum of the MSN–CA bioconjugate shows the appearance of two strong bands at 1645 cm^{-1} and 1542 cm^{-1} due to the protein amide I and II vibrational modes. Thus, these data unequivocally demonstrate immobilization of the enzyme into the functionalized MSN. However, these data do not distinguish adsorption from covalent immobilization.

However, proof was obtained by being able to remove the CA from the MSN using 10 mM DTT but not with buffer. The activity of the released enzyme was measured and was compared with that obtained for CA-SPDP (see Experimental section for details). The enzyme retained 79 ± 11% of activity after immobilization and release. This demonstrates some detrimental impact of the procedure on enzyme integrity. While some inactivation of the enzyme is probably inevitable using such strategies, future experiments are being designed to minimize this by increasing protein thermodynamic stability and minimizing protein–surface interactions.

To identify potential changes in the morphology of the MSN due to enzyme immobilization, we employed SEM and dynamic light scattering. The SEM micrographs show that no major morphology changes (size and porosity) occurred due to enzyme immobilization (for details, see Supporting Information). Dynamic light scattering showed that the size of the MSN–CA bioconjugates was similar to that of nonmodified MSN (Table 1).

Controlled Release of CA from Nanoparticles. In vitro release studies were conducted to assess the release of immobilized CA from the nanoparticles under somewhat physiological conditions in PBS at pH 7.4 and 37 °C. Intracellular glutathione concentrations (1–10 mM) are sufficient to cleave disulfide bonds and thus should afford release of the immobilized enzyme while the concentration of 1 μM glutathione representing extracellular plasma conditions should have no effect.[16] However, release could also be promoted by other cell-produced antioxidants, such as NADH and dihydrolipoic acid.[39] It is consequently possible that the intracellular release in vivo could be faster than in our in vitro assay. Fresh glutathione had to be added daily to each sample during release due to limited glutathione stability in the in vitro release assays. We found that only a small amount of 1% and 3% of CA was released using no or 1 μM concentrations of glutathione (Figure 6). In contrast, when exposing the CA–

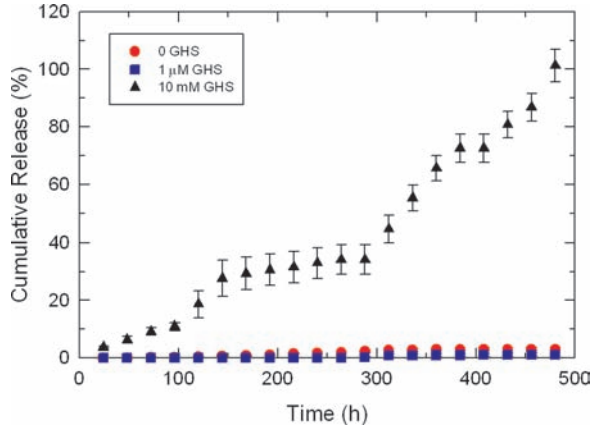

Figure 6. In vitro release profile of carbonic anhydrase from MSN at different glutathione concentrations.

MSN to 10 mM glutathione, CA was released from the nanoparticles (Figure 6). The fact that carbonic anhydrase release only occurred in the presence of glutathione proves that the enzyme was indeed covalently immobilized and not absorbed at the surface in agreement with our spectroscopic evidence.

The protein was completely released from the MSN under reducing conditions in 480 h. In contrast, in systems using adsorption for protein immobilization typically only 45–55% of the immobilized protein was released.[21] Figure 6 also shows that the CA release profile at intracellular glutathione concentrations is sigmoidal, which is characteristic of an energy-dependent release process. This type of system is characterized by slower release at initial stages followed by increased release at later stage.[40]

In summary, our results demonstrate the ability of our system to release the enzyme under intracellular conditions but not at extracellular conditions.

Cell Viability Studies. Cell viability is essential when creating a new drug delivery system to avoid nonselective cytotoxic events and was thus studied herein. Several publications have already established the noncytotoxity of MSN.[19,23,41] However, the cytotoxity of MSN–CA bioconjugates has not been investigated. Cell viability was studied via the measurement of cell metabolic activity. The mitochondrial function was measured using the MTS assay after incubating HeLa cells with different concentrations of MSN–CA

dx.doi.org/10.1021/bc200301a | Bioconjugate Chem. 2012, 23, 698–704

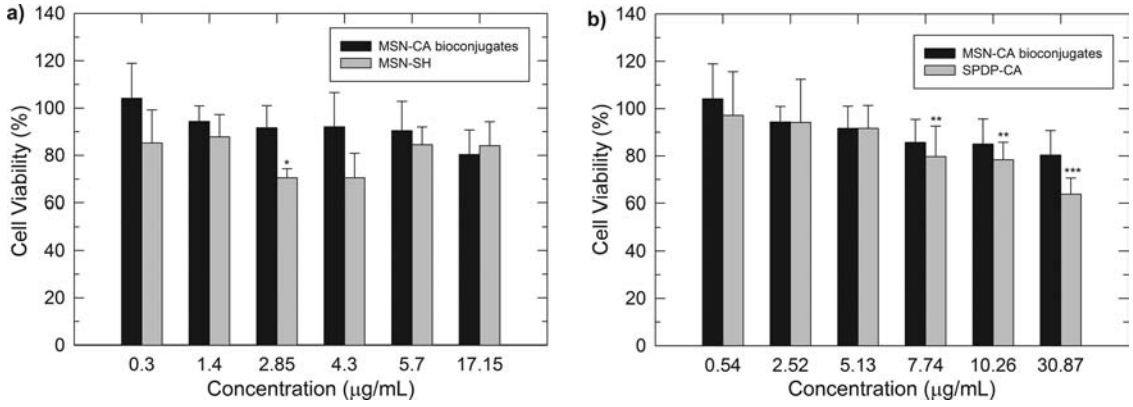

Figure 7. HeLa cell viability in the presence of different concentrations of MSN−SH and MSN−CA conjugates (A) and of SPDP−CA and MSN−CA conjugates (B) after incubation for 24 h.

bioconjugate for 24 h. Viable cells convert tetrazolium salts (MTS) to formazan dyes that are measured spectrophotometrically.[33] The assay was performed by varying the concentrations of the silica and the enzyme. Figure 7a shows the obtained results of the assay performed in terms of varying silica concentration. In general, the cytotoxic effect of the MSN−CA conjugate is lower than that of the MSN−SH alone (except for the 17.15 μg/mL concentration). Cell viability decreased from 97% to 63% at increasing CA concentration compared with 100% to 80% at increasing MSN−CA conjugate concentration, respectively (Figure 7b). However, statistical analysis by ANOVA demonstrated that there was no significant difference between the two groups ($p > 0.05$).

CONCLUSION

In summary, we have explored the covalent immobilization of a model protein into MSN to generate a stimulus−response controlled release. We demonstrate that the release of the immobilized enzyme occurs under intracellular but not extracellular redox conditions. The released enzyme was still functional and active, but some activity decrease was encountered. Cell viability studies establish good biocompatibility of the generated bioconjugate. Future experiments include studies related to endocytosis and endosomal escape of the bioconjugate. We envision that this bioconjugate could serve as a platform for the creation of a drug delivery system utilizing therapeutic proteins.

ASSOCIATED CONTENT

Supporting Information

Scanning electron microscopy micrographs of (A) MSN, (B) MSN−SH, and (C) MSN−CA. Residual activity of CA−SPDP bioconjugates at different levels of modification. This material is available free of charge via the Internet at http://pubs.acs.org.

AUTHOR INFORMATION

Corresponding Author

*E-mail: kai.griebenow@gmail.com. Tel: 787-764-0000 Ext. 7374, Fax: 787-756-8242.

Notes

The authors declare no competing financial interest.

ACKNOWLEDGMENTS

This publication was made possible by grant number SC1 GM086240 from the National Institute for General Medical Sciences (NIGMS) at the National Institutes of Health (NIH) through the Support of Competitive Research (SCORE) Program. Its contents are solely the responsibility of the authors and do not necessarily represent the official views of NIGMS. J.M. was supported by a fellowship from NASA (Puerto Rico Space Grant Consortium) and by the fellowship program of the Puerto Rico Industrial Development Company (PRIDCO). A.M. was supported by the NIH Research Initiative for Scientific Enhancement (RISE) Program. The authors thank all funding agencies for their ongoing support.

REFERENCES

(1) Ravichandran, R. (2009) Nanotechnology-based drug delivery systems. *NanoBioTechnology 5*, 17−33.
(2) Bulmus, V., Woodward, M., Lin, L., Murthy, N., Stayton, P., and Hoffman, A. (2003) A new pH-responsive and glutathione-reactive, endosomal membrane-disruptive polymeric carrier for intracellular delivery of biomolecular drugs. *J. Controlled Release 93*, 105−120.
(3) Salonen, J., Kaukonen, A. M., Hirvonen, J., and Lehto, V. P. (2008) Mesoporous silicon in drug delivery applications. *J. Pharm. Sci. 97*, 632−53.
(4) You, Y. Z., Hong, C. Y., and Pan, C. Y. (2007) Covalently immobilizing a biological molecule onto a carbon nanotube via a stimuli-sensitive bond. *J. Phys. Chem. C 111*, 16161−16166.
(5) Harris, J. M., and Chess, R. B. (2003) Effect of pegylation on pharmaceuticals. *Nat. Rev. Drug Discovery 2*, 214−221.
(6) Cho, K., Wang, X., and Nie, S. (2008) Therapeutic nanoparticles for drug delivery in cancer. *Clin. Cancer Res. 14*, 1310−1316.
(7) Kairemo, K., Erba, P., Bergström, K., and Pauwels, E. K. J. (2008) Nanoparticles in cancer. *Curr. Radiopharm. 1*, 30−36.
(8) Radu, D. R., Lai, C. Y., Jeftinija, K., Rowe, E. W., Jeftinija, S., and Lin, V. S. Y. (2004) A polyamidoamine dendrimer-capped mesoporous silica nanosphere-based gene transfection reagent. *J. Am. Chem. Soc. 126*, 13216−13217.
(9) Vivero-Escoto, J. L., Slowing, I. I., Wu, C. W., and Lin, V. S. Y. (2009) Photoinduced intracellular controlled release drug delivery in human cells by gold-capped mesoporous silica nanosphere. *J. Am. Chem. Soc. 131*, 3462.
(10) Zhu, Y. C., Liu, H. J., Li, F., Ruan, Q. C., Wang, H., Fujiwara, M., Wang, L. Z., and Lu, G. Q. (2010) Dipolar molecules as impellers achieving electric-field-stimulated release. *J. Am. Chem. Soc. 132*, 1450−1451.
(11) Zhao, Y. L., Li, Z. X., Kabehie, S., Botros, Y. Y., Stoddart, J. F., and Zink, J. I. (2010) pH-operated nanopistons on the surfaces of mesoporous silica nanoparticles. *J. Am. Chem. Soc. 132*, 13016−13025.
(12) Liu, R., Zhao, X., Wu, T., and Feng, P. Y. (2008) Tunable redox-responsive hybrid nanogated ensembles. *J. Am. Chem. Soc. 130*, 14418−14419.

(13) Trewyn, B. G., Giri, S., Slowing, I. I., and Lin, V. S. Y. (2007) Mesoporous silica nanoparticle based controlled release, drug delivery, and biosensor systems. *Chem. Commun.*, 3236−3245.
(14) Kam, N. W. S., Liu, Z., and Dai, H. J. (2005) Functionalization of carbon nanotubes via cleavable disulfide bonds for efficient intracellular delivery of siRNA and potent gene silencing. *J. Am. Chem. Soc. 127*, 12492−12493.
(15) Luo, Z., Cai, K. Y., Hu, Y., Zhao, L., Liu, P., Duan, L., and Yang, W. H. (2011) Mesoporous silica nanoparticles end-capped with collagen: redox-responsive nanoreservoirs for targeted drug delivery. *Angew. Chem. 50*, 640−643.
(16) Hong, R., Han, G., Fernandez, J. M., Kim, B. J., Forbes, N. S., and Rotello, V. M. (2006) Glutathione-mediated delivery and release using monolayer protected nanoparticle carriers. *J. Am. Chem. Soc. 128*, 1078−1079.
(17) Ganta, S., Devalapally, H., Shahiwala, A., and Amiji, M. (2008) A review of stimuli-responsive nanocarriers for drug and gene delivery. *J. Controlled Release 126*, 187−204.
(18) Meister, A.., and Anderson, M. E. (1983) Glutathione. *Annu. Rev. Biochem. 52*, 711−760.
(19) Lin, W. S., Huang, Y. W., Zhou, X. D., and Ma, Y. F. (2006) In vitro toxicity of silica nanoparticles in human lung cancer cells. *Toxicol. Appl. Pharmacol. 217*, 252−259.
(20) Yu, K. O., Grabinski, C. M., Schrand, A. M., Murdock, R. C., Wang, W., Gu, B. H., Schlager, J. J., and Hussain, S. M. (2009) Toxicity of amorphous silica nanoparticles in mouse keratinocytes. *J. Nanoparticle Res. 11*, 15−24.
(21) Slowing, I. I., Trewyn, B. G., and Lin, V. S. Y. (2007) Mesoporous silica nanoparticles for intracellular delivery of membrane-impermeable proteins. *J. Am. Chem. Soc. 129*, 8845−8849.
(22) Chung, T. H., Wu, S. H., Yao, M., Lu, C. W., Lin, Y. S., Hung, Y., Mou, C. Y., Chen, Y. C., and Huang, D. M. (2007) The effect of surface charge on the uptake and biological function of mesoporous silica nanoparticles 3T3-L1 cells and human mesenchymal stem cells. *Biomaterials 28*, 2959−2966.
(23) Lu, J., Liong, M., Zink, J. I., and Tamanoi, F. (2007) Mesoporous silica nanoparticles as a delivery system for hydrophobic anticancer drugs. *Small 3*, 1341−1346.
(24) Slowing, I., Trewyn, B. G., and Lin, V. S. Y. (2006) Effect of surface functionalization of MCM-41-type mesoporous silica nanoparticleson the endocytosis by human cancer cells. *J. Am. Chem. Soc. 128*, 14792−14793.
(25) Lin, Y. S., Tsai, C. P., Huang, H. Y., Kuo, C. T., Hung, Y., Huang, D. M., Chen, Y. C., and Mou, C. Y. (2005) Well-ordered mesoporous silica nanoparticles as cell markers. *Chem. Mater. 17*, 4570−4573.
(26) Huang, D. M., Hung, Y., Ko, B. S., Hsu, S. C., Chen, W. H., Chien, C. L., Tsai, C. P., Kuo, C. T., Kang, J. C., Yang, C. S., Mou, C. Y., and Chen, Y. C. (2005) Highly efficient cellular labeling of mesoporous nanoparticles in human mesenchymal stem cells: implication for stem cell tracking. *FASEB J. 19*, 2014−2016.
(27) Krishnamurthy, V. M., Kaufman, G. K., Urbach, A. R., Gitlin, I., Gudiksen, K. L., Weibel, D. B., and Whitesides, G. M. (2008) Carbonic anhydrase as a model for biophysical and physical-organic studies of proteins and protein-ligand binding. *Chem. Rev. 108*, 946−1051.
(28) Saito, R., Sato, T., Ikai, A., and Tanaka, N. (2004) Structure of bovine carbonic anhydrase II at 1.95 angstrom resolution. *Acta Crystallogr., Sect. D 60*, 792−795.
(29) Lindskog, S. (1997) Structure and mechanism of carbonic anhydrase. *Pharmacol. Ther. 74*, 1−20.
(30) Ozdemir, E. (2009) Biomimetic CO_2 sequestration: 1. Immobilization of carbonic anhydrase within polyurethane foam. *Energy Fuels 23*, 5725−5730.
(31) Montalvo, B. L., Pacheco, Y., Sosa, B. A., Velez, D., Sanchez, G., and Griebenow, K. (2008) Formation of spherical protein nanoparticles without impacting protein integrity. *Nanotechnology 19*, 465103.
(32) Barltrop, J. A., Owen, T. C., Cory, A. H., and Cory, J. G. (1991) 5-(3-Carboxymethoxyphenyl)-2-(4,5-dimethylthiazolyl)-3-(4-sulfophenyl)tetrazolium, inner salt (Mts) and related analogs of 3-(4,5-dimethylthiazolyl)-2,5-diphenyltetrazolium bromide (Mtt) reducing to purple water-soluble formazans as cell-viability indicators. *Bioorg. Med. Chem. Lett. 1*, 611.
(33) Cory, A. H., Owen, T. C., Barltrop, J. A., and Cory, J. G. (1991) Use of an aqueous soluble tetrazolium formazan assay for cell-growth assays in culture. *Cancer Commun. 3*, 207−212.
(34) Qu, X., and Qing, L. (2004) Abrin induces HeLa cell apoptosis by cytochrome c release and caspase activation. *Biochem. Mol. Biol. 37*, 445−453.
(35) Stevens, R., Stevens, L., and Price, N. C. (1983) The stabilities of various compounds used in protein purifications. *Biochem Educ 11*, 70.
(36) Hernández-Padrón, G., Rodríguez, R., and Castañro, V. M. (2005) In-situ thiol-modified silica nanoparticles. *Int. J. Nanotechnol.*, 1.
(37) Carlsson, J., Drevin, H., and Axen, R. (1978) Protein thiolation and reversible protein-protein conjugation. N-succinimidyl 3-(2-pyridyldithio)propionate, a new heterobifunctional reagent. *Biochem. J. 173*, 723−37.
(38) Habeeb, A. F. (1966) Determination of free amino groups in proteins by trinitrobenzenesulfonic acid. *Anal. Biochem. 14*, 328−36.
(39) Mortera, R., Vivero-Escoto, J., Slowing, I. I., Garrone, E., Onida, B., and Lin, V. S.-Y. (2009) Cell-induced intracellular controlled release of membrane impermeable cysteine from a mesoporous silica nanoparticles-based drug delivery system. *Chem. Commun.*, 3219−3221.
(40) Wei, X. L., Sun, N. Y., Wu, B. J., Yin, C. H., and Wu, W. (2006) Sigmoidal release of indomethacin from pectin matrix tablets: effect of in situ crosslinking by calcium cations. *Int. J. Pharm. 318*, 132−138.
(41) Liong, M., Lu, J., Kovochich, M., Xia, T., Ruehm, S. G., Nel, A. E., Tamanoi, F., and Zink, J. I. (2008) Multifunctional inorganic nanoparticles for imaging, targeting, and drug delivery. *ACS Nano 2*, 889−896.

Bioconjugate Chemistry

Article

pubs.acs.org/bc

Traceless Cross-Linker for Photocleavable Bioconjugation

Rong Wang,*[,†] Funing Yan,[†] Dengli Qiu,[†] Jae-Sun Jeong,[†] Qiaoling Jin,[‡] Tae-Young Kim,[†] and Liaohai Chen*[,‡]

[†]Department of Biological, Chemical and Physical Sciences, Illinois Institute of Technology

[‡]Biosciences Division, Argonne National Laboratory

Supporting Information

ABSTRACT: Photoresponsive bioconjugation empowers the development of novel methods for drug discovery, disease diagnosis, and high-throughput screening, among others. In this paper, we report on the characteristics of a traceless photocleavable cross-linker, di-6-(3-succinimidyl carbonyloxymethyl-4-nitro-phenoxy)-hexanoic acid disulfide diethanol ester (SCNE). The traceless feature and the biocompatibility of this photocleavable cross-linking reagent were corroborated. Consequently, we demonstrated its application in reversible phage particle immobilization that could provide a platform for direct single-phage screening. We also applied it in protein-photoprinting, where SCNE acts as a "photo-eraser" to remove the cross-linked protein molecules at a desired region in a simple, clean, and light-controllable fashion. We further demonstrated the two-tier atomic force microscopic (AFM) method that uses SCNE to carry out two subsequent AFM tasks *in situ*. The approach allows guided protein delivery and subsequent high-resolution imaging at the same local area, thus opening up the possibility of monitoring protein functions in live cells. The results imply that SCNE is a versatile cross-linker that can be used for a wide range of applications where photocleavage ensures clean and remote-controllable release of biological molecules from a substrate.

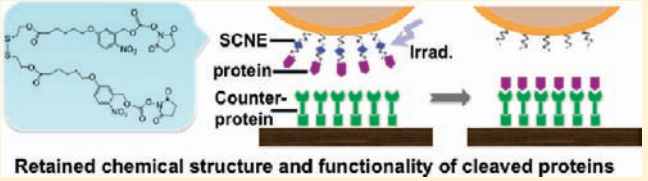

INTRODUCTION

Photocleavable cross-linkers play important roles in biological, pharmaceutical, and biotechnology research[1−4] in studies involving high-throughput target identification,[5,6] kinetic analysis of biorecognition,[7−9] dissection of signal transduction,[10,11] and ion transportation processes,[12] to name a few examples. The use of a photocleavable cross-linker as a remote control has become increasingly common in drug discovery processes for identifying the target of drugs,[13] determining the affinity and selectivity of drug-target interaction,[14] and identifying the binding site on a target.[15−17]

Among the photophores synthesized, *o*-nitrobenzyl derivative molecules show great promising. Upon photoirradiation, the nitro group is changed to a nitroso group, and the benzyl alcohol is oxidized to aldehyde or ketone.[18] Due to its rapid photoreaction, nitrobenzyl derivatives have become one of the most popular photolabile molecules in the field. Two strategies were engaged in applying nitrobenzyl derivatives. One is to deactivate a molecule by caging it with a nitrobenzyl group. Upon the photolysis of the nitrobenzyl group, the molecule is uncaged, and its function is resumed. A range of breakthrough applications have been established using this strategy, including (a) the creation of tunable surface active layers[19] and controllable protein micro/nano patterns[20,21] by activating biotin−avidin interactions[22] and nickel complex-His-tagged protein interactions;[23] (b) directing cell adhesion in selected regions by activating arginyl-glycyl-aspartic acid peptides;[24] (c) manipulating the bioactivity of metals or their coordinating ligands for potential therapeutic application;[25] (d) the intervention of DNA strand−strand interactions;[26] and (e) the establishment of near-field lithography, a new fabrication method for nanostructured patterns.[27,28] Another strategy is to position the nitrobenzyl group in the middle of a diad molecule. The nitrobenzyl group functions as a photocleavable cross-linker, thus conferring a photocontrollable way to dissociate the diad into two molecules. Intriguing applications established using this strategy include the generation of controllable substrates for protein adhesion and dissociation,[29] a precise fabrication method to generate supported bilayer structures,[30] and the rapid release of bioactive materials from inactive precursors.[31]

Previously, we reported the synthesis and characterization of a heterobifunctional photocleavable cross-linker, succinic acid succinimidyl ester 5-thioyloxy-2-nitrobenzyl ester (SSTN).[32] We demonstrated its application in manipulating protein attachment/detachment to substrates.[33] Recently, we synthesized a new multifunctional photocleavable cross-linker, di-6-(3-succinimidyl carbonyloxymethyl-4-nitro-phenoxy)-hexanoic acid disulfide diethanol ester (SCNE)[34] (see Supporting Information). The molecule was designed to include a disulfide bond, acting as the attaching group to a substrate (especially for a gold-coated substrate). SCNE is a homodimer containing two identical nitrobenzyl ester motifs with succinimidyl groups for photocleavable cross-linking of two identical or distinct

Received: June 30, 2011
Revised: March 6, 2012
Published: March 21, 2012

biomolecules at each terminal. Importantly, we placed the succinimidyl carbonyloxymethyl group next to the nitrobenzene ring to eliminate any residual tags on the biomolecules after photocleavage and decarboxylation, a way to prevent any possible change of functionality of the biomolecules upon their release by SCNE photocleavage.

In this paper, we first verify the traceless feature and the biocompatibility of SCNE. We then demonstrate its application in reversible phage particle attachment, protein-photoprinting, and the development of a two-tier AFM method. The results imply that SCNE can effectively conjugate biomaterials to a substrate, and warrant the photoreleased biomaterials to retain both chemical structure and biofunctionality.

MATERIALS AND METHODS

Chemicals and Reagents. All solvents as well as phosphate buffered saline (PBS) with pH 7.4, *N*-hydroxysyccinimidyl-11-mercapto-undecanoate (HSC11NHS), antihuman immunoglobulin G (anti-IgG), and human IgG (IgG) proteins were purchased from Sigma-Aldrich (St. Louis, MO) and were used as received. A succinimidyl derivative dye, 6-(((4-((,4-difluoro-5-(2-thienyl)-4-bora-*3a*,*4a*-diaza-*s*-indacene-3-yl)-phenoxy)acetyl)amino)hexanic acid succinimidyl ester (BODIPY TR), and a permanent cross-linker, succinimidyl 3-(2-pyridyldithio) propionate (SPDP), were purchased from Molecular Probes (Grand Island, NY). Ultrapure water (18.2 MΩ) was obtained with a Barnstead Nanopure filtration system (Thermo Fisher Scientific Inc., Franklin, MA) and was used throughout the experiments.

Surface Modification. Anti-IgG or phage particles were modified on a gold-coated Si wafer substrate via the previously synthesized cross-linker[34] (see Supporting Information), di-6-(3-succinimidyl carbonyloxymethyl-4-nitro-phenoxy)-hexanoic acid disulfide diethanol ester (SCNE). A precleaned Si substrate was coated with 7 nm of titanium, followed by 50 nm of gold using a vacuum evaporator (Denton Vacuum, Moorestown, NJ). The substrate was immediately immersed in SCNE solution (10^{-4} M in acetonitrile) and kept for 12 h at room temperature under N_2 gas protection. After thoroughly rinsing by acetonitrile and PBS buffer, the substrate was dipped in 10^{11} pfu/mL phage particle solution or 10^{-6} M protein solution, and incubated overnight at 4 °C under N_2 gas protection. After thoroughly rinsing with PBS buffer, the sample was subjected to phage particle photorelease or protein photoprinting experiment.

AFM tips were modified in a similar way. Si_3N_4 tips were cleaned via UV/ozone treatment for 30 min using a tip cleaner (BioForce Nanosciences, Inc., Ames, IA). Thinner metal coating (3 nm titanium and 15 nm gold) was applied to the tips. The freshly coated tips were modified by either SPDP or SCNE for permanent or photocleavable conjugation of IgG on the tip to perform lateral force measurement or to establish the two-tier AFM method.

Protein patterning was achieved by microcontact printing. A gold-coated Si substrate was immersed in a $HSC_{11}NHS$ solution (10^{-3} M in ethanol) overnight at 4 °C under N_2 gas protection. After thoroughly rinsing with ethanol and PBS buffer, the surface was printed with anti-IgG using a preinked PDMS stamp. It was immediately rinsed by PBS buffer and Tris-HCl buffer (pH 8.0) to passivate the hydroxysuccinimide groups at the unprinted regions of the surface.

Characterization of SCNE Photolysis. To monitor the photocleavage reactions, UV−vis spectra were collected using a HP 8453A diode array spectrophotometer (Agilent Technology Inc., Santa Clara, CA). The steady-state emission-spectral measurements were conducted using 1 cm × 1 cm quartz cells in a PTI C60 spectrofluorimeter (Photon Technology International, Inc., Birmingham, NJ) equipped with a 75 W mercury lamp as an irradiation source. Potassium ferrioxalate actinometry was utilized to determine the reaction quantum yield. Photolysis of SCNE for protein or phage particle detachment was achieved using a 60 W mercury lamp equipped with an IR filter and an interference filter (330 ± 5 nm, Andover Corporation Optical Filter) at a dose rate of 1 μW/cm^2.

Cross-Linking of Homodimeric pilM Protein (3HG9). Homodimeric pilM protein (Protein Data Bank code 3HG9) of 3.65×10^{-5} M was prepared in PBS (pH 7.4) and cross-linked by SCNE. To 300 μL of freshly prepared 3HG9 solution, 50 μL SCNE (5 mM in acetonitrile) was added, and the mixture was kept at room temperature for 8 h followed by the addition of 250 mM Tris-HCl buffer (pH 8.0) to passivate any unreacted SCNE. Prior to MALDI-TOF analysis, the samples were desalted/concentrated with a C4 ZipTip (Millipore Corporation, Billerica, MA) according to the manufacturer's instructions. To carry out the photolysis and recover the proteins, 20 μL of cross-linked protein solution was transferred to a quartz cuvette and irradiated under UV light at 330 nm for 2 h. Samples were desalted/concentrated with a C4 ZipTip after 30 min, 1 h, and 2 h, respectively, followed by MALDI-TOF analysis.

MALDI-TOF Mass Spectrometry. MALDI-TOF mass spectrometry analysis of the cross-linked peptides was performed on a Voyager Biospectrometry DE-STR Workstation (Applied Biosystems, Foster City, CA) equipped with a nitrogen laser (330 nm). The instrument was operated in positive ionization mode and the measurements were performed in linear mode (mass range m/z 10 000 to 40 000) using sinapinic acid as the matrix. A saturated matrix solution was prepared in 80% acetonitrile, 19.9% water, and 0.1% TFA (v/v/v). Samples were prepared using the dried droplet method by spotting 1 μL of matrix solution and 1 μL of zip-tipped sample solution onto the target. Spectra from 100 to 300 laser shots were accumulated to produce one spectrum. The instrument was calibrated using the monoisotopic masses of standard proteins (New England Biolabs Inc., Ipswich, MA): RNase A (Bovine), average MW 13 690.29 Da, monoisotopic MW 13 681.32; triose phosphate isomerase (*E. coli*), average MW 26 971.81 Da, monoisotopic MW 36 954.82; bovine serum albumin, average MW 66 462.98 Da, monoisotopic MW 66 419.87.

Plaque Assay. A plaque assay was applied in determining the phage activity. Serial dilution of the phage solution was conducted by gradually diluting the phage solution by 100-fold. The mixture of phage dilution, bacteria, and agarose was loaded on top of the LB/Agar. After incubation overnight at room temperature, individual plaques appeared as clear dots in the dish. The concentration of the original phage solution (pfu/mL) can be calculated by

$$\text{number of plaques}/(d \bullet V)$$

where d is the dilution factor, and V is the volume of the diluted phage added to the plate.

AFM Analysis. The AFM study was carried out using a multimode Nanoscope IIIa AFM (Digital Instruments, Santa Barbara, CA), equipped with a J-type scanner. Topographic

imaging was performed using oxide-sharpened Si_3N_4 tips in PBS buffer in a fluid cell. The images were acquired in the fluid-tapping mode at 512 pixels per line at a thermal resonance frequency of 8−10 kHz. The scan rate was less than 1.00 Hz. To detect the photoprinted anti-IgG, imaging in lateral force (LF) mode was carried out using an IgG modified tip at a scan angle of 90°. Line direction was set for both "trace" and "retrace" to compare and corroborate the high frictional force attributed to the specific interaction between IgG and anti-IgG. Alternatively, an IgG modified tip was utilized to scan a surface at a resolution of 32 pixels per line; a force−distance curve was collected at each pixel to detect the presence of anti-IgG via the specific interaction, indicated by an adhesive force in the retraction force curve.[35−38] The spring constant of the AFM cantilever was 0.07 ± 0.01 N/m, calibrated by using reference cantilevers with known spring constants.[39]

Protein delivery was achieved by applying direct irradiation to SCNE that conjugates IgG molecules to an AFM tip. The tip was positioned at an anti-IgG patterned region, engaged, and scanned at a preset area of 0.0001 × 0.0001 nm^2 and a scan rate of 0.02 Hz (in practice, the tip was fixed in position and in contact with the substrate). Twenty minutes of irradiation was applied to photorelease IgG molecules from the AFM tip. To minimize the light penetration through the sample, we applied irradiation parallel to the sample surface. The protein-free tip was then used to scan this local area to examine the delivered proteins.

RESULTS

SCNE Photolysis, Traceless Nature, and Biocompatibility. The photolytic reaction of SCNE was carried out by irradiating a SCNE solution in CH_3CN with a high-pressure mercury lamp equipped with a band-pass filter centered at 330 nm. On the basis of NMR, elementary analysis, and mass spectroscopic experimental results[34] (also see Supporting Information), we concluded the photolysis scheme as outlined in Figure 1A. The photolysis process was also monitored by UV−vis spectroscopy. Figure 1B illustrates the absorption spectral changes of the SCNE solution during photolysis with 10 min irradiation time intervals. The presence of an isosbestic point at 274 nm indicates a clean conversion from *o*-nitrobenzyl ester to nitrosobenzaldehyde.[40] The reaction is characterized quantitatively by monitoring the reduction of the peak at 313 nm. Using a potassium ferrioxalate actinometry,[32,41] the quantum yield of the photoreaction was calculated at 0.020 ± 0.005 under the irradiation at 330 nm.

SCNE conjugates to amine groups in a target molecule via the *N*-hydroxysuccinimidyl terminal. It was anticipated that the photocleavage of SCNE results in the recovery of the amine groups without any residues. We thus designed experiments to illustrate the reinstatement of the amine groups after SCNE photolysis. As shown in Figure 2A, a primary amine modified substrate was prepared by forming a monolayer of 2-aminoethanethiol on a gold-coated substrate. SCNE was then anchored to the substrate by amine-succinimidyl reaction to form a covalently bound monolayer. Such SCNE-anchored substrates were subjected to two separate treatments: (1) after exposure to irradiation of 330 nm light for 2 h, the substrate was rinsed (sample i) and then incubated with a succinimidyl derivative dye solution (BODIPY TR, 1 × 10^{-6} M in acetonitrile) for 2 h at room temperature, followed by thoroughly rinsing to remove any unbound dye molecules (sample ii); (2) without irradiation, the substrate was treated

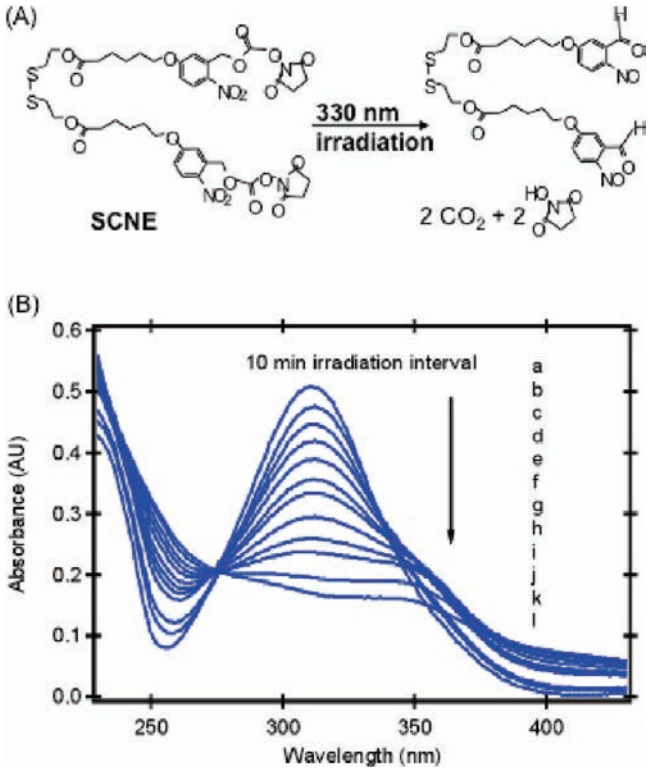

Figure 1. Photolysis reaction of SCNE. (A) Scheme of the photolysis of SCNE. (B) Absorption spectra of SCNE solution (5.6 × 10^{-5} M) under different period of irradiation: (a) 0 min, (b) 10 min, (c) 20 min, (d) 30 min, (e) 40 min, (f) 50 min, (g) 60 min, (h) 70 min, (i) 80 min, (j) 90 min, (k) 110 min, (l) 120 min.

with the same dye solution (sample iii). In sample i, no fluorescence signal was detectable. Strong fluorescence signal peaked at 625 nm was observed in sample ii (Figure 2B, green line); whereas negligible fluorescence signal was detected in sample iii in the absence of irradiation (Figure 2B, blue line). Apparently, the clean photocleavage of SCNE led to restoration of the amine groups on the substrate, and permitted the same amine-succinimidyl chemistry to couple the dye. The fluorescence intensity in sample ii is close to that obtained in sample iv (red line in Figure 2B), in which the amine modified substrate was incubated directly with the dye solution under the same conditions. It implies that ∼100% amine group recovery was achieved after photolysis of SCNE. We also carried out a negative control experiment, in which SCNE was replaced by a permanent cross-linker, SPDP, to react with the amine-modified substrate (data not shown). After the surface was irradiated and treated with dye solution under the same experimental conditions, dye molecules were undetectable. It provides further evidence that SCNE is a traceless, photocleavable cross-linker.

The traceless nature of SCNE was also examined when SCNE was applied in protein cross-linkage. The homodimeric pilM protein from *Pseudomonas aeruginosa* 2192 (3HG9) was chosen as a model system because of its simplicity, possessing only two lysines per monomer for convenient mass spectroscopic data analysis. Although the X-ray crystallographic analysis indicated that 3HG9 is a homodimer,[42] the protein was in the forms of both monomer (*m*/*z* 13 673) and dimer complex (*m*/*z* 27 348) when dissolved in solution as indicated by the MALDI data analysis (Figure 3A). Cross-linking by

dx.doi.org/10.1021/bc200343u | *Bioconjugate Chem.* 2012, 23, 705−713

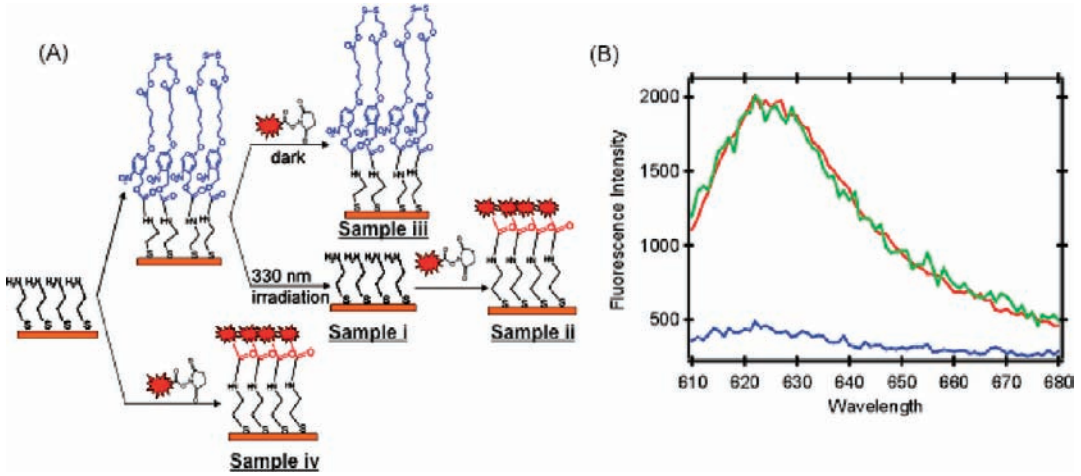

Figure 2. Surface reactions to demonstrate the traceless feature of SCNE. (A) Illustration of the paths of surface reactions. (B) Fluorescence spectra of substrates modified by SCNE and BODIPY TR. Red line: direct BODIPY TR modification without SCNE involvement (sample iv); blue line: BODIPY TR introduced to SCNE modified substrate without irradiation (sample iii); green line: BODIPY TR introduced to SCNE modified substrate after irradiation (sample ii).

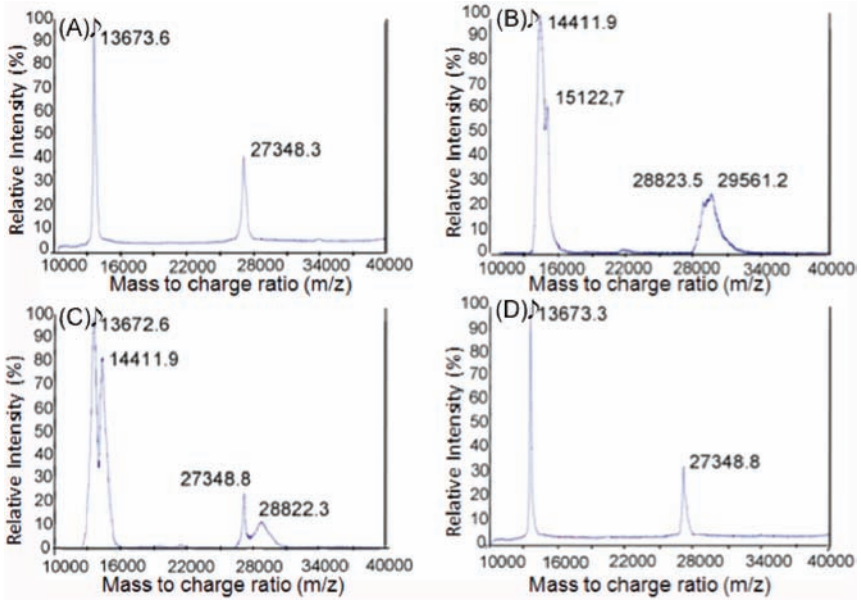

Figure 3. MALDI TOF spectra of protein cross-linking and recovery via irradiation of 330 nm light: (A) untreated protein 3HG9; (B) cross-linked 3HG9 by SCNE; (C) cross-linked 3HG9 after 30 min irradiation; (D) cross-linked 3HG9 after 2 h irradiation.

SCNE caused the increase of the monomer mass from 13 673 to 14 411 (Figure 3B), indicating that two lysines in the monomer were intra-cross-linked by SCNE. A shoulder peak at m/z 15 122 is likely a result of the reaction of SCNE with the amino group at the N-terminal, and the additional mass of 712 Da is attributed to the hydrolyzation of the carbonated ester at the other end of SCNE while a CO_2 is lost. In the dimer complex, there are six primary amines: four in lysines, and two in N-terminals. The cross-linking gave rise to several peaks. Among them, the peak at m/z 28 823 is associated with dimers with two intracomplex cross-links. Other peaks ranging from m/z 29 483 to m/z 29 615 are likely associated with dimers having various numbers of intra-cross-links and N-terminal labels. After 30 min irradiation (Figure 3C), we observed the partial recovery of the cross-linked proteins in both monomers and dimers. After 2 h irradiation (Figure 3D), the proteins were fully recovered, as evidenced by the clean peaks at m/z 13 673 and m/z 27 384 for the original protein monomer and dimer, respectively. Note that the laser of MALDI-TOF is significantly weaker than the UV light used for photolysis. Thus, the laser-induced SCNE cleavage during MALDI measurement is negligible.

One concern in SCNE application is that, the irradiation at a wavelength of 330 nm for SCNE photolysis may cause degradation of biofunctions of biomolecules (such as DNA, proteins) or living organisms. The results from MALDI analysis suggest that cross-linked proteins can fully resume their primary chemical structures upon 2 h irradiation by the light of 330 nm. To demonstrate the safety of SCNE photocleavage toward biofunctions, we further investigated the bioactivity of T7 phage particles under the same irradiation condition. Using a plaque assay, we found the number of infectious T7 phage particles remained constant after 2 h irradiation with light of 330 nm. However, the number decreased dramatically within

dx.doi.org/10.1021/bc200343u | *Bioconjugate Chem.* 2012, 23, 705–713

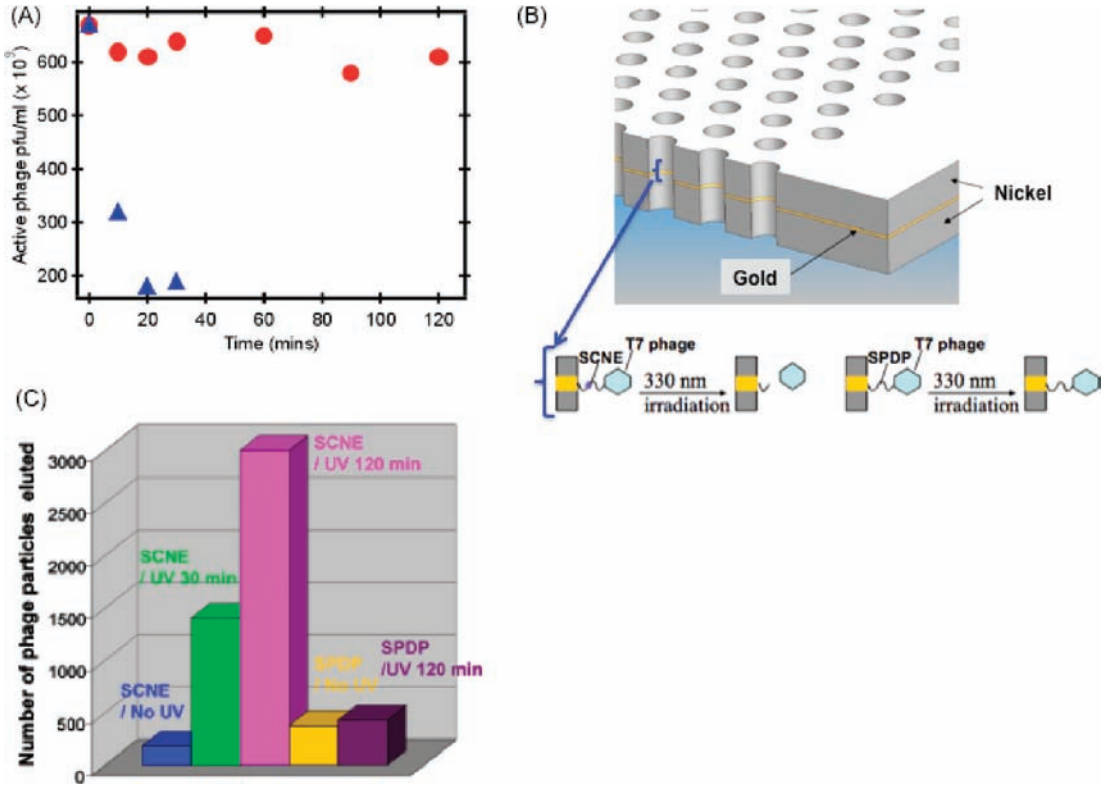

Figure 4. Response of phage particles to irradiations. (A) Irradiation time-dependence of the bioactivity of phage particles. Circles: under 330 nm irradiation; triangles: under 297 nm irradiation. (B) Illustration of the microchannel array, the surface modification and reactions. (C) Phage recovery from a SCNE or SPDP modified microchannel array under various conditions of irradiation. Blue: no UV irradiation with SCNE cross-linker; green: 30 min irradiation with SCNE cross-linker; pink: 120 min irradiation with SCNE cross-linker; yellow: no UV irradiation with SPDP cross-linker; 120 min irradiation with SPDP cross-linker.

30 min when the phage particles were irradiated with light of 297 nm (Figure 4A). The result implies that T7 phage particles survived the irradiation condition for SCNE photolysis well. Taken together, SCNE is a traceless cross-linker for protein conjugation; the irradiation condition of its photolysis has a negligible impact on the function of biomaterials. These are further evidenced when we demonstrate the application of SCNE in the following three areas.

Photorelease of Covalently Immobilized Phage Particles. In this study, we applied SCNE in achieving the photorelease of conjugated phage particles from a microchannel array (Figure 4B) with the potential application in direct phage screening (see Discussion section). The microchannel array has a total of 2682 channels. Each channel is 5 μm in diameter, 25 μm long, and the adjacent channels are separated 25 μm apart (center-to-center distance). A gold ring with a width of 1 μm is embedded in the microchannel for anchoring phage particles via SCNE. The effective volume of the compartment within each channel is ~20 fL. T7 phage particles were loaded at a solution concentration of 1.9×10^{11} pfu/mL, and conjugated to the gold ring via SCNE. Statistically, only one or two phage particles can be accommodated in each channel at this loading concentration. After thoroughly rinsing, the final wash solution was collected as the control sample. As shown in Figure 4C, less than 15 phage particles presented in the final washing elute before the photolysis, providing a baseline for counting the number of particles photocleaved from the surface. After irradiation with the light of 330 nm, the elutes from the experiment were collected for plaque assay analysis. 1340 ± 30 and 2970 ± 20 T7 phage particles (out of at least five measurements) were present in the post-irradiation elute upon 30 min and 2 h irradiation, respectively. It suggests efficient detachment and recovery of phage particles after 2 h irradiation. Control experiments were also conducted using SPDP, a permanent cross-linker, to anchor the T7 phage particles. Due to the noncleavable nature of SPDP, most phage particles remained even after two hours of irradiation (Figure 4C). Note that, when SPDP was used, the number of phage particles was higher in the final wash elute prior to irradiation. We speculate that the shorter chain in SPDP impedes its ordered monolayer assembly on gold, leaving more defects for physical adsorption of phage particles and consequently a larger number of particles in the wash elute.

Protein Photoprinting. We combined the use of SCNE with the photolithographic technique to achieve simple and clean protein photoprinting. Anti-IgG molecules were anchored on a gold-coated substrate via SCNE. As shown in the AFM images in Figure 5A, the surface is flat and featureless, except some bright dots which are likely protein aggregates or gold particle aggregates. A 1 h irradiation of 330 nm light was carried out through a Cr mask that possesses arrays of dots with a diameter of 3 μm. SCNE cleavage occurred at areas exposed to the irradiation, causing detachment of the antibody molecules, whereas antibodies in the shadow of the mask (within the circle in Figure 5B) remained intact. After thoroughly rinsing, protein patterns were visualized as shown in Figure 5B. The height of the anti-IgG patterns is 7.1 ± 0.9 nm above the surrounding areas, indicating a monolayer of anti-IgG covalently anchored on the substrate.[37,38,43−45]

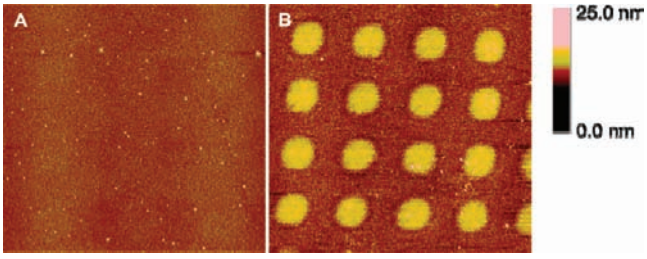

Figure 5. Tapping-mode AFM images of a gold-coated Si wafer substrate functionalized by anti-IgG via SCNE cross-linker before (A) and after (B) 330 nm light irradiation through a Cr mask. Image size: 30 × 30 μm^2; irradiation time: one hour.

To investigate the binding activity of the photoprinted protein layer, an IgG-modified AFM tip was used to perform measurements in LF mode. In this mode, when the line direction is set to "trace", high lateral (frictional) forces are indicated by bright contrast; the relative signal strength inverts as the scan direction is reversed to "retrace", thus high lateral forces are indicated by dark contrast.[46,47] Reversed contrast of the patterns is shown in the "trace" (Figure 6B) and "retrace" (Figure 6C) LF images. In contrast, when a BSA-modified tip was applied in repeating the experiment, no clear pattern was observed in LF images even though the patterns were clearly visible in topographic images. The results imply that the origin of the high friction force in Figure 6 is the anti-IgG−IgG specific interaction. It verifies the binding activity of the photoprinted proteins.

Two-Tier AFM. A two-tier AFM assay was established based on the use of SCNE in the AFM probe modification. It permits two sequential AFM tasks at the same site to locate specific protein species on a surface (tier 1) and to deliver its binding partner at a targeted position (tier 2). In addition, the postdelivery event can be monitored *in situ*.

We modified an AFM tip with human IgG via SCNE. Anti-IgG was patterned on a surface by microcontact printing, as shown in the height image in Figure 7A. When the tip scanned the surface in force mode, a force−distance curve was collected at each pixel. Typical adhesion force curves at the bright (M) and dark (N) pixels in Figure 7B are shown in Figure 7C. The adhesion force measured on the anti-IgG patterns was 1.2 ± 0.2 nN, in contrast to the low adhesion force of 0.2 ± 0.1 nN at the surrounding regions where anti-IgG was absent. Hence, the strong adhesion force is attributed to the specific interaction between IgG and anti-IgG, which identifies anti-IgG at the bright-contrasted regions.[35−38] This was verified by locating the same area in the height image in Figure 7A (highlighted region), in which the anti-IgG patterns (in bright contrast) elevate above the surrounding areas. Note that the tip apex of a gold-coated AFM probe was 35 nm in radius, much greater than the dimension of IgG.[43−45] Hence, multiple anti-IgG molecules were immobilized on the AFM probe. The measured adhesion force is ascribed to the specific interaction between multiple pairs of anti-IgG and IgG. Adhesion force based protein identification is particularly important when a surface contains a mixture of unknown proteins, as in the case of live cell membranes.[35−38] In the current experiment, we demonstrated that the IgG-modified tip provided guidance to identify the anti-IgG pattern for the follow-up IgG photodelivery. By selectively modifying IgG at the tip apex, we were able to restrict IgG delivery to a desired region of the anti-IgG pattern upon SCNE photocleavage (Figure 8A,B). After photocleavage, the protein-free tip was then employed to collect images to monitor the IgG and anti-IgG binding event. As illustrated in the height profile analysis (Figure 8C,D), the IgG is characterized by a 7.7 nm elevation above the round-shaped platform of anti-IgG pattern, and the anti-IgG in the pattern is 7.2 nm above the surrounding area. The measured height of IgG is consistent with the value reported in the literature.[43−45,48] IgG binding was not detected on other patterns of the same surface, indicating the successful local protein delivery and effective monitoring of the postdelivery event. The photodelivered IgG molecules are stable even after continuous scans of the local area, and remained for days when the sample was kept in PBS buffer. In the absence of anti-IgG on the substrate, the delivered proteins were visualized instantly, but disappeared from the surface upon continuous scans. It provides further evidence that the delivered proteins retained biofunctionality to recognize the binding partners on the substrate.

■ DISCUSSION

SCNE is a trifunctional cross-linker. The *N*-hydroxysuccinimidyl and the disulfide groups permit conjugation of proteins to a gold-coated substrate. The photolysis of the nitrobenzyl ester group in SCNE offers clean cleavage and reinstatement of the amine group of the conjugated protein. Thus, SCNE is capable of attaching proteins or organisms to a substrate, and subsequently releasing them from the substrate without a trace of alteration in structure and function. Note that the ether group in the 5′-position places the quantum yield of SCNE photolysis at the lower end among the *o*-nitrobenzyl compounds.[18] However, the presence of an ether group in the 5′-position renders SCNE a longer-wavelength absorption (absorption maximum at ∼310 nm) when compared to an absorption maximum at ∼260 nm for a pure *o*-nitrobenzyl molecule. This effectively prevents the photodamage of

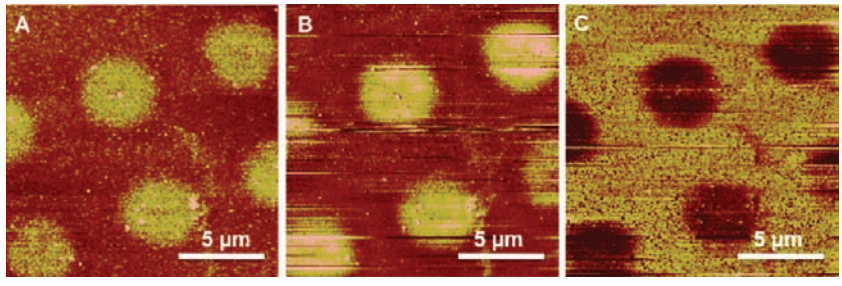

Figure 6. AFM images of Anti-IgG patterned surface collected by an IgG-functionalized AFM probe: (A) height image; (B) LF mode image in "trace" direction; (C) LF mode image in "retrace" direction". Image size: 16 × 16 μm^2.

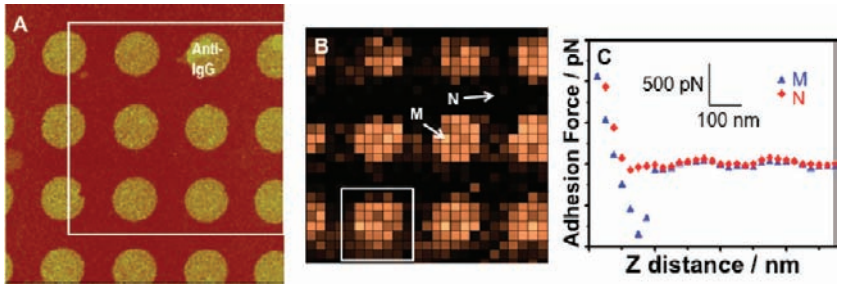

Figure 7. AFM study of an anti-IgG patterned surface. (A) 16 × 16 μm^2 height image of anti-IgG patterns in round shape with a diameter of 2.5 μm, captured at 512 pixels per line. (B) 12 × 12 μm^2 force map collected at the highlighted region in (A) at 32 pixels per line using an AFM tip conjugated with IgG via SCNE. (C) Typical force curves collected at bright (M) and dark (N) contrasted pixels in (B).

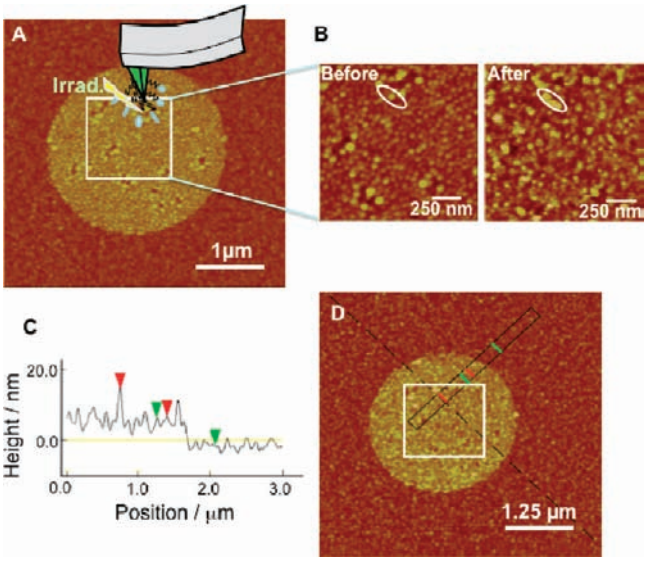

Figure 8. Protein delivery to an identified anti-IgG pattern followed by surface characterization. (A) 4 × 4 μm^2 height image of the identified anti-IgG pattern (highlighted in Figure 7B), where IgG was locally delivered by SCNE photocleavage. (B) Higher-resolution height images, captured at the highlighted region in (A), showing the structural difference before and after IgG local delivery (i.e., in the circled area). (C) Height profile at regions marked in (D), with the height differences of 7.7 and 7.2 nm between the pairs of red and green marks, respectively. (D) 5 × 5 μm^2 height image of the same anti-IgG pattern after IgG delivery.

proteins and other biomolecules when irradiation is employed for photocleavage, as was substantiated in our experiments (Figures 3–5).

We have demonstrated the application of SCNE in attaching and detaching phage particles from a microchannel array (Figure 4). The experiment was inspired by the need for new methods for phage particle based screening. Phage display has been the workhorse for mapping the protein–protein interactions of proteins of interest. In phage display, proteins or peptides are expressed as fusions to a capsid protein. The target-specific phage particles can be isolated by a biopanning process. The key advantage of phage display or a phage-particle-based screening method is the capability of linking the binding proteins with the genetic information that encodes them within the phage. It enables the identification of a protein sequence at the single molecule level, a capability that no other method can achieve so far. To fully attain this potential, it is critical to develop a method that is capable of collecting individual phage particles from a phage mixture. One strategy for such a challenge is (1) to compartmentalize the phage mixture at the single phage particle per compartment level; (2) to immobilize the phage particle to the compartment for binding reactions and subsequent washing; and (3) to release and recover the selected phage particle for corresponding protein identification. To implement this strategy, we designed the microchannel array with a total of 2682 channels that served as well-separated compartments. 2970 ± 20 phage particles were photocleaved from the channels, indicating that an average of one to two phage particles were accommodated in each channel. Individual phage particles are expected to be revealed against the target in each compartment for effective screening. This can be accomplished by introducing fluorescent-tagged targets to the substrate and visualizing the target-specific phage complexes by a fluorescence microscope. The efficient release of phage particles from the microarray, as demonstrated in Figure 4, permitted the recollection of selected phage particles from the compartments for further amplification and sequencing. Such a system has the potential to screen a mixture of phage particles in a one-by-one fashion to eliminate the tedious multistep enrichment procedure in conventional biopanning processes. The same principle can be applied to the screening of subpopulation cells within a cell mixture to understand the collective behavior of communicative cells. This research has been undertaken in our group.

Protein chips play increasingly important roles in modern biology and biotechniques.[49−51] One essential feature of chips is to array the proteins in a desired pattern. Current approaches rely on the fabrication of patterned substrate via lithography or microcontact printing, followed by selectively anchoring protein molecules at the patterned regions through specific chemistry. Herein, we introduced a simple and direct way to generate protein patterns applicable on a large scale. Starting with a uniform protein layer via SCNE conjugation to a substrate, we selectively removed unwanted proteins with light to transfer a geometric pattern from a photomask to the protein molecules on the substrate. Desired proteins within a pattern remain intact throughout the process, and the binding activity remains unchanged (Figure 6). While UV irradiation at a shorter wavelength can also remove the proteins by photodecomposition, products of photodecomposition will be left behind as small debris and intrude upon the protein patterns via random physical adsorption. Due to the traceless nature of SCNE, the proteins cleaved from the substrate are in their native form, and thus can be cleaned and eliminated from the surface by thoroughly rinsing. This has been demonstrated in the clear and reproducible protein patterns as shown in Figure 5.

dx.doi.org/10.1021/bc200343u | *Bioconjugate Chem.* 2012, 23, 705–713

One of the greatest challenges in cell biology is the ability to visualize and make measurements of individual proteins of an identified species in a living organism. We expect to tackle this challenge by the two-tier AFM assay established in the current study. Living cell membranes consist of a number of cell-surface proteins, generating a sophisticated surface. An antibody-modified AFM tip can distinguish a target protein from other species via force measurement, thus provide guidance to register a target protein. As demonstrated in the model system of the biomimic surface (Figures 7 and 8), the IgG-modified tip identifies anti-IgG patterns. Due to the use of SCNE as the cross-linker, natural IgG can be released from the tip and delivered to a local region by remotely switching on the light. Importantly, the postdelivery event can be *in situ* investigated immediately. This approach offers great potential in live cell studies, as it permits the monitoring of the initial ligand–receptor binding events, such as protein redistribution and rearrangement, associated with the protein function. We expect that the application of two-tier AFM will open up new avenues to elucidate cellular functions at the molecular level, and provide novel strategies for correcting cell dysfunction and for drug design.

In conclusion, SCNE is a versatile cross-linker that can be used for a wide range of applications where photocleavage ensures clean and remote-controllable release of biological molecules from a substrate.

■ ASSOCIATED CONTENT

Supporting Information

Synthesis and characterization of SCNE. This material is available free of charge via the Internet at http://pubs.acs.org.

■ AUTHOR INFORMATION

Corresponding Author

*Dr. Rong Wang, Illinois Institute of Technology, Life Sciences Building, 3101 S. Dearborn St., Chicago, IL 60616. E-mail: wangr@iit.edu, Tel: 312-567-3121, Fax: 312-567-3494. Dr. Liaohai Chen, Biosciences Division, Argonne National Laboratory, Lemont, IL 60439, USA. E-mail: l.hchen@anl.gov, Tel: 630-252-3975.

Notes

The authors declare no competing financial interest.

■ ACKNOWLEDGMENTS

This work was supported by the National Institute of Health (R01 NS047719).

■ REFERENCES

(1) Dormán, G., and Prestwich, G. D. (2000) Using photolabile ligands in drug discovery and development. *Trends Biotechnol. 18*, 64–77.

(2) Vodovozova, E. L. (2007) Photoaffinity labeling and its application in structural biology. *Biochemistry 72*, 1–20.

(3) Mourot, A., Grutter, T., Goeldner, M., and Kotzyba-Hibert, F. (2006) Dynamic structural instigations on the torpedo nicotinic acetylcholine receptor by time-resolved photoaffinity labeling. *ChemBioChem 7*, 570–583.

(4) Khoreva, S. N., and Lavrik, O. I. (2005) Photoaffinity labeling technique for studying DNA replication and DNA repair. *Curr. Med. Chem. 12*, 641–655.

(5) Murray, C. M., Hutchinson, R., Bantick, J. R., Belfield, G. P., Benjamin, A. D., Brazma, D., Bundic, R. V., Cook, I. D., Craggs, R. I., Edwards, S., Evans, L. R., Harrison, R., Holness, E., Jackson, A. P., Jackson, C. G., Kinston, L. P., Perry, M. W. D., Ross, A. R. J., Rugman, P. A., Sidhu, S. S., Sullivan, M., Taylor-Fishwick, D. A., Walker, P. C., Whitehead, Y. M., Wilkinson, D. J., Wright, A., and Donald, D. K. (2005) Monocarboxylate transporter MCT1 is a target for immunosuppression. *Nat. Chem. Biol. 1*, 371–376.

(6) Page, M. J., Amess, B., Rohlff, C., Stubberfield, C., and Parekh, R. (1999) Proteomics: a major new technology for the drug discovery process. *Drug Discovery Today 4*, 55–62.

(7) Berens, C., Courtoy, P. J., and Sonveaux, E. (1999) A fluorescent radioiodinated oligonucleotidic photoaffinity probe for protein labeling: synthesis and photolabeling of thrombin. *Bioconjugate Chem. 10*, 56–61.

(8) Scheibler, L., Mierke, D. F., Bitan, G., Rosenblatt, M., and Chorev, M. (2001) Identification of a contact domain between echistatin and hte integrin alpha (v) beta (3) by photoaffinity cross-linking. *Biochemistry 40*, 15117–15126.

(9) DeGraw, A. J., Zhao, Z., Strickland, C. L., Taban, A. H., Hsieh, J., Jefferies, M., Xie, W., Shintani, D. K., McMahan, C., Cornish, K., and Distefano, M. D. (2007) A photoactive isopreoid disphosphate analogue containing a stable phosphonate linkage: synthesis and biochemical studies with prenyltransferases. *J. Org. Chem. 72*, 4587–4595.

(10) Mourey, R. J., Estevez, V. A., Marecek, J. F., Barrow, R. K., Prestwich, G. D., and Snyder, S. H. (1993) Inositol 1,4,5-trisphosphate receptors: labeling the Inositol 1,4,5-trisphosphate binding site with photoaffinity ligands. *Biochemistry 32*, 1719–1726.

(11) Chaudhary, A., Chen, J., Gu, Q. M., Witke, W., Kwiatkowski, D. J., and Prestwich, G. D. (1998) Probing the phosphoinositide 4,5-bisphosphate binding site of human proflin I. *Chem. Biol. 5*, 273–281.

(12) Finch, E., and Augustine, G. (1999) Local calcium signaling by inositol-1,4,5-trisphosphate in Purkinje cell dendrites. *Nature 396*, 753–756.

(13) Woolley, G. A. (2005) Photo controlling Peptide Helices. *Acc. Chem. Res. 38*, 486–493.

(14) Smothers, J. F., Henikoff, S., and Carter, P. (2004) Affinity selection from biological libraries. *Science 298*, 621–622.

(15) Kaneda, M., Sadakane, Y., and Hatanaka, Y. (2003) A novel approach for affinity-based screening of target specific ligands: application of photoreactive D-glyceraldehyde-3-phosphate dehydrogenase. *Bioconjugate Chem. 14* (5), 849–852.

(16) Zhang, C. X., Chang, P. V., and Lippard, S. J. (2004) Identification of nuclear proteins that interact with platinum-modified DNA by photoaffinity labeling. *J. Am. Chem. Soc. 126* (21), 6536–6537.

(17) Chan, E. W. S., Chattopadhaya, S., Panicker, R. C., Huang, X., and Yao, S. Q. (2004) Developing photoactive affinity probes for proteomic profiling: hydroxamate-based probes for metalloproteases. *J. Am. Chem. Soc. 126* (44), 14435–14446.

(18) Aujard, I., Benbrahim, C., Gouget, M., Ruel, O., Baudin, J. B., Neveu, P., and Jullien, L. (2006) O-nitrobenzyl photolabile protecting groups with red-shifted absorption: syntheses and uncaging cross-sections for one- and two-photon excitation. *Chem.—Eur. J. 12*, 6865–6879.

(19) Alvarez, M., Alonso, J. M., Filevich, O., Bhagawati, M., Etchenique, R., Piehler, J., and del Campo, A. (2011) Modulating surface density of proteins via caged surfaces and controlled light exposure. *Langmuir 27*, 2789–2795.

(20) Pirrung, M. C., and Huang, C. (1996) A general method for the spatially defined immobilization of biomolecules on glass surfaces using "caged" biotin. *Bioconjugate Chem. 7*, 317–321.

(21) Driscoll, P. F., Milkani, E., Lambert, C. R., and McGimpsey, W. G. (2010) A multilayered approach to complex surface patterning. *Langmuir 26* (5), 3731–3738.

(22) Yang, Z., Frey, W., Oliver, T., and Chilkoti, A. (2000) Light-activated affinity micropatterning of proteins on self-assembled on gold. *Langmuir 16* (4), 1751–1758.

(23) Bhagawati, M., Lata, S., Tampe, R., and Piehler, J. (2010) Native laser lithography of His-tagged proteins by uncaging of multivalent chelators. *J. Am. Chem. Soc. 132* (17), 5932–5933.

(24) Petersen, S., Alonso, J. M., Specht, A., Duodu, P., Goeldner, M., and del Campo, A. (2008) Phototriggering of cell adhesion by caged cyclic RGD peptides. *Angew. Chem., Int. Ed. 47*, 3192−3195.
(25) Ciesienski, K. L., and Franz, K. J. (2011) Keys for unlocking photolabile metal-containing cages. *Angew. Chem., Int. Ed. 50*, 814−824.
(26) Sánchez, M. I., Vázquez, O., Vázquez, M. E., and Mascareñas, J. L. (2011) Light-controlled DNA binding of bisbenzamidines. *Chem. Commun. 47*, 11107−11109.
(27) ul Haq, E., Liu, Z., Zhang, Y., Ahmad, S. A. A., Wong, L. S., Armes, S. P., Hobbs, J. K., Leggett, G. J., Micklefield, J., Roberts, C. J., and Weaver, J. M. R. (2010) Parallel scanning near-field photolithography: the snomipede. *Nano Lett. 10* (11), 4375−4380.
(28) Ahmad, S. A. A., Wong, L. S., ul Haq, E., Hobbs, J. K., Leggett, G. J., and Micklefield, J. (2011) Protein micro- and nanopatterning using aminosilanes with protein-resistant photolabile protecting groups. *J. Am. Chem. Soc. 133* (8), 2749−2759.
(29) Nakayama, K., Tachikawa, T., and Majima, T. (2008) Spatial control of protein binding on lipid bimembrane using photoeliminative linker. *Langmuir 24* (13), 6425−6428.
(30) Han, X., Pradeep, S. N. D., Critchley, K., Sheikh, K., Bushby, R. J., and Evans, S. D. (2007) Supported bilayer lipid membrane arrays on photopatterned self-assembled monolayers. *Chem.—Eur. J. 13*, 7957−7964.
(31) Iwamto, M., Hasegawa, C., Sudo, Y., Shimono, K., Araiso, T., and Kamo, N. (2004) Proton release and uptake of *pharaonis* phoborhodopsin (sensory Rhodopsin II) reconstituted into phospholipids. *Biochemistry 43*, 3195−3203.
(32) Yan, F., Chen, L., Tang, Q., and Wang, R. (2004) Synthesis and characterization of a novel photolabile cross-linker and its application on tunable surface modification and protein photo-delivery. *Bioconjugate Chem. 15*, 1030−1036.
(33) Tang, Q., Zhang, Y., Chen, L., Yan, F., and Wang, R. (2005) Protein delivery with nanoscale precision. *Nanotechnology 16*, 1062−1068.
(34) Yan, F. (2006) Novel photocleavable cross-linkers and their applications in biotechnologies. PhD dissertation, Department of Biological, Chemical and Physical Sciences, Illinois Institute of Technology, Chicago IL. http://proquest.umi.com/pqdweb?index=0&did=1172109241&SrchMode=2&sid=3&Fmt=2&VInst=PROD&VType=PQD&RQT=309&VName=.
(35) Reddy, C. V. G., Krystina, M., Menhart, N., and Wang, R. (2004) Identification of TrkA on living PC12 cells by the atomic force microscopy. *Biochim. Biophys. Acta 1667*, 15−25.
(36) Qiu, D., Xiang, J., Li, Z., Krishnamoorthy, A., Chen, L., and Wang, R. (2008) Profiling TRA-1−81 antigen distribution on a human embryonic stem cell. *Biochem. Biophys. Res. Commun. 369*, 735−740.
(37) Li, Z., Qiu, D., Sridharan, I., Qian., X., Zhang, H., Zhang, C., and Wang, R. (2010) Spatially resolved quantification of E-cadherin on target hES cells. *J. Phys. Chem. B. 114*, 2894−2900.
(38) Li, Z., Qui, D., Xu, K., Sridharan, I., Qian, X., and Wang, R. (2011) Analysis of affinity maps of membrane proteins on individual human embryonic stem cells. *Langmuir 27* (13), 8294−8301.
(39) Tortonese, M., and Kirk, M. (1997) Characterization of application specific probes for SPMs. *Proc. SPIE 3009*, 53−60.
(40) Pearson, A. J., and Roush, W. R. (1999) *Handbook of reagents for organic synthesis: activating agents and protecting groups*, John Wiley & Sons Ltd., New York.
(41) Murov, S. L., Carmichael, I., and Hug, G. L. (1993) *Handbook of Photochemistry*, Marcel Dekker Inc., New York.
(42) Malashkevich, V. N., Toro, R., Sauder, M. J., Burley, S. K., and Almo, S. C. (2011) Crystal structure of putative pilM protein from pseudomonas aeruginosa 2192, *RCSB Protein Data Bank*, www.pdb.org/pdb/explore/explore.do?structureId=3hg9.
(43) Roberts, C. J., Williams, P. M., Davies, J., Dawkes, A. C., Sefton, J., Edwards, J. C., Haymes, A. G., Bestwick, C., Davies, M. C., and Tendler, S. J. B. (1995) Real-space differentiation of IgG and IgM antibodies deposited on microtiter wells by scanning force microscopy. *Langmuir 11*, 1822−1826.
(44) Lee, K. B., Park, S. J., Mirkin, C. A., Smith, J. C., and Mrksich, M. (2002) Protein nanoarrays generated by dip-pen nanolithography. *Science 295*, 1702−1705.
(45) Li, Z., Wang, J., Deng, L., and Chen, G. (2009) Preparation and characterization of covalently binding of rat anti-human IgG monolayer on thiol-modified gold surface. *Nanoscale Res. Lett. 4*, 1403−1408.
(46) Alessandrini, A., and Facci, P. (2005) AFM: a versatile tool in biophysics. *Meas. Sci. Technol. 16*, R65−R92.
(47) Lekka, M., Kulik, A. J., Jeney, S., Raczkowska, J., Lekki, J., Budkowski, A, and Forro, L. (2005) Friction force microscopy as an alternative method to probe molecular interactions. *J. Chem. Phys. 123*, 14702−14707.
(48) Silverton, E. W., Navia, M. A., and Davies, D. R. (1977) Three-dimensional structure of an intact human immunoglobulin. *Proc. Natl. Acad. Sci. U.S.A. 74*, 5140−5144.
(49) Becker, T., Hitzmann, B., Muffler, K., Pörtner, R., Reardon, K. F., Stahl, F., and Ulber, R. (2007) Future aspects of bioprocess monitoring. *Adv. Biochem. Eng. Biotechnol. 105*, 249−93.
(50) Spisák, S., and Guttman, A. (2009) Biomedical applications of protein microarrays. *Curr Med Chem. 16* (22), 2806−15.
(51) Naoghare, P. K., and Song, J. M. (2010) Chip-based high-throughout screening of herbal medicines. *Comb. Chem. High Throughput Screen. 13* (10), 923−31.

Bioconjugate Chemistry

Article

pubs.acs.org/bc

Site-Specific Immobilization of Enzymes on Magnetic Nanoparticles and Their Use in Organic Synthesis

Ching-Ching Yu, Yu-Ying Kuo, Chien-Fu Liang, Wei-Ting Chien, Huan-Ting Wu, Tsung-Che Chang, Fan-Dan Jan, and Chun-Cheng Lin*

Department of Chemistry, National Tsing Hua University, 101, Sec. 2, Kuang Fu Rd. Hsinchu, 30013, Taiwan

Supporting Information

ABSTRACT: Magnetic nanoparticles (MNPs) are attractive materials that serve as a support for enzyme immobilization and facilitate separations by applying an external magnetic field; this could facilitate the recycling of enzymes and broaden their applications in organic synthesis. Herein, we report the methods for the immobilization of water-soluble and membrane-bound enzymes, and the activity difference between free and immobilized enzymes is discussed. Sialyltransferase (PmST1, from *Pasteurella multocida*) and cytidine monophosphate (CMP)-sialic acid synthetase (CSS, from *Neisseria meningitides*) were chosen as water-soluble enzymes and expressed using an intein expression system. The enzymes were site-specifically and covalently immobilized on PEGylated-N-terminal cysteine MNPs through native chemical ligation (NCL). Increasing the length of the PEG linker between the enzyme and the MNP surface increased the activity of the immobilized enzymes relative to the free parent enzymes. In addition, the use of a fluorescent acceptor tag for PmST1 affected enzyme kinetics. In contrast, sialyltransferase from *Neisseria gonorrheae* (NgST, a membrane-bound enzyme) was modified with a biotin-labeled cysteine at the C-terminus using NCL, and the enzyme was then assembled on streptavidin-functionalized MNPs. Using a streptavidin−biotin interaction, it was possible to immobilize NgST on a solid support under mild ligation conditions, which prevented the enzyme from high-temperature decomposition and provided an approximately 2-fold increase in activity compared to other immobilization methods on MNPs. Finally, the ganglioside GM3-derivative (sialyl-lactose derivative) was synthesized in a one-pot system by combining the use of immobilized PmST1 and CSS. The enzymes retained 50% activity after being reused ten times. Furthermore, the results obtained using the one-pot two-immobilized-enzyme system demonstrated that it can be applied to large-scale reactions with acceptable yields and purity. These features make enzyme-immobilized MNPs applicable to organic synthesis.

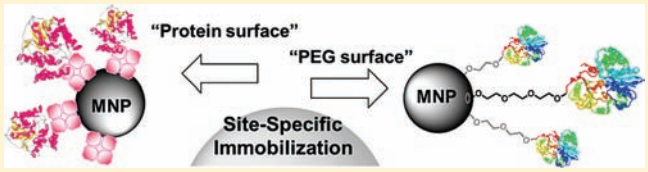

INTRODUCTION

Enzymes are versatile biocatalysts and are useful in many areas of research, including organic synthesis, immunoassays, and substrate sensing.[1] The specific chemo-, regio-, and stereoselectivity of enzyme-mediated transformations remarkably demonstrates their superiority compared to chemical catalytic reactions.[2−4] However, the reusability and long-term stability of enzymes have limited their applications in organic synthesis.[5] Due to the current high cost and time-consuming process of enzyme production, the effective recovery of stable, reusable enzymes should facilitate their application in organic synthesis. The use of immobilized enzymes simplifies enzyme recovery from aqueous solutions by providing a convenient route to recycle expensive biocatalysts through solid-phase separation. Such an approach would significantly reduce the separation time of enzyme recovery. In some cases, the denaturing of immobilized enzymes can be prevented.[6−8]

The most robust techniques to immobilize enzymes on solid support systems use covalent linkages.[9,10] However, in most immobilization approaches, the enzymes are attached to solid supports by random amide bonds or Schiff bases, resulting in a significant loss of enzyme activity.[11,12] One solution to these problems is to develop properly oriented site-specific immobilization techniques. Although enzymes have been noncovalently immobilized on solid supports with site-specific controls using recognition pairs, such as His-tag/Ni,[13,14] MBP/amylose,[15] anti-GST/antibody,[16] or biotin/streptavidin,[17] the enzyme can potentially dissociate from the solid surface, possibly interfering with the long-term storage and reusability of the immobilized enzyme.

Recently, many efforts have focused on the site-specific covalent immobilization of proteins on solid supports.[18,19] One of the most popular approaches used to achieve this goal is to fuse a protein of interest to a tagged peptide that reacts with a substrate immobilized on a solid support, forming a covalent adduct catalyzed by enzymes, such as PPTase,[20] FTase,[21,22] SrtA,[23] or TGase.[24] However, the efficiency of transforming or immobilizing enzyme-catalyzed functional groups could be jeopardized by the location of the tag due to steric effects. To circumvent this problem, a number of selective ligation chemistries have been developed, such as the intein-based system,[25] click chemistry,[26] Staudinger ligation,[27,28] the Diels−

Received: July 21, 2011
Revised: December 19, 2011
Published: March 18, 2012

   dx.doi.org/10.1021/bc200396r | *Bioconjugate Chem.* 2012, 23, 714−724

Alder reaction,[29] and native chemical ligation (NCL).[30,31] These chemoselective approaches for the conjugation or immobilization of proteins have attracted much attention due to the high reaction efficiency and their bioorthogonal reactivity for proteins.[32]

Magnetic nanoparticles (MNPs) have received increasing attention in biorelated research due to their distinct properties, such as their magnetic behavior, ease of surface modification, and high surface-area-to-volume ratio.[33] Various MNPs have been designed as powerful carriers in diverse areas of research.[34−41] MNPs should also function as ideal solid supports for enzyme immobilization because of their pseudohomogeneous properties in solutions and their ease of recovery using magnetic fields.[10,42,43] Thus, the combination of MNPs with site-specific enzyme immobilization strategies can be an efficient platform to retain high activity and facilitate recovery.

In principle, the stability, activity, and kinetic properties of an enzyme are significantly affected after immobilization by the choice of support material and immobilization method employed.[6,7] Blocking of MNPs with PEG suppresses nonspecific protein adsorption while enhancing the nanoparticle's water solubility. Therefore, PEG-functionalized MNPs may be attractive solid supports for the immobilization of water-soluble enzymes. However, membrane-bound enzymes, which are naturally hydrophobic, will not be suitable for immobilization on hydrophilic solid supports. Recently, some investigators have reported using "protein-friendly" surfaces to immobilize membrane-bound enzymes using lipid bilayers or self-assembling hybrid bilayers.[44−46] However, reproducing the formation of these lipid bilayers is difficult to control, and the resulting liposomes may be not stable. In this study, we fabricated MNPs with different surface properties to develop a suitable surface for the immobilization of membrane-bound enzymes.

Sialic acid is often found as a terminal, nonreducing end sugar in glycoproteins and glycolipids, and is associated with many biological processes. However, chemical sialylation requires multistep synthesis and the stereospecific control of α-sialosides, which is difficult. In contrast, the synthesis of sialic acid-containing carbohydrates using enzymatic sialylation via sialyltransferases (STs)[47−51] is very straightforward. STs catalyze glycosylation by transferring a sialic acid molecule to an acceptor sugar using CMP-sialic acid as the donor. Previously, the synthesis of CMP-sialic acid has been achieved on a 100 mg scale using MNP functionalized with CMP-sialic acid synthetase (CSS@MNP); the capability to recycle the immobilized enzyme in organic synthesis was also demonstrated in that case.[52] Hence, ST would be an ideal model enzyme for immobilization in conjugation with previously developed CSS@MNPs and could expand the application of sialoside production via a one-pot−two-enzyme@MNPs strategy. In this report, two α-2,3-sialyltransferases from *Pasteurella multocida* P-1059 (PmST1)[50] and *Neisseria gonorrheae* F62 (NgST)[53] were chosen as target enzymes. Truncated PmST1 is a soluble enzyme, whereas NgST, a membrane-bound enzyme, is relatively insoluble. Herein, we describe two strategies for the immobilization of water-soluble and membrane-bound enzymes in a site-specific manner (Figure 1). The water-soluble enzymes (PmST1 and CSS) were then site-specifically and covalently immobilized on the cysteine-poly(ethylene glycol)-functionalized MNPs (Cys@MNP) by NCL. The activity of the immobilized enzymes was noticeably

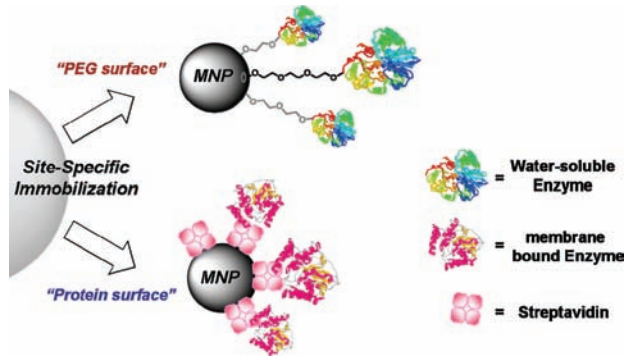

Figure 1. Strategies for site-specific enzyme immobilization. Poly(ethylene glycol) surface-functionalized magnetic nanoparticles were used for water-soluble enzyme immobilization, whereas protein surface-functionalized magnetic nanoparticles were suitable for membrane-bound enzyme immobilization.

higher when they were equipped with longer PEG linkers, indicating that the length of the linker is critical for its activity. In contrast, NgST was modified with a biotin-labeled cysteine at the C-terminus using NCL and assembled on streptavidin-functionalized MNP (SAv@MNP). Using the specific recognition between biotin and streptavidin, we immobilized NgST on the solid support under mild ligation conditions, preventing thermal enzyme decomposition and providing more acceptable activity.

■ EXPERIMENTAL PROCEDURES

Materials and Methods. Bacterial source of *Pasteurella multocida* genomic strain Pm70 and *Neisseria gonorrheae* were purchased from ATCC. All buffers and solutions were prepared by using Millipore water. The chemicals for the synthesis were all obtained from Sigma-Aldrich. HPLC was carried out on Agilent 1100 series system equipped with a UV detector. ^{1}H and ^{13}C NMR spectra were recorded on Bruker AV-400 or DMX-600 MHz. Assignment of ^{1}H NMR spectra was achieved using 2D methods (COSY). Chemical shifts are expressed in ppm using residual $CDCl_3$ (7.24 ppm) or CD_3OD (3.31 ppm) or D_2O (4.67 ppm at 298 k) as internal standard. Low-resolution and high-resolution mass spectra were recorded under ESI-TOF mass spectra conditions. Analytical thin-layer chromatography (TLC) was performed on precoated plates (Silica Gel 60). Silica gel 60 (E. Merck) was employed for all flash chromatography. All reactions were carried out in oven-dried glassware (120 °C) under an atmosphere of argon unless indicated otherwise. All solvents were dried and distilled by standard techniques.

Cloning, Overexpression, and Purification of the Full-Length Sialyltransferase from *Pasteurella multocida* (Pm0188Ph). A pair of primers: the forward primer 5′ CAT ATG AAA ACA ATC ACG CTG TAT TTA GAT CCT GCC TCC 3′ (the *Nde*I restriction site is underlined) and the reverse primer 5′ GCT CTT C CGC AGC CCA ACT GTT TTA AAC TGT CCC AAA AG 3′ (the *Sap*I restriction site is underlined) were used to amplify the full-length gene of Pm0188Ph using PCR from the *Pasteurella multocida* genomic strain Pm70. The reaction was performed in a total volume of 50 mL containing Tris-HCl (50 mM, pH 8.8), NaCl (50 mM), $MgCl_2$ (5 mM), template DNA (100 ng), each primer (400 nM), dNTPs (0.2 mM), and Easy-A high-fidelity PCR cloning enzyme (2.5 U, Stratagene). After heating at 95 °C for 3 min, we performed 30

cycles (denaturation at 95 °C for 30 s, annealing at 58.4 °C for 30 s, and elongation at 72 °C for 30 s). The elongation step was extended by 1 s each cycle, and a final elongation at 72 °C for 3 min was used. The amplified fragment (1.2 Kb) was cloned into a pGEM-T Easy Vector using the pGEM-T Easy Vector System I (Promega). The insert was further confirmed using blue/white screening and sequence analysis. The target gene was digested from a constructed T vector and inserted into an *Nde*I/*Sap*I-treated vector, pTXB1 (commercially available from NEB, USA). The ligated product was transformed into competent *E. coli* DH5α cells. Positive plasmids were selected and subsequently transformed into BL21 (DE3) competent cells. DNA sequencing was used to confirm in-frame cloning of the full length Pm0188Ph gene product. The *E. coli* BL21 (DE3) harboring the recombinant plasmid was grown in LB rich medium (10 g/L tryptone, 5 g/L yeast extract, and 10 g/L NaCl) containing ampicillin (100 μg/mL) at 37 °C until the OD_{600} reached 0.5−0.8. Protein expression was then induced by adding 0.1 mM of IPTG (isopropyl-1-thio-α-D-galacto-pyranoside) followed by incubation at 16 °C for 16 h with vigorous shaking at 200 rpm in a shaking incubator (Firstek S300R). The bacterial cells were harvested by centrifugation at 4 °C, 5000 *g*, for 15 min. The cell pellet was resuspended in column buffer (HEPES 20 mM pH 8.0, containing Triton X-100 0.1%, NaCl 500 mM, and EDTA 0.1 mM) and sonicated on ice for 2 min 50 s at 10 s intervals, before being centrifuged at 4 °C, 24 000 *g*, for 60 min. The cell lysate was collected and applied to a 6 mL chitin bead column, which had been pre-equilibrated with column buffer. After the sample was loaded onto the chitin column and incubated with the chitin affinity beads for 30 min at 4 °C, the column was washed with 20 volumes of the same buffer. The resin was then quickly washed with 1 column volume of the same buffer containing 50 mM DTT, and the effluent was reloaded. The column was clamped at both ends, and the intein tag was cleaved on-column from the fusion protein by incubating the column at 4 °C for 16 h. The purified protein was eluted using column buffer without DTT. The effluent was concentrated using a centrifugal filter device (Amicon Ultra, Millipore), divided into aliquots, and stored at 4 °C.

Cloning, Overexpression and Purification of the Full-Length Sialyltransferase from *Neisseria gonorrheae* (NgST). The steps performed for the cloning, overexpression, and purification of the full-length sialyltransferase from *Neisseria gonorrheae* (Genbank no. U60664) were performed exactly as previously mentioned except for the following distinctions. NgST used a pair of primers: the forward primer 5′ CCG GCA TAT GGG GTT GAA AAA AGT CTG TTT G 3′ (the *Nde*I restriction site is underlined) and the reverse primer 5′ GGC TCT TCC GCA GCC GCC ATT TTT ATC GTC AAA TGT 3′ (the *Sap*I restriction site is underlined) for PCR amplification of the full-length gene from *Neisseria gonorrheae*. NgST fusion protein expression was induced by adding 0.3 mM of IPTG followed by incubation at 16 °C for 16 h. NgST used Tris column buffer system (TrisHCl 20 mM pH 8.0, containing Triton X-100 0.1%, NaCl 500 mM, and EDTA 0.1 mM) for purification. After breaking cells, the insoluble fraction was pelleted by centrifugation at 4 °C, 24 000 *g*, for 1 h. The inclusion body pellet was resuspended in 10 mL of Tris column buffer. The suspension was stirred at 4 °C for 1 h and centrifuged at 4 °C, 24 000 *g* for 1 h to obtain NgST fusion protein, followed by affinity column purification as mentioned as PmST1.

Preparation of Amino-Functionalized Magnetic Nanoparticles (NH_2@MNP). Superparamagnetic nanoparticles (Fe_3O_4) were obtained by the coprecipitation of $FeCl_2$ and $FeCl_3$ under basic conditions. The surface of the particles was then transformed with a sol−gel process using tetraethyl orthosilicate (TEOS) followed by the addition of 3-amino-propyltrimethoxysilane (APS) to yield an amino-functionalized magnetic nanoparticle (NH_2@MNP). As shown in Scheme 1, the NH_2@MNP was used as starting material for the preparation of cysteine-functionalized magnetic nanoparticles.

Scheme 1[a]

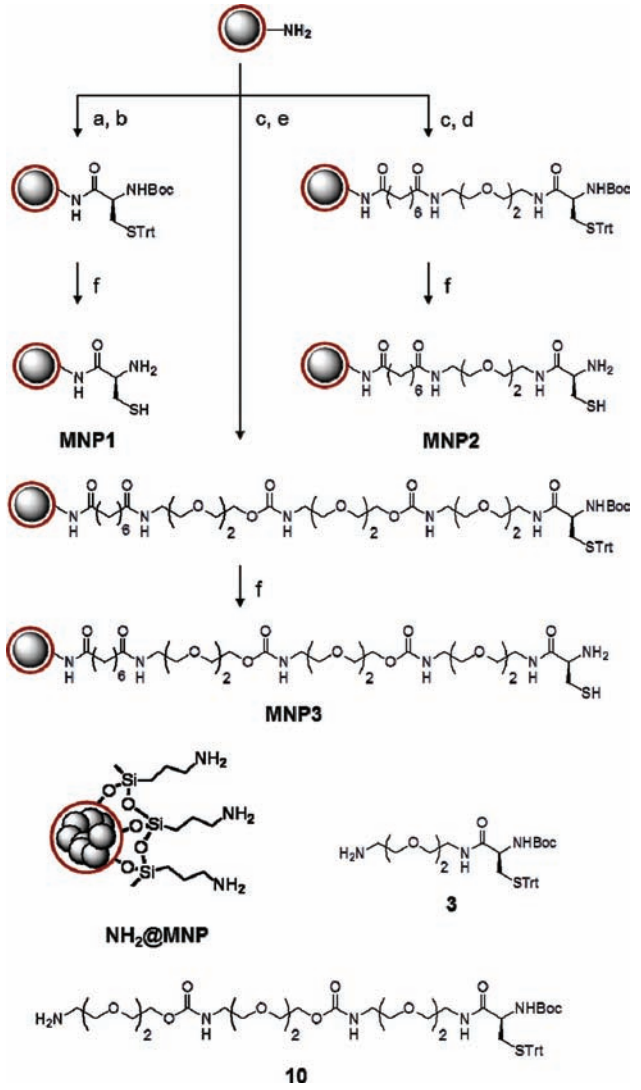

[a](a) Boc-Cys(Trt)-OH, EDC, HOBt, NEt_3, r.t., O/N, 97%; (b) acetic anhydride, pyridine, r.t., 3 h, 100%; (c) DSS, DMSO, r.t., 1 h, 81%; (d) **3**, DMF, 4 °C, O/N. 19%, then capping reagent; (e) **10**, DMF, 4 °C, O/N, 19%, then capping reagent; (f) TFA acid, triisopropylsilane, H_2O, r.t., 30 min, 100%.

Synthesis of Cysteine-Functionalized Magnetic Nanoparticles (MNP1). EDC (19.1 mg), HOBt (13.5 mg), triethylamine (15 μL), and Boc-Cys(Trt)-OH (47 mg) were added to a solution of amino-functionalized magnetic nanoparticles (50 mg) in dry dichloromethane (DCM, 2 mL). The resulting mixture was stirred for 12 h under nitrogen to obtain protected cysteine-functionalized magnetic nanoparticles. Then,

dx.doi.org/10.1021/bc200396r | *Bioconjugate Chem.* 2012, 23, 714−724

a pyridine/acetic anhydride mixture was added to the protected cysteine-functionalized magnetic nanoparticle, and the resulting solution was stirred at room temperature for 3 h. The acid-labile protecting group on the MNP was deprotected using a cocktail of reagents comprising trifluoroacetic acid (TFA, 1 mL), triisopropylsilane (TIPS, 33 μL), and deionized H_2O (32 μL) to obtain the cysteine-functionalized magnetic nanoparticle, **MNP1**.

Synthesis of Cysteine-Functionalized Magnetic Nanoparticles (MNP2). Aminated Fe_3O_4 nanoparticles (NH_2@MNPs) (1 mg) were dispersed into dimethyl sulfoxide (DMSO, 250 μL) and sonicated for 30 min. After sonication, suberic acid bis *N*-hydroxysuccinimide ester (DSS, 5 mg, 0.03 mmol) was added to the solution and stirred at room temperature for 1 h. The resulting nanoparticles were washed 3 times with DMSO (100 μL) to remove excess DSS. Cys **3** (200 μL, 50 mM) was added to the above black solid in DMF and shaken at room temperature for 12 h. The MNPs were separated using a magnet and washed 3 times with deionized H_2O. Ac_2O/pyridine (1/2, 300 μL) was then added and the mixture was stirred at room temperature for 3 h. Subsequently, 300 μL of 100 mM ethanolamine was added to the mixture and shaken at room temperature for 6 h. After separation by a magnet, the nanoparticles were washed 5 times with deionized H_2O to yield the protected cysteine-functionalized magnetic nanoparticle as a black powder. The acid-labile protecting groups on the MNPs were deprotected by following the procedures mentioned in the synthesis of **MNP1** above to yield **MNP2**.

Synthesis of Cys-Functionalized Magnetic Nanoparticles (MNP3). The synthesis of **MNP3** was similar to the described synthesis of **MNP2**, except that Cys **10** was used.

Site-Specific Immobilization of PmST1/NgST on Cys@MNPs. The cell lysate containing intein-fused PmST1/NgST was collected and applied to a 6 mL chitin bead column that had been pre-equilibrated with column buffer. After incubating at 4 °C for 30 min, the column was washed with 20 volumes of the same buffer. The resin was quickly washed with 1 volume of the same buffer containing 2-mercaptoethanesulfonic acid (MESNa, 300 mM) and tris(2-carboxyethyl)-phosphine hydrochloride (TCEP, 0.5 mM), and the effluent was then reloaded. The column was clamped at both ends, and the intein tag was cleaved on-column from the fusion protein by incubating the column at 4 °C for 16 h. The effluent was concentrated using a centrifugal filter device. To immobilize PmST1/NgST on the cysteine-functionalized MNPs, 30 μM of protein was reacted with 5 mg of cysteine-functionalized MNPs in 1 mL of HEPES buffer while vigorously shaking at room temperature for 12 h. The resulting enzyme@MNP complex was washed 3 times with HEPES column buffer.

Quantification of the Purified and MNP-Immobilized Proteins. The amount of protein on the MNPs was determined using the BCA Protein Assay Kit (PIERCE). To quantify the amount of protein on the MNPs, PmST1/NgST@MNPs were reacted with the BCA reagent at 60 °C for 30 min and then separated using a magnet. The absorbance of the separated reagent was measured at 562 nm. A standard curve was prepared by plotting the absorbance at 562 nm for each BSA standard vs its concentration (μg/mL). The standard curve was used to determine the protein concentration of each sample.

Sialyltransferase Activity Assay. Typically, the enzymatic assay was performed in a total volume of 50 μL in Tris-HCl buffer (100 mM, pH 8.5) containing $MgCl_2$ (20 mM), CMP-sialic acid (1 mM), lactose-Cy3 (0.59 mM), and the recombinant enzyme (22.5 ng). The reaction was allowed to proceed at 37 °C for 3 min and quenched by adding sodium dodecyl sulfate (SDS) (10%, 10 μL). The sample was analyzed using RP-HPLC with a reverse phase C18 column (Vydac 218TP54, GRACE) equipped with a C18 guard column system and a UV−vis detector. The fluorescent compounds, lactose-Cy3 and GM3-Cy3, were monitored at 550 nm and the system was controlled via the chromatography software. Solution A (deionized H_2O + 0.1% TFA) and solution B (acetonitrile) were prepared and used in two gradient conditions for the separation of the various compounds. The gradient conditions consisted of 100−64% A for 5 min, 64−53% A for 15 min, and 53−50% A for 5 min. The flow-rate was maintained at 1 mL/min for all separations. All assays were carried out in triplicate.

Kinetic Studies of PmST1 Sialyltransferase. Apparent kinetic parameters were obtained by varying the concentration of the fluorescent acceptor (0.25 mM, 0.5 mM, 1 mM, 2 mM, 4 mM, 8 mM) and using a fixed concentration of CMP-sialic acid (1 mM). All other components in the reaction mixture were the same as those described for the sialyltransferase activity assays. The reaction was then analyzed using RP-HPLC. The RP-HPLC peak areas were integrated, and the product concentration was calculated as a percentage of the total peak area. Initial velocity data were fit to the Michaelis−Menten equation using the computer software *KaleidaGraph*.

The synthetic scheme of linkers is shown in Scheme 2.

1-(*N*-α-*t*-Boc-*S*-Trityl-L-cysteinamido)-8-azido-3,6-dioxaoctane (2). Triethylamine (0.28 mL, 2 mmol) was added to a solution of Boc-Cys(Trt)-OH (463.6 mg, 1 mmol), **1** (209 mg, 1.2 mmol), EDC (382 mg, 2 mmol), and HOBt (270 mg, 2 mmol) in DCM. After stirring at room temperature for 16 h, the reaction was quenched using saturated $NaCl_{(aq)}$ and extracted with DCM. The organic layer was dried over $MgSO_4$, filtered, and evaporated. The crude product was purified by column chromatography to afford a white solid (497 mg, 80% yield); R_f: 0.2 (1:1 EtOAc-hexane); ^{1}H NMR (400 MHz, $CDCl_3$) δ 1.40 (s, 9H), 2.49 (dd, J = 5.2, 12.6 Hz, 1H), 2.68 (br, 1H), 3.33 (t, J = 5.0 Hz, 2H), 3.37−3.40 (m, 2H), 3.49 (t, J = 4.9 Hz, 2H), 3.56 (s, 4H), 3.62 (t, J = 4.8 Hz, 2H), 3.90 (br, 1H), 4.88 (br, 1H), 6.38 (br, 1H), 7.20 (t, J = 7.1 Hz, 3H), 7.24 (t, J = 7.8 Hz, 6H), 7.39 (d, J = 8.6 Hz, 6H); ^{13}C NMR (100 MHz, $CDCl_3$) δ 28.1, 34.1, 39.1, 50.4, 53.3, 66.9, 69.5, 69.8, 70.1, 70.3, 79.8, 126.7, 127.8, 129.4, 144.2, 155.1, 170.2; HRMS (ESI) calcd for $C_{33}H_{41}N_5O_5NaS$ $[M + Na]^+$: 642.2726, found: 642.2717.

1-(*N*-α-*t*-Boc-*S*-Trityl-L-cysteinamido)-8-amino-3,6-dioxaoctane (3). Palladium on charcoal (Pd/C) (30 mg; 5% Pd content) was added to a solution of **2** (310 mg, 0.5 mmol) in MeOH (5 mL). The flask was purged with H_2, and a hydrogen balloon was attached. After the mixture was stirred for 2.5 h, the catalyst was filtered out through a pad of Celite. The resulting solvent was removed *in vacuo*, and the residue was purified using flash silica gel column chromatography to obtain linker **3** as white foam (220 mg, 74% yield). R_f: 0.25 (1:4 MeOH−CH_2Cl_2); ^{1}H NMR (400 MHz, $CDCl_3$) δ 1.42 (s, 9H), 2.43−2.54 (m, 2H), 2.75 (t, J = 5.3 Hz, 2H), 3.27−3.36 (m, 2H), 3.47 (t, J = 5.3 Hz, 2H), 3.49 (br, 2H), 3.56 (s, 4H), 3.96 (t, J = 6.6 Hz, 1H), 7.21 (t, J = 6.1 Hz, 3H), 7.27 (t, J = 7.9 Hz, 6H), 7.38 (d, J = 7.6 Hz, 6H); ^{13}C NMR (100 MHz, $CDCl_3$) δ 28.27, 34.36, 39.26, 41.52, 53.38, 66.87, 69.68, 69.98, 70.32, 73.02, 79.89, 126.76, 127.95, 129.52, 144.42, 155.25 170.46;

dx.doi.org/10.1021/bc200396r | *Bioconjugate Chem.* 2012, 23, 714−724

Scheme 2[a]

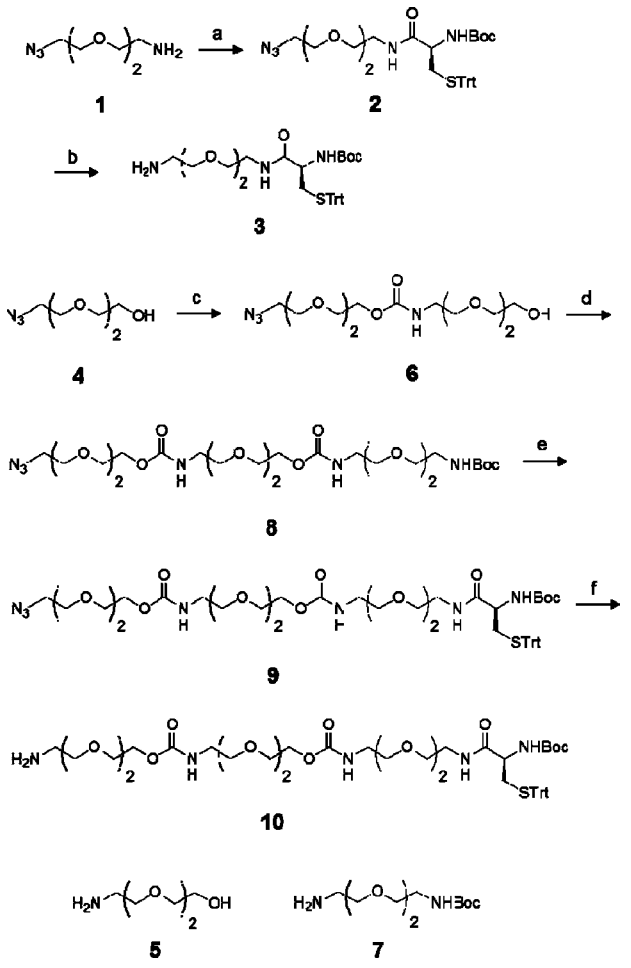

[a](a) Boc-Cys(Trt)-OH, EDC, HOBt, NEt_3, CH_2Cl_2, r.t., 16 h, 80%; (b) H_2, Pd/C, MeOH, r.t., 2.5 h, 74%; (c) NPCC, Pyr., CH_2Cl_2, r.t., 6 h, then **5**, NEt_3, CH_2Cl_2, r.t., 10 h, two steps 67%; (d) NPCC, Pyr., CH_2Cl_2, r.t., 6 h, then **7**, NEt_3, CH_2Cl_2, r.t., 10 h, two steps 70%; (e) TFA, MeOH. H_2O, r.t., 5 h, then Boc-Cys(Trt)-OH, HBTU, NEt_3, DMF, r.t., 10 h, two steps 83%; (f) PPh_3, THF, H_2O, r.t., 20 h, 85%.

HRMS (ESI) calcd for $C_{33}H_{44}N_3O_5S$ $[M + H]^+$: 594.3002, found: 594.3001.

***N*-{2-[2-(2-Hydroxyethoxy)ethoxy]ethyl}-2-[2-(2-azidoethoxy)ethoxy]ethoxy Ester (6).** Pyridine (1.84 mL, 22.7 mmol) was added to a solution of compound **4** (2.00 g, 11.36 mmol) in DCM (45 mL). After stirring at 0 °C for 5 min, 4-nitrophenyl chloroformate (2.52 g, 12.5 mmol) was added to the reaction mixture. The reaction mixture was then stirred for a further 6 h at room temperature, quenched using $NaHCO_3$ (10 mL), and diluted with ethyl acetate. The mixture was subsequently washed with saturated $NaCl_{(aq)}$ (10 mL). The organic phase was dried (using $MgSO_4$) and concentrated. The residue was used for the next reaction without further purification. A monoamine-linker **5** (2.03 g, 13.63 mmol) and triethylamine (2.37 mL, 17.04 mmol) were added to a solution of the residue in DCM (14 mL) at room temperature. After stirring at room temperature for 10 h, the reaction mixture was concentrated. The residue was purified using silica gel chromatography (50% gradient ethyl acetate in hexane + 10% MeOH) to afford **6** (2.66 g, 67% yield for two steps). ^{1}H NMR (400 MHz, $CDCl_3$) δ 2.78 (s, 1 H), 3.34 (q, J = 4.9 Hz, 4 H), 3.52 (t, J = 5.0 Hz, 2 H), 3.54−3.57 (m, 2 H), 3.59−3.65 (m, 12 H), 3.69−3.72 (m, 2 H), 4.17 (t, J = 4.2 Hz, 2 H), 5.53 (s, 1 H); ^{13}C NMR (100 MHz, $CDCl_3$) δ 40.56, 50.42, 61.36, 63.66, 69.44, 69.85, 70.04, 70.12, 70.29, 70.38, 72.38, 156.39. HRMS (ESI-TOF) Calcd for $C_{13}H_{26}N_4O_7Na$ $[M + Na]^+$: 373.1699, found: 373.1692.

5,8,13,16,19,24,27,30-Octaoxa-2,11,22-triazalacceroic acid,32-azido-12,23-dioxo-1,1-dimethylethyl Ester (8). Compound **8** was synthesized from compound **6** using a method similar to that described for the synthesis of compound **6** with 70% yield (yield for two steps): ^{1}H NMR (400 MHz, $CDCl_3$) δ 2.78 (s, 1 H), 3.34 (q, J = 4.9 Hz, 4 H), 3.52 (t, J = 5.0 Hz, 2 H), 3.54−3.57 (m, 2 H), 3.59−3.65 (m, 12 H), 3.69−3.72 (m, 2 H), 4.17 (t, J = 4.2 Hz, 2 H), 5.53 (s, 1 H); ^{13}C NMR (100 MHz, $CDCl_3$) δ 40.56, 50.42, 61.36, 63.66, 69.44, 69.85, 70.04, 70.12, 70.29, 70.38, 72.38, 156.39. HRMS (ESI-TOF) Calcd for $C_{13}H_{26}N_4O_7Na$ $[M + Na]^+$: 373.1699, found: 373.1692.

8,11,16,19,22,27,30,33-Octaoxa-2,5,14,25-tetraazaceroplastic acid,35-azido-4,15,26-trioxo-3-{[(triphenylmethyl)thio]methyl}-1,1-dimethylethyl Ester (9). A mixture of TFA (1.30 mL) and water (0.10 mL) was added dropwise to a solution of compound **8** (0.20 g, 0.32 mmol) in DCM (2.60 mL). After stirring at room temperature for 5 h, the reaction mixture was neutralized with DOWEX 550 (OH-) resin, filtered, and evaporated *in vacuo*. The resulting amine was used for the next reaction without further purification. To a solution of Boc-Cys(Trt)-OH (0.13 g, 0.28 mmol) in DCM (2.40 mL), *O*-benzotriazole-*N*,*N*,*N*′,*N*′-tetramethyl-uronium-hexafluoro-phosphate (0.16 g, 0.42 mmol) was added at 0 °C. The resulting solution was stirred at 0 °C for 10 min, and an aliquot of the amine crude product and diisopropylethylamine (87 mL, 0.56 mmol) in DMF (0.60 mL) were added slowly to the reaction vessel. After stirring at room temperature for 10 h, the reaction mixture was diluted with ethyl acetate, and the resulting organic layer was washed with $NaCl_{(aq)}$ (10 mL). The organic phase was dried (using $MgSO_4$) and concentrated. The residue was purified using silica gel chromatography (50% gradient ethyl acetate in hexane + 10% MeOH) to afford compound **9** (0.22 g, 83% yield for two steps): ^{1}H NMR (400 MHz, $CDCl_3$) δ 1.36 (s, 9 H), 2.58−2.70 (m, 2 H), 3.28−3.33 (m, 4 H), 3.36 (t, J = 4.7 Hz, 4 H), 3.44−3.52 (m, 10 H), 3.54−3.58 (m, 4 H), 3.60−3.68 (m, 10 H), 3.82−3.88 (m, 1 H), 4.15−4.23 (m, 4 H), 5.00 (s, 1 H), 5.48 (s, 1 H), 5.64 (s, 1 H), 6.53 (s, 1 H), 7.17 (t, J = 7.1 Hz, 3 H), 7.25 (t, J = 7.5 Hz, 6 H), 7.35 (d, J = 7.6 Hz, 6 H). ^{13}C NMR (100 MHz, $CDCl_3$) δ 28.14, 29.15, 33.84, 39.14, 40.61, 50.50, 63.78, 63.95, 66.99, 69.57, 69.75, 69.88, 69.99, 70.23, 70.28, 70.49, 80.20, 126.81, 127.95, 129.43, 144.27, 155.29, 157.12, 177.16. HRMS (ESI-TOF) Calcd for $C_{47}H_{67}N_7O_{13}NaS$ $[M + Na]^+$: 992.4415, found: 992.4426.

8,11,16,19,22,27,30,33-Octaoxa-2,5,14,25-tetraazaceroplastic acid,35-amino-4,15,26-trioxo-3-{[(triphenylmethyl)thio]methyl}-1,1-dimethylethyl Ester (10). To a solution of compound **9** (80 mg, 0.082 mmol) in tetrahydrofuran (0.40 mL) and water (0.40 mL), triphenylphosphine (43 mg, 0.165 mmol) was added. After stirring at room temperature for 20 h, the reaction mixture was concentrated. The residue was purified using silica gel column chromatography (50% gradient methanol in dichloromethane) to afford compound **10** (63 mg, 83% yield): ^{1}H NMR (400 MHz, D_2O/CD_3OD) δ 1.41 (s, 9 H), 2.48−2.54 (m, 2 H), 3.14 (t, J = 4.9 Hz, 2 H), 3.26−3.34 (m, 6 H), 3.48−3.58 (m, 10 H), 3.60−3.64 (m, 4 H), 3.66−3.74 (m, 10 H), 3.90 (t, J = 6.1 Hz,

dx.doi.org/10.1021/bc200396r | *Bioconjugate Chem.* 2012, 23, 714−724

1 H), 4.14−4.24 (m, 4 H), 7.23 (t, J = 6.9 Hz, 3 H), 7.29 (t, J = 7.4 Hz, 6 H), 7.35 (d, J = 7.3 Hz, 6 H). ^{13}C NMR (150 MHz, D_2O/CD_3OD) δ 28.69, 30.56, 35.36, 40.35, 40.60, 41.57, 55.07, 64.14, 64.97, 65.09, 67.73, 67.96, 70.37, 70.45, 70.85, 71.09, 71.15, 71.36, 81.22, 128.04, 129.07, 130.62, 145.80, 157.28, 158.92, 173.03. HRMS (ESI-TOF) Calcd for $C_{47}H_{70}N_5O_{13}S$ $[M + H]^+$: 944.4691, found: 944.4681.

C-terminal Cysteine Modified NgST. The cell lysate containing intein-fused NgST was collected and applied to a 6 mL chitin bead column that had been pre-equilibrated with column buffer. After incubating at 4 °C for 30 min, the column was washed with 20 volumes of column buffer. As shown in Scheme 3, the resin was then quickly washed with 1 column volume of the same buffer containing MESNa (300 mM), TCEP (0.5 mM), and 1 mM of the cysteine derivatives, and the effluent was reloaded. The column was clamped at both ends, and the intein tag was cleaved on-column from the fusion protein by incubating the column at 4 °C for 16 h. The effluent was concentrated using a centrifugal filter device, divided into aliquots, and stored at 4 °C.

Scheme 3. Site-Specific Immobilization of NgST on MNPs through the Biotin−Streptavidin Interaction[a]

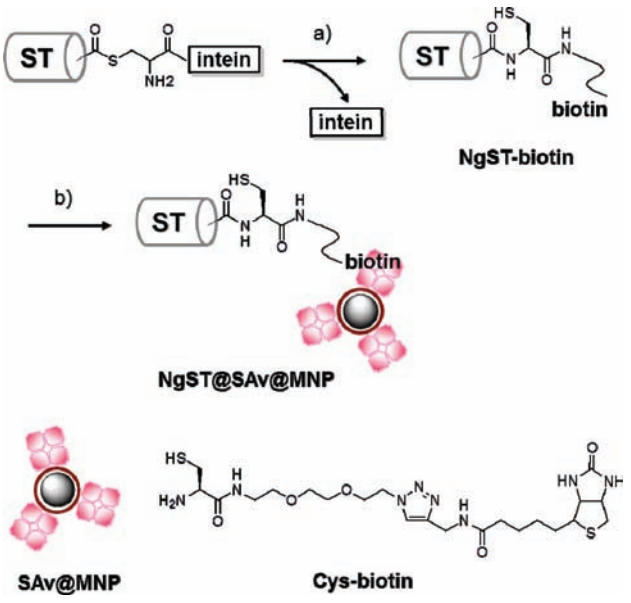

[a](a) Tris-HCl (20 mM), pH 8.0, MESNa (200 mM), TCEP 0.5 mM, Cys-biotin 1 mM, 16 h, 4 °C, then dialysis for 2 days, 4 °C; (b) Tris-HCl (20 mM), pH 8.0, SAv-MNP, 1 h, 4 °C. MESNa, 2-mercaptoethanesulfonic acid; TCEP, tris(2-carboxyethyl)phosphine; SAv@MNP, streptavidin-functionalized magnetic nanoparticles.

Immobilization of NgST-Biotin on Streptavidin@MNP. Cysteine-modified NgST (1 mL, 30 μM) was incubated with **SAv@MNP** (5 mg) in 1 mL of Tris column buffer and vigorously shaken at 4 °C for 1 h. The resulting enzyme@MNP complex was washed 3 times with Tris column buffer.

Recycling of Enzyme@MNPs. **PmST1@MNP3** and **CSS@MNP3** were used in a one-pot−two-enzyme@MNP system for the synthesis of GM3-Cy3. The reaction was carried out in 250 μL Tris-HCl buffer (100 mM, pH 8.5) containing lactose-Cy3 (1.1 mg, 1.25 mmol), CTP (1.32 mg, 2.5 mmol), sialic acid (0.775 mg, 2.5 mmol), $MgCl_2$ (20 mM), **PmST1@MNP3** (225 ng/PmST1), **CSS@MNP** (2.5 ng/CSS), and inorganic pyrophosphatase (0.4 U). After incubation at 37 °C for 3 min, the enzyme@MNPs were recovered by applying a magnet and washed with Tris buffer (100 mM, pH 8.5) for 3 times. The recovered enzyme@MNPs were used for next reaction. The procedure was repeated 10 times as described above.

RESULTS AND DISCUSSION

Synthesis and Characterization of Cys@MNPs. Recently, it was demonstrated that site-specific protein immobilization can provide higher protein activity than random immobilization.[26,41,52,54,55] However, compared to free protein, activity is decreased.[52] In an attempt to further increase immobilized protein activity in this study, different lengths of hydrophilic ethylene glycol linkers[56] were used to modify the surface of MNPs. The addition of a linker provided a spacer, which minimized steric hindrance between the enzyme and the solid supports, and also increased the flexibility of the immobilized enzyme.[57] Cysteine functionalized magnetic nanoparticles were then synthesized to react with the corresponding protein α-thioester through NCL[58] to achieve site-specific protein immobilization. The synthesis of the amine-functionalized MNP (NH_2@MNP) was achieved using a reported method (see Supporting Information, SI, Figures S1 and S2).[39] As shown in Scheme 1, Boc-Cys(Trt)-OH was conjugated with NH_2@MNP via amide bond formation and then capped with acetic anhydride in the presence of pyridine, forming a black powder. The product was then deprotected using trifluoroacetic acid (TFA) and triisopropylsilane (TIPS) to yield **MNP1**.

To investigate the effect of the length of the linker between the immobilized enzyme and the MNP surface, PEG-functionalized cysteine moieties **3** and **10** were synthesized (Schemes 1 and 2) and assembled on the MNP. As shown in Scheme 2, the amino group of compound **1**[57] was coupled with Boc-Cys(Trt)-OH to obtain compound **2**, which was then hydrogenated to yield linker **3**. To elongate the linker, 4-nitrophenyl chloroformate (NPCC) was used as bridge to conjugate ethylene glycol moieties.[59] In this way, the hydroxyl group of compound **4** was reacted with NPCC to form the carbamate compound, which was reacted with the amine group of compound **5**[56] to afford linker **6** with a total yield of 67% in two steps. Similar reactions were performed from **7**[56] to synthesize the long linker, **8**. The Boc group of linker **8** was deprotected and coupled with Boc-Cys(Trt)-OH using 2-(1*H*-benzotriazole-1-yl)-1,1,3,3-tetramethyluronium hexafluorophosphate (HBTU) to obtain compound **9**. The Staudinger reduction was applied to reduce the azide of compound **9** to obtain linker **10**. As shown in Scheme 1, linkers **3** and **10** were respectively incubated with *N*-hydroxy-succinimide (OSu)-activated MNPs (OSu@MNP), which were prepared by incubating NH_2@MNP with disuccinimidyl suberate (DSS) followed by capping with acetic anhydride and ethanolamine to obtain black powders. Removal of the protecting groups on the MNPs by TFA and TIPS yielded **MNP2** and **MNP3**, respectively. The introduction of an ethylene glycol linker on **MNP2** and **MNP3** resulted in a better suspension in aqueous solutions than **MNP1**. The capping steps were performed to block the nonreacted amine and activated ester on the MNP surface, thereby reducing the nonspecific reaction between the functionalized MNPs and the target molecule. The amount of cysteine on the MNPs was indirectly estimated by a colorimetric amine assay.[60] The amount of amino groups on the NH_2@MNPs was determined to be 95.56 nmol/mg MNP,

dx.doi.org/10.1021/bc200396r | Bioconjugate Chem. 2012, 23, 714−724

whereas that for the MNPs treated with DSS and ethylenediamine was estimated to be 17.75 nmol/mg MNP. The results demonstrate a low overall coupling efficiency when using DSS. Thus, **MNP2** and **MNP3** prepared by the OSu-activated ester coupling were anticipated to have a lower surface density of cysteine compared to **MNP1**, which was prepared by direct amino acid coupling.

Immobilization and Characterization of PmST1 and CSS. Glycosyltransferases are less robust than hydrolases, and therefore their activities may be more sensitive to the immobilization method used.[23] To test this hypothesis, we chose PmST1 as a target enzyme in this study. Accordingly, we overexpressed the gene-encoded PmST1 in *E. coli* using the commercially available IMPACT (intein-mediated purification with an affinity chitin-binding tag) vector system to produce the PmST1-intein fusion protein. To reduce potential nonspecific protein adsorption, we purified the PmST1 as a protein α-thioester by treating 2-mercaptoethanesulfonic acid (MESNa) during the affinity separation to exchange intein with MESNa. **MNP1**, **MNP2**, and **MNP3** were incubated with purified PmST1 in the presence of MESNa for 12 h at room temperature, and the enzyme was immobilized on the MNPs at its C-terminus using NCL to obtain **PmST1@MNP1**, **PmST1@MNP2**, and **PmST1@MNP3**, respectively (Figure 2a). The conjugation efficiency was determined by measuring

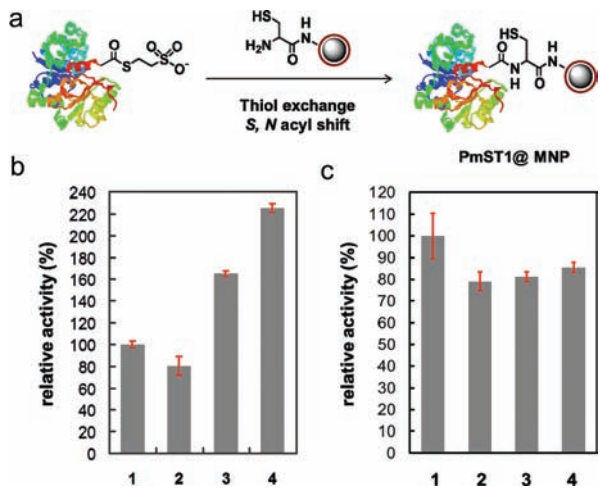

Figure 2. Relative activities of immobilized PmST1 and CSS. (a) Immobilization of PmST1 on MNPs. (b) Relative activities of immobilized PmST1: column 1, free PmST1; column 2, site-specific immobilized **PmST1@MNP1**; column 3, site-specific immobilized **PmST1@MNP2**; and column 4, site-specific immobilized **PmST1@MNP3**. (c) Relative activities of immobilized CSS: column 1, free CSS; column 2, site-specific immobilized **CSS@MNP1**; column 3, site-specific immobilized **CSS@MNP2**; and column 4, site-specific immobilized **CSS@MNP3**.

the amount of protein on the MNPs using a BCA protein assay.[52] The amount of protein per mg of enzyme@MNP complex was determined to be 38.4, 18.9, and 22.4 μg for **PmST1@MNP1**, **PmST1@MNP2**, and **PmST1@MNP3**, respectively. **PmST1@MNP1** contained a greater amount of protein on the surface of the nanoparticle than **PmST1@MNP2** or **PmST1@MNP3**. This may have resulted from the greater density of cysteine on the surface of **MNP1**, leading to a greater concentration of effective cysteine moieties available to react with protein. The greater amount of protein on **PmST1@MNP3** than on **PmST1@MNP2** may have resulted from steric effects. Because the thioester enzyme reacts with cysteine, which is located on the outermost surface, longer linkers result in a decrease in steric hindrance during NCL and provide greater coupling efficiency. We also prepared **MNP4**, a derivative of **MNP3**, from a high amine density MNP and subsequently immobilized PmST1 to give **PmST1@MNP4**, which was found to contain a high concentration of protein on its surface (57.7 μg/mg MNP), but the enzymatic activity was lower than that of **PmST1@MNP3**. Similarly, the lower enzyme activity was also observed in the case of **PmST1@MNP1** which shows related higher density of immobilized enzyme on the nanoparticle surface. Thus, the close packing of the enzyme on the surface of MNPs likely prevented enzyme flexibility, leading to a lower overall reaction yield.

Evaluation of PmST1@MNP Activity. To evaluate the activity of immobilized PmST1, we used a RP-HPLC assay to measure the decrease of a lactose-Cy3 substrate and the formation of the GM3-Cy3 product. The PmST1-catalyzed reaction was performed in Tris-HCl buffer (pH 8.5) containing $MgCl_2$, lactose-Cy3, and CMP-sialic acid. The reaction was initiated by adding sialyltransferase, and the resulting mixture was shaken at 37 °C for 3 min and stopped by adding SDS. The resultant precipitate was filtered through a 0.22 mm membrane and analyzed using RP-HPLC. The site-specifically immobilized **PmST1@MNP1** remained 80% active (compared to free PmST1) (Figure 2b). The loss of approximately 20% activity by the immobilized enzyme agrees with previous observations[52] (see Figure 2c). The decrease in activity may be caused by the large size of the MNP, which decreases the enzyme dynamics in solution resulting in a lower reaction rate. Surprisingly, the activities of **PmST1@MNP2** and **PmST1@MNP3** were enhanced to 165% and 225%, respectively, as shown in Figure 2b. The higher enzymatic activities of **PmST1@MNP2** and **PmST1@MNP3** may be caused by the increased length of the linker distancing the immobilized PmST1 away from the solid support, thereby increasing the enzyme dynamics and flexibility on the surface.

To further confirm the enhancement of enzyme activity after immobilization, CSS was overexpressed and immobilized on **MNP1**, **MNP2**, and **MNP3** to yield **CSS@MNP1**, **CSS@MNP2**, and **CSS@MNP3**, respectively. The initial rate of CMP-sialic acid production and the decrease in the CTP substrate were measured using RP-HPLC. Compared to free CSS, the relative activities of **CSS@MNP1**, **CSS@MNP2**, and **CSS@MNP3** were 80%, 81%, and 86%, respectively, as shown in Figure 2c. The activity of CSS@MNP1 measured here is almost fitted with earlier published data.[52] Although the activity of the immobilized enzyme increased with linker length, the activity of the immobilized enzyme did not exceed the activity of the free enzyme. In general, the activity of immobilized enzyme should not be greater than that of free enzyme, as the protein dynamics decrease after conjugation with a bulky solid support. However, for PmST1, the immobilized enzyme exhibited a promising enhancement of activity. To further understand the intrinsic properties of the differences in activity, we studied the kinetics of the immobilized enzyme.

Kinetics of Immobilized PmST1. The kinetic behavior of PmST1 was examined before and after immobilization. The kinetic parameters of free PmST1, **PmST1@MNP1**, **PmST1@MNP2**, and **PmST1@MNP3** were measured using RP-HPLC under saturating conditions of CMP-sialic acid and various concentrations of lactose-Cy3 in Tris buffer (pH 8.5). The

dx.doi.org/10.1021/bc200396r | *Bioconjugate Chem.* 2012, 23, 714–724

Table 1. Comparison of the Kinetic Parameters of PmST1 Immobilized on Different MNPs Using Lactose-Cy3 as the Acceptor[a]

enzyme@MNP complex	V_{max} (mM/min)	K_M (mM)	k_{cat} (min^{-1})	k_{cat}/K_M (mM^{-1} min^{-1})	protein loading rate (μg/mg MNP)
PmST1	0.559	9.80	5.59×10^4	5.70×10^3	-
PmST1@MNP1	0.128	3.85	1.28×10^4	3.32×10^3	38.36 ± 4.95
PmST1@MNP2	0.125	1.29	1.25×10^4	9.69×10^3	18.94 ± 0.25
PmST1@MNP3	0.136	0.95	1.36×10^4	1.43×10^4	22.45 ± 0.65

[a]Reactions were carried out under saturation concentration of CMP-sialic acid at 1 mM with varying concentrations of Lactose-Cy3.

results were obtained by fitting the curve to the Michaelis–Menten equation (Table 1). The specific activity of free PmST1 was determined to have a turnover number (k_{cat}) of 5.59×10^4 min^{-1}, a maximum reaction rate (V_{max}) of 0.559 mM/min, and a Michaelis–Menten constant (K_M) of 9.8 mM. The site-specifically immobilized **PmST1@MNP1**, **PmST1@MNP2**, and **PmST1@MNP3** exhibited low k_{cat} and V_{max} values, which were 1.28×10^4 min^{-1}, 1.25×10^4 min^{-1}, and 1.36×10^4 min^{-1}; and 0.128 mM/min, 0.125 mM/min, and 0.136 mM/min, respectively. Values of K_M were improved and found to be 3.85 mM, 1.29 mM, and 0.95 mM, respectively. The immobilization of the enzyme on bulky MNPs decreased enzyme flexibility, resulting in a decrease of catalytic activity. Thus, the apparent V_{max} and k_{cat} values of the immobilized enzyme were lower than those of free enzyme. Notably, the k_{cat} of PmST1@MNP remained constant while its K_M values exhibited significant differences. The K_M value of an enzyme reflects its affinity for a substrate. Thus, the decreased K_M of PmST1@MNPs indicated that the immobilized enzyme provided higher substrate affinity than free PmST1. The higher substrate affinity of immobilized PmST1 is most likely due to either partitioning effect,[6] which result in the nonspecific adsorption of lactose-Cy3 to the MNP surface, or a structural change in the active site of the enzyme after immobilization. **PmST1@MNP3**, which contains the longest linker, had the highest activity of the three immobilized PmST1@MNPs. This could be caused by the flexibility of the enzyme when linked with a long linker, providing greater substrate accessibility. However, the charged lactose fluorescent tag may have caused nonspecific interaction. To investigate the effect of the fluorescent tag, lactose-dansyl and lactose-FITC (fluorescein isothiocyanate) were synthesized, and their reaction rates were evaluated. The site-specifically immobilized **PmST1@MNP3** retained 53.5% and 38.4% of the activity of free PmST1 when using lactose-dansyl and lactose-FITC as substrates, respectively (see SI Figure S3). The results indicated that lactose-dansyl and lactose-FITC might not be favored to be adsorbed to the surface of **PmST1@MNP3** by nonspecific interaction. Therefore, the enzyme did not react with substrates easily, resulting in lower enzymatic activities. Additionally, the reactivity of free PmST1 with both lactose-dansyl and lactose-FITC was investigated. Neither substrate showed a substantial improvement of reaction rate over that observed when using lactose-Cy3 as the acceptor (see SI Figure S4), indicating that the fluorescent tag indeed affected the reaction.[61]

Immobilization of NgST on MNPs. To further evaluate enzyme immobilization, we tested membrane-bound α-2,3-sialyltransferase (NgST) from *Neisseria gonorrheae* F62, which was expressed and purified using previously described methods.[53] However, NgST is a membrane-bound protein, and this typically results in low expression yield and poor solubility.[53,62,63] The purified NgST α-thioester was incubated separately with **MNP1** and **MNP3** in the presence of MESNa to yield **NgST@MNP1** and **NgST@MNP3**, respectively. **NgST@MNP1** and **NgST@MNP3** retained only 7.5% and 18.1% of the activity of purified free NgST, respectively. Because NgST contains four cysteines, which may form two disulfide bonds, the presence of a large amount of cysteine on the MNP surface may cause the cleavage of such disulfide bonds, resulting in denaturation of the immobilized enzyme. For this reason, we adjusted the amount of cysteine on the surface of the MNPs by dilution with glycine moieties during the acid-amine coupling step (SI Table S1). However, reducing the cysteine density on the MNPs did not improve the enzyme activity. Therefore, we needed a different strategy for the site-specific immobilization of NgST. It has previously been demonstrated that the cycloaddition of 1,3-dipolar alkyne/azide using click chemistry is a very efficient chemical conjugation technique for the site-specific immobilization of proteins onto solid surfaces from their C-terminals while retaining protein activity.[54,55] Therefore, we fused the C-terminal of NgST with alkyne or azide using expression protein ligation.[55] Although the C-terminally modified NgST retained its activity (>95%), the enzyme completely lost its activity under click chemistry conditions due to the toxicity of Cu(I) to the enzyme[64] (Table 2 and SI Table S1). These results indicate

Table 2. Relative Activity of Immobilized NgSTs Obtained Using Different Site-Specific Immobilization Strategies

entry	ST	MNPs	ligation condition	relative activity (%)
1	azido ST	alkynated MNP	rt, 12 h	[a]
2	alkynated ST	azido MNP	rt, 12 h	[a]
3	NgST-MESNa	MNP1	rt, 12 h	7.5
4	NgST-MESNa	MNP3	rt, 12 h	18.1
5	NgST-biotin	SAv@MNP	4 °C, 1 h	34

[a]No product formation. The relative activity was measured by RP-HPLC.

that the small-molecule-modified MNPs might not provide a suitable surface for the site-specific immobilization of membrane-bound enzymes.

Previously, Wakarchuk and co-workers expressed CSS-fused NgST and demonstrated improved solubility of NgST while retaining activity.[63] These findings provide an attractive approach to the retention of immobilized enzyme activity by introducing a "protein surface" onto MNPs. Taking advantage of the specific recognition between streptavidin (SAv) and biotin ($K_D = 10^{-15}$ M^{-1}, almost as strong as a covalent bond), the biotin-tagged protein can be immobilized on a streptavidin-functionalized solid support. Thus, we fabricated SAv immobilized MNP (**SAv@MNP**) using random amide bond formation between the protein amines and OSu@MNP. As shown in Scheme 3, intein-fused NgST was purified using a chitin bead column and then treated with MESNa in the

dx.doi.org/10.1021/bc200396r | Bioconjugate Chem. 2012, 23, 714–724

presence of biotinylated cysteine (**Cys-biotin**). **NgST-biotin** was then obtained using NCL, which was performed under very mild reaction conditions (pH 8.0, 4 °C) to protect the enzyme from denaturation and degradation. Notably, the concentration of **Cys-biotin** was controlled at 1 mM to prevent any decrease in enzyme activity. Interestingly, **NgST-biotin** retained >95% enzymatic activity after modification. The desired **NgST-biotin** was analyzed using SDS-PAGE and Western blot analysis, and biotin-specific stain was used to verify the success of ligation (see SI Figure S5). After removal of the unreacted **Cys-biotin** using dialysis, we incubated the **NgST-biotin** with **SAv@MNP** under mild conditions (Tris buffer, pH 8.0, 4 °C, 1 h) to yield the site-specific and noncovalently bound immobilized **NgST-SAv@MNP** complex. The biotin–streptavidin immobilization method provided approximately a 2-fold increase in enzyme activity on the MNP compared to the direct NCL immobilization method and retained 34% of the **NgST-biotin** activity (Table 2, entry 5). The decreased effect of the "protein" linker on the activity of the immobilized enzyme compared to that observed using small molecules may arise from two factors: (1) the surface properties of **SAv@MNP** and (2) the lower reaction temperature and shorter reaction time of the immobilization procedure. Although the immobilized enzyme does not retain high activity, this study demonstrates that several approaches should be considered when immobilizing soluble and membrane-bound enzymes.

Reusability and Productivity of enzyme@MNPs. It is important that immobilized enzymes be operationally stable without significant loss of their activity for an immobilized enzyme to be economically advantageous in a synthetic process. Therefore, we evaluated the potential for reuse of the immobilized enzymes in the synthesis of the GM3 derivative. By combining **PmST1@MNP3** with **CSS@MNP3**, we developed a one-pot–two-enzyme@MNP system for the synthesis of GM3 (Figure 3a). Initially, the reusability of **PmST1@MNP3** and **CSS@MNP3** was determined by assessing the enzyme activities of the recovered enzyme@MNPs from repeated reactions. After vigorously mixing with substrates for 3 min to allow the reaction to proceed, the enzyme@MNPs were separated from the solution using a magnet. The remaining solution was analyzed by HPLC to determine how much GM3-Cy3 was formed. The enzyme@MNPs were recovered and washed with Tris buffer, and directly reused for the next, identical assay. As shown in Figure 3b, the total efficiency of the one-pot–two-enzyme@MNP system remained at 50% of its initial activity after 10 cycles. These results demonstrate the feasibility of recycling these immobilized enzymes.

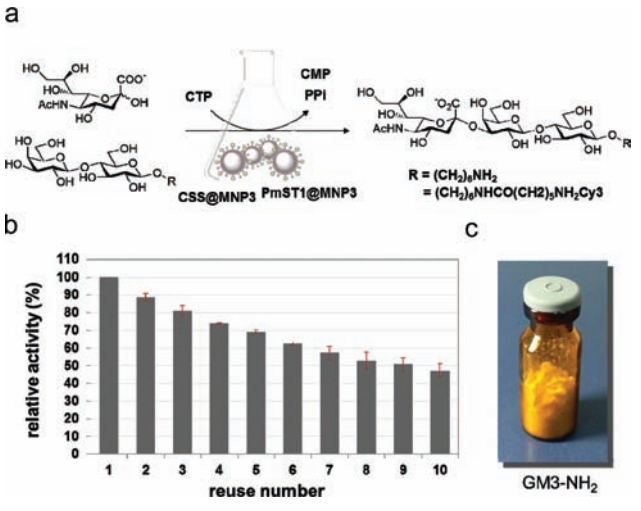

Figure 3. One-pot–two-enzyme@MNP system for reuse and synthesis of GM3-NH_2. (a) **PmST1@MNP3** and **CSS@MNP3** were used in a one-pot–two-enzyme@MNP system to synthesize GM3 derivatives. (b) The reusability of the one-pot–two-enzyme@MNP system. The relative activity was analyzed by RP-HPLC using lactose-Cy3 as the acceptor for UV–vis detection. (c) 100 mg scale synthesis of GM3-NH_2 was performed using a one-pot–two-enzyme@MNP system, and the crude product was further purified using size-exclusion column chromatography.

To further demonstrate the practical application of **PmST1@MNP3** and **CSS@MNP3** in carbohydrate synthesis, we used the one-pot–two-enzyme@MNP system to synthesize a GM3 derivative on 100 mg scale. **PmST1@MNP3** and **CSS@MNP3** were incubated with CTP, sialic acid, and lactose-NH_2, and the reaction mixture was vigorously stirred for 4 h at 37 °C. Subsequently, the enzyme@MNPs were easily separated using a magnet, and the solution was added to an equal volume of EtOH. Insoluble precipitates were removed by centrifugation, after which the supernatant was concentrated and applied to a P-2 gel filtration column to obtain 202 mg (61% yield) of the GM3 derivative of purity >98% after one trial (Figure 3c). These results demonstrate the advantage of using immobilized enzymes to simplify the purification of desired products.

■ CONCLUSIONS

PmST1 was site-specifically immobilized on ethylene glycol functionalized MNPs using NCL. The resulting enzyme demonstrated greater activity than the free enzyme. The increase of enzyme activity may be due to an intriguing nonspecific interaction between the fluorescent tag of the substrate and the surface of the MNP, which is supported by the observation that the charged fluorescent tag on the substrate affected the activities of the free enzyme and enzyme@MNPs. Therefore, the use of fluorescent tag-conjugated substrates in enzyme kinetic analysis should be considered cautiously. In addition, the length of the hydrophilic ethylene glycol linker affected enzyme activity: the longer the linker, the greater the activity of the immobilized enzyme and the higher the loading efficiency of the protein on the solid support. However, the close packing of the enzymes on the surface of the MNPs likely prevented their flexibility, leading to a lower overall reaction yield.

The hydrophilic surface of the MNP can be an attractive choice for the immobilization of water-soluble enzymes. However, to immobilize the membrane-bound α-2,3-sialyltransferase NgST, a protein surface was required on the MNP to retain the stability of the immobilized enzyme. By taking advantage of the specific recognition and tight binding between streptavidin and biotin, we were able to immobilize the C-terminal biotinylated NgST on the SAv@MNPs to prevent the enzyme deactivation caused by aggregation. Due to their small (nanoscale) size, the MNPs maximized the surface area available for enzyme attachment. In addition, the MNPs were easily recovered from aqueous suspensions by applying a magnetic field. By combining **PmST1@MNP3** and **CSS@MNP3**, we developed a one-pot–two-enzyme@MNP system to prepare a 100-mg-scale reaction of a desired carbohydrate while retaining 50% activity after ten consecutive uses. These

features of the enzyme@MNPs make them useful in organic synthesis.

■ ASSOCIATED CONTENT

Supporting Information

Additional figures and tables as described in the text. This material is available free of charge via the Internet at http://pubs.acs.org.

■ AUTHOR INFORMATION

Corresponding Author

*Tel: (+) 886-3-5753147. E-mail: cclin66@mx.nthu.edu.tw.

■ ACKNOWLEDGMENTS

This work was financially supported by the National Tsing Hua University, Academia Sinica, and the National Science Council, Taiwan.

■ REFERENCES

(1) Drauz, K., and Waldmann, H. (2002) *Enzyme Catalysis in Organic Synthesis: A Comprehensive Handbook*, Vol. *I-III*, Wiley-VCH, Weinheim.

(2) Koeller, K. M., and Wong, C.-H. (2001) Enzymes for chemical synthesis. *Nature 409*, 232−240.

(3) Schmid, A., Dordick, J. S., Hauer, B., Kiener, A., Wubbolt, M., and Witholt, B. (2001) Industrial biocatalysis today and tomorrow. *Nature 409*, 258−268.

(4) Toscano, M. D., Woycechowsky, K. J., and Hilvert, D. (2007) Minimalist active-site redesign: teaching old enzymes new tricks. *Angew. Chem., Int. Ed. 46*, 3212−3236.

(5) Sheldon, R. A. (2007) Enzyme immobilization: the quest for optimum performance. *Adv. Synth. Catal. 349*, 1289−1307.

(6) Hanefeld, U., Gardossi, L., and Magner, E. (2009) Understanding enzyme immobilization. *Chem. Soc. Rev. 38*, 453−468.

(7) Mateo, C., Palomo, J. M., Fernandez-Lorente, G., Guisan, J. M., and Fernandez-Lafuente, R. (2007) Improvement of enzyme activity, stability and selectivity via immobilization techniques. *Enzyme Microb. Technol. 40*, 1451−1463.

(8) Cao, L. (2005) Immobilised enzymes: science or art? *Curr. Opin. Chem. Biol. 9*, 217−226.

(9) Dyal, A., Loos, K., Noto, M., Chang, S. W., Spagnoli, C., Shafi, K. V. P. M., Ulman, A., Cowman, M., and Gross, R. A. (2003) Activity of Candida rugosa lipase immobilized on γ-Fe_2O_3 magnetic nanoparticles. *J. Am. Chem. Soc. 125*, 1684−1685.

(10) Wang, W., Xu, Y., Wang, D. I. C., and Li, Z. (2009) Recyclable nanobiocatalyst for enantioselective sulfoxidation: facile fabrication and high performance of chloroperoxidase-coated magnetic nanoparticles with iron oxide core and polymer shell. *J. Am. Chem. Soc. 131*, 12892−12893.

(11) Hermanson, G. T. (2008) *Bioconjugate Techniques*, Academic Press, San Diego.

(12) Niemeyer, C. M. (2008) *Bioconjugation Protocols*, Vol. *283*, Humana Press, Totowa, NJ.

(13) Xu, C., Xu, K., Gu, H., Zheng, R., Liu, H., Zhang, X., Guo, Z., and Xu, B. (2004) Dopamine as a robust anchor to immobilize functional molecules on the iron oxide shell of magnetic nanoparticles. *J. Am. Chem. Soc. 126*, 9938−9939.

(14) Chen, X., Fang, J., Zhang, J., Liu, Z., Shao, J., Kowal, P., Andreana, P., and Wang, G. P. (2001) Sugar nucleotide regeneration seads (Superbeads): a versatile tool for the practical synthesis of oligosaccharides. *J. Am. Chem. Soc. 123*, 2081−2082.

(15) Toda, A., Yamada, K., and Nishimura, S.-I. (2002) An engineered biocatalyst for the synthesis of glycoconjugates: utilization of β-1,3-N-acetyl-D-glucosaminyltransferase from Streptococcus agalactiae type Ia expressed in Escherichia coli as a fusion with maltose-binding protein. *Adv. Synth. Catal. 344*, 61−69.

(16) Ramachandran, N., Hainsworth, E., Bhuller, B., Eisenstein, S., Rosen, B., Lau, A. Y., Walter, J. C., and LaBaer, J. (2004) Self-assembling protein microarrays. *Science 305*, 86−90.

(17) Holland-Nell, K., and Beck-Sickinger, A. G. (2007) Specifically immobilised aldo/keto reductase AKR1A1 shows a dramatic increase in activity relative to the randomly immobilised enzyme. *ChemBioChem 8*, 1071−1076.

(18) Jonkheijm, P., Weinrich, D., Schröder, H., Niemeyer, C. M., and Waldmann, H. (2008) Chemical strategies for generating protein biochips. *Angew. Chem., Int. Ed. 47*, 9618−9647.

(19) Wong, L. S., Khan, F., and Micklefield, J. (2009) Selective covalent protein immobilization: strategies and applications. *Chem. Rev. 109*, 4025−4053.

(20) Yin, J., Liu, F., Li, X., and Walsh, C. T. (2004) Labeling proteins with small molecules by site-specific posttranslational modification. *J. Am. Chem. Soc. 126*, 7754−7755.

(21) Weinrich, D., Lin, P.-C., Jonkheijm, P., Nguyen, U. T. T., Schröder, H., Niemeyer, C. M., Alexandrov, K., Goody, R., and Waldmann, H. (2010) Oriented immobilization of farnesylated proteins by the thiol-ene reaction. *Angew. Chem., Int. Ed. 49*, 1252−1257.

(22) Gauchet, C., Labadie, G. R., and Poulter, C. D. (2006) Regio- and chemoselective covalent immobilization of proteins through unnatural amino acids. *J. Am. Chem. Soc. 128*, 9274−9275.

(23) Ito, T., Sadamoto, R., Naruchi, K., Togame, H., Takemoto, H., Kondo, H., and Nishimura, S.-I. (2010) Highly oriented recombinant glycosyltransferases: site-specific immobilization of unstable membrane proteins by using Staphylococcus aureus sortase A. *Biochemistry 49*, 2604−2614.

(24) Tanaka, Y., Tsuruda, Y., Nishi, M., Kamiya, N., and Goto, M. (2007) Exploring enzymatic catalysis at a solid surface: a case study with transglutaminase-mediated protein immobilization. *Org. Biomol. Chem. 5*, 1764−1770.

(25) Kwon, Y., Coleman, M. A., and Camarero, J. A. (2006) Selective immobilization of proteins onto solid supports through split-intein-mediated protein trans-splicing. *Angew. Chem., Int. Ed. 45*, 1726−1729.

(26) Lin, P.-C., Ueng, S.-H., Tseng, M.-C., Ko, J.-L., Huang, K.-T., Yu, S.-C., Adak, A. K., Chen, Y.-J., and Lin, C.-C. (2006) Site-specific protein modification through Cu^{I}-catalyzed 1,2,3-triazole formation and its implementation in protein microarray fabrication. *Angew. Chem., Int. Ed. 45*, 4286−4290.

(27) Soellner, M. B., Dickson, K. A., Nilsson, B. L., and Raines, R. T. (2003) Site-specific protein immobilization by Staudinger ligation. *J. Am. Chem. Soc. 125*, 11790−11791.

(28) Watzke, A., Köhn, M., Gutierrez-Rodriguez, M., Wacker, R., Schröder, H., Breinbauer, R., Kuhlmann, J., Alexandrov, K., Niemeyer, C. M., Goody, R. S., and Waldmann, H. (2006) Site-selective protein immobilization by Staudinger ligation. *Angew. Chem., Int. Ed. 45*, 1408−1412.

(29) Dantas de Araffljo, A., Palomo, J. M., Cramer, J., Köhn, M., Schröder, H., Wacker, R., Niemeyer, C. M., Alexandrov, K., and Waldmann, H. (2006) Diels-Alder ligation and surface immobilization of proteins. *Angew. Chem., Int. Ed. 45*, 296−301.

(30) Camarero, J. A., Kwon, Y., and Coleman, M. A. (2004) Chemoselective attachment of biologically active proteins to surfaces by expressed protein ligation and its application for "protein chip" fabrication. *J. Am. Chem. Soc. 126*, 14730−14731.

(31) Helms, B., van Baal, I., Merkx, M., and Meijer, E. W. (2007) Site-specific protein and peptide immobilization on a biosensor surface by pulsed native chemical ligation. *ChemBioChem 8*, 1790−1794.

(32) Sletten, E. M., and Bertozzi, C. R. (2009) Bioorthogonal chemistry: fishing for selectivity in a sea of functionality. *Angew. Chem., Int. Ed. 48*, 6974−6998.

(33) Laurent, S., Forge, D., Port, M., Roch, A., Robic, C., Vander Elst, L., and Muller, R. (2008) Magnetic iron oxide nanoparticles: synthesis, stabilization, vectorization, physicochemical characterizations, and biological applications. *Chem. Rev. 108*, 2064−2110.

(34) Gupta, A. K., and Gupta, M. (2005) Synthesis and surface engineering of iron oxide nanoparticles for biomedical applications. *Biomaterials 26*, 3995−4021.
(35) Lee, H., Yu, M. K., Park, S., Moon, S., Min, J. J., Jeong, Y. Y., Kang, H.-W., and Jon, S. (2007) Thermally cross-linked superparamagnetic iron oxide nanoparticles: synthesis and application as a dual imaging probe for cancer in vivo. *J. Am. Chem. Soc. 129*, 12739−12745.
(36) Gu, H., Ho, P.-L., Tsang, K. W. T., Wang, L., and Xu, B. (2003) Using biofunctional magnetic nanoparticles to capture vancomycin-resistant enterococci and other Gram-positive bacteria at ultralow concentration. *J. Am. Chem. Soc. 125*, 15702−15703.
(37) El-Boubbou, K., Gruden, C., and Huang, X. (2007) Magnetic glyco-nanoparticles: a unique tool for rapid pathogen detection, decontamination, and strain differentiation. *J. Am. Chem. Soc. 129*, 13392−13393.
(38) Chou, P.-H., Chen, S.-H., Liao, H.-K., Lin, P.-C., Her, G.-R., Lai, A. C.-Y., Chen, J.-H., Lin, C.-C., and Chen, Y.-J. (2005) Nanoprobe-based affinity mass spectrometry for selected protein profiling in human plasma. *Anal. Chem. 77*, 5990−5997.
(39) Lin, P.-C., Chou, P.-H., Chen, S.-H., Liao, H.-K., Wang, K.-Y., Chen, Y.-J., and Lin, C.-C. (2006) Ethylene glycol-protected magnetic nanoparticles for a multiplexed immunoassay in human plasma. *Small 2*, 485−489.
(40) Wang, K.-Y., Chuang, S.-A., Lin, P.-C., Huang, L.-S., Chen, S.-H., Ouarda, S., Pan, W.-H., Lee, P.-Y., Lin, C.-C., and Chen, Y.-J. (2008) Multiplexed immunoassay: quantitation and profiling of serum biomarkers using magnetic nanoprobes and MALDI-TOF MS. *Anal. Chem. 80*, 6159−6167.
(41) Lin, P.-C., Chen, S.-H., Wang, K.-Y., Chen, M.-L., Adak, A. K., Hwu, J.-R. R., Chen, Y.-J., and Lin, C.-C. (2009) Fabrication of oriented antibody-conjugated magnetic nanoprobes and their immunoaffinity application. *Anal. Chem. 81*, 8774−8782.
(42) Jin, M.-J., and Lee, D.-H. (2010) A practical heterogeneous catalyst for the Suzuki, Sonogashira, and Stille coupling reactions of unreactive aryl chlorides. *Angew. Chem., Int. Ed. 49*, 1119−1122.
(43) Hu, A., Yee, G. T., and Lin, W. (2005) Magnetically recoverable chiral catalysts immobilized on magnetite nanoparticles for asymmetric hydrogenation of aromatic ketones. *J. Am. Chem. Soc. 127*, 12486−12487.
(44) Casero, E., Darder, M., Pariente, F., and Lorenzo, E. (2002) Thiol-functionalized gold surfaces as a strategy to induce order in membrane-bound enzyme immobilization. *Nano Lett. 2*, 577−582.
(45) Jeuken, L. J. C. (2009) Electrodes for integral membrane enzymes. *Nat. Prod. Rep. 26*, 1234−1240.
(46) Naruchi, K., and Nishimura, S.-I. (2011) Membrane-bound stable glycosyltransferases: highly oriented protein immobilization by a C-terminal cationic amphipathic peptide. *Angew. Chem., Int. Ed. 50*, 1328−1331.
(47) Yu, H., Huang, S., Chokhawala, H., Sun, M., Zheng, H., and Chen, X. (2006) Highly efficient chemoenzymatic synthesis of naturally occurring and non-natural α-2,6-linked sialosides: a P. damsela α-2,6-sialyltransferase with extremely flexible donor-substrate specificity. *Angew. Chem., Int. Ed. 45*, 3938−3944.
(48) Teo, C.-F., Hwang, T.-S., Chen, P.-H., Hung, C.-H., Gao, H.-S., Chang, L.-S., and Lin, C.-H. (2005) Synthesis of sialyl T_N glycopeptides-enzymatic sialylation by α-2,6-sialyltransferase from Photobacterium damsela. *Adv. Synth. Catal. 347*, 967−972.
(49) Izumi, M., Shen, G.-J., Wacowich-Sgarbi, S., Nakatani, T., Plettenburg, O., and Wong, C.-H. (2001) Microbial glycosyltransferases for carbohydrate synthesis: α-2,3-sialyltransferase from Neisseria gonorrheae. *J. Am. Chem. Soc. 123*, 10909−10918.
(50) Yu, H., Chokhawala, H., Karpel, R., Yu, H., Wu, B., Zhang, J., Zhang, Y., Jia, Q., and Chen, X. (2005) A multifunctional Pasteurella multocida sialyltransferase: a powerful tool for the synthesis of sialoside libraries. *J. Am. Chem. Soc. 127*, 17618−17619.
(51) Yu, H., Cheng, J., Ding, L., Khedri, Z., Chen, Y., Chin, S., Lau, K., Tiwari, V. K., and Chen, X. (2009) Chemoenzymatic synthesis of GD3 oligosaccharides and other disialyl glycans containing natural and non-natural sialic acids. *J. Am. Chem. Soc. 131*, 18467−18477.
(52) Yu, C.-C., Lin, P.-C., and Lin, C.-C. (2008) Site-specific immobilization of CMP-sialic acid synthetase on magnetic nanoparticles and its use in the synthesis of CMP-sialic acid. *Chem. Commun.*, 1308−1310.
(53) Gilbert, M., Watson, D. C., Cunningham, A.-M., Jennings, M. P., Young, N. M., and Wakarchuk, W. W. (1996) Cloning of the lipooligosaccharide α-2,3-sialyltransferase from the bacterial pathogens Neisseria meningitidis and Neisseria gonorrhoeae. *J. Biol. Chem. 271*, 28271−28276.
(54) Chen, M.-L., Adak, A. K., Yeh, N.-C., Yang, W.-B., Chuang, Y.-J., Wong, C.-H., Hwang, K.-C., Hwu, J.-R. R., Hsieh, S.-L., and Lin, C.-C. (2008) Fabrication of an oriented Fc-fused lectin microarray through boronate formation. *Angew. Chem., Int. Ed. 47*, 8627−8630.
(55) Lin, P.-C., Ueng, S.-H., Yu, S.-C., Jan, M.-D., Adak, A. K., Yu, C.-C., and Lin, C.-C. (2007) Surface modification of magnetic nanoparticle via Cu(I)-catalyzed alkyne-azide [2 + 3] cycloaddition. *Org. Lett. 9*, 2131−2134.
(56) Iyer, S. S., Anderson, A. S., Reed, S., Swanson, B., and Schmidt, J. G. (2004) Synthesis of orthogonal end functionalized oligoethylene glycols of defined lengths. *Tetrahedron Lett. 45*, 4285−4288.
(57) Basso, A., Braiuca, P., Cantone, S., Ebert, C., Linda, P., Spizzo, P., Caimi, P., Hanefeld, U., Degrassi, G., and Gardossia, L. (2007) In silico analysis of enzyme surface and glycosylation effect as a tool for efficient covalent immobilisat ion of CalB and PGA on Sepabeads®. *Adv. Synth. Catal. 349*, 877−886.
(58) Dawson, P. E., Muir, T. W., Clark-Lewis, I., and Kent, S. B. H. (1994) Synthesis of proteins by native chemical ligation. *Science 266*, 776−779.
(59) Wang, Q., Graham, K., Schauer, T., Fietz, T., Mohammed, A., Liu, X., Hoffend, J., Haberkorn, U., Eisenhut, M., and Mier, W. (2004) Pharmacological properties of hydrophilic and lipophilic derivatives of octreotate. *Nucl. Med. Biol. 31*, 21−30.
(60) Bruce, I. J., and Sen, T. (2005) Surface modification of magnetic nanoparticles with alkoxysilanes and their application in magnetic bioseparations. *Langmuir 21*, 7029−7035.
(61) Aharoni, A., Thieme, K., Chiu, C. P. C, Buchini, S., Lairson, L. L., Chen, H., Strynadka, N. C. J., Wakarchuk, W. W., and Withers, S. G. (2006) High-throughput screening methodology for the directed evolution of glycosyltransferases. *Nat. Methods 3*, 609−614.
(62) Shell, D. M., Chiles, L., Judd, R. C., Seal, S., and Rest, R. F. (2002) The Neisseria lipooligosaccharide-specific α-2,3-sialyltransferase is a surface-exposed outer membrane protein. *Infect. Immun. 70*, 3744−3751.
(63) Gilbert, M., Bayer, R., Cunningham, A.-M., DeFrees, S., Gao, Y., Watson, D. C., Young, N. M., and Wakarchuk, W. W. (1998) The synthesis of sialylated oligosaccharides using a CMP-Neu5Ac synthetase/sialyltransferase fusion. *Nat. Biotechnol. 16*, 769−772.
(64) Kim, Y.-P., Daniel, W. L., Xia, Z., Xie, H., Mirkin, C. A., and Rao, J. (2010) Bioluminescent nanosensors for protease detection based upon gold nanoparticle-luciferase conjugates. *Chem. Commun. 46*, 76−78.

Bioconjugate Chemistry

Article

pubs.acs.org/bc

Developing Red-Emissive Ruthenium(II) Complex-Based Luminescent Probes for Cellular Imaging

Run Zhang,[†] Zhiqiang Ye,*[,†] Yuejiao Yin,[†] Guilan Wang,[†] Dayong Jin,[‡] Jingli Yuan,*[,†] and James A. Piper[‡]

[†]State Key Laboratory of Fine Chemicals, School of Chemistry, Dalian University of Technology, Dalian 116024, P. R. China

[‡]MQ Photonics Centre, Faculty of Science, Macquarie University, NSW 2109, Sydney, Australia

Supporting Information

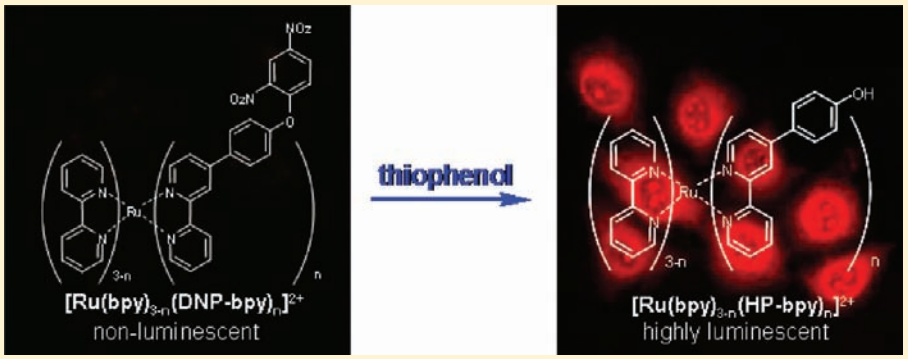

ABSTRACT: Ruthenium(II) complexes have rich photophysical attributes, which enable novel design of responsive luminescence probes to selectively quantify biochemical analytes. In this work, we developed a systematic series of Ru(II)-bipyrindine complex derivatives, $[Ru(bpy)_{3-n}(DNP\text{-}bpy)_n](PF_6)_2$ (n = 1, 2, 3; bpy, 2,2′-bipyridine; DNP-bpy, 4-(4-(2,4-dinitrophenoxy)phenyl)-2,2′-bipyridine), as luminescent probes for highly selective and sensitive detection of thiophenol in aqueous solutions. The specific reaction between the probes and thiophenol triggers the cleavage of the electron acceptor group, 2,4-dinitrophenyl, eliminating the photoinduced electron transfer (PET) process, so that the luminescence of on-state complexes, $[Ru(bpy)_{3-n}(HP\text{-}bpy)_n]^{2+}$ (n = 1, 2, 3; HP-bpy, 4-(4-hydroxyphenyl)-2,2′-bipyridine), is turned on. We found that the complex $[Ru(bpy)(DNP\text{-}bpy)_2]^{2+}$ remarkably enhanced the on-to-off contrast ratio compared to the other two (37.8 compared to 21 and 18.7). This reveals a new strategy to obtain the best Ru(II) complex luminescence probe via the most asymmetric structure. Moreover, we demonstrated the practical utility of the complex as a cell-membrane permeable probe for quantitative luminescence imaging of the dynamic intracellular process of thiophenol in living cells. The results suggest that the new probe could be a very useful tool for luminescence imaging analysis of the toxic thiophenol in intact cells.

INTRODUCTION

In the last two decades, fluorescent probes/sensors have revolutionized the fields of biochemistry, molecular biology, and clinical diagnostics. This analytical technology offers clear advances in simplicity, sensitivity, specificity, and robustness, enabling both *in vivo* and *in vitro* bioassays.[1] Recent efforts have been motivated to develop responsive fluorescence probes/sensors, whose overall fluorescence or relativity is a defined function of a specific-targeted biochemical variable. These "smart" probes/sensors enable intracellular dynamic imaging, so that both the presence and dynamic interactions of biologically important species can be visualized under a fluorescence microscope.[2−6]

In general, a responsive fluorescence probe consists of a fluorescent core and a switch moiety to be triggered by an analyte. There are several efficient transfer processes regulating the fluorescence switch, such as photoinduced electron transfer (PET), internal charge transfer (ICT), electronic energy transfer (EET), and monomer−excimer formation (MEF). These mechanisms have been demonstrated to render the fluorescence probes responsive to a variety of specific analytes, such as metal ions,[7−11] anions,[12−16] reactive small molecules,[17−19] proteins,[20,21] and nucleic acids.[22,23] The complexity in biological systems has been directing the current research to focus on the specificity of a responsive fluorescence probe to an analyte carrying rich biological signals. Another emphasis is on strategies to enhance the on/off contrast ratio and enlarge the dynamic range, to improve the detection limit.

Although there are a variety of fluorophores, such as organic dyes, fluorescent proteins, and emissive metal complexes, succeeding as the cores in various fluorescence probes, the recent attentions have been brought to the emissive transition metal complexes, especially those of Ru(II), Re(I), and Ir(III), thanks to their desirable features including large Stokes shifts;

Received: September 13, 2011
Revised: February 28, 2012
Published: March 21, 2012

high photo-, thermal, and chemical stabilities; and low cytotoxicities.[24−28] The Ru(II) complexes, for example, own rich photophysical and coordination chemistry attributes. Different from other fluorophores, the luminescent Ru(II) complexes typically entail three diimine ligands, mainly including bipyridine, phenanthroline, and bathophenanthroline derivatives. Since each diimine ligand can be modified to bind to a luminescence-switch group (generally an electron donor or acceptor group), a Ru(II) complex may incorporate with one, two, or three switch groups. This flexibility may be used to tune its recognition and luminescence responsive ability to a specific analyte. Though the influence of the substitution position of a switch group on the photophysical properties of Ru(II) complexes has been investigated,[29−31] the effect of the switch group number on the luminescence properties remains unclear.

Thiophenols are a class of thiols with high toxicity and are widely used for pharmaceuticals, pesticides, and polymer materials.[32] Exposure of either liquid or vapor of thiophenols to human beings can damage the central nervous system, showing symptoms such as wheezing, laryngitis, headache, nausea, vomiting, and even death.[33] In this work, we designed and synthesized a systematic series of Ru(II)-bipyridine complex derivatives, $[Ru(bpy)_{3-n}(DNP\text{-}bpy)_n]^{2+}$ (n = 1, 2, 3; bpy, 2,2′-bipyridine; DNP-bpy, 4-(4-(2,4-dinitrophenoxy)-phenyl)-2,2′-bipyridine), as luminescent probes for recognition and detection of thiophenol. The electron acceptor group, 2,4-dinitrophenyl (DNP), is the switch moiety capable of withholding the luminescence of the Ru(II) complexes in the dark state via a PET process. The reaction between the complexes and thiophenol triggers the cleavage of the DNP group to eliminate the PET process, so that the luminescence of the Ru(II) complexes is turned on (Scheme 1). Through a detailed characterization on the luminescence properties, an effective strategy to optimize the number of the electron acceptor groups was established for the rational design of the Ru(II) complex-based luminescence probes. The newly synthesized probes showed highly selective and sensitive luminescence response to thiophenol in aqueous solutions, and could be easily transferred into living cells using the ordinary coincubation method for imaging the intracellular thiophenol molecules. Our present work not only realized the Ru(II) complex-based luminescence probes quantifying the thiophenol in aqueous solutions, but also revealed the effect of the number of the electron acceptor moiety on the luminescence properties of the Ru(II) complexes.

Scheme 1. Luminescence Response Reaction of $[Ru(bpy)_{3-n}(DNP\text{-}bpy)_n]^{2+}$ (n = 1, 2, 3) towards Thiophenol

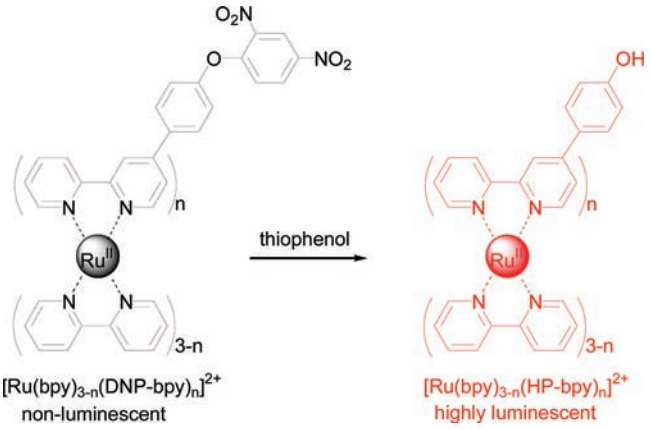

RESULTS AND DISCUSSION

Design, Synthesis, and Characterization of the Probe.

Recently, we demonstrated that the PET mechanism is a useful tool for developing Ru(II) complex-based luminescence probes.[34−36] In this work, to investigate the effect of the number of the electron acceptor moiety on the luminescence properties of Ru(II)-bipyridine complex derivatives, three Ru(II) complexes containing the increased number of 2,4-dinitrophenoxyphenyl-substituted bipyridine ligand, $[Ru(bpy)_{3-n}(DNP\text{-}bpy)_n]^{2+}$ (n = 1, 2, 3), were designed and synthesized as luminescence probes for recognition and detection of thiophenol. Due to the presence of intramolecular PET process from the excited Ru(II) complexes to the acceptor, 2,4-dinitrophenyl (DNP), the complexes themselves are almost non-luminescent. After reacting with thiophenol, following the cleavage of the DNP group in the complexes, highly luminescent Ru(II) complexes, $[Ru(bpy)_{3-n}(HP\text{-}bpy)_n]^{2+}$ (n = 1, 2, 3; HP-bpy, 4-(4-hydroxyphenyl)-2,2′-bipyridine), are generated. Thus, the metal-to-ligand charge transfer (MLCT)-based luminescence from the Ru(II)-bipyridine complexes is turned on.

The complexes $[Ru(bpy)_{3-n}(HP\text{-}bpy)_n](PF_6)_2$ and $[Ru(bpy)_{3-n}(DNP\text{-}bpy)_n](PF_6)_2$ (n = 1, 2, 3) were synthesized according to the procedures shown in Scheme 2. The key intermediate Ru(II) complexes **1**, **3**, and **4** were synthesized by reacting $RuCl_3$ with different bipyridine derivatives. After treating with BBr_3 in anhydrous CH_2Cl_2, the methyl ether bonds were cleaved, and $[Ru(bpy)_{3-n}(HP\text{-}bpy)_n](PF_6)_2$ (n = 1, 2, 3) were obtained with high yields. Then, the probe complexes, $[Ru(bpy)_{3-n}(DNP\text{-}bpy)_n](PF_6)_2$ (n = 1, 2, 3), were synthesized by reacting $[Ru(bpy)_{3-n}(HP\text{-}bpy)_n](PF_6)_2$ (n = 1, 2, 3) with 2,4-dinitrofluorobenzene in anhydrous CH_3CN in the presence of NaH. All the complexes were well-characterized by the NMR, ESI-MS, and elementary analyses. Both $[Ru(bpy)_{3-n}(HP\text{-}bpy)_n](PF_6)_2$ and $[Ru(bpy)_{3-n}(DNP\text{-}bpy)_n](PF_6)_2$ (n = 1, 2, 3) are stable in solid state and in aqueous buffers.

Figure 1 shows the UV−vis absorption spectra of $[Ru(bpy)_{3-n}(HP\text{-}bpy)_n]^{2+}$ and $[Ru(bpy)_{3-n}(DNP\text{-}bpy)_n]^{2+}$ (n = 1, 2, 3) in 20 mM HEPES buffer at pH 7.0. All the complexes exhibited two strong absorption bands at ~290 nm and ~460 nm, assigned to the spin-allowed ligand localized $\pi\rightarrow\pi^*$ transition and metal-to-ligand charge transfer (MLCT) transition, respectively. The two transitions of $[Ru(bpy)_{3-n}(DNP\text{-}bpy)_n]^{2+}$ (n = 1, 2, 3) displayed a gradual bathochromic shift with increasing number of the DNP-bpy ligand. However, there were no obvious differences in MLCT and $\pi\rightarrow\pi^*$ transitions between $[Ru(bpy)_{3-n}(DNP\text{-}bpy)_n]^{2+}$ and their corresponding reaction products with thiophenol, $[Ru(bpy)_{3-n}(HP\text{-}bpy)_n]^{2+}$, which suggests that the luminescence of $[Ru(bpy)_{3-n}(DNP\text{-}bpy)_n]^{2+}$ should be surely quenched via the PET mechanism, as expected.

The luminescence properties of both $[Ru(bpy)_{3-n}(DNP\text{-}bpy)_n]^{2+}$ and $[Ru(bpy)_{3-n}(HP\text{-}bpy)_n]^{2+}$ (n = 1, 2, 3) are listed in Table 1.[37] All the complexes exhibited the characteristic MLCT-based luminescence as typically observed in the spectra of Ru(II)-diimine complexes. Three luminescent Ru(II) complexes $[Ru(bpy)_{3-n}(HP\text{-}bpy)_n]^{2+}$ (n = 1, 2, 3) showed the luminescence quantum yields at the same level with long luminescence lifetimes, and their emission bands displayed a

dx.doi.org/10.1021/bc200506w | Bioconjugate Chem. 2012, 23, 725−733

Scheme 2. Synthesis Procedures of the New Ru(II) Complexes

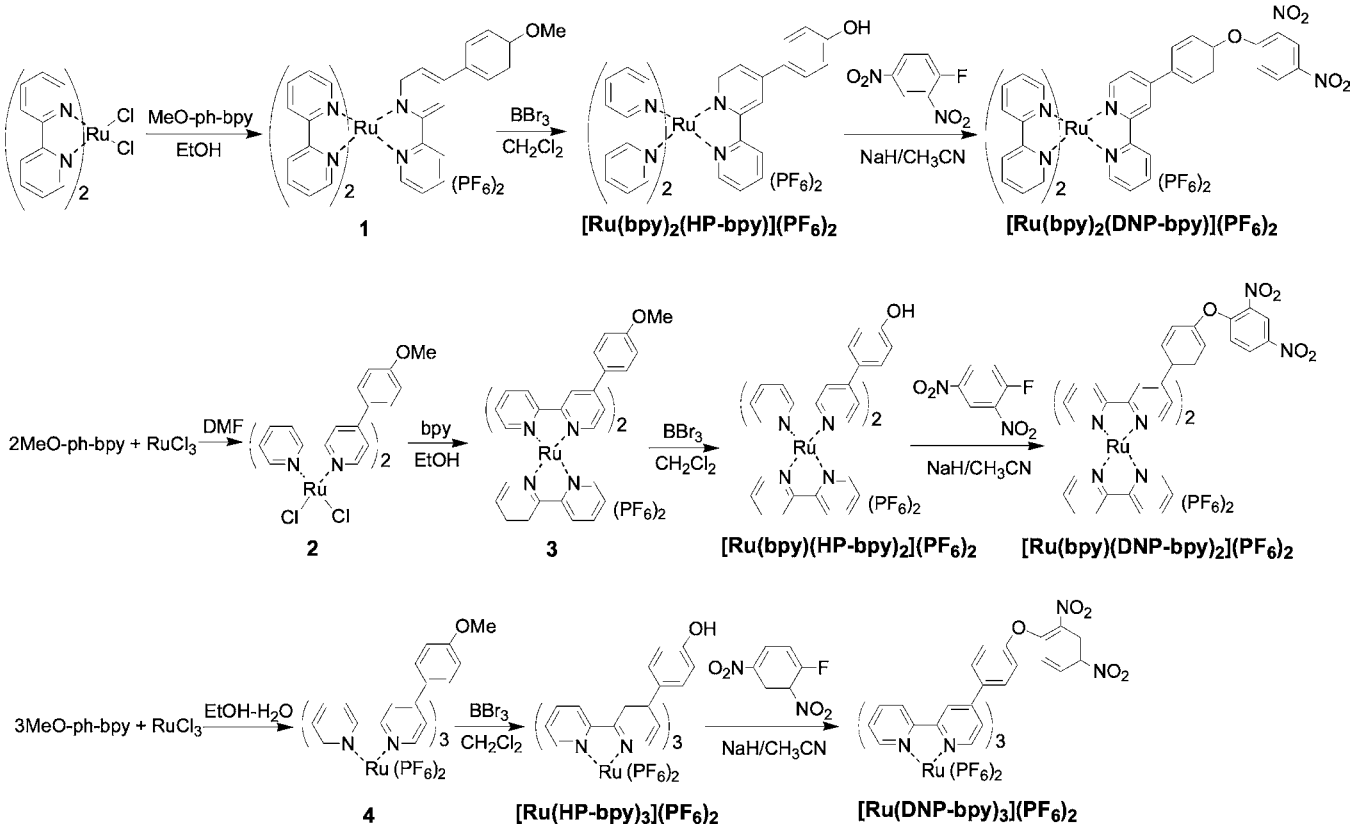

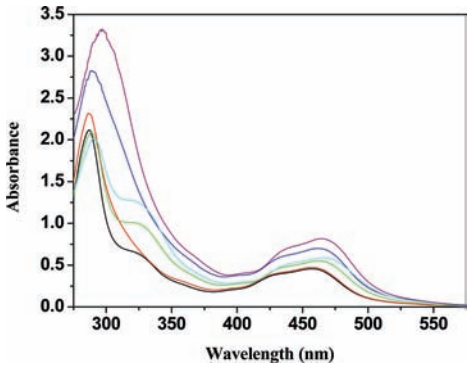

Figure 1. UV−vis absorption spectra of $[Ru(bpy)_2(HP\text{-}bpy)]^{2+}$ (black), $[Ru(bpy)_2(DNP\text{-}bpy)]^{2+}$ (red), $[Ru(bpy)(HP\text{-}bpy)_2]^{2+}$ (green), $[Ru(bpy)(DNP\text{-}bpy)_2]^{2+}$ (blue), $[Ru(HP\text{-}bpy)_3]^{2+}$ (cyan), and $[Ru(DNP\text{-}bpy)_3]^{2+}$ (purple) in 20 mM HEPES buffer at pH 7.0 (the complex concentration, 30 μM).

gradual red-shift with increasing number of the HP-bpy ligand. Incorporated with the 2,4-dinitrophenyl moiety, the luminescence of the Ru(II) complexes $[Ru(bpy)_{3-n}(DNP\text{-}bpy)_n]^{2+}$ (n = 1, 2, 3) was effectively quenched with very low luminescence quantum yields and short luminescence lifetimes. Interestingly, the dual-substitution complex, $[Ru(bpy)(DNP\text{-}bpy)_2]^{2+}$, displayed the largest red-shift of emission band and was the darkest with the lowest quantum yield among the three complexes of $[Ru(bpy)_{3-n}(DNP\text{-}bpy)_n]^{2+}$. The reason might be attributed to the quenching efficiency induced by the alteration of the symmetry. The structure of $[Ru(bpy)_3]^{2+}$ is highly symmetric with three identical ligands. After a Ru(II) center was coordinated by bipyridine derivatives having different numbers of substitution groups, the symmetry, as an important factor to influence the luminescence properties, could be changed.[29] A higher unsymmetric structure of Ru(II) complex should make the luminescence quenching by PET more effective, which further decreases the luminescence quantum yield in the dark state. The on-to-off contrast ratios of the synthesized Ru(II) complexes were calculated as 21, 37.8, and 18.7 with increased numbers of DNP groups from 1 to 3. Therefore, the off-state complex $[Ru(bpy)(DNP\text{-}bpy)_2]^{2+}$ is the darkest complex, which enables it to be the most responsive luminescence probe among the three DNP-containing Ru(II) complexes for the detection of thiophenol. Our results prove that the sophisticated combination of PET mechanism and the unsymmetry of Ru(II) complexes is a noteworthy approach for designing the Ru(II) complex-based luminescence probes.

Table 1. Luminescence Properties of $[Ru(bpy)_{3-n}(DNP\text{-}bpy)_n]^{2+}$ and $[Ru(bpy)_{3-n}(HP\text{-}bpy)_n]^{2+}$ (n = 1, 2, 3)[a]

complex	$\lambda_{ex,max}$ (nm)	$\varepsilon_{\lambda max}$ (cm^{-1} M^{-1})	$\lambda_{em,max}$ (nm)	ϕ^b (%)	τ (ns)
$[Ru(bpy)_2(DNP\text{-}bpy)]^{2+}$	456	1.58×10^4	612	0.11	20
$[Ru(bpy)_2(HP\text{-}bpy)]^{2+}$	456	1.53×10^4	612	2.31	305
$[Ru(bpy)(DNP\text{-}bpy)_2]^{2+}$	459	2.36×10^4	640	0.06	17
$[Ru(bpy)(HP\text{-}bpy)_2]^{2+}$	459	1.88×10^4	616	2.27	248
$[Ru(DNP\text{-}bpy)_3]^{2+}$	462	2.81×10^4	633	0.12	22
$[Ru(HP\text{-}bpy)_3]^{2+}$	462	1.95×10^4	620	2.24	202

[a]All data were obtained in 20 mM HEPES buffer of pH 7.0 at room temperature. [b]Luminescence quantum yield was measured by using $[Ru(bpy)_3]Cl_2$ (ϕ = 2.8%)[37] as a standard.

Reaction of the Probe with Thiophenol. Recently, a variety of fluorescence probes for sensing thiols have been developed and demonstrated in some applications.[38−41] However, only a few of probes can be used to selectively

dx.doi.org/10.1021/bc200506w | Bioconjugate Chem. 2012, 23, 725−733

discriminate thiophenol from aliphatic thiols.[38,40,41] Jiang and co-workers reported two PET and ICT based fluorescence probes for discriminating thiophenol,[38,40] but did not demonstrate their utilities for sensing thiophenol in environmental or living systems. Lin and co-workers developed a coumarin dye-based probe for thiophenol, but the probe could only be used in a mixture of water−DMF (11/9, v/v).[41] Thus, we expect that our new Ru(II) complex-based luminescence probes can be used for the selective and sensitive detection of thiophenol in aqueous media.

At first, the effect of pH on the reaction between $[Ru(bpy)(DNP\text{-}bpy)_2]^{2+}$ (10 μM) and thiophenol (50 μM) was examined in 50 mM phosphate buffers with different pHs. As shown in Figure 2, the luminescence intensity of $[Ru(bpy)(HP\text{-}bpy)_2]^{2+}$ was strong at acidic pHs, and decreased

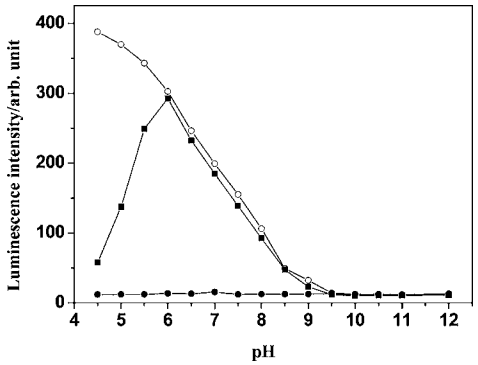

Figure 2. Effect of pH on the luminescence intensities of $[Ru(bpy)(DNP\text{-}bpy)_2]^{2+}$ (10 μM, ●), $[Ru(bpy)(HP\text{-}bpy)_2]^{2+}$ (10 μM, ○), and the product (■) of $[Ru(bpy)(DNP\text{-}bpy)_2]^{2+}$ (10 μM) reacted with thiophenol (50 μM) in 50 mM phosphate buffers with different pHs.

gradually with pH increase. This is due to the phenol/phenolate interconversion on the ligand of the complex. In contrast, $[Ru(bpy)(DNP\text{-}bpy)_2]^{2+}$ remained dark and stable in a pH range of 4.5−12.0. In the presence of thiophenol, the thiolysis of the dinitrophenyl ether in $[Ru(bpy)(DNP\text{-}bpy)_2]^{2+}$ proceeded through nucleophilic substitution by the nucleophilic thiolate yielded $[Ru(bpy)(HP\text{-}bpy)_2]^{2+}$. Due to the effect of pK_a (~6.5) of thiophenol on the thiolysis reaction and the effect of pH on the luminescence intensity of $[Ru(bpy)(HP\text{-}bpy)_2]^{2+}$, the luminescence intensity of the product of $[Ru(bpy)(DNP\text{-}bpy)_2]^{2+}$ reacted with thiophenol increased, reached a peak at the pH value of ~6.2, and then decreased along with the trend of $[Ru(bpy)(HP\text{-}bpy)_2]^{2+}$ at increased pHs. The pH effects on the reactions between $[Ru(bpy)_2(DNP\text{-}bpy)]^{2+}$/$[Ru(DNP\text{-}bpy)_3]^{2+}$ and thiophenol were also measured, respectively (SI Figure S1 and S2). Our results show that all these new Ru(II) complexes are useful luminescence probes for detecting thiophenol under the physiological pH condition.

Figure 3 shows the temporal dynamics of the luminescence responses of $[Ru(bpy)_{3-n}(DNP\text{-}bpy)_n]^{2+}$ (n = 1, 2, 3, 10 μM) to the addition of thiophenol (40 μM) in 20 mM HEPES buffer at pH 7.0. Upon the addition of thiophenol, a rapid increase in luminescence intensity was observed in a few minutes. After ~30 min reaction, the luminescence intensity reached a plateau and remained stable afterward. Moreover, the Job's plotting analyses of the reactions between $[Ru(bpy)_{3-n}(DNP\text{-}bpy)_n]^{2+}$ (n = 1, 2, 3) and thiophenol were conducted in 20 mM HEPES

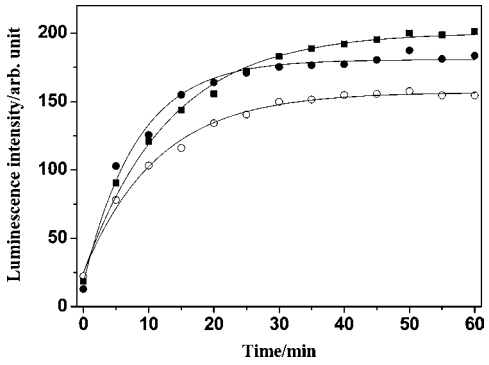

Figure 3. Temporal dynamics of the luminescence responses of $[Ru(bpy)_{3-n}(DNP\text{-}bpy)_n]^{2+}$ (n = 1, 2, 3, 10 μM) to the addition of thiophenol (40 μM) in 20 mM HEPES buffer of pH 7.0. $[Ru(bpy)_2(DNP\text{-}bpy)]^{2+}$ (○), $[Ru(bpy)(DNP\text{-}bpy)_2]^{2+}$ (●), $[Ru(DNP\text{-}bpy)_3]^{2+}$ (■).

buffer at pH 7.0, respectively (SI Figures S3, S4, S5). The maximum luminescence intensities were achieved at ~0.5, ~0.67, and ~0.76 molecular fractions for the reactions between $[Ru(bpy)_2(DNP\text{-}bpy)]^{2+}$/$[Ru(bpy)(DNP\text{-}bpy)_2]^{2+}$/$[Ru(DNP\text{-}bpy)_3]^{2+}$ and thiophenol, respectively. These results indicate that the reactions between $[Ru(bpy)_{3-n}(DNP\text{-}bpy)_n]^{2+}$ and thiophenol have the stoichiometries of 1:1, 1:2, and 1:3 for the three complexes (n = 1−3), which demonstrates that all the DNP groups, the luminescence quenchers, in the Ru(II) complexes can be removed by reacting with thiophenol.

To investigate the performance of $[Ru(bpy)_{3-n}(DNP\text{-}bpy)_n]^{2+}$ as luminescent probes for the quantitative detection of thiophenol, the excitation and emission spectra of $[Ru(bpy)_{3-n}(DNP\text{-}bpy)_n]^{2+}$ (n = 1, 2, 3, 10 μM) in the presence of different concentrations of thiophenol in 20 mM HEPES buffer at pH 7.0 were measured at room temperature (Figure 4, SI Figures S6 and S7). As expected, $[Ru(bpy)(DNP\text{-}bpy)_2]^{2+}$

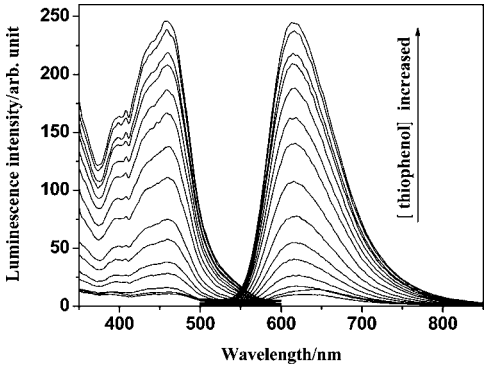

Figure 4. Excitation and emission spectra of $[Ru(bpy)(DNP\text{-}bpy)_2]^{2+}$ (10 μM) in the presence of different concentrations of thiophenol in 20 mM HEPES buffer at pH 7.0. The concentrations of thiophenol are 0, 5, 10, 12.5, 15, 17.5, 20, 25, 30, 35, 40, 45, 50, 75, and 100 μM, respectively.

showed the lowest background luminescence signal among the three DNP-containing complexes. Upon the addition of thiophenol, the luminescence of the three complexes was significantly enhanced. Interestingly, the enhancement in luminescence intensity was quantitatively proportional to the concentration of thiophenol from 1 to 12 μM for $[Ru(bpy)(DNP\text{-}bpy)_2]^{2+}$, from 12.5 to 30 μM for $[Ru(bpy)_2(DNP\text{-}bpy)]^{2+}$, and from 20 to 35 μM for $[Ru(DNP\text{-}bpy)_3]^{2+}$ (Figure

dx.doi.org/10.1021/bc200506w | Bioconjugate Chem. 2012, 23, 725−733

5). A sequential linearity relationship was obtained by using $[Ru(bpy)_{3-n}(DNP\text{-}bpy)_n]^{2+}$ (n = 1, 2, 3) to detect thiophenol.

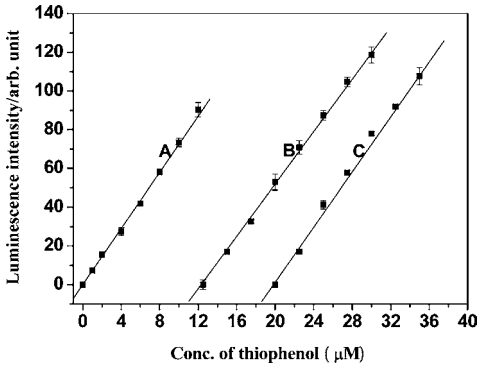

Figure 5. Dose-dependent luminescence responses of $[Ru(bpy)_{3-n}(DNP\text{-}bpy)_n]^{2+}$ (10 μM; A, n = 2; B, n = 1; C, n = 3) toward thiophenol in 20 mM HEPES buffers at pH 7.0.

According to the reported method defined by IUPAC,[42] the detection limit for thiophenol using $[Ru(bpy)(DNP\text{-}bpy)_2]^{2+}$ as a probe was calculated to be 32.9 nM. These results indicate that our new Ru(II) complex-based luminescence probes are remarkably sensitive with a large dynamic range and low detection limit for the quantitative detection of thiophenol in aqueous solutions.

The luminescence response specificity of $[Ru(bpy)(DNP\text{-}bpy)_2]^{2+}$ toward thiophenol was evaluated in 20 mM HEPES buffer at pH 7.0. As shown in Figure 6, $[Ru(bpy)(DNP\text{-}bpy)_2]^{2+}$ (10 μM) did not give any luminescence responses to the additions of 100 μM of various relevant aliphatic thiols, amino acids, and other common nucleophiles including valine (Val), lysine (Lys), aspartic acid (Asp), histidine (His), arginine

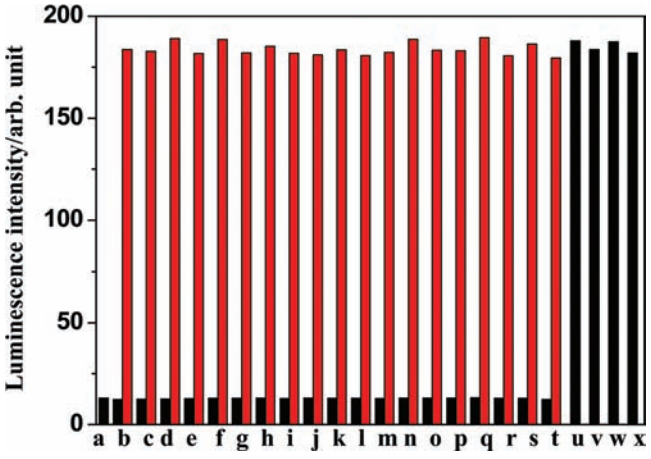

Figure 6. Luminescence intensities (616 nm) of the products of $[Ru(bpy)(DNP\text{-}bpy)_2]^{2+}$ (10 μM) reacted with various species (100 μM) and thiophenol (40 μM) in 20 mM HEPES buffer at pH 7.0 (black bars). The red bars show the luminescence intensities (616 nm) of the products of $[Ru(bpy)(DNP\text{-}bpy)_2]^{2+}$ (10 μM) reacted with thiophenol (40 μM) in the presence of various possible interfering species (100 μM) in 20 mM HEPES buffer at pH 7.0: (a) blank, (b) Val, (c) Lys, (d) Asp, (e) His, (f) Arg, (g) Met, (h) Leu, (i) GSH, (j) Cys, (k) Hcy, (l) Ser, (m) Tyr, (n) Na_2S, (o) KI, (p) PhOH, (q) Vc, (r) aniline, (s) $NH_2CH_2CH_2SH$, (t) the mixture of all possibly interfering species (10 μM for each), (u) thiophenol, (v) 4-bromo-thiophenol, (w) 4-amino-thiophenol, (x) 2-amino-thiophenol.

(Arg), methionine (Met), leucine (Leu), glutathione (GSH), cysteine (Cys), homocysteine (Hcy), serine (Ser), tyrosine (Tyr), sodium sulfide (Na_2S), potassium iodide (KI), phenol (PhOH), ascorbic acid (Vc), aniline, and cysteamine ($NH_2CH_2CH_2SH$), whereas the luminescence intensity was significantly enhanced in the presence of thiophenol or its derivatives such as 4-bromo-thiophenol, 4-amino-thiophenol, and 2-amino-thiophenol. These competition experiment results indicate that all the possible interfering species have no considerable influence on the luminescence detection of thiophenol, which reveals the fact that $[Ru(bpy)(DNP\text{-}bpy)_2]^{2+}$ can be used as a luminescence probe for the highly selective detection of thiophenol even in the presence of other interference species. Similar to $[Ru(bpy)(DNP\text{-}bpy)_2]^{2+}$, the other two complexes, $[Ru(bpy)_2(DNP\text{-}bpy)]^{2+}$ and $[Ru(DNP\text{-}bpy)_3]^{2+}$, also showed high luminescence response specificity toward thiophenol (SI Figure S8).

Luminescence Imaging of Thiophenol in Living Cells. In living cells, thiophenol is readily autoxidized at neutral pH to form its corresponding disulfide with the generations of superoxide radical ($O_2^{-\cdot}$) and hydrogen peroxide (H_2O_2) in the process.[32] These products can further generate other reactive oxygen/nitrogen species (ROS/RNS), such as singlet oxygen ($^1O_2$), hydroxyl radical (·OH), hypochlorite (ClO^-), and peroxynitrite ($ONOO^-$), to cause a high level of oxidative stress in living cells.[43,44] Moreover, the autoxidation reaction is strongly catalyzed in the presence of metal catalysts including copper, iron, or cobalt-containing protein, such as hemeatin and hemoglobin. The oxidation production, diphenyl disulfide, may be reduced back to thiophenol by intracellular glutathione.[32] The toxicity caused directly or indirectly by thiophenol will be amplified by these autoxidation/reduction reactions.

To examine the practical utility of the new Ru(II) complex luminescence probe for imaging thiophenol in living systems, the $[Ru(bpy)(DNP\text{-}bpy)_2]^{2+}$-loaded HeLa cells were prepared by coincubating the cells with the complex, and then the cells were used for the luminescence imaging of thiophenol. As shown in Figure 7A, no intracellular luminescence could be observed after HeLa cells were coincubated with 50 μM $[Ru(bpy)(DNP\text{-}bpy)_2]^{2+}$ at 37 °C for 2 h. When the $[Ru(bpy)(DNP\text{-}bpy)_2]^{2+}$-loaded cells were coincubated with thiophenol (50 μM), the specific red luminescence from the cells was gradually enhanced with the increase of the incubation time (Figure 7B–H). These results indicate the increasing formation of $[Ru(bpy)(HP\text{-}bpy)_2]^{2+}$ in the cells, and demonstrate that $[Ru(bpy)(DNP\text{-}bpy)_2]^{2+}$ can be easily transferred into the cultured HeLa cells by an ordinary coincubation method to trap the intracellular thiophenol molecules. By analyzing the recorded images, the exogenous thiophenol could be taken up into the cells in less than 10 min (Figure 7A–C). After 20 min incubation, the luminescence distribution of thiophenol in the cells could be clearly observed and the localization profiles remained unchanged for the extended incubation time (Figure 7D–H). Figure 8 shows the quantitative analysis result of the luminescence intensity distribution in the 1 h thiophenol-treated cells. It was notable that the strong luminescence mainly appeared in the nucleoli and around the nuclear membrane of the cells, and only the pale luminescence in the cytoplasm could be observed. The luminescence intensity of the nucleolus was found to be ~1.5 times higher than that of the nuclear membrane and ~2.3 times higher than that of the cytoplasm. These results clearly indicate

dx.doi.org/10.1021/bc200506w | Bioconjugate Chem. 2012, 23, 725–733

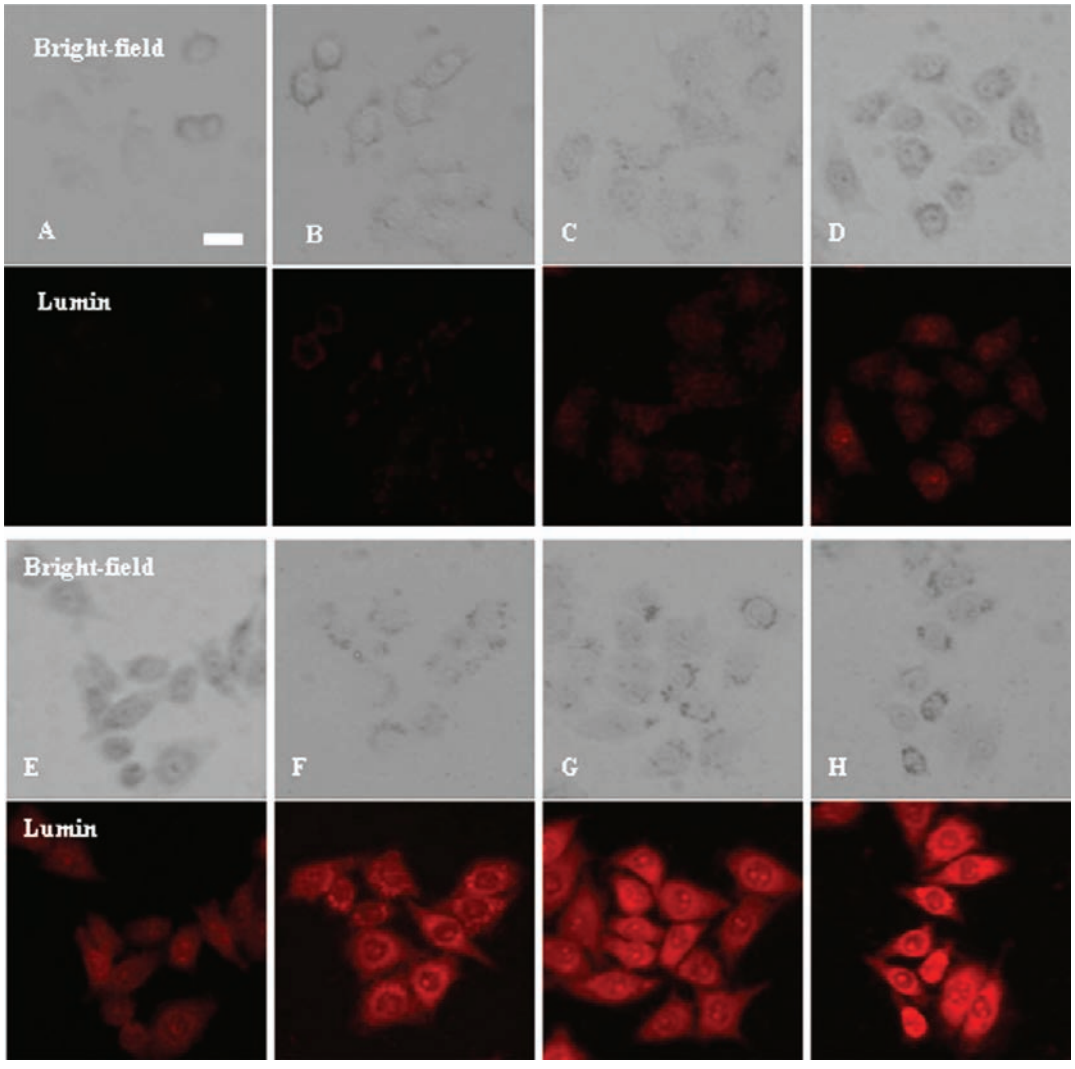

Figure 7. Luminescence images of the $[Ru(bpy)(DNP\text{-}bpy)_2]^{2+}$-loaded HeLa cells in the presence of thiophenol at different incubation times (A, 0 min; B, 5 min; C, 10 min; D, 20 min; E, 30 min; F, 40 min; G, 50 min; H, 60 min). Scale bar: 10 μm.

that the concentrations of probe molecules in nucleolus and perinuclear regions are significantly higher than that in cytoplasm, which is similar to the subcellular localization of the reported Eu^{3+}-azathiaxanthone complex.[45] Moreover, like some malignant cells, more than two nucleoli were also observed in the examined HeLa cells.[45,46]

The possible leakage of the probe molecules after internalization by the cells may be a concern to cell imaging for a new luminescence probe. To evaluate the intracellular retention of the probe, the $[Ru(bpy)(DNP\text{-}bpy)_2]^{2+}$-loaded cells were assessed by a time-lapse experiment: the HeLa cells were incubated with 50 μM of $[Ru(bpy)(DNP\text{-}bpy)_2]^{2+}$ for 2 h at 37 °C in a 5% CO_2/95% air incubator, and washed five times with the isotonic saline solution, and then treated with thiophenol for another 1 h. After washing, the luminescence images of the cells were recorded for a period of 60 at 10 min intervals. As shown in SI Figure S9, there were no significant changes in the luminescence intensity during the period of 60 min, suggesting that the reaction product of $[Ru(bpy)(DNP\text{-}bpy)_2]^{2+}$ and thiophenol, $[Ru(bpy)(HP\text{-}bpy)_2]^{2+}$, has excellent intracellular retention.

To examine the photostability of $[Ru(bpy)(HP\text{-}bpy)_2]^{2+}$ in the cells, the 1 h thiophenol-treated $[Ru(bpy)(DNP\text{-}bpy)_2]^{2+}$-loaded HeLa cells were illuminated for 15 min by successive intense irradiation of 450−490 nm light from a 100 W Hg lamp, and the luminescence images of the cells were acquired during the photobleaching experiment at 3 min intervals. As shown in SI Figure S10, the red signals from the cells could still be observed clearly after 15 min irradiation. This result indicates that the photobleaching of the Ru(II) complex in the cells is rather slow, suggesting that the dynamic intracellular process of thiophenol in living systems could be tracked long-term by using $[Ru(bpy)(DNP\text{-}bpy)_2]^{2+}$ as a luminescence probe.

As a new luminescence probe for monitoring the behavior of thiophenol in living cells, the cytotoxicity characteristic is another important factor to evaluate the practical utility of the probe. Therefore, the methyl thiazolyl tetrazolium (MTT) assay of $[Ru(bpy)(DNP\text{-}bpy)_2]^{2+}$ (0, 50, 100 μM) in HeLa cells was performed. As shown in SI Figure S11, no obvious effect on the cell proliferation was found after the cells were incubated with 50 μM of $[Ru(bpy)(DNP\text{-}bpy)_2]^{2+}$ for 4 h. When the concentration of $[Ru(bpy)(DNP\text{-}bpy)_2]^{2+}$ was increased to 100 μM, the cell viability still remained above 97%. These results indicate that the toxicity of $[Ru(bpy)(DNP\text{-}bpy)_2]^{2+}$ is low to the cultured HeLa cells.

dx.doi.org/10.1021/bc200506w | *Bioconjugate Chem.* 2012, 23, 725−733

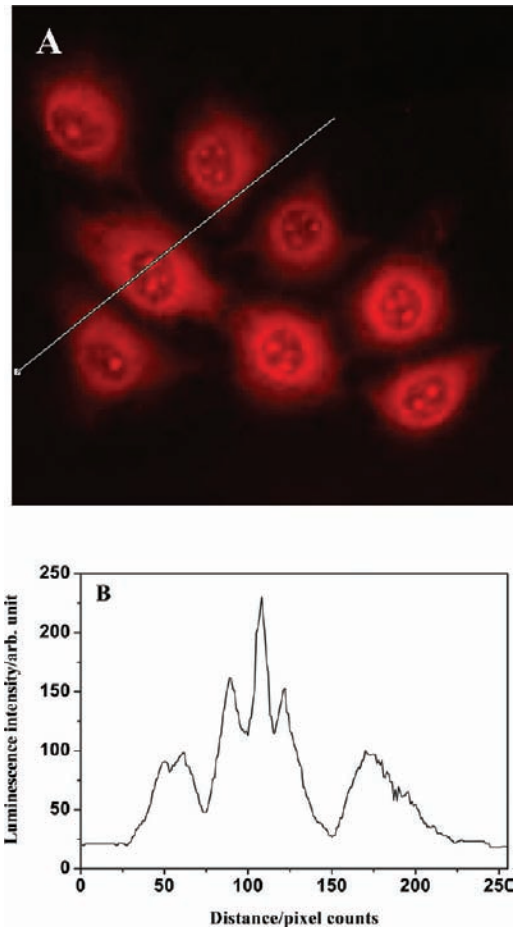

Figure 8. Luminescence image (A) of the 1 h thiophenol-treated $[Ru(bpy)(DNP\text{-}bpy)_2]^{2+}$-loaded HeLa cells, and the luminescence intensity profile along the line in the image (B).

CONCLUSIONS

In summary, we designed, synthesized, and characterized a systematic series of Ru(II)-bipyridine complex derivatives that can be used as luminescence probes for highly selective and sensitive detection of thiophenol in aqueous solutions with a large dynamic range and low detection limit. To further enhance the on-to-off switching contrast ratio for a Ru(II) complex, we discovered a new strategy by considering both the unsymmetry and the number of the electron acceptor groups in a complex. Our results reveal the fact that the luminescence quantum yields of the Ru(II) complexes are influenced by the alteration of the structure and symmetry of the unitary complex. A thorough investigation of the luminescence properties of $[Ru(bpy)_{3-n}(DNP\text{-}bpy)_n]^{2+}$ (n = 1, 2, 3) for sensing thiophenol indicates that the unsymmetric $[Ru(bpy)(DNP\text{-}bpy)_2]^{2+}$ has the lowest quantum yield in dark state, showing the highest on-to-off contrast ratio and best luminescence response to thiophenol. The complex was used as a luminescence probe for the quantitatively cellular imaging of thiophenol. The results demonstrated the practical utility and advantages of the probe for examining the distribution and dynamic process of thiophenol in living cells. These achievements provide a new flexible strategy for the rational design of Ru(II) complex-based luminescence bioprobes.

EXPERIMENTAL SECTION

Materials and Physical Measurements. HeLa cells were obtained from Dalian Medical University. The isotonic saline solution consisting of 140 mM NaCl, 10 mM glucose, and 3.5 mM KCl was prepared in our laboratory. The concentrated stock solution (10 mM) of thiophenol was prepared by dissolving thiophenol in acetonitrile and diluted to suitable concentrations with aqueous buffers before use. Unless otherwise stated, all chemical materials were purchased from commercial sources and used without further purification.

The NMR spectra were recorded on a Bruker Avance spectrometer (400 MHz for ^1H and 100 MHz for ^{13}C). ESI-MS spectra were measured on a Q-TOF Micro MS spectrometer. Absorption spectra were measured on a Perkin-Elmer Lambda 35 UV−vis spectrometer. Emission lifetimes were measured on an ISS-Chronos multifrequency cross-correlation phase and modulation lifetime spectrometer (ISS Inc., Champaign, IL). Elemental analysis was carried out on a Vario-EL analyzer. Luminescence spectra were measured on a Perkin-Elmer LS 50B luminescence spectrometer with excitation and emission slits of 10 nm. All bright-field imaging and luminescence imaging measurements were carried out on a Nikon TE2000-E luminescence microscope. The microscope, equipped with a 100 W mercury lamp, a Nikon B-2A filter (excitation filter, 450−490 nm; dichroic mirror, 505 nm; emission filter, >520 nm), and a color CCD camera system (RET-2000R-F-CLR-12-C, Qimaging Ltd.), was used for the luminescence imaging measurements with an exposure time of 2 s.

Syntheses of the Ru(II) Complexes. The details of the syntheses and characterizations of all the Ru(II) complexes are shown in Supporting Information.

Luminescence Responses of $[Ru(bpy)_{3-n}(DNP\text{-}bpy)_n]^{2+}$ (n = 1, 2, 3) toward Thiophenol. The luminescence titration experiments were performed in 20 mM HEPES buffer at pH 7.0. Typically, the solutions of $[Ru(bpy)_{3-n}(DNP\text{-}bpy)_n]^{2+}$ (n = 1, 2, 3, 10 μM) containing different concentrations of thiophenol were stirred at 37 °C for 40 min, and then subjected to the luminescence measurements at room temperature. The time dependences of the luminescence responses of $[Ru(bpy)_{3-n}(DNP\text{-}bpy)_n]^{2+}$ (n = 1, 2, 3, 10 μM) to the addition of thiophenol (40 μM) were measured with the same buffer and reaction temperature as above. For each reaction time point (0, 5, 10, 15, 20, 25, 30, 35, 40, 45, 50, 55, 60 min), the luminescence intensities of the solutions were measured.

The luminescence response selectivity experiments of $[Ru(bpy)_{3-n}(DNP\text{-}bpy)_n]^{2+}$ (n = 1, 2, 3) toward different species were also carried out in 20 mM HEPES buffer at pH 7.0. After $[Ru(bpy)_{3-n}(DNP\text{-}bpy)_n]^{2+}$ (10 μM) was reacted with different species (100 μM) for 40 min at 37 °C, respectively, the solutions were subjected to the luminescence measurements. The competition experiments were performed with the solutions containing $[Ru(bpy)_{3-n}(DNP\text{-}bpy)_n]^{2+}$ (10 μM), thiophenol (40 μM), and various possibly interfering species (100 μM). After stirring for 40 min at 37 °C, the solutions were subjected to the luminescence measurements.

Luminescence Imaging of Thiophenol in Living Cells. HeLa cells were cultured in RPMI-1640 medium (Sigma-Aldrich, Inc.), supplemented with 10% fetal bovine serum (Corning Incorporated), 1% penicillin (Gibco), and 1% streptomycin (Gibco) at 37 °C in a 5% CO_2/95% air incubator. The concentrated stock solution of $[Ru(bpy)(DNP\text{-}bpy)_2]^{2+}$ (50 mM) was prepared by dissolving $[Ru(bpy)(DNP\text{-}bpy)_2]$-

dx.doi.org/10.1021/bc200506w | Bioconjugate Chem. 2012, 23, 725−733

$(PF_6)_2$ in dimethylsulfoxide (DMSO). Before cell loading, the solution was 1000-fold diluted with the cell culture medium (final concentration of the complex: 50 μM). The cultured HeLa cells in a 25 cm^2 glass culture bottle were washed with the culture medium, and then incubated with 5 mL of the above Ru(II) complex solution. After incubation for 2 h at 37 °C in a 5% CO_2/95% air incubator, the cells were washed five times with an isotonic saline solution consisting of 140 mM NaCl, 10 mM glucose, and 3.5 mM KCl, and then further incubated with the isotonic saline solution containing 50 μM of thiophenol. The luminescence images of the cells were recorded at different incubation times.

MTT Assay. HeLa cells were cultured in RPMI-1640 medium (Sigma-Aldrich, Inc.), supplemented with 10% fetal bovine serum (Corning Incorporated), 1% penicillin (Gibco), and 1% streptomycin (Gibco) at a density of 5×10^5 cells/mL in a 25 cm^2 glass culture bottle. After $[Ru(bpy)(DNP\text{-}bpy)_2]^{2+}$ (final concentration: 0, 50, or 100 μM) was added to the medium, the cells were incubated at 37 °C in a 5% CO_2/95% air incubator for 4 h, and then the culture medium was removed. The cells were further incubated for 4 h in the culture medium containing 20 μL of a PBS solution of 3-(4,5-dimethyl-2-thiazoyl)-2,5-diphenyltetrazolium bromide (MTT, Sigma, final concentration: 250 μg/mL). After the supernatants were removed, the cells were dissolved in 1.5 mL DMSO. The DMSO solution was 15-fold diluted, and then the absorbance at 540 nm was measured.

■ ASSOCIATED CONTENT

Supporting Information

Details of syntheses and characterizations of all the Ru(II) complexes, and supplementary figures. This material is available free of charge via the Internet at http://pubs.acs.org.

■ AUTHOR INFORMATION

Corresponding Author

*Tel/Fax: +86-411-84986041. E-mail addresses: zhiqiangye2001@yahoo.com.cn (Z.Y.); jingliyuan@yahoo.com.cn (J.Y.).

Notes

The authors declare no competing financial interest.

■ ACKNOWLEDGMENTS

Financial supports from the National Natural Science Foundation of China (Grant Nos. 20835001, 20975017) are gratefully acknowledged.

■ REFERENCES

(1) Valeur, B. (2002) *Molecular Fluorescence: Principles and Applications*, Wiley-VCH, New York.

(2) Kikuchi, K. (2010) Design, synthesis and biological application of chemical probes for bio-imaging. *Chem. Soc. Rev. 39*, 2048−2053.

(3) Shao, Q., and Xing, B. G. (2010) Photoactive molecules for applications in molecular imaging and cell biology. *Chem. Soc. Rev. 39*, 2835−2846.

(4) Que, E. L., Domaille, D. W., and Chang, C. J. (2008) Metals in neurobiology: probing their chemistry and biology with molecular imaging. *Chem. Rev. 108*, 1517−1549.

(5) Ko, S. K., Chen, X. Q., Yoon, J., and Shin, I. (2011) Zebrafish as a good vertebrate model for molecular imaging using fluorescent probes. *Chem. Soc. Rev. 40*, 2120−2130.

(6) Stich, M. I. J., Fischer, L. H., and Wolfbeis, O. S. (2010) Multiple fluorescent chemical sensing and imaging. *Chem. Soc. Rev. 39*, 3102−3114.

(7) Valeur, B., and Leray, I. (2000) Design principles of fluorescent molecular sensors for cation recognition. *Coord. Chem. Rev. 205*, 3−40.

(8) Xu., Z. C., Yoon, J., and Spring, D. R. (2010) Fluorescent chemosensors for Zn^2. *Chem. Soc. Rev. 39*, 1996−2006.

(9) Nolan, E. M., and Lippard, S. J. (2008) Tools and tactics for the optical detection of mercuric ion. *Chem. Rev. 108*, 3443−3480.

(10) Quan, D. T., and Kim., J. S. (2010) Fluoro- and chromogenic chemodosimeters for heavy metal ion detection in solution and biospecimens. *Chem. Rev. 110*, 6280−6301.

(11) McRae, R., Bagchi, P., Sumalekshmy, S., and Fahrni, C. J. (2009) In situ imaging of metals in cells and tissues. *Chem. Rev. 109*, 4780−4827.

(12) Kim, S. Y., Lee, D. H., Hong, J. I., and Yoon, J. (2009) Chemosensors for pyrophosphate. *Acc. Chem. Res. 42*, 23−31.

(13) Duke, R. M., Veale, E. B., Pfeffer, F. M., Kruger, P. E., and Gunnlaugsson, T. (2010) Colorimetric and fluorescent anion sensors: an overview of recent developments in the use of 1,8-naphthalimide-based chemosensors. *Chem. Soc. Rev. 10*, 3936−3953.

(14) Li, A. F., Wang, J. H., Wang, F., and Jiang, Y. B. (2010) Anion complexation and sensing using modified urea and thiourea-based receptors. *Chem. Soc. Rev. 39*, 3729−3745.

(15) Galbraith, E., and James, T. D. (2010) Boron based anion receptors as sensors. *Chem. Soc. Rev. 39*, 3831−3842.

(16) Kubik, S. (2010) Anion recognition in water. *Chem. Soc. Rev. 39*, 3648−3663.

(17) Miller, E. W., Tulyathan, O., Isacoff, E. Y., and Chang., C. J. (2007) Molecular imaging of hydrogen peroxide produced for cell signaling. *Nat. Chem. Biol. 3*, 263−267.

(18) Nagno, T., and Yoshimura, T. (2002) Bioimaging of nitric oxide. *Chem. Rev. 102*, 1235−1269.

(19) Rosenthal, J., and Lippard, S. J. (2010) Direct detection of nitroxyl in aqueous solution using a tripodal copper(II) BODIPY complex. *J. Am. Chem. Soc. 132*, 5536−5537.

(20) Mizusawa, K., Ishida, Y., Takaoka, Y., Miyagawa, M., Tsukiji, S., and Hamachi, I. (2010) Disassembly-driven turn-on fluorescent nanoprobes for selective protein detection. *J. Am. Chem. Soc. 132*, 7291−7293.

(21) Yount, J. S., Tsou, L. K., Dossa, P. D., Kullas, A. L., van der Velden, A. W. M., and Hang, H. C. (2010) Visible fluorescence detection of type III protein secretion from bacterial pathogens. *J. Am. Chem. Soc. 132*, 8244−8245.

(22) Sassolas, A., Leca-Bouvier, B. D., and Blum, L. J. (2008) DNA biosensors and microarrays. *Chem. Rev. 108*, 109−139.

(23) Wang, Y. X., Li, J. S., Wang, H., Jin, J. Y., Liu, J. H., Wang, K. M., Tan, W. H., and Yang, R. H. (2010) Silver ions-mediated conformational switch: facile design of structure-controllable nucleic acid probes. *Anal. Chem. 82*, 6607−6612.

(24) Lo, K. K. W., Tsang, K. H. K., Sze, K. S., Chung, C. K., Lee, T. K. M., Zhang, K. Y., Hui, W. K., Li, C. K., Lau, J. S. Y., Ng, D. C. M., and Zhu, N. Y. (2007) Non-covalent binding of luminescent transition metal polypyridine complexes to avidin, indole-binding proteins and estrogen receptors. *Coord. Chem. Rev. 251*, 2292−2310.

(25) Campagna, S., Puntoriero, F., Nastasi, F., Bergamini, G., and Balzani, V. (2007) Photochemistry and photophysics of coordination compounds: ruthenium. *Top. Curr. Chem. 280*, 117−214.

(26) Zhao, Q., Li, F. Y., and Huang, C. H. (2010) Phosphorescent chemosensors based on heavy-metal complexes. *Chem. Soc. Rev. 39*, 3007−3030.

(27) Zhao, Q., Huang, C. H., and Li, F. Y. (2011) Phosphorescent heavy-metal complexes for bioimaging. *Chem. Soc. Rev. 40*, 2508−2524.

(28) Li, C. Y., Yu, M. X., Sun, Y., Wu, Y. Q., Huang, C. H., and Li, F. Y. (2011) A nonemissive iridium(III) complex that specifically lights-up the nuclei of living cells. *J. Am. Chem. Soc. 133*, 11231−11239.

(29) Glazer, E. C., Magde, D., and Tor, Y. (2007) Ruthenium complexes that break the rules: structural features controlling dual emission. *J. Am. Chem. Soc. 129*, 8544−8551.

(30) Damrauer, N. H., Boussie, T. R., Devenney, M., and McCusker, J. K. (1997) Effects of intraligand electron delocalization, steric tuning,

and excited-state vibronic coupling on the photophysics of aryl-substituted bipyridyl complexes of Ru(II). *J. Am. Chem. Soc. 119*, 8253−8268.
(31) Damrauer, N. H., Weldon, B. T., and McCusker, J. K. (1998) Theoretical studies of steric effects on intraligand electron delocalization: implications for the temporal evolution of MLCT excited states. *J. Phys. Chem. A 102*, 3382−3397.
(32) Amrolia, P., Sullivan, S. G., Stern, A., and Munday, R. (1989) Toxicity of aromatic thiols in the human red blood cell. *J. Appl. Toxicol. 9*, 113−118.
(33) Hathaway, G. J., and Proctor, N. H. (2004) *Proctor and Hughes' Chemical Hazards of the Workplace*, Wiley-VCH, New York.
(34) Zhang, R., Ye, Z. Q., Wang, G. L., Zhang, W. Z., and Yuan, J. L. (2010) Development of a ruthenium(II) complex-based luminescent probe for imaging nitric oxide production in living cells. *Chem.—Eur. J. 16*, 6884−6891.
(35) Zhang, R., Yu, X. J., Ye, Z. Q., Wang, G. L., Zhang, W. Z., and Yuan, J. L. (2010) Turn-on luminescent probe for cysteine/homocysteine based on a ruthenium(II) complex. *Inorg. Chem. 49*, 7898−7903.
(36) Zhang, R., Yu, X. J., Yin, Y. J., Ye, Z. Q., Wang, G. L., and Yuan, J. L. (2011) Development of a heterobimetallic Ru(II)-Cu(II) complex for highly selective and sensitive luminescence sensing of sulfide anions. *Anal. Chim. Acta 691*, 83−88.
(37) Juris, A., Balzani, V., Barigelletti, F., Campagna, S., Belser, P., and Von Zelewsky, A. (1988) Ruthenium(II) polypyridine complexes: photophysics, photochemistry, electrochemistry, and chemiluminescence. *Coord. Chem. Rev. 84*, 85−277.
(38) Jiang, W., Fu, Q. Q., Fan, H. Y., Ho, J., and Wang, W. (2007) A highly selective fluorescent probe for thiophenols. *Angew. Chem., Int. Ed. 46*, 8445−8448.
(39) Lee, J. H., Lim, C. S., Tian, Y. S., Han, J. H., and Cho, B. R. (2010) A two-photon fluorescent probe for thiols in live cells and tissues. *J. Am. Chem. Soc. 132*, 1216−1217.
(40) Jiang, W., Cao, Y. T., Liu, Y., and Wang, W. (2010) Rational design of a highly selective and sensitive fluorescent PET probe for discrimination of thiophenols and aliphatic thiols. *Chem. Commun. 46*, 1944−1946.
(41) Lin, W. Y., Long, L. L., and Tan, W. (2010) A highly sensitive fluorescent probe for detection of benzenethiols in environmental samples and living cells. *Chem. Commun. 46*, 1503−1505.
(42) Mocak, J., Bond, A. M., Mitchell, S., and Scollary, G. (1997) Analytical chemistry division commission on electroanalytical chemistry. *Pure Appl. Chem. 69*, 297−328.
(43) Ozben, T. (2007) Oxidative stress and apoptosis: impact on cancer therapy. *J. Pharm. Sci. 96*, 2181−2196.
(44) Muller, F. L., Lustgarten, M. S., Jang, Y., Richardson, A., and Remmen, H. V. (2007) Trends in oxidative aging theories. *Free Radic. Biol. Med. 43*, 477−503.
(45) Yu, J., Parker, D., Pal, R., Poole, R. A., and Cann, M. J. (2006) A europium complex that selectively stains nucleoli of cells. *J. Am. Chem. Soc. 128*, 2294−2299.
(46) Horky, M., Kotala, V., Anton, M., and Wesierska-Gadek, J. (2002) Nucleolus and apoptosis. *Ann. N.Y. Acad. Sci. 973*, 258−264.

Bioconjugate Chemistry

Article

pubs.acs.org/bc

Sensitive Detection of Proteins Using Assembled Cascade Fluorescent DNA Nanotags Based on Rolling Circle Amplification

Qingwang Xue,[†] Zhenguang Wang,[†] Lei Wang,*[,‡] and Wei Jiang*[,†]

[†]School of Chemistry and Chemical Engineering, [‡]School of Pharmacy, Shandong University, 250100 Jinan, P. R . China

ABSTRACT: A novel cascade fluorescence signal amplification strategy based on the rolling circle amplification (RCA)-aided assembly of fluorescent DNA nanotags as fluorescent labels and multiplex binding of the biotin−streptavidin system was proposed for detection of protein target at ultralow concentration. In the strategy, fluorescent DNA nanotags are prepared relying on intercalating dye arrays assembled on nanostructured DNA templates by intercalation between base pairs. The RCA product containing tandem-repeat sequences could serve as an excellent template for periodic assembly of fluorescent DNA nanotags, which were presented per protein recognition event to numerous fluorescent DNA nanotags for assay readout. Both the RCA and the multiplex binding system showed remarkable amplification efficiency, very little nonspecific adsorption, and low background signal. Using human IgG as a model protein, the designed strategy was successfully demonstrated for the ultrasensitive detection of protein target. The results revealed that the strategy exhibited a dynamic response to human IgG over a three-decade concentration range from 1.0 pM to 1.0 fM with a limit of detection as low as 0.9 fM. By comparison with the assay of multiple labeling antibodies with the dye/DNA conjugate, the limit of detection was improved by 4 orders. The designed signal amplification strategy would hold great promise as a powerful tool to be applied for the ultrasensitive detection of target protein in immunoassay.

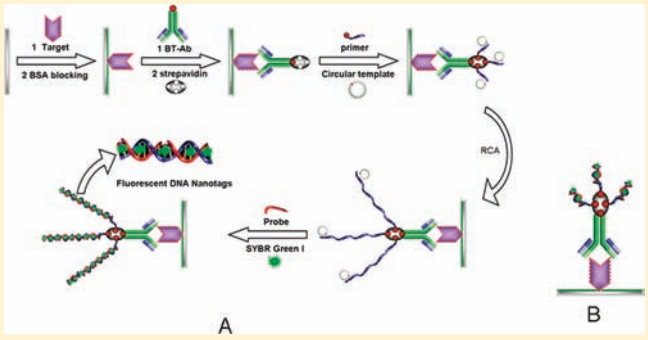

INTRODUCTION

Sensitive protein detection is critically important in basic discovery research and clinical practice, because a few molecules of protein are sufficient to affect the biological functions of cells and trigger pathophysiological processes.[1,2] Great efforts have been made to develop some new protein detection techniques to improve sensitivity.[2−10] Among them, fluorescence detection techniques combined with signal amplification are one of the most popular techniques.[11] In low-abundancy protein analysis, signal amplification is one of the most critical issues and is typically achieved by multiple fluorophore labeling, such as organic dyes. However, two major difficulties, low fluorescence signal intensity and poor photostability, limit the sensitivity when these fluorophores are used. To achieve strong and photostable fluorescence signals, a series of functionalized nanoparticle probes, such as quantum dots, dye-doped nanoparticles, and nanoparticles whose surfaces were modified with enzymes or nucleic acids, have been developed to enhance recognition events of targets and significantly lower the detection limit for protein analysis.[3−10] These nanoparticles were used as carriers by biofunctionalization with antibodies or aptamers for recognization of targets. However, there are some limitations involved in using functionalized nanoparticles as signal probe, such as the stability in different reaction systems, compatibility with biomolecules, and dispersion in aqueous solutions, and reaction kinetics.[5,9,12−14] An extra functionalized process on the surface of these particles adds a step to the assay and may decrease analytical accuracy.[5,12,13] Furthermore, the variability of the probes often affects reproducibility and quantification.[15,16] The synthesis of such functionalized fluorescent nanoparticle probes also requires a complicated and tedious process and considerable synthetic expertise, and it is time-consuming.[10,17]

Herein, aiming at the need for detection of low-abundancy proteins and the problems existing in the amplification techniques by multiple fluorophores and nanoparticle probes, this work proposed a novel cascade fluorescence signal amplification strategy for ultrasensitive detection of protein, based on the rolling circle amplification (RCA)-aided and assembled cascade fluorescent DNA nanotags as signal label and multiplex binding of the biotin−streptavidin system. As seen in Scheme 1A, it integrated two advanced amplification techniques, rolling circle amplification, the fluorescence signal amplification of fluorescent DNA nanotags, and a general signal amplification method, the multiplex binding of the biotin−streptavidin system. RCA, an isothermal DNA amplification procedure, can generate a linear concatenated DNA molecule containing up to 1000 complementary copies of the circular DNA in 1 h.[18,19] The RCA product contains tandem-repeat sequences.[20] In the proposed method, the RCA product containing tandem-repeat sequences serves as an excellent template for periodic assembly of fluorescent DNA nanotags.

Received: October 8, 2011
Revised: February 21, 2012
Published: March 4, 2012

   dx.doi.org/10.1021/bc200537g | *Bioconjugate Chem.* 2012, 23, 734−739

Scheme 1. Illustration of the Immunoassy Labeling Formats[a]

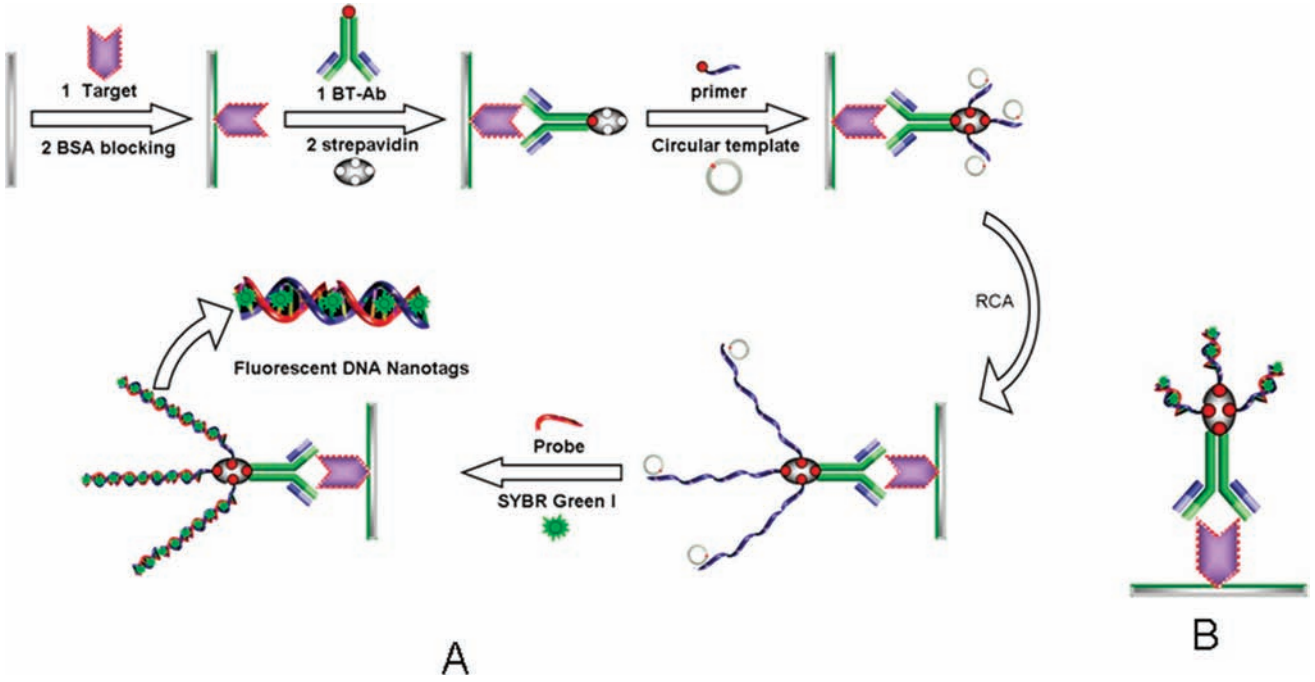

[a](A) Using assembled cascade fluorescent DNA nanotags based on rolling circle amplification. (B) Using a SYBR Green I/DNA conjugate. DNA: 30 bp.

The use of RCA provides a high ratio of assembled fluorescent DNA nanotags to labeling protein. This is an advantage for substantially improving the detection sensitivity. Moreover, the method does not require complicated conjugation chemistry and considerable synthetic expertise, and it shows fast reaction kinetics and simple manipulation in the process of assembling cascade fluorescent DNA nanotags as labels.

"Fluorescent DNA nanotags" represent a bright, self-assembling multichromophore array.[21] In the array, a fluorescent DNA probe is bound noncovalently to a double-helical DNA nanostructure at high ratios by the specific binding interaction with DNA. DNA nanostructures serve as a template for organizing and concentrating multiple fluorescent dye molecules into fluorescent arrays to amplify fluorescence. DNA steric constraints impede multiple dyes from binding at the same intercalation site and keep them far enough away from each other to prevent self-quenching. Also, the free (unbound) probe does not emit fluorescence; measurement can be performed without a separation step.[9,14] "Fluorescent DNA nanotags" resolve the self-quenching of electronically excited dyes by ground-state dyes at high labeling densities and amplify fluorescence.[21] Furthermore, the signal amplification efficiency of the fluorescent DNA nanotags can potentially be enhanced substantially by using longer DNAs to carry more fluorescent dyes. To the best of our knowledge, there is no previous report on using the RCA-aided and assembled cascade fluorescent DNA nanotags as signal labels to further amplify the fluorescence signal. Here, the integration of a series of amplification techniques further extends the application of fluorescent DNA nanotags.

This work used human IgG as a model protein to verify the practicability of the proposed strategy. As seen in Scheme 1A, in our experiment, human IgG was first immobilized on an epoxy-coated glass slide. Human IgG captured on the substrate was then detected by its immunoreaction with biotinylated mouse antihuman antibody. The streptavidin bound to the biotinylated immunocomplex could anchor three biotinylated single-strand oligonucleotides to act as RCA primers for binding of the circular template. In the presence of nucleotides and phi29 DNA polymerase, the RCA was initiated to produce micrometer-long single-strand DNA, which contained hundreds of tandem-repeat sequences for linear periodic assembly of a large number of DNA complementary detection probes. A highly fluorescent DNA probe, SYBR Green I (SG), is bound to the double-stranded oligonucleotide at high ratios by the specific binding interaction to assemble cascade fluorescent DNA nanotags for enhancement of recognition event.[9] Because the free (unbound) probe does not emit fluorescence, measurement can be performed without a wash step. Fluorescence intensity increase of the cascade fluorescent DNA nanotags further enhanced the sensitivity of the proposed protocol for monitoring the recognition events of low-abundancy protein.

EXPERIMENTAL SECTION

Materials and Reagents. Human immunoglobulin G (IgG), monoclonal antihuman IgG-Biotin conjugate (Clone HP-6017), 3-glycidyloxypropyltrimethoxysilane, and bovine serum albumin were purchased from Sigma-Aldrich Co. (St. Louis, MO, USA). The oligonucleotides with the following sequences were obtained from the Genscript Corporation (Nanjing, China): biotinylated primer, 5′-biotin-AAA AAA AAA AAA AAA CAC AGC TGA GGA TAG GAC AT-3′; circular template, 5′-p-CTC AGC TGT GTA ACA ACA TGA AGA TTG TAG GTC AGA ACT CAC CTG TTA GAA ACT GTG AAG ATC GCT TAT TAT GTC CTA TC-3′; DNA probe, 5′-TCA GAA CTC ACC TGT TAG-3′. Phi29 DNA polymerase, T4 DNA ligase, and dNTP were obtained from Fermentas (Lithuania). Streptavidin was obtained from Sigma-Aldrich Co. (St. Louis, MO, USA). Other chemicals (analytical

dx.doi.org/10.1021/bc200537g | Bioconjugate Chem. 2012, 23, 734–739

grade) were obtained from standard reagent suppliers. Microscope cover glasses (22 × 22 mm^2) were purchased from Cole-Parmer (Illinois, USA).

The physiological buffer saline (PBS) consisted of 0.15 M NaCl, 7.6 mM NaH_2PO_4, and 2.4 mM Na_2HPO_4 (pH 7.4). PBS-T buffer consisted of 0.15 M NaCl, 7.6 mM Na_2HPO_4, 2.4 mM NaH_2PO_4, and 0.05% Tween-20 (pH 7.4). TE buffer consisted of 10 mM Tris HCl and 1.0 mM Na_2EDTA (pH 8.0). A phosphate buffer (pH 7.0) containing 1% BSA was used as a buffer for blocking.

Apparatus. We used an inverted microscope (model IX81, Olympus, Tokyo, Japan) equipped with a high-numerical-aperture 60× objective lens (PlanApo, Olympus, Tokyo, Japan), a mercury lamp (OSRAM, HBO, 103w/2, Germany), a mirror unit consisting of a 470−490 nm excitation filter (BP470−490), a 505 nm dichromatic mirror (DM 505), a 510−550 nm emission filter (IF510−550), and a 16 bit thermoelectrically cooled EMCCD (Cascade 512B, Tucson, AZ, USA). The EMCCD was used for collecting the fluorescent images. Imaging acquisition and data analysis were performed using the *MetaMorph* software (Universal Imaging, Downingtown, PA, USA).

Circularization of DNA Template. 1.465 nmol of biotinylated primer oligonucleotide and 1.465 nmol of circular template oligonucleotide were mixed in 200 μL of ligation buffer (50 mM, pH 7.5 Tris-HCl buffer, 10 mM $MgCl_2$, 10 mM dithiothreitol, and 0.5 mM ATP) and incubated at 37 °C for 30 min. Then, 2.5 units of T4 DNA ligase was added and incubated at 37 °C for 2 h. After ligation, T4 DNA ligase was inactivated by heating the reaction mixture at 65 °C for 10 min. The resulting mixture could be used directly or stored at −20 °C.

Substrate Preparation and Antigen Coating. The epoxy-functionalized glass surfaces were prepared according to the modification described in the literature.[9] The freshly prepared substrate surface was coated with 100 μL human IgG solutions of various concentrations (1.0, 0.5, 0.1, 0.05, 0.01, 0.001 pM). The substrate was immediately placed in a sealed Petri dish at 37 °C for 5 h. After that, the substrate was washed three times with PBS-T washing buffer to remove unbound human IgG and impurities.

Blocking. We used a phosphate buffer containing 1% BSA as a blocking buffer. To the substrate of antigen coating was added 100 μL of blocking, and then, the substrate was incubated for 3 h. After that, the substrate was washed three times with PBS-T washing buffer.

Immunoreaction. Antihuman IgG-biotin solution was 40-fold diluted with a phosphate buffer (pH 7.4) before being used, and 100 μL of the diluted solution of various concentrations (40, 20, 4.0, 2.0, 0.4, 0.04 pM) was then added to the substrate. The biotinylated monoclonal antihuman IgG (BT-Ab) molecule was bound to the human IgG through the immunoreaction. After that, the substrate was deposited hermetically for 2 h at 37 °C. Finally, nonspecifically absorbed antibodies were washed by PBS-T washing buffer.

Rolling Circle Amplification and Assembly of Fluorescent DNA Nanotags. After the immunoreaction, the wells were incubated with 100 μL of 1.0 nM streptavidin solution (SA) (0.15 M NaCl, 7.6 mM NaH_2PO_4, and 2.4 mM Na_2HPO_4, pH 7.4, 0.2% BSA, 100 μg/mL salmon sperm DNA) per well at 37 °C for 120 min. After washing three times with 600 μL of PBS-T washing buffer, 100 μL of circularization mixture containing 4.0 nM circular template DNA and 4.0 nM biotinylated primer DNA was added to each well and incubated at 37 °C for 30 min. After the wells were washed three times with 600 μL of PBS-T washing buffer, RCA reaction was carried out at 37 °C for 80 min in 50 μL of reaction buffer (50 mM, pH 7.5 Tris HCl buffer, 10 mM magnesium acetate, 33 mM potassium acetate, 1 mM dithiothreitol, and 0.1% Tween 20) with 0.8 units of phi29 DNA polymerase and 50 μL of 10 mM dNTP. After the wells were carefully washed three times with 600 μL of PBS-T washing buffer, 100 μL of 60 nM complementary detection DNA probe was added to each well and hybridized at 37 °C for 30 min. After the well were carefully washed three times with 600 μL of washing buffer to remove the nonhybridized DNA detection probe, 100 μL 0.2 μM of a highly fluorescent DNA probe, SYBR Green I, was added to each well and incubated to assemble cascade fluorescent DNA nanotags for 10 min at room temperature.[9] Because the free (unbound) probe does not emit fluorescence, measurement can be performed without a wash step.

Imaging System. An inverted epi-fluorescence imaging system was used to acquire all fluorescence images for the array. The system included a mercury light source, a mirror unit consisting of a 470−490 nm excitation filter (BP470−490), a 505 nm dichromatic mirror (DM 505), a 510−550 nm emission filter (IF510−550), microscope objectives (model IX81, Olympus, Tokyo, Japan), and a 16 bit thermoelectrically cooled EMCCD (Cascade 512B, Tucson, AZ, USA). The fluorescence images were obtained by the excitation light within the wavelength 470−490 nm of the mercury lamp. Thirty images on the coverslip substrate were acquired one by one by moving the coverslip. The images were analyzed with *MetaMorph* software. Fluorescence quantitation was performed by the *MetaMorph* software. Fluorescence intensity values were acquired for background and signal images using a 90 ms image exposure time and 60× magnification.

RESULTS AND DISCUSSION

Characterization of RCA Reaction. To verify the amplification of the RCA reaction, the agarose gel electrophoresis experiment was performed. The RCA products were investigated by gel electrophoresis. It is observed that the RCA products in lane 2 reaction show extremely low mobility in Figure 1A. The anticipated high molecular weight of the RCA product was confirmed in lane 2. Compared with lane 2, lane 1 displayed no bands in the negative control experiment. These results give immediate evidence for the high molecular weight of these products, indicating that the proposed method could provide enormous signal amplification in immunoassay.[20] In addition, the amplification of the RCA reaction was also verified using fluorescent imaging experiment. In the experiments, although most of the ss-DNA molecules generated by RCA were condensed into small, compact objects, we observed many extended molecules, which were several micrometers long, lying on the surface of the glass slide. The discernible strands of RCA product were observed in Figure 1B with very low frequency by the assembled fluorescent DNA nanotags.

Effects of SA Concentration and Time-Dependent Signal Amplification of RCA. With a fixed design strategy, the performance of the developed immunoassay based on RCA-aided and assembled cascade fluorescent DNA nanotags and multiplex binding of the biotin−streptavidin system is still strongly influenced by the assay conditions such as SA concentration and RCA reaction conditions. Figure 2 shows the response of the concentration used for SA in the assembled

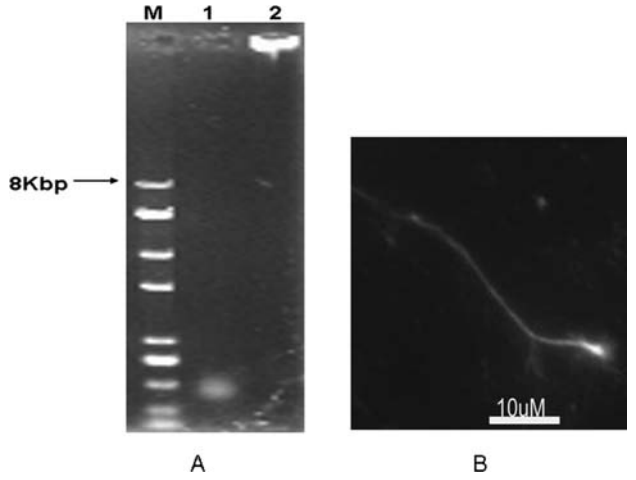

Figure 1. (A) Agarose gel (0.7%) electrophoresis experiments. The products of RCA reaction (1 h) (indicated by 1−2) were denatured at 95 °C for 5 min and quenched with ice-cooled water for 10 min. The marker was indicated by M. The high-molecular-weight RCA products are observed in lines 2. (B) Observation of fluorescent image of the assembled cascade fluorescent DNA nanotags based on noncondensed rolling circle DNA product, lying on the surface of a slide.

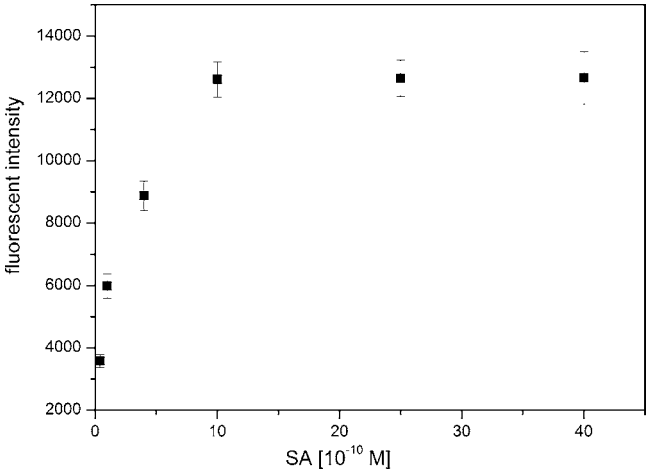

Figure 2. Influence of SA concentration on the fluorescent intensity signal responding to 1 pM of human IgG.

fluorescent DNA nanotag−RCA assay. In these cases, different concentrations of SA were incubated with the biotinylated mouse antihuman antibody in the assay. It is clear from Figure 2 that the response increases substantially when the concentration of SA changes from 40 pM to 1.0 nM. No significant increase in the sensor response occurred from 1.0 to 4.0 nm. As a result, the optimal concentration of SA for the assay was selected as 1.0 nM in subsequent studies.

To generate more tandem repeat complementary copies of the circular template, a long RCA reaction time is expected to yield enhanced signal amplification. The effect of RCA reaction time on the fluorescent signal was shown in Figure 3. It is clear that the fluorescence intensity response was very slow when the RCA reaction time is at the initial 10 min, indicating a relatively slow rate of RCA reaction. The fluorescence intensity response exhibits a rapid increase with a further increase in the RCA reaction time after 10 min and trends to a constant value at 60 min, indicating saturation of the RCA product due to the exhaustion of RCA substrates or inactivation of the phi 29

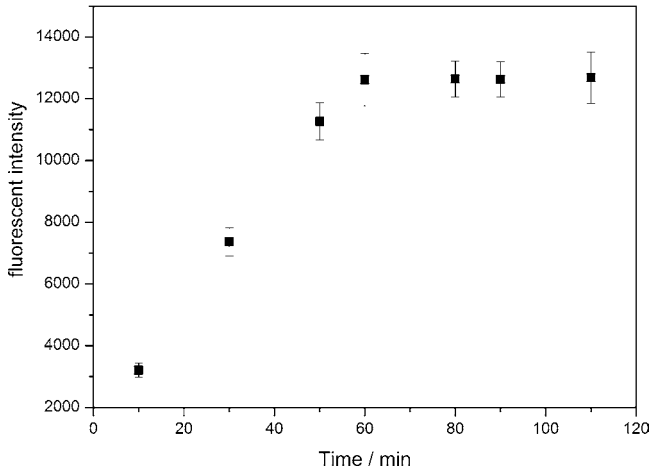

Figure 3. Influence of RCA reaction time on the fluorescence intensity signal responding to 1 pM of human IgG.

DNA polymerase. Thus, 80 min was selected as the optimum time for the RCA reaction in the experiment.

Signal Amplification Performance of Fluorescent DNA Nanotags Based on RCA Strategy. As seen in Scheme 1B, to further test the signal amplification of the assembled cascade fluorescent DNA nanotags based on RCA strategy, a signal amplification method based on SG/DNA (DNA: 30 bp) conjugate as labels was designed as a control (Scheme 1B). Figure 4 shows that the responses of the assembled cascade

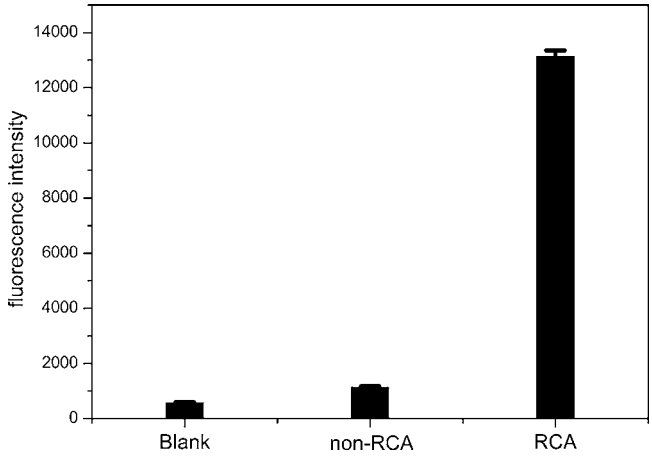

Figure 4. Fluorescence intensity signals using the assembled cascade fluorescent DNA nanotags based on RCA and using the SYBR Green I/ds-DNA conjugate as signal amplification methods for detection of human IgG. Conditions: 1.0 pM human IgG. ds-DNA: 30 bp.

fluorescent DNA nanotag based on the RCA method for human IgG at the same concentrations were significantly higher than those of the SG/DNA conjugate-label method. After subtracting the response to blank solution, the fluorescence intensity obtained with the assembled cascade fluorescent DNA nanotags based on RCA as labeling method for 1.0 pM of human IgG was about ∼10 times those based on the SG/DNA conjugate as labeling method, showing remarkable amplification performance. More interestingly, these methods showed nearly similar responses to the human IgG-free sample, indicating that the RCA process did not visibly increase the background response. Also, we found that a larger-scale assembled fluorescent DNA nanotag based on an RCA product

dx.doi.org/10.1021/bc200537g | *Bioconjugate Chem.* 2012, 23, 734−739

could be generated at lower analyte concentration due to the excess substrates and decreasing steric inhibition. Thus, the amplification efficiency increased with the decreasing protein concentration, which greatly improved the sensitivity of the designed strategy for detection of low-abundancy protein.

Analytical Performance of the Assembled Fluorescent DNA Nanotags Based on Rolling Circle Amplification as Labeling Strategy. In view of the outstanding ability of the assembled cascade fluorescent DNA nanotags based on RCA for signal amplification, the dynamic range of the designed method for detection of human IgG analyte was examined. The fluorescence intensity was proportional to the logarithm value of human IgG concentration over a three-decade range from 1 fM to 1 pM with a linear correlation coefficient of 0.995 (Figure 5). The calculated limit of lower detection is 0.9 fM in a 3 σ

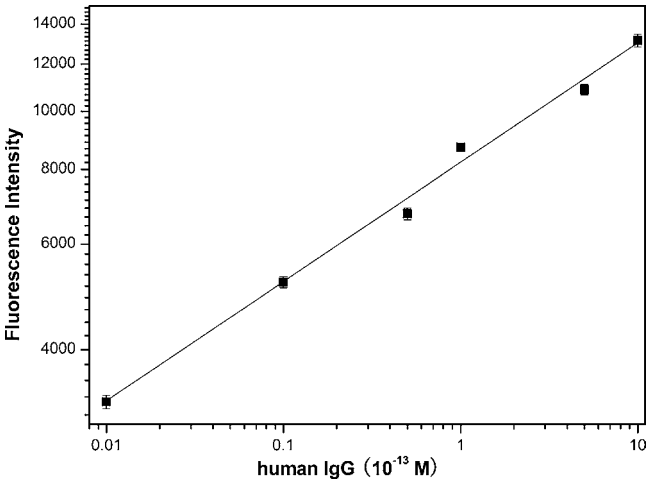

Figure 5. Linear relationship between the fluorescence intensity and the concentration of human IgG (n = 3). Each data point represents an average of three measurements (each error bar indicates the standard deviation).

rule. By comparison with the assay of multiple labeling antibodies with the dye/DNA conjugate, the limit of detection was improved by 4 orders.[14] The ultrahigh sensitivity and the broad dynamic range were attributed to the following causes: (i) a high ratio of assembled fluorescent DNA nanotags to labeling Ab; (ii) excellent signal amplification capability of RCA and fluorescent DNA nanotags; and (iii) multiplex binding of the biotin−streptavidin and very little nonspecific adsorption.

To estimate the reproducibility of the assembled cascade fluorescent DNA nanotags based on RCA strategy, the intra-assay imprecision of five different wells at one assay and interassay imprecision at five different assays for detection of 1.0 pM human IgG were examined. The intra-assay fluorescent signal intensity differed by 2.2%, and the coefficient of variation of interassay fluorescent signal intensity was 4.6%, indicating that the assembled cascade fluorescent DNA nanotags based on RCA amplification strategy was robust and could be used for protein analysis with acceptable reproducibility.

The specificity and matrix effect were further examined. The fluorescence intensities responding to 1 pM mouse IgG and BSA were similar to that of blank phosphate buffer (Figure 6), demonstrating that the designed strategy was specific for the target protein. The fluorescence intensities obtained after treatment with 1 pM human IgG in phosphate buffer, 50% cell culture fluid, 50% fetal calf serum, and 5% BSA did not show

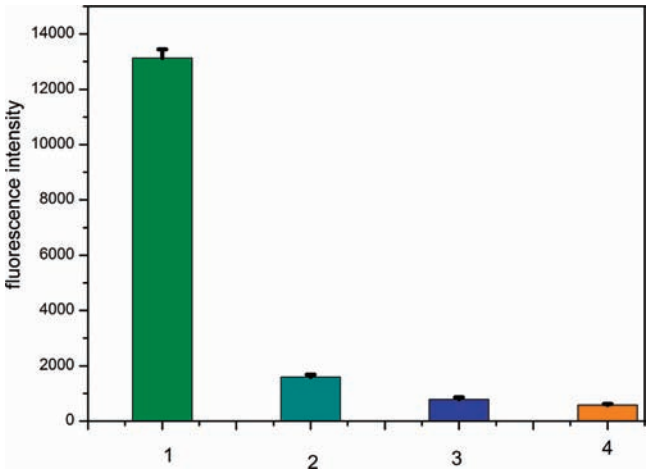

Figure 6. Fluorescence intensities responding to 1 pM human IgG (1), 1 pM mouse IgG (2), 1 pM BSA (3), and 0 (4). Conditions: Each data point represents an average of three measurements (each error bar indicates the standard deviation).

any significant difference (Figure 7), indicating very little interference of complex matrices on the designed strategy. The

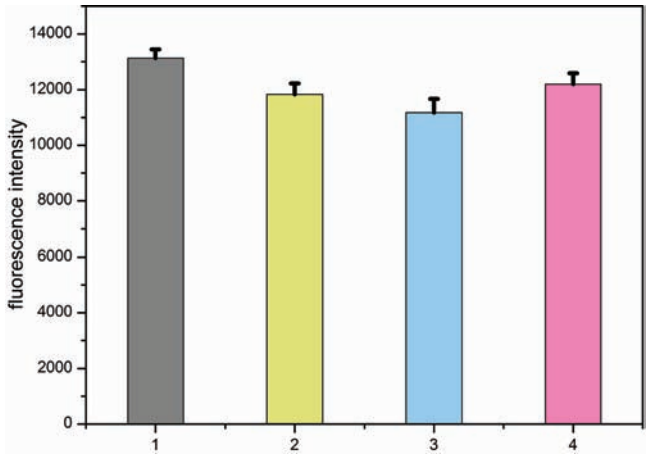

Figure 7. Fluorescence intensities responding to 1 pM human IgG (1) in phosphate buffe, and 1 pM IgG in 50% cell culture fluid (2), 50% fetal calf serum (3), and 5% BSA (4). Conditions: Each data point represents an average of three measurements (each error bar indicates the standard deviation).

high specificity and low matrix effect could further ensure the practicality of the proposed strategy.

CONCLUSION

In conclusion, a versatile cascade fluorescence signal amplification strategy was developed to implement ultrasensitive protein detection by using the assembled cascade fluorescent DNA nanotags based on RCA technique as fluorescent labels and the multiplex binding of the biotin−streptavidin system. It was demonstrated that the proposed strategy offers an enormous ratio of fluorescent DNA nanotags to label target molecules and shows a broad dynamic range, ultrahigh sensitivity, acceptable reproducibility, excellent specificity, and a low matrix effect. Futhermore, the method does not require complicated conjugation chemistry and shows fast reaction kinetics and simply manipulation in assembly of

dx.doi.org/10.1021/bc200537g | Bioconjugate Chem. 2012, 23, 734−739

fluorescent DNA nanotags. Compared with functionalized nanoparticles labels, it avoids the complicated and tedious synthesis process. The proposed strategy would become a powerful tool to be applied for the ultrasensitive detection of target protein in immunoassay.

AUTHOR INFORMATION

Corresponding Author

*Tel: +86 531 88363888. fax: +86 531 88564464. E-mail: wjiang@sdu.edu.cn; wangl-sdu@sdu.edu.cn.

Notes

The authors declare no competing financial interest.

ACKNOWLEDGMENTS

This project was supported by the National Natural Science Foundation of China (Grant Nos. 20875056, 21175081, 21175082) and the Natural Science Foundation of Shandong Province in China (Grant No. Z2008B05).

REFERENCES

(1) Gosling, J. P. (1990) A decade of development in immunoassay methodology. *Clin. Chem. 36*, 1408−27.

(2) Schweitzer, B., Wiltshire, S., Lambert, J., O'Malley, S., Kukanskis, K., Zhu, Z., Kingsmore, S. F., Lizardi, P. M., and Ward, D. C. (2000) Immunoassays with rolling circle DNA amplification: a versatile platform for ultrasensitive antigen detection. *Proc. Natl. Acad. Sci. U. S. A. 97*, 10113−9.

(3) Fu, A., Gu, W., Boussert, B., Koski, K., Gerion, D., Manna, L., Le Gros, M., Larabell, C. A., and Alivisatos, A. P. (2007) Semiconductor quantum rods as single molecule fluorescent biological labels. *Nano Lett. 7*, 179−82.

(4) Nam, J. M., Thaxton, C. S., and Mirkin, C. A. (2003) Nanoparticle-based bio-bar codes for the ultrasensitive detection of proteins. *Science 301*, 1884−6.

(5) Oh, B. K., Nam, J. M., Lee, S. W., and Mirkin, C. A. (2006) A fluorophore-based bio-barcode amplification assay for proteins. *Small 2*, 103−8.

(6) Mani, V., Chikkaveeraiah, B. V., Patel, V., Gutkind, J. S., and Rusling, J. F. (2009) Ultrasensitive immunosensor for cancer biomarker proteins using gold nanoparticle film electrodes and multienzyme-particle amplification. *ACS Nano 3*, 585−94.

(7) Nam, J. M., Jang, K. J., and Groves, J. T. (2007) Detection of proteins using a colorimetric bio-barcode assay. *Nat. Protoc. 2*, 1438−44.

(8) Fan, A., Lau, C., and Lu, J. (2005) Magnetic bead-based chemiluminescent metal immunoassay with a colloidal gold label. *Anal. Chem. 77*, 3238−42.

(9) Xue, Q., Jiang, D., Wang, L., and Jiang, W. (2010) Quantitative detection of single molecules using enhancement of Dye/DNA conjugate-labeled nanoparticles. *Bioconjugate Chem. 21*, 1987−93.

(10) Liu, G., Wang, J., Wu, H., and Lin, Y. (2006) Versatile apoferritin nanoparticle labels for assay of protein. *Anal. Chem. 78*, 7417−23.

(11) Zhu, H., and Snyder, M. (2003) Protein chip technology. *Curr. Opin. Chem. Biol. 7*, 55−63.

(12) Zhao, X., Tapec-Dytioco, R., and Tan, W. (2003) Ultrasensitive DNA detection using highly fluorescent bioconjugated nanoparticles. *J. Am. Chem. Soc. 125*, 11474−5.

(13) Xiang, D. S., Zeng, G. P., and He, Z. K. (2011) Magnetic microparticle-based multiplexed DNA detection with biobarcoded quantum dot probes. *Biosens. Bioelectron. 26*, 4405−10.

(14) Zhang, Q., and Guo, L. H. (2007) Multiple labeling of antibodies with dye/DNA conjugate for sensitivity improvement in fluorescence immunoassay. *Bioconjugate Chem. 18*, 1668−72.

(15) Cheng, W., Yan, F., Ding, L., Ju, H., and Yin, Y. (2010) Cascade signal amplification strategy for subattomolar protein detection by rolling circle amplification and quantum dots tagging. *Anal. Chem. 82*, 3337−42.

(16) Zhang, H., Zhao, Q., Li, X. F., and Le, X. C. (2007) Ultrasensitive assays for proteins. *Analyst 132*, 724−37.

(17) Wang, J., Liu, G., and Merkoci, A. (2003) Electrochemical coding technology for simultaneous detection of multiple DNA targets. *J. Am. Chem. Soc. 125*, 3214−5.

(18) Konry, T., Hayman, R. B., and Walt, D. R. (2009) Microsphere-based rolling circle amplification microarray for the detection of DNA and proteins in a single assay. *Anal. Chem. 81*, 5777−82.

(19) Baner, J., Nilsson, M., Mendel-Hartvig, M., and Landegren, U. (1998) Signal amplification of padlock probes by rolling circle replication. *Nucleic Acids Res. 26*, 5073−8.

(20) Zhou, L., Ou, L. J., Chu, X., Shen, G. L., and Yu, R. Q. (2007) Aptamer-based rolling circle amplification: a platform for electrochemical detection of protein. *Anal. Chem. 79*, 7492−500.

(21) Benvin, A. L., Creeger, Y., Fisher, G. W., Ballou, B., Waggoner, A. S., and Armitage, B. A. (2007) Fluorescent DNA nanotags: supramolecular fluorescent labels based on intercalating dye arrays assembled on nanostructured DNA templates. *J. Am. Chem. Soc. 129*, 2025−34.

Bioconjugate Chemistry

Article

pubs.acs.org/bc

Solid-Phase N-Terminus PEGylation of Recombinant Human Fibroblast Growth Factor 2 on Heparin-Sepharose Column

Zhifeng Huang,[†,‡,#] Chaohui Ye,[†,#] Zhijun Liu,[§,#] Xiaojie Wang,[†] Huaibin Chen,[†] Yanlong Liu,[†] Lu Tang,[†] Hongxin Zhao,[§] Junfeng Wang,[§] Wenke Feng,*[,†,∥] and Xiaokun Li*[,†,‡]

[†]Key Laboratory of Biotechnology and Pharmaceutical Engineering of Zhejiang Province, Wenzhou Medical College, Wenzhou 325035, China

[‡]Normal Bethune Medical College, Jilin University, Changchun, 130021, China

[§]High Magnetic Field Laboratory, Chinese Academy of Sciences, Hefei 230031, China

[∥]Department of Medicine, University of Louisville, Louisville, Kentucky 40202, United States

ABSTRACT: Recombinant fibroblast growth factor-2 (FGF-2) has been extensively studied and used in several clinical applications including wound healing, bone regeneration, and neuroprotection. Poly(ethylene glycol) (PEG) modification of recombinant human FGF-2 (rhFGF-2) in solution phase has been studied to increase the in vivo biostabilities and therapeutic potency. However, the solution-phase strategy is not site-controlled and the products are often not homogeneous due to the generation of multi-PEGylated proteins. In order to increase mono-PEGylated rhFGF-2 level, a novel solid-phase strategy for rhFGF-2 PEGylation is developed. RhFGF-2 proteins were loaded onto a heparin-sepharose column and the PEGylaton reaction was carried out at the N-terminus by PEG20 kDa butyraldehyde through reductive alkylation. The PEGylated rhFGF-2 was purified to near homogeneity by SP sepharose anion-exchange chromatography and the purity was more than 95% with a yield of mono-PEGylated rhFGF-2 of 58.3%, as confirmed by N-terminal sequencing and MALDI-TOF mass spectrometry. In vitro biophysical and biochemical measurements demonstrated that PEGylated rhFGF-2 has an unchanged secondary structure, receptor binding activity, cell proliferation, and MAP kinase stimulating activity, and an improved bio- and thermal stability. Animal assay showed that PEGylated rhFGF-2 has an increased half-life and reduced immunogenicity. Compared to conventional solution-phase PEGylation, the solid-phase PEGylation is advantageous in reaction time, production of mono-PEGylated protein, and improvement of biochemical and biological activity.

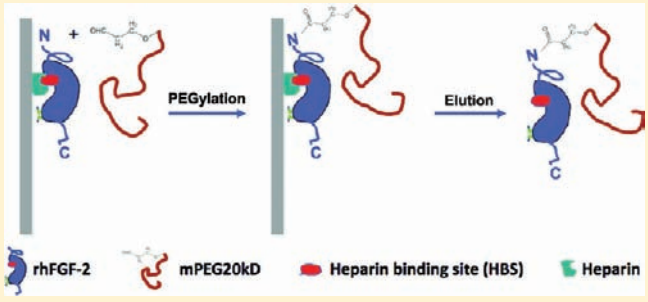

INTRODUCTION

Fibroblast growth factor 2 (FGF-2) belongs to the heparin binding growth factor family. It is widely expressed in developing and adult tissues.[1] It plays critical roles in multiple physiological functions including organ and tissue development,[2] wound healing,[3] angiogenesis,[4,5] bone regeneration,[6,7] and neurogenesis and neuroprotection, which have been tested both in experimental models of spinal cord injury[8] and in patients clinically for the treatment of stroke.[9] However, its short half-life time in vivo due to the sensitivity to proteolytic enzymes, kidney filtration, and neutralization by their specific antibodies and significant immunogenicity and antigenicity[7,10] significantly impedes its clinical applications. Moreover, frequent administration of FGF-2 often results in impaired homeostasis in vivo and may cause severe adverse effects.

To overcome these common problems of therapeutic proteins, molecular modification of protein with synthetic water-soluble macromolecules such as poly(ethylene glycol) (PEG)[11] has attracted considerable attention.[12−14] PEGylation is a process of covalently attaching PEG polymer to protein. This modification can reduce immunogenicity and antigenicity of the protein. It can also increase the half-life time of protein in vivo by increasing molecular size and steric hindrance to reduce the renal excretion and proteolytic digestion, thus stabilizing the protein structure.[15,16] As reported previously, PEGylation of some proteins, such as interleukin-2 (IL-2),[17] interferon α-2b,[17,18] bone morphogenetic protein,[19] and immunotoxin,[20] could enhance their therapeutic potency and reduce undesirable side/negative effects. However, non-site-specificity and multiple attachments of PEG to the protein might mask or interfere with the receptor binding sites and cause a dramatic decrease in in vitro bioactivity, thus partially limiting the practical application of the solution-phase PEGylation.[21−23] Reductive alkylation of N-terminal residue of the peptide has been reported as a useful selective target for homogeneous PEGylation without change of the protein structure.[24,25] However, even at optimized conditions, byproducts

Received: October 10, 2011
Revised: March 16, 2012
Published: March 21, 2012

such as di- and tri-PEGylated proteins and their isoforms are also produced.[26] Furthermore, solution-phase reductive alkylation often needs multiple purification steps to remove undesired impurities, such as the reducing agent, unreacted PEG, and multi-PEGylates.[22,27] Therefore, more site-specific and controlled mono-PEGylation strategies are needed for improving therapeutic protein biofunction.

Recent studies demonstrate that protein PEGylation can be achieved on ion-exchange media. Proteins were absorbed on the media by passing the protein solution through the ion-exchange column. PEG reagent solution was then circulated in the column allowing reaction with the absorbed protein for PEGylation.[27,28] The PEGylated protein is then separated from the unreacted protein and undesirable PEGylated forms by gradient elution. The higher site-specificity of PEGylation has been obtained by this strategy.[27] These studies provided a new strategy for protein PEGylation in the solid phase.

In the present work, we used heparin-sepharose as the solid-phase matrix for PEGylation of N-terminal residues of rhFGF-2. The biological function of FGF-2 is mainly through signaling that begins with the formation of a ternary complex of FGF-2, FGFR, and heparan sulfate.[29] The heparin and cell surface heparan sulfate proteoglycan have been shown to modulate FGF activity.[1] In addition, heparin-sepharose chromatography has been routinely used for the separation and purification of some therapeutic proteins.[30−33] Therefore, heparin-sepharose may provide an environment favorable for maintaining rhFGF-2 bioactivity during mono-PEGylation. Using the heparin-sepharose strategy, we successfully modified the rhFGF-2 at the N-terminal residue with 20 kDa mPEG-butyraldehyde (mPEG20K) and produced a highly homogeneously mono-PEGylated rhFGF-2. The bioactivity and secondary structure of the protein did not change after the solid-phase PEGylation, and the in vitro and in vivo biostability of PEGylated rhFGF-2 was significantly improved compared to the native rhFGF-2.

EXPERIMENTAL PROCEDURES

Materials. PEG20 kDa butyraldehyde (mPEG20K) and FGF receptor 1 (FGFR1) were purchased from Sigma−Aldrich (St. Louis, MO, USA). Heparin-sepharose column, Sepharose G25 column, and AKTA purifier were purchased from GE Healthcare (Piscataway, NJ, USA). Purified rhFGF-2 was produced by Key Laboratory of Biotechnology and Pharmaceutical Engineering of Zhejiang Province, Wenzhou Medical College, China. The enhanced chemiluminescence (ECL) detection kit was from Pierce (Rockford, IL, USA). Anti-Erk1/Erk2 rabbit mAb, antiphospho-Erk1/Erk2 rabbit mAb, antistathmin rabbit mAb, and goat antirabbit IgG conjugated with horseradish peroxidase (HRP) antibody were purchased from Cell Signaling Technology (Danvers, MA, USA). FGF-2 ELISA Kit was purchased from PeproTech (Princeton, NJ, USA). The protein assay reagent used for quantitative protein analysis was purchased from Bio-Rad (Hercules, CA, USA). All chemicals were of analytical grade.

PEGylation of rhFGF-2 in Solution Phase. Solution-phase PEGylation of rhFGF-2 with mPEG20K was performed at room temperature in a sodium phosphate buffer (SPB, 20 mM, pH 6.0) in the presence of 20 mM $NaBH_3CN$. mPEG20K was allowed to react with the protein at the PEG-to-protein molar ratios of 2, 4, 8, and 12, respectively, for various time durations. Reaction was terminated by adding 2% (w/v) glycine and subjected to 12% SDS-PAGE. The gels stained with Coomassie Blue were scanned by optical density scanner (Beckman AppraiseT Densitometer, USA) and protein products were quantified.

PEGylation of rhFGF-2 in Solid Phase. Three major procedures were performed for rhFGF-2 PEGylation in solid phase: (1) 2 mL of 0.1 mM rhFGF-2 in 20 mM SPB (pH 6.0) (the same solution was used in solution-phase PEGylation) was applied and bound on heparin-sepharose column. Due to the high binding affinity, rhFGF-2 completely bound on the column as evidenced by the fact that no protein was detected in the flowthrough after application of the protein sample on the column. (2) A solution containing 4.8 mL of 0.5 mM mPEG20K, which was used in the solution-phase PEGylation, and 20 mM $NaBH_3CN$ in various volumes was circulated in the column at low flow rate (0.01 mL/min) for 8 h (the same reaction time was also used in the solution-phase process). Therefore, one molecule of the immobilized rhFGF-2 was exposed to 12 molecules of PEG during 8 h reaction time, which was in the same molar ratio of PEG/rhFGF-2 used in the solution-phase process. At the end, 30 mL of equilibrium buffer (20 mM SPB, pH 6.0) was used to wash unreacted mPEG20K. (3) The reaction complex was completely eluted by applying 2 M NaCl in SPB at a rate of 1 mL/min. The eluate was collected and desalted by Sepharose G25 column and stored at −20 °C for subsequent experiments. PEGylation yield was estimated by SDS-PAGE and densitometry quantification as previously reported.[27,34]

Purification of Solid-Phase PEGylated rhFGF-2. The reaction mixture was applied to a SP Sepharose Fast Flow column (1 mL bed volume) pre-equilibrated with 15 column volumes (CVs) of binding buffer (20 mM sodium phosphate buffer, SPB, pH 7.0) at a rate of 0.5 mL/min. The sample was washed with 10 CVs of binding buffer, and then eluted with elution buffer A (0.3 M NaCl, 20 mM SPB, pH 7.0) and B (1.0 M NaCl, 20 mM SPB, pH 7.0) over 10 CVs. All elution fractions were collected and analyzed by SDS-PAGE.

The purity of PEGylated rhFGF-2 was further examined by reversed-phase high-performance liquid chromatography (RP-HPLC) analysis. The conditions of RP-HPLC were as follows: Agilent 1100 RP-HPLC (Agilent Technologies, Palo Alto, CA) equipped with a manual injector and a 300SB-C18 column (Agilent Technologies, Palo Alto, CA). The mobile phase comprised two buffers: Buffer A (distilled H_2O, 0.1% TFA) and Buffer B (acetonitrile, 0.1% TFA). Twenty microliters of the sample was injected into the RP column, and the column was eluted by an isocratic gradient of 10% (v/v) acetonitrile−water for 10 min, followed by a 10−60% (v/v) acetonitrile−water gradient over 20 min, at a total solvent flow rate of 0.5 mL/min. Absorbance was measured at 280 nm.

Mass Spectrometry and N-Terminal Analysis of Solid-Phase PEGylated rhFGF-2. Mass spectra were acquired using an Applied Biosystems Voyager System DE PRO MALDI-TOF mass spectrometer with a nitrogen laser. The matrix was a saturated solution of *R*-cyano-4-hydroxycinnamic acid in a 50:50 mixture of acetonitrile and water containing 0.1% trifluoroacetic acid. The mono-PEGylate and matrix were mixed at a ratio of 1:1, and then 1 μL sample was spotted onto a 100-well sample plate. All spectra were recorded on a Bruker Ultraflex instrument (Bruker Daltonik, Germany) and acquired in positive mode over the range 600−2500 Da under reflection conditions (20 kV accelerating voltage, 350 ns extraction delay time) and 2−100 kDa under linear conditions (25 kV accelerating voltage, 750 ns extraction delay time). The N-terminal amino acid sequence of PEGylated rhFGF-2 was examined by Edman degradation method,[35] and followed by MALDI-TOF mass spectroscopy as above.

dx.doi.org/10.1021/bc200550f | *Bioconjugate Chem.* 2012, 23, 740−750

Mitogenic Activity Analysis of the PEGylated rhFGF-2. We used NIH3T3 cell line (American Type Culture Collection, Rockville, MD) to determine the activity of proliferation of the PEGylated rhFGF-2. First, the cells were seeded in 96-well plates with 5×10^3 cells per well and incubated for 24 h. Then, they were washed with PBS and starved-cultured in the corresponding low-glucose Dulbecco's Modified Eagle's Medium (DMEM) containing 0.4% fetal bovine serum (FBS) for 24 h. Finally, the cells were treated with 1 nM rhFGF-2, 1 nM solid-phase or solution-phase PEGylated rhFGF-2 for 24 h, and the number of viable cells was detected by the methylthiazolete-trazolium (MTT) method as previously reported.[36]

Western Blot Analysis for the MAP Kinase Activation of Solid-Phase PEGylated rhFGF-2. NIH3T3 cells were treated with native rhFGF-2 or PEGylated rhFGF-2 in three doses at 2 nM, 1 nM, and 0.5 nM. After washing with PBS three times, the cells were homogenized in the lysis buffer. Total cellular proteins were collected by centrifuging at 12 000 rpm at 4 °C for 10 min. The protein concentration was determined by bicinchoninic acid (BCA) kit, and the samples were mixed with loading buffer and then subjected to electrophoresis on a 12% SDS-PAGE gel at 110 V for 100 min, followed by transferring to polyvinylidine fluoride (PVDF) membrane (Millipore-Billerica, MA, USA). After blocking with 5% nonfat milk for 2 h at room temperature, the membrane was washed three times with Tris-buffered saline containing 0.1% Tween-20 (TBST) and incubated with primary antibody at 4 °C overnight. The membrane was then washed three times with TBST, and secondary HRP-conjugated antibody was applied and the membrane was incubated for 1 h at room temperature. Finally, immunoreactive protein bands were visualized by ECL system and quantified by optical densitometer.

Analysis of the Binding Constants for FGFR1/rhFGF-2/heparin and FGFR1/PEG-rhFGF-2/heparin by SPR Biosensor. The Biacore 3000 biosensor from Biacore AB (Uppsala, Sweden) was used for all SPR measurements. The differences in binding constants between FGFR1/rhFGF-2/heparin and FGFR1/PEG-rhFGF-2/heparin were studied at 25 °C in 100 mM PBS (pH 7.4). FGFR1 was immobilized by amine coupling on flow channels of research-grade CM5 chips (Biacore AB) by a standard method. The mixed sample of rhFGF-2/heparin or PEG-rhFGF-2/heparin, with a fixed concentration ratio of 1:1 between the protein and the heparin, was injected over the CM5 chip at a flow rate of 50 μL/min. At the end of each sample injection (180 s), PBS (50 μL/min) was flowed over the chip to monitor the complex dissociation for 180 s. The chip surface was then regenerated by injecting 50 μL of 2.0 M NaCl in 10 mM sodium acetate (pH 4.5). A control channel was used by passing PBS buffer at same flow rate. The influences of alterations in flow rate (10−100 μL/min) or the addition of glycerol (1−10% v/v) to the running buffer on the kinetics of each sample were negligible, thereby indicating that mass transport limitations were minimal. For all the samples, the measurement was repeated in duplicate at five different concentrations ranging from 0.39 nM to 100 nM. Data were evaluated with the *BIAevaluation* software (v 3.0) using Kinetic Analysis, and a simple 1:1 Langmuir binding model.

Circular Dichroism Spectroscopy Analysis. The secondary structure of native rhFGF-2 and solid-phase PEGylated rhFGF-2 were determined with a circular dichroism (CD) spectropolarimeter (model J-810, Jasco, Japan). Far-UV CD spectra were recorded at wavelengths between 190 and 250 nm using a 0.1 cm path length cell at 25 °C with a protein concentration of 6 μM in 10 mM PBS, pH 7.4. Each spectrum was a representative of three scans. The CD spectra were corrected for buffer contributions.

Effect of Solid-Phase PEGylation on the Thermal and Structural Stabilities of rhFGF-2. The effects of solid-phase PEGylation on the thermal stability of rhFGF-2 at a physiologically relevant temperature were determined. PEGylated rhFGF-2 and its nonmodified control were incubated at a concentration of 10 μM at 37 °C in rat serum for various time durations as indicated. The samples were then subjected to the mitogenic activity assay as described above. Similarly, the effects of PEGylation on resistance of proteolysis of rhFGF-2 were tested in vitro by incubating PEGylated and native rhFGF-2 with trypsin (2 mM) at a molar ratio of 10: 1 (peptide/trypsin) at 37 °C for various times as indicated. The samples were then subjected to SDS-PAGE to examine the protein integrity.

Immunoreactivity in Vitro and Immunogenicity in Vivo Assay of Solid-Phase PEGylated rhFGF-2. To assess the immunoreactivity of PEGylated rhFGF-2 in vitro, the antibody binding activities of two forms of rhFGF-2 were evaluated by a double-antibody sandwich ELISA assay. Native rhFGF-2 or PEGylated rhFGF-2 at concentration of 0.3 μM were added into precoated FGF-2 monoclonal antibody microplate wells and incubated for 30 min at 37 °C. The plate was washed three times and 50 μL of HRP-conjugate reagent was added. The plate was incubated for 30 min at 37 °C, and then washed three times, followed by adding 100 μL color-developing solution and incubation for 15 min at 37 °C. Finally, the reaction was stopped with 50 μL stopping solution. The absorbance was measured by spectrometer at a wavelength of 450 nm immediately.

To investigate the immunogenicity of PEGylated rhFGF-2 in vivo, the normal female BALB/c mice (18−21 g) were used based on the procedures approved by the Wenzhou Medical College Animals Care and Use Committee. Mice were immunized by intraperitoneal (i.p.) injection of native rhFGF-2 or PEGylated rhFGF-2 (six mice in each group) at a dose of 2 nmol/mouse in 20 mM sodium acetate containing 1 mL Freund Complete Adjuvant (FCA). Two weeks after the first immunization, mice were immunized once again. Serum samples were collected every 7 days after the first immunization. The specific IgG levels in serum were determined by ABC-ELISA, as described previously.[37]

Pharmacokinetic Evaluation of Solid-Phase PEGylated rhFGF-2 in Rats. Normal male SD rats (220−250 g) were used based on the procedures approved by the Institutional Animal Care and Use Committee of Jilin University, China, and performed in accordance with institutional guidelines for animal experiments. Following intravenous (i.v.) injection of the original and PEGylated proteins at a dose of 100 μg/kg body weight (six animals in each group), blood samples were obtained at time points indicated. Serum levels of the test proteins were quantitated using Human FGF-basic Mini ELISA Development Kit (PeproTech, USA; sensitivity range 63−4000 pg/mL). Pharmacokinetic parameters of the test proteins were determined by *Drug and Statistics Software* (DAS, v 2.0; Mathematical Pharmacology Professional Committee of China). The elimination half-life ($t_{1/2}$) was calculated using the formula $t_{1/2} = 0.693/K_e$ (K_e stands for elimination rate constant).

Statistical Analysis of the Experimental Data. The in vitro experiments were performed three times with triplicate samples for each individual experiment. All data were expressed

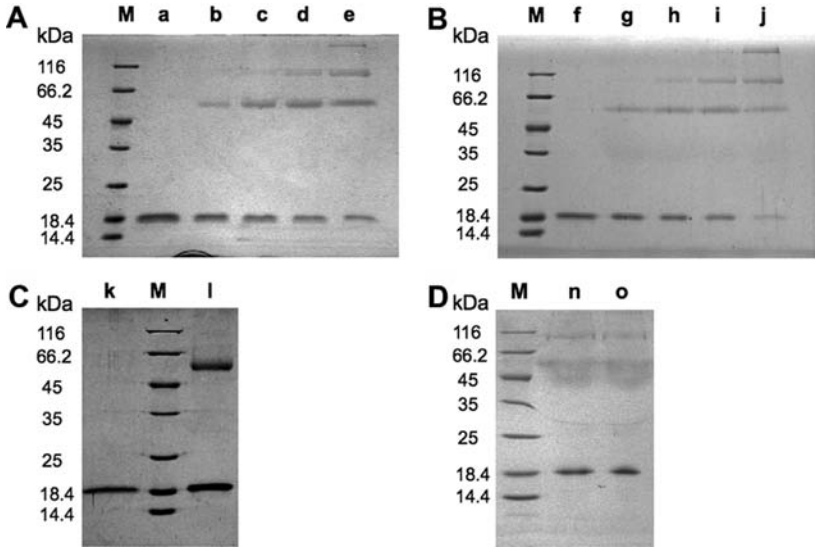

Figure 1. SDS-PAGE analysis of PEGylated rhFGF-2. Panel A. SDS-PAGE analysis of solution-phase PEGylation of rhFGF-2 at different PEG-to-protein molar ratio: lane M, molecular weight standards; lane a, native rhFGF-2; lanes b–e, PEGylation products obtained at the PEG-to-protein molar ratio of 2, 4, 8, and 12, respectively. Panel B. SDS-PAGE analysis of solution-phase PEGylation of rhFGF-2 at different reaction times: lane M, molecular weight standards; lane f, native rhFGF-2; lanes g–j, PEGylation products obtained at the reaction time of 2, 4, 8, and 12 h, respectively. Panel C. SDS-PAGE analysis of solid-phase PEGylation of rhFGF-2: lane M, molecular weight standards; lane k, native rhFGF-2; lane l, solid-phase PEGylation products obtained at PEG-to-protein ratio of 12:1 and reaction time of 8 h. Panel D. SDS-PAGE analysis of solution-phase PEGylation of rhFGF-2 in the presence of heparin: Lane M, molecular weight standards; lanes n,o, liquid-phase PEGylation products obtained in the presence of heparin at a molar amount same to rhFGF-2 in the reaction, at PEG-to-protein ratio of 12:1, reaction time of 8 h.

as mean ± SD and subjected to statistical analysis by ANOVA and Student *t*-test using statistical software *NASDAQ: SPSS* from SPSS Inc.

RESULTS AND DISCUSSION

PEGylation of rhFGF-2 in Solution-Phase and in Solid-Phase. PEG-to-protein molar ratio and reaction time are the two most crucial factors affecting the yield of PEGylated rhFGF-2 in both solution- and solid-phase PEGylation. As shown in Figure 1A, in solution-phase PEGylation, when the molar ratio was 2 and the reaction time was 8 h, the mono-PEGylation yield was nearly 20.1%. Increasing the molar ratio to 4, 8, and 12 improved the mono-PEGylation yield, but also increased the yield of multi-PEGylation. The effects of reaction time on the mono-PEGylation yield were investigated at a 12:1 PEG-to-protein ratio. As shown in Figure 1B, the yield of mono-PEGylated protein increased with increasing reaction time and reached the maximum at 8 h, but decreased at a later time point (12 h), probably due to the conversion between mono- and multi-PEGylated forms. On the other hand, multi-PEGylated proteins increased with the reaction time. On the basis of the conditions used in solution-phase PEGylation, the effects of PEG-to-protein molar ratio and reaction time on the PEGylation of rhFGF-2 in solid phase were studied. When PEG-to-protein ratio was about 12:1 and reaction time was 8 h at the pH of 6.0, optimized mono-PEGylation was obtained. As shown in Figure 1C, mono-PEGylated rhFGF-2 reached a yield up to 58.3%. Under the same condition, the solution-phase PEGylation reached a yield of mono-PEGylated rhFGF-2 only at 36.19%. The primary structure of FGF-2 includes 13 lysine residues located at positions 18, 21, 26, 46, 52, 66, 77, 86, 110, 119, 125, 129, and 135. According to the 3D structure of FGF-2, all lysine residues are on the surface of FGF-2 but 26, 110, 125, 129, and 135 lysine residues might be buried by the affinitic interactions between the protein and the resin.[38] Multi-PEGylation, seen in solution-phase PEGylation, was avoided by solid-phase PEGylation for several different reasons: first, the reactivity of the lysine residues was suppressed by the reductive alkylation condition (e.g., a low pH);[39] second, certain lysine residues might be buried by the affinitic interactions between the protein and the resin;[40] third, the frequency of protein contact with the PEG molecules was reduced because the protein was attached to a solid surface.[27]

In the present study, we tried to add heparin directly to the solution-phase protein sample to compare the PEGylation efficiency with solid-phase PEGylation. Regretfully, the results showed that this strategy not only lowered the mono-PEGylation yield (Figure 1D) but also led to one more step purification, since a separation of rhFGF-2 (or PEGylated rhFGF-2) from heparin by size exclusion chromatography using a high salt buffer is needed. Moreover, using a heparin column rather than heparin solution to PEGylate rhFGF-2 would be more cost-effective, because the heparin column is very stable and can be reused for many times.

Separation Behavior of Solid-Phase Mono-PEGylated rhFGF-2. The PEGylated rhFGF-2 was efficiently separated with non-PEGylated rhFGF-2 by HiTrap SPFF ion exchange chromatography (Figure 2A,B), suggesting that the modification alters the electrophilic property of rhFGF-2. RP-HPLC analysis indicated that the purity of the target protein exceeded 95% and the mono-PEGylated rhFGF-2 was eluted at a retention time of 18.64 min after the native rhFGF-2 (Figure 2C). This is likely due to the increased hydrophobicity by PEGylation, which has also been reported by others.[41]

Initially, our attempts to purify the modified rhFGF-2 by eluting the reaction mixture from heparin-sepharose column with PBS (pH 7.0) at a NaCl gradient from 0 to 2 M failed to produce satisfactory purification. The majority of both PEGylated rhFGF-2 and native rhFGF-2 were coeluted at 1.0–1.3 M NaCl (Figure 2D,E). Our previous studies demonstrated that[37] the PEGylated rhFGF-10 in solution-phase had altered heparin binding ability,

dx.doi.org/10.1021/bc200550f | *Bioconjugate Chem.* 2012, 23, 740–750

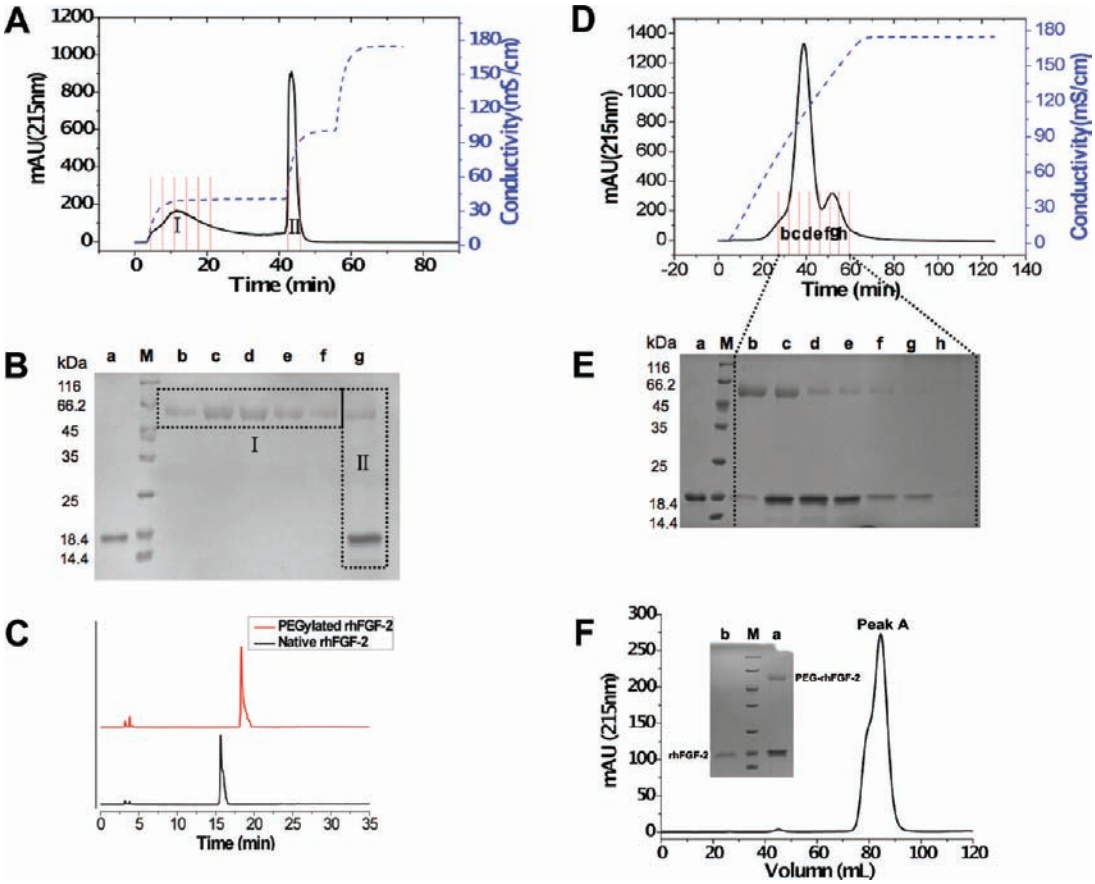

Figure 2. Elution chromatogram and SDS-PAGE analysis of solid-phase PEGylation mixture. Panel A. Elution chromatogram PEGylation mixture from SP Sepharose Fast Flow column. Panel B. SDS-PAGE analysis of the fractions collected from SP Sepharose chromatography. Panel C. RP-HPLC analysis of PEGylated rhFGF-2 purified using SP Sepharose chromatography. Panel D. Elution chromatogram of PEGylation mixture from heparin-sepharose column. Panel E. SDS-PAGE analysis of the fractions collected from heparin-sepharose chromatography. Panel F. Elution chromatogram of PEGylation mixture from size-exclusion column. Inset Panel. SDS-PAGE analysis of the fractions collected from size-exclusion chromatography: lane b, native rhFGF-2; lane M, molecular weight standards; lane a, eluted fraction of Peak A of size-exclusion chromatography.

since it could be separated from native rhFGF-10 readily by heparin-sepharose affinity chromatography. Heparin binding is essential for FGF signaling, and decreased binding could result in a FGF dysfunction.[29,42,43] Co-elution of PEGylated rhFGF-2 with native rhFGF-2 in heparin-affinity chromatography suggests that solid-phase PEGylation has no significant effect on the protein heparin binding capability. The potential reason of PEGylated rhFGF-2 eluted a bit earlier is that the molecular weight of rhFGF-2 was markedly increased by conjugating with 20 kDa PEG−butyraldehyde. Furthermore, the results of bioactivity, immune imprinting, CD, and other biophysical assays confirmed that the binding ability of PEGylated rhFGF-2 to heparin has no significant change compared with non-PEGylated rhFGF-2.

Moreover, we also tried to purify the solid-phase PEGylated rhFGF-2 with HiPrepTM 16/60 SephacrylTMS-100HR size-exclusion column (GE Healthcare), but our attempts failed to produce satisfactory purification (Figure 2F). The potential reason is that the spatial size of the protein might not be increased sufficiently by PEGylation due to the possible random twining of PEG around the protein surface.

Site Specificity of N-Terminus Mono-PEGylate. We performed MALDI-TOF-MS and Edman degradation of the N-terminus amino acid of the PEGylated rhFGF-2 to verify whether rhFGF-2 is modified by single molecule of mPEG20K to the N-terminus by solid-phase coupling. PEGylated rhFGF-2 has a molecular weight of 37 733.95 Da (Figure 3B), suggesting a single 20 kDa PEG conjugation to native rhFGF-2 (16292.84 Da) (Figure 3A). The broad peak of PEGylated rhFGF-2 was likely due to PEG polydispersity as reported before.[44] Moreover, the N-terminus sequencing by Edman degradation revealed that the N-terminus could not be degraded after five cycles of reactions (Figure 3C), as the covalently modified α-amine resists peptide cleavage by FDNB.[25] These data clearly indicated that a PEG molecule was attached to the N-terminus of rhFGF-2 by solid-phase PEGylation.

Mitogenic Activity Analysis of the PEGylated rhFGF-2. As shown in Table 1, solid-phase mono-PEGylated rhFGF-2 had no significant change in proliferation activity compared to native rhFGF-2 evaluated by NIH3T3 cell proliferation assay. The proliferation activity of the solution-phase PEGylated rhFGF-2 was only approximately 35.81% that of the native rhFGF-2. It is likely that solid-phase mono-PEGylation on a heparin column is more favorable to retain heparin binding ability, leaving an intact functional complex comprising the FGF, FGFRs, and heparin.[29,42,43] Furthermore, we investigated solid-phase mono-PEGylated rhFGF-2-stimulated MAP kinase activation, which is one of the major signal transduction pathways of FGF-2-induced proliferation, in NIH3T3 cells. As shown in Figure 4, solid-phase mono-PEGylated rhFGF-2 triggered intense phosphorylation of Erk1 and Erk2, which was comparable with the effects using native rhFGF-2 (Figure 4),

dx.doi.org/10.1021/bc200550f | Bioconjugate Chem. 2012, 23, 740−750

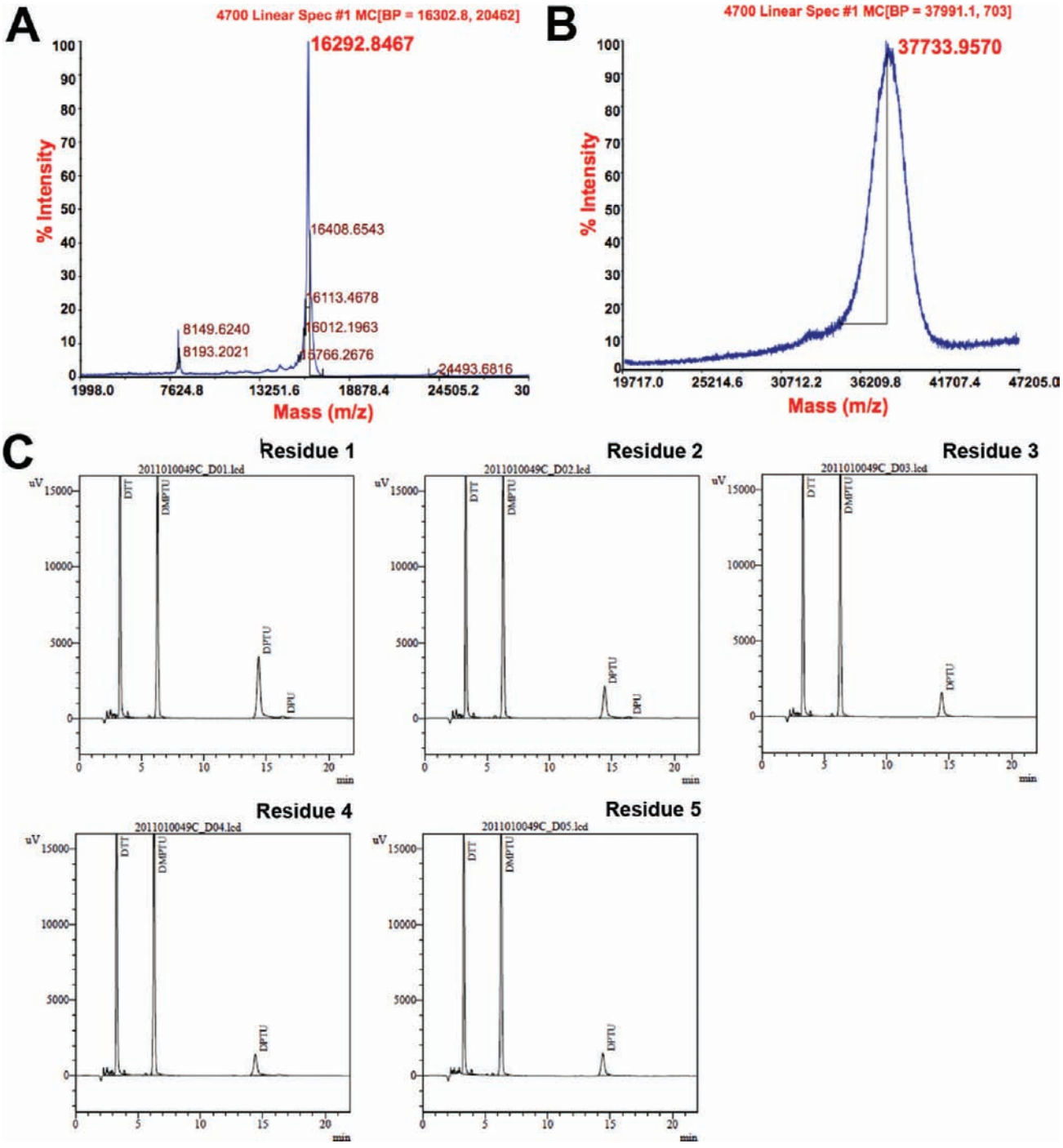

Figure 3. Identifying solid-phase PEGylated rhFGF-2. Panel A: MALDI-TOF mass spectrometry of native rhFGF-2 showing the molecular mass of native rhFGF-2 as 16 292.84 Da. Panel B. MALDI-TOF mass spectrometry of PEGylated rhFGF-2 showing the molecular mass of PEGylated rhFGF-2 as 37 733.95 Da. Panel C. N-terminus sequences of PEGylated rhFGF-2 was examined by Edman degradation method.

Table 1. Biological Activity of Native rhFGF-2 and PEGylated rhFGF-2

	mean biological activity (IU/μmol)	relative activity(%)	SD (n = 4)	CV (%)
Native rhFGF-2	1.48×10^7	100.00	2.45×10^6	16.48
PEGylated rhFGF-2 by solution-phase	0.53×10^7	35.81	3.86×10^6	0.73
PEGylated rhFGF-2 by solid-phase	1.56×10^7	105.41	1.93×10^6	12.40

further supporting the notion that solid-phase PEGylation does not alter the bioactivity of rhFGF-2.

Analysis of Binding Affinities of PEG-rhFGF-2 and rhFGF-2 for FGFR1. Previous studies have shown that solution-phase PEGylation significantly decreased the receptor binding affinity of the PEGylated proteins.[45−47] The binding affinities of the native rhFGF-2 and solid-phase PEGylated rhFGF-2 for FGF receptor 1 (FGFR1) were compared and quantified using surface plasmon resonance (SPR) spectroscopy. As shown in Figure 5, the FGFR1 binding affinity of solid-phase

dx.doi.org/10.1021/bc200550f | *Bioconjugate Chem.* 2012, 23, 740−750

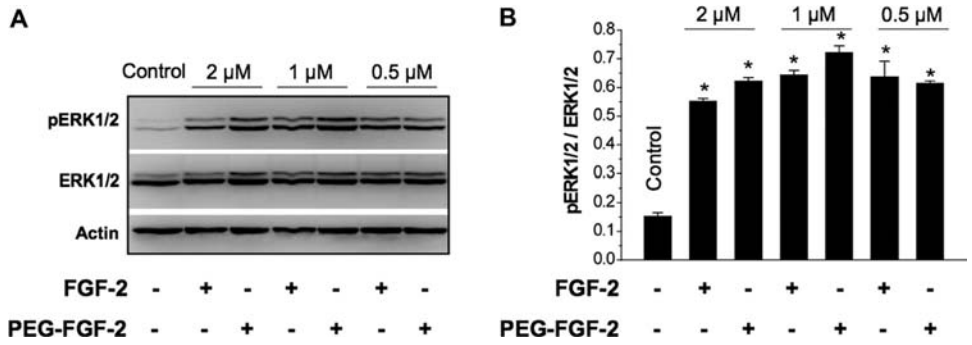

Figure 4. Effect of PEGylation on MAP kinase activation of rhFGF-2. Panel A. Western blot analysis. Panel B. Semiquantitative analysis of the protein bands in Panel A. * $p < 0.05$ vs Control.

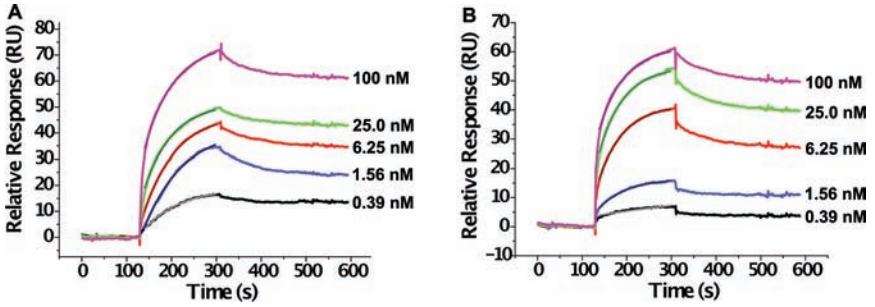

Figure 5. SPR analysis of the molecular interaction for FGFR1/rhFGF-2/heparin and FGFR1/PEG-rhFGF-2/heparin. Panel A. Interaction between FGFR1 and rhFGF-2/heparin complex. Concentrations of rhFGF-2 are 0.39, 1.56, 6.25, 25, and 100 nM, respectively, as indicated. Panel B. Interaction between FGFR1 and PEG-rhFGF-2/heparin complex. Concentrations of PEG-rhFGF-2 are 0.39, 1.56, 6.25, 25, and 100 nM, respectively, as indicated.

PEGylated rhFGF-2 was 2.52 nM (K_D), while that of native rhFGF-2 was 1.41 nM (K_D), which are in same order and comparable. The slightly lower affinity to FGFR1 for PEG-rhFGF-2 binding than for rhFGF-2 could be explained by steric hindrance imposed by the PEG moiety in PEGylation. Taken together, the solid-phase PEGylation does not have a significant effect on the receptor binding ability.

Circular Dichroism Spectroscopy Analysis of the Structure Difference between Solid-Phase PEGylated rhFGF-2 and Native rhFGF-2. The CD spectra of PEGylated rhFGF-2 and native rhFGF-2 were approximately overlapped in wavelength from 200 to 250 nm (Figure 6). The relative population of secondary structures calculated from the CD spectra also showed no difference between the PEGylated rhFGF-2 and the native rhFGF-2. This result indicated that the solid-phase PEGylation does not change the structure of native rhFGF-2.

Effect of Solid-Phase PEGylation on the Thermal and Structural Stabilities of rhFGF-2. Thermal resistance is one of the major factors for keeping the drug intact since the proteases are more active at higher temperatures. The thermal stability in rat serum of native and PEGylated rhFGF-2 was assessed by incubating the protein at 37 °C for various time periods. The mitogenic activity of native rhFGF-2 and PEGylated rhFGF-2 was decreased upon incubation in a time-dependent manner. After 96 h of incubation, native rhFGF-2 retained only 37.2% of the original mitogenic activity, whereas the PEGylated rhFGF-2 retained 70.4% of the original activity (Figure 7A), indicating increased thermal tolerance of PEGylated rhFGF-2. Next, the potent resistance of PEGylated rhFGF-2 to proteolysis was examined. RhFGF-2 and PEGylated rhFGF-2 were incubated with trypsin at 2 mM for various time periods, and the products were subsequently analyzed by SDS-PAGE to visualize their

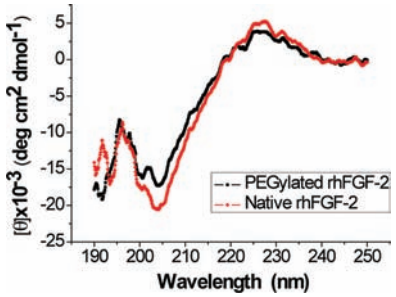

Figure 6. Far-UV CD spectra of native (red line) and solid-phase PEGylated rhFGF-2 (black line). The ellipticities are reported as mean residue ellipticity (MRE) (deg cm^2 dmol^{-1}).

integrity. As shown in Figure 7B, there was significant difference in the amount of degradation between the native and the PEGylated rhFGF-2 incubated with trypsin for various time periods. After incubation with trypsin for 30 min at 37 °C, nearly 72% of PEGylated rhFGF-2 still remained intact, whereas only about 25% non-PEGylated rhFGF-2 was left, indicating that the PEGylation of rhFGF-2 significantly increased its resistance to proteolysis. This is largely due to the modification-added mPEG20K, which protects the proteolytic sites in the peptide from trypsin attacks.[37] Such protection helps rhFGF-2 to maneuver through the body and approach target sites without being hydrolyzed by proteolytic enzymes.

Immunoreactivity in Vitro and Immunogenicity in Vivo of Solid-Phase PEGylated rhFGF-2. Figure 8A showed that the antibody binding activity of the mono-PEGylated rhFGF-2 in vitro was approximately 51% of the native rhFGF-2, and it is highly likely that PEG chain enveloped the N-terminus of rhFGF-2 and restricted the accessibility of the antibody.

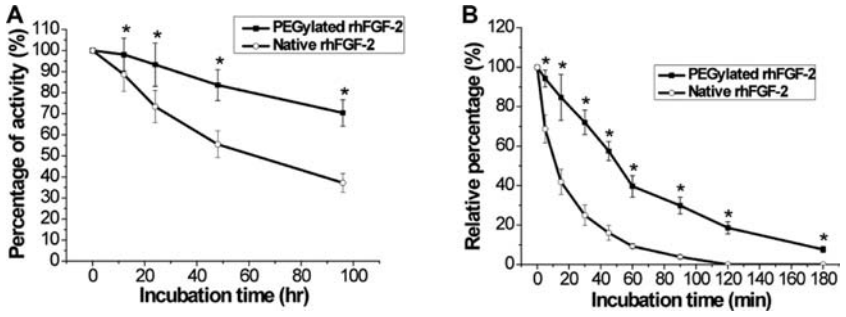

Figure 7. Effects of solid-phase PEGylation on the thermal stability in mouse serum and proteolysis resistance of rhFGF-2. Panel A. Thermal stability. Native and PEGylated rhFGF-2 were incubated in mouse serum at 37 °C for indicated times, then added to 3T3 cells for which proliferative activity was measured to determine the functional integrity of each form of rhFGF-2. Panel B. The relative resistance to trypsinization. PEGylated and native rhFGF-2 were incubated with trypsin at 2 mM for indicated times. Trypsin-treated rhFGF-2 was examined for the protein integrity by SDS-PAGE. The bands representing PEGylated and native rhFGF-2 were quantified by densitometry scanning. The band densities of non-trypsin-treated native and PEGylated rhFGF-2 are considered as 100% (indicated by control), while the band densities of trypsin-treated PEGylated or native rhFGF-2 are presented as relative percentage to the control. * $p < 0.05$ vs the corresponding native rhFGF-2 group.

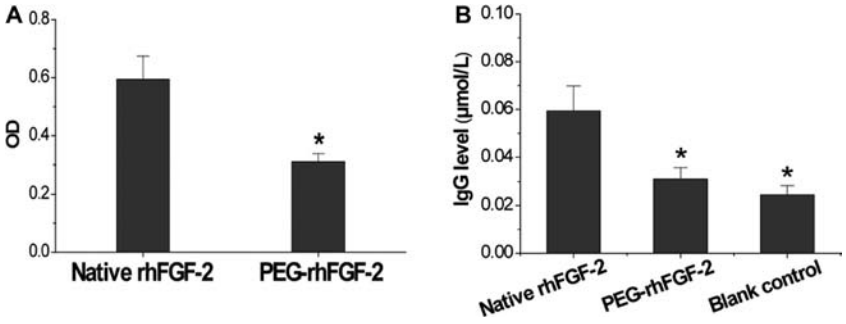

Figure 8. Immunoreactivity in vitro and immunogenicity in vivo of solid-phase PEGylated rhFGF-2. Panel A. Immunoreactivity of native and PEGylated rhFGF-2 in vitro was evaluated by a double-antibody sandwich ELISA assay. Panel B. Immunogenicity in vivo of native and PEGylated rhFGF-2. BALB/c mice were immunized with either PEGylated rhFGF-2 or native rhFGF-2 in 20 mM sodium acetate buffer by i.p. injection (2 nmol/mouse at the first day and the 14th day). Serum samples were collected on the 21st day after the first immunization. Anti-rhFGF-2 IgG levels were detected by indirect ELISA using native rhFGF-2 as the coating antigen. In addition, a group of mice were given same volume of sodium acetate for sodium acetate control. * $p < 0.01$ vs the corresponding native rhFGF-2 group.

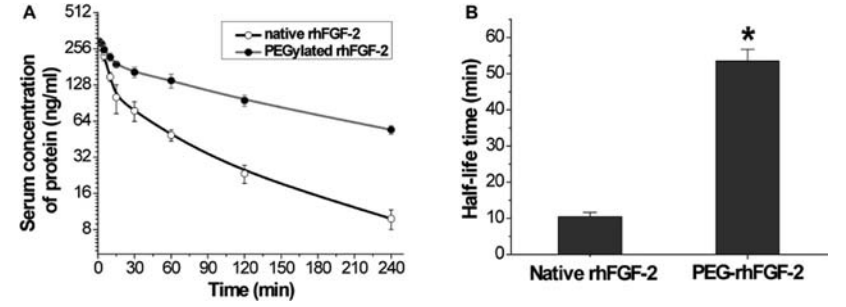

Figure 9. Pharmacokinetics study of solid-phase PEGylated rhFGF-2 in rats. Panel A. Normal male SD rats were injected intravenously with 100 μg/kg native rhFGF-2 (open circle), PEGylated rhFGF-2 (solid circle). Blood samples were collected at various time points. The amount of rhFGF-2 was measured by Human FGF-basic Mini ELISA Development Kit. A standard curve was made for each rhFGF-2, $n = 6$. Values are the mean ± SD. Panel B. Comparison of half-life of native rhFGF-2 and PEGylated rhFGF-2.

To assess the immunogenicity of PEGylated rhFGF-2 in vivo, BALB/c mice were given PEGylated or native rhFGF-2 (2 nmol/mouse) in 20 mM sodium acetate containing 1 mL FCA by i.p. injection twice with an interval of 14 days. Serum samples were collected on the 21st day after the first immunization, and the serum levels of anti-FGF-2 IgG were detected by indirect ELISA with native rhFGF-2 as the coating antigen. Native rhFGF-2, but not PEGylated rhFGF-2, induced a significant production of the antibody, indicating that PEGylated rhFGF-2 has less immunogenicity (Figure 8B). The reduced immunogenicity of PEGylated rhFGF-2 in vivo is likely due to the decreased binding of PEGylated rhFGF-2 to the FGF-2 antibody as described in Figure 8A. In addition, the presence of PEG chains that envelop the protein surface restrict the accessibility of host IgG to the antigenic moiety of rhFGF-2, and decrease PEGylated rhFGF-2 transportability from blood to immune tissues such as spleen, bone marrow, and lymphoid tissue.[48]

Pharmacokinetic Study of Solid-Phase PEGylated rhFGF-2 in Rats. The in vivo half-life times of two forms of rhFGF-2 were analyzed by i.v. injecting a single dose of 100 μg/kg of native or PEGylated rhFGF-2 to male SD rats and then measuring the dynamic levels of two forms of rhFGF-2 in the

dx.doi.org/10.1021/bc200550f | Bioconjugate Chem. 2012, 23, 740–750

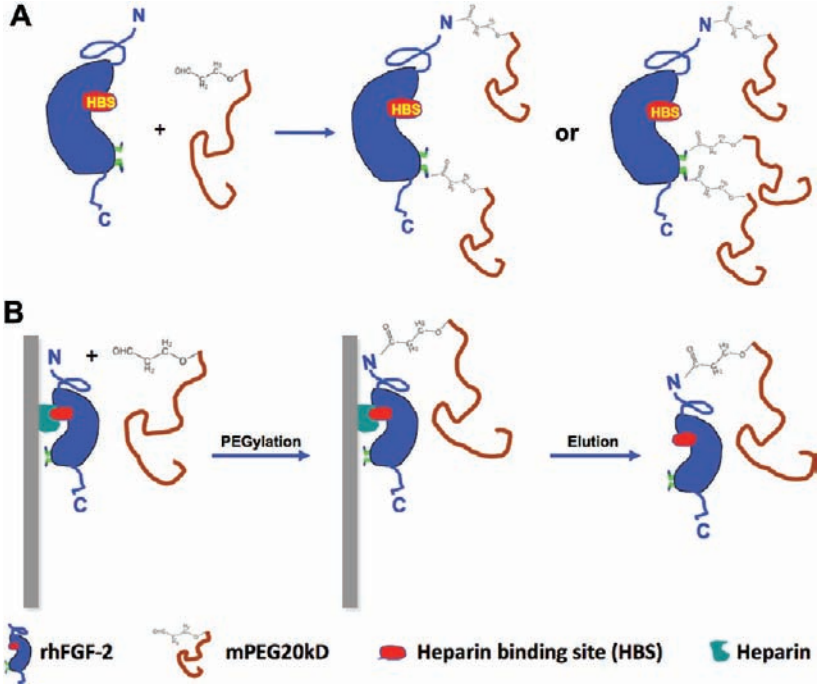

Figure 10. Schematic illustration of the two PEGylation strategies. Panel A. Solution phase. Panel B. Solid phase on heparin-sepharose column.

blood by ABC-ELISA method. On the basis of the pharmacokinetic curves shown in Figure 9A, the eliminated plasma half-life ($t_{1/2}$) was calculated with *Drug and Statistics Software* (DAS, v 2.0; Mathematical Pharmacology Professional Committee of China) and the equation described in the Experimental Procedures. The eliminated plasma half-life ($t_{1/2}$) of the nonmodified rhFGF-2 was about 10.39 min, which is consistent with the previous report.[49] After PEGylation, the $t_{1/2}$ of the protein increased to 53.45 min, a 5.2-fold increase (Figure 9B). The elongated half-life time of rhFGF-2 by solid-phase PEGylation may be explained by slower clearance from the circulation due to its larger size. In addition, conjugation of mPEG to rhFGF-2 may decrease filtration through the glomeruli of the kidney.[50]

■ CONCLUSION

In this study, we, for the first time, conjugated PEG to rhFGF-2 by site-specific PEGylation with mPEG20 kDa butyraldehyde at N-terminal residue through heparin-sepharose chromatography in a solid-phase reaction. The mono-PEGylated rhFGF-2 was purified to homogeneity by a single purification step. The PEGylated rhFGF-2 by this strategy retains its secondary structure and FGFR-1 binding activity. Compared to native rhFGF-2, the mono-PEGylated rhFGF-2 has improved bio- and thermal stability, decreased immunoreactivity in vitro and immunogenicity in vivo, and increased in vivo half-life. Importantly, the solid-phase PEGylation of rhFGF-2 is superior to the solution-phase PEGylation as indicated by the increase of the yield of mono-PEGylated form. Moreover, as shown in Figure 10, solution-phase PEGylation may mask the heparin binding site of the protein leading to a decrease of biological activity, whereas solid-phase PEGylation on heparin column effectively protects the heparin binding site preserving the bioactivity of the PEGylated protein. The PEGylation strategy described in the present study could be readily applied for the production of modified rhFGF-2 or other therapeutically recombinant protein for clinical practice.

■ AUTHOR INFORMATION

Corresponding Author

*W. Feng: Tel. 502 314 0452; fax 502 852 6904; E-mail address: wenke_feng@yahoo.com. X. Li: Tel. +86 13676701796; E-mail address: xiaokunli@163.net.

Author Contributions

#These authors contributed equally to the work.

Notes

The authors declare no competing financial interest.

■ ACKNOWLEDGMENTS

This study was supported, in part, by grants from Natural Science Foundation of China, 81102486 (to Z.H.); Natural Science Foundation of Zhejiang Province of China, Y4100067, R2090550 (to Z.H. and X.L.); Key Science Grant of Wenzhou Economic and Technological Development Zone, KK2010003 (to Z.H.); Emerging Artists Talents Scheme of Zhejiang Province of China, 2010R413059 (to C.Y.); Graduate Student Innovation Research Projects of Zhejiang Province of China, YK2010085 (to C.Y.)

■ REFERENCES

(1) Baird, A., and Klagsbrun, M. (1991) The fibroblast growth factor family. *Cancer Cells 3*, 239–43.

(2) McKeehan, W. L., Wang, F., and Kan, M. (1998) The heparan sulfate-fibroblast growth factor family: diversity of structure and function. *Prog. Nucleic Acid Res. Mol. Biol. 59*, 135–76.

(3) Marks, M. G., Doillon, C., and Silver, F. H. (1991) Effects of fibroblasts and basic fibroblast growth factor on facilitation of dermal wound healing by type I collagen matrices. *J. Biomed. Mater. Res. 25*, 683–96.

(4) Raimondi, A. R., Molinolo, A. A., and Itoiz, M. E. (2006) Fibroblast growth factor-2 expression during experimental oral carcinogenesis. Its possible role in the induction of pre-malignant fibrosis. *J. Oral Pathol. Med. 35*, 212–7.

(5) Gerwins, P., Skoldenberg, E., and Claesson-Welsh, L. (2000) Function of fibroblast growth factors and vascular endothelial growth

factors and their receptors in angiogenesis. *Crit. Rev. Oncol. Hematol. 34*, 185−94.
(6) Kurane, A., Simionescu, D. T., and Vyavahare, N. R. (2007) In vivo cellular repopulation of tubular elastin scaffolds mediated by basic fibroblast growth factor. *Biomaterials 28*, 2830−8.
(7) Jiang, X., Zou, S., Ye, B., Zhu, S., Liu, Y., and Hu, J. (2010) bFGF-Modified BMMSCs enhance bone regeneration following distraction osteogenesis in rabbits. *Bone 46*, 1156−61.
(8) Rabchevsky, A. G., Fugaccia, I., Turner, A. F., Blades, D. A., Mattson, M. P., and Scheff, S. W. (2000) Basic fibroblast growth factor (bFGF) enhances functional recovery following severe spinal cord injury to the rat. *Exp. Neurol. 164*, 280−91.
(9) Bogousslavsky, J., Victor, S. J., Salinas, E. O., Pallay, A., Donnan, G. A., Fieschi, C., Kaste, M., Orgogozo, J. M., Chamorro, A., and Desmet, A. (2002) Fiblast (trafermin) in acute stroke: results of the European-Australian phase II/III safety and efficacy trial. *Cerebrovasc. Dis. 14*, 239−51.
(10) Kawaguchi, H., Nakamura, K., Tabata, Y., Ikada, Y., Aoyama, I., Anzai, J., Nakamura, T., Hiyama, Y., and Tamura, M. (2001) Acceleration of fracture healing in nonhuman primates by fibroblast growth factor-2. *J. Clin. Endocrinol. Metab. 86*, 875−80.
(11) Katre, N. V. (1990) Immunogenicity of recombinant IL-2 modified by covalent attachment of polyethylene glycol. *J. Immunol. 144*, 209−13.
(12) Bory, C., Boulieu, R., Souillet, G., Chantin, C., Guibaud, P., and Hershfield, M. S. (1991) Effect of polyethylene glycol-modified adenosine deaminase (PEG-ADA) therapy in two ADA-deficient children: measurement of erythrocyte deoxyadenosine triphosphate as a useful tool. *Adv. Exp. Med. Biol. 309A*, 173−6.
(13) DeSantis, G., and Jones, J. B. (1999) Chemical modification of enzymes for enhanced functionality. *Curr. Opin. Biotechnol. 10*, 324−30.
(14) Poynard, T., McHutchison, J., Manns, M., Trepo, C., Lindsay, K., Goodman, Z., Ling, M. H., and Albrecht, J. (2002) Impact of pegylated interferon alfa-2b and ribavirin on liver fibrosis in patients with chronic hepatitis C. *Gastroenterology 122*, 1303−13.
(15) Veronese, F. M., and Pasut, G. (2005) PEGylation, successful approach to drug delivery. *Drug Discovery Today 10*, 1451−8.
(16) Caliceti, P., and Veronese, F. M. (2003) Pharmacokinetic and biodistribution properties of poly(ethylene glycol)-protein conjugates. *Adv. Drug Delivery Rev. 55*, 1261−77.
(17) George, S., Hutson, T. E., Mekhail, T., Wood, L., Finke, J., Elson, P., Dreicer, R., and Bukowski, R. M. (2008) Phase I trial of PEG-interferon and recombinant IL-2 in patients with metastatic renal cell carcinoma. *Cancer Chemother. Pharmacol. 62*, 347−54.
(18) Tamai, H., Shingaki, N., Shiraki, T., Tukuda, H., Mori, Y., Moribata, K., Enomoto, S., Deguchi, H., Ueda, K., Inoue, I., Maekita, T., Iguchi, M., Yanaoka, K., Oka, M., and Ichinose, M. (2011) Prediction of sustained response to low-dose pegylated interferon alpha-2b plus ribavirin in patients with genotype 1b and high hepatitis C virus level using viral reduction within 2 weeks after therapy initiation. *Hepatol. Res.,*.
(19) Hu, J., Duppatla, V., Harth, S., Schmitz, W., and Sebald, W. (2010) Site-specific PEGylation of bone morphogenetic protein-2 cysteine analogues. *Bioconjugate Chem. 21*, 1762−72.
(20) Filpula, D., Yang, K., Basu, A., Hassan, R., Xiang, L., Zhang, Z., Wang, M., Wang, Q. C., Ho, M., Beers, R., Zhao, H., Peng, P., Zhou, J., Li, X., Petti, G., Janjua, A., Liu, J., Wu, D., Yu, D., Longley, C., FitzGerald, D., Kreitman, R. J., and Pastan, I. (2007) Releasable PEGylation of mesothelin targeted immunotoxin SS1P achieves single dosage complete regression of a human carcinoma in mice. *Bioconjugate Chem. 18*, 773−84.
(21) Lee, H., Jang, I. H., Ryu, S. H., and Park, T. G. (2003) N-terminal site-specific mono-PEGylation of epidermal growth factor. *Pharm. Res. 20*, 818−25.
(22) Fee, C. J., and Alstine, J. M. V. (2006) PEG-protein:reaction engineering and separation issues. *Chem. Eng. Sci. 61*, 924−939.
(23) Basu, A., Yang, K., Wang, M., Liu, S., Chintala, R., Palm, T., Zhao, H., Peng, P., Wu, D., Zhang, Z., Hua, J., Hsieh, M. C., Zhou, J., Petti, G., Li, X., Janjua, A., Mendez, M., Liu, J., Longley, C., Mehlig, M., Borowski, V., Viswanathan, M., and Filpula, D. (2006) Structure-function engineering of interferon-beta-1b for improving stability, solubility, potency, immunogenicity, and pharmacokinetic properties by site-selective mono-PEGylation. *Bioconjugate Chem. 17*, 618−30.
(24) Marsac, Y., Cramer, J., Olschewski, D., Alexandrov, K., and Becker, C. F. (2006) Site-specific attachment of polyethylene glycol-like oligomers to proteins and peptides. *Bioconjugate Chem. 17*, 1492−8.
(25) Xiao, J., Burn, A., and Tolbert, T. J. (2008) Increasing solubility of proteins and peptides by site-specific modification with betaine. *Bioconjugate Chem. 19*, 1113−8.
(26) Dou, H., Zhang, M., Zhang, Y., and Yin, C. (2007) Synthesis and purification of mono-PEGylated insulin. *Chem. Biol. Drug Des. 69*, 132−8.
(27) Lee, B. K., Kwon, J. S., Kim, H. J., Yamamoto, S., and Lee, E. K. (2007) Solid-phase PEGylation of recombinant interferon alpha-2a for site-specific modification: process performance, characterization, and in vitro bioactivity. *Bioconjugate Chem. 18*, 1728−34.
(28) Suo, X., Lu, X., Hu, T., Ma, G., and Su, Z. (2009) A solid-phase adsorption method for PEGylation of human serum albumin and staphylokinase: preparation, purification and biochemical characterization. *Biotechnol. Lett. 31*, 1191−6.
(29) Wu, Z. L., Zhang, L., Yabe, T., Kuberan, B., Beeler, D. L., Love, A., and Rosenberg, R. D. (2003) The involvement of heparan sulfate (HS) in FGF1/HS/FGFR1 signaling complex. *J. Biol. Chem. 278*, 17121−9.
(30) Berman, B., Ostrovsky, O., Shlissel, M., Lang, T., Regan, D., Vlodavsky, I., Ishai-Michaeli, R., and Ron, D. (1999) Similarities and differences between the effects of heparin and glypican-1 on the bioactivity of acidic fibroblast growth factor and the keratinocyte growth factor. *J. Biol. Chem. 274*, 36132−8.
(31) Spielberger, R., Stiff, P., Bensinger, W., Gentile, T., Weisdorf, D., Kewalramani, T., Shea, T., Yanovich, S., Hansen, K., Noga, S., McCarty, J., LeMaistre, C. F., Sung, E. C., Blazar, B. R., Elhardt, D., Chen, M. G., and Emmanouilides, C. (2004) Palifermin for oral mucositis after intensive therapy for hematologic cancers. *N. Engl. J. Med. 351*, 2590−8.
(32) Seeger, A., and Rinas, U. (1996) Two-step chromatographic procedure for purification of basic fibroblast growth factor from recombinant Escherichia coli and characterization of the equilibrium parameters of adsorption. *J. Chromatogr., A 746*, 17−24.
(33) Anspach, F. B., Spille, H., and Rinas, U. (1995) Purification of recombinant human basic fibroblast growth factor: stability of selective sorbents under cleaning in place conditions. *J. Chromatogr., A 711*, 129−39.
(34) Balan, S., Choi, J. W., Godwin, A., Teo, I., Laborde, C. M., Heidelberger, S., Zloh, M., Shaunak, S., and Brocchini, S. (2007) Site-specific PEGylation of protein disulfide bonds using a three-carbon bridge. *Bioconjugate Chem. 18*, 61−76.
(35) Niall, H. D. (1973) Automated Edman degradation: the protein sequenator. *Methods Enzymol. 27*, 942−1010.
(36) Wu, X., Yan, Q., Huang, Y., Huang, H., Su, Z., Xiao, J., Zeng, Y., Wang, Y., Nie, C., Yang, Y., and Li, X. (2010) Isolation of a novel basic FGF-binding peptide with potent antiangiogenetic activity. *J. Cell Mol. Med. 14*, 351−6.
(37) Huang, Z., Ni, C., Chu, Y., Wang, S., Yang, S., Wu, X., Wang, X., Li, X., Feng, W., and Lin, S. (2009) Chemical modification of recombinant human keratinocyte growth factor 2 with polyethylene glycol improves biostability and reduces animal immunogenicity. *J. Biotechnol. 142*, 242−9.
(38) Schlessinger, J., Plotnikov, A. N., Ibrahimi, O. A., Eliseenkova, A. V., Yeh, B. K., Yayon, A., Linhardt, R. J., and Mohammadi, M. (2000) Crystal structure of a ternary FGF-FGFR-heparin complex reveals a dual role for heparin in FGFR binding and dimerization. *Mol. Cell 6*, 743−50.
(39) Zalipsky, S. (1995) Chemistry of polyethylene glycol conjugates with biologically active molecules. *Adv. Drug Delivery Rev. 16*, 157−182.

(40) Conover, C. D., Greenwald, R. B., Pendri, A., and Shum, K. L. (1999) Camptothecin delivery systems: the utility of amino acid spacers for the conjugation of camptothecin with polyethylene glycol to create prodrugs. *Anti-Cancer Drug Des. 14*, 499−506.
(41) Cai, Y., and Yue, P. (2011) Separation of exenatide analogue mono-PEGylated with 40 kDA polyethylene glycol by cation exchange chromatography. *J. Chromatogr., A 1218*, 6953−60.
(42) Zern, B. J., Chu, H., and Wang, Y. (2010) Control growth factor release using a self-assembled [polycation:heparin] complex. *PLoS One 5*, e11017.
(43) Chu, H., Johnson, N. R., Mason, N. S., and Wang, Y. (2011) A [polycation:heparin] complex releases growth factors with enhanced bioactivity. *J. Controlled Release 150*, 157−63.
(44) Huang, Z., Wang, H., Lu, M., Sun, C., Wu, X., Tan, Y., Ye, C., Zhu, G., Wang, X., Cai, L., and Li, X. (2011) A better anti-diabetic recombinant human fibroblast growth factor 21 (rhFGF21) modified with polyethylene glycol. *PLoS One 6*, e20669.
(45) Kubetzko, S., Sarkar, C. A., and Pluckthun, A. (2005) Protein PEGylation decreases observed target association rates via a dual blocking mechanism. *Mol. Pharmacol. 68*, 1439−54.
(46) Dhalluin, C., Ross, A., Huber, W., Gerber, P., Brugger, D., Gsell, B., and Senn, H. (2005) Structural, kinetic, and thermodynamic analysis of the binding of the 40 kDa PEG-interferon-alpha2a and its individual positional isomers to the extracellular domain of the receptor IFNAR2. *Bioconjugate Chem. 16*, 518−27.
(47) Yang, K., Basu, A., Wang, M., Chintala, R., Hsieh, M. C., Liu, S., Hua, J., Zhang, Z., Zhou, J., Li, M., Phyu, H., Petti, G., Mendez, M., Janjua, H., Peng, P., Longley, C., Borowski, V., Mehlig, M., and Filpula, D. (2003) Tailoring structure-function and pharmacokinetic properties of single-chain Fv proteins by site-specific PEGylation. *Protein Eng. 16*, 761−70.
(48) Scott, M. D., and Chen, A. M. (2004) Beyond the red cell: pegylation of other blood cells and tissues. *Transfus. Clin. Biol. 11*, 40−6.
(49) Abe, K., and Saito, H. (2001) Effects of basic fibroblast growth factor on central nervous system functions. *Pharmacol. Res. 43*, 307−12.
(50) Kuan, C. T., Wang, Q. C., and Pastan, I. (1994) Pseudomonas exotoxin A mutants. Replacement of surface exposed residues in domain II with cysteine residues that can be modified with polyethylene glycol in a site-specific manner. *J. Biol. Chem. 269*, 7610−6.

Bioconjugate Chemistry

Article

pubs.acs.org/bc

Deposition Gene Transfection Using Bioconjugates of DNA and Thermoresponsive Cationic Homopolymer

Ryosuke Iwai,[†] Shota Kusakabe,[†] Yasushi Nemoto,[†,‡] and Yasuhide Nakayama*[,†]

[†]Division of Medical Engineering and Materials, National Cerebral and Cardiovascular Center Research Institute, Japan

[‡]Development Department, Chemical Products Division, Bridgestone Company, Japan

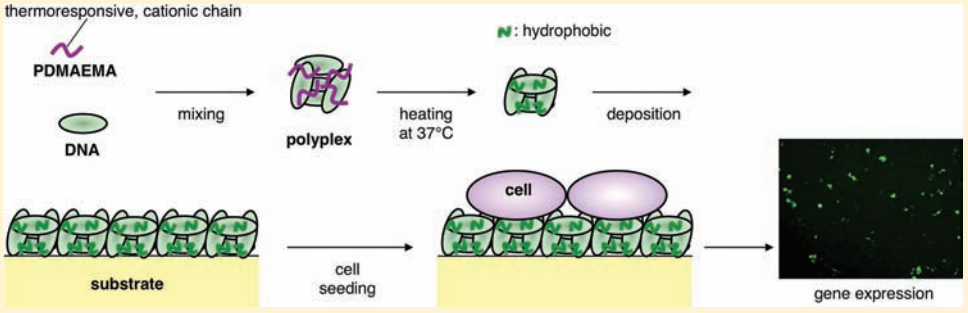

ABSTRACT: A poly(*N*,*N*-dimethylaminoethylmethacrylate) (PDMAEMA) homopolymer with both thermoresponsive and cationic characteristics was applied to a vector for use in deposition transfection. PDMAEMA with a molecular weight of 2.5×10^5 g mol^{-1} was synthesized by photoinduced radical polymerization. Polyplexes approximately 750 nm in size were formed by mixing PDMAEMA with luciferase-encoding plasmid DNA. The polyplexes had a lower critical solution temperature (LCST) of approximately 30 °C. In addition, they exhibited excellent adsorption and durability on a polystyrene surface, as confirmed by a surface chemical compositional analysis. When HeLa cells and primary cells were cultured on a substrate coated with the polyplexes, high transgene expression and cell viability of more than 90% were obtained at low charge ratios (PDMAEMA/plasmid DNA ratio) ranging from 2 to 8. In addition, transgene expression was sustained for over 2 weeks post-transfection whereas decreased expression was observed 5 days post-transfection when the conventional solution-mediated transfection method was used. Thus, high and sustained transgene expression as well as high cell viability can be realized by using small amounts of PDMAEMA as a deposition transfection material.

INTRODUCTION

Controlled gene delivery, e.g., by transfection, using biomaterial surfaces (substrate-mediated transfection) and transfection of specific tissues or cells (targeted transfection) are important in fields such as regenerative medicine and gene therapy.[1,2] In general, viral transfection is highly efficient, but it has several drawbacks. These include the potential for inducing acute inflammatory responses, integrating viral genes into the host genome, and limiting the DNA loading capacity.[3,4] Moreover, the use of viral carriers for controlled transfection is technically difficult because they cannot be readily modified. Cationic liposomes and polymers that can be used to generate gene-deliverable nanoparticles by forming polyion complexes (polyplexes) with plasmid DNA (pDNA) have been developed as nonviral carriers.[5,6] The transfection efficiency of nonviral carriers is lower than that of viral carriers; however, for controlled transfection, it is easier to introduce functional molecules such as signal peptides,[7,8] bioactive molecules,[9,10] thermoresponsive molecules,[11,12] or pH-responsive molecules[13,14] into nonviral carriers than viral carriers.

In a previous study, we designed a surfactant polymer for the thermoresponsive surface immobilization of pDNA.[15] The polymer comprised four AB-type block branches, each incorporating two different chemicals: a cationic poly(*N*,*N*-dimethylaminopropylacrylamide) (PDMAPAAm) block and a thermoresponsive poly(*N*-isopropylacrylamide) (PNIPAM) block (PDMAPAAm-PNIPAM). PNIPAM is the most popular thermally sensitive water-soluble nonionic polymer available and has a lower critical solution temperature (LCST) of approximately 32 °C. As shown in Figure 1A, the tertiary branched PDMAPAAm-PNIPAM block copolymer formed polyplexes with pDNA and was deposited on a cell culture surface at 37 °C. High transgene expression was achieved by using the cells seeded on to the polyplex culture surface. This surface-mediated transfection method is referred to as deposition transfection.

PDMAEMA is a cationic polymer and is used widely as a nonviral gene delivery carrier.[16−18] On the other hand, it is also a thermoresponsive polymer that has LCST, ranging from 34 to 37 °C.[19−21] However, little biomedical research has been carried out on the dual characteristics of this polymer. Recently, we developed a novel aqueous anti-thrombogenic coating

Received: October 26, 2011
Revised: January 13, 2012
Published: March 22, 2012

dx.doi.org/10.1021/bc2005768 | *Bioconjugate Chem.* 2012, 23, 751−757

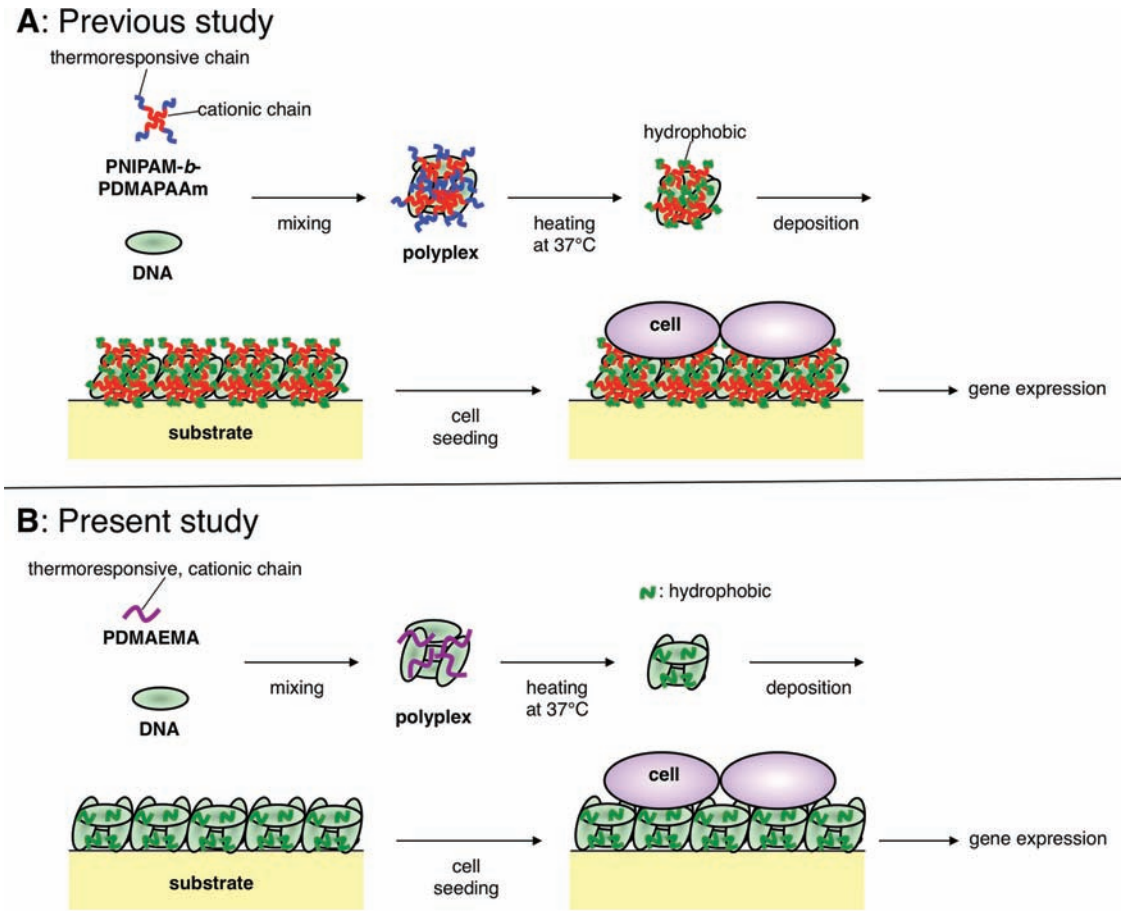

Figure 1. Deposition transfection method using (A) the tertiary branched thermoresponsive cationic block copolymer (PNIPAM-b-PDMAPAAm) in our previous study[15] and (B) thermoresponsive cationic homopolymer (PDMAEMA) in this study.

material that combines the thermoresponsive and cationic characteristics of PDMAEMA and can effectively immobilize heparin/PDMAEMA bioconjugates onto biomaterial surfaces at physiological temperatures.[22] By using PDMAEMA, the amount of polymer necessary to produce the heparin bioconjugate was reduced by more than 25% as compared to that required for our previous PDMAPAAm-PNIPAM block copolymer.[23]

In this study, we used PDMAEMA as the surfactant to carry out deposition transfection. Similar to heparin immobilization, we thought that a small amount of surfactant would suffice for immobilizing DNA. We also hypothesized that the reduced amount of polymer would increase transgene expression. Therefore, we investigated the characteristics of PDMAEMA and its ability to combine with DNA to produce polyplexes. We then proceeded to optimize the deposition transfection conditions. Finally, we evaluated the effects of transfecting primary cells with PDMAEMA.

EXPERIMENTAL SECTION

N-(2-(Dimethylamino)ethyl)methacrylate (DMAEMA) and all other chemical reagents were purchased from Wako Pure Chemical Ind., Ltd. (Osaka, Japan). DMAEMA was distilled under reduced pressure before use to remove the stabilizer.

General Methods. ^{1}H NMR spectra were recorded using a 300 MHz NMR spectrometer (Gemini 300; Varian, Palo Alto, CA) with deuterium oxide at room temperature. Gel permeation chromatography (GPC) analyses using *N*,*N*-dimethylformamide as a solvent were carried out by using an HPLC-8320 GPC instrument (Tosoh, Tokyo, Japan) in conjunction with Tosoh TSKgel SuperAW-4000 and SuperAW-5000 columns. The columns were calibrated prior to use with narrow distribution poly(ethylene glycol) standards (Tosoh).

Synthesis of Thermoresponsive Cationic Homopolymer. PDMAEMA was synthesized by photoradical polymerization. DMAEMA (2.0 g) was poured into a glass tube (35 × 65 mm^2; wall thickness, 1 mm, Maruemu Corp., Osaka, Japan), and N_2 gas was bubbled into it at 2 L/min for 10 min to remove O_2. DMAEMA was irradiated for 72 h using 100 mW visible light (FML27 EX-N; Panasonic Co., Osaka, Japan). After irradiation, reprecipitation was carried out using methanol solution in hexanes, and the precipitate was dried under reduced pressure, following which PDMAEMA was obtained (383 mg, 19% conversion). The molecular weight (M_n) of PDMAEMA was determined to be 2.5 × 10^5 g mol^{-1} (polydispersity: 2.5) by GPC analysis. Analysis of the ^{1}H NMR (in chloroform-d_1) spectra yielded the following results: δ 0.8−1.2 ppm (br, 3H, $-CH_3$), 1.6−2.0 (br, 2H, $-CH_2-CH_3$), 2.2−2.4 (br, 6H, $N-CH_3$), 2.5−2.7 (br, 2H, CH_2-N), 4.0−4.2 (br, 2H, $O-CH_2$). The mean diameters of PDMAEMA in deionized water (concentration: 10 mg/mL) were determined by dynamic light scattering (DLS) on Zetasizer Nano S (Malvern Instruments Ltd., Worcestershire, UK) equipped with a 10 mW He−Ne laser (n = 5).

dx.doi.org/10.1021/bc2005768 | *Bioconjugate Chem.* 2012, 23, 751−757

Preparation of Polyplexes. PDMAEMA was dissolved in saline. Aliquots (60 μL) were added to the firefly luciferase-encoding plasmid DNA (pGL3 control vector; Promega, WI, USA) or green fluorescent protein-encoding plasmid DNA (pQBI25 vector; Wako) dissolved in 90 μL of DNase-free water (Invitrogen, CA, USA) to obtain polymer/pDNA ratios from 1 to 32, which corresponded to cation/anion (C/A) ratios. The solutions (total volume, 150 μL) were mixed using a pipet to generate DNA complexes. The mean diameters of the DNA complexes in deionized water (concentration: 10 mg/mL, C/A ratio: 4) were determined by dynamic light scattering (DLS) on Zetasizer Nano S (n = 5).

Surface Characterization. The chemical composition of the outermost surface layer was determined by X-ray photoelectron spectroscopy (XPS 3400; Shimazu Co., Kyoto, Japan) using a magnesium anode (Mg Kα radiation) at room temperature, a pressure of 5×10^{-6} Torr (10 kV, 20 mA), and a takeoff angle of 90°. The takeoff angle was defined as the angle between the sample surface and the electron optics of the energy analyzer.

Primary Cell Culture. Adipose-derived adherent cell populations were isolated from beagle adipose tissue by modifying a method described previously by Manini et al.[24] Briefly, approximately 1 g of adipose tissue was obtained from the fatty layer under the skin and digested using 0.1% collagenase type I solution (Wako) at 37 °C for 1 h with gentle agitation. After filtering the digest through a 100 μm nylon mesh (BD Biosciences, NJ, USA) and centrifuging it at 1300 rpm for 3 min, the cell pellet was collected. The cell pellet was resuspended in Dulbecco's modified Eagle's medium (DMEM) (Gibco, Invitrogen Corp., Carlsbad, CA) containing 10% fetal bovine serum (Hyclone Laboratories Inc., Logan, UT), penicillin (200 units/mL; ICN Biomedicals Inc., Aurora, OH), and streptomycin (200 mg/mL; ICN) (growth medium). Then, it was filtered through a 70 μm nylon mesh (BD Biosciences). The cells were placed on a dish (55 cm^2; Asahi Glass Co., Ltd., Tokyo) with the growth medium and cultured in an atmosphere of 5% CO_2 at 37 °C. When the culture was nearly confluent, it was harvested and subcultivated at 1.0×10^4 cells/cm^2. The cells were used for experiments before they reached the fifth passage.

In Vitro Transfection Assays. In vitro transfection by the deposition transfection method was performed as reported previously.[15] Briefly, an aqueous solution of the DNA complexes (50 μL; plasmid concentration, 20 μg/mL) was diluted with 150 μL of saline and then added into each well of a 24-well dish (amount of DNA added to each well, 1.0 μg). After incubation at 37 °C for 6 h, HeLa cells or adipose-derived primary cells (approximately 1.5×10^5 cells per well) in 1.5 mL of growth medium were seeded and cultured in an atmosphere of 5% CO_2 at 37 °C for 2−15 days, with the medium being changed every 3 days. The expression of pGL3-control-plasmid transfected cells was analyzed by a luciferase assay as follows. After 2−15 days of cultivation, the cells were lysed with 0.2 mL of cell lysis buffer (Promega). The lysate was centrifuged at 15 000 rpm for 3 min at 4 °C, and 20 μL of the supernatant was analyzed for luciferase activity using a Luminus CT-9000 luminometer (Dia-Iatron, Tokyo, Japan). The relative light unit (RLU) measurements were standardized by using the total protein amounts of the cell lysates, which were measured by performing BioRad protein assays (BIO-RAD, Hercules, CA) using bovine serum albumin as a standard. The GFP expression of pQBI25 transfected cells (transfection efficiency) was analyzed by using a fluorescence microscope fitted with a fluoroisothiocyanate filter.

In vitro transfection by the conventional solution transfection method was performed under optimized conditions as follows. HeLa cells (approximately 1.5×10^5 cells/well) were seeded prior to treatment in a 24-well dish and cultivated for 24−48 h in the growth medium in an atmosphere of 5% CO_2 at 37 °C. After 15 min of complex formation, transfection was performed by adding 100 μL of the complex solutions into each well of the 24-well dish with 0.5 mL of Opti-Mem I (Invitrogen, amount of DNA added to each well, 0.5 μg). After 6 h of incubation, the cells were washed once with PBS(−) and cultivated in 1.5 mL of the growth medium for 2−15 days. Lipofectamine 2000 (Invitrogen) was used according to the manufacturer's procedures. Briefly, 2 μL of Lipofectamine 2000 reagent that was complexed with 0.5 μg of pDNA was added to each well. The luciferase and GFP expression were analyzed as described above.

Cell Viability Assays. Cytotoxicity was assessed by performing a cell viability assay using the water-soluble tetrazolium (WST)-8 method (Dojindo, Kumamoto, Japan). Polyplex solutions at different C/A ratios from 1 to 32 were added to each well in a 96-well plate (Asahi Glass Co. Ltd.). After incubating at 37 °C for 6 h, HeLa cells (approximately 1.5×10^4 cells per well) in 100 μL of the growth medium were seeded and cultured for 24 h at 37 °C in a 5% CO_2 atmosphere. To each well, 10 μL of WST-8 reagent (5 mmol/L) was added. After 2 h incubation at 37 °C, the absorbance at 450 nm was determined using a BioRad microplate reader (model 680).

RESULTS

Synthesis of PDMAEMA. PDMAEMA was synthesized by photoinduced radical polymerization by irradiating the bulk DMEMA using visible light. The resulting PDMAEMA was a solid white mass with a molecular weight of 2.5×10^5 g mol^{-1} and relatively narrow polydispersity. We were able to verify the chemical structure of the polymer by ^{1}H NMR spectroscopy (see Experimental Section for chemical shifts).

Characterization of DNA Complexes. The PDMAEMA thus obtained was dissolved in water at room temperature. The diameter of the polymer particles was 96 ± 3 nm. The polymer precipitated at approximately 28 °C, confirming its thermoresponsive nature (Figure 2). When an aqueous solution of PDMAEMA was mixed with an aqueous solution of the luciferase-encoding plasmid DNA (pGL3 control plasmid), the particle size increased by more than seven times (745 ± 46 nm), indicating the formation of polymer/pDNA complexes (polyplexes). The polyplexes precipitated (equilibrium transmittance, 15%; LCST, 30 °C) (Figure 2), which implies that PDMAEMA was sensitive to temperature even after polyplex formation.

Polyplex deposition was analyzed by XPS. Polystyrene (PS) was used as a model material. It was coated with PDMAEMA in saline or as a complex with pGL3 plasmid, subsequently air-dried, and then washed with water for 24 h at 37 °C. After coating, an N_{1s} signal, which originated mainly from the dimethylamino groups in the side chains of PDMAEMA, was detected on the surface. The changes in chemical composition are summarized in Table 1. For the polymer coating, the N/C elemental ratio determined from the peak area of C_{1s} and N_{1s} was 0.08 before and after washing with water, which was close to the theoretical ratio of PDMAEMA (0.12). On the other hand, when the polyplexes were coated on to the PS surface, a

dx.doi.org/10.1021/bc2005768 | Bioconjugate Chem. 2012, 23, 751−757

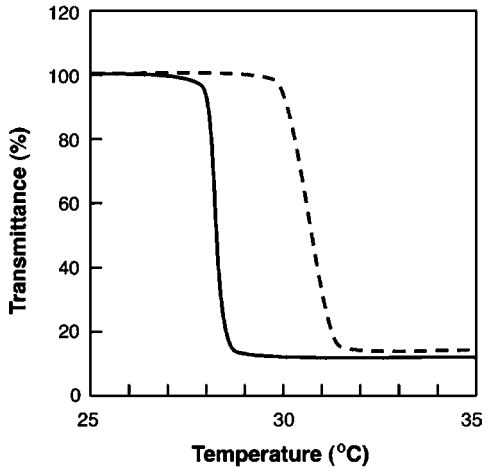

Figure 2. Thermoresponsive changes in transmittance of PDMAEMA (solid line) and its polyplex with pGL3 control plasmid DNA (broken line). Polymer and its polyplex (C/A ratio: 4) concentration: 10 mg/mL, Heating rate: 0.5 °C/min.

Table 1. Change in Surface Chemical Composition of the PS Film before and after Coating with PDMAEMA and its Polyplex with pGL3 Control Plasmid[a]

surface	chemical ratio	
	N/C	P/C
PS	0 (0)	0 (0)
coating with PDMAEMA	0.08 (0.12)	0 (0)
washing at 37 °C for 24 h	0.08 (0.12)	0 (0)
coating with polyplex	0.13 (0.26)	0.02 (0.05)
washing at 37 °C for 24 h	0.11 (0.26)	0.02 (0.05)

[a]Theoretical ratios are shown in parentheses. The data are presented as means (n = 5).

new P_{1s} signal was detected that mainly originated from the phosphate group in addition to the N_{1s} group. The N/C and P/C ratios were 0.13 and 0.02, respectively. Each ratio remained nearly stable even after washing for 24 h. Therefore, the polyplexes of PDMAEMA with pDNA could be immobilized thermally on the PS surface with high durability at 37 °C.

In Vitro Transfection and Cell Viability. HeLa cells were transfected by the deposition transfection method and the conventional transfection method. Polyplexes of PDMAEMA and the luciferase-encoding pGL3 control plasmid were created with C/A ratios ranging from 1 to 32. The luciferase activity was estimated through the levels of transgene expression 2−15 days post-transfection. When the cells were transfected by the conventional method, relatively high transgene expression levels were detected over the C/A ratio range 8−16. On the other hand, significantly high transgene expressions were observed at low C/A ratios of 2 and 4 for the deposition method, which were higher than the highest transgene expression C/A ratio of 32 obtained for the conventional method (Figure 3).

The high transgene expression of the deposition method was maintained for over 2 weeks, whereas the transgene expression of the conventional method decreased dramatically after 2 days. Fifteen days post-transfection, the transgene gene expression activity resulting from the deposition method was more than 100 times that resulting from the conventional method (Figure 4A). The number of GFP positive cells as a transfection

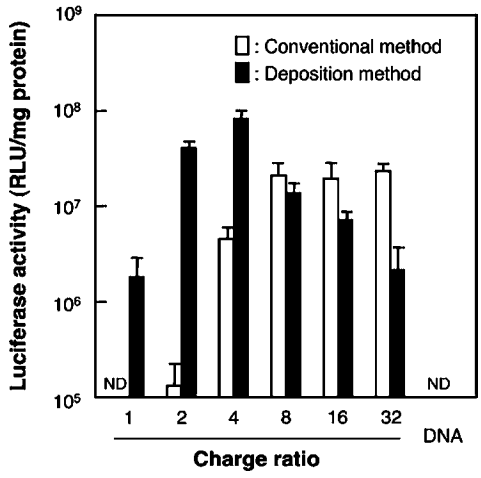

Figure 3. Effect of C/A ratio on transgene expression levels of HeLa cells transfected by using conventional method and deposition method with PDMAEMA. The luciferase activities of the conventional and the deposition method were measured at 2 and 5 days of post-transfection, respectively. The values represent the mean ± SD (n = 3). DNA indicates transfection without polymer. ND: not detected.

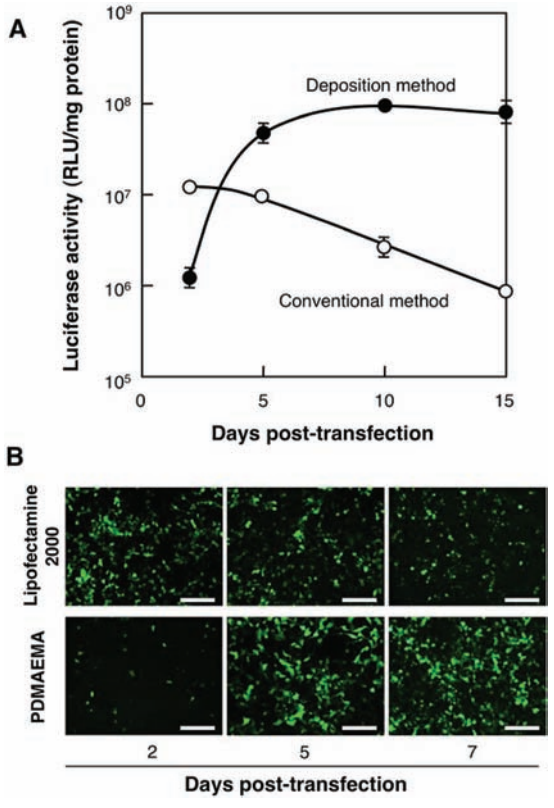

Figure 4. (A) Time course of the luciferase expression levels of HeLa cells transfected by conventional transfection method (○) and deposition transfection method (●) using polyplexes of PDMAEMA with pGL3-control plasmid DNA having C/A ratio of 16 and 4, respectively. The values represent the mean ± SD (n = 3). (B) Fluorescence microscopy observations of the HeLa cells transfected with pQBI25 plasmid DNA by conventional transfection method using Lipofectamine 2000 and deposition transfection method using PDMAEMA having C/A ratio of 4. Bar = 200 μm.

efficiency of deposition transfection method using PDMAEMA was significantly increased between 2 and 5 days of post-

dx.doi.org/10.1021/bc2005768 | Bioconjugate Chem. 2012, 23, 751−757

transfection (Figure 4B), which was the same tendency of the time course of transgene expression level of the deposition method shown in Figure 4A. Moreover, the transfection efficiency obtained by the deposition transfection using PDMAEMA was the same as or higher than that obtained by the conventional transfection using commercially available Lipofectamine 2000 at 5 days post-transfection (Figure 4B).

The viability of the HeLa cells transfected by employing the deposition method using PDMAEMA was evaluated for C/A ratios ranging from 1 to 32. Although the cell viability decreased slightly with increasing C/A ratio, significantly high cell viability (more than 90%) was obtained for C/A ratios ranging from 2 to 8, which were higher than those obtained by using commercially available Lipofectamine 2000 (Figure 5).

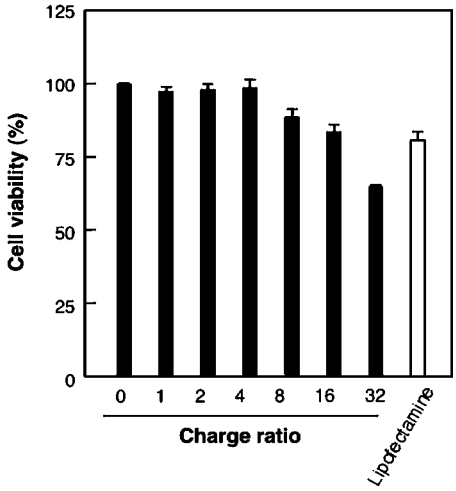

Figure 5. Cytotoxicity of polyplexes prepared by mixing PDMAEMA and pGL3 control plasmid DNA in different charge ratios (black bars) and lipoplexes prepared by mixing Lipofectamine 2000 and pGL3 control plasmid (white bar). The values represent the mean ± SD (n = 3).

Notably, a C/A ratio of 4, which showed the highest transgene expression for the deposition transfection method, also resulted in the highest cell viability (97%). This result was almost identical to that for the nontreated cells.

To evaluate the applicability of PDMAEMA to gene therapy, a preliminary study of in vitro transfection using adipose-derived primary cells was conducted. Adipose-derived primary cells were separated from beagle adipose tissue and transfected by using the deposition method and pQBI25 plasmid. As shown in Figure 6, the GFP positive primary cell populations were clearly visible in the fluorescence microscope images.

DISCUSSION

In a previous study, we developed the substrate-mediated deposition transfection method by using a custom-designed, tertiary-branched thermoresponsive cationic block copolymer (tertiary branched PDMAPAAm-PNIPAM block copolymer).[15] PDMAPAAm had cationic blocks for forming polyplexes with DNA and PNIPAM blocks for thermoresponsive surface immobilization of the polyplexes. The long chains of the PNIPAM blocks were effective for surface immobilization, but they reduced transgene expression because of DNA coverage by the polymer. On the other hand, the long chains of the PDMAPAAm blocks enabled firm binding of the polymer with DNA, but the deposited polyplex layer was delaminated easily

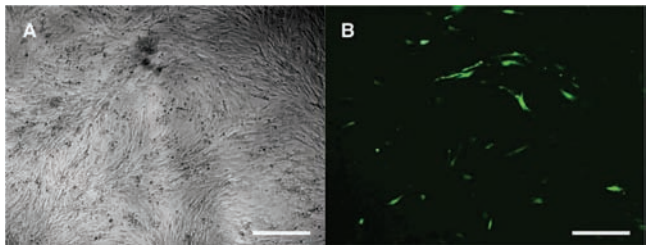

Figure 6. Fluorescence microscopy observations of adipose-derived primary cells transfected by using deposition method with polyplexes of PDMAEMA and pQBI25 plasmid DNA at C/A ratio of 4. Microscopic observation: 5 days post-transfection. (A) phase contrast microscopic image and (B) fluorescence microscopic image. Bar = 100 μm.

by washing. Therefore, a balance between the thermoresponsive and cationic blocks was needed for effective transgene expression by deposition transfection. We found through optimization that the chain length of PNIPAM should be twice as long as the PDMAPAAm chain length.

In this study, we attempted to use PDMAEMA, which has both thermoresponsive and cationic characteristics, for deposition transfection. As expected, PDMAEMA formed polyplexes with DNA and they could be immobilized on the substrate surface with high durability. Therefore, we could obtain high transgene expression using the deposition transfection method in conjunction with low amounts of PDMAEMA. For example, PDMAEMA was mixed with the same amount of pDNA to form polyplexes at a C/A ratio of 4. In comparison, for the previous tertiary branched PDMAPAAm-PNIPAM block copolymer, a 3-fold excess of the polymer relative to the pDNA was necessary to form polyplexes at the same C/A ratio.[15] Interestingly, significantly high cell viabilities (more than 90%) were obtained when the cells were cultured on the PDMAEMA/pDNA polyplex culture surface over C/A ratios ranging from 2 to 8 (Figure 5). This might have been due to the effect on cell growth of reducing the use of the polymer.

Positively charged polyplexes prepared at high C/A ratios performed better in terms of transfecting cells because of their enhanced ability to bind to negatively charged proteoglycans on cell surfaces.[25] Indeed, a high transfection efficiency was achieved by using the conventional solution-mediated transfection method with polyplexes of PDMAEMA at high C/A ratios ranging from 15 to 30.[16,26] These results agree well with the results that we obtained by using the conventional transfection method at a C/A ratio of 32 (Figure 3). On the other hand, the highest level of transgene expression that we achieved in this study occurred at a C/A ratio of 4 for the deposition transfection method. The reason this occurred is unclear. In our previous study, when the polyplexes were formed from tertiary branched PDMAPAAm-PNIPAM block copolymers, they were fixed firmly to the culture substrate by drying (reverse transfection method). In addition, the transgene expression level was decreased by more than four times as compared to deposition transfection where the polyplexes were attached weakly to the culture substrate.[15] Therefore, the effect of the C/A ratio on transgene expression that we observed in this study may have been due to the polyplexes being prepared by mixing pDNA with high amounts of PDMAEMA (C/A = 16, 32). Through this, the polyplexes may have more strongly attached to the culture surface than those that were prepared by

dx.doi.org/10.1021/bc2005768 | Bioconjugate Chem. 2012, 23, 751–757

mixing pDNA with low amounts of PDMAEMA (C/A = 2, 4). Adsorption occurred likely through hydrophobic interactions between the PDMAEMA and hydrophobic cell culture surface. As a result, if the polyplexes with high C/A ratios were too tightly bound to the surface, their uptake by cells may have been inhibited.[15] A detailed analysis of the relationship between the C/A ratios of the polyplexes and cellular uptake via the deposition transfection method is required. The results derived from such a study would be helpful for clinical applications of PDMAEMA with the aim of achieving high transgene expression using the deposition transfection method in conjunction with low amounts of PDMAEMA.

In general, strong transgene expression is achieved within the first 2−5 days post-transfection using the conventional transfection method. However, expression decreases dramatically 1 week post-transfection.[27] This observation is in agreement with the time course evaluation of transgene expression that we carried out for the conventional transfection method in this study (Figure 4A). On the other hand, sustained transgene expression even after 2 weeks post-transfection was observed by using cells that had been transfected through deposition transfection (Figure 4A). Short-term transgene expression achieved using the conventional transfection method is thought to be due to mainly two rate-limiting factors. First, polyplexes cannot be supplied continuously to the cells. It is necessary to exchange the serum-free medium with serum containing growth medium to foster cell growth. Any polyplexes that would be present in the new medium would lose their transfection activity because they would interact with the serum components. Second, for nonviral, plasmid-mediated transfection, incorporating a transgene into the genome of a host cell is extremely difficult.[28] In this study, the first rate-limiting factor did not exist for the deposition transfection method because the polyplexes were deposited and adsorbed on to the culture surface and they were kept in contact with the culture surface even after washing and the medium exchange as shown in Table 1. Therefore, the polyplexes were supplied continuously to the cells from the culture surface, and as a result, sustained transgene expression was achieved. Indeed, Okazaki et al. also reported that transgene expression was sustained at least 8 days post-transfection for the substrate-mediated transfection method using cationic pullulan, whereas transgene expression was decreased significantly just 4 days post-transfection for the conventional transfection method.[29]

Although the transgene expression level and transfection efficiency at 2 days of post-transfection in the deposition method were relatively low compared to those in the conventional method, they were significantly increased between 2 and 5 days of post-transfection (Figure 4A,B). The conventional solution-mediated transfection was performed by adding polyplexes to log growth-phase cells, which have high activity against polyplex uptake through cell endocyosis. On the other hand, deposition transfection was performed by seeding cells on the polyplex deposited culture surface, in which the activity of polyplex uptake by the cells would be very low until cells reach log growth phase, because they initiate uptake of polyplexes and other molecules after their adhesion to culture surface and then log-phase growth. Therefore, we considered that the difference in the time course of transgene expression profile between conventional and deposition transfection method was caused by the difference in cell state when the cells were exposed to polyplexes.

In the conventional transfection method, cells are needed to precultivate for several days before transfection to obtain growth-phase cells. On the other hand, in the deposition method, cells are directly seeded on the polyplex-deposited culture well, and they are transfected according with their growth. So, the time to obtain transgene expression from the starting point of cell cultivation is not so different between conventional and deposition methods. Therefore, we consider that the delay of transgene expression in the deposition transfection is not a disadvantage for the use of cell culture applications.

As shown in Figure 6, we successfully transfected the GFP gene into the primary cells isolated from beagle adipose tissue on the polyplex culture surface. Stem-cell-mediated tissue engineering and gene therapy are promising approaches for many areas of tissue regenerative medicine.[30] In particular, adipose-derived adherent cell populations including adipose-derived stem cells are useful for those approaches because they can differentiate into mesodermal tissues including adipocytes, chondrocytes, smooth muscle cells, and cardiac cells. Moreover, they are noninvasive and can be easily isolated from the human body.[31,32] Therefore, our results for transfecting adipose-derived primary cells by utilizing deposition transfection mean that deposition transfection using PDMAEMA may be a potential tool for stem-cell-mediated tissue engineering and gene therapy.

■ CONCLUSION

By using small amounts of PDMAEMA with both thermoresponsive and cationic characteristics, high and sustained transgene expression was achieved via deposition transfection, thus resulting in high cell viability. Further, the PDMAEMA-mediated transfection of adipose-derived primary cells in vitro was highly efficient. We believe that our findings confirm the applicability of PDMAEMA as a deposition transfection material and as a valuable tool for gene therapy.

■ AUTHOR INFORMATION

Corresponding Author

*Tel: +81-6-6833-5012(ex2624). Fax: +81-6-6872-8090. E-mail: nakayama.yasuhide.ri@mail.ncvc.go.jp.

Notes

The authors declare no competing financial interest.

■ REFERENCES

(1) Adler, A. F., and Leong, K. W. (2010) Emerging links between surface nanotechnology and endocytosis: impact on nonviral gene delivery. *Nano Today 5*, 553−569.

(2) Zhang, S., Zhao, Y., Zhao, B., and Wang, B. (2010) Hybrids of nonviral vectors for gene delivery. *Bioconjugate Chem. 21*, 1003−1009.

(3) Marshall, E. (1999) Gene therapy death prompts review of adenovirus vector. *Science 286*, 2244−2245.

(4) Li, Z., Düllmann, J., Schiedlmeier, B., Schmidt, M., von Kalle, C., Meyer, J., Forster, M., Stocking, C., Wahlers, A., Frank, O., Ostertag, W., Kühlcke, K., Eckert, H. G., Fehse, B., and Baum, C. (2002) Murine leukemia induced by retroviral gene marking. *Science 296*, 497.

(5) Ewert, K. K., Ahmad, A., Bouxsein, N. F., Evans, H. M., and Safinya, C. R. (2008) Non-viral gene delivery with cationic liposome-DNA complexes. *Methods Mol. Biol. 433*, 159−175.

(6) Nakayama, Y. (2012) Hyperbranched polymeric "star vectors" for effective DNA and siRNA delivery. *Acc. Chem. Res.*, in press.

(7) Pandita, D., Santos, J. L., Rodrigues, J., Pêgo, A. P., Granja, P. L., and Tomás, H. (2011) Gene delivery into mesenchymal stem cells: a

biomimetic approach using RGD nanoclusters based on poly(amidoamine) dendrimers. *Biomacromolecules 12*, 472−481.
(8) Santos, J. L., Pandita, D., Rodrigues, J., Pêgo, A. P., Granja, P. L., Balian, G., and Tomás, H. (2010) Receptor-mediated gene delivery using PAMAM dendrimers conjugated with peptides recognized by mesenchymal stem cells. *Mol. Pharmaceutics 7*, 763−774.
(9) Numata, K., Reagan, M. R., Goldstein, R. H., Rosenblatt, M., and Kaplan, D. L. (2011) Spider silk-based gene carriers for tumor cell-specific delivery. *Bioconjugate Chem. 22*, 1605−1610.
(10) Park, K., Lee, M. Y., Kim, K. S., and Hahn, S. K. (2010) Target specific tumor treatment by VEGF siRNA complexed with reducible polyethyleneimine-hyaluronic acid conjugate. *Biomaterials 31*, 5258−5265.
(11) Cheng, H., Zhu, J. L., Sun, Y. X., Cheng, S. X., Zhang, X. Z., and Zhuo, R. X. (2008) Novel thermoresponsive nonviral gene vector: P(NIPAAm-co-NDAPM)-b-PEI with adjustable gene transfection efficiency. *Bioconjugate Chem. 19*, 1368−1374.
(12) Hinrichs, W. L., Schuurmans-Nieuwenbroek, N. M., van de Wetering, P., and Hennink, W. E. (1999) Thermosensitive polymers as carriers for DNA delivery. *J. Controlled Release 60*, 249−259.
(13) Agut, W., Brûlet, A., Schatz, C., Taton, D., and Lecommandoux, S. (2010) pH and temperature responsive polymeric micelles and polymersomes by self-assembly of poly[2-(dimethylamino)ethyl methacrylate]-b-poly(glutamic acid) double hydrophilic block copolymers. *Langmuir 26*, 10546−10554.
(14) Su, J., Chen, F., Cryns, V. L., and Messersmith, P. B. (2011) Catechol polymers for pH-responsive, targeted drug delivery to cancer cells. *J. Am. Chem. Soc. 133*, 11850−11853.
(15) Zhou, Y. M., Ishikawa, A., Okahashi, R., Uchida, K., Nemoto, Y., Nakayama, M., and Nakayama, Y. (2007) Deposition transfection technology using a DNA complex with a thermoresponsive cationic star polymer. *J. Controlled Release 123*, 239−246.
(16) Layman, J. M., Ramirez, S. M., Green, M. D., and Long, T. E. (2009) Influence of polycation molecular weight on poly(2-dimethylaminoethyl methacrylate)-mediated DNA delivery in vitro. *Biomacromolecules 10*, 1244−1252.
(17) de Wolf, H. K., de Raad, M., Snel, C., van Steenbergen, M. J., Fens, M. H., Storm, G., and Hennink, W. E. (2007) Biodegradable poly(2-dimethylamino ethylamino)phosphazene for in vivo gene delivery to tumor cells. Effect of polymer molecular weight. *Pharm. Res. 24*, 1572−1580.
(18) Jiang, X., Lok, M. C., and Hennink, W. E. (2007) Degradable-brushed pHEMA-pDMAEMA synthesized via ATRP and click chemistry for gene delivery. *Bioconjugate Chem. 18*, 2077−2084.
(19) Xue, J., Chen, L., Wang, H. L., Zhang, Z. B., Zhu, X. L., Kang, E. T., and Neoh, K. G. (2008) Stimuli-responsive multifunctional membranes of controllable morphology from poly(vinylidene fluoride)-graft-poly[2-(N,N-dimethylamino)ethyl methacrylate] prepared via atom transfer radical polymerization. *Langmuir 24*, 14151−11458.
(20) Jana, S., Rannard, S. P., and Cooper, A. I. (2007) Structure-LCST relationships for end-functionalized water-soluble polymers: an "accelerated" approach to phase behaviour studies. *Chem. Commun. (Camb.) 28*, 2962−2964.
(21) Liu, G., Wu, D., Ma, C., Zhang, G., Wang, H., and Yang, S. (2007) Insight into the origin of the thermosensitivity of poly(2-(dimethylamino)ethyl methacrylate]. *ChemPhysChem 8*, 2254−2259.
(22) Nakayama, Y., Yamaoka, S., Nemoto, Y., Alexey, B., and Uchida, K. (2011) Thermoresponsive heparin bioconjugate as novel aqueous antithrombogenic coating material. *Bioconjugate Chem. 22*, 193−199.
(23) Nakayama, Y., Okahashi, R., Iwai, R., and Uchida, K. (2007) Heparin bioconjugate with a thermoresponsive cationic branched polymer: a novel aqueous antithrombogenic coating material. *Langmuir 23*, 8206−8211.
(24) Manini, I., Gulino, L., Gava, B., Pierantozzi, E., Urina, C. C., Rossi, D., Brafa, A., D'Aniello, C., and Sorrentino, V. (2011) Multipotent progenitors in freshly isolated and cultured human mesenchymal stem cells: a comparison between adipose and dermal tissue. *Cell Tissue Res. 344*, 85−95.
(25) Ruponen, M., Ylä-Herttuala, S., and Urtti, A. (1999) Interactions of polymeric and liposomal gene delivery systems with extracellular glycosaminoglycans: physicochemical and transfection studies. *Biochim. Biophys. Acta 1415*, 331−341.
(26) Funhoff, A. M., van Nostrum, C. F., Lok, M. C., Kruijtzer, J. A., Crommelin, D. J., and Hennink, W. E. (2005) Cationic polymethacrylates with covalently linked membrane destabilizing peptides as gene delivery vectors. *J. Controlled Release 101*, 233−246.
(27) van Gaal, E. V., Hennink, W. E., Crommelin, D. J., and Mastrobattista, E. (2006) Plasmid engineering for controlled and sustained gene expression for nonviral gene therapy. *Pharm. Res. 23*, 1053−1074.
(28) Wang, Z., Troilo, P. J., Wang, X., Griffiths, T. G., Pacchione, S. J., Barnum, A. B., Harper, L. B., Pauley, C. J., Niu, Z., Denisova, L., Follmer, T. T., Rizzuto, G., Ciliberto, G., Fattori, E., Monica, N. L., Manam, S., and Ledwith, B. J. (2004) Detection of integration of plasmid DNA into host genomic DNA following intramuscular injection and electroporation. *Gene Ther. 11*, 711−721.
(29) Okazaki, A., Jo, J., and Tabata, Y. (2007) A reverse transfection technology to genetically engineer adult stem cells. *Tissue Eng. 13*, 245−251.
(30) Sheyn, D., Mizrahi, O., Benjamin, S., Gazit, Z., Pelled, G., and Gazit, D. (2010) Genetically modified cells in regenerative medicine and tissue engineering. *Adv. Drug Delivery Rev. 62*, 683−698.
(31) Cherubino, M., Rubin, J. P., Miljkovic, N., Kelmendi-Doko, A., and Marra, K. G. (2011) Adipose-derived stem cells for wound healing applications. *Ann. Plast. Surg. 66*, 210−215.
(32) Zuk, P. A., Zhu, M., Mizuno, H., Huang, J., Futrell, J. W., Katz, A. J., Benhaim, P., Lorenz, H. P., and Hedrick, M. H. (2001) Multilineage cells from human adipose tissue: implications for cell-based therapies. *Tissue Eng. 7*, 211−228.

Bioconjugate Chemistry

Article

pubs.acs.org/bc

Cholesterol-Based Nucleolipid-Ruthenium Complex Stabilized by Lipid Aggregates for Antineoplastic Therapy

Luca Simeone,[†] Gaetano Mangiapia,[‡,∥] Giuseppe Vitiello,[‡,∥] Carlo Irace,[§] Alfredo Colonna,[§] Ornella Ortona,[‡,∥] Daniela Montesarchio,*[,†] and Luigi Paduano*[,‡,∥]

[†]Dipartimento di Chimica Organica e Biochimica, [‡]Dipartimento di Chimica "Paolo Corradini", Università "Federico II" di Napoli, Complesso Universitario di Monte S. Angelo, via Cintia, 4, 80126 Naples, Italy

[∥]CSGI – Consorzio interuniversitario per lo sviluppo dei Sistemi a Grande Interfase

[§]Dipartimento di Farmacologia Sperimentale, Università "Federico II" di Napoli, via D. Montesano 49, 80131 Naples, Italy

Supporting Information

ABSTRACT: A novel ruthenium complex, linked to a cholesterol-containing nucleolipid (named ToThyCholRu), stabilized by lipid aggregates for antineoplastic therapy is presented. In order to retard the degradation kinetics typically observed for several ruthenium-based antineoplastic agents, ToThyCholRu is incorporated into a liposome bilayer formed by POPC. The resulting nanoaggregates contain up to 15% in moles of the ruthenium complex, and are shown to be stable for several weeks. The liposomes host the ruthenium–nucleolipid complex with the metal ion surrounded by POPC lipid headgroups and the steroid moiety inserted in the more external acyl chain region. These ruthenium-containing liposomes are more effective in inhibiting the growth of cancer cells than a model NAMI-A-like ruthenium complex, prepared for a direct evaluation of their antiproliferative activity. These results introduce new perspectives in the design of innovative transition-metal-based supramolecular systems for anticancer drug vectorization.

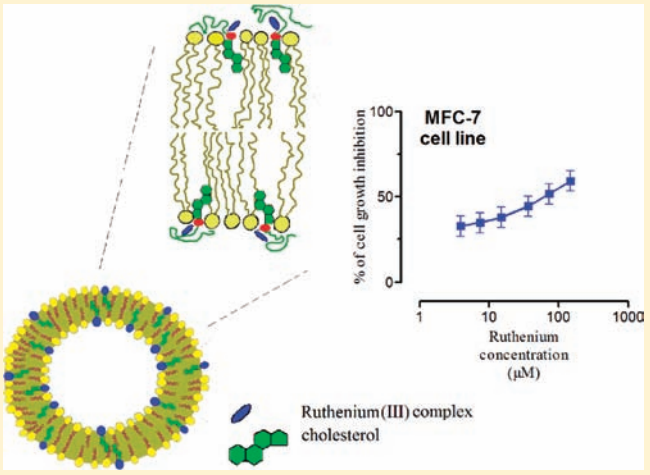

INTRODUCTION

In the past three decades, a number of ruthenium-based drugs have been proposed as antineoplastic agents, and some of them have been successfully tested for potential antitumor activity.[1] In several cases, the design of these compounds was largely inspired by well-known Pt complexes. Indeed, Cisplatin is still the most widely used chemotherapeutic drug for the treatment of several malignancies,[2,3] though its use is associated with severe side effects, and limited in many anticancer therapeutic protocols by primary and acquired resistance to it. These drawbacks have led to exploration of other transition metal complexes as efficient alternatives to Pt-based agents. Osmium, ruthenium, and titanium complexes offer some very interesting examples.[4]

As confirmed by the large number of papers appearing in the literature in the last two decades, ruthenium complexes have emerged as the most promising alternatives to Pt-based antineoplastic agents in biological screenings. Since the early 1980s, Sava and co-workers have been pioneers in studying the perspectives of transition-metal complexes, developing, among others, the ruthenium complex named NAMI-A, found to be a very active anticancer agent in *in vitro* assays. This compound, along with KP1019 and RAPTA-C, has reached human clinical testing and has completed Phase I clinical trials.[5]

Even if a large number of studies on Ru complexes have been published in recent years, to the best of our knowledge the unique example of nanovector-carrying ruthenium complexes for anticancer therapy has been reported by some of us only.[6−8]

As is well-known, amphiphilic self-assembly allows an efficient bottom-up strategy in order to obtain nanosized aggregates whose volume and shape are quite easily tunable. The incorporation of appropriate complex structural motifs in suitable amphiphilic building blocks, used as starting monomers, may lead to functional aggregates of great interest in the development of novel smart materials, with applications in both nanotechnology and nanomedicine. In this framework, with the aim of obtaining efficient delivery and controlled release of anticancer agents, we recently synthesized a new nucleolipid-based ruthenium complex that spontaneously incorporates into the phospholipid membrane of a liposome. As an evolution of

Received: October 31, 2011
Revised: February 13, 2012
Published: February 28, 2012

dx.doi.org/10.1021/bc200565v | *Bioconjugate Chem.* 2012, 23, 758–770

our previous work, we describe here the synthesis, molecular, and aggregation characterization along with bioactivity investigations of a novel cholesterol-containing ruthenium complex, baptized ToThyCholRu. This system has been studied as such and in parallel, when lodged in the biomimetic membrane formed by the naturally occurring lipid 1-palmitoyl-2-oleoyl-*sn*-glycero-3-phosphocholine, POPC.

Our purposes are to develop highly biomimetic liposomes able to preserve the bioactive ruthenium complex core from degradation and to deliver a higher amount of antineoplastic agent to the target cells, thus resulting into a more active anticancer drug.

By exploiting the high affinity of cholesterol with phospholipids, ToThyCholRu has been designed so to achieve easy penetration through the cell membrane, thus facilitating ruthenium complex internalization. This strategy has been successfully applied in the antisense strategy for gene therapy using oligonucleotides end-modified with a cholesterol motif. In fact, it has been observed that cholesterol conjugation to oligonucleotides results in high accumulation of the oligomers in various liver[9] and spleen cell types.[10]

Regarding the NAMI-A ruthenium complex, in spite of the quite encouraging clinical results, some questions are still open about its *in vivo* applicability, mainly due to its low stability in physiological conditions. In analogy with Cisplatin, the chloride ligands of the ruthenium complex are replaced by hydroxide ligands in a few hours. This leads to partial hydrolysis of the complex and to poly-oxo species formation.[11,12] Although it is guessed that the formation of poly-oxo species does not really alter the ruthenium activity, at least for some tumor cell lines,[13] as far as Cisplatin is concerned it has been shown that its premature aquation and hydrolysis in the extracellular medium deactivate up to 98% of the Pt complex administered. Thus, in order to drastically reduce the degradation process, our basic idea was to move *in vivo* ToThyCholRu using POPC-based liposomes as carrier. The ruthenium complex anchored to the cholesteryl−thymidine nucleolipid is incorporated by force into the liposome bilayer, in a region where the contact with water or hydroxy groups is reduced, thus sensibly retarding the degradation kinetics. The amphiphilic nanoaggregates described here contain up to 15 mol % ruthenium complex, which at this composition is stable for several weeks.

The study was carried out through the following steps: *(i)* synthesis of the Ru(III) complex, built on a thymidine scaffold incorporating the lipophilic cholesterol moiety and a hydrophilic polyoxyethylene chain; *(ii)* structural characterization of the aggregates generated by this complex, in the absence and in the presence of POPC; *(iii)* control of the stability of the Ru complexes in both forms; and *(iv)* antiproliferative *in vitro* investigations of the formulation.

The self-aggregation properties were studied by dynamic light scattering, DLS, and small-angle neutron scattering, SANS, whereas the degradation process was studied by UV−vis measurements and electron paramagnetic resonance, EPR. A limited panel of human tumor cell lines (HeLa cervical cancer cells, CaCo-2 and WiDr epithelial colorectal adenocarcinoma cells, MCF-7 breast adenocarcinoma cells, SH-SY5Y neuroblastoma cells) have been used to evaluate the cytotoxic activity of the Ru-containing aggregates.

MATERIALS AND METHODS

General Synthetic Methods. All the reagents were of the highest commercially available quality and were used as received. TLC analyses were carried out on silica gel plates from Merck (60, F254). Reaction products on TLC plates were visualized by UV light and then by treatment with a 10% $Ce(SO_4)_2/H_2SO_4$ aqueous solution. For column chromatography, silica gel from Merck (Kieselgel 40, 0.063−0.200 mm) was used.

1-Palmitoyl-2-oleoyl-*sn*-glycero-3-phosphocholine, POPC, from Avanti Polar and cholesterol, Chol, from Sigma, purity >99%, were used as received. Water used for liposome preparation was obtained by Millipore Elix 3 apparatus.

NMR spectra were recorded on Bruker WM-400, Varian Gemini 200, and Varian Inova 500 spectrometers, as specified. All the chemical shifts are expressed in ppm with respect to the residual solvent signal. Peak assignments have been carried out on the basis of standard H−H COSY and HSQC experiments. For the ESI MS analyses, a Waters Micromass ZQ instrument—equipped with an electrospray source—was used in the positive and/or negative mode. MALDI TOF mass spectrometric analyses were performed on a PerSeptive Biosystems Voyager-De Pro MALDI mass spectrometer in the linear mode using 3,4-dihydroxybenzoic acid as the matrix.

The NMR and MS characterization of ToThyCholRu and related synthetic intermediates are described in detail in the Supporting Information.

Synthesis. *Synthesis of 3-(4-Pyridylmethyl), 3′-O-Cholesteroxyacetyl, 5′-O-(4,4′-Dimethoxytriphenyl-methyl)-thymidine (**4**).* 5′-*O*-(4,4′-Dimethoxytriphenylmethyl)-thymidine **2** (396 mg, 0.73 mmol) was dissolved in 5 mL of dry DMF. K_2CO_3 (302 mg, 2.18 mmol) and 4-(bromomethyl)-pyridine hydrobromide (276 mg, 1.09 mmol) were sequentially added to the reaction mixture, left under stirring at 60 °C. After 12 h, TLC analysis indicated the presence of one main product in the reaction mixture. Alkylated compound **3** was not isolated, but directly converted into its 3′-conjugated derivative **4** (see Scheme 1). To this purpose, the solvent was removed and the residual solid was taken up in DCM, washed with water, dried over anhydrous Na_2SO_4, and concentrated in vacuo. Successively, the residue was dissolved in 3 mL of dry DCM, and then DMAP (32 mg, 0.266 mmol), cholesteroxy-acetic acid **8** (118 mg, 0.266 mmol), and DCC (55 mg, 0.266 mmol) were sequentially added. The reaction mixture was stirred for 12 h at room temperature, and then the solvent was removed in vacuo; the crude product was purified by chromatography on a silica gel column with *n*-hexane/AcOEt (1:1, v/v, containing 1% of TEA) as eluent, yielding the desired compound **4** in 19% yields for the two steps (144 mg, 0.14 mmol, unoptimized yield).

*Synthesis of 3-(4-Pyridylmethyl), 3′-O-Cholesteroxyacetyl Thymidine (**5**).* **4** (140 mg, 0.13 mmol) was dissolved in 3 mL of a 1% TCA solution in DCM and stirred for 1 h at room temperature (see Scheme 1). The reaction mixture was then concentrated in vacuo and purified by chromatography on a silica gel column with $CHCl_3/CH_3OH$ (99:1, v/v) as eluent, giving the desired compound **5** in almost quantitative yields (100 mg, 0.13 mmol).

*Synthesis of 3-(4-Pyridylmethyl), 3′-O-Cholesteroxyacetyl, 5′-O-Monomethoxy-triethylene Glycol Acetyl Thymidine (**6**, ToThyChol).* **5** (96 mg, 0.13 mmol) was dissolved in 2 mL of dry DCM, and then DMAP (46 mg, 0.38 mmol), carboxylic acid **10** (41 mg, 0.18 mmol), and DCC (38 mg, 0.18 mmol) were sequentially added (see Scheme 1). The reaction mixture was stirred for 12 h at room temperature and the solvent was then removed in vacuo; the crude product was purified by chromatography on a silica gel column with *n*-hexane/acetone

Scheme 1. Synthetic Scheme for the Preparation of Ruthenium Complex 1 (ToThyCholRu)[a]

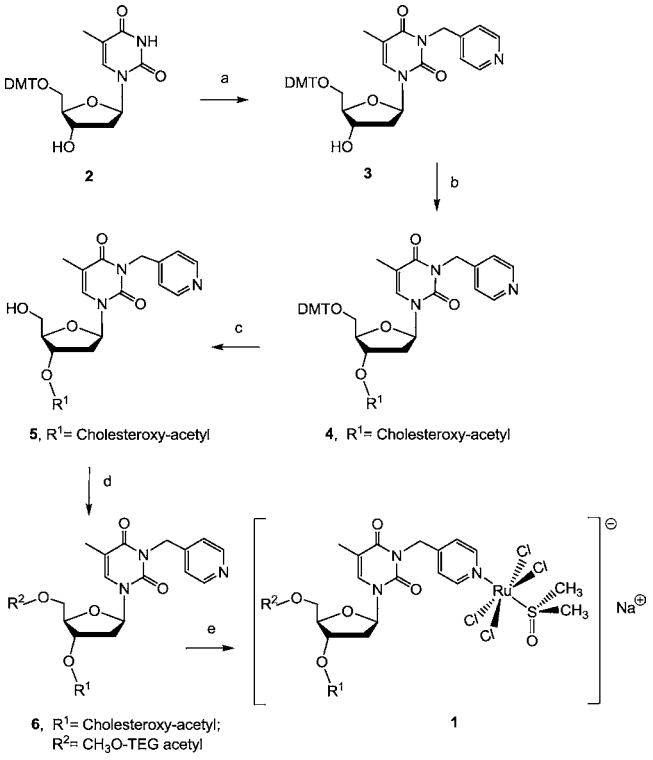

[a]Reaction conditions: (a) 4-(bromomethyl)pyridine, K_2CO_3, DMF, 12 h, 60 °C; (b) cholesteroxy acetic acid (**8**), DCC, DMAP, CH_2Cl_2, 12 h, r.t.; (c) 1% TCA in CH_2Cl_2, 1 h, r.t.; (d) CH_3O-TEG acetic acid (**10**), DCC, DMAP, CH_2Cl_2, 4 h, r.t.; (e) [trans-$RuCl_4(DMSO)_2$]$^-$ Na^+, CH_3CN, 4 h, 50 °C.

(1:1, v/v) as eluent, giving the desired compound **6** in 85% yields (106 mg, 0.11 mmol).

*Synthesis of tert-Butyl Cholesteroxy-Acetate (**7**).* Cholesterol (963 mg, 2.5 mmol) was dissolved in 4 mL of dry THF, and NaH 60% p.p. (200 mg, 4.98 mmol) and then *t*-butyl bromoacetate (920 μL, 6.22 mmol) were sequentially added to the reaction mixture taken at 0 °C. After 24 h at room temperature, the reaction was quenched by addition of CH_3OH (2 mL) and the solvent removed in vacuo (see Scheme 2). The residual solid was taken up in DCM, washed with water, dried over anhydrous Na_2SO_4, and concentrated in vacuo. The residue was then purified by chromatography on a silica gel column using *n*-hexane/AcOEt (9:1, v/v) as eluent, yielding the desired compound **7** in 31% yield (392 mg, 0.77 mmol).

*Synthesis of Cholesteroxy-Acetic Acid (**8**).* Ester **7** (300 mg, 0.59 mmol) was dissolved in 3.0 mL of formic acid and stirred at room temperature for 2 h. The solvent was then removed in vacuo and the residue coevaporated three times with $CHCl_3$ (3 × 3 mL), yielding the desired compound **8** in almost quantitative yields (266 mg, 0.59 mmol) (see Scheme 2).

*Synthesis of tert-Butyl(Monomethoxy)Triethylene Glycol Acetate (**9**).* Monomethoxytriethylene glycol (1.5 g, 9.13 mmol) was dissolved in 6.0 mL of dry THF, and NaH 60% p.p. (730 mg, 18.3 mmol) and then *t*-butyl bromoacetate (3.37 mL, 22.8 mmol) were sequentially added (see Scheme 3). The solution was stirred at room temperature for 12 h, then CH_3OH (1 mL) was added and the solvent removed in vacuo. The crude product, dissolved in $CHCl_3$ and filtered on Celite,

Scheme 2. Synthetic Scheme for the Preparation of Cholesteroxy Acetic Acid (8)[a]

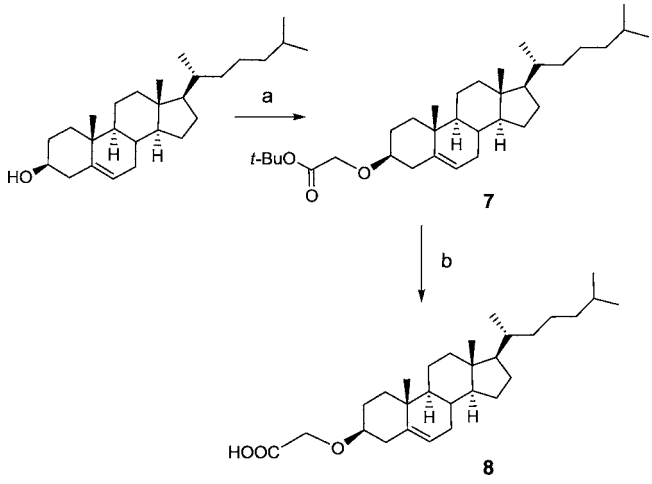

[a]Reaction conditions: (a) NaH, *tert*-butyl bromoacetate, THF, 12 h, r.t.; (b) HCOOH, 2 h, r.t.

Scheme 3. Synthetic Scheme for the Preparation of CH_3O-TEG Acetic Acid (10)[a]

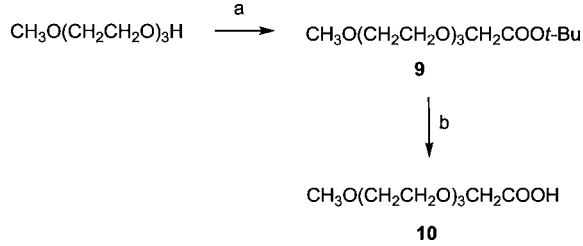

[a]Reaction conditions: (a) NaH, *tert*-butyl bromoacetate, THF, 12 h, r.t.; (b) HCOOH, 2 h, r.t.

was then purified by chromatography on a silica gel column with $CHCl_3$ as eluent, yielding the desired ester **9** in 98% yield (2.5 g, 8.96 mmol).

*Synthesis of (Monomethoxy)Triethylene Glycol Acetic Acid (**10**).* Ester **9** (630 mg, 2.26 mmol) was dissolved in 1.5 mL of formic acid and stirred at room temperature for 2 h (see Scheme 3). The solvent was then removed in vacuo, and the residue was coevaporated three times with $CHCl_3$ (3 × 3 mL), yielding the desired carboxylic acid **10** in 99% yield (500 mg, 2.25 mmol).

*Synthesis of Complex **1** (ToThyCholRu).* **6** (32 mg, 0.033 mmol) was dissolved in 1 mL of dry acetonitrile and then [*trans*-$RuCl_4(DMSO)_2$]$^-$ Na^+ (14 mg, 0.033 mmol) was added. The reaction mixture was stirred at 50 °C and the solvent was then removed in vacuo (see Scheme 1). The reaction, monitored by TLC on alumina, showed in 4 h the total disappearance of **6** to give the desired product **1** in quantitative yields.

*Synthesis of Complex **11** (AziRu).* In analogy to the synthesis of **1**, pyridine (3.0 μL, 0.037 mmol) was dissolved in 0.3 mL of dry acetonitrile and then [trans-$RuCl_4(DMSO)_2$]$^-$ Na^+ (15.6 mg, 0.037 mmol) was added. The reaction mixture was stirred at 50 °C for 2 h and the solvent was then removed in vacuo, giving the desired product AziRu, identified on the basis of its NMR and ESI-MS data (data not shown), in quantitative yields.

dx.doi.org/10.1021/bc200565v | *Bioconjugate Chem.* 2012, 23, 758−770

Lipid-Based Aggregate Preparation. The samples containing ToThyChol and ToThyCholRu were dissolved in a pseudophysiological solution. This latter solution was prepared in double-distilled and degassed water dissolving appropriate amounts of NaCl and KH_2PO_4 so that their final concentrations were 0.140 mol dm^{-3} and 0.010 mol dm^{-3}, respectively. pH was then adjusted to 7.4 by adding appropriate amounts of KOH. This value was checked to be within 0.1 pH units by means of a Radiometer pHM220 pH-meter equipped with a combined glass electrode previously calibrated with IUPAC standard buffer solutions.

For the samples containing POPC and ToThyCholRu, a standard procedure to form vesicles was applied: weighed amounts of ToThyCholRu and POPC were dissolved in chloroform, favoring the process by a slight warming (~40 °C) and sonication treatment (~5 min). Then, the solutions were transferred in round-bottom glass tubes, and a thin film of the solutes was obtained through evaporation of the solvent with dry nitrogen and keeping the samples under vacuum for at least 24 h. The film was then hydrated with H_2O or the pseudophysiological solution.

The vesicle suspensions were slightly heated at 40 °C and sonicated for 15 min at 59 kHz with a FALC LBS2 ultrasonic bath and, finally, repeatedly extruded through polycarbonate membranes of 100 nm pore size, for at least 11 times.

Samples for SANS measurements were prepared in heavy water (D_2O, isotopic enrichment >99.8%, molar mass 20.03 g mol^{-1}) purchased from Aldrich, in order to minimize the incoherent contribution to the scattering cross sections arising from the system. Samples to be analyzed by EPR also included 1% (w/w) of spin-labeled phosphatidylcholine (1-palmitoyl-2-[*n*-(4,4-dimethyloxazolidine-*N*-oxyl)]stearoyl-*sn*-glycero-3-phosphocholine, *n*-PCSL, *n* = 5, 7, 10, 14), purchased from Avanti Polar Lipids and stored at −20 °C in ethanol solutions.

Lipid-Based Aggregate Characterization. The lipid-based aggregate characterization has been achieved by different experimental techniques such as DLS, to get information on particle dimensions; SANS, to reach a deeper insight into the aggregate structure; UV−vis measurements, to evaluate their stability in time; and EPR, to confirm aggregate stability and investigate the membrane microstructure.

Dynamic Light Scattering (DLS). Dynamic light scattering investigations were performed with a setup composed of a Photocor compact goniometer, a SMD 6000 Laser Quantum 50 mW light source operating at 5325 Å, and a PMT-120-OP/B and a correlator (Flex02−01D) purchased from Correlator.com. All the measurements were performed at (25.00 ± 0.05) °C with the temperature controlled through the use of a thermostat bath. In dynamic light scattering, the intensity autocorrelation function $g^{(2)}(t)$ is measured and related to the electric field autocorrelation function $g^{(1)}(t)$ by the Siegert relation[14]

$$g^{(2)}(t) = 1 + \beta |g^{(1)}(t)|^2 \tag{1}$$

where β is the coherence factor, which accounts for the deviation from ideal correlation and depends on the experimental geometry. The function $g^{(1)}(t)$ can be written as the Laplace transform of the distribution of the relaxation rates, Γ, used to calculate the translational diffusion coefficient, D

$$g^{(1)}(t) = \int_{-\infty}^{+\infty} \tau A(\tau) \exp\left(-\frac{t}{\tau}\right) \mathrm{d} \ln \tau \tag{2}$$

where $\tau = 1/\Gamma$. Laplace transforms were performed using a variation of CONTIN algorithm incorporated in *Precision Deconvolve* software. From the relaxation rates, the *z*-average of the diffusion coefficient D may be obtained as follows:[15]

$$D = \lim_{q \to 0} \frac{\Gamma}{q^2} \tag{3}$$

where $q = (4\pi n_0)/(\lambda \sin(\theta/2))$ is the modulus of the scattering vector, n_0 the refractive index of the solution, λ the incident wavelength, and θ the scattering angle. An example of Γ fit vs q^2, to get the slope of the straight line, is shown in Figure S1 of the Supporting Information.

Provided that the solutions are quite dilute, the Stokes−Einstein equation, which rigorously holds at infinite dilution for non-interacting spherical species[16] diffusing in a continuous medium, may legitimately be used to evaluate the hydrodynamic radius R_H of the aggregates:[17,18]

$$R_H = \frac{kT}{6\pi\eta D} \tag{4}$$

where k is the Boltzmann constant, T is the absolute temperature, and η is the medium viscosity. In the case of nonspherical particles, R_H in eq 4 represents the radius of equivalent spherical aggregates with the same diffusion coefficient.

Small-Angle Neutron Scattering (SANS). Small angle neutron scattering measurements were performed at 25 °C with the KWS2 instrument located at the Heinz Maier-Leibnitz neutron source of the Jülich Centre for Neutron Science (Garching, Germany). Neutrons with an average wavelength of 7 Å and 19 Å and a wavelength spread $\Delta\lambda/\lambda \leq 0.2$ were used. A two-dimensional 128 × 128 array scintillation detector at three different wavelength (W)/collimation (C)/sample-to-detector (D) distances ($W_{7Å}C_{8m}D_{8m}$, $W_{7Å}C_{8m}D_{2m}$, and $W_{19Å}C_{8m}D_{8m}$) was used. These configurations allowed collection of data in a range of the scattering vector modulus $q = 4\pi/\lambda \sin(\theta/2)$ located between 0.002 and 0.25 $Å^{-1}$. The obtained raw data were corrected for background and empty cell scattering. Detector efficiency corrections, radial average, and transformation to absolute scattering cross sections were made with a secondary plexiglass standard.[19]

Depending on the scattering intensity profiles, different models were adopted to fit the collected date. For cylindrical aggregates (as in the case of the ToThyCholRu aggregates, see below), the following equation was used:

$$\frac{\mathrm{d}\Sigma}{\mathrm{d}\Omega} = \frac{\phi_{cyl}(1-\phi_{cyl})\pi^2 R^2 \Delta^2 \rho}{q} \exp\left(-\frac{q^2 R^2}{4}\right) + \left(\frac{\mathrm{d}\Sigma}{\mathrm{d}\Omega}\right)_{\mathrm{incoh}} \tag{5}$$

where R is the radius of the base, ϕ_{cyl} the cylinder volume fraction, and $\Delta\rho$ the scattering length density difference between the cylinders and the solvent.

dx.doi.org/10.1021/bc200565v | *Bioconjugate Chem.* 2012, 23, 758−770

In the presence of vesicles, the system was modeled as a collection of unilamellar and multilamellar vesicles:[20]

$$\frac{d\Sigma}{d\Omega} = \frac{1}{q^2}\langle |f(q)|^2\rangle\left(1 + \frac{\langle |f(q)|\rangle^2}{\langle |f(q)|^2\rangle}(S(q) - 1)\right) + \left(\frac{d\Sigma}{d\Omega}\right)_{incoh} \quad (6)$$

In eq 6, $f(q)$ is the form factor of a bilayer containing information on the shape of the scattering objects, whereas $S(q)$ is the structure factor that takes into account the interferences occurring among the bilayers belonging to a single stack of lamellae. $(d\Sigma/d\Omega)_{incoh}$ represents the incoherent contribution to the cross section measured, mainly due to the presence of hydrogenated molecules.

UV−vis Measurements. All the UV−vis measurements were acquired on a Cary Varian 5000 spectrophotometer equipped with a multicell holder. Temperature within the cell was controlled using the Peltier thermocouple. Quartz cuvettes with a path length of 1.0 cm were used for the measurements. Wavelength scans were performed at 25 °C from 200 to 800 nm, with a 300 nm/min scan speed.

Electron Paramagnetic Resonance (EPR). EPR spectra were recorded on a 9 GHz Bruker Elexys E-500 spectrometer (Bruker, Rheinstetten, Germany). Capillaries containing the samples were placed in a standard 4 mm quartz sample tube containing light silicone oil for thermal stability. The temperature of the sample was regulated at 25 °C and maintained constant during measurement by blowing thermostatted nitrogen gas through a quartz Dewar. The instrumental settings were as follows: sweep width, 120 G; resolution, 1024 points; modulation frequency, 100 kHz; modulation amplitude, 1.0 G; time constant, 20.5 ms, incident power, 5.0 mW. Several scans, typically 64, were accumulated to improve the signal-to-noise ratio. Values of the outer hyperfine splitting, $2A_{max}$, were determined by measuring, through a homemade MATLAB-based routine, the difference between the low-field maximum and the high-field minimum. This parameter is a useful empirical measure of the lipid chain dynamics and order in both gel and fluid phases of lipid bilayers.[21,22] The main source of error on the $2A_{max}$ value is the uncertainty in composition of samples prepared by mixing few microliters of mother solutions. For this reason, reproducibility of $2A_{max}$ determination was estimated by evaluating its value for selected independently prepared samples with the same nominal composition. It was found that the uncertainty was ±0.2 G.

Cell Cultures, Proliferation, and Viability. Bioactivity and cytotoxicity of ruthenium-containing nucleolipidic nanoparticles and of AziRu was investigated using a limited panel of human tumor cell lines (HeLa cervical cancer cells, CaCo-2 and WiDr epithelial colorectal adenocarcinoma cells, MCF-7 breast adenocarcinoma cells, SH-SY5Y neuroblastoma cells), all purchased from ATCC (American Type Culture Collection, Manassas, Virginia, USA). Cells were cultured at 37 °C in a humidified 5% CO_2 atmosphere and were grown in Dulbecco's modified Eagle's medium (DMEM, Invitrogen, Paisley, U.K.) containing high glucose (4.5 g/L) or in RPMI medium (Invitrogen, Paisley, U.K.). Media were supplemented with 10% fetal bovine serum (FBS, Cambrex, Verviers, Belgium), L-glutamine (2 mM, Sigma, Milan, Italy), penicillin (100 units/mL, Sigma), and streptomycin (100 μg/mL, Sigma), according to ATCC recommendations. For cytotoxicity studies, cells were washed with PBS buffer solution (Sigma), collected by trypsine (Sigma), and then inoculated in a 96-microwell culture plate at density of 10^4 cells/well. Cells were allowed to grow for 24 h; then, the medium was replaced with fresh medium and cells were treated for a further 72 h with a range of concentrations (25−1000 μM) of (i) AziRu and POPC liposomes, and (ii) of the nucleolipidic aggregates ToThyChol (**6**, Scheme 1), ToThyCholRu (**1**, Scheme 1), and ToThyCholRu/POPC. In more detail, 1 or 2 μL of physiological solutions containing POPC, AziRu, ToThyChol, ToThyCholRu, and ToThyCholRu/POPC were added to cell culture medium to give concentrations ranging from 25 to 1000 μM.

Cell number and proliferation were determined by the trypan blue dye exclusion test. After these treatments, the medium was removed and the cells were washed twice with PBS buffer solution (Sigma) and then incubated with a trypsin−EDTA solution (Sigma) at 37 °C for 5 min. Trypsin was inactivated by resuspending the cells in medium containing 10% FBS (Cambrex). The cells were pelleted at 250*g* and resuspended in PBS. Viable cells, cells that excluded 0.4% trypan blue (Sigma), were then counted with a hemocytometer. Concurrently, cell viability was evaluated with an MTT assay procedure, which measures the level of mitochondrial dehydrogenase activity using the yellow 3-(4,5-dimethyl-2-thiazolyl)-2,5-diphenyl-2*H*-tetrazolium bromide (MTT, Sigma) as substrate.[23] The assay was based on the redox ability of living mitochondria to convert dissolved MTT into insoluble purple formazan. Briefly, after the treatments the medium was removed and the cells were incubated with 20 μL/well of an MTT solution (5 mg/mL) for 1 h in a humidified 5% CO_2 incubator at 37 °C. The incubation was stopped by removing the MTT solution and by adding 100 μL/well of DMSO to solubilize the purple formazan. Finally, the absorbance was monitored at 530 nm by using a multiwell plate reader in a Perkin-Elmer LS 55 Luminescence Spectrometer (Perkin-Elmer Ltd., Beaconsfield, U.K.).[24]

The calculation of the concentration required to inhibit the net increase in the cell number and viability by 50% (IC_{50}) is based on plots of data carried out in triplicate and repeated three times. IC_{50} values were obtained using a dose response curve by nonlinear regression using a curve fitting program, *GraphPad Prism 5.0*, and are expressed as mean ± SEM.

RESULTS AND DISCUSSION

Synthesis. Thymidine-based ruthenium complex **1** (Figure 1*a*)—following the design of a uridine-based system previously described by some of us[6]—was prepared in five straightforward steps as depicted in Scheme 1.

As a privileged ligand for transition metal complexes, one pyridine residue, attached through a methylene linker at the N-3 position of thymidine, was selected to provide the functional group useful for ruthenium trapping. Its insertion on the pyrimidine nucleobase was achieved in almost quantitative yields by treatment of the 5′-DMT protected nucleoside **2** with 4-(bromomethyl)pyridine in DMF using K_2CO_3 as the base (Scheme 1).

In order to obtain the target amphiphilic nucleolipid, the ribosidic hydroxy groups of alkylated nucleoside **3** were conjugated with hydrophilic and lipophilic chains. Ester linkages were chosen to attach these components to hydroxy moieties, and thus obtain effective pro-drugs, on the basis of several advantages. First of all, they can be realized by simple and high-yielding couplings of suitable carboxylic acids; second,

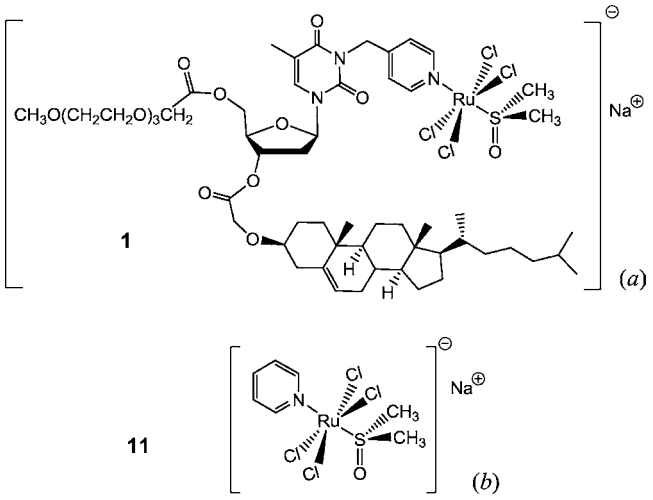

Figure 1. Molecular structure of (*a*): cholesterol-based nucleolipid-ruthenium complex **1** (ToThyCholRu); (*b*) pyridine-based ruthenium complex **11** (AziRu).

esters are stable covalent bonds in neutral and extracellular media, but are easily reversible once inside the cells, being rapidly degraded by esterases.

The desired nucleolipid **6** was synthesized by sequential insertion on **3** of two diverse appendages: one hydrophilic oligo(ethylene glycol) chain at the 5′-OH moiety, and one cholesterol residue, as the lipophilic component, attached at the 3′-OH position.

Cholesterol, selected here as the lipophilic decoration of the target functional nucleolipid in consideration of both its affinity with lipid membrane constituents and its easy availability, was first converted into ester **7** by reaction with *tert*-butyl bromoacetate and NaH in THF, followed by treatment with formic acid, assuring *tert*-butyl removal and recovery of target acid **8** in almost quantitative yields (Scheme 2).

A similar synthetic scheme was adopted to obtain the selected hydrophilic component, i.e., monomethoxy-triethylene glycol (TEG), in the form of carboxylic acid. This oligoether was first converted into *tert*-butyl ester **9**, then subjected to formic acid-promoted cleavage, giving oligoether-derivatized acetic acid **10** (Scheme 3).

Reaction of **3** with cholesterol derivative **8**, first, followed by detritylation and condensation of the resulting **5** with monomethoxy-TEG acetic acid **10**, with both couplings carried out using DCC as the activating agent, led to target nucleolipid **6**. Successive complexation with ruthenium was achieved by mixing **6** with the salt $[\text{trans-RuCl}_4(\text{DMSO})_2]^-\text{Na}^+$, prepared following literature procedures,[25] in CH_3CN at 50 °C for 4 h.

All the intermediate compounds were purified by silica gel column chromatography and characterized by ^{1}H and ^{13}C NMR spectroscopy and MS analysis. Target salt **1**, purified on alumina, was identified by ESI-MS spectrometry in the negative mode, showing m/z values in accordance with the expected mass. More difficult was the NMR characterization of the complex, with the ^{1}H and ^{13}C NMR spectra showing broadened signals, due to the presence of the paramagnetic Ru(III) nucleus. In the ^{1}H NMR spectrum in $CDCl_3$ of salt **1**, this also induced a dramatic upfield shift of the pyridine protons and of the methyl protons of the DMSO ligand, here found at $\delta = -1.87$ ppm and $\delta = -12.66$ ppm, respectively, as very broad signals, which can be considered diagnostic of the effective complex formation.[26,27]

Dynamic Light Scattering (DLS). ToThyChol (**6**, Scheme 1) exhibits a quite high solubility in water (>1−2 mmol/kg) with respect to the almost insoluble pure cholesterol. Furthermore, it shows self-aggregation properties due to its amphiphilic characteristics. DLS measurements carried out on ToThyChol at increasing sample concentration in pseudophysiological conditions reveal the presence of a monomodal radii distribution centered around 150 nm in the whole concentration range studied (see Figure 2 graph *a*). The dimensions of ToThyChol aggregates are shown in SI Table S1.

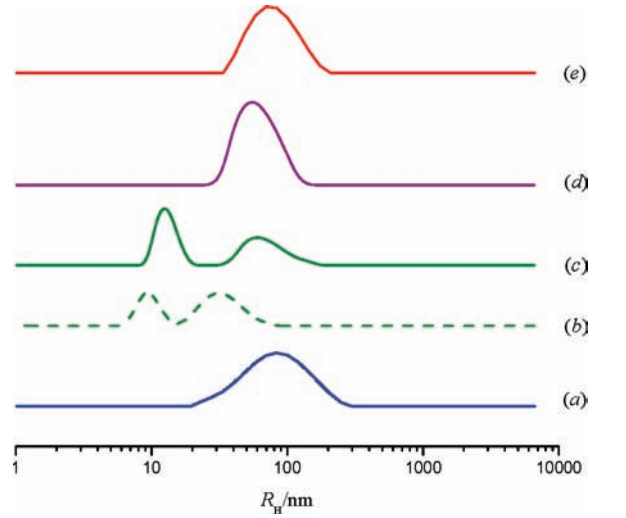

Figure 2. Example of size distribution of the ToThyChol and ToThyCholRu aggregates at 90°: (*a*) ToThyChol in pseudophysiological conditions, (*b*) ToThyCholRu in water, (*c*) ToThyCholRu in pseudophysiological conditions, (*d*) ToThyCholRu-POPC 15:85, (*e*) pure POPC in pseudophysiological conditions.

ToThyCholRu (**1**, Scheme 1) shows ability in nanostructuring, though its stability is limited in time. In fact, depending on the environmental conditions, we observed a clear change of the Ru-complex properties in a few hours (pseudophysiological conditions) or a few days (pure water).

DLS measurements performed on ToThyCholRu fresh solution both in water and in pseudophysiological conditions show a bimodal relaxation time distribution corresponding to the presence of two different aggregates whose mean hydrodynamic radii are ∼10 and ∼30 nm, respectively (see Figure 2 graphs *b*, *c*). However, the aggregate size progressively tends to increase, leading to the formation of small dark particles after 78 h in water and after 4−6 h in pseudophysiological conditions.

UV−vis. As in the case of NAMI-A,[11,12,28] ToThyCholRu complex in aqueous solution also suffers the replacement of its four chloride ligands by hydroxide ions, water molecules, or even buffer components, resulting in degradation of the initial complex. This effect is shown by the time evolution of the UV−vis spectra of ToThyCholRu both in pure water and in pseudophysiological conditions (see Figure 3 *a*, *b*).

Small-Angle Neutron Scattering (SANS). Information on the aggregate structure can be achieved by SANS measurements. The morphology of the aggregates has been obtained by means of small-angle neutron scattering. As shown in Figure 4*a*, the scattering profile of ToThyCholRu in pure heavy water

dx.doi.org/10.1021/bc200565v | *Bioconjugate Chem.* 2012, 23, 758−770

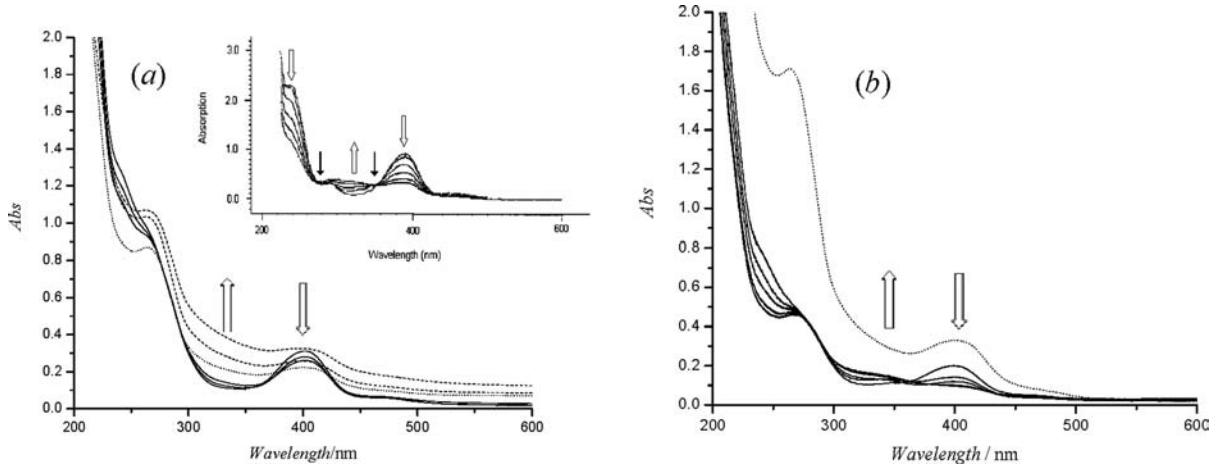

Figure 3. Absorbance evolution with time of 0.1 mmol kg^{-1} ToThyCholRu solution in (*a*) water (72 h), (*b*) pseudophysiological conditions (4 h). Two isosbestic points are present at 274 and 358 nm, respectively. The dashed lines refer to the formation of dark particles in solution, and the arrows indicate the direction of evolution with time. The inset represents the absorbance evolution with time of NAMI-A solution (reproduced with permission of *International Journal of Pharmaceutics*, Elsevier Limited, The Boulevard, Langford Lane Kidlington, Oxford, OX5 1GB, U.K. License number 2757030300954 released on Sep 27, 2011).

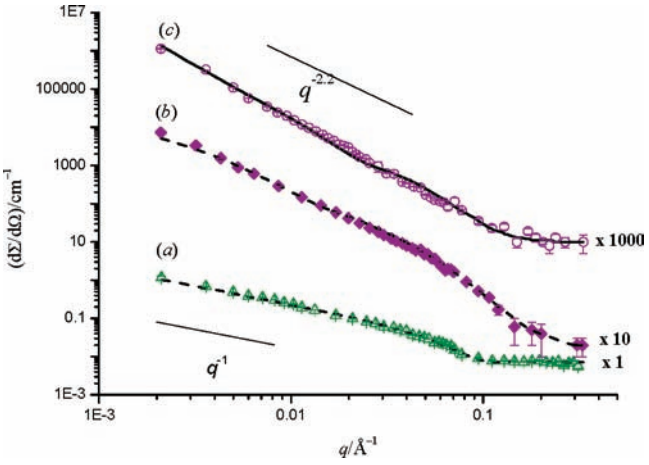

Figure 4. Scattering cross-section profiles for (*a*) ToThyCholRu in pure D_2O, (*b*) ToThyCholRu-POPC 5:95, and (*c*) ToThyCholRu-POPC 15:85 (in pseudophysiological conditions). The curves correspond to the appropriate fit equations. For a better visualization, data have been multiplied by a scale factor, as indicated.

shows a power law decay $d\Sigma/d\Omega \propto q^{-1}$. The slope −1 in a double log representation suggests the presence of cylindrical or near-cylindrical aggregates. Furthermore, this slope is quite constant over a large q range, changing to a −4 value only at high q, as expected in the Porod region.[29] Nevertheless, DLS measurements revealed the presence of two aggregates quite different in size (see Figure 2*b*,*c*).

This different experimental evidence can be matched either by admitting that both aggregates shown by DLS have a cylindrical shape or that the long cylindrical objects detected by SANS dominate in number and in size over the smaller ones. The former interpretation seems unrealistic on the basis of the very low value of the mean hydrodynamic radius (7÷10 nm) of the smaller aggregates. Thus, it appears more reasonable to admit that in the studied system there is coexistence of spherical or almost-spherical objects and long cylinders. In order to clarify this point, we simulated the scattering profile due to the simultaneous contribution to the form factor of spheres and cylinders. The results are shown in Figure S2 of the Supporting Information. The simulation suggests that a quite satisfactory reproduction of the experimental SANS data is only possible by admitting that the cylindrical objects represent more than 99% of the total volume of the aggregates, so that it is likely that in the ToThyCholRu systems the dominating population of aggregates presents a cylindrical shape.

On this basis, the experimental scattering data were modeled through eq 5. Model fit allows the estimation of the micelle radius R that results as (3.1 ± 0.5) nm. Unfortunately, the lack of the Guinier regime[29] in the scattering profile does not provide the possibility to calculate the length of the cylindrical micelles, l. Nonetheless, an estimation of its value can be obtained from the knowledge of the DLS hydrodynamic radius R_H that for a cylinder is given by[30]

$$R_H = \sqrt[3]{\frac{3}{4}R^2 l}\left[1.0304 + 0.0193x + 0.06229x^2 + 0.00476x^3 + 0.00166x^4 + \left(2.66\cdot10^{-7}\right)x^7\right] \quad (7)$$

where $x = \ln[l/(2R)]$ and R is the cylinder radius.

In order to avoid an overestimation of the experimental data, the above equation has been applied only to the larger aggregates in Figure 2. Upon application of eq 7 to ToThyCholRu aggregates, and on the basis of the hydrodynamic radius obtained by DLS, namely, 85−120 nm, it is possible to estimate that the cylinder length ranges between 1000 and 1400 nm.

Stabilization of ToThyCholRu. In order to increase the stability of ToThyCholRu in aqueous solution, the complex was lodged into POPC phospholipid bilayers.

Several samples of the system ToThyCholRu-POPC at different molar ratio (5:95, 10:90, 15:85, 20:80) in pseudophysiological solutions have been prepared, and their evolution with time has been monitored by UV−vis measurements.

As for the pure ToThyCholRu solutions, all the systems were light yellow immediately after preparation, giving superimposable spectra. However, while 5:95, 10:90, and 15:85 samples remained substantially unchanged for weeks, the 20:80 sample turned brown after 5−6 days. An example of the UV−

dx.doi.org/10.1021/bc200565v | *Bioconjugate Chem.* 2012, 23, 758−770

vis spectra over a time of 6 days (150 h) for the 15:85 sample is depicted in Figure 5. The absence of significant changes with

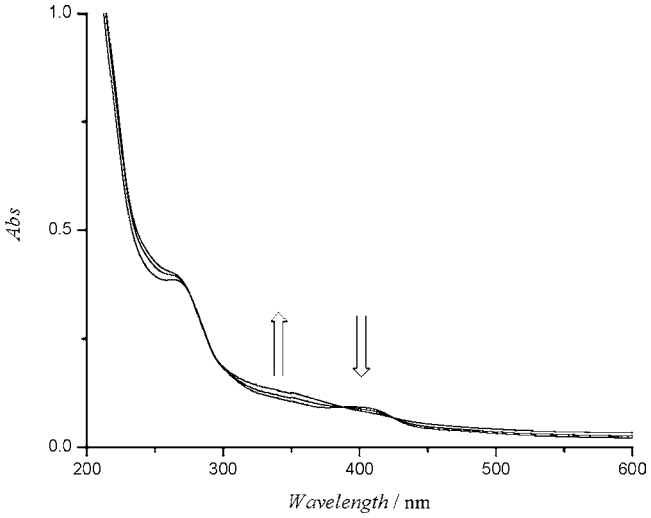

Figure 5. UV−vis time evolution of the ToThyCholRu-POPC 15:85 sample at 0.3 mmol kg^{-1} total concentration in pseudophysiological conditions over a period of 150 h. The arrows indicate the sense of the spectra evolution with time.

time in the spectra is a good indication of the formulation stability; no precipitation was observed as well. Furthermore, neither DLS nor EPR detected substantial changes with time in the aggregate dimensions and bilayer fluidity, as discussed below.

DLS measurements performed on the same 15:85 formulation, both in water and in pseudophysiological conditions, revealed for both systems the presence of aggregates with monomodal distribution having a mean hydrodynamic radius of 60 and 90 nm, respectively (see Figure 2*d*). Their size was invariant with time up to 5−6 days.

From the data obtained through SANS experiments, it was possible to identify the aggregates as liposomes. In fact, as shown in Figure 4*b*,*c*, the scattering profile of ToThyChol-POPC vs q shows slopes with a power law decay, $q^{-\alpha}$, with $\alpha > 2$ both in water and in pseudophysiological conditions. This is typical of bilayer structures that in the present case reflect the presence of liposomes.

It is worth noting that in both profiles the slope α in the intermediate q range is constantly ≥ 2, indicating the absence of coexisting pure ToThyCholRu cylindrical micelles, for which q^{-1} dependence should occur. It is thus possible to conclude that ToThyCholRu is quantitatively inserted in the liposome bilayer.

Since the α exponent is larger than 2, the aggregates were modeled as multilamellar systems (see eq 6). However, α value is only slightly larger than 2, and this is consistent with a small number of lamellae. It is likely that both single lamellar and some multilamellar vesicles are present.

The thickness of the layer changes from ∼4.0 nm for pure POPC liposomes to ∼4.5 nm for ToThyCholRu-POPC (5:95) and to ∼5.0 nm for ToThyCholRu-POPC (15:85) (see Table 1), indicating that the housing of the ToThyCholRu in the bilayer produces a slight increase of its thickness.

Electron Paramagnetic Resonance (EPR). Spin-label EPR spectroscopy has been proven to give substantial information on the acyl chains structuring in the lipid bilayers.[31−34] In this study, different spin-labels were used. They presented a nitroxide group, positioned at the levels of the 5, 7, 10, and 14 carbon atom of a phosphocholine backbone of a *sn*-2 chain, from here on called *n*-PCSL. 5-PCSL bears the radical label close to the molecule headgroup and consequently allows monitoring of the behavior of the region of the membrane inner core closer to the polar external layers. In contrast, 14-PCSL bears the radical label close to the terminal methyl group of the acyl chain, thus giving information on the more internal region of the membrane hydrophobic core. The goal has been to investigate how the membrane microstructure is influenced by the presence of ToThyCholRu at different ToThyCholRu/POPC ratios.

EPR spectra of *n*-PCSL in ToThyCholRu-POPC liposomes at 15:85 molar ratio are shown in Figure 6. In the same figure, the EPR spectra of the spin-labels in pure POPC vesicles are also presented.

For pure POPC, the 5-, 7-, and 10-PCSL spectra present a clearly defined axial anisotropy (see Figure 6, solid lines). In contrast, 14-PCSL spectrum shows an almost isotropic three-line signal, indicative of a rather free motion of the radical label. The higher isotropy of the 14-PCSL spectrum indicates a

Table 1. SANS, UV−vis, and DLS Results on Different ToThyCholRu/POPC Systems[a]

		SANS	UV−vis	DLS	SANS	
solvent	molar ratio	shape	degradation time/h	R_H/nm	lamellae number	layer thickness/nm
			ToThyCholRu			
pseudophys. buffer	100:0	cylinder	−	∼150 ± 15		3.1 ± 0.5 (cylinder radius)
			ToThyCholRu:POPC			
water	100:0	sphere	72	7.4 ± 0.5		
		cylinder		120 ± 30		
pseudophys. conditions	100:0	sphere	4	12 (*)		
		cylinder		85 (*)		
pseudophys. conditions	0:100	vesicles	stable	75 ± 7	1−2	4.0 ± 0.4
water	15:85		stable	64 ± 5		
pseudophys. conditions	5:95	vesicles	stable	78 ± 7	1−2	4.5 ± 0.7
pseudophys. conditions	15:85	vesicles	stable	80 ± 6	1−2	5.0 ± 0.5

[a]Measurements marked with * have been only evaluated at 90°.

dx.doi.org/10.1021/bc200565v | *Bioconjugate Chem.* 2012, 23, 758−770

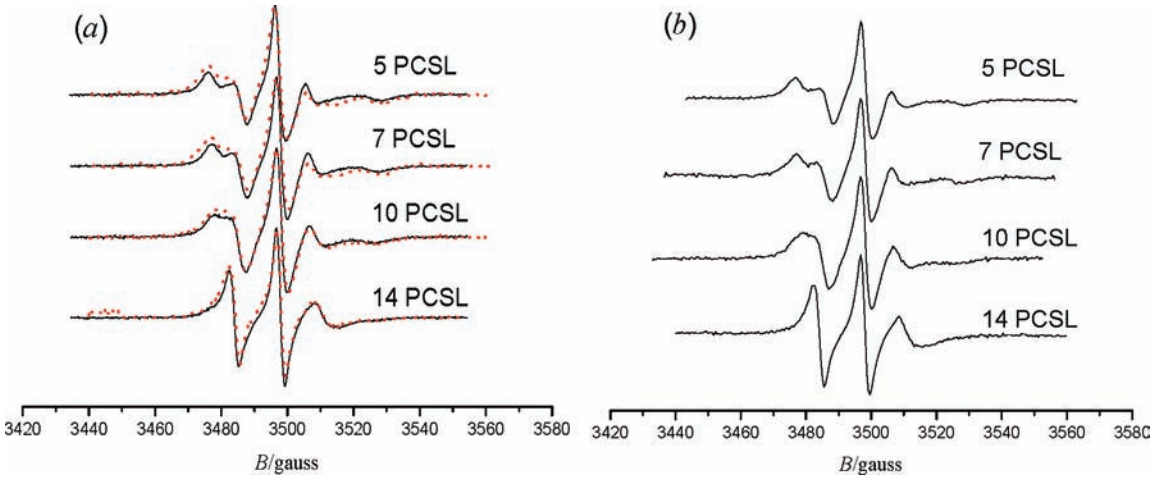

Figure 6. EPR spectra of *n*-PCSL in POPC (continuous line) and in ToThyCholRu/POPC bilayers at the ratio of 15:85 mol/mol (dashed line) freshly prepared (*a*) and ToThyCholRu/POPC bilayers at the molar ratio of 15:85 after 30 days (*b*).

flexibility increase in the segmental chain mobility going from the polar head groups to the inner hydrophobic core, which is a characteristic hallmark of the liquid-crystalline state of fluid phospholipid bilayers.[35]

Spectra of the spin-labels at 15:85 molar ratio in Figure 6, together with the $2A_{max}$ corresponding values in Table 2, show

Table 2. Outer Hyperfine Splitting Parameter $2A_{max}$ of *n*-PCSL in POPC and ToThyCholRu/POPC Liposomes at 25 °C[a]

	ToThyCholRu-POPC					Chol-POPC
	Ru/POPC molar ratio					Chol/POPC molar ratio
n-PCSL	0:100	5:95	10:95	15:85	20:80	20:80
	$2A_{max}$/G					
5-PCSL	52.4	52.7	53.1	53.2	54.0	53.4
7-PCSL	50.6	50.7	51.2	51.4	51.9	51.7
10-PCSL	47.2	46.7	46.1	45.5	45.9	48.5
14-PCSL	33.1	33.4	33.6	33.4	33.5	34.9

[a]The error on $2A_{max}$ value is ±0.2 G.

that the presence of ToThyCholRu complex induces a stiffening effect on the acyl carbon atoms closer to the hydrophilic region of the complex as shown by the increased value of $2A_{max}$ of 5-and 7-PCSL. An opposite effect, connected with an increased fluidity of the membrane, is observed for 10-PCSL. In the case of 14-PCSL, the fluidity of the more hydrophobic region of the bilayer explored by this spin-label is almost invariant. This complex behavior can be rationalized admitting that the presence of a cholesterol moiety at C5 and C7 vicinity creates more room at the level of the inner carbon atom C10 that is not directly interested in the aliphatic chain-cholesterol interaction, thus increasing the local segmental mobility of the acyl chains, while for C14, the presence of the Ru complex is ineffective.

Thus, the experimental results are a clear indication of the perturbation caused by the presence of ToThyCholRu in the phospholipid bilayers, which induces an increase in lipid packing density of the more external acyl chain segments ($n \leq 7$) and enhanced fluidity of the inner chains region ($n \geq 10$). It is interesting to note that pure cholesterol reduces dynamics and increases order of the whole lipid acyl chains in POPC bilayers, as indicated by the $2A_{max}$ values reported in Table 2 (Chol-POPC column). This effect could probably be due to the headgroup of ToThyCholRu, which causes a more intense change in the lipid packing density than that caused by cholesterol, such as to affect the acyl chain mobility.

EPR measurements were repeated several times over a period of 30 days obtaining substantial reproducibility of the results. No degradation was observed for all the samples up to 15:85 molar ratio. An example of the invariance of the EPR spectra with time is reported in Figure 6*b*.

In Vitro Bioactivity Study. We first analyzed the effect on the cell viability of cholesterol-based nucleolipidic nanoaggregates by culturing a panel of human tumor cell lines (HeLa cervical cancer cells, CaCo-2 and WiDr epithelial colorectal adenocarcinoma cells, MCF-7 breast adenocarcinoma cells, SH-SY5Y neuroblastoma cells). As shown in panels A and C of Figure 7 with respect to MCF-7 and WiDr cell lines after 72 h of incubation, ToThyChol did not exhibit a significant cytotoxic effect. The cell viability was also determined in the presence of conventional POPC liposomes, currently used in a broad range of biotechnological applications.[36] As expected, POPC liposomes did not induce cell growth inhibition at all the concentrations and time intervals tested. Substantially, ToThyChol showed little if any divergence compared to POPC liposomes. In this way, as demonstrated by parallel biochemical and toxicological investigations, we can assume that the cholesterol-containing nucleolipidic technological platform ToThyChol is a safe precursor potentially useful for drug delivery applications. Consequently, we further investigated the conversion of ToThyChol aggregates into Ru(III) complexes (ToThyChol-Ru), as such or lodged in the biomimetic membrane formed by the lipid POPC (ToThyCholRu/POPC). To gain an insight into the antiproliferative activity of this novel cholesterol-based nucleolipid–ruthenium complex, its cytotoxicity profile toward human cancer cells was compared to that of a NAMI-A-like ruthenium complex, named AziRu and prepared here for a direct evaluation of their antiproliferative activity. Cell lines were exposed to AziRu for 72 h in a growth inhibition assay, and the cytotoxicity was determined in terms of IC_{50} values. The detected cytotoxicities were rather moderate, and the IC_{50} values for AziRu were 900, 690, 515, 405, and 1500 μM in HeLa, CaCo-2, WiDr, MCF-7, and SH-SY5Y cells, respectively.

dx.doi.org/10.1021/bc200565v | *Bioconjugate Chem.* 2012, 23, 758–770

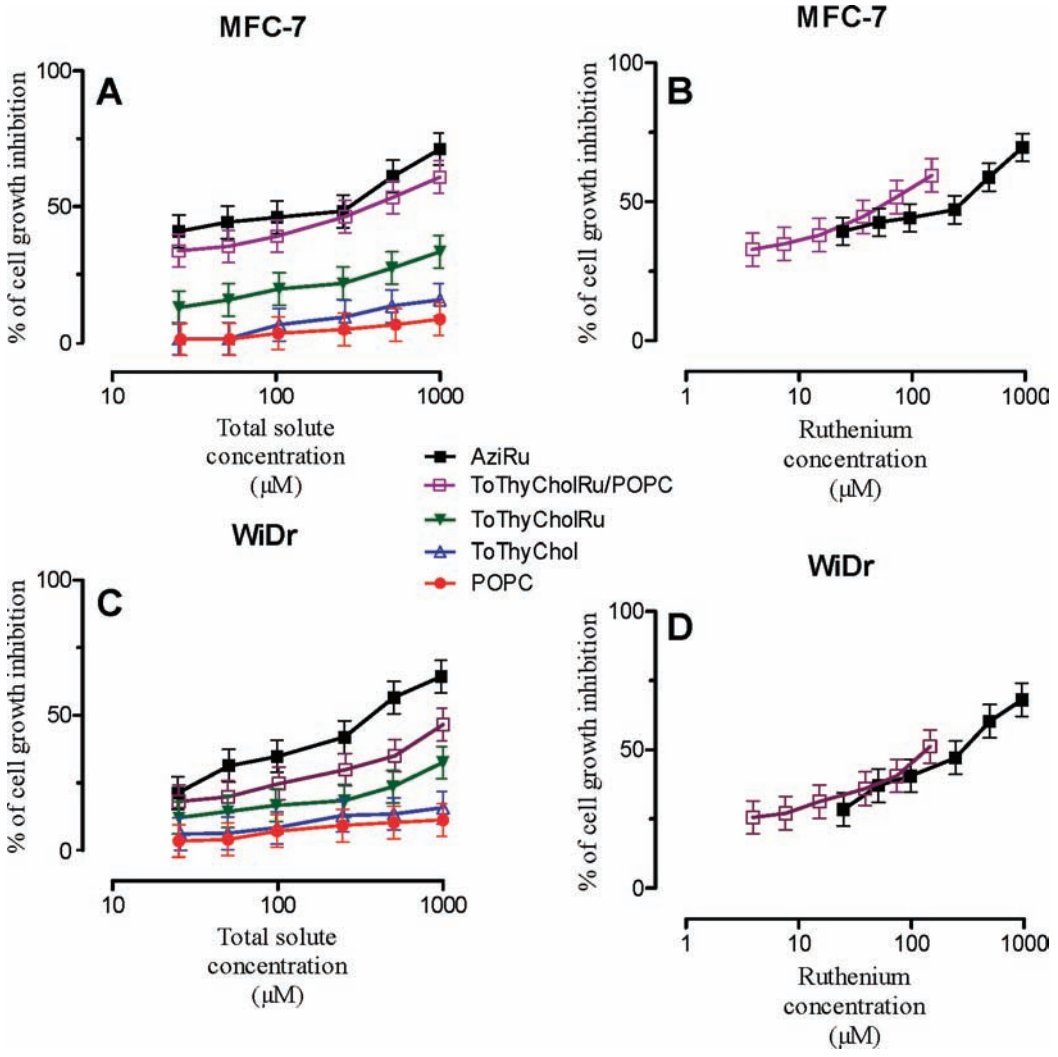

Figure 7. Growth inhibition of MCF-7 (panel A) and WiDr cells (panel C) treated for 72 h with different formulations and with AziRu as indicated in the legend, evaluated by MTT assay and cell counting. In panels B and D, for MCF-7 and WiDr cells, respectively, are reported the corresponding concentration–effect curves obtained by normalizing for the actual amount of ruthenium contained within the ToThyCholRu/POPC liposome. Data are expressed as percentage of untreated cells and are reported as mean of three independent experiments ± SEM.

First, under the same incubation conditions these results indicate a significant difference in ruthenium cytotoxicity exclusively depending on the cell line, suggestive of a selective cell-dependent mechanism of action.[37] Moreover, according to many published studies on ruthenium complexes, our results also showed that AziRu cytotoxicity was much lower than that of a well-known reference drug based on transition metals as the antitumor Cisplatin.[38] However, concerning NAMI-A, it should be considered that the concentration needed to reach cytotoxicity *in vitro* is much higher than the NAMI-A concentration capable of inhibiting the formation of metastases, suggesting that the recognized anti-metastatic activity of NAMI-A is probably not due exclusively to a reduction in cell viability.[39]

Then, focusing on the more sensitive cells (MCF-7 and WiDr lines) to ruthenium action in our *in vitro* experimental model, we assessed the potential cytotoxic effect of ruthenium-containing liposomes, and interestingly, we found that ToThyCholRu/POPC liposome, even if containing only 15 mol % of ruthenium, was able to induce cell growth inhibition in a similar manner to that induced by the same concentrations of AziRu. In other words, the same cytotoxicity shown by AziRu is reached at a ruthenium concentration ~6 times smaller if the metal is lodged in POPC liposomes. In particular, in MCF-7 cells ToThyCholRu/POPC the concentration–response curve was virtually identical to that of AziRu (Figure 7 panel A). Moreover, as reported in panels B and D of Figure 7, by normalizing concentration–effect curves for the actual amount of ruthenium contained within the liposomes, we found that ToThyCholRu/POPC was more active than AziRu in both cell lines. The latter is a noteworthy finding in the design and biological evaluation of innovative supramolecular systems for vectorization of the anticancer drugs. The calculated IC_{50} values reported in Table 3 for the real amount of ruthenium delivered to cells after 72 h of incubation in cell culture media also suggested that the ToThyCholRu/POPC complex was more effective than AziRu in inducing growth inhibition in MCF-7 and WiDr cell lines. In addition, evaluation of the potentiating factor (PF) values demonstrated that ruthenium vectorization by this liposome potentiated the growth inhibition induced by AziRu, reaching values higher than 3 in cancer cells of different histogenesis (see Table 3).

Similar *in vitro* results emerged from bioassays on other human cancer cell lines (data reported in the Supporting

dx.doi.org/10.1021/bc200565v | *Bioconjugate Chem.* 2012, 23, 758–770

Table 3. IC_{50} Values of AziRu (a NAMI-A-like Ru Complex) and of ToThyCholRu/POPC Liposome in the Indicated Cell Lines Following 72 h of Incubation, And Potentiating Factors (P.F.) of ToThyCholRu/POPC

	IC_{50}[a]/μM		P.F.[b]
cell lines	AziRu	ToThyCholRu/POPC	ToThyCholRu/POPC
MCF-7	405 ± 10	70 ± 12	5.7
WiDr	515 ± 15	165 ± 10	3.1

[a]IC_{50} values are reported as mean ± SEM. [b]Potentiating factor calculated as the ratio of IC_{50} values of ToThyCholRu/POPC complex to the IC_{50} of AziRu complex.

Information), albeit generally less sensitive to the action of the antiproliferative ruthenium.

Hence, consistent with our recent report,[40] different aggregate compositions differentially impacts cell viability. As demonstrated by a cytotoxic effect higher than that of AziRu, the cholesterol containing nucleolipidic liposome stabilized with POPC seems to deliver the ruthenium within the cells in a very effective way. Within this context, it is believed that free ruthenium complexes such as NAMI-A enter cells via a passive or facilitated passive transport molecular mechanism, albeit apparently with more difficulty than other antitumor drugs based on transition metal such as Cisplatin.[41] Together with other considerations, this outcome may account for the lower cytotoxicity of emerging ruthenium-based molecules assayed for antineoplastic activity, thus emphasizing the critical role of a proper vehiculation. The importance of liposome stabilization by the presence of the naturally occurring POPC is also supported by the fact that ToThyCholRu liposome per se resulted in a significantly lower cytotoxic effect. In fact, the absence of POPC within these novel liposomal formulations always reduces the effectiveness of the vehiculated anticancer drug. In addition, stable liposome formulations can probably more easily merge with target cell membranes, where the presence of sterols and of other typical membrane constituents might together play a crucial role in both liposome stability and its affinity for cell membranes.

CONCLUSIONS

Herein, we report on a novel cholesterol-based nucleolipidic ruthenium complex stabilized by lipid-based aggregates for antineoplastic therapy. This work was aimed toward the optimization of long-lived nanoaggregates containing high amount of ruthenium complex.

This paper presents the synthesis and assembly properties of the molecules settled, in the "bottom-up" engineering process of the proposed nanovectors. Using thymidine as the central, polyfunctional scaffold, a pyridine-methyl arm was introduced on the nucleobase as a functional ligand able to form an octaedric complex with Ru(III) ion. Insertion of one oligo-(ethylene glycol) chain and one cholesterol residue on the ribosidic moiety confers the desired amphiphilic behavior to this nucleolipid in aqueous solution. The role of the cholesterol moiety, inserted at the level of the sugar ring, is to favor the inclusion of the polyfunctional molecule inside the POPC liposome bilayer thus protecting the Ru complex from degradation. A qualitative picture of the structure of the ruthenium-cholesterol lipid vectors is depicted in Figure 8. Moreover, the presence of the cholesterol residue within the thymidine-based nucleolipidic ruthenium complex gives rise to a safe precursor that results in an attractive platform with useful

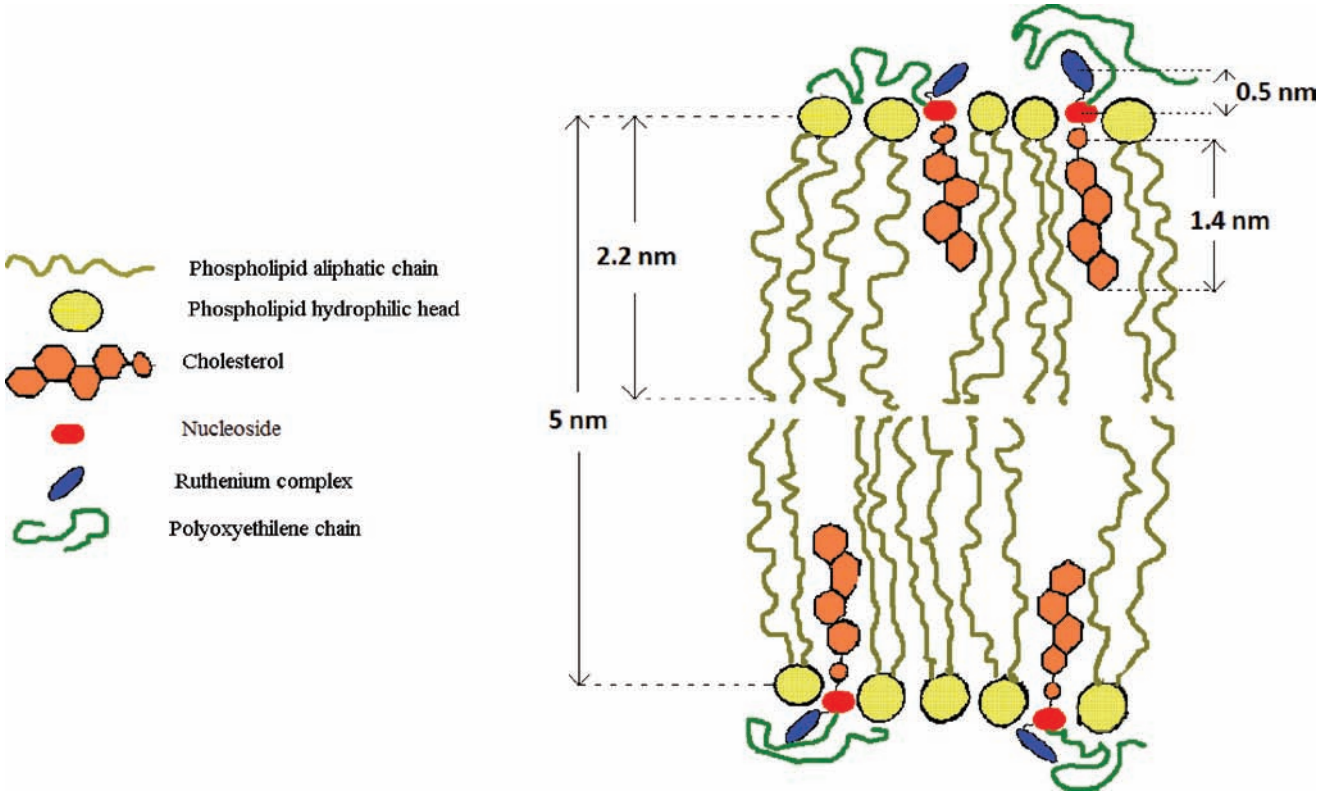

Figure 8. Qualitative graphical representation of ToThyCholRu lodged into a bilayer with indication of some structural parameters.

dx.doi.org/10.1021/bc200565v | *Bioconjugate Chem.* 2012, 23, 758–770

biotechnological features such as molecular carrier abilities for potential applications in drug delivery.

A detailed study of the aggregation behavior has shown that the synthesized compound forms a wide variety of supramolecular aggregates, spanning from spheres and cylinders to oligolamellar vesicles. Aggregates formed only by the Ru-based complex show a degradation kinetics that, depending on pH, is almost complete from a few hours to days, as reported for NAMI-A. However, when the ruthenium complex is lodged in POPC liposomes up to 15 mol %, the degradation is markedly reduced and the formulation is stable for at least several weeks. According to the experimental data, the lipophilic cholesterol residue of ToThyCholRu is lodged well inside the bilayer in the typical position observed for pure cholesterol; meanwhile, the ruthenium is hidden among the phospholipid heads.

It is worth mentioning that *in vitro* bioscreenings based on the evaluation of concentration−effect curves reveal that ToThyCholRu/POPC liposomes are more effective in inhibiting the growth of human cancer cells of different histogenesis with respect to the reference ruthenium-complex NAMI-A-like AziRu. Therefore, this study introduces new perspectives in the synthesis and formulation of highly biocompatible transition-metal-based aggregates having potential application as antineoplastic agents.

■ ASSOCIATED CONTENT

Supporting Information

Molecular characterization of ToThyColRu and its synthesis intermediates, along with supplementary DLS and antiproliferative activity plots,is provided in a separate file. This material is available free of charge via the Internet at http://pubs.acs.org.

■ AUTHOR INFORMATION

Corresponding Author

*E-mail: luigi.paduano@unina.it. Tel. +39 081 674250. Fax. +39 081 674090. E-mail: daniela.montesarchio@unina.it. Tel. +39 081 674126.

Notes

The authors declare no competing financial interest.

■ ACKNOWLEDGMENTS

Project has been funded by MIUR (PRIN 2008 - prot. 20087K9A2J). We thank Forschungszentrum Jülich for provision of beam time. The SANS experiments were supported by the European Commission, NMI3 contract RII3-CT-2003-505925.

■ ABBREVIATIONS

AcOEt, ethyl acetate; Chol, cholesteryl residue; DCC, *N,N*-dicyclohexylcarbodiimide; DCM, dichloromethane; DMAP, 4-(*N,N*-dimethylamino)-pyridine; DMF, *N,N*-dimethylformamide; DMT, 4,4′-dimethoxytriphenylmethyl; Py, pyridine; r.t., room temperature; *t*-Bu, *tert*-butyl; TEA, triethylamine; TEG, triethylene glycol; THF, tetrahydrofuran; Thy, thymidine residue; SANS, small angle neutron scattering; DLS, dynamic light scattering; EPR, electron paramagnetic spectroscopy

■ REFERENCES

(1) Levina, A., Mitra, A., and Lay, P. A. (2009) Recent developments in ruthenium anticancer drugs. *Metallomics 1*, 458−470.

(2) Ryu, M.-H., and Kang, Y.-K. (2009) ML17032 trial: capecitabine/Cisplatin versus 5-fluorouracil/Cisplatin as first-line therapy in advanced gastric cancer. *Expert Rev. Anticancer Ther. 9*, 1745−1751.

(3) Saloustros, E., and Georgoulias, V. (2008) Docetaxel in the treatment of advanced non-small-cell lung cancer. *Expert Rev. Anticancer Ther. 8*, 1207−1222.

(4) Rafique, S., Idrees, M., Nasim, A., Akbar, H., and Athar, A. (2010) Transition metal complexes as potential therapeutic agents. *Biotechnol. Mol. Biol. Rev. 5*, 38−45.

(5) Groessl, M., Tsybin, Y. O., Hartinger, C. G., Keppler, B. K., and Dyson, P. J. (2010) Ruthenium versus platinum: interactions of anticancer metallodrugs with duplex oligonucleotides characterised by electrospray ionisation mass spectrometry. *J. Biol. Inorg. Chem. 15*, 677−688.

(6) Vaccaro, M., Del Litto, R., Mangiapia, G., Carnerup, A. M., D'Errico, G., Ruffo, F., and Paduano, L. (2009) Lipid based nanovectors containing ruthenium complexes: a potential route in cancer therapy. *Chem. Commun. (Cambridge, U.K.)*, 1404−1406.

(7) Mangiapia, G., Vaccaro, M., D'Errico, G., Frielinghaus, H., Radulescu, A., Pipich, V., Carnerup, A. M., and Paduano, L. (2011) Cubosomes for ruthenium complex delivery: formulation and characterization. *Soft Matter. 7*, 10577−10580.

(8) Mangiapia, G., D'Errico, G., Simeone, L., Irace, C., Radulescu, A., Di Pascale, A., Colonna, A., Montesarchio, D., and Paduano, L. (2012) Ruthenium-based complex nanocarriers for Cancer Therapy. *Biomaterials 33*, 3770−3782.

(9) Bijsterbosch, M. K., Rump, E. T., De Vrueh, R. L. A., Dorland, R., Van Veghel, R., Tivel, K. L., Biessen, E. A. L., Van Berkel, T. J. C., and Manoharan, M. (2000) Modulation of plasma protein binding and *in vivo* liver cell uptake of phosphorothioate oligodeoxynucleotides by cholesterol conjugation. *Nucleic Acids Res. 28*, 2717−2725.

(10) Krieg, A. M., Tonkinson, J., Matson, S., Zhao, Q., Saxon, M., Zhang, L. M., Bhanja, U., Yakubov, L., and Stein, C. A. (1993) Modification of antisense phosphodiester oligodeoxynucleotides by a 5′ cholesteryl moiety increases cellular association and improves efficacy. *Proc. Natl. Acad. Sci. U.S.A. 90*, 1048−52.

(11) Mestroni, G., Alessio, E., Sava, G., Pacor, S., Coluccia, M., and Boccarelli, A. (1994) Water-soluble ruthenium(III)-dimethylsulfoxide complexes: chemical behavior and pharmaceutical properties. *Metal-Based Drugs 1*, 41−63.

(12) Sava, G., Alessio, E., Bergamo, A., and Mestroni, G. (1999) Sulfoxide ruthenium complexes: non-toxic tools for the selective treatment of solid tumor metastases. *Topics Biol. Inorg. Chem. 1*, 143−169.

(13) Bacac, M., Hotze, A. C. G., van der Schilden, K., Haasnoot, J. G., Pacor, S., Alessio, E., Sava, G., and Reedijk, J. (2004) The hydrolysis of the anti-cancer ruthenium complex NAMI-A affects its DNA binding and antimetastatic activity: an NMR evaluation. *J. Inorg. Biochem. 98*, 402−412.

(14) Berne, B. J., and Pecora, R. (1975) *Dynamic Light Scattering: with Applications to Chemistry, Biology, and Physics*

(15) Brehm, G. A., and Bloomfield, V. A. (1975) Analysis of polydispersity in polymer solutions by inelastic laser light scattering. *Macromolecules 8*, 663−5.

(16) Paduano, L., Sartorio, R., and Vitagliano, V. (1998) Diffusion Coefficients of the Ternary System α-Cyclodextrin-Sodium Benzenesulfonate-Water at 25 °C: The Effect of Chemical Equilibrium and Complex Formation on the Diffusion Coefficients of a Ternary System. *J. Phys. Chem. B 102*, 5023−5028.

(17) Vaccaro, M., Accardo, A., Tesauro, D., Mangiapia, G., Loef, D., Schillen, K., Soederman, O., Morelli, G., and Paduano, L. (2006) Supramolecular Aggregates of Amphiphilic Gadolinium Complexes as Blood Pool MRI/MRA Contrast Agents: Physicochemical Characterization. *Langmuir 22*, 6635−6643.

(18) Vergara, A., Paduano, L., and Sartorio, R. (2001) Multicomponent Diffusion in Systems Containing Molecules of Different Size. 4. Mutual Diffusion in the Ternary System Tetra(ethylene glycol)-Di(ethylene glycol)-Water. *J. Phys. Chem. B 105*, 328−334.

(19) Wignall, G. D., and Bates, F. S. (1987) Absolute calibration of small-angle neutron scattering data. *J. Appl. Crystallogr. 20*, 28−40.
(20) Kotlarchyk, M., and Ritzau, S. M. (1991) Paracrystal model of the high-temperature lamellar phase of a ternary microemulsion system. *J. Appl. Crystallogr. 24*, 753−8.
(21) Schorn, K., and Marsh, D. (1996) Lipid chain dynamics and molecular location of diacylglycerol in hydrated binary mixtures with phosphatidylcholine: spin label ESR studies. [Erratum to document cited in CA124:196780]. *Biochemistry 35*, 9286.
(22) D'Errico, G., Vitiello, G., Ortona, O., Tedeschi, A., Ramunno, A., and D'Ursi, A. M. (2008) Interaction between Alzheimer's Abeta (25−35) peptide and phospholipid bilayers: The role of cholesterol. *Biochim. Biophys. Acta, Biomembranes 1778*, 2710−2716.
(23) Hansen, M. B., Nielsen, S. E., and Berg, K. (1989) Re-examination and further development of a precise and rapid dye method for measuring cell growth/cell kill. *J. Immunol. Methods 119*, 203−10.
(24) Santamaria, R., Fiorito, F., Irace, C., De Martino, L., Maffettone, C., Granato, G. E., Di Pascale, A., Iovane, V., Pagnini, U., and Colonna, A. (2011) 2,3,7,8-Tetrachlorodibenzo-p-dioxin impairs iron homeostasis by modulating iron-related proteins expression and increasing the labile iron pool in mammalian cells. *Biochim. Biophys. Acta 1813*, 704−12.
(25) Alessio, E., Balducci, G., Calligaris, M., Costa, G., Attia, W. M., and Mestroni, G. (1991) Synthesis, molecular structure, and chemical behavior of hydrogen trans-bis(dimethyl sulfoxide)-tetrachlororuthenate(III) and mer-trichlorotris(dimethyl sulfoxide)-ruthenium(III): the first fully characterized chloride-dimethyl sulfoxide-ruthenium(III) complexes. *Inorg. Chem. 30*, 609−18.
(26) Mestroni, G., Alessio, E., and Sava, G. (1998) New salts of anionic complexes of Ru(III), as antimetastatic and antineoplastic agents, 1997-EP3401; 9800431
(27) Velders, A. H., Bergamo, A., Alessio, E., Zangrando, E., Haasnoot, J. G., Casarsa, C., Cocchietto, M., Zorzet, S., and Sava, G. (2004) Synthesis and Chemical-Pharmacological Characterization of the Antimetastatic NAMI-A-Type Ru(III) Complexes (Hdmtp)[trans-RuCl4(dmso-S)(dmtp)], (Na)[trans-RuCl4(dmso-S)(dmtp)], and [mer-RuCl3(H2O)(dmso-S)(dmtp)] (dmtp = 5,7-Dimethyl[1,2,4]-triazolo[1,5-a]pyrimidine). *J. Med. Chem. 47*, 1110−1121.
(28) Bouma, M., Nuijen, B., Jansen, M. T., Sava, G., Flaibani, A., Bult, A., and Beijnen, J. H. (2002) A kinetic study of the chemical stability of the antimetastatic ruthenium complex NAMI-A. *Int. J. Pharm. 248*, 239−246.
(29) Brumberger, H. (1967) *Small-Angle X-Ray Scattering*, Gordon & Breach, New York.
(30) Hansen, S. (2004) Translational friction coefficients for cylinders of arbitrary axial ratios estimated by Monte Carlo simulation. *J. Chem. Phys. 121*, 9111−9115.
(31) D'Errico, G., Silipo, A., Mangiapia, G., Vitiello, G., Radulescu, A., Molinaro, A., Lanzetta, R., and Paduano, L. (2010) Characterization of liposomes formed by lipopolysaccharides from Burkholderia cenocepacia, Burkholderia multivorans and Agrobacterium tumefaciens: from the molecular structure to the aggregate architecture. *Phys. Chem. Chem. Phys. 12*, 13574−13585.
(32) Lange, A., Marsh, D., Wassmer, K. H., Meier, P., and Kothe, G. (1985) Electron spin resonance study of phospholipid membranes employing a comprehensive line-shape model. *Biochemistry 24*, 4383−92.
(33) Marsh, D. (2010) Structural and thermodynamic determinants of chain-melting transition temperatures for phospholipid and glycolipids membranes. *Biochim. Biophys. Acta 1798*, 40−51.
(34) Moser, M., Marsh, D., Meier, P., Wassmer, K. H., and Kothe, G. (1989) Chain configuration and flexibility gradient in phospholipid membranes. Comparison between spin-label electron spin resonance and deuteron nuclear magnetic resonance, and identification of new conformations. *Biophys. J. 55*, 111−23.
(35) D'Errico, G., D'Ursi, A. M., and Marsh, D. (2008) Interaction of a Peptide Derived from Glycoprotein gp36 of Feline Immunodeficiency Virus and Its Lipoylated Analogue with Phospholipid Membranes. *Biochemistry 47*, 5317−5327.
(36) Walde, P., and Ichikawa, S. (2001) Enzymes inside lipid vesicles: preparation, reactivity and applications. *Biomol. Eng. 18*, 143−177.
(37) Sava, G., Pacor, S., Bregant, F., Ceschia, V., and Mestroni, G. (1990) Metal complexes of ruthenium: antineoplastic properties and perspectives. *Anti-Cancer Drugs 1*, 99−108.
(38) Pluim, D., van Waardenburg Robert, C. A. M., Beijnen Jos, H., and Schellens Jan, H. M. (2004) Cytotoxicity of the organic ruthenium anticancer drug Nami-A is correlated with DNA binding in four different human tumor cell lines. *Cancer Chemother. Pharmacol. 54*, 71−8.
(39) Sava, G., Clerici, K., Capozzi, I., Cocchietto, M., Gagliardi, R., Alessio, E., Mestroni, G., and Perbellini, A. (1999) Reduction of lung metastasis by IMH[trans-RuCl4(DMSO)Im]: mechanism of the selective action investigated on mouse tumors. *Anti-Cancer Drugs 10*, 129−138.
(40) Simeone, L., Mangiapia, G., Irace, C., Di Pascale, A., Colonna, A., Ortona, O., De Napoli, L., Montesarchio, D., and Paduano, L. (2011) Nucleolipid nanovectors as molecular carriers for potential applications in drug delivery. *Mol. BioSyst. 7*, 3075−86.
(41) Bergamo, A., Zorzet, S., Cocchietto, M., Carotenuto, M. E., Magnarin, M., and Sava, G. (2001) Tumour cell uptake G2-M accumulation and cytotoxicity of NAMI-A on TS/A adenocarcinoma cells. *Anticancer Res. 21*, 1893−1898.

Bioconjugate Chemistry

Article

pubs.acs.org/bc

Design, Evaluation, and Comparison of Ghrelin Receptor Agonists and Inverse Agonists as Suitable Radiotracers for PET Imaging

Constance Chollet,*[,†] Ralf Bergmann,[‡] Jens Pietzsch,[‡] and Annette G. Beck-Sickinger[†]

[†]Institute of Biochemistry, Universität Leipzig, Leipzig, Germany

[‡]Institute of Radiopharmacy, Helmholtz-Zentrum Dresden-Rossendorf, Dresden, Germany

ABSTRACT: Ghrelin agonist and inverse agonist radiotracers, suitable for positron emission tomography (PET), were developed to study the behavior of ghrelin receptor ligands in vivo and for further design of druggable peptides. The target peptides were synthesized on solid support and conjugated to the bifunctional chelator 1,4,7-triazacyclononane,1-glutaric acid-4,7-acetic acid (NODAGA), which is known to form a stable complex with Ga^{3+}. Complexation with ^{68}Ga could be achieved under mild conditions and led to radiotracers with high radiochemical purity and specific activity. The biological activity of the radiotracers was evaluated in vitro by an inositol phosphate turnover assay. Pharmacokinetic profile and metabolic stability of the ^{68}Ga-NODAGA-radiotracers were investigated by small animal PET in rodent. Ghrelin derived agonists presented very high kidney accumulation, negligible tissue distribution, fast blood clearance, and poor stability in blood. Contrarily, the inverse agonist radiotracer exhibited very high stability in blood, large diffusion in tissues, reasonable kidney and liver metabolism, and slow blood clearance. This pharmacokinetic profile makes the ghrelin inverse agonist motif KwFwLL-$CONH_2$ suitable for further development of radiotracers and a promising lead to design peptide-based therapeutics against obesity.

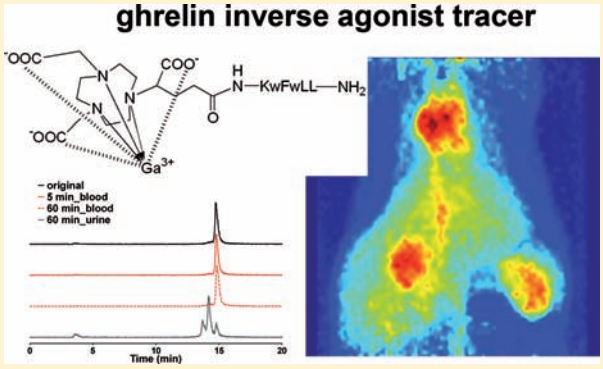

INTRODUCTION

Ghrelin is a peptide hormone acting as a predominant orexigenic signal. It triggers the preprandrial hunger and meal initiation and also acts as a positive adiposity signal favoring energy storage.[1,2] Physiologically, ghrelin activates the endogenous ghrelin receptor (formerly called GHS-R1a), and stimulates the secretion of the orexigenic neurotransmitter NPY and agouti related peptides (AgRP) in the arcuate nucleus of hypothalamus.[3−5] Ghrelin is a 28 amino acid peptide produced by the oxyntic mucosa of the stomach.[4,6] Its sequence contains a unique *n*-octanoylation at serine 3, introduced post-translationally by ghrelin-*O*-acyltransferase (GOAT) and essential for binding the ghrelin receptor.[7,8] Being the only known orexigenic signal from the periphery, the role of ghrelin in obesity has been widely studied. Indeed, although ghrelin levels are low in the obese, weight loss is correlated with an increase in ghrelin level and GHS-R1a expression.[9] In addition, the ghrelin receptor possesses a naturally high constitutive activity thought to induce constant appetite and to trigger food intake between meals.[10] Consequently, the ghrelin receptor has emerged as a new target to design drugs against not only obesity, but also cachexia and anorexia.[11−13]

However, ghrelin is an endogenous peptide and its short half-life and low stability in the organism limits its use as a drug. In addition, little is known about the peptide behavior in vivo. With the aim to develop peptide-based therapeutics targeting the ghrelin receptor, we developed radiotracers suitable for PET imaging. Indeed, the use of noninvasive imaging techniques, especially small animal PET, should provide better knowledge on biodistribution, biokinetics, metabolic stability, and mode of action of ghrelin receptor ligands in vivo. To obtain peptide-based radiotracers, we used the bifunctional chelator (BFC) 1,4,7-triazacyclononane, 1-glutaric acid-4,7-acetic acid (NODAGA), that can be easily branched to different peptide cores and can chelate radionuclides in mild conditions.

Hence, in this paper, we evaluate ghrelin agonist and inverse agonist peptides as radiotracers. [^{68}Ga]-NODAGA-conjugates were synthesized using solid-phase peptide synthesis. The biological activity of the radiotracers was evaluated in vitro in a functional assay. Peptides behavior in vivo was investigated in rodents with biodistribution, biokinetics, and metabolism studies and with PET imaging.

EXPERIMENTAL PROCEDURES

Materials. Fmoc amino acid derivatives, Boc-L-Gly-OH, diisopropylcarbodiimide (DIC), 1-hydroxybenzotriazole (HOBt), piperidine, Wang resin, and Fmoc-L-Arg(Pmc)-Wang resin were purchased from Iris Biotech (Marktredwitz, Germany) or Novabiochem (Läufelfingen, Switzerland). If not specified, the side chain protecting groups are *t*Bu for Glu, Ser, Thr, and Tyr; Boc for Lys and D-Trp; Trt for Gln; and His and Pbf for Arg. Fmoc-L-Lys(Dde)-OH, Fmoc-L-Ser(Trt)-OH, and Fmoc-L-Dpr(Mtt)-OH were also purchased from Iris Biotech

Received: November 4, 2011
Revised: February 28, 2012
Published: February 28, 2012

dx.doi.org/10.1021/bc2005889 | *Bioconjugate Chem.* 2012, 23, 771−784

(Marktredwitz, Germany) and used for orthogonal modification. Thioanisole, *p*-thiocresol, ethandithiol, piperidine, hydrazine monohydrate, 4-dimethylaminopyridine (DMAP), triisopropylsilane (TIPS), and *tert*-butanol was purchased from Fluka (Taufkirchen, Germany). NODAGA(tBu)$_3$ (4-(4,7-bis(2-*tert*-butoxy-2-oxoethyl)-1,4,7-triazonan-1-yl)-5-*tert*-butoxy-5-oxopentanoic acid) was obtained from CheMatec (Dijon, France). Dichloromethane (DCM) and *N*,*N*-dimethylformamide (DMF) were purchased from Biosolve (Valkenswaard, Netherlands). Trifluoroacetic acid (TFA), acetic anhydride, diisopropylethylamine (DIPEA), octanoic acid, and $Ga(NO_3)_3$ were obtained from Sigma-Aldrich (Taufkirchen, Germany). Gradient-grade high-performance liquid chromatography (HPLC) solvent acetonitrile (ACN) was from VWR (Darmstadt, Germany). All reagents and solvents were used without purification as provided from the commercial suppliers. Nonmodified ghrelin used as a control in biological assays was obtained from Polypeptide (Hillerød, Denmark). For cell culture and in vitro assays, Dulbecco's phosphate buffered saline without calcium and magnesium (PBS), DMEM, high glucose (4.5 g·L^{-1}) with L-glutamine, heat-inactivated fetal bovine serum (FBS), penicillin/streptavidin, and trypsin/EDTA (1:250) were purchased from PAA (Pasching, Austria). Metafectene was purchased from Biontex (Martinsried, Germany). myo-[^{3}H] Inositol (681 MBq.mmol^{-1}; 25.0 Ci.mmol^{-1}) was from GE Healthcare Europe GmbH (Braunschweig, Germany). Cell culture flasks (75 cm^2) and 24-well plates were from TPP (Trasadingen, Switzerland).

Instruments. Automated peptide synthesis was performed with a multiple peptide synthesizer MultiSynTech Syro II or MultiSynTech Syro XP (Bochum, Germany). Preparative and semipreparative HPLC were performed using a Merck-Hitachi system on a Shimadzu RP18-column (12.5 × 250 mm; 5 μm/300 Å). Analytical HPLC were performed using a Merck-Hitachi system with a Vydac RP18-column (4.6 × 250 mm; 5 μm/300 Å, Merck Hitachi, Darmstadt, Germany). All peptides were analyzed by matrix-assisted LASER desorption ionization−time-of-flight (MALDI-ToF) using a Bruker Daltonics Ultraflex III mass spectrometer. The 1.85-GBq (50-mCi) ^{68}Ge/^{68}Ga generator was purchased from iThemba Laboratories (Somerset West, South Africa) with the ^{68}Ge on a SnO_2-cartrige and eluted according to the manufacturer's recommendations using a remote-controlled module.

Synthesis of Ghrelin Derivative Tracers. The peptides were synthesized on solid support, following a fluorenylmethoxycarbonyl/*tert*-butyl (Fmoc/*t*Bu) strategy. Preloaded Fmoc-Arg(Pmc)-Wang was used for peptides **1**−**3a** and Rink amide resin for peptide **5a**. For peptide **4a**, Wang resin was manually loaded with Fmoc-L-Lys(Dde)-OH.

Manual Loading of Wang Resin with Fmoc-L-Lys-(Dde)-OH for the Synthesis of Peptide 4a. The Wang resin (0.015 mmol, 0.64 mmol.g^{-1}) was swollen in 500 μL of DMF for 15 min. Fmoc-L-Lys(Dde)-OH (0.075 mmol, 5 equiv) and HOBt (0.075 mmol, 5 equiv) were dissolved in DMF to a concentration of 0.5 M. The solution was added to the resin with DIC (0.075 mmol, 5 equiv), and the reaction mixture was shaken overnight at room temperature. The resin was successively washed five times with DMF, DCM, MeOH, and Et_2O, and dried in vacuo. The coupling was repeated once, followed by an end-capping of the free hydroxyl residues of the Wang resin. For this purpose, the resin was swollen for 15 min in 500 μL of DCM. Acetic anhydride (50 μL) and DIPEA (50 μL) were then added to the resin with 400 μL DCM, and the mixture was incubated 15 min at room temperature. The resin was successively washed five times with DMF, DCM, MeOH, and Et_2O, and dried in vacuo. The loaded resin was elongated automatically and manually as described above to yield peptide **4a** on solid support.

Automated Peptide Synthesis. To synthesize peptides **1**−**5a**, amino acids were introduced automatically with a multiple peptide synthesis robot system, following the procedure recently described.[14] For all peptides, the resin was first swollen for 15 min in DMF. Then, a 10-fold excess of the corresponding Fmoc-protected amino acid was coupled through an in situ activation with a 10-fold excess of both HOBt and DIC in 400 μL of DMF. Each amino acid was coupled twice for 40 min, followed by a washing step and the removal of the Fmoc group by adding 400 μL of 40% piperidine in DMF (v/v), twice, for 10 min. The last amino acid introduced was Fmoc-L-Gly-OH for peptide **1a**, and Boc-L-Gly-OH for peptides **2**−**4a**, and Fmoc-L-Lys(BOC)-OH for peptide **5a**.

Manual Peptide Synthesis. Fmoc-L-Lys(Dde)-OH at position 16 of peptide **3a**, Fmoc-L-Ser(Trt)-OH at position 3 of peptides **1**−**2a**, Fmoc-L-Dpr(Mtt)-OH at position 3 of peptides **3**−**4a** were introduced manually to be further modified. First, each peptide was swollen in 500 μL of DMF for 15 min. The respective Fmoc-amino acid (0.075 mmol, 5 equiv) and HOBt (0.075 mmol, 5 equiv) were then dissolved in 200 μL DMF and the solution was added to the resins with DIC (0.075 mmol, 5 equiv). The reaction mixtures were shaken for at least 3 h at room temperature. The peptides were then washed successively five times with DMF, DCM, MeOH, and Et_2O, and dried in vacuo. The completion of the coupling reaction was checked with a Kaiser test.

Selective Dde Cleavage at Lys^{16} of Peptides 2−4a. 500 μL of a hydrazine solution (2% v/v) was added to each peptide for 10 min. The cleavage was repeated 10 times. The peptides were then washed successively five times with DMF, DCM, MeOH, and Et_2O, and dried in vacuo.

NODAGA(*t*Bu)$_3$ Coupling for Peptides 1−5a. NODAGA(*t*Bu)$_3$ was introduced at the *N*-terminus of peptides **1a** and **5a** and at the N^{ε} of K^{16}, after Dde cleavage, for peptides **2**−**4a**. Each peptide was first swollen in 500 μL of DMF for 15 min. NODAGA(*t*Bu)$_3$ (0.03 mmol, 2 equiv) and HOBt (0.03 mmol, 2 equiv) were dissolved in 150 μL DMF and the solution was added to the resins with DIC (0.03 mmol, 2 equiv). The reaction mixtures were shaken overnight at room temperature. The peptides were then washed successively five times with DMF, DCM, MeOH, and Et_2O, and dried in vacuo to yield peptides **1**−**5b**. The completion of the coupling reaction was monitored with a Kaiser test.

Selective Trt/Mtt Cleavage for Peptides 1−4b. Mtt at Ser^3 of peptides **1**−**2b** and Trt at Dpr^3 of peptides **3**−**4b** were selectively cleaved following the same procedure. The peptides were incubated at room temperature for 5 min with 500 μL of the cleavage solution: TFA 1%, triisopropylsilane 5%, DCM 94% (v/v). The cleavage was repeated 15 times. At the end of the cleavage reaction, the peptides were washed successively five times with DMF, DCM, MeOH, and Et_2O, and dried in vacuo.

Octanoic Acid Coupling at Ser^3 of Peptides 1−2b. After Trityl cleavage, both peptides were swollen in 500 μL of NMP for 15 min. Octanoic acid (0.15 mmol, 10 equiv), DMAP (0.09 mmol, 6 equiv), and DCC (0.09 mmol, 6 equiv) were then dissolved in 200 μL NMP, and the solution was added to the resins. The reaction mixtures were shaken for 1 h at room temperature. The peptides were then washed twice with NMP

Table 1. Analytical Data of Conjugates 1−4d, 5c, and Chelates 1−4e, 5d

	compound	exact mass (g.mol^{-1})	$[M+H]^+$ found	purity (%)	yield (%)	elution (% ACN)
1d	N^{α}-NODAGA-ghrelin(1−28)	3726.0	3727.0	99	32	73
1e	N^{α}-NODAGA(Ga)-ghrelin(1−28)	3791.9	3792.9	99	-	74
2d	[K^{16}(NODAGA)]ghrelin(1−28)	3726.2	3727.2	97	37	72
2e	[K^{16}(NODAGA(Ga))]ghrelin(1−28)	3792.1	3793.1	99	-	78
3d	[Dpr^3;K^{16}(NODAGA)]ghrelin(1−28)	3725.0	3726.0	97	20	38
3e	[Dpr^3;K^{16}(NODAGA(Ga))]ghrelin(1−28)	3791.8	3792.1	100	-	23
4d	[Dpr^3;K^{16}(NODAGA)]ghrelin(1−16)	2365.3	2366.3	100	21	26
4e	[Dpr^3;K^{16}(NODAGA(Ga))]ghrelin(1−16)	2431.95	2432.2	100	-	25
5c	N^{α}-NODAGA-KwFwLL-$CONH_2$	1247.67	1248.7	95	28	70
5d	N^{α}-NODAGA(Ga)-KwFwLL-$CONH_2$	1313.5	1314.5	98	-	88

and the reaction repeated three more times. Subsequently, the peptides were successively washed five times with NMP, DMF, DCM, MeOH, and Et_2O, and dried in vacuo to yield peptides **1**−**2c** on solid support. The completion of the coupling reaction was monitored with a sample cleavage of the peptides from the resin.

Octanoic Acid Coupling at Dpr^3 of Peptides 3−4b. After Mtt cleavage, both peptides were swollen in 500 μL of DMF for 15 min. Octanoic acid (0.15 mmol, 10 equiv) and HOBt (0.15 mmol, 10 equiv) were dissolved in 200 μL DMF and the solution was added to the resin with DIC (0.15 mmol, 10 equiv). The reaction mixture was shaken for 4 h at room temperature. The peptides were then successively washed five times with DMF, DCM, MeOH, and Et_2O, and dried in vacuo to yield peptides **3**−**4c** on solid support. The completion of the coupling reaction was monitored with a Kaiser test.

Cleavage from the Resin and Side-Chain Deprotection of Peptide 1−4c and 5b. Cleavage from the resin and side-chain deprotection were simultaneously achieved by incubating the resins for 3 h at room temperature with 1 mL of different cleavage mixtures: Peptides **1**−**4c** were incubated with 90% of TFA, 5% of thioanisole, and 5% of thiocresol (v/v). Peptide **5c** was incubated with 90% of TFA, 3% of thioanisole, and 7% of ethandithiol (v/v). After 3 h, filtration of the resins allows collection of the cleavage mixtures containing the peptides. Peptides were then precipitated in 10 mL of ice-cold diethyl ether for 20 min and collected by centrifugation. After removal of the supernatant, the precipitates were washed four times by resuspension in ice-cold ether and centrifugation to yield conjugates **1**−**4d** and **5c** as white powders.

Identity of the following conjugates was confirmed by MALDI-ToF mass spectrometry (see Table 1): **1d**, N^{α}-NODAGA-ghrelin(1−28); **2d**, [K^{16}(NODAGA)]ghrelin(1−28); **3d**, [Dpr^3;K^{16}(NODAGA)]ghrelin(1−28); **4d**, [Dpr^3;K^{16}(NODAGA)]ghrelin(1−16); **5c**, N^{α}-NODAGA-KwFwLL-$CONH_2$.

Purification of Conjugates 1−4d and 5c. All peptides were purified by preparative RP-HPLC using a linear gradient of 0.1% TFA in water (A) and 0.08% TFA in acetonitrile (B) at a flow rate of 10 mL.min^{-1} with different gradient systems. All conjugates showed a purity higher than 95% as determined by analytical RP-HPLC and identity of the conjugates was confirmed by MALDI-ToF mass spectrometry (see Table 1).

Complexation of Conjugates 1−4d and 5c with Ga for in Vitro Assay. 0.5 μmol of each peptide was dissolved in 700 μL of an ammonium acetate solution (0.1 M in H_2O). 300 μL of a $Ga(NO_3)_3$ solution (0.04 M in H_2O) were added, and the pH adjusted to 4.5 with diluted HCl. The solutions were then incubated for 30 min at 37 °C and directly purified by semipreparative HPLC to yield the following chelates: **1e**, N^{α}-NODAGA(Ga)-ghrelin(1−28); **2e**, [K^{16}(NODAGA(Ga))]-ghrelin(1−28); **3e**, [Dpr^3;K^{16}(NODAGA(Ga))]ghrelin(1−28); **4e**, [Dpr^3;K^{16}(NODAGA(Ga))]ghrelin(1−16); **5d**, N^{α}-NODAGA(Ga)-KwFwLL-$CONH_2$. Identity and purity of the chelates **1**−**4e** and **5d** were confirmed by MALDI-ToF mass spectrometry and HPLC (see Table 1).

TFA-HCl Exchange for Conjugates 2−4d and 5c for in Vivo Assays. Each conjugate (15 μmol) was dissolved in 4 mL of a 50 mM HCl solution in H_2O and stirred at room temperature for 1 h. The conjugates were dried in a freeze−dryer and the procedure repeated two more times. Integrity and purity of the conjugates were controlled by MALDI-ToF mass spectrometry and HPLC.

Signal Transduction Assay. *Cell Culture.* COS-7 cells (African green monkey, kidney) were cultured in DMEM containing 10% FCS (v/v), 100 units.mL^{-1} penicillin, and 100 μg.mL^{-1} streptomycin. Cells were grown as monolayers at 37 °C in a humidified atmosphere of 5% CO_2.

Measurement of Inositol Phosphate Accumulation. The functional assay to measure ghrelin receptor ligand potency was previously described in detail.[14] Briefly, COS-7 cells were seeded into 24-well plates (8×10^5 cells/well) and transiently transfected with 0.3 μg of a vector GHS-R_EYFP_pVITRO2_mcs (containing hygromycin resistance), using 0.9 μL of Metafectene. At confluency, cells were then incubated with 4 μCi.mL^{-1} of myo-[^{3}H] Inositol (25.0 Ci.mmol^{-1}) about 16 h prior to stimulation. Cells were then washed once and stimulated in DMEM containing 10 mM LiCl and 0.1% BSA, in the absence or with increasing concentrations of ghrelin and chelates **1e**−**4e** and **5d** for 2 h at 37 °C. The stimulation was stopped by aspiration of medium and cell lysis with 0.1 M NaOH (150 μL/well). After adding 0.2 M formic acid (50 μL/well) and sample dilution, intracellular inositol phosphate levels were determined by anion-exchange chromatography. Data were analyzed with *GraphPad Prism 3.0* program (GraphPad Software, San Diego, USA). EC_{50} and E_{max} values were obtained from concentration−response curves. All signal transduction assays were performed in duplicate and repeated at least two times independently.

Small Animal PET Assay. *^{68}Ga-Production.* ^{68}Ga ($T_{1/2}$ = 68 min, β^+ = 89%, and EC = 11%) was available from two ^{68}Ge/^{68}Ga-generator-systems (Cyclotron Co., Ltd., Obninsk, Russia (Eckert & Ziegler, Germany), iThemba, South Africa (IDB Holland bv, The Netherlands)) where ^{68}Ge ($T_{1/2}$ = 270.8 d) was attached to a column of an inorganic matrix based on titanium dioxide or tin oxide. The ^{68}Ga was eluted with 1 M hydrochloric acid or water. The final HCl concentrations of the eluates of both generators were approximately 1 M

dx.doi.org/10.1021/bc2005889 | *Bioconjugate Chem.* 2012, 23, 771−784

hydrochloric acid. The pH of the fractionated [^{68}Ga]-eluate (300 μL) was adjusted to pH 4.0−4.5 using 2 M NH_4OAc.

Radiolabeling. The solution of $^{68}Ga(OAc)_3$ in acetate buffer was added to 20 nmol of each NODAGA-peptide **2**−**4d** and **5c**. The reaction mixture was shaken for 15 min at 37 °C to afford [^{68}Ga]-labeled **2**−**4f** and **5e** in solution. The reaction mixture was analyzed by radio-HPLC. Analysis was performed on a Zorbax C18 300SB (250 × 9.4 mm; 4 μm) column with an eluent system C (water + 0.1% TFA) and D (acetonitrile +0.1% TFA) in a gradient 5 min 95% C, 10 min to 95% D, and 5 min at 95% D at a flow rate of 3 mL.min^{-1}. Radiolabeled conjugates with radiochemical purity higher than 95% were used for radiopharmacological studies. Before formulation for the in vitro or in vivo application, the reaction mixture was filtrated (45 μm pore size, REZIST 13/0.45 PTFE, Schleicher & Schuell, Dassel, Germany). The filtrates were then diluted with electrolyte solution E-153 (140 mmol.L^{-1} Na^+, 5 mmol.L^{-1} K^+, 2.5 mmol.L^{-1} Ca^{2+}, 1.5 mmol.L^{-1} Mg^{2+}, 50 mmol.L^{-1} acetate, 103 mmol.L^{-1} Cl^-, Serumwerk Bernburg, Germany) to reach concentration of about 80 MBq.mL mmol.L^{-1} and directly used for the radiopharmacological studies.

Animals, Feeding, Husbandry, and Animal Preparation. The local animal research committee at the Landesdirektion Dresden approved the animal facilities and the experiments according to institutional guidelines and the German animal welfare regulations (permission number: 24−9168.21−4/2004−1 from 04/27/2004 valid up to 03/31/2014). The experimental procedure used conforms to the *European Convention for the Protection of Vertebrate Animals used for Experimental and other Scientific Purposes (ETS No. 123)*, to the *Deutsches Tierschutzgesetz*, and to the *Guide for the Care and Use of Laboratory Animals* published by the U. S. National Institutes of Health [DHEW Publication No. (NIH) 82−23, Revised 1996, Office of Science and Health Reports, DRR/NIH, Bethesda, MD 20205]. Wistar rats (Wistar Unilever, HsdCpb:WU, Harlan Winkelmann, Borchen, Germany) were housed under standard conditions with free access to food (2016 Teklad Global 16% Protein Rodent Diet, Harlan Laboratories, Inc., Germany) and tap water. Rats were housed (5 rats per cage) in Uni Protect airflow cabinet (Ehret GmbH Labor and Pharmatechnik, Schönwalde, Germany) in polysulfone cages (380 × 200 × 590 mm^3; floor area, 1815 cm^2). The caging had a solid bottom and stainless steel wire lid. The cage floor was covered with chipped wood. The cages were changed weekly. Tap water was provided in polycarbonate bottles, changed twice weekly, and refilled once between the cage changes. The room temperature was 22 ± 1 °C and relative humidity was 53% ± 6%, but the temperature was 1−4 °C higher in the airflow cabinets. Artificial lighting was in 12 h light and dark cycles with fluorescent tubes (light color, warm white).

Surgery. Male Wistar-Unilever rats weighing 183 ± 56 g (mean ± SD, n = 19) were anesthetized with desflurane. The guide value for breathing frequency was 65 breaths/min. Animals were put in the supine position and placed on a heating pad to maintain body temperature. The spontaneously breathing rats were treated with 100 units.kg^{-1} heparin (Heparin-Natrium 25.000-ratiopharm, Ratiopharm, Germany) by subcutaneous injection to prevent blood clotting on intravascular catheters. After local anesthesia by injection of Lignocaine 1% (Xylocitin loc, Mibe, Jena, Germany) into the right groin, catheter was introduced into the right femoral artery (0.8 mm Umbilical Vessel Catheter, Tyco Healthcare, Tullamore, Ireland) for blood samples for metabolite analysis, for gas analysis, arterial blood pressure measurements and a second needle (35 G) catheter into one tail vein was used for administration of the **2**−**4f**, **5e**.

Measurement of Original Compounds and Radioactive Metabolites. Metabolic stability studies were performed on male Wistar rats. Arterial blood samples were collected at 1, 3, 5, 10, 20, 30, and 60 min after injections and the activity (% ID.mL^{-1}) was measured to give the arterial activity of **2**−**4f**, **5e**. Blood cells were separated by centrifugation (5 °C, 5 min, 8000 rpm), and plasma proteins were precipitated using 60% acetonitrile and subsequent centrifugation (5 °C, 5 min, 8000 rpm). The supernatant was analyzed by radio-HPLC. The radio-HPLC system (Agilent 1100 series) applied for metabolite analysis was equipped with UV detection (254 nm) and an external radiochemical detector (Ramona, Raytest GmbH, Straubenhardt, Germany). Analysis was performed on a Zorbax C18 300SB (250 × 9.4 mm; 4 μm) column with an eluent system C (water + 0.1% TFA) and D (acetonitrile + 0.1% TFA) in a gradient 5 min 95% C, 10 min to 95% D, and 5 min at 95% D at a flow rate of 3 mL.min^{-1}. HPLC were performed on **2**−**4e**, **5f** added to a rat blood sample, and arterial blood samples from 1 to 60 min after injections and on urine sample from 60 min after injection. The metabolite fraction in blood was calculated as % of the parent compound in blood in HPLC. The extracts from other tissues were prepared by ultrasound homogenization as 10% solution in PBS, centrifugation (5 °C, 70 000 g × min) and subsequent precipitation by 60% acetonitrile. The supernatant was analyzed by the described radio-HPLC.

Small Animal PET. Anesthetized, spontaneously breathing animals were allowed to stabilize for 10 min after preparation. A 10 min transmission scan was recorded during this time for each subject by using a rotating point source of ^{57}Co. The transmission scan was used to correct the emission scan for γ-ray attenuation caused by body tissues and supporting structures; it was also used to demarcate the body field for image registration. After the transmission scans, physiological data [mean arterial blood pressure (MAP), heart rate (HR), respiration rate (RR), and body temperature (T)] were measured and arterial blood samples were taken for pH, PaO_2, $PaCO_2$, hemoglobin (Hb), and hematocrit (Hct). The radioactivity of the injection solution was measured in a well counter (Isomed 2000, Dresden, Germany) cross-calibrated to the microPET P4 scanner (Siemens preclinical solutions, Knoxville, TN). The PET acquisition of 60 or 120 min emission scan was started and the infusion of the ^{68}Ga-labeled compound was initiated with a delay of 30 s. 0.5 mL of [^{68}Ga]-peptide solutions **2**−**4f** and **5e**, containing 90 ± 33 MBq was infused over 1 min (with a Harvard apparatus 44 syringe pump) into a tail vein. At the end of the experiment, the animals were deeply anesthetized and sacrificed by an intravenous injection of potassium chloride.

Data Acquisition. Acquisition was performed in 3D list mode. Emission data were collected continuously. The list mode data were sorted into sinograms with 32 or 38 frames (15 × 10 s, 5 × 30 s, 5 × 60 s, 4 × 300 s, 3 × 600 s, or 9 × 600 s). The data were decay-, scatter-, and attenuation-corrected. The frames were reconstructed by Ordered Subset Expectation Maximization applied to 3D sinograms (OSEM3D) with 14 subsets, 15 OSEM3D iterations, 25 maximum a posteriori (MAP) iterations, and 1.8 mm resolution using the FastMAP algorithm (Siemens Preclinical Solutions, Knoxville, TN). The voxel size was 0.07 by 0.07 by 0.12 cm, and the resolution in the center of

field of view was 1.8 mm. No correction for partial volume effects was applied. The image volume data were converted to Siemens ECAT7 format for further processing. The image files were then processed using the ROVER software (ABX GmbH, Radeberg, Germany). Masks for defining three-dimensional regions of interest (ROI) were set and the ROI's were defined by thresholding and ROI time activity curves (TAC) were derived for the subsequent data analysis. The ROI data and TAC were further analyzed using R (R is available as Free Software under the terms of the Free Software Foundation's GNU General Public License in source code form) and especially developed program packages (Jörg van den Hoff, Helmholtz-Zentrum Dresden-Rossendorf, Dresden, Germany). The standardized uptake values (SUV = (activity.mL^{-1} tissue)/(injected activity/body weight), mL.g^{-1})) were calculated in the ROI.

Biodistribution. The male Wistar rats (Wistar Unilever, HsdCpb:WU, Harlan Winkelmann GmbH, Borchen, Germany) were between 7 and 9 weeks of age. Two groups of four animals (mean body weight ± SD, 186 ± 11 g) for each time point were intravenously injected into a tail vein with approximately 0.3 MBq of the 0.5 mL of [^{68}Ga]-tracer solutions **2**−**4f** and **5e**, Ga-68-labeled compound dissolved in 0.5 mL of electrolyte solution E-153. The specific activity ranged between 5 and 30 GBq.mmol^{-1} at the time of injection. Animals were sacrificed at 5 and 60 min post injection. Blood and the major organs were collected, weighed, and counted in a Wallac WIZARD automatic gamma counter (PerkinElmer, Germany). The radioactivity of the tissue samples was decay-corrected and calibrated by comparing the counts in tissue with the counts in aliquots of the injected tracer that had been measured in the gamma counter at the same time. The activity amount in the selected tissues and organs was expressed as percent of injected dose (% ID). The activity concentration in the biodistribution measurements were calculated as SUV (SUV = (activity/g tissue)/(injected activity/body weight)) and expressed as means ± standard deviation (mean ± SD) for each group of four animals.

Statistical Analysis. Values are expressed as mean ± SD or median and interquartile range (IQR). IQR is defined as the range of the values extending from the 25th percentile to the 75th percentile. Values were compared using an unpaired Student's *t*-test with Welch's correction and an *F*-test to compare the variances (*GraphPad Prism* 5.02 for Windows, GraphPad Software, San Diego, CA). The nonparametric Wilcoxon signed rank test and the D'Agostino-Pearson normality test were used for statistical evaluation for some of the data. A *P* value of <0.05 was considered significant and is indicated by an asterisk.

RESULTS

Peptide Synthesis. Wang resin was used as solid support to synthesize ghrelin agonist derivatives **1**−**4a**. Amino acids were automatically coupled with a robot synthesizer, except Fmoc-L-Lys(Dde)-OH at position 16 of peptides **2**−**4a**; Fmoc-L-Ser(Trt)-OH at position 3 of peptides **1**−**2a** and Fmoc-L-Dpr(Mtt)-OH at position 3 of peptides **3**−**4a**, which were introduced manually. Peptide **4a** is a truncated analogue of peptide **3a** lacking the *C*-terminal fragment [17−28]. *N*-Terminal and orthogonal modifications were achieved on peptides **1**−**4a** as detailed in Schemes 1 and 2. NODAGA(tBu)$_3$ was introduced at the *N*-terminus of peptide **1a** and at N^{ε} of Lys^{16} for peptides **2**−**4b**, after a selective cleavage of the Dde protecting group and led to peptides **1**−**4b**. Octanoylation was performed at Ser^3 of compounds **1**−**2b**, after a selective trityl

Scheme 1. Synthesis of Conjugate 1d[a]

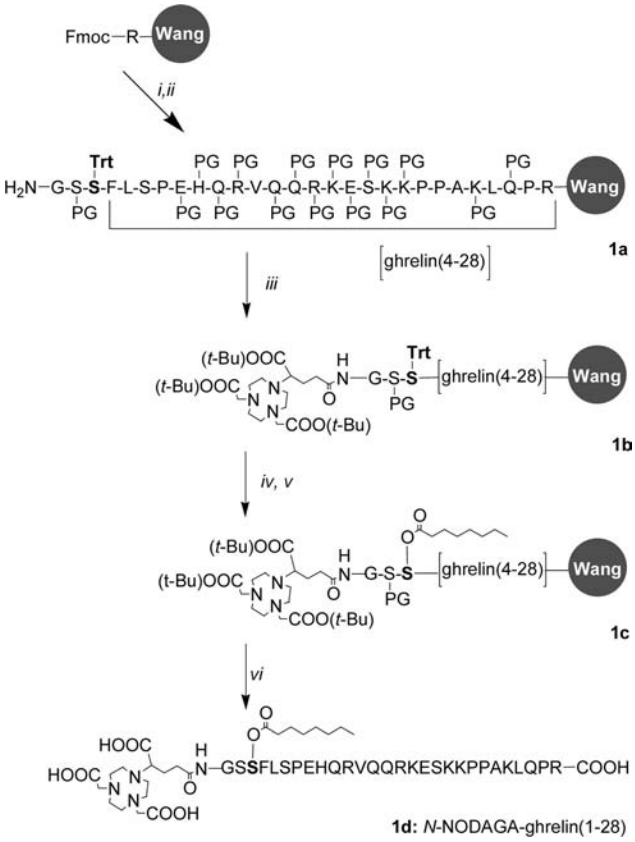

[a]Automatic and manual peptide synthesis: (i) Fmoc-AA-OH, HOBt, DIC, DMF, r.t., 2 h. (ii) piperidine 20% in DMF, 2 × 15 min. (iii) NODAGA(tBu)$_3$, HOBt, DIC, DMF, r.t., overnight. (iv) TFA/TIPS/DCM: 1/5/94, r.t., 15 × 2 min. (v) $CH_3(CH_2)_6COOH$, DCC, DMAP, r.t., 4 × 1 h. (vi) TFA/thioanisole/thiocresol: 90/5/5, r.t., 3 h.

cleavage in low acidic conditions, and yield the *O*-octanoylated peptides **1**−**2c**. Similarly, N^{β} of Dpr^3 of peptides **3**−**4b** was octanoylated after the selective cleavage of 4-methyl trityl (Mtt) to afford the *N*-octanoylated peptides **3**−**4c**. Finally, peptides **1**−**4c** were simultaneously deprotected and cleaved from the resin in TFA to obtain the conjugates **1**−**4d** after purification (Table 1). The inverse agonist derivative **5c** was obtained with a similar strategy. Automated synthesis of the hexapeptide **5a** was performed on a Rink amide resin (Scheme 3). NODAGA-(tBu)$_3$ was then coupled to the *N*-terminus to obtain **5b**. Finally, simultaneous side chain deprotection and cleavage from the resin in TFA/scavenger led to the conjugate **5c** after purification. Prior to the in vivo experiments, a TFA−HCl exchange was performed for conjugates **2**−**4d** and **5c**, simply by incubating three times the peptides in diluted HCl and subsequent lyophilization. Integrity of the peptides was controlled by MS and HPLC at each step.

Complexation with Cold Ga. For complexation with cold Ga, conjugates **1**−**4d** and **5c** were incubated for 30 min with Ga(NO$_3$)$_3$ in acetate buffer (pH 5) and at 37 °C. The cold chelates **1**−**4e** and **5d** (Scheme 4) were directly purified to remove the excess of metal, and the peptides were used for in vitro assay.

Radiolabeling with ^{68}GaCl$_3$. The radiolabeling procedure was adapted for the two ^{68}Ge/^{68}Ga-generator systems used. The reaction conditions were optimized for the reproducibility

dx.doi.org/10.1021/bc2005889 | *Bioconjugate Chem.* 2012, 23, 771−784

Scheme 2. Synthesis of Conjugates 2−4d[a]

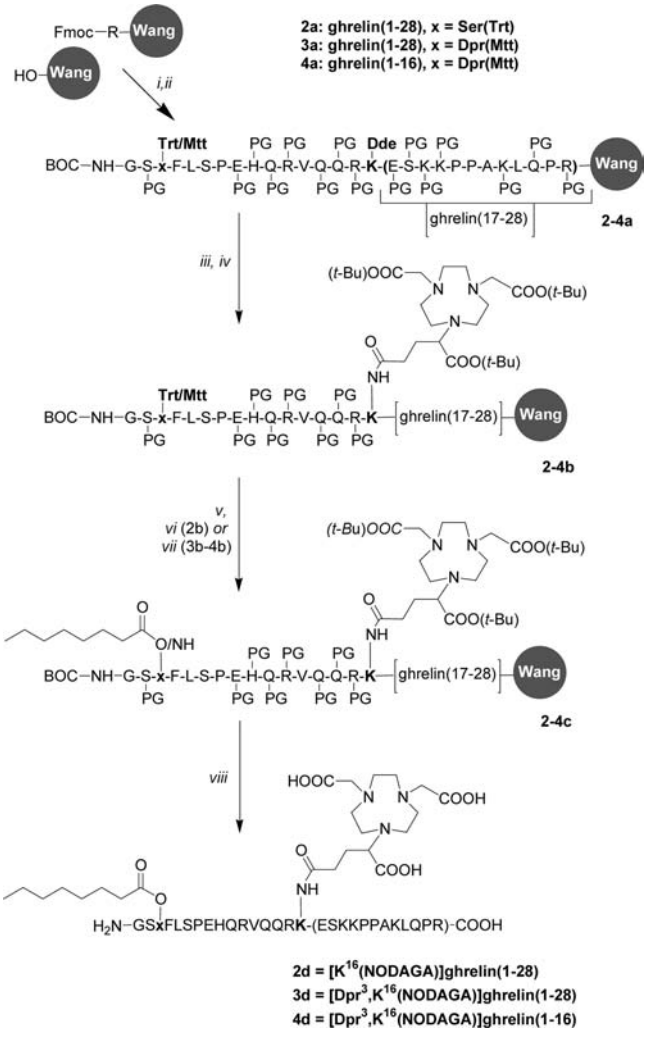

[a]Automatic and manual peptide synthesis: (i) Fmoc-AA-OH, HOBt, DIC, DMF, r.t., 2 h. (ii) Piperidine 20% in DMF, 2 × 15 min. (iii) Hydrazine 2% in DMF, 10 × 10 min. (iv) NODAGA(tBu)$_3$, HOBt, DIC, DMF, r.t., overnight. (v) TFA/TIPS/DCM: 1/5/94, r.t., 15 × 2 min. (vi) $CH_3(CH_2)_6COOH$, DCC, DMAP, r.t., 4 × 1 h. (vii) $CH_3(CH_2)_6COOH$, DCC, DMAP, r.t., 4 × 1 h. (viii) TFA/thioanisole/thiocresol: 90/5/5, r.t. 3 h.

of the radiolabeling process of conjugates **2**−**4d** and **5c** and were used for all compounds. 20 nmol of **2**−**4d** and **5c** were shaken 15 min with $^{68}Ga(OAc)_3$, in acetate buffer (pH 4.0 to 4.5) at 37 °C, and led to ^{68}Ga-radiotracers **2**−**4f** and **5c** in solution (Scheme 4). The radiochemical purity and integrity of the peptides after radiolabeling was confirmed by radio-HPLC, and the data are summarized in Table 2. High amounts of radiolabeled conjugates were obtained (280 to 430 MBq), which allowed us to carry out parallel experiments for biodistribution and PET. The high radiochemical purity and specific activity (8.4−16.1 GBq.μmol^{-1}) allowed the direct application of the **2**−**4f**, **5e**. A further purification of the products was not necessary since the radiochemical purity was higher than 95%. In spite of our great care in storage of **2e** (T < −60 °C), the radiochemical purity of **2f** decreased after several weeks; however, after HPLC purification of the conjugate **2e** the radiochemical purity again reached 96.7 ± 4.0%. The acetate concentration in the final formulation did not exceed 150 mmol.L^{-1} and was suitable for intravenous injection. Hence, the results support the previous reports on efficient complexation of NODAGA with $^{68}GaCl_3$.[15,16]

In Vitro Functional Assay. The activity of the cold chelates **1**−**4e** and **5d** was evaluated by inositol phosphate turnover assay (Figure 1 and Table 3). As expected, chelates **1**−**4e** showed agonist behavior at ghrelin receptor. Peptide **1e** with NODAGA(Ga) at *N*-terminus presented a 1000-fold loss of activity compared to ghrelin. Chelate **2e**, bearing NODAGA-(Ga) at Lys^{16} was equipotent to ghrelin. On the other hand, *N*-octanoylated chelates **3e** and **4e** with NODAGA(Ga) at Lys^{16} presented both a slight loss of activity compared to ghrelin (respectively 3.2- and 1.9-fold). Nevertheless, both chelates **3e** and **4e** showed an EC_{50} in the low nanomolar range and the same efficacy as ghrelin. Chelate **5d** showed inverse agonist activity in low micromolar range at the ghrelin receptor (EC_{50} = 643.2 ± 9.1 nM), whereas the native inverse agonist KwFwLL-$CONH_2$ possesses a higher activity (EC_{50} = 45.6 ± 5.4 nM). *N*-terminal modification of this short inverse agonist has not been reported so far to reduce the inverse agonist activity, but to increase the efficacy at the receptor (91% toward 37%). Accordingly, tracers **2**−**4f** were selected for in vivo studies due to their high potency at the receptor. Tracer **5e** was also included in the in vivo study to obtain the first pharmacokinetic data of a ghrelin inverse agonist, which might be an interesting drug candidate.

Biodistribution in Rats. Ghrelin agonist radiotracers **2f**, **3f**, and **4f** present a very similar biodistribution pattern. The kidney uptake is highly predominant and almost exclusive. It represents respectively 26.6%, 33.2% and 27.7% ID of the tracers **2f**, **3f**, and **4f** after 5 min (Figure 2A,C,E and Table 4). At 60 min, doses increase to 63.3−65.3% ID for **2f**−**3f** and 52.3% ID for **4f**, showing an accumulation of the tracers **2**−**4f** in the kidney. Interestingly, **3f** also presents an important accumulation in the liver, with high and stable doses at 5 and 60 min (22.6% and 22.3% ID). In comparison, concentrations of both **2f** and **4f** are lower at 5 min (11.1% and 6.2% ID) and a slight decrease is measured at 60 min (respectively, 8.1% and 3.4% ID). The combined doses measured in both liver and intestine show a hepatobiliary elimination of the agonist tracers **2**−**4f**, although it represents a minor metabolism pathway compared with the renal metabolism. The uptake of agonist tracers **2**−**4f** in all other organs is negligible (SUV < 1) and concentrations decrease at 60 min, showing no accumulation. Importantly, the brain shows the lowest uptake values after 5 min (SUV = 0.04 to 0.06 for **2**−**4f**, Figure 2B,D,F and Table 5) and only traces after 60 min (SUV = 0.01 for **2**−**4f**). In the blood, the three peptides are found at low concentration after 5 min (1.3 to 1.8 SUV for **2**−**4f**) and are almost eliminated after 60 min (0.15 to 0.26 SUV for **2**−**4f**).

Interestingly, the inverse agonist tracer **5e** presents a very different pharmacologic profile. The kidney uptake is important but much lower than for all agonist tracers **2**−**4f**. No accumulation is visible in the kidney, since an equal doses of **5e** are found at 5 and 60 min (4.4% ID, Figure 2G and Table 4). The liver uptake of **5e** is important as it represents 11.6% and 9.4% ID, respectively, after 5 and 60 min. Moreover, concentration in intestine is in the same order with a minor increase from 5 to 60 min (9.1−10.7% ID), showing a predominant hepatobiliary elimination (Table 4). Importantly, the uptake in all organs is higher for **5e** compared to agonist tracers **2**−**4f**. Particularly in blood, the concentration of **5e** is

dx.doi.org/10.1021/bc2005889 | *Bioconjugate Chem.* 2012, 23, 771−784

Scheme 3. Synthesis of Conjugates 5c[a]

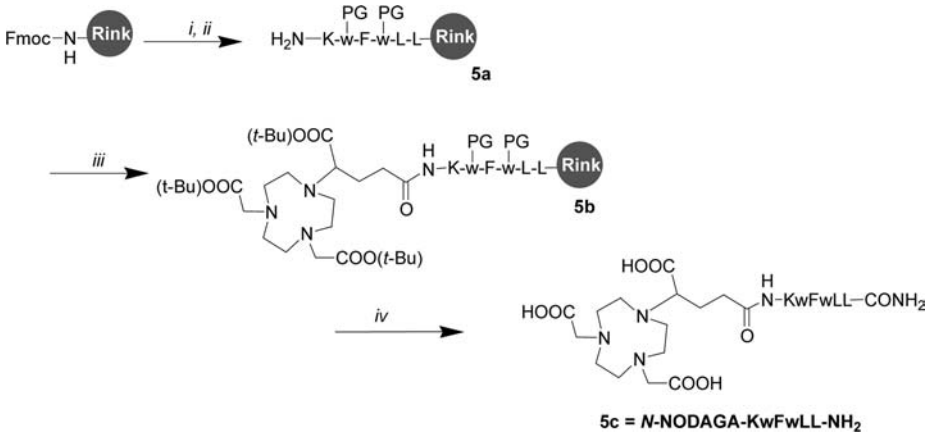

[a](i) Fmoc-AA-OH, HOBt, DIC, DMF, r.t., 2 h. (ii) Piperidine 20% in DMF, 2 × 15 min. (iii) NODAGA(tBu)$_3$, HOBt, DIC, DMF, r.t., overnight. (iv) TFA/thioanisole/thiocresol: 90/5/5, r.t. 3 h.

Scheme 4. Complexation with Cold Ga and Radiolabeling with ^{68}Ga to Yield Chelates 1−4e, 5d, and Radiotracers 2−4f, 5e

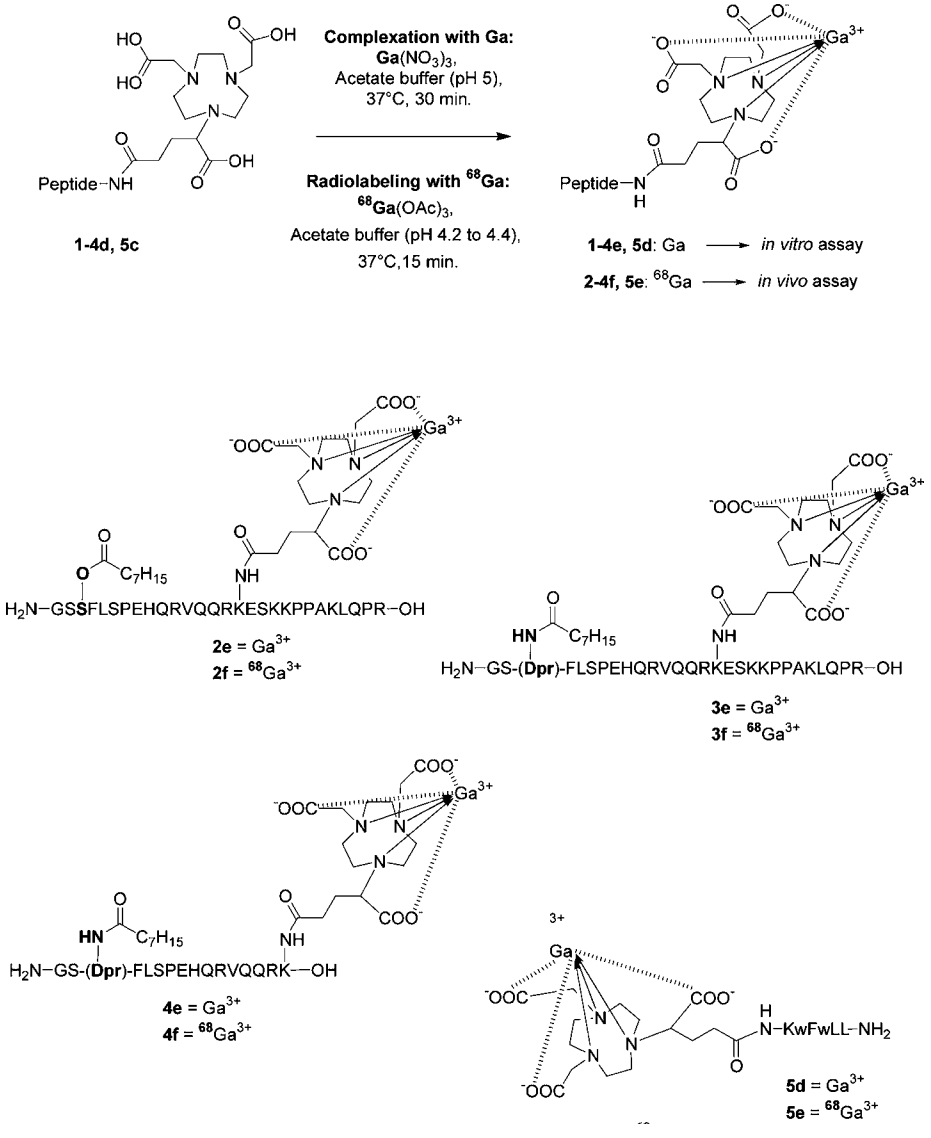

high at 5 min and still significant after 60 min (respectively, 3.78 and 1.53 SUV, Figure 2H and Table 5). On the other hand, the brain uptake is very low at 5 min (0.11 SUV) and negligible after 60 min.

dx.doi.org/10.1021/bc2005889 | Bioconjugate Chem. 2012, 23, 771−784

Table 2. Radiochemical Characterization of Conjugates 2−4f and 5e

	[^{68}Ga]Ga-labeled compound	activity (MBq)	radiochemical purity (%)	specific activity (GBq.μmol^{-1})	n
2f	[K^{16}(NODAGA(^{68}Ga))]ghrelin(1−28)	391 ± 4	96.7 ± 4.0	23.4 ± 6.6	3
3f	[Dpr^3;K^{16}(NODAGA(^{68}Ga))]ghrelin(1−28)	339 ± 30	99.5 ± 0.5	12.6 ± 1.1	6
4f	[Dpr^3;K^{16}(NODAGA(^{68}Ga))]ghrelin(1−16)	282 ± 74	95.8 ± 4.5	8.4 ± 6.2	6
5e	N^{α}-NODAGA(^{68}Ga)-KwFwLL-CONH$_2$	393 ± 67	96.2 ± 4.3	16.1 ± 2.4	6

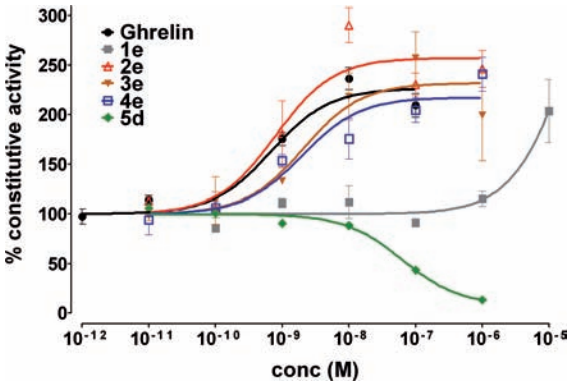

Figure 1. Concentration−response curves of chelates **1**−**4e** and **5d** in inositol phosphate turnover assay. All compounds were tested in COS-7 cells expressing human ghrelin receptor (GHS-R1a) in a signal transduction assay. The response is expressed in % of constitutive activity of the receptor.

Metabolic Stability in Rats. The clearance of the total radioactivity related to each tracer was measured in arterial blood (Figure 3A). The clearances of the original compounds (Figure 3B) and the metabolite fraction (Figure 3C) were then calculated for each tracer after quantification of metabolites by HPLC analysis (Figure 3D−G). According to those results, the concentration of **2f** in blood drops from 5.5% ID.mL^{-1} after injection to 1.7% ID.mL^{-1} after 5 min and reaches 0.1% ID.mL^{-1} after 60 min (Figure 3A,B). **3f** displays a comparable clearance in arterial blood with concentrations decreasing from 5.3% to 2.3% ID.mL^{-1} at 5 min and then 0.2% ID.mL^{-1} at 60 min. **4f** presents a dramatically higher clearance in arterial blood, which is directly due to a very low metabolic stability. Although the total radioactivity related to **4f** in blood follows the same clearance as **2f** and **3f** (Figure 3B), concentration of the original compound falls from 5.8 to 1.2% ID.mL^{-1} in 5 min, 0.3% ID.mL^{-1} in 10 min, and finally 0.001% ID.mL^{-1} after 20 min. Indeed, the tracers **2**−**4f** show discrepancies in metabolic stability. At 5 min, the metabolite fraction is low for **3f** (5%), moderate for **2f** (15%), and extremely high for **4f** (50%). After 20 min, the metabolite fractions of **2f** and **3f** reach 35%, whereas **4f** is fully metabolized (100% of metabolite fraction). At 60 min, **2f** and **3f** present 40% of metabolite fraction.

Chromatograms clearly exhibit the conversion of **2f** into 2 metabolites in blood at 5 and 60 min, and the appearance of a third metabolite in both blood and urine at 60 min (Figure 3D). Importantly, the conversion of **2f** in its major metabolite was already observed before injection (2f_original, Figure 3D). Thus, this side product appeared during the radiolabeling step and indicates a spontaneous decomposition of **2f**. For tracer **3f**, no metabolites are detectable in blood at 5 min, although two metabolites are visible in both blood and urine at 60 min (Figure 3E). Exemplarily in Figure 4, radiochromatogram of compound **3f** presents the resulting pattern of the liver extract at 5 min after injection. Thus, only 7% of **3f** remains in the liver after 5 min. In addition, **4f** showed a sole metabolite, for both blood and urine after 5 and 60 min (Figure 3F).

Interestingly, the inverse agonist tracer **5e** presents a very different metabolism compared to agonist tracers **2**−**4f** with an impressively slow clearance and a high stability in blood. Indeed, concentration of **5e** in blood initially decreases significantly from 7% to 5.4% ID.mL^{-1} in 3 min and then gently drops to 2% ID.mL^{-1} after 60 min (Figure 3A and B). A metabolite fraction lower than 5% is detected in blood after 60 min and the integrity of the tracer **5e** is maintained at 5 and 60 min in blood without any metabolite detected in HPLC (Figure 3C and G). However, three radioactive metabolites are detected at low concentration in urine after 60 min (Figure 3G).

PET Studies. The maximum intensity images confirm the biodistribution experiments (Figure 5). After 5 min, the radioactivity is only visible in the kidney for **2f** and **4f**. Image of tracer **3f** clearly shows high concentration of radioactivity in the kidney and the liver. Radioactivity related to **5e** is broadly spread in all the organs with higher concentrations visible in liver, kidney, and intestine. According to the time−activity curves, the activity in the kidneys increases over time. The kidney accumulation is high and fast for **2f** and **4f**, intermediate for **3f** and moderate for **5e** (Figure 6A). In the liver, **3f** shows the highest activity and the increase of activity over the time indicates hepatic accumulation (Figure 6B). The time−activity curves of the other tracers in the liver demonstrate a hepatic clearance over time with a high (**4f**) or low (**2f** and **5e**) velocity. The blood clearance of the ^{68}Ga activity is comparable for all compounds studied (Figure 6C).

Table 3. In Vitro Activity of Chelates 1−4e and 5d in Inositol Phosphate Turnover Assay[a]

	compound	EC$_{50}$ (nM)	x fold over ghrelin	Δ efficacy (%)	n	behavior
	ghrelin	0.55 ± 0.24	1	112 ± 25	4	agonist
1e	N^{α}-NODAGA(Ga)-ghrelin(1−28)	>1000	>1000	n.d.	3	agonist
2e	[K^{16}(NODAGA(Ga))]ghrelin(1−28)	0.72 ± 0.06	1.3	122 ± 7	3	agonist
3e	[Dpr^3;K^{16}(NODAGA(Ga))]ghrelin(1−28)	1.91 ± 0.40	3.5	111 ± 11	3	agonist
4e	[Dpr^3;K^{16}(NODAGA(Ga))]ghrelin(1−16)	1.41 ± 0.60	2.6	150 ± 8	3	agonist
5d	N^{α}-NODAGA(Ga)-KwFwLL-CONH$_2$	643.2 ± 9.1	n.c.*	91 ± 1	2	inverse agonist

[a]EC$_{50}$ values (mean ± SD) were obtained from concentration−response curves and showed the potency of the chelates. Efficacy values (ΔEfficacy) are the mean ± SD of |Efficacy$_{max}$ − Efficacy$_{min}$|. *n.c.: noncalculated.

dx.doi.org/10.1021/bc2005889 | Bioconjugate Chem. 2012, 23, 771−784

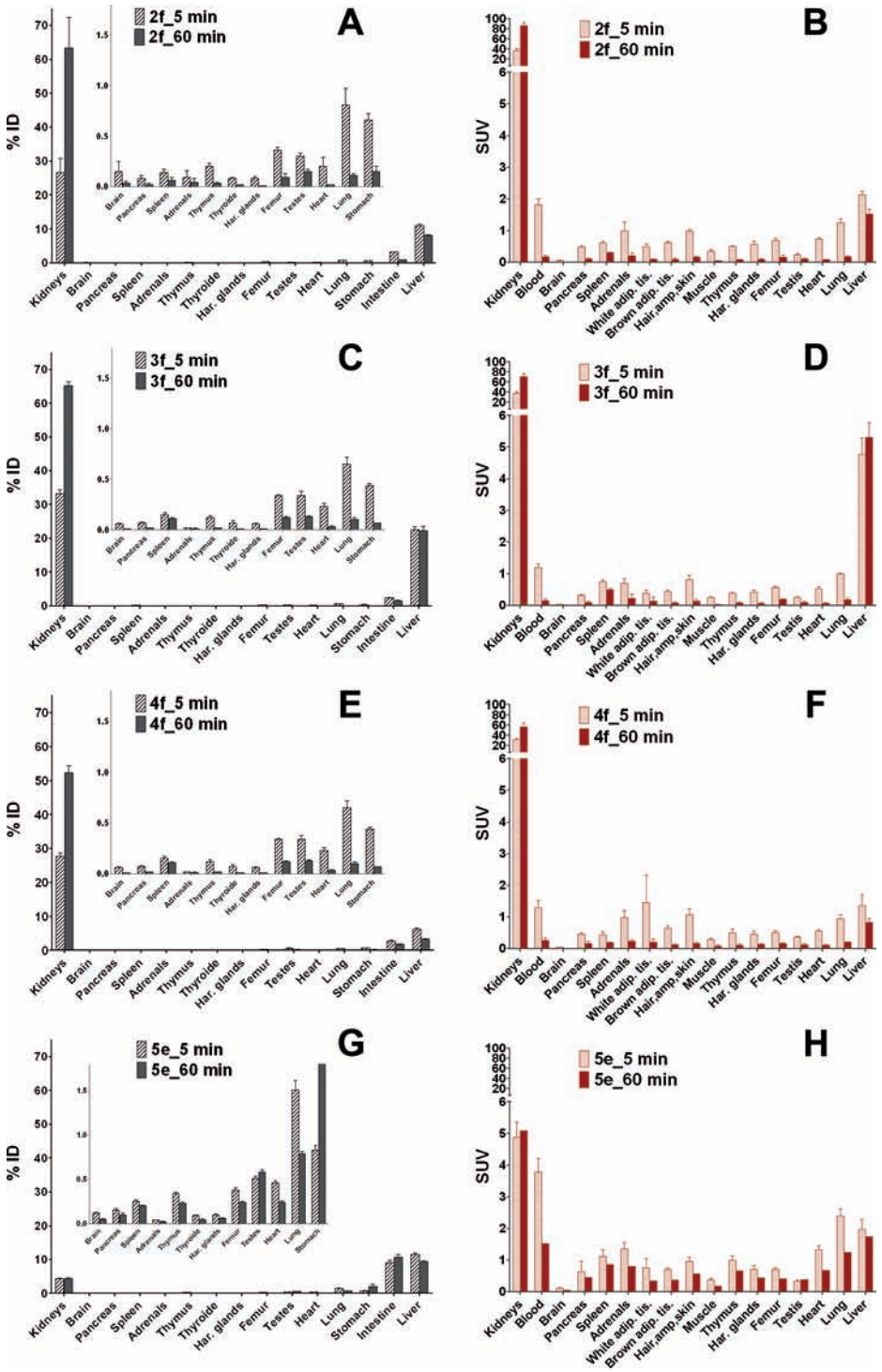

Figure 2. Biodistribution profiles of tracers **2**–**4f** and **5e** in male Wistar rats. Activity amount in selected organs were measured at 5 and 60 min after injection of radiotracers **2**–**4f** and **5e**. Values are given as mean ± SD for each group of four animals. Biodistribution profiles are expressed as percent of the injected dose (%ID) for **2f** (A), **3f** (C), **4f** (E), and **5e** (G). Biodistribution profiles are expressed as standard uptake values (SUV) for **2f** (B), **3f** (D), **4f** (F) and **5e** (H).

However, the absolute retention of compound **5e** in blood is higher than of **2**–**4f**. The mean plasma retention times were consistent with the metabolic studies. The typical pattern of high blood activity of **5e** is also visible in the PET image (Figure 5). The heart and the large vessels (jugular vein, vena cava) are clearly visible at midframe time of 5 min. At this time, the liver is prominent in the animal injected with **3f**.

■ DISCUSSION

In this study, we developed both agonist and inverse agonist probes targeting the ghrelin receptor. Indeed, suitable probes with opposed behavior would be highly valuable for studying the hormone signalization in vivo. Radiotracers could be of major interest as diagnostic tools in hormonal dysfunctions and for further development of therapeutic peptides for diseases

dx.doi.org/10.1021/bc2005889 | *Bioconjugate Chem.* 2012, 23, 771–784

Table 4. Elimination Pathways: Comparison of the Renal Metabolism (Kidney) toward the Hepatobiliary Metabolism (Liver + Intestine) for Radiotracer 2−4f and 5e[a]

	renal metabolism		hepathobiliary metabolism			
	kidney		liver		intestine	
%ID	5 min	60 min	5 min	60 min	5 min	60 min
2f	26.6 ± 11.8	63.3 ± 25.9	11.1 ± 0.9	8.1 ± 0.8	3.2 ± 0.3	0.9 ± 0.1
3f	33.2 ± 2.2	65.3 ± 2.2	22.6 ± 1.6	22.3 ± 2.4	2.3 ± 0.2	1.5 ± 0.4
4f	27.7 ± 2.9	52.3 ± 5.9	6.2 ± 1.3	3.4 ± 0.2	2.8 ± 0. 6	1.7 ± 0.5
5e	4.4 ± 0.2	4.4 ± 0.6	11.6 ± 1.4	9.4 ± 0.7	9.1 ± 2.0	10.7 ± 2.1

[a]Values are given as mean ± SD for each group of four animals and are as expressed as percent of the injected dose (%ID).

Table 5. Concentrations of the Radiotracers 2−4f and 5e in Blood, Kidney, Liver, and Brain of Male Wistar Rat at 5 and 60 min after the Injection[a]

	blood (mean ± SD)		kidney (mean ± SD)		liver (mean ± SD)		brain (mean ± SD)	
SUV	5 min	60 min	5 min	60 min	5 min	60 min	5 min	60 min
2f	1.82 ± 0.19	0.18 ± 0.04	36.58 ± 4.02	85.70 ± 6.2	2.13 ± 0.11	1.53 ± 0.15	0.06 ± 0.01	0.01 ± 0.00
3f	1.19 ± 0.12	0.15 ± 0.05	37.02 ± 3.95	70.39 ± 6.51	4.77 ± 0.52	5.31 ± 0.45	0.04 ± 0.00	0.01 ± 0.00
4f	1.30 ± 0.23	0.26 ± 0.09	30.93 ± 3.15	56.31 ± 7.99	1.36 ± 0.34	0.83 ± 0.12	0.05 ± 0.01	0.01 ± 0.00
5e	3.78 ± 0.43	1.53 ± 0.25	4.88 ± 0.48	5.09 ± 0.58	1.96 ± 0.33	1.75 ± 0.43	0.11 ± 0.02	0.05 ± 0.01

[a]Values are given as mean ± SD for each group of four animals and are as expressed in standard uptake value SUV = (activity.g^{-1} tissue)/(injected activity/body weight).

associated with ghrelin dysregulation like obesity, cachexia, or anorexia nervosa. The probes consist of a ghrelin agonist or inverse agonist peptides bound to the bifunctional chelator NODAGA and further labeled with the positron emitting radionuclide ^{68}Ga to allow in vivo imaging of the radiolabeled peptides. NODAGA is derived from the NOTA ring (1,4,7-triazacyclononane-1,4,7-triacetic acid), and the protected precursor NODAGA(tBu)$_3$ was suitable for solid-phase peptide synthesis. Peptide synthesis and coupling of NODAGA were straightforward, as they could both be achieved on solid support. Complexation of cold gallium for in vitro studies was easily achieved under mild conditions and supported the existing reports on NODAGA chemistry and stability.[17,18] Moreover, all [Ga]-NODAGA−peptide complexes were stable and could easily be purified.

Potency of the chelates was evaluated at the ghrelin receptor by an in vitro inositol phosphate turnover assay, and results were consistent with previous ghrelin SAR studies.[19] Tracers **1−4f** are agonists derived from the ghrelin motif. The agonist activity was maintained when the bifunctional chelator was introduced at position 16 of the ghrelin sequence (**2−4e**), whereas modification at the *N*-terminus was not tolerated (**1e**). Introduction of an amide bond instead of the native ester bond at position 3 (**3e**) or truncation of the *C*-terminal segment (17−28) (**4e**) were both tolerated and did not affect the agonist activity at the receptor. Compound **5e** is an inverse agonist tracer derived from the short inverse agonist KwFwLL-CONH$_2$, developed in our group.[20] Previous SAR showed that Lys^1 was essential for the inverse agonist activity of the hexapeptide. Hence, modification at Lys^1 side chain was excluded. Introduction of NODAGA was restricted to the peptide *N*-terminus and led to an important loss of activity compared with the native peptide (KwFwLL-CONH$_2$). Nevertheless, **5e** was included in the in vivo studies to gain information on the peptide pharmacokinetic and nonspecific biodistribution of the native peptide. Indeed, the development of an inverse agonist tracer could be very interesting for a dynamic receptor mapping, as inverse agonists are less likely to mediate receptor internalization and thus increase receptor concentration on membranes. Moreover, the hexapeptide is a current lead for development of antiobesity peptides, and in vivo data for **5e** could guide further SAR.

In vivo studies highlighted a very distinct behavior between agonists **2−4f** and the inverse agonist **5e**. Agonist tracers **2f**, **3f**, and **4f** were mainly found in the kidney, and the high increase in concentration reflected an accumulation in this organ over time. The renal metabolism and the hepatobiliary metabolism were also compared. Although the renal metabolism was predominant, accumulation in the kidney is a high bias to measure the renal elimination and longer biodistribution studies (i.e., with radionuclide having longer half-life) need to be performed to get an exact picture of metabolism pathways. However, agonists **2f** and **4f** presented a low hepatobiliary metabolism, whereas accumulation of **3f** could be observed in the liver. On the other hand, the inverse agonist **5e** was mainly excreted via the hepatobiliary system, and accumulation was visible neither in the kidney nor in the liver. In addition, very low doses of agonists **2−4f** were found in blood and in all other tissues, whereas inverse agonist **5e** presented a significant perfusion in all tissues, and especially a high concentration in blood even after 1 h.

Metabolic stability studies gave us extremely valuable insight for further development of radiotracers. Compounds **2−4f** all presented a fast blood clearance but showed differences in stability. The *N*-octanoylated ghrelin analogue **3f** appeared stable within 5 min after injection, but was degraded after 1 h. The *O*-octanoylated ghrelin tracer **2f** showed a spontaneous conversion into a main metabolite, detected before injection in a low proportion and increasing in blood over the time. This metabolite is probably the desoctanoylated form of tracer **2f** as desoctanoylation of ghrelin occurs very fast under physiological conditions. Interestingly, **4f** was completely metabolized after 5 min and a unique metabolite was found in blood and urine. **4f** is a *N*-octanoylated and C-terminally truncated ghrelin analogue. The *C*-terminal (17−28) segment, although not essential for ghrelin receptor recognition, appeared to stabilize

dx.doi.org/10.1021/bc2005889 | *Bioconjugate Chem.* 2012, 23, 771−784

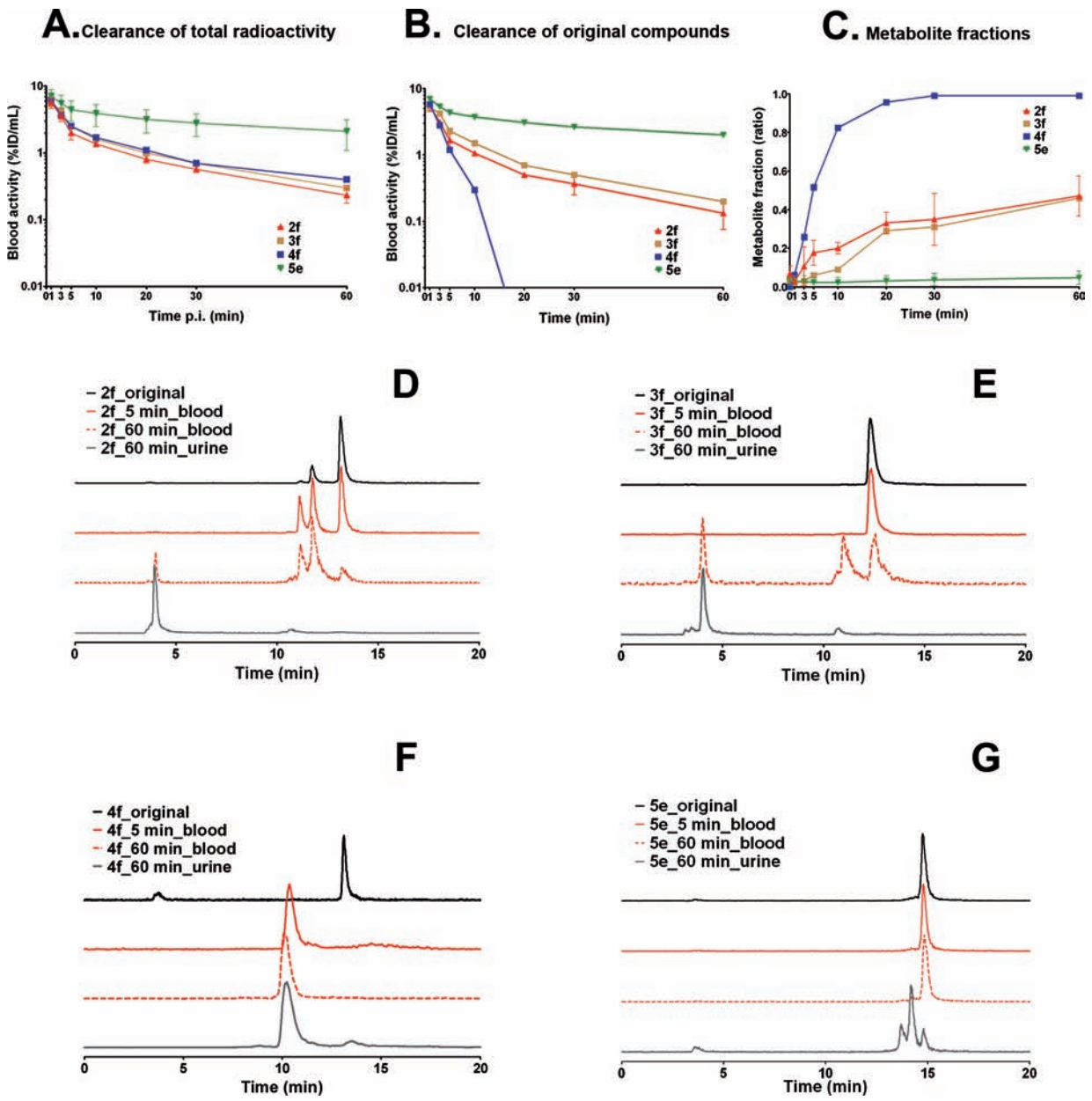

Figure 3. Blood clearance, metabolite fractions after injection of tracers **2**–**4f** and **5e** in rats and HPLC analysis. (A) Blood clearance was measured for the total radioactivity related to each tracer. (B) Blood clearance of original compounds and (C) metabolite fractions corresponding to each tracer were calculated according to HPLC analysis. (D) Chromatogram of tracer **2f**. (E) Chromatogram of tracer **3f**. (F) Chromatogram of tracer **4f**. (G) Chromatogram of tracer **5e**. For each chromatogram, pick intensities are normalized over the pick intensity of the major compound and the baselines are shifted to avoid overlapping.

the peptide sequence. Indeed, a recent study showed that *C*-terminal truncation of (8–28) and (21–28) segments dramatically decreased ghrelin half-life in rats.[21] It was also reported that ghrelin interaction with plasma lipoprotein via both its *N*- and *C*-terminus may confer protection against esterases.[22] Consequently, *C*-terminal truncation is not suitable for the development of stable ghrelin agonist motifs. On the other hand, **5e** exhibited a slow blood clearance and appeared impressively stable in blood and urine after 60 min. Indeed, the peptidomimetic structure of **5e** with two D-amino acids and an amidated *C*-terminus certainly protects the tracer from peptidases. Moreover, the peptide hydrophobicity, normally correlated with an elevated binding to plasma protein, can be the reason for a slow blood clearance.

The differences in peptide structures and metabolic stability can explain the divergence in biodistribution and metabolism. Indeed, peptides **2**–**4f** are hydrophilic biomolecules, structurally derived from the endogenous ghrelin. They present a molecular weight of, respectively, 3792, 3791, and 2431 Da and a high charge ratio. Thus, the three tracers **2**–**4f** present high renal elimination and poor tissue perfusion, characteristic for hydrophilic macromolecules. In addition, **3f** is more stable than **2f** and **4f** toward metabolism. This can explain the higher hepatobiliary elimination of the original compound **3f**, whereas renal elimination is favored for metabolites of **2f** and **4f**. It is important to mention that the renal accumulation of the tracers **2**–**4f** could also be attributed to the bifunctional chelator (BFC) increasing the charge ratio of the peptides. Indeed, renal

dx.doi.org/10.1021/bc2005889 | *Bioconjugate Chem.* 2012, 23, 771–784

accumulation of BFC-functionalized peptides has often been reported.[23] However, it cannot be considered an intrinsic property of the NOTA motif (1,4,7-triazacyclononane-1,4,7-triacetic acid),

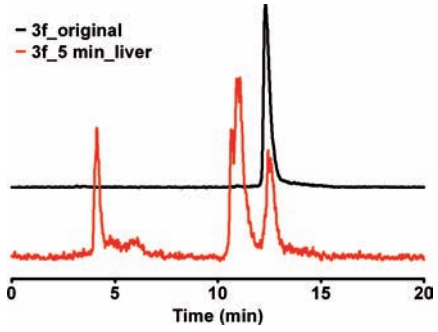

Figure 4. Radioactive metabolites in rat liver 5 min after injection of **3f**. For each chromatogram, pick intensities are normalized over the pick intensity of the major compound and the baseline are shifted to avoid overlapping.

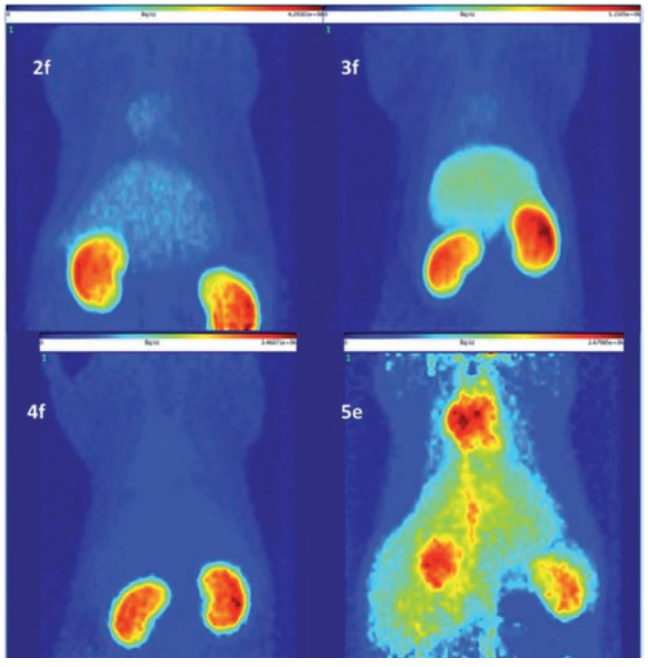

Figure 5. Maximum intensity projection of PET studies of Ga^{68} labeled compounds **2**–**4f** and **5e** at 5 min midframe time (duration of measurement 6 min). The images were scaled to the maximum activity ($Bq.cm^{-3}$) in each image.

as tracer **5e** in the present study and other NOTA or NODAGA based tracers in earlier reports did not display any renal accumulation.[18,24] Nevertheless, a high renal uptake can lead to renal toxicity, and is a serious drawback for PET imaging. Hence, other bifunctional chelator and different agonist moieties should be investigated in the future to overcome this issue.

On the other hand, the inverse agonist tracer **5e** is a short peptidomimetic (MW = 1315 Da). It presents hydrophobic properties that can directly be correlated with (a) a favored hepatobiliary elimination; (b) a high perfusion in tissues due to unspecific and passive membrane diffusion; and (c) a high concentration in blood due to a high affinity for plasma protein.

Importantly, none of the tracers were detected in the brain. The concentration gradient between the blood plasma and the brain tissue seems too small to transfer significant amounts of radiotracers through the blood-brain barrier (BBB) for all tracers **2**–**4f** and **5e**. As a consequence, we could not detect any active transport into the brain at the investigated tracer concentrations. However, ghrelin response is thought to be mediated via the arcuate nucleus of hypothalamus where ghrelin receptors are mainly expressed.[5,25,26] Interestingly, a previous study reported the accumulation in hypothalamus of a [^{11}C]quinazolinone ligand of the ghrelin receptor, at tracer concentration.[27] Low concentrations of the tracer could also be detected in the brain region with low ghrelin receptor density (cortex, cerebellum, and hippocampus). Therefore, in the current study, the lack of tracers **2**–**4f** in the brain may be due to their hydrophilic nature or an excessively high charge ratio. In addition, the higher hydrophobicity and lower charge ratio of **5e** made it more likely to cross the BBB although no trace of the tracer could be detected in the brain. Accordingly, the moderate in vitro activity of **5e** could limit the tracer detection in the brain if the uptake was specific. Importantly, as the NODAGA motif highly modifies the physicochemical properties of the compounds, no conclusion can be drawn concerning the blood-brain barrier passage of the native peptide KwFwLL-$CONH_2$. Therefore, extensive SAR should be conducted on **5e** to identify a radiotracer with higher binding affinity at the receptor.

To conclude, the in vitro and in vivo evaluation of four [^{68}Ga]Ga-NODAGA-peptide conjugates provides an interesting insight for the development of imaging probes and peptide-based therapeutics targeting the ghrelin receptor. On one hand, despite a very good affinity for the receptor, ghrelin derived agonists **2**–**4f** presented very high kidney accumulation, negligible tissue distribution, fast blood clearance, and poor stability in blood. Consequently, the ghrelin motif does not

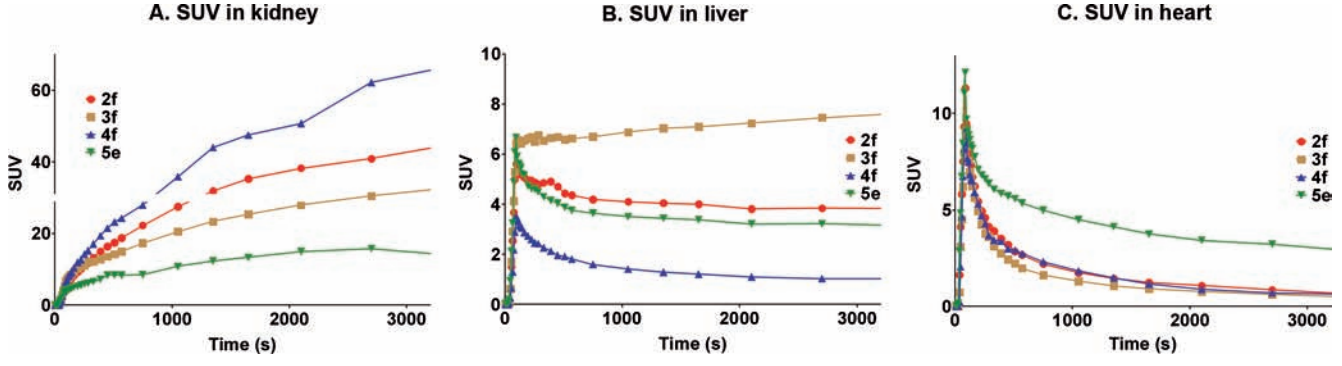

Figure 6. Time–activity curves of ^{68}Ga-labeled compounds **2f**–**4f** and **5e** for three regions of interest (ROI) in rats. (A) kidneys, (B) liver, and (C) heart. Values are given as mean ± SD for each group of four animals and are expressed in standard uptake values (SUV).

dx.doi.org/10.1021/bc2005889 | *Bioconjugate Chem.* 2012, 23, 771–784

appear suitable to develop radiotracer for imaging. Moreover, the ghrelin motif as such is not an appropriate lead for drug development. However, we demonstrated that structural modifications on the ghrelin sequence influence the peptide behavior in vivo. Indeed, the *N*-octanoylated ghrelin derivatives were more stable than the *O*-octanoylated ghrelin derivatives toward metabolism in blood, and the *C*-terminal (17−28) segment appeared essential for ghrelin metabolic stability.

On the other hand, tracer **5e** exhibited very high stability in blood, large diffusion in tissues, reasonable kidney and liver metabolism without accumulation, and slow blood clearance. Consequently, the unspecific diffusion of the inverse agonist limits its use as a radiotracer for understanding ghrelin receptor signaling. Nevertheless, the pharmacokinetic profile of **5e** is excellent for further development of druggable peptides targeting the ghrelin receptor. Hence, the ghrelin inverse agonist sequence KwFwLL-$CONH_2$ emerges as a promising lead to design peptide-based therapeutics against obesity.

AUTHOR INFORMATION

Corresponding Author

*Tel: +49 341 97 36904. Fax: +49 341 97 36909. E-mail: chollet@rz.uni-leipzig.de.

Notes

The authors declare no competing financial interest.

If not specified, amino acids are L and written in the standard one or three letter codes.

ACKNOWLEDGMENTS

This project was financially supported by the EU (Gastrointestinal Peptides in Obesity, GIPIO, Grant Agreement Number 223057) and the Alexander von Humboldt foundation. Regina Reppich-Sacher and Kristin Löbner are kindly acknowledged for technical assistance during the synthesis and in vitro experiments. The authors also thank Regina Herrlich, Andrea Suhr, Natalie Thieme, Mareike Barth, and Catharina Heinig for contributing to the in vivo experiments.

ABBREVIATIONS

BBB, blood-brain barrier; BFC, bifunctional chelator; Boc, *tert*-butyloxycarbonyl; Dde, 1-(4,4-dimethyl-2,6-dioxocyclohex-1-ylidene)ethyl; Dpr, diaminopropionic acid; Fmoc, 9-fluorenylmethyloxycarbonyl; Mtt, 4-methyltrityl; NODAGA(tBu)$_3$, 4-(4,7-bis(2-(tert-butoxy)-2-oxoethyl)-1,4,7-triazacyclononan-1-yl)-5-(*tert*-butoxy)-5-oxopentanoic acid; NOTA, 1,4,7-triazacyclononane-1,4,7-triacetic acid; Pbf, 2,2,4,6,7-pentamethyldihydrobenzofurane-5-sulfonyl; Pmc, 2,2,5,7,8-pentamethylchroman; SAR, structure−activity relashionship; tBu, *tert*-butyl; Trt, trityl

REFERENCES

(1) Nakazato, M., Murakami, N., Date, Y., Kojima, M., Matsuo, H., Kangawa, K., and Matsukura, S. (2001) A role for ghrelin in the central regulation of feeding. *Nature 409* (6817), 194−8.

(2) Cummings, D. E. (2006) Ghrelin and the short- and long-term regulation of appetite and body weight. *Physiol. Behav. 89* (1), 71−84.

(3) Howard, A. D., Feighner, S. D., Cully, D. F., Arena, J. P., Liberator, P. A., Rosenblum, C. I., Hamelin, M., Hreniuk, D. L., Palyha, O. C., Anderson, J., Paress, P. S., Diaz, C., Chou, M., Liu, K. K., McKee, K. K., Pong, S. S., Chaung, L. Y., Elbrecht, A., Dashkevicz, M., Heavens, R., Rigby, M., Sirinathsinghji, D. J., Dean, D. C., Melillo, D. G., Patchett, A. A., Nargund, R., Griffin, P. R., DeMartino, J. A., Gupta, S. K., Schaeffer, J. M., Smith, R. G., and Van der Ploeg, L. H. (1996) A receptor in pituitary and hypothalamus that functions in growth hormone release. *Science 273* (5277), 974−7.

(4) Kojima, M., Hosoda, H., Date, Y., Nakazato, M., Matsuo, H., and Kangawa, K. (1999) Ghrelin is a growth-hormone-releasing acylated peptide from stomach. *Nature 402* (6762), 656−60.

(5) Ferrini, F., Salio, C., Lossi, L., and Merighi, A. (2009) Ghrelin in central neurons. *Curr. Neuropharmacol. 7* (1), 37−49.

(6) Kojima, M., and Kangawa, K. (2005) Ghrelin: structure and function. *Physiol. Rev. 85* (2), 495−522.

(7) Gutierrez, J. A., Solenberg, P. J., Perkins, D. R., Willency, J. A., Knierman, M. D., Jin, Z., Witcher, D. R., Luo, S., Onyia, J. E., and Hale, J. E. (2008) Ghrelin octanoylation mediated by an orphan lipid transferase. *Proc. Natl. Acad. Sci. U. S. A. 105* (17), 6320−5.

(8) Yang, J., Brown, M. S., Liang, G., Grishin, N. V., and Goldstein, J. L. (2008) Identification of the acyltransferase that octanoylates ghrelin, an appetite-stimulating peptide hormone. *Cell 132* (3), 387−96.

(9) Cummings, D. E., Weigle, D. S., Frayo, R. S., Breen, P. A., Ma, M. K., Dellinger, E. P., and Purnell, J. Q. (2002) Plasma ghrelin levels after diet-induced weight loss or gastric bypass surgery. *N. Engl. J. Med. 346* (21), 1623−30.

(10) Holst, B., and Schwartz, T. W. (2006) Ghrelin receptor mutations--too little height and too much hunger. *J. Clin. Invest. 116* (3), 637−41.

(11) Leite-Moreira, A. F., and Soares, J. B. (2007) Physiological, pathological and potential therapeutic roles of ghrelin. *Drug Discovery Today 12* (7−8), 276−88.

(12) Chollet, C., Meyer, K., and Beck-Sickinger, A. G. (2009) Ghrelin--a novel generation of anti-obesity drug: design, pharmacomodulation and biological activity of ghrelin analogues. *J. Pept. Sci. 15* (11), 711−30.

(13) Depoortere, I. (2009) Targeting the ghrelin receptor to regulate food intake. *Regul. Pept. 156* (1−3), 13−23.

(14) Els, S., Beck-Sickinger, A. G., and Chollet, C. (2010) Ghrelin receptor: high constitutive activity and methods for developing inverse agonists. *Methods Enzymol. 485*, 103−21.

(15) Eisenwiener, K. P., Prata, M. I., Buschmann, I., Zhang, H. W., Santos, A. C., Wenger, S., Reubi, J. C., and Macke, H. R. (2002) NODAGATOC, a new chelator-coupled somatostatin analogue labeled with [67/68Ga] and [111In] for SPECT, PET, and targeted therapeutic applications of somatostatin receptor (hsst2) expressing tumors. *Bioconjugate Chem. 13* (3), 530−41.

(16) Velikyan, I., Maecke, H., and Langstrom, B. (2008) Convenient preparation of 68Ga-based PET-radiopharmaceuticals at room temperature. *Bioconjugate Chem. 19* (2), 569−73.

(17) de Sa, A., Matias, A. A., Prata, M. I., Geraldes, C. F., Ferreira, P. M., and Andre, J. P. (2010) Gallium labeled NOTA-based conjugates for peptide receptor-mediated medical imaging. *Bioorg. Med. Chem. Lett. 20* (24), 7345−8.

(18) Knetsch, P. A., Petrik, M., Griessinger, C. M., Rangger, C., Fani, M., Kesenheimer, C., von Guggenberg, E., Pichler, B. J., Virgolini, I., Decristoforo, C., and Haubner, R. (2011) [(68)Ga]NODAGA-RGD for imaging alpha(v)beta (3) integrin expression. *Eur. J. Nucl. Med. Mol. Imaging 38* (7), 1303−12.

(19) Bednarek, M. A., Feighner, S. D., Pong, S. S., McKee, K. K., Hreniuk, D. L., Silva, M. V., Warren, V. A., Howard, A. D., Van Der Ploeg, L. H., and Heck, J. V. (2000) Structure-function studies on the new growth hormone-releasing peptide, ghrelin: minimal sequence of ghrelin necessary for activation of growth hormone secretagogue receptor 1a. *J. Med. Chem. 43* (23), 4370−6.

(20) Holst, B., Lang, M., Brandt, E., Bach, A., Howard, A., Frimurer, T. M., Beck-Sickinger, A., and Schwartz, T. W. (2006) Ghrelin receptor inverse agonists: identification of an active peptide core and its interaction epitopes on the receptor. *Mol. Pharmacol. 70* (3), 936−46.

(21) Morozumi, N., Hanada, T., Habara, H., Yamaki, A., Furuya, M., Nakatsuka, T., Inomata, N., Minamitake, Y., Ohsuye, K., and Kangawa, K. (2011) The role of C-terminal part of ghrelin in pharmacokinetic profile and biological activity in rats. *Peptides 32* (5), 1001−7.

(22) De Vriese, C., Hacquebard, M., Gregoire, F., Carpentier, Y., and Delporte, C. (2007) Ghrelin interacts with human plasma lipoproteins. *Endocrinology 148* (5), 2355−62.
(23) Tornesello, A. L., Aurilio, M., Accardo, A., Tarallo, L., Barbieri, A., Arra, C., Tesauro, D., Morelli, G., and Aloj, L. (2011) Gastrin and cholecystokinin peptide-based radiopharmaceuticals: an in vivo and in vitro comparison. *J. Pept. Sci. 17* (5), 405−12.
(24) Fani, M., Del Pozzo, L., Abiraj, K., Mansi, R., Tamma, M. L., Cescato, R., Waser, B., Weber, W. A., Reubi, J. C., and Maecke, H. R. (2011) PET of Somatostatin Receptor-Positive Tumors Using 64Cu- and 68Ga-Somatostatin Antagonists: The Chelate Makes the Difference. *J. Nucl. Med. 52* (7), 1110−8.
(25) Gnanapavan, S., Kola, B., Bustin, S. A., Morris, D. G., McGee, P., Fairclough, P., Bhattacharya, S., Carpenter, R., Grossman, A. B., and Korbonits, M. (2002) The tissue distribution of the mRNA of ghrelin and subtypes of its receptor, GHS-R, in humans. *J. Clin. Endocrinol. Metab.* No. 6, 2988.
(26) Zigman, J. M., Jones, J. E., Lee, C. E., Saper, C. B., and Elmquist, J. K. (2006) Expression of ghrelin receptor mRNA in the rat and the mouse brain. *J. Comp. Neurol. 494* (3), 528−48.
(27) Potter, R., Horti, A. G., Ravert, H. T., Holt, D. P., Finley, P., Scheffel, U., Dannals, R. F., and Wahl, R. L. (2011) Synthesis and in vivo evaluation of (S)-6-(4-fluorophenoxy)-3-((1-[11C]methylpiperidin-3-yl)-methyl)-2-o-tolylquinazolin-4(3H)-one, a potential PET tracer for growth hormone secretagogue receptor (GHSR). *Bioorg. Med. Chem. 19* (7), 2368−72.

Bioconjugate Chemistry

Article

pubs.acs.org/bc

Design, Synthesis, and Initial Biological Evaluation of a Steroidal Anti-Estrogen–Doxorubicin Bioconjugate for Targeting Estrogen Receptor-Positive Breast Cancer Cells

Kinh-Luan Dao,[†] Rupa R. Sawant,[‡] J. Adam Hendricks, Victoria Ronga,[†] Vladimir P. Torchilin,[‡] and Robert N. Hanson*[,†]

[†]Department of Chemistry and Chemical Biology [‡]Center for Pharmaceutical Biotechnology and Nanomedicine 360 Huntington Avenue, Northeastern University, Boston, Massachusetts 02115-5000, United States

Supporting Information

ABSTRACT: As part of our program to develop breast cancer specific therapeutic agents, we have synthesized a conjugate agent that is a conjugate of the steroidal anti-estrogen and the potent cytotoxin doxorubicin. In this effort, we employed a modular assembly approach to prepare a novel 11β-substituted steroidal anti-estrogen functionalized with an azido-tetraethylene glycol moiety, which could be coupled to a complementary doxorubicin benzoyl hydrazone functionalized with a propargyl tetraethylene glycol moiety. Huisgen [3 + 2] cycloaddition chemistry gave the final hybrid that was evaluated for selective uptake and cytotoxicity in ER(+)-MCF-7 and ER(−)-MDA-MB-231 breast cancer cell lines. The results demonstrated that the presence of the anti-estrogenic component in the hybrid compound was critical for selectivity and cytotoxicity in ER(+)-MCF-7 human breast cancer cells as the hybrid was ~70-fold more potent than doxorubicin in inhibition of cell proliferation and promoting cell death.

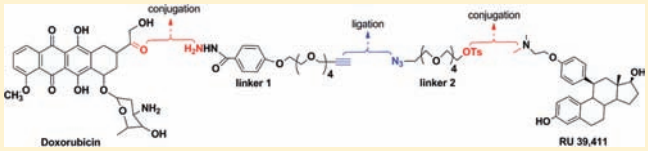

INTRODUCTION

Breast cancer is the most common cancer diagnosis among women, with the majority of cases linked with the hormone-responsive form of the disease.[1] Because of the well-established association of estradiol with estrogen receptors (ER), endocrine therapy using anti-estrogens, such as tamoxifen (TAM) and Faslodex, is the typical regimen for the treatment of hormone-responsive breast cancer.[2−5] Unfortunately, prolonged treatment of breast cancer patients with anti-estrogens frequently leads within 2−5 years to the emergence of recurrent disease that no longer responds to endocrine therapy. More aggressive and nonselective interventions are required that produce significant side-effects and morbidity to the patient population. Therefore, there is a continued need to develop therapeutic agents that are more effective from the very beginning and/or that do not develop resistance.

One approach to develop such agents involves combining two drugs into a single entity as a conjugate that can interact with two relevant components of the disease process. The general criteria and challenges associated with such an approach have been the subject of several reviews.[6−12] In addition to fundamental concerns related to choice of targeting strategies (e.g., receptor vs antibody), of single target versus independent/related targets, and of pathway interactions between the biological targets, one also needs to address the issues related to the chemical synthesis of such an agent. In particular, the two components need to be joined in a fashion that does not compromise the activity of either, and ultimately, the synthetic approach needs to be sufficiently robust to tolerate structural variants that would enhance or optimize the activity of the product.

In the field of hormone-responsive breast cancer, this approach typically involved linking a potent estrogen receptor targeting agent to a second component, such as an antimetabolite, intercalating agent, antimitotic, alkylating agent, or metal chelating group.[13−28] In the case of estrogen receptor-targeted hybrids, these efforts have been almost invariably unsuccessful. To a significant extent, the lack of success can be traced to an over-reliance on chemical transformations of readily available estrogens or easily modified sites on those estrogens to prepare the target compounds. While the attachment of functional groups at the 17β-,17α-, 16α-, and 7α-positions of estradiol (Figure 1) is readily achieved through simple transformations of estradiol or its derivatives, the analysis of the crystal structures of agonist and antagonist−estrogen receptor−ligand binding domain (ER-LBD) complexes suggests that such modifications seriously impair receptor binding.[29] Several examples of recent 17β-, 17α-, and 16α -substituted estradiol hybrids with specific therapeutic R groups have shown low ER binding affinity.[30−35] While the introduction of substituents at the 7α-position of estradiol (such as those found in the anti-estrogen Faslodex) is synthetically more challenging, the resultant products retain significant ER binding capacity and modest ER-based

Received: December 2, 2011
Revised: February 15, 2012
Published: March 11, 2012

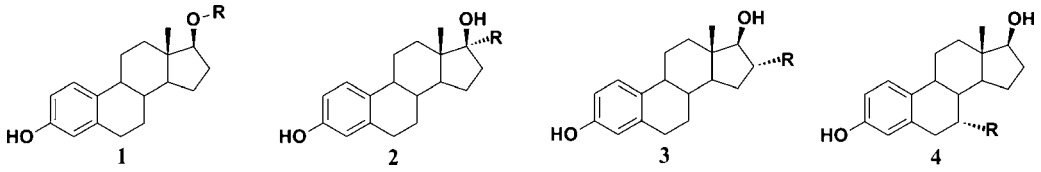

Figure 1. (**1**) 17-β substituted estradiol;[28] (**2**) 17-α substituted estradiol;[27,31−33] (**3**) 16-α substituted estradiol;[30,34,35] and (**4**) 7-α substituted estradiol.[36−40]

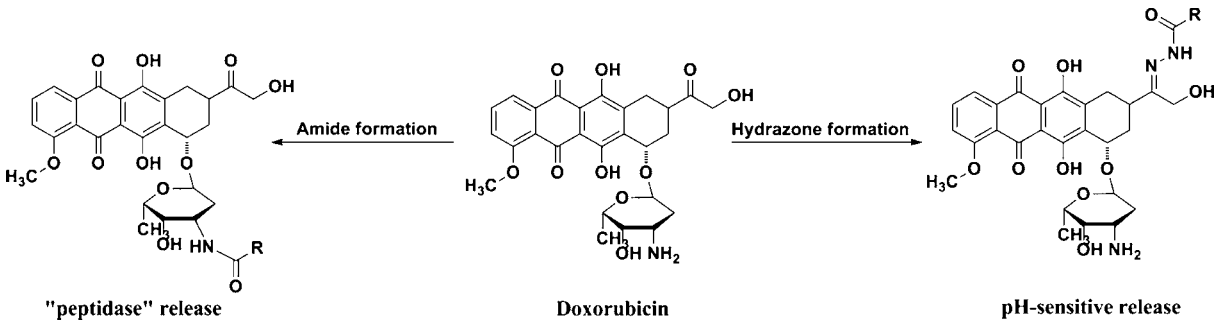

Figure 2. Prodrug approaches in the development of doxorubicin conjugates.

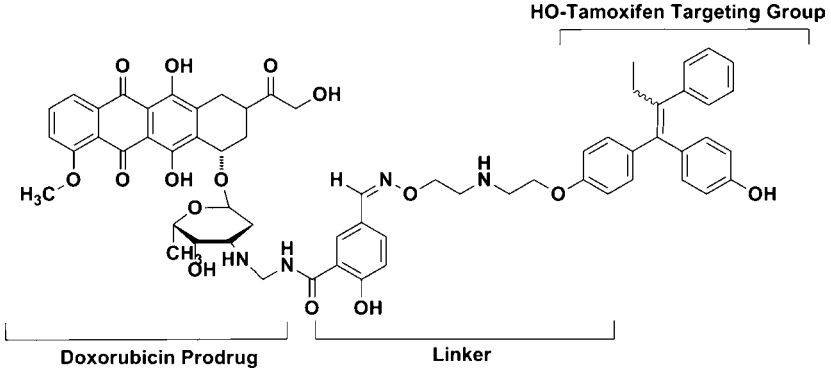

Figure 3. Tamoxifen−doxorubicin conjugate.[50,51]

selectivity.[36−40] X-ray crystal structures of complexes of similarly 7α-substituted ligands with ERα-LBD indicated that the steroidal scaffold was rotated around the 3−17 axis, and there was a disorder associated with helix-12, suggesting that the significant steric interactions were involved.[41]

The second component of the bioconjugate involves the therapeutic agent. To address the need for more effective drugs for estrogen-responsive breast cancer, we have chosen the clinically effective anthracycline doxorubicin. While highly effective as a cytotoxic agent, its use is compromised by dose-limiting cardiotoxic side effects.[42−44] Strategies to improve its clinical utility have focused on pro-drug approaches to reduce side effects and on targeted drug delivery to improve its efficacy. Some of the most promising doxorubicin derivatives involve hydrazone formation through the ketone or amide conjugation on the carbohydrate amino-group (Figure 2).[42,45,46] In both approaches, intracellular processes, such as pH-dependent hydrolysis or enzymatic cleavage of the amide bond lead to free doxorubicin that generates the observed therapeutic response. While such conjugation strategies may reduce cardiotoxic effects, selective or enhanced delivery of the agent to the tumor is not improved.[42]

Enhanced tumor delivery of doxorubicin requires the incorporation of an appropriate targeting agent. Several examples of doxorubicin derivatives bearing tumor-selective groups, including breast cancer selective agents, have been described.[47−49] For example, a nonsteroidal anti-estrogen, such as tamoxifen (Figure 3), has been used to target doxorubicin to ER(+)-breast cancer; however, it is associated with significant problems. The parent compound, tamoxifen, has low ER affinity and exhibits substantial non-ER binding capacity. Although the hydroxylated metabolite, 4-hydroxytamoxifen, has higher ER affinity, this compound exists as a mixture of *E*/*Z*-isomers and is chemically less stable.[5,50] Nevertheless, preliminary studies suggested that an enhanced and selective cytotoxicity in breast cancer cells may be achieved using a better targeting group. The conjugation of amino-sugar component doxorubicin to the amino terminus of hydroxyl tamoxifen using a releasable linker led to an increase of potency (antiproliferative activity) in a variety of breast cancer cell lines. The investigators suggested that the targeting in this case was due to a combination of ER and anti-estrogen binding site (AEBS) effects.[47,48]

Much of the (anti-)estrogen−doxorubicin conjugate research has focused on the targeting and therapeutic groups; however, the linking moiety is also important. For the hybrid to be effective *in vitro* or *in vivo*, the linker must be long enough to permit the ER-binding component to interact with the target protein while maintaining a stable bond with the doxorubicin. Likewise, the interaction with doxorubicin must be stable in the

dx.doi.org/10.1021/bc200645n | *Bioconjugate Chem.* 2012, 23, 785−795

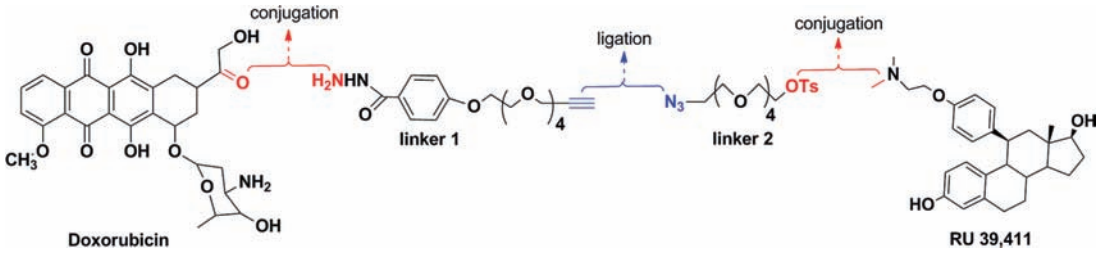

Figure 4. Strategy for conjugate AE-Dox synthesis.

Scheme 1. Synthesis of Anti-Estrogen–Doxorubicin (AE-Dox) Conjugate 15

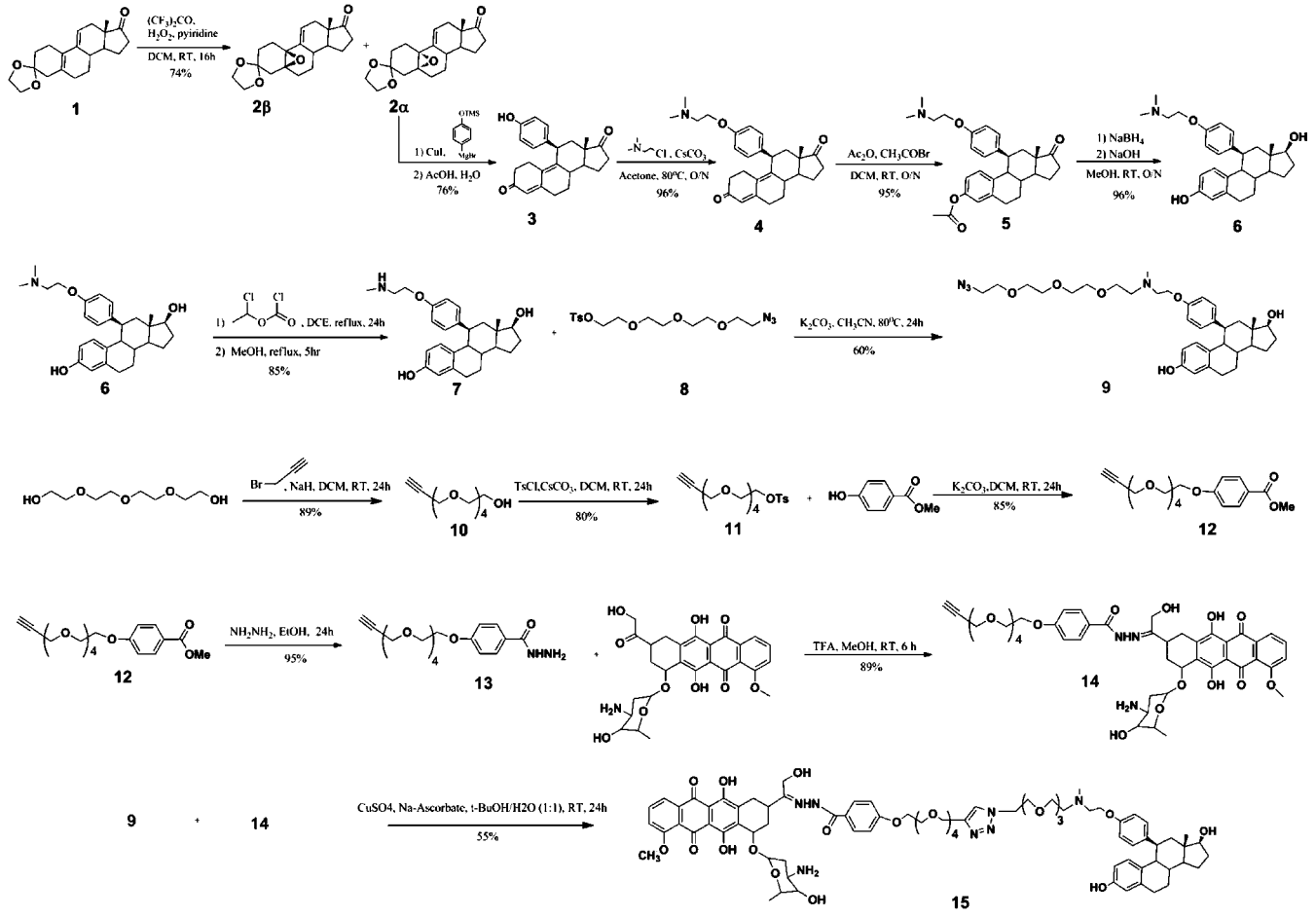

extracellular environment while permitting facile dissociation within the target breast cancer cells. The linker also needs to have physicochemical properties that do not compromise its formulation or biological compatibility. Therefore, our strategy in this study considered all three components of hybrid drug design—the estrogen targeting component, the doxorubicin drug delivery component, and the linker component—that would tether the targeting, readily release mechanism, and chemotherapeutic units.

In our design of the anti-estrogen–doxorubicin conjugate, we have used a strategy involving modular assembly, i.e., each component can be developed independently and ultimately incorporated in a modular fashion. We selected an analogue of steroidal anti-estrogen similar to RU39411, as our targeting component. Not only is the parent compound a pure antagonist, it possesses significantly higher ER binding affinity compared to most nonsteroidal anti-estrogens such as tamoxifen and raloxifene, and it is less lipophilic.[51,52] The elimination of the triarylethylene pharmacophore would also reduce interactions with the anti-estrogen binding sites not associated with the estrogen receptor. The analysis of its binding in comparison to tamoxifen-ERα-LBD complexes suggested that the ligation of linker groups via the tertiary amine should retain ER affinity, as the linker would be external to the ligand-binding pocket. The modified anti-estrogen **9** is chemically accessible via the multistep synthesis from the steroidal intermediate deltenone (as shown in the Experimental section), a process with which we have significant experience.[53−56] The preparation of doxorubicin hydrazones is well-described as is their intracellular release under acidic conditions;[45,46,57−62] however, we needed to develop a specific linker derivative to form the desired hydrazone. A key aspect of our approach involves the use of half-linkers that would be ligated in the final step to form the final conjugate. Each part

dx.doi.org/10.1021/bc200645n | *Bioconjugate Chem.* 2012, 23, 785–795

would consist of a heterobifunctional tetraethylene glycol, in which one functional group consists of a "click" partner and the other functionality would interact with the targeting (anti-estrogen) or chemotherapeutic (doxorubicin) moiety. Our ultimate approach is shown in Figure 4, in which we take each component, attach it to the appropriate half-linker, and finally ligate them to form the intact bioconjugate. We hypothesize that the resultant bioconjugate should retain antiproliferative effects comparable to doxorubicin in all cancer cell lines, but demonstrate selective antiproliferative effects in membrane ER-expressing cancer cells. We suggest that endosomal uptake of our AE-Dox hybrid is selectively mediated through membrane ER.[63] Once within the acidic cytoplasm compartment, hydrolysis of the hydrazone-Dox linkage releases the free doxorubicin to generate the antiproliferative response. As our results illustrate, the final compound achieves these target properties and demonstrates selectivity toward ER(+)-breast cancer cells and promotes enhanced cytotoxicity against those cells compared to the unmodified parent components.

EXPERIMENTAL SECTION

General Methods. All solvents and reagents involved in the synthesis were reagent grade, purchased from either Sigma-Aldrich or Fisher Scientific, and used without further purification. Thin-layer chromatography (TLC) was done on polyester sheets precoated with silica gel matrix 60 F254 obtained from Sigma-Aldrich. Separations were performed using automated flash chromatography (Argonaut FlaskMaster) or packed column chromatography with Sorbent Technologies silica gel particle size 32−63 μm and 60 Å pore size. Liquid chromatography−mass spectroscopy (LC-MS) was performed using Alliance HT -LCT Premier 2489, Waters instrument equipped with time-of-flight (TOF) MS module. High-performance liquid chromatography (HPLC) trace analysis was performed using a Waters HPLC system, equipped with a Waters 2695 binary pump, a Waters 2998 fluorescence photodiode array detector, and an XBridge C18 column (3.5 μm, 4.6 × 75 mm). ^{1}H and ^{13}C NMR spectra were recorded on 400 or 500 MHz Varian FT-NMR spectrometers. Chemical shifts (δ) are reported in parts per million (ppm) by reference to proton resonances resulting from incomplete deuteration of the NMR solvent. The concentrations of test compounds were determined spectrophotometrically with a diode array UV mini 1240, Shimadzu spectrophotometer. Ultracentrifugation of cell lysates was accomplished with Sorvall RT 6000B Refrigerated Centrifuge. All tissue culture materials were obtained from Gibco Life Technologies (Grand Island, NY) unless otherwise stated. MCF-7 and MDA-MB-231 cells were obtained from American Type Culture Collection (Rockville, MD).

Synthesis. *3,3-Ethylenedioxy-5(10)-α-epoxy-ester-9(11)-ene* ***2α***. To a solution of estra-5(10),9(11)-diene-3,17-dione 3-ethylenedioxy ketal **1** (10.0 g, 31.8 mmol), hexafluoroacetone (0.46 mL, 3.6 mmol), and pyridine (0.23 mL, 2.86 mmol) in 10 mL of dichloromethane was added hydrogen peroxide (50%, 2.28 mL, 74 mmol) at 0 °C. After 18 h stirring at ambient temperature, the reaction was terminated by the addition of 4 g of sodium thiosulfate in 100 mL of water and extracted with dichloromethane (3 × 100 mL). The organic layer was dried over magnesium sulfate, filtered, and the solvent removed under reduced pressure. The resulting colorless solid was triturated with diethyl ether (35 mL). The precipitate was collected by filtration and rinsed with diethyl ether (25 mL) to yield 5.23 g (15.8 mmol) 49.8% of the **2α**-isomer. The mother liquor was purified via flash chromatography to afford 2.0 g (5.8 mmol, 18.2%) of the β-isomer, and an additional 600 mg (1.8 mmol, 5.7%) of **2α**-isomer. Overall 3,3-ethylenedioxy-5(10)-α-epoxy-estr-9(11)-ene-17-one (5.8 g, 17.5 mmol, 56% yield) and 3,3-ethylenedioxy-5(10)-β-epoxy-estr-9(11)-ene-17-one (2.0 g, 5.8 mmol, 18% yield) were obtained in a final ratio of 3:1 in favor of the α-isomer and a total yield of 74%. For **2α**-isomer: ^{1}H NMR ($CDCl_3$, 400 MHz): δ 0.88 (3H, s), 1.32−1.12 (1H, s), 2.52−2.44 (2H, m), 3.98−3.88 (4H, m), 6.06 (1H, s). ^{13}C NMR ($CDCl_3$, 100 MHz): δ 14.89, 22.05, 22.33, 25.23, 28.19, 31.73, 33.76, 36.05, 37.23, 40.40, 46.13, 46.81, 60.18, 61.73, 64.24, 64.45, 107.04, 125.80, 136.81, 221.37; mp 154 °C. For **β**-isomer: ^{1}H NMR (400 MHz, $CHCl_3$): δ 0.87 (s, 3H), 1.32−1.12 (m, 1H), 2.52−2.44 (m, 2H), 3.98−3.88 (m, 4H), 5.87(s, 1H); $C_{20}H_{26}O_4$, TOF-MS: m/z 330.18 (calcd); 353.42 $[M+Na]^+$ (found).

11β-(4-Hydroxy-phenyl)-estra-4,9-diene-3,17-dione ***3***. 3,3-Ethylenedioxy-5(10)-α-epoxy-estr-9-ene-17-one **2α** (2.014 g, 6.1 mmol) was dissolved in anhydrous THF (15 mL) under an argon atmosphere. Copper(I) iodide (0.160 g, 0.840 mmol) was added to the solution at −10 °C and stirred for 15 min. Freshly prepared Grignard reagent, (4-((trimethylsilyl)oxy)-phenyl)magnesium bromide, was added dropwise in 5.0 mL aliquots. The reaction was gradually warmed to ambient temperature, and stirring was continued for 16 h. The reaction was quenched by the addition of ammonium chloride (0.8 g, 15 mmol) in 35 mL of water and 35 mL of EtOAc at 10 °C. The organic layer was washed with water (2 × 35 mL). The organic solvent was removed under reduced pressure, and the resulting residue was dissolved in a mixture of acetic acid (14 mL) and water (6 mL). The resultant mixture was warmed at 50−60 °C for 1.5 h, after which it was diluted with ethyl acetate (20 mL). The solution was neutralized by the addition of saturated aqueous sodium bicarbonate. The organic layer was separated, washed with brine solution, dried over magnesium sulfate, and evaporated to dryness to give a crude, yellow oil. Purification using silica gel column chromatography (70:30 hexane/ethyl acetate) afforded the product **3** (2.00 g, 76%) as a yellow solid: ^{1}H NMR ($CDCl_3$, 400 MHz): δ 0.53 (3H, s), 4.38 (1H, d, J = 6.9), 5.78 (1H, s), 6.71 (2H, d), 6.97 (2H, d). ^{13}C NMR ($CDCl_3$, 100 MHz): δ 14.17, 21.76, 25.99, 27.06, 30.68, 35.02, 36.87, 38.14, 38.34, 39.71, 47.53, 50.77, 115.53, 122.82, 128.30, 129.83, 135.52, 145.62, 155.59, 155.99, 197.54, 217.44; $C_{24}H_{26}O_3$, TOF-MS: m/z 363.19 (calcd); 384.99 $[M+Na]^+$ (found); m.p. 248 °C.

11β-[4-(2-Dimethylamino-ethoxy)-phenyl]-estra-4,9-diene-3,17-dione ***4***. To a solution of **3** (250 mg, 0.69 mmol) and cesium carbonate (1.1 g, 3.45 mmol) in 10 mL acetone was added 2-*N*,*N*-dimethyl chloroethyl amine hydrochloride (223 mg, 2.07 mmol). The reaction mixture was heated at reflux for 16 h. The solvent was removed under reduced pressure, and the residue was extracted with ethyl acetate. The organic layer was washed with water, brine solution, dried over magnesium sulfate, and evaporated under reduced pressure to give a crude oil. Purification using flash chromatography yielded the product **4** (287 mg, 96%) as light yellow oil. ^{1}H NMR ($CDCl_3$, 400 MHz): δ 0.56 (3H, s), 1.22−1.41 (2H, m), 1.48−1.72 (2H, m), 1.91 (2H, dd, J = 13.92, 6.60 Hz), 1.99−2.23 (6H, m), 2.28−2.52 (6H, m), 2.59−2.67 (2H, m), 2.67−2.89 (2H, m), 4.03 (1H, t, J = 5.86 Hz), 4.38 (2H, d, J = 7.33 Hz), 5.79 (1H, s), 6.84 (2H, d, J = 8.79 Hz), 7.08 (2H, d, J = 8.06 Hz). ^{13}C NMR ($CDCl_3$, 100 MHz): δ 15.6, 22.1, 26.1, 27.0, 29.6, 31.1, 32.0, 35.6, 37.0, 38.0, 39.8, 46.1, 47.9, 50.9, 54.0, 58.5, 66.1, 114.9,

dx.doi.org/10.1021/bc200645n | Bioconjugate Chem. 2012, 23, 785−795

123.6, 127.9, 128.0, 128.2, 130.2, 136.1, 145.2, 156.2, 157.2, 199.6; $C_{28}H_{35}NO_3$, TOF-MS: *m/z* 433.26 (calcd); 457.99 [M +Na]+ (found).

3-Acetoxy-11β-[4-(2-dimethylamino-ethoxy)-phenyl]-estra-1,3,5(10)-triene-17-one ***5***. To a solution of **4** (200 mg, 0.42 mmol) in dichloromethane (10 mL) was added acetic anhydride (47 mg, 0.46 mmol) and acetyl bromide (142 mg, 1.15 mmol) at room temperature. The reaction solution was stirred for 16 h, after which the product was extracted with ethyl acetate and washed with water. The organic layer was separated, dried over magnesium sulfate, and evaporated under reduced pressure to give a yellow crude oil. Column chromatography afforded the desired product **5** (207 mg, 95%). ^{1}H NMR ($CDCl_3$, 400 MHz): δ 0.45 (3H, s), 1.25 (2H, s), 1.47−1.73 (2H, m), 1.84−2.02 (2H, m), 2.03−2.20 (6H, m), 2.22−2.29 (6H, m), 2.35 (3H, d, *J* = 10.26 Hz), 2.41−2.64 (2H, m), 2.87−3.03 (2H, m), 3.07 (1H, br. s.), 4.00−4.22 (2H, m), 6.59−6.76 (3H, m), 6.86 (1H, d, *J* = 2.20 Hz), 6.96 (2H, d, *J* = 8.79 Hz). ^{13}C NMR ($CDCl_3$, 100 MHz): δ 15.4, 21.6, 22.3, 23.1, 27.3, 30.2, 35.1, 35.5, 38.3, 40.2, 44.8, 47.8, 48.3, 48.4, 52.4, 57.4, 64.7, 64.9, 114.0, 119.4, 121.9, 128.6, 130.9, 135.6, 135.7, 137.7, 148.3, 155.7, 169.9, 176.1; $C_{30}H_{37}NO_4$, TOF-MS: *m/z* 475.27 (calcd); 498.26 $[M+Na]^+$ (found).

11β-[4-(2-Dimethylamino-ethoxy)-phenyl]-estra-1,3,5(10)-triene-3,17β-diol ***6***. To a solution of **5** (200 mg, 0.42 mmol) in methanol (5 mL) was added sodium borohydride (24 mg, 0.63 mmol) and the reaction mixture was stirred at room temperature. After 1 h, 10 N sodium hydroxide (0.025 mL, 0.25 mmol) was added and the reaction continued for 16 h. The reaction solution was poured into an ice-cold mixture of ethyl acetate (20 mL) and water (20 mL), after which the organic layer was separated, washed sequentially with water and brine, and dried over magnesium sulfate. The solvent was removed under reduced pressure to give a yellow crude oil. Silica column chromatography afforded the product **6** (176 mg, 96%). ^{1}H NMR ($CDCl_3$, 400 MHz): δ 0.36 (3H, s), 1.17−1.29 (2H, m), 1.29−1.44 (2H, m), 1.70 (2H, d, *J* = 8.79 Hz), 1.78 (2H, dd, *J* = 13.18, 5.86 Hz), 1.86−1.99 (2H, m), 2.03−2.14 (2H, m), 2.27−2.38 (6H, m), 2.51 (3H, d, *J* = 12.21 Hz), 2.61−2.67 (2H, m), 2.69−2.85 (2H, m), 3.68 (1H, t, *J* = 8.06 Hz), 3.89−4.04 (2H, m), 6.37 (1H, dd, *J* = 8.30, 2.44 Hz), 6.44−6.58 (3H, m), 6.76 (1H, d, *J* = 8.79 Hz), 6.95 (2H, d, *J* = 8.30 Hz). ^{13}C NMR ($CDCl_3$, 100 MHz): δ 15.4, 21.6, 22.3, 23.1, 27.3, 30.2, 35.1, 35.5, 38.3, 40.2, 44.8, 47.8, 48.3, 48.4, 52.4, 57.4, 64.7, 64.9, 82.5, 114.0, 116.4, 128.6, 130.4, 131.6, 138.2, 139.1, 158.6, 155.7; $C_{28}H_{37}NO_3$, TOF-MS: *m/z* 435.26 (calcd); 437.99 $[M+Na]^+$ (found).

11β-[4-(2-methylamino-ethoxy)-phenyl]-estra-1,3,5(10)-triene-3,17β-diol ***7***. To a solution of **6** (100 mg, 0.23 mmol) in anhydrous dichloromethane (10 mL) was added α-chloroethyl chloroformate (53 μL, 0.48 mmol). The reaction mixture was stirred at 0 °C for 30 min, and then heated at reflux for 24 h. The solvent was removed by rotary evaporation, methanol (3 mL) was added, and the reaction solution was heated at reflux for 3 h. The solvent was removed by rotary evaporation to give the crude product as clear oil. Purification using silica gel chromatography gave the product **7** (82 mg, 85%) as yellow oil. ^{1}H NMR ($CDCl_3$, 400 MHz) δ 0.34 (3H, s), 1.20−1.45 (2H, m), 1.63−1.87 (2H, m), 1.90−2.18 (2H, m), 2.32 (1H, s), 2.51 (4H, m), 2.72−2.97 (4H, m), 3.69 (1H, t, *J* = 8.43 Hz), 3.88−4.03 (2H, m), 6.39 (1H, dd, *J* = 8.43, 2.56 Hz), 6.47−6.61 (3H, m), 6.79 (1H, d, *J* = 8.06 Hz), 6.97 (2H, d, *J* = 8.06 Hz). ^{13}C NMR ($CDCl_3$, 100 MHz): δ 15.4, 21.6, 22.3, 23.1, 27.3, 30.2, 35.5, 38.3, 40.2, 44.8, 47.8, 48.3, 48.4, 52.4, 57.4, 64.7, 64.9, 82.5, 114.0, 116.4, 128.6, 130.4, 131.6, 138.2, 139.1, 158.6, 155.7; $C_{27}H_{35}NO_3$, TOF-MS: *m/z* 422.26 (calcd); 443.99 $[M+Na]^+$ (found).

2-{2-[2-(2-Azido-ethoxy)-ethoxy]-ethoxy}-ethyl Tosylate ***8***. To a solution of tetraethylene glycol di-*para*-toluene sulfonate (2 g, 4 mmol) in ethanol (25 mL) was added sodium azide (0.28 g, 4.3 mmol). The resulting solution was heated at 80 °C overnight. The reaction mixture was poured into ice water (125 mL), and the product was extracted with ethyl acetate. The combined organic extracts were washed sequentially with water and brine solution, and dried over magnesium sulfate. The crude material was purified using silica gel chromatography to yield the product as clear oil **8** (1.2 g, 79%). ^{1}H NMR ($CDCl_3$, 400 MHz): δ 1.21 (2H, td, *J* = 6.96, 2.93 Hz), 2.45 (3H, s), 3.40 (2H, m), 3.52−3.75 (10H, m), 3.93 (2H, m), 7.37 (2H, d), 7.79 (2H, d); $C_{15}H_{23}N_3O_7S$, TOF-MS: *m/z* 389.42 (calcd); 412.56 $[M+Na]^+$ (found).

11β-(4-{2-[(2-{2-[2-(2-Azido-ethoxy)-ethoxy]-ethoxy}-ethyl)-methyl-amino]-ethoxy}-phenyl)-estra-1,3,5(10)-triene-3,17β-diol ***9***. To a solution of **7** (8 mg, 0.205 mmol) and potassium carbonate (43 mg, 0.31 mmol) in acetonitrile (10 mL) was added dropwise at ambient temperature under an inert atmosphere a solution of **8** (69 mg, 0.16 mmol) in acetonitrile. The solution was heated at reflux for 16 h. The reaction solvent was evaporated under reduced pressure, and the resulting residue was extracted with ethyl acetate. The solvent was evaporated under reduced pressure and the crude material was purified using silica gel column chromatography to yield a light yellow oil **9** (77 mg, 60%). ^{1}H NMR ($CDCl_3$, 400 MHz): δ 0.31 (3H, s), 1.18−1.45 (2H, m), 1.66−1.81 (2H, m), 1.99−2.20 (2H, m), 2.33−2.41 (4H, m), 2.51 (1 H, d, *J* = 12.46 Hz), 2.68 (2H, t, *J* = 5.86 Hz), 2.77−2.90 (2H, m), 3.34−3.42 (2H, m), 3.45−3.71 (14H, m), 3.81 (2H, t, *J* = 4.76 Hz), 3.92−4.00 (4H, m), 4.00−4.07 (3H, m), 6.49 (1H, dd, *J* = 8.43, 2.56 Hz), 6.56−6.67 (2H, m), 6.86 (2H, d, *J* = 8.79 Hz), 6.94 (2H, d, *J* = 8.79 Hz). ^{13}C NMR ($CDCl_3$, 100 MHz): δ 13.0, 17.5, 23.4, 28.2, 30.5, 30.7, 35.6, 38.4, 43.6, 43.8, 45.8, 47.6, 50.9, 52.1, 56.8, 57.4, 67.4, 69.6, 70.0, 70.3, 70.6, 70.9, 71.0, 76.9, 82.8, 112.6, 113.7, 114.8, 127.7, 130.7, 131.1, 136.0, 137.7, 155.9, 156.3; $C_{35}H_{50}N_4O_6$, TOF-MS: *m/z* 622.37 (calcd); 657.99 [M+Na]+ (found).

2-{2-[2-(2-Prop-2-ynyloxy-ethoxy)-ethoxy]-ethoxy}-ethanol ***10***. To a solution of tetraethylene glycol (2.00 g, 10.3 mmol) in tetrahydrofuran (10.0 mL) was slowly added sodium hydride (60% in paraffin, 580 mg, 15 mmol) at −20 °C. To the reaction vessel was added dropwise at −20 °C a solution of propargyl bromide (3.0 g, 22 mmol) in 5.0 mL tetrahydrofuran. The reaction mixture was stirred at −20 °C for 30 min, allowed to warm to ambient temperature, and then stirred for an additional 24 h. The reaction was partitioned between ethyl acetate (20 mL) and water (20 mL), after which the organic layer was washed with water and brine. The organic layer was dried over magnesium sulfate, filtered, and the solvent removed via rotary evaporation. The crude product was purified using silica gel column chromatography to yield 1.55 g (65%) of the product **10** as oil. ^{1}H NMR ($CDCl_3$, 400 MHz): δ 1.26 (1H, t, *J* = 7.1 Hz), 2.08−2.09 (1H, m), 2.17 (1H, s), 2.44 (2H, t, *J* = 2.4 Hz), 3.65−3.77 (14H, m), 4.21 (2H, d, *J* = 2.4 Hz). ^{13}C NMR (CDCl3, 100 MHz): δ 58.3, 61.5, 69.0, 70.3, 70.3, 70.5, 70.5, 70.6, 72.7, 75.1, 79.7; $C_{11}H_{20}O_5$, TOF-MS: *m/z* 233.42 (calcd); 256.34 $[M+Na]^+$ (found).

*2-(2-(2-(2-(Prop-2-ynnyloxy)-ethoxy)-ethoxy)-ethoxy)-ethanol Tosylate **11**.* To a solution of propargyl tetraethylene glycol **10** (1.0 g, 4.31 mmol) in CH_2Cl_2 (15.0 mL) was added triethylamine (1.2 mL, 8.6 mmol) and *p*-toluenesulfonyl chloride (0.99 g, 5.2 mmol). The reaction mixture was stirred at ambient temperature for 16 h. The solvent was under reduced pressure to give a crude product as dark oil. Separation using silica gel column chromatography gave the product **11** (1.53 g, 92%) as a yellow oil. ^{1}H NMR ($CDCl_3$, 400 MHz): δ. 2.45 (3H, s), 2.49 (1H, J = 2.2 Hz), 3.59−3.64 (14H, m), 3.65−3.72 (2H, m), 4.13−4.17 (2 H, m), 4.18 (2H, J = 2.2 Hz), 7.36 (2H, J = 8.1 Hz), 7.79 (2H, d, J = 8.1 Hz). ^{13}C NMR ($CDCl_3$, 100 MHz): δ 21.9, 21.9, 58.6, 68.9, 69.3, 69.5, 70.6, 70.7, 70.7, 70.8, 70.9, 74.8, 74.8, 79.9, 128.2, 130.1, 133.2, 145.0; $C_{18}H_{26}O_7S$, TOF-MS: m/z 402.13 (calcd); 422.99 $[M+Na]^+$ (found).

*Methyl 4-(2-(2-(2-(2-(Prop-2-ynyloxy)-ethoxy)-ethoxy)-ethoxy)-ethoxybenzoate **12**.* To a solution of **11** (1.0 g, 2.6 mmol) in dichloromethane (10 mL) was added dropwise a mixture of cesium carbonate (126 mg, 388 mmol) and methyl 4-hydroxybenzoate (590 mg, 3.9 mmol) in 5 mL of dichloromethane. The reaction was heated at reflux for 16 h. The reaction mixture was filtered and then concentrated under rotary evaporation. The residue was purified using silica gel column chromatography to afford the product **12** (1.1 g, 70%) as clear oil. ^{1}H NMR ($CDCl_3$, 400 MHz): δ 2.05 (1H, s), 2.44 (3H, t, J = 2.56 Hz), 3.62−3.75 (12H, m), 3.82−3.92 (2H, m), 4.09−4.22 (4H, m), 6.93 (2H, d, J = 8.79 Hz), 7.98 (2H, d, J = 8.79 Hz). ^{13}C NMR ($CDCl_3$, 100 MHz): δ 22.6, 52.1, 52.3, 58.6, 67.8, 69.3, 69.7,70.4, 70.6, 70.8, 71.1, 74.8, 79.9, 114.4, 122.9, 131.7, 162.8, 167.0; $C_{19}H_{26}O_7$, TOF-MS: m/z 366.16 (calcd); 389.10 $[M+Na]^+$ (found).

*4-(2-{2-[2-(2-Prop-2-ynyloxy-ethoxy)-ethoxy]-ethoxy}-ethoxy)-benzoic Acid Hydrazide **13**.* To a solution of **12** (200 mg, 0.55 mmol) in ethanol (10 mL) was added hydrazine hydrate (44 mg, 1.4 mmol). The solution was heated at reflux for 10 h. The solvent was removed by rotary evaporation to give a crude material that was purified by using amino column chromatography. The product **13** was isolated (144 mg, 72%) as a pale, yellow oil. ^{1}H NMR ($CDCl_3$, 400 MHz): δ d 1.81 (2H, s), 2.16 (1H, s), 2.21−2.35 (2H, m), 3.66−3.81 (14H, m), 4.2 (2H, m), 6.96 (2H, d), 7.78 (2H, d), 7.82 (1H, s). ^{13}C NMR ($CDCl_3$, 100 MHz): δ 67.7, 69.7, 70.1, 70.7, 71.0, 73.2, 114.5, 114.6, 125.2, 126.0, 129.0, 129.5, 144.0, 161.8, 161.9, 168.5, 169.8, 173.6; $C_{18}H_{26}N_2O_6$, TOF-MS: m/z 371.17 (calcd); 371.3 $[M]^+$ (found).

*4-(2-(2-(2-(2-(Prop-2-ynyloxy)ethoxy)ethoxy)ethoxy)-ethoxybenzohydrazone−Doxorubicin Conjugate **14**.* To a solution of **12** (14 mg, 0.04 mmol) in ethanol (5 mL) was added doxorubicin hydrochloride (20 mg, 0.004 mmol) and trifluoroacetic acid (64.5 mg, 0.6 mmol). The reaction mixture was stirred at 20 °C for 24 h, concentrated to approximately 1.0 mL, and triturated with ether to yield a red precipitate. The red precipitate was collected by filtration, washed with ether, and dried under vacuum to afford the product (28.5 mg, 85%). ^{1}H NMR ($CDCl_3$, 400 MHz): δ 1.29 (3H, d, J = 6.6 Hz), 1.81−1.94 (3H, m), 1.97−2.10 (2H, m), 2.11−2.22 (1H, m), 2.30−2.47 (1H, m), 2.89−3.03 (1H, m), 3.06−3.15 (1H, m), 3.22−3.37 (12H, m), 3.52−3.74 (3H, m), 3.78−3.89 (1H, m), 4.04 (3H, s), 4.14−4.24 (2H, m), 4.26−4.33 (1H, m), 4.71 (2H, d, J = 2.2 Hz), 5.03−5.17 (1H, m), 5.39−5.52 (2H, m), 6.97−7.13 (2H, m), 7.51−7.62 (1H, m), 7.74−7.89 (3H, m), 7.94−8.00 (1H, m). ^{13}C NMR ($CDCl_3$, 100 MHz): δ 11.6, 20.5, 28.6, 38.3, 48.1, 51.2, 61.0, 67.6, 69.4, 70.1, 70.3, 70.4, 72.4, 114.2, 117.3, 122.4, 125.8, 131.4, 140, 153.2, 155.4, 163.1, 167.4, 187.2; $C_{45}H_{53}N_3O_{15}$, TOF-MS: m/z 875.35 (calcd); 898.39 $[M+Na]^+$ (found).

*Anti-Estrogen−Doxorubicin Conjugate **15**.* To a solution of **9** (10 mg, 0.015 mmol) in 500 μL of *tert*-butanol/water (1:1) was added a solution of **14** (13.1 mg, 0.015 mmol) in 500 μL of *tert*-butanol/water (1:1). The reaction was stirred at room temperature for 30 min, followed by the addition of copper(II) sulfate pentahydrate (3.75 μL, 0.15 μmol) and (+)-sodium L-ascorbate (14.8 μL, 0.75 μmol). The reaction mixture was warmed to 40 °C, stirred for 24 h, and then partitioned between water (10 mL) and dichloromethane (10 mL). The organic layer was washed with water (2 × 10 mL). The aqueous layers were combined; sodium chloride was added and then back-extracted with dichloromethane (10 mL). The organic fractions were combined, dried over magnesium sulfate, filtered, and concentrated leaving a dark red residue. The product was isolated using column chromatography (85:15 dichloromethane/methanol) to yield the product **15** (12.7 mg, 55%) as a red solid. TLC (Si_2O, 80:20 dichloromethane/methanol) R_f = 0.25. ^{1}H NMR (CH_3OH-*d*, 500 MHz): δ = 7.93 (d, J = 7.2, 2H), 7.89 (s, 1H), 7.85 (s, 1H), 7.76 (s, 1H), 7.61−7.67 (m, 3H), 7.56 (s, 1H), 7.49 (s, 1H), 7.25 (d, J = 7.8 Hz, 2H), 7.03 (d, J = 8.8 Hz, 2H), 6.99 (d, J = 8.8 Hz, 2H), 6.90 (s, 1H), 6.83 (s, 2H), 6.75−6.79 (m, 2H), 4.36 (t, J = 7.3 Hz, 1H), 4.27 (m, 2H), 4.16−4.20 (m, 1H), 4.03 (d, J = 5.9 Hz, 1H), 3.86−3.90 (m, 2H), 3.71−3.75 (m, 3H), 3.63−3.71 (m, 28H), 3.55−3.61 (m, 2H), 3.50−3.54 (m, 1H), 3.39−3.44 (m, 1H), 2.39 (s, 2H), 2.27 (s, 3H), 1.93 (s, 1H), 1.64−1.74 (m, 2H), 1.41−1.50 (m, 6H), 1.33−1.41 (m, 2H), 1.30 (s, 2H), 1.28 (br. s., 1H), 1.26 (m, 3H), 1.15 (m, 3H), 1.00 ppm (m, 3H). $C_{45}H_{53}N_3O_{15}$, TOF-MS: m/z 1277.59 (calcd); 1299.91 $[M+Na]^+$ (found).

High-Performance Liquid Chromatography (HPLC) Trace Analysis. The compounds were analyzed with Waters HPLC system, equipped with a Waters 2695 binary pump, a Waters 2998 fluorescence photodiode array detector, and a XBridge C18 column (3.5 μm, 4.6 × 75 mm). HPLC-grade acetonitrile/water/trifluoroacetic acid (50/50/0.1%, v/v) was used as the mobile phase at 25 °C with a flow rate of 1.0 mL min^{-1}. Fluorescence detector was set at 254 nm for excitation and 570 nm for emission and linked to *Empower III* software for data analysis.

Cell Cultures. The ER(+)MCF7 (human breast adenocarcinoma) and ER(−)MBA-MD-231 (human breast adenocarcinoma) cell lines were maintained in Dulbecco's Modified Eagle Medium (DMEM) at 37 °C, 5% CO_2. DMEM were supplemented with 10% fetal bovine serum (FBS), 50 U/mL penicillin, and 50 μg/mL streptomycin.

Cytotoxicity Assays. Cells were plated at a 5 × 10^3 cells per well density in 96-well plates (Corning Inc., Corning, NY, USA). The stock solutions of free drug or drug-conjugates were prepared in DMSO and diluted in complete media before adding to cells. After 24 h, the medium was replaced with medium containing free drug or drug-conjugates. After 24 h incubation, each well was washed twice with complete media, and cell survival was measured using the Cell Titer-Blue Cell Viability Assay method. The conversion of Resaruzin to Resorufin by viable cells results in the fluorescence excitation at 550 nm. The fluorescence produced is proportional to the number of viable cells. The emitted fluorescence was measured at 590 nm (the measurement of the cytotoxicity) using a

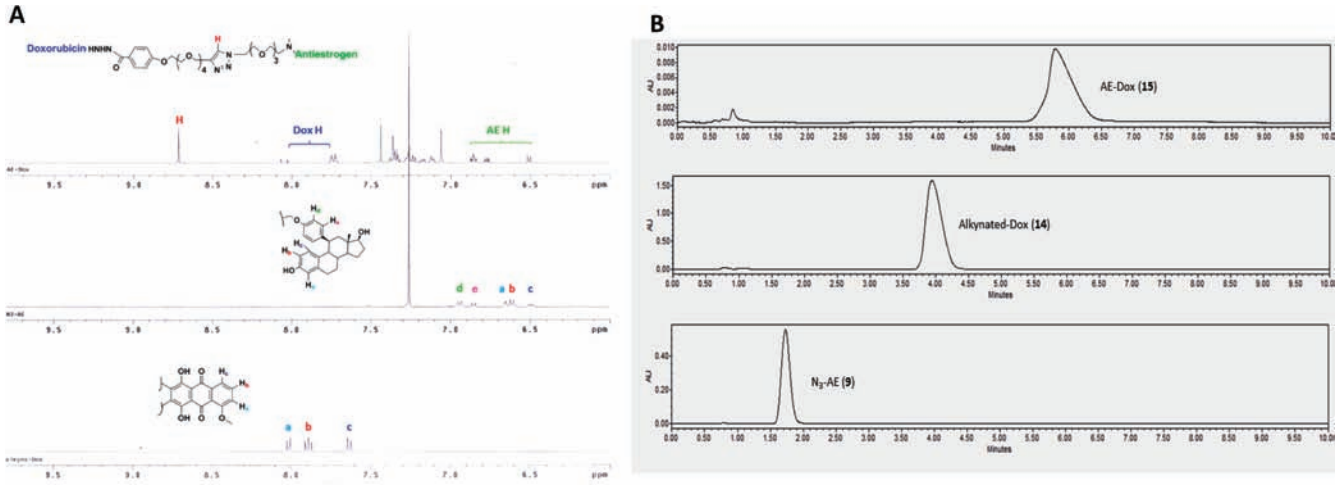

Figure 5. (A) Partial stacking ^{1}H NMR of AE-Dox **15**; (B) HPLC of AE-Dox **15** and its components.

Labsystems Multiskan MCC/340 microplate reader (Labsystems and Life Sciences International, UK).

For estradiol competition assay, the cells were pretreated with 17β-estradiol (ES) (50 μM) for 1 h, followed by addition of free drug or drug-conjugates in complete media with 50 μM of ES. After 24 h incubation, cell viability was analyzed as described above.

Flow Cytometry. The ER(+)MCF-7 and ER(−)MDA-MB-231 cells were grown in 12-well tissue culture plates until 70−80% confluency. The medium was removed from the wells; cells were washed with complete media and incubated with or without 50 μM ES for 1 h. After incubation, the cells were washed twice with complete media, and exposed to 0.1 μM of Dox, AE-Dox in complete media with or without 50 μM of ES. After 1 h, cells were washed, trypsinized, and finally resuspended in 800 μL of 4% paraformaldeyhde in phosphate buffered saline (PBS) pH 7.4. The cell-associated fluorescence was quantified by Becton Dickinson FACScan (Becton Dickinson, San Jose, CA) at the emission wavelength of 580 nm (channel FL-2).The data analysis was performed using *CellQuest* software (Becton Dickinson). A total of 10 000 events were acquired for each sample. Data shown were derived from three separate experiments.

Fluorescence Microscopy. The ER(+) MCF-7 cells were seeded on a coverslip in six-well tissue culture plates at a concentration of 1 × 10^5 cells per well. After 24 h, the cells were washed twice with complete media and then incubated with 0.1 μM Dox or AE-Dox **15**. After 1 h incubation, medium was removed, and cells were washed twice with sterile PBS followed by fixation of the cells with 4% paraformaldehyde (15 min at room temperature). Hoechst 33342 (1 μg/mL) was added to the cells for 15 min, and cells were washed twice with sterile PBS. Cells were observed immediately on a Nikon Eclipse E400 fluorescence microscope equipped with appropriate filters for Rhodamine and Hoechst detection. For estradiol competition assay, the cells were pretreated with 17β-estradiol (ES) (50 μM) for 1 h, followed by addition of 0.1 μM of AE-Dox in complete media with 50 μM of ES.

RESULTS AND DISCUSSION

Synthesis. The convergent modular approach proved to be a successful strategy for assembling the target anti-estrogen doxorubicin conjugate AE-Dox **15**. The starting materials were transformed to the requisite components in high yields and purity. In particular, the conversion of the readily available tetra(oligo)ethylene glycols to heterobifunctional half-linkers **8** and **13** is notable because of the possibility of subsequent variations that one can generate. If necessary, one can control the length of the spacer groups as well as the modes of ligation to address concerns not apparent at the outset of the study. In this example, the use of small tetraethylene glycol moieties facilitated the individual reactions, purifications, and subsequent ligations. The conjugation the propargylated-tetraethylene glycol benzohydrazide **13** to doxorubicin to form the alkynylated intermediate **14**, proceeded with good yield, and remained stable under neutral and basic conditions. The preparation of the steroidal anti-estrogen **9** was readily achieved from the key starting material **1** and transformed via N-demethylation into the reactive intermediate **7**. The subsequent alkylation with the azido-tetraethylene glycol tosylate **8** gave the stable component **9.** The conversion into the final product **15** was achieved with good yield using the classical "click" conditions.

To verify the ligation of the AE-Dox conjugate **15** from its two intermediates, the azido anti-estrogen **9** and the alkynylated Dox **14**, we performed stacking ^{1}H NMR analysis, FT-IR, and HPLC. AE-Dox formation was indicated by the signature triazole proton, shown at approximately 8.7 ppm in the ^{1}H NMR spectrum, and the presence of the characteristic aromatic signature protons for both Dox and AE components (Figure 5A). The FTIR spectrum supported the ligation of the two intermediates by the disappearance of the azide stretch approximately at 2100 cm^{-1} from compound **9**, and the alkyne stretch at 2050 cm^{-1} (SI) from compound **14**. In addition, the HPLC data (Figure 5B) showed the elution of a single peak for **15** that was distinct from the azide **15** or the alkyne **14**.

Cell Studies. The preliminary evaluation of the parent compounds (Dox and RU39411), linker modified components **14** and **9**, and the final AE-Dox hybrid **15** was determined using ER(+)-MCF-7 and ER(−)-MDA-MB-231 breast cancer cell lines. ER(+)-MCF-7 is a human breast adenocarcinoma cell line that overexpresses ER and is an excellent *in vitro* assay system to demonstrate anti-estrogenic effects,[64−66] while ER(−)-MDA-MB-231 cells are insensitive to antihormonal interventions.[67] Both cell lines are responsive to doxorubicin, such that structural modifications affecting the activity should be readily apparent. Under the conditions of the bioassay, neither cell line

dx.doi.org/10.1021/bc200645n | *Bioconjugate Chem.* 2012, 23, 785−795

metabolizes doxorubicin or the anti-estrogen to a significant degree, so that any activity observed would be due primarily to the parent drug and not potential metabolites.[50,68]

Initial cell-based assays evaluated whether the presence of the linker groups would affect the individual components as inhibitors of cell proliferation (cytotoxicity). The steroidal anti-estrogen and its azido-linker modified derivative (N_3-AE **9**) had no significant cytotoxic effects on ER(+)-MCF-7 cells at concentrations below 1 μM and only modest effects at 10 μM (see SI). In the same cell line, doxorubicin and its alkynyl hydrazone derivative **14** displayed statistically similar IC_{50} values (Table 1) and *in vitro* cytotoxicity profiles (results also in SI). Therefore, the introduction of the tetraethylene glycol (TEG) linker onto the amino terminus of the steroidal anti-estrogen and the TEG hydrazone linker onto the ketone of doxorubicin had no observable effect on the cytotoxic properties of the parent compounds. However, the AE-Dox conjugate **15** showed a significant enhancement of cytotoxicity (approximately 70-fold) in ER(+)-MCF-7 cells compared to the other formulations (Figure 6A). The IC_{50} for the AE-Dox conjugate **15** was 0.011 μM compared to 0.602 μM and 0.597 μM for the free Dox and the linker-Dox **14**, respectively. In the ER(−)-MDA-MB-231 cell line (Figure 6B), the presence of the anti-estrogenic component had no significant effect. The cytotoxicity curves for all three compounds in this cell line were essentially superimposable, with IC_{50} values in a narrow range (0.125−0.080 μM).

Table 1. Inhibition Concentration, IC_{50} (nM), of Various Dox Compounds

compound	MCF-7	MDA-MB-231	MCF-7 (+ES)
Dox	602 ± 20	89 ± 7	585 ± 30
Dox-Linker **14**	597 ± 20	86 ± 5	594 ± 20
AE-Dox **15**	11 ± 6	90 ± 8	589 ± 3

Then, we determined whether the effect of the anti-estrogenic component in the hybrid AE-Dox **15** could be reversed by the addition of estradiol (ES). Cytotoxicity of Dox and the hybrid AE-Dox **15** were analyzed in ER(+)MCF-7 cells in the presence or absence of ES. The results (Table 1) show that the enhanced cytotoxicity of the AE-Dox hybrid was completely abolished by the addition of ES, whereas ES has virtually no effect on either Dox itself, or the linker-Dox **14**. Therefore, it appeared that the effect was ER-dependent and not a nonspecific process.

The IC_{50} was estimated by using *GraphPad 3* parameters curve fitting for 24 h drug exposure data points. All values are represented here were evaluated in a duplicate of a triplicate count. Standard deviation was measured from the mean of six wells for each compound.

The subsequent study was undertaken both to support the ER-related effect and to identify the nature of that effect. Cell uptake/targeting of the hybrid AE-Dox **15** with ER(+)-MCF-7 and ER(−)-MDA-MB-231 cells was evaluated using fluorescence activated cell sorting (FACS), in both presence and absence of ES, as shown in Figure 7. The AE-Dox **15** demonstrated enhanced cell binding only to ER(+)-MCF-7 cells in the absence of ES. In presence of ES, cell binding of AE-Dox **15** was similar to that of Dox alone. Also, the ER(−)-MDA-MB-231cells did not show any significant change in cell binding of Dox and AE-Dox **15**, and as expected, the presence or absence of ES had no effect on cell binding of the drugs. The results in Figure 7 illustrated a marked targeting effect imparted by the presence of the steroidal anti-estrogen component in the hybrid agent **15**. These effects were consistent with the interaction selective for the membrane ER.

Since FACS studies do not distinguish among membrane, cytoplasmic, or nuclear localization of the fluorescent group, we undertook cellular studies using fluorescence microscopy. The results shown in Figure 8 clearly support enhanced AE-Dox **15** targeting to the ER-positive breast cancer cells. The cellular localization of the fluorescence from AE-Dox **15** and Dox was evaluated via ER(+)-MCF-7 cells in the presence (+) and absence (−) of ES. The low level of fluorescence for cells treated with Dox alone (panel B) is associated primarily with the nucleus since the drug is known as DNA binding agent and accumulates in nucleus.[69,70] AE-Dox **15** (panel C) shows a significantly enhanced uptake within the ER(+)-MCF-7 cells, compared to Dox alone (panel B), suggesting that the AE component of the conjugate has substantially facilitated uptake by cells. Moreover, the fluorescence appeared to be associated with nucleus, suggesting Dox should have been hydrolyzed from the targeting group coupled with the translocation of free Dox. The incubation of the cells with AE-Dox **15** and ES (panel D) decreased the uptake of the AE-Dox (panel B) confirming that the uptake is ER-mediated. This study supported the observation for the initial cytotoxicity results in which AE-Dox **15** would generate a higher intracellular concentration of Dox and therefore more rapid cell death.

CONCLUSION

In this study, we have demonstrated that we can prepare the anti-estrogen−doxorubicin conjugate **15** efficiently and in high yield using our modular assembly approach. Because the

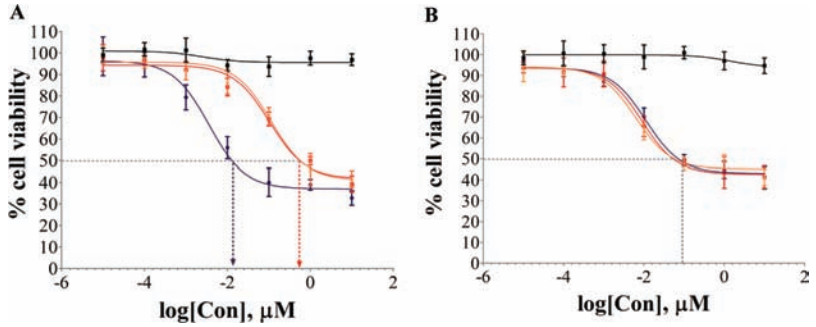

Figure 6. Cytotoxicity of compounds 11β-AE **9** (black), Dox-linker **14**-red, Dox (orange), and AE-Dox **15** (purple), in (A) ER(+)MCF-7 and (B) ER(−)MDA-MB-231 cell lines.

dx.doi.org/10.1021/bc200645n | *Bioconjugate Chem.* 2012, 23, 785−795

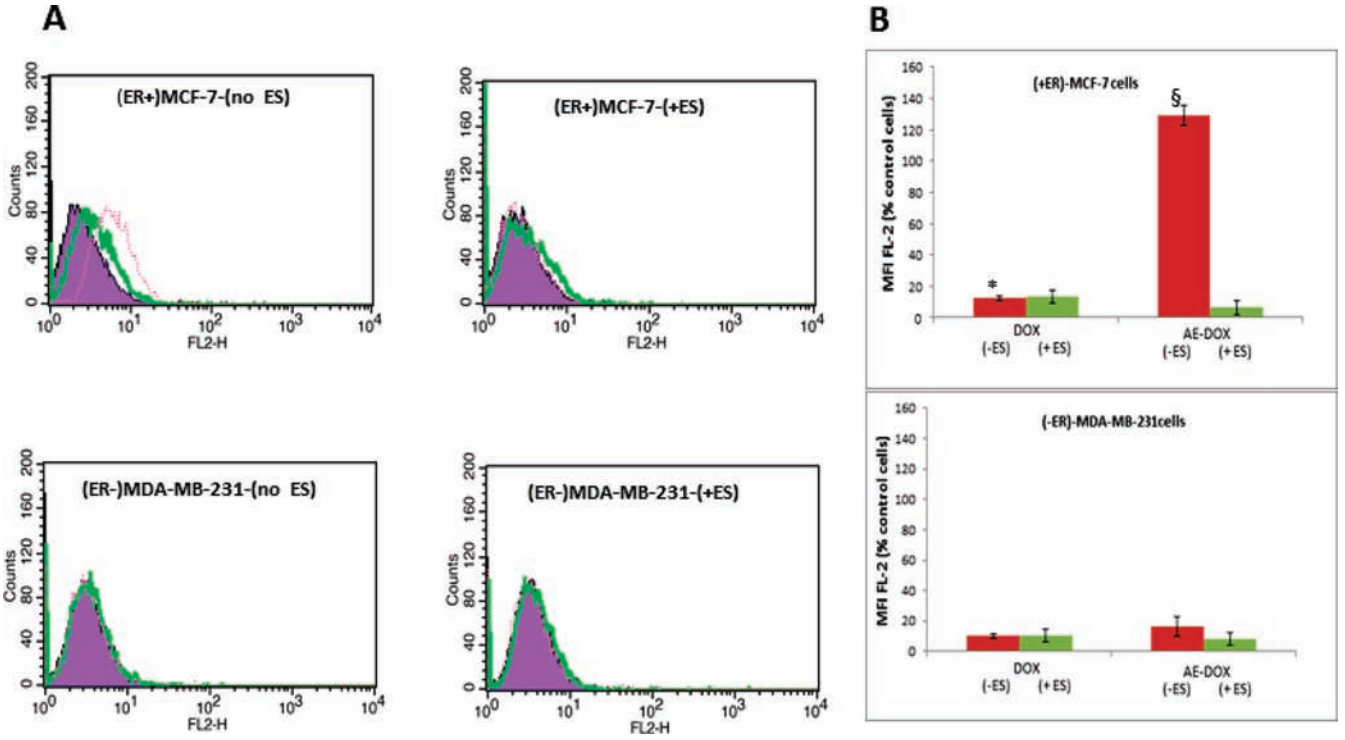

Figure 7. FACS analysis of ER(+)MCF-7 and ER(−)MDA-MB-231 cells. (A) Histogram analysis of cells treated with 0.1 μM of Dox and AE-Dox **15** with and without ES; (purple) cells only, (green) Dox treated cells, and (red) AE-Dox treated cells. (B) The percentage of Dox-positive cells in ER(+)MCF-7 and ER(−)MDA-MB-231cells. *P < 0.01 (Dox vs AE-DOX (-ES)); §P < 0.01 (AE-Dox (-ES) vs AE-Dox(+ES).

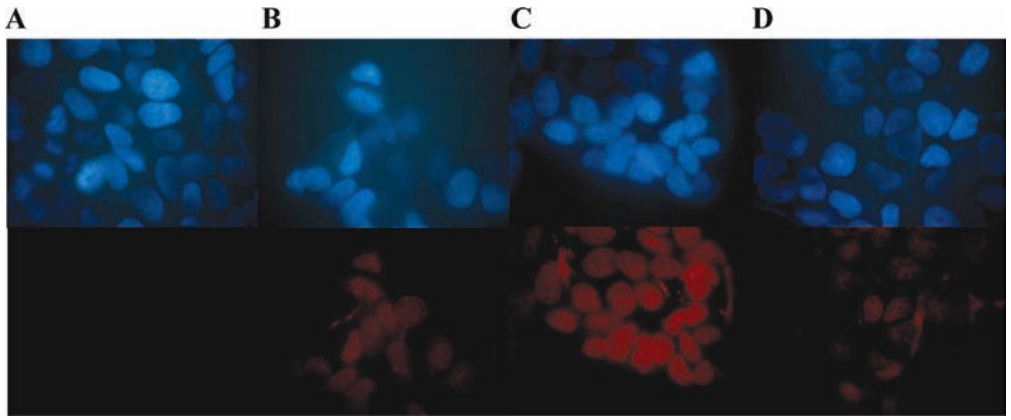

Figure 8. Fluorescence microscopy images ER(+)MCF-7 cells treated for 1 h with 0.1 μM of (B) Dox; (C) AE-Dox **15**; (D) AE-Dox **15** after pretreatment with 50 μM estradiol; and (A) untreated cell. Hoechst fluorescent (upper panel). Red fluorescence (lower panel).

components can be prepared independently and conjugated using simple chemistry, potential modifications of the conjugate properties are relatively easy. Initial cytotoxicity experiments demonstrated that the AE-Dox conjugate **15** was 70-fold more potent than Dox alone in ER(+)-MCF-7 cells, but equipotent compared to Dox in ER(−)-MDA-MB-231 cells. The enhanced cytotoxic effect in MCF-7 cells was reversed by preincubation with ES, suggesting an ER-mediated process. Subsequent FACS studies on both cell lines in the presence or absence of ES supported this hypothesis. Additional studies using fluorescence microscopy in MCF-7 cells suggested that the uptake proceeded via a membrane ER-mediated effect leading to an enhanced cellular accumulation of Dox. Within the cell, the pH-sensitive hydrazone release mechanism incorporated into the conjugate leads ultimately to the elevated levels of free Dox in nucleus. Studies to further characterize the individual steps of the process are in progress.

■ ASSOCIATED CONTENT

Supporting Information

^{1}H and ^{13}C NMR spectra for compounds **2**−**15** are provided. Infrared spectra for **15**, and cytotoxicity data for **9** and **14** are provided. This material is available free of charge via the Internet at http://pubs.acs.org.

■ AUTHOR INFORMATION

Corresponding Author

*E-mail: r.hanson@neu.edu.

Notes

The authors declare no competing financial interest.

■ ACKNOWLEDGMENTS

We acknowledge the financial support from the Northeastern University and the Department of Defense- Congressional Directed Medical Research Programs (W81XWH-10-1-0262) [K.-L.D.], Department of Energy (DE-SC0001781)[RNH], Komen Foundation (BCTR0600659)[RNH], and Public Health Service (NIH - 1R01CA121838)[VPT].

■ REFERENCES

(1) Garcia, M., Jemal, A., Ward, E. M., Center, M. M., Hao, Y., and Siegel, R. L. *Global Cancer Facts and Figures 2007* (2007) American Cancer Society, Atlanta, GA.

(2) Coezy, E., Borgna, J.-L., and Rochefort, E. (1982) Tamoxifen and metabolites in MCF7 cells: Correlation between binding to estrogen receptor and inhibition of cell growth. *Cancer Res. 42*, 317−323.

(3) Langan Fahey, S. M., Jordan, V. C., Fritz, N. F., Robinson, S. P., Waters, D., and Tormey, D. C. (1994) Clinical pharmacology and endocrinology of long-term tamoxifen therapy. In *Long-term tamoxifen treatment for breast cancer* (Jordan, V. C., Ed.) pp 27−56, University of Wisconsin Press, Madison.

(4) Shiau, A. K., Barstad, D., Loria, P. M., Cheng, L., Kushner, P. J., Agard, D. A., and Greene, G. L. (1998) The structural basis of estrogen receptor/coactivator recognition and the antagonism of this interaction by tamoxifen. *Cell (Cambridge, Mass.) 95*, 927−937.

(5) Jordan, V. C. (2003) Tamoxifen: A most unlikely pioneering medicine. *Nat. Rev. Drug Discovery 2*, 205−213.

(6) Du, D.-M., and Carlier, P. R. (2004) Development of bivalent acetylcholinesterase inhibitors as potential therapeutic drugs for Alzheimer's disease. *Curr. Pharm. Des. 10*, 3141−3156.

(7) Messer, W. S. (2004) Bivalent ligands for G protein-coupled receptors. *Curr. Pharm. Des. 10*, 2015−2020.

(8) Antonello, A., Tarozzi, A., Morroni, F., Cavalli, A., Rosini, M., Hrelia, P., Bolognesi, M. L., and Melchiorre, C. (2006) Multitarget-directed drug design strategy: a novel molecule designed to block epidermal growth factor receptor (EGFR) and to exert proapoptotic effects. *J. Med. Chem. 49*, 6642−6645.

(9) Morphy, R., and Rankovic, Z. (2006) The physicochemical challenges of designing multiple ligands. *J. Med. Chem. 49*, 4961−4970.

(10) Ojima, I. (2008) Guided molecular missiles for tumor-targeting chemotherapy-case studies using the second-generation taxoids as warheads. *Acc. Chem. Res. 41*, 108−119.

(11) Aspland, S. E., Ballatore, C., Castillo, R., Desharnais, J., Eustaquio, T., Goelet, P., Guo, Z., Li, Q., Nelson, D., Sun, C., Castellino, A. J., and Newman, M. J. (2006) Kinase-mediated trapping of bi-functional conjugates of paclitaxel or vinblastine with thymidine in cancer cells. *Bioorg. Med. Chem. Lett. 16*, 5194−5198.

(12) Reddy, J. A., Westrick, E., Santhapuram, H. K. R., Howard, S. J., Miller, M. L., Vetzel, M., Vlahov, I., Chari, R. V. J., Goldmacher, V. S., and Leamon, C. P. (2007) Folate receptor-specific antitumor activity of EC131, a folate-maytansinoid conjugate. *Cancer Res. 67*, 6376−6382.

(13) Swamy, N., Purohit, A., Fernandez-Gacio, A., Jones, G. B., and Ray, R. (2006) Nuclear estrogen receptor targeted photodynamic therapy: selective uptake and killing of MCF-7 breast cancer cells by a C17α-alkynylestradiol-porphyrin conjugate. *J. Cell. Biochem. 99*, 966−977.

(14) Eisenbrand, G., Berger, M. R., Fischer, J., Schneider, M. R., Tang, W., and Zeller, W. J. (1998) Development of more selective *anti-cancer* nitrosoureas. *Anti-Cancer Drug Des. 2*, 231.

(15) Eisenbrand, G., Fischer, J., Muhlbauer, K., Schied, G., Schreiber, J., Tang, W., and Zelezny, O. (1998) Synthesis and characterization of steroid-linked N-(2-chloroethyl)nitrosoureas. *Arch. Pharm. (Weinheim) 322*, 863−72.

(16) Delbarre, A., Oberlin, R., Roques, B. P., Borgna, J. L., Rochefort, H., Le, P. J. B., and Jacquemin-Sablon, A. (1985) Ellipticine derivatives with an affinity to the estrogen receptor. An approach to develop intercalating drugs with a specific effect on the hormone-dependent breast cancer. *J. Med. Chem. 28*, 752−61.

(17) Devraj, R., Barrett, J. F., Fernandez, J. A., Katzenellenbogen, J. A., and Cushman, M. (1996) Design, synthesis, and biological evaluation of ellipticine-estradiol conjugates. *J. Med. Chem. 39*, 3367−3374.

(18) Kasiotis, K. M., Magiatis, P., Pratsinis, H., Skaltsounis, A., Abadji, V., Charalambous, A., Moutsatsou, P., and Haroutounian, S. A. (2001) Synthesis and biological evaluation of novel daunorubicin-estrogen conjugates. *Steroids 66*, 785−91.

(19) Fernandez-Gacio, A., Fernandez-Marcos, C., Swamy, N., Dunn, D., and znd Ray, R. (2006) Photodynamic cell-kill analysis of breast tumor cells with a tamoxifen-pyropheophorbide conjugate. *J. Cell. Biochem. 99*, 665−670.

(20) Ali, H., Ahmed, N., Tessier, G., and Van, L. J. E. (2006) Synthesis and biological activities of nucleoside-estradiol conjugates. *Bioorg. Med. Chem. Lett. 16*, 317−319.

(21) Jones, G. B., Huber, R. S., Matthews, J. E., and Li, A. (1996) Target directed enediyne prodrugs: cytotoxic estrogen conjugates. *Tetrahedron Lett. 37*, 3643−3646.

(22) Kuduk, S. D., Zheng, F. F., Sepp-Lorenzino, L., Rosen, N., and Danishefsky, S. J. (1999) Synthesis and evaluation of geldanamycin-estradiol hybrids. *Bioorg. Med. Chem. Lett. 9*, 1233−1238.

(23) Liu, C., Strobl, J. S., Bane, S., Schilling, J. K., McCracken, M., Chatterjee, S. K., Rahim-Bata, R., and Kingston, D. G. I. (2004) Design, synthesis, and bioactivities of steroid-linked taxol analogues as potential targete drugs for prostate and breast cancer. *J. Nat. Prod. 67*, 152−159.

(24) Bednarski, P. J., Gust, R., Spruss, T., Knebel, N., Otto, A., Farbel, M., Koop, R., Holler, E., Von, A. E., and Schoenenberger, H. (1990) Platinum compounds with estrogen receptor affinity. *Cancer Treat. Rev. 17*, 221−31.

(25) Banerjee, S., Das, T., Chakraborty, S., Samuel, G., Korde, A., Venkatesh, M., and Pillai, M. R. A. (2005) An estradiol-conjugate for radiolabelling with ^{177}Lu: an attempt to prepare a radiotherapeutic agent. *Bioorg. Med. Chem. 13*, 4315−4322.

(26) Gagnon, V., St-Germain, M.-E., Descoteaux, C., Provencher-Mandeville, J., Parent, S., Mandal, S. K., Asselin, E., and Berube, G. (2004) Biological evaluation of novel estrogen-platinum(II) hybrid molecules on uterine and ovarian cancers-molecular modeling studies. *Bioorg. Med. Chem. Lett. 14*, 5919−5924.

(27) Gabano, E., Cassino, C., Bonetti, S., Prandi, C., Colangelo, D., Ghiglia, A., and Osella, D. (2005) Synthesis and characterisation of estrogenic carriers for cytotoxic Pt(II) fragments: biological activity of the resulting complexes. *Org. Biomol. Chem. 3*, 3531−3539.

(28) Barnes, K. R., Kutikov, A., and Lippard, S. J. (2004) Synthesis, characterization, and cytotoxicity of a series of estrogen-tethered platinum(IV) complexes. *Chem. Biol. 11*, 557−564.

(29) Jordan, V. C. (2007) Chemoprevention of breast cancer with selective oestrogen-receptor modulators. *Nat. Rev. Cancer 7*, 46−53.

(30) Cyrus, K., Wehenkel, M., Choi, E.-Y., Lee, H., Swanson, H., and Kim, K.-B. (2010) Jostling for position: optimizing linker location in the design of estrogen receptor-targeting protacs. *ChemMedChem 5*, 979−985.

(31) Gunanathan, C., Pais, A., Furman-Haran, E., Seger, D., Eyal, E., Mukhopadhyay, S., Ben-David, Y., Leitus, G., Cohen, H., Vilan, A., Degani, H., and Milstein, D. (2007) Water-soluble contrast agents targeted at the estrogen receptor for molecular magnetic resonance imaging. *Bioconjugate Chem. 18*, 1361−1365.

(32) Kim, S. H., Tamrazi, A., Carlson, K. E., Daniels, J. R., Lee, I. Y., and Katzenellenbogen, J. A. (2004) Estrogen receptor microarrays: subtype-selective ligand binding. *J. Am. Chem. Soc. 126*, 4754−4755.

(33) Hannon, M. J., Green, P. S., Fisher, D. M., Derrick, P. J., Beck, J. L., Watt, S. J., Ralph, S. F., Sheil, M. M., Barker, P. R., Alcock, N. W., Price, R. J., Sanders, K. J., Pither, R., Davis, J., and Rodger, A. (2006) An estrogen-platinum terpyridine conjugate: DNA and protein binding and cellular delivery. *Chem.—Eur. J. 12*, 8000−8013.

(34) Gupta, A., Saha, P., Descoteaux, C., Leblanc, V., Asselin, E., and Berube, G. (2010) Design, synthesis and biological evaluation of estradiol-chlorambucil hybrids as anticancer agents. *Bioorg. Med. Chem. Lett. 20*, 1614−1618.

(35) Kuduk, S. D., Harris, C. R., Zheng, F. F., Sepp-Lorenzino, L., Ouerfelli, O., Rosen, N., and Danishefsky, S. J. (2000) Synthesis and evaluation of geldanamycin-testosterone hybrids. *Bioorg. Med. Chem. Lett. 10*, 1303−1306.
(36) Mitra, K., Marquis, J. C., Hillier, S. M., Rye, P. T., Zayas, B., Lee, A. S., Essigmann, J. M., and Croy, R. G. (2002) A rationally designed genotoxin that selectively destroys estrogen receptor-positive breast cancer cells. *J. Am. Chem. Soc. 124*, 1862−1863.
(37) Jiang, W., and Sui, Z. (2007) Preparation of 11-phosphorus steroid derivatives useful as progesterone receptor modulators. World Patent, WO2007098381A2, Aug 30, 2007.
(38) Jiang, X.-R., Wang, P., Fu, X., and Zhu, B. T. (2008) Chemical synthesis and biochemical characterization of a biotinylated derivative of 17α-estradiol with a long side chain covalently attached to its C-7α-position. *Steroids 73*, 1252−1261.
(39) Sharma, U., Marquis, J. C., Dinaut, A. N., Hillier, S. M., Fedeles, B., Rye, P. T., Essigmann, J. M., and Croy, R. G. (2004) Design, synthesis, and evaluation of estradiol-linked genotoxicants as anti-cancer agents. *Bioorg. Med. Chem. Lett. 14*, 3829−3833.
(40) Hussey, S. L., He, E., and Peterson, B. R. (2001) A synthetic membrane-anchored antigen efficiently promotes uptake of antifluorescein antibodies and associated protein a by mammalian cells. *J. Am. Chem. Soc. 123*, 12712−3.
(41) Pike, A. C., Brzozowski, A. M., Walton, J., Hubbard, R. E., Thorsell, A.-G., Li, Y.-L., Gustafsson, J.-A., and Carlquist, M. (2001) Structural insights into the mode of action of a pure antiestrogen. *Structure 9*, 145−153.
(42) Jayaprakash, S., Wang, X., Heston, W. D., and Kozikowski, A. P. (2006) Design and synthesis of a PSMA inhibitor-doxorubicin conjugate for targeted prostate cancer therapy. *ChemMedChem 1*, 299−302.
(43) Rajski, S. R., and Williams, R. M. (1998) DNA cross-linking agents as antitumor drugs. *Chem. Rev. 98*, 2723−2796.
(44) Skladanowski, A., and Konopa, J. (1993) Adriamycin and daunomycin induce programmed cell death (apoptosis) in tumour cells. *Biochem. Pharmacol. 46*, 375−82.
(45) Aryal, S., Grailer, J. J., Pilla, S., Steeber, D. A., and Gong, S. (2009) Doxorubicin conjugated gold nanoparticles as water-soluble and pH-responsive anticancer drug nanocarriers. *J. Mater. Chem. 19*, 7879−7884.
(46) Lee, C. C., Cramer, A. T., Szoka, F. C., and Frachet, J. M. J. (2006) An intramolecular cyclization reaction is responsible for the in vivo inefficacy and apparent ph insensitive hydrolysis kinetics of hydrazone carboxylate derivatives of doxorubicin. *Bioconjugate Chem. 17*, 1364−1368.
(47) Burke, P. J., Kalet, B. T., and Koch, T. H. (2004) Antiestrogen binding site and estrogen receptor mediate uptake and distribution of 4-hydroxytamoxifen-targeted doxorubicin -formaldehyde conjugate in breast cancer cells. *J. Med. Chem. 47*, 6509−6518.
(48) Burke, P. J., and Koch, T. H. (2004) Design, synthesis, and biological evaluation of doxorubicin-formaldehyde conjugates targeted to breast cancer cells. *J. Med. Chem. 47*, 1193−1206.
(49) Dreaden, E. C., Mwakwari, S. C., Sodji, Q. H., Oyelere, A. K., and El-Sayed, M. A. (2009) Tamoxifen-poly(ethylene glycol)- thiol gold nanoparticle conjugates: enhanced potency and selective delivery for breast cancer treatment. *Bioconjugate Chem. 20*, 2247−2253.
(50) Jordan, V. C. (2007) New insights into the metabolism of tamoxifen and its role in the treatment and prevention of breast cancer. *Steroids 72*, 829−842.
(51) Nique, F., Van de Velde, P., Bremaud, J., Hardy, M., Philibert, D., and Teutsch, G. J. (1994) 11β-Amidoalkoxyphenyl estradiols, a new series of pure antiestrogens. *Steroid Biochem. Mol. Biol. 50*, 21−29.
(52) Prat, D., Benedetti, F., Bouda, L. N., and Girard, G. F. (2004) Recent developments in the synthesis of 11β-aryl-estrone derivatives. *Tetrahedron Lett. 45*, 765−768.
(53) Hanson, R. N., Napolitano, E., and Fiaschi, R. (1998) Novel high-affinity steroidal estrogenic ligands: synthesis and receptor binding of 11β-vinyl-17α-[(E/Z)-(phenylselenovinyl)]estradiols. *Steroids 63*, 479−483.
(54) Hanson, R. N., Napolitano, E., and Fiaschi, R. (1998) Synthesis and evaluation of 11β-substituted 21-chloro/iodo-(17α,20E/Z)-19-norpregna-1,3,5(10),20-tetraene-3,17α-diols: high-affinity ligands for the estrogen receptor. *J. Med. Chem. 41*, 4686−4692.
(55) Hanson, R. N. Steroidal anti-hormone hybrids with quinone antibiotics as antitumor agents. World Patent WO2010085747A1, Jul 25, 2010.
(56) Hanson, R. N., Hua, E. Y., Labaree, D. C., Hochberg, R. B., Essigmann, J. M., and Croy, R. G. (2007) *AAPS J. 9*, 128−147.
(57) Torchilin, V. P. (2006) Multifunctional nanocarriers. *Adv. Drug Delivery Rev. 58*, 1532−1555.
(58) Torchilin, V. P. (2007) Targeted pharmaceutical nanocarriers for cancer therapy and imaging. *AAPS J. 9*, 128−147.
(59) Prabaharan, M., Grailer, J. J., Pilla, S., Steeber, D. A., and Gong, S. (2009) Amphiphilic multi-arm-block copolymer conjugated with doxorubicin via pH-sensitive hydrazone bond for tumor-targeted drug delivery. *Biomaterials 30*, 5757−5766.
(60) Chen, Q., Sowa, D. A., Cai, J., and Gabathuler, R. (2003) Synthesis of doxorubicin conjugates through hydrazone bonds to melanotransferrin P97. *Synth. Commun. 33*, 2377−2390.
(61) Rodrigues, P. C. A., Beyer, U., Schumacher, P., Roth, T., Fiebig, H. H., Unger, C., Messori, L., Orioli, P., Paper, D. H., Mülhaupt, R. M., and Kratz, F. (1999) Acid-sensitive polyethylene glycol conjugates of doxorubicin: preparation, in vitro efficacy and intracellular distribution. *Bioorg. Med. Chem. 7*, 2517−2524.
(62) Rodrigues, P. C. A., Roth, T., Fiebig, H. H., Unger, C., Mülhauptc, R., and Kratz, F. (2006) Correlation of the acid-sensitivity of polyethylene glycol daunorubicin conjugates with their in vitro antiproliferative activity. *Bioorg. Med. Chem. 14*, 4110−4117.
(63) Pietras, R. J., and Marquez-Garban, D. C. (2007) Membrane-associated estrogen receptor signaling pathways in human cancer. *Clin. Cancer Res. 13*, 4672−4676.
(64) Jordan, V. C. (2007) SERMs: meeting the promise of multifunctional medicines. *J. Natl. Cancer Inst. 99*, 350−356.
(65) Kasiotis, K. M., Magiatis, P. P., Pratsinis, H., Skaltsounis, A. L., Abadji, V., Charlambous, A., Moutsatsou, P., and Haroutounian, S. A. (2001) Synthesis and biological evaluation of novel daunorubicin-estrogen conjugates. *Steroids 66*, 785.
(66) Olofson, R. A., Martz, J. T., Senet, J. P., Piteau, M., and Malfroot, T. (1984) A new reagent for the selective, high-yield N-dealkylation of tertiary amines: improved syntheses of naltrexone and nalbuphine. *J. Org. Chem. 49*, 2081−2082.
(67) Mimnaugh, E. G., Fairchild, C. R., Fruehauf, J. P., and Sinha, B. K. (1991) Biochemical and pharmacological characterization of MCF-7 drug-sensitive and Adr multidrug-resistant human breast tumor xenografts in athymic mice. *Biochem. Pharmacol. 42*, 391−402.
(68) King, H. D., Dubowchik, G. M., Mastalerz, H., Willner, D., Hofstead, S. J., Firestone, R. A., Lasch, S. J., and Trai, P. A. (2002) Monoclonal antibody conjugates of doxorubicin prepared with branched peptide linkers: inhibition of aggregation by methoxytriethyleneglycol chains. *J. Med. Chem. 45*, 4336−4343.
(69) Taatjes, D. J, Fenick, D. J., and Koch, T. H. (1999) Nuclear targeting and nuclear retention of anthracycline-formaldehyde conjugates implicates dna covalent bonding in the cytotoxic mechanism of anthracyclines. *Chem. Res. Toxicol. 12*, 588−596.
(70) Taatjes, D. J., and Koch, T. H. (1999) Growth inhibition, nuclear uptake, and retention of anthracycline-formaldehyde conjugates in prostate cancer cells relative to clinical anthracyclines. *Anticancer Res. 19*, 1201−1208.

Bioconjugate Chemistry

Article

pubs.acs.org/bc

Dual Function of RGD-Modified VEGI-192 for Breast Cancer Treatment

Jueheng Wu,[†,‡,#] Yi Jiang,[§,¶,#] Wan Yang,[⊥,#] Zhenjian He,[†,‡] Shiyu Meng,[⊥] Qianhui Zhang,[⊥] Min Lin,[⊥] Henan Zhang,[⊥] Weifeng Li,[⊥] Yaochao Yang,[⊥] Yiqun Jia,[⊥] Liang Qian,[⊥] Dihan Lu,[⊥] Wenjia Cai,[⊥] Guotian Luo,[⊥] Yesong Wang,[*,§] Xun Zhu,[*,†,‡] and Mengfeng Li[†,‡]

[†]Key Laboratory of Tropical Disease Control (Sun Yat-sen University), Ministry of Education, 74 Zhongshan Road II, Guangzhou 510080, China

[‡]Department of Microbiology, [⊥]Department of Clinical Medicine, Zhongshan School of Medicine, Sun Yat-sen University, 74 Zhongshan Road II, Guangzhou 510080, China

[§]Department of Cardiology, The First Affiliated Hospital of Sun Yat-Sen University, 58 Zhongshan Road II, Guangzhou 510080, China

[¶]Department of Cardiology, The First People's Hospital of Zigong, 42 Shangyihao Road I, Zigong 643000, China

Supporting Information

ABSTRACT: Identification of endogenous angiogenesis inhibitors has led to development of an increasingly attractive strategy for cancer therapy and other angiogenesis-driven diseases. Vascular endothelial growth inhibitor (VEGI), a potent and relatively nontoxic endogenous angiogenesis inhibitor, has been intensively studied, and this work shed new light on developing promising anti-angiogenic strategies. It is well-documented that the RGD (Arg-Gly-Asp) motif exhibits high binding affinity to integrin $\alpha_v\beta_3$, which is abundantly expressed in cancer cells and specifically associated with angiogenesis on tumors. Here, we designed a fusion protein containing the special RGD-4C motif sequence and VEGI-192, aimed at offering more effective multiple targeting to tumor cells and tumor vasculature, and higher anti-angiogenic and antitumor efficacy. Functional tests demonstrated that the purified recombinant human RGD-VEGI-192 protein (rhRGD-VEGI-192) potently inhibited endothelial growth in vitro and suppressed neovascularization in chicken chorioallantoic membrane in vivo, to a higher degree as compared with rhVEGI-192 protein. More importantly, rhRGD-VEGI-192, but not rhVEGI-192 protein, could potentially target MDA-MB-435 breast tumor cells, significantly inhibiting growth of MDA-MB-435 cells in vitro, triggered apoptosis in MDA-MB-435 cells by activation of caspase-8 as well as caspase-3, which was mediated by activating the JNK signaling associated with upregulation of pro-apoptotic protein Puma, and consequently led to the observed significant antitumor effect in vivo against a human breast cancer xenograft. Our study indicated that the RGD-VEGI-192 fusion protein might represent a novel anti-angiogenic and antitumor strategy.

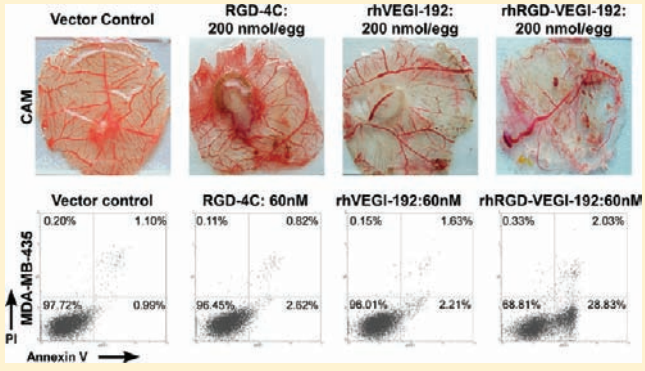

INTRODUCTION

Angiogenesis as a biological process is key to many physiological functions as well as pathological conditions in humans.[1] In the scenario of cancer, it has been widely recognized that angiogenesis is essential for tumor growth and dissemination. Discovery of numerous endogenous anti-angiogenic factors or development of angiogenesis inhibitors during the past decades has led to development of the anti-angiogenic strategy using tumor vasculature as a therapeutic target.[1,2] Numerous anti-angiogenic agents are under active development to achieve effective and safe anti-angiogenic cancer therapy.

Vascular endothelial growth inhibitor (VEGI), a cytokine belonging to the tumor necrosis factor (TNF) superfamily,[3] was identified as an endothelial cell-specific gene and a potent endogenous inhibitor of endothelial cell proliferation, angiogenesis, and tumor growth. Three distinguishable splicing isoforms of VEGI have been found, namely, VEGI-174, VEGI-251, and VEGI-192, which differ in their N-terminal regions but share an identical C-terminal 151-residue segment.[4−8] These isoforms displayed various degrees of anti-angiogenic activities when tested in their natural or recombinant forms. The initially reported VEGI protein was composed of 174 amino acids and designated VEGI-174. Previous reports have demonstrated that the recombinant human VEGI-174 (rhVEGI-174) inhibits angiogenesis in vitro as well as in animal models bearing

Received: December 5, 2011
Revised: February 29, 2012
Published: March 29, 2012

experimental tumors, in spite of the fact that the molecule is essentially insoluble in aqueous solutions.[4,5] VEGI-251, the product of the most abundant VEGI variants, was found to be a secreted protein. Ectopic expression of VEGI-251 in tumor cells causes apoptosis of endothelial cells in the tumor vasculature, reduction of microvessel density, and inhibition of tumor growth, although purified recombinant VEGI-251 protein lacks anti-angiogenic activity.[7,9,10] A new isoform of VEGI, VEGI-192, consisting of 192 amino acids, was identified by Chew et al. recently. Previous experiments showed that VEGI-192 was approximately 20-fold more potent than endostatin in its anti-angiogenic effect in vitro. In vivo study showed that purified recombinant human VEGI-192 (rhVEGI-192) gave rise to a significant inhibition of tumor growth and angiogenesis when systemically administrated to LLC tumor-bearing C57BL/6 mice. Meanwhile, treatment with rhVEGI-192 exhibited no toxicity to liver and kidneys, and did not damage endothelial cells in normal and quiescent vasculature.[7,8,11] Moreover, rhVEGI-192 has better solubility than rhVEGI-174. It was previously reported that VEGI could mediate the following two activities in endothelial cells: (1) early G1 arrest in G0/G1 cells responding to growth stimuli, and (2) programmed death in proliferating cells.[6] The mechanism underlying the VEGI-induced increase of endothelial cell apoptosis had been described as VEGI directly activating c-Jun N-terminal kinase (JNK), which is required for VEGI-mediated apoptosis of proliferating endothelial cells. In one previous study, we developed an improved preparation method for producing rhVEGI-192 with high yield, solubility, and bioactivity, and first demonstrated that VEGI-192 is capable of forming a polymeric structure, which is possibly essential for its anti-angiogenic activity.[12]

On the other hand, it is well-established that amino acid sequence Arg-Gly-Asp (RGD) binds cell adhesion receptors, including numerous integrins, and is capable of triggering signals that leads to cell adhesion.[13,14] Among RGD-binding integrins, integrin $\alpha_v\beta_3$ is highly expressed on the surface of tumor cells and neovascular endothelial cells. Furthermore, integrin $\alpha_v\beta_3$ is responsible for capillary regression by inducing apoptosis when it binds to RGD peptides.[15,16] Interestingly, integrin $\alpha_v\beta_3$ is not expressed in normal and quiescent vessels, which makes the receptor a potential target for cancer-specific anti-angiogenic therapy.[15,17] It has been reported that coupling tumor necrosis factor-alpha (TNF-α),[18] Fc fragment of mouse immunoglobulin G,[19] or endostatin[20,21] with the RGD motif could improve the anti-angiogenic and antineoplastic activities of the proteins. Furthermore, various fusion proteins carrying the RGD motif peptides have been designed to target integrin $\alpha_v\beta_3$, and among them, RGD-4C with sequence ACDCRGDCFC peptide showed highly selective activity.[22−24]

Recently, it was reported that death receptor 3 (DR3), a member of the TNF receptor superfamily, might be the receptor of VEGI-251 in T cells and dendritic cells.[9,25] The crystal structure, receptor-binding property, and pharmacokinetics of VEGI-192, however, have not been clearly defined. In order to investigate whether the vascular inhibition approach based on the use of VEGI-192 could be targeted to other molecular targets of tumor cells and tumor blood vessels, such as integrin $\alpha_v\beta_3$, so that VEGI-192 can be selectively delivered to the endothelial lining of tumor vessels while sparing normal vessels, we conducted a study evaluating the anti-angiogenic and antineoplastic properties of RGD-4C fused VEGI-192 conjugate (rhRGD-VEGI-192). We found that the rhRGD-VEGI-192 fusion protein exhibited a higher level of anti-angiogenic activity as compared with the parental rhVEGI-192. We further demonstrated that rhRGD-VEGI-192 reagent could target the breast cancer-orignating cell line MDA-MB-435 in which α_v integrin was predominately expressed, leading to significantly antitumor effect in breast tumor-bearing animals.

EXPERIMENTAL PROCEDURES

Preparation of rhVEGI-192, RGD, and RGD-rhVEGI-192. Unless otherwise stated, routine laboratory chemicals, bacterial culture reagents, antibiotics, and disposable labware were purchased from the Sangon Biotech (Shanghai, China), Sigma-Aldrich (St. Louis, MO), or BBI (Gaithersburg, MD). rhVEGI-192 expression plasmid pET-19b-rhVEGI-192 was constructed as previously described.[8] The cDNA coding region for RGD-VEGI-192 (human VEGI-192 fused with the COOH-terminus of ACDCRGDCFCG motif) was obtained by PCR engineering of plasmid containing the VEGI-192 cDNA sequence, using the following primers: 5′-TTCCATATGG-CTTGCGACTGCCGTGGTGACTGCTTCTGCGGTC-AACTCACAAAGGGCCGTCT-3′ (5′primer); 5′-CGCG-GATCCCTATAGTAAGAAGGCTCCAAAGAAGGTT-3′ (3′primer). Primer sequences were designed to include the *Nde I* and *Bam*HI restriction sites for PCR-cloning into a prokaryotic expression vector pET-19b (Novagen, Darmstadt, Germany). Briefly, expression and purification of rhVEGI-192 or rhRGD-VEGI-192 protein were performed according to a standard method as previously described,[12] by using a combination of Origami B (DE3) strain, autoinduction expression system, and affinity chromatography. Vector control was the product obtained by expression of the pET-19b vector, without rhVEGI-192 or rh-RGD-VEGI-192, using the same purification procedure as described above. RGD-4C (ACDCRGDCFCG) peptides were synthesized and purified by the Chinese Peptide Company (Hangzhou, China).

Cell Viability Assay. Human umbilical endothelial cells (HUVEC) were grown in human umbilical endothelial cell serum-free medium (Gibco-Invitrogen, Carlsbad, CA), supplemented with 15 g/mL endothelial cell growth supplements (Upstate, Billerica, MA, USA). Human breast cancer-originated cell line MDA-MB-435 and adult bovine aortic endothelial cells (ABAE) were cultured in DMEM (Invitrogen, Carlsbad, CA), supplemented with 10% fetal bovine serum (FBS) (Hyclone, Logan, UT), 2 ng/mL bFGF, 2 mM L-glutamine, 100 μg/mL streptomycin, and 100 units/mL penicillin (Invitrogen, Carlsbad, CA). All of the cells used in this study were maintained at 37 °C in a humidified atmosphere of 5% CO_2.

For cell viability assays, cells were seeded in 96-well flat-bottom plates at a density of 1×10^4 cells/well, and cultured for 24 h, followed by exposure to various concentrations of RGD-4C, rhVEGI-192, or rhRGD-VEGI-192, respectively, for 48 h. Subsequently, the MTT (3-(4, 5-dimethylthiazol-2-yl)-2,5-diphenyl tetrazolium bromide) reagent (Genview, Houston, TX) was added to each well to a final concentration of 0.5 mg/mL, followed by an additional incubation for 4 h. The MTT-formazan crystals formed were dissolved in 150 μL DMSO, and the absorbance was measured at 570 nm with a reference wavelength of 630 nm using a microplate reader (Bio-Tek Synergy 2, Winooski, VT). Cell viabilities of the vector control group and the tested groups were expressed as a percentage of mean cell viability value of the vector control group as previously described.[12,26] All experiments were performed in triplicate, and the half-maximal inhibitory concentration (IC_{50})

dx.doi.org/10.1021/bc2006576 | *Bioconjugate Chem.* 2012, 23, 796−804

was calculated with the Bliss's software[12,26] and analyzed using the *SPSS* statistics software.

MDA-MB-435 Cell Adhesion Assay. The cell adhesion assay was done as previously described.[18,27] Briefly, 48-well flat-bottom plates (Greiner Bio-One, Frickenhausen, Germany) were coated with rhVEGI-192 or rhRGD-VEGI-192 proteins at various concentrations, and uncoated wells were used as the control group. Then, each well was rinsed with PBS, and blocked with DMEM containing 2% BSA for 1 h at 37 °C. Plates were washed again and air-dried. MDA-MB-435 cells were serum-starved for 45 min, and seeded in 200 μL basic DMEM (5×10^4) and allowed to attach for 1 h at 37 °C, 5% CO_2. Non-adherent cells were removed by washing with basic DMEM three times. The MTT assay was performed to quantify the numbers of adherent cells, by measuring the absorbance of each well at 570 nm using a microplate reader (Bio-Tek Synergy 2, Winooski, VT). Cell adhesion (%) = (OD of treated cells/OD of control cells) × 100%.[18,27]

Annexin V-FITC/PI Staining Assay. Cells were seeded in 60 mm plates and allowed to settle down for 24 h before treatment with purified RGD-4C, rhVEGI-192, and rhRGD-VEGI-192 protein, respectively, for 12 h. Subsequently, cells were trypsinized after washing with PBS three times, incubated in 500 μL binding buffer containing annexin V-FITC and propidium iodide (PI) in the dark for 15 min at room temperature, according to the manufacturer's instructions (Keygen Biotech, Nanjing, China), and measured for Annexin V-FITC binding and PI staining using flow cytometric analysis (FACS Calibur cytometer, Becton-Dickinson, San Jose, CA). The percentage of stained cells was defined by their distribution in a fluorescence dot plot using *WinMdi 2.8* software (Scripps Research Institute, La Jolla, CA).

Western Blotting Analysis. After treatment with rhVEGI-192, RGD-4C, or rhRGD-VEGI-192 at a final concentration of 10 nM or 60nM for 24 h, floating cells, and adherent cells were collected and lysed in 1× sample buffer containing 50 mM Tris-HCl (pH 7.4), 1 mM PMSF, 10% glycerol, 6% SDS, 5% mercaptoethanol, and 0.1% bromophenol blue before sonication. The protein concentration of the extracts was determined by the Bicinchoninic Acid Protein Assay Kit (Thermo Fisher Scientific, Rockford, IL) according to the manufacturer's instructions with BSA as the standard. The total cell lysate (40 μg of protein) was subjected to SDS-PAGE, and then transferred to PVDF membranes. After blocking with blocking buffer (Tris-buffered saline, TBS, containing 5% nonfat milk) for 1 h at room temperature, the membranes were incubated overnight at 4 °C with specific primary antibodies, namely, mouse antihuman caspase-8 antibody (BD Biosciences, San Jose, CA); rabbit antihuman caspase-3, Phospho-SAPK-JNK (Thr183-Tyr185) (81E11), phospho-c-Jun (Ser63), phospho-c-Jun (Ser73), SAPK/JNK, c-Jun (60A8), or Puma antibodies (Cell Signaling, Beverly, MA); and monoclonal anti-actin antibody (Sigma-Aldrich, St. Louis, MO); and further incubated with the corresponding horseradish peroxidase (HRP)-conjugated secondary antibody for 1.5 h at room temperature. Membranes were washed three times in Tris-buffered saline containing 0.1% Tween-20 for 10 min after each incubation step. The bands were detected using enhanced chemiluminescence kit (Thermo Fisher Scientific, Rockford, IL) with a Kodak film. Actin was used as a loading control for quantity normalization. Intensities of the bands of interest on the PVDF membranes were quantitatively calculated with the *Quantity One 4.6.3* measurement software (Bio-Rad, Hercules, CA).

Chicken Chorioallantoic Membrane Assay. To determine anti-angiogenic activity, chorioallantoic membrane (CAM) assay was performed as previously described.[12,28] Briefly, a window of 1 cm in diameter was opened in the shell of each egg with 8-day-old chicken embryo (Yueqin Breeding Co. Ltd., Guangdong, China). The surface of the dermic sheet on the floor of the air sac was removed to expose the CAM. A filter paper of 0.5 cm in diameter was suspended in 200 nmol rhVEGI-192, rhRGD-VEGI-192, RGD-4C preparation, or the vector control as described above, respectively, and subsequently placed on top of the CAM. After the window was closed with sterile adhesive tape, the eggs were incubated at 37 °C under 80−90% relative humidity for 48 h. Following fixation with stationary solution (methanol:acetone = 1:1) for 15 min, the CAM was cut and harvested, and gross photos of each CAM were taken under a digital camera (Panasonic, Osaka, Japan). Microscopic photos of each CAM were taken under an inverted microscope (Zeiss Axiovert100M, Carl Zeiss, Germany). The angiogenic score was determined by scoring from 0 to 3 the appearance of the brush-like capillary formation by two independent observers, and the angiogenic inhibition of the tested groups was expressed as a percentage of mean angiogenic score value of the vehicle-control group, as previously described.[12,28]

Mice Xenograft Tumor Model and in Vivo Antitumor Effects by rhRGD-VEGI-192. Female BALB/c-nu mice (18−20 g) were purchased from Center of Experiment Animal of Guangzhou University of Chinese Medicine, and were housed in barrier facilities on a 12 h light/dark cycle. On day zero, MDA-MB-435 cells (5×10^6 cells in 0.1 mL) were implanted subcutaneously just in the right mammary gland of each mouse. Mice were then ear-tagged and randomly divided into three groups in a blinded fashion before treatment. On day 6, the tumors were measured and the mice were divided into treated and control groups. The three groups of treated animals received an intraperitoneal (i.p.) dosage of 100 μL rhVEGI-192 protein (1 mg/kg body weight) and rhRGD-VEGI-192 (1 mg/kg body weight) every four days, while the control animals received daily i.p. doses of 100 μL deionized−distilled H_2O (Vector Control). Tumors were measured every four days in a blinded manner, and the tumor size was assessed by measuring perpendicular diameters with a digital caliper. The volumes were determined using the formula, volume = width × width × length × $\pi/6$. Data were expressed as the mean ± standard deviation (S.D.) of six mice in each group. Approximately 30 days later, the tumors were extracted. All experimental procedures were approved by The Institutional Animal Care and Use Committee at the University of Sun Yat-sen University.

Statistical Analysis. The data given in the text were presented as means ± standard deviation (S.D.). Comparison between two groups was evaluated by the two-tailed Student's *t* test, with 0.05 as the cutoff *P* value.

RESULTS

rhRGD-VEGI-192 Exhibited an Enhanced Inhibitory Effect on the Growth of Endothelial Cells and Breast Cancer Cells. rhVEGI-192 and rhRGD-VEGI-192 proteins were produced by autoinduction techniques and immobilized-metal affinity chromatography on Ni-NTA column. The purified products were examined using nonreducing SDS−

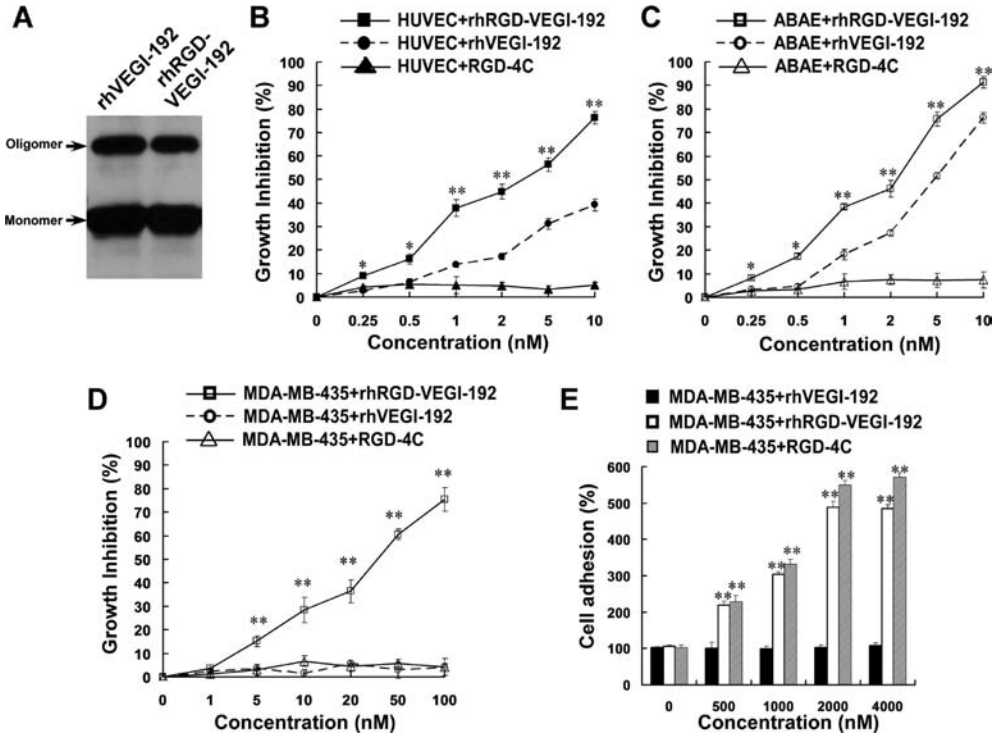

Figure 1. Angiogenesis inhibition by purified rhVEGI-192 and rhRGD-VEGI-192 protein in vitro. (A) Western blotting analysis of purified rhVEGI-192 and rhRGD-VEGI-192 proteins by nonreducing SDS-PAGE. (B,C,D) Dose−response curve of RGD-4C peptides, rhVEGI-192, and rhRGD-VEGI-192, respectively, on the growth of HUVEC (B), ABAE (C), and MDA-MB-435 cells (D) after treatment for 48 h. Cell viabilities were determined by MTT assay. (E) Adhesion of MDA-MB-435 cells to solid phases coated with rhVEGI-192 or rhRGD-VEGI-192 protein. Data points are presented as means ± SD of triplicated experiments. Student's two-tailed *t* test was performed and statistical differences are shown with asterisks (* indicates $P < 0.05$, and ** indicates $P < 0.01$).

PAGE, as well as Western blotting analysis. The results revealed that rhVEGI-192 and rhRGD-VEGI-192 preparations contained the same proportion of oligomers, namely, 25.93% and 24.89% of total protein, respectively (Figure 1A), and it achieved the high degree of purity (>95%) for the target protein (Supporting Information Figure S1). The effects of rhVEGI-192 and rhRGD-VEGI-192 protein on the growth of HUVEC, ABAE, and MDA-MB-435 were investigated using the MTT assay. Upon treatment of RGD-4C, rhVEGI-192, or rhRGD-VEGI-192 for 48 h with varying concentrations, as shown in Figure 1 (B,C), cultured HUVEC and ABAE exhibited marked inhibition of growth as compared with vehicle-controlled cells in a dose-dependent manner. rhRGD-VEGI-192, but not rhVEGI-192 protein, significantly inhibited growth of MDA-MB-435 in vitro (Figure 1D). The IC_{50} values of rhVEGI-192 were 25.9 nM and 5.7 nM, respectively, against HUVEC and ABAE, in comparison with the IC_{50} of 4.5 nM, 2.6 nM, and 35.6 nM against HUVEC, ABAE, and MDA-MB-435, respectively, for rhRGD-VEGI-192. Meanwhile, the RGD-4C peptides within these same concentrations showed no cytotoxicity on HUVEC, ABAE, and MDA-MB-435. These data suggested that rhRGD-VEGI-192 protein possessed higher inhibitory activity on endothelial growth, and exhibited a marked inhibition on the survival of the human breast cancer cell.

rhRGD-VEGI-192 Promotes Cell Adhesion and Spreading. To assess whether the RGD domain of rhRGD-VEGI-192 protein is functional and accessible to integrins, we compared the cell pro-adhesive properties of rhVEGI-192 and rhRGD-VEGI-192 in a MDA-MB-435 cell adhesion assay. This assay takes advantage of the fact that RGD motif is the minimal recognition sequence of many integrins so that it can serve as an adhesion motif, and the MDA-MB-435 breast carcinoma highly expresses α_v integrins. We observed adhesion and spreading of MDA-MB-435 cells on plates coated with rhRGD-VEGI-192 but not with rhVEGI-192 (Figure 1E). These results strongly suggested that the RGD domain of rhRGD-VEGI-192 was properly folded and able to interact with adhesion receptors, very likely integrins, on tumor cell membrane.

rhRGD-VEGI-192 Induced Stronger Apoptosis in HUVEC and MDA-MB-435. To determine whether the stronger loss of endothelial and cancer cell viability induced by rhRGD-VEGI-192 was associated with enhanced apoptosis, Annexin V/Propidium iodide (PI) dual staining assay was employed. Following treatment with 20 nM of RGD-4C, rhVEGI-192, or rhRGD-VEGI-192 on proliferating HUVEC cells, and 60 nM of each protein on MDA-MB-435 cells for 12 h, 10.13% and 52.82% of rhVEGI-192 and rhRGD-VEGI-192-treated HUVEC, and 28.83% of rhRGD-VEGI-192-treated MDA-MB-435, respectively, were identified as annexin V+/PI- cells (Figure 2A,B). To further understand the apoptotic pathway involved in rhRGD-VEGI-192-induced cell death, key caspases were examined using Western blotting. As shown in Figure 2C,D, rhRGD-VEGI-192 protein treatment led to stronger-activating cleavage of caspase-8 and caspase-3, displaying a dramatic increase of cleaved bands accompanied by a reduction in the level of the pro-caspases. However, the effect of rhVEGI-192 protein on apoptosis in MDA-MB-435, and RGD-4C peptides on apoptosis in HUVEC and MDA-MB-435 was far milder. These data suggested that the rhRGD-VEGI-192 fusion protein triggered stronger apoptosis in endothelial cells as well as breast cancer cells.

dx.doi.org/10.1021/bc2006576 | *Bioconjugate Chem.* 2012, 23, 796−804

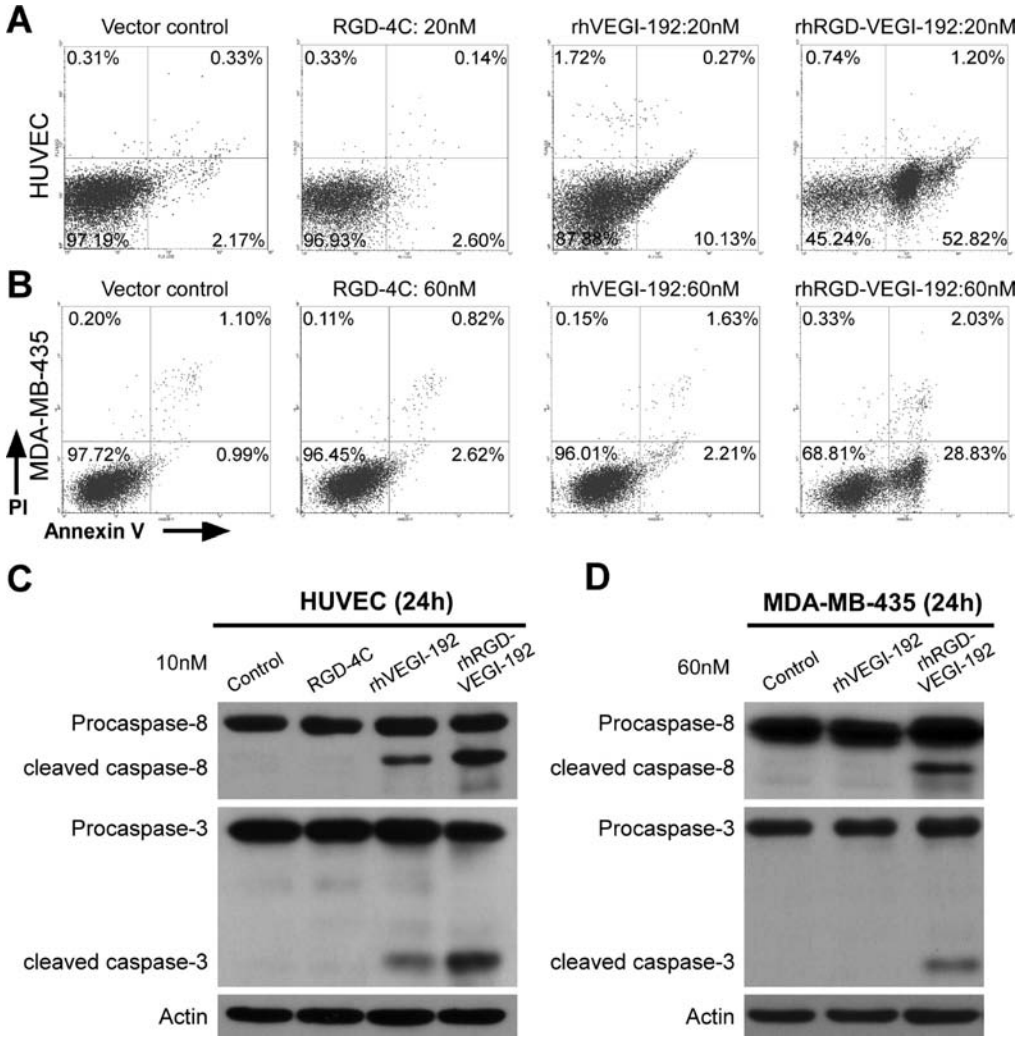

Figure 2. Induction of apoptosis in proliferating HUVEC by purified rhVEGI-192 or rhRGD-VEGI-192 protein. (A,B) Annexin V-FITC/PI staining of HUVEC and MDA-MB-435 treated with rhVEGI-192 or rhRGD-VEGI-192 as indicated. 24 h after the time of seeding (when the cells were undergoing proliferation), cells were exposed to vector control, RGD-4C peptides, rhVEGI-192, and rhRGD-VEGI-192 protein (20 nM or 60 nM) for 12 h. Cells were collected and subjected to Annexin V-FITC/PI double staining and analyzed using flow cytometry. (C,D) Western blotting analysis of caspases-8 and -3 in HUVEC or MDA-MB-435 after RGD-4C (10 nM), rhVEGI-192 (10 nM or 60 nM), or rhRGDVEGI-192 (10 nM or 60 nM) treatment for 24 h using antibodies against caspase-8 and caspase-3. Actin was used as an internal control.

Differential Activation of JNK Signaling in HUVEC and MDA-MB-435 by rhRGD-VEGI-192 versus rhVEGI-192. Because VEGI can directly activate c-Jun N-terminal kinase (JNK) in proliferating endothelial cells, which is required for VEGI-mediated apoptosis,[6] to further understand the signaling cascade that mediates the pro-apoptotic effect of rhRGD-VEGI-192 on HUVEC and MDA-MB-435, changes in phosphorylation status of JNK and its downstream substrates such as c-Jun and Puma were examined. As shown in Figure 3A, the RGD-4C peptide at 10 nM showed little effect on the activation of JNK signaling pathway, while rhRGD-VEGI-192 at 10 nM led to a drastic increase of the levels of p46 and p54 JNKs when tested for the phosphorylation at Thr183 or Tyr185 without an effect on the expression of total JNK in HUVEC, as compared with rhVEGI-192 protein. Such an effect was accompanied by significantly elevated levels of phosphorylated c-Jun at serine 63 and serine 73. More importantly, the peak activities of JNK, c-Jun (Ser63), and c-Jun (Ser73) in MDA-MB-435 cells were significantly increased by rhRGD-VEGI-192 but not by rhVEGI-192 treatment (Figure 3B). In parallel with the increased c-Jun phosphorylation, the downstream substrate of c-Jun, Puma, a pro-apoptotic protein, was upregulated to a higher level in response to the rhRGD-VEGI-192 treatment.

Enhanced Anti-Angiogenic Activity of rhRGD-VEGI-192 in Vivo. The inhibitory effect of rhRGD-VEGI-192 on new blood vessel formation was investigated using the CAM model, and the angiogenic scores were evaluated. While no inhibitory effect of the RGD-4C peptide on new blood vessel formation was detected, treatment with rhVEGI-192 or rhRGD-VEGI-192 protein led to a strong brush-like capillary inhibition and a marked reduction in vessel density (Figure 4A–D), achieving a 39.39% or 73.69% reduction of vessel density, respectively, when applied at 200 nmol protein per egg (Figure 4E,F), indicating that the rhRGD-VEGI-192 fusion protein was more effective in suppressing neovascularization.

Improved Antitumor Effect of rhRGD-VEGI-192 in Vivo. Then, we evaluated the in vivo anticancer activity of the rhRGD-VEGI-192 compared to rhVEGI-192 proteins in human breast cancer xenograft nude mice model. Following injection with 1 mg/kg of rhVEGI-192 or rhRGD-VEGI-192, a

dx.doi.org/10.1021/bc2006576 | *Bioconjugate Chem.* 2012, 23, 796–804

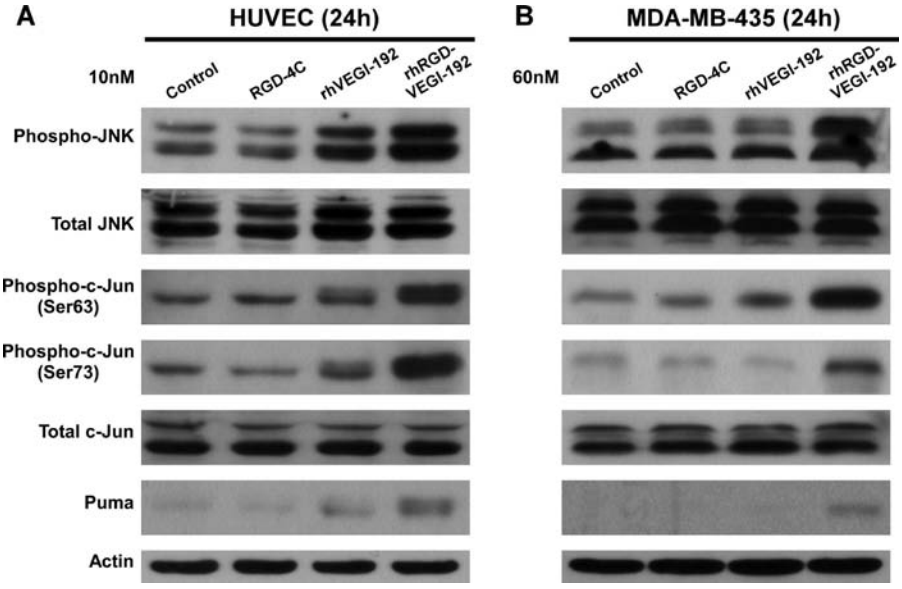

Figure 3. Effects of rhVEGI-192 and rhRGD-VEGI-192 protein on the JNK signaling pathway in HUVEC and MDA-MB-435 cells. Representative blots of phosphorylated and total JNK1/2 and c-Jun in HUVEC cells (A) and MDA-MB-435 (B) treated as indicated. Cells were treated with RGD-4C, rhVEGI-192, or rhRGD-VEGI-192 at 10 nM or 60 nM for 24 h as noted. Western blotting analysis was performed using antibodies against phospho-JNK, total JKN, phospho-c-Jun (ser 63), phosphoc- Jun (ser73), total c-Jun, or Puma, actin was used as a loading control.

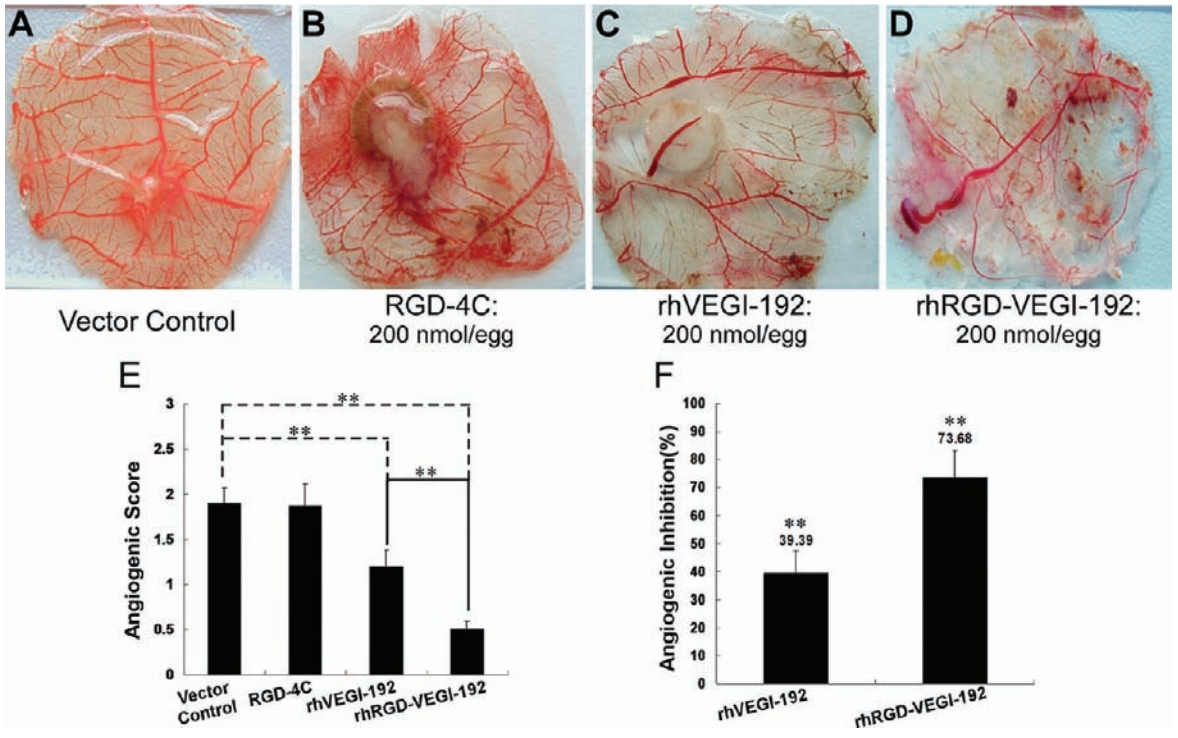

Figure 4. Anti-angiogenic activity of rhVEGI-192 and rhRGD-VEGI-192 tested by CAM assay. Direct camera images (A–D) of representative CAMs treated with indicated conditions: A, vehicle-control, $n = 6$; B, RGD-4C, $n = 6$; C, rhVEGI-192, $n = 6$; D, rhRGD-VEGI-192, $n = 6$. Angiogenic score (E) and inhibition rates (F) of new blood vessel formation within CAM by rhVEGI-192 or rhRGD-VEGI-192. Data for the quantitative assessment of angiogenesis inhibition are presented as means ± SD. Student's two-tailed t test was performed to show significant differences (* $P < 0.05$; ** $P < 0.01$).

marked inhibition of the growth of the xenograft tumors formed by the MDA-MB-435 cells was observed, and RGD-4C peptides itself showed no antitumor effect (Figure 5A, and Supporting Information Figure S2). When the tumor volumes were assessed on day 6 after inoculation, all the group of animals had developed tumors (6 of 6 or 100%), with a mean volume (±S.D.) of about 30 mm^3. After 6 times of administration, the volume of the xenografted breast tumor was significantly inhibited by 65.74% in 1 mg/kg rhRGD-VEGI-192-treated nude mice, respectively, while inhibited by 35.11% in 1 mg/kg rhVEGI-192-treated nude mice. In addition, the mean weight of the transplanted tumors was significantly

dx.doi.org/10.1021/bc2006576 | Bioconjugate Chem. 2012, 23, 796–804

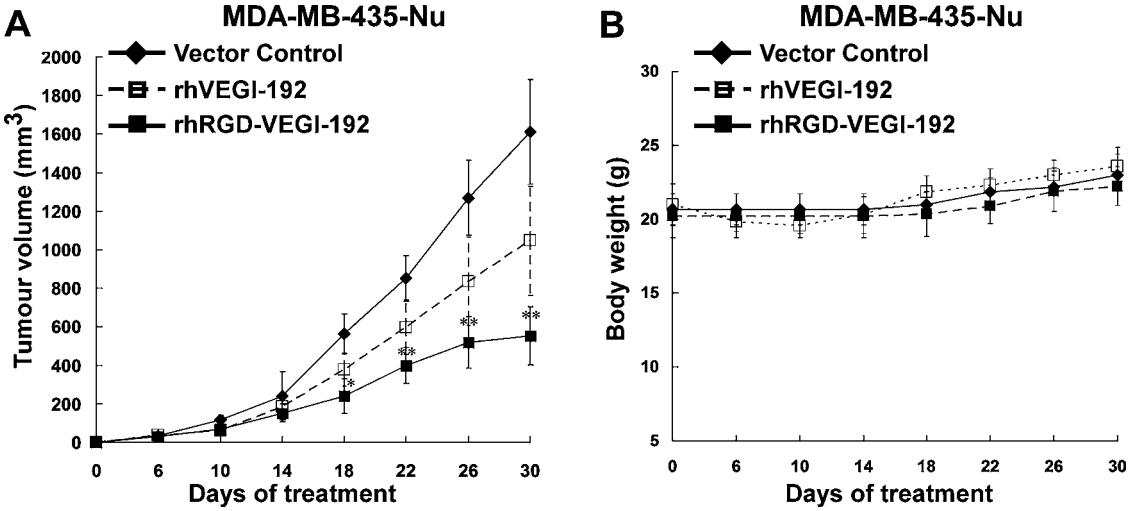

Figure 5. In vivo antitumor effect of rhRGD-VEGI-192 on xenografted MDA-MB-435 tumor in nude mice. Viable MDA-MB-435 cells (5 × 106 cells/mouse) were inoculated subcutaneously in the right mammary gland of female nude mice (six mice each group). After solid tumor formation, the mice received an intraperitoneal injection of rhRGD-VEGI-192 (1 mg/kg), rhVEGI-192 (1 mg/kg), or vehicle control (deionized−distilled H_2O) every four days. Data are expressed in the format of mean ± standard deviation (S.D.) of six mice in each group. Student's two-tailed *t* test was performed, and statistical differences are shown with asterisks (* indicates $P < 0.05$, and ** indicates $P < 0.01$).

inhibited by by 41.97% and 71.89%, respectively. However, we did not observe any signs of discomfort, behavioral changes, or weight loss (Figure 5B) in the rhVEGI-192 or rhRGD-VEGI-192-treated animals compared to the untreated animals. These data strongly suggested that systemically delivered rhRGD-VEGI-192 was able to inhibit the growth of established breast tumor in mice, and rhRGD-VEGI-192 was much more effective than rhVEGI-192 in inhibiting tumor formation.

DISCUSSION

It has been well-documented that VEGI represents a potent endogenous inhibitor of angiogenesis. Our previous work was the first report on developing a preparative system for efficient expression and purification of intact and biologically active rhVEGI-192 protein, for which the choice of bacterial strain, method of expression induction, purification protocol, and refolding strategy were determined to achieve optimal production of pure and highly bioactive rhVEGI-192 protein. It is also of note, as demonstrated by our previous study, that VEGI-192 was capable of forming polymeric structure and such polymerization might be essential for its anti-angiogenic activity.[12] To explore a strategy that leads to a more effective neovascular-targeted anti-angiogenic activity of the rhVEGI-192, we investigated the feasibility of employing an integrin-targeting approach to enhance the efficacy selectively against tumor angiogenesis and tumor formation. In addition, the main finding of the present study demonstrates that these can be achieved by fusing VEGI-192 with the RGD-4C motif (ACDCRGDCFC peptide), a ligand of $\alpha_v\beta_3$ integrin.

Recently, a number of different RGD peptides, linear or cyclic, have been developed, and chemically designed peptidomimetics are currently being tested for their therapeutic efficacies.[13,16,18,19,22,24] Wadih Arap et al. found that three main peptide motifs were able to interact with angiogenic endothelium markers, and to home selectively to the tumor blood vessels, including several tumor types such as carcinoma, sarcoma, and melanoma.[22] One of these motifs, ACDCRGDCFC (termed RGD-4C), embedded in a peptide structure could bind selectively to integrins $\alpha_v\beta_3$ and $\alpha_v\beta_5$ of the cell membrane, and home to tumor vasculature in a highly selective manner. The RGD-4C motif has proven useful for delivering various antitumor compounds, such as chemotherapeutic drugs and pro-apoptotic peptides, to tumor vessels.[22,23] Furthermore, several lines of evidence have suggested that a cyclic RGD peptide with the possibility of two pairs of disulfide bonds altered the binding activity of the peptide and exhibited a greater affinity than a linear RGD peptide.[29] Such an observation may be largely attributable to the fact that a cyclic, multivalent RGD peptide is able to simultaneously bind several $\alpha_v\beta_3$ molecules. In our current study, such an 11-residue peptide, namely, the ACDCRGDCFCG sequence, was chosen to fuse with the N-terminal regions of VEGI-192 for the construction of a targeted VEGI molecule. Consequently, the resultant VEGI fusion protein exhibited far stronger anti-angiogenic activity than the parental rhVEGI-192, and the observed enhancement efficacy was in close association with an elevated pro-apoptotic effect and increased endothelial JNK phosphorylation. It is of note that the RGD-4C sequence has four cysteines in the structure, which is presumably essential for the formation of disulfide bonds and cyclic structure. It would be of great interest, therefore, to further elucidate whether such a structure underlies the enhancement of specific anti-angiogenic and pro-apoptotic effects of the fusion protein on endothelial cells and tumor cells.

In summary, our current study demonstrates the feasibility of employing an RGD-4C peptide to increase the endothelial-targeting capability of angiogenesis inhibitor VEGI-192. We further demonstrated that rhRGD-VEGI-192 reagent could target the breast cancer cell line in which the α_v integrin was predominately expressed, leading to improving the antitumor activity of VEGI-192 in breast tumor-bearing animals. Further investigation on the possibility of blocking tumor cell migration and metastasis, as well as tumor endothelial cells by rhRGD-VEGI-192 protein, the underlying molecular mechanisms of how JNK signaling was activated by rhRGD-VEGI-192, and the potential significance in further improving the anti-metastasis

dx.doi.org/10.1021/bc2006576 | *Bioconjugate Chem.* 2012, 23, 796−804

activity of VEGI-192 in tumor-bearing animals, is underway in the laboratory.

CONCLUSION

In conclusion, our study provided the evidence that that the rhRGD-VEGI-192 fusion protein exhibited a higher level of anti-angiogenic activity as compared with the parental rhVEGI-192. We further demonstrated that rhRGD-VEGI-192 reagent could target the breast cancer cell line MDA-MB-435 in which α_v integrin was predominately expressed, which was mediated by activated the JNK signaling associated with upregulation of pro-apoptotic protein Puma, leading to significant antitumor effect in breast tumor-bearing animals. Our study indicated that the application of RGD-VEGI-192 fusion protein might be a promising anti-angiogenic and antitumor strategy, as a combination therapeutic approach against multiple targets.

ASSOCIATED CONTENT

Supporting Information

Reducing SDS-PAGE analysis of the purified rhRGD-VEGI-192 protein, and in vivo antitumor effect of rhRGD-VEGI-192 on xenografted MDA-MB-435 tumor in nude mice. This material is available free of charge via the Internet at http://pubs.acs.org.

AUTHOR INFORMATION

Corresponding Author

*Xun Zhu: Voice +86(20)87335868; Fax +86(20)87335868; E-mail zhuxun8@mail.sysu.edu.cn. Yesong Wang: Voice +86(20)87332200 x8164; E-mail yesong_wang@yahoo.com.cn.

Author Contributions

#These authors contributed equally to this work.

Notes

The authors declare no competing financial interest.

ACKNOWLEDGMENTS

The Natural Science Foundation of China (No. 81102370, No. 81071762); Guangdong Provincial Natural Science Foundation (No. S2011040003876); National Science and Technique Major Project (201005022-2, 2012ZX09102101-017); High-Tech Research (863) projects (2011AA09070201); The Key Science and Technique Research Project of Guangdong Province (2007A03260001, 2010B030600003); China Post-doctoral Science Foundation (20100480825, 20110490954, 3181404); National innovative training projects for university students (111055855); and the 12th "Challenge Cup" Guangdong Extracurricular Sci-Tech Project, and the 13th "Challenge Cup" China Extracurricular Sci-Tech Project. We thank Prof. Luyuan Li for kindly providing us with pET-19b-rhVEGI-192; Guangdong Provincial Innovative Training Projects for University (201002250); The Laboratory Opening Foundation of Sun Yat-sen University (KF201133).

REFERENCES

(1) Folkman, J. (2006) Angiogenesis. *Annu. Rev. Med. 57*, 1−18.

(2) Folkman, J. (1971) Tumor angiogenesis: therapeutic implications. *N. Engl. J. Med. 285*, 1182−6.

(3) Tan, K. B., Harrop, J., Reddy, M., Young, P., Terrett, J., Emery, J., Moore, G., and Truneh, A. (1997) Characterization of a novel TNF-like ligand and recently described TNF ligand and TNF receptor superfamily genes and their constitutive and inducible expression in hematopoietic and non-hematopoietic cells. *Gene 204*, 35−46.

(4) Zhai, Y., Ni, J., Jiang, G. W., Lu, J., Xing, L., Lincoln, C., Carter, K. C., Janat, F., Kozak, D., Xu, S., Rojas, L., Aggarwal, B. B., Ruben, S., Li, L. Y., Gentz, R., and Yu, G. L. (1999) VEGI, a novel cytokine of the tumor necrosis factor family, is an angiogenesis inhibitor that suppresses the growth of colon carcinomas in vivo. *Faseb J. 13*, 181−9.

(5) Zhai, Y., Yu, J., Iruela-Arispe, L., Huang, W. Q., Wang, Z., Hayes, A. J., Lu, J., Jiang, G., Rojas, L., Lippman, M. E., Ni, J., Yu, G. L., and Li, L. Y. (1999) Inhibition of angiogenesis and breast cancer xenograft tumor growth by VEGI, a novel cytokine of the TNF superfamily. *Int. J. Cancer 82*, 131−136.

(6) Yu, J., Tian, S., Metheny-Barlow, L., Chew, L. J., Hayes, A. J., Pan, H., Yu, G. L., and Li, L. Y. (2001) Modulation of endothelial cell growth arrest and apoptosis by vascular endothelial growth inhibitor. *Circ. Res. 89*, 1161−7.

(7) Chew, L. J., Pan, H., Yu, J., Tian, S., Huang, W. Q., Zhang, J. Y., Pang, S., and Li, L. Y. (2002) A novel secreted splice variant of vascular endothelial cell growth inhibitor. *Faseb J. 16*, 742−4.

(8) Hou, W., Medynski, D., Wu, S., Lin, X., and Li, L. Y. (2005) VEGI-192, a new isoform of TNFSF15, specifically eliminates tumor vascular endothelial cells and suppresses tumor growth. *Clin. Cancer Res. 11*, 5595−602.

(9) Migone, T. S., Zhang, J., Luo, X., Zhuang, L., Chen, C., Hu, B., Hong, J. S., Perry, J. W., Chen, S. F., Zhou, J. X., Cho, Y. H., Ullrich, S., Kanakaraj, P., Carrell, J., Boyd, E., Olsen, H. S., Hu, G., Pukac, L., Liu, D., Ni, J., Kim, S., Gentz, R., Feng, P., Moore, P. A., Ruben, S. M., and Wei, P. (2002) TL1A is a TNF-like ligand for DR3 and TR6/DcR3 and functions as a T cell costimulator. *Immunity 16*, 479−92.

(10) Bamias, G., Martin, C. 3rd, Marini, M., Hoang, S., Mishina, M., Ross, W. G., Sachedina, M. A., Friel, C. M., Mize, J., Bickston, S. J., Pizarro, T. T., Wei, P., and Cominelli, F. (2003) Expression, localization, and functional activity of TL1A, a novel Th1-polarizing cytokine in inflammatory bowel disease. *J. Immunol. 171*, 4868−74.

(11) O'Reilly, M. S., Boehm, T., Shing, Y., Fukai, N., Vasios, G., Lane, W. S., Flynn, E., Birkhead, J. R., Olsen, B. R., and Folkman, J. (1997) Endostatin: an endogenous inhibitor of angiogenesis and tumor growth. *Cell 88*, 277−85.

(12) Chen, X., Wu, J., Liu, H., He, Z., Gu, M., Wang, N., Ma, J., Hu, J., Xia, L., He, H., Yuan, J., Li, J., Li, L., Li, M., and Zhu, X. (2010) Approaches to efficient production of recombinant angiogenesis inhibitor rhVEGI-192 and characterization of its structure and antiangiogenic function. *Protein Sci. 19*, 449−57.

(13) Ruoslahti, E. (1996) RGD and other recognition sequences for integrins. *Annu. Rev. Cell Dev. Biol. 12*, 697−715.

(14) Pasqualini, R., Koivunen, E., and Ruoslahti, E. (1997) Alpha v integrins as receptors for tumor targeting by circulating ligands. *Nat. Biotechnol. 15*, 542−6.

(15) Brooks, P. C., Clark, R. A., and Cheresh, D. A. (1994) Requirement of vascular integrin alpha v beta 3 for angiogenesis. *Science 264*, 569−71.

(16) Meyer, A., Auernheimer, J., Modlinger, A., and Kessler, H. (2006) Targeting RGD recognizing integrins: drug development, biomaterial research, tumor imaging and targeting. *Curr. Pharm. Des. 12*, 2723−47.

(17) Ginsberg, M. H., Partridge, A., and Shattil, S. J. (2005) Integrin regulation. *Curr. Opin. Cell Biol. 17*, 509−16.

(18) Curnis, F., Gasparri, A., Sacchi, A., Longhi, R., and Corti, A. (2004) Coupling tumor necrosis factor-alpha with alphaV integrin ligands improves its antineoplastic activity. *Cancer Res. 64*, 565−71.

(19) Li, J., Ji, J., Holmes, L. M., Burgin, K. E., Barton, L. B., Yu, X., Wagner, T. E., and Wei, Y. (2004) Fusion protein from RGD peptide and Fc fragment of mouse immunoglobulin G inhibits angiogenesis in tumor. *Cancer Gene Ther. 11*, 363−70.

(20) Li, S., Wei, J., Yuan, L., Sun, H., Liu, Y., Zhang, Y., Li, J., and Liu, X. (2011) RGD-modified endostatin peptide 30 derived from endostatin suppresses invasion and migration of HepG2 cells through the alphavbeta3 pathway. *Cancer Biother. Radiopharm.*

(21) Jing, Y., Lu, H., Wu, K., Subramanian, I. V., and Ramakrishnan, S. (2011) Inhibition of ovarian cancer by RGD-P125A-endostatin-Fc fusion proteins. *Int. J. Cancer 129*, 751−61.
(22) Arap, W., Pasqualini, R., and Ruoslahti, E. (1998) Cancer treatment by targeted drug delivery to tumor vasculature in a mouse model. *Science 279*, 377−80.
(23) Ellerby, H. M., Arap, W., Ellerby, L. M., Kain, R., Andrusiak, R., Rio, G. D., Krajewski, S., Lombardo, C. R., Rao, R., Ruoslahti, E., Bredesen, D. E., and Pasqualini, R. (1999) Anti-cancer activity of targeted pro-apoptotic peptides. *Nat. Med. 5*, 1032−8.
(24) Zitzmann, S., Ehemann, V., and Schwab, M. (2002) Arginine-glycine-aspartic acid (RGD)-peptide binds to both tumor and tumor-endothelial cells in vivo. *Cancer Res. 62*, 5139−43.
(25) Wen, L., Zhuang, L., Luo, X., and Wei, P. (2003) TL1A-induced NF-kappaB activation and c-IAP2 production prevent DR3-mediated apoptosis in TF-1 cells. *J. Biol. Chem. 278*, 39251−8.
(26) Xie, G., Zhu, X., Li, Q., Gu, M., He, Z., Wu, J., Li, J., Lin, Y., Li, M., She, Z., and Yuan, J. (2010) SZ-685C, a marine anthraquinone, is a potent inducer of apoptosis with anticancer activity by suppression of the Akt/FOXO pathway. *Br. J. Pharmacol. 159*, 689−97.
(27) Palmieri, D., Lee, J. W., Juliano, R. L., and Church, F. C. (2002) Plasminogen activator inhibitor-1 and -3 increase cell adhesion and motility of MDA-MB-435 breast cancer cells. *J. Biol. Chem. 277*, 40950−7.
(28) Zilberberg, L., Shinkaruk, S., Lequin, O., Rousseau, B., Hagedorn, M., Costa, F., Caronzolo, D., Balke, M., Canron, X., Convert, O., Lain, G., Gionnet, K., Goncalves, M., Bayle, M., Bello, L., Chassaing, G., Deleris, G., and Bikfalvi, A. (2003) Structure and inhibitory effects on angiogenesis and tumor development of a new vascular endothelial growth inhibitor. *J. Biol. Chem. 278*, 35564−73.
(29) Haier, J., Goldmann, U., Hotz, B., Runkel, N., and Keilholz, U. (2002) Inhibition of tumor progression and neoangiogenesis using cyclic RGD-peptides in a chemically induced colon carcinoma in rats. *Clin. Exp. Metastasis 19*, 665−72.

Bioconjugate Chemistry

Article

pubs.acs.org/bc

[^{18}F]Fluoro-Deoxy-Glucose Folate: A Novel PET Radiotracer with Improved in Vivo Properties for Folate Receptor Targeting

Cindy R. Fischer,[†] Cristina Müller,[‡] Josefine Reber,[‡] Adrienne Müller,[†] Stefanie D. Krämer,[†] Simon M. Ametamey,[†] and Roger Schibli*[,†,‡]

[†]Center for Radiopharmaceutical Sciences of ETH, PSI and USZ, Institute of Pharmaceutical Sciences, ETH Zurich, Zurich, Switzerland

[‡]Center for Radiopharmaceutical Sciences of ETH, PSI and USZ, Paul Scherrer Institute, Villigen-PSI, Switzerland

ABSTRACT: The folate receptor (FR) is upregulated in various cancer types (FR-α isoform) and in activated macrophages (FR-β isoform) which are involved in inflammatory and autoimmune diseases, but its expression in healthy tissues and organs is highly restricted to only a few sites (e.g kidneys). Therefore, the FR is a promising target for imaging and therapy of cancer and inflammation using folate-based radiopharmaceuticals. Herein, we report the synthesis and evaluation of a novel folic acid conjugate with improved properties suitable for positron emission tomography (PET).

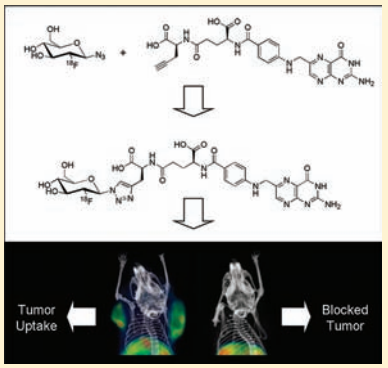

[^{18}F]-fluoro-deoxy-glucose folate ([^{18}**F**]**3**) was synthesized based on the click chemistry approach using 2-deoxy-2-[^{18}F]fluoroglucopyranosyl azide and a folate alkyne derivative. The novel radiotracer [^{18}**F**]**3** was produced in good radiochemical yields (25% d.c.) and high specific radioactivity (90 GBq/μmol). Compared to previously published ^{18}F-folic acid derivatives, an increase in hydrophilicity was achieved by using a glucose entity as a prosthetic group. Biodistribution and PET imaging studies in KB tumor-bearing mice showed a high and specific uptake of the radiotracer in FR-positive tumors (10.03 ± 1.12%ID/g, 60 min p.i.) and kidneys (42.94 ± 2.04%ID/g, 60 min p.i.). FR-unspecific accumulation of radioactivity was only found in the liver (9.49 ± 1.13%ID/g, 60 min p.i.) and gallbladder (17.59 ± 7.22%ID/g, 60 min p.i.). No radiometabolites were detected in blood, urine, and liver tissue up to 30 min after injection of [^{18}**F**]**3**. [^{18}F]-fluoro-deoxy-glucose-folate ([^{18}**F**]**3**) is thus a promising PET radioligand for imaging FR-positive tumors.

INTRODUCTION

The folate receptor (FR) is a membrane-anchored protein which binds the vitamin folic acid with high affinity (K_D ~10^{-9} M). Binding induces internalization via endocytosis. Upregulation of the FR was identified in various cancer types (FR-α isoform) and activated macrophages (FR-β isoform), which are involved in inflammatory and autoimmune diseases.[1,2] The fact that the expression of the FR in healthy tissues is limited to only a few sites (kidneys, choroid plexus, lungs, and placenta) makes this receptor a relevant target for imaging and therapy of cancer and inflammation.[3,4]

A number of folate-based radiopharmaceuticals have been developed and preclinically evaluated as diagnostic tools for positron emission tomography (PET) and single photon emission tomography (SPECT) of FR-positive cancer and inflammatory diseases.[5−8] So far, ^{99m}Tc-EC20 is the only folate-based radiotracer currently used in the clinics.[9] This SPECT tracer is used for identification and selection of patients with FR-positive tumors who could potentially benefit from FR-targeted therapies such as, e.g., the application of folic acid targeted chemotherapeutics[10,11] or FR-alpha targeted antibodies.[12] Furthermore, ^{99m}Tc-EC20 has been used for detection of active inflammation in patients with rheumatoid arthritis or osteoarthritis.[6,13] FR-targeted therapies for the treatment of rheumatoid arthritis, based on folic acid conjugates of anti-inflammatory chemotherapeutics,[14] folate-targeted hapten immunotherapy,[15] or FR-beta targeted antibodies,[16] are currently under evaluation for clinical use.

However, for the purposes mentioned above a folate radiotracer for PET imaging would be superior since PET is a more accurate nuclear imaging technology than SPECT.[17] The high spatial resolution and high sensitivity which can be achieved by PET would allow detection of marginal accumulation of radioactivity as is expected in the case of small metastases and sites of inflammation. Moreover, the characteristics of the positron decay which establish the basis for a quantitative measurement of accumulated radioactivity[18] would allow determination of FR-expression levels as an important criterion for the application of FR-targeted therapies. Fluorine-18 [^{18}F] is the most widely used PET isotope because of its optimal physical decay properties ($t_{1/2}$ = 110 min, $E_{\beta+,\max}$ = 0.6 MeV) that allow multistep syntheses and PET images of high quality. Its relatively long physical half-life allows a distribution of ^{18}F-labeled radiopharmaceuticals to more distant PET centers.

Received: December 9, 2011
Revised: February 28, 2012
Published: February 29, 2012

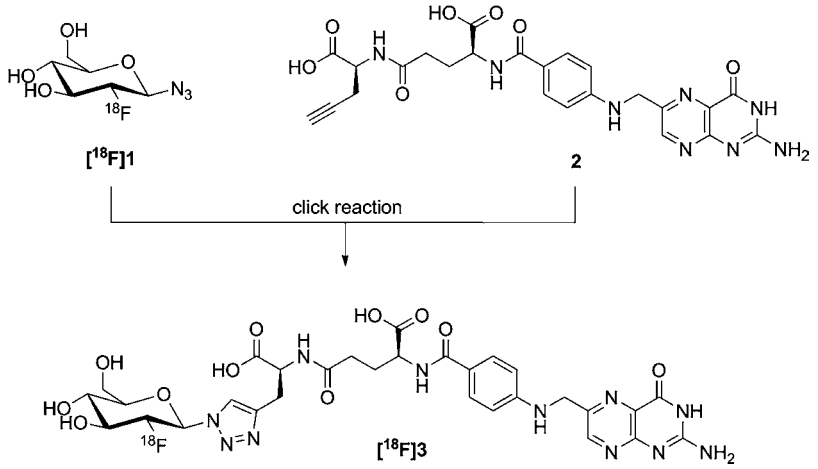

Figure 1. Schematic diagram of the radiosynthesis of [^{18}F]fluoro-deoxy-glucose folate ([^{18}F]**3**).

Several ^{18}F-based folate tracers have been developed using different labeling approaches. The radioisotope was either introduced by coupling folic acid with a ^{18}F-radiolabeled prosthetic group[19−21] or by direct radiolabeling of the folic acid molecule.[22] In our group, a ^{18}F-labeled folate tracer was synthesized that made use of a click chemistry approach ([^{18}F]fluoro-click-folate), which resulted in an excellent overall yield (25−35%).[20] In contrast, adaption of a direct ^{18}F-labeling strategy where the ^{18}F-label was introduced at the 2′-position of the 4-amino-benzoyl moiety of folic acid (2′-[^{18}F]fluorofolate) resulted in an only low yield (1−5%).[22] The [^{18}F]fluoro-click-folate tracer revealed unfavorable in vivo distribution characteristics in mice as a consequence of its high overall lipophilicity.[20] However, application of the more hydrophilic 2′-[^{18}F]-fluorofolate allowed excellent tumor visualization via PET with only negligible retention of radioactivity in nontargeted tissues and organs.[22] These results suggest a need for a hydrophilic folate radiotracer which can be produced in high radiochemical yields.

The aim of this study was to combine the advantage of the click chemistry approach for the coupling reaction of a ^{18}F-radiolabeled prosthetic group with the application of a hydrophilic prosthetic group of a well established radiolabeling procedure. Thus, we employed a ^{18}F-labeled glucose entity as a prosthetic group for coupling to a folate alkyne derivative (Figure 1). This ^{18}F-labeled glucose prosthetic group was previously described by Maschauer et al. for peptide labeling.[23,24] The novel [^{18}F]fluoro-deoxy-glucose-folate radiotracer was investigated with regard to its in vitro characteristics and in vivo distribution in mice bearing FR-positive tumor xenografts.

EXPERIMENTAL PROCEDURES

General. Reagents and solvents were purchased from Sigma-Aldrich, Merck AG or VWR International AG. All chemicals were used as supplied unless stated otherwise. The N^2-*N*,*N*-dimethylaminomethylene-10-formylpteoric acid (protected pteroic acid, **8**) was generously provided by Merck & Cie (Schaffhausen, Switzerland). Nuclear magnetic resonance spectra were recorded on a Bruker 400 or 500 MHz spectrometer with the corresponding solvent signals as an internal standard. Chemical shifts are reported in parts per million (ppm) relative to tetramethylsilane (0.00 ppm). Values of the coupling constant, *J*, are given in hertz (Hz); the following abbreviations are used in this section for the description of ^{1}H NMR spectra: singlet (s), doublet (d), triplet (t), quartet (q), multiplet (m), doublet of doublets (dd), and bs (broad singlet). The chemical shifts of complex multiplets are given as the range of their occurrence. For signal assignment, H/D exchange and 2D-NMR experiments (COSY, HSQC) were performed for all new compounds. Low resolution mass spectra (LR-MS) were recorded with a Micromass Quattro micro API LC-ESI and high resolution mass spectra (HR-MS) with a Bruker FTMS 4.7 T BioAPEXII (ESI). Reactions were monitored by thin layer chromatography (TLC, performed on Merck precoated silica gel 60 F-254 aluminum plates) or HPLC.

HPLC was performed on a Merck-Hitachi L-7000 system equipped with a L-7400 tunable absorption detector. Analytical HPLC was performed with a reversed-phase column (Gemini C18, 5 μm, 4.6 × 250 mm, Phenomenex) using 50 mM NH_4HCO_3 solution (solvent A) and acetonitrile (solvent B) as a solvent system with a gradient from 0−4 min 100% A, 4−5 min 100−93% A, 5−15 min 93% A, 15−25 min 93−30% A, and 25−30 min 30% A, and a flow rate of 1 mL/min. Semipreparative HPLC was performed with a reversed-phase semipreparative column (Gemini C18, 5 μm, 10 × 250 mm, Phenomenex) at a flow rate of 3 mL/min with 50 mM NH_4HCO_3 solution (solvent A) and methanol (solvent B) as the solvent system and a gradient as follows: 0−3 min 100% A, 3−28 min 100−40% A, 28−30 min 40−30% A, and 30−35 min 30% A.

Analytical radio-HPLC was performed on a Merck-Hitachi L-2130 system equipped with a L-2450 diode array detector and a Berthold radiodetector with a reversed-phase column (Gemini C18, 5 μm, 4.6 × 250 mm, Phenomenex) using the above-mentioned gradient for the analytical HPLC.

For the stability studies in vitro and radiometabolites ex vivo, an ultraperformance liquid chromatography (UPLC, Waters) system with an Acquity UPLC BEH C18 column (2.1 × 50 mm, 1.7 μm, Waters) and an attached coincidence detector (FlowStar LB513, Berthold) was used with 50 mM NH_4HCO_3 solution (solvent A) and acetonitrile (solvent B) as solvents and a gradient from 0−0.5 min 100% A, 0.5−3.5 min 100−30% A, and 3.5−3.9 min 30% A at a flow rate of 0.5 mL/min.

Semipreparative radio-HPLC was performed on a HPLC system equipped with a Merck-Hitachi L-6200A intelligent pump, a Knauer variable-wavelength ultraviolet detector and an Eberline RM-14 radiodetector. [^{18}F]fluoro-deoxy-glucose folate

dx.doi.org/10.1021/bc200660z | *Bioconjugate Chem.* 2012, 23, 805−813

Scheme 1. Synthesis of Folate Alkyne (2)[a]

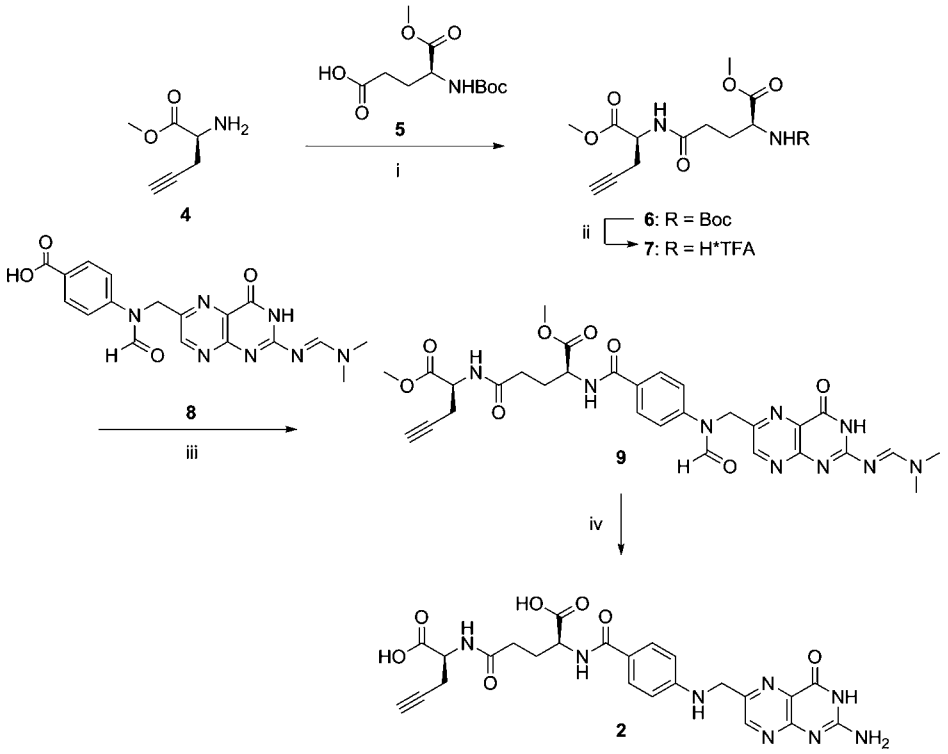

[a](i) HBTU, Et_3N, DMF, 0°C to rt, 20 h, 82%; (ii) TFA/CH_2Cl_2 (1:9), rt, 5 h, quant.; (iii) HBTU, Et_3N, DMF, 0°C to rt, 6 h; (iv) aq. NaOH (1 M), rt, 15 h, 38% (over 2 steps).

([^{18}F]**3**) was purified on a reversed-phase column (Gemini C18, 5 μm, 250 × 10 mm, Phenomenex) using an isocratic solvent system of 5% ethanol in 50 mM NaH_2PO_4/Na_2HPO_4 Soerensen buffer solution (pH 7.5) at a flow rate of 3 mL/min.

Specific radioactivity was determined from a calibration curve obtained from different concentrations of the nonradioactive reference compound [^{19}F]fluoro-deoxy-glucose folate (**3**).

Synthesis of Intermediate 7. To a solution of BocGluOMe (**5**, 402 mg, 1.54 mmol) in dry DMF (4 mL) and Et_3N (428 μL, 2 equiv), HBTU (700 mg, 1.85 mmol) was added at 0 °C. The mixture was stirred for 30 min at 0 °C. The activated acid was added to a solution of H-Pra-OMe·HCl (**4**, 205 mg, 1.62 mmol) in dry DMF (4 mL) containing Et_3N (856 μL, 4 equiv) at 0 °C. The mixture was stirred for 1 h at 0 °C, warmed to rt, and stirred overnight. The product was extracted with citric acid (1 M, 50 mL) and ethyl acetate (50 mL), and the organic phase was rinsed with brine, dried over Na_2SO_4, and concentrated under reduced pressure. Purification was achieved by flash chromatography on silica gel with CH_2Cl_2/MeOH (50:1). Product **6** was obtained as a white solid (467 mg, 82%). ^{1}H NMR (DMSO-d_6) δ/ppm 8.40 (d, 1H, J = 7.3 Hz), 7.27 (d, 1H, J = 7.7 Hz), 4.45 (q, 1H, J = 7.3 Hz), 4.00 (m, 1H), 3.68 (s, 3H), 3.66 (s, 3H), 2.92 (t, 1H, J = 2.5 Hz), 2.62 (m, 2H), 2.26 (t, 2H, J = 7.6 Hz), 2.04−1.71 (m, 2H), 1.42 (s, 9H); ^{13}C NMR (DMSO-d_6) δ/ppm 173.8, 172.4, 171.8, 156.4, 80.9, 79.1, 74.1, 53.9, 53.0, 52.6, 51.9, 32.2, 29.1, 27.5, 21.9. HR-MS (ES$^+$) calculated for $C_{17}H_{27}N_2O_7$: 371.1813; found, 371.1816

Boc-protected intermediate **6** (460 mg, 1.24 mmol) was dissolved in CH_2Cl_2 (4.5 mL), and trifluoroacetic acid (TFA; 0.5 mL) was added. The mixture was left at rt for 5 h and then concentrated under reduced pressure to yield the TFA salt of amine **7** as a yellow oil (332 mg, quantitative). ^{1}H NMR (DMSO-d_6) δ/ppm 8.56 (d, 1H, J = 7.3 Hz), 8.48 (bs, 1H), 4.46 (q, 1H, J = 7.3 Hz), 4.10 (bs, 1H), 3.79 (s, 3H), 3.68 (s, 3H), 2.95 (t, 1H, J = 2.6 Hz), 2.64 (m, 2H), 2.38 (m, 2H), 2.04 (m, 2H); ^{13}C NMR (DMSO-d_6) δ/ppm 171.9, 171.7, 170.6, 81.0, 74.3, 53.8, 53.0, 52.5, 52.0, 31.1, 26.8, 21.9. HR-MS (ES$^+$) calculated for $C_{12}H_{19}N_2O_5$: 271.1288; found, 271.1298

Synthesis of Folate Alkyne (2). To a suspension of protected pteroic acid (**8**, 246 mg, 0.62 mmol) in dry DMF (2 mL) and Et_3N (165 μL, 2 equiv), HBTU (314 mg, 0.83 mmol) was added at 0 °C. The suspension was stirred for 5 min until a clear orange solution appeared. The resulting solution was added at 0 °C to a solution of amine **7** (TFA salt; 160 mg, 0.59 mmol) in dry DMF (3 mL) containing Et_3N (165 μL, 2 equiv). The clear yellow solution was stirred at 0 °C for 4 h and then allowed to warm to rt and stirred for 2 h. Removal of volatile components under reduced pressure and purification of the residue by flash chromatography on silicagel with CH_2Cl_2/MeOH (10:1) provided product **9** as a yellow solid (238 mg, 62%). LR-MS [M + H]$^+$: 647.83

NMR and HPLC indicated partial deprotection of the product; thus, compound **9** was deprotected directly to yield folate alkyne **2** using the procedure described below.

Protected folate alkyne **9** (203 mg, 0.35 mmol) was dissolved in 1 M NaOH (6 mL) and stirred overnight at rt. The aqueous solution was extracted with small amounts of ethyl acetate (3× 1 mL), and afterward, the pH was adjusted to 8 with 2 M HCl (3 mL). The solution was passed through a reversed-phase cartridge (Sep-Pak C18, 12 cm^3, 2 g; Waters; preconditioned with MeOH (5 mL) and H_2O (5 mL)). The cartridge was first washed with H_2O (3 mL), and then the product was eluted with H_2O (12 mL). After lyophilization of the product fraction,

dx.doi.org/10.1021/bc200660z | Bioconjugate Chem. 2012, 23, 805−813

the folate alkyne **2** was obtained as a yellow powder (121 mg, 63%, purity according to HPLC >95%). ^{1}H NMR (D_2O/NaOD) δ/ppm 8.62 (s, 1H), 7.69 (d, 2H, J = 8.8 Hz), 6.86 (d, 2H, J = 8.8 Hz), 4.63 (s, 2H), 4.37 (q, 1H, J = 4.5 Hz), 4.24 (t, 1H, J = 5.7 Hz), 2.56 (m, 2H), 2.44 (m, 2H), 2.29 (m, 1H), 2.07 (m, 1H). HR-MS (ES$^+$) calculated for $C_{24}H_{25}N_8O_7$: 537.1841; found, 537.1834

Synthesis of [^{19}F]Fluoro-deoxy-glucose Folate (3). The synthesis of 2-deoxy-2-fluoroglucopyranosyl azide (**1**) was prepared according to the procedure described by Maschauer et al.[23] To a solution of folate alkyne (**2**, 10 mg, 19 μmol) in ^{t}BuOH/H_2O (1:1, 1 mL) in an Eppendorf tube, 2-deoxy-2-fluoroglucopyranosyl azide (**1**, 11.6 mg, 56 μmol), 0.1 M $Cu(OAc)_2$ solution (0.1 eq., 19 μL) and 0.1 M sodium ascorbate solution (0.2 eq., 38 μL) were added. The solution was shaken at rt and 500 rpm for 1 h until complete conversion. The reaction progress was followed by analytical HPLC. For isolation of the product, the mixture was submitted to semipreparative HPLC. The desired fraction was collected and lyophilized to provide product **3** as a yellow powder (7.2 mg, 52%, purity according to HPLC >98%). ^{1}H NMR (D_2O/NaOD) δ/ppm 8.74 (s, 1H), 7.98 (s, 1H), 7.61 (d, 2H, J = 8.8 Hz), 6.76 (d, 2H, J = 8.8 Hz), 5.89 (dd, 1H, J_1 = 2.6 Hz, J_2 = 9.0 Hz), 4.91 (t, 1H, J = 9.0 Hz), 4.61 (s, 2H), 4.44 (q, 1H, J = 4.7 Hz), 4.35 (q, 1H, J = 4.3 Hz), 4.02−3.86 (m, 2H), 3.79−3.62 (m, 2H), 3.20 (dd, 1H, J_1 = 4.7 Hz, J_2 = 14.8 Hz), 3.04 (dd, 1H, J_1 = 8.4 Hz, J_2 = 14.8 Hz), 2.37 (m, 2H), 2.17 (m, 1H), 2.01 (m, 1H). HR-MS (ES$^+$) calculated for $C_{30}H_{35}FN_{11}O_{11}$: 744.2496; found, 744.2508.

Radiochemistry. No-carrier-added [^{18}F]fluoride was produced via the ^{18}O(p,n)^{18}F nuclear reaction at a Cyclone 18/9 cyclotron (IBA) by irradiation of enriched ^{18}O-water. [^{18}F]-fluoride was immobilized on an anion-exchange cartridge (QMA Light; Waters; preconditioned with 0.5 M K_2CO_3-solution (5 mL) and H_2O (5−10 mL)) and eluted with a solution of Kryptofix $K_{2.2.2}$ (5 mg) and K_2CO_3 (1 mg) in acetonitrile (1.4 mL) and water (0.6 mL) into a 10 mL sealed reaction vessel. The [^{18}F]fluoride (ca. 50−55 GBq) was dried by azeotropic distillation of acetonitrile at 110 °C under vacuum with a stream of nitrogen. The azeotropic drying process was repeated 3 times with 1 mL of acetonitrile.

The synthesis of 2-deoxy-2-[^{18}F]fluoroglucopyranosyl azide ([^{18}F]**1**) was prepared according to the procedure described by Maschauer et al..[23]

To the dried [^{18}F]fluoride-cryptate complex, the precursor solution of 3,4,6-tri-*O*-acetyl-2-*O*-trifluoromethanesulfonyl-β-D-mannopyranosyl azide (**10**, 3.0 mg, 6.5 μmol) in anhydrous acetonitrile (300 μL) was added. The mixture was stirred for 5 min at 80 °C. After 5 min of cooling, 8 mL of water was added to the reactive vial. The mixture was passed through a reversed-phase cartridge (Sep-Pak C18 Plus; Waters; preconditioned with MeOH (5 mL) and H_2O (5 mL)). The cartridge was washed with 5 mL of water, then ^{18}F-labeled protected intermediate, 3,4,6-tri-*O*-acetyl-2-deoxy-2-[^{18}F]-fluoroglucopyranosyl azide ([^{18}F]**11**) was eluted with 2.0 mL of acetonitrile into another 5 mL sealed reaction vessel and dried under reduced pressure with a stream of nitrogen at 80 °C. For hydrolysis, sodium hydroxide solution (250 μL, 60 mM) was added, and the mixture was heated to 65 °C for 5 min. After cooling, the mixture was neutralized with hydrogen chloride solution (250 μL, 60 mM) and directly used for the click reaction without further purification. The deprotected [^{18}F]**1** was transferred into another reaction vessel containing the folate alkyne **2**, followed by the addition of ethanol (300 μL), $Cu(OAc)_2$ solution (10 μL, 0.1 M), and sodium ascorbate solution (20 μL, 0.1 M). The reaction mixture was stirred at 50 °C for 15 min, and after the addition of phosphate buffer solution (3 mL, 0.15 M), the mixture was purified by semipreparative radio-HPLC. The product fraction of [^{18}F]**3** was collected and passed through a sterile filter into a sterile, pyrogen-free vial without further formulation.

Determination of Distribution Coefficient. The distribution coefficient (log $D_{7.4}$) was determined by the shake flask method.[25] In brief, [^{18}F]**3** was dissolved in a mixture of phosphate buffer (500 μL, pH 7.4) and *n*-octanol (500 μL) at 20 °C. The sample was equilibrated for 15 min in an overhead shaker. The two phases were separated by centrifugation (3 min, 5000 rpm), and 50 μL aliquots each of both phases were analyzed in a γ-counter (Wizard, PerkinElmer). The partition coefficient is expressed as the ratio between the radioactivity concentrations (cpm/mL) of the octanol and the buffer phase. Values represent the mean ± standard deviation of eight determinations from two independent experiments.

Binding Affinity Assays in Vitro. Binding affinity assays were performed with KB cells derived from human cervical carcinoma (DSMZ ACC136). The cells were cultured in a folate-free culture medium FFRPMI (modified RPMI, without folic acid, vitamin B_{12}, and phenol red, Cell Culture Technologies GmbH) supplemented with 10% heat-inactivated fetal calf serum (as the only source of folate), L-glutamine and antibiotics (penicillin/streptomycin/fungizone) at 37 °C in a humidified atmosphere (5% CO_2). For the binding assay, a cell suspension in FFRPMI medium (no additives, ice-cold, 7000 cells in 240 μL) was incubated in triplicate with ^{3}H-folic acid (0.82 nM, 0.94 TBq/mmol, Moravek Biochemicals Inc.) and increasing concentrations of the nonradioactive reference compound **3** (5.0×10^{-6} to 5.0×10^{-12} M) at 4 °C for 30 min. Nonspecific binding was determined in the presence of excess folic acid (10^{-4} M). After incubation, the suspension was centrifuged at 1000 rpm and 4 °C for 5 min, and the supernatant was removed. The cells were lysed by addition of 0.5 mL of 1 N NaOH, stirred on a vortex mixer, and transferred into scintillation tubes containing 5 mL of scintillation cocktail (Ultima Gold; Perkin-Elmer). Radioactivity was measured using a β-counter (LS6500; Beckman), and the inhibitory concentrations of 50% were determined from displacement curves using GraphPad Prism 4.0 software. The relative binding affinity of **3** was determined based on the binding affinity of folic acid which was set to 1.0. A value equal to that of folic acid indicates an equal affinity for the FR, a value lower than 1.0 reflects weaker affinity, and a value higher than 1.0 reflects stronger affinity.[26,27]

Stability Studies in Vitro. Stability of [^{18}F]**3** was investigated in human plasma and phosphate buffered saline (PBS) at various incubation times (0−120 min) and 37 °C. After incubation, plasma proteins were precipitated with ice-cold methanol and centrifuged for 10 min at 13500 rpm and 20 °C. The samples of [^{18}F]**3** incubated in PBS were diluted with the same volume of methanol. The supernatants of the plasma samples and the PBS samples were analyzed by analytical radio-UPLC. To test metabolism by hepatic microsomal enzymes, [^{18}F]**3** was incubated with human and murine liver microsomes (0.5 mg/mL protein, BD Biosciences). Each sample contained a NADPH regenerating system consisting of solution A containing 31 mM $NADP^+$, 66 mM glucose-6-phosphate, and 66 mM $MgCl_2$ in water and solution B containing 40 U/mL

dx.doi.org/10.1021/bc200660z | Bioconjugate Chem. 2012, 23, 805−813

Scheme 2. Radiosynthesis of 2-Deoxy-2-[^{18}F]fluoroglucopyranosyl Azide ([^{18}F]1)[a]

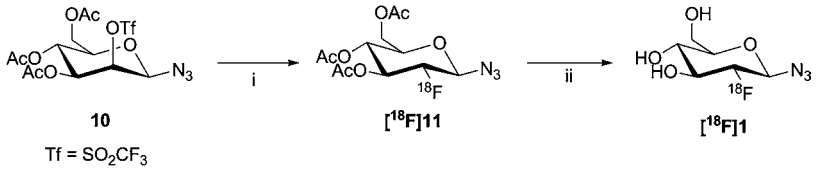

[a](i) [^{18}F]KF-$K_{2.2.2}$, MeCN, 80°C, 5 min, 75%; (ii) aq. NaOH (60 mM), 65°C, 5 min, quant.

glucose-6-phosphate dehydrogenase in 5 mM sodium citrate. These two reagents were combined to provide the reducing agent for the reaction with cytochrome P450 (CYP). Control samples were incubated without microsomes or without the NADPH regenerating system. Proteins were precipitated by addition of ice-cold methanol at different time points between 0 and 60 min and centrifugation for 5 min at 13400 rpm. Aliquots of the supernatants were analyzed by radio-UPLC.

Biodistribution Studies. All animal experiments complied with Swiss and local laws on animal protection. Female CD-1 nude mice were purchased from Charles River (Germany) and maintained on a folate-deficient rodent diet (Harlan Laboratories, US). After a 5−7 day acclimatization period, 0.1 mL of a KB tumor cell suspension (5×10^6 cells) was inoculated subcutaneously on both shoulders of each mouse. The animal experiments were performed 12 days after tumor cell inoculation. Animals were injected with ∼5 MBq (0.05−0.07 nmol) of [^{18}F]**3** in a volume of 100 μL via a lateral tail vein (n = 4 per time point). Blocking studies (n = 3) were performed with excess folic acid dissolved in PBS (100 μg in 100 μL) which was intravenously injected 10 min before the radiotracer injection. Animals were sacrificed at the indicated time points, and organs and tissues were collected and measured in the γ-counter. The incorporated radioactivity was expressed as percentage injected dose [% ID] per gram of tissue.

PET Imaging Studies. PET experiments were performed with an eXplore VISTA PET/CT tomograph (GE). Animals were injected with 10−14 MBq (0.15−0.23 nmol) of [^{18}F]**3** (100−150 μL per injection) via a lateral tail vein. For blocking studies, the animals received excess folic acid (100 μg in 100 μL) via intravenous injection 10 min prior to the radiotracer injection. Animals were anesthetized with isoflurane in an air/oxygen mixture and scanned as described previously.[28] The PET scans were acquired from 75 to 105 min p.i.. After acquisition, PET data were reconstructed in user-defined time frames. The fused data sets of PET and CT were analyzed with Amira (version 4.0) postprocessing software.

Metabolite Studies ex Vivo. For the determination of radiometabolites in vivo, [^{18}F]**3** (50−70 MBq; 0.35 nmol-0.49 nmol) was intravenously injected into mice without tumors (n = 3). After 5 min, blood samples were withdrawn from the opposite vein, and the animals were sacrificed 30 min after radiotracer injection. Whole blood, liver, and urine were collected. Blood samples were centrifuged at 5000g for 5 min at 4 °C. The proteins of the plasma samples were precipitated by addition of ice-cold methanol followed by centrifugation. The supernatants of the plasma samples and the urine samples were analyzed by radio-UPLC and radio-TLC, respectively. Liver tissue was homogenized in an equal volume of PBS using a PT 1200 C Polytron (Kinematica AG). After centrifugation (5000g, 5 min, 4 °C), the supernatant was cleared from proteins by addition of ice-cold methanol and centrifugation. The supernatant was analyzed by radio-UPLC and radio-TLC, respectively.

RESULTS

Chemistry and Radiochemistry. The synthesis of folate alkyne **2** was obtained in 4 steps in an overall yield of 31% (Scheme 1). The first step involving the coupling of two commercially available amino acids BocGluOMe (**5**) and H-Pra-OMe (**4**) yielded the Boc-protected glutamic acid intermediate **6** in 82% yield. Deprotection of intermediate **6** with TFA afforded amine **7**, which was obtained in quantitative yield. Protected folate alkyne **9** was prepared by the coupling of amine **7** with protected pteroic acid (**8**) following a published procedure.[29] The final product folate alkyne **2** was obtained after deprotection of compound **9** and was purified using a reversed-phase cartridge.

The synthesis of the azide component, 2-deoxy-2-fluoroglucopyranosyl azide (**1**), was accomplished using the procedure described by Maschauer et al.[23] The Cu(I)-catalyzed cycloaddition of azide **1** and folate alkyne **2** was performed in an aqueous system, and after semipreparative HPLC purification the nonradioactive reference compound **3** was achieved in high purity (>98%) and good yield (52%).

The protected glucose azide [^{18}F]**11** was obtained by nucleophilic ^{18}F-substitution of the mannosyl-precursor **10**[23] in 75% radiochemical yield after purification by C18 reversed-phase cartridge (Scheme 2). After hydrolysis, crude [^{18}F]**1** was neutralized and used for the click reaction without further purification. A complete conversion to [^{18}F]**3** was observed by UPLC after 15 min at 50 °C. [^{18}F]**3** was purified by reversed-phase semipreparative HPLC. The desired product peak (retention time 20 min) was directly collected into a sterile, pyrogen-free product vial after passing through a sterile filter. The solution was either immediately used for biological applications or diluted with PBS. After an overall synthesis time of 3 h, a maximum activity amount of 1−3 GBq isolated product [^{18}F]fluoro-deoxy-glucose folate ([^{18}F]**3**) was obtained in decay-corrected radiochemical yields of 5−25%, with a radiochemical purity ≥95% and a specific activity (EOS) of 90 ± 38 GBq/μmol. [^{18}F]**3** was identified by coinjection with its nonradioactive reference compound **3** by analytical HPLC (Figure 2).

In Vitro Characterization. The relative binding affinity of the nonradioactive fluoro-deoxy-glucose folate (**3**) was obtained from three independent experiments and was 0.63 ± 0.05 compared to folic acid which was set to 1.0. The displacement curves of one representative experiment are shown in Figure 3. The log $D_{7.4}$ value of [^{18}F]**3** was −4.2 ± 0.1. Stability studies in human plasma and human and murine liver microsomes revealed no defluorination or radioactive degradation products of [^{18}F]**3** within 120 and 60 min, respectively, at 37 °C.

dx.doi.org/10.1021/bc200660z | Bioconjugate Chem. 2012, 23, 805−813

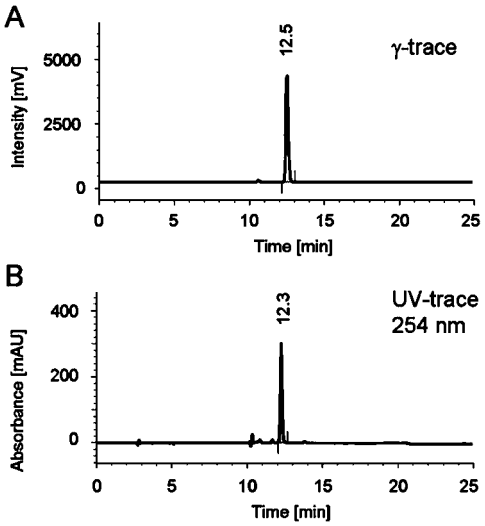

Figure 2. HPLC chromatogram of [^{18}F]fluoro-deoxy-glucose folate ([^{18}F]**3**) (A) with coinjection of the nonradioactive reference compound fluoro-deoxy-glucose folate (**3**) (B).

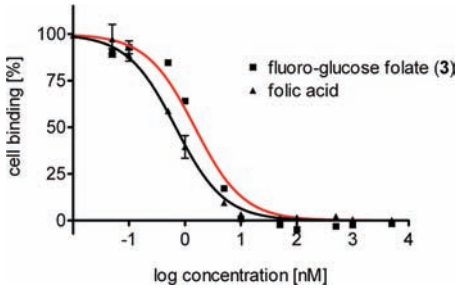

Figure 3. Displacement curves of fluoro-deoxy-glucose folate (**3**) and folic acid using ^{3}H-folic acid and human KB tumor cells.

Biodistribution Studies. The results of the biodistribution studies are shown in Table 1, including previously reported data of the SPECT tracer $^{99\,m}$Tc-EC20.[30] The tumor uptake already reached a value of 9.61 ± 1.73% ID/g 30 min after injection of ~5 MBq [^{18}F]**3**, which was similar to the values obtained at 60 min (10.03 ± 1.12% ID/g) and 90 min p.i. (9.05 ± 2.12 %ID/g). Radioactivity in the tumor xenografts was reduced by 89% to 1.19 ± 1.04% ID/g under blockade conditions. High specific uptake was also found in the kidneys and in the salivary glands, organs with known FR expression.[31] The kidney uptake was high under baseline conditions (42.94 ± 2.04% ID/g; 60 min p.i.) and was reduced to 3.48 ± 0.14% ID/g in the blockade group. This means a reduction of 92%, which indicates the high specific binding of [^{18}F]**3** to the FR. A similar observation was made in the salivary glands, where the uptake was reduced by 95% from 5.93 ± 0.77% ID/g in the baseline group to 0.30 ± 0.01% ID/g under blockade conditions. [^{18}F]**3** exhibited a fast blood clearance, which resulted in a high tumor-to-blood ratio of 36.09 ± 15.37 at 90 min p.i.. A high nonspecific accumulation was observed in the liver (10.82 ± 1.68% ID/g ; 30 min p.i.), which slightly decreased to 8.37 ± 1.19% ID/g at 90 min after injection. This uptake leads to tumor-to-liver ratios of ~1 at all time points after injection. Furthermore, high radioactivity was found in the gallbladder, urine, and feces, indicating biliary and renal excretion of [^{18}F]**3**.

PET Imaging Studies. The excellent tumor targeting properties of [^{18}F]**3** found in biodistribution studies ex vivo were confirmed by PET imaging studies. Both KB tumors on the shoulders and the FR-positive kidneys were clearly imaged under baseline conditions, whereas uptake of [^{18}F]**3** in tumors and kidneys was negligible under blockade conditions (Figure 4). Under baseline conditions, high radioactivity was also observed in the liver, gallbladder, and urinary bladder. Uptake of radioactivity in the liver and gallbladder was not reduced under blockade conditions.

Table 1. Biodistribution Data of [^{18}F]Fluoro-deoxy-glucose Folate ([^{18}F]3) in Nude Mice Bearing KB Tumor Xenografts[a] in Comparison to the SPECT Tracer ^{99m}Tc-EC20[30]

organ or tissue	30 min p.i. (n = 4)	60 min p.i. (n = 4)	90 min p.i. (n = 4)	60 min p.i. blockade[b] (n = 3)	$^{99\,m}$Tc-EC20[30] 60 min p.i. (n = 4)
% ID/g in					
blood	0.94 ± 0.31	0.44 ± 0.09	0.25 ± 0.08	1.37 ± 1.80	0.38 ± 0.12
brain	0.38 ± 0.06	0.59 ± 0.08	0.45 ± 0.07	0.04 ± 0.02	n.d.
heart	1.04 ± 0.14	1.15 ± 0.13	0.81 ± 0.01	1.66 ± 2.05	n.d.
lungs	1.18 ± 0.14	0.92 ± 0.07	0.71 ± 0.12	0.46 ± 0.06	1.14 ± 0.24
spleen	0.61 ± 0.13	0.73 ± 0.21	0.60 ± 0.22	0.23 ± 0.05	0.46 ± 0.12
liver	10.82 ± 1.68	9.49 ± 1.13	8.37 ± 1.19	10.00 ± 3.53	5.12 ± 1.57
gallbladder	9.53 ± 6.01	17.59 ± 7.22	27.42 ± 7.57	22.49 ± 12.25	n.d.
kidneys	32.44 ± 1.84	42.94 ± 2.04	27.08 ± 1.53	3.48 ± 0.14	89.18 ± 10.73
stomach	1.27 ± 0.20	1.42 ± 0.53	1.03 ± 0.01	0.33 ± 0.08	1.60 ± 0.32
intestine	1.48 ± 0.46	3.45 ± 1.61	3.69 ± 0.04	4.56 ± 2.05	0.95 ± 0.38
feces	6.56 ± 4.41	10.95 ± 4.33	18.40 ± 6.83	20.48 ± 0.21	n.d.
salivary glands	4.61 ± 0.44	5.93 ± 0.77	4.90 ± 0.01	0.30 ± 0.01	8.08 ± 2.51
bone	0.90 ± 0.13	0.87 ± 0.05	0.72 ± 0.04	0.29 ± 0.01	0.70 ± 0.18
muscle	0.89 ± 0.15	0.69 ± 0.05	0.57 ± 0.12	0.26 ± 0.04	0.73 ± 0.18
tumor	9.61 ± 1.73	10.03 ± 1.12	9.05 ± 2.12	1.19 ± 1.04	11.39 ± 3.24
ratios					
tumor/liver	0.89 ± 0.14	1.06 ± 0.02	1.28 ± 0.22	0.15 ± 0.16	2.28 ± 0.58
tumor/kidneys	0.29 ± 0.04	0.23 ± 0.04	0.34 ± 0.07	0.33 ± 0.28	0.13 ± 0.04
tumor/blood	10.57 ± 1.65	24.10 ± 7.44	36.09 ± 15.37	10.61 ± 14.77	30.09 ± 3.39

[a]Mice were injected with ~5 MBq (0.05−0.07 nmol) of [^{18}F]**3** via the lateral tail vein. [b]In the blockade group, each animal received 100 μg of folic acid in PBS 10 min before the radiotracer injection.

dx.doi.org/10.1021/bc200660z | *Bioconjugate Chem.* 2012, 23, 805−813

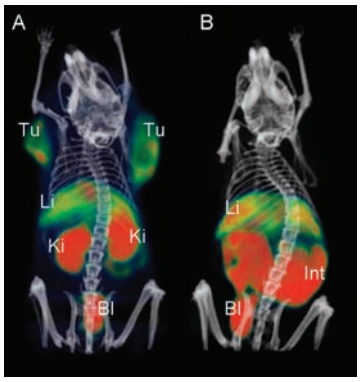

Figure 4. Three-dimensional PET/CT images of KB tumor-bearing mice 75−105 min after injection of 10−14 MBq (0.15−0.23 nmol) [^{18}F]fluoro-deoxy-glucose folate ([^{18}F]**3**): (A) baseline and (B) mouse injected with folic acid prior to radiotracer (Tu, tumor; Li, liver; Ki, kidneys; Bl, urinary bladder; and Int, intestines/feces).

Metabolite Studies ex Vivo. To determine whether a radiometabolite was responsible for the liver uptake, ex vivo metabolite studies were carried out to determine potential metabolites. [^{18}F]**3** was injected into mice (without tumors). Analysis of plasma, urine, and liver tissue taken 30 min after injection revealed only intact parent compound [^{18}F]**3** (Figure 5).

DISCUSSION

The radiosynthesis of the prosthetic group, 2-deoxy-2-[^{18}F]-fluoroglucopyranosyl azide ([^{18}F]**1**), proceeded in a manner similar to the highly reliable and efficient radiosynthesis of 2-deoxy-2-[^{18}F]fluoroglucose (FDG).[32] For the synthesis of the folate alkyne derivative **2**, a fragment coupling strategy was employed. As the main step, a condensation reaction of protected pteroic acid and an alkyne substituted glutamic acid part was performed. By combining the click chemistry approach and the well established prosthetic group [^{18}F]**1**, an efficient procedure was found to synthesize a novel hydrophilic ^{18}F-labeled folic acid derivative. The radiosynthesis allowed a regiospecific reaction which resulted only in the γ-isomer without the need to perform cumbersome separation of regioisomers.

Compared to our previously published ^{18}F-labeled folic acid derivatives, [^{18}F]fluoro-deoxy-glucose folate ([^{18}F]**3**) was produced in excellent radiochemical yields of up to 25% d.c. (up to 3 GBq isolated product) in a total synthesis time of 3 h. The overall time could potentially be reduced by the employment of an automated modular system allowing a standardization of the synthesis and radiolabeling procedure, which will be required for the routine production of the radiotracer. Because of the high selectivity of the 1,3-dipolar cycloaddition in the presence of Cu(I),[33−35] protection of functional groups was not necessary, and thus by application of this strategy, a further deprotection step during the radiosynthesis could be avoided. The use of physiological phosphate buffer as solvent system for the reversed-phase HPLC purification provided the final product [^{18}F]**3** in a solution formulated for direct in vitro and in vivo application of the radiotracer.

An increase in hydrophilicity, compared to previously investigated ^{18}F-labeled folic acid derivatives of our group[19,20,22] was achieved by using a glucose entity as a prosthetic group. The log $D_{7.4}$ value of −4.2 ± 0.1 was in a range similar to that of the log $D_{7.4}$ value of the ^{111}In-DOTA-folate conjugate, which showed excellent tissue distribution properties, recently published by Müller et al.[36] The presence of only intact radiotracer [^{18}F]**3** after 120 min incubation in human plasma or 60 min incubation with human and murine liver microsomes proved its high stability toward hydrolases and oxidoreductases. As expected from these results, the radiotracer was stable in vivo, and no radiometabolites were detected in liver, urine, and blood. Potential release of the ^{18}F-labeled glucose entity would most probably have resulted in an accumulation of radioactivity in the brain and myocardium, similar to [^{18}F]-FDG.[37] Free [^{18}F]fluoride potentially produced by the defluorination reaction would accumulate in the bones.[38] However, the fact of only background radioactivity in the brain, heart, and bone clearly demonstrated the absence of a glucose-like molecule or [^{18}F]fluoride as potential radiometabolites.

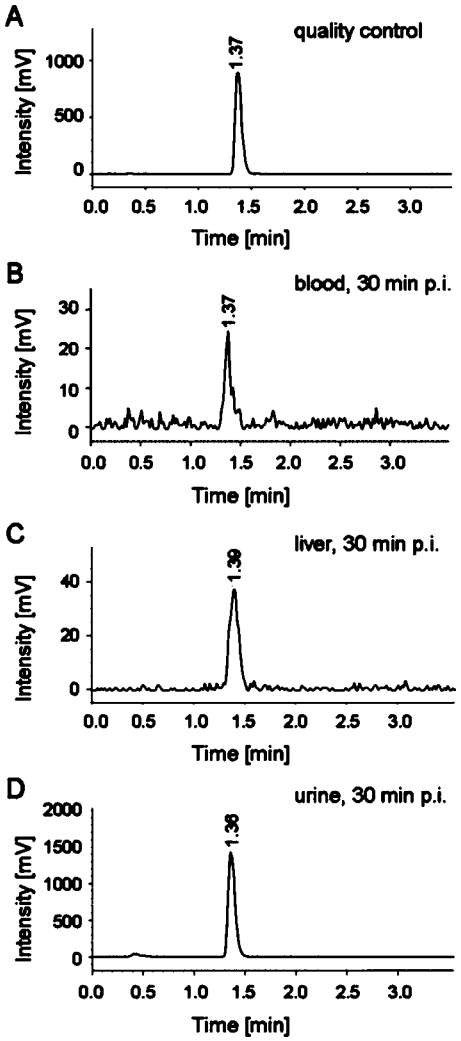

Figure 5. Radio-UPLC chromatograms of reference radiotracer [^{18}F]**3** (A), blood sample (B), liver tissue (C), and urine sample (D) 30 min after [^{18}F]fluoro-deoxy-glucose folate ([^{18}F]**3**) injection.

Biodistribution data and PET imaging experiments with [^{18}F]**3** confirmed the proposed characteristics of this new radiotracer. [^{18}F]**3** showed a comparative tissue distribution to the SPECT tracer $^{99\,m}$Tc-EC20 (Table 1). Uptake of [^{18}F]**3** in FR-positive KB tumors was high already at 30 min p.i. and remained between 9 and 10% ID/g for the entire study period. Furthermore, a high and specific uptake was found in the

dx.doi.org/10.1021/bc200660z | *Bioconjugate Chem.* 2012, 23, 805−813

kidneys (42.94 ± 2.04% ID/g; 60 min p.i.), where the FR is expressed on the proximal tubule cells.[4]

Because of the hydrophilic properties of [^{18}F]**3**, favorable tumor-to-background contrast was achieved shortly after injection and allowed excellent tumor visualization by PET. These results were clearly superior to those obtained with the [^{18}F]fluoro-click-folate, previously synthesized by Ross et al.[20] The lipophilic character of this [^{18}F]fluoro-click-folate and a pronounced hepatobiliary elimination resulted in a high accumulation of radioactivity in the abdominal region. With regard to the tumor-to-background contrast, our novel [^{18}F]fluoro-deoxy-glucose folate ([^{18}F]**3**) was comparable to 2′-[^{18}F]fluorofolate, where the ^{18}F label was directly introduced at the 2′-position of the 4-amino-benzoyl moiety in folic acid. The 2′-[^{18}F]fluorofolate also showed a comparable high uptake of ∼9% ID/g (75 min p.i.) in FR-positive KB tumors,[22] but a routine production of that radiotracer would not have been possible due to the unfavorably low radiochemical yield which was achievable.

Despite the hydrophilic character of [^{18}F]**3**, a relatively high uptake of radioactivity was observed in the liver resulting in a tumor-to-liver ratio of ∼1, which was in the same range as that for 2′-[^{18}F]fluorofolate. The SPECT tracer ^{99m}Tc-EC20, which was evaluated in the same animal model, showed better tumor-to-liver ratios due to a lower uptake of the radiotracer in the liver.[30] Since liver cells do not express the FR,[4] and only parent radiotracer [^{18}F]**3** was detected in liver tissue, a carrier-mediated uptake of the folic acid derivative into the hepatocytes is assumed. These results are in agreement with the findings with the clinically established folate-based radiotracer ^{99m}Tc-EC20[9] and correlate well with the oberservations made by Leamon et al. proposing a liver uptake via promiscuous organic anion transporters.[39]

CONCLUSIONS

A novel ^{18}F-labeled folic acid derivative [^{18}F]**3** was synthesized using a hydrophilic glucose entity as a radiolabeled prosthetic group to increase the overall hydrophilicity of the radiotracer. The coupling reaction of the [^{18}F]-glucose entity and the folic acid precursor was carried out via the well established click chemistry approach. A folate precursor with a mannosyl moiety for a direct radiolabeling could be an alternative strategy. The new [^{18}F]fluoro-deoxy-glucose folate ([^{18}F]**3**) can be produced by a reliable and high-yielding radiosynthesis and shows high affinity and specificity for the FR, both in vitro and in vivo.

Thus, [^{18}F]fluoro-deoxy-glucose folate is a highly promising ^{18}F-radiotracer for clinical use as it would be suitable for routine production potentially allowing application in patients for PET imaging of FR-positive cancer and inflammatory diseases.

AUTHOR INFORMATION

Corresponding Author

*Center for Radiopharmaceutical Sciences of ETH, PSI and USZ, Department of Chemistry and Applied Biosciences, ETH Hönggerberg, Wolfgang-Pauli-Strasse 10, CH-8093 Zurich, Switzerland. Phone: +41 44 633 74 64. Fax: +41 44 633 13 67. E-mail: roger.schibli@pharma.ethz.ch.

Notes

The authors declare no competing financial interest.

ACKNOWLEDGMENTS

We thank Dr. Linjing Mu, Dr. Selena Milicevic-Sephton, Dr. Alexander Hohn, Dr. Harriet Struthers, Dr. Thomas Betzel, Nadja Romano, Claudia Keller, Petra Wirth, and Dominique Leutwiler for their support and technical assistance.

REFERENCES

(1) Low, P. S., Henne, W. A., and Doorneweerd, D. D. (2008) Discovery and development of folic-acid-based receptor targeting for imaging and therapy of cancer and inflammatory diseases. *Acc. Chem. Res. 41*, 120−129.

(2) Sega, E. I., and Low, P. S. (2008) Tumor detection using folate receptor-targeted imaging agents. *Cancer Metastasis Rev. 27*, 655−664.

(3) Weitman, S. D., Lark, R. H., Coney, L. R., Fort, D. W., Frasca, V., Zurawski, V. R., and Kamen, B. A. (1992) Distribution of the folate receptor GP38 in normal and malignant cell lines and tissues. *Cancer Res. 52*, 3396−3401.

(4) Parker, N., Turk, M. J., Westrick, E., Lewis, J. D., Low, P. S., and Leamon, C. P. (2005) Folate receptor expression in carcinomas and normal tissues determined by a quantitative radioligand binding assay. *Anal. Biochem. 338*, 284−293.

(5) Ke, C. Y., Mathias, C. J., and Green, M. A. (2004) Folate-receptor-targeted radionuclide imaging agents. *Adv. Drug Deliv. Rev. 56*, 1143−1160.

(6) Paulos, C. M., Turk, M. J., Breur, G. J., and Low, P. S. (2004) Folate receptor-mediated targeting of therapeutic and imaging agents to activated macrophages in rheumatoid arthritis. *Adv. Drug Delivery Rev. 56*, 1205−1217.

(7) Müller, C., and Schibli, R. (2011) Folic acid conjugates for nuclear imaging of folate receptor-positive cancer. *J. Nucl. Med. 52*, 1−4.

(8) Müller, C., and Schibli, R. (2011) Folate Receptor-Targeted Radionuclide Imaging Agents, *Targeted Drug Strategies for Cancer and Inflammation* (Jackman, A. L., and Leamon, C. P., Eds.) pp 65−92, Chapter 4, Springer Science, New York.

(9) Fisher, R. E., Siegel, B. A., Edell, S. L., Oyesiku, N. M., Morgenstern, D. E., Messmann, R. A., and Amato, R. J. (2008) Exploratory study of ^{99m}Tc-EC20 imaging for identifying patients with folate receptor-positive solid tumors. *J. Nucl. Med. 49*, 899−906.

(10) Leamon, C. P., and Reddy, J. A. (2004) Folate-targeted chemotherapy. *Adv. Drug Delivery Rev. 56*, 1127−1141.

(11) Li, J., Sausville, E. A., Klein, P. J., Morgenstern, D., Leamon, C. P., Messmann, R. A., and LoRusso, P. (2009) Clinical pharmacokinetics and exposure-toxicity relationship of a folate-vinca alkaloid conjugate EC145 in cancer patients. *J. Clin. Pharmacol. 49*, 1467−1476.

(12) Konner, J. A., Bell-McGuinn, K. M., Sabbatini, P., Hensley, M. L., Tew, W. P., Pandit-Taskar, N., Els, N. V., Phillips, M. D., Schweizer, C., Weil, S. C., Larson, S. M., and Old, L. J. (2010) Farletuzumab, a humanized monoclonal antibody against folate receptor alpha, in epithelial ovarian cancer: a phase I study. *Clin. Cancer Res. 16*, 5288−5295.

(13) Matteson, E. L., Lowe, V. J., Prendergast, F. G., Crowson, C. S., Moder, K. G., Morgenstern, D. E., Messmann, R. A., and Low, P. S. (2009) Assessment of disease activity in rheumatoid arthritis using a novel folate targeted radiopharmaceutical Folatescan™. *Clin. Exp. Rheum. 27*, 253−259.

(14) Lu, Y. J., Stinnette, T. W., Westrick, E., Klein, P. J., Gehrke, M. A., Cross, V. A., Vlahov, I. R., Low, P. S., and Leamon, C. P. (2011) Treatment of experimental adjuvant arthritis with a novel folate receptor-targeted folic acid-aminopterin conjugate. *Arthritis Res. Ther. 13*, R56.

(15) Yi, Y. S., Ayala-Lopez, W., Kularatne, S. A., and Low, P. S. (2009) Folate-targeted hapten immunotherapy of adjuvant-induced arthritis: comparison of hapten potencies. *Mol. Pharmaceutics 6*, 1228−1236.

(16) Feng, Y., Shen, J. Y., Streaker, E. D., Lockwood, M., Zhu, Z. Y., Low, P. S., and Dimitrov, D. S. (2011) A folate receptor beta-specific

human monoclonal antibody recognizes activated macrophage of rheumatoid patients and mediates antibody-dependent cell-mediated cytotoxicity. *Arthritis Res. Ther. 13*, R59.
(17) Herzog, H. (2001) In vivo functional imaging with SPECT and PET. *Radiochim. Acta 89*, 203−214.
(18) Ametamey, S. M., Honer, M., and Schubiger, P. A. (2008) Molecular imaging with PET. *Chem. Rev. 108*, 1501−1516.
(19) Bettio, A., Honer, M., Müller, C., Brühlmeier, M., Müller, U., Schibli, R., Groehn, V., Schubiger, A. P., and Ametamey, S. M. (2006) Synthesis and preclinical evaluation of a folic acid derivative labeled with ^{18}F for PET imaging of folate receptor-positive tumors. *J. Nucl. Med. 47*, 1153−1160.
(20) Ross, T. L., Honer, M., Lam, P. Y. H., Mindt, T. L., Groehn, V., Schibli, R., Schubiger, P. A., and Ametamey, S. M. (2008) Fluorine-18 click radiosynthesis and preclinical evaluation of a new ^{18}F-labeled folic acid derivative. *Bioconjugate Chem. 19*, 2462−2470.
(21) Al Jammaz, I., Al-Otaibi, B., Amer, S., and Okarvi, S. M. (2011) Rapid synthesis and *in vitro* and *in vivo* evaluation of folic acid derivatives labeled with fluorine-18 for PET imaging of folate receptor-positive tumors. *Nucl. Med. Biol. 38*, 1019−1028.
(22) Ross, T. L., Honer, M., Müller, C., Groehn, V., Schibli, R., and Ametamey, S. M. (2010) A new ^{18}F-labeled folic acid derivative with improved properties for the PET imaging of folate receptor-positive tumors. *J. Nucl. Med. 51*, 1756−1762.
(23) Maschauer, S., and Prante, O. (2009) A series of 2-O-trifluoromethylsulfonyl-D-mannopyranosides as precursors for concomitant ^{18}F-labeling and glycosylation by click chemistry. *Carbohydr. Res. 344*, 753−761.
(24) Maschauer, S., Einsiedel, J., Haubner, R., Hocke, C., Ocker, M., Hübner, H., Kuwert, T., Gmeiner, P., and Prante, O. (2010) Labeling and glycosylation of peptides using click chemistry: a general approach to ^{18}F-glycopeptides as effective imaging probes for positron emission tomography. *Angew. Chem., Int. Ed. 49*, 976−979.
(25) Baumann, C. A., Mu, L. J., Wertli, N., Krämer, S. D., Honer, M., Schubiger, P. A., and Ametamey, S. M. (2010) Syntheses and pharmacological characterization of novel thiazole derivatives as potential mGluR5 PET ligands. *Bioorg. Med. Chem. 18*, 6044−6054.
(26) Leamon, C. P., Parker, M. A., Vlahov, I. R., Xu, L. C., Reddy, J. A., Vetzel, M., and Douglas, N. (2002) Synthesis and biological evaluation of EC20: A new folate-derived, ^{99m}Tc-based radiopharmaceutical. *Bioconjugate Chem. 13*, 1200−1210.
(27) Reddy, J. A., Xu, L. C., Parker, N., Vetzel, M., and Leamon, C. P. (2004) Preclinical evaluation of ^{99m}Tc-EC20 for imaging folate receptor-positive tumors. *J. Nucl. Med. 45*, 857−866.
(28) Honer, M., Brühlmeier, M., Missimer, J., Schubiger, A. P., and Ametamey, S. M. (2004) Dynamic imaging of striatal D_2-receptors in mice using quad-HIDAC PET. *J. Nucl. Med. 45*, 464−470.
(29) Mindt, T. L., Müller, C., Melis, M., de Jong, M., and Schibli, R. (2008) "Click-to-Chelate": In vitro and in vivo comparison of a ^{99m}Tc(CO)$_3$-labeled N(tau)-histidine folate derivative with its isostructural, clicked 1,2,3-triazole analogue. *Bioconjugate Chem. 19*, 1689−1695.
(30) Müller, C., Reddy, J. A., Leamon, C. P., and Schibli, R. (2010) Effects of the antifolates Pemetrexed and CB3717 on the tissue distribution of ^{99m}Tc-EC20 in xenografted and syngeneic tumor-bearing mice. *Mol. Pharmaceutics 7*, 597−604.
(31) Müller, C., Forrer, F., Schibli, R., Krenning, E. P., and de Jong, M. (2008) SPECT study of folate receptor-positive malignant and normal tissues in mice using a novel ^{99m}Tc-radiofolate. *J. Nucl. Med. 49*, 310−317.
(32) Hamacher, K., Coenen, H. H., and Stöcklin, G. (1986) Efficient stereospecific synthesis of no-carrier-added 2-[^{18}F]-fluoro-2-deoxy-D-glucose using aminopolyether supported nucleophilic-substitution. *J. Nucl. Med. 27*, 235−238.
(33) Rostovtsev, V. V., Green, L. G., Fokin, V. V., and Sharpless, K. B. (2002) A stepwise Huisgen cycloaddition process: Copper(I)-catalyzed regioselective "ligation" of azides and terminal alkynes. *Angew. Chem., Int. Ed. 41*, 2596−2599.
(34) Tornoe, C. W., Christensen, C., and Meldal, M. (2002) Peptidotriazoles on solid phase: [1,2,3]-triazoles by regiospecific copper(I)-catalyzed 1,3-dipolar cycloadditions of terminal alkynes to azides. *J. Org. Chem. 67*, 3057−3064.
(35) Moses, J. E., and Moorhouse, A. D. (2007) The growing applications of click chemistry. *Chem. Soc. Rev. 36*, 1249−1262.
(36) Müller, C., Mindt, T. L., de Jong, M., and Schibli, R. (2009) Evaluation of a novel radiofolate in tumour-bearing mice: promising prospects for folate-based radionuclide therapy. *Eur. J. Nucl. Med. Mol. Imaging 36*, 938−946.
(37) Goodman, M. M., Elmaleh, D. R., Kearfott, K. J., Ackerman, R. H., Hoop, B., Brownell, G. L., Alpert, N. M., and Strauss, H. W. (1981) ^{18}F-Labeled 3-deoxy-3-fluoro-*D*-glucose for the study of regional metabolism in the brain and heart. *J. Nucl. Med. 22*, 138−144.
(38) Czernin, J., Satyamurthy, N., and Schiepers, C. (2010) Molecular mechanisms of bone ^{18}F-NaF deposition. *J. Nucl. Med. 51*, 1826−1829.
(39) Leamon, C. P., Reddy, J. A., Klein, P. J., Vlahov, I. R., Dorton, R., Bloomfield, A., Nelson, M., Westrick, E., Parker, N., Bruna, K., Vetzel, M., Gehrke, M., Nicoson, J. S., Messmann, R. A., LoRusso, P. M., and Sausville, E. A. (2011) Reducing undesirable hepatic clearance of a tumor-targeted vinca alkaloid via novel saccharopeptidic modifications. *J. Pharmacol. Exp. Ther. 336*, 336−343.

Bioconjugate Chemistry

Article

pubs.acs.org/bc

Cellular Uptake of Gold Nanoparticles Bearing HIV gp120 Oligomannosides

Blanca Arnáiz,[†,‡] Olga Martínez-Ávila,[†] Juan M. Falcon-Perez,[§,∥] and Soledad Penadés*[,†,‡]

[†]Laboratory of Glyconanotechnology, Biofunctional Nanomaterials Unit, CIC biomaGUNE, [‡]Biomedical Research Networking Center in Bioengineering, Biomaterials, and Nanomedicine (CIBER-BBN), P° de Miramón 182, 20009 San Sebastian, Spain

[§]IKERBASQUE, Basque Foundation for Science; [∥]Metabolomics Unit, CIC bioGUNE, CIBERehd, Bizkaia Technology Park Bldg 801-A, Derio, 48160, Bizkaia, Spain

Supporting Information

ABSTRACT: Dendritic cells are the most potent of the professional antigen-presenting cells which display a pivotal role in the generation and regulation of adaptive immune responses against HIV-1. The migratory nature of dendritic cells is subverted by HIV-1 to gain access to lymph nodes where viral replication occurs. Dendritic cells express several calcium-dependent C-type lectin receptors including dendritic cell-specific ICAM-3 grabbing non-integrin (DC-SIGN), which constitute a major receptor for HIV-1. DC-SIGN recognizes *N*-linked high-mannose glycan clusters on HIV gp120 through multivalent and Ca^{2+}-dependent protein−carbohydrate interactions. Therefore, mimicking the cluster presentation of oligomannosides from the virus surface is a strategic approach for carbohydrate-based microbicides. We have shown that gold nanoparticles (*manno*GNPs) displaying multiple copies of structural motifs (di-, tri-, tetra-, penta-, or heptaoligomanosides) of the *N*-linked high-mannose glycan of viral gp120 are efficient inhibitors of DC-SIGN-mediated *trans*-infection of human T cells. We have now prepared the corresponding fluorescent-labeled glyconanoparticles (FITC-*manno*GNPs) and studied their uptake by DC-SIGN expressing Burkitt lymphoma cells (Raji DC-SIGN cell line) and monocyte-derived immature dendritic cells (iDCs) by flow cytometry and confocal laser scanning microscopy. We demonstrate that the 1.8 nm oligomannoside coated nanoparticles are endocytosed following both DC-SIGN-dependent and -independent pathways and part of them colocalize with DC-SIGN in early endosomes. The blocking and sequestration of DC-SIGN receptors by *manno*GNPs could explain their ability to inhibit HIV-1 *trans*-infection of human T cells *in vitro*.

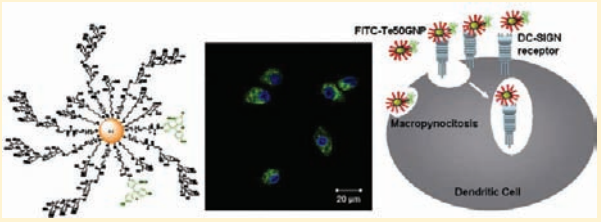

INTRODUCTION

In the fight against the transmission of the human immunodeficiency virus (HIV), extraordinary efforts have been made to prevent (vaccines and microbicides) or eliminate infection (anti-retrovirals, therapeutic vaccines). None of these strategies have yet eradicated HIV infection or prevented transmission. A renewed effort is needed to understand the molecular basis of the complex mechanism of virus infection.[1] The recent development of biofunctional nanoparticles and their applications in biomedicine opens new opportunities to address this problem.

Among the early targets of HIV-1 are immature dendritic cells (iDCs) and Langerhans cells in mucosal epithelium, and $CD4^+CCR5^+$ T cells and macrophages in the subepithelium.[2,3] Some studies point to iDCs as the main migratory cell populations involved in HIV-1 disseminations from intravaginal transmission.[4−6] iDCs, especially those in epithelia, can recognize, bind, and ingest whole pathogens and/or their related antigens, transporting them between peripheral and lymphoid tissues. Through subversion of the migration mechanisms of DCs, HIV-1 gains access to $CD4^+$ lymphocytes in lymphoid tissue through the so-called *trans*-infection mechanism and enters these cells through a series of sequential interactions between the envelope glycoprotein (Env) and cellular receptor CD4 and coreceptors CCR5 or CXCR4. The involvement of iDCs in the transfer of HIV-1 to $CD4^+$ lymphocytes has been described in two distinct phases. First, iDCs divert virus from the endolysosomal pathway (clathrin-coated vesicles) to the DC-T cell synapse (*trans*-infection). This phase is temporally limited by the degradation of significant amounts of virus within 24 h postinfection. Second, residual virus replicates by "de novo production" and is transferred from iDCs to CD4+T cells (*cis*-infection).[7] Other studies postulate that the vast majority of virions are transmitted in *trans* originating from the plasma membrane rather than from intracellular vesicles.[8]

DCs are equipped with C-type lectin receptors (CLRs) involved in HIV-1 capture such as dendritic-cell specific intercellular adhesion molecule-3 (ICAM-3) grabbing non-integrin (DC-SIGN; CD209) and mannose receptor (MR; CD206).[9,10] CLRs are characterized by one or several carbohydrate recognition domains (CRD) that interact in a

Received: December 13, 2011
Revised: March 2, 2012
Published: March 21, 2012

   dx.doi.org/10.1021/bc200663r | *Bioconjugate Chem.* 2012, 23, 814−825

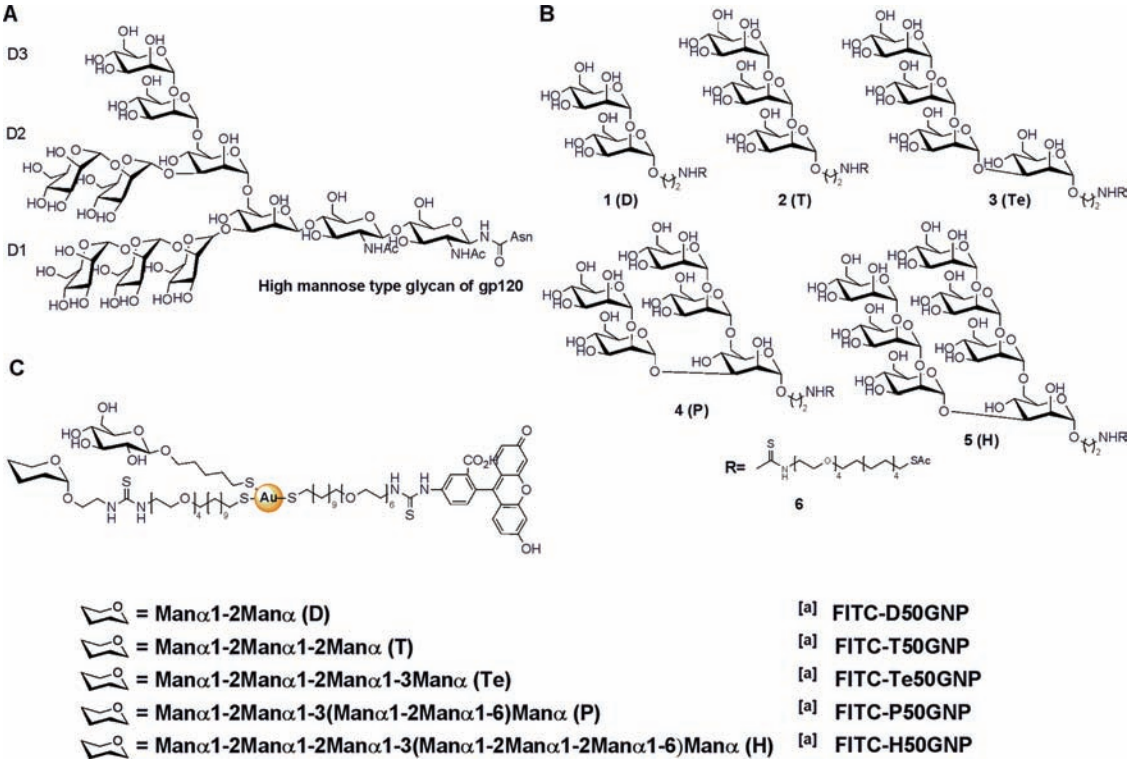

Figure 1. (A) High-mannose undecasaccharide of viral gp120. (B) Di-, tri-, tetra-, penta-, and hepta-oligomannoside conjugates, structural motifs of the gp120 high-mannose glycan, used for the preparation of glyconanoparticles. (C) Schematic representation of fluorescein-labeled oligomannoside gold nanoparticles (FITC-*manno*GNPs). [a] The numbers indicate the percentage of mannose oligosaccharides on GNPs, with the rest being the stealthy component 5-mercaptopentyl β-D-glucopyranoside ($GlcC_5S$) and fluorescein conjugates.

calcium-dependent manner. DC-SIGN has a single CRD which specifically recognizes high-mannose clusters on gp120.[11] The HIV-1 glycoprotein gp120 is highly glycosylated with high-mannose type glycans.[12−15] The high-mannose glycans (Figure 1) are arranged in clusters, which mediate virus attachment to DCs through multivalent carbohydrate−lectin interactions.[16,17] Mimicking the cluster presentation of high-mannose glycans on the virus surface is a strategy for the generation of carbohydrate-based antiviral agents. Approaches mimicking the multivalent presentation of high-mannose oligosaccharides on proteins,[18] peptides,[19] dendrimers,[20,21] polymers,[22] liposomes,[23] microspheres,[24] and nanoparticles,[25,26] as scaffolds, are emerging for the development of potent and selective inhibitors with potential applications as vaginal microbicides and HIV vaccines. Among these scaffolds, gold nanoparticles offer additional advantageous features, as they allow display of a large number of carbohydrates with a high density and multifunctionality by simultaneous incorporation, in a single gold cluster, of different ligands in a controlled way.[27]

To target the DC-SIGN receptor on DCs, we prepared a small library of glyconanoparticles bearing multiple copies of oligosaccharidic motifs of the *N*-linked high-mannose glycan of viral gp120 (*manno*GNPs).[28] These GNPs mimic the cluster presentation of the high-mannose glycans on gp120. The *manno*GNPs efficiently inhibit DC-SIGN mediated *trans*-infection of human T-cells in a cellular assay that mimics the natural route of virus transmission from DCs to T-lymphocyte.[29] DC-SIGN-mediated uptake of HIV is required for *trans*-enhancement of T cell infection.[30] We hypothesized that the ability of *manno*GNPs to inhibit HIV-1 *trans*-infection of human T cells could be explained by binding and sequestration of DC-SIGN receptor of dendritic cells in competition with the virus.[31] To investigate this hypothesis, we have now prepared fluorescently labeled analogues of the *manno*GNPs (FITC-*manno*GNPs) bearing 50% density of di-, tri-, tetra-, penta-, or heptamannosides (Figure 1) and monitored their binding and entry into DC-SIGN expressing cells by flow cytometry (FC) and confocal laser scanning microscopy (CLSM).

EXPERIMENTAL PROCEDURES

Reagents and Methods. Reagent-grade solvents and chemicals were used without further purification. 3-(4,5-Dimethylthiazol-2-yl)-2,5-diphenyl tetrazolium bromide (MTT), sodium borohydride ($NaBH_4$), and ethylene diamine-tetraacetic acid (EDTA) were purchased from Sigma-Aldrich. Chloroauric acid was purchased from Strem Chemicals. The PBS buffer was purchased in tablets and prepared following manufacturer procedures (Sigma-Aldrich) corresponding to 10 mM phosphate buffer containing 137 mM NaCl and 2.7 mM KCl at pH 7.4. UV−vis spectra were carried out with a Beckman Coulter DU 800 spectrometer. ^{1}H NMR spectra were recorded in D_2O on a Bruker AVANCE (500 MHz) spectrometer. Chemical shifts (δ) are given in ppm relative to the residual signal of D_2O. For transmission electron microscopy (TEM) examinations, a single drop (10 μL) of the aqueous solution (ca. 0.1 mg/mL in Milli-Q water) of GNPs was placed onto a copper grid coated with a carbon film (Electron Microscopy Sciences). The grid was left to dry in air for several hours at room temperature. TEM analysis was carried out in a Philips JEOL JEM-2100F working at 200 kV. Milli-Q reagent-grade water was used in all experiments. Fluorescein conjugate (FITC) was prepared as reported.[32] 5-

dx.doi.org/10.1021/bc200663r | *Bioconjugate Chem.* 2012, 23, 814−825

Mercaptopentyl β-D-glucopyranoside ($GlcC_5S$) and the di- (D), tri- (T), tetra- (Te), penta- (P), and hepta- (H) mannoside conjugates described in Figure 1 were synthesized as previously reported.[28]

General Procedure for the Preparation of Fluorescent Gold *manno*-Glyconanoparticles. The fluorescent di-, tri-, tetra-, penta-, and heptamannosylated (FITC-D50, FITC-T50, FITC-Te50, FITC-P50, and FITC-H50) GNPs were synthesized following a modified protocol.[28,32] A solution (0.012 M) of a 50:45:5 mixture of the oligomannoside conjugate (D, T, Te, P, or H), glucose conjugate ($GlcC_5S$), and fluorescein conjugate (FITC) in methanol/water (3:1) was added (3 equiv) to a solution of tetrachloroauric acid (0.025 M, 1 equiv) in water. An aqueous solution of $NaBH_4$ (1 M, 22 equiv) was then added in four portions, with rapid shaking. The black suspension formed was shaken for an additional 2 h at 25 °C, and the supernatant was then removed. The residue was dissolved in the minimum amount of Milli-Q water, and the solution was loaded into 5−10 cm segments of SnakeSkin pleated dialysis tubing (Pierce, 3500 MWCO), placed in a 3 L beaker of water, and stirred slowly, replacing with fresh water every 3−4 h over the course of 72 h. The dialyzed solution was lyophilized to afford the GNPs (see also Supporting Information). ^1H NMR spectra of the glycoconjugate mixture used for the GNP synthesis and of the products recovered from the supernatant after GNP formation were recorded to confirm the ratio of the ligands attached in the GNPs. The particle size distribution of the gold nanoparticles was evaluated from several TEM micrographs by means of an automatic image analyzer. The average diameter and the number of gold atoms of the GNPs were deduced as reported.[28,32] Fluorescein content on GNPs was evaluated by interpolation from a calibration curve of commercial fluorescein isothiocyanate. The fluorescence of each FITC-*manno*GNP was measured in quadruplicates at λ_{em} 530 nm (λ_{ex} 485 nm) with a plate reader (GENios Pro, TECAN). These values were taken as reference to normalize the fluorescence of cells after incubation with GNPs. Nanoparticle solutions were freshly prepared (Milli Q sterile water) and sterilized (Minisart filters 0.20 μm, Sartorius) before using in cell assays. For statistical calculations of the mean fluorescence values by the *FACSDiva* software of the Canto II flow cytometer (BD biosciences), fluorescent cells were gated for live populations, homogeneous in size (side scatter or SSC) and granularity (forward scatter or FSC).

Cell Lines. The Raji line of lymphoblast-like cells, established from a Burkitt's lymphoma, and same line stably expressing DC-SIGN were a generous gift from Dr. J. Alcamí (Instituto de Salud Carlos III, Madrid). This cell line was grown in RPMI-1640 medium supplemented with 10% fetal calf serum. Media also contained 2 mM L-glutamine and streptomycin/penicillin (100 U/mL penicillin and 100 μg/mL streptomycin). Cells were subcultured following ATCC recommendations.

Generation of Human Immature DCs. Immature DCs were obtained by differentiation of monocytes isolated from buffy coat packs from healthy donors (Basque Center for Transfusions and Human Tissues, San Sebastian, Spain). Peripheral blood mononuclear cells (PBMCs) were prepared by Ficoll-Paque Premium (GE, Heathcare, Sweden) density gradient centrifugation. Monocytes were isolated by positive selection of $CD14^+$ cells using CD14 microbeads (Miltenyi Biotec, Germany) and cultured for 6 days in RPMI-1640 medium (Sigma-Aldrich) supplemented with 10% low endotoxin fetal bovine serum (PAN Biotech Gmbh, Germany), 2 mM L-glutamine, 50 U/mL penicillin/streptomycin, 2 μg/mL amphotericin B, 1000 U/mL recombinant human IL-4 (Becton Dickinson), and 1000 U/mL granulocyte macrophage colony stimulating factor (GM-CSF). Medium and cytokines were replaced every 2 days. At day 6, the resulting cells displayed the characteristic phenotype;[33] moderate levels of CD14, MHCII (HLA-DR), and DC-SIGN, high levels of CD11c, and negligible CD80 as determined by flow cytometry (SI Figure S11A and B).

Analysis of Surface Receptor Expression. Cell surface receptor expression was analyzed in a BD Canto II flow cytometer (Becton Dickinson). Cells were washed in PBS, blocked for 30 min at 4 °C with 10% low-endotoxin heat-inactivated FBS (Fetal Bovine Serum, Biochrom AG) and incubated in ice for 30 min in staining buffer (1% FBS, 0.09% sodium azide, PBS) containing saturation concentrations of the phycoerythrin(PE)-labeled anti-CD80, anti-DC-SIGN, anti-CCR5, and CXCR4 mAb; APC-labeled HLA-DR and CD83 mAb; PerCP-cy5.5-labeled CD14 mAb, and PE-cy7-labeled CD11c mAb. As control, isotype-matched fluorophore-matched mouse mAb were used. Before analysis, cells were fixed in PBS containing 4% paraformaldehyde for 15 min at 4 °C, washed twice, and resuspended in staining buffer. A gate (M1) that excluded the isotypic control signal determined the percentage of positive cells. The mean fluorescence intensity was determined for those cells stained with the specific marker antibody. All the antibodies were purchased from BD biosciences. Detachment of DCs from the flask immediately prior to each experiment was committed by tapping or harsh flushing.

ELISA for Secretion of IL10 and IL-12p40. To detect IL-12p40 and IL-10 production by DCs, 96-well flat-bottom plates were coated for 12−15 h with 4 μg/mL antihuman IL-12p40 antibody or 2 μg/mL antihuman IL-10 antibody, respectively. The plates were blocked with PBS containing bovine serum albumin (BSA, 1%), sucrose (5%), and sodium azide (0.05%) for 2 h and incubated for 12−15 h with 100 μL of human recombinant IL-12p40 (hrIL-12p40), IL-10 (hrIL10) standards, or supernatants of iDCs (10^4) incubated with LPS (1 μg/mL), gp120 (35 ng/mL), Te50GNPs (3500 ng/mL, 350 ng/mL, and 35 ng/mL) or media alone for 24 h at 37 °C. Following the incubation, biotinylated anti-IL12p40 (175 ng/mL) or biotinylated anti-IL-10 (300 ng/mL) antibody was added, respectively, and the incubation continued for 2 h. Levels of IL-12p40 and IL-10 were detected using streptavidin−horseradish peroxidase (SA-HRP, 1:2500) in PBS and its substrate *p*-nitrophenyl phosphate according to manufacturer's instructions. The reaction was stopped with 50 μL of H_2SO_4. Absorbance was measured at 492 nm. All the incubations and reactions were performed at room temperature. After each incubation, all the wells were washed three times with distilled water containing NaCl (150 mM) and Tween-20 (0.05%).The antibodies and standards (DuoSet human IL-12p40) used were purchased from R&D Systems.

Cellular Uptake of FITC-*manno*GNPs. For internalization assays, 10^5 cells (Raji, Raji DC-SIGN, and iDCs) were incubated in 300 μL of supplemented medium (RPMI-1640) containing 25 μg/mL of FITC-*manno*GNPs (FITC-D50, FITC-T50, FITC-Te50, FITC-P50, and FITC-H50) or media alone (untreated) for 3 h at 37 °C, 5% CO_2. Unbound *manno*GNPs were removed by two washes with cold PBS before FC analysis. Raji DC-SIGN cells incubated with FITC-

Te50GNPs were stained with DAPI (100 ng/mL) for 20 min, washed with PBS, and deposited on a coverslip for confocal imaging. For inhibition of energy-dependent uptake, cells were incubated for 3 h at 4 °C, 5% CO_2. For receptor digestion, cells were incubated with 1 mg/mL trypsin/EDTA PBS (Sigma-Aldrich) at 37 °C for 15 min previous to FC analysis. For inhibition assays, cells were preincubated with the corresponding inhibitors (EDTA or anti-DC-SIGN IgG1 mAb) in supplemented RPMI-1640 medium for 30 min at 37 °C, 5% CO_2, before addition of FITC-*manno*GNPs. The final concentrations of the inhibitors used were 50 mM of EDTA[34] (Sigma), 10 μg/mL of anti-DC-SIGN IgG1 mAb (clone AZND1, Beckman Coulter, France), and 10 μg/mL of anti-immunoglobulin IgG1 isotype mAb as a control (BD biosciences). GNP uptake is expressed as a ratio between the mean fluorescence intensity of cells treated with GNPs and untreated samples (fluorescence background) and normalized to the fluorescence content of GNPs (relative fluorescence intensity). GNP uptake inhibition is presented as the percentage of the mean cell fluorescence signal in the presence of EDTA, AZND1, or isotype control to the signal in its absence. For each acquisition, the autofluorescence was eliminated from the fluorescent signal up to a residual 10%. Cells incubated in the absence of FITC-*manno*GNPs were set in the cytometer to give the lowest signal in the histogram (first decade, around 50 U.A). Then, the cells incubated in the presence of FITC-*manno*GNPs were acquired under the same voltage conditions.

Kinetics of FITC-Te50GNPs Uptake. For uptake time course determination, cells were incubated with FITC-Te50GNP (25 μg/mL) for up to 11 h. Cell aliquots (10^5) were washed with cold PBS at different incubation times (2.5, 5, 10, 30 min; and 1, 1.5, 2, 2.5, 3, 4, 4.5, 5, 5.5, 6, 6.5, 7.5, 9, 10, and 11 h) and the internalized FITC-Te50GNP measured by FC. For FITC detection in the FC, all the samples were excited with a 488 nm laser, and both a 502 nm long-pass and a 530/30 nm band-pass filter were used.

At 2 h incubation time, the cell sample was split, and one part was washed with PBS and incubated in fresh media for up to 9 additional hours. At times 2.5, 3, 4, 4.5, 5, 5.5, 6, 6.5, 7.5, 9, 10, and 11 h, a cell aliquot was washed and resuspended in cold PBS and fluorescence decrease measured by FC. The fluorescence time course was plotted as time versus relative fluorescence intensity obtained by dividing the mean fluorescence intensities of cells treated with FITC-Te50GNP by the untreated samples and normalized with the fluorescence content of FITC-Te50GNPs.

The fluorescence time course of iDCs was also followed by CLSM. Cells were incubated with FITC-Te50GNPs (25 μg/mL) and imaged at 5 min, 2.5 h, and 5 h. At 2 h incubation time, the cell sample was split, and one part was washed with PBS and incubated in fresh media for 3 h and imaged. For imaging, 3×10^5 cells were deposited at 37 °C and 5% CO_2 on polylysine-coated coverslips to allow adherence. Cells were washed twice in PBS, fixed with 4% paraformaldehyde PBS for 30 min at 37 °C, and washed twice with PBS and mounted with DAPI-containing oil (Vectashield, Vector Laboratories).

Gold content of cells incubated with FITC-Te50GNP for 2.5 h was determined by inductive couple plasma−mass spectrometry (ICP-MS). Cells (10^5) were washed with media and the cell pellet lyophilized and digested by addition of 180 μL of HNO_3 and 20 μL of HCl, heated at 60 °C overnight before the addition of 3.8 mL thiourea (200 μg/mL) in HCl 1% for analysis in an Agilent 7500 CE.

Localization of Intracellular FITC-Te50GNP. Confocal microscopy was performed on a Zeiss LSM 510 META microscope equipped with 63× magnification oil lens. iDCs were incubated with FITC-Te50GNPs (25 μg/mL) in media. Following 3 h incubation, 3×10^5 cells were deposited on polylysine-coated coverslips and left for 1 h at 37 °C to allow adherence. Cells were washed three times with PBS at 37 °C, fixed with 4% paraformaldehyde PBS (37 °C) for 15 min and washed again three times with PBS. Cells were permeabilized with PBS containing 0.05% saponin and 10% BSA for 10 min at room temperature and then blocked with 3% BSA in PBS at 4 °C overnight. For double immunostaining, permeabilized iDCs were incubated at 37 °C for 2 h with both rabbit antihuman DC-SIGN mAb (Abcam, 10 μg/mL) and mouse antihuman mAb against LAMP-1 (BD Pharmigen, 0.5 μg/mL), EEA-1 (BD Pharmigen, 5 μg/mL), HLA-DP, DQ&DR (Ancell, 50 μg/mL), Cav-1 (BD Pharmigen, 5 μg/mL), or Clathrin (BD Pharmigen, 5 μg/mL) in 1% BSA PBS buffer. After extensive washes with 0.5% Tween-20 in PBS, cells were first incubated with 1% BSA in PBS containing secondary goat antirabbit antibody−Alexa Fluor 405 (Invitrogen, 5 μg/mL) at 37 °C for 1 h, washed three times with 0.5% Tween-20 PBS and then incubated 1 h with rabbit antimouse antibody−Alexa Fluor 594 (Invitrogen, 5 μg/mL) and washed again. In an attempt to palliate the low pH of some organelles that leads to FITC fluorescence quenching, labeled iDCs were mounted in FluorSave oil (Merck, pH 10.5−10.7) and examined under the confocal microscope with a 63× objective at excitation wavelengths of 488, 405, and 561 nm for fluorescein, Alexa Fluor 405, and Alexa Fluor 594, respectively. Images of cells photographed with CLSM were analyzed with Zeiss LSM Image Browser or *ImageJ* software.

Quantification Analysis of Colocalization. For intensity quantification of each color along a defined line, two-color overlays were analyzed with the *Zen 2007* software and generated fluorescence intensity histograms. Colocalization coefficients displayed in Table S1 were obtained by *ImageJ* software analysis of pairs of 8-bit images (488/561 nm or 405/488 nm) using automatic threshold and background correction.[35] Quantification of the degree of colocalization of the different vesicular markers was carried out as previously reported using imaging software.[36,37] A total of 1413 fluorescein-positive objects with a mean area of 0.62 μm^2, each of them corresponding to independent vesicles, were detected in the 90 iDCs (mean = 15.7 and SD = 8.9) and processed to evaluate the colocalization degree with DC-SIGN and EEA1 positive compartments by using the imaging software *Volocity v 5.5.* (Perkin-Elmer).

RESULTS AND DISCUSSION

Synthesis of FITC-*manno*GNPs. Fluorescein-labeled oligomannoside gold nanoparticles (FITC-*manno*GNPs) coated with different structural motifs of HIV-1 gp120 high-mannose glycan were prepared to study their binding/internalization into DC-SIGN expressing cells. FITC-*manno*GNPs having an average density of 50% linear di-(D), tri-(T), or tetra-(Te), or branched penta-(P) and hepta-(H) mannoside conjugates, 45% of 5-mercaptopentyl β-D-glucopyranoside ($GlcC_5S$) and 5% of fluorescein conjugate (FITC) (Figure 1) were prepared and characterized following a modification of previously described methodologies.[28,32] The

dx.doi.org/10.1021/bc200663r | *Bioconjugate Chem.* 2012, 23, 814−825

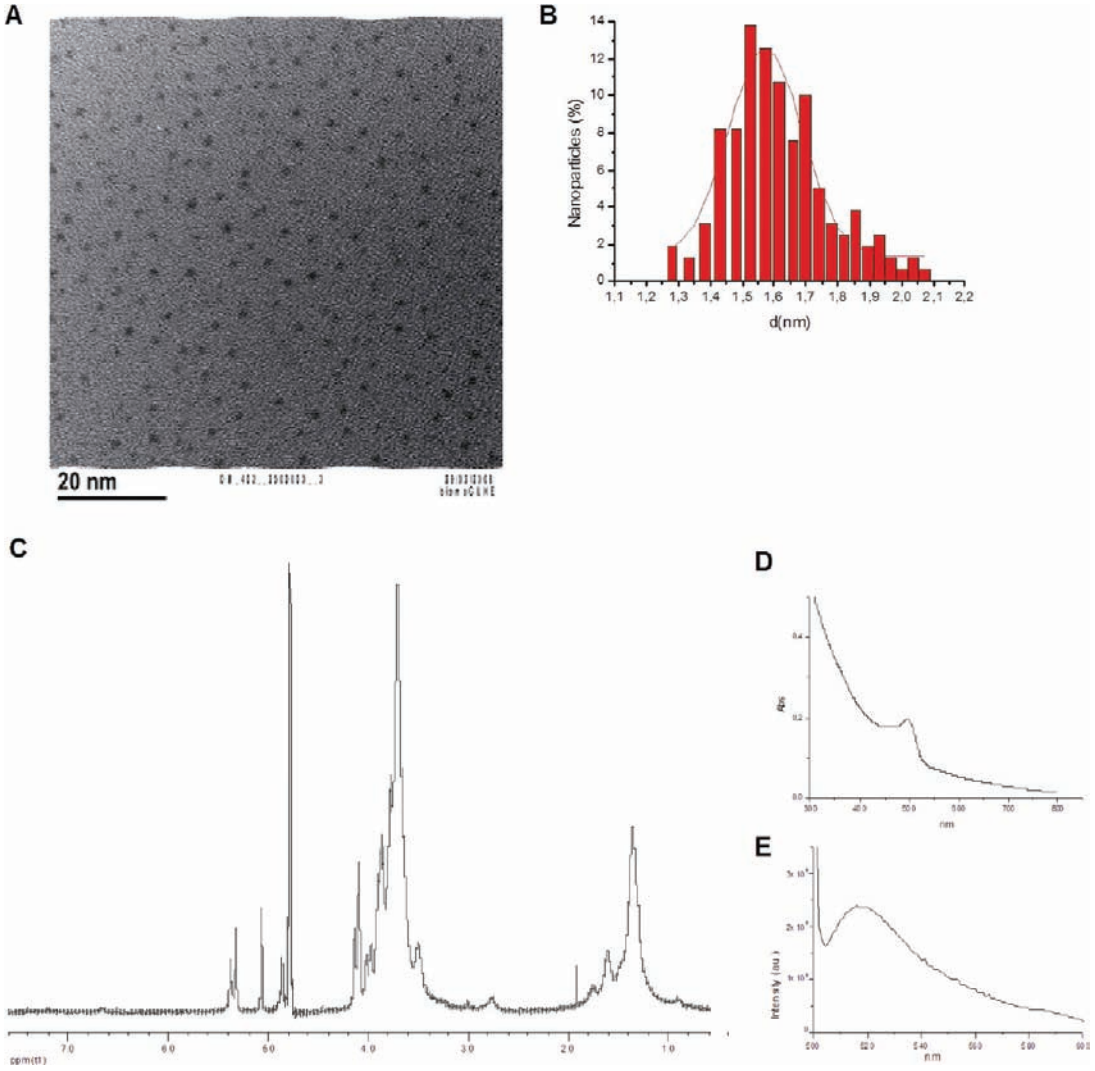

Figure 2. Characterization of FITC-Te50GNP. (A) TEM micrograph in H_2O. (B) Size distribution histogram. (C) ^1H NMR spectrum in D_2O. (D) UV−visible spectrum. (E) Fluorescence spectrum.

average number of ligands on the gold surface is between 100 and 120. Mannoside conjugates **1**−**5** were synthesized by thiourea coupling of the corresponding 2-aminoethyl α-oligomannosides and the isothiocyanate linker **6** followed by subsequent removal of the acetyl group, affording compounds **1**−**5** as disulfide derivatives.[28] The fluorescein conjugate was synthesized as previously reported.[32] The length and flexibility of the linker of the fluorescein conjugate were chosen in order to avoid fluorescence quenching. To control the density of oligomannosides and fluorescein on the GNPs, the $GlcC_5S$ conjugate was selected as the stealthy component because its insignificant contribution to DC-SIGN mediated *trans*-infection had been proven.[29] An aqueous solution of tetrachloroauric acid was added to a methanol−water mixture containing the three different conjugates in the desired ratio. The resulting mixture was reduced with an excess of $NaBH_4$, and the suspension was vigorously shaken for 2 h at 25 °C. The supernatant was removed and the residue was dissolved in Milli-Q water and purified by dialysis. The resulting FITC-*manno*GNPs were characterized by transmission electron microscopy (TEM), ^1H NMR, UV−vis, and fluorescence spectroscopy. The average diameter of the gold core was 1.2−2.0 nm, and the fluorescein molecules per cluster are around 5% of the total number of glycoconjugates as determined by fluorescence (Figure 2 and SI Figures S1−S5).

Binding and Uptake of FITC-*manno*GNPs by Raji DC-SIGN and iDCs. Application of the FITC-*manno*GNPs to cells was preceded by viability assays. Incubation of monocyte derived iDCs, Raji, or Raji DC-SIGN cell lines with 100 μg/mL FITC-*manno*GNPs for 24 h indicates the absence of cytotoxic effects on Raji and Raji DC-SIGN cells and moderate effects on the viability of monocyte-derived iDCs (SI Figure S6). The incorporation of fluorescein in the *manno*GNPs did not induce apparent cytotoxicity when compared with the analogous nonfluorescent *manno*GNPs tested at the same concentration in the Raji DC-SIGN cell line.[29] Subsequently, FITC-*manno*GNPs at 25 μg/mL were employed safely for all the experiments described in this work.

The binding of FITC-*manno*GNPs by monocyte-derived iDCs or Raji and DC-SIGN stably transfected Raji cells was explored under different experimental conditions by FC. DC-SIGN expression was confirmed in both Raji DC-SIGN cell line and iDCs by immunolabeling with PE-conjugated antihuman DC-SIGN antibody (SI Figure S7). FITC-*manno*GNP binding and uptake was first assessed by incubation with Raji or Raji DC-SIGN cells for 3 h at 37 or 4 °C, and cellular fluorescence

dx.doi.org/10.1021/bc200663r | *Bioconjugate Chem.* 2012, 23, 814−825

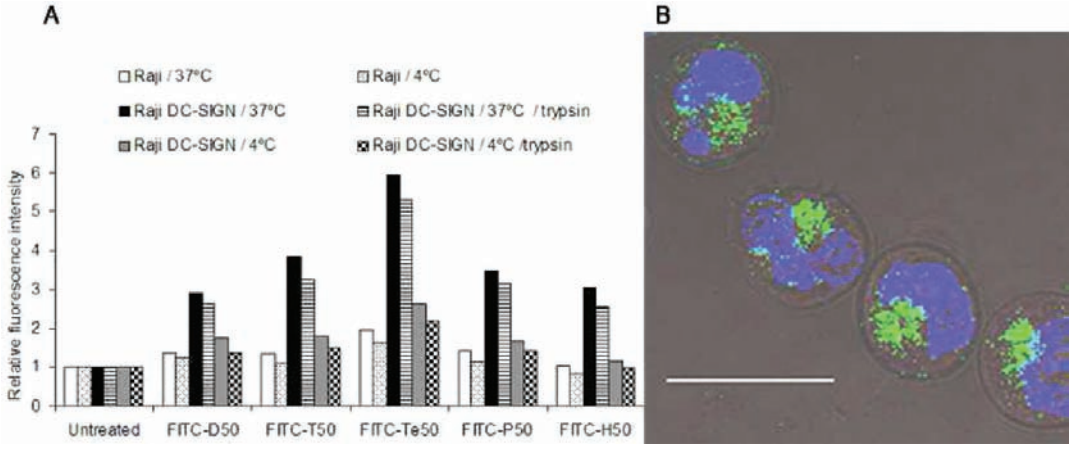

Figure 3. DC-SIGN receptor-mediated internalization of FITC-*manno*GNPs. (A) GNPs or media alone were incubated with Raji or Raji DC-SIGN cells for 3 h at 37 or 4 °C. Raji DC-SIGN cells were treated with trypsin to distinguish internalized from cell-surface-bound GNPs. Cell fluorescence intensity was measured by flow cytometry (FC) and expressed as a ratio between the mean fluorescence intensity of cells treated with GNPs and untreated samples, and normalized to the fluorescence content of GNP (relative fluorescence intensity). (B) Confocal image of Raji DC-SIGN cells incubated with FITC-Te50GNPs (green) for 3 h at 37 °C. Nuclei were stained with DAPI (blue). Transmitted light overlay shows the delimited plasma membrane. Data are from a representative experiment carried out twice with similar results.

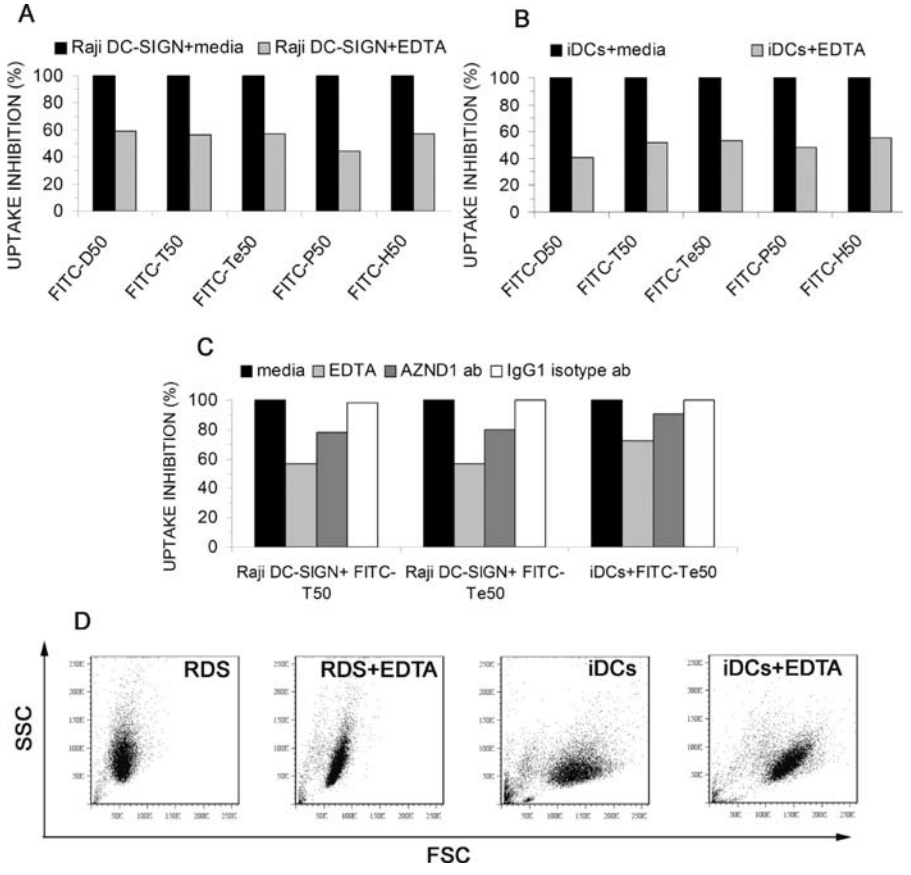

Figure 4. Flow cytometry of the specific FITC-*manno*GNPs uptake by C-type lectins (CLRs) and DC-SIGN receptors. Uptake of GNPs (25 μg/mL) after 3 h by Raji DC-SIGN cells (A) or iDCs (B) in the absence or presence of EDTA (50 mM). (C) Comparison of FITC-Te50GNP and FITC-T50GNP uptake in the presence of EDTA or anti-DC-SIGN IgG1 mAb (AZN-D1, 10 μg/mL), specific for DC-SIGN carbohydrate recognition domain. A control sample with an anti-IgG1 isotype mAb (10 μg/mL) is included. FITC-*manno*GNPs uptake is presented as the percentage of the mean cell fluorescence signal in the presence of EDTA, AZND1, or isotype control to the signal in its absence. Values were normalized to the FITC content per *manno*GNP. (D) Dot plots of the effect of 50 mM EDTA on the size (side scatter, SSC) and granularity (forward scatter, FSC) of Raji DC-SIGN cells and iDCs after a 3 h incubation. A representative experiment out of three with similar results is shown.

was detected by FC (Figure 3). In the presence of DC-SIGN-expressing cells, all FITC-*manno*GNPs were efficiently internalized at 37 °C reaching fluorescence levels at least 3 times above the cell autofluorescence levels (Figure 3A, Raji DC-SIGN/37 °C). FITC-Te50GNP showed a preferential uptake in comparison with the rest of the GNPs. In the absence

dx.doi.org/10.1021/bc200663r | *Bioconjugate Chem.* 2012, 23, 814–825

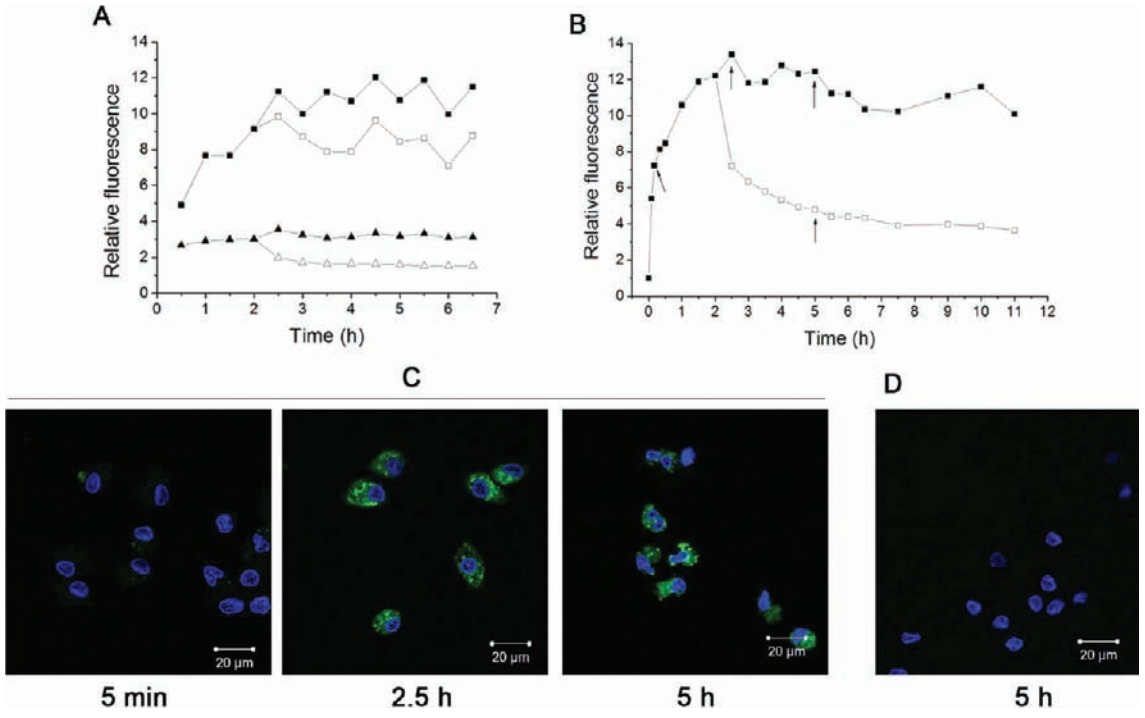

Figure 5. Time course of the FITC-Te50GNP uptake at 37 °C. FC analysis of the uptake of GNPs (25 μg/mL) by Raji DC-SIGN (A, filled squares) and Raji cells (A, filled triangle), and iDCs (B, filled squares). After 2 h of FITC-Te50GNP uptake, medium containing GNPs was replaced with medium alone and cultured again (empty symbols). Data are expressed as a ratio of the mean fluorescence intensity of Te50-FITC-treated cells to untreated cells. (C) CLSM analysis of iDCs after 5 min, 2.5 h, and 5 h of FITC-Te50GNP incubation and (D) 3 h after GNP removal from the media (arrows). The images are overlays of fluorescein (green) and DAPI (blue) of a single section of the *Z*-stacks acquired at each time point.

of DC-SIGN (Raji cells), FITC-*manno*GNPs were barely internalized (Figure 3A, Raji/37 °C). The entry in Raji DC-SIGN was mostly inhibited by incubation at 4 °C (Figure 3A, Raji DC-SIGN/4 °C). The incubation of cells at 4 °C has been extensively described as a method to inhibit energy-dependent internalization. Confocal imaging of Raji DC-SIGN after incubation with FITC-Te50GNPs corroborates that internalization occurs (Figure 3B). Together, these results show that the entry of fluorescently labeled oligomannoside-coated GNPs in Raji DC-SIGN is mediated by active mechanisms and, to a much less extent, by passive mechanisms. Trypsination before FC measurements (Figure 3A) showed a small reduction of fluorescence. This result indicates that a high fraction of FITC-*manno*GNPs is internalized via receptor-mediation, and only a small fraction remains bound to plasma membrane.

In order to prove the involvement of the Ca^{2+}-dependent CLRs in the active uptake of *manno*GNPs, Raji DC-SIGN and iDC were incubated with the nanoparticles in the presence of ethylenediaminetetraacetic acid (EDTA) (Figure 4). EDTA inhibits the binding of oligosaccharides to CLRs by chelating calcium cations. Dot plots in Figure 4D show the lack of drastic effects of 50 mM EDTA on the size and granularity homogeneity of Raji DC-SIGN cells and iDCs after a 3 h incubation. The uptake of *manno*GNPs by Raji DC-SIGN cells or iDCs for 3 h at 37 °C was partially inhibited by 50 mM EDTA (Figure 4A,B). The rest of the total uptake observed (~50%) could be attributed to CLR-independent pathways. As expected, EDTA treatment did not decrease the uptake of FITC-*manno*GNP by Raji cells (data not shown) indicating that CLRs are not involved.

In order to investigate the role of DC-SIGN in the cellular uptake of *manno*GNPs, we selected the anti-DC-SIGN mAb AZN-D1 to block specifically the carbohydrate recognition domain (CRD) of DC-SIGN. This antibody has been shown to inhibit HIV-1 gp120/DC-SIGN interaction[38] and HIV transmission to CD4+T cells.[39] The fluorescently labeled FITC-T50GNP and FITC-Te50GNP, whose analogues (T50GNP and Te50GNP) showed the highest inhibitory activity in the DC-SIGN mediated HIV-1 *trans*-infection of T-cells,[29] were used as probes to test whether the uptake in Raji DC-SIGN and iDCs is dependent on the mannoside/DC-SIGN interaction. We found that the GNP entry in monocyte-derived iDCs and Raji DC-SIGN was specifically diminished by 10 μg/mL of antibody (Figure 4C). Higher concentrations of mAb AZN-D1 (15 μg/mL and 20 μg/mL) improved the inhibition levels (SI Figure S8). As control, we used an antibody of the same isotype as AZN-D1 (IgG 1), which did not inhibit the uptake of FITC-T50GNP and FITC-Te50GNP (Figure 4C). The entry inhibition of the FITC-T50GNP and FITC-Te50GNP by mAb AZN-D1 in Raji DC-SIGN and iDCs and the *trans*-infection inhibitory activity observed for both GNPs suggest that the multivalent display of the mannosides on the GNPs competes with HIV-1 for the carbohydrate recognition domain of the DC-SIGN receptor.

Kinetics of the Uptake Process of FITC-Te50GNPs by iDCs, Raji, or Raji DC-SIGN cells. Cell uptake of FITC-Te50GNP was monitored by FC and CLSM at different incubation times (Figure 5). iDCs, Raji, or Raji DC-SIGN cells were incubated with FITC-Te50GNP (25 μg/mL) for up to 11 h at 37 °C allowing uptake (Figure 5A,B, filled symbols). As expected, FITC-Te50GNP was efficiently internalized in Raji DC-SIGN cells and iDC. The uptake reaches a plateau (equilibrium state) at 2−2.5 h in Raji DC-SIGN cells and iDCs. This uptake was 4 times higher than in Raji cells. The

dx.doi.org/10.1021/bc200663r | *Bioconjugate Chem.* 2012, 23, 814−825

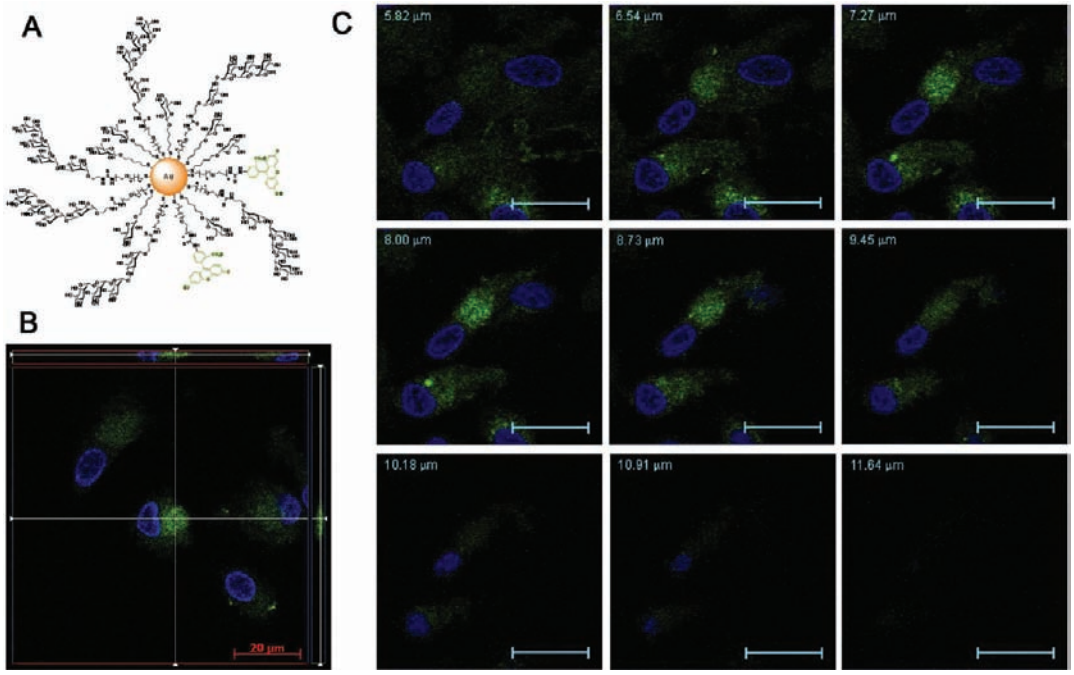

Figure 6. (A) Schematic representation of FITC-Te50GNP. (B) Orthogonal view of a *Z*-stack. (C) Gallery view of single plane series of a *Z*-stack. iDCs were incubated with FITC-Te50GNP (green) for 3 h at 37 °C, plated on glass coverslips, and fixed before mounting. Nuclei were counterstained with DAPI (blue). Confocal optical 2 μm sections in 730 nm intervals taken through the whole cells show intracellular localization of FITC-Te50GNP (scale bars = 20 μm).

small uptake observed in Raji cells remains constant (Figure 5A). After 2 h incubation half of the cell sample was washed with PBS and centrifuged to remove the free FITC-Te50 nanoparticles and the cells were incubated in fresh medium for additional 9 h. Maximum fluorescence decrease is reached after 1.5 h for Raji DC-SIGN (Figure 5A, empty squares) and 5−6 h for iDCs (Figure 5B, empty squares). The decrease in iDC was 4-fold higher than the decrease in Raji DC-SIGN. The curves indicate that 80−90% of fluorescence remains in Raji DC-SIGN and 40−60% in iDCs. Confocal imaging confirmed the cellular internalization of FITC-Te50GNPs in iDCs (Figure 5C and SI Figure S9 upper panel). After removing the free GNPs, a fluorescence decrease was observed (Figure 5D). Inductively coupled plasma mass spectrometry (ICP-MS) analysis after 2.5 h uptake of FITC-Te50GNPs showed ∼90% and ∼95% of gold content inside Raji DC-SIGN and iDCs, respectively. The discrepancy between the fluorescence values and the gold content in iDCs deserves further investigation. It has been reported that the quantum yield of fluorescein is pH-dependent.[40] Accumulation of FITC-Te50GNPs in subcellular acidic compartments such as late endosomes could explain the loss of fluorescence signal in iDCs.[41]

Analysis of Intracellular Localization of FITC-Te50GNP. Additional evidence of intracellular distribution of FITC-Te50GNP was supplied by confocal fluorescent optical *z* sections (Figure 6). As shown in Figure 6, FITC-Te50GNP shows a punctuated pattern distribution after 3 h uptake of nanoparticles. To study the intracellular compartment distribution and routing of FITC-Te50GNP in iDCs, mAbs specific for DC-SIGN, caveolin (Cav-1), clathrin, early endosome antigen 1 (EEA1), lysosomal-associated membrane protein 1 (LAMP-1), and major histocompatibility complex class II (HLA-DP, -DQ, and -DR) were used to specifically label intracellular organelles in iDCs. Some of these organelles are thought to be potentially involved in the endocytic pathway of DC-SIGN and gp120/HIV-1.[42−45]

Qualitative analysis of the images using fluorescence intensity histograms did not allowed us to obtain conclusive colocalization results (SI Figure S9). As an attempt to overcome this problem, we followed a quantitative protocol based on coefficient calculations.[35] Overlap coefficient according to Manders indicated that both GNPs and DC-SIGN colocalize between 60% and 70% with Cav-1, clathrin, EEA1, LAMP-1, and MHCII positive compartments. However, Pearson's correlation coefficients (0−0.3) indicated absence of colocalization (SI Table S1). To clarify this contradiction, a comprehensive quantitative analysis using the imaging software *Volocity* v 5.5 (Perkin-Elmer) was carried out on iDCs loaded with FITC-Te50GNPs (Figure 7). In the 90 iDCs that were processed, a total of 1413 FITC-positive objects (GNPs) with a mean area of 0.62 μm^2, each of them corresponding to independent organelles, were detected. 62% of the FITC-Te50GNPs-positive objects were positive for DC-SIGN, 43% were positive for the early endosome marker, and only 36% were positive for the both markers. Apart from early endosomes, FITC-Te50GNPs were also observed in organelles labeled with the late endocytic marker, LAMP1 (SI Figure S9). Together, these results confirm that at least half of the Te50GNP-containing organelles also contain DC-SIGN receptor, and indicate that GNPs can enter the cells by binding to DC-SIGN and routing through the early endosomes similarly to gp120.[7,44] Remarkably, 38% of the FITC-Te50GNPs do not colocalize with the DC-SIGN receptor, which can be interpreted as DC-SIGN-independent modes of entry for GNPs could exist or that, after DC-SIGN-dependent entry occurs, GNPs and DC-SIGN follow different intracellular fates. Further investigations to differentiate between these alternatives are certainly required.

dx.doi.org/10.1021/bc200663r | *Bioconjugate Chem.* 2012, 23, 814−825

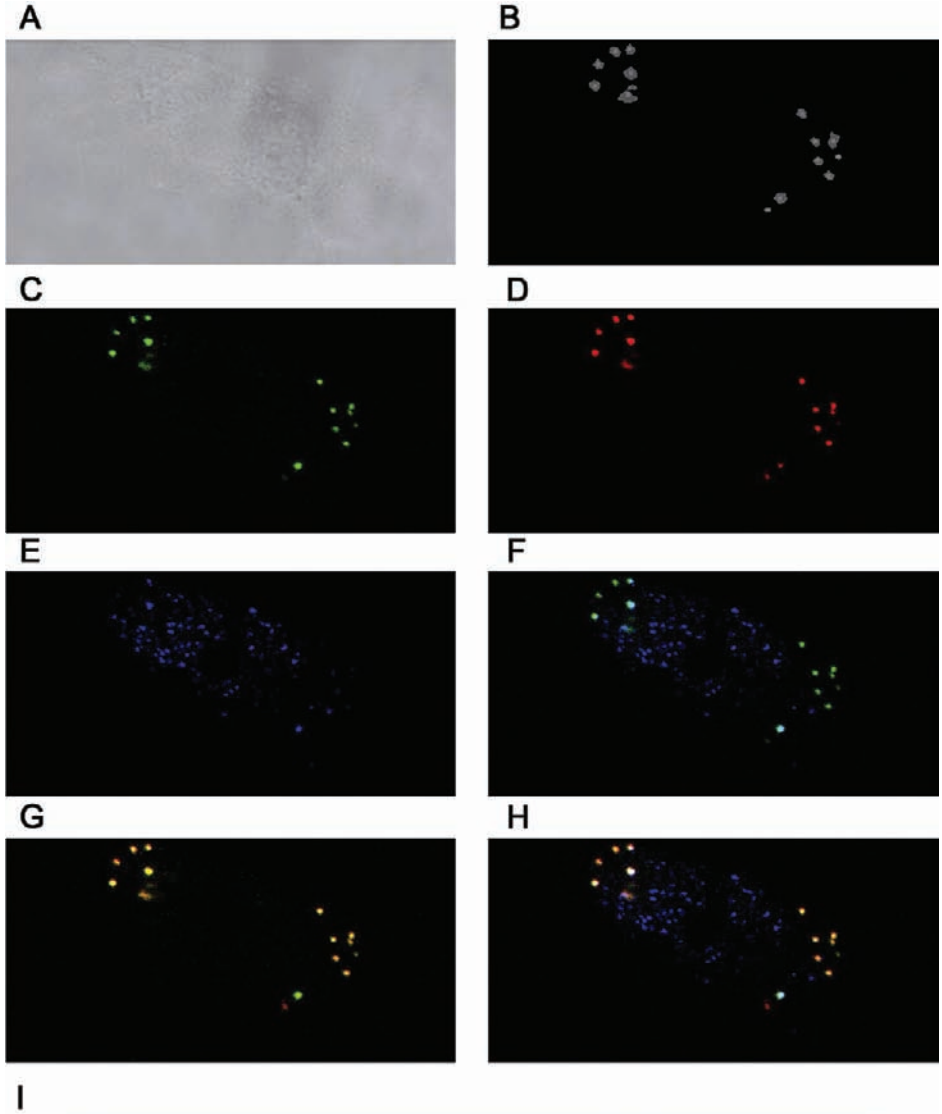

Objects	Nr. Counts	Percentage (%)
FITCTe50GNPs^{+} organelles	1413	100
EEA1^{+} organelles	603	43
DC-SIGN^{+} organelles	871	62
Triple colocalization	518	36

Figure 7. Representative images of quantitative colocalization analysis. (A) Bright-field image of a selected representative iDC. (B). FITC-Te50GNP^{+} objects selected by *Volocity* software in a single cell image with an intensity threshold established from the fluorescence background observed outside the cell. (C,D,E) Single image of FITC-Te50GNP (green), early endosomes (red), and DC-SIGN (blue). Overlay images of (F) FITC-Te50GNP and DCSIGN; (G) FITC-Te50GNP and early endosomes; (H) FITC-Te50GNP, DC-SIGN, and early endosomes; and (I) colocalization degree of FITC-Te50GNPs, with DC-SIGN receptor and the early endosomal marker EEA-1. Values represent percentages of the structures conforming to the definitions indicated in the table out of the total number of structures scored positive for FITC-Te50GNPs.

The multivalent oligomannoside-coated GNPs are able to enter Raji DC-SIGN and iDCs by CRL-dependent and -independent ways. We have demonstrated that GNPs incorporating D1 branch tri- and tetramannosides of the gp120 in 50% density enter partially Raji DC-SIGN and iDCs by binding specifically to DC-SIGN lectin. This indicates that multimerization of the D1 branch oligomannosides on gold nanoparticles mimics the interaction of HIV/gp120 high-mannose glycan clusters with DC-SIGN. Thus, the most plausible explanation for the inhibitory effect of *mannoGNPs* in HIV-1 *trans*-infection[29] may be their competition with the virus for binding to DC-SIGN. In an *in vivo* scenario, DCs are vulnerable to productive HIV-1 infection.[3] Therefore, in addition to inhibiting *trans*-infection by binding DC-SIGN, *manno*GNPs could also down-regulate other receptors (CCR5 and CXCR4) involved in the HIV infection of DCs. In order to

dx.doi.org/10.1021/bc200663r | *Bioconjugate Chem.* 2012, 23, 814–825

test this possible effect, the level of DC-SIGN, CCR5, and CXCR4 on iDC plasma membrane upon 3 h treatment with FITC-Te50GNP was determined by FC. The expression of the receptors in GNP-treated cells was the same as in the untreated cells (SI Figure S10). Phenotypic characteristics and/or cytokine secretion of DC after longer incubation periods was also evaluated. iDCs incubated for 24 h with Te50GNPs (350 ng/mL and 3500 ng/mL) showed the opposite maturing effect on DC-SIGN and CD83 expression than lipopolysaccharide (LPS, 1 μg/mL), while no effect was observed on CD80 expression, or IL12p40 or IL10 secretion (SI Figure S11 B&C). Te50GNPs down-regulate the expression of CD83 in iDCs in a dose-dependent manner (SI Figure S11B) and up-regulate the expression of DC-SIGN. Te50GNPs showed a similar but more pronounced effect on CD83 and DC-SIGN expression than gp120. The results suggest a lack of maturing effect by Te50GNPs at the concentrations tested and a certain opposite effect on the iDC maturation phenotype.

CONCLUSIONS

Gold glyconanoparticles bearing multiple copies of structural motifs of the high-mannose glycan clusters of gp120 (*manno*GNPs) are internalized by C-type lectin-expressing cells. We demonstrate that entry of the 1.5−1.8-nm-sized *manno*GNPs is mediated by both CLR-dependent and CLR-independent mechanisms. The internalization mediated by CLRs accounts for about 50% of the total entry in iDCs. The rest of *manno*GNP seems to enter by other active mechanisms (i.e., constitutive macropinocytosis). The tetramannoside coated nanoparticle (FITC-Te50GNP) mimics the behavior of gp120 in their ability to bind to DC-SIGN and internalize into the early endosomes in iDCs. These results support our idea that the multivalent presentation of oligomannosides onto the GNP surface provides a tool for the development of HIV microbicides and vaccines. The incorporation into the GNPs of T cell peptide epitopes and/or immunostimulant adjuvants could be a strategy to break the immunotolerance promoted by high-mannose-type glycans.[33]

Understanding the interaction of engineered biofunctional nanoparticles with cells has implications in their design and improvement and in clarifying the impact of these nanomaterials on human and environmental health.[46] Previous studies have shown that size, shape,[47,48] surface modifications,[49] and even sedimentation and diffusion[50] play a role in cellular uptake, trafficking, and removal of nanoparticles. The great diversity in the size, shape, and surface of nanoparticles as well as the multiple portals[51] that regulate the uptake by cells makes it difficult to establish a common mechanism of internalization for nanomaterials. Furthermore, for *in vivo* applications, the pitfalls in performing studies of endocytosis and intracellular transport of nanoparticles must be taken into account.[52]

ASSOCIATED CONTENT

Supporting Information

Characterization data of FITC-*manno*GNPs and results on cell viability. DC-SIGN expression in Raji DC-SIGN and iDC. FITC-Te50GNP intracellular distribution and quantitation, and their effect on DC-SIGN, CCR5, and CXR4 expression on iDC. Phenotype and cytokine secretion of DC before and after 24 h incubation with Te50GNPs. This material is available free of charge via the Internet at http://pubs.acs.org.

AUTHOR INFORMATION

Corresponding Author

*E-mail: spenades@cicbiomagune.es.

Notes

The authors declare no competing financial interest.

ACKNOWLEDGMENTS

This work was supported by the Spanish Ministry of Science and Innovation (grant CTQ2011-27268), the EU (grant CHAARM), and the Department of Industry and Innovation of the Basque Country Government (grant ETORTEK). The reagent ARP971 GM-CSF Recombinant and gp120 from the HIV-1 CN54 clone (repository reference ARP683) were obtained from the Programme EVA Centre for AIDS Reagents, NIBSC, UK, supported by the EC FP6/7 Europrise Network of Excellence, AVIP and NGIN consortia, and the Bill and Melinda Gates GhRC-CAVD Project and was donated by Invitrogen. We thank Dr. J. M. Cárdenas, director of the Basque Centre for Transfusions and Human Tissue for the access to blood samples from healthy donors.

REFERENCES

(1) Desrosiers, R. C. (2004) Prospects for an AIDS vaccine. *Nat. Med. 10* (3), 221−3.

(2) Figdor, C. G., van Kooyk, Y., and Adema, G. J. (2002) C-type lectin receptors on dendritic cells and Langerhans cells. *Nat. Rev. Immunol. 2* (2), 77−84.

(3) Shattock, R. J., and Moore, J. P. (2003) Inhibiting sexual transmission of HIV-1 infection. *Nat. Rev. Microbiol. 1* (1), 25−34.

(4) Spira, A. I., Marx, P. A., Patterson, B. K., Mahoney, J., Koup, R. A., Wolinsky, S. M., and Ho, D. D. (1996) Cellular targets of infection and route of viral dissemination after an intravaginal inoculation of simian immunodeficiency virus into rhesus macaques. *J. Exp. Med. 183* (1), 215−25.

(5) Hu, Q., Frank, I., Williams, V., Santos, J. J., Watts, P., Griffin, G. E., Moore, J. P., Pope, M., and Shattock, R. J. (2004) Blockade of attachment and fusion receptors inhibits HIV-1 infection of human cervical tissue. *J. Exp. Med. 199* (8), 1065−75.

(6) Hu, J., Gardner, M. B., and Miller, C. J. (2000) Simian immunodeficiency virus rapidly penetrates the cervicovaginal mucosa after intravaginal inoculation and infects intraepithelial dendritic cells. *J. Virol. 74* (13), 6087−95.

(7) Turville, S. G., Santos, J. J., Frank, I., Cameron, P. U., Wilkinson, J., Miranda-Saksena, M., Dable, J., Stossel, H., Romani, N., Piatak, M. Jr., Lifson, J. D., Pope, M., and Cunningham, A. L. (2004) Immunodeficiency virus uptake, turnover, and 2-phase transfer in human dendritic cells. *Blood 103* (6), 2170−9.

(8) Cavrois, M., Neidleman, J., and Greene, W. C. (2008) The achilles heel of the trojan horse model of HIV-1 trans-infection. *PLoS Pathog. 4* (6), e1000051.

(9) Geijtenbeek, T. B., Torensma, R., van Vliet, S. J., van Duijnhoven, G. C., Adema, G. J., van Kooyk, Y., and Figdor, C. G. (2000) Identification of DC-SIGN, a novel dendritic cell-specific ICAM-3 receptor that supports primary immune responses. *Cell 100* (5), 575−85.

(10) Turville, S. G., Arthos, J., Donald, K. M., Lynch, G., Naif, H., Clark, G., Hart, D., and Cunningham, A. L. (2001) HIV gp120 receptors on human dendritic cells. *Blood 98* (8), 2482−8.

(11) Drickamer, K. (1995) Increasing diversity of animal lectin structures. *Curr. Opin. Struct. Biol. 5* (5), 612−6.

(12) Lifson, J., Coutre, S., Huang, E., and Engleman, E. (1986) Role of envelope glycoprotein carbohydrate in human immunodeficiency virus (HIV) infectivity and virus-induced cell fusion. *J. Exp. Med. 164* (6), 2101−6.

(13) Mizuochi, T., Spellman, M. W., Larkin, M., Solomon, J., Basa, L. J., and Feizi, T. (1988) Carbohydrate structures of the human-

immunodeficiency-virus (HIV) recombinant envelope glycoprotein gp120 produced in Chinese-hamster ovary cells. *Biochem. J. 254* (2), 599−603.
(14) Leonard, C. K., Spellman, M. W., Riddle, L., Harris, R. J., Thomas, J. N., and Gregory, T. J. (1990) Assignment of intrachain disulfide bonds and characterization of potential glycosylation sites of the type 1 recombinant human immunodeficiency virus envelope glycoprotein (gp120) expressed in Chinese hamster ovary cells. *J. Biol. Chem. 265* (18), 10373−82.
(15) Zhu, X., Borchers, C., Bienstock, R. J., and Tomer, K. B. (2000) Mass spectrometric characterization of the glycosylation pattern of HIV-gp120 expressed in CHO cells. *Biochemistry 39* (37), 11194−204.
(16) Feinberg, H., Mitchell, D. A., Drickamer, K., and Weis, W. I. (2001) Structural basis for selective recognition of oligosaccharides by DC-SIGN and DC-SIGNR. *Science 294* (5549), 2163−6.
(17) Guo, Y., Feinberg, H., Conroy, E., Mitchell, D. A., Alvarez, R., Blixt, O., Taylor, M. E., Weis, W. I., and Drickamer, K. (2004) Structural basis for distinct ligand-binding and targeting properties of the receptors DC-SIGN and DC-SIGNR. *Nat. Struct. Mol. Biol. 11* (7), 591−8.
(18) Adams, E. W., Ratner, D. M., Seeberger, P. H., and Hacohen, N. (2008) Carbohydrate-mediated targeting of antigen to dendritic cells leads to enhanced presentation of antigen to T cells. *ChemBioChem 9* (2), 294−303.
(19) Frison, N., Taylor, M. E., Soilleux, E., Bousser, M. T., Mayer, R., Monsigny, M., Drickamer, K., and Roche, A. C. (2003) Oligolysine-based oligosaccharide clusters: selective recognition and endocytosis by the mannose receptor and dendritic cell-specific intercellular adhesion molecule 3 (ICAM-3)-grabbing nonintegrin. *J. Biol. Chem. 278* (26), 23922−9.
(20) Wang, S. K., Liang, P. H., Astronomo, R. D., Hsu, T. L., Hsieh, S. L., Burton, D. R., and Wong, C. H. (2008) Targeting the carbohydrates on HIV-1: Interaction of oligomannose dendrons with human monoclonal antibody 2G12 and DC-SIGN. *Proc. Natl. Acad. Sci. U.S.A. 105* (10), 3690−5.
(21) Sattin, S., Daghetti, A., Thepaut, M., Berzi, A., Sanchez-Navarro, M., Tabarani, G., Rojo, J., Fieschi, F., Clerici, M., and Bernardi, A. (2010) Inhibition of DC-SIGN-mediated HIV infection by a linear trimannoside mimic in a tetravalent presentation. *ACS Chem. Biol. 5* (3), 301−12.
(22) Garber, K. C., Wangkanont, K., Carlson, E. E., and Kiessling, L. L. (2010) A general glycomimetic strategy yields non-carbohydrate inhibitors of DC-SIGN. *Chem. Commun. (Camb.) 46* (36), 6747−9.
(23) Espuelas, S., Thumann, C., Heurtault, B., Schuber, F., and Frisch, B. (2008) Influence of ligand valency on the targeting of immature human dendritic cells by mannosylated liposomes. *Bioconjugate Chem. 19* (12), 2385−93.
(24) Wattendorf, U., Coullerez, G., Voros, J., Textor, M., and Merkle, H. P. (2008) Mannose-based molecular patterns on stealth microspheres for receptor-specific targeting of human antigen-presenting cells. *Langmuir 24* (20), 11790−802.
(25) Wang, X., Uto, T., Akagi, T., Akashi, M., and Baba, M. (2007) Induction of potent CD8+ T-cell responses by novel biodegradable nanoparticles carrying human immunodeficiency virus type 1 gp120. *J. Virol. 81* (18), 10009−16.
(26) Rieger, J., Freichels, H., Imberty, A., Putaux, J. L., Delair, T., Jerome, C., and Auzely-Velty, R. (2009) Polyester nanoparticles presenting mannose residues: toward the development of new vaccine delivery systems combining biodegradability and targeting properties. *Biomacromolecules 10* (3), 651−7.
(27) Ojeda, R., de Paz, J. L., Barrientos, A. G., Martin-Lomas, M., and Penadés, S. (2007) Preparation of multifunctional glyconanoparticles as a platform for potential carbohydrate-based anticancer vaccines. *Carbohydr. Res. 342* (3−4), 448−59.
(28) Martínez-Avila, O., Hijazi, K., Marradi, M., Clavel, C., Campion, C., Kelly, C., and Penadés, S. (2009) Gold manno-glyconanoparticles: multivalent systems to block HIV-1 gp120 binding to the lectin DC-SIGN. *Chemistry 15* (38), 9874−88.
(29) Martinez-Avila, O., Bedoya, L. M., Marradi, M., Clavel, C., Alcami, J., and Penadés, S. (2009) Multivalent manno-glyconanoparticles inhibit DC-SIGN-mediated HIV-1 trans-infection of human T cells. *ChemBioChem 10* (11), 1806−9.
(30) Kwon, D. S., Gregorio, G., Bitton, N., Hendrickson, W. A., and Littman, D. R. (2002) DC-SIGN-mediated internalization of HIV is required for trans-enhancement of T cell infection. *Immunity 16* (1), 135−44.
(31) Wu, L., and KewalRamani, V. N. (2006) Dendritic-cell interactions with HIV: infection and viral dissemination. *Nat. Rev. Immunol. 6* (11), 859−68.
(32) Barrientos, A. G., de la Fuente, J. M., Rojas, T. C., Fernandez, A., and Penadés, S. (2003) Gold glyconanoparticles: synthetic polyvalent ligands mimicking glycocalyx-like surfaces as tools for glycobiological studies. *Chemistry 9* (9), 1909−21.
(33) Shan, M., Klasse, P. J., Banerjee, K., Dey, A. K., Iyer, S. P., Dionisio, R., Charles, D., Campbell-Gardener, L., Olson, W. C., Sanders, R. W., and Moore, J. P. (2007) HIV-1 gp120 mannoses induce immunosuppressive responses from dendritic cells. *PLoS Pathog. 3* (11), e169.
(34) Lozach, P. Y., Burleigh, L., Staropoli, I., Navarro-Sanchez, E., Harriague, J., Virelizier, J. L., Rey, F. A., Despres, P., Arenzana-Seisdedos, F., and Amara, A. (2005) Dendritic cell-specific intercellular adhesion molecule 3-grabbing non-integrin (DC-SIGN)-mediated enhancement of dengue virus infection is independent of DC-SIGN internalization signals. *J. Biol. Chem. 280* (25), 23698−708.
(35) Zinchuk, V., and Zinchuk, O. (2008) Quantitative colocalization analysis of confocal fluorescence microscopy images. In *Current Protocols in Cell Biology*, Wiley Interscience, Chapter 4, Unit 4.19.1−4.19.15.
(36) Nazarian, R., Falcon-Perez, J. M., and Dell'Angelica, E. C. (2003) Biogenesis of lysosome-related organelles complex 3 (BLOC-3): a complex containing the Hermansky-Pudlak syndrome (HPS) proteins HPS1 and HPS4. *Proc. Natl. Acad. Sci. U. S. A. 100* (15), 8770−5.
(37) Falcon-Perez, J. M., Nazarian, R., Sabatti, C., and Dell'Angelica, E. C. (2005) Distribution and dynamics of Lamp1-containing endocytic organelles in fibroblasts deficient in BLOC-3. *J. Cell. Sci. 118* (Pt 22), 5243−55.
(38) Geijtenbeek, T. B., Kwon, D. S., Torensma, R., van Vliet, S. J., van Duijnhoven, G. C., Middel, J., Cornelissen, I. L., Nottet, H. S., KewalRamani, V. N., Littman, D. R., Figdor, C. G., and van Kooyk, Y. (2000) DC-SIGN, a dendritic cell-specific HIV-1-binding protein that enhances trans-infection of T cells. *Cell 100* (5), 587−97.
(39) Engering, A., Van Vliet, S. J., Geijtenbeek, T. B., and Van Kooyk, Y. (2002) Subset of DC-SIGN(+) dendritic cells in human blood transmits HIV-1 to T lymphocytes. *Blood 100* (5), 1780−6.
(40) Sjoback, R, N. J., and Kubista, M. (1995) Absorption and Fluorescence Properties of Fluorescein. *Spectrochim. Acta, Part A 51* (6), L7−L21.
(41) Fuchs, R., Male, P., and Mellman, I. (1989) Acidification and ion permeabilities of highly purified rat liver endosomes. *J. Biol. Chem. 264* (4), 2212−20.
(42) Daecke, J., Fackler, O. T., Dittmar, M. T., and Krausslich, H. G. (2005) Involvement of clathrin-mediated endocytosis in human immunodeficiency virus type 1 entry. *J. Virol. 79* (3), 1581−94.
(43) Cambi, A., Beeren, I., Joosten, B., Fransen, J. A., and Figdor, C. G. (2009) The C-type lectin DC-SIGN internalizes soluble antigens and HIV-1 virions via a clathrin-dependent mechanism. *Eur. J. Immunol. 39* (7), 1923−8.
(44) Cambi, A., Lidke, D. S., Arndt-Jovin, D. J., Figdor, C. G., and Jovin, T. M. (2007) Ligand-conjugated quantum dots monitor antigen uptake and processing by dendritic cells. *Nano Lett. 7* (4), 970−7.
(45) Miyauchi, K., Kim, Y., Latinovic, O., Morozov, V., and Melikyan, G. B. (2009) HIV enters cells via endocytosis and dynamin-dependent fusion with endosomes. *Cell 137* (3), 433−44.
(46) Nel, A. E., Madler, L., Velegol, D., Xia, T., Hoek, E. M., Somasundaran, P., Klaessig, F., Castranova, V., and Thompson, M.

(2009) Understanding biophysicochemical interactions at the nano-bio interface. *Nat. Mater. 8* (7), 543−57.
(47) Chithrani, B. D., Ghazani, A. A., and Chan, W. C. (2006) Determining the size and shape dependence of gold nanoparticle uptake into mammalian cells. *Nano Lett. 6* (4), 662−8.
(48) Jiang, W., Kim, B. Y., Rutka, J. T., and Chan, W. C. (2008) Nanoparticle-mediated cellular response is size-dependent. *Nat. Nanotechnol. 3* (3), 145−50.
(49) Verma, A., and Stellacci, F. (2010) Effect of surface properties on nanoparticle-cell interactions. *Small 6* (1), 12−21.
(50) Cho, E. C., Zhang, Q., and Xia, Y. (2011) The effect of sedimentation and diffusion on cellular uptake of gold nanoparticles. *Nat. Nanotechnol. 6* (6), 385−91.
(51) Conner, S. D., and Schmid, S. L. (2003) Regulated portals of entry into the cell. *Nature 422* (6927), 37−44.
(52) Iversen, T.-G., Skotland, T., and Sandving, K. (2011) Endocytosis and intracellular transport of nanoparticles: Present Knowledge and need for future studies. *Nanotoday 6* (7), 176−185.

Bioconjugate Chemistry

Article

pubs.acs.org/bc

Site-Specific Fluorescent Labeling and Oriented Immobilization of a Triple Mutant of CYP3A4 via C64

Amélie Ménard, Yue Huang, Pierre Karam, Gonzalo Cosa, and Karine Auclair*

Department of Chemistry, McGill University, 801 Sherbrooke Street West, Montréal, Québec, Canada, H3A 0B8

Supporting Information

ABSTRACT: The generation of site-specific bioconjugates of proteins is highly desired for a number of biophysical and nanotechnological applications. To this end, many strategies have been developed that allow the specific modification of certain canonical amino acids and, more recently, noncanonical functional groups. P450 enzymes are heme-dependent monooxygenases involved in xenobiotic metabolism and in the biosynthesis of a variety of secondary metabolites. We became interested in the site-specific modification of these enzymes, CYP3A4 in particular, through our studies of their *in vitro* biocatalytic properties and our desire to exploit their remarkable ability to oxidize unactivated C−H bonds in a regio- and stereospecific manner. Obtained via a partial cysteine-depletion approach, a functional triple mutant of CYP3A4 (C98S/C239S/C468G) is reported here which is singly modified at C64 by maleimide-containing groups. While cysteine-labeling of the wild-type enzyme abolished >90% of its enzymatic activity, this mutant retained ≥75% of the activity of the unmodified wild-type enzyme with 9 of the 18 maleimides that were tested. These included both fluorescent and solid-supported maleimides. The loss of activity observed after labeling with some maleimides is attributed to direct enzyme inhibition rather than to steric effects. We also demonstrate the functional immobilization of this mutant on maleimide-functionalized agarose resin and silica microspheres.

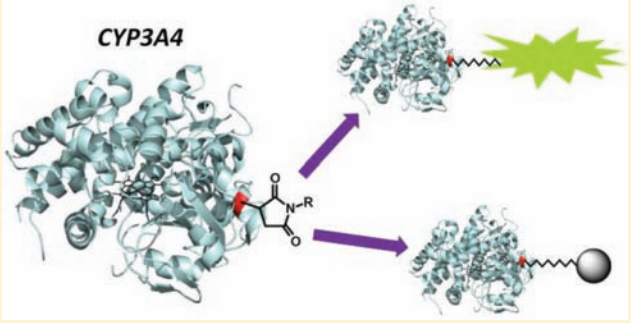

INTRODUCTION

In recent years, the desire to generate covalent protein conjugates has exploded with the rise of more sophisticated biochemical and biophysical analytical techniques, and applications such as single-molecule spectroscopy (SM fluorescence and SM force experiments),[1] the fabrication of protein microarrays, biosensors, and bioreactors, and the *in vivo* visualization and tracking of biomolecules. The difficulty remains in obtaining conjugates that retain the activity, functionality, and stability found in the native systems. Because of the great diversity of proteins, meeting all these demands is often quite challenging and involves a great deal of trial and error. It is widely acknowledged, however, that employing site-specific bioconjugation strategies significantly improves the probability of success.[2,3] By restricting bioconjugation to a single and precise position, one can more easily avoid modifications near residues known to be important for function and stability. An added advantage of generating such conjugates is the resulting uniformity in the population to be studied. This is especially important, for example, in SM experiments in which one wishes to detect biologically significant heterogeneities within a given population.

During our various investigations geared toward the use of human cytochrome P450 enzymes (CYPs or P450s) as *in vitro* biocatalysts, it was envisaged that the successful generation of functional and site-specific covalent conjugates of these enzymes could potentially open up opportunities to study and apply these catalysts in new ways. P450s form a family of widespread heme-dependent monooxygenases known mainly for their role in xenobiotic metabolism and their notable ability to regio- and stereoselectively oxidize unactivated C−H bonds. Unfortunately, our ability to study and make use of these properties *in vitro* has been limited by the low activity, the low stability, the requirement for expensive cofactors, and the poor product predictability of P450s. Our attention in addressing these issues has been focused mainly on CYP3A4[4−7] because of its highly promiscuous yet predictable behavior, which boosts this P450 enzyme's potential as a useful and versatile biocatalyst.

A variety of bioconjugation methods that target either specific amino acids (usually cysteine or lysine) or functional groups that are not found in the canonical amino acids (e.g., alkynes, azides, alkenes, phosphines, thioesters, ketones, aldehydes, and anilines), termed "bioorthogonal", have been reported.[8] The former often requires the use of mutagenesis in order to achieve complete site-specificity, while the latter requires the incorporation of non-native functional groups such as unnatural amino acids,[9,10] or protein fusions either with modified inteins[11] or enzymatically modifiable peptide tags.[8] Unfortunately, most of the bioorthogonal reactions suffer from

Received: December 19, 2011
Revised: March 5, 2012
Published: March 21, 2012

slow, second-order kinetics and therefore often require high reagent concentrations, harsh conditions (i.e. high temperatures and extreme pHs), and long reaction times that would result in loss of P450 activity. A few improvements in this area have been reported recently however, namely, for the Cu^{I}-catalyzed azide−alkyne cycloaddition reaction,[12] the hydrazone-ligation,[13] and the oxidative coupling of anilines to *o*-aminophenols.[14] Considering our observations on the stability of CYP3A4 at room temperature (Figure 1), we thought it

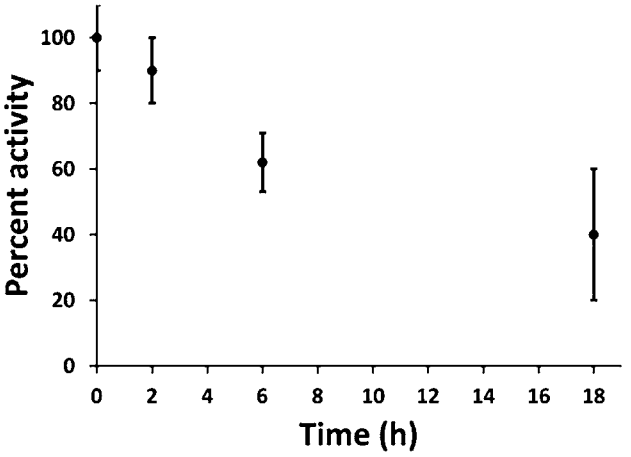

Figure 1. Thermodynamic stability of CYP3A4 at 25 °C in 0.1 M potassium phosphate buffer, pH 7.4. The activity was assayed with testosterone as the substrate and cumene hydroperoxide (CHP) as the cofactor.[4] All values represent an average of three separate experiments, each performed in duplicate or triplicate ±1 standard deviation.

prudent to attempt bioconjugation using cysteine-specific maleimide chemistry which can be achieved at room temperature and neutral pH, and proceed to completion within a few hours. There is also precedent in generating functional, partially cysteine-depleted mutants of CYP3A4. Reactions of a quadruple mutant (C98S/C239S/C377S/C468A) with cysteine-reactive fluorescent probes have generated C64-specific labeled CYP3A4 used to study the mechanism of α-naphthoflavone binding by FRET.[15] Here, we present our efforts, by way of this same partial cysteine-depletion strategy, in generating and characterizing site-specific cysteine-modified bioconjugates of CYP3A4 with a variety of maleimide tags, both soluble and solid-supported. Others have reported the immobilization of CYP3A4 on solid matrices such as gold electrodes allowing electrochemically driven drug metabolism,[16] monolithic chromatographic supports in the development of immobilized enzyme reactors (IMERs),[17] glass slides for analysis by total internal reflection microscopy (TIRFM),[18] or silver nanoparticles in the development of a localized surface plasmon resonance (LSPR) spectroscopy-based biosensor.[19] Various other surfaces have also been employed in the development of CYP3A4-based amperometric[20−22] and oxygen-sensing[23] drug metabolism biosensors. However, in all the above cases, CYP3A4 was immobilized in a random manner, either covalently or noncovalently in biological membranes (microsomal or *E. coli*-derived) or in synthetic membranes such as Nanodiscs.[18,24] We report here what is, to our knowledge, the first functional immobilization of CYP3A4 in a covalent and oriented fashion, through site-specific modification of a single cysteine residue on its surface.

EXPERIMENTAL PROCEDURES

Site-Directed Mutagenesis. Cysteine mutants of CYP3A4 were generated using the QuikChange Multi Site-Directed Mutagenesis Kit (Stratagene, Agilent) and pSE3A4His encoding *N*-terminally truncated and tetrahistidine-tagged CYP3A4 wild-type cDNA as the template.[25] The following PCR primers were used: for C64S, 5′-GGCTTTTGTATGTTTGACATGGAAAGTCATAAAAAGTATGGAAAAGTG-3′; for C98S, 5′-CAAAACAGTGCTAGTGAAAGAAAGTTATTCTGTCTTCACAAACCG-3′; for C239S, 5′-TCCCAATTCTTGAAGTATTAAATATCAGTGTGTTTCCAAGAGAAGT-3′; for C337S, 5′-CTATGAGACTTGAGAGGGTCAGCAAAAAAGATGTTGAGATC-3′, and for C468G, 5′-GAACTTCTCCTTCAAACCTGGTAAAGAAACACAGATCCC-3′. The following mutants were constructed: C98S (mutant 1), C98S/C377S/C468G (mutant 2), C98S/C239S/C468G (mutant 3), and C64S/C98S (mutant 4).

Expression of Wild-Type and Mutant CYP3A4. Protein expression was adapted from a protocol described previously.[4] Briefly, *Escherichia coli* DH5α competent cells were transformed with the desired plasmid. A starter culture was generated by inoculation of LB medium (100 mL) containing ampicillin (100 μg/mL) and allowed to grow overnight at 37 °C and 250 rpm. Culture flasks (2 L) containing TB medium (750 mL) supplemented with ampicillin (50 μg/mL) were inoculated each with the overnight starter culture (10 mL). The flasks were shaken at 250 rpm and 37 °C until an OD_{600} of 0.6 was reached. Protein expression was then induced by the addition of isopropyl β-D-1-thiogalactopyranoside (1 mM) and δ-aminolevulinic acid (80 mg/L). Incubation was continued for 48 h at 30 °C and 190 rpm. The cells were harvested at 4000 × *g* and 4 °C for 15 min.

Purification of Wild-Type and Mutant CYP3A4. All the following steps were performed at 4 °C. The pellet obtained from 5 × 750 mL cultures was resuspended in Buffer A (150−200 mL, 0.1 M potassium phosphate, or KPi, at pH 7.4, containing 10% glycerol) supplemented with phenylmethylsulfonyl fluoride (PMSF, 2 mM). The following protease inhibitors were also added: leupeptin (1.6 μg/mL), aprotinin (1 μg/mL), bestatin (0.8 μg/mL), and pepstatin A (0.7 μg/mL), along with lysozyme (10 mg per g of cells) and CHAPS (1% w/v). The resulting mixture was stirred slowly for 30 min and then sonicated at 60% cycle duty and power 8 for 4 cycles of 30 s each. The lysate was centrifuged for 1 h at 54 000 × *g*. The supernatant was supplemented with imidazole (5 mM) and KCl (0.5 M) before being loaded onto a column containing Ni-NTA agarose resin (5 mL, Qiagen) pre-equilibrated with Buffer A. The flow rate was adjusted to ca. 1 mL/min. The resin was washed with 10 column volumes of Buffer A containing KCl (0.5 M), CHAPS (0.5% w/v), and imidazole (5 mM), followed by 10 column volumes of Buffer A containing imidazole (20 mM). The protein was eluted with Buffer A containing more imidazole (200 mM). The fractions containing the protein of interest were combined and dialyzed against Buffer A. The protein was further purified by ion-exchange using Macro-Prep High S Support resin (Bio-Rad). Thus, the protein was loaded onto a column containing the said resin (15 mL) pre-equilibrated with Buffer A. The column was next washed with Buffer A (50 mL), followed by elution with Buffer A containing KCl (0.5 M). Finally, the fractions of interest were combined, dialyzed against Buffer A, and stored at −80 °C. Protein concentration was measured using the Bradford

dx.doi.org/10.1021/bc200672s | *Bioconjugate Chem.* 2012, 23, 826−836

method (Pierce, 23236) while the concentration of P450 was calculated from its reduced-CO spectrum.[26]

Expression and Purification of Cytochrome P450 Reductase (CPR). CPR was expressed and purified as described elsewhere.[4] Protein concentration was measured by the Bradford method (Pierce, 23236). The concentration of holo-CPR was estimated from its flavin content using an extinction coefficient of 21.4 mM^{-1} cm^{-1} at 456 nm.[27]

Cysteine-Specific Protein Labeling with Maleimides. Maleimide labels were purchased or generated from the corresponding amine as described below. Stock solutions (20 mM) of the maleimides were prepared in anhydrous DMSO. In a small glass vial, wild-type or mutant CYP3A4 (typically ~10 μM, based on Bradford assay) was combined with 9 equiv of TCEP (10 mM stock in Milli-Q water) in KPi buffer (0.1 M at pH 7.4), and incubated at 25 °C and 250 rpm for 20 min. Then, 100 equiv of the desired maleimide label were added, and the reaction was incubated for 2 h under the same conditions. Note, equivalents are reported relative to the concentration of CYP3A4. The reaction was quenched by the addition of DTT (2 mM from a 0.1 M stock solution in Milli-Q water) and incubation for 5−10 min. Control reactions were also performed in which pure anhydrous DMSO was added instead of the maleimide label with and without the 2 h incubation period.

Generation of Maleimide Labels from Their Corresponding Amines. Maleimides **1b**, **1c**, **2c**, **3b**, and **3c** were prepared as follows (see Supporting Information for full product characterization). All other maleimides were purchased and used as is. In a typical reaction, heterobifunctional cross-linker **15b** or **15c** (6−23 nmol) was combined with 1.05 equiv of **1a**, **2a**, or **3a** in anhydrous DMSO (final concentration of ~45 mM) and stirred at 25 °C. The reaction was monitored by ESI-MS and was usually complete within 4 h after which the cross-linker (**15b** or **15c**) had been consumed and the major peak corresponded to the desired amide bond formation product between the amine and the NHS-ester. A small amount (10−15%) of double addition product (conjugate addition of the amine to the maleimide) was also observed. Purification was usually not necessary, but was possible using chromatography (see Supporting Information). The products were stored at −20 °C. The final maleimide concentration was quantified spectrophotometrically from the difference in the amount of 4-thiopyridone product formed when 2-mercaptoethanol reacts with 4,4′-dithiodipyridine in the presence and absence of the maleimide reaction mixture (maleimides react with 2-mercaptoethanol but not with 4,4′-dithiodipyridine).[28] Briefly, an aliquot (5 μL) of the reaction mixture in DMSO was diluted into KPi buffer (195 μL of 0.1 M at pH 7.4). A sample of this diluted stock (2−5 μL) was combined with 2-mercaptoethanol (10 μL from a 1.5 mM stock solution prepared fresh in Milli-Q water) and KPi buffer (0.1 M at pH 7.4), to a final volume of 450 μL. Control reactions containing only 2-mercaptoethanol were also prepared. These were incubated 10 min at room temperature after which a saturated solution of 4,4′-dithiodipyridine (50 μL in Milli-Q water) was added before incubation for another 15 min. Absorbance was read at 324 nm against a blank containing only 4,4′-dithiodipyridine. The concentration of the 4-thiopyridone formed from the reaction between 2-mercaptoethanol and 4,4′-dithiodipyridine in the presence and absence of the maleimide was calculated using $\varepsilon_{224\ nm}$ = 19 800 M^{-1} cm^{-1}. The difference gave the maleimide concentration in the reaction mixture.

Assessing the Effect of Quenched Maleimide Labels on Enzymatic Activity. Samples were prepared in the same manner described above for the cysteine-specific labeling except that the maleimides were quenched with DTT prior to mixing with enzyme. The enzymatic activity was then assayed immediately using testosterone as the substrate and CPR/NADPH as the cofactors (end-point assay, see below), omitting the 2 h incubation period usually required for complete labeling. SDS-PAGE analysis followed by fluorescence visualization of the gels confirmed that CYP3A4 remained essentially label-free when the maleimides were prequenched in this manner.

Estimating the Labeling Yield of CYP3A4 Mutant 3 with the Maleimide DyLight 549. CYP3A4 mutant 3 was labeled with 10 or 100 equiv of DyLight 549 maleimide as described above. The excess label was removed by size-exclusion using Zeba Spin Desalting Columns (3 × 0.5 mL, Pierce). The absorbance spectrum of the flowthrough containing the labeled protein was obtained and the degree of labeling was calculated as per the manufacturer's instructions using $\varepsilon_{280\ nm}$ = 40 340 M^{-1} cm^{-1} (ExPASy ProtParam tool) to determine the protein concentration.

Sample Preparation for Single-Molecule Photobleaching Analysis. An aliquot of DyLight 549 maleimide **10**-labeled wild-type or mutant CYP3A4 (see above) was combined with SDS sample buffer (4 μL of 0.13 M Tris pH 6.8, 20% glycerol, 4% SDS, 1.25% bromophenol blue, 1.4 M 2-mercaptoethanol) and boiled for 1 min. The sample was then loaded onto a precast 12.5% polyacrylamide gel and subjected to SDS-PAGE (with PhastSystem, Pharmacia) in order to ensure complete removal of excess label. The fluorescent band of appropriate molecular weight (ca. 57 kDa) was excised and subjected to syringe−maceration−extraction[29] in order to extract the labeled protein. Coverslips were cleaned in Piranha solution following a procedure reported earlier and used without any further modification of the surface.[30] Predrilled polycarbonate films with an adhesive gasket (Grace Bio-Laboratories, Bend, OR) were assembled on top of the cleaned coverslips yielding a chamber with a total volume of 10 μL. Inlet and outlet ports (Nanoport, Upchurch Scientific, Oak Harbor, WA) were glued on top of the chambers.[30,31] In order to increase the dye photostability, all experiments were run under a constant flow of an oxygen scavenger solution consisting of 2-mercaptoethanol (1% v/v), β-D(+)glucose (3% w/v), glucose oxidase (0.1 mg/mL), and catalase (0.02 mg/mL).[30,32,33] All experiments were conducted at room temperature (22−23 °C). Purified labeled proteins were diluted (ca. 1000-fold) and then injected into a clean coverslip until a satisfactory surface density was observed.

Quantification of Labeling via Single-Molecule Photobleaching Analysis: Single Molecule Imaging. Total internal reflection fluorescence microscopy (TIRF) was utilized to quantify the number of fluorescent dyes per single protein. The setup consisted of an inverted microscope (Olympus IX71) equipped with a laser-based TIRFM illumination module (IX2-RFAEVA-2, Olympus) coupled to a diode-pumped solid-state green laser with 532 nm output (CrystaLaser). The beam position was adjusted using the illuminator to attain total internal reflection through a 60×, N.A. 1.45, oil-immersion objective (Olympus U PLAN SAPO). Fluorescence emission was collected through the objective, and images were captured with an electron-multiplied back-illuminated charged-coupled device (EMCCD) camera (CascadeII:512, Photometrics,

dx.doi.org/10.1021/bc200672s | Bioconjugate Chem. 2012, 23, 826−836

Roper Scientific). The camera was controlled using *Image-Pro Plus 5.1* (Media Cybernetics), capturing 8-bit 512 × 512 pixel images with an exposure time of 200 ms per frame, a conversion gain of 3, and a multiplication gain of 4095. Excitation was carried out at a full power setting (25 mW) with a power output of 6.6 mW measured at the objective.

Quantification of Labeling via Single-Molecule Photobleaching Analysis: Intensity Analysis. A *Matlab* algorithm was utilized, which first maps the ca. hundreds of single molecule spots, and following background subtraction, it then extracts intensity−time trajectories from the stack of images for each individual molecule. Upon inspecting individual trajectories, photobleaching events were observed as steps. The number of fluorophores per protein was next calculated from the number of photobleaching steps recorded.

In-gel BrCN Digestion of Labeled Protein. An aliquot of the dye-labeled sample (20 μL) was combined with SDS sample buffer (4 μL, see Sample preparation for single-molecule photobleaching analysis above). Exceptionally, for dansyl-labeled (**1b**) samples, an aliquot (500 μL) was first concentrated (to 20 μL) with a centrifugal filter (10 kDa MWCO, Millipore) before combination with SDS sample buffer (4 μL). Samples were boiled for 1 min and separated by SDS-PAGE using a classical vertical separation system. The appropriate bands were excised, washed, and treated with cyanogen bromide.[34] The resulting peptides were analyzed by tricine-SDS-PAGE.[35] Optimal resolution was achieved with a 1.7-mm-thick gel when a 10% spacer gel was included between the 4% stacking gel above and the 16%/6 M urea separating gel below. Gels were imaged with a Typhoon Trio + scanner using the Green-excited mode (λ_{ex} = 532 nm) and the 580 nm band-pass filter (580 BP 30, which transmits light between 565 and 595 nm with a transmission peak centered on 580 nm).

Preparation of Maleimide-Functionalized Resin. Maleimide-functionalized resins were generated through modification at the terminal amine of CarboxyLink resin (**4a**, Pierce) with **15b** or **15c**. Aliquots of the resin (1 mL) were washed with KPi buffer (3 × 2 mL, 0.1 M at pH 7.4) through centrifugation/resuspension cycles resulting ultimately in removal of as much supernatant as possible. The cross-linkers (**15b** or **15c**, 22 μmol) were dissolved in anhydrous DMSO (0.5 mL), diluted with the same KPi buffer (0.5 mL), and immediately added to the resin. After brief vortexing, the resin was incubated at room temperature and ∼100 rpm for 1.5 h to give **4b** or **4c**. Reaction completion was confirmed with a ninhydrin test[36] as follows. A small aliquot of the resin was transferred to a glass vial and the supernatant was removed. Two drops each of pyridine, 4:1 phenol:ethanol, and 4% (w/v) ninhydrin in EtOH were added to the resin, which was then heated to 100 °C for 2 min. No color change indicated that all free amines on the resin had reacted with the cross-linkers. Unmodified resin turned deep blue under the same conditions. The resin was then washed with buffer (5 × 2 mL) to remove excess cross-linker. The degree of maleimide loading was quantified from mixtures of resin aliquots (20 μL, supernatant removed) and 4,4′-dithiodipyridine as described above in Generation of maleimide labels from their corresponding amines. The degree of loading was generally ∼12 nmol maleimide/20 μL resin.

Immobilization of CYP3A4 Mutant 3 onto Maleimide-Functionalized Resins. CYP3A4 (∼1 nmol based on Bradford assay, ∼0.18 nmol active P450,[26] from a stock in Buffer A) was combined with TCEP (9 nmol, 0.9 μL from a 10 mM stock in Milli-Q water). The volume was adjusted to 100 μL with KPi buffer (0.1 M at pH 7.4) before incubation at 25 °C and 250 rpm for 20 min. This TCEP-reduced enzyme solution was then added to an aliquot of resin (200 μL, supernatant removed, contained ca. 120 nmol maleimide) and incubated for 2 h. The enzyme activity was measured both in the supernatant and on the resin. To evaluate the immobilization yield, an aliquot of the supernatant collected after the immobilization reaction was assayed for P450 activity using BFC as the substrate (initial rate measurement, see below). The immobilization yield was calculated from the difference in P450 activity found in the supernatant versus the control containing unmodified resin **4a** mixed with free mutant 3 enzyme. This was also compared to the standard enzyme activity of mutant 3 in solution to rule out nonspecific interaction of the enzyme with the resin. The activity of the enzyme immobilized on the resin was measured using the testosterone assay (end-point assay, see below) after washing the resin with KPi buffer (0.1 M at pH 7.4).

Preparation of Maleimide-Functionalized Silica Microspheres. To an aliquot (427 μL) of silica microspheres (89.5 nM of 0.1 μm, colloidal, Polysciences Inc.) was added 3-(aminopropyl)trimethoxysilane (2 μL). The mixture was vortexed briefly and incubated at room temperature for 5 min. The reaction was then quenched with the addition of HCl (conc., 8 μL). The resulting aminosilanized beads (**14a**) were then washed with KPi buffer (3 × 1 mL, 0.1 M at pH 7.4) using centrifugation and resuspension cycles. The beads were finally resuspended in the same buffer (500 μL). The beads were then mixed with cross-linker **15c** (22 μmol in 500 μL DMSO) and incubated at 25 °C and 250 rpm for 1.5 h. Reaction completion was confirmed using the ninhydrin test (see Preparation of maleimide-functionalized resin above). The beads were washed again to remove excess cross-linker **15c** and resuspended in buffer (500 μL). The degree of maleimide loading was quantified from mixtures of bead aliquots (20 μL washed, supernatant included) and 4,4′-dithiodipyridine as described in Generation of maleimide labels from their corresponding amines above. The degree of loading was generally ∼4.3 nmol maleimide/20 μL beads or 5.6 nmols of maleimide/pmol of beads. Finally, the microspheres were concentrated by centrifugation and resuspension in KPi buffer (200 μL).

Immobilization of CYP3A4 Mutant 3 onto Maleimide-Functionalized Silica Microspheres. An aliquot of TCEP-reduced CYP3A4 mutant 3 (43 μL, see Immobilization of CYP3A4 mutant 3 onto maleimide functionalized resins above) was combined with the maleimide-functionalized microsphere suspension prepared as above (100 μL, contained ca. ∼54 nmol maleimide) and incubated at 25 °C and 250 rpm for 2 h. Controls were also performed in which the beads were quenched with DTT (2 mM from a 0.1 M stock solution in Milli-Q water) prior to combining with mutant 3, or in which no beads were included. At the end of the incubation period, the reactions were quenched with DTT, and the enzyme activity in the supernatant was assayed with BFC (initial rate measurement, see below) in order to estimate the immobilization yield. The immobilization yield was calculated from the difference in P450 activity found in the supernatant versus the control containing prequenched resin. The beads were washed (2 × 1 mL) and resuspended in KPi buffer (final volume ∼150 μL, 0.1 M at pH 7.4) before the activity of the immobilized enzyme was assayed using either testosterone or BFC (end-point assays, see below).

dx.doi.org/10.1021/bc200672s | *Bioconjugate Chem.* 2012, 23, 826−836

CYP3A4 Activity Assays with Testosterone. End-point CYP3A4 activity was assayed from the conversion of testosterone to 6β-hydroxytestosterone. To assay the activity of CYP3A4 in solution, each enzymatic reaction contained P450 (0.4 μM), testosterone (50 μM), and either CPR (1.6 μM)/NADPH (2 mM) or cumene hydroperoxide (CHP, 100 μM) in KPi buffer (0.1 M at pH 7.4) in a final volume of 75 μL. For agarose resin-immobilized P450, each reaction contained P450 (ca. ~0.4 μM, 70 μL resin, supernatant removed), testosterone (667 μM), and either CPR (1.6 μM) and NADPH (1 mM) or CHP (1 mM) in KPi buffer (0.1 M at pH 7.4) in a final volume of 150 μL. Similarly, for microsphere-immobilized P450, each reaction contained P450 (ca. 0.4 μM, 150 μL microsphere suspension), testosterone (667 μM), and CHP (1 mM) in KPi buffer (0.1 M at pH 7.4) in a final volume of 300 μL. The buffer, testosterone, P450, and CPR (if required) were combined and preincubated for 5 min at 37 °C. The reactions were initiated by the addition of NADPH or CHP, and the reaction was allowed to proceed for 1 h at 37 °C with shaking at 250 rpm. At the end of the reaction, the tubes were spiked with internal standard cortexolone (5 μL from a 200 μM stock solution in methanol) and extracted with ethyl acetate (0.5 mL). The extracts were evaporated and redissolved in acetonitrile (75 μL for the resin or 150 μL for the microspheres) before HPLC analysis. Separation and quantification of the product (relative to the internal standard cortexolone) was achieved using a 250 × 4.60 mm Synergi 4 μm Hydro-RP 80 Å column in line with a UV detector (set to monitor at 244 nm) using mobile phases A (Milli-Q water) and B (acetonitrile) at a flow rate of 0.5 mL/min. Elution consisted of an initial isocratic step at 50% phase B for 5 min followed by an increase to 70% phase B over the next 7 min and finally to 95% phase B over the final 8 min. The retention times were generally 7.1 min for the product 6β-hydroxytestosterone, 10.1 min for the internal standard cortexolone and 15.8 min for the substrate testosterone.

Determination of Initial Rates for CYP3A4 Using the Substrate 7-Benzyloxy-4-Trifluoromethylcoumarin (BFC). To assay initial enzyme activity rates, the debenzylation of BFC to the fluorescent product 7-hydroxy-4-trifluoromethylcoumarin (HFC) was monitored over time with a microtiter plate fluorimeter (SpectraMax Gemini XS). CYP3A4 (~50 nM), CPR (150 nM), and BFC (30 μM) were first combined in KPi buffer (0.1 M at pH 7.4, used to adjust the final reaction volume to 150 μL) and preincubated for 5 min at 37 °C. The reaction was initiated with the addition of NADPH (1 mM). Product formation was monitored over time with an excitation wavelength of 410 nm and an emission wavelength of 530 nm.

End-Point Activity Determination for CYP3A4 Using the Substrate 7-Benzyloxy-4-trifluoromethylcoumarin (BFC). End-point activity of microsphere-immobilized CYP3A4 mutant 3 was also assayed with BFC. Each enzymatic reaction contained P450 (ca. ~0.4 μM from a 150 μL microsphere suspension), BFC (67 μM), and CHP (1 mM) in KPi buffer (0.1 M at pH 7.4) in a final volume of 300 μL. The buffer, BFC, and P450 were combined and preincubated for 5 min at 37 °C. The reactions were initiated by the addition of CHP, and the reaction was allowed to proceed for 1 h at 37 °C with shaking at 250 rpm. At the end of the reaction, the tubes were spiked with the internal standard 7-hydroxycoumarin (5 μL from a 200 μM stock solution in ethyl acetate) and extracted with ethyl acetate (0.5 mL). The extracts were evaporated and redissolved in acetonitrile (150 μL) before HPLC analysis. Separation and quantification of the product (relative to the internal standard 7-hydroxycoumarin) was achieved using a 250 × 4.60 mm Synergi 4 μm Hydro-RP 80 Å column in line with a UV detector (set to monitor at 335 nm) using mobile phases A (Milli-Q water) and B (acetonitrile) at a flow rate of 0.5 mL/min. Elution consisted of a linear gradient from 50% phase B to 95% phase B over 20 min followed by an isocratic step at 95% phase B for 5 min. The retention times were 10.1 min for the product HFC, 6.5 min for the internal standard 7-hydroxycoumarin, and 20.8 min for the substrate BFC.

RESULTS AND DISCUSSION

Analysis of Fluorescently Labeled Wild-Type CYP3A4. Information about the number and identity of CYP3A4 cysteine residues available for reactions with maleimides is desirable to achieve regioselective conjugation of CYP3A4. The primary sequence of CYP3A4 lists 7 cysteine residues (Figure 2). Upon careful inspection of the crystal structure of CYP3A4, one notes that C442 is coordinated to the heme prosthetic group and buried at the center of the protein, making it inaccessible to maleimide modification when CYP3A4 is in its correctly folded holo-form. After chemical reaction of wild-type CYP3A4 with maleimide-containing molecules **1b** and **3b** (Scheme 1, Figure 3), MS analysis gave ambiguous results with

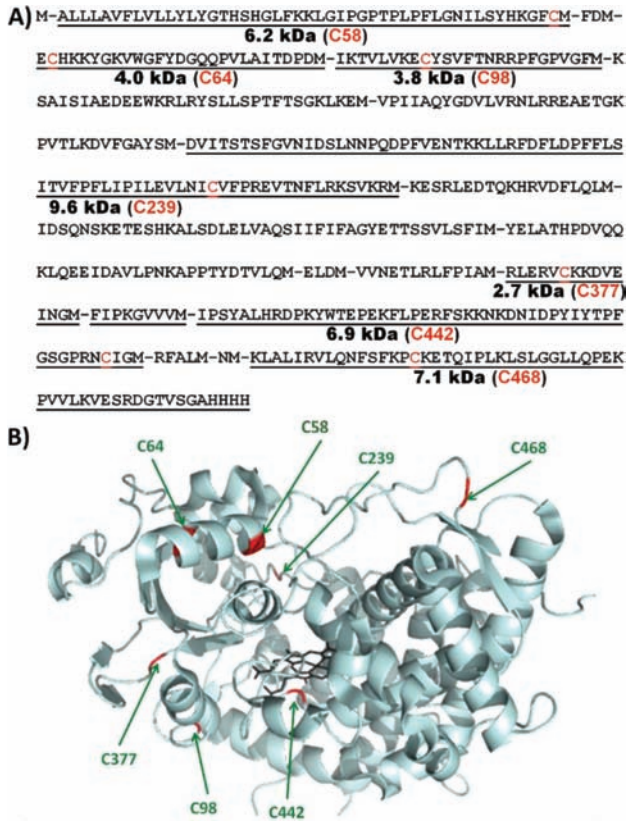

Figure 2. (A) Primary sequence of human CYP3A4 used here (referred to as the wild-type). Theoretical Cys-containing BrCN digestion peptides are underlined, and their approximate molecular weight when labeled with **10** is shown with the sequence number of the cysteine residue included in each peptide. (B) Crystal structure of CYP3A4 (PDB: 1TQN) with cysteine residues highlighted in red.

dx.doi.org/10.1021/bc200672s | *Bioconjugate Chem.* 2012, 23, 826–836

Scheme 1. (A) General Reaction Used to Label Wild-Type and Mutant CYP3A4 Enzymes with Maleimides 1−13. (B) General Approach to Preparing the Non-Commercial Maleimide Labels[a]

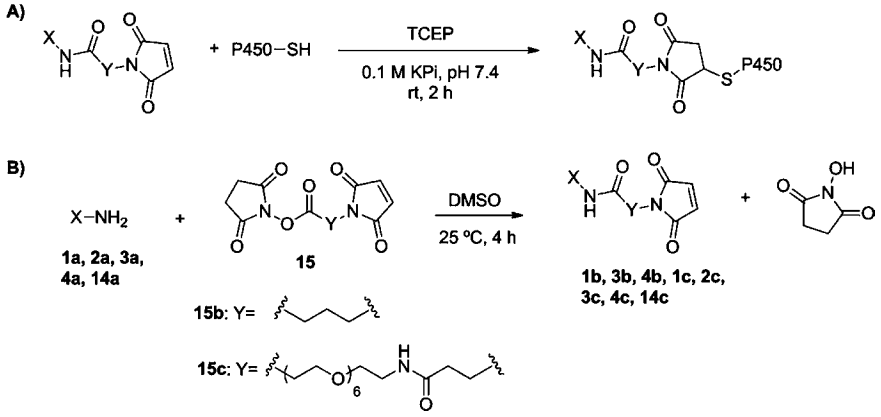

[a]See Figure 3 for detailed structures.

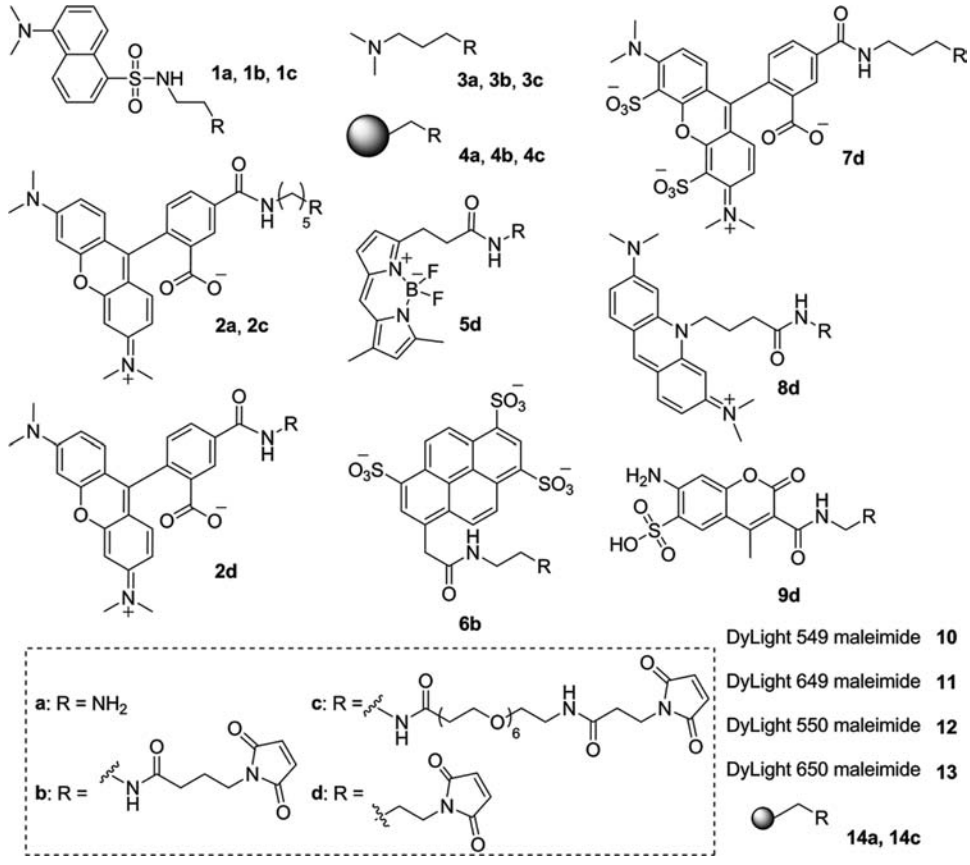

Figure 3. Structures for molecules **1**−**9** and **14**. The structures for commercial compounds **10**−**13** are not disclosed by the vendor. The larger sphere represents CarboxyLink resin in **4a**−**4c**. The smaller sphere represents the silica microsphere in **14a** and **14c**.

poor reproducibility (data not shown). Failure of MS to provide the desired information is likely due to the low stability of CYP3A4 and its notorious tendency to form aggregates.

A combination of methods was used here to characterize the CYP3A4 conjugates. These include single-molecule fluorescence spectroscopy, electrophoresis, UV and fluorescence spectroscopy, and enzymatic assays. For detailed characterization of the conjugates, wild-type CYP3A4 was reacted with an excess of fluorescent maleimide DyLight 549 (**10**, structure not disclosed by vendor) as shown in Scheme 1A. A sample of CYP3A4 labeled with **10** was imaged with a single molecule total internal reflection fluorescence microscopy setup (TIRF, see Experimental Procedures section for details). Analysis of the images acquired allowed us to count the number of fluorescent moieties present per labeled protein molecule (Figure 4). Results indicated that modification with **10** gave predominantly singly modified CYP3A4 (76.9%), with a significant proportion being doubly and triply modified (18.6% and 4.2%, respectively). On the down side, this same conjugate only retained ∼5% of its original enzymatic activity when assayed with testosterone as the substrate and cytochrome P450 reductase (CPR)/NADPH as the cofactors

dx.doi.org/10.1021/bc200672s | *Bioconjugate Chem.* 2012, 23, 826−836

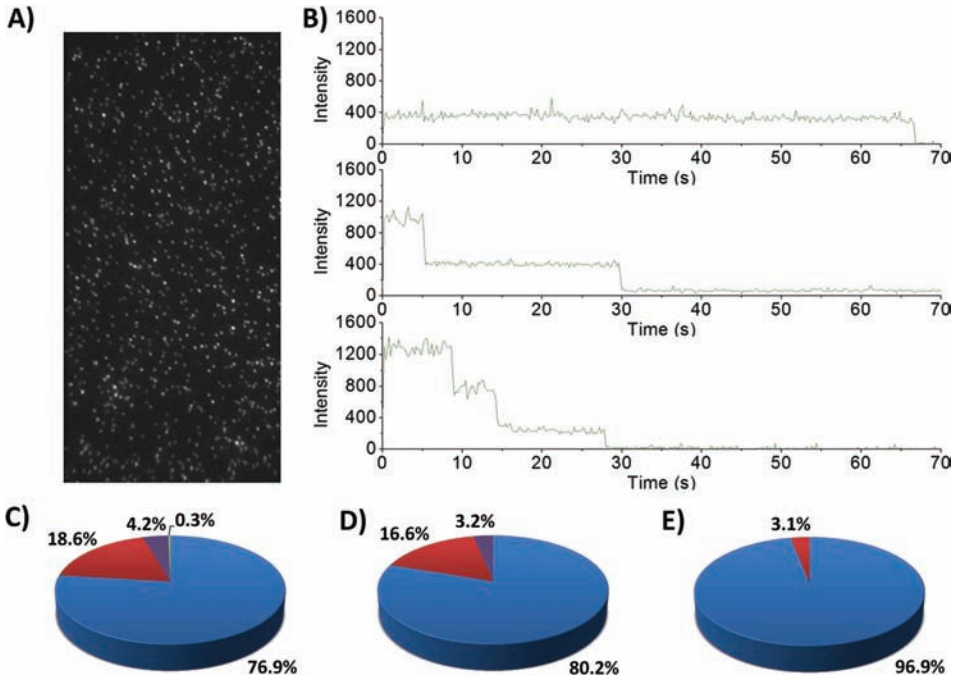

Figure 4. Single-molecule photobleaching experiments on individual variant CYP3A4 enzymes labeled with DyLight 549 maleimide (**10**). (A) Representative example of a wide-field single molecule total internal reflection fluorescence (TIRF) microscope image obtained for fluorescently labeled CYP3A4 upon excitation at 532 nm. (B) Representative intensity−time trajectories observed when the protein has one fluorophore/protein molecule (one step), two fluorophores/protein molecule (two steps), and three fluorophores/protein molecule (three steps). These trajectories were tallied for CYP3A4 wild-type, n = 2212 (C); mutant 1, n = 1778 (D); and mutant 3, n = 703 (E). Pie colors used: blue = one step, red = two steps, purple = three steps, green = four steps.

(Figure 5, wild-type in blue). Replacing the native cofactors with cumene hydroperoxide (CHP) marginally improved the retained activity to ~10%. This deleterious effect on the activity hints at C98 being the main site of modification, based on recent studies indicating that substitutions with large aromatic groups at this residue result in loss of activity.[37] The C98W and C98F mutations were indeed reported to result in a conformational shift that led to a subsequent loss in catalytic activity, due in part to a reduction in the ability of CYP3A4 to properly interact with its reductase CPR. The C98S CYP3A4 mutant on the other hand was reported to display unchanged activity.[37]

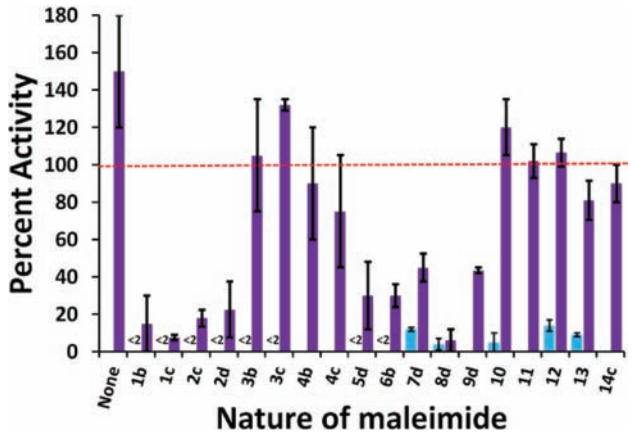

Figure 5. Relative activity of CYP3A4 wild-type (in blue, left side) and mutant 3 (in purple, right side) after labeling with maleimides **1**−**14**. Percent activity is reported relative to that of nonlabeled wild-type CYP3A4. All values are the average of duplicates or triplicates ± 1 standard deviation.

These results do not eliminate the possibility of different singly labeled regioisomers being formed concurrently. To gain a better handle on the identity of the residues being modified, we turned to an approach combining SDS-PAGE and BrCN digestion of fluorescently labeled P450 samples. BrCN is known to cleave proteins selectively after methionine residues. Sequence and molecular weight of the cysteine-containing peptides expected from BrCN digestion of CYP3A4 are shown in Figure 2. All of the expected digestion peptides contain a maximum of one cysteine residue. Digestion and peptide analysis of **10**-labeled wild-type CYP3A4 revealed that at least 5 of the cysteine positions were accessible for modification (Figure 6). Indeed, SDS-PAGE of the digested protein revealed 5 peptide bands exhibiting fluorescence emission between 565 and 595 nm (580 nm band-pass filter) when excited at 532 nm (green-excited mode), as suggested by vendor for DyLight 549 (**10**). The bands corresponding to the C239- and C377-containing peptides are significantly fainter than the other ones, possibly suggesting minor reactivity at these sites.

Design of Cysteine-Depleted CYP3A4 Mutants for Site-Specific Cysteine Modification. As alluded to above, a C98S substitution was desirable in order to prevent conjugation at C98 which is expected to incur a loss in activity. It was also desirable to minimize the number of mutations in order to increase the likelihood of obtaining fully active and stable mutants. Thus, mutant 1 contained only one mutation, C98S. Mutant 2 (C98S/C377S/C468G) and mutant 3 (C98S/C239S/C468G) were also generated to confirm the sites of modifications (especially since some peptides comigrate on the gel), and in the hopes of producing variants that would be singly modified by maleimides.

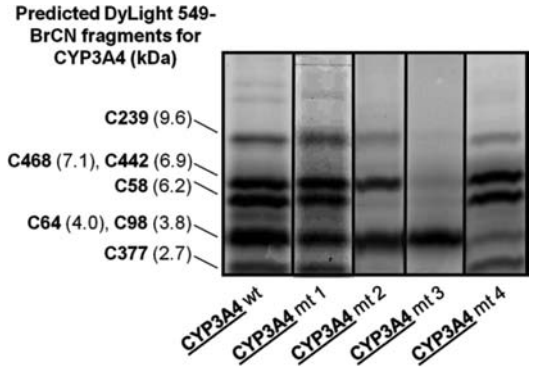

Figure 6. Tricine-SDS-PAGE analysis of BrCN digestion peptides of CYP3A4 variants labeled with DyLight 549 maleimide **10**. The image was acquired with a Typhoon Trio + scanner using the green-excited mode (λ_{ex} = 532 nm), with a 580 nm band-pass filter (580 BP 30, transmits light between 565 and 595 nm with a transmission peak centered on 580 nm). Mutations include C98S for mt 1, C98S/C377S/C468G for mt 2, C98S/C239S/C468G for mt 3, and C64S/C98S for mt 4.

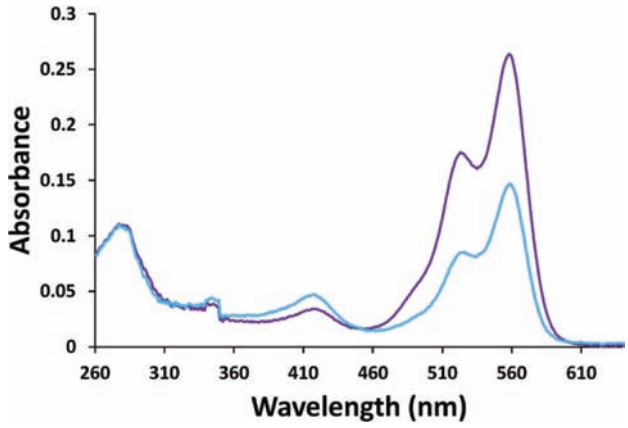

Figure 7. Absorbance spectrum of CYP3A4 mutant 3 labeled with DyLight 549 Maleimide (**10**). In blue, 10 maleimide equiv were used resulting in ca. ~0.4 labels/protein molecule. In purple, 100 maleimide equiv were used resulting in ca. ~0.8 labels/protein molecule. An $\varepsilon_{280\ nm}$ of 40 340 M^{-1} cm^{-1} was used to calculate the concentration of CYP3A4.

The photobleaching profile of mutant 1 labeled with **10** was very similar to that of labeled wild-type enzyme (Figure 4). The key difference was revealed by gel analysis of the digested protein (Figure 6) which shows a decrease in the fluorescence intensity of the band with a molecular weight corresponding to the C98-containing peptide. Because of their very similar predicted molecular weights (4.0 kDa and 3.8 kDa, respectively), the C64- and C98-containing peptides are not resolved under the electrophoretic conditions used. Since C98 was mutated to Ser in mutant 1, we do not expect the 98th-residue-containing peptide to have reacted with maleimide **10**, thus reducing the fluorescence of the band at ~3.9 kDa. The remainder of fluorescence at this MW implies that C64 is modified in mutant 1, and both C64 and C98 are labeled in the wild-type enzyme. Taken together, these results suggest that, under our conditions, most of the cysteine residues can be modified, although only up to 2 (or 3, but rarely) are labeled at a time. This is consistent with previous reports suggesting that more than 2 cysteine-modifications per CYP3A4 protein resulted in protein denaturation.[15]

As for mutants 2 (C98S/C377S/C468G) and 3 (C98S/C239S/C468G), however, our data suggest that both mutants are modified primarily at C64 (Figure 6). They cannot be labeled at the co-migrating peptide containing C98 because of the C98S mutation. In the case of mutant 2, a minor band corresponding to labeling at C442 is observed. The latter is likely due to partial denaturation of the enzyme resulting in exposure of the heme-ligated cysteine residue (C442). Since this band is not observed with mutant 3, a detrimental effect of C377S is inferred. On the other hand, we were delighted to see one major band with labeled mutant 3, suggesting very specific modification by **10** at the C64 position. For reasons that we do not understand, C377 was not modified despite sequence analysis confirming that it had not been mutated. This is likely due to a conformational difference found in mutant 3 rendering C377 unavailable for reactions with maleimides.

Corroborating results were also obtained by UV−vis spectroscopy indicating the presence of ~0.8 DyLight groups (fluorophore of **10**) per protein molecule under saturating conditions (Figure 7), and by photobleaching analysis, which indicated that 96.9% of the mutant 3 conjugates were singly labeled (Figure 6). According to the analysis of the gel, the remaining 3−4% is likely to result from a small proportion of the protein being denatured and exposing C442 for labeling. Moreover, this high regioselectivity was consistently observed with all other fluorescent maleimide-conjugates of mutant 3 that were characterized, namely, those of **1b**, **5d**, **8d**, **11**, **12**, and **13** (data not shown).

The identity of the main residue being modified in mutant 3 was further verified with mutant 4, consisting of C64S and C98S mutations. As seen in Figure 6, characterization of **10**-labeled mutant 4 shows that the band corresponding to the C64-containing peptide does not fluoresce anymore. This confirms that mutant 3 is modified almost exclusively at C64.

In addition, we were gratified to find that mutant 3 is as stable as and even more active (150 ± 30%) than wild-type CYP3A4. And whereas labeled wild-type CYP3A4 lost >90% of its activity, **10**-labeled mutant 3 remained at least as active, if not more, than unlabeled wild-type CYP3A4 (120 ± 20%).

Effect of Varying the Maleimide Label on Enzyme Activity. Next, we wanted to expand our scope of maleimides used to label the CYP3A4 mutant 3. This mutant was therefore reacted with a variety of structurally diverse maleimides, either commercially available or synthesized by our group (Scheme 1, Figure 3). Unlike the wild-type enzyme, mutant 3 retained some degree of activity upon labeling with most maleimides that were tested (Figure 5, labeled mutant in purple). DyLight maleimides **10**−**13** were especially interesting, producing mutant 3 conjugates with 80−120% of the activity of nonmodified wild-type. On the other hand, addition of maleimides **1b**−**c**, **2c**−**d**, and **8d** proved quite noxious to enzymatic activity. To assess the role that the linker portion (as opposed to the fluorophore portion) plays in the observed loss of activity, maleimides **3b** and **3c** were prepared and coupled to mutant 3. As seen in Figure 5, when modified with these maleimides, mutant 3 retains most of its activity. This suggests that the fluorophore portions are likely the main culprits causing the loss of activity observed upon labeling of mutant 3. It was envisaged that the fluorophores themselves might inhibit the activity of CYP3A4. This hypothesis was verified by monitoring the enzyme activity of unlabeled wild-type and mutant enzyme in the presence of the free fluorophores. As

dx.doi.org/10.1021/bc200672s | *Bioconjugate Chem.* 2012, 23, 826−836

depicted in Figure 8, in general, the degree of inhibition observed in the presence of free fluorophores correlates with

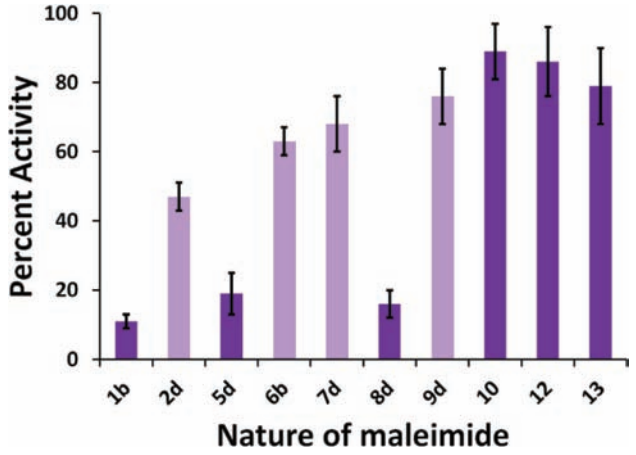

Figure 8. Effect of free fluorophores (dark purple: 100 μM, light purple: 1 mM) on the enzymatic activity of nonlabeled CYP3A4 mutant 3. The data are normalized against the activity of nonlabeled mutant 3 in the absence of free fluorophore. All values are the average of duplicates or triplicates ± 1 standard deviation.

the loss of activity seen upon labeling (Figure 5). We can further explain the effect of modifying mutant 3 on its activity by observing changes in its reduced-CO spectrum. As seen in Figure 9, labeling with maleimides **2d** and **9d** caused an observable loss in intensity of the band at 450 nm and an increase in absorbance at 420 nm. This is characteristic of a switch to the nonfunctional P420 form of the enzyme. These results allow us to rule out steric effects and to attribute the loss of activity observed with selected labels to varying degrees of enzyme inhibition by the fluorophores themselves. In the end, it would seem prudent to test a variety of molecular structures when attempting to label CYP3A4.

Immobilization of CYP3A4 Mutant 3 onto Maleimide-Functionalized CarboxyLink Resin. As an extension of our work with soluble, fluorescent labels, we sought to modify mutant 3 with solid supports derivatized with maleimide groups. Thus, commercial CarboxyLink resin (**4a**) was modified to display a maleimide group at the end of a chain of varying length (see **4b** and **4c**). Maleimide coverage of the resin was calculated to be ~0.6 nmol/μL resin. This derivatization was followed by reaction with CYP3A4 mutant 3. No attempts were made to immobilize the wild-type enzyme in light of the fact that attachment of the linker alone (**3b** or **3c**) to wild-type CYP3A4 suffices to bring the enzymatic activity below 5% (Figure 5). Attachment of **3b** or **3c** to mutant 3 on the other hand did not affect the enzyme activity significantly, and to our satisfaction, covalent bond formation with the modified resins **4b** and **4c** did not cause significant decrease in activity either. To assess the efficiency of CYP3A4 immobilization, the enzyme activity present in the supernatant was assayed using BFC as the substrate. The activity detected in the supernatants was <5% compared to 100% for a control containing **4a**, indicating an immobilization yield of ≥95%. Moreover, once immobilized, the activity of CYP3A4 mutant 3 was retained (Figure 5), and no penalty was incurred on the thermodynamic stability of the mutant over the 16 h observation period. These results were very promising with respect to applications that require oriented immobilization of

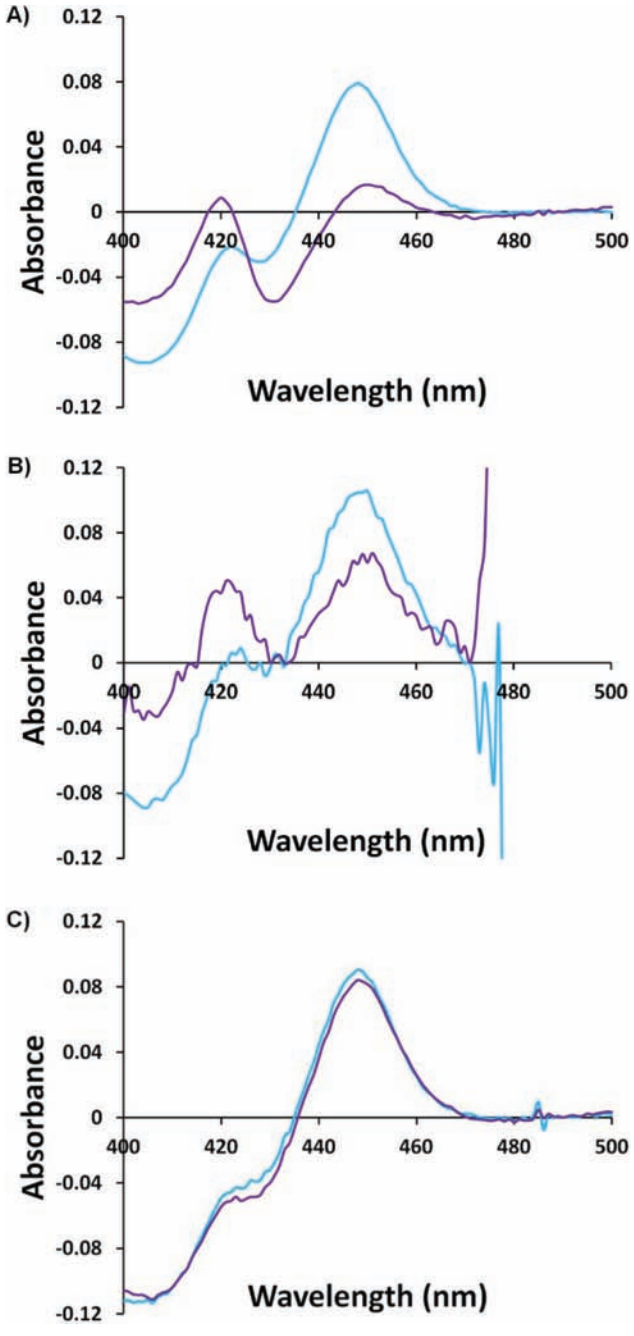

Figure 9. Effect of labeling with maleimides **9d** (A) and **2d** (B) on the CO-difference spectrum of CYP3A4 mutant 3 compared to the nonlabeled control (C). Each plot compares the CO-difference spectrum before (in blue) and after (in purple) labeling. The CO-difference spectra were acquired in the manner reported by Omura and Sato.[26] Note that **2d** absorbs maximally in the region around 500 nm.

enzymes onto solid surfaces such as single-molecule spectroscopy and the production of protein microarrays.

Immobilization of CYP3A4 Mutant 3 onto Maleimide-Functionalized Silica Microspheres. Finally, we sought to assess the activity mutant 3 upon immobilization to a surface that would be more appropriate for applications such as those mentioned above. Thus, 0.1 μm colloidal silica microspheres were aminosilanized and treated with cross-linker **15c** to produce a PEG-maleimide surface analogous to that used to immobilize biomolecules on glass slides for single-molecule

dx.doi.org/10.1021/bc200672s | *Bioconjugate Chem.* 2012, 23, 826–836

experiments[38] or the production of microarrays. In fact, biomolecule-modified microspheres are often used directly in single molecule experiments[39,40] and in the production of liquid bead arrays. CYP3A4 mutant 3 was then immobilized onto these beads as described above for the CarboxyLink agarose resin. Under the conditions used here (see Experimental Procedures section for details), the immobilization yield was ~70%. Once immobilized, mutant 3 retained 60 ± 10% of its activity compared to the activity of mutant 3 in solution when assayed with testosterone as the substrate, and 90 ± 10% activity retained versus the wild-type enzyme (Figures 5 and 10). Activity of the microsphere-immobilized mutant 3 was also observed with BFC as the substrate (60 ± 10% versus wild-type and 40 ± 10% versus mutant 3).

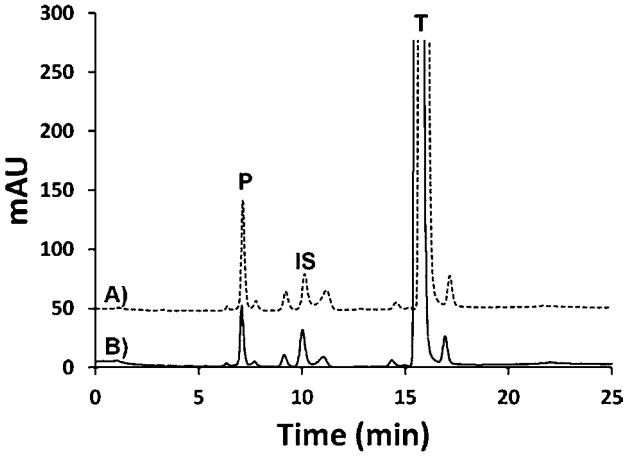

Figure 10. Immobilization of CYP3A4 mutant 3 on silica microspheres. (A) Control: representative HPLC UV-chromatogram of 6β-hydroxytestosterone (P, 7.1 min) formation by CYP3A4 mutant 3 in solution. (B) Representative HPLC UV-chromatogram of 6β-hydroxytestosterone (P, 7.1 min) formation by microsphere-immobilized CYP3A4 mutant 3. The peaks at 10.1 and 15.8 min correspond to the internal standard cortexolone (IS) and the substrate testosterone (T), respectively. Note: a very large excess of testosterone was used in these assays.

CONCLUSION

In summary, we have generated a triple mutant of CYP3A4 (C98S/C239S/C468G) that is singly modified at C64 by a variety of soluble and solid-supported maleimides. While the actual chemical modification at C64 incurs a minor cost to activity, this is made up for in many cases by the fact that this mutant is more active (150 ± 30%) than the wild-type enzyme. Bioconjugation of mutant 3 with some dyes (**1**, **2**, and **8**) had a detrimental effect on the enzyme activity. We were able to rule out the implication of steric effects in this observed loss in activity and demonstrated instead that enzyme inhibition by some fluorophore moieties on the maleimide labels played a predominant role. Finally, our bioconjugation strategy was successfully applied toward the immobilization of this CYP3A4 mutant on maleimide-functionalized CarboxyLink resin and silica microspheres. The fact that the enzyme, attached via C64, remained active on these solid matrices is promising with respect to applications that favor oriented immobilization and suggests that this mutant of CYP3A4 would be an appropriate choice in the development of protein microarrays, biosensors, or bioreactors.

ASSOCIATED CONTENT

Supporting Information

Preparation, characterization, and spectra of noncommercial maleimides. This material is available free of charge via the Internet at http://pubs.acs.org.

AUTHOR INFORMATION

Corresponding Author

*E-mail: karine.auclair@mcgill.ca; Tel: (+1)514-398-2822; Fax: (+1)514-398-3797.

Notes

The authors declare no competing financial interest.

ACKNOWLEDGMENTS

We thank Dr. Hsiao-Wei Liu for aminosilanization of the microspheres. This work was funded by research grants from the National Science and Engineering Research Council of Canada (NSERC) to K.A. and also to G.C. while A.M. was supported by scholarships from NSERC and the Center for Green Chemistry and Catalysis. Y.H.'s stipend was partly covered by an NSERC undergraduate scholarship. P.K. was supported by the McGill Chemical Biology Fellowship Program (Canadian Institutes of Health Research).

REFERENCES

(1) Claridge, S. A, Schwartz, J. J., and Weiss, P. S. (2011) Electrons, photons, and force: quantitative single-molecule measurements from physics to biology. *ACS Nano 5*, 693−729.

(2) Wong, L. S., Khan, F., and Micklefield, J. (2009) Selective covalent protein immobilization: strategies and applications. *Chem. Rev. 109*, 4025−4053.

(3) Kalia, J., and Raines, R. T. (2010) Advances in bioconjugation. *Curr. Org. Chem. 14*, 138−147.

(4) Chefson, A., Zhao, J., and Auclair, K. (2006) Replacement of natural cofactors by selected hydrogen peroxide donors or organic peroxides results in improved activity for CYP3A4 and CYP2D6. *ChemBioChem 7*, 916−919.

(5) Chefson, A., Zhao, J., and Auclair, K. (2007) Sugar-mediated lyoprotection of purified human CYP3A4 and CYP2D6. *J. Biotechnol. 130*, 436−440.

(6) Chefson, A., and Auclair, K. (2007) CYP3A4 activity in the presence of organic cosolvents, ionic liquids, or water-immiscible organic solvents. *ChemBioChem 8*, 1189−1197.

(7) Larsen, A., May, E., and Auclair, K. (2011) Predictable stereoselective and chemoselective hydroxylations and epoxidations with P450 3A4. *J. Am. Chem. Soc. 133*, 7853−7858.

(8) Sletten, E. M., and Bertozzi, C. R. (2009) Bioorthogonal chemistry: fishing for selectivity in a sea of functionality. *Angew. Chem., Int. Ed. 48*, 2−27.

(9) Wang, L., and Schultz, P. G. (2002) Expanding the genetic code. *Chem. Commun. 1*, 1−11.

(10) Kiick, K. L., and Tirrell, D. A. (2000) Protein engineering by in vivo incorporation of non- natural amino acids: control of incorporation of methionine analogues by methionyl-tRNA synthetase. *Tetrahedron 56*, 9487−9493.

(11) Muralidharan, V., and Muir, T. W. (2006) Protein ligation: and enabling technology for the biophysical analysis of proteins. *Nat. Methods 3*, 429−438.

(12) Besanceney-Webler, C., Jiang, H., Zheng, T., Feng, L., Soriano del Amo, D., Wang, W., Klivanski, L. M., Marlow, F. L., Liu, Y, and Wu, P. (2011) Increasing the efficacy of bioorthogonal click reactions for bioconjugation: a comparative study. *Angew. Chem., Int. Ed. 50*, 8051−8056.

(13) Blanden, A. R., Mukherjee, K, Dilek, O., Loew, M., and Bane, S. (2011) 4-Aminophenylalanine as a biocompatible nucleophilic catalyst

for hydrazone-ligations at low temperature and neutral pH. *Bioconjugate Chem. 22*, 1954−1961.
(14) Behrens, C. R., Hooker, J. M., Obermeyer, A. C., Romanini, D. W., Katz, E. M., and Francis, M. B. (2011) Rapid chemoselective bioconjugation through the oxidative coupling of anilines and aminophenols. *J. Am. Chem. Soc. 133*, 16398−16401.
(15) Tsalkova, T. N., Davydova, N. Y., Halpert, J. R., and Davydov, D. R. (2007) Mechanism of interactions of R-naphthoflavone with cytochrome P450 3A4 explored with an engineered enzyme bearing a fluorescent probe. *Biochemistry 46*, 106−119.
(16) Mie, Y., Suzuki, M., and Komatsu, Y. (2009) Electrochemically driven drug metabolism by membranes containing human cytochrome P450. *J. Am. Chem. Soc. 131*, 6646−6647.
(17) Nicoli, R., Bartolini, M., Rudaz, S., Andrisano, V., and Veuthey, J.-L. (2008) Development of immobilized enzyme reactors based on human recombinant cytochrome P450 enzymes for phase I drug metabolism studies. *J. Chromatogr., A 1206*, 2−10.
(18) Nath, A., Koo, P. K., Rhoades, E., and Atkins, W. M. (2008) Allosteric effects on substrate dissociation from cytochrome P450 3A4 in Nanodiscs observed by ensemble and single-molecule fluorescence spectroscopy. *J. Am. Chem. Soc. 130*, 15746−15747.
(19) Das, A., Zhao, J., Schatz, G. C., Sligar, S. G., and Van Duyne, R. P. (2009) Screening of Type I and II drug binding to human cytochrome P450−3A4 in nanodiscs by localized surface plasmon resonance spectroscopy. *Anal. Chem. 81*, 3754−3759.
(20) Shumyantseva, V. V., Bulko, T. V., Kuznetsova, G. P., Samenkova, N. F., and Archakov, A. I. (2009) Electrochemistry of cytochromes P450: analysis of current-voltage characteristics of electrodes with immobilized cytochromes P450 for the screening of substrates and inhibitors. *Biochemistry (Mosc.) 74*, 438−444.
(21) Shumiantseva, V. V., Shikh, E. V., Makhova, A. A., Bylko, T. V., Kukes, V. G., Sizova, O. S., Ramenskaia, G. V., Usanov, S. A., and Archakov, A. I. (2011) The influence of vitamin B group on monooxygenase activity of cytochrome P450 3A4: pharmacokinetics and electro analysis of catalytic properties. *Biomed. Khim. 57*, 343−54.
(22) Ignaszak, A., Hendricks, N., Waryo, T., Songa, E., Jahed, N., Ngece, R., Al-Ahmed, A., Kgarebe, B., Baker, P., and Iwuoha, E. I. (2009) Novel therapeutic biosensor for indinavir-a protease inhibitor antiretroviral drug. *J. Pharm. Biomed. Anal. 49*, 498−501.
(23) Chang, G., Morigaki, K., Tatsu, Y., Hikawa, T., Goto, T., and Imaishi, H. (2011) Vertically integrated human P450 and oxygen sensing film for the assays of P450 metabolic activities. *Anal. Chem. 83*, 2956−2963.
(24) Nath, A., Grinkova, Y. V., Sligar, S. G., and Atkins, W. M. (2007) Ligand binding to cytochrome P450 3A4 in phospholipid bilayer nanodiscs. *J. Biol. Chem. 282*, 28309−28320.
(25) Domanski, T. L., Liu, J., Harlow, G. R., and Halpert, J. R. (1990) Analysis of four residues within substrate recognition site 4 of human cytochrome P450 3A4: role in steroid hydroxylase activity and a-naphthoflavone stimulation. *Arch. Biochem. Biophys. 350*, 223−232.
(26) Omura, T., and Sato, R. (1964) The carbon monoxide-binding pigment of liver microsomes. *J. Biol. Chem. 239*, 2370−2378.
(27) Oprian, D. D., and Coon, M. J. (1982) Oxidation-reduction states of FMN and FAD in NADPH-cytochrome P-450 reductase during reduction by NADPH. *J. Biol. Chem. 257*, 8935−8944.
(28) Grassetti, D. R., and Murray, J. F. Jr. (1967) Determination of sulfhydryl groups with 2,2′- or 4,4′-dithiodipyridine. *Arch. Biochem. Biophys. 119*, 41−49.
(29) Scheer, J. M., and Ryan, C. A. (2001) A method for the quantitative recovery of proteins from polyacrylamide gels. *Anal. Biochem. 298*, 130−132.
(30) Karam, P., Ngo, A. T., Rouiller, I., and Cosa, G. (2010) Unraveling electronic energy transfer in single conjugated polyelectrolytes encapsulated in lipid vesicles. *Proc. Natl. Acad. Sci. U.S.A. 107*, 17480−17485.
(31) Ngo, A. T., Karam, P., Fuller, E., Burger, M, and Cosa, G. (2008) Liposome encapsulation of conjugated polyelectrolytes: toward a liposome beacon. *J. Am. Chem. Soc. 130*, 457−459.
(32) Ha, T. (2001) Single-molecule fluorescence energy transfer. *Methods 25*, 78−86.
(33) Harada, Y., Sakurada, K., Aoki, T., Thomas, D. D., and Yanagida, T. (1990) Mechanochemical coupling in actomyosin energy transduction studied by *in vitro* movement assay. *J. Mol. Biol. 216*, 49−68.
(34) Cordoba, O. L., Linskens, S. B., Dacci, E., and Santome, J. A. (1997) 'In gel' cleavage with cyanogen bromide for protein internal sequencing. *J. Biochem. Biophys. Methods 35*, 1−10.
(35) Schagger, H. (2006) Tricine-SDS-PAGE. *Nat. Protoc. 1*, 16−22.
(36) Moss, J. A. (2005) Guide for resin and linker selection in solid-phase peptide synthesis. In *Current Protocols in Protein Science*, Unit 18.7.8, John Wiley & Sons Inc.
(37) Wen, B., Lampe, J. N., Arthur, G., Roberts, A. G., Atkins, W. M., Rodrigues, A. D., and Nelson, S. D. (2006) Cysteine 98 in CYP3A4 contributes to conformational integrity required for P450 interaction with CYP reductase. *Arch. Biochem. Biophys. 454*, 42−54.
(38) Zimmermann, J. L., Nicolaus, T., Neuret, G., and Blank, K. (2010) Thiol-based, site-specific and covalent immobilization of biomolecules for single molecule experiments. *Nat. Protoc. 5*, 975−985.
(39) English, B. P, Min, W., van Oijen, A. M., Lee, K. T., Luo, G., Sun, H., Cherayol, B. J., Kou, S. C., and Xie, X. S. (2006) Ever-fluctuating single molecules: Michaelis-Menten equation revisited. *Nat. Chem. Biol. 2*, 87−94.
(40) Neuman, K. C., and Nagy, A. (2008) Single-molecule force spectroscopy: optical tweezers, magnetic tweezers and atomic force microscopy. *Nat. Methods 5*, 491−505.

Bioconjugate Chemistry

Article

pubs.acs.org/bc

Tris[2-(acryloyloxy)ethyl]isocyanurate Cross-Linked Low-Molecular-Weight Polyethylenimine as Gene Delivery Carriers in Cell Culture and Dystrophic *mdx* Mice

Mingxing Wang,*[,†] Jay D. Tucker,[†,‡] Peijuan Lu,[†] Bo Wu,[†] Caryn Cloer,[†] and Qilong Lu*[,†]

[†]Department of Neurology, McColl–Lockwood Laboratory for Muscular Dystrophy Research, Neuromuscular/ALS Center, Carolinas Medical Center, 1000 Blythe Boulevard, Charlotte, North Carolina 28231, United States

[‡]Department of Biology, University of North Carolina, Charlotte, 9201 University City Boulevard, Charlotte, North Carolina 28223, United States

Supporting Information

ABSTRACT: Hyperbranched poly(ester amine)s (PEAs) were successfully synthesized by Michael addition reaction between tris[2-(acryloyloxy)ethyl]isocyanurate (TAEI) and low-molecular-weight polyethylenimine (LPEI, M_w 0.8k, 1.2k, and 2.0k) and evaluated *in vitro* and *in vivo* as gene carriers. PEAs effectively condensed plasmid DNA with particle sizes below 200 nm and surface charges between 11.5 and 33.5 mV under tested doses [at the ratios 2−10:1 of polymer/pDNA(w/w)]. The PEAs showed significantly lower cytotoxicities when compared with PEI 25k in two different cell lines. The PEAs (C series) composed of PEI 2k showed higher transgene expression compared to PEAs of PEI 0.8k (A series) or 1.2k (B series). Highest gene transfection efficiency in CHO, C2C12 myoblast, and human skeletal muscle (HSK) cell lines was obtained with TAEI/PEI-2K (C12) at a ratio of 1:2. Both C12, C14(TAEI/PEI-2K at a ratio of 1:4) demonstrated 5−8-fold higher gene expression as compared with PEI 25k in *mdx* mice *in vivo* through intramuscular administration. No obvious muscle damage was observed with these new polymers. Higher transfection efficiency and lower toxicity indicate the potential of the biodegradable PEAs as safe and efficient transgene delivery vectors.

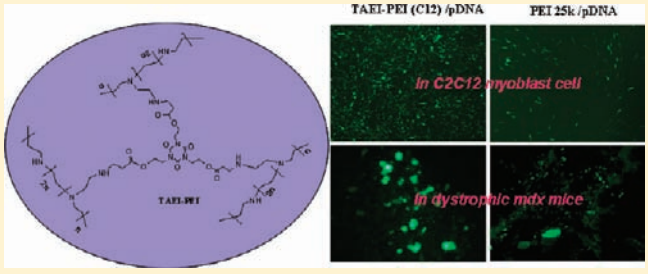

INTRODUCTION

As a therapeutic approach, gene therapy has great potential for treating heritable and acquired diseases, but also faces significant challenges. The precarious balance between efficient gene transfer and possible negative effects of a given delivery system limits a successful therapeutic application. Viral vectors have been shown to be effective delivery vehicles due to their high ability to enter and utilize the transcription machinery of host cells. Limited insert size, insertional mutagenesis, and host immune response, however, limit the applications of viral vectors.[1,2] Polymer-based nonviral vectors remain an attractive alternative, because they possess some unique advantages for practical use such as easy manipulation, controlled release, stimuli-reactivity, and even targeted delivery, although delivery efficiency is still lower than seen in viral vector systems.[3−11] Among them, high-molecular-weight polyethylenimine (HPEI) has demonstrated high gene transfection efficiency in various types of cells *in vitro* and *in vivo*, due to its ability to effectively condense plasmid DNA and its proton-sponge effect. However, its nondegradability, aggregation, and cytotoxicity especially *in vivo* have hindered clinical applications. Modifications of PEI to reduce cytotoxicity while retaining its high potential to bind and condense plasmid DNA for gene delivery have been investigated previously, with limited success.[4−7] One such effort has been to modify HPEI (25k) with hydrophilic poly(ethylene glycol) (PEG) aimed at primarily shielding the surface charges of PEI, potentially reducing toxicity. Nevertheless, this resulted in reduced transfection efficiency when compared to HPEI alone. One alternative for lower toxicity is to use lower-molecular-weight PEIs (LPEI) such as those of M_w 0.8k, 1.2k, or 2.0k Da. However, while LPEIs are effective in binding pDNA, their efficiency in gene delivery is limited both *in vitro* and *in vivo*.[12,13] One possible explanation for the differential effect between HPEI and LPEI is that the LPEI/transgene complex does not form particles with optimal size(s) for effective internalization. To overcome this dilemma, one possible approach is to develop cross-linked LPEI to form conjugates with optimal sizes via stimuli-responsive linkages. Cross-linked LPEI modifications based on poloxamer diacrylate (GDM), poly(ethylene glycol) diacrylate (PEGDA), polycaprolactone diacrylate (PCLDA), glycerol dimethacrylate, and glycerol triacrylate have been explored as ways to reduce cytotoxicity with improved transfection efficiency *in vitro* and have been applied to the central nervous system, lung, and

Received: December 21, 2011
Revised: February 27, 2012
Published: March 25, 2012

tumors *in vivo*.[14−19] We report here the synthesis of biodegradable poly(ester amine)s (PEAs) with the combinations of cross-linker tris[2-(acryloyloxy)ethyl]isocyanurate (TAEI) and LPEIs to enhance transfection efficiency, with the following considerations. (1) TAEI is one of the derivatives of 1,3,5-triazine, which have found widespread applications in the pharmaceutical, textile, plastic, and rubber industries.[20,21] The triazine core is an electron-deficient heterocycle, that has the potential to disperse the positive charges of electron-rich PEI by cross-linking with each other. (2) LPEIs have low cytotoxicity while maintaining its high potential to condense plasmid DNA or antisense oligomer. (3) Cross-linking would raise the effective molecular weight of polycation and hence elevate the effectiveness of complexes with optimal sizes and transfection efficiency. The cross-linked PEIs could show dispersed positive charge density compared with HPEI, thus maintaining proton-sponge capacity and leading to faster endosomal release of polymer-cargo polyplex. (4) Branched cationic polyesters undergo slower degradation under physiological condition when compared to linear ones.[15,18,22] In this study, a series of hyperbranched PEAs (TAEI cross-linked PEIs) have been prepared and characterized. The effects of the PEAs on gene delivery and toxicity were investigated in different cell lines (CHO, C2C12, and HSK). The results indicate that PEI 2k-based PEAs are highly effective for the delivery of plasmid transgene in cell cultures and in dystrophic *mdx* mice *in vivo* with lower cytotoxicity as compared to PEI 25k.

EXPERIMENTAL PROCEDURES

Materials. Polyethylenimines (M_w: 0.8, 1.2, 2.0, and 25 kDa), tris[2-(acryloyloxy)ethyl]isocyanurate (TAEI) and anhydrous methanol were purchased from Sigma (St. Louis, MO, USA). Cell Titer 96 Aqueous One Solution Reagent for cell viability, pEGFP (4.7 kb), was obtained from BD Biosciences. Cell culture media RPMI 1640, Dulbecco's Modified Eagle's Medium (DMEM), penicillin−streptomycin, fetal bovine serum, L-glutamine, and HEPES buffer solution (1 M) were purchased from GIBCO, Invitrogen Corp (USA). All other chemicals were reagent-grade without further treatments. Fluorescence was visualized using both the Olympus IX71 and BX51fluorescent microscopy. Digital images were taken using Olympus DP70 camera and DP manager software.

Synthesis and Characterization of PEAs. PEAs were successfully synthesized by Michael addition reaction as reported.[16,19] Briefly, TAEI and LPEI were separately dissolved in methanol, and TAEI solution was slowly added to PEI solution at three different TAEI/PEI feed ratios (Table 1). The reaction was kept at room temperature with constant stirring for 48 h. Subsequently, the reaction mixtures were dialyzed at 4 °C for 24 h using Spectra/Por membrane (molecular mass cutoff 2 kDa) against 20% methanol and followed by distilled water. The final products were lyophilized and stored at 4 °C.

^{1}H NMR spectra of samples were recorded in $CDCl_3$ using JEOL500 spectrometer. Capillary viscosity measurements were carried out to estimate molecular weights. The polymers were dissolved in 0.9% NaCl at concentration from 20 mg/mL to 5 mg/mL, and the molecular weights of polymers were calculated using the Mark−Houwink equation $[\eta] = KM^{\alpha}$, where M is the molecular weight and K and α are Mark−Houwink parameters determined from PEI standards of known molecular weights (PEI 0.8, 2.0, and 25 kDa) at 25 °C.[23,24]

Table 1. Characteristics of Synthesized PEAs

series	code	feed ratio of TEAI/PEI	M_w PEI (kDa)	Mv [a]	PEI mol (%) [b]	yield of copolymer (%)
A	A11	1:1	0.8	4980	63.2	28.1
	A12	1:2	0.8	4570	72.5	32.4
	A14	1:4	0.8	4390	53.4	40.5
B	B11	1:1	1.2	7160	51.7	33.6
	B12	1:2	1.2	5940	70.3	37.8
	B14	1:4	1.2	5580	63.5	43.3
C	C11	1:1	2.0	9870	54.8	38.5
	C12	1:2	2.0	8430	65.6	41.3
	C14	1:4	2.0	7650	71.4	53.2

[a]Determined by viscosity measurements in 0.9% NaCl solution at 25 °C. [b]Determined by ^{1}H NMR in $CDCl_3$.

Degradation of PEAs. The degradability of the new PEAs was estimated by measuring the reduction in molecular weight. Polymers dissolved in phophate buffered saline (PBS, 0.1 g/mL) were incubated in a shaking incubator (37 °C) and sampled at various time intervals. Subsequently, the lyophilized samples were subjected to capillary viscosity analysis to estimate molecular weights.

Preparation and Purification of pDNA. One Shot TOP10 chemically competent *Escherichia coli* (Invitrogen) were transformed with pEGFP vector as reporter gene (Clontech Laboratories, Inc.) per manufacturer's instructions. The transformed bacteria were grown on LB agar overnight at 37 °C with selection antibiotic, ampicillin. Single clones were selected and grown for 8 h in broth media. The plasmid was extracted from the bacterial cultures using the Concert Miniprep protocol, digested with Eco R1 restriction enzyme, and electrophoresed on 1% agarose gel to confirm the correct size. The pDNA was purified using the Qiafilter plasmid purification kit from Qiagen, dissolved in purified water, and stored at −80 °C until further use. Plasmid concentration was determined by UV spectrophotometry at 260/280 nm and further confirmed by 1% agarose gel electrophoresis.

Polymer/DNA Complexation. All polymer/DNA complexes were prepared immediately before use by gently vortexing a mixture of DNA and polymer solution at various polymer/DNA weight ratios. The complexes were incubated at room temperature for 30 min in 24 μL volume and loading dye was added. Samples were then loaded onto 1% agarose gel with ethidium bromide (EB, 0.1 μg/mL) in Tris-acetate (TAE) buffer (100 V, 40 min). The gel was analyzed on UV illuminator.

Particle Size, Zeta Potential, and Morphology Analysis. The hydrodynamic diameters of polymer/pDNA complexes were determined by light scattering. Two milliliters of polyplex solution containing 5 μg of pDNA was prepared at various weight ratios (polymer/pDNA = 2, 5, 10). After 30 min incubation, polyplex sizes were measured by photon correlation spectroscopy using Zetaplu Zeta Potential Analyzer (Brookhaven Instrument Co.) equipped with a 15 mV solid-state laser operated at a wavelength of 635 nm. Scattered light was detected at a 90° measurement angle. The refractive index (1.33) and the viscosity (0.89) of 0.9% sodium chloride were used at 25 °C. The zeta potentials were also measured using the same instrument with different software. The sampling time was set to automatic. Values were presented as the average of six runs.

Scheme 1. Synthesis of PEAs Based on TAEI Cross-Linked LPEI

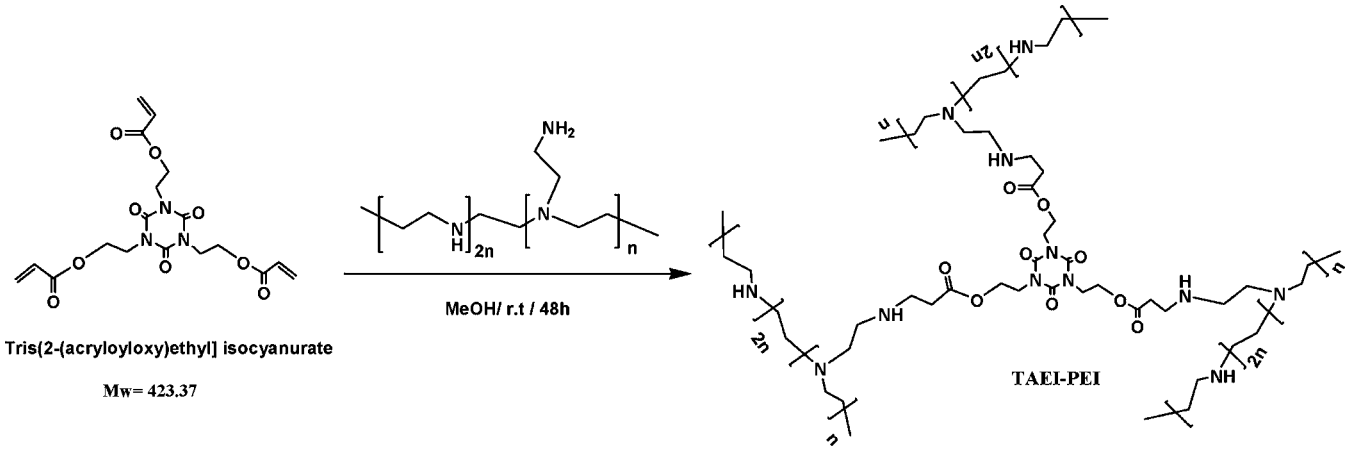

The morphologies of the polymer/DNA complexes were analyzed using transmission electron microscopy (TEM, Phllips CM-10). The samples were prepared using negative staining with 1% phosphotungstic acid. Briefly, one drop of polymer/DNA complex solution was placed on a Formvar- and carbon-coated carbon grid (Electron Microscopy Sciences, Hatfield, PA) for 1 h, and the grid was blotted dry. Samples were then stained for 3 min. The grids were blotted dry again. Samples were analyzed at 60 kV. Digital images were captured with a digital camera system from 4 pi Analysis (Durham, NC).

Resistance to Serum and Heparin. To determine the stability of the polymer/DNA complexes in the presence of serum, 10 μL of 5:1 ratio of polymer/DNA complexes were added to 0.5 mL Eppendorf tubes. Fetal bovine serum (FBS) was then added by volume to achieve final concentrations relative to physiological conditions, mixed, and incubated for 30 min at 37 °C. These samples were then electrophoresed in 1% agarose gel to determine the stability of the complexes. For the analysis of their resistance to heparin, varying amounts of 1 μg /μL heparin sodium was added to polymer/DNA complexes of 5:1 ratio to achieve final concentrations of 0, 10, 25, 50 μg/mL. Samples were then incubated at 37 °C for 20 min and electrophoresed in a 1% agarose gel to determine stability.[25]

Cell Viability Assay. Cytotoxicity was evaluated using the MTS assay by Cell Titer 96Aqueous One Solution Proliferation Kit 24 h after the treatment with different doses of polymers. Cells were seeded in a 96-well tissue culture plate at 10^4 cell per well in 100 μL medium containing 10% FBS. Cells achieving 70−80% confluence were exposed to different doses of polymers for 24 h in the presence of 10% FBS. Cells not exposed to samples were taken as controls with 100% viability and wells without cells as blanks. The relative cell viability was calculated by $(A_{\text{treated}} - A_{\text{background}}) \times 100/(A_{\text{control}} - A_{\text{background}})$. All cell viability assays were carried out in triplicate.

Transfection *in Vitro*. GFP reporter C2C12 myoblasts (ATCC), chinese hamster ovary (CHO), and human skeletal muscle cell (HSkMC, Cell Applications, Inc.) were grown in DMEM or RPMI-1640, respectively, and maintained at 37 °C and 10% CO_2 in a humidified incubator. 5 $\times 10^4$ cells per well were seeded in a 24 well plate in 500 μL medium containing 10% FBS and grown to reach 70−80% confluence prior to transfection. Cell culture medium was replaced with either serum-free or serum-containing media prior to addition of polymer/DNA polyplexes formulated with varying ratio of polymer/DNA. Formulation of 1 μg GFP vector and appropriate amount of polymers was added into the wells 20 min after combination. PEI 25k was used as control for delivery. Transfection efficiencies were determined quantitatively with flow cytometry (BD FACS calibur, BD) and relative efficiency was also recorded using Olympus IX71 inverted microscopy.

Transfection *in Vivo*. Ten *mdx* mice aged 4 to 6 weeks were used for each experimental group. For each tibialis anterior (TA) muscle, 10 μg of plasmid DNA with or without 10 μg polymer in 40 μL saline was used . The muscles were examined 5 days after injection by Olympus BX51 upright fluorescent microscopy for the expression of GFP. The numbers of GFP expressing muscle fibers were counted from a minimum of 6 sections spanning at least half the length of the muscles. A maximum number of GFP positive fibers in one section for each TA muscle was used for comparison of transfection efficiency. Experimental protocols were approved by the Institutional Animal Care and Use Committee (IACUC), Carolinas Medical Center.

RESULTS AND DISCUSSION

Synthesis and Characterization of PEAs. One essential feature of new polymers required for effective gene delivery *in vivo* is the high DNA binding affinity and, moreover, ability to form stable DNA complexes. This character is strongly influenced by charge density and molecular weight.[26] Furthermore, toxicity of polymers has to be minimized for *in vivo* applications.[27] Cross-linking of the small polycation using degradable linkages can potentially meet these requirements, enhancing DNA binding capacity, polyplex stability, and high transfection efficiency with low toxicity. The ester bonds in these PEAs are susceptible to hydrolysis at physiological conditions to form the respective triol and corresponding acids, thereby generating low-molecular-weight, low-toxicity by-product.[28,29] In this study, we design, characterize, and evaluate a novel class of biodegradable, hyperbranched poly(ester amine)s (PEAs) based on TAEI and LPEI. The PEAs were prepared from nucleophilic addition of amines to acrylates under mild reaction conditions with low molecular weight PEI (M_w: 0.8, 1.2, and 2.0 kDa) as amine nucleophile and TAEI as a cross-linker at different feed ratios (Scheme 1). Triacrylate linker reacts with PEI by Michael addition reaction to either primary or secondary amines, generating ester-based polymers. The compositions of synthesized PEAs were confirmed through ^{1}H NMR spectroscopy. The signals at δ 4.6 ppm were related

dx.doi.org/10.1021/bc200674e | Bioconjugate Chem. 2012, 23, 837−845

to TAEI (−$COOCH_2$−) protons. The signals at δ 2.2−3.0 ppm belong to PEI (−CH_2−) and TAEI (−CH_2−) protons. The molecular weights of PEAs ranged from around 4 to 10 kDa determined by viscosity at 25 °C. No significant difference in the M_w of PEAs was observed at variation in feed ratio of TAEI to LPEI for each series, although slightly higher-molecular-weight PEAs were obtained using equal feed ratio of TAEI/PEI (1:1) than the ratio 1:2 or 1:4. This is probably due to reactions of some of the secondary amines in PEIs with TAEI. The characteristics of synthesized PEAs at different TAEI/PEI feed ratios are summarized in Table 1.

Biodegradability of a gene delivery polymer could circumvent long-term toxicity.[22] The kinetics of ester bond degradation of PEAs was investigated by measuring the molecular weight. Figure 1 indicates the typical degradation pattern of PEAs under mimic physiological condition. The PEA underwent hydrolysis forming respective acid and alcohol, thereby generating LMW by-product. A biphasic degradation pattern was observed in that only a small proportion of the PEAs underwent cleavage within 4 days. However, a more rapid degradation was observed 4 days later (Figure 1).

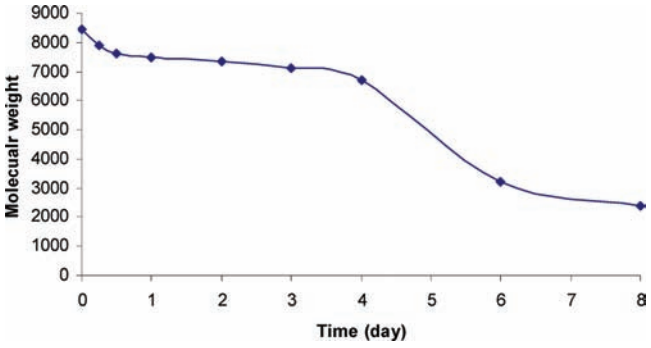

Figure 1. Degradation pattern of TAEI-PEI 2.0k (C12) under mimic physiological condition.

PEA/DNA Polyplex Characteristics. The ability of polymers to complex with plasmid DNA was assessed using agarose gel electrophoresis. The binding of the PEAs to DNA retarded the migration of DNA in the gel due to increase in molecular size and/or changes in charge of the DNA when bound with PEAs. As shown in Figure 2, all PEAs bound pDNA effectively with DNA completely retarded within the original loading wells when the weight ratio of the polymer/pDNA was 2.0. In the B series, B12 and B14 showed stronger binding affinity to DNA than B11 when used at the same concentration. This is likely due to the fact that B12 and B14 have relatively higher PEI content compared with B11. This was further supported by the strong DNA binding capacity of A12 and C14, which also have higher PEI content. Almost all pDNA was retained in the loading well even when the ratio of polymer/pDNA was only 0.5 for these two polymers. In contrast, B11 had relatively lower PEI composition and retained all DNA in the loading well only when the ratio of polymer/pDNA reached 2.0. The results are consistent with our earlier observation that the density of positively charged groups within a polymer determines the binding affinity to negatively charged DNA (unpublished data).

The size and surface charge of PEA/DNA complexes were measured using dynamic light scattering (DLS) as shown in Figure 3. All three series of the PEAs effectively condensed DNA into nanosized, positively charged complexes at the ratio of 2:1. Lower amounts of polymer tended to give larger nanoparticles owing to aggregation. An increase in PEA/DNA weight ratio (up to 5) produced smaller-sized nanoparticles (below 150 nm). Most PEAs formed DNA polyplexes with sizes below 200 nm except for A11 (2 μg) and A14 (5 and 10 μg), which are considered optimal for intracellular delivery. All polyplexes had positive surface charges in the range of 11.5−33.5 mV, with an increase in the weight ratio from 2 to 10 of polymer/pDNA (an example was given in Figure 3b). The results of zeta potential with the PEA/DNA polyplexes are therefore consistent with previous findings that DNA binding neutralizes cationic groups including those within the PEAs.[16,18] The charge neutralization was also consistent with the retardation of DNA in gel analysis described above. The particle sizes and zeta potentials indicated that polymer/DNA complexes were cationic with effective diameters around 200 nm and surface charges strong enough for attachment to anionic cell surfaces, possibly promoting endocytosis. Figure 4 shows polyplex particle morphologies of PEA/pDNA at weight ratio 5. All the results taken together indicate that the PEAs bind and condense DNA effectively. These polyplexes formed spherical nanoparticles with an average diameter below 100 nm observed under TEM. The sizes of the polyplexes were therefore smaller than that obtained by DLS measurement, which is largely attributed to the dry process in the sample preparation of TEM. PEI 25k/DNA formulation yielded aggregated particles.[3,9,10]

Stability of PEA/Plasmid DNA Polyplexes in the Presense of Serum and Heparin. Serum, containing a variety of negatively charged molecules from proteins to glycosaminoglycans (GAG), has a significant effect on gene transfection efficiency *in vitro*, and especially *in vivo*, when positively charged polymers are used as carriers. Strongly charged serum components can compete with DNA for the binding of positively charged polymers, leading to the dissociation of DNA from the carrier and reduced gene delivery effect. The presence of DNAase in the serum can additionally degrade plasmid DNA, thus contributing to the low efficiency of gene delivery. The stability of the DNA/polymer complex in the presence of serum is therefore important for both *in vitro* and *in vivo* applications of gene carriers. To determine the stability of the PEAs, the complexes were

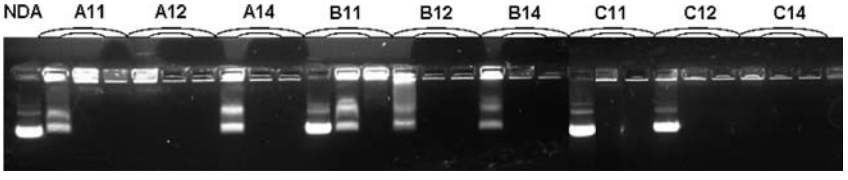

Figure 2. Agarose gel electrophoresis of PEA/DNA complexes at different weight ratios (the weight ratios of PEA/DNA = 0.5, 1.0, 2.0 from left to right for each sample).

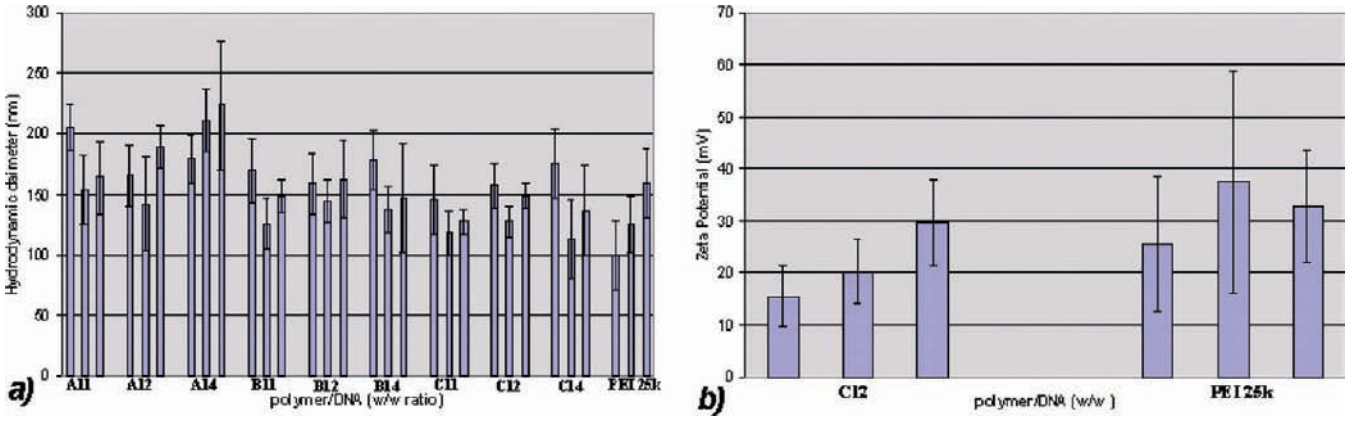

Figure 3. Biophysical properties of PEA/DNA complexes at various weight ratios (2, 5, 10). (a) Particle size of PEA/DNA complexes, (b) Zeta potential of PEA/DNA complexes (error bars represent standard deviation).

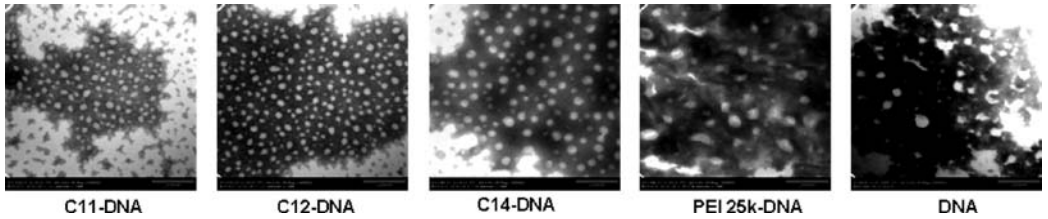

Figure 4. TEM images of polymer/DNA (5:1) complexes (scale bar 200 nm).

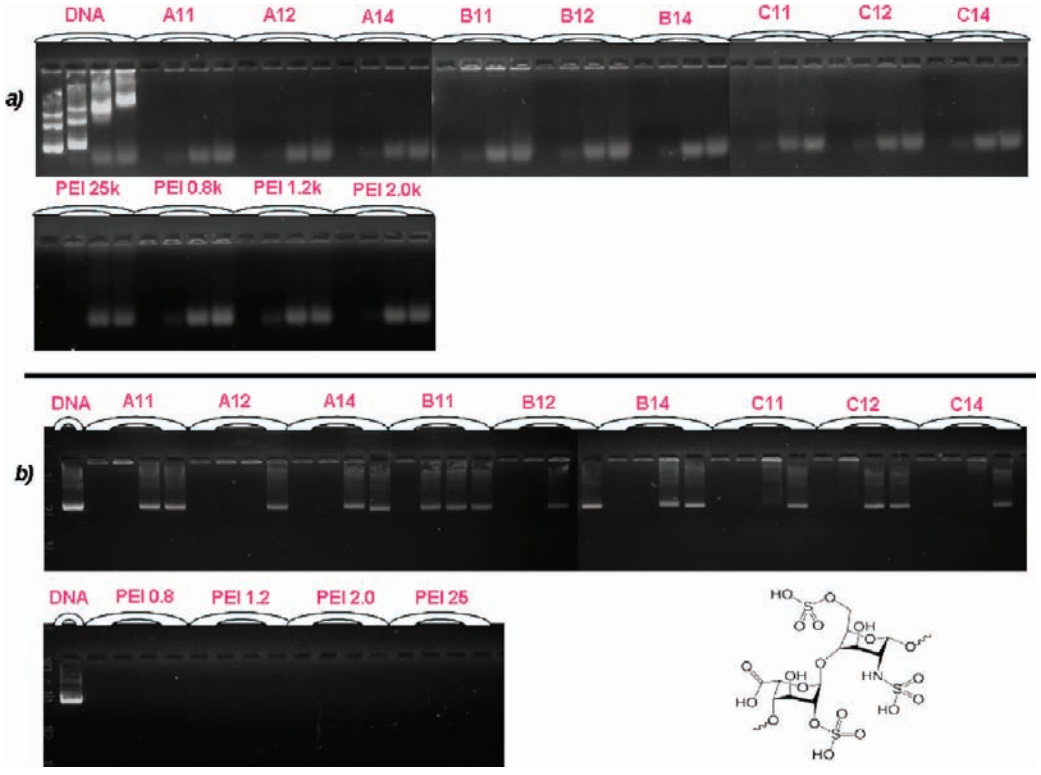

Figure 5. Stability of Complexes [Polymer/DNA = 5/1(weight ratio)] to serum or heparin: (a) In the presence of serum. Four lanes for each polymer with FBS concentration of 0%, 10%, 25%, 50% from left to right. The lowest bands are nonspecific binding of EB to serum components. (b) Sodium heparin (0, 10, 25, 50 μg/mL) from left to right.

prepared at different ratios and bovine serum was added to a final concentration of 0%, 10%, 25%, and 50%, and the mixture was analyzed by gel electrophoresis. As shown in Figure 5a, plasmid DNA reacted with serum components to form complexes indicated by an increase in the size of the DNA bands when the amount of FBS increased. This is in agreement with previous reports by Hao et al.[25] When plasmid DNA was bound to the PEAs at polymer/DNA ratio of 5, however, serum had no effect on the polymer-bound DNA at the concentration, and this was similar to the complexed DNA with all PEIs. This

dx.doi.org/10.1021/bc200674e | *Bioconjugate Chem.* 2012, 23, 837–845

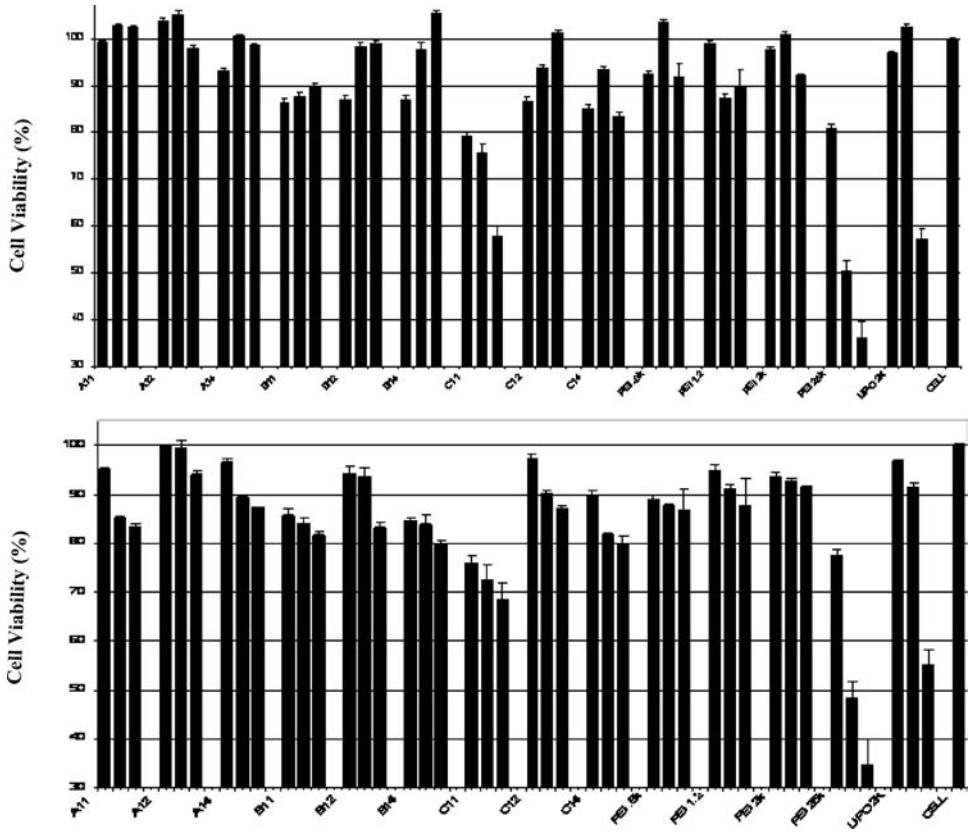

Figure 6. Cell viability of PEA at various concentrations (10, 25, 50 μg/mL in different cell lines: (top) CHO, (bottom) C2C12 by MTS assay (mean ± SD, n = 3).

result suggests that LPEIs in the PEAs maintain their binding affinity and strength, preventing the bound DNA from being replaced by serum components.

Sodium heparin with strong negative charges has been used to evaluate binding strength between polymer and plasmid DNA.[30,31] At a polymer/DNA weight ratio of 5 in the presence of 10 μg/mL sodium heparin, EB signals for DNA remained in the loading well in all samples with PEAs except B11. Nearly all DNA was dissociated from the B11/pDNA complex indicated by the similarity of the EB signal pattern to that observed in samples with DNA alone. This may be related to the lower PEI contents in B11 compared to other PEAs. Increasing concentration of sodium heparin to 25 μg/mL led to near complete dissociation of DNA from more PEAs including A11, A14, B11, B12, B14 and C12. However, the majority of DNA with the A12 and C14 remained PEA-bound, probably due to their higher PEI composition. Almost all DNA was dissociated from the PEA/DNA complexes when the concentration of sodium heparin increased to 50 μg/mL (Figure 5b). In contrast to all PEAs, all PEI/DNA complexes remained compacted in the presence of sodium heparin even at 50 μg/mL. The results further confirm the increased affinity of PEAs with increasing M_w, and the presence of TAEI in the PEAs weakens the binding of LPEI to DNA. The concentration-dependent release of DNA from polymer/DNA complexes in the presence of highly negative charged heparin, the abundance of which varies considerably among tissues, may help to design polymers for controlled release of cargo DNA when specific tissues are targeted.

Cell Cytotoxicity. Among the many attempts to reduce cytotoxicity of gene carriers so far, the most popular strategy is the use of biodegradable polymers through ester linkages.[15−18,27,32] The PEA polymers with LPEI and biodegradable linkage are expected to reduce cytotoxicity due to the low toxicity of building blocks and biodegradation products from the ester backbone in physiological conditions. Using both C2C12 myoblasts and CHO cells with MTS -based cell viability assay 24 h after the treatment, PEI 25K showed much higher cytotoxicity reflected by the fact that over 50% of the cells were killed at the concentration of 25 μg/mL. In contrast, the PEAs have remarkably low cytotoxicity in both cell lines, with most PEAs showing above 80% cell viability even at a high dose of 50 μg/mL as depicted in Figure 6. Only C11 showed slightly higher toxicity than the LPEIs, likely by reason of the higher molecular weight compared with other PEAs. The low cytotoxicity of the PEAs is undoubtedly due to the low toxicity of LPEIs. The increase in the total unites of LPEI within the PEAs without significantly increase in toxicity may be attributed to a more dispersed PEI components within the TAEI cross-linked structures. High-molecular-weight PEI 25k aggregates with DNA and impairs important membrane function, therefore reducing cell viability.[33] Lipofectamine-2000 also reduced the cell viability down below 60% in both cell lines at the dose of 50 μg/mL. The favorable cytotoxicity results of the new PEAs clearly demonstrate their potential as a safe gene delivery carrier.

Transfection Efficiency of PEAs *in Vitro*. The efficiency of PEAs to deliver pDNA in cell culture was determined using GFP as the transgene with its expression levels measured by flow cytometry quantitatively and also recorded with microscopy semiquantitatively in CHO, C2C12, and HSK cell lines. pDNA was complexed with each PEA at various

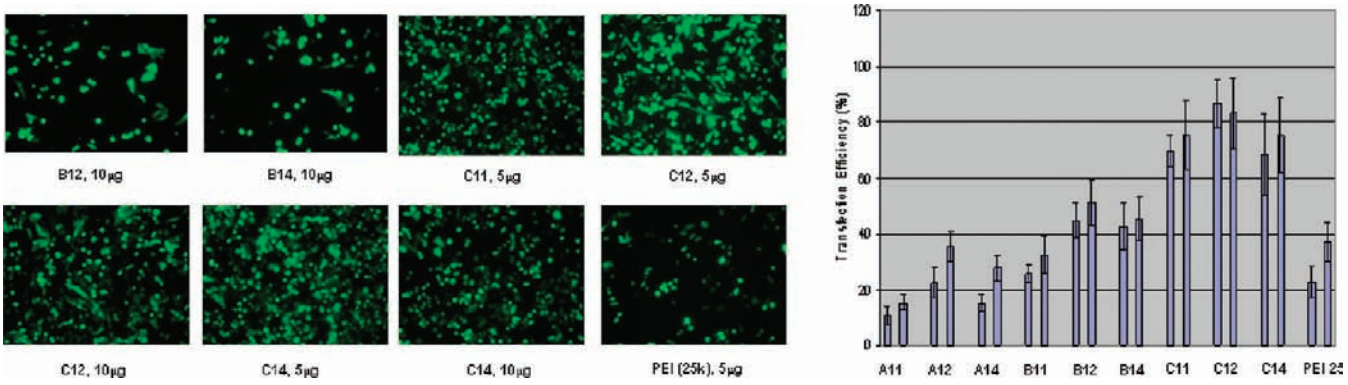

Figure 7. GFP expressed in CHO cell line transfected with PEA/pDNA complexes at weight ratios of 5 and 10 after 48 h incubation (PEI 25K used at 2 and 5 due to its high toxicity): (Left) Fluorescent images of pEGFP reporter gene expression. (Right) Flow cytometry analysis (n = 3, Error bar represents SD).

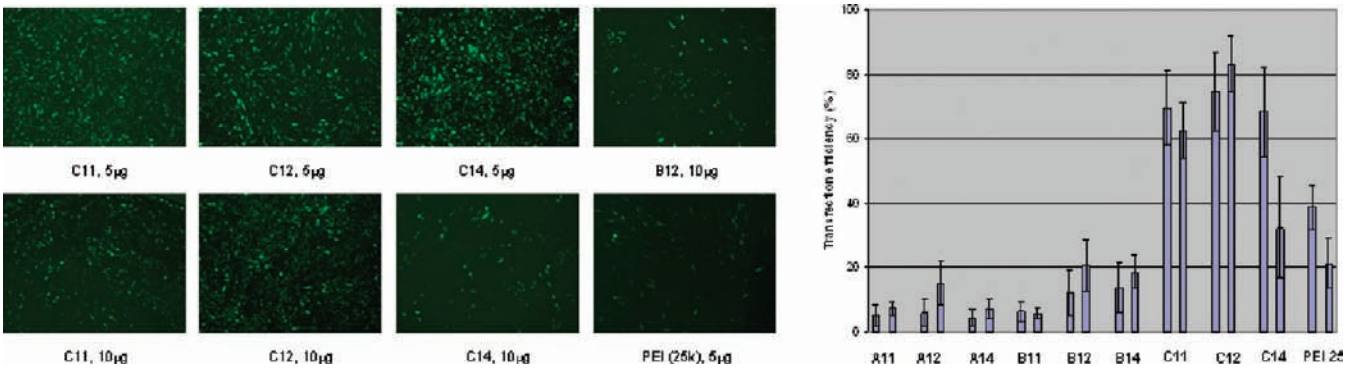

Figure 8. GFP expressed in C2C12 cell line transfected with PEA/pDNA complexes at the weight ratios of 5 and 10 after 48 h incubation. (Left) Fluorescent images of pEGFP reporter gene expression. (Right) Flow cytometry analysis (n = 3, Error bar represents SD).

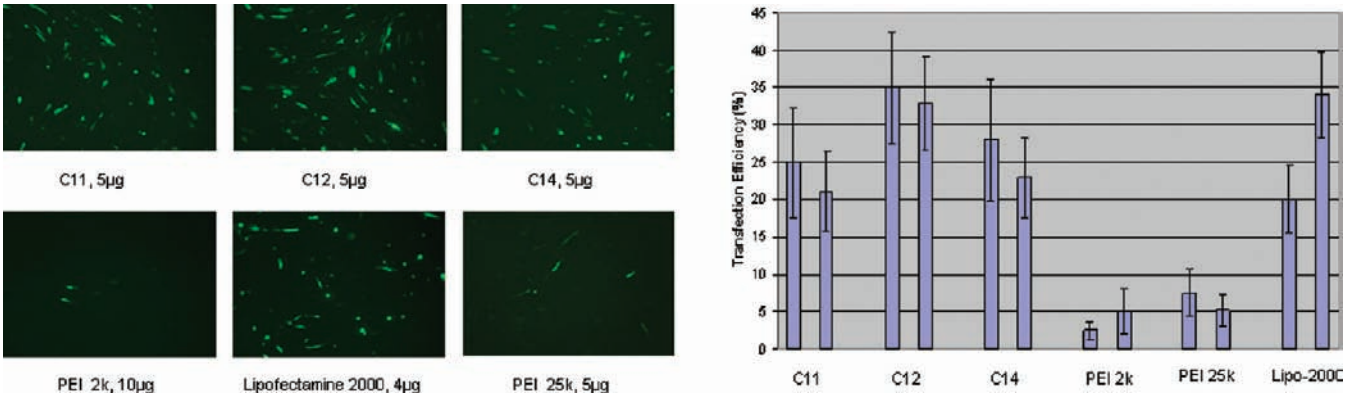

Figure 9. GFP expressed in HSK cell line treated with PEA/pDNA complexes at the weight ratios of 5 and 10 after 48 h incubation. (Lipofectamine-2000 used at 2 and 4): (Left) Fluorescent images of pEGFP reporter gene expression. (Right) Flow cytometry analysis (n = 3, Error bar represents SD).

weight ratios of 2, 5, and 10. All PEAs showed an increase in reporter gene expression when compared to the cells treated with GFP only. As depicted in Figure 7, increasing transfection efficiency (TE) in CHO cells was detected in the order of C12 > C11,C14 ≫ Bs > As. The highest transgene expression was observed in the cells treated with C12 (5 μg) with 87% TE. Similar efficiencies in transgene expression were detected in the C2C12 cells, with C12 (10 μg) producing up to 82% GFP expression (Figure 8). However, levels of transgene expression were much lower in the HSK cells (Figure 9), indicating a cell-type-dependent nature for TE with PEAs. Nevertheless, relative transgene expression remained accordant with that observed in the other two cell lines. The efficiency of transgene expression with the C serial polymers was clearly higher than that of commercially available Lipofectamine-2000 and PEI 25k. The fact that TE of C series is higher than the TEs of A or B series as well as PEI 25k indicates the importance of a balanced positive charge for effective gene delivery. Specifically, the size of cross-linked PEIs, the structural arrangement of the positive charge, as well as toxicity of polymers could all contribute to TE. Transfection efficiency with PEAs was affected by the presence of serum, with GFP expression decreasing from 80% to 64% without serum to 55−30% in the presence of serum (SI Figure S1). Nevertheless, TE with PEI 25K was even more

dx.doi.org/10.1021/bc200674e | Bioconjugate Chem. 2012, 23, 837−845

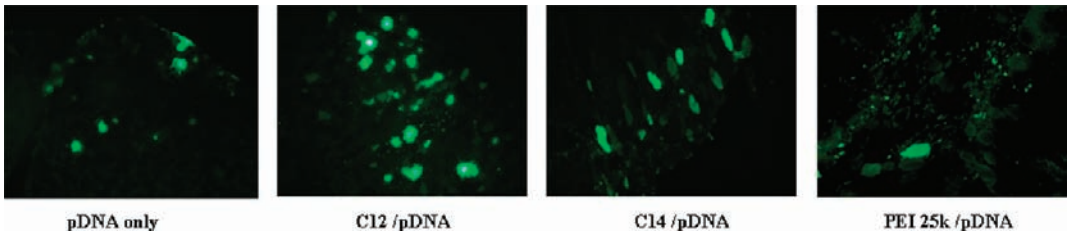

Figure 10. Restoration of dystrophin in muscles of *mdx* mice (age 4−6 weeks) 5 days after i.m. injection.

significantly affected, decreasing from 22% without serum to only 5% in the presence of serum.

Transfection Efficiency of PEAs *in Vivo*. Based on the TE and cytotoxicity data obtained from *in vitro* systems, we selected C12 and C14 as candidates to further examine their potential for gene delivery in muscle by intramuscular (i.m.) injection. Plasmid GFP expression vector at the dose of 10 μg combined with 10 μg corresponding polymer was injected into the TA muscles of the *mdx* mice, a model of Duchenne muscular dystrophy, with GFP expression examined 5 days after the injection. The numbers of GFP expressing muscle fibers were 125 ± 15 and 72 ± 13 for C12 and C14, respectively. As a control, PEI 25k at the dose of 5 μg induced only 15−20 positive muscle fibers (Figure 10). Histologically, there was limited muscle damage after the treatment with the two polymers at the dose tested. However, similar damage was also observed in the muscles injected with saline only. In contrast, 5 μg PEI 25k induced significantly larger areas of muscle damage indicated by the presence of necrotic fibers and focal infiltrations. These results therefore indicate that the PEA polymers, especially the TAEI cross-linked PEI 2k polymers, have the potential for *in vivo* applications as gene delivery carriers.

CONCLUSIONS

Biodegradable PEAs were successfully prepared through the Michael addition reaction between TAEI and LPEI and exhibited biophysical properties suitable as gene delivery carrier. These properties include a desirable polyplex size below 200 nm, a surface charge in the range 11.5−33.5 mV under the tested concentration, and stability in the presence of serum and sodium heparin. The LPEI-based PEAs, although larger than their corresponding parent PEIs, still have relatively low molecular weight when compared to PEI 25k. This together with a more dispersed positive charge likely explains their low toxicity in cell culture and *in vivo*. The use of TAEI linkage provides hydrolytic degradation of PEAs, thus could also contribute the low toxicity. The higher levels of transgene expression with PEAs over parent PEIs suggest that optimization of polymer size and density of the positively charged PEI group in combination with consideration of biodegradability could achieve enhanced gene delivery of PEI-based polymers without increasing toxicity.

ASSOCIATED CONTENT

Supporting Information

In vitro transfection examined in CHO cell line with and without serum. This material is available free of charge via the Internet at http://pubs.acs.org.

AUTHOR INFORMATION

Corresponding Author

*Mingxing Wang: Tel. 1-7043555588; Fax 1-704-355-1679; E-mail: mingxing.wang@carolinashealthcare.org. Qilong Lu: Tel. 1-7043551701; Fax 1-704-355-1679; E-mail: qi.lu@carolinashealthcare.org.

Notes

The authors declare no competing financial interest.

ACKNOWLEDGMENTS

The authors would like to thank Dr. Craig A. Ogle at Department of Chemistry, University of North Carolina, Charlotte, for help in measuring ^{1}H NMR and DLS. We also thank Ms. Daisy Ridings and Mr. David Radoff for TEM analysis; Dr. David M. Foureau for FACS analysis, and Dr. Tony Blaeser for constructive proof reading. The authors gratefully acknowledge the support from Carolinas Muscular Dystrophy Research Endowment at the Carolinas HealthCare Foundation and Carolinas Medical Center, Charlotte, NC. This work is also supported by Department of Defense (USAMRMC) W81XWH-09-1-0599.

REFERENCES

(1) Kay, M. A., Glorioso, J. C., and Naldini, L. (2001) Viral vectors for gene therapy: the art of turning infectious agents into vehicles of therapeutics. *Nat. Med. 7*, 33−40.

(2) Robbins, P. D., Tahara, H., and Ghivizzani, S. C. (1998) Viral vectors for gene therapy. *Trends Biotechnol. 16*, 35−40.

(3) Lungwitz, U., Breunig, M., Blunk, T., and Gopferich, A. (2005) Polyethylenimine-based non-viral gene delivery systems. *Eur. J. Pharm. Biopharm. 60*, 247−266.

(4) Neu, M., Fischer, D., and Kissel, T. (2005) Recent advances in rational gene transfer vector design based on poly(ethylene imine) and its derivatives. *J. Gene Med. 7*, 992−1009.

(5) Verbaan, F. J., Oussoren, C., van Dam, I. M., Takakura, Y., Hashida, M., Crommelin, D. J. A., Hennink, W. E., and Storm, G. (2001) The fate of poly(2-dimethyl amino ethyl)methacrylate-based polyplexes after intravenous administration. *Int. J. Pharm. 214*, 99−101.

(6) Garrett, S. W., Davies, O. R., Milroy, D. A., Wood, P. J., Pouton, C. W., and Threadgill, M. D. (2000) Synthesis and characterisation of polyamine-poly(ethylene glycol) constructs for DNA binding and gene delivery. *Bioorg. Med. Chem. 8*, 1779−1797.

(7) Williams, J. H., Sirsi, S. R., Latta, D. R., and Lutz, G. J. (2006) Induction of dystrophin expression by exon skipping in mdx mice following intramuscular injection of antisense oligonucleotides complexed with PEG-PEI copolymers. *Mol. Ther. 14*, 88−96.

(8) Luo, D., and Saltzman, W. M. (2000) Synthetic DNA delivery systems. *Nat. Biotechnol. 18*, 33−37.

(9) Boussif, O., Lezoualch, F., Zanta, M. A., Mergny, M. D., Scherman, D., Demeneix, B., and Behr, J. P. (1995) A versatile vector for gene and oligonucleotide transfer into cells in culture and in vivo: polyethylenimine. *Proc. Natl. Acad. Sci. U.S.A. 92*, 7297−7301.

(10) Tang, M. X., and Szoka, F. C. (1997) The influence of polymer structure on the interactions of cationic polymers with DNA and morphology of the resulting complexes. *Gene Ther. 4*, 823−832.
(11) Vijayanathan, V., Thomas, T., and Thomas, T. J. (2002) DNA nanoparticles and development of DNA delivery vehicles for gene therapy. *Biochemistry 41*, 14085−14094.
(12) Kunath, K., von Harpe, A., Fischer, D., Petersen, H., Bickel, U., Voigt, K., and Kissel, T. (2003) Low-molecular-weight polyethylenimine as non-viral vetor for DNA delivery; comparison of physicochemical properties, transfection efficiency and in vivo distribution with high-molecualr weight polyethylenimine. *J. Controlled Release 89*, 113−125.
(13) Godbey, W. T., Wu, K. K., and Mikos, A. G. (1999) Size matters: molecular weight affects the efficiency of poly(ethylenimine) as a gene delivery. *J. Biomed. Mater. Res. 45*, 268−275.
(14) Thomas, M., Ge, Q., Lu, J. J., Chen, J., and Klibanov, A. M. (2005) Cross-linked small polyethylenimines: while still nontoxic, deliver DNA efficiently to mammalian cells in vitro and in vivo. *Pharm. Res. 22*, 373−380.
(15) Park, M. R., Han, K. O., Cho, M. H., Nah, J. W., Choi, Y. J., and Cho, C. S. (2005) Degradable polyethylenimine-alt-poly(ethylene glycol) copolymers as novel gene carriers. *J. Controlled Release 105*, 367−380.
(16) Arote, R. B., Kim, T. H., Kim, Y. K., Hwang, S. K., Jiang, H. L., Song, H. H., Nah, J. W., Cho, M. H., and Cho, C. S. (2007) A biodegradable poly(ester amine) based on polycaprolactone and polyethylenimine as a gene carrier. *Biomaterials 28*, 735−744.
(17) Kim, T. H., Cook, S. E., Arote, R. B., Cho, M. H., Nah, J. W., Choi, Y. J., and Cho, C. S. (2007) A degradable hyperbranched poly(ester amine) based on poloxamer diacrylate and polyethylenimine as a gene carrier. *Macromol. Biosci. 7*, 611−619.
(18) Arote, R. B., Hwang, S. K., Yoo, M. K., Jere, D., Jiang, H. L., Kim, Y. K., Choi, Y. J., Nah, J. W., Cho, M. H., and Cho, C. S. (2008) Biodegradable poly(ester amine) based on glycerol dimethacrylate and polyethylenimine as a gene carrier. *J. Gene. Med. 10*, 1223−1235.
(19) Arote, R. B., Lee, E. S., Jiang, H. L., Kim, Y. K., Choi, Y. J., Cho, M. H., and Cho, C. S. (2009) Efficient gene delivery with osmotically active and hyperbranched poly(ester amine)s. *Bioconjugate Chem. 20*, 2231−2241.
(20) Seifer, G. B. (2002) Cyanuric acid and cyanurates. *Russian Journal of Coordinate Chemistry 28*, 301−324.
(21) Grzegorz, B. (2006) Recent applications of 2,4,6-trichloro-1,3,5-triazine and its derivatives in organic synthesis. *Tetrahedron 62*, 9507−9522.
(22) Lim, Y. B., Kim, S. M., Suh, H., and Park, J. S. (2002) Biodegradable, endosome disruptive, and cationic network-type polymer as a highly efficient and nontoxic gene delivery carrier. *Bioconjugate Chem. 13*, 952−957.
(23) von Harpe, A., Petersen, H., Li, Y., and Kissel, T. (2000) Characterization of commercially available and synthesized polyethylenimines for gene delivery. *J. Controlled Release 69*, 309−322.
(24) Dong, W., Jin, G. H., Li, S. F., Sun, Q. M., Ma, D. Y., and Hua, Z. C. (2006) Cross-linked polyethylenimine as potential DNA vector for gene delivery with high efficiency and low cytotoxicity. *Acta Biochim. Biophys. Sin. 38*, 780−787.
(25) Hao, J., Sha, X., Tang, Y., Jiang, Y., Zhang, Z., Zhang, W., Li, Y., and Fang, X. (2009) Enhanced transfection of polyplexes based on pluronic-polypropylenimine dendrimer for gene transfer. *Arch. Pharm. Res 32*, 1045−1054.
(26) Plank, C., Tang, M. X., Wolfe, A. R., and Szoka, F. C., Jr. (1999) Branched cationic peptides for gene delivery: role of type and number of cationic residues in formation and in vitro activity of DNA polyplexes. *Hum. Gene Ther. 10*, 319−332.
(27) Lynn, D. M., and Langer, R. (2000) Degradable poly(b-amino esters): synthesis, characterization, and self-assembly with plasmid DNA. *J. Am. Chem. Soc. 122*, 10761−10768.
(28) Lynn, D., Anderson, D., Putnam, D., and Langer, R. (2001) Accelerated discovery of synthetic transfection vectors: Parallel synthesis and screening of a degradable polymer library. *J. Am. Chem. Soc. 123*, 8155−8156.
(29) Forrest, M. L., Koerber, J. K., and Pack, D. W. (2003) A degradable polyethylenimine derivative with low toxicity for highly efficient gene delivery. *Bioconjugate Chem. 14*, 934−940.
(30) Clamme, J. P., Azoulay, J., and Mely, Y. (2003) Monitoring of the formation and dissociation of polyethyleneimine/dNA complexes by two photon flurorescence correlation spectroscopy. *Biophys. J. 84*, 1960−1968.
(31) Moret, I., Peris, J. E., Guillem, V. M., Benet, M., Revert, F., Dasi, F., Crespo, A., and Alino, S. F. (2001) Stability of PEI DNA and DOTAP DNA complexes: effect of alkaline pH, heparin and serum. *J. Controlled Release 76*, 169−181.
(32) Lim, Y. B., Han, S. O., Kong, H. U., Lee, Y., Park, J. S., Jeong, B., and Kim, S. W. (2000) Biodegradable polyester, poly[alpha-(4-aminobutyl)-L-glycolic acid], as a non-toxic gene carrier. *Pharm. Res. 17*, 811−816.
(33) Fischer, D., Bieber, T., Li, Y., Elsasser, H. P., and Kissel, T. (1999) A novel non-viral vector for DNA delivery based on low molecular weight, branched polyethylenimine: effect of molecular weight on transfection efficiency and cytotoxicity. *Pharm. Res. 16*, 1273−1279.

Bioconjugate Chemistry

Article

pubs.acs.org/bc

Vinyl Sulfone Functionalization: A Feasible Approach for the Study of the Lectin−Carbohydrate Interactions

Francisco Javier Lopez-Jaramillo,[†] Mariano Ortega-Muñoz,[†] Alicia Megia-Fernandez, Fernando Hernandez-Mateo,[†] and Francisco Santoyo-Gonzalez*[,†]

[†]Departamento de Química Orgánica, Instituto de Biotecnología, Facultad de Ciencias, Universidad de Granada, 18071 Granada, Spain

Supporting Information

ABSTRACT: Carbohydrate-mediated molecular recognition is involved in many biological aspects such as cellular adhesion, immune response, blood coagulation, inflammation, and infection. Considering the crucial importance of such biological events in which proteins are normally involved, synthetic saccharide-based systems have emerged as powerful tools for the understanding of protein−carbohydrate interactions. As a new approach to create saccharide-based systems, a set of representative monosaccharides (D-mannose, D-glucose, *N*-acetyl-D-glucosamine, and L-fucose) and disaccharides (lactose, maltose, and melibiose) were derivatized at their anomeric carbon with a vinyl sulfone group spanned by an ethylthio linker. This vinyl sulfone functionalization is demonstrated to be a general strategy for the covalent linkage of a saccharide in mild conditions via Michael-type additions with the amine and thiol groups from functionalized supports and those naturally present in biomolecules. The introduction of the ethylthio linker between the biorecognizable element (i.e., saccharide) and the reactive group (i.e., vinyl sulfone) was found to preserve the functionality of the former. The capability of the vinyl sulfone saccharides for the study of lectin−carbohydrate interactions was demonstrated by (i) immobilizing them on both amine-functionalized supports (glass slides and microwell plates) and polylysine-coated glass slides to create sugar arrays that selectively bind lectins (ii) coupling to model proteins to yield neoglycoproteins that are recognized by lectins and (iii) using vinyl sulfone saccharides as tags to allow the detection of the labeled biomolecule by HRP-lectins. The above results were further put tothe test with a real case: detection of carbohydrate binding proteins present in rice (*Oryza sativa*).

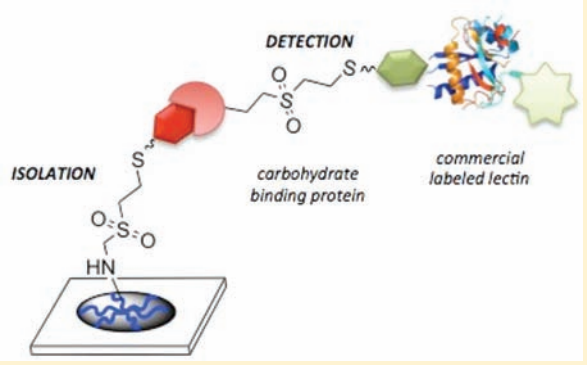

INTRODUCTION

Among the different post-translational modifications of proteins, glycosylation is the most prevalent one, occurring in at least 50% of all proteins.[1] Carbohydrate-mediated molecular recognition is involved in many biological aspects. At the cell membrane, it plays an important role in physiological events such as cellular adhesion, immune response, or host−pathogen interactions[2−4] and many molecular processes as diverse as blood coagulation,[5] inflammation,[6] or host recognition; and immune responses to parasitic helminths[7] are also regulated by carbohydrate biosignals. Thus, Glycomics (the study of the *glycocode*) is an emergent field in the postgenomic era. However, carbohydrate research has to face several challenges: (i) the range of carbohydrate structures is enormously diverse; (ii) the biosynthesis of carbohydrates is not template-driven, as nucleic acid or proteins, their obtention in large quantities and/or homogeneous form being far from trivial; (iii) traditional methods to analyze carbohydrate−protein interactions (isothermal calorimetry, plasmon resonance, enzyme-linked lectin assay) are time-consuming and labor-intensive and require large quantities of each carbohydrate to study; (iv) carbohydrate−protein interactions are of low affinity and poor selectivity, multivalent presentation of the carbohydrate being necessary for effective binding.[8−11]

Array technology has been proven as a convenient approach to study the protein−carbohydrate interactions that overcome some of these challenges.[12−14] Historically, several array formats have been used for many years, and glycoconjugates have been immobilized on silica plates,[15] synthesized on beads,[16] or immobilized in wells of ELISA plates.[17] The advent of robotic arraying and high-resolution imaging has permitted a degree of miniaturization that allows the simultaneous analysis of several thousands of carbohydrates on a single standard microscope slide. In past years, there has been an explosion of methods for creating modern versions of glycan microarrays, most of which use (or can be adapted to use) state-of-the-art array technology developed for printing DNA microarrays on glass slides. They can be divided into two main categories

Received: December 22, 2011
Revised: March 1, 2012
Published: March 21, 2012

depending on the type of glycan immobilization: by covalent attachment or by physical adsorption. Polysaccharide materials derived from natural sources can be readily and randomly immobilized on supports by hydrophobic physical adsorption[18−20] or by charge-based interaction.[21] However, the immobilization of oligosaccharides is less straightforward due to their hydrophilic nature, and many different methodologies have been described in a number of reviews.[13,14,22] One approach is to conjugate the oligosaccharide to a tag to promote noncovalent interactions with the support. Thus, saccharides have been conjugated to (i) lipids to generate neoglycolipids (NGL) with amphipathic properties[23−25] and (ii) biotin to exploit the biotin−streptavidin affinity.[26,27] An alternative approach relies on the derivatization of the carbohydrate to incorporate specific functional groups that yield a covalent bond with the support. The most popular strategies are the amide bond formation via an activated ester,[28−33] the use of click chemistry,[31,34−37] and the thiol maleimide ligation.[38−43] Another alternative is based on the coupling of the saccharide to a protein[39,44] or DNA[45,46] that acts as a tag to yield the immobilization on a conveniently functionalized support. Regardless of the approach, the immobilization strategy is important from the point of view of the presentation of the glycan, since the low affinity and multivalent character of the carbohydrate−protein interactions make the presentation of the glycan one of the key factors to be taken into account in the fabrication of arrays.[47] Features of presentation such as spacing and orientation of carbohydrates, nature of the linker, or ligand density are relevant.[48−50] Passive adsorption of large oligosaccharides leads to a random orientation that may not reflect their orientation in living systems, while potential disadvantages of the direct covalent immobilization methods are the high concentration of the saccharide required, the variation of the immobilization efficiency depending on the saccharide, and the role of the linker in nonspecific protein adsorption.[51] As a result, the immobilization method plays a major role and different array platforms may yield significantly different results.[47]

Another important topic in Glycomics is protein glycosylation, since it has been demonstrated to be involved in processes as diverse and important as protein folding, protein stabilization, or intracellular trafficking, and altered glycosylation patterns have been involved in diseases.[52] On the other hand, the effect of the carbohydrate fraction on the physicochemical properties of glycoproteins, such as viscosity, solubility, isoelectric point, degree of hydration, and structural roles have been known for some time.[53] Studies on native glycosylated, carbohydrate-depleted, and recombinant non-glycosylated proteins have revealed the influence of the carbohydrate moiety on the stabilization of proteins, their conformation, protection from proteolysis, and enhancement in solubility.[54,55] However, the fact that glycosylation is not template-driven makes the large-scale production of glycoproteins a challenging task that has been approached by biological, enzymatic, and chemical strategies.[56−59] Biological strategies comprise approaches such as site-directed mutagenesis to introduce a glycosylation site, molecular and cell biological techniques to increase the biosynthesis, codon suppression technology, and expressed protein ligation. Enzymatic strategies make use of in vitro enzyme-catalyzed techniques based on glycosyltransferases and glycoprotein remodeling. Finally, chemical strategies rely on the formation of glycan−protein bonds via reactions that can be either chemoselective and site-specific or generic and non-site-specific. Among the chemical strategies currently in use, Cys and Lys are the two naturally occurring residues most commonly targeted for reaction with suitable derivatized saccharides. The abundance and exposure of the Lys lead to non-site-specific glycosylation, whereas the rarity and nucleophility of the Cys make it a good nucleophile to react with thiol-specific electrophiles and yield site-specific glycosylation.

In this general frame, new functionalizations to efficiently promote the reaction of oligosaccharides with solid supports and yield their immobilization or the glycosylation of proteins are desirable. Vinyl sulfone (VS) derivatization may be an attractive strategy, since vinyl sulfone is a very stable functional group whose reactivity toward amine and/or thiol groups by means of the so-called Michael-type addition[60,61] is well-known although not fully exploited in the context of biomolecules.[62−65] The applications of this function on Proteomics have been recently reviewed,[66] and our previous results have demonstrated the feasibility of the vinyl sulfone derivatization as a versatile function to yield the coupling of tags to proteins.[64−69] In the context of carbohydrate research, vinyl sulfone derivatized carbohydrates have been synthesized as enofuranosides and enopyranosides with the sulfone group directly attached either to the endocyclic double bond or to an exocyclic carbon, and their reactivity toward nucleophiles and applications as synthetic intermediates have been reviewed.[70,71] However, the vinyl sulfone derivatization of the anomeric carbon has not been subjected to such a systematic study despite its biological relevance as the attachment point to other biomolecules, such as lipids or amino acids, through glycosidic linkages. We have already demonstrated the feasibility of the vinyl sulfone functionalization of the anomeric carbon as a procedure for the chemical glycosylation of proteins,[67−69] and in this paper we focused on its application in the context of glycoscience to explore protein−carbohydrate interactions.

EXPERIMENTAL PROCEDURE

Immobilization of Vinyl Sulfone Saccharides (VS-SCH) on Solid Supports. *Immobilization of Vinyl Sulfone D-Mannose (VS-D-Man, 1) on Commercial Amino-Functionalized Glass Slides and Interaction with FITC-ConA.* Commercial amino-functionalized glass slides (Nunc) were coated with silicone isolators (Sigma-Aldrich) to define the wells that were functionalized by reaction with 75 μL of 42 mM, 4.2 mM, 2.15 mM, 1.05 mM, 0.5 mM, 0.25 mM, and 0.125 mM **VS-D-Man** (**1**) solutions in 100 mM HEPES pH 8, 10% glycerol for 24 h at 37 °C in a recipient containing a large volume of 100 mM HEPES pH 8, 10% glycerol, and 685 mM NaCl to prevent desiccation. The unreacted **1** was removed by washing with 50 mM HEPES pH 7.4, 134 mM NaCl, 0.1% (v/v) Tween 20 (3 × 90 μL well). The amount of **1** reacted in each well was revealed by incubation with 75 μL of a solution of 1 μg/mL FITC-ConA in 50 mM HEPES pH 7.4, 134 mM NaCl, 1 mM $CaCl_2$, 1 mM $MnCl_2$, Tween 20 for 1 h at 37 °C, and the unbound FITC-ConA was removed by washing with 50 mM HEPES pH 7.4, 134 mM NaCl, 1 mM $CaCl_2$, 1 mM $MnCl_2$, and Tween 20 (3 × 90 μL well). The fluorescence was estimated from the images taken with an epifluorescence microscope (Olympus IX71 equipped with a U-MNB2 fluorescence mirror unit) at 200 and 50 ms.

Immobilization of Vinyl Sulfone Saccharides (VS-SCH) on Commercial Amino-Functionalized Plates. Commercial polystyrene wells functionalized with secondary amine groups

dx.doi.org/10.1021/bc200681c | Bioconjugate Chem. 2012, 23, 846−855

(CovaLink NH plates, Nunc) were reacted with the pool of **VS-SCH**. Each well was incubated with 100 μL of 1 mM of the **VS-SCH** in 100 mM carbonate buffer pH 9 at 37 °C for 8 h. The unreacted carbohydrate was removed by washing with PBST (3 × 300 μL/well for 5 min). Covalent immobilized carbohydrate was incubated with 100 μL of HRP coupled lectin (ConA, 2 μg/mL and 1 mM $CaCl_2/MnCl_2$; UEA, 1 μg/mL; PNA, 1 μg/mL; WGA, 0.2 μg/mL) in PBST at 37 °C for 1 h, and the unbound lectin was washed with PBST (3 × 400 μL/well for 3 min), revealed by incubation with 200 μL of 100 mM PO_4Na_2H, 50 mM citrate pH 5, 0.04% (w/v) *o*-phenylenediamine dihydrochloride, 0.05% (v/v) H_2O_2 at 37 °C for 40 min and then addition of 100 μL 1.5 M H_2SO_4. The resulting optical density was measured with a Sunrise absorbance reader (Tecan).

Immobilization of Vinyl Sulfone Saccharides (VS-SCH) on Polylysine-Coated Glass Slides. Commercial glass slides were cleaned by soaking in a liquid wash solution thoroughly rinsed with distilled water and then flamed. Wells were defined with silicone isolators (Sigma-Aldrich) and coated by incubation with 40 μL of 0.1 mg/mL polylysine solution in water (Sigma) at room temperature for 5 min. After rinsing thoroughly with distilled water, each well was reacted with 30 μL of the suitable solutions of vinyl sulfone saccharide (ranging from 19 μM to 5 mM) in 250 mM HEPES pH 8 at 37 °C for 30 min, and the unreacted species were removed by incubation with PBST (3 × 45 μL/well for 3 min). When the unreacted amine groups from polylysine were blocked, two additional steps were introduced: (i) reaction with 30 μL of 5 mM methoxytetra(ethylene glycol)vinyl sulfone (2,5,8,11,14-pentaoxa-17-thianonadec-18-ene 17,17-dioxide) in 250 mM HEPES pH 8 at 37 °C for 30 min and (ii) incubation with PBST (3 × 45 μL for 3 min) to remove the excess tetra(ethylene glycol) derivative.

The biological functionality of the carbohydrates covalently linked to the polylysine-coated glass slides was assayed by incubation with HRP-coupled lectins (ConA, 2 μg/mL and 1 mM $CaCl_2/MnCl_2$; UEA, 1 μg/mL; PNA, 1 μg/mL; WGA, 0.2 μg/mL; and dilutions 1/10 and 1/100 of them) in PBST supplemented with ionic strength (from 0% to 12% (w/v) NaCl) at 37 °C for 30 min. The presence of HRP-coupled lectins was revealed by incubation of each well with 30 μL of 100 mM PO_4Na_2H, 50 mM citrate pH 5, 0.2% (w/v) *o*-phenylenediamine dihydrochloride, 0.13% (v/v) H_2O_2 at 37 °C for 30 min, and then addition of 10 μL of 1.5 M H_2SO_4 .

Synthesis of Neoglycoproteins and Interaction with Lectins. VS-SCH (1 μequiv) was reacted with model proteins (0.625 μequiv, i.e., molecular weight divided by the number of reactive groups toward vinyl sulfone) in 250 μL of 275 mM HEPES pH 8 at room temperature overnight, except for reaction with lumazine in which the buffer was 56 mM phospate buffer pH 8.7. The interaction with HRP-coupled lectins was carried out by adsorption of 28.5 μg, 57.4 μg, 79.8 μg, or 57.0 μg of glycosylated BSA, ConA, HEW lysozyme, or lumazine synthase, respectively, on ELISA plate wells by incubation in 200 μL 100 mM carbonate buffer pH 9 at 4 °C overnight. Wells were washed with 300 μL PBST (3 × 3 min) and then incubated with 200 μL of HRP coupled lectin (ConA, 2 μg/mL and 1 mM $CaCl_2/MnCl_2$; UEA, 1 μg/mL; PNA, 1 μg/mL; WGA, 0.2 μg/mL) at 37 °C for 1 h. After washing with PBST (3 × 300 μL/3 min), the presence of lectin was detected by the peroxidase activity after stopping with 100 μL of 2 M H_2SO_4 the 30 min incubation at 37 °C with 200 μL of 100 mM PO_4Na_2H, 50 mM citrate pH 5, 0.04% (w/v) *o*-phenylenediamine dihydrochloride, 0.05% (v/v) H_2O_2. Quantification was carried out by measurement of the absorbance at 495 nm with a Sunrise absorbance reader (Tecan).

Application of Vinyl Sulfone Saccharides (VS-SCH) to the Detection of Carbohydrate Binding Proteins. Glass slides were coated with polylysine and reacted with the pool of **VS-SCH 1−7** to create an array as described above. A crude extract of *Oryza sativa* was prepared from rice seedlings previously soaked overnight in PBS buffer (20 g in 70 mL) by homogenization with a mixer and centrifugation at 14 000 rpm to isolate the supernatant. An amount of 30 μL of crude extract per well of the array was incubated at 37 °C for 15 min and then washed with PBS (3 × 30 μL/well for 3 min). The proteins bound to the array were labeled "in situ" by reaction with 20 μL of 3.75 mM **VS-L-Fuc 3** in 125 mM HEPES pH 8 at 37 °C for 1 h, and the excess of **3** was removed by washing with PBS (3 × 30 μL/well for 3 min). The presence of protein bound to the array was detected by incubation of each well with 30 μL of a solution of HRP-coupled lectin in PBST (0.2 μg/mL) supplemented with 8% (w/v) NaCl at 37 °C for 15 min, washing with PBST (3 × 30 μL/3 min), incubation with 30 μL of 100 mM PO_4Na_2H, 50 mM citrate pH 5, 0.2% (w/v) *o*-phenylenediamine dihydrochloride, 0.13% (v/v) H_2O_2 at 37 °C for 30 min and addition of 10 μL of 1.5 M H_2SO_4.

RESULTS AND DISCUSSION

Synthesis of Vinyl Sulfone Saccharides (VS-SCH). Saccharides are branched complex structures comprising core residues, that function primarily as a supporting framework, and terminal residues (antennae), that often serve as recognition markers and modulate biological functions.[52] Thus, the vinyl sulfone functionalization of physiologically relevant carbohydrates to promote their coupling to other biomolecules was first envisaged as a valid approach to easily access saccharide-based systems with biological function. In the present study, four monosaccharides (D-mannose, D-glucose, *N*-acetyl-D-glucosamine, and L-fucose) and three disaccharides (lactose, maltose, and melibiose) were chosen as model sugars and functionalized at the anomeric carbon with a vinyl sulfone group by a simple two-step procedure consisting of (i) preparation of the corresponding glycosyl thiols and (ii) generation of the vinyl sulfone function from those intermediates (Scheme 1). For the implementation of this strategy, the glycosyl thiols were first

Scheme 1. Synthesis of Vinyl Sulfone Saccharides (VS-SCH)[a]

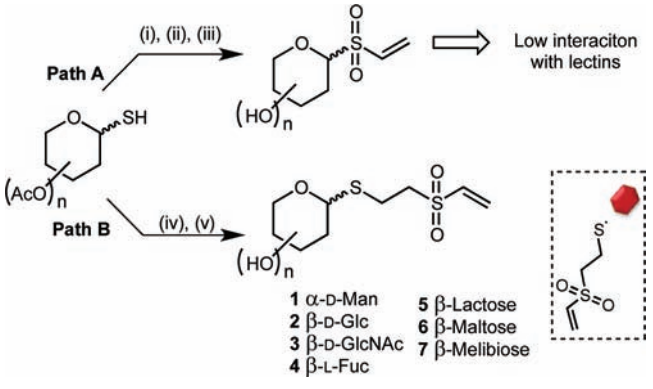

[a]Reagents: (i) $Br(CH_2)_2Cl$; (ii) H_2O_2, AcOH; (iii) MeOH, Et_3N; (iv) NaOMe, MeOH; (v) DVS, SiO_2.

dx.doi.org/10.1021/bc200681c | *Bioconjugate Chem.* 2012, 23, 846−855

synthesized by an approach based on the Lewis acid-catalyzed displacement of an anomeric halide atom or an acetyl group by a thionucleophile[72] that for our particular case was thiourea in the presence of boron trifluoride, since this is a high-yielding procedure that allows the introduction of an alkyl halide.[73] By this way, the per-*O*-acetylated derivative of the 1-thiol glycosides (the α-anomer for D-mannose and the β-anomer of the rest of the selected carbohydrates) were easily prepared in a straightforward manner and isolated as stable solids (for D-mannose, D-glucose, and lactose) or used directly with neither further purification nor isolation (for *N*-acetyl-D-glucosamine, L-fucose, maltose, and mellobiose). Initially, the introduction of the vinyl sulfone group was carried out by reaction of these glycosyl thiols with 1-bromo-2-chloroethane and then sequential oxidation−elimination of the resulting 2-haloethylthioether (Scheme 1, Path A). This approach led to vinyl sulfone saccharide (**VS-SCH**) with the sulfone group directly linked to the anomeric carbon.[70] However, preliminary biological assays (vide infra) showed that the interaction of such sulfone derivatives with lectins was poor,[74] in concordance with previous reports.[75] To overcome this difficulty, a longer spacer between the biorecognizable element (i.e., saccharide) and the reactive group (i.e., VS function) was considerer to be more adequate on the basis of our previous results.[67−69] Simple reaction of the de-*O*-acetylated glycosyl thiols intermediates with commercial divinyl sulfone (DVS) yielded the 1-(vinylsulfonyl) ethylthio saccharides **1**−**7** (Scheme 1, Path B) (see Supporting Information).

Immobilization of Vinyl Sulfone Saccharides on Solid Supports. The reactivity of the vinyl sulfone group toward amines and thiols[60,61] makes feasible the immobilization of the prepared **VS-SCH** on conveniently functionalized supports. In the context of glycoscience, the derivatization of hydroxyl-terminated surfaces with VS groups has been reported.[76] However, amino-functionalized glass slides and microwell plates are common supports used for the analysis of the protein−carbohydrate interactions. For this reason, the suitability of the immobilization of vinyl sulfone saccharides on these supports was evaluated (Figure 1).

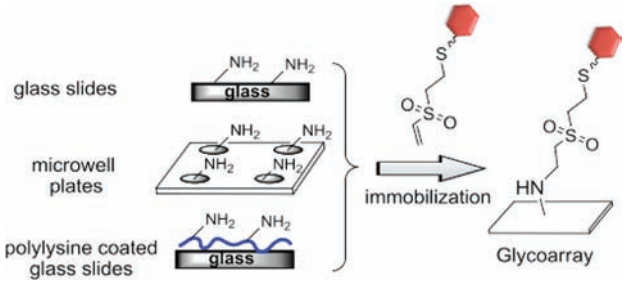

Figure 1. Immobilization of vinyl sulfone saccharides (**VS-SCH**) on amino-functionalized solid supports.

Immobilization of Vinyl Sulfone D-Mannose (VS-D-Man) on Commercial Amino-Functionalized Glass Slides. One critical factor in glycoarrays is carbohydrate presentation, and both linker and ligand density play a major role. It has been reported that long aliphatic chains and aromatic- or charge-containing linkers lead to nonspecific protein adsorption[51] and that high ligand densities decrease protein−carbohydrate recognition, probably due to steric hindrance that inhibits the interactions.[77] In fact, the **VS-SCH** with the sulfone group directly linked to the anomeric carbon yielded saccharides that were poorly recognized by lectins, in full agreement with other authors,[75] although reactive toward proteins.[62] Thus, the assessment of the biological functionality of those saccharides and the determination of the optimal density when immobilized on solid supports are prerequisites to evaluate their feasibility to explore protein−carbohydrate interactions. To this aim, commercial amino-functionalized glass was printed by overnight incubation at pH 8 and 37 °C with different concentrations of vinyl sulfone D-mannose (**VS-D-Man**, **1**) and the interaction with FITC-ConA was analyzed by fluorescence. Results (Figure S1, Supporting Information) reveal the existence of a linear relationship between the fluorescence and the concentration of **1** used to print the support, supporting the validity of the vinyl sulfone derivatization when an ethylthio spacer is introduced between the anomeric carbon and the sulfone group. The linear relationship holds up to 1 mM, diminishing the affinity of ConA by the immobilized **VS-D-Man** beyond this concentration, which was established as the optimum saccharide density.

Immobilization of Vinyl Sulfone Saccharides on Commercial Amino-Functionalized Plates. The use of microwell plates and horseradish peroxidase (HRP) conjugated lectins is another standard approach to analyze the interaction between carbohydrates and saccharide binding proteins. Polysaccharides are immobilized on plates mainly by adsorption,[18−20] but the less hydrophobic nature of oligosaccharides demands other methodologies,[13,14,22] the derivatization of the carbohydrate to yield a covalent bond with the support being one of them.[28−43] The feasibility of the functionalization with vinyl sulfone was further put to the test by reacting the model system comprising the **VS-SCH 1**−**7** with commercial amino-functionalized plates at pH 9 for 8 h at 37 °C and then quantifying the interaction with HRP-coupled ConA, PNA, UEA, and WGA lectins. Results are depicted in Table 1 and show that the main carbohydrate−lectin interactions were Man-ConA, Lac-PNA, Fuc-UEA, and GlcNAc-WGA, demonstrating that the derivatization of the anomeric carbon with a vinyl sulfone group containing a two carbon spacer is a general strategy that, besides yielding a covalent bond between commercial supports and saccharides, is compatible with the high specificity of the carbohydrate−lectin interactions.

Secondary minor carbohydrate−lectin interactions were also detected, but when compared to the primary ones and with the blank, only Mal-ConA and Mel-PNA were significant. In fact, Mel-PNA affinity has been described in BSA-Mel semisynthetic glycoproteins, and this affinity has been exploited to purify PNA by affinity chromatography on melibiose−Sepharose,[78] emphasizing the galactose specificity of PNA. On the other hand, the interactions between ConA and maltose and the importance of the anomeric position is well-documented,[79] and they explain the affinity of ConA for vinyl sulfone maltose (**VS-Mal**, **6**) and the null interaction with vinyl sulfone glucose (**VS-Glc**, **2**), since the derivatization of the latter yields the β-anomer. At this point, it is important to recall that the differences in the values of peroxidase activity among the different lectins are not directly linked to the lectin−carbohydrate affinity but to the specific activity of the peroxidase coupled to the lectin.

Immobilization of Vinyl Sulfone Saccharides (VS-SCH) on Polylysine-Coated Glass Slides. Polylysine coating is a

dx.doi.org/10.1021/bc200681c | *Bioconjugate Chem.* 2012, 23, 846−855

Table 1. Interaction of HRP-Coupled Lectins with Vinyl Sulfone Saccharides (VS-SCH, 1−7) Covalently Immobilized on Commercial Amino-Functionalized Plates[a]

VS-SCH	ConA	PNA	UEA	WGA
α-Man (**1**)	**2.69 (0.20)**	0.85 (0.07)	0.93 (0.04)	0.92 (0.05)
β-Glc (**2**)	0.71 (0.05)	0.83 (0.04)	0.89 (0.08)	0.87 (0.05)
β-GlcNAc (**3**)	0.78 (0.08)	0.95 (0.09)	0.93 (0.07)	**18.26 (2.27)**
β-Fuc (**4**)	0.51 (0.02)	0.82 (0.07)	**7.17 (0.83)**	0.85 (0.09)
β-Lac (**5**)	0.25 (0.01)	**5.17 (1.15)**	0.64 (0.05)	1.05 (0.12)
β-Mal (**6**)	1.54 (0.22)	0.87 (0.22)	0.82 (0.04)	0.97 (0.22)
β-Mel (7)	0.62 (0.04)	1.23 (0.17)	1.1 (0.06)	0.99 (0.05)
blank	1.00	1.00	1.00	1.00

[a]Primary and secondary interactions are shown in bold and underlined, respectively. Values are normalized to that of the blank (in absence of carbohydrate), and the standard deviations are shown in brackets.

well-known procedure to fix cells on surfaces on the basis of interactions between cationic sites of the adsorbed polylysine and the anionic sites of the biomolecules.[80] The fact that the polylysine coating provides a high density of amine groups ready to react with **VS-SCH**[67] encouraged us to explore the feasibility of combining polylysine coating and vinyl sulfone derivatization as a general strategy of immobilization of carbohydrates on nonfunctionalized glass slides.

A first round of experiments to optimize the saccharide density on polylysine-coated glass slides revealed that 2.5 mM was a suitable concentration, since higher values do not improve the signal, and the four lectins (ConA, PNA, UEA, and WGA) interact in an isoelectric point dependent manner with those coated wells that were not reacted with vinyl sulfone saccharides (Figure S2, Supporting Information). Thus, the interaction of PNA and UEA, with isoelectric points of 5.7−6.7[81] and 4.8 (estimated from the sequence), respectively, yields a peroxidase activity similar to that obtained from the carbohydrate-functionalized wells, whereas those for the less acidic ConA and WGA, with isoelectric points of 7.1[82] and 8.7,[83] respectively, were lower.

In order to screen the electrostatic interactions, three complementary strategies were assayed: (i) dilution of the lectin solutions, (ii) blockage of the unreacted amine groups from polylysine with a vinyl sulfone derivatized tetra(ethylene glycol) (2,5,8,11,14-pentaoxa-17-thianonadec-18-ene 17,17-dioxide), and (iii) increase of the ionic strength of the lectin solutions to screen the electrostatic interactions. Results showed that a 10-fold dilution of the lectin concentration weakened the carbohydrate−lectin signal for ConA, UEA, and WGA (Figure 2 slides A, B, and C, lane 1) and the comparison between blocked (Figure 2 lane 2) and unblocked (Figure 2 lane 3) polylysine-coated wells did not reveal a clear benefit of the former. As expected from the electrostatic nature of the unspecific interactions, the use of ionic strength overcame the unspecific interaction of PNA and UEA, especially when amine groups from polylysine were blocked (Figure 3, lanes 2) or when the solution with the lectin was supplemented with 12% NaCl, although the latter also led a diminished signal as a consequence of the disruption of the carbohydrate−lectin specific interactions. Additional experiments led to the conclusion that the optimal conditions to minimize the unspecific interactions without introducing an additional step to block the unreacted amine groups from polylysine are 4% NaCl for ConA and WGA at 2 μg/mL and 0.2 μg/mL, respectively, and for UEA and PNA 8% NaCl at 1 μg/mL and 0.2 μg/mL, respectively. At this point, it should be recalled the importance of the use of ionic strength to screen unspecific

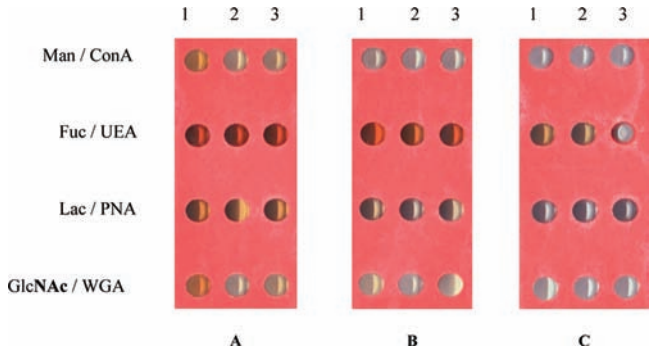

Figure 2. Effect of the dilution of the lectin and blockage on the unspecific interactions. Wells were coated with polylysine; and columns 3 were not further modified (blank), columns 1 and 2 were reacted with **VS-SCH**, and the unreacted amine groups from polylysine in columns 2 were blocked with methoxytetra(ethylene glycol) VS. Concentrations of HRP coupled lectins were 2 μg/mL for ConA, 1 μg/mL for PNA and UEA, and 0.2 μg/m for WGA (slide A), and dilutions 1/10 (slide B) and 1/100 (slide C).

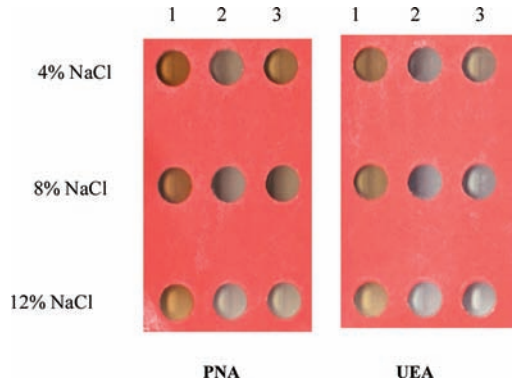

Figure 3. Effect of the blockage and the ionic strength to minimize the unspecific interactions of the HRP-coupled PNA (left) and UEA (right). Wells were coated with polylysine and **1** and **2** were functionalized with VS-L-Fuc 4 (right) or VS-Lac 5 (left), but only wells 2 were blocked with methoxytetra(ethylene glycol) vinyl sulfone. Lanes 3 are controls without carbohydrate.

interactions. Both ELISA and ELLA imply unspecific adsorption of antigen and carbohydrate on the surface of the plate and the detection of the adsorbed biomolecules by specific interactions with antibodies or lectins, respectively. The coverage of the surface of the well with the adsorbed biomolecule is a critical issue, and BSA is used as a standard blockage agent that (i) is adsorbed on those spots of surface

dx.doi.org/10.1021/bc200681c | Bioconjugate Chem. 2012, 23, 846−855

Table 2. Main Features of the Proteins Used to Synthesize Neoglycoconjugates[a]

protein	quaternary structure	MW (kDa)	isoelectric point	nucleophilic residues (per monomer)			
				H	K	free C	S−S bonds
lysozyme	monomer	14.3	10.7[87]	1	6	none	4
BSA	monomer	66.5	4.7[88]	17	56	1	17
ConA	tetramer	4 × 26.6	7.1[82]	6	12	none	none
mutant Lumazine[89]	icosahedral	60 × 16.2	5.7	2	9	none	none

[a]Molecular weights were estimated from the sequence. Experimental isoelectric points were taken from bibliography, except for the mutant lumazine that was estimated from the sequence.

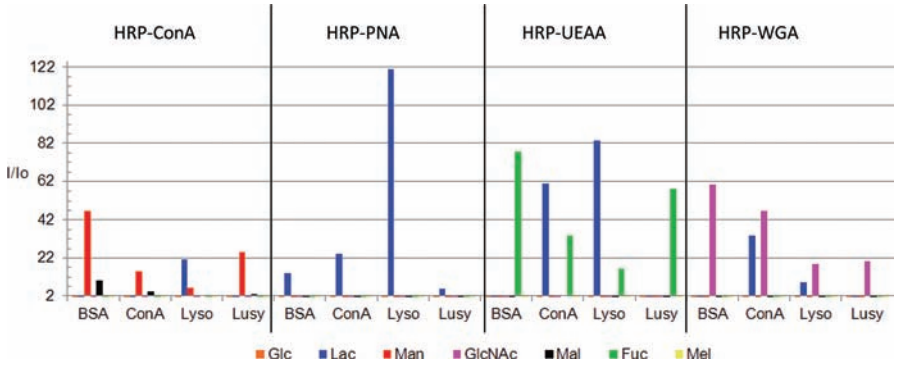

Figure 4. Interaction of the neoglycoconjugates with HRP-coupled lectins. Values are normalized by dividing the signal of the glycoconjugate (*I*) by that of the protein (*Io*).

that remain uncoated by the adsorbed biomolecule and (ii) is included in the buffers to compete with the unspecific interactions between the immobilized biomolecules and the antibody or lectin. However, the surface of the polystyrene ELISA/ELLA plates is completely different from that of polylysine-coated glass slides, ionic strength being a better candidate than BSA to screen the strong unspecific ionic interactions expected from the unreacted amine groups of the polylysine coating. Additionally, for the particular case of arrays with immobilized carbohydrate the blockage with BSA is not exempt of difficulties, since unspecific interactions with some lectins that yield high background signals have been reported.[84]

Synthesis of Neoglycoproteins. The large-scale production of glycoproteins is a challenging task that has been approached by biological and chemical strategies.[56−59] One chemical approach relies on the derivatization to promote the reaction between the carbohydrate moiety and the protein. In this context, the reactivity in mild conditions of the VS function toward amine and thiol groups naturally present in proteins as side chains of Lys and Cys has been reported as compatible with the biological nature of the biomolecules and an attractive option to couple tags.[67−69] Thus, having demonstrated the preservation of the biorecognizable features of the carbohydrate by the introduction of the two-carbon spacer and the reactivity of vinyl sulfone glucose toward lysozyme,[67] we focused on the synthesis of neoglycoproteins and their interaction with model lectins. To this aim, four model proteins (BSA, ConA, lysozyme, and lumazine) comprising the representative features of proteins (Table 2) were selected and reacted with the full set of **VS-SCH (1−7)** to generate a pool of 28 neoglycoproteins and their interaction with four lectins was evaluated (Table S1, Supporting Information). As depicted in Figure 4, the glycosylation of BSA and lumazine synthase makes them recognizable by the expected lectin, supporting the hypothesis that carbohydrate recognition is insensitive to the underlying polypeptide chain.[39] Thus, the neoglycoproteins resulting from reaction with **VS-D-Man 1** and **VS-Mal 6** interacted with ConA and those from reaction with **VS-D-GlcNAc**, **3 VS-L-Fuc 4**, and **VS-Lac 5** interacted with WGA, UEA, and PNA, respectively. However, unpredicted cross reactions were also detected when **VS-Lac 5** is reacted with ConA and lysozyme, the former being recognized by UEA and WGA and the latter by ConA, UEA, and WGA. These results were not unexpected since cross reactions of neoglycoproteins have been previously reported,[44] but the fact that they were not detected when the saccharides were immobilized on microwell plates (section 2.2) highlights the role of the surface where the saccharide is attached and demonstrates the feasibility of mischaracterization of proteins, cells, and tissues with lectins.

Application of the Vinyl Sulfone Saccharides (VS-SCH) to Detection of Carbohydrate Binding Proteins. Carbohydrate binding proteins are expressed in many species and are involved in a wide variety of biological processes ranging from cell adhesion to cell proliferation and apoptosis,[85] their characterization being one of the most widely used applications of glycoarrays. However, upon binding to the array their presence has to be detected either directly by labeling or indirectly by coupling to a labeled molecule (typically an antibody). In this context, the capability of **VS-SCH** to (i) be linked to polylysine-coated glass slides to yield arrays and (ii) turn proteins into glycoproteins that can be detected with commercial horseradish coupled lectins may be exploited as a general strategy of detection of carbohydrate binding proteins (Figure 5).

Finding the experimental conditions that minimize unspecific interactions is a prerequisite that was approached by incubation of ConA (i.e., model of carbohydrate binding protein) and BSA (i.e., model of nonbinding carbohydrate protein) with polylysine-coated glass slides previously reacted with **VS-D-Man 1**. Then, the proteins interacting with the wells were reacted with **VS-GlcNAc 3**, **VS-L-Fuc 4**, and **VS-Lac 5** and detected by the HRP activity coupled to WGA, UEA, and PNA,

dx.doi.org/10.1021/bc200681c | *Bioconjugate Chem.* 2012, 23, 846−855

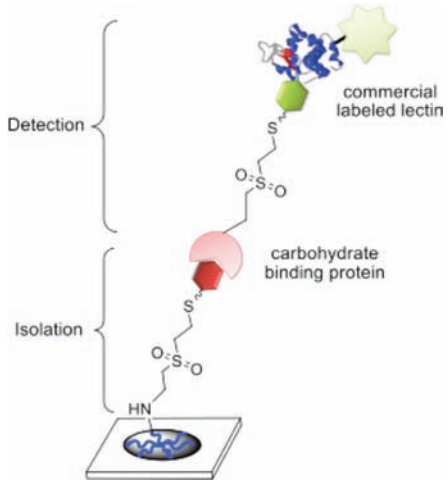

Figure 5. Application of the **VS-SCH** for both isolation and detection of carbohydrate binding proteins.

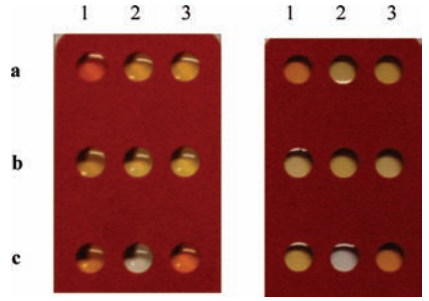

Figure 6. Application of the **VS-SCH** to the detection of carbohydrate binding proteins from *Oryza sativa* seeding in glass slides. Wells were coated with polylysine and then reacted with **VS-L-Fuc** (a1), **VS-D-Glc** (a2), **VS-Lac** (a3), **VS-Mal** (b1), **VS-D-Man** (b2), **VS-Mel** (b3), **VS-GlcNAc** (c1) and H_2O (c2). After incubation with the crude extract from rice (left) or with BSA as negative control (right), the retained proteins were labeled with vinyl sulfone L-fucose and detected by the peroxidase activity coupled to the HRP–UEA lectin.

respectively. As ionic strength was demonstrated to suffice for screening unspecific interactions, it was a variable to optimize. Thus, the interaction between the model proteins and the immobilized carbohydrates was evaluated at different values of ionic strength, and the interaction between the glycosylated protein and the corresponding lectin was carried out at the ionic strength found optimal for the analysis of **VS-SCH** on polylysine-coated glass (section 2.3). Promising results were obtained when the labeling was carried out with **VS-L-Fuc** and revealed with HRP-coupled UEA (Figure S3, Supporting Information): regardless of the ionic strength, fucosylated ConA is well-detected and unspecific interactions are negligible. This result supports the use of vinyl sulfone derivatized saccharide for detection purposes.

The application of the vinyl sulfone derivatization for the study of protein–carbohydrate interactions was further put to the test with a real case: detection of carbohydrate binding proteins present in a extract of seeds from rice (*Oryza sativa*). To this end, glass slides were coated with polylysine and then reacted with the pool of seven **VS-SCH** to yield an array. After incubation with the extract from rice and washing to break unspecific interactions, the retained proteins were labeled with **VS-L-Fuc 4** and then revealed by incubation with HRP-coupled UEA. A blank consisting of a solution of BSA was also analyzed as a negative control. A clear positive hit was detected for GlcNAc (Figure 6, left c1) and to a lesser extent for Glc, Lac, and Mal (Figure 6, left a2, a3, b1) in the rice extract and none in the slide incubated with BSA (Figure 6 right). These results are coherent with the plant lectin database lectinbdb[86] where proteins with affinity for GlcNAc, Man, and Gal are reported. As expected, a hit is also found in wells functionalized with L-Fuc (Figure 6, wells 1a) that acts as a positive control of the interaction HRP coupled UEA-L-Fuc.

CONCLUSION

The derivatization of the anomeric carbon of mono- and disaccharides (**VS-SCH**) with a vinyl sulfone group spanned by an ethylthio linker is a general strategy to covalently link a saccharide in mild conditions that are compatible with the biological nature of the biomolecules and preserves the high specificity of the carbohydrate–lectin interactions.

The reaction of **VS-SCH** with solid supports leads to their immobilization. Besides their reactivity toward commercial amino-functionalized glass slides and microwell plates, polylysine-coated slides are also a suitable support providing that the unspecific electrostatic interactions are screened. Among the different strategies assayed, the use of ionic strength was found to suffice to overcome the unspecific interaction without introducing an additional step to block unreacted amine groups from polylysine.

The reaction of **VS-SCH** with proteins yields neoglycoproteins that selectively interact with model lectins. The glycosylation of four model proteins (BSA, ConA, lysozyme, and lumazine) makes them recognizable by the expected lectin. However, unpredicted cross reactions are also detected, highlighting the role of the surface where the saccharide is attached and demonstrating the feasibility of mischaracterization of proteins, cells, and tissues with lectins. One important application that derives from the interactions between the glycosylated protein and lectins is the use of **VS-SCH** as tags that make the protein detectable by HRP-coupled lectins.

The capability of the **VS-SCH** was further demonstrated by detecting the carbohydrate binding proteins present in commercial rice. The interaction of a sample with an array prepared on a polylysine-coated glass slide was revealed by reacting the immobilized proteins with VS-L-Fuc and ulterior detection with HRP-coupled UEA.

In summary, the results reported herein demonstrate the potential of the vinyl sulfone derivatization in glycoscience research as a general strategy of activation of saccharide to yield the formation of a covalent bond with solid supports to create glycoarrays and with proteins to synthesize neoglycoproteins as well as tags that make the proteins detectable by labeled lectins.

ASSOCIATED CONTENT

Supporting Information

Synthesis and spectroscopic characterization of vinyl sulfone saccharides (**VS-SCH**) **1**–**7**. This material is available free of charge via the Internet at http://pubs.acs.org.

AUTHOR INFORMATION

Corresponding Author

*Fax: (+34) 958-243186; E-mail: fsantoyo@ugr.es.

Notes

The authors declare no competing financial interest.

■ ACKNOWLEDGMENTS

We acknowledge Dr. Salto and Dra. Girón for their assistance with the epifluorescence microscope and Prof. Weinkanf and Dra. Rodriguez-Fernandez for the gift of lumazine synthase. The authors acknowledge Direccion General de Investigacion Cientıfica y Tecnica (DGICYT) (CTQ2008-01754) and Junta de Andalucia (P07-FQM-02899) for financial support. A. Megia-Fernandez thanks the University of Granada for a research grant (Programa Puente).

■ REFERENCES

(1) Apweiler, R., Hermjakob, H., and Sharon, N. (1999) On the frequency of protein glycosylation, as deduced from analysis of the SWISS-PROT database. *Biochim. Biophys. Acta 1473*, 4−8.

(2) Marth, J. D., and Grewal, P. K. (2008) Mammalian glycosylation in immunity. *Nat. Rev. Immunol. 8*, 874−887.

(3) Sharon, N. (2006) Carbohydrates as future anti-adhesion drugs for infectious diseases. *Biochim. Biophys. Acta 1760*, 527−37.

(4) Ohtsubo, K., and Marth, J. D. (2006) Glycosylation in cellular mechanisms of health and disease. *Cell 126*, 855−867.

(5) Capila, I., and Linhardt, R. J. (2002) Heparin - Protein interactions. *Angew. Chem., Int. Ed. 41*, 390−412.

(6) Rabinovich, G. A., and Toscano, M. A. (2009) Turning 'sweet' on immunity: galectin-glycan interactions in immune tolerance and inflammation. *Nat. Rev. Immunol. 9*, 338−352.

(7) van Die, I., and Cummings, R. D. (2010) Glycan gimmickry by parasitic helminths: A strategy for modulating the host immune response? *Glycobiology 20*, 2−12.

(8) Jayaraman, N. (2009) Multivalent ligand presentation as a central concept to study intricate carbohydrate-protein interactions. *Chem. Soc. Rev. 38*, 3463−3483.

(9) Lee, R. T., and Lee, Y. C. (2000) Affinity enhancement by multivalent lectin-carbohydrate interaction. *Glycoconjugate J. 17*, 543−551.

(10) Mammen, M., Choi, S. K., and Whitesides, G. M. (1998) Polyvalent interactions in biological systems: Implications for design and use of multivalent ligands and inhibitors. *Angew. Chem., Int. Ed. 37*, 2755−2794.

(11) Gestwicki, J. E., Cairo, C. W., Strong, L. E., Oetjen, K. A., and Kiessling, L. L. (2002) Influencing receptor-ligand binding mechanisms with multivalent ligand architecture. *J. Am. Chem. Soc. 124*, 14922−14933.

(12) Yue, T. T., and Haab, B. B. (2009) Microarrays in glycoproteomics research. *Clin. Lab. Med. 29*, 15−29.

(13) Feizi, T., Fazio, F., Chai, W. C., and Wong, C. H. (2003) Carbohydrate microarrays - a new set of technologies at the frontiers of glycomics. *Curr. Opin. Struc. Biol. 13*, 637−645.

(14) Liu, Y., Palma, A. S., and Feizi, T. (2009) Carbohydrate microarrays: key developments in glycobiology. *Biol. Chem. 390*, 647−656.

(15) Tang, P. W., Gooi, H. C., and Hardy, M. (1985) Novel approach to the study of the antigenicities and receptor functions of carbohydrate chains of glycoproteins. *Biochem. Biophys. Res. Commun. 132*, 474−480.

(16) Liang, R., Yan, L., Loebach, J., Ge, M., Uozumi, Y., Sekanina, K., Horan, N., Gildersleeve, J., Thompson, C., Smith, A., Biswas, K., Still, W. C., and Kahne, D. (1996) Parallel synthesis and screening of a solid phase carbohydrate library. *Science 274*, 1520−1522.

(17) Roy, R. (1996) Syntheses and some applications of chemically defined multivalent glycoconjugates. *Curr. Opin. Struct. Biol. 6*, 692−702.

(18) Wang, D., Liu, S., Trummer, B. J., Deng, C., and Wang, A. (2002) Carbohydrate microarrays for the recognition of cross-reactive molecular markers of microbes and host cells. *Nat. Biotechnol. 20*, 275−81.

(19) Willats, W. G., Rasmussen, S. E., Kristensen, T., Mikkelsen, J. D., and Knox, J. P. (2002) Sugar-coated microarrays: a novel slide surface for the high-throughput analysis of glycans. *Proteomics 2*, 1666−71.

(20) Moller, I., Sørensen, I., Bernal, A. J., Blaukopf, C., Lee, K., Øbro, J., Pettolino, F., Roberts, A., Mikkelsen, J. D., Knox, J. P., Bacic, A., and Willats, W. G. T. (2007) High-throughput mapping of cell-wall polymers within and between plants using novel microarrays. *Plant J. 50*, 1118−1128.

(21) Shipp, E. L., and Hsieh-Wilson, L. C. (2007) Profiling the sulfation specificities of glycosaminoglycan interactions with growth factors and chemotactic proteins using microarrays. *Chem. Biol. 14*, 195−208.

(22) Laurent, N., Voglmeir, J., and Flitsch, S. L. (2008) Glycoarrays - tools for determining protein-carbohydrate interactions and glycoenzyme specificity. *Chem. Commun.*, 4400−4412.

(23) Feizi, T., Stoll, M. S., Yuen, C. T., Chai, W. G., and Lawson, A. M. (1994) Neoglycolipids - probes of oligosaccharide structure, antigenicity, and function. *Methods Enzymol. 230*, 484−519.

(24) Feizi, T., and Chai, W. G. (2004) Oligosaccharide microarrays to decipher the glyco code. *Nat. Rev. Mol. Cell Biol. 5*, 582−588.

(25) Fukui, S., Feizi, T., Galustian, C., Lawson, A. M., and Chai, W. (2002) Oligosaccharide microarrays for high-throughput detection and specificity assignments of carbohydrate-protein interactions. *Nat. Biotechnol. 20*, 1011−1017.

(26) Alvarez, R. A., and Blixt, O. (2006) Identification of ligand specificities for glycan-binding proteins using glycan arrays. *Glycobiology 415*, 292−310.

(27) Shao, M. C. (1992) The use of streptavidin biotinylglycans as a tool for characterization of oligosaccharide-binding specificity of lectin. *Anal. Biochem. 205*, 77−82.

(28) Blixt, O., Head, S., Mondala, T., Scanlan, C., Huflejt, M. E., Alvarez, R., Bryan, M. C., Fazio, F., Calarese, D., Stevens, J., Razi, N., Stevens, D. J., Skehel, J. J., Van Die, I., Burton, D. R., Wilson, I. A., Cummings, R., Bovin, N., Wong, C. H., and Paulson, J. C. (2004) Printed covalent glycan array for ligand profiling of diverse glycan binding proteins. *Proc. Natl. Acad. Sci. U.S.A. 101*, 17033−17038.

(29) de Paz, J. L., Noti, C., and Seeberger, P. H. (2006) Microarrays of synthetic heparin oligosaccharides. *J. Am. Chem. Soc. 128*, 2766−2767.

(30) Disney, M. D., and Seeberger, P. H. (2004) The use of carbohydrate microarrays to study carbohydrate-cell interactions and to detect pathogens. *Chem. Biol. 11*, 1701−1707.

(31) Huang, C. Y., Thayer, D. A., Chang, A. Y., Best, M. D., Hoffmann, J., Head, S., and Wong, C. H. (2006) Carbohydrate microarray for profiling the antibodies interacting with Globo H tumor antigen. *Proc. Natl. Acad. Sci. U.S.A. 103*, 15−20.

(32) Liang, P. H., Wang, S. K., and Wong, C. H. (2007) Quantitative analysis of carbohydrate-protein interactions using glycan microarrays: Determination of surface and solution dissociation constants. *J. Am. Chem. Soc. 129*, 11177−11184.

(33) Shilova, N. V., Galanina, O. E., Rubina, A. Y., Butvilovskaya, V. I., Huflejt, M. E., Chambers, J., Roucoux, A., and Bovin, N. V. (2008) 2-Aminopyridine - a label for bridging of oligosaccharides HPLC profiling and glycoarray printing. *Glycoconjugate J. 25*, 11−14.

(34) Fazio, F., Bryan, M. C., Blixt, O., Paulson, J. C., and Wong, C. H. (2002) Synthesis of sugar arrays in microtiter plate. *J. Am. Chem. Soc. 124*, 14397−14402.

(35) Houseman, B. T., and Mrksich, M. (2002) Carbohydrate arrays for the evaluation of protein binding and enzymatic modification. *Chem. Biol. 9*, 443−454.

(36) Sun, X. L., Stabler, C. L., Cazalis, C. S., and Chaikof, E. L. (2006) Carbohydrate and protein immobilization onto solid surfaces by sequential Diels-Alder and azide-alkyne cycloadditions. *Bioconjugate Chem. 17*, 52−57.

(37) Zhang, Y., Luo, S. Z., Tang, Y. J., Yu, L., Hou, K. Y., Cheng, J. P., Zeng, X. Q., and Wang, P. G. (2006) Carbohydrate-protein interactions by "clicked" carbohydrate self-assembled monolayers. *Anal. Chem. 78*, 2001−2008.

(38) Park, S., Lee, M. R., Pyo, S. J., and Shin, I. (2004) Carbohydrate chips for studying high-throughput carbohydrate-protein interactions. *J. Am. Chem. Soc. 126*, 4812−4819.
(39) Adams, E. W., Ratner, D. M., Bokesch, H. R., McMahon, J. B., O'Keefe, B. R., and Seeberger, P. H. (2004) Oligosaccharide and glycoprotein Microarrays as tools in HIV glycobiology: Glycan-dependent gp120/protein interactions. *Chem. Biol. 11*, 875−881.
(40) Brun, M. A., Disney, M. D., and Seeberger, P. H. (2006) Miniaturization of microwave-assisted carbohydrate functionalization to create oligosaccharide microarrays. *ChemBioChem 7*, 421−424.
(41) Park, S., and Shin, I. (2002) Fabrication of carbohydrate chips for studying protein-carbohydrate interactions. *Angew. Chem., Int. Ed. 41*, 3180−3182.
(42) Ratner, D. M., Adams, E. W., Disney, M. D., and Seeberger, P. H. (2004) Tools for glycomics: Mapping interactions of carbohydrates in biological systems. *ChemBioChem 5*, 1375−1383.
(43) Ratner, D. M., Adams, E. W., Su, J., O'Keefe, B. R., Mrksich, M., and Seeberger, P. H. (2004) Probing protein-carbohydrate interactions with microarrays of synthetic oligosaccharides. *ChemBioChem 5*, 379−382.
(44) Manimala, J. C., Roach, T. A., Li, Z., and Gildersleeve, J. C. (2006) High-throughput carbohydrate microarray analysis of 24 lectins. *Angew. Chem., Int. Ed. 45*, 3607−3610.
(45) Chevolot, Y., Bouillon, C., Vidal, S., Morvan, F., Meyer, A., Cloarec, J. P., Jochum, A., Praly, J. P., Vasseur, J. J., and Souteyrand, E. (2007) DNA-based carbohydrate biochips: A platform for surface glyco-engineering. *Angew. Chem., Int. Ed. 46*, 2398−2402.
(46) Zhang, J., Pourceau, G., Meyer, A., Vidal, S., Praly, J.-P., Souteyrand, E., Vasseur, J.-J., Morvan, F., and Chevolot, Y. (2009) DNA-directed immobilisation of glycomimetics for glycoarrays application: Comparison with covalent immobilisation, and development of an on-chip IC50 measurement assay. *Biosens. Bioelectron. 24*, 2515−2521.
(47) Oyelaran, O., and Gildersleeve, J. C. (2009) Glycan arrays: recent advances and future challenges. *Curr. Opin. Chem. Biol. 13*, 406−13.
(48) Leteux, C., Stoll, M. S., Childs, R. A., Chai, W., Vorozhaikina, M., and Feizi, T. (1999) Influence of oligosaccharide presentation on the interactions of carbohydrate sequence-specific antibodies and the selectins: Observations with biotinylated oligosaccharides. *J. Immunol. Methods 227*, 109−119.
(49) Lewallen, D. M., Siler, D., and Iyer, S. S. (2009) Factors affecting protein−glycan specificity: effect of spacers and incubation time. *ChemBioChem 10*, 1486−1489.
(50) Dhayal, M., and Ratner, D. M. (2009) XPS and SPR analysis of glycoarray surface density. *Langmuir 25*, 2181−2187.
(51) Dyukova, V. I., Shilova, N. V., Galanina, O. E., Rubina, A. Y., and Bovin, N. V. (2006) Design of carbohydrate multiarrays. *Biochim. Biophys. Acta 1760*, 603−609.
(52) Bhatia, P. K., and Mukhopadhyay, A. (1999) Protein glycosylation: implications for in vivo functions and therapeutic applications. *Adv. Biochem. Eng. Biot. 64*, 155−201.
(53) Wyss, D. F., and Wagner, G. (1996) The structural role of sugars in glycoproteins. *Curr. Opin. Biotechnol. 7*, 409−416.
(54) Kern, G., Kern, D., Jaenicke, R., and Seckler, R. (1993) Kinetics of folding and association of differently glycosylated variants of invertase from saccharomyces-cerevisiae. *Protein Sci. 2*, 1862−1868.
(55) Rudd, P. M., Joao, H. C., Coghill, E., Fiten, P., Saunders, M. R., Opdenakker, G., and Dwek, R. A. (1994) Glycoforms modify the dynamic stability and functional-activity of an enzyme. *Biochemistry 33*, 17−22.
(56) Bennett, C. S., and Wong, C.-H. (2007) Chemoenzymatic approaches to glycoprotein synthesis. *Chem. Soc. Rev. 36*, 1227−1238.
(57) Bernardes, G. J. L., Castagner, B., and Seeberger, P. H. (2009) Combined approaches to the synthesis and study of glycoproteins. *ACS Chem. Biol. 4*, 703−713.
(58) Davis, B. G. (2002) Synthesis of glycoproteins. *Chem. Rev. 102*, 579−601.
(59) Gamblin, D. P., Scanlan, E. M., and Davis, B. G. (2009) Glycoprotein synthesis: an update. *Chem. Rev. 109*, 131−163.
(60) Meadows, D. C., and Gervay-Hague, J. (2006) Vinyl sulfones: Synthetic preparations and medicinal chemistry applications. *Med. Res. Rev. 26*, 793−814.
(61) Simpkins, N. S. (1990) The chemistry of vinyl sulfones. *Tetrahedron 46*, 6951−6984.
(62) Masri, M. S., and Friedman, M. (1988) Protein reactions with methyl and ethyl vinyl sulfones. *J. Protein Chem. 7*, 49−54.
(63) Houen, G., and Jensen, O. M. (1995) Conjugation to preactivated proteins using divinylsulfone and iodoacetic acid. *Immunol. Methods 181*, 187−200.
(64) Morpurgo, M., Veronese, F. M., Kachensky, D., and Harris, J. M. (1996) Preparation and characterization of poly(ethylene glycol) vinyl sulfone. *Bioconjugate Chem. 7*, 363−368.
(65) Porath, J., and Axén, R. (1976) Immobilization of enzymes to agar, agarose, and sephadex support. *Methods Enzymol. 44*, 19−45.
(66) Lopez-Jaramillo, F. J., Hernandez-Mateo, F., and Santoyo-Gonzalez, F. (2011) Vinyl sulfone: a multi-purpose function in proteomics, in *Proteomics, Book 2* (Leung, E., Ed.) In press.
(67) Lopez-Jaramillo, F. J., Perez-Banderas, F., Hernandez-Mateo, F., and Santoyo-Gonzalez, F. (2005) Production, crystallization and x-ray characterization of chemically glycosylated hen egg-white lysozyme. *Acta Crystallogr., Sect. F F61*, 435−438.
(68) Morales-Sanfrutos, J., Lopez-Jaramillo, J., Ortega-Munoz, M., Megia-Fernandez, A., Perez-Balderas, F., Hernandez-Mateo, F., and Santoyo-Gonzalez, F. (2010) Vinyl sulfone: a versatile function for simple bioconjugation and immobilization. *Org. Biomol. Chem. 8*, 667−675.
(69) Valero, E., Tambalo, S., Marzola, P., Ortega-Muñoz, M., Lopez-Jaramillo, F. J., Santoyo-Gonzalez, F., Lopez, J. D., Delgado, J. J., Calvino, J. J., Cuesta, R., Dominguez-Vera, J. M., and Galvez, N. (2011) Magnetic nanoparticles-templated assembly of protein subunits: a new platform for carbohydrate-based MRI nanoprobes. *J. Am. Chem. Soc. 133*, 4889−4895.
(70) Pathak, T. (2008) Vinyl sulfone-modified carbohydrates: An inconspicuous group of chiral building blocks. *Tetrahedron 64*, 3605−3628.
(71) Pathak, T., and Bhattacharya, R. (2008) A vinyl sulfone-modified carbohydrate mediated new route to aminosugars and branched-chain sugars. *Carbohydr. Res. 343*, 1980−1998.
(72) Oscarson, S. (2008) Glycoscience (Fraser-Reid, B., Tatsuta, K., and Thiem, J., Eds.) pp 661−697, Springer-Verlag, Berlin-Heidelberg.
(73) Ibatullin, F. M., Shabalin, K. A., Janis, J. V., and Shavva, A. G. (2003) Reaction of 1,2-trans-glycosyl acetates with thiourea: a new entry to 1-thiosugars. *Tetrahedron Lett. 44*, 7961−7964.
(74) Perez-Balderas, F. PhD Thesis (2005), University of Granada. http://tinyurl.com/7yf887u
(75) Poretz, R. D., and Goldstein, I. J. (1970) An examination of topography of saccharide binding sites of concanavalin-A and of forces involved in complexation. *Biochemistry 9*, 2890−2896.
(76) Cheng, F., Shang, J., and Ratner, D. M. (2011) A versatile method for functionalizing surfaces with bioactive glycans. *Bioconjugate Chem. 22*, 50−57.
(77) Houseman, B. T., and Mrksich, M. (1999) The role of ligand density in the enzymatic glycosylation of carbohydrates presented on self-assembled monolayers of alkanethiolates on gold. *Angew. Chem., Int. Ed. 38*, 782−785.
(78) Chacko, B. K., and Appukuttan, P. S. (2001) Peanut (Arachis hypogaea) lectin recognizes alpha-linked galactose, but not N-acetyl lactosamine in N-linked oligosaccharide terminals. *Int. J. Biol. Macromol. 28*, 365−371.
(79) Goldstein, I. J., and Iyer, R. N. (1966) Interaction of concanavalin a a phytohemagglutinin with model substrates. *Biochim. Biophys. Acta 121*, 197−200.
(80) Mazia, D., Schatten, G., and Sale, W. (1975) Adhesion of cells to surfaces coated with polylysine - applications to electron-microscopy. *J. Cell Biol. 66*, 198−200.

(81) Miller, R. L. (1983) Purification of peanut (Arachis hypogaea) agglutinin isolectins by chromatofocusing. *Anal. Biochem. 131*, 438–446.
(82) Agrawal, B. B. L., and Goldstein, I. J. (1967) Physical and chemical characterization of concanavalin a hemagglutinin from jack bean (Canavalia ensiformis). *Biochim. Biophys. Acta 133*, 376–379.
(83) Rice, R. H., and Etzler, M. E. (1975) Chemical modification and hybridization of wheat-germ agglutinins. *Biochemistry 14*, 4093–4099.
(84) Roisin, T., Aileen, C., Michael, O. C., Brendan, O. C., and Paul, C. (2011) Optimization of the enzyme-linked lectin assay for enhanced glycoprotein and glycoconjugate analysis. *Anal. Biochem. 413*, 114–122.
(85) Nakahara, S., and Raz, A. (2008) Biological modulation by lectins and their ligands in tumor progression and metastasis. *Anticancer Agents Med. Chem. 8*, 22–36.
(86) Chandra, N. R., Kumar, N., Jeyakani, J., Singh, D. D., Gowda, S. B., and Prathima, M. N. (2006) Lectindb: a plant lectin database. *Glycobiology 16*, 938–946.
(87) Li-Chan, E., and Nakai, S. G. (1989) *Crit. Rev. Poult. Biol. 2*, 21.
(88) Anfinsen, C. B., Edsall, J. T., and Richards, F. M. (1985) Academic Press, New York.
(89) Rodríguez-Fernández, L., López-Jaramillo, F. J., Bacher, A., Fischer, M., and Weinkauf, S. (2008) Improvement of the quality of lumazine synthase crystals by protein engineering. *Acta Crystallogr., Sect. F 64*, 625–628.

Bioconjugate Chemistry

Article

pubs.acs.org/bc

Construction and Assembly of Branched Y-Shaped DNA: "Click" Chemistry Performed on Dendronized 8-Aza-7-deazaguanine Oligonucleotides

Hai Xiong,[†,‡] Peter Leonard,[†] and Frank Seela*[,†,‡]

[†]Laboratory of Bioorganic Chemistry and Chemical Biology, Center for Nanotechnology, Heisenbergstraße 11, 48149 Münster, Germany

[‡]Laboratorium für Organische und Bioorganische Chemie, Institut für Chemie, Universität Osnabrück, Barbarastraße 7, 49069 Osnabrück, Germany

Supporting Information

ABSTRACT: Branched DNA was synthesized from tripropargylated oligonucleotides by the Huisgen-Meldal-Sharpless cycloaddition using "stepwise and double click" chemistry. Dendronized oligonucleotides decorated with 7-tripropargylamine side chains carrying two terminal triple bonds were further functionalized with bis-azides to give derivatives with two terminal azido groups. Then, the branched side chains with two azido groups or two triple bonds were combined with DNA-fragments providing the corresponding clickable function. Both concepts afforded branched (Y-shaped) three-armed DNA. Annealing of branched DNA with complementary oligonucleotides yielded supramolecular assemblies. The concept of "stepwise and double click" chemistry combined with selective hybridization represents a flexible tool to generate DNA nanostructures useful for various purposes in DNA diagnostics, delivery, and material science applications.

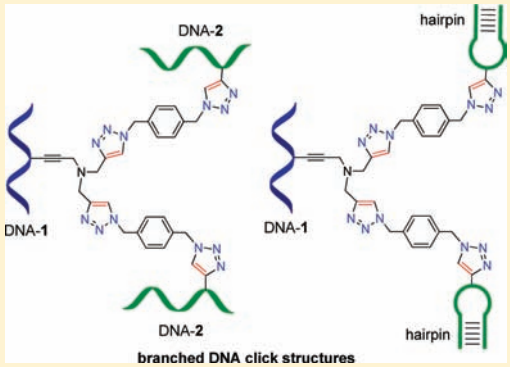

INTRODUCTION

Branched oligonucleotides have been found to represent an important class of molecules acting in nature as structural intermediates of RNA splicing.[1−4] They can form multistranded structures or hairpin motifs. Branched DNA was also prepared chemically following various concepts. One approach uses the self-assembly by hybridization of predesigned complementary oligonucleotides leading to DNA three- or four-way junctions, so-called X- or Y-shaped DNA.[5−9] In another more synthetic approach, branched DNA was synthesized with preformed branching elements including dendronized molecules. Nucleoside or non-nucleosidic building blocks were used for this purpose.[10−22] Dendronized materials find applications in catalysis, drug delivery, nanomedicine, and nanoscale electronics.[23−30] Branched or dendronized oligonucleotides were synthesized, modified, or further assembled to dendritic nucleic acid structures.[31−33] However, these approaches show drawbacks and are often laborious and low-yielding. The Huisgen-Meldal-Sharpless copper(I) cycloaddtion[34−36]—"click" chemistry—was recently used to covalently connect DNA oligonucleotides.[37−42] Our laboratory introduced tripropargylamine side chains as branching units into the 5-position of pyrimidine nucleosides[43] as well as in the 7-position of 7-deazapurine and 7-deaza-8-azapurine 2′-deoxyribonucleosides[44−46] to generate dendronized DNA. Both terminal triple bonds were simultaneously "double clicked" to azido functions of azido reporter groups.[43−46] We also described DNA cross-linking of dendronized DNA by a "bis-click" or "stepwise click" protocol.[41,42]

This manuscript reports on the "stepwise and double click" concept employing tripropargylated **3** as branching point for the defined construction of three-armed (Y-shaped) dendronized DNA. 8-Aza-7-deaza-2′-deoxyguanosine with short (**1**), long (**2**), and branched (**3**) linker arms together with *p*-azidoxylene **4**[47] were used for this purpose. Azido-functionalized oligonucleotides incorporating **5**, **6**, or **7** were linked to alkynylated DNA-fragments affording branched oligonucleotides. Hybridization experiments of branched oligonucleotides and single-stranded chains were performed. The controlled synthesis via click chemistry and intra- or intermolecular base-pairing leads to self-assembly resulting in unique DNA nanoconstructs applicable to material science and nanomedicine.[48,49]

EXPERIMENTAL PROCEDURES

General Methods and Materials. All chemicals and solvents were of laboratory grade as obtained from Acros, Aldrich, Sigma, or Fluka (Sigma-Aldrich Chemie GmbH, Deisenhofen, Germany) and were used without further purification. Standard phosphoramidites were purchased from

Received: January 11, 2012
Revised: March 14, 2012
Published: March 25, 2012

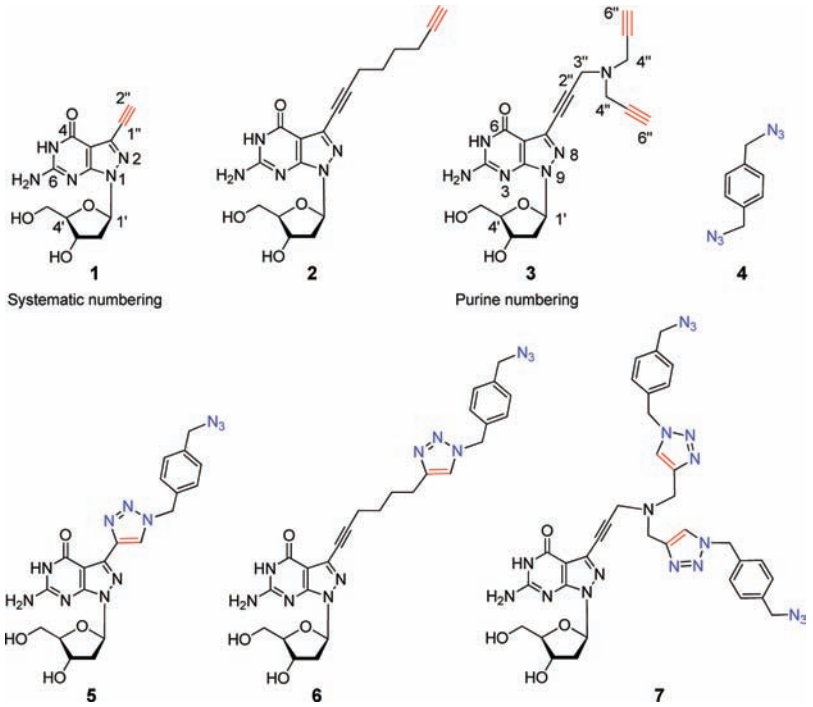

Figure 1. Structures of mono- and bisfunctionalized "clickable" nucleosides used in this study.

Sigma (Sigma-Aldrich Chemie GmbH, Deisenhofen, Germany). The 5′-MMT-amino-modifier C6-CE phosphoramidite **11** was purchased from Link Technologies (Bellshill, Lanarkshire, UK). Thin layer chromatography (TLC) was performed on TLC aluminum sheets covered with silica gel 60 F254 (0.2 mm, VWR International, Germany). Flash column chromatography (FC): silica gel 60 (40−60 μM, VWR International, Germany) at 0.4 bar. UV spectra were recorded on a U-3000 spectrophotometer (Hitachi, Japan); λ_{max} (ε) in nm, ε in $dm^3\ mol^{-1}\ cm^{-1}$. NMR spectra: DPX 300 spectrophotometer (Bruker, Germany) at 300.15 MHz for ^1H and 75.48 MHz for ^{13}C. The J values are given in Hz and δ values in ppm relative to Me_4Si as internal standard. For NMR spectra recorded in DMSO, the chemical shift of the solvent peak was set to 2.50 ppm for ^1H NMR and 39.50 ppm for ^{13}C NMR. Elemental analysis was performed by the Mikroanalytisches Laboratorium Beller, Göttingen, Germany. Reversed-phase HPLC was carried out on a 250 × 4 mm RP-18 LiChrospher 100 column with a HPLC pump connected with a variable wavelength monitor, a controller, and an integrator. Gradients used for HPLC chromatography are as follows: A = MeCN; B = 0.1 M (Et_3NH)OAc (pH 7.0)/MeCN, 95:5. (*I*): 3 min 15% A in B, 12 min 15−50% A in B, and 5 min 50−10% A in B, flow rate 0.7 mL min^{-1}; (*II*): 0−25 min 0−20% A in B, flow rate 0.7 mL min^{-1}; (*III*): 0−15 min 0−20% A in B, 15−18 min 20−40% A in B, flow rate 0.7 mL min^{-1}; (*IV*): 0−30 min with 20−80% D in C with a flow rate of 0.75 mL min^{-1} (C: 25 mM Tris-HCl, 10% MeCN, pH 7.0; D: 25 mM Tris-HCl, 1.0 M NaCl, 10% MeCN, pH 7.0). Melting curves were measured with a Cary-100-Bio UV−vis spectrophotometer (Varian, Australia) equipped with a Cary thermoelectrical controller with a heating rate of 1 °C/min. Nanopure water (resistance <0.055 μS/cm) from MembraPure water system (Astacus) was used for all experiments. ESI-TOF mass spectra of the nucleosides were measured with a Micro-TOF spectrometer. The molecular masses of oligonucleotides were determined by LC-ESI-TOF (Agilent 1200 Series, Bruker Micro-TOF Q2) or MALDI-TOF (MS Autoflex, Bruker) mass spectrometry in the linear positive mode with 3-hydroxypicolinic acid (3-HPA) as a matrix.

6-Amino-1-(2-deoxy-β-D-*erythro*-pentofuranosyl)-1,5-dihydro-3-[di(1′,2′,3′-triazoyl-1-methyl-4-azidomethylbenzyl)propargylamino}-4*H*-pyrazolo[3,4-*d*]pyrimidin-4-one (7). To a solution of compound **3**[44] (59.4 mg, 0.15 mmol) and **4**[47] (282 mg, 1.5 mmol) in THF/H_2O/*t*-BuOH, 3: 1: 1 (2 mL) was added a freshly prepared 1 M solution of sodium ascorbate (120 μL, 0.12 mmol) in water, followed by the addition of copper(II) sulfate pentahydrate 7.5% in water (96 μL, 0.0285 mmol). The reaction mixture was stirred in the dark at r.t. for 12 h. After completion of the reaction (monitored by TLC), the mixture was filtered. The solvent was evaporated, and the residue was applied to FC (silica gel, column 8 × 3 cm, eluted with CH_2Cl_2/MeOH, 95:5 → 90:10). Evaporation of the main zone gave **7** as a pale yellow solid (70 mg, 60%). TLC (CH_2Cl_2/MeOH, 90:10): R_f 0.46; UV λ_{max} (MeOH)/nm 246 (ε/$dm^3\ mol^{-1}\ cm^{-1}$ 20 500), 260 (11 600), 280 nm (4800). Anal. ($C_{35}H_{36}N_{18}O_4$) C, H, N. ^1H NMR (300 MHz, DMSO-d_6): δ = 10.70 (s, 1H, NH), 8.21 (s, 2H, 2× H-triazole), 7.37−7.30 (m, 8H, 2× H-phenylene), 6.79 (br s, 2H, NH_2), 6.30 (t, J = 6.3 Hz, 1H, 1′-H), 5.60 (s, 4H, 2× $PhCH_2$), 5.24−5.23 (d, J = 4.5 Hz, 1H, 3′-OH), 4.73 (t, J = 5.7 Hz, 1H, 5′-OH), 4.43 (s, 4H, 2× $PhCH_2$), 4.39−4.35 (m, 1H, 3′-H), 3.82−3.75 (m, 5H, 2× NCH_2, 4′-H), 3.52−3.44 (m, 2H, NCH_2), 3.40−3.36 (m, 2H, 5′-H), 2.63−2.72 (m, 1H, 2′-H_β), 2.14−2.19 (m, 1H, 2′-H_α). (ESI-TOF): m/z calcd for $C_{35}H_{36}N_{18}O_4 + Na^+$: 795.3067 [M + Na^+]; found: 795.3059.

Synthesis, Purification, and Characterization of Oligonucleotides. The syntheses of oligonucleotides were performed on a DNA synthesizer on a 1 μmol scale in the trityl-on mode using the phosphoramidites **8**−**10**[41,42,44] (Figure 2) and the standard phosphoramidite building blocks following the synthesis protocol for 3′-*O*-(2-cyanoethyl)phosphoramidites.[50]

dx.doi.org/10.1021/bc300013k | *Bioconjugate Chem.* 2012, 23, 856−870

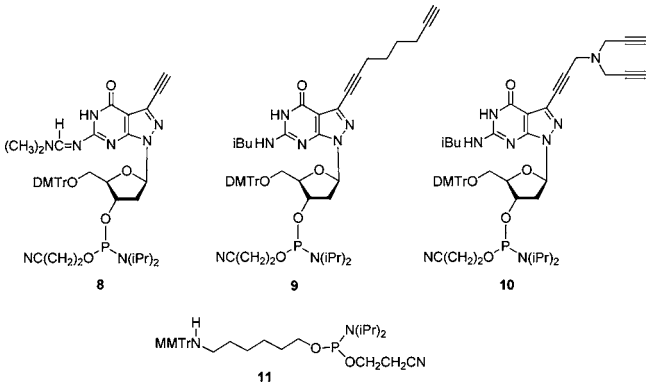

Figure 2. Structure of phosphoramidite building blocks **8**−**11** used in this study.

After cleavage from the solid support, the oligonucleotides were deprotected in 25% aq. ammonia solution in a sealed tube for 12−16 h at 60 °C. The 5′-aminoalkyl oligonucleotides were synthesized starting from 5′-MMT-amino-modifier C6-CE phosphoramidite **11** (Link Technologies Ltd., Bellshill, Lanarkshire, UK). The oligonucleotides were cleaved from the solid support and deprotected by heating the oligonucleotides in a 25% aq. ammonia solution in a sealed tube for 5 h at 55 °C. The purification of the "trityl-on" oligonucleotides was carried out on reversed-phase HPLC (RP-18 column; gradient system *I*). The purified "trityl-on" oligonucleotides were treated with 2.5% $Cl_2CHCOOH/CH_2Cl_2$ for 5 min at 0 °C to remove the mono- or dimethoxytrityl residues. The detritylated oligomers were purified by reversed-phase HPLC (gradient *II*). The oligomers were desalted on a short column using distilled water for elution of salt, while the oligonucleotides were eluted with H_2O/MeOH (2: 3). Then, the solvent was evaporated using a SpeedVac evaporator to yield colorless solids which were frozen at −24 °C. The molecular masses of the oligonucleotides were determined by LC-ESI-TOF or MALDI-TOF mass spectrometry (Table 1 and 2). Extinction coefficients ε_{260} (MeOH) of nucleosides: dA, 15400; dG, 11700; dT, 8800; dC, 7300; **1**, 10900;[42] **2**, 11500;[42] **3**, 14000;[44] **5**, 26000;[42] **6**, 23100;[42] **7**, 11600.

Ion-Exchange HPLC Analysis of Branched Oligonucleotides. The ion-exchange chromatography was performed on a 4 × 250 mm DNA PA-100 column with a precolumn using a HPLC apparatus. Elution profiles were recorded at 260 nm. The azidomethylbenzyl-labeled oligonucleotides as well as the nonbranched and branched oligonucleotides (0.2 A_{260} units each) were dissolved in 100 μL of water and were then directly injected into the HPLC apparatus. The compounds were eluted using gradient *IV:* 0−30 min

Table 1. Structures and Mass Spectrometric Data of Nonbranched Oligonucleotides ODN-1−ODN-5 and Branched Oligonucleotides BR-1 and BR-2

Oligonucleotides	MS [calc.] found	Oligonucleotides	MS [calc.] found
3′-d(TATATATATATA)-O-P(=O)(-O)-O-$(CH_2)_6NH_2$ (ODN-**1**)	[3820.6[a]] 3820.7[b]	3′-d(TAGGTCAATACT)-O-P(=O)(-O)-O-$(CH_2)_6NH_2$ (ODN-**2**)	[3821.7[c]] 3821.7[d]
3′-d(TATATATATATA)-O-P(=O)(-O)-O-$(CH_2)_6$HN-C(=O)-$(CH_2)_4N_3$ (ODN-**3**)	[3945.7[a]] 3944.8[b]	3′-d(TAGGTCAATACT)-O-P(=O)(-O)-O-$(CH_2)_6$HN-C(=O)-$(CH_2)_4N_3$ (ODN-**4**)	[3946.8[c]] 3946.8[d]
5′-d(A3T ATT GAC CTA) (ODN-**5**)[44]	[3772.6[a]] 3772.6[b]	5′-d(AGTATTGACCTA) (ODN-**6**)	[3644.4[a]] 3640.3[b]
5′-d(TAGGTCAATACT) (ODN-**7**)	[3644.4[a]] 3643.7[b]		
3′-d(TATATATATATA)-O-P(=O)(-O)-O-$(CH_2)_6$HN—Linker—NH$(CH_2)_6$O-P(=O)(-O)-O-d(ATATATATATAT)-3′ 5′-d(A3T ATT GAC CTA)-3′ **BR-1**	[11666.0[a]] 11667.2[b]		
3′-d(TAGGTCAATACT)-O-P(=O)(-O)-O-$(CH_2)_6$HN—Linker—NH$(CH_2)_6$O-P(=O)(-O)-O-d(TCATAACTGGAT)-3′ 5′-d(A3T ATT GAC CTA)-3′ **BR-2**	[11665.3[c]] 11666.1[d]		

Linker (3) = 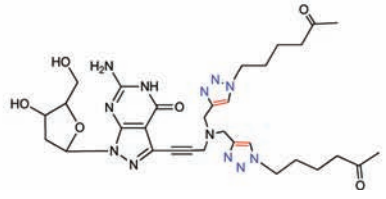

[a]Calculated on the basis of molecular weight as $[M+1]^+$. [b]Determined by Maldi-TOF mass spectrometry as $[M+1]^+$ in the linear positive mode. [c]Calculated on the basis of exact mass. [d]Determined by LC-ESI-TOF mass spectrometry.

dx.doi.org/10.1021/bc300013k | *Bioconjugate Chem.* 2012, 23, 856−870

Table 2. Structure and Mass Spectrometric Data of Nonbranched and Branched Oligonucleotides[e]

Oligonucleotides	MS [calc.] found	ODN Intermediates with Azido Groups	MS [calc.] found
5'-d(TAG**1**TCAATACT) (ODN-**8**)[42]	[3666.7][c] 3666.6[d]	5'-d(TAG **5**TCAAT ACT) (ODN-**14**)[42]	[3855.6][a] 3854.5[b]
5'-d(**1**ATATATATATAT) (ODN-**9**)	[3994.7][a] 3995.1[b]	5'-d(**5**ATATATATATAT) (ODN-**15**)	[4181.8][c] 4181.8[d]
5'-d(**2**ATATATATATAT) (ODN-**12**)	[4074.8][a] 4075.0[b]	5'-d(**6**ATATATATATAT) (ODN-**16**)	[4261.9][c] 4261.9[d]
5'-d(AGTATT**3**ACCTA) (ODN-**13**)[44]	[3772.6][a] 3772.0[b]	5'-d(AGT ATT**7**AC CTA) (ODN-**17**)	[4147.9][c] 4147.9[d]
5'-d(T_6AGTATT**2**ACCTAA_6) (ODN-**18**)[53]	[7452.0][a] 7452.4[b]	5'-d(T_6 AGTATT**6**ACCTA A_6) (ODN-**19**)	[7641.2][a] 7642.4[b]
5'-d(T_6AGTATTGACCTAA_6) (ODN-**20**)	[7398.9][a] 7398.9[b]		
5'-d(AGTATT**1**ACCTA) (ODN-**10**)[42]	[3667.4][a] 3667.2[b]		
5'-d(AGTATT**2**ACCTA) (ODN-**11**)[41]	[3747.6][a] 3746.9[b]		

Branched oligonucleotides		Branched oligonucleotides	
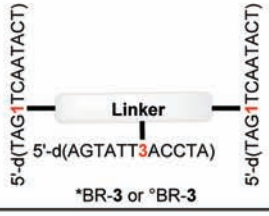	[11481.5][c] 11483.2[d,*] 11483.2[d,°]	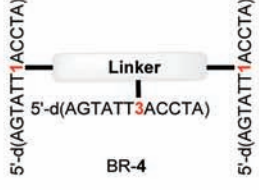	[11481.5][c] 11482.0[d]
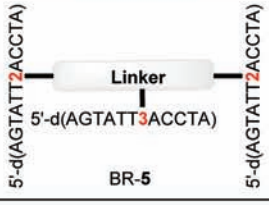	[11641.3][c] 11643.4[d]	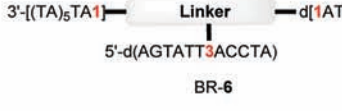	[12135.3][c] 12137.3[d]
	[12295.4][c] 12297.4[d]	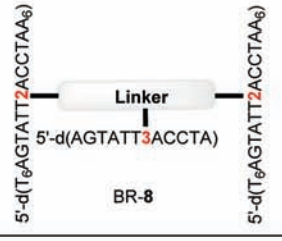	[19051.6][c] 19055.0[d]
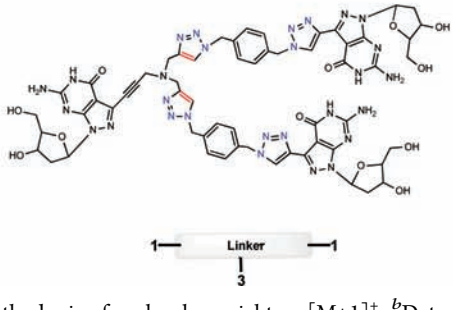		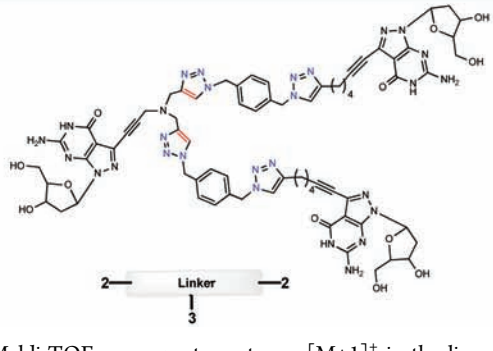	

[a]Calculated on the basis of molecular weight as $[M+1]^+$. [b]Determined by Maldi-TOF mass spectrometry as $[M+1]^+$ in the linear positive mode. [c]Calculated on the basis of exact mass. [d]Determined by LC-ESI-TOF mass spectrometry. [*]BR-**3** from azido-ODN-**14** and °BR-**3** from azido-ODN-**17**. [e]**1-3-1** (branched-short) and **2-3-2** (branched-long) represent the cross-linked nucleosides formed by the cycloaddition of the azido group within one side chain and the terminal triple bond of the other side chain.

dx.doi.org/10.1021/bc300013k | *Bioconjugate Chem.* 2012, 23, 856–870

with 20−80% D in C with a flow rate of 0.75 mL min^{-1} (C: 25 mM Tris-HCl, 10% MeCN, pH 7.0; D: 25 mM Tris-HCl, 1.0 M NaCl, 10% MeCN, pH 7.0).

Denaturing Polyacrylamide Gel Electrophoresis (PAGE) of Oligonucleotides. Analysis of nonbranched and branched oligonucleotides as well as cross-linked oligonucleotide ODN-**22**[42] was carried out by polyacrylamide gel electrophoresis (17% polyacrylamide gel, 19:1, acryl:bisacrylamide, containing 7 M urea). The gel was prerun for 30 min at rt using 1× tris-borate-EDTA (TBE) buffer containing 20 mM $MgCl_2$ (pH 8.4). The individual oligonucleotides (1−2 μM) were dissolved in 2−5 μL of distilled water at rt. Then, 10 μL of gel loading buffer containing formamide was added, and the oligonucleotide solution was loaded onto the gel. Electrophoresis was run at rt for 6 h using 1× TBE buffer containing 20 mM $MgCl_2$ (pH 8.4) at a constant field strength of 12 V/cm. The gel was stained with 0.02% methylene blue for 20 min and was then incubated in water for 1 h to remove excess dye from the background.

Native Polyacrylamide Gel Electrophoresis (PAGE). Analysis of hybridization of nonbranched and branched oligonucleotides was carried out by native polyacrylamide gel electrophoresis (15% polyacrylamide gel, 19:1 acryl:bisacrylamide). The gel was prerun for 30 min at 0 °C using 1× tris-borate-EDTA (TBE) buffer containing 20 mM $MgCl_2$ (pH 8.4). The individual oligonucleotides (2 μM) were dissolved in 2−5 μL of 10× tris-borate-EDTA buffer containing 20 mM $MgCl_2$ (pH 8.4), and the solutions were heated to 85 °C for 10 min. The oligonucleotides were annealed by cooling the solution to room temperature followed by incubation at rt for 1 h. Then, 10 μL of gel loading buffer containing 30% glycerol was added, and the oligonucleotide solution was loaded onto the gel. Electrophoresis was run at 0 °C for 6 h using 1× TBE buffer containing 20 mM $MgCl_2$ (pH 8.4) at a constant field strength of 10 V/cm. The gel was stained with 0.02% methylene blue for 20 min and then incubated in water for 1 h to remove excess dye from the background.

T_m Measurements. For the T_m measurements, the oligonucleotides were dissolved in 1 M NaCl, 100 mM $MgCl_2$, and 60 mM Na-cacodylate buffer, pH 7.0. For the self-complementary oligonucleotides ODN-**3**, ODN-**15**, and ODN-**16**, 4 μM of single-strand concentration was used. Hairpin-forming oligonucleotides were measured with 2.0 μM and 5.0 μM single-strand concentration (Table S3, Supporting Information). Hybridization experiments with branched oligonucleotides containing self-complementary oligonucleotide strands (BR-**1**, BR-**6**, or BR-**7**) were performed with 2 μM single-strand concentration. Hybridization experiments with complementary oligonucleotide strands were carried out with 2 μM of the branched oligonucleotide (BR-**1**, BR-**3**−BR-**7**) and 2 μM, 4 μM, or 6 μM of the complementary single-stranded oligonucleotide. The melting temperature curves were measured with a UV−vis spectrophotometer equipped with a thermoelectrical controller. The temperature was measured continuously in the reference cell with a Pt-100 resistor with a heating rate of 1 °C min^{-1}, and the absorbance at 260 nm was recorded as a function of the temperature. For melting profiles, see Figures S9−13 (Supporting Information).

Synthesis of 5′-Azidovalerate-Labeled Oligonucleotides ODN-3 and ODN-4. The C6-aminoalkyl oligonucleotide ODN-**1** or ODN-**2** (10 A_{260} units) in 160 μL of 0.5 M $Na_2CO_3/NaHCO_3$ buffer (pH 8.7) was incubated for 5 h at room temperature with 34 μmol of succinimidyl-5-azidovalerate **13** in 40 μL of DMSO. The reaction mixture was concentrated in a SpeedVac, dissolved in 1 mL bidistilled water, and centrifuged for 20 min at 12 000 rpm. The supernatant was collected and further purified by reversed-phase HPLC (gradient *III*) to give about 90% isolated yield of the 5′-azidovalerate-labeled oligonucleotide ODN-**3** or ODN-**4** (Supporting Information, Figure S3a,b). The molecular masses of ODN-**3** and ODN-**4** were determined by LC-ESI-TOF or MALDI-TOF mass spectrometry (Table 1).

Synthesis of Branched BR-1. To ODN-**5**[44] (1.2 A_{260} units) and 5′-azidovalerate-labeled ODN-**3** (2.8 A_{260} units), $CuSO_4$-TBTA ligand complex (25 μL of a 20 mM stock solution in H_2O/DMSO/*t*-BuOH, 4:3:1 for TBTA; 25 μL of a 20 mM stock solution in H_2O/DMSO/*t*-BuOH 4:3:1 for $CuSO_4$), tris(carboxyethyl)phosphine (TCEP; 25 μL of a 20 mM stock solution in water), sodium bicarbonate (10 μL of a 200 mM aq. solution), and 30 μL of DMSO were added, and the reaction proceeded at room temperature for 12 h. The reaction mixture was concentrated in a SpeedVac, dissolved in 0.3 mL bidistilled water and centrifuged for 20 min at 12 000 rpm. The supernatant was collected and further purified by reversed-phase HPLC (gradient *III*). The peak containing the "click" product BR-**1** was collected (Figure S3c, Supporting Information) and concentrated to dryness in a SpeedVac. The integrity of BR-**1** was confirmed by MALDI-TOF mass spectrometry (Table 1).

Synthesis of Branched BR-2. To ODN-**5** (1.2 A_{260} units) and 5′-azidovalerate-labeled ODN-**4** (2.8 A_{260} units), $CuSO_4$−TBTA ligand complex (25 μL of a 20 mM stock solution in H_2O/DMSO/*t*-BuOH, 4:3:1 for TBTA; 25 μL of a 20 mM stock solution in H_2O/DMSO/*t*-BuOH, 4:3:1 for $CuSO_4$), tris(carboxyethyl)phosphine (TCEP; 25 μL of a 20 mM stock solution in water), benzoic acid (10 μL of a 100 mM stock solution in DMSO), and 30 μL of DMSO were added, and the reaction proceeded at room temperature for 20 min. Then, sodium bicarbonate (100 μL of a 200 mM aq. solution) was used to neutralize the excess of benzoic acid. The reaction mixture was concentrated in a SpeedVac, dissolved in 0.3 mL bidistilled water and centrifuged for 20 min at 12 000 rpm. The supernatant was collected and further purified by reversed-phase HPLC (gradient *III*) to give the "click" product BR-**2** (Figure S3d, Supporting Information). The integrity of BR-**2** was confirmed by LC-ESI-TOF mass spectrometry (Table 1).

General Protocol for the Combined "Stepwise Click" and "Double Click" Procedure: "First Click": Synthesis of Azidomethylbenzyl-Labeled Oligonucleotides ODN-14−ODN-17 and ODN-19 from Alkynylated Oligonucleotides ODN-8, ODN-9, ODN-12, ODN-13, and ODN-18 with Bis-Azide 4. To the single-stranded oligonucleotide (5 A_{260} units), a mixture of $CuSO_4$−TBTA ligand complex (50 μL of a 20 mM stock solution in H_2O/DMSO/*t*-BuOH, 4:3:1 for TBTA; 50 μL of a 20 mM stock solution in H_2O/DMSO/*t*-BuOH, 4:3:1 for $CuSO_4$), tris(carboxyethyl)phosphine (TCEP; 50 μL of a 20 mM stock solution in water), 1,4-bis-azidomethylbenzene **4**[47] (37.5 μL of a 20 mM stock solution in dioxane/H_2O, 1:1), sodium bicarbonate (50 μL of a 20 mM aq. solution), and 30 μL of DMSO were added, and the reaction proceeded at room temperature for 12 h. The reaction mixture was concentrated in a SpeedVac, dissolved in 1 mL bidistilled water, and centrifuged for 20 min at 12000 rpm. The supernatant was collected and further purified by reversed-phase HPLC (gradient *III*) to give about 80% isolated yield of the azidomethylbenzyl oligonucleotides ODN-**14**−ODN-**17**

dx.doi.org/10.1021/bc300013k | *Bioconjugate Chem.* 2012, 23, 856−870

Scheme 1. Synthesis of the Double-Functionalized "Click" Conjugate 7

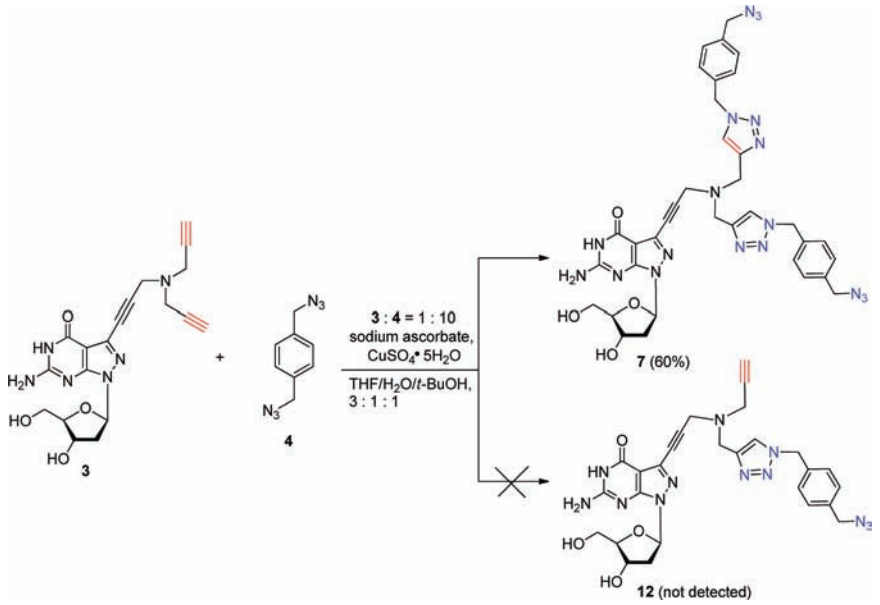

and ODN-**19**. For the preparation of ODN-**17**, 70 μL of 1,4-bis-azidomethylbenzene **4** was used. The molecular masses of the azidomethylbenzyl oligonucleotides ODN-**14**–ODN-**17** and ODN-**19** were determined by MALDI-TOF or LC-ESI-TOF mass spectrometry (Table 2).

"Second Click": Synthesis of Branched Y-shaped Oligonucleotides BR-3–BR-8 from Azidomethylbenzyl Oligonucleotides ODN-14–ODN-17 and ODN-19 with Alkynylated Oligonucleotides ODN-8–ODN-13 and ODN-18. To the alkynylated oligonucleotide (1.2 A_{260} units) and azidomethylbenzyl oligonucleotide (2.8 A_{260} units), a mixture of the $CuSO_4$–TBTA ligand complex (25 μL of a 20 mM stock solution in H_2O/DMSO/*t*-BuOH, 4:3:1 for TBTA; 25 μL of a 20 mM stock solution in H_2O/DMSO/*t*-BuOH, 4:3:1 for $CuSO_4$), tris(carboxyethyl)phosphine (TCEP; 25 μL of a 20 mM stock solution in water), benzoic acid (10 μL of a 100 mM stock solution in DMSO), and 30 μL of DMSO were added, and the reaction proceeded at room temperature for 20 min. Then, sodium bicarbonate (100 μL of a 200 mM aq. solution) was used to neutralize the excess of benzoic acid. The reaction mixture was concentrated in a SpeedVac, dissolved in 1 mL bidistilled water, and centrifuged for 20 min at 12 000 rpm. The supernatant was collected and further purified by reversed-phase HPLC (gradient *III*) to give the branched oligonucleotide. After purification by reversed-phase HPLC, the branched oligonucleotides BR-**3**–BR-**8** were isolated in 50–60% yield. The molecular masses of branched BR-**3**–BR-**8** were determined by MALDI-TOF or ESI-TOF mass spectrometry (Table 2).

RESULTS AND DISCUSSION

Synthesis and Characterization of Monomers. Recently, we have reported on the "stepwise click" reaction of modified oligonucleotides containing one terminal triple bond with the bis-azido compound **4**.[42] Now, this protocol is applied to the construction of branched oligonucleotides. To evaluate the efficiency of the "double click" reaction as the crucial step ("first click") in the "stepwise click" protocol, this reaction was first performed on monomeric nucleosides. For that, tripropargylated 8-aza-7-deaza-2′-deoxyguanosine (**3**)[44] and bis-azide **4**[47] were employed as starting materials. The "double click" reaction was performed on nucleoside **3** with bis-azide **4** in a mixture of THF/H_2O/*t*-BuOH at r.t. using $CuSO_4 \cdot 5H_2O$ as catalyst and sodium ascorbate as reducing agent. The starting material **3** was consumed within 12 h. Under these conditions, double-functionalization occurred when the molar excess of the bis-azide **4** over nucleoside **3** was 10:1 (Scheme 1). We found that both terminal triple bonds were functionalized simultaneously by two bis-azido residues **4**, even though they are space demanding. Formation of the monofunctionalized derivative **12** was not observed. "Double click" functionalization might result from the enhanced catalytic action of copper(I) being bound to the tripropargylamine side chain or to a monofunctionalized intermediate, thereby increasing the reaction rate for the "second click" reaction. The double-functionalized compound **7** was characterized by elemental analyses, as well as by ^{1}H and ^{13}C NMR spectra. The ^{13}C NMR chemical shifts are listed in the Supporting Information (Table S1). ^{13}C NMR chemical shift signals were assigned by ^{1}H–^{13}C gated-decoupled spectra (Table S2, Supporting Information) as well as by DEPT-135 NMR spectra (Figure S16, Supporting Information).

Construction and Base Pair Stability of Branched Oligonucleotides. *Principles of Construction.* For the construction of branched oligonucleotides by the "click" reaction, triple bonds as well as azido groups have to be introduced into individual oligonucleotides. While triple bonds are compatible to solid-phase phosphoramidite chemistry, azido groups are prone to react with phosphites used in phosphoramidite chemistry (Staudinger reaction). Consequently, azido groups were introduced into oligonucleotides by postmodification. Our first concept for the construction of branched DNA comprises the preparation of monoazido functionalized oligonucleotides (azido-DNA) following a reported protocol.[37,42] The azido-DNA was employed in a subsequent "double click" reaction to yield branched DNA structures as illustrated in Scheme 2.

For our second concept, a combination of the "stepwise click" and "double click" reaction was used to generate azido-modified oligonucleotides. Two routes were evaluated: (i) the "stepwise click" reaction was performed on dendronized

dx.doi.org/10.1021/bc300013k | *Bioconjugate Chem.* 2012, 23, 856–870

Scheme 2. Illustration of the First Concept for the Construction of Branched DNA Structures: DNA Conjugation of Dendronized DNA-1 with 5′-Azido-DNA

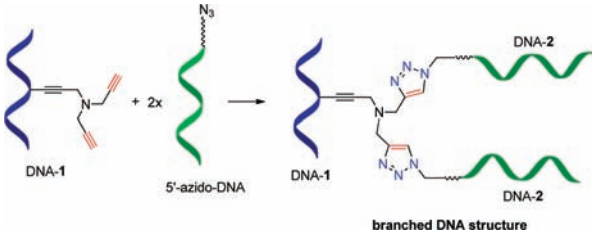

tripropargylamine oligonucleotides ("double click") with bis-azido-*p*-xylene (**4**) resulting in the formation of bis-functionalized azido-DNA carrying two azido groups at the branching position (Scheme 3, route 1). (ii) The triple bond of monoalkynylated oligonucleotides was functionalized with the bis-azido linker **4** to yield monoazido DNA (Scheme 3, route 2).[37,42] In both cases, "second click" reactions were performed with alkynylated oligonucleotides yielding branched DNA oligonucleotides.

Construction of Branched Oligonucleotides from 5′-Azido-oligonucleotides and Oligonucleotides with Tripropargylamine Side Chains by the "Double Click" Reaction. Following our first concept, 5′-alkylamino-modified oligonucleotides (ODN-**1** and ODN-**2**) were synthesized from MMT (monomethoxytrityl) protected 5′-aminolink oligonucleotides by removal of the MMT protecting group (2.5% DCA/CH_2Cl_2). Following a literature protocol, the oligomers were treated with succinimidyl-5-azidovalerate **13**[51] in a mixture of DMSO/bicarbonate buffer (pH 8.7) to give the 5′-azidovalerate-functionalized oligonucleotides ODN-**3** and ODN-**4** (Scheme 4 and Table 1).[37] The starting oligonucleotides and the 5′-azido oligonucleotides were purified by reversed-phase HPLC and characterized by LC-ESI-TOF or MALDI-TOF mass spectrometry (Table 1). For additional details, see the Experimental section and the Supporting Information.

Next, the "double click" reaction was performed with 5′-azido-labeled oligonucleotide ODN-**3** and dendronized ODN-**5** bearing a tripropargylamine side chain which resulted in the selective formation of the three-armed (Y-shaped) oligonucleotide BR-**1**. The reaction was carried out at r.t. in a mixture of H_2O/DMSO/*t*-BuOH employing a premixed 1:1 complex of $CuSO_4$–TBTA (tris(benzyltriazoylmethyl)amine), TCEP (tris-(carboxyethyl)phosphine), and $NaHCO_3$. The 5′-azido oligonucleotide ODN-**3** was used in a slight excess (7:3) compared to the tripropargylated ODN-**5**. By this, chromatographic purification was simplified as ODN-**5** was completely consumed. The reaction proceeded smoothly, and a reaction time of 12 h was necessary to drive the reaction to completeness (Scheme 4). The branched BR-**1** was obtained as the sole product confirmed by HPLC (Supporting Information, Figure S3c) and MALDI-TOF mass spectrometry (Table 1).

Recently, it was shown that the "click" reaction can be performed with high efficiency by the catalysis of carboxylic acids as demonstrated on small molecules.[52] Now, this method was applied for the synthesis of branched oligonucleotide BR-**2**. Benzoic acid was used as catalyst instead of an aq. $NaHCO_3$ solution for the "double click" reaction of ODN-**5** containing a tripropargylamine side chain and two entities of 5′-azido-labeled oligonucleotide ODN-**4**. Compared to the synthesis of the Y-shaped branched BR-**1** ($NaHCO_3$), the reaction time for the synthesis of the Y-shaped BR-**2** (benzoic acid) was now significantly shortened. The branched oligonucleotide BR-**2** was characterized by RP-18 HPLC (Figure S3d, Supporting Information), and its integrity was confirmed by LC-ESI-TOF mass spectrometry (Table 1). Table 1 displays the structures of the synthesized oligonucleotides following the first concept for the construction of branched DNA and compiles the molecular masses obtained from mass spectrometry.

*Construction of Branched Oligonucleotides BR-**3**–BR-**8** by a Combined "Stepwise Click" and "Double Click" Approach.* Next, the synthesis of a variety of three-armed branched DNA structures employing branching points at different positions and linkers of different length was performed following the protocol of a combined "stepwise click" and "double click" reaction according to our second concept. For that, oligonucleotides with short or long linkers and various linking positions were functionalized to monoazido intermediates. Two different routes were employed. Route 1 utilized ODN-**8** bearing the 7-ethynylated 7-deaza-8-azaguanine nucleoside **1** and bis-azide **4** as starting material to afford the monofunctionalized "click" intermediate ODN-**14** (Scheme 5). The ratio of **4** over ODN-**8** was 15:1 and $NaHCO_3$ was used as catalyst ("first click"). In the "second click" reaction, azidomethylbenzyl ODN-**14** and dendronized ODN-**13** yielded branched oligonucleotide *BR-**3** employing benzoic acid as catalyst (Figure S4a–d, Supporting Information). Route 2 utilized tripropargylated ODN-**13** as starting material together with a 30-fold excess of bis-azide **4** resulting in the formation of the double-functionalized dendron ODN-**17** ($NaHCO_3$, "first

Scheme 3. Illustration of the Second Concept for the Construction of Branched DNA Structures: Combined "Stepwise Click" and "Double Click" Approach for the Construction of Branched DNA Structures via Two Different Routes

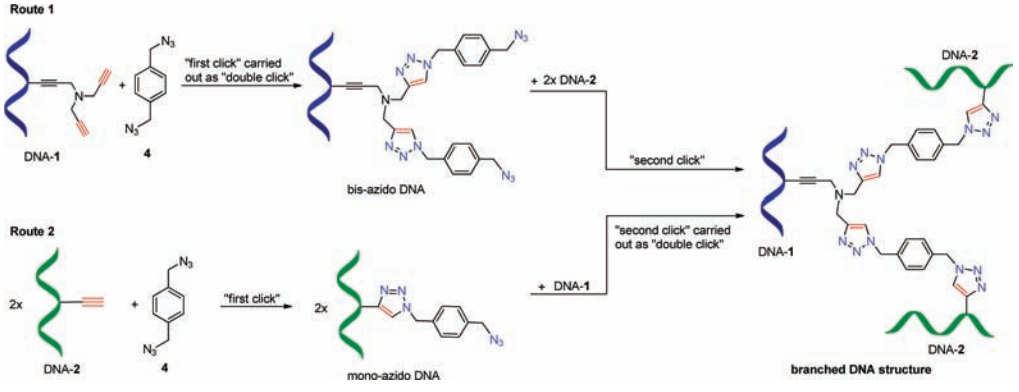

dx.doi.org/10.1021/bc300013k | *Bioconjugate Chem.* 2012, 23, 856–870

Scheme 4. Synthesis of the Branched Y-Shaped Oligonucleotide BR-1 by "Double Click" Chemistry Using ODN-5 Containing a Tripropargylamine Side Chain and 5′-Azido-Labeled ODN-3

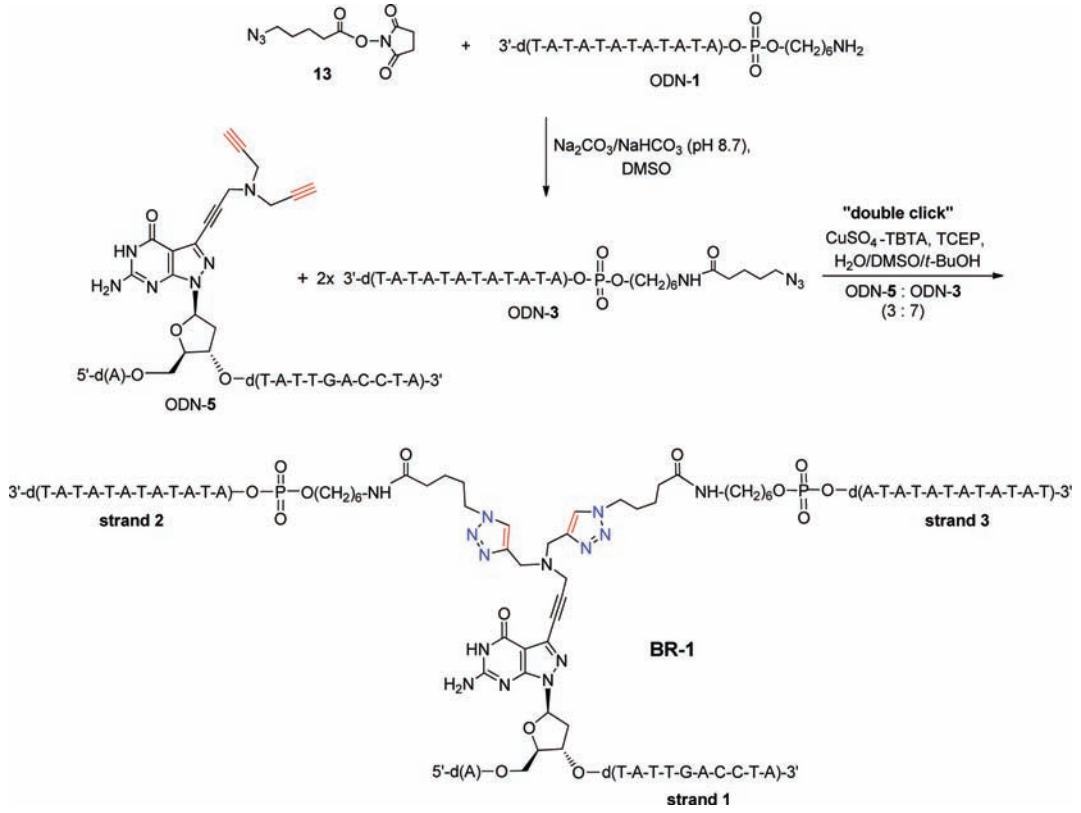

click"). ODN-**17** was clicked with ethynylated ODN-**8** leading to the formation of °BR-**3** (Figure S4e–i, Supporting Information).

It is widely accepted that the click reaction proceeds with high efficiency;[30] thus, it is predestinated to be employed in the construction of dendronic oligonucleotides. Nevertheless, by serendipity, we observed formation of a side product (BR-**3b**) during the click reaction of dendron ODN-**13** with an additional mass of +3965 Da compared to the main product (LC-ESI-TOF). This compound resulted from an incomplete "double click" reaction of ODN-**13** with azide **4** yielding a monofunctionalized adduct with one azido group and one free triple bond. A "bis-click" reaction occurring during the "first click" reaction leads to formation of BR-**3a**, while the "second click" of BR-**3a** and two ODN-**8** entities affords the four-armed branched BR-**3b**.

However, functionalization of only one triple bond (→ compound **12**, Scheme 1) was not observed on the nucleoside level nor in many other oligonucleotide examples. We assume that, during the reaction illustrated in Scheme 6, the amount of Cu(I) present in the reaction mixture was not sufficient to drive the reaction to completeness, probably resulting from the oxidation of Cu(I) to Cu(II) during the reaction.

Following route 1 or 2 shown in Scheme 5 and using a large excess of **4**, a series of branched oligonucleotides (BR-**3**–BR-**8**) was synthesized. The linker within the oligonucleotide chains were changed in length and position. The branched oligonucleotides show the following structural features: (i) one branched linker was combined with two short linkers or (ii) one branched linker was combined with two long linkers. The linking positions were placed at central or terminal positions of the oligonucleotides. Purification of the crude products was performed by reversed-phase HPLC (Figures S5–6, Supporting Information), and LC-ESI-TOF or MALDI-TOF mass spectrometry were used for characterization (Table 2). The structures of the branched oligonucleotides BR-**3**–BR-**8** as well as the alkynylated starting oligonucleotides (ODN-**8**–ODN-**13**, ODN-**18**[53]) and the azido-functionalized intermediates ODN-**14**–ODN-**17** and ODN-**19** are shown in Table 2.

Characterization of Branched Oligonucleotides by Ion-Exchange Chromatography and PAGE. The purified (RP-18 HPLC chromatography) branched oligonucleotides were characterized by ion-exchange chromatography and denaturing polyacrylamide gel electrophoresis (PAGE). As it cannot be excluded that an individual peak isolated during RP-18 chromatography contains more than one compound, we used ion-exchange chromatography to distinguish between compounds by their different number of negative charges and to proof their purity. Oligonucleotides ODN-**8**, ODN-**13**, and ODN-**14** (starting materials), as well as the branched oligonucleotide BR-**3**, were characterized by this method as demonstrated in Figure 3. Other examples are shown in the Supporting Information (Figure S7). Figure 3a,b displays the elution profiles of the starting materials, and Figure 3c shows the elution profile of the branched oligonucleotide BR-**3**. From these profiles, it is apparent that BR-**3** (36 negative charges) migrates significantly more slowly than the starting materials ODN-**8**, ODN-**13**, and ODN-**14** (12 negative charges). An ion-exchange profile of an artificial mixture of all three components is shown in Figure 3d. In this experiment, the complementary oligonucleotides ODN-**13** and ODN-**14** form a duplex. Only the excess of dendronic ODN-**13** gives a separate peak. The duplex ODN-**13**·ODN-**14** migrates between ODN-**13** and BR-**3**.

dx.doi.org/10.1021/bc300013k | *Bioconjugate Chem.* 2012, 23, 856–870

Scheme 5. Formation of Branched Oligonucleotides by a Combined "Stepwise Click" and "Double Click" Approach Using ODN-8 (Short Linker) or Dendronic ODN-13 (Branched Linker) in the "First Click" and ODN-14 (Short Linker) or the Dendronic ODN-17 (Branched Linker) in the "Second Click" Reaction

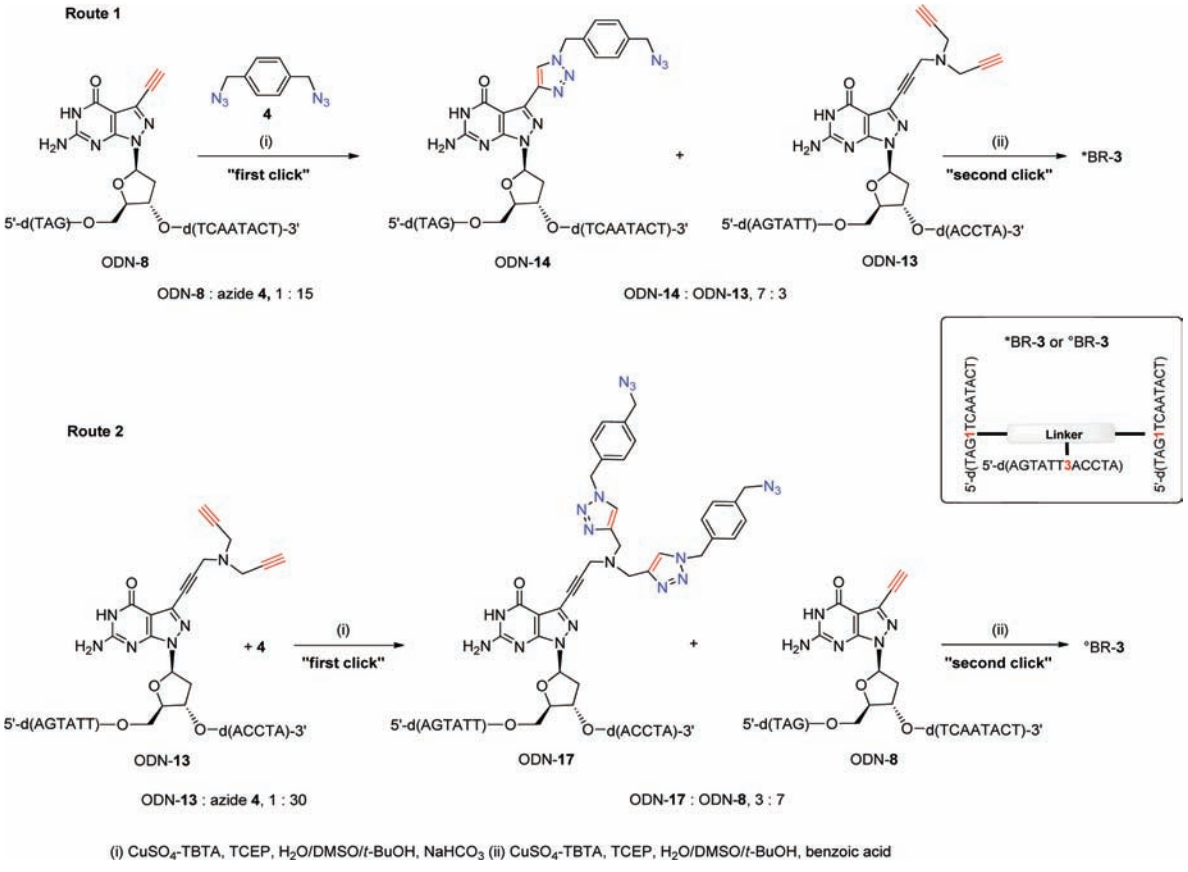

Scheme 6. "Bis-Click" Reaction of Two ODN-13 Entities during the "First Click" Reaction Followed by the Reaction of Bis-Functionalized BR-3a with Two ODN-8 Entities in the "Second Click" Reaction Affording the Four-Armed Branched BR-3b

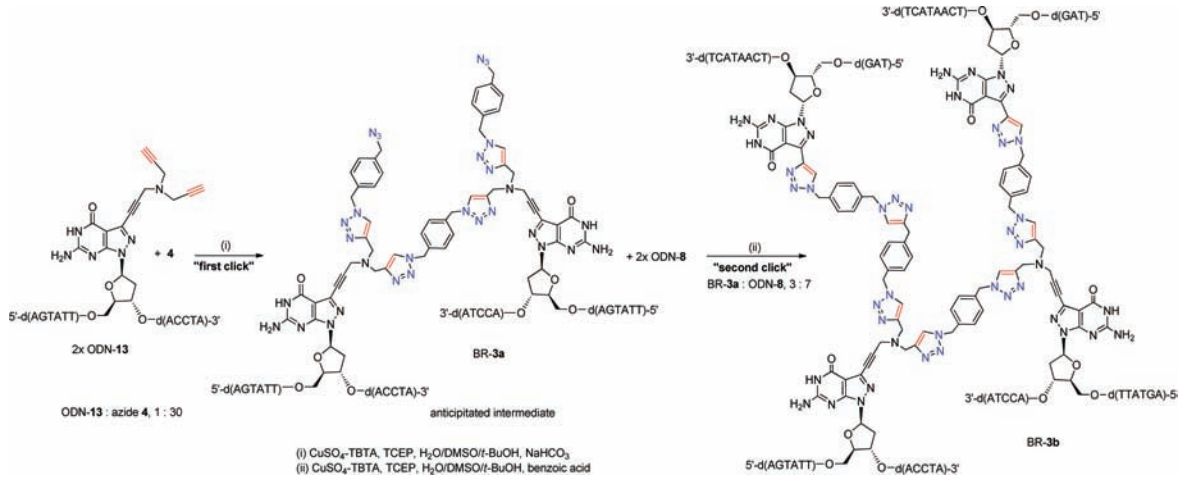

Next, the electrophoretic mobility analysis of nonbranched oligonucleotides utilized as starting materials and branched oligonucleotides obtained after "click reactions" following our first or second concept was performed by denaturing PAGE. Representative examples are shown in Figure 4 (for additional examples, see Figure S8, Supporting Information). Figure 4a depicts the relative mobilities of dendronic ODN-**13** (12-mer, lane 1), interstrand cross-linked ODN-**22**[42] as comparison (24-mer, lane 2) and the branched oligonucleotides *BR-**3** (36-mer, lane 3), BR-**4** (36-mer, lane 4), and BR-7 (38-mer, lane 5). On the basis of the different number of nucleotides (38-mer compared to 36-mers) and the different flexibility or rigidity of the linker arms, BR-**7** is migrating slower than *BR-**3** and BR-**4** (36-mers each). The slightly different migration velocity of *BR-**3** and BR-**4** can be attributed to intramolecular duplex formation of *BR-**3**, which is not possible in the case of BR-**4** (see Table 3). The PAGE analysis of branched BR-**8** (60-mer, line 3), as well as the azidomethylbenzyl-labeled ODN-**19**

dx.doi.org/10.1021/bc300013k | Bioconjugate Chem. 2012, 23, 856−870

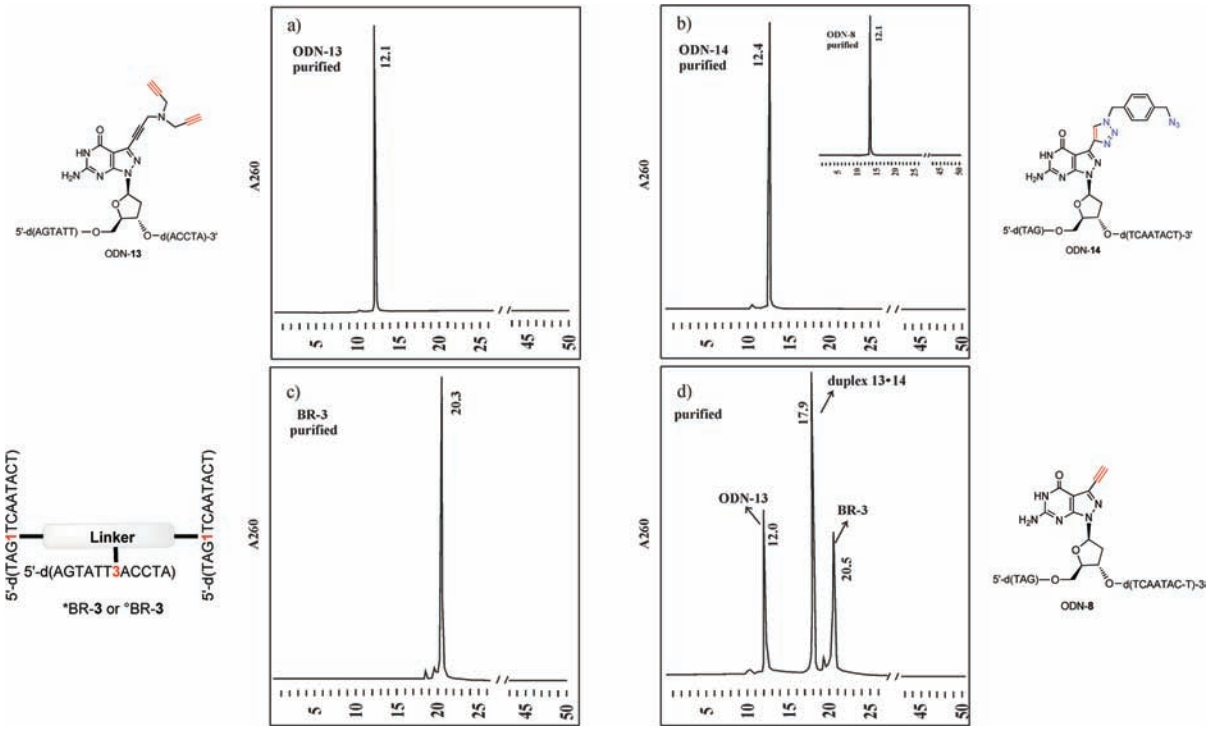

Figure 3. Ion-exchange HPLC elution profiles of (a) ODN-**13**, (b) the starting material ODN-**8** and azidomethylbenzyl-labeled ODN-**14**, (c) the branched oligonucleotide BR-**3**, (d) an artificial mixture of ODN-**13** (excess over complementary ODN-**14**), ODN-**14**, and BR-**3** on a 4 × 250 mm DNA PA-100 column using the following buffer system: (C) 25 mM Tris-HCl, 10% MeCN, pH 7.0; (D) 25 mM Tris-HCl, 1.0 M NaCl, and 10% MeCN, pH 7.0. Elution gradient *IV*: 0−30 min 20−80% D in C with a flow rate of 0.75 mL min^{-1}.

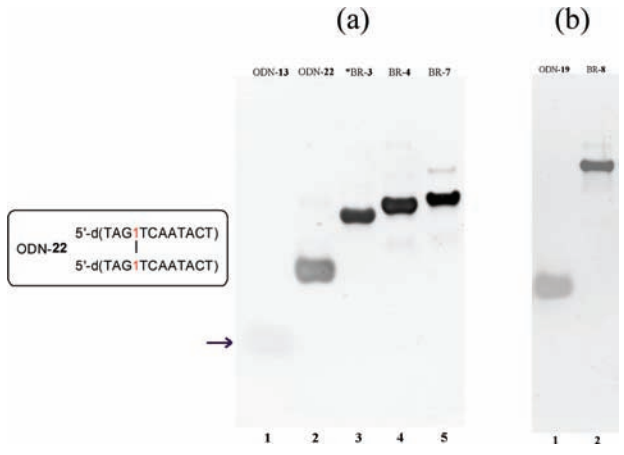

Figure 4. Denaturing PAGE analysis of oligonucleotides on a 17% polyacrylamide/7 M urea gel. (a) Lane 1, 12-mer ODN-**13**; lane 2, 24-mer cross-linked ODN-**22**;[42] lane 3, 36-mer branched *BR-**3**; lane 4, 36-mer branched BR-**4**; and lane 5, 38-mer branched BR-7. (b) Lane 1, 24-mer ODN-**19**; and lane 2, 60-mer branched BR-**8**.

(24-mer, lane 2), is shown in Figure 4b. Apart from its branched structure, BR-**8** comprises an additional unique feature, as two of its branches were designed to form hairpin structures.[53]

Chain Assembly and Base Pairing of Branched Oligonucleotides. Branched oligonucleotides are expected to form multistranded assemblies upon hybridization with complementary strands. To evaluate the type of assembly, T_m measurements were performed, and the results were summarized in Table 3. Incorporation of the tripropargylamine nucleoside **3** resulted in a duplex with a slightly increased T_m value (**5**•**7**). The self-complementary 5′-azido-labeled ODN-**3** showed a similar T_m value as the parent unmodified duplex 5′-d[(A-T)$_6$]$_2$.[54] Next, the assembly of branched oligonucleotides was studied. For branched BR-**1** containing two arms with the identical self-complementary 5′-d(A-T)$_6$ sequence, a T_m value of 35.5 °C is observed. This molecule can only form dA-dT base pairs, but several hybridization patterns are possible, affording different types of assemblies. Some examples are outlined in Figure 5. The intramolecular monomeric motif (I) requires a parallel orientation of the 5′-d(A-T) arms, while in motifs (II) and (III), dimeric and multimeric assemblies with antiparallel chain orientation are shown. We anticipate that an extended network-like assembly is formed, which, however, remains to be proven.

Interestingly, when we added ODN-7 to BR-**1**, a higher T_m value was obtained (48.5 °C) indicating that ODN-7 hybridized to its complementary arm in BR-**1**. It was not possible to determine a lower T_m value in the range 32−35 °C. Probably, the lower T_m melting profile was superimposed by the high T_m melting profile.

The branched oligonucleotides BR-**6** and BR-**7** are closely related to BR-**1**, but were constructed following our second concept of combined "stepwise click" and "double click" reactions. Also, the 5′-d(A-T)$_6$ arms of BR-**6** and BR-**7** can form only dA-dT base pairs. The somewhat lower T_m values of BR-**6** (28.5 °C) and BR-7 (26.0 °C) compared to BR-**1** might result from the different linker types. Exemplarily, nondenaturing PAGE was performed with BR-7 (Figure 6), indicating that different assemblies are formed consisting of presumably 72 nucleosides (2 molecules) or 108 nucleosides (3 molecules). After addition of ODN-7 to BR-**6** or BR-7, T_m values of 37 °C were observed indicating that ODN-7 formed a duplex with the remaining complementary chains of BR-**6** or BR-7 as shown in Table 3.

dx.doi.org/10.1021/bc300013k | *Bioconjugate Chem.* 2012, 23, 856−870

Table 3. T_m Values of DNA Duplexes, Hairpins, and Branched Oligonucleotide Assemblies

Hybridization of oligonucleotides	T_m [a,b] [°C]	Hybridization of oligonucleotides	T_m [a,b] [°C]
5'-d(AGTATTGACCTA) (ODN-**6**) 3'-d(TCATAACTGGAT) (ODN-**7**)	49.0	5'-d(A**3**TATTG ACCTA) (ODN-**5**) 3'-d(TCATAACTGGAT) (ODN-**7**)	54.0[44]
		5'-[d(A-T)$_6$]$_2$[c]	32.0[54]
5'-d(**5**ATATATATATAT) (ODN-**15**) 3'-d(TATATATATATA**5**) (ODN-**15**)	28.0	5'-d(**6**ATATATATATAT) (ODN-**16**) 3'-d(TATATATATATA**6**) (ODN-**16**)	29.5
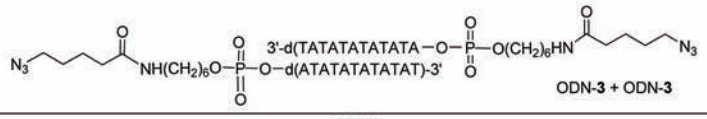 ODN-**3** + ODN-**3**			31.0
BR-1 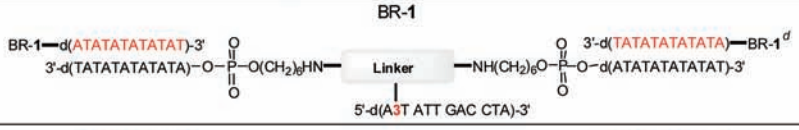			35.5
			48.5
BR-6 	28.5	BR-6 + ODN-7 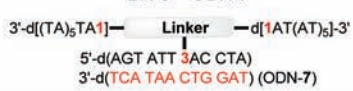	37.0
BR-7 	26.0	BR-7 + ODN-7 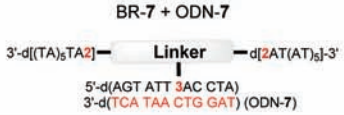	37.0
BR-4 + 3x ODN-7 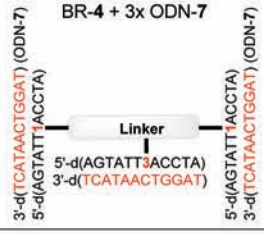	38.0	BR-5 + 3x ODN-7 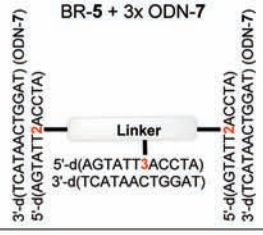	44.5[c]
BR-3 	74.0	BR-3 + ODN-6 	74.0 39.5
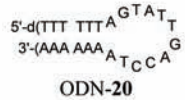 ODN-**20** + ODN-7	58.0 58.0	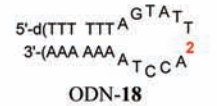 ODN-**18** + ODN-7	59.0 59.0
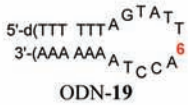 ODN-**19** + ODN-7	57.0 57.5	5'-d(T$_6$AGTATT2ACCTAA$_6$) (ODN-**18**) 3'-d(A$_6$TCATAACTGGATT$_6$) (ODN-**21**)	64.0
5'-d(T$_6$AGTATT6ACCTAA$_6$) (ODN-**19**) 3'-d(A$_6$TCATAACTGGATT$_6$) (ODN-**21**)	62.0	BR-8 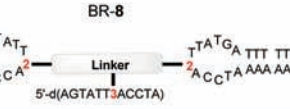	56.0

dx.doi.org/10.1021/bc300013k | Bioconjugate Chem. 2012, 23, 856−870

Table 3. continued

Hybridization of oligonucleotides	T_m [a,b] [°C]	Hybridization of oligonucleotides	T_m [a,b] [°C]
BR-8 + ODN-7	53.5	BR-8 + 2x ODN-21	61.5[e]

[a]Measured at 260 nm in a 1 M NaCl solution containing 100 mM $MgCl_2$ and 60 mM Na-cacodylate (pH 7.0). [b]The concentration of nonbranched oligonucleotides and branched compounds was 2 μM each. [c]The nonbranched oligonucleotide concentration was 6 μM. [d]For possible hybridization pattern of BR-**1**, see Figure 5. [e]The nonbranched oligonucleotide concentration was 4 μM. For linker details see Tables 1 and 2.

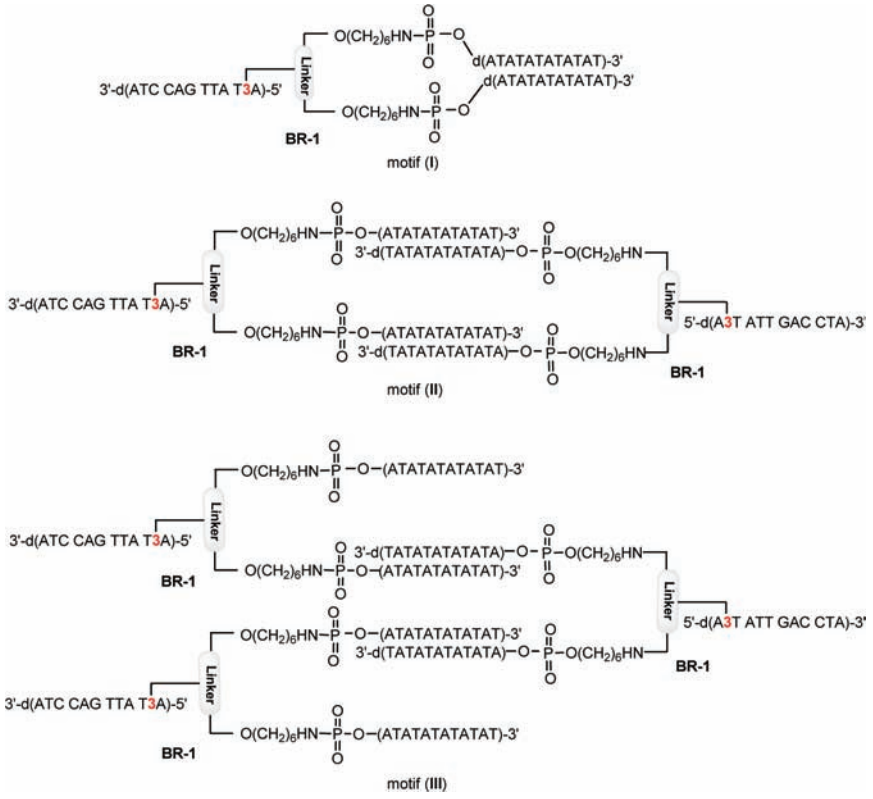

Figure 5. Possible hybridization motifs for the 5′-d(A-T) arms of BR-**1**: (i) intramolecular parallel duplex formation, (ii) bimolecular antiparallel duplex formation of two BR-**1** residues, and (iii) multistranded intermolecular network formation by several BR-**1** residues.

The branched oligonucleotides BR-**4** and BR-**5** were composed of noncomplementary 12-mer sequences. By adding complementary ODN-**7**, each arm of BR-**4** and BR-**5** is supposed to form a duplex. However, T_m values of about 40 °C were detected, while the closely related parent duplex **6**·**7** shows a T_m value of 49.0 °C. Apparently, duplex stability is reduced by the linker units situated at central positions of each duplex. This finding correlates with the observation that the destabilization is less pronounced for the long linker in BR-**5** (ΔT_m = −4.5 °C) compared to the short linker in BR-**4** (ΔT_m = −11.0 °C).

In contrast, branched oligonucleotide BR-**3** forms a highly stable intramolecular duplex (T_m = 74.0 °C; for melting profile, see Figure 7a). Pronounced duplex stabilization caused by cross-linking has previously been reported.[41,42,55−57] Native PAGE supported that no intermolecular network formation took place (Figure 6, lane 4). When ODN-**6** was added to BR-**3**, a biphasic melting was observed as shown in Figure 7b. Now, two duplexes are formed. The higher T_m value (74.0 °C) can be attributed to the cross-linked duplex, while the newly formed duplex gives the lower T_m value of 39.5 °C.

The branched oligonucleotide BR-**8** contains an additional unique feature, as two of its branches were designed to form a hairpin structure.[53] Alkynylated ODN-**18**[53] and azido-functionalized ODN-**19** as well as the parent unmodified ODN-**20** form hairpin structures with T_m values in the range 57−59 °C (Table 3 and Table S3, Supporting Information). The addition of ODN-**7** being complementary to the loop region of ODN-**18**−ODN-**20** did not impair the hairpin structures as demonstrated by the unchanged T_m values. However, the hairpins were

dx.doi.org/10.1021/bc300013k | *Bioconjugate Chem.* 2012, 23, 856−870

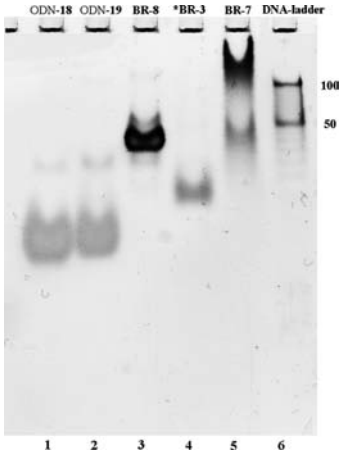

Figure 6. Nondenaturing PAGE analysis of oligonucleotides on a 15% polyacrylamide gel: lane 1, 24-mer ODN-**18**;[53] lane 2, azido-functionalized 24-mer ODN-**19**; lane 3, 60-mer branched BR-**8**; lane 4, 36-mer branched *BR-**3**; lane 5, 38-mer branched BR-**7**; and lane 6, 50-mer and 100-mer DNA ladder.

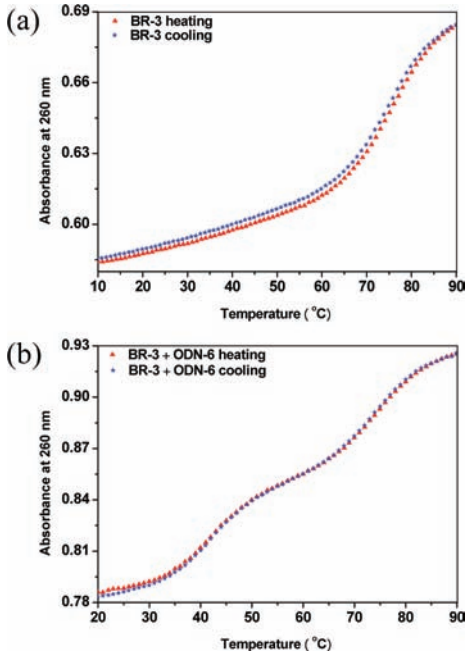

Figure 7. Melting profiles obtained from heating (red triangles) and cooling (blue stars) experiments monitored at 260 nm in 1 M NaCl, 100 mM $MgCl_2$, and 60 mM Na-cacodylate, pH 7.0, with 2 μM oligonucleotide concentration for (a) BR-**3** and (b) with 2 μM + 2 μM single-strand concentration for BR-**3** and ODN-**6**.

opened upon addition of the fully complementary oligonucleotide ODN-**21** (T_m values around 62−64 °C). Accordingly, results were obtained for the branched BR-**8** (56.0 °C) and for the combination of BR-**8** with ODN-7 (53.5 °C) and ODN-**21** (61.5 °C). The T_m value of BR-**8** with ODN-7 (53.5 °C) is somewhat lower than for the individual BR-**8** (56.0 °C), which can be attributed to the overlap of a lower melting profile of the duplex part and the higher melting profile of the hairpins.

As shown in Figure 6, ODN-**18**,[53] ODN-**19**, and the branched product BR-**8** were also analyzed by nondenaturing PAGE. As expected, only single bands were obtained, demonstrating that no higher aggregates were formed in all three cases.

This study demonstrates the versatility of the combined "stepwise and double click" chemistry approach to construct well-defined branched oligonucleotides including dendronized molecules. This protocol is applicable to most different sequence motifs and was herein exemplified for self-complementary and nonself-complementary DNA chains as well as for hairpin forming oligonucleotides.

CONCLUSION AND OUTLOOK

Dendronized oligonucleotides decorated with 7-tripropargylamine side chains carrying two terminal triple bonds were synthesized. Further functionalization with bis-azides yielded conjugates with two terminal azido groups. Both types of dendronized oligonucleotides were applied to the Huisgen-Meldal-Sharpless cycloaddition using "stepwise and double click" chemistry thereby affording hyperbranched (Y-shaped) three-armed DNA. Annealing of hyperbranched DNAs with complementary oligonucleotides resulted in supramolecular assemblies. The CuAAC chemistry used in this study shows the necessary efficiency to make dendronized DNA accessible which would be extremely difficult to be synthesized by other means. As tripropargylated phosphoramidites of all four building blocks of DNA have been reported,[43−46] a variety of branched oligonucleotides differing in linking position, linking number, or base pairing are now available. Dendronized DNA gives rise to a number of interesting properties which cannot be realized by linear biopolymers. Dendronized DNA can be utilized to stabilize hydrogels after cross-linking alkynyl chain with bifunctional azides. Dendronized DNA can be used for the signal amplification in DNA detection and quantification.[12,58] The incorporation of photoresponsive units[59] in dendronized DNA offers the possibility of creating light-sensitive DNA devices. Consequently, the concept of a combined "stepwise and double click" chemistry followed by selective hybridization expands the application of DNA conjugates to DNA diagnostics, delivery, and nanobiotechnology.

ASSOCIATED CONTENT

Supporting Information

^{13}C NMR chemical shifts, $^{1}H-^{13}C$ NMR coupling constants, synthetic procedure for **13**, HPLC purification profiles of nonbranched and branched oligonucleotides, ion-exchange HPLC profiles of nonbranched and branched oligonucleotides, denaturing PAGE analysis of oligonucleotides, additional T_m values of hairpin forming oligonucleotides, melting profiles, ^{1}H NMR, ^{13}C NMR, DEPT-135 spectra, and $^{1}H-^{13}C$-gated decoupled NMR spectra of the new compounds. This material is available free of charge via the Internet at http://pubs.acs.org.

AUTHOR INFORMATION

Corresponding Author

*Phone: +49 (0)251 53406 500. Fax: +49 (0)251 53406 857. E-mail: Frank.Seela@uni-osnabrueck.de.

Notes

The authors declare no competing financial interest.

ACKNOWLEDGMENTS

We thank Dr. Simone Budow for her continuous support throughout the preparation of the manuscript. We thank Mr. N. Q. Tran for the oligonucleotide synthesis, and Dr. Uhlmann, Coley Pharmaceuticals GmbH for LC-ESI-TOF, and Dr. Luftmann, Organisch-Chemisches Institut, WWU Münster,

Germany for MALDI-TOF mass spectra. Financial support by ChemBiotech, Münster, Germany is gratefully acknowledged.

REFERENCES

(1) Lilley, D. M. J. (1998) Folding of branched RNA species. *Biopolymers 48*, 101−112.
(2) Edmonds, M. (1987) Branched RNA. *Bioessays 6*, 212−216.
(3) Padgett, R. A., Konarska, M. M., Grabowski, P. J., Hardy, S. F., and Sharp, P. A. (1984) Lariat RNA's as intermediates and products in the splicing of messenger RNA precursors. *Science 225*, 898−903.
(4) Damha, M. J., and Ogilvie, K. K. (1988) Synthesis and spectroscopic analysis of branched RNA fragments: Messenger RNA splicing intermediates. *J. Org. Chem. 53*, 3710−3722.
(5) Agback, P., Glemarec, C., Sund, C., and Chattopadhyaya, J. (1992) Solution structures of nonameric and decameric branched-RNA modelling the lariat of group II and nuclear pre-mRNA introns (splicing) by 500 MHz NMR spectroscopy. *Tetrahedron 48*, 6537−6554.
(6) Duckett, D. R., and Lilley, D. M. J. (1990) The three-way DNA junction is a Y-shaped molecule in which there is no helix − helix stacking. *EMBO J. 9*, 1659−1664.
(7) Lin, C., Liu, Y., Rinker, S., and Yan, H. (2006) DNA tile based self-assembly: Building complex nanoarchitectures. *ChemPhysChem 7*, 1641−1647.
(8) Aldaye, F. A., Palmer, A. L., and Sleiman, H. F. (2008) Assembling materials with DNA as the guide. *Science (Washington D.C., U.S.) 321*, 1795−1799.
(9) LaBean, T. H., and Li, H. (2007) Constructing novel materials with DNA. *Nano Today 2*, 26−35.
(10) Chandra, M., Keller, S., Gloeckner, C., Bornemann, B., and Marx, A. (2007) New branched DNA constructs. *Chem.—Eur. J. 13*, 3558−3564.
(11) Scheffler, M., Dorenbeck, A., Jordan, S., Wüstefeld, M., and von Kiedrowski, G. (1999) Self-assembly of trisoligonucleotidyls: The case for nano-acetylene and nano-cyclobutadiene. *Angew. Chem., Int. Ed. 38*, 3311−3315.
(12) Horn, T., Chang, C.-A., and Urdea, M. S. (1997) Chemical synthesis and characterization of branched oligodeoxyribonucleotides (bDNA) for use as signal amplifiers in nucleic acid quantification assays. *Nucleic Acids Res. 25*, 4842−4849.
(13) Shchepinov, M. S., Udalova, I. A., Bridgman, A. J., and Southern, E. M. (1997) Oligonucleotide dendrimers: synthesis and use as polylabelled DNA probes. *Nucleic Acids Res. 25*, 4447−4454.
(14) Rosemeyer, H., Feiling, E., Nierling, W., and Seela, F. (1999) Glycerol-furcated oligonucleotides: Synthesis and aggregation. *Nucleosides Nucleotides 18*, 1563−1564.
(15) Hudson, R. H. E., and Damha, M. J. (1993) Nucleic acid dendrimers: Novel biopolymer structures. *J. Am. Chem. Soc. 115*, 2119−2124.
(16) Thrane, H., Fensholdt, J., Regner, M., and Wengel, J. (1995) Novel linear and branched oligodeoxynucleotide analogues containing 4'-C-(hydroxymethyl)thymidine. *Tetrahedron 51*, 10389−10402.
(17) Heinonen, P., and Lönnberg, H. (2004) Synthesis of phosphate-branched oligonucleotides. *Bioconjugate Chem. 15*, 1158−1160.
(18) Stewart, K. M., and McLaughlin, L. W. (2004) Four-arm oligonucleotide Ni(II)-cyclam-centered complexes as precursors for the generation of supramolecular periodic assemblies. *J. Am. Chem. Soc. 126*, 2050−2057.
(19) Gothelf, K. V., Thomsen, A., Nielsen, M., Cló, E., and Brown, R. S. (2004) Modular DNA-programmed assembly of linear and branched conjugated nanostructures. *J. Am. Chem. Soc. 126*, 1044−1046.
(20) Probst, M., Wenger, D., Biner, S. M., and Häner, R. (2012) The DNA three-way junction as a mould for tripartite chromophore assembly. *Org. Biomol. Chem. 10*, 755−759.
(21) Ueno, Y., Shibata, A., Matsuda, A., and Kitade, Y. (2003) Synthesis of 3,3′-linked oligonucleotides branched by a pentaerythritol linker and the thermal stabilities of the triplexes with single-standed DNA or RNA. *Bioconjugate Chem. 14*, 684−689.
(22) Burley, G. A., Gierlich, J., Mofid, M. R., Nir, H., Tal, S., Eichen, Y., and Carell, T. (2006) Directed DNA metallization. *J. Am. Chem. Soc. 128*, 1398−1399.
(23) Buhleier, E., Wehner, W., and Vögtle, F. (1978) "Cascade"- and "non-skid-chain-like" syntheses of molecular cavity topologies. *Synthesis*, 155−158.
(24) Grayson, S. M., and Fréchet, J. M. J. (2001) Convergent dendrons and dendrimers: from synthesis to applications. *Chem. Rev. 101*, 3819−3867.
(25) Urbani, C. N., Bell, C. A, Whittaker, M. R., and Monteiro, M. J. (2008) Convergent synthesis of second generation AB-type miktoarm dendrimers using "click" chemistry catalyzed by copper wire. *Macromolecules 41*, 1057−1060.
(26) Ornelas, C., Aranzaes, J. R., Cloutet, E., Alves, S., and Astruc, D. (2008) Click assembly of 1,2,3-triazole-linked dendrimers, including ferrocenyl dendrimers, which sense both oxo anions and metal cations. *Angew. Chem., Int. Ed. 46*, 872−877.
(27) Helms, B., Mynar, J. L., Hawker, C. J., and Fréchet, J. M. J. (2004) Dendronized linear polymers via "click chemistry. *J. Am. Chem. Soc. 126*, 15020−15021.
(28) Ornelas, C., Broichhagen, J., and Weck, M. (2010) Strain-promoted alkyne azide cycloaddition for the functionalization of poly(amide)-based dendrons and dendrimers. *J. Am. Chem. Soc. 132*, 3923−3931.
(29) Voit, B. (2007) The potential of cycloaddition reactions in the synthesis of dendritic polymers. *New J. Chem. 31*, 1139−1151.
(30) Johnson, J. A., Finn, M. G., Koberstein, J. T., and Turro, N. J. (2008) Construction of linear polymers, dendrimers, networks, and other polymeric architectures by copper-catalyzed azide-alkyne cycloaddition "click" chemistry. *Macromol. Rapid Commun. 29*, 1052−1072.
(31) Caminade, A.-M., Turrin, C.-O., and Majoral, J.-P. (2008) Dendrimers and DNA: Combinations of two special topologies for nanomaterials and biology. *Chem.—Eur. J. 14*, 7422−7432.
(32) DeMattei, C. R., Huang, B., and Tomalia, D. A. (2004) Designed dendrimer syntheses by self-assembly of single-site, ssDNA functionalized dendrons. *Nano Lett. 4*, 771−777.
(33) Endo, M., and Majima, T. (2006) Thermodynamic properties of branched DNA complexes with full-matched and mismatched DNA strands. *Chem. Commun. (Cambridge U. K.)*, 2329−2331.
(34) Huisgen, R. (1989) Kinetics and reaction mechanisms: Selected examples from the experience of forty years. *Pure Appl. Chem. 61*, 613−628.
(35) Meldal, M., and Tornøe, C. W. (2008) Cu-catalyzed azide-alkyne cycloaddition. *Chem. Rev. 108*, 2952−3015.
(36) Rostovtsev, V. V., Green, L. G., Fokin, V. V., and Sharpless, K. B. (2002) A stepwise Huisgen cycloaddition process: Copper(I)-catalyzed regioselective "ligation" of azides and terminal alkynes. *Angew. Chem., Int. Ed. 41*, 2596−2599.
(37) Kumar, R., El-Sagheer, A., Tumpane, J., Lincoln, P., Wilhelmsson, L. M., and Brown, T. (2007) Template-directed oligonucleotide strand ligation, covalent intramolecular DNA circularization and catenation using click chemistry. *J. Am. Chem. Soc. 129*, 6859−6864.
(38) Jacobsen, M. F., Ravnsbæk, J. B., and Gothelf, K. V. (2010) Small molecule induced control in duplex and triplex DNA-directed chemical reactions. *Org. Biomol. Chem. 8*, 50−52.
(39) Lietard, J., Meyer, A., Vasseur, J.-J., and Morvan, F. (2008) New strategies for cyclization and bicyclization of oligonucleotides by click chemistry assisted by microwaves. *J. Org. Chem. 73*, 191−200.
(40) Peng, X., Li, H., and Seidman, M. (2010) A template-mediated click-click reaction: PNA-DNA, PNA-PNA (or peptide) ligation and single nucleotide discrimination. *Eur. J. Org. Chem.*, 4194−4197.
(41) Pujari, S. S., Xiong, H., and Seela, F. (2010) Cross-linked DNA generated by "bis-click" reactions with bis functional azides: Site independent ligation of oligonucleotides via nucleobase alkynyl chains. *J. Org. Chem. 75*, 8693−8696.
(42) Xiong, H., and Seela, F. (2011) Stepwise "click" chemistry for the template independent construction of a broad variety of cross-linked

oligonucleotides: Influence of linker length, position, and linking number on DNA duplex stability. *J. Org. Chem. 76*, 5584−5597.
(43) Sirivolu, V. R., Chittepu, P., and Seela, F. (2008) DNA with branched internal side chains: Synthesis of 5-tripropargylamine-dU and conjugation by an azide-alkyne double click reaction. *ChemBioChem 9*, 2305−2316.
(44) Seela, F., Xiong, H., and Budow, S. (2010) Synthesis and 'double click' density functionalization of 8-aza-7-deazaguanine DNA bearing branched side chains with terminal triple bonds. *Tetrahedron 66*, 3930−3943.
(45) Seela, F., and Ingale, S. A. (2010) "Double click" reaction on 7-deazaguanine DNA: Synthesis and excimer fluorescence of nucleosides and oligonucleotides with branched side chains decorated with proximal pyrenes. *J. Org. Chem. 75*, 284−295.
(46) Ingale, S. A., Pujari, S. S., Sirivolu, V. R., Ding, P., Xiong, H., Mei, H., and Seela, F. (2012) 7-Deazapurine and 8-aza-7-deazapurine nucleoside and oligonucleotide pyrene "click" conjugates: Synthesis, nucleobase controlled fluorescence quenching and duplex stability. *J. Org. Chem. 77*, 188−199.
(47) Thomas, J. R., Liu, X., and Hergenrother, P. J. (2005) Size-specific ligands for RNA hairpin loops. *J. Am. Chem. Soc. 127*, 12434−12435.
(48) Astruc, D., Liang, L., Rapakousiou, A., and Ruiz, J. (2012) Click dendrimers and triazole-related aspects: Catalysts, mechanism, synthesis, and functions. A bridge between dendritic architectures and nanomaterials. *Acc. Chem. Res.*, DOI: 10.1021/ar200235m.
(49) Feldkamp, U., and Niemeyer, C. M. (2006) Rational design of DNA nanoarchitectures. *Angew. Chem., Int. Ed. 45*, 1856−1876.
(50) *User's Manual of the DNA Synthesizer*, Applied Biosystems, Weiterstadt, Germany.
(51) Seo, T. S., Li, Z., Ruparel, H., and Ju, J. (2003) Click chemistry to construct fluorescent oligonucleotides for DNA sequencing. *J. Org. Chem. 68*, 609−612.
(52) Shao, C., Wang, X., Xu, J., Zhao, J., Zhang, Q., and Hu, Y. (2010) Carboxylic acid-promoted copper(I)-catalyzed azide-alkyne cycloaddition. *J. Org. Chem. 75*, 7002−7005.
(53) Qing, G., Xiong, H., Seela, F., and Sun, T. (2010) Spatially controlled DNA nanopatterns by "click" chemistry using oligonucleotides with different anchoring sites. *J. Am. Chem. Soc. 132*, 15228−15232.
(54) Seela, F., and Kaiser, K. (1988) 8-Aza-7-deazaadenine N^8 and N^9-(β-D-2'-deoxyribofuranosides): Building blocks for automated DNA synthesis and properties of oligodeoxyribonucleotides. *Helv. Chim. Acta 71*, 1813−1823.
(55) Noronha, A. M., Noll, D. M., Wilds, C. J., and Miller, P. S. (2002) N^4-C-Ethyl-N^4C cross-linked DNA: Synthesis and characterization of duplexes with interstrand cross-links of different orientations. *Biochemistry 41*, 760−771.
(56) El-Sagheer, A. H., Kumar, R., Findlow, S., Werner, J. M., Lane, A. N., and Brown, T. (2008) A very stable cyclic DNA miniduplex with just two base pairs. *ChemBioChem 9*, 50−52.
(57) Kočalka, P., El-Sagheer, A. H., and Brown, T. (2008) Rapid and efficient DNA strand cross-linking by click chemistry. *ChemBioChem 9*, 1280−1285.
(58) Detmer, J., Lagier, R., Flynn, J., Zayati, C., Kolberg, J., Collins, M., Urdea, M., and Sánchez-Pescador, R. (1996) Accurate quantification of hepatitis C virus (HCV) RNA from all HCV genotypes by using branched-DNA technology. *J. Clin. Microbiol. 34*, 901−907.
(59) Shen, X., Liu, H., Li, Y., and Liu, S. (2008) Click-together azobenzene dendrons: Synthesis and characterization. *Macromolecules 41*, 2421−2425.

Bioconjugate Chemistry

Technical Note

pubs.acs.org/bc

Polyamidoamine Dendron-Bearing Lipids as a Nonviral Vector: Influence of Dendron Generation

Kenji Kono,* Ryuji Ikeda, Kota Tsukamoto, Eiji Yuba, Chie Kojima, and Atsushi Harada

Department of Applied Chemistry, Graduate School of Engineering, Osaka Prefecture University, 1-1 Gakuen-cho, Naka-ku, Sakai, Osaka 599-8531, Japan

Supporting Information

ABSTRACT: Recently, we demonstrated that octadecyl chains are important as alkyl chain moieties of polyamidoamine (PAMAM) dendron-bearing lipids for their serum-resistant transfection activity [*Bioconjugate Chem.* **2007**, *18*, 1349−1354]. Toward production of highly potent vectors, we examined the influence of the generation of dendron moiety on transfection activity of PAMAM dendron-bearing lipids having two octadecyl chains. We synthesized dendron-bearing lipids with PAMAM G1, G2, and G3 dendrons, designated respectively as DL-G1−$2C_{18}$, DL-G2−$2C_{18}$, and DL-G3−$2C_{18}$. The DL-G2−$2C_{18}$ and DL-G3−$2C_{18}$ interacted with plasmid DNA effectively and formed stable lipoplexes with small sizes and spherical shape. However, DL-G1−$2C_{18}$ interacted with plasmid DNA less effectively and formed tubular-shaped lipoplexes with lower stability and larger size. Cells took up DL-G2−$2C_{18}$ and DL-G3−$2C_{18}$ lipoplexes efficiently, but cellular uptake of the DL-G1−$2C_{18}$ lipoplexes was less efficient. Nevertheless, DL-G1−$2C_{18}$ lipoplexes achieved 100−10 000 times higher levels of transgene expression, which was evaluated using luciferase gene as a reporter gene. Confocal scanning laser microscopic analysis of intracellular behaviors of the lipoplexes revealed that DL-G1−$2C_{18}$ lipoplexes generated free plasmid DNA molecules in the cytosol more effectively than other lipoplexes did. Moderate binding ability of DL-G1−$2C_{18}$ might be responsible for generation of lipoplexes which deliver plasmid DNA into cells, liberate it in the cytoplasm, and induce efficient transgene expression.

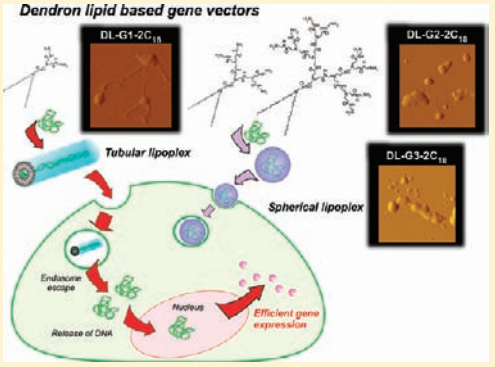

INTRODUCTION

Development of nonviral vectors that deliver therapeutic genes to target cells has been demanded for efficient and safe gene therapy and iPS cell-based regenerative medicine.[1−3] Among these nonviral vectors, various types of cationic lipids and cationic polymers have been studied intensively, but their activity requires improvement. These vectors can associate with plasmid DNA and form complexes, which are respectively designated as lipoplexes and polyplexes.[4−6] These vector−DNA complexes bind to the cell surface through electrostatic interactions and are taken up by cells mainly via endocytosis.[6,7] Subsequently, some parts of plasmid DNA contained in the complexes reach the nucleus, where gene transcription occurs. Nevertheless, most complexes are likely to be trapped in the endosome, where they are eventually degraded in the lysosome. Therefore, avoidance of plasmid DNA degradation in the lysosome and its transfer into cytosol is regarded as a key process for efficient transfection.[7]

To date, various strategies have been explored to promote transfer of plasmid DNA into cytosol, including membrane fusion[8−10] and proton sponge effect,[11,12] which are, respectively, typical functions of lipid-based and polymer-based vectors. We regarded the combination of these polymer-based and lipid-based functions as an efficient strategy for producing efficient nonviral vectors. With respect to polymer-based vectors, while various types of polymers have been shown to induce gene transfection into cells,[11−15] polyamidoamine (PAMAM) dendrimers are one of the most extensively studied.[16−18] Indeed, PAMAM dendrimers exhibit efficient gene transfection by generating the proton sponge effect through their tertiary amines.[16−18] In addition, attachment of PAMAM dendrimer functional moieties, such as L-argnine,[19] L-phenylalanine,[20] and hydrophobic alkyl chains,[21,22] to the periphery of PAMAM dendrimers was shown to increase transfection activity of the corresponding unmodified dendrimers, indicating that PAMAM dendrimers can be used as a base material for the production of highly efficient gene vectors.[13,23] Therefore, we chose PAMAM dendrimers as a polymer-based functional component and derivatized them to generate a new type of lipids that consisted of a PAMAM dendron and two dodecyl chains.[24,25] Transfection activity of the PAMAM dendron-bearing lipids was shown to increase concomitantly with increasing dendron generation because of the proton sponge effect increase with dendron generation.[24] In addition, we found recently that serum-resistant transfection activity of the PAMAM G3 dendron-based lipid can be improved greatly by increasing their alkyl chain length from dodecyl to octadecyl chains.[26] Indeed, we expected that optimization of the generation of

Received: July 12, 2011
Revised: December 14, 2011
Published: February 29, 2012

   dx.doi.org/10.1021/bc200368b | *Bioconjugate Chem.* 2012, 23, 871−879

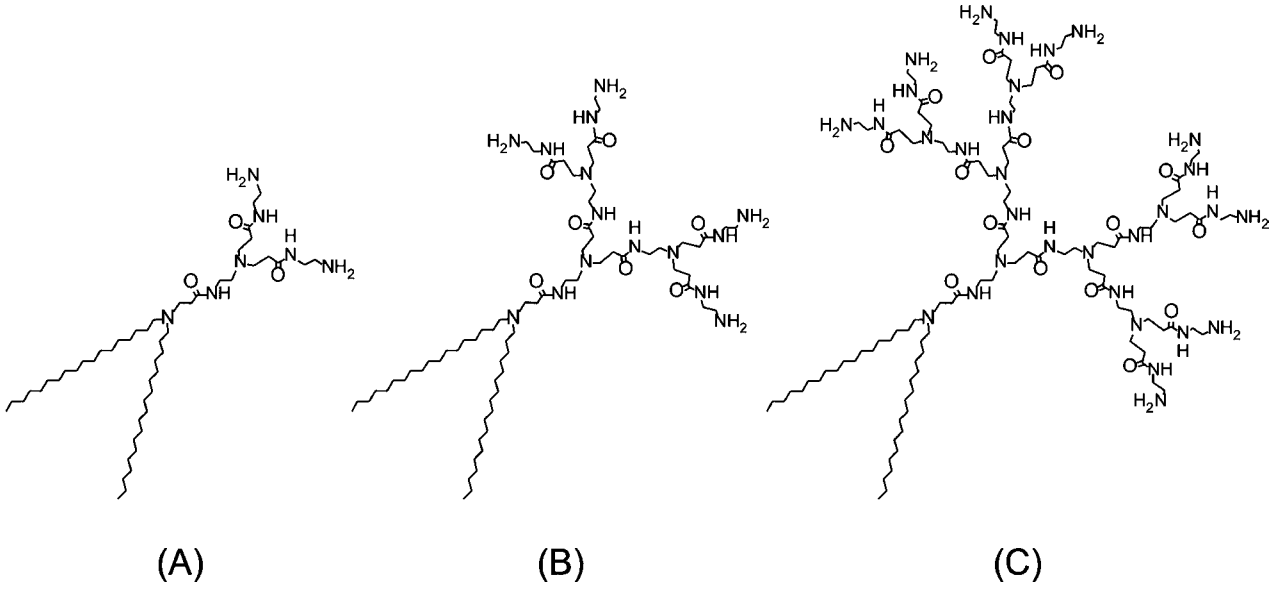

Figure 1. Structures of DL-G1−$2C_{18}$ (A), DL-G2−$2C_{18}$ (B), and DL-G3−$2C_{18}$ (C).

PAMAM dendron moiety of the octadecyl-type PAMAM dendron-based lipids might generate highly potent vectors, which achieve efficient transfection in the presence of serum.

In this study, toward production of highly potent vectors, we examined the influence of the generation of dendron moiety on transfection activity of the PAMAM dendron-bearing lipids having two octadecyl chains. We synthesized dendron-bearing lipids of three kinds with PAMAM G1, G2, and G3 dendrons, which are designated DL-G1−$2C_{18}$, DL-G2−$2C_{18}$, and DL-G3−$2C_{18}$ (Figure 1), and examined transfection of cells using these dendron-bearing lipids. Unexpected but marked increases of transfection activity with decreasing generation were found.

EXPERIMENTAL SECTION

General Methods. Dioctadecylamine was purchased from Fluka (Tokyo, Japan). Methyl acrylate, ethylenediamine, and tris(hydroxymethyl)aminomethane (Tris) were obtained from Kishida Chemical (Osaka, Japan). Sodium cyanide and ethidium bromide were supplied from Wako Pure Chemical Industries (Osaka, Japan). Merck Kieselgel 60 (230−400 mesh) was used for silica gel chromatography. 3-(4,5-Dimethyl-2-thiazolyl)-2,5-diphenyl-2*H*-tetrazolium bromide (MTT) was obtained from Dojin Laboratories (Kumamoto, Japan). Fetal bovine serum (FBS) was from PAA Laboratories GmbH (Pasching, Austria). Dulbecco's modified Eagle's medium (DMEM) was from Nissui Pharmaceutical (Tokyo, Japan). Agarose was purchased from Nacalai Tesque (Kyoto, Japan). Plasmid DNA pCMV-Luc, which contains the cDNA of firefly luciferase driven by a human cytomegalovirus immediate−early promoter, was a gift from Dr. Kazuo Maruyama, Teikyo University, and amplified in *E. coli*, isolated, and purified using a QIAGEN plasmid Maxi Kit. Dendron-based lipids DL-G1−$2C_{18}$, DL-G2−$2C_{18}$, and DL-G3−$2C_{18}$ were synthesized as previously reported.[26]

Preparation of Lipoplexes. To a dry, thin membrane of the dendron-bearing lipid, phosphate-buffered saline (PBS) was added and sonicated for 2 min using a bath-type sonicator to afford a lipid suspension. Plasmid DNA (1 μg) was dissolved in 20 mM Tris-HCl buffer (pH 7.4, 50 μL), mixed with the lipid suspension (50 μL), and incubated for 30 min at room temperature to afford a lipoplex with a given ratio of primary amine of DL-G3 to DNA phosphate (N/P ratio).

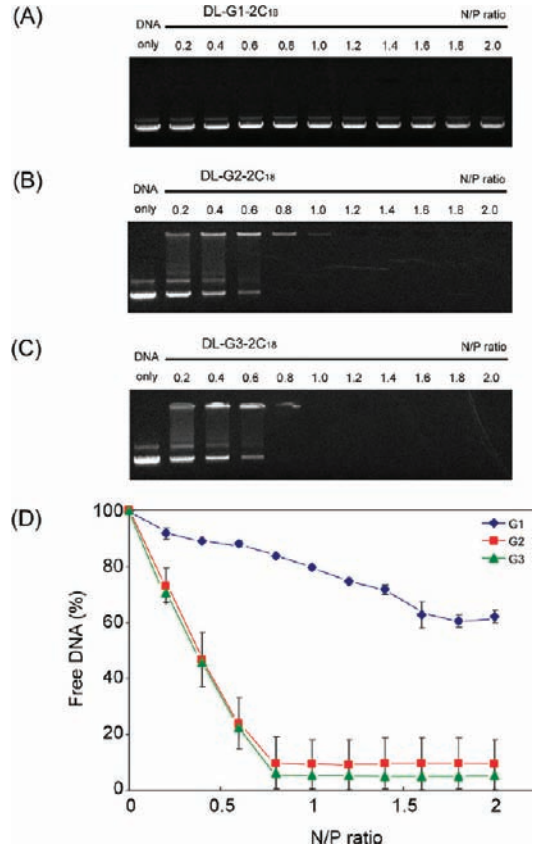

Figure 2. Agarose gel electrophoretic analysis for complexation of DL-G1−$2C_{18}$ (A), DL-G2−$2C_{18}$ (B), and DL-G3−$2C_{18}$ (C), with plasmid DNA at varying N/P ratios. The percentage of free plasmid DNA was evaluated and plotted against N/P ratio (D) for complexation of DL-G1−$2C_{18}$ (diamonds), DL-G2−$2C_{18}$ (squares), and DL-G3−$2C_{18}$ (triangles) with plasmid DNA. Each point represents the mean ± SD (n = 2).

Agarose Gel Electrophoresis. The dendron-bearing lipid−DNA complexes with varying N/P ratios were prepared

dx.doi.org/10.1021/bc200368b | *Bioconjugate Chem.* 2012, 23, 871−879

by mixing plasmid DNA (1 μg) dissolved in 20 mM Tris-HCl buffer (5 μL) and lipid suspension (5 μL). After 30 min incubation at room temperature, the samples (10 μL) were electrophoresed on 0.6 wt % agarose gel in 40 mM Tris, 20 mM sodium acetate, and 2 mM EDTA buffer (pH 8.0) containing 1 μg/mL ethidium bromide at 100 V for 30 min. The ethidium bromide-stained bands were visualized using a LAS-1000UV mini (Fujifilm, Tokyo, Japan) and analyzed with *Science Lab 2003 Multi Gauge* software (Fujifilm, Tokyo, Japan).

Dynamic Light Scattering (DLS) Measurement. The diameters of lipoplexes were estimated by DLS using an electrophoretic light scattering spectrometer ELS-8000F (Otuka Electronics Co, Ltd., Osaka, Japan). Lipoplexes with various N/P ratios were prepared by mixing plasmid DNA (20 μg) and a given amount of the dendron-bearing lipid and incubated for 30 min as described above. The data were obtained at a detection angle of 90° at 25 °C and were analyzed by the cumulant method.

Atomic Force Microscopy (AFM). AFM measurements were performed by SPI3800 probe station and SPA400 unit system of the scanning probe microscopy system (Seiko Instruments Inc., Japan). The cantilever was made of silicon (SI-DF40; Seiko Instruments Inc., Japan), and its spring constant was 16 N/m. Lipoplexes were formed at a total of 100 μg/mL of plasmid DNA concentration. Lipoplexes containing 1 μg of plasmid DNA were applied to freshly cleaved mica and incubated on the mica for 30 min. The measurements were performed in a dynamic force mode (noncontact mode).

Transfection. Transfection of CV1 cells or HeLa cells was done according to the following procedures. The cells were seeded in 0.5 mL of DMEM supplemented with 10% FBS in 24-well culture plates at 5.0×10^4 cells per well the day before transfection. The cells were washed with PBS containing 0.36 mM $CaCl_2$ and 0.42 mM $MgCl_2$ [PBS(+)] and then covered with DMEM in the presence or absence of 10% FBS (1 mL). The lipoplexes containing plasmid DNA were added gently to the cells and incubated for 4 h at 37 °C. Then, the cells were rinsed with PBS(+), covered with DMEM containing 10% FBS, and incubated at 37 °C. After 40 h, the cells were lysed by adding 50 μL of Luc-PGC-50 detergent (Toyo Ink, Tokyo, Japan). A 20 μL aliquot was taken from each dish and used for one luciferase assay using a kit (Toyo Ink) and a Lumat LB9507 luminometer (Berthold, Bad Wildbad, Germany). The protein content of the lysate was measured by Coomassie Protein Assay Reagent (Pierce, IL, USA) using bovine serum albumin as the standard. Transfection with Lipofectamine LTX was also performed according to the protocol recommended by the manufacturer.

Cytotoxicity. HeLa cells (5×10^4 cells per well) were seeded in a 24 well plate and grown in DMEM supplemented with 10% FBS for 20 h. The cells were washed with PBS(+) and covered with DMEM supplemented with 10% FBS (1 mL). Then, the lipoplex suspension (100 μL) containing plasmid DNA (1 μg) at N/P ratio of 2.0 was added to the cells and incubated at 37 °C for 4 h. The cells were rinsed with PBS(+), covered with DMEM containing 10% FCS, and incubated at 37 °C for 40 h and their viability was evaluated using an assay with 3-(4,5-dimethyl-2-thiazolyl)-2,5-diphenyl-2*H*-tetrazolium bromide (MTT).[27] The cell viability was defined as the ratio to that without treatment.

RESULTS AND DISCUSSION

Lipoplex Formation with Plasmid DNA. The ability of the dendron-bearing lipids with varying dendron generations to form a lipoplex with plasmid DNA was investigated using gel retardation assay. The plasmid DNA (1 μg) was incubated with varying amounts of DL-G1−$2C_{18}$, DL-G2−$2C_{18}$, and DL-G3−$2C_{18}$ for 30 min and electrophoresed on an agarose gel. Figure 2A−C shows that the amount of free plasmid DNA decreased concomitantly with the increasing N/P ratio for all dendron-based lipids, indicating that these lipids can form a lipoplex with plasmid DNA. No free plasmid DNA was observed at N/P ratios higher than 0.8 for DL-G2−$2C_{18}$ and DL-G3−$2C_{18}$, indicating that these lipids formed lipoplexes efficiently with plasmid DNA. However, for DL-G1−$2C_{18}$, more than 60% of plasmid DNA existed as free after electrophoresis, even at the N/P ratio of 2 (Figure 2D), and the lipoplex formation became complete above the N/P ratio of 8 (see Figure S1 of Supporting Information). It is possible that dissociation of plasmid DNA from DL-G1−$2C_{18}$ lipoplexes was induced during electrophoresis, but the result might indicate that its lipoplex formation ability is weak. Indeed, electrostatic interaction between the dendron moiety and plasmid DNA are expected to play an important role in their lipoplex formation. The number of terminal amino groups increases concomitantly with increasing dendron generation. Therefore, multivalent interaction of positively charged terminal groups of the dendron moiety of higher generations with negatively charged DNA molecules might result in efficient lipoplex formation.[18,24,28]

Lipoplex Particle Size. Influence of the generation of the dendron moiety of the dendron-bearing lipids on their lipoplex size was investigated using DLS (Figure 3 and Figure S2).

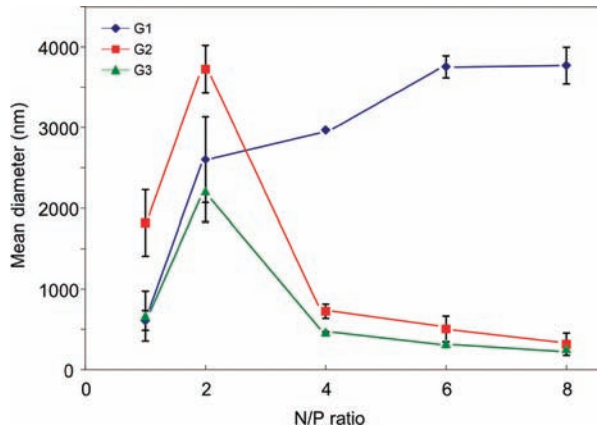

Figure 3. Mean diameter of DL-G1−$2C_{18}$ (diamonds), DL-G2−$2C_{18}$ (squares), and DL-G3−$2C_{18}$ (triangles) lipoplexes as a function of N/P ratio. The mean diameter was estimated using DLS. The lipid suspension was added to plasmid DNA solution and incubated for 30 min at 25 °C. Each point represents the mean ± SD (n = 2 or 3).

Although DL-G1−$2C_{18}$ was shown to have a weak ability to form lipoplexes from the electrophoresis experiment (Figure 2), this lipid actually formed lipoplexes whose sizes were generally large. In addition, DL-G2−$2C_{18}$ formed large lipoplexes of around 2000−3500 nm at the N/P ratio of 2, although their size decreased to about 500 nm above the N/P ratio of 4. A similar N/P ratio dependence was observed for the DL-G3−$2C_{18}$ lipoplexes, although their sizes were somewhat smaller than those of the DL-G2−$2C_{18}$ lipoplexes.

dx.doi.org/10.1021/bc200368b | *Bioconjugate Chem.* 2012, 23, 871−879

Charge-neutralized lipoplexes are known to tend to form large aggregates because of their hydrophobic interaction.[29] For that reason, these dendron-based lipids might form large lipoplexes around N/P ratio of 2, where their charge density was low. In contrast, at an N/P ratio higher than 4, the lipoplexes might possess sufficient net charge to suppress aggregation of small lipoplexes with G2 and G3 dendron-bearing lipids.

In contrast, lipoplexes with the G1 dendron-bearing lipid exhibited a large size of 3000−4000 nm above the N/P ratio of 4, which suggests that the DL-G1−$2C_{18}$ lipoplexes retain hydrophobic character at high N/P ratios. Because DL-G1−$2C_{18}$ molecules have fewer positive charges than the G2 and G3 dendron-bearing lipid molecules, the DL-G1−$2C_{18}$ lipoplexes contain more octadecyl chains than those of the G2 and G3 dendron-bearing lipids at the same N/P ratio. Therefore, the hydrophobic character of the DL-G1−$2C_{18}$ lipoplexes might be derived from higher contents of the octadecyl chains of the DL-G1−$2C_{18}$ lipoplexes than those of the DL-G2−$2C_{18}$ and DL-G2−$2C_{18}$ lipoplexes of the same N/P ratio.

Morphology of the lipoplexes was also investigated using AFM. As is seen in Figure 4, their morphology is quite heterogeneous, which is consistent with their large size distribution estimated using DLS (Figure S2). The DL-G2−$2C_{18}$ and DL-G3−$2C_{18}$ lipoplexes displayed particles with spherical shape, although some particles seem to be formed by fusion of spherical lipoplexes. The DL-G1−$2C_{18}$ lipoplex also exhibited spherical particles, but these particles contained many tubular structures. The overall dynamic molecular shape of amphiphiles is known to affect their assembly morphology.[30] These dendron-based lipids have the same long alkyl chains as the hydrophobic moiety but different generation of dendron as the polar head moiety, which would result in the different molecular shape among these dendron-based lipids. Probably, the DL-G1−$2C_{18}$ molecule having a relatively small headgroup may enable formation of complexes with a tubular shape, although correlation between the molecular shape of the dendron-based lipids and their lipoplex morphology is still to be clarified. To confirm that the tubular structures of the DL-G1−$2C_{18}$ lipoplexes contained plasmid DNA, we prepared the lipoplexes using FITC-labeled plasmid DNA. We observed that the tubular structures displayed rhodamine fluorescence using a confocal laser scanning microscope, indicating that these tubular structures indeed contain plasmid DNA (Figure S3).

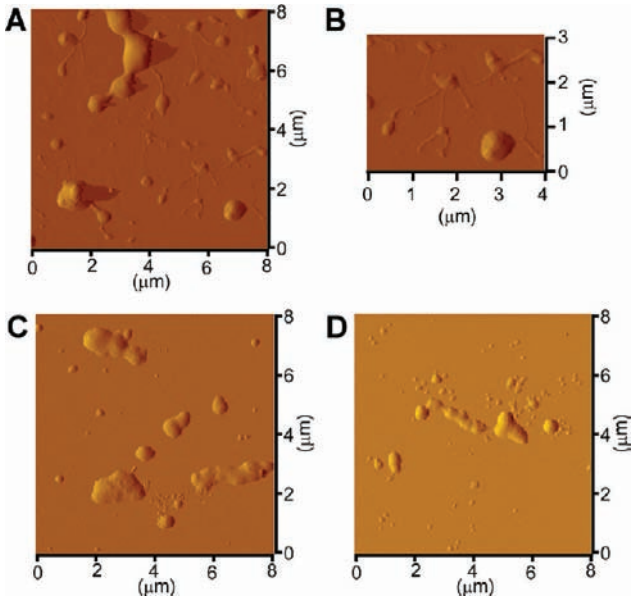

Figure 4. AFM images of DL-G1−$2C_{18}$ (A,B), DL-G2−$2C_{18}$ (C), and DL-G3−$2C_{18}$ (D) lipoplexes. N/P ratio of lipoplex was 2. (B) A portion of image (A) was enlarged.

Transfection Activity of Dendron-Bearing Lipid−DNA Lipoplexes. We investigated the influence of dendron generation of dendron-bearing lipids on their transfection activity. The transfection activity of lipoplexes generally varies depending on their N/P ratio. Therefore, we prepared lipoplexes consisting of the dendron-bearing lipids having different dendron generations and plasmid DNA containing luciferase gene at various N/P ratios. Then, we examined transfection of CV1 cells using these lipoplexes.

Figure 5A presents the expression of luciferase in the cells treated with these lipoplexes in the presence of 10% serum. Although both DL-G2−$2C_{18}$ and DL-G3−$2C_{18}$ lipoplexes exhibited very low transfection activities at the N/P ratio of 1, their activity increased concomitantly with the increasing N/P ratio from 1 to 2 and reached the maximum value at N/P ratio of 2, where these lipoplexes achieved expression of luciferase of around 1×10^7 RLU/mg protein. However, a further increase in the N/P ratio rather decreased their transfection activity. An increase of the N/P ratio might increase positive charges of the lipoplexes, which causes elevation of their affinity to the cells and increase of their transfection activity. However, a further increase of the N/P ratio might engender cellular toxicity derived from too much positive charge and decreased gene expression in the cells.[31] In fact, we have already observed similar N/P ratio dependence of transfection activities for the dendron-based lipids having the same dendron moieties and dodecyl chains instead of octadecyl chains.[24−26]

In contrast to cases of the G2 and G3 dendron-based lipoplexes, DL-G1−$2C_{18}$ lipoplexes exhibited extremely high transfection activity irrespective of the N/P ratio. Even the lipoplex with the N/P ratio of 1 induced a very high level of luciferase expression in the cells, at which 4 orders of magnitude higher expression of luciferase gene was achieved compared to the cases of the G2 and G3 dendron-based lipoplexes. An increase in the N/P ratio for the G1-dendron-based lipoplexes increased their transfection activity to some degree and the high level of transfection activity was retained at N/P ratios of 1.5−8, where about 1×10^9 RLU/mg protein of luciferase activity was induced.

We also examined the activity of these dendron-bearing lipids for transfection of HeLa cells (Figure 5B). Considerably high activity of DL-G1−$2C_{18}$ lipoplex was again observed for transfection of HeLa cells, compared to the G2 and G3 dendron-bearing lipid lipoplexes with the same N/P ratio of 2, where these dendron-bearing lipid lipoplexes achieved efficient transfection (Figure 5A). Its activity was of the same level as that of Lipofectamine LTX, which was used as a positive control with high transfection activity. We further checked cytotoxicity for these dendron-based lipid lipoplexes during the transfection. As is seen in Figure 5C, these lipoplexes showed a low level of cytotoxicity under the transfection condition.

Dendron-based lipids were originally designed to achieve efficient gene transfection of cells through the synergetic effect of hydrophobic interaction derived from their long alkyl chain moieties and the so-called proton sponge effect derived from the ability of PAMAM dendron moiety to buffer the acidification of endosome, which promotes the transfer of gene from

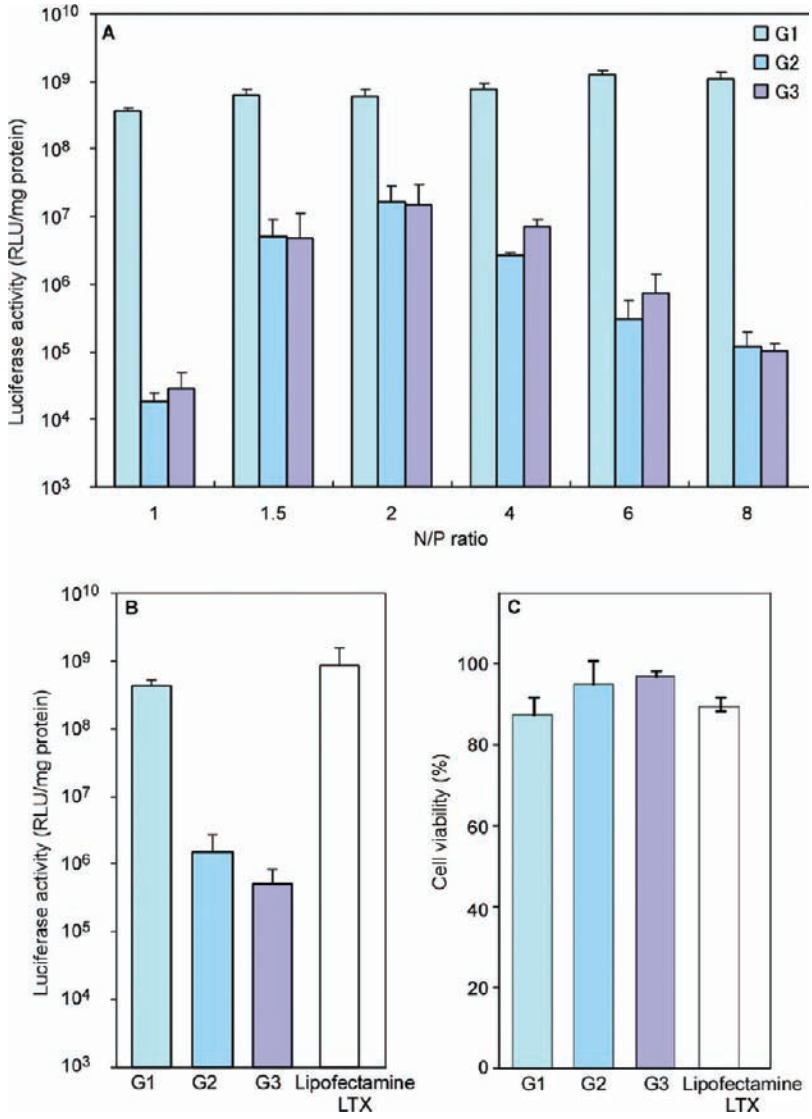

Figure 5. (A) Luciferase activities of CV1 cells treated with DL-G1−$2C_{18}$, DL-G2−$2C_{18}$, and DL-G3−$2C_{18}$ lipoplexes with varying N/P ratios. Luciferase activity (B) and viability (C) for HeLa cells treated with DL-G1−$2C_{18}$, DL-G2−$2C_{18}$, and DL-G3−$2C_{18}$ lipoplexes with N/P ratio of 2. Transfection with Lipofectamine LTX was performed as a control. The cells (5×10^4) were treated with the lipoplexes containing 1 μg DNA in the presence of 10% FBS. Each bar represents the mean ± SD (n = 3) for (A) and (B) or (n = 2) for (C).

endosome into cytosol and enables their efficient expression.[24] Because the number of tertiary amines of the dendron-bearing lipids, which generate the proton sponge effect, increases in the order of DL-G1−$2C_{18}$ < DL-G2−$2C_{18}$ < DL-G3−$2C_{18}$, we expected that their transfection activity would increase in the same order. In fact, we observed that the dendron-based lipids with dodecyl chains increased their transfection activity with increasing dendron generation (DL-G1−$2C_{12}$ < DL-G2−$2C_{12}$ < DL-G3−$2C_{12}$). In addition, the DL-G1−$2C_{18}$ lipoplexes have low ability to form lipoplexes (Figure 2). Therefore, the high transfection activity of the G1-based dendron lipid lipoplexes was completely unexpected.

Synthetic vectors without the endosome-buffering ability, such as poly(lysine), are known to increase their transfection efficiency in the presence of an endosomotropic agent, chloroquine, because it causes destabilization of endosome and promotes transfer of plasmid DNA into cytosol.[32] Therefore, the effect of chloroquine on the dendron-bearing lipid-mediated transfection was examined to estimate their ability to promote the endosome escape of plasmid DNA (Figure 6). HeLa cells were transfected with the dendron-bearing lipid lipoplexes with the N/P ratio of 2 in the presence or absence of chloroquine. As presented in Figure 6A, the presence of chloroquine decreased luciferase for the cells treated with the G1 and G2 dendron-bearing lipids to some degree, probably because cellular toxicity of chloroquine might suppress the gene expression.[33] However, for transfection with the G3 dendron-bearing lipid, cellular luciferase expression was 2.5-fold higher in the presence of chloroquine than in the case of transfection in the absence of chloroquine (Figure 6B). This result suggests that G1 and G2 dendron-bearing lipids have sufficient ability to achieve efficient endosome escape of plasmid DNA, whereas the ability of the G3-dendron-bearing lipid is insufficient. In an earlier report, we described that the dendron-bearing lipids having dodecyl chains, such as DL-G1−$2C_{12}$, DL-G2−$2C_{12}$, and DL-G3−$2C_{12}$, exhibited enhancement of transfection in the presence of chloroquine.[24] Considering the difference of the alkyl chain length of these dendron-based lipids, more hydrophobic character of octadecyl chains of the dendron-bearing lipids

dx.doi.org/10.1021/bc200368b | *Bioconjugate Chem.* 2012, 23, 871−879

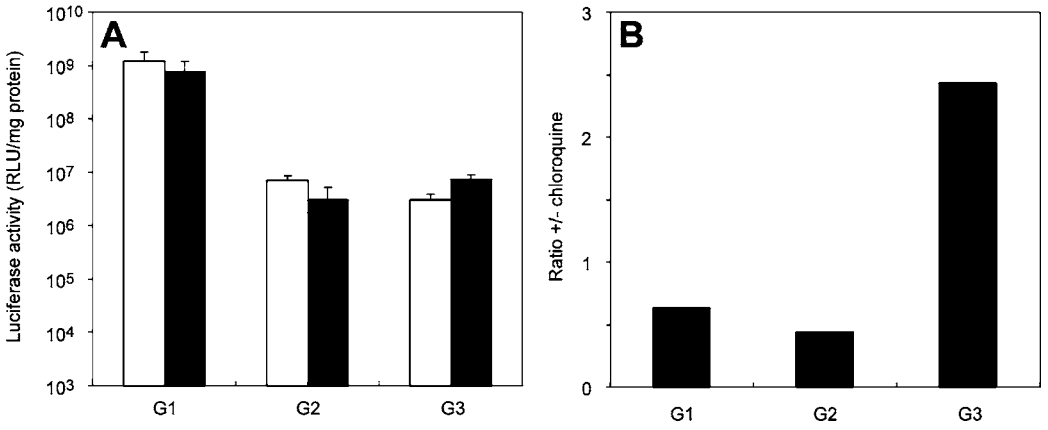

Figure 6. Influence of chloroquine on transfection activity of HeLa cells treated with DL-G1−2C_{18}, DL-G2−2C_{18}, and DL-G3−2C_{18} lipoplexes with N/P ratio of 2. Luciferase activities of the cells treated with the lipoplexes without chloroquine (open bar) or with 100 μM chloroquine (closed bar) in the presence of 10% FBS. Each bar represents the mean ± SD (n = 3). (B) Ratio of cellular luciferase activity in the presence of chloroquine to that in the absence of chloroquine.

might enhance destabilization of endosome membranes through strong hydrophobic interaction.

Another strategy to promote the endosomal escape of plasmid DNA introduced with lipid-based vectors is to use fusogenic phospholipids, such as dioleoylphosphatidylethanolamine (DOPE), as an additional component of lipoplexes.[34,35] In fact, we observed that the inclusion of DOPE in the dendron-based lipids having dodecyl chains greatly increased their transfection activity.[24] Therefore, we examined the effect of DOPE on the transfection activity of the dendron−lipid lipoplexes. The CV1 cells were transfected using dendron−lipid-based lipoplexes with varying DOPE contents and N/P ratios (Figure S4), which showed that the optimum DOPE/dendron−lipid molar ratio and N/P ratio were, respectively, 0.1/1 and 4 for DL-G1−2C_{18} lipoplex, 2/1 and 6 for DL-G2−2C_{18} lipoplex, and 4/1 and 4 for DL-G3−2C_{18} lipoplex. We compared the transfection activity of DOPE-containing lipoplexes and DOPE-free lipoplexes with their optimal compositions. As presented in Figure 7, CV-1 cells treated with these lipoplexes containing luciferase gene expressed 10−100 times as high a level of luciferase activity when treated with DOPE-containing lipoplexes of G2- and G3-dendron-bearing lipids. In contrast, no fundamental increase of the gene expression induced by the DOPE inclusion was observed for the case of the G1-dendron-bearing lipoplexes. Some reports in the literature describe that DOPE might increase gene transfection by enhancing destabilization and fusion of endosomal membrane, which promotes transfer of plasmid DNA into the cytosol.[34,35] Therefore, the results suggest that the G1and G2 dendron-bearing lipid lipoplexes can destabilize the endosomal membrane strongly without support of DOPE.

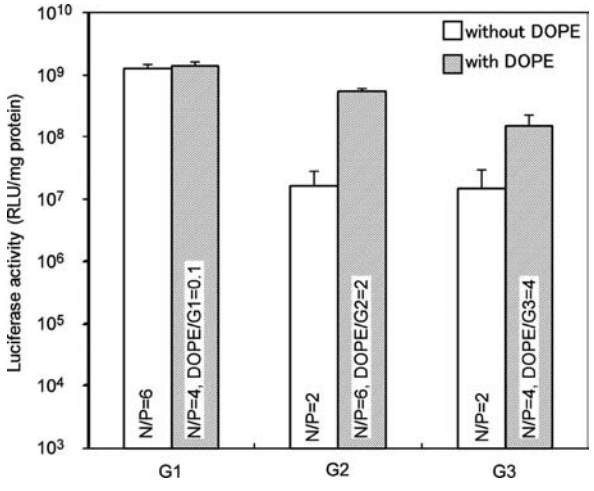

Figure 7. Luciferase activities of CV1 cells treated with DL-G1−2C_{18}, DL-G2−2C_{18}, and DL-G3−2C_{18} lipoplexes without (open bar) or with DOPE (closed bar). The N/P ratio and DOPE/dendron-bearing lipid ratio of the lipoplex are shown in figure. Cells were treated with lipoplexes in the presence of 10% FBS. Each bar represents the mean ± SD (n = 3).

We sought an explanation for why the DL-G1−2C_{18} lipoplexes achieved markedly higher transgene expression efficiency than the lipoplexes with the larger dendron moieties. We expected that the efficiency of plasmid DNA introduction into the cells might be influenced by the generation of dendron moiety of the lipids. Therefore, to estimate the amount of plasmid DNA introduced into the cells, plasmid DNA labeled with FITC was used for the lipoplex preparation with the dendron lipids. CV1 cells were treated with the lipoplexes for 4 h and the cellular fluorescence was evaluated by flow cytometry (Figure S5). The percentages of cellular association for the G1, G2, and G3 dendron-bearing lipid lipoplexes were estimated to be 77.1 ± 2.3%, 89.5 ± 2.0%, and 88.9 ± 0.8%, respectively, indicating that the lipoplexes were efficiently taken up by the cells. Although these lipoplexes had relatively larger sizes, which might be formed by aggregation of these small lipoplexes, such lipoplexes may be dissociated into lipoplexes of smaller size after adsorption onto the cellular membrane and be taken up by the cells through endocytosis. Figure 8 depicts the average of cellular fluorescence intensity of FITC for cells treated with lipoplexes with various dendron-bearing lipids. Contrary to our expectation, the cellular fluorescence intensities suggested that the amount of plasmid DNA delivered into the cells using DL-G1−2C_{18} was much smaller than the cases of DL-G2−2C_{18} and DL-G3−2C_{18} for DNA delivery, which might result from the low ability of DL-G1−2C_{18} to form lipoplexes, compared to other dendron lipids with larger dendron moieties (Figure 2).

We also expected that intracellular behavior of the lipoplexes might affect their transgene expression efficiency. We prepared lipoplexes from FITC-labeled plasmid DNA, the dendron lipids, and a small aliquot (0.6 mol %) of Rh-PE, which was used for detection of lipid component of lipoplexes in the cell.

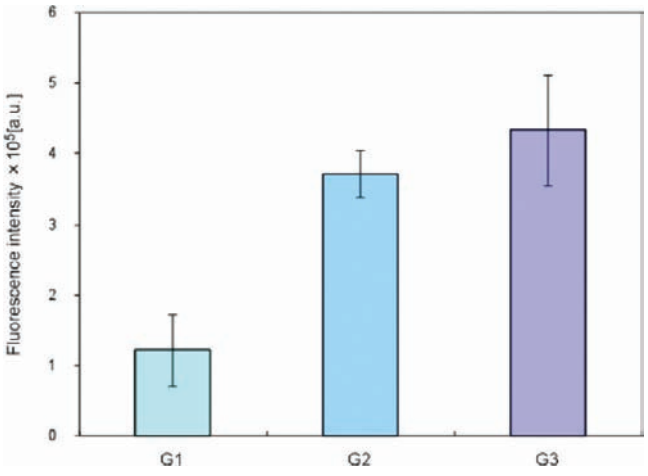

Figure 8. Fluorescence intensities of CV1 cells treated with DL-G1−$2C_{18}$, DL-G2−$2C_{18}$, and DL-G3−$2C_{18}$ lipoplexes with N/P ratio of 2 prepared using FITC-labeled plasmid DNA. Cells (1×10^5) were treated with the lipoplexes and the complex containing 2 μg DNA in the presence of 10% FBS. Each bar represents the mean ± SD ($n = 3$).

HeLa cells were treated with doubly labeled lipoplexes and viewed with a confocal laser scanning microscope (CLSM) (Figure 9). The cells displayed both FITC and Rh fluorescence, indicating that the plasmid DNA component and the lipid components were internalized into the cells. Spots exhibiting fluorescence in the cells are generally smaller than the size of lipoplexes evaluated by DLS (Figure 3), suggesting that the lipoplexes dissociated into smaller particles after internalization in the cell. As presented in the merged image of the cells treated with the DL-G1−$2C_{18}$ lipoplex (Figure 9A), these cells displayed many spots emitting green fluorescence, which was indicative of the existence of free plasmid DNA, which might be liberated from the lipoplex. Compared to cases of the DL-G1−$2C_{18}$ lipoplex-treated cells, in the merge images of the cells treated with the DL-G2−$2C_{18}$ and DL-G3−$2C_{18}$ lipoplexes, the quantities of green spots apparently decreased, and yellow fluorescence-emitting spots became predominant (Figure 9B,C). The result indicates that green fluorescence-emitting FITC-labeled plasmid DNA and red fluorescence-emitting Rh-PE coexisted in the same places, suggesting that plasmid DNA and the dendron lipids were still bound in these cells. Considering that stability of the DL-G1−$2C_{18}$ lipoplex might be much lower than that of the DL-G2−$2C_{18}$ and DL-G3−$2C_{18}$ lipoplexes (Figure 2), the former lipoplex was able to liberate plasmid DNA in the cells readily through interaction with cellular components, such as proteins of various kinds, thereby enabling more efficient transcription of the luciferase gene. The results underscore the importance of the balance of polar head moiety and hydrophobic tail moiety, which reconciles stabilization and destabilization of the lipoplexes, respectively, for efficient delivery of plasmid DNA into cells and effective liberation of plasmid DNA in the intracellular space. In addition, morphology of the lipoplexes may be another factor which affects their high transfection efficiency. Relatively large surface area of the tubular DL-G1−$2C_{18}$ lipoplexes should enhance interaction with endosomal membrane, resulting in efficient liberation of plasmid DNA from the dendron-based lipid and transfer into cytosol. The lipid having small G1 dendron and two highly hydrophobic octadecyl chains forms moderately stable lipoplexes with a hydrophobic nature, which enables

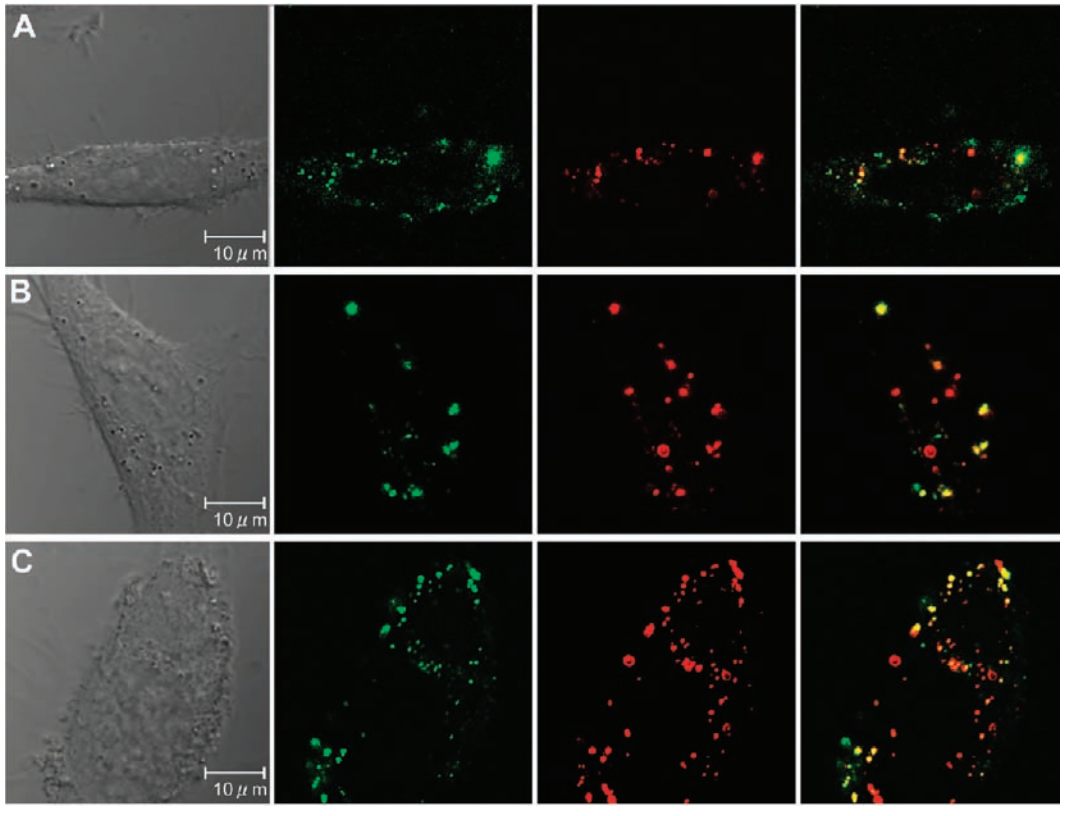

Figure 9. Fluorescence microscopic observation of HeLa cells treated with DL-G1−$2C_{18}$ lipoplexes. Differential interference contrast image (A), green shows the fluorescence of FITC-labeled pDNA (B), red shows the fluorescence of Rhodamine-PE (C), and overlay image (D). Cells (1×10^5) were treated with the lipoplexes containing 2 μg DNA in the presence of 10% FBS.

dx.doi.org/10.1021/bc200368b | *Bioconjugate Chem.* 2012, 23, 871−879

efficient cellular internalization, efficient endosomal escape, and efficient liberation of plasmid DNA, resulting in efficient gene expression.

In conclusion, we demonstrated that the transfection activity of the PAMAM dendron-bearing lipids having two octadecyl chains varied significantly depending on their generation of dendron moiety. The dendron lipid having the smallest dendron DL-G1−$2C_{18}$ exhibited significantly higher transfection activity among the dendron lipids. Results demonstrated the importance of the dendron moiety of the PAMAM dendron-bearing lipids for their lipoplex formation with plasmid DNA having appropriate stability to reconcile efficient cellular delivery and liberation of plasmid DNA. In this sense, the dendron-bearing lipids are advantageous because their characteristics which are necessary to achieve efficient transfection can be controlled precisely by selecting a backbone structure and generation of dendron moiety. Synthetic vectors of many types are known to need helper lipids, such as DOPE, to achieve efficient transfection. In addition, their transfection activity is often decreased in the presence of serum. Therefore, it is noteworthy that the DL-G1−$2C_{18}$ achieved efficient gene transfection in the presence of serum without the help of fusogenic lipid DOPE. We expect that structural optimization for alkyl chain moieties, such as introduction of double bonds, and for dendron moiety, such as hydrophobicity, might engender further improvement of transfection activity of the dendron-based lipids. Therefore, dendron-based lipids might be promising for the production of potent synthetic vectors.

■ ASSOCIATED CONTENT

Ⓢ Supporting Information

Agarose gel electrophoretic analysis for complexation of DL-G1−$2C_{18}$ with plasmid DNA at varying N/P ratios, size distribution for G1, G2, and G3 dendron-bearing lipid lipoplexes, CLSM analysis of lipoplex containing FITC-labeled DNA, the effects of N/P ratio and DOPE/dendron-lipid ratio on the transfection activity of DL-G1−$2C_{18}$, DL-G2−$2C_{18}$, and DL-G3−$2C_{18}$ lipoplexes, and flow cytometry analysis for CV1 cells treated with DL-G1−$2C_{18}$, DL-G2−$2C_{18}$, and DL-G3−$2C_{18}$ lipoplexes containing FITC-labeled plasmid DNA. This material is available free of charge via Internet at http://pubs.acs.org.

■ AUTHOR INFORMATION

Corresponding Author

*E-mail: kono@chem.osakafu-u.ac.jp. Tel: +81-722549330. Fax: +81-722549330.

Present Address

C. Kojima, Nanoscience and Nanotechnology Research Center, Research Organization for the 21st Century, Osaka Prefecture University, 1−2 Gakuen-cho, Naka-ku, Sakai, Osaka 599−8570, Japan.

■ REFERENCES

(1) Mintzer, M. A., and Simanek, E. E. (2009) Nonviral vectors for gene delivery. *Chem. Rev. 109*, 259−302.

(2) Okita, K., Nakagawa, M., Hyenjong, H., Ichisaka, T., and Yamanaka, S. (2008) Generation of mouse induced pluripotent stem cells without viral vectors. *Science 322*, 949−953.

(3) Niidome, T., and Huang, L. (2002) Gene therapy progress and prospects: nonviral vectors. *Gene Ther. 9*, 1647−1652.

(4) de Lima, M. C. P., Simoes, S., Pires, P., Faneca, H., and Duzgunes, N. (2001) Cationic lipid-DNA complexes in gene delivery: from biophysics to biological applications. *Adv. Drug Delivery Rev. 47*, 277−294.

(5) Wagner, E., and Kloeckner, J. (2006) Gene delivery using polymer therapeutics. *Adv. Polym. Sci. 192*, 135−173.

(6) Tros de Ilarduya, C., Sun, Y., and Duzgunes, N. (2010) Gene delivery by lipoplexes and polyplexes. *Eur. J. Pharm. Sci. 40*, 159−170.

(7) Pouton, C. W., and Seymour, L. W. (1998) Key issues in non-viral gene delivery. *Adv. Drug Delivery Rev. 34*, 3−19.

(8) Zelphati, O., and Szoka, F. C. Jr. (1996) Mechanism of oligonucleotide release from cationic liposomes. *Proc. Natl. Acad. Sci. U.S.A. 93*, 11493−11498.

(9) Monkkonen, J., and Urtti, A. (1998) Lipid fusion in oligonucleotide and gene delivery with cationic lipids. *Adv. Drug Delivery Rev. 34*, 37−49.

(10) Mok, K. W. C., and Cullis, P. R. (1997) Structural and fusogenic properties of cationic liposomes in the presence of plasmid DNA. *Biophys. J. 73*, 2534−2545.

(11) Boussif, O., Lezoualc'h, F., Zanta, M. A., Mergny, M. D., Scherman, D., Demeneix, B., and Behr, J. P. (1995) A versatile vector for gene and oligonucleotide transfer into cells in culture and in vivo: Polyethylenimine. *Proc. Natl. Acad. Sci. U.S.A. 92*, 7297−7301.

(12) Sonawane, N. D., Szoka, F. C., and Verkman, A. S. (2003) Chloride accumulation and swelling in endosomes enhances DNA transfer by polyamine-DNA polyplexes. *J. Biol. Chem. 278*, 44826−44831.

(13) Dufes, C., Uchegbu, I. F., and Schatzlein, A. G. (2005) Dendrimers in gene delivery. *Adv. Drug Delivery Rev. 57*, 2177−2202.

(14) Miyata, K., Oba, M., Nakanishi, M., Fukushima, S., Yamasaki, Y., Koyama, H., Nishiyama, N., and Kataoka, K. (2008) Polyplexes from poly(aspartamide) bearing 1,2-diaminoethane side chains induce pH-selective, endosomal membrane destabilization with amplified transfection and negligible cytotoxicity. *J. Am. Chem. Soc. 130*, 16287−16294.

(15) Lim, Y., Kim, S., Suh, H., and Park, J. (2002) Biodegradable, endosome disruptive, and cationic network-type polymer as a highly efficient and nontoxic gene delivery carrier. *Bioconjugate Chem. 13*, 952−957.

(16) Haensler, J., and Szoka, F. C. Jr. (1993) Polyamidoamine cascade polymers mediate efficient transfection of cells in culture. *Bioconjugate Chem. 4*, 372−379.

(17) Tang, M., Redemann, C. T., and Szoka, F. C. Jr. (1996) In vitro gene delivery by degraded polyamidoamine dendrimers. *Bioconjugate Chem. 7*, 703−714.

(18) Kukowska-Latallo, J. F., Bielinska, A. U., Johnson, J., Spindler, R., Tomalia, D. A., and Baker, J. R. Jr. (1996) Efficient transfer of genetic material into mammalian cells using Starburst polyamidoamine dendrimers. *Proc. Natl. Acad. Sci. U.S.A. 93*, 4897−4902.

(19) Choi, J. S., Nam, K., Park, J., Kim, J. B., Lee, J. K., and Park, J. (2004) Enhanced transfection efficiency of PAMAM dendrimer by surface modification with L-argnine. *J. Controlled Release 99*, 445−456.

(20) Kono, K., Akiyama, H., Takahashi, T., Takagishi, T., and Harada, A. (2005) Transfection activity of polyamidoamine dendrimers having hydrophobic amino acid residues in the periphery. *Bioconjugate Chem. 16*, 208−214.

(21) Santos, J. L., Oliveira, H., Pandita, D., Rodrigues, J., Pego, A. P., Grnja, P. L., and Tomas, H. (2010) Functionalization of poly(amidoamine) dendrimers with hydrophobic chains for improved gene delivery in mesenchymal stem cells. *J. Controlled Release 144*, 55−64.

(22) Morales-Sanfrutos, J., Megia-Fernandez, A., Hernandez-Mateo, F., Giron-Gonzalez, M. D., Salto-Gonzalez, and Santoyo-Gonzalez, F. (2011) Alkyl sulfonyl derivatized PAMAM-G2 dendrimers as nonviral gene delivery vectors with improved transfection efficiencies. *Org. Biomol. Chem. 9*, 851−864.

(23) Guillot-Nieckowski, M., Eisler, S., and Diederrich, F. (2007) Dendritic vectors for gene transfection. *New J. Chem. 31*, 1111−1127.

(24) Takahashi, T., Kono, K., Itoh, T., Emi, N., and Takagishi, T. (2003) Synthesis of novel cationic lipids having polyamidoamine dendrons and their transfection activity. *Bioconjugate Chem. 14*, 764−773.

(25) Takahashi, T., Harada, A., Emi, N., and Kono, K. (2005) Preparation of efficient gene carriers using a polyamidoamine dendron-bearing lipid: improvement of serum resistance. *Bioconjugate Chem. 16*, 1160−1165.
(26) Takahashi, T., Kojima, C., Harada, A., and Kono, K. (2007) Alkyl chain moieties of polyamidoamine dendron-bearing lipids influence their function as a nonviral gene vector. *Bioconjugate Chem. 18*, 1349−1354.
(27) Mosmann, T. (1983) Rapid colorimetric assay for cellular growth and survival:application to proliferation and cytotoxicity assays. *J. Immunol. Methods 65*, 55−63.
(28) Tang, M. X., and Szoka, F. C. (1997) The influence of polymer structure on the interactions of cationic polymers with DNA and morphology of the resulting complexes. *Gene Ther. 4*, 823−832.
(29) Pitard, B., Aguerre, O., Airiau, M., Lachages, A. M., Boukhnikachvili, T., Byk, G., Dubertret, C., Herviou, C., Scherman, D., Mayaux, J. F., and Crouzet, J. (1997) Virus-sized self-assembling lamellar complexes between plasmid DNA and cationic micelles promote gene transfer. *Proc. Natl. Acad. Sci. U.S.A. 94*, 14412−14417.
(30) Israelachvili, J. N., Marcelja, S., and Horn, R. G. (1980) Physical principles of membrane organization. *Q. Rev. Biophys. 13*, 121−200.
(31) Masotti, A., Mossa, G., Cametti, C., Ortaggi, G., Bianco, A., Del Grosso, N., Malizia, D., and Esposito, C. (2009) Comparison of different commercially available cationic liposome-DNA lipoplexes: parameters influencing toxicity and transfection efficiency. *Colloids Surf., B 68*, 136−144.
(32) Brown, M. D., Schatzlein, A. G., and Uchegbu, I. F. (2001) Gene delivery with synthetic (non viral) carriers. *Int. J. Pharm. 229*, 1−21.
(33) Hardy, J. G., Kostianen, M. A., Smith, D. K., Gabrielson, N. P., and Pack, D. W. (2006) Dendrons with spermine surface groups as potential building blocks for nonviral vectors in gene therapy. *Bioconjugate Chem. 17*, 172−178.
(34) Farhood, H., Serbina, N., and Huang, L. (1995) The role of dioleoylphosphatidylethanolamine in cationic liposome mediated gene transfer. *Biochim. Biophys. Acta 1235*, 289−295.
(35) Hui, S. W., Langner, M., Zhao, Y. L., Ross, P., Hurley, E., and Chan, K. (1996) The role of helper lipids in cationic liposome-mediated gene transfer. *Biophys. J. 71*, 590−599.

Bioconjugate Chemistry

Review

pubs.acs.org/bc

Analytical Measurement of PEGylated Molecules

Tian-Lu Cheng,[†] Kuo-Hsiang Chuang,[†] Bing-Mae Chen,[‡] and Steve R. Roffler*[,‡]

[†]Department of Biomedical Science and Environmental Biology, Kaohsiung Medical University, Kaohsiung, Taiwan

[‡]Institute of Biomedical Sciences, Academia Sinica, Taipei, Taiwan

ABSTRACT: Attachment of poly(ethylene glycol) (PEG) to proteins, peptides, liposomes, drugs, and nanoparticles can improve pharmaceutical pharmacokinetic properties and enhance in vivo biological efficacy. Since the first PEGylated product was approved by the Food and Drug Administration in 1990, increasing numbers of PEGylated compounds have entered clinical use. Successful clinical development of PEGylated pharmaceuticals requires accurate methods for the qualitative and quantitative analysis of intact PEG conjugates in biological fluids. In this article, we review assay methods that can be utilized for the detection and measurement of PEGylated pharmaceuticals in complex biological samples for determination of biodistribution and pharmacokinetic properties. In particular, we describe relevant colorimetric, chromatographic, radiolabeled, biological, and enzyme-linked immunosorbent assays for the pharmacokinetic study of PEGylated molecules.

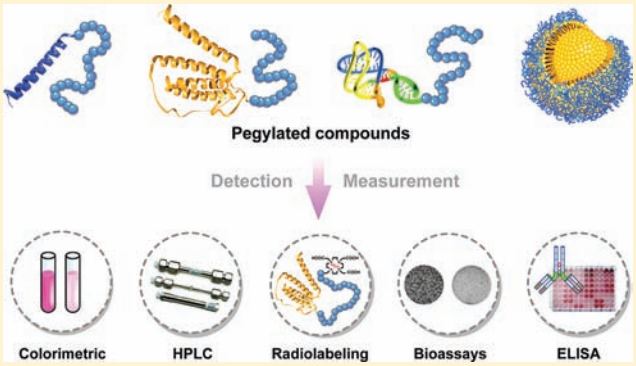

INTRODUCTION

PEG is a water-soluble, nontoxic, non-antigenic, biocompatible polymer that has been approved by the Food and Drug Administration for human intravenous, oral, and dermal applications.[1,2] Attachment of PEG (PEGylation) to drugs, peptides, proteins, nanoparticles, micelles, and liposomes is a mature technology for enhancing the bioavailability, stability, safety, and efficacy of a wide range of therapeutic agents. Therefore, PEGylated molecules are increasingly employed as mainstream therapeutic and diagnostic agents, which in turn have created great demand for methods facilitating the qualitative and quantitative analysis of PEG-derivatized molecules for both drug development and clinical applications.

PEGylation of peptides and proteins can reduce immunogenicity,[3] minimize proteolytic cleavage,[4] and increase serum half-life,[5] which in turn can increase drug efficacy and reduce injection frequency to enhance patient compliance and quality of life. Several PEGylated protein conjugates are now commercially available including Pegasys (PEG-interferon alpha-2a)[6,7] and PEG-Intron (PEG-interferon alpha-2b)[8] for hepatitis, Somavert (PEG-human growth hormone receptor antagonist) for acromegaly,[9] Cimzia (certolizumab pegol, PEGylated anti-human TNF-alpha Fab′) for rheumatoid arthritis,[10] Neulasta (pegfilgrastim, PEG-recombinant human granulocyte colony-stimulating factor analogue) for neutropenia associated with cancer chemotherapy,[11,12] PEG-erythropoietin (EPO) for anemia,[13] Adagen (PEG-adenosine deaminase) for immunodeficiency,[14] PEG-Hirudin for thrombosis,[15] and Oncaspar (PEG-asparaginase) for cancer treatment.[16] PEGylation of protein drugs has become routine and there is a trend of PEGylating established protein drugs for new uses.

PEGylation of polymeric nanoparticles, liposomes, and micelles can improve drug bioavailability and efficacy by reducing unintended uptake in normal tissues, decreasing systemic toxicity, prolonging circulation time in the blood, and enhancing tumor accumulation.[17−21] For example, PEG-modified liposomal doxorubicin (Doxil), approved by the FDA for the clinical treatment of ovarian and breast carcinomas and Kaposi's sarcoma,[22,23] displays comparable efficacy to doxorubicin but with significantly reduced cardiotoxicity, myelosuppression, vomiting, and alopecia.[24,25] Several polymeric micelle formulations (paclitaxel (Genexol) and cisplatin) are currently undergoing phase I/II clinical trials, and have shown improved antitumor efficacy and reduced systemic toxicity.[26] PEGylation of nanoparticles such as superparamagnetic iron oxide (PEG-SPIO/phase III, MRI contrast agent),[27] PEG-microbubbles,[28] ultrasound contrast agents, and quantum dots[29] improves their biocompatibility and reduces receptor-mediated uptake by the reticuloendothelial system,[30] but can also influence their imaging contrast properties.[31,32] These nanoparticles have been extensively studied in cells and animal models for cell trafficking studies,[33,34] tumor targeting,[35,36] and diagnostics.[37,38] PEGylated nanoparticles are being increasingly employed for clinical applications.

PEG has also been employed to prolong the circulation and increase the water solubility of small molecules such as camptothecin (PEG-CPT/phase II),[39] SN-38,[40] and paclitaxel.[41−43] In addition, PEGylation of indomethacin has been examined in animal models for improved anti-inflammatory effects.[44] Novel

Received: September 1, 2011
Revised: December 27, 2011
Published: January 15, 2012

dx.doi.org/10.1021/bc200478w | *Bioconjugate Chem.* 2012, 23, 881−899

functions are also continually being discovered for PEG. For example, PEG molecules have been investigated as therapeutic agents for neuronal injury,[45] as chemopreventive agents for chemically induced colitis,[46,47] and as tumor suppressive agents for cancer.[47,48] New treatment modalities using PEG are likely to be developed in the future.

All trends indicate that PEG will be increasingly employed to improve the properties of therapeutic or diagnostic agents as more proteins, macromolecular drugs, and nanoparticles enter clinical trials in the 21st century. The successful translation of PEGylated molecules to the clinic depends on accurate methods for the quantitative analysis of pharmacokinetic parameters in animals and patients. Measurement of drug exposure and tissue distribution is critical for interpretation of preclinical and clinical therapeutic efficacy and toxicity. Sensitive in vivo quantification is also important for assessing stability, metabolism, and bioavailability of PEGylated compounds. Here, we provide an overview of analytical methods for the quantitative measurement of PEGylated molecules in biological mixtures.

COLORIMETRIC METHODS

Colorimetric methods have been employed for more than 60 years to detect PEG and PEGylated molecules (Table 1). Shaffer and colleagues developed the first and most commonly cited method for quantification of PEG molecules based on the formation of insoluble complexes between PEG and heteropoly inorganic acids (phosphomolybdic and silicotungstic acid) in the presence of barium chloride. The method can detect 0.05 to 1 mg of PEG at concentrations as low as 0.01 mg/mL.[49] Treatment with barium and iodine to form a barium−iodide complex produced a linear response at 535 nm from 1.25 to 7.5 μg/mL of PEG4000.[50,51] This approach can also measure the concentration of distearoylphosphatidylethanolamine-PEG (DSPE−PEG), used for the formation of PEGylated liposomes, at concentrations as low as 25 μg/mL.[52] These methods, however, are technically demanding and time-consuming due to the need to collect and wash precipitates and are therefore not ideal for rapid quantification of PEG in multiple, complex biological samples. Ingham and colleagues developed a more convenient assay for determination of PEG based on the nephelometric quantitation of turbidity which appears when PEG is added to Nessler's solution (an alkaline solution of potassium mercuric iodide).[53] However, plasma proteins drastically diminish the scattering intensity; as little as 1 μg/mL albumin in the final assay mixture destroys the quantitative relationship.

Two-phase systems can be employed to detect PEG and PEGylated compounds in the presence of proteins. Guermant and colleagues measured PEG indirectly by determining the influence of PEG on the partitioning of a fluorescein dye between water and aqueous ammonium sulfate phases.[54] A more general assay developed by Nag and colleagues is based on the partitioning of colored PEG-Fe(SCN)$_3$ complexes from an aqueous ammonium ferrothiocyanate phase to chloroform (Figure 1). The visible absorbance at 510 nm in the chloroform phase is linearly dependent on PEG concentration over a range of 5−100 μg PEG5000 (PEG with a molecular weight of 5000 Da).[55] This assay can be employed for estimation of PEG in plasma samples containing as much as 5 mg plasma proteins in a 50 μL sample. Amphipathic compounds, such as Triton X-100, which possesses repeating ethylene oxide units like PEG, also influence the partitioning of the chromophore and thus may interfere with the assay. In addition, PEGylated compounds that partition poorly into chloroform are difficult

Table 1. Colorimetric Methods for Measuring PEG and PEGylated Molecules

PEGylated compound	PEG length	method	possible interference	sensitivity	ref
Free PEG	1000−6000	Formation of insoluble complexes between PEG and heteropoly inorganic acids in the presence of barium chloride	Plasma, Urine	10 μg/mL	49
Free PEG	400−6000	Nessler's solution	Proteins	20 μg/mL for PEG4000 500 μg/mL for PEG400	53
Free PEG	1000−5000	Spectrophotometric measurement of fluorescein dye absorbance in an aqueous two-phase system containing PEG in the upper phase and ammonium sulfate in the lower phase	Triton X-100 CTAB	5 μg/mL for PEG5000	54
Free PEG PEG-protein	750−15000	Measurement of absorbance in the chloroform phase in an aqueous ammonium ferrothiocyanate and chloroform two-phase system	Triton X-100 dioxan	5 μg	55
PEG-protein	5000	Alkaline hydrolysis of PEG-protein before analysis in an aqueous ammonium ferrothiocyanate/chloroform biphasic system	Triton X-100 dioxan	1 μg/mL	56
PEG-liposome	2000	Phospholipase C treated PEG-liposome are analyzed in an ammonium ferrothiocyanate and chloroform biphasic system	Triton X-100 dioxan	1 μg/mL	57
PEG-liposome	5000	Measurement of the absorbance at 234 nm of PEG-dichlorotriazine in liposomes	None reported	250 μg/mL	194

dx.doi.org/10.1021/bc200478w | Bioconjugate Chem. 2012, 23, 881−899

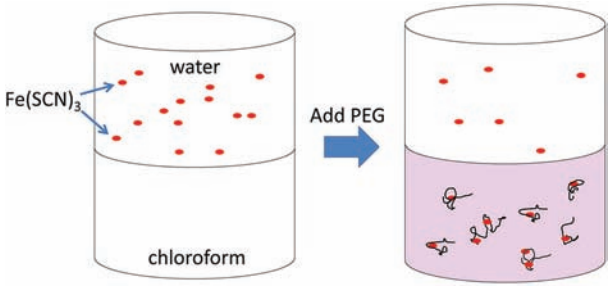

Figure 1. Two-phase system for PEG determination. Partitioning of ferrothiocyanate−PEG complexes into the chloroform phase produces a visible purple−pink coloration in proportion to PEG concentration that can be detected at 510 nm.

to assay. However, sample hydrolysis can extend analysis to PEGylated compounds that do not partition well into the organic phase. For example, alkaline hydrolysis of a chloroform-insoluble PEGylated protein prior to measurement of the released PEG allowed determination of the amounts of free and coupled PEG in the biphasic system.[56] Likewise, phospholipase-C digestion of PEG-conjugated distearoylphosphatidylethanolamine (PEG-DSPE) stealth liposomes to remove interfering phospholipids before analysis in the biphasic system allowed measurement of PEG2000 in amounts as low as 1 μg/mL with a linear response over a range of 1−100 μg.[57,58]

Colorimetric assays are simple and utilize commonly available lab equipment for analysis and detection (Table 2). On the other hand, colorimetric assays are sensitive to interference from proteins and detergents and are therefore most applicable to monitoring PEGylation reactions in relatively defined samples rather than for accurate determination of PEGylated compound concentrations in complex biological fluids.

HIGH-PERFORMANCE LIQUID CHROMATOGRAPHY (HPLC)

HPLC is a powerful analytical technique that is widely used for the measurement of PEG, PEGylated small drugs, and PEGylated liposomes and micelles (Table 3). HPLC analysis of clinical samples usually requires pretreatment steps to reduce sample complexity. Typically, proteins are first removed by precipitation with chloroform,[59,60] acetonitrile,[61] 5-sulfosalicylic acid,[62] trifluoroacetic acid,[63] $ZnSO_4$/acetone,[64] or $ZnSO_4$−methanol.[65] Acetonitrile and chloroform are preferred precipitation agents because nonvolatile salts can precipitate in analytical columns.

PEG molecules separated by HPLC can be directly measured with a refractive index detector, which has been commonly employed to measure PEG concentrations in urine samples during studies examining intestinal permeability. Early methods suffered from poor sensitivity with detection limits ranging from 0.2 to 5 mg/mL for PEG400.[66−68] Assay sensitivity can be improved by more extensive sample preparation to remove substances that interfere with refractive index measurements. Utilization of sized regenerated cellulose membranes and mixed ion exchange resin for sample preparation combined with size-exclusion HPLC allowed measurement of as little as 5 μg/mL PEG3350 and 50 μg/mL PEG400 in urine.[69] Size exclusion HPLC with refractive index detection was also used to measure residual unconjugated PEG in a PEGylated protein preparation with a limit of detection of 10 μg/mL by utilizing two tandem Shodex Protein KW803 and KW804 columns.[70] Refractive index, however, suffers from low sensitivity and is sensitive to changes in ambient temperature, pressure, and flow rate. In general, refractive index detection is only suitable when relatively noncomplex samples, such as urine, contain at least 10−100 μg of PEG per injection.

PEG can also be detected by UV absorption at wavelengths shorter than 200 nm, but sensitivity is only comparable to that obtained with an refractive index detector.[71] The limit of detection can be improved by modification of the PEG chain. For example, attachment of a dibenzoate group at the terminal end of PEG600 allowed UV detection at 230 nm, thereby greatly improving the limit of detection to 1 μg per injection.[60] However, the hydrophobic properties of the benzoate group may alter the pharmacokinetic behavior of PEG, limiting the general utility of this method.

High-performance liquid chromatography coupled with tandem mass spectrometry (HPLC-MS/MS) allows sensitive quantitation of free PEG in biological fluid samples. Pelham and colleagues used HPLC-MS/MS for the determination of PEG3350 in human urine and plasma with quantification limits of 30 ng/mL and 100 ng/mL, respectively. Samples were treated with metaphosphoric acid to precipitate proteins, extracted with chloroform, and separated on a SUPELCO TSK gel column.[72]

HPLC is an excellent choice for the quantification of PEGylated drugs and small molecules that can be detected on UV or fluorescence detectors. Liu and colleagues measured PEGylated puerarin (PEG-PUE), an isoflavone C-glycoside, in rat plasma samples by gradient elution of PEG-PUE on a CAPCELL PAK C18 column with 0.2% aqueous phosphoric acid and acetonitrile as the mobile phase and detection at 250 nm with a limit of quantitation of 80 ng/mL.[73] PEGylated SN38, a camptothecin derivative, was measured in tumor-bearing mice after precipitation of proteins with acetonitrile, separation on a C18 reversed-phase column, and fluorescence detection with a limit of detection of 10 ng/mL.[63] Posey and colleagues also applied this method in a phase 1 pharmacokinetic study of weekly pegamotecan (polyethylene glycol-camptothecin, PEG-CPT) in patients with advanced solid tumors and lymphomas.[74] Although generally useful, the HPLC conditions and detection method must be optimized for each compound based on the chromatographic and spectral properties of the conjugated drug or small molecule.

HPLC approaches are also useful to measure encapsulated drug concentrations in PEGylated liposomes and micelles. Typically, lysosomes are disrupted to release free drug which can then be assayed by traditional HPLC methods. For example, Wei and colleagues measured micelle-encapsulated or liposome-encapsulated doxorubicin formulations in rat plasma with a lower limit of quantitation of 5 ng/mL by precipitating proteins with acetonitrile, evaporation and sample reconstitution in mobile phase before separation on a C18 reversed-phase column, and measurement of doxorubicin fluorescence.[61] UV−visible detection can help avoid potential interfering species commonly observed when using fluorescent detection; doxorubicin and PEGylated liposomal doxorubicin were separated on a C_{16} reversed-phase column and then were determined by measuring UV absorption at 487 nm, giving a linear response in the range 10−25 μg/mL.[62]

Sophisticated HPLC and detection combinations have been developed for detailed characterization of PEG and PEGylated proteins, peptides, and nanoparticles including accurate determination of conjugate molecular weight, polymer mass distribution, degree and sites of PEG modification, positional isomers, and other physiochemical properties.[75−91] LC-MS/MS, however, has been more difficult to apply for the quantitative analysis of PEGylated proteins because of the generation of broad continuous mass spectrum due to the size and charge

Table 2. Advantages and Disadvantages of PEG-Quantification Methods

	advantages	disadvantages
Colorimetric method	1 Simple assays based on turbidity or chromophore formation between chemical agents and PEG 2 Suitable for monitoring PEGylation reactions	1 Relatively insensitive and may produce erratic results in the presence of plasma proteins or detergents 2 Not generally applicable for analysis of pharmacokinetic samples 3 Sample pretreatment required for PEGylated compounds that partition poorly into organic phase
HPLC	1 High reproducibility and sensitivity 2 Appropriate for PEGylated drug-containing liposomes and drug conjugates 3 LC-MS/MS measure peptide-PEG and protein-PEG conjugates at low ng/mL concentrations	1 Usually requires multiple processing steps to reduce sample complexity before analysis 2 Limited throughput compared to multiplex methods 3 Extensive method development required for PEGylated peptides and proteins 4 Sophisticated equipment may be required
Radiolabeling	1 Highly specific and sensitive 2 Simple analysis and high throughput 3 Compatible with complex biological samples 4 May allow noninvasive imaging of compound biodistribution	1 Safety and disposal issues 2 Radioactivity may be released from compounds (ie., deiodination) 3 Pharmacokinetic properties of compounds may be altered
Bioactivity assay	1 Can directly quantify PEGylated molecules in complex biological samples 2 Can assess the bioactivity and function of PEGylated molecules	1 PEG can affect interactions and catalytic activity of substrates and enzymes, resulting in lower detection sensitivity 2 Requires an appropriate and sensitive bioassay 3 Assays using a complex biological system may introduce experimental uncertainty 4 Endogenous compounds may interfere with the assay
Protein ELISA	1 Can directly quantify PEGylated molecules in serum samples 2 Simple analysis and high throughput 3 Can assess the binding activity of PEGylated antibodies or the native state of PEGylated proteins	1 PEG chains usually mask the epitopes of proteins, which can decrease detection sensitivity 2 ELISA assay using antiprotein antibodies cannot differentiate between PEGylated and non-PEGylated molecules
Anti-PEG ELISA	1 Can directly quantify PEGylated molecules in serum sample 2 Simple analysis and high throughput 3 No need to develop specific antibodies against the compound of interest such as peptides, proteins or drugs 4 Provide a universal assay format for nearly all PEGylated compounds	1 Cannot recognize the integrity of PEG-compounds, if the compounds were hydrolyzed or decomposed 2 Assay sensitivity is decreased for molecules containing a single short PEG molecule

dx.doi.org/10.1021/bc200478w | *Bioconjugate Chem.* 2012, 23, 881–899

Table 3. HPLC Quantitation of PEG and PEGylated Molecules

HPLC type	sample preparation	separation column	mobile phase	analytes	sensitivity	ref.
Refractive index HPLC (RI-HPLC)	Lyophilization and chloroform extraction	Styrene divinylbenzene beads, 5 μm particles (Polymer Laboratories, Amherst, MA)	Water/methanol	PEG 400 in urine	4 mg/mL	66
RI-HPLC	0.22 μm filtration	Styrene divinylbenzene 250 mm × 4.6 mm, 5 μm particles (Polymer Laboratories, Amherst, MA)	Water/methanol	PEG 400 in urine	0.2 mg/mL	67
RI-HPLC	Size-based filtration, concentration, mixed ion-exchange (for PEG400)	TSK3000PW, TSK2000PW and TSK2000SW size-exclusion gel filtration columns (Tosoh Bioscience)	Water	PEG3350 and PEG400 in urine	5 μg/mL for PEG3350 50 μg/mL for PEG400	69
RI-HPLC	None	Protein KW803 300 mm × 8 mm, 5 μm particles and KW804 300 mm × 8 mm, 7 μm particles size-exclusion columns in tandem (Shodex)	20 mM HEPES, pH 6.5	PEG43,000 and PEGylated protein	5 μg/mL	70
RI-HPLC	Saturated with ammonium sulfate, dichloromethane extraction	μBondapak C18 reversed-phase 300 mm × 3.9 mm, 10 μm particles (Waters Corporation)	Water/methanol	PEG400 in urine	0.25 mg/mL	68
UV based HPLC	Introduce dibenzoate group to PEG, chloroform extraction	Nucleosil 10 C18 reversed-phase 250 mm × 4.6 mm, 10 μm particles (Macherey-Nagel) or Spherisorb 10 ODS reversed-phase 250 mm × 4.6 mm, 10 μm particles (Waters Corporation)	Water/methanol or water/acetonitrile gradient	PEG600 in urine	1 μg per injection	60
UV based HPLC	4-hydroxybenzaldehyde precipitation, methanol extraction	CAPCELL PAK C18 reversed-phase 250 mm × 4.6 mm, 5 μm particles (Shiseido Fine Chemicals)	H_3PO_4/water/acetonitrile gradient	PEG4700-PUE	80 ng/mL	73
UV based HPLC	Triton X-100 extraction, 5-sulfosalicylic acid precipitation	Discovery RP-amide C16 reversed-phase 250 mm × 3 mm, 5 μm particles (Supelco)	0.05 M sodium acetate/acetonitrile	Doxorubicin and PEG2000 liposomal doxorubicin	10 ng/mL	62
Fluorescence based HPLC	Trifluoroacetic acid precipitation, evaporative concentration	Juniper C18 reversed-phase 150 mm × 2 mm, 5 μm particles (Phenomenex)	Ammonium acetate/acetonitrile gradient	PEG40K-SN38, SN38 or CPT-11 in human serum	10 ng/mL	63,74
Fluorescence based HPLC	Acetonitrile precipitation, evaporative concentration.	Diamonsil C18 reversed-phase 200 mm × 4.6 mm, 5 μm particles (Dikma)	Formic acid/ammonia/water/methanol	PEG2000 liposomal doxorubicin and micelle doxorubicin	5 ng/mL	61
HPLC/MS/MS	Meta-phosphoric acid precipitation, chloroform extraction	TSK-GEL 300 mm × 7.8 mm, 6 μm particles (Supelco)	Ammonium acetate/acetonitrile	PEG3350 in urea or plasma	30 ng/mL in urine, 100 ng/mL in plasma	72
LC-MS/MS	Proteins were denatured and alkylated, enriched on 96 well SPE C18 plate, filtered, trypsin digested, cleaned up on 96-well Oasis MCX plate.	ACE C8 reversed-phase 50 mm × 2.8 mm, 5 μm particles (Advanced Chromatography Technologies)	Formic acid/water/acetonitrile gradient	Pegasys	3.6 ng/mL	92
LC-MS/MS	Acidic isopropanol precipitation, extraction, trypsin digestion	Zorbax Eclipse XDB C8 column reversed-phase 500 mm × 2.1 mm, 3.5 μm particles (Agilent)	Formic acid/water/methanol gradient	PEGylated protein	10 ng/mL	195
LC-MS/MS	Plasma proteins precipitated with PEG6000, immunoaffinity purification, filtration, concentration, trpsin digestion	Wide-pore Zorbax 300SB C18 reversed-phase 50 mm × 1.0 mm, 3.5 μm particles (Agilent)	Water/acetonitrile/formic acid gradient	Mircera	0.3 ng/mL	94
LC-MS/MS	Extraction on a 96-well SPE plate, gas-phase dePEGylation by in-source collision-induced dissociation	Acquity UPLC BEH C18 reversed-phase 50 mm × 2.1 mm, 1.7 μm particles (Waters)	Formic acid/acetonitrile/water gradient	human calcitonin peptide receptor antagonist conjugated with PEG20000	5 ng/mL	95

dx.doi.org/10.1021/bc200478w | *Bioconjugate Chem.* 2012, 23, 881–899

distributions of PEG and proteins. However, utilization of clever pretreatment steps before analysis to reduce sample complexity is allowing utilization of LC-MS/MS for analysis of larger PEGylated compounds. For example, measurement of Pegasys in human serum samples was accomplished by denaturing and alkylating proteins, enriching Pegasys on 96-well solid-phase extraction C18 plates, enzymatically digesting the eluants and concentrating proteins on a 96-well Oasis MCX plate before separation on an ACE C8 column and analysis by LC-MS/MS of a signature peptide derived from the target protein. The quantitation limit of this assay was 3.6 ng/mL.[92] Similarly, the concentration of an investigational peptide linked to a 40 kDa PEG in monkey plasma was accomplished by acidic isopropanol precipitation and tryptic digestion to produce a unique tryptic peptide arising from the PEGylated therapeutic protein for detection by LC-MS/MS with a lower limit of quantitation of 10 ng/mL on a Zorbax Eclipse XDB C8 column.[93] Mircera (C.E.R.A., a continuous erythropoietin receptor activator conjugated with a single 30 kDa PEG chain) could be detected in horse plasma at a concentration of 0.3 ng/mL by an optimized process entailing pretreatment of equine plasma with PEG 6000 to precipitate proteins, immunoaffinity collection of Mircera on magnetic beads coated with specific antibodies, buffer exchange, tryptic digestion, separation on a wide-pore Zorbax 300SB C18 column under gradient elution conditions and MS/MS analysis of a signature tryptic peptide.[94] The concentration of an investigational human calcitonin peptide receptor antagonist conjugated with PEG20,000 in cynomolgus monkey serum was also determined with a lower limit of quantitation of 5 ng/mL by performing solid phase extraction on a 96-well solid phase extraction plate before gas phase dePEGylation by in-source collision-induced dissociation to generate surrogate peptide fragments for quantitative analysis of the peptide by LC-MS/MS.[95]

A drawback of LC-MS/MS for PEGylated protein and peptide determination is the need to develop appropriate conditions for cleanup and analysis for each protein (Table 2). In general, protein precipitation in an organic solvent, solid phase extraction or affinity purification can be employed to deplete serum proteins and concentrate PEGylated proteins before enzymatic digestion and analysis. Methods for sample cleanup and preparation for HPLC analysis have been recently reviewed.[96−98] Besides the need for sample cleanup, the presence of PEG chains may also sterically hinder tryptic digestion and quantitative generation of small peptides.[94] In addition, LC-MS/MS may overestimate PEGylated protein concentrations due to detection of intact surrogate peptides from dePEGylated peptides as well as other truncated metabolite species present in clinical samples.[99]

RADIOLABELING

Radiolabeling offers a straightforward and sensitive method to determine the pharmacokinetics of PEG and PEGylated compounds. Typically, a radioisotope (a radionuclide tracer atom) is included in the chemical composition of PEG or PEGylated molecules, and is administrated in small amounts to minimize interference with the experimental system. The radionuclide atom continually emits radiation which can be detected and quantified by a gamma counter to monitor X-ray and gamma-ray emissions or by a scintillation counter (also known as an α/β counter) to monitor α and β particle emissions. A variety of radioisotopes have been employed to measure PEG and PEGylated compound pharmacokinetics (Table 4).

Because methoxy-PEG is difficult to directly label, it is usually necessary to use other functional end groups for radiolabeling.

Table 4. Radioisotopes Commonly Used to Measure PEG and PEGylated Compound Pharmacokinetic Properties

radioisotope	emission type	half-life	detector
^{18}F	gamma-ray	109.8 min	gamma counter
^{32}P	β particle	14.3 days	liquid scintillation counter
^{59}Fe	β particle gamma-ray	44.5 days	liquid scintillation counter gamma counter
^{64}Cu	β particle gamma-ray	12.7 days	liquid scintillation counter gamma counter
^{99m}Tc	gamma-ray	6 h	gamma counter
^{111}In	gamma-ray	2.8 days	gamma counter
^{123}I	gamma-ray	13.3 h	gamma counter
^{125}I	gamma-ray	59.4 days	gamma counter
^{186}Re	gamma-ray	3.7 days	gamma counter

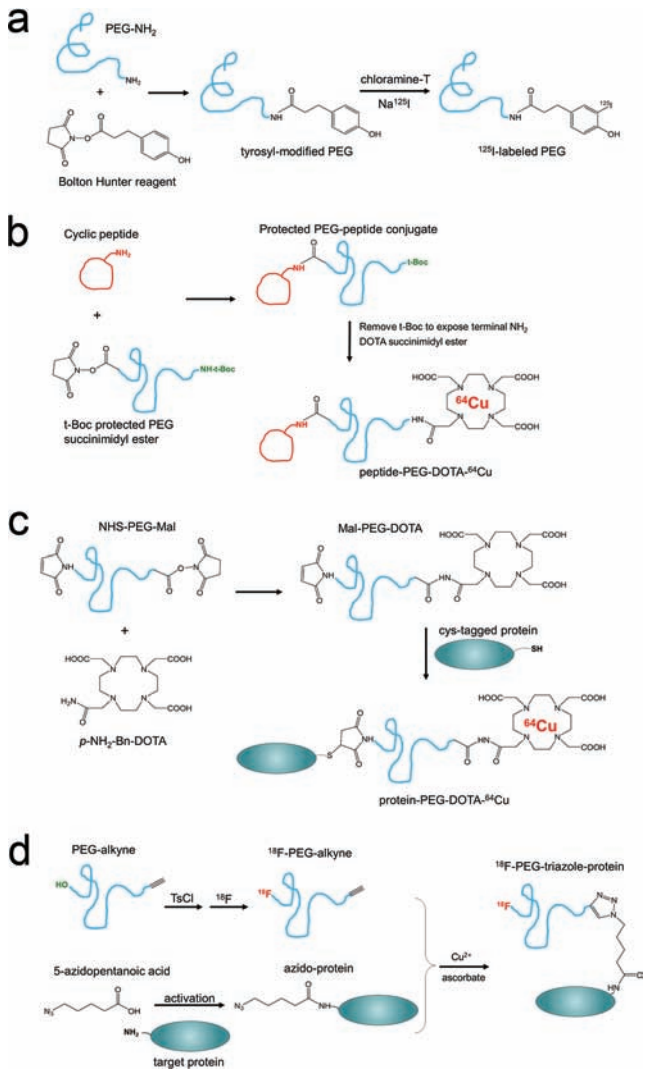

Figure 2. Radiolabeling of PEG for pharmacokinetic analysis. (a) Amino-PEG is reacted with Bolton-Hunter reagent to introduce a tyrosyl moiety for subsequent iodination by the chloramine-T procedure. (b) A t-Boc protected PEG succinimidyl ester is reacted with the primary amine group of a cyclic peptide. Removal of the t-Boc protective group allows reaction of DOTA succinimydyl ester to the terminal amine group on PEG to form a peptide-PEG-DOTA conjugate for ^{64}Cu labeling. (c) 2-(4-Aminobenzyl)-DOTA is reacted with NHS-PEG-Mal, which is then reacted to the cysteine-tag in the protein for chelation of ^{64}Cu. (d) A PEG-alkane labeled with ^{18}F and a azido-derivatized protein are combined in a click reaction to form a ^{18}F-PEG-triazole-protein conjugate.

dx.doi.org/10.1021/bc200478w | Bioconjugate Chem. 2012, 23, 881−899

Table 5. Radiolabeling Methods for the Quantitative Measurement of PEG and PEGylated Molecules

isotopes	PEG compounds	labeling method	measurement	ref.
^{125}I	PEG 3−190KDa	Conjugate tyramine to terminal hydroxyl groups of PEG molecules and then label ^{125}I to the tyramine residues by the chloramine T method	Directly detect by a gamma counter	101
^{125}I	PEG 5−20KDa	Conjugate Bolton Hunter reagent to terminal amine groups of PEG molecules and then label ^{125}I by the chloramine T method	Directly detect by a gamma counter	100
^{125}I	PEG2K-RGD peptide	Directly label ^{125}I to the tyrosine residue of RGD peptide or PEG-RGD peptide by the chloramine T method	Directly detect by a gamma counter	102
^{123}I ^{127}I	PEG10K- cholecystokinin	Directly label ^{123}I or ^{127}I to the tyrosine residue of cholecystokinin by the chloramine T method	Directly detect by a gamma counter	108
^{125}I	PEG-superoxide dismutase (PEG-SOD)	Directly label ^{125}I to the tyrosine residue of PEG-SOD by the chloramine T method	Directly detect by a gamma counter	103
^{125}I	Somavert (B2036-PEG)	Directly label ^{125}I to the tyrosine residue of B2036-PEG by the chloramine T method	Radioimmunoassay & gamma counter	158
^{111}In	PEG-LLP2A peptide	Conjugate DOTA to the amine group of PEG-LLP2A peptide and label with ^{111}In	Directly detect by a gamma counter	196
^{111}In	PEG2000-anti-EGFR antibody (PEG-528MAb)	Labeling 528Mab with PEG2000 and DTPA, followed by labeling with ^{111}In	Directly detect by a gamma counter	109
^{111}In	PEG3400-anti-EGFR antibody (PEG-C225)	A heterofunctional PEG with one end attached to DTPA, and the other end attached to C225, followed by labeling with ^{111}In	Directly detect by a gamma counter	114
^{111}In	PEG-immunoliposome	Incorporate ^{111}In-DTPA in PEGylated liposomes	Directly detect by a gamma counter	121
^{111}In	Lymphoma-binding peptide-PEG-DOTA	Peptide bearing a branched chain amine-terminated PEG chain was reacted with *p*-isothiocyanatobenzyl-DOTA to allow labeling with ^{111}In	Directly detect by a gamma counter	113
^{64}Cu	RGD-PEG3400-DOTA	React DOTA sulfosuccinimydyl ester to the terminal amine group of NH_2−PEG attached to a cyclic RGD peptide to allow labeling with ^{64}Cu	Directly detect by a gamma counter	111
^{64}Cu	EGF-PEG5000-DOTA	React 2-(4-aminobenzyl)-DOTA to NHS-PEG5000-Mal, react DOTA-PEG5000-Mal to a cysteine-tag in EGF for chelation of ^{64}Cu	Directly detect by a gamma counter	115
^{64}Cu	scVEGF-PEG5000-DOTA	Label 2-(4-aminobenzyl)-DOTA to NHS-PEG5000-Mal, react DOTA-PEG5000-Mal with the cysteine-tag in scVEGF for chelation of ^{64}Cu	Directly detect by a gamma counter	116
^{64}Cu	PEG-liposome	A ^{64}Cu specific chelator, BAT, was conjugated to an artificial lipid to form a BAT-PEG-lipid	Directly detect by a gamma counter	124
^{64}Cu	PEG-liposome	Conjugate bifunctional ^{64}Cu chelators, TETA-PDP and CB-TE2A-PDEA, to liposomes via attachment to a maleimide lipid	Directly detect by a gamma counter	125
^{64}Cu	SPIO core coated with DOTA-PEG-DSPE	NHS-DOTA reacted with NH_2−PEG-DSPE on SPIO cores to allow labeling with ^{64}Cu	Directly detect by a gamma counter	128
^{99m}Tc	PEG-liposome	Label ^{99m}Tc to the HYNIC derivative of DSPE and incorporate into PEG-liposomes	Directly detect by a gamma counter	123
^{99m}Tc	PEG-liposomal doxorubicin (Doxil)	Use ^{99m}Tc-BMEDA complex loading to label Doxil	Directly detect by a gamma counter	127
^{186}Re	Doxil	Use an ammonium sulfate gradient to load ^{186}Re-BMEDA complexes into Doxil	Directly detect by a gamma counter	120
^{18}F	RGD dimer peptide with 4 arm PEG linkers	^{18}F-fluoropropionate reacted with NH_2−PEG-peptide conjugate	Directly detect by a gamma counter	112
^{18}F	Fluoro-PEG-Triazole-E(RGDyK)$_2$	Cu(I)-catalyzed Huisgen cycloaddition to label RGD peptides with ^{18}F by forming 1,2,3-triazoles	Directly detect by a gamma counter	118
^{18}F	PEG-liposome	Incorporate 3-[^{18}F]fluoro-1,2-dipalmitoylglycerol into PEG-liposomes	Directly detect by a gamma counter	122
^{32}P	PEI(-PEG)/siRNA complex	siRNA was [^{32}P] end-labeled using T4 polynucleotide kinase	Directly detect by a scintillation counter	129
^{3}H	PEG-liposome	[^{3}H]cholesteryl hexadecyl ether was incorporated in liposomes	Directly detect by a scintillation counter	197

Amine-PEG can be conveniently labeled with ^{125}I using Bolton Hunter reagent (Figure 2a).[100] Similarly, a tyramine group can be introduced to the terminal hydroxyl group of PEG to allow radiolabeling with ^{125}I by the chloramine T method (Table 5).[101]

For the pharmacokinetic study of PEGylated peptides, radioiodine can be conveniently incorporated if tyrosine residues are present in the polypeptide backbone. A RGD peptide conjugated with PEG2000 was labeled with ^{125}I by the chloramine T method for pharmacokinetic and biodistribution studies.[102] Likewise, plasma and brain levels of PEG-conjugated superoxide dismutase (PEG-SOD), which is being explored as an agent to reduce oxygen radical-mediated damage following brain injury in normal and fluid percussion rats, were determined by gamma counter detection of ^{125}I-labeled PEG-SOD.[103] Similar experimental procedures were also used for the pharmacokinetic study of ^{125}I-labeled PEG-salmon calcitonin,[104] ^{125}I-labeled PEG-recombinant human growth hormone,[105] ^{125}I-labeled PEG-recombinant human interleukin-6,[93] and ^{125}I-labeled PEG-recombinant tissue plasminogen activator.[106] Because radioiodinated peptides are susceptible to deiodiniation, complementary methods such as HPLC should be employed to confirm that radioactivity remains associated with the PEGylated peptide.[107,108]

Labeling of PEGylated proteins that do not possess accessible tyrosine residues can be accomplished by introducing a chelating agent into the protein for subsequent binding of radiometals such as ^{111}In, ^{99m}Tc, ^{186}Re, or ^{59}Fe. Reactive derivatives of chelating agents such as 1,4,7,10-tetraazacyclododecane-*N*,*N*′,*N*″,*N*‴-tetraacetic acid (DOTA) and diethylenetriaminepentaacetic acid (DTPA) are commercially available for labeling the primary amine group (−NH_2) in lysine or the thiol

dx.doi.org/10.1021/bc200478w | *Bioconjugate Chem.* 2012, 23, 881−899

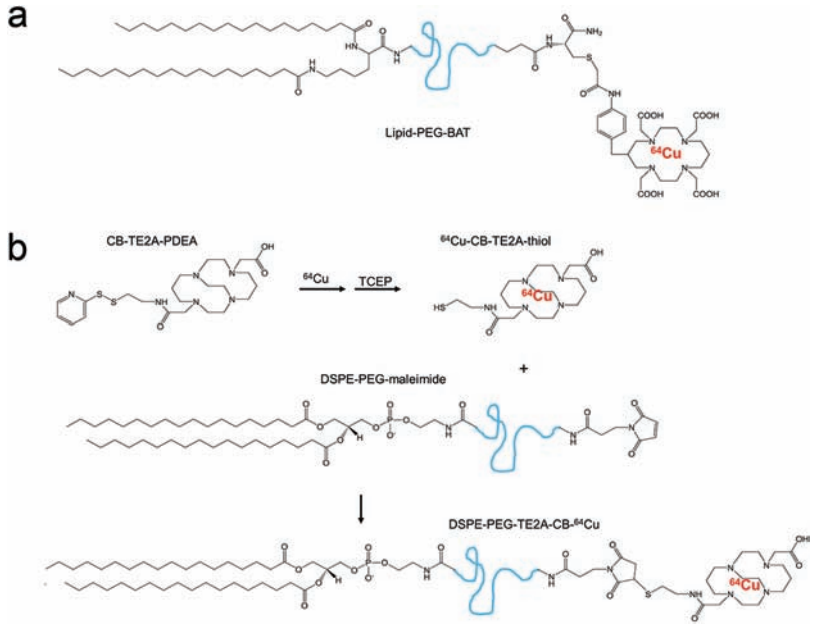

Figure 3. Surface labeling of PEGylated liposomes. (a) 6-[*p*-(Bromoacetamido)benzyl]-1,4,8,11-tetraazacyclotetradecane-*N*,*N*′,*N*″,*N*‴-tetraacetic acid (BAT) is attached to stearic acid via a PEG spacer to allow anchorage of ^{64}Cu on liposomes for PET imaging. (b) CB-TE2A-PDEA is loaded with ^{64}Cu at elevated temperature and then reduced to generate a sulfhydryl group for reaction with maleimide-PEG2000-DSPE to generate DSPE-PEG-TE2A-CB−^{64}Cu for liposome labeling.

group (−SH) in cysteine. For example, Lee and colleagues sequentially modified an anti-EGFR antibody (528 mAb) with PEG2000 and DTPA dianhydride to allow labeling with ^{111}In for pharmacokinetic analysis of the PEGylated antibody.[109] ^{111}In conjugates prepared with DTPA anhydride, however, can produce intermolecular and intramolecular cross-linking and alter in vivo pharmacokinetics.[109,110]

Chelating agents can also be directly introduced to one end of a bifunctional PEG molecule to allow chelation of an isotope and covalent attachment to the target protein or peptide. To facilitate positron emission tomography (PET) imaging of brain tumor $\alpha_v\beta_3$ integrin expression, Chen and colleagues first reacted an amine-PEG-succinimidyl ester with a cyclic peptide followed by reaction of DOTA sulfosuccinimydyl ester to the exposed terminal amine group of NH_2−PEG for labeling with ^{64}Cu (Figure 2b).[111] Peptides possessing amine-terminated PEG chains can be reacted with *p*-isothiocyanatobenzyl-DOTA to allow labeling with ^{111}In or with *N*-succinimidyl 4-[^{18}F]fluorobenzoate to incorporate ^{18}F.[112,113]

Heterofunctional PEG molecules have also been synthesized with one end attached to the radiometal chelator^{111}In-DTPA and the other to a protected S-acetylthioacetate group. Deprotection of the S-acetylthioacetate allowed reaction of the resulting DTPA-PEG-SH to maleimide-activated anti-EGFR antibody (C225) for labeling with ^{111}In.[114] Site directed radiolabeling of proteins can be achieved by first introducing a cysteine tag into the target protein; Conjugates formed by reaction of 2-(4-aminobenzyl)-DOTA to the amine-reactive NHS group of NHS-PEG5000-Mal can be selectively reacted via the thiol-reactive maleimide to the cysteine-tag in the protein for chelation of radioactive metals such as ^{64}Cu (Figure 2c).[115,116]

Recently, the Cu(I)-catalyzed azide−alkyne cycloaddition of organo azides with terminal alkynes to form 1,2,3-triazoles, also known as the click reaction, is finding increasing use for labeling PEGylated peptides,[117] typified by utilization of a ^{18}F-labeled PEG-aldehyde to label a dimeric RGD peptide, resulting in favorable pharmacokinetic properties for tumor imaging (Figure 2d).[118] A variety of alkyne-PEG and azide-PEG derivatives are now commercially available for use in click reactions (i.e., Nanocs, Creative PEGWorks, Iris Biotech GMBH).

Radiolabeling of PEGylated liposomes and micelles is useful for biodistribution and pharmacokinetic studies.[119−121] In general, radioisotopes can either be attached to the surface of a liposome or trapped inside the liposome. Two major approaches have been employed to label the surface of liposomes: membrane-soluble chelating agents can be used to anchor metallic radioisotopes on the liposome surface, or radiolabeled chelating agents can be covalently linked to the surface of liposomes. Torchilin and colleagues anchored ^{111}In-DTPA-sterylamide in PEGylated liposomes to study in vivo half-life and accumulation in infracted rabbit myocardium.[121] Incorporation of 3-[^{18}F]fluoro-1,2-dipalmitoylglycerol into PEGylated liposomes allowed PET imaging and determination of liposome biodistribution in rats.[122] Laverman and colleagues incorporated a hydrazine nicotinyl (chelator) derivative of distearoylphosphatidyl-ethanolamine (DSPE) into PEGylated liposomes for subsequent labeling with ^{99m}Tc.[123]

Besides lipid insertion methods, PEGylated liposomes can also be labeled by covalent attachment of a chelator to the liposome surface. 6-[*p*-(Bromoacetamido)benzyl]-1,4,8,11-tetraazacyclotetradecane-*N*,*N*′,*N*″,*N*‴-tetraacetic acid (BAT) was attached to stearic acid via a PEG spacer to allow anchorage of ^{64}Cu on liposomes for PET imaging (Figure 3a).[124] The longer half-life of ^{64}Cu (12.7 h) as compared to ^{18}F (110 min) can facilitate longer biodistribution studies. ^{64}Cu can also be linked to liposomes via the disulfide protected chelators (6-(6-(3-(2-pyridyldithio)propionamido)hexanamido)benzyl)-1,4,8,11-tetraazacyclotetradecane-1,4,8,11-tetraacetic acid (TETA-PDP) or 4-(2-(2-pyridyldithioethyl)ethanamido)-11-carboxymethyl-1,4,8,11-tetraazabicyclo(6.6.2)hexadecane (CB-TE2A-PDEA).

These chelators require loading of ^{64}Cu at elevated temperature before the disulfide group is reduced and reacted with the maleimide group on the commercially available maleimide-PEG2000-DSPE (1,2-distearoyl-*sn*-glycero-3-phosphoethanolamine) lipid on the surface of the liposomes (Figure 3b).[125]

A disadvantage of surface labeling of liposomes is the possibility that the surface modifications may change the in vivo behavior of the liposomes, and it may be argued as to whether these surface-altered liposomes can represent the clinically used liposomal therapeutic drugs. In fact, it has been observed that the location of a ^{64}Cu-chelator complex can alter liposome uptake in the liver and spleen.[124] To reduce the surface effects of radiolabeling liposomes, radioisotopes can be introduced inside liposomes by remote loading in which a chemical gradient is formed between the inner and outer space of the liposome. A commonly employed labeling method utilizes glutathione encapsulated liposomes to load and trap ^{99m}Tc-*N*,*N*-bis(2-mercaptoethyl)-*N*′,*N*″-diethyl-ethylenediamine (^{99m}Tc-BMEDA) with good efficiency and stability (Figure 4).[126] ^{99m}Tc-BMEDA and ^{186}Re-BMEDA can also be directly loaded into the commercially available PEGylated liposomal doxorubicin, Doxil,[120,127] allowing determination of liposome pharmacokinetics and biodistribution.

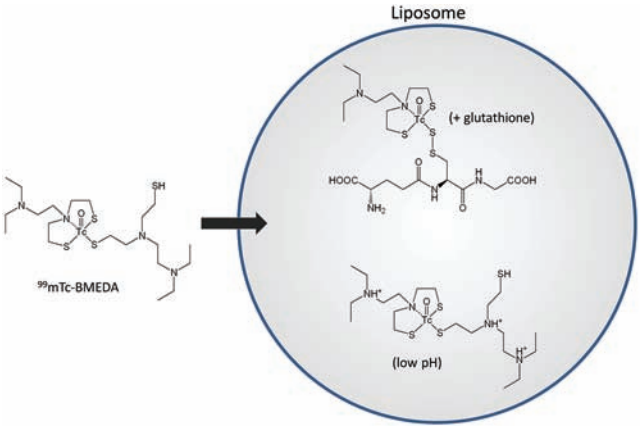

Figure 4. Internal labeling of liposomes. Lipophilic BMEDA can shuttle radioactive metals (^{99m}Tc, ^{86}Re) into liposomes. Radioactive BMEDA complexes are retained inside liposome by conversion of BMEDA to a more hydrophilic species, either by reaction with preloaded glutathione or by protonization by a low pH environment inside liposomes.

Other PEGylated compounds can also be radiolabeled for pharmacokinetic studies. Superparametric iron oxide nanoparticles coated with amine-PEG-DSPE were reacted with DOTA-NHS-ester to append the chelating agent at the amine group at the PEG termini for binding of ^{64}Cu. The biodistribution of these nanoparticles in mice could be followed by both PET and magnetic resonance imaging (MRI).[128] PEGylated nucleotides, such as small interfering RNAs (siRNA), can be conveniently end-labeled with ^{32}P using T4 polynucleotide kinase and γ-[^{32}P]ATP to allow measurement of siRNA-PEG biodistribution and pharmacokinetics.[129]

Radiolabeling offers highly sensitive and specific measurement of PEGylated compounds in vivo (Table 2). In addition, they offer the advantage of allowing noninvasive visualization of biodistribution by multiple imaging methods. The major disadvantages include possible alterations of the physical properties of the pharmaceutical and additional safety and cost issues associated with radioisotope handling and disposal.

BIOACTIVITY ASSAYS

Bioactivity assays can be employed for quantitation of PEGylated molecules in serum samples if a suitable and sensitive bioassay is available. PEGylated enzymes are particularly suited to this approach since a wide variety of detectable substrates are commercially available. For example, Hoffmann and colleagues measured PEG-hirudin (thrombin inhibitor) in blood by a chromogenic method based on inhibition of thrombin hydrolysis of the substrate S-2238.[130,131] Similarly, Hempel and colleagues measured the pharmacokinetics of PEG-asparaginase based on the generation of indooxine for photometric detection at 710 nm.[132] Enzyme assays have also been employed to measure PEG-uricase,[133,134] antibody-β-glucuronidase-PEG conjugates,[5,135] PEG-organophosphorus hydrolase,[136] PEG-recombinant human acetylcholinesterase hypolysine variants,[137] and PEG-arginine deiminase[138] in serum samples.

PEGylated cytokines often can be assayed in clinical samples by established bioassays. The proliferation of an IL-2 dependent HT2 murine cell line was used to measure the serum pharmacokinetics of PEGylated-IL-2.[139] The pharmacokinetic properties of PEGylated IL-2 have also been measured using the cytopathic effect assay (CPE assay) in which the protective effect of IL-2 against vesicular stomatitis virus challenged MDBK cells are determined.[140] Likewise, PEGylated human IFN-β-1a pharmacokinetics in mice, rats, and monkeys was determined by assessing the antiviral activity of samples against A549 cells exposed to encephalomyocarditis (EMC) virus.[141] The pharmacokinetics of PEGylated GM-CSF in Sprague–Dawley rats were determined by measuring the proliferative effects of serum samples on C3H/He mouse bone-marrow derived cells.[142] François and colleagues developed an interesting bioassay for the measurement of PEGylated interferon based on the IFN-α induced activation of a MxA promoter-chloramphenicol acetyltransferase reporter gene.[143]

There are several considerations when utilizing bioassays for pharmacokinetic studies. An appropriate and sensitive bioassay is required for the compound of interest. The assay should provide a specific readout for the PEGylated compound without interference by related compounds. For measurement of human proteins such as enzymes and cytokines, one must ensure that endogenous and related compounds are not detected by the assay.[143] Bioassays tend to lack high reproducibility due to the reliance on a complex biological system for the readout. Attachment of PEG chains to proteins and peptides can also reduce their biological activity and hinder receptor binding,[144,145] which can decrease assay sensitivity. For example, PEG chain on proteins can decrease their apparent association rate when assayed by surface plasmon resonance.[146] Also, Pegasys displayed only 7% of wild-type activity in a cytopathic effect assay measuring antiviral activity.[147] Likewise, PEG-modified granulocyte colony stimulating factor displayed greatly reduced activity in a cell proliferation assay.[148] In some cases, PEGylation can even alter the spectrum of a proteins biological activity.[149,150] Finally, biological assays assume that the PEGylated compound displays constant activity in vivo. Alterations in biological activity with time (i.e., dePEGylation, interaction with inhibitors, degradation) may affect biological activity and provide false results.[151] These caveats suggest that bioassays are most suitable for in vitro determination of the biological activity of PEGylated compounds and are generally less desirable for in vivo pharmacokinetic studies if alternative analytical approaches are available.

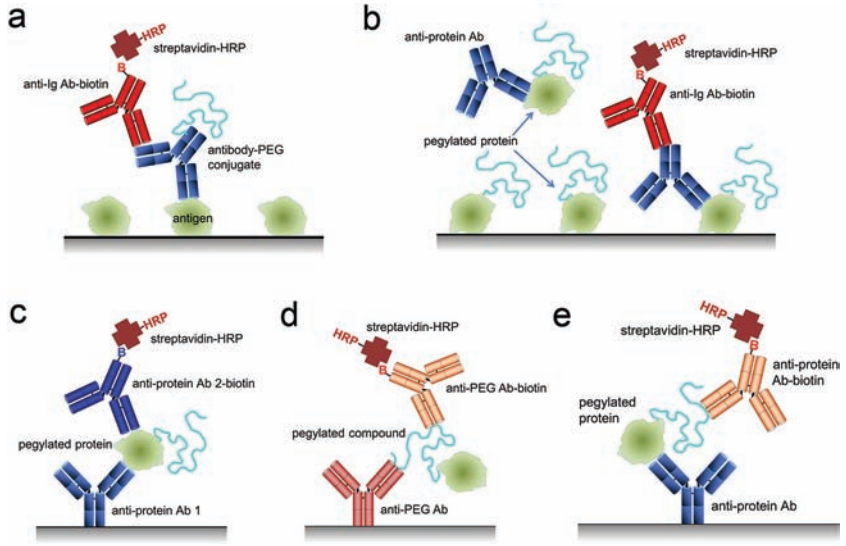

Figure 5. ELISA detection of PEGylated compounds. (a) In direct ELISA, PEGylated antibody binding to antigen-coated microtiter wells is detected with biotin-labeled anti-immunoglobulin antibody and streptavidin-HRP. (b) In competition ELISA, PEGylated protein (or any PEGylated compound) is coated in wells of microtiter plates. The concentration of PEGylated compound in samples is determined by measuring how completely the binding of antiprotein antibodies to the coated antigen is blocked (competed) by the soluble protein. (c) In sandwich ELISA, antibodies that bind distinct epitopes on the PEGylated protein are employed to capture and detect the PEGylated protein. (d) In sandwich PEG ELISA, anti-PEG antibodies are employed for both capture and detection of the PEG portion of the PEGylated compound. Note that this assay can use the same antibody for both capture and detection. (e) In combination sandwich ELISA, the PEGylated protein is captured by an antiprotein antibody coated in microtiter plate wells and detected by a biotin-conjugated anti-PEG antibody.

■ DIRECT ELISA

Direct enzyme-linked immunosorbent assay (direct ELISA) is useful for measuring the concentration of PEGylated antibodies in serum samples. In this approach, a specific antigen is coated in the wells of microtiter plates for capture of PEGylated antibodies in the sample (Figure 5a). The amount of antibody bound to the antigen is then determined by adding a detection antibody, typically a horseradish peroxidase (HRP) conjugate. For example, a PEGylated humanized antitumor necrosis factor (TNF) Fab fragment (CDP870) developed for treatment of rheumatoid arthritis (RA) was captured in wells coated with recombinant human TNF-α and then detected with HRP-conjugated goat antihuman κ light chain antibody followed by addition of tetramethyl benzidine (TMB) substrate.[152] Direct ELISA employing antigen-coated microtiter plates were also used to measure the pharmacokinetics of a PEGylated single chain Fv fragment in monkeys[153] and the pharmacokinetics in rats of a PEGylated Fab′ fragment of an antibody against LINGO-1.[154]

Direct ELISA can also be employed to measure the concentration of other PEGylated compounds by using a competition assay format. PEGylated compound is typically coated in the wells of a microtiter plate. The degree that serum samples block binding of a specific antibody to plate-coated PEGylated compound provides a measure of the serum concentration of the PEGylated compound (Figure 5b). Using this format, Song and colleagues measured serum PEG-hirudin at concentrations as low as 87 ng/mL by coating PEG-hirudin in microtiter plates and then determining the ability of serum PEG-hirudin to compete the binding of rabbit antihirudin to the immobilized antigen.[155] A similar ELISA was used to measure serum levels of PEGylated asparaginase with a limit of detection of 0.004 IU/mL[156,157] and PEGylated consensus interferon with a limit of quantification of 8.4 ng/mL in rhesus monkey serum.[151] The competition assay can also be performed by coating a specific antibody in the microtiter plate and then measuring competition of serum samples for radiolabeled or tagged antigen. Using this approach, Muto and colleagues detected serum concentrations of Somavert with a competitive binding radioimmunoassay in which serum Somavert competed with trace amounts of radiolabeled antigen (^{125}I-Somavert) for binding to rabbit anti-Somavert antibodies immobilized in microtiter plates.[158] A competitive ELISA using ^{3}H-radiolabeled peptide antigen was also employed to measure the pharmacokinetics of a PEGylated thromobopoietin peptide in rats and monkeys.[159] Although direct ELISA possesses the advantage of requiring only one specific antibody for compound detection, they may not be able to distinguish between PEGylated and dePEGylated metabolites.[151] Direct ELISA may also produce anomalous results if neutralizing antibodies are present in the sample. For example, the development of neutralizing antibodies in monkeys blocked binding of a PEGylated scaffold protein to antigen coated in microtiter plates, resulting in underestimation of serum levels of the PEGylated protein.[160]

■ SANDWICH ELISA

Sandwich ELISA is a powerful approach to measure the concentration of PEGylated conjugates in complex biological samples. Sandwich ELISA employs two antibodies, one to capture the analyte on a solid surface and a second to detect the concentration of the captured analyte (Figure 5c). The analyte must possess at least two antigen-binding sites, usually distinct binding epitopes on the analyte. However, the same epitope can be used for multimeric analytes since the capture and detection antibodies can still bind to the same molecule. Sandwich ELISA is usually more sensitive (ng/mL to pg/mL) and more specific (when using two distinct antibodies) than direct and competitive ELISA and is therefore a good choice when very low concentrations of analyte must be determined.

Bruno and colleagues analyzed the pharmacokinetics of Pegasys and PEG-Intron with a quantitative sandwich ELISA

dx.doi.org/10.1021/bc200478w | *Bioconjugate Chem.* 2012, 23, 881–899

Table 6. Quantitation of PEGylated Molecules by Protein-Specific Antibody-Based ELISA

PEGylated proteins	PEG length	ELISA type	Capture/detection layers	sensitivity	ref
Pegasys	40-kDa branched PEG	Sandwich ELISA	Mouse monoclonal antihuman IFN-α antibodies/HRP-conjugated antihuman-IFN-α antibody	125 pg/mL	161,162
PEG-Intron	12 kDa	Sandwich ELISA	Mouse antihuman interferon-alpha monoclonal antibody/ HRP-conjugated monoclonal anti-interferon-alpha antibody	100 pg/mL	163
Neulasta	20 kDa	Sandwich ELISA	Mouse monoclonal anti-G-CSF antibody/HRP-conjugated polyclonal anti-G-CSF antibody	166 pg/mL	165
Mircera	30 kDa	Sandwich ELISA	Mouse monoclonal anti-EPO antibody/HRP-conjugated rabbit anti-EPO polyclonal antibody	500 pg/mL	166
Cimzia	40 kDa	Direct ELISA	Recombinant human TNF-α/ HRP-conjugated goat antihuman κ light chain antibody	Not reported	152
NNC126−0083 (PEGylated recombinant Human Growth Hormone)	43 kDa	Sandwich ELISA	Mouse monoclonal anti-NNC126−0083 antibody/biotin-labeled rhGH-specific monoclonal antibody	Not reported	198
PEG-EPO	5 kDa	Sandwich ELISA	Mouse monoclonal anti-EPO antibody/HRP-conjugated rabbit anti-EPO polyclonal antibody	500 pg/mL	199
PEG-Hirudin	5 kDa	Competition ELISA	PEG-hirudin/rabbit IgG antihirudin antibody	87 ng/mL	155
PEG-asparaginase	5 kDa	Competition ELISA	Asparaginase/Rabbit anti-asparaginase serum + biotinylated goat antirabbit IgG	0.004 IU/mL	156,157

using two mouse monoclonal antihuman IFN-α antibodies that recognize different epitopes of IFN-α with a sensitivity of 125 pg/mL (Table 6).[161] Motzer and colleagues also applied this method in a phase II trial of Pegasys in patients with advanced renal cell carcinoma with an analytical sensitivity of about 125 pg/mL.[162] Similar sandwich ELISA approaches were used to measure PEG-Intron,[163] Neulasta,[164,165] and Mircera.[166] Eggermont and colleagues measured serum PEG-Intron concentrations in melanoma patient serum samples with a validated and highly sensitive electrochemiluminescent immunoassay with a lower limit of quantitation (LLOQ) of 40 pg/mL. PEG-Intron was captured on streptavidin paramagnetic beads via a biotinylated sheep polyclonal antibody against PEG-Intron and detected with an anti-PEG-Intron mouse monoclonal antibody labeled with ruthenium trisbipyridine chelate, which produces an electrochemiluminescent signal in the presence of tripropylamine in an ORIGIN analyzer.[167]

ELISA approaches possess important advantages over other analytical approaches including the ability to detect compounds in their native state (i.e., no need to radiolabel or otherwise modify the analyte), superb specificity, and sensitivity and compatibility with complex samples such as serum without the need to perform sample cleanup. However, ELISA assays using antiprotein antibodies generally cannot differentiate between PEGylated and non-PEGylated molecules and therefore assume that measurements represent the PEGylated compound. This can be solved in some cases by separating PEGylated from non-PEGylated proteins. For example, the pharmacokinetics of recombinant human leptin modified with a single branched 42 kDa PEG molecule were measured in human blood samples by sandwich ELISA using an antileptin antibody after size exclusion chromatography to remove unmodified leptin.[168] However, this greatly complicates assay of multiple samples. In addition, protein-specific antibody-based ELISA can be affected by the presence of PEG chains. PEG is well-known for its ability to decrease protein antigenicity, principally by shielding antigenic epitopes on the surface of proteins from antibody binding.[77] The shielding effect of PEG can also mask antibody-binding epitopes during ELISA, resulting in weaker interactions with capture and detection antibodies, thereby decreasing assay sensitivity. For example, attachment of branched 40 kDa PEG to IFN-α 2b significantly inhibited monoclonal antibody binding to IFN.[169] Antibody binding to PEGylated asparaginase was also significantly reduced by attachment of multiple linear 10 kDa PEG molecules and even more dramatically reduced by attachment of multiple 10 kDa branched PEG chains.[170] Generally, large, branched PEG molecules and attachment of multiple PEG chains to proteins more effectively shields antibody-binding epitopes, reducing assay sensitivity. For maximal accuracy, purified PEG-conjugate should be used for construction of the standard curve.

■ ANTI-PEG ELISA

The development of antibodies that specifically bind to PEG has allowed the development of highly sensitive and accurate ELISAs for PEGylated molecules. Richter and Akerblom were the first to generate antibodies against PEG by immunizing rabbits with PEG linked to ovalbumin, bovine superoxide dismutase, and ragweed pollen in Freund's complete adjuvant.[171] These polyclonal antibodies allowed detection of PEGylated proteins down to about 1 μg/mL. To overcome the inherent limitations of polyclonal antibodies, we[135,172−174] and others[175] generated mouse monoclonal antibodies that can specifically bind to PEG molecules (Table 7). Anti-PEG antibodies were generated by attaching PEG to highly immunogenic carrier proteins and immunizing mice multiple times to overcome the very low immunogenicity of PEG. For example, we developed two mouse monoclonal anti-PEG antibodies (AGP3/IgM and E11/IgG1) by sequentially immunizing mice with an antibody-PEG-β-glucuronidase conjugate.[135,173] Both antibodies bind the repeating subunits of the PEG backbone and can detect PEG-modified proteins by ELISA, immunoblotting, and flow cytometry.

Anti-PEG sandwich ELISA allows detection of PEGylated compounds by direct binding to PEG independent of the attached compound (Figure 5d). A sandwich ELISA in which E11/AGP3 were employed as the capture/detection antibodies was developed to detect PEG-modified proteins at concentrations as low as 1.2 ng/mL. The ELISA could also quantify, in the presence of 10% fetal bovine serum, PEG2000-quantum dots and PEG2000-liposomes at concentrations as low as 1.4 ng/mL (3.1 pM) and 2.4 ng/mL (3.13 nM phospholipids), respectively (Table 8). AGP3 and E11 have been widely used in proprietary assays throughout the pharmaceutical and biotechnology industries for pharmacokinetic measurements of PEGylated compounds.[176,177] An advantage of anti-PEG ELISA is general application to the detection of a wide variety of PEGylated compounds since the antibodies bind to PEG.

Table 7. Anti-PEG Antibodies

name	species	specificity	biotin version?	applications[a]	source[b]	refs
PEG-B-47	Rabbit IgG_1	Terminal methoxy group of PEG	Yes	ELISA, WB, FC	Epitomics	99,160,174,184,186
PEG-2−128−7	Rabbit IgM	PEG backbone	No	ELISA, WB	Epitomics	
AGP3	Mouse IgM	PEG backbone	Yes	ELISA, WB, FC, IHC	Academia Sinica	135,147,172−174,176−182,185,187,189−191
E11	Mouse IgG_1	PEG backbone	No	ELISA, WB, FC, IHC	Academia Sinica	135,172−174,176,177,188,192
AGP4	Mouse IgM	PEG backbone	Yes	ELISA, WB, FC, IHC	Academia Sinica	174,200
3.3	Mouse IgG_1	PEG backbone	Yes	ELISA, WB, FC, IHC	Academia Sinica	174
B139M	Mouse IgG_1	PEG backbone[c]	No	ELISA	Acris Antibodies	174
B141M	Mouse IgG_1	PEG backbone[c]	No	ELISA	Acris Antibodies	174

[a]ELISA, Enzyme-linked immunosorbent assay; WB, Western blot; FC, flow cytometry, IHC, immunohistochemistry. [b]Supplier Addresses: Epitomics, Inc., 863 Mitten Road, Suite 103, Burlingame, California; Academia Sinica, Academia Road, Section 2, No. 128, Taipei 11529, Taiwan; Acris Antibodies, Inc., 6815 Flanders Drive, Suite 140, San Diego, CA 92121. [c]Antibody binding is blocked by detergents containing PEG-like structures such as Tween-20.

Table 8. Anti-PEG Antibody-Based ELISA

PEGylated proteins	PEG length	capture/detection layers	sensitivity	ref
Pegylated quantum dots	2000	E11 anti-PEG antibody/AGP3 anti-PEG antibody and HRP-conjugated goat antimouse IgM μ chain antibody	1.4 ng/mL	173
Lipodox	2000	E11 anti-PEG antibody/AGP3 anti-PEG antibody and HRP-conjugated goat antimouse IgM μ chain antibody	2.4 ng/mL	173
PEG-β-glucuronidase	3400	E11 anti-PEG antibody/AGP3 anti-PEG antibody and HRP-conjugated goat antimouse IgM μ chain antibody	1.2 ng/mL	173
Pegylated thrombopoietin peptide	20 kDa	Rabbit antipeptide antibody/AGP3 anti-PEG antibody and HRP-conjugated antimouse immunoglobulin antibody	6.2 ng/mL	178,179
Mircera	30 kDa	Rabbit antierythropoietin antibody/AGP3 anti-PEG antibody and HRP-conjugated goat antimouse IgM μ chain antibody	150 pg/mL	180,181
Mircera	30 kDa	Rabbit antierythropoietin antibody/digoxigenin-labeled AGP3 anti-PEG antibody and HRP-conjugated antidigoxigenin Fab	30 pg/mL	181
PEG-human growth hormone	20 kDa	AGP3 anti-PEG antibody/sulfo-tag labeled goat anti-hGH antibody	0.5 ng/mL	182
PEG-human growth hormone	43 kDa	Anti-PEG antibody/anti-hGH antibody	Not specified	183
Lipodox	2000	AGP4 anti-PEG antibody/biotin-labeled 3.3 anti-PEG antibody and streptavidin-HRP	0.32 ng/mL	174
PEG-quantum dots	2000	AGP4 anti-PEG antibody/biotin-labeled 3.3 anti-PEG antibody and streptavidin-HRP	0.36 ng/mL	174
Pegasys	43 kDa branched	AGP4 anti-PEG antibody/biotin-labeled 3.3 anti-PEG antibody and streptavidin-HRP	0.32 ng/mL	174
PEG-Intron	12 kDa	AGP4 anti-PEG antibody/biotin-labeled 3.3 anti-PEG antibody and streptavidin-HRP	4.1 ng/mL	174
Neulasta	20 kDa	AGP4 anti-PEG antibody/biotin-labeled 3.3 anti-PEG antibody and streptavidin-HRP	1.2 ng/mL	174
PEG-peptide	40 kDa branched	Rabbit antipeptide antibody/10F05 anti-PEG antibody and HRP-labeled goat antimouse antibody	0.1 ng/mL	175

Anti-PEG antibodies can also be used in combination with antiprotein antibodies in sandwich ELISA format (Figure 5e). For example, a sandwich ELISA was used to measure a PEGylated thrombopoietin mimetic peptide (PEG-TPOm, RWJ-800088) in human serum samples by using an anti-thrombopoietin antibody for capture and AGP3 anti-PEG antibody for detection with a limit of detection of 6.25 ng/mL.[178,179] Mircera in human serum samples was measured by adding biotin-labeled rabbit polyclonal antibodies against human erythropoietin in commercially available microtiter plates precoated with streptavidin, adding serum samples, and then detecting with AGP3 anti-PEG antibody followed by peroxidase-conjugated goat anti-mouse IgM.[180,181] The assay allowed measurement of serum Mircera concentrations over the range 150−4000 pg/mL. Modification of the assay by using digoxigenin-labeled AGP3 followed by detection with peroxidase-conjugated polyclonal antidigoxigenin Fab fragment increased the dynamic detection range of the assay to 30−1000 pg/mL.[181] Myler and colleagues detected PEGylated human growth hormone (PEG-hGH) in growth hormone deficient patients in a sandwich electrochemiluminescent immunosorbent assay. Biotinylated AGP3 was bound to streptavidin-coated microtiter plates as the capture layer, whereas goat anti-hGH polyclonal antibody labeled with Sulfo Tag succinimidyl ester was used for detection by measuring electrochemiluminescence.[182] Interestingly, acid treatment of samples before analysis greatly increased assay specificity, presumably by dissociating PEG-hGH from serum resident growth hormone binding protein (GHBP), thereby reducing detection of endogenous GHBP by goat anti-hGB secondary antibody.

The pharmacokinetics of NNC126−0083, rhGH with a 43 kDa PEG molecule attached at glutamine 141, were determined in a validated sandwich ELISA using an anti-PEG antibody for capture and a biotin-labeled hGH-specific monoclonal antibody for detection.[183] Combined use of anticompound and anti-PEG antibodies allows highly specific detection of PEGylated compounds in complex biological samples.

We recently generated two second-generation monoclonal antibodies to PEG (AGP4/IgM and 3.3/IgG) that also bind to the repeating subunits of the PEG backbone but with greater affinity than AGP3 and E11.[174] A sandwich ELISA in which AGP4 was employed as the capture antibody and biotinylated 3.3 (3.3-biotin) was used as the detection antibody allowed quantification with detection limits of 0.79 pM for PEG-Qdot 525, 0.32 ng/mL for Lipo-Dox, 0.32 ng/mL for Pegasys, 4.1 ng/mL for PEG-Intron, and 1.2 ng/mL for Neulasta, respectively. 3.3-Biotin was also found to allow detection of several PEGylated compounds in combination with other commercially available monoclonal antibodies.[174]

Comparison of anti-PEG antibody binding to different sizes of PEG indicates that E11, AGP3, and AGP4 can bind PEG750 (~16 repeating oxyethylene repeat units) but binding increased for longer chain PEG molecules.[174] By contrast, the anti-PEG antibody 3.3 bound PEG2000 but did not bind to PEG750, indicating that 3.3 recognizes a larger antigen-binding epitope than the other antibodies. Both AGP4 capture and 3.3-biotin detection antibodies could bind to the same PEG chain as shown by the ability to detect PEG-Intron (possessing a single 12 kDa methoxy PEG), Neulasta (incorporating a single 20 kDa monomethoxy PEG), and Pegasys (with a single 40 kDa branched-chain methoxy PEG). Detection sensitivity was greater for proteins possessing longer PEG chains (Pegasys > Nuelasta ≫ PEG-Intron). Nanoparticles and liposomes decorated with multiple short PEG chains provided the highest assay sensitivities, likely due to binding of multiple anti-PEG antibodies to the surface of the particles. The anti-PEG ELISA was insensitive to the presence of 50% human serum, demonstrating suitability for analysis of human samples.

Wunderlich and colleagues also developed a mouse monoclonal anti-PEG antibody (10F05) by immunizing mice with keyhole limpet hemocynanin (KLH) conjugated with PEG-2000. 10F05 could recognize a PEGylated peptide conjugated with a branched 40 kDa PEG in serum at concentrations lower than 100 pg/mL.[175] Xu and colleagues quantified a 38 amino acid therapeutic peptide (MK-2662) modified with a single branched 40 kDa PEG in human plasma by an immunoaffinity purification method (IAP) using streptavidin-coated magnetic beads decorated with biotinylated rabbit monoclonal antibody PEG-B-47, which binds to the terminal methoxy group of mPEG along with 16 oxyethylene repeat units,[184] to concentrate PEGylated peptide followed by tryptic digestion and measurement of surrogate peptide concentration by LC-MS/MS with a dynamic range of 2−200 nM.[99] Preconcentration of pepylated peptides or proteins by anti-PEG antibody immunopurification is a promising method to replace precipitation and solid-phase extraction methods for LC-MS/MS analysis.

In addition to ELISA, anti-PEG antibodies are useful to characterize PEGylated compounds and for detection of PEG or PEGylated compounds in tissues. Anti-PEG antibodies can visualize PEGylated proteins and compounds on immunoblots.[173,174,185] For example, Bailon and colleagues characterized the integrity and predominant mono-PEGylation of Pegasys by immunoblotting using AGP3 anti-PEG antibody for detection.[147] Anti-PEG antibodies can also help visualize PEGylated compound in tissue sections.[186−188] Ton and colleagues used AGP3 anti-PEG antibody for immunohistochemical detection of tissue localization of CDP791, a PEGylated di-Fab′ conjugate that binds VEGFR-2, in a phase I clinical trial in patients with hemangioma.[187] White and colleagues studied the localization of PEGLA, a PEGylated leukemia inhibitory factor antagonist which can block the action of leukemia inhibitory factor, in the uterus by immunohistochemistry using E11 anti-PEG antibody for detection.[188]

For reasons not clearly understood, anti-PEG antibodies can strongly bind PEG molecules immobilized on a surface such as a protein, liposome, nanoparticle, or microtiter plate but bind less effectively to unconjugated PEG molecules in solution. Therefore, sandwich ELISA using anti-PEG antibodies cannot readily detect unconjugated PEG molecules.[174] By contrast, recombinant AGP3 anti-PEG Fab fragments expressed on the surface of 3T3 fibroblasts effectively bound both conjugated and unconjugated PEG molecules.[189−191] An anti-PEG cell-based competition ELISA allowed PEG quantification by measuring the ability of PEG to compete binding of biotinylated PEG5000 (CH_3-PEG5000-biotin) to the cells. The αPEG cell-based competition ELISA could measure the concentrations of PEG and small compounds linked to PEG2000, PEG5000, PEG10000, and PEG20000 with detection limits ranging from 3 to 60 ng/mL. The αPEG cell-based competition ELISA accurately delineated the pharmacokinetics of PEG5000, comparable to those determined by direct measurement of radioactivity in blood after intravenous injection of CH_3−PEG5K−^{131}I into mice. This quantitative strategy may provide a simple and sensitive method for quantifying PEG and PEGylated small molecules in vivo.

■ SUMMARY

Increasing numbers of pegylated proteins and small peptides are expected to reach preclinical and clinical trials in the near future. A multitude of nanoparticle PEGylated therapeutic and diagnostic agents are also under active development, indicating a continued demand for accurate, robust, and high throughput methods for the quantitative measurement of PEGylated compounds. Improved HPLC methods are expected to play an important role in the characterization of PEGylated compounds and increasingly be used for defining pharmacokinetic parameters of new PEGylated compounds. Anti-PEG ELISA or combined anticompound/anti-PEG ELISA should continue to play an important role in pharmacokinetic studies due to the high throughput, ability to assay complex biological samples, and good sensitivity and specificity of these immunological methods. Combination of technologies should facilitate creation of powerful assays as typified by the use of anti-PEG antibodies to capture PEGylated compounds for subsequent analysis by LC-MS/MS[99] or the combination of immunological and nanoscale technologies.[192] Adoption of established technologies and development of new methods will accelerate clinical translation of novel PEGylated agents such as carbon nanotubes, nanodiamonds, microbubbles, dendrimers, and other nanoparticles.[193]

■ AUTHOR INFORMATION

Corresponding Author

*Dr. Steve R. Roffler, Institute of Biomedical Sciences, Academia Sinica, Academia Road, Section 2, No. 128, Taipei 11529, Taiwan. E-mail: sroff@ibms.sinica.edu.tw.

■ ACKNOWLEDGMENTS

This work was supported by grants from the National Science Council (NSC 100-2811-B-001-048, NSC 100-2325-B-037-001), Academia Sinica (AS-98-TP-B09), the Department of Health, Executive Yuan, Taiwan (DOH100-TD-C-111-002 and DOH100-TD-N-111-010) and the Cancer Center, Kaohsiung Medical University Hospital.

■ REFERENCES

(1) Harris, J. M., and Chess, R. B. (2003) Effect of pegylation on pharmaceuticals. *Nat. Rev. Drug Discovery 2*, 214−221.
(2) Veronese, F. M., and Pasut, G. (2005) PEGylation, successful approach to drug delivery. *Drug Discovery Today 10*, 1451−1458.
(3) Chaffee, S., Mary, A., Stiehm, E. R., Girault, D., Fischer, A., and Hershfield, M. S. (1992) IgG antibody response to polyethylene glycol-modified adenosine deaminase in patients with adenosine deaminase deficiency. *J. Clin. Invest. 89*, 1643−1651.
(4) Brinckerhoff, L. H., Kalashnikov, V. V., Thompson, L. W., Yamshchikov, G. V., Pierce, R. A., Galavotti, H. S., Engelhard, V. H., and Slingluff, C. L. Jr. (1999) Terminal modifications inhibit proteolytic degradation of an immunogenic MART-1(27−35) peptide: implications for peptide vaccines. *Int. J. Cancer 83*, 326−334.
(5) Cheng, T. L., Chen, B. M., Chan, L. Y., Wu, P. Y., Chern, J. W., and Roffler, S. R. (1997) Poly(ethylene glycol) modification of beta-glucuronidase-antibody conjugates for solid-tumor therapy by targeted activation of glucuronide prodrugs. *Cancer Immunol. Immunother. 44*, 305−315.
(6) Heathcote, E. J., Shiffman, M. L., Cooksley, W. G., Dusheiko, G. M., Lee, S. S., Balart, L., Reindollar, R., Reddy, R. K., Wright, T. L., Lin, A., Hoffman, J., and De Pamphilis, J. (2000) Peginterferon alfa-2a in patients with chronic hepatitis C and cirrhosis. *N. Engl. J. Med. 343*, 1673−1680.
(7) Reddy, K. R., Wright, T. L., Pockros, P. J., Shiffman, M., Everson, G., Reindollar, R., Fried, M. W., Purdum, P. P. 3rd, Jensen, D., Smith, C., Lee, W. M., Boyer, T. D., Lin, A., Pedder, S., and DePamphilis, J. (2001) Efficacy and safety of pegylated (40-kd) interferon alpha-2a compared with interferon alpha-2a in noncirrhotic patients with chronic hepatitis C. *Hepatology 33*, 433−438.
(8) Manns, M. P., McHutchison, J. G., Gordon, S. C., Rustgi, V. K., Shiffman, M., Reindollar, R., Goodman, Z. D., Koury, K., Ling, M., and Albrecht, J. K. (2001) Peginterferon alfa-2b plus ribavirin compared with interferon alfa-2b plus ribavirin for initial treatment of chronic hepatitis C: a randomised trial. *Lancet 358*, 958−965.
(9) Goffin, V., and Touraine, P. (2002) Pegvisomant. Pharmacia. *Curr. Opin. Invest. Drugs 3*, 752−757.
(10) Schreiber, S., Khaliq-Kareemi, M., Lawrance, I. C., Thomsen, O. O., Hanauer, S. B., McColm, J., Bloomfield, R., and Sandborn, W. J. (2007) Maintenance therapy with certolizumab pegol for Crohn's disease. *N. Engl. J. Med. 357*, 239−250.
(11) Lyman, G. H. (2005) Pegfilgrastim: a granulocyte colony-stimulating factor with sustained duration of action. *Expert Opin. Biol. Ther. 5*, 1635−1646.
(12) Molineux, G. (2004) The design and development of pegfilgrastim (PEG-rmetHuG-CSF, Neulasta). *Curr. Pharm. Des. 10*, 1235−1244.
(13) Sanchez-Fructuoso, A., Guirado, L., Ruiz, J. C., Torregrosa, V., Gonzalez, E., Suarez, M. L., and Gallego, R. (2010) Anemia control in kidney transplant patients treated with methoxy polyethylene glycol-epoetin beta (mircera): the Anemiatrans Group. *Transplant. Proc. 42*, 2931−2934.
(14) Hershfield, M. S. (1995) PEG-ADA replacement therapy for adenosine deaminase deficiency: an update after 8.5 years. *Clin. Immunol. Immunopathol. 76*, S228−S232.
(15) Bossavy, J. P., Sakariassen, K. S., Rubsamen, K., Thalamas, C., Boneu, B., and Cadroy, Y. (1999) Comparison of the antithrombotic effect of PEG-hirudin and heparin in a human ex vivo model of arterial thrombosis. *Arterioscler. Thromb. Vasc. Biol. 19*, 1348−1353.
(16) Keating, M. J., Holmes, R., Lerner, S., and Ho, D. H. (1993) L-asparaginase and PEG asparaginase--past, present, and future. *Leuk. Lymphoma 10* (Suppl), 153−157.
(17) Papahadjopoulos, D., Allen, T. M., Gabizon, A., Mayhew, E., Matthay, K., Huang, S. K., Lee, K. D., Woodle, M. C., Lasic, D. D., Redemann, C., et al. (1991) Sterically stabilized liposomes: improvements in pharmacokinetics and antitumor therapeutic efficacy. *Proc. Natl. Acad. Sci. U. S. A. 88*, 11460−11464.
(18) Allen, T. M., Hansen, C., Martin, F., Redemann, C., and Yau-Young, A. (1991) Liposomes containing synthetic lipid derivatives of poly(ethylene glycol) show prolonged circulation half-lives in vivo. *Biochim. Biophys. Acta 1066*, 29−36.
(19) Allen, T. M., and Cullis, P. R. (2004) Drug delivery systems: entering the mainstream. *Science 303*, 1818−1822.
(20) Torchilin, V. P. (2005) Recent advances with liposomes as pharmaceutical carriers. *Nat. Rev. Drug Discovery 4*, 145−160.
(21) Klibanov, A. L. (2006) Microbubble contrast agents: targeted ultrasound imaging and ultrasound-assisted drug-delivery applications. *Invest. Radiol. 41*, 354−362.
(22) Chao, T. C., Wang, W. S., Yen, C. C., Chiou, T. J., Liu, J. H., and Chen, P. M. (2003) A dose-escalating pilot study of sterically stabilized, pegylated liposomal doxorubicin (Lipo-Dox) in patients with metastatic breast cancer. *Cancer Invest. 21*, 837−847.
(23) Hsiao, S. M., Chen, C. A., Lin, H. H., Hsieh, C. Y., and Wei, L. H. (2009) Phase II trial of carboplatin and distearoylphosphatidylcholine pegylated liposomal doxorubicin (Lipo-Dox) in recurrent platinum-sensitive ovarian cancer following front-line therapy with paclitaxel and platinum. *Gynecol. Oncol. 112*, 35−39.
(24) Safra, T., Muggia, F., Jeffers, S., Tsao-Wei, D. D., Groshen, S., Lyass, O., Henderson, R., Berry, G., and Gabizon, A. (2000) Pegylated liposomal doxorubicin (doxil): reduced clinical cardiotoxicity in patients reaching or exceeding cumulative doses of 500 mg/m2. *Ann. Oncol. 11*, 1029−1033.
(25) O'Brien, M. E. R., Wigler, N., Inbar, M., Rosso, R., Grischke, E., Santoro, A., Catane, R., Kieback, D. G., Tomczak, P., Ackland, S. P., Orlandi, F., Mellars, L., Alland, L., and Tendler, C. (2004) Reduced cardiotoxicity and comparable efficacy in a phase III trial of pegylated liposomal doxorubicin HCl (CAELYX/Doxil®) versus conventional doxorubicin for first-line treatment of metastatic breast cancer. *Ann. Oncol. 15*, 440−449.
(26) Blanco, E., Kessinger, C. W., Sumer, B. D., and Gao, J. (2009) Multifunctional micellar nanomedicine for cancer therapy. *Exp. Biol. Med. 234*, 123−131.
(27) Zhang, Y., Sun, C., Kohler, N., and Zhang, M. (2004) Self-assembled coatings on individual monodisperse magnetite nanoparticles for efficient intracellular uptake. *Biomed. Microdevices 6*, 33−40.
(28) Rapoport, N. Y., Efros, A. L., Christensen, D. A., Kennedy, A. M., and Nam, K. H. (2009) Microbubble generation in phase-shift nanoemulsions used as anticancer drug carriers. *Bubble Sci. Eng. Technol. 1*, 31−39.
(29) Ballou, B., Lagerholm, B. C., Ernst, L. A., Bruchez, M. P., and Waggoner, A. S. (2004) Noninvasive imaging of quantum dots in mice. *Bioconjugate Chem. 15*, 79−86.
(30) Yowell, S. L., and Blackwell, S. (2002) Novel effects with polyethylene glycol modified pharmaceuticals. *Cancer Treat. Rev. 28* (Suppl A), 3−6.
(31) Chen, Y. J., Tao, J., Xiong, F., Zhu, J. B., Gu, N., and Geng, K. K. (2010) Characterization and in vitro cellular uptake of PEG coated iron oxide nanoparticles as MRI contrast agent. *Pharmazie 65*, 481−486.
(32) LaConte, L. E., Nitin, N., Zurkiya, O., Caruntu, D., O'Connor, C. J., Hu, X., and Bao, G. (2007) Coating thickness of magnetic iron oxide nanoparticles affects R2 relaxivity. *J. Magn. Reson. Imaging 26*, 1634−1641.
(33) Kircher, M. F., Allport, J. R., Graves, E. E., Love, V., Josephson, L., Lichtman, A. H., and Weissleder, R. (2003) In vivo high resolution three-dimensional imaging of antigen-specific cytotoxic T-lymphocyte trafficking to tumors. *Cancer Res. 63*, 6838−6846.

(34) Tkachenko, A. G., Xie, H., Liu, Y., Coleman, D., Ryan, J., Glomm, W. R., Shipton, M. K., Franzen, S., and Feldheim, D. L. (2004) Cellular trajectories of peptide-modified gold particle complexes: comparison of nuclear localization signals and peptide transduction domains. *Bioconjugate Chem. 15*, 482−490.
(35) Gao, X., Cui, Y., Levenson, R. M., Chung, L. W., and Nie, S. (2004) In vivo cancer targeting and imaging with semiconductor quantum dots. *Nat. Biotechnol. 22*, 969−976.
(36) Kim, S., Lim, Y. T., Soltesz, E. G., De Grand, A. M., Lee, J., Nakayama, A., Parker, J. A., Mihaljevic, T., Laurence, R. G., Dor, D. M., Cohn, L. H., Bawendi, M. G., and Frangioni, J. V. (2004) Near-infrared fluorescent type II quantum dots for sentinel lymph node mapping. *Nat. Biotechnol. 22*, 93−97.
(37) Denis, M. C., Mahmood, U., Benoist, C., Mathis, D., and Weissleder, R. (2004) Imaging inflammation of the pancreatic islets in type 1 diabetes. *Proc. Natl. Acad. Sci. U. S. A. 101*, 12634−12639.
(38) Kloepfer, J. A., Mielke, R. E., Wong, M. S., Nealson, K. H., Stucky, G., and Nadeau, J. L. (2003) Quantum dots as strain- and metabolism-specific microbiological labels. *Appl. Environ. Microbiol. 69*, 4205−4213.
(39) Rowinsky, E. K., Rizzo, J., Ochoa, L., Takimoto, C. H., Forouzesh, B., Schwartz, G., Hammond, L. A., Patnaik, A., Kwiatek, J., Goetz, A., Denis, L., McGuire, J., and Tolcher, A. W. (2003) A phase I and pharmacokinetic study of pegylated camptothecin as a 1-h infusion every 3 weeks in patients with advanced solid malignancies. *J. Clin. Oncol. 21*, 148−157.
(40) Zhao, H., Rubio, B., Sapra, P., Wu, D., Reddy, P., Sai, P., Martinez, A., Gao, Y., Lozanguiez, Y., Longley, C., Greenberger, L. M., and Horak, I. D. (2008) Novel prodrugs of SN38 using multiarm poly(ethylene glycol) linkers. *Bioconjugate Chem. 19*, 849−859.
(41) Greenwald, R. B., Gilbert, C. W., Pendri, A., Conover, C. D., Xia, J., and Martinez, A. (1996) Drug delivery systems: water soluble taxol 2′-poly(ethylene glycol) ester prodrugs-design and in vivo effectiveness. *J. Med. Chem. 39*, 424−431.
(42) Li, C., Yu, D., Inoue, T., Yang, D. J., Milas, L., Hunter, N. R., Kim, E. E., and Wallace, S. (1996) Synthesis and evaluation of water-soluble polyethylene glycol-paclitaxel conjugate as a paclitaxel prodrug. *Anticancer Drugs 7*, 642−648.
(43) Pendri, A., Conover, C. D., and Greenwald, R. B. (1998) Antitumor activity of paclitaxel-2′-glycinate conjugated to poly-(ethylene glycol): a water-soluble prodrug. *Anti-Cancer Drug Des. 13*, 387−395.
(44) Lele, B. S., and Hoffman, A. S. (2000) Mucoadhesive drug carriers based on complexes of poly(acrylic acid) and PEGylated drugs having hydrolysable PEG-anhydride-drug linkages. *J. Controlled Release 69*, 237−248.
(45) Borgens, R. B., and Shi, R. (2000) Immediate recovery from spinal cord injury through molecular repair of nerve membranes with polyethylene glycol. *FASEB J. 14*, 27−35.
(46) Roy, H. K., Kunte, D. P., Koetsier, J. L., Hart, J., Kim, Y. L., Liu, Y., Bissonnette, M., Goldberg, M., Backman, V., and Wali, R. K. (2006) Chemoprevention of colon carcinogenesis by polyethylene glycol: suppression of epithelial proliferation via modulation of SNAIL/beta-catenin signaling. *Mol. Cancer Ther. 5*, 2060−2069.
(47) Wali, R. K., Kunte, D. P., Koetsier, J. L., Bissonnette, M., and Roy, H. K. (2008) Polyethylene glycol-mediated colorectal cancer chemoprevention: roles of epidermal growth factor receptor and Snail. *Mol. Cancer Ther. 7*, 3103−3111.
(48) Corpet, D. E., Parnaud, G., Delverdier, M., Peiffer, G., and Tache, S. (2000) Consistent and fast inhibition of colon carcinogenesis by polyethylene glycol in mice and rats given various carcinogens. *Cancer Res. 60*, 3160−3164.
(49) Shaffer, C. B., and Critchfield, F. H. (1947) Solid polyethylene glycols (carbowax compounds). *Anal. Chem. 19*, 32−34.
(50) Skoog, B. (1979) Determination of polyethylene glycols 4000 and 6000 in plasma protein preparations. *Vox Sang. 37*, 345−349.
(51) Sims, G. E., and Snape, T. J. (1980) A method for the estimation of polyethylene glycol in plasma protein fractions. *Anal. Biochem. 107*, 60−63.
(52) Chung, T. W., Chung, C. H., and Lue, Y. F. (2000) A colorimetric method for determining distearoylphosphatidylethanolamine-polyethylene glycol 2000 in blood suspension. *Anal. Biochem. 285*, 264−266.
(53) Ingham, K. C., and Ling, R. C. (1978) A quantitative assay for poly(ethylene glycol) without interference by proteins. *Anal. Biochem. 85*, 139−145.
(54) Guermant, C., Brygier, J., Baeyens-Volant, D., Nijs, M., Vincentelli, J., Paul, C., and Looze, Y. (1995) Quantitative determination of polyethylene glycol based upon its salting out and partitioning of a dye into the resulting aqueous two-phase system. *Anal. Biochem. 230*, 254−258.
(55) Nag, A., Mitra, G., and Ghosh, P. C. (1996) A colorimetric assay for estimation of polyethylene glycol and polyethylene glycolated protein using ammonium ferrothiocyanate. *Anal. Biochem. 237*, 224−231.
(56) Li, S., Yang, Z., Sun, X., Tan, Y., Yagi, S., and Hoffman, R. M. (2003) A simultaneous colorimetric assay of free and protein-coupled polyethylene glycol. *Anal. Biochem. 313*, 335−337.
(57) Nag, A., Mitra, G., and Ghosh, P. C. (1997) A colorimetric estimation of polyethyleneglycol-conjugated phospholipid in stealth liposomes. *Anal. Biochem. 250*, 35−43.
(58) Stewart, J. (1980) Colorimetric determination of phospholipids with ammonium ferrothiocyanate. *Anal. Biochem. 104*, 10−14.
(59) Parlesak, A., Bode, J. C., and Bode, C. (1994) Parallel determination of gut permeability in man with M(r) 400, M(r) 1500, M(r) 4000 and M(r) 10,000 polyethylene glycol. *Eur. J. Clin. Chem. Clin. Biochem. 32*, 813−820.
(60) Kinahan, I. M., and Smyth, M. R. (1991) High-performance liquid chromatographic determination of PEG 600 in human urine. *J. Chromatogr., B 565*, 297−307.
(61) Wei, G., Xiao, S., Si, D., and Liu, C. (2008) Improved HPLC method for doxorubicin quantification in rat plasma to study the pharmacokinetics of micelle-encapsulated and liposome-encapsulated doxorubicin formulations. *Biomed. Chromatogr. 22*, 1252−1258.
(62) Chin, D. L., Lum, B. L., and Sikic, B. I. (2002) Rapid determination of PEGylated liposomal doxorubicin and its major metabolite in human plasma by ultraviolet-visible high-performance liquid chromatography. *J. Chromatogr., B 779*, 259−269.
(63) Sapra, P., Zhao, H., Mehlig, M., Malaby, J., Kraft, P., Longley, C., Greenberger, L. M., and Horak, I. D. (2008) Novel delivery of SN38 markedly inhibits tumor growth in xenografts, including a camptothecin-11-refractory model. *Clin. Cancer Res. 14*, 1888−1896.
(64) Al-Abd, A. M., Kim, N. H., Song, S. C., Lee, S. J., and Kuh, H. J. (2009) A simple HPLC method for doxorubicin in plasma and tissues of nude mice. *Arch. Pharm. Res. 32*, 605−611.
(65) Afshar, M., and Rouini, M. (2004) A rapid HPLC assay for the simultaneous determination of propafenone and its major metabolites in human serum. *Anal. Sci. 20*, 1307−1311.
(66) Delahunty, T., and Hollander, D. (1986) New liquid-chromatographic method for measuring polyethylene glycol in urine. *Clin. Chem. 32*, 351−353.
(67) Young, G. O., Ruttenberg, D., and Wright, J. P. (1990) Measurement of polyethylene glycol 400 in urine by direct-injection high-performance liquid chromatography. *Clin. Chem. 36*, 1800−1802.
(68) Schwertner, H. A., Patterson, W. R., Cissik, J. H., and Wilson, K. W. (1992) New extraction procedure and high-performance liquid chromatographic method for analyzing polyethylene glycol-400 in urine. *J. Chromatogr., B 578*, 297−301.
(69) Ryan, C. M., Yarmush, M. L., and Tompkins, R. G. (1992) Separation and quantitation of polyethylene glycols 400 and 3350 from human urine by high-performance liquid chromatography. *J. Pharm. Sci. 81*, 350−352.
(70) Li, N., Ziegemeier, D., Bass, L., and Wang, W. (2008) Quantitation of free polyethylene glycol in PEGylated protein conjugate by size exclusion HPLC with refractive index (RI) detection. *J. Pharmaceut. Biomed. 48*, 1332−1338.
(71) Wal, S. V. D., and Snyder, L. R. (1983) Photometric detection at 185 nm for high-performance liquid chromatography with either

isocratic or gradient elution: Assay of mixtures of polyethylene glycol oligomers. *J. Chromatogr., A 255*, 463−474.
(72) Pelham, R. W., Nix, L. C., Chavira, R. E., Cleveland, M. V., and Stetson, P. (2008) Clinical trial: single- and multiple-dose pharmacokinetics of polyethylene glycol (PEG-3350) in healthy young and elderly subjects. *Aliment. Pharm. Ther. 28*, 256−265.
(73) Liu, X., Zhi, H., Du, F., Ye, Z., Wang, N., Qin, W., and Li, J. (2010) A HPLC-UV method for the determination of puerarin in rat plasma after intravenous administration of PEGylated puerarin conjugate. *J. Chromatogr., B 878*, 3297−3302.
(74) Posey, J. A. 3rd, Saif, M. W., Carlisle, R., Goetz, A., Rizzo, J., Stevenson, S., Rudoltz, M. S., Kwiatek, J., Simmons, P., Rowinsky, E. K., Takimoto, C. H., and Tolcher, A. W. (2005) Phase 1 study of weekly polyethylene glycol-camptothecin in patients with advanced solid tumors and lymphomas. *Clin. Cancer Res. 11*, 7866−7871.
(75) Monkarsh, S. P., Spence, C., Porter, J. E., Palleroni, A., Nalin, C., Rosen, P., and Bailon, P. (1997) *Isolation of positional isomers of mono-poly (ethylene glycol) ylated interferon/ 2a and the determination of their biochemical and biological characteristics*; ACS Symposium Series; American Chemical Society: Washington, DC.
(76) Lee, K. C., Moon, S. C., Park, M. O., Lee, J. T., Na, D. H., Yoo, S. D., Lee, H. S., and DeLuca, P. P. (1999) Isolation, characterization, and stability of positional isomers of mono-PEGylated salmon calcitonins. *Pharm. Res. 16*, 813−818.
(77) Grace, M., Youngster, S., Gitlin, G., Sydor, W., Xie, L., Westreich, L., Jacobs, S., Brassard, D., Bausch, J., and Bordens, R. (2001) Structural and biologic characterization of pegylated recombinant IFN-alpha2b. *J. Interferon Cytokine Res. 21*, 1103−1115.
(78) Zillies, J. C., Zwiorek, K., Winter, G., and Coester, C. (2007) Method for quantifying the PEGylation of gelatin nanoparticle drug carrier systems using asymmetrical flow field-flow fractionation and refractive index detection. *Anal. Chem. 79*, 4574−4580.
(79) Youn, Y. S., Na, D. H., Yoo, S. D., Song, S. C., and Lee, K. C. (2004) Chromatographic separation and mass spectrometric identification of positional isomers of polyethylene glycol-modified growth hormone-releasing factor (1−29). *J. Chromatogr., A 1061*, 45−49.
(80) Yu, P., Qin, G., Qin, D., and Zhang, Z. (2010) A liquid chromatographic method for determination of the modification degree of proteins: PEGylated arginase as an example. *Anal. Biochem. 396*, 325−327.
(81) Yoo, C., Suckau, D., Sauerland, V., Ronk, M., and Ma, M. (2009) Toward top-down determination of PEGylation site using MALDI in-source decay MS analysis. *J. Am. Soc. Mass Spectrom. 20*, 326−333.
(82) Tom, I., Lee, V., Dumas, M., Madanat, M., Ouyang, J., Severs, J., Andersen, J., Buxton, J. M., Whelan, J. P., and Pan, C. Q. (2007) Reproductible production of a PEGylated dual-acting peptide for diabetes. *AAPS J. 9*, 227−234.
(83) Szostek, B., Zajac, J., and Koropchak, J. A. (1997) Coupling condensation nucleation light scattering detection with capillary electrophoresis using electrospray. *Anal. Chem. 69*, 2955−2962.
(84) Schneiderheinze, J., Walden, Z., Dufield, R., and Demarest, C. (2009) Rapid online proteolytic mapping of PEGylated rhGH for identity confirmation, quantitation of methionine oxidation and quantitation of UnPEGylated N-terminus using HPLC with UV detection. *J. Chromatogr., B 877*, 4065−4070.
(85) Kou, D., Manius, G., Zhan, S., and Chokshi, H. P. (2009) Size exclusion chromatography with Corona charged aerosol detector for the analysis of polyethylene glycol polymer. *J. Chromatogr., A 1216*, 5424−5428.
(86) Huang, L., Gough, P. C., and DeFelippis, M. R. (2008) Characterization of poly (ethylene glycol) and PEGylated products by LC/MS with postcolumn addition of amines. *Anal. Chem. 81*, 567−577.
(87) Fekete, S., Ganzler, K., and Fekete, J. (2010) Simultaneous determination of polysorbate 20 and unbound polyethylene-glycol in protein solutions using new core-shell reversed phase column and condensation nucleation light scattering detection. *J. Chromatogr., A 1217*, 6258−6266.
(88) Foser, S., Schacher, A., Weyer, K. A., Brugger, D., Dietel, E., Marti, S., and Schreitmüller, T. (2003) Isolation, structural characterization, and antiviral activity of positional isomers of monopegylated interferon [alpha]-2a (PEGASYS). *Protein Expres. Purif. 30*, 78−87.
(89) Díaz-López, R., Libong, D., Tsapis, N., Fattal, E., and Chaminade, P. (2008) Quantification of pegylated phospholipids decorating polymeric microcapsules of perfluorooctyl bromide by reverse phase HPLC with a charged aerosol detector. *J. Pharmaceut. Biomed. 48*, 702−707.
(90) Cindric, M., Cepo, T., Galic, N., Bukvic-Krajacic, M., Tomczyk, N., Vissers, J. P. C, Bindila, L., and Peter-Katalinic, J. (2007) Structural characterization of PEGylated rHuG-CSF and location of PEG attachment sites. *J. Pharmaceut. Biomed. 44*, 388−395.
(91) Bagal, D., Zhang, H., and Schnier, P. D. (2008) Gas-phase proton-transfer chemistry coupled with TOF mass spectrometry and ion mobility-MS for the facile analysis of poly (ethylene glycols) and PEGylated polypeptide conjugates. *Anal. Chem. 80*, 2408−2418.
(92) Yang, Z., Ke, J., Hayes, M., Bryant, M., and Tse, F. L. (2009) A sensitive and high-throughput LC-MS/MS method for the quantification of pegylated-interferon-alpha2a in human serum using monolithic C18 solid phase extraction for enrichment. *J. Chromatogr., B 877*, 1737−1742.
(93) He, X. L., Yin, H. L., Wu, J., Zhang, K., Liu, Y., Yuan, T., Rao, H. L., Li, L., Yang, G., and Zhang, X. M. (2011) A multiple-dose pharmacokinetics of polyethylene glycol recombinant human interleukin-6 (PEG-rhIL-6) in rats. *J. Zhejiang Univ. Sci. B 12*, 32−39.
(94) Guan, F., Uboh, C. E., Soma, L. R., Maylin, G., Jiang, Z., and Chen, J. (2010) Confirmatory analysis of continuous erythropoietin receptor activator and erythropoietin analogues in equine plasma by LC- MS for doping control. *Anal. Chem. 82*, 9074−9081.
(95) Li, H., Rose, M., Holder, J., Wright, M., Miranda, L., and James, C. (2011) Direct quantitative analysis of a 20 kDa PEGylated human calcitonin gene peptide antagonist in cynomolgus monkey serum using in-source CID and UPLC-MS/MS. *J. Am. Soc. Mass Spectrom. 22*, 1660−1667.
(96) Korfmacher, W. A. (2005) Principles and applications of LC-MS in new drug discovery. *Drug Discovery Today 10*, 1357−1367.
(97) Chen, Y., Guo, Z., Wang, X., and Qiu, C. (2008) Sample preparation. *J. Chromatogr., A 1184*, 191−219.
(98) Nováková, L., and Vlckova, H. (2009) A review of current trends and advances in modern bio-analytical methods: chromatography and sample preparation. *Anal. Chim. Acta 656*, 8−35.
(99) Xu, Y., Mehl, J. T., Bakhtiar, R., and Woolf, E. J. (2010) Immunoaffinity purification using anti-PEG antibody followed by two-dimensional liquid chromatography/tandem mass spectrometry for the quantification of a PEGylated therapeutic peptide in human plasma. *Anal. Chem. 82*, 6877−6886.
(100) Veronese, F. M., Schiavon, O., Pasut, G., Mendichi, R., Andersson, L., Tsirk, A., Ford, J., Wu, G., Kneller, S., Davies, J., and Duncan, R. (2005) PEG-doxorubicin conjugates: influence of polymer structure on drug release, in vitro cytotoxicity, biodistribution, and antitumor activity. *Bioconjugate Chem. 16*, 775−784.
(101) Yamaoka, T., Tabata, Y., and Ikada, Y. (1994) Distribution and tissue uptake of poly(ethylene glycol) with different molecular weights after intravenous administration to mice. *J. Pharm. Sci. 83*, 601−606.
(102) Chen, X., Park, R., Shahinian, A. H., Bading, J. R., and Conti, P. S. (2004) Pharmacokinetics and tumor retention of 125I-labeled RGD peptide are improved by PEGylation. *Nucl. Med. Biol. 31*, 11−19.
(103) Yoshida, K., Burton, G. F., McKinney, J. S., Young, H., and Ellis, E. F. (1992) Brain and tissue distribution of polyethylene glycol-conjugated superoxide dismutase in rats. *Stroke 23*, 865−869.
(104) Yoo, S. D., Jun, H., Shin, B. S., Lee, H. S., Park, M. O., Deluca, P. P., and Lee, K. C. (2000) Pharmacokinetic disposition of polyethylene glycol-modified salmon calcitonins in rats. *Chem. Pharm. Bull. 48*, 1921−1924.
(105) Jiang, L., Cai, Y. M., Zeng, Y., Huang, J., and Chen, Z. M. (2009) Pharmacokinetics of rhGH decorated by polyethylene glycol in rat in vivo. *Yao Xue Xue Bao 44*, 506−509.

(106) Berger, H. Jr., and Pizzo, S. V. (1988) Preparation of polyethylene glycol-tissue plasminogen activator adducts that retain functional activity: characteristics and behavior in three animal species. *Blood 71*, 1641−1647.
(107) Bakker, W. H., Krenning, E. P., Breeman, W. A., Kooij, P. P. M, Reubi, J.-C., Koper, J. W., de Jong, M., Laméris, J. S., Visser, T. J., and Lamberts, S. W. (1991) In vivo use of a radioiodinated somatostatin analogue: dynamics, metabolism, and binding to somatostatin receptor-positive tumors in man. *J. Nucl. Med. 32*, 1184−1189.
(108) Leon-Tamariz, F., Verbaeys, I., Van Boven, M., De Cuyper, M., Buyse, J., de Witte, P., Verbruggen, A., and Cokelaere, M. (2010) Biodistribution and pharmacokinetics of PEG-10 kDa-cholecystokinin-10 in rats after different routes of administration. *Curr. Drug Delivery 7*, 137−143.
(109) Lee, H. J., and Pardridge, W. M. (2003) Monoclonal antibody radiopharmaceuticals: cationization, pegylation, radiometal chelation, pharmacokinetics, and tumor imaging. *Bioconjugate Chem. 14*, 546−553.
(110) Maisano, F., Gozzini, L., and De Haen, C. (1992) Coupling of DTPA to proteins: a critical analysis of the cyclic dianhydride method in the case of insulin modification. *Bioconjugate Chem. 3*, 212−217.
(111) Chen, X., Hou, Y., Tohme, M., Park, R., Khankaldyyan, V., Gonzales-Gomez, I., Bading, J. R., Laug, W. E., and Conti, P. S. (2004) Pegylated Arg-Gly-Asp peptide: 64Cu labeling and PET imaging of brain tumor $\alpha v\beta 3$-integrin expression. *J. Nucl. Med. 45*, 1776−1783.
(112) Liu, Z., Liu, S., Wang, F., Liu, S., and Chen, X. (2009) Noninvasive imaging of tumor integrin expression using 18F-labeled RGD dimer peptide with PEG4 linkers. *Eur. J. Nucl. Med. Mol. I 36*, 1296−1307.
(113) DeNardo, S. J., Yao, Z., Lam, K. S., Song, A., Burke, P. A., Mirick, G. R., Lamborn, K. R., O'Donnell, R. T., and DeNardo, G. L. (2003) Effect of molecular size of pegylated peptide on the pharmacokinetics and tumor targeting in lymphoma-bearing mice. *Clin. Cancer Res. 9*, 3854S−3864S.
(114) Wen, X., Wu, Q. P., Lu, Y., Fan, Z., Charnsangavej, C., Wallace, S., Chow, D., and Li, C. (2001) Poly(ethylene glycol)-conjugated anti-EGF receptor antibody C225 with radiometal chelator attached to the termini of polymer chains. *Bioconjugate Chem. 12*, 545−553.
(115) Levashova, Z., Backer, M. V., Horng, G., Felsher, D., Backer, J. M., and Blankenberg, F. G. (2009) SPECT and PET imaging of EGF receptors with site-specifically labeled EGF and dimeric EGF. *Bioconjugate Chem. 20*, 742−749.
(116) Backer, M. V., Levashova, Z., Patel, V., Jehning, B. T., Claffey, K., Blankenberg, F. G., and Backer, J. M. (2007) Molecular imaging of VEGF receptors in angiogenic vasculature with single-chain VEGF-based probes. *Nat. Med. 13*, 504−509.
(117) Wangler, C., Schafer, M., Schirrmacher, R., Bartenstein, P., Wangler, B. (2010) DOTA derivatives for site-specific biomolecule-modification via click chemistry: Synthesis and comparison of reaction characteristics. *Bioorg. Med. Chem.*.
(118) Li, Z. B., Wu, Z., Chen, K., Chin, F. T., and Chen, X. (2007) Click chemistry for (18)F-labeling of RGD peptides and microPET imaging of tumor integrin alphavbeta3 expression. *Bioconjugate Chem. 18*, 1987−1994.
(119) Cahouet, A., Denizot, B., Hindre, F., Passirani, C., Heurtault, B., Moreau, M., Le Jeune, J., and Benoit, J. (2002) Biodistribution of dual radiolabeled lipidic nanocapsules in the rat using scintigraphy and gamma counting. *Int. J. Pharm. 242*, 367−371.
(120) Soundararajan, A., Bao, A., Phillips, W. T., Perez, R. 3rd, and Goins, B. A. (2009) [(186)Re]Liposomal doxorubicin (Doxil): in vitro stability, pharmacokinetics, imaging and biodistribution in a head and neck squamous cell carcinoma xenograft model. *Nucl. Med. Biol. 36*, 515−524.
(121) Torchilin, V. P., Klibanov, A. L., Huang, L., O'Donnell, S., Nossiff, N. D., and Khaw, B. A. (1992) Targeted accumulation of polyethylene glycol-coated immunoliposomes in infarcted rabbit myocardium. *FASEB J. 6*, 2716−2719.
(122) Marik, J., Tartis, M. S., Zhang, H., Fung, J. Y., Kheirolomoom, A., Sutcliffe, J. L., and Ferrara, K. W. (2007) Long-circulating liposomes radiolabeled with [18F]fluorodipalmitin ([18F]FDP). *Nucl. Med. Biol. 34*, 165−171.
(123) Laverman, P., Dams, E. T., Oyen, W. J., Storm, G., Koenders, E. B., Prevost, R., van der Meer, J. W., Corstens, F. H., and Boerman, O. C. (1999) A novel method to label liposomes with 99mTc by the hydrazino nicotinyl derivative. *J. Nucl. Med. 40*, 192−197.
(124) Seo, J. W., Zhang, H., Kukis, D. L., Meares, C. F., and Ferrara, K. W. (2008) A novel method to label preformed liposomes with 64Cu for positron emission tomography (PET) imaging. *Bioconjugate Chem. 19*, 2577−2584.
(125) Seo, J. W., Mahakian, L. M., Kheirolomoom, A., Zhang, H., Meares, C. F., Ferdani, R., Anderson, C. J., and Ferrara, K. W. (2010) Liposomal Cu-64 labeling method using bifunctional chelators: poly(ethylene glycol) spacer and chelator effects. *Bioconjugate Chem. 21*, 1206−1215.
(126) Bao, A., Goins, B., Klipper, R., Negrete, G., Mahindaratne, M., and Phillips, W. T. (2003) A novel liposome radiolabeling method using 99mTc-"SNS/S" complexes: in vitro and in vivo evaluation. *J. Pharm. Sci. 92*, 1893−1904.
(127) Bao, A., Goins, B., Klipper, R., Negrete, G., and Phillips, W. T. (2004) Direct 99mTc labeling of pegylated liposomal doxorubicin (Doxil) for pharmacokinetic and non-invasive imaging studies. *J. Pharmacol. Exp. Ther. 308*, 419−425.
(128) Glaus, C., Rossin, R., Welch, M. J., and Bao, G. (2010) In vivo evaluation of (64)Cu-labeled magnetic nanoparticles as a dual-modality PET/MR imaging agent. *Bioconjugate Chem. 21*, 715−722.
(129) Malek, A., Merkel, O., Fink, L., Czubayko, F., Kissel, T., and Aigner, A. (2009) In vivo pharmacokinetics, tissue distribution and underlying mechanisms of various PEI(-PEG)/siRNA complexes. *Toxicol. Appl. Pharmacol. 236*, 97−108.
(130) Pöschel, K. A., Bucha, E., Esslinger, H. U., Nörtersheuser, P., Jansa, U., Schindler, S., Nowak, G., and Stein, G. (2000) Pharmacodynamics and pharmacokinetics of polyethylene glycol-hirudin in patients with chronic renal failure. *Kidney Int. 58*, 2478−2484.
(131) Hoffmann, J. J., and Janssen, W. C. (2001) Comparison of three methods for measuring PEG-hirudin in blood. *Blood Coagul. Fibrinolysis 12*, 577−581.
(132) Hempel, G., Muller, H. J., Lanvers-Kaminsky, C., Wurthwein, G., Hoppe, A., and Boos, J. (2010) A population pharmacokinetic model for pegylated-asparaginase in children. *Br. J. Hamaetol. 148*, 119−125.
(133) Sundy, J. S., Ganson, N. J., Kelly, S. J., Scarlett, E. L., Rehrig, C. D., Huang, W., and Hershfield, M. S. (2007) Pharmacokinetics and pharmacodynamics of intravenous PEGylated recombinant mammalian urate oxidase in patients with refractory gout. *Arthritis Rheum. 56*, 1021−1028.
(134) Ganson, N., Kelly, S., Scarlett, E., Sundy, J., and Hershfield, M. (2005) Control of hyperuricemia in subjects with refractory gout, and induction of antibody against poly (ethylene glycol)(PEG), in a phase I trial of subcutaneous PEGylated urate oxidase. *Arthritis Res. Ther. 8*, R12.
(135) Cheng, T. L., Wu, P. Y., Wu, M. F., Chern, J. W., and Roffler, S. R. (1999) Accelerated clearance of polyethylene glycol-modified proteins by anti-polyethylene glycol IgM. *Bioconjugate Chem. 10*, 520−528.
(136) Novikov, B. N., Grimsley, J. K., Kern, R. J., Wild, J. R., and Wales, M. E. (2010) Improved pharmacokinetics and immunogenicity profile of organophosphorus hydrolase by chemical modification with polyethylene glycol. *J. Controlled Release 146*, 318−325.
(137) Kronman, C., Cohen, O., Mazor, O., Ordentlich, A., Raveh, L., Velan, B., and Shafferman, A. (2009) Next generation OP-bioscavengers: A circulatory long-lived 4-PEG hypolysine mutant of F338A-HuAChE with optimal pharmacokinetics and pseudo-catalytic characteristics. *Chem.-Biol. Interact. 187*, 253−258.
(138) Holtsberg, F. W., Ensor, C. M., Steiner, M. R., Bomalaski, J. S., and Clark, M. A. (2002) Poly (ethylene glycol)(PEG) conjugated arginine deiminase: effects of PEG formulations on its pharmacological properties. *J. Controlled Release 80*, 259−271.

(139) Meyers, F. J., Paradise, C., Scudder, S. A., Goodman, G., and Konrad, M. (1991) A phase I study including pharmacokinetics of polyethylene glycol conjugated interleukin-2. *Clin. Pharmacol. Ther. 49*, 307−313.
(140) Jo, Y. W., Youn, Y. S., Lee, S. H., Kim, B. M., Kang, S. H., Yoo, M., Choi, E. C., and Lee, K. C. (2006) Long-acting interferon-alpha 2a modified with a trimer-structured polyethylene glycol: preparation, in vitro bioactivity, in vivo stability and pharmacokinetics. *Int. J. Pharm. 309*, 87−93.
(141) Pepinsky, R. B., LePage, D. J., Gill, A., Chakraborty, A., Vaidyanathan, S., Green, M., Baker, D. P., Whalley, E., Hochman, P. S., and Martin, P. (2001) Improved pharmacokinetic properties of a polyethylene glycol-modified form of interferon-beta-1a with preserved in vitro bioactivity. *J. Pharmacol. Exp. Ther. 297*, 1059−1066.
(142) Tanaka, H., Satake-Ishikawa, R., Ishikawa, M., Matsuki, S., and Asano, K. (1991) Pharmacokinetics of recombinant human granulocyte colony-stimulating factor conjugated to polyethylene glycol in rats. *Cancer Res. 51*, 3710−3714.
(143) François, C., Bernard, I., Castelain, S., Charleston, B., Fray, M. D., Capiod, J. C., and Duverlie, G. (2005) Quantification of different human alpha interferon subtypes and pegylated interferon activities by measuring MxA promoter activation. *Antimicrob. Agents Chemother. 49*, 3770−3775.
(144) Schiavon, O., Caliceti, P., Ferruti, P., and Veronese, F. M. (2000) Therapeutic proteins: a comparison of chemical and biological properties of uricase conjugated to linear or branched poly(ethylene glycol) and poly(N-acryloylmorpholine). *Farmaco 55*, 264−269.
(145) Pearce, K. H. Jr, Cunningham, B. C., Fuh, G., Teeri, T., and Wells, J. A. (1999) Growth hormone binding affinity for its receptor surpasses the requirements for cellular activity. *Biochemistry 38*, 81−89.
(146) Kubetzko, S., Sarkar, C. A., and Pluckthun, A. (2005) Protein PEGylation decreases observed target association rates via a dual blocking mechanism. *Mol. Pharmacol. 68*, 1439−1454.
(147) Bailon, P., Palleroni, A., Schaffer, C. A., Spence, C. L., Fung, W. J., Porter, J. E., Ehrlich, G. K., Pan, W., Xu, Z. X., Modi, M. W., Farid, A., Berthold, W., and Graves, M. (2001) Rational design of a potent, long-lasting form of interferon: a 40 kDa branched polyethylene glycol-conjugated interferon alpha-2a for the treatment of hepatitis C. *Bioconjugate Chem. 12*, 195−202.
(148) Bowen, S., Tare, N., Inoue, T., Yamasaki, M., Okabe, M., Horii, I., and Eliason, J. F. (1999) Relationship between molecular mass and duration of activity of polyethylene glycol conjugated granulocyte colony-stimulating factor mutein. *Exp. Hematol. 27*, 425−432.
(149) Knüsli, C., Delgado, C., Malik, F., Dómine, M., Tejedor, M., Irvine, A., Fisher, D., and Francis, G. (1992) Polyethylene glycol (PEG) modification of granulocyte-macrophage colony stimulating factor (GM-CSF) enhances neutrophil priming activity but not colony stimulating activity. *Br. J. Hamaetol. 82*, 654−663.
(150) Pettit, D., Bonnert, T., Eisenman, J., Srinivasan, S., Paxton, R., Beers, C., Lynch, D., Miller, B., Yost, J., and Grabstein, K. (1997) Structure-function studies of interleukin 15 using site-specific mutagenesis, polyethylene glycol conjugation, and homology modeling. *J. Biol. Chem. 272*, 2312−2318.
(151) Cao, J., Du, Y., Tian, H., Gao, X., and Yao, W. (2009) Quantitative determination of pegylated consensus interferon in rhesus monkey serum using a competitive enzyme-linked immunosorbent assay. *Immunopharm. Immunother. 31*, 543−549.
(152) Choy, E. H., Hazleman, B., Smith, M., Moss, K., Lisi, L., Scott, D. G., Patel, J., Sopwith, M., and Isenberg, D. A. (2002) Efficacy of a novel PEGylated humanized anti-TNF fragment (CDP870) in patients with rheumatoid arthritis: a phase II double-blinded, randomized, dose-escalating trial. *Rheumatology 41*, 1133−1137.
(153) Lee, L. S., Conover, C., Shi, C., Whitlow, M., and Filpula, D. (1999) Prolonged circulating lives of single-chain Fv proteins conjugated with polyethylene glycol: a comparison of conjugation chemistries and compounds. *Bioconjugate Chem. 10*, 973−981.
(154) Pepinsky, R., Walus, L., Shao, Z., Ji, B., Gu, S., Sun, Y., Wen, D., Lee, X., Wang, Q., and Garber, E. (2011) Production of a PEGylated Fab′of the anti-LINGO-1 Li33 antibody and assessment of Its biochemical and functional properties in vitro and in a rat model of remyelination. *Bioconjugate Chem. 22*, 200−210.
(155) Song, X. H., Huhle, G., Wang, L. C., and Harenberg, J. (2000) Quantitative determination of PEG-hirudin in human plasma using a competitive enzyme-linked immunosorbent assay. *Thromb. Res. 99*, 195−202.
(156) Avramis, V. I., Sencer, S., Periclou, A. P., Sather, H., Bostrom, B. C., Cohen, L. J., Ettinger, A. G., Ettinger, L. J., Franklin, J., Gaynon, P. S., Hilden, J. M., Lange, B., Majlessipour, F., Mathew, P., Needle, M., Neglia, J., Reaman, G., Holcenberg, J. S., and Stork, L. (2002) A randomized comparison of native Escherichia coli asparaginase and polyethylene glycol conjugated asparaginase for treatment of children with newly diagnosed standard-risk acute lymphoblastic leukemia: a Children's Cancer Group study. *Blood 99*, 1986−1994.
(157) Asselin, B. L., Whitin, J. C., Coppola, D. J., Rupp, I. P., Sallan, S. E., and Cohen, H. J. (1993) Comparative pharmacokinetic studies of three asparaginase preparations. *J. Clin. Oncol. 11*, 1780−1786.
(158) Muto, C., Chiba, K., and Suwa, T. (2011) Population pharmacokinetic and pharmacodynamic modeling of pegvisomant in asian and western acromegaly patients. *J. Clin. Pharmacol. 51*, 1628−1643.
(159) de Serres, M., Yeager, R. L., Dillberger, J. E., Lalonde, G., Gardner, G. H., Rubens, C. A., Simkins, A. H., Sailstad, J. M., McNulty, M. J., and Woolley, J. L. (1999) Pharmacokinetics and hematological effects of the PEGylated thrombopoietin peptide mimetic GW395058 in rats and monkeys after intravenous or subcutaneous administration. *Stem Cells 17*, 316−326.
(160) Wang, S. J., Wu, S. T., Gokemeijer, J., Fura, A., Krishna, M., Morin, P., Chen, G., Price, K., Wang-Iverson, D., and Olah, T. (2011) Attribution of the discrepancy between ELISA and LC-MS/MS assay results of a PEGylated scaffold protein in post-dose monkey plasma samples due to the presence of anti-drug antibodies. *Anal. Bioanal. Chem*.
(161) Bruno, R., Sacchi, P., Ciappina, V., Zochetti, C., Patruno, S., Maiocchi, L., and Filice, G. (2004) Viral dynamics and pharmacokinetics of peginterferon alpha-2a and peginterferon alpha-2b in naive patients with chronic hepatitis c: a randomized, controlled study. *Antivir. Ther. 9*, 491−497.
(162) Motzer, R. J., Rakhit, A., Thompson, J., Gurney, H., Selby, P., Figlin, R., Negrier, S., Ernst, S., Siebels, M., Ginsberg, M., Rittweger, K., and Hooftman, L. (2002) Phase II trial of branched peginterferon-alpha 2a (40 kDa) for patients with advanced renal cell carcinoma. *Ann. Oncol. 13*, 1799−1805.
(163) Rozenberg, L., Haagmans, B. L., Neumann, A. U., Chen, G., McLaughlin, M., Levy-Drummer, R. S., Masur, H., Dewar, R. L., Ferenci, P., Silva, M., Viola, M. S., Polis, M. A., and Kottilil, S. (2009) Therapeutic response to peg-IFN-alpha-2b and ribavirin in HIV/HCV co-infected African-American and Caucasian patients as a function of HCV viral kinetics and interferon pharmacodynamics. *AIDS 23*, 2439−2450.
(164) Roskos, L. K., Lum, P., Lockbaum, P., Schwab, G., and Yang, B. B. (2006) Pharmacokinetic/pharmacodynamic modeling of pegfilgrastim in healthy subjects. *J. Clin. Pharmacol. 46*, 747−757.
(165) Yang, B. B., Kido, A., Salfi, M., Swan, S., and Sullivan, J. T. (2008) Pharmacokinetics and pharmacodynamics of pegfilgrastim in subjects with various degrees of renal function. *J. Clin. Pharmacol. 48*, 1025−1031.
(166) Macdougall, I. C., Robson, R., Opatrna, S., Liogier, X., Pannier, A., Jordan, P., Dougherty, F. C., and Reigner, B. (2006) Pharmacokinetics and pharmacodynamics of intravenous and subcutaneous continuous erythropoietin receptor activator (C.E.R.A.) in patients with chronic kidney disease. *Clin. J. Am. Soc. Nephrol. 1*, 1211−1215.
(167) Eggermont, A., Bouwhuis, M., Kruit, W., Testori, A., ten Hagen, T., Yver, A., and Xu, C. (2010) Serum concentrations of pegylated interferon alpha-2b in patients with resected stage III melanoma receiving adjuvant pegylated interferon alpha-2b in a randomized phase III trial (EORTC 18991). *Cancer Chemother. Pharm. 65*, 671−677.

(168) Hukshorn, C. J., Saris, W. H. M., Westerterp-Plantenga, M. S., Farid, A. R., Smith, F. J., and Campfield, L. A. (2000) Weekly subcutaneous pegylated recombinant native human leptin (PEG-OB) administration in obese men. *J. Clin. Endocr. Metab.*, 4003−4009.
(169) Ramon, J., Saez, V., Baez, R., Aldana, R., and Hardy, E. (2005) PEGylated interferon-alpha2b: a branched 40K polyethylene glycol derivative. *Pharm. Res. 22*, 1374−1386.
(170) Veronese, F. M., Monfardini, C., Caliceti, P., Schiavon, O., Scrawen, M. D., and Beer, D. (1996) Improvement of pharmacokinetic, immunological and stability properties of asparaginase by conjugation to linear and branched monomethoxy poly(ethylene glycol). *J. Controlled Release 40*, 199−209.
(171) Richter, A. W., and Akerblom, E. (1983) Antibodies against polyethylene glycol produced in animals by immunization with monomethoxy polyethylene glycol modified proteins. *Int. Arch. Allergy Appl. Immunol. 70*, 124−131.
(172) Tsai, N. M., Cheng, T. L., and Roffler, S. R. (2001) Sensitive measurement of polyethylene glycol-modified proteins. *Biotechniques 30*, 396−402.
(173) Cheng, T. L., Cheng, C. M., Chen, B. M., Tsao, D. A., Chuang, K. H., Hsiao, S. W., Lin, Y. H., and Roffler, S. R. (2005) Monoclonal antibody-based quantitation of poly(ethylene glycol)-derivatized proteins, liposomes, and nanoparticles. *Bioconjugate Chem. 16*, 1225−1231.
(174) Su, Y. C., Chen, B. M., Chuang, K. H., Cheng, T. L., and Roffler, S. R. (2010) Sensitive quantification of PEGylated compounds by second-generation anti-poly(ethylene glycol) monoclonal antibodies. *Bioconjugate Chem. 21*, 1264−1270.
(175) Wunderlich, D. A., Macdougall, M., Mierz, D. V., Toth, J. G., Buckholz, T. M., Lumb, K. J., and Vasavada, H. (2007) Generation and characterization of a monoclonal IgG antibody to polyethylene glycol. *Hybridoma 26*, 168−172.
(176) Ehrlich, G. K., Michel, H., Chokshi, H. P., and Malick, A. W. (2009) Affinity purification and characterization of an anti-PEG IgM. *J. Mol. Recognit. 22*, 99−103.
(177) Bailon, P., Won, C. Y. (2009) PEG-modified biopharmaceuticals.
(178) Liem-Moolenaar, M., Cerneus, D., Molloy, C., End, D., Brown, K., De Kam, M., Cohen, A., Van Hensbergen, Y., and Burggraaf, J. (2008) Pharmacodynamics and pharmacokinetics of the novel thrombopoietin mimetic peptide RWJ-800088 in humans. *Clin. Pharmacol. Ther. 84*, 481−487.
(179) Samtani, M. N., Perez-Ruixo, J. J., Brown, K. H., Cerneus, D., and Molloy, C. J. (2009) Pharmacokinetic and pharmacodynamic modeling of pegylated thrombopoietin mimetic peptide (PEG-TPOm) after single intravenous dose administration in healthy subjects. *J. Clin. Pharmacol. 49*, 336−350.
(180) Fishbane, S., Pannier, A., Liogier, X., Jordan, P., Dougherty, F. C., and Reigner, B. (2007) Pharmacokinetic and pharmacodynamic properties of methoxy polyethylene glycol-epoetin beta are unaffected by the site of subcutaneous administration. *J. Clin. Pharmacol. 47*, 1390−1397.
(181) Lamon, S., Giraud, S., Egli, L., Smolander, J., Jarsch, M., Stubenrauch, K. G., Hellwig, A., Saugy, M., and Robinson, N. (2009) A high-throughput test to detect C.E.R.A. doping in blood. *J. Pharm. Biomed. Anal. 50*, 954−958.
(182) Myler, H. A., McVay, S., and Kratzsch, J. (2010) Troubleshooting PEG-hGH detection supporting pharmacokinetic evaluation in growth hormone deficient patients. *J. Pharmacol. Toxicol. 61*, 92−97.
(183) Rasmussen, M. H., Bysted, B. V., Anderson, T. W., Klitgaard, T., and Madsen, J. (2010) Pegylated long-acting human growth hormone Is well-tolerated in healthy subjects and possesses a potential once-weekly pharmacokinetic and pharmacodynamic treatment profile. *J. Clin. Endocr. Metab.*, 3411−3417.
(184) Armstrong, J. K. (2009) *The occurrence, induction, specificity and potential effect of antibodies against poly (ethylene glycol)*; Birkhauser Verlag: Switzerland.
(185) Elinav, E., Niv-Spector, L., Katz, M., Price, T. O., Ali, M., Yacobovitz, M., Solomon, G., Reicher, S., Lynch, J. L., and Halpern, Z. (2009) Pegylated leptin antagonist is a potent orexigenic agent: preparation and mechanism of activity. *Endocrinology 150*, 3083−3091.
(186) Sakai, H., Seishi, Y., Obata, Y., Takeoka, S., Horinouichi, H., Tsuchida, E., and Kobayashi, K. (2009) Fluid resuscitation with artificial oxygen carriers in hemorrhaged rats: profiles of hemoglobin-vesicle degradation and hematopoiesis for 14 days. *Shock 31*, 192−200.
(187) Ton, N. C., Parker, G. J., Jackson, A., Mullamitha, S., Buonaccorsi, G. A., Roberts, C., Watson, Y., Davies, K., Cheung, S., Hope, L., Power, F., Lawrance, J., Valle, J., Saunders, M., Felix, R., Soranson, J. A., Rolfe, L., Zinkewich-Peotti, K., and Jayson, G. C. (2007) Phase I evaluation of CDP791, a PEGylated di-Fab′ conjugate that binds vascular endothelial growth factor receptor 2. *Clin. Cancer Res. 13*, 7113−7118.
(188) White, C. A., Zhang, J. G., Salamonsen, L. A., Baca, M., Fairlie, W. D., Metcalf, D., Nicola, N. A., Robb, L., and Dimitriadis, E. (2007) Blocking LIF action in the uterus by using a PEGylated antagonist prevents implantation: a nonhormonal contraceptive strategy. *Proc. Natl. Acad. Sc.i U. S. A. 104*, 19357−19362.
(189) Chuang, K. H., Tzou, S. C., Cheng, T. C., Kao, C. H., Tseng, W. L., Shiea, J., Liao, K. W., Wang, Y. M., Chang, Y. C., Huang, B. J., Wu, C. J., Chu, P. Y., Roffler, S. R., and Cheng, T. L. (2010) Measurement of poly(ethylene glycol) by cell-based anti-poly(ethylene glycol) ELISA. *Anal. Chem. 82*, 2355−2362.
(190) Chuang, K. H., Wang, H. E., Cheng, T. C., Tzou, S. C., Tseng, W. L., Hung, W. C., Tai, M. H., Chang, T. K., Roffler, S. R., and Cheng, T. L. (2010) Development of a universal anti-polyethylene glycol reporter gene for noninvasive imaging of PEGylated probes. *J. Nucl. Med. 51*, 933−941.
(191) Chuang, K. H., Wang, H. E., Chen, F. M., Tzou, S. C., Cheng, C. M., Chang, Y. C., Tseng, W. L., Shiea, J., Lin, S. R., Wang, J. Y., Chen, B. M., Roffler, S. R., and Cheng, T. L. (2010) Endocytosis of PEGylated agents enhances cancer imaging and anticancer efficacy. *Mol. Cancer Ther. 9*, 1903−1912.
(192) Hyotyla, J., Deng, J., and Lim, R. (2011) Synthetic protein targeting by the intrinsic biorecognition functionality of poly (ethylene glycol) using PEG-antibodies as biohybrid molecular adaptors. *ACS nano 5*, 5180−5187.
(193) Doshi, N., and Mitragotri, S. (2009) Designer biomaterials for nanomedicine. *Adv. Funct. Mater. 19*, 3843−3854.
(194) Boada, J., Gallardo, M., and Estelrich, J. (1997) Determination of polyethylene glycol activated with cyanuric chloride in liposomes. *Anal. Biochem. 253*, 33−6.
(195) Wu, S. T., Ouyang, Z., Olah, T. V., and Jemal, M. (2011) A strategy for liquid chromatography/tandem mass spectrometry based quantitation of pegylated protein drugs in plasma using plasma protein precipitation with water-miscible organic solvents and subsequent trypsin digestion to generate surrogate peptides for detection. *Rapid Commun. Mass Spectrom. 25*, 281−290.
(196) Denardo, S. J., Liu, R., Albrecht, H., Natarajan, A., Sutcliffe, J. L., Anderson, C., Peng, L., Ferdani, R., Cherry, S. R., and Lam, K. S. (2009) 111In-LLP2A-DOTA polyethylene glycol-targeting {alpha}-4{beta}1 integrin: comparative pharmacokinetics for imaging and therapy of lymphoid malignancies. *J. Nucl. Med. 50*, 625−634.
(197) Immordino, M. L., Brusa, P., Arpicco, S., Stella, B., Dosio, F., and Cattel, L. (2003) Preparation, characterization, cytotoxicity and pharmacokinetics of liposomes containing docetaxel. *J. Controlled Release 91*, 417−429.
(198) Sondergaard, E., Klose, M., Hansen, M., Hansen, B. S., Andersen, M., Feldt-Rasmussen, U., Laursen, T., Rasmussen, M. H., and Christiansen, J. S. (2011) Pegylated long-acting human growth hormone possesses a promising once-weekly treatment profile, and multiple dosing is well tolerated in adult patients with growth hormone deficiency. *J. Clin. Endocrinol. Metab.*, 681−688.
(199) Jolling, K., Ruixo, J. J., Hemeryck, A., Piotrovskij, V., and Greway, T. (2004) Population pharmacokinetic analysis of pegylated human erythropoietin in rats. *J. Pharm. Sci. 93*, 3027−3038.
(200) Myler, H. A., Given, A., Kolz, K., Mora, J. R., and Hristopoulos, G. (2011) Biotherapeutic bioanalysis: a multi-indication case study review. *Bioanalysis 3*, 623−643.

Bioconjugate Chemistry

Article

pubs.acs.org/bc

Enhanced Cellular Uptake of a New, *in Silico* Identified Antitubercular Candidate by Peptide Conjugation

Kata Horváti,[†] Bernadett Bacsa,[†] Nóra Szabó,[‡] Sándor Dávid,[†,‡] Gábor Mező,[†] Vince Grolmusz,[§,#] Beáta Vértessy,[∥,⊥] Ferenc Hudecz,[†,○] and Szilvia Bősze*[,†]

[†]Research Group of Peptide Chemistry, Hungarian Academy of Sciences, Eötvös L. University, Budapest, Hungary

[‡]Laboratory of Bacteriology, Korányi National Institute for Tuberculosis and Respiratory Medicine, Budapest, Hungary

[§]Protein Information Technology Group, Eötvös L. University, Budapest, Hungary

[∥]Institute of Enzimology, Hungarian Academy of Science, Budapest, Hungary

[⊥]Department of Applied Biotechnology, Budapest University of Technology and Economics, Budapest, Hungary

[#]Uratim Ltd., Budapest, Hungary

[○]Department of Organic Chemistry, Eötvös L. University, Budapest, Hungary

Supporting Information

ABSTRACT: *Mycobacterium tuberculosis* is a successful pathogen, and it can survive in infected macrophages in dormant phase for years and decades. The therapy of tuberculosis takes at least six months, and the slow-growing bacterium is resistant to many antibiotics. The development of novel antimicrobials to counter the emergence of bacteria resistant to current therapies is urgently needed. *In silico* docking methods and structure-based drug design are useful bioinformatics tools for identifying new agents. A docking experiment to *M. tuberculosis* dUTPase enzyme, which plays a key role in the bacterial metabolism, has resulted in 10 new antitubercular drug candidates. The uptake of antituberculars by infected macrophages is limited by extracellular diffusion. The optimization of the cellular uptake by drug delivery systems can decrease the used dosages and the length of the therapy, and it can also enhance the bioavailability of the drug molecule. In this study, improved *in vitro* efficacy was achieved by attaching the TB5 antitubercular drug candidate to peptide carriers. As drug delivery components, (i) an antimicrobial granulysin peptide and (ii) a receptor specific tuftsin peptide were used. An efficient synthetic approach was developed to conjugate the *in silico* identified TB5 coumarone derivative to the carrier peptides. The compounds were effective on *M. tuberculosis* $H_{37}Rv$ culture *in vitro*; the chemical linkage did not affect the antimycobacterial activity. Here, we show that the OT20 tuftsin and GranF2 granulysin peptide conjugates have dramatically enhanced uptake into human MonoMac6 cells. The TB5−OT20 tuftsin conjugate exhibited significant antimycobacterial activity on *M. tuberculosis* $H_{37}Rv$ infected MonoMac6 cells and inhibited intracellular bacteria.

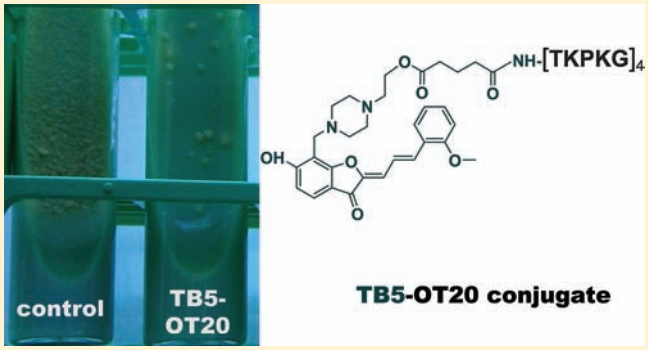

INTRODUCTION

It is estimated that more than one-third of the world's population are infected with *Mycobacterium tuberculosis*, the causative agent of tuberculosis (TB). Latent TB is an asymptomatic phase of the disease during which bacilli do not multiply but persist within their host cells. Individuals with latent TB are assumed to harbor viable tubercle bacilli in their body. These bacilli have the potential to reactivate and cause disease. Around 10% of infected individuals will become sick with active TB during their lifetime. The risk of active TB is 20 to 40 times higher among patients living with HIV/AIDS, those with diabetes, cancer patients, organ transplant recipients, and those undergoing treatment for autoimmune diseases.[1] Among all TB cases, 5% are multidrug-resistant TB (MDR-TB), and in 2010, MDR-TB caused at least 150 000 deaths. MDR-TB strains are resistant to at least isoniazid and rifampicin, the two most effective first-line antituberculars. Additionally, a growing number of XDR-TB (extensively drug-resistant TB; resistant to isoniazid, rifampicin, any fluoroquinolones, and any of the second-line anti-TB injectable drugs) was reported.[2] The therapy of resistant TB can take up to two years with drugs that are less effective, more expensive, and more toxic.

The alarming number of bacterial strains resistant to current therapies led to the development of antituberculotics with novel mechanisms of action. *M. tuberculosis* dUTPase enzyme, which is required for mycobacterial growth, is one of the potential

Received: April 30, 2011
Revised: January 19, 2012
Published: April 19, 2012

dx.doi.org/10.1021/bc200221t | *Bioconjugate Chem.* 2012, 23, 900−907

target enzymes.[3−5] The dUTPase enzyme (EC 3.6.1.23; Rv2697) plays an important role in preventive DNA repair mechanism and thymidilate biosynthesis.[5] The X-ray crystal structure and the catalytic mechanism of *Mycobacterial* dUTPase was published previously.[6] It has been proposed that binding to the species-specific loop of dUTPase protein might be an effective tool to inhibit the growth of *M. tuberculosis*.[7,8]

Small molecular ligands which are capable of binding to and perturbing the function of an essential enzyme of *M. tuberculosis* can be identified using a high-throughput *in silico* docking method. *In silico* docking is a promising approach for fast screening of high numbers of drug-like compounds. Inputs for this process require three key components: (i) 3D structure of target proteins, (ii) a small molecular ligand database containing drug-like compounds, and (iii) an adequately performing docking protocol.

The commercial protein−ligand docking programs were quite secretive about their *exact* optimization methods and *exact* scoring functions, and fine-tuning for the specific needs of the application were not possible since the users cannot interfere with the inner settings of the program. This problem led us to develop our own energy based protein−ligand docking algorithm: the FRIGATE. This program was used to (i) analyze the structure of crucial bacterial enzymes for possible binding sites, (ii) generate candidate molecule conformations, (iii) dock these molecules with the target, and (iv) rank them according to their binding affinities. The software uses different strategies for local and global energy optimization in the typically 10−22 dimensional conformational space by a state-of-the art method combining continuous and discrete optimization techniques.

As a ligand library, we used the free ZINC database[9] of the Shoichet laboratory of the University of California at San Francisco (http://zinc.docking.org/). The database contains the three-dimensional description (SDF and mol2 files) of more than 12 million compounds collected and updated regularly from the catalogues of chemical compound manufacturers worldwide. For the ligand search, the subset generated according to the Lipinski's rule of five[10] was used; this subset contains approximately 2 million drug-like molecules.

Considering that *M. tuberculosis* can survive in host cells, the elimination from infected phagocytes could be more efficient with cell directed delivery of antituberculars. The optimization of the uptake rate using peptide based drug delivery systems can increase the efficacy of the compounds. We describe new peptidic conjugates of the *in silico* identified TB5 coumarone derivative: (i) an antimicrobial peptide (AMP) and (ii) a tuftsin receptor specific conjugate.

However, in many cases, the exact mechanism of bacterial killing of the AMPs is not known; these evolutionarily conserved peptides can interact with the lipid membrane, induce cell lysis, and provoke a broad spectrum of antimicrobial activity against bacteria, viruses, and fungi.[11] Granulysin, a 9 kDa protein found in granules of cytotoxic T lymphocytes and natural killer cells, lyses a variety of tumor and bacterial cells *in vitro* and directly kills *M. tuberculosis*, altering the membrane integrity.[12,13] GranF2, a 23-mer peptide analogue of granulysin, represents a helix−loop−helix region, which is postulated to be the membrane-docking part of the protein.[14] At a relatively high concentration (400 μg/mL, 132 μM), GranF2 inhibits the *in vitro* growth of multidrug resistant cultures. In the presence of a pore forming protein, such as perforin, GranF2 was found to be active against intracellular *M. tuberculosis*.[15,16] The cytolytic and ion channel-forming property of perforin is located at the N-terminus;[17] thus, the peptide represents this part of the protein that can be used in combination with granulysin. Conjugation of the TB5 molecule to the GranF2 peptide is proposed to intensify the antimycobacterial effect by a double mode of action: binding and inhibiting a crucial bacterial enzyme and causing bacterial cell lysis.

Receptor mediated endocytosis can also enhance the intracellular killing of *M. tuberculosis*.[18,19] More efficient inhibition of *M. tuberculosis* from infected phagocytes would be based on the internalization through receptors which are expressed mainly on macrophages. On the basis of the literature, the tuftsin receptor is used for targeted drug delivery.[20−22] Recently, the relevance of tuftsin conjugates as macrophage specific imaging biomarkers was also demonstrated.[23,24] Tuftsin is a natural phagocytosis stimulating peptide produced by enzymatic cleavage of the Fc-domain of the heavy chain of immunoglobulin G. Binding of tuftsin to its receptor causes macrophage activation. An activated macrophage has the ability to enhance phagocytosis and lysis of intracellular parasites.[25] During the past decade, a new group of sequential oligopeptide carriers with discrete molecular masses and defined sequences has been developed in our laboratory: oligotuftsin derivatives consisting of tandem pentapeptide repeat unit $[TKPKG]_n$ (n = 2, 4, 6, and 8) based on the canine tuftsin sequence TKPK.[26,27] These compounds are nontoxic and nonimmunogenic and exhibit tuftsin-like biological properties, e.g., receptor binding, immunostimulatory activity, and chemotactic activity on monocytes and macrophages. In this study, a tetramer tuftsin derivative $[TKPKG]_4$ (OT20) was used as a carrier peptide for the TB5 molecule.

Here, we report the synthesis, characterization, *in vitro* antimycobacterial activity, cytotoxicity, cellular uptake, and intracellular antitubercular efficacy of TB5−peptide conjugates. As the carrier/targeting moiety, a granulysin derived peptide (GranF2) and a tetra-tuftsin derivative (OT20) were used. Our primary aim was to enhance the cellular uptake and intracellular antimycobacterial efficacy of the TB5 *in silico* identified drug candidate.

EXPERIMENTAL PROCEDURES

Materials. Glutaric anhydride, *N,N*-diisopropylethylamine (DIEA), *N,N′*-diisopropylcarbodiimide (DIC), triisopropylsilane (TIS), and phenol were purchased from Fluka (Buchs, Schwitzerland). The amino acid derivatives were obtained from Reanal (Budapest, Hungary) and IRIS Biotech (Marktredwitz, Germany). 1-Hydroxybenzotriazole (HOBt) and 1,8-diazabicyclo-[5.4.0]undec-7-ene (DBU) were also from IRIS Biotech. Fmoc-Rink Amide MBHA resin was purchased from NovaBiochem (Läufelfingen, Schwitzerland). Acetonitrile, trifluoroacetic acid (TFA), *N*-methylpyrrolidone (NMP), and dimethyl sulfoxide (DMSO) were from Merck (Darmstadt, Germany). Ninhydrin, RPMI-1640 medium, Löwenstein−Jensen medium base and the components of the Sula medium was from Sigma-Aldrich (St. Louis, MO, USA). *N,N*-Dimethylformamide (DMF) and dichloromethane (DCM) were from Reanal (Budapest, Hungary). The TB5 molecule was purchased from Ubichem (Budapest, Hungary). HPMI buffer contains 9 mM glucose, 10 mM $NaHCO_3$, 119 mM NaCl, 9 mM HEPES, 5 mM KCl, 0.85 mM $MgCl_2$, 0.053 mM $CaCl_2$, and 5 mM $Na_2HPO_4 \times 2H_2O$ (pH 7.4). ^1H NMR and ^{13}C NMR spectra were recorded on a Bruker 300 MHz instrument. Chemical shifts (δ) are expressed in ppm downfield from TMS as an internal standard.

dx.doi.org/10.1021/bc200221t | *Bioconjugate Chem.* 2012, 23, 900−907

***In Silico* Docking Experiment.** The FRIGATE docking program unites discretization approaches of the energy field around the target protein, similar to that of AUTODOCK[28] with optimization techniques, completely different from AUTODOCK. The FRIGATE program stores the precomputed energy field around the target protein in a grid format. That grid needs to be placed into the RAM during the computation phase. Flexible small molecules are evaluated in that grid, but naturally, the atoms of the small molecules almost never coincide with the point of the grid. Therefore, the forces for the atoms of small molecules between grid points need to be approximated from the grid. FRIGATE uses continuously differentiable B-spline approximation. The main advantage of the B-splines is that for the energy functions we can apply highly developed continuous optimization techniques, namely, the conjugate gradient method, together with stochastic global optimization techniques. The hybrid of the discrete and continuous approaches retains the best from both worlds: discrete storage of the precomputed energy data on a grid makes possible storage at reasonable cost, while the conjugate gradient method yields fast and reliable local energy optimization, lacking in most of the docking programs used today.

Evaluation of Antimycobacterial Activity. *In vitro* antimycobacterial activity of the compounds was determined on *M. tuberculosis* $H_{37}Rv$ (ATCC 27294) by serial dilution in Sula semisynthetic medium, which was prepared in-house (pH 6.5).[29−31] Compounds were added to the medium as DMSO solutions at 10 various doses (range of final concentration was between 0.5 and 100 μg/mL). MIC was determined after incubation at 37 °C for 28 days. MIC was the lowest concentration of a compound at which the visible inhibition of the growth of *M. tuberculosis* $H_{37}Rv$ occurred. In order to confirm growth inhibition, colony forming unit (CFU) was determined by subculturing from the Sula medium onto drug-free Löwensten−Jensen solid medium. Samples were incubated for 28 days. Experiments were repeated at least two times.

Derivatization of TB5 with Glutaric Anhydride. Fifty milligrams (0.115 mmol) of TB5 was dissolved in 2 mL of DCM, and in the presence of 5 equiv of DIEA (98 μL, 0.575 mmol), it was reacted with 3 equiv of glutaric anhydride (39 mg, 0.345 mmol). After 2 h of stirring, the solvent was removed *in vacuo*, and the resulting product was subjected to flash chromatography to afford the desired compound as a bright yellow oil. The synthesized TB5−glutaric acid derivative (pentanedioic acid mono-[2-(4-{6-hydroxy-2-[3-(2-methoxy-phenyl)-allylidene]-3-oxo-2,3-dihydro-benzofuran-7-ylmethyl}-piperazin-1-yl)-ethyl] ester) was purified using an automated chromatography system (SP1, Biotage) using cartridges packed with KP-SIL, 60 Å (40−63 μm particle size), and a chloroform/methanol mixture (gradient from 0 to 10% methanol) as eluent (43 mg, 68%). ^{1}H NMR ($CDCl_3$, 300 MHz, 25 °C): δ = 1.88−2.00 (m, 6H), 2.34−2.43 (m, 8H), 2.79 (t, J = 4.3 Hz, 2H), 2.85 (br s, 1H), 3.88 (s, 3H), 4.00 (s, 2H), 4.26 (t, J = 4.8 Hz, 2H), 6.61 (dd, J = 7.8 and 3.1 Hz, 1H), 6.75 (dd, J = 11.3 and 3.4 Hz, 1H), 6.85−7.00 (m, 2H), 7.20−7.42 (m, 3H), 7.58 (dd, J = 8.4 and 3.1 Hz, 1H), 7.66 (dd, J = 7.7 and 1.2 Hz, 1H), 8.26 (br s, 1H). ^{13}C NMR ($CDCl_3$, 75 MHz, 25 °C): δ = 20.0, 33.1, 33.2, 51.6, 52.3, 53.0, 55.6, 56.1, 60.3, 103.6, 111.2, 113.5, 114.3, 114.5, 120.7, 120.8, 125.3, 125.4, 127.1, 130.5, 135.7, 148.1, 157.5, 165.1, 166.9, 172.9, 173.6, 178.0, 182.1. MS (pos. ESI): calcd 550.2 (M_{mo}); found, 550.2. R_t (RP-HPLC): 26.3 min.

To ease further handling, the product was next prepared in larger amounts as a TFA-salt as follows: after 2 h of stirring, 10 mL of 0.1% TFA/H2O (v/v) was added to the solution, and the yellow precipitate was filtered, washed with water, and dried over P_2O_5 under vacuum. The isolated salt was obtained as a yellow solid and used without further purification.

Synthesis of Tuftsin and Granulysin Derived Carrier Peptides. The tetramer analogue of the canine tuftsin sequence (TKPKGTKPKGTKPKGTKPKG) and GranF2, a granulysin derivative (^{33}VCRTGRSRWRDVCRNFMRRYQSR^{55}) were produced on Fmoc-Rink Amide MBHA resin in an automated peptide synthesizer (Syro-I, Biotage, Uppsala, Sweeden) using Fmoc/^{t}Bu strategy. The protocol of the synthesis was the following: (i) Fmoc deprotection with 40% piperidine/DMF (v/v), 2 min; 20% piperidine/DMF (v/v), 20 min; (ii) washing with DMF (5 × 1 min); (iii) coupling twice with 4 equiv of Fmoc-amino acid derivative−DIC−HOBt dissolved in NMP (2 × 60 min); and (iv) washing with DMF (5 × 1 min). Peptides were cleaved from the resin with the TFA/H_2O/TIS (9.5:2.5:2.5 v/v) mixture (2 h, RT). After filtration, compounds were precipitated in cold diethyl ether, centrifuged (4000 rpm, 5 min), and freeze-dried in water. Crude products were purified by semipreparative RP-HPLC as described below. Purified peptides were analyzed by analytical RP-HPLC, ESI MS, and amino acid analysis.

Conjugation of TB5−glut to Tuftsin and Granulysin Derived Carrier Peptides. TB5−glut compound, which contains a free carboxylic group, was conjugated to the *N*-terminus of the previously synthesized peptides on solid phase. Two equiv of TB5−glut−DIC−HOBt−DIEA dissolved in NMP was mixed with the peptide−resin. After 60−120 min, the efficacy of the coupling was monitored by ninhydrin assay. TB5−tuftsin and TB5−granulysin conjugates were cleaved from the resin with TFA in the presence of H_2O and TIS (9.5:2.5:2.5 v/v; 2 h, RT). After filtration, conjugates were precipitated in cold diethyl ether, centrifuged (4000 rpm, 5 min), and freeze-dried. Crude conjugates were purified by semipreparative RP-HPLC and characterized by analytical RP-HPLC and ESI MS.

Cell Culturing. MonoMac6 human monocytic cell line[32] (DSMZ no.: ACC 124, Deutsche Sammlung von Mikroorganismen and Zellkulturen GmbH, Braunschweig, Germany) was maintained in RPMI-1640 medium containing 10% FCS, 2 mM L-glutamine, and 160 μg/mL gentamycin at 37 °C in 5% CO_2 atmosphere.

Cell Viability and Uptake Studies by Flow Cytometry. The measurement of cell viability and cellular uptake of the compounds were evaluated by flow cytometry (BD LSR II, BD Biosciences, San Jose, CA, USA) and fluorescent microscopy (Olympus CKX41, Hamburg, Germany) on MonoMac6 human monocytic cell line. Cells were harvested in the logarithmic phase of growth and plated on a 24-well tissue culture plate (10^5 cells/1 mL medium/well) 24 h prior to the experiment. Compounds were dissolved in serum free RPMI-1640 medium, and running dilutions were prepared. The highest concentration of the compounds on the cells was 300 μM. Cells were incubated with compounds TB5, TB5−glut, TB5−OT20, TB5−GranF2, GranF2, and OT20 for 60 min (37 °C, 5% CO_2 atmosphere). After centrifugation (1000 rpm, 5 min), the supernatant was removed, and 100 μL of 1 mM trypsin was added to the cells. After 5 min of incubation at 37 °C, 1 mL of 10% FCS/RPMI-1640 medium was added, and then cells were washed two times with medium and resuspended in 0.5 mL

dx.doi.org/10.1021/bc200221t | *Bioconjugate Chem.* 2012, 23, 900−907

HPMI. Cell viability and cellular uptake were determined by BD LSR II using a 488 nm (Coherent Sapphire, 22 mW) laser. The cell viability was assessed using propidium iodide (PI). The cells in suspension were mixed 1:1 with 10 μg/mL PI solution. Viable cells did not stain significantly with PI, whereas the nonviable cell population demonstrated significant PI staining (see Supporting Information, Figure S1). The intracellular fluorescence intensity of the cells was measured on channel PE LP550 (emission at λ = 550 nm). Data were analyzed with FACSDiva 5.0 software (BD Biosciences, San Jose, CA, USA). All measurements were performed in duplicate. In parallel with flow cytometry measurements, microscopic images of the cells were captured with an Olympus CKX41 microscope.

Infection of MonoMac6 Monolayers with *M. tuberculosis* H_{37}Rv and Determination of Efficacy against Intracellular Bacteria (Modified Method Based On Refs 33 and 34). Briefly, MonoMac6 monocytes (2×10^5 cells/1 mL medium/well) were cultured with RPMI-1640 medium containing 10% FCS in a 24-well plate 24 h prior to the experiment. Adherent cells were infected with *M. tuberculosis* H_{37}Rv at a multiplicity of infection (MOI) of 10 for 4 h. Nonphagocytosed extracellular bacteria were removed, and the culture was washed three times with serum free RPMI-1640. The infected monolayer was incubated for 1 day before antitubercular treatment. Infected cells were then treated with TB5 conjugates at 50 μM final concentration with or without 100 μM perforin peptide. After 3 days, the treatment was repeated with fresh solution of the compounds for an additional 3 days. Untreated cells were considered as the negative control. As the control compound, isoniazid (INH) was used at 50 μg/mL (365 μM) concentration. After washing steps, in order to remove the antituberculars, infected cells were lysed with 2.5% sodium dodecyl sulfate solution. The CFU of *M. tuberculosis* was enumerated on Löwenstein–Jensen solid media after 4 weeks of incubation.

RESULTS

Results of *in Silico* Docking. The FRIGATE program generated docking energies for each of the more than 2 million small molecules from the ZINC database. The best 1000 scored molecules were filtered according to their log *P* and predicted solubility properties. We also checked for their drug likeness and ranked them according to their binding affinities.[35] In the first run of the experiments, we ordered the 20 best molecules from compound manufacturers, using the ZINC database. The *in vitro* antimycobacterial activity of the compounds was characterized by the determination of the minimal inhibitory concentration (MIC) on *M. tuberculosis* H_{37}Rv culture with 4-week exposure period (Table 1). One compound was not soluble at the used concentration. Fifty-three percent (10/19) of the tested molecules showed relevant MIC values (lower than 100 μg/mL). Chemical structure of the effective compounds is given in Figure 1. For peptide conjugation, a fluorescent compound, TB5 coumarone derivative, was chosen. The fluorescent property of the TB5 compound (Figure 2) can be used conveniently to determine the cellular uptake rate by flow cytometry and fluorescent microscopy.

Conjugation of the TB5 Molecule to Carrier Peptides. Carrier peptides were synthesized using the standard Fmoc/^{t}Bu strategy. All of the peptides were obtained with amide *C*-termini after final cleavage. These peptides were also used as control compounds in further experiments. Data concerning analytical characterization of peptides are presented in Table 2.

Table 1. Antimycobacterial Effect of the *in Silico* Identified Compounds

compd	MIC[a] (μg/mL)	MIC (μM)	CFU[b]
control	no inhibition		+++[c]
isoniazid (INH)[d]	0.16	1.2	12
norfloxacin[d]	5	15	1
TB1	25	51	n.d.
TB2	5	12	5
TB3	15	31	42
TB4	30	63	n.d.
TB5	20	46	2
TB6	45	100	7
TB7	25	53	20
TB8	1	3.7	8
TB9	45	93	70
TB10	45	110	2

[a]MIC (minimal inhibitory concentration) was determined on the *M. tuberculosis* H_{37}Rv strain in Sula semisynthetic media, pH 6.5 (4 weeks). [b]To confirm the growth inhibition, CFU (colony forming unit) was determined on Löwenstein–Jensen solid media (4 weeks). [c]+++: confluent colonies. [d]As positive control, bacteria were inoculated in the absence of drugs. Izoniazid (a first line antitubercular drug) and norfloxacin (a fluoroquinolone) were used to compare the MIC results.

All purified peptides demonstrated a single peak on analytical RP-HPLC with a mass coinciding with the theoretically calculated molecular mass. The amino acid composition of peptides was proved by amino acid analysis where the accuracy was less than 5%.

In order to prepare TB5–peptide conjugates, the TB5 molecule was first esterificated with glutaric anhydride (Figure 3). Through the free carboxylic group, TB5–glut was conjugated to tuftsin and granulysin derived peptides on solid phase using the standard DIC/HOBt coupling method. After the final cleavage with TFA, TB5–tuftsin and TB5–granulysin conjugates were purified and carefully characterized (Table 2).

Antitubercular Effect of TB5 and TB5–glut. The *in vitro* antimycobacterial activity of the new compounds was characterized by the determination of the minimal inhibitory concentration (MIC) using *M. tuberculosis* H_{37}Rv strain with a 4-week exposure period. TB5–glut was effective against the bacteria and exhibited almost the same MIC value as free TB5. MIC(TB5) = 20 μg/mL; 46 μM) and MIC(TB5–glut) = 40 μg/mL; 73 μM. These results suggested that chemical modification did not influence the antitubercular effect of TB5 molecule.

Cell Viability. Viability of MonoMac6 human monocytic cells was measured by flow cytometry after 1 h of treatment with TB5, TB5–glut, TB5–GranF2, TB5–OT20 conjugates, GranF2, and OT20 carrier peptides. Relative percentage of living cells was determined compared to that of the untreated control (Figure 4). The most cytotoxic compound was TB5–GranF2, where the IC_{50} value is close to that of the free GranF2 carrier peptide (42 and 85 μM). The microscopic images (Figure 5C and E) clearly demonstrate that the GranF2 peptide and TB5–GranF2 conjugate disrupted the membrane integrity. The tuftsin conjugated TB5–OT20 compound is less cytotoxic on MonoMac6 cells; the IC_{50} value (201 μM) is 5 times higher than the IC_{50} of TB5–GranF2. Treatment with TB5, TB5–glut compounds, and OT20 peptide did not influence the cell viability up to 300 μM concentration.

dx.doi.org/10.1021/bc200221t | *Bioconjugate Chem.* 2012, 23, 900–907

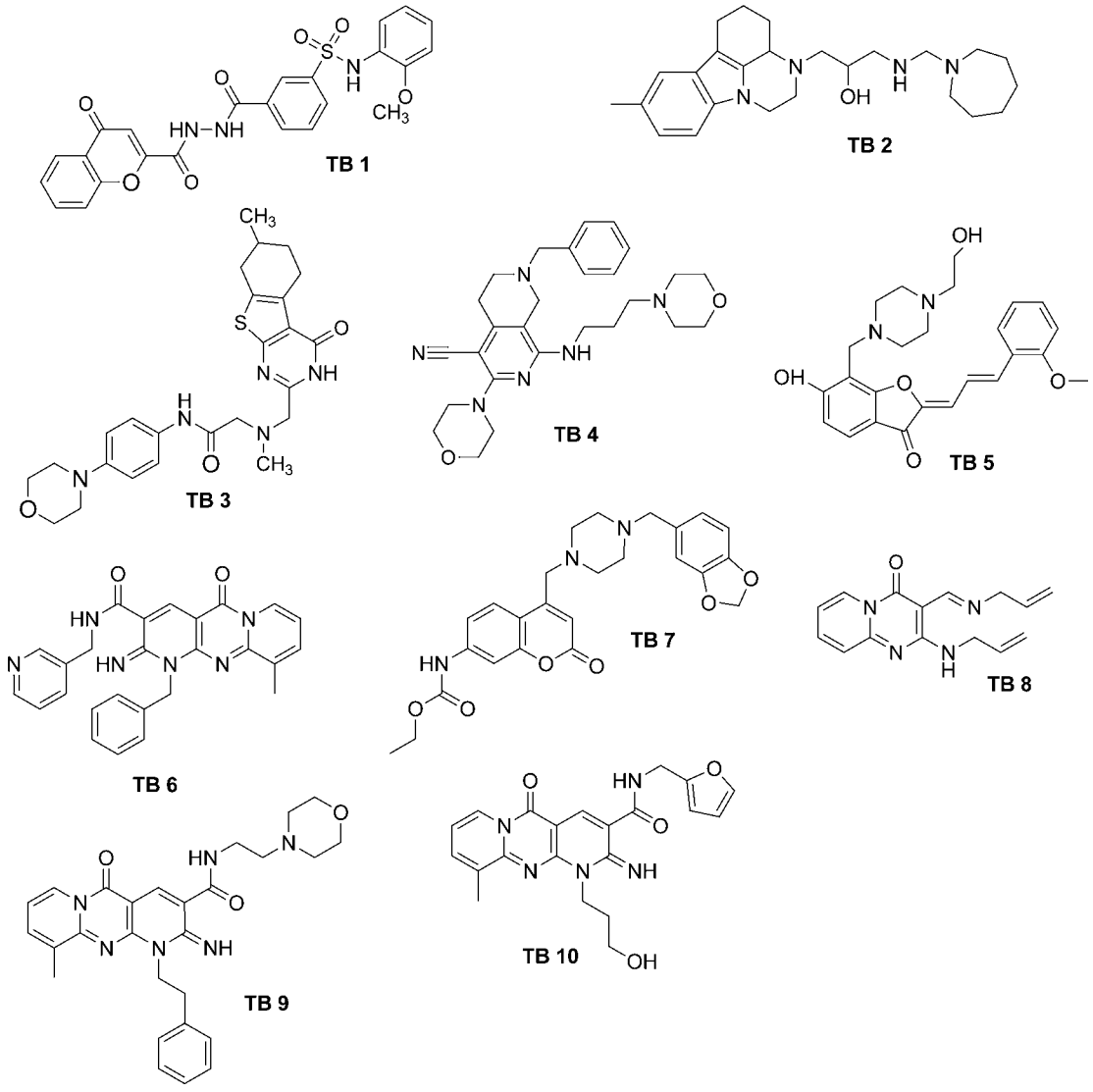

Figure 1. Chemical structure of the *in silico* identified antitubercular drug candidates.

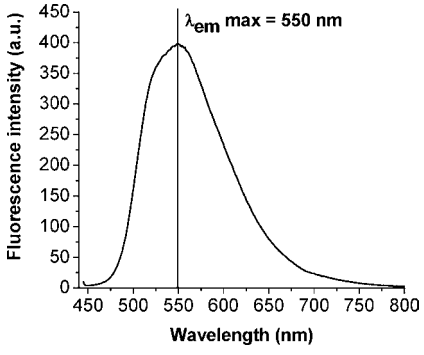

Figure 2. Fluorescent emission spectra of the TB5 compound. The sample was measured on a VARIAN Cary Eclipse fluorescence spectrophotometer in HPMI media at 10 μM concentration. The emission spectra indicate the use of TB5 and its peptide conjugates in flow cytometry and fluorescent microscopy.

Cellular Uptake of TB-5 Conjugates. Cellular uptake was evaluated on the MonoMac6 human monocytic cell line using flow cytometry (BD LSRII, Figure 6) and fluorescent microscopy (Olympus CKX41, Figure 5) after trypsinization. The treatment of MonoMac6 monocytic cells with TB5 and TB5−glut compounds has resulted in the same intracellular fluorescent intensity as that of the untreated control. In contrast, the internalization rates of TB5−OT20 and TB5−GranF2 conjugates were more than ten-times higher than the rates of TB5 compounds.

Intracellular Killing of *M. tuberculosis*. Intracellular efficacy of antitubercular drug candidates was evaluated on MonoMac6 human monocytes using a modified previously described method.[33,34] At 100 μM or higher concentration, TB5−GranF2 and GranF2 are cytotoxic for the monocytes (IC_{50} = 42 and 85 μM), and false intracellular inhibition can be detected. Therefore, 50 μM final concentration was used in this experiment. When infected, MonoMac6 cells were treated with only carrier peptides (GranF2, OT20), no antitubercular activity was observed on intracellular bacteria. In the case of TB5−GranF2 conjugate, significantly reduced CFU was enumerated compared to CFU of the lysed untreated control cells. Applying the combination of GranF2 and perforin resulted in 10 times higher activity, but in the case of the TB5−GranF2 conjugate in the presence of perforin, no further improvement in efficacy was detected. Isoniazid (INH), a first-line

dx.doi.org/10.1021/bc200221t | *Bioconjugate Chem.* 2012, 23, 900−907

Table 2. Analytical Characterization of Peptide−Drug Conjugates and Free Carrier Peptides[a]

compd	composition	M_{av}[b] calcd/found	R_t[d] (min)
TB5		436.4/436.4[c]	24.5
TB5−glut		550.5/550.5[c]	26.3
OT20	$[TKPKG]_4$	2063.5/2063.5	14.8[e]
TB5−OT20	TB5−$[TKPKG]_4$	2596.0/2596.0	28.4[e]
GranF2	^{33}VCRTGRSRWRDVCRNFMRRYQSR^{55}	2988.5/2988.7	21.6
TB5−GranF2	TB5−^{33}VCRTGRSRWRDVCRNFMRRYQSR^{55}	3521.0/3520.8	30.1

[a]The *C*-termini of the peptides and peptide conjugates were in amidated form. [b]Measured average molecular mass by Bruker Esquire 3000+ ESI-MS. Samples were dissolved in a mixture of acetonitrile/water = 1/1 (v/v) containing 0.1% acetic acid and introduced by a syringe pump with a flow rate of 10 μL/min. [c]Monoisotopic molecular mass. [d]RP-HPLC, Knauer, Eurospher-100, C18, 5 μm, 250 × 4 mm column; 1 mL/min flow rate; detection at λ = 214 nm. A eluent: 0.1% TFA/H_2O. B eluent: 0.1% TFA/acetonitrile/H_2O = 80:20 (v/v). Gradient: 10% B, 5 min; 10−80% B, 35 min. [e]Gradient: 5% B, 5 min; 5−60% B, 35 min.

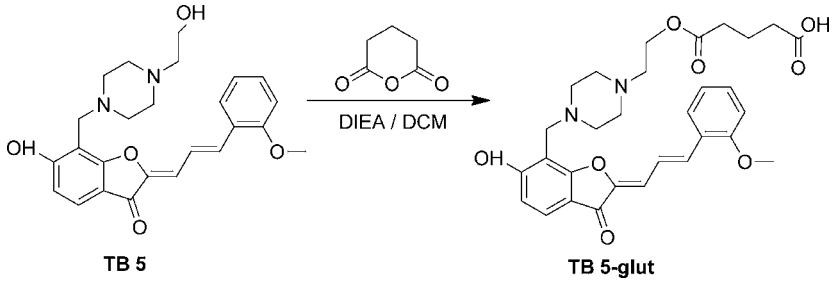

Figure 3. Outline of the esterification of the TB5 molecule with glutaric anhydride (TB5−glut).

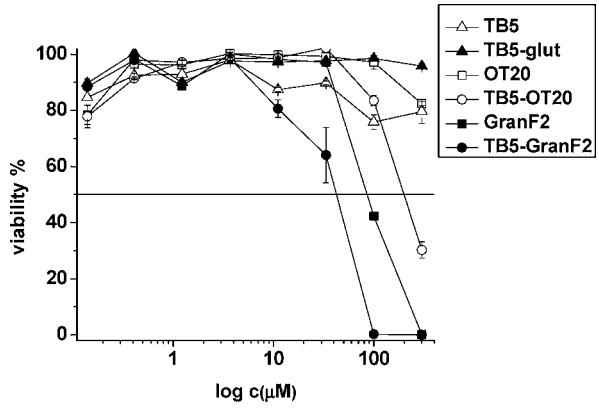

Figure 4. Viability of MonoMac6 human monocytic cells after 1 h of treatment with TB5, TB5−glut, TB5−GranF2, TB5−OT20 conjugates, GranF2, and OT20 carrier peptides. Relative percentage of viable cells was determined compared to that of the untreated control. Each point represents the mean ± SD of triplicate measurements. GranF2 and TB5−GranF2 are the most cytotoxic compounds *in vitro*. IC_{50}(GranF2) = 85 μM; IC_{50}(TB5−GranF2) = 42 μM.

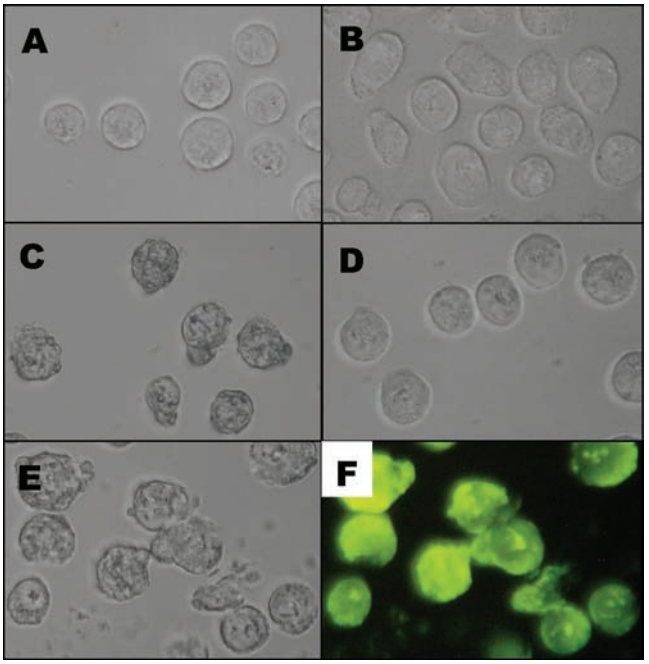

Figure 5. Microscopic images of MonoMac6 human monocytic cells treated with TB5 compounds. Untreated control (A), TB5 (B), GranF2 (C), OT20 (D), and TB5−GranF2 (E), fluorescent image of TB5−GranF2 (F). Treatment with TB5 and the OT20 peptide did not change the morphology of the cells, while GranF2 and TB5−GranF2 induced cell lysis and membrane disruption.

antitubercular drug, was also tested and did not show antitubercular activity even at 365 μM concentration against intracellular bacteria. Treatment with TB5−OT20 dramatically reduced the intracellular growth of *M. tuberculosis* (Figure 7).

DISCUSSION

An *in silico* docking experiment to *M. tuberculosis* dUTPase enzyme has resulted in 10 new antimycobacterial compounds (TB1-TB10). Considering MIC values, solubility features, and chemical structure, the TB5 compound was chosen for conjugation to oligotuftsin and granulysin derived carrier peptides. Furthermore, the fluorescent property of TB5 molecule gives us the possibility to study cellular uptake and cell viability by flow cytometry and fluorescence microscopy. Efficient synthetic pathway was introduced to conjugate the TB5 compound to peptidic carriers. The antitubercular activity of TB5 coumarone derivative was preserved after chemical modification.

The main goal of our study was to improve the antimycobacterial efficacy of the compound against intracellular

dx.doi.org/10.1021/bc200221t | *Bioconjugate Chem.* 2012, 23, 900−907

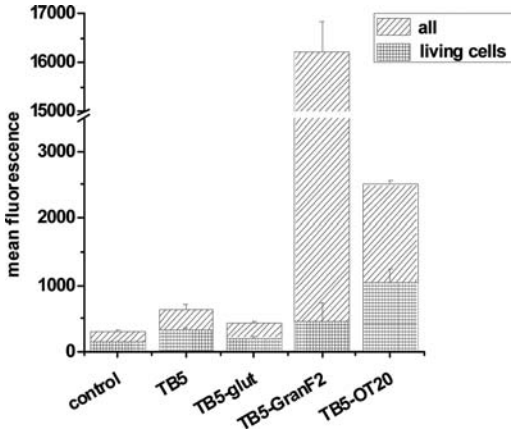

Figure 6. MonoMac6 human monocytic cells were treated with the TB5 compound and conjugates at 100 μM concentration. The cellular uptake was determined after trypsination by flow cytometry (BD LSRII) measuring the intracellular fluorescent intensity. No internalization was detected for TB5 and TB5−glut compare to that of the untreated control. Conjugation to GranF2 and the OT20 peptide significantly increased cellular uptake. TB5−OT20 treatment has resulted in the highest intracellular fluorescence intensity of viable cells.

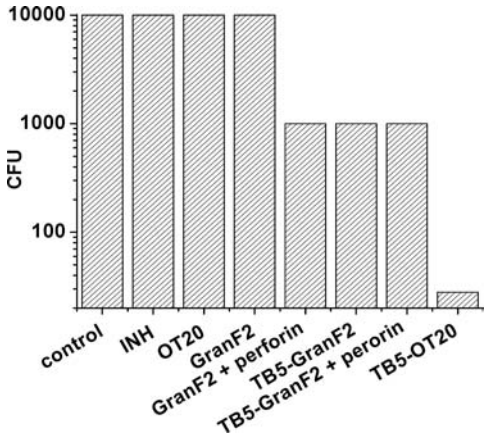

Figure 7. Inhibition of intracellular *M. tuberculosis* by TB5−peptide conjugates. Cultured MonoMac6 cells were infected with *M. tuberculosis* H_{37}Rv and treated with compounds at 50 μM final concentration. As the control, untreated cells were used. In the case of the GranF2 peptide, perforin peptide was added at 100 μM concentration. After SDS lysis, the colony forming units (CFU) of *M. tuberculosis* was enumerated on Löwenstein−Jensen solid media.

M. tuberculosis. To determine the efficacy against intracellular bacteria, MonoMac6 human monocytes were infected with *M. tuberculosis* H_{37}Rv and treated with the new compounds. MonoMac6 cells are phagocytic and express the CR3 receptor, which is important for the entry of *M. tuberculosis* bacteria. MonoMac6 was established as a cell line, which appears to have phenotypic and functional characteristics of mature blood monocytes; therefore, it is frequently used as a host cell model to measure activity against phagocytosed intracellular bacteria.

In order to adjust the experimental parameters on infected MonoMac6, first the cellular uptake of the compounds was determined. The treatment of MonoMac6 cells with the TB5 compound evoked almost the same intracellular fluorescent intensity as that of the untreated control, which means that the uptake rate of the free drug candidates is limited. In contrast, the mean fluorescent intensity was significantly higher after the incubation with the tuftsin and granulysin conjugated TB5 compound. The most efficient internalization was measured for TB5−granF2, but the antimicrobial granulysin derived peptide provoked membrane disruption and lysis of MonoMac6 cells. Coupling TB5 to OT20 peptide has resulted in a less cytotoxic conjugate, and the intracellular fluorescent intensity of TB5−OT20 treated cells was five-times higher than that of TB5 treated cells. The TB5−OT20 conjugate was remarkably effective against phagocytised intracellular *M. tuberculosis bacteria*: a significant decrease in CFU was enumerated at 50 μM concentration. At this concentration, GranF2 and TB5−GranF2 conjugates resulted in 35-times higher CFU even in the presence of a pore forming perforin.

We can conclude that conjugation of antitubercular agents to a peptidic carrier is a promising approach to enhance cellular uptake and *in vitro* selectivity. In this study, we showed that the OT20 tuftsin conjugate efficiently inhibited the intracellular *M. tuberculosis* bacteria.

■ ASSOCIATED CONTENT

Supporting Information

Gating strategy in flow cytometry. This material is available free of charge via the Internet at http://pubs.acs.org.

■ AUTHOR INFORMATION

Corresponding Author

*Research Group of Peptide Chemistry, Hungarian Academy of Sciences, Eötvös L. University, Pázmány P. stny. 1/A, Budapest, Hungary 1117. Tel: +36-1-372-2500 ext. 1736. Fax: +36-1-372-2620. E-mail: bosze@chem.elte.hu.

Notes

The authors declare no competing financial interest.

■ ACKNOWLEDGMENTS

This work was supported by NKFP_07_1-TB_INTER-HU; Hungarian Research Fund (T68358, T68258, CK78646, NK-84008). New Hungary Development Plan (TAMOP-4.2.1/B-09/1/KMR-2010-0002, 0003); Baross program of the New Hungary Development Plan (3DSTRUCT, OMFB-00266/2010 REG-KM-09-1-2009-0050). We thank Dr. Hedvig Medzihradszky-Schweiger for the amino acid analysis and Dr. Toma N. Glasnov for the characterization of the TB5−glut compound.

■ REFERENCES

(1) Dyer, C. M. (2010) *Tuberculosis*, pp 89−121, Chapters 7 and 8, Greenwood Press, Santa Barbara, CA

(2) Wright, A., and Zignol, M. (2008) *Anti-Tuberculosis Drug Resistance in the World: Fourth Global Report (WHO/HTM/TB/2008.394)*, WHO Press, Geneva, Switzerland

(3) Sassetti, C. M., Boyd, D. H., and Rubin, E. J. (2003) Genes required for mycobacterial growth defined by high density mutagenesis. *Mol. Microbiol. 48*, 77−84.

(4) Mészáros, B., Tóth, J., Vértessy, B. G., Dosztányi, Z., and Simon, I. (2011) Proteins with complex architecture as potential targets for drug design: a case study of *Mycobacterium tuberculosis*. *PLoS Comput. Biol.* 7 (7), e1002118.

(5) Vértessy, B. G, and Tóth, J. (2009) Keeping uracil out of DNA: physiological role, structure and catalytic mechanism of dUTPases. *Acc. Chem. Res. 42*, 97−106.

(6) Chan, S., Segelke, B., Lekin, T., Krupka, H., Cho, U. S., Kim, M. Y., So, M., Kim, C. Y., Naranjo, C. M., Rogers, Y. C., Park, M. S., Waldo, G. S., Pashkov, I., Cascio, D., Perry, J. L., and Sawaya, M. R.

(2004) Crystal structure of the *Mycobacterium tuberculosis* dUTPase: insights into the catalytic mechanism. *J. Mol. Biol. 341*, 503−517.
(7) Varga, B., Barabás, O., Takács, E., Nagy, N., Nagy, P., and Vértessy, B. G. (2008) Active site of mycobacterial dUTPase: structural characteristics and a built-in sensor. *Biochem. Biophys. Res. Commun. 373*, 8−13.
(8) Takács, E., Nagy, G., Leveles, I., Harmat, V., Lopata, A., Tóth, J., and Vértessy, B. G. (2010) Direct contacts between conserved motifs of different subunits provide major contribution to active site organization in human and mycobacterial dUTPases. *FEBS Lett. 584*, 3047−3054.
(9) Irwin, J. J., and Shoichet, B. K. (2005) ZINC - a free database of commercially available compounds for virtual screening. *J. Chem. Inf. Model. 45*, 177−182.
(10) Lipinski, C. A., Lombardo, F., Dominy, B. W., and Feeney, P. J. (2001) Experimental and computational approaches to estimate solubility and permeability in drug discovery and development settings. *Adv. Drug Delivery Rev. 46*, 3−26.
(11) Reddy, K. V., Yedery, R. D., and Aranha, C. (2004) Antimicrobial peptides: premises and promises. *Int. J. Antimicrob. Agents 24*, 536−547.
(12) Stenger, S., Hanson, D. A., Teitelbaum, R., Dewan, P., Niazi, K. R., Froelich, C. J., Ganz, T., Thoma-Uszynski, S., Melián, A., Bogdan, C., Porcelli, S. A., Bloom, B. R., Krensky, A. M., and Modlin, R. L. (1998) An antimicrobial activity of cytolytic T cells mediated by granulysin. *Science 282*, 121−125.
(13) Clayberger, C., and Krensky, A. M. (2003) Granulysin. *Curr. Opin. Immunol. 15*, 560−565.
(14) Andreu, D., Carreño, C., Linde, C., Boman, H. G., and Andersson, M. (1999) Identification of an anti-mycobacterial domain in NK-lysin and granulysin. *Biochem. J. 344*, 845−849.
(15) Toro, J. C., Hoffner, S., Linde, C., Andersson, M., Andersson, J., and Grundström, S. (2006) Enhanced susceptibility of multidrug resistant strains of *Mycobacterium tuberculosis* to granulysin peptides correlates with a reduced fitness phenotype. *Microbes Infect. 8*, 1985−1993.
(16) Walch, M., Latinovic-Golic, S., Velic, A., Sundstrom, H., Dumrese, C., Wagner, C. A., Groscurth, P., and Ziegler, U. (2007) Perforin enhances the granulysin-induced lysis of Listeria innocua in human dendritic cells. *BMC Immunol. 8*, 14.
(17) Ojcius, D. M., Persechini, P. M., Zheng, L. M., Notaroberto, P. C., Adeodato, S. C., and Young, J. D. (1991) Cytolytic and ion channel-forming properties of the N terminus of lymphocyte perforin. *Proc. Natl. Acad. Sci. U.S.A. 88*, 4621−4625.
(18) Majumdar, S., and Basu, S. K. (1991) Killing of intracellular *Mycobacterium tuberculosis* by receptor-mediated drug delivery. *Antimicrob. Agents Chemother. 35*, 135−140.
(19) Horváti, K., Mező, G., Szabó, N., Hudecz, F., and Bősze, Sz. (2009) Peptide conjugates of therapeutically used antitubercular isoniazid-design, synthesis and antimycobacterial effect. *J. Pept. Sci. 15*, 385−391.
(20) Amoscato, A. A., Davies, P. J., Babcock, G. F., and Nishioka, K. (1983) Receptor-mediated internalization of tuftsin. *Ann. N.Y. Acad. Sci. 419*, 114−134.
(21) Gottlieb, P., Hazum, E., Tzehoval, E., Feldman, M., Segal, S., and Fridkin, M. (1984) Receptor-mediated endocytosis of tuftsin by macrophage cells. *Biochem. Biophys. Res. Commun. 119*, 203−211.
(22) Agrawal, A. K., and Gupta, C. M. (2000) Tuftsin-bearing liposomes in treatment of macrophage-based infections. *Adv. Drug Delivery Rev. 41*, 135−146.
(23) Feng, J., Meloni, M. M., Allan, S. M., Faulkner, S., Narvainen, J., Vidyasagar, R., and Kauppinen, R. (2010) Tuftsin derivatives of FITC, Tb-DOTA or Gd-DOTA as potential macrophage-specific imaging biomarkers. *Contrast Media Mol. Imaging 5*, 223−230.
(24) Wong, E., Bennett, S., Lawrence, B., Fauconnier, T., Lu, L. F., Bell, R. A., Thornback, J. R., and Eshima, D. (2001) Tuftsin receptor-binding peptide labeled with technetium: chemistry and preliminary in vitro receptor-binding study. *Inorg. Chem. 40*, 5695−5700.
(25) Najjar, V. A. (1983) Tuftsin, a natural activator of phagocyte cells: an overview. *Ann. N.Y. Acad. Sci. 419*, 1−11.
(26) Mező, G., Kalászi, A., Reményi, J., Majer, Zs., Hilbert, A., Láng, O., Kőhidai, L., Barna, K., Gaál, D., and Hudecz, F. (2004) Synthesis, conformation, and immunoreactivity of new carrier molecules based on repeated tuftsin-like sequence. *Biopolymers 73*, 645−656.
(27) Bai, K. B., Láng, O., Orbán, E., Szabó, R., Kőhidai, L., Hudecz, F., and Mező, G. (2008) Design, synthesis, and *in vitro* activity of novel drug delivery systems containing tuftsin derivatives and methotrexate. *Bioconjug. Chem. 19*, 2260−2269.
(28) Morris, G. M., Goodsell, D. S., Halliday, R. S., Huey, R., Hart, W. E., Belew, R. K., and Olson, A. J. (1998) Automated docking using a Lamarckian genetic algorithm and an empirical binding free energy function. *J. Comput. Chem. 19*, 1639−1662.
(29) Sula, L. (1963) WHO Co-operative studies on a simple culture technique for the isolation of mycobacteria. 1. Preparation, lyophilization and reconstitution of a simple semi-synthetic concentrated liquid medium; culture technique; growth pattern of different mycobacteria. *Bull. W. H. O. 29*, 589−606.
(30) Sula, L. (1963) WHO cooperative studies on a simple culture technique for the isolation of mycobacteria: 2. Comparison of the efficacy of lyophilized liquid medium with that of Lowenstein-Jensen (L-J) medium. *Bull. W. H. O. 29*, 607−625.
(31) Vinsova, J., Cermakova, K., Tomeckova, A., Ceckova, M., Jampilek, J., Cermak, P., Kunes, J., Dolezal, M., and Staud, F. (2006) Synthesis and antimicrobial evaluation of new 2-substituted 5,7-di-tert-butylbenzoxazoles. *Bioorg. Med. Chem. 14*, 5850−5865.
(32) Ziegler-Heitbrock, H. W. L., Thiel, E., Fütterer, A., Herzog, V., Wirtz, A., and Riethmüller, G. (1988) Establishment of a human cell line (Mono Mac 6) with characteristics of mature monocytes. *Int. J. Cancer 41*, 456−461.
(33) Wright, E. L., Quenelle, D. C., Suling, W. J., and Barrow, W. W. (1996) Use of Mono Mac 6 human monocytic cell line and J774 murine macrophage cell line in parallel antimycobacterial drug studies. *Antimicrob. Agents Chemother. 40*, 2206−2208.
(34) Tomioka, H., Sato, K., Kajitani, H., Akaki, T., and Shishido, S. (2000) Comparative antimicrobial activities of the newly synthesized quinolone WQ-3034, levofloxacin, sparfloxacin, and ciprofloxacin against *Mycobacterium tuberculosis* and *Mycobacterium avium* complex. *Antimicrob. Agents Chemother. 44*, 283−286.
(35) Schnöller, D., Pénzes, Cs. B., Horváti, K., Bősze, Sz., Hudecz, F., and Kiss, É. (2011) Membrane affinity of new antitubercular drug candidates using a phospholipid Langmuir monolayer model and LB technique. *Prog. Colloid Polym. Sci. 138*, 131−137.

Bioconjugate Chemistry

Article

pubs.acs.org/bc

Impact of Spacer and Strand Length on Oligonucleotide Conjugation to the Surface of Ligand-Free Laser-Generated Gold Nanoparticles

A. Barchanski,[†,#] N. Hashimoto,[†,‡,#] S. Petersen,[†] C. L. Sajti,*[,†] and S. Barcikowski*[,§]

[†]Laser Zentrum Hannover e.V., Hollerithallee 8, 30419 Hannover, Germany

[‡]Chuo University, 1-13-27, Kasuga, Bunkyo-ku, 112-8551 Tokyo, Japan

[§]University of Duisburg-Essen, Institute for Technical Chemistry, Technical Chemistry I and Center for Nanointegration Duisburg-Essen (CeNIDE), Universitätsstraße 7, 45141 Essen, Germany

Supporting Information

ABSTRACT: Gold nanoparticles conjugated to nucleic acids are widely used for biomedical targeting and sensing applications; however, little is known about the conjugation chemistry covering the impact of steric dimension and strand orientation of single-stranded oligonucleotides (ssO) on the conjugation process and binding efficiencies. In this context, we present an extensive investigation concerning the attachment of thiolated ssO to the surface of laser-generated gold nanoparticles, altering both strand length and binding orientation by the insertion of different spacer types at either the 3′ or 5′ ssO terminus. A significant reduction of conjugation efficiency of about 30−50% is determined for spacer-prolonged bionanoconjugates due to coiling effects of the flexible ssO strand on the particle surface which increases deflection angle of oligonucleotides and limits the number of biomolecules attached to the nanoparticles.

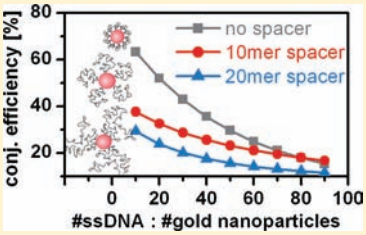

INTRODUCTION

Noble metal nanoparticles have attracted great attention for biomedical applications, as they show interesting and versatile properties that are a function of their size dimensions. Especially, gold nanoparticles (AuNP) are of outstanding use for nanobiotechnology because of their attributes regarding low cytotoxicity[1] and feasible visualization due to optical characteristics[2] with high photostability[3] compared to molecular fluorophores. Concerning these properties, gold nanoparticles are established analytical tools for biological and medical applications, especially when conjugated to functional biomolecules as nucleic acids.[4−6] Single-stranded oligonucleotides (ssO) are routinely used in the lab as fluorochrome-labeled probes for fluorescence in situ hybridization (FISH) analysis and for sensory applications, but their adoption is usually limited due to the low photostability and long-term visualization of the fluorescent dyes. Thus, conjugation of ssO to the photostable AuNPs is the focus of current research, as these bionanoconstructs facilitate the imaging process significantly. So far, several studies have been reported in the past decade concerning the successful application of ssO-conjugated gold nanoparticles (AuNP-ssO).[7−9]

The generation of AuNPs is conventionally achieved by chemical synthesis which often employs cell-toxic preservatives.[10,11] However, laser ablation of a metal in a liquid environment has also been applied for the production of metal nanoparticles. As Kabashin et al. have shown, nanoparticles can be generated by laser ablation of a target in solution in a single-step process using ultrashort pulses.[12,13] The fabrication process features high purity and partial charging of the generated nanoparticles, as well as concentration and size control due to modulation of laser parameters.[14,15] AuNPs can be functionalized in situ subsequent to fabrication[16] with biomolecules like cell-penetrating-peptides,[17] aptamers,[18] or ssO,[19] for example, while the observed degradation of biomolecules during laser irradiation[20] is avoided due to the use of femtosecond pulses with low thermal effects.[16,21] In this context, Petersen et al. have described both unspecific adsorption of negatively net-charged biomolecules on positively net-charged laser-generated AuNP via electrostatic interactions,[22] as well as their covalent conjugation using thiolated ligands.[16,23]

Laser-generated gold nanoparticles may be conjugated to ssO in order to develop modern hybrid nanomarkers with the long-term visualization benefit of AuNP. In this context, we have recently investigated the in situ and ex situ bioconjugation of laser-generated gold nanoparticles with a thiolated 18mer ssO regarding conjugation efficiencies and surface coverages.[23] In comparison to the conventional conjugation method by ligand exchange on chemically synthesized AuNP, we observed up to five times higher maximal surface coverage values for laser-fabricated AuNP. Conjugation efficiencies of in situ conjugated oligonucleotides were about four times higher compared to the ex situ conjugated ssO.[23]

The conjugation of biomolecules to chemically synthesized gold nanoparticles by a spacer molecule has also been investigated by numerous groups.[24−26] For instance, Liu et al. reported a systematic investigation of an adenine-linked

Received: August 24, 2011
Revised: April 3, 2012
Published: April 5, 2012

Table 1. Sequence, Length, and Label of Analyzed ssO Species

sequence	length	conjugate ID
HS-$(CH_2)_6$-(T_{10})-**5'**-GGCGACTGTGCAAGCAGA-3'	28mer	ssO28-T10-5'
HS-$(CH_2)_6$-(T_{20})-**5'**-GGCGACTGTGCAAGCAGA-3'	38mer	ssO38-T20-5'
5'-GGCGACTGTGCAAGCAGA-**3'**-(T_{10})-$(CH_2)_3$-SH	28mer	ssO28-T10-3'
5'-GGCGACTGTGCAAGCAGA-**3'**-(T_{20})-$(CH_2)_3$-SH	38mer	ssO38-T20-3'
5'-GGCGACTGTGCAAGCAGA-**3'**-$(CH_2)_3$-SH	18mer	ssO18-3'

aptamer−gold nanoparticle system. Varying the relative position of aptamers to the AuNP by insert of nucleotide spacers, they found the stability and activity of the bioconjugate systems to change drastically, even though all thermodynamic conditions and base pairing interactions were kept constant.[24] There was a linear relationship between the number of adenines and the melting temperature of the aptamer, demonstrating that the spacer length has an intrinsic impact on the temperature stability of the system.

Impact of spacer length was studied recently by Malicki et al. using various alkyl groups between gold nanoparticles and a conjugated chromophore in order to analyze the resulting excited-state dynamics of the dye. They found a propyl spacer imposing a closer dye−dye distance than a dodecyl spacer, thus allowing dye−dye interactions that lead to the formation of a charge-transfer species.[26] The length of alkyl spacer therefore has a profound effect on the ultrafast dynamics of chromophore systems.

In another approach, Walter et al. functionalized gold nanoparticles with aptamers in situ during the ultrashort-pulsed laser technique. Using a specific spacer design consisting of a hexa(ethylene glycol) followed by an oligothymidine (T10) spacer, they were able to ensure the steric condition for the correct aptamer folding in buffer.[25]

However, there is still little known about the impact of ssO strand length on their conjugation efficiency and the attachment mechanisms to laser-generated gold nanoparticle surfaces. Furthermore, oligonucleotides are tethered to surfaces typically via 5′-end linkage, exposing a free hydroxyl group at the 3′ strand end.[27] Although conjugation via 3′-thioliated as well as via 5′-thiolated termini has already been described,[28] a systematic study of the coupling behavior of oppositely orientated oligonucleotides to gold nanoparticles has not yet been performed.

Hybrid nanomarkers may be used in DNA array technology with applications in expression screening, sequencing, and drug discovery. One of the main characteristics of a DNA array is the availability of single-stranded DNA (ssDNA) for hybridization with targets. Thus, knowing the physical structure of ssO on the nanoparticles is essential.[29] Unfortunately, there is no reliable model for predicting the shape and diameter of the random coil form,[30] complicating the determination of ssO conformation on AuNP surface. Unlike double-stranded DNA (dsDNA), ssDNA is more flexible, and reports like the atomic force microscopy measurements from Shlyakhtenko et al.[31] suggested that ssDNA immobilized on a surface exists in a globular, freely jointed, and flexible worm-like chain conformation.[32] However, there are also reports assuming that, because of steric hindrance from nearby molecules, ssDNA may change its conformation from a random coil to more extended forms.[33]

In this context, we investigate the influence of different spacer designs and binding orientations on the in situ attachment of single-stranded oligonucleotides to gold nanoparticles, fabricated by femtosecond-pulsed laser ablation in liquids. Conjugation efficiencies, surface coverages, footprints, and deflection angles of the generated ssO-spacer conjugates are compared to a spacerless model conjugate, in order to determine conjugation mechanisms and ssO conformation and in order to optimize conditions for the stable and reproducible ssO-AuNP attachment.

EXPERIMENTAL PROCEDURES

All chemicals used in the experiments were purchased from Fluka Chemie AG (D-82024 Taufkirchen) and Sigma-Aldrich Chemie GmbH (D-89555 Steinheim).

Five kinds of thiolated, single-stranded oligonucleotides with the same basic sequence were purchased from Eurofins MWG Synthesis GmbH (D-85560 Ebersberg). Four species varied in both spacer insert position at the ssO sequence endings (3′ vs 5′) as well as the spacer length using 10 thymidine (28mer) or 20 thymidine nucleotides (38mer) and were systematically compared to a sequence without nucleotide spacer (18mer) (Table 1). Thymidine was chosen, since this nucleotide has the lowest affinity toward the gold surface[34] and because it was demonstrated by Demers et al. that higher surface coverage values were obtained for gold nanoparticle conjugation using an oligonucleotide with a dT spacer instead of a dA spacer.[35] A gold foil (area 5 × 5 mm^2; thickness 0.1 mm; purity 99.99%) for the nanoparticle fabrication was received from Goodfellow GmbH (D-61213 Bad Nauheim).

The AuNP-ssO conjugates were fabricated by laser ablation in liquid using a femtosecond-pulsed laser system (Spritfire Pro, Newport Spectra-Physics GmbH, D-64291 Darmstadt) which delivers 120 fs laser pulses at a wavelength of 800 nm (maximum pulse energy 400 μJ; beam diameter 4 mm). Ablation parameters (pulse energy 100 μJ; repetition rate 5 kHz) were adopted from our previous study presenting in situ conjugation of ssO to laser-generated AuNP without photodegradation.[16] Nanoparticle fabrication was performed in a 48-well plate, filled with 500 μL double-distilled aqueous solution (ddH_2O) per well. For in situ conjugation, ssO18−3′ solution or spacer-ssO solution of 1 μM, 2.5 μM, or 5 μM concentration was chosen as ablation medium. The laser beam was focused through a 40 mm lens to the gold foil, which was positioned at the bottom of the well, and the target position was set 1 mm below the determined focus point on the target in air. An axis-system (micro FS 150−2, 3D-Micromac AG, D-09126 Chemnitz) was used for well-plate movement at constant speed of 1 mm s^{-1} in a spiral with inner radius of 0.4 mm, outer radius of 1 mm, and line distance of 0.05 mm. Irradiation time was set to 159 s due to previously determined parameters. Ablation in ssO18−3′ solution was performed once in order to validate reproducibility of results from a former, complex study,[16] whereas spacer-ssO conjugation to AuNP was performed in three single runs per spacer design and ssO concentration for statistics.

Zeta-potential and hydrodynamic size measurements of the AuNP and AuNP-ssO colloids were performed by dynamic light scattering with the Zetasizer ZS (Malvern Instruments GmbH, D-71083 Herrenberg). In general, 100 μL of the

dx.doi.org/10.1021/bc200462b | Bioconjugate Chem. 2012, 23, 908−915

solution was added to 900 μL water and the diluted solution was injected into the disposal cuvette. The average value of three consecutive measurements was then taken for documentation.

The optical absorbance of AuNP and AuNP-ssO conjugates was recorded in the spectral range 190−900 nm with a Shimadzu 1650 UV−vis spectrometer (Shimadzu Europa GmbH, D-47269 Duisburg). Concentration of AuNP was estimated by converting the absorbance intensity at 380 nm to concentrations by interpolation from a previously reordered standard calibration (Figure S1, Supporting Information). The relationship between the absorbance intensity at 380 nm and the concentration of the gold nanoparticles was referenced to a report of Muto et al. who found the absorbance intensity at this wavelength to be predominantly contributed by interband transition of AuNP and therefore usable for determining the concentration of the dispersed nanoparticles in solution.[36]

Aggregation level of colloids was described by the ratio of absorbance intensity at 800 nm to the absorbance intensity at 380 nm, demonstrating the amount of aggregated primary particles within a specified particle concentration.

Analyzing the optical properties of spherical AuNP in aqueous solutions, both theoretically and experimentally, for diameters from 3 to 120 nm, Haiss and co-workers set up several calculation formulas for determination of gold nanoparticle diameters.[37] The equations are derived from UV−vis spectra and are based on analytical relations between absorbance efficiency and diameter. With experimentally determined fitting parameters (B1 and B2), the calculation results in an average deviation of 11%. According to the work of other research groups using Haiss calculations,[38] the average Feret diameter of the gold nanoparticles in this study was estimated using eq 1 from Haiss et al., where A_{spr} is the absorbance at the surface plasmon resonance peak, A_{450} represents the absorbance at 450 nm, and the experimentally determined fit parameters are B_1 = 3.00 and B_2 = 2.20. This approach was used since the UV−vis spectra of bioconjugates differ significantly from ligand-free AuNP only in the UV regime; thus, the calculation parameters are not affected by the presence of biomolecules on the AuNP surface.

$$d = \exp\left[B_1 \frac{A_{spr}}{A_{450}} - B_2\right] (\mathrm{nm}) \quad (1)$$

In order to enhance long-term stability of the colloid for further usage and to increase surface loading of oligonucleotides,[39,40] the AuNP-ssO conjugates were transferred into physiological salt solution by adding 100 mM phosphate buffer and 2 M NaCl in successive steps over a three-day period, resulting in a final concentration of 10 mM phosphate buffer and 100 mM NaCl.

After transfer of the colloids into physiological solution, ssO which had not bound to the AuNP were removed by ultracentrifugation of the colloids for 20 min at 14.850 *g* and a second centrifugation step for 30 min at 59.400 *g*. The AuNP-ssO conjugate-containing pellet was resuspended in PBS buffer (10 mM) for further application, while the spare ssO-containing supernatant was taken for absorbance intensity measurement by UV−vis spectroscopy in order to quantify conjugation efficiency and surface coverage values. The absorbance spectra of supernatant for different ssO concentrations are exemplarily shown in Figure 1 for ssO38-T20−5′. Intensities at 260 nm were converted to molar concentrations

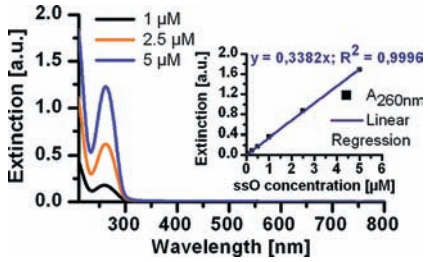

Figure 1. Absorbance spectra of ssO38-T20−5′ supernatants containing unbound ssO: 1 μM ssO concentration, solid line; 2.5 μM ssO concentration, dashed line; 5 μM ssO concentration, dot−dashed line. Absorbance intensities of ssO at 280 nm wavelength were converted into concentrations by interpolation from a previously reordered standard calibration, presented in the inset.

of ssO by interpolation from a previously reordered calibration with known ssO concentrations. The molar concentration of AuNP-bound ssO was determined by subtraction of ssO molar concentration of supernatant from ssO molar concentration prior ablation and conjugation efficiencies were determined on a percentage basis. Finally, the average number of ssO per nanoparticle was obtained by dividing the measured ssO molar concentration of supernatant by the determined nanoparticle concentration. For a comparable overview, the nanoparticle concentration was normalized for all ssO-spacer samples based on the results for ssO18−3′ calculation.

The average area each ssO molecule occupies on the AuNP surface (footprint) and deflection angles between ssO attached to AuNP were calculated based on eqs 2−4 from Hill et al.,[40] assuming the particles are perfect spheres as described in our previous work.[41] Within the equations, *K* represents the ssO footprint in nm^2, *N* is the average number of ssO per AuNP for a given particle radius *r*, *R* represents the radius of footprint approximation on the nanoparticle surface, and deg represents the deflection angle in degrees.

$$K = \left[\frac{4\pi r^2}{N_r}\right]\left(\frac{\mathrm{nm}^2}{n}\right) \quad (2)$$

$$R = \sqrt[2]{\frac{K}{\pi}}\ (\mathrm{nm}) \quad (3)$$

$$\mathrm{deg} = \left[\frac{2R}{r}\right] \times \frac{180}{\pi}(^\circ) \quad (4)$$

RESULTS AND DISCUSSION

Aiming at the study of the in situ conjugation process and adjustment of single-stranded oligonucleotides to laser-generated AuNP, the influence of different oligonucleotide designs with varied spacer lengths of 10 and 20 nucleotides and spacer insert positions at the two ssO sequence endings were investigated and results were compared to spacer-less model conjugates.

Characterization of Laser-Generated AuNP and AuNP−ssO Conjugates. Owing to the deeper understanding of the impact of biomolecule conjugation to AuNP, we characterized laser-generated AuNP and AuNP−ssO conjugates concerning colloidal stability, bioconjugate properties, and nanoparticle size.

The stability of laser-generated, red-colored colloids was determined by zeta-potential analysis (Figure S2, Supporting

Information) as −31 mV for unconjugated AuNP due to electrostatic stabilization of the partially charged particles in solution. In contrast, zeta-potential values of −30 mV to −40 mV were found for all generated conjugates indicating additional electrosteric stability via conjugation with biomolecules that carry a negatively net-charged phosphate backbone. In this context, we found that 38mer ssO38-T20−5′ and ssO38-T20−3′ conjugates with long phosphate backbone feature a higher absolute zeta potential of −33 to −40 mV than 28mer ssO28-T10−5′ and ssO28-T10−3′ conjugates with absolute values of −30 to −35 mV. This effect is assumed to result from an enhanced negative net charge of the conjugates with increasing length of conjugated oligonucleotide sequence and therefore prolonged phosphate backbone.

Bioconjugate properties were investigated by UV−vis spectroscopy of the laser-generated colloids in comparison to unconjugated AuNP. The normalized optical absorbance spectra of unconjugated AuNP and in situ conjugated AuNP−ssO are illustrated in Figure 2.

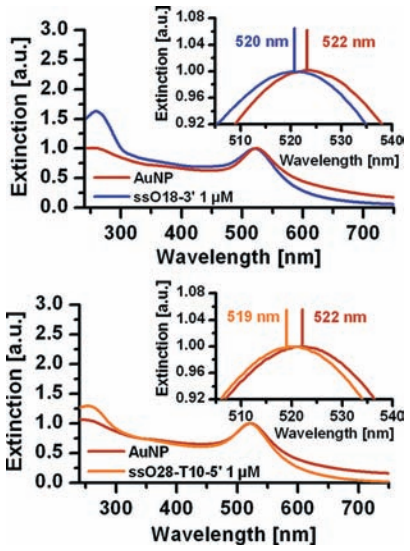

Figure 2. Normalized absorbance spectra of unconjugated gold nanoparticles (solid line) and AuNP conjugated to 1 μM ssO18−3′ (dotted line) and for AuNP conjugated to 1 μM ssO28-T10−5′ (dash−dotted line). Magnifications of plasmon resonance peak maxima are presented in the insets.

All spectra exhibit the characteristic peak of the gold surface plasmon resonance band (SPR) which has a maximum at 522 nm for unconjugated AuNP. The peak maximum of the spacerless model conjugate (ssO18−3′) is shifted to 520 nm indicating a change in size distribution of AuNP toward smaller particles.[42] This effect is due to size quenching of the ablated nanoparticles by coordination of biomolecules during the nanoparticle nucleation and growth process in the colloidal state. In addition, AuNP conjugation with ssO18−3′ lowered the aggregation level significantly from 0.21 for unconjugated AuNP to 0.06, indicating a reduced ratio of primary particles and particle aggregates as a result of the described size quenching effect (Figure S3, Supporting Information).

SPR peak maximum of the conjugates with different spacer designs is found to be centered at 517−520 nm (data exemplarily shown in Figure 2 for ssO28-T10−5′), indicating the formerly described shift toward smaller particles caused by biomolecule coordination. Moreover, the aggregation level is lowered to 0.09 compared to that of unconjugated AuNP (Figure S3, Supporting Information).

In contrast to the unconjugated AuNP spectrum, all AuNP−ssO spectra exhibit the characteristic peak of nucleic acids at 260 nm[43] (Figure 3), indicating the presence of oligonucleotides in the colloid while allowing bioconjugate quantification, since higher absorbance intensities for increasing ssO concentrations have been observed.

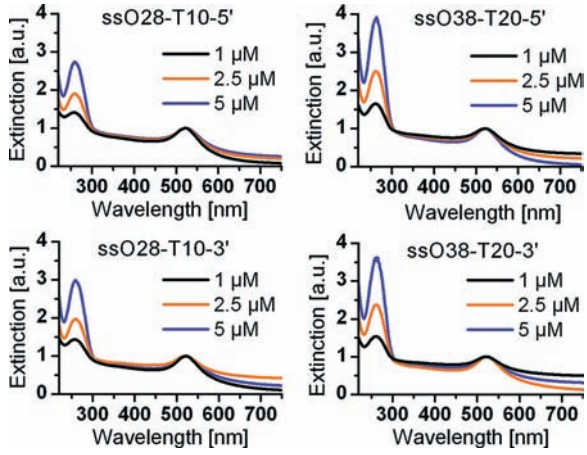

Figure 3. Normalized absorbance spectra of the four AuNP−ssO conjugates with different ssO concentrations of 1 μM (solid line), 2.5 μM (dashed line), and 5 μM (dot−dashed line) displayed by increased absorbance intensity values at 260 nm.

Comparing among the absorbance spectra of single ssO−spacer conjugates, we find all featuring the SPR peak indicating gold nanoparticles. A noticeable difference is observed between the 28mer ssO28-T10−5′ and ssO28-T10−3′ samples and the 38mer ssO38-T20−5′ and ssO38-T10−3′ samples concerning the aggregation level (Figure S4, Supporting Information). In detail, for 28mer conjugates, aggregation level of 2.5 μM samples increases up to four times compared to the 1 μM colloid, indicating an aggregation of primary nanoparticles to bigger clusters. This effect might be a result of reduced electrostatic repulsion between the partially charged AuNP because of a probably higher surface coverage with densely packed ssO for the increased ssO concentration. The reduction of electrostatic repulsion might further be supported by unspecific attraction between the conjugated biomolecules.

We revealed an inverse situation for the 38mer conjugates with an aggregation level up to three times higher for the 1 μM colloids in comparison to 2.5 μM concentrated samples. In this case, electrostatic repulsion between the nanoparticles seems to be enhanced by steric support of the longer and therefore more flexible ssO molecules, which probably cover the AuNP surface in higher number when used in high concentrations. Nevertheless, we found all aggregation levels of the nanoparticle bioconjugates to be smaller than 0.6 and could not observe a visual flocculation of the colloids, still presenting stable solutions as proven previously by high zeta potential values.

The average Feret diameter of primary particles in the colloids was determined by eq 1 (Table S1, Supporting Information). Compared to an average diameter of 15 nm for unconjugated AuNP, the ssO18−3′-conjugated sample was determined to systematically feature nanoparticles of 13 nm in diameter which results in a blue shift of the SPR maximum, according to the size-quenching effect reported earlier.[15,16]

dx.doi.org/10.1021/bc200462b | *Bioconjugate Chem.* 2012, 23, 908−915

In comparison, ssO28-T10−5′- and ssO38-T20−5′-conjugated AuNP with spacer inserts at the 5′-ending were found to exhibit an average diameter of 12 nm, while ssO28-T10−3′- and ssO38-T10−3′-conjugated AuNP with spacer inserts at 3′ end possessed a diameter of 13 nm. Since the difference of 1 nm between the two spacer classes is not significant (average deviation 10%), spacer insert position as well as spacer presence seem to have no impact on the AuNP primary size by coordinative ligands. Furthermore, ssO concentrations above 1 μM appear to have no influence on size quenching, since the mean particle size of three independent measurements does not differ significantly for colloids with 1 μM, 2.5 μM, and 5 μM oligonucleotide concentration (Table S1 in the Supporting Information). This result corresponds to our previous work, showing no increase in average Feret diameter of laser-generated gold nanoparticles after their in situ conjugation to single-stranded oligonucleotides of either 0.1 μM or 5 μM concentration.[23]

In summary, ssO18−3′ and ssO−spacer conjugates may be generated by pulsed laser ablation in liquids, resulting in red-colored, stabilized colloids with high zeta potential. From the study of colloids by UV−vis spectroscopy, all oligonucleotides were found to induce significant reduction of primary particle size by surface coordination during laser ablation, independent of spacer design. Furthermore, stability of the corresponding NP colloids was enhanced, presumably by electrosteric stabilization of AuNP due to biomolecule coordination.

Conjugation Efficiency and Surface Coverage of ssO on AuNP. Conjugation efficiencies of ssO and surface coverages on AuNP were systematically quantified for all conjugate sequences and ssO concentrations in order to reveal the impact of biomolecule composition on the conjugation mechanism and plotted against the ratio of ssO molecules to the number of laser-generated AuNP for a comparable overview (Figure S5 in the Supporting Information).

Each conjugate species was compared to the results of the AuNP-ssO18−3′ spacerless model, which we found to have a conjugation efficiency up to 62% for an ssO:AuNP ratio of 16. Increasing the ssO:AuNP ratio up to 59, we found the conjugation efficiency dropping down exponentially to 28% due to different molecular distributions and limited binding places on the AuNP surface (Figure 4). Additional insight into ssO18−3′ conjugation was already given in a prior study.[23] A similar exponential trend of conjugation is displayed for all ssO−spacer conjugates, while the maximal efficiency is slightly lower, with 30−43% at the ssO:AuNP ratio of 16 and 20% at the ssO:AuNP ratio of 59, respectively (Figure 4). This leads to a lowered conjugation efficiency of 30−50% and therefore reduced conjugation of oligonucleotides if a spacer is introduced into the 18mer sequence.

However, quantitative comparability is limited due to different ssO:AuNP ratios as well as significant standard deviations resulting from the variance of three in situ conjugation runs per ssO concentration and spacer design (Figure S5 in the Supporting Information).

Mean conjugation efficiencies for the shorter 28mer ssO28-T10−5′ and ssO28-T10−3′ seem to exceed conjugation efficiencies of the 38mer ssO38-T20−5′ and ssO38-T10−3′ conjugates by 5−30%. Moreover, mean efficiencies for conjugates with spacer insert at the 3′ end (ssO28-T10−3′ and ssO38-T10−3′) exceed conjugation efficiencies of the spacer insert at the 5′ end (ssO28-T10−5′ and ssO38-T20−5′) by 7−33%. Results illustrate a significant impact of both spacer length and spacer insert position, favoring no spacer or a short spacer type and an insert position at the 3′ ssO sequence ending.

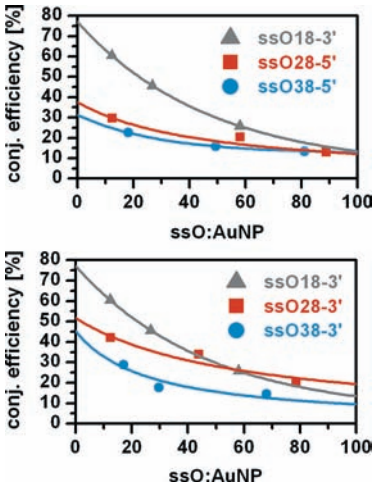

Figure 4. Mean conjugation efficiency values of AuNP−ssO conjugates are exponentially fitted and plotted against the ratio of ssO molecules to the number of laser-generated AuNP in solution. Left panel illustrates difference between 18mer model conjugates and 5′-conjugates while right panel shows data of 18mer model conjugates and 3′-conjugates.

In order to verify these results, surface coverage values of AuNP were determined for a normalized AuNP concentration and illustrated in Figure S6 in the Supporting Information. For the spacerless model conjugate, we observed a logarithmic rise in surface coverage from 7 ssO to up to maximal 15 ssO per nanoparticle with increasing ssO:AuNP ratio from 16 to 59, due to the enhanced concentration of biomolecules in the solution. An increasing trend is also determined for all spacer-containing sequences, although neither linear nor logarithmic relationship could be observed clearly due to high standard deviations of three test runs.

For the ssO−spacer conjugates, surface coverage values of 4 and 6 ssO per AuNP were determined at the ssO:AuNP ratios of 16 and 59, respectively, yielding a lower surface coverage of 30−62% compared to spacerless ssO18−3′ conjugate. These results support our previous assumption regarding a reduced conjugation of spacer-prolonged ssO to AuNP and it also corresponds to findings of Steel et al. who determined surface coverages of a gold substrate as decreased significantly for oligonucleotide strands longer than 24 bases.[33]

Besides, we found the 28mer ssO28-T10−5′ and ssO28-T10−3′ conjugates to exhibit higher mean coverage values of 15−45% than the 38mer ssO38-T20−5′ and ssO38-T10−3′ conjugates, and we discovered conjugates with spacer insert at 3′ ssO sequence ending (ssO28-T10−3′ and ssO38-T10−3′) to feature higher mean coverage values of 5−45% than the conjugates with spacer insert at 5′ ssO sequence ending (ssO28-T10−5′ and ssO38-T20−5′). These results correspond to determined conjugation efficiencies, favoring no spacer or a short spacer type and insert position at the 3′ sequence ending.

Since enthalpy of the conjugation process is determined by thiol function only, we speculate that enhanced values of conjugation efficiency and surface coverage for 3′-conjugates are due to synthesis-dependent production of capped "failure" sequences. When a 3′-modification is used, every subsequent molecule resulting in full-length ssO or capped failure sequence

will contain the modification, as synthesis direction is conventionally completed from 3′ to 5′ end. In contrast, for a 5′-modification only the full-length product is modified, because the modification is added as the last step. Therefore, compared to 5′-ssO a higher amount of 3′-ssO bears thiol function and may attach to AuNP surfaces, resulting in increased conjugation efficiency and surface coverage.

Steric Conformation of ssO on AuNP. Analyzing hydrodynamic diameter, footprint, and deflection angle of ssO on AuNP and taking all these cross-related results into account, we concluded a hypothesis about the steric attachment behavior. For increasing ssO concentration, footprint and deflection angles decreased significantly for all AuNP−ssO conjugate species (Table S2, Supporting Information), whereas hydrodynamic size of conjugates was determined as being constant for 1 μM and 2.5 μM ssO concentration, while increased significantly for 5 μM ssO concentration (Table S3, Supporting Information). In the case of ssO18−3′ conjugates, a reduction of footprint from 75 nm^2 to 26 nm^2 combined with a reduction of deflection angle from 84° to 59° were identified for 1 μM and 5 μM ssO concentrations, respectively, while hydrodynamic size increased from 59 to 69 nm.

From these results, we conclude that for a low ssO to AuNP ratio only a few nucleotides can bind to a single nanoparticle, leaving enough space for nonspecific attraction of amino-containing bases[44] or DNA phosphate backbone,[45,46] which results in the formation of a worm-like structure with high deflection angle. By increasing the ssO to AuNP ratio, a more saturated and tight ssO loading is achieved on the nanoparticle, which omits the wrapping of ssO around the particle surface and hence features decreased deflection angles (Figure 5). A similar conformation behavior was already revealed by Parak et al. studying electrophoretic mobility of AuNP−ssO conjugates within agarose gels for different surface coverages and ssO lengths.[47]

For increased AuNP to ssO ratios, as for 5 μM ssO concentration within our test series, the formation of biomolecule bilayer or clustering behavior of AuNP−ssO conjugates would explain the enhanced hydrodynamic diameter, due to decreased electrostatic repulsion of ssO within the concentrated sample (Figure 5). This conclusion is in good agreement with the descriptions of Zhang et al. who found the strong electrostatic repulsive potential in low-salt solutions to exclude ssO bases from getting close into the Watson−Crick base-pair range, while in contrast, electrostatic and complementary base-pairing interactions took place in high-salt solution only.[32]

For increasing ssO length from 18mer to 38mer, we found significantly increased total values of ssO footprint, deflection angles, and hydrodynamic diameters (Table S2 and Table S3, Supporting Information). In the exemplary case of 28mer ssO28−10T-3′ conjugates, footprint and deflection angle of ssO are increased from 75 nm^2 to 110 nm^2 and from 84° to 101°, respectively, for 1 μM ssO concentration compared to 18mer ssO18−3′ conjugates, while a footprint of even 151 nm^2 and deflection angle of 122° were identified for 38 mer ssO38−20T-3′ conjugates using 1 μM ssO concentration. In addition, hydrodynamic diameter was increased significantly from 59 nm (ssO18−3′) to 74 nm (ssO28−10T-3′) and 84 nm (ssO38−20T-3′), respectively.

We assume from these results that, with increasing ssO length from 18 to 38 nucleotides, the steric dimensions of the conjugated oligonucleotides increase, resulting from the

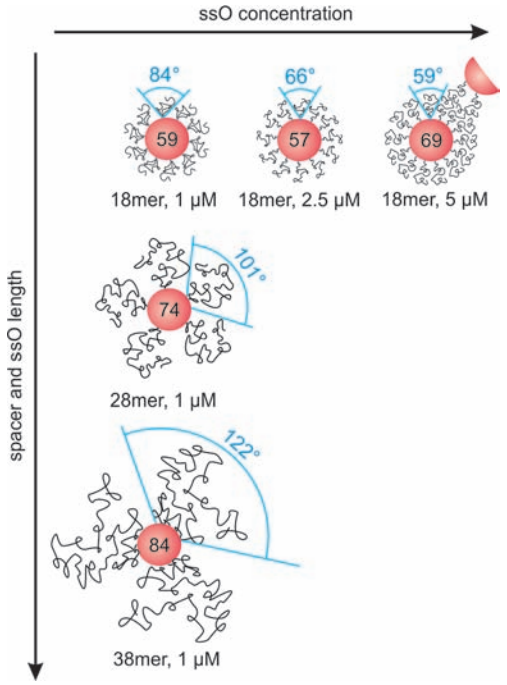

Figure 5. Schematic illustration of the impact of spacer length on ssO conjugation to laser-generated AuNP. First raw: scenario (I) − "stretched" conformation of 18mer, spacer-less model conjugates (AuNP-ssO18−3′). From left to right: increasing surface coverage and decreasing deflection angle corresponding to ssO concentration from 1 μM to 5 μM. Second raw: scenario (II) − increased steric dimension and hairpin-coiling of 28mer ssO−spacer conjugates (AuNP-ssO28-T10−5′, AuNP-ssO28-T10−3′). Third raw: scenario (III) − 38mer ssO−spacer conjugates (AuNP-ssO38-T20−5′, AuNP-ssO38-T10−3′) wrapping the AuNP surface as flexible, coil-like polymer chains due to unspecific adsorption. Hydrodynamic diameters of conjugates in nanometers are written into the nanoparticles, diameters of AuNP core are almost invariant (12−14 nm, Table S1).

enhanced flexibility of the elongated ligand. This theory is in good agreement with results of Steel et al.[33] who found less ordered arrangement of a long oligonucleotide chain on a planar gold surface compared to shorter ssO chains. These findings presumably reflect increasingly polymeric behavior as the effect of a single thiol group on ssO attachment becomes less significant when compared to the large number of adsorptive nucleotide− and phosphate backbone−gold interactions that arise between each ssO and the gold surface.

On the basis of these arguments, we conclude three scenarios for ssO−AuNP conjugation of different sequence lengths, illustrated in Figure 5:

(I) Short 18mer oligonucleotides are aligned in a mostly stretched configuration pointing perpendicular to the gold nanoparticle surface, while the occupied surface area is a function of ssO concentration and number of adsorptive nucleotide− and phosphate backbone−gold interactions. This confirmation facilitates densely packed ssO ligands on the AuNP, resulting in high surface coverage values.

(II) The higher flexibility of 28mer spacer-prolonged sequence increases the steric dimension of the ligand by random hairpin-coiling. Thus, the conjugated ssO number on the AuNP surface decreases due to a reduced density.

dx.doi.org/10.1021/bc200462b | Bioconjugate Chem. 2012, 23, 908−915

(III) The flexibility increase of 38mer spacer-prolonged ssO sequence enables the ssO to wrap around the gold nanoparticle surface resulting in a polymer-like coiled formation and reduced surface area for single ssO to coordinate to. We presume that flexibility of the increased ssO chain and therefore enhanced coiling and steric hindrance of ligands limit the ssO surface coverage on the AuNP surface. Consequently, increasing ssO length results in an exponential decrease in conjugation efficiency and surface coverages compared to the spacer-less model conjugate.

In summary, we found all ssO spacerless conjugates exhibiting 50% increased conjugation efficiency and surface coverage compared to the spacer−ssO conjugates, indicating short nucleotide sequences to be favored for efficient gold nanoparticle conjugation. On the basis of this overall clear trend, we assume that the reduced values for oligonucleotide−spacer sequences are due to an increased steric dimension of spacer-prolonged ssO by coiling effects and therefore enhanced captured area on the gold nanoparticles, which might enable them to wind around the nanoparticle core while blocking potential binding places for further ligands and featuring higher deflection angles.

■ ASSOCIATED CONTENT

Supporting Information

Additional figures and tables, covering a standard calibration curve on gold nanoparticle concentration and data on zeta-potential and aggregation level of conjugates, conjugation efficiency, and surface coverage raw data of gold nanoparticles with single-stranded oligonucleotides, Feret diameter, and hydrodynamic diameter of unconjugated nanoparticles and conjugates, as well as footprint and deflection angle of oligonucleotides. This material is available free of charge via the Internet at http://pubs.acs.org.

■ AUTHOR INFORMATION

Corresponding Author

*C.L.S.: E-mail l.sajti@lzh.de, Phone +49-511-2788-149, Fax +49-511-2788-100. S.B.: E-mail stephan.barcikowski@uni-due.de.

Author Contributions

#Both authors contributed equally.

Notes

The authors declare no competing financial interest.

■ ACKNOWLEDGMENTS

This work was funded by the German Research Foundation (DFG) within the excellence cluster REBIRTH. The authors thank Prof. C. Urbanke, PD U. Curth, and Frank Hartmann (Medizinische Hochschule Hannover) for the use of the ultracentrifugation facilities.

■ REFERENCES

(1) Lewinski, N., Colvin, V., and Drezek, R. (2008) Cytotoxicity of nanoparticles. *Small 4*, 26−49.

(2) El-Sayed, I. H., Huang, X., and El-Sayed, M. A. (2005) Surface plasmon resonance scattering and absorption of anti-EGFR antibody conjugated gold nanoparticles in cancer diagnostics: applications in oral cancer. *Nano Lett. 5*, 829−834.

(3) Jain, P. K., El-Sayed, I. H., and El-Sayed, M. A. (2007) Au nanoparticles target cancer. *Nano Today 2*, 18−29.

(4) Mirkin, C. A., Letsinger, R. L., Mucic, R. C., and Storhoff, J. J. (1996) A DNA-based method for rationally assembling nanoparticles into macroscopic materials. *Nature 382*, 607−609.

(5) Fischler, M., and Simon, U. J. (2009) Metal nanoparticle−DNA hybrids − from assembly towards functional conjugates. *J. Mater. Chem. 19*, 1518−1523.

(6) Sato, K., Hosokawa, K., and Maeda, M. (2003) Rapid aggregation of gold nanoparticles induced by non-cross-linking DNA hybridization. *J. Am. Chem. Soc. 125*, 8102−8103.

(7) Zhou, X. C., O'Shea, S. J., and Li, S. F. Y. (2000) Amplified microgravimetric gene sensor using Au nanoparticle modified oligonucleotides. *Chem. Commun. 11*, 953−954.

(8) Taton, T. A., Mirkin, C. A., and Letsinger, R. L. (2000) Scanometric DNA array detection with nanoparticle probes. *Science 289*, 1757−1760.

(9) Zheng, G. F., Daniel, W. L., and Mirkin, C. A. (2008) A new approach to amplified telomerase detection with polyvalent oligonucleotide nanoparticle conjugates. *J. Am. Chem. Soc. 130*, 9644−9645.

(10) Brust, M., Walker, M., Bethell, D., Schiffrin, D. J., and Whyman, R. (1994) Synthesis of thiol derivatised gold nanoparticles in a two-phase liquid-liquid system. *J. Chem. Soc., Chem. Commun. 801*, 801−802.

(11) Turkevich, J., Stevenson, P. C., and Hillier, J. (1951) A study of the nucleation and growth processes in the synthesis of colloidal gold. *Discuss. Faraday Soc. 11*, 55−75.

(12) Kabashin, A. V., Meunier, M., Kingston, C., and Luong, J. H. T. (2003) Fabrication and characterization of gold nanoparticles by femtosecond laser ablation in an aqueous solution of cyclodextrins. *J. Phys. Chem. B 107*, 4527−4531.

(13) Sylvestre, J.-P., Poulin, S., Kabashin, A. V., Sacher, E., Meunier, M., and Luong, J. H. T. (2004) Surface chemistry of gold nanoparticles produced by laser ablation in aqueous media. *J. Phys. Chem. B 108*, 16864−16869.

(14) Barcikowski, S., Hahn, A., Kabashin, A. V., and Chichkov, B. N. (2007) Properties of nanoparticles generated during femtosecond laser machining in air and water. *Appl. Phys. A: Mater. Sci. Process. 87*, 47−55.

(15) Amendola, V., and Meneghetti, M. (2007) Controlled size manipulation of free gold nanoparticles by laser irradiation. *J. Mater. Chem. 17*, 4705−4710.

(16) Petersen, S., and Barcikowski, S. (2009) In-situ bioconjugation - single step approach to tailored nanoparticle-bioconjugates by ultrashort pulsed laser ablation. *Adv. Funct. Mater. 19*, 1167−1172.

(17) Berry, C. C., La Fuente, J. M., Mullin, M., Chu, S. W. L., and Curtis, A. S. G. (2007) Nuclear localization of HIV-1 Tat functionalized gold nanoparticles. *IEEE Trans. Nanobiosci. 6*, 262−269.

(18) Huang, Y.-F., Lin, Y.-W., Lin, Z.-H., and Chang, H.-T. (2009) Aptamer-modified gold nanoparticles for targeting breast cancer through light scattering. *J. Nanopart. Res. 11*, 775−783.

(19) Dougan, J. A., Karlsson, C., Smith, W. E., and Graham, D. (2007) Enhanced oligonucleotide−nanoparticle conjugate stability using thioctic acid modified oligonucleotides. *Nucleic Acid Res. 35*, 3668.

(20) Takeda, Y., Kondow, T., and Mafuné, F. (2006) Degradation of protein in nanoplasma generated around gold nanoparticles in solution by laser irradiation. *J. Phys. Chem. B 110*, 2393−2397.

(21) Besner, S., Kabashin, A. V., Winnik, F. M., and Meunier, M. (2009) Synthesis of size-tunable polymer-protected gold nanoparticles by femtosecond laser-based ablation and seed growth. *J. Phys. Chem. C 113*, 9526−9531.

(22) Petersen, S., Soller, J. T., Wagner, S., Richter, A., Bullerdiek, J., Nolte, I., Barcikowski, S., and Escobar, H. M. (2009) Co-transfection of plasmid DNA and laser-generated gold nanoparticles does not disturb the bioactivity of GFP-HMGB I fusion protein. *J. Nanobiotechnol. 7*, 6.

(23) Petersen, S., and Barcikowski, S. (2009) Conjugation efficiency of laser-based bioconjugation of gold nanoparticles with nucleic acids. *J. Phys. Chem. C 113*, 19830−19835.

(24) Liu, J., and Lu, Y. (2007) Non-base pairing DNA provides a new dimension for controlling aptamer-linked nanoparticles and sensors. *J. Am. Chem. Soc. 129*, 8634−8643.
(25) Walter, J., Petersen, S., Stahl, F., Scheper, T., and Barcikowski, S. (2010) Laser ablation-based one-step generation and bio-functionalization of gold nanoparticles conjugated with aptamers. *J. Nanobiotechnol. 8*, 21 DOI: DOI: 10.1186/1477-3155-8-21.
(26) Malicki, M., Hales, J. M., Rumi, M., Barlow, S., McClary, L., Marder, S. R., and Perry, J. W. (2010) Excited-state dynamics and dye-dye interactions in dye-coated gold nanoparticles with varying alkyl spacer lengths. *Phys. Chem. Chem. Phys. 12*, 6267−6277.
(27) Hacia, J. G. (1999) Resequencing and mutational analysis using oligonucleotide microarrays. *Nat. Genet. 21*, 42−47.
(28) Liu, J., and Lu, Y. (2004) Adenosine-dependent assembly of aptazyme-functionalized gold nanoparticles and its application as a colorimetric biosensor. *Anal. Chem. 76*, 1627−1632.
(29) Moiseev, L., Ünlü, M. S., Swan, A. K., Goldberg, B. B., and Cantor, C. R. (2006) DNA conformation on surfaces measured by fluorescence self-interference. *Proc. Natl. Acad. Sci. U.S.A. 103*, 2623−2628.
(30) Murphy, M. C., Rasnik, I., Cheng, W., Lohman, T. M., and Ha, T. (2004) Probing single-stranded DNA conformational flexibility using fluorescence spectroscopy. *Biophys. J. 86*, 2530−2537.
(31) Shlyakhtenko, L. S., Gall, A. A., Weimer, J. J., Hawn, D. D., and Lyubchenko, Y. L. (1999) Atomic force microscopy imaging of DNA covalently immobilized on a functionalized mica substrate. *Biophys. J. 77*, 568−576.
(32) Zhang, Y., Zhou, H., and Ou-Yang, Z.-C. (2001) Stretching single-stranded DNA: interplay of electrostatic, base-pairing, and base-pair stacking interactions. *Biophys. J. 81*, 1133−1143.
(33) Steel, A. B., Levicky, R. L., Herne, T. M., and Tarlov, M. J. (2000) Immobilization of nucleic acids at solid surfaces - effect of oligonucleotide length on layer assembly. *Biophys. J. 79*, 975−981.
(34) Kimura-Suda, H., Petrovykh, D. Y., Tarlov, M. J., and Whitman, L. J. J. (2003) Base-dependent competitive adsorption of single-stranded DNA on gold. *J. Am. Chem. Soc. 125*, 9014−9015.
(35) Demers, L. M., Mirkin, C. A., Mucic, R. C., Reynolds, R. A., III, Letsinger, R. L., Elghanian, R., and Viswanadham, G. (2000) A fluorescence-based method for determining the surface coverage and hybridization efficiency of thiol-capped oligonucleotides bound to gold thin films and nanoparticles. *Anal. Chem. 72*, 5535−5541.
(36) Muto, H., Yamada, K., Miyajima, K., and Mafune, F. J. (2007) Estimation of surface oxide on surfactant-free gold nanoparticles laser-ablated in water. *J. Phys. Chem. C 111*, 17221−17226.
(37) Haiss, W., Thanh, N. T. K., Aveyard, J., and Fernig, D. G. (2007) Determination of size and concentration of gold nanoparticles from UV-Vis spectra. *Anal. Chem. 79*, 4215−4221.
(38) Uppal, M. A., Kafizas, A., Lim, T. H., and Parkin, I. P. (2010) The extended time evolution size decrease of gold nanoparticles formed by the Turkevich method. *New J. Chem. 34*, 1401−1407.
(39) Hurst, S. J., Lytton-Jean, A. K. R., and Mirkin, C. A. (2006) Maximizing DNA loading on a range of gold nanoparticle sizes. *Anal. Chem. 78*, 8313−8318.
(40) Hill, H. D., Millstone, J. E., Banholzer, M. J., and Mirkin, C. A. (2009) The role radius of curvature plays in thiolated oligonucleotide loading on gold nanoparticles. *ACS Nano 3*, 418−424.
(41) Barchanski, A., Sajti, C. L., Sehring, C., Petersen, S., and Barcikowski, S. (2011) Design of bi-functional bioconjugated gold nanoparticles by pulsed laser ablation with minimized degradation. *J. Laser- & Micro/Nanoeng. 6*, 124−130.
(42) Peng, S., McMahon, J. M., Schatz, G. C., Gray, S. K., and Sun, Y. P. (2010) Reversing the size-dependence of surface plasmon resonances. *Proc. Natl. Acad. Sci. U.S.A. 107*, 14530−14534.
(43) Doshi, R., Day, P. J. R., Carampin, P., Blanch, E., Stratford, I. J., and Tirelli, N. (2010) Spectrophotometric analysis of nucleic acids oxygenation-dependant hyperchromism of DNA. *Anal. Bioanal. Chem. 396*, 2331−2339.
(44) Herne, T. M., and Tarlov, M. J. (1997) Characterization of DNA probes immobilized on gold surfaces. *J. Am. Chem. Soc. 119*, 8916−8920.
(45) Levicky, R., Herne, T. M., Tarlov, M. J., and Satija, S. K. (1998) Using self-assembly to control the structure of DNA monolayers on gold: a neutron reflectivity study. *J. Am. Chem. Soc. 120*, 9787−9792.
(46) Park, S., Brown, K. A., and Hamad-Schifferli, K. (2004) Changes in oligonucleotide conformation on nanoparticle surfaces by modification with mercaptohexanol. *Nano Lett. 4*, 1925−1929.
(47) Parak, W. J., Pellegrino, T., Micheel, C. M., Gerion, D., Wiliams, S. C., and Alivisatos, A. P. (2003) Conformation of oligonucleotides attached to gold nanocrystals probed by gel electrophoresis. *Nano Lett. 3*, 33−36.

Bioconjugate Chemistry

Article

pubs.acs.org/bc

Synthesis and Assembly of Conjugates Bearing Specific Numbers of DNA Strands per Gold Nanoparticle

Natalia Borovok,[†] Elad Gillon,[†,‡] and Alexander Kotlyar*[,†,‡]

[†]Department of Biochemistry, George S. Wise Faculty of Life Sciences and [‡]The Center of Nanoscience and Nanotechnology, Tel-Aviv University, Ramat Aviv 69978, Israel

ABSTRACT: Here, we present a relatively simple, efficient, and high-yielding polymerase-based method for the synthesis of 15 nm gold nanoparticle conjugates bearing a specific number of 25 base oligonucleotide strands. We have shown that the conjugates bearing one or two oligonucleotide strands per particle, with the conjugates comprising a single complementary strand, self-assemble into nanoparticle dimers and trimers, respectively. Incubation of fully coated AuNPs, containing tens of oligonucleotide strands, with a conjugate bearing a single complementary strand leads to the formation of flower-shaped structures. The assembly of particles into nanoparticle structures shown here is a prerequisite for more complex controlled assembly of particles into three-dimensional macrostructures.

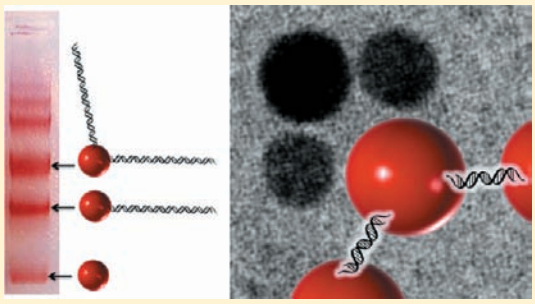

INTRODUCTION

Conjugates of various metal nanoparticles including gold nanoparticles (AuNPs) with DNA[1−4] and other biomaterials exhibit unique optical properties and have been used as bases for development of various applications in nanobiotechnology,[5] nanomedicine,[6−9] material science,[10,11] and nanoelectronics.[10−13] The ability of nucleic acids to self-assemble into well-defined supramolecular architectures offers a variety of possibilities for the design and production of novel two- and three-dimensionally organized DNA-based nanostructures.[14,15] The use of DNA−nanoparticle conjugates bearing specific numbers of DNA strands as a starting material is of particular importance for the creation of novel nanomaterials.

Alivisatos and colleagues demonstrated that binding of single-stranded oligonucleotides produces a significant effect on particle mobility in an electric field and succeeded in separating conjugates bearing different numbers of oligonucleotide strands per particle by electrophoresis.[16,17] Increasing the particle size and decreasing the DNA length, however, substantially reduce the separation efficiency. Good separation of the conjugates can be achieved only for relatively small particles (2−10 nm) bearing relatively long (50−100 bases) sequences. Separation of conjugates of bigger AuNPs (diameter more than 10 nm) with relatively short (less than 50 bases) single- or double-stranded DNA molecules is very challenging. To overcome this separation problem and to produce stable DNA−nanoparticle conjugates, several enzyme-based methods have been recently employed.[18−23] The polymerase-based approach was used to synthesize long double-stranded DNA, containing a thiol-group at the end of the polymer.[23] The conjugates of the synthesized thiolated DNA with nanoparticles bearing a different number of nucleic acid molecules per particle have been efficiently separated from each other by electrophoresis.

The ligase-based method was also used to covalently join the ends of DNA molecules and thus produce a stable connection between the particles in DNA−nanoparticle conjugates.[18,21] Another enzyme, the restriction endonuclease, was shown to disassemble the DNA−nanoparticle structures by cleaving the double-stranded DNA connections between particles.[19]

In this work, we present a novel polymerase-based method for the synthesis of AuNP−DNA conjugates bearing a specific number of oligonucleotide strands. We have demonstrated that the conjugates bearing complementary strands self-assemble into uniform multiparticle structures. The optical properties and the molecular morphology of individual AuNP−DNA conjugates and complexes between them were elucidated by AFM and TEM analysis.

EXPERIMENTAL PROCEDURES

Unless otherwise stated, reagents and chemicals were obtained from Sigma-Aldrich (USA) and were used without further purification. Klenow fragment exonuclease minus of DNA polymerase I from *E. coli* lacking the 3′-, 5′-exonuclease activity (Klenow exo$^-$) was purchased from Epicenter Biotechnologies (USA).

DNA Samples. All DNA samples were purchased from Alpha DNA (Montreal, Canada). The following sequences were used in this study: 1, 5′-$a_{10}A_5$-3′ oligonucleotide comprising 10 phosphorothioated adenine nucleotides (a_{10}) and 5 regular ones (A_5); 2, 5′-GCTGACTATCCATCCTT-CATCCTTGaaaaaaaaaa-3′ (R1-a_{10}), containing a 25 base random sequence (R1) and 10 phosphorothioated adenine

Received: September 5, 2011
Revised: April 8, 2012
Published: April 20, 2012

nucleotides; 3, 5′-CAAGGATGAAGGATGGATAGTCAG-Caaaaaaaaaa-3′ (R2-a_{10}), containing a 25 base random sequence (R2) complementary to R1 (see above) and 10 phosphorothioated adenine nucleotides; 4, 5′-GCTGACTATC-CATCCTTCATCCTTG-A_{15}-3′ (R1-A_{15}), containing a 25 base random sequence (R1) and 15 regular adenine nucleotides; 5, 5′-CAAGGATGAAGGATGGATAGTCAGC-A_{15}-3′ (R2-A_{15}), containing a 25 base random sequence (R2) and 15 regular adenine nucleotides; 6, 15 base deoxythymidine oligonucleotide $(dT)_{15}$. The oligonucleotides (~1 mg) were dissolved in ~200 μL of double-distilled water and subsequently passed through a prepacked Sephadex G-25 DNA-grade column (Amersham Biosciences) equilibrated with 2 mM Tris-Ac, pH 8.5. The oligonucleotide, eluted in the void volume, was collected in 0.4−0.5 mL and purified by ion-exchange HPLC to homogeneity as described in our previous studies.[24] Concentrations of the oligonucleotides were calculated using extinction coefficients at 260 nm of 356, 407, 475, 424, 140, and 122 mM^{-1} cm^{-1} for R1-a_{10}, R2-a_{10}, R2-A_{15}, R1-A_{15}, $a_{10}A_5$, and $(dT)_{15}$, respectively.

DNA Synthesis Reaction. Syntheses of long (hundreds of base pairs) double-stranded poly(dA)-poly(dT) homopolymers, containing either R1 or R2 sequence at 5′-end of the poly(dA) strand, 5′-R1-poly(dA)-poly(dT), and 5′-R2-poly-(dA)-poly(dT), respectively, was performed as previously described.[24,25] A standard reaction mixture contained the following: 60 mM KPi, pH 6.5, 5 mM $MgCl_2$, 5 mM DTT, 1.5 mM dATP, 1.5 mM dTTP, 0.2 μM Klenow exo$^-$, and HPLC purified template-primers, 5′-R1-$(dA)_{15}$-$(dT)_{15}$ or 5′-R2-$(dA)_{15}$-$(dT)_{15}$. The enzymatic extension of a 15-base-pair double-stranded fragment of the template-primer was conducted for 2 h at 37 °C. The reaction was halted by the addition of EDTA to a final concentration of 20 mM.

HPLC Purifications. The separation of synthesized DNA molecules from nucleotides and other reaction components was achieved with a TSK-gel G-5000-PW HPLC column (7.8 × 300 mm) from TosoHaas (Japan) by isocratic elution with 20 mM Tris-Ac, pH 7.5, in the presence of 0.1 M NaCl for 30 min at a flow rate of 0.5 mL/min. HPLC purification of the oligonucleotides and the synthesized DNA was conducted on a Finnigan Surveyor LC (Thermo Electron Corporation, USA) HPLC system with a photodiode array detector. Peaks were identified from their retention times obtained from the absorbance at 260 nm for DNA. Eluted products were concentrated by Amicon Ultra-30K-50K MWCO filter devices (Millipore, USA). The length of synthesized molecules was determined by 1.5% agarose gel electrophoresis.

Electrophoresis. The DNA or DNA-nanoparticle samples were loaded onto 1.5% agarose gel 7 × 7 cm, and electrophoresed at 130 V for 40 min in an ice bath. TAE buffer, in addition to being used to prepare the agarose, also served as the running buffer.

AuNPs. Spherical gold nanoparticles with a diameter of 15 nm were prepared by $HAuCl_4$ reduction in the presence of citric acid essentially as described.[26] The resulting nanoparticles were screened for their size and uniformity by TEM, revealing an average diameter of 15 ± 2 nm. The UV−vis spectra showed a characteristic absorption peak at 520 nm. The particles were coated with $a_{10}A_5$ (or in a few cases with R1-a_{10} or R2-a_{10}) as follows. The particles with absorption of approximately 30 at 520 nm were incubated with 20 μM $a_{10}A_5$ in the presence of 10 mM NaPi buffer, pH 7.5, for 30 min at 50 °C. The buffer concentration was increased stepwise from 10 to 50 mM. Each time, 10 mM of NaPi was added and the sample was incubated for 30 min at 50 °C. The particles were purified from the excess oligonucleotides and from a minor fraction of multiparticle structures formed during the incubation by size-exclusion chromatography as follows. The sample was loaded onto a Sepharose CL-6B 1.6 × 40 cm column equilibrated with 10 mM NaPi buffer, pH 7.5, at a flow rate of 0.5 mL/min. The particles were eluted in approximately half the column volume and were completely separated from the excess of nonbound $a_{10}A_5$ oligonucleotides. The particles were collected and concentrated by centrifugation at 10 000 rpm for 20 min on an Eppendorf Table 5424 centrifuge (Eppendorf, Germany). Concentration of the particles was calculated using an extinction coefficient of 7.4×10^8 M^{-1} cm^{-1} at 520 nm.[27,28]

TEM Measurements. TEM images were acquired by using carbon-coated grids (400 mesh). 2.5 μL of a sample in 40 mM Tris-Ac, pH 7.8, was dropped onto a grid surface. After incubation for 5 min at ambient temperature, the excess solution was removed by blotting with a filter paper. TEM imaging was performed on a TEM (JEM model 1200 EX instrument) operated at an accelerating voltage of 120 kV. The TEM analysis showed that the particles are uniform and spherical with diameters of 15 ± 2 nm.

Atomic Force Microscopy. AFM was performed on the molecules adsorbed onto muscovite mica surfaces. A 20 μL aliquot of 1.0−2.0 nM AuNP−DNA solution, containing 2.0 mM $MgCl_2$ and 25 mM NaCl, were deposited on freshly cleaved 1 cm^2 mica plates for 5 min. The surface was then washed with distilled water and dried by nitrogen blow. AFM imaging was performed on a Solver PRO AFM system (NT-MDT, Russia), in semicontact (tapping) mode, using 130 μm Si-gold-coated cantilevers (NT-MDT, Russia) with resonance frequency of 119−180 kHz. The images were "flattened" (each line of the image was fitted to a second-order polynomial, and the polynomial was then subtracted from the image line) by the *Nova* image processing software (NT-MDT, Russia). The images were analyzed and visualized using a Nanotec Electronica S.L (Madrid) *WSxM* imaging software.[29]

Absorption Spectroscopy. Absorption spectra were recorded with a Jasco V-630 spectrophotometer (Japan).

RESULTS

The procedure of AuNP−DNA conjugate production (see Scheme 1) includes the following steps:

1. Synthesis of the DNA Polymer. The DNA polymer, 5′-R1-poly(dA)-poly(dT), contains a 0.8 Kbp poly(dA)-poly(dT) and 25 base overhang fragment, R1 at the 5′-end of the poly(dA) strand (see stage 1 of Scheme 1). The molecules were synthesized using a polymerase-based method that we recently invented.[24,25] This enzymatic method enables extension of short (tens of base pairs) blunt-ended double-stranded template primers into long (varying from several nanometers to several micrometers) uniform double-stranded homopolymers, poly(dA)-poly(dT) or poly(dG)-poly(dC), functionalized with oligonucleotide sequences or (and) other moieties at one or both ends of the DNA. 5′-R1-poly(dA)-poly(dT) was synthesized and purified by HPLC as described in the Experimental Procedures section.

2. Annealing of the Overhang End Fragment. The overhang end fragment, R1 of the synthesized polymer was annealed with the complementary sequence flanked by 10 phosphorothioated adenosine residues at its 3′ ends, R2-a_{10} (see stage 2 of Scheme 1). The synthesized polymer, 5′-R1-

dx.doi.org/10.1021/bc200485r | *Bioconjugate Chem.* 2012, 23, 916−922

Scheme 1. AuNP−Oligonicleotide Conjugate Preparation

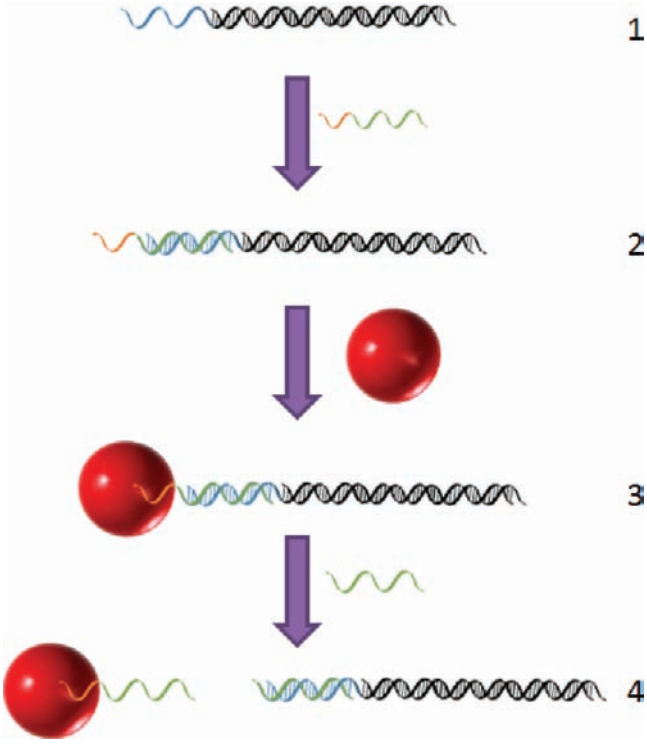

1: Synthesis of a 0.8 Kbp R1-poly(dA)-poly(dT), a double-stranded DNA polymer, containing a 25 base random overhang fragment sequence (R1, shown in blue) at the 5′-end of the poly(dA)-strand. 2: Hybridization of R2-oligonucleotide (shown in green), comprising 10 phosphorothioated adenine bases (shown in orange) at the 3′-end of the sequence, with R1-poly(dA)-poly(dT). 3: Formation of a complex between a_{10}-R2-R1-poly(dA)-poly(dT) and AuNPs. 4: Separation of R1-poly(dA)-poly(dT) from AuNP-a_{10}-R2 by heat treatment in the presence of R2.

poly(dA)-poly(dT), was mixed with 10-fold molar excess of R2-a_{10} and incubated for 0.5 h at room temperature in 20 mM Tris-Ac buffer, pH 7.5, in the presence of 0.1 M NaCl. The excess of nonbound R2-a_{10} was removed by size-exclusion HPLC as described in the Experimental Procedures. The eluted product, a_{10}-R2-R1-poly(dA)-poly(dT), was collected and concentrated by ultrafiltration (see Experimental Procedures) .

3. Synthesis of AuNP−DNA Conjugates. A a_{10}-R2-R1-poly(dA)-poly(dT) polymer prepared as shown above was incubated with AuNPs in 20 mM Tris-Ac buffer, pH 7.5, in the presence of 0.1 M NaCl, for 48 h at 42 °C (see stage 3 of Scheme 1). The incubation yielded a mixture of AuNP−DNA conjugates bearing different numbers of DNA molecules per particle. In contrast to nanoparticles conjugated with short oligonucleotides, the mobility of the AuNP conjugates comprising long (hundreds and thousands of base pairs) DNA is governed by the nucleic acid content. The latter conjugates, bearing different numbers of DNA molecules, can, therefore, be completely and efficiently separated from each other by electrophoresis. Electrophoresis of the conjugate mixture in a 1.5% agarose gel is shown in Figure 1. The red-colored bands in the gel (see Figure 1) correspond to the conjugates bearing distinct number of a_{10}-R2-R1-poly(dA)-poly(dT) molecules per AuNP. As seen in the figure (lanes 2−4), the relative amounts of conjugates comprising different numbers of DNA molecules depend on the ratio between the

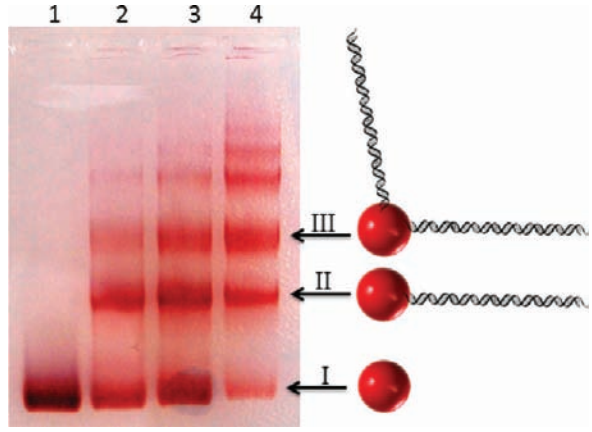

Figure 1. Electrophoretic separation of AuNP-a_{10}-R2-R1-poly(dA)-poly(dT) conjugates. Lane 1: 0.1 μM AuNPs were incubated with 0.1 (lane 2), 0.2 (lane 3), and 0.4 (lane 4) μM of 0.8 Kbp a_{10}-R2-R1-poly(dA)-poly(dT) for 72 h at 42 °C in 10 mM NaPi buffer, pH 7.5, containing 0.1 M NaCl. Electrophoresis was conducted on 1.5% agarose gel (7 × 7 cm^2) in TEA buffer at 130 V for 40 min in an ice bath.

DNA and the particles in the incubation. At 1 to 1 ratio, the major (most intensive) band corresponds to the conjugate containing one DNA molecule (Figure 1, lane 2); at higher ratios, the relative amounts of conjugates bearing 2, 3, and even larger numbers of DNA molecules are increased (compare lanes 2 and 4). In this study, we were mainly focused on the conjugates bearing one and two DNA molecules per particle. These conjugates were prepared by the incubation of AuNP with DNA at 1 to 2 molar ratio (see Figure 1, lane 3). The gel areas corresponding to mono- and bimolecular conjugates, bearing one and two DNA molecules per particle (two red bands indicated by arrows II and III in Figure 1), were cut out of the gel with a razor blade. Each of the colored gel slices was placed in a dialysis bag containing TAE buffer, and the compounds were electroeluted from gel. The molecular morphology of the conjugates was elucidated by AFM. The molecules were deposited onto freshly cleaved muscovite mica and imaged by AFM in a noncontact mode as described in Experimental Procedures. As seen in Figure 2, the vast majority of conjugates extracted from bands II and III (see Figure 1) are composed of 1 and 2 DNA molecules connected to a nanoparticle, respectively. The average estimated contour length of DNA molecules connected to the particles is equal to 250 ± 10 nm. This value corresponds well with the contour length of 0.8 Kbp poly(dA)-poly(dT) molecules.[25]

4. Removing R1-poly(dA)-poly(dT) from AuNP-a_{10}-R2-R1-poly(dA)-poly(dT). R1-poly(dA)-poly(dT) was separated from AuNP-a_{10}-R2 during incubation of AuNP-a_{10}-R2-R1-poly(dA)-poly(dT) with 100-molar excess of R2 oligonucleotides for 10 min at 70 °C in the presence of 50 mM NaCl. This treatment results in a complete dissociation of the double-stranded DNA fragment from the nanoparticle. The sample was then centrifuged at 12 000 rpm for 30 min, and the supernatant containing R1-poly(dA)-poly(dT) was discarded. The pellet containing a_{10}-R2-AuNP was resuspended and analyzed by electrophoresis. As seen in Figure 3, the band corresponding to the conjugate moves in the gel similarly to that of nonmodified AuNP (compare lanes 1 and 3, Figure 3). This clearly shows that the treatment results in dissociation of the DNA polymer from the particle. In order to confirm that a short

dx.doi.org/10.1021/bc200485r | *Bioconjugate Chem.* 2012, 23, 916−922

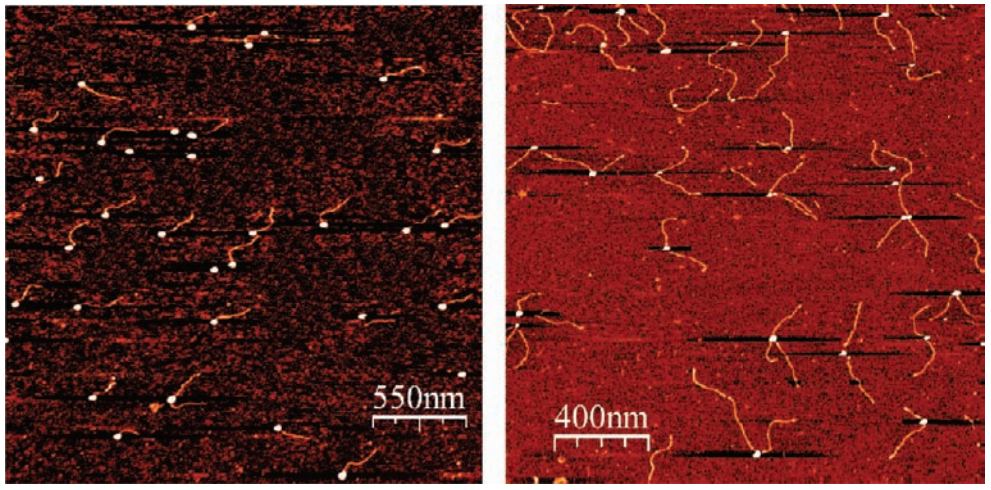

Figure 2. AFM images of AuNPa_{10}-R2-R1-poly(dA)-poly(dT) conjugates. The conjugates extracted from the gel (see Figure 1) were deposited on a mica surface in 2 mM $MgCl_2$ and scanned in a semicontact mode as described in Experimental Procedures. Left and right panels present images of the conjugates extracted from bands II and III (see Figure 1), respectively.

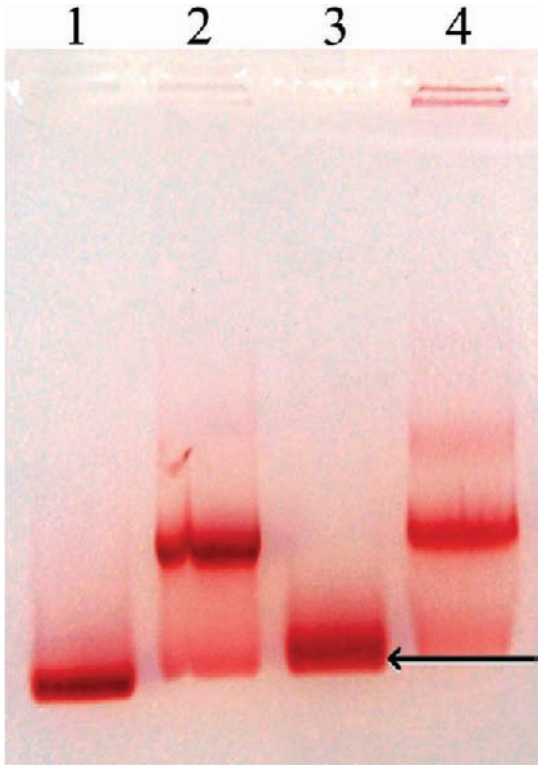

Figure 3. Electrophoretic analysis of AuNP−DNA conjugates. AuNPs (lane 1) and a conjugate extracted from band II in Figure 1 (lane 2) treated for 10 min at 70 °C in the presence of 100 molar excess of a R2 (lane 3). Lane 4: A conjugate electroeluted from the gel area indicated by the arrow in lane 3 and incubated with 10-fold molar excess of R1-poly(dA)-poly(dT) in the presence of 0.1 M NaCl for 1 h at 4 °C. Samples were run in 1.5% agarose gel in TEA buffer at 130 V for 40 min in an ice bath.

oligonucleotide fragment (a_{10}-R2) remained bound to the particle we have incubated the pellet fraction, containing the conjugate, with an excess of R1-poly(dA)-poly(dT). As seen in Figure 3 (compare lanes 3 and 4), the incubation results in restoring the band mobility back to the initial level, corresponding to AuNP-a_{10}-R2-R1-poly(dA)-poly(dT). These results confirm that the heat treatment results in dissociation of AuNP-a_{10}-R2-R1-poly(dA)-poly(dT) into R1-poly(dA)-poly(dT) and AuNP-a_{10}-R2. The same approach was applied for synthesis of AuNP-conjugates bearing two R1, one R2, or two R2 strands.

The conjugates containing complementary sequences (R1 and R2) were assembled to form nanoparticle dimers and trimers. We have shown (see Figure 4, lane 1) that mixing equal amounts of AuNP-a_{10}-R1 and AuNP-a_{10}-R2 (prepared as described above) together results in their association. The gel

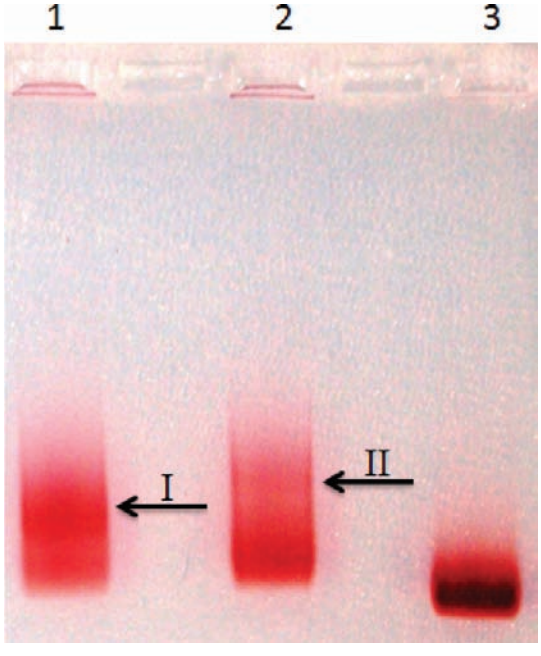

Figure 4. Electrophoresis of AuNP assemblies. Lane 1: Equimolar amounts of AuNP-a_{10}-R1 and AuNP-a_{10}-R2 conjugates (each bearing a single oligonucleotide strand per particle) were incubated in 10 mM NaPi buffer, pH 7.5, containing 0.1 M NaCl for 16 h at room temperature. Lane 2: AuNP-a_{10}-R2 was incubated with AuNP-$(a_{10}$-R1$)_2$, a conjugate bearing two R2 strands, at a 2 to 1 molar ratio in identical conditions (see above). Lane 3: AuNPs. Samples were run in 1.5% agarose gel at 110 V for 40 min in 2×TAE buffer. The bands corresponding to AuNP assemblies are indicated by arrows.

dx.doi.org/10.1021/bc200485r | *Bioconjugate Chem.* 2012, 23, 916−922

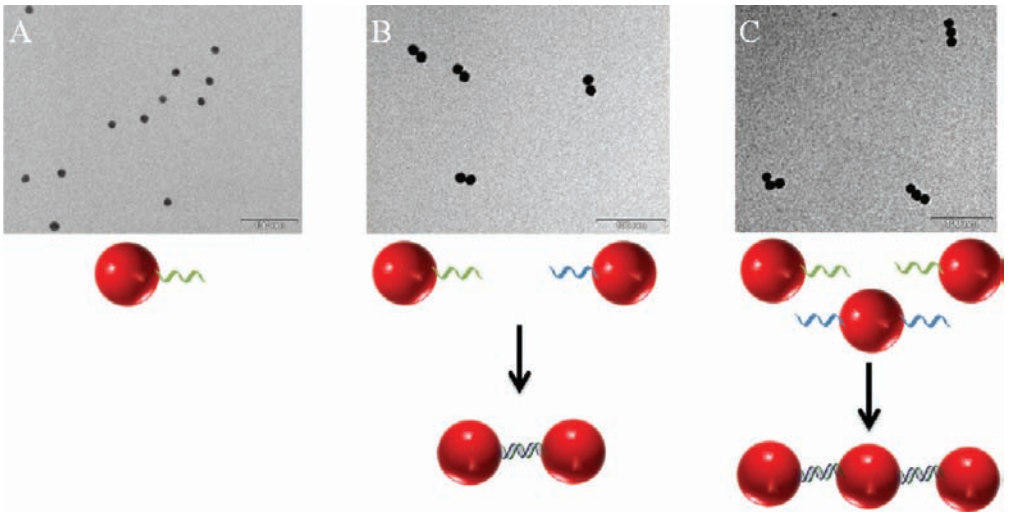

Figure 5. TEM images of AuNP-assemblies. The structures were electroeluted from gel areas indicated by arrows in Figure 4. Panel B: lane I. Panel C: lane II. Panel A: AuNPs. Moelcules were deposited on 400 mesh copper carbon grids and visualized by TEM. Below the images are schematic drawings of the structures.

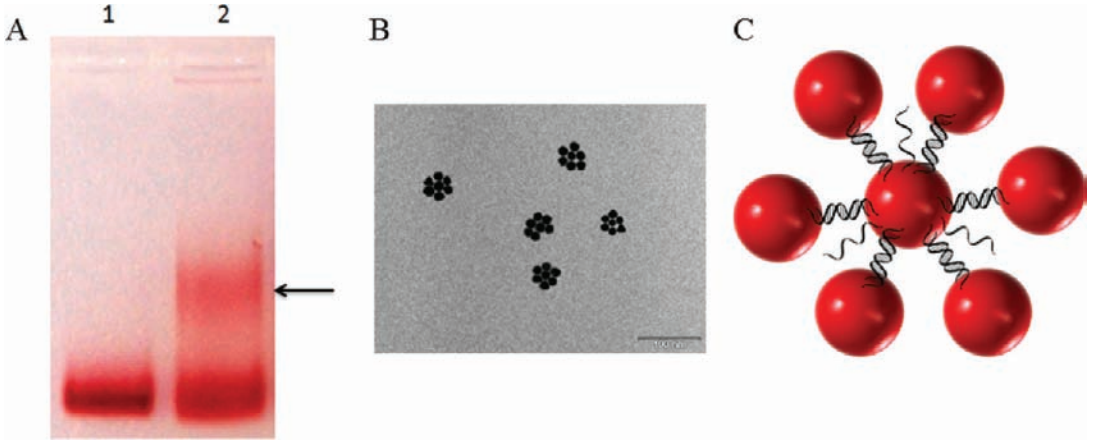

Figure 6. Electrophoresis (panel A) and TEM image (panel B) of complexes between AuNPs fully coated with R1 and a monomolecular AuNP-a_{10}-R2 conjugate. The fully coated particles, AuNP-$(a_{10}\text{-R1})_n$ containing a large number (tens) of R1-strands were prepared as described in Experimental Procedures; AuNP-a_{10}-R2 conjugate was prepared as described in Figure 3. Panel A: Lane 1, fully coated particles; lane 2, the fully coated particles were incubated with 10-fold excess of AuNP-a_{10}-R2 in 10 mM NaPi buffer, pH 7.5, containing 0.1 M NaCl for 72 h at room temperature. The sample was loaded on 1.5% agarose gel and electrophoresed at 110 V for 40 min in an ice bath in 2×TAE buffer. Panel B: The slice corresponding to a band indicated by the arrow in panel A (lane 2) was cut out, and the molecules were electroeluted from the gel. They were subsequently deposited on 400 mesh copper carbon grids and visualized by TEM. Panel C: Schematic drawings of the structure.

area corresponding to the complex (indicated by arrow I, Figure 4) was cut out of the gel with a razor blade; the red compound was electroeluted and analyzed by TEM. As clearly seen in the TEM image (see Figure 5B), the structures are composed of a pair of particles. We thus suggest that the two complementary strands (R1 and R2) attached to different particles associate with each other forming a double-stranded DNA bridge between the particles (see drawing below panel B in Figure 5). We have also shown that incubation of a monomolecular AuNP-a_{10}-R1 conjugate with a bimolecular one, AuNP-a_{10}-$(R2)_2$ (bearing two R2 strands), at a 2 to 1 molar ratio also results in the association of the conjugates (see lane 2, Figure 4). The complex was electroeluted from the gel area (indicated by arrow II, Figure 4) and imaged by TEM. As seen in the image (Figure 5, panel C), the structures are composed of three particles. The particles in the trimer are connected to each other by a double-stranded R1-R2 bridge (see drawing below panel C, Figure 5).

By increasing the number of DNA strands in the conjugate, following the above strategy, one can gradually increase the number of particles in the cluster. We have shown that incubation of AuNPs fully coated with R1-oligonucleotide with more than 10-fold molar excess of the conjugates bearing a single R2-strand leads to the formation of a complex that moves through the gel more slowly than AuNPs (indicated by the arrow, Figure 6A, lane 2). The slice corresponding to the indicated complex was cut out of the gel, and the compound was electroeluted and analyzed by TEM. As clearly seen from the TEM image (Figure 6B), the structures are flower-shaped and consist of a central AuNP surrounded by several (5−6) peripheral particles. The central particle in the structure is connected to each peripheral one via a double-stranded R1-R2 linker.

dx.doi.org/10.1021/bc200485r | *Bioconjugate Chem.* 2012, 23, 916−922

DISCUSSION

In this study, we present a novel method for synthesis of AuNP conjugates bearing a specific number of short (25 base) ssDNA molecules. The method is relatively simple and characterized by high yield of individual conjugates. In the conjugates, DNA is anchored to the particle by phosphorothioated bases at the 5′-end of the polynucleotide strand. We have demonstrated in our recent works that phosphorothioated oligonucleotides are capable of efficient covalent binding to silver [30] and gold nanoparticle surfaces.[31]

The method of NP−oligonucleotide conjugate production described here is not limited to AuNPs. We have shown (data not presented) that an identical approach can be applied for production of conjugates between silver nanoparticles and DNA. One can also vary over a wide range the diameter of NPs, as well as the length and the number of oligonucleotide strands in the conjugate. The efficiency of the DNA−NP conjugate separation in gels decreases as the particle size increases, and increases as the DNA length increases. Therefore, in order to prepare conjugates of bigger (diameter larger than 20 nm) particles, the length of poly(dA)-poly(dT) polymer can be increased to several thousand base pairs. The enzymatic method of extension[24,25] allows us to synthesize tens of Kbase pair long dsDNA homopolymers. The use of very long poly(dA)-poly(dT), we believe, will make it possible to achieve good electrophoretic separation of individual conjugates of big (tens or even hundreds of nm) nanoparticles and other nanostructures (nanorods and nanoshells) with DNA.

We have demonstrated that mixing of two monomolecular AuNP−DNA conjugates, each bearing a single DNA strand, results in the formation of a dimer (see Figure 5B). The complementary strands attached to different particles recognize each other and form a double-stranded DNA bridge between the particles. We have also shown that incubation of the AuNP conjugate bearing two DNA strands with a 2-fold molar excess of the conjugate functionalized with a single complementary sequence yielded nanoparticle trimers (see Figure 5C). By increasing the number of DNA strands in the conjugate, following the above strategy, one can increase the number of particles in the cluster. Indeed, mixing of the AuNPs bearing a single R2 sequence to AuNPs and the nanoparticle fully coated with R1-strands yields structures composed of a central nanoparticle and 5−6 peripheral ones (see Figure 6B). The results of preliminary experiments (data not presented) show that mixing together equal amounts of AuNP-$(R1)_2$ and AuNP-$(R2)_2$ conjugates, each bearing two identical strands, yields chains of nanoparticles. Each particle in the chain is bridged to the two neighboring ones by a 25 bp double-stranded R1-R2 molecule.

The results demonstrated here are a prerequisite for complex controlled self-assembly of nanoparticle conjugates bearing a large number of DNA strands into two- and three-dimensional macrostructures. The method of NP−oligonucleotide conjugate production described here allows one to vary the size of nanoparticles, the distance between them (by changing the length of a DNA linker), and a number of connections that each particle establishes with neighboring ones. Nanostructures composed of silver or gold nanoparticles, as well as heterogeneous structures composed of both types of particles can also be synthesized. We believe that these structures will possess interesting plasmonic and conductive properties and will lead to development of new multiparticle functional materials.

AUTHOR INFORMATION

Corresponding Author

*E-mail: s2shak@post.tau.ac.il.

Notes

The authors declare no competing financial interest.

ACKNOWLEDGMENTS

This work was supported by the Israel Science Foundation, 172/10.

REFERENCES

(1) Mirkin, C. A., Letsinger, R. L., Mucic, R. C., and Storhoff, J. J. (1996) A DNA-based method for rationally assembling nanoparticles into macroscopic materials. *Nature 382*, 607−609.

(2) Alivisatos, A. P., Johnsson, K. P., Peng, X., Wilson, T. E., Loweth, C. J., Bruchez, M. P., Jr., and Schultz, P. G. (1996) Organization of 'nanocrystal molecules' using DNA. *Nature 382*, 609−611.

(3) Loweth, C. J., Caldwell, W. B., Peng, X., Alivisatos, A. P., and Schultz, P. G. (1999) *Angew. Chem., Int. Ed. 38*, 1808−1812.

(4) Dujardin, E., Hsin, L. B., Wang, C. R. C., and Mann, S. (2001) DNA-driven self-assembly of gold nanorods. *Chem. Commun. 14*, 1264−1265.

(5) Goluch, E. D., Nam, J. M., Georganopoulou, D. G., Chiesl, T. N., Shaikh, K. A., Ryu, K. S., Barron, A. E., Mirkin, C. A., and Liu, C. (2006) A bio-barcode assay for on-chip attomolar-sensitivity protein detection. *Lab Chip 6*, 1293−1299.

(6) Huang, X., El-Sayed, I. H., Qian, W., and El-Sayed, M. A. (2006) Cancer cell imaging and photothermal therapy in the near-infrared region by using gold nanorods. *J. Am. Chem. Soc. 128*, 2115−2120.

(7) Durr, N. J., Larson, T., Smith, D. K., Korger, B. A., Sokolov, K., and Ben-Yakar, A. (2007) Two-photon luminescence imaging of cancer cells using molecularly targeted gold nanorods. *Nano Lett. 7*, 941−945.

(8) Huang, X., El-Sayed, I. H., Qian, W., and El-Sayed, M. A. (2006) Cancer cell imaging and photothermal therapy in the near-infrared region by using gold nanorods. *J. Am. Chem. Soc. 128*, 2115−2120.

(9) Yu Cheng, J. D., Meyers, A. M., Broome, M. E., Kenney, J. P., Basilion, and Burda, C. (2011) Deep penetration of a PDT drug into tumors by noncovalent drug-gold nanoparticle conjugates. *J. Am. Chem. Soc. 133*, 2583−2591.

(10) He, Y., Zhang, S., Zhang, X., Baloda, M., Gurung, S., Xu, H., Zhang, X., and Liu, G. (2011) Ultrasensitive nucleic acid biosensor based on enzyme-gold nanoparticle dual label and lateral flow stop biosensor. *Biosens. Bioelectron. 26*, 2018−2024.

(11) Alivisatos, P. A. (2008) Birth of a nanoscience building block. *ACS Nano 2*, 1514−1516.

(12) Choi, C. L., and Alivisatos, A. P. (2010) From artificial atoms to nanocrystal molecules: preparation and properties of more complex nanostructures. *Annu. Rev. Phys. Chem. 61*, 369−389.

(13) Burda, C., Chen, X. B., Narayanan, R., and El-Sayed, M. A. (2005) Chemistry and properties of nanocrystals of different shapes. *Chem. Rev. 105*, 1025−1102.

(14) Kim, M. R., Kim, J. Y., and Jang, D. J. (2007) Electrochemical fabrication of arrayed alumina nanowires showing strong blue emission. *Eur. Phys. J. D 43*, 279−282.

(15) Kumar, A., Pattarkine, M., Bhadbhade, M., Mandale, A. B., Ganesh, K. N., Datar, S. S., Dharmadhikari, C. V., and Sastry, M. (2001) Linear superclusters of colloidal gold particles by electrostatic assembly on DNA templates. *Adv. Mater. 13*, 341−344.

(16) Zanchet, D., Micheel, C. M., Parak, W. J., Gerion, D., and Alivisatos, A. P. (2001) Electrophoretic isolation of discrete Au nanocrystal/DNA conjugates. *Nano Lett. 1*, 32−35.

(17) Zanchet, D., Micheel, C. M., Parak, W. J., Gerion, D., Williams, S. C., and Alivisatos, A. P. (2002) Electrophoretic and structural

studies of DNA-directed Au nanoparticle groupings. *J. Phys. Chem. B 106*, 11758−11763.
(18) Claridge, S. A., Mastroianni, A. J., Au, Y. B., Liang, H. W., Micheel, C. M., Fréchet, J. M. J., and Alivisatos, A. P. (2008) Enzymatic ligation creates discrete multinanoparticle building blocks for self-assembly. *J. Am. Chem. Soc. 130*, 9598−9605.
(19) Kanaras, A. G., Wang, Z. X., Brust, M., Cosstick, R., and Bates, A. D. (2007) Enzymatic disassembly of DNA−gold nanostructures. *Small 3*, 590−594.
(20) Kanaras, A. G., Wang, Z., Hussain, I., Brust, M., Cosstick, R., and Bates, A. D. (2007) Site-specific ligation of DNA-modified gold nanoparticles activated by the restriction enzyme StyI. *Small 3*, 67−70.
(21) Kanaras, A. G., Wang, Z. X., Bates, A. D., Cosstick, R., and Brust, M. (2003) Towards multistep nanostructure synthesis: programmed enzymatic self-assembly of DNA/gold systems. *Angew. Chem., Int. Ed. 42*, 191−194.
(22) Pena, S. R. N., Raina, S., Goodrich, G. P., Fedoroff, N. V., and Keating, C. D. (2002) Hybridization and enzymatic extension of Au nanoparticle-bound oligonucleotides. *J. Am. Chem. Soc. 124*, 7314−7323.
(23) Zikich, D., Borovok, N., Molotsky, T., and Kotlyar, A. (2010) Synthesis and AFM characterization of poly(dG)-poly(dC)-gold nanoparticle conjugates. *Bioconjugate Chem. 21*, 544−547.
(24) Kotlyar, A. B., Borovok, N., Molotsky, T., Fadeev, L., and Gozin, M. (2005) In Vitro synthesis of uniform poly(dG)−poly(dC) by Klenow exo$^-$ fragment of polymerase I. *Nucleic Acids Res. 33*, 525−535.
(25) Borovok, N., Molotsky, T., Ghabboun, J., Cohen, H., Porath, D., and Kotlyar, A. (2007) Poly(dG)−poly(dC) DNA appears shorter than poly(dA)−poly(dT) and possibly adopts an A-related conformation on a mica surface under ambient conditions. *FEBS Lett. 581*, 5843−5846.
(26) Nasir, S. M., and Nur, H. (2008) Gold nanoparticles embedded on the surface of polyvinyl alcohol layer. *J. Fund. Sci. 4*, 245−252.
(27) Reynolds, R. A., III, Mirkin, C. A., and Letsinger, R. L. (2000) Homogeneous, nanoparticle-based quantitative colorimetric detection of oligonucleotides. *J. Am. Chem. Soc. 122*, 3795−3796.
(28) Jana, N. R., Gearheart, L., and Murphy, C. J. (2001) Seeding growth for size control of 5−40 nm diameter gold nanoparticles. *Langmuir 17*, 6782−6786.
(29) Horcas, I., Fernandez, R., Gomez-Rodriguez, J. M., Colchero, J., Gomez-Herrero, J., and Baro, A. M. (2007) WSXM: a software for scanning probe microscopy and a tool for nanotechnology. *Rev. Sci. Instrum. 78*, 013705.
(30) Lubitz, I., and Kotlyar, A. (2011) Self-assembled G4-DNA-silver nanoparticle structures. *Bioconjugate Chem. 22*, 482−487.
(31) Lubitz, I., and Kotlyar, A. (2011) G4-DNA-coated gold nanoparticles: synthesis and assembly. *Bioconjugate Chem. 22*, 2043−2047.

Bioconjugate Chemistry

Article

pubs.acs.org/bc

Measuring CREB Activation Using Bioluminescent Probes That Detect KID−KIX Interaction in Living Cells

Tetsuya Ishimoto,[†] Hiroki Mano,[†] Takeaki Ozawa,[‡] and Hisashi Mori*[,†]

[†]Department of Molecular Neuroscience, Graduate School of Medicine and Pharmaceutical Sciences, University of Toyama, Toyama, Japan

[‡]Department of Chemistry, Graduate School of Science, The University of Tokyo, Bunkyo-Ku, Tokyo, Japan

Supporting Information

ABSTRACT: The cyclic adenosine monophosphate response element-binding protein (CREB) is a transcription factor that contributes to memory formation. The transcriptional activity of CREB is induced by its phosphorylation at Ser-133 and subsequent interaction with the CREB-binding protein (CBP)/p300. We designed and optimized firefly split luciferase probe proteins that detect the interaction of the kinase-inducible domain (KID) of CREB and the KIX domain of CBP/p300. The increase in the light intensity of the probe proteins results from the phosphorylation of the responsible serine corresponding to Ser-133 of CREB. Because these proteins have a high signal-to-noise ratio and are nontoxic, it has become possible for the first time to carry out long-term measurement of KID−KIX interaction in living cells. Furthermore, we examined the usefulness of the probe proteins for future high-throughput cell-based drug screening and found several herbal extracts that activated CREB.

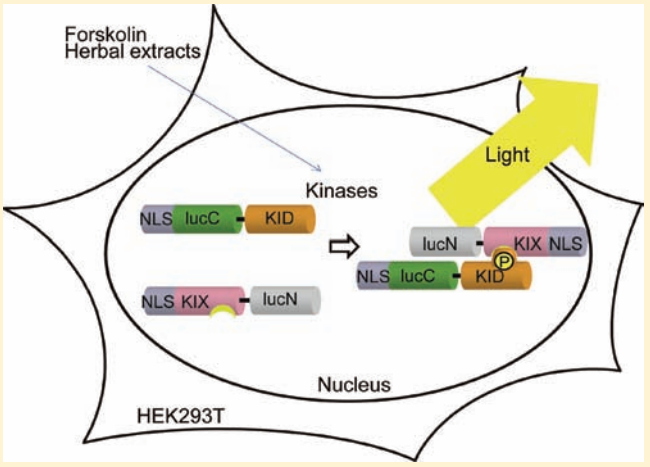

INTRODUCTION

The cyclic adenosine monophosphate (cAMP) response element-binding protein (CREB) was first identified as a protein that binds to the upstream sequence of somatostatin (TGACGTCA), which was referred to as the cAMP response element (CRE).[1,2] Later, it was found that the phosphorylation at a serine residue in the kinase-inducible domain (KID) of CREB increases the transcriptional activity of CREB following the recruitment of the CREB-binding protein (CBP) or its paralogue p300, a transcription coactivator that has histone acetyltransferase activity.[3] We refer to this phosphorylation site (133rd serine in CREB) as S133 in this study. Many studies have suggested the relationship of CREB with synaptic plasticity and memory formation.[4−6] Thus, monitoring the phosphorylation of CREB and subsequent KID-KIX interaction during memory formation is important to elucidate the mechanism underlying memory formation. The screening for CREB activators may lead to the development of therapies for memory disorders.

Although CREB was originally reported to be phosphorylated by protein kinase A (PKA), it has been revealed that S133 of CREB is phosphorylated not only by PKA but also by many other kinases such as protein kinase C (PKC), calcium calmodulin-dependent protein kinase (CaMK), and mitogen-activated protein kinase kinase (MEK).[7] This means that measuring PKA activity is not sufficient for measuring the CREB activation level. There are some PKA probes in which catalytic, regulatory subunit of PKA and fluorescent or luminescent proteins are used;[8−11] however, they detect cAMP level but not CREB phosphorylation and subsequent CREB-CBP/p300 binding. To detect the phosphorylation of CREB specifically, Western blotting and immunohistochemistry using the antibody specific to phosphorylated S133 are widely used in *in vitro* studies. However, these methods do not enable the detection of the phosphorylation of CREB in living cells. CRE-dependent transcription can be detected by CRE-luciferase reporter assay in living cells. However, this assay not only detects CREB-dependent transcription, but is also influenced by other transcription-regulating proteins that bind to CRE, such as AP-1.[12]

A detection method for CREB phosphorylation using fluorescence resonance energy transfer (FRET) has been reported.[13] This method was designed to detect changes in emission properties induced by the interaction of two distinct fluorescent proteins induced by the KID−KIX interaction. Under the conditions in which fluorescent proteins can be excited by light and autofluorescence noise is very low, this method enables the measurement of phosphorylation level

Received: September 7, 2011
Revised: December 28, 2011
Published: April 16, 2012

dx.doi.org/10.1021/bc200491j | *Bioconjugate Chem.* 2012, 23, 923−932

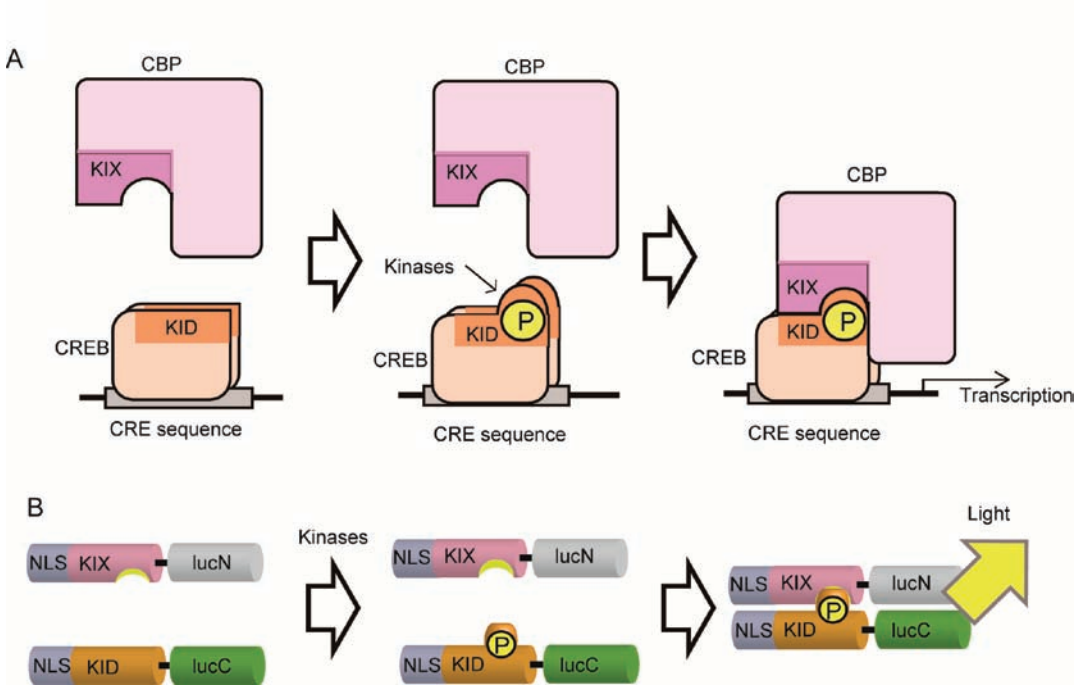

Figure 1. Schematic diagram of split luciferase for detecting interaction between KID and KIX. (A) Phosphorylation-dependent interaction between KID and KIX domains. When the S133 residue of CREB is phosphorylated (represented as 'P' in the figure), the KID interacts with the KIX domain of CBP. (B) Schema of measurement of the KID−KIX interaction with light emission. Probe proteins consist of the N-terminal and C-terminal domains of luciferase (LucN and LucC) and KID and KIX domains attached through short peptide linkers. Both fusion proteins contain nuclear localization signals (NLS) that allow nuclear translocation. Once S133 of the KID domain is phosphorylated, two probe proteins interact with each other and luciferase activity is restored to emit light.

using living cells. However, changes in emission ratio are usually small and are principally less quantitative in the FRET method. Furthermore, excitation light is toxic to cells. These disadvantages make long-term measurement of CREB phosphorylation level difficult in living cells. Therefore, a simple and quantitative method of measuring CREB activation in living cells has been desired.

Complementation and reconstitution assay of firefly split luciferase has been established in this decade.[14−16] Because this method has the advantages of viability of cells and linearity of signal intensity, we attempted to develop a new probe protein that can be used for the detection of CREB activation in real time and for a long period by employing firefly split luciferase technique. On the other hand, the optimization of domain combination and a linker sequence are required to establish practical split luciferase probes that have a sufficient light intensity from living cells.[17] In this study, we designed and optimized the probe proteins with a high light intensity depending on phosphorylation at S133 and subsequent KID−KIX interaction. Then, we determined whether long-term observation of KID−KIX interaction is possible in living cells. Furthermore, we examined the usability of our probe proteins in cell-based drug screening using a herbal extract library and found some extracts that activated CREB.

■ EXPERIMENTAL PROCEDURES

Plasmid Construction. Plasmids that coded probe proteins were constructed using a MultiSite Gateway Three-Fragment Vector Construction kit (Invitrogen) as described in previous reports.[17−19] In accordance with the manufacturer's instructions, PCR-amplified DNA fragments of interest were inserted by BP reaction in a defined order of 5′, center, and 3′ entry clones. The SV40 enhancer promoter sequence amplified from pGL4.13 (Promega) was inserted in 5′ entry clones, and then the start codon and nuclear localization signal (DPKKKRKVDPKKKRKV) were inserted using a KOD plus mutagenesis kit (Toyobo). The amino-terminal part (nucleotide numbers 1−1245) of firefly luciferase ORF (LucN), carboxyl-terminal part of firefly luciferase (LucC) sequence corresponding to nucleotide numbers 1246−1650 of the luciferase ORF, nucleotide numbers 417−596 of CREB cDNA (Genbank: BC021649) (KID), and nucleotide numbers 1923-2165 of CBP cDNA (Genbank: BC072594) (KIX) were amplified and inserted into the center and 3′ entry clones. The obtained clones were reacted with a destination vector pDEST R4-R3 using LR clonase plus II (Invitrogen) to generate the expression clones A1, A2, B1, B2, C1, C2, D1, and D2. The linker sequences of these clones were modified using a KOD plus mutagenesis kit (Toyobo). All the expression clones are illustrated in Figure 2A. All the constructs were confirmed by DNA sequencing using ABI3100 (Applied Biosystems). For the CRE-luc assay, pGL4.29 (Promega), and a plasmid which expressed enhanced green fluorescent protein (EGFP) driven by SV40 promoter were used.

Cell Culture and DNA Transfection. HEK293T (0.27×10^5 cells/cm^2) cells were cultured in DMEM supplemented with 10% FCS at 37 °C in 5% CO_2 on 24-well or 96-well dishes (Falcon). The cells were transiently transfected using Lipofectamine 2000 (Invitrogen) in accordance with the manufacturer's instructions.

Cell Viability Assay. HEK293T cells 0, 1, and 2 days after transfection were used for the assay. Cell viability was determined by 3-(4,5-dimethyl-2-thizolyl)-2,5-diphenyl-2*H*-tetrazolium bromide (MTT) assay in accordance with the manual

dx.doi.org/10.1021/bc200491j | *Bioconjugate Chem.* 2012, 23, 923−932

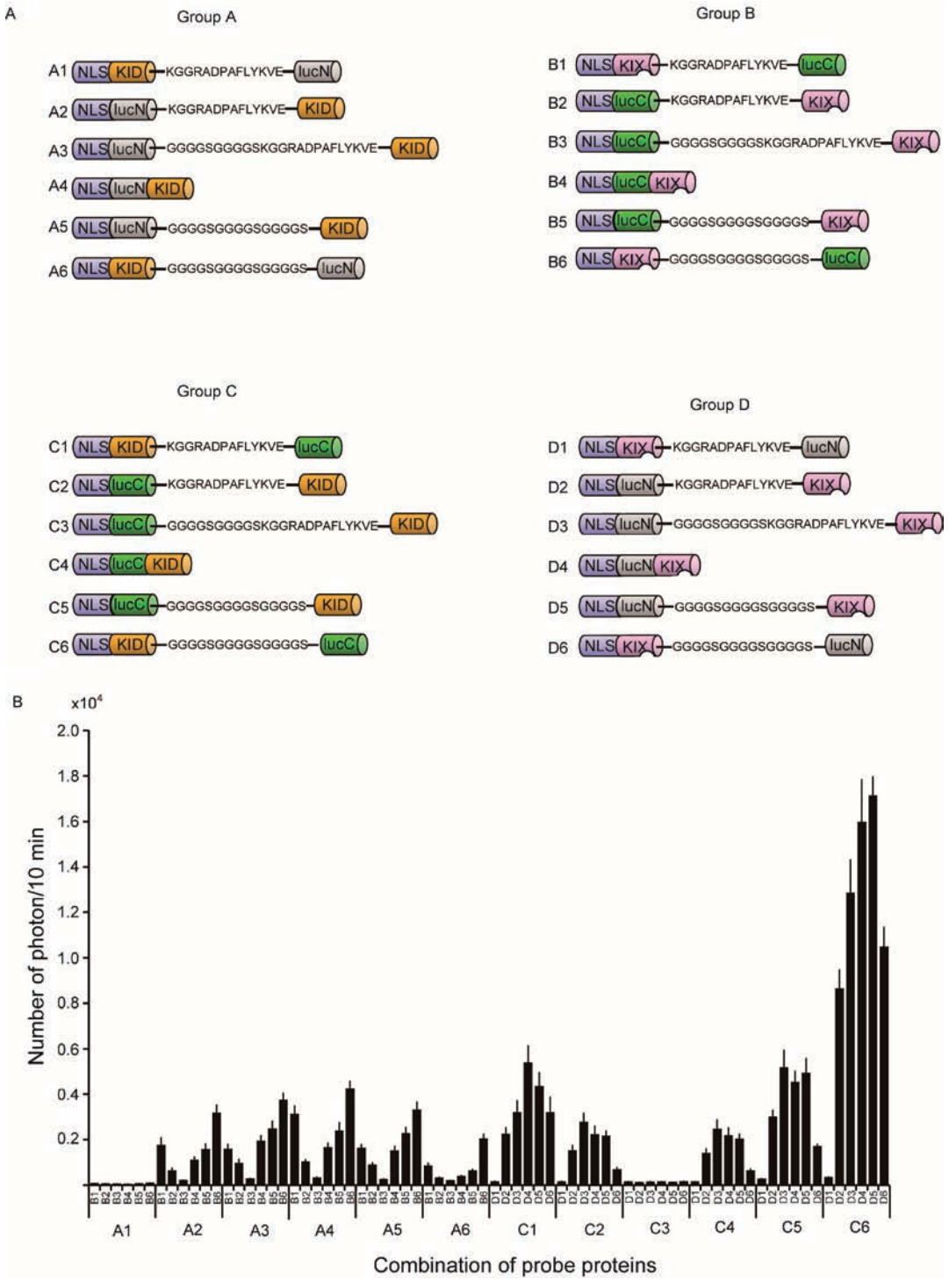

Figure 2. Development of probe proteins to measure KID−KIX interaction. (A) Schematic structures of probe proteins A1−D6, in which the linker sequences, domain combinations, and domain location were modified. Combinations of probe proteins from groups A and B or groups C and D were coexpressed in HEK293T cells, and the emitted photons were counted for 10 min using an image intensifier/CCD camera. (B) Numbers of photons emitted from all the combinations of probe proteins for 10 min. Data are presented as mean ± SEM, n = 4.

attached to the MTT cell viability assay kit (Biotium Inc.). After incubation with the tetrazolium salt MTT (1 mg/mL) for 2 h at room temperature, the harvested cells were solubilized with 1 mL of dimethyl sulfoxide. We measured the absorbance at wavelengths of 570 and 630 nm using a spectrophotometer (Gene Quant 1300, GE Healthcare). Sample signal intensity was obtained by subtraction of OD at 630 nm from OD at 570 nm and indicated as a percentage of the control value.

Western Blotting. Cells were harvested and lysed using M-PER solution (Thermo Scientific). Proteins separated by SDS-PAGE were electrically transferred onto a PVDF membrane (GE Healthcare). The membranes were incubated with goat anti-luciferase (1:1000, Promega), rabbit anti-phospho CREB (1:500, Upstate), rabbit anti-CREB (1:500, Cell Signaling Technology), or rabbit anti-actin (1:1000, Santa Cruz) primary antibody in the Can Get Signal solution (Toyobo) at 4 °C

dx.doi.org/10.1021/bc200491j | Bioconjugate Chem. 2012, 23, 923−932

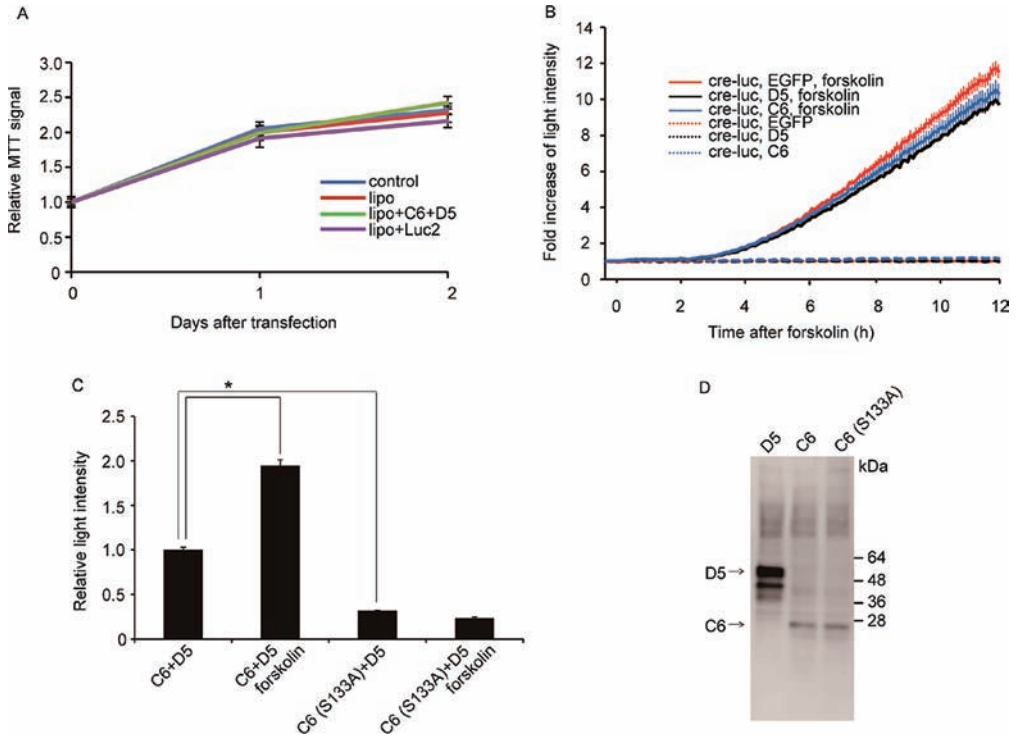

Figure 3. Characterization of KID−KIX interaction probe proteins expressed in cells. (A) Effect of probe protein expression on cell proliferation. HEK293T cells were transfected with the plasmids encoding probe proteins (C6 + D5) or wild-type luciferase (Luc2) using lipofectamine 2000 (lipo). Cell viability was measured by the MTT method 1−2 days after transfection. Data are presented as mean ± SEM, $n = 4$. (B) Effect of probe protein expression on CRE-dependent gene expression. HEK293T cells were transfected with CRE-luc reporter plasmid with the expression plasmid of C6, D5, or EGFP. The relative increase in light intensity in response to forskolin treatment was measured for 12 h. Dotted lines represent control experiments without forskolin treatment. (C) Effect of point mutation at phosphorylation site of probe proteins on light emission. The probe proteins (C6 + D5) and point-mutated C6 probe C6 (S133A) with D5 were expressed in HEK293T cells. Light intensity was measured 1 h after forskolin treatment. (D) Western blot analysis of probe proteins. The expression levels of probe proteins in experiment (C) were analyzed using the anti-luc antibody. The bands corresponding to the expected sizes of D5 and C6 are indicated by arrows. The locations of protein size markers (kDa) are indicated on the right side. Data are presented as mean ± SEM, $n = 4$ in (A, B, and C).

overnight. The membranes were reacted with secondary rabbit anti-goat IgG HRP-conjugated and goat anti-rabbit IgG HRP-conjugated antibodies (1:2000, Bio Rad) and visualized using an ECL plus Western blotting reagent (GE Healthcare). Chemiluminescence signals were detected using the LAS-4000 system (Fujifilm).

Measuring Light Intensity from Cultured Cells. The Aequoria-2D/C8600 system (Hamamatsu Photonics) and *Wasabi* software (U9304−02) were used for data acquisition and analysis, as described in a previous report.[17] Briefly, cultured cells were taken out from a CO_2 incubator 48 h after transfection. The culture medium was replaced with L15 medium containing 0.5 mM luciferin EF (Promega). The culture plate was placed in a dark box for 30 min. Then, the number of photons emitted from one culture dish well was determined using a CCD camera with an image intensifier attached to the top of the dark box. Light intensity was measured every 5 min continuously for 12 h after the stimulation. The numbers of emitted photons from wells were normalized to those from nontreated wells (control) and were plotted as relative intensity. All the measurement of light intensity was done at room temperature.

Herbal Extracts. The library of herbal extract was a kind gift from the Institute of Natural Medicine, University of Toyama. Each herb (45 g in 900 mL water) was boiled for 70 min and filtered. Freeze−dried extracts were resuspended in water at 10 mg/mL. The cells in the 96-well dish were treated with the extracts (500 μg/mL).

Statistical Analyses. Data are presented as mean ± standard error of the mean (SEM). In Figures 3A,C and 5A, a two-tailed Student's t test was used to determine statistical significance. Two-factor repeated measure ANOVA was performed for Figure 3B.

RESULTS

Design of Split Luciferase Probes for Detecting KID−KIX Interaction. KID of CREB interacts with KIX domain of CBP/p300[3]. Phosphorylation of KID at S133 of the CREB residue triggers interaction with KIX (Figure 1A), and the KID−KIX interaction activates the subsequent transcription machinery.[20] On the basis of these features, we designed split luciferase probe proteins for detecting KID−KIX interaction (Figure 1B). The LucN (1−415 aa) and LucC (416−550 aa) domains of firefly (*Photinus pyralis*) luciferase were attached to the KID and KIX domains with short linker peptides. Each probe protein contains a nuclear localization signal. The interaction between KID and KIX leads to complementation of LucN and LucC, restoration of luciferase activity, and subsequent photon emission.

Development of Probe Proteins to Measure KID−KIX Interaction Level. Because the linker sequence and domain combination markedly affect the ability of photon emission from split luciferase probes, as described in a previous report,[17]

dx.doi.org/10.1021/bc200491j | *Bioconjugate Chem.* 2012, 23, 923−932

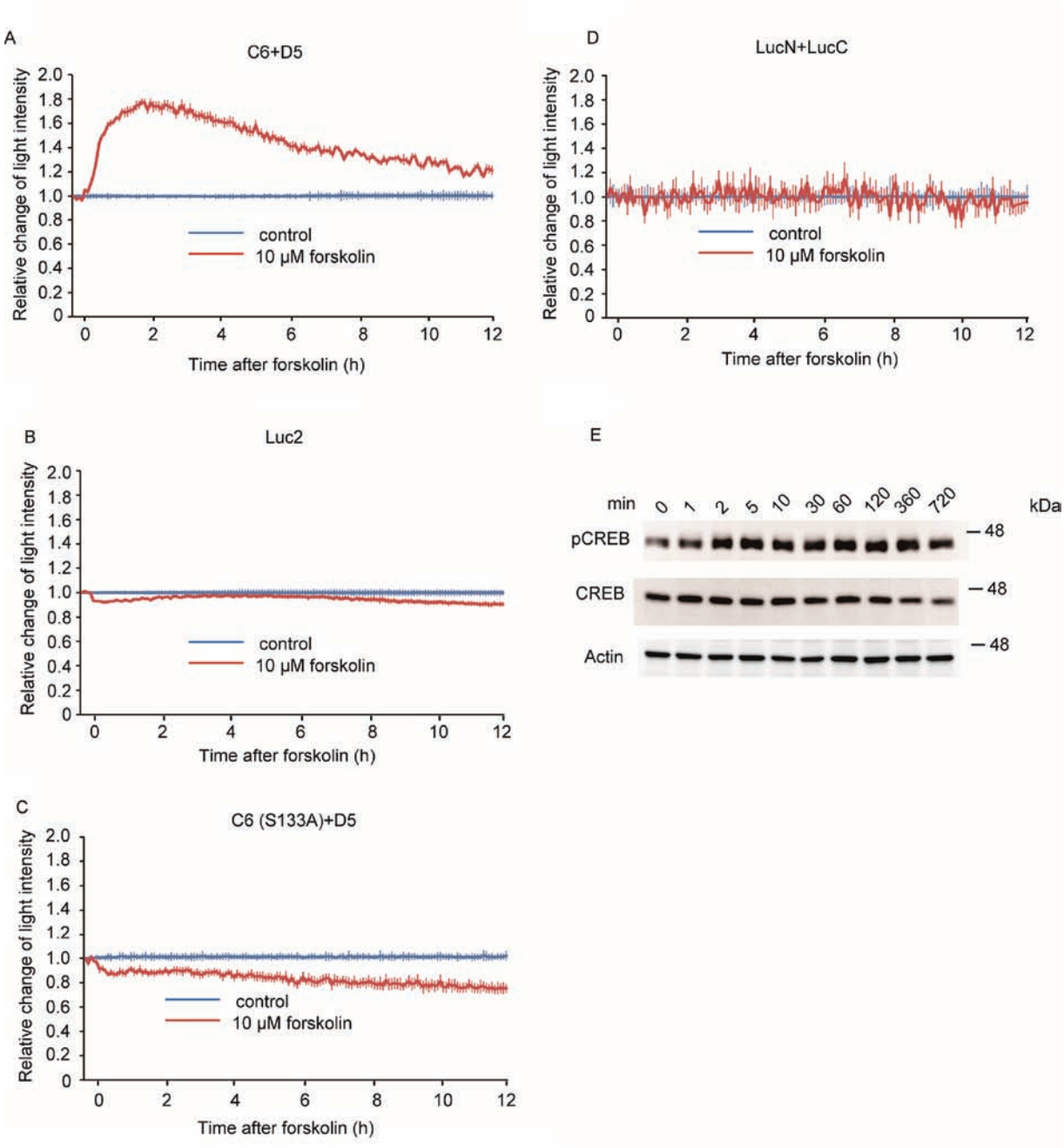

Figure 4. Long-term measurement of KID−KIX interaction in living cells. (A) Change in light intensity of cells expressing probe proteins after forskolin treatment. HEK293T cells were transfected with C6+D5 probe proteins. Forskolin was added to the culture medium at time 0, and the relative change in light intensity was measured for 12 h. (B, C, D) Same measurements as in (A) were performed using the cells transfected with Luc2, C6 (S133A)+D5, and LucN+LucC. Data in A, B, C, and D are presented as mean ± SEM, $n = 4$. (E) Western blotting of endogenous CREB, phosphorylated CREB (pCREB), and actin in HEK293T cells after forskolin treatment. HEK293T cells treated with forskolin were analyzed by Western blotting to detect the phosphorylation of endogenous CREB.

we constructed several plasmids that expressed fusion proteins with modifications in the linker sequence and domain combination, as shown in Figure 2A. A MultiSite Gateway Three-Fragment Vector Construction kit was employed to obtain A1, A2, B1, B2, C1, C2, D1, and D2 probe expression plasmids. The linkers of these plasmids were modified by the inverse PCR method to construct the other plasmids. Each combination of probes from groups A and B or groups C and D was expressed in HEK293T cells, and the emitted photons were counted for 10 min using an image intensifier/charge-coupled device (CCD) camera. Among all combinations of probe proteins, we found that the cells expressed the combination C6+D5 emitted more photons than any other combination of probes (Figure 2B) including control probes LucN and LucC (Supporting Information Figure S1A). The expression levels of probe proteins (C1, C6, D1, and D5) were not significantly different (Figure S1B). The probe protein combination C6+D5 was used in the following experiments.

Characterization of KID−KIX Interaction Probe Proteins Expressed in Cells. Since split luciferase probes are

dx.doi.org/10.1021/bc200491j | *Bioconjugate Chem.* 2012, 23, 923−932

exogenous proteins, they may interfere with some biological processes in cells. In order to test these interferences of our probe proteins, we determined whether the probes affect on HEK293T proliferation rate. HEK293T cells were transfected with probe proteins or wild-type luciferase (Luc) expression plasmids, and cell viability was measured after transfection for 2 days. We did not find any difference in the intensity of the 3-(4,5-dimethyl-2-thizolyl)-2,5-diphenyl-2*H*-tetrazolium bromide (MTT) signal between the probe-protein- or Luc-expressing cells and the cells treated with transfection reagent alone (Figure 3A). This finding demonstrates that the probe proteins do not affect cell proliferation.

Next, we examined whether the expression of probe proteins interferes with CRE-mediated transcription in HEK293T cells. Expression plasmid of C6, D5, or EGFP was co-transfected with CRE-luc plasmid that could indicate CRE-mediated transcription by photon emission. Two days after transfection, we found that at least 90% of HEK293T cells expressed EGFP (Figure S2). Under this condition, cells were treated with 10 μM forskolin, a compound that upregulates cAMP production followed by PKA activation and CRE-dependent transcription, and light intensity was measured for 12 h. All the CRE-luc-expressing cells showed an increased light intensity following forskolin treatment. We did not find a significant inhibition of upregulation of light emission when each probe protein (C6 or D5) was coexpressed with CRE-luc, as compared with EGFP coexpression with CRE-luc (Figure 3B). Furthermore, no increase in light intensity was observed without forskolin treatment. These findings indicate that probe proteins do not have any effect on CRE-mediated transcription.

We determined whether forskolin enhanced the photon emission from C6+D5 probe proteins in HEK293T cells. We found that 1 h incubation with 10 μM forskolin markedly enhanced the photon emission from the cells expressing C6+D5 probe proteins (Figure 3C). Next, we examined whether the point mutation at the phosphorylation site diminished the response to forskolin. S133 of C6 probe was replaced with alanine, which was termed C6 (S133A), and was expressed in HEK293T cells with the D5 probe. We found that HEK293T cells expressing C6(S133A)+D5 probes exhibited no increase in light intensity in response to the forskolin treatment. This result strongly suggests that our probes upregulate the light intensity by binding of phosphorylated KID and KIX domain. Furthermore, the light intensity of the cells expressing C6 (S133A)+D5 proteins was lower than that of C6+D5-expressing cells without forskolin treatment. We then compared the amount of expressed C6 and C6 (S133A) probe proteins. The cells expressing the probes were analyzed by Western blotting, and we found no significant difference in the intensity of band signals between C6 and C6 (S133A) (Figure 3D). These findings indicate that the difference in light intensity seen in Figure 3C is not due to the difference in expression level between C6 and C6 (S133A). From the results shown in Figure 3C and D, the forskolin-induced upregulation of light emission from the probes was considered to be induced by phosphorylation at S133 and subsequent KID−KIX interaction.

Long-Term Measurement of Light Intensity from KID−KIX Interaction Probes in Living Cells. We then determined whether the long-term measurement of KID−KIX interaction was possible using living cells. HEK293T cells were transfected with C6+D5, Luc2, C6 (S133A)+D5, or LucN +LucC. Then, the cells were treated with 10 μM forskolin for 12 h at room temperature. During the treatment, the light intensity from each culture dish was measured continuously. We found that the temporal increase in light intensity from the cells expressing C6+D5 (Figure 4A) peaked at 2 h, whereas other cells expressing Luc2 (Figure 4B), C6 (S133A)+D5 (Figure 4C), and LucN+LucC (Figure 4D) did not show any increase in light intensity in response to forskolin. We examined whether the phosphorylation of endogenous CREB level increases in response to forskolin. HEK293T cells were treated with 10 μM forskolin and analyzed by Western blotting. Phosphorylated CREB level increased within 2 min and peaked at 5 min; this peaking remained for 6 h after the treatment. The total amount of CREB was unchanged during the treatment with forskolin. These findings indicate that our probes enable long-term evaluation of KID−KIX interaction in living cells. We also confirmed that a sufficient amount of luciferin for the activity of luciferase remained in the culture medium after 12 h measurement (Figure S3A). This indicates that light intensity was not decreased because of luciferin depletion. We also observed that the expression level of Luc2 driven by SV40 promoter was unchanged during measurement (Figure S3B), which indicated changes in light intensity in Figure 4, was not due to the expression level of proteins.

Effect of Kinase Inhibitors on Light Intensity. The photon emission shown in Figure 4A is considered to be a result of PKA activation, because forskolin increases cAMP concentration. We examined whether our probe proteins are capable of evaluating the level of CREB phosphorylation when two or more kinases induce the phosphorylation in living cells. HEK293T cells expressing the C6+D5 probe proteins were treated with H89 (a PKA inhibitor), KN93 (a CaMK II inhibitor), calphostin C (a PKC inhibitor), and a mixture of three inhibitors for 8 h. After the treatment, we measured light intensity and found H89 and KN93 but not calphostin C significantly decreased light intensity. An additional decrease in light intensity was observed when the cells were treated with a mixture of inhibitors (Figure 5A). To determine whether the change in light intensity correlated with endogenous CREB phosphorylation, cells treated with inhibitors were analyzed by Western blotting. We found that H89, KN93, and the mixture of inhibitors significantly attenuated pCREB signals (Figure 5B). On the other hand, cells treated with calphostin C showed only slight attenuation of pCREB signals. In the control experiments, we found that kinase inhibitor treatment resulted in slight decreases in MTT signals of HEK293T cells when KN93 and inhibitor mixture were added (Figure S4A). Since these changes in MTT signal are smaller than the changes in light intensity shown in Figure 5A, a major cause of reduced light intensity in Figure 5A was not the toxic effects of inhibitors. We also found that forskolin treatment together with kinase inhibitors canceled the forskolin-induced upregulation of light intensity (Figure S4B). These findings show that CREB is phosphorylated by mainly PKA and CaMKII and not by PKC in nontreated HEK293T cells, and our probe proteins are useful for evaluating the level of CREB phosphorylation when other kinases contribute to phosphorylation simultaneously.

Screening for CREB Activators Using Herbal Extract Library. Some herbal extracts or molecules purified from herbal extracts show the activity to phosphorylate CREB.[21−24] To determine the capability of our probe proteins to screen for molecules that induce CREB phosphorylation, we used a library consisting of 120 herbal extracts. Each extract was added to a culture dish of cells expressing probe proteins, and the light intensity from each dish was measured at times 0 and 4 h. Most

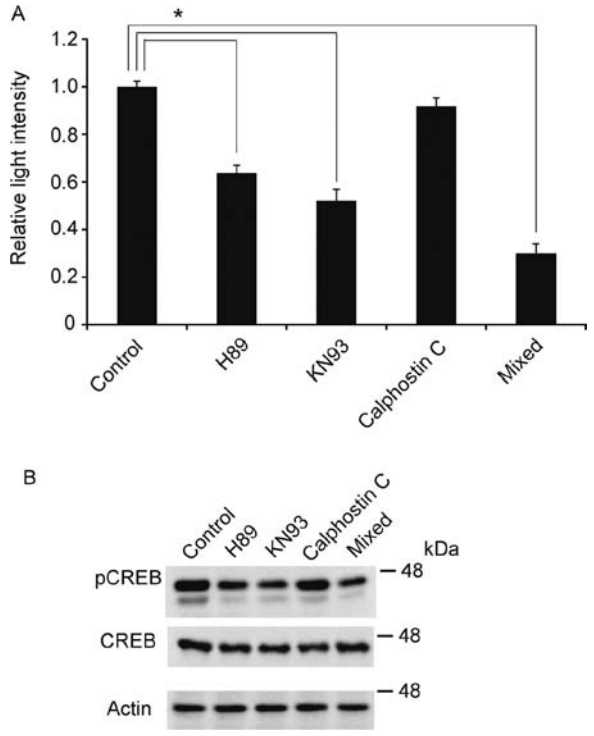

Figure 5. Effect of kinase inhibitors on light intensity. (A) Changes in light intensity of cells expressing probe proteins after the treatment with protein kinase inhibitors. HEK293T cells transfected with C6+D5 probes were treated with kinase inhibitors (10 μM H89, 10 μM KN93, 100 nM calphostin C, and mixture of all) for 8 h. Control cells were treated with DMSO at a concentration equivalent to that of inhibitor mixture. Data are presented as relative light intensity (mean ± SEM, n = 4). (B) Western blotting of endogenous CREB and phosphorylated CREB (pCREB) after the treatment with protein kinase inhibitors. Inhibitor-treated cells are analyzed by Western blotting using anti-pCREB, anti-CREB, and anti-actin antibodies.

of the cells treated with an extract and control cells did not show an increased light intensity. We chose 8 extracts that increased light intensity from among the 120 extracts, whose ID numbers are indicated on the bars, and further analysis was carried out (Figure 6A). The cells treated with these 8 extracts were analyzed by Western blotting using anti-pCREB and -CREB antibodies. Seven extracts (*Chrysanthemi flos*, *Schisandrae fructus*, *Cimicifugae rhizoma*, *Caryophylli flos*, *Moutan cortex*, *Viticis fructus*, and *Myrrha*) showed increased pCREB signal, whereas one extract (*Aurantii nobilis pericarpium*) did not show an increased signal intensity. Three extracts (*Chrysanthemi flos*, *Cimicifugae rhizome*, and *Caryophylli flos*) increased the expression level of the CREB protein. Because the results of photon measurement were consistent with those of Western blotting with high probability, our probe proteins are therefore useful for screening for molecules that affect CREB phosphorylation.

■ DISCUSSION

Development of Split Luciferase Probes for Detection of KID−KIX Interaction. We developed probe proteins for detection of KID−KIX interaction in living cells (Figure 2). On the basis of the reported optimized cleavage site of firefly luciferase,[16,17,25] we constructed various fusion probe proteins. Light intensity from probe proteins (C6+D5) was more than 100-fold higher than that of probe proteins without linker sequence modulation (C1+D1). Because the expression levels of C1, D1 probe proteins and C6,D5 probe proteins in HEK293T cells were not significantly different (Figure S1B), this increase in light intensity is probably caused by the optimal interaction between LucN and LucC. As the $(GGGGS)_3$ linker[26] worked well in other split luciferase probes,[17] using flexible peptides may be important for the development of split luciferase. We did not find any interference with normal cellular activities such as proliferation and CRE-dependent transcription caused by probe protein expression (Figure 3). These findings confirm that our probe proteins do not have any harmful effects on normal cellular activities.

Characterization of Developed Probe Proteins. HEK293T cells expressing probe proteins showed an increased light intensity when treated with forskolin (Figure 3C). Because forskolin activates protein kinase A by upregulating intracellular cAMP production, this increase in light intensity is considered to be the result of KID−KIX interaction initiated by phosphorylation of probe proteins. Furthermore, we found that the single amino acid mutation (S133A) in the C6 probe protein abolished the increase in light intensity in response to forskolin treatment. Thus, the photon emission of our probe proteins originates from single amino acid phosphorylation at S133 in the C6 probe protein and subsequent interaction with D5. We found that the time course of phosphorylation of endogenous CREB after forskolin treatment (Figure 4E) was correlated with that of light intensity from probes (Figure 4A). Furthermore, levels of phosphorylated CREB match the light intensity from probes (Figure 5). These results indicate that the time course of CREB phosphorylation overlaps well with that of the KID−KIX interaction; thus, the photon emission from probes is considered to reflect the phosphorylation state of CREB. The level of phosphorylated CREB is considered to be low in nonstimulated neurons; however, we found photon emission in HEK293T cells expressing probe proteins under nonstimulated condition. It is assumed that the photon emission is caused by constitutive phosphorylation of some probe proteins in HEK293T cells. Consistent with this idea, endogenous CREB is phosphorylated in nonstimulated HEK293T cells (Figure 4E).

A significant increase in light intensity from HEK293T cells expressing probe proteins was observed from 15 min and peaked 1−2 h after forskolin treatment (Figure 4A). This time course is similar to that of chromatin binding of p300 reported previously, peaked 1 h after serum treatment of T98G cells, as determined by chromatin immunoprecipitation (ChIP) assay.[27] Because endogenous CREB phosphorylation occurred 2 min after forskolin treatment (Figure 4E), the photon emission from probe proteins was delayed 10−15 min compared with endogenous CREB phosphorylation. On the other hand, CRE-dependent transcription is upregulated 4 h after forskolin treatment and it occurs much later than photon emission from probe proteins (Figure 3B). This might be because transcriptional activation after CREB-CBP/p300 interaction requires 4 h. We conclude that the photon emission of our probe proteins originates from the phosphorylation of S133 and the timing of photon emission is similar to that of CREB-CBP/p300 interaction.

Specificity and Advantages of Our Probe Proteins. There are some probes that detect PKA activity.[8−11] These probes are based on the interaction between catalytic and regulatory subunits of PKA. Thus, these probes detect the enhancement of cAMP production and subsequent activation

dx.doi.org/10.1021/bc200491j | Bioconjugate Chem. 2012, 23, 923−932

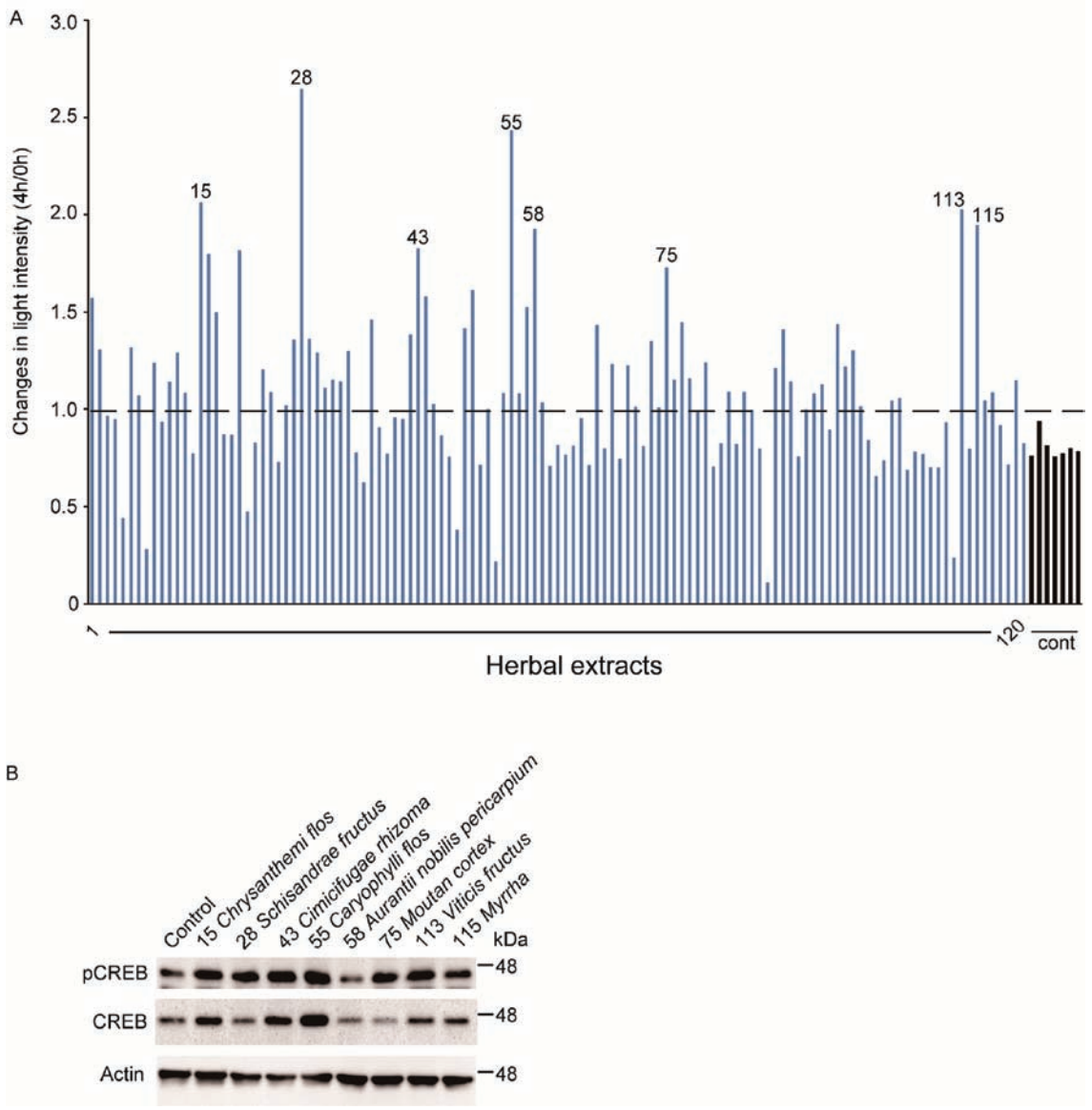

Figure 6. Screening for CREB activators using herbal extract library. (A) Changes in light intensity of cells expressing probe proteins after treatment with herbal extracts. HEK293T cells expressing C6+D5 probe proteins were treated with oriental herbal extracts for 4 h. Each bar represents changes in light intensity induced by each extract. Black bars are control experiments without extract treatment. (B) Western blotting of endogenous CREB, pCREB, and actin after treatment with herbal extracts. Cells with increased light intensity numbered in (A) were analyzed 4 h after the treatment by Western blotting using anti-pCREB, anti-CREB, and anti-actin antibodies.

of PKA. Although CREB phosphorylation was considered to be induced mainly by PKA, it is widely accepted that many kinases phosphorylate S133 of CREB and increase CREB transcriptional activity depending on the cell type and stimulus used.[7] This means that PKA-detecting probes are not sufficient for measuring CREB activity. On the other hand, our probes are based on KID phosphorylation and subsequent KID−KIX interaction. Even when KID is phosphorylated by kinases other than PKA, our probes can emit light. Hence, we conclude that our probes are useful for the specific detection of CREB activation. As shown in Figure 5, our probe proteins can detect KID−KIX interaction induced by CaMKII.

A FRET probe that detects CREB phosphorylation has been reported.[13] The FRET probe is capable of detecting CREB activation with a high spatiotemporal resolution. However, methods based on FRET have the limitations of autofluorescence noise and phototoxicity, which makes them inappropriate for measuring CREB activity for a long time in living cells. On the other hand, our split luciferase probe proteins have little noise and no phototoxicity because no excitation light is required. These advantages enable us to carry out long-term measurement of KID−KIX interaction in living cells (Figure 4A).

Screening Herbal Extracts That Induce CREB Activation. In this report, we screened and analyzed the extracts that increased the light intensity of our probe proteins. Because CREB phosphorylation in neurons is an important event for plastic changes in synaptic transmission, the extracts that activate CREB are expected to have the potential as drugs that improve memory and cognition.[28,29] On the other hand, CREB phosphorylation is considered to be important in oncogenesis and some tumor cells show overexpressed or constitutively activated CREB.[30,31] Hence, screening for molecules that

decrease light intensity from the probe proteins may contribute to the search for the antitumor compounds.

We analyzed 8 extracts that increased the light intensity from the probe proteins. Among them, some extracts (*Schisandrae fructus*, *Moutan cortex*, *Viticis fructus*, and *Myrrha*) induced CREB phosphorylation, which is probably caused by the activation of kinases induced by some constituents in the extracts. Other extracts (*Chrysanthemi flos*, *Cimicifugae rhizoma*, and *Caryophylli flos*) induced not only the phosphorylation but also the expression of CREB. In the case of these extracts, the increase in kinase activity and CREB expression level occurred simultaneously. This might be due to the upregulation of transcriptional activation induced by some extract constituents. As an increased expression level of CREB in leukemia cells has been reported,[32] the CREB upregulation seen in leukemia cells and HEK293T cells treated with these herbal extracts may share the same signal transduction pathway. Because each herbal extract consists of many kinds of molecules, we presently cannot specify which constituent is responsible for CREB activation. Some studies suggest that candidates responsible molecules. Schizandrin[33] and Gomisin A,[34] compounds purified from *Schisandrae fructus*, are reported to reverse the scopolamine-induced memory impairment. Paeonol from *Moutan cortex* is reported to improve the learning ability of mice with D-galactose-induced aging in the Morris water maze test.[35] Because memory formation is closely related to CREB activation, it is of interest to investigate whether these molecules induce improvements of memory via CREB phosphorylation. Interestingly, the extract of *Aurantii nobilis pericarpium* that increased the light intensity of probe proteins did not show an increased CREB phosphorylation level in Western blotting. Although we do not have any data that can explain why this pseudopositive reaction occurred, some constituents in *Aurantii nobilis pericarpium* extract may affect LucN and LucC directly and increase light intensity. Taken together, we conclude that our probe protein is useful for screening for molecules that affect CREB phosphorylation with high probability, simplicity in method, and good signal-to-noise ratio compared with the FRET technique. In addition, this cell-based approach can exclude compounds that are toxic to cells and identify the molecules that permeate across the cell membrane and activate CREB. Furthermore, high-throughput screening will be possible if sample application and photon detection are automated.

For the future application of our probe proteins, we expect to apply them in the monitoring of CREB activation in the brain of living animals. Imaging the activity of a particular protein in the brain of a living animal has been impossible using fluorescence-based methods such as FRET because animal tissues have a marked autofluorescence and a change in FRET signal intensity is undetectable. Because our probes do not require excitation light, we do not have to consider the problem of autofluorescence. Furthermore, the luciferase substrate luciferin can reach the brain even when administered by intraperitoneal injection.[36] Using transgenic mice that express the probe proteins, behavioral analysis in parallel with the observation of CREB activation in the brain will be possible. This experiment will elucidate when and where CREB activation is required for memory formation.

■ ASSOCIATED CONTENT

Supporting Information

Additional figures as described. This material is available free of charge via the Internet at http://pubs.acs.org.

■ AUTHOR INFORMATION

Corresponding Author

*Tel: +81-76-434-7230, Fax: +81-76-434-5015, E-mail: hmori@med.u-toyama.ac.jp.

Notes

The authors declare no competing financial interest.

■ ACKNOWLEDGMENTS

This work was supported by PRESTO of the Japan Science and Technology Corporation (JST, No. 2602), Japan Society for the Promotion of Science (JSPS, No. 2070331), and Grant-in-Aid for the Cooperative Research Project from Joint Usage/Research Center (Joint Usage/Research Center for Science-Based Natural Medicine), Institute of Natural Medicine, University of Toyama in 2010.

■ REFERENCES

(1) Montminy, M. R., Sevarino, K. A., Wagner, J. A., Mandel, G., and Goodman, R. H. (1986) Identification of a cyclic-AMP-responsive element within the rat somatostatin gene. *Proc. Natl. Acad. Sci. U. S. A. 83*, 6682−6.

(2) Montminy, M. R., and Bilezikjian, L. M. (1987) Binding of a nuclear protein to the cyclic-AMP response element of the somatostatin gene. *Nature 328*, 175−8.

(3) Parker, D., Ferreri, K., Nakajima, T., LaMorte, V. J., Evans, R., Koerber, S. C., Hoeger, C., and Montminy, M. R. (1996) Phosphorylation of CREB at Ser-133 induces complex formation with CREB-binding protein via a direct mechanism. *Mol. Cell. Biol. 16*, 694−703.

(4) Benito, E., and Barco, A. (2010) CREB's control of intrinsic and synaptic plasticity: implications for CREB-dependent memory models. *Trend. Neurosci. 33*, 230−40.

(5) Bourtchuladze, R., Frenguelli, B., Blendy, J., Cioffi, D., Schutz, G., and Silva, A. J. (1994) Deficient long-term memory in mice with a targeted mutation of the cAMP-responsive element-binding protein. *Cell 79*, 59−68.

(6) Lonze, B. E., and Ginty, D. D. (2002) Function and regulation of CREB family transcription factors in the nervous system. *Neuron 35*, 605−23.

(7) Johannessen, M., Delghandi, M. P., and Moens, U. (2004) What turns CREB on? *Cell. Signal. 16*, 1211−27.

(8) Adams, S. R., Harootunian, A. T., Buechler, Y. J., Taylor, S. S., and Tsien, R. Y. (1991) Fluorescence ratio imaging of cyclic AMP in single cells. *Nature 349*, 694−7.

(9) Bagorda, A., Das, S., Rericha, E. C., Chen, D., Davidson, J., and Parent, C. A. (2009) Real-time measurements of cAMP production in live Dictyostelium cells. *J. Cell Sci. 122*, 3907−14.

(10) Zaccolo, M., De Giorgi, F., Cho, C. Y., Feng, L., Knapp, T., Negulescu, P. A., Taylor, S. S., Tsien, R. Y., and Pozzan, T. (2000) A genetically encoded, fluorescent indicator for cyclic AMP in living cells. *Nat. Cell Biol. 2*, 25−9.

(11) Stefan, E., Aquin, S., Berger, N., Landry, C. R., Nyfeler, B., Bouvier, M., and Michnick, S. W. (2007) Quantification of dynamic protein complexes using Renilla luciferase fragment complementation applied to protein kinase A activities in vivo. *Proc. Natl. Acad. Sci. U. S. A. 104*, 16916−21.

(12) Hai, T., and Curran, T. (1991) Cross-family dimerization of transcription factors Fos/Jun and ATF/CREB alters DNA binding specificity. *Proc. Natl. Acad. Sci. U. S. A. 88*, 3720−4.

(13) Friedrich, M. W., Aramuni, G., Mank, M., Mackinnon, J. A. G., and Griesbeck, O. (2010) Imaging CREB activation in living cells. *J. Biol. Chem. 285*, 23285−95.
(14) Paulmurugan, R., Umezawa, Y., and Gambhir, S. S. (2002) Noninvasive imaging of protein-protein interactions in living subjects by using reporter protein complementation and reconstitution strategies. *Proc. Natl. Acad. Sci. U. S. A. 99*, 15608−13.
(15) Ozawa, T., Kaihara, A., Sato, M., Tachihara, K., and Umezawa, Y. (2001) Split luciferase as an optical probe for detecting protein-protein interactions in mammalian cells based on protein splicing. *Anal. Chem. 73*, 2516−21.
(16) Luker, K. E., Smith, M. C., Luker, G. D., Gammon, S. T., Piwnica-Worms, H., and Piwnica-Worms, D. (2004) Kinetics of regulated protein-protein interactions revealed with firefly luciferase complementation imaging in cells and living animals. *Proc. Natl. Acad. Sci. U. S. A. 101*, 12288−93.
(17) Ishimoto, T., Ozawa, T., and Mori, H. (2011) Real-time monitoring of actin polymerization in living cells using split luciferase. *Bioconjugate Chem. 22*, 1136−44.
(18) Hartley, J. L., Temple, G. F., and Brasch, M. A. (2000) DNA cloning using in vitro site-specific recombination. *Genome Res. 10*, 1788−95.
(19) Sasaki, Y., Sone, T., Yoshida, S., Yahata, K., Hotta, J., Chesnut, J. D., Honda, T., and Imamoto, F. (2004) Evidence for high specificity and efficiency of multiple recombination signals in mixed DNA cloning by the Multisite Gateway system. *J. Biotechnol. 107*, 233−43.
(20) Vo, N., and Goodman, R. H. (2001) CREB-binding protein and p300 in transcriptional regulation. *J. Biol. Chem. 276*, 13505−8.
(21) Cheung, W. M., Hui, W. S., Chu, P. W., Chiu, S. W., and Ip, N. Y. (2000) Ganoderma extract activates MAP kinases and induces the neuronal differentiation of rat pheochromocytoma PC12 cells. *FEBS Lett. 486*, 291−6.
(22) Lin, Y. L., Lee, Y. C., Huang, C. L., Lai, W. L., Lin, Y. R., and Huang, N. K. (2007) Ligusticum chuanxiong prevents rat pheochromocytoma cells from serum deprivation-induced apoptosis through a protein kinase A-dependent pathway. *J. Ethnopharmacol. 109*, 428−34.
(23) Kim, D. H., Kim, S., Jeon, S. J., Son, K. H., Lee, S., Yoon, B. H., Cheong, J. H., Ko, K. H., and Ryu, J. H. (2009) Tanshinone I enhances learning and memory, and ameliorates memory impairment in mice via the extracellular signal-regulated kinase signalling pathway. *Br. J. Pharmacol. 158*, 1131−42.
(24) Hou, Y., Aboukhatwa, M. A., Lei, D. L., Manaye, K., Khan, I., and Luo, Y. (2010) Anti-depressant natural flavonols modulate BDNF and beta amyloid in neurons and hippocampus of double TgAD mice. *Neuropharmacology 58*, 911−20.
(25) Kim, S. B., Kanno, A., Ozawa, T., Tao, H., and Umezawa, Y. (2007) Nongenomic activity of ligands in the association of androgen receptor with SRC. *ACS Chem. Biol. 2*, 484−92.
(26) Huston, J. S., Levinson, D., Mudgett-Hunter, M., Tai, M. S., Novotny, J., Margolies, M. N., Ridge, R. J., Bruccoleri, R. E., Haber, E., Crea, R., et al. (1988) Protein engineering of antibody binding sites: recovery of specific activity in an anti-digoxin single-chain Fv analogue produced in Escherichia coli. *Proc. Natl. Acad. Sci. U. S. A. 85*, 5879−83.
(27) Ramos, Y. F., Hestand, M. S., Verlaan, M., Krabbendam, E., Ariyurek, Y., van Galen, M., van Dam, H., van Ommen, G. J., den Dunnen, J. T., Zantema, A., and Hoen, P. A. (2010) Genome-wide assessment of differential roles for p300 and CBP in transcription regulation. *Nucleic Acids Res. 38*, 5396−408.
(28) Glannon, W. (2006) Psychopharmacology and memory. *J. Med. Ethics 32*, 74−8.
(29) Scott, R., Bourtchuladze, R., Gossweiler, S., Dubnau, J., and Tully, T. (2002) CREB and the discovery of cognitive enhancers. *J. Mol. Neurosci. 19*, 171−7.
(30) Siu, Y. T., and Jin, D. Y. (2007) CREB--a real culprit in oncogenesis. *FEBS J. 274*, 3224−32.
(31) Shankar, D. B., Cheng, J. C., and Sakamoto, K. M. (2005) Role of cyclic AMP response element binding protein in human leukemias. *Cancer 104*, 1819−24.
(32) Crans-Vargas, H. N., Landaw, E. M., Bhatia, S., Sandusky, G., Moore, T. B., and Sakamoto, K. M. (2002) Expression of cyclic adenosine monophosphate response-element binding protein in acute leukemia. *Blood 99*, 2617−9.
(33) Egashira, N., Kurauchi, K., Iwasaki, K., Mishima, K., Orito, K., Oishi, R., and Fujiwara, M. (2008) Schizandrin reverses memory impairment in rats. *Phytother. Res. 22*, 49−52.
(34) Kim, D. H., Hung, T. M., Bae, K. H., Jung, J. W., Lee, S., Yoon, B. H., Cheong, J. H., Ko, K. H., and Ryu, J. H. (2006) Gomisin A improves scopolamine-induced memory impairment in mice. *Eur. J. Pharmacol. 542*, 129−35.
(35) Zhong, S. Z., Ge, Q. H., Qu, R., Li, Q., and Ma, S. P. (2009) Paeonol attenuates neurotoxicity and ameliorates cognitive impairment induced by d-galactose in ICR mice. *J. Neurol. Sci. 277*, 58−64.
(36) Izumi, H., Ishimoto, T., Yamamoto, H., Nishijo, H., and Mori, H. (2011) Bioluminescence imaging of Arc expression enables detection of activity-dependent and plastic changes in the visual cortex of adult mice. *Brain Struct. Funct. 216*, 91−104.

Bioconjugate Chemistry

Article

pubs.acs.org/bc

Development of a Low Toxicity, Effective pDNA Vector Based on Noncovalent Assembly of Bioresponsive Amino-β-cyclodextrin:Adamantane−Poly(vinyl alcohol)−Poly(ethylene glycol) Transfection Complexes

Aditya Kulkarni,[†] Wei Deng,[†] Seok-hee Hyun, and David H. Thompson*

Departments of Chemistry and Biomedical Engineering, Purdue University, 560 Oval Drive, West Lafayette, Indiana 47907, United States

Supporting Information

ABSTRACT: A host:guest-derived gene delivery vector has been developed, based on the self-assembly of cationic β-CD derivatives with a poly(vinyl alcohol) (MW 27 kDa) (PVA) main chain polymer bearing poly(ethylene glycol) (MW 750) (PEG) or MW 2000 PEG and acid-labile adamantane-modified (Ad) grafts through an acid-sensitive benzylidene acetal linkage. These components were investigated for their ability to promote supramolecular complex formation with pDNA using two different assembly schemes, involving either precomplexation of the pendent Ad-PVA-PEG polymer with the cationic β-CD derivatives before pDNA condensation (method A) or pDNA condensation with the cationic β-CD derivatives prior to addition of Ad-PVA-PEG to engage host:guest complexation (method B). The pendent polymers were observed to degrade under acidic conditions while remaining intact for more than 5 days at pH 7. HeLa cell culture data show that these materials have 10^3-fold lower cytotoxicities than 25 kDa bPEI while maintaining transfection efficiencies that are superior to those observed for this benchmark cationic polymer transfection reagent when the method A assembly scheme is employed. These findings suggest that degradable cationic polymer constructs employing multivalent host:guest interactions may be an effective and low-toxicity vehicle for delivering nucleic acid cargo to target cells.

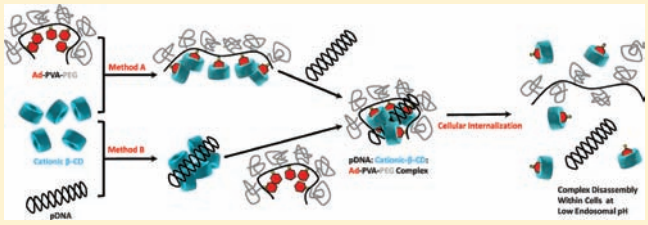

INTRODUCTION

Safe and efficient delivery of nucleic acid constructs to target cells has great potential for the treatment of genetic diseases;[1−4] however, the clinical success of this approach greatly depends on the development of effective delivery vehicles with low toxicity. Viral and nonviral vectors both have been studied for this purpose but suffer from several key limitations. Although efficient and persistent, viral vectors are challenged by issues of large-scale production, immunogenicity, and safety, whereas nonviral vectors are limited primarily by lack of efficiency. Nonetheless, nonviral gene delivery has attracted considerable attention because of its scalability and modest host immunogenicity compared to viral vectors.[5−7] A variety of nonviral vectors have been explored, including cationic lipids, cationic peptides, and cationic polymers such as polyethylenimines (PEIs),[8,9] poly-(L-lysine),[10] PAMAM dendrimers,[11,12] polyaminoesters,[13,14] polyamidoamines,[15] polyphosphoesters,[16] chitosans,[17] and cyclodextrin (CD) oligomers.[4,18−22] These vectors are all capable of condensing DNA at high N/P ratios to form positively charged particles that enter cells via nonspecific uptake mechanisms. These particles also protect the genetic material from degradation and enhance their cell permeability; however, they often display significant cytotoxicity at the concentrations needed for effecting nucleic acid cargo bioactivity. Thus, the challenge remains to create nonviral vectors that have high transfection efficiencies while maintaining low toxicity. This requires an integration of various factors such as serum stability, specific binding to target cells, and efficient unpackaging and release of the cargo upon cellular internalization.

β-Cyclodextrin (CD) is a widely used host molecule capable of internalizing guest molecules in water with binding constants in the $10^{0.5}$−10^5 M^{-1} range.[23] CDs have been extensively used for gene delivery because of their ability to stabilize the nucleic acids in biological media and their ability to destabilize and permeate biological membranes and for obviating undesirable side effects. A variety of CD-based systems such as CD polymers, CD dendrimers, and CD polyrotaxanes are promising materials for nonviral vector development. Davis and co-workers have reported a diverse class of β-CD oligomers coupled via cationic linkers.[24−27] Recently, one of these derivatives was successfully used as a vector for siRNA delivery in a clinical trial for treatment of melanoma in humans.[4] Cationic CD polyrotaxanes have also been reported where the

Received: September 18, 2011
Revised: March 26, 2012
Published: May 2, 2012

dx.doi.org/10.1021/bc2005158 | Bioconjugate Chem. 2012, 23, 933−940

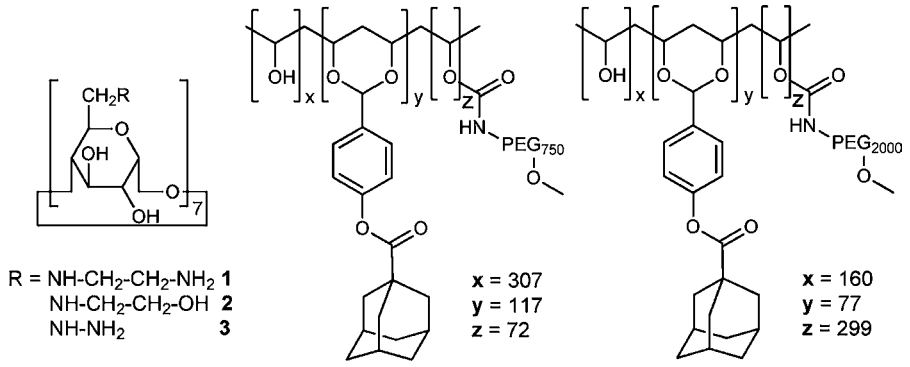

Figure 1. Structures of amino-β-CDs, Ad-PVA-PEG$_{750}$, and Ad-PVA-PEG$_{2000}$.

cationic substituents have been introduced by postmodification reactions after the macrocycle has been threaded onto the polymer backbone.[19,28,29] The limited flexibility and highly polycationic nature of these constructs can impede efficient DNA complexation, thus requiring high N/P ratios for nucleic acid compaction that may affect their efficiency.

Herein we report a nucleic acid delivery vector designed to avoid these limitations by employing the self-assembly of cationic β-CD derivatives with a pendent polymer comprising adamantane-modified (Ad) poly(vinyl alcohol)−poly(ethylene glycol) (PVA-PEG), whose Ad units are linked through an acid-labile acetal motif (Figure 1). It was anticipated that pDNA compaction could be achieved via complexation with self-assembled amino-β-CD$^+$:Ad-PVA-PEG host:guest pendent polymer complexes via multivalent electrostatic interactions between the cationic β-CD derivatives and the nucleic acid cargo. These amino-β-CD units are then held into place via hydrophobic interactions between the β-CD host cavities and the pendent benzylidene acetal-linked Ad groups on the PVA backbone. This design enables the compaction of nucleic acid cargo into stable nanometer-size particles that can then be internalized and degraded within the acidic endosomes of target cells by acid-catalyzed cleavage of the acetal-linked adamantyl pendent groups (Scheme 1).

Scheme 1

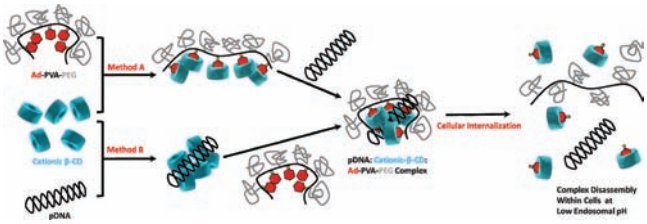

EXPERIMENTAL PROCEDURES

Materials. All solvents were reagent grade, purchased from commercial sources, and used without further purification except DMF and toluene, which were dried over CaH_2 under N_2, filtered, and distilled under reduced pressure. β-CD, NaOH, I_2, Ph_3P 1-adamantanecarbonyl chloride (Ad-CO-Cl), 4-hydroxybenzaldehyde, Na_2CO_3, 1,1-carbonyldiimidazole (CDI), β-CD, *p*-toluenesulfonyl acid (TSA), and *p*-toluenesulfonyl chloride were obtained from Aldrich-Sigma, Inc. ^{1}H NMR spectra were recorded on a 300 MHz Varian INOVA 300 NMR spectrometer at 30 °C. Chemical shifts were referenced to the residual protonated solvent peak. Qiagen kits were purchased from Qiagen. mhGFP plasmid vector was purchased from Promega. Plasmid DNA was amplified in *Escherichia coli* and purified according to the supplier's protocol (Qiagen, Hilden, Germany). The purity and concentration of the purified plasmid DNA were determined by agarose gel electrophoresis and by absorption at 260 and 280 nm. The purified plasmid DNA was resuspended in TE buffer (10 mM Tris-Cl, pH 7.5, 1 mM EDTA) and kept in aliquots at 0.5 mg/mL.

Synthesis of Hepta-6-(2′-aminoethyl)amino-β-CD (1). Hepta-6-iodo-β-CD (1.0 g, 0.5 mmol) was dissolved in 50 mL of 1,2-diaminoethane, then stirred at 60 °C under an atmosphere of N_2 for 24 h. The solution was then concentrated under reduced pressure to a few milliliters before pouring into acetone (300 mL). A fine white precipitate was formed and gathered by filtration. The precipitate was washed with acetone and dried under vacuum to yield a stable white powder. Yield = 0.47 g (66%). ^{1}H NMR (270 MHz, D_2O): δ = 5.21−5.15 (s, 7H, C1H of CD), 4.10−3.82 (m, 21H, C3H and C5H of CD and NH), 3.77−3.54 (m, 28H, C2H, C4H, and C6H of CD), 3.21−2.97 (m, 2H, N1-CH_2), 2.97−2.88 (t, 2H, N2-CH_2), 2.68−2.56 (b, 14H, NH_2). ^{13}C NMR (75 MHz, $CDCl_3$): δ = 102.0 (C(1) of β-CD), 82.3 (C(4) of β-CD), 73.2 (C(3) of β-CD), 72.5 (C(2) of β-CD), 72.1 (C(5) of β-CD), 55.2 (C(6) of β-CD), 53.9 (NH-CH_2), 45.2(CH_2-NH_2).

Synthesis of Hepta-6-(2′-hydroxyethyl)amino-β-CD (2). This was prepared as described for compound **1** except that 2-aminoethanol was used as nucleophile instead of 1,2-diaminoethane. Yield = 0.51 g (70%). ^{1}H NMR (270 MHz, D_2O): δ = 5.10−5.05 (s, 7H, C1H of CD), 4.00−3.85 (m, 14H, C3H and C5H of CD) 3.75−3.42 (m, 28H, C2H, C4H, and C6H of CD), 3.01−2.82 (m, 2H, ethanolamine CH_2O), 2.78−2.72 (t, 2H, ethanolamine CH_2N). ^{13}C NMR (75 MHz, D_2O): δ = 104.1 (C(1) of β-CD), 84.6 (C(4) of β-CD), 74.0 (C(3) of β-CD), 73.2 (C(2) of β-CD), 72.5 (C(5) of β-CD), 67.5(CH_2−OH), 58.7 (C(6) of β-CD), 57.5 (CH_2-N).

Synthesis of Hepta-6-hydrazyl-β-CD (3). This was prepared as described for compound **1** except that hydrazine was used as nucleophile instead of 1,2-diaminoethane. Yield = 0.52 g (54%). ^{1}H NMR (270 MHz, D_2O): δ = 5.13−5.09 (s, 7H, C1H of CD), 4.28−4.02 (b, 7H, NH), 4.02−3.22 (m, 42H, C2H, C3H, C4H, C5H, and C6H of CD), 2.00−1.80 (b, 14H, NH_2). ^{13}C NMR (75 MHz, D_2O): δ = 101.9 (C(1) of β-CD), 81.6 (C(4) of β-CD), 73.0 (C(3) of β-CD), 72.4 (C(2) of β-CD), 72.0 (C(5) of β-CD), 45.9 (C(6) of β-CD).

Synthesis of 4-Benzaldehyde Adamantanecarboxyl Ester (Ad-Ph-CHO). To a solution of 4-hydroxybenzaldehyde

dx.doi.org/10.1021/bc2005158 | *Bioconjugate Chem.* 2012, 23, 933−940

(2.44 g, 20 mmol) in THF (10 mL) was added 3 mL of NEt_3. The solution was cooled with ice before adding dropwise a solution of AdCOCl (5.94 g, 30 mmol) in THF (10 mL). After 6 h, the THF was removed using a rotary evaporator. The residue was dissolved in 50 mL of ether and then washed three times with 1 M Na_2CO_3 and one time with saturated NaCl solution. The solution was dried over Na_2SO_4 and the solvent removed using a rotary evaporator to yield a pale yellow solid. Yield = 5.11 g (90%). ^{1}H NMR (400 MHz, $CDCl_3$): δ = 9.99 (s, 1H, CHO), 7.91 (d, J = 8.4 Hz, 2H, Ph), 7.23 (d, J = 8.0 Hz, 2H, Ph), 2.09−2.05 (m, 9H, Ad), 1.81−1.74 (m, 6H, Ad).

Synthesis of Ad-PVA. PVA (MW = 27 kDa) (460 mg, 10 mmol) was dissolved in 10 mL of dry DMSO, and then Ad-PhCHO (568 mg, 1.0 mmol) and 50 mg of TSA were added. This solution was stirred for 2 days at 50 °C. The solution was then poured into acetone (300 mL). A fine white precipitate was formed and gathered by filtration. The precipitate was washed with acetone and dried under vacuum to yield a stable white solid. Yield = 850 mg (85.2%). ^{1}H NMR (400 MHz, DMSO-d_6): δ = 7.42 (w, 2H, Ph), 7.03 (w, 2H, Ph), 5.51 (s, 1H, PhCH), 4.66−4.02 (m, 3H, PVA-OH), 3.96-3.74 (m, 5H, PVA-CH), 2.02−1.95 (m, 9H, Ad), 1.70 (m, 6H, Ad), 1.59−1.21 (m, 10H, PVA-CH_2).

Synthesis of Ad-PVA-PEG. A solution of CDI (162 mg, 1 mmol in 10 mL of DMSO) was added dropwise to a solution of Ad-PVA (720 mg in 20 mL of DMSO). The solution was stirred for 1 day at 50 °C, then processed by addition of 300 mL of dry THF three times to precipitate the CDI-activated polymer, which was used directly in the next step after redissolving in 10 mL of DMSO. After the addition of methoxypolyethylene glycol amine (MW = 750 or 2000), NH_2-PEG-OMe (750 mg, 100 equiv, 1 mmol of PEG750, or 6.4 g, 320 equiv, 3.2 mmol of PEG2000), to the solution, the mixture was stirred overnight. The product was dialyzed against DMSO and deionized water three times each (Spectra/Por membrane, MWCO 6000−8000) to remove low MW impurities. After removal of the solvent, the polymer was redissolved in DMSO and precipitated into acetone. The Ad-PVA-PEG was isolated as a pale yellow solid. Yield = 1.1 g. ^{1}H NMR (400 MHz, H_2O): δ = 7.61−7.45 (br, Ph), 7.12−7.01 (br, Ph), 5.2−4.6 (br m, PVA-OH, overlapped with HDO), 4.01−3.05 (br m, PVA-CH and PEG-CH_2), 2.2−1.5 (br, Ad). MW Ad-PVA-PEG_{750} = 112 kDa; MW Ad-PVA-PEG_{2000} = 645 kDa.

^{1}H NMR Evidence for Acid Catalyzed Cleavage of Acetal Linker. Ad-PVA (50 mg) was dissolved by sonication in 2 mL of 10 mM β-CD D_2O solution for 10 min, followed by removal of undissolved material via centrifugation at 5400 rpm for 1 h. The sample was then transferred to an NMR tube for analysis. Trifluoroacetic acid (TFA) was added to get the desired pH (pH 4 and pH 7), and the ^{1}HNMR spectra were recorded at 4 and 48 h.

Dynamic Light Scattering and Atomic Force Microscopy. The sizes and size distributions of the materials were evaluated by dynamic light scattering using a particle size analyzer (Zetasizer Nano S, Malvern Instruments Ltd.) at room temperature (25 °C) with a scattering angle of 90°. AFM imaging of the nanoparticles was conducted in tapping mode (MultiMode, Veeco, U.S.) using dry samples on mica. The AFM tips (PPP-NCH, Nanoscience Instruments, Inc., U.S.) had a typical radius of 7 nm or less, and the images were recorded with a scan rate of 0.5 or 1 Hz. Samples were prepared by dropping 2 mL of solution on a mica surface, followed by overnight drying at 20 °C.

Gel Shift Assay. The complexation ability of the systems was studied by gel shift assay. Agarose gels (1% w/v) containing ethidium bromide were made in 1× TE buffer. All transfection complexes were loaded onto the gel at various N/P ratios, and 200 ng of DNA was added to each well. The gels were run at 50 V for about 1 h and visualized.

Cell Viability Assay. The cytotoxicity of the amino-β-CD$^+$ complexes relative to bPEI (25 kDa) was evaluated using the MTT assay in HeLa cells. The cells were cultured in complete DMEM medium supplemented with 10% FBS at 37 °C, 5% CO_2, and 95% relative humidity. The cells were seeded in 96-well microtiter plates (Nunc, Wiesbaden, Germany) at densities of 10 000 cells/well. After 24 h, the culture medium was replaced with serum-supplemented culture medium containing serial dilutions of amino-β-CD$^+$, and the cells were incubated for an additional 24 h. Then 10 μL of sterile-filtered MTT stock solution in PBS (5 mg/mL) was added to each well, reaching a final MTT concentration of 0.5 mg/mL. After 5 h, unreacted dye was removed by aspiration. The formazan crystals were dissolved in DMSO (100 μL/well), and the absorbance at 570 nm was measured using a microplate reader (Spectra Plus, TECAN). The percent cell viability, compared to control cells cultured in medium without polymers, was calculated as $[A]_{test}/[A]_{control} \times 100\%$, where $[A]_{test}$ is the absorbance of the wells with polymers and $[A]_{control}$ is the absorbance of the control wells. All experiments were conducted for three samples and averaged. The median lethal dose (LD_{50}) is the dose of a toxic material that kills half (50%) of the cells tested. In this study, LD_{50} was taken as the concentration of a gene carrier causing a relative cell viability decrease to 50%.

In Vitro Transfection of mhGFP pDNA. HeLa cells were cultured in complete DMEM medium supplemented with 10% FBS at 37 °C, 5% CO_2, and 95% relative humidity. Cells were seeded in 24-well plates at a density of 100 000 cells/well. After 48 h, the culture medium was replaced with medium (serum-free or 10% serum-supplemented) containing the transfection complexes prepared at a 20:1 N/P ratio using mhGFP pDNA. The cells were incubated with the transfection complexes for 24 h, after which the spent medium was aspirated and fresh serum-supplemented medium was added. After incubation for 24 h, the medium was aspirated and the cells were washed with PBS, trypsinized, and analyzed by FACS using excitation and emission filters of 488 and 530 nm, respectively.

RESULTS AND DISCUSSION

Synthesis of Amino-β-CD$^+$ and Ad-PVA-PEG Host:-Guest Polymer Components. On the basis of the design shown in Scheme 1, we synthesized three cationic β-CD derivatives (Figure 1) to test the amino-β-CD$^+$:pendent polymer concept, i.e., hepta-6-(1′,2′-diaminoethyl)-β-CD (**1**), hepta-6-(2′-hydroxyethylamino)-β-CD (**2**), and hepta-6-(hydrazino)-β-CD (**3**). The amino-β-CD$^+$ components were synthesized from hepta-6-iodo-β-CD by a simple one step procedure. Ad-PhCHO was prepared from 4-hydroxybenzaldehyde and 1-adamantanecarbonyl chloride. Ad-PhCHO was further used to synthesize Ad-PVA and Ad-PVA-PEG from PVA (27 kDa). The Ad-PVA was prepared from Ad-PhCHO and PVA in the presence of a catalytic amount of TSA to give the acetal-based pendent polymer. Ad-PVA was isolated by precipitation in acetone. This was further activated by 1,1′-carbonyldiimidazole to give the PEGylated pendent polymer Ad-PVA-PEG. The Ad-PVA and Ad-PVA-PEG_{750} were prepared with 19 mol % Ad acetal modifications and 12 mol

dx.doi.org/10.1021/bc2005158 | Bioconjugate Chem. 2012, 23, 933−940

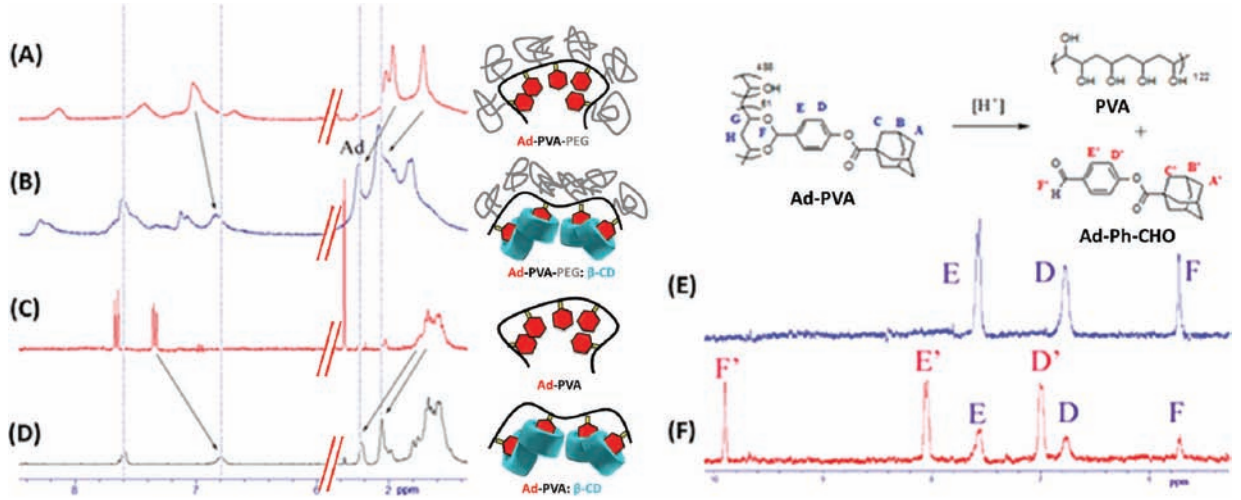

Figure 2. 400 MHz ^{1}H NMR spectra of Ad-PVA-PEG in the absence (A) and in the presence (B) of β-CD; Ad-PVA in the absence (C) and presence (D) of β-CD in D_2O after 48 h at 20 °C; and Ad-PVA with β-CD at pH 7 (E) and pH 4 (F) in D_2O at 20 °C.

% PEG750 carbamate modifications (MW = 112 kDa), while Ad-PVA-PEG$_{2000}$ was prepared with 13 mol % Ad acetal modifications and 48 mol % PEG2000 carbamate modifications (MW = 645 kDa) as determined by ^{1}H NMR. These pendent polymer constructs then were investigated for their ability to promote pDNA:host:guest complex formation and acid-responsive disassembly.

Characterization of Amino-β-CD$^+$:Ad-PVA-PEG Interaction. Complexation of Ad-PVA and Ad-PVA-PEG$_{750}$ with the amino-β-CD$^+$ derivatives was confirmed by ^{1}H NMR (Figure 2A–D). The phenyl and Ad resonances of the PVA derivatives showed significant upfield shifts upon the addition of amino-β-CD host ligands in aqueous medium, indicating the formation of host:guest polymer complexes via Ad ↔ CD inclusion. The complexation of the pendent polymer with α-CD and γ-CD as studied by ^{1}H NMR revealed that there was no detectable binding of the α-CD or γ-CD to the polymer (i.e., no upfield shift was observed for the phenyl or Ad resonances upon their addition to the aqueous solution of the pendent polymer; Supporting Information). Next, we tested the acid-catalyzed cleavage of the acetal bond used to connect the Ad guest ligand to the polymer backbone. ^{1}H NMR spectra of Ad-PVA in D_2O in the presence of equimolar unmodified β-CD were measured as a function of pH. At pH 7, the resonances of the benzylidene acetal pendent group protons were observed at 7.6, 6.8, and 5.6 ppm. After treatment of this solution at pH 4 for 48 h, the ^{1}H NMR spectra exhibited three new peaks at 7.0, 8.1, and 9.8 ppm that were attributed to the cleaved benzaldehyde-4-adamantanecarboxyl ester unit (Figure 2E,F). Detailed hydrolysis kinetics were studied by a pyrene fluorescence assay to study the time-dependent degradation of the polymer.[38] Evidence from NMR and the pyrene fluorescence assay of the pendent group cleavage from the polymer main chain at low pH suggests that a similar process may occur upon cellular internalization. Hydrolysis of the pendent groups from the PVA backbone within the acidic endosomal environment would be expected to promote complex disassembly, pDNA unpackaging, and escape.

Characterization of the Particles Formed by pDNA:Amino-β-CD$^+$:Ad-PVA-PEG Complexation. The ability of these noncovalent pendent polymer assemblies to condense pDNA was then evaluated with respect to particle size and net charge. Two different complexation methods (Scheme 1) were used to evaluate the relative capacity of amino-β-CD$^+$:Ad-PVA-PEG$_{750}$ host:guest polymer assemblies toward pDNA condensation. In method A, Ad-PVA-PEG$_{750}$ was preassociated with amino-β-CD$^+$s before addition to the pDNA solution. In method B, the pDNA was first complexed with the respective amino-β-CD$^+$, followed by addition of Ad-PVA-PEG$_{750}$.

Gel shift assays of pDNA complexes with the amino-β-CD$^+$ and the amino-β-CD$^+$:Ad-PVA-PEG$_{750}$ pendent polymer assemblies indicate that both methods of formulation had comparable pDNA complexation abilities. Also, in the absence of polymer, much higher N/P ratios were required to condense pDNA effectively. Comparison of the three amino-β-CD$^+$ compounds indicated that **3** has the greatest capacity for condensing pDNA compared to **1** and **2** (Supporting Information). This improved condensation capability of **3** relative to **1** and **2** can be attributed to the availability of both the nitrogens on the hydrazine moiety for interaction with pDNA. In the cases of **1** and **2**, the more basic 2° amines are not as easily accessible to the pDNA, resulting in less effective condensation.

The ζ potentials were measured for both types of complexes with Ad-PVA-PEG$_{750}$ to determine the surface charge of the resulting transfection particles (Figure 3A). We observed that complexes formed by both methods, as well as polymer-free amino-β-CD$^+$:pDNA complexes, had positive ζ when N/P > 5.

Hydrazine derivative **3** was an unusual case in that complexes of this species prepared either via method B or in the absence of Ad-PVA-PEG$_{750}$ gave similar results, whereas complexes of **3** produced using method A had a positive charge that was significantly higher and comparable to bPEI:pDNA complexes. Interestingly, we observed that complexes formulated from Ad-PVA-PEG$_{2000}$ had a surface charge that was slightly negative. Similar trends were observed with Ad-PVA-PEG; such complexes formulated with **3** produced nearly neutral surface charges at N/P = 20.

Dynamic light scattering (DLS) was used to determine the transfection complex sizes produced using these different materials and methods. Our data show that both **1** and **3** had plasmid condensation abilities that were similar to bPEI when method A was used (i.e., the particle diameters were below 300 nm when N/P > 5) (Figure 3B). Compound **2** also condensed

dx.doi.org/10.1021/bc2005158 | Bioconjugate Chem. 2012, 23, 933–940

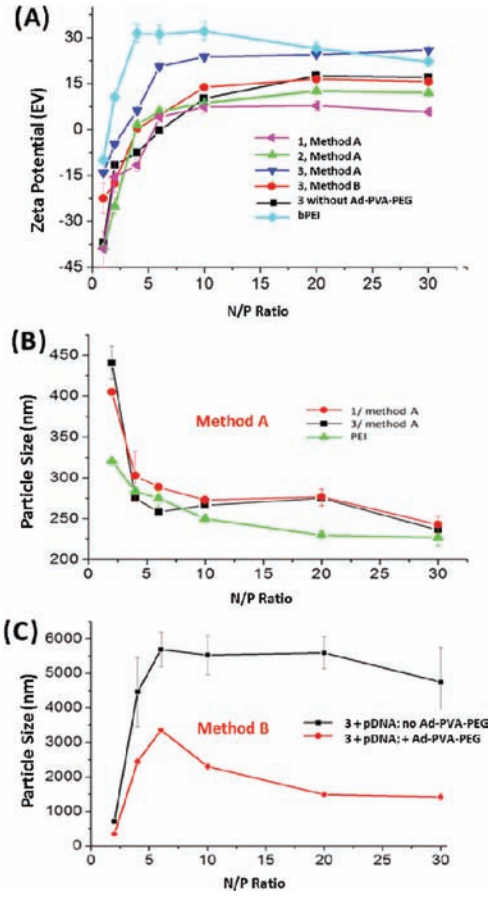

Figure 3. (A) ζ potential measurements of pDNA:amino-β-CD complexes and pDNA:bPEI complexes. DLS measurements of (B) pDNA:**1**:Ad-PVA-PEG$_{750}$ and pDNA:**3**:Ad-PVA-PEG$_{750}$ complexes formulated by method A and (C) pDNA:**3** and pDNA:**3**:Ad-PVA-PEG$_{750}$ complexes formulated by method B.

pDNA to form particles of ~400 nm at high N/P ratios (≥40) using method A (Supporting Information). In stark contrast, method B complexes of **3**:pDNA showed a sharp increase in particle size across a narrow N/P ratio range of 2:1 →5:1 (500 → 5500 nm), indicating that extensive aggregation occurs with these complexes in the absence of polymer. Interestingly, the particle sizes of pDNA:**3**:Ad-PVA-PEG$_{750}$ complexes initially increased over this same range of N/P ratios, followed by a decrease to below 2000 nm at N/P ≥ 10. We infer from these results that the PEG-grafted polymer helps to sterically stabilize the **3**:pDNA particles (Figure 3C). Our findings indicate that method A is much better than method B for producing small transfection complexes, presumably because of improved steric stabilization and a reduced propensity for Ad-PVA-PEG$_{750}$ to promote particle aggregation via host:guest interactions of a single polymer chain between two or more preformed amino-β-CD$^+$:pDNA particles. DLS measurements of complexes made with Ad-PVA-PEG$_{2000}$ showed that the particles were less than 300 nm for all the CD variants. Ad-PVA-PEG complexes prepared by method B were larger than those prepared by method A. Another notable observation is that at similar N/P ratios (e.g., 20), complexes formulated from Ad-PVA-PEG$_{2000}$ are significantly smaller than those prepared from Ad-PVA-PEG$_{750}$ (225 vs 295 nm, respectively, for **1**). This indicates that the increased PEG MW and grafting density on the polymer backbone sterically stabilizes the complexes and helps condense them into smaller particles (Supporting Information).

AFM images of Ad-PVA-PEG$_{750}$ samples revealed the presence of spherical particles (Figure 4A) that were formed by aggregation of the pendent Ad units in aqueous medium. Upon addition of amino-β-CD$^+$ derivatives, the spherical particles were transformed into granular fibrillar shaped objects (Figure 4B). We infer from these observations that β-CD complexation with the polymer Ad groups via host:guest interaction causes a transformation of the spherical micelle geometry to an elongated, flexible rod structure due to the combined effects of electrostatic repulsion between the neighboring cationic amino-β-CD$^+$s that are appended to the polymer backbone via host:guest inclusion and the excluded volume occupied by the pendent PEG750 segments. When pDNA was added to this system at low N/P ratios, the samples were observed to be a mixture of fibers and particles, presumably due to the presence of both partially complexed flexible rod structures and more fully compacted pDNA complexes (Figure 4C). When N/P = 6, only particles with diameters of about 100 nm were observed (Figure 4D). Ad-PVA-PEG$_{2000}$ formed complexes that were smaller than the complexes formed by Ad-PVA-PEG$_{750}$ but showed similar trends with respect to shape and morphology (Supporting Information). The sizes determined by AFM are smaller than those measured by DLS because of the absence of solvent-swollen polymer in the AFM samples. These results support the conclusion that host:guest complexation of Ad-PVA-PEG with amino-β-CD$^+$ produces a noncovalent assembly that is capable of condensing pDNA into compact, relatively uniform particles

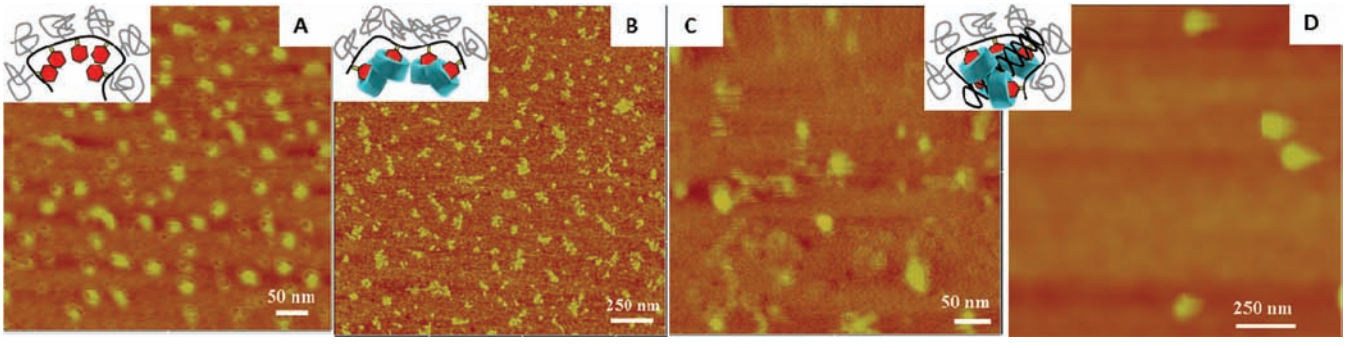

Figure 4. AFM images of (A) Ad-PVA-PEG$_{750}$ and (B) 1:1 β-CD:Ad-PVA-PEG$_{750}$. Images of pDNA:**3**:Ad-PVA-PEG$_{750}$ prepared by method B at (C) N/P = 2 and (D) N/P = 6. The insets illustrate the possible structures in these images. The samples were prepared by adding a drop of solution to the mica surface and then slowly evaporating the sample at 25 °C overnight.

dx.doi.org/10.1021/bc2005158 | *Bioconjugate Chem.* 2012, 23, 933–940

that are sufficiently small to be internalized by cells via endocytosis.

Acute Cytotoxicity and Transfection Properties of Amino-β-CD$^+$:Ad-PVA-PEG Complexes. The in vitro cytotoxicity of amino-β-CD$^+$ compounds, Ad-PVA-PEG$_{750}$, and their host:guest complexes are a highly relevant factor for their long-term consideration as a safe nonviral nucleic acid vector. Figure 5 shows that Ad-PVA-PEG$_{750}$, all of the amino-β-CD$^+$ compounds, and the **1**:Ad-PVA-PEG$_{750}$ host:guest complex were nearly 3 orders of magnitude less cytotoxic than bPEI, a benchmark reagent for in vitro and in vivo transfections. Specifically, we found that the LD_{50} values of bPEI, **1**, **2**, **3**, Ad-PVA-PEG, and 1:1 **1**:Ad-PVA-PEG$_{750}$ were 0.01, 4.5, 8.9, 1.6, 1.77 and 2 mM, respectively.

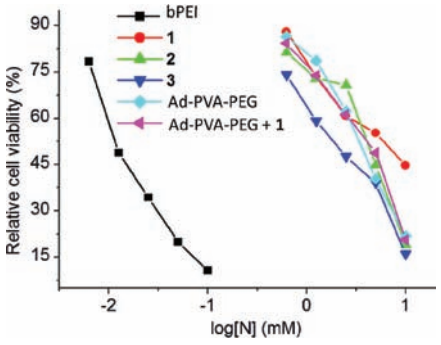

Figure 5. Cytotoxicities of **1**, **2**, **3**, Ad-PVA-PEG$_{750}$, and **1**:Ad-PVA-PEG$_{750}$ host:guest complexes in HeLa cells using 25 kDa bPEI as a control. The cells were treated with increasing concentrations of amino-β-CDs, **1**:Ad-PVA-PEG$_{750}$ complexes, and bPEI for 24 h in serum-free medium before analysis by MTT assay.

The in vitro performance of the transfection complexes generated by complexation of pDNA (mhGFP) and the amino-β-CD$^+$:Ad-PVA, amino-β-CD$^+$:Ad-PVA-PEG$_{750}$, or amino-β-CD$^+$:Ad-PVA-PEG$_{2000}$ host:guest pendent polymer systems was assessed in HeLa cells at N/P = 20 in both serum-free and 10% serum-supplemented medium (Figure 6). The transfection efficiencies were calculated using the transfection efficiency of bPEI as 100%. The amino-β-CD$^+$:Ad-PVA complexes showed less than 20% transfection efficiency, with method A complexes performing marginally better than method B complexes. We attribute this low level of transfection to the formation of poorly internalized large aggregates that are formed because of the absence of sterically stabilizing PEG segments in this host:guest pendent polymer construct.

In the absence of serum, method A amino-β-CD$^+$:Ad-PVA-PEG$_{750}$ complexes produced transfection efficiencies in the 15−55% range, depending on the amino-β-CD type, whereas complexes generated using method B showed transfection efficiencies in the 10−25% range. In the presence of serum, complexes made from Ad-PVA-PEG$_{750}$ showed less than 10% efficiency. This can be attributed to the low serum stability of the particles due to the relatively low PEG density. Complexes made from Ad-PVA-PEG$_{2000}$ produced transfection efficiencies in the range of 40−140% of bPEI in the absence of serum and 30−130% of bPEI in the presence of serum. We observed that the presence of serum has little effect on the transfection efficiency of PEG$_{2000}$ constructs because of the impact of either the higher PEG MW or higher PEG loading on improved serum stability. Complexes made from the hydrazino-modified β-CD (**3**) and ethylenediamine-modified β-CD (**2**) showed

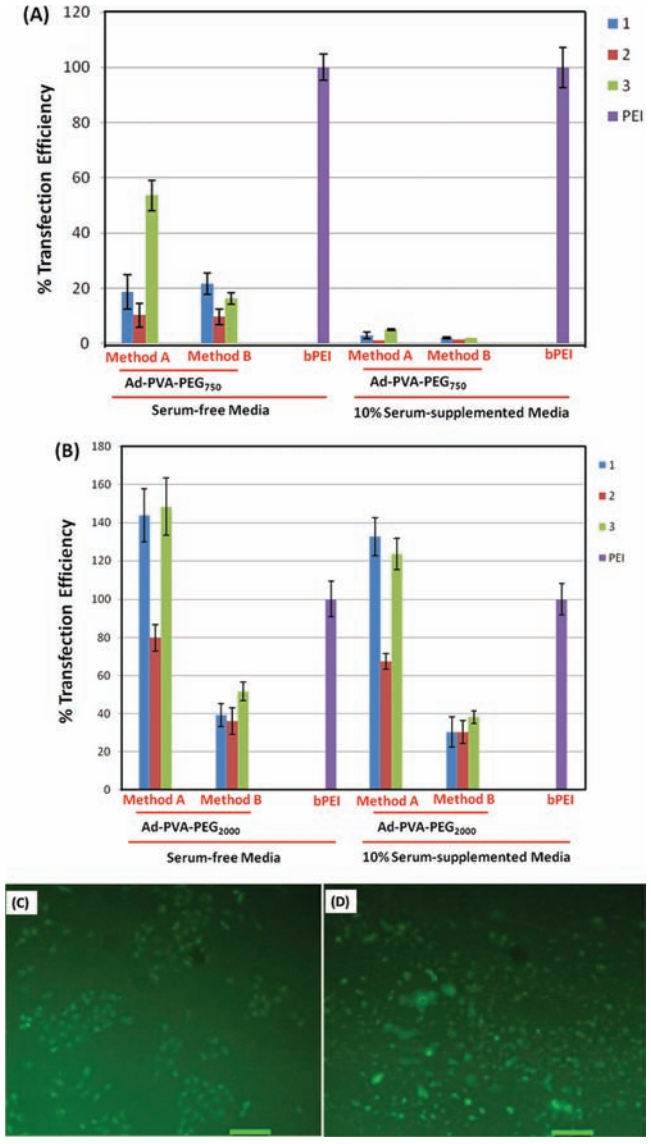

Figure 6. In vitro transfection efficiencies of amino-β-CD host:guest complexes with (A) Ad-PVA-PEG$_{750}$ and mhGFP pDNA, (B) Ad-PVA-PEG$_{2000}$ and mhGFP pDNA in HeLa cells, with 25 kDa bPEI (control) considered as 100% transfection efficiency. Fluorescence microscope images of transfected HeLa cells (C) bPEI 25k, (D) **3**:Ad-PVA-PEG$_{750}$ using method A at N/P = 20 in serum-free medium using GFP gene as a reporter gene. Scale bar: 100 μm.

better transfection efficiency than the ethanolamine (**1**) derivative. We attribute this finding to the lower charge density on these derivatives (due to the lower pK_a expected for **3** and **1** relative to the 2° amines present on **2**) that makes them capable of more facile exchange off the pDNA core.

The transfection experimental conditions used were those that had been previously optimized for bPEI in order to provide the most accurate comparison with this widely used transfection reagent. It is important to note, however, that the performance of bPEI is almost 2-fold lower and nearly 1000 times more toxic than the amino-β-CD$^+$:Ad-PVA-PEG$_{2000}$ complexes reported here (Figure 5). Indeed, the widely reported dose-limiting toxicity of bPEI has been a major impediment to the further development of gene delivery strategies *in vivo* using this vector. In view of this limitation, the apparent low toxicity of amino-β-CD$^+$:Ad-PVA-PEG complexes

dx.doi.org/10.1021/bc2005158 | *Bioconjugate Chem.* 2012, 23, 933−940

suggests that higher doses may be possible with this vector while still maintaining good cell viability.

Three other observations deserve note for all the amino-β-CD$^+$:Ad-PVA-PEG complexes studied: (i) method A complexes tend to produce higher transfection efficiencies than the analogous method B complexes; (ii) Ad-PVA-PEG$_{2000}$ complexes were significantly more effective than Ad-PVA-PEG$_{750}$ complexes, which in turn were more effective than Ad-PVA complexes; and (iii) increased PEG loading and use of longer PEG result in complexes that are stable in presence of serum. Smaller transfection complex sizes, improved solubility due to the presence of PEG, and improved steric stabilization are likely to be responsible for these findings. The smaller sizes of the transfection complexes may have led to an increase in extent of cellular internalization of the particles, thereby leading to better transfection efficiencies for method A. Conversely, the low solubility of the Ad-PVA complexes results in aggregation, giving rise to larger particles that may be too large to be effectively internalized, thus leading to lower transfection efficiencies. On the basis of our encouraging findings, we plan to evaluate the effect of various material parameters (e.g., pendent group density, pendent group spacing, pendent group hydrolysis rate) on the performance of this novel self-assembled vector strategy in future studies.

CONCLUSIONS

A low toxicity and efficient gene delivery system has been developed based on the self-assembly of cationic CD derivatives with adamantane-modified PVA. PVA, linked to Ad via a pH-sensitive acetal linkage, provides a scaffold for binding of cationic amino-β-CD$^+$ that is capable of condensing pDNA into nanoparticles in the <300 nm size range using a multilayer strategy.[30−32] This system employs reversible host:guest interactions that have also been used to construct cross-linked hydrogels, particles, transfection and RNAi complexes.[33−37,39] The pendent guest ligands have been attached using acid-sensitive acetal linkages so that they are capable of degrading within acidic endosomes to effect pDNA release. These cationic host:guest pendent polymers are capable of achieving transfections efficiencies that are comparable and superior to those of 25 kD bPEI while being nearly 1000-fold less toxic than this conventional cationic polymer transfection agent.

ASSOCIATED CONTENT

Supporting Information

Characterization of amino-β-CD$^+$ compounds and Ad-PVA-PEG. This material is available free of charge via the Internet at http://pubs.acs.org.

AUTHOR INFORMATION

Corresponding Author

*Phone: 765-494-0386. Fax; 765-496-2592.

Author Contributions

†These authors contributed equally to this work.

Notes

The authors declare no competing financial interest.

ACKNOWLEDGMENTS

The authors express their special thanks for the support of this work by NIH Grant GM087016, the Showalter Foundation, the Purdue University Center for Cancer Research, and the Purdue University Department of Chemistry.

REFERENCES

(1) Mancuso, K., Hauswirth, W. W., Li, Q., Connor, T. B., Kuchenbecker, J. A., Mauck, M. C., Neitz, J., and Neitz, M. (2009) Gene therapy for red-green colour blindness in adult primates. *Nature 461*, 784−788.

(2) Waehler, R., Russell, S. J., and Curiel, D. T. (2007) Engineering targeted viral vectors for gene therapy. *Nat. Rev. Genet. 8*, 573−587.

(3) Semple, S. C., Akinc, A., Chen, J., Sandhu, A. P., Mui, B. L., Cho, C. K., Sah, D. W. Y., Stebbing, D., Crosley, E. J., Yaworski, E., Hafez, I. M., Dorkin, J. R., Qin, J., Lam, K., Rajeev, K. G., Wong, K. F., Jeffs, L. B., Nechev, L., Eisenhardt, M. L., Jayaraman, M., Kazem, M., Maier, M. A., Srinivasulu, M., Weinstein, M. J., Chen, Q., Alvarez, R., Barros, S. A., De, S., Klimuk, S. K., Borland, T., Kosovrasti, V., Cantley, W. L., Tam, Y. K., Manoharan, M., Ciufolini, M. A., Tracy, M. A., de Fougerolles, A., MacLachlan, I., Cullis, P. R., Madden, T. D., and Hope, M. J. (2010) Rational design of cationic lipids for siRNA delivery. *Nat. Biotechnol. 20*, 172−176.

(4) Davis, M. E., Zuckerman, J. E., Choi, C. H. J., Seligson, D., Tolcher, A., Alabi, C. A., Yen, Y., Heidel, J. D., and Ribas, A. (2010) Evidence of RNAi in humans from systemically administered siRNA via targeted nanoparticles. *Nature 464*, 1067−1070.

(5) Nayak, S., and Herzog, R. W. (2010) Progress and prospects: immune responses to viral vectors. *Gene Ther. 17*, 295−304.

(6) Li, S. D., and Huang, L. (2007) Non-viral is superior to viral gene delivery. *J. Controlled Release 123*, 181−3.

(7) Xu, L., and Anchordoquy, T. (2011) Drug delivery trends in clinical trials and translational medicine: challenges and opportunities in the delivery of nucleic acid-based therapeutics. *J. Pharm. Sci. 100*, 38−52.

(8) Yu, H. J., and Wagner, E. (2009) Bioresponsive polymers for nonviral gene delivery. *Curr. Opin. Mol. Ther. 11*, 165−178.

(9) Vachutinsky, Y., and Kataoka, K. (2010) PEG-based polyplex design for gene and nucleotide delivery. *Isr. J. Chem. 50*, 175−184.

(10) Kawano, T., Okuda, T., Aoyagi, H., and Niidome, T. (2004) Long circulation of intravenously administered plasmid DNA delivered with dendritic poly(L-lysine) in the blood flow. *J. Controlled Release 99*, 329−337.

(11) Majoros, I. J., Williams, C. R., and Baker, J. R. (2008) Current dendrimer applications in cancer diagnosis and therapy. *Curr. Top. Med. Chem. 8*, 1165−1179.

(12) Mintzer, M. A., and Grinstaff, M. W. (2011) Biomedical applications of dendrimers: a tutorial. *Chem. Soc. Rev. 40*, 173−190.

(13) Zhang, J., and Lynn, D. M. (2006) Multilayered films fabricated from combinations of degradable polyamines: tunable erosion and release of anionic polyelectrolytes. *Macromolecules 39*, 8928−8935.

(14) Zhang, J., Montañez, S. I., Jewell, C. M., and Lynn, D. M. (2007) Multilayered films fabricated from plasmid DNA and a side-chain functionalized poly(beta-amino ester): surface-type erosion and sequential release of multiple plasmid constructs from surfaces. *Langmuir 23*, 11139−11146.

(15) Peng, L., Gao, Y., Xue, Y.-N., Huang, S.-W., and Zhuo, R.-X. (2010) Cytotoxicity and in vivo tissue compatibility of poly(amidoamine) with pendant aminobutyl group as a gene delivery vector. *Biomaterials 31*, 4467−4476.

(16) Huang, S.-W., and Zhuo, R.-X. (2008) Recent advances in polyphosphoester and polyphosphoramidate-based biomaterials. *Phosphorus, Sulfur Silicon Relat. Elem. 183*, 340−348.

(17) Duceppe, N., and Tabrizian, M. (2010) Advances in using chitosan-based nanoparticles for in vitro and in vivo drug and gene delivery. *Expert Opin. Drug Delivery 7*, 1191−1207.

(18) Yui, N., Katoono, R., and Yamashita, A. (2009) Functional cyclodextrin polyrotaxanes for drug delivery. *Adv. Polym. Sci. 222*, 55−77.

(19) Yang, C., Wang, X., Li, H., Tan, E., Lim, C. T., and Li, J. (2009) Cationic polyrotaxanes as gene carriers: physicochemical properties and real-time observation of DNA complexation, and gene transfection in cancer cells. *J. Phys. Chem. B 113*, 7903−7911.

(20) Mellet, C. O., Fernandez, J. M. G., and Benito, J. M. (2011) Cyclodextrin-based gene delivery systems. *Chem. Soc. Rev. 40*, 1586−1608.
(21) Srinivasachari, S., Fichter, K. M., and Reineke, T. M. (2011) Polycationic beta-cyclodextrin "click clusters": monodisperse and versatile scaffolds for nucleic acid delivery. *J. Am. Chem. Soc. 130*, 4618−4627.
(22) Srinivasachari, S., and Reineke, T. M. (2009) Versatile supramolecular pDNA vehicles via "click polymerization" of beta-cyclodextrin with oligoethyleneamines. *Biomaterials 30*, 928−938.
(23) Rekharsky, M. V., and Inoue, Y. (1998) Complexation thermodynamics of cyclodextrins. *Chem. Rev. 98*, 1875−1918.
(24) Gonzalez, H., Hwang, S. J., and Davis, M. E. (1999) New class of polymers for the delivery of macromolecular therapeutics. *Bioconjugate Chem. 10*, 1068.
(25) Reineke, T. M., and Davis, M. E. (2003) Structural effects of carbohydrate-containing polycations on gene delivery. 1. Carbohydrate size and its distance from charge centers. *Bioconjugate Chem. 14*, 247−254.
(26) Reineke, T. M., and Davis, M. E. (2003) Structural effects of carbohydrate-containing polycations on gene delivery. 2. Charge center type. *Bioconjugate Chem. 14*, 255−261.
(27) Popielarski, S. R., Mishra, S., and Davis, M. E. (2003) Structural effects of carbohydrate-containing polycations on gene delivery. 3. Cyclodextrin type and functionalization. *Bioconjugate Chem. 14*, 672−678.
(28) Yamashita, A., Kanda, D., Katoono, R., Yui, N., Ooya, T., Maruyama, A., Akita, H., Kogure, K., and Harashima, H. (2008) Supramolecular control of polyplex dissociation and cell transfection: efficacy of amino groups and threading cyclodextrins in biocleavable polyrotaxanes. *J. Controlled Release 131*, 137−144.
(29) Ooya, T., Choi, H. S., Yamashita, A., Yui, N., Sugaya, Y., Kano, A., Maruyama, A., Akita, H., Ito, R., Kogure, K., and Harashima, H. (2006) Biocleavable polyrotaxane-plasmid DNA polyplex for enhanced gene delivery. *J. Am. Chem. Soc. 128*, 3852−3853.
(30) Jewell, C. M., and Lynn, D. M. (2008) Multilayered polyelectrolyte assemblies as platforms for the delivery of DNA and other nucleic acid-based therapeutics. *Adv. Drug Delivery Rev. 60*, 979−999.
(31) Becker, A. L., Johnston, A. P. R, and Caruso, F. (2010) Layer-by-layer-assembled capsules and films for therapeutic delivery. *Small 6*, 1836−1852.
(32) Hatakeyama, H., Akita, H., Kogure, K., and Harashima, H. (2010) A novel nonviral gene delivery system: multifunctional envelope-type nano device. *Adv. Biochem. Eng. Biotechnol. 119*, 197−230.
(33) Charlot, A., and Auzely-Vélty, R. (2007) Synthesis of novel supramolecular assemblies based on hyaluronic acid derivatives bearing bivalent β-cyclodextrin and adamantane moieties. *Macromolecules 40*, 1147−1158.
(34) Li, L., Guo, X. H., Wang, J., Liu, P., Prud'homme, R. K., May, B. L., and Lincoln, S. F. (2008) Polymer networks assembled by host−guest inclusion between adamantyl and β-cyclodextrin substituents on poly(acrylic acid) in aqueous solution. *Macromolecules 41*, 8677−8681.
(35) Wang, H., Wang, S., Su, H., Chen, K.-J., Armijo, A. L., Lin, W.-Y., Wang, Y., Sun, J., Kamei, K., Czernin, J., Radu, C. G., and Tseng, H.-R. (2009) A supramolecular approach for preparation of size-controlled nanoparticles. *Angew. Chem., Int. Ed. 48*, 4344−4348.
(36) Zhang, J. X., Sun, H. L., and Ma, P. X. (2010) Host−guest interaction mediated polymeric assemblies: multifunctional nanoparticles for drug and gene delivery. *ACS Nano 4*, 1049−1059.
(37) Kim, S. K., Park, K. M., Singha, K., Kim, J., Ahn, Y., Kim, K., and Kim, W. J. (2010) Galactosylated cucurbituril-inclusion polyplex for hepatocyte-targeted gene delivery. *Chem. Commun. 46*, 692−694.
(38) Deng, W., Chen, J., Kulkarni, A., and Thompson, D. H. (2012) Poly(ethylene glycol)-poly(vinyl alcohol)-adamantanate: synthesis and stimuli-responsive micelle properties. *Soft Matter*, DOI: 10.1039/c2sm06394h.
(39) Kulkarni, A., DeFrees, K., Hyun, S.-H., and Thompson, D. H. (2012) Pendant polymer:amino−cyclodextrin:siRNA guest:host nanoparticles as efficient vectors for gene silencing. *J. Am. Chem. Soc.*, DOI: 10.1021/ja300690j.

Bioconjugate Chemistry

Article

pubs.acs.org/bc

Nanoclusters of Iron Oxide: Effect of Core Composition on Structure, Biocompatibility, and Cell Labeling Efficacy

Geralda A. F. van Tilborg,*[,†] David P. Cormode,[‡] Peter A. Jarzyna,[‡] Annette van der Toorn,[†] Susanne M. A. van der Pol,[§] Louis van Bloois,[∥] Zahi A. Fayad,[‡] Gert Storm,[∥] Willem J. M. Mulder,[‡] Helga E. de Vries,[§] and Rick M. Dijkhuizen[†]

[†]Biomedical MR Imaging and Spectroscopy Group, Image Sciences Institute, University Medical Center Utrecht, Utrecht, The Netherlands

[‡]Translational and Molecular Imaging Institute, Mount Sinai School of Medicine, New York, New York, United States

[§]Department of Molecular Cell Biology and Immunology, VU University Medical Center, Amsterdam, The Netherlands

[∥]Department of Pharmaceutics, Utrecht Institute for Pharmaceutical Sciences, Utrecht University, Utrecht, The Netherlands

Supporting Information

ABSTRACT: Inorganic nanocrystals have a variety of applications in medicine. They may serve as contrast agents, therapeutics, and for in vitro diagnostics. Frequently, the synthesis route yields hydrophobically capped nanocrystals, which necessitates their subsequent coating to render a water-soluble and biocompatible probe. Biocompatibility is crucial for cellular imaging applications, which require large quantities of diagnostically active nanoparticles to be loaded into cells. We have previously reported the design and synthesis of a fluorescent and magnetic resonance imaging-detectable core–shell nanoparticle that encapsulates hydrophobically coated iron oxide nanocrystals. The core of soybean oil and iron oxide is covered by a shell mixture of phospholipids, some of which contained polyethylene glycol. Despite the biocompatibility of these components, we hypothesize that we can improve this formulation with respect to *in vitro* toxicity. To this aim, we measured the effect of six different core compositions on nanoparticle structure, cell labeling efficacy, and cell viability, as well as cell tracking potential. We methodically investigated the causes of toxicity and conclude that, even when combining biocompatible materials, the resulting formulation is not guaranteed to be biocompatible.

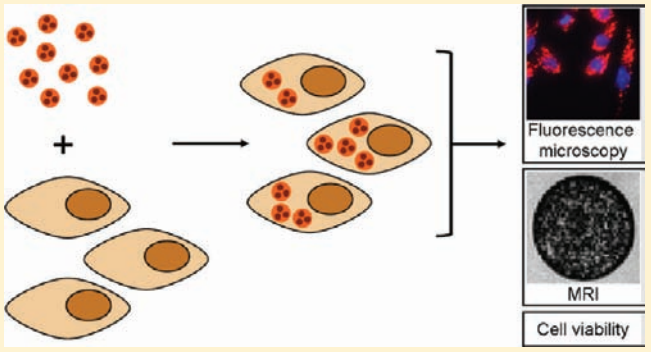

INTRODUCTION

Inorganic nanocrystals such as quantum dots, gold nanoparticles, and iron oxides have a wide variety of applications in the field of biomedicine. Semiconductor nanocrystals, also known as quantum dots, are useful in a variety of fluorescence related applications,[1] such as fluorescence imaging,[2] and for probing biological systems using Förster resonance energy transfer (FRET).[3] Gold nanostructures can be used as computed tomography contrast agents,[4,5] as tracers for optical[6,7] and photoacoustic imaging,[8] for photothermal ablation,[9] and for in vitro diagnostics.[10] Iron oxide nanoparticles can be used in magneto-hyperthermia therapies,[11] for in vitro diagnostics,[12] and as magnetic resonance imaging (MRI) contrast agents.[13] One of the most important uses of iron oxide based contrast agents is to label cells to allow them to be tracked noninvasively by MRI. In vivo cell tracking may provide an important tool in (pre)clinical diagnostics and therapeutics, for instance, by enabling monitoring of leukocyte infiltration[14] or stem cell migration.[15]

Inorganic nanocrystals may be ideally synthesized under hydrophobic conditions, which produce nanocrystals of highly defined size and high stability. For instance, synthesis of iron oxides in octadecene and other hydrophobic solvents result in very monodisperse cores of controllable diameter, which can be coated with oleic acid and dispersed in hydrophobic solvents.[16,17] In contrast, aqueous phase synthesis of iron oxides via the Molday method results in amorphous iron oxide cores.[18] However, despite their advantageous properties, such hydrophobically coated nanocrystals are not miscible with biological media. Therefore, the development of methods to render hydrophobically coated nanocrystals biocompatible is of great importance and is pivotal for biomedical applications. This is particularly relevant for cell tracking studies, which require cell loading with large quantities of contrast agent, while preserving biological function.

Received: October 5, 2011
Revised: April 2, 2012
Published: April 3, 2012

There have been several methods proposed for making hydrophobic nanocrystals biocompatible. For example, Dubertret et al. used phospholipids to suspend quantum dots in aqueous media.[19] Polymers such as poly maleic anhydride-alt-1-octadecene derivatives have been used by the group of Colvin and others, to solubilize quantum dots and iron oxides.[20−23] A variety of nanocrystals have been encapsulated in lipoprotein-like coatings.[24−26] We have previously reported a method to create biocompatible, core−shell nanoparticles of controllable diameter via the use of a carefully chosen phospholipid mixture for the shell and soybean oil as the core material.[27] These nanoemulsions were utilized to suspend oleic acid coated iron oxides in aqueous media, creating iron oxide nanoclusters and allowing their use as an MRI contrast agent, as demonstrated in tumor-bearing mice. Fluorophores were included in the lipid coating to provide contrast for fluorescence imaging. The formulation was well-tolerated by mice. Furthermore, we have lately used this platform for the delivery of hydrophobic glucocorticoid drugs, where we observed significant reductions in tumor growth compared to controls.[28] Nevertheless, at moderate to high incubation doses we also observed in vitro toxicity of the formulation *without drug*, indicating an adverse reaction to this soybean oil−iron oxide platform, even though it was composed of biocompatible building blocks.

In the current study, we developed this core−shell platform for simultaneous fluorescent and magnetic labeling of cells and tested the effect of a variety of core materials on nanoparticle formation and biocompatibility. To be specific, we compared nanoparticles with nanoclusters of iron oxide and soybean oil, medium chain triglycerides, olive oil, cottonseed oil, corn oil, or no oil as core materials, with the aim of developing an improved formulation for cell tracking applications. Of the two formulations with highest biocompatibility, we extensively characterized the nanoparticles as well as their cellular uptake by means of MRI, confocal microscopy, transmission electron microscopy, and other methods, in comparison with the original formulation. Furthermore, we methodically assessed to what extent nanoparticle composition, storage conditions, and storage time affect cell viability and activity.

EXPERIMENTAL PROCEDURES

Information on the materials, nanoparticle characterization, intracellular iron content determination, and thiobarbituric acid reactive substances assay can be found in the Supporting Information.

Nanoparticle Formation. Nanoparticles were prepared according to a solvent evaporation method, as described by Jarzyna et al.[27] First, oleic acid-coated iron oxide nanocrystals were retrieved from the toluene carrier fluid by evaporation under nitrogen flow. Next, lipids, oil, and dry iron oxide nanocrystals were individually dissolved in chloroform to obtain the following stock solutions: 25 mg/mL DSPC, 100 mg/mL PEG2000-DSPE, 1 mg/mL Rhodamine-PE, 0.5 g/mL oil, and 100 mg/mL iron oxide. Stock solutions were used to obtain fresh lipid/oil/iron oxide mixtures, containing 2.8 mg of DSPC, 10 mg of PEG2000-DSPE, and 8.4 mg of iron oxide nanocrystals. In the case of oil inclusion, 29.5 mg of soybean oil (d = 0.919 g/mL), 30.5 mg of MCT (d = 0.945 g/mL), 28.9 mg of corn oil (d = 0.9 g/mL), 29.5 mg cottonseed oil (d = 0.918 g/mL), or 29.2 mg of olive oil (d = 0.91 g/mL) was also added to the mixture. Fluorescent nanoparticles were obtained by inclusion of 1 mol % (8.1 μg) Rhodamine-PE in the lipid mixture. Oil-containing nanoparticles without iron were prepared by inclusion of 11% extra oil in the lipid/oil mixture, thereby correcting for the volume of the iron oxide nanocrystals. Directly following its preparation, the lipid/oil/iron oxide/chloroform mixture, with a maximum volume of 447 μL, was added dropwise under stirring to 8 mL of boiling reverse osmosis water. In order to evaporate all chloroform, the resulting nanoparticle suspension was continuously heated and concentrated to 3 mL. Next, the suspension was placed under nitrogen or air and homogenized by 45 min of sonication in an ultrasonic water bath (UR = 198, Retsch GmbH, Haan, Germany). Following sonication, the nanoparticle suspension was cooled to room temperature, filtered through a 0.2 μm filter (Minisart, Sartorius Stedim Biotech GmbH, Goettingen, Germany), and concentrated to approximately 1 mL using a 300 kDa MWCO Vivaspin concentrator (Sartorius Stedim Biotech GmbH, Goettingen, Germany) for 10 min at 3500 rpm. Iron concentrations were measured, and all nanoparticle preparations were diluted in reverse osmosis water to a concentration of 3.5 mg Fe/mL. Nanoparticles were stored in the dark at 4 °C under nitrogen or air, similar to the conditions used during sonication.

Cell culture and incubations. The murine macrophage cell line RAW 264.7 was grown in RPMI 1640 medium (Gibco, Invitrogen, Breda), supplemented with 10% FCS and 1% PSG. Cells were cultured at 37 °C in a humified atmosphere and 5% CO_2.

For each experiment, cells were plated at a concentration of 0.5×10^6 cells/mL RPMI 1640 at 24 h before incubation. At the onset of the experiment, the medium was changed, and nanoparticles were added to a final concentration of 200 μg Fe/mL. Microscopy, MRI, and labeling efficiency experiments were performed with freshly prepared nanoparticles, whereas nanoparticles at 1, 7, 14, and 24 days post preparation were used for viability assays. Cells were incubated for three hours, followed by extensive washing in PBS and harvesting for subsequent analyses, unless stated otherwise.

Flow Cytometry of Fluorescently Labeled Cells. Cells were incubated with fluorescent nanoparticles in 24 well plates, washed, and harvested by incubation with 1 mM EGTA in PBS for 5 min at 37 °C. Cell suspensions were centrifuged for 5 min at 1500 rpm, and the resulting pellets were resuspended in 100 μL of PBS/0.1% BSA. Cellular fluorescence, excited with a 488 nm argon-ion laser, was measured in fluorescent channel 2 (FL-2: 575/25 nm) of a FACSCalibur flow cytometer (BD Biosciences, Breda, The Netherlands), counting 20,000 cells per sample.

Fluorescence and Light Microscopy of Labeled Cells. Cells were grown on coverslips in 24 wells plates, incubated with fluorescent nanoparticles, washed, and fixed in 4% formalin for 20 min. Subsequently, cells were either stained for iron with Prussian Blue or prepared for fluorescence microscopy. For Prussian Blue staining, cells were incubated for 30 min with a fresh mixture of 20 mg/mL potassium ferricyanide ($K_3[Fe(CN)_6]$) and 2 N HCl. Nuclei were counterstained for 10 min with nuclear fast red (NFR), dehydrated, and mounted with Entellan. For fluorescence microscopy, nuclei were counterstained with Hoechst (5 min; 1:1000 dilution), washed in PBS, and mounted in fluorescence mounting medium. Fluorescence microcopy images were obtained on a Leica DM6000 microscope (Leica, Rijswijk, The Netherlands), whereas Prussian Blue labeled cells were visualized on a Nikon light microscope (Nikon, Amstelveen, The Netherlands).

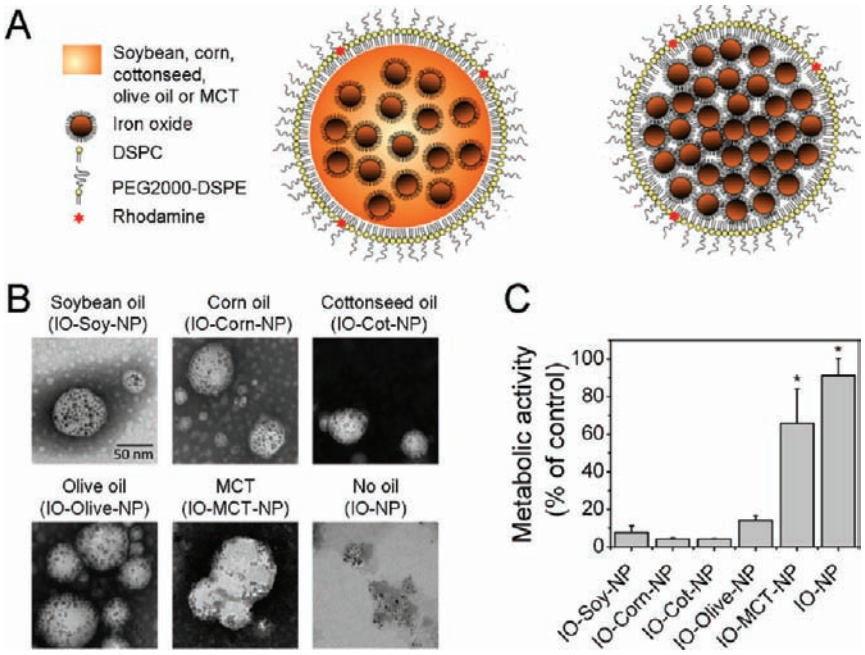

Figure 1. Schematic overview of the different nanoparticles either with or without incorporated oil (A). Negative stain TEM of the different nanoparticles (B) and metabolic activity of RAW cells after 3 h of incubation at 200 μg Fe/mL with the six different nanoparticle formulations (C). Cell incubations were performed at 14 days post nanoparticle preparation. Bars represent the mean ± standard deviation (n = 6 for IO-Soy-NP, IO-MCT-NP, and IO-NP; n = 4 for IO-Corn-NP, IO-Cot-NP, and IO-Olive-NP). * $p < 0.05$ compared to IO-Soy-NP.

Transmission Electron Microscopy of Labeled Cells. Cells were incubated with nonfluorescent nanoparticles in 6 wells plates, washed, and harvested by scraping in RPMI 1640 medium. Subsequently, cells were pelleted (5 min, 1500 rpm) and resuspended in 2.5% glutaraldehyde in PBS for fixation. The cells were embedded and stained using standard TEM pathology tissue processing techniques.[29] The grids were imaged using a Hitachi H7650 instrument (Hitachi High Technologies, Pleasanton, CA). A minimum of 15 cells per sample was imaged at a range of magnifications (2−50k).

MRI of Labeled Cells. Cells were incubated with nonfluorescent nanoparticles in T25 flasks, washed, harvested in RPMI 1640 by scraping and counted using a hemocytometer. Next, cells were pelleted by centrifugation (5 min, 1500 rpm) and resuspended to a concentration of 2×10^3 cells/μL PBS. Part of the cell sample was used to determine the intracellular iron content, while the other part was further diluted in PBS to obtain 4 samples within a range of 0.25×10^3−2×10^3 cells/μL. The obtained samples were carefully mixed with 0.8% warm agarose, at a 1:1 volume ratio in 250 μL PCR tubes, and rapidly cooled on ice. MRI experiments were performed in a 9.4 T horizontal bore MR system (Varian Inc., Palo Alto, CA, USA). Cell-containing PCR tubes were placed in a water container, and T_2 as well as T_1 values of homogeneously distributed cells in agarose were obtained using sequences and parameters similar to those described for nanoparticle characterization (see Supporting Information). T_2*-weighted MR images were acquired using a gradient echo sequence (TR/TE = 100/15 ms, α = 35°, 16 averages and 100 × 100 × 100 μm^3 voxel resolution).

T_2*-weighted images were analyzed in Matlab. First, a relatively large region-of-interest (ROI) was manually drawn on the image of the water reservoir surrounding the cell samples. Next, the mean signal intensity (SI_{ref}) and standard deviation (SD_{ref}) within this reference ROI were calculated and used to define the threshold for detection of contrast enhancement: threshold = $SI_{ref} - (5 \cdot SD_{ref})$. Pixels in the cell-containing tubes were considered contrast-enhanced in case their signal intensity (SI_{pixel}) dropped below the defined threshold: $SI_{pixel} \leq$ threshold. ROIs were manually drawn within the images of the individual sample containers, and the fraction of contrast-enhanced pixels was determined for each ROI.

Cell Viability. Cells were incubated with nonfluorescent nanoparticles in 24 and 96 wells plates at 1, 7, 14, and 28 days after nanoparticle preparation. Following incubation, cells were directly washed in PBS and subjected to viability assays (3/0 h). Alternatively, cells were washed in RPMI 1640 and cultured up to 24 h postincubation, followed by washing in PBS and viability assays (3/24 h).

The viability of labeled cells was assessed with fluorescent 7-amino-actinomycin D (7-AAD) and a colorimetric MTT assay (3-(4,5-dimethylthiazol-2-yl)-2,5-diphenyl-tetrazolium bromide). For 7-AAD staining, cells from the 24 wells plates were harvested by incubation with 1 mM EGTA in PBS (5 min at 37 °C), pelleted by centrifugation (5 min at 1500 rpm), and resuspended in 50 μL of PBS/0.1% BSA. A 1:500 dilution of 7-AAD staining solution (BD Pharmingen, BD Biosciences, Breda, The Netherlands) was added to each cell sample in a 1:1 volume ratio, and fluorescence, excited with a 488 nm argon-ion laser, was directly measured in fluorescent channel 3 (FL-3) of a FACSCalibur flow cytometer (BD Biosciences, Breda, The Netherlands), counting 20,000 cells per sample. Untreated control cells were also stained with 7-AAD to determine baseline levels of cell death within the population, which is typically less than 15%. For the MTT assay, cells were directly incubated with MTT in the 96 wells plate (100 μL/well, 1:10 diluted in RPMI 1640) for 1.5 h at 37 °C and 5% CO_2. Next, MTT was removed and the formed water-insoluble formazan was dissolved in a mixture of dimethylsulfoxide and glycine (6:1 volume ratio; 175 μL/well). The absorption of the resulting

dx.doi.org/10.1021/bc200543k | Bioconjugate Chem. 2012, 23, 941−950

Table 1. Properties of the Different Nanoparticles in Reverse Osmosis Water[a]

nanoparticle	diameter (nm)	zeta potential (mV)	r_1 ($mM^{-1}\cdot s^{-1}$)	r_2 ($mM^{-1}\cdot s^{-1}$)
IO-Soy-NP	76.2 ± 8.6	−51.3 ± 2.1	0.29 ± 0.06	268.89 ± 17.80
IO-MCT-NP	78.9 ± 5.7	−50.4 ± 0.4	0.55 ± 0.08	267.19 ± 19.25
IO-NP	62.4 ± 4.1*	−46.0 ± 0.3*	0.62 ± 0.12	402.48 ± 8.82*

[a]Diameters were obtained with dynamic light scattering, as given by the number-weighted average of three different nanoparticle preparations (n = 9). Zeta potentials were determined on a single nanoparticle sample (n = 3). Relaxivities, expressed in $mM^{-1}s^{-1}$ iron were measured at 9.4 T on two different nanoparticle preparations (n = 2). Values represent the mean ± standard deviation. * $p < 0.05$ compared to IO-Soy-NP.

purple solution was measured at 540 nm. Untreated control cells were used as a reference with 100% metabolic activity.

Statistics. Statistical analysis was performed in SPSS (16.0). A one-way ANOVA with a posthoc Bonferroni multiple-comparison procedure was applied to test for significant differences in cellular iron content, mean fluorescent intensity per cell (MFI), metabolic activity, thiobarbituric acid reactive substances (TBARS), and nanoparticle properties compared to IO-Soy-NP and, if applicable, nanoparticles without iron and/or untreated control cells. A two-way ANOVA with Bonferroni pairwise comparisons was applied to test for significant effects of storage time and storage conditions on cell viability for each of the nanoparticles. $P < 0.05$ was considered statistically significant.

RESULTS

Initial Screening. In order to obtain a more biocompatible platform than the previously described soybean oil−iron oxide formulations,[27,28] we first synthesized five alternatives to the original soybean oil−iron oxide formulation, with medium chain triglycerides (MCT), olive oil, cottonseed oil, corn oil, or no oil as core materials (Figure 1A). The described solvent-evaporation technique resulted in stable suspensions of lipid-coated nanoparticles with nanoclusters of iron oxide. Our initial screening step was characterization of the nanoparticles with TEM, to ensure that the nanoparticles had correctly formed. As can be seen in Figure 1B, inclusion of corn, cottonseed, or olive oil allowed homogeneous dispersion of the oleic-acid coated iron oxide nanocrystals throughout the nanoparticle core, similar to that of soybean oil (included for comparison). MCT forced the encapsulated iron oxides outward, to the interface of the MCT core and lipid coating (IO-MCT-NP). In the absence of the oil phase (IO-NP), iron oxide nanocrystals were densely packed inside the lipid monolayer (Figure 1B) and resulted in more irregularly shaped nanoparticles compared with the spherically shaped oil-containing nanoparticles. As the oleic acid coating of the iron oxide nanoparticle and all the oils are hydrophobic, similar iron oxide incorporation patterns were expected. The differing behavior of the iron oxide in the MCT compared to the other oils likely reflects a favorable interaction between the oleic acid (C18, unsaturated) coating of the iron oxide with the long chain unsaturated fatty acids of soybean, corn, cottonseed, and olive oils, whereas such an interaction with the saturated, short fatty acids of MCT is disfavored. Nevertheless, every formulation allowed good incorporation of the iron cores and oil within lipid coatings, and were thus included in the next screening step.

The second screening step was the in vitro MTT cell viability assay, which measures metabolic activity. We used murine macrophage RAW 264.7 cells to study the nanoparticles as these cells are known to efficiently internalize contrast agents. We tested the metabolic activity of these cells incubated with 200 μg Fe/mL of media, with formulations synthesized 14 days earlier (*infra vide*). Incubation with corn, cottonseed, or olive oil-based formulations resulted in considerable loss of metabolic activity to less than 20% of control values, which was comparable with the soybean oil-based formulation (Figure 1C). However, incubation with formulations using MCT or no oil resulted in significantly higher metabolic activity. The latter formulations were therefore selected for in depth characterization, along with the soybean oil formulation for cell labeling purposes and for further assessment of effects on cell viability.

Nanoparticle Characteristics. Dynamic light scattering (DLS) measurements showed that IO-NP were significantly smaller than IO-Soy-NP, while IO-MCT-NP and IO-Soy-NP were of comparable size (Table 1). Nanoparticle size was highly reproducible between different batches and demonstrated a polydispersity index (PDI) < 0.2 for each preparation. Zeta potentials varied marginally from −51.3 ± 2.1 mV for IO-Soy-NP to −46.0 ± 0.3 mV for IO-NP (Table 1). Lipid-coated oil-containing nanoparticle formulations without entrapped iron oxide crystals showed equivalent size and zeta potentials compared to those of their corresponding iron-containing nanoparticle (Table S1, Supporting Information), indicating that the zeta potential was predominantly determined by the lipid coating.

Relaxivities r_1 and r_2, measures of the efficiency of the contrast agent to reduce T_1 and T_2, respectively, and thereby generate contrast in T_1- and T_2-weighted MR images, were determined for each nanoparticle at 9.4 T. IO-Soy-NP and IO-MCT-NP showed similar r_2 values, whereas the r_2 of IO-NP was significantly higher (Table 1). In all cases, the r_2/r_1 ratio was high (≥400), which indicates that the nanoparticles are extremely potent $T_2^{(*)}$ contrast agents that can induce strong hypointensities on $T_2^{(*)}$-weighted MR images. The distinctive distribution of iron oxide within the nanoparticle core apparently induces differences in r_1 and r_2 relaxivities (Table 1). Most importantly, elimination of the oil phase caused a significant increase in relaxivity r_2, which agrees with studies demonstrating that r_2 increases with iron oxide core size or aggregation of iron oxide particles in suspension.[30] Longitudinal relaxivities (r_1) were rather low (<1 $mM^{-1}s^{-1}$), which is expected at high field strength, but may also be ascribed to restricted exchange of water protons with iron oxide particles in the hydrophobic core, especially when iron oxide is homogeneously distributed throughout the entire oil phase as is the case for soybean oil. The relaxivity values for IO-Soy-NP differ from those we reported previously;[27] however, this is expected as the previous measurements were acquired at a different field strength, i.e., 1.5 T.

Inclusion of Rhodamine-PE within the lipid monolayer provided multimodal nanoparticles that additionally allowed their detection with optical techniques. Nevertheless, it is important to note that nanoparticle fluorescence was largely quenched in the presence of iron oxide (Figure S1, Supporting Information).

Cell Labeling Efficacy. RAW 264.7 cells, i.e., murine macrophages, were incubated with IO-Soy-NP, IO-MCT-NP, and IO-NP to assess and compare their labeling efficiency. Following 3 h of incubation at 200 μg Fe/mL, cells labeled with IO-Soy-NP contained 1.0 ± 0.1 pg iron per cell, which was significantly less than the iron content of RAWs labeled with IO-MCT-NP (2.6 ± 0.4 pg iron) or IO-NP (5.3 ± 0.7 pg iron) (Figure 2A). Fluorescence measurements also showed sig-

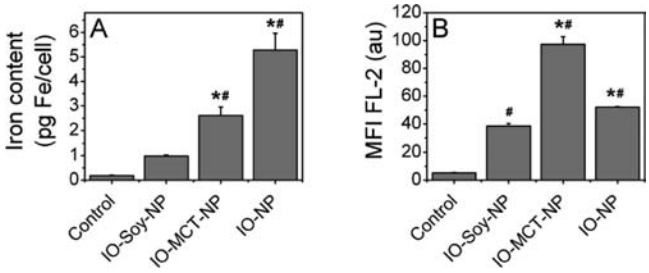

Figure 2. Cellular iron content (A) and flow cytometry-based mean fluorescent intensity (MFI) in fluorescent channel 2 (FL-2: 575/25 nm) (B) after 3 h of incubation with 200 μg Fe/mL RPMI 1640. Bars represent the mean ± standard deviation (n = 3). * p < 0.05 compared to IO-Soy-NP incubation. # p < 0.05 compared to untreated control cells.

nificantly increased uptake of IO-MCT-NP and IO-NP compared to that of IO-Soy-NP (Figure 2B). However, in contrast to the iron uptake, fluorescence was higher for IO-MCT-NP than for IO-NP labeled cells. Possibly, this may be attributed to the quenching of fluorescence in the presence of high iron concentrations.

Additional fluorescence measurements of cells labeled with oil-containing nanoparticles without incorporated iron oxide revealed significantly reduced uptake compared to their iron-containing counterparts (Figure S2, Supporting Information). Considering fluorescence is quenched by the presence of iron oxide within the nanoparticles (Figure S1, Supporting Information), this suggests that actual differences in uptake between nanoparticles with and without iron oxide are larger than those observed by the mean fluorescent intensity per cell.

Microscopy of Labeled Cells. Following internalization, nanoparticles were easily detected by fluorescence microscopy and light microscopy (Figure 3). In the latter case, cells were stained for iron by Prussian Blue. Compartmentalized intense areas of fluorescence and iron were observed throughout the cytoplasm for all nanoparticles. Transmission electron microscopy (TEM) images of labeled cells revealed nanoparticle accumulation in endolysosomal compartments (Figure 4), which corresponded with the localized areas of fluorescence and iron observed with fluorescence and light microscopy (Figure 3). In case of IO-Soy-NP, internalized iron oxide was predominantly restricted to the endosomal membrane (Figure 4C,D), while cells labeled with IO-MCT-NP showed a characteristic dispersion and circular shaped distribution of iron oxide throughout the entire endosome, similar to that observed in TEM images of the IO-MCT-NP alone (Figure 4E,F). Labeling of cells with IO-NP resulted in completely filled endosomes with high amounts of densely packed iron oxide (Figure 4G,H).

MRI of Labeled Cells. Labeling of cells with iron oxide encapsulating nanoparticles (Figure 3F,I,L) induced a visibly detectable reduction in signal intensity on T_2*-weighted MR

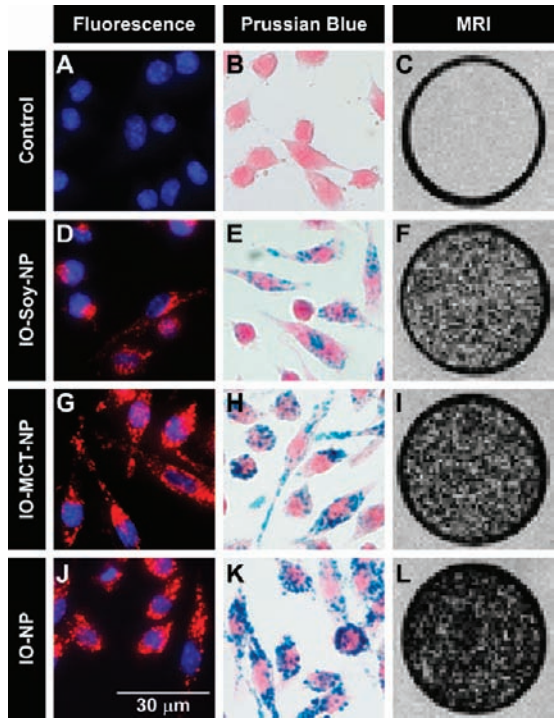

Figure 3. Fluorescence microscopy, Prussian Blue staining, and MRI of unlabeled control cells (A–C) and cells labeled with IO-Soy-NP (D–F), IO-MCT-NP (G–I), or IO-NP (J–L) nanoparticles. Fluorescence: fluorescent nanoparticles, containing Rhodamine lipids, are shown in red, while nuclei, stained with Hoechst, are shown in blue. Prussian Blue: iron, stained by Prussian Blue, is shown in blue, while nuclei, stained by Nuclear Fast Red, are shown in red. MRI: T_2*-weighted gradient echo images of homogeneously dispersed labeled cells in 0.4% agarose at a concentration of 1000 cells/μL (TR/TE = 100/15 ms, 100 μm isotropic resolution, 9.4 T).

images compared to images of unlabeled control cells (Figure 3C). This signal decrease was most pronounced for IO-NP, followed by IO-MCT-NP and IO-Soy-NP, and corresponded with reductions in T_1 and T_2 values in the same cell samples (Figure S3, Supporting Information). Decreasing the density of labeled cells from 1000 cells/μL to 125 cells/μL agarose allowed us to study the potential of these lipid-coated clusters of iron oxide for MR-based detection of small cell clusters or even individual cells (Figure 5). Contrast-enhanced pixels were not observed in samples containing unlabeled cells, while cells labeled with IO-NP and IO-MCT-NP showed contrast-enhanced pixels even at cell concentrations as low as 125 cells/μL, i.e., 0.125 cell/voxel (Figure 5A). At such a low cell density, the measured fraction of contrast-enhanced pixels underestimated the actual cell density for each of the nanoparticles (Figure 5B). This data suggests that cells were either clustered or that some cells were insufficiently labeled for single cell detection. Furthermore, we have to take into account that the blooming T_2* effect of extensively labeled cells also affects neighboring voxels, which further complicates accurate cell density measurements based on the extent of contrast enhancement. Nevertheless, the MRI data convincingly demonstrate that IO-NP and IO-MCT-NP allowed the detection of small numbers of cells.

Nanoparticle-Related Cytotoxicity. Nanoparticle-induced cytotoxicity was assessed by flow cytometric analysis of fluorescently stained late-apoptotic and/or necrotic cells with 7-

dx.doi.org/10.1021/bc200543k | Bioconjugate Chem. 2012, 23, 941–950

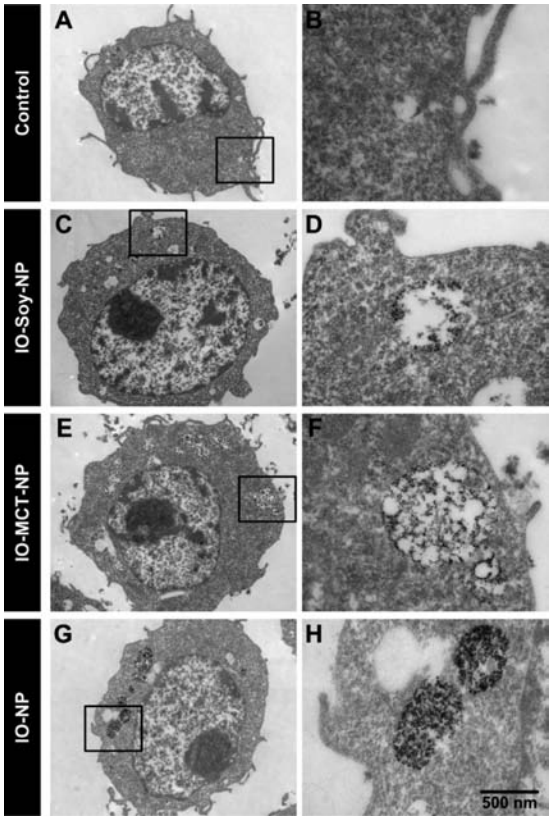

Figure 4. TEM images of unlabeled cells (A,B) and cells labeled with IO-Soy-NP (C,D), IO-MCT-NP (E,F), or IO-NP (G,H) nanoparticles. Single cells are shown in the left column (A,C,E,G) and magnifications of the corresponding images in the right column (B,D,F,H).

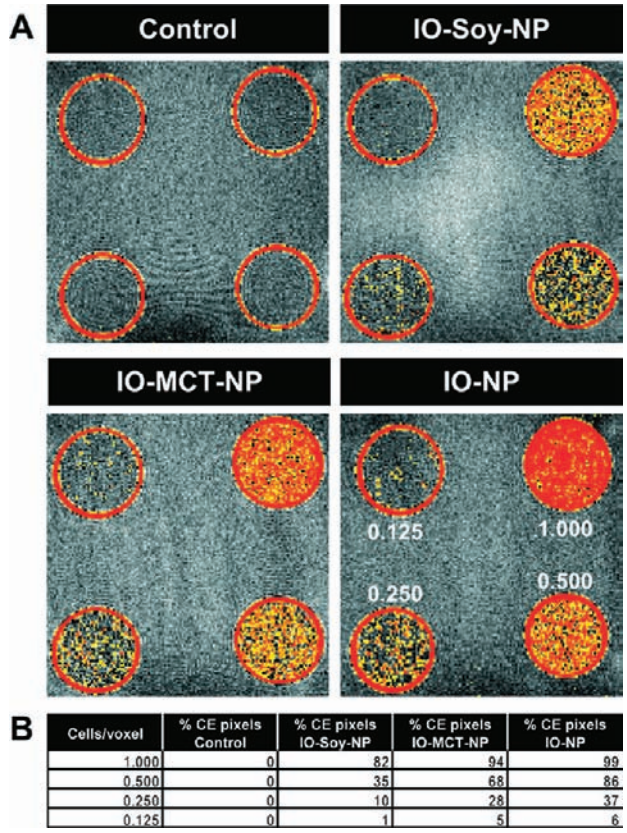

Cells/voxel	% CE pixels Control	% CE pixels IO-Soy-NP	% CE pixels IO-MCT-NP	% CE pixels IO-NP
1.000	0	82	94	99
0.500	0	35	68	86
0.250	0	10	28	37
0.125	0	1	5	6

Figure 5. (A) T_2*-weighted MR images (100 μm isotropic resolution) of homogeneously distributed cells in 0.4% agarose, at concentrations varying from 125 to 1000 cells per μL (i.e., 0.125−1 cells/voxel), overlaid by color-coded significantly contrast-enhanced (CE) pixels. (B) Percentage of CE pixels measured within each cell sample.

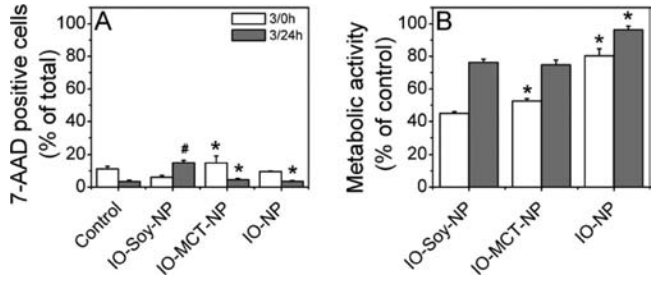

Figure 6. Effect of cell labeling on cell death, as determined from 7-AAD staining (A), and metabolic activity, as determined with an MTT assay (B). 3/0 h = 3 h of incubation, harvesting directly after incubation, and 3/24 h = 3 h of incubation, harvesting 24 h after incubation. Bars represent the mean ± standard deviation (n = 3). Degree of 7-AAD staining was defined as the percentage of 7-AAD positive cells within a population of 20,000 cells, whereas normal metabolic activity was set at 100%, based on the levels in untreated control cells. * p < 0.05 compared to IO-Soy-NP incubation at the corresponding time point. # p < 0.05 compared to untreated control cells at the corresponding time point.

AAD, while a second measure of cell viability, i.e., metabolic activity, was assessed with the MTT assay. Directly following 3 h of incubation with freshly prepared nanoparticles, only cells treated with IO-MCT-NP showed a small, yet significant, particle-related increase in 7-AAD staining compared to that of untreated control cells (Figure 6A). Metabolic activity was also reduced, and significant differences between the three nanoparticles were observed. IO-NP showed the most preserved metabolic activity, followed by IO-MCT-NP and IO-Soy-NP (Figure 6B). Metabolic activity was partially restored at 24 h after labeling with IO-Soy-NP and IO-MCT-NP, and activity in cells labeled with IO-NP returned to reference levels. Only cells labeled with IO-Soy-NP showed a small but significantly increased percentage of 7-AAD positive cells within the culture after 24 h.

IO-Soy-NP-induced cytotoxicity was also found to progress with nanoparticle storage time, as the fraction of 7-AAD positive cells after 3 h of incubation consistently and significantly increased with time after nanoparticle preparation (Figure 7A). These results were corroborated by the metabolic activity measurements, which showed significant loss of metabolic activity as a function of nanoparticle storage time (Figure 7D). In both assays, it was demonstrated that this is a partially oxygen-dependent process, as storage under nitrogen significantly delayed the storage time-dependent increase in nanoparticle-induced cytotoxicity (Figure 7A,D). IO-MCT-NP and IO-NP nanoparticles did not demonstrate such a storage time effect, and significant differences with nitrogen storage were not observed (Figure 7B,C,E,F).

The storage time-dependent cytotoxic effects of IO-Soy-NP could not be attributed to nanoparticle degradation during storage, as DLS measurements demonstrated that particle size and PDI remained stable over a time period of at least 18 weeks after production (own observations; data not shown). The fact that oxygen deprivation during nanoparticle storage significantly delayed this time-dependency strongly suggests that

dx.doi.org/10.1021/bc200543k | Bioconjugate Chem. 2012, 23, 941−950

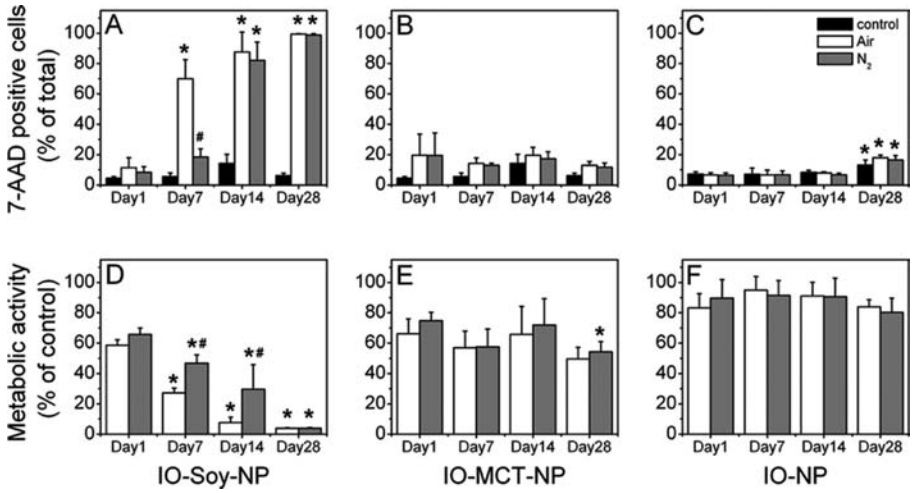

Figure 7. Cell viability as a function of time after nanoparticle preparation, as assessed by 7-AAD staining (A–C) and an MTT assay (D–F). Nanoparticles were prepared on day 0, followed by storage under normal conditions (Air) or nitrogen (N_2). Cells were incubated with nanoparticles or remained untreated (control) for 3 h at 200 μg Fe/mL. Bars represent the mean ± standard deviation (n = 4 for 7-AAD, n = 6 for metabolic activity). * $p < 0.05$ compared to its corresponding storage condition on day 1 after preparation. # $p < 0.05$ compared to its corresponding nanoparticle treatment under storage in air at the same time point after nanoparticle preparation.

cytotoxicity may be partially ascribed to the oxidative formation of fatty acid hydroperoxides and secondary degradation products from polyunsaturated fatty acids in the soybean oil. We hypothesize that this effect is enhanced by the dispersion of the iron oxide crystals throughout the oil phase, as iron acts as a catalyst in the oxidation of unsaturated fatty acids.[31] This was confirmed by a thiobarbituric acid reactive substances (TBARS) assay, which demonstrated significantly increased production of fatty acid hydroperoxide degradation products in IO-Soy-NP compared to that in Soy-NP, IO-MCT-NP, MCT-NP, and IO-NP (Figure 8).

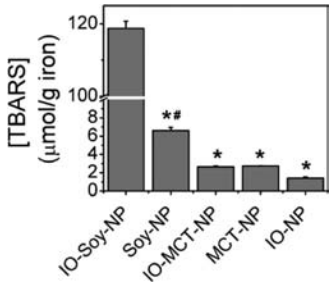

Figure 8. Thiobarbituric acid reactive substances (TBARS) in nanoparticle suspension at day 1 after nanoparticle preparation under air storage. Bars represent the mean ± standard deviation (n = 3). * $p < 0.05$ compared to IO-Soy-NP. # $p < 0.05$ compared to its iron-containing counterpart.

■ DISCUSSION

Recent developments in nanoparticulate agents for multimodal imaging have opened a window of opportunities for advanced biomedical research.[32] In the current study, a relatively simple solvent evaporation procedure was applied to prepare six different fluorescently labeled lipid-coated nanoparticles, with a diameter <100 nm and characteristic distributions of the iron oxide crystals throughout the nanoparticle core, depending on the oil phase (Figure 1). We characterized structural properties of formulations composed of combinations of biocompatible materials and measured the effect of such combinations on nanoparticle characteristics, cell labeling potential, and cell viability. We found that combinations of individually biocompatible materials do not necessarily result in biocompatible nanoparticles, with the catalytic or oxidizing properties of iron oxides potentially degrading the oil core, depending on its composition.

The increasing interest in nanomaterials for in vivo cell imaging studies requires development of particles that allow efficient cell labeling with minimal effects on cell viability and function. In general, nanoparticle internalization is affected by numerous factors, including cell type and cell density,[33,34] as well as nanoparticle size, charge, shape, and concentration.[35−38] We found that incubations of RAW cells with the negatively charged lipid-coated nanoparticle preparations resulted in an intracellular iron content ranging from 1.0 ± 0.1 pg iron/cell for IO-Soy-NP to 5.3 ± 0.7 pg iron/cell for IO-NP (Figure 2A). Labeling of human monocytes with negatively charged carboxydextran-coated SPIO (65 nm) was found to be higher.[35] On the basis of size, charge, and cell type (Table 1), one may also expect higher labeling efficiency of RAW cells with IO-Soy-NP, IO-MCT-NP, and IO-NP. However, internalization of these nanoparticles is most probably hampered by the high amount of PEG polymers (50 mol %) in the lipid coating, which sterically stabilizes these nanoparticles and decreases their interaction with macrophages due to reduced absorption of serum proteins on the nanoparticle surface.[39] This is corroborated by other studies in macrophages, demonstrating reduced uptake of PEGylated iron oxide particles compared to that of carboxy-dextran coated SPIO[40] and dextran-coated nanoparticles.[41] We chose the RAW macrophage cell line as a test bed, as these cells are known to efficiently internalize contrast agents. Cells that extensively internalize nanoparticles were a prerequisite for efficient evaluation of cytotoxicity and detectability. The investigation of nanoparticle internalization by a variety of different cell types would be an interesting future extension of this work.

Our study demonstrates that coating and size, which were comparable between the nanoparticles, are not the only factors affecting nanoparticle uptake, as substantial differences in labeling efficiency were observed between IO-Soy-NP, IO-

MCT-NP, and IO-NP (Figure 2), as well as their non-iron containing counterparts (Figure S2, Supporting Information). These differences could also not be explained by dissimilarities in charge (Tables 1 and S1, Supporting Information) but may originate from differences in nanoparticle weight, caused by differences in core density due to inclusion/exclusion of iron oxide nanocrystals, shape, and/or cytotoxicity.

Cells labeled with the selected nanoparticles generated visibly detectable hypointensities on T_2*-weighted images with an isotropic resolution of 100 μm, which reflects the potential to detect small clusters of cells (Figure 5). We expect that the actual detection threshold in our experimental setting could be further optimized, as single cell MR imaging studies have already been conducted at lower magnetic field strength (1.5 T) and lower intracellular iron content (0.2 pg iron/cell).[42]

The inclusion of fluorescent entities additionally allowed the detection of labeled cells with optical techniques (Figures 2−3), which extends the application of these nanoparticles for biodistribution studies using optical in vivo imaging systems,[27] phenotyping of intravenously labeled cells with flow cytometry,[43] and validation of MRI data at the subcellular level with (confocal) fluorescence microscopy. Unfortunately, fluorescence measurements did not permit quantitative analysis of labeling efficiency due to fluorescent quenching in the presence of iron, especially at high concentrations (Figure S1, Supporting Information). Most probably, this also explains the discrepancy between measurements of nanoparticle load based on iron content and mean fluorescent intensity for IO-NP-labeled cells (Figure 2), in which nanoparticles are densely packed within endolysosomal compartments (Figure 4H). Such effects may be minimized by coupling the fluorescent label to the distal end of the PEG chain, instead of directly to the phospholipid.

Despite the regular assumption that iron oxide particles are nontoxic at concentrations typically applied for cellular MR imaging, recent studies revealed that excessive intracellular labeling with iron oxide particles may seriously affect cell proliferation, migration, and differentiation.[44] In the current study, we evaluated the cytotoxicity of the different nanoparticle preparations and found that cellular metabolic activity as assessed with an MTT assay was initially lowered but recovered after 24 h, while the degree of cell death observed from flow cytometric analysis of 7-AAD stained cells remained relatively stable or increased somewhat (Figure 6). The measured increase in metabolic activity at 24 h post cell labeling may be associated with increased reactive oxygen species (ROS) production, which is in agreement with earlier studies demonstrating transiently increased ROS production within 3−24 h of labeling with magnetoliposomes,[45] VSOP,[46] and dextran-coated nanoparticles.[47]

Cytotoxicity after nanoparticle loading is dependent on a number of factors, including intracellular iron concentration and nanoparticle coating.[44] However, in our study the differences in cytotoxicity between formulations were likely not caused by these two factors as all nanoparticles had the same coating, and the formulations with highest iron content had lowest toxicity. Potentially, these differences may be ascribed to lipotoxicity since the uptake of triglycerides, irrespective of their degradation in free fatty acids, has been associated with oxidative stress and consequent cell death in J774 macrophages.[48,49] Especially polyunsaturated fatty acids (PUFA), which are abundantly present in soybean oil (59%), are known to be highly susceptible to oxidation into hydroperoxides, followed by rapid degradation into more stable and toxic secondary products such as reactive aldehydes.[50] In contrast to PUFA, monounsaturated fatty acids (MUFA), such as the oleic acid coating of the iron oxide crystals, and saturated fatty acids (SFA), as present in MCT and the DSPC/PEG2000 coating, are more resistant to oxidation. Accordingly, replacement of the soybean oil core by alternative vegetable oils consisting of long chain triglycerides with varying fractions of MUFA and polyunsaturated PUFA, i.e., corn, cottonseed, or olive oil, was expected to result in nanoparticles with reduced toxicity after cell labeling. Highest cell viability at 14 days after nanoparticle preparation was achieved with olive oil preparations (Figure 1C), which may be attributed to the relatively low PUFA content of olive oil (7%) compared to corn (59%) and cottonseed (48%) oil. Nevertheless, each nanoparticle reduced the cell viability to 10−20%, suggesting that MUFA peroxidation in the oil phase may also play a role in oxidative deterioration, perhaps by propagation of a chain reaction initiated in PUFA.

The nanoparticle platform presented in the current study is considered highly flexible and allows a wide range of variations in its coating as well as materials encapsulated within the core. Present formulations contained high amounts of PEGylated phospholipids and may therefore be suitable for future applications requiring a long blood half-life, such as in vivo labeling of circulating monocytes. However, in the case of in vitro labeling, the labeling efficiency of phagocytes as well as nonphagocytic cells may be increased by decreasing the PEG content and/or by inclusion of different phospholipids, such as cationic lipids. Alternatively, functionalized PEG lipids may be incorporated and covalently conjugated to peptides, proteins, or antibodies that induce nanoparticle internalization. Finally, nanocrystals such as gold or quantum dots may also be loaded as cargoes for alternative applications such as CT or fluorescence imaging.

■ CONCLUSIONS

Lipid-coated nanoparticles containing nanoclusters of iron oxide, either in the presence or absence of an oil phase, allowed the detection of single cells with MRI, fluorescence microscopy, and flow cytometry. Nanoparticles without incorporated oil exhibited superior properties in terms of MR relaxivities, cell labeling efficiency, biocompatibility, and shelf life, whereas medium-chain triglycerides (MCT) and long-chain triglycerides (soybean, corn, cottonseed, and olive oil) were associated with lipotoxicity. The inclusion of vegetable oils caused a further increase in cytotoxicity as a function of storage time, which we ascribe to iron-catalyzed peroxidation of (poly)unsaturated fatty acids in the oil phase. We therefore conclude that lipid-coated iron oxide nanoparticles without an oil phase are most suitable for future cellular imaging studies and represent an attractive, potent, and flexible platform that can be easily adjusted for alternative multimodal imaging setups or therapeutic purposes.[28] Additionally, this study emphasizes that nanoparticles for in vivo applications, even when composed of biocompatible compounds such as phospholipids, iron oxide, and vegetable oils, should be carefully designed and evaluated in terms of cell homeostasis, as the combination of biologically safe building blocks may still lead to cytotoxic products.

■ ASSOCIATED CONTENT

Supporting Information

Information on materials, nanoparticle characterization, intracellular iron content determination, and thiobarbituric acid reactive substances assay. This material is available free of charge via the Internet at http://pubs.acs.org.

■ AUTHOR INFORMATION

Corresponding Author

*Yalelaan 2, 3584 CM Utrecht, The Netherlands. Phone: +31 30 2535515. E-mail: gtilborg@gmail.com

Notes

The authors declare no competing financial interest.

■ ACKNOWLEDGMENTS

We thank Marina Talelli (Department of Pharmaceutics, Institute for Pharmaceutical Sciences, Utrecht, The Netherlands) for assistance with the iron quantification. This research was supported by The Netherlands Organization for Scientific Research (NWO-Vidi 917.76.351 to R.M.D.), the European Union's Seventh Framework Programme (FP7/2007-2013) under grant agreements numbers 201024 and 202213 (European Stroke Network), and NIH grant K99 EB012165 (to D.P.C.).

■ REFERENCES

(1) Medintz, I. L., Uyeda, H. T., Goldman, E. R., and Mattoussi, H. (2005) Quantum dot bioconjugates for imaging, labelling and sensing. *Nat. Mater. 4*, 435−446.

(2) Choi, H. S., Liu, W., Misra, P., Tanaka, E., Zimmer, J. P., Ipe, B. I., Bawendi, M. G., and Frangioni, J. V. (2007) Renal clearance of quantum dots. *Nat. Biotechnol. 25*, 1165−1170.

(3) Medintz, I. L., Clapp, A. R., Mattoussi, H., Goldman, E. R., Fisher, B., and Mauro, J. M. (2003) Self-assembled nanoscale biosensors based on quantum dot FRET donors. *Nat. Mater. 2*, 630−638.

(4) Hainfeld, J. F., Slatkin, D. N., Focella, T. M., and Smilowitz, H. M. (2006) Gold nanoparticles: a new X-ray contrast agent. *Br. J. Radiol. 79*, 248−253.

(5) Cormode, D. P., Roessl, E., Thran, A., Skajaa, T., Gordon, R. E., Schlomka, J. P., Fuster, V., Fisher, E. A., Mulder, W. J. M., Proksa, R., and A., F. Z. (2010) Atherosclerotic plaque composition: analysis with multicolor CT and targeted gold nanoparticles. *Radiology 256*, 774−782.

(6) Wang, H. F., Huff, T. B., Zweifel, D. A., He, W., Low, P. S., Wei, A., and Cheng, J. X. (2005) In vitro and in vivo two-photon luminescence imaging of single gold nanorods. *Proc. Natl. Acad. Sci. U.S.A. 102*, 15752−15756.

(7) Qian, X., Peng, X.-H., Ansari, D. O., Yin-Goen, Q., Chen, G. Z., Shin, D. M., Yang, L., Young, A. N., Wang, M. D., and Nie, S. (2008) In vivo tumor targeting and spectroscopic detection with surface-enhanced Raman nanoparticle tags. *Nat. Biotechnol. 26*, 83−90.

(8) Song, K. H., Kim, C., Cobley, C. M., Xia, Y., and Wang, L. V. (2009) Near-infrared gold nanocages as a new class of tracers for photoacoustic sentinel lymph node mapping on a rat model. *Nano Lett. 9*, 183−188.

(9) von Maltzahn, G., Park, J. H., Agrawal, A., Bandaru, N. K., Das, S. K., Sailor, M. J., and Bhatia, S. N. (2009) Computationally guided photothermal tumor therapy using long-circulating gold nanorod antennas. *Cancer Res. 69*, 3892−3900.

(10) Rosi, N. L., and Mirkin, C. A. (2005) Nanostructures in biodiagnostics. *Chem. Rev. 105*, 1547−1562.

(11) Jordan, A., Scholz, R., Wust, P., Fähling, H., and Felix, R. (1999) Magnetic fluid hyperthermia (MFH): Cancer treatment with AC magnetic field induced excitation of biocompatible superparamagnetic nanoparticles. *J. Magn. Magn. Mater. 201*, 413−419.

(12) Haun, J. B., Castro, C. M., Wang, R., Peterson, V. M., Marinelli, B. S., Lee, H., and Weissleder, R. (2011) Micro-NMR for rapid molecular analysis of human tumor samples. *Sci. Transl. Med. 3*, 71ra16.

(13) Bulte, J. W. M., and Kraitchman, D. L. (2004) Iron oxide MR contrast agents for molecular and cellular imaging. *NMR Biomed. 17*, 484−499.

(14) Stoll, G., and Bendszus, M. (2009) Imaging of inflammation in the peripheral and central nervous system by magnetic resonance imaging. *Neuroscience 158*, 1151−1160.

(15) de Vries, I. J. M., Lesterhuis, W. J., Barentsz, J. O., Verdijk, P., van Krieken, J. H., Boerman, O. C., Oyen, W. J. G., Bonenkamp, J. J., Boezeman, J. B., Adema, G. J., Bulte, J. W. M., Scheenen, T. W. J., Punt, C. J. A., Heerschap, A., and Figdor, C. G. (2005) Magnetic resonance tracking of dendritic cells in melanoma patients for monitoring of cellular therapy. *Nat. Biotechnol. 23*, 1407−1413.

(16) Kwon, S. G., Piao, Y., Park, J., Angappane, S., Jo, Y., Hwang, N.-M., Park, J.-G., and Hyeon, T. (2007) Kinetics of monodisperse iron oxide nanocrystal formation by "heating-up" process. *J. Am. Chem. Soc. 129*, 12571−12584.

(17) Hyeon, T., Lee, S. S., Park, J., Chung, Y., and Na, H. B. (2001) Synthesis of highly crystalline and monodisperse maghemite nanocrystallites without a size-selection process. *J. Am. Chem. Soc. 123*, 12798−12801.

(18) Molday, R. S., and Mackenzie, D. (1982) Immunospecific ferromagnetic iron-dextran reagents for the labeling and magnetic separation of cells. *J. Immun. Methods 52*, 353−367.

(19) Dubertret, B., Skourides, P., Norris, D. J., Noireaux, V., Brivanlou, A. H., and Libchaber, A. (2002) In vivo imaging of quantum dots encapsulated in phospholipid micelles. *Science 298*, 1759−1762.

(20) Qi, L. F., and Gao, X. H. (2008) Quantum dot-amphipol nanocomplex for intracellular delivery and real-time imaging of siRNA. *ACS Nano 2*, 1403−1410.

(21) Cormode, D. P., Skajaa, G. O., Delshad, A., Parker, N., Jarzyna, P. A., Calcagno, C., Galper, M. W., Skajaa, T., Briley-Saebo, K. C., Bell, H. M., Gordon, R. E., Fayad, Z. A., Woo, S. L., and Mulder, W. J. (2011) A versatile and tunable coating strategy allows control of nanocrystal delivery to cell types in the liver. *Bioconjugate Chem. 22*, 353−361.

(22) Yu, W. W., Chang, E., Falkner, J. C., Zhang, J., Al-Somali, A. M., Sayes, C. M., Johns, J., Drezek, R., and Colvin, V. L. (2007) Forming biocompatible and nonaggregated nanocrystals in water using amphiphilic polymers. *J. Am. Chem. Soc. 129*, 2871−2879.

(23) Muir, B. W., Moffat, B. A., Harbour, P., Greg Coia, G., Zhen, G., Waddington, L., Scoble, J., Krah, D., Thang, S. H., Chong, Y. K., Mulvaney, P., and Hartley, P. (2009) Combinatorial discovery of novel amphiphilic polymers for the phase transfer of magnetic nanoparticles. *J. Phys. Chem. C 113*, 16615−16624.

(24) Bruns, O. T., Ittrich, H., Peldschus, K., Kaul, M. G., Tromsdorf, U. I., Lauterwasser, J., Nikolic, M. S., Mollwitz, B., Merkel, M., Bigall, N. C., Sapra, S., Reimer, R., Hohenberg, H., Weller, H., Eychmuller, A., Adam, G., Beisiegel, U., and Heeren, J. (2009) Real-time magnetic resonance imaging and quantification of lipoprotein metabolism in vivo using nanocrystals. *Nat. Nano 4*, 193−201.

(25) Cormode, D. P., Skajaa, T., van Schooneveld, M. M., Koole, R., Jarzyna, P., Lobatto, M. E., Calcagno, C., Barazza, A., Gordon, R. E., Zanzonico, P., Fisher, E. A., Fayad, Z. A., and Mulder, W. J. M. (2008) Nanocrystal core high-density lipoproteins: A multimodal molecular imaging contrast agent platform. *Nano Lett. 8*, 3715−3723.

(26) McMahon, K. M., Mutharasan, R. K., Tripathy, S., Veliceasa, D., Bobeica, M., Shumaker, D. K., Luthi, A. J., Helfand, B. T., Ardehali, H., Mirkin, C. A., Volpert, O., and Thaxton, C. S. (2011) Biomimetic high density lipoprotein nanoparticles for nucleic acid delivery. *Nano Lett. 11*, 1208−1214.

(27) Jarzyna, P. A., Skajaa, T., Gianella, A., Cormode, D. P., Samber, D. D., Dickson, S. D., Chen, W., Griffioen, A. W., Fayad, Z. A., and Mulder, W. J. (2009) Iron oxide core oil-in-water emulsions as a multifunctional nanoparticle platform for tumor targeting and imaging. *Biomaterials 30*, 6947−6954.

(28) Gianella, A., Jarzyna, P. A., Mani, V., Ramachandran, S., Calcagno, C., Tang, J., Kann, B., Dijk, W. J. R., Thijssen, V. L., Griffioen, A. W., Storm, G., Fayad, Z. A., and Mulder, W. J. (2011) A multifunctional nanoemulsion platform for imaging guided therapy evaluated in experimental cancer. *ACS Nano 5*, 4422−4433.
(29) Horak, D., Babic, M., Jendelova, P., Herynek, V., Trchova, M., Pientka, Z., Pollert, E., Hajek, M., and Sykova, E. (2007) D-mannose-modified iron oxide nanoparticles for stem cell labeling. *Bioconjugate Chem. 18*, 635−644.
(30) Perez, J. M., Josephson, L., and Weissleder, R. (2004) Use of magnetic nanoparticles as nanosensors to probe for molecular interactions. *ChemBioChem 5*, 261−264.
(31) Minotti, G., and Aust, S. D. (1989) The role of iron in oxygen radical mediated lipid peroxidation. *Chem.-Biol. Interact. 71*, 1−19.
(32) Mulder, W. J., Strijkers, G. J., van Tilborg, G. A., Cormode, D. P., Fayad, Z. A., and Nicolay, K. (2009) Nanoparticulate assemblies of amphiphiles and diagnostically active materials for multimodality imaging. *Acc. Chem. Res. 42*, 904−914.
(33) Boutry, S., Brunin, S., Mahieu, I., Laurent, S., Vander Elst, L., and Muller, R. N. (2008) Magnetic labeling of non-phagocytic adherent cells with iron oxide nanoparticles: a comprehensive study. *Contrast Media Mol. Imaging 3*, 223−232.
(34) Arbab, A. S., Bashaw, L. A., Miller, B. R., Jordan, E. K., Bulte, J. W., and Frank, J. A. (2003) Intracytoplasmic tagging of cells with ferumoxides and transfection agent for cellular magnetic resonance imaging after cell transplantation: methods and techniques. *Transplantation 76*, 1123−1130.
(35) Metz, S., Bonaterra, G., Rudelius, M., Settles, M., Rummeny, E. J., and Daldrup-Link, H. E. (2004) Capacity of human monocytes to phagocytose approved iron oxide MR contrast agents in vitro. *Eur. Radiol. 14*, 1851−1858.
(36) Matuszewski, L., Persigehl, T., Wall, A., Schwindt, W., Tombach, B., Fobker, M., Poremba, C., Ebert, W., Heindel, W., and Bremer, C. (2005) Cell tagging with clinically approved iron oxides: feasibility and effect of lipofection, particle size, and surface coating on labeling efficiency. *Radiology 235*, 155−161.
(37) Roser, M., Fischer, D., and Kissel, T. (1998) Surface-modified biodegradable albumin nano- and microspheres. II: effect of surface charges on in vitro phagocytosis and biodistribution in rats. *Eur. J. Pharm. Biopharm. 46*, 255−263.
(38) Sharma, G., Valenta, D. T., Altman, Y., Harvey, S., Xie, H., Mitragotri, S., and Smith, J. W. (2010) Polymer particle shape independently influences binding and internalization by macrophages. *J. Controlled Release 147*, 408−12.
(39) Verma, A., and Stellacci, F. (2009) Effect of surface properties on nanoparticle-cell interactions. *Small 6*, 12−21.
(40) Tromsdorf, U. I., Bruns, O. T., Salmen, S. C., Beisiegel, U., and Weller, H. (2009) A highly effective, nontoxic T1MR contrast agent based on ultrasmall PEGylated iron oxide nanoparticles. *Nano Lett. 9*, 4434−4440.
(41) Xie, J., Xu, C., Kohler, N., Hou, Y., and Sun, S. (2007) Controlled PEGylation of monodisperse Fe3O4 nanoparticles for reduced non-specific uptake by macrophage cells. *Adv. Mater. 19*, 3163−3166.
(42) Smirnov, P., Poirier-Quinot, M., Wilhelm, C., Lavergne, E., Ginefri, J. C., Combadiere, B., Clement, O., Darrasse, L., and Gazeau, F. (2008) In vivo single cell detection of tumor-infiltrating lymphocytes with a clinical 1.5 T MRI system. *Magn. Reson. Med. 60*, 1292−1297.
(43) Flogel, U., Ding, Z., Hardung, H., Jander, S., Reichmann, G., Jacoby, C., Schubert, R., and Schrader, J. (2008) In vivo monitoring of inflammation after cardiac and cerebral ischemia by fluorine magnetic resonance imaging. *Circulation 118*, 140−148.
(44) Soenen, S. J., Himmelreich, U., Nuytten, N., and De Cuyper, M. (2011) Cytotoxic effects of iron oxide nanoparticles and implications for safety in cell labelling. *Biomaterials 32*, 195−205.
(45) Soenen, S. J., Brisson, A. R., and De Cuyper, M. (2009) Addressing the problem of cationic lipid-mediated toxicity: the magnetoliposome model. *Biomaterials 30*, 3691−3701.
(46) Stroh, A., Zimmer, C., Gutzeit, C., Jakstadt, M., Marschinke, F., Jung, T., Pilgrimm, H., and Grune, T. (2004) Iron oxide particles for molecular magnetic resonance imaging cause transient oxidative stress in rat macrophages. *Free Radical Biol. Med. 36*, 976−984.
(47) Bulte, J. W., Arbab, A. S., Douglas, T., and Frank, J. A. (2004) Preparation of magnetically labeled cells for cell tracking by magnetic resonance imaging. *Methods Enzymol. 386*, 275−299.
(48) Aronis, A., Madar, Z., and Tirosh, O. (2005) Mechanism underlying oxidative stress-mediated lipotoxicity: exposure of J774.2 macrophages to triacylglycerols facilitates mitochondrial reactive oxygen species production and cellular necrosis. *Free Radical Biol. Med. 38*, 1221−1230.
(49) Aronis, A., Madar, Z., and Tirosh, O. (2008) Lipotoxic effects of triacylglycerols in J774.2 macrophages. *Nutrition 24*, 167−176.
(50) Gueraud, F., Atalay, M., Bresgen, N., Cipak, A., Eckl, P. M., Huc, L., Jouanin, I., Siems, W., and Uchida, K. (2010) Chemistry and biochemistry of lipid peroxidation products. *Free Radical Res. 44*, 1098−1124.

Bioconjugate Chemistry

Article

pubs.acs.org/bc

DNA Surface Modified Gadolinium Phosphate Nanoparticles as MRI Contrast Agents

Matthieu F. Dumont,[†,§] Celine Baligand,[‡] Yichen Li,[†] Elisabeth S. Knowles,[§] Mark W. Meisel,[§] Glenn A. Walter,[‡] and Daniel R. Talham*[,†]

[†]Department of Chemistry, University of Florida, Gainesville, Florida 32611-7200, United States

[‡]Department of Physiology and Functional Genomic, University of Florida and the National High Magnetic Field Laboratory, Gainesville, Florida 32610-0274, United States

[§]Department of Physics, University of Florida and the National High Magnetic Field Laboratory, Gainesville, Florida 32611, United States

Supporting Information

ABSTRACT: Oligonucleotide modified gadolinium phosphate nanoparticles have been prepared and their magnetic resonance relaxivity properties measured. Nanoparticles of $GdPO_4 \cdot H_2O$ were synthesized in a water/oil microemulsion using IGEPAL CO-520 as surfactant, resulting in 50 to 100 nm particles that are highly dispersible and stable in water. Using surface modification chemistry previously established for zirconium phosphonate surfaces, the particles are directly modified with 5′-phosphate terminated oligonucleotides, and the specific interaction of the divalent phosphate with Gd^{3+} sites at the surface is demonstrated. The ability of the modified nanoparticles to act as MRI contrast agents was determined by performing MR relaxivity measurements at 14.1 T. Solutions of nanopure water, Feridex, and Omniscan (FDA approved contrast agents) in 0.25% agarose were used for comparison and control purposes. MRI data confirm that $GdPO_4 \cdot H_2O$ nanoparticles have relaxivities (r_1, r_2) comparable to those of commercially available contrast agents. In addition, the data suggest that biofunctionalization of the surface of the nanoparticles does not prevent their function as MRI contrast agents.

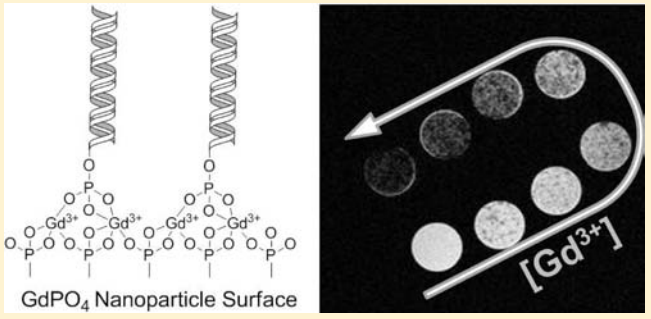

INTRODUCTION

Magnetic resonance imaging (MRI) is a noninvasive medical imaging technique that allows both morphological and functional evaluation of tissues, making it a powerful diagnosis and research tool. MRI contrast depends on a number of factors including proton density, longitudinal relaxation time (T_1), and transverse relaxation time (T_2). This contrast varies depending on the tissue type and can be altered with pathology, making it especially useful in neurological and oncological imaging.[1−3]

Despite the ability to image, in some cases, an increase in the endogenous contrast is needed to distinguish between two tissues that naturally produce very similar MR signal. This fact is particularly relevant to *in vivo* cell therapy protocols or gene expression tracking, where the therapeutic material does not offer any natural contrast with the tissue.[4] Improved MR contrast is made possible by the use of contrast agents (CAs) that modify the rates of relaxation of the water protons in their vicinity. The efficiency of CAs is usually estimated as the magnitude of their effect on the water proton relaxation rates and is related to the concentration and relaxivity of the agents by the following equation:

$$\frac{1}{T_{iapp}} = \frac{1}{T_i} + r_i(s^{-1}\cdot mM^{-1}) \times [CA](mM) \qquad i = 1, 2 \tag{1}$$

where T_{iapp} is the apparent T_1 or T_2 of the tissue, r_i are the relaxivities r_1 or r_2, and [CA] is the concentration of contrast agent.[1,5,6] Magnetic resonance CAs are conventionally divided into two main classes depending on their superparamagnetic or paramagnetic properties. The first class is exemplified by superparamagnetic iron oxide nanoparticles (SPIOs). Superparamagnetic particles affect the transverse relaxation rate, R_2, of the protons in their vicinity through spin−lattice interactions and are known as T_2 or negative contrast agents.[6,7] The second class of agent is mainly based on chelates of gadolinium(III). These molecules are strongly paramagnetic as a result of unpaired electrons giving a spin state of S = 7/2. Chelation is required to reduce their toxicity and make their use *in vivo* possible. These complexes operate through an inner-sphere spin−spin relaxation mechanism, show a high longitudinal

Received: October 19, 2011
Revised: February 1, 2012
Published: April 2, 2012

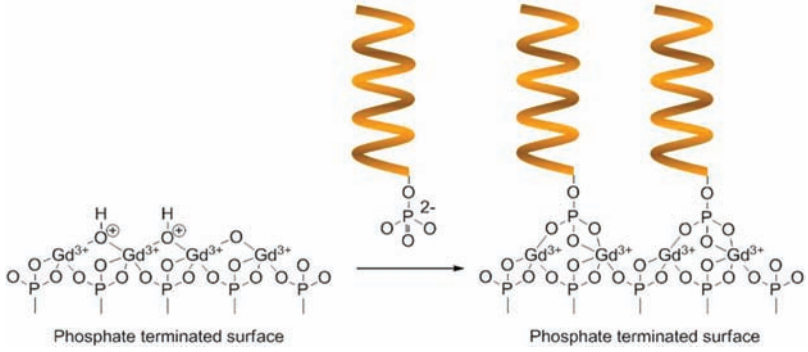

Figure 1. Illustration of the surface of the gadolinium phosphate nanoparticles. Hydroxide and oxide ions present on the surface can be displaced by divalent phosphate terminated oligonucleotide, creating a coordinate covalent linkage.

relaxivity r_1 and generate a positive contrast by brightening of the image. They are known as T_1 or positive contrast agents.[5]

Recent studies have raised some concerns about the release of Gd^{3+} in the body, leading to pathology such as nephrogenic systemic fibrosis.[8−11] The need to keep gadolinium in a more stable form has led to the investigation of different types of gadolinium-based nanomaterials. Some recent examples are small particulate gadolinium oxides,[12−14] GdF_3 nanoparticles,[15] Gd-DOTA attached to SiO_2-coated semiconductor quantum dots (DOTA is tetraazacyclododecanetetraacetic acid),[16] and $Gd(BDC)_{1.5}(H_2O)_2$ nanorods (BDC is 1,4-benzendicarboxylate).[17] Similarly, Hifumi et al.[18,19] reported the use of dextran-coated gadolinium phosphate nanoparticles that act as a positive contrast agent. Gadolinium phosphate is potentially highly desirable because of its extremely low solubility and its predisposition to form paramagnetic nanoparticles.[20,21]

For many nanoparticle CAs, targeting of the agents relies on the effects of particle size, localizing where they are not excluded by their size, such as tumor sites with high vascularity. Driven by the goal to improve efficiency and to lower dosage, techniques have been developed to modify the surface of nanoparticles with bioactive targeting molecules such as oligonucleotides, antibodies, or proteins. Surface modification has the added benefit of facilitating biocompatibility, reducing toxicity, and avoiding immediate elimination from the body. Methods to modify nanoparticles with bioactive molecules include approaches such as using the avidin/biotin interaction to link groups to the surface and passivating particles with functionalized polymers.[2,22−24] These techniques have been successful, but often require significant effort through specialized synthesis and multiple steps.

Recent studies in our laboratories have shown that oligonucleotides bearing a 5′-terminus phosphate covalently bind directly to zirconium phosphonate-modified surfaces through the 5′-phosphate and that this interaction can be used to immobilize oligonucleotide probes for applications such as DNA arrays.[25−27] In the present article, we report that the same type of chemistry can be applied to the surface of gadolinium phosphate nanoparticles ($GdPO_4$NP) (Figure 1). Since the K_a values of Gd^{3+} and Zr^{4+} are close, the metal ions show similar affinity for divalent phosphate. A phosphorylated oligonucleotide was selected as the surface modifier because of its potential for cancer-cell marker recognition and its high biocompatibility, mandatory for *in vivo* applications. Specific binding of the terminal phosphate of an oligonucleotide on the $GdPO_4$NPs has been established by confocal laser scanning microscopy. In order to demonstrate that the oligonucleotides covalently attached to the nanoparticle surface remain bioactive, hybridization experiments were performed with a fluorescently labeled complement. Subsequent relaxivity measurements established that the biofunctionalization of the surface of the $GdPO_4$NPs does not alter their role as MRI contrast agents. The DNA-modified $GdPO_4$ nanoparticles ($GdPO_4$NP-DNA) exhibit relaxivities comparable to those of FDA approved contrast agents.

EXPERIMENTAL PROCEDURES

Materials. All oligonucleotides were custom synthesized and purchased from Sigma-Aldrich (St. Louis, MO) and used as received. The oligonucleotide strands were HPLC-purified by Sigma-Aldrich before use. The appropriate amount of sodium saline citrate (SSC) buffer (pH 8) was added to the oligonucleotide to make 100 μM solutions, and the DNA solutions were subsequently aliquoted into one-time-use volumes (10 μL). The aliquots were stored at −20 °C. All other reagents were of analytical grade and used as received from commercial sources.

High Resolution Transmission Electron Microscopy (HRTEM). Microscopy was performed on a JEOL 2010F HRTEM at 200 kV. TEM grids (carbon film on holey carbon support film, 400 mesh, copper from Ted-Pella, Inc.) were prepared by dropping onto the grid 20 μL of a solution containing 5 mg of sample in 2 mL of H_2O dispersed by sonication for 30 min.

Energy Dispersive X-ray Spectroscopy (EDS). Analysis was performed with an Oxford Instruments EDS X-ray Microanalysis System coupled to the HRTEM microscope. A total of 4 scans were completed on different parts of the sample and averaged to give relative atomic percentages for gadolinium and phosphorus.

X-ray Powder Diffraction (XRD). Powder data were obtained using a Philips APD 3720 powder diffractometer. One hundred milligrams of nanoparticles were mounted on double-sided tape backed by a glass slide.

Confocal Laser Scanning Microscopy (CLSM). DNA-modified gadolinium phosphate nanoparticles were imaged using a confocal microscope setup consisting of an Olympus IX-81 inverted microscope with an Olympus FluoView 500 confocal scanning system.

METHODS

$Gd(PO_4)\cdot H_2O$ Nanoparticle ($GdPO_4$NP) synthesis. $GdPO_4$NPs were obtained by combining two precursor mixtures. The first was prepared by adding 500 mg of

$Gd(NO_3)_3$ in 5 mL of H_2O to a solution of IGEPAL CO-520 (20 mL) dissolved in 100 mL of cyclohexane under vigorous stirring. The second was a mixture of NaH_2PO_4 (700 mg) in 5 mL of H_2O combined with a solution of IGEPAL CO-520 (20 mL) dissolved in 100 mL of cyclohexane. The two precursor mixtures were combined by dropwise addition using a peristaltic pump (10 mL/hour). Once the addition was complete, the mixture was left under vigorous stirring. After one hour, the microemulsion was broken with 200 mL of acetone. The nanoparticles were collected by centrifugation, washed with 50 mL of water and 2 × 50 mL of acetone, and left to dry under N_2. The composition was confirmed by comparison to published X-ray data.

Gadolinium Surface Preparation. $GdPO_4$NP (20 mg) were redispersed by sonication in 20 mL of nanopure water. A solution of 2 mg of $Gd(NO_3)_3$ in 5 mL of H_2O was then added to the nanoparticle suspension and sonicated for 20 min. The nanoparticles were subsequently washed by 3 successive cycles consisting of isolation by centrifugation and redispersion in nanopure water. The Gd-modified $GdPO_4$NPs were kept redispersed in 10 mL of water.

DNA Functionalization of $GdPO_4$NP. A solution of phosphorylated-single-stranded DNA 5′-[phos]-ATC-TAACTGCTGCGCCCGCCG-3′ (250 nM,100 μL) was added to 20 mg of Gd-modified $GdPO_4$NPs in 10 mL of water and left to incubate for 24 h. The nanoparticles were then washed with nanopure water to eliminate unbound DNA and kept in 10 mL of nanopure water. Control experiments were carried out using the nonphosphorylated probe (5′-ATC-TAACTGCTGCGCCCGCCG-3′).

Probe Hybridization. A solution (100 μL, 250 nM) of Cy3-labeled complement (5′-[Cy3]-CGGCGGCGCAGCAGT-TAGAT-3′) was added to 5 mL of the DNA modified $GdPO_4$NP ($GdPO_4$NP-DNA) and left to incubate for 24 h. The nanoparticles were then washed with nanopure water to eliminate unbound Cy3-DNA and kept in 10 mL of nanopure water. The changing surface properties of the nanoparticles through the synthesis and modification steps were monitored using zeta potential. The measured zeta potential value of $GdPO_4$NP immediately after synthesis is −17 mV. Following treatment with $Gd(NO_3)_3$, the zeta potential increased to 25 mV, confirming the formation of a cationic layer on the surface of the particles. This Gd^{3+} layer proved to be robust to rinsing. After incubation with the phosphorylated oligonucleotide, the measured surface potential was again negative; −23 mV corresponded to surface binding of the negatively charged DNA. Values of the zeta potential measurements confirm the successive changes at every stage of the surface modification.

Phantom Preparation. The $GdPO_4$NP-DNA (2 mM) MR contrast agent was compared to commercial iron oxide (Feridex, 11.2 mg·mL^{-1}, Berlex Laboratories, Montville, NJ), and gadolinium chelate (Omniscan, Gd-DTPA-BMA, 500 mM, Berlex Laboratories, Montville, NJ). $GdPO_4$NP-DNA standards were prepared in concentrations of 2, 1.5, 1, 0.5, 0.25, 0.12, and 0.06 mM in a 0.25% agarose solution prepared with agar gelose (Acros Organics, Pittsburgh, PA). Omniscan and Feridex standards were made using the same procedure, in concentrations of 25, 12.5, 6.25, 3.13, 1.56, and 0.78 mM and 2.5, 1.87, 1.25, 0.63, 0.31, 0.16, and 0.08 mM, respectively. Borosilicate capillary tubes (Curtin-Matheson Scientific, Broomall, PA) were then filled with the solutions and sealed with clay (Critoseal, McCormick Scientific, Richmond, IL). The use of agarose averts possible sedimentation during relaxation measurements. Control phantoms consisting of 0.25% agarose alone were concurrently imaged. All samples were secured together inside a 10 mm NMR glass tube (Wilmad-LabGlass, Vineland, NJ) to prevent movement. The NMR tube was filled with perfluorotri-*n*-butylamine (FC-43 Fluorinert, 3M, Maplewood, MN) in order to avoid magnetic susceptibility artifacts from the air−glass interfaces.

MR Relaxation Time Measurements. All MR measurements were performed at a constant temperature of 22 °C in a vertical 14.1 T magnet (Avance 600, Bruker Instruments, Billerica, MA) equipped with microimaging gradients (micro-5, Bruker Instruments). Samples were placed into a 10 mm-diameter Helmholtz probe. The spectrometer was interfaced with ParaVision 3.0.2 software (Bruker).

For each of the tested contrast agents, T_1 and T_2 relaxation times were measured in the same axial 0.5 mm-thick slice, positioned across the middle of the different capillaries. A variable repetition time (TR) spin echo sequence was used for T_1 measurements (variable TR = (15; 7.5; 4; 3; 2; 1.5; 1; 0.75; 0.5; 0.25; 0.15; 0.1; 0.075; 0.05; 0.015 s); echo time (TE) = 4 ms; matrix size = 128 × 128, FOV = 1 × 1 cm^2). T_2 was measured with a multiple spin echo sequence (TR/TE = 4.5 ms/15 s, interecho spacing ΔTE = 5 ms (32 echoes), matrix size = 128 × 128, FOV = 1 × 1 cm^2).

MR Data Analysis. All MR data were analyzed using ParaVision 3.0.2 software (Bruker) and Excel (Microsoft Inc.). For each sample, the signal intensity on magnitude images was averaged within regions of interest (ROIs) and plotted against TR for T_1 recovery curves or TE for T_2 decay curves. Data were then fitted to the following monoexponential functions:

$$T_1\text{: (TR)} = A(1 - e^{(-TR/T_1)}) + y_0 \quad (2)$$

$$T_2\text{: (TE)} = A(1 - e^{(-TE/T_2)}) + y_0 \quad (3)$$

In both cases, the constant y_0 was set to zero, and the low signal intensity values were excluded from the fit when inferior to 3 times the standard deviation of the noise in the images.[28] The obtained T_1 and T_2 values were converted into R_1 and R_2 relaxation rates ($1/T_1$ (s^{-1}), $1/T_2$ (s^{-1})).

Finally, R_1 and R_2 values were plotted against the concentration of the corresponding contrast agent, and r_1 and r_2 (mM^{-1} s^{-1}) relaxivities were obtained as the slope of the resulting linear plots using the following equations:

$$R_1 = r_1 \times [CA](mM) + R_{1_{agarose}} \quad (4)$$

$$R_2 = r_2 \times [CA](mM) + R_{2_{agarose}} \quad (5)$$

RESULTS

Nanoparticle Synthesis. The nanoparticles were synthesized in a water-in-oil microemulsion containing $Gd(NO_3)_3$ and NaH_2PO_4. The assembly was formed by adding the precursors in an aqueous phase to a cyclohexane solution containing a surfactant (IGEPAL CO-520) to form reverse micelles containing microdroplets of the precursors dispersed in the reaction media. When the two precursor solutions were mixed, the reverse micelles coalesced leading to formation of gadolinium phosphate. The use of a peristaltic pump to mix the reactants gave particles with well-defined shapes and surfaces.

High resolution transmission electron microscopy images show rod-shaped nanoparticles averaging 50 nm in length and

dx.doi.org/10.1021/bc200553h | *Bioconjugate Chem.* 2012, 23, 951−957

10 nm in width as seen in Figure 2. Lattice fringes visible in the images are consistent with a highly crystalline product. To

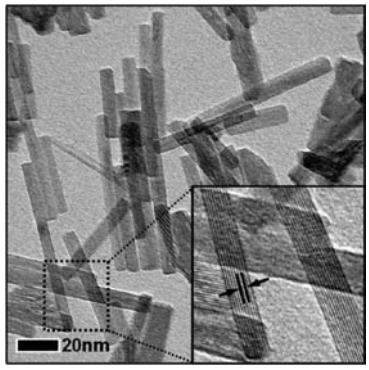

Figure 2. TEM images of $GdPO_4{\cdot}H_2O$ nanoparticles modified with DNA. The lattice planes are visible on the close up (inset).

further prove the composition and the crystallinity of the synthesized materials, a powder X-ray diffraction (XRD) analysis was performed (Figure 3). The XRD patterns are

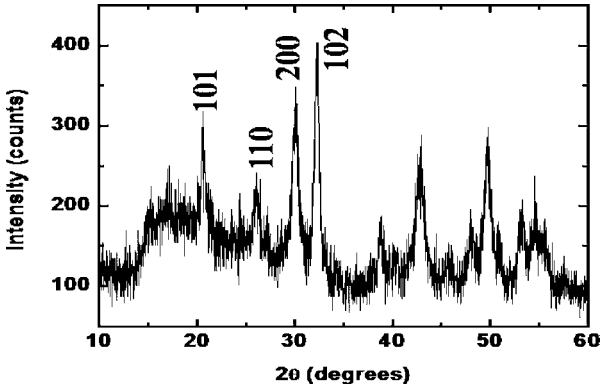

Figure 3. X-ray diffraction pattern of the gadolinium phosphate nanoparticles indexed to $GdPO_4{\cdot}H_2O$. (JCPDS no. 39-232; space groupn $P3_121$, #152).

consistent with the known hexagonal $GdPO_4{\cdot}H_2O$ with a = 6.90 Å and c = 6.35 Å (JCPDS no. 39-232; space group, $P3_121$, #152).[21,29,30] Magnetic susceptibility measurement of the $GdPO_4{\cdot}H_2O$ nanoparticles show paramagnetic behavior at room and physiological temperatures (Supporting Information).

Surface Modification of the $GdPO_4$NPs. The phosphate-terminated oligonucleotides are expected to specifically bind the particle surface through the divalent phosphate, in line with observations made for zirconium phosphate and zirconium phosphonate surfaces.[25−27] The specific Gd^{3+}-divalent phosphate linkage requires that Gd^{3+} sites are accessible at the particle surface (Figure 1). The as-synthesized $GdPO_4{\cdot}H_2O$ are phosphate-rich at the surface, as confirmed by zeta potential measurements (Supporting Information). Therefore, a postsynthesis treatment of the particles with excess Gd^{3+} is employed to ensure a Gd^{3+}-rich surface for oligonucleotide binding.

The specific interaction depicted in Figure 1 was verified by monitoring phosphate-terminated oligonucleotide binding to Gd^{3+} treated particles and comparing it to three control experiments. The controls include particles that were pretreated with Gd^{3+} and incubated in nonphosphorylated DNA, particles that were not pretreated with Gd^{3+} and incubated in phosphorylated DNA, and particles that were not pretreated with Gd^{3+} and incubated in nonphosphorylated DNA. The four conditions are shown schematically in Figure 4.

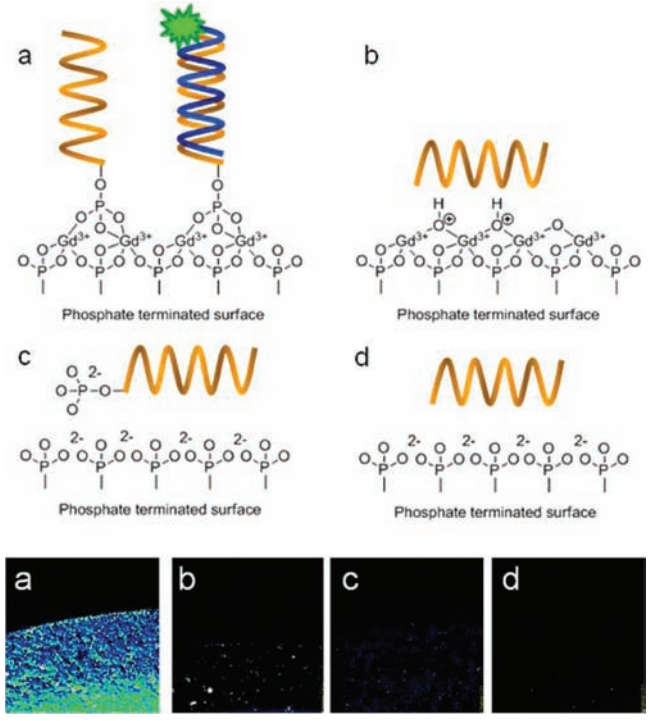

Figure 4. Schematic of different modification procedures (top) and confocal laser scanning microscopy images of drops of dispersions of the $GdPO_4{\cdot}H_2O$ nanoparticles in water following each procedure (bottom). (a) Nanoparticles treated with Gd^{3+} and followed by phosphorylated oligonucleotide; (b) treated with Gd^{3+} and followed by nonphosphorylated oligonucleotide; (c) without postsynthesis treatment with Gd^{3+} but with phosphorylated oligonucleotide; and (d) without postsynthesis treatment with Gd^{3+} and with nonphosphorylated oligonucleotide. In each case, the nanoparticles are shown after incubation with Cy3-labeled complement and methodical rinsing. Because the fluorophore is attached to the complementary strand, robust fluorescence indicates successful modification and hybridization steps. The fluorescence intensities are color coded from blue (low) to green, yellow, red, and white (saturation).

A fluorescently labeled complementary oligonucleotide strand (target) was used to confirm the modification of the particles. Confocal microscopy detects fluorescence on nanoparticles dispersed in water. When the fluorescence is maintained after successive rinsing procedures, the target is successfully hybridized to the probe strands covalently attached to the surface of the particle (Figure 4). Confocal microscopy shows that the greatest binding affinity is for the phosphorylated DNA with $GdPO_4$NP treated with Gd^{3+}. This result points out that nonspecifically bound DNA is removed from the particles following the wash procedures. Particles pretreated with $Gd(NO_3)_3$ and incubated with nonphosphorylated oligonucleotides showed some areas of saturated fluorescence, but it is not uniform, which can be explained by a few aggregates of particles trapping nonspecifically bound DNA. By far, the greatest extent of hybridization occurred on Gd^{3+}-treated $GdPO_4$NPs that were subsequently modified with phosphorylated oligonucleotides.

dx.doi.org/10.1021/bc200553h | *Bioconjugate Chem.* 2012, 23, 951−957

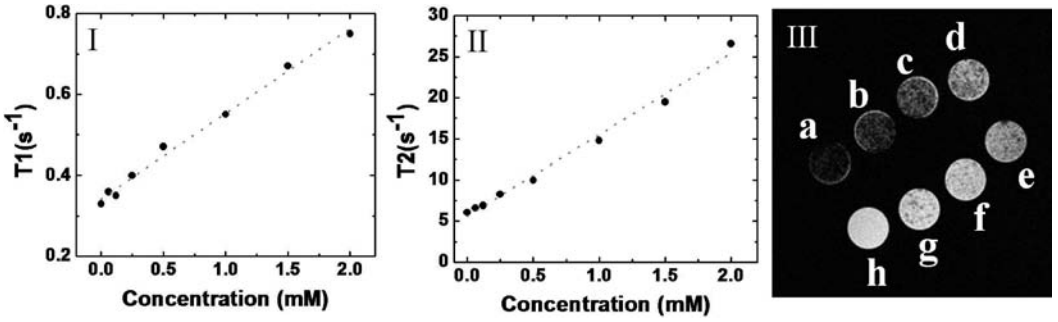

Figure 5. MR relaxivity data and image of serial dilutions of DNA modified $GdPO_4 \cdot H_2O$ nanoparticles ($GdPO_4$NP-DNA). (I) and (II) Plots of the values of longitudinal (T_1) and transverse (T_2), relaxation respectively, measured against the concentration of Gd^{3+}. (III) T_2 weighted images of successive dilutions of $GdPO_4$NP-DNA (in sequence, from a to h: 2, 1.5, 1, 0.5, 0.25, 0.12, 0.06 mM, and pure agarose).

Table 1. Comparison of the Chemical and Magnetic Characteristics of Functionalized $GdPO_4 \cdot H_2O$ Nanoparticles, Omniscan, and Feridex

				relaxivity ($mM^{-1}s^{-1}$)[c]		
contrast agent	structure[a]	magnetism[b]	chemical composition	r_1	r_2	r_2 / r_1
$GdPO_4$NP-DNA	NP	P	$GdPO_4$	0.2	12.8	60.9
Omniscan	C	P	Gd^{3+}-DTPA-BMA	4.6	5.4	1.1
Feridex	NP	SP	iron oxide	1.9	313	164.7

[a]NP, nanoparticles; C, chelate. [b]P, paramagnetic; SP, superparamagnetic. [c]MR measurements were performed at 600 MHz (14.1 T field).

MR Measurements. Dispersions of the DNA-modified nanoparticles in agarose were used to evaluate the r_2/r_1 values. Longitudinal and transversal relaxation rates, R_1 and R_2, were measured in the same phantom consisting of solutions containing increased concentrations of $GdPO_4$NP-DNA in agarose.

As expected, a linear relationship was established between the relaxation rates and the agent concentration (Figure 5). Longitudinal and transversal relaxivities were derived from the linear fits of R_1 and R_2 versus gadolinium concentration. Relaxivities were found to be r_1 = 0.2 $mM^{-1} \cdot s^{-1}$ and r_2 = 12.8 $mM^{-1} \cdot s^{-1}$ from which we calculated the ratio r_2/r_1 = 60.9 (Table 1). A T_2 weighted image of successive dilutions of $GdPO_4$NP-DNA showed an obvious negative contrast, increasing with the agent concentration (Figure 5). All together, these data confirmed the efficacy of $GdPO_4$NP-DNA as an MR contrast agent. Identical measurements were carried out with commercial gadolinium chelate and SPIO, using the same sequences. The values of r_1 and r_2 are reported in Table 1. Omniscan, a Gd-chelate positive contrast agent was found to have an r_2/r_1 value of 1.1 at 14.1 T, whereas Feridex, an SPIO negative contrast agent, had an r_2/r_1 of 164.7. These results were consistent with the specifications of these agents. The value of r_2/r_1 = 60.9 obtained for $GdPO_4$NP-DNA and the loss of signal observed with increasing concentration confirmed that $GdPO_4$NP-DNA has the characteristics of a T_2 or negative contrast agent.

DISCUSSION

Surface Modification. The results demonstrate specific binding of phosphate terminated DNA oligonucleotides to the surface of $GdPO_4 \cdot H_2O$ nanoparticles. The result is consistent with previous work on zirconium phosphate and zirconium phosphonate surfaces that showed that coordinate covalent bonds can be formed between the divalent phosphate group at the terminus of oligonucleotides and Zr^{4+} ions at the surface. The acidic Zr^{4+} surface sites are bound by oxide and hydroxide groups, and the specificity comes from the fact that the divalent phosphate can displace the oxides and hydroxides on the surface, whereas the phosphodiester backbone $[(RO)_2PO_2^-]$ of a DNA molecule is not sufficiently basic, only forming electrostatic or hydrogen bonding interactions.[25−27] In the absence of the terminal phosphate, the DNA probe is easily washed away. Interaction between phosphate terminating the DNA and the surfaces of acidic metal phosphates and phosphonates has been shown to be stable under a range of conditions.[25−27]

The same principle applies for DNA binding to $GdPO_4$NP. Oligonucleotide binding to these particles occurs through a coordinate covalent linkage with the terminal 5′-phosphate of the oligonucleotides. Therefore, binding to these particles does not require any modification of the DNA molecule to obtain specific immobilization or any polymer or organic coating of the particles. Furthermore, the phosphate-terminated oligonucleotides specifically bound to the $GdPO_4$NP were able to hybridize with their complementary sequence, demonstrating sustained biological activity. The procedures should enable efficient surface modification with targeting markers associated with pathological conditions while simultaneously providing a biocompatible outer-shell to the nanoparticles.

MR Measurements. Despite their content in Gd^{3+}, which is usually utilized as a positive contrast agent, the $GdPO_4$NP-DNA nanoparticles developed in this study proved to generate negative MR contrast. This observation was confirmed by the high r_2/r_1 value of 60.9 and the generation of a negative contrast on T_2-weighted images at 14.1 T. In general, the development of positive MR contrast agents at high magnetic fields is challenging. Indeed, the sensitivity of such compounds depends on the complex interplay between different structural and dynamics properties, such as rotational mobility or the residence lifetime of the water protons at the metal site.[31] High r_1 relaxivities have been achieved in a few cases. For example, using similar gadolinium phosphate nanoparticles to those studied here but coated with dextran, Hifumi et al.[18,19] reported

dx.doi.org/10.1021/bc200553h | Bioconjugate Chem. 2012, 23, 951−957

small r_2/r_1 values of 1.1, although at very low magnetic field (0.47 T). Relaxivity measurements of the oligonucleotide modified $GdPO_4$NPs at 1.47 T gave r_2/r_1 of 1.7 ± 0.2, confirming the positive contrast agent properties observed by these authors at low field (Supporting Information). At higher fields (> 3 T), the relaxivity of gadolinium-based agents decreases rapidly due to their frequency dependence, making the achievement of high r_1 a bigger challenge.[31]

The DNA-modified $GdPO_4{\cdot}H_2O$ particles induced an important change in the relaxivity of surrounding water, indicating high sensitivity as a negative MRI contrast agent. The ability to easily functionalize the particles with phosphate-terminated DNA, such as that enzymatically produced by polymerase chain reaction (PCR), suggests this system could potentially enable cancer-cell recognition in order to specifically enhance the contrast of the tumors with surrounding tissue.[32,33] In addition, surface modification combined with the low solubility of $GdPO_4{\cdot}H_2O$ means that Gd^{3+} release is slow. Measurements of the supernatant of suspensions kept for 18 months showed no significant discharge of Gd^{3+} (Supporting Information). Additionally, data suggesting *in vivo* stability and low cytotoxicity have been reported for similar gadolinium phosphate nanoparticles by Hifumi et al.[18]

CONCLUSIONS

Using surface modification chemistry previously demonstrated on zirconium phosphonate surfaces, it is shown that $GdPO_4{\cdot}H_2O$ nanoparticles can be easily functionalized with DNA probes. The key interaction is coordinate covalent binding of the oligonucleotide terminal phosphate to active Gd^{3+} sites on the surface of the particles. The single-step binding of phosphate-terminated oligonucleotides avoids complicated surface modification schemes that involve multiple synthetic steps. The binding is achieved in one step, in biological conditions, and in the case of a DNA oligonucleotide, the bioactivity is retained. The MR relaxivity measurements confirmed that the DNA-modified $GdPO_4{\cdot}H_2O$ nanoparticles have relaxivities comparable to those of commercially available contrast agents and that the biofunctionalization of the surface of the nanoparticles does not prevent their function as MRI contrast agents.

ASSOCIATED CONTENT

Supporting Information

Details of the magnetic measurement and the magnetic susceptibility, χ, as a function of temperature, T; titration of free Gd^{3+} with xylenol orange; and low field relaxivity measurements on $GdPO_4$NP-DNA. This material is available free of charge via the Internet at http://pubs.acs.org.

AUTHOR INFORMATION

Corresponding Author

*Phone: (352) 392-9016. Fax (352) 392-3255. E-mail: talham@chem.ufl.edu.

Notes

The authors declare no competing financial interest.

ACKNOWLEDGMENTS

This work was supported, in part, by the U.S. National Science Foundation and the National Institutes of Health through grants CHE-0957155 (to D.R.T.), DMR-0701400 (to M.W.M.) and P01HL059412 (to G.A.W.). The MRI work was performed in the Advanced Magnetic Resonance Imaging and Spectroscopy facility (AMRIS) in the McKnight Brain Institute (MBI) at the University of Florida, which is supported by the National High Magnet Field Laboratory and the State of Florida. We gratefully acknowledge Weihong Tan and Suwussa Bamrungsap from the Chemistry Department at University of Florida for MR relaxivity studies, Kerry Siebein at the UF Major Analytical Instrument Center for HRTEM imaging and EDS analysis work, and Dan Plant at AMRIS/MBI for MRI work.

REFERENCES

(1) Fukumori, Y., and Ichikawa, H. (2006) Nanoparticles for cancer therapy and diagnosis. *Adv. Powder Technol. 17*, 28−33.

(2) Louie, A. (2010) Multimodality imaging probes: design and challenges. *Chem. Rev. 110*, 3146−3171.

(3) Oghabian, M. A., and Farahbakhsh, N. M. (2010) Potential use of nanoparticle based contrast agents in MRI: a molecular imaging perspective. *J. Biomed. Nanotechnol. 6*, 203−207.

(4) Cahill, K. S., Germain, S., Byrne, B. J., and Walter, G. A. (2004) Non-invasive analysis of myoblast transplants in rodent cardiac muscle. *Int. J. Cardiovasc. Imaging 20*, 593−597.

(5) Caravan, P., Ellison, J. J., McMurry, T. J., and Lauffer, R. B. (1999) Gadolinium(III) chelates as MRI contrast agents: structure, dynamics, and applications. *Chem. Rev. 99*, 2293−2321.

(6) Sharma, P., Brown, S., Walter, G., Santra, S., and Moudgil, B. (2006) Nanoparticles for bioimaging. *Adv. Colloid Interface Sci. 123*, 471−476.

(7) Laurent, S., Forge, D., Port, M., Roch, A., Robic, C., Vander Elst, L., and Muller, R. N. (2008) Magnetic iron oxide nanoparticles: synthesis, stabilization, vectorization, physicochemical characterizations, and biological applications. *Chem. Rev. 108*, 2064−2069.

(8) Boyd, A. S., Zic, J. A., and Abraham, J. L. (2007) Gadolinium deposition in nephrogenic fibrosing dermopathy. *J. Am. Acad. Dermatol. 56*, 27−31.

(9) DaSilva, M., Deming, M. O., Fligiel, S. E. G., Dame, M. K., Johnson, K. J., Swartz, R. D., and Varani, J. (2010) Responses of human skin in organ culture and human skin fibroblasts to a gadolinium-based MRI contrast agent comparison of skin from patients with end-stage renal disease and skin from healthy subjects. *Invest. Radiol. 45*, 733−737.

(10) Ersoy, H., and Rybicki, F. J. (2007) Biochemical safety profiles of gadolinium-based extracellular contrast agents and nephrogenic systemic fibrosis. *J. Magn. Reson. Im. 26*, 1190−1194.

(11) Thakral, C., and Abraham, J. L. (2009) Gadolinium-induced nephrogenic systemic fibrosis is associated with insoluble Gd deposits in tissues: in vivo transmetallation confirmed by microanalysis. *J. Cutananeous Pathol. 36*, 1244−1248.

(12) Bridot, J.-L., Faure, A.-C., Laurent, S., Riviere, C., Billotey, C., Hiba, B., Janier, M., Josserand, V., Coll, J.-L., Vander Elst, L., Muller, R., Roux, S., Perriat, P., and Tillement, O. (2007) Hybrid gadolinium oxide nanoparticles: a multimodal contrast agents for in vivo imaging. *J. Am. Chem. Soc. 129*, 5076−5081.

(13) McDonald, M. A., and Watkin, K. L. (2006) Investigations into the physicochemical properties of dextran small particulate gadolinium oxide nanoparticles. *Acad. Radiol. 13*, 421−426.

(14) Park, J. Y., Baek, M. J., Choi, E. S., Woo, S., Kim, J. H., Kim, T. J., Jung, J. C., Chae, K. S., Chang, Y., and Lee, G. H. (2009) Paramagnetic ultrasmall gadolinium oxide nanoparticles as advanced T1MRI contrast agent: account for large longitudinal relaxivity, optimal particle diameter, and in vivo T1MR images. *ACS Nano 3*, 3663−3668.

(15) Cheung, E. N., Alvares, R. D. A., Oakden, W., Chaudhary, R., Hill, M. L., Pichaandi, J., Mo, G. C. H., Yip, C., Macdonald, P. M., Stanisz, G. J., van Veggel, F. C., and Prosser, R. S. (2010) Polymer-stabilized lanthanide fluoride nanoparticle aggregates as contrast agents for magnetic resonance imaging and computed tomography. *Chem. Mater. 22*, 4728−4733.

(16) Gerion, D., Herberg, J., Bok, R., Gjersing, E., Ramon, E., Maxwell, R., Kurhanewicz, J., Budinger, T. F., Gray, J. W., Shuman, M. A., and Chen, F. F. (2007) Paramagnetic silica-coated nanocrystals as an advanced MRI contrast agent. *J. Phys. Chem. C 111*, 12542−12546.
(17) Rieter, W. J., Taylor, K. M. L., An, H., Lin, W., and Lin, W. (2006) Nanoscale metal-organic frameworks as potential multimodal contrast enhancing agents. *J. Am. Chem. Soc. 128*, 9024−9029.
(18) Hifumi, H., Yamaoka, S., Tanimoto, A., Akatsu, T., Shindo, Y., Honda, A., Citterio, D., Oka, K., Kuribayashi, S., and Suzuki, K. (2009) Dextran coated gadolinium phosphate nanoparticles for magnetic resonance tumor imaging. *J. Mater. Chem. 19*, 6393−6397.
(19) Hifumi, H., Yamaoka, S., Tanimoto, A., Citterio, D., and Suzuki, K. (2006) Gadolinium-based hybrid nanoparticles as a positive MR contrast agent. *J. Am. Chem. Soc. 128*, 15090−15094.
(20) Fang, Y. P., Xu, A. W., Song, R. Q., Zhang, H. X., You, L. P., Yu, J. C., and Liu, H. Q. (2003) Systematic synthesis and characterization of single-crystal lanthanide orthophosphate nanowires. *J. Am. Chem. Soc. 125*, 16025−16029.
(21) Lessing, P. A., and Erickson, A. W. (2003) Synthesis and characterization of gadolinium phosphate neutron absorber. *J. Eur. Ceramic Soc. 23*, 3049−3054.
(22) Huang, Y.-F., Sefah, K., Bamrungsap, S., Chang, H.-T., and Tan, W. (2008) Selective photothermal therapy for mixed cancer cells using aptamer-conjugated nanorods. *Langmuir 24*, 11860−11863.
(23) Medley, C. D., Smith, J. E., Tang, Z., Wu, Y., Bamrungsap, S., and Tan, W. (2008) Gold nanoparticle-based colorimetric assay for the direct detection of cancerous cells. *Anal. Chem. 80*, 1067−1070.
(24) Villaraza, L. A. J., Bumb, A., and Brechbiel, M. W. (2010) Macromolecules, dendrimers, and nanomaterials in magnetic resonance imaging: the interplay between size, function, and pharmacokinetics. *Chem. Rev. 110*, 2921−2924.
(25) Cinier, M., Petit, M., Williams, M. N., Fabre, R. M., Pecorari, F., Talham, D. R., Bujoli, B., and Tellier, C. (2009) Bisphosphonate adaptors for specific protein binding on zirconium phosphonate-based microarrays. *Bioconjugate Chem. 20*, 2270−2276.
(26) Lane, S., Monot, J., Petit, M., Bujoli, B., and Talham, D. (2007) XPS investigation of DNA binding to zirconium-phosphonate surfaces. *Colloid. Surf. B 58*, 34−37.
(27) Monot, J., Petit, M., Lane, S. M., Guisle, I., Lager, J., Tellier, C., Talham, D. R., and Bujoli, B. (2008) Towards zirconium phosphonate-based microarrays for probing DNA-protein interactions: critical influence of the location of the probe anchoring groups. *J. Am. Chem. Soc. 130*, 6243−6247.
(28) Hutton, C., Bork, A., Josephs, O., Deichmann, R., Ashburner, J., and Turner, R. (2002) Image distortion correction in fMRI: a quantitative evaluation. *NeuroImage 16*, 217−240.
(29) Huo, Z. Y., Chen, C., Chu, D., Li, H. H., and Li, Y. D. (2007) Systematic synthesis of lanthanide phosphate nanocrystals. *Chem. Eur. J. 13*, 7708.
(30) Parreu, I., Sola, R., Gavalda, J., Massons, J., Diaz, F., and Aguila, M. (2005) Crystal growth, structural characterization, and linear thermal evolution of $KGd(PO_3)_4$. *Chem. Mater. 17*, 822−826.
(31) Terreno, E., Castelli, D. D., Viale, A., and Aime, S. (2010) Challenges for molecular magnetic resonance imaging. *Chem. Rev. 110*, 3019−3046.
(32) Wang, H., Yang, R., Yang, L., and Tan, W. (2009) Nucleic acid conjugated nanomaterials for enhanced molecular recognition. *ACS Nano 3*, 2451−2460.
(33) Tang, Z., Parekh, P., Turner, P., Moyer, R. W., and Tan, W. (2009) Generating aptamers for recognition of virus-infected cells. *Clin. Chem. 55*, 813−822.

Bioconjugate Chemistry

Article

pubs.acs.org/bc

Size Dependent Biodistribution and SPECT Imaging of ^{111}In-Labeled Polymersomes

René P. Brinkhuis,[†,∥] Katica Stojanov,[‡,∥] Peter Laverman,[§] Jos Eilander,[†] Inge S. Zuhorn,[‡] Floris P. J. T. Rutjes,[†] and Jan C. M. van Hest*[,†]

[†]Institute for Molecules and Materials, Radboud University Nijmegen, Heijendaalseweg 135, 6525 AJ, Nijmegen, The Netherlands

[‡]Department of Cell Biology, section Membrane Cell Biology, University Medical Center Groningen, University of Groningen, A. Deusinglaan 1, 9713 AV Groningen, The Netherlands

[§]Department of Nuclear Medicine, Radboud University Nijmegen Medical Centre, Geert Grooteplein Zuid 8, 6525 GA Nijmegen, The Netherlands

Supporting Information

ABSTRACT: Polymersomes, self-assembled from the block copolymer polybutadiene-*block*-poly(ethylene glycol), were prepared with well-defined diameters between 90 and 250 nm. The presence of ∼1% of diethylene triamine penta acetic acid on the polymersome periphery allowed to chelate radioactive ^{111}In onto the surface and determine the biodistribution in mice as a function of both the polymersome size and poly(ethylene glycol) corona thickness (i.e., PEG molecular weight). Doubling the PEG molecular weight from 1 kg/mol to 2 kg/mol did not change the blood circulation half-life significantly. However, the size of the different polymersome samples did have a drastic effect on the blood circulation times. It was found that polymersomes of 120 nm and larger become mostly cleared from the blood within 4 h, presumably due to recognition by the reticuloendothelial system. In contrast, smaller polymersomes of around 90 nm circulated much longer. After 24 h more than 30% of the injected dose was still present in the blood pool. This sharp transition in blood circulation kinetics due to size is much more abrupt than observed for liposomes and was additionally visualized by SPECT/CT imaging. These findings should be considered in the formulation and design of polymersomes for biomedical applications. Size, much more than for liposomes, will influence the pharmacokinetics, and therefore, long circulating preparations should be well below 100 nm.

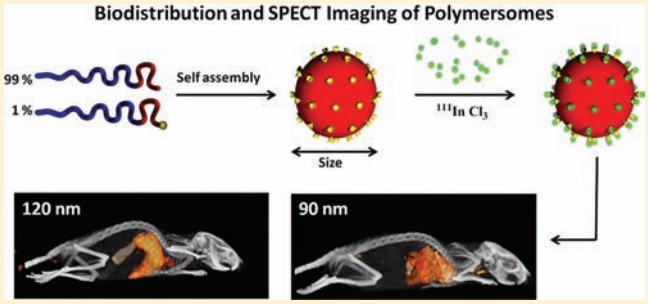

INTRODUCTION

Polymersomes, or polymer vesicles, are a relatively new class of nanocapsules that are formed by the self-assembly of amphiphilic block copolymers in aqueous media.[1] Polymersomes can be regarded as the polymeric analogues of liposomes with a thicker, more stable and less leaky membrane. These characteristics make polymersomes an interesting class of nanocarriers for the delivery of diagnostic and therapeutic agents. For these applications, it is generally desired to have long circulating particles which are not readily cleared from the bloodstream by the reticuloendothelial system (RES).[2] From liposomal *in vivo* studies, it is known that size, next to PEGylation and charge, is a major factor that influences the blood circulation kinetics and biodistribution. Liposomes of more than 200 nm have been shown to accumulate in the spleen and liver, whereas liposomes of less than 70 nm tend to accumulate predominantly in the liver.[3,4] Liposomes with a size between 90 and 150 nm have the longest blood circulation times. The blood circulation times of liposomes can be further enhanced by the introduction of up to 10% PEGylated phospholipids.[5,6] Polyethylene glycol (PEG) prevents the opsonization by blood proteins and the subsequent recognition and degradation by macrophages of the reticuloendothelial system. PEGylated liposomes may exhibit blood circulation half-lives ($t_{1/2}$) of more than 15 h, depending on the PEG chain length, charge, and size of liposomes.[3,4,7] Finally, the effect of surface charge in liposomal formulations[8] and nano carriers[9] has been studied. Both slightly negative and positive surface charges were reported to have a positive effect on blood circulation kinetics.

The number of reports on biodistribution of neutral polymersomes is limited and is basically restricted to the work of Discher,[10,11] who used fluorescently labeled polymersomes to determine the effect of longer PEG chains and surface charge on $t_{1/2}$ values, the work of Lee et al.,[12] and the recent work by Kataoka et al., who studied the size dependence of fluorescently labeled polyelectrolyte vesicles (PICsomes) for the preferred accumulation in tumor tissue compared to healthy

Received: October 27, 2011
Revised: January 30, 2012
Published: April 2, 2012

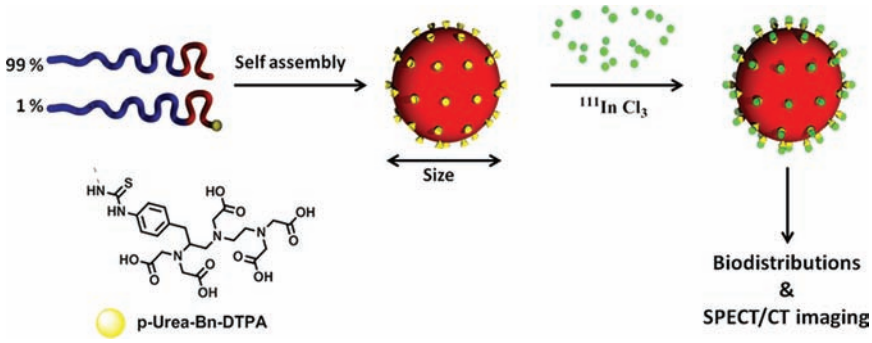

Figure 1. Schematic presentation of polymersome formation, ^{111}In labeling, and *in vivo* SPECT/CT imaging.

tissue.[13] Also, near-infrared dyes have been encapsulated in order to visualize tumors in mice.[14,15] Discher et al. reported that polymersomes exhibit blood circulation half-lives up to 28 h. These high $t_{1/2}$ values are partly due to the fact that polymersomes are fully PEGylated upon choosing PEG as the hydrophilic part of the block copolymer that constitutes the polymersome bilayer. It was furthermore shown that neutral polymersomes circulate with the highest $t_{1/2}$ values. Finally, Tsourkas et al.[16] encapsulated a Gd-based magnetic resonance imaging (MRI) contrast agent for enhanced MRI imaging. By measuring the concentration of Gd in blood, they were also able to determine a concentration−time profile.

One of the most quantitative methods to determine the biodistribution of drug delivery vehicles *in vivo* is by radio isotope labeling. This technique is often used for liposomal formulations but has until now been hardly explored for polymersomes. There is one report on the biodistribution and radiolabeling (^{14}C/^{3}H) of negatively charged polymersomes[12] and one study that shows data on the encapsulation and biodistribution of a radiolabeled model drug encapsulated in polymersomes.[17] However, the effect of polymersome size on biodistribution has not been analyzed before with this technique. If radiolabeling of polymersomes with a suitable isotope such as ^{111}In would be performed, this would not only allow quantitative determination of organ distribution but also visualization with SPECT/CT imaging, as has previously been demonstrated for 50 nm polymer micelles.[18,19]

In this article, we present a systematic study into the effect of size on the biodistribution of polymersomes via the quantitative technique of ^{111}In radiolabeling, in combination with SPECT/CT imaging as depicted schematically in Figure 1. It is shown that polymersomes of around 90 nm in diameter have long circulation times in male Balb/C mice. Upon increasing the diameter to 120 nm and above, the long circulating properties are lost, and polymersomes are cleared from the bloodstream within a few hours by mainly the liver and spleen. The effect on circulation time upon changing the size from 90 to 120 nm is also clearly visualized by SPECT/CT imaging.

EXPERIMENTAL PROCEDURES

Materials. *sec*-Butyllithium (Aldrich 1.4 M in hexane), tetrabutylammonium fluoride (TBAF) (Aldrich, 1.0 M in THF), sodium hydride (Aldrich, 60% dispersion in mineral oil, *p*-isothiocyanate-benzyl diethylenetriamine penta-acetic acid (MACROCYCLICS >94%), and Chelex resin (Aldrich) were used as received. Tetrahydrofuran (THF) (ACROS ORGANICS, 99+% extra pure, stabilized with BHT) was distilled under argon from sodium/benzophenone, and triethyl amine (TEA) (BAKER) was distilled from calcium hydride under an argon atmosphere prior to use. Polymersome extrusions were performed using 200 nm filters (Acrodisc 13 mm Syringe Filter, 0.2 μm Nylon membrane) and 0.1 μm PC membrane (WHATMAN). $^{111}InCl_3$ was purchased from Covidien, Petten, The Netherlands. Instant Thin-Layer Chromatography Silica Gel impregnated glass fiber (ITLC-SG) strips were purchased from Varian. Column chromatography was carried out using silica gel (Acros (0.035−0.070 mm, pore diameter ca. 6 nm)). Note that other silica suppliers gave less satisfactory results for α- azido ω-carboxy poly(ethylene glycol).

Instrumentation. Infrared (IR) spectra were obtained using a Thermo Matson IR 300 FTIR spectrometer. Data are presented as the frequency of absorption (cm^{-1}). Proton nuclear magnetic resonance (^{1}H NMR) spectra were recorded on a Varian Unity Inova 400 FTNMR spectrometer. Chemical shifts are expressed in parts per million (δ scale) relative to the internal standard tetramethylsilane (δ = 0.00 ppm). Molecular weight distributions were measured using size exclusion chromatography (SEC) on a Shimadzu (CTO-20A) system equipped with a guard column and a PL gel 5 μm mixed D column (Polymer Laboratories) with differential refractive index and UV (λ = 254 nm, and λ = 345 nm) detection, using tetrahydrofuran (SIGMA Aldrich chromasolv 99.9%) as an eluent at 1 mL/min and T = 35 °C. Particle size distributions were measured on a Malvern instruments Zetasizer Nano-S, and zeta potentials were measured on a NanoSight NS 500 instrument.

*Propyne- End-Capped Polybutadiene (**1**).* A Schlenk tube was thoroughly cleaned, rinsed with butyllithium, flushed with Milli-Q, and oven-dried overnight. The Schlenk tube was evacuated, and an argon atmosphere was applied, after which 7.1 g of 1,3-butadiene was condensed at −78 °C. THF was distilled under argon over sodium/benzophenone, and 10 mL was added to the flask. The polymerization was initiated by the addition of 1.4 mL of *sec*-butyllithium (1.4 M in hexane). The mixture was allowed to heat up to −35 °C as the color changed from pale yellow to orange. After the color changed back to yellow, the reaction was terminated by the addition of 10 mL of dry THF and 400 mg of trimethylsilyl propargylbromide. After all of the color had disappeared, 4 mL of tetrabutyl ammonium fluoride (1 M in THF) was added, and the mixture was stirred for 1 h. All solvents were removed, and the product was dissolved in dichloromethane, after which it was filtered over a slab of silica, eluting with dichloromethane. The final product was obtained by coevaporation with 4 times 50 mL of toluene to remove any traces of propargyl bromide. The product contained two molecular weight distributions as determined by size exclusion chromatography (THF): 3.7 kg/mol (60%) and

dx.doi.org/10.1021/bc200578s | *Bioconjugate Chem.* 2012, 23, 958−965

7.4 kg/mol (40%). The higher molecular weight, a polymer dimer as reported and explained by Tohyama et al.,[20] is not reactive toward azides and was easily removed by silica column chromatography, after the block copolymers were formed as shown in Figures S1−S3 (Supporting Information). ^{1}HNMR: δ 5.45 (m, 67H, C$\underline{H}$CH$_2$), 4.94 (m, 134H, CHC$\underline{H}_2$), 2.11 (m, 67H, CH$_2$C$\underline{H}$), 1.16 (m, 134H, C$\underline{H}_2$CH).

*α-Azido ω-Methoxy Poly(ethylene glycol) (**2a/b**): General Procedure.* Poly(ethylene glycol) monomethyl ether (5 mmol, 1 or 2 kg/mol to obtain, respectively, **2a** or **2b**) was coevaporated with benzene three times and dissolved in 250 mL of dry and under argon distilled THF. The general procedure is further described for the preparation of **2a**. The flask was cooled on an ice bath, and air was replaced by argon before 5 mL of freshly distilled triethyl amine was added. The mixture was stirred for 3 h, after which 1.14 g (2 equiv, 10 mmol) of mesyl chloride in 10 mL of THF was added. The mixture was allowed to warm to room temperature and was stirred for 6 h. All THF was removed, and 100 mL of methanol containing 3.25 g (10 eq 50 mmol) of sodium azide was added. The mixture was refluxed overnight after which methanol was removed and 100 mL of water was added. The product was extracted with 5× 100 mL of dichloromethane. The combined organic layers were dried over magnesium sulfate, and DCM was removed, yielding 4.5 g (90%) of product **2a**. The SEC traces of both **2a** (Figure S1, Supporting Information) and **2b** (Figure S2, Supporting Information) can be found in Supporting Information. ^{1}HNMR (**2a**): δ 3.37 (s, 3H, C$\underline{H}_3$O), 3.39 (t, 2H, C$\underline{H}_2$N$_3$), 3.64 (m, 90H, C$\underline{H}_2$C$\underline{H}_2$O). FTIR: 2098 cm^{-1} (azide). SEC (THF): Mn (**2a**) = 1 kg/mol, M_w/M_n = 1.19.

α-Azido ω-Carboxy Poly(ethylene glycol). Five grams of poly(ethylene glycol) (5 mmol, 1 kg/mol) was coevaporated with benzene three times and dissolved in 250 mL dry and under argon distilled THF. The flask was cooled on ice, and air was replaced by argon, followed by the addition of 5 mL of distilled triethyl amine. The mixture was stirred for 3 h, after which 0.6 g (1.1 eq 5.1 mmol) of mesyl chloride in 10 mL of THF was added over 1 h. The reaction was allowed to warm to room temperature and stirred for 6 h. THF was removed, and 100 mL of methanol containing 3.25 g (10 eq 50 mmol) of sodium azide was added. The reaction was heated to reflux overnight, whereafter methanol was removed, and 100 mL of water was added. The mixture of statistical products was extracted with 5× 100 mL of dichloromethane. The combined organic layers were dried over MgSO$_4$, and dichloromethane was removed.

The products were coevaporated with benzene, dissolved in 250 mL of freshly distilled THF, and cooled on an ice bath. An argon atmosphere was applied, and 400 mg of 60% sodium hydride (2 equiv) was added. After three hours, 2.9 g of *t*-butyl bromoacetate (3eq. 14 mmol) in 10 mL of THF was added, and the temperature was raised to 50 °C. The reaction was allowed to proceed overnight, after which all solids were filtered off, and THF was removed. The products were dissolved in 100 mL of 2 M HCl and heated to reflux for 5 h. The final product was extracted with 5× 100 mL of dichloromethane. The combined organic layers were dried over MgSO$_4$, and all solvents were removed. The product (R_f = 0.5) was purified using silica column chromatography (eluent MeOH/DCM/NH$_3$ =15:85:5) yielding 1.5 g (30%) of product. TLC: R_f = 0.5, permanganate staining, eluent DCM/MeOH = 92:8. ^{1}HNMR: δ 3.39 (t, 2H, C$\underline{H}_2$N$_3$), 3.64 (m, 90H, C$\underline{H}_2$C$\underline{H}_2$O), 4.00 (s, 2H, OC$\underline{H}_2$COOH). FTIR: 2098 cm^{-1} (azide), 1570 (C═O of carboxylic acid salt). SEC (THF): M_n = 1 kg/mol, M_w/M_n = 1.19.

*α-Azido ω-Amino Poly(ethylene glycol) (**3**).* One gram (1 mmol) of α-azido ω-carboxy poly(ethylene glycol) was dissolved in 50 mL of methanol, and 5 drops of concentrated sulphuric acid were added. The mixture was heated under reflux overnight, after which methanol was removed. The product was dissolved in 50 mL of water and extracted with 5 times 50 mL of dichloromethane. The organic layer was dried over MgSO$_4$, and all solvents were removed. TLC: R_f = 0.65, permanganate staining, eluent DCM/MeOH = 92:8. Indicative ^{1}HNMR shifts: δ 4.17 (s, 2H, OC$\underline{H}_2$COOMe), 3.75 (s, 3H, COOC$\underline{H}_3$) and IR: 1748 cm^{-1} (carbonyl/ester).

The product was dissolved in 50 mL of methanol, and 0.5 mL of 1,2-diamino ethane was added (large excess). The mixture was heated under reflux for 48 h, after which all methanol was removed. The product was dissolved in 50 mL of 1 M hydrochloric acid and extracted with 5 times 50 mL of dichloromethane. The combined organic layers were dried over MgSO$_4$, and all solvents were removed to yield 800 mg of product (80%). TLC: R_f = 0.55, permanganate and nynhydrin staining, eluent DCM/MeOH = 92:8. ^{1}HNMR: δ 2.99 (t, 2H CH$_2$C$\underline{H}_2$NH$_2$), 3.39 (t, 2H, C$\underline{H}_2$N$_3$), 3.64 (m, 90H, C$\underline{H}_2$C$\underline{H}_2$O), 4.01 (s, 2H, OC$\underline{H}_2$CONH). FTIR: 2098 cm^{-1} (azide), 1696 cm^{-1} (amide). SEC (THF): M_n = 1 kg/mol, M_w/M_n = 1.24.

*Polybutadiene-block-Poly(ethylene glycol): General Procedure (**4a/b, 5**).* Poly(ethylene glycol) **2a**, **2b**, or **3** (**2a**, **3**, 80 mg 0.08 mmol; **2b**, 160 mg 0.08 mmol) and **1** (800 mg, 2.6 equiv 0.21 mmol) were dissolved in 10 mL of dry tetrahydrofuran under an argon atmosphere. The general procedure is further described for the coupling of **2a** and **1**. The temperature was raised to 55 °C, and 30 mg of CuBr and 70 mg of PMDETA were added. The reaction was allowed to proceed for 12 h after which all solvents were removed. The crude product was redissolved in 50 mL of dichloromethane and washed three times with 25 mL of 0.33 M EDTA. The organic layer was dried over MgSO$_4$ and poured on a short silica column, which was eluted with dichloromethane. After all nonreacted polybutadiene was flushed off, the product was eluted with 8 v% methanol in dichloromethane. After the removal of all solvents, 250 mg of the product was obtained in 60% yield (**4a**). The product was analyzed by size exclusion chromatography, showing a single size distribution (PDI = 1.14) with a shift toward higher hydrodynamic volume compared to that of polybutadiene. ^{1}NMR: δ 1.16 (m, 134H, C$\underline{H}_2$CH), 2.11 (m, 67H, CH$_2$C$\underline{H}$), 3.37 (s, 3H, C$\underline{H}_3$O), 3.64 (m, 90H, C$\underline{H}_2$C$\underline{H}_2$O), 4.94 (m, 134H, CHC$\underline{H}_2$), 5.45 (m, 67H, C$\underline{H}$CH$_2$). Mn was determined by NMR (**4a**, 4.7 kg/mol; **4b**, 5.7 kg/mol; and **5**, 4.7 kg/mol). All SEC traces are shown in Supporting Information Figures S1 (**4a**), S2 (**4b**), and S4 (**5**).

*Conjugation of Diethylene Triamine Penta Acetic Acid (DTPA) (**6**).* Amine end-functional polybutadiene-*block*-poly(ethylene glycol) (110 mg) (23 μmol) was dissolved in 10 mL of THF. To the solution, 14 mg (0.95 eq 22 μmol) of *p*-isothiocyanate-benzyl diethylene-triamine-penta-acetic-acid and 5 mL of triethylamine were added. The mixture was stirred at room temperature for 48 h, after which all solvents were removed. The products were dissolved in 5 mL of THF and cooled on ice for 6 h, after which the solution was filtered through a 200 nm syringe filter. The product was obtained by removing all THF. The DTPA end groups were not quantified,

dx.doi.org/10.1021/bc200578s | *Bioconjugate Chem.* 2012, 23, 958−965

Scheme 1. Overview of Polymers and the Reaction Path Toward These Compounds[a]

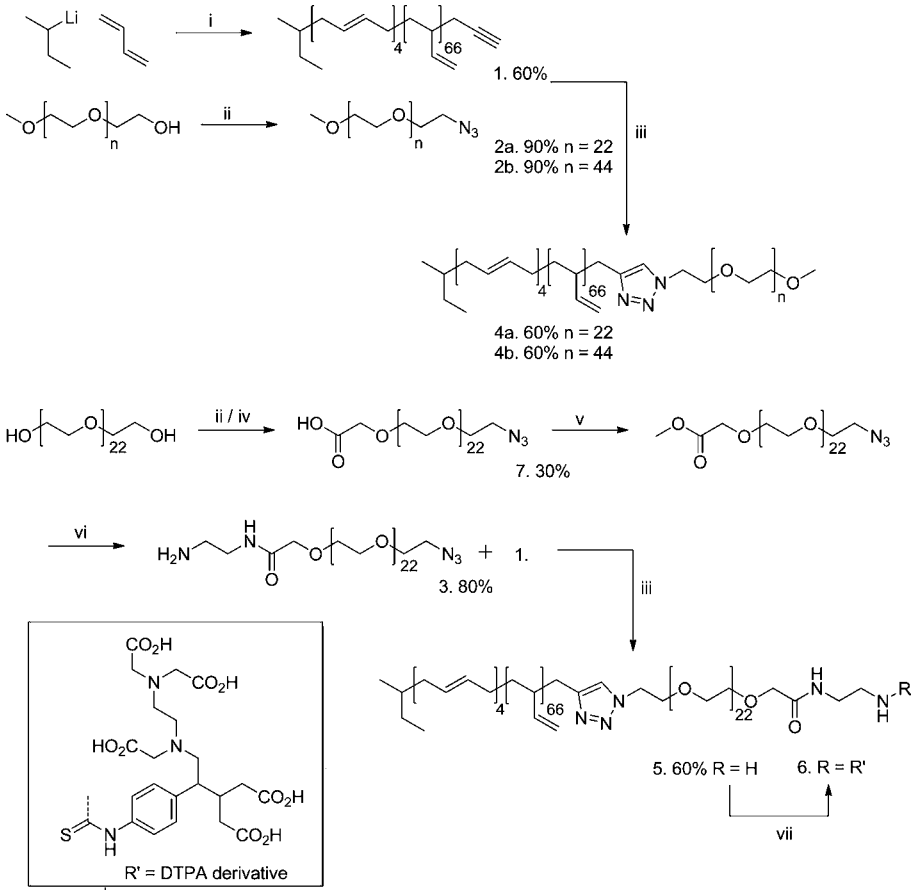

[a]Exact details of the synthesis can be found in the Experimental Procedures section of the article. (i) Anionic polymerisation of 1,3 butadiene followed by end-capping and deprotection; (ii) azidation with MsCl followed by NaN_3; (iii) coupling of polymers via copper catalysed (2 + 3) cycloaddition; (iv) NaH, *t*-butyl bromoacetate in THF, followed by deprotection in 1 M HCl; (v) esterification in $MeOH/H_2SO_4$; (vi) nucleophilic acyl substitution by 1,2 diamino ethane in MeOH; (vii) amine coupling of p-SCN-Bn-DTPA.

yet their presence was confirmed by FTIR and ^{111}In test labeling. FTIR: 1730 cm^{-1} (carboxylic acid). SEC (THF): M_w/M_n = 1.26, M_w (theoretical) = 5.3 kg/mol.

Polymersome Formation (General). Compound **4a** (9.9 mg) (2.1 μmol) or **4b** (1.7 μmol) and 0.1 mg (0.02 μmol) of diethylene-triamine-penta-acetic-acid functional polybutadiene-*block*-poly(ethylene glycol) **6** were dissolved in 200 μL of THF. Polymersomes were formed by the slow addition of 0.6 mL of 0.1 M. 2-(*N*-morpholino)ethanesulfonic acid (MES) buffer of pH 5.5. The samples were passed three times through a 200 nm syringe filter to yield polymersomes of ~250 nm. Polymersomes of ~120 nm were obtained by multiple extrusion through 100 nm filters (one pass will yield ~160 nm polymersomes), and polymersomes of less than 100 nm were obtained by treating the sample with ultrasonic sound waves (48 kHz, 200 W) for 30 min at 35 °C. Samples were washed and concentrated to 200 μL by means of a spin column (100 kD MWCO, 3000 rpm). Note that for the biodistribution samples a stock solution containing 9.9 mg of **4a** and 0.1 mg of **6** per 200 μL of THF was prepared to prevent variation in concentration and ratio of polymers.

^{111}In Labeling. To 30 μL of polymersomes, 150 μL of 0.1 M 2-(*N*-morpholino)ethanesulfonic acid (MES) buffer (pH 5.5) and 15 MBq $^{111}InCl_3$ were added. The labeling mixture was incubated at room temperature for 30 min. Labeling efficiency was analyzed by Instant Thin-Layer Chromatography Silica Gel impregnated glass fiber (ITLC-SG), developed in 0.1 M NH_4Ac (pH 5.5)/0.1 M EDTA (1:1, v/v). Samples with a labeling efficiency of more than 95% were used without purification and diluted with PBS buffer prior injection. Samples with a coupling efficiency of less than 95% were purified over a PD10 desalting column and diluted with PBS.

Blood Plasma Stability. To study the stability of polymersome preparations, 20 μL of radiolabeled polymersomes was incubated in 500 μL of blood serum for 4 and 24 h at 37 °C. Association of ^{111}In with the polymersomes was analyzed by ITLC-SG, developed in 0.1 M NH_4Ac (pH 5.5)/0.1 M EDTA (1:1, v/v).

Biodistribution Studies. Biodistribution was analyzed in male BALB/c mice (6 weeks of age, 20−23 g per animal). The animals were divided in 8 groups of 4 animals and injected in their tail vein with 250 kBq (0.2 mL or 0.42 mg/kg) of ^{111}In-labeled polymersome preparation. Mice were sacrificed by CO_2 inhalation 4 or 24 h postinjection (p.i.), a blood sample was drawn, and tissues of interest were dissected, weighed, and counted in a gamma-counter along with a standard of the injected activity to allow calculation of the injected dose per gram tissue (% ID/g). Animal experiments were approved by the local animal welfare committee and carried out according to national regulations.

SPECT/CT Imaging. Two animals were selected for SPECT/CT imaging and injected with 15 MBq (0.2 mL, 25.2 mg/kg)

dx.doi.org/10.1021/bc200578s | *Bioconjugate Chem.* 2012, 23, 958−965

Table 1. Overview of Polymersome Characteristics

ID	size (nm)	PDI	M_w PEG (kg/mol)	ζ potential[a]	^{111}In labeling efficiency	specific activity (MBq/mg)	4 h plasma	24 h plasma
1k90	94	0.15	1	−14.76	97%	10	85%	79%
1k120	115	0.05	1	−13.11	95%	10	84%	78%
1k250	259	0.14	1	−12.42	94%	10	87%	80%
2k90	87	0.13	2	−9.96	60%	6	77%	73%

[a]Zeta potentials were measured on a NanoSight NS500 in tap water with an applied voltage of 24. Polymersomes (250 nm) formed from only polymer **4a**, i.e., no DTPA chelated to the surface, have a zeta potential of −6.32 mV.

^{111}In-polymersomes in the tail vein. The animals were sacrificed by CO_2 inhalation and scanned with the U-SPECT-II (MILabs) 4 h post-injection.

RESULTS AND DISCUSSION

The amphiphilic block copolymer used in this study was polybutadiene-*block*-poly(ethylene glycol) (PBd-PEG) because of its well known biocompatibility and glass transition temperature (T_g) well below room temperature. Because of this low T_g, the membrane of polymersomes formed from PBd-PEG remains fluidic, which allows good control over the size via standard sizing techniques such as extrusion.

The general synthetic route toward the three block copolymers used in this study is depicted in Scheme 1. As can be seen from this Scheme, we adopted a modular approach based on the copper-catalyzed (2 + 3) cycloaddition reaction.[21] One of the main advantages of this modular approach is the possibility to vary the molecular weight of PEG between 1 and 2 kg/mol, while keeping the molecular weight (distribution) of PBd exactly constant at 3.7 kg/mol. Polybutadiene was synthesized by means of anionic polymerization. The reaction was initiated with *sec*-butyllithium at −35 °C. After all of the monomer was consumed, the living polymer was end-capped with 3-bromo-1-(trimethylsilyl)-1-propyne.[22] Deprotection with tetrabutyl ammonium fluoride yielded the alkyne-functional polybutadiene **1**. Poly(ethylene glycol) monomethyl ether was purchased with a molecular weight of either 1 or 2 kg/mol. The introduction of an azide was straightforward by mesylation and azidation as published elsewhere.[23] PBd and PEG were coupled in THF at 60 °C by the addition of copper bromide and PMDETA as the ligand. This reaction yielded the nonfunctional block copolymers PBd-PEG with a molecular weight of approximately 4.7 kg/mol (**4a**) or 5.7 kg/mol (**4b**) depending on the PEG molecular weight. These inert block copolymers served as the basic building blocks for polymersome formation.

To allow radiolabeling of polymersomes with ^{111}In, a third block copolymer was synthesized with diethylene triamine penta acetic acid (DTPA) as chelating end group. Polybutadiene was coupled to α-amino-ω-azido-poly(ethylene glycol) via the same click approach as described above to obtain amine end-functional PBd-PEG (**5**) with a molecular weight of 4.7 kg/mol (PEG molecular weight of 1 kg/mol). DTPA is a metal chelating agent that coordinates well to bi- and trivalent metals. Copper, as used in the coupling reaction of PBd and PEG, can also coordinate strongly to DTPA. To prevent undesired occupation of DTPA by copper, all traces of copper in the different PBd-PEG analogues were removed by treating the polymers with Chelex resin in THF (as confirmed by ICP-MS). Finally, *p*-benzyl-isothiocyanate DTPA was introduced in block copolymer **5** by reacting the amine end group and isothiocyanate in THF with triethylamine as base to form polymer **6**.

Polymersomes were formed by slowly diluting a solution of **4a**/**6** or **4b**/**6** = 99:1 (w/w) in THF with 2-(*N*-morpholino)-ethanesulfonic acid (MES) buffer with a pH of 5.5. After the addition of MES buffer, the samples were extruded through 0.2 μm syringe filters to yield polymersomes of around 250 nm diameter. To size the polymersomes even further down, the samples were either extruded through 100 nm filters (to yield ∼120 nm polymersomes) or treated with ultrasonic sound waves at 35 °C (to yield ∼90 nm polymersomes). After resizing, the samples were washed with MES buffer and concentrated. It should be noted that extrusion through 100 nm membranes yielded the narrowest particle size distribution, whereas ultrasound waves and extrusion through syringe filters gave broader distributions. All particle polydispersities were found to be below 0.15, which is comparable to results often encountered for liposomal formulations (see Figures S5 and S6, Supporting Information, for the full DLS curves). The characteristics of the polymersomes are summarized in Table 1, as is the ^{111}In labeling efficiency and blood plasma stability of the different samples which will be discussed next.

^{111}In labeling was performed by adding 15 MBq $^{111}InCl_3$ to 30 μL of polymersome solution. Samples that labeled with an efficiency of more than 95% were used without further purification and were diluted with PBS to 1.25 MBq per mL. The one sample that had a labeling efficiency of only 60% (2k90) was purified over a PD10 desalting column after which it was also diluted with PBS. The stability of the ^{111}In-labeled preparations was tested by adding 20 μL of each sample to 500 μL of human blood serum. After 24 h, about 80% of the Indium-111 radioactivity was still associated with the polymersomes as summarized in Table 1. These results show that these polymersomes of well-defined size allow for stable radio isotope labeling for *in vivo* applications.

After establishing polymersome synthesis and evaluation of the radiolabeling stability, we studied the biodistribution as a function of size and peripheral PEG thickness. As might be expected from similar studies based on liposomes, larger particles will influence the circulation kinetics negatively. In order to study if a similar trend is also valid for polymersomes, we injected male Balb/c mice (6 weeks old, 20−23 g/animal) with 250 kBq (0.2 mL or 0.42 mg/kg) of ^{111}In-labeled polymersome solution in the tail vein. Each group contained four animals which were sacrificed after 4 or 24 h. Tissues of interest were collected, weighed, and counted for radioactivity. The tissue distribution is depicted in Figure 2.

Upon looking at the blood levels, a clear effect of polymersome size can be recognized immediately. Vesicles of 90 nm circulate much longer than vesicles of 120 nm and larger. After 4 h, more than 50% of the 90 nm polymersomes were still present in the blood pool, which after 24 h was reduced to 25% (based on a blood volume assumption of 1.5 g per animal). This allows us to estimate the blood half-lives of these 90 nm polymersomes to be around 20 h, a number

dx.doi.org/10.1021/bc200578s | *Bioconjugate Chem.* 2012, 23, 958−965

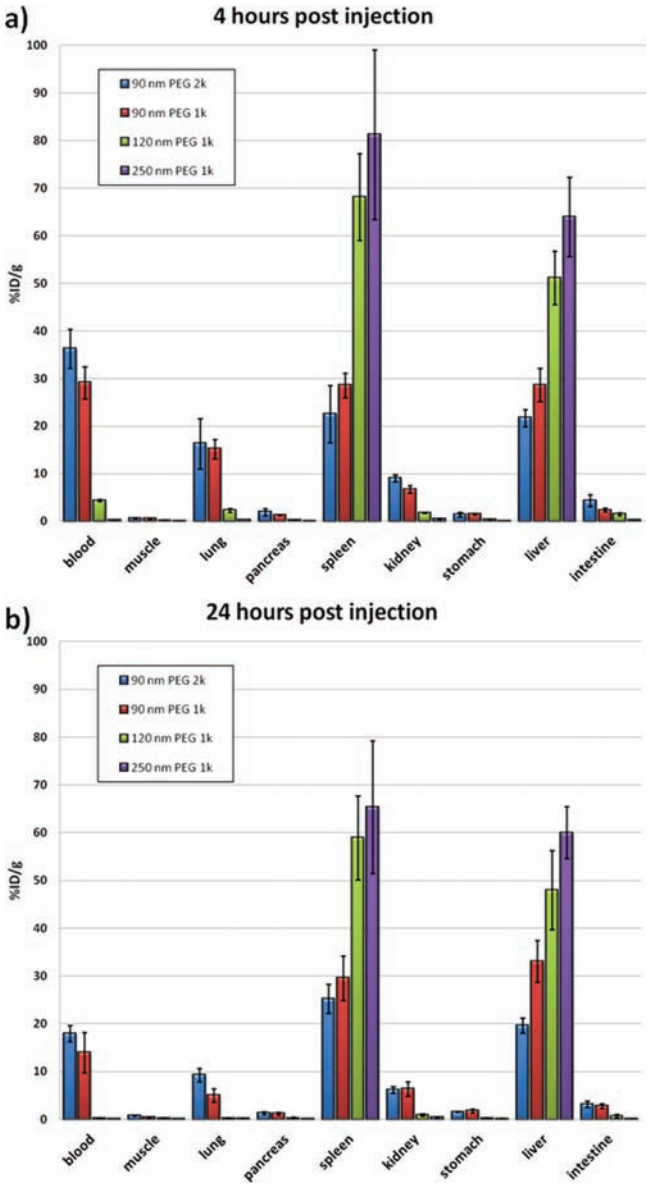

Figure 2. Biodistribution of differently sized ^{111}In-labeled polymersomes in Balb/C mice (n = 4/group). (a) 4 h post-injection and (b) 24 h post-injection.

comparable to blood circulation half-lives as reported by Photos et al.[10] Upon increasing the particle size, both the liver and spleen accumulation became higher, an effect that is more abrupt for the liver than for the spleen. The abundance of 90 nm polymersomes in lungs was relatively high, which most likely is caused by high blood levels in lung tissue. These data show that similar to liposomes smaller polymersomes circulate longer. However, there is a major difference in the correlation between size and blood circulation kinetics of these polymersomes and liposomes. For polymersomes, the transition from long-circulating to short-circulating, upon increasing the size, is much more abrupt than for liposomes. A possible explanation might be found in the more rigid[1] structure of polymersomes, which results in less flexibility. This feature could be of practical use since it could have a beneficial effect on tumor accumulation via the enhanced permeability and retention (EPR) effect.[13,24]

In order to investigate the effect of the PEG corona on biodistribution, two polymersome samples were included in these experiments with an average diameter of ~90 nm but with different PEG lengths of 1 and 2 kg/mol (Table 1 and Figure 2). Although the sample with the thicker PEG corona seemed to circulate longer in the bloodstream and showed lower liver and spleen accumulation, this effect is not significant, especially because there is also a small size difference between both samples.

A powerful method of imaging organs/tissue particle distributions in living animals (and humans) is by Single Photon Emission Computed Tomography (SPECT) imaging. SPECT/CT imaging is a tool often used in nuclear medicine to obtain three-dimensional images in a noninvasive manner. The polymersomes as described in this article have a high enough specific activity to image them by this technique. Typically, for imaging of mice 15 MBq of activity is needed, an amount easily accessible via the route described herein.

In order to illustrate by SPECT/CT the abrupt transition from long circulating to fast clearance upon increasing the polymersome size, we prepared samples of 90 nm polymersomes and 120 nm polymersomes with 15 MBq of ^{111}In. The procedure was analogous to that described above; only the dilution factor with PBS was adjusted to end up with a sample of 75 MBq per mL. Each animal was injected intravenously with 15 MBq (0.2 mL, 25.2 mg/kg) ^{111}In-polymersomes in the tail vein and was scanned after 4 h. The resulting images are depicted in Figure 3. The top panel of Figure 3a–c shows the results for the long circulating polymersomes of 90 nm with a PEG molecular weight of 1 kg/mol. As visualized by radioactivity in the heart and lungs, the polymersomes are still present in the blood circulation. The lower panel of Figure 3d–f shows 4 h post-injection scans of the 120 nm polymersomes. All of the radioactivity is present in the liver and spleen. This is in agreement with the biodistribution data as discussed above. These scans again show the strong size dependence of polymersomes with regard to blood circulation kinetics.

■ CONCLUSIONS

We have demonstrated that for polymersomes, size is an important factor in the blood circulation kinetics. Polymersomes of 120 nm and larger are readily cleared from the blood, whereas smaller polymersomes of approximately 90 nm are long circulating with an estimated blood half-life of 24 h. We have shown that polymersomes containing 1% of a DTPA end-functional amphiphilic block copolymer of polybutadiene-*block*-poly(ethylene glycol) can be prepared with a sufficient specific activity for SPECT/CT imaging. The effect of size on the biodistribution could therefore also be illustrated by this technique to confirm that 90 nm polymersomes are long circulating, whereas 120 nm polymersomes readily accumulate in the liver and spleen. The effect of increasing the PEG molecular weight from 1 to 2 kg/mol was not found to be significant in this case. These findings should be taken into account upon designing polymersome formulations for imaging or drug delivery purposes. Polymersome size, much more than for liposomes, will influence the circulation kinetics of polymersomes.

dx.doi.org/10.1021/bc200578s | *Bioconjugate Chem.* 2012, 23, 958–965

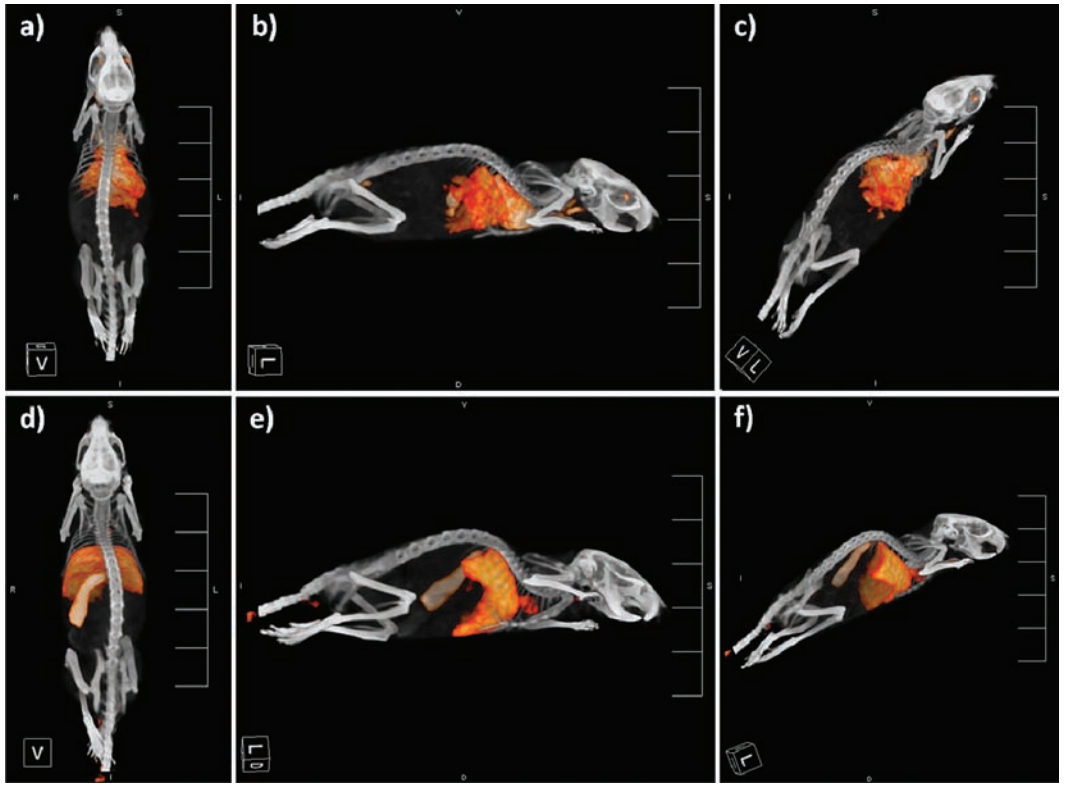

Figure 3. SPECT/CT images (4 h p.i.) of polymersomes injected in male BalB/c mice. Top (a–c): long circulating 90 nm polymersomes clearly show circulation through the liver, lungs, and carotid artery. Bottom (d–f): 120 nm polymersomes show fast accumulation in the liver and the spleen.

■ ASSOCIATED CONTENT

Ⓢ Supporting Information

Size exclusion chromatography data of the main polymers and dynamic light scattering measurements of the polymersomes. This material is available free of charge via the Internet at http://pubs.acs.org.

■ AUTHOR INFORMATION

Corresponding Author

*Tel: +31 243653204. Fax: +31 243653393. E-mail: j.vanhest@science.ru.nl.

Author Contributions

‖These authors contributed equally to this work.

Notes

The authors declare no competing financial interest.

■ ACKNOWLEDGMENTS

This study/work was performed within the framework of the Dutch Top Institute Pharma project # T5-105.

■ REFERENCES

(1) Discher, B. M., Won, Y. Y., Ege, D. S., Lee, J. C. M., Bates, F. S., Discher, D. E., and Hammer, D. A. (1999) Polymersomes: Tough vesicles made from diblock copolymers. *Science 284*, 1143–1146.

(2) Brinkhuis, R. P., Rutjes, F. P. J. T., and van Hest, J. C. M. (2011) Polymeric vesicles in biomedical applications. *Polym. Chem. 2*, 13.

(3) Harashima, H., and Kiwada, H. (1996) Liposomal targeting and drug delivery: Kinetic consideration. *Adv. Drug Delivery Rev. 19*, 425–444.

(4) Litzinger, D. C., Buiting, A. M. J., Vanrooijen, N., and Huang, L. (1994) Effect of liposome size on the circulation time and intraorgan distribution of amphipathic poly(ethylene glycol)-containing liposomes. *Biochim. Biophys. Acta Biomembr. 1190*, 99–107.

(5) Klibanov, A. L., Maruyama, K., Torchilin, V. P., and Huang, L. (1990) Amphipathic polyethyleneglycols effectively prolong the circulation time of liposomes. *FEBS Lett. 268*, 235–237.

(6) Allen, T. M., Hansen, C., Martin, F., Redemann, C., and Yauyoung, A. (1991) Liposomes containing synthetic lipid derivatives of poly(ethylene glycol) show prolonged circulation half-lives in vivo. *Biochim. Biophys. Acta 1066*, 29–36.

(7) Lian, T., and Ho, R. J. Y. (2001) Trends and developments in liposome drug delivery systems. *J. Pharm. Sci. 90*, 667–680.

(8) Gabizon, A., and Papahadjopoulos, D. (1992) The role of surface-charge and hydrophilic groups on liposome clearance in vivo. *Biochim. Biophys. Acta 1103*, 94–100.

(9) Yamamoto, Y., Nagasaki, Y., Kato, Y., Sugiyama, Y., and Kataoka, K. (2001) Long-circulating poly(ethylene glycol)-poly(D,L-lactide) block copolymer micelles with modulated surface charge. *J. Controlled Release 77*, 27–38.

(10) Photos, P. J., Bacakova, L., Discher, B., Bates, F. S., and Discher, D. E. (2003) Polymer vesicles in vivo: correlations with PEG molecular weight. *J. Controlled Release 90*, 323–334.

(11) Christian, D. A., Garbuzenko, O. B., Minko, T., and Discher, D. E. (2010) Polymer vesicles with a red cell-like surface charge: microvascular imaging and in vivo tracking with near-infrared fluorescence. *Macromol. Rapid Commun. 31*, 135–141.

(12) Lee, J. S., Ankone, M., Pieters, E., Schiffelers, R. M., Hennink, W. E., and Feijen, J. (2011) Circulation kinetics and biodistribution of dual-labeled polymersomes with modulated surface charge in tumor-bearing mice: Comparison with stealth liposomes. *J. Controlled Release 155*, 282–288.

(13) Anraku, Y., Kishimura, A., Kobayashi, A., Oba, M., and Kataoka, K. (2011) Size-controlled long-circulating PICsome as a ruler to measure critical cut-off disposition size into normal and tumor tissues. *Chem. Commun. 47*, 6054–6056.

(14) Ghoroghchian, P. P., Frail, P. R., Susumu, K., Blessington, D., Brannan, A. K., Bates, F. S., Chance, B., Hammer, D. A., and Therien, M. J. (2005) Near-infrared-emissive polymersomes: Self-assembled soft matter for in vivo optical imaging. *Proc. Natl. Acad. Sci. U.S.A. 102*, 2922−2927.
(15) Tanisaka, H., Kizaka-Kondoh, S., Makino, A., Tanaka, S., Hiraoka, M., and Kimura, S. (2008) Near-infrared fluorescent labeled peptosome for application to cancer imaging. *Bioconjugate Chem. 19*, 109−117.
(16) Cheng, Z. L., Thorek, D. L. J., and Tsourkas, A. (2009) Porous polymersomes with encapsulated gd-labeled dendrimers as highly efficient MRI contrast agents. *Adv. Funct. Mater. 19*, 3753−3759.
(17) Upadhyay, K. K., Bhatt, A. N., Castro, E., Mishra, A. K., Chuttani, K., Dwarakanath, B. S., Schatz, C., Le Meins, J. F., Misra, A., and Lecommandoux, S. (2010) In vitro and in vivo evaluation of docetaxel loaded biodegradable polymersomes. *Macromol. Biosci. 10*, 503−512.
(18) Damen, D. M. (2008) Chelating Amphiphilic Polymers, EP 2 161 020 A1.
(19) Allen, C., Hoang, B., Lee, H., and Reilly, R. M. (2009) Noninvasive monitoring of the fate of (111)In-labeled block copolymer micelles by high resolution and high sensitivity micro-SPECT/CT imaging. *Mol. Pharmaceutics 6*, 581−592.
(20) Tohyama, M., Hirao, A., and Nakahama, S. (1996) Synthesis of end-functionalized polymer by means of living anionic polymerization. *Macromol. Chem. Phys. 197*, 3135−3148.
(21) Opsteen, J. A., and van Hest, J. C. M. (2005) Modular synthesis of block copolymers via cycloaddition of terminal azide and alkyne functionalized polymers. *Chem. Commun.*, 57−59.
(22) Hirao, A., and Hayashi, M. (1999) Recent advance in syntheses and applications of well-defined end-functionalized polymers by means of anionic living polymerization. *Acta Polym. 50*, 219−231.
(23) Brinkhuis, R. P., Visser, T. R., Rutjes, F. P. J. T., and van Hest, J. C. M. (2011) Shedding the hydrophilic mantle of polymersomes. *Polym. Chem. 2*, 550−552.
(24) Maeda, H., Wu, J., Sawa, T., Matsumura, Y., and Hori, K. (2000) Tumor vascular permeability and the EPR effect in macromolecular therapeutics: a review. *J. Controlled Release 65*, 271−284.

Bioconjugate Chemistry

Article

pubs.acs.org/bc

Lysosomal Delivery of a Lipophilic Gemcitabine Prodrug Using Novel Acid-Sensitive Micelles Improved Its Antitumor Activity

Saijie Zhu, Dharmika S. P. Lansakara-P., Xinran Li, and Zhengrong Cui*

College of Pharmacy, Pharmaceutics Division, The University of Texas at Austin, Austin, Texas, 78712, United States

Supporting Information

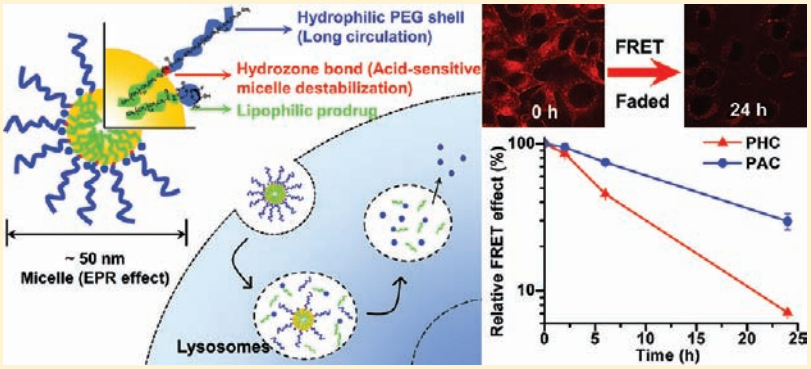

ABSTRACT: Stimulus-sensitive micelles are attractive anticancer drug delivery systems. Herein, we reported a novel strategy to engineer acid-sensitive micelles using a amphiphilic material synthesized by directly conjugating the hydrophilic poly(ethylene glycol) (PEG) with a hydrophobic stearic acid derivative (C18) using an acid-sensitive hydrazone bond (PHC). An acid-insensitive PEG-amide-C18 (PAC) compound was also synthesized as a control. 4-(*N*)-Stearoyl gemcitabine (GemC18), a prodrug of the nucleoside analogue gemcitabine, was loaded into the micelles, and they were found to be significantly more cytotoxic to tumor cells than GemC18 solution, likely due to the lysosomal delivery of GemC18 by micelles. Moreover, GemC18 in the acid-sensitive PHC micelles was more cytotoxic than in the acid-insensitive PAC micelles, which may be attributed to the acid-sensitive release of GemC18 from the PHC micelles in lysosomes. In B16−F10 melanoma-bearing mice, GemC18-loaded PHC or PAC micelles showed stronger antitumor activity than GemC18 or gemcitabine solution, likely because of the prolonged circulation time and increased tumor accumulation of the GemC18 by the micelles. Importantly, the *in vivo* antitumor activity of GemC18-loaded PHC micelles was significantly stronger than that of the PAC micelles, demonstrating the potential of the novel acid-sensitive micelles as an anticancer drug delivery system.

INTRODUCTION

The last several decades have witnessed great progress in cancer chemotherapy, specifically the development of nanoparticulates as delivery systems for anticancer drugs, which have become increasingly attractive to researchers because of their ability to efficiently accumulate in tumors by the enhanced permeability and retention (EPR) effect.[1,2] Among the nanoparticulate drug delivery systems, micelles that are self-assembled from amphiphilic molecules provide a core−shell architecture, wherein the hydrophobic core serves as a natural carrier environment for hydrophobic drugs, and the hydrophilic shell allows particle stabilization in aqueous solution.[3−5] Micelle drug delivery systems have several documented advantages, such as ease of preparation, small and uniform particle size (10−100 nm), high drug loading, and controllable drug release profiles.[6−8] In addition, due to their unique structure, micelles are characteristic of hydrophilic corona, mostly composed of poly(ethylene glycol) (PEG), which create a highly water-bound barrier, block the adhesion of opsonins, and prolong the blood circulation time of micelles.[9]

Recently, stimulus-sensitive drug release strategies have been frequently utilized in the design of micelle drug delivery systems.[10] Among these stimuli, changes in acidity are particularly useful for treating solid tumors, because tumor tissues have a relatively acidic extracellular environment (pH ~6.8), compared with surrounding normal tissues. In addition, more acidic conditions (pH 5−6) are also encountered in endosomes and lysosomes once the micelles enter cells via endocytosis.[11,12] There are several general approaches to construct acid-sensitive micelles. One approach relies on the hydrophobic-to-hydrophilic transition of the hydrophobic segment in slightly acidic condition, which results in the destabilization of micelles and the release of drug.[13,14] Another approach is to covalently conjugate drug to the hydrophobic segment using acid-sensitive chemical bonds (such as hydrazone).[11,15] Finally, some researchers incorporate acid-

Received: November 7, 2011
Revised: March 9, 2012
Published: April 4, 2012

Scheme 1. Schematic Reaction Process and Micelle Formation[a]

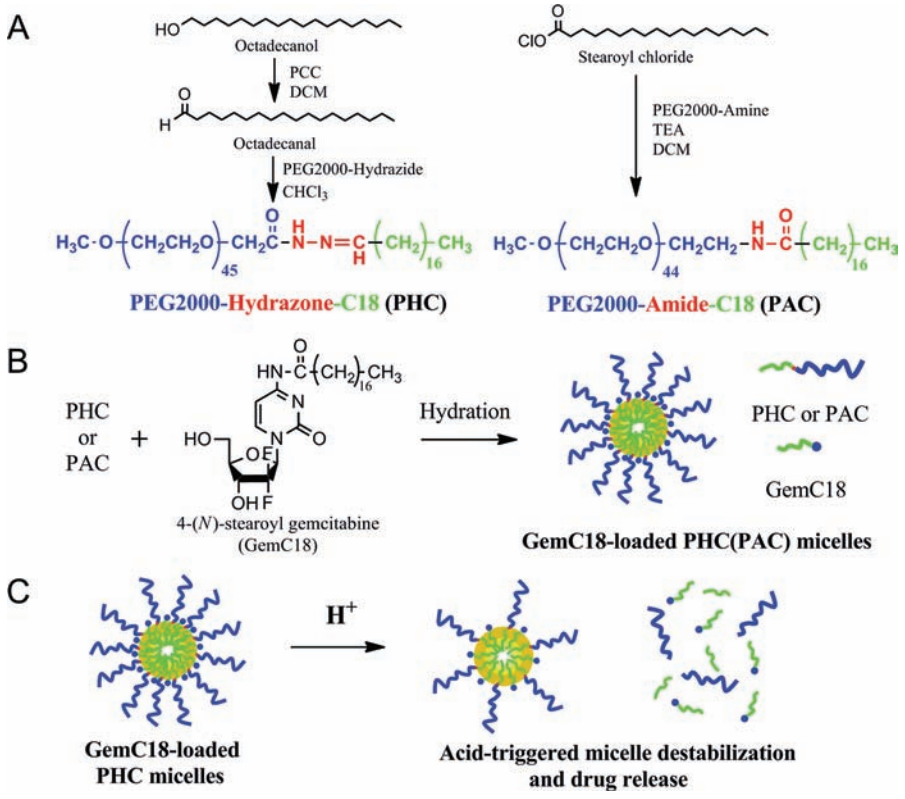

[a](A) Schemes of the synthesis of PHC and PAC conjugates. (B) Illustration of the preparation of GemC18-loaded micelles. (C) Schematic illustration of the acid-sensitive release of GemC18 from PHC micelles.

sensitive bonds into the hydrophobic polymer block, and drug release is expected when the micelles dissociate in acidic condition due to the degradation of the hydrophobic segment.[16] In the present study, we introduced a simple yet novel strategy for the construction of acid-sensitive micelles, by directly conjugating the hydrophilic PEG segment to a hydrophobic stearic acid derivative with an acid-sensitive hydrazone bond (Scheme 1A). The hydrolysis of the hydrazone bond in acidic condition is expected (Scheme 1B,C).

Gemcitabine (2′,2′-difluoro-2′-deoxycytidine) is a deoxycytidine nucleoside analogue, which is approved for the treatment of pancreatic, non-small cell lung, breast, and ovarian cancers.[17] Clinical trials using gemcitabine for melanoma therapy have also been reported.[18,19] Despite its effective anticancer activity, gemcitabine suffers from various drawbacks, such as rapid deamination to inactive 2′,2′-difluorodeoxyuridine (dFdU) by cytidine deaminase after intravenous (i.v.) injection, resulting in a short *in vivo* half-life (8−17 min).[20] A lipophilic prodrug strategy has been explored by conjugating gemcitabine with a long fatty acid chain, which was shown to prevent the deamination.[21] In addition, it is relatively easier to load the lipophilized gemcitabine into lipid-based nanoparticulate drug delivery systems, as compared with the highly hydrophilic gemcitabine.[22,23] For example, Couvreur's group covalently coupled gemcitabine with 1,1′,2-tris-*nor*-squalenic acid and formulated the resultant 4-(*N*)-tris-*nor*-squalenoyl-gemcitabine (SQdFdC) into nanoparticles,[24,25] which were shown to increase the survival of mice with murine metastatic leukemia (L1210 wt), as compared with gemcitabine alone. Similarly, 4-(*N*)-stearoyl-gemcitabine (GemC18), a stearic acid amide derivative of gemcitabine,[21] also showed improved antitumor activity in mouse models when delivered using liposomes or solid lipid nanoparticles, again as compared with gemcitabine alone.[21,23]

In the present study, the feasibility of using the novel acid-sensitive micelles as a carrier for the gemcitabine prodrug, GemC18, was evaluated both *in vitro* and *in vivo*. Furthermore, a lipophilic fluorescence resonance energy transfer (FRET) pair was incorporated into the micelles to confirm the acid-sensitivity of the micelles at the cellular level, and the significance of the lysosomal delivery of the amide prodrug, GemC18, was discussed accordingly.

EXPERIMENTAL PROCEDURES

Materials. Gemcitabine hydrochloride (GemHCl) was from U. S. Pharmacopeia (Rockville, MD). Methoxy-poly(ethylene glycol) 2000-hydrazide (PEG2000-hydrazide) and methoxy-poly(ethylene glycol) 2000-amine (PEG2000-amine) were from Creative PEGWorks (Wiston Salem, NC). Pyridinium chlorochromate (PCC) and pyrene were from Acros Organics (Morris Plains, NJ). 1-Hydroxy-7-azabenzotriazole (HOAt) was from CreoSalus, Inc. (Louisville, KY). Octadecanol, stearoyl chloride, stearic acid, sodium dodecyl sulfate (SDS), 1-ethyl-3-(3-dimethylaminopropyl)carbodiimide (EDCI), 3-(4,5-dimethylthiazol-2-yl)-2,5-diphenyltetrazolium bromide (MTT), uracil 1-β-D-arabinofuranoside (AraU), 1,1′-dioctadecyl-3,3,3′,3′-tetramethylindocarbocyanine perchlorate (DiI), and 3,3′-dioctadecyloxacarbocyanine perchlorate (DiO) were from Sigma-Aldrich (St. Louis, MO). Lysotracker Red DND-99 was from Molecular Probes (Eugene, OR). Hoechst 33342 was from AnaSpec, Inc. (Fremont, CA). The *in situ* cell death detection kit, TMR red, was from Roche Diagnostics

dx.doi.org/10.1021/bc2005945 | *Bioconjugate Chem.* 2012, 23, 966−980

(Indianapolis, IN). Bromodeoxyuridine (BrdU) and primary BrdU monoclonal antibody were from BD Biosciences (San Jose, CA). Biotinylated rabbit-antimouse F(ab)′ was from Accurate Chem (Westbury, NY). HPLC-grade tetrahydrofuran (THF) and methanol were used during HPLC analysis, and other solvents used in chemical synthesis and cell culture work were of analytical grade. Water was purified using a Millipore filtration system (Millipore Corporation, Billerica, MA).

Murine melanoma B16−F10 cells and human pancreatic cancer BxPC-3 cells were from (American Type Culture Collection, ATCC, Manassas, VA) and grown in RPMI 1640 medium and DMEM medium, respectively. All media were supplemented with 10% fetal bovine serum (FBS), 100 U/mL of penicillin, and 100 μg/mL of streptomycin, all from Invitrogen (Carlsbad, CA).

Proton NMR (^{1}H NMR) spectra were recorded using a 300 MHz Varian UNITY Plus instrument. The molecular weights of PEG derivatives were determined with a Varian 12T FTICR equipped with a Nd:YAG laser emitting at 355 nm (Varian, Inc., Palo Alto, CA) using matrix-assisted laser desorption/ionization (MALDI). For other compounds, the molecular weight was determined on a Thermo Scientific TSQ Quantum GC Triple Quad (Thermo Scientific, Pittsburgh, PA) using chemical ionization.

Synthesis of PEG2000-hydrazone-C18 (PHC). Synthesis of octadecanal. The synthetic procedure of octadecanal was adapted from Easton et al.[26] Briefly, PCC (600.0 mg, 2.78 mmol) was suspended in dichloromethane (DCM) (6 mL), and octadecanol (600.0 mg, 2.22 mmol) in DCM (12 mL) was then rapidly added at room temperature. The reaction was kept at room temperature for 2 h with magnetic stirring (750 rpm), after which diethyl ether (Et_2O) (36 mL) was added to the reaction mixture. Insoluble reduced reagent was removed by centrifugation, and the crude product was obtained by drying the supernatant. Final purification of the product was performed on silica gel (hexane/Et_2O, 96:4) to give octadecanal (320.0 mg, 53.7% yield) as a white solid. R_f = 0.52 (chloroform ($CHCl_3$)). ^{1}H NMR (300 MHz, $CDCl_3$): δ = 9.74 (t, 1H, C(O)*H*), 2.39 (t, 2H, COCH_2), 1.61 (m, 2H, COCH$_2$CH_2), 1.23 (m, 28H, (CH_2)$_{14}$), 0.86 ppm (t, 3H, CH_3). MS [M+H]$^+$ m/z calculated for $C_{18}H_{36}O$: 268.2766, found: 268.2769. **Synthesis of PHC.** Octadecanal (100.0 mg, 0.372 mmol) was reacted with PEG2000-hydrazide (200.0 mg, 0.1 mmol) in 4.8 mL of dry $CHCl_3$ at 50 °C under argon and molecular sieves. After 24 h of reaction, the mixture was concentrated with a rotary evaporator and then applied to a silica gel column. Chloroform was first used as the mobile phase to separate excessive octadecanal, after which $CHCl_3$/methanol (10:1) was used to collect PHC (151.3 mg, 67.6% yield) as a white solid. R_f = 0.22 ($CHCl_3$/methanol, 9:1). ^{1}H NMR (300 MHz, $CDCl_3$): δ = 9.82 (t, 1H, CONHN=CH), 7.46(s, 1H, N=C*H*), 3.5−3.7 (m, 180H, (CH_2CH_2O)$_{45}$), 3.36 (s, 3H, OCH_3), 2.34 (t, 2H, COCH_2), 1.49 (m, 2H, COCH$_2$CH_2), 1.23 (m, 28H, (CH_2)$_{14}$), 0.85 ppm (t, 3H, CH_3).

Synthesis of PEG2000-amide-C18 (PAC). To the solution of PEG2000-amine (220 mg, 0.11 mmol) in 3 mL dry DCM, 46 μL (0.33 mmol) of triethylamine (TEA) was added at room temperature, followed by dropwise addition of stearoyl chloride (100 mg, 0.33 mmol) in 2 mL of dry DCM. The reaction mixture was then placed on a plate of 30 °C, while stirring at 500 rpm. About 20 h later, the solvent was evaporated with a rotary evaporator, and the crude product was recrystallized twice with 5 mL of Et_2O. The solid obtained was further purified with a silica gel column ($CHCl_3$/methanol, 4:1) to give PEG2000-amide-C18 (205.2 mg, 82.3% yield) as a white solid. R_f = 0.41 ($CHCl_3$/methanol, 9:1). ^{1}H NMR (300 MHz, $CDCl_3$): δ = 6.06 (s, 1H, N*H*CO), 3.5−3.7 (m, 176H, (CH_2CH_2O)$_{44}$), 3.36 (s, 3H, OCH_3), 2.14 (t, 2H, COCH_2), 1.59 (m, 2H, COCH_2CH$_2$), 1.23 (m, 28H, (CH_2)$_{14}$), 0.85 ppm (t, 3H, CH_3).

Synthesis of 4-(*N*)-Stearoyl Gemcitabine (GemC18). 4-(*N*)-Stearoyl gemcitabine (GemC18) was synthesized according to literature procedures with slight modifications.[23,27] The primary and secondary alcohols of the deoxyribofuranose ring of gemcitabine were first Boc(*tert*-butoxycarbonyl)-protected to produce 3′,5′-*O*-bis(*tert*-butoxycarbonyl) gemcitabine.[27] Next, Boc-protected gemcitabine (219 mg, 0.47 mmol), stearic acid (149 mg, 0.52 mmol), and HOAt (70 mg, 0.52 mmol) were dissolved in anhydrous DCM at 4 °C, followed by the addition of 109 mg of EDCI (0.57 mmol). After degassing by vacuum sonication, the reaction mixture was kept at room temperature for another 40 h in argon atmosphere. Water (15 mL) was added, and the mixture was extracted with ethyl acetate (EtOAc)/hexane (2:1). The organic phase was washed with saturated ammonium chloride (NH_4Cl) and brine, dried over anhydrous Na_2SO_4, and then evaporated. The residue obtained was purified using a silica gel column (EtOAc/Hexane, 3:7) to give Boc-protected-*N*-stearoyl gemcitabine as a white powder. The obtained product (319 mg, 0.44 mmol) was then dissolved in 7 mL of DCM, followed by the addition of 1.5 mL of trifluoroacetic acid (TFA). After 2 h of stirring at room temperature, excessive TFA was removed under reduced pressure, and the concentrated sample was co-distilled with DCM 5 times. A silica gel column was used to purify this crude sample (DCM/ethanol, 94:6), and the desired product of GemC18 was obtained as a white powder (162 mg, 64.4% yield).[23] R_f = 0.36 (DCM/methanol 10:1). ^{1}H NMR (300 MHz, pyridine-d_5): δ = 12.01 (s, 1H, N*H*CO), 8.76 (d, 1H, 6-C*H*), 7.76 (d, 1H, 5-C*H*), 7.00 (t, 1H, 1′-C*H*), 5.14 (m, 1H, 3′-C*H*), 4.47−4.27 (overlapping m, 3H, 4′-C*H* and 5′-CH_2), 2.67 (t, 2H, COCH_2), 1.79 (m, 2H, COCH$_2$CH_2), 1.28 (m, 28H, (CH_2)$_{14}$), 0.87 (t, 3H, CH_3). ESI-HRMS [M+H]$^+$ m/z calculated for $C_{27}H_{46}F_2N_3O_5$: 530.3406, found: 530.3401.

Acid-Sensitive Degradation. UV−vis spectroscopy. PEG-C18 (i.e., PHC or PAC) was dissolved in phosphate buffered saline (PBS, 5 mM; pH 5.5, 6.8, or 7.4) to achieve the final concentration of 2 mg/mL and then incubated at 37 °C in a water bath. At predetermined time points, 0.2 mL of sample was withdrawn, and its absorbance at 500 nm was immediately measured using a BioTek Synergy HT Multi-Mode Microplate Reader (Winooski, VT). **High-resolution ^{1}H NMR spectroscopy.** PEG-C18 in PBS (5 mM, pH 5.5, 6.8, or 7.4) at 2 mg/mL was incubated at 37 °C in a water bath. At predetermined time points, the pH value was adjusted to 8.0 using sodium hydroxide (NaOH, 0.25 or 0.5 N), and the samples were then lyophilized followed by high-resolution ^{1}H NMR analysis using a Varian DirectDrive 600. The percentage of hydrolysis was calculated using the following equation:

$$\text{Percentage of hydrolysis (\%)} = \frac{S_{\delta 8.42}}{S_{\delta 8.42} + S_{\delta 9.82}} \times 100 \quad (1)$$

where S is the area of peak in ^{1}H NMR spectrum and δ is the chemical shift of the peak.

Determination of the Critical Micellar Concentrations (CMC) of PEG-C18. The CMC values of PHC and PAC in

water were determined using a pyrene 1:3 ratio method.[28] Briefly, 0.25 mL of pyrene in acetone (4.69 μg/mL) was added to a glass vial and dried under vacuum. Each vial was then supplemented with 2 mL of various concentrations (0.001−1 mg/mL) of PHC or PAC in aqueous solution. The glass vials were then capped and incubated overnight at room temperature while shaking at 200 rpm before further experiments. The samples were then subjected to fluorescence spectrometry (Fluorolog3 Fluorimeter, HORIBA Scientific, Edison, NJ). The emission spectra of pyrene were recorded between 350 to 450 nm (Ex = 335 nm, slit = 1 nm; Em slit = 2 nm). Five peaks were identified within this wavelength range and referred to as I_1, I_2, I_3, I_4, and I_5 from shorter to longer wavelengths. The intensity ratio between the first peak (I_1, 371 nm) and third peak (I_3, 383 nm) (I_1/I_3) was calculated.

The values of CMC were obtained from the plot of the I_1/I_3 ratio versus the logarithm of the concentration of PHC or PAC, which could be described by a decreasing sigmoid of the Boltzmann type using the following equation:[28]

$$y = \frac{A_1 - A_2}{1 + e^{(x-x_0)/\Delta x}} + A_2 \quad (2)$$

where the variable y corresponds to the I_1/I_3 ratio, the independent variable x is the concentration of PHC or PAC, A_1 and A_2 are the upper and lower limits of the sigmoid, respectively, x_0 is the center of the sigmoid, and Δx is directly related to the independent variable range where the abrupt change of the dependent variable occurs. For nonionic surfactants, x_0 stands for the CMC value.

Preparation and Characterization of GemC18-loaded PEG-C18 Micelles. PEG-C18 micelles with different percentages of GemC18 (3%, 5%, or 10%, $W_{GemC18}/W_{PEG\text{-}C18}$) were prepared using a modified thin-film hydration method. Briefly, 0.25 mL of THF containing 0.3, 0.5, or 1 mg of GemC18 was dried under vacuum and then hydrated with 1 mL of PAC or PHC aqueous solution (10 mg/mL) under vigorous stirring in a 75 °C water bath. Micelles were obtained within 5 min and then cooled down to room temperature with constant water bath sonication. The resultant micelle preparation was filtrated through a 0.2 μm PTFE syringe filter (Nalge Nunc International, Rochester, NY), followed by lyophilization to obtain a white solid. Micelles with different percent of GemC18 were referred to as PHC3%, PHC5%, PHC10%, PAC3%, PAC5%, and PAC10%. To compare the intracellular fate of PHC and PAC micelles, a lipophilic fluorescence resonance energy transfer (FRET) pair, DiO and DiI were loaded into the micelles using the same method. DiI (0.25 mg) and DiO (0.25 mg) were added into each formulation (10 mg PHC or PAC) to achieve a theoretical loading of 5% ($W_{FRET\ pair}/W_{PEG\text{-}C18}$). Finally, PHC and PAC micelles loaded with DiO (1%, $W_{DiO}/W_{PEG\text{-}C18}$) only were also prepared to detect the intracellular localization of the micelles.

Determination of Entrapment Efficiency and Percentage of Drug Loading. To determine the concentration of GemC18, the lyophilized GemC18-loaded micelles were dissolved in THF and subjected to HPLC analysis using an Agilent 1260 Infinity Quaternary Liquid Chromatographic System with an UV detector operated at 248 nm and an Aglient ZORBAX Eclipse Plus C18 column (5 μm, 4.6 mm × 150 mm). The mobile phase was methanol. The flow rate was 1 mL/min. The drug loading and the entrapment efficiency were calculated using the following equations:

$$\text{Percent of drug loading (\%)} = \frac{\text{Weight of GemC18 in micelles}}{\text{Weight of GemC18 containing micelles}} \times 100 \quad (3)$$

$$\text{Entrapment efficiency (\%)} = \frac{\text{Weight of GemC18 in micelles}}{\text{Weight of total GemC18 added}} \times 100 \quad (4)$$

Determination of Particle Size and Zeta Potential. The hydrodynamic diameters of blank micelles and GemC18-loaded micelles were determined using a Malvern Zetasizer Nano ZS (Malvern Instruments Ltd., MA). Lyophilized sample (1 mg) was dissolved in 1 mL of water and filtered through a 0.2 μm PTFE filter prior to measurement. The zeta potential was determined using the same equipment, but lyophilized samples were dissolved in PBS (pH 7.4, 10 mM) at a final concentration of 1 mg/mL.

Transmission Electron Micrographs (TEM). The size and morphology of the micelles were examined using a Tecnai transmission electron microscope (FEI Company, Hillsboro, OR) in the Institute for Cellular and Molecular Biology Microscopy and Imaging Facility at The University of Texas at Austin. A carbon-coated 400-mesh copper specimen grid (Ted Pella, Inc., Redding, CA) was glow-discharged for 2 min. Micelle solutions (10 mg/mL) were deposited on the grid, and uranyl acetate staining were completed as described previously.[29]

Drug Release from Micelles at Different pH. GemC18-loaded micelles were dissolved in PBS (5 mM) with pH values of 5.5, 6.8, or 7.4 (50 μg/mL GemC18) and incubated at 37 °C under constant shaking (150 rpm). At predetermined time points, 0.5 mL aliquots of sample were withdrawn, filtered through 0.2 μm filter, and lyophilized. The lyophilized samples were dissolved in 0.5 mL of THF and centrifuged at 13 000 rpm for 10 min. The supernatants were subjected to HPLC analysis.

***In Vitro* Stability in 10% FBS.** The stability of GemC18-loaded micelles was investigated by evaluating the changes in particle size and drug content after incubation in 10% FBS. Briefly, 450 μL of GemC18-loaded micelles (1 mg/mL in water) were mixed with 50 μL FBS. Particle sizes were recorded immediately and after 1 h of incubation at 37 °C. For drug content determination, the mixture was filtered (0.2 μm) after 1 h of incubation at 37 °C, and the filtrate was diluted with THF before applied to HPLC.

***In Vitro* Cytotoxicity.** B16−F10 or BxPC-3 cells were seeded into 96-well plates (5000 cells/well). After overnight incubation, the culture medium was replaced with 200 μL fresh medium containing GemHCl, GemC18 (less than 1.5% (v/v) dimethyl sulfoxide (DMSO) as a solubilizer), PHC5%, or PAC5%, with GemHCl-equivalent concentrations ranging from 0.7 to 7000 nM. After 48 h of incubation, the medium was replaced with 200 μL of fresh culture medium containing 100 μg of MTT. For BxPC-3 cells, formulations including GemHCl, PHC5%, PHC10%, PAC5%, and PAC10% were tested at GemHCl-equivalent concentrations of 14 and 140 nM. GemC18-free Blank PHC and PAC micelles were also tested at a concentration equivalent to 140 nM of GemHCl at 5% loading. Cells were incubated for four additional hours, followed by the addition of 200 μL of DMSO to dissolve the purple formazan crystals formed after the removal of the MTT solution. The absorbance at 570 nm was measured using a

dx.doi.org/10.1021/bc2005945 | Bioconjugate Chem. 2012, 23, 966−980

BioTek Synergy HT Multi-Mode Microplate Reader. Cell viability was calculated, and the IC_{50} values were obtained using *Graphpad Prism* software (GraphPad Software, Inc., CA).

Cellular Uptake and Metabolism. B16−F10 cells (2.5×10^5/well) were seeded in a 6-well plate and incubated overnight at 37 °C, 5% CO_2. The medium was then replaced with 1 mL of fresh medium containing 20 μg/mL of GemC18, PHC5%, or PAC5% and incubated at 37 °C, 5% CO_2. GemC18 solution was prepared by diluting GemC18 stock solution in DMSO with culture media (DMSO concentration at 1.35%, v/v). At predetermined time points (0.5, 1, 3, and 6 h), the culture medium was removed, cells were washed three times with cold PBS and then lysed with 1% SDS. The cell lysates were lyophilized and redissolved in methanol. The supernatant was collected after centrifugation and subjected to HPLC analysis to determine GemC18 concentration. To evaluate the cellular metabolism of GemC18, the GemC18-containing medium was removed after 6 h of incubation and replaced by fresh medium. After 16 additional hours of incubation, the amount of GemC18 in the medium and cells was determined using the same method as described above, which was divided by the amount of GemC18 initially taken up by the cells to obtain the percentage of GemC18 remaining.

Intracellular Fate of PEG-C18 Micelles. B16−F10 cells (5×10^4/well) were seeded in a 35 mm glass-bottom dish (Mattek Corporation, Ashland, MA) and incubated overnight. To study the intracellular localization of PHC and PAC micelles, the cells were first treated with DiO-loaded PHC or PAC micelles (100 μg/mL in culture medium) (Ex/Em, 488/501 nm) for 3 h, followed by incubation with 500 nM Lysotracker Red DND-99 (an acidic organelle dye, Ex/Em, 577/590 nm) for 20 min and 5 μg/mL Hoechst 33342 (a nuclear dye, Ex/Em, 345/478 nm) for 5 min. Finally, the cells were rinsed with PBS and examined with a Leica TCS-SP5 confocal microscope with an oil immersion objective (63 × 1.4 NA) (Leica Microsystems GmbH, Mannheim, Germany).

For the purpose of comparing the intracellular fate of PHC and PAC micelles, the cells were first treated with 1.5 mL of medium containing 100 μg/mL of DiI/DiO-loaded PHC or PAC micelles for 3 h, followed by 0, 2, 6, or 24 h incubation after replacing the micelle-containing medium with fresh medium. Finally, the cells were examined using a Leica TCS-SP5 confocal microscope. Fluorescence images were acquired with the excitation wavelength of 488 nm, and the spectral filter of 555−655 nm (for DiI detection) was used to record FRET effect. All images were obtained with the same gain and offset. To further quantify the intracellular degradation of the micelles, cells pretreated with the DiI/DiO-loaded PHC or PAC micelles were incubated for 0, 2, 6, or 24 h with fresh medium, and then trypsinized and resuspended in PBS before being subjected to flow cytometry. Cell-associated fluorescence was analyzed using a Guava easyCyte 8HT Flow Cytometry System (Millipore Corporation, Billerica, MA) equipped with an argon laser (488 nm) and emission filter for 583 nm. Data collection involved 10 000 counts per sample. Data were analyzed using the *FlowJo 9.3.1* software (Tree Star, Inc., Ashland, OR) and expressed as the geometric mean of the entire population. Cells incubated without micelles were used to account for background fluorescence.

***In Vivo* Antitumor Activity.** All care and handling of animals were performed in accordance with National Institutes of Health guidelines, and the animal protocol was approved by the Institutional Animal Care and Use Committee at the University of Texas at Austin. Female C57BL/6 mice (6−8 weeks) were from Charles River Laboratories (Wilmington, MA). The antitumor activity of the GemC18-loaded PEG-C18 micelles was evaluated in C57BL/6 mice with subcutaneously inoculated B16−F10 cells (5.0×10^5 /mouse) in the right flank. Treatments were given 6 days after tumor cell inoculation by tail vein injection with normal saline, GemHCl solution, GemC18 solution, blank PAC micelles, blank PHC micelles, PAC5% micelles, or PHC5% micelles. The dose was 0.283 mg of GemHCl or 0.283 mg of GemHCl-equivalent GemC18. GemC18 solution was prepared according to a previously reported method,[21] and all other formulations, including GemHCl and micelles, were dissolved in normal saline. All groups received a second dose three days after the first dose, while the PHC5% and PAC5% groups also received a third dose 3 days after the second dose. Tumor sizes were measured with calipers in two perpendicular diameters every day and reported as tumor volume ($V = 1/2[a \times b^2]$, a = longest diameter, b = shortest diameter).

Determination of Gemcitabine Concentration in Tumor Tissues and Plasma. B16−F10 tumors were allowed to grow to ~1 cm^3 in C57BL/6 mice as mentioned above. GemHCl solution, GemC18 solution, PHC5%, or PAC5% was injected via the tail veil at a dose of 0.283 mg GemHCl-equivalent per mouse. Mice were sacrificed 4 h later, and the blood was collected into heparinized tubes and centrifuged (8000 rcf, 10 min) to isolate plasma. Tumor tissues were also collected, rinsed with cold saline, paper dried, and weighed before storing at −80 °C until analysis.

A hydrolysis method was used to detect the concentration of GemC18 in plasma.[30] Briefly, to 75 μL of plasma, 25 μL of AraU solution (10 μg/mL) was added as an internal standard, followed by the addition of 100 μL of 2 N NaOH. The mixture was vortexed and incubated at 40 °C for 1 h. After incubation, 0.8 mL of acetonitrile and 75 μL of 1.4 M H_3PO_4 were added, followed by centrifugation at 13 000 rpm for 10 min. The supernatant was collected and dried under vacuum. The residue was redissolved in 100 μL of PBS (2.5 mM, pH 7.4) and centrifuged (13 000 rpm 10 min) again to collect the supernatant, which was then subjected to HPLC to measure gemcitabine concentration. The mobile phase was 5 mM sodium acetate (pH 6.0) and methanol (95/5, v/v), and the detection wavelength was 266 nm.

A direct extraction method was used to determine the concentration of GemC18 in tumor tissues. Briefly, around 100 mg of tumor tissue was homogenized in DCM using a bead beater (Biospec Products, Inc., Bartlesville, OK) at 4800 rpm for 80 s. Organic layers were collected after centrifugation (13 000 rpm, 10 min) and dried under vacuum. The residue was redissolved in 100 μL of methanol and centrifuged (13 000 rpm, 10 min) to collect the supernatant. The GemC18 concentration in the supernatant was determined using the same method as described above, while the detection wavelength of 308 nm was used.

Histological Analyses. For histological analyses, three representative tumors were harvested per experimental group at the end of treatment (day 6 for GemHCl solution, GemC18 solution, and normal saline groups; day 8 for PAC5% and PHC5% groups). Bromodeoxyuridine (BrdU) was injected intraperitoneally at a dose of 2 mg/mouse 30 min before euthanization. Tumor tissues were fixed with 10% buffered formalin phosphate, embedded in paraffin, sectioned (4 μm), stained with hematoxylin and eosin (H&E), and examined

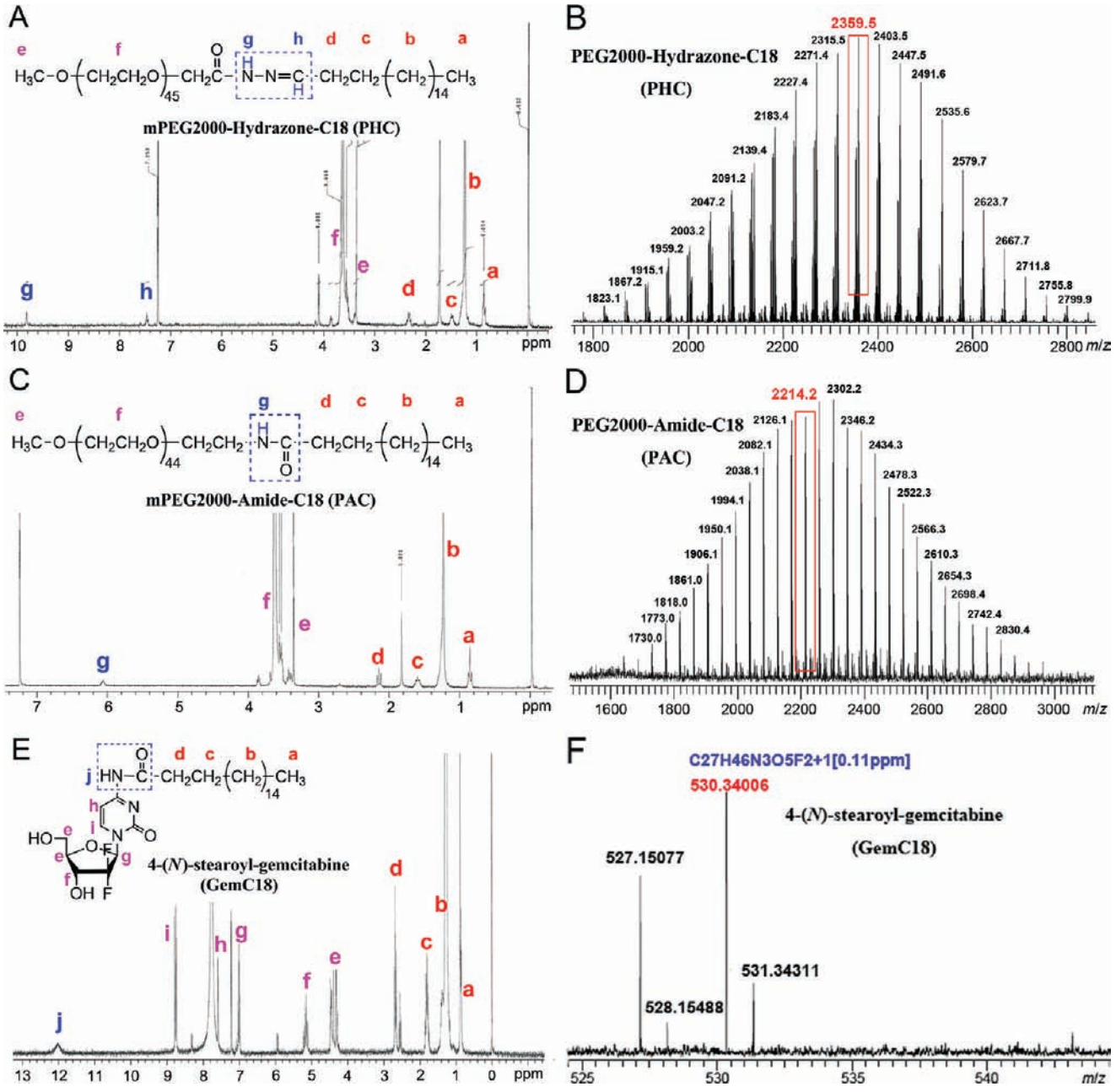

Figure 1. Characterization of PHC, PAC, and GemC18. (A) ^{1}H NMR spectrum of PHC in $CDCl_3$. (B) MALDI mass spectrum of PHC. (C) ^{1}H NMR spectrum of PAC in $CDCl_3$. (D) MALDI mass spectrum of PAC. (E) ^{1}H NMR spectrum of GemC18 in pyridine-d_5. (F) ESI-MS spectrum of GemC18.

under a light microscope. To detect the extent of tumor cell apoptosis, the slides were stained with TUNEL (Terminal deoxynucleotidyl Transferase Biotin-dUTP Nick End Labeling) and counterstained with 4',6-diamidino-2-phenylindole (DAPI) before visualized under an Olympus fluorescence microscope. The slides were also stained using anti-BrdU antibody at the University of Texas MD Anderson Cancer Center Science Park Research Division (Smithville, TX) to detect the extent of cell proliferation.

Data Analysis. All data are presented as mean ± standard deviation (SD). Statistical analyses were completed by performing ANOVA followed by Fisher's protected least significant difference (LSD) procedure. A P value of ≤ 0.05 (two-tail) was considered significant.

RESULTS

Synthesis and Characterization of PHC, PAC, and GemC18. PHC was synthesized by reacting PEG2000-hydrazide with octadecanal, which was first synthesized by oxidizing octadecanol. The appearance of aldehyde proton peak at 9.74 ppm in ^{1}H NMR spectrum indicated the successful conversion of octadecanol to octadecanal (Figure S1 in Supporting Information). The most significant evidence of the formation of hydrazone bond after PEG2000-hydrazide was reacted with octadecanal includes (1) the chemical shift of the aldehyde proton from 9.74 ppm to 7.42 ppm (Figure 1A), which was due to the replacement of the aldehyde oxygen by the less electronegative nitrogen, and (2) the chemical shift of hydrazide proton ($CONHNH_2$) from 8.42 ppm (Figure S2A)

dx.doi.org/10.1021/bc2005945 | Bioconjugate Chem. 2012, 23, 966–980

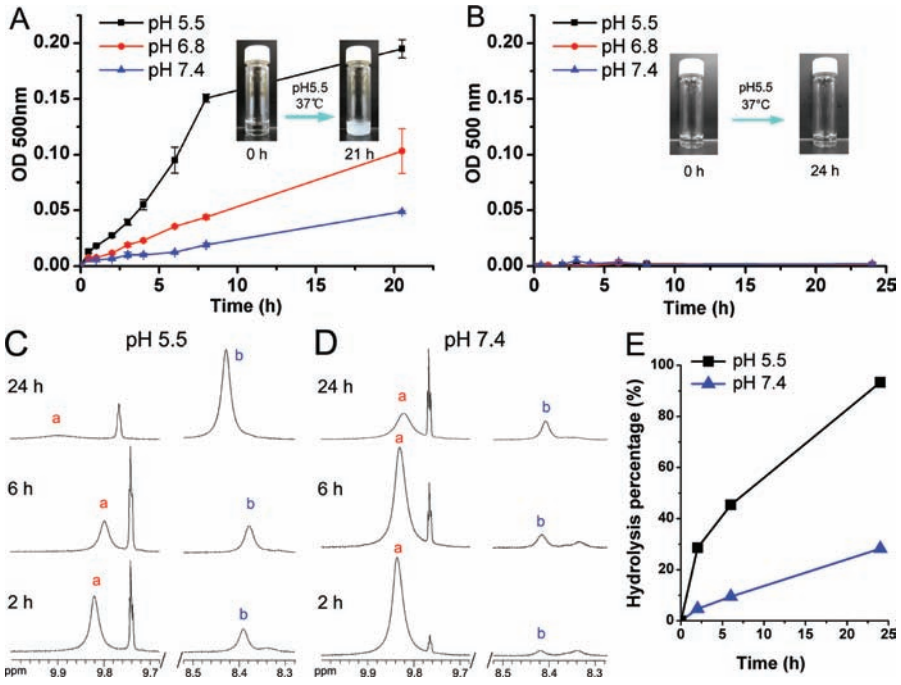

Figure 2. Acid sensitivity of PHC and PAC. (A) Time- and pH-dependent changes of the turbidity of PHC solution (insets are digital photographs taken after 0 and 21 h of incubation at pH 5.5, 37 °C). (B) Time- and pH-dependent changes of the turbidity of PAC solution. (C) ^{1}H NMR spectra of PHC in $CDCl_3$ after incubation for different periods of time at pH 5.5, 37 °C. (D) ^{1}H NMR spectra of PHC in $CDCl_3$ after incubation for different period of time at pH 7.4, 37 °C. (E) Time- and pH-dependent degradation of PHC based on ^{1}H NMR spectra shown in C and D. a, CONHN=CH from PHC, 9.82 ppm; b, $CONHNH_2$ from PEG2000-hydrazide, 8.42 ppm.

to 9.82 ppm (CON*H*N=CH) (Figure 1A), which was due to the effect of π-bond from the newly formed carbon−nitrogen double bond. As will be shown later, these characteristic changes in chemical shift were also useful in quantifying the hydrolysis of PHC. The synthesis of PHC was further confirmed by matrix-assisted laser desorption/ionization (MALDI) mass spectrometry. The starting material of PEG2000-hydrazide has a molecular weight (MW) of 2087 (H^+ adduct) (Figure S2B). After conjugation with octadecanal (MW 268, Figure S1B), a peak with m/z of 2359 (Na^+ adduct) was observed in the MALDI mass spectrum of PHC (Figure 1B), which was in agreement with the expected MW of 2336.

PAC was synthesized by conjugating stearoyl chloride with PEG2000-amine. The ^{1}H NMR spectrum of PAC is shown in Figure 1C, where the peak of 6.06 ppm (N*H*CO) confirmed the formation of amide. For a comparison, the ^{1}H NMR spectrum of PEG2000-amine could be found in Figure S3A. The MALDI mass data also supported the formation of PAC. The MW of PEG2000-amine was 1925 (H^+ adduct) (Figure S3B), which was expected to increase to 2191 after conjugation with the stearoyl chloride (MW 303). The appearance of a peak with m/z of 2214 (Na^+ adduct) confirmed the successful conjugation (Figure 1D).

GemC18 was synthesized by forming an amide bond between the aromatic amine of gemcitabine and stearic acid. Amide bond formation was confirmed by the appearance of a peak at 12.01 ppm in ^{1}H NMR spectrum (Figure 1E). The electrospray ionization mass (ESI-MS) spectrum also provided evidence of the formation of GemC18 (Figure 1F).

Acid Sensitivity of PEG-C18. The acid sensitivity of the PEG-C18 (i.e., PHC or PAC) was first examined by UV−vis spectroscopy. The degradation of PHC and PAC was expected to produce water-insoluble octadecanal and stearic acid, respectively, and result in an increase in the turbidity of the solution, providing a means to evaluate the degradation of the PEG-C18 by measuring the optical density of the solution at 500 nm ($OD_{500\ nm}$).[31] As shown in Figure 2A, PHC aqueous solution was transparent immediately after solubilization and did not have significant absorbance at 500 nm ($OD_{500\ nm}$ of 0). However, when incubated at pH 5.5, 37 °C, the PHC solution slowly became turbid, and the value of $OD_{500\ nm}$ increased to 0.195 after 21 h of incubation, which was likely due to the formation of water-insoluble octadecanal after the degradation of PHC. The increase of the $OD_{500\ nm}$ value for the PHC solution was slower at pH 6.8 than at pH 5.5; similarly, a slower increase in the $OD_{500\ nm}$ value was observed at pH 7.4 than at pH 6.8, indicating that the degradation of PHC was pH-dependent, faster at lower pH. In contrast, the turbidity of the PAC aqueous solution did not increase during 24 h of incubation at pH 5.5, 6.8, and 7.4, indicating that the PAC was stable at the pH tested (Figure 2B).

High-resolution ^{1}H NMR spectroscopy (600 MHz) was used to further examine the pH-dependent degradation of PHC. As shown in Figure 2C, when PHC was incubated at pH 5.5, 37 °C, the peak area of the NH proton (CON*H*N=CH, 9.82 ppm) in the PHC molecule decreased as a function of time, while the peak area of the NH proton (CON*H*NH_2, 8.42 ppm) in the PEG2000-hydrazide increased gradually, indicating the disappearance of the PHC and the appearance of the PEG2000-hydrazide. A significant degradation was observed as early as after only 2 h of incubation, and almost all the PHC was degraded after 24 h of incubation (Figure 2C). A similar trend was observed at pH 7.4 (Figure 2D), but the degradation rate was much lower than at pH 5.5. Shown in Figure 2E are the changes of the peak area of characteristic protons as a function of time. Twenty-eight percent of PHC was hydrolyzed after

dx.doi.org/10.1021/bc2005945 | *Bioconjugate Chem.* 2012, 23, 966−980

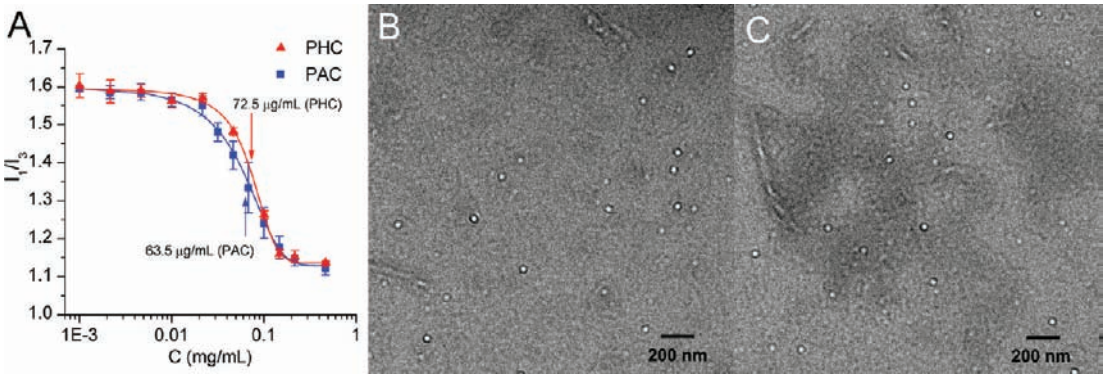

Figure 3. (A) Plots of I_1/I_3 values versus the concentrations of PHC and PAC in water (n = 3). (B) TEM image of PHC5% micelles. (C) TEM image of PAC5% micelles. Bar, 200 nm.

only 2 h of incubation at pH 5.5, and the percentage of hydrolysis increased to 45.4% and 93.3% after 6 and 24 h of incubation, respectively. In contrast, when incubated at pH 7.4, only 28.3% of PHC degraded after 24 h of incubation, again demonstrating the acid-sensitive degradation of the PHC. As to the PAC, ^{1}H NMR data did not reveal any significant degradation after 24 h of incubation at pH 5.5 (data not shown).

Preparation and Characterization of PEG-C18 Micelles. The CMC value is an important characteristic of amphiphilic molecules, indicating the ability to form micelles. In the present study, the aggregation behavior of PEG-C18 was investigated by fluorescence spectroscopy using pyrene as a probe, which is sensitive to the polarity change of the microenvironment it is in. Figure 3A shows the fluorescence intensity ratio (I_1/I_3) of pyrene as a function of the PEG-C18 concentration. At low PEG-C18 concentrations, pyrene mainly existed in the aqueous solution, and the I_1/I_3 values remained constant (~1.6). As the concentration of PEG-C18 was increased, a substantial decrease in the I_1/I_3 value was observed, indicating that pyrene was gradually transferred from the polar aqueous solution to the nonpolar core of the micelles. I_1/I_3 values became constant (~1.1) again once all pyrene was completely incorporated into the micelles. After fitting the data into a decreasing sigmoid of the Boltzmann type, the CMC values of PHC and PAC were calculated to be 72.5 ± 0.3 μg/mL and 63.5 ± 14.2 μg/mL, respectively.

Formulation preparation was then performed by incorporating different amounts of GemC18 into PHC or PAC micelles. Micelles with different percentages of GemC18 (w/w) were referred to as PHC3%, PHC5%, PHC10%, PAC3%, PAC5%, and PAC10%. All micelles with or without GemC18 have similar slightly negative zeta potentials in PBS (10 mM, pH 7.4) (Table 1). Entrapment efficiency of more than 95% was obtained for all formulations (Table 1), and as expected, increasing the percentage of GemC18 included in the PHC or PAC micelles led to a decreased entrapment efficiency. Blank PHC and PAC micelles were 21.6 ± 0.6 nm and 12.8 ± 0.1 nm, respectively. The particle size increased after the incorporation of GemC18. For example, the size of PHC micelles increased to 29.6, 43.1, and 51.8 nm, respectively, when 3%, 5%, and 10% of GemC18 (w/w) was included (Table 1). Similar results were observed for the GemC18-loaded PAC micelles. The particle size was further confirmed by TEM. Both PHC5% micelles and PAC5% micelles exhibited uniform spherical shape, and the particle size determined from the TEM images was around 50 nm (Figure 3B,C), in agreement with that measured by the dynamic laser scattering technique (Table 1).

Table 1. Characterization of PHC and PAC Micelles Loaded with or without GemC18 (n = 3)

	entrapment efficiency (%)	drug loading (%)	particle size (nm)	zeta potential (mV)
PHC	-	-	21.6 ± 0.6	−3.3 ± 1.1
PHC 3%	99.5 ± 3.0	3.3 ± 0.1	29.6 ± 3.7	−2.7 ± 1.2
PHC 5%	96.7 ± 2.5	5.0 ± 0.1	43.1 ± 3.8	−2.0 ± 0.7
PHC 10%	95.9 ± 6.5	9.7 ± 1.3	51.8 ± 3.2	−2.2 ± 0.9
PAC	-	-	12.8 ± 0.1	−1.6 ± 0.5
PAC 3%	102.1 ± 2.5	3.5 ± 0.3	28.1 ± 1.0	−1.8 ± 0.6
PAC 5%	101.1 ± 7.7	5.5 ± 0.4	40.8 ± 2.8	−1.6 ± 0.4
PAC 10%	95.6 ± 11.3	9.7 ± 0.5	45.3 ± 2.7	−1.7 ± 0.5

***In Vitro* Stability of GemC18-Loaded Micelles.** The GemC18-loaded micelles are intended to be administrated intravenously. Therefore, the physical and chemical stabilities of them in 10% FBS were evaluated to estimate the extent to which they would aggregate upon i.v. injection. As seen in Figure 4A, the size of the GemC18-loaded micelles did not change after 1 h of incubation in 10% FBS (P > 0.05). It should be noted that, due to the small size (~10 nm) of the proteins in the FBS, the overall average particle size of GemC18-loaded micelles measured using the dynamic light scattering technique decreased slightly after mixing with FBS. Figure 4B showed the percentage of GemC18 remaining in micelles after 1 h of incubation with FBS at 37 °C; more than 94% of the GemC18 remained in the micelles after 1 h of incubation with FBS at 37 °C when the drug loading percentage was at 3% and 5%. However, for PHC10% and PAC10%, the percentage of GemC18 remaining decreased to about 86% after the same period of incubation. According to the stability data in Figure 4, the PHC5% and PAC5% were chosen for further *in vitro* and *in vivo* studies, considering the relatively high concentration of GemC18 in them and their relatively higher stability.

***In Vitro* Release of GemC18 from PHC5% and PAC5%.** Acid-sensitive release of GemC18 from PHC5% and PAC5% was investigated at different pH. As seen in Figure 5A, the rate of release of GemC18 from PHC5% was pH-dependent. At pH 5.5, 93.1 ± 7.2% of the GemC18 was still in the micelles after 2 h of incubation, but almost all the GemC18 was released after another 2 h of incubation. At pH 6.8, PHC5% remained stable for at least 8 h, and a complete release was observed only after 24 h of incubation. At pH 7.4, about 80% of the GemC18 still

dx.doi.org/10.1021/bc2005945 | *Bioconjugate Chem.* 2012, 23, 966−980

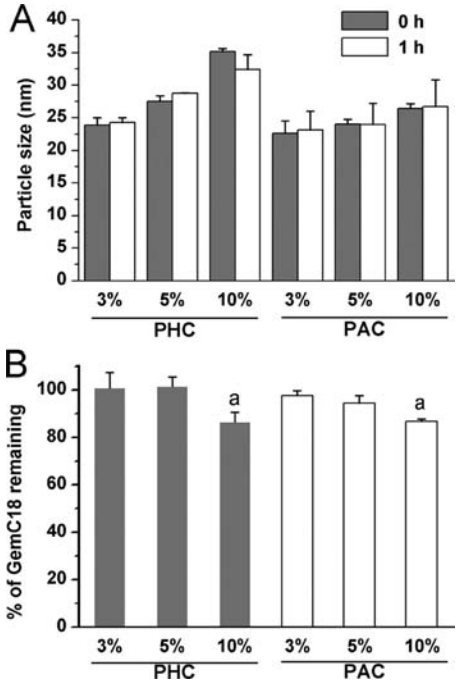

Figure 4. *In vitro* stability of GemC18-loaded PHC and PAC micelles. (A) Particle sizes of PHC and PAC micelles loaded with various percentages of GemC18 after 1 h of incubation with 10% FBS at 37 °C. (B) The percentage of GemC18 remained in PHC and PAC micelles after 1 h of incubation with 10% FBS at 37 °C (n = 3). a, P < 0.05 vs 3% and 5%.

remained in the micelles even after 24 h of incubation. In contrast, no apparent pH-dependent GemC18 release was observed from the PAC5% micelles (Figure 5B). Close to 90%

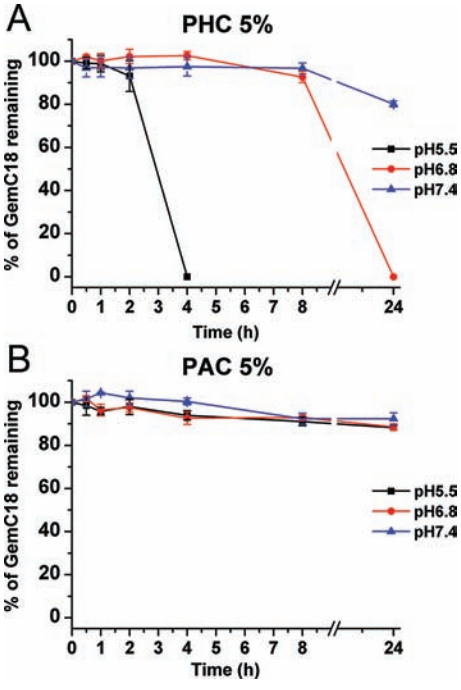

Figure 5. Release of GemC18 from PHC5% (A) and PAC5% (B) micelles in PBS of different pH values (5.5, 6.8, and 7.4) at 37 °C (n = 3).

of the GemC18 still remained in the micelles after 24 h of incubation at all pH values.

***In Vitro* Cytotoxicity.** The cytotoxicity of the GemC18 in PHC or PAC micelles was evaluated by determining the viability of cells after incubation with the micelles using the MTT assay. The BxPC-3 human pancreatic cancer cell line was used first in a preliminary study. It was reported that the IC_{50} value of GemHCl was around 14 nM in BxPC-3 cells.[23] Therefore, we tested the cytotoxicity of the GemC18 in micelles at 14 and 140 nM. As shown in Figure 6A, the PHC

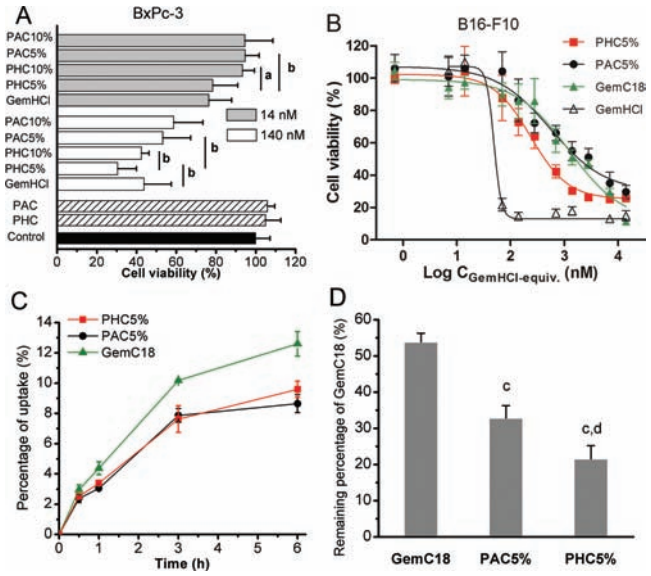

Figure 6. (A) Viability of BxPC-3 cells after 48 h of incubation with 14 nM or 140 nM of GemHCl or GemC18 in micelles (n = 5). a, P < 0.05; b, P < 0.01. The concentrations of blank PHC and PAC micelles were equivalent to 140 nM of GemC18 at 5% loading. (B) Viability of B16−F10 cells after 48 h of incubation with GemHCl, GemC18, PHC5%, or PAC5% micelles (n = 4). (C) Percentage of GemC18 internalized by B16−F10 cells after incubation with GemC18 in solution or in PHC5% or PAC5% micelles (n = 3). (D) Percentage of GemC18 remaining in B16−F10 cells 16 h after internalization (n = 3). c, P < 0.01 vs GemC18; d, P < 0.01 vs PAC5%.

micelles were more cytotoxic than PAC micelles, and for the PHC micelles, micelles with 5% of GemC18 were more cytotoxic than those with 10% GemC18 (P < 0.05 and P < 0.01 at 14 nM and 140 nM, respectively). In addition, it was also found that the cytotoxicity of PHC5% was comparable to that of the GemHCl at 14 nM, and was even higher at 140 nM (P < 0.01). Finally, we have also tested the cytotoxicity of the blank micelles. As seen in Figure 6A, blank PHC and PAC micelles, at a concentration equivalent to 140 nM of GemC18 at 5% loading, did not shown any significant cytotoxicity, confirming that the cytotoxicity of GemC18 in micelles was not due to the PHC or PAC molecules themselves. The cytotoxicity data were also supportive of using 5% drug loading in the future work.

Figure 6B showed the viability of B16−F10 cells after 48 h of incubation with GemHCl, GemC18, PHC5%, or PAC5%. GemHCl had the strongest cytotoxicity with an IC_{50} value of 48.9 nM. The prodrug GemC18 was significantly less cytotoxic than GemHCl, with an IC_{50} value almost 20 times higher (1227 nM). However, incorporation of the GemC18 into PHC or PAC micelles significantly decreased the IC_{50} values to 233.7 nM and 556.7 nM, respectively, indicating an increase in the cytotoxicity of the GemC18 after incorporation into micelles.

dx.doi.org/10.1021/bc2005945 | *Bioconjugate Chem.* 2012, 23, 966−980

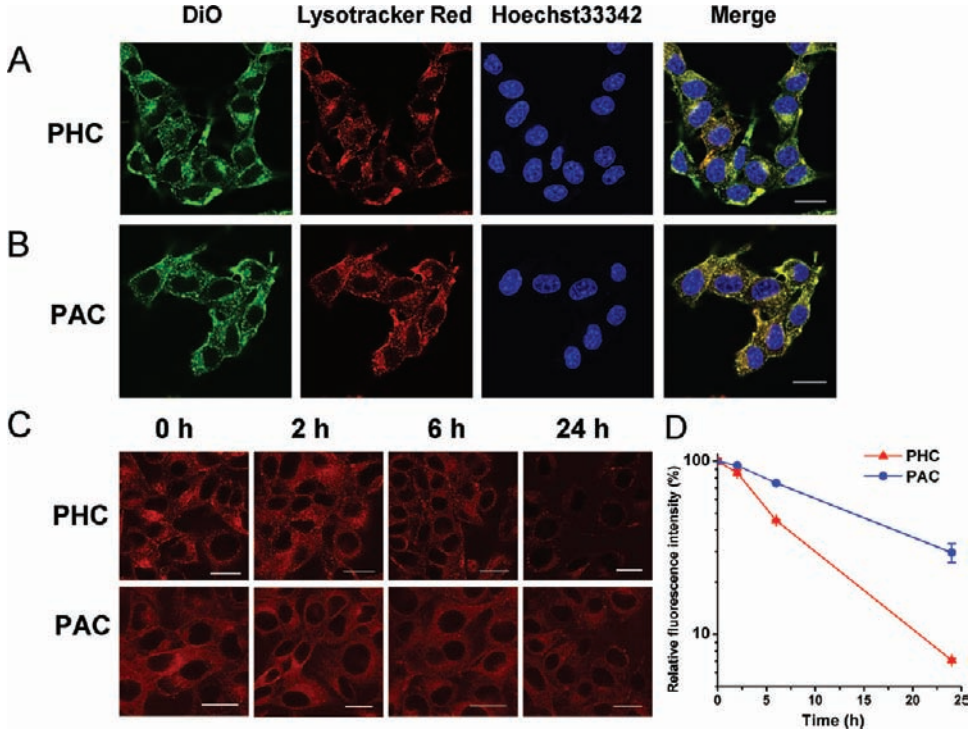

Figure 7. Comparison of intracellular fate of PHC and PAC micelles. (A) Colocalization of DiO-loaded PHC micelles (green) with lysosomes (red). Cell nuclei are in blue. (B) Colocalization of DiO-loaded PAC micelles with lysosomes. (C) Time-dependent decrease of FRET effect in B16−F10 cells preincubated with DiI/DiO-loaded PHC micelles or PAC micelles. (D) Time-dependent decrease of FRET effect quantified by flow cytometry (n = 3).

Finally, PHC5% was more cytotoxic than PAC5% against B16−F10 cells (Figure 6B).

Cellular Uptake of GemC18 in Micelles and Its Intracellular Metabolism. The cellular uptake of GemC18 in solution and in micelles was studied by directly determining the concentration of GemC18 in cells using an HPLC method. As seen in Figure 6C, the uptake of GemC18 was time-dependent. GemC18 dissolved in culture medium (with 1.35% DMSO, v/v) was more efficiently taken up by B16−F10 cells than GemC18 in micelles, with 12.6 ± 0.8% of GemC18 in solution being internalized after 6 h of incubation, while the percentage of GemC18 in PHC5% and PAC5% that was internalized was 9.6 ± 0.5% and 8.7 ± 0.6%, respectively.

Figure 6D showed the intracellular stability of the internalized GemC18. When the GemC18 was internalized as GemC18 in solution, 53.9 ± 2.4% of it was recovered after 16 h in cells. However, only 32.8 ± 3.4% and 21.6 ± 3.7% of GemC18 remained in the cells 16 h after it was internalized as PAC5% or PHC5%, respectively, indicating a higher degree of cellular metabolism of GemC18 when it was taken up by the cells as GemC18-loaded micelles, especially in the acid-sensitive PHC micelles.

Intracellular Localization and Acid Sensitivity of GemC18 in Micelles. Localization of acid-sensitive micelles in acidic organelles after cellular uptake is a prerequisite for acid-sensitive drug release. In the present study, DiO-loaded PHC or PAC micelles were used to identify the intracellular localization of the micelles. As seen in Figure 7A, almost all the PHC micelles were located in the lysosomes, showing an almost complete overlap with LysoTracker red, which was a marker specific to late endosomes and lysosomes. A similar overlap was observed with the PAC micelles (Figure 7B), indicating the efficient accumulation of both micelles into the acidic organelles after cellular uptake.

FRET is a physical property of energy transfer from a donor dye to an acceptor dye. If both dyes existed within the range of Förster distance, nonradiative fluorescence from the excited donor dye could be effectively used as the excitation energy for the acceptor dye, resulting in the emission of the acceptor fluorescence.[32] Therefore, for micelles with both DiO (donor, Ex/Em 488/501 nm) and DiI (acceptor, Ex/Em 501/565 nm) inside, when they are excited at wavelength of 488 nm, the energy generated from DiO can be transferred to DiI, which subsequently emits a red fluorescence. With the degradation of micelles and/or the release of DiO/DiI from them, the FRET effect is expected to decrease, accompanied by the decrease of red fluorescence. As seen in Figure 7C, cells preincubated with the DiO/DiI-loaded PHC and PAC micelles gave bright red color when observed under a confocal microscope. For the PHC micelles, a significant decrease in fluorescence intensity was observed 6 h later, and almost all the fluorescence disappeared 24 h later. However, cells preincubated with the PAC micelles kept almost the same fluorescence intensity 6 h later, and a significant decrease in fluorescence intensity was observed only 24 h later. Moreover, flow cytometric data also confirmed the observation from the confocal microscope. As seen in Figure 7D, the mean fluorescence intensity of cells preincubated with DiI/DiO-loaded PHC micelles decreased significantly faster than that of cells preincubated with the PAC micelles.

***In Vivo* Antitumor Activity.** To evaluate the *in vivo* antitumor activity of the GemC18 in micelles, B16−F10-tumor-bearing mice were treated with normal saline, GemHCl solution, GemC18 solution, blank PAC, blank PHC, PAC5% micelles, or PHC5% micelles. As seen in Figure 8A, tumors in

dx.doi.org/10.1021/bc2005945 | *Bioconjugate Chem.* 2012, 23, 966−980

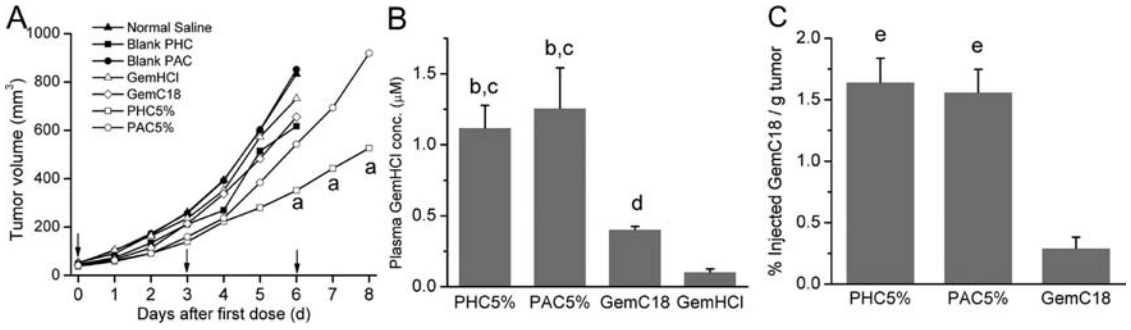

Figure 8. (A) Effect of normal saline, GemHCl in solution, GemC18 in solution, blank PHC micelles, blank PAC micelles, PHC5%, or PAC5% on the growth of murine B16−F10 tumors in C57BL/6 mice (n = 5−8). Arrows indicated the days of injection. a, $P < 0.05$ vs PAC5%. (B) Plasma concentration of gemcitabine after i.v. injection of GemHCl in solution, GemC18 in solution, PHC5%, or PAC5% (expressed as GemHCl-equiv, n = 4). b, c, $P < 0.01$ vs GemC18 and GemHCl, respectively; d, $P < 0.01$ vs GemHCl. (C) Percentage of GemC18 accumulated into tumor tissues 4 h after i.v. injection of GemC18 in solution, PHC5%, or PAC5% at a dose of 0.5 mg GemC18 per mouse (n = 4). e, $P < 0.01$ vs GemC18.

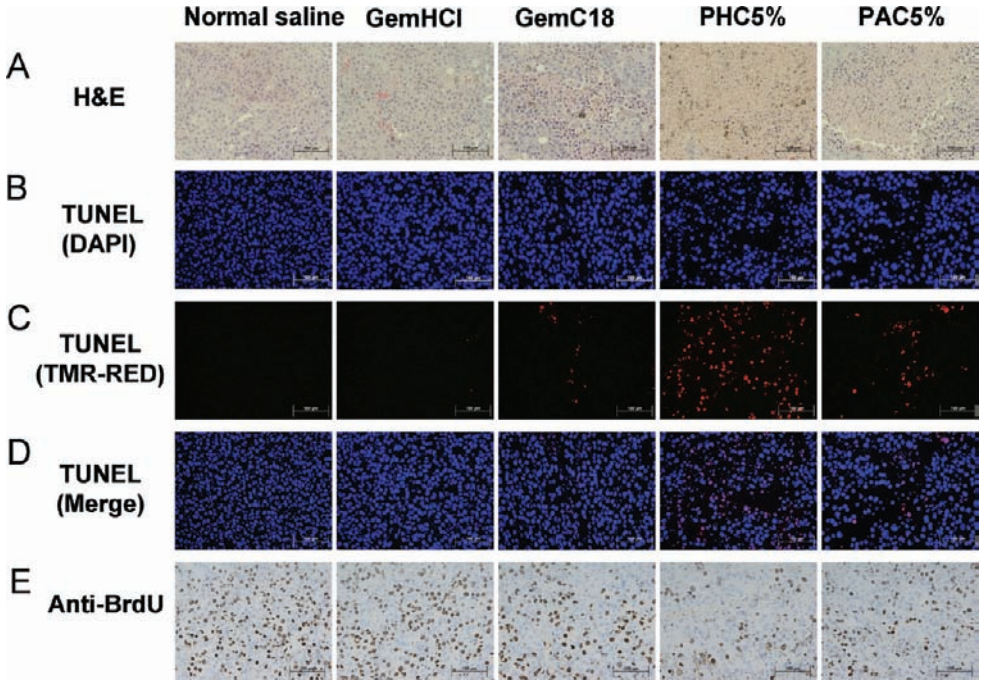

Figure 9. (Immuno)histograms of murine B16−F10 tumors after mice were treated with normal saline, GemHCl in solution, GemC18 in solution, PHC5%, or PAC5%. (A) H&E staining. (B−D) TUNEL staining. (E) Anti-BrdU staining.

mice that were injected with normal saline grew aggressively and uncontrolled, and the tumor volume reached 833 ± 274 mm^3 six days after the first injection. No significant difference in tumor volume was observed between mice that were injected with the blank micelles and normal saline, indicating that the blank micelles were pharmaceutically inert, and any therapeutic effect from the PAC5% and PHC5% micelles should be attributed to the GemC18 in the micelles. The sizes of the tumors in mice that were injected with GemHCl or GemC18 in solution were not significantly different from that in mice that were injected with normal saline at the end of treatment (day 6, P = 0.50 and 0.19 compared to GemHCl and GemC18, respectively). In contrast, PAC5% and PHC5% significantly inhibited the tumor growth compared with normal saline, which was significant as early as on the second day after the first dose ($P < 0.05$). On the first 5 days after the first dose, PHC5% and PAC5% were equally effective in inhibiting tumor growth (day 5, P = 0.11). Starting on day 6, the mean size of tumors in mice that were treated with the PHC5% micelles became significantly smaller than that in mice that were treated with the PAC5% micelles. Finally, the body weights of mice that received various treatments were also recorded. A slight increase in body weight was observed at the end of treatment, but no significant difference was observed among the different groups of mice (data not shown).

Plasma Concentration and Tumor Accumulation of Gemcitabine or GemC18. After i.v. injection, GemHCl was quickly cleared from the circulation, with a plasma GemHCl concentration of only 0.11 ± 0.02 μM 4 h after i.v. injection (Figure 8B). The clearance of GemC18 was slightly slower with a plasma GemC18 concentration of 0.40 ± 0.02 μM 4 h after i.v. injection of GemC18 in solution. When GemC18 was incorporated into micelles, its clearance was further slowed down. For example, the plasma GemC18 concentration was 1.12 ± 0.16 μM and 1.26 ± 0.28 μM for the PHC5% and PAC5% micelles, respectively, 4 h after i.v. injection.

The PHC and PAC micelles also increased the accumulation of GemC18 in tumors. As shown in Figure 8C, 4 h after i.v.

dx.doi.org/10.1021/bc2005945 | *Bioconjugate Chem.* 2012, 23, 966−980

injection, the concentrations of GemC18 in tumors reached 1.64 ± 0.19% and 1.56 ± 0.18% of the injected amount (per g of tumor), when mice were injected with PHC5% and PAC5%, respectively, which are more than 5 times higher than when mice were injected with GemC18 in solution.

Histology. Hematoxylin and eosin (H&E) staining revealed that tumors in mice that were treated with normal saline were characteristic of large nuclei, with small intercellular spaces (Figure 9A). Tumors in mice that were treated with GemHCl or GemC18 displayed similar characteristics, indicating a limited therapeutic effect. However, treatment with PHC5% or PAC5% micelles led to a significant shrinkage of the nuclei and much larger intercellular spaces, with the PHC5% being stronger than PAC5% (Figure 9A). Apoptotic cells (purple) were detected only in tumors in mice that were treated with GemC18 in PHC or PAC micelles, and the GemC18 in PHC micelles (PHC5%) appeared to induce more apoptosis in tumor tissues than the GemC18 in PAC micelles (PAC5%) (Figure 9B–D). Antibromodeoxyuridine (BrdU) staining showed extensive cell proliferation in tumors in mice that were injected with normal saline. Treatment with GemHCl or GemC18 solution did not significantly decrease the extent of cell proliferation. However, a significant decrease in BrdU positive staining was observed in tumors in mice that were treated with PHC5% or PAC5% micelles, as compared with that in mice that were treated with normal saline, and it appeared that the BrdU positive staining was significantly less extensive in tumors in mice that were treated with the PHC5% micelles than with the PAC5% micelles (Figure 9E).

■ DISCUSSION

In the present study, we reported a new method to construct acid-sensitive micelles by directly conjugating hydrophilic PEG with a hydrophobic stearic acid derivative (C18) using an acid-sensitive hydrazone bond. The acid sensitivity of the PHC micelles was validated both in test tube and in cells in culture. Specifically, to the best of our knowledge, this represents the first report using FRET technique to confirm the cellular-level acid sensitivity of acid-sensitive micelles. The PHC micelles as a carrier to a lipophilic prodrug, 4-(*N*)-stearoyl gemcitabine (GemC18), significantly enhanced the *in vitro* and *in vivo* antitumor activity. The enhanced antitumor activity may be attributed to the enhanced plasma retention and tumor accumulation of GemC18 by the micelles, the lysosomal delivery of GemC18, and faster acid-sensitive release of GemC18 from the PHC micelles in lysosomes.

The lack of stability after systemic injection is a major obstacle preventing the development of effective micelle drug delivery systems, which could be reflected as follows:[33] (1) micelle dissociation upon dilution in the blood, (2) particle size increase due to micelle aggregation or protein binding, (3) and drug loss caused by plasma protein extraction or protein-induced micelle disassembly. The effect of blood dilution could be alleviated by using amphiphilic molecules with a low CMC value. Because of the lower molecular weight of the hydrophobic C18 group, the CMC values of the PEG-C18 synthesized in the present study (~70 μg/mL) were relatively higher than that of previously reported synthetic block copolymers (~4 μg/mL),[34,35] yet they were still much lower than that of commonly used nonionic surfactants, such as Tween 80 and Tween 20 (both ~300 μg/mL),[36] and comparable with that of Pluronic block copolymers (25, 35, and 299 μg/mL for Pluronic P123, F127, and P85, respectively).[37] On the basis of the blood volume of a mouse (58.5 mL of blood per kg of body weight)[38] and the dose of the micelles injected (9.5 mg of PEG-C18), we estimated that the concentration of PEG-C18 in the blood of a mouse of 25 g can be as high as 6.75 mg/mL, which was about 100 times higher than the CMC values of PEG-18 (60–70 μg/mL). Therefore, it is expected that micelles formed by PEG-C18 are potentially stable against dilution when used as drug carriers. The effect of serum/plasma proteins on the stability of the micelles formed was also evaluated by measuring the particle size changes and the loss of GemC18 from the micelles after incubation with 10% FBS. The fact that no significant change in particle size was observed and that more than 94% of the GemC18 still remained in the micelles (at lower loading percentages of 3–5%) after 1 h of incubation with 10% FBS suggested that the GemC18-loaded micelles were resistant to protein-induced aggregation and extraction (Figure 4).

The results from the release study also demonstrated the stability of the GemC18-loaded micelles. For acid-insensitive PAC micelles, only 10% of GemC18 was released after 24 h of incubation (Figure 5B); for acid-sensitive PHC micelles, the percent of GemC18 released after 24 h of incubation at pH 7.4 was around 20% (Figure 5A), indicating that the GemC18-loaded PEG-C18 micelles were able to retain the incorporated GemC18. Rijcken et al. stated that the slow release of drugs from micelles could be attributed to the solid-like core of the polymeric micelles and the high affinity between drug molecules and the hydrophobic core of micelles.[10] It is unlikely that the PEG-C18 micelles had a solid-like core, since similar micelles prepared with 1,2-distearoyl-*sn*-glycero-3-phosphoethanolamine (DSPE)-PEG2000 were reported to have a fluid core.[39] A possible explanation for the slow release of GemC18 from the PEG-C18 micelles may be attributed to the high affinity between the C18 chains of GemC18 and the PEG-C18. It is well-recognized that fatty acid chains stabilize and hold together the phospholipid bilayers of the cell membrane by a variety of forces such as van der Waals interactions.[40]

Being stable in the blood circulation after i.v. injection is beneficial to the therapeutic effect of micelle drug delivery systems against tumors. However, for acid-sensitive micelles, it is also critical for them to readily release drug in an acidic condition. Polymeric micelles with a semisolid core suffer from the risk of core precipitation after the removal of the hydrophilic segment, which may explain why there is no report of constructing acid-sensitive micelles by directly conjugating a hydrophobic polymer with a hydrophilic polymer using an acid-sensitive bond. It is unlikely that the current PEG-C18 micelles have a hydrophobic core as "solid" as that of a polymeric micelle. Therefore, core precipitation was unlikely after the cleavage of the hydrazone bond. This was confirmed by the confocal microscopy data using DiI/DiO-loaded PEG-C18 micelles. The almost complete disappearance of FRET effect (i.e., the red fluorescence in Figure 7C) indicated the release of DiI and DiO from the micelle core. Otherwise, the FRET effect should not have disappeared if core precipitation happened. Therefore, the GemC18-loaded PEG-C18 micelles are expected to be stable at neutral pH in the blood circulation, but able to readily release GemC18 in an acidic condition.

In fact, the acid sensitivity of the PHC molecule and GemC18-loaded PHC micelles was demonstrated both in test tubes and in cells in culture. The acid sensitivity of the PHC was first examined by UV–vis spectroscopy and high-resolution ^{1}H NMR spectroscopy. PHC was found to be acid-sensitive,

while the control PAC was stable at pH 5.5, 6.8, and 7.4 (Figure 2B). The degradation data of PHC (Figure 2E) showed that 29−40% of PHC was hydrolyzed after 2−4 h of incubation at pH 5.5. Meanwhile, within 2−4 h of incubation at the same pH, the percentage of GemC18 released from the PHC micelles sharply increased from 7% to 100% (Figure 5). Similarly, at pH 7.4, the release of GemC18 from the micelles was negligible at 6 h when only 9.5% of PHC was degraded, while 28.3% of PHC degradation led to 20% of release of GemC18. Taken together, it appears that, when 30−40% of the PHC was hydrolyzed, the PHC micelles underwent dissociation, resulting in the complete release of GemC18.

The cellular-level acid sensitivity of acid-sensitive micelles had rarely been investigated previously. Previously, FRET technique was used to study the stability of PEG-polylactic acid (PLA) micelles after i.v. administration[41] or after incubation with cells.[42] Xiao et al. also used FRET technique to evaluate the interaction between PEG-PLA micelles and the cell membrane.[43] In the present study, we evaluated the acid sensitivity of the PEG-C18 micelles at the cellular level using FRET. Using the intensity of red fluorescence generated from the FRET effect as the indicator, both confocal microscopic images and the flow cytometric data revealed that the FRET effect diminished faster in cells preincubated with the PHC micelles than in cells preincubated with the PAC micelles (Figure 7C,D), which was likely caused by the acidic lysosomal condition, confirming the cellular-level acid sensitivity of PHC micelles. This finding is in agreement with the lysosomal delivery of the PEG-C18 micelles (Figure 7A,B) and the different release profiles of the GemC18 from the micelles in acidic conditions in tubes (Figure 5). Finally, although to a lesser degree, a decrease in red fluorescence was also observed when cells were preincubated with the PAC micelles, indicating that the micelles also underwent destabilization inside cells independent of the acidic condition.

Acid-sensitive destabilization of micelles either extracellularly or intracellularly followed by the quick release of anticancer drugs incorporated in them should be beneficial to the antitumor activity of the anticancer drug. However, GemC18 is a prodrug, which needs to be hydrolyzed to produce the active gemcitabine. The amide bond is relatively stable in physiological and slightly acidic conditions,[44] but its hydrolysis is enzymatically catalyzed by enzymes such as cathepsin B (a cysteine protease) and cathepsin D (an aspartic protease),[21] which are important enzymes in lysosomes and play a key role in the degradation of amide-bearing drugs, polypeptides, and proteins inside cells.[45] Therefore, it is preferable to specifically deliver the GemC18 into the lysosomes. The *in vitro* cellular uptake and cytotoxicity data are also supportive of the delivery of the GemC18 into lysosomes by the micelles. Even though the cellular uptake of the GemC18 in solution was 30−40% higher than the uptake of the GemC18 in PHC or PAC micelles (Figure 6C), the cytotoxicity of the GemC18 in solution was lower (Figure 6B), likely because the GemC18 in solution entered the cells by passive diffusion and was distributed randomly over the whole cell. In contrast, the micelles entered cells by endocytosis, were transferred into the lysosomes, and then released the GemC18 by acid-sensitive micelle destabilization. The GemC18 released into the lysosomes was then enzymatically hydrolyzed to generate gemcitabine. The faster disappearance of GemC18 in cells when delivered using the micelles than using GemC18 in solution and, more importantly, the faster disappearance of the GemC18 in cells when delivered using the acid-sensitive PHC micelles than using the acid-insensitive PAC micelles (Figure 6D) are supportive of the reasoning above. The newly generated gemcitabine may cross the lysosome membrane and reach the cytoplasm by passive diffusion[46] and/or with the help of human equilibrative nucleoside transporter 3 (hENT3), which is localized in the late endosomes/lysosomes.[47]

Finally, the *in vivo* antitumor activity of GemC18 in the acid-sensitive PHC micelles was evaluated in C57BL/6 mice with the model of B16−F10 melanoma. The B16−F10 mouse melanoma model was chosen because the B16−F10 tumor cells grew aggressively in the syngeneic C57BL/6 mice, which allowed us to readily determine whether the delivery of the GemC18 in the acid-sensitive PHC micelles can improve its *in vivo* antitumor activity. After all, melanoma is the most dangerous skin cancer, causing the majority of deaths related to skin cancer, and clinical data showed that melanoma is responsive to gemcitabine.[18,19] GemHCl or GemC18 in solution did not show any significant antitumor activity (Figure 8A). It is possible that a higher dose of GemHCl or GemC18 in solution is needed for them to show antitumor activity against the B16−F10 tumor in mice. In addition, both GemHCl and GemC18 are small molecules and could be quickly eliminated after i.v. injection. They may have also distributed to organs and tissues other than tumors. Data in Figure 8A showed that the GemC18 in micelles was more effective than GemC18 in solution and GemHCl in solution in inhibiting the tumor growth, which may be attributed to the following: (1) The hydrophilic PEG corona on the micelles created a barrier layer to block the adhesion of opsonins present in the serum, thus preventing the recognition of the micelles by phagocytic cells, reducing the accumulation them in the reticuloendothelial system (RES), and prolonging their circulation in blood.[9] (2) The nanoscaled size (40−50 nm) of the micelles permitted the passive accumulation of them in tumor tissues due to the EPR effect.[33] (3) The micelles delivered GemC18 into the lysosomes, where enzymatic hydrolysis facilitated the generation of the active parent drug of gemcitabine after GemC18 release. More importantly, we have found that the acid-sensitive PHC5% micelles were more effective than the acid-insensitive PAC5% micelles in inhibiting the tumor growth (Figure 8A). Possible explanations are summarized as follows: (1) intravenous injection of either PHC5% or PAC5% resulted in comparable plasma GemC18 concentrations and accumulations of GemC18 in the tumor tissues (Figure 8B,C); (2) the cellular uptakes of PHC5% and PAC5% were also similar (Figure 6C); (3) the GemC18 was more quickly released from acid-sensitive PHC5% micelles than from the acid-insensitive PAC5% micelles, which was confirmed both in test tube in acidic condition (Figure 5) and in cultured cells (Figure 7); (4) due to the faster release of GemC18 from the PHC micelles than from the PAC micelles, the GemC18 delivered using the PHC micelles can be more quickly hydrolyzed to regenerate gemcitabine, which was supported by Figure 6D. The histological data, including H&E, TUNEL, and anti-BrdU staining, also confirmed that the acid-sensitive PHC5% micelles induced more tumor cell apoptosis and more effectively inhibited tumor cell proliferation than the acid-insensitive PAC5% micelles, supporting the finding that the PHC5% micelles were more effective than the PAC5% micelles in inhibiting tumor growth (Figure 8A).

CONCLUSION

In the present study, we reported a novel strategy to construct acid-sensitive micelles by directly conjugating the hydrophilic PEG with a hydrophobic stearic acid derivative (C18) using an acid-sensitive hydrazone bond. Furthermore, the anticancer drug gemcitabine was conjugated with stearic acid (C18) to produce the lipophilic prodrug, namely, GemC18, which was then incorporated into the micelles. Acid-sensitive release was observed when the micelles were incubated in slightly acidic conditions, while the control PAC micelles were stable at the same incubation conditions. Cellular-level acid sensitivity was confirmed using a FRET technique. Lysosomal delivery of GemC18 by micelles was found to be critical for the cytotoxicity of the GemC18 because it was necessary for the GemC18 to be hydrolyzed by lysosomal enzymes to generate the active parent drug of gemcitabine. Most importantly, GemC18 carried by the pH-sensitive PHC micelles showed a significantly stronger *in vivo* antitumor activity than gemcitabine HCl in solution, GemC18 in solution, and GemC18 in the pH-insensitive PAC micelles, suggesting the acid-sensitive micelles as an effective delivery system for the lipophilized gemcitabine amide derivative, GemC18, and possibly the amide derivatives of other anticancer drugs.

ASSOCIATED CONTENT

Supporting Information

^{1}H NMR and MS spectra of octadecanal; ^{1}H NMR and MALDI MS spectra of PEG2000-hydrazide; ^{1}H NMR and MALDI MS spectra of PEG2000-amine. This material is available free of charge via the Internet at http://pubs.acs.org.

AUTHOR INFORMATION

Corresponding Author

*Tel.: +1 512 495 4758; fax: +1 512 471 7474. E-mail address: zhengrong.cui@austin.utexas.edu.

Notes

The authors declare no competing financial interest.

ACKNOWLEDGMENTS

This work was supported in part by a National Cancer Institute grant CA135274 (to Z.C.). We would like to thank Dr. Yue Li at the Microscopy Core Facility at the Dell Pediatric Research Institute at The University of Texas at Austin for assistance in acquiring the confocal microscopic images. The Fluorolog3 Fluorimeter was funded by the National Science Foundation Grant CHE-094750.

REFERENCES

(1) Matsumura, Y., and Maeda, H. (1986) A new concept for macromolecular therapeutics in cancer chemotherapy: mechanism of tumoritropic accumulation of proteins and the antitumor agent smancs. *Cancer Res. 46*, 6387−6392.

(2) Iyer, A. K., Khaled, G., Fang, J., and Maeda, H. (2006) Exploiting the enhanced permeability and retention effect for tumor targeting. *Drug Discovery Today 11*, 812−818.

(3) Kwon, G. S. (2003) Polymeric micelles for delivery of poorly water-soluble compounds. *Crit. Rev. Ther. Drug Carrier Syst. 20*, 357−403.

(4) Otsuka, H., Nagasaki, Y., and Kataoka, K. (2003) PEGylated nanoparticles for biological and pharmaceutical applications. *Adv. Drug Delivery Rev. 55*, 403−419.

(5) Torchilin, V. P. (2001) Structure and design of polymeric surfactant-based drug delivery systems. *J. Controlled Release 73*, 137−172.

(6) Wang, Y., Wang, X., Zhang, Y., Yang, S., Wang, J., Zhang, X., and Zhang, Q. (2009) RGD-modified polymeric micelles as potential carriers for targeted delivery to integrin-overexpressing tumor vasculature and tumor cells. *J. Drug Targeting 17*, 459−467.

(7) Nishiyama, N., and Kataoka, K. (2006) Current state, achievements, and future prospects of polymeric micelles as nanocarriers for drug and gene delivery. *Pharmacol. Ther. 112*, 630−648.

(8) Huh, K. M., Lee, S. C., Cho, Y. W., Lee, J., Jeong, J. H., and Park, K. (2005) Hydrotropic polymer micelle system for delivery of paclitaxel. *J. Controlled Release 101*, 59−68.

(9) Owens, D. E., 3rd., and Peppas, N. A. (2006) Opsonization, biodistribution, and pharmacokinetics of polymeric nanoparticles. *Int. J. Pharm. 307*, 93−102.

(10) Rijcken, C. J., Soga, O., Hennink, W. E., and van Nostrum, C. F. (2007) Triggered destabilisation of polymeric micelles and vesicles by changing polymers polarity: an attractive tool for drug delivery. *J. Controlled Release 120*, 131−148.

(11) Haag, R. (2004) Supramolecular drug-delivery systems based on polymeric core-shell architectures. *Angew. Chem., Int. Ed. Engl. 43*, 278−282.

(12) Engin, K., Leeper, D. B., Cater, J. R, Thistlethwaite, A. J., Tupchong, L., and McFarlane, J. D. (1995) Extracellular pH distribution in human tumours. *Int. J. Hyperthermia 11*, 211−216.

(13) Lee, E. S., Na, K., and Bae, Y. H. (2003) Polymeric micelle for tumor pH and folate-mediated targeting. *J. Controlled Release 91*, 103−113.

(14) Boudier, A., Aubert-Pouëssel, A., Louis-Plence, P., Gérardin, C., Jorgensen, C., Devoisselle, J. M., and Bégu, S. (2009) The control of dendritic cell maturation by pH-sensitive polyion complex micelles. *Biomaterials 30*, 233−241.

(15) Gillies, E. R., Jonsson, T. B., and Fréchet, J. M. (2004) Stimuli-responsive supramolecular assemblies of linear-dendritic copolymers. *J. Am. Chem. Soc. 126*, 11936−11943.

(16) Toncheva, V., Schacht, E., Ng, S. Y., Barr, J., and Heller, J. (2003) Use of block copolymers of poly(ortho esters) and poly (ethylene glycol) micellar carriers as potential tumour targeting systems. *J. Drug Targeting 11*, 345−353.

(17) Barton-Burke, M. (1999) Gemcitabine: a pharmacologic and clinical overview. *Cancer Nurs. 22*, 176−183.

(18) Schmittel, A., Schuster, R., Bechrakis, N. E., Siehl, J. M., Foerster, M. H., Thiel, E., and Keilholz, U. (2005) A two-cohort phase II clinical trial of gemcitabine plus treosulfan in patients with metastatic uveal melanoma. *Melanoma Res. 15*, 447−451.

(19) Corrie, P. G., Shaw, J., Spanswick, V. J., Sehmbi, R., Jonson, A., Mayer, A., Bulusu, R., Hartley, J. A., and Cree, I. A. (2005) Phase I trial combining gemcitabine and treosulfan in advanced cutaneous and uveal melanoma patients. *Br. J. Cancer 92*, 1997−2003.

(20) Brusa, P., Immordino, M. L., Rocco, F., and Cattel, L. (2007) Antitumor activity and pharmacokinetics of liposomes containing lipophilic gemcitabine prodrugs. *Anticancer Res. 27*, 195−199.

(21) Immordino, M. L., Brusa, P., Rocco, F., Arpicco, S., Ceruti, M., and Cattel, L. (2004) Preparation, characterization, cytotoxicity and pharmacokinetics of liposomes containing lipophilic gemcitabine prodrugs. *J. Controlled Release 100*, 331−346.

(22) Celano, M., Calvagno, M. G., Bulotta, S., Paolino, D., Arturi, F., Rotiroti, D., Filetti, S., Fresta, M., and Russo, D. (2004) Cytotoxic effects of gemcitabine-loaded liposomes in human anaplastic thyroid carcinoma cells. *BMC Cancer 4*, 63.

(23) Sloat, B. R., Sandoval, M. A., Li, D., Chung, W. G., Lansakara-P, D. S., Proteau, P. J., Kiguchi, K., DiGiovanni, J., and Cui, Z. (2011) In vitro and in vivo anti-tumor activities of a gemcitabine derivative carried by nanoparticles. *Int. J. Pharm. 409*, 278−288.

(24) Reddy, L. H., Dubernet, C., Mouelhi, S. L., Marque, P. E., Desmaele, D., and Couvreur, P. (2007) A new nanomedicine of gemcitabine displays enhanced anticancer activity in sensitive and resistant leukemia types. *J. Controlled Release 124*, 20−27.

(25) Arias, J. L., Reddy, L. H., and Couvreur, P. (2008) Magnetoresponsive squalenoyl gemcitabine composite nanoparticles for cancer active targeting. *Langmuir 24*, 7512−7519.
(26) Easton, C. J., Xia, L., Pitt, M. J., Ferrante, A., Poulos, A., and Rathjen, D. A. (2001) Polyunsaturated nitroalkanes and nitro-substituted fatty acids. *Synthesis 3*, 451−457.
(27) Guo, Zw., and Gallo, J. M. (1999) Selective protection of 2′,2′-difluorodeoxycytidine (gemcitabine). *J. Org. Chem. 64*, 8319−8322.
(28) Aguiar, J., Carpena, P., Molina-Bolívar, J. A., and Carnero Ruiz, C. (2003) On the determination of the critical micelle concentration by the pyrene 1:3 ratio method. *J. Colloid Interface Sci. 258*, 116−122.
(29) MacLaughlin, F. C., Mumper, R. J., Wang, J., Tagliaferri, J. M., Gill, I., Hinchcliffe, M., and Rolland, A. P. (1998) Chitosan and depolymerized chitosan oligomers as condensing carriers for in vivo plasmid delivery. *J. Controlled Release 56*, 259−272.
(30) Pasut, G., Canal, F., Dalla Via, L., Arpicco, S., Veronese, F. M., and Schiavon, O. (2008) Antitumoral activity of PEG-gemcitabine prodrugs targeted by folic acid. *J. Controlled Release 127*, 239−248.
(31) Sethuraman, V. A., Lee, M. C., and Bae, Y. H. (2008) A biodegradable pH-sensitive micelle system for targeting acidic solid tumors. *Pharm. Res. 25*, 657−666.
(32) Berney, C., and Danuser, G. (2003) FRET or no FRET: a quantitative comparison. *Biophys. J. 84*, 3992−4010.
(33) Kim, S., Shi, Y., Kim, J. Y., Park, K., and Cheng, J. X. (2010) Overcoming the barriers in micellar drug delivery: loading efficiency, in vivo stability, and micelle-cell interaction. *Exp. Opin. Drug Delivery 7*, 49−62.
(34) Aryal, S., Hu, C. M., and Zhang, L. (2010) Polymer-cisplatin conjugate nanoparticles for acid-responsive drug delivery. *ACS Nano 4*, 251−258.
(35) Tang, R., Ji, W., Panus, D., Palumbo, R. N., and Wang, C. (2011) Block copolymer micelles with acid-labile ortho ester side-chains: Synthesis, characterization, and enhanced drug delivery to human glioma cells. *J. Controlled Release 151*, 18−27.
(36) Lo, Y. L. (2003) Relationships between the hydrophilic-lipophilic balance values of pharmaceutical excipients and their multidrug resistance modulating effect in Caco-2 cells and rat intestines. *J. Controlled Release 90*, 37−48.
(37) Kabanov, A. V., Batrakova, E. V., and Miller, D. W. (2003) Pluronic block copolymers as modulators of drug efflux transporter activity in the blood-brain barrier. *Adv. Drug Delivery Rev. 55*, 151−164.
(38) http://www.nc3rs.org.uk/bloodsamplingmicrosite/page.asp?id=419
(39) Kastantin, M., Ananthanarayanan, B., Karmali, P., Ruoslahti, E., and Tirrell, M. (2009) Effect of the lipid chain melting transition on the stability of DSPE-PEG(2000) micelles. *Langmuir 25*, 7279−7286.
(40) Pandit, N. K. (2007) *Membranes and Tissues. Introduction to the Pharmaceutical Sciences* (Pandit, N. K., Eds.) pp 65, Lippincott Williams & Wilkins, Philadelphia.
(41) Chen, H., Kim, S., He, W., Wang, H., Low, P. S., Park, K., and Cheng, J. X. (2008) Fast release of lipophilic agents from circulating PEG-PDLLA micelles revealed by in vivo forster resonance energy transfer imaging. *Langmuir 24*, 5213−5217.
(42) Chen, H., Kim, S., Li, L., Wang, S., Park, K., and Cheng, J. X. (2008) Release of hydrophobic molecules from polymer micelles into cell membranes revealed by Forster resonance energy transfer imaging. *Proc. Natl. Acad. Sci. U. S. A. 105*, 6596−6601.
(43) Xiao, L., Xiong, X., Sun, X., Zhu, Y., Yang, H., Chen, H., Gan, L., Xu, H., and Yang, X. (2011) Role of cellular uptake in the reversal of multidrug resistance by PEG-b-PLA polymeric micelles. *Biomaterials 32*, 5148−5157.
(44) Kono, K., Kojima, C., Hayashi, N., Nishisaka, E., Kiura, K., Watarai, S., and Harada, A. (2008) Preparation and cytotoxic activity of poly(ethylene glycol)-modified poly(amidoamine) dendrimers bearing adriamycin. *Biomaterials 29*, 1664−1675.
(45) Dosio, F., Brusa, P., Crosasso, P., Arpicco, S., and Cattel, L. (1997) Preparation, characterization and properties in vitro and in vivo of a paclitaxel−albumin conjugate. *J. Controlled Release 47*, 293−304.
(46) Calvagno, M. G., Celia, C., Paolino, D., Cosco, D., Iannone, M., Castelli, F., Doldo, P., and Frest, M. (2007) Effects of lipid composition and preparation conditions on physical-chemical properties, technological parameters and in vitro biological activity of gemcitabine-loaded liposomes. *Curr. Drug Delivery 4*, 89−101.
(47) Baldwin, S. A., Yao, S. Y., Hyde, R. J., Ng, A. M., Foppolo, S., Barnes, K., Ritzel, M. W., Cass, C. E., and Young, J. D. (2005) Functional characterization of novel human and mouse equilibrative nucleoside transporters (hENT3 and mENT3) located in intracellular membranes. *J. Biol. Chem. 280*, 15880−15887.

Bioconjugate Chemistry

Article

pubs.acs.org/bc

Development of Biocompatible Polymeric Nanoparticles for in Vivo NIR and FRET Imaging

Anil Wagh, Steven Y. Qian, and Benedict Law*

Department of Pharmaceutical Sciences, North Dakota State University, Fargo, North Dakota 58108-6050, United States

Supporting Information

ABSTRACT: The majority of near-infrared (NIR) fluorophores are organic molecules that show significant overlap between the excitation and emission spectra and therefore exhibit high fluorescence backgrounds during in vivo imaging. Recently, cyanine dyes with a large Stokes shift have shown great promise for NIR imaging but often undergo rapid photodegradation and nonspecific protein adsorption. Alternatively, fluorescence resonance energy transfer (FRET) is a promising technique to generate a larger gap between the excitation and emission maxima and thus can reduce the background signal. Here, we report the rational design of FRET-based polymeric nanoparticles for NIR and FRET imaging. The particles were assembled from diblock copolymers of poly(D,L-lactic-*co*-glycolic acid) and maleimide-activated poly(ethylene glycol), which were also encapsulated with both the donor (1,1′-dioctadecyl-3,3,3′,3′-tetramethylindodicarbocyanine) and acceptor (1,1′-dioctadecyl-3,3,3′,3′-tetramethylindotricarbocyanine) fluorophores. Because of their extreme hydrophobicity, thousands of fluorophores could be encapsulated inside a single particle without causing leakage. FRET resulted in a large Stokes shift (>100 nm) of the emission maxima, and the transfer efficiency could be fine-tuned by further adjusting the doping ratio of the donor and acceptor fluorophores. The optimized formulation was less than 100 nm in size, brighter than quantum dots, stable in biological media, and demonstrated similar biodistribution to most nanomaterials. Additional animal phantom studies demonstrated that the FRET imaging platform developed could have far-reaching applications in optical imaging.

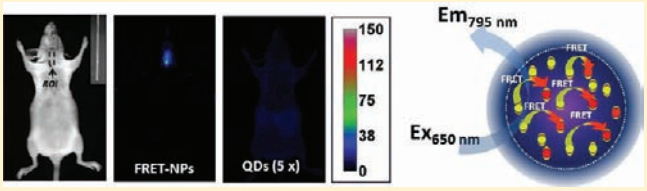

INTRODUCTION

Optical imaging has become an emerging diagnostic tool that provides several advantages, including higher sensitivity, lower cost, and avoidance of using ionizing radiation, over other imaging modalities.[1] Optical contrast agents are often required to enhance detection sensitivity in vivo. To improve tissue penetration, most contrast agents are incorporated with fluorescence reporters that excite and emit photons at the NIR region (650−900 nm).[2] The majority of these reporters are organic molecules that exhibit high background fluorescence while imaging, because of the small Stokes shift (difference between the excitation and emission maxima of the fluorophore). Heptamethine cyanine fluorophores with a larger Stokes shift (>100 nm) were synthesized.[3,4] These fluorophores are water-soluble and can be easily coupled with a variety of the biological entities including biomolecules such as antibodies and peptides. However, due to their rapid photodegradation, nonspecific protein adsorption, and biological or chemical degradation, they are not suitable for use in prolonged imaging.[5,6] Inorganic fluorescent nanocrystals such as quantum dots (QDs) can be used as an alternative.[7] They are known to be more sensitive (brighter) and less susceptible to photodegradation than organic fluorophores, but the unsure long-term toxicities hinder their future application in clinical settings.[8]

One of the approaches to improve the stability of fluorophores is through doping them into/onto the nanoparticles.[9,10] Fluorophore molecules can be incorporated into the nanoparticles via ionic interaction, entrapment, or covalent conjugation.[11] Unlike organic fluorophores, nanoparticle-based contrast agents are less prone to photobleaching and thus allow long-term and sensitive tracking of the signal. Furthermore, nanoparticles possess unique physicochemical properties that can be exploited in specific disease conditions. For example, in cancer, these contrast agents may accumulate at the tumor site via enhanced permeability and retention (EPR) effect and thus help in the early detection. Another advantage of nanoparticles is that more than one type of fluorophore can be easily incorporated inside a single particle to favor the fluorescence resonance energy transfer (FRET),[12] a process that transfers radiationless energy from an excited-state donor fluorophore to a ground-state acceptor molecule via dipole−dipole interaction.[13−15] Since the energy transfer is highly dependent on the distance between the donor and acceptor molecules (1−10 nm), FRET can also be employed to monitor the integrity of nanoparticles. For example, polymeric micelles that encapsulated with a FRET pair (DiO and Dil) showed a significant change in FRET efficiency upon the release of fluorophore molecules, which could be useful for monitoring the stability of polymeric micelles in both in vitro and in vivo systems.[16−18]

Received: November 27, 2011
Revised: April 5, 2012
Published: April 7, 2012

   dx.doi.org/10.1021/bc200637h | *Bioconjugate Chem.* 2012, 23, 981−992

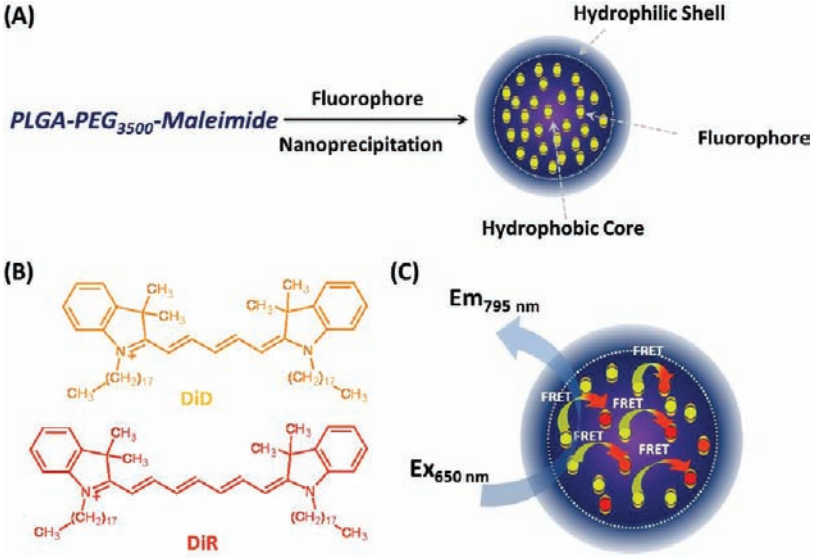

Figure 1. Design of FRET-NPs. (A) Nanoparticles were synthesized by the nanoprecipitation method.[23,24] DiD fluorophore, with excitation λ_{max} at 644 nm and emission λ_{max} at 665 nm in methanol, and DiR fluorophore, with excitation λ_{max} at 750 nm and emission λ_{max} at 780 nm, in methanol were encapsulated inside the FRET-NPs. (B) Chemical structures of DiD and DiR fluorophores. (C) The close proximity between the entrapped DiD and DiR fluorophores favored the fluorescence resonance energy transfer (FRET).

However, the employed FRET pairs do not absorb and/or emit photons at the NIR region and therefore limit their use for in vivo applications.[19] Until now, no one has explored the utility of the FRET in the development of a NIR contrast agent for in vivo imaging.

In the present study, we reported the development of biocompatible polymeric nanoparticles for in vivo NIR and FRET imaging. These particles were composed of diblock copolymers of poly(D,L-lactic-*co*-glycolic acid) (PLGA) and maleimide-activated poly(ethylene glycol) (PLGA-PEG_{3500}-maleimide),[20] and were encapsulated with two lipophilic NIR fluorophores, DiD and DiR, as the donor and acceptor, respectively (Figure 1).[21] One of the advantages of FRET over single fluorophores as the optical reporters is that it has a relatively larger gap between the excitation and emission maxima and thus can significantly reduce the background while imaging.[22] We also observed that the FRET transfer was efficient, despite less overlap between the donor (DiD) and acceptor (DiR) spectra (Table S1) as compared to previously reported Di series analogues (DiO and DiI).[17,18] Energy transfer from DiD to DiR resulted in a decrease of the emission maxima at 668 nm and was accomplished with an increase of the emission maxima at 795 nm. We further demonstrated that these nanoparticles have tremendous potential for in vivo imaging.

EXPERIMENTAL PROCEDURES

Chemicals and Materials. All solvents were purchased from Fischer Scientific (Pittsburgh, PA). Poly(D,L-lactic-*co*-glycolic acid) (PLGA-COOH, monomer ratio 50:50, 17 kDa) was received as gift samples from PURAC Biomaterials (Netherland). Maleimide-activated PEG (Mal-PEG_{3500}-NH_2, 3.5 kDa) was purchased from JenKem Technology USA, Inc. (Allen, TX). 1,1′-Dioctadecyl-3,3,3′,3′-tetramethylindodicarbocyanine, 4-chlorobenzenesulfonate salt (DiD) and 1,1′-dioctadecyl-3,3,3′,3′-tetramethylindotricarbocyanine iodide (DiR), and Qdot 800 ITK carboxyl quantum dots (QDs-800) were obtained from Life Technologies Corporation (Grand Island, NY). Cy5 and Cy7 monofunctional hydroxysuccinimide esters were purchased from GE Healthcare Biosciences (Piscataway, NJ). Trilite fluorescent nanocrystal 665 nm (QDs-665) was purchased from Cytodiagnostics, Inc. (Burlington, Ontario). Uranyl acetate and copper grids were obtained from Electron Microscopy Sciences (Hatfield, PA). 1-Ethyl-3-(3-dimethylaminopropyl) carbodiimide (EDC) and *N*-hydroxysuccinimide (NHS) were purchased from Advanced ChemTech (Louisville, KY) and Alfa Aesar (Ward Hill, MA), respectively. Bovine serum albumin (BSA), *N,N*-diisopropylethylamine (DIEA), Intralipid emulsion (20% w/v), and agar powder were obtained from Sigma-Aldrich (St. Louis, MO). Whole human blood was purchased from Biochemed Services (Winchester, VA). Ellman's reagent was purchased from Enzo Biochem, Inc. (New York, NY). CellTiter 96 AQueous One Solution Cell Proliferation Assay (MTS) was provided by Promega Corporation (Madison, WI).

Synthesis of Polymeric Constructs (PLGA-PEG_{3500}-maleimide). The copolymer was synthesized by standard carbodiimide chemistry, as previously described.[23] PLGA-COOH (1 g, 0.06 mmoL) dissolved in anhydrous dichloromethane (DCM, 10 mL) was activated by adding excess NHS (0.035 g, 0.30 mmoL) and EDC (0.056 g, 0.30 mmoL). After 4 h, the activated PLGA-NHS ester was precipitated in ice-cold diethyl ether (25 mL), washed with a mixture of ice-cold methanol and diethyl ether (30:70, 3 × 5 mL) to remove the unreacted NHS, and dried under the vacuum. The collected precipitate (0.8 g, 0.047 mmoL) was then dissolved in chloroform (8 mL). Mal-PEG-NH_2 (0.217 g, 0.062 mmoL) was then added to the solution mixture, in the presence of DIEA (0.028 g, 0.22 mmoL). The solution mixture was stirred in the dark for 12 h at room temperature. The copolymer was then precipitated in ice-cold diethyl ether (25 mL) and washed with ice-cold methanol (3 × 5 mL) to remove the unreacted PEG. The final product, PLGA-PEG_{3500}-maleimide, was dried under vacuum to remove the residual solvents and further characterized by ^{1}H NMR spectroscopy. ^{1}H NMR (400 Hz, $CDCl_3$): δ 6.70 (2H, −C<u>H</u>═, s), δ 5.22 (1H, −C(O)C<u>H</u>-

dx.doi.org/10.1021/bc200637h | *Bioconjugate Chem.* 2012, 23, 981−992

(CH_3)O−, m), δ 4.83 (2H, −C(O)C$\underline{H_2}$O−, m), δ 3.64 (4H, −OC$\underline{H_2}$C$\underline{H_2}$−, s), δ 1.58 (3H, −C(O)CH(C$\underline{H_3}$)O−, dd).

Nanoparticle Assembly. All the nanoparticles were fabricated by the nanoprecipitation method as described previously.[24,25] The single fluorophore-doped nanoparticles were synthesized by mixing PLGA-PEG_{3500}-maleimide (2 mg) with different amounts of DiD or DiR fluorophores (0.05% to 3% w/w) in DMF (0.2 mL). The solution mixtures were then added dropwise in deionized water (2 mL). The resulting particles were allowed to stir for 2 h at room temperature. Nanoparticles were then purified by ultracentrifugation (3000 × *g*, 15 min) using SPIN-X UF concentrators with 10 kDa MWCO (Corning Incorporated, Lowell, MA) and washed with deionized water (2 × 5 mL) to remove the free fluorophores. The purified nanoparticles were resuspended in deionized water (0.2 mL) and stored at 4 °C. Using the same protocol, FRET nanoparticles (FRET-NPs) were synthesized by adding a mixture of DiD and DiR fluorophores (1:1 ratio) to the copolymer.

Physical Characterization of the Particles. Particle size and zeta potential were measured by dynamic light scattering (Zetasizer, Malvern Instruments, Worcestershire, U.K.). The equipment was first calibrated according to the manufacturer's instruction, using the certified zeta potential transfer standard (DTS1050). For the size measurement, the samples (0.2 mg/mL) were loaded into a disposable polystyrene cuvette. All measurements were recorded with the same particle concentration in deionized water at 25 °C. The solvent parameters such as refractive index and viscosity were set at 1.33 and 0.8872 cP, respectively. The intensity-weighted mean values were recorded as the average of three independent measurements. The zeta potentials of the particles (0.2 mg/mL) were measured in a disposable capillary cell (Malvern Instruments, Worcestershire, U.K).

The surface morphology and the size of the particles were confirmed by high-resolution transmission electron microscope (JEM-2100, Jeol Ltd., Peabody, MA). Samples were negatively stained with uranyl acetate.[26] Briefly, nanoparticles (2 mg/mL) in deionized water (10 μL) were adsorbed onto 200 mesh Formvar/carbon-coated grids for 5 min and the excess samples were blotted off by a filter paper. The grids were stained with 3% (w/v) uranyl acetate in deionized water (10 μL) for 5 min and then blotted off. Finally, the grids were air-dried and images were acquired using computer-controlled station.

Determination of Particle Numbers. The number of nanoparticles (n) in the stock solution was estimated as previously described from the following equation:[27]

$$n = \frac{6c}{\pi \times d^3 \times \rho_p} \quad (1)$$

where c is the polymer concentration, d is the particle hydrodynamic diameter obtained by dynamic light scattering, and ρ_p is the density of PLGA nanoparticle core (estimated to be 1.27 g cm^{-3} at 20 °C).

Determination of Fluorophore Contents in the Particles. The fluorophore loading (% w/w) of the particles was determined by UV absorbance. The numbers of particles in the stock solutions were first determined by using eq 1. The solution mixtures (~3 × 10^{13} particles/mL) were then freeze−dried, weighed (~0.5 mg), and redissolved in DMSO (1 mL) to extract the encapsulated fluorophores. The resulting mixtures were centrifuged (10 000 × *g*, 5 min) to remove any visible aggregates. The amount of the fluorophores in the solution mixtures were further quantified by absorbance according to our predetermined extinction coefficient values in DMSO ($\varepsilon_{DiD\ at\ 655\ nm}$ = 173 000 M^{-1} cm^{-1} and $\varepsilon_{DiR\ at\ 760\ nm}$ = 207 000 M^{-1} cm^{-1}).

The percentage of fluorophore loading was calculated from the following equation:[28]

$$\%\text{fluorophore loading} = \frac{\text{weight of the encapsulated fluorophore}}{\text{total weight of the particles}} \times 100\% \quad (2)$$

The loading efficiency was calculated from the following equation:[28]

$$\%\text{loading efficiency} = \frac{\text{weight of the encapsulated fluorophore}}{\text{weight of the fluorophore used for the particle assembly}} \times 100\% \quad (3)$$

The number of fluorophores per particle was calculated from the following equation:

$$\text{number of fluorophores per particle} = \frac{\text{weight of the encapsulated fluorophore}}{\text{molecular weight of the fluorophore} \times \text{number of particles}} \quad (4)$$

To accurately determine the amount of the individual fluorophore in FRET-NPs, the absorbance at λ_{max1} and λ_{max2} were first corrected from the degree of spectral overlap of the DiD and DiR fluorophores.[29]

Measurement of Absorbance and Fluorescence. All measurements were recorded in deionized water at room temperature, using a submicrocuvette for absorbance or fluorescence (Starna Cells, Inc., Atascadero, CA). For ease of comparison, all samples were diluted to the same particle number (1 × 10^{12} particles/mL) in deionized water (100 μL). Absorption spectra were collected from a spectrophotometer (Spectramax, Molecular Devices, LLC, Sunnyvale, CA). Fluorescence spectra were measured on a spectrofluorometer (Cary Eclipse, Agilent Technologies, Inc., Santa Clara, CA). The DiD-doped nanoparticles and FRET-NPs were excited at 650 nm, and the DiR-doped nanoparticles were excited at 755 nm. Fluorescence emissions were recorded from 660 to 850 nm with a scanning interval of 0.2 nm. The excitation and emission slit widths were set at 2.5 and 5 nm, respectively.

Measurement of Extinction Coefficient (ε) and Quantum Yield (Φ). The number of particles in stock solutions and the number of fluorophores in each particle were first determined from eqs 1 and 4, respectively. The extinction coefficient of the particles (ε_p) was determined from the Lambert−Beer's law.[30] Note: The extinction coefficient based on the amount of fluorophore (ε_f) was calculated by dividing the ε_p value by the total number of fluorophores in the respective particles.

The relative quantum yield was determined in deionized water by previously described comparative method,[31,32] using Cy5 and Cy7 as the reference standards for DiD- and DiR-doped nanoparticles, respectively.[21] Each particle sample was prepared in a series of four dilutions (0.1−0.5 μM of the fluorophore). The DiD- and DiR-doped nanoparticles were excited at 640 and 740 nm, respectively. The entire fluorescence spectrum (from 660 to 850 nm) was then

recorded and integrated using *Prism* software (GraphPad Software, Inc., La Jolla, CA). The relative quantum yield was then calculated from the following equation as previously described:[33]

$$\Phi = \Phi_R\left(\frac{M}{M_R}\right)\left(\frac{n^2}{n_R{}^2}\right) \quad (5)$$

where Φ and Φ_R are the quantum yields of the sample and its corresponding reference, respectively; M and M_R are the slopes calculated from a plot of the absorbance at excitation wavelength versus the integrated fluorescence spectra, and n is the refractive index of the solvent, i.e., deionized water.

Calculation of Net FRET (nFRET), FRET Ratio (R_{FRET}), and FRET Efficiency (E_{FRET}) of FRET-NPs. FRET signals were converted to the net FRET value (nFRET) as previously described.[34,35] Briefly, the fractional cross-talks of the DiD and DiR fluorophores in the FRET setting were first determined from the following equations:

$$a = \frac{I_{\text{DiD at775nm}(\lambda_{650nm})}}{I_{\text{DiD at668nm}(\lambda_{650nm})}} \quad (6)$$

$$b = \frac{I_{\text{DiR at775nm}(\lambda_{650nm})}}{I_{\text{DiR at775nm}(\lambda_{755nm})}} \quad (7)$$

where a = 0.04 was determined by dividing the fluorescence intensity of DiD-doped nanoparticles (excited at 650 nm) at the acceptor emission λ_{max} (775 nm) with the intensity at the donor emission λ_{max} (668 nm), and b = 0.03 was determined by dividing the fluorescence intensity of DiR-doped nanoparticles at the acceptor emission λ_{max} (775 nm) when excited at 650 nm by the intensity when excited at 755 nm.

The net FRET (nFRET) was then calculated from the following equation:[34]

$$n\text{FRET} = I_{FRET} - a \times I_{DiD} - b \times I_{DiR} \quad (8)$$

where I_{FRET}, I_{DiD}, and I_{DiR} are the fluorescence intensities of FRET-NPs at the FRET, DiD, and DiR settings. The FRET ratio (R_{FRET}) was calculated by dividing the nFRET values by I_{DiD}.[36]

FRET efficiencies (E_{FRET}) were determined according to the donor-based and acceptor-based methods as previously described.[37,38] Briefly, following steady-state fluorescence emission spectra (excited at 650 nm) were recorded: (1) the emission of FRET-NPs (F_{FRET}; recorded at 660−850 nm), (2) emission of DiD-doped nanoparticles consisting of the same total fluorophore contents as the FRET-NPs (F_{DiD}; recorded at 660−850 nm), and (3) the acceptor emission of DiR-doped nanoparticles consisting of the same total fluorophore contents as the FRET-NPs (F_{DiR}; recorded at 660−850 nm). The emission spectra were further integrated using *Prism* software. The donor-based FRET efficiency (E_D) was calculated from the following equation:[37,38]

$$E_D = 1 - \frac{\int_{660}^{774} F_{FRET}\, d(\text{nm})}{\int_{660}^{774} F_{DiD}\, d(\text{nm})} \quad (9)$$

The acceptor-based FRET efficiency (E_A) was calculated from the following equation:[37,38]

$$E_A = \frac{\varepsilon_{\text{DiD at650nm}}}{\varepsilon_{\text{DiR at650nm}}}\left(\frac{\int_{775}^{850} F_{FRET}\ \text{d(nm)} - \int_{775}^{850} F_{DiD}\ \text{d(nm)}}{\int_{775}^{850} F_{DiR}\ \text{d(nm)}} - 1\right) \quad (10)$$

where $\varepsilon_{\text{DiD at 650 nm}}$ and $\varepsilon_{\text{DiR at 650 nm}}$ are the extinction coefficients of DiD- and DiR-doped nanoparticles at 650 nm, respectively.

Comparison of the Brightness of the Particles. The brightness of single-fluorophore doped nanoparticles was determined using a reflectance imaging system (In Vivo system FX, Carestream Health, Inc., Rochester, NY) as described previously.[39] The imaging system was equipped with a halogen lamp (150 W) as an excitation light source. Band pass filters (Carestream Health, Inc., Rochester, NY) were employed to adjust the corresponding excitation wavelengths for DiD (615/645 nm) and DiR (700/740 nm) fluorophores. Briefly, the particles (1×10^{12} particles/mL) suspended in deionized water (100 μL) were added to the wells of a clear-bottom 96-well black plate (Corning Incorporated, Lowell, MA). The plates were then exposed to the excitation light source. The emitted light was collected using the corresponding band-pass filters (Carestream Health, Inc., Rochester, NY) for DiD (680/720 nm) and DiR (770/810 nm). All images were acquired with a single exposure time of 5 min and were further analyzed using Kodak molecular imaging software (Carestream Health, Inc., Rochester, NY). The region of interest (ROI) of individual wells was selected for the determination of the relative fluorescence intensities.

The brightness of particles was also compared with the commercially available quantum dots (QDs-650 and QDs-800) using a spectrofluorometer (Cary Eclipse, Agilent Technologies, Inc., Santa Clara, CA). The samples were first diluted to the same number of particles ($(1-5) \times 10^{12}$ particles/mL) in deionized water (100 μL). For ease of comparison, QDs were prepared in a series of four different particle concentrations ($(1-5) \times 10^{12-14}$ particles/mL) in deionized water (100 μL). The QDs were excited at 465 nm and fluorescence emissions were recorded (from 600 to 850 nm).

MTS Assay. MTS assay was performed as previously described.[40] Both mouse leukemic monocyte macrophage (RAW 264.7) and human embryonic kidney (HEK-293) cell lines were obtained from American Type Culture Collection (Manassas, VA) and maintained in Dulbecco's Modified Eagle Medium (DMEM) supplemented with 10% (v/v) fetal bovine serum (FBS), penicillin (50 000 units/L), and streptomycin (50 mg/L) at 37 °C. The cells (5000/well) were seeded in a clear-bottom 96-well plate (Corning Incorporated, Lowell, MA). After 12 h, fresh medium (150 μL) mixed with FRET-NPs (0.4−2 mg/mL) in PBS (50 μL) was added to the cells and further incubated for 24 h at 37 °C. Cells incubated with PBS served as a negative control. MTS reagent (20 μL) in fresh culture medium (100 μL) was then added to each well, and the cell viability was determined by measuring the absorbance (A) at 490 nm after 1 h. The percentage cell viability relative to the negative control was determined by using the following equation: $(A_{sample})/(A_{control}) \times 100\%$.

In Vitro Hemolysis Assay. The hemocompatibility of the particles was tested on the erythrocytes as previously described.[41] The erythrocytes were isolated from fresh citrated whole human blood by centrifugation (800 × g, 15 min) and further washed with PBS. The stock erythrocyte dispersion (3.5×10^8 cells/mL) in PBS (100 μL) was mixed with FRET-NPs (0.2−2 mg/mL) in PBS (100 μL) and then incubated at 37 °C.

dx.doi.org/10.1021/bc200637h | *Bioconjugate Chem.* 2012, 23, 981−992

Triton X-100 (10% v/v) in deionized water and PBS were used as the positive and negative controls, respectively. After 3 h, the intact erythrocytes were separated by centrifugation (800 × *g*, 15 min) and the absorbance of the supernatant (100 μL) was measured at 540 nm to detect the presence of the released hemoglobin. All the absorption values were corrected for the intrinsic absorbance of the particles. The percentage of hemolysis was calculated using the following equation: $[(A_{sample} - A_{negative})/(A_{positive} - A_{negative}) \times 100]$.

Stability Studies. To determine the long-term colloidal stability, FRET-NPs (1 mg) were first suspended in deionized water (1 mL) and then kept at room temperature. The particle size and the zeta potential were measured by dynamic light scattering (DLS) for 7 days. The physical stability of particles was tested in different biological media as previously described.[42] Briefly, FRET-NPs (1 mg) suspended in deionized water (500 μL) were added to different media (500 μL), including PBS alone, 9.0% (w/v) of BSA in PBS, and 20% (v/v) of FBS in minimum essential medium (MEM). Deionized water was used as a negative control. The solution mixtures were incubated at 37 °C. At different time points, an aliquot of nanoparticle solutions (100 μL) was collected to measure their sizes. Similarly, the changes in the optical properties of the particles (0.1 mg/mL) with time were determined.[17] After each time point, an aliquot of the media (100 μL) was collected, and the fluorescence intensities were recorded between 660 and 850 nm after excitation at 650 nm. The FRET ratio (R_{FRET}) was calculated by dividing the *n*FRET values by I_{DiD}. All the FRET ratio values were normalized according to the corresponding samples at t = 0 h (R_{FRET} = 1).

Biodistribution Studies. Four- to five-week-old female, severe combined immunodeficiency (SCID) hairless outbred (*SHO-Prkdc*^{scid}*Hr*^{hr}) mice (approximately 20 g in weight) were purchased from Charles River Laboratories (Wilmington, MA). The animals were maintained in a pathogen-free and temperature-controlled environment and were provided with sterilized food and water. All the animal experiments were performed according to the guidelines of the Institutional Animal Care and Use Committees (IACUC) at North Dakota State University. For the biodistribution study, mice were injected with the same number of FRET-NPs (5 × 10^{12} particles/mL) in PBS (100 μL) via tail-vein. After 24 h, the mice were euthanized by intraperitoneal injection of pentobarbital (100 mg/kg) and different organs including livers, hearts, bladders, kidneys, spleens, brains, lungs, stomachs, pancreas, and intestines were excised, washed, and imaged using a reflectance imaging system by employing the FRET channel (excited at 615/645 nm and recorded at 770/810 nm). All images were collected with a single exposure time of 5 min and were further processed using Kodak molecular imaging software. Following imaging, each organ was weighed (50 mg), homogenized with DMSO (200 μL), and centrifuged (5000 × *g*, 5 min). The fluorescence intensity of the supernatant (100 μL) was recorded on a spectrofluorometer and the amount of FRET-NPs was quantitatively determined according to the standard curve. The standard curve was generated by mixing known amounts of FRET-NPs in deionized water with the corresponding isolated organs (50 mg) from an uninjected mouse and extracted as described above. All the data were normalized in units of percentage of injected dose per gram of the tissue (% ID/g).

Phantom Studies. For phantom study, the mice were first euthanized by intraperitoneal injection of pentobarbital (100 mg/kg). A glass capillary tube (1.1 × 90 mm) filled with FRET-NPs or DiR-doped nanoparticles (5 × 10^{12} particles/mL) in deionized water (10 μL) was then carefully inserted into the thoracic region via the mouth of the animal. The images were then acquired at the respective channels: DiD (excited at 615/645 nm and recorded at 680/720 nm), DiR (excited at 700/740 nm and recorded at 770/810 nm), and FRET (excited at 615/645 nm and recorded at 770/810 nm). Water-soluble QDs-800 (2.5 × 10^{13} particles/mL) in deionized water (10 μL) was used as a positive control, and the images were acquired with excitation at 445/485 nm and recorded at 770/810 nm. All images were recorded with a single exposure time of 5 min and were further processed using Kodak molecular imaging software.

Imaging Data Processing and Analysis. All the raw images were processed using PixFRET *ImageJ* plug-in freeware as previously described.[43] Briefly, the fractional cross-talk values of DiD (a = 0.09) and DiR (b = 0.26) fluorophores were first determined from eqs 6 and 7, using the phantom containing only the DiD- and DiR-doped nanoparticles (2.10% w/w), respectively. The FRET image of FRET-NPs phantom was then corrected from the fractional cross-talk values, as well as the background fluorescence to obtain the *n*FRET image. For the data analysis, the signal-to-phantom background ratio was determined by dividing the signal intensity of the sample with the phantom background at the ROIs. The phantom images of DiR-doped nanoparticles and QDs-800 were corrected from the background fluorescence. A constant Gaussian blur (2.0) and a threshold (1.0) values were applied to all the images.

RESULTS AND DISCUSSION

Synthesis of the Polymeric Constructs (PLGA-PEG_{3500}-maleimide). The nanoparticles were composed of PLGA-PEG_{3500}-maleimide copolymers (Figure 1A), which were synthesized by reacting an equivalent amount of maleimide-activated poly(ethylene glycol) (Mal-PEG_{3500}-NH_2) with poly-(D,L-lactic-*co*-glycolic acid) carboxylic acid (PLGA-COOH) in DCM.[23] The resulting copolymer was recovered by precipitation in diethyl ether and further washed with methanol to remove the unreacted Mal-PEG_{3500}-NH_2. The final product, PLGA-PEG_{3500}-maleimide, was confirmed by ^{1}H NMR (Figure S1). When compared to the ^{1}H NMR spectrum of PLGA-COOH (Figure S2), an additional peak (−OCH_2CH_2−, s) appeared at 3.64 ppm indicated that the reaction was successful.[23] A small peak observed at 6.70 ppm (−CH═, s) also confirmed the preservation of the maleimide groups.[44] The coupling efficiency of the reaction was calculated based on the relative integration of the peaks at 3.64 and 5.22 ppm for PEG and PLGA, respectively, and was estimated to be approximately 50%.

Particle Assembly. All particles were assembled from the PLGA-PEG_{3500}-maleimide copolymers by the previously described nanoprecipitation method.[25] This method is simple and does not require the use of surfactant or toxic solvent.[45] Nanoparticles of various sizes (65 to 300 nm) can be synthesized simply by changing the solvent parameters[46] and polymer concentrations.[23] To synthesize nanoparticles of less than 100 nm in size, a mixture of copolymer constructs and fluorophores in DMF was added dropwise to deionized water. This procedure has been employed previously to encapsulate a large amount of hydrophobic drug molecules (~18% w/w) in the nanoparticles.[47]

dx.doi.org/10.1021/bc200637h | *Bioconjugate Chem.* 2012, 23, 981−992

Table 1. Physical Properties of Single Fluorophore-Doped Nanoparticles

fluorophore content						
used (% w/w)	loading (% w/w)	loading efficiency (%)	particle size (nm)	zeta potential (mV)	polydispersity	number of fluorophores/particle
0	0.00 ± 0.00	00 ± 0	57 ± 2	−17.0 ± 2.0	0.17 ± 0.02	0
			DiD-doped nanoparticles			
0.05	0.04 ± 0.01	88 ± 9	58 ± 2	−17.5 ± 0.5	0.15 ± 0.05	33
0.10	0.08 ± 0.01	87 ± 11	61 ± 2	−17.7 ± 1.5	0.13 ± 0.04	70
0.25	0.20 ± 0.04	83 ± 13	60 ± 1	−17.7 ± 1.5	0.16 ± 0.05	161
0.50	0.38 ± 0.05	75 ± 10	66 ± 3	−15.4 ± 0.8	0.16 ± 0.04	419
1	0.72 ± 0.09	72 ± 10	68 ± 5	−17.0 ± 0.7	0.14 ± 0.03	756
2	1.46 ± 0.09	73 ± 5	71 ± 4	−16.8 ± 0.2	0.11 ± 0.03	2048
3	2.10 ± 0.17	70 ± 6	84 ± 8	−17.3 ± 0.5	0.17 ± 0.03	4908
			DiR-doped nanoparticles			
0.05	0.04 ± 0.01	90 ± 7	56 ± 3	−15.2 ± 0.7	0.16 ± 0.03	31
0.10	0.08 ± 0.02	88 ± 9	58 ± 4	−16.5 ± 0.8	0.15 ± 0.02	68
0.25	0.20 ± 0.03	80 ± 10	64 ± 2	−16.3 ± 0.9	0.17 ± 0.04	205
0.50	0.38 ± 0.08	76 ± 14	60 ± 3	−18.2 ± 0.3	0.15 ± 0.01	323
1	0.74 ± 0.04	75 ± 4	61 ± 4	−17.1 ± 1.8	0.11 ± 0.02	666
2	1.50 ± 0.18	76 ± 9	72 ± 4	−15.6 ± 2.3	0.12 ± 0.02	2295
3	2.10 ± 0.14	69 ± 5	85 ± 5	−16.0 ± 1.0	0.15 ± 0.03	5104

Physical Characterization of the Single-Fluorophore Doped Nanoparticles. DiD and DiR are carbocyanine derivatives and are conjugated with lipophilic alkyl tails (C_{18}) at the imine nitrogens. The fluorophores were originally developed as organelle sensors for cell membrane, mitochondria, and endoplasmic reticulum.[48,49] To investigate whether particles composed of PLGA-PEG_{3500}-maleimide copolymers could be used as fluorophore carriers, a series of particles encapsulated with various amounts of DiD or DiR fluorophores (0.0−2.10% w/w) were prepared. DiD and DiR fluorophores were chosen because of their extreme hydrophobicity; therefore, hundreds to thousands of the fluorophores could be easily encapsulated inside a single particle (Table 1). Here, all the single fluorophore-doped particles synthesized were less than 100 nm, as the sizes were confirmed by DLS (Table 1) and TEM analysis (Figure 2). There was no significant difference in

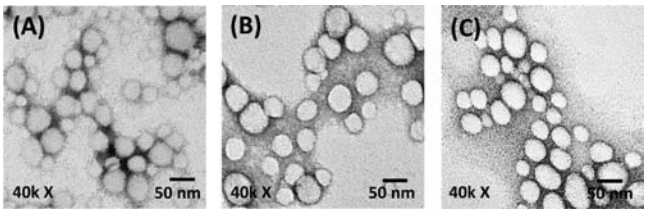

Figure 2. The transmission electron microscope (TEM) images of (A) blank nanoparticles, (B) DiD-doped nanoparticles (0.72% w/w), and (C) DiR-doped nanoparticles (0.74% w/w). The particles were negatively stained with 3% (w/v) uranyl acetate in deionized water (Scale bar = 50 nm).

their zeta potentials, which suggested that the fluorophores were trapped inside the hydrophobic PLGA matrices (Table 1). However, increasing the fluorophore loadings (from 0.0 to 2.10% w/w) resulted in a gradual increase of the particle size (from ∼56 to 85 nm).

Optical Properties of the Single-Fluorophore Doped Nanoparticles. Encapsulating a large number of organic fluorophores in a single particle may cause significant fluorescence self-quenching, presumably because the fluorophores are constrained in close proximity.[50] To compare the optical properties between the single fluorophore-doped nanoparticles, all the particles were first diluted to the same particle concentration (1×10^{12} particles/mL) prior to recording the absorbance and emission spectra. Our result demonstrated that, with increasing the fluorophore loading, both the absorbance and fluorescence emission increased (Figure 3A and B), accompanied with continuous blue-shift and red-shift of the absorption and emission λ_{max}, respectively (Table 2), which suggested that the entrapped fluorophores gradually experienced an increasing hydrophobic environment.[51] Particles encapsulated with ∼0.70% w/w of fluorophores were among the brightest (Figure 3A and B) and were stable from continuous light irradiation (SI Figure S3). On the other hand, significant fluorescence self-quenching was observed in the particles with fluorophore loading ≥0.70% w/w.

To study the quenching effect, we determined the quantum yield (Φ) of the particles as previously described.[33] For particles that consisted of a minimal fluorophore content, i.e., 0.04% w/w, the Φ values were comparable to those of the corresponding free DiD and DiR fluorophores in methanol (Table 2),[21] as well as other reported carbocyanine derivatives.[52] As expected, the Φ values declined with further increase in fluorophore content. Surprisingly, a plot of the normalized fluorescence intensity (according to the total fluorophore content) versus the fluorophore loading revealed that quenching even occurred in particles consisting of low fluorophore content (Figure 3C and D). This suggested that there might be a nonuniform absorption of the incident light by the encapsulated fluorophores inside the particles, as reflected by the linear decrease in the extinction coefficient values (ε_f) increasing fluorophore contents (Table 2). Next, we compared the brightest single fluorophore-doped nanoparticles with the corresponding water-soluble quantum dots (QDs-665 and QDs-800). The optimized DiD- and DiR-doped nanoparticles were more than 100 and 70 times brighter than their corresponding QDs, respectively (Figure 4).

FRET-Based Nanoparticles. FRET is known to be affected by the distance between the donor and acceptor fluorophores and the orientation factor of the employed FRET pair.[12] To determine an optimum fluorophore loading for the efficient

dx.doi.org/10.1021/bc200637h | Bioconjugate Chem. 2012, 23, 981−992

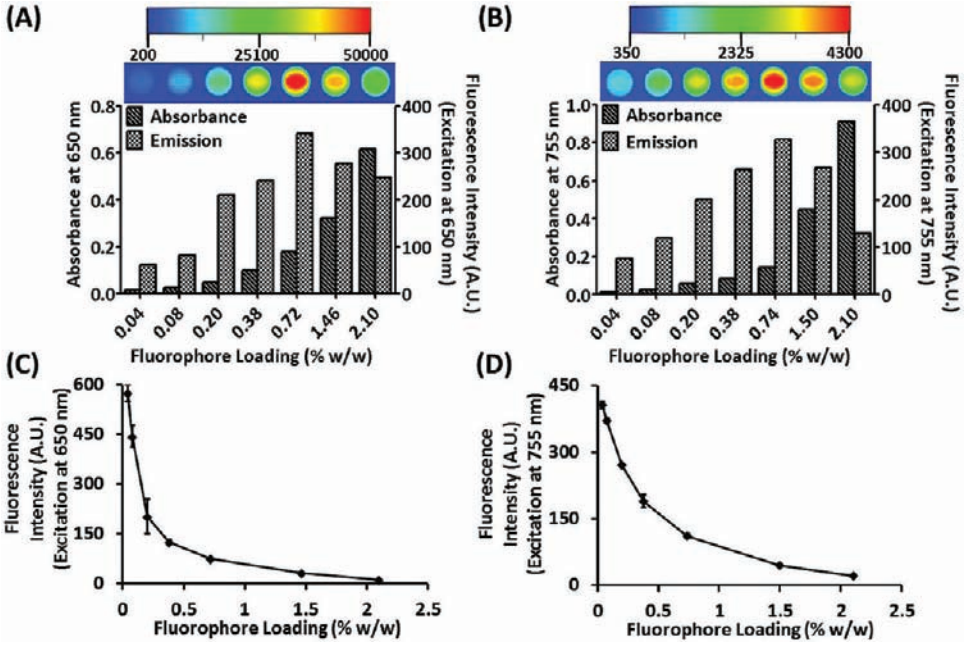

Figure 3. Optical properties of the single fluorophore-doped nanoparticles. A bar chart showing the absorbance and fluorescence emission of (A) DiD- and (B) DiR-doped nanoparticles (0.0−2.10% w/w). All samples consisted of the same number of particles (1×10^{11} particles) in deionized water (100 μL). Insets: The fluorescence images of the particles in a 96-well plate were acquired by a NIRF reflectance imaging system. A plot of the normalized fluorescence intensities of (C) DiD- and (D) DiR-doped nanoparticles versus fluorophore loadings. The fluorescence intensities were normalized to same fluorophore content (400 nM).

Table 2. Optical Properties of Single Fluorophore-Doped Nanoparticles

fluorophore content				extinction coefficient (ε)		
used (% w/w)	loading (% w/w)	absorbance λ_{max} (nm)	emission λ_{max} (nm)	per particle (ε_p) $\times 10^7$ (M^{-1} cm^{-1})	per fluorophore (ε_f) $\times 10^5$ (M^{-1} cm^{-1})[a]	quantum yield (Φ)
			DiD-doped nanoparticles			
0.05	0.04 ± 0.01	652	665	0.84	2.55	0.34
0.10	0.08 ± 0.01	652	665	1.51	2.14	0.27
0.25	0.20 ± 0.04	651	666	2.94	1.82	0.26
0.50	0.38 ± 0.05	650	667	5.99	1.43	0.21
1	0.72 ± 0.09	650	668	10.7	1.42	0.10
2	1.46 ± 0.09	650	668	19.5	0.95	0.05
3	2.10 ± 0.17	649	668	37.1	0.75	0.02
			DiR-doped nanoparticles			
0.05	0.04 ± 0.01	759	769	0.79	2.56	0.46
0.10	0.08 ± 0.02	758	771	1.54	2.27	0.31
0.25	0.20 ± 0.03	755	772	3.43	1.68	0.24
0.50	0.38 ± 0.08	755	774	4.94	1.53	0.16
1	0.74 ± 0.04	755	773	8.61	1.29	0.08
2	1.50 ± 0.18	755	775	27.1	1.18	0.04
3	2.10 ± 0.14	754	781	54.8	1.07	0.02

[a]The extinction coefficient per fluorophore (ε_f) was calculated by dividing by ε_p value with the number of fluorophores per particle.

FRET, a series of particles were synthesized by encapsulating an equal mixture of DiD and DiR but different total fluorophore contents (0.20, 0.38, 0.72, 1.48, and 2.10% w/w) inside our developed polymeric platform. The resulting FRET-NPs were characterized and found to have similar physical properties as the single-fluorophore-doped nanoparticles (Tables 1 and 3). The two absorption maxima, λ_{max1} and λ_{max2}, appearing in the absorption spectra of the FRET-NPs indicated the presence of both DiD and DiR fluorophores, respectively (Figure 5A). It was estimated that all the FRET-NPs were composed of a 1:1 ratio of donor (DiD) and acceptor (DiR) fluorophores (Table 3).

We then compared the optical properties among all the FRET-NPs formulations by recording their absorbance and fluorescence spectra in deionized water (Figure 5A and B). As expected, the absorbance of the particles increased with increasing the total fluorophore content. Increasing the fluorophore loading from 0.20 to 2.10% w/w resulted in a significant red-shift (24 nm) of the acceptor emission λ_{max} (Table 4). It was found that 0.38% w/w of FRET-NPs was among the brightest (Table 4), and similar results were obtained when the FRET intensities were further converted to net FRET (*n*FRET) in order to remove the cross-talk between the DiD and DiR fluorophores.[34] On the other hand, particles

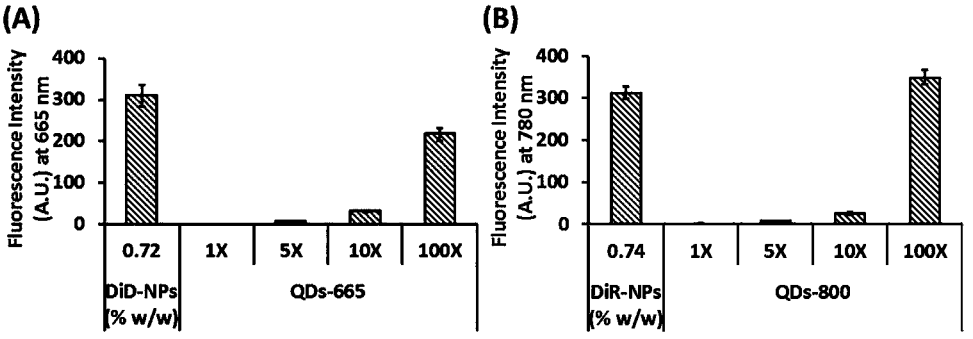

Figure 4. Comparison of fluorescence intensity between the single fluorophore-doped nanoparticles with the water-soluble quantum dots. A bar chart showing the relative fluorescence intensities of (A) DiD-doped nanoparticles (1×10^{11} particles) and QDs-665 ($1 \times 10^{11-13}$ particles) and (B) DiR-doped nanoparticles (1×10^{11} particles) and QDs-800 ($1 \times 10^{11-13}$ particles) in deionized water (100 μL).

Table 3. Physical Properties of FRET-NPs

FRET-NPs (% w/w)	DiD/DiR ratio	particle size (nm)	zeta potential (mV)	polydispersity	total number of fluorophores/particle
0.20	1:1	64 ± 3	−17.3 ± 2.5	0.18 ± 0.02	213
0.38	1:1	69 ± 4	−17.4 ± 2.0	0.19 ± 0.01	478
0.72	1:1	72 ± 3	−16.8 ± 1.5	0.16 ± 0.03	1065
1.48	1:1	84 ± 5	−16.5 ± 3.9	0.17 ± 0.02	3439
2.10	1:1	93 ± 8	−16.4 ± 0.5	0.16 ± 0.04	6563

consisting of 2.10% w/w fluorophore content were most efficient for FRET (Figure 5B), and the results were also confirmed by the calculated donor-based E_{FRET} (E_D) and acceptor-based E_{FRET} (E_A) values (Table 4).[37] The optimized particles (2.10% w/w) were brighter than QD-800 (Figure 5D), but lost some of the brightness (2.5 times dimer) when compared to the 0.38% w/w, presumably because of some self-quenching. To confirm the occurrence of FRET, the particles were further dissolved in DMF and the emission spectra were recorded with excitation at 650 nm. As expected, after decomposition, the FRET emission disappeared (Figure 5C). FRET-NPs also consisted of multiple thiol-activated maleimide groups on the surface. Therapeutic molecules such as antibodys could be attached to the particles in the future (SI Figure S4).

Stability of FRET-NPs. To examine the long-term stability of FRET-NPs, the particles were monitored by DLS for changes in physical behavior. FRET-NPs were found to be stable in deionized water, with no significant changes in both the size and zeta potential for 7 days (Figure 6A).[53] In addition, there was no observable change in the size of FRET-NPs that were stored in PBS only or 10% (v/v) of FBS in MEM media (Figure 6B). However, in the presence of 4.5% (w/v) of BSA, the particles were slightly increased in size after 24 h. This could be due to the adsorption of proteins on the particle surfaces. Similarly, there was a slightly decrease in the normalized R_{FRET} of FRET-NPs when stored in 4.5% (w/v) of BSA in PBS or 10% (v/v) of FBS in MEM culture media,

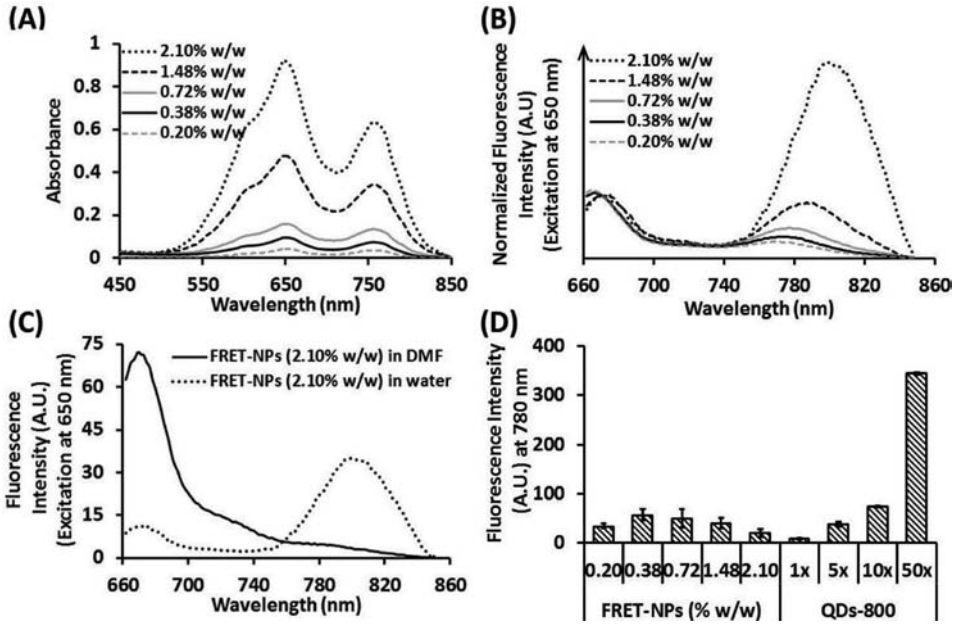

Figure 5. Optical properties of FRET-NPs (0.20−2.10% w/w). (A) Absorption spectra of FRET-NPs (1×10^{11} particles) in deionized water (100 μL). (B) Emission spectra of FRET-NPs (5×10^{11}) in deionized water (100 μL). All emission spectra were normalized at 666 nm and the excitation and emission slit widths were set at 2.5 and 5 nm, respectively. (C) Emission spectra of FRET-NPs (5×10^{11} particles) after dilution in DMF (100 μL) and deionized water (100 μL). (D) Comparison of the *n*FRET intensities of FRET-NPs (5×10^{11} particles) with the fluorescence intensities of quantum dots ($2.5 \times 10^{11-13}$ particles) in deionized water (100 μL).

dx.doi.org/10.1021/bc200637h | *Bioconjugate Chem.* 2012, 23, 981−992

Table 4. Optical Properties of FRET-NPs

FRET-NPs (% w/w)	absorbance λ_{max} (nm)		extinction coefficient (ε) per particle × 10^7 (M^{-1} cm^{-1})		FRET λ_{max} (nm)	FRET intensity	nFRET	R_{FRET}	E_{FRET}	
	λ_{max1}	λ_{max2}	λ_{max1}	λ_{max2}					E_D	E_A
0.20	651	757	2.55	2.20	771	60 ± 7	34 ± 5	0.14 ± 0.012	0.66	0.47
0.38	651	756	5.77	4.47	776	89 ± 15	57 ± 11	0.22 ± 0.021	0.67	0.91
0.72	649	756	9.60	8.09	778	76 ± 23	50 ± 19	0.29 ± 0.089	0.79	1.25
1.48	649	756	28.7	20.6	790	53 ± 11	40 ± 10	0.70 ± 0.144	0.90	1.70
2.10	649	756	55.3	38.1	795	24 ± 8	20 ± 8	2.25 ± 0.490	0.97	2.30

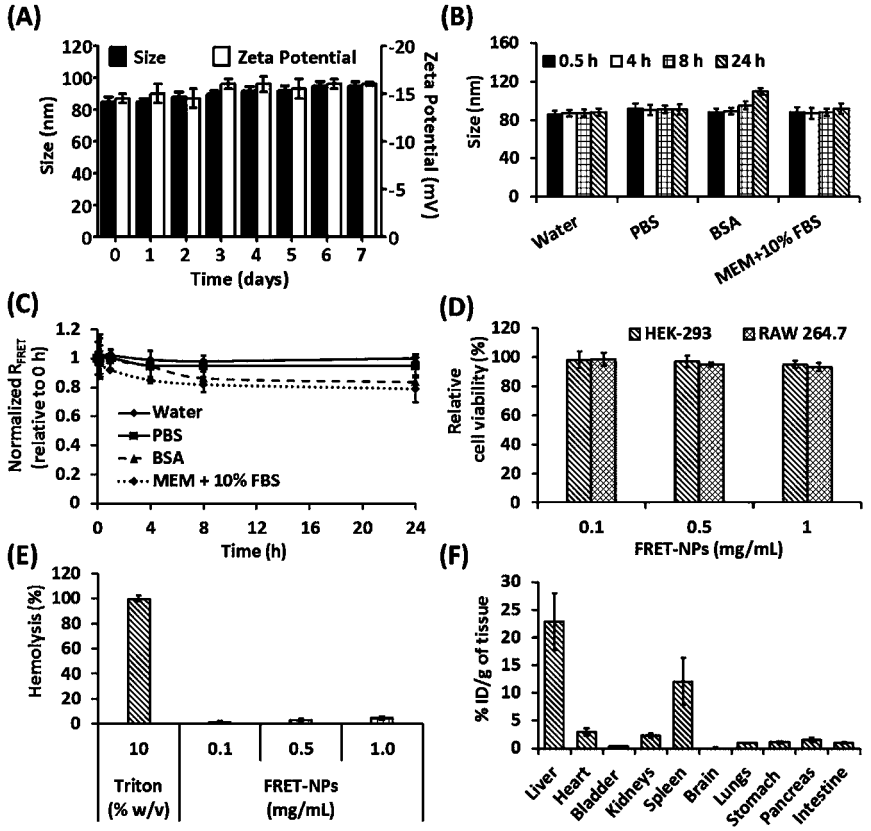

Figure 6. (A) Colloidal stability of FRET-NPs (1 mg/mL) in deionized water at room temperature. The size (nm) and zeta potential (mV) of the particles were measured over a period of 7 days. (B) Bar chart showing the temporal changes in the size of FRET-NPs (1 mg/mL) in different biological media at 37 °C. (C) Comparison of the normalized FRET ratio (Normalized R_{FRET}) of FRET-NPs (0.1 mg/mL) versus time in different biological media at 37 °C. The R_{FRET} was normalized according to the corresponding samples at t = 0 h. (D) Relative cell viability of RAW 264.7 and HEK-293 cells in the presence of FRET-NPs at 24 h. Cell viability was determined by MTS assay. (E) In vitro hemolysis assay. The particles were incubated with the RBCs for 3 h at 37 °C, and the amount of released hemoglobin was determined by absorbance at 540 nm. The results were expressed as the percentage of hemolysis with respect to the positive control (Triton X-100). (F) Bar chart showing the organ distribution at 24 h after intravenous administration of FRET-NPs (5×10^{12}/mL) in PBS (100 μL) to the SCID mice (n = 3, mean ± SEM).

which suggested that there might be some leakage of encapsulated fluorophores from the particles with time (Figure 6C).

Biocompatibility of FRET-NPs. Next, we investigated the biocompatibility of FRET-NPs using MTS assay (Figure. 6D). Mouse leukemic monocyte macrophage (RAW 264.7) and human embryonic kidney (HEK-293) cells were used as the model phagocytic and nonphagocytic cell lines. After 24 h of incubation with FRET-NPs, no significant difference was observed in the cell viability, suggesting that they were nontoxic.

We also studied the hemocompatibility of FRET-NPs. According to the standard of the American Society for Testing and Materials (ASTM), if the percentage of hemolysis is <5%, the material is considered to cause damage to the erythrocytes.[41] Here, hemolysis assay was performed using isolated erythrocytes from the citrated whole human blood as previously described.[41] Triton X-100 and PBS were used as the positive and negative controls, respectively. The percentage of hemolysis increased in a concentration-dependent manner (Figure 6E), with 4.5% of hemolysis in the sample containing the highest concentration (1 mg/mL) of FRET-NPs. Our results indicated that FRET-NPs did not induce any damage to erythrocytes and thus were considered to be hemocompatible.

Biodistribution of FRET-NPs. Next, we studied the biodistribution of FRET-NPs. To prevent the possible interaction of nanoparticles with the serum proteins, the maleimide groups on the particle surfaces were first quenched

dx.doi.org/10.1021/bc200637h | Bioconjugate Chem. 2012, 23, 981–992

by reacting with cysteine, prior to injecting the FRET-NPs to the SCID mice (n = 3) via tail-vein. Ellman's assay confirmed that nearly 85% of initial maleimide groups were successfully quenched (SI Table S2). Similar to other nanoparticles, FRET-NPs showed a typical tissue distribution pattern with a majority of uptake in the liver and spleen at 24 h after injection (Figure 6F).[54] The FRET signal in these organs indirectly suggested that FRET-NPs were remaining intact in the body (SI Figure S5). While not a focus of this study, the length and terminal functional groups of PEG chains could be varied to bypass the uptake from the reticuloendothelial system (including liver and spleen) in the future.[54]

Phantom Studies. Prior to administration of FRET-NPs in a preclinical animal model for imaging, phantom studies were performed to evaluate their efficacy as an imaging agent. An animal phantom was constructed to simulate the tissue fluorescence while imaging. The phantom was composed of a capillary tube prefilled with FRET-NPs, DiR-doped nanoparticles, or QDs-800 in deionized water, which was inserted into the thoracic region of a SCID mouse via its mouth (Figure 7). FRET-NPs consisting of 2.10% w/w fluorophore content

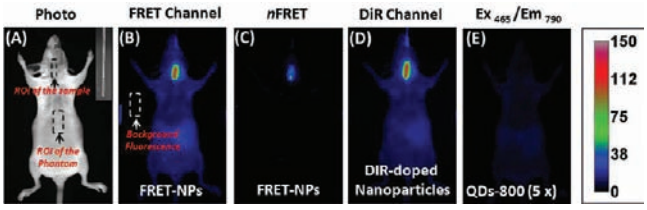

Figure 7. Phantom studies. (A) Photo, (B) FRET, and (C) nFRET images of a mouse inserted with a glass capillary tube (1.1 × 90 mm) filled with FRET-NPs in deionized water (5×10^{12} particles/mL, 10 μL). The fluorescence images of a mouse inserted with (D) DiR-doped nanoparticles (5×10^{12} particles/mL, 10 μL) and (E) QDs-800 (2.5×10^{13} particles/mL, 10 μL). For the data analysis, all the images were corrected from the corresponding background fluorescence. The signal-to-phantom background ratio was determined by dividing the signal intensity of the samples with the phantom at the regions of interest (ROIs).

were chosen in this study. These particles had the highest FRET efficiency (Table 4) and thus were considered more applicable for FRET imaging. In the present study, both the raw FRET image of FRET-NPs and NIRF image of DiR-doped nanoparticles showed similar brightness and signal-to-phantom background ratio (1:11) and were also more sensitive than the QDs-800 (Figure 7). Our results indicated that FRET-NPs had no advantage over the DiR-doped nanoparticles alone in terms of the detection sensitivity and the ability to increase the contrast between the tested sample and the animal. On the other hand, when the FRET signal was converted into nFRET as previously described,[34] the processed image of the FRET-NPs showed significant improvement of the signal-to-phantom background ratio (from 1:11 to 1:39), presumably as a result of removing the fractional cross-talk of the fluorophores and reducing the background contributed by the phantom (Figure 7). Similar results were also obtained when agarose was used as the substitute for the phantom (SI Figure S6). Overall, our results suggested that FRET-NPs can be used for time-resolved imaging in the future, which will further improve the spatial and temporal resolution, by discriminating against light scattering, reflection, autofluorescence, and extraneous prompt fluorophores.[55]

CONCLUSION

Numerous types of near-infrared (NIR) fluorescent materials such as organic fluorophores,[56] rare-earth emitters,[57] quantum dots,[7] gold nanoparticles,[58] long circulating polymers with tagged fluorophore,[59] and fluorescent proteins[60] have been employed for in vivo imaging. However, there is only a limited number of FRET-based contrast agents developed for in vivo NIR imaging. In the present study, we investigated polymeric nanoparticles composed of PLGA-PEG_{3500}-maleimide copolymers as a fluorophore carrier and DiD and DiR fluorophores as the FRET pair. The particles (FRET-NPs) were synthesized by the nanoprecipitation method. The energy transfer was found to be more efficient in particles that consisted of higher fluorophore contents. The optimized FRET-NPs were brighter than the quantum dots, stable in biological media, and hemocompatible. Most importantly, the energy transfer from DiD (donor) to DiR (acceptor) fluorophore resulted in a large Stokes shift (>100 nm) between the excitation and emission maxima. Similar to other nanoparticles, FRET-NPs revealed the expected tissue distribution in the mice model. For proof-of-principle, an animal phantom was also constructed to demonstrate the potential imaging application of FRET-NPs. Our results showed that simply applying eq 8 during image processing would significantly improve the signal-to-phantom background ratio.

ASSOCIATED CONTENT

Supporting Information

Experimental procedures of quenching the maleimide groups of FRET-NPs and preparation of the IgG-conjugated FRET-NPs. Tables showing the optical properties of FRET pairs and results of the Ellman's assay. ^{1}H NMR spectra of PLGA-PEG-maleimide and PLGA copolymer. Photostability studies, SDS-PAGE gel of IgG-conjugated FRET-NPs, agarose phantom studies, and ex vivo organ imaging. This material is available free of charge via the Internet at http://pubs.acs.org.

AUTHOR INFORMATION

Corresponding Author

*E-mail: Shek.law@ndsu.edu.

Notes

The authors declare no competing financial interest.

ACKNOWLEDGMENTS

The authors would like to thank Erin Nyren-Erickson for editorial assistance. This research was supported in part by North Dakota EPSCoR Program, Department of Pharmaceutical Sciences (NDSU), and Darryle and Clare Schoepp Research Fund to B.L.

REFERENCES

(1) Bremer, C., Ntziachristos, V., and Weissleder, R. (2003) Optical-based molecular imaging: contrast agents and potential medical applications. *Eur. Radiol. 13*, 231−43.

(2) Ntziachristos, V., Bremer, C., and Weissleder, R. (2003) Fluorescence imaging with near-infrared light: new technological advances that enable in vivo molecular imaging. *Eur. Radiol. 13*, 195−208.

(3) Peng, X., Song, F., Lu, E., Wang, Y., Zhou, W., Fan, J., and Gao, Y. (2005) Heptamethine cyanine dyes with a large Stokes shift and strong fluorescence: a paradigm for excited-state intramolecular charge transfer. *J. Am. Chem. Soc. 127*, 4170−1.

(4) Bertolino, C. A., Caputo, G., Barolo, C., Viscardi, G., and Coluccia, S. (2006) Novel heptamethine cyanine dyes with large Stoke's shift for biological applications in the near infrared. *J. Fluoresc. 16*, 221−5.
(5) Altinoglu, E. I., and Adair, J. H. (2010) Near infrared imaging with nanoparticles. *Wiley Interdiscip. Rev. Nanomed. Nanobiotechnol. 2*, 461−77.
(6) Luo, S., Zhang, E., Su, Y., Cheng, T., and Shi, C. (2011) A review of NIR dyes in cancer targeting and imaging. *Biomaterials 32*, 7127−38.
(7) Kim, S., Lim, Y. T., Soltesz, E. G., De Grand, A. M., Lee, J., Nakayama, A., Parker, J. A., Mihaljevic, T., Laurence, R. G., Dor, D. M., Cohn, L. H., Bawendi, M. G., and Frangioni, J. V. (2004) Near-infrared fluorescent type II quantum dots for sentinel lymph node mapping. *Nat. Biotechnol. 22*, 93−7.
(8) Rzigalinski, B. A., and Strobl, J. S. (2009) Cadmium-containing nanoparticles: perspectives on pharmacology and toxicology of quantum dots. *Toxicol. Appl. Pharmacol. 238*, 280−8.
(9) He, X., Wang, K., and Cheng, Z. (2010) In vivo near-infrared fluorescence imaging of cancer with nanoparticle-based probes. *Wiley Interdiscip. Rev. Nanomed. Nanobiotechnol. 2*, 349−66.
(10) Koo, H., Huh, M. S., Ryu, J. H., Lee, D.-E., Sun, I.-C., Choi, K., Kim, K., and Kwon, I. C. (2011) Nanoprobes for biomedical imaging in living systems. *Nano Today 6*, 204−220.
(11) Jiang, S., Gnanasammandhan, M. K., and Zhang, Y. (2010) Optical imaging-guided cancer therapy with fluorescent nanoparticles. *J. R. Soc. Interface 7*, 3−18.
(12) Wang, L., and Tan, W. (2006) Multicolor FRET silica nanoparticles by single wavelength excitation. *Nano Lett. 6*, 84−8.
(13) Lakowicz, J. R. (1999) *Principle of fluorescence spectroscopy*, 2nd ed., Kluwer Academic/Plenum Publishers, New York.
(14) Day, R. N., Periasamy, A., and Schaufele, F. (2001) Fluorescence resonance energy transfer microscopy of localized protein interactions in the living cell nucleus. *Methods 25*, 4−18.
(15) Zhang, S., Metelev, V., Tabatadze, D., Zamecnik, P. C., and Bogdanov, A., Jr. (2008) Fluorescence resonance energy transfer in near-infrared fluorescent oligonucleotide probes for detecting protein-DNA interactions. *Proc. Natl. Acad. Sci. U. S. A. 105*, 4156−61.
(16) Chen, H., Kim, S., He, W., Wang, H., Low, P. S., Park, K., and Cheng, J. X. (2008) Fast release of lipophilic agents from circulating PEG-PDLLA micelles revealed by in vivo forster resonance energy transfer imaging. *Langmuir 24*, 5213−7.
(17) Lu, J., Owen, S. C., and Shoichet, M. S. (2011) Stability of self-assembled polymeric micelles in serum. *Macromolecules 44*, 6002−6008.
(18) Chen, H., Kim, S., Li, L., Wang, S., Park, K., and Cheng, J. X. (2008) Release of hydrophobic molecules from polymer micelles into cell membranes revealed by Forster resonance energy transfer imaging. *Proc. Natl. Acad. Sci. U. S. A. 105*, 6596−601.
(19) Lee, S., Park, K., Lee, S. Y., Ryu, J. H., Park, J. W., Ahn, H. J., Kwon, I. C., Youn, I. C., Kim, K., and Choi, K. (2008) Dark quenched matrix metalloproteinase fluorogenic probe for imaging osteoarthritis development in vivo. *Bioconjugate Chem. 19*, 1743−7.
(20) Gref, R., Minamitake, Y., Peracchia, M. T., Trubetskoy, V., Torchilin, V., and Langer, R. (1994) Biodegradable long-circulating polymeric nanospheres. *Science 263*, 1600−3.
(21) Texier, I., Goutayer, M., Da Silva, A., Guyon, L., Djaker, N., Josserand, V., Neumann, E., Bibette, J., and Vinet, F. (2009) Cyanine-loaded lipid nanoparticles for improved in vivo fluorescence imaging. *J. Biomed. Opt. 14*, 054005.
(22) Peng, X., Song, F., Lu, E., Wang, Y., Zhou, W., Fan, J., and Gao, Y. (2005) Heptamethine cyanine dyes with a large Stokes shift and strong fluorescence: a paradigm for excited-state intramolecular charge transfer. *J. Am. Chem. Soc. 127*, 4170−1.
(23) Cheng, J., Teply, B. A., Sherifi, I., Sung, J., Luther, G., Gu, F. X., Levy-Nissenbaum, E., Radovic-Moreno, A. F., Langer, R., and Farokhzad, O. C. (2007) Formulation of functionalized PLGA-PEG nanoparticles for in vivo targeted drug delivery. *Biomaterials 28*, 869−76.
(24) Townsend, S. A., Evrony, G. D., Gu, F. X., Schulz, M. P., Brown, R. H., Jr., and Langer, R. (2007) Tetanus toxin C fragment-conjugated nanoparticles for targeted drug delivery to neurons. *Biomaterials 28*, 5176−84.
(25) Fessi, H., Puisieux, F., Devissaguet, J. P., Ammoury, N., and Benita, S. (1989) Nanocapsule formation by interfacial polymer deposition following solvent displacement. *Int. J. Pharm. 55*, R1−R4.
(26) Panyam, J., Sahoo, S. K., Prabha, S., Bargar, T., and Labhasetwar, V. (2003) Fluorescence and electron microscopy probes for cellular and tissue uptake of poly(D,L-lactide-co-glycolide) nanoparticles. *Int. J. Pharm. 262*, 1−11.
(27) Vauthier, C., Schmidt, C., and Couvreur, P. (1999) Measurement of the density of polymeric nanoparticulate drug carriers by isopycnic centrifugation. *J. Nanopart. Res. 1*, 411−418.
(28) Chen, Y., Wang, F., and Benson, H. A. (2008) Effect of formulation factors on incorporation of the hydrophilic peptide dalargin into PLGA and mPEG-PLGA nanoparticles. *Biopolymers 90*, 644−50.
(29) Mujumdar, R. B., Ernst, L. A., Mujumdar, S. R., Lewis, C. J., and Waggoner, A. S. (1993) Cyanine dye labeling reagents: sulfoindocyanine succinimidyl esters. *Bioconjugate Chem. 4*, 105−11.
(30) Yu, W. W., Qu, L., Guo, W., and Peng, X. (2003) Experimental determination of the extinction coefficient of CdTe, CdSe, and CdS nanocrystals. *Chem. Mater. 15*, 2854−2860.
(31) Bringley, J. F., Penner, T. L., Wang, R., Harder, J. F., Harrison, W. J., and Buonemani, L. (2008) Silica nanoparticles encapsulating near-infrared emissive cyanine dyes. *J. Colloid Interface Sci. 320*, 132−9.
(32) Russin, T. J., Altinoglu, E. I., Adair, J. H., and Eklund, P. C. (2010) Measuring the fluorescent quantum efficiency of indocyanine green encapsulated in nanocomposite particulates. *J. Phys.: Condens. Matter 22*, 334217.
(33) Herz, E., Marchincin, T., Connelly, L., Bonner, D., Burns, A., Switalski, S., Wiesner, U. Relative quantum yield measurements of coumarin encapsulated in core-shell silica nanoparticles. *J. Fluoresc. 20*, 67−72.
(34) Xia, Z., and Liu, Y. (2001) Reliable and global measurement of fluorescence resonance energy transfer using fluorescence microscopes. *Biophys. J. 81*, 2395−402.
(35) Kaufmann, A. M., Goldman, S. D., and Krise, J. P. (2009) A fluorescence resonance energy transfer-based approach for investigating late endosome-lysosome retrograde fusion events. *Anal. Biochem. 386*, 91−7.
(36) Feinstein, T. N., Wehbi, V. L., Ardura, J. A., Wheeler, D. S., Ferrandon, S., Gardella, T. J., and Vilardaga, J. P. (2011) Retromer terminates the generation of cAMP by internalized PTH receptors. *Nat. Chem. Biol. 7*, 278−84.
(37) Grunberg, R., Ferrar, T. S., van der Sloot, A. M., Constante, M., and Serrano, L. Building blocks for protein interaction devices. *Nucleic Acids Res. 38*, 2645−62.
(38) Teo, Y. N., and Kool, E. T. (2009) Polyfluorophore excimers and exciplexes as FRET donors in DNA. *Bioconjugate Chem. 20*, 2371−80.
(39) Law, B., Weissleder, R., and Tung, C. H. (2007) Protease-sensitive fluorescent nanofibers. *Bioconjugate Chem. 18*, 1701−4.
(40) Law, B., Quinti, L., Choi, Y., Weissleder, R., and Tung, C. H. (2006) A mitochondrial targeted fusion peptide exhibits remarkable cytotoxicity. *Mol. Cancer Ther. 5*, 1944−9.
(41) Dobrovolskaia, M. A., Clogston, J. D., Neun, B. W., Hall, J. B., Patri, A. K., and McNeil, S. E. (2008) Method for analysis of nanoparticle hemolytic properties in vitro. *Nano Lett 8*, 2180−7.
(42) Fang, R. H., Aryal, S., Hu, C. M., and Zhang, L. (2010) Quick synthesis of lipid-polymer hybrid nanoparticles with low polydispersity using a single-step sonication method. *Langmuir 26*, 16958−62.
(43) Feige, J. N., Sage, D., Wahli, W., Desvergne, B., and Gelman, L. (2005) PixFRET, an ImageJ plug-in for FRET calculation that can accommodate variations in spectral bleed-throughs. *Microsc. Res. Technol. 68*, 51−8.
(44) Toti, U. S., Guru, B. R., Grill, A. E., and Panyam, J. (2010) Interfacial activity assisted surface functionalization: a novel approach

to incorporate maleimide functional groups and cRGD peptide on polymeric nanoparticles for targeted drug delivery. *Mol. Pharmaceutics 7*, 1108−17.
(45) Bilati, U., Allemann, E., and Doelker, E. (2005) Nanoprecipitation versus emulsion-based techniques for the encapsulation of proteins into biodegradable nanoparticles and process-related stability issues. *AAPS PharmSciTech 6*, E594−604.
(46) Galindo-Rodriguez, S., Allemann, E., Fessi, H., and Doelker, E. (2004) Physicochemical parameters associated with nanoparticle formation in the salting-out, emulsification-diffusion, and nanoprecipitation methods. *Pharm. Res. 21*, 1428−39.
(47) Dhar, S., Gu, F. X., Langer, R., Farokhzad, O. C., and Lippard, S. J. (2008) Targeted delivery of cisplatin to prostate cancer cells by aptamer functionalized Pt(IV) prodrug-PLGA-PEG nanoparticles. *Proc. Natl. Acad. Sci. U. S. A. 105*, 17356−61.
(48) Garcia-Saez, A. J., Chiantia, S., and Schwille, P. (2007) Effect of line tension on the lateral organization of lipid membranes. *J. Biol. Chem. 282*, 33537−44.
(49) Han, J., Goldstein, L. A., Gastman, B. R., and Rabinowich, H. (2006) Interrelated roles for Mcl-1 and BIM in regulation of TRAIL-mediated mitochondrial apoptosis. *J. Biol. Chem. 281*, 10153−63.
(50) Law, B., Curino, A., Bugge, T. H., Weissleder, R., and Tung, C. H. (2004) Design, synthesis, and characterization of urokinase plasminogen-activator-sensitive near-infrared reporter. *Chem. Biol. 11*, 99−106.
(51) Altinoglu, E. I., Russin, T. J., Kaiser, J. M., Barth, B. M., Eklund, P. C., Kester, M., and Adair, J. H. (2008) Near-infrared emitting fluorophore-doped calcium phosphate nanoparticles for in vivo imaging of human breast cancer. *ACS Nano 2*, 2075−84.
(52) Lin, Y., Weissleder, R., and Tung, C. H. (2002) Novel near-infrared cyanine fluorochromes: synthesis, properties, and bioconjugation. *Bioconjugate Chem. 13*, 605−10.
(53) Schadlich, A., Rose, C., Kuntsche, J., Caysa, H., Mueller, T., Gopferich, A., and Mader, K. (2011) How stealthy are PEG-PLA nanoparticles? An NIR in vivo study combined with detailed size measurements. *Pharm. Res. 28*, 1995−2007.
(54) Gu, F., Zhang, L., Teply, B. A., Mann, N., Wang, A., Radovic-Moreno, A. F., Langer, R., and Farokhzad, O. C. (2008) Precise engineering of targeted nanoparticles by using self-assembled biointegrated block copolymers. *Proc. Natl. Acad. Sci. U. S. A. 105*, 2586−91.
(55) Akers, W., Lesage, F., Holten, D., and Achilefu, S. (2007) In vivo resolution of multiexponential decays of multiple near-infrared molecular probes by fluorescence lifetime-gated whole-body time-resolved diffuse optical imaging. *Mol. Imaging 6*, 237−46.
(56) Becker, A., Hessenius, C., Licha, K., Ebert, B., Sukowski, U., Semmler, W., Wiedenmann, B., and Grotzinger, C. (2001) Receptor-targeted optical imaging of tumors with near-infrared fluorescent ligands. *Nat. Biotechnol. 19*, 327−31.
(57) Bouzigues, C., Gacoin, T., and Alexandrou, A. (2011) Biological applications of rare-earth based nanoparticles. *ACS Nano 5*, 8488−505.
(58) Wu, X., He, X., Wang, K., Xie, C., Zhou, B., and Qing, Z. (2010) Ultrasmall near-infrared gold nanoclusters for tumor fluorescence imaging in vivo. *Nanoscale 2*, 2244−9.
(59) Hsiao, J. K., Law, B., Weissleder, R., and Tung, C. H. (2006) In-vivo imaging of tumor associated urokinase-type plasminogen activator activity. *J. Biomed. Opt. 11*, 34013.
(60) Shcherbo, D., Merzlyak, E. M., Chepurnykh, T. V., Fradkov, A. F., Ermakova, G. V., Solovieva, E. A., Lukyanov, K. A., Bogdanova, E. A., Zaraisky, A. G., Lukyanov, S., and Chudakov, D. M. (2007) Bright far-red fluorescent protein for whole-body imaging. *Nat. Methods 4*, 741−6.

Bioconjugate Chemistry

Article

pubs.acs.org/bc

Lower Rim Guanidinocalix[4]arenes: Macrocyclic Nonviral Vectors for Cell Transfection

Valentina Bagnacani,[†,§] Valentina Franceschi,[‡,§] Laura Fantuzzi,[†] Alessandro Casnati,[†] Gaetano Donofrio,[*,‡] Francesco Sansone,[*,†] and Rocco Ungaro[†]

[†]Dipartimento di Chimica Organica e Industriale, Università di Parma, Parco Area delle Scienze 17/A, I-43124, Parma, Italy

[‡]Dipartimento di Salute Animale, Università degli Studi di Parma, Via del Taglio 6, I-43126 Parma, Italy

Supporting Information

ABSTRACT: Guanidinium groups were introduced through a spacer at the lower rim of calix[4]arenes in the cone conformation to give new potential nonviral vectors for gene delivery. Several structural modifications were explored, such as the presence or absence of a macrocyclic scaffold, lipophilicity of the backbone, length of the spacer, and nature of the charged groups, in order to better understand the factors which affect the DNA condensation ability and transfection efficiency of these derivatives. The most interesting compound was a calix[4]arene unsubstituted at the upper rim and having four guanidinium groups linked at the lower rim through a three carbon atom spacer. This compound, when formulated with DOPE, showed low toxicity and transfection efficiency higher than the commercially available lipofectamine LTX in the treatment of human Rhabdomiosarcoma and Vero cells. Most of the investigated compounds showed a tendency to self-aggregate in pure water or in the presence of salts, as evidenced by NMR and AFM studies, and it was found that the ability to condense DNA plasmids in nanometric globules is a necessary but not sufficient condition for transfection. The superiority of macrocyclic vectors over linear Gemini-type analogues and of guanidinium compared to other ammonium head groups in determining the biological activity of the vectors was also ascertained.

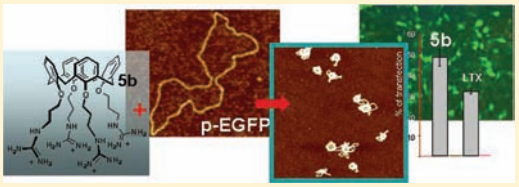

INTRODUCTION

The design and synthesis of new nonviral vectors for cell transfection as an alternative to viruses is still an active area of research,[1−3] due to the well-known problems related to the use of viruses, such as high toxicity, immunogenicity, and potential mutagenicity, and the limits experienced by the currently available synthetic gene delivery systems, such as poor efficiency and selectivity together with a not always negligible cytotoxicity. One of the most successful approaches in this field is the combination of a cationic lipid (cytofectin) with a neutral colipid,[4] called "helper lipid", because it allows a good balance between efficiency and toxicity. Since the first studies reported by Felgner,[5] cationic lipids appear still as the most effective and widely exploited vectors for transfection protocols.[1−3,6] Other systems, in particular based on polymers[1,7−9] and dendrimers[1,10−12] but also on nanoparticles[1,13,14] and, more recently, macrocycles,[15−18] have been tested and are used for these purposes. In the case of macrocyclic scaffolds, their conformational features can be exploited to obtain more preorganized vectors with possible positive effects on transfection efficiency. Cyclodextrins functionalized with cationic groups have been proposed as promising gene ligands and vectors,[18−25] but before them, we reported several calixarene derivatives as the first examples of cationic lipids based on a macrocyclic structure. These compounds (e.g., **I**) were calix[*n*]arenes bearing guanidinium groups directly linked to the aromatic nuclei (upper rim)[16,26] able to condense plasmid and linear DNA and to perform cell transfection in a way which resulted strongly dependent on the macrocycle size, lipophilicity, and conformation. Unfortunately, they were characterized by low transfection efficiency and high cytotoxicity,[16] especially at the vector concentration required for observing cell transfection (10−20 μM), even in the presence of the helper lipid DOPE[27] (dioleoylphosphatidylethanolamine).

With the aim of improving the transfection properties of this new type of nonviral vectors, we decided to shift the cationic head groups from the upper to the lower rim, privileging the calix[4]arene platform since the previous work with upper rim guanidinocalixarenes had shown that the calix[6]- and calix[8]-arene derivatives were not able to compact DNA and give transfection.[16] This manuscript reports the full details of the studies performed in our laboratories on lower rim guanidinocalix[4]arenes, which were partly described in a preliminary communication.[28]

EXPERIMENTAL SECTION

Procedures for DNA preparation, gel electrophoresis, melting curve determination, fluorescence and AFM experiments, cell culture, transient transfection, luciferase reporter, and MTT survival assays are reported in Supporting Information. Here, we report the procedure corresponding to the last step of the

Received: December 23, 2011
Revised: February 16, 2012
Published: April 2, 2012

Chart 1. Upper rim guanidinocalix[4]arenes

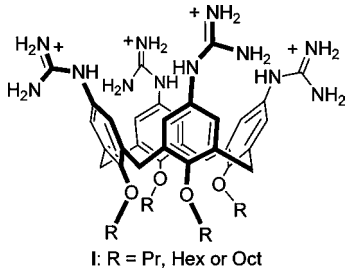

synthesis of the ligands and their characterization. Synthetic procedures for all the new intermediates and their characterization are reported in Supporting Information.

Melting points were determined on an electrothermal apparatus in capillaries sealed under nitrogen. ^{1}H and ^{13}C NMR spectra were recorded on Bruker AC300, AV300, and AV400 spectrometers. Partially deuterated solvents were used as internal standards; for ^{1}H NMR spectra recorded in D_2O at values higher than the room temperature, the correction of chemical shifts was performed using the expression $\delta = 5.060 - 0.0122 \times T$ (°C) + $(2.11 \times 10^{-5}) \times T^2$ (°C) to determine the resonance frequency of water protons.[29] MS-ESI spectra were recorded on a Waters single quadrupole instrument SQ detector. HRMS-ESI spectra were recorded on an LTQ Orbitrap XL instrument. Elemental analyses were performed using a Termoquest 1112 CHN instrument and are reported as percentages. TLC was performed on Merck 60 F_{254} silica gel and flash column chromatography on 230−400 mesh Merck 60 silica gel.

General Procedure for the Synthesis of the Guanidino-Calixarenes and Guanidino-Gemini from the Corresponding Boc Protected Precursors. Concentrated HCl (10 equiv for each Boc group) was added dropwise to a solution of the protected guanidinocalixarenes or guanidinylated Gemini derivatives in 1,4-dioxane (0.1 mmol/10 mL). The reaction mixture was stirred for 24−72 h, and the solvent was removed under reduced pressure to obtain the pure product.

5,11,17,23-Tetra-*tert*-butyl-25,26,27,28-tetrakis(3-guanidiniumpropoxy)calix[4]arene, Tetrachloride (5a). The pure compound was obtained as a white powder in quantitative yield. Hygroscopic. Mp >250 °C dec.; ^{1}H NMR (300 MHz, D_2O) δ = 7.02 (s, 8H, Ar*H*), 4.33 (d, J = 12.3 Hz, 4H, ArCH_2Ar), 3.99 (t, J = 7.7 Hz, 8H, OCH_2), 3.38−3.29 (m, 12H, OCH$_2$CH$_2$CH_2 and ArCH_2Ar), 2.29−2.25 (m, 8H, OCH$_2$CH_2), 1.10 (s, 36H, *t*Bu); ^{13}C NMR (75 MHz, CD_3OD) δ = 158.7, 154.4, 146.1, 135.0, 126.4, 73.4, 40.0, 34.8, 32.3, 32.0, 30.9. MS (ESI) m/z calcd for $C_{60}H_{96}N_{12}O_4Cl_4$: 1045.7 [M-3H-4Cl]$^+$; found, 1045.7. Elemental analysis calcd (%) for $C_{60}H_{96}N_{12}O_4Cl_4 \times 4H_2O$: C 57.04, H 8.30, N 13.30; found, C 56.90, H 7.95, N 12.92.

25,26,27,28-Tetrakis(3-guanidiniumpropoxy)calix[4]arene, Tetrachloride (5b). The pure compound was obtained as a white powder in quantitative yield. Hygroscopic. Mp >250 °C dec.; ^{1}H NMR (300 MHz, D_2O) δ = 6.86−6.80 (m, 8H, Ar*H*), 6.80−6.70 (m, 4H, Ar*H*), 4.40 (d, J = 13.3 Hz, 4H, ArCH_2Ar), 4.08 (t, J = 7.0 Hz, 8H, OCH_2), 3.40−3.33 (m, 12H, OCH$_2$CH$_2$CH_2 and ArCH_2Ar), 2.25 (quint, J = 6.9 Hz, 8H, OCH$_2$CH_2); ^{13}C NMR (75 MHz, CD_3OD) δ = 158.7, 157.2, 136.0, 129.6, 123.6, 73.2, 40.0, 32.1, 30.9. MS (ESI) m/z calcd for $C_{44}H_{64}N_{12}O_4Cl_4$: 843.6 [M-3H-4Cl]$^+$; found, 843.6. Elemental analysis calcd (%) for $C_{44}H_{64}N_{12}O_4Cl_4 \times 4H_2O$: C 54.66, H 6.67, N 17.38; found, C 54.51, H 6.49, N 17.28.

5,11,17,23-Tetra-*n*-hexyl-25,26,27,28-tetrakis(3-guanidiniumpropoxy)calix[4]arene, Tetrachloride (5c). The pure compound was obtained as a white powder in quantitative yield. Hygroscopic. Mp >250 °C dec.; ^{1}H NMR (300 MHz, CD_3OD) δ = 7.75 (t, J = 5.4 Hz, 4H, NHCH_2), 6.47 (s, 8H, Ar*H*), 4.35 (d, J = 13.0 Hz, 4H, ArCH_2Ar), 3.99 (t, J = 7.2 Hz, 8H, OCH_2), 3.46−3.35 (m, 8H, OCH$_2$CH$_2$CH_2), 3.13 (d, J = 13.0 Hz, 4H, ArCH_2Ar), 2.32−2.15 (m, 16H, OCH$_2$CH_2 and ArCH_2), 1.50−1.16 (m, 32H, ArCH$_2$CH_2CH_2CH_2CH_2), 0.89 (t, J = 6.5 Hz, 12H, CH_3); ^{13}C NMR (75 MHz, CD_3OD) δ = 159.0, 155.4, 137.8, 135.8, 129.7, 73.5, 40.3, 36.6, 33.3, 33.1, 32.3, 31.1, 30.3, 24.2, 14.9. MS (ESI) m/z calcd for $C_{68}H_{112}N_{12}O_4Cl_4$: 1157.8 [M-3H-4Cl]$^+$; found, 1158.0. Elemental analysis calcd (%) for $C_{68}H_{112}N_{12}O_4Cl_4 \times 4H_2O$: C 59.37, H 8.79, N 12.22; found, C 59.14, H 8.52, N 12.03.

25,26,27,28-Tetrakis(6-guanidiniumhexyloxy)calix[4]arene, Tetrachloride (5d). The pure compound was obtained as a white powder in 87% yield. Mp >250 °C dec.; ^{1}H NMR (300 MHz, D_2O) δ = 6.89 (d, J = 7.6 Hz, 8H, Ar*H*), 6.73 (t, J = 7.6 Hz, 4H, Ar*H*), 4.51 (d, J = 13.1 Hz, 4H, ArCH_2Ar), 4.00 (t, J = 6.8 Hz, 8H, OCH_2), 3.33 (d, J = 13.1 Hz, 4H, ArCH_2Ar), 3.22 (t, J = 6.3 Hz, 8H, CH_2N), 2.06−1.95 (m, 8H, OCH$_2$CH_2), 1.71−1.57 (m, 8H, CH_2CH$_2$N), 1.57−1.41 (m, 16H, OCH$_2$CH$_2$CH_2CH_2); ^{13}C NMR (75 MHz, CD_3OD) δ = 158.9, 158.0, 136.5, 129.6, 123.4, 76.2, 42.9, 32.3, 31.6, 30.4, 28.2, 27.5. HRMS (ESI) m/z calcd for $C_{56}H_{88}N_{12}O_4Cl_4$: 495.34420 [M-2H-4Cl]$^+$; found, 495.34408.

49,50,51,52,53,54,55,56-Octakis(3-guanidiniumpropoxy)calix[8]arene, Octachloride (7). The crude was dissolved in water and purified by semipreparative RP-HPLC, with a C_{12} column using 30−60% gradient of CH_3CN/TFA 100/0.05 v/v in H_2O/TFA 100/0.05 v/v over 20 min. The fractions corresponding to the pure product were collected, and the solvent was evaporated under reduced pressure. The residue was solved (3×) in 10 mM HCl aqueous solution (5 mL), and each time, the solvent was removed under reduced pressure. The pure compound was obtained as a white powder in 27% yield. Mp >250 °C dec.; ^{1}H NMR (300 MHz, D_2O) δ = 6.91 (s, 24H, Ar*H*), 4.04 (s, 16H, ArCH_2Ar), 3.88 (t, J = 5.9 Hz, 16H, OCH_2), 3.24 (t, J = 6.7 Hz, 16H, OCH$_2$CH$_2$CH_2), 1.98 (quint, J = 6.2 Hz, 16H, OCH$_2$CH_2); ^{13}C NMR (75 MHz, CD_3OD) δ = 158.9, 156.4, 135.8, 130.5, 125.8, 71.9, 40.1, 31.2, 30.8; HRMS (ESI) m/z calcd for $C_{88}H_{128}N_{24}O_8Cl_8$: 411.25030 [M-4H+8Cl]$^{4+}$; found, 411.50098.

5-Guanidinium-25,26,27,28-Tetrakis(3-guanidiniumpropoxy)calix[4]arene, Pentachloride (11). The pure compound was obtained as a light yellow powder in quantitative yield. Hygroscopic. Mp 223−225 °C; ^{1}H NMR (300 MHz, D_2O) δ = 7.22−7.12 (m, 4H, Ar*H*), 6.97 (t, 2H, J = 7.5 Hz, Ar*H*), 6.54 (s, 3H, Ar*H*), 6.37 (s, 2H, Ar*H*), 4.40 (d, 4H, J = 13.4 Hz, ArCH_2Ar), 4.18 (t, 4H, J = 7.1 Hz, OCH_2), 3.99 (t, 2H, J = 6.9 Hz, OCH_2), 3.96 (t, 2H, J = 6.9 Hz, OCH_2), 3.48−3.28 (m, 12H, NHCH_2 and ArCH_2Ar), 2.35−2.16 (m, 8H, OCH$_2$CH_2); ^{13}C NMR (75 MHz, CD_3OD) δ = 159.0, 158.3, 157.7, 156.8, 156.1, 137.9, 137.6, 137.1, 135.4, 130.8, 130.4, 130.0, 129.3, 126.0, 124.3, 123.8, 74.1, 73.9, 73.5, 40.3, 40.2, 32.3, 31.2, 31.0; HRMS (ESI) m/z calcd for $C_{45}H_{68}N_{15}O_4Cl_5$: 439.76665 [M-2H-4Cl]$^{2+}$; found, 439.76602.

dx.doi.org/10.1021/bc2006829 | *Bioconjugate Chem.* 2012, 23, 993−1002

Scheme 1. Synthesis of the Lower Rim Guanidinocalix[4]arenes 5a–d[a]

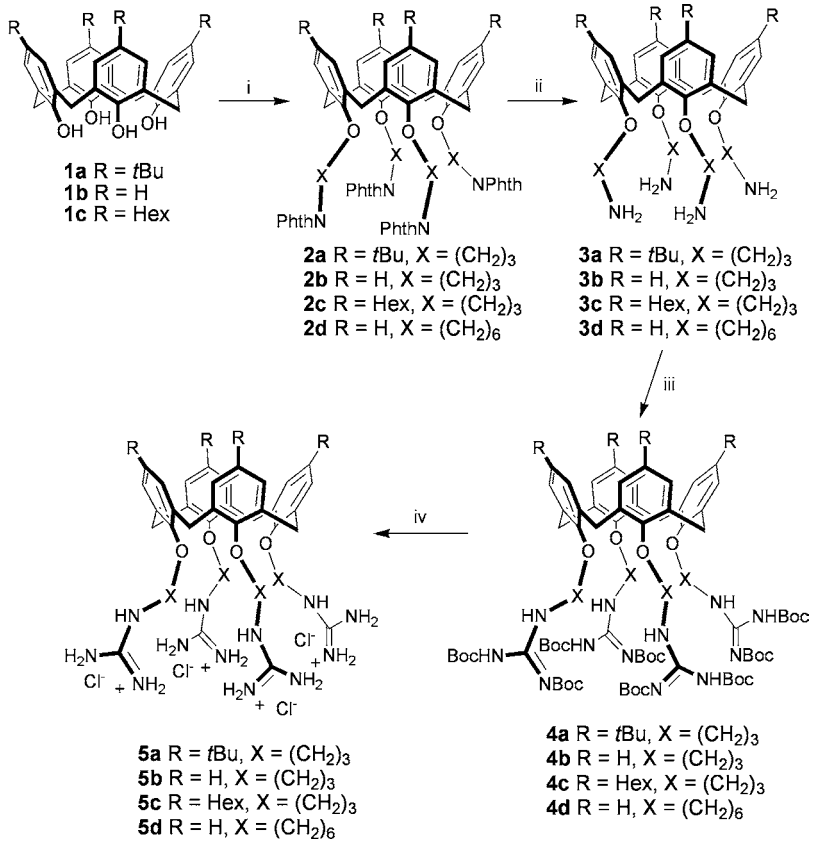

[a]Reagents and conditions: (i) *N*-(3-bromopropyl)phthalimide or *N*-(6-bromohexyl)phthalimide, NaH, dry DMF, N_2, rt; (ii) $NH_2NH_2{\cdot}H_2O$, abs EtOH, N_2, reflux; (iii) *N,N′*-di-Boc-*N″*-triflylguanidine, CH_2Cl_2, N_2, rt; (iv) HCl 37%, 1,4-dioxane, rt.

Bis[5-*tert*-butyl-2-(3-guanidiniumpropoxy)-3-methylphenyl]methane, Dichloride (21a). The pure compound was obtained as a white powder in quantitative yield. Hygroscopic. Mp >250 °C dec; ^{1}H NMR (300 MHz, D_2O) δ = 7.21 (s, 2H, Ar*H*), 6.93 (s, 2H, Ar*H*), 4.01 (s, 2H, ArCH_2Ar), 3.79 (bt, 4H, OCH_2), 3.35 (t, J = 6.0 Hz, 4H, OCH$_2$CH$_2$CH_2), 2.27 (s, 6H, ArCH_3), 2.07–1.90 (m, 4H, OCH$_2$CH_2), 1.17 (s, 18H, *t*Bu); ^{13}C NMR (75 MHz, CD_3OD) δ = 159.0, 154.6, 148.0, 134.4, 131.5, 127.6, 127.5, 71.0, 40.3, 35.3, 32.2, 31.2, 30.8, 17.2. HRMS (ESI) m/z calcd for $C_{31}H_{52}N_6O_2Cl_2$: 539.40680 $[M\text{-}H\text{-}2Cl]^+$; found, 539.40695.

Bis{[2-(3-guanidiniumpropoxy)-3-methyl]phenyl}methane, Dichloride (21b). The pure compound was obtained as a white powder in quantitative yield. Hygroscopic. Mp >250 °C dec.; ^{1}H NMR (300 MHz, D_2O) δ = 7.17 (d, J = 7.4 Hz, 2H, Ar*H*), 7.00 (t, J = 7.4 Hz, 2H, Ar*H*), 6.88 (d, J = 7.4 Hz, 2H, Ar*H*), 3.99 (s, 2H, ArCH_2Ar), 3.82 (t, J = 6.2 Hz, 4H, OCH_2), 3.33 (t, J = 6.7 Hz, 4H, OCH$_2$CH$_2$CH_2), 2.29 (s, 6H, ArCH_3), 2.02 (quint, J = 6.4 Hz, 4H, OCH$_2$CH_2); ^{13}C NMR (75 MHz, CD_3OD) δ = 159.0, 156.9, 135.3, 132.4, 130.9, 130.0, 125.6, 71.0, 68.4, 40.2, 31.1, 30.8, 21.1, 16.9. MS (ESI) m/z calcd for $C_{23}H_{36}N_6O_{22}Cl_2$: 427.3 $[M\text{-}H\text{-}2Cl]^+$; found, 427.5. Elemental analysis calcd (%) for $C_{23}H_{36}N_6O_{22}Cl_2 \times 2H_2O$: C 51.59, H 7.53, N 15.69; found, C 51.72, H 7.66, N 15.58.

Bis[2-(3-guanidiniumpropoxy)-5-hexyl-3-methylhenyl]methane, Dichloride (21c). The pure compound was obtained as a white powder in 76% yield. Mp > 250 °C dec.; ^{1}H NMR (300 MHz, CD_3OD) δ = 7.44 (t, J = 5.1 Hz, 2H, CH$_2$N*H*), 6.86 (d, J = 1.9 Hz, 2H, Ar*H*), 6.63 (d, J = 1.9 Hz, 2H, Ar*H*), 3.98 (s, 2H, ArCH_2Ar), 3.78 (t, J = 5.9 Hz, 4H, OCH_2), 3.42–3.32 (m, 4H, OCH$_2$CH$_2$CH_2), 2.43 (t, J = 7.3 Hz, 4H, ArCH_2), 2.27 (s, 6H, ArCH_3), 2.02 (quint, J = 6.3 Hz, 4H, OCH$_2$CH_2), 1.55–1.40 (m, 4H, ArCH$_2$CH_2), 1.32–1.16 (m, 12H, ArCH$_2$CH$_2$CH_2CH_2CH_2), 0.86 (t, J = 6.5 Hz, 6H, CH$_2$CH_3); ^{13}C NMR (75 MHz, CD_3OD) δ = 159.0, 154.8, 139.9, 134.9, 132.0, 130.7, 129.9, 71.0, 40.4, 36.5, 33.2, 33.0, 31.0, 30.8, 30.1, 24.0, 16.9, 14.8. HRMS (ESI) m/z calcd for $C_{35}H_{60}N_6O_2Cl_2$: 595.46940 $[M\text{-}H\text{-}2Cl]^+$; found, 595.46979.

25,26,27,28-Tetrakis(3-aminopropoxy)calix[4]arene, Tetrahydrochloride (12). Calixarene **3b** was dissolved in aqueous 2 M HCl (2 mL) and stirred for 15 min, then the water was evaporated under reduced pressure to obtain the tetra salt as a white solid. Mp >250 °C dec.; ^{1}H NMR (300 MHz, D_2O) δ = 6.88 (d, 8H, J = 7.3 Hz, Ar*H*), 6.80–6.73 (m, 4H, Ar*H*), 4.39 (d, J = 13.3 Hz, 4H, ArCH_2Ar), 4.14 (t, J = 7.2 Hz, 8H, OCH_2), 3.41 (d, J = 13.3 Hz, 4H, ArCH_2Ar), 3.14 (t, J = 7.4 Hz, 8H, CH_2N$^+$), 2.26 (quint, J = 7.8 Hz, 8H, OCH$_2$CH_2); ^{13}C NMR (75 MHz, CD_3OD) δ = 157.2, 136.3, 129.9, 124.0, 73.4, 38.8, 32.3, 29.6. HRMS (ESI) m/z calcd for $C_{40}H_{56}N_4O_4Cl_4$: 653.40613 $[M\text{-}3H\text{-}4Cl]^+$; found, 653.40568.

25,26,27,28-Tetrakis[3-(trimethylammonium)-propoxy]calix[4]arene, Tetrachloride (13). The tetraminocalix[4]arene **3b** (0.26 g, 0.4 mmol) was dissolved in MeOH (8 mL), then $KHCO_3$ (0.41 g, 4.1 mmol) and MeI (0.8 mL, 12.7 mmol) were added and the mixture stirred at room temperature. The reaction was followed by mass spectroscopy and stopped after 7 days. A mixture MeOH/CH_2Cl_2 9/1 v/v (10 mL) was added, the insoluble inorganic

dx.doi.org/10.1021/bc2006829 | *Bioconjugate Chem.* 2012, 23, 993–1002

salts were filtered off, and the solvent removed under reduced pressure. The residue (0.53 g, 0.4 mmol) was dissolved in H_2O (5 mL), and 5 mL of Cl^- DOWEX11 resin were added and the mixture stirred for 30 min. After removal of the resin, pure compound **13** was obtained by evaporation of the solvent under reduced pressure as a white solid in 98% yield. Mp 220 °C dec.; ^{1}H NMR (300 MHz, D_2O, 323 K) δ = 6.84−6.79 (m, 12H, Ar*H*), 4.38 (d, J = 13.6 Hz, 4H, ArCH_2Ar), 4.24 (t, J = 6.8 Hz, 8H, OCH_2), 3.46 (d, J = 13.6 Hz, 4H, ArCH_2Ar), 3.42−3.28 (m, 8H, OCH$_2$CH$_2$CH_2), 3.14 (s, 36H, CH_3), 2.40−2.24 (m, 8H, OCH$_2$CH_2); ^{13}C NMR (100 MHz, CD_3OD) δ = 155.0, 134.8, 128.4, 122.5, 70.6, 63.7, 52.5, 31.1, 23.7. HRMS (ESI) m/z calcd for $C_{52}H_{80}N_4O_4Cl_4$: 206.15394 $[M\text{-}4Cl]^{4+}$; found, 206.15393.

RESULTS AND DISCUSSION

Synthesis. In order to obtain potential gene vectors with a different degree of lipophilicity, the three calix[4]arene scaffolds **1a**, **1b**, and **1c**[30] were selected for the functionalization with guanidinium units at their lower rim. This functionalization was performed by alkylation of the OH groups with propylphthalimido chains, subsequent removal of the amino protecting groups, reaction with bis-Boc-triflylguanidine, and final deprotection from Boc groups by reaction with HCl in dioxane, which gave the guanidinocalix[4]arenes **5a−c** (Scheme 1). Using derivative **5b** as a reference, we also performed a series of structural modifications in order to dissect the factors affecting DNA condensation and cell transfection in this family of ligands. We thus synthesized compound **5d** (Scheme 1) to evaluate the effects of an increased distance between the apolar cavity and the charged groups, and we prepared octamer **7** (Scheme 3 and Scheme SI1, Supporting Information) to assess the influence of the platform conformational features and the higher number of charged head groups. As further modification, an additional guanidinium moiety with respect to **5b** was introduced at the upper rim, synthesizing compound **11** through the reaction sequence described in Scheme 2.

The last variation was the introduction of other positively charged groups instead of the guanidinium by the synthesis of compounds **12** and **13** (Scheme 3) bearing primary and quaternary ammonium cations, respectively. They were both prepared from **3b**, the former by treatment with 2 M HCl and the latter by reaction with methyl iodide and a relatively weak base ($KHCO_3$).[31] To evaluate the importance of the macrocyclic structure in relation to the transfection properties, we also synthesized the series of Gemini-type compounds **21a−c** (Scheme 3). These derivatives were obtained starting from the corresponding 2,2′-dihydroxydiphenylmethane precursors (Scheme SI2, Supporting Information) following the same reaction sequence (Scheme SI3, Supporting Information) used for their calix[4]arene analogues.

Solubility and Aggregation Properties. All of the compounds synthesized were water-soluble, although within different concentration limits. They revealed aggregation properties which depend on their structure and could, in some cases, be responsible for their different behavior shown in DNA condensation and cell transfection (*vide infra*). The macrocyclic derivatives **5a**, **5b**, **5d**, **11**, **12**, and **13** and the Gemini **21a** and **21b** gave rise to ^{1}H NMR spectra in D_2O at rt with sharp signals. On the contrary, the spectra of **5c** and the corresponding model **21c** showed broad signals as a reasonable consequence of hydrophobic aggregation due to the lipophilic hexyl chains on the aromatic nuclei. The sharpening of the

Scheme 2. Synthesis of Derivative 11[a]

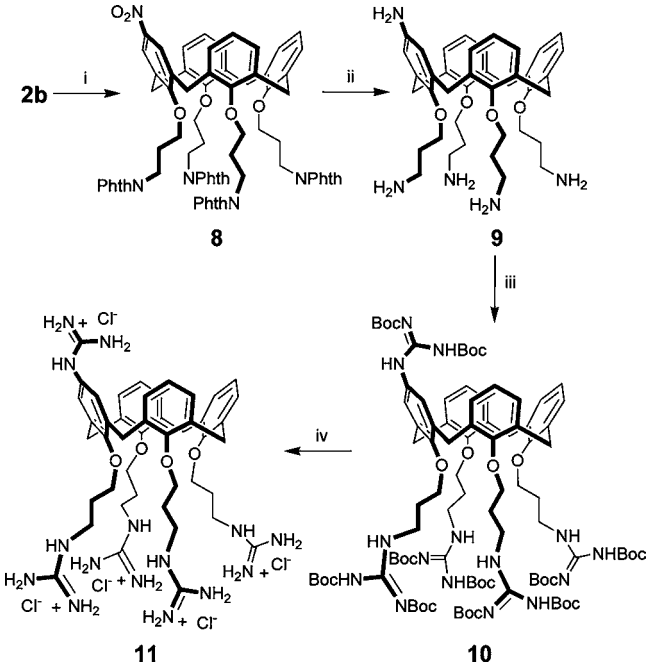

[a]Reagents and conditions: (i) HNO_3, glacial CH_3COOH, dry CH_2Cl_2, N_2; (ii) $NH_2NH_2{\cdot}H_2O$, Pd/C, abs EtOH, reflux, N_2; (iii) *N,N′*-di-Boc-*N″*-triflylguanidine, Et_3N, $CHCl_3$, N_2, rt; (iv) HCl 37%, 1,4-dioxane, rt.

signals upon dilution (e.g., Figure SI1 (Supporting Information) for compound **21c**) confirmed the occurrence of this phenomenon. The signals of 5 mM **5c** even at 363 K (Figure SI2a, Supporting Information) remained still rather broad, even though they could be recognized and assigned. Quite different was the situation in CD_3OD (Figure SI2b, Supporting Information) where all the signals of **5c** appeared sharp, indicating that in this solvent the aggregates are disrupted. Surprisingly, although apparently less amphiphilic compared to the calix[4]arene derivatives due to its conformational mobility, calix[8]arene **7** gave ^{1}H NMR spectra in D_2O (Figure SI3, Supporting Information) in which the signal shape and width are strongly dependent on the concentration, changing from broad to sharp by dilution and suggesting also for this derivative a high propensity to aggregation. A deeper investigation in water solution under varied conditions revealed further differences on the behavior of the members of this family of guanidinylated calixarenes. In particular, compounds **5a**, **5b**, **5d**, **11**, **12**, and **13**, which showed no evidence of aggregation in pure D_2O at mM concentration, indeed act quite differently in the presence of inorganic salts. The addition of $MgCl_2$ (2 mM) and NaCl (10 mM), both components of the deposition buffer used in the AFM experiments with DNA (*vide infra*), to a 1 mM sample of **5a** in D_2O determined a drastic reduction of the peak intensity in the ^{1}H NMR spectrum, although no precipitation was observed. This suggests the formation of water-soluble aggregates in equilibrium with monomeric **5a**. Analogously, calixarene **5b** and **5d** aggregate in the presence of the salt as evidenced by a significant broadening of their NMR signals, even if for **5b** (Figure SI4, Supporting Information) a higher concentration of the two salts ($MgCl_2$ 50 mM and NaCl 250 mM) was necessary to cause clear changes in the spectrum. A polarity decrease of the medium determines disaggregation as demonstrated by the progressive sharpening of the NMR

dx.doi.org/10.1021/bc2006829 | *Bioconjugate Chem.* 2012, 23, 993−1002

Scheme 3. Structures of Octamer 7, Ammonium Containing Ligands 12 and 13, and Gemini-Type Ligands 21a–c

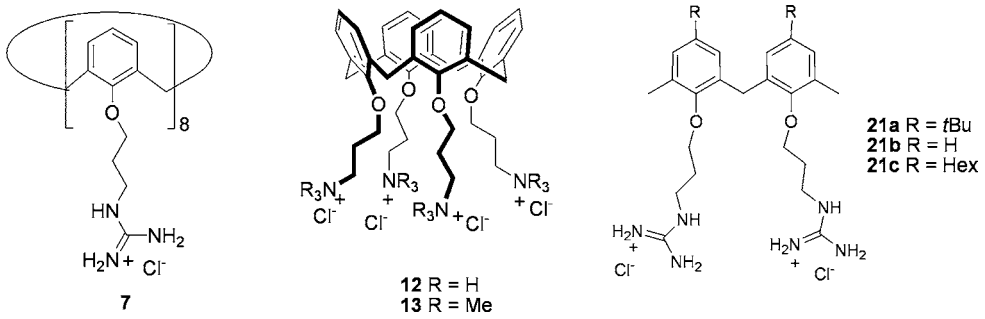

signals upon addition of increasing volumes of EtOH to the ligand samples in D_2O solution containing salts (e.g., see the case of **5d** in Figure SI5, Supporting Information). The data qualitatively revealed that this tendency to the aggregation follows the order **5c** > **5a** ≈ **5d** > **5b**. The self-assembly shown even by compounds **5b** and **5d**, although less markedly for the former one, indicates that also the unfunctionalized aromatic rings of the calixarenes themselves can actively participate in the formation of aggregated species through hydrophobic interactions not excluding for both compounds the possibility of condensing DNA and transfection. This represents an uncommon observation because, while it is well known that amphiphilic calixarenes functionalized with hydrophobic alkyl chains at the upper or lower rim tend to aggregate in aqueous solution,[32,33] those without such substituents[34] at the upper rim and with charged groups at the lower rim resulted as monomers in water,[32] although no investigation of their behavior in presence of salts was reported so far. Accordingly, compound **11** did not show self-association at all since the additional charged group at the upper rim perturbs the polarity of the whole molecule disrupting any amphiphilic character. The presence of ammonium units, instead of guanidinium, eliminates the tendency to aggregate for the macrocycles **12** and **13** at least up to the investigated concentration of 1 mM, also with the simultaneous presence of $MgCl_2$ and NaCl.

AFM experiments with **5b** and **5d** (Figure SI6, Supporting Information) evidenced the same differences of behavior in pure water and in solutions containing salts (10 mM NaCl and 2 mM $MgCl_2$) observed by NMR. The small aggregates visible on the mica surface by using buffer made clear that the two macrocycles at 1–2 μM are still able to aggregate despite a concentration much lower than that of the NMR studies (μM vs mM), probably thanks to the much higher salt concentration compared to that of the calixarene ligand.

DNA Binding. The compounds obtained were then studied with different techniques to verify their binding properties toward DNA. All of the experiments were performed using the pEGFP-C1 plasmid DNA (4731 bp), encoding for the enhanced green fluorescent protein and subsequently used for the cell transfection assays. The ability of compounds to bind this plasmid was initially assessed through gel electrophoresis. The electrophoretic data (Figure SI7, Supporting Information) revealed that the guanidinium containing macrocycles strongly affect DNA mobility already at a concentration of 50 μM (cationic over anionic charges ratio N/P between ~1/1 and ~2/1 depending on the number of positively charged units on the ligand). It is also significant to notice that the efficiency of the lower rim guanidinocalix[4]arenes is higher than that observed, always by EMSA, for the previously described upper rim analogues.[16] The Gemini analogues of **5a–c** and the macrocycles containing ammonium instead of guanidinium head groups are not able to interact efficiently with DNA even at a ligand concentration of 200 μM (Figure SI7, Supporting Information).

Determination of the plasmid DNA melting curves in the presence of the ligands and evaluation of their ability to displace ethidium bromide from its complexes with the nucleic acid gave further, qualitative indication that binding between the DNA and all our ligands was taking place (Figures SI8 and SI9, Supporting Information).

Using AFM in tapping mode on air, we could visualize and observe different effects of our compounds on DNA folding. After incubation of the circular plasmid pEGFP-C1 DNA (0.5 nM) with the *p-tert*-butyl calixarene **5a** (0.6 μM) (N/P = 0.5) in the deposition buffer (4 mM Hepes, 10 mM NaCl, and 2 mM $MgCl_2$, pH 7.4), the plasmids detected on the mica were 50–60 nm globular species (Figure 1b) each consisting of a single plectoneme.[35] The presence of 10% of ethanol (v/v) in the deposition buffer where DNA and ligand molecules were dissolved during the incubation time caused a partial relaxation of the nucleic acid condensates (Figure SI10a, Supporting Information). A comparable behavior related to the presence or the absence of alcohol in the buffer was observed for compound **5c**, although the condensates generated by this ligand (2.5 μM, N/P = 2) appeared even much larger and was often constituted of more than one plasmid (Figure 1c). On the contrary, compound **5b** at 1–2 μM concentration, having no alkyl chains on the aromatic nuclei, did not form tight DNA condensates in the deposition buffer. Compared to their relaxed state (Figure 1a), the single plectomenes, however, appeared much more constrained, which proves the interaction of **5b** with plasmid DNA. The addition of alcohol determined the formation of single plectoneme condensates, some of them detectable in the globular form (Figure 1d), others with a toroid-like[36] shape (Figure SI10b, Supporting Information). Compound **5d**, although lacking alkyl chains at the upper rim as **5b**, seemed able to give, at 1 μM concentration, small condensates also in the absence of ethanol (Figure 1e). For all four calix[4]arenes **5a–d**, it was also possible to observe on the mica surface very small aggregates of few nanometers not containing nucleic acid molecules, which could therefore be ascribed to the macrocycle aggregates previously observed in the absence of DNA.

On the whole, ligands **5a–d** seem to generate DNA globular species, of proper size for transfection in the case of **5a**, **5b**, and **5d**, thanks to their ability to self-assemble through hydrophobic interactions between the alkyl chains at the upper rim (**5a** and **5c**) or the aromatic nuclei of the calixarene (**5b** and **5d**).

dx.doi.org/10.1021/bc2006829 | *Bioconjugate Chem.* 2012, 23, 993–1002

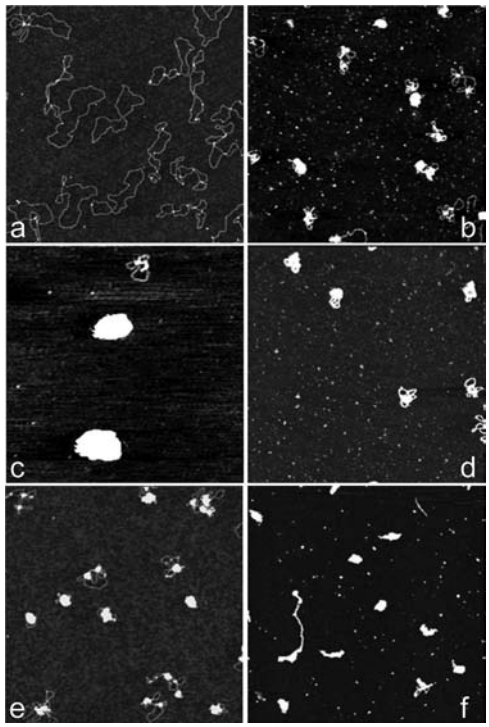

Figure 1. AFM images showing the effects induced on plasmid DNA by the guanidinylated ligands. All images were obtained with the microscope operating in tapping mode in air and with supercoiled pEGFP-C1 plasmid deposited onto mica at a concentration of 0.5 nM. (a) Plasmid alone. Plasmid incubated with (b) 0.6 μM **5a**; (c) 2.5 μM **5c**; (d) 1.8 μM **5b** + 10 % EtOH; (e) 1 μM **5d**; and (f) 2 μM **5b** + 4 μM DOPE using the cell growth medium as deposition buffer (90% DMEM, 10% FBS, 2 mM L-glutamine,100 IU/mL penicillin, and 10 μg/mL streptomycin). Each image represents a 2 × 2 μm scan.

Because of the particular efficiency in transfection characterizing the *para*-H lower rim guanidinocalix[4]arene **5b** (*vide infra*), additional AFM experiments were performed upon incubation of the macrocycle with plasmid DNA in the cell growth medium (90% DMEM, 10% FBS, 2 mM L-glutamine, and 100 IU/mL penicillin and 10 μg/mL streptomycin) where DNA and a nonviral vector are indeed mixed for the treatment of cells. Having preliminarily verified that the medium allows the deposition of filaments on mica (Figure SI11a, Supporting Information), we proceeded with the analysis of samples coming from the incubation in such an environment of DNA and **5b** with and without DOPE (ligand/DOPE 1:2), analogously to the used transfection experiment formulations. Condensates with proper shape and size for gene delivery were detected on the mica surface only for samples containing DOPE (Figure 1f and Figure SI11b, Supporting Information), similar to those previously observed with the same ligand in the absence of DOPE but upon the addition of 10% ethanol to the buffer solution (Figure 1d). This clearly evidenced the beneficial role of the helper lipid to obtain tight condensates and also how the experimental conditions given by the simpler deposition buffer represent a good model to collect information about DNA binding and the compacting abilities of these ligands in the more complex conditions of the transfection protocol.

Fluorescence experiments with compounds **5a**−**c**, at the same concentrations and with the same buffer of the AFM studies, were performed using Nile Red (Figure SI12, Supporting Information) to verify if the interaction with DNA plasmids visualized by AFM involves the macrocycles either as monomers or, following a hierarchical process,[15,34,37−39] as self-assembled aggregates. In the case of **5c**, a blueshift of the emission band and a strong enhancement of the fluorescence intensity were observed upon addition of the guanidinocalixarene (2 μM) to a buffer solution of the dye (0.2 μM). Subsequent addition of pEGFP-C1 DNA (0.5 nM) caused only a slight redshift of the emission band maintaining the same intensity. This suggests that, as recently reported for an amphiphilic tetrammonium-tetraoctyloxycalix[4]arene,[34] compound **5c**, endowed with long hexyl chains at the upper rim, forms aggregates that trap Nile Red and binds to DNA as self-assembled species. This conclusion, however, could not be clearly reached with **5a** and **5b** which showed a different effect on the Nile Red spectrum respect to **5c**. Addition of these compounds to the solution containing the dye did not substantially change the fluorescence band which underwent a shift and an intensity increase only when DNA was added. In both cases, Nile Red did not interact with the calixarene aggregates, which we know from AFM experiments to be present in solution in these conditions, but it seemed instead to be included in the calixarene−DNA complexes. Therefore, for **5a** and **5b**, both possibilities are open: (i) the interaction with plasmid through a hierarchical assembly, in analogy with **5c**, or (ii) the binding to DNA as monomeric species because of the lower aggregate stability due to the lack of long alkyl chains at the upper rim.

AFM images relative to mixtures of DNA with the pentaguanidinium compound **11** at 1 μM concentration showed expected marked changes in the folding of the plasmids which, however, were mainly involved in the formation of very large aggregates (200−300 nm) (Figure SI10c, Supporting Information). Large aggregates were formed also by the guanidinocalix[8]arene **7**, but together with other smaller condensates (Figure SI10d, Supporting Information) comparable in size with those observed, for example, with **5a** and which, similarly, were relaxed by the addition of ethanol to the deposition buffer. Calix[8]arene **7** showed this behavior, which is in agreement with its observed self-aggregation ability even if it lacks alkyl chains at the upper rim and possesses a high conformational mobility compared to the rigid and amphiphilic cone calix[4]arene **5a**. As previously verified by EMSA, the AFM experiments confirmed the lower efficiency of the two ammonium containing ligands **12** and **13** in the binding to DNA and their inability to condense it even when modifying the concentration (from 10^{-6} to 5×10^{-6} M) and the pH of the sample solutions (5.9 and 7.4) (Figures SI10e,f, Supporting Information). The data collected relative to these two compounds reveal that the presence of positive charges in this type of vectors is not sufficient to achieve efficient DNA binding and condensation and that guanidinium cations play a special role in this respect.

While no substantial differences were revealed by EMSA in the binding properties of Gemini-type derivatives **21a**−**c**, different effects on DNA folding attributable to the substituents at the aromatic nuclei of these compounds were observed by AFM measurements (Figure SI13, Supporting Information) also considering a higher N/P ratio not explored in gel electrophoresis. However, what was detected could not be related with the transfection properties of these ligands mainly because of their toxicity (*vide infra*).

dx.doi.org/10.1021/bc2006829 | *Bioconjugate Chem.* 2012, 23, 993−1002

Transfection Properties. On the basis of the biophysical evidence of DNA binding and condensation, transfection experiments were performed on RD-4 human Rhabdomyosarcoma cells using plasmid pEGFP-C1 DNA (1 nM) encoding for the green fluorescent protein whose production in cells is easily detectable by fluorescence microscopy. This cell line was chosen because, beyond the medical relevance, it is easy to grow and difficult to transfect by traditional methods, especially if compared to other cell lines that are more widely used, such as HEK 293 cells.

A first important observation is that no transfection occurred when either DOPE or ligands were used alone, also in the case of compounds which demonstrated DNA condensation ability in AFM experiments. On the contrary, the formulation calixarene/DOPE (1/2 molar ratio) especially at 10 μM (N/P = 4) ligand concentration was effective for some of them and, in particular, for compound **5b** which turned out to be a very efficient transfectant agent for RD-4 human Rhabdomyosarcoma cells. Remarkably, the amount of transfected cells for **5b** (Figure 2), going from 35 to 50%, was higher than that achieved by the commercially available lipofectamine LTX (never more than 30% in our comparison experiments) and by our previously investigated upper rim tetraguanidinocalix[4]arenes **I** (less than 20%, Figure 2b). The presence of 10% of serum in the transfection mixture decreased to 11% the efficiency of **5b**. Little transfection activity was observed for compounds **5a** (3−4%) and **5c** (6−7%). Quite rewarding was also the finding that the most active compound **5b** has low cytotoxicity showing 70−75% of cell viability in MTT (3-(4,5-dimethylthiazol-2-yl)-2,5-diphenyltetrazolium bromide) assays at 30 h from the treatment both by simple incubation (in the absence of DNA, Figure 3a) and in transfection conditions (in the presence of DNA, Figure 3b). On the contrary, cytotoxicity of **5a** and particularly of **5c** significantly increased going from their simple incubation with cells to transfection conditions (Figure 3). Rather surprisingly, also **5d**, which showed a much lower efficiency in transfection experiments compared to **5b**, overall appeared characterized by a very high cytotoxicity (Figure 3) which made irrelevant the determination of the transfection percentage. No significant differences in toxicity were revealed in the presence or in absence of DOPE for the four compounds. For a further elaboration of the transfection results, **5b** and **5d** were also compared by luciferase assays which supported the higher activity of **5b** respect to both LTX (Figure SI14, Supporting Information) and **5d**.

Calix[8]arene **7** showed a maximum of 5% of transfection in the presence of adjuvant. The three derivatives **11**, **12**, and **13**, all not showing self-aggregation propensity, were all unable to transfect Rhabdomyosarcoma cells. For compound **11**, this result could be related to the formation of the very large aggregates of DNA observed on mica whereas for the other two to their inability to condense DNA (see the AFM studies above). The very low transfection found for Gemini compounds **21a** and **21c** is reasonably due also to their high toxicity. They were incubated at a double concentration with respect to the calixarene derivatives to have the same N/P ratio, and only **21b** showed detectable transfection (ca. 6% at 20 μM). Since it is well known in the field of synthetic nonviral vectors that transfection efficiency may depend on the type of cell used, our lead compound **5b** was tested in a different cell line setting using again LTX as reference. With Vero cells, again the calixarene based vector, together with DOPE, proved to be better than the lipofectamine, transfecting 30 and 20% of the

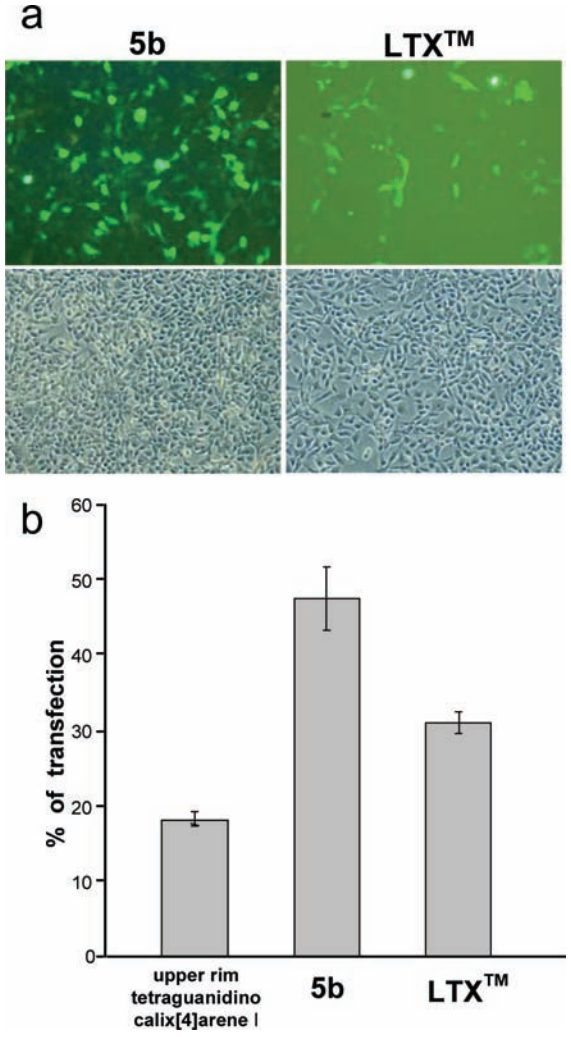

Figure 2. Transfection experiments performed with 1 nM pEGFP-C1 plasmid, guanidinocalixarene **5b**/DOPE (1/2 molar ratio, 10/20 μM) formulation, and lipofectamine LTX to Rhabdomyosarcoma cells. (a) Fluorescence microscopy images (upper row) of the transfected cells as visualized thanks to the expression of the enhanced green fluorescent protein EGFP and phase contrast images (lower row) of the corresponding experiments. (b) In vitro transfection efficiency as percentage of transfected cells upon treatment with guanidino derivative/DOPE formulations and lipofectamine LTX.

treated cells, respectively.[40] Comparable results between the two formulations were on the contrary obtained with AUBEK and BoMAK cells, whereas LTX was definitely more efficient in the case of hMSC and N2a cell lines.

Experiments finalized at disclosing the uptake mechanism through which the complexes **5b**/DOPE/DNA are internalized into the cells were also performed. Transfection of Rhabdomyosarcoma cells was carried out in presence of chemical compounds that inhibit different uptake pathways. On the basis of the preliminary results collected, macropinocytosis appeared as the most probable mechanism and caveolae-dependent endocytosis as a secondary pathway for the transport of these lipoplexes across the cell membrane. Wortmannin and amiloride, in fact known as inhibitors of macropinocytosis, and filipin, an inhibitor of caveolae-mediated uptake, significantly suppressed the transfection induced by **5b** (Figure SI15, Supporting Information). In agreement with this assumption, we found that also monesine acts as an inhibitor of

dx.doi.org/10.1021/bc2006829 | *Bioconjugate Chem.* 2012, 23, 993−1002

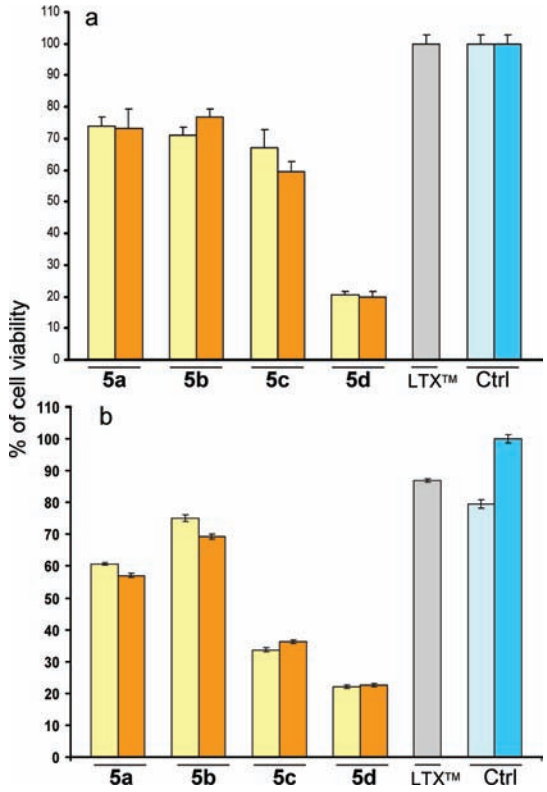

Figure 3. Cell viability (Rhabdomyosarcoma cells) at 30 h from the treatment in MTT assays (a) after incubation with 10 μM ligands **5a–c** and (b) in transfection conditions, with ligand alone (yellow bars), ligand/DOPE (10 μM/20 μM) formulation (orange bars), LTX (gray bar), DOPE alone (light blue bar), and without any treatment (blue bar).

transfection, and it is known that this compound blocks the pH induced degradation typical of the macropinocytosomes in which our complexes should reasonably be included. No effects on transfection were evidenced by inhibition of clathrin mediated endocytosis, which was indeed recently found out as one of the uptake mechanisms for cyclodextrin based vectors.[41]

We can thus put forward some hypotheses to explain, in particular, the superior performance found for the lower rim guanidinocalix[4]arene **5b** as a nonviral vector compared to the upper rim guanidinocalixarenes **I** previously reported and shown to be less efficient and more toxic. We can rule out the fact that the different efficiencies could be linked to a possible different protonation degree between the lower and upper rim derivatives since we know that in all cases, the four guanidinium groups are fully protonated at physiological pH.[42] A first reason could then be the flexibility of the chains linking the guanidinium groups to the macrocyclic scaffold of **5b** which could favor the binding to DNA and cell membrane phospholipids. A further aspect seems related to the role played by DOPE on vector activity, which is in fact particularly relevant in the case of the lower rim guanidinocalixarenes and substantially unimportant for the upper rim derivatives **I**. The hydrophobic calixarene cavity of the former could allow an optimized interaction with the phospholipid helper exalting its functions and determining the formation of peculiar calixarene–DOPE supramolecular assemblies more suitable for transfection and endowed with much lower toxicity. This appears especially in the case of the most active *para*-H compound **5b** for which the addition of DOPE, as observed by AFM, significantly helps in the condensation of the DNA plasmids.

CONCLUSIONS

In summary, attaching the guanidinium groups at the lower rim of calix[4]arenes disclosed the possibility to significantly enhance the cell transfection ability of the synthetic vectors based on this scaffold and reduce their toxicity to cells, if compared to the analogues **I** with the charged groups directly linked to the aromatic nuclei (upper rim). In particular, the macrocycle **5b** was, in formulation with DOPE, even better than the widely used, commercially available lipofectamine LTX in the transfection of RD-4 human Rhabdomyosarcoma. The possibility to study and compare **5b** with a series of analogues, in which structural modifications were introduced, evidenced that subtle variations in conformational freedom, distance of the charges from the cavity, nature of the cationic head groups and of the substituents decorating the apolar cavity, determine changes in the lipophilicity–hydrophilicity balance which in turn cause drastic changes in the biological properties also when relevant differences in DNA binding and condensation are not found by EMSA and AFM experiments. Moreover, we found evidence that the ability for these calixarene based vectors to self-assemble in water and condense DNA, as detected by AFM experiments,[43] is a necessary but not sufficient condition for getting significant transfection activity. It is also interesting that, at least for lower rim derivatives in the cone conformation, the guanidinium is essential as a cationic group to observe transfection activity, and its replacement with other ammonium moieties is definitely detrimental, although some of these have been reported as effective when attached at the upper rim of calix[4]arene derivatives.[34,44]

The superior biological properties of these calixarene derivatives with respect to the linear Gemini-type compounds **21a–c** indicate that a macrocyclic effect is operating and that the presence of a cavity and the preorganization of the charged groups make these derivatives promising systems to further develop interesting nonviral vectors.

ASSOCIATED CONTENT

Supporting Information

Further synthetic schemes, experimental procedures, characterization, and ^{1}H and ^{13}C NMR spectra relative to all the new compounds; and pictures and graphics from gel electrophoresis analysis, AFM, fluorescence, melting curve determination, and cell transfection studies. This material is available free of charge via the Internet at http://pubs.acs.org.

AUTHOR INFORMATION

Corresponding Author

*E-mail: gaetano.donofrio@unipr.it (G.D.); francesco.sansone@unipr.it (F.S.).

Author Contributions

[§]These authors equally contributed to the work.

Notes

The authors declare no competing financial interest.

ACKNOWLEDGMENTS

We acknowledge the Ministero dell'Istruzione, Università e Ricerca (MIUR, PRIN-project number 2008HZJW2L) and Fondazione Cassa di Risparmio di Parma which financially

supported this research, and the Centro Interdipartimentale Misure "G. Casnati" for the use of NMR, HRMS, and AFM facilities. This work was carried out in the frame of COST Actions CM1005 and CM1102.

REFERENCES

(1) Mintzer, M. A., and Simanek, E. E. (2009) Nonviral vectors for gene delivery. *Chem. Rev. 109*, 259−302.
(2) Bhattacharya, S., and Bajaj, A. (2009) Advances in gene delivery through molecular design of cationic lipids. *Chem. Commun.*, 4632−4656.
(3) Srinivas, R., Samanta, S., and Chaudhuri, A. (2009) Cationic amphiphiles: promising carriers of genetic materials in gene therapy. *Chem. Soc. Rev. 38*, 3326−3338.
(4) Zuhorn, I. S., Engberts, J. B. F. N., and Hoekstra, D. (2007) Gene delivery by cationic lipid vectors: overcoming cellular barriers. *Eur. Biophys. J. 36*, 349−362.
(5) Felgner, P. L., Gadek, T. R., Holm, M., Roman, R., Chan, H. W., Wenz, M., Northrop, J. P., Ringold, G. M., and Danielsen, M. (1987) Lipofection - A highly efficient, lipid-mediated DNA-transfection procedure. *Proc. Natl. Acad. Sci. U.S.A. 84*, 7413−7417.
(6) Dass, C. R. (2004) Lipoplex-mediated delivery of nucleic acids: factors affecting in vivo transfection. *J. Mol. Med. Immunol. 82*, 579−591.
(7) Boussif, O., Lezoualch, F., Zanta, M. A., Mergny, M. D., Scherman, D., Demeneix, B., and Behr, J. P. (1995) A versatile vector for gene and oligonucleotide transfer into cells in culture and in vivo: polyethylenimine. *Proc. Natl. Acad. Sci. U.S.A. 92*, 7297−7301.
(8) Merdan, T., Kopecek, J., and Kissel, T. (2002) Prospects for cationic polymers in gene and oligonucleotide therapy against cancer. *Adv. Drug Delivery Rev. 54*, 715−758.
(9) Sizovs, A., McLendon, P. M., Srinivasachari, S., and Reineke, T. M. (2010) Carbohydrate polymers for nonviral nucleic acid delivery. *Top. Curr. Chem. 296*, 131−190.
(10) Haensler, J., and Szoka, F. C. J. (1993) Polyamidoamine cascade polymers mediate efficient transfection of cells in culture. *Bioconjugate Chem. 4*, 372−379.
(11) Bielinska, A. U., Chen, C., Johnson, J., and Baker, J. R. J. (1999) DNA complexing with polyamidoamine dendrimers: Implications for transfection. *Bioconjugate Chem. 10*, 843−850.
(12) Guillot-Nieckowski, M., Eisler, S., and Diederich, F. (2007) Dendritic vectors for gene transfection. *New J. Chem. 31*, 1111−1127.
(13) Bertling, W. M., Gareis, M., Paspaleeva, V., Zimmer, A., Kreuter, J., Nuernberg, E., and Harrer, P. (1991) Use of liposomes, viral capsids, and nanoparticles as DNA carriers. *Biotechnol. Appl. Biochem. 13*, 390−405.
(14) Sandhu, K. K., McIntosh, C. M., Simard, J. M., Smith, S. W., and Rotello, V. M. (2002) Gold nanoparticle-mediated transfection of mammalian cells. *Bioconjugate Chem. 13*, 3−6.
(15) Aoyama, Y. (2004) Macrocyclic glycoclusters: from amphiphiles through nanoparticles to glycoviruses. *Chem.—Eur. J. 10*, 588−593.
(16) Sansone, F., Dudic, M., Donofrio, G., Rivetti, C., Baldini, L., Casnati, A., Cellai, S., and Ungaro, R. (2006) DNA condensation and cell transfection properties of guanidinium calixarenes: Dependence on macrocycle lipophilicity, size, and conformation. *J. Am. Chem. Soc. 128*, 14528−14536.
(17) Ortiz Mellet, C., Benito, J. M., and García Fernández, J. M. (2010) Preorganized, macromolecular, gene-delivery systems. *Chem.—Eur. J. 16*, 6728−6742.
(18) Ortiz Mellet, C., García Fernández, J. M., and Benito, J. M. (2011) Cyclodextrin-based gene delivery systems. *Chem. Soc. Rev. 40*, 1586−1608.
(19) Srinivasachari, S., Fichter, K. M., and Reineke, T. M. (2008) Polycationic beta-cyclodextrin "click clusters": monodisperse and versatile scaffolds for nucleic acid delivery. *J. Am. Chem. Soc. 130*, 4618−4627.
(20) Mourtzis, N., Paravatou, M., Mavridis, I. M., Roberts, M. L., and Yannakopoulou, K. (2008) Synthesis, characterization, and remarkable biological properties of cyclodextrins bearing guanidinoalkylamino and aminoalkylamino groups on their primary side. *Chem.—Eur. J. 14*, 4188−4200.
(21) Diaz-Moscoso, A., Le Gourrierec, L., Gomez-Garcia, M., Benito, J. M., Balbuena, P., Ortega-Caballero, F., Guilloteau, N., Di Giorgio, C., Vierling, P., Defaye, J., Ortiz Mellet, C., and García Fernández, J. M. (2009) Polycationic amphiphilic cyclodextrins for gene delivery: synthesis and effect of structural modifications on plasmid DNA complex stability, cytotoxicity, and gene expression. *Chem.—Eur. J. 15*, 12871−12888.
(22) Diaz-Moscoso, A., Guilloteau, N., Bienvenu, C., Mendez-Ardoy, A., Blanco, J. L. J., Benito, J. M., Le Gourrierec, L., Di Giorgio, C., Vierling, P., Defaye, J., Ortiz Mellet, C., and García Fernández, J. M. (2011) Mannosyl-coated nanocomplexes from amphiphilic cyclodextrins and pDNA for site-specific gene delivery. *Biomaterials 32*, 7263−7273.
(23) Bennevault-Celton, V., Urbach, A., Martin, O., Pichon, C., Guégan, P., and Midoux, P. (2011) Supramolecular assemblies of histidinylated α-cyclodextrin in the presence of DNA scaffold during CDplexes formation. *Bioconjugate Chem. 22*, 2404−2414.
(24) Méndez-Ardoy, A., Urbiola, K., Aranda, C., Ortiz Mellet, C., García-Fernández, J. M., and Tros de Ilarduya, C. (2011) Polycationic amphiphilic cyclodextrin-based nanoparticles for therapeutic gene delivery. *Nanomedicine 6*, 1697−1707.
(25) Méndez-Ardoy, A., Guilloteau, N., Di Giorgio, C., Vierling, P., Santoyo-González, F., Ortiz Mellet, C., and García Fernández, J. M. (2011) β-Cyclodextrin-based polycationic amphiphilic "click" clusters: effect of structural modifications in their DNA complexing and delivery properties. *J. Org. Chem. 76*, 5882−5894.
(26) Dudic, M., Colombo, A., Sansone, F., Casnati, A., Donofrio, G., and Ungaro, R. (2004) A general synthesis of water soluble upper rim calix[n]arene guanidinium derivatives which bind to plasmid DNA. *Tetrahedron 60*, 11613−11618.
(27) Farhood, H., Serbina, N., and Huang, L. (1995) The role of dioleoyl phosphatidylethanolamine in cationic liposome mediated gene transfer. *Biochim. Biophys. Acta, Biomembr. 1235*, 289−295.
(28) Bagnacani, V., Sansone, F., Donofrio, G., Baldini, L., Casnati, A., and Ungaro, R. (2008) Macrocyclic nonviral vectors: high cell transfection efficiency and low toxicity in a lower rim guanidinium calix[4]arene. *Org. Lett. 10*, 3953−3956.
(29) Gottlieb, H. E., Kotlyar, V., and Nudelman, A. (1997) NMR chemical shifts of common laboratory solvents as trace impurities. *J. Org. Chem. 62*, 7512−7515.
(30) Shinkai, S., Nagasaki, T., Iwamoto, K., Ikeda, A., He, G. X., Matsuda, T., and Iwamoto, M. (1991) New syntheses and physical properties of para-alkylcalix[n]arenes. *Bull. Chem. Soc. Jpn. 64*, 381−386.
(31) Chen, F. C. M., and Benoiton, N. L. (1976) A new method of quaternizing amines and its use in amino acid and peptide chemistry. *Can. J. Chem. 54*, 3310−3311.
(32) Shinkai, S., Arimura, T., Araki, K., Kawabata, H., Satoh, H., Tsubaki, T., Manabe, O., and Sunamoto, J. (1989) Syntheses and aggregation properties of new water-soluble calixarenes. *J. Chem. Soc., Perkin Trans. 1*, 2039−2045.
(33) Helttunen, K., and Shahgaldian, P. (2010) Self-assembly of amphiphilic calixarenes and resorcinarenes in water. *New J. Chem. 34*, 2704−2714.
(34) Rodik, R. V., Klymchenko, A. S., Jain, N., Miroshnichenko, S. I., Richert, L., Kalchenko, V. I., and Mely, Y. (2011) Virus-sized DNA nanoparticles for gene delivery based on micelles of cationic calixarenes. *Chem.—Eur. J. 17*, 5526−5538.
(35) Zinchenko, A. A., Pyshkina, O. A., Lezov, A. V., Sergeyev, V. G., and Yoshikawa, K. (2008) Single DNA Molecules: Compaction and Decompaction, *DNA Interactions with Polymers and Surfactants* (Dias, R. S., and Lindman, B., Eds.) pp 59−88, John Wiley & Sons, Inc., Hoboken, NJ.
(36) Golan, R., Pietrasanta, L. I., Hsieh, W., and Hansma, H. G. (1999) DNA toroids: stages in condensation. *Biochem. 38*, 14069−14076.

(37) Sternberg, B., Sorgi, F. L., and Huang, L. (1994) New structures in complex formation between DNA and cationic liposomes visualized by freeze-fracture electron microscopy. *FEBS Lett. 356*, 361−366.
(38) Pitard, B., Aguerre, O., Airiau, m., Lachages, A. M., Boukhnikachvili, T., Byk, G., Dubertret, C., Herviou, C., Scherman, D., Mayaux, J. F., and Crouzet, J. (1997) Virus-sized self-assembling lamellar complexes between plasmid DNA and cationic micelles promote gene transfer. *Proc. Natl. Acad. Sci. U.S.A. 94*, 14412−14417.
(39) Nakai, T., Kanamori, T., Sando, S., and Aoyama, Y. (2003) Remarkably size-regulated cell invasion by artificial viruses. saccharide-dependent self-aggregation of glycoviruses and its consequences in glycoviral gene delivery. *J. Am. Chem. Soc. 125*, 8465−8475.
(40) The discrepancy between the percentages of transfected cells of the Vero line reported here with respect to those indicated in ref 25 is due to the different clone used in the new experiments performed for this article. However, the substantial accordance found now and before in the gap (10%) between the efficiency of LTX and **5b**/DOPE confirms the data reproducibility and goodness.
(41) Diaz-Moscoso, A., Vercauteren, D., Rejman, J., Benito, J. M., Mellet, C. O., De Smedt, S. C., and Fernandez, J. M. G. (2010) Insights in cellular uptake mechanisms of pDNA-polycationic amphiphilic cyclodextrin nanoparticles (CDplexes). *J. Controlled Release 143*, 318−325.
(42) No significant deprotonation of guanidium groups directly linked at the upper rim of a calix[4]arene was observed till pH 8 in titration experiments. Baldini, L., Cacciapaglia, R., Casnati, A., Mandolini, L., Salvio, R., Sansone, F., and Ungaro, R. (2012) Upper Rim Guanidinocalix[4]arenes as Artificial Phosphodiesterases. *J. Org. Chem. 77*, 3381−3389.
(43) Hansma, H. G., Golan, R., Hsieh, W., Lollo, C. P., Mullen-Ley, P., and Kwoh, D. (1998) DNA condensation for gene therapy as monitored by atomic force microscopy. *Nucleic Acids Res. 26*, 2481−2487.
(44) Lalor, R., Di Gesso, J. L., Mueller, A., and Matthews, S. E. (2007) Efficient gene transfection with functionalised multicalixarenes. *Chem. Commun.*, 4907−4909.

Bioconjugate Chemistry

Article

pubs.acs.org/bc

Recognition of Dextran–Superparamagnetic Iron Oxide Nanoparticle Conjugates (Feridex) via Macrophage Scavenger Receptor Charged Domains

Ying Chao,[†] Milan Makale,[‡,§] Priya Prakash Karmali,[∥] Yuriy Sharikov,[‡] Igor Tsigelny,[‡,⊥] Sergei Merkulov,[¶] Santosh Kesari,[‡,§] Wolf Wrasidlo,[†,‡] Erkki Ruoslahti,[∥,#] and Dmitri Simberg[†,*]

[†]Moores Cancer Center, School of Medicine, [‡]Department of Neurosciences, and [⊥]San Diego Supercomputer Center, University of California San Diego, La Jolla, California, United States

[§]Neuro-Oncology Program, Moores Cancer Center, University of California, San Diego

[∥]Cancer Research Center, Sanford-Burnham Medical Research Institute, La Jolla, California, United States

[¶]Virogene LLC, Solon, Ohio, United States

[#]Vascular Mapping Center, Sanford-Burnham Medical Research Institute at University of California Santa Barbara, Santa Barbara, California, United States

Supporting Information

ABSTRACT: Dextran-coated superparamagnetic iron oxide nanoparticles (dextran–SPIO conjugates) offer the attractive possibility of enhancing MRI imaging sensitivity so that small or diffuse lesions can be detected. However, systemically injected SPIOs are rapidly removed by macrophages. We engineered embryonic cells (HEK293T) to express major macrophage scavenger receptor (SR) subtypes including SR-AI, MARCO, and endothelial receptor collectin-12. These SRs possess a positively charged collagen-like (CL) domain and they promoted SPIO uptake, while the charge neutral lipoprotein receptor SR-BI did not. In silico modeling indicated a positive net charge on the CL domain and a net negative charge on the cysteine-rich (CR) domain of MARCO and SR-AI. In vitro experiments revealed that CR domain deletion in SR-AI boosted uptake of SPIO 3-fold, while deletion of MARCO's CR domain abolished this uptake. These data suggest that future studies might productively focus on the validation and further exploration of SR charge fields in SPIO recognition.

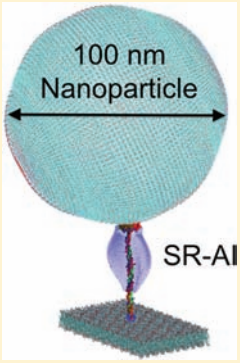

INTRODUCTION

Magnetic resonance imaging (MRI) is a modality that has long attracted considerable interest for early disease detection and staging. However, to be useful for small, indistinct lesions MRI often requires enhancement.[1] FDA-approved superparamagnetic iron oxide (SPIO) contrast agents are the most detectable and effective medium for enhancing contrast in MRI acquisitions.[2−6] A major difficulty with current SPIO formulations, viz., dextran-coated SPIO nanoparticles, is that they are avidly taken up by macrophages, which results in premature clearance, reduced effectiveness of imaging, and toxicity.[7−10] The mechanism of macrophage SPIO uptake is incompletely characterized, and we along with others[11−13] have sought to further elucidate this process to identify possible inhibitory strategies.

Much remains to be learned about the key specifics of particle uptake by macrophages, although it is known that uptake is opsonin-independent for many types of nanoparticles, including gold, silica,[14−16] polystyrene,[17] and liposomes.[18] SPIO-dextran uptake has recently been shown by us to be complement and IgG independent in mouse knockout models.[19] Although several classes of macrophage receptors could conceivably mediate SPIO recognition, multiple studies have collectively provided convincing data that SPIO uptake is coordinated by scavenger receptors (SRs).[11,12]

What remains to be elucidated is the specific mechanism of SPIO recognition by SRs. This is important, as it may provide an opportunity for selectively inhibiting or manipulating SPIO nanoparticle uptake by macrophages. Current evidence reveals that often it is polyanionic pathogen-associated molecular patterns that are eliminated by SRs.[12,15,17,20−22] Moreover, the major macrophage SR AI subtype (SR-AI) recognizes negatively charged surfaces via a positively charged collagen-like domain (CL-domain).[12,17,20,23] Therefore, we hypothesized that SPIO–dextran nanoparticles, which are weakly anionic, are recognized by the CL-domain of SRs. We further hypothesized that this mode of recognition might be differentially modulated among various SR subtypes.

Our hypotheses were addressed using in silico modeling of the SR domain charge field, together with a defined system in which human embryonic kidney cells (HEK293T) were engineered to individually express the major macrophage SR

Received: January 4, 2012
Revised: April 9, 2012
Published: April 19, 2012

   dx.doi.org/10.1021/bc200685a | *Bioconjugate Chem.* 2012, 23, 1003–1009

subtypes SR-AI, MARCO, SR-PSOX, SR-BI, and the primary endothelial SR collectin-12 (CL-P1). The experiments indicated that the net positively charged collagen-like domain mediated SPIO uptake by SR-AI, and deletion of a net negatively charged cysteine rich (CR) domain adjacent to the CL domain differentially affected SPIO binding to SR-AI versus MARCO.

The results of this modeling and in vitro study provide an essential step for followup investigations of SR mediated macrophage nanoparticle recognition and a comprehensive validation of various SR domains according to the fine structure of charge fields. This will lead to strategies for (i) inhibiting nanoparticle clearance, (ii) minimizing undesired labeling of macrophages, and (iii) targeting specific subpopulations of macrophages.

EXPERIMENTAL PROCEDURES

SPIO−Dextran Nanoparticle Preparation and Physical Characterization -. *Preparation and Storage of Nanoparticles.* Commercial Feridex I.V. nanoparticles were used for this study and were obtained from a commercial source on our behalf by the UCSD Department of Radiology. Feridex consists of a suspension of SPIO−dextran composites. Each composite is 50−160 nm across and contains multiple SPIO particles approximately 5−6 nm in diameter embedded in a meshwork of linear dextran (10 kDa, T-10). Particles were resuspended in PBS at 1−2 mg (Fe)/mL, filtered through a 0.2 μm membrane filter, and stored at 4 °C.

Nanoparticle Size Determination. The size distribution and ζ-potential of diluted aliquots of the nanoparticle suspension were measured with a Zetasizer Nano (Malvern, UK). To determine any effects of adherent plasma proteins on nanoparticle size, SPIO was mixed with citrated mouse plasma (1:3 volume ratio), incubated for 10 min, and applied to a MINI magnetic column (Miltenyi Biotech), then eluted and sized.

Nanoparticle Structure Determination. Nanoparticle structure was confirmed using transmission electron microscopy; 5 μL of 0.5 mg/mL of SPIO−dextran in double-distilled water was applied to Formvar/carbon-coated grids (Ted Pella, Redding, CA). After drying, grids were viewed using a JEOL 1200EX II (JEOL, Peabody, MA) transmission electron microscope at 75 keV and photographed using a Gatan digital camera (Gatan, Pleasanton, CA).

Scavenger Receptor Gene Cloning, Amplification, and Expression in HEK293T Cells. In order to provide a general characterization of SPIO recognition according to major SR subtypes, we transfected HEK293T cells using equal amounts of constructs coding for the following receptors: SR-AI, which is expressed on macrophages and monocytes;[24] MARCO, which is a macrophage receptor with collagenous structure expressed on macrophages resident in the lung alveoli, in the spleen, and in the liver (Kupffer cells);[25] lectin SR Collectin-12 (collectin placenta 1 or CL-P1, expressed on endothelial cells);[26] chemokine SR for phosphatidylserine and oxidized lipoproteins (PSOX/CXCL16, expressed on dendritic cells and atherogenic macrophages[27]); and ubiquitous lipoprotein receptor SR-BI.[28] The details of cloning, amplification, and expression are given below.

SR MARCO. A pCMV6-AC plasmid carrying full-length human macrophage receptor with collagenous structure (MARCO) as transfection-ready DNA (catalog SC319619) was purchased from OriGene (Rockville, MD). Human MARCO with the truncated cysteine domain and MARCO with charged collagen were designed with flanking *Bam*HI and XhoI restriction sites and synthesized by Epoch Life Sciences (Missouri City, TX); see Supporting Information for sequences of the construct and primers. The inserts were cloned into pCDNA3.1+(Zeo).

SR-AI (CR Domain +) and SR-AII (CR Domain −). Full-length mouse cDNA of SR-AI (splicing variant A, NM_001113326) was amplified from mouse liver mRNA by RT-PCR and cloned into a pCDNA 3.1+ plasmid using the *Bam*HI and XhoI restriction sites. pCMV-SPORT6 plasmid encoding mouse scavenger receptor SR-AII (splicing variant B; without the cysteine-rich domain) was obtained from ATCC (catalog MGC-6140), PCR amplified, and cloned into pCDNA 3.1. All inserts were verified by forward and reverse sequencing. Full details for the primers are provided in the Supporting Information.

SR-BI and Collectin-12 (Endothelial). A transfection-ready clone encoding human macrophage scavenger receptor SR-BI was obtained from ATCC in pCMV-SPORT6 cassette. A transfection-ready human Collectin Placenta 1 (CL-P1) or Collectin-12 in $pCMV_6$-XL4 cassette was obtained from OriGene.

Transfection of HEK293T Cells. HEK293T (ATCC) were transiently transfected using Lipofectamine 2000 (Invitrogen) with 0.5 μg of receptor plasmids or empty vector pCDNA 3.1 (Invitrogen) per 1×10^6 cells in 24 well plates. The mRNA expression of SR-AI, MARCO, CL-P1, and SR-BI was compared via quantitative PCR as described in Supporting Information.

Determination of Receptor Expression on the HEK293T Cell Surface. Comparisons of SPIO binding between receptor subtypes required equal SR densities on the cell surface to be valid or a measure of relative density by which to normalize binding data between receptor subtypes. Our assessment of receptor expression did not rely on one type of measure alone and was determined using three different approaches for cross-validation. First, we used immunostaining with MARCO rabbit anti-human polyclonal AP9891a, SR-BI rabbit anti-human monoclonal AJ1734a (both from Abgent, San Diego, CA), and rat anti-mouse SR-AI (R&D). The second approach involved Western blotting using rabbit anti-human MARCO (Abgent) and rat anti-mouse SR-AI (AbD Serotec MAB 1322). Cells were transfected with SR-AI and MARCO and fractionated with Mem-PER membrane isolation kit (Thermo). The quality of fractionation was determined with anti-HSP90 antibody (Cell Signaling Technology, Danvers, MA) as a cytoplasmic marker and anti-alpha1 sodium−potassium ATPase antibody (Abcam, Cambridge, MA) as a membrane marker. The level of SR-AI and MARCO in each fraction was compared with Western blotting using the above-described antibodies. The final measure of cell receptor expression was based on real-time PCR of the receptor transcripts (details in the SI).

SPIO Uptake and Binding Experiments. Nanoparticle uptake experiments in receptor-transfected HEK293T cells and in J774A.1 cells were performed similarly.

Uptake Measured by Optical Absorbance. Cells in 24 well plates were incubated with 0.1 mg/mL SPIO−dextran nanoparticles for 2 h in complete medium at 37 °C. For the ligand inhibition experiment, polyinosinic acid, dextran sulfate 500 kDa, fucoidan, dextran, or gelatin (all from Sigma) were incubated with J774A.1 cells for 15 min prior to the addition of

nanoparticles. SPIO uptake was quantified by adding 200 μL of QuantiChrom Iron Assay reagent (BioAssay Systems), overnight incubation, and measurements of relative absorbance (570 nm). For cell binding experiments, SPIO was added to cells at 4 °C at 3-fold higher concentration (0.3 mg/mL) for 15 min, washed, and assayed as above.

Microscopy-Based Measurements of SPIO Uptake. Cells were seeded into 8-well chamber slides (NalgeNunc) and incubated for 2 h with 0.1 mg/mL SPIO, washed, fixed with 4% formaldehyde, and stained with Prussian blue dye[29] to visualize iron inside the cells.

SPIO Binding to Type I Collagen. To determine whether SPIO does in fact bind to collagen, which comprises the CL domain of SRs, microwell 96-well plates (Costar) were coated with either calf skin type I collagen (100 μg/mL 0.1 M acetic acid/PBS; Sigma, C3511) or BSA/PBS (controls) and blocked with 1% BSA/PBS. SPIO solution (3, 10, 30, or 100 μg/mL of Fe in PBS) was added and bound iron quantified using the QuantiChrom Iron Assay as described previously.

In Silico Modeling of SR Domains. We sought to predict whether SR domains might possess charge differences that form the basis of differential recognition between SR receptor subtypes. Therefore, modeling of the SR-AI and MARCO electrostatic charge fields was performed using the homology module of Insight II software (Accelrys, San Diego) on the San Diego supercomputer at UCSD. Collagen-like domains were modeled based on the type I collagen (PDB ID 3HQV). The cysteine-rich domain models were based on the crystal structure of the monomeric cysteine-rich domain of mouse MARCO (PDB ID 2OY3). Equipotential maps of receptor charges were plotted using the NAMD program.[30] For human SR-BI, the charge was estimated as the number of charged ionizable residues (positive, ARG and LYS (+1); negative, GLU and ASP (−1)) per 10 residues at pH 7.5.

RESULTS

SPIO−Dextran Nanoparticle Physical Characteristics. *SPIO Nanoparticle Size and Structure.* We used the commercial SPIO MRI contrast agent Ferridex I.V., which is essentially a SPIO−dextran nanoparticle, to study SPIO recognition by macrophage SRs. The measured diameter of the SPIO dextran particles (composites) was between 80 and 150 nm (average 112 nm), and zeta potential was slightly negative, −13 mV (Figure 1A,B). TEM confirmed our expectation that the particles consisted of several 5 nm cores of crystalline iron oxide embedded in a meshwork of dextran. The clusters exhibited a worm-like shape, although irregular aggregates were also visible (Figure 1C).

SPIO Uptake by SRs. *SPIO Uptake by Macrophages Is Mediated via SRs and Blocked by Charged Polymers.* Previously reported SR-dependent recognition/uptake of Feridex by J774a.1 macrophages was confirmed by inhibition experiments using various SR ligands (Figure 2). Addition of the polyanionic scavenger receptor ligands fucoidan (10 μg/mL) or dextran sulfate (3 μg/mL) to J774A.1 macrophages prior to the addition of SPIO produced up to 80% inhibition of SPIO uptake (P value = 0.0003 for dextran sulfate). The addition of positively charged gelatin (hydrolyzed collagen) at 1 mg/mL also inhibited the uptake, whereas branched 20 kDa dextran at 1 mg/mL had no effect (data not shown). The suppression of Feridex uptake by known SR polyanionic ligands confirms that in J774A.1 macrophages recognition is mostly SR-dependent, and inhibition by both positively and negatively charged polymers provides a preliminary indication that charge interactions may play an important role in the uptake.

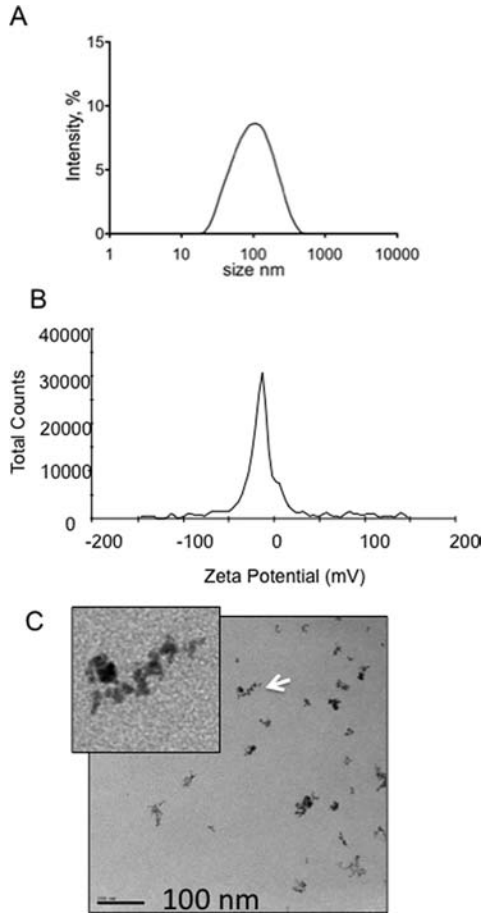

Figure 1. Physical characterization of Feridex (SPIO nanoparticles). (A) SPIO nanoparticle size (intensity) distribution. Particles were processed as described in Experimental Procedures; (B) zeta potential of particles; (C) TEM of SPIO nanoparticle (Feridex), magnification 60 000×. Size bar = 100 μm. Inset, cropped area showing a representative nanoparticle consisting of a cluster of electron-dense magnetite−maghemite crystals (white arrow on the main image).

Charged SRs Exhibited Greater SPIO Uptake. Transiently transfected MARCO, SR-BI, and CL-PI showed similar levels of mRNA expression based on quantitative PCR, while SR-AI showed about 50% lower mRNA expression (SI Figure S1A-B). For SR-AI, SR-BI, and MARCO, we also verified the expression with Western blotting and confirmed membrane expression with immunostaining (see SI Figure S2 and data below).

According to the Prussian blue staining and iron quantification (Figure 3A,B), SR-AI, CL-P1, SR-PSOX, and MARCO, which have positively charged SRs, significantly promoted the binding and uptake of SPIO by HEK293T cells (5−20-fold increase compared to vector-transfected), while the charge-neutral SR-BI did not show any uptake despite being expressed on the cell surface (SI Figure S2). According to charge calculations, the SR-BI extracellular domain has a neutral charge of +0.05, and no charged domains were detected in the sequence.

SPIO Binds to Type I Collagen. SR-AI, MARCO, and CL-P1 each possess a positively charged CL domain (Figure 4A), and we sought to determine if the SPIO−dextran nanoparticle could bind collagen alone. Collagen type I has a cationic heparin-binding site with affinity of 150 nM.[31,32] We tested the

dx.doi.org/10.1021/bc200685a | Bioconjugate Chem. 2012, 23, 1003−1009

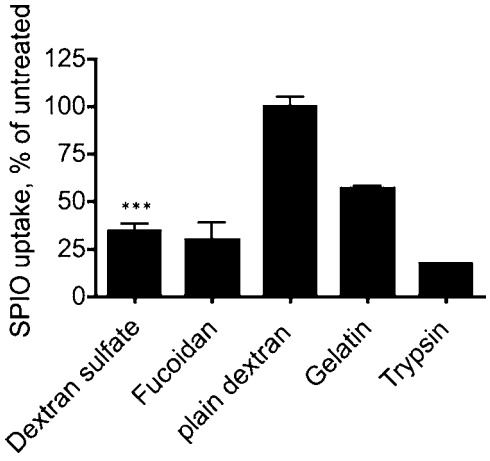

Figure 2. SR ligand tests confirm SPIO uptake mediated by SRs. SPIO nanoparticle uptake by the macrophages in the presence of various inhibitors (n = 3–5). Addition of polyanionic SR ligands fucoidan (10 μg/mL) and dextran sulfate (3 μg/mL) to J774A.1 macrophages prior to SPIO resulted in 65–76% inhibition of uptake (nonparametric Mann–Whitney test, p value = 0.0003, n = 3). The uptake was also inhibited by 1 mg/mL gelatin. These data suggest that the mechanism of SPIO nanoparticle uptake is SR-dependent and may be based on electrical charge. Pretreatment of J774A.1 cells with 0.1 mg/mL trypsin reduced the uptake by 80%, confirming that a protein receptor is needed.

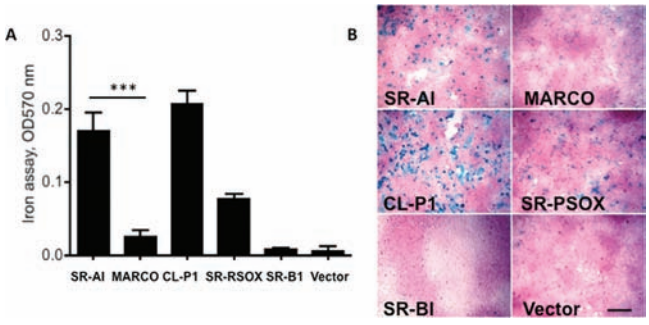

Figure 3. SPIO nanoparticle uptake of transiently expressed macrophage SRs. HEK293T cells were transiently transfected with the same amounts of receptor-coding plasmids and then incubated with 0.1 mg/mL SPIO (Feridex) in 10% FBS-supplemented medium for 2 h. (A) Uptake of SPIO by cells transfected with SRs quantified with QuantiChrom Iron Assay Kit (see Experimental Section), p-value 0.0007, nonpaired t test, n = 5. Only receptors with charged domains show uptake. (B) Example images of cells were stained with Prussian Blue and Nuclear Fast Red and the images were taken at low magnification (4× objective). A representative experiment out of five is shown. Size bar = 200 μm.

binding of Feridex to a collagen type I-coated plate. There was a concentration-dependent binding that was completely inhibited by addition of polyanionic dextran sulfate 500 kDa to the plate prior to the addition of nanoparticles (Figure 4B, SI Figure S3).

SR Domain Effects on SPIO Binding and Uptake by MARCO and SR-AI. *MARCO and SR-AI Exhibited Different Uptake.* SPIO uptake by Prussian blue (Figure 5A) showed major differences between SR-AI and MARCO (quantitatively 8-fold difference, Figure 3A). We tested whether this difference is due to the unequal cell surface expression. Immunostaining of the cell surface receptors (Figure 5A bottom panel) and Western blot analysis of the membrane fraction (Figure 5B)

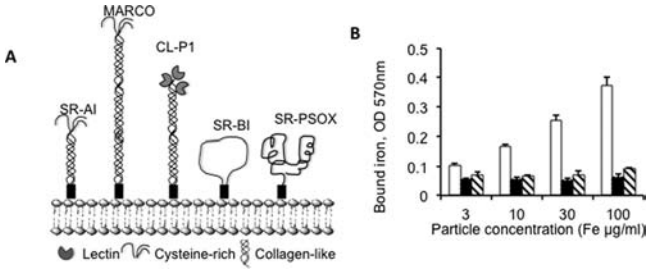

Figure 4. SPIO binding to collagen-coated surface. (A) Schematic representation of SRs based on previously published literature. SR-AI, MARCO, and CL-P1 contain collagen-like domains (stem) in the extracellular portion. (B) In order to mimic the binding to cationic collagenous receptors, microplate wells were coated with charged collagen type I, and SPIO nanoparticles were incubated in PBS as described in Experimental Section. The binding was only to collagen-coated wells (open bars) and not to BSA-coated wells (solid bars). The binding was inhibited by 10 μg/mL dextran sulfate (striped bars).

showed that both receptors are expressed on the cell surface at the approximately same level. The binding of SPIO to receptor-transfected cells showed about 5-fold higher binding to SR-AI than to MARCO (Figure 5C).

Predicted Charge Differences between SRs. We sought to determine whether differences between SR-AI and MARCO are due to differences in SR domains. As an initial strategy, we modeled charge, which is the most obvious, but not necessarily the only, possible basis for any differential domain effects on SPIO binding. After predicting possible differences between the domains, according to charge, we were prompted to follow up with uptake experiments in which the CR domain was either added or deleted.

Using well-validated and widely used structural modeling approaches and software (see Experimental Procedures), 3D crystal structure-based models of the extracellular region and its electrostatic profile were built for human SR-AI and for murine MARCO (Figure 6). The crystal structure of human MARCO is not available, but murine and human MARCO share >70% sequence identity[33] and 96% charge amino acid identity (Supporting Information). According to the 3D equipotential (from +1.8 to −1.8) surface charge map for both SRs (Figure 6), the CL domain positive charge field extends well outside the protein backbone. In contrast, the C-terminal CR domain of both SRs had a negative charge field (Figure 6). Interestingly, the net positive charge field of MARCO was lower than SR-AI, suggesting the possibility of differential effects on recognition by the CR domain.

CL/CR Domain Effects on SPIO Uptake in SR Subtypes. Functional tests were made to determine in vitro whether the CL versus thr CR domain has differential effects on SR–SPIO binding. SR-AI and MARCO were compared since they are structurally very similar, and we made the working assumption that uptake differences between them would be more influenced by the CL and CR domains rather than overall SR structure.

We prepared shortened isoforms of SR-AI (known as SR-AII) and MARCO in which the entire CR domain was deleted (Figure 7A). In addition, we prepared a chimeric MARCO/SR-AI receptor by fusing a highly charged collagen fragment of SR-AI to the C-terminal part of MARCO's CL domain (Figure 7A). This charged collagen fragment is known to mediate the binding of acetylated LDL to SR-AI and to inhibit ligand binding.[23] The expression of the constructs on the cell surface

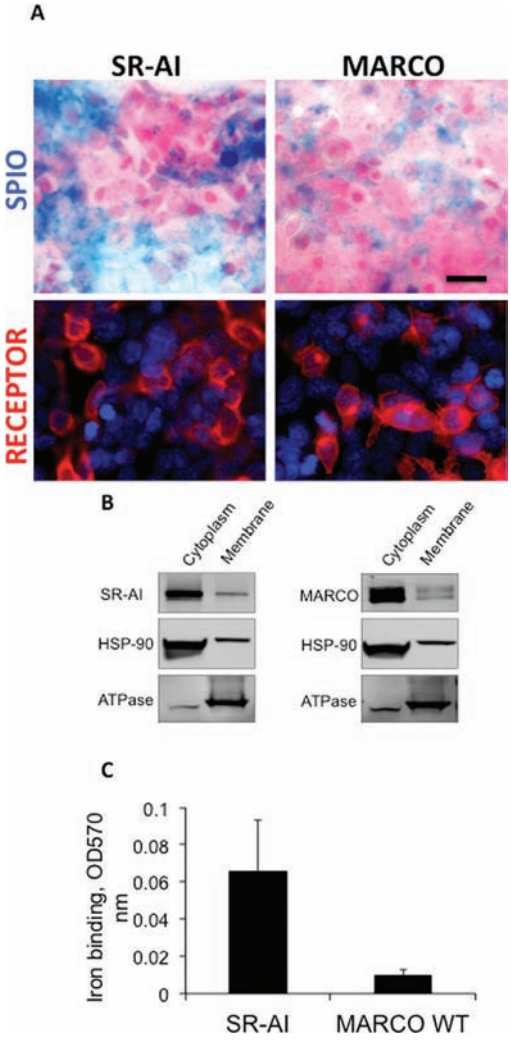

Figure 5. Comparison of SPIO uptake by SR-AI and MARCO. (A) Upper panel: SPIO uptake by receptor-transfected HEK293T cells. The experiment was performed as in Figure 3B. Cropped areas are shown. Size bar = 50 μm. Lower panel: Staining of the receptors on the cell surface (described in Experimental Section). (B) Western blotting of SR-AI and MARCO after cell fractionation. Both cytoplasmic and membrane fractions are positive for the receptors. Majority of the receptor is in intracellular compartment. HSP90 and Na+, K+ ATPase staining confirms fractionation efficiency. (C) SPIO binding to cells at 4 °C shows the difference in binding efficiency between SR-AI and MARCO.

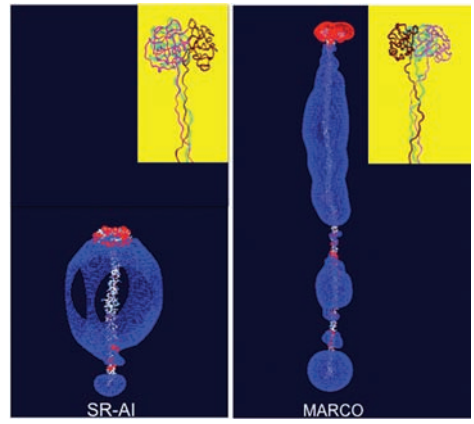

Figure 6. Molecular models of SRs and their electrostatic profiles. Electrostatic profiles of mouse MARCO and mouse SR-AI receptors are shown as equipotential surfaces for the values of +1.8 (blue) or −1.8 (red) charges. Note the higher positive charge density of SR-AI and MARCO CL-domain per unit length versus the overall negative charge of the C-terminal CR-domain (red color). Inset: Ribbon presentation of the 3D models of MARCO and SR-AI receptors used for charge profile reconstruction. Different colors denote the three subunits of each receptor.

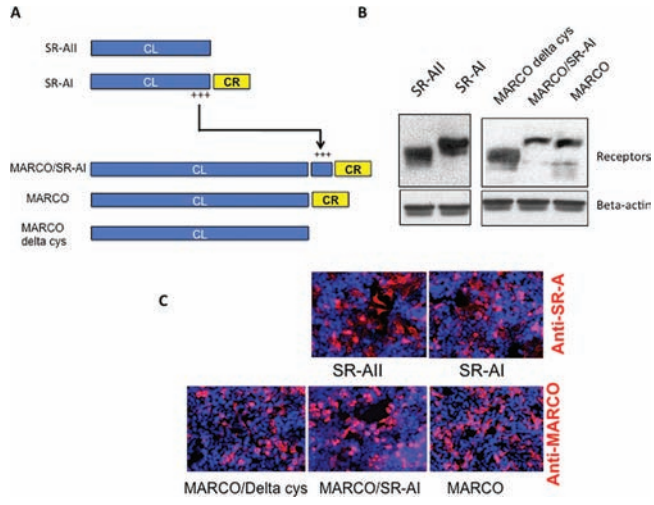

Figure 7. Modifications and expression of SR-AI and MARCO. (A) CR DOMAIN of SR-AI was deleted. The charged collagen sequence from SR-AI was fused to C-terminal portion of MARCO's CL DOMAIN. CR DOMAIN of MARCO was deleted. (B) SRs were expressed on HEK293T cells and the levels of expression were verified by Western blotting. (C) To demonstrate equal efficiency of transfection, the cells were stained with antibodies against the SRs. High-magnification images of MARCO receptor staining in the membrane are provided in Supporting Information.

was verified with Western blotting and immunostaining (Figure 7B,C; SI Figure S4).

Deletion of the CR domain in SR-AI boosted SPIO uptake almost 3-fold (Figure 8A). The cell binding studies performed at 4 °C showed similar effect of CR domain deletion on SR-AI mediated uptake (Figure 8B). Deletion of MARCO's CR domain abolished the uptake (Figure 8C), whereas fusion of the SR-AI collagen fragment to MARCO increased MARCO uptake 2-fold (Figure 8C). These results suggest that the CL and CR domains on different SRs may produce a different net effect, and future experiments will examine in greater detail the mechanims of iron nanoparticle recognition in the context of domain charge fields in different SRs.

■ DISCUSSION

SPIO nanoparticle-based contrast media for MRI are recognized and scavenged by macrophages. This clearance of circulating contrast agent reduces the amount of MRI label available for target tissue contrast enhancement. Moreover, interpretation of MRI volumes becomes complicated because the scavenging macrophages end up being labeled and detected. This obstacle to effective MR imaging may potentially be addressed by selective macrophage SR inhibitors, but currently available polyanionic SR antagonists are not selective and are toxic. The present study was intended to contribute to our

dx.doi.org/10.1021/bc200685a | Bioconjugate Chem. 2012, 23, 1003−1009

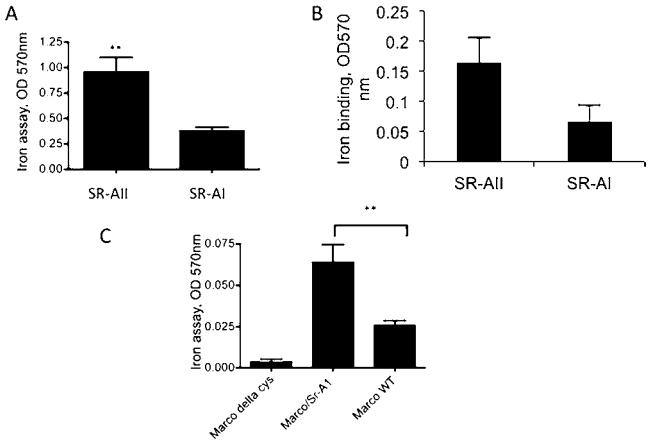

Figure 8. CL-CR domains influence SR mediated SPIO uptake in vitro. Uptake of the constructs shown in Figure 6 was quantified with an iron assay. (A) SR-AI and SR-AII mediated uptake. Deletion of SR-AI CR DOMAIN increases the SPIO uptake 3-fold (nonparametric Mann–Whitney test, p-value 0.0026, n = 3). (B) Binding of SPIO to SR-AI and SR-AII transfected HEK293T cells at 4 °C. Cells were grown, transfected in 24 well plates, and incubated with 0.3 mg/mL SPIO at 4 °C for 15 min. Results of a triplicate measurement are shown. (C) MARCO-mediated uptake. Addition of the charged CL to MARCO increased the uptake 2-fold (non-parametric Mann–Whitney test, p-value 0.013, n = 5), but the uptake was still much lower than that of SR-AI cells. Deletion of the CR DOMAIN in MARCO completely blocked SPIO uptake.

understanding of SPIO recognition to provide a basis for further work leading to selective inhibitors of SR-mediated SPIO recognition.

Our data confirmed previous observations that SPIO uptake by macrophages is mediated by SRs[11,12] and demonstrated that physical differences in collagen-like (CL) and cysteine-rich (CR) domains very likely charge-related and may provide a basis for differential recognition and uptake of SPIO and other nanoparticles according to SR subtype. These results provide an initial point of departure for more detailed investigations of SR recognition and specificity, and the precise contribution of charge field fine structure.

Our test platform was the embryonic kidney cell (HEK293T) expression system, and we were able to acquire consistent results and successfully confirm previous reported findings for SRs and SPIO. SPIO nanoparticles were recognized by two major and well-defined SRs, SR-AI and MARCO, by the SR Collectin-12, which is expressed on endothelial cells,[26] and by SR-PSOX, which is mainly expressed on dendritic cells and macrophages in atherosclerotic lesions.

According to our in vitro uptake data, and in agreement with our hypothesis that the CL domain plays a key role in SPIO uptake, the CL domain appears to involve mediate recognition of SPIO nanoparticles by SR-AI. We found that the common feature of tested receptors that bound and internalized SPIO–dextran was the presence of a positively charged CL domain, and in agreement with this observation, it has been reported that the positively charged fragment of the SR-AI CL domain mediates the binding of polyanionic ligands and negatively charged, acetylated LDL.[23]

Importantly, there was a distinct difference in the uptake mechanism between SR-AI and MARCO despite their similar overall structures. Differences in recognition between these two receptor subtypes are suggested by previous reports indicating that MARCO recognizes other anionic nanoparticles and recognizes larger iron oxide particulates.[4,22] There was no evidence of iron aggregation, which might favor MARCO, in our experiments, and transiently transfected MARCO in fact had lower uptake than SR-AI, despite the two having similar levels of cell surface expression. The reason for this difference is not clear but could be related to the difference in charge properties of the receptor domains. Deletion of the CR domain from SR-AI boosted uptake, and a similar effect was observed by Doi et al.[23] for the uptake of acetylated lipoprotein. However, deletion of MARCO's CR domain abolished uptake, indicating a differential effect of the CR domain depending on SR subtype.

Our in silico models show a net negative charge for the CR domain, and other studies have reported that MARCO's CR domain has a fine structure comprising positive and negative subdomains.[34] This could influence nanoparticle recognition in subtle ways. Bacteria and nanoparticle uptake studies of MARCO and SR-AI have uncovered different SR specificities,[25,34,35] and deletion of the MARCO CR domain abolishes the uptake of bacteria.[34] Since MARCO may recognize SPIO–dextran and other particles through a somewhat different binding mechanism than SR-AI, there is a need for future, specific in vitro experiments that would be conceptually linked with what is known about SR behavior and with further, detailed modeling of the fine structure of charge domains and charge interactions between closely spaced receptors. For example, SRs have been reported to form clusters on the cell surface,[36] and such receptor clustering could have important implications on local charge fields and on SPIO binding.

In conclusion, we demonstrated that a variety of SRs are able to promote the uptake of dextran-coated SPIO (Feridex) in vitro, with the positively charged CL domain largely responsible for uptake by SR-AI. The precise role of the CR domain and charge fields in SPIO uptake by different SR subtypes remains to be elucidated. Specific further investigations suggested by the present study may provide a basis for defined strategies by which to selectively inhibit macrophage uptake of SPIO.

■ ASSOCIATED CONTENT

Supporting Information

The methods for receptor cloning and expression by PCR are described. In addition, we provide and explain data that documents the expression of the receptor subtypes in HEK293T cells. This material is available free of charge via the Internet at http://pubs.acs.org.

■ AUTHOR INFORMATION

Corresponding Author

*Tel: 858-822-6922. E-mail: dsimberg@ucsd.edu.

Notes

The authors declare no competing financial interest.

■ ACKNOWLEDGMENTS

We would like to thank Dr. Yuko Kono (UCSD Department of Medicine) for providing us with Feridex I.V. This work was supported by NCI Grant 5U54CA119335 to E.R. and CA 137721-01 to D.S., and by the UCSD Cancer Center Specialized Support Grant P30 CA23100.

REFERENCES

(1) Rosen, E. L., Blackwell, K. L., Baker, J. A., Soo, M. S., Bentley, R. C., Yu, D., Samulski, T. V., and Dewhirst, M. W. (2003) Accuracy of MRI in the detection of residual breast cancer after neoadjuvant chemotherapy. *Am. J. Roentgenol. 181*, 1275−82.

(2) Gupta, A. K., and Gupta, M. (2005) Synthesis and surface engineering of iron oxide nanoparticles for biomedical applications. *Biomaterials 26*, 3995−4021.

(3) Coroiu, I. (1999) Relaxivities of different superparamagnetic particles for application in NMR tomography. *J. Magn. Magn. Mater. 201*, 449−452.

(4) Le Duc, G., Elst, L. V., Colet, J. M., Roch, A., Gillis, P., Le Bas, J. F., and Muller, R. N. (2001) Ultrasmall particulate iron oxides as contrast agents for magnetic resonance spectroscopy: A dose-effect study. *J. Magn. Reson. Imaging 13*, 619−626.

(5) Bulte, J. W. M., Hoekstra, Y., Kamman, R. L., Magin, R. L., Webb, A. G., Briggs, R. W., Go, K. G., Hulstaert, C. E., Miltenyi, S., The, T. H., and Deleij, L. (1992) Specific MR imaging of human-lymphocytes by monoclonal antibody-guided dextran-magnetite particles. *Magn. Reson. Med. 25*, 148−157.

(6) Josephson, L., Tung, C. H., Moore, A., and Weissleder, R. (1999) High-efficiency intracellular magnetic labeling with novel superparamagnetic-tat peptide conjugates. *Bioconjugate Chem. 10*, 186−191.

(7) Dobrovolskaia, M. A., and McNeil, S. E. (2007) Immunological properties of engineered nanomaterials. *Nat. Nanotechnol. 2*, 469−78.

(8) Berry, C. C., Wells, S., Charles, S., Aitchison, G., and Curtis, A. S. (2004) Cell response to dextran-derivatised iron oxide nanoparticles post internalisation. *Biomaterials 25*, 5405−13.

(9) Oberdorster, G., Oberdorster, E., and Oberdorster, J. (2005) Nanotoxicology: an emerging discipline evolving from studies of ultrafine particles. *Environ. Health Perspect. 113*, 823−39.

(10) Weissleder, R., Stark, D. D., Engelstad, B. L., Bacon, B. R., Compton, C. C., White, D. L., Jacobs, P., and Lewis, J. (1989) Superparamagnetic iron oxide: pharmacokinetics and toxicity. *Am. J. Roentgenol. 152*, 167−73.

(11) Lunov, O., Zablotskii, V., Syrovets, T., Rocker, C., Tron, K., Nienhaus, G. U., and Simmet, T. (2011) Modeling receptor-mediated endocytosis of polymer-functionalized iron oxide nanoparticles by human macrophages. *Biomaterials 32*, 547−55.

(12) Raynal, I., Prigent, P., Peyramaure, S., Najid, A., Rebuzzi, C., and Corot, C. (2004) Macrophage endocytosis of superparamagnetic iron oxide nanoparticles: mechanisms and comparison of ferumoxides and ferumoxtran-10. *Invest. Radiol. 39*, 56−63.

(13) Moore, A., Weissleder, R., and Bogdanov, A., Jr. (1997) Uptake of dextran-coated monocrystalline iron oxides in tumor cells and macrophages. *J. Magn. Reson. Imaging 7*, 1140−5.

(14) Demoy, M., Andreux, J. P., Weingarten, C., Gouritin, B., Guilloux, V., and Couvreur, P. (1999) In vitro evaluation of nanoparticles spleen capture. *Life Sci. 64*, 1329−37.

(15) Kobzik, L. (1995) Lung macrophage uptake of unopsonized environmental particulates. Role of scavenger-type receptors. *J. Immunol. 155*, 367−76.

(16) Leroux, J. C., De Jaeghere, F., Anner, B., Doelker, E., and Gurny, R. (1995) An investigation on the role of plasma and serum opsonins on the internalization of biodegradable poly(D,L-lactic acid) nanoparticles by human monocytes. *Life Sci. 57*, 695−703.

(17) Kanno, S., Furuyama, A., and Hirano, S. (2007) A murine scavenger receptor MARCO recognizes polystyrene nanoparticles. *Toxicol. Sci. 97*, 398−406.

(18) Kamps, J. A., and Scherphof, G. L. (1998) Receptor versus non-receptor mediated clearance of liposomes. *Adv. Drug Delivery Rev. 32*, 81−97.

(19) Simberg, D., Park, J. H., Karmali, P. P., Zhang, W. M., Merkulov, S., McCrae, K., Bhatia, S. N., Sailor, M., and Ruoslahti, E. (2009) Differential proteomics analysis of the surface heterogeneity of dextran iron oxide nanoparticles and the implications for their in vivo clearance. *Biomaterials 30*, 3926−33.

(20) Nagayama, S., Ogawara, K., Minato, K., Fukuoka, Y., Takakura, Y., Hashida, M., Higaki, K., and Kimura, T. (2007) Fetuin mediates hepatic uptake of negatively charged nanoparticles via scavenger receptor. *Int. J. Pharm. 329*, 192−8.

(21) Shnyra, A., and Lindberg, A. A. (1995) Scavenger receptor pathway for lipopolysaccharide binding to Kupffer and endothelial liver cells in vitro. *Infect. Immun. 63*, 865−73.

(22) Xu, Z., Tian, J., Smith, J. S., and Byrnes, A. P. (2008) Clearance of adenovirus by Kupffer cells is mediated by scavenger receptors, natural antibodies and complement. *J. Virol.,*.

(23) Doi, T., Higashino, K., Kurihara, Y., Wada, Y., Miyazaki, T., Nakamura, H., Uesugi, S., Imanishi, T., Kawabe, Y., Itakura, H., et al. (1993) Charged collagen structure mediates the recognition of negatively charged macromolecules by macrophage scavenger receptors. *J. Biol. Chem. 268*, 2126−33.

(24) Kodama, T., Freeman, M., Rohrer, L., Zabrecky, J., Matsudaira, P., and Krieger, M. (1990) Type I macrophage scavenger receptor contains alpha-helical and collagen-like coiled coils. *Nature 343*, 531−5.

(25) Arredouani, M. S., and Kobzik, L. (2004) The structure and function of marco, a macrophage class a scavenger receptor. *Cell. Mol. Biol. (Noisy-le-grand) 50 Online Pub*, OL657−65.

(26) Ohtani, K., Suzuki, Y., Eda, S., Kawai, T., Kase, T., Keshi, H., Sakai, Y., Fukuoh, A., Sakamoto, T., Itabe, H., Suzutani, T., Ogasawara, M., Yoshida, I., and Wakamiya, N. (2001) The membrane-type collectin CL-P1 is a scavenger receptor on vascular endothelial cells. *J. Biol. Chem. 276*, 44222−8.

(27) Shimaoka, T., Kume, N., Minami, M., Hayashida, K., Kataoka, H., Kita, T., and Yonehara, S. (2000) Molecular cloning of a novel scavenger receptor for oxidized low density lipoprotein, SR-PSOX, on macrophages. *J. Biol. Chem. 275*, 40663−6.

(28) Ryeom, S. W., Silverstein, R. L., Scotto, A., and Sparrow, J. R. (1996) Binding of anionic phospholipids to retinal pigment epithelium may be mediated by the scavenger receptor CD36. *J. Biol. Chem. 271*, 20536−9.

(29) Litovsky, S., Madjid, M., Zarrabi, A., Casscells, S. W., Willerson, J. T., and Naghavi, M. (2003) Superparamagnetic iron oxide-based method for quantifying recruitment of monocytes to mouse atherosclerotic lesions in vivo: enhancement by tissue necrosis factor-alpha, interleukin-1beta, and interferon-gamma. *Circulation 107*, 1545−9.

(30) Phillips, J. C., Braun, R., Wang, W., Gumbart, J., Tajkhorshid, E., Villa, E., Chipot, C., Skeel, R. D., Kale, L., and Schulten, K. (2005) Scalable molecular dynamics with NAMD. *J. Comput. Chem. 26*, 1781−802.

(31) Sweeney, S. M., Guy, C. A., Fields, G. B., and San Antonio, J. D. (1998) Defining the domains of type I collagen involved in heparin-binding and endothelial tube formation. *Proc. Natl. Acad. Sci. U. S. A. 95*, 7275−80.

(32) San Antonio, J. D., Lander, A. D., Karnovsky, M. J., and Slayter, H. S. (1994) Mapping the heparin-binding sites on type I collagen monomers and fibrils. *J. Cell Biol. 125*, 1179−88.

(33) Kraal, G., van der Laan, L. J., Elomaa, O., and Tryggvason, K. (2000) The macrophage receptor MARCO. *Microbes Infect. 2*, 313−6.

(34) Ojala, J. R., Pikkarainen, T., Tuuttila, A., Sandalova, T., and Tryggvason, K. (2007) Crystal structure of the cysteine-rich domain of scavenger receptor MARCO reveals the presence of a basic and an acidic cluster that both contribute to ligand recognition. *J. Biol. Chem. 282*, 16654−66.

(35) Jozefowski, S., Arredouani, M., Sulahian, T., and Kobzik, L. (2005) Disparate regulation and function of the class A scavenger receptors SR-AI/II and MARCO. *J. Immunol. 175*, 8032−41.

(36) Peng, Y., Akmentin, W., Connelly, M. A., Lund-Katz, S., Phillips, M. C., and Williams, D. L. (2004) Scavenger receptor BI (SR-BI) clustered on microvillar extensions suggests that this plasma membrane domain is a way station for cholesterol trafficking between cells and high-density lipoprotein. *Mol. Biol. Cell 15*, 384−96.

Bioconjugate Chemistry

Article

pubs.acs.org/bc

Luminescent/Magnetic Hybrid Nanoparticles with Folate-Conjugated Peptide Composites for Tumor-Targeted Drug Delivery

Jian-Min Shen,[†,‡] Xing-Mei Guan,[†] Xiao-Yan Liu,[†] Jing-Feng Lan,[†] Ting Cheng,[†] and Hai-Xia Zhang*[,†]

[†]Key Laboratory of Nonferrous Metal Chemistry and Resources Utilization of Gansu Province and [‡]School of Life Sciences, Lanzhou University, Lanzhou 730000, China

Supporting Information

ABSTRACT: We developed a novel chitosan-based luminescent/magnetic hybrid nanoparticles with folate-conjugated tetrapeptide composites (CLMNPs-tetrapeptide-FA) by conjugation in situ. First, chitosan, CdTe quantum dots (QDs), and superparamagnetic iron oxide were directly gelled into ternary hybrid nanogels. Subsequently, tetrapeptides (GFFG and LGPV) and folate were conjugated orderly into the hybrid nanoparticles. The morphology, composition, and properties of the as-prepared copolymers have also been characterized and determined using TEM, EDX, XRD, FTIR spectra, DLS, fluorescence spectroscopy, VSM, and fluorescence microscopy imaging studies. The size range of the end product CLMNPs-tetrapeptide-FA copolymers was from 150 to 190 nm under simulated physiological environment. In vivo, the experimental results of magnetic accumulation showed that the copolymers could be trapped in the tumor tissue under magnetic guidance. Under the present experimental conditions, the loading efficiencies of CPT were approximately 8.6 wt % for CLMNPs-GFFG-FA and 1.1 wt % for CLMNPs-LGPV-FA, respectively. The CPT cumulative release under dialysis condition mainly occurred for the first 28 h, and could reach 55% at pH 5.3 and 46% at pH 7.4 from CPT-loaded CLMNPs-GFFG-FA, and 69% at pH 5.3 and 57% at pH 7.4 from CPT-loaded CLMNPs-LGPV-FA within 28 h, respectively. The hemolysis percentages (<2%) and coagulation properties of blank and CPT-loaded copolymers were within the scope of safe values. Compared to free CPT, the CPT-loaded CLMNPs-tetrapeptide-FA copolymers showed specific targeting to A549 cells in vitro. More than 75% viability in L02 cells were seen in CLMNPs-GFFG-FA and CLMNPs-LGPV-FA copolymer concentration of 500 μg/mL, respectively. It was found that the two kinds of copolymers were transported into the A549 cells by a folate-receptor-mediated endocytosis mechanism. These results indicate that the multifunctional CLMNPs-tetrapeptide-FA copolymers possess a moderate CPT loading efficiency, low cytotoxicity, and favorable biocompatibility, and are promising candidates for tumor-targeted drug delivery.

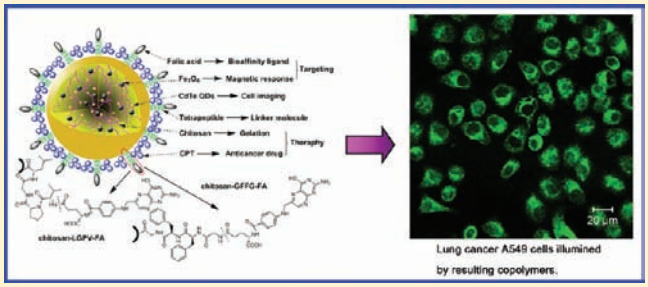

INTRODUCTION

Camptothecin (CPT) is regarded as the broad-spectrum anticancer agent that can inhibit effectively the relaxation process of DNA related to replication and transcription by the stable combination with topoisomerase I and DNA.[1,2] However, the severe side effects, including leukopenia and hemorrhagic cystitis, limited its clinical applications.[3] In addition, CPT molecule is easy to transform from the lactone form to carboxylate form in the medium, which leads to a complete loss of anticancer activity.[4] The poor water solubility of CPT is another problem hindering the development of CPT as a chemotherapy agent.[5] As a consequence, a variety of micelles and carriers for CPT delivery were developed to decrease potent toxicities and improve its properties.[6−8] However, some results may not necessarily be satisfactory due to excessively slow release of CPT from micelles.[9,10] In fact, two critical measures should be adopted in the course of CPT delivery, i.e., specific targeting and appropriate shelter for CPT.

In recent years, a variety of ferroferric oxide magnetic nanoparticles (MNPs) have been widely applied in biomedical fields, including drug delivery,[11,12] magnetic targeting,[13] and cell imaging.[14] It has been achievable to synthesize multifunctional MNPs based on a specific application objective.[15] Delivering CPT under magnetic induction for targeting chemotherapy will permit CPT to preferentially anchor them to the site of the tumor, which would potentially maximize therapeutic effect with minimal toxicity.[13] Further, the magnetic drug carrier labeled fluorescent dye (e.g., quantum dots, QDs) could be tracked to obtain imaging of migration and anchoring of drug in vivo.[16] In the course of assembly of the multifunctional drug carriers, MNPs and QDs introduced must be precoated with proper matrix to ensure their stability, biocompatibility, and nontoxicity in the physiological medium.[17] Chitosan is an available gelation material that has been broadly used for drug delivery due to its precious properties, such as biological functionality, safety, and biodegradability.[18,19]

Received: January 8, 2012
Revised: April 7, 2012
Published: April 10, 2012

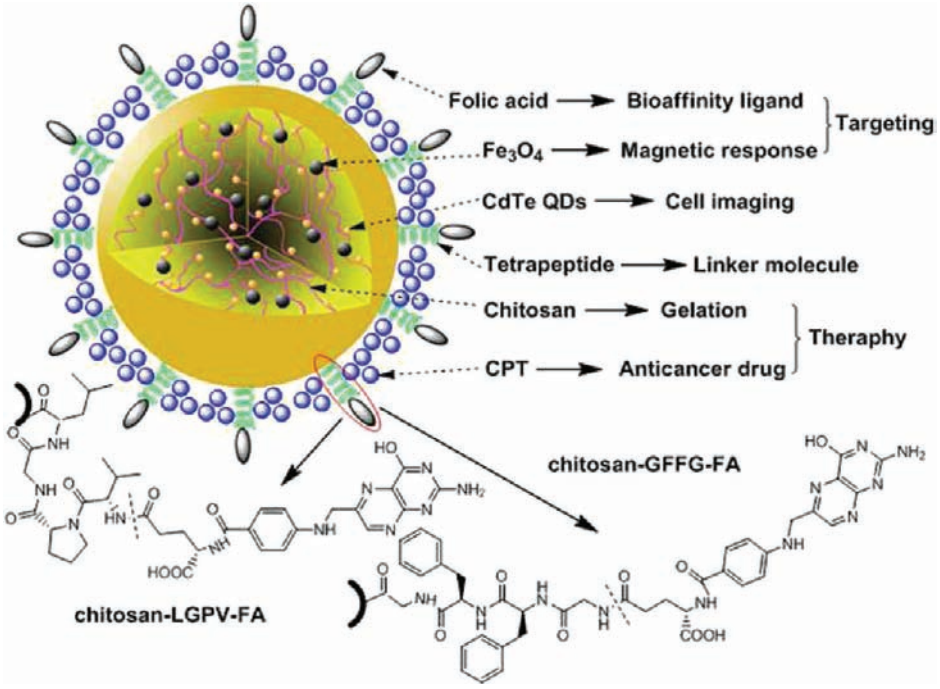

Figure 1. Schematic diagram of designing multifunctional CLMNPs-tetrapeptide-FA copolymers and their potential applications in biomedicine.

Furthermore, it is reported that the low-molecular-weight chitosan can restrain tumor growth and possess anti-transfer activity in tumor-bearing mice by activating lymphocyte factor and enhancing immune regulation.[20,21] At the same time, chitosan can serve as a scavenger because it can react with the degradation products of anticancer drugs and form complexes before drug residue was eliminated from the body through liver, kidney, and intestinal canal. Therefore, chitosan is an ideal matrix to meet simultaneous demand in gelation and therapy. The development of integrating therapy system of CPT with chitosan is promising in the treatment of various cancers.

Moreover, folic acid, as an effective and non-immunogenic target ligand, possesses high binding affinity with folate receptor, which overexpresses on the surface of many human malignant cell membranes, such as ovarian, colon, lung, breast, and liver cancers.[22,23] On the contrary, the expression level of folate receptor on other normal cells is low and only limited to some epithelial cells.[24] If FA is conjugated to drug carrier equipped with the MNPs and QDs, this multifunctional copolymer will have dual magnetic/folate targeting by magnetic guidance and folate-receptor-mediated cellular uptake.[13,25,26] In general, there must be a linker molecule with specific functional groups as arms connecting folate to multifunctional drug carrier.[27] Peptide linker may be a suitable candidate due to its small molecular weight, favorable cell permeability, tailored amino acid sequence, and easy synthesis.[28] In fact, the peptide delivery systems as anticancer drug carriers have been widely fabricated.[29,30] In the present drug carrier system, folate can be directly conjugated to the end amino groups of the peptide by amide bonds, while the terminal carboxyl group of the peptide can readily conjugate with an amino group on the chitosan shell gelling functional materials (MNPs and QDs). In addition, with the use of hydrophobic peptide linker, it will provide a more flexible and convenient platform for the loading and release of hydrophobic CPT under a certain triggerable condition such as a change in pH. Besides these, the folate-conjugated peptide composites can be regarded as pocket shielding CPT from hydrolyzation and diffusion of toxicity.

In the present study, we synthesized chitosan-based luminescent/magnetic hybrid nanoparticles with folate-conjugated tetrapeptide composites (CLMNPs-tetrapeptide-FA). The coupling reaction was performed by direct gelation of chitosan, CdTe QDs, and superparamagnetic iron oxide into the hybrid nanogels, and subsequent orderly conjugation of tetrapeptide and folate on hybrid nanogels (Figure 1). After a series of characterizations, in vivo a magnetic copolymer accumulation experiment was conducted. In vitro release profiles, blood compatibility, and cytotoxicity were assayed. Human hepatocytes normal L02 cell and lung cancer A549 cells were used to observation of binding and morphological changes in vitro in order to examine antitumor activity of CPT-loaded CLMNPs-tetrapeptide-FA copolymers.

MATERIALS AND METHODS

Materials. Ferric trichloride hexahydrate, ferrous chloride tetrahydrate, aqueous ammonia, tellurium powder (purity above 99%), sodium borohydride, cadmium chloride (99%), thioglycolic acid (TGA, 99%), chitosan (80 mesh, MW 22.4 kDa, deacetylation degree above 95%), *N*-hydroxysuccinimide (NHS), 1-ethyl-3-(3-dimethylaminopropyl) carbodiimide hydrochloride (EDAC), folate (MW 441.41 Da), and camptothecin (CPT) were purchased from Sigma. RPMI-1640 medium was obtained from Gibco (USA). Dimethyl sulfoxide (DMSO) was analytical grade and obtained from Gansu Yinguang Chemical Industry Co. (China). Human red blood cells (HRBCs) and plasma were freshly obtained from Red Cross Blood Center (Gansu, China). Calf serum was acquired from Sijiqing Biological Engineering Materials Co., Ltd. (Hangzhou, China). Human normal hepatocytes L02 cell line and lung cancer A549 cell line were obtained from the cell bank of Shanghai Science Academe (China). All other chemicals were of analytical grade. The water used in the study was

dx.doi.org/10.1021/bc300008k | *Bioconjugate Chem.* 2012, 23, 1010−1021

prepared using a Milli-Q Water Purification System (Milli-Pore, Bedford, MA, USA).

Synthesis of Chitosan-Based Luminescent/Magnetic Nanoparticles (CLMNPs). The preparation methods of Fe_3O_4 MNPs and TGA-capped CdTe QDs solution were described in our previous literature.[17] Briefly, 4 mmol of Fe_3O_4 MNPs and 10 mmol of the TGA-capped CdTe QDs solution irradiated for 24 h in natural light were added to 2 mL of PBS buffer (5 mM, pH 6.0) containing 0.1 M NaCl and sonicated for 5 min. Afterward, 24 mL of the chitosan solution (3.125 mg/mL) was added with vigorous stirring, and then was further sonicated for 40 min. The resulting CLMNPs were washed three times with above PBS to completely remove the excessive unbound precursors in aqueous solution.

Synthesis of CLMNPs-Tetrapeptide with End Amino Group. Gly-Phe-Phe-Gly-NH-Fmoc (GFFG-NH-Fmoc, M_w 648.5 Da) and Lue-Gly-Pro-Val-NH-Boc (LGPV-NH-Boc, M_w 484.6 Da) were designed according to the different hydrophobic properties to conjugate folate to CLMNP surface via tetrapeptides and load CPT on copolymers. Two tetrapeptide linkers were synthesized manually by the solid-phase synthesis method, using the Fmoc/Boc strategy and starting from Rink Amide resin (Tianjin Nankai Hecheng Science and Technology Co., Ltd., China; 0.5 mmol/g). The purity of the resulting tetrapeptides was analyzed (>98%) by HPLC. The ESI-mass spectrometry of the resulting peptides was performed on Bruker maXis 4G spectrometer equipped with a nebulizer-assisted electrospray source (see SI 1). Then, 53.7 μmol of GFFG-NH-Fmoc and LGPV-NH-Boc were dissolved in 7 mL of anhydrous DMSO and 7 mL of methanol, respectively. After shaking gently for 5 min, the mixtures were kept at room temperature overnight. The absorbances of the GFFG-NH-Fmoc and the LGPV-NH-Boc solution were recorded from 250 to 450 nm (see SI 2). Afterward, to conjugate the tetrapeptide linkers with chitosan on the CLMNPs surface by amido bond, the end carboxyl groups on two tetrapeptides were activated by adding 30 mg of NHS and 53 mg of EDAC and stirring at room temperature for 2 h. Finally, the previous resulting CLMNPs were divided equally into two parts and added to the two mixtures, respectively. After shaking on a level swing bed at room temperature for 12 h, the reaction mixtures were centrifuged at 10 000 rpm for 5 min. The precipitate containing GFFG was washed three times with DMSO, and the precipitate containing LGPV was washed three times with methanol. The products were denoted as CLMNPs-GFFG-Fmoc and CLMNPs-LGPV-Boc. All supernatants from the two systems were collected, respectively, and the absorbance values were measured at 296 nm for free GFFG-Fmoc and at 374 nm for free LGPV-Boc. The loading amounts of two tetrapeptides on CLMNPs were calculated by deducting free tetrapeptide content from added total amount.

To obtain the final compound CLMNPs-GFFG-NH_2 and CLMNPs-LGPV-NH_2, the deprotection procedures of CLMNPs-GFFG-Fmoc and CLMNPs-LGPV-Boc were indispensable. In the case of CLMNPs-GFFG-Fmoc, 3 mL of 5% piperidine solution (in anhydrous dimethyl formamide, DMF) was added. After shaking gently for 5 min at room temperature, the mixture was centrifuged at 10 000 rpm for 5 min. The precipitate was treated again with 3 mL of 5% piperidine solution by shaking for 20 min. Afterward, the precipitate was washed three times with cold anhydrous DMF in order to obtain purified CLMNPs-GFFG-NH_2. With respect to the deprotection of CLMNPs-LGPV-Boc, 10 mL of trifluoroacetic acid (TFA) was added dropwise with stirring in an ice bath. The mixture was stirried for another 3 h at room temperature, and then centrifuged at 10 000 rpm for 5 min. The precipitate was washed once with 1 mL of NaOH (1 M), four times with 20 mL of a saturated NaCl solution, and again three times with 20 mL of PBS buffer (5 mM, pH 6.0) containing 0.1 M NaCl by centrifugation. The product, CLMNPs-LGPV-NH_2 with free end amino groups, was obtained.

Synthesis of FA-Conjugated CLMNPs-Tetrapeptide Copolymers. To conjugate folic acid molecule with CLMNPs-GFFG-NH_2 and CLMNPs-LGPV-NH_2, two aliquots of 0.1 mmol of folic acid were dissolved in 10 mL of anhydrous DMF in a round-bottom flask under nitrogen, respectively, and activated by adding 23.1 mg NHS and 39 mg EDAC, and then mixed with the as-prepared CLMNPs-GFFG-NH_2 and CLMNPs-LGPV-NH_2. After shaking overnight at room temperature in the absence of light, the mixtures were centrifuged at 10 000 rpm for 5 min, and the precipitates were washed twice with cold anhydrous DMF by means of centrifugation, and again several times with 20 mL of PBS buffer (5 mM, pH 6.0) containing 0.1 M NaCl. The end products, CLMNPs-GFFG-FA and CLMNPs-LGPV-FA copolymers, were obtained. In order to make certain subsequent CPT-loading mechanism on copolymers, CLMNPs-FA was also prepared by directly conjugating FA to CLMNPs under the activation of NHS and EDAC.

Characterization. UV−vis absorption spectra were measured on a UV−vis spectrophotometer (Puxi TU-1810, China). Transmission electron microscopy (TEM) images were measured with a TecnaiG^2 F30 (FEI, USA) by placing one drop of the samples on copper grids coated with carbon. X-ray energy-dispersive (EDX) spectra were obtained on a S-4800 field emission scanning electron microscope with a EDX spectroscopy (Hitachi, Japan). Large-angle powder X-ray diffraction (XRD) patterns from 10° to 80° were recorded at X'Pert PRO (PANalytical, Holand) using Cu Kα radiation. The Fourier transform infrared (FTIR) spectra were acquired with an FTIR spectrometer (NEXUS 670 FT-IR, Nicolet, USA). The hydrodynamic diameter of the copolymers were determined by dynamic light scattering (DLS) with angle detection at 90° (BI-200SM, Brookharen Instruments Corporation, USA). Fluorescence spectra were recorded on a RF-5310 PC spectrofluorophotometer (Shimadzu, Japan). The magnetic properties were recorded using a vibrating sample magnetometer (VSM) (Lake Shore, USA). The fluorescence images were taken with a fluorescence microscope (Nikon TE2000-S, Japan). The cellular images were acquired with a laser scanning confocal microscope (LCSM, ZEISS, LSM 510 Meta, Germany). Others also employed in this work were a high-speed refrigerated centrifuge (Himac, CR 21G, Hitachi, Japan) and level swing bed with temperature controller (Heo Bio-Tech Co., Ltd., Beijing, China).

Drug Loading and Release in Vitro. The loading of CPT was achieved as follows: 30 mg of CLMNPs-GFFG-FA or CLMNPs-LGPV-FA copolymers were dispersed in 30 mL of CPT solution (1 mg/mL in DMF) by ultrasonication for 30 s, respectively, and shaken for 24 h at room temperature until CPT concentration in the solution stabilized. Then, the suspension was centrifuged at 10 000 rpm for 10 min. To remove unbound CPT, the copolymers were further rinsed three times with DMF. All the supernatants in every system were collected, respectively, and the concentration of the unbound CPT was assayed by UV−visible spectrophotometer

at 366 nm. The loading efficacy and loading amount of CPT were determined according to the decrease in initial CPT solution. All the experiments were carried out in triplicate.

In order to evaluate the effect of pH on the release mechanism, the release profiles of CPT were obtained by the dialysis method in a simulated normal body fluid (PBS, pH 7.4) and an acidic environment (PBS, pH 5.3) at 37 ± 1 °C. First, 30 mg of the CPT-loaded CLMNPs-GFFG-FA and CLMNPs-LGPV-FA copolymers were dispersed in 5 mL of medium and placed in a dialysis bag (molecular weight cutoff of 14 kDa), respectively. The dialysis bags were then soaked in 45 mL of the release medium in a water bath with gentle shaking. 3.0 mL aliquots of sample in the solution were withdrawn at defined time periods, and as soon as the amount of CPT released was analyzed by UV spectrophotometry at 366 nm, the measuring solution was returned to the medium. Each experiment was conducted in triplicate and results are presented as mean (standard deviation).

Magnetic Targeting in Vivo. In order to assess magnetic targeting of copolymers in vivo, S-180 sarcoma-bearing Kunming mice (male, body weight 18−20 g) were used. After mice were anesthetized by intraperitoneal injection of 20% chloral hydrate, 0.2 mL of the blank CLNMPs-GFFG-FA copolymer with a concentration of 200 μg/mL in sterile PBS were injected by tail vein. Subsequently, mice were fastened and treated with a constant magnet field (about 1500 Oe) laid outside the skin of the belly near the tumor site at 25 °C (Figure 4C). After three hours, the mice were killed, and the tumor tissues were quickly removed and cut into slices (thickness about 20 μm) on a freezing microtome (Leica CM1100, Germany). The magnetic copolymer accumulation in the tumor slice was detected on a fluorescence microscope (Nikon TE2000-S, Japan) by observing luminescence imaging under excitation wavelength of 488 nm. The statistics of the magnetic copolymer trapped in the tumor tissue or cells were measured via photoluminescence (PL) intensity in a microscopic field. The control experiment was also performed (other operations similar except no magnet field applied). Each experiment was conducted in triplicate and results are presented as mean (standard deviation).

Haemacompatibility Assessment in Vitro. *Hemolysis Assay in Vitro.* Three mL of human blood was centrifuged at 1500 rpm for 10 min to acquire human red blood cells (HRBCs). After removing the serum by suction, HRBCs were washed five times with sterile physiological saline solution by centrifugation and suction, and diluted to 10-fold volume to make the absorbance value of the positive control supernatant located in the range 0.5−0.6 at 541 nm. Then, experiments were divided into four sample groups: (a) CLMNPs-GFFG-FA, (b) CLMNPs-LGPV-FA, (c) CLMNPs-GFFG-FA-CPT, and (d) CLMNPs-LGPV-FA-CPT. In every group, eight aliquots of 100 μL of the diluted HRBC suspension were added in a series of centrifuge tubes containing (1) 1.9 mL of physiological saline solution as a negative control; (2) 1.9 mL of deionized water as a positive control; (3−8) 1.9 mL of samples at concentrations of 31.25, 62.5, 125, 250, 500, and 1000 μg/mL. After shaking gently and placing at a standstill for 3 h at room temperature, the eight aliquots of the mixtures in every group were centrifuged at 1500 rpm for 10 min, and the absorbance of the supernatants was recorded from 500 to 650 nm. The hemolysis percentages of the samples were calculated according to the equation below:

$$\left(\text{Sample O.D.}_{541} - \text{Negative control O.D.}_{541}\right) / \left(\text{Positive control O.D.}_{541} - \text{Negative control O.D.}_{541}\right) \times 100\%$$

Coagulation Assay in Vitro. Seven aliquots of 100 μL of fresh human plasma were added in centrifuge tubes containing 900 μL of physiological saline solution as a control, and a series of 900 μL of samples (CLMNPs-GFFG-FA, CLMNPs-LGPV-FA, CLMNPs-GFFG-FA-CPT, CLMNPs-LGPV-FA-CPT copolymers) at concentrations of 31.25, 62.5, 125, 250, 500, and 1000 μg/mL. After shaking gently and incubating at 37 °C for 5 min, the mixtures were centrifuged at 2500 rpm for 10 min, and 700 μL of the supernatant was extracted by suction for analysis of prothrombin time (PT) and activated-partial-thromboplastin time (APTT) on a fully automatic blood-coagulation analyzer (ACL TOP 9000, USA) by using the SynthAsil kit (Instrumentation Laboratory Company, Orangeburg, USA).

In Vitro Cytotoxicity Study. The cytotoxicity of the blank and the CPT-loaded CLMNPs-GFFG-FA or CLMNPs-LGPV-FA copolymers was assessed by using the MTT assay. L02 cells and A549 cells (1×10^4 cells/well) were grown at 37 °C and under 5% CO_2 atmosphere in folate-free RPMI-1640 medium in a 96-well plate, supplemented with calf serum (10%) and 1% penicillin−streptomycin in a fully humidified incubator. Then, the blank and CPT-loaded CLNMPs-GFFG-FA or CLNMPs-LGPV-FA copolymers with a concentration of 25, 50, 100, 200, 300, 400, and 500 μg/mL, and the free CPT with a concentration of 1.23, 3.27, 6.53, 13.06, 19.59, 26.12, and 32.65 μg/mL were added to cell dishes, respectively, and then these cell dishes were put into incubators at 37 °C for 12 h. In order to demonstrate folate targeting, the cytotoxicity of the blank and CPT-loaded CLNMPs-GFFG or CLNMPs-LGPV copolymers with a concentration of 200 μg/mL against A549 cells was also measured. After incubation for a defined time, the culture medium was removed and 20 μL of MTT reagent (diluted in culture medium, 0.5 mg/mL) was added, followed by incubating for another 2 h. The MTT/medium was removed carefully and DMSO (150 μL) was added to each well to dissolve the formazan crystals. Absorbance of the colored solution was measured at 570 nm using a microplate reader (Bio-Rad, iMark). All experiments were performed in triplicate.

Cell Imaging. After confirming the powerful fluorescence from two copolymers and no distinct autofluorescence from the cell itself under similar conditions, the cellular images were obtained with a laser scanning confocal microscope (LSCM, ZEISS, LSM 510 Meta, Germany). L02 cells and A549 cells (6×10^4 cells/well) were seeded on a 6-well plate at 37 °C for 24 h. After that, the blank and CPT-loaded CLNMPs-GFFG-FA or CLNMPs-LGPV-FA copolymers with a concentration of 200 μg/mL were added to the cell dishes, respectively. After a further 2 h incubation, these copolymer-loaded cells were washed with PBS three times to remove the free copolymers attached on the outer surface of cell membrane. Cell targeting was detected on LSCM for luminescence imaging under excitation wavelength of 488 nm. Cell imaging of three control experiments was also performed: L02 cells and A549 cells incubated with free CPT, and A549 cells incubated with CPT-loaded CLMNPs-GFFG copolymer. All experiments were performed in triplicate.

RESULTS AND DISCUSSION

Synthesis and Characterization of CLMNPs-Tetrapeptide-FA Copolymers. Synthesis of CLMNPs-tetrapeptide-FA copolymers consisted of the following three steps. In the first step, the CLMNPs were prepared for cellular imaging and magnetic targeting. First, the MNPs were treated with 5% aqueous ammonia to obtain MNPs with sufficient hydroxyl groups on the surface, which can facilitate coating MNPs with chitosan. Then, QDs photoactivated and MNPs were mixed together using the chitosan as a gelation agent according to ratios of 1/32/12 (chitosan/QD/MNP, wt/wt/wt) under sonication mode. Figure 2 show TEM images of Fe_3O_4 and the as-prepared CLMNPs. It is clear that the CLMNPs tend to form a sphere in moderate sizes (about 140−160 nm) according to TEM. The QDs and the MNPs were randomly distributed all over the hybrid nanogel particle. The EDX analysis (Figure 3A) indicated that the elemental compositions of the CLMNPs were primarily Fe, O, Cd, Te, and N, which further confirmed the structure ingredients of the CLMNPs. On the basis of XRD pattern (Figure 3B(b)), the intensities of (311) Fe_3O_4 diffraction peaks from CLMNPs were weaker than those of pure Fe_3O_4 (Figure 3B(a), which manifested the presence of amorphous materials (chitosan) on the surface of Fe_3O_4. Furthermore, the FTIR spectra of the CLMNPs (Figure 3C(b)) showed that the characteristic peak at 1650 cm^{-1} corresponding to an amino group, two weak peaks at 2925 cm^{-1} and 1380 cm^{-1} corresponding to the stretching and bending vibration of methylene groups, and the broad peak situated at 1060−1030 cm^{-1} related to C−O stretching resulting from chitosan were observed, while these peaks were negligible in pure Fe_3O_4 MNPs (Figure 3C(a)). All these results verified that the chitosan-based luminescent/magnetic nanoparticles have been synthesized.

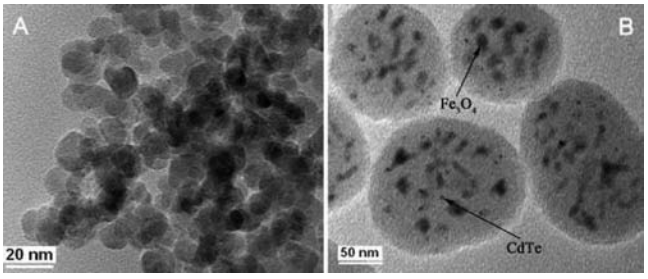

Figure 2. TEM images of (A) Fe_3O_4MNPs and (B) the as-prepared CLMNPs.

In the second step, the end carboxyl groups of two kinds of tetrapeptide linkers (HOOC-GFFG-Fmoc and HOOC-LGPV-Boc) were conjugated with the amino groups in chitosan molecules exposed to the CLMNPs surface by amido bond under activation of NHS and EDAC. After the intermediate products with blocking groups were subsequently processed by deprotection procedures, the CLMNPs-GFFG-NH_2 and CLMNPs-LGPV-NH_2 copolymers were obtained. On the basis of the FTIR spectra of two copolymers

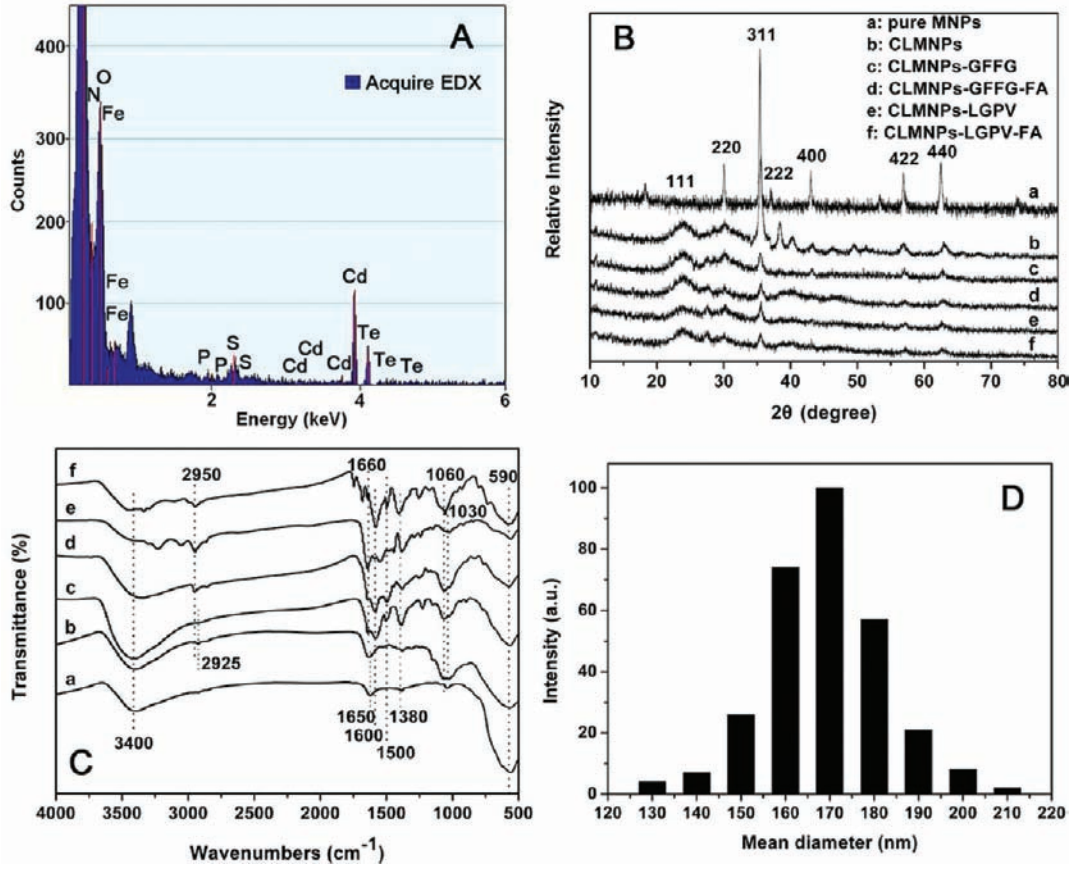

Figure 3. (A) Representative EDX spectra of the CLMNPs-tetrapeptide-FA copolymer. (B) XRD patterns of the products prepared step by step. (C) FTIR spectra of (a) Fe_3O_4, (b) CLMNPs, (c) CLMNPs-GFFG, (d) CLMNPs-GFFG-FA, (e) CLMNPs-LGPV, and (f) CLMNPs-LGPV-FA. (D) The size distribution of the blank CLMNPs-tetrapeptide-FA measured by DLS.

dx.doi.org/10.1021/bc300008k | Bioconjugate Chem. 2012, 23, 1010−1021

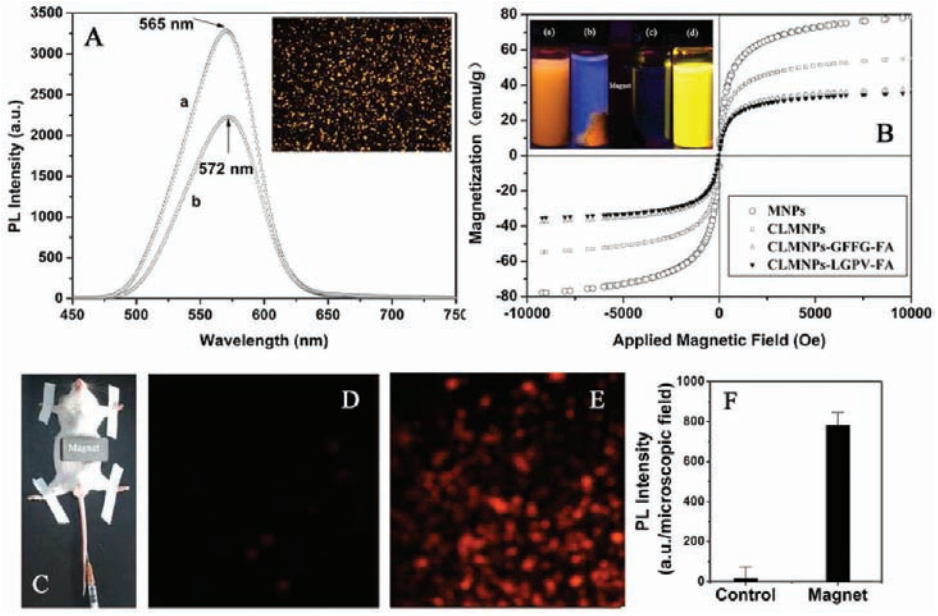

Figure 4. (A) PL spectra of the as-prepared CLMNPs-GFFG-FA (a) and CLMNPs-LGPV-FA (b); the inset in right top shows the fluorescence microscope image of the CLMNPs-GFFG-FA copolymer (10×, excitation wavelength = 488 nm). (B) VSM magnetization curves of Fe_3O_4MNPs, CLMNPs, CLMNPs-GFFG-FA, and CLMNPs-LGPV-FA in applied magnetic field at 305 K. The inset in left top shows photograph taken under a 365 nm UV lamp: (a) CLMNPs, (b) CLMNPs-GFFG-FA, (c) Fe_3O_4MNPs, (d) TGA-capped CdTe QDs in deionized water. (b) and (c) are attracted by a permanent magnet. (C) Male S-180 sarcoma-bearing Kunming mouse being guided with a magnet after the CLMNPs-GFFG-FA copolymer was injected into the bloodstream by tail vein. (D,E) Representative fluorescence microscope images of the tumor slices indued without (D, control experiment) and with (E) magnet (10×, excitation laser wavelength = 488 nm). (F) Average value of PL intensity per microscopic field on the slice of control and magnet guidance.

(Figure 3C(c,e)), a new characteristic peak appeared at 1660 cm^{-1}, which indicated that the new bond of $CONH_2$ groups linking tetrapeptides to the CLMNPs has emerged. Further, two absorption peaks at 1600 cm^{-1} and 1500 cm^{-1} corresponding to the stretching vibration of the aromatic ring skeleton derived from phenylalanine appeared in the CLMNPs-GFFG-NH_2 copolymer, while a distinct peak at 2950 cm^{-1} related to the stretching vibration of methyl groups derived from leucine and valine was present in CLMNPs-LGPV-NH_2 copolymers. All the above results suggest that the two CLMNPs-tetrapeptide-NH_2 copolymers have been successfully prepared.

In the third step, to obtain CLMNPs-GFFG-FA and CLMNPs-LGPV-FA copolymers, the end amino groups on CLMNPs-GFFG-NH_2 and CLMNPs-LGPV-NH_2 were coupled with the γ-carboxyl group of folate by the amide bond. The coupling reaction was achieved in anhydrous DMF at room temperature in the presence of NHS and EDAC as the activating agent for the carboxylic group. The mean diameter of the CLMNPs-tetrapeptide-FA copolymer was determined to be about 150−190 nm by DLS (Figure 3D). Compared with the average diameters of CLMNPs based on TEM (Figure 2B), those of the CLMNPs-tetrapeptide-FA copolymers only increased by about 10−20 nm, reflecting that the agglomeration of copolymers is very little. Furthermore, the intensities of Fe_3O_4 diffraction peaks of the end products were weaker than those of the previous products based on XRD pattern (Figure 3B(b-f)), which indicated the presence of more amorphous materials (tetrapeptide and FA) on the surface of the copolymers. On the basis of FTIR spectra of the CLMNPs-GFFG-FA and CLMNPs-LGPV-FA copolymers (Figure 3C(d,f)), two absorption peaks of benzene ring derived from folate at 1600 cm^{-1} and 1500 cm^{-1} were also stronger than those of CLMNPs-tetrapeptide, confirming successful conjugation of folate to CLMNPs-tetrapeptide copolymers.

Properties of CLMNPs-GFFG-FA/CLMNPs-LGPV-FA Copolymers. The PL spectra of CLMNPs-GFFG-FA and CLMNPs-LGPV-FA copolymer aqueous solutions at the same concentration (1 mg/mL) was shown in Figure 4A(a,b), respectively. The fluorescent CLMNPs-GFFG-FA and CLMNPs-LGPV-FA copolymers showed emission peaks at 565 and 572 nm when excited at 450 nm. According to the representative fluorescence microscopy image of the CLMNPs-GFFG-FA (inset in Figure 4A), it is clear that highly fluorescent copolymers with orange−yellow emissions was prepared successfully. As shown in the VSM magnetization curves (Figure 4B), with step-by-step fabrication, the saturation magnetization declined accordingly due to the thickening of the shells. At the same time, two kinds of copolymers showed a similar saturation magnetization, which displayed negligible variation in magnetic properties although different precursors and operating steps were used in the course of synthesis. The saturation magnetization of two as-prepared copolymers (approximately 36 emu/g) accounted for about 45.6% of that of the MNPs (79 emu/g), reflecting an adequate magnetic responsiveness in the applications for magnetic targeting. According to the photographs of MNPs, CLMNPs, CLMNPs-GFFG-FA, and CdTe QDs in deionized water at 365 nm (inset in Figure 4B), the color conversion from bright yellow (pure CdTe QDs) to orange−yellow (CLMNPs-GFFG-FA) showed the realization of effective reaction; at the same time, the achievement of magnetic copolymers with orange−yellow color fluorescence also verified success of conjugation. All the above results suggest that the end products, CLMNPs-GFFG-FA and CLMNPs-LGPV-FA cpoplymers, integrated magnetic and fluorescent properties.

dx.doi.org/10.1021/bc300008k | *Bioconjugate Chem.* 2012, 23, 1010−1021

Magnetic Targeting in Vivo. To estimate tumor target capability, we have also conducted in vivo copolymer accumulation experiments under magnetic attraction using male S-180 sarcoma-bearing Kunming mice (Figure 4C). As displayed in Figure 4D,E, the fluorescence imaging on tumor tissue slices indicates the presence of accumulated copolymers (dark orange fluorescence). The more intense fluorescence of magnetic copolymer on the magnet-field-exposed tumor slice (Figure 4E) is apparent as compared to the control slice (without magnet-field-exposed tumor) (Figure 4D). On the basis of the fluorescence distribution, it can be judged that some copolymers have even been transported into tumor cells by endocytosis. By further measurement for the fluorescence intensity on tumor tissue slices, the average PL intensity of the magnetic copolymers trapped in the tumor tissue per microscopic field was quite significant (Figure 4F), i.e., approximately 50 times greater with magnetic induction as compared to that for the control group sample. These results indicate that the magnetic copolymers were trapped successfully in the tumor tessue, even tumor cells under external magnetic field guidance.

Drug Loading and Release. Under present experimental condition, the loading efficiency of CPT was 8.6 wt % for CLMNPs-GFFG-FA copolymer, namely, the actual loading amount of CPT on this copolymer reached approximately 70.2 mg/g. Moreover, CLMNPs-FA and CLMNPs-VPGL-FA were used to replace CLMNPs-GFFG-FA for further confirmation of the CPT-loaded mechanism. The results showed that the loading efficiency of CPT on CLMNPs-VPGL-FA copolymer was only 1.1 wt %, while there was nothing on CLMNPs-FA. Clearly, the binding site of CPT is right on the peptide linker, and the CPT loading efficiency has a significantly positive correlation with the hydrophobic degree of the peptide. In fact, CPT is conjugated to CLMNPs-GFFG-FA by means of both hydrophobic force and aromatic-ring stack force between CPT and phenylalanine in GFFG tetrapeptide. In the case of CLMNPs-FA, that is not appropriate for the CPT loading due to the hydrophilic chitosan surface of the CLMNPs. With respect to CLMNPs-LGPV-FA, although there was a length of LGPV tetrapeptide as linker on the chitosan shell, the CPT loading on CLMNPs-LGPV-FA only relied on the hydrophobic stacking force, and the binding force was relatively vulnerable. In addition, the traditional CPT-loading approach was to connect CPT to one end of the peptides through covalent bond.[28,31] The present way was to combine CPT with side chain groups of the peptides, which prevented CPT from hydrolysis and toxicity diffusion to some extent by means of peptide pockets. This is a new concept having both drug loading and drug protecting.

Figure 5 reveals the release behaviors of CPT-loaded CLMNPs-GFFG-FA and CLMNPs-LGPV-FA in a simulated normal body fluid (50 mM PBS, pH 7.4) and an acidic environment (50 mM PBS, pH 5.3) under dialysis condition at 37 °C. As shown in Figure 5, first, the CPT releasing results clearly demonstrated an initial burst release of CPT. For example, about 15% and 25% of CPT from CLMNPs-GFFG-FA-CPT and CLMNPs-LGPV-FA-CPT copolymers can be released at the initial 1 h, respectively, while approximately ~55% (pH 5.3) or ~46% (pH 7.4) of CPT from the former and ~69% (pH 5.3) or ~57% (pH 7.4) of CPT from the latter can be released within 28 h. The initial burst release of the CPT may be related with the loading mode of CPT. Although the binding maintained by hydrophobic force may be unstable,

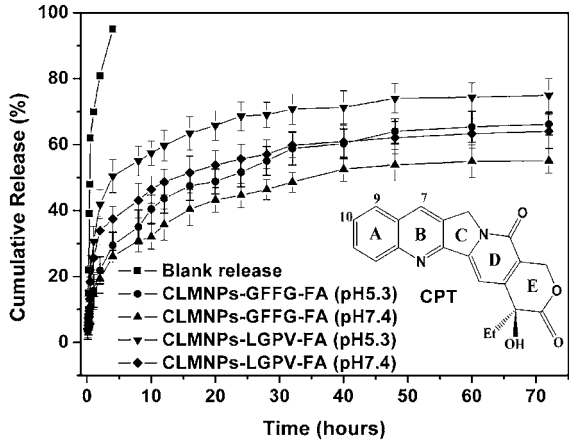

Figure 5. Release profiles of CPT from CPT-loaded CLMNPs-GFFG-FA and CLMNPs-LGPV-FA copolymers in PBS solutions at pH 5.3 and pH 7.4 at 37 °C, respectively.

CPT was not readily removed by motionless washing. In fact, there were no differences in the release profiles after washing three times or more, indicating that the noncomplexed CPT molecules were nearly completely washed off before the releasing experiments. Therefore, we think that the initial burst release of the CPT should be triggered by shaking in a water bath. Second, the release efficiencies from two copolymers were higher at pH 5.3 than at pH 7.4. A possible reason may be that the quinoline ring (B ring) in the CPT molecule (insert in Figure 5) is extremely likely to generate positively charged salt under acidic condition (pH 5.3), which results in not only a decrease of binding force between CPT and peptide, but also mutual repulsion between CPT and the cation chitosan shell on CLMNPs. The another possible reason is the solubility of chitosan. At pH 5.3, chitosan polymer is probably soluble to water,[17] so the water content of the shell would be high, and accordingly the repulsion would be more powerful due to hydrophobic effects of CPT; while at pH 7.4, chitosan polymer is insoluble, so the water content of the shell would be low, and accordingly the repulsion would be weaker. This is exactly what we expect, i.e., CPT could mainly be distributed around tumor tissues (acidic microenvironment) rather than located in a normal section. Finally, in comparison with the release capacity of CPT-loaded CLMNPs-LGPV-FA copolymer, that of the CPT-loaded CLMNPs-GFFG-FA copolymer is distinctly lower under similar pH condition, which may be attributed to higher binding force between CPT and the latter. Even so, the absolute release quantity of CPT from CPT-loaded CLMNPs-GFFG-FA was still significantly higher than from CPT-loaded CLMNPs-LGPV-FA, because the former possessed more CPT-loaded quantity.

Blood Compatibility Assay. When materials are administrated by vein injection, excellent blood compatibility is a prerequisite to their applications in vivo, such as low hemolysis and coagulation effects.[32] The investigation showed that no significant hemolysis effects were found for blank and CPT-loaded CLMNPs-GFFG-FA/CLMNPs-LGPV-FA copolymers within the experimental concentration range (Figure 6A,B). The hemolysis percentages of both blank and CPT-loaded copolymers increased only slightly with an increased copolymer concentration in the range 31.25−1000 μg/mL. Even at a high concentration of 1000 μg/mL, as low as 1.66% and 1.75% hemolysis percentages were detected for CPT-loaded

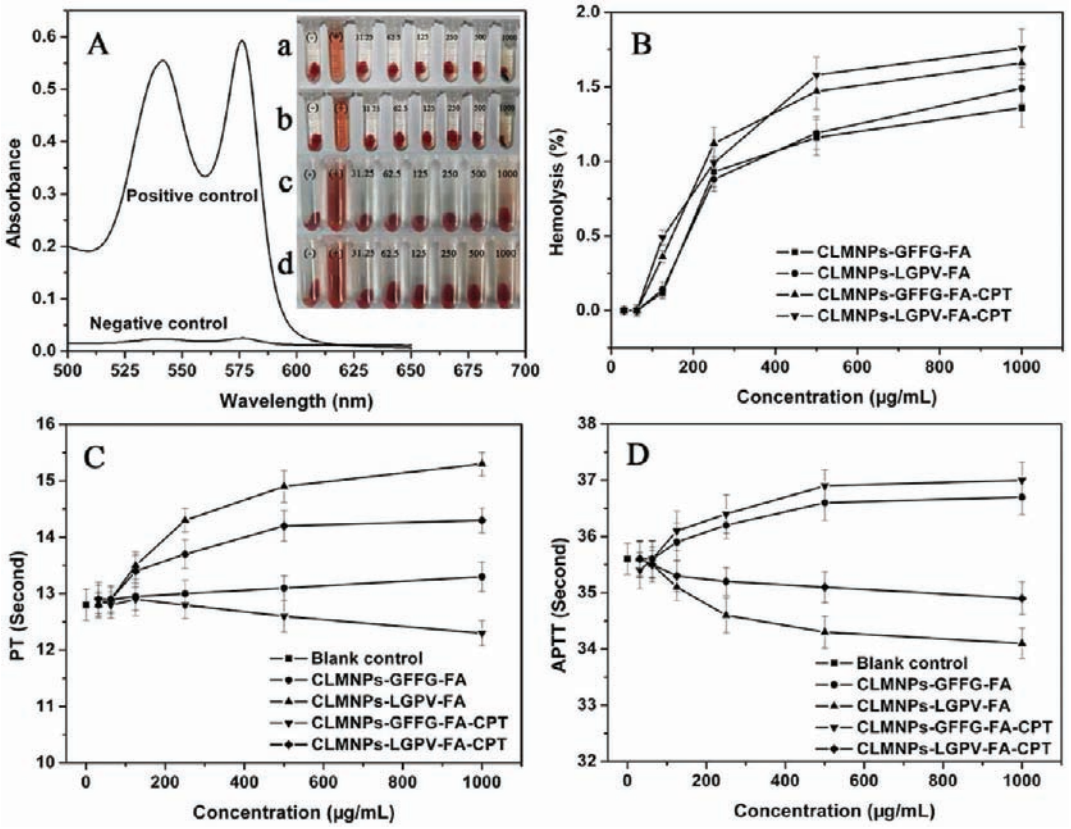

Figure 6. Blood compatibility studies in vitro. (A) Representative absorption spectra in the supernatant of copolymer in PBS after incubation with HRBCs using water and PBS as the positive and negative controls. Inset on the right is a photograph of the hemolysis assay to detect the presence of hemoglobin in the supernatant of copolymer in PBS at the concentrations of 31.25, 62.5, 125, 250, 500, and 1000 μg/mL: (a) CLMNPs-GFFG-FA, (b) CLMNPs-LGPV-FA, (c) CLMNPs-GFFG-FA-CPT, (d) CLMNPs-LGPV-FA-CPT. (B) Hemolysis percentages of blank and CPT-loaded copolymers in PBS at above concentrations. (C,D) Coagulation properties of blank and CPT-loaded copolymers at above concentrations after incubation with fresh plasma for 5 min.

CLMNPs-GFFG-FA and CPT-loaded CLMNPs-LGPV-FA copolymers, respectively, and still fell within the negligible scope (<5%).[33] It was reported that smaller, porous particles presented higher toxicity than larger, nonporous particles, because the former had larger surface area per mass, and were apt to penetrate positively into cells.[34] The present copolymers are nonporous nanoparticles with a size distribution of 150−190 nm and are less likely to achieve direct transmembrane transport accompanied by red blood cell membrane damage. Moreover, sphere-shaped copolymers have difficulty rupturing the membrane of HRBC to cause subsequent release of hemoglobin.[33] Miyake believed that metal ions were able to lead to hemolysis effect through changing holes and flexibility of cell membrane.[35] In the present copolymers, however, the Cd ion-induced hemolysis can potentially be eliminated by gelation with a chitosan coating. Therefore, no matter which aspect of the resulting copolymers we examine (morphology or composition), they do not trigger the obvious hemolysis.

In order to predict the possible thrombosis induced by copolymers, another parameter, coagulation effect including PT and APTT, has been evaluated. Figure 6C,D indicates that the PT and APTT values of the plasma mixed with different concentrations of copolymers (blank and CPT-loaded CLMNPs-GFFG-FA/CLMNPs-LGPV-FA) did not display a prominent difference from those of the control experiment. Furthermore, PTR (PT ratios between the test samples and the reference sample) and APTT values of plasma exposed to different copolymers under all analytical concentrations were within their normal ranges of 0.8−1.2 and 25.4−38.4 s,[32] respectively. These results show that extrinsic (PT) and intrinsic (APTT) coagulation pathways were not influenced by these copolymers.

In Vitro Cytotoxicity. To investigate cytotoxicity and tumor targeting of two copolymers, normal human hepatocytes L02 cell lines and lung cancer A549 cell lines were chosen to incubate with various types of the as-prepared copolymers. The results are presented on the following four aspects: (I) The viability of the A549 cells was much lower than that of the L02 cells after incubation with CPT-loaded CLMNPs-GFFG-FA or CLMNPs-LGPV-FA copolymers (Figure 7A,B), which demonstrates that two copolymers possessed higher growth inhibition properties for cancer cells than for normal cells due to folate receptor-mediated specific endocytosis on the tumor cell membrane, and the CPT released from the CPT-loaded copolymers still held high anticancer activity. Furthermore, more than 75% of viability in L02 cells was observed even at a CPT-loaded copolymer concentration of 500 μg/mL, which displayed low cytotoxicity and favorable cell compatibility as drug carrier. The effect of CPT-loaded CLMNPs-GFFG-FA copolymers on the cell viability in the same cell line was more prominent in comparison with those of CPT-loaded CLMNPs-LGPV-FA copolymers (Figure 7A,B), which was attributed to increased CPT released from the former. (II) The potential cytotoxicity of the free CPT solutions corresponding to the

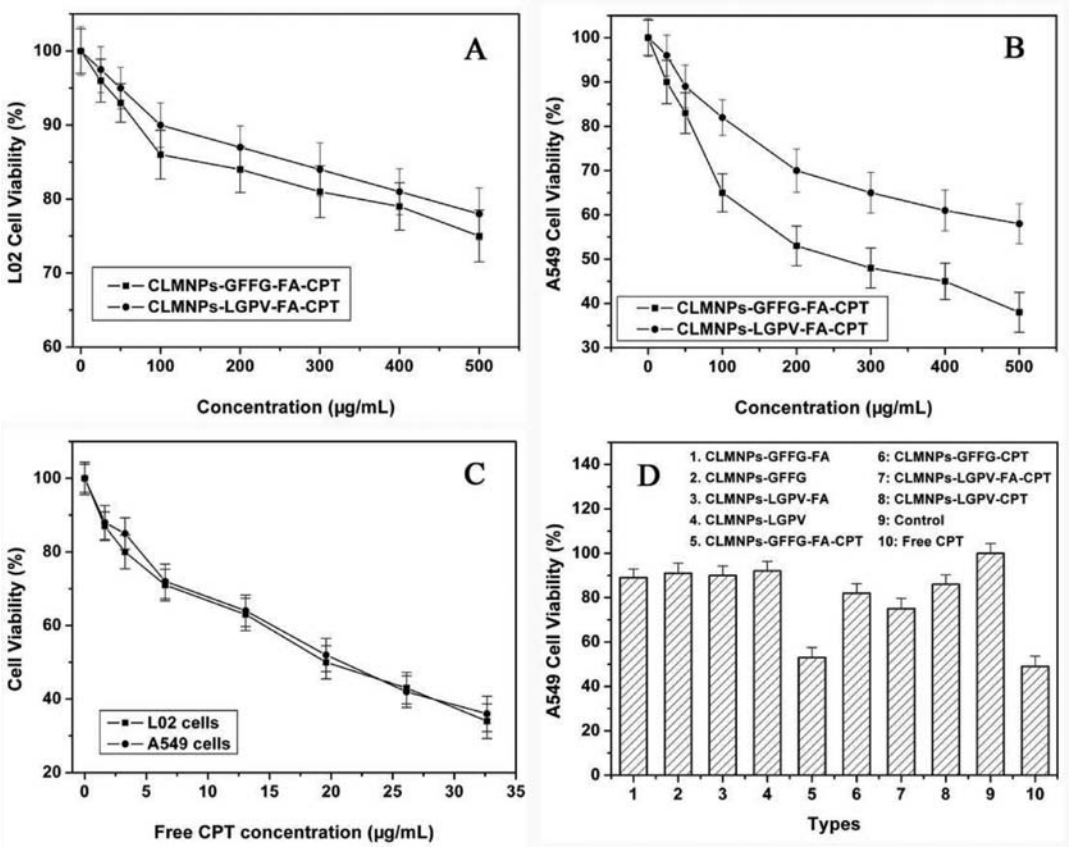

Figure 7. (A,B) In vitro cytotoxicity of CPT-loaded CLMNPs-GFFG-FA and CLMNPs-LGPV-FA copolymers at the different concentration against L02 cells and A549 cells, respectively. (C) Control experiment in the free CPT solution for comparison against L02 cells and A549 cells, respectively. (D) Cytotoxicity of the blank CLMNPs-GFFG-FA, CLMNPs-GFFG, CLMNPs-LGPV-FA, and CLMNPs-LGPV copolymers (1−4), and the CPT-loaded CLMNPs-GFFG-FA, CLMNPs-GFFG, CLMNPs-LGPV-FA, and CLMNPs-LGPV copolymers (5−8) under a concentration of 200 μg/mL against A549 cells for verifying folate targeting, respectively. Two control experiment groups, including the group with no added copolymer (9) and the group in free CPT solutions (10) corresponding to the CPT concentrations loaded on copolymers, were also studied.

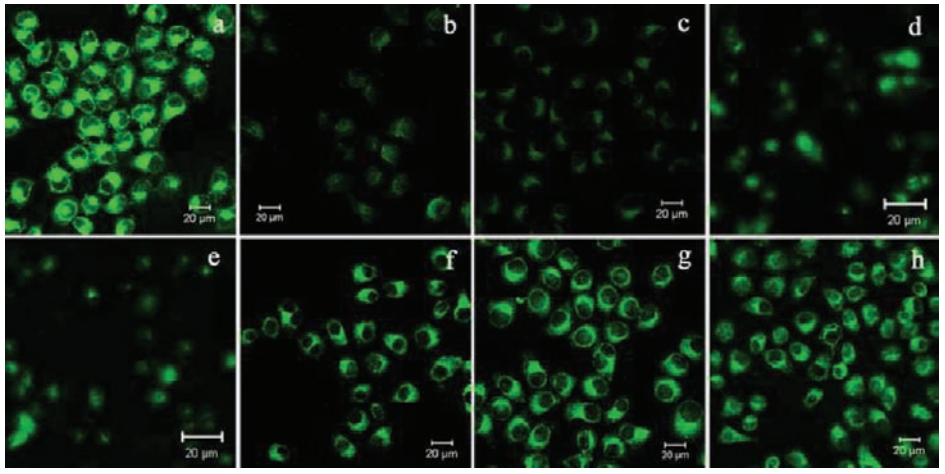

Figure 8. Laser scanning confocal images of representative A549 cells and L02 cells incubated with the different copolymers (200 μg/mL) or free CPT solutions (6.53 μg/mL) corresponding to the CPT concentrations loaded on copolymers for 2 h. (a) A549 cells + CPT-loaded CLMNPs-GFFG-FA, (b) L02 cells + CPT-loaded CLMNPs-GFFG-FA, (c) A549 cells + CPT-loaded CLMNPs-GFFG, (d) A549 cells + free CPT, (e) L02 cells + free CPT, (f) A549 cells + blank CLMNPs-GFFG-FA, (g) A549 cells + blank CLMNPs-LGPV-FA, (h) A549 cells + CPT-loaded CLMNPs-LGPV-FA. Excitation laser wavelength = 488 nm.

CPT concentrations loaded on copolymers was also studied. The results showed that a nonspecific permeation for free CPT led to a similar cell viability in L02 cells and A549 cells (Figure 7C). (III) In order to assess cytotoxicity of blank copolymers, a series of experiments have been performed with blank CLMNPs-GFFG-FA, CLMNPs-GFFG, CLMNPs-LGPV-FA, and CLMNPs-LGPV copolymers. The results showed that the effects of these blank copolymers on cell viability were

dx.doi.org/10.1021/bc300008k | *Bioconjugate Chem.* 2012, 23, 1010−1021

almost uniform (Figure 7D1−4), and there was a relatively high cell viability (more than 88% at a concentration of 200 μg/mL) in A549 cells, which displays low cytotoxicity and favorable cell compatibility for carriers. This also indicates that the discrepancy of inhibition of growth activity of copolymers appears only when CPT is loaded to the FA-conjugated copolymers. (IV) In the case of CPT-loaded copolymers, the viability in A549 cells incubated with folate-conjugated copolymers only accounted for 64.6% (for CLMNPs-GFFG-FA) and 87.2% (for CLMNPs-LGPV-FA) of that incubated with non-folate-conjugated copolymers, respectively (Figure 7D5−8). This indicates that the inhibition growth activity to A549 cancer cells can be facilitated by conjugating FA on copolymers.

Although the blank copolymers presented a relatively high cell viability, there is partly toxicity associated with Cd if the resulting drug carriers are used in clinical applications. Because this work is in the experimental stage, the CdTe QDs were used as imaging agents in order to track the tumor-targeted drug delivery of nanoparticles and establish a system along with our previous work.[17] The imaging portion (CdTe QDs) can be cast aside if the nanoparticles are used solely for therapeutic applications in humans. Even if the imaging function is still necessary for future applications, we are trying to substitute the CdTe QDs with other nontoxic imaging agents, such as silicon nanocrystal, gold nanoclusters, and so forth.

Cell Imaging. Figure 8 shows laser scanning confocal images of representative A549 cells and L02 cells incubated with the different copolymers (200 μg/mL) or free CPT solutions (6.53 μg/mL) corresponding to the CPT concentrations loaded on copolymers for 2 h. In the case of CPT-loaded CLMNPs-GFFG-FA copolymer, it is clear that the amount of distributing copolymer within the A549 cells (Figure 8a) was much higher than within the L02 cells (Figure 8b) under corresponding conditions. In order to verify this mechanism, the first control experiment has been performed with non-folate-conjugated CLMNPs-GFFG-CPT. It is discovered that the non-folate-conjugated copolymers could also enter the cells (Figure 8c). This may be because the non-folate-conjugated copolymers were transported into cells through a nonspecific endocytosis process. In here, the smart nanoparticles should play a critical role in the course of overcoming cell membrane barriers to enter the intracellular space. However, the uptake of folate-conjugated copolymer into A549 cells (Figure 8a) was more significant than that of non-folate-conjugated copolymer (Figure 8c), indicating that the cellular uptake of the copolymer into tumor cells can be enhanced by conjugating folate on their surface. In fact, the folate-conjugated copolymer was transported into the A549 cells by a folate-receptor-mediated endocytosis mechanism due to high expression of folate receptor on the surface of A549 cell membrane. Thus, the copolymer targeting to tumor cells can be enhanced by conjugating folate on copolymer.

In addition, the second control experiment has been also carried out to clarify differences in transportation mechanism for free CPT and CPT-loaded copolymers. It is found that the cellular uptake of free CPT was faster than that of copolymers through comparison of fluorescence within the cells, and the cellular uptake of free CPT in tumor cells (Figure 8d) was consistent with that in normal cells (Figure 8e), indicating that the transport of the small molecules (free CPT) was a nonspecific passive diffusion mechanism.[36] Furthermore, the free CPT was dramatically accumulated in the nucleus (Figure 8d,e) due to rapid binding of the free CPT to topoisomerase I and the chromosomal DNA,[1] while after endocytosis by the cells, the copolymers were mainly located in the cytoplasm due to the large sizes of the copolymers. The fluorescence within the cells from the CPT-loaded CLMNPs-GFFG-FA (Figure 8a) is more intense in comparison to free CPT (Figure 8d,e) or blank copolymers (Figure 8f,g) alone due to the integration effects of CPT and copolymers in CPT-loaded copolymers. However, the CPT-loaded copolymers were still mainly located in the cytoplasm. Thus, the fluorescence crosstalk from the free CPT can be eliminated by comparing the distribution of intracellular fluorescence.

Finally, it was found that the cellular uptake of blank CLMNPs-GFFG-FA and CLMNPs-LGPV-FA presented an identical pattern on the basis of their fluorescence within A549 cells (Figure 8f,g). However, the fluorescence from the CPT-loaded CLMNPs-LGPV-FA within A549 cells (Figure 8h) is slightly weaker in comparison with that from the CPT-loaded CLMNPs-GFFG-FA (Figure 8a), which may be attributed to less CPT loading on the former.

In this section, nanoparticle targeting and cell imaging occurred in the absence of magnetic guidance. Indeed, magnetic targeting can bring the copolymers to the tumor tissue, while ligand targeting (e.g., folate receptor-mediated cell uptake) can enhance the endocytosis of the copolymers due to higher specificity to the tumor cell membrane. The examination of cell uptake in different situations will be the content of our next work, including sole magnetic targeting, sole folate targeting, and dual magnetic/folate targeting. By then, we may make certain whether dual targeting is more effective than sole targeting.

■ CONCLUSION

In this study, we synthesized novel lminescent/magnetic nanoparticles with folate-conjugated tetrapeptide composites by assembly in situ for tumor-targeted drug delivery. The resulting end product, CLMNPs-GFFG-FA and CLMNPs-LGPV-FA cpoplymers, integrated magnetic and fluorescent properties. It was found that the CLMNPs-tetrapeptide-FA copolymers could be successfully trapped in the tumor tissue, even tumor cells under external magnetic field guidance. The loading efficiency of CPT were 8.6 wt % and 1.1 wt % on CLMNPs-GFFG-FA and CLMNPs-LGPV-FA copolymers, respectively. It can indicate that the binding site of CPT is right on peptide linkers, and the CPT loading efficiency has a significantly positive correlation with hydrophobic degree of peptides. The CPT release efficiency from CPT-loaded copolymers was higher at pH 5.3 than at pH 7.4 due to mutual repulsion between positively charged CPT and the cation chitosan shell of CLMNPs in acidic system. Furthermore, even at a high concentration of 1000 μg/mL, the hemolysis effect induced by the CPT-loaded copolymers was still negligible, extrinsic (PT) and intrinsic (APTT) coagulation pathways were not influenced by these copolymers, indicating their excellent blood compatibility. At the same time, more than 75% of viability in L02 cells was observed at a CPT-loaded copolymer concentration of 500 μg/mL, which displayed a low cytotoxicity and favorable cell compatibility as drug carriers. Additionally, the study confirmed that two CPT-loaded copolymers possess higher growth inhibition properties for cancer cells than for normal cell, and the CPT released from the CPT-loaded copolymers still holds high anticancer activity. Compared to free CPT, CPT-loaded

copolymers demonstrated specific targeting against A549 cells in vitro due to folate receptor-mediated endocytosis on the tumor cell membrane.

■ ASSOCIATED CONTENT

Supporting Information

ESI-mass spectrometry of the resulting GFFG-NH-Fmoc and the LGPV-NH-Boc tetrapeptides (SI 1), and the absorbance spectra of the two tetrapeptides solution (SI 2). This material is available free of charge via the Internet at http://pubs.acs.org.

■ AUTHOR INFORMATION

Corresponding Author

*Tel.: +86-931-891-2510; fax: +86-931-891-2582. E-mail address: zhanghx@lzu.edu.cn (Haixia Zhang).

Notes

The authors declare no competing financial interest.

■ ACKNOWLEDGMENTS

This study was supported by the National Natural Science Foundation of China Fund (no. 21105039), and the Fundamental Research Funds for the Central University (no. lzujbky-2012-k09). State Key Laboratory of Environmental Chemistry and Ecotoxicology, Research Center for Eco-Environmental Sciences, Chinese Academy of Sciences (KF2010-19).

■ REFERENCES

(1) Galbiati, A., Tabolacci, C., Rocca, B. M. D., Mattioli, P., Beninati, S., Paradossi, G., and Desideri, A. (2011) Targeting tumor cells through chitosan-folate modified microcapsules loaded with camptothecin. *Bioconjugate Chem. 22*, 1066−1072.

(2) Bandyopadhyay, K., and Gjerset, R. A. (2011) Protein kinase CK2 is a central regulator of topoisomerase I hyperphosphorylation and camptothecin sensitivity in cancer cell lines. *Biochemistry 50*, 704−714.

(3) Mi, Z. H., and Burke, T. G. (1994) Marked interspecies variations concerning the interactions of camptothecin with serum albumins: A frequency-domain fluorescence spectroscopic study. *Biochemistry 33*, 12540−12545.

(4) Burke, T. G., Staubus, A. E., and Mishra, A. K. (1992) Liposomal stabilization of camptotbecin's lactone ring. *J. Am. Chem. Soc. 114*, 8318−8319.

(5) Mi, Z. H., and Burke, T, G. (1994) Differential interactions of camptothecin lactone and carboxylate forms with human blood components. *Biochemistry 33*, 10325−10336.

(6) Thambi, T., Yoon, H. Y., Kim, K., Kwon, I. C., Yoo, C. K., and Park, J. H. (2011) Bioreducible block copolymers based on poly(ethylene glycol) and poly(γ-benzyl L-glutamate) for intracellular delivery of camptothecin. *Bioconjugate Chem. 22*, 1924−1931.

(7) Zhang, K., Wang, Y. J., Yu, A., Zhang, Y., Tang, H., and Zhu, X. X. (2010) Cholic acid-modified dendritic multimolecular micelles and enhancement of anticancer drug therapeutic efficacy. *Bioconjugate Chem. 21*, 1596−1601.

(8) Meenach, S. A., Kim, Y. J., Kauffman, K. J., Kanthamneni, N., Bachelder, E. M., and Ainslie, K. M. (2011) Synthesis, optimization and characterization of camptothecin-loaded acetalated dextran porous microparticles for pulmonary delivery. *Mol. Pharmaceutics* DOI: 10.1021/mp2003785.

(9) Machida, Y., Onishi, H., Kurita, A., Hata, H., and Morikawa, A. (2000) Pharmacokinetics of prolonged-release CPT-11-loaded microspheres in rats. *J. Controlled Release 66*, 159−175.

(10) Musumeci, T., Ventura, C. A., Giannone, I., Ruozi, B., Montenegro, L., Pignatello, R., and Puglisi, G. (2006) PLA/PLGA nanoparticles for sustained release of docetaxel. *Int. J. Pharm. 325*, 172−179.

(11) Guo, J., Yang, W. L., Wang, C. C., He, J., and Chen, J. Y. (2006) Poly(N-isopropylacrylamide)-coated luminescent/magnetic silica microspheres: Preparation, characterization, and biomedical applications. *Chem. Mater. 18*, 5554−5562.

(12) Chen, J. P., Yang, P. C., Ma, Y. H., and Wu, T. (2011) Characterization of chitosan magnetic nanoparticles for in situ delivery of tissue plasminogen activator. *Carbohydr. Polym. 84*, 364−372.

(13) Kong, S. D., Zhang, W. Z., Lee, J. H., Brammer, K., Lal, R., Karin, M., and Jin, S. (2010) Magnetically vectored nanocapsules for tumor penetration and remotely switchable on-demand drug release. *Nano Lett. 10*, 5088−5092.

(14) Mathew, M. E., Mohan, J. C., Manzoor, K., Nair, S. V., Tamura, H., and Jayakumar, R. (2010) Folate conjugated carboxymethyl chitosan-manganese doped zinc sulphide nanoparticles for targeted drug delivery and imaging of cancer cells. *Carbohydr. Polym. 80*, 442−448.

(15) Mangeney, C., Bousalem, S., Connan, C., Vaulay, M., Bernard, S., and Chehimi, M. M. (2006) Latex and hollow particles of reactive polypyrrole: Preparation, properties, and decoration by gold nanospheres. *Langmuir 22*, 10163−10169.

(16) Cho, H. S., Dong, Z. Y., Pauletti, G. M., Zhang, J. M., Xu, H., Gu, H. C., Wang, L. M., Ewing, R. C., Huth, C., Wang, F., and Shi, D. L. (2010) Fluorescent, superparamagnetic nanospheres for drug storage, targeting, and imaging: A multifunctional nanocarrier system for cancer diagnosis and treatment. *Nano 4*, 5398−5404.

(17) Shen, J. M., Xu, L., Lu, Y., Cao, H. M., Xu, Z. G., Chen, T., Zhang, H. X. (2012) Chitosan-based luminescent/magnetic hybrid nanogels for insulin delivery, cell imaging, and antidiabetic research of dietary supplements. *Int. J. Pharm.* 2012, *427* (2): 400-409.

(18) Jayakumar, R., Menon, D., Manzoor, K., Nair, S. V., and Tamura, H. (2010) Biomedical applications of chitin and chitosan based nanomaterials-A short review. *Carbohydr. Polym. 82*, 227−232.

(19) Corato, R. D., Bigall, N. C., Ragusa, A., Dorfs, D., Genovese, A., Marotta, R., Manna, L., and Pellegrino, T. (2011) Multifunctional nanobeads based on quantum dots and magnetic nanoparticles: Synthesis and cancer cell targeting and sorting. *Nano 5*, 1109−1121.

(20) Xia, W. S., Liu, P., Zhang, J. L., and Chen, J. (2011) Biological activities of chitosan and chitooligosaccharides. *Food Hydrocolloid 25*, 170−179.

(21) Suzuki, K., Mikami, T., Okawa, Y., Tokoro, A., Suzuki, S., and Suzuki, M. (1986) Antitumor effect of hexa-N-acetylchitohexaose and chitohexaose. *Carbohydr. Res. 151*, 403−408.

(22) Yang, S. J., Lin, F. H., Tsai, K. C., Wei, M. F., Tsai, H. M., Wong, J. M., and Shieh, M. J. (2010) Folic acid-conjugated chitosan nanoparticles enhanced protoporphyrin IX accumulation in colorectal cancer cells. *Bioconjugate Chem. 21*, 679−689.

(23) Prabaharan, M., Grailer, J. J., Pilla, S., Steeber, D. A., and Gong, S. Q. (2009) Folate-conjugated amphiphilic hyperbranched block copolymers based on Boltorn H40, poly(L-lactide) and poly(ethylene glycol) for tumor-targeted drug delivery. *Biomaterials 30*, 3009−3019.

(24) Mahato, R., Tai, W. Y., and Cheng, K. (2011) Prodrugs for improving tumor targetability and efficiency. *Adv. Drug Delivery Rev. 63*, 659−670.

(25) Shi, Z. L., Neoh, K. G., Kang, E. T., Shuter, B., Wang, S. C., Poh, C., and Wang, W. (2009) (Carboxymethyl)chitosan-modified superparamagnetic iron oxide nanoparticles for magnetic resonance imaging of stem cells. *ACS Appl. Mater. Interfaces 1*, 328−335.

(26) Wu, W. T., Shen, J., Banerjee, P., and Zhou, S. Q. (2010) Chitosan-based responsive hybrid nanogels for integration of optical pH-sensing, tumor cell imaging and controlled drug delivery. *Biomaterials 31*, 8371−8381.

(27) Moody, T. W., Mantey, S. A., Fuselier, J. A., Coy, D. H., and Jensen, R. T. (2007) Vasoactive intestinal peptide−camptothecin conjugates inhibit the proliferation of breast cancer cells. *Peptides 28*, 1883−1890.

(28) Pozzo, A. D., Ni, M. H., Esposito, E., Dallavalle, S., Musso, L., Bargiotti, A., Pisano, C., Vesci, L., Bucci, F., Castorina, M., Foderà., R., Giannini, G., Aulicino, C., and Penco, S. (2010) Novel tumor-targeted

RGD peptide−camptothecin conjugates: Synthesis and biological evaluation. *Bioorg. Med. Chem. 18*, 64−72.
(29) Aluri, S., Janib, S. M., and Mackay, J. A. (2009) Environmentally responsive peptides as anticancer drug carriers. *Adv. Drug Delivery Rev. 61*, 940−952.
(30) Zhang, X. X., Eden, H. S., and Chen, X. Y. (2011) Peptides in cancer nanomedicine: Drug carriers, targeting ligands and protease substrates. *J. Controlled Release*, DOI: 10.1016/j.jconrel.2011.10.023.
(31) Henne, W. A., Doorneweerd, D. D., Hilgenbrink, A. R., Kularatne, S. A., and Low, P. S. (2006) Synthesis and activity of a folate peptide camptothecin prodrug. *Bioorg. Med. Chem. Lett. 16*, 5350−5355.
(32) Wu, H. X., Zhang, S. J., Zhang, J. M., Liu, G., Shi, J. L., Zhang, L. X., Cui, X. Z., Ruan, M. L., He, Q. J., and Bu, W. B. (2011) A hollow-core, magnetic, and mesoporous double-shell nanostructure: In situ decomposition/reduction synthesis, bioimaging, and drug-delivery properties. *Adv. Funct. Mater. 21*, 1850−1862.
(33) Sun, Y. N., Wang, C. D., Zhang, X. M., Ren, L., and Tian, X. H. (2011) Shape dependence of gold nanoparticles on in vivo acute toxicological effects and biodistribution. *J. Nanosci. Nanotechnol. 11*, 1210−1216.
(34) Lin, Y. S., and Haynes, C. L. (2010) Impacts of mesoporous silica nanoparticle size, pore ordering, and pore integrity on hemolytic activity. *J. Am. Chem. Soc. 132*, 4834−4842.
(35) Miyakem, M., Honda, T., and Miwatani, T. (1989) Effect of divalent cations and saccharides on Vibrio metschnikovii cytolysin-induced hemolysis of rabbit erythrocytes. *Infect. Immun. 57*, 158−163.
(36) Yoo, H. S., and Park, T. G. (2004) Folate-receptor-targeted delivery of doxorubicin nano-aggregates stabilized by doxorubicin−PEG−folate conjugate. *J. Controlled Release 100*, 247−256.

Bioconjugate Chemistry

Article

pubs.acs.org/bc

Iodinated Photosensitizing Chitosan: Self-Assembly into Tumor-Homing Nanoparticles with Enhanced Singlet Oxygen Generation

Chang-Keun Lim,[†,§] Jiyoung Shin,[‡,§] Ick Chan Kwon,[†] Seo Young Jeong,*[,‡] and Sehoon Kim*[,†]

[†]Center for Theragnosis, Korea Institute of Science and Technology, 39-1 Hawolgok-dong, Seongbuk-gu, Seoul 136-791, Korea

[‡]Department of Life and Nanophaceutical Science, Kyung Hee University, 1 Hoegi-dong, Dongdaemun-gu, Seoul 130-701, Korea

Supporting Information

ABSTRACT: A novel iodinated chitosan-backboned conjugate (GC−I−Ce6) was designed and prepared to fabricate self-assembled biopolymeric nanoparticles with heavy atom-effected enhanced singlet oxygen generation as well as biological merits. The heavy atom-rich nature of the hydrophobic particle interior was characterized with X-ray absorption and the modified photophysical properties of a chemically embedded photosensitizer, chlorin e6 (Ce6). From the comparative spectroscopic studies as well as cellular and animal experiments, it has been shown that the self-assembled GC−I−Ce6 nanoparticles have enhanced capability of singlet oxygen generation by the intraparticle heavy-atom effect, along with high tumor targetability in vitro and in vivo thanks to the glycol chitosan-surfaced exterior with biocompatible, positively charged and tumor-homing characteristics. Actual efficacy improvement in the photodynamic therapy of a human breast cancer cell line (MDA-MB-231) demonstrates potential of our photophysically and pharmaceutically motivated hybrid bioconjugate approach for nanomedicine applications.

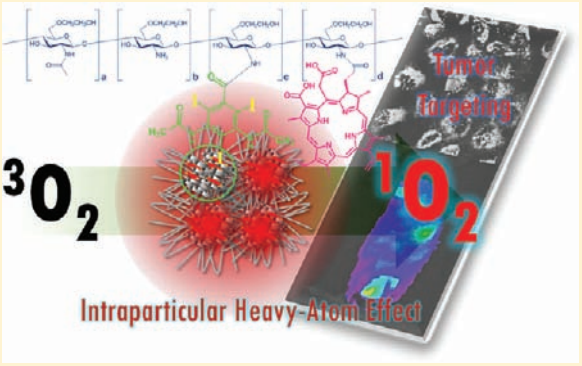

INTRODUCTION

Hydrophobically modified polysaccharides are an emerging class of biohybrid materials that, in an aqueous milieu, spontaneously form nanometer-sized colloids with the interfacial-free energy-minimized structure comprising a hydrophilic shell and hydrophobic multicores. The self-assembled polysaccharide nanoparticles have intensively been exploited as useful nanocarriers for the delivery of drugs and imaging agents in vivo and in cells.[1−8] Their advantages include (1) high biocompatibility,[1−8] (2) enhanced cell permeability with less cytotoxicity,[1,5] (3) prolonged blood circulation to manifest passive tumor targeting in vivo by the enhanced permeability and retention (EPR) effect,[4,6] and (4) lots of reactive chemical groups available for multifunctional bioconjugation and active targeting of therapeutic/signaling payloads.[1−8] Hydrophobically modified glycol chitosan (GC) is a representative example exhibiting all these advantageous features in a self-assembled nanoparticulate formulation.[3−6]

Recently, it has been shown that self-assembled polysaccharide nanoparticles can significantly improve the efficacy of photodynamic therapy (PDT) by carrying a photosensitizer (PS; PDT drug) that is physically entrapped or chemically conjugated in their hydrophobic cores.[9,10] PDT is a light-activated modality of treatment for several types of cancer.[11,12] Its therapeutic efficacy is attained by utilizing the PS molecules capable of generating cytotoxic reactive oxygen species (ROS), particularly singlet oxygen ($^1O_2$), after light excitation. Co-localization of light and the PS molecules at cancerous cells is a prerequisite to the selectivity of treatment by PDT without collateral damage to healthy tissues. However, most existing PSs are aromatic and hydrophobic in nature with poor solubility in physiological media, which limits selective accumulation of the PS molecules in malignant cells by systemic administration. In this respect, the incorporation of PS in water-dispersible polymeric nanoparticle carriers can enhance the PDT efficacy by preventing the undesired PS aggregation as well as promoting tumor targeting and intracellular delivery of the PS payload.[13−16]

Another possible advantage attainable by nanoparticle incorporation of the PS molecules is the photophysical modulation by coencapsulating functional molecules that impose the intraparticle intermolecular interaction on the PS payload to enhance the overall capability of $^1O_2$ generation.[17−19] Recently, we have demonstrated that iodine-concentrated nanoformulation can enhance the $^1O_2$ generation efficiency.[18,19] This is attributed to the intraparticle heavy-atom effect that facilitates intersystem crossing (ISC) of the photoexcited PS from the singlet state (^{1}PS*) to the long-lived triplet state (^{3}PS*), where the latter photoproduct sensitizes surrounding molecular oxygen ($^3O_2$) into $^1O_2$.

In this study, we designed and prepared an iodinated photosensitizing polysaccharide amphiphile (GC−I−Ce6), to

Received: January 11, 2012
Revised: April 16, 2012
Published: April 19, 2012

   dx.doi.org/10.1021/bc300012g | Bioconjugate Chem. 2012, 23, 1022−1028

Scheme 1. Schematic Representation of Iodinated (GC−I−Ce6) or noniodinated (GC−Me−Ce6) GC Amphiphile and Its Bionanoparticles Implemented Therewith

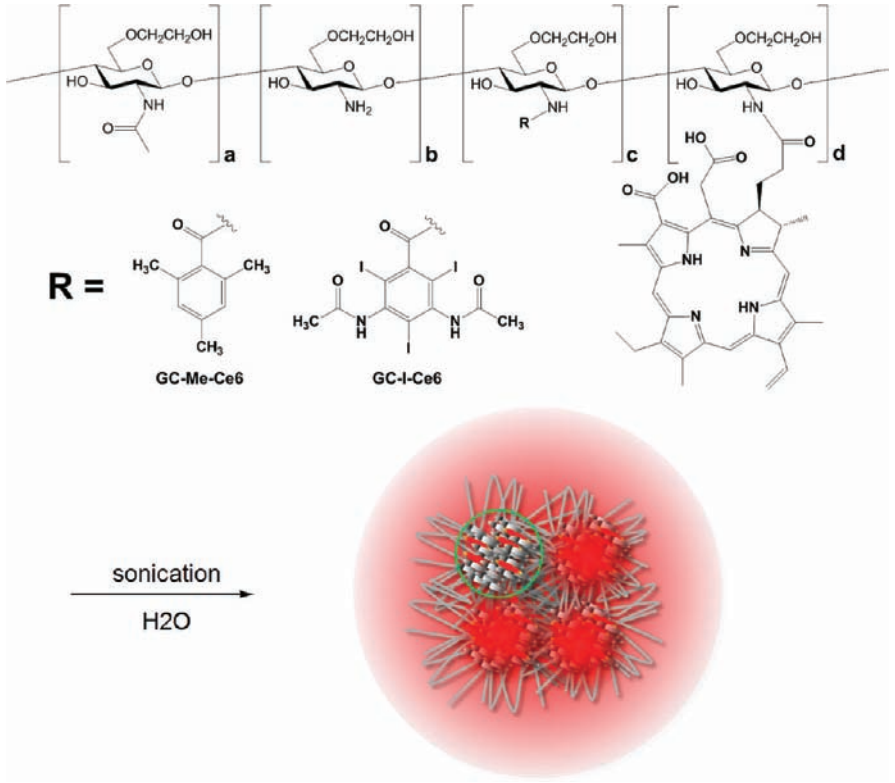

integrate all the above concepts into a polymeric bioconjugate monolith. As shown in Scheme 1, the designed amphiphilic bioconjugate is composed of water-soluble glycol chitosan (GC), photosensitizing chlorin e6 (Ce6), and densely conjugated diatrizoic acid (3,5-bis(acetamido)-2,4,6-triiodobenzoic acid) as an iodine-rich hydrophobic pendant. It is hence anticipated that GC−I−Ce6 will self-assemble into nanoparticles in water due to the given amphiphilicity and construct the heavy atom-effected particulate interior surrounded by the GC constituent on the surface. In the structure design, the amine-rich polysaccharide backbone (GC) provides hydrophilicity and chemical conjugation sites as well as other biologically favorable properties, as mentioned above. Diatrizoic acid was chosen because it has been shown to be safe in vivo and is being used clinically as a radiocontrast agent for X-ray imaging and computed tomography (CT).[20,21] Overall, the designed biohybrid is expected to be an biocompatible nanoplatform that has great potential for PDT. Here are reported the experimental results that validate the heavy atom-conjugated biohybrid approach for the enhanced $^1O_2$ generation and tumor cell targeting in vitro and in vivo.

EXPERIMENTAL SECTION

Instrumentation. Transmission electron microscopic (TEM) images of negatively stained particles (2 wt % uranyl acetate) was obtained with a CM30 electron microscope (FEI/Philips) operated at 200 kV. Absorption and fluorescence spectra were acquired using a UV−visible spectrometer (Agilent 8453) and a fluorescence spectrophotometer (Hitachi F-7000, wavelength calibrated for excitation and emission), respectively. The CT image of the phentom study was acquired using micro CT (Skyscan 1076, Skyscan Inc.) with the following parameters: 70 KV, 140 μA, 35 μm of resolution, 632 ms of exposure time.

Preparation of GC−I−Ce6 and GC−Me−Ce6 Amphiphiles and Nanoparticles Thereof. Glycol chitosan (GC, M_W = 250; degree of deacetylation = 82.7%; Sigma) (10 mg, 0.0488 mmol (unit)) was dissolved in 3 mL of distilled water with sonication, and a DMSO (10 mL) solution containing diatrizoic acid (or trimethylbenzoic acid), 1-ethyl-3-(3-dimethylaminopropyl) carbodiimide hydrochloride (EDC), and *N*-hydroxysuccinimide (NHS) was added. The feed ratio of diatrizoic acid (or trimethylbenzoic acid) was 20% with respect to the total GC repeating unit. For each amphiphile, 1.5 equiv coupling agents (EDC and NHS) with respect to the hydrophobic benzoic acids were fed, then the reaction mixtures were stirred at ambient temperature for 24 h. Then, a DMSO solution containing Ce6 (0.5 mol%), EDC (1.5 equiv), and NHS (1.5 equiv) was added to the reaction mixture, followed by stirring at ambient temperature for 24 h. For purification, the coupling reaction mixtures were subjected to the successive dialysis against DMSO (2 days) and water (2 days) using a cellular separation membrane (Membrane Filtration Products, Inc., molecular cutoff = 50 kDa). The resulting dispersions of nanoparticles were freeze-dried or used as is for characterization and imaging experiments. The dried GC−I−Ce6 (or GC−Me−Ce6) nanoparticles were able to be redispersed in water at 1 mg mL^{-1} under probe sonication at 90 W for 2 min (Sigma Ultrasonic Processor, GEX-600). However, they were not able to be dissolved into separate chains in DMSO or other relevant solvents after complete drying, which does not allow for NMR measurement or other solution characterizations. Therefore, the substitution yields were determined before purification by quantifying the unreacted hydrophobic pendants and Ce6. For

dx.doi.org/10.1021/bc300012g | *Bioconjugate Chem.* 2012, 23, 1022−1028

this, the reaction mixtures (200 μL) were mixed with THF (800 μL) and centrifuged to remove precipitates of reacted GC−I−Ce6 (or GC−Me−Ce6) conjugates. The substitution ratios were indirectly calculated through the measurements of the unreacted diatrizoic acid (or trimethylbenzoic acid) and free Ce6 concentrations in the supernatant of the centrifuged mixture by UV absorbance-based quantification.

Measurement of Singlet Oxygen Generation Quantum Yield with RNO Test. Singlet oxygen generation was monitored by a decrease in the absorbance of the mixed RNO at 440 nm under laser excitation. Each mixture solution was prepared by mixing 0.21 mL of GC−I−Ce6 (1 mg mL^{-1}) or GC−Me−Ce6 (concentration was adjusted to get the same absorbance at 671 nm as GC−I−Ce6) in water with 0.11 mL of RNO stock solution (0.12 mM in water), 0.7 mL of histidine (0.03 M in water) and 0.18 mL water. The excitation at 671 nm was performed by irradiating the collimated laser beam through the sample. The relative quantum yields of $^1O_2$ generation (Φ_Δ) were estimated by using free Ce6 as a reference and comparing the derived slopes of RNO absorbance plots against the irradiation time.

Nanoparticle Uptake and NIR Fluorescence Imaging with Tumor Cells. HeLa (human cervical epithelioid carcinoma) cells were cultivated in RPMI1640 medium supplemented with 10% FBS, 100 U/mL penicillin, and 100 mg/mL streptomycin in a humidified 5% CO_2 incubator at 37 °C. The tested cells were seeded onto 35 mm cover glass bottom dishes and allowed to grow until a confluence of 70% was reached. Prior to the experiment, cells were washed twice with PBS (pH 7.4) to remove the remnant growth medium and then incubated in a serum-free medium (2 mL) containing GC−I−Ce6 nanoparticles (0.2 mg) for 2 h. The cells were then washed twice with ice-cold PBS (pH 7.4) and directly imaged using a fluorescence microscope (Ziess Axioskop2 FS Plus).

In Vivo NIRF Imaging with Tumor Bearing Mouse. The animal studies have been approved by the animal care and use committee of the Korea Institute of Science and Technology, and all handling of mice was performed in accordance with the institutional regulations. Tumor xenografts were created via subcutaneous injection of 1×10^7 SCC7 (squamous cell carcinoma) cells suspended in RPMI1640 cell culture media in 5-week-old male BALB/c nude mice (Orient. Korea). After 2 weeks postinoculation, the mice were intravenously injected with the GC−I−Ce6 nanoparticles suspension (0.2 mg GC−I−Ce6 in 200 μL of DPBS). Their tissue distribution and time-dependent excretion profiles in a murine tumor model were imaged by positioning mice on an animal plate heated to 37 °C in the eXplore Optix System (Advanced Research Technologies Inc., Canada). Laser power and count time settings were optimized at 100 μW and 0.3 s per point. A 670 nm pulsed laser diode was used to excite the nanoparticles.

Determination of the Dark- and Phototoxicity with MTT Cell Viability Assay. MDA-MB-231 cells (human breast-cancer cell) were cultured in two 96-well plates and treated with GC−I−Ce6 nanoparticles (1 mg) or GC−Me−Ce6 nanoparticles (1 mg) for 5 h. After washing with fresh media, one plate was incubated for 14 h after laser irradiation (671 nm, 6.4 W/cm^2) to separated five groups with irradiation times of 0 min, 1 min, 2 min, 4 min, and 6 min, to determine the dark- and phototoxicity as a light dose. Then, the cell viability was evaluated via MTT assay.

RESULTS AND DISCUSSION

For comparative studies, iodinated, and noniodinated GC amphiphiles (GC−I−Ce6 and GC−Me−Ce6, respectively) were synthesized by sequential amidation of free amines of GC with hydrophobic benzoic acids and then Ce6 (20 mol % and 0.5 mol % fed with respect to the GC monomeric units, respectively) in DMSO/water (Scheme 1). The purification was conducted by successive dialysis against DMSO and excess pure water. Table 1 summarizes the feed ratio of pendants and the resulting degree of substitution for hydrophobic benzoic acids and Ce6, estimated through the measurements of the unreacted free substituents by UV absorbance-based quantification. It was found that both the lyophilized GC amphiphiles form clear solutions in water by sonication. When the solution was sampled, dried on a grid, and examined with a transmission electron microscope (TEM), spherical nanoparticles were observed with average diameters of 19.2 ± 6.1 and 22.5 ± 4.8 nm for GC−I−Ce6 and GC−Me−Ce6, respectively (Figure 1 and Supporting Information Figure S1; at least 80 particles were counted for the size analysis). This suggests that the obtained GC amphiphiles undergo aqueous self-assembly into nanoparticles with an appropriate size for facile endocytosis.[22−24] The ζ potentials of both GC nanoparticles were measured as similar (18−20 mV) in deionized water, implying that a similar portion of the positively charged glycol chitosan chains covers the nanoparticle surface through amphiphilic self-assembly to stabilize the colloidal dispersion.

Table 1. Synthesis of Hydrophobically Modified GC Amphiphiles

	hydrophobic benzoic acid pendant[a]			Ce6[a]		
	fed	substituted	yield (%)	fed	substituted	yield (%)
GC−I−Ce6	20	14.6	73	0.5	0.49	98
GC−Me−Ce6	20	13.2	66	0.5	0.49	98

[a]The fed and substituted values are expressed as a molar ratio (in percent) with respect to the total GC repeating unit.

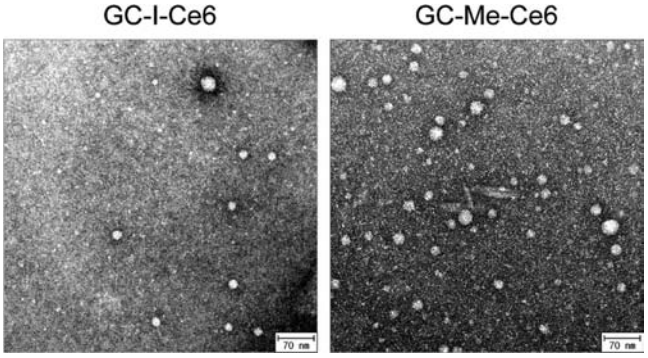

Figure 1. TEM images of GC−I−Ce6 and GC−Me−Ce6 nanoparticles. Both of the scale bars present 70 nm.

The heavy atom-rich construction of the self-assembled GC−I−Ce6 nanoparticles was confirmed by comparing the X-ray absorption with the iodine-free GC-Me-Ce6 control. As shown in Figure 2, the phantom CT image of GC−I−Ce6 nanoparticles revealed a linear increment of the X-ray absorption with increasing concentration. Importantly, the X-

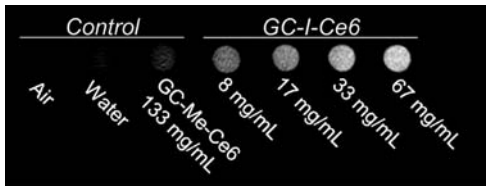

Figure 2. MicroCT image of GC−I−Ce6 and GC−Me−Ce6 nanoparticles dispersed in water at varying concentrations.

ray absorption of dilute GC−I−Ce6 (328 HU at 8 mg/mL) is much higher than that of concentrated GC−Me−Ce6 (71 HU at 133 mg/mL). In spite of the same surface characteristics of the self-assembled nanoparticles given by the hydrophilic GC constituent, the intraparticle environments are different depending on the chemical nature of the hydrophobic pendant. Strong X-ray absorption of GC−I−Ce6 nanoparticles is attributable to the high intraparticle content of iodine (atomic weight = 126.9) possessing a high X-ray density.[20,21] This suggests that the iodine-rich construction of the hydrophobic interior is capable of exerting the heavy-atom effect on the photophysics of the colocalized Ce6 sensitizer.

The optical spectra of both of GC−I−Ce6 and GC−Me−Ce6 nanoparticles dispersed in water (Figure 3) clearly exhibit

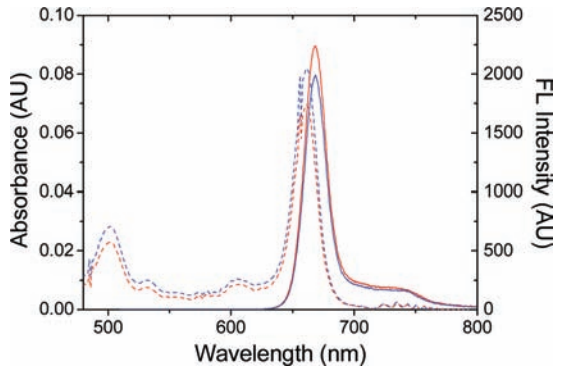

Figure 3. Absorption (dotted) and fluorescence (solid) spectra of GC−I−Ce6 (blue) and GC−Me−Ce6 (red) nanoparticles dispersed in water.

the light absorption and emission in the near-infrared (NIR) region ($\lambda_{max.abs}$ = 662 nm, $\lambda_{max.fl}$ = 668 nm). No indication of Ce6 aggregation (spectral broadening and fluorescence quenching) was observed in the spectra.[25−27] GC−I-Ce6 nanoparticles are NIR fluorescent and the spectra are sharp without notable broadening (fwhm = 24 nm for the longest-wavelength Q-band absorption and 21 nm for fluorescence), which suggests that hydrophobic Ce6 is molecularly dispersed in aqueous milieu by chemical conjugation to the water-soluble GC backbone. The prepared bioconjugate nanoparticles exhibited almost identical spectral features except for the fluorescence intensity that was 7% reduced in the iodine-rich GC−I−Ce6 nanoparticles in comparison to the iodine-free GC−Me−Ce6 counterpart. The observed reduction in relative fluorescence intensity is ascribable to the promoted ISC over fluorescence due to the intraparticle heavy-atom effect,[18,19] which indicates that the chemically conjugated Ce6 is located close to the iodinated aromatic pendants in the self-assembled nanostructure through the hydrophobic interaction.

The capability of the self-assembled nanoparticles to sensitize $^1O_2$ under laser irradiation was assessed by monitoring the absorption bleaching of *p*-nitroso-*N*,*N*′-dimethylaniline (RNO) in the presence of histidine.[28] Figure 4A is a representative

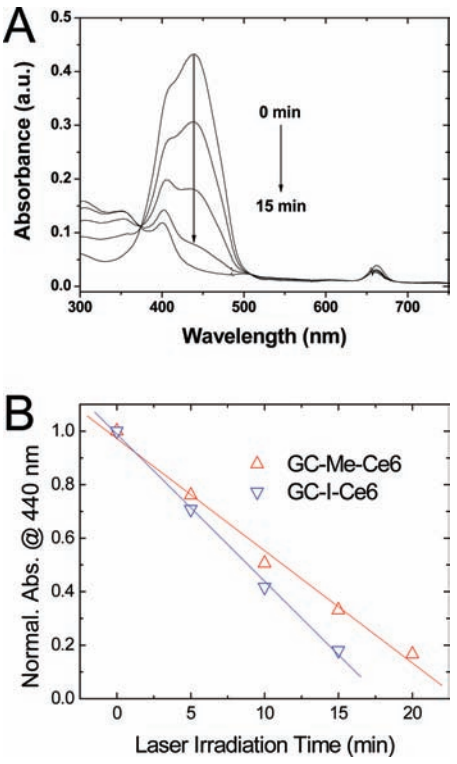

Figure 4. (A) Photochemical bleaching of RNO by $^1O_2$ generated upon laser excitation of GC−I−Ce6 nanoparticles at 671 nm. Temporal evolutions are indicated by the arrows. (B) Temporal dependence of RNO absorbance at 440 nm during the irradiation of samples (GC−I−Ce6 and GC−Me−Ce6 suspensions) containing the same amount of Ce6 under the identical photobleaching condition. The lines are linear fits of the absorbance plots.

spectral evolution showing the RNO bleaching in the presence of GC−I−Ce6 nanoparticles and laser irradiation at 671 nm, where the RNO absorption band at 440 nm decreased continuously over the course of irradiation. It should be noted that the observed bleaching was not caused by its own photochemical oxidation of RNO as it has no absorption at the irradiation wavelength and thus cannot reach the excited state. Rather, it is attributable to the oxidation of RNO caused by the photosensitized $^1O_2$ by the Ce6-conjugated nanoparticles. Temporal traces of the RNO bleaching by both nanoparticles are shown in Figure 4B. Importantly, the GC−I−Ce6 nanoparticles showed markedly rapid absorption bleaching compared to the GC−Me−Ce6 control possessing the same optical density of Ce6 at 671 nm. From the slopes of Figure 4B, the relative quantum yields of $^1O_2$ generation (Φ_Δ) were estimated as 0.59 and 0.45 for GC−I−Ce6 and GC−Me−Ce6 nanoparticles, respectively. The enhanced oxidation capability of the iodine-rich nanoparticles over the iodine-free control is direct evidence for the increased efficiency of $^1O_2$ generation by the intraparticle heavy-atom effect.

Given enhanced $^1O_2$ photosensitization of the GC−I-Ce6 nanoparticles, their tumor targeting capability was further studied in vitro and in vivo to evaluate the possible utility for PDT application. For this, the fluorescence imaging technique was used because the Ce6 pendant itself has absorption and fluorescence in the NIR, as discussed in Figure 3. Recently,

dx.doi.org/10.1021/bc300012g | *Bioconjugate Chem.* 2012, 23, 1022−1028

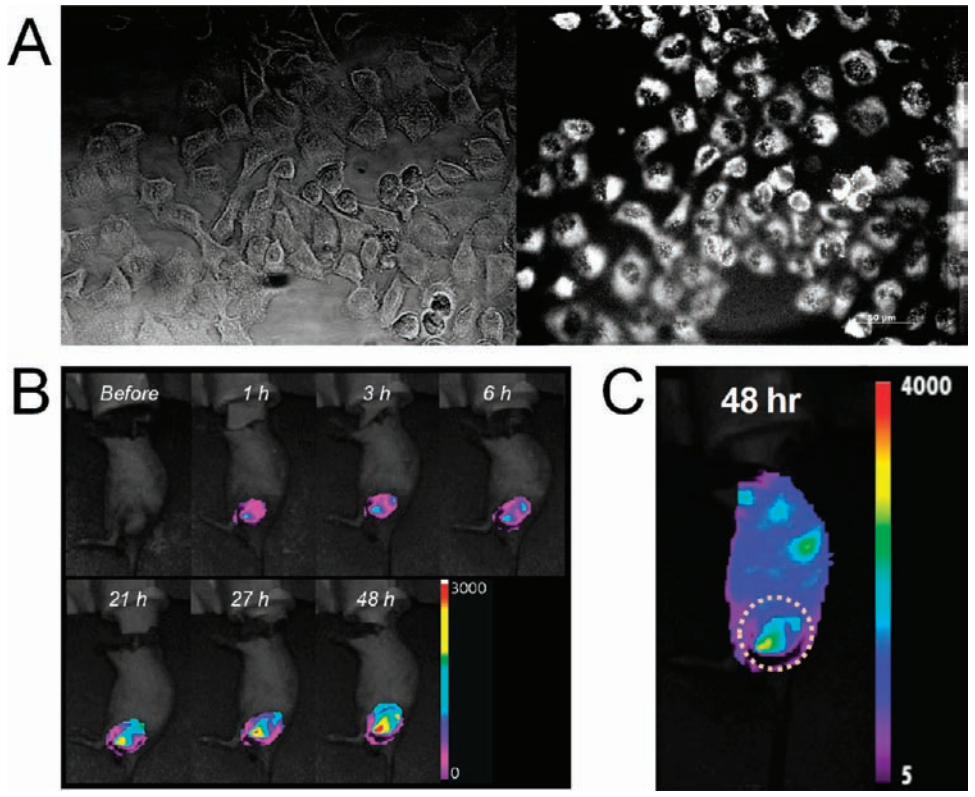

Figure 5. (A) Optical (left) and NIRF (right) images of HeLa cells treated with GC−I−Ce6 nanoparticles. (B) In vivo NIRF images at tumor tissue of SCC7 tumor-bearing mouse before and after tail vein injection of GC−I−Ce6 nanoparticles. Imaging time points postinjection are indicated. (C) In vivo whole body NIRF image of the mouse at 48 h after the tail vein injection. White circle indicates the tumor location. Laser excitation and image acquisition were scanned around the tumor area only (B) or throughout the body (C).

noninvasive and real-time NIR fluorescence imaging has been widely employed to visualize the tissue distribution of the objects of interest because the technique allows for better in vitro/in vivo signal-to-noise ratio and deeper light penetration into biological materials.[29,30] To assess the cancer cell targeting behavior in vitro, HeLa (human cervical epithelioid carcinoma) cells were incubated with GC−I−Ce6 nanoparticles and examined under a NIR-filtered fluorescence microscope. After 2 h of incubation at 37 °C, the nanoparticle-treated cells manifested a clear NIR fluorescence signal from the cytoplasmic region (Figure 5A). This avid cellular uptake indicates that the positively charged biopolymeric surface properties of the hybrid nanoparticles facilitates their internalization into cells by several nondestructive endocytic pathways that are operative in GC-based nanoparticles.[5] Indeed, hydrophobically modified GC nanoparticles have a greater advantage in the in vivo tumor targeting by intravenous administration.[3,4] In this regard, we monitored the temporal tumor accumulation of the self-assembled GC−I−Ce6 nanoparticles after systemic administration into SCC7 (squamous cell carcinoma) tumor-bearing mice via tail vein injection. As shown in the NIR fluorescence images taken at selected time points (Figure 5B and Supporting Information Figure S2), a notable signal was observed at the tumor at 1 h postinjection. Importantly, the tumor signal was further increased in the course of time, indicating significant tumor accumulation of GC−I−Ce6 nanoparticles. The whole body image taken at 48 h postinjection suggests that GC−I−Ce6 nanoparticles were mainly taken up by the tumor so as to readily identify the tumor location (Figure 5C). This behavior is well accordant to our earlier result that GC nanoparticles displayed prolonged blood circulation, decreased time-dependent excretion from the body, and elevated tumor accumulation in vivo.[3,4] All the imaging results conclude that the self-assembled GC−I−Ce6 nanoparticles has great tumor targetability in vitro as well as in vivo, validating our design strategy based on the GC-incorporated bioconjugation.

By taking advantage of the enhanced $^1O_2$ generation and high tumor targetability, we explored possible utility of GC−I−Ce6 nanoparticles for phototherapy of cancer cells. For comparative evaluation of the phototoxicity, human breast-cancer cells (MDA-MB-231) were incubated with GC−I−Ce6 and GC−Me−Ce6 nanoparticles for 5 h and then subjected to the cell viability (MTT) assay[31] with or without light irradiation (Figure 6). Without phototreatment, both nanoparticles showed minimal cytotoxicity. To induce the intracellular $^1O_2$ generation, nanoparticle-treated cells were irradiated with a laser (671 nm, 6.4 W/cm^2) for varying times of irradiation. Under laser illumination, the phototoxic impact was clearly seen in cells treated with both nanoparticles but not in sample-free control cells. Importantly, the iodine-rich GC−I−Ce6 nanoparticles exhibited significantly enhanced phototoxicity over the iodine-free GC−Me−Ce6 nanoparticles at the same light dose. This comparison clearly elucidates that highly iodinated biopolymeric nanoparticles with the intraparticle heavy-atom effect have great potential for the PDT application.

■ CONCLUSION

We have synthesized a highly iodinated photosensitizing bioconjugate (GC−I−Ce6) by densely conjugating glycol

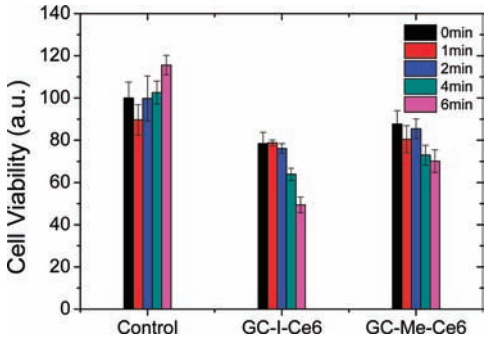

Figure 6. In vitro phototoxicity of GC−I−Ce6 and GC−Me−Ce6 nanoparticles against human breast cancer cells (MDA-MB-231), evaluated by the colorimetric MTT assay done 14 h after laser irradiation of sample-stained cells. Control is phototreated sample-free cells. The legend presents the laser irradiation time. The error bars indicate the standard deviations for independent experiments (n = 10).

chitosan with diatrizoic acid. It was found that amphiphilic GC−I−Ce6 self-assembles into water-dispersed nanoparticles that present the intraparticle heavy-atom effect on the photosensitizing Ce6 pendant and thereby the enhanced $^1O_2$ generation through the modified photophysics. Owing to the biologically favorable surface characteristics arising from the glycol chitosan constituent, the self-assembled GC−I−Ce6 nanoparticles exhibited high tumor targeting capability in vitro and in vivo. By virtue of these combined merits, the iodine-rich bioconjugate nanoparticles demonstrated possible utility as a PDT agent with improved efficacy for the treatment of cancer cells.

■ ASSOCIATED CONTENT

Ⓢ Supporting Information

TEM images as well as in vivo whole body NIRF images of the tumor xenograft model before and after the injection of GC−I−Ce6 nanoparticles suspension. This material is available free of charge via the Internet at http://pubs.acs.org.

■ AUTHOR INFORMATION

Corresponding Author

*for S.Y.J.: E-mail, syjeong@khu.ac.kr. For S.K.: phone, +82-2-958-5924; fax, +82-2-958-5909; E-mail, sehoonkim@kist.re.kr.

Author Contributions

§These authors contributed equally to this work.

Notes

The authors declare no competing financial interest.

■ ACKNOWLEDGMENTS

This work was supported by grants from the Korea Ministry of Education, Science and Technology (MEST) (nos. 2011-0029930 and 2011-0002139).

■ REFERENCES

(1) Janes, K. A., Calvo, P., and Alonso, M. J. (2001) Polysaccharide colloidal particles as delivery systems for macromolecules. *Adv. Drug Deliv. Rev. 47*, 83−97.

(2) Baldwin, A. D., and Kiick, K. L. (2010) Polysaccharide-modified synthetic polymeric biomaterials. *Biopolymers 94*, 128−140.

(3) Kim, K., Kwon, S., Park, J. H., Chung, H., Jeong, S. Y., and Kwon, I. C. (2005) Physicochemical characterizations of self-assembled nanoparticles of glycol chitosan-deoxycholic acid conjugates. *Biomacromolecules 6*, 1154−1158.

(4) Park, K., Kim, J.-H., Nam, Y. S., Lee, S., Nam, H. Y., Kim, K., Park, J. H., Kim, I.-S., Choi, K., Kim, S. Y., and Kwon, I. C. (2007) Effect of polymer molecular weight on the tumor targeting characteristics of self-assembled glycol chitosan nanoparticles. *J. Controlled Release 122*, 305−314.

(5) Nam, H. Y., Kwon, S. M., Chung, H., Lee, S.-Y., Kwon, S.-H., Jeon, H., Kim, Y., Park, J. H., Kim, J., Her, S., Oh, Y.-K., Kwon, I. C., Kim, K., and Jeong, S. Y. (2009) Cellular uptake mechanism and intracellular fate of hydrophobically modified glycol chitosan nanoparticles. *J. Controlled Release 135*, 259−267.

(6) Lee, S., Ryu, J. H., Park, K., Lee, A., Lee, S.-Y., Youn, I.-C., Ahn, C.-H., Yoon, S. M., Myung, S.-J., Moon, D. H., Chen, X., Choi, K., Kwon, I. C., and Kim, K. (2009) Polymeric nanoparticle-based activatable near-infrared nanosensor for protease determination in vivo. *Nano Lett. 9*, 4412−4416.

(7) Lim, C.-K., Kim, S., Kwon, I. C., Ahn, C.-H., and Park, S. Y. (2009) Dye-condensed biopolymeric hybrids: chromophoric aggregation and self-assembly toward fluorescent bionanoparticles for near infrared bioimaging. *Chem. Mater. 21*, 5819−5825.

(8) Lim, C.-K., Seo, J., Kim, S., Kwon, I. C., Ahn, C.-H., and Park, S. Y. (2011) Concentration and pH-modulated dual fluorescence in self-assembled nanoparticles of phototautomerizable biopolymeric amphiphile. *Dyes Pigm. 90*, 284−289.

(9) Lee, S. J., Park, K., Oh, Y.-K., Kwon, S.-H., Her, S., Kim, I.-S., Choi, K., Lee, S. J., Kim, H., Lee, S. G., Kim, K., and Kwon, I. C. (2009) Tumor specificity and therapeutic efficacy of photosensitizer-encapsulated glycol chitosan-based nanoparticles in tumor-bearing mice. *Biomaterials 30*, 2929−2939.

(10) Bae, B.-C., and Na, K. (2009) Self-quenching polysaccharide-based nanogels of pullulan/folate-photosensitizer conjugates for photodynamic therapy. *Biomaterials 31*, 6325−6335.

(11) Dolmans, D. E. J. G. J., Fukumura, D., and Jain, R. K. (2003) Photodynamic therapy for cancer. *Nature Rev. Cancer 3*, 380−387.

(12) Dougherty, T. J., Gomer, C. J., Henderson, B. W., Jori, G., Kessel, D., Korbelik, M., Moan, J., and Peng, Q. (1998) Photodynamic therapy. *J. Natl. Cancer Inst. 90*, 889−905.

(13) Konan, Y. N., Gurny, R., and Allémann, E. (2002) State of the art in the delivery of photosensitizers for photodynamic therapy. *J. Photochem. Photobiol., B 66*, 89−106.

(14) van Nostrum, C. F. (2004) Polymeric micelles to deliver photosensitizers for photodynamic therapy. *Adv. Drug Delivery Rev. 56*, 9−16.

(15) Chatterjee, D. K., Fong, L. S., and Zhang, Y. (2008) Nanoparticles in photodynamic therapy: an emerging paradigm. *Adv. Drug Delivery Rev. 60*, 1627−1637.

(16) Bechet, D., Couleaud, P., Frochot, C., Viriot, M.-L., Guillemin, F., and Barberi-Heyob, M. (2008) Nanoparticles as vehicles for delivery of photodynamic therapy agents. *Trends Biotechnol. 26*, 612−621.

(17) Kim, S., Ohulchanskyy, T. Y., Pudavar, H. E., Pandey, R. K., and Prasad, P. N. (2007) Organically modified silica nanoparticles co-encapsulating photosensitizing drug and aggregation-enhanced two-photon absorbing fluorescent dye aggregates for two-photon photodynamic therapy. *J. Am. Chem. Soc. 129*, 2669−2675.

(18) Kim, S., Ohulchanskyy, T. Y., Bharali, D., Chen, Y., Pandey, R. K., and Prasad, P. N. (2009) Organically modified silica nanoparticles with intraparticle heavy-atom effect on the encapsulated photosensitizer for enhanced efficacy of photodynamic therapy. *J. Phys. Chem. C 113*, 12641−12644.

(19) Lim, C.-K., Shin, J., Lee, Y.-D., Kim, J., Park, H., Kwon, I. C., and Kim, S. (2011) Heavy-atomic construction of photosensitizer nanoparticles for enhanced photodynamic therapy of cancer. *Small 7*, 112−118.

(20) McIntire, G. L., Bacon, E. R., Toner, J. L., Cornacoff, J. B., Losco, P. E., Illig, K. J., Nikula, K. J., Muggenburg, B. A., and Ketai, L. (1998) Pulmonary delivery of nanoparticles of insoluble, iodinated CT x-ray contrast agents to lung draining lymph nodes in dogs. *J. Pharm. Sci. 87*, 1466−1470.

(21) El-Gendy, N., Aillon, K. L., and Berkland, C. (2010) Dry powdered aerosols of diatrizoic acid nanoparticle agglomerates as a lung contrast agent. *Int. J. Pharm. 391*, 305−312.
(22) Lee, K. D., Nir, S., and Papahadjopoulos, D. (1993) Quantitative analysis of liposome−cell interactions in vitro: rate constants of binding and endocytosis with suspension and adherent J774 cells and human monocytes. *Biochemistry 32*, 889−899.
(23) Davda, J., and Labhasetwar, V. (2002) Characterization of nanoparticle uptake by endothelial cells. *Int. J. Pharm. 233*, 51−59.
(24) Nie, S. M., Xing, Y., Kim, G. J., and Simons, J. W. (2007) Nanotechnology applications in cancer. *Annu. Rev. Biomed. Eng. 9*, 257−288.
(25) Bonnett, R. (1995) Photosensitizers of the porphyrin and phthalocyanine series for photodynamic therapy. *Chem. Soc. Rev. 24*, 19−33.
(26) Zenkevich, E., Sagun, E., Knyukshto, V., Shulga, A., Mironov, A., Efremova, O., Bonnett, R., Songca, S. P., and Kassem, M. (1996) Photophysical and photochemical properties of potential porphyrin and chlorin photosensitizers for PDT. *J. Photochem. Photobiol., B 33*, 171−180.
(27) Nyman, E. S., and Hynninen, P. H. (2004) Research advances in the use of tetrapyrrolic photosensitizers for photodynamic therapy. *J. Photochem. Photobiol., B 73*, 1−28.
(28) Kraljic, I., El Mohsni, S., and Arvis, M. (1978) A general method for the identification of primary reactions in sensitized photo-oxidations. *Photochem. Photobiol. 27*, 531−537.
(29) Weissleder, R., and Ntziachristos, V. (2003) Shedding light onto live molecular targets. *Nature Med. 9*, 123−128.
(30) Prasad, P. N. *Introduction to Biophotonics*, (2003) John Wiley & Sons, Hoboken, NJ.
(31) Mosmann, T. (1983) Rapid colorimetric assay for cellular growth and survival: application to proliferation and cytotoxicity assays. *J. Immunol. Methods 65*, 55−63.

Bioconjugate Chemistry

Article

pubs.acs.org/bc

Comparison of ^{64}Cu-Complexing Bifunctional Chelators for Radioimmunoconjugation: Labeling Efficiency, Specific Activity, and *in Vitro*/*in Vivo* Stability

Maggie S. Cooper,*[,†] Michelle T. Ma,[‡] Kavitha Sunassee,[†] Karen P. Shaw,[†] Jennifer D. Williams,[†] Rowena L. Paul,[†] Paul S. Donnelly,[‡] and Philip J. Blower[†]

[†]King's College London, Division of Imaging Sciences and Biomedical Engineering, 4th Floor Lambeth Wing, St. Thomas' Hospital, SE1 7EH, London, United Kingdom

[‡]School of Chemistry and Bio21 Molecular Science and Biotechnology Institute, University of Melbourne, Parkville, Melbourne, Victoria 3010, Australia

Supporting Information

ABSTRACT: High radiolabeling efficiency, preferably to high specific activity, and good stability of the radioimmunoconjugate are essential features for a successful immunoconjugate for imaging or therapy. In this study, the radiolabeling efficiency, *in vitro* stability, and biodistribution of immunoconjugates with eight different bifunctional chelators labeled with ^{64}Cu were compared. The anti-CD20 antibody, rituximab, was conjugated to four macrocyclic bifunctional chelators (*p*-SCN-Bn-DOTA, *p*-SCN-Bn-Oxo-DO3A, *p*-SCN-NOTA, and *p*-SCN-PCTA), three DTPA derivatives (*p*-SCN-Bn-DTPA, *p*-SCN-CHX-A″-DTPA, and ITC-2B3M-DTPA), and a macrobicyclic hexamine (sarcophagine) chelator (sar-CO_2H) = (1-NH_2-8-NHCO-$(CH_2)_3CO_2H$)sar where sar = sarcophagine = 3,6,10,13,16,19-hexaazabicyclo[6.6.6]icosane). Radiolabeling efficiency under various conditions, *in vitro* stability in serum at 37 °C, and *in vivo* biodistribution and imaging in normal mice over 48 h were studied. All chelators except sar-CO_2H were conjugated to rituximab by thiourea bond formation with an average of 4.9 ± 0.9 chelators per antibody molecule. Sar-CO_2H was conjugated to rituximab by amide bond formation with 0.5 chelators per antibody molecule. Efficiencies of ^{64}Cu radiolabeling were dependent on the concentration of immunoconjugate. Notably, the ^{64}Cu-NOTA-rituximab conjugate demonstrated the highest radiochemical yield (95%) under very dilute conditions (31 nM NOTA-rituximab conjugate). Similarly, sar-CO-rituximab, containing 1/10th the number of chelators per antibody compared to that of other conjugates, retained high labeling efficiency (98%) at an antibody concentration of 250 nM. In contrast to the radioimmunoconjugates containing DTPA derivatives, which demonstrated poor serum stability, all macrocyclic radioimmunoconjugates were very stable in serum with <6% dissociation of ^{64}Cu over 48 h. *In vivo* biodistribution profiles in normal female Balb/C mice were similar for all the macrocyclic radioimmunoconjugates with most of the activity remaining in the blood pool up to 48 h. While all the macrocyclic bifunctional chelators are suitable for molecular imaging using ^{64}Cu-labeled antibody conjugates, NOTA and sar-CO_2H show significant advantages over the others in that they can be radiolabeled rapidly at room temperature, under dilute conditions, resulting in high specific activity.

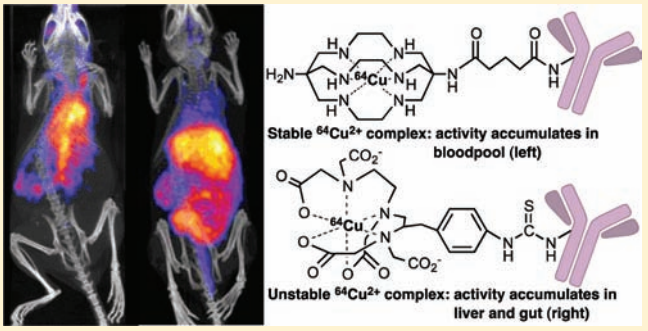

INTRODUCTION

Radioimmunoconjugates comprising antibodies attached to a bifunctional chelator (BFC) and radiolabeled with a metallic radioisotope provide an excellent way of delivering radioactivity selectively to a tumor target. An appropriate choice of both antibody and radioisotope is essential whether the purpose is imaging or therapy.[1]

^{64}Cu ($t_{1/2}$ = 12.7 h), with both β^+ and β^- emissions, allows for both PET imaging and radionuclide therapy, and ^{64}Cu labeled antibodies have attracted considerable interest in the field of targeted radionuclide therapy and diagnosis. In addition, copper has several other medically relevant isotopes (^{60}Cu, ^{61}Cu, ^{62}Cu, and ^{67}Cu) that are potentially useful for either diagnosis or therapy.[2,3] Although direct labeling approaches for labeling antibodies with ^{64}Cu have been proposed,[4] indirect labeling using a BFC is the preferred method to control stability of the ^{64}Cu−antibody complex formed. Improvements in chelators and radiolabeling methods will provide radioimmunoconjugates that are better able to target these copper isotopes to the tumor site.

Numerous chelators have been reported for complexing copper,[5−16] and several of these have been functionalized to

Received: January 24, 2012
Revised: March 20, 2012
Published: April 4, 2012

allow attachment to antibodies[17−34] and are now commercially available. The choice of antibody/BFC combination will affect efficacy as an imaging or therapy agent. While some side-by-side standardized comparisons of chelators conjugated to antibodies have previously been described,[18−23] a comparative investigation of radiolabeling efficiencies for the most readily available bifunctional chelators has not been reported. Moreover, many of the reported chelators have been evaluated under labeling conditions that are not sufficiently exacting to demonstrate superiority over others or real practical utility as high quality radiopharmaceutical components.

Several key factors must be considered when optimizing an immunoconjugate for its designed purpose. The method of conjugation must not result in degradation of the antibody, and radiolabeling should be rapid and result in high specific activity. *In vivo*, the radioimmunoconjugate must provide sufficient target-to-background ratio to provide high quality diagnostic images or target-selective therapy, in turn requiring high *in vivo* integrity as loss of copper from the BFC will cause accumulation in nontarget tissues, such as the liver. The radiolabeling should be rapid and easily performed at low antibody concentration to achieve high specific activity.

The choice of BFC can influence the biodistribution of radioactivity *in vivo*,[18−24,35−41] with biodistribution related to the *in vivo* stability of the $^{64}Cu^{2+}$−BFC complex. Generally, high liver activity is assumed to be indicative of instability of the $^{64}Cu^{2+}$−BFC complex *in vivo*. Transchelation of ^{64}Cu to serum components (e.g., albumin[18,42]) or in the liver to ceruloplasmin,[43] metallothionein, or superoxide dismutase, may occur.[44]

In this study, we compared six commercially available isothiocyanatobenzyl BFCs (Figure 1): *S*-2-(4-isothiocyanatobenzyl)-1,4,7-triazacyclononane-1,4,7-triacetic acid (*p*-SCN-Bn-NOTA); 2-(4-isothiocyanatobenzyl)-1,4,7,10-tetraazacyclododecane-1,4,7,10-tetraacetic acid (*p*-SCN-Bn-DOTA); 1-oxa-4,7,1-tetraazacyclododecane-5-*S*-(4-isothiocyanatobenzyl)-4,7,10-triacetic acid (*p*-SCN-Bn-oxo-DO3A); 3,6,9,15-tetraazabicyclo[9.3.1]-pentadeca-1(15),11,13-triene-4-*S*-(4-isothiocyanatobenzyl)-3,6,9-triacetic acid (*p*-SCN-Bn-PCTA); 2-(4-isothiocyanatobenzyl)-diethylenetriaminepentaacetic acid (*p*-SCN-Bn-DTPA); and *N*-[*R*-2-amino-3-(*p*-isothiocyanatophenyl)propyl]-*trans*-(*S*,*S*)-cyclohexane-1,2-diamine-*N*,*N*,*N*′,*N*″,*N*″-pentaacetic acid (CHX-A″-DTPA). We also included 2-benzyl-3-methyl-isothiocyanato-diethylenetriaminepentaaceticacid (2B3M-ITC-DTPA) and a sarcophagine ligand, (1-NH_2-8-$NHCO(CH_2)_3CO_2H$)sar, where sar = sarcophagine = 3,6,10,13,16,19-hexaazabicyclo[6.6.6]icosane (sar-CO_2H).[45,46] Encapsulating hexaamine sarcophagine ligands, first prepared by Sargeson and co-workers,[47−51] form extraordinary stable complexes with copper(II) and benefit from rapid complexation rates.[52,53] Methods have been developed to introduce reactive functional groups to the ligand framework,[54−56] to allow the ligands to be conjugated to peptides and antibodies with a goal of synthesizing copper radiopharmaceuticals that benefit from the special properties of sarcophagine ligands.[21,45,46,57−61] Each BFC was conjugated to the anti-CD20 antibody, rituximab, as a model antibody with clinical utility. We assessed radiolabeling efficiency under increasing dilution, stability in serum, and *in vivo* biodistribution in normal female Balb/C mice to identify the best BFC for radioimmunotherapy and diagnostic studies with copper radioisotopes.

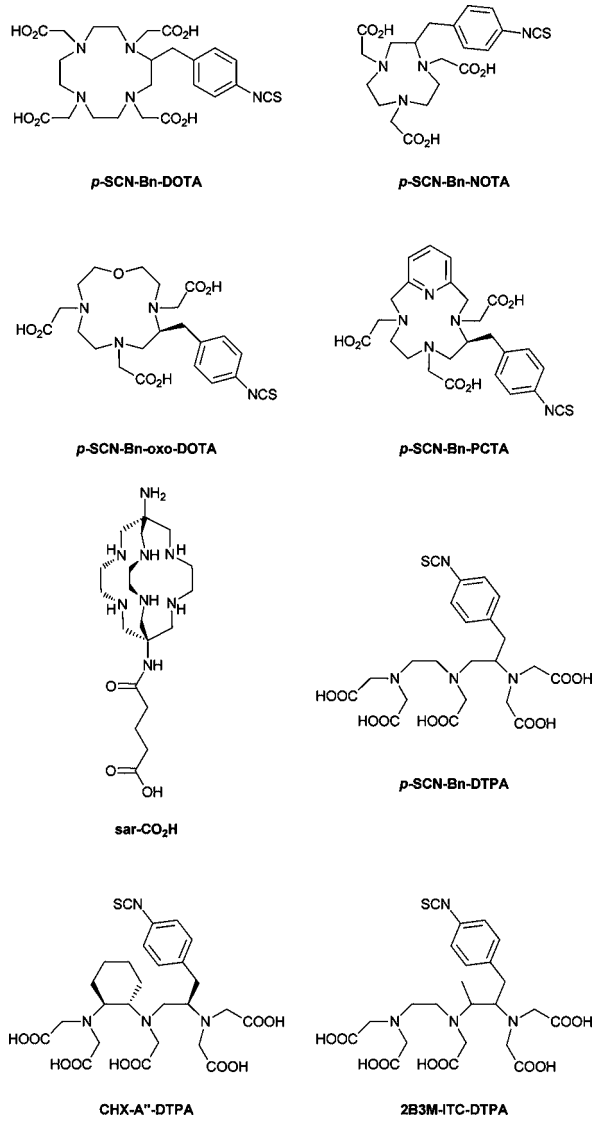

Figure 1. Structures of bifunctional chelators *p*-SCN-Bn-DOTA, *p*-SCN-Bn-NOTA, *p*-SCN-Bn-oxo-DO3A, *p*-SCN-Bn-PCTA, sar-CO_2H, *p*-SCN-Bn-DTPA, CHX-A″-DTPA, and 2B3M-ITC-DTPA.

MATERIALS AND METHODS

General. Chemicals and reagents were obtained from Sigma-Aldrich (Dorset, UK) unless otherwise specified. The highest available purity (lowest metal ion-containing) chemicals were used. Sterile water for injection, used to prepare buffers, was obtained from Baxter Healthcare (Newbury, UK). G-25 (Sephadex) size exclusion columns were purchased from GE Healthcare (Chalfont St. Giles, UK) and washed with 0.1 M ammonium acetate solution, pH 6. Vivaspin 2 ultracentrifugation tubes were purchased from Sartorius (Epsom, UK). BFCs were purchased from Macrocyclics, Inc. (Dallas, TX) except for 2B3M-ITC-DTPA, which was a gift from Dr. Kim Orchard (Haematology Department, Southampton General Hospital), and sar-CO_2H, which was prepared as previously described.[45,46] Rituximab (MabThera, Roche) was obtained as a 10 mg/mL solution from the Pharmacy Department at Guy's and St. Thomas' NHS Trust, London. Male AB type human serum was obtained from Sigma (product H4522, this serum contains sodium citrate which is added as part of the preparation process). High-performance liquid chromatography (HPLC)

analysis was carried out on an Agilent 1200 series system with an in-line UV (280 nm) and gamma detector (Flow-Count, LabLogic). Instant thin layer chromatography strips (ITLC-SA) were obtained from Varian Medical Systems UK, Ltd. (Crawley, UK).

Antibody Conjugation of *p*-SCN-Bn-Derivatized BFCs. To rituximab (10 mg, 1 mL) was added 50 mM EDTA (50 μL) to complex any free trace metal ion. The antibody was buffer exchanged and concentrated to approximately 10 mg/mL in 0.1 M HEPES buffer, pH 8.9, in Vivaspin 2 ultracentrifugation tubes. The antibody was transferred to a cryovial (Nalgene), and conjugation to the BFCs was carried out as previously described with a slight modification.[62] A 40-fold molar excess of each BFC over antibody in DMSO (40 μL) was added to the antibody in 0.1 M HEPES buffer, pH 8.9. Conjugation was allowed to proceed at room temperature for 2 h and continued overnight at 2−8 °C. Excess chelator was removed initially by G25 Sephadex size exclusion purification (PD-10 column). The immunoconjugate was eluted with 0.1 M ammonium acetate solution, pH 6. Fractions containing the immunoconjugate were combined and then further purified by centrifugal ultrafiltration (Vivaspin 2). The volume was reduced to approximately 0.5 mL during centrifugation. After each centrifugation step, the immunoconjugate was resuspended and diluted to 2 mL with 0.1 M ammonium acetate solution, pH 6. The immunoconjugate was finally concentrated to 2 mg/mL in 0.1 M ammonium acetate solution, pH 6.

Antibody Conjugation of sar-CO_2H. To rituximab (10 mg, 1 mL) was added 50 mM EDTA (50 μL) to complex any free trace metal ion. The antibody was buffer exchanged and concentrated to approximately 10 mg/mL in 0.1 M phosphate buffer, pH 7, in Vivaspin 2 ultracentrifugation tubes. The antibody was transferred to a cryovial (Nalgene).

The NHS ester of sar-CO_2 was prepared by first mixing sulfo-*N*-hydroxysuccinimide (4 mg) in 0.1 M phosphate buffer, pH 7 (40 μL), with sar-CO_2 (4.7 mg) in 0.1 M phosphate buffer, pH 7 (80 μL), and then adding 1-ethyl-3-(3-dimethylaminopropyl)carbodiimide (1.5 mg) in 0.1 M phosphate buffer, pH 7 (15 μL). This solution (32 μL) was added to the antibody and the mixture left at room temperature (21 °C) for 90 min. The immunoconjugate was purified as detailed above.

^{64}Cu Production. ^{64}Cu was prepared by ^{64}Ni(p,n)^{64}Cu nuclear reaction on a CTI RDS 112 11 MeV cyclotron. The irradiated ^{64}Ni (10 mg) was dissolved from the gold target on which it was electroplated in minimal concentrated hydrochloric acid (100−150 μL) and ^{64}Cu purified to yield $^{64}CuCl_2$ by loading onto an anion exchange column (Biorad AG1-X8 resin). Excess ^{64}Ni was removed by elution in 9 M HCl. Six molar HCl was then used to reduce the pH before elution of the $^{64}Cu^{2+}$ in 0.1 M HCl (Figure 2). Fraction 9 (the fraction after the main ^{64}Cu elution) was used because fraction 8 consistently gave poorer labeling and more aggregation and precipitation of the antibody even when the pH of the ^{64}Cu solution was adjusted adequately. Fraction 9 was diluted with an equal volume of 1 M ammonium acetate solution bringing the pH to 6. This solution contains approximately 0.5 M chloride and 0.5 M acetate.

Radiolabeling. Typically, the ^{64}Cu solution prepared as described above (37 MBq, 120 μL) was added to 240 μg (120 μL) of immunoconjugate solution prepared as described above and the resulting solution incubated at room temperature for 20 min. In the case of DOTA-rituximab, the solution was heated at 37 °C for 90 min in light of literature precedent; however, it was subsequently found that the radiolabeling proceeded adequately at room temperature in 20 min (see below). Analysis was performed by instant thin layer chromatography using ITLC-SA (Varian) with a mobile phase of 0.1 M citrate buffer (pH 5) and by size exclusion HPLC using a BioSep SEC-S-2000 column (Phenomenex, Macclesfield, UK) with an isocratic mobile phase of 0.1 M phosphate buffer containing 2 mM EDTA, pH 7, and a flow rate of 1 mL/min. The retention time of the immunoconjugate was typically 7 min and that of the unbound ^{64}Cu impurities was approximately 11 min.

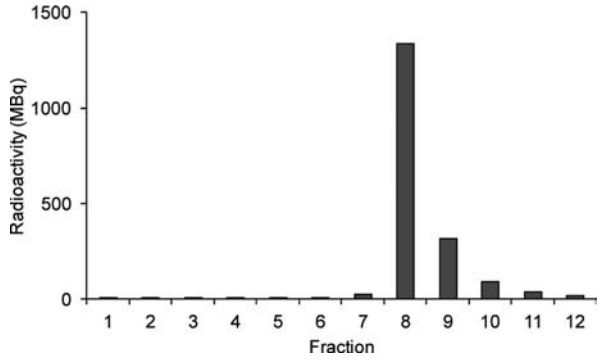

Figure 2. Elution profile for ^{64}Cu purification. Initial elution is with 5 mL of 9 M HCl (fraction 1), followed by 2 fractions of 3 and 2 mL of 6 M HCl (fractions 2−3), then 1 mL of 0.1 M HCl (fraction 4) with all other fractions (5−12) being eluted with 0.5 mL of 0.1 M HCl.

Radiolabeling of DOTA-Rituximab under Different Conditions. To each of three samples of DOTA-rituximab (20 μL, 40 μg) was added ^{64}Cu solution (15 MBq, 20 μL). One sample was incubated at 4−8 °C for 20 min, another at ambient temperature (25 °C) for 20 min, and a third at 37 °C for 20 min. Following incubation, a 20 μL sample was analyzed by HPLC, and a 2000-fold molar excess of EDTA (50 mM, 5 μL) was added to the remaining solution. The samples were left at room temperature for 40 min then analyzed by HPLC.

BFC to Antibody Ratio. The average number of chelators per antibody was assessed using a modification of the method of Meares et al.[63,64] using a mixture of ^{64}Cu and cold copper rather than cobalt. A small amount of ^{64}Cu solution was added to a known concentration of copper(II) chloride solution to give a 0.25 mM Cu^{2+} solution. To the immunoconjugate (1.25×10^{-10} moles) were added increasing ratios of copper (1.25×10^{-9}−1.25×10^{-8} mol), and the total volume of the reaction was adjusted to 100 μL by addition of 0.1 M ammonium acetate solution, pH 6. The solution was incubated at room temperature for 20 min (or at 37 °C for 90 min in the case of DOTA-rituximab) after which time a solution of 50 mM EDTA (2 μL, approximately 1000:1 molar ratio of EDTA/immunonconjugate) was added to complex any unbound copper. Five minutes after the addition of EDTA, the reaction solution was analyzed on ITLC-SA (0.75 × 9 cm) with the origin at 1 cm from the bottom of the strip and the solvent front at 8 cm. Then, 1.5 μL of the radiolabeled immunoconjugate was spotted at the origin, and the strip was allowed to air-dry and then developed in 0.1 M citrate buffer, pH 5. The strip was cut in half and the radioactivity in each half counted using a gamma counter. It had previously been determined from visualizing the strip on a PhosphorImager that EDTA-complexed copper moved to the upper half of the TLC

dx.doi.org/10.1021/bc300037w | *Bioconjugate Chem.* 2012, 23, 1029−1039

strip and the radiolabeled antibody remained at the origin. The labeling efficiency at different copper to immunoconjugate ratios was calculated, and from this, the number of moles of copper specifically bound at each ratio was determined for each immunoconjugate. Knowing the moles of immunoconjugate used initially, we determined the number of chelators per antibody (see Supporting Information).

Radiolabeling Dilution Assay. Serial dilutions of immunoconjugates were prepared in 0.1 M ammonium acetate solution, pH 6, and ^{64}Cu solution (~1.3 MBq, ~1−5 μL) added to give immunoconjugate concentrations of 500 nM−15.6 nM in 100 μL. Mixtures were incubated at room temperature for 20 min (or at 37 °C for 90 min in the case of DOTA-rituximab) and 50 mM EDTA solution (2 μL, a 2000-fold excess over immunoconjugate at the highest antibody concentration) added. After incubation for 5 min at room temperature, the radiolabeling efficiency was assessed by ITLC as described above. The complete assay was carried out in triplicate, and each ITLC was also run in triplicate.

Serum Stability Assay. To 50 μg (25 μL) of each immunoconjugate was added ^{64}Cu solution (12.5 MBq, 25 μL). Reactions were incubated at room temperature for 20 min (or at 37 °C for 90 min in the case of DOTA-rituximab). The radioimmunoconjugates were added to 450 μL of male AB type human serum and incubated at 37 °C for 48 h. Samples were analyzed by size exclusion HPLC at 0, 24, and 48 h using a BioSep SEC-S-2000 column (Phenomenex, Macclesfield, UK) with an isocratic mobile phase of 0.1 M phosphate buffer containing 2 mM EDTA, pH 7, and a flow rate of 1 mL/min. For the later time points when the signal from the HPLC in-line radionuclide detector was low, fractions from the HPLC were collected and counted in a gamma counter to measure the radioactivity. The amount of radioactivity associated with the antibody was assessed based on the retention time.

Biodistribution Study. Animal studies were carried out in accordance with UK Research Councils' and Medical Research Charities' guidelines on Responsibility in the Use of Animals in Bioscience Research, under a UK Home Office license. Female BALB/c mice (n = 3 per group, aged 9 weeks, 20.6 ± 1.1 g) were purchased from Harlan Laboratories, UK. Each group received i.v. (tail vein) injections of approximately 6 MBq (35 μL) of a ^{64}Cu-labeled immunoconjugate. The feces and urine of each set of 3 mice were pooled due to logistic issues of housing the animals separately over 48 h. Animals were culled at 48 h postinjection and tissues explanted, weighed (except thyroid, *vide infra*), and counted on a gamma counter. The whole body activity (excluding tail) was measured with an ionization chamber cross-calibrated with the gamma counter, prior to dissection. Because of the small size and intimate attachment to trachea, normal thyroid glands were explanted along with a small piece of trachea and counted on the gamma counter. A small piece of trachea was also counted as a control. For all biodistribution calculations, a standard thyroid tissue mass of 0.0169 g (±0.0052) previously obtained from age-matched BALB/c mice (n = 14) was used. A separate piece of thyroid-free trachea was taken and weighed to confirm that activity in trachea tissue did not significantly affect the thyroid activity measurement. Uptake in each tissue was expressed as the percentage injected dose per gram of tissue (% ID/g). Excreted radioactivity, radioactivity in the tail, and mass of the tail were excluded from the calculation.

Imaging Study. BALB/c mice (age and weight as described above) received i.v. (tail vein) injections of 12 or 6 MBq of each radioimmunoconjugate (70 μL). With the mice under isofluorane anesthesia in a Minerve imaging chamber, PET/CT scans were acquired 4, 24, and 48 h postinjection using a NanoPET/CT scanner (Bioscan, Paris, France) with PET acquisition time 1800, 1800, and 3600 s respectively, and coincidence relation, 1−3. Image reconstruction, OSEM with SSRB 2D LOR; energy window, 400−600 keV; filter, Ramlak cutoff 1; number of iterations/subsets, 8/6. The biodistribution of the tracer in the imaged mice was then determined by dissection and organ counting after sacrificing at 48 h p.i.

RESULTS

Conjugation and Radiolabeling. Immunoconjugates were prepared by conjugation of the BFCs through free amine groups on lysine residues within the antibody, either via a thiourea linkage (isothiocyanato derivatized chelators) or, in the case of sar-CO_2H, by amide formation (active *N*-hydroxysuccinimide ester-derived chelator). The average number of BFCs per antibody was 4.9 ± 0.9 (±SD, n = 4) for the isothiocyanato-derivatized chelators and 0.5 ± 0.1 (±SD, n = 4) for sar-CO_2H (Table 1).

Table 1. Average Number of Bifunctional Chelators per Antibody Molecule (±SD, n = 4)

bifunctional chelator	average number of chelators per antibody
p-SCN-Bn-DOTA	5.0 ± 0.3
p-SCN-Bn-NOTA	5.2 ± 0.2
p-SCN-Bn-oxo-DO3A	4.5 ± 0.6
p-SCN-Bn-PCTA	4.9 ± 1.2
Sar-CO_2H	0.5 ± 0.1
p-SCN-Bn-DTPA	3.6 ± 1.0
CHX-A″-DTPA	5.6 ± 0.5
2B3M-ITC-DTPA	5.4 ± 0.5

At a radioimmunoconjugate concentration of 13 μM, all immunoconjugates were labeled with $^{64}Cu^{2+}$ with high efficiency (see Figure 3 for example HPLC chromatograms). Size exclusion HPLC was able to resolve radiolabeled antibody from radiolabeled antibody aggregates and low molecular weight radiolabeled impurities. Radiochemical purity of all unpurified ^{64}Cu-labeled immunoconjugates was 99.5% ± 0.5% except in the case of DTPA-rituximab where radiochemical purity was 96.8% ± 1.8%. It is reported in the literature that DOTA-rituximab does not label well at room temperature,[10,65] so in this case the radiolabeling mixture was heated at 37 °C, but all other immunoconjugates were efficiently labeled at room temperature in 20 min.

However, further investigations into the radiolabeling of DOTA-rituximab under different conditions showed that, in our hands, there was no difference in the radiolabeling efficiency at the three temperatures studied (4−8 °C, 25 and 37 °C). Labeling efficiency was 98.9% at all temperatures. There was also no difference in the amount of activity still associated with the immunoconjugate following challenge with EDTA (2000-fold molar excess), with 98.1% still associated with DOTA-rituximab that had been labeled at 4−8 °C and 98.2% still associated with DOTA-rituximab that had been labeled at 25 or 37 °C.

To determine the relative efficacy of radiolabeling of the conjugates, increasingly dilute samples of the conjugates were studied. The most efficacious chelators were taken to be those that resulted in comparatively high radiochemical yields at the

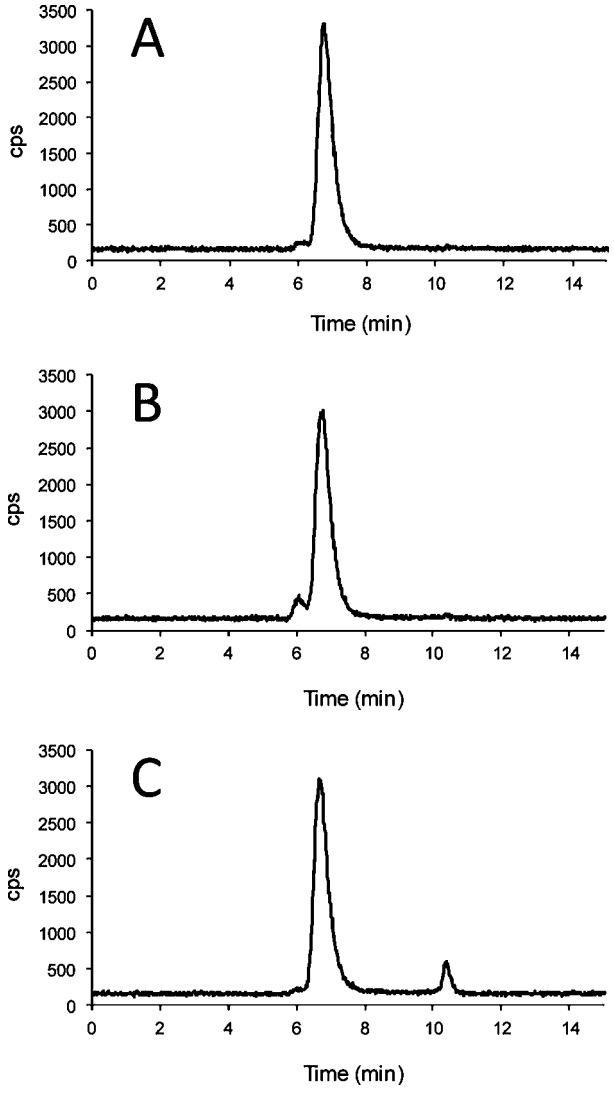

Figure 3. Exemplar HPLC radiochromatograms of ^{64}Cu labeled rituximab conjugated with different bifunctional chelators (A) *p*-SCN-Bn-NOTA (B) *p*-SCN-Bn-PCTA (C) *p*-SCN-Bn-DTPA. NOTA- and PCTA-rituximab show very high radiolabeling efficiency, while DTPA-rituximab shows a significant level of ^{64}Cu impurities. The level of antibody aggregates (the peak eluting at 6 min, prior to the antibody peak) was higher for PCTA-rituximab compared with the other immunoconjugates. Similar data acquired for the other three bifunctional chelator conjugates are shown in Supporting Information.

lowest concentration of conjugate. Since the BFC-to-antibody ratio varied among the chelators, the concentrations were standardized on the effective BFC concentration rather than antibody concentration (by multiplying antibody concentration by the appropriate measured BFC-to-antibody-ratio). All immunoconjugates, with the exception of DTPA-rituximab (74.5%), were labeled with >97% efficiency at an effective BFC concentration of 2500 nM (174 MBq/mg immunoconjugate). On reducing the immunoconjugate concentration to give an effective BFC concentration of 1250 nM, the radiolabeling efficiency after 20 min remained >90% for all immunconjugates, except for DTPA-rituximab. At further reduced BFC concentrations, however, only NOTA-rituximab, sar-CO-rituximab, CHX-A″-DTPA-rituximab, and 2B3M-ITC-DTPA-rituximab had labeling efficiency >90% (Figure 4). NOTA-rituximab and sar-CO-rituximab achieved high radiolabeling

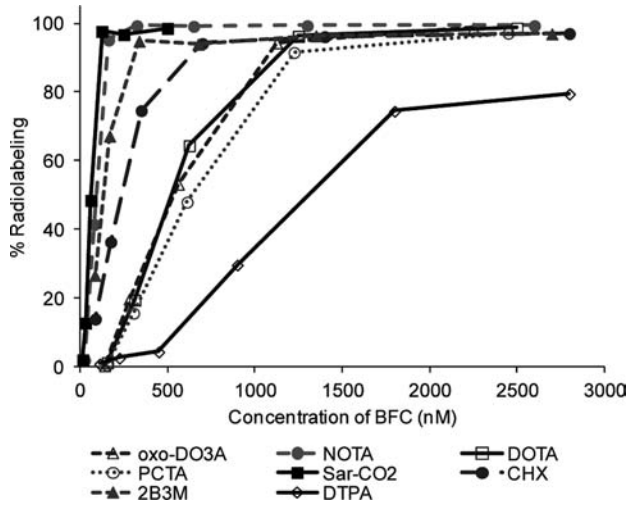

Figure 4. Radiolabeling efficiency of immunoconjugates under increasingly dilute conditions expressed as % labeling efficiency against effective concentration of bifunctional chelator.

efficiency under the most dilute conditions with 95.2% (±0.2%) and 97.7% (±0.7%) labeling at approximately 120–150 nM effective BFC concentration (2775 MBq/mg or 416 MBq/nmol immunoconjugate in the case of NOTA-rituximab).

Serum Stability. Serum stability of all ^{64}Cu-rituximab immunoconjugates was measured at 37 °C over 48 h (Figure 5). A control using unconjugated rituximab subjected to the

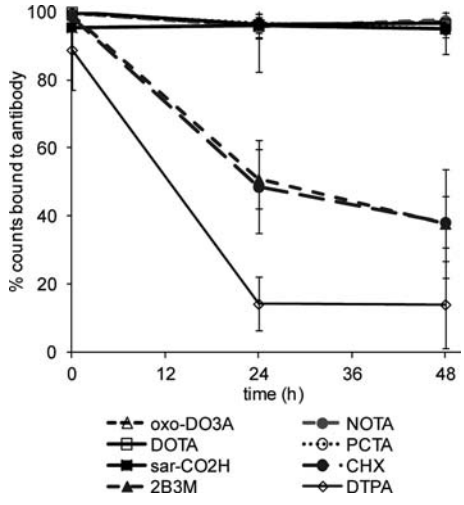

Figure 5. Serum stability of ^{64}Cu-rituximab immunoconjugates at 37 °C over 48 h (mean ± SD, n = 3) determined by size exclusion radiochromatography.

same labeling procedure as the conjugated rituximab showed minimal labeling (<2%) and "free" ^{64}Cu eluted after the antibody peak on HPLC at approximately 11 min. ^{64}Cu-rituximab immunoconjugates containing a macrocyclic BFC (*p*-SCN-Bn-DOTA, *p*-SCN-Bn-NOTA, *p*-SCN-Bn-oxo-DO3A, *p*-SCN-Bn-PCTA, or sar-CO_2H) demonstrated greater radiochemical stability than immunoconjugates containing DTPA BFC derivatives. All macrocyclic conjugated immunoconjugates showed high stability in serum over 48 h with ^{64}Cu-NOTA-rituximab showing the greatest stability (97.5% ± 0.3%) at 48 h. The stability of DTPA-based conjugates was much lower: 38.2% and 37.8% for ^{64}Cu-CHX-A″-DTPA-rituximab and ^{64}Cu-

dx.doi.org/10.1021/bc300037w | *Bioconjugate Chem.* 2012, 23, 1029–1039

2B3M-DTPA-rituximab, respectively. The most unstable radioimmunoconjugate was the unsubstituted ^{64}Cu-DTPA-rituximab with only 14.0% of the radioactivity associated with the antibody at 48 h.

Biodistribution and Imaging. Biodistribution and PET imaging studies were done on normal female Balb/c mice. Images were taken at 4, 24, and 48 h postinjection and biodistribution analyzed at 48 h. The results of the biodistribution (48 h) and imaging (24 h) studies are presented in Figures 6 and 7. For the immunoconjugates containing

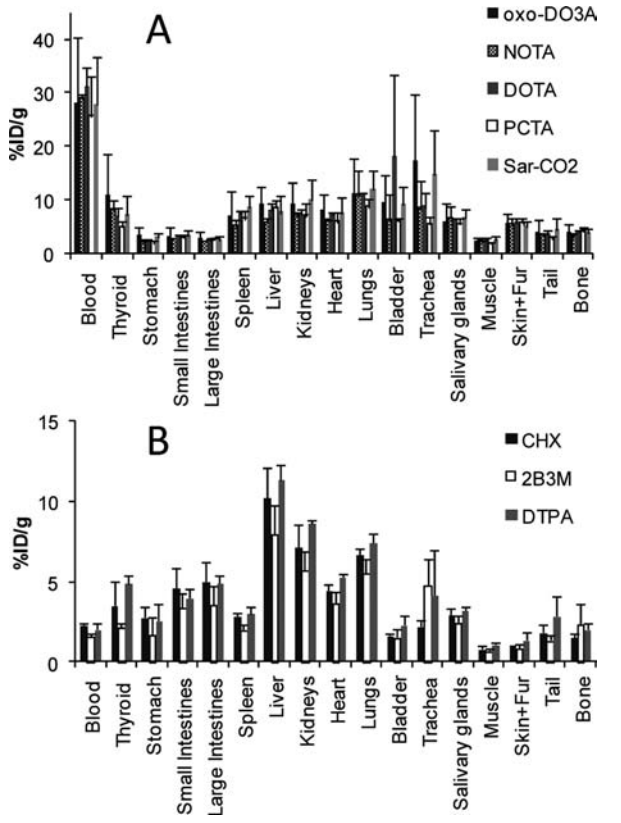

Figure 6. Biodistribution of ^{64}Cu-rituximab-immunoconjugates in normal female Balb/C mice at 48 h postinjection. The biodistribution patterns fall into two distinct groups, those containing macrocyclic chelators (A) and those containing DTPA derivatives (B).

macrocycles, the activity was predominantly seen in the blood pool at all time points (4, 24, and 48 h postinjection) with little difference seen in the biodistribution between the different macrocycles. Importantly, there is no difference between the macrocycle conjugates in the uptake in the kidneys and liver suggesting that all the macrocyclic radioimmunoconjugates show good stability *in vivo*. The clearance of the immunoconjugates containing DTPA derivatives from the blood pool was much faster compared with the immunoconjugates containing macrocycles, giving rise to higher liver to blood ratios and images dominated by liver and gut activity.

There was a higher level of excretion into the feces for the immunoconjugates containing DTPA derivatives (mean 29.8% ID) compared to the macrocyclic immunoconjugates (mean 3.0% ID) over 48 h. In addition, ^{64}Cu-Oxo-DO3A-rituximab and ^{64}Cu-PCTA-rituximab showed higher levels of excretion into the feces (3.7% ID and 4.6% ID respectively) than ^{64}Cu-DOTA-rituximab, ^{64}Cu-NOTA-rituximab, and ^{64}Cu-sar-CO-

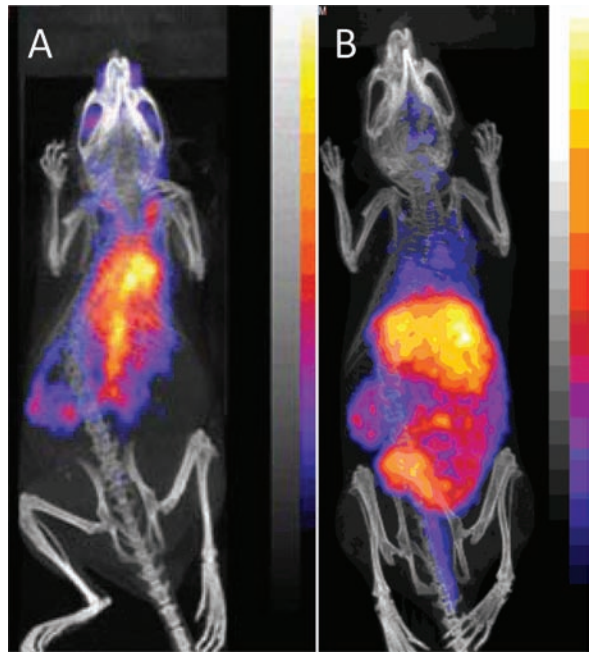

Figure 7. PET/CT images (maximum intensity projection) of Balb/C mice 24 h postinjection with ^{64}Cu-rituximab-immunoconjugates. (A) ^{64}Cu-Sar-CO-rituximab and (B) ^{64}Cu-DTPA-rituximab are given as examples of macrocycle containing immunoconjugates (A, showing predominantly blood pool activity) and immunoconjugates containing DTPA derivatives (B, showing predominantly liver and gut activity). Corresponding images for the other chelators tested are presented in Supporting Information.

rituximab over 48 h (2.2% ID, 2.9% ID, and 1.6% ID; see Figure 8).

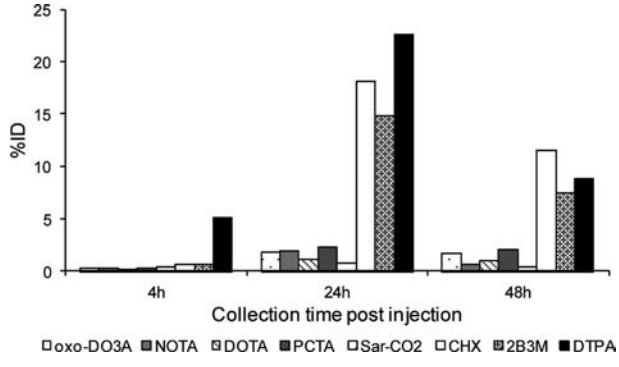

Figure 8. Radioactivity (% ID) in the feces of normal female Balb/C mice at 4, 24, and 48 h postinjection with ^{64}Cu-rituximab-immunoconjugates.

DISCUSSION

For the purposes of this study, rituximab was used as a model antibody to study the radiolabeling and stability of ^{64}Cu-immunoconjugates. It is envisaged that the most propitious conjugation and radiolabeling conditions elucidated here for rituximab can be translated to other antibodies, proteins, and peptides.

Conjugation to each of the isothiocyanate-derivatized BFCs yielded approximately 5 chelators per antibody using identical conjugation conditions for each BFC. Where a different

conjugation method was used (i.e., active ester, in the case of sar-CO_2H), the number of chelators per antibody was markedly reduced (0.5 chelator per antibody), but no attempt was made at this stage to optimize the conjugation to increase the number of chelators per antibody. It is possible that increasing the number of chelators bound to each antibody can lead to a decrease in immunoreactivity.

All of the rituximab immunoconjugates studied showed good radiolabeling efficiency at concentrations that are not kinetically or thermodynamically exacting (13 μM). Radiolabeling was carried out over 20 min at room temperature, except in the case of DOTA-rituximab. The slower radiolabeling for DOTA-metal ion complexes is well-documented.[17] Efficient radiolabeling of DOTA-peptides in short incubation periods is reported at high temperatures, but antibodies will not tolerate these conditions; therefore, radiolabeling of DOTA-immunoconjugates has usually been carried out at 40−43 °C over a longer period of time,[66−72] in order to achieve satisfactory labeling efficiency. In view of this, in this study, DOTA-rituximab radiolabeling was carried out at 37 °C over 90 min.

To discriminate between the performance of the different BFC's under investigation, the immunoconjugate concentration was reduced to determine radiolabeling efficiency under progressively more challenging conditions. It was found that whereas the labeling efficiency of several chelators (including the widely used DOTA) dropped significantly when the chelator concentration dropped below 1 μM, NOTA-rituximab and Sar-CO-rituximab could be radiolabeled efficiently under very dilute conditions (>90% radiolabeling efficiency at 125 nM chelator concentration in 20 min at room temperature when radiolabeled with 1.3 MBq ^{64}Cu). This suggests that complex formation with NOTA and Sar-CO_2H conjugates is faster than the other BFC's investigated in this study, although it does not imply that they form the most kinetically or thermodynamically stable complexes. Even in the cases of NOTA-rituximab and Sar-CO-rituximab, where the specific activity achieved under these mild conditions is significantly higher than that for the other chelators, the specific activities equate to roughly 1% of chelator molecules being occupied by a ^{64}Cu ion. It is possible that yields and specific activities might be increased further by prolonging the incubation time or raising the temperature, and by introducing further steps to remove trace metals during the purification of ^{64}Cu from the target material.

During the course of this work, it was observed that in our hands radiolabeling of DOTA-rituximab could be achieved in high yields (98.9%) in 20 min at temperatures as low as 4−8 °C, despite literature consensus that elevated temperatures are required for labeling DOTA-conjugated biomolecules with copper isotopes. Although neither we nor other groups working with ^{64}Cu can provide analytical data to explain the contrasting experience, we note that in the work described here we used fraction 9 from the ion exchange purification of ^{64}Cu, rather than fraction 8 which contains the most ^{64}Cu, because fraction 9 consistently gave better labeling yields and less antibody aggregation and precipitation. Fraction 8 is more acidic before buffering (as determined with a pH elecetrode), has higher chloride concentration, and may have a different trace metal content than fraction 9; one or more of these factors may contribute to the less efficient labeling using this fraction. Further investigation is required to identify the cause of inefficient labeling with fraction 8 and to improve the purification procedure accordingly since fraction 8 contains the majority of the ^{64}Cu radioactivity.

The stability of the radioimmunoconjugates was assessed in serum and *in vivo*. In the control, there was no evidence of ^{64}Cu transchelation to serum proteins that was not in turn transchelated to EDTA during the HPLC analysis; therefore, it is reasonable to assume that radioactivity eluting in the high molecular weight fraction is antibody-bound. All the macrocyclic chelated immunoconjugates were very stable in serum, but the immunoconjugates containing DTPA derivatives were unstable with released copper which appeared at an elution time corresponding to the copper EDTA complex. Ferreira et al.[72] observed a difference in the stability of three ^{64}Cu-trastuzumab radioimmunoconjugates: the immunoconjugates ^{64}Cu-PCTA-trastuzumab and ^{64}Cu-Oxo-DO3A-trastuzumab (>95% intact at 24 h and ∼80% intact at 48 h) were more stable in serum than ^{64}Cu-DOTA-trastuzumab (54% intact at 24 h and 26% intact at 48 h). In contrast, we found little difference between the macrocyclic immunoconjugates with all showing high labeling efficiency and >95% stability at 24 h and >94.9% at 48 h. The labeled conjugates could be used without additional purification. We speculate that the comparatively high labeling efficiency and stability we found compared to those of others[21,72,73] may be related to our use of fraction 9 from the ^{64}Cu purification.

It is interesting to note that while the efficiency of labeling for ^{64}Cu-2B3M-DTPA-rituximab and ^{64}Cu-CHX-A″-DTPA-rituximab is favorable, the resulting radiolabeled immunoconjugates do not demonstrate adequate serum stability. In contrast, ^{64}Cu-NOTA-rituximab and ^{64}Cu-sar-CO-rituximab were both found to offer both favorable rapid labeling and very high complex stability in serum. In the biodistribution study, ^{64}Cu-DTPA-, ^{64}Cu-2B3M-DTPA-, and ^{64}Cu-CHX-A″-DTPA-rituximab, which all showed poor serum stability, were rapidly cleared from the blood pool, and the activity was predominantly excreted into the feces (approximately 30% of the injected dose) by 48 h. In contrast, the macrocycle-containing immunoconjugates showed predominantly blood pool activity, and there was no difference in the biodistribution of these immunoconjugates at 48 h. Most notably, there was no difference in the liver and kidney uptake among the radioimmunoconjugates. It has been reported that ^{64}Cu-DOTA conjugates can lose ^{64}Cu to proteins such as superoxide dismutase, possibly via bioreductive mechanisms, with the ^{64}Cu being retained in the liver.[44] There was no evidence of a higher liver retention of ^{64}Cu in these studies. It was noted, however, that there was slightly higher activity in the feces of animals injected with ^{64}Cu-Oxo-DO3A-rituximab and ^{64}Cu-PCTA-rituximab over the course of the study. Ferreira et al.[72] showed similar biodistribution results for ^{64}Cu-DOTA-trastuzumab, ^{64}Cu-Oxo-DO3A-trastuzumab, and ^{64}Cu-PCTA-trastuzumab but noted higher uptake in the tumors of tumor-bearing animals for ^{64}Cu-Oxo-DO3A-trastuzumab and ^{64}Cu-PCTA-trastuzumab.

The biodistribution of ^{64}Cu-complex conjugates has previously been shown to be influenced by the charge and lipophilicity of the complexes,[23,35] but these studies were carried out on antibody fragments rather than intact antibodies. The smaller size of these fragments will make their biodistribution more susceptible to the influence of the nature of the BFC, compared to intact antibodies. For intact antibodies, the performance of the BFC itself in terms of the stability of the ^{64}Cu-complex, the stability of the chelate−antibody conjugate, the radiolabeling efficiency, and conven-

ience of radiolabeling are much more important factors. From the *in vivo* study presented here, where the different immunoconjugates were labeled to the same specific activity and achieved the same radiolabeling efficiency, we found little difference in the stability of the complexes, and the physical characteristics of the chelators did not influence the biodistribution.

Quadri and Vriesendorf[74] demonstrated that the linker could be a crucial determinant of biodistribution. Labile linkers can be cleaved from the antibody by enzymes in the serum and liver giving rise to low molecular weight radioactive metabolites, which will tend to be cleared via the kidneys. Isothiocyanatobenzyl (*p*-SCN-Bn) derivatives form a stable thiourea bond with the amino side chain of lysine residues and are therefore a good choice of linker for connecting the chelator to the antibody. However, we found no difference in the *in vivo* stability of the thiourea conjugated immunoconjugates and the amide conjugated sar-CO-rituximab.

It is intuitively clear that thermodynamic stability alone (as expressed, for example, by low metal−ligand dissociation constants) is not a sound basis on which to select a chelator to make immunoconjugates with the best *in vivo* stability since under biological conditions at tracer levels, if allowed to come to equilibrium, even complexes with very high stability constants (such as the NOTA and DTPA complexes of copper) would not withstand challenge from endogenous metal-binding proteins, endogenous metal ions, metabolism, and extreme dilution. Our results show no correlation between Cu^{2+} complex stability constants and serum stability. Indeed, reported stability constants for Cu^{2+} complexes of NOTA and DTPA are comparable (log *K* values of 21.6 and 21.4, respectively[5]), yet the serum stability of the ^{64}Cu-labeled conjugates is markedly different (97.5 ± 3.0% vs 14.0 ± 12.9% antibody-bound ^{64}Cu after 48 h, respectively). Dearling et al.[21] also recently showed that differences in the thermodynamic stability of ^{64}Cu-BFC complexes were not associated with significant differences in uptake of radioimmunoconjugates by tumors; indeed, the least thermodynamically stable copper complex that they studied, ^{64}Cu-NOTA, produced the lowest concentration of ^{64}Cu in the liver. Similarly, Cole et al.[18] found that thermodynamic equilibrium constants of ^{67}Cu-, ^{111}In-, and ^{57}Co-radiometal complexes bore little relation to the serum stability of the complexes. In particular, the published thermodynamic equilibrium constants suggest that ^{67}Cu-TETA would be less stable than ^{67}Cu-DTPA or ^{67}Cu-EDTA, whereas ^{67}Cu-TETA was the only complex of the three to show any stability in serum. Such macrocyclic or macrobicyclic Cu^{2+} complexes possess sufficiently high thermodynamic stability to allow efficient radiolabeling, as well as relatively rigid geometries that enhance their kinetic stability.[8,10,75,76] Individual bond dissociation is rapidly followed by recoordination, as the coordinating ligand remains spatially close to the metal center. A sufficiently low reduction potential of the bound Cu^{2+} metal center is also desirable, as intracellular endogenous reductants, such as thiol-rich proteins, are capable of reducing Cu^{2+} to Cu^{+}.[75,77] Cu^{+}, with a d^{10} configuration, possesses markedly different coordination preferences to Cu^{2+}, is more kinetically labile, and can dissociate from the chelate in the presence of *in vivo* endogenous cuprous-binding ligands.

To achieve the needed *in vivo* stability requires that equilibration is delayed as long as possible, maximizing kinetic stability by imposing high activation free energy barriers to dissociation. However, these same free-energy barriers have to be overcome in order to perform the radiolabeling; therefore, the optimal chelator design will require balancing both efficiency of labeling (requiring a low free energy barrier between complexed and dissociated states) and resistance to dissociation *in vivo* (requiring a high free energy barrier). Identifying chelators with the appropriate compromise is at present largely an empirical matter, and side-by-side comparison of chelators in the context of a bioconjugate is necessary. Assessing the *in vivo* stability and biodistribution combined with the stability in serum and the ability of the ligand to complex radiometal under increasingly dilute conditions, as described here, provides a discriminating and systematic approach for assessing which BFC is appropriate for any given radiometal.

■ CONCLUSIONS

The results presented here suggest that *p*-SCN-NOTA and sar-CO_2H stand out from the other chelators, including the commonly used DOTA, as the most promising BFCs for radiolabeling antibodies with ^{64}Cu. Dearling et al.[21] report good efficacy for *p*-SCN-NOTA, and Liu et al.[78] found that employing the NOTA chelator in studies using ^{64}Cu-labeled heat-stable enterotoxin analogues for detecting colorectal cancer gave superior tumor/liver and tumor/kidney ratios relative to DOTA- and TETA-functionalized peptides. The prolonged retention in blood pool and the low amount of activity in the feces and urine in our study suggest that ^{64}Cu-NOTA-rituximab and ^{64}Cu-sar-CO-rituximab are extremely stable *in vivo*, while labeling is rapid and easy under mild conditions and achieves high specific activity under very dilute conditions. These properties make them very attractive as ^{64}Cu-complexing BFCs for radiolabeling antibodies.

■ ASSOCIATED CONTENT

Supporting Information

Experimental data regarding radiolabeling efficiencies of each immunoconjugate under increasingly dilute conditions, bifunctional chelator to antibody ratio determination, PET images for all radioimmunoconjugates, and HPLC radiochromatograms of radioimmunoconjguates. This material is available free of charge via the Internet at http://pubs.acs.org.

■ AUTHOR INFORMATION

Corresponding Author

*Phone: +44 (0)20 7188 8376. E-mail: Margaret.s.cooper@kcl.ac.uk.

Notes

The authors declare no competing financial interest.

■ ACKNOWLEDGMENTS

M.S.C., K.P.S., and J.D.W. were supported by the King's College London-UCL Comprehensive Cancer Imaging Centre funded by Cancer Research UK & EPSRC, in association with MRC and DoH (UK). M.T.M. acknowledges Cancer Council Victoria for providing a Sydney Parker Smith Postdoctoral Cancer Research Fellowship; The State Government of Victoria for a Victoria Fellowship; and a Kaye Merlin Brutton Bequest. P.S.D. acknowledges financial support from the Australian Research Council. We thank Wellcome Trust for grant support to P.J.B. enabling the purchase of the PET-CT scanner. R.P. was supported in part by a National Institute for Health Research (NIHR) comprehensive Biomedical Research Centre

award to Guy's & St. Thomas' NHS Foundation Trust in partnership with King's College London and King's College Hospital NHS Foundation Trust, and in part by the Guy's and St. Thomas' Charity. We thank Stephen Clarke (supported by the Centre of Excellence in Medical Engineering funded by the Wellcome Trust and EPSRC under grant WT 088641/Z/09/Z) for assistance with PET/CT imaging. We thank Levente Meszeros (supported by a Cancer Research UK studentship), Alex Koers (supported by a National Institute for Health Research-funded Biomedical Research Centre studentship), and Alex O'Neill (supported by the Harris studentship) for assistance with biodistribution studies.

REFERENCES

(1) Meares, C. F., and Goodwin, D. A. (1984) Linking radiometals to proteins with bifuntional chelating agents. *J. Protein Chem. 3*, 215−228.
(2) Blower, P. J., Lewis, J. S., and Zweit, J. (1996) Copper radionuclides and radiopharmaceuticals in nuclear medicine. *Nucl. Med. Biol. 23*, 957−980.
(3) Donnelly, P. S. (2011) The role of coordination chemistry in the development of copper and rhenium radiopharmaceuticals. *Dalton Trans. 40*, 999−1010.
(4) Zamora, P. O., Mercer-Smith, J. A., Marek, M. J., Schulte, L. D., and Rhodes, B. A. (1992) Similarity of copper and technetium binding sites in human IgG. *Nucl. Med. Biol. 19*, 797−802.
(5) Wadas, T. J., Wong, E. H., Weisman, G. R., and Anderson, C. J. (2010) Coordinating radiometals of copper, gallium, indium, yttrium, and zirconium for PET and SPECT imaging of disease. *Chem. Rev. 110*, 2858−2902.
(6) Motekaitis, R. J., Rogers, B. E., Reichert, D. E., Martell, A. E., and Welch, M. J. (1996) Stability and structure of activated macrocycles. Ligands with biological applications. *Inorg. Chem. 35*, 3821−3827.
(7) Sun, X., Wuest, M., Weisman, G. R., Wong, E. H., Reed, D. P., Boswell, C. A., Motekaitis, R., Martell, A. E., Welch, M. J., and Anderson, C. J. (2002) Radiolabeling and in vivo behavior of copper-64-labeled cross-bridged cyclam ligands. *J. Med. Chem. 45*, 469−477.
(8) Ma, M. T., and Donnelly, P. S. (2011) Peptide targeted copper-64 radiopharmaceuticals. *Curr. Top. Med. Chem. 11*, 500−520.
(9) Wong, E. H., Weisman, G. R., Hill, D. C., Reed, D. P., Rogers, M. E., Condon, J. S., Fagan, M. A., Calabrese, J. C., Lam, K.-C., Guzei, I. A., and Rheingold, A. L. (2000) Synthesis and characterization of cross-bridged cyclams and pendant-armed derivatives and structural studies of their copper(II) complexes. *J. Am. Chem. Soc. 122*, 10561−10572.
(10) Smith, S. V. (2004) Molecular imaging with copper-64. *J. Inorg. Biochem. 98*, 1874−1901.
(11) McMurry, T. J., Brechbiel, M., Wu, C., and Gansow, O. A. (1993) Synthesis of 2-(*p*-thiocyanatobenzyl)-1,4,7-triazacyclononane-1,4,7-triacetic acid: Application of the 4-methoxy-2,3,6-trimethylbenzenesulfonamide protecting group in the synthesis of macrocyclic polyamines. *Bioconjugate Chem. 4*, 236−245.
(12) Anderson, C. J., and Welch, M. J. (1999) Radiometal-labeled agents (non-technetium) for diagnostic imaging. *Chem. Rev. 99*, 2219−2234.
(13) Eisenwiener, K. P., Powell, P., and Macke, H. R. (2000) A convenient synthesis of novel bifunctional prochelators for coupling to bioactive peptides for radiometal labelling. *Bioorg. Med. Chem. Lett. 10*, 2133−2135.
(14) Gasser, G., Tjioe, L., Graham, B., Belousoff, M. J., Juran, S., Walther, M., Kuenstler, J.-U., Bergmann, R., Stephan, H., and Spiccia, L. (2008) Synthesis, copper(II) complexation, ^{64}Cu-labeling, and bioconjugation of a new bis(2-pyridylmethyl) derivative of 1,4,7-triazacyclononane. *Bioconjugate Chem. 19*, 719−730.
(15) Juran, S., Walther, M., Stephan, H., Bergmann, R., Steinbach, J., Kraus, W., Emmerling, F., and Comba, P. (2009) Hexadentate bispidine derivatives as versatile bifunctional chelate agents for copper(II) radioisotopes. *Bioconjugate Chem. 20*, 347−359.
(16) Roehrich, A., Bergmann, R., Kretzschmann, A., Noll, S., Steinbach, J., Pietzsch, J., and Stephan, H. (2011) A novel tetrabranched neurotensin(8−13) cyclam derivative: Synthesis, ^{64}Cu-labeling and biological evaluation. *J. Inorg. Biochem. 105*, 821−832.
(17) Brechbiel, M. W. (2008) Bifunctional chelates for metal nuclides. *Q. J. Nucl. Med. Mol. Imaging 52*, 166−173.
(18) Cole, W. C., DeNardo, S. J., Meares, C. F., McCall, M. J., DeNardo, G. L., Epstein, A. L., O'Brien, H. A., and Moi, M. K. (1986) Serum stability of ^{67}Cu chelates: comparison with ^{111}In and ^{57}Co. *Int. J. Rad. Appl. Instrum. B 13*, 363−368.
(19) Kukis, D. L., Diril, H., Greiner, D. P., DeNardo, S. J., DeNardo, G. L., Salako, Q. A., and Meares, C. F. (1994) A comparative study of copper-67 radiolabeling and kinetic stabilities of antibody-macrocycle chelate conjugates. *Cancer 73*, 779−786.
(20) Lewis, M. R., Boswell, C. A., Laforest, R., Buettner, T. L., Ye, D., Connett, J. M., and Anderson, C. J. (2001) Conjugation of monoclonal antibodies with TETA using activated esters: Biological comparison of ^{64}Cu-TETA-1A3 with ^{64}Cu-BAT-2IT-1A3. *Cancer Biother. Radiopharm. 16*, 483−494.
(21) Dearling, J. L. J., Voss, S. D., Dunning, P., Snay, E., Fahey, F., Smith, S. V., Huston, J. S., Meares, C. F., Treves, S. T., and Packard, A. B. (2011) Imaging cancer using PET: the effect of the bifunctional chelator on the biodistribution of a ^{64}Cu-labeled antibody. *Nucl. Med. Biol. 38*, 29−38.
(22) Zimmermann, K., Grunberg, J., Honer, M., Ametamey, S., Schubiger, P. A., and Novak-Hofer, I. (2003) Targeting of renal carcinoma with $^{67/64}$Cu-labeled anti-L1-CAM antibody chCE7: selection of copper ligands and PET imaging. *Nucl. Med. Biol. 30*, 417−427.
(23) Rogers, B. E., Anderson, C. J., Connett, J. M., Guo, L. W., Edwards, W. B., Sherman, E. L. C., Zinn, K. R., and Welch, M. J. (1996) Comparison of four bifunctional chelates for radiolabeling monoclonal antibodies with copper radioisotopes: Biodistribution and metabolism. *Bioconjugate Chem. 7*, 511−522.
(24) Roselli, M., Schlom, J., Gansow, O. A., Brechbiel, M. W., Mirzadeh, S., Pippin, C. G., Milenic, D. E., and Colcher, D. (1991) Comparative biodistribution studies of DTPA-derivative bifunctional chelates for radiometal labeled monoclonal antibodies. *Int. J. Rad. Appl. Instrum. B 18*, 389−394.
(25) Novak-Hofer, I., Amstutz, H. P., Maecke, H. R., Schwarzbach, R., Zimmermann, K., Morgenthaler, J.-J., and Schubiger, P. A. (1995) Cellular processing of copper-67-labeled monoclonal antibody chCE7 by human neuroblastoma cells. *Cancer Res. 55*, 46−50.
(26) Smith, A., Alberto, R., Blaeuenstein, P., Novak-Hofer, I., Maecke, H. R., and Schubiger, P. A. (1993) Preclinical evaluation of copper-67-labeled intact and fragmented anti-colon carcinoma monoclonal antibody MAb35. *Cancer Res. 53*, 5727−5733.
(27) Smith-Jones, P. M., Fridrich, R., Kaden, T. A., Novak-Hofer, I., Siebold, K., Tschudin, D., and Maecke, H. R. (1991) Antibody labeling with copper-67 using the bifunctional macrocycle 4-[(1,4,8,11-tetraazacyclotetradec-1-yl)methyl]benzoic acid. *Bioconjugate Chem. 2*, 415−421.
(28) Anderson, C. J., Connett, J. M., Schwarz, S. W., Rocque, P. A., Guo, L. W., Philpott, G. W., Zinn, K. R., Meares, C. F., and Welch, M. J. (1992) Copper-64-labeled antibodies for PET imaging. *J. Nucl. Med. 33*, 1685−1690.
(29) Anderson, C. J., Schwarz, S. W., Connett, J. M., Cutler, P. D., Guo, L. W., Germain, C. J., Philpott, G. W., Zinn, K. R., Greiner, D. P., Meares, C. F., and Welch, M. J. (1995) Preparation, biodistribution and dosimetry of copper-64-labeled anti-colorectal carcinoma monoclonal antibody fragments 1A3-F(ab′)$_2$. *J. Nucl. Med. 36*, 850−858.
(30) Connett, J. M., Anderson, C. J., Guo, L.-W., Schwarz, S. W., Zinn, K. R., Rogers, B. E., Siegel, B. A., Philpott, G., and Welch, M. J. (1996) Radioimmunotherapy with a ^{64}Cu-labeled monoclonal antibody: a comparison with ^{67}Cu. *Proc. Natl. Acad. Sci. U.S.A. 93*, 6814−6818.
(31) Franz, J., Freeman, G. M., Barefield, E. K., Volkert, W. A., Ehrhardt, G. J., and Holmes, R. A. (1987) Labeling of antibodies with

copper-64 using a conjugate containing a macrocyclic amine chelating agent. *Nucl. Med. Biol. 14*, 479−484.
(32) Lewis, M. R., Wang, M., Axworthy, D. B., Theodore, L. J., Mallet, R. W., Fritzberg, A. R., Welch, M. J., and Anderson, C. J. (2003) In vivo evaluation of pretargeted ^{64}Cu for tumor imaging and therapy. *J. Nucl. Med. 44*, 1284−1292.
(33) Morphy, J. R., Parker, D., Alexander, R., Bains, A., Carne, A. F., Eaton, M. A. W., Harrison, A., Millican, A., Phipps, A., Rhind, S. K., Titmas, R., and Weatherby, D. (1988) Antibody labeling with functionalized cyclam macrocycles. *J. Chem. Soc., Chem. Commun.*, 156−158.
(34) Wu, A. M., Yazaki, P. J., Tsai, S.-W., Nguyen, K., Anderson, A.-L., McCarthy, D. W., Welch, M. J., Shively, J. E., Williams, L. E., Raubitschek, A. A., Wong, J. Y. C., Toyokuni, T., Phelps, M. E., and Gambhir, S. S. (2000) High-resolution microPET imaging of carcinoembryonic antigen-positive xenografts by using a copper-64-labeled engineered antibody fragment. *Proc. Natl. Acad. Sci. U.S.A. 97*, 8495−8500.
(35) Jones-Wilson, T. M., Deal, K. A., Anderson, C. J., McCarthy, D. W., Kovacs, Z., Motekaitis, R. J., Sherry, A. D., Martell, A. E., and Welch, M. J. (1998) The in vivo behavior of copper-64-labeled azamacrocyclic complexes. *Nucl. Med. Biol. 25*, 523−530.
(36) Prasanphanich, A. F., Nanda, P. K., Rold, T. L., Ma, L., Lewis, M. R., Garrison, J. C., Hoffman, T. J., Sieckman, G. L., Figueroa, S. D., and Smith, C. J. (2007) [^{64}Cu-NOTA-8-Aoc-BBN(7−14)NH_2] targeting vector for positron-emission tomography imaging of gastrin- releasing peptide receptor-expressing tissues. *Proc. Natl. Acad. Sci. U.S.A. 104*, 12462−12467.
(37) Boswell, C. A., Sun, X., Niu, W., Weisman, G. R., Wong, E. H., Rheingold, A. L., and Anderson, C. J. (2004) Comparative in vivo stability of copper-64-labeled cross-bridged and conventional tetraazamacrocyclic complexes. *J. Med. Chem. 47*, 1465−1474.
(38) Fani, M., Del Pozzo, L., Abiraj, K., Mansi, R., Tamma, M. L., Cescato, R., Waser, B., Weber, W. A., Reubi, J. C., and Maecke, H. R. (2011) PET of somatostatin receptor-positive tumors using ^{64}Cu- and ^{68}Ga-somatostatin antagonists: the chelate makes the difference. *J. Nucl. Med. 52*, 1110−1118.
(39) Lewis, J. S., Lewis, M. R., Srinivasan, A., Schmidt, M. A., Wang, J., and Anderson, C. J. (1999) Comparison of four ^{64}Cu-labeled somatostatin analogs in vitro and in a tumor-bearing rat model: Evaluation of new derivatives for positron emission tomography imaging and targeted radiotherapy. *J. Med. Chem. 42*, 1341−1347.
(40) Hausner, S. H., Kukis, D. L., Gagnon, M. K. J., Stanecki, C. E., Ferdani, R., Marshall, J. F., Anderson, C. J., and Sutcliffe, J. L. (2009) Evaluation of [^{64}Cu]Cu-DOTA and [^{64}Cu]Cu-CB-TE2A chelates for targeted positron emission tomography with an $\alpha v\beta 6$-specific peptide. *Mol. Imaging 8*, 111−121.
(41) Heroux, K. J., Woodin, K. S., Tranchemontagne, D. J., Widger, P. C. B., Southwick, E., Wong, E. H., Weisman, G. R., Tomellini, S. A., Wadas, T. J., Anderson, C. J., Kassel, S., Golen, J. A., and Rheingold, A. L. (2007) The long and short of it: The influence of *N*-carboxyethyl versus *N*-carboxymethyl pendant arms on in vitro and in vivo behavior of copper complexes of cross-bridged tetraamine macrocycles. *Dalton Trans.*, 2150−2162.
(42) Meares, C. F., Moi, M. K., Diril, H., Kukis, D. L., McCall, M. J., Deshpande, S. V., DeNardo, S. J., Snook, D., and Epenetos, A. A. (1990) Macrocyclic chelates of radiometals for diagnosis and therapy. *Br. J. Cancer 62* (Suppl. X), 21−26.
(43) Mirick, G. R., O'Donnell, R. T., DeNardo, S. J., Shen, S., Meares, C. F., and DeNardo, G. L. (1999) Transfer of copper from a chelated ^{67}Cu-antibody conjugate to ceruloplasmin in lymphoma patients. *Nucl. Med. Biol. 26*, 841−845.
(44) Bass, L. A., Wang, M., Welch, M. J., and Anderson, C. J. (2000) In vivo transchelation of copper-64 from TETA-octreotide to superoxide dismutase in rat liver. *Bioconjugate Chem. 11*, 527−532.
(45) Ma, M. T., Cooper, M. S., Paul, R. L., Shaw, K. P., Karas, J. A., Scanlon, D., White, J. M., Blower, P. J., and Donnelly, P. S. (2011) Macrobicyclic cage amine ligands for copper radiopharmaceuticals: A single bivalent cage amine containing two Lys^3-bombesin targeting peptides. *Inorg. Chem. 50*, 6701−6710.
(46) Ma, M. T., Karas, J. A., White, J. M., Scanlon, D., and Donnelly, P. S. (2009) A new bifunctional chelator for copper radiopharmaceuticals: A cage amine ligand with a carboxylate functional group for conjugation to peptides. *Chem. Commun.*, 3237−3239.
(47) Sargeson, A. M. (1984) Encapsulated metal ions. *Pure Appl. Chem. 56*, 1603−1619.
(48) Geue, R. J., Hambley, T. W., Harrowfield, J. M., Sargeson, A. M., and Snow, M. R. (1984) Metal ion encapsulation: Cobalt cages derived from polyamines, formaldehyde, and nitromethane. *J. Am. Chem. Soc. 106*, 5478−5488.
(49) Sargeson, A. M. (1996) The potential for the cage complexes in biology. *Coord. Chem. Rev. 151*, 89−114.
(50) Sargeson, A. M. (1986) Developments in the synthesis and reactivity of encapsulated metal ions. *Pure Appl. Chem. 58*, 1511−1522.
(51) Bottomley, G. A., Clark, I. J., Creaser, I. I., Engelhardt, L. M., Geue, R. J., Hagen, K. S., Harrowfield, J. M., Lawrance, G. A., Lay, P. A., Sargeson, A. M., See, A. J., Skelton, B. W., White, A. H., and Wilner, F. R. (1994) The synthesis and structure of encapsulating ligands: Properties of bicyclic hexamines. *Aust. J. Chem. 47*, 143−179.
(52) Bernhardt, P. V., Harrowfield, J. M., Hockless, D. C. R., and Sargeson, A. M. (1994) *N*-Methylated macrobicyclic hexaamines of copper(II) and nickel(II): Large steric effects. *Inorg. Chem. 33*, 5659−5670.
(53) Di Bartolo, N. M., Sargeson, A. M., Donlevy, T. M., and Smith, S. V. (2001) Synthesis of a new cage ligand, SarAr, and its complexation with selected transition metal ions for potential use in radioimaging. *J. Chem. Soc., Dalton Trans.*, 2303−2309.
(54) Donnelly, P. S., and Harrowfield, J. M. (2002) Synthesis with coordinated ligands: Biomolecule attachment to cage amines. *J. Chem. Soc., Dalton Trans.*, 906−913.
(55) Donnelly, P. S., Harrowfield, J. M., Skelton, B. W., and White, A. H. (2000) Carboxymethylation of cage amines: Control of alkylation by metal ion coordination. *Inorg. Chem. 39*, 5817−5830.
(56) Donnelly, P. S., Harrowfield, J. M., Skelton, B. W., and White, A. H. (2001) Carboxymethylated cage amines: Coordination and lactamization. *Inorg. Chem. 40*, 5645−5652.
(57) Di Bartolo, N., Sargeson, A. M., and Smith, S. V. (2006) New 64Cu PET imaging agents for personalised medicine and drug development using the hexa-aza cage. *Org. Biomol. Chem. 4*, 3350−3357.
(58) Voss, S. D., Smith, S. V., DiBartolo, N., McIntosh, L. J., Cyr, E. M., Bonab, A. A., Dearling, J. L. J., Carter, E. A., Fischman, A. J., Treves, S. T., Gillies, S. D., Sargeson, A. M., Huston, J. S., and Packard, A. B. (2007) Positron emission tomography (PET) imaging of neuroblastoma and melanoma with ^{64}Cu-SarAr immunoconjugates. *Proc. Natl. Acad. Sci. U.S.A.*, 1−5.
(59) Ma, M. T., Neels, O. C., Denoyer, D., Roselt, P., Karas, J. A., Scanlon, D. B., White, J. M., Hicks, R. J., and Donnelly, P. S. (2011) Gallium-68 complex of a macrobicyclic cage amine chelator tethered to two integrin-targeting peptides for diagnostic tumor imaging. *Bioconjugate Chem. 22*, 2093−2103.
(60) Lears, K. A., Ferdani, R., Liang, K., Zheleznyak, A., Andrews, R., Sherman, C. D., Achilefu, S., Anderson, C. J., and Rogers, B. E. (2011) In vitro and in vivo evaluation of ^{64}Cu-labeled SarAr-bombesin analogs in gastrin-releasing peptide receptor-expressing prostate cancer. *J. Nucl. Med. 52*, 470−477.
(61) Cai, H., Li, Z., Huang, C.-W., Shahinian, A. H., Wang, H., Park, R., and Conti, P. S. (2010) Evaluation of copper-64 labeled AmBaSar conjugated cyclic RGD peptide for improved microPET imaging of integrin $\alpha v\beta 3$ expression. *Bioconjugate Chem. 21*, 1417−1424.
(62) Cooper, M. S., Sabbah, E., and Mather, S. J. (2006) Conjugation of chelating agents to proteins and radiolabeling with trivalent metallic isotopes. *Nat. Protoc. 1*, 314−317.
(63) Meares, C. F., McCall, M. J., Reardan, D. T., Goodwin, D. A., Diamanti, C. I., and McTigue, M. (1984) Conjugation of antibodies with bifunctional chelating agents: isothiocyanate and bromoacetamide

reagents, methods of analysis, and subsequent addition of metal ions. *Anal. Biochem. 142*, 68−78.
(64) Langford, J. H., Cooper, M. S., and Orchard, K. H. (2011) Development and validation of the ^{57}Co assay for determining the ligand to antibody ratio in bifunctional chelate/antibody conjugates for use in radioimmunotherapy. *Nucl. Med. Biol. 38*, 1103−1110.
(65) Huang, C.-W., Li, Z., Cai, H., Shahinian, T., and Conti Peter, S. (2011) Biological stability evaluation of the $\alpha 2\beta 1$ receptor imaging agents: Diamsar and DOTA conjugated DGEA peptide. *Bioconjugate Chem. 22*, 256−263.
(66) Li, W. P., Meyer, L. A., Capretto, D. A., Sherman, C. D., and Anderson, C. J. (2008) Receptor-Binding, Biodistribution, and Metabolism Studies of ^{64}Cu-DOTA-Cetuximab, a PET-Imaging Agent for Epidermal Growth-Factor Receptor-Positive Tumors. *Cancer Biother. Radiopharm. 23*, 158−171.
(67) Cai, W., Chen, K., He, L., Cao, Q., Koong, A., and Chen, X. (2007) Quantitative PET of EGFR expression in xenograft-bearing mice using ^{64}Cu-labeled cetuximab, a chimeric anti-EGFR monoclonal antibody. *Eur. J. Nucl. Med. Mol. Imaging 34*, 850−858.
(68) Lewis, M. R., Kao, J. Y., Anderson, A.-L. J., Shively, J. E., and Raubitschek, A. (2001) An improved method for conjugating monoclonal antibodies with *N*-hydroxysulfosuccinimidyl DOTA. *Bioconjugate Chem. 12*, 320−324.
(69) Cai, W., Wu, Y., Chen, K., Cao, Q., Tice David, A., and Chen, X. (2006) In vitro and in vivo characterization of ^{64}Cu-labeled Abegrin, a humanized monoclonal antibody against integrin $\alpha v\beta 3$. *Cancer Res. 66*, 9673−9681.
(70) Paudyal, P., Paudyal, B., Hanaoka, H., Oriuchi, N., Iida, Y., Yoshioka, H., Tominaga, H., Watanabe, S., Watanabe, S., Ishioka, N. S., and Endo, K. (2010) Imaging and biodistribution of Her2/neu expression in non-small cell lung cancer xenografts with ^{64}Cu-labeled trastuzumab PET. *Cancer Sci. 101*, 1045−1050.
(71) Martin, S. M., O'Donnell, R. T., Kukis, D. L., Abbey, C. K., McKnight, H., Sutcliffe, J. L., and Tuscano, J. M. (2009) Imaging and pharmacokinetics of ^{64}Cu-DOTA-HB22.7 administered by intravenous, intraperitoneal, or subcutaneous injection to mice bearing non-Hodgkin's lymphoma xenografts. *Mol. Imaging Biol. 11*, 79−87.
(72) Ferreira, C., L., Yapp, D., T. T., Crisp, S., Sutherland, B., W., Ng Sylvia, S. W., Gleave, M., Bensimon, C., Jurek, P., and Kiefer, G., E. (2010) Comparison of bifunctional chelates for (64)Cu antibody imaging. *Eur. J. Nucl. Med. Mol. Imaging 37*, 2117−2126.
(73) Ferreira, C. L., Yapp, D. T., Lamsa, E., Gleave, M., Bensimon, C., Jurek, P., and Kiefer, G. E. (2008) Evaluation of novel bifunctional chelates for the development of Cu-64-based radiopharmaceuticals. *Nucl. Med. Biol. 35*, 875−882.
(74) Quadri, S. M., and Vriesendorp, H. M. (1998) Effects of linker chemistry on the pharmacokinetics of radioimmunoconjugates. *Q. J. Nucl. Med. 42*, 250−261.
(75) Woodin, K. S., Heroux, K. J., Boswell, C. A., Wong, E. H., Weisman, G. R., Niu, W., Tomellini, S. A., Anderson, C. J., Zakharov, L. N., and Rheingold, A. L. (2005) Kinetic inertness and electrochemical behavior of copper(II) tetraazamacrocyclic complexes: Possible implications for in vivo stability. *Eur. J. Inorg. Chem.*, 4829−4933.
(76) Shokeen, M., and Anderson, C. J. (2009) Molecular imaging of cancer with copper-64 radiopharmaceuticals and positron emission tomography (PET). *Acc. Chem. Res. 42*, 832−841.
(77) Xiao, Z., Donnelly, P. S., Zimmermann, M., and Wedd, A. G. (2008) Transfer of copper between bis(thiosemicarbozone ligands and intracellcular copper-binding proteins. Insights in mechanisms of copper uptake and selectivity. *Inorg. Chem. 47*, 4338−4347.
(78) Liu, D., Overbey, D., Watkinson, L. D., Smith, C. J., Daibes-Figueroa, S., Hoffman, T. J., Forte, L. R., Volkert, W. A., and Giblin, M. F. (2010) Comparative evaluation of three 64Cu-labeled E. Coli heat-stable enterotoxin analogues for PET imaging of colorectal cancer. *Bioconjugate Chem. 21*, 1171−1176.

Bioconjugate Chemistry

Article

pubs.acs.org/bc

Efficient siRNA Targeted Delivery into Cancer Cells by Gastrin-Releasing Peptides

Mouldy Sioud* and Anne Mobergslien

Department of Immunology, Molecular Medicine Group, Institute for Cancer Research, Oslo University Hospital, Montebello, N-0310, Oslo, Norway

ABSTRACT: Small interfering RNAs (siRNAs) have displayed considerable promise for the treatment of cancer. However, their delivery to the desired cell population remains a challenging task. Here we have covalently conjugated a siRNA against survivin to gastrin-releasing peptides (GRPs) to direct siRNA molecules to cancer cells that express the GRP receptor. The cellular uptake of the peptide−siRNA conjugates was tested in breast MDA-MB 231 cancer cells, which express the GRP receptor. Fluorescein-tagged GRP−siRNA conjugates were taken up by cancer cells but not normal mammary epithelial cells or human blood monocytes. By 120 min of incubation, most of the cells have taken up the conjugates. Excess free peptide inhibited uptake, implying dependence of uptake on GRP receptor. Moreover, bitargeting of siRNA molecules by GR and luteinizing hormone-releasing peptides accelerated the uptake kinetics by MDA-MB 231 cells when compared to monotargeted siRNAs. Peptide−siRNA conjugates, but not free siRNAs, inhibited the expression of survivin, an endogenous gene involved in cancer cell survival. None of the peptide−siRNA conjugates induced the expression of inflammatory cytokines or interferon α in human blood leukocytes. Overall, the data demonstrate the feasibility of GRP receptor-mediated targeted delivery of siRNAs to cancer cells, an important step for RNA interference therapy in humans.

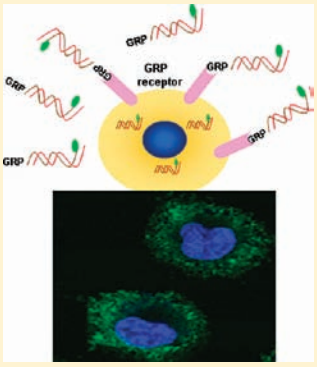

INTRODUCTION

RNA interference (RNAi) has recently emerged not only as a powerful tool to study gene function but also as a therapeutic strategy to silence genes involved in the initiation and/or perpetuation of disease.[1−3] Although much has been achieved about the mechanisms of RNAi, there are a number of challenges that applications of this gene-silencing technology need to overcome, including off-target effects and delivery.[3,4]

To date, siRNA delivery has been achieved by a number of strategies including lipid-based agents, nanoparticles, magnetofection, and electroporation.[1,5] As the most used delivery agents enter all cell types, specificity must be built into the delivery agents or directly attached to the siRNA molecules. With respect to peptides, a wide range of cell penetrating peptides (CPPs) have been identified and used as a vehicle for intracellular delivery of siRNAs. Well-known examples of CPPs are TAT-transactivator protein from human immunodeficiency virus type 1, penetratin from the homeodomain protein of *Antennapaedia*, transportan, a hybrid amino acid sequence, and MGP peptide.[6−9] Although the current CPP siRNA-delivery approaches have gained some merits, they generally target the entire cell population.[10]

To achieve specific delivery to target cells, a variety of siRNA targeting strategies have been used, including antibodies, CpG oligonucleotides, RNA aptamers, peptides, and chemical modifications.[11−17] Peptides that target specifically one given cell type have been identified using different techniques such as peptide libraries.[18−20] For example, we have identified a short peptide (LTVSPWY) capable of delivering antisense oligonucleotides to breast carcinoma cell lines.[20] Recently, this peptide was able to deliver therapeutics and imaging agents to cancer cells in vitro and in vivo.[21,22] Similarly, a RGD peptide targeting tumor vasculature expressing $\alpha v\beta 3$ integrin was shown to deliver VEGF siRNAs to tumor cells.[23] A peptide mimetic of the insulin-like growth factor 1 (IGF-1) was conjugated to siRNAs, and about 60% of the target gene was inhibited by the peptide−siRNA conjugates.[14] Furthermore, a 29-amino acid peptide derived from rabies virus glycoprotein facilitated the delivery of siRNAs to the brain through the binding to acetylcholine receptor expressed by neuronal cells.[15]

Given their exogenous origin, microorganism-derived peptides and peptides selected from random peptide libraries or artificially designed may activate the immune system and induce some side effects.[24] By contrast, naturally occurring peptides are expected to be nonimmunogenic and more stable in extracellular microenvironment where they are expected to function. Immunogenicity and stability are likely to be more of an issue for any artificial delivery formats for siRNAs.

A number of hormone receptor binding peptides have been successfully explored for magnetic resonance imaging of tumors.[25] More importantly, the receptors of these naturally circulating peptides are overexpressed in a large variety of human cancers but not normal human tissues, thus permitting an in vivo targeting of tumor cells. For example, the BB2 receptor for the human gastrin-releasing peptide (GRP) is overexpressed on the cell surfaces of several malignant tissues, particularly in the cases of colon cancer, breast cancer, lung cancer, and prostate cancer.[26−28] Another receptor, which also represents an attractive targeting molecule, is the gonadotropin releasing hormone receptor (GnRHR), which is

Received: February 3, 2012
Revised: March 22, 2012
Published: March 25, 2012

   dx.doi.org/10.1021/bc300050j | *Bioconjugate Chem.* 2012, 23, 1040−1049

strongly expressed by tumors such as ovarian, colon, breast, prostate, and lung cancer.[29] The ability of GRP agonists to be internalized is one factor that has led to their use as vehicles for radionuclide imaging and therapy.[28,30] In this work, first we tested whether the covalent linkage of GRP to siRNA against survivin would enable the delivery of the siRNA to cancer cells that express the GRP receptor. Second, we bitargeted the siRNA molecules to breast cancer cell line MDA-MB 231 using GRP and GnRH peptide. Third, we investigated gene silencing by peptide−siRNA conjugates.

MATERIALS AND METHODS

Cells. The breast MDA-MB-231 cancer cell line was purchased from American Type Culture Collection. Cells were cultured in RPMI medium supplemented with 10% FCS or in X-vivo 15 medium. Human mammary epithelial cells (HMECs) were obtained from Clonetics/BioWhittaker (San Diego, CA, U.S.) and cultured in MEGM, Ham's F12 medium supplemented with 10% FCS. Human peripheral monocytes, dendritic cells, T cells, and B cells were prepared from buffy coats obtained from normal volunteers as described previously.[31]

Peptides, siRNAs, and Oligonucleotides. Synthetic peptides were obtained from Eurogentec (Seraing, Belgium). The amino acid sequences of GRP1, GRP2, GnRH peptide, and control peptide are CGGNHWAVGHLM, CKMYPRGNHWAVGHLM, CQHWSYGLRP, and ADGGAQGTAC, respectively. A cysteine residue was added to the NH_2- or C-terminus to allow conjugation of the peptides to thiol-containing siRNAs, 6-(iodoacetamide)fluorescein (6-IAF), or biotin. Survivin siRNA sense strand with 5′-thiol group and 3′-fluorescein, unmodified siRNA sense and antisense strands were made and purified by Eurogentec (Seraing, Belgium). 5′-biotinylated siRNA duplexes with or without 3′-fluorescein at the 3′-end of the sense strand, and DNA oligonucleotides were made by Eurofins MWG (Ebersberg, Germany). The sequences of siRNA sense strand were the following: survivin, 5′-GAGCCAAGAACAAAAUUGC-3′; control siRNA (scrambled sequence), 5′-UAUAGCAAGACAGCAGAAC-3′.

Conjugation of the 6-IAF to Peptides. Peptides were dissolved in water at 1 mg/mL. Around 0.5 nmol of each peptide was mixed with 5 nmol of the fluorescein 6-iodoacetamide in PBS buffer, and then the mixture was incubated at room temperature for 2 h with agitation. The labeled peptide conjugates were purified on a gel filtration column, Sephadex G-10, in PBS buffer as described by the manufacturer's instructions (Nuclear Probes, Invitrogen). Aliquots from all fractions were analyzed on 15% native PAGE gels, and fluorescein-conjugated peptides were visualized by UV exposure. Positive fractions were collected and stored at −20 °C until use.

Conjugation of GRP1 to siRNAs. The siRNA targeting human survivin with a thiol group at the 5′-end and fluorescein at the 3′-end of the sense strand was dissolved in 10 mM HEPES and 1 mM EDTA, pH, 8.0, at 20 μM. The conjugation of the siRNA to the peptide-containing a thiol group was mainly performed as described by Muratovska and Eccles.[32] Briefly, equimolar concentrations of siRNA, peptide, and the thiol oxidant diamide (20 nmol) were mixed and incubated for 1 h at 40 °C. Subsequently, the mixture was run on 15% PAGE and the band corresponding to the peptide−siRNA conjugates was cut out, crushed into a fine slurry, and then incubated in RNase free water at 37 °C for 6 h with agitation. Subsequent to centrifugation at 12000*g* for 10 min, supernatants were collected and concentrated to 200 μL using a Centricon-3 device (Ambion). To increase RNA stability, the sense and antisense strands were annealed before chemical modification and purification. In some experiments, siRNA coupling to the GRP1 peptide was done as described by Davidson et al.[33] The final concentration of the conjugates was adjusted at 0.5 μg/μL. The samples were stored in aliquots at 20 °C until use.

Peptide and siRNA Conjugation to Streptavidin. Equimolar amounts (10 nmol) of the 5′-biotin siRNA with 3′ fluorescein, biotin-GRP1 peptide, and biotin-GnRH peptide were mixed with 8 nmol of streptavidin (Promega) in PBS buffer. The mixture was incubated at room temperature for 30 min and was then stored at 4 °C in the dark until use. As controls, streptavidin was incubated with siRNA combined with either GRP1 or GnRH peptide. Peptide−streptavidin−siRNA conjugates were added directly to cells at a final concentration of 50 nM. The attachment of the siRNA molecules and peptides to streptavidin protein was verified with PAGE shift assay. Under our experimental conditions, all siRNAs and peptide molecules were bound to the streptavidin protein.

Cellular Uptake of the Peptide−siRNA Conjugates. The cells were seeded onto a six-well plate (5×10^5/well) 1 day before the experiment. Subsequently, they were washed and replenished with 2 mL of fresh X-vivo 15 medium (2 mL/well) and then incubated with peptide−siRNA conjugates (50 nM) or free siRNA (50 nM) for 3 h at 37 °C, 5% CO_2. At the end of the uptake period, Hoechst 33342 dye was added for 10 min to visualize nuclei. The cells were washed twice with PBS to remove fluorescent siRNAs and then analyzed by epifluorescence microscope (Leica). To confirm internalization, the cells were cultured on Lab-Tek chamber slides (Nalge Nunc International), incubated with the siRNA conjugates, washed, and then analyzed by a Zeiss LSM 510 confocal microscope.

Flow Cytometry Analysis. For GRP and GnRH receptor analysis, the cells were stained for 30 min at 4 °C with goat anti-GRPR or anti-GnRHR polyclonal IgG antibodies in phosphate buffered saline (PBS) containing 1% fetal calf serum (staining buffer). Subsequent to washing, the cells were incubated with FITC-conjugated anti-goat IgG antibody for 30 min in staining buffer, washed, and then analyzed on a BD LSR II flow cytometer (BD Biosciences). Cells were also stained with control antibody isotypes. For peptide binding, the cells were incubated with fluorescein-tagged peptides (5 μg/mL) in phosphate-buffered saline (PBS)/1% FCS for 30 min at room temperature. Subsequently, they were washed and analyzed by flow cytometry. The uptake of peptide−siRNA conjugates was also analyzed by flow cytometry. In these experiments the cells were seeded into six-well plates (3×10^5 cells/well) in RPMI medium and cultured for 24 h. Prior to treatment, RPMI medium was replaced by X-vivo 15 medium (2 mL/well) and the cells were incubated with peptide−siRNA conjugates (50 nM) for the desired time at 37 °C in 5% CO_2. Subsequent to incubation, the cells were harvested by scraping, washed 3 times with PBS/1% FCS, and then analyzed by flow cytometry. Cellular uptake was also performed in RPMI supplemented with 10% FCS. All data were analyzed by FlowJo software.

Real-Time Quantitative Reverse-Transcription PCR. Total RNA was isolated from cells using the TRIzol reagent (Invitrogen). GRP and GnRH receptor expression was analyzed in MDA-BM 231 cells by quantitative RT-PCR using SYBR Green. Survivin mRNA expression in controls and siRNA-treated samples was also analyzed by RT-PCR. All reactions were performed in triplicate and normalized to GAPDH mRNA. Relative expression was calculated using the Ct method. The sequences of

the used primers are the following: GRP receptor, 5′-CTCC-CCGTGAACGATGACTGG-3′ (forward) and 5′-ATCTTCA-TCAGGGCATGGGAG-3′ (reverse); GnRH receptor, 5′-CCA-GAGACACAAGGCTTGAAG-3′ (forward) and 5′-TGACAA-TCAGAGTCTCCAACAG-3′ (reverse); survivin 5′-AGGT-TCCTTATCTGTCACAC-3′ (forward) and 5′-TCCCCAAT-GACTTAGAATGG-3′ (reverse); GAPDH, 5′-CTTCCAAG-GAGTAAGACCCC-3′ (forward) and 5′-TGTGAGGAGGGA-GATTCAC-3′ (reverse).

Western Blot Analysis. Subsequent to treatments, cells were collected by scraping and washed with PBS, and cytoplasmic proteins were prepared as previously described.[31] Equal amount of proteins (50 μg) were resolved by denaturing electrophoresis in 0.1% sodium dodecyl sulfate (SDS) on 12% PAGE and electrotransferred to nitrocellulose membrane. After blocking in 5% milk in TBST (0.1% Tween) for 2 h, membranes were probed with primary antibodies against survivin (Santa Cruz Biotechnology) and HRP-conjugated secondary antibodies. Immunoreactive proteins were detected using the enhanced chemiluminescence (ECL) system (GE Healthcare). In order to control for protein loading, membranes were stripped and then incubated with anti-β-actin polyclonal antibodies.

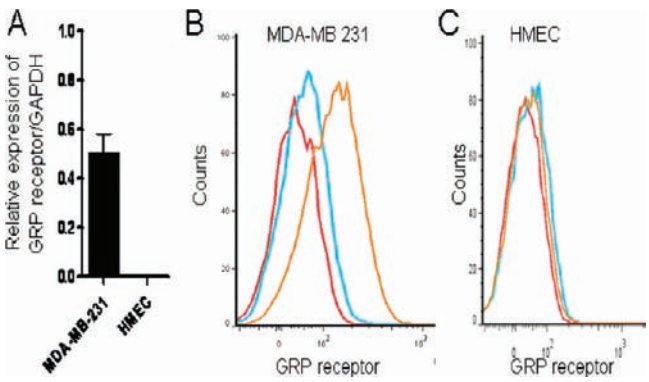

Figure 1. MDA-MB cancer cells express the GRP receptor. (A) GRP receptor expression was analyzed by quantitative real time PCR in MDA-MB 231 and human mammary epithelial cells (HMEC). (B) GRP receptor expression (orange lines), compared with isotype control (blue lines) and unstained cells (red lines), was analyzed by flow cytometry in both cell types. Data are representative of at least three independent experiments.

Gene Silencing. One day prior to transfection, the breast MDA-MB 231 cancer cells were seeded in a six-well plate at a density of 5×10^5 cells per well in RPMI supplemented with 10% FCS. Subsequently, the medium was replaced by X-vivo 15 medium (2 mL/well) containing 50 nM either peptide−siRNA conjugates or unconjugated siRNAs. Cells were harvested 24 h after the addition of the test molecules and monitored for survivin gene expression by real-time PCR and Western blots. In some experiments, the conjugates were directly added to cells cultured in RPMI medium supplemented with 10% FCS.

Cytokine ELISA. Peripheral blood mononuclear cells were prepared from buffy coats from healthy donors. Cells were plated in a 96-well plate (2×10^5/well/200 μL) and than incubated with either free siRNA or siRNA−peptide conjugates. DOTAP-formulated siRNA was used as positive control. Culture supernatants were collected at 24 h after treatment and assayed for TNF-α and IFN-α by ELISA according to the manufacturer's protocol (R&D Systems). All molecules were tested at 100 nM in triplicate.

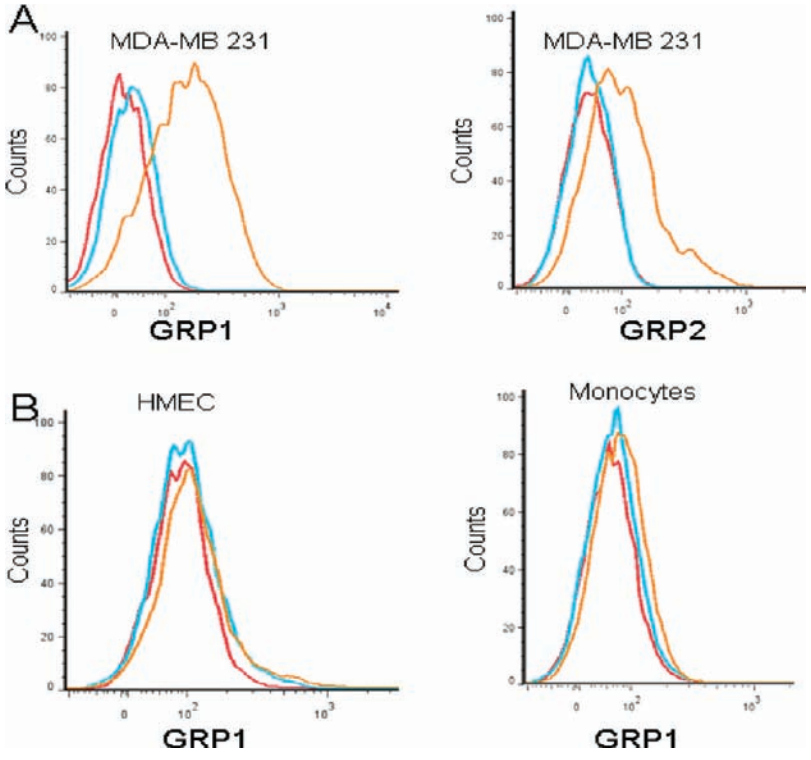

Figure 2. Binding of GRP peptides to human cells. Binding of the carboxyfluorescein-tagged GRP1 and GRP2 peptides (orange lines), or control peptide (blue lines) to MDA-MB 231 (A). The binding to HMEC and blood monocytes is shown in (B). The cells were incubated with the peptides (5 μg/mL) for 30 min at room temperature, washed three times, and then analyzed by flow cytometry. The cells incubated with only the staining buffer are represented by the red lines. Data are representative of three independent experiments.

Statistical Analysis. Statistical analysis was performed with a Student's t test. Values with $P < 0.05$ were considered significant.

RESULTS

Analysis of Peptide Binding by Flow Cytometry. The overexpression of GRP receptor BB2 in various neoplasias relative to normal tissues has been a major factor for driving the development of GRP-based radiopharmaceuticals.[34] To assess the utility of this receptor as a targeting strategy for siRNAs, first we have examined its expression in the breast MDA-MB 231 cancer cell line at the mRNA level by RT-PCR (Figure 1A) and at the protein level by flow cytometry (Figure 1B and Figure 1C). The receptor is expressed by breast MDA-MB 231 cancer cells but not normal human mammary epithelial cells (HMEC).

To investigate the targeting potential of GRP receptor, two synthetic peptides (GRP1, **C**GGNHWAVGHLM; GRP2, **C**KMYPRGNHWAVGHLM) were designed, conjugated to 6-iodoacetamidofluorescein (6-IAF), and tested for binding to MDA-MB 231 cells (Figure 2A). A significant binding to both peptides when compared to control peptide was found ($P < 0.001$). HMEC and blood monocytes did not express the receptor, and they did not bind to GRP1 or GRP2 (Figure 2B and data not shown). Collectively, these results confirm the binding specificity of the GR peptides and indicated that the addition of a cysteine and a fluorescent dye to the NH_2 terminus of the peptides does not hamper their binding to the GRP receptor expressed by breast MDA-MB 231 cancer cells.

Cellular Uptake of the Peptide–siRNA Conjugates. To determine whether the short peptide (GRP1) could deliver siRNAs to cancer cells, we prepared peptide–siRNA conjugates with fluorescently labeled sense strand and then evaluated their cellular uptake. The peptide was covalently attached to the 5′-end of the sense siRNA strand via disulfide linkage. Breast MDA-MB 231 cancer cells were incubated with the conjugates for 3 h at 37 °C in ex vivo 15 medium. Subsequent to incubation, Hoechst 33342 dye was added to the cultures for 10 min to visualize the nuclei in living cells, and then the cells were washed and analyzed with an epifluorescence microscope (Figure 3A). The conjugation of the peptide to survivin siRNA dramatically facilitated the uptake of siRNA by breast MDA-MB 231 cells. The same results were obtained with breast T47D cancer cells (data not shown). In contrast, free siRNA molecules were not taken up by the cells when compared to peptide–siRNA conjugates (Figure 3A). We further validated peptide–siRNA delivery to MDA-MB 231 cells by confocal microscopy. Fluorescently labeled siRNA delivered with GRP1 exhibited a punctate pattern characteristic of intracellular delivery and compartmentalization (Figure 3B).

To investigate the kinetics of uptake, MDA-MB 231 cells were incubated with GRP1–siRNA conjugates at 37 °C, and then they were harvested at various time points, washed, and analyzed with flow cytometry (Figure 4). GRP1–siRNA conjugates were efficiently taken up by the cells. Indeed, within 120 min of incubation nearly 70% of the cells have taken up the siRNAs. To validate that the uptake is receptor-dependent, we performed competition experiments. As shown in Figure 5A, excess free peptide inhibited uptake (58% vs 22.4%; 58% vs 9.0%, $P < 0.001$), implying dependence of uptake on the GRP receptor. In contrast to cancer cells, the peptide–siRNA conjugates were not taken up by blood monocytes (Figure 5B) or HMEC that do not express the GRP receptor (Figure 5C).

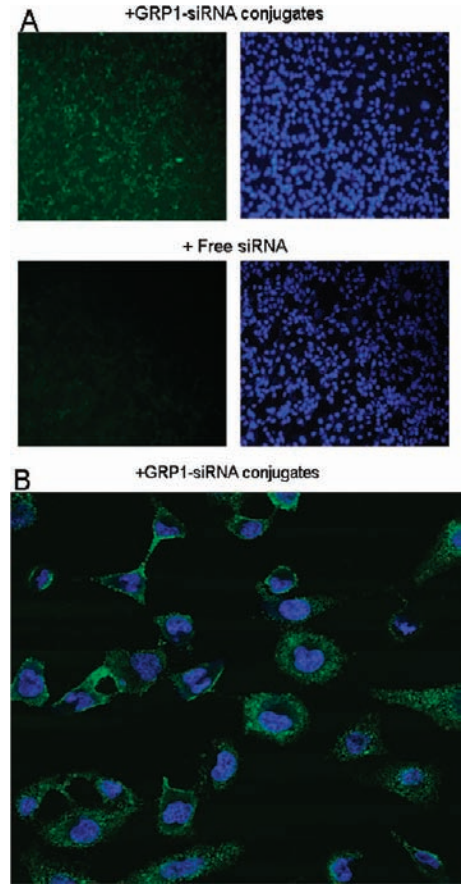

Figure 3. Fluorescence microscopy images of MDA-MB 231 cells. (A) The cells were incubated with GRP1–siRNA conjugates (50 nM) or free siRNA (50 nM) for 3 h at 37 °C in X-vivo 15 medium and then processed as described in Materials and Methods. Hoechst 33342 staining, shown in blue, was added to visualize nuclei. Green signals represent 3′-fluorescein-labeled siRNA molecules. Data are representative of at least four independent experiments. (B) Confocal microscopy showing cytoplasmic localization of the peptide–siRNA conjugates. The cells were cultured in chamber slides and then processed as in (A). Green signals represent 3′-fluorescein-labeled siRNA molecules.

Enhancement of siRNA Uptake by the Combined Use of GRP and GnRH Peptides. Although the rate of uptake of the GRP1–siRNA conjugates by breast cancer cell line MDA-MB 231 cells is relatively good, we have tested the possibility of accelerating the uptake by simultaneously targeting GRP and GnRH receptors. Theoretically, the recognition of two cell surface receptors is expected to increase targeting specificity and uptake by cells that express both receptors. MDA-MB 231 cells expressed the GnRH receptor at mRNA and protein levels (Figure 6A and Figure 6B). In the next experiment, we tested whether a 10 amino acids (**C**QHWSYGLRP) GnRH peptide bind to MDA-MB 231 cells. Flow cytometry analysis revealed the binding of the 6-iodoacetamidofluorescein (6-IAF) conjugated GnRH peptide to MDA-MB 231 cells (Figure 6C).

We used streptavidin–biotin technology to investigate the delivery of siRNA molecules by the combined use of GRP and GnRH peptides. Equimolar amounts of biotinylated peptides and biotinylated siRNA were incubated with streptavidin protein, and then the complexes were added to MDA-MB 231 cells. The siRNA is biotinylated at the 5′-end, and it has fluorescein at the 3′-end. Streptavidin has the ability to bind up

dx.doi.org/10.1021/bc300050j | Bioconjugate Chem. 2012, 23, 1040–1049

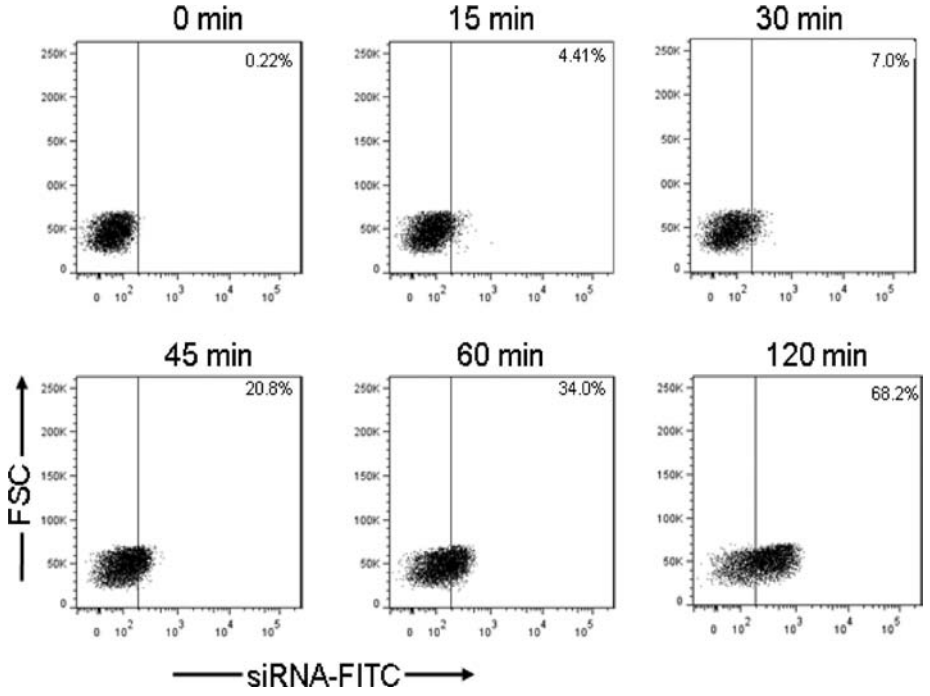

Figure 4. Uptake kinetics of the GRP1−siRNA conjugates. The cells were cultured in six-well plates and then incubated at 37 °C with GRP1−siRNA conjugates (50 nM) for 0, 15, 30, 45, 60, or 120 min. Subsequent to incubation, the cells were scraped, washed three times, and then analyzed by flow cytometry. Data are representative of three independent experiments.

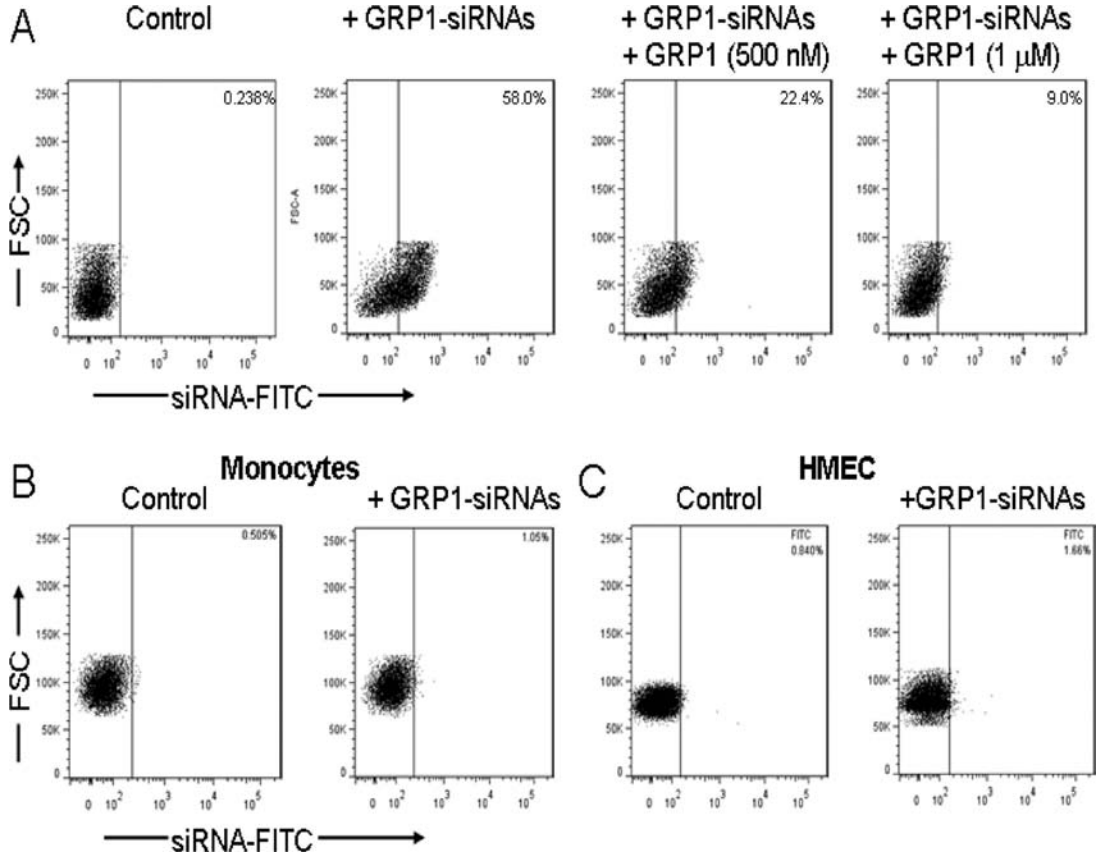

Figure 5. Competition assays and GRP1−siRNA conjugates binding to normal cells. (A) The competition experiments were performed by adding free peptide (500 nM or 1 μM) to MDA-MB 231 cells 60 min prior to addition of GRP1−siRNA conjugates (50 nM) and further incubation for 120 min. Subsequently, the cells were processed as in Figure 4. (B, C) Uptake of GRP1−siRNA conjugates by monocytes and HMEC, respectively. The cells were incubated with the peptide−siRNA conjugates (50 nM) at 37 °C for 120 min. Subsequently, they were washed and then analyzed by flow cytometry.

dx.doi.org/10.1021/bc300050j | *Bioconjugate Chem.* 2012, 23, 1040−1049

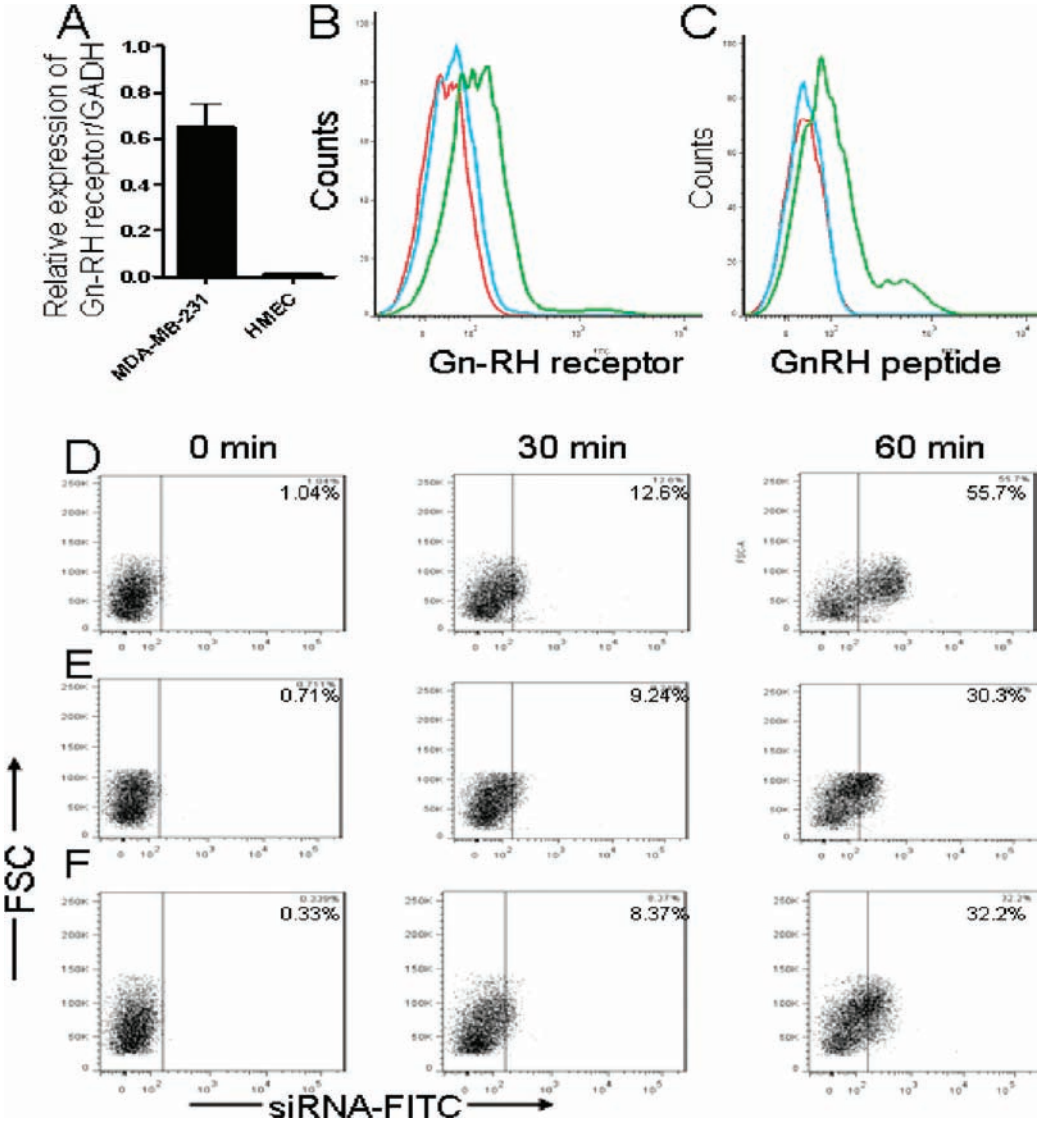

Figure 6. GnRH receptor expression and uptake kinetics. (A) The expression of Gn-RH receptor in cancer (MDA-MB 231) and normal (HMEC) cells was analyzed by RT-PCR. (B) Gn-RH receptor expression (green line), compared with isotype control (blue lines) and unstained cells (red lines), was analyzed by flow cytometry using specific antibodies. (C) Binding of the carboxyfluorescein-tagged GnRH peptide (green line) or of control peptide (blue line) to MDA-MB 231 cells. The cells were incubated with the peptides (5 μg/mL) for 30 min at room temperature, washed, and then analyzed by flow cytometry. The red line represents unstained cells. (D) Uptake kinetics of steptavidin−GRP-Gn-RHP−siRNA conjugates. The cells were cultured in six-well plates and then incubated at 37 °C with streptavidin−GRP-Gn-RHP−siRNA conjugates (50 nM) for various time points. Subsequent to incubation, the cells were scraped, washed three times, and then analyzed by flow cytometry. The cells were also incubated with either streptavidin−GRP1−siRNA (E) or streptavidin−Gn-RHP−siRNA (F) conjugates and processed as in (D). Results are representative of three independent experiments.

to four biotin molecules, and therefore, each streptavidin molecule is expected to bind to at least two different peptides and one siRNA molecule. As shown in Figure 6D, bitargeting led to accelerated uptake of the siRNA conjugates by MDA-MB 231 cancer cells when compared to cells incubated with either streptavidin−GRP1−siRNA or streptavidin−Gn-RHP−siRNA conjugates (Figure 6E and Figure 6F, respectively). Indeed, within 60 min, nearly 56% of the cells have taken up the bitargeted siRNA, while around 31% of the cells have taken up the monotargeted siRNA molecules ($P < 0.05$).

Endogenous Gene Knockdown Using Peptide−siRNA Conjugates. Having confirmed the delivery of siRNAs using short peptides, subsequently we investigated the targeting of survivin, an endogenous gene, by measuring mRNA and protein levels. Increased survivin expression in cancer cells has been associated with poor prognosis.[35] In initial studies, several siRNAs targeting survivin were designed, tested and the most active siRNA was conjugated to GRP1. The cells were incubated for 24 h with either GRP1−siRNA formulations or free siRNA. The disulfide linkage was used for the conjugation of the GRP1 to the 5′-terminus of the sense strand of siRNA. This linkage was chosen to allow the uncoupling of the siRNA from the peptide by reduction in the cytoplasm. We also chose to have the 3′-end of the sense unconjugated. As shown in Figure 7A, treatment of the cells with GRP1−siRNA conjugates resulted in significant gene silencing (15 ± 5% survivin expression relative to untreated cell, $P < 0.001$). Unconjugated siRNA did not reduce survivin mRNA (94 ± 3% relative to untreated control) nor did the scrambled siRNA conjugated to GRP1 (92 ± 5%, relative to the untreated control). Western

dx.doi.org/10.1021/bc300050j | Bioconjugate Chem. 2012, 23, 1040−1049

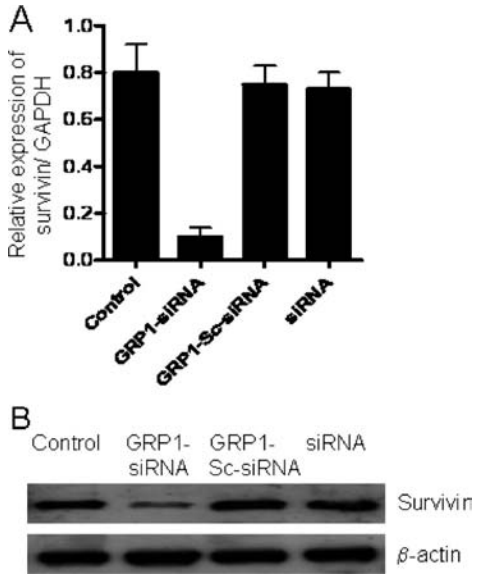

Figure 7. Inhibition of survivin gene expression by the GRP1−siRNA conjugates. Survivin siRNA was directly conjugated to the GRP1 via disulfide linkage. The GRP1−siRNA conjugates (GRP1−siRNA) or unconjugated siRNAs (50 nM) were added to MDA-MB 231 cells cultured in X-vivo 15 medium. As a control for gene silencing, a scrambled siRNA conjugated to GRP1 was included (GRP1-Sc−siRNA). Subsequent to 24 h of incubation time, total RNA and cytoplasmic protein extracts were prepared and then the expression of the survivin was analyzed by RT-PCR (A) and Western blots (B). Control = untreated cells. Data are representative of at least three independent experiments.

blot analysis was also used to investigate the relative knockdown of survivin expression (Figure 7B). GRP1−siRNA conjugates significantly reduced survivin protein level in breast MDA-MD 231 cancer cells when compared to control molecules (18 ± 5%, relative to untreatred cells, $P < 0.001$). These results clearly demonstrate that GRP1 is an efficient siRNA escort agent and indicate that siRNA molecules have reached the cytoplasm for gene silencing, which is consistent with the confocal microscopy data (Figure 3B).

Having demonstrated that the conjugates are active in human cells cultured in X-vivo 15 medium, in the next experiments we have tested the uptake in RPMI medium supplemented with 10% FCS. The cells were incubated for 3 h with GRP1−siRNAs conjugates at various concentrations and then analyzed by flow cytometry. As shown in Figure 8A, the peptide−siRNA conjugates were taken up by MDA-MB 231 cells. When tested at 100 nM, the level of survivin mRNA in GRP1−siRNA-treated cells was significantly reduced (46 ± 6%, relative to cell treated with GRP1-scrambled siRNA conjugates, $P < 0.05$) (Figure 8B). Consistent with mRNA level, treatment of cells with GPR1−siRNA conjugates yielded a significant decrease in survivin protein level (42% relative to cells treated with GRP1-scrambled siRNA conjugates, $P < 0.05$) (Figure 8 and Figure 8D). Collectively, these results indicate that gene silencing in mammalian cells can be achieved with GRP−siRNA conjugates in the presence of serum.

Peptide−siRNA Formulations Did Not Trigger Cytokine Production by Blood Leukocytes. We have previously shown that both chemically made single-stranded and double-stranded siRNAs can activate innate immunity leading to the production of cytokines such as tumor necrosis factor-α (TNF-α), interleukin-6 (IL-6), and interferon-α (IFN-α).[36] Such nonspecific immune activation by siRNAs could contribute to antitumoral effects of siRNA but can also create unwanted toxicities.[37] Therefore, we have assessed the induction of TNF-α and IFN-α by PBMC in response to GRP1−siRNA conjugates. We used DOTAP-delivered siRNA as positive control.[36] In contrast to DOTAP-delivered siRNA, we did not observe TNF-α or IFN-α production following treatment with GRP1−siRNA conjugates (Figure 9).

■ DISCUSSION

RNAi has been applied as tool to gain insights into gene functions or to understand cellular mechanisms in the context of infection or cancer.[2] Also, it has been considered as a promising strategy for the treatment of human diseases.[3] Yet in order to exploit the full therapeutic potential of this technology, it is necessary to overcome certain constraints related to delivery, targeting, and activation of innate immunity. Here, we covalently linked a siRNA against survivin to naturally occurring peptides whose receptors are strongly expressed on the majority of tumors, including, breast, colon, ovarian, and prostate cancers to achieve cell-type-specific delivery of the siRNA molecules. The siRNA−peptide conjugates were effectively taken up by cancer cells but not normal cells. In contrast to free siRNAs, the siRNA−peptide conjugates inhibited gene expression. Moreover, none of the conjugates induced the expression of inflammatory cytokines and IFN-α in human blood leukocytes.

In general specific interaction between a specific ligand and its cell surface receptor normally enhances the cellular uptake by the aid of a mechanism called receptor-mediated endocytosis. Cell-specific ligands, including aptamers, antibodies, and vitamins, have been used to confer cell-specificity of siRNAs.[3,4] The antibody-targeted delivery has attracted much attention owing to the high selectiveness toward cell surface receptors.[38] In this respect, a monoclonal antibody targeting the transferrin receptor was directly conjugated to siRNAs via a biotin−streptavidin linkage, and intravenous administration of these formulations blocked the expression of a reporter gene in a rat model bearing intracranially transplanted brain tumor.[39] Similarly, single-chain Fv antibody−siRNA conjugates targeting either gp120-expressing cells or the T cell-specific CD7 receptor delivered anti- HIV-1 siRNAs to cells in vitro and in vivo.[11]

In contrast to antibodies, small peptides are expected to be less immunogenic, cost-effective, and easy to conjugate to small molecules such as siRNAs. Because of their small size, they are also expected to have more tumor penetrance than antibodies. It is interesting to note that GRP and GnRH peptides also have high affinity for their receptors expressed on the cell surface of cancer cells.[26,29] Such high affinity would allow the use of low concentrations of peptide−siRNA conjugates, which likely reduces potential nonspecific side effects while being cost-effective. Moreover, the clinical usefulness of certain GRP radiopharmaceutical analogues as cancer specific imaging agents was demonstrated in patients with either prostate or breast cancer.[40] Overall, the published data indicate that GRP analogues can localize in tumors with high specificity. Again, these promising results in patients may facilitate the therapeutic testing of GRP1−siRNA conjugates in humans.

In order to preserve the silencing potency of siRNAs, we have used a disulfide linkage between the peptide and siRNA molecules. This strategy is expected to facilitate the intracellular delivery of siRNAs by the action of the GRP peptides and to release intact siRNA by reductive cleavage of the disulfide

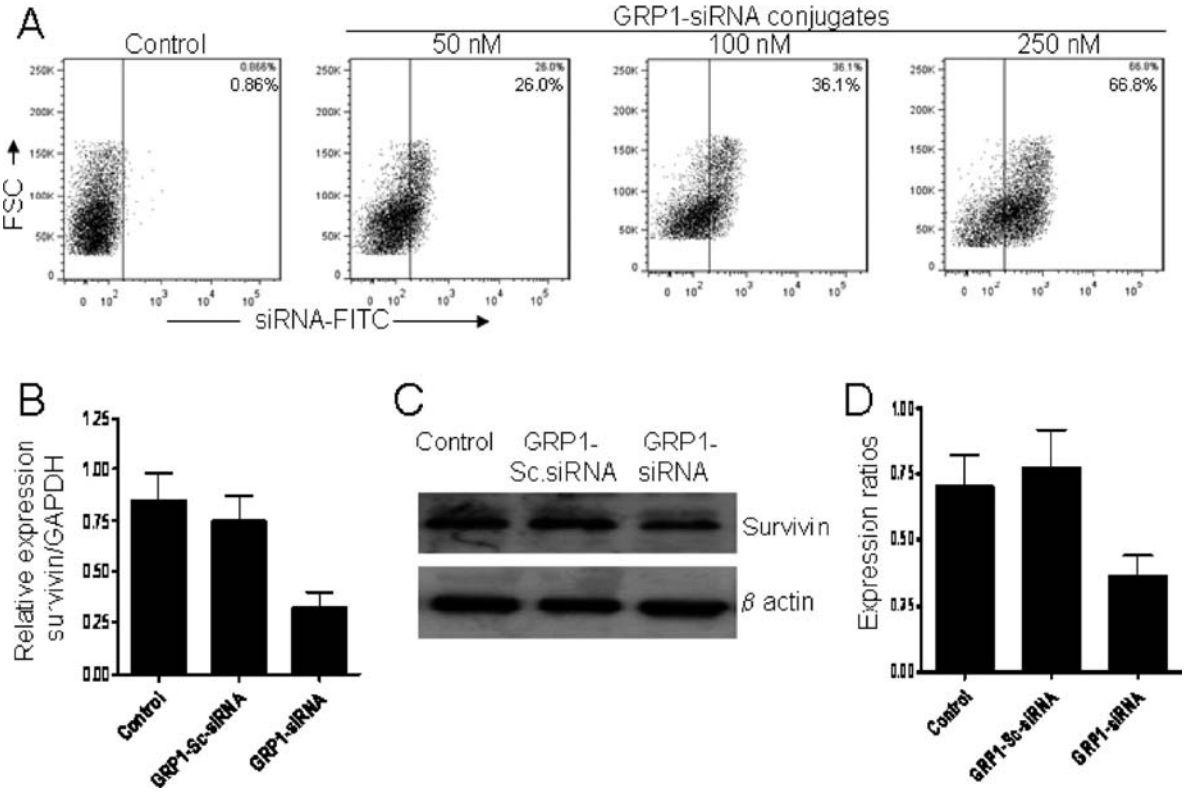

Figure 8. Uptake and silencing potency of GRP−siRNA conjugates in the presence of 10% FCS. (A) Various concentrations of GRP1−siRNA conjugates were added to MDA-MB 231 cells cultured in RPMI medium supplemented with 10% FCS. Subsequent to 3 h of incubation time, the cells were washed three times and then analyzed by flow cytometry. The silencing potency of the peptide−siRNA conjugates (100 nM) was also tested in RPMI medium supplemented with 10% FCS. Subsequent to 24 h of incubation time, total RNA and cytoplasmic protein extracts were prepared and the expression of the survivin was analyzed by RT-PCR (B) and Western blots (C). (D) Densitometry analysis of survivin protein level and normalization with β-actin level (mean ± SD of three experiments). Control = untreated cells. All data are representative of at least three experiments.

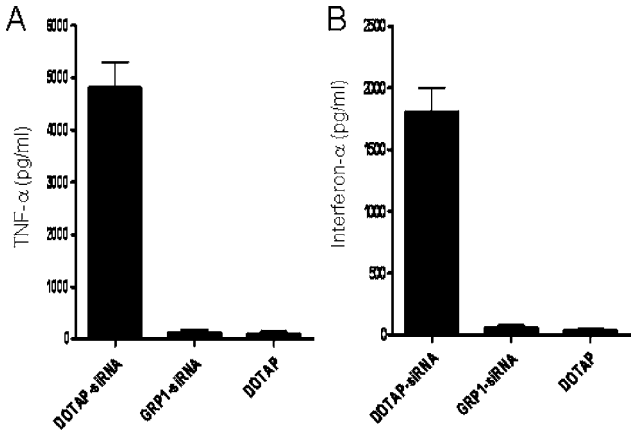

Figure 9. Immunostimulatory potential of GRP−siRNA conjugates. Peripheral blood mononuclear cells were incubated with either GRP1−siRNA conjugates or DOTAP-formulated siRNAs (100 nM) for 18 h. Subsequently, culture supernatants were harvested and cytokine contents were determined by ELISA. Data are representative of at least three independent experiments.

linkage between the peptide and the siRNAs in the reductive cytoplasmic environment. Gene silencing was achieved at lower siRNA concentrations. Indeed, we obtained around 80% inhibition of survivin gene at 50 nM in X-vivo 15 medium. Other studies have reported high concentration in vitro.[14,12,41,42]

Serum effect on the activity of peptide−siRNA conjugates is an important issue when considering potential in vivo applications. The GRP−siRNA conjugates were active in medium supplemented with 10% FCS. At 100 nM, a significant gene silencing (58% inhibition of protein expression, $P < 0.05$) effect was obtained with GRP1−siRNA conjugates. Previous studies have shown that peptide−siRNA conjugates can be active in the presence of serum. In a recent study, the authors have treated M21 + GL3 cells RGD−siRNA conjugates for 4 h in serum free medium and then added serum to a final concentration of 2%.[41] Under these conditions, a 40% reduction in luciferase activity at 50 nM was obtained with one siRNA. A second siRNA showed 70% inhibition at 25 nM; however, there was no difference in potency between 25 and 100 nM concentrations. In another study, the breast MCF-7 cancer cells growing in DMEM/F12 medium supplemented with 5% FCS was treated with a nuclease resistant siRNA conjugated to a peptide analogue of insulin-like growth factor. A 57% inhibition of the insulin receptor substrate-1 protein was obtained at 200 nM.[14] Notably, most of the published data on peptide delivery of siRNAs have been carried in serum free medium for 4−6 h, and then serum was added to cell culture. One reason for this has been that the siRNA molecules and/or peptides are not so stable in serum. Neither the suvivin siRNA nor the GRP peptides used in this study are modified; therefore, there is room for improvement. By use of stabilized siRNA and/or peptides in combination with optimized conjugation protocols, the GRP−siRNA conjugates are likely to work at lower concentrations in

medium containing serum. With regard to siRNA stability, a recent study showed that a group of siRNAs are extremely stable in their native form in 10% serum and in vivo.[43]

Although it exceeded our expectations, the uptake of GRP−siRNA conjugates by breast cancer MDA-MB 231 cells was somehow slow when compared to other targeting strategies.[12] The kinetic of uptake seems to be receptor-dependent. Indeed, increasing the peptide−siRNA concentration from 50 to 100 nM did not significantly accelerate the kinetics of uptake in X-vivo 15 medium (data not shown). To enhance cell uptake and/or specificity, one might use bispecific or trispecific branched peptides targeted to different receptors expressed by the same cell type. Enhancement of uptake was achieved by conjugation of siRNA molecules to GRP and GnRH peptide. Therefore, bitargeting of siRNAs to tumor cells is possible and should be further explored.

Another problem encountered during siRNA delivery is the activation of innate immunity through the binding of siRNA molecules to TLR7 and TLR8, expressed by immune cells, particularly monocytes and dendritic cells.[36,44] These early findings highlight the necessity of testing the immunostimulatory potential of each therapeutic siRNA. We found no significant binding of the peptide−siRNA conjugates to human blood cells such as monocytes, dendritic cells, and T cells (Figure 5B and data not shown). Moreover, no TNF-α or IFN-α was produced after overnight incubation of blood leukocytes with peptide−siRNA conjugates. Depending on the intended therapy, immunostimulation could be a wanted or unwanted effect. For treatments like cancer therapy and infection medicine, the immunostimulatory effect could be wanted and beneficial, and in that respect siRNAs can intentionally be designed to induce such an adjuvant effect.[45]

In summary, the current study shows that naturally occurring peptides are suitable for carrying siRNAs to breast cancer cells. There are other types of cancer that show overexpression of GRP receptor and therefore may also benefit from the use of this targeting strategy. Although further work is needed, the conjugation of two synergistic peptides on the same assembling agents such as streptavidin and nanoparticles will strengthen the targeting specificity and facilitate the uptake in vitro and in vivo.[46] In addition to its therapeutic applications, the targeting method described here could potentially be adapted for basic research and target screening in cancer cells that express GRP and/or GnRH receptors.

AUTHOR INFORMATION

Corresponding Author

*E-mail: mosioud@medisin.uio.no. Phone: +47 22 78 14 14.

Notes

The authors declare no competing financial interest.

ACKNOWLEDGMENTS

The authors acknowledge support from Helse Sør Øst, the Norwegian Cancer Society, and the gene therapy program at the Norwegian Radium Hospital.

REFERENCES

(1) Elbashir, S. M., Harborth, J., Lendeckel, W., Yalcin, A., Weber, K., and Tuschl, T. (2001) Duplexes of 21-nucleotide RNAs mediate RNA interference in cultured mammalian cells. *Nature 411*, 494−498.

(2) Behlke, M. A. (2006) Progress towards in vivo use of siRNAs. *Mol. Ther. 13*, 644−670.

(3) Lares, M. R., Rossi, J. J., and Ouellet, D. L. (2010) RNAi and small interfering RNAs in human disease therapeutic applications. *Trends Biotechnol. 28*, 129−138.

(4) Sioud, M. (2005) On the delivery of small interfering RNAs into mammalian cells. *Expert Opin. Drug Delivery 2*, 639−651.

(5) Mykhaylyk, O., Zelphati, O., Rosenecker, J., and Plank, C. (2008) siRNA delivery by magnetofection. *Curr. Opin. Mol. Ther. 10*, 493−505.

(6) Torchilin, V. P., Rammohan, R., Wissig, V., and Levchenko, T. S. (2001) TAT peptide on the surface of liposomes affords their efficient intracellular delivery even at low temperature and in the presence of metabolic inhibitors. *Proc. Natl. Acad. Sci. U.S.A. 98*, 8786−8791.

(7) Morris, M. C., Vidal, P., Chaloin, L., Heitz, F., and Divita, G. (1997) A new peptide vector for efficient delivery of oligonucleotides into mammalian cells. *Nucleic Acids Res. 25*, 2730−2736.

(8) Derossi, D., Joliot, A. H., Chassaing, G., and Prochiantz, A. (1994) The third helix of the antennapedia homeodomain translocates through biological membranes. *J. Biol. Chem. 269*, 10444−10450.

(9) Ishihara, T., Goto, M., Kodera, K., Kanazawa, H., Murakami, Y., Mizushima, Y., and Higaki, M. (2009) Intracellular delivery of siRNA by cell-penetrating peptides modified with cationic oligopeptides. *Drug Delivery 16*, 153−159.

(10) Meade, B. R., and Dowdy, S. F. (2007) Exogenous siRNA delivery using peptide transduction domains/cell penetrating peptides. *Adv. Drug Delivery Rev. 59*, 134−140.

(11) Song, E., Zhu, P., Lee, S. K., Chowdhury, D., Kussmann, S., Dykxhoorn, D. M., Feng, Y., Palliser, D., Weiner, D. B., Shankar, P., Marasco, W. A., and Lieberman, J. (2005) Antibody mediated in vivo delivery of small interfering RNAs via cell-surface receptors. *Nat. Biotechnol. 23*, 709−717.

(12) Kortylewski, M., Swiderski, P., Herrmann, A., Wang, L., Kowolik, C., Kujawski, M., Lee, H., Scuto, A., Liu, Y., Yang, C., Deng, J., Soifer, H. S., Raubitschek, A., Forman, S., Rossi, J. J., Pardoll, D. M., Jove, R., and Yu, H. (2009) In vivo delivery of siRNA to immune cells by conjugation to a TLR9 agonist enhances antitumor immune responses. *Nat. Biotechnol. 27*, 925−932.

(13) McNamara, J. O., Andrechek, E. R., Wang, Y., Viles, K. D., Rempel, E. R., Gilboa, E., Sullenger, B. A., and Giangrande, P. H. (2006) Cell type-specific delivery of siRNAs with aptamer−siRNA chimeras. *Nat. Biotechnol. 24*, 1005−1015.

(14) Cesarone, G., Edupuganti, O. P., Chen, C. P., and Wickstrom, E. (2007) Insulin receptor substrate 1 knockdown in human MCF7 ER+ breast cancer cells by nuclease-resistant IRS1 siRNA conjugated to a disulfide-bridged D-peptide analogue of insulin-like growth factor 1. *Bioconjugate Chem. 18*, 1831−1840.

(15) Kumar, P., Wu, H., McBride, J. L., Jung, K. E., Kim, M. H., Davidson, B. L., Le, S. K., Shankar, P., and Manjunath, N. (2007) Transvascular delivery of small interfering RNA to the central nervous system. *Nature 448*, 39−43.

(16) Peer, D., Zhu, P., Carman, C. V., Lieberman, J., and Shimaoka, M. (2007) Selective gene silencing in activated leukocytes by targeting siRNAs to the integrin lymphocyte function-associated antigen-1. *Proc. Natl. Acad. Sci. U.S.A. 104*, 4095−4100.

(17) McNamara, J. O., Andrechek, E. R., Wang, Y., Viles, K. D., Rempel, E. R., Gilboa, E., Sullenger, B. A., and Giangrande, P. H. (2006) Cell type-specific delivery of siRNAs with aptamer−siRNA chimeras. *Nat. Biotechnol. 24*, 1005−1015.

(18) Pasqualini, R., and Ruoslahti, E. (1996) Organ targeting in vivo using phage display peptide libraries. *Nature 380*, 364−366.

(19) Shadidi, M., and Sioud, M. (2003) Selective targeting of cancer cells using synthetic peptides. *Drug Resist. Updates 6*, 363−371.

(20) Shadidi, M., and Sioud, M. (2003) Identification of novel carrier peptides for the specific delivery of therapeutics into cancer cells. *FASEB J. 17*, 256−258.

(21) Wang, X. F., Birringer, M., Dong, L. F., Veprek, P., Low, P., Swettenham, E., Stantic, M., Yuan, L. H., Zobalova, R., Wu, K., Ledvina, M., Ralph, S. J., and Neuzil, J. (2007) A peptide conjugate of vitamin E succinate targets breast cancer cells with high ErbB2 expression. *Cancer Res. 67*, 3337−3344.

(22) Luo, H., Yang, J., Jin, H., Huang, C., Fu, J., Yang, F., Gong, H., Zeng, S., Luo, Q., and Zhang, Z. (2011) Tetrameric far-red fluorescent protein as a scaffold to assemble an octavalent peptide nanoprobe for enhanced tumor targeting and intracellular uptake in vivo. *FASEB J. 25*, 1−9.
(23) Schiffelers, R. M., Ansari, A., Xu, J., Zhou, Q., Tang, Q., Storm, G., Molema, G., Lu, P. Y., Scaria, P. V., and Woodle, M. C. (2004) Cancer siRNA therapy by tumor selective delivery with ligand-targeted sterically stabilized nanoparticle. *Nucleic Acids Res. 32*, e149.
(24) Moschos, S. A., Jones, S. W., Perry, M. M., Williams, A. E., Erjefalt, J. S., Turner, J. J., Barnes, P. J., Sproat, B. S., Gait, M. J., and Linda, M. A. (2007) Lung delivery studies using siRNA conjugated to TAT (48−60) and penetratin reveal peptide induced reduction in gene expression and induction of innate immunity. *Bioconjugate Chem. 18*, 1450−1459.
(25) Riccabona, G., and Decristoforo, C. (2003) Peptide targeted imaging of cancer. *Cancer Biother. Radiopharm. 18*, 675−687.
(26) Preston, S. R., Woodhouse, L. F., Jones-Blackett, S., Miller, G. V., and Primrose, J. N. (1995) High-affinity binding sites for gastrin-releasing peptide on human colorectal cancer tissue but not uninvolved mucosa. *Br. J. Cancer 71*, 1097−1089.
(27) Smith, C. J., Volkert, W. A., and Hoffman, T. J. (2003) Gastrin releasing peptide (GRP) receptor targeted radiopharmaceuticals: a concise update. *Nucl. Med. Biol. 30*, 861−868.
(28) Smith, C. J., Volkert, W. A., and Hoffman, T. J. (2005) Radiolabeled peptide conjugates for targeting of the bombesin receptor superfamily subtypes. *Nucl. Med. Biol. 32*, 733−740.
(29) Montagnani-Marelli, M., Moretti, R. M., Januszkiewcz-Caulier, J., Motta, M., and Limonata, P. (2006) Gonadotropin-releasing hormone (GnRH) receptors in tumors: a new rationale for the therapeutical application of GnRH analogs in cancer patients? *Curr. Cancer Drug Targets 6*, 257−269.
(30) Schumann, M., Nakagawa, T., Mantey, S. A., Howell, B., and Jensen, R. T. (2008) Function of non-visual arrestins in signalling and endocytosis of the gastrin-releasing peptide receptor (GRP receptor). *Biochem. Pharmacol. 75*, 1170−1185.
(31) Flatekval, G. F., and Sioud, M. (2009) Modulation of dendritic cell maturation and function with mono- and bifunctional small interfering RNAs targeting indoleamine 2,3-dioxygenase. *Immunology 128*, e837−e848.
(32) Muratovska, A., and Eccles, M. R. (2004) Conjugate for efficient delivery of short interfering RNA (siRNA) into mammalian cells. *FEBS Lett. 558*, 63−68.
(33) Davidson, T. J., Harel, S., Arboleda, V. A., Prunel, G. F., Shelanski, M. L, Greene, L. A., and Troy, C. M. (2004) Highly efficient small interfering RNA delivery to primary mammalian neurons induces microRNA-like effects before mRNA degradation. *J. Neurosci. 24*, 10040−10046.
(34) Patel, O., Shulkes, A., and Baldwin, G. S. (2006) Gastrin-releasing peptide and cancer. *Biochim. Biophys. Acta 1766*, 23−41.
(35) Altieri, D. C. (2008) Survivin, cancer networks and pathway-directed drug discovery. *Nat. Rev. Cancer 8*, 61−70.
(36) Sioud, M. (2005) Induction of inflammatory cytokines and interferon responses by double-stranded and single-stranded siRNAs is sequence-dependent and requires endosomal localization. *J. Mol. Biol. 348*, 1079−1090.
(37) Sioud, M. (2007) RNA interference and innate immunity. *Adv. Drug Delivery Rev. 59*, 153−163.
(38) Rudnick, S. I., and Adams, G. P. (2009) High affinity antibody for targeting. Affinity and avidity in antibody-based tumor targeting. *Cancer Biother. Radiopharm. 24*, 155−161.
(39) Xia, C. F., Zhang, Y., Zhang, Y., Boado, R. J., and Pardridge, W. M. (2007) Intravenous siRNA of brain cancer with receptor targeting and avidin−biotin technology. *Pharmacol. Res. 24*, 2309−2316.
(40) Van de Wiele, C., Dumont, F., Broecke, R. V., Oosterlinck, W., Cocquyt, V., Serrenyn, R., Peers, S., Thornback, J., Slegers, G., and Dierckx, R. A. (2000) Technetium-99m RP527, a GRP analogue for visualization of GRP receptor-expressing malignancies: a feasible study. *Eur. J. Nucl. Med. 27*, 1694−1699.
(41) Alam, M. R., Ming, X., Fischer, M., Lackey, J. G., Rajeev, K. G., Manoharan, M., and Juliano, R. L. (2011) Multivalent cyclic RGD conjugates for targeted delivery of small interfering RNA. *Bioconjugate Chem. 22*, 1673−1681.
(42) Tumer, J. J., Jones, S., Fabani, M. M., Ivanova, G., Arzumanov, A. A., and Gait, M. J. (2007) RNA targeting with peptide conjugates of oligonucleotides, siRNA and PNA. *Blood Cells, Mol. Dis. 38*, 1−7.
(43) Hong, J., Huang, Y., Li, J., Yi, F., Zheng, J., Huang, H., Wei, N., Shan, Y., An, M., Zhang, H., Ji, J., Zhang, P., Xi, Z., Du, Q., and Liang, Z. (2010) Comprehensive analysis of sequence-specific stability of siRNA. *FASEB J. 24*, 4844−4855.
(44) Judge, A. D., Sood, V., Shaw, J. R., Fang, D., McClintock, K., and MacLachlan, I. (2005) Sequence-dependent stimulation of the mammalian innate immune response by synthetic siRNA. *Nat. Biotechnol. 23*, 457−462.
(45) Furset, G., and Sioud, M. (2007) Design of bifunctional siRNAs: combining immunostimulation and gene-silencing in one single siRNA molecule. *Biochem. Biophys. Res. Commun. 352*, 642−649.
(46) Jeong, J. H., Mok, H, Oh, Y.-K., and Park, T. G. (2009) siRNA conjugate delivery systems. *Bioconjugate Chem. 20*, 5−14.

Bioconjugate Chemistry

Article

pubs.acs.org/bc

Hyperbranched Glycopolymers for Blood Biocompatibility

Marya Ahmed,[†] Benjamin F. L. Lai,[‡] Jayachandran N. Kizhakkedathu,[‡,§] and Ravin Narain*[,†]

[†]Department of Chemical and Materials Engineering, Alberta Glycomics Centre, University of Alberta, Edmonton, Alberta, Canada

[‡]Department of Pathology and Laboratory Medicine and Centre for Blood Research, University of British Columbia, Vancouver, British Columbia, Canada

[§]Department of Chemistry, University of British Columbia, Vancouver, British Columbia, Canada

Supporting Information

ABSTRACT: Carbohydrate-based drug and gene delivery carriers are becoming extremely popular for in vitro and in vivo applications. These carriers are found to be nontoxic and can play a significant role in targeted delivery. However, the interactions of these carriers with blood cells and plasma components are not well explored. To the best of our knowledge, there are currently no reports that explore the role of carbohydrate based carriers for blood biocompatibility. Hyperbranched glycopolymers of varying molecular weights are synthesized by reversible addition−fragmentation chain transfer polymerization (RAFT) and are studied in detail for their biocompatibility, including hemocompatibility and cytotoxicity against different cell lines in vitro. The hemocompatibility studies (such as hemolysis and platelet activation) indicate that hyperbranched glycopolymers of varying molecular weights produced are highly hemocompatible and do not induce clot formation, red blood cell aggregation, and immune response. Hence, it can be concluded that glycopolymers functionalized carriers can serve as an excellent candidate for various biomedical applications. In addition, cytotoxicity of these hyperbranched polymers is studied in primary and malignant cell lines at varying concentrations using cell viability assay.

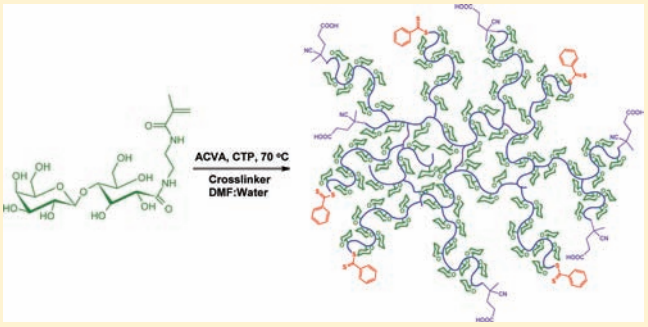

INTRODUCTION

Biocompatibility of polymers is directly related to their architecture, molecular weight, and surface chemistry.[1−5] Dendrimers and hyperbranched polymers hold great potential as gene or drug delivery agents because of their three-dimensional shapes and availability of a large number of surface functional groups amenable to various modification chemistries for drug conjugation and targeting purposes. The facile synthesis of hyperbranched polymers as compared to dendrimers makes them ideal structures for further studies for biological applications.[6−10] The nonspecific adsorption of proteins on foreign materials is a major event that activates a cascade of biochemical reactions leading to complement activation and inflammation.[2] The research in our laboratory shows that passivation of cationic polyplexes with linear glycopolymers or MPC segments significantly reduces the interaction of polyplexes with serum proteins while maintaining their higher cellular uptake and gene expression.[11,12] It is hypothesized that hyperbranched glycopolymers (due to the presence of a large number of functional units on the surface) should be efficient in preventing the protein adsorption and hence would not activate immune response.[13,14] Polyethylene glycol (PEG) is one of the most studied polymers to incorporate biocompatibility to foreign materials (including drug and gene delivery vectors);[15−17] however, the presence of PEG on a foreign material also decreases its interaction with living tissues, which is not desirable for many biomedical applications.[18] The carbohydrate-based cationic vectors have also been synthesized to decrease the toxicity of delivery carriers.[17] The natural polysaccharides such as chitosan and cellulose are used for a variety of biological applications such as in bone regeneration and hemodialysis; however, there are no reports that discuss the hemocompatible properties of synthetic hyperbranched glycopolymers. Starch and dextran based polymers and their scaffolds have also been studied for their toxicity profiles, and they are shown to be highly cell viable.[16,19] The improved biocompatibility of these polymers is associated with their high hydrophilicity.[9,16] Some synthetic hydrophilic polymers such as polyglycolic acid (PGA), poly(glycerol), polyanhydrides, and PEG are also synthesized and are studied to mimic the biocompatible properties of those materials. Linear and branched analogues of PEG have also been produced and are studied for their blood biocompatibility.[2,9,13] The synthesis of glycopolymers of controlled architectures and molecular weights is a novel and rapidly growing approach. The synthesis of hyperbranched glycopolymers has been reported by living radical polymerization (LRP).[10,20] However, their use for in vitro and in vivo applications is not well explored.

Received: February 12, 2012
Revised: April 11, 2012
Published: April 15, 2012

   dx.doi.org/10.1021/bc3000723 | *Bioconjugate Chem.* 2012, 23, 1050−1058

Scheme 1. Structures of Glycomonomers 3-Gluconamidopropylmethacrylamide (GAPMA) and 2-Lactobionamidoethylmethacrylamide (LAEMA), Cross-Linker (CL), Chain Transfer Agent (CTP), and Initiator (ACVA)

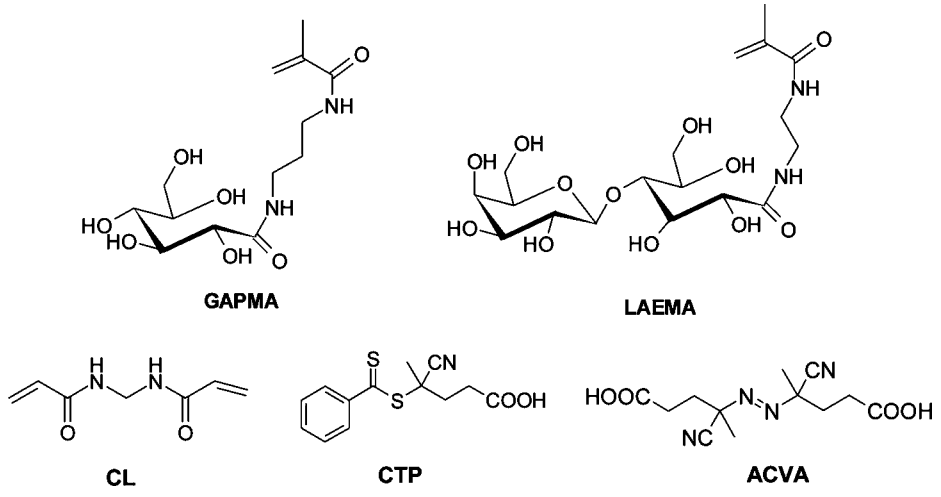

Scheme 2. Synthesis of Hyperbranched Glycopolymers via RAFT Polymerization

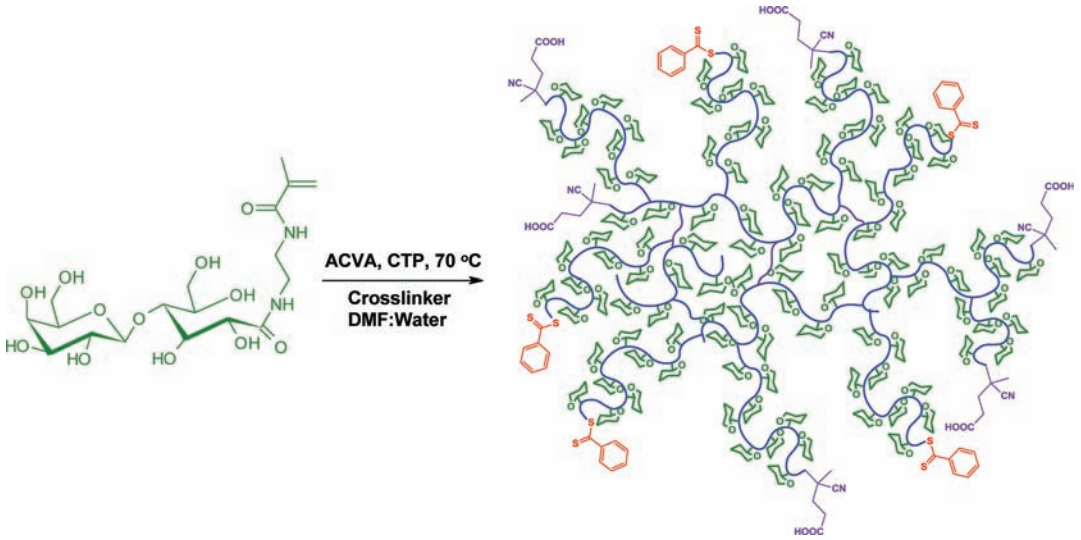

To the best of our knowledge, this is the first report where synthesis of hyperbranched carbohydrate based polymers of varying molecular weights (15−40 kDa) is reported by RAFT. The molecular weights of the polymers were carefully chosen, as cationic glycopolymers are shown to serve as excellent gene delivery vectors as a function of their molecular weights ranging from 5 to 40 kDa, compositions, and architectures.[11] Moreover, polymers having these molecular weights are expected to show high renal clearance during in vivo studies. The chemical structures of the glycomonomers, 3-glyconamidopropylmethacrylamide (GAPMA) and 2-lactobionamidoethylmethacrylamide (LAEMA), used to synthesize hyperbranched glycopolymers, are shown in Scheme 1. The schematics of polymerization of the glycomonomers via RAFT is depicted in Scheme 2.

These hyperbranched glycopolymers are then studied for their hemocompatibility and in vitro cell toxicity. Blood compatibility of the polymers is investigated by measuring the activation of coagulation system, activation of complement system, platelet activation, and their interaction with red blood cells in vitro. The cell toxicity of these carbohydrate based hyperbranched polymers is evaluated as a function of effective molecular weight and concentration in primary and malignant cell lines (adherent and suspension) using MTT assay.

MATERIALS AND METHODS

Materials. 4,4′-Azobis(4-cyanovaleric acid) (ACVA) and MTT assay kit were purchased from Sigma Aldrich. *N*,*N*′-Methylenebis(acrylamide) was obtained from Bio-Rad Laboratories. Cell culture Dulbecco's modified Eagle medium (DMEM, low glucose with L-glutamine and sodium pyruvate), RPMI medium with HEPES and L-glutamine, penicillin (10000 U/mL), and streptomycin (10 mg/mL), 0.25% trypsin, Dulbecco's modified phosphate buffer saline (DPBS), and fetal bovine serum (FBS) were obtained from Invitrogen.

Synthesis of Hyperbranched Glycopolymers. The monomers 3-gluconamidopropylmethacrylamide (GAPMA) and 2-lactobionamidoethylmethacrylamide (LAEMA) were synthesized according to previously reported protocols.[21,22] The hyperbranched glycopolymers of GAPMA) or LAEMA were synthesized at 70 °C in the presence of 4-cyanopentanoic acid dithiobenzoate (CTP) and 4,4′-azobis(4-cyanovaleric acid) (ACVA) as chain transfer agent and initiator, respectively. *N*,*N*′-Methylenebis(acrylamide) was used as a cross-linker. In a

dx.doi.org/10.1021/bc3000723 | *Bioconjugate Chem.* 2012, 23, 1050−1058

typical synthesis, GAPMA (0.25 g, 0.75 mmol) was dissolved in doubly distilled water (1.25 mL) followed by the addition of *N*,*N*′-methylenebis(acrylamide) (27.5 mg, 54 μmol), CTP (5 mg, 15 μmol), and ACVA (2 mg, 5 μmol) in 1 mL of DMF (targeted DP_n of 50, targeted molecular weight of 17 kDa). The mixture was purged with nitrogen for 30 min in a sealed reaction tube and was placed in an oil bath for polymerization under nitrogen atmosphere for 24 h. The polymerization was quenched using liquid nitrogen, and the polymer was precipitated in acetone. The product was extensively washed with methanol to remove the excess of monomers and was dried under vacuum. The number average molecular weight (M_n) and polydispersity (M_w/M_n) of the polymers was studied using a Viscotek conventional gel permeation chromatography (GPC) instrument connected to two Waters Ultrahydrogel linear WAT011545 columns (pore size, blend; exclusion limit of 7.0×10^6) and with a Viscotek model 250 dual detector. An acidic buffer of 0.50 M sodium acetate/0.50 M acetic acid was used as eluent. Calibration of the GPC instrument was done by six monodisperse pullulan standards (M_p of 5.9×10^3 to 212×10^3 g mol^{-1}). The chemical structures of hyperbranched polymers are confirmed using a Varian 500 ^1H NMR instrument.

Biological Experiments. Blood from healthy consented donors was collected in 3.8% sodium citrated tube with a blood/anticoagulant ratio of 9:1 or in an empty non-anticoagulant tube at Centre for Blood Research, University of British Columbia, Canada. Platelet-rich plasma (PRP) was prepared by centrifuging citrated whole blood samples at 150*g* for 20 min in an Allegra X-22R centrifuge (Beckman Coulter, Canada). Platelet-poor plasma (PPP) was prepared by centrifuging citrated whole blood samples at 1200*g* for 20 min. Serum was prepared by centrifuging nonanticoagulated whole blood samples at 1200*g* for 30 min.

All of the polymer samples and lyophilized products were dissolved in 150 mM saline solution. Reagents for conventional coagulation assays, such as actin FSL and recombinant thromboplastin, were purchased from Dade Behring (Marburg, Germany). Anti-CD62pPE and goat anti-mouse PE antibodies were purchased from Immunotech. GVB^{2+} (0.1% gelatin, 5 mM Veronal, 145 mM NaCl, 0.025% NaN_3 with 0.15 mM $CaCl_2$, and 0.5 mM $MgCl_2$, pH 7.3) and antibody-sensitized sheep erythrocytes (EA) were purchased from CompTech (Tyler, TX).

Stock concentrations of the polymers were diluted to 1, 10, and 50 mg/mL, with HEPES-buffered saline (10 mM HEPES in 150 mM saline, pH 7.4). One in ten dilutions of the polymer samples was made with plasma, whole blood, or serum in order to achieve final polymer concentrations 0.1, 1, and 5 mg/mL of the polymer, respectively.

Blood Coagulation Assays: Prothrombin Time (PT) and Activated Partial Thromboplastin Time (APTT). Sodium citrate anticoagulated PPP was used for PT and APTT analyses. The effect of polymers on the coagulation cascade was examined by mixing PPP with the polymer solution (9:1 v/v, 1 mg/mL final concentration) at 37 °C. Protamine in HEPES buffer solution was used as positive control, and PPP in HEPES buffer solution, as that in polymer solution, was used as a normal control. Coagulation initiation reagents actin FSL and recombinant thromboplastin were used for APTT and PT analyses, respectively. Each experiment was repeated in triplicate on the STart4 coagulometer (Diagnostica Stago, France) with plasma from two separate donors, and the average ± SD was reported.

Thromboelastography Analysis. Fresh whole blood in sodium citrate anticoagulant was mixed with different polymers for coagulation studies using Thromboelastograph hemostasis system 5000 (TEG) (from Haemoscope Corporation) at 37 °C. Whole blood added with identical volume of HEPES buffer was used as a normal control. TEG measures the clot's physical and kinetic properties by means of fibrin formation. In this study, citrated whole blood (360 μL) was mixed with 40 μL of polymer solution. Then 340 μL of this blood−polymer solution was transferred into the TEG cup. The TEG coagulation analysis was initiated by using 20 μL of 0.2 M calcium chloride solution. All TEG measurements were performed within 10 min of blood collection.

Platelet Activation Analysis. The level of platelet activation in PRP was quantified by flow cytometry. An amount of 90 μL of PRP was incubated with 10 μL of polymer solution (final concentrations of the polymer of 0.1, 1, and 5 mg/mL) at 37 °C. After 1 h, aliquots of the incubation mixtures were removed for assessment of the platelet activation. After 1 h of incubation, PRP/polymer mixture was diluted in HEPES buffer and was incubated with 5 μL of monoclonal anti-CD62P-PE (Immunotech) and with 5 μL of anti-CD62P-FITC for 20 min in the dark. The samples were then fixed with 0.5 mL of formalin solution. The level of platelet activation was analyzed in a BD FACSCanto II flow cytometer (Becton Dickinson) by gating platelets specific events based on their CD62P-FITC fluorescence and light scattering profile. Duplicate measurements were performed using PRP from two separate donors, and the average ± SD values were reported. PRP incubated with HEPES buffer was used as normal control, and PRP incubated with bovine thrombin (1 U/mL) (Sigma, Ontario, Canada) was used as positive control. PE conjugated goat anti-mouse IgG polyclonal antibodies (Immunotech) were used as the nonspecific binding control.

Complement Activation Analysis. The level of complement activation was measured by CH50 sheep erythrocyte lysis assay. A amount of 10 μL of polymer solutions was mixed with 90 μL of fresh serum for 1 h at 37 °C. The final concentrations of polymer in serum were 0.1, 1, and 5 mg/mL. Serum incubated with HEPES buffer was used as normal control. Heat-activated human IgG (1 mg/mL) and 5 mM EDTA solution in saline (5 mM) were used as positive and negative controls, respectively. After 1 h of incubation, 60 μL of this mixture was diluted with 120 μL of GVB^{2+} (CompTech), followed by the incubation of this mixture (75 μL) with 75 μL of antibody-sensitized sheep erythrocytes (CompTech). The reaction was stopped by addition of 300 μL of cold GVB-EDTA to each sample. The samples were centrifuged, and the optical density of supernatant at 540 nm was measured. Antibody-sensitized sheep erythrocytes incubated with distilled H_2O was used as 100% lysis control.

Red Blood Cell Morphology, Aggregation, and Hemolysis Studies. Red blood cell (RBC) morphology and aggregation were measured in whole blood incubated with different polymers at 37 °C. Washed RBCs were used for the hemolysis assay.

In RBC morphology study, an amount of 10 μL of polymer solutions was mixed with whole blood in the ratio 1:9 to obtain final polymer concentrations of 0.1, 1, and 5 mg/mL. The incubation mixtures were placed at 37 °C for 1 h. PEI (1 mg/mL) was used a positive control for the RBC aggregation study,

and HEPES buffer mixed whole blood was used as normal control. RBC morphology was assessed by examining the incubation mixture on a wet mounted slide with a bright field light microscope (Zeiss Axioskop 2 Plus, Carl Zeiss Microimaging Inc.). Color images were captured using the digital microscope camera (AxioCam ICc 1, Carl Zeiss Microimaging Inc.).

In the RBC hemolysis study, 30 μL of each of the polymer solutions was mixed with 270 μL of 10% hematocrit RBC suspension for 1 h at 37 °C. RBCs incubated with distilled H_2O were used as positive control (100% lysis). The percent of RBC lysis was measured by the Drabkin method.[6,7] Then 20 μL of the RBC/polymer mixture was added to 1 mL of Drabkin's solution and the optical density (OD) of the solution was measured using the spectrophotometer at 540 nm. The remaining RBC/polymer mixture was centrifuged, and 200 μL of the supernatant was added to 1 mL of Drabkin's solution. The OD of the solution was measured. The percent lysis was calculated using the following equation.

$$\%\,\text{lysis} = [(6 \times \text{OD of supernatant}) / (51 \times \text{OD of suspension})] \times 100$$

The values reported were from replicates measurements of two separate donor RBCs, and the average ± SD values were reported.

Tissue Culture. Human dermal fibroblasts (CRL-2522) isolated from human tissue[23] and Hep G2 were maintained in low glucose DMEM supplemented with 10% fetal bovine serum (FBS), 1% penicillin/streptomycin in a humidified atmosphere at 37 °C and 5% CO_2. HL-60 monocytes were maintained in RPMI medium supplemented with HEPES buffer and L-glutamine with 10% FBS and 1% antibiotic. The cells were maintained in humidified atmosphere at 37 °C and 5% CO_2. The cells were cultured at 80% confluency and were seeded in 96-well tissue culture plates to study the optimum cell density for MTT assay according to the manufacturer's protocol.

MTT Assay of Cell Viability. Human dermal fibroblasts (8000 cells/well) and Hep G2 cells (30 000 cells/well) were seeded in 96-well tissue culture plates in low glucose DMEM supplemented with 10% fetal bovine serum (FBS) and 1% antibiotic and were allowed to adhere overnight. HL-60 monocytes (40,000 cells/well) were seeded in 96-well tissue culture plates in RPMI medium with HEPES buffer and L-glutamine, supplemented with 10% FBS and 1% antibiotic. The cells were treated with varying concentrations of hyperbranched glycopolymers (0.1−5 mg/mL) for 24 h. Then 25 μL of MTT dye was added per well followed by the addition of 100 μL of lysis buffer, after the incubation of polymers with cells. The absorbance was read at 570 nm using TECAN plate reader. The untreated cells and medium alone were used as positive and negative controls, respectively. The percent cell viability was calculated: % cell viability = [(treated cells − negative control)/(untreated cells − negative control)] × 100.

RESULTS AND DISCUSSION

Hyperbranched Polymer Synthesis by RAFT Method. Synthetic polymers with pendent carbohydrate moieties are finding increasing use in the biomedical fields because of their high hydrophilicity, biological recognition, facile synthesis, low cost, and remarkable control over their physical and chemical properties.[10] These glycopolymers have been used as tools to investigate carbohydrate based interactions in living systems.[10] Hyperbranched glycopolymers, because of their facile synthesis, present an ideal alternative to glycodendrimers, with the presence of multivalent functional groups on the surface. A major aspect in the use of hyperbranched glycopolymers for biomedical applications is their biocompatibility.[14,16] Polysaccharides are reported to be biocompatible materials, and these macromolecules are now used in clinics to enhance the biocompatibility of surfaces and for drug and gene delivery applications. Therefore, synthetic carbohydrate based polymers hold great promise, as they are expected to show excellent biocompatibility. Polymers with branched architecture have low intrinsic viscosity because of their globular structure and high solubility with a high density of functional groups on their surface. This may affect their biological properties, including their interactions with blood components and their cytotoxicity.[1,16] Living radical polymerization allows the facile synthesis of hyperbranched polymers, with a better control over branching density, as the primary chains are near monodisperse. Living radical polymerization of monomers in the presence of a suitable cross-linker yields polymers ranging from stars to gels, depending upon the cross-linker concentrations. Stimuli responsive hyperbranched polymers are recently prepared by RAFT and are shown to possess temperature sensitive behavior.[10] In the present work, hyperbranched glycopolymers of varying molecular weights (M_n = 15−40 kDa) are synthesized by RAFT and are studied for their blood compatibility and cell toxicity. (Table 1, Supporting Information Figure S1). These hyperbranched polymers are synthesized at constant cross-linker concentration and are analyzed by gel permeation chromatography for their molecular weights and polydispersities. The hyperbranched polymers are further characterized using ^{1}H NMR (Supporting Information Figures S2 and S3).

Table 1. Synthesis of Hyperbranched Glycopolymers of Varying Effective Molecular Weights by Reversible Addition−Fragmentation Chain Transfer (RAFT) Polymerization Technique

polymer	cross-linker (mol %)	M_n (kDa)	polydispersity index
$P(LAEMA)_{51}$	7	24	1.74
$P(LAEMA)_{77}$	7	36	2.20
$P(GAPMA)_{59}$	7	19	2.0
$P(GAPMA)_{118}$	7	38	2.5

Blood Coagulation Analysis. *Prothrombin Time (PT) and Activated Partial Thromboplastin Time (APTT) Analysis.* The introduction of foreign material in the body leads to the deposition of plasma proteins on the surface, followed by the platelet adhesion and clot formation.[16] The polymers can also inhibit clot formation, similar to heparin or other highly anionic macromolecules. Blood coagulation pathways include both intrinsic and extrinsic pathways. Prothrombin time (PT) is used to evaluate extrinsic pathway. Thrombin is a proteolytic enzyme that converts fibrinogen to fibrin and helps in clot formation.[24] PT reflects the formation of clots in seconds after the addition of tissue thromboplastin to citrated platelet poor blood plasma.[16] Activated partial thromboplastin time (APTT) is used to evaluate intrinsic pathway and indicates the time in seconds required to make a clot after the addition of thromboplastin (in the presence of Ca^{2+} ions).[9] The blood coagulation in the presence of new hyperbranched glycopol-

dx.doi.org/10.1021/bc3000723 | Bioconjugate Chem. 2012, 23, 1050−1058

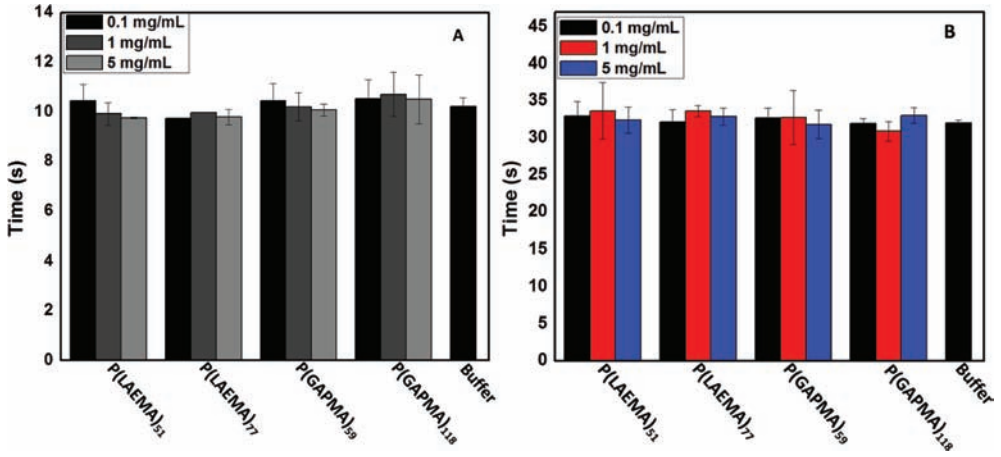

Figure 1. Effect of hyperbranched glycopolymers of varying effective molecular weights on prothrombin time (PT) (A) and activated partial prothrombin time (APTT) (B) at varying concentrations compared to buffer.

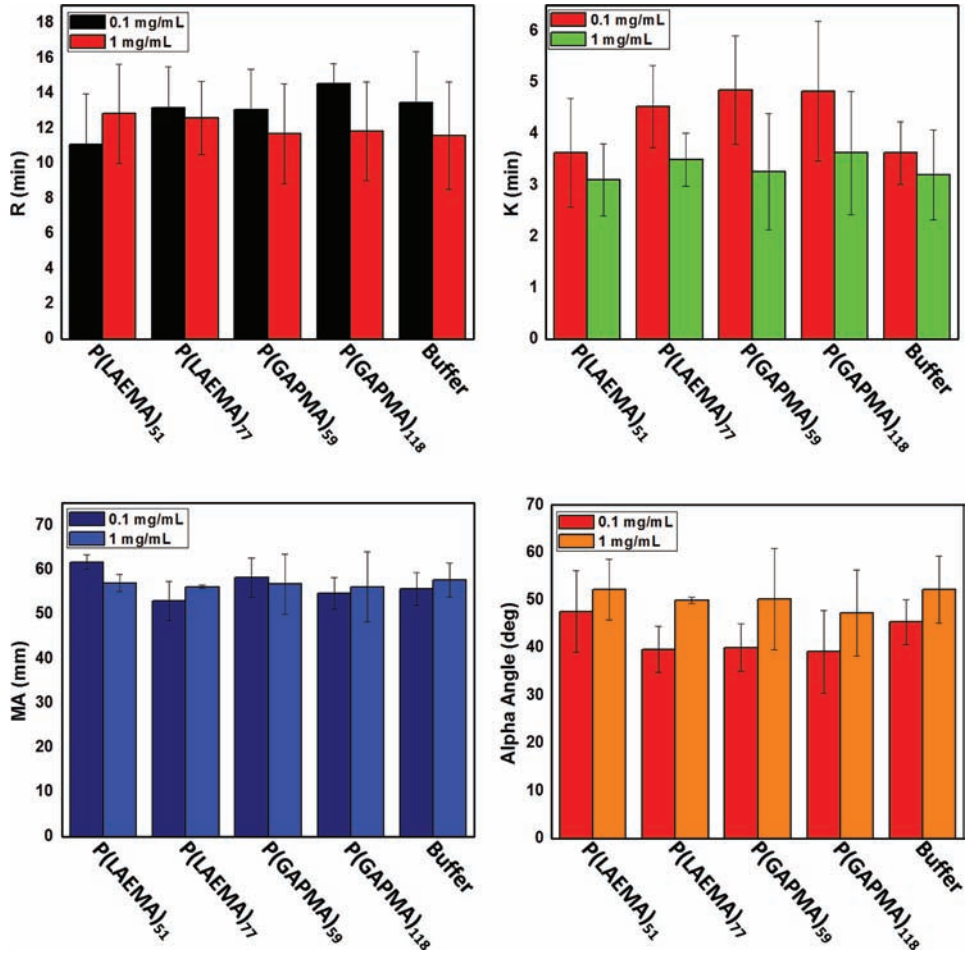

Figure 2. Effect of hyperbranched glycopolymers on thromboelastograph (TEG) parameters, compared to buffer control. The values given are the average ± SD from three independent measurements.

ymers is measured by PT and APTT assays to study whether they behave like anticoagulant or procoagulant.

The new hyperbranched glycopolymers show no significant change in PT values compared to the normal control (HEPES buffer) (Figure 1A). The effective molecular weights and the concentration of the glycopolymers do not have any influence. Similarly, APTT values are not affected in presence of various polymers at different concentrations (Figure 1B). Thus, it can be concluded that these hyperbranched polymers of varying molecular weights do not behave like anticoagulant or procoagulant under the conditions studied (0.1−5 mg/mL final concentrations). The results are in agreement with previous reports where the effect of hyperbranched polyglycerols on blood biocompatibility is studied, and it is found that branched polyglycerols of varying molecular weights do not impact the blood coagulation time.[1]

dx.doi.org/10.1021/bc3000723 | *Bioconjugate Chem.* 2012, 23, 1050−1058

Thromboelastography (TEG) Analysis. Plasma coagulation tests (PT, APTT) evaluate the rapidity of clot formation, while thrombelastography (TEG) monitors the kinetic changes in whole blood sample during clot formation (also a measure of clot strength), by monitoring its shear elasticity. TEG analysis is closer to in vivo conditions, as all the blood components are present during analysis and as initiation of coagulation is natural. The four parameters of TEG, namely, *R*, *K*, α, and MA are obtained. The reaction time, R-time, is the time from the start of sample run to the initiation of clot formation and is expressed in minutes. *K* is the time of start of clot formation (*R*) until the clot reached a fixed level of firmness. It measures the relationship between speed and clot strength. The α-angle is a measurement of rate of clot formation. MA measures the maximum strength or stiffness of the clot formed. The strength of clot is dependent on the contribution of two components of blood, fibrin and platelets. Increase in MA reflects in increased platelet functions and hence is a measure of platelet dysfunction or fibrin binding.[13] Hyperbranched glycopolymers of varying effective molecular weights are added to citrated whole blood at 0.1 and 1 mg/mL, and blood is recalcified to induce clot formation at 37 °C. The results are compared to HEPES buffer diluted whole blood as control. Our data show that all the new hyperbranched glycopolymers do not affect blood coagulation as a function of concentration (Figure 2).

There is no significant difference in TEG parameters compared to the control and to the normal values reported in the literature at both studied concentrations.[1] These results in combination with PT and APTT confirm that the presence of hyperbranched glycopolymers does not alter the coagulation of blood.

Platelet Activation. Activation of platelets involves the interaction of specific receptors on the plasma membrane of platelets with biomaterials, followed by the overexpression of P-selectin-CD62 on the surface of platelets. P-selectin CD62 is a glycoprotein presented on activated platelet cell surface. It plays a critical role in platelet mediated interactions with leukocytes and leads to thrombin generation.[1,25] The hyperbranched polymers are studied for platelet activation by measuring the expression of P-selectin CD62 on platelets surface using antibody based flow cytometry analysis. (Figure 3). Hyperbranched glycopolymers do not cause platelet activation at different concentrations or at different molecular weights.

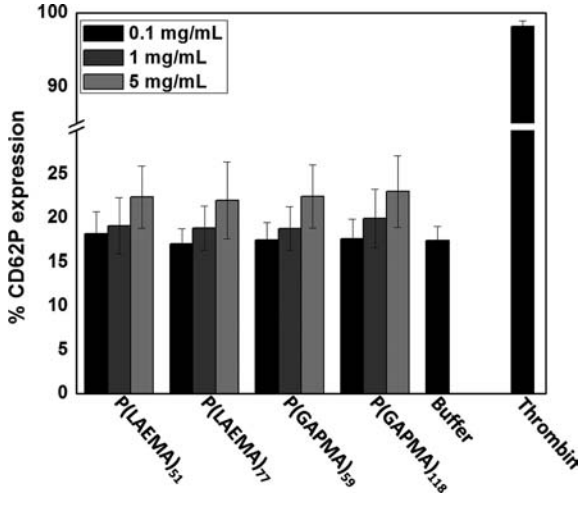

Figure 3. Platelet activation induced by hyperbranched polymers at varying concentrations, as determined by % CD62P expression.

Although a slight increase in platelet activation as a function of concentration is observed, the activation is not significant as determined from statistical analysis of data ($p > 0.05$). The thrombin activated platelets which show enhanced expression of CD62P on the surface of platelets (98%) are used as positive control. This shows that platelets used in the analysis have normal physiological function. The hyperbranched polymers show positive expression of P-selectin -CD62 ranging from 17% to 23%, and the expression is similar to that of the negative control. These results together with TEG analysis (no change in R-time as well as MA values) support that our hyperbranched glycopolymers do not influence the platelet functions. Thus, other analyses to investigate platelet function such as fibrinogen binding to platelets are not explored further.

Erythrocytes Aggregation and Hemolysis. The viscosity of the blood depends on a number of factors, including hematocrit, aggregation, and deformation of red blood cells. Aggregation of erythrocytes in the presence of plasma proteins is a common reversible process and is called "rouleaux". Nonreversible aggregation of erythrocytes in the presence of macromolecules increases the blood viscosity and is considered harmful for vital organs. PEG is a commonly used molecule for biomedical applications. High molecular weight PEG (40 kDa) is found to enhance the aggregation of red blood cells at a concentration as low as 1 mg/mL.[1] The hyperbranched glycopolymers of different concentrations (0.1, 1, and 5 mg/mL) are incubated with anticoagulated blood, and the effects on erythrocyte shape and aggregation are studied in vitro by optical microscopy (Figure 4).

The cationic polymers are known to aggregate erythrocytes, followed by their lysis. PEI is used as a positive control, which shows significant aggregation at 1 mg/mL for an incubation period of 1 h. In contrast, the new hyperbranched glycopolymers do not show significant aggregation of erythrocytes at all studied concentrations and are similar to the normal control samples (Figure 4). These results are similar to those for hyperbranched polyglycerols, which have no effect on erythrocytes aggregation. In contrast, hetastarch (a derivative of natural polysaccharide) is shown to significantly increase the viscosity and aggregation of RBCs.[1,13]

The membrane disruption ability of these hyperbranched polymers is then studied using hemolysis assay, and the amount of hemoglobin released is detected at 570 nm using the Drabkin method. Distilled water is used as a positive control, which shows 100% lysis of the cells at 37 °C. The hyperbranched glycopolymers of varying molecular weights at all the studied concentrations do not show any disruption of plasma membrane of red blood cells, and the percent red blood cell lysis is comparable to the normal control (HEPES buffer) (3−5%) (Figure 5).

These results are in agreement with the previous studies where hyperbranched polyglycerols are shown to have no effect on red blood cells aggregation and hemolysis.[1,13] Because of their biocompatible nature, the hyperbranched polyglycerols (HPGs) are shown to successfully graft the surface of red blood cells and hydrophobically modified HPGs are used as a human serum albumin substitute.[7,8] The nondisruptive property of hyperbranched glycopolymers further reflects their biocompatible nature.

Complement Activation. The complement system is the main immune-surveillance system in living species. Comple-

dx.doi.org/10.1021/bc3000723 | *Bioconjugate Chem.* 2012, 23, 1050−1058

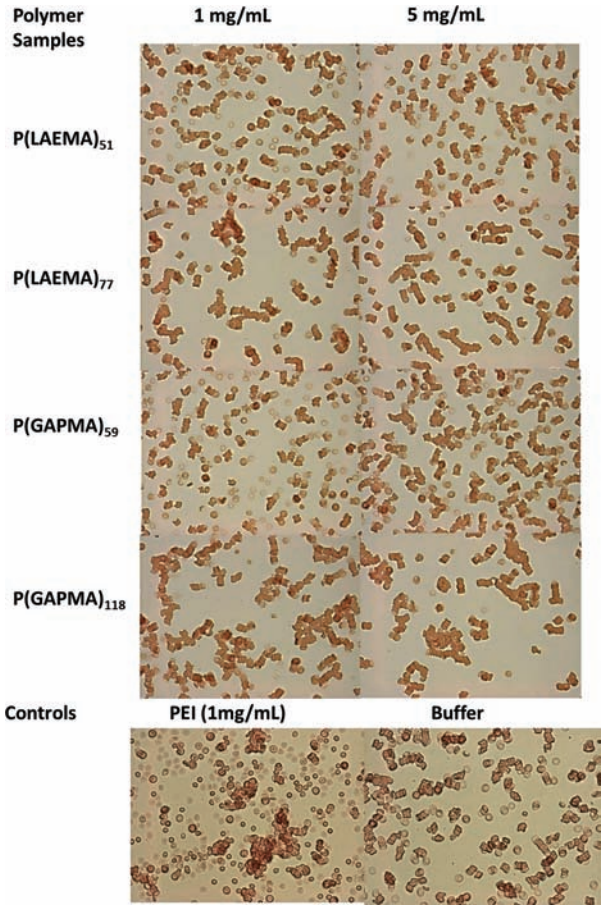

Figure 4. Erythrocytes aggregation in the presence of hyperbranched glycopolymers at 1 and 5 mg/mL. A cationic polymer, PEI, is used as a positive control.

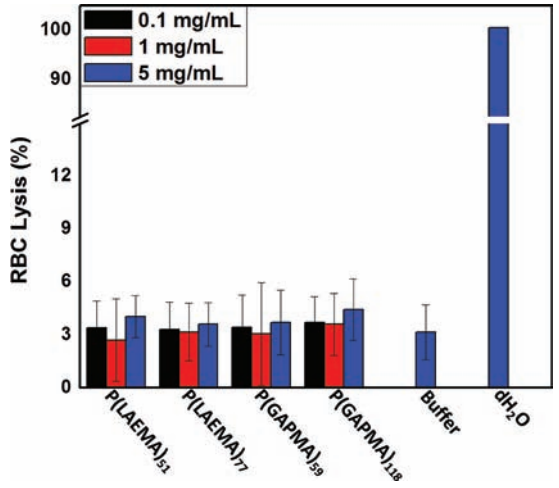

Figure 5. Effect of hyperbranched glycopolymer concentration on RBC hemolysis. HEPES buffer is used as a normal control, and distilled water (dH_2O) is used as positive control.

ment system and coagulation systems are two critical components that regulate hemostasis and innate immunity. The findings suggest that serine proteases of coagulation system are able to activate complement system. The coagulation factors are also known to cleave C3 and C5 to generate C3a and C5a. The generation of anaphylatoxin, C3a, C5a and complement consumption play a key role in complement activation.[1,26] Our results from blood coagulation analysis presented earlier (PT, APTT, and TEG analysis), clearly demonstrate that our hyperbranched polymers do not change the blood coagulation. Thus, we investigated whether our hyperbranched polymer can activate the complement system. We used a complement consumption analysis (CH50 assay) to study the complement activation by the hyperbranched glycopolymers synthesized by RAFT polymerization. The 50% hemolytic component assay (CH50) is a simple quantitative assay to determine the functioning of classical pathway of complement system. The CH50 assay depends on sequential activation of classical pathway components (C1−C9) to lyse antibody sensitized sheep erythrocytes.[27] The degree of cell lysis is proportional to the activity of classical complement pathway in serum.[28] Immunoglobulin G (IgG) and EDTA are used as positive and negative controls, respectively. IgG is the most common type of antibody, which is crucial for protection against pathogens and foreign substances. Aggregation of IgG in response to foreign elements activates the complement system via classical and alternative pathways. The addition of heat activated IgG in serum shows 100% complement consumption.[29] In contrast, hyperbranched polymers show very low complement consumption, and results are similar to those of buffer control. This indicates that the presence of hyperbranched glycopolymers at all studied concentrations (0.1−5 mg/mL) do not cause complement activation (Figure 6).

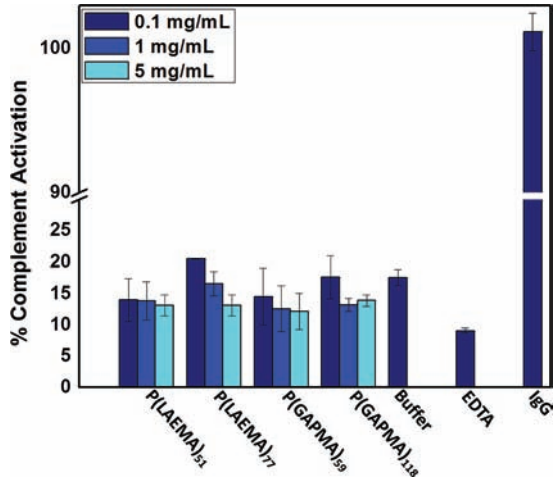

Figure 6. Percent complement consumption (% complement activation) caused by hyperbranched glycopolymers at different concentrations in serum after incubation for 1 h. IgG is used as a positive control, and EDTA is used as a negative control.

It is reported that the presence of nucleophiles such as hydroxyl groups on the surface of biomaterials activates clot formation because of the binding of C3b on the surface of biomaterials.[21] Most polymeric materials studied for biocompatibility purposes like dextran, Sephadex, regenerated cellulose, poly(methylmethacrylate), and poly(hydroxyethyl methacrylate) are known to activate complement system. Our soluble hyperbranched polymers do not show complement consumption and any changes in blood coagulation. Hence, our hyperbranched polymers are found to be neutral toward complement activation. Because of the low amount complement consumption, enzyme linked immunosorbent assay

dx.doi.org/10.1021/bc3000723 | Bioconjugate Chem. 2012, 23, 1050−1058

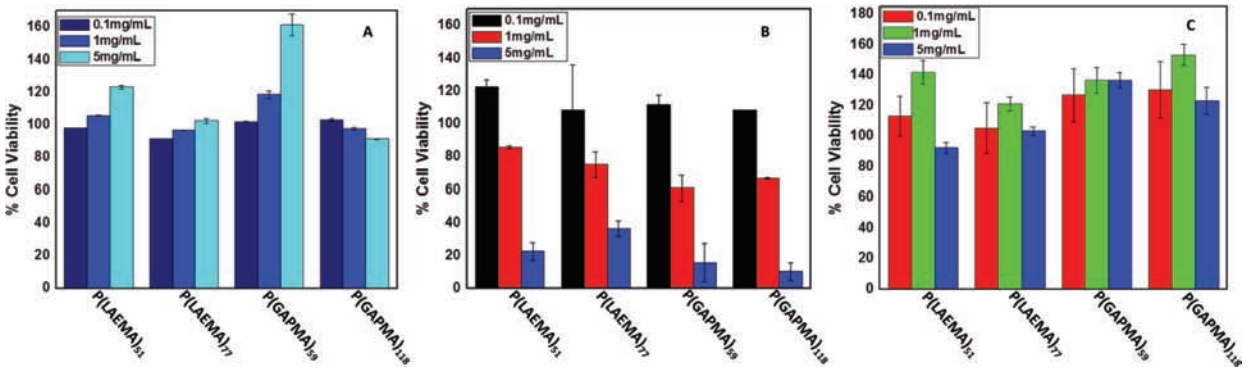

Figure 7. In vitro cell viability of hyperbranched glycopolymers at varying concentrations in human dermal fibroblasts (A), Hep G2 cells (B), and HL-60 leukemia cells (C), as determined by MTT assay after 24 h of incubation with cells.

(ELISA) is not performed to detect the presence of C3a or C5a, byproducts of complement activation.

Cytotoxicity of Hyperbranched Polymers. The cytotoxicity of hyperbranched polymers in human cell lines is determined using MTT assay. Human dermal fibroblasts (CRL-2522), (primary adherent cells), leukemia cells (HL-60) (malignant suspension cells), and hepatocytes (HepG2, malignant adherent cells) are used for this purpose. The hyperbranched polymers are incubated with varying concentrations of polymer for 24 h with different cell lines, and mitochondrial activity of cells is determined by the production of formazan crystal. The results show that cytotoxicity of hyperbranched polymers is dependent on the concentration of polymers as well as on the type of cell line used for the study (Figure 7).

The fibroblasts and HL-60 leukemia cells show less sensitivity toward the presence of hyperbranched glycopolymers of all studied effective molecular weights over the period of 24 h, as shown in Figure 7. In general, hyperbranched glycopolymers show no toxicity in fibroblasts up to 5 mg/mL, regardless of the molecular weights of polymers. These results are similar to the previously reported data, where dermal fibroblasts are found to be less sensitive toward the presence of polyglycerols.[1,13] In contrast, Hep G2 cells (malignant hepatoma cells) show high sensitivity toward hyperbranched glycopolymers as a function of concentration of polymers studied. At low concentration (0.1 mg/mL) of these polymers the cell viability is not compromised; however, at high concentrations a proportional decrease in cell viability has been observed, regardless of the effective molecular weight and type of carbohydrate studied. The high toxicity of these hyperbranched glycopolymers is not dependent upon their molecular weights. In this study, two different types of glycopolymers are studied for their toxicity as a function of their effective molecular weights. It is found that both glucose and galactose derived hyperbranched glycopolymers show similar cytotoxic profiles in all studied cell lines, and no change in toxicity as a function of carbohydrate types or effective molecular weights is observed. Some preliminary results in our lab show that glucose and galactose derived polymers are both well uptaken by hepatocytes. These results are further supported by this toxicity profile in Hep G2 cells, where all hyperbranched glycopolymers show similar toxicity profiles. HepG2 cell line is a cancer cell line with overexpressed ASGP-R receptors (50000−150000) on the surface of the cells. The high toxicity of the hyperbranched glycopolymers toward Hep G2 cells might be associated with their high interactions with those glycoproteins. Hence, this high sensitivity of malignant hepatocytes toward hyperbranched glycopolymers is expected to be due to the high receptor mediated uptake of these polymers in Hep G2 as compared to other cell lines studied. These results are also consistent with a previous work, where sugar modified methacrylate based polymers were studied for their uptake in hepatocytes.[30] The study showed that all saccharide conjugates were well uptaken in Hep G2 cells. However, the binding affinities of ASGPR with copolymers were dependent upon the extent of glycosylation and the three-dimensional arrangement of galactose residues on the surface of glycoprotein.[30] Further mechanistic studies are required to explore the toxicity issues of these hyperbranched glycopolymers toward hepatocytes. In vivo studies in mice model are currently underway to confirm the toxicity of these glycopolymers to cancer liver cells.

■ CONCLUSION

The synthesis of hyperbranched glycopolymers of varying molecular weights is obtained by RAFT method, and these polymers are further studied for their biocompatibility. The biological evaluation of these hyperbranched polymers using blood coagulation assays, hemolysis assays, platelet and complement activation analysis, and in vitro cytotoxicity assays confirms their biocompatibility. It is found that at all studied concentrations, hyperbranched glycopolymers of effective molecular weights ranging from 15 to 38 kDa are hemocompatible in vitro. The cytotoxicity of these polymers is found to be dependent on the type of cell line used as well as on the concentration of polymers. The fibroblasts (primary cells) and leukemia cells show less toxicity in response to hyperbranched polymers, as compared to Hep G2 cells. In future, statistical hyperbranched glycopolymers containing ionic or hydrophobic moieties will be synthesized and their biocompatibility will be studied in detail.

■ ASSOCIATED CONTENT

Ⓢ Supporting Information

GPC data for the hyperbranched polymers and ^{1}H NMR specta. This material is available free of charge via the Internet at http://pubs.acs.org.

■ AUTHOR INFORMATION

Corresponding Author

*Phone: (780) 492-1736 or (780) 492 6101. Fax: (780) 492-2881. E-mail: narain@ualberta.ca.

Notes

The authors declare no competing financial interest.

■ ACKNOWLEDGMENTS

The authors acknowledge support from Natural Sciences and Engineering Research Council of Canada (NSERC) for the funding for this work. The authors also thank Dr. Hasan Uludag for providing human dermal fibroblasts and leukemia cell line. J.N.K. thanks Canadian Institutes of Health Research and Canadian Blood Services for support. J.N.K. thanks infrastructure facilities supported by the Canadian Foundation for Innovation (CFI) and the MSFHR at Centre for Blood Research. J.N.K. also acknowledges the Michael Smith Foundation for Health Research (MSFHR) Career Scholar Award.

■ REFERENCES

(1) Kainthan, R. K., Hester, S. R., Levin, E., Devine, D. V., and Brooks, D. E. (2007) In vitro biological evaluation of high molecular weight hyperbranched polyglycerols. *Biomaterials 28*, 4581−4590.

(2) Frey, H., and Haag, R. (2002) Dendritic polyglycerols: a new versatile biocompatible material. *Rev. Mol. Biotechnol. 90*, 257−267.

(3) Saad, B., Keiser, O. M., Welti, M., Uhlschmid, G. K., Neuenschwander, P., and Suter, U. W. (1997) Multiblock copolyesters as biomaterials: in vitro biocompatibility testing. *J. Mater. Sci.: Mater. Med. 8*, 497−505.

(4) Belanger, M.-C., and Marois, Y. (2001) Hemocompatibility, biocompatibility, inflammatory and in vivo studies of primary reference materials low density poly(ethylene) and poly(dimethylsiloxane): a review. *J. Biomed. Mater. Res. 58*, 467−477.

(5) Malik, N., Wiwattanapatapee, R., Kolpsch, R., Lorenz, K., Frey, H., Weener, J. W., Meijer, E. W., Paulus, W., and Duncan, R. (2000) Dendrimers: relationship between structure and biocompatibility in vitro, and preliminary studies on the biodistribution of I^{125}-labelled polyamidoamine dendrimers in vivo. *J. Controlled Release 65*, 133−148.

(6) Rossi, N. A. A., Mustafa, I., Jackson, J. K., Burt, H. M., Horte, S. A., Scott, M. D., and Kizhakkedathu, J. N. (2009) In vitro chelating, cytotoxicity, and blood compatibility of degradable poly-(ethyleneglycol)-based macromolecular iron chelators. *Biomaterials 30*, 638−648.

(7) Rossi, N. A. A., Constantinescu, I., Kainthan, R. K., Brooks, D. E., Scott, M. D., and Kizhakkedathu, J. N. (2010) Red blood cell membrane grafting of multi-functional hyperbranched polyglycerols. *Biomaterials 31*, 4167−4178.

(8) Kainthan, R. K., Janzen, J., Kizhakkedathu, J. N., Devine, D. V., and Brooks, D. E. (2008) Hydrophobically derivatized hyperbranched polyglycerol as a human serum albumin substitute. *Biomaterials 29*, 1693−1704.

(9) Kainthan, R. K., Ganamani, M., Ganguli, M., Ghosh, T., Brooks, D. E., Maiti, S., and Kizhakkedathu, J. N. (2006) Blood compatibility of novel water soluble hyperbranchedpolyglycerol-based multivalent cationic polymers and their interaction with DNA. *Biomaterials 27*, 5377−5390.

(10) Muthukrishnan, S., Mori, H., and Muller, E. H. A. (2005) Synthesis and characterization of methacrylate-type hyperbranched glycopolymers via self-condensing atom transfer radical copolymerization. *Macromolecules 38*, 3108−3119.

(11) Ahmed, M., and Narain, R. (2011) The effect of polymer architecture, composition, and molecular weight on the properties of glycopolymer-based non-viral gene delivery systems. *Biomaterials 32*, 5279−5290.

(12) Ahmed, M., Bhuchar, N., and Narain, R. (2011) Well-controlled cationic water-soluble phospholipid polymer−DNA nanocomplexes for gene delivery. *Bioconjugate Chem. 22*, 1228−1238.

(13) Kainthan, R. K., Janzen, J., Levin, E., Devine, D. V., and Brooks, D. E. (2006) Biocompatibility testing of branched and linear polyglycidol. *Biomacromolecules 7*, 703−709.

(14) Chen, H., Yuan, L., Song, W., Wu, Z., and Li, D. (2008) Biocompatibility testing of branched and linear polyglycidol. *Prog. Polym. Sci. 33*, 1059−1087.

(15) Siegers, C., Biesalski, M., and Haag, R. (2004) Self-assembled monolayers of dendritic polyglycerol derivatives on gold that resist the adsorption of proteins. *Chem.—Eur. J. 10*, 2831−2838.

(16) Wang, Y.-X., Robertson, J. L., Spillman, W. B., Jr., and Claus, R. O. (2004) Effects of the chemical structure and the surface properties of polymeric biomaterials on their biocompatibility. *Pharm. Res. 21*, 1362−1373.

(17) Mintzer, A. M., and Simanek, E. E. (2009) Nonviral vectors for gene delivery. *Chem. Rev. 109*, 259−302.

(18) Lutz, J.-F. (2008) Polymerization of oligo(ethylene glycol) (meth)acrylates: toward new generations of smart biocompatible materials. *J. Polym. Sci., Part A: Polym. Chem. 46*, 3459−3470.

(19) Marques, A. P., Reis, R. L., and Hunt, J. A. (2002) The biocompatibility of novel starch-based polymers and composites: in vitro studies. *Biomaterials 23*, 1471−1478.

(20) Sevastianov, V. I., and Tseytlina, E. A. (1984) The activation of the complement system by polymer materials and their blood compatibility. *J. Biomed. Mater. Res. 18*, 969−978.

(21) Deng, Z., Ahmed, M., and Narain, R. (2008) Novel well-defined glycopolymers synthesized via the reversible addition fragmentation chain transfer process in aqueous media. *J. Polym. Sci., Part A: Polym. Chem. 46*, 4984−4996.

(22) Deng, Z., Li, S., Jiang, X., and Narain, R. (2009) Well-define galactose-containing multifunctional copolymers and glyconanoparticles for biomolecular recognition processes. *Macromolecules 42*, 6393−6405.

(23) Wang, J., Dodd, C., Shankowsky, H. A., Scott, P. G., Tredget, E. E., and Wound Healing Research Group. (2008) Deep dermal fibroblasts contribute to hypertrophic scarring. *Lab. Invest. 88*, 1278−1290.

(24) Luzon, M., Boyer, C., Peinado, C., Corrales, T., Whittaker, M., Tao, L., and Davis, P. T. (2010) Water-soluble, thermoresponsive, hyperbranched copolymers based on PEG-methacrylates: synthesis, characterization, and LCST behavior. *J. Polym. Sci., Part A: Polym. Chem. 48*, 2783−2792.

(25) Gorbet, M. B., and Sefton, M. V. (2004) Biomaterial-associated thrombosis: roles of coagulation factors, complement, platelets and leukocytes. *Biomaterials 25*, 5681−5703.

(26) Amara, U., Rittirsch, D., Flierl, M., Bruckner, U., Klos, A., Gebhard, F., Lambris, J. D., and Huber-Lang, M. (2008) Interaction between the coagulation and complement system. *Adv. Exp. Med. Biol. 632*, 71−79.

(27) Sohn, H.-J., Kaplan, H. J., Suk, H.-J., Bora, P. S., and Bora, N. S. (2000) Complement regulatory activity of normal human intraocular fluid is mediated by MCP, DAF, and CD59. *Invest. Ophthalmol. Visual Sci. 41*, 4195−4202.

(28) Jaskowski, T. D., Martins, T. B., Litwin, C. M., and Hill, H. R. (1999) Comparison of three different methods for measuring classical pathway complement activity. *Clin. Diagn. Lab. Immunol. 6*, 137−139.

(29) Avirutnan, P., Mehihop, E., and Diamond, M. S. (2008) Complement and its role in protection and pathogenesis of flavivirus infections. *Vaccines 26S*, 1100−1107.

(30) David, A., Kopeckova, P., Rubinstein, A., and Kopecek, J. (2001) Enhanced biorecognition and internalization of HPMA copolymers containing multiple or multivalent carbohydrate side-chains by human hepatocarcinoma cells. *Bioconjugate Chem. 12*, 890−899.

Bioconjugate Chemistry

Article

pubs.acs.org/bc

Peripheral Functionalization of Dendrimers Regulates Internalization and Intracellular Trafficking in Living Cells

Lorenzo Albertazzi,*[,∥,†,‡,#] Marcos Fernandez-Villamarin,[§,#] Ricardo Riguera,[§] and Eduardo Fernandez-Megia*[,§]

[†]NEST, Scuola Normale Superiore and Istituto Nanoscienze-CNR, I-56127 Pisa, Italy

[‡]IIT@NEST, Center for Nanotechnology Innovation, Pisa, Italy

[§]Department of Organic Chemistry and Center for Research in Biological Chemistry and Molecular Materials (CIQUS), University of Santiago de Compostela, Jenaro de la Fuente s/n, 15782 Santiago de Compostela, Spain

Supporting Information

ABSTRACT: GATG (gallic acid-triethylene glycol) dendrimers represent appealing nanostructures for biomedical applications. The incorporation of specific ligands and targeting and imaging agents on their surface has resulted in promising tools in diagnosis and drug delivery. With the aim to further explore the versatility of GATG dendrimers in the biomedical field, in this work we study the effect of peripheral substitution on their uptake and intracellular trafficking in living cells. To this end, peripheral groups with different physicochemical properties and biological relevance have been installed on the surface of GATG dendrimers, and their interactions, uptake efficacy, and specificity for certain cell populations studied by confocal microscopy. Finally, this information was used to design a pH-sensitive drug delivery system for the selective release of cargo molecules inside cells after lysosomal localization. These results along with the easy functionalization and modular architecture of GATG dendrimers reveal these systems as promising nanotools in biomedicine.

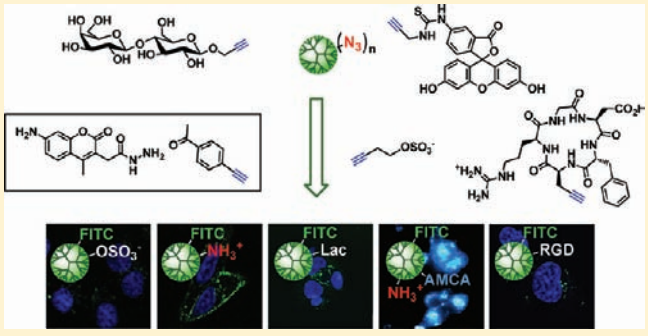

INTRODUCTION

Dendrimers are promising nanostructures for biomedical applications such as drug and gene delivery, diagnosis, and biosensing.[1−4] Their characteristic monodispersity and tree-like structure endows dendrimers with unique properties such as controlled physicochemical properties and globular morphology. In addition, their inherent multivalency allows for the display of specific ligands, drugs, targeting, and imaging agents.[5−9] The Vögtle "cascade synthesis" constituted the first strategy toward dendritic structures.[10] This was followed by reports on polyamidoamine (PAMAM) dendrimers by Tomalia[11] and arborols by Newcome.[12] Since then, alternative dendritic architectures and synthetic strategies have been proposed in the search of novel and improved properties.[13−16]

Our group has recently reported on the preparation of dendrimers and their block copolymers with poly(ethylene glycol) (PEG), that incorporate a gallic acid-triethylene glycol repetition unit (GATG dendrimers) ([G*n*]-N_3 and PEG-[G*n*]-N_3, where *n* is the generation number, Scheme 1).[17−20] These structures are characterized by peripheral azides which facilitate their direct surface functionalization by means of the Cu(I)-catalyzed azide−alkyne cycloaddition (CuAAC).[21,22] Alternatively, reduction of the azides by hydrogenation or Staudinger reaction affords terminal amino groups which can be further elaborated by classical means (e.g.; amide or thiourea formation, reductive amination). The incorporation of the PEG chain in the block copolymers pursues to improve the biocompatibility, solubility, and biodistribution of the final conjugates.[23,24] GATG dendrimers and block copolymers have emerged as promising tools for bioapplications, such as the study of the multivalent carbohydrate−receptor interaction[25] and the dynamics of glycodendrimers,[26] or the preparation of drug and gene delivery nanosystems.[27,28] More recently, GATG dendrimers have been also developed as contrast agents for MRI[29] and as inhibitors of the dimerization of the capsid protein of HIV-1.[30]

With the aim of further exploring the versatility of GATG dendrimers as tools in the biomedical field, in this work we exploit their easy click functionalization to synthesize a small library of dendrimers and PEG-dendritic block copolymers carrying different peripheral groups, and we evaluate their behavior in living cells. Two series of dendritic systems were studied: one peripherally functionalized with charged/neutral groups having different physicochemical properties, and another one decorated with biologically relevant ligands such as carbohydrates and peptides. Confocal microscopy was used

Received: February 16, 2012
Revised: March 22, 2012
Published: April 7, 2012

Scheme 1

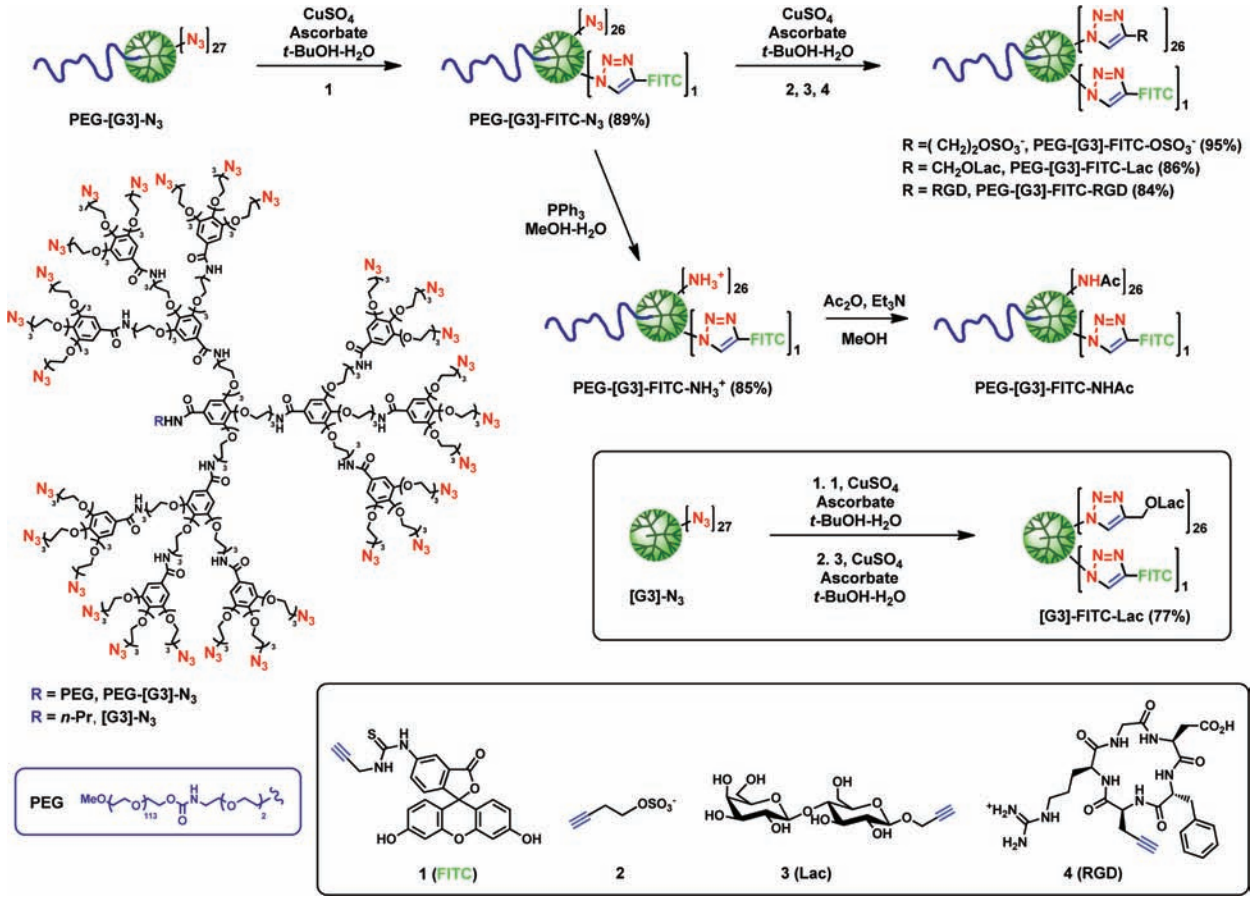

to study the effect of functionalization on cell-uptake and intracellular trafficking, both properties of particular interest in drug delivery and other biomedical applications. Finally, this information was used to design a tailored carrier for the intracellular delivery and selective release of biologically active molecules. A PEG-dendritic copolymer carrying cargo molecules bound through a pH-sensitive linker was designed for selective cell uptake and release after lysosomal localization. The performance of this system was evaluated with a double fluorescent-labeling allowing for simultaneous monitoring the localization of the dendritic carrier and payload molecules.

EXPERIMENTAL SECTION

Materials and Methods. $CuSO_4 \cdot 5H_2O$ and sodium bicarbonate were obtained from Prolabo. 4′-Ethynyl acetophenone and sodium ascorbate were purchased from Acros Organics. AMCA-hydrazide (AMCA, aminomethylcoumarin acetate) was purchased from Pierce Thermo Fisher Scientific. Triphenylphosphine and *t*-butanol were obtained from Sigma-Aldrich. PEG_{5000}-[G3]-N_3[17] and [G3]-N_3[18] were prepared following procedures previously described by our group. Alkynated fluorescein (FITC) (**1**),[31] sodium 3-butyn-1-sulfate (**2**),[27] and 2-propynyl β-D-lactopyranoside (**3**)[18] were prepared following reported procedures. Alkynated RDG peptide cyclo(RGDfPra) (**4**) was purchased from Peptide Synthetics. H_2O was of Milli-Q grade. All other reagents were of analytical grade. Ultrafiltration was performed on Amicon stirred cells with Amicon YM3 membranes. NMR spectra were recorded on a Bruker DRX 500 MHz and Varian Mercury 300 MHz spectrometers. Chemical shifts are reported in ppm (δ units) downfield from internal tetramethylsilane ($CDCl_3$), the HOD solvent peak (D_2O), or residual solvent peak (DMSO-d_6). Resonances corresponding to FITC are only visible when spectra recorded in DMSO-d_6. UV−vis spectra were performed on a HP 8452A Diode Array and Jasco V-630 spectrophotometers. FT-IR spectra were recorded on a Bruker IFS-66v (neat samples, CsI window) or a Varian 670-IR equipped with a Varian 610-IR microscope.

Synthesis and Labeling. *PEG-[G3]-FITC-N_3.* PEG-[G3]-N_3 (15 mg, 1.15 μmol) was dissolved in *t*-BuOH (0.16 mL) and H_2O (0.12 mL). Then, alkynated FITC **1** (1.5 mg, 3.46 μmol) and freshly prepared aqueous solutions of $NaHCO_3$ (7 μL, 6.92 μmol, 1 M), $CuSO_4$ (14 μL, 0.69 μmol, 0.05 M), and sodium ascorbate (17 μL, 3.46 μmol, 0.2 M) were added. The resulting mixture was stirred at rt for 48 h, and then was purified by ultrafiltration (H_2O, 5 × 30 mL) to afford PEG-[G3]-FITC-N_3 (13.9 mg, 89%) as an orange foam. ^{1}H NMR (500 MHz, DMSO-d_6) δ: 8.54 (s, 1.2H), 8.50−8.39 (m, 10.8H), 7.25−7.10 (m, 26H), 4.50−3.93 (m, 82H), 3.88−3.43 (m, ∼808H), 3.25 (s, 3H), 3.13−3.04 (m, 2H); (methylene protons adjacent to the azide groups are buried by the H_2O signal). IR (KBr, cm^{-1}): 3278, 2871, 2106, 1112. UV−vis (H_2O) λ_{max}: 296, 490 nm. UV−vis (DMSO) λ_{max}: 520 nm. An average of 1.2 fluorescein molecules in PEG-[G3]-FITC-N_3 was determined by absorbance at 520 nm in DMSO, applying an extinction coefficient of 60 800 M^{-1} cm^{-1}. Same functionalization degree was obtained by integration of the triazol protons at 8.54 ppm in the ^{1}H NMR (DMSO-d_6) spectrum.

dx.doi.org/10.1021/bc300079h | Bioconjugate Chem. 2012, 23, 1059−1068

PEG-[G3]-FITC-NH_3^+. PPh_3 (9.5 mg, 34.0 μmol) was added to a solution of PEG-[G3]-FITC-N_3 (13.9 mg, 1.03 μmol) in 2% H_2O/MeOH (1.0 mL). The resulting mixture was stirred at rt for 12 h. After addition of aqueous HCl (21 μL, 0.1 M), reaction was purified by ultrafiltration (50% MeOH/H_2O, 5 × 30 mL) to afford PEG-[G3]-FITC-NH_2·HCl (12.2 mg, 85%) as an orange foam. ^{1}H NMR (500 MHz, D_2O) δ: 7.21−7.08 (m, 26H), 4.32−4.07 (m, 80H), 3.98−3.50 (m, ∼805H), 3.43 (s, 3H), 3.29−3.18 (m, 54H). IR (ICs window, MeOH, cm^{-1}): 2924, 1109. UV−vis (H_2O) λ_{max}: 298, 490 nm. Peracetylation of this material with excess Ac_2O in the presence of Et_3N in MeOH (overnight, rt) afforded PEG-[G3]-FITC-NHAc after purification by extensive dialysis against H_2O (MWCO 10 KDa).

PEG-[G3]-FITC-OSO_3^-. PEG-[G3]-FITC-N_3 (13.2 mg, 0.97 μmol) was dissolved in *t*-BuOH (0.13 mL) and H_2O (0.07 mL). Then, sulfate **2** (9.1 mg, 52.6 μmol) and freshly prepared aqueous solutions of $CuSO_4$ (26 μL, 1.32 μmol, 0.05 M) and sodium ascorbate (33 μL, 6.58 μmol, 0.2 M) were added. The resulting mixture was stirred at rt for 48 h, and then was purified by ultrafiltration (H_2O, 5 × 30 mL) to afford PEG-[G3]-FITC-OSO_3Na (16.7 mg, 95%) as an orange foam. ^{1}H NMR (500 MHz, D_2O) δ: 8.14−7.83 (m, 27H), 7.30−7.00 (m, 26H), 4.62−4.50 (m, 54H), 4.47−4.01 (m, 132H), 4.00−3.49 (m, ∼803H), 3.42 (s, 3H), 3.28−3.22 (m, 2H), 3.14−2.90 (m, 52H). IR (ICs window, neat, cm^{-1}): 3312, 2874, 1105. UV−vis (H_2O) λ_{max}: 296, 490 nm.

PEG-[G3]-FITC-Lac. PEG-[G3]-FITC-N_3 (12.4 mg, 0.92 μmol) was dissolved in *t*-BuOH (0.12 mL) and H_2O (0.07 mL). Then, lactoside **1** (19.6 mg, 49.4 μmol) and freshly prepared aqueous solutions of $CuSO_4$ (25 μL, 1.24 μmol, 0.05 M) and sodium ascorbate (31 μL, 6.18 μmol, 0.2 M) were added. The resulting mixture was stirred at 65 °C for 60 h, and then was purified by ultrafiltration (H_2O, 5 × 30 mL) to afford PEG-[G3]-FITC-Lac (18.6 mg, 86%) as an orange foam. ^{1}H NMR (500 MHz, D_2O) δ: 8.09−8.00 (m, 27H), 7.13−6.96 (m, 26H), 4.61−4.37 (m, 106H), 4.24−3.42 (m, ∼1164H), 3.38 (s, 3H), 3.31−3.24 (m, 28H); (anomeric protons in lactose residues are buried by the HOD signal). IR (KBr, cm^{-1}): 3392, 2876, 1112. UV−vis (H_2O) λ_{max}: 300, 490 nm.

[G3]-FITC-Lac. [G3]-N_3 (15 mg, 1.91 μmol) was dissolved in *t*-BuOH (0.26 mL) and H_2O (0.19 mL). Then, alkynated FITC **1** (2.6 mg, 5.73 μmol) and freshly prepared aqueous solutions of $NaHCO_3$ (12 μL, 11.5 μmol, 1 M), $CuSO_4$ (23 μL, 1.15 μmol, 0.05 M), and sodium ascorbate (29 μL, 5.73 μmol, 0.2 M) were added. After 48 h of stirring at rt, lactoside **1** (40.9 mg, 0.103 mmol) and additional portions of $CuSO_4$ (14 μL, 1.43 μmol, 0.1 M) and sodium ascorbate (14 μL, 7.16 μmol, 0.5 M) were added. The resulting mixture was stirred at 65 °C for 48 h, and then was purified by ultrafiltration (H_2O, 5 × 30 mL) to afford [G3]-FITC-Lac (27.3 mg, 77%) as an orange foam. ^{1}H NMR (500 MHz, D_2O) δ: 8.20−7.97 (m, 27H), 7.25−6.85 (m, 26H), 4.94−4.85 (m, 26H), 4.76−4.69 (m, 26H), 4.61−4.38 (m, 106H), 4.18−3.39 (m, 700H), 3.36−3.27 (m, 26H), 3.26−3.19 (m, 2H), 1.60−1.45 (m, 2H), 0.94−0.81 (m, 3H). IR (KBr, cm^{-1}) 3418, 2925, 1077. UV−vis (H_2O) λ_{max}: 262, 495 nm. UV−vis (DMSO) λ_{max}: 520 nm. An average of 1.0 fluorescein molecules in [G3]-FITC-Lac was determined by absorbance at 502 nm in 50% DMSO/H_2O, applying an extinction coefficient of 61 000 M^{-1} cm^{-1}.

PEG-[G3]-FITC-RGD. PEG-[G3]-FITC-N_3 (2 mg, 0.15 μmol) was dissolved in *t*-BuOH (20 μL). Then, alkynated RGD peptide **4** (5.5 mg, 7.97 μmol) and freshly prepared aqueous solutions of $CuSO_4$ (10 μL, 0.20 μmol, 0.02 M) and sodium ascorbate (10 μL, 1.02 μmol, 0.1 M) were added. The resulting mixture was stirred at 65 °C for 60 h, and then was purified by ultrafiltration [0.02 M EDTA (2 × 30 mL), H_2O (2 × 30 mL), 0.01 M HCl (2 × 30 mL), H_2O (5 × 30 mL)] to afford PEG-[G3]-FITC-RGD·HCl (3.6 mg, 84%) as an orange foam. IR (ICs window, MeOH, cm^{-1}): 2866, 1582, 1496, 1109. UV−vis (H_2O) λ_{max}: 234, 262, 502 nm.

PEG-[G3]-AP-N_3. PEG-[G3]-N_3 (36 mg, 2.77 μmol) was dissolved in *t*-BuOH (0.37 mL) and H_2O (0.32 mL). Then, 4′-ethynyl acetophenone (0.8 mg, 5.53 μmol) and freshly prepared aqueous solutions of $CuSO_4$ (22 μL, 1.11 μmol, 0.05 M) and sodium ascorbate (28 μL, 5.53 μmol, 0.2 M) were added. The resulting mixture was stirred at rt for 48 h, and then was purified by ultrafiltration (50% MeOH/H_2O, 5 × 30 mL) to afford PEG-[G3]-AP-N_3 (36.1 mg, 98%) as a white foam. ^{1}H NMR (500 MHz, $CDCl_3$) δ: 8.27−8.02 (m, 1.4H), 8.00−7.69 (m, 5.6H), 7.22−7.01 (m, 26H), 4.68−4.47 (m, 2.8H), 4.46−3.96 (m, 80H), 3.95−3.44 (m, ∼798), 3.42−3.21 (m, 56H), 2.58 (s, 2.1H), 2.54 (s, 2.1H). IR (KBr, cm^{-1}): 3438, 2874, 2108, 1113. An average of 1.4 acetophenone groups in PEG-[G3]-AP-N_3 was determined by integration of the characteristic aromatic signals of the acetophenone and dendritic scaffold in the ^{1}H NMR spectrum in $CDCl_3$.

PEG-[G3]-AP-FITC-N_3. PEG-[G3]-AP-N_3 (18 mg, 1.37 μmol) was dissolved in *t*-BuOH (0.18 mL) and H_2O (0.15 mL). Then, **1** (1.8 mg, 4.10 μmol) and freshly prepared aqueous solutions of $NaHCO_3$ (8 μL, 8.21 μmol, 1 M), $CuSO_4$ (16 μL, 0.82 μmol, 0.05 M), and sodium ascorbate (20 μL, 4.10 μmol, 0.2 M) were added. The resulting mixture was stirred at rt for 48 h, and then was purified by ultrafiltration (H_2O, 5 × 30 mL) to afford PEG-[G3]-AP-FITC-N_3 (16.2 mg, 87%) as an orange foam. ^{1}H NMR (500 MHz, DMSO-d_6) δ: 8.63 (s, 1.2H), 8.58 (s, 1.4H), 8.52−8.39 (m, 10.8H), 8.00−7.83 (m, 5.6H), 7.25−7.08 (m, 26H), 4.69−4.48 (m, 5.2H), 4.45−3.94 (m, 80H), 3.88−3.44 (m, ∼805H), 3.25 (s, 3H), 3.13−3.04 (m, 2H); (methylene protons adjacent to the azide groups are buried by the H_2O signal and methyl protons in acetophenone by residual DMSO). IR (KBr, cm^{-1}): 3381, 2873, 2106, 1116. UV−vis (H_2O) λ_{max}: 296, 495 nm. UV−vis (DMSO) λ_{max}: 520 nm. An average of 1.2 fluorescein molecules in PEG-[G3]-AP-FITC-N_3 was determined by absorbance at 520 nm in DMSO, applying an extinction coefficient of 60 800 M^{-1} cm^{-1}.

PEG-[G3]-AMCA-FITC-N_3. PEG-[G3]-AP-FITC-N_3 (16.2 mg, 1.18 μmol) and AMCA-hydrazide (2.5 mg, 10.1 μmol, 620 mol % per ketone) were dissolved in DMF (0.12 mL). Then, a pyridine/acetic acid mixture (3:1, 120 μL) was added. The resulting solution was stirred at rt for 48 h, and then it was concentrated and purified by ultrafiltration (50% MeOH/H_2O, 5 × 30 mL) to afford PEG-[G3]-AMCA-FITC-N_3 (16.1 mg, 97%) as a yellow foam. ^{1}H NMR (500 MHz, $CDCl_3$) δ: 8.22−8.05 (m, 1.4H), 7.98−7.77 (m, 5.6H), 7.27−6.91 (m, 26H), 4.63−4.38 (m, 2.8H), 4.26−3.95 (m, 80H), 3.93−3.50 (m, ∼800H), 3.36−3.17 (m, 54H), 2.61−2.45 (m, 4.2H); (because of their low intensity, AMCA signals are not included). UV−vis (H_2O) $_{\lambda max}$: 298, 350, 496 nm.

PEG-[G3]-AMCA-FITC-NH_2. PPh_3 (10.0 mg, 38.4 μmol) was added to a solution of PEG-[G3]-AMCA-FITC-N_3 (16.1 mg, 1.15 μmol) in 2% H_2O/MeOH (1.1 mL). The resulting mixture was stirred at rt for 12 h, and then it was purified by ultrafiltration (50% MeOH/H_2O, 5 × 30 mL) to afford PEG-[G3]-AMCA-FITC-NH_2 (14.7 mg, 95%) as a yellow foam. IR (ICs window, $CHCl_3$, cm^{-1}): 3270, 2870, 1107. UV−vis (H_2O)

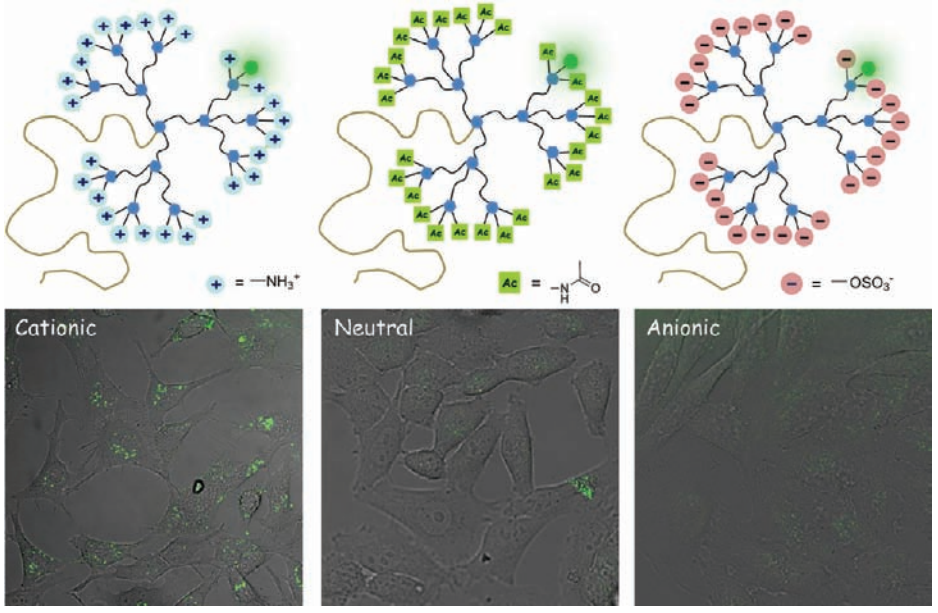

Figure 1. Confocal images of HeLa cells treated with PEG-GATG copolymers carrying different surface charge. Cells were incubated with labeled dendrimers for 1 h and then were washed with PBS and imaged after 8 h.

λ_{max}: 302, 350, 500 nm. An average of 1.0 AMCA in PEG-[G3]-AMCA-FITC-NH_2 was determined by measuring the increase in absorbance at 350 nm in H_2O with respect to PEG-[G3]-AP-FITC-N_3, applying an extinction coefficient of 19 000 M^{-1} cm^{-1}.

Cell Culture. HeLa, MCF7, and HepG2 cells were purchased from ATCC and cultured following manifacturer's instructions. For live cell microscopy, cells were plated onto 35 mm glass-bottom dishes (WillCo-dish GWSt-3522) and imaged at 37 °C, 5% CO_2.

Confocal Imaging. Cell imaging was performed on a Leica TCS SP2 inverted confocal microscope (Leica Microsystems) equipped with a 40 × 1.25 NA oil immersion objective (Leica Microsystems). Imaging was obtained illuminating the samples with the inline Ar and He−Ne lasers of the microscope and with a 403 nm pulsed diode laser (M8903−01; Hamamatsu) at 50 MHz repetition rate. Fluorescence emission was collected with the AOBS-based built-in detectors of the confocal microscope (Hamamatsu R6357). Nuclei were stained with Hoechst and imaged using the 403 nm laser. Simultaneous AMCA and fluorescein imaging was performed by means of a Leica AF6000 wide-field setup.

Propidium Iodide (PI) Assay. HeLa cells were incubated for 2 h at 37 °C with DMEM (Dulbecco's Modified Eagle Medium) containing 8 μg/mL propidium iodide and different concentrations of dendrimer. The medium was then discarded and cells were washed with PBS buffer containing the same concentration of propidium iodide before confocal imaging.

Flow Cytometry Measurements. Cells were grown in a six-well plate and after treatment with labeled dendrimer were detached using trypsin-EDTA, washed with PBS buffer, and fixed with 4% paraformaldheyde (PFA). Cells were washed with PBS until complete removal of PFA and finally resuspended in 250 μL of PBS. Flow cytometry was performed on a FACScalibur system (BD biosciences) by counting 10 000 events. Histogram plots were analyzed using *WinMDI 2.9* (http://facs.scripps.edu/software.html).

Toxicity Assay. HeLa cells were incubated for 1 h at 37 °C with DMEM containing 8 μg/mL propidium iodide and different concentrations of dendrimer. The medium was then discarded and the cells were washed with PBS buffer three times. Calcein-AM was then added and incubated for 15 min before confocal imaging.

Internalization Assay and Colocalization Studies. To monitor dendrimer internalization, cells were incubated with 100 nM fluorescein-labeled dendrimers in DMEM for 1 h at 37 °C. To remove unbound molecules in the medium, cells were rinsed twice with PBS. After the initial preloading and subsequent washing, cells were incubated again in DMEM and imaged at the indicated time point. In order to identify the endocytic vesicles involved in dendrimer internalization, colocalization assays were performed in living cells. HeLa cells were coincubated with dendrimers (as described above) and different dyes: 1 mg/mL of a 70 kDa dextran−TRITC conjugate at 37 °C for 30 min to label macropinosomes, 50 mM Lysotracker for 10 min to label lysosomes, and 2 μg/mL of a transferrin−Alexa568 conjugate to label clathrin-coated endosomes. Images were analyzed using *ImageJ* software v 1.37 (NIH Image; http://rsbweb.nih.gov/ij).

■ RESULTS AND DISCUSSION

With the aim of analyzing the effect of the peripheral substitution of GATG dendrimers on their uptake and intracellular trafficking in living cells, biologically relevant ligands and groups with different physicochemical properties were selected to functionalize the surface of a dendrimer and a PEG_{5000}-dendritic block copolymer of G3 ([G3]-N_3 and PEG-[G3]-N_3) (Scheme 1). The 27 peripheral azides on these structures provide a large degree of multivalency for the easy incorporation of several tags and ligands, and for a subsequent effective interaction with cell surfaces. To this end, a common synthetic strategy was followed that involved an initial functionalization of PEG-[G3]-N_3 and [G3]-N_3 with the alkynated FITC derivative **1** by CuAAC ($CuSO_4$, sodium ascorbate, *t*-BuOH-H_2O) in excellent yields (Scheme 1). The

dx.doi.org/10.1021/bc300079h | *Bioconjugate Chem.* 2012, 23, 1059−1068

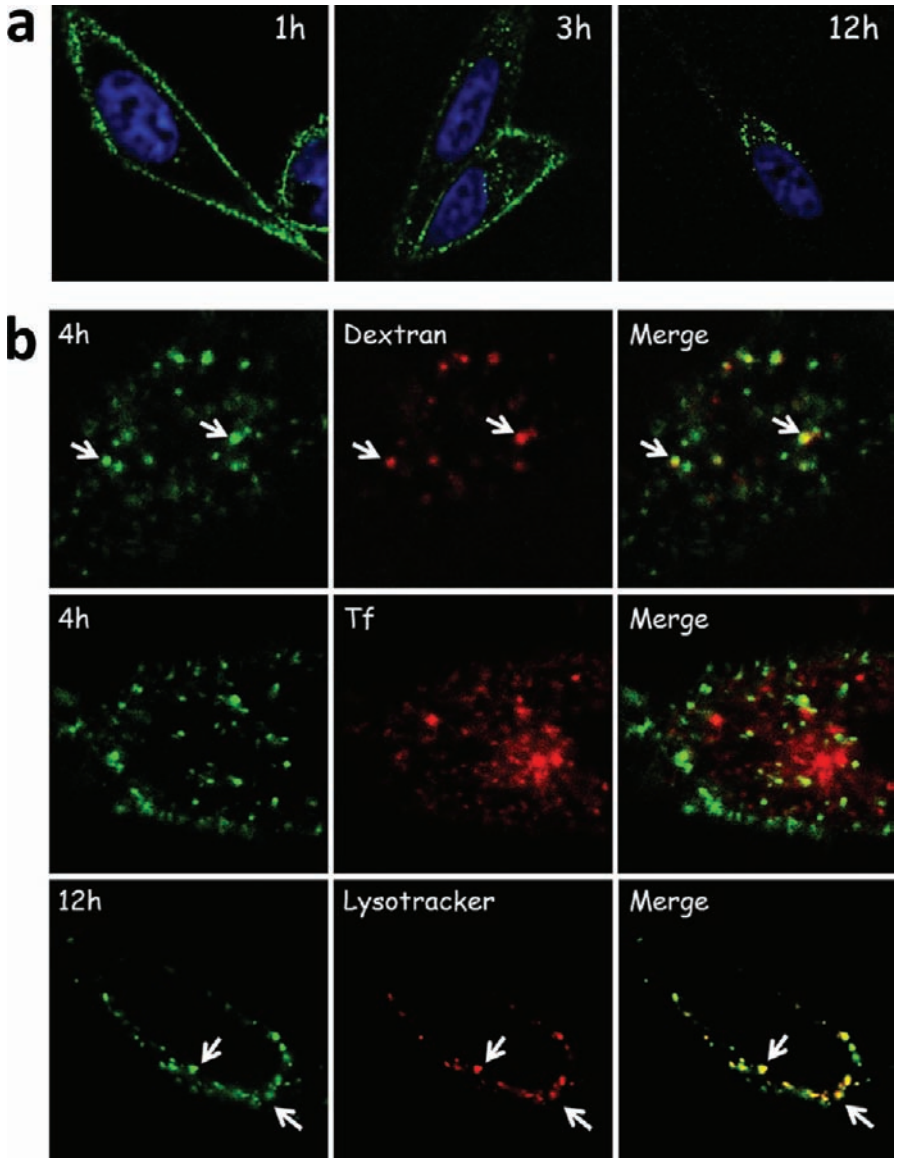

Figure 2. (a) Time-lapse imaging of PEG-[G3]-FITC-NH_3^+ (green) in HeLa cells and (b) colocalization assays with different endocytic markers (red): dextran for macropinocytosis (top), transferrin for clathrin pathway (middle), and lysotracker (bottom).

incorporation of one FITC molecule on average, determined by absorbance and NMR, resulted in dendritic structures that can be monitored by confocal microscopy. Decoration of the remaining azides with cationic/neutral/anionic groups or biologically relevant ligands, such as carbohydrates and peptides, afforded a small library of dendritic structures as tools to evaluate the effect of peripheral groups on the cell-uptake and intracellular trafficking of GATG dendrimers (Scheme 1).

To this end, anionic sulfate residues were easily introduced on the block copolymer by CuAAC (**2**, $CuSO_4$, sodium ascorbate, *t*-BuOH-H_2O) to give PEG-[G3]-FITC-OSO_3^- in 95% yield. Cationic and neutral groups were incorporated via Staudinger reaction (PPh_3, H_2O-MeOH) and subsequent acetylation to afford, respectively, PEG-[G3]-FITC-NH_3^+·and PEG-[G3]-FITC-NHAc in excellent yields. In a similar way, the biologically relevant carbohydrate and peptide ligands, lactose and RGD, were introduced by CuAAC (**3** or **4**, $CuSO_4$, sodium ascorbate, *t*-BuOH-H_2O) leading to [G3]-FITC-Lac, PEG-[G3]-FITC-Lac, and PEG-[G3]-FITC-RGD in excellent yields. Complete functionalization of peripheral azides in all these conjugates was confirmed by ^1H NMR (D_2O) by disappearance of the characteristic signal of the methylene protons adjacent to the azide groups (3.40 ppm). IR spectroscopy additionally confirmed complete functionalization by disappearance of the intense azide signal at around 2100 cm^{-1}.

Peripheral Functionalization of PEG-GATG Regulates Cell Uptake. To address the ability of PEG-GATG block copolymers to cross the plasma membrane and to be internalized into living cells, we studied their interactions with cultured HeLa cells by confocal microscopy as a function of the physicochemical properties (charge and hydrophobicity) on their surface. In particular, we initially focused our attention on three surface groups: (i) primary amines (PEG-[G3]-FITC-NH_3^+), (ii) acetylated amines (PEG-[G3]-FITC-NHAc), and (iii) sulfate groups (PEG-[G3]-FITC-OSO_3^-), which display cationic, neutral, and anionic character at physiological pH, respectively.

Figure 1 shows confocal images of HeLa cells treated with these three groups of FITC-labeled structures. A strong effect

dx.doi.org/10.1021/bc300079h | *Bioconjugate Chem.* 2012, 23, 1059−1068

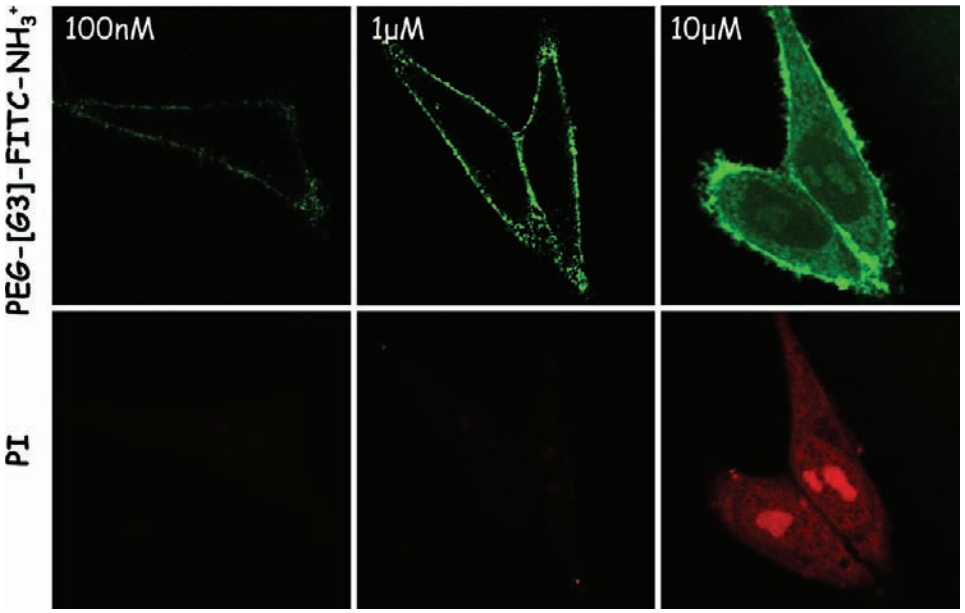

Figure 3. Localization of FITC-labeled cationic PEG-[G3]-FITC-NH_3^+ in HeLa cells after 15 min at different concentrations (top). Cells were treated with the copolymer in the presence of propidium iodide (bottom) to study the membrane permeability during treatment.

of the surface charge on cell uptake was observed in agreement with previous reports with alternative dendritic families.[32,33] While cationic PEG-[G3]-FITC-NH_3^+ showed a strong internalization consistent with its ability to bind cell membranes through ionic interactions, anionic PEG-[G3]-FITC-OSO_3^- showed only a weak internalization because of its lower affinity for cell membranes. This behavior is even more evident for neutral PEG-[G3]-FITC-NHAc, showing no internalization at all in HeLa cells. A strong difference between cationic and anionic dendritic structures has been also observed in the kinetics of internalization (see Figure S1 in the Supporting Information). Thus, PEG-[G3]-FITC-NH_3^+ showed a long residence time on the plasma membrane and slow internalization, while no accumulation on the membrane and fast internalization (perinuclear localization after 1 h) was observed for the anionic counterpart. This observed relationship between charge and internalization efficiency is of great interest for the application of these materials in nanomedicine, as it would allow control of the behavior of dendritic carriers by selecting the physicochemical properties on their surface.

Further studies with the most internalizing derivative, PEG-[G3]-FITC-NH_3^+, were performed to unveil the details of its uptake properties. Figure 2a shows time-lapse imaging of this copolymer where three main phases of internalization can be observed: (i) membrane binding, (ii) formation of intracellular vesicles, and (iii) delivery to the perinuclear region. These results are in good agreement with previous observations with PAMAM dendrimers and suggest endocytosis as the main way of entry for these macromolecules inside cells. Next, we decided to investigate the mechanism of cell uptake by means of colocalization assays using red-labeled endocytic markers (Figure 2b). After 4 h of administration, a good colocalization of PEG-[G3]-FITC-NH_3^+ (100 nM) was observed with a 70 kDa dextran, a specific marker of macropinocytosis. In contrast, no colocalization was observed with transferrin, indicating that the copolymer does not localize in clathrin-coated vesicles. This result differs slightly from previous observations with PAMAM dendrimers that showed a prevalence of macropinocytosis accompanied by a significant population of dendrimers entering cells through a clathrin-mediated pathway. In general, macropinocytosis is the preferred pathway for nonspecific cell binding, and although it converges with the clathrin pathway at a later stage, some significant differences between both exist; in particular, the kinetic of internalization for macropinocytosis is usually slower. Further studies of colocalization with endocytic markers and inhibitors of the different pathways will be of help to confirm these results.

Moreover, the final fate of PEG-[G3]-FITC-NH_3^+ trafficking in HeLa cells was identified (Figure 2b). Colocalization with lysotroacker, a well-known lysosome marker, clearly showed the copolymer fully localizing in the lysosomes after 12 h, a fact which is considered of great interest for drug delivery applications, as lysosomes are endowed with a peculiar chemical environment (low pH, high ionic strength, and abundance of hydrolytic enzymes). As shown below, advantage was taken of these internalization properties for the design of a drug delivery system with the ability to trigger the release of drugs.

Concentration-Dependent Uptake Mechanism. Internalization studies with PEG-[G3]-FITC-NH_3^+ were performed in HeLa cells that shed light on the concentration-dependence of the process. Figure 3 shows the cellular localization of the copolymer at different concentrations after 15 min of incubation. At concentrations up to 1 μM, PEG-[G3]-FITC-NH_3^+ showed membrane binding as previously described. However, at higher concentrations, a completely different localization pattern appeared with copolymers widely spread in the cytoplasm and accumulated into the nucleoli. This localization suggested the possibility of a direct membrane translocation mechanism in agreement with previous reports by Holl and co-workers on the ability of PAMAM dendrimers of high generations (from G7) to create temporary holes in the plasma membrane.[34] To confirm this mechanism in our case, a propidium iodide assay was performed that revealed altered permeability of the cell membrane for PEG-[G3]-FITC-NH_3^+ at a concentration 10 μM. It is interesting to note that, while this phenomenon operates in PEG-GATG copolymers of G3

dx.doi.org/10.1021/bc300079h | Bioconjugate Chem. 2012, 23, 1059−1068

with only 27 amines, an order of magnitude higher in peripheral amines is required for PAMAM dendrimers to alter cell membranes. This difference could be related to the higher flexibility of the GATG dendritic scaffold which may exploit more efficiently the peripheral cationic groups as ionic binders. Interestingly, the observed nucleolar localization is in good agreement with previously reported intracellular studies with cationic PAMAM dendrimers.[35]

Carbohydrate-Decorated Copolymers. Carbohydrates regulate a plethora of biological and pathological processes in Nature. Recognition events such as fertilization, toxin and hormone mediation, pathogen invasion, and cell−cell interactions rely on multivalent carbohydrate−receptor interactions.[36−38] This cluster glycoside effect has prompted the development of glycodendrimers with the ability to interact with target lectins and promote/inhibit natural carbohydrate−receptor interactions.[25,39] In this context, an approach of our laboratory to speed up the preparation of glycodendrimers has taken advantage of the chemical compatibility of unprotected carbohydrates with the typical reaction conditions of CuAAC. This way, not only are subsequent deprotection reactions avoided, but also functionalization is facilitated by reduced steric hindrance.[17,18]

Lactose (Lac) represents an especially attractive carbohydrate of low molecular weight. Thanks to its high biocompatibility and ability to target specific cell populations, Lac has already been proposed as a coating agent for dendrimers with potential applications in antiadhesive therapy[40] and drug delivery toward hepatocytes.[41] Focusing our attention on this latter application, HepG2 cells derived from hepatocarcinoma and endowed with the asialoglycoprotein receptor (ASGPR, that can recognize and internalize lactose moieties) were incubated with lactose-decorated PEG-[G3]-FITC-Lac (Figure 4). [G3]-FITC-Lac

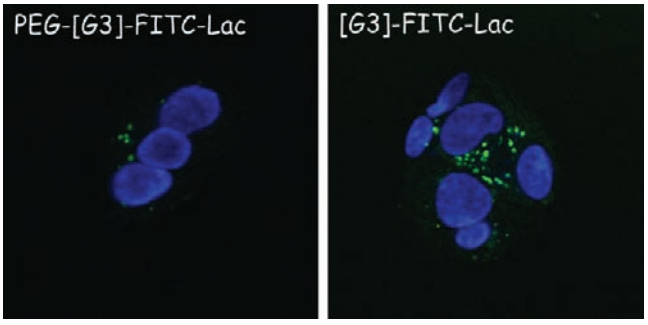

Figure 4. Localization of PEG-[G3]-FITC-Lac (left) and [G3]-FITC-Lac (right) after 2 h incubation with HepG2 cells.

was also included in this study to investigate the influence of PEG on the ability of GATG dendrimers to interact with cell surfaces. Confocal microscopy revealed that both structures were taken up by cells, but with very different efficacy. Indeed, it is evident from Figure 4 that PEG-[G3]-FITC-Lac is much less internalized by HepG2 cells compared to the non-PEGylated dendrimer, a difference that might arise from the ability of PEG to shield lactose ligands and, hence, limit cell−dendrimer interactions. Notably, when experiments were performed in the presence of an excess of free lactose (up to 150 mM), internalization was unaffected. In the same way, comparable levels of internalization were observed with HeLa cells, indicating that receptor-mediated endocytosis is not the only pathway of internalization in the case of these dendrimers. On the basis of this significant cell uptake and the known biocompatibility associated with carbohydrates, we believe these carbohydrate-coated dendrimers deserve further investigation as tools for cell internalization as an alternative to classical cationic dendrimers, while avoiding the characteristic higher toxicity of the latter (Supporting Information Figure S2).

Peptide-Decorated Copolymers. Peptides are common targeting vectors in nanobiotechnology thanks to their small size, easy large-scale synthesis, and activity retained upon conjugation. Solid-phase synthesis of peptides allows their easy modification with chemical handles for incorporation into nanostructures. In this work, we report the synthesis and biological evaluation of a peptide-decorated PEG-[G3]-FITC-RGD which incorporates multiple copies of a cyclic RGD (Arg-Gly-Asp) peptide. RGD peptides are of great interest for their ability to be effectively recognized by integrins. These are heterodimeric cell-surface proteins that play important roles in cell adhesion and signaling,[42] and are overexpressed in pathologies such as cancer and atherosclerosis.[43] The clustered arrangement of integrins on cell surfaces has stimulated the preparation of RGD-coated dendrimers for enhanced affinity through multivalent interactions.[44] The alkynated cyclo-(RGDfPra) peptide **4** incorporated in PEG-[G3]-FITC-RGD is a mimetic of Cilengitide, a peptide with superior integrin binding affinity, currently under clinical trials in patients with glioblastoma.[45−47]

Figure 5 shows the internalization efficacy of PEG-[G3]-FITC-RGD in two cell lines: HeLa cells that overexpress the

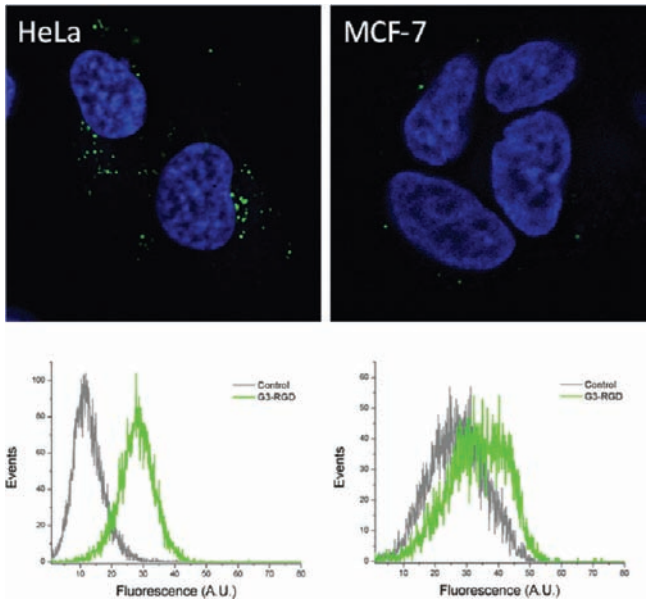

Figure 5. (a) Localization of PEG-[G3]-FITC-RGD in HeLa cells (left) and MCF7 (right). (b) Flow cytometry quantification of cell uptake in the two cell lines.

$\alpha v\beta 3$ integrin, and MCF7 which are reported to have low expression level of this membrane protein. Both confocal imaging and flow cytometry show a strong internalization in HeLa cells, but a response comparable to a negative control in MCF7 cells. Clearly, the presence of RGD peptides on the surface of PEG-[G3]-FITC-RGD grants the whole nanostructure targeting and internalization properties to specific cell populations. These results along with the modular synthetic

dx.doi.org/10.1021/bc300079h | *Bioconjugate Chem.* 2012, 23, 1059−1068

Scheme 2

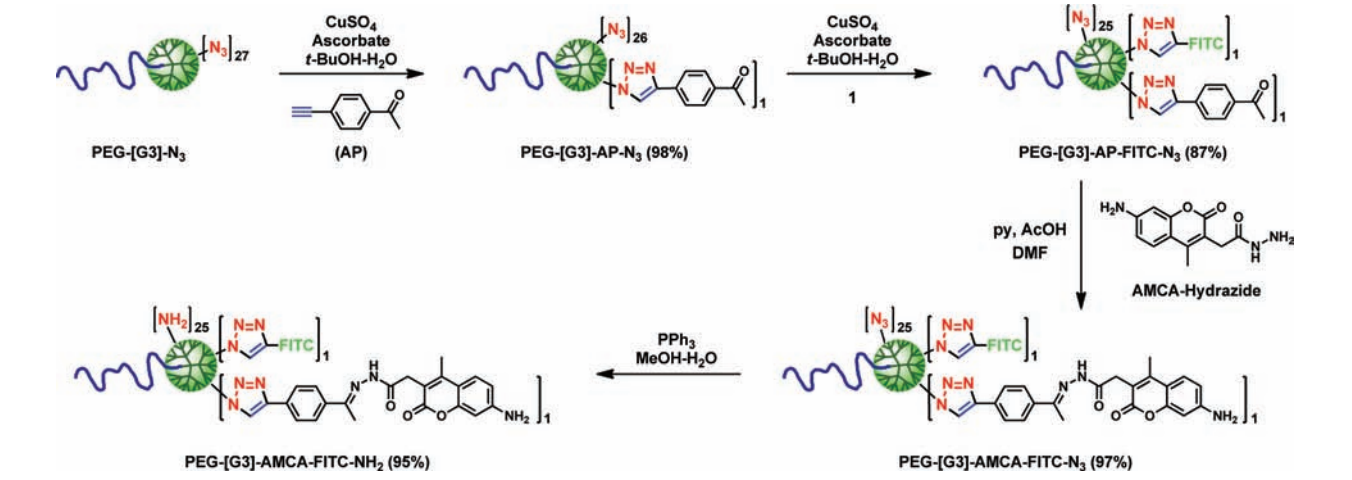

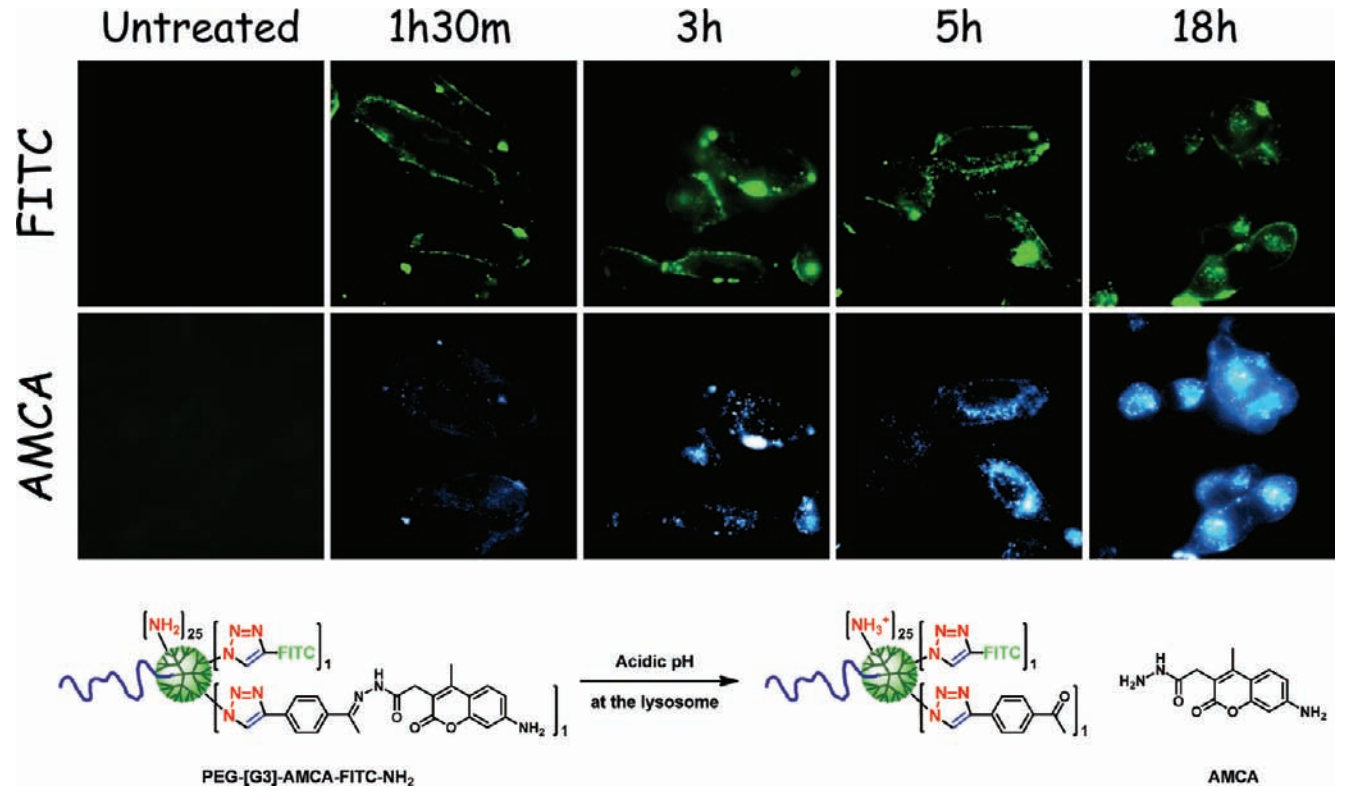

Figure 6. HeLa cells treated for 18 h with PEG-[G3]-AMCA-FITC-NH_2. Fluorescent signals from fluorescein (top panels) and AMCA (bottom panels) were recorded at different times.

approach and easy functionalization of GATG dendrimers reveal PEG-[G3]-FITC-RGD as a prototype of a family of peptide-driven targeted nanostructures with promising biological applications.

Development of a Dendritic pH-Sensitive Drug Delivery System for Selective Release after Lysosomal Localization. The possibility of delivering nanostructures to specific cell compartments with particular biochemical environments (pH, ionic strength, enzymatic activity) is of crucial interest for drug delivery applications.[48] Lysosomes are especially interesting in this context, as their characteristic acidic pH (usually below 5.0) can be exploited to trigger the release of active species inside cells.[49] In the previous sections, we have demonstrated the internalization mechanism of PEG-[G3]-FITC-NH_3^+ through macropinocytosis and its final delivery to the lysosomal compartment. In this section, we describe a drug delivery prototype that based on this structure exploits pH-cleavable hydrazone linkers (stable at physiological pH but hydrolyzable under acidic media) for the selective delivery of cargo molecules inside cells (Scheme 2). With the aim of simultaneously monitoring the localization of the dendritic carrier and payload molecules in this system, a dual fluorescent-labeling strategy was pursued combining FITC and a coumarin dye (AMCA-Hydrazide) as model cargo molecule (Scheme 2).

For the preparation of this delivery system, an ethynyl acetophenone linker (**AP**) was first introduced by CuAAC into PEG-[G3]-N_3 as a chemical handle for subsequent hydrazone

dx.doi.org/10.1021/bc300079h | Bioconjugate Chem. 2012, 23, 1059−1068

formation ($CuSO_4$, sodium ascorbate, *t*-BuOH-H_2O, 98% yield). The resulting PEG-[G3]-AP-N_3 conjugate carrying one acetophenone on average (as determined by NMR) was then tagged by CuAAC with a FITC dye (**1**, $NaHCO_3$, $CuSO_4$, sodium ascorbate, *t*-BuOH-H_2O). PEG-[G3]-AP-FITC-N_3 was obtained in 87% yield with an average of one FITC as determined by absorbance. The appearance of two singlets at 8.63 and 8.58 ppm corresponding to two triazol protons in the ^1H NMR spectrum of PEG-[G3]-AP-FITC-N_3 confirms the dual CuAAC labeling. Incorporation of AMCA-Hydrazide at this stage was followed by reduction of the remaining azides via Staudinger conditions to afford the desired PEG-[G3]-AMCA-FITC-NH_2 in excellent overall yield. Complete functionalization/reduction of peripheral azides in this system was confirmed by disappearance of the intense azide signal at around 2100 cm^{-1} in the IR spectrum.

Fluorescence experiments with PEG-[G3]-AMCA-FITC-NH_2 were performed in HeLa cells over a period of 18 h (Figure 6). At short incubation times, high colocalization between FITC and AMCA was seen in the endolysosomal system in agreement with the integrity of the conjugate. The low fluorescence intensity of AMCA at this stage is probably due to a probe−probe quenching effect. At longer incubation times, two main phenomena are revealed in dendrimer-treated cells: (i) an increase in the fluorescence intensity of AMCA; and (ii) a reduced colocalization of AMCA and FITC. These observations have been interpreted as resulting from hydrolysis of the hydrazone linkers at the lysosome and release of the AMCA molecules. Moreover, as AMCA seems to be localized in the cytoplasm, this suggests the ability of this small and hydrophobic dye to escape the endosome, while the hydrophilic and bulky dendrimer prevents the endosomal escape of the covalently attached fluorescein. Accordingly, this GATG-based conjugate is able to accomplish the main requirements for a successful drug delivery system: cell internalization, intracellular release, and endosome escape. This promising proof-of-principle opens the way for the application of GATG dendrimers for specific issues in pharmacology.

■ CONCLUSIONS

In this paper, we exploit the versatility of GATG dendrimers to obtain a wide array of surface functionality. The interaction of these materials with cells has been studied by confocal microscopy, unveiling a strong relationship between peripheral decoration at the dendrimer and relevant properties for their bioapplications, such as cell internalization and localization. This information has been exploited to design a drug delivery vector able to intracellularly release a model compound. These results disclose relevant insights about the behavior of GATG dendrimers in the biological environment and represent an important step toward their use for clinical purposes.

■ ASSOCIATED CONTENT

Supporting Information

Additional figures. This material is available free of charge via the Internet at http://pubs.acs.org.

■ AUTHOR INFORMATION

Corresponding Author

*L.Albertazzi@tue.nl; ef.megia@usc.es.

Present Address

[‖]Lorenzo Albertazzi, TU/e, Den Dolech 2, 5612 AZ Eindhoven, The Netherlands.

Author Contributions

[#]These authors equally contribute to the work.

Notes

The authors declare no competing financial interest.

■ ACKNOWLEDGMENTS

This work was financially supported by the Spanish MICINN (CTQ2009-10963 and CTQ2009-14146-C02-02) and the Xunta de Galicia (10CSA209021PR and CN2011/037). M.F.-V. thanks the Spanish Ministry of Education for a FPU fellowship.

■ REFERENCES

(1) Menjoge, A. R., Kannan, R. M., and Tomalia, D. A. (2010) Dendrimer-based drug and imaging conjugates: design considerations for nanomedical applications. *Drug Discovery Today 15*, 171−185.

(2) Gillies, E. R., and Fréchet, J. M. J. (2005) Dendrimers and dendritic polymers in drug delivery. *Drug Discovery Today 10*, 35−43.

(3) Lee, C. C., MacKay, J. A., Fréchet, J. M. J., and Szoka, F. C. (2005) Designing dendrimers for biological applications. *Nat. Biotechnol. 23*, 1517−1526.

(4) Shcharbin, D., Pedziwiatr, E., Blasiak, J., and Bryszewska, M. (2010) How to study dendriplexes II: Transfection and cytotoxicity. *J. Controlled Release 141*, 110−127.

(5) Rolland, O., Turrin, C.-O., Caminade, A.-M., and Majoral, J.-P. (2009) Dendrimers and nanomedicine: multivalency in action. *New J. Chem. 33*, 1809−1824.

(6) Tekade, R. K., Kumar, P. V., and Jain, N. K. (2009) Dendrimers in oncology: an expanding horizon. *Chem. Rev. 109*, 49−87.

(7) Villaraza, A. J. L., Bumb, A., and Brechbiel, M. W. (2010) Macromolecules, dendrimers, and nanomaterials in magnetic resonance imaging: the interplay between size, function, and pharmacokinetics. *Chem. Rev. 110*, 2921−2959.

(8) Sakadžić, S., Roussakis, E., Yaseen, M. A., Mandeville, E. T., Srinivasan, V. J., Arai, K., Ruvinskaya, S., Devor, A., Lo, E. H., Vinogradov, S. A., and Boas, D. A. (2010) Two-photon high-resolution measurement of partial pressure of oxygen in cerebral vasculature and tissue. *Nat. Methods 7*, 755−759.

(9) Albertazzi, L., Brondi, M., Pavan, G. M., Sato, S. S., Signore, G., Storti, B., Ratto, G. M., and Beltram, F. (2011) Dendrimer-based fluorescent indicators: in vitro and in vivo applications. *PLoS ONE 6*, e28450.

(10) Buhleier, E., Wehner, W., and Vögtle, F. (1978) "Cascade"- and "nonskid-chain-like" syntheses of molecular cavity topologies. *Synthesis*, 155−158.

(11) Tomalia, D. A., Baker, H., Dewald, J., Hall, M., Kallos, G., Martin, S., Roeck, J., Ryder, J., and Smith, P. (1985) A new class of polymers: starburst-dendritic macromolecules. *Polym. J. 17*, 117−132.

(12) Newkome, G. R., Yao, Z.-q., Baker, G. R., and Gupta, V. K. (1985) Cascade molecules: a new approach to micelles. A [27]-arborol. *J. Org. Chem. 50*, 2003−2004.

(13) Hawker, C. J., and Fréchet, J. M. J. (1990) Preparation of polymers with controlled molecular architecture. A new convergent approach to dendritic macromolecules. *J. Am. Chem. Soc. 112*, 7638−7647.

(14) Astruc, D., Boisselier, E., and Ornelas, C. (2010) Dendrimers designed for functions: from physical, photophysical, and supramolecular properties to applications in sensing, catalysis, molecular electronics, photonics, and nanomedicine. *Chem. Rev. 110*, 1857−1959.

(15) Vögtle, F., Richardt, G., and Werner, N. (2009) *Dendrimer Chemistry*, Wiley-VCH, Weinheim, .

(16) *Dendrimers and Other Dendritic Polymers*, John Wiley & Sons, Ltd., Chichester, 2001.

(17) Fernandez-Megia, E., Correa, J., and Riguera, R. (2006) "Clickable" PEG-dendritic block copolymers. *Biomacromolecules 7*, 3104−3111.
(18) Fernandez-Megia, E., Correa, J., Rodríguez-Meizoso, I., and Riguera, R. (2006) A click approach to unprotected glycodendrimers. *Macromolecules 39*, 2113−2120.
(19) Amaral, S. P., Fernandez-Villamarin, M., Correa, J., Riguera, R., and Fernandez-Megia, E. (2011) Efficient multigram synthesis of the repeating unit of gallic acid-triethylene glycol dendrimers. *Org. Lett. 13*, 4522−4525.
(20) Meunier, S. J., Wu, Q., Wang, S.-N., and Roy, R. (1997) Synthesis of hyperbranched glycodendrimers incorporating α-thiosialosides based on a gallic acid core. *Can. J. Chem. 75*, 1472−1482.
(21) Tornøe, C. W., Christensen, C., and Meldal, M. (2002) Peptidotriazoles on solid phase: [1,2,3]-triazoles by regiospecific copper(i)-catalyzed 1,3-dipolar cycloadditions of terminal alkynes to azides. *J. Org. Chem. 67*, 3057−3064.
(22) Rostovtsev, V. V., Green, L. G., Fokin, V. V., and Sharpless, K. B. (2002) A stepwise huisgen cycloaddition process: copper(I)-catalyzed regioselective "ligation" of azides and terminal alkynes. *Angew. Chem., Int. Ed. 41*, 2596−2599.
(23) Harris, J. M., and Chess, R. B. (2003) Effect of pegylation on pharmaceuticals. *Nat. Rev. Drug Discovery 2*, 214−221.
(24) Joralemon, M. J., McRae, S., and Emrick, T. (2010) PEGylated polymers for medicine: from conjugation to self-assembled systems. *Chem. Commun. 46*, 1377−1393.
(25) Munoz, E. M., Correa, J., Fernandez-Megia, E., and Riguera, R. (2009) Probing the relevance of lectin clustering for the reliable evaluation of multivalent carbohydrate recognition. *J. Am. Chem. Soc. 131*, 17765−17767.
(26) Novoa-Carballal, R., Säwén, E., Fernandez-Megia, E., Correa, J., Riguera, R., and Widmalm, G. (2010) The dynamics of GATG glycodendrimers by NMR diffusion and quantitative 13C relaxation. *Phys. Chem. Chem. Phys. 12*, 6587−6589.
(27) Sousa-Herves, A., Fernandez-Megia, E., and Riguera, R. (2008) Synthesis and supramolecular assembly of clicked anionic dendritic polymers into polyion complex micelles. *Chem. Commun.*, 3136−3138.
(28) Raviña, M., de la Fuente, M., Correa, J., Sousa-Herves, A., Pinto, J., Fernandez-Megia, E., Riguera, R., Sanchez, A., and Alonso, M. J. (2010) Core−shell dendriplexes with sterically induced stoichiometry for gene delivery. *Macromolecules 43*, 6953−6961.
(29) Fernández-Trillo, F., Pacheco-Torres, J., Correa, J., Ballesteros, P., Lopez-Larrubia, P., Cerdán, S., Riguera, R., and Fernandez-Megia, E. (2011) Dendritic MRI contrast agents: an efficient prelabeling approach based on CuAAC. *Biomacromolecules 12*, 2902−2907.
(30) Doménech, R., Abian, O., Bocanegra, R., Correa, J., Sousa-Herves, A., Riguera, R., Mateu, M. G., Fernandez-Megia, E., Velázquez-Campoy, A., and Neira, J. L. (2010) Dendrimers as potential inhibitors of the dimerization of the capsid protein of HIV-1. *Biomacromolecules 11*, 2069−2078.
(31) Ikeda, M., Minari, J., Shimada, N., Numata, M., Sakurai, K., and Shinkai, S. (2007) Complex formation between cationic β-1,3-glucan and hetero-sequence oligodeoxynucleotide and its delivery into macrophage-like cells to induce cytokine secretion. *Org. Biomol. Chem. 5*, 2219−2224.
(32) Perumal, O. P., Inapagolla, R., Kannan, S., and Kannan, R. M. (2008) The effect of surface functionality on cellular trafficking of dendrimers. *Biomaterials 29*, 3469−3476.
(33) Albertazzi, L., Serresi, M., Albanese, A., and Beltram, F. (2010) Dendrimer internalization and intracellular trafficking in living cells. *Mol. Pharmaceutics 7*, 680−688.
(34) Hong, S., Bielinska, A. U., Mecke, A., Keszler, B., Beals, J. L., Shi, X., Balogh, L., Orr, B. G., Baker, J. R., Jr., and Banaszak Holl, M. M. (2004) Interaction of poly(amidoamine) dendrimers with supported lipid bilayers and cells: hole formation and the relation to transport. *Bioconjugate Chem. 15*, 774−782.
(35) Albertazzi, L., Storti, B., Marchetti, L., and Beltram, F. (2010) Delivery and subcellular targeting of dendrimer-based fluorescent pH sensors in living cells. *J. Am. Chem. Soc. 132*, 18158−18167.
(36) Kiessling, L. L., Young, T., Gruber, T. D., and Mortell, K. H. (2008) In *Glycoscience* (Fraser-Reid, Tatsuta, and Thiem, Eds.) pp 2483−2523, Springer, Berlin.
(37) Dam, T. K., and Brewer, C. F. (2008) Effects of clustered epitopes in multivalent ligand-receptor interactions. *Biochemistry 47*, 8470−8476.
(38) Lundquist, J. J., and Toone, E. J. (2002) The cluster glycoside effect. *Chem. Rev. 102*, 555−578.
(39) Imberty, A., Chabre, Y. M., and Roy, R. (2008) Glycomimetics and glycodendrimers as high affinity microbial anti-adhesins. *Chem.—Eur. J. 14*, 7490−7499.
(40) Vrasidas, I., de Mol, N. J., Liskamp, R. M. J., and Pieters, R. J. (2001) Synthesis of lactose dendrimers and multivalency effects in binding to the cholera toxin B subunit. *Eur. J. Org. Chem. 2001*, 4685−4692.
(41) Arima, H., Yamashita, S., Mori, Y., Hayashi, Y., Motoyama, K., Hattori, K., Takeuchi, T., Jono, H., Ando, Y., Hirayama, F., and Uekama, K. (2010) In vitro and in vivo gene delivery mediated by lactosylated dendrimer/α-cyclodextrin conjugates (G2) into hepatocytes. *J. Controlled Release 146*, 106−117.
(42) Hynes, R. O. (2002) Integrins: bidirectional, allosteric signaling machines. *Cell 110*, 673−687.
(43) Desgrosellier, J. S., and Cheresh, D. A. (2010) Integrins in cancer: biological implications and therapeutic opportunities. *Nat. Rev. Cancer 10*, 9−22.
(44) Welsh, D. J., and Smith, D. K. (2011) Comparing dendritic and self-assembly strategies to multivalency-RGD peptide-integrin interactions. *Org. Biomol. Chem. 9*, 4795−4801 and references therein..
(45) Burke, P. A., DeNardo, S. J., Miers, L. A., Lamborn, K. R., Matzku, S., and DeNardo, G. L. (2002) Cilengitide targeting of αvβ3 integrin receptor synergizes with radioimmunotherapy to increase efficacy and apoptosis in breast cancer xenografts. *Cancer Res. 62*, 4263−4272.
(46) Mas-Moruno, C., Rechenmacher, F., and Kessler, H. (2010) Cilengitide: the first anti-angiogenic small molecule drug candidate. design, synthesis and clinical evaluation. *Anti-Cancer Agents Med. Chem. 10*, 753−768.
(47) Reardon, D. A., Neyns, B., Weller, M., Tonn, J. C., Nabors, L. B., and Stupp, R. (2011) Cilengitide: an RGD pentapeptide αvβ3 and αvβ5 integrin inhibitor in development for glioblastoma and other malignancies. *Future Oncol. 7*, 339−354.
(48) Rajendran, L., Knölker, H.-J., and Simons, K. (2010) Subcellular targeting strategies for drug design and delivery. *Nat. Rev. Drug Discovery 9*, 29−42.
(49) Ulbrich, K., and Subr, V. (2004) Polymeric anticancer drugs with pH-controlled activation. *Adv. Drug Delivery Rev. 56*, 1023−1050.

Bioconjugate Chemistry

Article

pubs.acs.org/bc

In Vivo Biodistribution and Small Animal PET of ^{64}Cu-Labeled Antimicrobial Peptoids

Jiwon Seo,[#,§] Gang Ren,[#,†] Hongguang Liu,[†] Zheng Miao,[†] Minyoung Park,[⊥] Yihong Wang,[†] Tyler M. Miller,[‡] Annelise E. Barron,*[,‡] and Zhen Cheng*[,†]

[†]Molecular Imaging Program at Stanford (MIPS), Department of Radiology, Bio-X Program, Canary Center at Stanford for Cancer Early Detection, Stanford University, California, 94305-5344, United States

[‡]Department of Bioengineering, [⊥]Department of Chemical and Systems Biology, Stanford University, California, 94305-5440, United States

[§]School of General Studies, Gwangju Institute of Science and Technology, Gwangju 500-712, Republic of Korea

Supporting Information

ABSTRACT: Peptoids are a rapidly developing class of biomimetic polymers based on oligo-*N*-substituted glycine backbones, designed to mimic peptides and proteins. Inspired by natural antimicrobial peptides, a group of cationic amphipathic peptoids has been successfully discovered with potent, broad-spectrum activity against pathogenic bacteria; however, there are limited studies to address the *in vivo* pharmacokinetics of the peptoids. Herein, ^{64}Cu-labeled DOTA conjugates of three different peptoids and two control peptides were synthesized and assayed *in vivo* by both biodistribution studies and small animal positron emission tomography (PET). The study was designed in a way to assess how structural differences of the peptidomimetics affect *in vivo* pharmacokinetics. As amphipathic molecules, major uptake of the peptoids occurred in the liver. Increased kidney uptake was observed by deleting one hydrophobic residue in the peptoid, and **^{64}Cu-3** achieved the highest kidney uptake of all the conjugates tested in this study. In comparison to peptides, our data indicated that peptoids had general *in vivo* properties of higher tissue accumulation, slower elimination, and higher *in vivo* stability. Different administration routes (intravenous, intraperitoneal, and oral) were investigated with peptoids. When administered orally, the peptoids showed poor bioavailability, reminiscent of that of peptide. However, remarkably longer passage through the gastrointestinal (GI) tract without rapid digestion was observed for peptoids. These unique *in vivo* properties of peptoids were rationalized by efficient cellular membrane permeability and protease resistance of peptoids. The results observed in the biodistribution studies could be confirmed by PET imaging, which provides a reliable way to evaluate *in vivo* pharmacokinetic properties of peptoids noninvasively and in real time. The pharmacokinetic data presented here can provide insight for further development of the antimicrobial peptoids as pharmaceuticals.

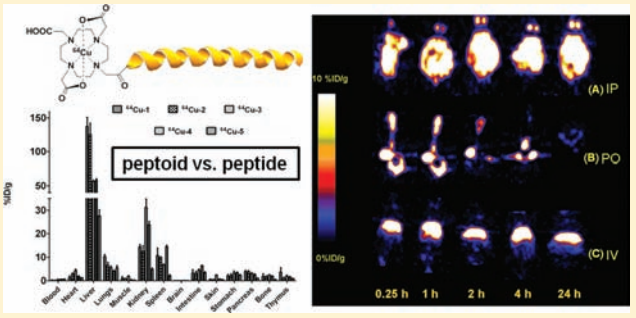

INTRODUCTION

Over recent decades, a number of antimicrobial peptides (AMPs) have been identified as a front-line defense in various host organisms.[1,2] AMPs have drawn great scientific interest because they not only belong to the intrinsic host-defense system,[3−6] but also are promising candidates for the development of novel anti-infective agents.[7,8] Natural AMP-based therapeutics demonstrate activities against broad-spectrum pathogens *in vitro*; however, they exhibit major drawbacks *in vivo* such as their low resistance against proteolysis and rapid clearance by the kidneys.[9,10] Recently, the challenges associated with peptides are being addressed owing to the use of non-natural amino acids and modified peptide structures;[11,12] hence, various peptidomimetics that are designed to reproduce critical AMP structural characteristics, such as spatially segregated cationicity and hydrophobicity in an amphipathic secondary structure, have been developed.[13−18] Particularly, short (<40 amino acids), cationic, linear, and α-helical AMPs are amenable to mimicry, and peptoids are among the front-runners in mimicking this class of AMPs.

Peptoids (oligo-*N*-substituted glycines) are a novel class of peptidomimetics that differ from peptides only in that side chains are attached to the backbone amide nitrogen instead of the α-carbon (Figure 1).[19,20] This unique structural feature of peptoids leads to quite different pharmacological properties from natural peptides: (1) they are highly stable against proteases;[21,22] (2) they lack hydrogen-bonding potential, which further prevents backbone-driven aggregation and thus increases bioavailability;[23,24] (3) they show increased cell permeability over

Received: February 23, 2012
Revised: April 3, 2012
Published: April 9, 2012

A

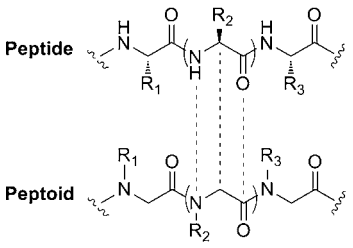

B

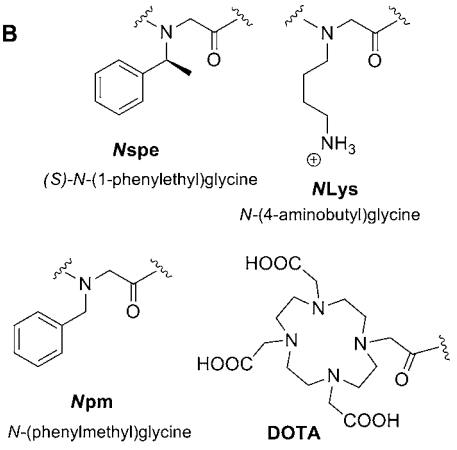

C

compound name		sequence
unmetalated	radiolabeled	
1	**^{64}Cu-1**	DOTA-(*N*Lys-*N*spe-*N*spe)$_4$-NH_2
2	**^{64}Cu-2**	DOTA- *N*Lys-*N*spe-*N*pm-(*N*Lys-*N*pm-*N*pm)$_3$-NH_2
3	**^{64}Cu-3**	DOTA-(*N*Lys-*N*spe-*N*spe)$_3$-*N*Lys-*N*spe -NH_2
4	**^{64}Cu-4**	DOTA-(Lys-Phe-Phe)$_4$-NH_2
5	**^{64}Cu-5**	DOTA-Gly-Ile-Gly-Lys-Phe-Leu-Lys-Lys-Ala-Lys-Lys-Phe-Gly-Lys-Ala-Phe-Val-Lys-Ile-Leu-Lys-Lys-NH_2

Figure 1. (A) Comparison of peptide and peptoid. (B) Chemical structures of peptoid submonomers and DOTA. (C) Sequences of the synthesized DOTA conjugates and corresponding compound names.

peptides;[23,25] and (4) they may evade immune recognition.[26] Peptoids can be readily synthesized using a conventional solid-phase peptide synthesis (SPPS) method, and diverse sequences of peptoids can be prepared at relatively low cost. They are also precisely tunable in conjugation with established synthetic methods.[27] Since their development in the early 1990s, peptoids have become attractive scaffolds for many different biological applications.[28−30] For example, the use of peptoids as antimicrobial agents,[31−36] molecular transporters for intracellular drug delivery,[37] or ligands for tumor receptor binding has been reported.[25]

Among many peptidomimetic systems under study, peptoids are particularly well suited for structural mimicry of AMPs[31,32] because they can readily form helical secondary structures via a periodic incorporation of bulky, α-chiral side chains.[38−40] The structures of the peptoid helices have been characterized to be stable polyproline type-I-like helices which exhibit a pitch of 6.0−6.7 Å and a periodicity of approximately three residues per turn.[41−43] The threefold periodicity of the peptoid helix makes it easier to mimic the facially amphipathic structures similar to those found in many AMPs; for example, the trimer repeat $(X\text{-}Y\text{-}Z)_n$ forms a peptoid helix with three faces, composed of X, Y, and Z residues. Previously, a group of cationic amphipathic peptoids, with broad-spectrum antimicrobial activity against both Gram-positive and Gram-negative bacteria including clinically relevant biosafety level 2 (BSL-2) pathogens, has been discovered.[31−34] Interestingly, these antimicrobial peptoids also show potential in treating multidrug resistant strains such as *Pseudomonas aeruginosa* biofilms[35] and *Micobacterium tuberculosis*.[36] Furthermore, we recently found that the cationic amphipathic peptoids were potent against several cancer cell lines at low micromolar concentrations, and their actions were not affected by multidrug resistance (MDR) developed in cancer cells.[44] Therefore, cationic amphipathic peptoids represent an excellent molecular platform for the development of antimicrobials as well as cytotoxic chemotherapeutics and warrant systematic investigations on their *in vivo* behaviors.

The *in vivo* pharmacokinetic studies on antimicrobial peptides have been reported using radiolabeled peptides;[45,46] however, we cannot simply extrapolate peptoid biodistribution from previous peptide biodistribution data. First, due to the lack of hydrogen-bond donors in the peptoid backbone, the hydrodynamic radii of peptides and peptoids are expected to be significantly different.[24] Second, peptoids are protease-resistant and metabolically more stable than peptides.[21,22] For these reasons, the pharmacokinetic profiles of peptoids are likely to be different from what was observed with peptides, and a new set of pharmacokinetic data are required for better understanding the *in vivo* behavior of this unique family of peptidomimetics.

Recently, we found that antimicrobial peptoids showed different *in vitro* antimicrobial activity depending on their degree of helicity, chain length, and hydrophobicity (Table 1; note that the biological data are for oligomers without DOTA conjugation). Then, we reasoned that the different structural and physicochemical properties could also cause distinct *in vivo* pharmacokinetic profiles of the peptoids. Herein, three cationic amphipathic peptoids and two control peptides were selected, and their *in vivo* profiles were evaluated using both biodistribution and small animal positron emission tomography (PET). Peptoids **1**, **2**, and **3** represent N-terminal 1,4,7,10-tetraazacyclododecane-1,4,7,10-tetraacetic acid (DOTA) conjugates of cationic amphipathic peptoids (Table 1 and Figure 1). Peptoids **1** and **3**, where the latter is almost identical to **1** except that it has one less C-terminal Nspe monomer, are linear peptoid

Table 1. Properties of 1−5

compounds	class	chain length[a]	secondary structure[b]	hydrophobicity (t_R in minutes)[d]	antimicrobial activity[e]	
					E. coli MIC, μM	selectivity ratio[f]
1	peptoid	12	helical	25.0	3.5−6.3	6.0
2	peptoid	12	almost unstructured	24.1	6.3	205
3	peptoid	11	helical	23.9	6.3	132
4	peptide	12	helix-like	24.0	ND	ND
5	peptide	22	random coil[c]	21.3	3.1−6.3	24

[a]Number of peptoid or peptide residues. [b]Determined by circular dichroism spectroscopy. [c]Fold into helical conformation upon binding to lipid membranes.[47,48] [d]Detailed HPLC conditions are provided in the Experimental Procedure section. HPLC chromatograms are shown in the Supporting Information (t_R: retention time in reverse phase HPLC column). [e]Biological data are for peptoids or peptides without DOTA conjugation. MIC (minimum inhibitory concentration) values and selectivity ratios for **1** and **5** are from ref 32, and for **2** and **3** are unpublished results. [f]Selectivity ratio = (HD_{10})/(*E. coli* MIC). HD_{10}: 10% hemolytic dose.

helices. Peptoid **3** (without DOTA) has lower hydrophobicity than peptoid **1** (without DOTA) and was recently found to have substantially higher selectivity in killing bacterial cells without significant loss in potency (Table 1). Peptoid **2** (without DOTA) is a nonstructured peptoid, which nonetheless can adopt a helical conformation in the presence of the anionic bacterial membrane that serves as an organizing surface. For comparison, we tested two cationic amphipathic peptide controls: (1) peptide **4** has a direct sequence homology to peptoid **1**, and the effect of the peptoid backbone versus the peptide backbone was examined; and (2) peptide **5** is based on a well-known antimicrobial peptide, namely, pexiganan,[47,48] which advanced to phase 3 clinical trials.[49] Also known as MSI-78, pexiganan exhibits a random coil conformation, which folds into a helical conformation upon binding to a bacterial membrane (Table 1). To obtain kinetic data for the biodistribution and clearance for 24 h, a radionuclide with an appropriate half-life was needed. Therefore, DOTA-chelated ^{64}Cu was used due to its relatively long half-life (762 min) and numerous precedent biodistribution data of the DOTA-^{64}Cu labeled peptides.[50−52] With the radiolabeled peptoids and peptides, three different administration routes (intravenous, intraperitoneal, and oral) were examined. The results reported here can provide insight for future development of peptoids as antimicrobial chemotherapeutics.

EXPERIMENTAL PROCEDURES

Materials. All reagents were purchased from Sigma-Aldrich, Fisher, and Novabiochem. They were used without further purification unless stated otherwise. DOTA-tris(*t*-Bu ester) (or tri-*tert*-butyl 1,4,7,10-tetraazacyclododecane-1,4,7,10-tetraacetate) was purchased from Macrocyclics, TX, USA. *N,N′*-Diisopropylcarbodiimide was purchased from Advanced ChemTech, KY, USA. Radioisotope ^{64}Cu was purchased from the Department of Medical Physics, University of Wisconsin, Madison, WI, USA. Six-week-old Balb/c mice were ordered from Harlan, CA, USA.

Synthesis and Purification. The peptoid oligomers were synthesized by solid-phase submonomer method using an automated peptide synthesizer (ABI 433A, Applied Biosystems, CA, USA).[20,53] Rink amide resin (0.60 mmol/g, Novabiochem, San Diego, CA) was used to generate C-terminal amide peptoids. After Fmoc deprotection, each monomer was added by a series of bromoacetylation and displacement by an amine. These two steps were iterated with appropriate amines until the desired peptoid sequence was obtained. Typically, 0.06 mmol reaction scale was used (0.1 g of the resin). For bromoacetylation, the addition of bromoacetic acid (1 mL, 1.2 M in *N,N*-dimethylformamide (DMF), 1.2 mmol) followed by *N,N′*-diisopropylcarbodiimide (0.15 mL, neat, 1.0 mmol), and then agitation at room temperature for 20 min were performed. For the displacement reaction, primary amine (1 mL, 1.5 M in *N*-methylpyrrolidone (NMP), 1.5 mmol) was added, and the reactor was agitated at room temperature for 1 h. The resin was washed with DMF (6 mL × 5) between each step. Peptide oligomers were prepared by the automated solid-phase peptide synthesis according to standard Fmoc/tBu-methodology and HBTU/HOBt/DIEA coupling.[54] Rink amide resin (0.60 mmol/g) was used to obtain C-terminal amide peptides. After completion of the solid-phase synthesis, the DOTA chelator was manually conjugated at the N-terminus of the pepoids or peptides by activating the carboxylic acid of DOTA-tris(*t*-Bu ester) with HATU. Peptoid (or peptide) attached on resin (properly protected, 0.025 mmol) was swelled in DMF (2 mL). To this was added DOTA-tris(*t*-Bu ester) (0.15 mmol), 2-(7-aza-1*H*-benzotriazole-1-yl)-1,1,3,3-tetramethyluronium hexafluorophosphate (HATU) (0.30 mmol), and *N,N*-diisopropylethylamine (DIPEA) (0.75 mmol), and the reaction continued at room temperature overnight.[55] Cleavage from the resin and deprotection were performed with 95:2.5:2.5 TFA/water/triisopropylsilane (v/v/v) for 2−3 h at room temperature. It should be noted that shorter cleavage time resulted in incomplete *tert*-butyl ester deprotection of DOTA-tris(*t*-Bu ester). The cleavage solution was filtered by solid-phase extraction (SPE) cartridges (Applied Separations, Allentown, PA, USA) and the volatiles were removed by a stream of nitrogen. The crude peptoid was dissolved in acetonitrile/water, lyophilized, and analyzed by ESI-MS (or MALDI-TOF) and analytical HPLC.

Analytical HPLC was performed on a Waters 2695 separations module system with Waters 2998 photodiode array detector and Waters Alliance column heater. Phenomenex Jupiter C18 (250 × 2.0 mm, 5 μ, 300 Å) column was used for the analytical HPLC and the column was heated at 55 °C. Sample purity was monitored by absorbance at 220 nm. The mobile phase was used as follows: [A, water + 0.1% trifluoroacetic acid (TFA); B, CH_3CN + 0.1% TFA] 3 min using 1% B, then a linear gradient to 99% B over 30 min, a linear gradient back to 1% B over 10 min, and then 2 min using 1% B. Flow rate of the analytical HPLC was 0.2 mL/min.

The peptoids or peptides were purified by a preparative HPLC system (Waters PrepLC system, Waters 2489 UV/Visible detector, Waters fraction collector III) using a C18 column (Phenomenex Jupiter C18, 250 × 21.20 mm, 10 μm, 300 Å) at a flow rate of 25 mL/min. Sample elution was detected by absorbance at 220 and 260 nm. The purity of the product fractions was confirmed by analytical HPLC, and fractions containing pure product (>98% purity) were collected, lyophilized, and stored at −80 °C.

dx.doi.org/10.1021/bc300091d | *Bioconjugate Chem.* 2012, 23, 1069−1079

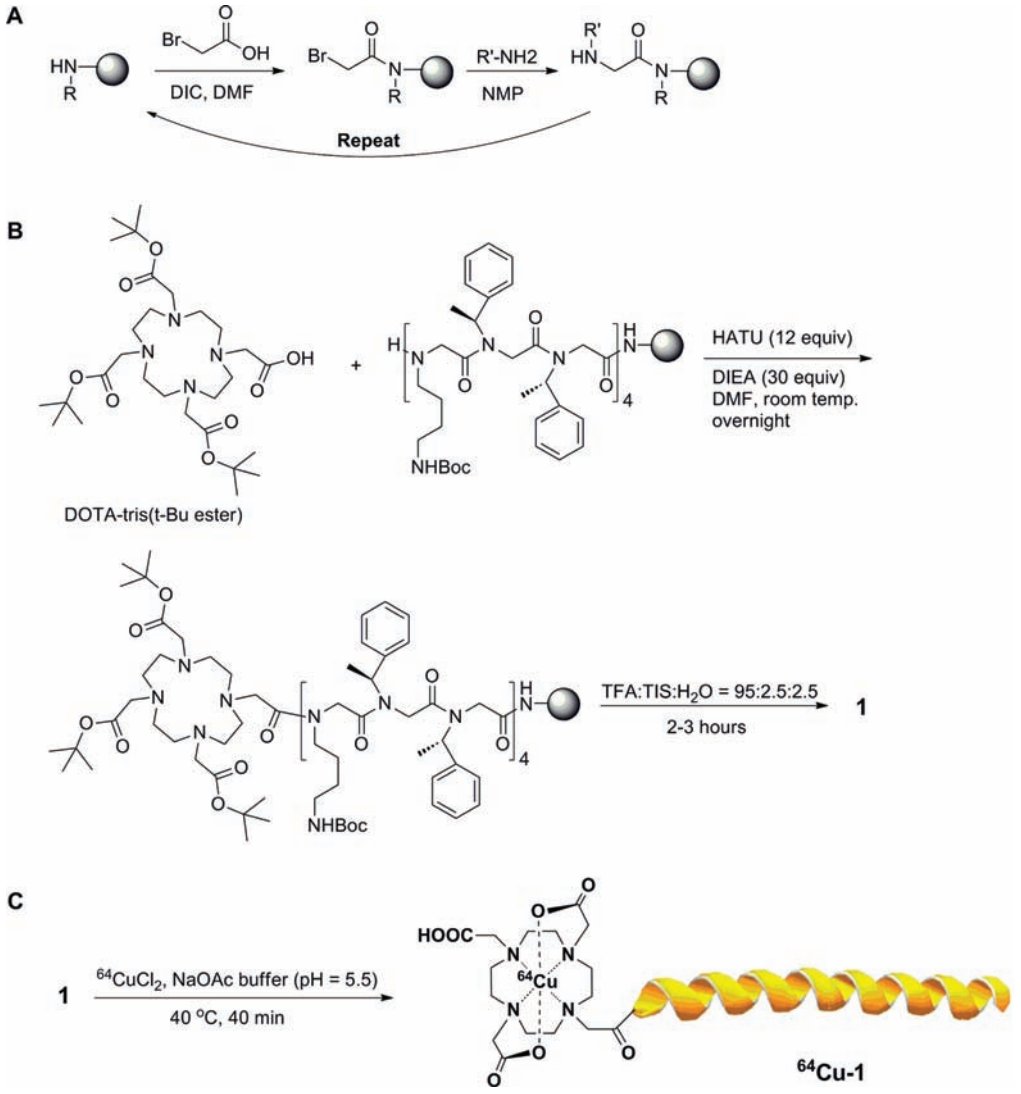

Figure 2. (A) Peptoid submonomer synthesis protocol. (B) Representative synthetic scheme of DOTA conjugates. (C) Illustrative structure of ^{64}**Cu-1** prepared by ^{64}Cu radiolabeling of DOTA conjugate **1**.

For electrospray ionization mass spectrometry (ESI-MS) analysis of compounds, ThermoFinnigan LCQ "Classic" ion trap LC-MS instrument was used (Stanford University Mass Spectrometry facility). Voyager-DE RP Biospectrometry instrument was used for matrix-assisted laser desorption/ionization time-of-flight (MALDI-TOF) mass spectrometry (Stanford University PAN facility).

Circular Dichroism Spectroscopy. Typical procedure for the preparation of **Cu-1**−**Cu-4** (for CD study) is as follows. Compound **1** (1.0 mg) was dissolved in NaOAc buffer (0.1 M, pH 5.5, 940 μL). To this was added 10 mM $CuCl_2$ (60 μL, approximately 2.0 mol equiv). The reaction mixture was incubated at room temperature overnight with gentle agitation. The reaction was monitored by analytical HPLC and stopped when the starting material (compound **1**) was consumed. D-Salt polyacrylamide desalting column (Pierce, Rockford, IL, USA) was used to purify the crude product. The purification was carried out according to the manufacturer's instruction. The column fractions were monitored by measuring the absorbance at 220 nm using Nanodrop spectrophotometer. Fractions containing **Cu-1** were combined and lyophilized.

Circular dichroism measurements were carried out at 20 °C with a Jasco J-815 circular dichroism spectrometer (Jasco, Inc., Easton, MD, USA). CD spectra were obtained in an 1 mm path length quartz cell and recorded from 190 to 260 nm in 1 nm increments with a scanning speed of 20 nm/min and a response time of 4 s. Three scans for each sample were averaged. Sample concentrations were in 50 μM. Data are expressed in terms of per-residue molar ellipticity (deg cm^2/dmol) calculated per number of amides in a molecule.

Radiolabeling. DOTA-conjugated compounds (10 μg) were used for labeling. The bioconjugate was radiolabeled with ^{64}Cu by addition of $^{64}CuCl_2$ (111 MBq, 3 mCi) in NaOAc buffer (pH 5.5, 0.1 N) followed by a 40 min incubation at 40 °C. EDTA (5 μL, 10 mM) was then added to quench free $^{64}Cu^{2+}$. The radiolabeled complex was purified by analytical radio-HPLC. The mobile phase was used as follows: [A, water + 0.1% TFA; B, CH_3CN + 0.1% TFA] 3 min using 5% B, then a linear gradient to 65% B over 30 min, then going to 85% B over 3 min, maintaining this solvent composition for another 3 min, and then a linear gradient back to 5% B over 3 min (total 42 min). Flow rate of the radio-HPLC was 1.0 mL/min. Fractions containing pure radiolabeled peptoid (or peptide) were

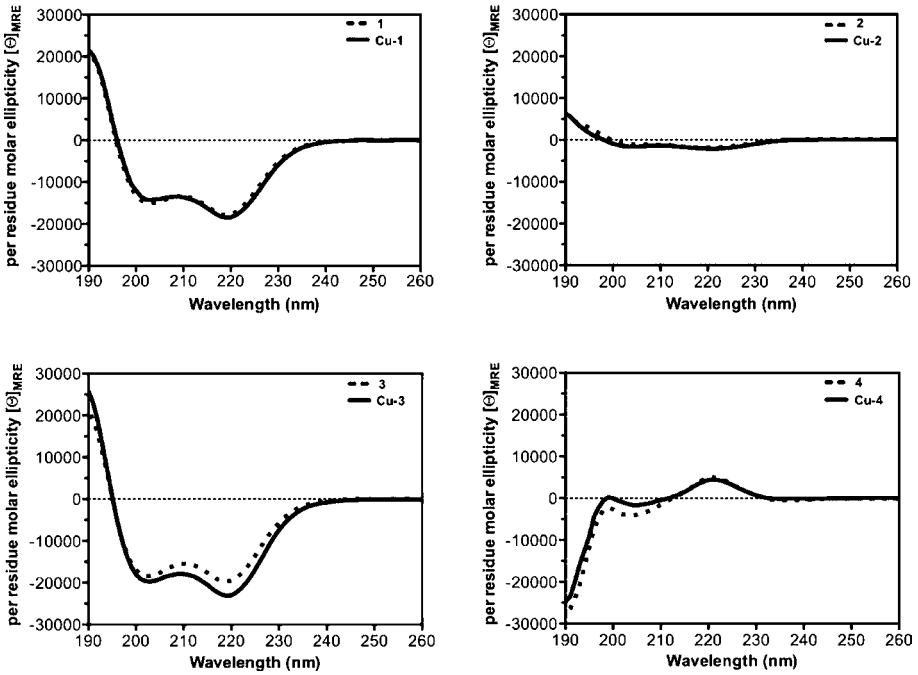

Figure 3. CD spectra of **1**−**4** and **Cu-1**−**Cu-4** in water (50 μM, 20 °C) were recorded as per-residue molar ellipticity (deg cm^2/dmol).

combined and dried under reduced pressure using rotary evaporator. The radiolabeled compound was reconstituted in phosphate-buffered saline (PBS) and passed through a 0.22 μm Millipore filter into a sterile vial for *in vitro* and animal experiments.

Biodistribution. ^{64}Cu-DOTA-peptoids or peptides (30−40 μCi) were injected into a tail vein in Balb/c mice (n = 4 for each group), and then the mice were sacrificed at 2 and 24 h p.i. For peptoid **^{64}Cu-1**, three administration routes including intraperitoneal (i.p.), intravenous (i.v.) or gavages needle (p.o.) injection were used to compare the *in vivo* profiles of the peptoid. Major organs were excised and weighed, and their radioactivity was measured in a Wallac 1480 automated γ-counter (Perkin-Elmer, MA, USA). The radioactivity uptake in the organs was expressed as a percentage of the injected radioactive dose per gram of tissue (% ID/g).

Small Animal PET Imaging. Small animal PET imaging of Balb/c mice was performed on a microPET R4 rodent model scanner (Siemens Medical Solutions USA, Inc., Knoxville, TN, USA). The mice were injected with ^{64}Cu-DOTA-peptoids or peptides (~40 μCi) through the tail vein. A dynamic image of the first 35 min and a series of static images were acquired. During the scan, anesthesia was maintained with 2% isofluorane in 1 L/min oxygen, and imaging was performed in a prone position. For dynamic scan, image acquisition was initiated once the mice were centered in the field of view. Radiolabeled peptoid was administered with immediate data collection and image acquisition. Acquisition lasted about 35 min. Image reconstruction was performed by a two-dimensional OSEM (ordered subsets expectation maximum) algorithm with a spatial resolution of 1.66−1.85 mm. No attenuation or partial volume corrections were performed. Regions of interest (ROIs) were selected using ASIPro VM software (Siemens Medical Solutions USA Inc., Knoxville, TN, USA). For static scan at different times p.i. (0.25, 1, 2, 4, and 24 h), the mice were anesthetized with 2% isofluorane and placed in the prone position and in the center of the field of view of microPET. The 5 min static scans were obtained, and the images were reconstructed by the OSEM algorithm. PET images were imported using ASIPro VM. ROIs were drawn manually over the organ of interest on decay-corrected whole-body coronal images. The mean counts per pixel per minute were obtained from the ROIs and converted to counts per milliliter per minute by using a calibration constant. No attenuation correction was performed.

Statistical Methods. Statistical analysis was performed using the Student's t-test for unpaired data. A 95% confidence level was chosen to determine the significance between groups, with $P < 0.05$ being significantly different.

RESULTS

Synthesis and Radiolabeling. Five DOTA conjugated compounds (three different cationic amphipathic peptoids **1**−**3** and two peptide controls **4**−**5** in Figure 1) were successfully synthesized by solid-phase synthesis followed by N-terminal DOTA conjugation. Both peptoid and peptide sequences were synthesized by automated peptide synthesizer according to the submonomer protocol[20] and standard Fmoc/*t*Bu method,[54] respectively (Figure 2A). Then, the DOTA chelator was manually conjugated at the N-terminus of the pepoids or peptides by activating the carboxylic acid of DOTA-tris(*t*-Bu ester) with HATU (Figure 2B).[55] After deprotection and cleavage from the resin with trifluoroacetic acid, the DOTA conjugates were purified by preparative HPLC. It should be noted that less than 2 h of cleavage/deprotection resulted in incomplete *tert*-butyl ester deprotection of DOTA-tris(*t*-Bu ester); therefore, 2−3 h of cleavage reaction were used for all five compounds. The identity of each compound was confirmed by mass spectrometry (Supporting Information, Table S1).

Subsequently, the conjugates were radiolabeled with ^{64}Cu in order to monitor their *in vivo* behaviors (Figure 2C). The purification of radiolabeled complex, using a PD-10 column, afforded ^{64}Cu-DOTA-peptoid/peptide (**^{64}Cu-1**−**^{64}Cu-5**) with >95% radiochemical purity and modest specific activity of 3.98−6.83 MBq/nmol. Further mouse serum stability test

dx.doi.org/10.1021/bc300091d | *Bioconjugate Chem.* 2012, 23, 1069−1079

demonstrated that over 95% radiolabeled complexes remained intact after 1 h incubation at 37 °C (Supporting Information, Figure S5).

Circular Dichroism Studies. Conformational information of unmetalated **1**−**4** as well as copper-incorporated conjugates **Cu-1**−**Cu-4** was obtained by circular dichroism (CD) spectroscopy (Figure 3). CD study of pexiganan was previously reported (Table 1);[56] therefore, compound **5** was not included in this study. For the CD study, nonradioactive copper-bound DOTA conjugates, namely, **Cu-1**−**Cu-4**, was prepared, and the physicochemical properties of radioactive and nonradioactive copper compounds are assumed to be the same.

For helical peptoid conjugates **1** and **3**, the maintenance of helical folds was observed after copper incorporation (**Cu-1** and **Cu-3**). In addition, conformations of **1** and **Cu-1** at body temperature (37 °C) were examined and indicated minimal temperature dependence at 20 and 37 °C (Supporting Information, Figure S2). As predicted, compounds **2** and **Cu-2** indicated an almost unstructured conformation due to the lack of structure-inducing residue, *N*spe or (*S*)-*N*-(1-phenylethyl)glycine, in the peptoid sequence. Uncharacteristic, but α-helix-like, CD signatures were obtained for **4** and **Cu-4**, and the handedness was the opposite of the peptoid conjugates' handedness. The CD spectra in this study clearly showed that the influence of copper incorporation on the overall conformation was minimal.

Biodistribution. Radiolabeled peptoids and peptides ^{64}**Cu-1**−^{64}**Cu-5** were injected intravenously into a tail vein in Balb/c mice. After 2 and 24 h postinjection (p.i.), the mice were euthanized, and the radioactivity of the organs and the blood was determined. The activity in the selected organs was expressed as a percentage of the injected radioactivity per gram of tissue (%ID/g). The results of the biodistribution studies are summarized in Figure 4.

Peptoid conjugates ^{64}**Cu-1** and ^{64}**Cu-2** exhibited prominent uptake in the liver, with lower liver uptake for ^{64}**Cu-2** than ^{64}**Cu-1**. The detected activity in the liver was 137.6 ± 13.4%ID/g for ^{64}**Cu-1** and 125.3 ± 16.8%ID/g for ^{64}**Cu-2** at 2 h p.i., and the activity remained at 95.6 ± 10.5%ID/g for ^{64}**Cu-1** and 72.2 ± 11.3%ID/g for ^{64}**Cu-2** at 24 h p.i. Compared with ^{64}**Cu-1** and ^{64}**Cu-2**, ^{64}**Cu-3** exhibited lower liver uptake at both 2 and 24 h p.i. with 56.7 ± 1.8%ID/g and 47.3 ± 4.4%ID/g, respectively. Unlike the liver uptake, ^{64}**Cu-3** showed the highest kidney uptake, which was around 31.2 ± 3.6%ID/g at 2 h, while it was 14.4 ± 0.9%ID/g and 12.55 ± 2.3%ID/g for ^{64}**Cu-1** and ^{64}**Cu-2**, respectively. At 24 h p.i., the activity of ^{64}**Cu-3** in the kidney remained 19.3 ± 2.6%ID/g, which was the highest level of all the conjugates tested in this study.

As for the peptide controls, both ^{64}**Cu-4** and ^{64}**Cu-5** showed lower liver uptake and faster liver clearances compared to all three peptoid conjugates ($P < 0.05$). ^{64}**Cu-4** has a direct sequence homology to ^{64}**Cu-1** and a similar hydrophobicity to ^{64}**Cu-2** (Table 1). Compared to both peptoids, ^{64}**Cu-4** showed lower liver uptake and higher kidney uptake at 2 h p.i. (Figure 4A), reminiscent of the different hydrodynamic radii coming from the lack of hydrogen-bond donors in the peptoid backbone. Then, the kidney activity of ^{64}**Cu-4** decreases faster and becomes similar to that of ^{64}**Cu-2** at 24 h p.i. (Figure 4B), which can be explained by the higher *in vivo* stability of peptoids over peptides. Between the two peptides, less hydrophobic ^{64}**Cu-5** exhibited lower liver uptake than ^{64}**Cu-4** did. In addition, ^{64}**Cu-5** had a much lower spleen uptake than the other four conjugates tested at both 2 and 24 h. All three peptoids and two peptides showed minimal brain uptake (lower than 1%ID/g), suggesting their incapability of crossing the blood-brain-barrier.

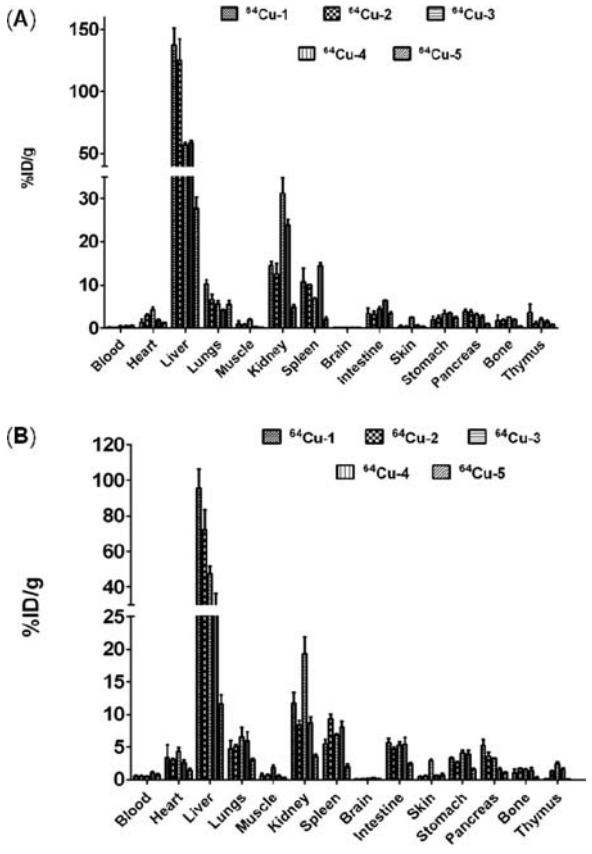

Figure 4. Biodistribution of ^{64}**Cu-DOTA-peptoids/peptides** (^{64}**Cu-1**−^{64}**Cu-5**) in Balb/c mice at 2 h (A) and 24 h (B). Data were expressed as mean ± SD, indicating the percentage administered activity (injected dose) per gram of tissue (%ID/g) after intravenous injection of about 40 μCi (1.48 MBq) tracers (n = 4).

The effects of different administration routes (oral, intravenous, and intraperitoneal) on the *in vivo* biodistribution were then examined using ^{64}**Cu-1** (Supporting Information, Figure S3). When administered intraperitoneally, predominant disposition of ^{64}**Cu-1** was in the abdomen region. After intraperitoneal injection, activity was detected in most abdomen organs including intestine, colon, stomach, liver, spleen, and pancreas, and the activity persisted through 24 h. Significant kidney and thymus uptake was also observed after the intraperitoneal injection. When administered orally, the activity in stomach reached up to 4.82 ± 1.44%ID/g at 2 h and then dropped to 0.54 ± 0.22%ID/g at 24 h. The uptake of ^{64}**Cu-1** could only be measured in the digestive system (i.e., stomach, small intestine, colon), suggesting that ^{64}**Cu-1** cannot be absorbed into blood circulations when administered orally.

Small-Animal PET Imaging. Imaging studies were conducted at 0.25, 1, 2, 4, and 24 h after tail vein injection of ^{64}**Cu-1**−^{64}**Cu-5**. Decay-corrected coronal microPET images are shown in Figure 5. Three peptoids and two peptides displayed different *in vivo* distribution patterns; particularly, uptakes in liver and in kidney were noticeable. For ^{64}**Cu-1** and ^{64}**Cu-2**, the main excretion route is likely hepatic; little kidney activity was observed. ^{64}**Cu-3** demonstrated the highest kidney activity of all three peptoids. Compared to peptoids, higher kidney activity and lower liver activity were observed for peptides.

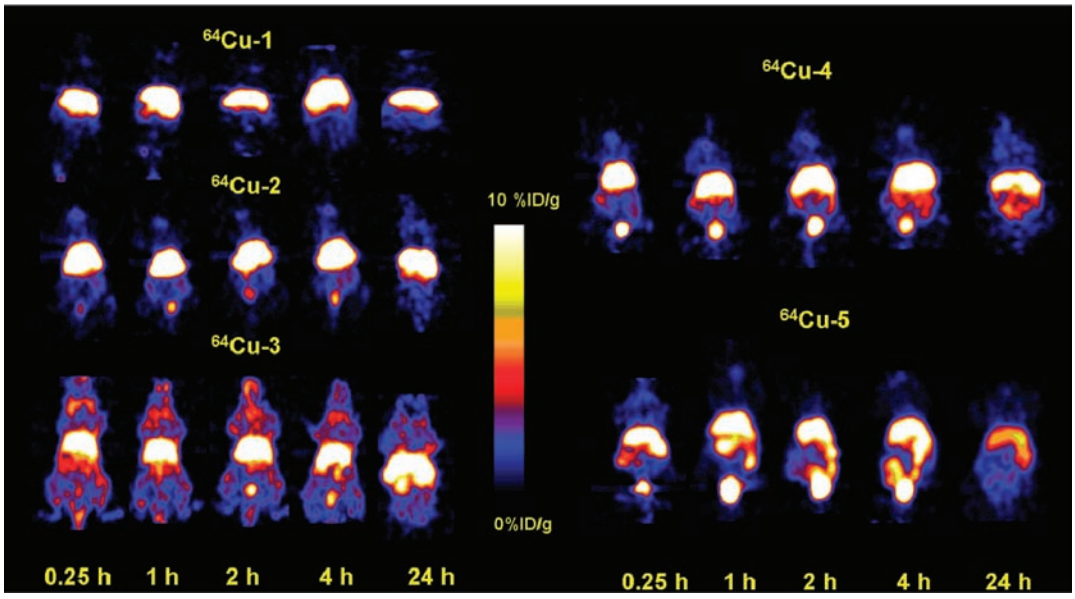

Figure 5. Representative decay-corrected coronal small-animal PET images of Balb/c mice at different time points after intravenous (iv) injection of ^{64}**Cu-1**–^{64}**Cu-5** (n = 4 for each group).

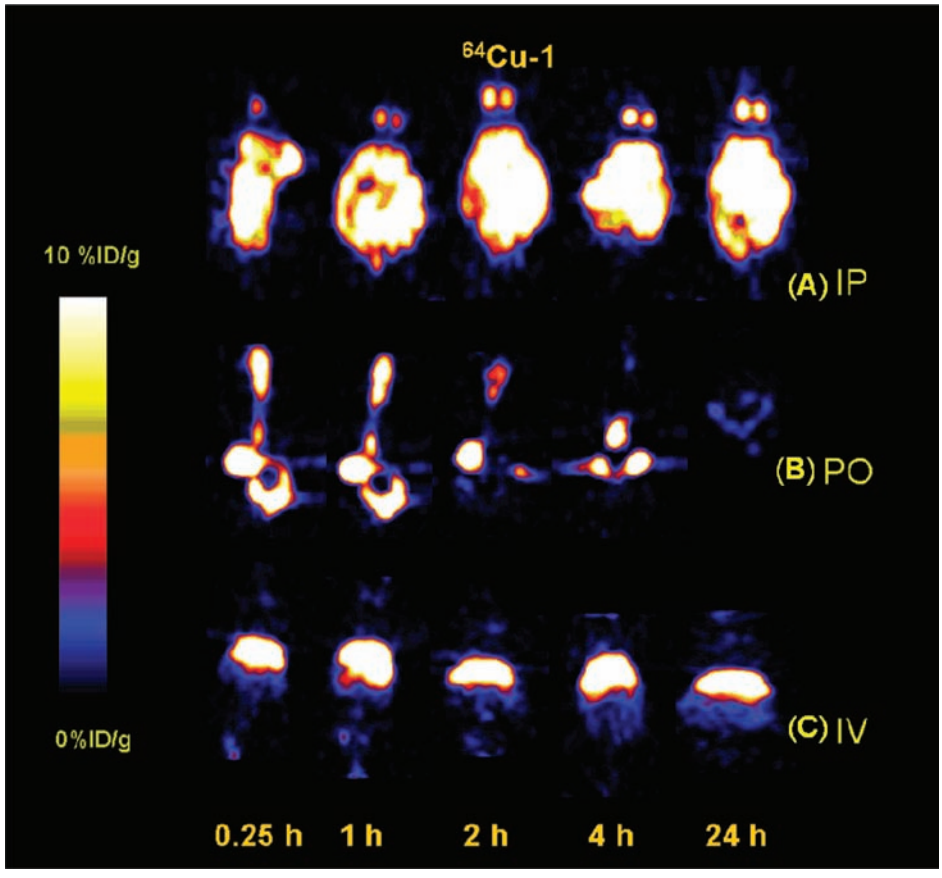

Figure 6. Representative decay-corrected coronal small-animal PET images of Balb/c mice at different time points after administration of ^{64}**Cu-1** through peritoneal (A), oral (B), and intravenous (C) injections (n = 4 for each group).

Among the tested conjugates, ^{64}**Cu-5** showed fastest clearance in both hepatic and renal pathways. Activity in the gastrointestinal (GI) tract could also be observed for all tested compounds, but markedly lower for ^{64}**Cu-1**.

The distribution patterns of ^{64}**Cu-1** with different administration routes were compared and shown by PET imaging (Figure 6). Radioactivity was found throughout the whole abdominal cavity when ^{64}**Cu-1** was administered intraperitoneally. The permissive activity in abdomen clears rather slowly; therefore, it was complicated to differentiate organs in 24 h based upon PET imaging. Interestingly, a symmetrical anatomical structure was distinctly visible inside the upper body

dx.doi.org/10.1021/bc300091d | *Bioconjugate Chem.* 2012, 23, 1069–1079

of the mice after the intraperitoneal administration of ^{64}**Cu-1**, and biopsy confirmed the symmetrical organ as thymus. Thymic uptake has been reported for several radioactive pharmaceuticals such as ^{18}F-fluorodeoxyglucose (^{18}F-FDG), radioiodine, and gallium-67 citrate; however, the mechanism through which it occurs is not completely understood.[57,58] When ^{64}**Cu-1** was administered through the tail vein, the compound essentially accumulated in the liver through 24 h as described above. Very low GI activity and kidney activity were observed in 24 h. In mice with orally administrated ^{64}**Cu-1**, only GI activity was observed initially, and the peptoid conjugate was eliminated after 24 h as seen from PET imaging at 24 h p.i. A similar distribution pattern was observed for the oral administration of ^{64}**Cu-3** (Supporting Information, Figure S4).

DISCUSSION

Designed to mimic naturally occurring proteins and peptides, peptoids are interesting materials whose properties lie in between natural biopolymers and non-natural synthetic polymers. The structural similarity to peptides enabled peptoids to exhibit an impressive diversity of biological activity;[28−30] however, the slight variation of backbone structure provides peptoids with distinct pharmacological properties such as resistance to proteolysis.[21−23]

Previously, a library of cationic amphipathic peptoids were synthesized based upon defined sequences and variations of secondary structures. It was demonstrated that the main chain length, helicity, charge, and hydrophobicity of peptoids could alter the *in vitro* antimicrobial activity.[31,32] Similarly, we envisioned that the modulation of peptoid structure could influence the *in vivo* pharmacokinetic profiles and biodistribution, which is critical information for further development of antimicrobial peptoids as therapeutic agents.

Previous *in vivo* data on biodistribution of peptoids are limited. Wang et al. used a ^{3}H-labeled tripeptoid to test the absorption and disposition in rats and compared the labeled tripeptoid to a ^{3}H-labeled tetrapeptide.[59] The tripeptoid appeared to be more metabolically stable, but showed lower oral absorption and more rapid biliary excretion. Although the *in vivo* pharmacokinetic properties of peptoid were investigated, the peptoids tested by Wang et al. can be classified as a small molecule with molecular weight less than 500 Da. In our present study, we examined antimicrobial peptoids that have secondary structures and molecular weight higher than 1500 Da, which render the peptoids similar to small proteins rather than to small molecules. Since distinct pharmacological properties between small and large molecules are reported,[60] biodistribution study of the antimicrobial peptoids is important for further *in vivo* applications.

When designing radiolabeled conjugates, we chose ^{64}Cu-DOTA labeling at the N-terminus of peptoids because we expected (1) more straightforward synthesis and (2) less impact on the peptoid secondary structure. The latter was confirmed by CD study. The comparison of CD spectra before and after N-terminal DOTA conjugation indicated nearly identical CD signatures: the intensity of spectral maxima at 190 nm and minima at 220 nm did not change much.[32] If the labeling was made on the side chain, the impact on the peptoid conformation could be larger. CD spectra in Figure 3 clearly demonstrate minimal conformational change after Cu^{2+} binding. Although our observation proves neither DOTA conjugation nor metalation changed the CD signature of peptoid, this does not prove that the peptoid with complexed Cu^{2+} has the same pharmacokinetic characteristics. Nonetheless, the CD data prove useful as a preliminary indicator of intact peptoid conformation after radiolabeling.

The hepatobiliary system and the kidneys are the major routes by which drugs and their metabolites are eliminated from the body. Generally, small and hydrophilic organic compounds are preferentially excreted via the kidneys. In contrast, compounds with relatively high molecular weight (>500 Da) and amphipathic structure are mainly excreted via the liver (and then into bile).[60,61] As large and amphipathic compounds, ^{64}**Cu-1**−^{64}**Cu-5** all showed that major uptake and excretion occurred in the liver; however, different uptake profiles in the liver and in the kidney are observed for each conjugate by the combined effect of the structure, hydrophobicity, and resistance to proteolysis (Figures 4 and 5).

After intravenous administration, biodistribution studies of ^{64}**Cu-1** demonstrated highest liver accumulations at both 2 and 24 h (Figure 4). A slow elimination from the liver region was observed by PET images (Figure 5). Although the secondary structures of ^{64}**Cu-1** and ^{64}**Cu-2** are very distinct, they showed similar *in vivo* pharmacokinetics based on biodistribution and microPET studies, suggesting their overall hydrophobicity and amphipathicity. At both 2 and 24 h p.i., ^{64}**Cu-3** showed the highest level of kidney uptake among all three peptoids and two peptides tested (Figure 4). With only one shorter hydrophobic residue than ^{64}**Cu-1**, ^{64}**Cu-3** showed more than 50% lower liver uptake and noticeably higher kidney uptake; and this result exemplifies the strong influence of structural modification on *in vivo* biodistribution. Both biodistribution and PET results indicated faster clearance of peptide controls compared to peptoids (Figures 4 and 5). ^{64}**Cu-5** indicated lowest uptake in both the liver and the kidney and fastest elimination. Along with the hydrophilic property of ^{64}**Cu-5**, the random coil structure, therefore vulnerability to proteolysis, can explain the result.

Different administration routes were investigated with ^{64}**Cu-1** and ^{64}**Cu-3**. When administered orally, the peptoids showed poor bioavailability. The minimal absorption was indicated by high activity in the GI tract and little activity in the liver or in the kidney system (Supporting Information, Figure S3 and S4). For peptides, poor oral bioavailability has been widely accepted,[62] and our result suggests the similarity between peptides and peptoids in terms of the poor absorption after oral administration. However, it should be noted that peptides usually have rapid elimination kinetics in the range of minutes due to the extensive hydrolysis in the GI tract by peptidases.[63,64] Therefore, the 24 h passage through the GI tract without rapid digestion constitutes a unique aspect of peptoids, which originates from the protease resistance and the property as a non-natural biopolymer. The high *in vivo* stability of peptoids can be advantageous for some applications. If the site of action of a designed peptoid is in the GI tract, such as peptoid-based bacterial toxin sequestrants developed by Kodadek et al.[65] or antimicrobial peptoids for bacterial digestive infections, oral administration may provide a better therapeutic effect. Prolonged localized exposure to the pathogens and fewer side effects are expected due to the longer retention in the GI tract and the poor absorption to the systemic circulation, respectively.

Our data indicated that peptoids, compared to peptides, had a general *in vivo* property of higher tissue accumulation and slower elimination as well as higher stability. These observations can be rationalized in two ways: membrane permeability and protease resistance. Studies have shown that the cellular uptake could be improved by directly translating peptides into peptoids

due to the lipophilic nature and the stability of peptoids compared to those of peptides.[24,37,66] In addition, peptoids used in this study are cationic and amphipathic, which are recently found to be effective in cell membrane penetration.[44] As the first step for the tissue uptake is transport across the cell membrane (i.e., proximal tubular cells for the kidney uptake or hepatocyte cells for the liver uptake),[60,61] the efficient membrane permeability of the cationic amphipathic peptoids appears to play an important role in the higher tissue uptake. Second, the *in vivo* stability of peptoids against proteolysis provides longer circulation time, which leads to the higher tissue uptake and slower elimination.

Unique *in vivo* properties of cationic amphipathic peptoids are demonstrated in our study. Applications of the peptoids, for example, as a long-lasting liver targeting carrier or as an antimicrobial therapeutic agent against digestive infections or against urinary tract infections, now seem to be reasonable.

In conclusion, our results suggest that the *in vivo* pharmacokinetics of peptoids can be tuned by varying the structure and modifying the physicochemical properties of peptoids. In comparison to peptides, peptoids exhibited higher *in vivo* stability, higher tissue uptake, and a slower elimination rate. The *in vivo* biodistribution of peptoids can be confirmed by real-time small animal PET imaging. Using the noninvasive *in vivo* imaging approaches described here, pharmacokinetic properties of various peptoids can be predicted, which will provide useful information for suitable application and development of the peptoids.

■ ASSOCIATED CONTENT

Ⓢ Supporting Information

Supplementary figures and tables including HPLC, ESI-MS, CD spectra, biodistribution data, and PET images. This material is available free of charge via the Internet at http://pubs.acs.org.

■ AUTHOR INFORMATION

Corresponding Author

*Zhen Cheng, Ph.D.: 650-723-7866 (Phone), 650-736-7925 (Fax), E-mail: zcheng@stanford.edu. Annelise E. Barron, Ph.D.: 650-721-1151 (Phone), E-mail: aebarron@stanford.edu.

Author Contributions

#These authors contributed equally to this work.

Notes

The authors declare no competing financial interest.

■ ACKNOWLEDGMENTS

This work was supported by the DOD-PCRP-NIA (PC094646 to Z. C.), the National Institutes of Health (RO1 AI072666 to A. E. B.), and the GIST specialized research program (GIST-K02360 to J. S.).

■ ABBREVIATIONS:

AMP, antimicrobial peptide; PET, positron emission tomography; CD, circular dichroism; MBq, megabecquerel; Ci, curie; I.P., intraperitoneal; I.V., intravenous; P.O., oral; P.I., post-injection; % ID/g, percentage of injected dose per gram of tissue; GI, gastrointestinal; DOTA, 1,4,7,10-tetraazacyclododecane-1,4,7,10-tetraacetic acid; TFA, trifluoroacetic acid; TIS, triisopropylsilane; HATU, 2-(7-aza-1*H*-benzotriazole-1-yl)-1,1,3,3-tetramethyluronium hexafluorophosphate; DIEA, *N,N*-diisopropylethylamine; DMF, *N,N*-dimethylformamide; Nspe, (*S*)-*N*-(1-phenylethyl)glycine; MIC, minimum inhibitory concentration

■ REFERENCES

(1) Hancock, R. E. W., and Sahl, H. G. (2006) Antimicrobial and host-defense peptides as new anti-infective therapeutic strategies. *Nat. Biotechnol. 24*, 1551−1557.

(2) Mygind, P. H., Fischer, R. L., Schnorr, K. M., Hansen, M. T., Sonksen, C. P., Ludvigsen, S., Raventos, D., Buskov, S., Christensen, B., De Maria, L., Taboureau, O., Yaver, D., Elvig-Jorgensen, S. G., Sorensen, M. V., Christensen, B. E., Kjaerulff, S., Frimodt-Moller, N., Lehrer, R. I., Zasloff, M., and Kristensen, H. H. (2005) Plectasin is a peptide antibiotic with therapeutic potential from a saprophytic fungus. *Nature 437*, 975−980.

(3) Brown, K. L., and Hancock, R. E. W. (2006) Cationic host defense (antimicrobial) peptides. *Curr. Opin. Immunol. 18*, 24−30.

(4) Zasloff, M. (1992) Antibiotic peptides as mediators of innate immunity. *Curr. Opin. Immunol. 4*, 3−7.

(5) Hamill, P., Brown, K., Jenssen, H., and Hancock, R. E. (2008) Novel anti-infectives: is host defence the answer? *Curr. Opin. Biotechnol. 19*, 628−636.

(6) Scott, M. G., Dullaghan, E., Mookherjee, N., Glavas, N., Waldbrook, M., Thompson, A., Wang, A., Lee, K., Doria, S., Hamill, P., Yu, J. J., Li, Y., Donini, O., Guarna, M. M., Finlay, B. B., North, J. R., and Hancock, R. E. (2007) An anti-infective peptide that selectively modulates the innate immune response. *Nat. Biotechnol. 25*, 465−472.

(7) Nolan, E. M., and Walsh, C. T. (2009) How nature morphs peptide scaffolds into antibiotics. *ChemBioChem 10*, 34−53.

(8) Marr, A. K., Gooderham, W. J., and Hancock, R. E. (2006) Antibacterial peptides for therapeutic use: obstacles and realistic outlook. *Curr. Opin. Pharmacol. 6*, 468−472.

(9) Radzishevsky, I. S., Rotem, S., Zaknoon, F., Gaidukov, L., Dagan, A., and Mor, A. (2005) Effects of acyl versus aminoacyl conjugation on the properties of antimicrobial peptides. *Antimicrob. Agents Chemother. 49*, 2412−2420.

(10) Scott, R. W., DeGrado, W. F., and Tew, G. N. (2008) De novo designed synthetic mimics of antimicrobial peptides. *Curr. Opin. Biotechnol. 19*, 620−627.

(11) Vagner, J., Qu, H., and Hruby, V. J. (2008) Peptidomimetics, a synthetic tool of drug discovery. *Curr. Opin. Chem. Biol. 12*, 292−296.

(12) Thayer, A. M. (2011) Improving peptides. *Chem. Eng. News 89*, 13−20.

(13) Radzishevsky, I. S., Rotem, S., Bourdetsky, D., Navon-Venezia, S., Carmeli, Y., and Mor, A. (2007) Improved antimicrobial peptides based on acyl-lysine oligomers. *Nat. Biotechnol. 25*, 657−659.

(14) Liu, D., and DeGrado, W. F. (2001) De novo design, synthesis, and characterization of antimicrobial beta-peptides. *J. Am. Chem. Soc. 123*, 7553−7559.

(15) Porter, E. A., Weisblum, B., and Gellman, S. H. (2002) Mimicry of host-defense peptides by unnatural oligomers: antimicrobial beta-peptides. *J. Am. Chem. Soc. 124*, 7324−7330.

(16) Fernandez-Lopez, S., Kim, H. S., Choi, E. C., Delgado, M., Granja, J. R., Khasanov, A., Kraehenbuehl, K., Long, G., Weinberger, D. A., Wilcoxen, K. M., and Ghadiri, M. R. (2001) Antibacterial agents based on the cyclic D,L-alpha-peptide architecture. *Nature 412*, 452−455.

(17) Srinivas, N., Jetter, P., Ueberbacher, B. J., Werneburg, M., Zerbe, K., Steinmann, J., Van der Meijden, B., Bernardini, F., Lederer, A., Dias, R. L., Misson, P. E., Henze, H., Zumbrunn, J., Gombert, F. O., Obrecht, D., Hunziker, P., Schauer, S., Ziegler, U., Kach, A., Eberl, L., Riedel, K., DeMarco, S. J., and Robinson, J. A. (2010) Peptidomimetic antibiotics target outer-membrane biogenesis in Pseudomonas aeruginosa. *Science 327*, 1010−1013.

(18) Goodson, B., Ehrhardt, A., Ng, S., Nuss, J., Johnson, K., Giedlin, M., Yamamoto, R., Moos, W. H., Krebber, A., Ladner, M., Giacona, M. B., Vitt, C., and Winter, J. (1999) Characterization of novel antimicrobial peptoids. *Antimicrob. Agents Chemother. 43*, 1429−1434.

(19) Simon, R. J., Kania, R. S., Zuckermann, R. N., Huebner, V. D., Jewell, D. A., Banville, S., Ng, S., Wang, L., Rosenberg, S., Marlowe, C.

K., et al. (1992) Peptoids: a modular approach to drug discovery. *Proc. Natl. Acad. Sci. U.S.A. 89*, 9367−9371.
(20) Zuckermann, R. N., Kerr, J. M., Kent, S. B. H., and Moos, W. H. (1992) Efficient method for the preparation of peptoids [oligo(N-substituted glycines)] by submonomer solid-phase synthesis. *J. Am. Chem. Soc. 114*, 10646−10647.
(21) Miller, S. M., Simon, R. J., Ng, S., Zuckermann, R. N., Kerr, J. M., and Moos, W. H. (1995) Comparison of the proteolytic susceptibilities of homologous L-amino acid, D-amino acid, and N-substituted clycine peptide and peptoid oligomers. *Drug Dev. Res. 35*, 20−32.
(22) Miller, S. M., Simon, R. J., Ng, S., Zuckermann, R. N., Kerr, J. M., and Moos, W. H. (1994) Proteolytic studies of homologous peptide and N-substituted glycine peptoid oligomers. *Bioorg. Med. Chem. Lett. 4*, 2657−2662.
(23) Kwon, Y. U., and Kodadek, T. (2007) Quantitative evaluation of the relative cell permeability of peptoids and peptides. *J. Am. Chem. Soc. 129*, 1508−1509.
(24) Tan, N. C., Yu, P., Kwon, Y. U., and Kodadek, T. (2008) High-throughput evaluation of relative cell permeability between peptoids and peptides. *Bioorg. Med. Chem. 16*, 5853−5861.
(25) Udugamasooriya, D. G., Dineen, S. P., Brekken, R. A., and Kodadek, T. (2008) A peptoid "antibody surrogate" that antagonizes VEGF receptor 2 activity. *J. Am. Chem. Soc. 130*, 5744−5752.
(26) Astle, J. M., Udugamasooriya, D. G., Smallshaw, J. E., and Kodadek, T. (2008) A VEGFR2 antagonist and other peptoids evade immune recognition. *Int. J. Pept. Res. Ther. 14*, 223−227.
(27) Fowler, S. A., and Blackwell, H. E. (2009) Structure-function relationships in peptoids: recent advances toward deciphering the structural requirements for biological function. *Org. Biomol. Chem. 7*, 1508−1524.
(28) Yoo, B., and Kirshenbaum, K. (2008) Peptoid architectures: elaboration, actuation, and application. *Curr. Opin. Chem. Biol. 12*, 714−721.
(29) Zuckermann, R. N., and Kodadek, T. (2009) Peptoids as potential therapeutics. *Curr. Opin. Mol. Ther. 11*, 299−307.
(30) Seo, J., Lee, B.-C., and Zuckermann, R. N. (2011) Peptoids: synthesis, characterization and nanostructures, in *Comprehensive Biomaterials* (Ducheyne, P., Healy, K. E., Hutmacher, D. W., Grainger, D. W., and Kirkpatric, C. J., Ed.) pp 53−76, Elsevier.
(31) Patch, J. A., and Barron, A. E. (2003) Helical peptoid mimics of magainin-2 amide. *J. Am. Chem. Soc. 125*, 12092−12093.
(32) Chongsiriwatana, N. P., Patch, J. A., Czyzewski, A. M., Dohm, M. T., Ivankin, A., Gidalevitz, D., Zuckermann, R. N., and Barron, A. E. (2008) Peptoids that mimic the structure, function, and mechanism of helical antimicrobial peptides. *Proc. Natl. Acad. Sci. U.S.A. 105*, 2794−2799.
(33) Chongsiriwatana, N. P., Miller, T. M., Wetzler, M., Vakulenko, S., Karlsson, A. J., Palecek, S. P., Mobashery, S., and Barron, A. E. (2011) Short alkylated peptoid mimics of antimicrobial lipopeptides. *Antimicrob. Agents Chemother. 55*, 417−420.
(34) Chongsiriwatana, N. P., Wetzler, M., and Barron, A. E. (2011) Functional synergy between antimicrobial peptoids and peptides against gram-negative bacteria. *Antimicrob. Agents Chemother. 55*, 5399−5402.
(35) Kapoor, R., Wadman, M. W., Dohm, M. T., Czyzewski, A. M., Spormann, A. M., and Barron, A. E. (2011) Antimicrobial peptoids are effective against pseudomonas aeruginosa biofilms. *Antimicrob. Agents Chemother. 55*, 3054−3057.
(36) Kapoor, R., Eimerman, P. R., Hardy, J. W., Cirillo, J. D., Contag, C. H., and Barron, A. E. (2011) Efficacy of antimicrobial peptoids against mycobacterium tuberculosis. *Antimicrob. Agents Chemother. 55*, 3058−3062.
(37) Schroder, T., Niemeier, N., Afonin, S., Ulrich, A. S., Krug, H. F., and Brase, S. (2008) Peptoidic amino- and guanidinium-carrier systems: targeted drug delivery into the cell cytosol or the nucleus. *J. Med. Chem. 51*, 376−379.
(38) Wu, C. W., Sanborn, T. J., Huang, K., Zuckermann, R. N., and Barron, A. E. (2001) Peptoid oligomers with alpha-chiral, aromatic side chains: Sequence requirements for the formation of stable peptoid helices. *J. Am. Chem. Soc. 123*, 6778−6784.
(39) Sanborn, T. J., Wu, C. W., Zuckermann, R. N., and Barron, A. E. (2002) Extreme stability of helices formed by water-soluble poly-N-substituted glycines (polypeptoids) with alpha-chiral side chains. *Biopolymers 63*, 12−20.
(40) Armand, P., Kirshenbaum, K., Falicov, A., Dunbrack, R. L., Jr., Dill, K. A., Zuckermann, R. N., and Cohen, F. E. (1997) Chiral N-substituted glycines can form stable helical conformations. *Fold. Des. 2*, 369−375.
(41) Kirshenbaum, K., Barron, A. E., Goldsmith, R. A., Armand, P., Bradley, E. K., Truong, K. T., Dill, K. A., Cohen, F. E., and Zuckermann, R. N. (1998) Sequence-specific polypeptoids: a diverse family of heteropolymers with stable secondary structure. *Proc. Natl. Acad. Sci. U.S.A. 95*, 4303−4308.
(42) Wu, C. W., Kirshenbaum, K., Sanborn, T. J., Patch, J. A., Huang, K., Dill, K. A., Zuckermann, R. N., and Barron, A. E. (2003) Structural and spectroscopic studies of peptoid oligomers with alpha-chiral aliphatic side chains. *J. Am. Chem. Soc. 125*, 13525−13530.
(43) Armand, P., Kirshenbaum, K., Goldsmith, R. A., Farr-Jones, S., Barron, A. E., Truong, K. T., Dill, K. A., Mierke, D. F., Cohen, F. E., Zuckermann, R. N., and Bradley, E. K. (1998) NMR determination of the major solution conformation of a peptoid pentamer with chiral side chains. *Proc. Natl. Acad. Sci. U.S.A. 95*, 4309−4314.
(44) Huang, W., Seo, J., Willingham, S. B., Czyzewski, A. M., Gonzalgo, M. L., Weissman, I. L., and Barron, A. E. unpublished results.
(45) Akhtar, M. S., Qaisar, A., Irfanullah, J., Iqbal, J., Khan, B., Jehangir, M., Nadeem, M. A., Khan, M. A., Afzal, M. S., ul-Haq, I., and Imran, M. B. (2005) Antimicrobial peptide Tc-99m-ubiquicidin 29−41 as human infection-imaging agent: Clinical trial. *J. Nucl. Med. 46*, 567−573.
(46) Brouwer, C. P. J. M., Wulferink, M., and Welling, M. M. (2008) The pharmacology of radiolabeled cationic antimicrobial peptides. *J. Pharm. Sci. 97*, 1633−1651.
(47) Ge, Y., MacDonald, D. L., Holroyd, K. J., Thornsberry, C., Wexler, H., and Zasloff, M. (1999) In vitro antibacterial properties of pexiganan, an analog of magainin. *Antimicrob. Agents Chemother. 43*, 782−788.
(48) Gottler, L. M., and Ramamoorthy, A. (2009) Structure, membrane orientation, mechanism, and function of pexiganan--a highly potent antimicrobial peptide designed from magainin. *Biochim. Biophys. Acta 1788*, 1680−1686.
(49) Lipsky, B. A., Holroyd, K. J., and Zasloff, M. (2008) Topical versus systemic antimicrobial therapy for treating mildly infected diabetic foot ulcers: a randomized, controlled, double-blinded, multicenter trial of pexiganan cream. *Clin. Infect. Dis. 47*, 1537−1545.
(50) Ametamey, S. M., Honer, M., and Schubiger, P. A. (2008) Molecular imaging with PET. *Chem. Rev. 108*, 1501−1516.
(51) Miao, Z., Ren, G., Liu, H., Jiang, L., and Cheng, Z. (2010) Small-animal PET imaging of human epidermal growth factor receptor positive tumor with a 64Cu labeled affibody protein. *Bioconjugate Chem. 21*, 947−954.
(52) Cheng, Z., Xiong, Z., Subbarayan, M., Chen, X., and Gambhir, S. S. (2007) 64Cu-labeled alpha-melanocyte-stimulating hormone analog for microPET imaging of melanocortin 1 receptor expression. *Bioconjugate Chem. 18*, 765−772.
(53) Burkoth, T. S., Fafarman, A. T., Charych, D. H., Connolly, M. D., and Zuckermann, R. N. (2003) Incorporation of unprotected heterocyclic side chains into peptoid oligomers via solid-phase submonomer synthesis. *J. Am. Chem. Soc. 125*, 8841−8845.
(54) Montalbetti, C. A. G. N., and Falque, V. (2005) Amide bond formation and peptide coupling. *Tetrahedron 61*, 10827−10852.
(55) Cheng, Z., Chen, J. Q., Miao, Y., Owen, N. K., Quinn, T. P., and Jurisson, S. S. (2002) Modification of the structure of a metallopeptide: Synthesis and biological evaluation of (111)in-labeled DOTA-conjugated rhenium-cyclized alpha-MSH analogues. *J. Med. Chem. 45*, 4588−4588.

(56) Ramamoorthy, A., Thennarasu, S., Lee, D. K., Tan, A., and Maloy, L. (2006) Solid-state NMR investigation of the membrane-disrupting mechanism of antimicrobial peptides MSI-78 and MSI-594 derived from magainin 2 and melittin. *Biophys. J. 91*, 206−216.
(57) Mello, M. E., Flamini, R. C., Corbo, R., and Mamede, M. (2009) Radioiodine concentration by the thymus in differentiated thyroid carcinoma: report of five cases. *Arq. Bras. Endocrinol. Metabol. 53*, 874−879.
(58) Connolly, L. P., and Connolly, S. A. (2003) Thymic uptake of radiopharmaceuticals. *Clin. Nucl. Med. 28*, 648−651.
(59) Wang, Y., Lin, H., Tullman, R., Jewell, C. F., Jr., Weetall, M. L., and Tse, F. L. (1999) Absorption and disposition of a tripeptoid and a tetrapeptide in the rat. *Biopharm. Drug Dispos. 20*, 69−75.
(60) Hagenbuch, B. (2010) Drug uptake systems in liver and kidney: a historic perspective. *Clin. Pharmacol. Ther. 87*, 39−47.
(61) van Montfoort, J. E., Hagenbuch, B., Groothuis, G. M., Koepsell, H., Meier, P. J., and Meijer, D. K. (2003) Drug uptake systems in liver and kidney. *Curr. Drug Metab. 4*, 185−211.
(62) Silverman, R. B. (2004) *The Organic Chemistry of Drug Design and Drug Action*, 2nd ed., Elsevier Academic Press, USA.
(63) Foltz, M., van der Pijl, P. C., and Duchateau, G. S. (2010) Current in vitro testing of bioactive peptides is not valuable. *J. Nutr. 140*, 117−118.
(64) Lee, H. J. (2002) Protein drug oral delivery: the recent progress. *Arch. Pharm. Res. 25*, 572−584.
(65) Simpson, L. S., Burdine, L., Dutta, A. K., Feranchak, A. P., and Kodadek, T. (2009) Selective toxin sequestrants for the treatment of bacterial infections. *J. Am. Chem. Soc. 131*, 5760−5762.
(66) Wender, P. A., Mitchell, D. J., Pattabiraman, K., Pelkey, E. T., Steinman, L., and Rothbard, J. B. (2000) The design, synthesis, and evaluation of molecules that enable or enhance cellular uptake: peptoid molecular transporters. *Proc. Natl. Acad. Sci. U.S.A. 97*, 13003−13008.

Bioconjugate Chemistry

Article

pubs.acs.org/bc

Enhancing Peptide Ligand Binding to Vascular Endothelial Growth Factor by Covalent Bond Formation

Bernadette V. Marquez,[†] Heather E. Beck,[†] Tolulope A. Aweda,[†] Brett Phinney,[§] Cynthia Holsclaw,[‡] William Jewell,[‡] Diana Tran,[§] Jeffrey J. Day,[†] Malalage N. Peiris,[†] Charles Nwosu,[†] Carlito Lebrilla,[†] and Claude F. Meares*[,†]

[†]Department of Chemistry, [§]Genome Center Proteomics Core Facility, and [‡]Campus Mass Spectrometry Facilities, University of California, One Shields Avenue, Davis, California 95616, United States

Supporting Information

ABSTRACT: Formation of a stable covalent bond between a synthetic probe molecule and a specific site on a target protein has many potential applications in biomedical science. For example, the properties of probes used as receptor-imaging ligands may be improved by increasing their residence time on the targeted receptor. Among the more interesting cases are peptide ligands, the strongest of which typically bind to receptors with micromolar dissociation constants, and which may depend on processes other than simple binding to provide images. The side chains of cysteine, histidine, or lysine are attractive for chemical attachment to improve binding to a receptor protein, and a system based on acryloyl probes attaching to engineered cysteine provides excellent positron emission tomographic images in animal models (Wei et al. (2008) *J. Nucl. Med. 49*, 1828−1835). In nature, lysine is a more common but less reactive residue than cysteine, making it an interesting challenge to modify. To seek practically useful cross-linking yields with naturally occurring lysine side chains, we have explored not only acryloyl but also other reactive linkers with different chemical properties. We employed a peptide-VEGF model system to discover that a 19mer peptide ligand, which carried a lysine-tagged dinitrofluorobenzene group, became attached stably and with good yield to a unique lysine residue on human vascular endothelial growth factor (VEGF), even in the presence of 70% fetal bovine serum. The same peptide carrying acryloyl and related Michael acceptors gave low yields of attachment to VEGF, as did the chloroacetyl peptide.

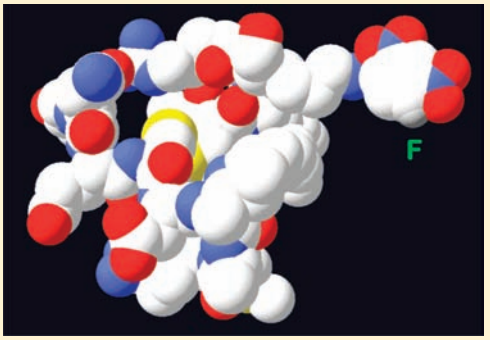

INTRODUCTION

Specific binding of one molecule to another is a widespread phenomenon in biology and is the basis of numerous practical applications directed at analysis, imaging, or therapy. In most familiar cases, the binding is reversible and may be characterized by an equilibrium constant K_D; a common rule of thumb in medicinal chemistry is that a drug should have a K_D value on the order of 10^{-9} M for its specific target, and negligible binding to other sites. At equilibrium, half the target sites will be occupied when the concentration of free drug equals K_D; so for nanomolar K_D, nanomolar free drug will achieve half-saturation. In a living body, clearance of the drug from the tissues and other effects of molecular transport and chemical modification complicate this simple picture. Receptor ligands used as target-imaging probes may have properties similar to drugs, but often have a stronger constraint to remain on target for periods of hours or even days.

The development of a drug, or ligand, that binds with at least nanomolar affinity without loss of other desirable properties is usually not a simple matter, even though sophisticated technologies have been developed for this purpose. Among the more challenging examples is the improvement of peptide ligands, the best of which typically bind in the micromolar instead of nanomolar range. This has attracted the attention of several laboratories that have chosen to explore the use of covalent attachment to deal with the shortcomings of low peptide affinity. A notable recent instance is the work of Holm et al., who used 58-residue affibody peptides carrying acryloyl groups to cross-link cysteine, histidine, or lysine side chains on protein targets.[1]

Previously, we had developed antibodies with infinite affinity, which employed imaging probes carrying acryloyl groups to covalently label engineered cysteine side chains in the binding sites of antiprobe antibodies.[2−4] Cysteine not involved in disulfide bonds is uncommon in extracellular proteins, usually making it necessary to use protein engineering to introduce a cysteine side chain at a desired site *in vitro*.[5]

Unlike cysteine and histidine, lysine residues are abundantly present on practically all proteins; if the covalent methodology were developed further to target naturally occurring lysine residues, it could lead to a new and interesting class of infinite-affinity ligands for biomedical use. Similar to the report by Holm et al.,[1] our efforts to employ ligands bearing acryloyl

Received: March 11, 2012
Published: April 26, 2012

dx.doi.org/10.1021/bc300114d | *Bioconjugate Chem.* 2012, 23, 1080−1089

groups to cross-link specific lysine residues have achieved limited success, resulting in specific reactions but low yields. Here, we explore some alternative reactive groups, finding one in particular that gives better yields in a relevant example. The system we use for illustration is a small 19-residue peptide ligand with modest K_D $\sim 10^{-6}$ M affinity for the 165-residue human signal protein vascular endothelial growth factor (VEGF).[6]

EXPERIMENTAL PROCEDURES

Chemicals. Maleic anhydride and chloroacetyl chloride were purchased from Sigma-Aldrich. Biotin-PEG_4-NHS, 1,5-difluoro-2,4-dinitrobenzene, 1-step TMB-Blotting substrate, and 1-step TMB-ELISA substrate were purchased from Thermo Fisher Scientific Pierce products (Rockford, IL). SYPRO Ruby total protein stain was purchased from Bio-Rad (Hercules, CA).

Proteins. Recombinant human VEGF ($VEGF_{165}$ or VEGF-A) produced in *E. coli* was first purchased from Prospec-Tany (Rehovot, Israel). To obtain larger amounts, we turned to expression of VEGF in *E. coli*. Prof. Samuel Gellman and Holly Haase (University of Wisconsin-Madison) kindly provided plasmid pET-3d-VEGF165 transformed in *E. coli* BL21(DE3). Expression of VEGF was carried out as described.[7,8] Recombinant human VEGFR1-Fc chimera (rhFlt-1-Fc) was purchased from R&D Systems (Minneapolis, MN). Polyclonal rabbit anti-VEGF was purchased from Santa Cruz Biotech (Santa Cruz, CA). Streptavidin-AP and -HRP conjugates were purchased from Southern Biotech (Birmingham, AL). Goat antirabbit-HRP (1 mg/mL) was purchased from Abcam (Cambridge, MA). Rabbit antihuman Fc was purchased from Jackson Immunoresearch (West Grove, PA). Trypsin and chymotrypsin were purchased from Promega (Madison, WI). Bovine serum albumin fraction V was purchased from Fisher Scientific (Pittsburgh, PA).

Miscellaneous. For control experiments, mutant VEGF K48A was cloned using QuikChangeXL site-directed mutagenesis kit (Stratagene, La Jolla, CA). Primers were purchased from Invitrogen (Carlsbad, CA), and expressed following the same procedures as VEGF. Competent *E. coli* BL21(DE3) was purchased from New England Biolabs (Ipswich, MA). The DNA mini-prep kit was purchased from Qiagen (Valencia, CA). Monomeric avidin resin was purchased from Thermo Fisher Scientific Pierce products (Rockford, IL).

Mass Spectrometry. High-resolution mass spectra were acquired on an LTQ Orbitrap XL mass spectrometer equipped with an electrospray ionization source (ThermoFisher, San Jose, CA), operating in the positive ion mode. Samples were introduced into the source via direct infusion at a rate of 10 μL/min. Collision-induced dissociation (CID) was used for MS^n experiments; the precursor ions were isolated with an isolation width of 3 Da, the ions were activated with a 25−35% normalized collision energy for 100 ms, and the q_z value was maintained at 0.250. The ions were subjected to CID in the ion trap portion of the instrument, and transferred to the Orbitrap for detection for high-resolution MS^n measurements. Spectra were acquired using *Xcalibur*, version 2.0.7 SP1 (ThermoFinnigan), and are an average of 16−53 scans. The spectra were externally calibrated using the manufacturer's standard calibration mixture, and then further calibrated internally with the lock mass tool.

Additional high-resolution mass spectra were acquired using Liquid Chromatography Tandem Mass spectrometry (LC-MS/MS). Peptides were separated and analyzed using a Michrom Paradigm MG4 HPLC system, (Michrom Bioresources, Auburn, CA) coupled with a Thermo Scientific LTQ-FT Ultra hybrid linear ion trap Fourier transform ion cyclotron resonance mass spectrometer (Thermo-Scientific, San Jose, CA) through a Michrom Bioresources Captivespray source (Michrom Bioresources, Auburn, CA). Peptides were loaded onto a C18 trap column (Zorbax 300SB-C18, 5 μm, 0.3 mm × 5 mm: Agilent) and desalted online. Peptides are then eluted from the trap and separated with a reverse-phase Michrom Magic C18AQ (200 μm × 150 mm) capillary column at a flow rate of 2 μL/min. Peptides are eluted using a 45 min gradient of 2% B to 35% B over 30 min, 35% B to 80% B for 7.5 min, held at 80% B for 1 min, 80% B to 2% B in 0.5 min, and re-equilibrated for 11 min at 2% B (solvent A = aqueous 0.1% HCOOH; solvent B = 100% CH_3CN). The mass spectrometer was operated using a standard top 10 method where one high-resolution survey scan (FT, 50 000 resolution) was followed by 10 low-energy CID MS/MS LTQ ion-trap scans of the most intense ions eluting from the column. Dynamic exclusion was enabled.

Protein and peptide identification were performed using *Peaks Studio 5.3* (Bioinformatics Solutions Inc.). Raw mass spectrometry files were loaded directly into *Peaks Studio* and searched against the VEGF protein sequence appended to the Common Repository of Adventitious Proteins database (www.thegpm.org/crap), which contains 112 sequences of common laboratory protein contaminants. The data were searched using a parent ion mass of 25 ppm and fragment ion mass of 0.5 Da, with trypsin and chymotrypsin enzyme specificity. Carboxamidomethylation of cysteine was searched as a fixed modification and the following masses were searched as variable modifications to lysine (*K*(amide) + linker = 309.11, ERK(amide) + linker = 594.25, EC(CAM)FERK(amide) + linker = 1030.39) . In addition, oxidation of methionine and deamidation of asparagine and glutamine were searched as variable modifications. A false discovery rate was calculated using an appended decoy database.

Low-resolution mass spectra were acquired in the positive ion mode with an AB Sciex Qtrap 2000 (Foster City, CA). Source parameters were 5 kV spray voltage, with a curtain plate temperature of 275 °C and sheath gas setting of 15. Samples were analyzed via flow injection analysis by injecting 20 μL samples into a stream of 50% CH_3CN:50% 0.1% HCOOH flowing at 200 μL/min. Protein Prospector (www.prospector.ucsf.edu) was used to calculate theoretical m/z values.

Molecular Modeling and Peptide Synthesis. To determine candidate sites for cross-linking on VEGF and peptide v107, the NMR structure of the complex (PDB 1KAT) was visualized using PyMOL Molecular Viewer. We explored possible modifications of peptide v107 to introduce a reactive side chain for cross-linker attachment. Distances between reactive residues on VEGF and potential v107 reactive side chains were modeled, resulting in the hypothesis that mutating Leu-19 to Lys would give the closest proximity to VEGF Lys-48 with no apparent steric hindrance from neighboring residues.

Solid-phase peptide synthesis of v107 L19K, consisting of the sequence GGNECDAIRMWEWECFERK-NH_2 with either free or acetylated N-terminus, was performed by Biomatik (Wilmington, DE). Note that residues A7 and I8 were transposed from the original sequence.[6] The two cysteine residues were bridged by a disulfide bond. The peptide was characterized via HPLC and electrospray ionization mass spectrometry (ESI-MS).

N-Terminal Biotinylation of Peptide v107 L19K to form "L19K". This protocol was modified from Sèlo and coworkers.[9] The v107 L19K peptide (1.4 μmol, 1.8 mM) was prepared in 150 μL DMF and 650 μL of aqueous 0.1 M

dx.doi.org/10.1021/bc300114d | *Bioconjugate Chem.* 2012, 23, 1080−1089

Et_3N·HOAc (pH 6.5). Peptide concentration was determined by measuring absorbance at 280 nm using ε_{280} = 11 500 M^{-1} cm^{-1}.[8] Biotin-PEG_4-NHS (2 mg, 3.4 μmol) was dissolved in 100 μL of 0.1 M Et_3N·HOAc (pH 6.5) and immediately added to the peptide solution to a final concentration of 4 mM biotin-PEG_4-NHS and 1.5 mM peptide. The reaction was incubated at 4 °C overnight with shaking. The crude product was purified by RP-C18 HPLC using a semiprep column (Phenomenex Luna 5 μ C18 300 Å 250 × 10 mm). Mobile phases were A, aqueous 50 mM Et_3N·HOAc (pH 7), and B, CH_3CN with 0.1% CF_3COOH; gradient 25−50% B (0−50 min); flow rate = 3 mL/min. Yield = 90% for the product conjugated only at the N terminus (retention time = 18.1 min), determined by HPLC peak areas. Free peptide eluted at 15.4 min with a yield of 4%, biotinylation only at the lysine side chain eluted at 19.5 min with a yield of 2%, and doubly biotinylated peptide (both the N-terminus and the lysine side chain) eluted at 21.4 min with a yield of 4%. Identification of biotinylated species was performed by tandem mass spectrometry (see Supporting Information).

Synthesis of L19K-Chloroacetamide (L19K−Cl). Neat chloroacetyl chloride (0.5 μL) was added to 100 μL of 1 mM L19K dissolved in 1:1 CH_3CN/aqueous 0.1 M Et_3N·HOAc (pH 9). The reaction mixture was readjusted to pH 9 with neat Et_3N and incubated at RT with shaking for 15 min. The reaction was monitored by fluorescamine spot test for free amines until negative.[10,11] Hydrolysis of the acid chloride formed chloroacetic acid, significantly acidifying the reaction mixture to pH ≈ 2. The mixture was extracted with EtOAc several times to remove the chloroacetic acid. A modified 4-(4′-nitrobenzyl)pyridine (NBP) spot test for alkylating agents was used to monitor the progress of extraction.[12,13] EtOAc extracts were spotted on a silica plate. NBP (5% w/v in acetone) was sprayed on the plate and heated at 100 °C for 5 min. A drop of neat Et_3N was applied to each spot, resulting in a violet color if chloroacetyl chloride or chloroacetic acid was present in the extract. Mass spec confirmed the chloroacetyl adduct (see Supporting Information).

Synthesis of L19K-Maleyl (L19K-M). Maleic anhydride (10 μL of 100 mM) in CH_3CN was added to 100 μL of 1 mM L19K dissolved in 1:1 CH_3CN/aqueous 0.1 M Et_3N·HOAc (pH 8) and incubated at RT with shaking for 3 h. Completion of reaction was monitored by fluorescamine spot test. Purification was performed by several EtOAc extractions. Baeyer's test was used to confirm the efficiency of extraction for maleic anhydride, wherein a drop of 1% aqueous $KMnO_4$ was added to the ethyl acetate extracts to check for alkenes.[14] HR-MS confirmed the maleyl adduct (in the absence of formic acid due to the instability of the adduct under acidic conditions; see Supporting Information).

Synthesis of L19K-5-fluoro-2,4-dinitrobenzene (L19K-FDNB). As shown in Scheme 1, 1 μmol (10 μL of 100 mM) 1,5-difluoro-2,4-dinitrobenzene (DFDNB) was added to 0.1 μmol (100 μL of 1 mM) L19K dissolved in 1:1 CH_3CN/aqueous 0.1 M Et_3N·HOAc (pH 9) and incubated at RT for 2 h. Completion of the reaction was monitored by fluorescamine spot test. Purification was performed with several EtOAc extractions. A simple UV quench test was used to determine the efficiency of DFDNB extraction, with 254 nm radiation from a hand-held lamp applied to the EtOAc extracts spotted on a fluorescent silica TLC plate. Mass spec confirmed the FDNB adduct (see Supporting Information).

All the L19K-electrophiles were evaporated under reduced pressure and resuspended in DMF as 1 mM solutions.

Scheme 1. Electrophiles Attached to Peptide L19K (denoted R)[a]

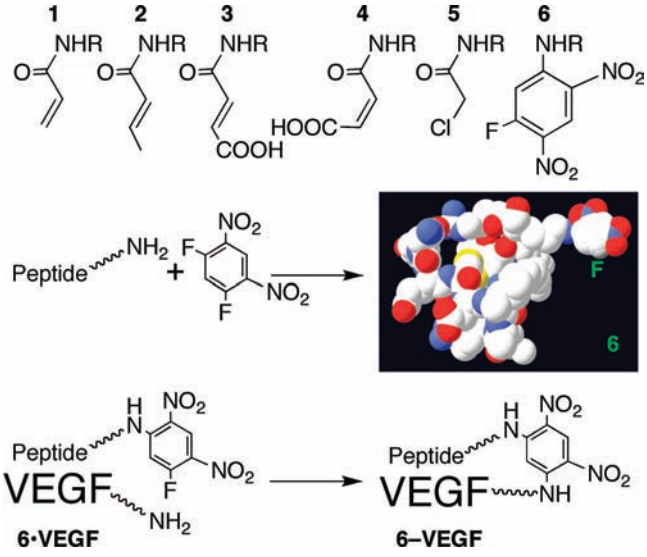

[a]**1** acryloyl, **2** crotonoyl, **3** fumaryl, **4** maleyl, **5** chloroacetyl, **6** FDNB. Example reactions: tagging the peptide's unique lysine with DFDNB, and cross-linking of **6** (peptide L19K-FDNB) to VEGF Lys-48 in the peptide·VEGF complex. The structure of unmodified peptide was taken from PDB 1KAT; the fluorodinitroaryl group may interact with the peptide surface in ways not suggested by the drawing.

Reaction of L19K-Electrophiles with VEGF. For all reactions, concentrations of 0.5 μM VEGF (1 μM binding sites) and 1 μM peptides (-M, -FDNB, and -Cl derivatives) were studied in PBS (pH 7.2), unless stated otherwise. All reactions were performed at 37 °C with shaking. VEGF concentrations are stated in terms of binding sites hereafter.

For *comparing electrophilic linker reactivity*, 4 μL of 10 μM (40 pmol) peptide analogue prepared in PBS was added to 10 μL of 4 μM VEGF sites (40 pmol binding sites) plus PBS to a total volume of 40 μL. The reactions were stopped after 24 h by adding 5× SDS-PAGE sample application buffer containing 20% v/v β-mercaptoethanol (5× SABR20) for subsequent Western blot analysis.

For *pH-dependent* reactions, in addition to pH 7.2, additional samples were prepared using PBS adjusted to pH 8 and 9. These reactions were stopped after 1 h.

For *competitive binding* with unlabeled L19K, a 10-fold dilution series (5 mM, 500 μM, 50 μM, and 5 μM) of N-terminal acetylated v107 L19K (competitor) was first prepared in PBS. A 2.5 μL aliquot of each concentration (containing 12 500; 1250; 125; and 12.5 pmol, respectively) was added to 4.3 μL of 5.8 μM VEGF binding sites (25 pmol), 2.5 μL of 10 μM L19K-FDNB (25 pmol), and PBS to a total volume of 25 μL in this order. These reactions were stopped after 1 h.

For *time-dependent* covalent attachment, 7.5 μM L19K-FDNB was reacted with 6 μM VEGF binding sites. A 10 μL aliquot from the reaction was collected after each time point (0.1, 0.2, 0.4, 0.8, 1.5, 3, 6, 9, and 24 h) and quickly frozen in liquid N_2 until electrophoretic analysis.

For *off-target reactions* of L19K-electrophile with other VEGF residues, L19K-FDNB and -Cl were each added to mutant VEGF K48A (1 μM binding site final concentration), in which lysine-48 has been replaced by alanine. Each L19K-electrophile was also reacted with parental VEGF as a positive control.

For *protein selectivity* of L19K-FDNB for VEGF in the presence of serum proteins, fetal bovine serum was added to a final concentration of 2, 20, or 70% v/v. These reactions were stopped after 1 h. Control reactions include no added FBS, no VEGF, no peptide, or no electrophile.

Western Blot to Characterize L19K-Electrophiles Covalently Bound to VEGF. L19K-electrophile-VEGF reaction mixtures were diluted with 5× sample application buffer containing 20% v/v β-mercaptoethanol (5× SABR20). Each 10 μL sample was loaded on 10−20% Novex Tris-glycine gels for SDS-PAGE at 200 V for 50 min. Protein was electroblotted onto a PVDF membrane and blocked with 50 mL of 3% w/v bovine serum albumin (BSA) in Tris-buffered saline (TBS), for 1 h at 37 °C. For anti-VEGF Western blots, the membrane was probed with 25 mL rabbit polyclonal anti-VEGF (1:500) in binding buffer (TBS containing 0.05% Tween-20 and 3% BSA) for 1 h at RT. The membrane was washed 3× with TBST. Secondary antibody conjugate goat antirabbit-HRP (1:500 dilution from 10 μg/mL) in binding buffer was incubated for 1 h at RT. The membrane was washed 5× with TBST. Turbo TMB-Blotting substrate (10 mL) was added and incubated at 37 °C until blue color developed.

Stripping Western Blots for Reprobing. After anti-VEGF analysis, the blot was stripped of its antibody probes in 40 mL stripping buffer (62.5 mM Tris-HCl pH 7, 2% SDS, and 100 mM β-mercaptoethanol) and incubated at 50 °C with shaking at 70 rpm for 30 min. The blot was washed several times with H_2O and reblocked with BSA for streptavidin-AP probing.

For *streptavidin-AP* Western blots, the membrane was probed with 25 mL of streptavidin-AP (1:10 000) in binding buffer at RT for 1 h. The membrane was washed 4× with TBST and 1× with AP developing buffer (100 mM Tris-HCl, 100 mM NaCl, and 5 mM $MgCl_2$, pH 9.5). Protein bands were stained with 5-bromo-4-chloro-3-indolyl phosphate and nitro blue tetrazolium (BCIP/NBT, 0.4 mM) substrates in AP developing buffer until color developed.

Site-Directed Mutagenesis of VEGF K48A. The VEGF K48A mutant gene was constructed using a QuikChange II XL site-directed mutagenesis kit according to the supplier's instructions. Plasmid pET-3d-$VEGF_{165}$ was used as the DNA template, in which the VEGF gene is located between Nco1 and BamH1 restriction sites and under control of a phage T7 promoter. Sequences of primers were as follows, with the mutation underlined in bold letters: Forward 5′-GATCGAGTACATCTTC**GCG**C-CATCCTGTGTGCCCC; Reverse 5′-GGGGCACACAG-GATGG**CGC**GAAGATGTACTCGATC.

DNA template (50 ng) was mixed with 100 ng of each primer along with 1× reaction buffer, dNTPs, Quick solution, DNA polymerase (2.5 μL), and DNase-free water to a total volume of 50 μL. The reaction was thermally cycled with an initial cycle at 95 °C for 1 min followed by 18 cycles (95 °C for 50 s, 68 °C for 50 s, 68 °C for 15 min), and a final cycle at 68 °C for 7 min. Note that the annealing temperature was optimal at 68 °C and is the same temperature as the elongation cycle. Dpn 1 was added and incubated at 37 °C for 3 h. The mutant plasmid was transformed into ultracompetent XL2-Blue *E. coli* following standard transformation protocol. Each reaction was plated onto LB (+100 μg/mL carbenicillin) plates. Selected colonies were purified using a Qiagen mini-prep kit, characterized using a 1.2% agarose gel, and submitted for DNA sequencing (Davis Sequencing, Davis, CA). The resulting sequence was analyzed using *Bioedit* (Supporting Information). The selected plasmid was transformed into competent *E. coli* BL21(DE3) for protein expression and isolation as described for parental VEGF by Peterson and co-workers.[8]

Characterization of Binding Activity of VEGF Mutant K48A by Competitive ELISA. The activity of mutant VEGF K48A was characterized by competitive ELISA with biotinylated parental VEGF conjugate (biotin-VEGF) against immobilized recombinant human VEGFR1-Fc chimera (rhFlt-1-Fc). Biotin-VEGF was prepared by conjugating 1 mM biotin-PEG_4-NHS with 200 μg/mL parental VEGF in 50 μL PBS at 4 °C overnight, and desalted with gel filtration spin columns. For ELISA, 50 μL of 5 μg/mL rhFlt-1-Fc in PBS was immobilized in a 96-well microtiter plate at 4 °C overnight. The wells were washed with PBS and blocked with 300 μL of 1% BSA in PBS at RT for 1 h. 4-fold serial dilutions (50 μL) of VEGF mutant K48A starting from 200 nM in binding buffer (1% BSA in PBS) were added to rhFlt-1-Fc and incubated at RT for 1 h in triplicate wells. The wells were washed 2× with PBST. Biotin-VEGF (50 μL of 6 nM sites) in binding buffer was added and incubated at RT for 1 h. The wells were washed 3× with PBST. Streptavidin-HRP (1:4000) in binding buffer was added and incubated at RT for 1 h. The wells were washed 5× with PBST. I-Step Turbo-TMB ELISA (100 μL) was added and incubated at 37 °C until blue color developed. Final yellow color was stabilized with 100 μL of 1 M H_2SO_4. Absorbance was read at 450 nm. As a positive control, rhFlt-1-Fc was detected using rabbit antihuman Fc (1:5000), followed by goat anti-rabbit-HRP conjugate (1:500 dilution from 10 μg/mL). Negative controls included omission of Flt-1-Fc, biotin-VEGF, or streptavidin-HRP.

Affinity Purification of L19K-FDNB-VEGF and Enzymatic Digestion for Mass Spectrometric Analysis. Using the biotin tag on the peptide, cross-linked L19K-FDNB-VEGF (100 μg, 900 μL) was purified from unreacted VEGF using 1 mL of monomeric avidin resin (Pierce), following the manufacturer's protocol. The conjugate was eluted with 5 mM biotin in PBS containing 0.02% NaN_3, in 1 mL fractions. A Bradford colorimetric assay was used to determine which fractions contained the conjugate. The conjugate was precipitated using trichloroacetic acid with sodium deoxycholate, followed by acetone precipitation, as described by Pierce protocols (Tech Tip #8).

The pellet was resuspended in 50 μL of 50 mM NH_4HCO_3 (pH 8.5) and up to 10% of CH_3CN by volume. Trypsin digestion was performed following standard procedures. Briefly, the conjugate was reduced and denatured first by the addition of TCEP (1 μL of 500 mM; final 10 mM) and heated at 95 °C for 10 min. The conjugate was alkylated with 15 mM iodoacetamide at RT in the dark for 1 h, and quenched with 5 mM DTT for 10 min. Trypsin (1.5 μg) was added and the mixture incubated at 37 °C overnight. The reaction was stopped by heating to 95 °C for 5 min. Chymotrypsin (1.6 μg) was added and the mixture incubated at 37 °C overnight. The reaction was stopped by heating to 95 °C for 5 min.[15] The peptides were desalted using a Sep Pak C18 cartridge, and the solvent was evaporated using a speed-vac. The peptide fragments were resuspended in aqueous 10% CH_3CN. LC-MS/MS was performed by UC Davis Proteomics Core facility.

RESULTS

N-Terminal Biotinylation of L19K. The NMR structure[16] indicated that labeling with a tag at the N-terminus of the peptide would not interfere with binding to VEGF (Figure 1). We chose biotin-PEG_4- as the tag because it is convenient for

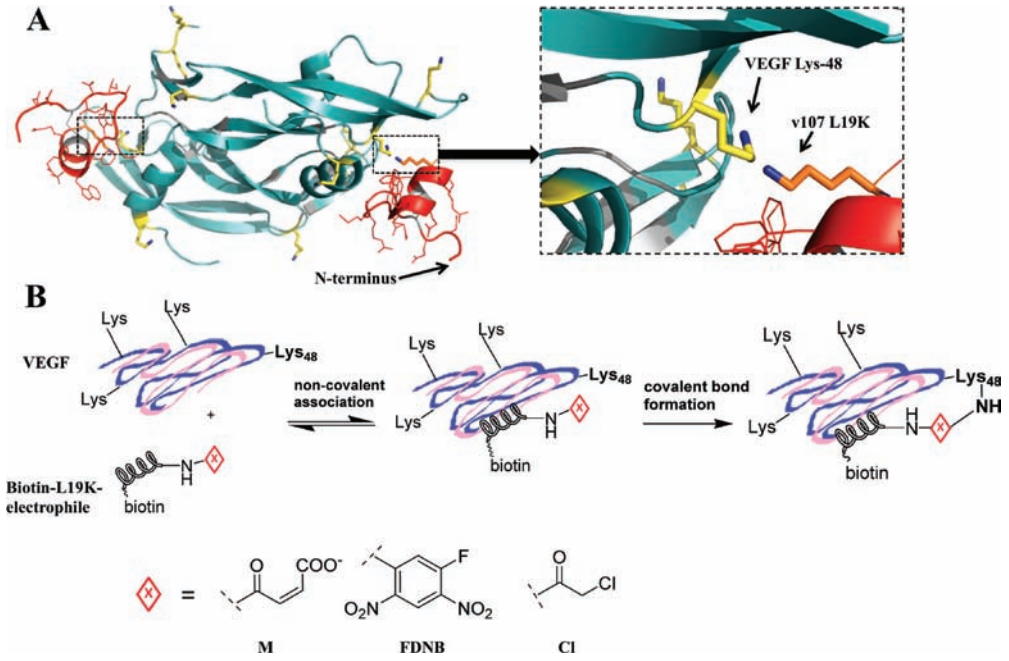

Figure 1. Covalent labeling of VEGF Lys-48 with biotinylated L19K-electrophiles. (A) Molecular modeling of NMR structure PDB 1KAT, showing ribbon structures of peptide in red and VEGF in teal. Peptide N-terminus does not participate in binding to VEGF. Lysine side chains are shown in yellow (CPK coloring). Boxed area was enlarged to show v107 L19K side chain (orange) in close proximity to VEGF Lys-48. (B) Schematic representation of reversible interaction between peptide-electrophile and VEGF, followed by covalent labeling to VEGF Lys-48 with electrophiles maleyl (**M**), 5-fluoro-2,4-dinitrobenzene (**FDNB**), or chloroacetamide (**Cl**).

subsequent Western blotting with streptavidin conjugates. In addition, the PEG_4 spacer between biotin and the peptide should allow room for streptavidin to capture biotin without steric hindrance from the L19K-VEGF cross-linked product. Analytical results demonstrating isolation of the pure N-terminal conjugate are provided in Supporting Information.

Conjugation of Peptides to VEGF: Yields with L19K-FDNB, -M, and -Cl. As an example, the L19K-FDNB reaction chemistry is shown in Scheme 1. Reducing, denaturing conditions were employed for anti-VEGF Western blot analysis to confirm irreversible covalent reactions and to obtain distinguishable bands between unreacted monomer VEGF (~20 kDa) and the cross-linked VEGF-peptide (~23 kDa). Next, the blot was stripped of its anti-VEGF probes and reprobed with streptavidin-AP to detect the biotinylated peptide (~3 kDa) and its 23 kDa VEGF conjugate.

After 24 h incubation of 1 μM L19K-electrophiles with 1 μM VEGF (sites) at pH 7.2 and 37 °C, biotin-tagged peptide in conjugates was detected at ~23 kDa using the sensitive streptavidin Western blot (Figure 2A). Control reactions with no electrophile or no peptide did not show bands at ~23 kDa. Free biotinylated peptide was observed to migrate below 10 kDa.

Using the less sensitive anti-VEGF Western blot, 1 μM L19K-FDNB gave a modest conversion of 1 μM VEGF to the conjugate migrating at ~23 kDa (Figure 2B), while the ~23 kDa conjugates of VEGF with L19K-M and -Cl were not detected. Free VEGF was observed at ~20 kDa.

The reactivity of L19K-FDNB was further investigated by varying the pH of the reaction. As shown in Figure 2C, after 1 h the bands corresponding to L19K-FDNB-VEGF (~23 kDa) had higher intensities at pH 8 and 9 compared to pH 7.2. SYPRO total protein stain confirmed the presence of unconjugated VEGF at ~20 kDa, but the conjugated product was not detectable during the first hour (Figure 2D).

Competitive binding between excess peptide L19K and 1 μM L19K-FDNB for VEGF (1 μM sites) was briefly explored. After 1 h, the highest concentration of the competitor (500 μM) completely prevented the permanent attachment of L19K-FDNB to VEGF (Figure 2E).

A time course study of a small excess of L19K-FDNB (7.5 μM) binding to 6 μM VEGF sites was performed at pH 7.2 from 5 min to 24 h of incubation at 37 °C (Figure 3, lanes 0.1–24 h). The yield of covalent product increased over 24 h, approaching saturation of VEGF (~23 kDa) as shown on a total protein-stained gel under reducing conditions. A control lane under nonreducing conditions (lane 24*) shows that after 24 h almost no monomer VEGF is visible at ~20 kDa, indicating that the VEGF dimer is stable under these incubation conditions.

To confirm that L19K-FDNB reacts specifically with VEGF residue Lys-48, we performed trypsin and chymotrypsin double digests of the L19K-FDNB-VEGF conjugate and analyzed the peptide fragments by LC-MS/MS as described in Experimental Procedures. A possible solution to the VEGF peptide fragment containing Lys-48 was identified as IFK(309.11)PSC(CAM)-VPL (Figures 4 and 5). Mass modification of 309.11 on VEGF Lys-48 corresponds to the L19K-FDNB fragment, 2,4-dinitrobenzyl-5-lysine. CAM represents a carboxamidomethyl modification on the cysteine.

Mutating VEGF Lys-48 to Ala eliminates reaction between 1 μM L19K-FDNB and 1 μM VEGF mutant. Though the reported affinity of v107 for VEGF K48A (K_D > 10 μM) is weaker than for parental VEGF ($K_D \approx 1$ μM),[16] we can still gain valuable information regarding the background reactivity of L19K-electrophiles with the other 10 lysine residues on the protein. L19K-FDNB and -Cl were each incubated with equimolar 1 μM mutant VEGF K48A sites at 37 °C for 24 h, comparing parental VEGF as positive control. A streptavidin

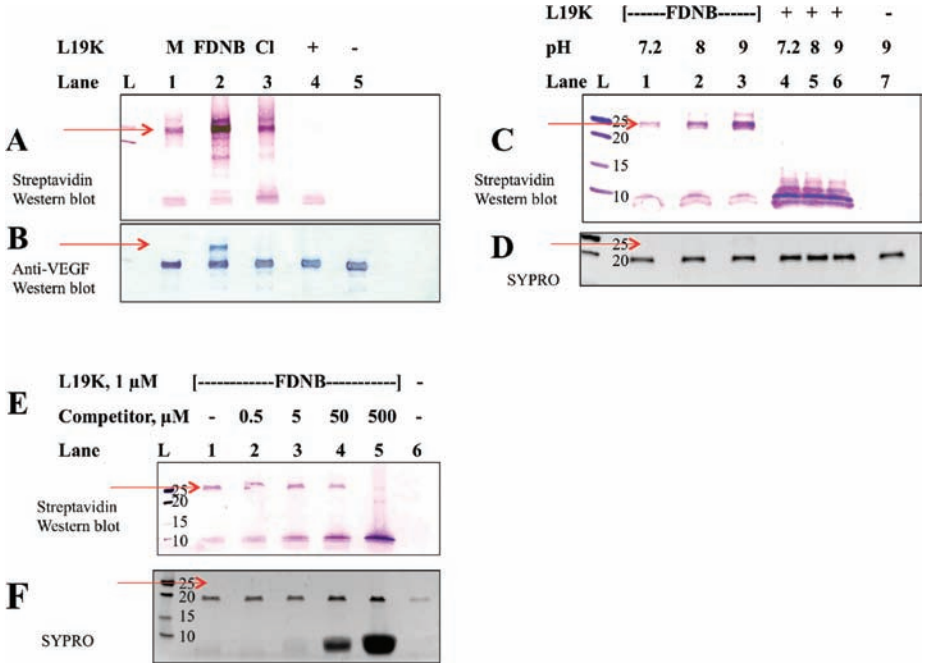

Figure 2. Western blots and SYPRO total protein stain characterization of VEGF-peptide conjugates under reducing conditions. Red arrows indicate the position of bands representing the conjugate on the blot or gel at ~23 kDa. Unreacted peptide (~3 kDa) is shown below 10 kDa. Protein standards (L) are labeled in kDa units. (A) The maleyl analogue was included as a representative aza-Michael acceptor for comparison with electrophiles −Cl and −FDNB. After 24 h incubation of 1 μM L19K-electrophiles with 1 μM VEGF (sites) at pH 7.2 and 37 °C, comparison of reactivity with VEGF by detecting peptide with streptavidin. Bands corresponding to unreacted peptide are at the bottom of the blot. Control reactions: no electrophile (lane 4) and no peptide (lane 5). (B) The same blot as **A** probed with the less sensitive anti-VEGF shows that only L19K-FDNB gave a detectable product (lane 2). The bottom of the blot is not shown because no bands were visible. (C) Reaction of L19K−FDNB and VEGF after 1 h at pH 7.2, 8, or 9 (lanes 1−3, respectively) probed with streptavidin, showing increasing product band intensities with pH 8 and 9. Control reactions: no electrophile (lanes 4−6) and no peptide (lane 7). (D) SYPRO stain of **C** confirmed the same amount of VEGF loaded on each lane, but is not sensitive enough to detect VEGF conjugate after 1 h. (E) Competition between 1 μM L19K−FDNB and 0.5, 5, 50, and 500 μM unlabeled L19K (lanes 2−5, respectively) for 1 μM VEGF sites shows that during 1 h incubation, 500 μM competitor prevents L19K−FDNB reaction with VEGF (lane 5). Control reactions: no competitor (lane 1) and VEGF alone (lane 6). (F) SYPRO stain of E confirmed the same amount of VEGF. Covalent product was not yet detectable after 1 h. Unreacted peptide competitor is visible at higher concentrations (lanes 4 and 5).

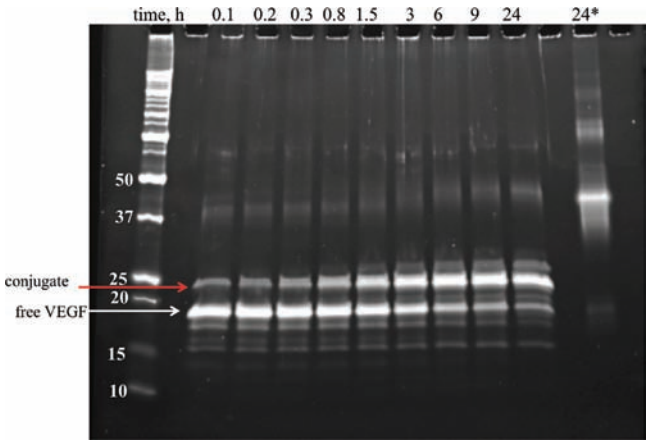

Figure 3. SYPRO stain from time course study of 7.5 μM L19K−FDNB and 6 μM VEGF sites from 5 min (lane 0.1) up to 24 h (lane 24) at pH 7.2, 37 °C, showing almost quantitative conversion of VEGF to the conjugate after ~9 h of incubation. Red arrow indicates the position of VEGF conjugate migration on the gel. Control: nonreducing aliquot from 24 h reaction, showing practically no monomer VEGF at ~20 kDa.

Western blot showed that the analogues did not yield covalent products with the mutant, while they did yield covalent products with parental VEGF (see Supporting Information). This supports the expectation that L19K-FDNB and -Cl do not react with the other lysines on parental VEGF or mutant K48A under these conditions.

To ensure that VEGF mutant K48A was folded properly, we measured its ability to compete with biotinylated parental VEGF for binding to an immobilized VEGF receptor (rhFlt-1-Fc). Concentrations of VEGF K48A >10 nM reduce the binding of 6 nM parental VEGF to Flt-1-Fc in a dose-dependent manner (see Supporting Information), implying that the mutant is functional and binds to the same site on the receptor as parental VEGF.

In the presence of 2, 20, or 70% v/v fetal bovine serum, L19K-FDNB (1 μM) reacted with VEGF (1 μM sites), but showed minimal attachment to serum proteins after 1 h (Figure 6). Streptavidin Western blots showed that the band for L19K-FDNB-VEGF conjugate at ~23 kDa is significantly darker than the smeared background in the lane due to serum. The bloom from the large concentration of serum albumin loaded on the gel (see SYPRO, Figure 6 inset) gives an idea of the selectivity of the reaction.

DISCUSSION

Previous work by our colleagues successfully used a DOTA-acrylamide ligand to tag an engineered cysteine adjacent to the binding pocket of an antibody for imaging *in vivo*.[3,4] We wished to extend this approach to specific attachment of a probe to a

dx.doi.org/10.1021/bc300114d | *Bioconjugate Chem.* 2012, 23, 1080−1089

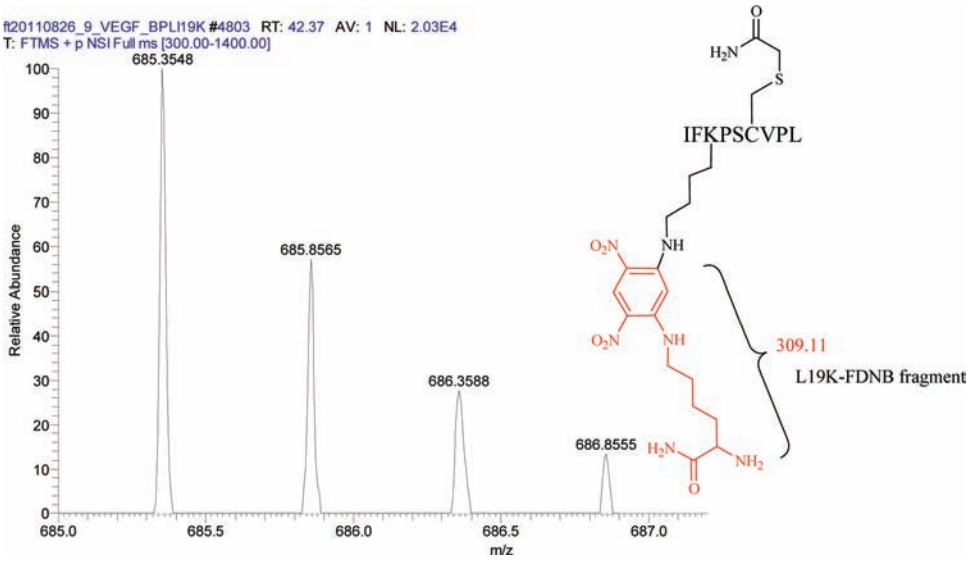

Figure 4. FT-ICR-MS1 of trypsin and chymotrypsin fragment of VEGF conjugate, IFK(309.11)PSC(CAM)VPL. Doubly charged $[M+2H]^{2+}$ m/z calcd 685.3516, observed 685.3548. A modification of mass 309.11 corresponds to the L19K-FDNB fragment.

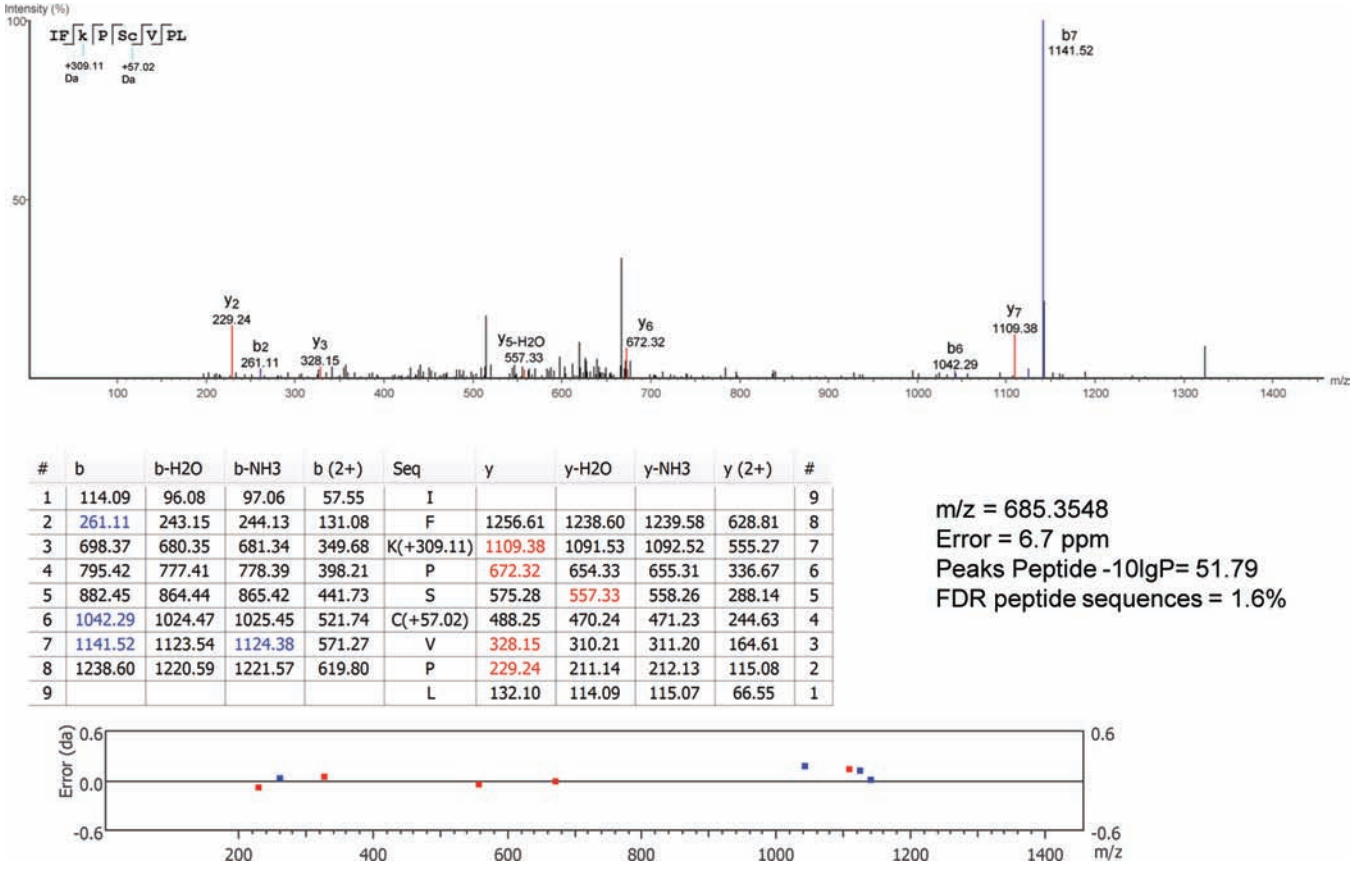

#	b	b-H2O	b-NH3	b (2+)	Seq	y	y-H2O	y-NH3	y (2+)	#
1	114.09	96.08	97.06	57.55	I					9
2	261.11	243.15	244.13	131.08	F	1256.61	1238.60	1239.58	628.81	8
3	698.37	680.35	681.34	349.68	K(+309.11)	1109.38	1091.53	1092.52	555.27	7
4	795.42	777.41	778.39	398.21	P	672.32	654.33	655.31	336.67	6
5	882.45	864.44	865.42	441.73	S	575.28	557.33	558.26	288.14	5
6	1042.29	1024.47	1025.45	521.74	C(+57.02)	488.25	470.24	471.23	244.63	4
7	1141.52	1123.54	1124.38	571.27	V	328.15	310.21	311.20	164.61	3
8	1238.60	1220.59	1221.57	619.80	P	229.24	211.14	212.13	115.08	2
9					L	132.10	114.09	115.07	66.55	1

m/z = 685.3548
Error = 6.7 ppm
Peaks Peptide -10lgP= 51.79
FDR peptide sequences = 1.6%

Figure 5. MS2 of IFK(309.11)PSC(CAM)VPL. Theoretical values were calculated using *Protein Prospector*. *Peaks Studio 5.3* software was used to identify the modified peptide. A modification of 309.11 corresponding to the L19K-FDNB fragment is indicated on VEGF Lys-48, as K(+309.11). The spectrum and table highlight the observed *y* ions in red and *b* ions in blue. The table lists the peptide sequence along with m/z values corresponding to theoretical *b* and *y* ions. Errors for the observed masses are plotted on the graph and are within 0.5 Da.

naturally occurring lysine residue on a protein target. Our initial results were similar to those of Holm and co-workers, who used an affibody-acrylamide ligand to target lysine, cysteine, and histidine near the binding pocket of its protein target.[1] For our initial studies, we prepared derivatives of peptide L19K not only with acryloyl, but also with closely related crotonoyl, fumaryl, and maleyl tags as potential aza-Michael acceptors to explore whether adding substituents would enhance the conjugation yield with the VEGF site (structures are provided in Scheme 1). As a typical representative of this class of tagged peptides, the maleyl derivative **4** is included in the experiments below.

dx.doi.org/10.1021/bc300114d | *Bioconjugate Chem.* 2012, 23, 1080−1089

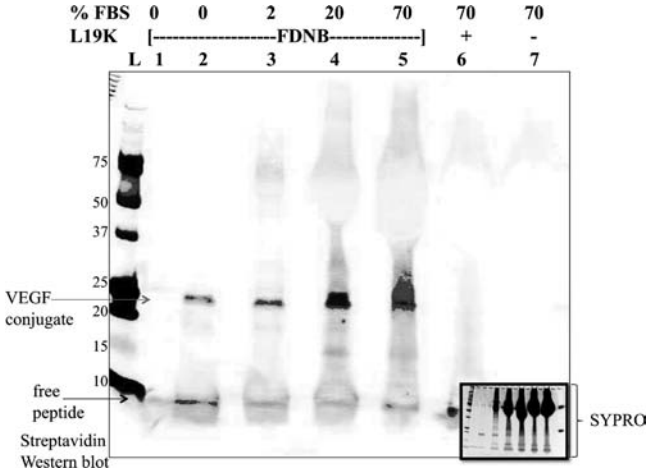

Figure 6. Streptavidin Western blot of 1 μM L19K−FDNB and 1 μM VEGF sites in the presence of 2, 20, and 70% fetal bovine serum (lanes 3−5) showing selectivity of L19K−FDNB for VEGF after 1 h. Inset: SYPRO stain shows an overwhelming amount of proteins, particularly albumin, in these reactions. On the left side, L denotes protein standards. Controls: peptide only (lane 1), no serum (lane 2), no electrophile (lane 6), and no peptide (lane 7).

All the aza-Michael acceptors above gave low conjugation yields with VEGF under physiological conditions. While streptavidin Western blots detected the biotin-tagged peptide in conjugation products, yields were so low that anti-VEGF Western blots and also SYPRO total protein stain showed that practically all the VEGF remained unmodified. These low yields could be due to multiple factors such as weak affinity of L19K-acrylamide for VEGF, steric constraints on reaction between the bound acryloyl and the Lys-48 nucleophile, and a small population of the unprotonated free amine available to undergo an aza-Michael addition with the acryloyl moiety during its noncovalent bound lifetime. Other systems of affinity-induced covalent capture by Michael addition rely on stronger noncovalent association and a sulfur nucleophile.[3,4,17] The acryloyl-affibody ligand model system of Holm and co-workers, which reacts covalently with an engineered lysine near the protein binding pocket, gave a significantly lower yield than its engineered cysteine counterpart.[1]

To seek improved cross-linking yields with lysine, we explored other electrophilic linkers with different chemistry. While they react with nitrogen nucleophiles, chloroacetamide groups are typically more reactive with sulfur, and can attach fluorescent tags with affinity to a molecular probe via alkylation of a nearby cysteine side chain.[18] We examined the reaction of L19K−Cl **5** with VEGF Lys-48; similar to the acrylamide analogues and perhaps for similar reasons, the yield was poor.

Next, we examined the classic reagent DFDNB, which has been used to cross-link molecules via primary amines in a variety of circumstances such as attaching peptides to protein binding sites,[19,20] amino acids to each other,[21] or phospholipids to cell-surface proteins.[22] Due to the electron withdrawing and resonance properties of $-NO_2$ groups in the 2- and 4-positions of the benzene ring of 1,5-difluoro-2,4-dinitrobenzene (DFDNB), in addition to the activating effect of the 5-fluorine on the 1-fluorine,[23−25] DFDNB appears to be a very reactive cross-linker. The symmetric nature of DFDNB may give the impression that the reactivity of both fluorine leaving groups is equal. However, after displacement of the first fluorine by an amine nucleophile to form **6** (Scheme 1), the reactivity of the remaining fluorine is significantly lower owing to the amine's inductive effect. This makes L19K-FDNB **6** intrinsically less reactive than the similar-looking small molecule 1-fluoro-2, 4-dinitrobenzene (FDNB or DNFB), which Sanger famously used in the sequencing of insulin.[26] The markedly low reactivity of L19K-FDNB with serum proteins (Figure 6) is likely to depend on steric hindrance by the L19K peptide in addition to the electronic properties of the fluorodinitroaryl group. The latter group is not hydrophilic and so might interact favorably with the peptide surface, while the rather restricted geometry for nucleophilic attack by a protein-bound lysine could further disfavor reactions with all but specifically bound proteins. Such effects may be important, since any applications beyond these *in vitro* experiments would depend on the reagent maintaining its specificity in biological environments similar to serum.

Another topic to consider is the classical experiments of Landsteiner and Jacobs, who prepared guinea pig immunogens from 1-halo-2,4-dinitrobenzenes.[27,28] Landsteiner used intracutaneous administration techniques designed to efficiently produce sensitization in order to study the immunological properties of these electrophilic small molecules, which are much less shielded than **6** in Scheme 1. Nevertheless, the possibility that *in vivo* applications of molecules related to L19K-FDNB would stimulate an immune response requires further investigation.

The reaction of L19K-FDNB **6** with VEGF gave yields superior to L19K−Cl **5** or L19K−M **4** in PBS (pH 7.2) at 37 °C under equimolar reaction conditions and at low micromolar concentration (Figure 2A,B). The size and shape of the cross-linker, nature of the reaction, and microenvironment of the peptide-VEGF binding pocket could all affect the yield of the covalent product. In this case, the "reach" of all three cross-linkers is comparable (lysine-$(CH_2)_4$NH- plus ∼2−3 Å), but their shapes are distinct and the relative bulk of the −FDNB is evident. The local environment of the peptide-VEGF binding pocket contains aromatic residues such as VEGF Phe-17 and Tyr-21, which may interact favorably with the aromatic ring of −FDNB and aid in prolonging the residence lifetime of the peptide on VEGF prior to covalent labeling. Our time-course study (Figure 3) shows that covalent labeling can be observed as early as 5 min and increases to almost quantitative after several hours. This yield is comparable to systems with engineered cysteines near the protein binding pocket and acryloyl-based ligands.[1,29]

The mass spectrometric analysis of the VEGF conjugate tryptic fragments (Figures 4 and 5) agrees with our expectation that VEGF Lys-48 was the site of covalent labeling with L19K−FDNB. Other products were not detected by mass spectrometry. Study of the VEGF mutant K48A indicates that L19K−FDNB does not react detectably with any of the other 10 lysine residues or the N-terminus of mutant K48A. Both mass spectrometry and Western blotting with mutant K48A imply that the peptide's affinity for parental VEGF drives L19K−FDNB to selectively tag Lys-48. Previous studies with intramolecular cross-linking of insulin chains and also a peptide with affinity for thrombin using DFDNB, are consistent with these findings of site-selective cross-linking to a nearby lysine.[19,20]

■ CONCLUSIONS

The covalent attachment of ligand to target is interesting as an alternative strategy to the extensive use of combinatorial library technology to seek synthetic ligands that bind usefully to naturally occurring proteins. In order for covalent attachment to be useful,

the chemistry involved must be so mild (or so shielded) that reactions with off-target molecules are negligible, but a significant portion of the target protein should be affected. This need not be a high percentage in all cases, since applications such as imaging do not require it. When designing covalent ligands for natural biological targets, engineering highly nucleophilic residues such as cysteine near the ligand-binding site on the protein target is usually not an option. Since lysine side chains occur in high abundance, finding a suitable lysine cross-linker is an important challenge. The results described here suggest that electrophiles inspired by aryl halides may provide a way forward.

■ ASSOCIATED CONTENT

Ⓢ Supporting Information

Experimental results for L19K-FDNB reaction with mutant VEGF K48A, and mass spectra of peptide-electrophiles. This material is available free of charge via the Internet at http://pubs.acs.org.

■ AUTHOR INFORMATION

Corresponding Author

*Phone: (530) 752-0936, Fax: (530) 752-8938, E-mail: cfmeares@ucdavis.edu.

Notes

The authors declare no competing financial interest.

■ ACKNOWLEDGMENTS

We thank Prof. Samuel Gellman and Holly Haase for providing PET-3D-$VEGF_{165}$ *E. coli* clones; Dr. Robert Chalkley and Dr. Peter Baker for Protein Prospector support; and Dr. Sarah Cheal for helpful discussions. Supported by NIH research grants CA016861 and CA136639 (C.F.M.).

■ ABBREVIATIONS:

DFDNB, 1,5-difluoro-2,4-dinitrobenzene; Et_3N·HOAc, triethylammonium acetate; FBS, fetal bovine serum; L19K, biotin-peptide v107 L19K; L19K−Cl, biotin-peptide v107 L19K-Chloroacetamide; L19K-M, biotin-peptide v107 L19K-Maleyl; L19K-FDNB, biotin-peptide v107 L19K-5-Fluoro-2,4-dinitrobenzene; NBP, 4-(4′-nitrobenzyl)pyridine; PBST, PBS containing 0.05% Tween-20; streptavidin-AP, conjugate of streptavidin with alkaline phosphatase; RT, room temperature; TCEP, *tris*(2-carboxyethyl)phosphine; DTT, dithiothreitol; VEGF, human vascular endothelial growth factor (Human $VEGF_{165}$ or VEGF-A)

■ REFERENCES

(1) Holm, L., Moody, P., and Howarth, M. (2009) Electrophilic affibodies forming covalent bonds to protein targets. *J. Biol. Chem. 284*, 32906−32913.

(2) Chmura, A. J., Orton, M. S., and Meares, C. F. (2001) Antibodies with infinite affinity. *Proc. Natl. Acad. Sci. U.S.A. 98*, 8480−8484.

(3) Corneillie, T. M., Lee, K. C., Whetstone, P. A., Wong, J. P., and Meares, C. F. (2004) Irreversible engineering of the multielement-binding antibody 2D12.5 and its complementary ligands. *Bioconjugate Chem. 15*, 1392−1402.

(4) Wei, L. H., Olafsen, T., Radu, C., Hildebrandt, I. J., McCoy, M. R., Phelps, M. E., Meares, C., Wu, A. M., Czernin, J., and Weber, W. A. (2008) Engineered antibody fragments with infinite affinity as reporter genes for PET imaging. *J. Nucl. Med. 49*, 1828−1835.

(5) Levitsky, K., Boersma, M. D., Ciolli, C. J., and Belshaw, P. J. (2005) Exo-mechanism proximity-accelerated alkylations: Investigations of linkers, electrophiles and surface mutations in engineered cyclophilin-cyclosporin systems. *ChemBioChem 6*, 890−899.

(6) Fairbrother, W., Christinger, H., Cochran, A., Fuh, G., Keenan, C., Quan, C., Shriver, S., Tom, J., Wells, J., and Cunningham, B. (1998) Novel peptides selected to bind vascular endothelial growth factor target the receptor-binding site. *Biochemistry 37*, 17754−64.

(7) Siemeister, G., Schnurr, B., Mohrs, K., Schächtele, C., Marmé, D., and Martiny-Baron, G. (1996) Expression of biologically active isoforms of the tumor angiogenesis factor VEGF in Escherichia coli. *Biochem. Biophys. Res. Commun. 222*, 249−255.

(8) Peterson, K. J., Sadowsky, J. D., Scheef, E. A., Pal, S., Kourentzi, K. D., Willson, R. C., Bresnick, E. H., Sheibani, N., and Gellman, S. H. (2008) A fluorescence polarization assay for identifying ligands that bind to vascular endothelial growth factor. *Anal. Biochem. 378*, 8−14.

(9) Sélo, I., Négroni, L., Créminon, C., Grassi, J., and Wal, J. M. (1996) Preferential labeling of [alpha]-amino N-terminal groups in peptides by biotin: application to the detection of specific anti-peptide antibodies by enzyme immunoassays. *J. Immunol. Meth. 199*, 127−138.

(10) Udenfriend, S., Stein, S., Böhlen, P., Dairman, W., Leimgruber, W., and Weigele, M. (1972) Fluorescamine: a reagent for assay of amino acids, peptides, proteins, and primary amines in the picomole range. *Science (Washington, DC)*, 871−872.

(11) Stein, S., Böhlen, P., and Udenfriend, S. (1974) Studies on the kinetics of reaction and hydrolysis of fluorescamine. *Arch. Biochem. Biophys.*, 400−403.

(12) Thomas, J. J., Kim, J. H., and Mauro, D. M. (1992) 4-(4-nitrobenzyl)pyridine tests for alkylating agents following chemical oxidative activation. *Arch. Environ. Contam. Toxicol. 22*, 219−227.

(13) Epstein, J., Rosenthal, R. W., and Ess, R. J. (1955) Use of γ-(4-nitrobenzyl)pyridine as analytical reagent for ethylenimines and alkylating agents. *Anal. Chem. 27*, 1435−1439.

(14) Pavia, D. L. (2005) Introduction to organic laboratory techniques: a small scale approach, Thomson Brooks/Cole.

(15) Skutnik, J. M., Assink, R. A., and Celina, M. (2004) High-sensitivity chemical derivatization NMR analysis for condition monitoring of aged elastomers. *Polymer 45*, 7463−7469.

(16) Pan, B., Li, B., Russell, S. J., Tom, J. Y., Cochran, A. G., and Fairbrother, W. J. (2002) Solution structure of a phage-derived peptide antagonist in complex with vascular endothelial growth factor. *J. Mol. Biol. 316*, 769−87.

(17) Chmura, A. J., Schmidt, B. D., Corson, D. T., Traviglia, S. L., and Meares, C. F. (2002) Electrophilic chelating agents for irreversible binding of metal chelates to engineered antibodies. *J. Controlled Release 78*, 249−258.

(18) Nonaka, H., Fujishima, S.-h., Uchinomiya, S.-h., Ojida, A., and Hamachi, I. (2010) Selective covalent labeling of tag-fused GPCR proteins on live cell surface with a synthetic probe for their functional analysis. *J. Am. Chem. Soc. 132*, 9301−9309.

(19) Bourdon, P., Fenton, J. W., and Maraganore, J. M. (1990) Affinity labeling of lysine-149 in the anion-binding exosite of human .alpha.-thrombin with an N.alpha.-(dinitrofluorobenzyl)hirudin C-terminal peptide. *Biochemistry 29*, 6379−6384.

(20) Klosterm, H., and Humbel, R. E. (1966) Chemistry and biochemistry of insulin. *Angew. Chem., Int. Ed. Engl. 5*, 807−822.

(21) Marfey, P. (1984) Determination of D-amino acids: use of a bifunctional reagent, 1,5-difluoro-2,4-dinitrobenzene. *Carlsberg Res. Comm. 49*, 591−596.

(22) Marinetti, G. V., Baumgarten, R., Sheeley, D., and Gordesky, S. (1973) Cross-linking of phospholipids to proteins in the erythrocyte membrane. *Biochem. Biophys. Res. Commun. 53*, 302−308.

(23) McDaniel, D. H., and Brown, H. C. (1958) An extended table of hammett substituent constants based on the ionization of substituted benzoic acids. *J. Org. Chem. 23*, 420−427.

(24) Bunnett, J. F., Garbisch, E. W., and Pruitt, K. M. (1957) The element effect as a criterion of mechanism in activated aromatic nucleophilic substitution reactions. *J. Am. Chem. Soc. 79*, 385−391.

(25) Ji, P., Atherton, J. H., and Page, M. I. (2011) The kinetics and mechanisms of aromatic nucleophilic substitution reactions in liquid ammonia. *J. Org. Chem. 76*, 3286−3295.

(26) Sanger, F. (1945) The free amino groups of insulin. *Biochem. J. 39*, 507−515.
(27) Landsteiner, K., and Jacobs, J. (1935) Studies on the sensitization of animals with simple chemical compounds. *J. Exp. Med. 61*, 643−U8.
(28) Landsteiner, K., and Jacobs, J. (1936) Studies on the sensitization of animals with simple chemical compounds. II. *J. Exp. Med. 64*, 625−639.
(29) Corneillie, T. M., Lee, K. C., Whetstone, P. A., Wong, J. P., and Meares, C. F. (2004) Irreversible engineering of the multielement-binding antibody 2D12.5 and its complementary ligands. *Bioconjugate Chem. 15*, 1392−1402.

Bioconjugate Chemistry

Review

pubs.acs.org/bc

Lipid Conjugated Oligonucleotides: A Useful Strategy for Delivery

Mouna Raouane,[†,‡] Didier Desmaële,[†] Giorgia Urbinati,[‡] Liliane Massaad-Massade,*[,‡] and Patrick Couvreur*[,†]

[†]Laboratoire de physicochimie, Pharmacotechnie et biopharmacie, UMR CNRS 8612, Université Paris Sud 11, Faculté de pharmacie, 5 rue J. B. Clément, 92296 Châtenay-Malabry, France

[‡]Laboratoire de Vectorologie et transfert de gènes, UMR CNRS 8203, Institut Gustave Roussy, 114 rue Edouard Vaillant, 94805 Villejuif, France

ABSTRACT: Oligonucleotides, including antisense oligonucleotides and siRNA, are promising therapeutic agents against a variety of diseases. Effective delivery of these molecules is critical in view of their clinical application. Therefore, cation-based nanoplexes have been developed to improve the stability as well as the intracellular penetration of these short fragments of nucleic acids. However, this approach is clearly limited by the strong interaction with proteins after administration and by the inherent toxicity of these positively charged transfection materials. Neutral lipid−oligonucleotide conjugates have become a subject of considerable interest to improve the safe delivery of oligonucleotides. These molecules have been chemically conjugated to hydrophobic moieties such as cholesterol, squalene, or fatty acids to enhance their pharmacokinetic behavior and trans-membrane delivery. The present review gives an account of the main synthetic methods available to conjugate lipids to oligonucleotides and will discuss the pharmacological efficacy of this approach.

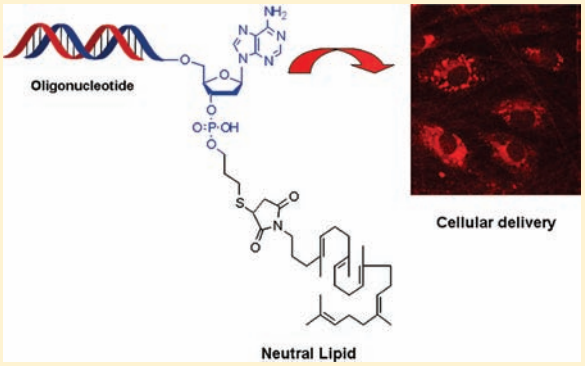

INTRODUCTION

The therapeutic use of oligonucleotides (ONs) (either antisense oligonucleotides AS-ON or siRNA) has gained a lot of attention. Their high specificity covering a wide range of biomedical applications allows the inhibition of target proteins that are not easily accessed and modulated by conventional small molecular weight or protein drugs.[1−8] As a prelude, it is important to recall that ONs do not cross the intact cell membranes to any significant degree via simple diffusion. This is primarily due to the highly hydrophilic and anionic character of these molecules which have poor affinity for the negatively charged cell membranes. Thus, development of efficient delivery systems is one of the most challenging hurdles to turn ONs into clinically acceptable therapeutic drugs. So far, a wide variety of approaches including viral vectors as well as nonviral delivery systems, such as liposomes, nanoparticles, micelles, and polyplexes[9−15] have been investigated to enhance target cells uptake and silencing potency in vivo. However, the safety of viral vectors is questionable due to immunogenicity and possible recombination of oncogenes. On the other hand, most of the nonviral vectors are designed using polycations, either polymers or lipids, whose (cyto)toxicity is now well-documented.[16,17] That is the reason the conjugation of nucleic acids with neutral lipids offers an interesting alternative, since it has been reported that this approach could (i) significantly enhance cellular uptake of AS-ONs and siRNA, (ii) prolong the half-life of these molecules in plasma, and (iii) increase the efficiency of siRNA-induced gene silencing in vivo.[13,18−20] Despite the richness of the different synthetic strategies developed for the modification of the ONs,[21] the synthesis of lipid−ON conjugates (LOC) is anything but trivial and requires extensive expertise in organic chemistry and solid-phase synthesis. These covalently attached LOCs can be synthesized either by postsynthetic coupling of prepurified lipids and ONs or by stepwise solid-phase synthesis without intermediate purification. This short review attempts to provide an overview of the vast repertoire of chemical protocols developed so far for the chemical synthesis of LOCs.

BACKGROUND

Antisense and RNAi Mechanisms. Antisense oligonucleotides (AS-ONs) and RNA interference (RNAi) are the two major approaches for therapeutic gene expression. Although the activity of both types of molecules is due to their base-pairing capacity with complementary cellular nucleic acids, the method by which they inhibit gene expression is different. An understanding of the mechanisms of action of AS-ON and RNAi is a prerequisite for the design of efficient lipid conjugates of these molecules.

AS-ON. AS-ONs are single-stranded DNA sequences of 13−25 bases, which can highly selectively inhibit the expression of target genes by hybridizing with their specific "sense" sequences in mRNA (mRNA) or DNA molecules.[22,23] Ribonuclease H

Received: August 1, 2011
Revised: January 23, 2012
Published: February 29, 2012

(RNase H)-mediated degradation of complementary mRNA is the major mode of action of AS-ONs.[24] This enzyme specifically cleaves the RNA strand of RNA-DNA heteroduplexes, leading to the release of the AS-ON which can further bind to a new mRNA strand; this mechanism is therefore catalytic.[24]

RNAi. Suppression by double-stranded RNA (dsRNA) is an important endogenous mechanism of gene regulation.[25] Briefly, the "Dicer" enzyme and its cofactors cleave dsRNA into 21- to 23-mer segments called short interfering RNAs (siRNAs) and assist its loading onto the Argonaute 2 (Ago 2)-containing "RISC" proteic complex. In the RISC assembly process, Ago2 cleaves the passenger strand, thereby liberating the guide strand from the siRNA duplex and producing active RISC capable of cleaving target mRNA.[26,27] The guide strand serves as a template for the recognition of homologous mRNA, which upon binding to RISC is cleaved by the catalytic activity of Ago2 between bases 10 and 11 relative to the 5′ end of the guide siRNA strand;[5,28−31] therefore, the RNA is degraded and the translation is arrested. Noteworthy, the template siRNA is not affected by this reaction, so the RISC can undergo numerous cycles of mRNA cleavage that explain the high efficiency of RNAi and its use as a therapeutic target.

Major Challenges for Oligonucleotides and siRNA Delivery in Vivo. As polyanionic macromolecules, ONs face multiple obstacles including plasma membrane, cytoplasm, and nuclear membrane to reach their intracellular site of action. Moreover, naked AS-ONs and siRNA are relatively unstable in the blood due to nonspecific uptake by the reticulo-endothelial system (RES) and aggregation with serum proteins and are rapidly cleared from the body by rapid renal excretion owing to degradation by nucleases (half-life in serum is few minutes).[32] Issues of stability have been solved in part by the introduction of chemical modifications that provide greater metabolic stability or improved bioavailability. There have been several recent reviews that provide a good overview of chemical modification strategies for siRNA[33,34] and AS-ONs.[35,36] Nonetheless, ON delivery still faces many challenges. As illustrated in Figure 1, ONs have to overcome several obstacles to reach their intracellular site. Then, an effective delivery strategy must take account the need to (i) protect the ON from the enzymatic digestion, (ii) improve the pharmacokinetics by avoiding uptake via the RES and rapid renal filtration, (iii) allow better translocation through the endothelium, (iv) facilitate the diffusion through the extracellular matrix, and (v) enhance cellular uptake and (vi) intracellular endolysosomal escape. Such delivery systems would also minimize potential ON-induced toxicities.[37]

Mechanisms of Endocytosis and Intracellular Trafficking. Endocytosis covers multiple distinct uptake pathways that are subdivided into three major classes: (i) phagocytosis (that mainly takes place in "professional phagocytes" such as macrophages and granulocytes); (ii) macropinocytosis (in which macromolecules being internalized as simply dissolved in the ambient medium); and (iii) receptor mediated endocytosis (that often involve a cell surface receptor). The last class comprises three diverse uptake pathways: (i) the "classic" clathrin-coated pit pathway, (ii) the caveolar pathway, and (iii) one or more noncaveolar, clathrin-independent pathways (CLIC pathways).[38]

It is generally believed that ONs are internalized into the cytoplasm by cell surface receptors via receptor-mediated endocytosis[39,40] which includes three major steps. The first step consists of the ligand−receptor binding. In fact, the complex enters vesicles that bud from the cytosolic face of the plasma membrane. In the second step, the initial uptake is followed by sequential intracellular trafficking into a variety of low pH endomembrane compartments, including early/sorting endosomes, late endosomes/multivesicular bodies, and lysosomes. The last step leads to the endosomal escape of ON to reach the cell cytoplasm (or nucleus) and to exert pharmacological activity. The general aspects of the cellular uptake of ONs have been studied and extensively reviewed.[35,40−42]

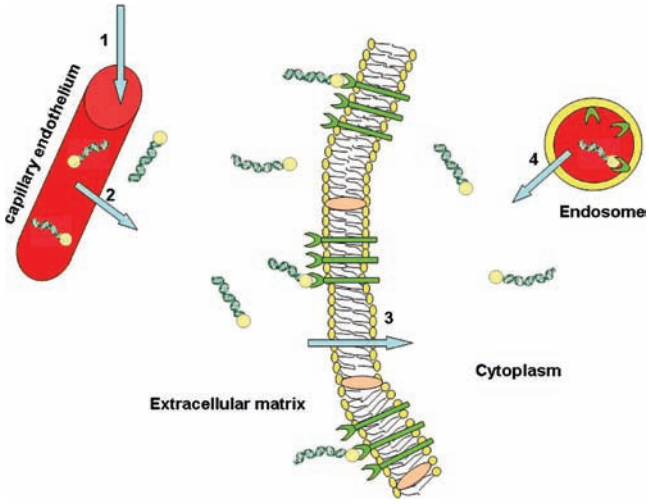

Figure 1. In vivo barriers for the effective delivery of antisense and siRNA oligonucleotides. There are four major barriers for oligonucleotides to gain access to cells and take effect on their intracellular targets. After administration into the blood circulation, the oligonucleotide must avoid rapid degradation by serum nucleases, clearance by the reticulo-endothelial system, and rapid excretion by renal filtration.[1] Further, the oligonucleotide must gain access to the target cells by crossing the capillary endothelium and diffusing through the extracellular matrix.[2] The oligonucleotide has to be further taken up by the target cells, typically through a receptor-mediated endocytosis process.[3] Inside the cells, the oligonucleotide must be released from the endosomes to reach their intracellular targets.[4]

Approaches to Deliver Oligonucleotides. Two major approaches, based on either chemistry or formulation, were adopted to overcome the above-mentioned limitations concerning ONs administration. The chemical approach consists either of synthesizing nucleic acids with variations in their natural structure (in order to improve resistance toward degradation) and/or of attaching a lipid, peptide, or polymer moiety associated or not with a cell targeting ligand. The potential advantages of the chemical strategy are as follows: (i) ON preferential targeting toward specific tissues and cells which express specific receptors, (ii) delivery of ON to appropriate intracellular compartments, i.e., cytoplasm or nucleus, and (iii) better ON away from the blood and widespread distribution in tissues due to the small size of the chemical conjugates in comparison to the nanoformulations mentioned below.

The formulation approach generally uses cationic lipids or polymers which can interact with ONs through strong electrostatic interactions, leading to the so-called "nanoplexes" with size between ten and a few hundred nanometers. The expected advantages of the nanoformulation approach are better stability in biological fluids and also improved cell penetration and tissue biodistribution. This strategy has already

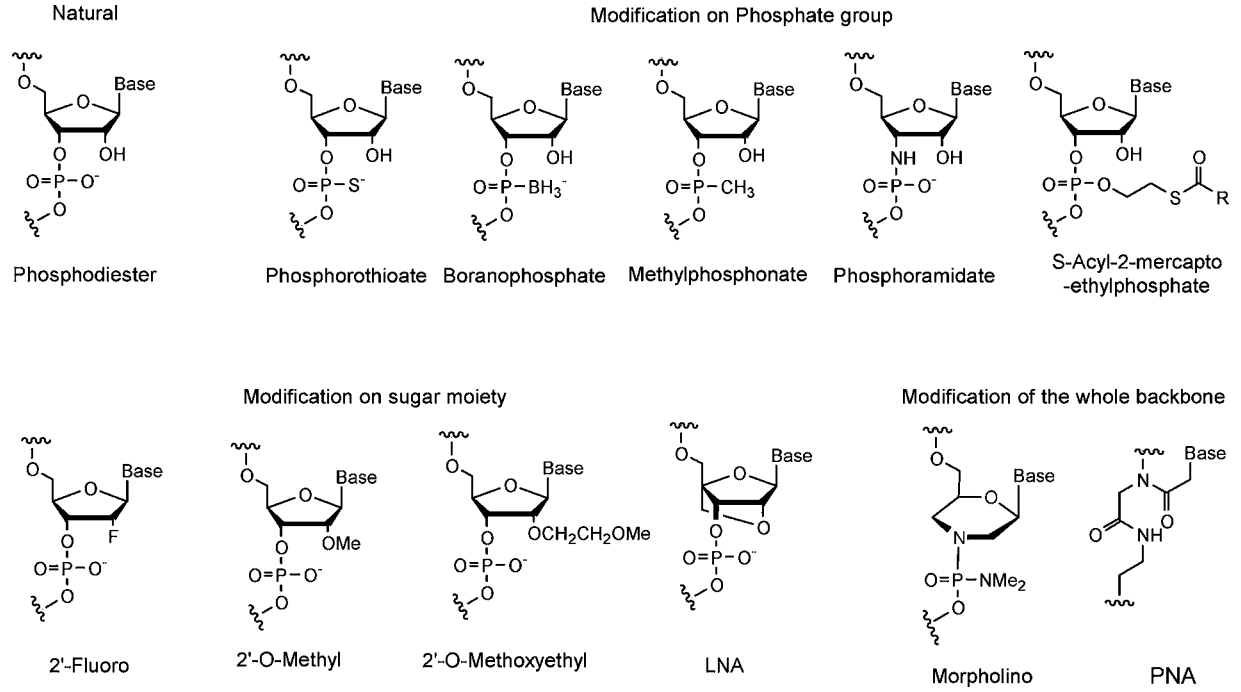

Figure 2. Chemical modifications: structures of the various chemically modified oligonucleotide residues.

achieved significant success in both cellular and animal studies.[43−45] However, the toxicity of cationic transfectants either lipidic or polymeric may raise major issues for clinical utilization.[16] Indeed, creating a positive surface charge promotes serum protein binding, so that cationic components are typically toxic even when biodegradable linkages are employed.[46] For instance, concerning cationic liposomes, significant toxicity including cell contraction, mitotic inhibition, formation of aggregates in blood, and the tendency to induce inflammatory response has been reported.[47,48] Similarly, polymers like PEI have shown marked cytotoxicity due to induction of cell death (necrosis and apoptosis).[49] This explains why, although hundreds of compounds have been in the discovery phase, only fourteen entered clinical trials, among which four are designed for ocular administration or inhalant administration and only five for systemic administration (QPI-1002 by Quark Pharm., ALN-TTR01, TKM-ApoB, ALN-VSP by Alnylam Pharm, TKM-PLK1 by Protiva Biotherapeutics and CALAA-01 by Calando Pharm) (www.clinicaltrials.gov). Since these clinical trials are, to our knowledge, only in Phase I, further data concerning toxicity and efficacy are not yet available. In this context, the use of non-ionic lipids for ON delivery represents an attractive methodology, since many lipids are safe, nontoxic, and biocompatible, with some of them being of natural origin. However, the association of ONs through physical interactions (i.e., adsorption or encapsulation) with neutral lipid nanoparticles or liposomes suffers from lower ON loading and encapsulation yield as compared to cationic transfectants.[50−52] Thus, it is our opinion that the chemical linkage of nucleic acids with neutral lipids has been insufficiently exploited, although it may combine biocompatibility and important drug loading capacity, therefore representing an interesting delivery strategy.

It is noteworthy that an additional strategy to maintain intracellular penetration without using cationic lipids is the design of ligand-decorated nanocarriers allowing transport of ON into cells (also called "active targeting"). However, important issues have to be mentioned about active drug targeting: as an example, the use of human transferrin as targeting ligand for cyclodextrin-based siRNA delivery (i.e., CALAA-01) raises the question of the difficulty realizing success on a commercial scale due to difficulty of manufacturing, conjugation, processing, and storage as reported by Xu and Anchordoquy.[46]

CHEMICAL STRATEGIES FOR THE SYNTHESIS OF LIPID−OLIGONUCLEOTIDE CONJUGATES

Below are discussed the main synthetic methods for performing covalent conjugation of lipids to ONs. In many cases, changes in pharmacokinetic and pharmacodynamic properties were observed.

Site of Conjugation and Chemical Modification. Conjugation of lipids to ONs generally occurs at the 5′- or 3′-ends.[53,54] In siRNA, there are four terminal ends for potential conjugation sites, since siRNA is a hybridized product of two complementary strands (sense and antisense). The antisense (guide) siRNA strand needs to be incorporated into the RISC complex to initiate the RNAi mechanism as previously described. Therefore, for steric reasons this strand should not be chemically modified. On the contrary, the presence of the inactive sense strand makes it an ideal site for chemical conjugation.

Argonaute2 is a key component of the RISC complex and responsible for mRNA cleavage in the RNAi pathway as discussed before.[55] It is composed of PAZ, Mid, and PIWI domains. The X-ray structural analysis of a cocrystal between a PIWI protein and an siRNA reveals that the 5′-phosphate of the siRNA guide strand is recognized by the PIWI domain and the 5′-phosphate interacts with the carboxyl group of a C-terminal residue of the domain through a divalent metal ion.[56,57] Previous observations showed that the modification of the 5′-hydroxyl groups of the siRNA guide strand by methoxy groups completely hampered the siRNA function in *Drosophila* embryo lysate and HeLa cell extract.[58,59] Thus, these observations have

dx.doi.org/10.1021/bc200422w | *Bioconjugate Chem.* 2012, 23, 1091−1104

suggested that the 5′-end of a guide strand is not suitable for modification by lipophilic groups. On the contrary, the 3′- and 5′-ends of the sense strand are primarily considered as potential sites for conjugation with minimal influence on RNAi activity.[60−63]

Although duplex RNA is more resistant to nuclease attack than single-stranded ON, unmodified siRNAs are nevertheless rapidly degraded when administered intravenously in mammals. Therefore, before conjugation of ONs to lipids, it is of prime importance to protect them from degradation. Thus, a number of chemically modified ONs have been developed to enhance stability and to confer other desirable properties in single-stranded AS-ONs and siRNA. Chemical modifications may occur at three different sites: (i) at phosphate groups, (ii) on the sugar moiety, and/or (iii) on the entire backbone structure of the ON.

The most common stabilizing modification for both antisense and siRNA is substitution at the phosphorus atom of sulfur for oxygen (S → O) to form phosphorothioate ONs. Several phosphorothioate oligoribonucleotides are now in various clinical trials, often in combination with other anticancer drugs. It is worth mentioning that a phase II clinical trial combining Oblimersen (Bcl2 antisense) and rituximab (monoclonal antibody against CD20) for the treatment of recurrent non-Hodgkin's lymphoma has been just completed. Moreover, a phosphorothioate oligodeoxynucleotide agonist of Toll-like Receptor 9 (IMO 2055) is now being tested in Phase Ib trial in combination with cetuximab and FOLFIRI (folinic acid, 5-FU, irinotecan) in patients with colorectal cancer who have progressed following chemotherapy for advanced or metastatic diseases (http://www.clinicaltrials.gov/). However, extensive phosphorothioate modification can lead to unwanted side effects due to a variety of nonspecific cellular protein bindings.[64] So, it may be preferable to limit the use of this modification to terminal positions (or 3′ overhangs) where nuclease resistance is probably most important. Nevertheless, this modification can be safely used to improve the stability of siRNA.[65−68] It can also be mentioned that the replacement of a nonbridging oxygen with a boron (boranophosphate), nitrogen (phosphoramidate), or methyl (methylphosphonate) group will provide nuclease resistance and has been used to help stabilize single-stranded AS-ONs. Figure 2 shows various such modifications that improve nuclease stability and can also be employed in siRNAs. Boranophosphate-modified DNA or RNA resistant to nuclease degradation and the boron modification appears to be compatible with siRNA function. However, boranophosphates are not easily prepared using chemical synthesis.[69,70] In contrast, PS modification is easier and has been extensively used to improve nuclease stability of both antisense ONs and siRNAs. Phosphoramidate and methylphosphonate derivatives were extensively explored for antisense applications but were found to significantly alter the interaction between the nucleic acid and cellular enzymes such as RNase H.[66,71−74] Hydrophobic moieties can also be used for the same protective purpose by masking the internucleosidic phosphodiester bonds of an AS-ON with biodegradable or thermolabile protecting groups. *S*-Acyl-2-mercaptoethyl and alkoxymethyl-protected AS-ONs are the most representative example of this approach.[75,76]

A further important class of modified ONs is represented by derivatives with substitutions at the 2′ position of the sugar. *O*-Methyl group (2′-O-Me), 2-methoxyethyl (2′-O-MOE) group, and fluoro (2′-F) group substitutions have been made. These modifications increase the nuclease resistance and the stability of the complexes formed with native RNA. However, these modifications also have consequences for ON activity. This is not the case for 2′-*O*-methyl RNA, which is a naturally occurring base present in mammalian rRNA. A number of reports have described patterns of 2′-*O*-methyl incorporation that retain full potency of the siRNA compared with unmodified RNA and are stable in serum.[61,65,77] According to Layzer et al. (2004), fluoro-substituted siRNA did not show increased in vivo activity, despite better stability in plasma.[61,66] However, in another study *O*-methoxyethyl derivatives were found to have the same activity as the unmodified sequence.[78] Another recent approach has shown that the ribose moiety can also be used to produce locked nucleic acid (LNA), in which a covalent bridge is formed between the 2′ oxygen and the 4′ carbon of the ribose, fixing it in the 3′-endo configuration. These constructs, referred to as inaccessible RNA, are extremely stable in biological medium, able to activate RNase H and form tight hybrids with complementary RNA and DNA.[79,80] LNAs can be incorporated into siRNAs; however, location of the modified ribose to achieve the best effect is more restricted than for 2′-*O*-methyl or 2′-F modified bases.[81]

Other highly improved ON chemistries consist of modification of the whole backbone structure. For example, the phosphodiester backbone can be completely replaced by a peptide backbone consisting of (2-aminoethyl)-glycine residues. These are known as peptide nucleic acids.[82] They have the advantages of strong hybridization, low toxicity, and good biological stability with respect to nucleases, but also the disadvantages of low solubility in water, poor intracellular penetration, and a lack of ability to activate RNase H. Another completely modified structure is the morpholino AS-ON, in which the ribose is mimicked by a morpholino ring while phosphoramidate intersubunit linkages are used as a substitute for phosphodiester bonds. They have low toxicity and show affinity for their targets similar to that of unmodified AS-ON.[83,84] A Phase II clinical trial for morpholino-oligomer directed against exon 5 (AVI-4658 PMO) for Duchenne muscular dystrophy treatment has just been completed in April, 2011. Another example of phosphorodiamidate morpholino-antisense oligomer already in Phase I clinical trial is AVI-6002, by AVI BioPharma, for the treatment of Ebola hemorrhagic fever. The final data collection started in November, 2011.

Synthetic Approaches. The synthetic approaches employed for LOC synthesis fall into two major categories: the postsynthetic conjugation approach (or solution-phase approach) and the presynthetic conjugation approach (or stepwise solid-phase synthesis approach). In the postsynthetic conjugation approach, the ON is equipped with an appropriate functionality, to which the lipid moiety is coupled in solution after release and purification of the ON. When using the stepwise solid-phase approach, the LOC is prepared on a single support by assembling the conjugate group (i.e., lipophilic group) by a stepwise process prior to or after the ON synthesis and using suitable protecting groups or/and functional moieties which minimize side reactions. The advantage of the solid-supported approach compared to conjugation in solution is a less laborious purification method. To achieve high coupling efficiency, the conjugate group is indeed generally used in considerable excess which complicates the purification when the conjugation is carried out in solution. By contrast, on a solid support, the unreacted conjugated group and the possible side products may be removed by simple washing, which markedly

Table 1. Summary of Strategies Used for the Synthesis of Lipid−Oligonucleotide Conjugates

ON conjugate	site of conjugation on the ON	linker and/or functional group	covalent linkage	conjugate chemistry	target siRNA	ref
Cholesterol-siRNA	3′-end of sense strand	cholesterol-aminocaproic acid-4-hydroxyproline linker	not specified	solid-phase synthesis (phosphoramidite)	Apo-B-1 siRNA	13
Cholesterol-siRNA	5′-end of sense strand	cholesterol phosphoramidite coupled to (CH_2)−S-S-$(CH_2)_6$ linker	reducible (disulfide)	solid-phase synthesis (phosphoramidite)	p38 MAP kinase siRNA	88
Squalene-siRNA	3′-end of sense strand	maleimide modified squalenic acid	thioether	postsynthesis conjugation (Michael addition)	RET/PTC1 siRNA	85
α-tocopherol-siRNA	5′-end of anti sense strand	R-tocopherol phosphoramidite	phosphodiester cleavage (site of Dicer	solid-phase synthesis (phosphoramidite)	Apo-B-1 siRNA	86
Lipid- and steroid-siRNA	3′-end	not specified	trans-4-hydroxyprolinol-aminohexanoic linker	solid-phase synthesis phosphoramidite)	Apo-B-1 siRNA	18
Lipid- and cholesteryl siRNA	3′-end of sense strand	not specified	glycerol scaffold with 2-hydroxy-ethoxycarbonylamino-butyl-carbamic acid linker	solid-phase synthesis (phosphoramidite)	Apo-B-1 siRNA	19

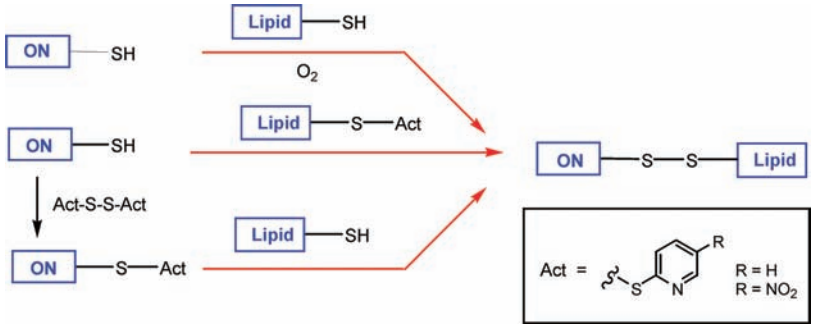

Figure 3. Routes for formation of disulfide-linked conjugates.

facilitates the chromatographic purification after the conjugate is released from the support. The use of a solid support may also help to avoid the problems otherwise arising from the limited solubility of one of the reactants. These approaches can be further categorized into different categories depending on the type of covalent bond generated between the ON and the lipid. The covalent linkages frequently used for connecting lipids to the termini of ONs are as follows: thioether,[85] disulfide,[117] phosphate,[86] or phosphoramidate.[87,88] In order to avoid eventual steric hindrance, a simple alkyl chain[88] is often used as a spacer arm and may be introduced between the ON and the lipid, whereas aminocaproic−pyrrolidine linker,[13] ether linker,[85] and non-scissile triazole linker[89] are other spacers used for LOC synthesis. Some conjugation strategies of LOCs are summarized in Table 1.

Post-Synthetic approach. It is noteworthy that stepwise solid-phase synthesis of LOC is difficult and expensive due to the conflicting chemistries and different solubility profiles of ONs and lipids. One of the simplest approaches to overcome this issue is to prepare separately both functionalized components, i.e., by exploiting standard lipid and ON synthetic methodologies before proceeding toward the final conjugation of the ON and the lipid. Of course, prior to the conjugation, it is required to ensure a unique and specific linkage between the lipids and ONs when attaching certain reactive functionalities to both molecules. Recently, Raouane and co-workers established a new, efficient method to synthesize the lipid conjugates of ONs via a thioether linkage.[85] However, at the beginning, these authors have chosen the covalent linkage of the thiolated siRNA sense strand (with sequence toward the RET/PTC1 fusion oncogene) to squalene derivative (SQ) through a disulfide linkage, taking advantage of the 3-mercaptopropyl phosphate group introduced at the 3′-terminal of the ON during its manufacture on solid support, since thiol groups have a specific reactivity and afford rapid conjugation with a wide variety of substrates. The disulfide linkage can be formed either by direct oxidation of two thiols[90] or by preliminary activation of one thiol with pyridyldisulfanyl or 5-nitropyridyldisulfanyl groups followed by nucleophilic substitution[91] as illustrated in Figure 3. Attempts to couple thiol-containing ON with thiopyridyl-activated SQ via disulfide linkage met with repeated failure even after activation of both substrates.[85] Thus, the challenging squalenoylation was more efficiently achieved by the use of the maleimide group as thiol acceptor as previously described by Weber et al.[92] It was described (see Scheme 1) that thiolated siRNA 1 could selectively react with maleimide-derivatized SQ 2 possessing an ether linker to form the nonreducible thioether bond.[85] This chemical construct was found to self-organize as nanoparticles in water and was found to inhibit tumor growth in a mice xenografted experimental model of the thyroid papillary carcinoma.[85]

Presynthesic Approach. The strategy of modifying the ON during solid-phase synthesis is by far the most widely used approach to add hydrophobic moieties to ONs. Due to the elongation of the ON chain in the 3′-5′ direction during solid-phase synthesis, the modification is more conveniently incorporated at the 5′-end as compared to the 3′-end, which requires substantial additional synthetic efforts.[93,94]

The LOCs are usually obtained by one of the three following solid-phase approaches: either (i) 3′-conjugates by chain assembly on a support bearing the desired hydrophobic group or (ii) 5′-conjugates by introducing the conjugate group as a phosphoramidite reagent; (iii) intrachain conjugates

dx.doi.org/10.1021/bc200422w | *Bioconjugate Chem.* 2012, 23, 1091−1104

Scheme 1. Postsynthetic Strategy for the Direct Hydrophobization of siRNA by Squalene Conjugation

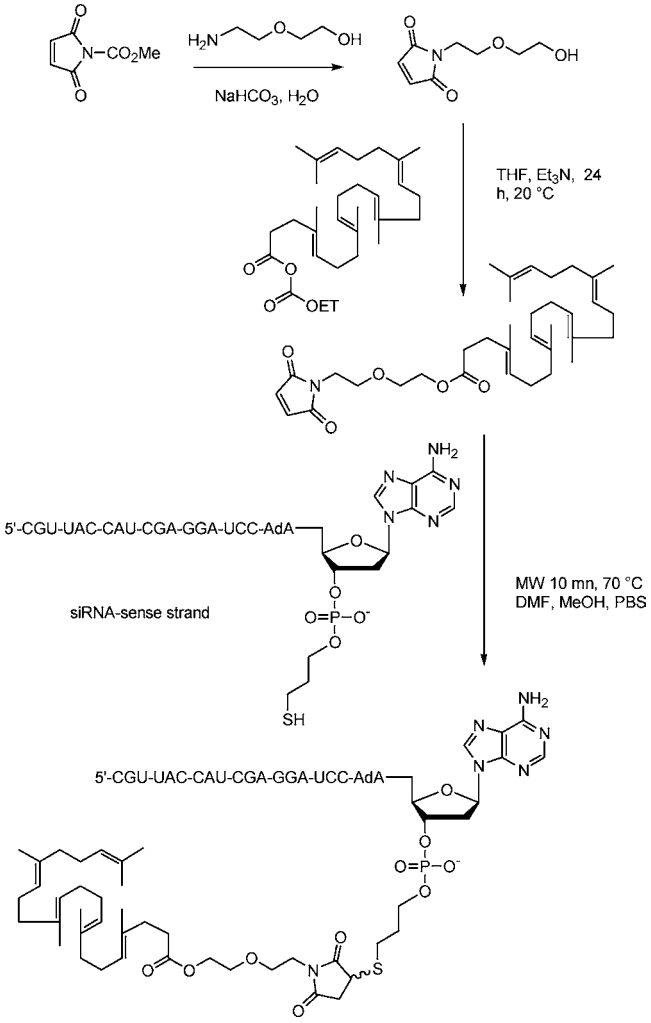

may also be obtained by making use of prefabricated nucleosidic building blocks or their congeners incorporating the conjugate group.

Preparation of Oligonucleotide 3′-Lipid Conjugates. For the synthesis of lipid 3′-conjugates ONs, an accessible solid-phase method has been described by Stetsenko et al. (2001). This method involves the use of a branched alcohol bearing orthogonally protected amino and hydroxyl groups which is attached to the support via a succinyl linker as illustrated in Scheme 2. The conjugate group (i.e., cholesterol) bearing a hydroxyl function is first attached to the deprotected amino group of a homoserine scaffold as a chloroformate ester and the ON is then assembled on the deprotected hydroxyl function.[95] A similar amino-alcohol supported CPG−resin allowing stepwise immobilization of cholesterol and 3′-ON had previously been proposed.[96] Related supports have more often been prepared by immobilization of a prefabricated linker−cholesterol conjugate.[19,97−102] Supports derived from *trans*-L-4-hydroxyprolinol have additionally been used for the preparation of ON conjugates of many other steroids and diacylated glycerols,[103] 2′-*O*-[94] and 3′-*O*-succinylated uridine.[104]

Interestingly, instead of conventional succinyl linker, an aminoalkyl support was acylated with 3-chloro-4-hydroxyphenylacetic acid and the 3′-terminal nucleoside was coupled to the

Scheme 2. Solid-Phase Synthetic Strategy Developed by Stetsenko for Preparation of 3′-ODN Conjugate

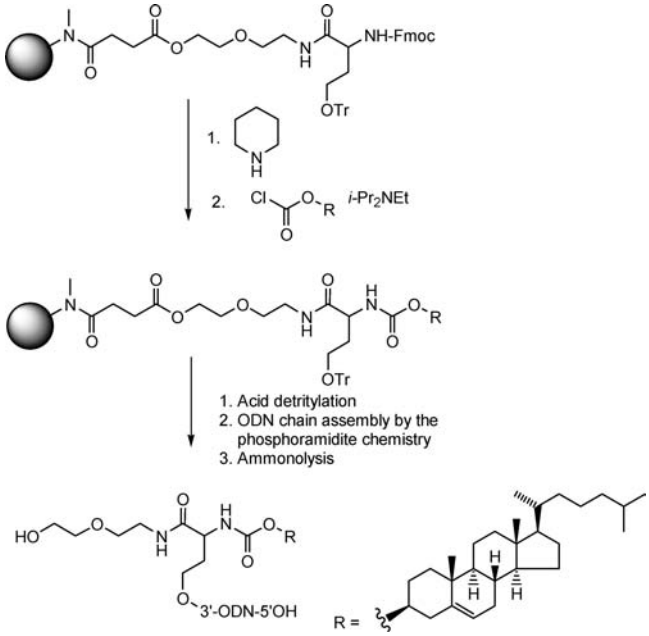

hydroxyl function by the normal phosphoramidite chemistry.[105] The 2-cyanoethyl protection was then removed with triethylamine in pyridine and the lipid group, e.g., cholesterol was coupled to the exposed phosphodiester linkage by the phosphotriester chemistry. The ON was then assembled using standard phosphoramidite protocols and the LOC was obtained after normal ammonolysis.

Soutschek et al. (2004)[13] used 4-hydroxyprolinol as a linker to connect RNAs and lipophilic groups, while Ueno et al. (2008)[106] selected glycerol which was more flexible than hydroxyprolinol as a linker to join lipophilic groups at the 3′-terminus of RNAs (Scheme 3). It is worth noting that a report in 2004 by Soutschek and co-workers using a cholesterol−siRNA conjugate provided the first mechanistic in vivo proof of concept for RNAi. Chemical conjugation of siRNA to cholesterol has indeed been shown to facilitate intracellular siRNA uptake in vitro[107] and in vivo[13] In the latter case, intravenous administration of cholesterol conjugated siRNA oriented toward apolipoprotein B (ApoB) was shown to silence endogenous ApoB gene expression by 55% in the liver and by 70% in the jejunum, the two principal sites for ApoB expression, resulting in decreased plasma levels of ApoB protein and consequently to a remarkable reduction in the cholesterol levels by 35−40%.[13] Cholesterol conjugation imparted critical pharmacokinetic and cellular uptake properties to the duplex as evidenced by the fact that the unconjugated ApoB siRNA was rapidly cleared after administration and unable to induce any mRNA silencing.[13] Radiolabeled cholesterol conjugates of siRNA displayed an elimination half-life of 95 min, whereas unconjugated siRNAs had a half-life of only 6 min. The prolonged half-life of the cholesterol conjugates relative to naked siRNA was explained, at least in part, by an enhanced binding to serum proteins. The mechanism of improved biodistribution and cellular uptake of siRNA through cholesterol conjugation has been further investigated in a recent study:[18] cholesterol−siRNA conjugates were found to incorporate into circulating lipoproteins, especially in LDL, allowing liver targeting, i.e., improved

dx.doi.org/10.1021/bc200422w | *Bioconjugate Chem.* 2012, 23, 1091−1104

Scheme 3. Synthesis of 3′-Lipid-Conjugated Oligonucleotides According to Ueno et al. and D'Onofrio et al.

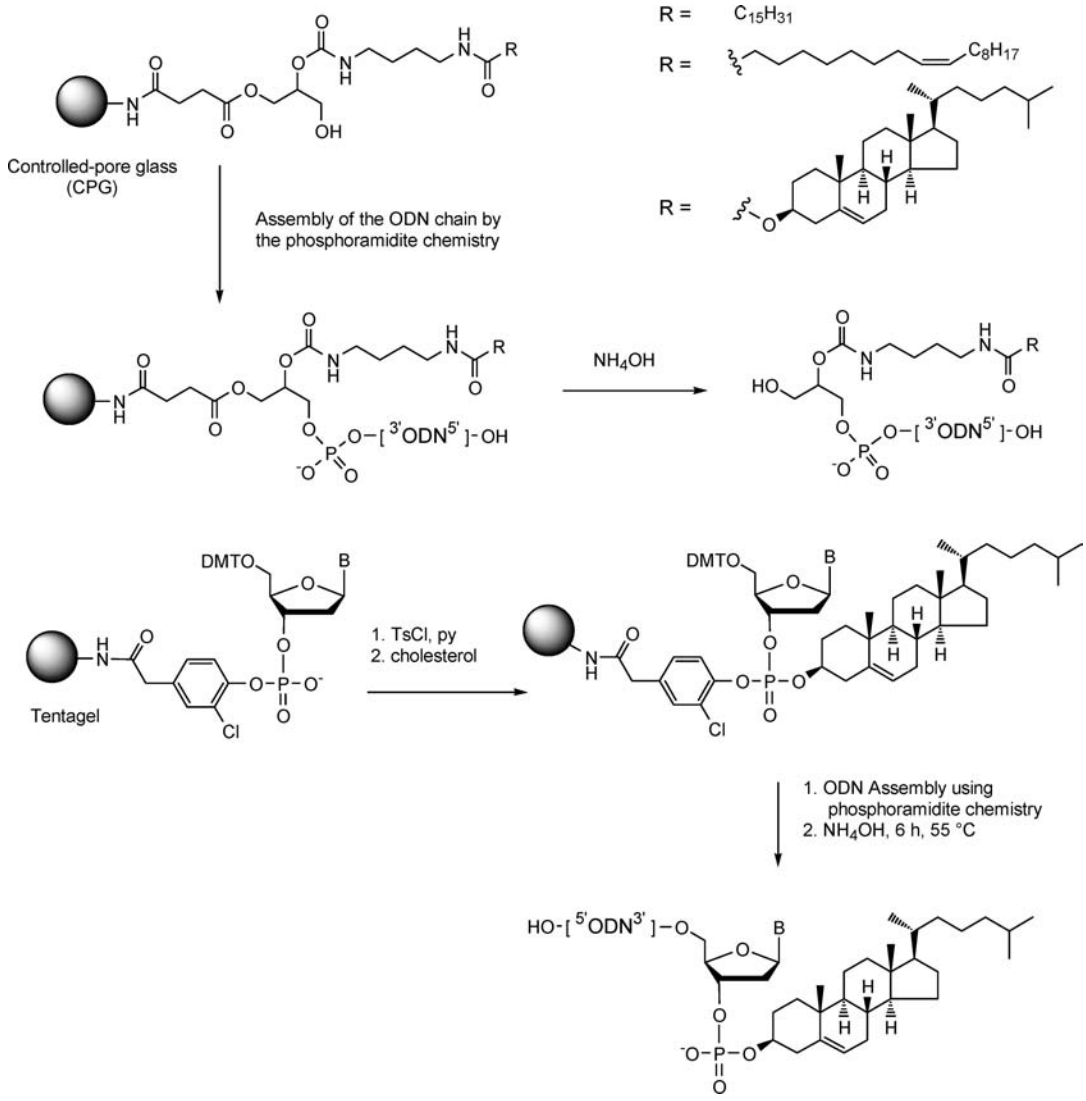

distribution in vivo, whereas efficient hepatocyte internalization occurred via receptor-mediated processes (i.e., efficient cellular uptake).[18] Besides, preloading of cholesterol–siRNA bioconjugates to natural lipoparticles dramatically improved silencing efficacy in mice, whereas the nanoparticle type was found to affect cholesterol–siRNA conjugate distribution in various tissues especially in favor of the liver as explained before (see mechanisms of endocytosis and intracellular trafficking).[18] Wolfrum et al. have elegantly extended the in vivo efficacy seen with cholesterol to other conjugates such as bile acids and long-chain fatty acids. It has been shown that conjugation to bile acids and long-chain fatty acids mediated siRNA uptake into cells and gene silencing in vivo and that efficient and selective uptake of these siRNA conjugates not only depended on interactions with lipoprotein particles, lipoprotein receptors, and transmembrane proteins, but was also affected by the nature of the conjugated lipid. Thus, a variety of lipophilic siRNA conjugates were synthesized using cholesterol or fatty acids of different chain lengths as lipid moieties. The fatty acid conjugates with longer saturated alkyl chains such as stearoyl and docosanyl, but not those with shorter chains, reduced target gene expression in mouse livers.[18] The efficacy of the conjugation of nucleic acids with cholesterol has been further confirmed in another study, showing enhanced cellular uptake in cell culture as well as hepatic deposition after systemic administration.[108] Finally, other authors have demonstrated that the conjugation with cholesterol may enhance siRNA uptake not only via receptor-mediated endocytosis, but also by increased membrane permeability of the otherwise negatively charged RNA.

Using a transgenic mouse model for Huntington's disease, it was also established that a single intrastriatal injection of cholesterol–siRNA conjugate allowed significant inhibition of a mutant Huntingtin gene, attenuating neuronal pathology as well as delaying the abnormal behavioral phenotype.[109]

Preparation of Oligonucleotide 5′-Lipid Conjugates. Apart from 3′ linkage, there are also some LOCs which have been prepared carrying lipids at the 5′-end of the ONs. Figure 4 illustrates different LOCs bearing lipids at the 5′-end of the ONs. Many phosphoramidite and H-phosphonate reagents, both non-nucleosidic and nucleosidic, were designed to introduce hydrophobic conjugate groups into the 5′-terminus of ONs.[89,93,101–104] An archtypical one is the phosphoramidite reagent derived from the allyl ester of 3-α-(2-hydroxyethoxy)-cholic acid obtained by selective phosphitylation of the primary hydroxyl group with 2-cyanoethyl-*N*,*N*-diisopropylphosphoro-

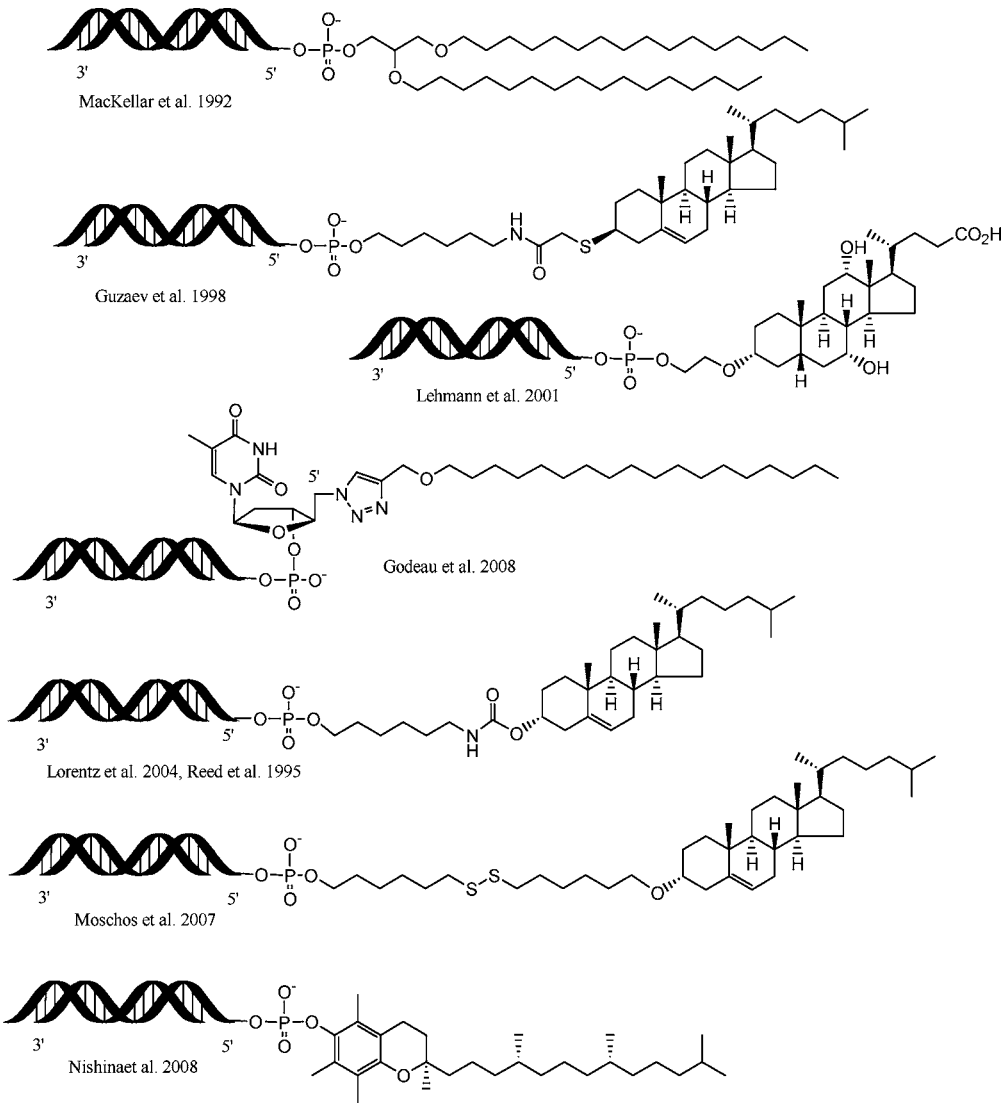

Figure 4. Selected lipid–oligonucleotide conjugates bearing lipids at 5′-ends of the oligonucleotide.

chloridite without interference of the secondary hydroxyl functions.[110] The allyl protection may then be removed on-support using $Pd[PPh_3]_4$-catalyzed deallylation.

Another straightforward approach for the synthesis of 5′-lipid ON conjugates has been developed for ON conjugation to fatty acids.[111] In this approach, 5′-palmitoyl ONs have been obtained by using base-labile *t*-butylphenoxyacetyl protecting groups for base moiety amino functions and oxalyl-CPG anchor group. These modifications to the standard phosphoramidite strategy allowed mild deprotection with ethanolamine, and hence, the 5′-ester linkage remained intact.[111]

In addition, the method mentioned below, described by Letsinger, had been used by Krieg to conjugate cholesteryl moiety at the 5′-end of AS-ON targeted against an mRNA encoding immunosuppressive protein.[112] It was described that a cholesteryl–AS-ON conjugate increased cellular association (by enhance binding to LDL) and improved efficacy.[112] Conjugation of lipids to ONs by 1,3-dipolar cycloaddition reaction involves reaction between alkyne and azide to form 1,2,3-triazoles. This so-called "click chemistry" reaction has been added to the repertoire of ON modifying methods, because the 1,3-dipolar cycloaddition chemistry is very chemoselective, only occurring between terminal alkynyl and azido functional groups with high yield. In addition, the resulting 1,2,3-triazoles are stable under aqueous conditions and high temperature. The use of the Huisgen 1,3-dipolar cyclo-addition for postsynthetic modification of ONs has been the subject of an interesting recent minireview.[113] Practically, the "click chemistry" reaction has been employed to synthesize LOC in three steps starting from alkyne-modified lipids derived from cholesterol and octadecanol.[89] The resulting 1,3-dipolar cycloaddition reaction provided the expected 1,2,3-triazole intermediates, which were next converted into phosphoramidites in one step. The phosphoramidites were further coupled to the 17-mer 2′-*O*-methylribonucleotide antisense chain of the hepatitis C virus (HCV) RNA, using a classical solid support synthesis, in which the ON was elongated in the 3′-5′ direction. This reaction could be carried out in either water or organic medium and be employed postsynthetically on purified units modified with alkynyl and azido functionalities without additional functional group protecting strategies. Godeau et al. (2008) reported that the incorporation of a lipid moiety via a nonscissile triazole linker noticeably increased the lipophilicity of the ONs, which had a positive impact on their intracellular delivery (Scheme 4). ONs conjugated with cholesterol or octadecanol moiety induced a dose-dependent reduction of

Scheme 4. Synthesis of 5′-cholic Acid-Conjugated Oligonucleotides According to Lehmann et al. and Conjugation of Lipid Moiety via "Click Chemistry" According to Godeau et al.

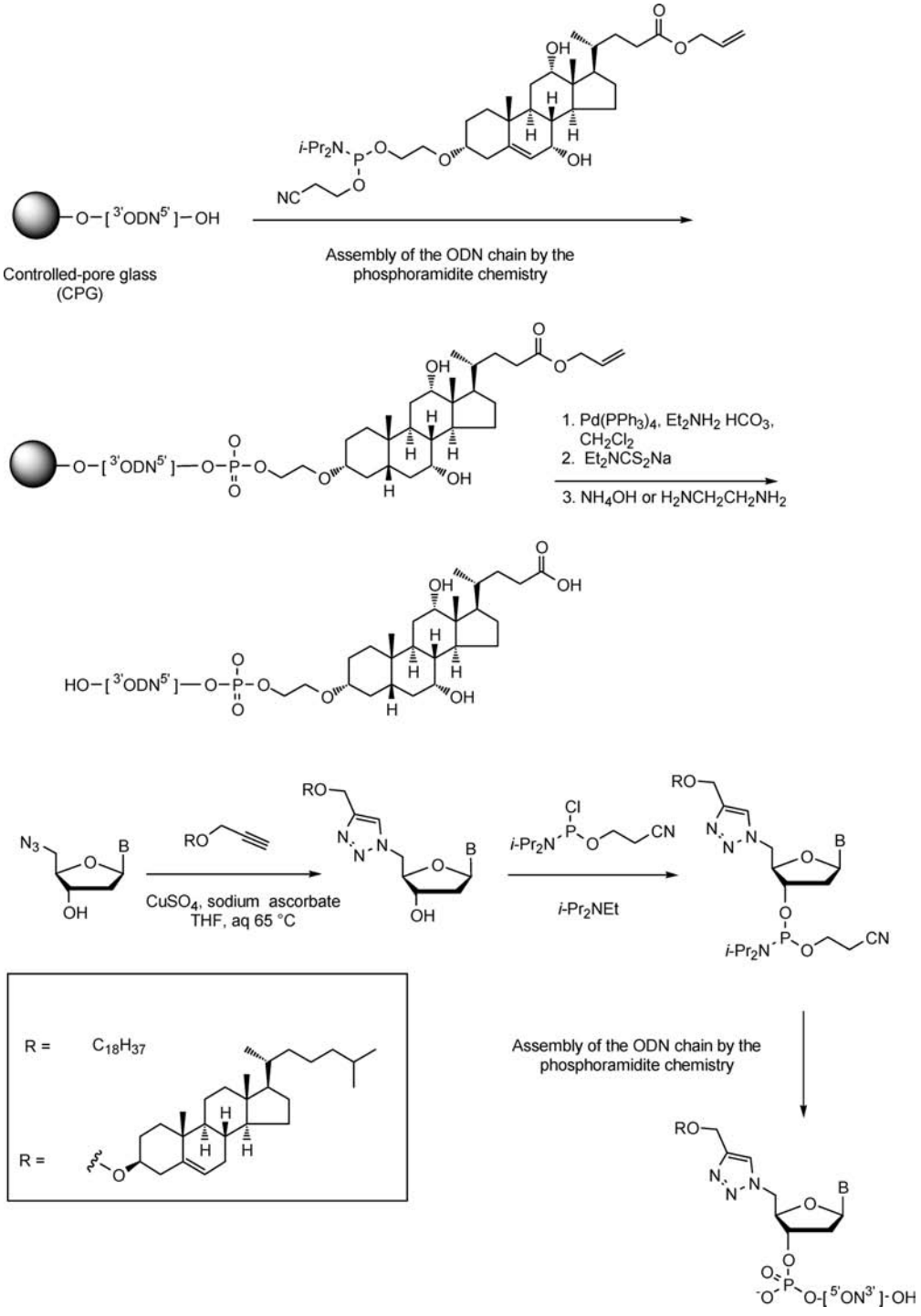

HCV-internal ribosome entry site (IRES)-dependent translation in the Huh7 cell line. More importantly, the toxicity of the LOCs was negligible and biological activity of the LOCs was not affected by the presence of serum.[89]

Lorenz et al. (2004) conjugated the siRNA β-galactosidase to cholesterol at the 5′ end of the sense strand. The cellular uptake of siRNA β-galactosidase in human liver cells was increased when it was conjugated to cholesterol. In fact, incubation of cells with 50 nM of siRNA β-galactosidase during 4 h with a modified sense strand down-regulated β-galactosidase expression to a higher extent than siRNAs with a modified antisense strand or two modified strands.[107] Cholesterol-conjugated siRNA has also been administered directly into the lung via intratracheal instillation. In this case, the target was p38 MAP kinase mRNA. The cholesterol-conjugated sense strand RNA was synthesized using a cholesterol phosphoramidite coupled to a C6-SS-C6 linker at the 5′-end of the RNA. The so-obtained cholesterol−siRNA conjugate was shown to have a target-specific RNAi effect in mice. The escalation of lipophilic siRNA doses improved the duration of the RNAi effect.[88]

dx.doi.org/10.1021/bc200422w | Bioconjugate Chem. 2012, 23, 1091−1104

Evidence of the utility of cholesterol for oligonucleotide delivery was provided in a recent report showing cholesterol-mediated delivery of 2′-*O*-methyl and phosphorothioate-modified single-stranded RNA for the knockdown of microRNA expression in various tissues, e.g., liver, lung, kidney, and heart, following intravenous injection.[114]

Another interesting LOC, α-tocopherol (vitamin E)-siRNA, was introduced for systemic siRNA delivery to the liver.[86] Lipophilic vitamin E was covalently conjugated to the 5′-terminus of the antisense strand of 27/29-mer siRNA and was partially modified with 2′-*O*-methylated ribose and phosphorothioate linkage. After intracellular delivery, the 27/29-mer siRNA was processed by the action of Dicer to generate 21/21-mer siRNA, which caused the simultaneous release of the vitamin E moiety. The intravenous administration of the conjugate achieved a significant reduction of the target protein ApoB in the liver without any induction of inflammatory interferons, i.e., interferon-α or -β.[86] Such as with cholesterol, conjugation with α-tocopherol promoted siRNA delivery via binding to serum proteins and lipoproteins. α-Tocopherol was also incorporated into intrachain positions of the siRNA as described below.

Dodecylamine, octadecanethiol, and thiocholesterol have been conjugated to the 5′-terminus of a support-bound ODN by elongation of the chain with 6-chloroacetamidohexanol phosphoramidite and displacing the chlorosubstituent with nitrogen sulfur nucleophiles in dioxane in the presence of DBU, and normal ammonolysis then released the conjugate.[115]

Several lipophilic alcohols including cholesterol, borneol, menthol, and heptadecanol have been converted to 2-alkoxy-2-thiono-1,3,2-oxathiaphospholane and reacted in DCM in the presence of DBU with the 5′-hydroxy group of a support-bound ODN. Again, a normal ammonolysis was finally carried out.[116] However, those constructions have been tested neither in vitro nor in vivo.

Lipid Incorporation into Intrachain Positions of the Oligonucleotide Chain. The incorporation of hydrophobic groups into intrachain positions of the oligonucleotide chain is usually performed with the aid of prefabricated nucleosidic building blocks bearing a lipid moiety either on the base or on the 2′-position of the ribose. Alternatively, the phosphate linker has been replaced by a phosphoramidate group allowing tethering of the hydrophobic chain on the internucleoside phosphorus linker. The exploited nucleosidic building blocks include the phosphoramidites of C5-derivatized pyrimidine 2′-deoxyribonucleosides,[117,118] 2′-*O*-derivatized uridine, and a thymine amino-LNA monomer.[119] Several lipophilic moieties such as cholesterol,[117,119] α-tocopherol,[118] adamantanylacetic acid,[94] long-chain fatty acids,[94] and diacylglycerol[94] have been introduced in this manner. In fact, the first solid-phase synthesis of a cholesterol conjugate is a nice example of such an approach involving oxidative phosphoramidation of a support-bound dinucleoside-3′,5′-(*H*-phosphonate) with cholester-3-yloxycarbonylaminoethylamine and subsequent assembly of the ODN chain.[87] This elegant strategy to functionalize the 3′-end and 5′-end internucleoside phosphorus was developed by Letsinger, from the corresponding *H*-phosphonate manually attached beforehand to the solid support (Scheme 5). The ODN chain is then assembled by phosphoramidite chemistry, and upon ammonolysis, only the ODN bearing the conjugate group is released from the support, since the phosphodiester and phophoramidate linkages are not cleaved by ammonolysis. The advantages of this method are as follows: first, there is an ability

Scheme 5. Strategy Developed by Letsinger to Modify the 3′-End of Oligonucleotide

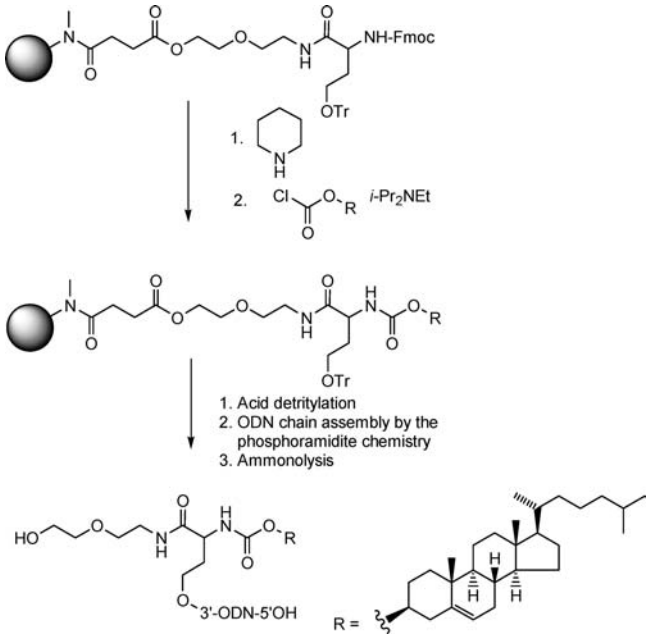

to attach more than one lipid to ONs at defined sites and the freedom to attach additional moieties, i.e., fluorescent groups at both the 3′- and 5′-ends of the ON; second, linkage by this process did not interfere with ON-to-target hybridization. Thus, Letsinger et al. (1989) showed that the antiviral activity of a 20-mer cholesteryl−phosphorothioate derivative was significantly increased. A complete inhibition of the human immunodeficiency virus type 1 replication, as judged by inhibition of syncytia formation and expression of viral proteins p17, p24 in Molt-3 cells, was obtained with an oligomer concentration of 0.2 μM.[87]

Non-nucleosidic hydrophobic building blocks have been incorporated at either the 3′ or 5′ terminus of ODNs using a phosphoramidite reagent derived from dioctyl 2,2-bis-(hydroxymethyl)malonate.[120] Again, a prolonged coupling time of 10 min is required for high coupling yield (>98%), and the subsequent detritylation has to be carried out with TFA. Interestingly, the ester linkages at internucleosidic positions withstand normal ammonolysis. Besides exploitation of prefabricated solid supports and phosphoramidite reagents bearing the conjugate group, several on-support conjugation procedures have been reported.

■ SUPRAMOLECULAR ORGANIZATION

There are only a few studies which have investigated in deep detail the structure of LOCs in water, although these molecules have a natural tendency to self-assemble and to form supramolecular organizations, due to their strong amphiphilic character.[121,122] For example, Wu et al.[123] have described the formation of DNA aptamer micelles by linking a simple lipid tail phospholipid with diacyl chains onto the end of an aptamer inserted with PEG linker. This amphiphilic unit self-assembled spontaneously in water into a spherical micelle structure of 68 nm. In a similar way, the linkage of squalene to RET/PTC1 siRNA led to the formation of spherical nanoassemblies with a size of around 170 nm. Transmission electron microscopy examinations have revealed the formation of nanoparticles

rather than micelles.[85] In another study, a series of charge-reversal amphiphiles with different spacers separating the headgroup from the hydrophobic chains are described for the delivery of DNA and siRNA.[124] Given their polar headgroup and long hydrophobic alkyl chains, these amphiphiles self-assembled to form bilayer vesicles in aqueous solution. X-ray diffraction investigation has shown that the DNA is located between the adjacent lipid bilayers.

CONCLUSION

The literature is full of studies using cationic polymers or lipids to promote the delivery of antisense oligonucleotides or siRNA.[10] If the strong ionic interactions of these transfectants may appear as an advantage for the delivery of small fragments of nucleic acids, their (cyto)toxicity remains the major toxicological issue even if few cationic nanoformulations are currently in early clinical trial. Surprisingly, the use of neutral, safe, and biocompatible lipids has not drawn so much attention for nucleic acids administration, probably because loading these hydrophilic molecules onto neutral lipid based nanocarriers raises difficulties from a formulation point of view. Thus, chemical conjugation of oligonucleotides/siRNA to neutral lipids is an interesting option, which is insufficiently exploited today. In our opinion, this approach should avoid the toxicological issue inherent to (poly)cations, even if the conjugation of oligonucleotides/siRNA with a neutral lipid is less obvious than the design of ion pairs of nucleic acids with polycations. Additionally, the chemical strategies used for LOC synthesis need to use a hydrolyzable spacer able to release, in a controlled manner, these short fragments of nucleic acids both in vitro and in vivo. The relevance of LOCs for the treatment of human diseases has, however, never been demonstrated until now in clinical trials, probably because additional preclinical studies are still needed. Thus, the aim of the present review was to give account of the availability of the many chemical conjugation methodologies that allow construction of lipid nucleic acids capable of in vivo gene silencing.

AUTHOR INFORMATION

Corresponding Author

*P.C.: Phone 33 1 46 83 53 96, Fax 33 1 46 61 93 34, E-mail: patrick.couvreur@u-psud.fr. L.M.: Phone 33 1 42 11 62 42, Fax 33 1 42 11 53 14, E-mail: liliane.massade@igr.fr.

Notes

The authors declare no competing financial interest.

ACKNOWLEDGMENTS

This work was supported by the European Research Council under the European Community's Seventh Framework Programme FP7/2007-2013 Grant Agreement No 249835 and by the ANR P2N (Nanosqualonc program).

ABBREVIATIONS:

AS-ON, antisense oligonucleotide; ApoB, apolipo protein B; Ago 2, Argonaute 2; DBU, 1,8-Diazabicyclo[5.4.0]undec-7-ene; dsRNA, double-stranded RNA; EPR, enhanced permeability and retention; ECM, extracellular matrix; GFP, green fluorescent protein; HCV, hepatitis C virus; HDL, high density lipoprotein; IRES, internal ribosome entry site; LOC, lipid oligonucleotide conjugate; LNA, locked nucleic acid; LDL, low density lipoprotein; mRNA, mRNA; miRNA, microRNA; PNA, peptide nucleic acid; ODN, oligodeoxyribonucleotide; ON, oligonucleotide; RES, reticulo-endothelial system; RET/PTC1, rearranged during transfection/papillary thyroid carcinoma type 1; RNase H, Ribonuclease H; RISC, RNA-induced silencing complex; RNAi, RNA interference; SR-BI, scavenger receptor; siRNA, small interfering RNA; SQ, squalene.

REFERENCES

(1) Crooke, S. T. (1992) Oligonucleotide therapy. *Curr. Opin. Biotechnol. 3*, 656−661.

(2) Da Ros, T., Spalluto, G., Prato, M., Saison-Behmoaras, T., Boutorine, A., and Cacciari, B. (2005) Oligonucleotides and oligonucleotide conjugates: a new approach for cancer treatment. *Curr. Med. Chem. 12*, 71−88.

(3) Opalinska, J. B., and Gewirtz, A. M. (2002) Nucleic-acid therapeutics: basic principles and recent applications. *Nat. Rev. Drug Discovery 1*, 503−514.

(4) Kim, D. H., and Rossi, J. J. (2007) Strategies for silencing human disease using RNA interference. *Nat. Rev. Genet. 8*, 173−184.

(5) Dorsett, Y., and Tuschl, T. (2004) siRNAs: applications in functional genomics and potential as therapeutics. *Nat. Rev. Drug Discovery 3*, 318−329.

(6) Manoharan, M. (2002) Oligonucleotide conjugates as potential antisense drugs with improved uptake, biodistribution, targeted delivery, and mechanism of action. *Antisense Nucleic Acid Drug Dev. 12*, 103−128.

(7) de Fougerolles, A., Vornlocher, H. P., Maraganore, J., and Lieberman, J. (2007) Interfering with disease: a progress report on siRNA-based therapeutics. *Nat. Rev. Drug Discovery 6*, 443−453.

(8) Chan, J. H., Lim, S., and Wong, W. S. (2006) Antisense oligonucleotides: from design to therapeutic application. *Clin. Exp. Pharmacol. Physiol. 33*, 533−540.

(9) Davis, M. E., Zuckerman, J. E., Choi, C. H., Seligson, D., Tolcher, A., Alabi, C. A., Yen, Y., Heidel, J. D., and Ribas, A. (2011) Evidence of RNAi in humans from systemically administered siRNA via targeted nanoparticles. *Nature 464*, 1067−1070.

(10) Geisbert, T. W., Lee, A. C., Robbins, M., Geisbert, J. B., Honko, A. N., Sood, V., Johnson, J. C., de Jong, S., Tavakoli, I., Judge, A., Hensley, L. E., and Maclachlan, I. (2010) Postexposure protection of non-human primates against a lethal Ebola virus challenge with RNA interference: a proof-of-concept study. *Lancet 375*, 1896−1905.

(11) Gondi, C. S., and Rao, J. S. (2009) Concepts in in vivo siRNA delivery for cancer therapy. *J. Cell Physiol. 220*, 285−291.

(12) Halder, J., Kamat, A. A., Landen, C. N. Jr., Han, L. Y., Lutgendorf, S. K., Lin, Y. G., Merritt, W. M., Jennings, N. B., Chavez-Reyes, A., Coleman, R. L., Gershenson, D. M., Schmandt, R., Cole, S. W., Lopez-Berestein, G., and Sood, A. K. (2006) Focal adhesion kinase targeting using in vivo short interfering RNA delivery in neutral liposomes for ovarian carcinoma therapy. *Clin. Cancer Res. 12*, 4916−4924.

(13) Soutschek, J., Akinc, A., Bramlage, B., Charisse, K., Constien, R., Donoghue, M., Elbashir, S., Geick, A., Hadwiger, P., Harborth, J., John, M., Kesavan, V., Lavine, G., Pandey, R. K., Racie, T., Rajeev, K. G., Rohl, I., Toudjarska, I., Wang, G., Wuschko, S., Bumcrot, D., Koteliansky, V., Limmer, S., Manoharan, M., and Vornlocher, H. P. (2004) Therapeutic silencing of an endogenous gene by systemic administration of modified siRNAs. *Nature 432*, 173−178.

(14) Tanaka, T., Mangala, L. S., Vivas-Mejia, P. E., Nieves-Alicea, R., Mann, A. P., Mora, E., Han, H. D., Shahzad, M. M., Liu, X., Bhavane, R., Gu, J., Fakhoury, J. R., Chiappini, C., Lu, C., Matsuo, K., Godin, B., Stone, R. L., Nick, A. M., Lopez-Berestein, G., Sood, A. K., and Ferrari, M. (2010) Sustained small interfering RNA delivery by mesoporous silicon particles. *Cancer Res. 70*, 3687−3696.

(15) Zimmermann, T. S., Lee, A. C., Akinc, A., Bramlage, B., Bumcrot, D., Fedoruk, M. N., Harborth, J., Heyes, J. A., Jeffs, L. B., John, M., Judge, A. D., Lam, K., McClintock, K., Nechev, L. V., Palmer, L. R., Racie, T., Rohl, I., Seiffert, S., Shanmugam, S., Sood, V., Soutschek, J., Toudjarska, I., Wheat, A. J., Yaworski, E., Zedalis, W., Koteliansky, V., Manoharan, M., Vornlocher, H. P., and MacLachlan, I.

(2006) RNAi-mediated gene silencing in non-human primates. *Nature 441*, 111−114.
(16) Al-Brahim, N., and Asa, S. L. (2006) Papillary thyroid carcinoma: an overview. *Arch. Pathol. Lab. Med. 130*, 1057−1062.
(17) Kuo, W. T., Huang, H. Y., and Huang, Y. Y. (2009) Intracellular trafficking, metabolism and toxicity of current gene carriers. *Curr. Drug Metab. 10*, 885−894.
(18) Wolfrum, C., Shi, S., Jayaprakash, K. N., Jayaraman, M., Wang, G., Pandey, R. K., Rajeev, K. G., Nakayama, T., Charrise, K., Ndungo, E. M., Zimmermann, T., Koteliansky, V., Manoharan, M., and Stoffel, M. (2007) Mechanisms and optimization of in vivo delivery of lipophilic siRNAs. *Nat. Biotechnol. 25*, 1149−1157.
(19) Ueno, Y., Kawada, K., Naito, T., Shibata, A., Yoshikawa, K., Kim, H. S., Wataya, Y., and Kitade, Y. (2008) Synthesis and silencing properties of siRNAs possessing lipophilic groups at their 3′-termini. *Bioorg. Med. Chem. 16*, 7698−7704.
(20) de Smidt, P. C., Le Doan, T., de Falco, S., and van Berkel, T. J. (1991) Association of antisense oligonucleotides with lipoproteins prolongs the plasma half-life and modifies the tissue distribution. *Nucleic Acids Res. 19*, 4695−4700.
(21) Gissot, A., Camplo, M., Grinstaff, M. W., and Barthelemy, P. (2008) Nucleoside, nucleotide and oligonucleotide based amphiphiles: a successful marriage of nucleic acids with lipids. *Org. Biomol. Chem. 6*, 1324−1333.
(22) Branch, A. D. (1996) A hitchhiker's guide to antisense and nonantisense biochemical pathways. *Hepatology 24*, 1517−1529.
(23) Akhtar, S., and Agrawal, S. (1997) In vivo studies with antisense oligonucleotides. *Trends Pharmacol. Sci. 18*, 12−18.
(24) Walder, R. Y., and Walder, J. A. (1988) Role of RNase H in hybrid-arrested translation by antisense oligonucleotides. *Proc. Natl. Acad. Sci. U. S. A. 85*, 5011−5015.
(25) Valencia-Sanchez, M. A., Liu, J., Hannon, G. J., and Parker, R. (2006) Control of translation and mRNA degradation by miRNAs and siRNAs. *Genes Dev. 20*, 515−524.
(26) Matranga, C., Tomari, Y., Shin, C., Bartel, D. P., and Zamore, P. D. (2005) Passenger-strand cleavage facilitates assembly of siRNA into Ago2-containing RNAi enzyme complexes. *Cell 123*, 607−620.
(27) Leuschner, P. J., Ameres, S. L., Kueng, S., and Martinez, J. (2006) Cleavage of the siRNA passenger strand during RISC assembly in human cells. *EMBO Rep. 7*, 314−320.
(28) Elbashir, S. M., Lendeckel, W., and Tuschl, T. (2001) RNA interference is mediated by 21- and 22-nucleotide RNAs. *Genes Dev. 15*, 188−200.
(29) Hannon, G. J. (2002) RNA interference. *Nature 418*, 244−251.
(30) Hammond, S. M. (2005) Dicing and slicing: the core machinery of the RNA interference pathway. *FEBS Lett. 579*, 5822−5829.
(31) Paddison, P. J., and Hannon, G. J. (2002) RNA interference: the new somatic cell genetics? *Cancer Cell 2*, 17−23.
(32) Juliano, R., Bauman, J., Kang, H., and Ming, X. (2009) Biological barriers to therapy with antisense and siRNA oligonucleotides. *Mol. Pharm. 6*, 686−695.
(33) Juliano, R. L., Kang, H., Alam, M. R., Dixit, V., and Fisher, M. (2008) Cellular delivery and biological activity of antisense oligonucleotides conjugated to a targeted protein carrier. *Bioconjugate Chem. 19*, 2182−2188.
(34) Behlke, M. A. (2008) Chemical modification of siRNAs for in vivo use. *Oligonucleotides 18*, 305−319.
(35) Crooke, S. T. (2004) Progress in antisense technology. *Annu. Rev. Med. 55*, 61−95.
(36) Juliano, R. L. (2005) Peptide-oligonucleotide conjugates for the delivery of antisense and siRNA. *Curr. Opin. Mol. Ther. 7*, 132−136.
(37) Jain, R. K. (1999) Transport of molecules, particles, and cells in solid tumors. *Annu. Rev. Biomed. Eng. 1*, 241−263.
(38) Mayor, S., and Pagano, R. E. (2007) Pathways of clathrin-independent endocytosis. *Nat. Rev. Mol. Cell Biol. 8*, 603−612.
(39) Bennett, R. M. (1993) As nature intended? The uptake of DNA and oligonucleotides by eukaryotic cells. *Antisense Res. Dev. 3*, 235−241.
(40) Le Doan, T. (2001) Cell binding and internalisation of oligonucleotides. *STP Pharm. Sci. 11*, 75−82.
(41) Juliano, R. L., Alahari, S., Yoo, H., Kole, R., and Cho, M. (1999) Antisense pharmacodynamics: critical issues in the transport and delivery of antisense oligonucleotides. *Pharm. Res. 16*, 494−502.
(42) Wang, L., Prakash, R. K., Stein, C. A., Koehn, R. K., and Ruffner, D. E. (2003) Progress in the delivery of therapeutic oligonucleotides: organ/cellular distribution and targeted delivery of oligonucleotides in vivo. *Antisense Nucleic Acid Drug Dev. 13*, 169−189.
(43) Gao, K., and Huang, L. (2009) Nonviral methods for siRNA delivery. *Mol. Pharm. 6*, 651−658.
(44) Wu, S. Y., and McMillan, N. A. (2009) Lipidic systems for in vivo siRNA delivery. *AAPS J. 11*, 639−652.
(45) Frank-Kamenetsky, M., Grefhorst, A., Anderson, N. N., Racie, T. S., Bramlage, B., Akinc, A., Butler, D., Charisse, K., Dorkin, R., Fan, Y., Gamba-Vitalo, C., Hadwiger, P., Jayaraman, M., John, M., Jayaprakash, K. N., Maier, M., Nechev, L., Rajeev, K. G., Read, T., Rohl, I., Soutschek, J., Tan, P., Wong, J., Wang, G., Zimmermann, T., de Fougerolles, A., Vornlocher, H. P., Langer, R., Anderson, D. G., Manoharan, M., Koteliansky, V., Horton, J. D., and Fitzgerald, K. (2008) Therapeutic RNAi targeting PCSK9 acutely lowers plasma cholesterol in rodents and LDL cholesterol in nonhuman primates. *Proc. Natl. Acad. Sci. U. S. A. 105*, 11915−11920.
(46) Xu, L., and Anchordoquy, T. (2011) Drug delivery trends in clinical trials and translational medicine: challenges and opportunities in the delivery of nucleic acid-based therapeutics. *J. Pharm. Sci. 100*, 38−52.
(47) Gao, Y., Liu, X. L., and Li, X. R. (2011) Research progress on siRNA delivery with nonviral carriers. *Int. J. Nanomed. 6*, 1017−1025.
(48) Filion, M. C., and Phillips, N. C. (1997) Toxicity and immunomodulatory activity of liposomal vectors formulated with cationic lipids toward immune effector cells. *Biochim. Biophys. Acta 1329*, 345−356.
(49) Ozpolat, B., Sood, A. K., and Lopez-Berestein, G. (2009) Nanomedicine based approaches for the delivery of siRNA in cancer. *J. Intern. Med. 267*, 44−53.
(50) Mendonca, L. S., Moreira, J. N., de Lima, M. C., and Simoes, S. (2010) Co-encapsulation of anti-BCR-ABL siRNA and imatinib mesylate in transferrin receptor-targeted sterically stabilized liposomes for chronic myeloid leukemia treatment. *Biotechnol. Bioeng. 107*, 884−893.
(51) Mendonca, M., Tanji, M. M., Silva, L. C., Silveira, G. G., Oliveira, S. C., Duarte, A. J., and Benard, G. (2007) Deficient in vitro anti-mycobacterial immunity despite successful long-term highly active antiretroviral therapy in HIV-infected patients with past history of tuberculosis infection or disease. *Clin. Immunol. 125*, 60−66.
(52) Vrignaud, S., Benoit, J. P., and Saulnier, P. (2011) Strategies for the nanoencapsulation of hydrophilic molecules in polymer-based nanoparticles. *Biomaterials 32*, 8593−8604.
(53) Grijalvo, S., Ocampo, S. M., Perales, J. C., and Eritja, R. (2010) Synthesis of oligonucleotides carrying amino lipid groups at the 3′-end for RNA interference studies. *J. Org. Chem. 75*, 6806−6813.
(54) Grijalvo, S., Ocampo, S. M., Perales, J. C., and Eritja, R. (2011) Synthesis of lipid-oligonucleotide conjugates for RNA interference studies. *Chem. Biodivers. 8*, 287−299.
(55) Tolia, N. H., and Joshua-Tor, L. (2007) Slicer and the argonautes. *Nat. Chem. Biol. 3*, 36−43.
(56) Parker, J. S., Roe, S. M., and Barford, D. (2005) Structural insights into mRNA recognition from a PIWI domain-siRNA guide complex. *Nature 434*, 663−666.
(57) Ma, J. B., Yuan, Y. R., Meister, G., Pei, Y., Tuschl, T., and Patel, D. J. (2005) Structural basis for 5′-end-specific recognition of guide RNA by the A. fulgidus Piwi protein. *Nature 434*, 666−670.
(58) Nykanen, A., Haley, B., and Zamore, P. D. (2001) ATP requirements and small interfering RNA structure in the RNA interference pathway. *Cell 107*, 309−321.
(59) Schwarz, D. S., Hutvagner, G., Haley, B., and Zamore, P. D. (2002) Evidence that siRNAs function as guides, not primers, in the Drosophila and human RNAi pathways. *Mol. Cell 10*, 537−548.

(60) Cazorla, S. I., Becker, P. D., Frank, F. M., Ebensen, T., Sartori, M. J., Corral, R. S., Malchiodi, E. L., and Guzman, C. A. (2008) Oral vaccination with Salmonella enterica as a Cruzipain-DNA delivery system confers protective immunity against Trypanosoma cruzi. *Infect. Immun. 76*, 324−333.
(61) Chiu, Y. L., and Rana, T. M. (2003) siRNA function in RNAi: a chemical modification analysis. *RNA 9*, 1034−1048.
(62) Khvorova, A., Reynolds, A., and Jayasena, S. D. (2003) Functional siRNAs and miRNAs exhibit strand bias. *Cell 115*, 209−216.
(63) Schwarz, D. S., Hutvagner, G., Du, T., Xu, Z., Aronin, N., and Zamore, P. D. (2003) Asymmetry in the assembly of the RNAi enzyme complex. *Cell 115*, 199−208.
(64) Krieg, A. M., and Stein, C. A. (1995) Phosphorothioate oligodeoxynucleotides: antisense or anti-protein? *Antisense Res. Dev. 5*, 241.
(65) Amarzguioui, M., Holen, T., Babaie, E., and Prydz, H. (2003) Tolerance for mutations and chemical modifications in a siRNA. *Nucleic Acids Res. 31*, 589−595.
(66) Braasch, D. A., Jensen, S., Liu, Y., Kaur, K., Arar, K., White, M. A., and Corey, D. R. (2003) RNA interference in mammalian cells by chemically-modified RNA. *Biochemistry 42*, 7967−7975.
(67) Li, Z. Y., Mao, H., Kallick, D. A., and Gorenstein, D. G. (2005) The effects of thiophosphate substitutions on native siRNA gene silencing. *Biochem. Biophys. Res. Commun. 329*, 1026−1030.
(68) Choung, S., Kim, Y. J., Kim, S., Park, H. O., and Choi, Y. C. (2006) Chemical modification of siRNAs to improve serum stability without loss of efficacy. *Biochem. Biophys. Res. Commun. 342*, 919−927.
(69) Hall, A. H., Wan, J., Shaughnessy, E. E., Ramsay Shaw, B., and Alexander, K. A. (2004) RNA interference using boranophosphate siRNAs: structure-activity relationships. *Nucleic Acids Res. 32*, 5991−6000.
(70) Hall, A. H., Wan, J., Spesock, A., Sergueeva, Z., Shaw, B. R., and Alexander, K. A. (2006) High potency silencing by single-stranded boranophosphate siRNA. *Nucleic Acids Res. 34*, 2773−2781.
(71) Froehler, B., Ng, P., and Matteucci, M. (1988) Phosphoramidate analogues of DNA: synthesis and thermal stability of heteroduplexes. *Nucleic Acids Res. 16*, 4831−4839.
(72) Iwase, R., Toyama, T., and Nishimori, K. (2007) Solid-phase synthesis of modified RNAs containing amide-linked oligoribonucleosides at their 3′-end and their application to siRNA. *Nucleosides Nucleotides Nucleic Acids 26*, 1451−1454.
(73) Prakash, T. P., Allerson, C. R., Dande, P., Vickers, T. A., Sioufi, N., Jarres, R., Baker, B. F., Swayze, E. E., Griffey, R. H., and Bhat, B. (2005) Positional effect of chemical modifications on short interference RNA activity in mammalian cells. *J. Med. Chem. 48*, 4247−4253.
(74) Prakash, T. P., Kraynack, B., Baker, B. F., Swayze, E. E., and Bhat, B. (2006) RNA interference by 2′,5′-linked nucleic acid duplexes in mammalian cells. *Bioorg. Med. Chem. Lett. 16*, 3238−3240.
(75) Alvarez, K., Vasseur, J. J., Beltran, T., and Imbach, J. L. (1999) Photocleavable protecting groups as nucleobase protections allowed the solid-phase synthesis of base-sensitive SATE-prooligonucleotides. *J. Org. Chem. 64*, 6319−6328.
(76) Spinelli, N., Meyer, A., Hayakawa, Y., Imbach, J. L., and Vasseur, J. J. (2002) Use of allylic protecting groups for the synthesis of base-sensitive prooligonucleotides. *Eur. J. Org. Chem.*, 49−56.
(77) Czauderna, F., Fechtner, M., Dames, S., Aygun, H., Klippel, A., Pronk, G. J., Giese, K., and Kaufmann, J. (2003) Structural variations and stabilising modifications of synthetic siRNAs in mammalian cells. *Nucleic Acids Res. 31*, 2705−2716.
(78) Kraynack, B. A., and Baker, B. F. (2006) Small interfering RNAs containing full 2′-O-methylribonucleotide-modified sense strands display Argonaute2/eIF2C2-dependent activity. *RNA 12*, 163−176.
(79) Vester, B., and Wengel, J. (2004) LNA (locked nucleic acid): high-affinity targeting of complementary RNA and DNA. *Biochemistry 43*, 13233−13241.
(80) Wahlestedt, C., Salmi, P., Good, L., Kela, J., Johnsson, T., Hokfelt, T., Broberger, C., Porreca, F., Lai, J., Ren, K., Ossipov, M., Koshkin, A., Jakobsen, N., Skouv, J., Oerum, H., Jacobsen, M. H., and Wengel, J. (2000) Potent and nontoxic antisense oligonucleotides containing locked nucleic acids. *Proc. Natl. Acad. Sci. U. S. A. 97*, 5633−5638.
(81) Grunweller, A., Wyszko, E., Bieber, B., Jahnel, R., Erdmann, V. A., and Kurreck, J. (2003) Comparison of different antisense strategies in mammalian cells using locked nucleic acids, 2′-O-methyl RNA, phosphorothioates and small interfering RNA. *Nucleic Acids Res. 31*, 3185−3193.
(82) Hanvey, J. C., Peffer, N. J., Bisi, J. E., Thomson, S. A., Cadilla, R., Josey, J. A., Ricca, D. J., Hassman, C. F., Bonham, M. A., Au, K. G., et al. (1992) Antisense and antigene properties of peptide nucleic acids. *Science 258*, 1481−1485.
(83) Summerton, J. (1999) Morpholino antisense oligomers: the case for an RNase H-independent structural type. *Biochim. Biophys. Acta 1489*, 141−158.
(84) Summerton, J., and Weller, D. (1997) Morpholino antisense oligomers: design, preparation, and properties. *Antisense Nucleic Acid Drug Dev. 7*, 187−195.
(85) Raouane, M., Desmaele, D., Gilbert-Sirieix, M., Gueutin, C., Zouhiri, F., Bourgaux, C., Lepeltier, E., Gref, R., Ben Salah, R., Clayman, G., Massaad-Massade, L., and Couvreur, P. (2010) Synthesis, characterization, and in vivo delivery of siRNA-squalene nanoparticles targeting fusion oncogene in papillary thyroid carcinoma. *J. Med. Chem. 54*, 4067−4076.
(86) Nishina, K., Unno, T., Uno, Y., Kubodera, T., Kanouchi, T., Mizusawa, H., and Yokota, T. (2008) Efficient in vivo delivery of siRNA to the liver by conjugation of alpha-tocopherol. *Mol. Ther. 16*, 734−740.
(87) Letsinger, R. L., Zhang, G. R., Sun, D. K., Ikeuchi, T., and Sarin, P. S. (1989) Cholesteryl-conjugated oligonucleotides: synthesis, properties, and activity as inhibitors of replication of human immunodeficiency virus in cell culture. *Proc. Natl. Acad. Sci. U. S. A. 86*, 6553−6556.
(88) Moschos, S. A., Jones, S. W., Perry, M. M., Williams, A. E., Erjefalt, J. S., Turner, J. J., Barnes, P. J., Sproat, B. S., Gait, M. J., and Lindsay, M. A. (2007) Lung delivery studies using siRNA conjugated to TAT(48−60) and penetratin reveal peptide induced reduction in gene expression and induction of innate immunity. *Bioconjugate Chem. 18*, 1450−1459.
(89) Godeau, G., Staedel, C., and Barthelemy, P. (2008) Lipid-conjugated oligonucleotides via "click chemistry" efficiently inhibit hepatitis C virus translation. *J. Med. Chem. 51*, 4374−4376.
(90) Chaloin, L., Vidal, P., Lory, P., Mery, J., Lautredou, N., Divita, G., and Heitz, F. (1998) Design of carrier peptide-oligonucleotide conjugates with rapid membrane translocation and nuclear localization properties. *Biochem. Biophys. Res. Commun. 243*, 601−608.
(91) Bongartz, J. P., Aubertin, A. M., Milhaud, P. G., and Lebleu, B. (1994) Improved biological activity of antisense oligonucleotides conjugated to a fusogenic peptide. *Nucleic Acids Res. 22*, 4681−4688.
(92) Tuschl, T. (2002) Expanding small RNA interference. *Nat. Biotechnol. 20*, 446−448.
(93) MacKellar, C., Graham, D., Will, D. W., Burgess, S., and Brown, T. (1992) Synthesis and physical properties of anti-HIV antisense oligonucleotides bearing terminal lipophilic groups. *Nucleic Acids Res. 20*, 3411−3417.
(94) Manoharan, M., Tivel, K. L., and Cook, P. D. (1995) Lipidic Nucleic-Acids. *Tetrahedron Lett. 36*, 3651−3654.
(95) Stetsenko, D. A., and Gait, M. J. (2001) A convenient solid-phase method for synthesis of 3′-conjugates of oligonucleotides. *Bioconjugate Chem. 12*, 576−586.
(96) Marasco, C. J., Angelino, N. J., Paul, B., and Dolnick, B. J. (1994) A simplified synthesis of acridine and/or lipid containing oligodeoxynucleotides. *Tetrahedron Lett. 35*, 3029−3032.
(97) Habus, I., Zhao, Q., and Agrawal, S. (1995) Synthesis, hybridization properties, nuclease stability, and cellular uptake of the oligonucleotide--amino-beta-cyclodextrins and adamantane conjugates. *Bioconjugate Chem. 6*, 327−331.

(98) Rait, A., Pirollo, K., Will, D. W., Peyman, A., Rait, V., Uhlmann, E., and Chang, E. H. (2000) 3′-End conjugates of minimally phosphorothioate-protected oligonucleotides with 1-O-hexadecylglycerol: synthesis and anti-ras activity in radiation-resistant cells. *Bioconjugate Chem. 11*, 153−160.
(99) Reed, M. W., Adams, A. D., Nelson, J. S., and Meyer, R. B. Jr. (1991) Acridine- and cholesterol-derivatized solid supports for improved synthesis of 3′-modified oligonucleotides. *Bioconjugate Chem. 2*, 217−225.
(100) Vu, H., Hill, T. S., and Jayaraman, K. (1994) Synthesis and properties of cholesteryl-modified triple-helix forming oligonucleotides containing a triglycyl linker. *Bioconjugate Chem. 5*, 666−668.
(101) Vu, H., Singh, P., Joyce, N., Hogan, M. E., and Jayaraman, K. (1993) Synthesis of cholesteryl supports and phosphoramidites containing a novel peptidyl linker for automated synthesis of triple-helix forming oligonucleotides (TFOs). *Nucleic Acids Symp. Ser.*, 19−20.
(102) Will, D. W., and Brown, T. (1992) Attachment of vitamin-E derivatives to oligonucleotides during solid-phase synthesis. *Tetrahedron Lett. 33*, 2729−2732.
(103) Reed, M. W., Lukhtanov, E. A., Gorn, V. V., Lucas, D. D., Zhou, J. H., Pai, S. B., Cheng, Y. C., and Meyer, R. B. Jr. (1995) Structure-activity relationships of cytotoxic cholesterol-modified DNA duplexes. *J. Med. Chem. 38*, 4587−4596.
(104) Matysiak, S., Frank, R., and Pfleiderer, W. (1997) Acetal oligonucleotide conjugates in antisense strategy. *Nucleosides Nucleotides 16*, 855−861.
(105) D'Onofrio, J., Montesarchio, D., De Napoli, L., and Di Fabio, G. (2005) An efficient and versatile solid-phase synthesis of 5′- and 3′-conjugated oligonucleotides. *Org. Lett. 7*, 4927−4930.
(106) Ueno, Y., Inoue, T., Yoshida, M., Yoshikawa, K., Shibata, A., Kitamura, Y., and Kitade, Y. (2008) Synthesis of nuclease-resistant siRNAs possessing benzene-phosphate backbones in their 3′-overhang regions. *Bioorg. Med. Chem. Lett. 18*, 5194−5196.
(107) Lorenz, C., Hadwiger, P., John, M., Vornlocher, H. P., and Unverzagt, C. (2004) Steroid and lipid conjugates of siRNAs to enhance cellular uptake and gene silencing in liver cells. *Bioorg. Med. Chem. Lett. 14*, 4975−4977.
(108) Cheng, K., Ye, Z., Guntaka, R. V., and Mahato, R. I. (2006) Enhanced hepatic uptake and bioactivity of type alpha1(I) collagen gene promoter-specific triplex-forming oligonucleotides after conjugation with cholesterol. *J. Pharmacol. Exp. Ther. 317*, 797−805.
(109) DiFiglia, M., Sena-Esteves, M., Chase, K., Sapp, E., Pfister, E., Sass, M., Yoder, J., Reeves, P., Pandey, R. K., Rajeev, K. G., Manoharan, M., Sah, D. W., Zamore, P. D., and Aronin, N. (2007) Therapeutic silencing of mutant huntingtin with siRNA attenuates striatal and cortical neuropathology and behavioral deficits. *Proc. Natl. Acad. Sci. U. S. A. 104*, 17204−17209.
(110) Lehmann, T. J., and Engels, J. W. (2001) Synthesis and properties of bile acid phosphoramidites 5′-tethered to antisense oligodeoxynucleotides against HCV. *Bioorg. Med. Chem. 9*, 1827−1835.
(111) Polushin, N. N., and Cohen, J. S. (1994) Antisense pro-drugs: 5′-ester oligodeoxynucleotides. *Nucleic Acids Res. 22*, 5492−5496.
(112) Krieg, A. M., Tonkinson, J., Matson, S., Zhao, Q., Saxon, M., Zhang, L. M., Bhanja, U., Yakubov, L., and Stein, C. A. (1993) Modification of antisense phosphodiester oligodeoxynucleotides by a 5′ cholesteryl moiety increases cellular association and improves efficacy. *Proc. Natl. Acad. Sci. U. S. A. 90*, 1048−1052.
(113) Gramlich, P. M., Wirges, C. T., Manetto, A., and Carell, T. (2008) Postsynthetic DNA modification through the copper-catalyzed azide-alkyne cycloaddition reaction. *Angew. Chem., Int. Ed. Engl. 47*, 8350−8358.
(114) Krutzfeldt, J., Rajewsky, N., Braich, R., Rajeev, K. G., Tuschl, T., Manoharan, M., and Stoffel, M. (2005) Silencing of microRNAs in vivo with 'antagomirs'. *Nature 438*, 685−689.
(115) Guzaev, A., and Manoharan, M. (1998) Conjugation of oligonucleotides via an electrophilic tether: N-chloroacetamidohexyl phosphoramidite reagent. *Bioorg. Med. Chem. Lett. 8*, 3671−3676.
(116) Kobylanska, A., Okruszek, A., Stec, and J., W. (1998) Application of oxathiaphospholane method for the synthesis of oligodeoxyribonucleotide 5′-O-conjugates. *Nucleosides Nucleotides 17*, 1977−1982.
(117) Durand, A., and Brown, T. (2007) Synthesis and properties of oligonucleotides containing a cholesterol thymidine monomer. *Nucleosides Nucleotides Nucleic Acids 26*, 785−794.
(118) Kurz, A., Bunge, A., Windeck, A. K., Rost, M., Flasche, W., Arbuzova, A., Strohbach, D., Muller, S., Liebscher, J., Huster, D., and Herrmann, A. (2006) Lipid-anchored oligonucleotides for stable double-helix formation in distinct membrane domains. *Angew. Chem., Int. Ed. Engl. 45*, 4440−4444.
(119) Bryld, T., and Lomholt, C. (2007) Attachment of cholesterol to amino-LNA: synthesis and hybridization properties. *Nucleosides Nucleotides Nucleic Acids 26*, 1645−1647.
(120) Guzaev, A., and Lonnberg, H. (1999) Solid support synthesis of ester linked hydrophobic conjugates of oligonucleotides. *Tetrahedron 55*, 9101−9116.
(121) Kwak, M., and Herrmann, A. (2011) Nucleic acid amphiphiles: synthesis and self-assembled nanostructures. *Chem. Soc. Rev. 40*, 5745−5755.
(122) Patwa, A., Gissot, A., Bestel, I., and Barthelemy, P. (2011) Hybrid lipid oligonucleotide conjugates: synthesis, self-assemblies and biomedical applications. *Chem. Soc. Rev. 40*, 5844−5854.
(123) Wu, Y., Sefah, K., Liu, H., Wang, R., and Tan, W. (2010) DNA aptamer-micelle as an efficient detection/delivery vehicle toward cancer cells. *Proc. Natl. Acad. Sci. U. S. A. 107*, 5−10.
(124) Barthelemy, P., Prata, C. A., Filocamo, S. F., Immoos, C. E., Maynor, B. W., Hashmi, S. A., Lee, S. J., and Grinstaff, M. W. (2005) Supramolecular assemblies of DNA with neutral nucleoside amphiphiles. *Chem. Commun. (Camb.)*, 1261−1263.

Bioconjugate Chemistry

Communication

pubs.acs.org/bc

Controlling the DNA Cleavage Activity of Light-Inducible Chimeric Endonucleases by Bidirectional Photoactivation

Benno Schierling* and Alfred Pingoud

Institute of Biochemistry, Justus-Liebig University, Heinrich-Buff-Ring 58, D-35392 Giessen, Germany

ABSTRACT: A functional coupling of photosensory domains derived from photoreceptors to effector proteins is a promising strategy for engineering novel photoresponsive proteins in optogenetics. Here, we have fused the light-sensitive LOV2 domain from *Avena sativa* phototropin1 to the restriction enzyme PvuII to generate a genetically encoded, light-controllable endonuclease. By analyzing several LOV-PvuII fusion enzymes, variants were obtained that show a 3-fold difference in DNA cleavage activity, when illuminated with blue light or kept in the dark. The effect is fully reversible over multiple photocycles. Depending on the particular fusion interface, the LOV-PvuII variants obtained had a bidirectional polarity in photoactivation; i.e., increased DNA cleavage activity was observed either in the dark state, with a compact folded LOV domain, or in the blue light photoexcitation state, when the LOV domain is partially unfolded.

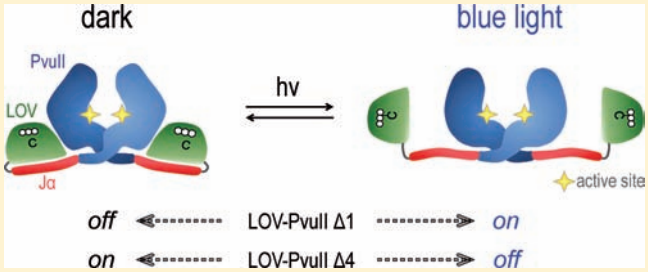

Using light to trigger photosensitive biomolecules *in vivo* allows the precise regulation of biological processes by an external stimulus with a high spatial and temporal resolution.[1,2] Besides the naturally evolved photoreceptor proteins,[3] novel photoresponsive proteins have been engineered by conjugating light-sensitive sensors that make the effector proteins controllable in their activity by illumination with light.[4,5] For the same purpose, small photoswitchable compounds,[6] such as azobenzene derivatives, have been used, because of their light-inducible *cis*/*trans*-photoisomerization.[7]

The light-sensory domains of photoreceptors have been conjugated to several effector proteins,[8] resulting in novel photosensitive proteins, which can be expressed *in vivo* and allow photocontrolling of, for example, gene expression,[9−11] cellular motility,[12] enzymatic function,[13,14] or protein−protein interactions.[15−17] The conformational change within the sensory domain upon photoexcitation, i.e., in the signaling state, acts in this case as a light-sensitive trigger of the activity of the fused effector protein.

The LOV2 domain of *Avena sativa* phototropin1 is one of the best studied photosensitive modules and belongs to the PAS-family of sensory domains (Figure 1A).[18] Upon blue light photoexcitation, a covalent adduct between the flavin mononucleotide cofactor and a conserved cysteine residue is formed, resulting in a conformational change in the core domain and a displacement and unfolding of the carboxy-terminal Jα-helix.[19] In this study, an improved variant of the LOV2 domain (*A. sativa* LOV2 domain containing the amino acid substitutions G528A and N538E) was used that had been developed by Strickland et al.,[20] in which the docking of the Jα-helix to the LOV domain core in the dark state is stabilized, thus increasing the output signal (unfolding/refolding of the Jα-helix) within the photocycle.

Recently, we developed two strategies to control the enzymatic activity of restriction endonucleases by light using (i) azobenzene modifications at the entrance of the DNA binding site of SsoII to form a light-controllable "molecular gate"[21] or (ii) bifunctional azobenzene cross-linkers as "molecular springs" near the active site of PvuII.[22] Both strategies resulted in a reversible regulation of DNA cleavage *in vitro* with a 2- and, respectively, 16-fold difference in DNA cleavage activity when the tethered azobenzene moieties were in the light-induced *cis* or *trans* configuration. Since highly specific nucleases that contain restriction endonucleases as cleavage modules are commonly used in gene targeting,[23] making use of engineered light-controllable nucleases may contribute another level of control for genomic integrity *in vivo*. With a photoswitch, DNA cleavage at off-target sites could be prevented before binding of the fusion protein to the target site on the DNA and after cleavage at the specific target site had occurred.[24]

We recently developed a novel zinc-finger nuclease platform by fusing the restriction endonuclease PvuII to specific zinc-finger DNA binding modules; the fusion protein specifically cleaves DNA at tripartite target sequences only, comprising the two zinc-finger binding sites flanking the 6 bp palindromic recognition site of PvuII.[25] In the present study, as proof-of-concept, our focus is on the development of a light-controllable and genetically encoded variant of PvuII, which in future might be used as a light-controllable cleavage module in an endogenous, highly specific nuclease for gene targeting approaches.

Received: March 16, 2012
Revised: April 27, 2012
Published: May 6, 2012

   dx.doi.org/10.1021/bc3001326 | *Bioconjugate Chem.* 2012, 23, 1105−1109

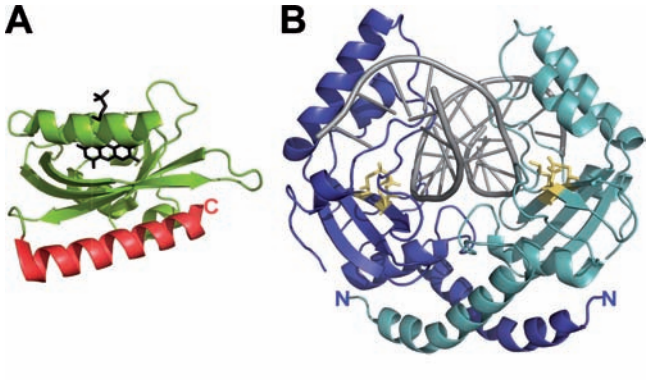

C

LOV2 GANE ...DAAEREAVMLIKKTAEEIDEAA 543
PvuII 2 SHPDLNKLLELWPH...

LOV-PvuII Δ1 ...DAAEREAVMLIKKTAEEIDEAASHPDLNKLLELWPH...
LOV-PvuII Δ3 ...DAAEREAVMLIKKTAEEIDEAAPDLNKLLELWPH...
LOV-PvuII Δ4 ...DAAEREAVMLIKKTAEEIDEAADLNKLLELWPH...
LOV-PvuII Δ5 ...DAAEREAVMLIKKTAEEIDEAALNKLLELWPH...
LOV-PvuII Δ7 ...DAAEREAVMLIKKTAEEIDEAAKLLELWPH...

Figure 1. (A) Ribbon presentation of the structure of the *Avena sativa* LOV2 domain (2V0U). The core domain, containing the FMN cofactor (black), is indicated in green, and the terminal Jα-helix is indicated in red. (B) The crystal structure of PvuII bound to its cognate DNA recognition sequence (1PVI). The two subunits of the homodimeric restriction endonuclease are shown in blue and light blue ribbon; the amino acid residues of the active site (D58, E68, and K70) are indicated in yellow. (C) Compilation of the sequences of the Jα-helix [improved LOV2 domain[20] containing the amino acid substitutions G528A N538E; red] through Ala543 and the amino terminus of PvuII (blue) beginning with Ser2, as well as the sequences of the fusion site in the chimeric LOV-PvuII variants. The Jα-helix was fused to successive truncations of the amino-terminal helix of PvuII (from Δ1 to Δ7), as indicated.

Table 1. Photoswitching Effect of Different LOV-PvuII Fusion Variants[a]

	absolute activity [nM substrate/(min × nM enzyme)]		relative activity
variant	dark	blue	dark vs. blue
PvuII	1.07 ± 0.04	1.02 ± 0.07	1:1
LOV-PvuII Δ1	0.050 ± 0.004	0.135 ± 0.004	1:2.7
LOV-PvuII Δ3	0.00066 ± 0.00001	0.00057 ± 0.00001	1.2:1
LOV-PvuII Δ4	0.0025 ± 0.0002	0.0008 ± 0.0001	3.3:1
LOV-PvuII Δ5	0.0021 ± 0.0002	0.0020 ± 0.0002	1:1
LOV-PvuII Δ7	0.0015 ± 0.0002	0.0011 ± 0.0000	1.4:1

[a]The absolute activities of the various chimeric proteins in the dark and the blue light state, as well as their activity ratio, are given, as derived from plasmid cleavage assays in the dark or during saturating blue light photoexcitation, under otherwise identical conditions (see legend to Figure 2 for details). It must be mentioned that all PvuII variants used in this study contain the high-fidelity amino acid substitution T46G that results in an increased specificity of PvuII.[30]

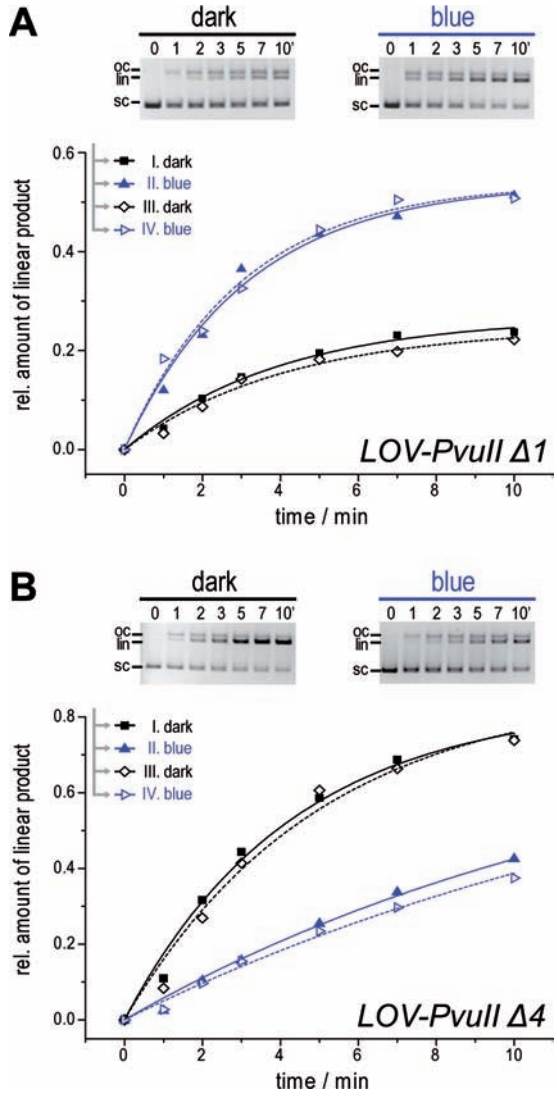

Figure 2. Reversible activity changes of LOV-PvuII Δ1 (A; using 5 nM enzyme) and LOV-PvuII Δ4 (B; using 300 nM enzyme) induced through a continuous photocycle: I. dark → II. blue light → III. dark → IV. blue light. After preincubation of the enzyme sample for 10 min in the dark or for 5 min with blue light illumination (470 ± 10 nm using a LED device), respectively, the cleavage activities were determined by subsequent DNA cleavage assays [addition of 4 nM plasmid DNA containing a singular PvuII site in cleavage buffer (10 mM Tris-HCl pH 7.4, 50 mM NaCl, 1 mM DTT, 0.1 mg/mL bovine serum albumin, 10 mM $MgCl_2$) at 37 °C] in the dark or under blue light photoexcitation, respectively. On top, the gel electrophoretic analyses of samples withdrawn from the incubation mixture at defined time intervals are shown, on the bottom the corresponding activity vs time profile. sc, oc, and lin denote the supercoiled, open circular, and linear forms, respectively, of the plasmid DNA substrate.

The homodimeric restriction enzyme PvuII has been thoroughly investigated in terms of structure[26,27] and function:[28,29] it contains an extended N-terminal α-helix that is part of the subunit dimerization region (Figure 1B), i.e., an interaction of the N-terminal helices of both PvuII monomers is required to form an active PvuII homodimer that supports DNA binding and catalysis. We figured that the fusion of a LOV2 domain via its C-terminal Jα-helix to both N-terminal helices of each PvuII subunit might result in a light-controllable chimeric restriction enzyme: LOV-PvuII. Similar to the fusion

dx.doi.org/10.1021/bc3001326 | *Bioconjugate Chem.* 2012, 23, 1105−1109

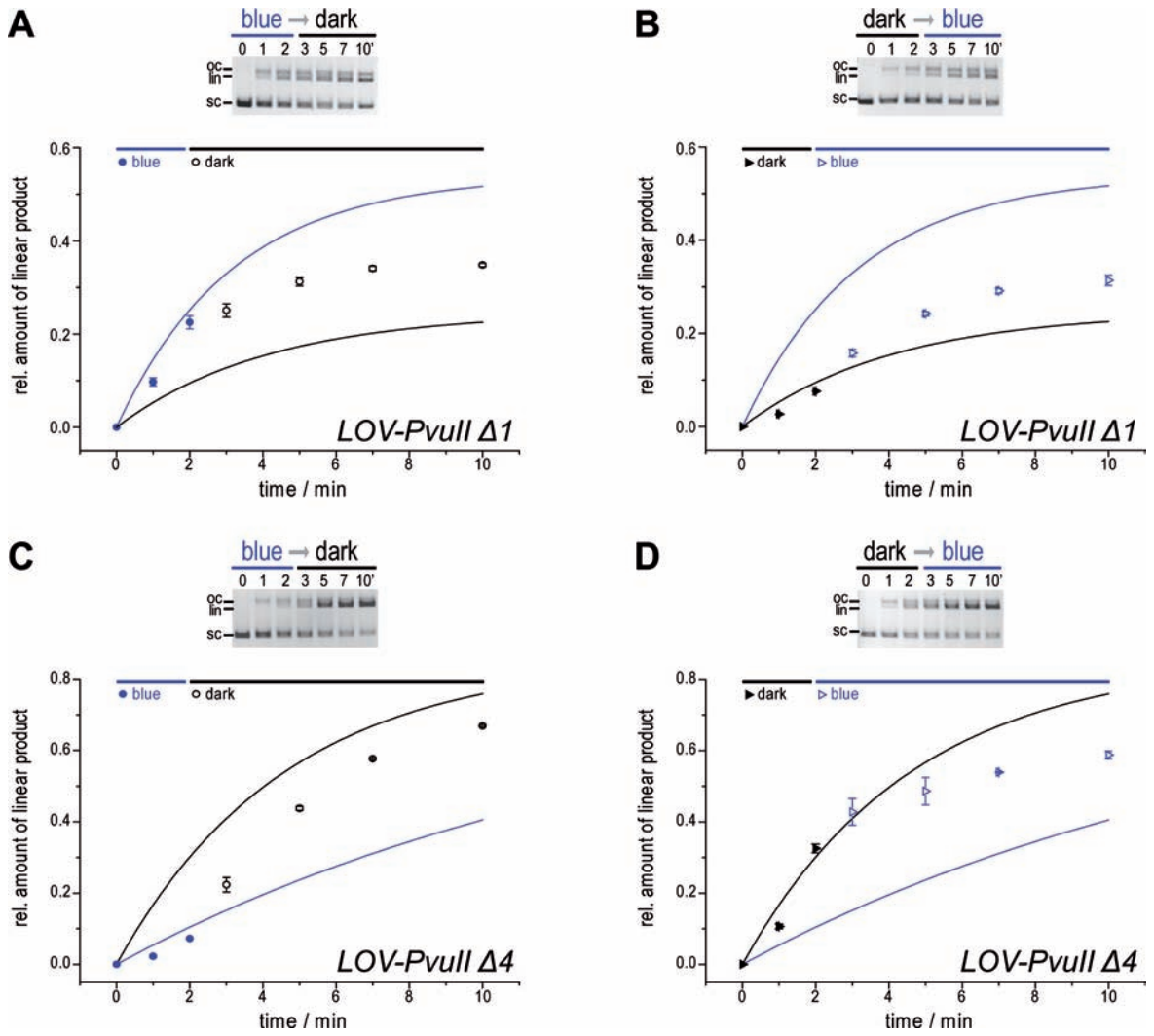

Figure 3. Photoswitching of the DNA cleavage activity of LOV-PvuII Δ1 (A: blue → dark; B: dark → blue) and LOV-PvuII Δ4 (C: blue → dark; D: dark → blue) observed *in situ*. After preincubating the enzyme (cf. Figure 2), the photoconversion of the LOV-PvuII variants was monitored by following the DNA cleavage activity *in situ* with variation of the illumination during cleavage (blue [or dark] 0–2 min, dark [or blue] 2–10 min). On top, the gel electrophoretic analyses of samples withdrawn from the incubation mixture at defined time intervals are shown, on the bottom the corresponding activity vs time profile. sc, oc, and lin denote the supercoiled, open circular, and linear forms, respectively, of the plasmid DNA substrate. The solid lines indicate the activity vs time profiles of cleavage assays with continuous photoexcitation (cf. Figure 2; black ≡ dark state; blue ≡ blue light excitation state).

approach of Strickland et al. for the engineered photosensitive tryptophan repressor LOV-TAP,[11] the fusion interface between the LOV domain and PvuII should result in one common, shared α-helix. According to this initial fusion approach, the Jα-helix should be docked to the LOV domain core in the dark state and sterical clashes of the core structures of the LOV domain, and the PvuII subunits might result in a structural perturbation of the PvuII dimerization interface. This sterical distortion might further restrict the dynamics of the DNA-binding cleft and/or catalytic site and, thus, decrease the DNA cleavage activity of LOV-PvuII in the dark. In contrast, a blue light photoexcitation should cause the chimeric enzyme to become active, since the unfolding of the Jα-helix should neutralize the distorting interactions of the protein core structures and an intact dimeric interface of PvuII should support full DNA cleavage activity.

For the analysis of our fusion approach, several different LOV-PvuII fusion variants were generated, in which the Jα-helix was fused to successive truncations of the amino-terminal helix of PvuII (from Δ1 to Δ7, as indicated in Figure 1C), and tested for differences in their DNA cleavage activity in the dark state vs the blue light photoexcitation state. The absolute activities of all variants in both states as well as the corresponding activity ratio dark/blue are summarized in Table 1. In general, the fusion of the sensory domain to the N-terminus of PvuII resulted in a 10- to 1000-fold reduced overall activity compared to wild-type PvuII, which by itself did not show any light-dependent difference in cleavage activity. In contrast, the variant LOV-PvuII Δ1 exhibited a 2.7-fold higher activity in the blue light photoexcitation state than in the dark state. Interestingly, the polarity of photoactivation was changed for LOV-PvuII Δ4. For this variant, a 3.3-fold higher DNA cleavage activity was observed in the dark compared to the activity under blue light illumination. The other variants tested, LOV-PvuII Δ3, Δ5, and Δ7 showed only marginal differences in the activity ratio dark/blue. The variants LOV-PvuII Δ1 and Δ4 were further subjected to a dark → blue light → dark → blue light illumination protocol, and the activity was measured

dx.doi.org/10.1021/bc3001326 | *Bioconjugate Chem.* 2012, 23, 1105–1109

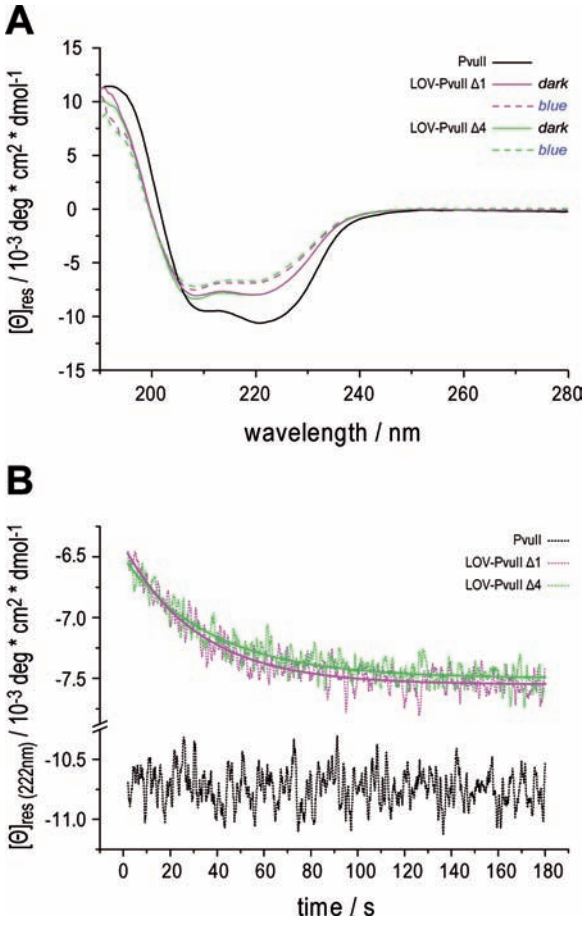

Figure 4. (A) Far-UV CD spectra of PvuII (solid black line), as well as LOV-PvuII Δ1 (magenta) and LOV-PvuII Δ4 (green), each recorded in the dark (solid line) or immediately after blue light photoexcitation (dashed line). CD measurements were performed using 10 μM protein in 10 mM Na-phosphate buffer pH 7.4 at 23 °C. (B) Time course of the recovery of the LOV-PvuII variants after blue light photoexcitation. After 1 min of blue light illumination, the respective mean residue ellipticity of each protein at 222 nm was monitored in the dark for 3 min, plotted against time, and fitted by nonlinear regression analysis (solid lines).

under each condition. As shown in Figure 2, the activity changes of both variants are fully reversible, independent of the directionality of photoactivation. The reversible photoconversion was also seen *in situ* by alternating the illumination conditions (dark → blue and blue → dark, respectively) during the cleavage reaction (Figure 3). For further investigation of the structural changes of LOV-PvuII during photoexcitation, a far-UV CD spectroscopic analysis was performed (Figure 4). Since the dark-state CD spectra of LOV-PvuII Δ1 and Δ4 are nearly identical, structural differences, if any, between the two variants do not affect the secondary structure without photoexcitation. However, the CD spectra observed directly after blue light illumination show a slight decrease in the intensity of the mean residue ellipticity in the 210−240 nm region for both variants, indicating similar light-induced structural differences. The small changes in ellipticity are compatible with the unfolding of the Jα-helix upon photoexcitation and show that no major structural changes of the full protein occur during the photocycle of LOV-PvuII. By following the mean residue ellipticity of LOV-PvuII Δ1 and Δ4 at 222 nm in the dark after a saturating blue light photoexcitation, the reversible recovery of the CD signal to the dark state could be observed directly *in situ*, i.e., the refolding of the Jα-helix in the absence of photoexcitation. Fitting the time course with a single exponential, the halftime of the photoconversion blue → dark at 23 °C could be determined to be approximately 26 and 22 s for LOV-PvuII Δ1 and Δ4, respectively, which is in line with the observed changes in DNA cleavage activity upon photoconversion *in situ*.

Our data show that the activity of both chimeric restriction enzymes, LOV-PvuII Δ1 and Δ4 can be controlled by light in a robust and, over multiple photocycles, fully reversible manner, but with a different polarity of photoactivation. How can this bidirectional control of DNA cleavage activity be explained for two variants that differ in approximately only one helical pitch at the fusion site of the shared helix? LOV-PvuII Δ1 behaves as expected with increased activity in the blue light photoexcitation state. In the absence of more detailed structural information, the answer to this question must be speculative. As already discussed when introducing the initial fusion setup, docking of the Jα-helix to the LOV domain core may cause sterical constraints on the dimerization interface and/or the catalytic center of PvuII that can be released by unfolding the Jα-helix through blue light illumination. In contrast, LOV-PvuII Δ4, with a ∼50-fold reduced over all activity compared to LOV-PvuII Δ1, shows an activity change of opposite polarity, with increased activity in the dark state with a properly folded and docked Jα-helix. This could mean that the compact LOV domain in the dark might stabilize the dimerization interface of PvuII, or that the partially unfolded LOV domain upon photoexcitation might destabilize the dimerization interface of PvuII, resulting in the observed photoactivation directionality. It might also be considered that the compact LOV domain in the dark induces structural distortions onto the PvuII subunits that stimulate the DNA cleavage activity of PvuII. This effect might result in a preferred DNA binding and/or catalytic conformation of PvuII in the dark state, which can be reversibly terminated by unfolding of the Jα-helix in the blue light photoexcitation state.

In summary, we have developed novel light-controllable chimeric endonucleases by fusing the light-sensory LOV2 domain to the restriction enzyme PvuII. Depending on the fusion site of the shared linking α-helix, the LOV-PvuII variants show a higher DNA cleavage activity either in the dark state or in the blue light photoexcitation state. The threefold bidirectional changes in activity are fully reversible and support the concept of generating an endogenous light-controllable restriction enzyme. For further applications, the activity ratio between the two photocycle states need to be further enhanced by engineering of the LOV-PvuII fusion interface for an increased sensor/effector-crosstalk, similar to the successful rational engineering of two designed photocontrollable transcription factors.[9,20] It is important to note that small changes in the fusion site between the sensory and effector modules can not only affect the extent of photoactivation, but also result in a change in the polarity activation → inhibition vs inhibition → activation upon illumination, which to our knowledge has not been observed yet.

■ AUTHOR INFORMATION

Corresponding Author

*E-mail: benno.schierling@chemie.bio.uni-giessen.de; +49 641 9935404 (phone); +49 641 9935409 (fax).

Notes

The authors declare no competing financial interest.

■ ACKNOWLEDGMENTS

We thank Dr. Tobin Sosnick (University of Chicago) for providing plasmids containing the LOV2 gene sequences, Dr. Wolfgang Wende & Dr. Marika Midon for fruitful discussions, Dr. Anja Drescher for critical reading of the manuscript and Birgit Reinhardt & Bedriska Reitz for technical assistance. This work was supported by the Justus-Liebig-University Giessen [program Just'us] and the DFG-RFBR program "International Research Training Groups" [Grants GRK 1384, 08-04-91974].

■ REFERENCES

(1) Kramer, R. H., Fortin, D. L., and Trauner, D. (2009) New photochemical tools for controlling neuronal activity. *Curr. Opin. Neurobiol. 19*, 544−52.
(2) Krauss, U., Drepper, T., and Jaeger, K. E. (2011) Enlightened enzymes: strategies to create novel photoresponsive proteins. *Chemistry 17*, 2552−60.
(3) van der Horst, M. A., and Hellingwerf, K. J. (2004) Photoreceptor proteins, "star actors of modern times": a review of the functional dynamics in the structure of representative members of six different photoreceptor families. *Acc. Chem. Res. 37*, 13−20.
(4) Drepper, T., Krauss, U., Meyer zu Berstenhorst, S., Pietruszka, J., and Jaeger, K. E. (2011) Lights on and action! Controlling microbial gene expression by light. *Appl. Microbiol. Biotechnol. 90*, 23−40.
(5) Moglich, A., and Moffat, K. (2010) Engineered photoreceptors as novel optogenetic tools. *Photochem. Photobiol. Sci. 9*, 1286−300.
(6) Fehrentz, T., Schonberger, M., and Trauner, D. (2011) Optochemical genetics. *Angew. Chem., Int. Ed. Engl. 50*, 12156−82.
(7) Beharry, A. A., and Woolley, G. A. (2011) Azobenzene photoswitches for biomolecules. *Chem. Soc. Rev. 40*, 4422−37.
(8) Herrou, J., and Crosson, S. (2011) Function, structure and mechanism of bacterial photosensory LOV proteins. *Nat. Rev. Microbiol. 9*, 713−23.
(9) Fan, H. Y., Morgan, S. A., Brechun, K. E., Chen, Y. Y., Jaikaran, A. S., and Woolley, G. A. (2011) Improving a designed photocontrolled DNA-binding protein. *Biochemistry 50*, 1226−37.
(10) Moglich, A., Ayers, R. A., and Moffat, K. (2009) Design and signaling mechanism of light-regulated histidine kinases. *J. Mol. Biol. 385*, 1433−44.
(11) Strickland, D., Moffat, K., and Sosnick, T. R. (2008) Light-activated DNA binding in a designed allosteric protein. *Proc. Natl. Acad. Sci. U. S. A. 105*, 10709−14.
(12) Wu, Y. I., Frey, D., Lungu, O. I., Jaehrig, A., Schlichting, I., Kuhlman, B., and Hahn, K. M. (2009) A genetically encoded photoactivatable Rac controls the motility of living cells. *Nature 461*, 104−8.
(13) Lee, J., Natarajan, M., Nashine, V. C., Socolich, M., Vo, T., Russ, W. P., Benkovic, S. J., and Ranganathan, R. (2008) Surface sites for engineering allosteric control in proteins. *Science 322*, 438−42.
(14) Moglich, A., Ayers, R. A., and Moffat, K. (2010) Addition at the molecular level: signal integration in designed Per-ARNT-Sim receptor proteins. *J. Mol. Biol. 400*, 477−86.
(15) Levskaya, A., Weiner, O. D., Lim, W. A., and Voigt, C. A. (2009) Spatiotemporal control of cell signalling using a light-switchable protein interaction. *Nature 461*, 997−1001.
(16) Pham, E., Mills, E., and Truong, K. (2011) A synthetic photoactivated protein to generate local or global Ca(2+) signals. *Chem. Biol. 18*, 880−90.
(17) Yazawa, M., Sadaghiani, A. M., Hsueh, B., and Dolmetsch, R. E. (2009) Induction of protein-protein interactions in live cells using light. *Nat. Biotechnol. 27*, 941−5.
(18) Halavaty, A. S., and Moffat, K. (2007) N- and C-terminal flanking regions modulate light-induced signal transduction in the LOV2 domain of the blue light sensor phototropin 1 from Avena sativa. *Biochemistry 46*, 14001−9.
(19) Harper, S. M., Neil, L. C., and Gardner, K. H. (2003) Structural basis of a phototropin light switch. *Science 301*, 1541−4.
(20) Strickland, D., Yao, X., Gawlak, G., Rosen, M. K., Gardner, K. H., and Sosnick, T. R. (2010) Rationally improving LOV domain-based photoswitches. *Nat. Methods 7*, 623−6.
(21) Hien le, T., Zatsepin, T. S., Schierling, B., Volkov, E. M., Wende, W., Pingoud, A., Kubareva, E. A., and Oretskaya, T. S. (2011) Restriction endonuclease SsoII with photoregulated activity--a "molecular gate" approach. *Bioconjugate Chem. 22*, 1366−73.
(22) Schierling, B., Noel, A. J., Wende, W., Hien le, T., Volkov, E., Kubareva, E., Oretskaya, T., Kokkinidis, M., Rompp, A., Spengler, B., and Pingoud, A. (2010) Controlling the enzymatic activity of a restriction enzyme by light. *Proc. Natl. Acad. Sci. U. S. A. 107*, 1361−6.
(23) Pingoud, A., and Wende, W. (2011) Generation of novel nucleases with extended specificity by rational and combinatorial strategies. *ChemBioChem 12*, 1495−500.
(24) Zaremba, M., and Siksnys, V. (2010) Molecular scissors under light control. *Proc. Natl. Acad. Sci. U. S. A. 107*, 1259−60.
(25) Schierling, B., Dannemann, N., Gabsalilow, L., Wende, W., Cathomen, T., and Pingoud, A. (2012) A novel zinc-finger nuclease platform with a sequence-specific cleavage module. *Nucleic Acids Res. 40*, 2623−38.
(26) Athanasiadis, A., Vlassi, M., Kotsifaki, D., Tucker, P. A., Wilson, K. S., and Kokkinidis, M. (1994) Crystal structure of PvuII endonuclease reveals extensive structural homologies to EcoRV. *Nat. Struct. Biol. 1*, 469−75.
(27) Cheng, X., Balendiran, K., Schildkraut, I., and Anderson, J. E. (1994) Structure of PvuII endonuclease with cognate DNA. *EMBO J. 13*, 3927−35.
(28) Nastri, H. G., Evans, P. D., Walker, I. H., and Riggs, P. D. (1997) Catalytic and DNA binding properties of PvuII restriction endonuclease mutants. *J. Biol. Chem. 272*, 25761−7.
(29) Xie, F., Qureshi, S. H., Papadakos, G. A., and Dupureur, C. M. (2008) One- and two-metal ion catalysis: global single-turnover kinetic analysis of the PvuII endonuclease mechanism. *Biochemistry 47*, 12540−50.
(30) Zhu, Z., Blanchard, A., Xu, S.-y., Wei, H., Zhang, P., Sun, D., and Chan, S.-h. (2009) (New England Biolabs, I. I., MA, US) U.S. Patent No 20090029376.

Bioconjugate Chemistry

Article

pubs.acs.org/bc

Effects of Enzymatic Activation on the Distribution of Fluorescently Tagged MMP-2 Cleavable Peptides in Cancer Cells and Spheroids

Natsuho Yamamoto,[†] Nicole S. Bryce,[†] Nils Metzler-Nolte,[‡] and Trevor W. Hambley*[,†]

[†]School of Chemistry, The University of Sydney, NSW 2006, Australia

[‡]Faculty of Chemistry and Biochemistry, Ruhr-Universitaet Bochum, Universitaetsstrasse 150, Bochum, 44801 Germany

Supporting Information

ABSTRACT: A peptide tagged at the N-terminus with FITC, at the C-terminus with coumarin-343, and incorporating a sequence selectively cleaved by the matrix metalloproteinase, MMP-2, was synthesized to investigate the effect of peptide cleavage on both cellular accumulation and distribution in cancer cell spheroids. The peptide was shown by HPLC and mass spectroscopy to be cleaved in the presence of MMP-2 at the expected site. The cellular and spheroid distribution of each of the fragments was monitored using confocal fluorescence microscopy. The intact peptide had minimal accumulation in 2D-cultured DLD-1 cells that do not express MMP-2 in these conditions. Following addition of serum containing MMP-2 to the cell media, the cleaved C-terminal fragment was seen to enter the cells, while the N-terminal fragment remained extracellular, evidently blocked by the presence of the FITC group. 3D culture of DLD-1 cells as spheroids resulted in measurable MMP-2 activity. Different distribution patterns of the two fluorophores were seen in spheroids treated with the intact peptide, consistent with cleavage occurring. Different rates of accumulation of each of the fragments were observed within the spheroid over time, which is attributed to the extent of accumulation and sequestration of the fragments by cells residing in the periphery of the spheroids. The outcomes suggest that tumor-associated enzymes have the potential to modify the distribution of peptides and peptide fragments in solid tumors by modifying the cellular uptake of those peptides.

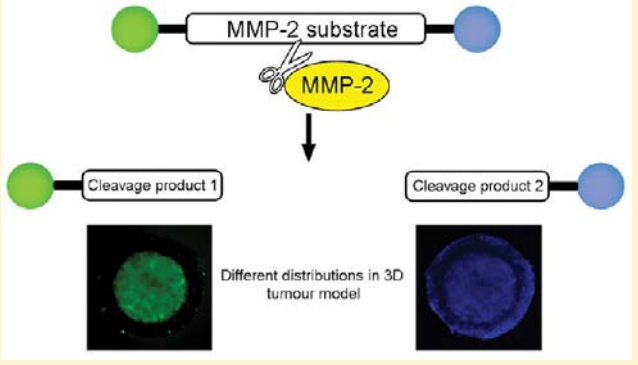

INTRODUCTION

Increasing the efficacy of antitumor agents is dependent on achieving higher selectivity of action against tumor cells than against healthy cells. This can be achieved by inhibition of enzymes expressed at much higher levels by tumor cells, an approach generally known as molecular targeting. However, it is also possible to exploit some of these overexpressed enzymes to activate inert prodrug forms of the anticancer agents.

Matrix metalloproteinases (MMPs) are zinc-containing endopeptidases that regulate the tumor microenvironment by tissue remodeling and degradation. There are 24 different types of mammalian MMPs, and some are known to have pro-metastatic roles while others act to inhibit metastasis.[1,2] MMP-2, also known as gelatinase A, is of particular interest since it is overexpressed and highly active in many cell lines derived from metastatic tissue,[3−5] consistent with its involvement in metastasis, the primary cause of death from cancer. There have been attempts to exploit the increased activity of MMPs in tumors to activate prodrugs.[6] For example, Tsien and co-workers showed that cellular association of polyarginine-based, cell-penetrating peptides (CPPs) was blocked when fused to an inhibitory domain made up of negatively charged residues, but cleavage of the linker between the polycationic and polyanionic domains by MMP-2 released the CPP portion and its attached fluorescent cargo to bind to and enter cells.[7] Further, an albumin binding octapeptide was attached to doxorubicin and the resultant adduct was found to be superior to doxorubicin alone in the treatment of an MMP-2 expressing human melanoma xenograft.[8] The octapeptide contained an MMP-2 cleavage site which was processed by the proteases, ultimately resulting in the release of free doxorubicin. The conjugate had a 4-fold higher maximum tolerated dose (MTD) than doxorubicin, demonstrating the potential of this approach.[6]

Here, we report a study of peptide sequences that are selectively cleaved by MMP-2 aimed at determining their effectiveness at targeting solid tumors and the effect of cleavage on the cellular accumulation and distribution in models of solid tumors. Orthogonally fluorescent fluorophores attached to each end of the peptide were employed to monitor MMP-2 cleavage of the peptide and the distribution of the peptide and its fragments in biological systems.

Received: October 26, 2011
Revised: May 23, 2012
Published: May 23, 2012

   dx.doi.org/10.1021/bc200561n | *Bioconjugate Chem.* 2012, 23, 1110−1118

EXPERIMENTAL PROCEDURES

Peptide Synthesis. All peptides were synthesized using standard solid-phase peptide synthesis (SPPS) methods using the Fmoc strategy.[9] Wang resins preloaded with Fmoc-Lys(Mtt) (0.56 mmol/g) (Mtt = 4-methyltrityl), or Fmoc-Ser(tBu) (0.69 mmol/g) (tBu = *tert*-butyl) were used. The resin was swollen in DMF for 1 h in a fritted syringe (Torviq). Fmoc groups were removed using 20% piperidine in DMF, first shaken for 2 min, then for 10 min with fresh 20% piperidine in DMF. Four equivalents of the respective Fmoc-protected amino acids along with *O*-(benzotriazol-1-yl)-*N*,*N*,*N*′,*N*′-tetramethyluronium tetrafluoroborate (TBTU: 3.9 equiv) and 1-hydroxy-benzotriazole (HOBt: 3.9 equiv) as coupling reagents were used to form the peptide bond. *N*,*N*-Diisopropylethylamine (DIPEA, 12 equiv) was used as a base, with an activation time of 1 min. The coupling mixture was shaken for 30 min and tested for free amines using the Kaiser test.[10] The process was repeated until no free amines could be observed. Once coupling was complete; the subsequent amino acids were added in turn, following the same procedure.

The side chains of the lysine residues were used for labeling with fluorophores. Mtt side-chain deprotection was performed by washing the resin first with DMF then with dichloromethane (DCM) to remove impurities and subsequently shrinking the resin with MeOH. The Mtt group was removed with a solution of 1% trifluoroacetic acid (TFA), 5% triisopropylsilane (TIS), and 94% DCM. The resin was treated with the deprotection mixture (2 mL) for 2 min, and this was repeated until the yellow color of the removed Mtt group was no longer visible. The resin was washed with DCM and again swollen for 30 min in DMF. For coupling with coumarin-343 (c343), the resin was shaken with a solution of c343, TBTU, and HOBt (all 2 equiv) in DCM and DIPEA (6 equiv) at room temperature for 4 h. For coupling with FITC, the resin was shaken with fluorescein-5-isothiocyanate (FITC, 4 equiv) and DIPEA (12 equiv) dissolved in DMF at room temperature for 4 h. For the peptide that contained both fluorophores, Mtt deprotection of the C-terminal lysine and subsequent coupling of the first fluorophore was performed before attaching the second Fmoc-Lysine(Mtt) residue at the N-terminus and coupling the second fluorophore.

At the end of the synthesis, the terminal Fmoc group was removed with 20% piperidine in DMF, and the resin was washed repeatedly with DMF then DCM and finally shrunk with MeOH. Cleavage from the resin was achieved with a solution of 95% TFA, 2.5% TIS, and 2.5% H_2O for 3 h. The solution containing the cleaved peptides was filtered through the fritted syringe and precipitated from the filtrate upon addition of Et_2O cooled in liquid N_2. The precipitated product was dried and lyophilized. The crude yield was quantitative in all cases. Purification was achieved by preparative HPLC (Linear gradient, 5−45% MeCN in 45 min; eluents, H_2O and MeCN, both containing 0.1% TFA).

Parameters and Characterization of Peptides. All peptides (Chart 1) were synthesized in a similar manner, purified with HPLC, and analyzed by analytical HPLC and mass spectrometry. HPLC retention times were obtained using analytical HPLC (linear gradient, 10−100% MeCN over 30 min; eluents, H_2O and MeCN, both containing 0.1% TFA). All analytical HPLC spectra are in the Supporting Information.

K(FITC)IPVSLRSK(c343)−OH (***1***). Resin: Fmoc-Lys(Mtt)-Wang (0.56 mmol/g). Mass Spectrometry (ESI positive ion): 1683.27 ($[M]^+$), 1294.67 ($[M\text{-FITC}]^+$), 942.27 ($[M+H]^{2+}$), 560.60 ($[M+2H]^{3+}$). HPLC retention time: 17.614 (Figure S1). Yield: 7.1 mg (4.2 μmol, 4.2%).

Chart 1. Peptides Synthesized in This Study

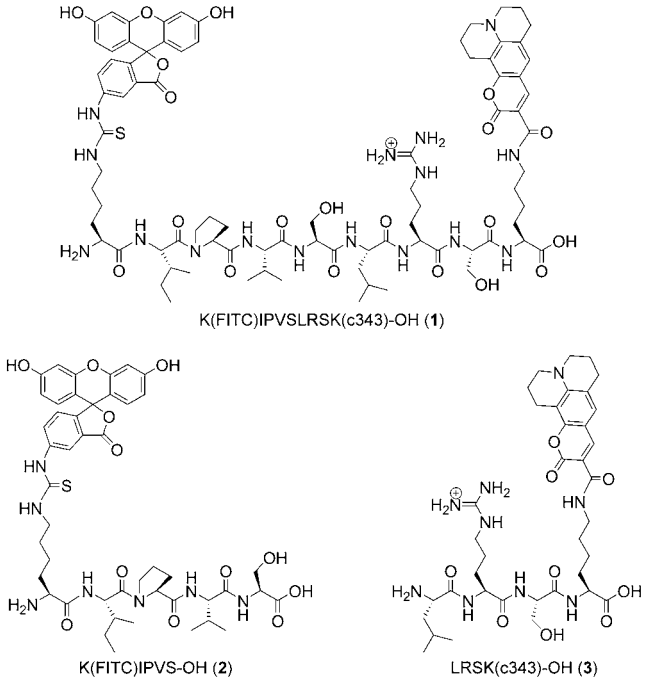

K(FITC)IPVS−OH (***2***). Resin: Fmoc-Ser(tBu)-Wang (0.69 mmol/g). Mass Spectrometry (ESI positive ion): 932.13-($[M]^+$), 466.73($[M+H]^{2+}$). HPLC retention time: 14.852 (Figure S2). Yield: 8.5 mg (9.1 μmol, 9.1%).

LRSK(c343)−OH (***3***). Resin: Fmoc-Lys(Mtt)-Wang (0.56 mmol/g). Mass Spectrometry (ESI positive ion): 770.40 ($[M]^+$), 383.60 ($[M+H]^{2+}$). HPLC retention time: 15.276 (Figure S3). Yield: 9.9 mg (12.8 μmol, 12.8%).

Analytical HPLC. Analytical HPLC was performed on an Alliance HPLC system using the Waters 2695 Separations Module. A linear gradient of 10−100% MeCN over 30 min was used, with the eluents H_2O and MeCN, both containing 0.1% TFA. A Waters Sunfire C18 (5 μm, 4.6 × 150 mm) analytical column was used at a flow rate of 0.2 mL/min. Signals were detected at 254 nm using a Waters 2998 Photodiode Array Detector.

Preparative HPLC. Preparative HPLC was performed on a Waters 600 HPLC system. A linear gradient of 5−45% MeCN over 45 min was used, with the eluents H_2O and MeCN, both containing 0.1% TFA. A Waters Sunfire C18 (5 μm, 19 × 150 mm) preparative column was used at a flow rate of 7 mL/min. Signals were detected at 254 nm on a Waters 2998 Photodiode Array Detector. Relevant fractions were collected manually.

Fluorescence Spectra. Fluorescence measurements were performed at room temperature using a Varian Cary Eclipse fluorescence spectrophotometer, with a 1 cm × 1 cm quartz cuvette (Starna). Scans were run as 1×10^{-5} M solutions in Tris/HCl buffer (50 mM Tris, 5 mM $CaCl_2$, 0.3 M NaCl, 0.05% Brij-35, pH adjusted to 7.4 using 1 M HCl) at 100 nm/min with excitation and emission slit widths of 2.5 nm. All solutions were prepared immediately prior to analysis.

Cleavage Assay Using LC-MS. 0.88 U MMP-2 catalytic domain (ProtEra) was added to 150 μL of the peptide solution (1×10^{-5} M) made up in Tris/HCl buffer (50 mM Tris, 5 mM

dx.doi.org/10.1021/bc200561n | *Bioconjugate Chem.* 2012, 23, 1110−1118

$CaCl_2$, 0.3 M NaCl, 0.05% Brij-35, pH adjusted to 7.4 using 1 M HCl) and heated at 37 °C for 18 h in a dry block heater (Ratek).

A Finigan LCQ-DECA LC-MS was used to analyze peptide cleavage by LC-MS. A linear gradient of 0−100% MeCN in 40 min was used, with the eluents H_2O and MeCN. A Waters Sunfire C18 (5 μm, 4.6 × 150 mm) analytical column was used at a flow rate of 0.2 mL/min.

Cell Lines. DLD-1 human colon carcinoma cells and HT1080 human fibrosarcoma cells were obtained from ATCC and used within 6 months of resuscitation. Cells were maintained in complete media which is Advanced DMEM (Invitrogen) supplemented with 2% FBS (Invitrogen) and 2 mM glutamine (Invitrogen) in a humidified environment at 37 °C and 5% CO_2. Cells were imaged in phenol red free DMEM, supplemented with 2 mM glutamine.

Retroviral knockdown constructs targeting MMP-2 were created using the following oligonucleotide sequences: MMP-2: GCGGTCACAGCTACTTCTTCA[11] (MMP-2 KD1) and GGAGAGCTGCAACCTGTTTG[12] (MMP-2 KD1) cloned into pRetroSuper (Oligoengine). Virus was produced and cells tranduced as previously described.[13,14] A polyclonal pool of knockdown cells was selected with 10 μg/mL of puromycin and maintained in 2 μg/mL of puromycin in complete media. Both knockdowns gave equivalent results and only MMP-2 KD1 is shown in the results for brevity.

Spheroids were formed by plating 100 μL of a 2.5 × 10^5 cells/mL single cell suspension of DLD-1 onto agarose (sterile, 0.75% (w/v) in PBS) coated 96 well plates. They were allowed to aggregate for 5 days without motion, resulting in the formation of single spheroid per well.[15]

MMP-2 Activity Assay. The activity of MMP-2 in spheroids was tested using a Novex Zymogram (gelatin) Gel Kit (Invitrogen). On day 4 of spheroid growth, the media were replaced with serum-free media. After 24 h, the media were collected from 10 spheroids and pooled for zymography. Positive control HT1080 cells were plated in a 6-well plate at a density of 200 000 cells/well in complete media. They were allowed to adhere overnight, then the media replaced with serum-free Advanced DMEM. Aliquots were taken after 48 h. Each sample was loaded onto a Novex 10% Zymogram gel (10 wells) and run in a Tris-Glycine SDS running buffer (25 mM Tris, 192 mM glycine and 0.1% SDS) at 125 V for 90 min. The Novex Sharp Standard (Invitrogen) was used as a mass marker. The gel was renatured using Novex Zymogram renaturing buffer and developed using Novex Zymogram developing buffer at 37 °C for 12 h according to the manufacturer's instructions. This was stained for 30 min using the Colloidal Blue Staining Kit (Invitrogen). A separate SDS page gel of the DLD-1 and DLD-1 MMP-2 knockdown conditioned media samples was performed and equal sample loading was visualized by Colloidal Blue staining.

Preparation of Monolayer Cell Cultures for Microscopy. Cells were plated onto black, μ-clear 96-well imaging plates (Greiner Bio-One) and grown to 40−60% confluence in complete media. The medium was replaced with serum-free, phenol red free medium prior to treating the cells with compound and the nuclear stain Draq5 (5 μM) (Abcam) for 4 h. The cells were subsequently imaged either with the compound still in the media or with the medium replaced with fresh serum free, phenol red free medium after washing with PBS.

Preparation of Spheroids for Microscopy. On day 5 of spheroid growth, the spheroids were treated with 10 μM of compound (in up to 2% DMSO) for 4 h, washed with PBS, then replaced in fresh PBS in black, μ-clear 96-well imaging plates (Greiner Bio-One) to be imaged within 10 min. A heated stage (Linkam Scientific) was used to maintain the temperature at 37 °C during imaging.

Inhibition of MMP-2 Activity. The MMP-2 blocking peptide (CA-4001, Pierce) was used at a concentration of 4 μg/mL and incubated for 30 min prior to any peptide addition. Inhibition of MMP-2 activity in spheroids was also carried out by incubating the spheroids with 5 μM Marimastat. The Marimastat was added to the media 10 min prior to adding the peptide.

Confocal Fluorescence Microscopy. Confocal fluorescence microscopy was performed using a Nikon Eclipse TE200 inverted fluorescence microscope and a Nikon Plan Fluor 40×/NA 0.75 DIC objective lens for imaging monolayer cells and a 10×/NA 0.3 DIC objective lens for imaging spheroids. Confocal images were collected using a Nikon DE-Eclipse microscope C1 and Coherent Radius 405−25 and Sapphire 488−20 optically pumped semiconductor laser systems. The emission ranges were 433−467 nm and 500−550 nm. A scan rate of 15 ms/pixel was used for all images and an average of 4 scans per image was collected. At least 3 spheroids were imaged on each occasion, and the experiment was repeated on at least 3 different occasions.

Live Confocal Microscopy of Compound Uptake. The spheroids were transferred onto a black, μ-clear 96-well imaging plate containing fresh phenol red free media, treated with the compound, and images were collected every 10 min in a humidified live-cell chamber maintained at 37 °C (Solent Scientific).

Images were collected on an Olympus FV1000 inverted microscope using an Olympus UPLAPO 10×/0.40 air objective lens. A scan rate of 4.0 μs/pixel and sequential collection of the green and blue channels were applied for all images. Blue fluorescence was collected by excitation with a 405 nm diode laser and green fluorescence was collected by excitation with a 488 nm argon laser. The emission ranges were 425−475 nm and 500−550 nm, respectively.

RESULTS

Discussion of Synthesis. The peptide K(FITC)-IPVSLRSK(c343)−OH (**1**) was constructed based on a study reported by Turk and co-workers, where the sequence Ile-Pro-Val-Ser-Leu-Arg-Ser was found to be preferentially cleaved by MMP-2 between the serine and leucine residues.[16] Two orthogonal fluorophores, FITC (ex. 488 nm, em 518 nm) and c343 (ex. 395 nm, em. 488 nm), were attached on either side of the peptide to monitor each fragment once cleaved by the enzyme. The expected fragments of the peptide on either side of the MMP-2 cleavage site, K(FITC)IPVS−OH (**2**) and LRSK(c343)−OH (**3**), were also synthesized.

The peptides were synthesized using standard solid-phase peptide synthesis (SPPS) techniques using the 9-fluorenylmethoxycarbonyl (Fmoc) strategy. The Mtt protecting group for lysine was chosen, as it is labile to weak acid, allowing the use of dilute TFA for its deprotection. This allows the side-chain amine to be liberated for further reaction without affecting the rest of the molecule. For K(FITC)IPVSLRSK(c343)−OH (**1**), the first fluorophore, c343, was attached to the peptide via the C-terminal lysine before the final N-terminal lysine residue was

added to the sequence. The second fluorophore, FITC, was then added via its isothiocyanate functional group to form a thiourea bond with the free side-chain amine of the N-terminal lysine. Coupling of the fluorophores was done in this order to minimize exposure of c343 to acidic and basic conditions encountered during the deprotection and coupling steps.

Fluorescence Properties of the Peptides. The fluorescence spectrum of K(FITC)IPVS−OH (**2**) is the same as that of free FITC (Figure 1A), whereas the excitation and

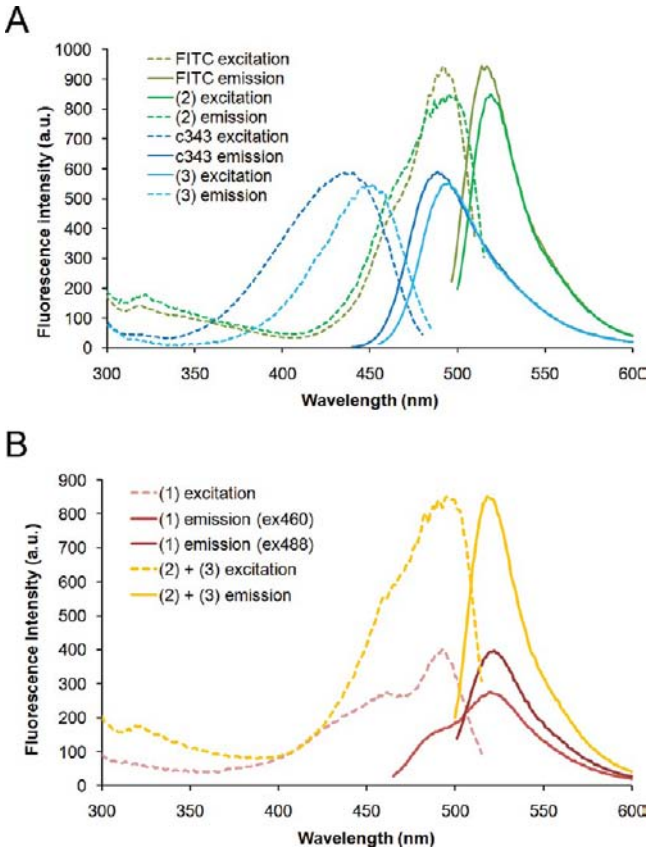

Figure 1. (A) Fluorescence excitation and emission spectra of fragments (**2**) and (**3**) and their respective free fluorophores. (B) Fluorescence excitation and emission spectra of K(FITC)IPVSLRSK-(c343)−OH (1) overlaid with that of the (1:1) mixture of its respective fragments K(FITC)IPVS−OH (2) and LRSK(c343)−OH (3).

emission spectra of LRSK(c343)−OH (**3**) are slightly red-shifted compared to those of free c343. However, the extent of the shift is not large enough to affect its use in fluorescence microscopy experiments.

As shown in Figure 1B, the fluorescence emission spectrum of LRSK(c343)−OH (**3**) overlaps with the fluorescence excitation spectrum of K(FITC)IPVS−OH. This raises the possibility that c343 and FITC could be a Förster resonance energy transfer (FRET) pair. If there is FRET interaction between the two fluorophores, then excitation of c343 would result in fluorescence emission in the FITC region via a nonradiative energy transfer, and thus could be used for monitoring the cleavage of the peptide. If cleavage of the peptide resulted in the two fluorophores no longer interacting with each other, the excitation of c343 would result only in emission from c343.

However, when the fluorescence excitation and emission spectra of K(FITC)IPVSLRSK(c343)−OH (**1**) were compared to that of a (1:1) mixture of the fragments K(FITC)IPVS−OH (**2**) and LRSK(c343)−OH (**3**), it was found that the spectral characteristics were not significantly different (Figure 1B). For both the uncleaved and cleaved peptides, excitation of the donor fluorophore caused emission at the acceptor fluorophore. This suggests that an energy transfer process is occurring, not only in the uncleaved peptide, but also between the fragments of the cleaved peptide, most likely indicating a strong association between the fragments. Since there is no significant difference between the fluorescence properties of the uncleaved and cleaved peptides, FRET could not be used for monitoring the cleavage of this peptide.

Cleavage Assay. In order to test the cleavage of the peptides, the 17.8 kDa catalytic domain of human recombinant MMP-2 was added to solutions of K(FITC)IPVSLSRK-(c343)−OH (**1**) and monitored using LC-MS. It was found that the peptide was cleaved into its component fragments at the expected site, as determined by the mass of the fragments (Figure S4). Moreover, only two major peaks, each corresponding to an expected fragment, were observed in the chromatogram, suggesting that the cleavage of K(FITC)-IPVSLRSK(c343)−OH (**1**) by the recombinant enzyme is almost complete.

Confocal Microscopy of Monolayer Cell Culture. Confocal microscopy was used to determine the cellular localization of the free fluorophores in DLD-1 cells (Figure S5). No intracellular localization of FITC was seen, as black shadows were observed where the cells are located, against a green fluorescent background. Images collected after the removal of excess FITC from the media confirmed the lack of intracellular FITC. In contrast, intracellular blue fluorescence was observed (Figure S5) indicating that c343 was able to enter the cells as we have reported previously.[17] The cellular localization of the fluorophores bound to the peptide fragments is similar to that of the free fluorophores. K(FITC)IPVS−OH (**2**) is not localized intracellularly (Figure 2A1) and images collected after the removal of the excess compound from the media (Figure 2A2) show only minor localized dots of fluorescence within the cells. This indicates that K(FITC)-IPVS−OH (**3**) is generally not accumulated by cells, most likely as a result of the uptake blocking effect of the FITC group or possibly the IPVS peptide sequence. Fluorescence was observed in cells treated with LRSK(c343)−OH (**3**) despite removing the excess compound, confirming that this fragment is able to enter cells (Figures 2B1, and B2, respectively). These results confirm that the two fragments can be monitored independently in biological systems.

DLD-1 cells incubated with the full-length peptide K(FITC)-IPVSLRSK(c343)−OH (**1**) show differential localization of the fluorophores both with the compound present in the media (Figure 3A) or after washout (Figure 3B). Since the cleaved peptides are shown to have different cellular uptake patterns, where LRSK(c343)−OH (**3**) enters cells, but K(FITC)IPVS−OH (**2**) does not (Figure 2), the cleavage of the peptide was visualized by the lack of colocalization of the blue and green fluorescence.

To validate the MMP-2 selectivity of K(FITC)IPVSLRSK-(c343)−OH (**1**), MMP-2 activity in DLD-1 cells was inhibited in two different ways: (a) by treating the cells with a MMP-2 blocking antibody (Ab) and (b) by creating MMP-2 knock-down DLD-1 cell lines (Figure 4A). In the control cells (Figure

dx.doi.org/10.1021/bc200561n | Bioconjugate Chem. 2012, 23, 1110−1118

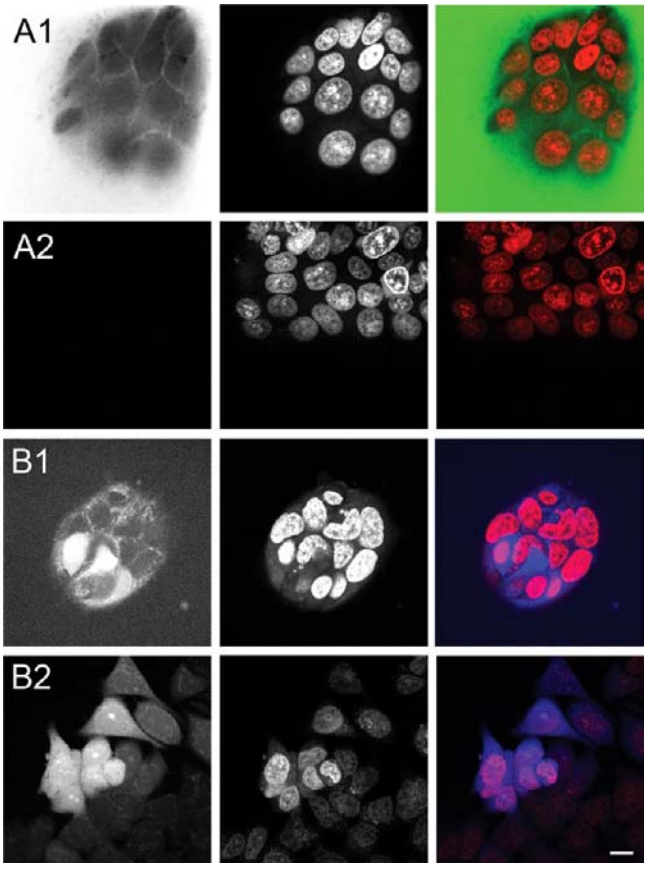

Figure 2. LRSK(c343)−OH (**3**) cleavage fragment is able to readily enter into cells in contrast to the K(FITC)IPVS−OH (**2**) cleavage fragment. Confocal microscopy images of DLD-1 cells treated with the fragments of K(FITC)IPVSLRSK(c343)−OH (**1**). (A) K(FITC)-IPVS−OH (**2**) imaged in the green channel and (B) LRSK(c343)−OH (**3**) imaged in the blue channel (shown in black and white for clarity) with their respective Draq5 nuclear stained images and merged images. 1 shows the cells with the compound still in the media, and 2 shows the cells washed with PBS prior to taking the images to remove excess compound from the media. Scale bar represents 10 μm.

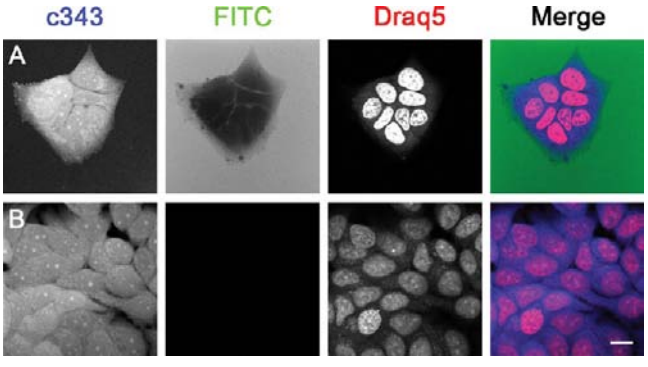

Figure 3. Presence of MMP-2 results in peptide cleavage and diffusion of the cell permeable peptide fragment LRSK(c343)−OH (**3**). Confocal microscopy images of cells treated with K(FITC)IPVSLRSK-(c343)−OH (**1**). (A) DLD cells with the compound still in the media. (B) DLD-1 cells washed with PBS prior to taking the images to remove excess compound from the media. The blue, green, and red individual images are shown in black and white for clarity. Scale bar represents 10 μm.

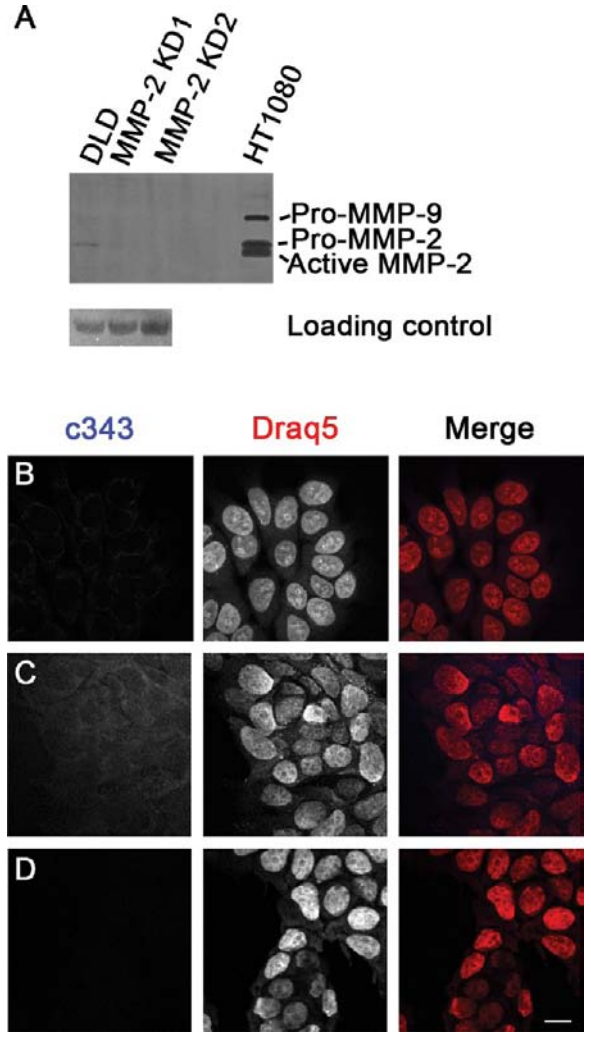

Figure 4. Cleavage of K(FITC)IPVSLRSK(c343)−OH (**1**) is MMP-2 specific in DLD-1 cells. (A) Zymogram showing reduced MMP-2 activity in the spheroids made from MMP-2 knockdown lines compared to spheroids made from control DLD-1 cells. The HT1080 lysate was used as a positive control for MMP expression. Confocal images of the cell-permeable fragment, Draq5 nuclear stain, and the respective merged images in (B) DLD-1 cells treated with the MMP-2 blocking antibody, (C) DLD-1 MMP-2 knockdown cells and (D) DLD-1 MMP-2 knockdown cells treated with the MMP-2 blocking antibody. The blue and red individual images are shown in black and white for clarity. Scale bar represents 10 μm.

4B), intracellular blue fluorescence resulting from the cellular uptake of the LRSK(c343)−OH (**3**) cleavage fragment was observed following treatment with K(FITC)IPVSLRSK-(c343)−OH (**1**). However, when MMP-2 inhibited cells were treated with K(FITC)IPVSLRSK(c343)−OH (**1**), minimal intracellular blue fluorescence was observed (Figure 4B,C) compared to the control. Treatment of MMP-2 knockdown cells with MMP-2 blocking Ab followed by K(FITC)-IPVSLRSK(c343)−OH (**1**) also showed no intracellular fluorescence (Figure 4D). This suggests that MMP-2 activity is necessary for the cleavage of K(FITC)IPVSLRSK(c343)−OH (**1**) and consequent cellular uptake of the LRSKC(c343)−OH (**3**) fragment.

Confocal Microscopy of Spheroids. To investigate the potential for selective cleavage of these peptide sequences in solid tumors, their behavior was studied in spheroids. Spheroids

dx.doi.org/10.1021/bc200561n | *Bioconjugate Chem.* 2012, 23, 1110−1118

are a type of three-dimensional cell culture whereby tumor cells are grown as spherical aggregates which mimic the distribution of drugs in tumor-like tissues.[18,19]

Figure 5A1 shows a DLD-1 spheroid treated with the cell-permeable peptide LRSK(c343)−OH (**3**). Fluorescence

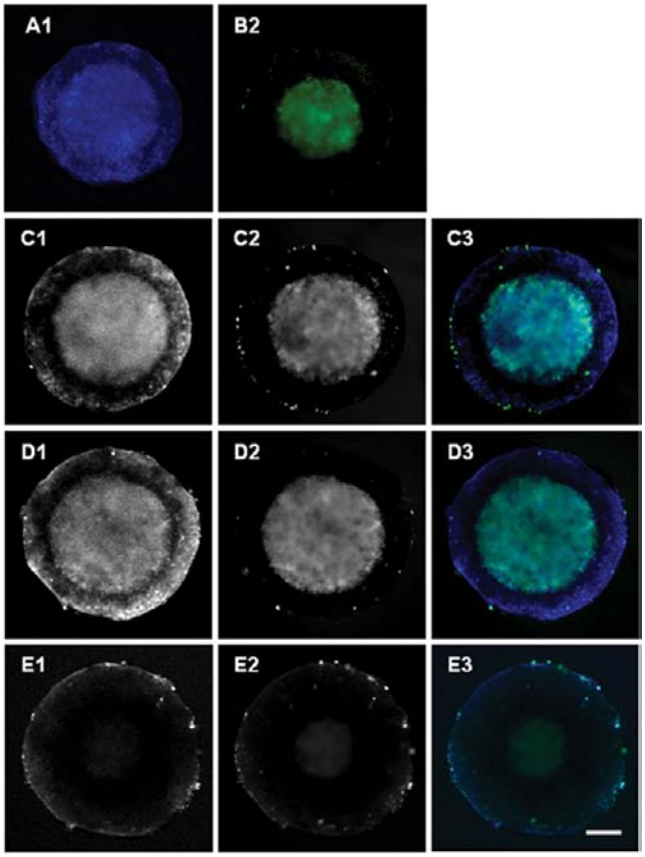

Figure 5. Differential localization of individual fluorophores in DLD-1 spheroids dosed with intact peptide is indicative of peptide cleavage. Confocal microscopy images of DLD-1 spheroids treated with K(FITC)IPVSLRSK(c343)−OH (**1**) and its fragments. (A) LRSK-(c343)−OH (**3**), (B) K(FITC)IPVS−OH (**2**), (C) K(FITC)-IPVSLRSK(c343)−OH (**1**), (D) a (1:1) mixture of LRSK(c343)−OH (**3**) and K(FITC)IPVS−OH (**2**), and (E) K(FITC)IPVSLRSK-(c343)−OH (**1**) cotreated with Marimastat. 1 shows the image in the blue channel, 2 shows the image in the green channel, and 3 shows the overlay image. For C−E, the blue and green images are shown in black and white for clarity. Scale bar represents 200 μm.

accumulation is observed at the periphery of the spheroid to a distance of approximately 85 μm, as well as in the central hypoxic/necrotic region of the spheroid (morphology of the spheroid shown in Figure S6). The central region of DLD-1 spheroids is hypoxic,[20] and hypoxic conditions are known to lead to the upregulation of MMP-2 expression.[21,22] Spheroids treated with K(FITC)IPVS−OH (**2**) have no significant fluorescence accumulation at the periphery (Figure 5B2), but diffuse fluorescence is observed in the central region of the spheroid. Cellular accumulation of K(FITC)IPVS−OH (**2**) is observed in some of the cells, indicated by bright dots of intense fluorescence, but these are limited to within one or two cell diameters of the spheroid periphery.

The differences between the diffusion patterns of the two fluorophores in the peripheries of the spheroids can be explained by the differences in their cellular uptake properties. LRSK(c343)−OH (**3**) was shown to be readily taken up by monolayer cultured cells, and it is most likely sequestered by the cells in the periphery of the spheroid. This is not observed for K(FITC)IPVS−OH (**2**) treated cells because it is not taken up by the cells. It should be noted that MTT assays of the compounds after a 4 h incubation period gave IC_{50} values above 150 μM, suggesting the compounds are not toxic on this time scale. This indicates that the observed pattern of fluorescence is not due to the compounds affecting the integrity of the cells in the spheroids.

When the spheroid is treated with a mixture of both the K(FITC)IPVS−OH (**2**) and LRSK(c343)−OH (**3**) fragments, the blue and green fluorescence patterns in the core of the spheroids are colocalized, but there is no colocalization at the periphery of the spheroid (Figure 5D). This further supports that the two fragments have different diffusion patterns into the spheroid, and that the individual fragments do not affect the diffusion pattern of the other.

The fluorescence in the core of the spheroids is diffuse, and no significant intense dots of fluorescence are observed, suggesting that there is no cellular accumulation. This indicates that the fluorescence observed in the core of these spheroids is due to the compounds in the interstitial space. The hypoxic/necrotic core of the spheroids is known to be less dense than the periphery of the spheroids (Figure S6), and therefore, the diffuse fluorescence observed in the core of the spheroids could be due to the compounds accumulating in this less dense space. It should be noted that, apart from the diffuse appearance, it is impossible to determine whether the observed fluorescence is intra- or extracellular, as nuclear or cytoplasmic dyes also have limited diffusion through the spheroid and cannot stain the cells in the core of the spheroids (Figure S7).

The fluorescence diffusion pattern seen on treatment with K(FITC)IPVSLRSK(c343)−OH (**1**) (Figure 5C) resembles that following treatment with the mixture of its fragments (Figure 5D). This suggests that K(FITC)IPVSLRSK(c343)−OH (**1**) has been cleaved.

To investigate whether the cleavage of the peptide is occurring as a result of MMP-2 activity, Marimastat, a well-established broad-spectrum MMP inhibitor[23] was added (Figure 5E). It can be seen that the fluorescence diffusion pattern observed in the blue channel (Figure 5E1) is significantly different from that observed in the absence of Marimastat (Figure 5C1), as the blue fluorescence is only observed within one or two cell diameters from the outer edge of the spheroid, whereas in Figure 5A1, the fluorescence at the periphery of the spheroid spans approximately 85 μm. Similarly, there is a higher level of fluorescence in the green channel at the periphery of the spheroid in the Marimastat treated spheroid (Figure 5E2) compared to that observed in Figure 5C2.

These results suggest that it is the uncleaved species giving rise to the fluorescence in Figure 5E as the blue and green fluorescence are colocalized. Marimastat successfully inhibited MMP-2 from cleaving the peptide, which allowed for the diffusion pattern of the intact peptide in spheroids to be observed. In general, less fluorescence is observed in the core of the spheroids cotreated with Marimastat. This is potentially due to the uncleaved peptide having a different diffusion rate compared to the cleaved fragments, whereby it diffuses more slowly through the interstitial space of the spheroid, and therefore is not able to penetrate to the core as effectively as the cleaved fragments.

Similar to the monolayer cell studies, MMP-2 blocking Ab and spheroids grown with MMP-2 knockdown DLD-1 cells were used to investigate whether the altered diffusion pattern of K(FITC)IPVSLRSK(c343)−OH (**1**) in the absence and presence of Marimastat was due to the specific inhibition of MMP-2. When MMP-2 inhibited spheroids were treated with K(FITC)IPVSLRSK(c343)−OH (**1**), less fluorescence was observed in the core of the spheroids (Figure 6). The observed

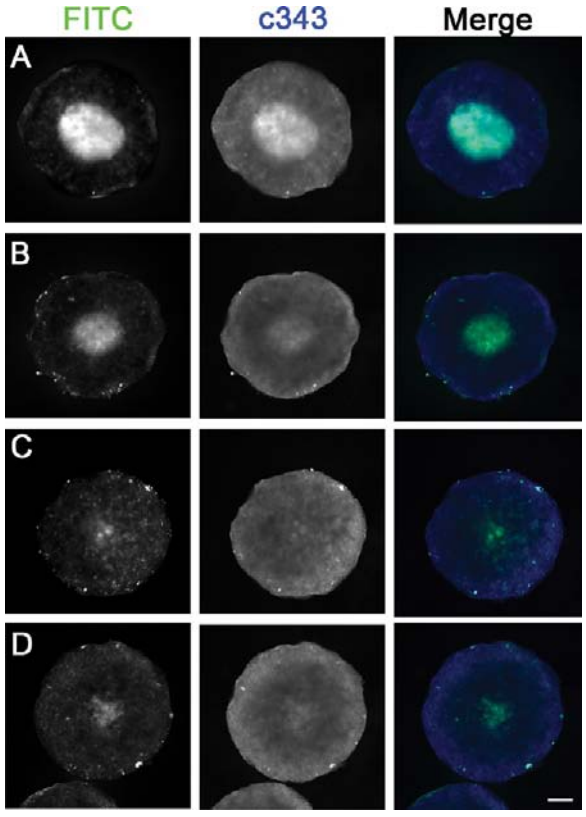

Figure 6. Inhibition of MMP-2 using a MMP-2 blocking antibody or a MMP-2 knockdown cell line inhibits peptide cleavage and alters the distribution of the peptide. Confocal microscopy images of DLD-1 spheroids treated with K(FITC)IPVSLRSK(c343)−OH (**1**). (A) DLD-1 cell spheroid in serum-free media, (B) DLD-1 cell spheroid in serum-free media with MMP-2 blocking Ab, (C) MMP-2 knockdown DLD-1 cell speroid in serum-free media, and (D) MMP-2 knockdown DLD-1 cell spheroid in serum-free media with MMP-2 blocking Ab. The FITC (green) and c343 (blue) images are shown in black and white for clarity. Scale bar represents 200 μm.

fluorescence pattern is similar to that of spheroids treated with Marimastat, confirming that the peptide is specifically cleaved by MMP-2. MMP-2 activity is necessary for peptide cleavage and consequent diffusion of its fragments.

Live Confocal Microscopy. The outcome of the confocal microscopy studies of spheroids suggests that the two fragments of K(FITC)IPVSLRSK(c343)−OH (**1**) have different rates of diffusion through the spheroids. To test this, the spheroids were treated with the uncleaved peptide, then imaged every 10 min in both the blue and green channels to monitor the rate of diffusion of the fragments into the spheroid (Figure 7). The images were obtained over 4 h, but no significant change was observed after 3 h, so only images up to 3 h are shown. At 0 min, the images are dark because the peptide had not distributed evenly throughout the media. Unlike the images

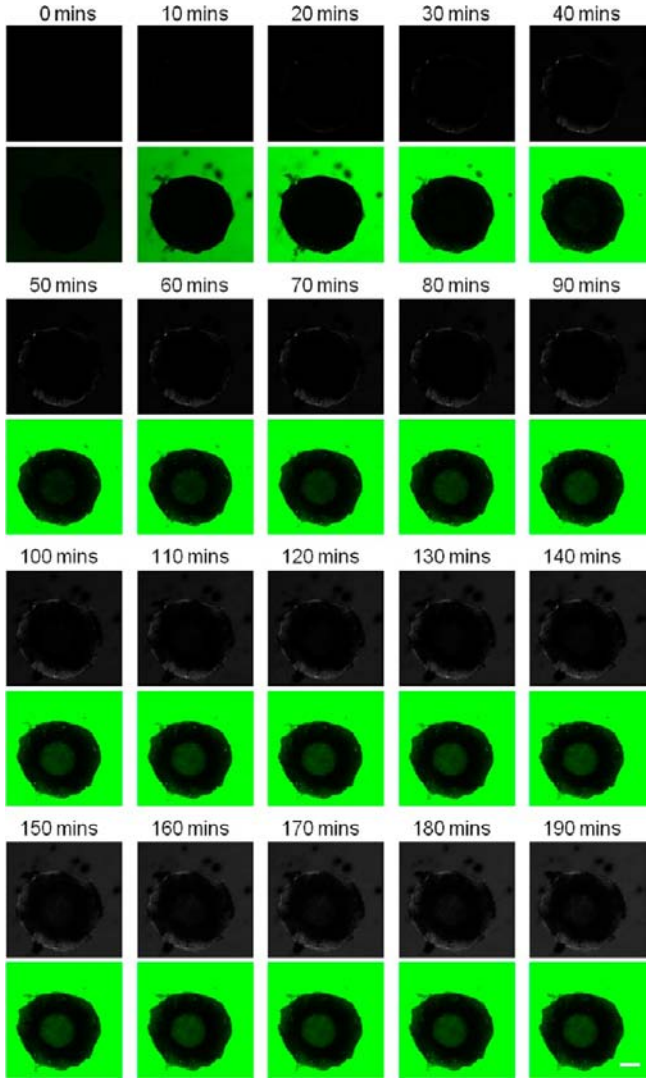

Figure 7. Live cell imaging shows differential diffusion characteristics of the cleaved peptides. DLD-1 spheroids treated with K(FITC)-IPVSLRSK(c343)−OH (**1**) and monitored every 10 min over 3 h. Images in the blue channel are shown in black and white for clarity. Scale bar 200 μm.

shown in Figure 6, the peptide remained in the media while the images were collected, so a significant amount of background fluorescence can be seen.

In the blue channel, the intensity and width of the fluorescent band observed at the periphery of the spheroid increase over time, showing the cellular accumulation of the c343 containing fragment. The fluorescence in the core of the spheroid becomes visible after approximately 90 min. In the green channel, bright dots of localized fluorescence appear in the spheroid periphery almost immediately, and fluorescence in the core of the spheroid is visible after approximately 40 min. The difference in the time at which fluorescence starts to become visible in the core of the spheroid is in agreement with the hypothesis that it originates from the cleaved fragments. LRSK(c343)−OH (**3**) is slower at accumulating in the core of the spheroid compared to K(FITC)IPVS−OH (**2**), presumably because its cellular uptake is more efficient, and as such, it is sequestered more by the peripheral cells of the spheroids. This is in contrast to K(FITC)IPVS−OH (**2**), which is not taken up by cells and diffuses directly into the core of the spheroid

without being sequestered by the outer layer cells. The results were not affected by fluorescence bleaching, as a control spheroid treated over the same time period and imaged once at the end of the incubation time had a diffusion pattern indistinguishable from that of the final image in Figure 7 (Figure S8).

DISCUSSION

The results from this study show that selective cleavage of a peptide by a tumor-associated enzyme modifies the delivery of the components in tumor models. Although there are many examples of activity-based probes, whereby protease activity is visualized by fluorescence output,[24,25] this system utilizes the protease activity to achieve visualization of differential and selective delivery of agents in cells and tumors. In doing so, it models the activation and fate of protease-activated prodrugs, such as the MMP-2 activated doxorubin prodrug.[8]

Using LC-MS, the synthesized peptide, K(FITC)IPVSLRSK-(c343)−OH (**1**) was shown to be cleaved by MMP-2 at the expected site to yield the anticipated fragments, K(FITC)-IPVS−OH (**2**) and LRSK(c343)−OH (**3**). It was found that FITC containing peptides were not taken up by cells, and this was essential for limiting uptake of any component to environments in which MMP-2 activation occurred.

The LRSK(c343)−OH (**3**) fragment was seen to enter monolayer cultured cells, while the other fragment remained extracellular. Moreover, cells treated with K(FITC)IPVSLRSK-(c343)−OH (**1**) showed different patterns of fluorescence in the blue and green channels in the presence of MMP-2, suggesting that the peptide was being cleaved in the presence of MMP-2 and the different fragments were giving rise to different fluorescence distribution patterns. In spheroids, which were shown to have some MMP-2 activity, cleavage of the peptide and consequently different fluorescence patterns were observed in the blue and the green channels. The specificity of the peptide for MMP-2 was confirmed in both the monolayer cell culture and spheroids by employing MMP-2 blocking Ab and MMP-2 knockdown cell lines. Inhibition of MMP-2 resulted in the inhibition of the cleavage of K(FITC)IPVSLRSK(c343)−OH (**1**), as shown by colocalization of the blue and green fluorescence. This showed that MMP-2 activity is necessary for peptide cleavage and consequent uptake/diffusion of the fragments. Inhibition of MMP-9, which is structurally similar and has a similar substrate specificity to MMP-2,[26] does not inhibit peptide cleavage, confirming that K(FITC)IPVSLRSK-(c343)−OH (**1**) is highly specific for MMP-2.

When the uptake of the intact peptide was tested over a 4 h period, it was found that the rate and pattern of diffusion of LRSK(c343)−OH (**3**) into the spheroid was different from that of K(FITC)IPVS−OH (**2**). LRSK(c343)−OH (**3**) accumulated at the periphery of the spheroids, and was consequently slower to reach the core of the spheroids, while K(FITC)-IPVS−OH (**2**) did not accumulate at the periphery of the spheroids and accumulated in the core of the spheroids more rapidly. This suggests that the fluorescence observed in the different channels is due to different species and the accumulation of fluorescence in the core of the spheroids is due to peptides not being taken up by the cells in the periphery.

Although it was shown that both fragments eventually accumulated in the core of the spheroids, the diffusion of K(FITC)IPVSLRSK(c343)−OH (**1**) and its fragments in the presence and absence of MMP-2 in both monolayer cells and spheroids confirmed that the cleavage of the peptide by MMP-2 does occur, and the resultant fragments have different cell and spheroid uptake properties. The results shed light on the mechanism of action and cellular uptake behavior of previously reported protease-cleavable agents.[8,27] The outcomes of this study successfully demonstrate the effectiveness of using a peptide sequence that is selectively cleaved by tumor-associated enzymes to modify the cellular uptake of compounds in solid tumor models.

ASSOCIATED CONTENT

Supporting Information

HPLC traces of synthesized peptides, LC-MS trace of peptide cleavage experiment, and images of control cells and spheroids. This material is available free of charge via the Internet at http://pubs.acs.org.

AUTHOR INFORMATION

Corresponding Author

*E-mail: trevor.hambley@sydney.edu.au, ph: +61-2-9351-3320, fax: +61-2-9351-3329.

Notes

The authors declare no competing financial interest.

ACKNOWLEDGMENTS

The authors acknowledge funding support from the Australian Research Council and Deutscher Akademischer Austauch Dienst. The authors would like to thank Dr. Renee Whan for technical assistance and acknowledge scientific and technical input and support from the Australian Microscopy & Microanalysis Research Facility (AMMRF) node at the University of Sydney.

REFERENCES

(1) Krueger, A., Kates, R. E., and Edwards, D. R. (2010) Avoiding spam in the proteolytic internet: Future strategies for anti-metastatic MMP inhibition. *Biochim. Biophys. Acta, Mol. Cell Res. 1803*, 95−102.

(2) Overall, C. M., and Kleifeld, O. (2006) Tumour microenvironment - Opinion: Validating matrix metalloproteinases as drug targets and anti-targets for cancer therapy. *Nat. Rev. Cancer 6*, 227−239.

(3) Cockett, M. I., Murphy, G., Birch, M. L., O'Connell, J. P., Crabbe, T., Millican, A. T., Hart, I. R., and Docherty, A. J. P. (1998) Matrix metalloproteinases and metastatic cancer. *Biochem. Soc. Symp. 63*, 295−313.

(4) Kleiner, D. E., and Stetler-Stevenson, W. G. (1999) Matrix metalloproteinases and metastasis. *Cancer Chemother. Pharmacol. 43* (Suppl), S42−51.

(5) Itoh, T., Tanioka, M., Yoshida, H., Yoshioka, T., Nishimoto, H., and Itohara, S. (1998) Reduced angiogenesis and tumor progression in gelatinase A-deficient mice. *Cancer Res. 58*, 1048−1051.

(6) Atkinson, J. M., Siller, C. S., and Gill, J. H. (2008) Tumour endoproteases: the cutting edge of cancer drug delivery? *Br. J. Pharmacol. 153*, 1344−1352.

(7) Jiang, T., Olson, E. S., Nguyen, Q. T., Roy, M., Jennings, P. A., and Tsien, R. Y. (2004) Tumor imaging by means of proteolytic activation of cell-penetrating peptides. *Proc. Natl. Acad. Sci. U.S.A. 101*, 17867−72.

(8) Mansour Ahmed, M., Drevs, J., Esser, N., Hamada Farid, M., Badary Osama, A., Unger, C., Fichtner, I., and Kratz, F. (2003) A new approach for the treatment of malignant melanoma: enhanced antitumor efficacy of an albumin-binding doxorubicin prodrug that is cleaved by matrix metalloproteinase 2. *Cancer Res. 63*, 4062−6.

(9) Kirin, S. I., Noor, F., Metzler-Nolte, N., and Mier, W. (2007) Manual solid-phase peptide synthesis of metallocene-peptide bioconjugates. *J. Chem. Educ. 84*, 108−111.

(10) Kaiser, E., Colescott, R. L., Bossinger, C. D., and Cook, P. I. (1970) Color test for detection of free terminal amino groups in the solid-phase synthesis of peptides. *Anal. Biochem. 34*, 595−8.
(11) Tremblay, P., Beaudet, M. J., Tremblay, E., Rueda, N., Thomas, T., and Vallieres, L. (2011) Matrix metalloproteinase 2 attenuates brain tumour growth, while promoting macrophage recruitment and vascular repair. *J. Pathol. 224*, 222−33.
(12) Sun, Y., Liu, M., Yang, B., Li, B., and Lu, J. (2008) Role of siRNA silencing of MMP-2 gene on invasion and growth of laryngeal squamous cell carcinoma. *Eur. Arch. Otorhinolaryngol. 265*, 1385−91.
(13) Bryce, N. S., Clark, E. S., Leysath, J. L., Currie, J. D., Webb, D. J., and Weaver, A. M. (2005) Cortactin promotes cell motility by enhancing lamellipodial persistence. *Curr. Biol. 15*, 1276−85.
(14) Ireton, R. C., Davis, M. A., van Hengel, J., Mariner, D. J., Barnes, K., Thoreson, M. A., Anastasiadis, P. Z., Matrisian, L., Bundy, L. M., Sealy, L., Gilbert, B., van Roy, F., and Reynolds, A. B. (2002) A novel role for p120 catenin in E-cadherin function. *J. Cell Biol. 159*, 465−476.
(15) Bryce, N. S., Zhang, J. Z., Whan, R. M., Yamamoto, N., and Hambley, T. W. (2009) Accumulation of an anthraquinone and its platinum complexes in cancer cell spheroids: the effect of charge on drug distribution in solid tumour models. *Chem. Commun. (Cambridge, U. K.)*, 2673−2675.
(16) Turk, B. E., Huang, L. L., Piro, E. T., and Cantley, L. C. (2001) Determination of protease cleavage site motifs using mixture-based oriented peptide libraries. *Nat. Biotechnol. 19*, 661−667.
(17) Yamamoto, N., Danos, S., Bonnitcha, P. D., Failes, T. W., New, E. J., and Hambley, T. W. (2008) Cellular uptake and distribution of cobalt complexes of fluorescent ligands. *J. Biol. Inorg. Chem. 13*, 861−871.
(18) Minchinton, A. I., and Tannock, I. F. (2006) Drug penetration in solid tumours. *Nat. Rev. Cancer 6*, 583−592.
(19) Kelm, J. M., Timmins, N. E., Brown, C. J., Fussenegger, M., and Nielsen, L. K. (2003) Method for generation of homogeneous multicellular tumor spheroids applicable to a wide variety of cell types. *Biotechnol. Bioeng. 83*, 173−180.
(20) Kim, B. J., Hambley, T. W., and Bryce, N. S. (2011) Visualising the hypoxia selectivity of cobalt(III) prodrugs. *Chem. Sci. 2*, 2135−2142.
(21) Furlan, D., Sahnane, N., Carnevali, I., Cerutti, R., Bertoni, F., Kwee, I., Uccella, S., Bertolini, V., Chiaravalli, A. M., and Capella, C. (2008) Up-regulation of the hypoxia-inducible factor-1 transcriptional pathway in colorectal carcinomas. *Hum. Pathol. 39*, 1483−1494.
(22) Luo, Y., He, D.-L., Ning, L., Shen, S.-L., Li, L., Li, X., Zhau Haiyen, E., and Chung Leland, W. K. (2006) Over-expression of hypoxia-inducible factor-1alpha increases the invasive potency of LNCaP cells *in vitro*. *BJU Int. 98*, 1315−9.
(23) Thomas, A. L., and Steward, W. P. (2000) Marimastat: the clinical development of a matrix metalloproteinase inhibitor. *Expert Opin. Invest. Drugs 9*, 2913−2922.
(24) Scherer, R. L., VanSaun, M. N., McIntyre, J. O., and Matrisian, L. M. (2008) Optical imaging of matrix metalloproteinase-7 activity in vivo using a proteolytic nanobeacon. *Mol. Imaging 7*, 118−31.
(25) Tedelind, S., Jordans, S., Resemann, H., Blum, G., Bogyo, M., Fuhrer, D., and Brix, K. (2011) Cathepsin B trafficking in thyroid carcinoma cells. *Thyroid Res. 4* (Suppl 1), S2.
(26) Bjoerklund, M., and Koivunen, E. (2005) Gelatinase-mediated migration and invasion of cancer cells. *Biochim. Biophys. Acta, Rev. Cancer 1755*, 37−69.
(27) McIntyre, J. O., Fingleton, B., Wells, K. S., Piston, D. W., Lynch, C. C., Gautam, S., and Matrisian, L. M. (2004) Development of a novel fluorogenic proteolytic beacon for in vivo detection and imaging of tumour-associated matrix metalloproteinase-7 activity. *Biochem. J. 377*, 617−628.

Bioconjugate Chemistry

Article

pubs.acs.org/bc

Development of an *Influenza virus* Protein Array Using Sortagging Technology

Antonia Sinisi,[†,‡,§] Maximilian Wei-Lin Popp,[†,∥] John M. Antos,[†] Werner Pansegrau,[‡] Silvana Savino,[‡] Mikkel Nissum,[‡] Rino Rappuoli,[‡] Hidde L. Ploegh,*[,†] and Ludovico Buti[†,‡,⊥]

[†]Whitehead Institute for Biomedical Research, 9 Cambridge Center, Cambridge, Massachusetts 02142, United States

[‡]Novartis Vaccines and Diagnostics, Via Fiorentina 1, 53100 Siena, Italy

Supporting Information

ABSTRACT: Protein array technology is an emerging tool that enables high-throughput screening of protein−protein or protein−lipid interactions and identification of immunodominant antigens during the course of a bacterial or viral infection. In this work, we developed an *Influenza virus* protein array using the sortase-mediated transpeptidation reaction known as "Sortagging". LPETG-tagged *Influenza virus* proteins from bacterial and eukaryotic cellular extracts were immobilized at their carboxyl-termini onto a preactivated amine-glass slide coated with a Gly_3 linker. Immobilized proteins were revealed by specific antibodies, and the newly generated Sortag-protein chip can be used as a device for antigen and/or antibody screening. The specificity of the Sortase A (SrtA) reaction avoids purification steps in array building and allows immobilization of proteins in an oriented fashion. Previously, this versatile technology has been successfully employed for protein labeling and protein conjugation. Here, the tool is implemented to covalently link proteins of a viral genome onto a solid support. The system could readily be scaled up to proteins of larger genomes in order to develop protein arrays for high-throughput screening.

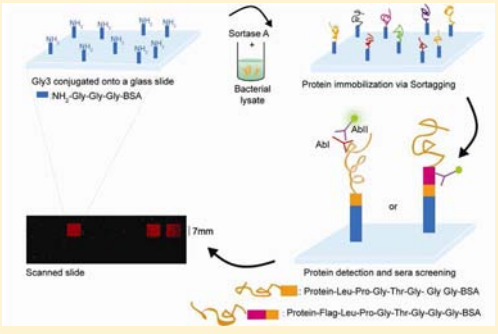

INTRODUCTION

In the past decade, applications of microarray technology have grown exponentially, but a simple and fast technique to immobilize functional proteins onto solid supports still represents a major challenge.[1] Various protein tags and several different strategies have been employed to attach proteins to solid supports. Examples include hexahistidine-tagged fusion proteins and in vivo/in vitro biotinylation procedures, which confer a specific orientation to the arrayed proteins. However, these approaches often give rise to a high level of background which may compromise the quality of the protein chip.[2] Chemical procedures or chemoselective reactions between protein α-thioesters and a cysteine-coated glass slide are examples of a more general but even less specific reaction to immobilize proteins onto a solid support due to the random cross-linking of lysines to carboxylic acid coated slides.[3,4]

To overcome these issues, we made use of the specificity of the Sortase-catalyzed transpeptidation reaction to develop a method to covalently anchor proteins to a solid support. The enzyme Sortase A (SrtA) from *Staphylococcus aureus* recognizes and cleaves the peptide bond between the threonine and glycine residue of an LPXTG motif, incorporated close to the C-terminus of a substrate.[5−7] Following sortase-mediated cleavage, SrtA and the substrate form a thioester intermediate, which is subsequently resolved by an oligoglycine nucleophile, resulting in the final transpeptidation product. Depending on the nature of the glycine derivative, this reaction may yield fluorescently labeled proteins, circularized proteins or proteins covalently linked by an intermolecular isopeptide bond.[8−13] Here, we used the transpeptidase reaction (also known as Sortagging) to covalently attach LPETGG-tagged antigens from *Influenza A* virus to a solid support, thereby creating a Sortagged-influenza protein array from unpurified cellular lysates.

Influenza virus is the cause of major respiratory illness in human populations, where the viral hemagglutinin (HA) and neuraminidase (NA) proteins are the two most prominent antigens recognized by the host immune system.[14] Early studies have shown that neutralizing antibodies are mainly directed against the receptor binding domain of hemagglutinin[15] (fragment HA1).

In addition, antibodies directed against the membrane-proximal and more conserved stem region of HA have also been described.[16,17] These antibodies have been shown to neutralize several subtypes among the virus clades which, in principle, could allow for a wide coverage.

Recombinant epitopes could be used for early identification of genetic variations among virus clades, and may therefore provide the basis for a universal flu vaccine.[17] From this perspective, it would be desirable to develop tools for generating protein arrays to screen and identify new viral epitopes. Moreover, a useful antigen chip with influenza virus

Received: October 26, 2011
Revised: April 19, 2012
Published: May 17, 2012

   dx.doi.org/10.1021/bc200577u | *Bioconjugate Chem.* 2012, 23, 1119−1126

proteins and/or fragments of HA and NA major antigens could be updated seasonally and used for yearly screening. At the moment, inactivated viruses, pseudoparticles, or proteins purified from virus isolates are used for testing immunogenic response[18] and for vaccine development purposes.[18−21] Here, we developed a simple process to Sortag proteins to a glass slide derivatized with oligoglycine groups. We show an efficient alternative to existing methods that avoids protein purification steps and allows a highly efficient immobilization reaction between the proteins of interest and the substrate.

EXPERIMENTAL PROCEDURES

Generation of an *Influenza virus* Library in *E. coli* and Cloning HA Constructs for Mammalian Expression. cDNA fragments from *Influenza A virus* (A/WSN/1933/H1N1) genome were amplified and inserted into a bacterial expression vector pET28 b(+) LPETG (Novagen). PCR primers containing ±20 bp of gene specific regions and adapter sequences were used (SI Table S1). The adapter sequence, which becomes incorporated into the termini flanking the amplified gene, is homologous to the outer ends of the linearized vector and ensures annealing and ligation of the PCR products into the expression vector, which is subsequently transformed in chemically competent TOP 10 cells (Invitrogen). Cloned genes contain at the C-terminus the following adapter sequence for ligation and sortagging: 5′-GAA GGA GAT ATA CAT ATG-3′ and 5′-CGG TAG GCC GCC GCT GCC GCC GCC GCC-3′. cDNA fragments from *Influenza A virus* HA A/Vietnam/1194/2004 (H5N1); HA A/Panama/2007/1999 (H3N2); HA A/NewYork/396/2005 (H3N2); HA A/California/7/2009 (H1N1) were amplified and inserted into the eukaryotic expression vector pcDNA 3.1(+)LPETG (Geneart) (Figure 1 SI). The constructs contain an in frame C-terminal Flag tag, an LPETG motif, followed by an HA tag and a His_6 tag. All cloned plasmids are sequence-verified (SI Table S2).

Expression and Cell Cultures. Sequence-confirmed plasmids were expressed in BL21 Codon Plus competent cells (Stratagene), grown in autoinduction media (15 g/L glycerol, 30 g/L yeast extract, 0,5 g/L $MgSO_4$, 20 g/L K_2HPO_4, and 5 g/L KH_2PO_4) for 12−18 h, and harvested after overnight (o/n) growth.[22] SrtA and mCherry proteins were expressed and purified as previously reported.[10]

HEK 293T cells were cultured in Dulbecco's modified Eagle's medium (DMEM) supplemented with 10% heat-inactivated FBS (fetal bovine serum) and vitamins at 37 °C under humidified air containing 5% CO_2. All transfections were carried out using Polymer and Xfect (Clontech) using the instructions provided by the manufacturer.

SDS-PAGE and Western Blot analysis. SDS-PAGE analysis was performed using Nu-PAGE 4−12% Bis-Tris gradient gel (Invitrogen) according to the manufacturer's instructions. Gels were stained with Colloidal Coomassie Blu G-250 (Invitrogen) or processed for Western Blot analysis using standard protocols. Polyclonal antibody specific for Influenza A-recognizing H1N1 and H3N2 and Flu A strains (Millipore) and polyclonal antibody specific for PB1 and NS1 were used at a dilution of 1/1000. Secondary rabbit antigoat IgG-HRP conjugated antibodies were used at a dilution of 1/10 000.

Chemically Derivatized Amine Glass Slides. Super amine slides were purchased from Arrayit (Arrayit, CA). BSA-coated slides were fabricated following the literature procedure.[23] Briefly, amine slides were treated with 100 mM *N,N*-disuccinimidyl carbonate (DSC) and 100 mM *N,N*-diisopropylethylamine (DIPEA) in a final volume of 400 mL anhydrous *N,N*′-dimethylformamide (DMF). Slides were agitated in this solution for 3 h at room temperature. The slides were rinsed twice with 95% ethanol and then incubated in 400 mL of PBS pH 7.5 containing 1% BSA for 12 h at room temperature. The slides were rinsed twice with H_2O, twice with 95% ethanol, and dried using a Microarray High-Speed Centrifuge (Arrayit, CA). The slides were then placed in a 2 × 8 multiwell cassette to provide discrete wells for further chemical derivatization. Attachment of Gly_3 to the slide surface was achieved by adding 100 μL of Gly_3 conjugation solution (100 mM Fmoc-Gly_3, 100 mM PyBOP, 100 mM HOBt, and 300 mM DIPEA in NMP) to each well. The reaction was quenched by replacing the Gly_3 conjugation solution with a solution of 100 mM ethanolamine and 300 mM DIPEA in NMP. Slides were then washed for 10 min in NMP and then rinsed in 20% piperidine NMP for 30 min. Following washing steps in NMP, ddH_2O and sortase buffer (150 mM NaCl, 50 mM Tris pH 8.0, 1 mM $CaCl_2$), slides were dried by centrifugation and stored.

Transpeptidation Reaction Conditions. Bacterial pellets were solubilized in lysis buffer (150 mM NaCl, 20 mM Tris-HCl pH 8.0, 1 mM $CaCl_2$, 0.5% NP40, 1 mM benzamidine HCl) and/or denaturing buffer (20 mM Tris-HCl pH 7.5, 150 mM NaCl, 20 mM imidazole, 0.5% Triton X-100, 0.3% SDS, 10% glycerol) and then sonicated. Protein concentrations were normalized by SDS PAGE analysis. HEK 293 cells were lysed by sonication in Nonidet P-40 containing buffer (150 mM NaCl, 20 mM Tris-HCl pH 8.0, 1 mM $CaCl_2$, 0.5% NP40, 1 mM benzamidine HCl) and cleared by centrifugation.

Sortase Reaction on Glass Slides. To perform the sortase reaction on glass slides, 100 μL of a solution containing sortase buffer (final concentrations: 150 mM NaCl, 20 mM Tris-HCl pH 8.0, 1 mM $CaCl_2$, 5% milk) was supplemented with 0.5−3 μM of various mammalian and bacterial lysates and 50 μM Sortase A. The mixture was applied to appropriate wells on the glass slides, and the sortagging reaction was carried out at room temperature. Slides were washed three times in sortase buffer in the presence of detergents (150 mM NaCl, 20 mM Tris-HCl pH 8.0, 1 mM $CaCl_2$, 0.5% NP40) and dried by centrifugation.

Serum Screening Probing and Scanner Analysis. Slides were blocked with 5% milk, 2% BSA, and 1% Tween in PBS at 4 °C for 4 h or o/n, and washed 3 times in 0.1% Tween PBS (PBST). The slide was incubated with a dilution of commercial *Influenza A virus* H1N1 serum (Millipore) and Influenza anti-A/New York/55/2004 HA, anti-A/Vietnam/1194/04 HA, and anti-A/California/7/2009(H1N1) (Nibsc) in blocking buffer for 1 h at 4 °C. Slides were washed 3 times in PBST and probed for 1 h at 4 °C with 1 μg/mL of Alexa-647-labeled antimouse or -goat secondary antibody (Invitrogen) in PBST. Washing steps in PBST and PBS were followed by a final step in ddH_2O. The slides were air-dried after brief centrifugation and analyzed using a Tecan Power scanner. Intensities were quantified using *Image J* software. All signal intensities were corrected for spot-specific background. Protein concentrations in bacterial lysates in each well were normalized with respect to internal protein standards.

RESULTS

Design and Expression of *Influenza A virus* Protein Antigens Compatible with Sortagging. An *Influenza virus*

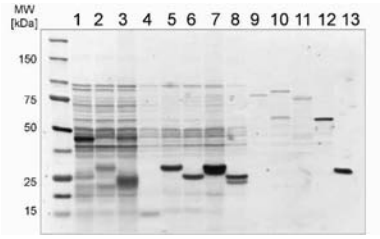

Figure 1. Expression of *Influenza A* virus protein array for Sortagging. SDS-Page analysis of bacterial lysates containing *Influenza* virus proteins stained with Coomassie Blue. The library represents each of 10 cDNA's encoding the viral genome (Lanes 1−12: HA chain A 38 kDa; HA chain B 24 kDa; NA/C_2 15 kDa; NA/C_3 9 kDa; M1 28 kDa; M2 26 kDa; NS1 30 kDa; NS2 25 kDa; PA 78 kDa; PB1 85 kDa; PB2 83 kDa; NP 55 kDa). Lane 13 represents purified SrtA protein.

Scheme 1. Sortagging Immobilization of an Expressed cDNA Protein Library[a]

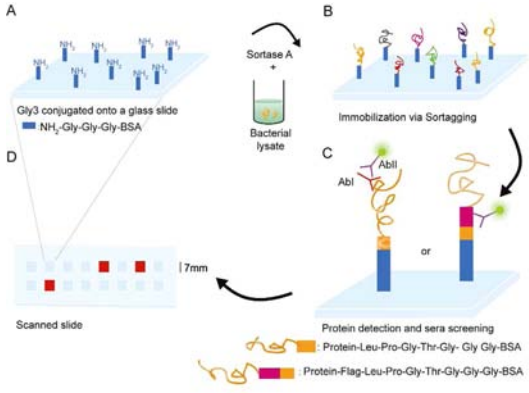

[a](A) Super amine glass slides were derivatized with Gly_3 attached to a layer of bovine serum albumin (BSA). (B) Bacterial lysates or eukaryotic expressing proteins containing the LPETG motif are incubated in separate wells in the presence of Sortase A. As a result, proteins are covalently linked to the slide. (C) Sortagged conjugates are detected using specific anti sera. (D) The slide is scanned to visualize protein interactions.

cDNA library was cloned into a dedicated bacterial expression vector. Proteins were expressed in frame with the C-terminal LPETG motif, followed by a His_6 tag. The *Influenza A viral* genome contains eight single (nonpaired) RNA strands encoding ten proteins with high antigenic variability that is relevant for applicative studies in vaccine research. The library represents each of ten genes present in the viral genome. In the case of Hemagglutinin (HA), two fragments were obtained, hereafter called HA chain A (1 to 342 aa) and HA chain B (343 to 566 aa). For Neuraminidase (NA), a fragment called NA/C_2 (141 to 273 aa) was cloned and expressed with a C-terminal Flag tag. Additional fragments were generated for HA and NA; however, because of their poor expression these were excluded from follow-up experiments (data not shown). The library was cloned and successfully expressed in BL21-Codon Plus cells using autoinduction medium (Figure 1). As further discussed below, the small LPETG motif at the C-terminus does not influence the expression or solubility of the recombinant proteins.

Chemical Derivation of the Solid Support and Conjugation of Gly_3 Peptide to Solid Support. Different types of chemically derivatized glass slides were tested to determine the optimal solid support for use as a Sortagging

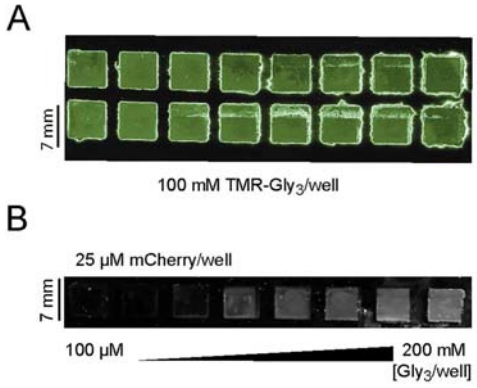

Figure 2. Laser scan analysis of derivatized slides. (A) The BSA-layer of a super amine glass slide was conjugated to a fluorescent peptide (TMR-Gly_3), allowing direct visualization of the coupling reaction with a microarray slide fluorescence scanner. (B) The concentration of Gly_3 peptide was varied between 100 μM and 200 mM during derivatization to find the optimal nucleophile concentration required to facilitate the transpeptidation reaction. Subsequently, 25 μM of fluorescent purified protein mCherry-LPETG-His_6 was immobilized by Sortagging using 150 μM of SrtA in sortase reaction buffer (50 mM Tris, pH 7.5, 150 mM NaCl, 10 mM $CaCl_2$) on the Gly_3-modified glass slides and the immobilized mCherry was detected with a microarray slide fluorescence scanner.

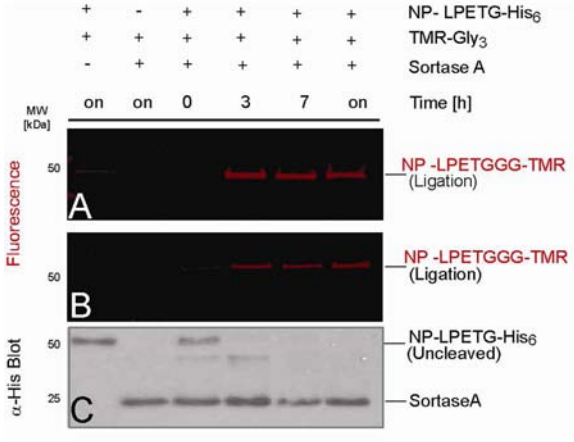

Figure 3. Labeling of NP protein in bacterial lysates with TMR-Gly_3 nucleophile under nondenaturing and denaturing conditions. Bacterial lysate of *Influenza* virus protein NP containing a C-terminal LPETG motif was incubated with SrtA for different times in the presence and absence of fluorescent TMR-Gly_3 peptide. 15 μM protein in the bacterial lysate was treated with 150 μM SrtA in sortase reaction buffer in (A) NP40 lysis buffer and in (B) SDS/Triton buffer (for 0, 4, 7 h and o.n. at 37 °C), (C) His_6/HRP immunoblot showing the presence of unlabeled protein in the absence of Sortase A, and at T_0, the band corresponding to 25 kDa demonstrates the presence of Sortase A.

platform. Aldehyde, epoxy, and amine glass slides were treated (data not shown), and the latter was found to be best suited for Sortagging experiments.

Scheme 1 illustrates the steps used to build the Sortag-protein array. First, BSA coated slides were fabricated via DSC (*N,N′*-disuccinimidyl carbonate) cross-linking following the reported procedure.[23] An amide linkage was then formed between free BSA lysine residues and the C-terminus of a Fmoc-protected triglycine peptide (Gly_3) using PyBOP mediated coupling. Finally, Fmoc removal with piperidine

dx.doi.org/10.1021/bc200577u | *Bioconjugate Chem.* 2012, 23, 1119−1126

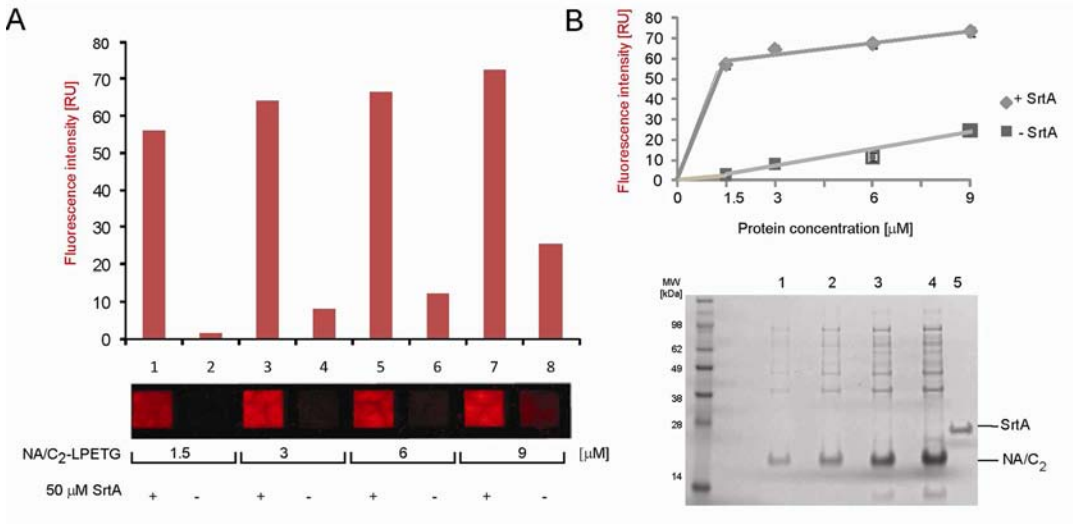

Figure 4. Effect of different concentrations of cellular lysate on protein immobilization to Gly_3 glass slides. (A) The lower part depicts direct visualization of immobilized NA/C_2 on a Gly_3 derivatized slide. Increasing concentrations of *Influenza* virus protein in crude extract of NA/C_2 ranging from 1.5 μM to 9 μM were incubated in the absence or presence of SrtA and detected by Anti-Flag 647 antibody. Upper part: graphical representation of the fluorescence intensity showing enzymatic activity. Data were analyzed using *Image J* software. (B) Linearity and sensivity of the protein array by experiments with lysates in triplicate. Lower part: a SDS-Page analysis of the different cellular protein concentrations used on in the Sortagging reaction.

unmasked the triglycine N-terminus, allowing it to function as a nucleophile in the sortase-mediated transpeptidation reaction.

As an initial demonstration of the efficiency of the slide modification procedure described above, a Gly_3 peptide with TMR attached at the N-terminus was conjugated to the slide to allow direct visualization of covalent linkage onto the solid support (Figure 2A). Next, the optimal concentration of Gly_3 nucleophile loaded onto the slide was determined for the Sortagging reaction. Purified mCherry-LPETGG-His_6 protein was used as a model protein. The fluorescence of immobilized mCherry-LPETGG His_6 tag protein was observed to correlate with the initial concentration of Gly_3 used in the slide derivatization procedure in a linear fashion (Figure 2B). 100 mM of Gly_3 was chosen as the optimal concentration to use in the following experiments. Thus, we were able to demonstrate that appropriately modified solid supports allow covalent attachment of proteins to a surface using Sortagging, and by altering the concentration of Gly_3, we can control and maximize the final transpeptidation yield on the activated slide. It should be also noted that sortase mediated transpeptidation has been used previously to attach proteins to other solid supports including beads and Biacore sensor chips.[24−26]

Different Experimental Conditions Do Not Affect the Enzymatic Activity of Sortase A. The purification of expressed proteins often represents a limiting step when building a protein array. Therefore, we sought to define the conditions that would allow us to avoid such steps. In previous studies, Sortagging was performed with high efficiency using purified starting materials, but sortase-mediated transpeptidation was also obtained in the presence of crude mammalian or bacterial cell extracts. The NP protein extracted from *E. coli* cells in both mild (A) NP40 lysis buffer (50 mM Tris, pH 7.5, 150 mM NaCl, 10 mM $CaCl_2$, 0.5% NP40) and harsh (B) SDS/Triton lysis buffer (50 mM Tris, pH 7.5, 150 mM NaCl, 10 mM $CaCl_2$, 0.5% SDS, 1% Triton) was briefly studied for its ability to participate in sortase mediated transpeptidation reactions. Crude bacterial extract was produced by sonication using (A) or (B) conditions (Figure 3). Lysates containing ~15 μM of LPETG-tagged substrate were incubated with 2 mM of the fluorescent TMR-Gly_3 peptide in the presence of 150 μM SrtA. Sortagging was detectable at 3 h and appeared complete after 7 h. The presence of SDS in the reaction mixture did not affect the overall reaction conversion. The sortase reaction was additionally monitored by anti-His_6 immunoblotting. In the absence of SrtA, or at the initial time point of the reaction (T_0), the C-terminal His_6 tag of the LPETG-tagged substrate remained intact. At later time points, the His_6 tag was cleaved and replaced by the fluorescent probe, indicating that Sortagging had occurred (Figure 3C).

Next, we determined the optimal concentration of SrtA necessary for optimal Sortagging when using cell extracts from stringent or mild lysis conditions. Although the Sortag-labeling still takes place in the presence of SDS at all enzyme concentrations tested, the reaction kinetics are more favorable at higher concentrations of SrtA. In contrast, SrtA concentration had little effect on reaction progress in the presence of milder NP40 lysis conditions (Figure 2 SI).

Altogether, the sortase remains active in the presence of crude cellular extracts or in the presence of detergents, indicating that the purification of recombinant proteins can be bypassed when fabricating the desired protein arrays.

Normalization and Validation of System for Bacterial Extracts. To further define the rules of the immobilization reaction on the solid support, the NA/C_2 fragment from our *Influenza* proteins library was used. Increasing concentrations of NA/C_2 protein (from 1.5 to 9 μM in crude extract) were incubated overnight with SrtA on the Gly_3 derivatized slide.

The Flag tag upstream of the LPETGG motif allowed us to detect conjugated NA/C_2. Following the immobilization procedure, the slide was probed with a FLAG antibody coupled to Alexa-647. This allows the conjugation efficiency to be measured, allows an estimation of the reproducibility of the system, and allows normalization of the data against the nonconjugated fraction. In the presence of increasing

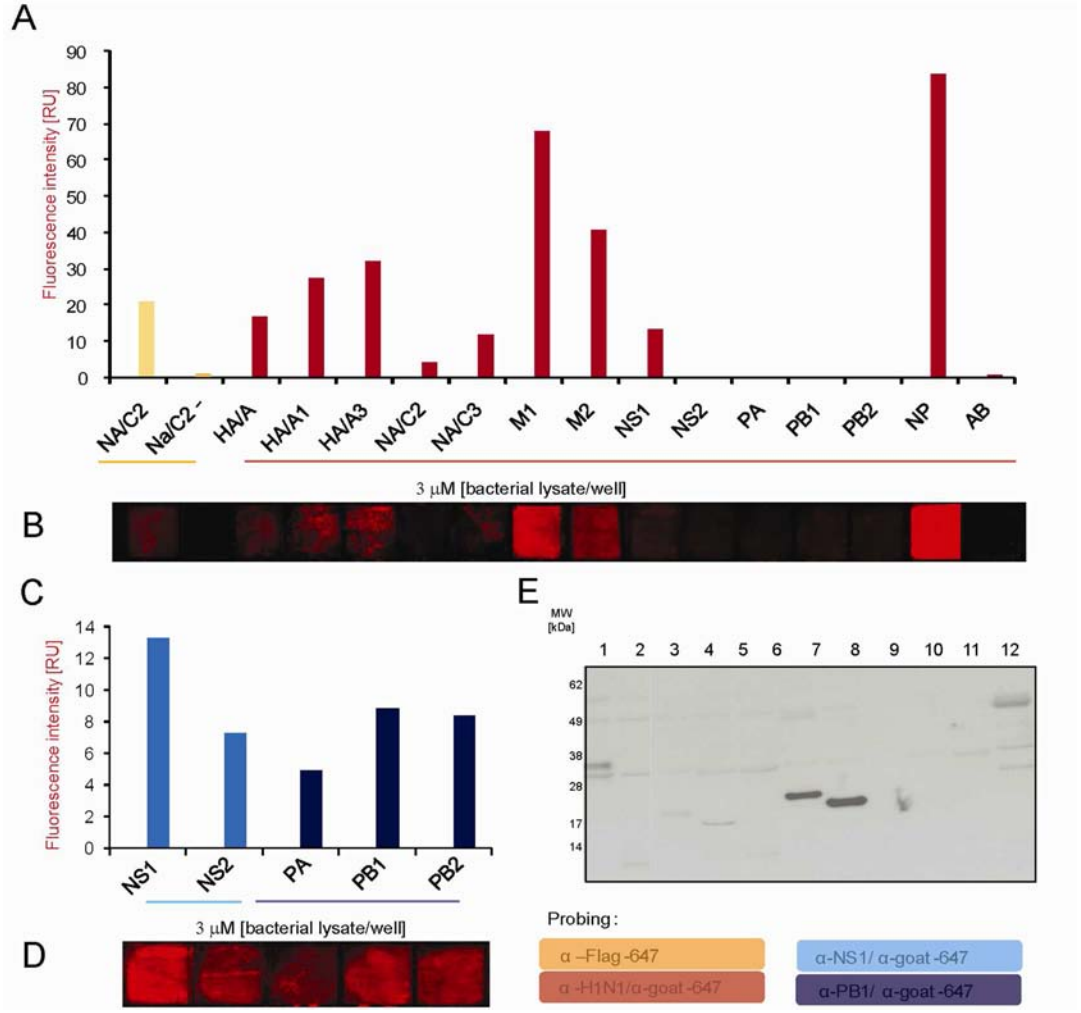

Figure 5. Probing an immobilized library of *Influenza* virus proteins. (A) 3 μM *Influenza* virus proteins in crude extract were incubated in the presence of 50 μM Sortase A and detected by H1N1 serum. Graphical representation of fluorescence intensity of the constructed protein array shows some interaction with H1N1 serum. The total extract from *E. coli* cells expressing NA/C_2 Flag-tag was printed on the array in the presence or absence of Sortase A, verifying that immobilization of the proteins and subsequent detection with specific antibodies was sortase-dependent. (B) Visualization of the detected immobilized proteins after fluorescence slide scanning. (C,D) Graphical representation of fluorescence intensity of constructed protein array shows some interaction with specific antibodies against NS and PB proteins. (E) SDS-Page analysis of bacterial lysates containing *Influenza virus* proteins from the library blotted against H1N1 antibodies (Lanes 1−12: HA chain A 38 kDa; NA/C_2 15 kDa; HA/A_1 7 kDa; HA/A_3 23 KDa; M1 28 kDa; M2 26 kDa; NS1 30 kDa; NS2 25 kDa; PA 78 kDa; PB1 85 kDa; PB283 kDa; NP 55 kDa).

concentrations of NA/C_2, the mean fluorescence intensity (FI) of the FLAG signal increased, while background staining remained relatively low (Figure 4A). A graphical representation of the FI attributable to immobilized NA/C_2 protein shows the activity of sortase during the reaction on the solid support (Figure 4A). In the absence of SrtA, the FI remained low, indicating that nonspecific binding of the substrate to the slide is minimal. Moreover, three independent experiments show similar FI, further demonstrating the reproducibility of the conjugation of NA/C_2 to the solid support (Figure 4B). We conclude that the sortase activity, either in solution or on the solid support, is not influenced by the presence of unpurified starting material (Figures 3 and 4), nor by the presence of SDS (Figure 2 SI).

Screening the *Influenza virus* Library. Given the good immobilization profile obtained with the NA/C_2 protein, we expanded the Sortag-ligation to include other flu proteins. To generate the protein array, proteins were manually spotted on the Gly_3 surface at a concentration of 3 μM in bacterial lysates. The array was incubated overnight with SrtA and then washed extensively to remove unbound material. Each well was probed with a commercial H1N1 antiserum and visualized by probing with an Alexa-647 coupled antigoat secondary antibody. NA/C_2 was additionally visualized by probing the well with anti-FLAG-647. After extensive washing, the array was scanned with a GenePrix microarray scanner. The fluorescence intensity of each protein on the slide was normalized for background FI. As expected, Flag staining only revealed immobilized NA/C_2 in the presence of sortase. In the absence of SrtA, no such staining was detected, indicating that immobilization is strictly dependent on the activity of SrtA (Figure 5A,B). The H1N1 antiserum recognizes most flu proteins immobilized on the array; however, NS2, PA, PB1, and PB2 were not detected. To verify that these proteins were successfully immobilized on the surface of the slide, we probed the slide with antibodies specific for NS1 and PB1. The FI obtained with these antibodies indicates that indeed these recombinant proteins were successfully conjugated to the glass slide (Figure 5C,D) but not detected

dx.doi.org/10.1021/bc200577u | *Bioconjugate Chem.* 2012, 23, 1119−1126

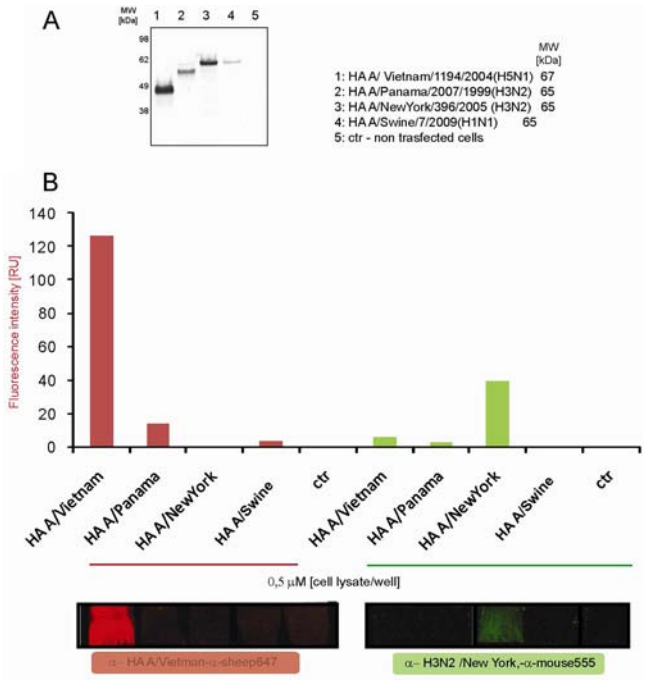

Figure 6. Probing an immobilized HA protein array produced in HEK293 T cells. (A) HA tag immunoblot showing the expression of HA full length in HEK 293 T cells. The higher MW of bands is correlated to post translational glycosylation processes. (B) 0.5 μM *Influenza* virus proteins in mammalian cell crude extract were incubated in the presence of 50 μM Sortase A and detected by Influenza anti-H3N2/New York or anti-A/Vietnam/1194/04 HA sera produced in mouse and sheep and subsequently recognized by anti-mouse Alexa 555 and anti-sheep Alexa 647, respectively. Fluorescence intensity of constructed protein array shows the interaction of HA sera with its specific antigen.

by the H1N1 serum. SDS-PAGE gel and immunoblotting of the same proteins confirms that only some of the overexpressed antigens were recognized by the H1N1 serum (Figure 5E), with a partial overlap with the results obtained with the glass slide (compare Figure 5A and E). In addition, using antibodies specific to PB1, we confirmed that PB1 is efficiently expressed (immunoblot analysis,Figure 3SI) and immobilized onto the slide (Figure 5C). A possible explanation for this result is that the proteins spotted on the array were solubilized using mild lysis conditions. In this experimental setting, a partial folding can be maintained by the protein, thus allowing the serum to recognize certain epitopes of the antigens. In contrast, sera will detect only linear epitopes in denatured proteins resolved by SDS-PAGE.

Screening HA *Influenza* Constructs Expressed in Eukaryotic Cell Shows Specific Interaction. Protein folding and post-translational modification of HA and NA may significantly affect their biological activity and immunogenicity. Therefore, we expressed four seasonal HA proteins in HEK 293 T cells: HA A/Vietnam/1194/2004 (H5N1), HA A/Panama/2007/1999 (H3N2), HA A/New York/396/2005 (H3N2), and HA A/California/7/2009 (H1N1). Each of these HA variants was equipped with an N-terminal ER signal peptide and a C-terminal LPETG motif, and their expression and post-translational modification were assessed in eukaryotic cells (Figure 6A). Glycanase, Sialidase A, and O-Glycanase sensitivity and distinct migration patterns on an acrylamide gel demonstrate that the exogenously expressed proteins have acquired their typical post-translational modifications (Figure 4 SI), suggesting that they also acquire the correct fold. Next, cell extracts solubilized under mild lysis conditions were incubated overnight on Gly3 derivatized glass slides in the presence of SrtA. A cellular extract not expressing any of the HA variants served as negative control. After incubation with SrtA, each well was probed with specific neutralizing antibodies raised against influenza anti-A/New York/HA or the anti-A/Vietnam/1194/04 HA[21] (Figure 6B). The FI of each protein was normalized for background FI. The specificity of the two different sera rigorously matched the HA protein that was spotted on the array. In addition, when the array was interrogated using an Influenza serum able to recognize different Flu strains, we were able to show that all the HA proteins were immobilized on the chip (Figure 5 SI). As the specific anti-HA antibodies used here have neutralizing activity against intact viral particles,[21] they are likely to be conformation-specific, suggesting that in our assay the immobilized proteins at least partially retained proper folding.

DISCUSSION

In summary, we have developed a general strategy to build protein arrays using the specificity of the sortase transpeptidase reaction to attach proteins of different molecular size, structure, and activity to a solid support. The immobilization method described here only requires the insertion of a small LPXTG motif at the C-terminus of the overexpressed protein, with minimal or no impact on the expression and folding of the substrate. The reaction takes place only in the presence of the enzyme SrtA and results in the exclusive conjugation of the selected substrate to the preactivated glass side, even in the presence of a complex cellular extract. As discussed above, proteins can be immobilized onto different kinds of solid supports by chemical reactions with aldehyde,[2] epoxide,[27] photocross-linking agents,[28] or amine groups, but with no control over the reaction. Alternatively, GST, His_6, or biotinylated tags are often used in order to obtain a uniformly oriented protein array. Although successfully used, these approaches require purification of the engineered substrates before conjugation to the solid support. Sortase has an excellent enzymatic activity under a wide range of experimental conditions, enabling substrate extraction, labeling, and covalent immobilization to occur simultaneously without intermittent purification steps. In addition, the specificity of the reaction allows anchoring of the recombinant protein to the solid support in a site-specific manner. In a previous study, the transpeptidase activity of SrtA was tested to link a purified model protein to a biacore chip.[24] Here, we show that different proteins can be successfully linked to a solid support, and we are now able to control critical parameters, i.e., concentration of Gly_3 and SrtA, which allow optimization of the reaction on the glass slide.

In a recent study, a proteome microarray expressing around 5000 candidate tumor antigens has been developed for the identification of novel autoantibody biomarkers in early detection of breast cancer. The following screening of sera has led to the identification of 28 biomarkers from patients with heterogeneous breast cancers.[29] Following this approach, an entire bacterial, viral, or eukaryotic genome can be randomly (or rationally) cut in order to generate fragments that can be expressed in the most suitable expression system and immobilized via sortase onto solid supports for subsequent screening.[23] To this end, we successfully expressed antigens

from *Influenza A* virus and selectively immobilized the recombinant proteins onto a glass slide. We confirmed that all expressed antigens are efficiently immobilized on the slide and that they are recognized by the respective serum. In this work, we used the small genome of *Influenza A* as a proof of concept to build a Sortag-protein array, and we envision that such a protein chip can easily become an efficient means for the early detection of seasonal flu. Additionally, it can be scaled up to proteins of larger genomes in order to develop a protein array for high-throughput screening.

■ ASSOCIATED CONTENT

Supporting Information

Experimental procedures describing the ELISA assay and deglycosylation reaction, tables of primers used in this study, and additional figures. This material is available free of charge via the Internet at http://pubs.acs.org.

■ AUTHOR INFORMATION

Corresponding Author

*E-mail: ploegh@wi.mit.edu.

Present Addresses

[§]Istituto Nazionale di Genetica Molecolare, Via F. Sforza 35, 20122 Milano, Italy.

[∥]University of Rochester School of Medicine and Dentistry 601 Elmwood AvenueRochester, NY 14642, USA.

[⊥]Ludwig Institute for Cancer Research, Nuffield Department of Clinical Medicine, University of Oxford, Old Road Campus Research Building, Headington, Oxford OX3 7DQ, UK.

Notes

The authors declare no competing financial interest.

■ ACKNOWLEDGMENTS

We thank Drs. Galli Grazia, Roberta Cozzi, Annemarthe van der Veen, Carlo Zambonelli, and Antonello Covacci for helpful discussion and critical review of the article. We are grateful to Barbara Capecchi for providing us with HA constructs and specific antibodies. We thank Thomas DiCesare for assistance with the original art work.

■ ABBREVIATIONS

BSA, Bovine Serum Albumin; DIPEA, *N,N*-Diisopropylethylamine; DMF, *N,N'*-Dimethylformamide; DSC, *N,N*-Disuccinimidyl carbonate; FMOC, 9-Fluorenylmethyloxycarbonyl; HOBT, 1-Hydroxybenzotriazole; NMP, *N*-Methyl-2-pyrrolidone; MFI, Mean fluorescence intensity; PyBOP, Benzotriazol-1-yl-oxytripyrrolidinophosphonium hexafluorophosphate

■ REFERENCES

(1) Zhu, H., and Snyder, M. (2003) Protein chip technology. *Curr. Opin. Chem. Biol. 7*, 55−63.

(2) Zhu, H., Bilgin, M., Bangham, R., Hall, D., Casamayor, A., Bertone, P., Lan, N., Jansen, R., Bidlingmaier, S., Houfek, T., Mitchell, T., Miller, P., Dean, R. A., Gerstein, M., and Snyder, M. (2001) Global analysis of protein activities using proteome chips. *Science 293*, 2101−5.

(3) Kindermann, M., George, N., Johnsson, N., and Johnsson, K. (2003) Covalent and selective immobilization of fusion proteins. *J. Am. Chem. Soc. 125*, 7810−1.

(4) Camarero, J. A., Kwon, Y., and Coleman, M. A. (2004) Chemoselective attachment of biologically active proteins to surfaces by expressed protein ligation and its application for "protein chip" fabrication. *J. Am. Chem. Soc. 126*, 14730−1.

(5) Ton-That, H., Mazmanian, S. K., Faull, K. F., and Schneewind, O. (2000) Anchoring of surface proteins to the cell wall of Staphylococcus aureus. Sortase catalyzed in vitro transpeptidation reaction using LPXTG peptide and NH(2)-Gly(3) substrates. *J. Biol. Chem. 275*, 9876−81.

(6) Ton-That, H., Liu, G., Mazmanian, S. K., Faull, K. F., and Schneewind, O. (1999) Purification and characterization of sortase, the transpeptidase that cleaves surface proteins of Staphylococcus aureus at the LPXTG motif. *Proc. Natl. Acad. Sci. U. S. A. 96*, 12424−9.

(7) Kruger, R. G., Otvos, B., Frankel, B. A., Bentley, M., Dostal, P., and McCafferty, D. G. (2004) Analysis of the substrate specificity of the Staphylococcus aureus sortase transpeptidase SrtA. *Biochemistry 43*, 1541−51.

(8) Wu, Z., Guo, X., Wang, Q., Swarts, B. M., and Guo, Z. (2010) Sortase A-catalyzed transpeptidation of glycosylphosphatidylinositol derivatives for chemoenzymatic synthesis of GPI-anchored proteins. *J. Am. Chem. Soc. 132*, 1567−71.

(9) Popp, M. W., Antos, J. M., and Ploegh, H. L. (2009) Site-specific protein labeling via sortase-mediated transpeptidation. In *Current Protocols in Protein Science*, Wiley Interscience: USA, Chapter 15.3.1-15.3.9.

(10) Popp, M. W., Antos, J. M., Grotenbreg, G. M., Spooner, E., and Ploegh, H. L. (2007) Sortagging: a versatile method for protein labeling. *Nat. Chem. Biol. 3*, 707−8.

(11) Antos, J. M., Popp, M. W., Ernst, R., Chew, G. L., Spooner, E., and Ploegh, H. L. (2009) A straight path to circular proteins. *J. Biol. Chem. 284*, 16028−36.

(12) Antos, J. M., Miller, G. M., Grotenbreg, G. M., and Ploegh, H. L. (2008) Lipid modification of proteins through sortase-catalyzed transpeptidation. *J. Am. Chem. Soc. 130*, 16338−43.

(13) Antos, J. M., Chew, G. L., Guimaraes, C. P., Yoder, N. C., Grotenbreg, G. M., Popp, M. W., and Ploegh, H. L. (2009) Site-specific N- and C-terminal labeling of a single polypeptide using sortases of different specificity. *J. Am. Chem. Soc. 131*, 10800−1.

(14) Hancock, K., Veguilla, V., Lu, X., Zhong, W., Butler, E. N., Sun, H., Liu, F., Dong, L., DeVos, J. R., Gargiullo, P. M., Brammer, T. L., Cox, N. J., Tumpey, T. M., and Katz, J. M. (2009) Cross-reactive antibody responses to the 2009 pandemic H1N1 influenza virus. *N. Engl. J. Med. 361*, 1945−52.

(15) Skehel, J. J., and Wiley, D. C. (2000) Receptor binding and membrane fusion in virus entry: the influenza hemagglutinin. *Annu. Rev. Biochem. 69*, 531−69.

(16) Ekiert, D. C., Bhabha, G., Elsliger, M. A., Friesen, R. H., Jongeneelen, M., Throsby, M., Goudsmit, J., and Wilson, I. A. (2009) Antibody recognition of a highly conserved influenza virus epitope. *Science 324*, 246−51.

(17) Bommakanti, G., Citron, M. P., Hepler, R. W., Callahan, C., Heidecker, G. J., Najar, T. A., Lu, X., Joyce, J. G., Shiver, J. W., Casimiro, D. R., ter Meulen, J., Liang, X., and Varadarajan, R. (2010) Design of an HA2-based Escherichia coli expressed influenza immunogen that protects mice from pathogenic challenge. *Proc. Natl. Acad. Sci. U. S. A. 107*, 13701−6.

(18) Lu, H., Khurana, S., Verma, N., Manischewitz, J., King, L., Beigel, J. H., and Golding, H. (2011) A rapid Flp-In system for expression of secreted H5N1 influenza hemagglutinin vaccine immunogen in mammalian cells. *PLoS One 6*, e17297.

(19) Lin, S. C., Huang, M. H., Tsou, P. C., Huang, L. M., Chong, P., and Wu, S. C. (2011) Recombinant trimeric HA protein immunogenicity of H5N1 avian influenza viruses and their combined use with inactivated or adenovirus vaccines. *PLoS One 6*, e20052.

(20) Audouy, S. A., van der Schaaf, G., Hinrichs, W. L., Frijlink, H. W., Wilschut, J., and Huckriede, A. (2011) Development of a dried influenza whole inactivated virus vaccine for pulmonary immunization. *Vaccine 29*, 4345−52.

(21) Alberini, I., Del Tordello, E., Fasolo, A., Temperton, N. J., Galli, G., Gentile, C., Montomoli, E., Hilbert, A. K., Banzhoff, A., Del Giudice, G., Donnelly, J. J., Rappuoli, R., and Capecchi, B. (2009) Pseudoparticle neutralization is a reliable assay to measure immunity

and cross-reactivity to H5N1 influenza viruses. *Vaccine 27*, 5998−6003.
(22) Studier, F. W. (2005) Protein production by auto-induction in high density shaking cultures. *Protein Expr. Purif. 41*, 207−34.
(23) MacBeath, G., and Schreiber, S. L. (2000) Printing proteins as microarrays for high-throughput function determination. *Science 289*, 1760−3.
(24) Clow, F., Fraser, J. D., and Proft, T. (2008) Immobilization of proteins to biacore sensor chips using Staphylococcus aureus sortase A. *Biotechnol. Lett. 30*, 1603−7.
(25) Chan, L., Cross, H. F., She, J. K., Cavalli, G., Martins, H. F., and Neylon, C. (2007) Covalent attachment of proteins to solid supports and surfaces via Sortase-mediated ligation. *PLoS One 2*, e1164.
(26) Wu, S., and Proft, T. (2010) The use of sortase-mediated ligation for the immobilisation of bacterial adhesins onto fluorescence-labelled microspheres: a novel approach to analyse bacterial adhesion to host cells. *Biotechnol. Lett. 32*, 1713−8.
(27) Zhu, H., Klemic, J. F., Chang, S., Bertone, P., Casamayor, A., Klemic, K. G., Smith, D., Gerstein, M., Reed, M. A., and Snyder, M. (2000) Analysis of yeast protein kinases using protein chips. *Nat. Genet. 26*, 283−9.
(28) Kanoh, N., Honda, K., Simizu, S., Muroi, M., and Osada, H. (2005) Photo-cross-linked small-molecule affinity matrix for facilitating forward and reverse chemical genetics. *Angew. Chem., Int. Ed. Engl. 44*, 3559−62.
(29) Anderson, K. S., Sibani, S., Wallstrom, G., Qiu, J., Mendoza, E. A., Raphael, J., Hainsworth, E., Montor, W. R., Wong, J., Park, J. G., Lokko, N., Logvinenko, T., Ramachandran, N., Godwin, A. K., Marks, J., Engstrom, P., and Labaer, J. (2011) Protein microarray signature of autoantibody biomarkers for the early detection of breast cancer. *J. Proteome Res. 10*, 85−96.

Bioconjugate Chemistry

Article

pubs.acs.org/bc

Binding and NMR Structural Studies on Indoloquinoline–Oligonucleotide Conjugates Targeting Duplex DNA

Andrea Eick, Fanny Riechert-Krause, and Klaus Weisz*

Institute of Biochemistry, Ernst-Moritz-Arndt University Greifswald, Felix-Hausdorff-Strasse 4, D-17487 Greifswald, Germany

Supporting Information

ABSTRACT: An 11-phenyl-indolo[3,2-*b*]quinoline (PIQ) was tethered through an aminoalkyl linker to the 5′-end of four pyrimidine oligonucleotides with T/C scrambled sequences at their two 5′-terminal positions. Binding to different double-helical DNA targets formed parallel triple helices with a PIQ-mediated stabilization that strongly depends on pH and the terminal base triad at the 5′-triplex–duplex junction. The most effective stabilization was observed with a TAT triplet at the 5′-junction under low pH conditions, pointing to a protonated ligand with a high triplex binding affinity and unfavorable charge repulsions in the case of a terminal C^+GC triplet at the junction. The latter preference of the PIQ ligand for TAT over CGC is alleviated yet still preserved at higher pH. Intercalation of PIQ at the 5′-triplex–duplex junction as suggested by the triplex melting experiments was confirmed by homonuclear and heteronuclear NMR structural studies on a specifically isotope-labeled triplex. The NMR analysis revealed two coexisting species that only differ by a 180° rotation of the indoloquinoline within the intercalation pocket. NOE-derived molecular models indicate extensive stacking interactions of the indoloquinoline moiety with the TAT base triplet and CG base pair at the junction and a phenyl substituent that is positioned in the major groove and oriented almost perpendicular to the plane of the indoloquinoline.

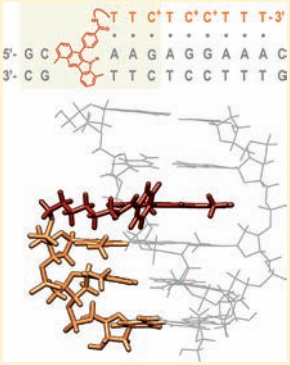

INTRODUCTION

The sequence-selective targeting of double-helical DNA bears enormous potential for various biotechnological applications, as well as in the area of DNA therapeutics and diagnostics.[1−3] For an effective recognition of longer stretches of DNA associated with a reliable readout of the corresponding base pair sequence, synthetic polyamides[4] as well as engineered zinc finger proteins[5] and single-stranded oligonucleotides[6] have been shown in the past to be the most promising tools when used under appropriate conditions. Thus, oligonucleotides can bind to double-helical DNA in its major groove based on a well-defined base–base recognition code to form triple-helical structures.[7] However, because formation of triple-stranded DNA is based on Hoogsteen hydrogen bond interactions between bases of the triplex-forming oligonucleotide (TFO) and available hydrogen bond donor and acceptor groups of purine bases in the double-helical DNA target, effective triplex formation is mostly limited to the presence of oligopyrimidine·oligopurine sequences. Also, in the pyrimidine-type triplex motif a pyrimidine third strand oriented parallel to the oligopurine strand of the cognate duplex forms isomorphous T·AT and C^+·GC base triplets through the formation of two Hoogsteen hydrogen bonds only after protonation of third strand cytosines, resulting in a considerable pH dependence of triplex stability and less stable triplexes under physiological pH conditions. On the other hand, many small cytotoxic and antitumor drugs bind to DNA through intercalation or groove binding with considerable affinity but often lack sufficient sequence discrimination due to their limited contact area with the duplex that hampers a readout of longer sequences. Consequently, clinical use of such drugs is compromised by their unspecific binding often associated with severe side effects.

Given the various limitations associated with the triplex methodology and with the duplex binding of low-molecular-weight ligands, a combination of both approaches is expected to provide for synergistic effects and for a more favorable recognition in terms of affinity and specificity. In fact, TFO conjugates have been employed in the past to improve the sequence-specific molecular recognition of duplex targets under physiological conditions.[8,9] Whereas triplex formation mostly benefits from additional stabilization through interactions of the covalently attached ligand with the duplex or triplex, a ligand employed for its chemical reactivity may considerably benefit from the high sequence specificity of the TFO. Thus, the TFO can be used as a delivery system that guides the agent to a particular target site to exert its cross-linking, strand-cleaving, or base-modifying effects.[10,11]

Several natural and synthetic members of indoloquinolines have been reported to exhibit a large spectrum of biological activities. We have recently shown that a synthetic 11-phenyl-substituted indolo[3,2-*b*]quinoline (PIQ) exhibits significant cytotoxic activity.[12] Interestingly, this polycyclic compound does not seem to bind duplex DNA with high affinity but is able to considerably stabilize triple-helical structures. The thermodynamics of triplex formation when binding a duplex target was recently determined for a corresponding indoloquinoline–TFO

Received: October 31, 2011
Revised: March 28, 2012
Published: May 2, 2012

conjugate with the PIQ drug covalently tethered to 5′-, 3′-, or internal positions of the oligonucleotide with different linkers.[13] However, details regarding the sequence selectivity of the drug, its favorable binding site and specific drug−DNA contacts are still vague, yet are a prerequisite for the further structural optimization of the ligand for future applications. Depending on its protonation at the quinoline ring nitrogen, the present PIQ drug may resemble some of the most efficient triplex binding compounds like benzo[*e*]pyrido[4,3-*b*]indoles (BePI)[14] or naphthylquinolines[15] in their sequence-selective binding. The ring chromophores of the latter ligands carry a positive charge at acidic or neutral pH and have been shown to prefer binding to TAT-rich over C^+GC-rich triplexes, pointing to charge repulsion between protonated third strand cytosines and the positively charged ligand. Unfortunately, even for the best characterized triplex binders there is a remarkable lack of experimental structural data that clearly define and pinpoint any specific binding interactions. To the best of our knowledge, there is no X-ray or NMR-derived structure of a triplex-bound ligand available. Rather, structural models reported for triplex-ligand complexes derive from indirect evidence, low-resolution spectroscopic methods, and computational methodologies.

In this report, we present studies on the pH dependence, on the sequence selectivity, and on structural details of duplex-targeting PIQ conjugates by UV, fluorescence, and NMR spectroscopy. The covalent attachment of the drug at the 5′-terminus of the TFO is expected not only to result in a more favorable free energy of binding, but also to promote well-defined binding interactions, amenable to a more detailed thermodynamic and structural analysis. In this respect, the PIQ drug may also serve as an excellent model for the study of triplex−drug interactions in general and of the factors governing their sequence and pH-dependent binding.

EXPERIMENTAL PROCEDURES

Materials. Unmodified oligonucleotides as well as oligonucleotides modified with 2-aminopurine, with isotope-labeled nucleosides and with 5′-C_6 amino linkers were synthesized employing the phosphoramidite method (TIB MOLBIOL, Berlin, Germany). All oligonucleotides carrying modifications were purified by HPLC. Uniformly ^{13}C (98%) and ^{15}N (98%) 2′-deoxyadenosine and thymidine phosphoramidites for the oligonucleotide synthesis were purchased from Cambridge Isotope Laboratories, Inc. (Andover, MA, USA). The NHS-functionalized indoloquinoline derivative 4,9-dimethyl-11-(4-succinimido-carboxyphenyl)-10*H*-indolo[3,2-*b*]quinoline[16] was used for the coupling reaction with the 5′-amino-modified oligonucleotides as previously described.[13] All conjugates were characterized by MALDI-TOF mass spectrometry (see Supporting Information).

The concentration of the oligonucleotides was calculated using molar extinction coefficients at 260 nm derived from a nearest-neighbor model.[17] For the TFO-PIQ conjugates, the molar extinction coefficient of the ligand ($\varepsilon_{260\ nm}$ = 26 818 L mol^{-1} cm^{-1}) was added to the calculated extinction coefficient of the oligonucleotide.

Mass Spectrometry. Mass spectral data were recorded on a Bruker Microflex Maldi-TOF with a linear detection method and negative ion mode using *Flexcontrol* and *Flexanalysis* software. The measurements were performed with 400 shots. The HPLC-purified conjugates and the matrix solution (saturated 3-hydroxypicolinic acid in water) were desalted via ammonium-activated cation exchange resin beads (Dowex 50 W × 8 100−200 mesh) and applied on a target plate. The main peak is equivalent to m/z M−1.

UV−vis Spectroscopy. All UV measurements were performed on a Cary 100 spectrophotometer equipped with a temperature control unit (Varian, Darmstadt, Germany). Melting curves were recorded with 1 data point/°C at 260 nm in a temperature interval from 1 to 90 °C. To prevent water condensation at temperatures below 25 °C on the 1-cm cuvettes, the sample chamber was constantly flushed with nitrogen gas. The lyophilized unmodified or conjugated TFO (1.7 μM) and target duplex (1.45 μM) were dissolved in cacodylate buffer pH 6.0 (0.1 M NaCl, 0.02 M cacodylate, 1 mM spermine) and annealed prior to each melting experiment by heating to 90 °C followed by slow cooling to room temperature. For pH-dependent melting experiments, the cacodylate buffer was adjusted with HCl or NaOH within a pH range 5.0 to 6.5. Measurements included one cooling (0.5 °C/min) followed by a heating period (0.5 °C/min). The melting temperature was determined by the maximum of the first derivative plot of the final heating curve after appropriate smoothing.

Fluorescence Measurements. Fluorescence data were acquired with a Jasco FP-6500 spectrofluorometer (Jasco, Tokyo, Japan) with an emission and excitation bandwidth of 5 nm, a response time of 1 s, and 1 data point/nm. Measurements were performed with single-strand concentrations from 1.45 μM up to 3 μM in cacodylate buffer (0.1 M NaCl, 0.02 M sodium cacodylate, 1 mM spermine) at pH values from 5.0 to 6.0. Fluorescence melting experiments were carried out within a temperature range from 20 to 90 °C, using an excitation wavelength of 350 nm to monitor changes in the PIQ fluorescence upon DNA melting. Denaturation temperatures were extracted from the first derivative of the sigmoidal curve obtained from the temperature-dependent fluorescence at 466 nm for the indoloquinoline emission. All data were blank and volume-corrected.

NMR Experiments. Samples for the NMR measurements were prepared by the stepwise addition of the TFO or TFO−PIQ conjugate to the target duplex up to a 1:1 molar ratio in an aqueous solution with 100 mM NaCl (TFO) or 84 mM NaCl (TFO−PIQ), 1 mM NaN_3, pH 5.0. One-dimensional ^1H NMR spectra acquired after each titration step confirmed the complete formation of triple-helical structures through the disappearance of resolved Watson−Crick imino protons of the duplex. Triplex concentrations of the final solutions varied between 0.42 and 0.76 mM. If necessary, the pH of the unbuffered solutions was readjusted after titrations or lyophilizations by the addition of HCl.

All NMR spectra were acquired on a Bruker Avance 600 MHz spectrometer equipped with an inverse $^1H/^{13}C/^{15}N/^{31}P$ quadruple resonance cryoprobehead and *z*-field gradients. Data were processed using *Topspin 2.1*. Proton chemical shifts were referenced relative to TSP by setting the H_2O or HDO signal in 90% H_2O/10% D_2O or 100% D_2O to δ_H = 4.95 ppm at 10 °C and δ_H = 4.84 ppm at 20 °C. For the one- and two-dimensional measurements in 90% H_2O/10% D_2O a Watergate with w5 element or the excitation sculpting sequence was employed for solvent suppression. NOESY experiments in 90% H_2O were performed at 283 K with several mixing times between 30 and 300 ms and a spectral width of 15 kHz. 2K × 800 data points with 32, 64, or 128 transients per t_1 increment and a recycle delay of 2 s were collected in t_2 and t_1. Prior to Fourier transformation data were zero-filled to give a 2K × 1K matrix

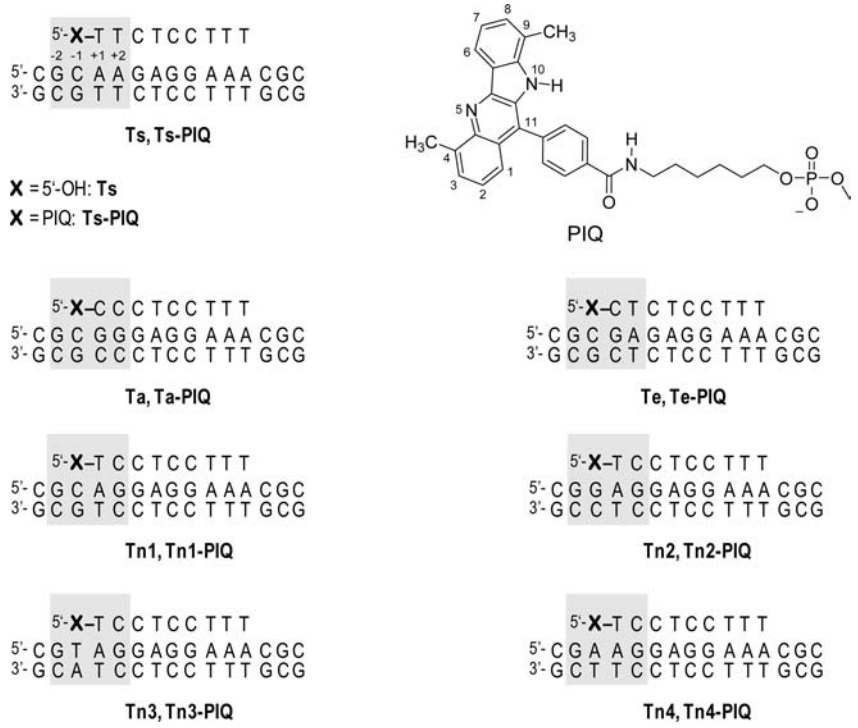

Figure 1. Sequences of triplexes with nonconjugated and PIQ-conjugated TFOs; positions −2, −1, +1, and +2 at the 5′-triplex−duplex junction are highlighted. The PIQ ligand is shown at the top (right) with atom numbering.

and both dimensions were apodized by squared sine bell window functions. 2D NOE experiments in D_2O were typically acquired with a spectral width of 6 kHz at 293 K with 32 transients per t_1 increment, mixing times of 100 and 200 ms and a recycle delay of 2 s. In total, 1024 t_1 increments with 4096 complex data points each were collected and finally zero-filled to give a matrix of 4K × 2K data points. The residual HDO signal was suppressed by presaturation during the recycle delay.

For DQF-COSY spectra in D_2O, 1024 t_1 increments with 2048 complex data points were acquired and zero-filled to give a final 4K × 2K data matrix. TOCSY experiments with a DIPSI2 isotropic mixing scheme and field strengths of 7.14 kHz (**T1s**) and 10.0 kHz (**T1s-PIQ**) were recorded with spin lock times of 80 ms. ROESY spectra were acquired with a spin-lock field applied for 60 ms at a field strength of 2.5 kHz. For off-resonance ROESY experiments in 90% H_2O, a spin-lock pulse of 4.16 kHz was applied 3.6 kHz off-resonance for 50 ms.

Phase-sensitive $^1H-^{15}N$ HSQC experiments on the DNA−drug complex in 90% H_2O were recorded with 256 increments and a spectral width of 7.3 kHz in the indirect ^{15}N dimension, 128 transients per t_1 increment, and a recycle delay of 1.5 s. Phase-sensitive $^1H-^{13}C$ HSQC experiments were acquired in D_2O with a sweep width of 25 kHz in the indirect ^{13}C dimension, 64 scans at each of 512 t_1 increments, and a relaxation delay of 1.5 s between scans. ^{15}N and ^{13}C chemical shifts were referenced relative to nitromethane and TMS by using the indirect referencing method.

Construction of Molecular Models. A fragment of the triplex conjugate that was studied by NMR spectroscopy and which consists of the two-base pair overhang, the first three base triads of the triplex stem and the covalently attached PIQ ligand was constructed starting with the published coordinates of a pyrimidine triplex with an intercalating non-natural base determined by NMR spectroscopic methods in solution (PBD ID 1WAN).[18] The intercalating nucleotide analogue and additional 5′-linked nucleotides of the third strand were removed, and the N5-protonated PIQ ligand was attached through the C_6 amino linker to the TFO at the intercalation site with the model builder of *Spartan'08* (Wave function Inc., Irvine, CA, USA). Also, to allow for the correct sequence, base triplets and base pairs were exchanged where necessary. Distortions and excessive strain in the resulting complex were initially removed by a simple energy minimization keeping hydrogen bonds of the Watson−Crick and Hoogsteen base pairs constrained.

The PIQ ligand was manually positioned within the intercalation site at the newly created triplex−duplex junction to give drug−DNA interproton distances for all observed NOE crosspeaks of <6 Å. Following a molecular mechanics geometry optimization with the MMFF94s force field without any restraints imposed on the structure, a final semiempirical optimization with the AM1 model in *Spartan'08* was employed for the intercalated ligand and the linker while keeping the oligonucleotide fixed.

RESULTS AND DISCUSSION

Sequence Selectivity of PIQ Triplex Stabilization. To evaluate any sequence selectivity in triplex binding for the TFO-bound indoloquinoline ligand, various third strand oligonucleotides and target duplexes were synthesized and employed in thermal melting experiments. Through its attachment to the TFO with a hexamethylene linker, PIQ interactions with the DNA are expected to not extend beyond the two base pairs and base triads flanking the 5′-triplex−duplex junction in the formed triplex construct between positions −2 and +2 (see Figure 1). Therefore, base substitutions were restricted to this short DNA tract. All TFOs, their target duplexes, and formed triplexes are summarized in Figure 1.

UV thermal melting experiments were performed in a buffer solution with 1 mM spermine[13] at pH 6.0 and analyzed in terms of the well separated triplex-to-duplex transition T_{m1} and the duplex-to-single strand transition T_{m2}. As expected, melting of the target duplexes at higher temperatures was not affected by the TFO-attached PIQ and corresponding melting temperatures T_{m2} in the absence or presence of the ligand were identical in all cases within the experimental uncertainty of <1 °C (not shown). As summarized in Table 1, **Ts** with two TAT base triads flanking the 5′-junction melts at 17 °C but is significantly stabilized by about 14 °C upon covalent attachment of the PIQ ligand in the triplex conjugate **Ts-PIQ**. Substituting the terminal TAT base triad for a CGC triad results in a slight stabilization of triplex **Te** under the present solution conditions. At the same time, a considerable decrease of the PIQ-mediated thermal stabilization in the corresponding triplex conjugate with a ΔT_{m1} of only 4 °C points to a significant loss of favorable ligand–DNA interactions at pH 6. The large impact of the 5′-terminal base triplet on the PIQ stabilization is also apparent in the melting data of triplex constructs **Ta** and **Tn1**. For **Ta**, three contiguous CGC base triads bordering the 5′-triplex–duplex junction impair its triplex thermal stability with a T_{m1} of only 9 °C. Most noticeably, however, a covalently attached PIQ ligand only yields a moderate thermal stabilization with a $\Delta T_{m1} \approx 7$ °C in **Ta-PIQ**. A similarly low triplex stability as observed for **Ta** is also found for **Tn1** with a 5′-terminal TAT followed by two adjacent CGC triplets. On the other hand, the corresponding conjugate considerably stabilizes the triplex by 14 °C comparable to **Ts-PIQ**. Apparently, in contrast to the base triad at position +2 the base triad at position +1 seems to have a significant impact on PIQ binding.

Table 1. Triplex-to-Duplex Melting Temperatures T_{m1} (°C) from Temperature-Dependent UV Experiments of Triplexes without and with TFO-Bound Indoloquinoline[a]

triplex	T_{m1} w/o PIQ	T_{m1} with PIQ	ΔT_{m1}[b]
Ts/Ts-PIQ	17.1 ± 0.7	31.5 ± 0.6	14.4 ± 0.9
Ta/Ta-PIQ	8.6 ± 0.5	15.7 ± 1.0	7.1 ± 1.1
Te/Te-PIQ	18.9 ± 1.2	23.0 ± 0.1	4.1 ± 1.2
Tn1/Tn1-PIQ	9.4 ± 0.1	24.1 ± 0.1	14.7 ± 0.1
Tn2/Tn2-PIQ	9.5 ± 0.4	23.6 ± 0.7	14.1 ± 0.8
Tn3/Tn3-PIQ	11.0 ± 0.4	25.9 ± 0.9	14.9 ± 0.9
Tn4/Tn4-PIQ	9.6 ± 0.4	24.5 ± 0.7	14.9 ± 0.8

[a]Measured in 20 mM sodium cacodylate, 100 mM NaCl, 1 mM spermine, pH 6.0; data are given as average values with standard deviations from three independent experiments. [b]ΔT_{m1} values refer to differences in T_{m1} between triplexes with and without covalently attached PIQ ligand; uncertainty calculated based on error propagation upon data subtraction.

In addition to sequence variations within the triplex stem, the first base pair flanking the 5′-junction was also subjected to base pair substitutions in triplexes **Tn2** to **Tn4** for assessing its potential influence on PIQ binding. Interestingly, although not directly involved in third strand binding a TA base pair at the junction seems to exert a positive influence on the TFO association with the target duplex as apparent from the small increase in the triplex melting temperature for **Tn3**. Otherwise, the substituted base pair at the junction does not result in a measurable change in the strength of the PIQ–DNA interaction, yielding an increase in T_{m1} for all **Tn-PIQ** triplex conjugates of 14–15 °C irrespective of the particular base pair located at position −1.

The results presented above can be attributed to the partial or full protonation of the indoloquinoline ligand as well as of third strand cytosines at pH 6. Clearly, positive charges through protonation of both a third strand cytosine within a CGC base triplet and of the ligand being in close contact will compromise favorable interactions through electrostatic repulsion. For the methyl-substituted PIQ ligand, an apparent pK_a of about 6.2 has previously been determined upon binding to an all-TAT triplex, suggesting a high degree of protonation at pH 6.[13] Likewise, cytosine bases in a triplex third strand are known to exhibit strongly increased pK_a values compared to the free base, depending upon their position within the triple-helical region.[19,20] Whereas cytosines in the central tract of a triplex have been found to exhibit pK_a values around 7, cytosines at the fraying triplex termini are less likely to be fully protonated at pH 6 but may nevertheless be partially charged. Also, the protonation of neighboring cytosine bases in the TFO is disfavored due to charge repulsion effects and further lowers their apparent pK_a.[20]

Accordingly, the sequence-dependent PIQ stabilization can be easily rationalized by a major interaction of the covalently attached ligand with the first base triad, leading to an unfavorable charge repulsion when a TAT triad is replaced by a partially protonated CGC base triplet. Likewise, there is no indication of a major interaction with the second triad (see **Ts** vs **Tn** triplex). Note that even more subtle differences in PIQ stabilization as observed between **Ta** and **Te** triplexes with 5′-CC and 5′-CT TFO sequences can be directly linked to the smaller extent of protonation for the 5′-cytosine in **Ta** having another cytosine neighboring base (see Table 1). Only involving uncharged bases, the Watson–Crick base pair at the junction has no noticeable effect on the PIQ triplex binding. It should be mentioned, however, that in addition to charge–charge repulsions variable stacking interactions through dispersion and dipole–dipole forces between an intercalated PIQ ligand and a CGC or TAT base triad cannot be excluded as other contributors to the observed sequence selectivity of the ligand–DNA interactions (vide infra). Anyway, invoking an intercalative mode of binding[16] the triplex–duplex junction seems to constitute the most probable intercalation site based on the present results.

To provide further evidence on a PIQ intercalation at the junction, triplex **Tn4** was additionally modified by replacing adenine in the purine-rich strand of the underlying duplex by the non-natural and fluorescent 2-aminopurine base (AP) at either position +1 or −1. Incorporated AP destabilizes triplexes formed by binding the nonconjugated TFO even if placed at the −1 position of the duplex overhang, but in particular when located at the +1 position within the first base triad. The considerable destabilization for the latter is expected based on the loss of a second Hoogsteen hydrogen bond between AP and the third strand thymine. However, triplex formation with the TFO–PIQ conjugate again results in a considerable triplex stabilization through the attached ligand. Most notably, when compared to unmodified **Tn4-PIQ** the PIQ-mediated triplex stabilization ΔT_{m1} even increases by 2 and 4 °C at pH 5 for triplex conjugates with AP located at the +1 and −1 positions, respectively (not shown). Thus, favorable direct contacts between the aminopurine base and PIQ likely contribute in addition to potential AP-induced conformational rearrangements to the enhanced stabilization. Because AP constitutes a

fluorophore with an emission spectrum partly overlapping the PIQ absorption, a fluorescence resonance energy transfer (FRET) in the AP-modified triple-helical conjugates from the AP donor to the PIQ acceptor may corroborate the suggested PIQ intercalation at the junction. In fact, a small but noticeable increase in the PIQ fluorescence quantum yield at excitation wavelengths in the absorption region of AP > 300 nm outside the absorption range of the natural DNA bases indicates a FRET process, albeit with low efficiency (see Supporting Information).

pH-Dependent PIQ Triplex Binding. If cytosine and ligand protonation are critical factors in the sequence-selective PIQ–triplex interactions, additional support is expected to come from pH-dependent triplex thermal stabilities without and with attached ligand. Corresponding measurements of the TFO dissociation temperature were performed with triplexes **Ts** and **Te** within the pH range 5 < pH < 6.5. Note that at higher pH T_{m1} values for nonconjugated triplex are too low to be measured accurately, whereas at strongly acidic pH, triplex-to-duplex and duplex-to-single strand transitions partially overlap, hampering the observation of a well-defined triplex denaturation process. To overcome the latter limitation, melting temperatures for the triplex conjugate at low pH values were also determined through PIQ fluorescence melting experiments, yielding a triplex denaturation temperature consistent with the results from the UV melting[16] but avoiding problems with any overlapping duplex dissociation.

Averaged triplex melting temperatures, each obtained from 2 to 3 independent experiments, are presented in Figure 2A together with associated standard deviations for the reference and PIQ-conjugated triplexes **Ts** and **Ts-PIQ**, as well as **Te** and **Te-PIQ**. Except for the lowest pH values, nonconjugated triplexes **Ts** and **Te** differing in their 5′-base triad exhibit closely similar thermal stabilities. Stabilization increases with decreasing pH as expected for a cytosine-rich third strand and the requirement for cytosine protonation to form two Hoogsteen hydrogen bonds with a CG base pair of the target duplex. In fact, the broad sigmoidal-like pH dependence must originate from the various superimposed protonation equilibria within the triplex. However, whereas T_{m1} of triplex **Ts** seems to approach a limiting value as a result of almost full cytosine protonation at low pH, triplex **Te** still exhibits a significant stabilization, pointing to only partial protonation of its terminal CGC base triad even at pH 5. With covalently attached ligand, triplex stabilization is increased for all pH values through additional PIQ–triplex interactions. Also, the smaller ligand stabilization in triplex **Te-PIQ** already discussed for pH 6 (vide supra) is preserved over the entire pH range.

The pH dependence of the thermal stability for the triplex conjugates must be attributed to (i) third strand cytosine protonation stabilizing the triplex, (ii) PIQ protonation, and (iii) potential charge–charge repulsion of protonated ligand and protonated cytosine in close vicinity. To separate general triplex-stabilizing effects through cytosine protonation and to better follow PIQ-associated contributions, ΔT_{m1} between conjugated and reference triplexes is plotted in Figure 2B as a function of pH. Protonated PIQ has been suggested to bind to triple helices with higher affinity.[13] Consequently, the PIQ-induced triplex thermal stabilization increases with decreasing pH and amplifies stabilizing effects through protonated cytosines at lower pH. Interestingly, however, ΔT_{m1} for the **Te** triplex passes a maximum and falls off again below pH 5.5. This is in contrast to the **Ts** construct where the course of

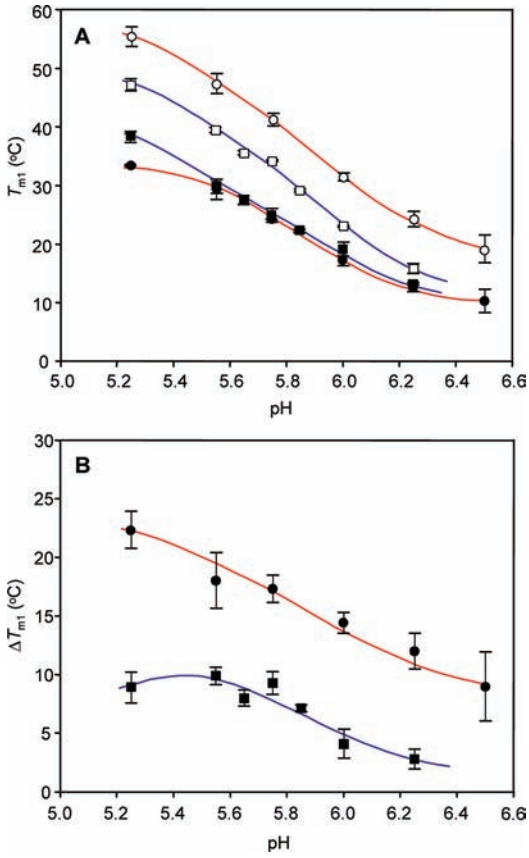

Figure 2. (A) Triplex melting temperatures T_{m1} for triplexes **Ts** (closed circles), **Te** (closed squares), **Ts-PIQ** (open circles), and **Te-PIQ** (open squares). (B) PIQ-mediated triplex stabilization ΔT_{m1} in triplexes **Ts-PIQ** (circles) and **Te-PIQ** (squares). Red and blue solid lines connecting the **Ts** and **Te** data only serve as visual guides.

increasing ΔT_{m1} seems to be attenuated but is still intact even at low pH. It should be mentioned that by accounting for error propagation during data subtraction relatively large uncertainties in ΔT_{m1} as indicated in Figure 2B have to be considered. Nonetheless, an unambiguous trend in the pH-dependent stabilization is clearly apparent and supports the idea that with progressively protonated ligand and 5′-terminal CGC triad unfavorable direct electrostatic interactions in triplex **Te-PIQ** severely compromise the stabilizing effects generally seen in low pH buffer. Accordingly, differences in the PIQ-mediated stabilization detected for **Ts-PIQ** and **Te-PIQ** diminish with increasing pH and an associated lower degree of cytosine and PIQ protonation. However, the data plotted in Figure 2B also suggest that the PIQ sequence discrimination in favor of an adjacent 5′-terminal TAT triad will not completely vanish even at higher pH with mostly unprotonated and thus uncharged ligand. Note that the thermal stability of the two unmodified triplexes **Ts** and **Te** are closely similar, excluding any additional influence of temperature-dependent binding equilibria on the different ΔT_{m1}. Apparently, other electronic and/or steric factors also contribute to the PIQ binding preference for neighboring TAT base triads. Interestingly, nearly all known triplex-specific intercalators including compounds with an uncharged polycyclic chromophore like anthraquinones are most effective in stabilizing TAT-rich sequences, albeit with a varying degree of sequence selectivity.[21]

dx.doi.org/10.1021/bc200582u | *Bioconjugate Chem.* 2012, 23, 1127–1137

NMR Structural Studies on the PIQ-Conjugated Triplex. For a spectral simplification in NMR structural studies, the unmodified **Ts** triplex and the **Ts-PIQ** hybrid triplex were shortened by one and two base pairs in the duplex overhang extending beyond the TFO 5′- and 3′-terminus, respectively. These new triple-helical constructs termed **T1s** and **T1s-PIQ** are shown in Figure 3 (top) together with their nucleotide numbering.

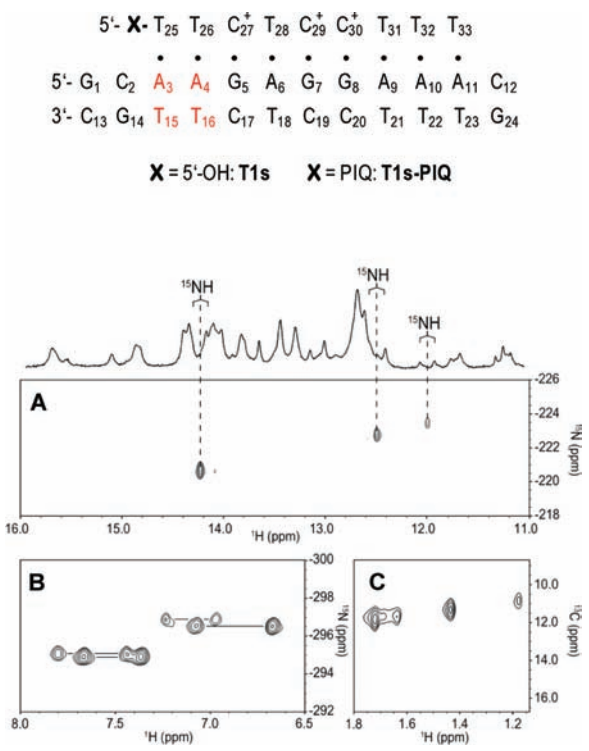

Figure 3. Top: Triplex constructs **T1s** and **T1s-PIQ** with numbering of nucleotides. Uniformly ^{15}N-, ^{13}C-labeled A and T incorporated in **T1s-PIQ** are colored red. Bottom: Imino (A) and amino (B) region of a ^{1}H−^{15}N HSQC spectrum and T methyl region of a ^{1}H−^{13}C HSQC spectrum (C) of the specifically ^{15}N-, ^{13}C-labeled complex **T1s-PIQ**; imino crosspeaks in (A) are correlated with the 1D imino proton spectral region (without ^{15}N decoupling); spectra were acquired in 90% H_2O/10% D_2O at 10 °C (A,B) or in 100% D_2O at 20 °C (C), 85 mM NaCl, 1 mM NaN_3, pH 5.0.

Having confirmed the formation of a stable triplex by UV melting experiments under the NMR solution conditions employed, protons of the unmodified triplex **T1s** were initially assigned based on 2D NOE and DQF-COSY spectra according to established procedures for triple-helical DNA.[22−24] Note that the pH for all NMR experiments was adjusted to 5.0 in order to stabilize the pyrimidine triplexes and to decrease imino proton exchange rates with the solvent. Continuous sequential imino−imino connectivities along the Hoogsteen and Watson−Crick base-paired strands enabled the straightforward assignment of the well-separated Hoogsteen and Watson−Crick imino resonances except for the 5′- and 3′-terminal Watson−Crick base pairs due to fraying effects (see Supporting Information). Confirmation of the imino assignments and additional assignments for other exchangeable and nonexchangeable protons are largely based on characteristic NOE contacts including (i) T·A·T intratriplet imino−imino contacts, (ii) intratriplet contacts of Hoogsteen hydrogen-bonded C^+ and T as well as Watson−Crick hydrogen-bonded T imino protons to purine H8 and AH2 protons, respectively, (iii) intra- and intertriplet imino-amino contacts, (iv) intrabase and sequential imino-TMe contacts, (v) interstrand contacts between purine H8 and H1′ of 3′-neighboring third strand pyrimidines, (vi) sequential C^+ amino-TMe contacts, and (vii) intranucleotide and sequential base-sugar proton contacts (see Supporting Information). Due to severe spectral overlap, no attempt was made to assign H2′, H2″, H4′, H5′, and H5″ protons. In general, relative crosspeak intensities observed in the region of crosspeaks between H6/H8−H2′/H2″, H6/H8−H3′, and H6/H8−H1′ suggest a regular B-type helical structure with bases in an anti conformation and with a sugar pucker mostly in the C2′-endo conformational range for all three strands. No major distortions are apparent as indicated by continuous base-H1′ and base-H3′ NOE connectivities along the entire length of the third strand (see Supporting Information). It should be noted that this also applies to the 5′-triplex−duplex junction despite the relatively short duplex overhang. Notwithstanding an interstrand NOE crosspeak from T_{25}H6 in the terminal base triad to C_2H5 and H6 protons located in the neighboring base pair of the duplex, noticeable aberrations in either intensity or line width for the observed intranucleotide and sequential base-sugar proton NOE contacts within the $C_2A_3{\cdot}T_{15}G_{14}$ dinucleotide are clearly absent. Apparently, the 5′-junction shows no significantly increased flexibility and only minor conformational perturbations.[25]

To facilitate the NMR analysis of triplexes with covalently attached PIQ ligand, uniformly ^{15}N-, ^{13}C-labeled A and T nucleotides were specifically incorporated at positions 3, 4, 15, and 16, constituting the first two base pairs targeted by the TFO and in close proximity to the tethered ligand (see Figure 3 top). Formation of the triple-helical conjugate **T1s-PIQ** was accomplished through the stepwise addition of the TFO−PIQ conjugate to the isotope-labeled target duplex up to a 1:1 molar ratio, accompanied by the disappearance of duplex-specific resonances in the imino proton spectral region.

Subsequent inspection of the imino signals for the triplex **T1s-PIQ** revealed the presence of more than one species in solution. This is easily noticeable when looking at the spectral region located above 14.7 ppm and expected to only include three downfield shifted C^+NH resonances of Hoogsteen-bound third strand cytosines (see, for example, 1D spectrum in Figure 3). Additional insight into the number of coexisting complexes comes from heteronuclear ^{1}H−^{15}N HSQC measurements in 90% H_2O/10% D_2O and ^{1}H−^{13}C HSQC experiments in 100% D_2O, taking advantage of the considerable spectral simplification of the ^{15}N, ^{13}C isotope-labeled sample. Although only two labeled thymidines and two adenosines are positioned within the underlying duplex, three resolved crosspeaks correlate ^{15}N-labeled T imino nitrogens resonating at around −222 ppm to their directly attached imino protons (Figure 3A). Also, crosspeak intensities vary, gradually decreasing from the most downfield shifted NH proton at 14.27 ppm to the rather strongly shielded T iminos resonating at 12.50 and 12.0 ppm. On the other hand, four pairs of crosspeaks each correlating adenine $^{15}NH_2$ amino nitrogens at around −296 ppm to their two directly attached amino protons are observed with intensity ratios estimated to be about 1:2:1:2 in the amino spectral region of the ^{1}H−^{15}N HSQC spectrum (Figure 3B). Likewise, the region of T methyl groups in a ^{1}H−^{13}C HSQC spectrum reveals four correlation signals with an intensity ratio of about 2:1:2:1 (from downfield to highfield ^{1}H, Figure 3C). Taken

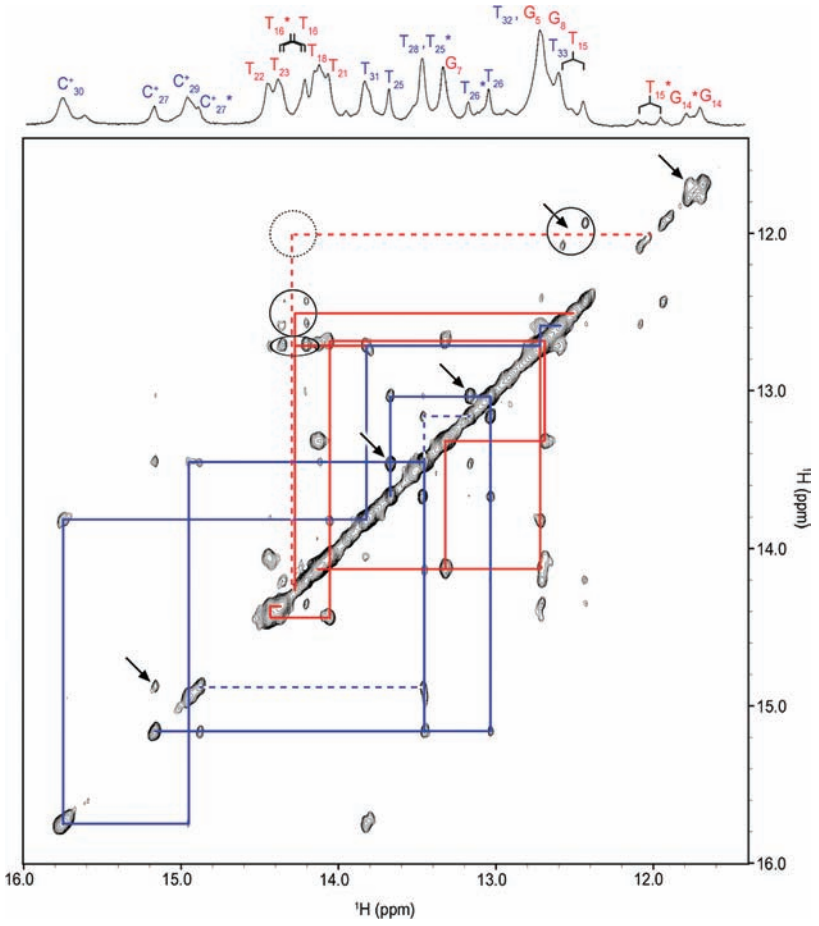

Figure 4. Portion of a NOESY spectrum (200 ms mixing time) of **T1s-PIQ** (0.42 mM) at 10 °C in 90% H_2O/10% D_2O, 84 mM NaCl, 1 mM NaN_3, pH 5.0. Sequential imino−imino crosspeaks connect Watson−Crick (red lines) and Hoogsteen hydrogen-bonded iminos (blue lines) in the major (continuous lines) and minor complex (broken lines). Circles enclose crosspeaks of the ^{15}N-labeled T_{15} and T_{16} imino resonances with their doublet structure due to $J_{NH} \sim 90$ Hz that collapses into a singlet in a corresponding ^{15}N decoupled spectrum (not shown). A T_{15}*-T_{16}* crosspeak only observable at a lower threshold level or in the ^{15}N decoupled spectrum is marked by a dotted circle. Arrows indicate chemical exchange crosspeaks. A corresponding nondecoupled 1D spectrum with imino resonance assignments is shown on top.

together, these observations suggest the coexistence of two complexes in solution, a major complex and a less populated minor complex. Two ^{1}H−^{15}N imino crosspeaks arising from a major and minor species must overlap in the corresponding HSQC spectrum in line with relative crosspeak intensities.

Imino resonances of ^{15}N-labeled thymines are convenient starting points for a sequential assignment of NH protons within the triplex. Excluding the rapidly exchanging iminos of the two fraying terminal base pairs, a continuous walk connects imino resonances along the Watson−Crick duplex from T_{15}·A_3 up to the T_{23}·A_{11} base pair (see Figure 4). However, even after careful examination no imino−imino contact was found between the T_{15}·A_3 Watson−Crick base pair of the triplex stem and the neighboring G_{14}·C_2 base pair of the duplex overhang at the 5′-triplex−duplex junction. Note that the strongly upfield shifted G_{14} imino proton could be clearly identified in the 1D proton spectrum and missing crosspeaks are therefore hardly related to a potential fast solvent exchange as is the case for unobservable iminos of terminal base pairs. The complete assignment of imino resonances in the Hoogsteen-bound third strand is based on nondisrupted sequential connectivities along the entire strand including the terminal bases. Additionally, intratriplet imino−imino crosspeaks are observed between T_{22}-T_{32}, T_{21}-T_{31}, and T_{18}-T_{28}, further corroborating the sequential assignment of the Hoogsteen and Watson−Crick iminos. Taken together, the crosspeak pattern of the imino protons supports the formation of a regular triple helix in the presence of the covalently attached PIQ.

Notably, imino protons of C^+_{27}, T_{26}, T_{25}, T_{15}, and G_{14} located in the vicinity of the 5′-triplex−duplex junction showed additional strong correlations with other remaining and yet unassigned imino resonances of lower intensity (see Figure 4). Acquiring off-resonance ROESY spectra, these crosspeaks could be unambiguously attributed to chemical exchange by their different sign when compared to a dipolar coupling mechanism (not shown). Obviously, two different species coexist in solution and slowly exchange on the NMR chemical shift time scale. Relative signal intensities between resolved pairs of exchanging imino protons in the 1D proton spectrum suggest a 2:1 population ratio of the two complexes at 10 °C, associated with a major and minor complex **T1s-PIQ** and **T1s-PIQ*** in full agreement with the ^{1}H−^{15}N and ^{1}H−^{13}C HSQC experiments (see Figure 3). Albeit weak, sequential imino−imino connectivities within the minor complex were also observed between the Watson−Crick base-paired T_{15}* and T_{16}* but not T_{15}* and G_{14}* imino protons. Also, NOE contacts along the third strand were found between T_{25}* and T_{26}*

dx.doi.org/10.1021/bc200582u | *Bioconjugate Chem.* 2012, 23, 1127−1137

iminos as well as between the C^{+}_{27}* imino and a proton resonating at the T_{28} imino proton chemical shift. Obviously, additional NOE connectivities within the minor complex more distant from the 5′-junction mostly coincide with the sequential walk of the major species due to small and therefore nonresolved chemical shift differences for the other imino protons, only resulting in some heterogeneous or homogeneous line-broadening effects.

Given the assignment of all imino resonances, other amino and nonlabile base protons were assigned for the triplex conjugate essentially through NOE contacts already outlined for the nonconjugated triplex **T1s**. However, given the severe signal overlap in some spectral regions of the complex with its two slowly exchanging species and due to the fact that we were primarily interested in structural details at the PIQ binding site, we did not attempt to do a more complete proton assignment. Rather, we focused on unambiguous assignments in the better defined spectral regions with the exclusion of deoxyribose protons (for a compiled list of proton chemical shifts in the nonconjugated and conjugated triplex, see the Supporting Information).

To map chemical shift changes upon ligand binding onto regions of the DNA triplex, a chemical shift footprint as given in Figure 5 was constructed based on the completely assigned

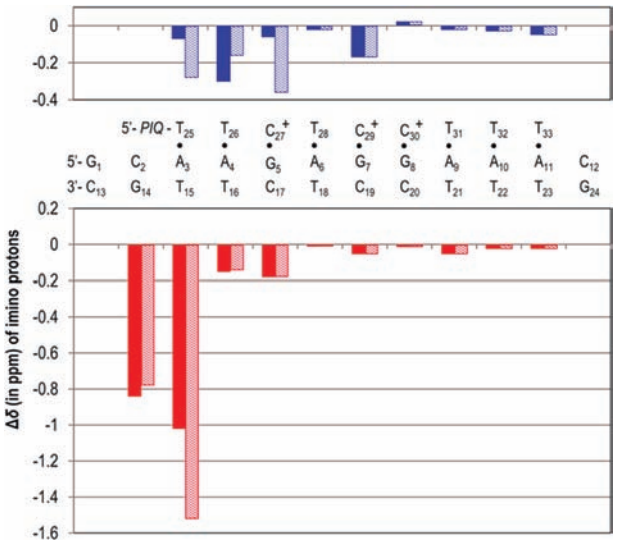

Figure 5. Chemical shift differences $\Delta\delta$ of Hoogsteen hydrogen-bonded (blue) and Watson–Crick hydrogen-bonded (red) imino resonances betweeen triplex **T1s** and the triplex conjugate **T1s-PIQ**; major and minor complex are indicated by filled and hatched bars, respectively.

imino protons. It shows the difference in chemical shifts between the free triplex **T1s** and the PIQ-conjugated triplex **T1s-PIQ** for both the major and minor complex. Clearly, noticeable upfield shifts upon PIQ binding are experienced by imino protons in the vicinity of the 5′-junction and vanish toward the 3′-junction as expected by their larger distance to the covalently bound ligand. However, for both complexes considerable upfield shifts between 0.8 and 1.5 ppm indicative of strong drug-induced shielding effects are restricted to the two Watson–Crick-bound imino protons in G_{14}·C_2 and T_{15}·A_3 directly located at the 5′-triplex–duplex junction. This pattern of chemical shift changes strongly suggests an intercalation of the polycyclic PIQ chromophore at the 5′-junction in full agreement with the disruption of NOE connectivities between base pairs G_{14}·C_2 and T_{15}·A_3 in both complexes (vide supra). Interestingly, the Hoogsteen-bound imino resonance in T_{25} was found to be considerably less perturbed in both conjugates, being upfield shifted by only 0.1–0.3 ppm upon ligand binding.

After the assignment of exchangeable DNA imino and amino resonances for the complex **T1s-PIQ** in H_2O, remaining exchangeable protons in the less crowded spectral region at around 9 and 10.5 ppm could easily be assigned to the amide NH of the PIQ linker moiety and to the PIQ indole NH10, showing NOE contacts to the adjacent α-methylene protons of the C6 linker between 3 and 4 ppm and to the indoloquinoline 9-methyl protons (vide infra), respectively. Both NH resonances also exhibit additional strong crosspeaks close to the diagonal (see Supporting Information). In line with two coexisting complexes, the latter are again identified as being due to chemical exchange between a major and minor species through ROESY experiments. Note that a single unassigned labile proton resonance observed at 11.21 ppm only showed a strong exchange crosspeak with water in the 2D NOE spectrum and may be attributed to NH^{+} of a protonated indoloquinoline.

Aromatic protons of the PIQ ligand were identified based on their scalar couplings as observed in DQF-COSY and TOCSY spectra. Moreover, initial 2D NOE spectra of the free TFO conjugate showed a characteristic pattern of NOE contacts between indoloquinoline protons of the two isolated spin systems, namely, 9Me–H8, H8–H7, and H7–H6 connectivities superimposed on a similar pattern involving 4Me, H3, H2, and H1 protons. These connectivities also enabled the unambiguous assignment of all indoloquinoline resonances in the major triple-helical complex (see Supporting Information). For the minor species, NOE and in particular chemical exchange crosspeaks clearly identified PIQ indole and amide NH as well as resonances of the two methyl substituents but failed to unambiguously identify the H1, H2, and H3 indoloquinoline spin system due to signal overlap and low signal intensity.

Indole as well as amide NH resonances showed additional NOE contacts to protons of the unfused phenyl ring. It should be mentioned, that the AA′XX′ spin system of the phenyl substituent in the free TFO conjugate changed upon duplex binding to give four chemically nonequivalent phenyl protons within the triplex environment. For a compilation of PIQ chemical shifts in the free TFO–PIQ and triple-helical **T1s–PIQ** conjugate, see the Supporting Information.

PIQ–Triplex Interactions. In both complexes, all indoloquinoline proton resonances exhibit an upfield shift with respect to the unbound TFO–PIQ conjugate, again pointing to stacking interactions with nucleobases through intercalation. To obtain a more detailed picture of the ligand binding in the two coexisting triplexes, drug–DNA contacts were identified in NOE spectra acquired with longer mixing times (Figure 6). We relied on the few but unambiguously assigned drug–DNA crosspeaks in the less crowded regions of the spectra to exclude any ambiguities that could possibly result in erroneous ligand–DNA distances within the formed triplex. As a result, only seven and three NOE contacts for the major and minor complex were used for a subsequent structural refinement of the intercalation site. These involve contacts to DNA imino and T methyl protons and are summarized in Table 2. For the major complex, NOE contacts between phenyl protons of the PIQ moiety and imino protons of T_{15}, T_{25}, and G_{14} unequivocally place the indoloquinoline at the 5′-triplex–

dx.doi.org/10.1021/bc200582u | *Bioconjugate Chem.* 2012, 23, 1127–1137

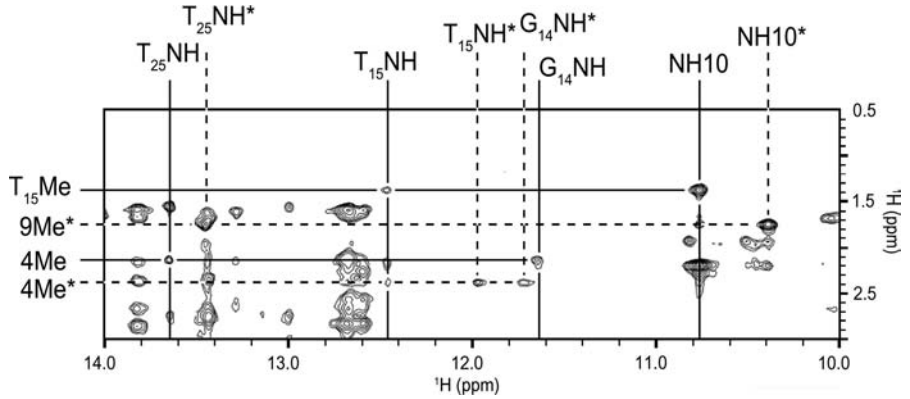

Figure 6. Portion of a ^{15}N-decoupled 2D NOE spectrum of triplex **T1s-PIQ** (0.76 mM) acquired at 10 °C with a mixing time of 200 ms in 90% H_2O/10% D_2O, 84 mM NaCl, 1 mM NaN_3, pH 5.0. Intermolecular PIQ–DNA connectivities are indicated by solid lines for the major complex and broken lines for the minor complex.

Table 2. NOE Contacts Observed Between DNA and PIQ Protons in T1s–PIQ for the Major and Minor Complexes

major complex		minor complex*
G_{14}NH – 4Me	T_{25}NH – 4Me	G_{14}NH* - 4Me*
G_{14}NH - phenyl-H	T_{25}NH - phenyl-H	T_{15}NH* - 4Me*
T_{15}NH - phenyl-H	T_{25}Me – amide-NH	T_{25}NH* - 9Me*
T_{15}Me – NH10		

duplex junction. Drug–DNA contacts for the minor species only include the well resolved 4Me and 9Me protons of the indoloquinoline at 2.41 and 1.80 ppm, respectively.

No attempt was made to quantify NOE intensities in terms of interproton distances because the isolated spin pair approximation is expected to be violated at the mixing times employed and NOE contacts involve exchangeable protons in all cases. Rather, all interproton distances were conservatively estimated to be within a range of 3.5 Å < d_{HH} < 5.5 Å. It should be stressed that in contrast to expectations the rigid indoloquinoline structure is sufficiently constrained by the evenly distributed NOE-derived distance limits to allow for a well-defined orientation with respect to the adjacent base triplet and base pair at the intercalation site even for the minor complex (see Supporting Information). Because major structural distortions for the base triad and Watson–Crick base pair bordering the intercalation site can be excluded based on the available NOE data, any more noticeable reorientations of the drug will ultimately result in a considerable increase of at least one of the critical interproton distances and thus in a severe violation of the experimental restraints. Also, although no NOE restraints were imposed for the final geometry optimizations of the manually docked intercalated ligand, the resulting complex geometries exhibit an excellent agreement with the experimental data with all NOE-associated DNA-ligand interproton distances being in the range 3.9 Å ≤ d_{HH} ≤ 5.3 Å.

Final NOE-based models of the PIQ intercalation site are shown in Figure 7. In both complexes, the ligand is intercalated at the 5′-triplex–duplex junction with the plane of the phenyl substituent almost perpendicular to the plane of the indoloquinoline ring system. As already indicated by a comparison of corresponding NOE data, the indoloquinoline is rotated by 180° when going from the major to the minor complex. A ring flip of the large tetracyclic indoloquinoline is hardly conceivable to take place within the intercalation pocket

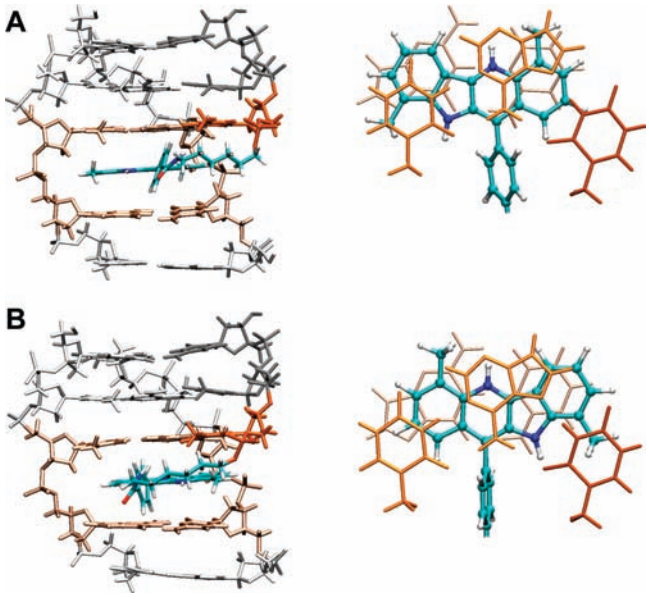

Figure 7. Molecular models for part of the (A) major and (B) minor triplex conjugate highlighting the PIQ intercalation site; view into the major groove (left) and top view of the intercalation site (right) showing (from top to bottom) the $T_{25}A_3T_{15}$ base triad, the intercalating PIQ ligand and the C_2G_{14} base pair. The TFO is distinguished from the target duplex by stronger colors.

as has previously been suggested for a naphthalimide intercalator[26,27] but is rather expected to involve dissociation, followed by a ring flip and reintercalation. In fact, exchange rates of <10 s^{-1} at 10 °C are derived from chemical shift differences of slowly exchanging protons. Whereas the detailed conformation of the linker moiety is not defined by experimental data, an NOE between the PIQ amide proton and T_{25} Me protons in the major complex demonstrate that the ligand penetrates the junction from the major groove. In line with the significant upfield shifts experienced by the imino proton of T_{15}·A_3 and G_{14}·C_2, the polycyclic indoloquinoline exhibits significant stacking interactions with the Watson–Crick base pairs. On the other hand, there is only poor stacking in both complexes with the Hoogsteen-bound T_{25} thymine in agreement with the imino proton chemical shift footprints (see Figure 5). Interestingly, in contrast to the major complex the PIQ 9Me protons in the minor complex were found to be

dx.doi.org/10.1021/bc200582u | Bioconjugate Chem. 2012, 23, 1127–1137

noticeably upfield shifted when compared to the other methyl group at the 4-position. This observation may be rationalized by the geometry of the minor species, pointing to a shielding effect of thymine T_{25} located above the PIQ 9-methyl substituent (Figure 7B).

According to simple molecular models, the C6 linker used in the present studies is expected to allow not only for the observed intercalation at the 5′-junction from the major groove, but also for an intercalation between the two terminal base triads, as well as base pairs of the duplex overhang bordering the 5′-junction. Previous studies on the PIQ ligand tethered within the central part of a TFO have suggested intercalative binding between base triads of the triplex stem,[13] indicating that the linker directs the ligand to the neighboring junction and constitutes the major determinant for the present binding site selectivity. However, favored binding at the triplex−duplex junction has also been found for several free intercalating molecules based on chemical footprinting experiments with diethylpyrocarbonate.[28] Thus, the observed preference for intercalation at the triplex−duplex junction may also be attributed to a more favorable balance of free energy contributions as a result of the energy gain by drug−DNA stacking interactions and the opposing energetic cost of base unstacking and helix unwinding to create an intercalation cavity.

CONCLUSION

Depending on pH, the PIQ ligand is able to significantly stabilize triplexes formed with a double-helical target when tethered to the TFO by a 5′-aminoalkyl linker. An intercalation of the ligand at the 5′-triplex−duplex junction is found to constitute the exclusive mode of interaction in such a conjugate, albeit with two different orientations of the indoloquinoline moiety within the intercalation pocket. The triplex binding affinity and sequence selectivity of the PIQ drug strongly depend on protonation equilibria involving the polycyclic indoloquinoline. Protonation of the drug at acidic pH strongly enhances its triplex affinity but also results in a strong preference for TAT triplets at the intercalation site. This is attributable to direct charge repulsions between the protonated ligand and a protonated third strand cytosine within a neighboring C^+GC base triplet, also discussed for other positively charged triplex-selective intercalators.[21] Thus, sequence selectivities are expected and also found to be alleviated with a less protonated drug. In fact, apparent pK_a values of the present indoloquinoline structure when bound to triplex DNA are within a pH range typical for in vitro and in vivo studies. This offers the option to furnish indoloquinolines with suitable substituents, tuning their basicity for pK_a values thought to be advantageous for a particular target and solution pH. A nonprotonated PIQ drug specifically substituted for a lower apparent pK_a will extend the range of potential target sequences to also include C^+GC at the intercalation site. However, even an uncharged ligand will likely discriminate between TAT and C^+GC base triplets, albeit with lower TAT selectivity. Also, the broader target recognition will inevitably compromise the strength of PIQ triplex binding. On the other hand, studies aimed at a high triplex binding affinity will benefit from a fully protonated PIQ with an increased pK_a value, expected to significantly stabilize triplexes even under physiological conditions.

ASSOCIATED CONTENT

Supporting Information

Molar extinction coefficients, synthesis yields and mass spectral data of the conjugates, details of fluorescence energy transfer experiments, 2D NOE spectra as well as proton resonance assignments for triplexes **T1s** and **T1s-PIQ**, molecular models of the PIQ intercalation site showing NOE-derived distance restraints. This material is available free of charge via the Internet at http://pubs.acs.org.

AUTHOR INFORMATION

Corresponding Author

*Tel: +49 (0)3834 864426. fax: +49 (0)3834 864427. E-mail address: weisz@uni-greifswald.de.

Notes

The authors declare no competing financial interest.

REFERENCES

(1) Biton, A., Ezra, A., Kasparkova, J., Brabec, V., and Yavin, E. (2010) DNA photocleavage by DNA and DNA-LNA amino acid-dye conjugates. *Bioconjugate Chem. 21*, 616−621.

(2) Ghosh, I., Stains, C. I., Ooi, A. T., and Segal, D. J. (2006) Direct detection of double-stranded DNA: molecular methods and applications for DNA diagnostics. *Mol. Biosyst. 2*, 1−11.

(3) Knauert, M. P., and Glazer, P. M. (2001) Triplex forming oligonucleotides: sequence-specific tools for gene targeting. *Hum. Mol. Genet. 10*, 2243−2251.

(4) Urbach, A. R., and Dervan, P. B. (2001) Toward rules for 1:1 polyamide:DNA recognition. *Proc. Natl. Acad. Sci. U.S.A. 98*, 4343−4348.

(5) Segal, D. J., and Barbas, C. F., III (2000) Design of novel sequence-specific DNA-binding proteins. *Curr. Opin. Chem. Biol. 4*, 34−39.

(6) Chan, P. P., and Glazer, P. M. (1997) Triplex DNA: fundamentals, advances, and potential applications for gene therapy. *J. Mol. Med. 75*, 267−282.

(7) Thuong, N. T., and Hélène, C. (1993) Sequence-specific recognition and modification of double-helical DNA by oligonucleotides. *Angew. Chem., Int. Ed. Engl. 32*, 666−690.

(8) Jain, A. K., Awasthi, S. K., and Tandon, V. (2006) Triple helix stabilization by covalently linked DNA-bisbenzimidazole conjugate synthesized by maleimide-thiol coupling chemistry. *Bioorg. Med. Chem. 14*, 6444−6452.

(9) Grimm, G. N., Boutorine, A. S., Lincoln, P., Nordén, B., and Hélène, C. (2002) Formation of DNA triple helices by an oligonucleotide conjugated to a fluorescent ruthenium complex. *ChemBioChem 3*, 324−331.

(10) Ziemba, A., Derosier, L. C., Methvin, R., Song, C.-Y., Clary, E., Kahn, W., Milesi, D., Gorn, V., Reed, M., and Ebbinghaus, S. (2001) Repair of triplex-directed DNA alkylation by nucleotide excision repair. *Nucleic Acids Res. 29*, 4257−4263.

(11) Liu, Y., Nairn, R. S., and Vasquez, K. M. (2008) Processing of triplex-directed psoralen DNA interstrand crosslinks by recombination mechanisms. *Nucleic Acids Res. 36*, 4680−4688.

(12) Riechert-Krause, F., Eick, A., Grünert, R., Bednarski, P. J., and Weisz, K. (2011) In vitro anticancer activity and evaluation of DNA duplex binding affinity of phenyl-substituted indoloquinolines. *Bioorg. Med. Chem. Lett. 21*, 2380−2383.

(13) Eick, A., Riechert-Krause, F., and Weisz, K. (2010) Spectroscopic and calorimetric studies on the triplex formation with oligonucleotide-ligand conjugates. *Bioconjugate Chem. 21*, 1105−1114.

(14) Mergny, J. L., Duval-Valentin, G., Nguyen, C. H., Perrouault, L., Faucon, B., Rougée, M., Montenay-Garestier, T., Bisagni, E., and Hélène, C. (1992) Triple helix-specific ligands. *Science 256*, 1681−1684.

(15) Wilson, W. D., Tanious, F. A., Mizan, S., Yao, S., Kiselyov, A. S., Zon, G., and Strekowski, L. (1993) DNA triple-helix specific intercalators as antigene enhancers: unfused aromatic cations. *Biochemistry 32*, 10614−10621.
(16) Eick, A., Xiao, Z., Langer, P., and Weisz, K. (2008) Spectroscopic studies on the formation and thermal stability of DNA triplexes with a benzoannulated δ-carboline-oligonucleotide conjugate. *Bioorg. Med. Chem. 16*, 9106−9112.
(17) Tataurov, A. V., You, Y., and Owczarzy, R. (2008) Predicting ultraviolet spectrum of single stranded and double stranded deoxyribonucleic acids. *Biophys. Chem. 133*, 66−70.
(18) Wang, E., Koshlap, K. M., Gillespie, P., Dervan, P. B., and Feigon, J. (1996) Solution structure of a pyrimidine·purine·pyrimidine triplex containing the sequence-specific intercalating non-natural base D_3. *J. Mol. Biol. 257*, 1052−1069.
(19) Leitner, D., Schröder, W., and Weisz, K. (1998) Direct monitoring of cytosine protonation in an intramolecular DNA triple helix. *J. Am. Chem. Soc. 120*, 7123−7124.
(20) Leitner, D., Schröder, W., and Weisz, K. (2000) Influence of sequence-dependent cytosine protonation and methylation on DNA triplex stability. *Biochemistry 39*, 5886−5892.
(21) Keppler, M. D., James, P. L., Neidle, S., Brown, T., and Fox, K. R. (2003) DNA sequence specificity of triplex-binding ligands. *Eur. J. Biochem. 270*, 4982−4992.
(22) Macaya, R., Wang, E., Schultze, P., Sklenář, V., and Feigon, J. (1992) Proton nuclear magnetic resonance assignments and structural characterization of an intramolecular DNA triplex. *J. Mol. Biol. 225*, 755−773.
(23) de los Santos, C., Rosen, M., and Patel, D. (1989) NMR studies of DNA $(R+)_n·(Y-)_n·(Y+)_n$ triple helices in solution: imino and amino proton markers of T·A·T and C·G·C^+ base-triple formation. *Biochemistry 28*, 7282−7289.
(24) Feigon, J., Koshlap, K. M., and Smith, F. W. (1995) ^{1}H NMR spectroscopy of DNA triplexes and quadruplexes. *Methods Enzymol. 261*, 225−255.
(25) Asensio, J. L., Dosanjh, H. S., Jenkins, T. C., and Lane, A. N. (1998) Thermodynamic, kinetic, and conformational properties of a parallel intermolecular DNA triplex containing 5′ and 3′ junctions. *Biochemistry 37*, 15188−15198.
(26) Gallego, J. (2004) Sequence-dependent nucleotide dynamics revealed by intercalated ring rotation in DNA-bisnaphthalimide complexes. *Nucleic Acids Res. 32*, 3607−3614.
(27) Rettig, M., Langel, W., Kamal, A., and Weisz, K. (2010) NMR structural studies on the covalent binding of a pyrrolobenzodiazepine-naphthalimide conjugate. *Org. Biomol. Chem. 8*, 3179−3187.
(28) Collier, D. A., Mergny, J.-L., Thuong, N. T., and Hélène, C. (1991) Site-specific intercalation at the triplex-duplex junction induces a conformational change which is detectable by hypersensitivity to diethylpyrocarbonate. *Nucleic Acids Res. 19*, 4219−4224.

Bioconjugate Chemistry

Article

pubs.acs.org/bc

Mannosylated Polyethyleneimine–Hyaluronan Nanohybrids for Targeted Gene Delivery to Macrophage-Like Cell Lines

Sunil Mahor,[#] Biraja C. Dash,[#] Stephen O'Connor, and Abhay Pandit*

Network of Excellence for Functional Biomaterials, National University of Ireland, IDA Business Park, Galway, Ireland

Supporting Information

ABSTRACT: Nonviral gene delivery systems have a number of limitations including low transfection efficiency, specificity, and cytotoxicity, especially when the target cells are macrophages. To address these issues, the hypothesis tested in this study was that mannose functionalized nanohybrids composed of synthetic and natural polymers will improve transfection efficiency, cell viability, and cell specificity in macrophages. Robust nanohybrids were designed from hyaluronic acid (HA) and branched polyethyleneimine (bPEI) using carbodiimide chemistry. The reaction product, i.e., branched polyethyleneimine-hyaluronic acid (bPEI-HA) copolymer was subsequently functionalized with mannose at the terminal end of the copolymer to obtain mannosylated-bPEI-HA (Man-bPEI-HA) copolymer. UV spectroscopy and gel retardation studies confirmed the formation of polyplexes at polymer to DNA weight ratio ≥2. Alamar Blue and MTT assay revealed that the cytotoxicity of the developed nanohybrids were significantly ($P < 0.05$) lower than that of unmodified bPEI. Mannose functionalization of these nanohybrids showed specificity for both murine and human macrophage-like cell lines RAW 264.7 and human acute monocytic leukemia cell line (THP1), respectively, with a significant level ($P < 0.05$) of expression of *gaussia* luciferase (GLuc) and green fluorescent reporter plasmids. Internalization studies indicate that a mannose mediated endocytic pathway is responsible for this higher transfection rate. These results suggest that hyaluronan-based mannosylated nanohybrids could be used as efficient carriers for targeted gene delivery to macrophages.

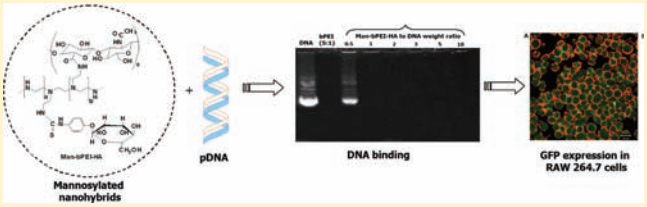

INTRODUCTION

In the past two decades, a number of new techniques have been investigated for the transfer of genetic materials into specific cells in order to achieve a therapeutic effect. One of the techniques involves the use of viral vectors because of their higher transfection efficiency; however, toxicity issues such as immunogenicity, inflammation, and oncogenic effects limit their potential clinical translation.[1,2] These limitations have led to the development of nonviral methods of gene transfer, e.g., lipid based and polymeric vectors.[3] Although the lipid based gene transfer methods have been used widely, there are limits in cargo carrying capacity and transfection efficiency. Therefore, the use of polymeric systems has been a focus of recent investigation. Specifically, polyethyleneimines (PEIs) have been extensively investigated for various gene transfer applications.[4,5] The transfection efficiency of PEIs can be attributed to the "proton sponge effect" allowing endosomal or lysosomal escape and transfer of DNA to the nucleus.[1−3] However, the inherent cytotoxicity of PEIs has limited their applications for in vivo gene delivery.[8−10] Furthermore, PEIs are also known to cause complement activation, coagulation of blood cells, and aggregation of serum proteins.[11] Several strategies have been investigated to overcome these limitations. One of the strategies has been to mask the strong cationic group by the use of maltose and dextran,[12] poly(ethylene glycol),[13] and hyaluronic acid.[14]

Hyaluronan or hyaluronic acid (HA) is a widely used biomaterial which is relatively unexplored as a delivery vehicle for gene transfer.[15,16] Hyaluronic acid is the only nonsulfated glycosaminoglycan (GAG) that is abundant in synovial fluid and extracellular matrix (ECM). Different molecular weights of HA have various physiological effects and molecular weight profiles in the range 10^3−10^7 Da have been studied for HA in numerous applications. Recently, hyaluronic acid was reported to mask cytotoxicity of PEI by covalent conjugation.[17]

For effective and successful gene delivery and expression in specific cell types, a selective targeting approach is often desirable.[18,19] To improve gene transfection efficiency and avoid nonspecific interaction between plasma proteins and the cell membrane, receptor-mediated endocytosis of the polymer/DNA complexes is required. Mannose receptors are abundantly expressed on antigen-presenting cells such as macrophages and dendritic cells.[20−22] The introduction of mannose to various nonviral gene delivery carriers such as polylysine,[23] polyethyleneimine,[4,24] cationic liposomes,[25] and chitosan[26] has shown an improved cellular uptake and transfection efficiency in macrophage cells.

The aim of this study was to synthesize mannose-functionalized nanohybrids based on branched PEI (bPEI)

Received: November 8, 2011
Revised: March 26, 2012
Published: May 2, 2012

Scheme 1. Schematic Representation of Synthesis of Man-bPEI-HA Nanohybrids

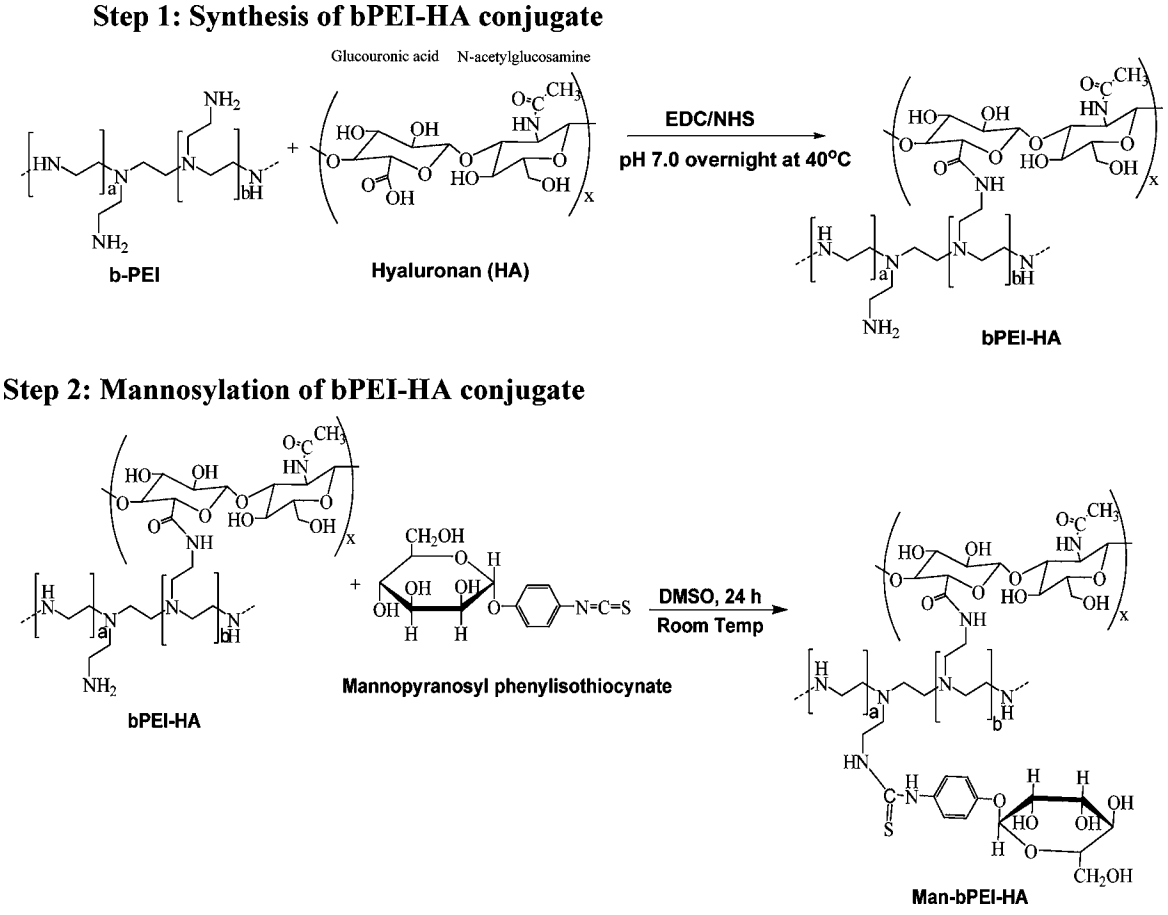

and HA with the goal of targeting macrophages. The first objective of this study was to reduce the toxicity of bPEI by coupling bPEI to hyaluronan to form a bPEI-HA copolymer using carbodiimide chemistry. The second objective was to modify bPEI-HA into Man-bPEI-HA nanohybrids by tethering mannose to terminal groups of bPEI-HA for increased transfection efficiency through receptor-mediated endocytosis in two different macrophage cells: RAW 264.7 and THP1 from murine and human source, respectively. These objectives were investigated by assessment of the physicochemical properties of Man-bPEI-HA/*p*DNA complexes by particle size measurement, zeta potential measurement, gel electrophoresis, UV spectroscopic analysis, and pDNA protection studies. The in vitro cytotoxicity, transfection efficiency, and internalization of the Man-bPEI-HA/*p*DNA complexes were also evaluated with respect to the selective use of these nanohybrids for both murine and human macrophages.

EXPERIMENTAL SECTION

Materials. Hyaluronan (M_w 750−1000 kDa) was purchased from CPN Ltd. (Czech Republic). D-Mannopyranosylphenyl isothiocyanate, branched PEI, 1-ethyl-3-(3-dimethylaminopropyl) carbodiimide) (EDC), and *N*-hydroxysuccinimide (NHS) and bovine serum albumin (BSA) were purchased from Sigma-Aldrich Ireland, and used without any purification. Deionized (DI) water was used throughout the studies unless otherwise stated.

Plasmid Propagation and Isolation. XL1-Blue (Stratagene USA) competent cells were transformed and selected twice in antibiotic containing LB broth and on LB agar plates. Plasmid amplification was carried out using a QIAGEN EndoFree Plasmid Giga Kit (QIAGEN, USA) following the manufacturer's instructions. Plasmid purity was confirmed by UV spectroscopy (NanoDrop ND1000 Spectrophotometer, Thermo Scientific) and gel electrophoresis. Also, in order to avoid recontamination of plasmid DNA after initial endotoxin removal, only new plasticware which is certified to be pyrogen- or endotoxin-free for storage was used. *Gaussia* princeps luciferase plasmid (pCMV-GLuc) was obtained from New England Biolabs UK and its expression was assayed with a kit from the same manufacturer. Plasmid DNA expressing green fluorescent protein (pCMV-GFP) was also amplified and propagated following the same protocol.

Preparation of Man-bPEI-HA Nanohybrids. Man-bPEI-HA conjugates were synthesized in a two-step reaction as shown in Scheme 1. In the first step, HA was conjugated with branched PEI using the method described previously with modifications.[27] Briefly, 25.0 mg of HA (5.0 mg/mL) was dissolved in 0.1 M phosphate buffer and the pH was adjusted to 7.0. *N*-Ethyl-*N*′-(3-dimethylaminopropyl)carbodiimide and NHS were added in a 20% molar excess based on the carboxyl group and the reaction mixture was stirred overnight at 40 °C. 125.0 mg of bPEI (10 mg/mL) was added to the reaction mixture under continuous stirring at 40 °C. The reaction was allowed to complete by incubation for another 12 h under the same conditions. The conjugates were purified by dialysis for 48 h using a dialysis membrane (MW cutoff 50 kDa Spectrapore) and washed four times with 0.1 M phosphate buffer. Finally, the

dx.doi.org/10.1021/bc200599k | *Bioconjugate Chem.* 2012, 23, 1138−1148

buffer was exchanged with distilled water (four washes). The bPEI-HA conjugates were collected and lyophilized (Virtis Advantage 2.0, UK).

In the second step, 100 mg of purified bPEI-HA conjugate obtained from the previous reaction was dissolved in 0.1 M carbonate buffer (pH 9.0). 2.5 mg of D-mannopyranosylphenyl isothiocyanate (15% molar excess) was dissolved in 1 mL of DMSO, and added to the reaction mixture and allowed to react for 24 h at room temperature to complete the reaction. Man-bPEI-HA conjugate was further purified by dialysis for 48 h using a dialysis membrane (MWCO 8 kDa Spectrapore) and washed four times with 0.1 M carbonate buffer (pH 9.0) and then with DI water (four washes). The bPEI-HA conjugates were then collected and lyophilized. FITC labeling was performed as described in a previous study.[28] Briefly, a weight ratio of 1:40 of FITC to bPEI-HA-Man was shaken at 4 °C overnight. The unbound FITC was removed by dialyzing in water for one day.

Fourier Transform Infrared (FTIR) Analysis of Man-bPEI-HA. Purified conjugate samples were prepared by the KBr pellet method and analyzed by FTIR spectroscopy using an FTIR AIM-8800 spectroscope (Shimadzu, Japan) (32 scans, resolution 4.0 and wavenumber range 4000−500 cm^{-1}).

^{1}H Nuclear Magnetic Resonance (^{1}H NMR) Assay. The Man-bPEI-HA nanohybrids were characterized using proton nuclear magnetic resonance (^{1}H NMR). ^{1}H NMR was carried out on a 400 MHz JEOL NMR with *DELTA* processing software. The chemical shifts were referenced to the lock D_2O.

Determination of Primary Amines in Man-bPEI-HA by Ninhydrin Assay. Unmodified bPEI, HA-bPEI, and Man-bPEI-HA were characterized for number of primary amine groups and estimated by ninhydrin assay.[29] The standard curve was prepared and plotted using polyamidoamine dendrimer G-4 (Sigma-Aldrich, UK) as a standard. Briefly, 100 μL of polymer solution (0.2 mg/mL) and a standard having different concentrations were added with 100 μL of sodium acetate buffer (pH 5.4) into 1.5 mL microcentrifuge tubes. 100 μL of freshly prepared ninhydrin reagent was added to each centrifuge tube, after which the tube was placed in a boiling water bath for 10 min and cooled to room temperature. After cooling, 300 μL of 50% v/v isopropyl alcohol in water was added to each tube. Finally, the absorbance of each solution was measured at 570 nm in triplicate against a reagent blank by a UV−vis spectrophotometer (VarioskanFlash-4.00.53).

Gel Retardation Studies of Man-bPEI-HA/*p*DNA Complexes. The binding ability of the Man-bPEI-HA with plasmid DNA was studied by agarose gel electrophoresis as described previously with slight modifications.[30] The Man-bPEI-HA/*p*DNA complexes containing luciferase plasmid were prepared with different polymer to DNA weight ratios ranging from 1:1 to 10:1 by keeping the plasmid DNA amount constant and varying the amount of Man-bPEI-HA. Thereafter, the complexes were loaded in individual wells of 0.8% (w/v) agarose gel in TAE buffer containing SYBR Safe stain (Invitrogen, USA). The samples were run at 100 V for 90 min, and the gel was then visualized on a UV transilluminator (G-Box, Syngene, UK).

Size and Zeta Potential of Man-bPEI-HA/*p*DNA Complexes. The particle size and surface charge of the Man-bPEI-HA/*p*DNA complexes were measured using a Malvern's zetasizer (Nano-ZS90, Malvern Instrument Ltd., UK). Man-bPEI-HA/*p*DNA complexes at different polymer to *p*DNA weight ratios from 0.5:1 to 10:1 were prepared in PBS (pH 7.4) following the same method as used in the previous section. The particle size measurement was performed with a He−Ne laser beam at 658 nm and a scattering angle of 90°. The particle size measurement was repeated for 3 runs for each sample, and the data were reported as the average of the effective mean diameters of 3 runs. The zeta potential measurement was repeated for 3 runs per sample, and the data were calculated automatically using the software from the electrophoretic mobility based on the Smoluchowski's formula. Before starting measurement, the complex solution was subjected to 10 times dilution with PBS (pH 7.4) to mimic the condition employed for in vitro transfection experiment.

Protection Studies of Man-bPEI-HA/*p*DNA Complexes against DNase I. For DNA digestion assay, the complexes were subjected to 2 μL of DNase I (2 IU to 1 μg of DNA) in DNase I buffer (400 mM Tris-HCl (pH 8.0), 100 mM $MgSO_4$, and 10 mM $CaCl_2$) for 30 min at 37 °C. The reaction was terminated with 4 μL of 0.5 M EDTA (pH 8.0) and then placed on ice for 10 min. The samples were divided in half before running in agarose gel electrophoresis. One-half of the samples were pretreated with a high concentration (10 mg/mL) of polyglutamic acid (PGA) for 30 min at 37 °C.[31] All samples were then subjected to 1% agarose gel electrophoresis stained with SYBR Safe in TAE buffer at 100 V for 60 min. DNA was visualized on a UV transilluminator (G-Box, Syngene, UK).

Cell Culture Experiments. Cellular metabolic activity (alamarBlue reduction, and MTT assay) and transfection activity (G-luciferase activity) of developed nanohybrids were studied using RAW 264.7 and THP1 cells. RAW 264.7 cells were cultured in Dulbecco's Modified Eagle's Medium (DMEM) supplemented with 10% fetal bovine serum (FBS) and 1% penicillin/streptomycin (P/S) at 37 °C in humidified 5% CO_2. THP1 nonadherent cells were cultured in RPMI-1640 supplemented with 10% FBS and 1% P/S and L-glutamine at 37 °C in humidified 5% CO_2. Culture of adherent macrophages from THP1 monocytes were achieved by using phorbolmyristate acetate (PMA) in a differentiation media.[32] Briefly, the THP1 cells, when they reached a density of 800 000−1 000 000 cells/mL, were cultured on tissue culture plates in a RPMI-1640 differentiation media containing 5 g/L glucose, 1% P/S, and L-glutamine and PMA at a final concentration of 100 ng/mL for 24 h.

MTT Assay. The effect of uncomplexed Man-bPEI-HA, bPEI-HA, and unmodified bPEI on RAW 264.7 and THP1 cells metabolic activity was evaluated by MTT test as described previously.[30−33] Briefly, RAW 264.7 and RAW cells were seeded in 96-well microtiter plates at a density of 1×10^4 cells/well. After 24 h, culture medium was replaced with complete medium (DMEM + 10%, FBS + 1% P/S for RAW 264.7 and RPMI-1640 + 10%, FBS + 1% P/S for THP1) with uncomplexed Man-bPEI-HA, bPEI-HA and unmodified bPEI and incubated for two different time points, i.e., 4 h and 24 h. Then, the medium was replaced with MTT solution in PBS and incubated for 2 h at 37 °C in humidified 5% CO_2. The unreacted dye was aspirated, formazan crystals were dissolved in 100 μL of DMSO, and absorbance was read at 570 nm with a background correction at 690 nm using a microplate reader (VarioskanFlash-4.00.53). Relative cell growth was related to untreated cells (control) and % cell viability was calculated by $[A_{(test)} \times 100]/A_{(control)}$. Similar protocol of MTT was followed to evaluate the metabolic activity of the complexed DNA of different polymer /*p*DNA weight ratio (0.1, 1, 2, 3, 5, and 10) on RAW 264.7 and THP1 macrophages. Also, the experimental

conditions were kept similar to those of in vitro transfection experiments mentioned below. They were kept in the incubator for 24 h before performing any experiments on them.

In Vitro Transfection Studies. All transfection studies were performed in triplicate. A total of 5×10^4 RAW 264.7 (specific for mannose receptor) and NIH3T3 (nonspecific for mannose receptor) cells per well were seeded on 48-well plates 24 h prior to transfection. The medium was replaced with the fresh medium (DMEM + 10% FBS + 1% P/S) immediately before transfection. Man-bPEI-HA/DNA complexes were prepared by adding the appropriate amount of Man-bPEI-HA or bPEI-HA in serum free DMEM to *p*DNA and incubated at room temperature for 30 min under mild agitation. The transfection complexes were appropriately diluted with serum-free DMEM. 50 μL of the complex solution was then added to each well and cells were incubated at 37 °C in 5% CO_2 atmosphere. After 4 h, the medium was replaced with fresh medium (DMEM + 10%, FBS + 1% P/S) and incubated for another 44 h. Cell supernatant was then collected and assayed for GLuc activity using a GLuc assay kit following the manufacturer's protocol. Results were then calculated and expressed as relative light units (RLU) normalized with untreated cells (negative control).

For competition studies, cells were treated with Man-bPEI-HA/*p*DNA complexes in the presence of mannosylated bovine serum albumin (Man-BSA) (a specific competitor for mannose receptors) and BSA (a nonspecific competitor).[23,34] Man-BSA was prepared using BSA and D-mannopyranosylphenyl isothiocyanate. Briefly, 100 mg BSA was dissolved in 0.1 M carbonate buffer (pH 9.0) and D-mannopyranosylphenyl isothiocyanate of 15% molar excess was dissolved in 1 mL of DMSO, and added to the reaction mixture and allowed to react overnight at room temperature to complete the reaction. Man-BSA conjugate was further purified by dialysis. Briefly, for these specific transfection studies a total of 5×10^4 RAW 264.7 and THP1 cells per well were seeded on 48-well plates 24 h prior to transfection. The medium was replaced with the aforesaid fresh medium immediately before pretreatment of Man-BSA and BSA. Both Man-BSA and BSA were used at a final concentration of 100 nmol and incubated for 30 min before the transfection studies.[35]Man-bPEI-HA/*p*DNA, bPEI-HA/*p*DNA, and bPEI/*p*DNA of different ratio (0.1, 1, 2, 3, 5, and 10) were used for these experiments and a similar protocol, as mentioned above, was followed for the quantification of the transfection efficiency.

*p*CMV-GFP reporter gene was used to investigate further the in vitro transfection efficiency of the nanohybrids. For these studies, a total of 1×10^5 RAW 264.7 and THP1 cells per well were seeded on 6-well plates 24 h prior to transfection. Then, the cells pretreated with Man-BSA and BSA were incubated with Man-bPEI-HA/*p*DNA complexes of ratio 2. The cells were mechanically harvested using cell scrapper and washed and resuspended in FACS buffer in order to analyze by FACS.

Fluorescence Microscopy Studies for Reporter Gene GFP Expression. RAW 264.7 and THP1 cells were seeded 24 h prior to transfection studies in a 35 mm MatTek's glass chamber tissue culture slide using 500 μL of complete medium and 10 000 cells/chamber, incubated at 37 °C, 5% CO_2. After 24 h of incubation, the medium was replaced with aforementioned fresh medium and incubated with Man-bPEI-HA/*p*DNA complexes at optimum polymer to *p*DNA weight ratio, i.e., 2. After 4 h, the medium was again replaced with fresh medium and cells were incubated for another 44 h at 37 °C, 5% CO_2. Cells were then washed with cold PBS solution and fixed with formaldehyde solution overnight at 4 °C. Cells were incubated with DAPI (Invitrogen, USA) for cell nucleus staining, mounted with Vectashield, and imaged with OLYMPUS fluorescence microscope.

Colocalization Studies. Man-bPEI-HA labeled with FITC was for the colocalization study. Man-bPEI-HA/*p*DNA at a ratio of 2 was prepared and incubated with both RAW 264.7 and THP1 cells for 6 h. The cells were pretreated with Man-BSA and BSA for the competitive study. The cells were washed after the required time of incubation in PBS. Lysotracker Blue was used as per manufacturer's instructions to stain the lysosomes in live cells. Cells were kept in the incubator for 2 h. The cells were fixed with 2% paraformaldehyde for 30 min, and this was followed by several washes with PBS. The cells were then observed under the fluorescence microscope (Olympus IX81). Lysotracker Blue staining was tinted as blue and the polyplex as green. The images were then merged to characterize the colocalization.

Statistical Analysis. One-way ANOVA was performed using *GraphPad Prism* v 5.1 to detect significant differences between various groups. Differences were considered significant for $p < 0.05$.

RESULTS

Synthesis and Characterization of Man-bPEI-HA Nanohybrids. The suitability of mannosylation in targeting of nanocarriers for macrophages has been explored in the present investigation. Man-bPEI-HA nanohybrids were successfully developed as target specific gene delivery carriers. As shown in Scheme 1, mannosylated nanohybrids of bPEI and HA were prepared by a two-step method. Because bPEI has been used in various gene delivery applications, it was coupled to HA by using water-soluble EDC to alleviate the cytotoxicity of bPEI in the form of bPEI-HA.[36] Man-bPEI-HA nanohybrids were prepared by thiourea reaction between the isothiocyanate group of mannopyranosylphenyl isothiocyanate and the amine groups of bPEI-HA with a lower degree of substitution for targeting both murine and human macrophages (RAW 264.7 and THP1) that have an overexpression of mannose receptors. To improve yields, reaction conditions were optimized for pH, reaction temperature, and time.

FTIR spectroscopy involves the measurement of the wavelength and intensity of absorption of infrared light through the excitation of molecular vibrations, which provides predictive information about representative functional groups and changes in the molecular structure of organic materials. The representative FTIR spectra of the various conjugates and intermediates were studied and are shown in Figure 1. Absorption peaks were observed in the region 3300−3350 cm^{-1} due to the N−H stretching in primary amines (Figure 1A). FTIR studies also revealed the characteristic peak in the region of 1600−1640 cm^{-1} due to the presence of C═O (carbonyl) groups in HA (Figure 1B). bPEI-HA copolymers showed characteristic peaks in the region of 3309 cm^{-1} and 1575.91 cm^{-1} due to N−H stretching and C═O stretching, respectively (Figure 1C). Upon mannosylation, characteristically strong peaks were observed in the region of 1146.35 cm^{-1} and 1550−1620 cm^{-1} due to C═S (thionyl) and C═C stretching, respectively (Figure 1D). The Man-bPEI-HA nanohybrids were characterized for conjugation using ^{1}H NMR (Figure 2). The ^{1}H NMR spectra of bPEI−HA as compared to that of HA and PEI has both a methyl peak of

dx.doi.org/10.1021/bc200599k | *Bioconjugate Chem.* 2012, 23, 1138−1148

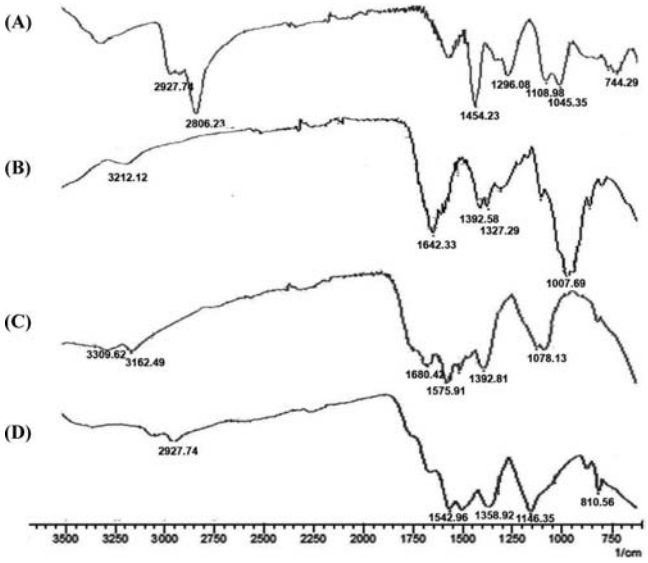

Figure 1. FTIR spectra of (A) branch-type polyethyleneimine (bPEI), (B) hyaluronic acid (HA), (C) bPEI-HA, and (D) Man-bPEI-HA.

acetoamide group of HA at 1.9 ppm and a bPEI peak at 2.5−3.2 ppm shifted from 2.5 ppm as reported in previous literatures (Figure 2A−C).[27] In the final step, the thiourea reaction between the isothiocyanate group of mannopyranosylphenyl isothiocyanate and the amine groups of bPEI-HA forms the nanohybrid Man-bPEI-HA. This is clearly evident in the ^{1}H NMR spectra of Man-bPEI-HA where three peaks corresponding to HA (1.9 ppm), PEI (2.5−3.2 ppm), and a relatively weak signal of mannose (7 ppm) can be seen as reported elsewhere (Figure 2D).[26] We hypothesize that the relatively weak signal of mannose at 7 ppm in ^{1}H NMR spectra can be attributed to the low proportion of mannose in the overall nanohybrid composition.

Determination of Primary Amines by Ninhydrin Assay. The ninhydrin assay was performed to quantify the number of primary amines in Man-bPEI-HA and bPEI-HA nanohybrids and compared with unmodified bPEI. The ninhydrin assay revealed that the unmodified bPEI possesses a higher number of primary amines than do bPEI-HA and Man-bPEI-HA nanohybrids and the conjugation of HA with bPEI reduced the number of primary amines in the conjugates (Figure 3). There was an almost comparable level of primary amines in Man-PEI-HA when compared with bPEI-HA. The degree of substitution for mannose residue in Man-HA-PEI was calculated and found to be nearly 8% of amines.

Gel Retardation Studies of Man-bPEI-HA/*p*DNA Complexes. Gel retardation studies of complexation of *p*DNA with Man-bPEI-HA conjugates revealed that polymers were able to bind with *p*DNA with an increase in polymer to *p*DNA ratio (Figure 4). At a low polymer to *p*DNA weight ratio such as 0.5:1, *p*DNA was observed in migrated lane (free *p*DNA) as well as in retarded form (complexed *p*DNA). At a polymer to *p*DNA weight ratio of 1:1 and higher, the *p*DNA was observed in the gel pocket, most probably due to the complexation of *p*DNA with polymers. *p*DNA retention in the gel pocket suggested that the migration ability of plasmid *p*DNA was retarded due to the polyplex formation.

Size and Zeta Potential Analysis of Man-bPEI-HA/*p*DNA Complexes. The hydrodynamic diameters of *p*DNA complexes of mannosylated and nonmannosylated bPEI-HA

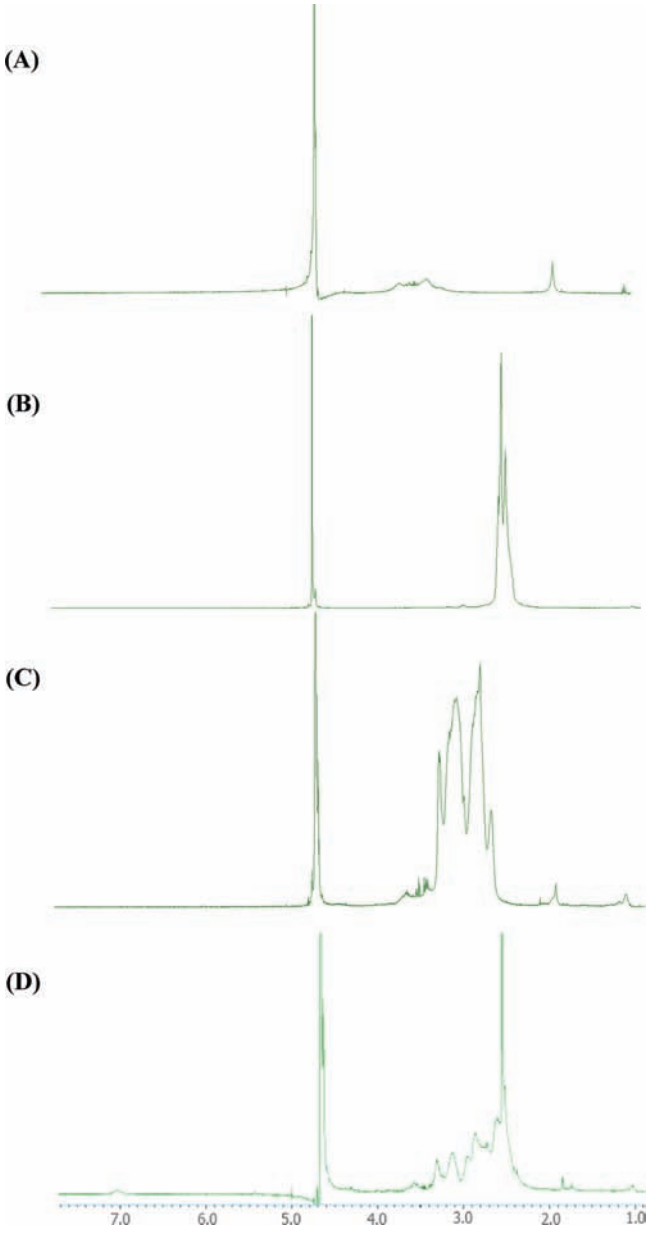

Figure 2. Representative ^{1}H NMR spectra of Man-bPEI-HA. ^{1}H NMR spectra of (A) HA, (B) bPEI, (C) bPEI-HA, conjugate and (D) Man-bPEI-HA nanohybrid.

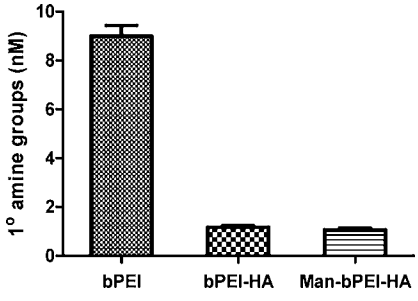

Figure 3. Physicochemical characteristics of Man-bPEI-HA conjugates. Quantification of primary amines by ninhydrin assay. Man-bPEI-HA, bPEI-HA, and unmodified bPEI were reacted with ninhydrin reagent and primary amino groups were estimated spectrophotometrically. Data are shown as mean ± SD (n = 3).

dx.doi.org/10.1021/bc200599k | *Bioconjugate Chem.* 2012, 23, 1138−1148

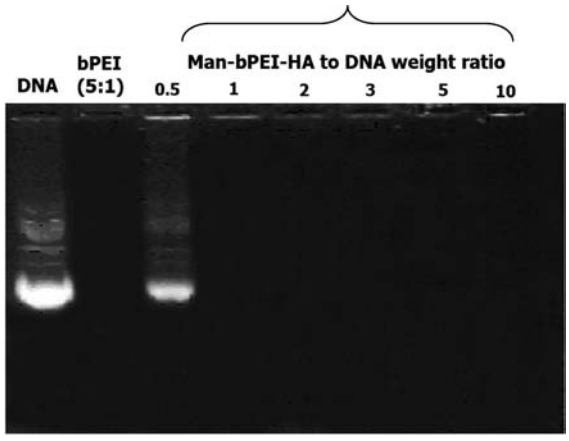

Figure 4. Polymer/*p*DNAcomplexation studies at different weight ratio of polymer to *p*DNA using agarose gel electrophoresis analysis.

nanohybrids were dependent upon weight ratio (Figure 5). Man-bPEI-HA/*p*DNA complexes were examined for size at

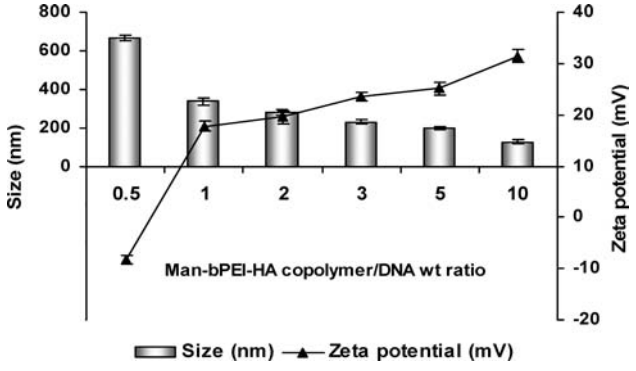

Figure 5. Size and zeta potential analysis of Man-bPEI-HA/*p*DNA complexes at polymer to *p*DNA weight ratio. (Data are shown as Mean ± SD, n = 3.)

different weight ratios ranging from 0.5 to 10. The higher polymer to *p*DNA weight ratios led to a decrease in complex size. A Man-bPEI-HA to *p*DNA weight ratio of 0.5 caused larger complexes (664.07 ± 13.32 nm) compared to a weight ratio of one (336.43 ± 18.79 nm). Furthermore, this increment of weight ratio indicates more condensation of polyplexes and further reduction in complexes size.

A linear relationship was observed between the zeta potential and Man-bPEI-HA to *p*DNA weight ratio (Figure 5). A Man-bPEI-HA to *p*DNA weight ratio of 0.5 showed negative zeta potential of −8.27 ± 0.85 because of incomplete *p*DNA condensation and complexes bearing more *p*DNA on their surface, and thereafter showed positive surface charge (17.77 ± 1.06, 19.5 ± 1.21, 23.53 ± 0.97, 25.1 ± 1.18, and 31.47 ± 1.09 for Man-bPEI-HA to *p*DNA weight ratios of 1, 2, 3, 5, and 10, respectively).

***p*DNA Protection Studies of Man-bPEI-HA/*p*DNA Complexes against DNase I.** The endonuclease activity of DNase I results in fragmentation of unprotected plasmid DNA. Plasmid DNA complexation with polymers is expected to protect plasmid DNA from enzymatic degradation. In this study, naked *p*DNA and Man-bPEI-HA/DNA complexes at different polymers to *p*DNA weight ratios were treated with DNase I and their protection ability was evaluated by agarose gel electrophoresis (Figure 6A). Naked *p*DNA was not seen in the lane because of complete degradation within 30 min of

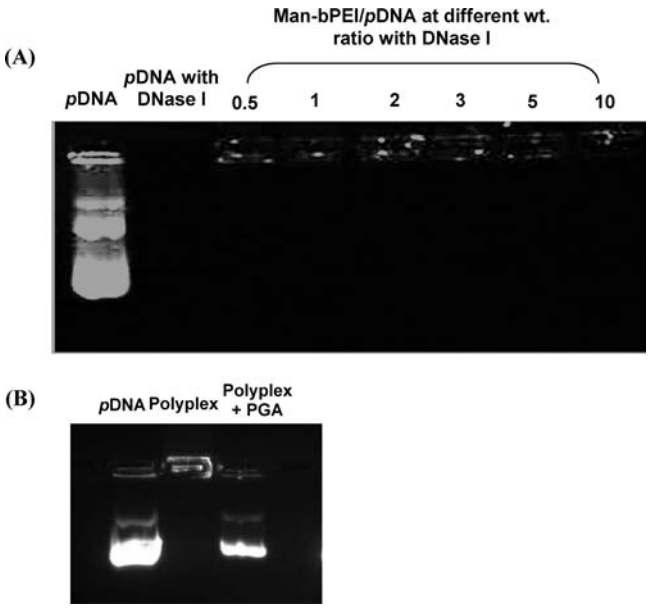

Figure 6. DNA protection studies against DNase I in DNase I buffer. Man-bPEI-HA/*p*DNA complexes were prepared at different weight ratio of polymer to *p*DNA and treated with DNase I and reaction were stopped by using 0.5 M EDTA. Samples (A) untreated with polyglutamic acid (PGA) and (B) treated with PGA (polymer/DNA ratio 2) were run on 1% agarose gel electrophoresis and visualized under UV transilluminator.

treatment of DNase I (lane 2), whereas complexed *p*DNA were detected in the gel pocket. These results illustrated that *p*DNA retention in the gel pockets, most likely due to the complexation of Man-bPEI-HA with *p*DNA, protected the *p*DNA from enzymatic degradation against DNase I. Further investigation of this was carried out by incubating these DNase I treated *p*DNA complexation with PGA (Figure 6B). The agarose gel electrophoresis in lane 1 showed migrated native *p*DNA (control), while the second lane is the polyplex (polymer/*p*DNA ratio 2) treated with DNase I and was found in the gel pocket as reported previously. The third lane is PGA treated sample which is found migrated in the gel as the native *p*DNA.

In Vitro Cell Viability Studies. Cell viabilities of Man-bPEI-HA conjugates were compared to bPEI-HA and unmodified bPEI using MTT assay. The MTT assay was employed to evaluate relative cell viability over a wide range of concentrations of uncomplexed polymers for incubation times of 4 and 24 h. MTT assay demonstrated that cellular viability was closely dependent on the HA conjugation (Figure 7A,B). Mannosylation of bPEI-HA did not affect the cell viability of RAW 264.7 cells, and nearly comparable cell viabilities were observed in all tested concentrations when compared with bPEI-HA. Unmodified bPEI caused a greater decrease in cell viability which dropped to nearly 5% or less at a concentration of 50 μg/mL. As expected, the cell viability of all conjugates and bPEI was reduced when the incubation time was increased from 4 to 24 h (Figure 7A,B). Similar trends in cell viability were obtained using MTT assay when THP1 cells were treated with Man-bPEI-HA, bPEI-HA, and unmodified bPEI (Supporting Information, Figure 3).

dx.doi.org/10.1021/bc200599k | *Bioconjugate Chem.* 2012, 23, 1138–1148

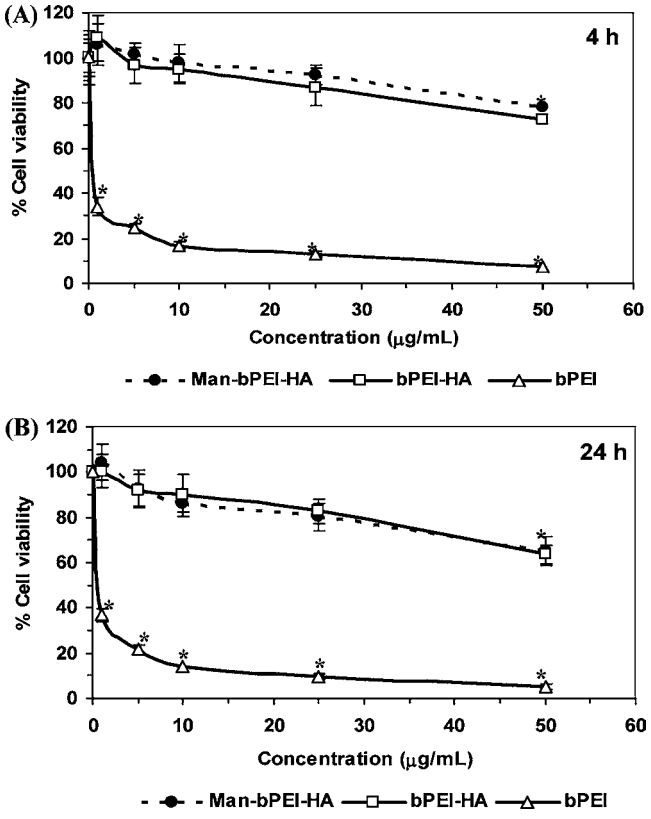

Figure 7. In vitro cell viability of RAW 264.7 cells using a MTT assay by incubating Man-bPEI-HA, bPEI-HA, and unmodified bPEI at different concentrations from 1 to 50 μg/mL for (A) 4 h and (B) 24 h. Data are shown as mean ± SD (n = 3) and considered significantly different if $^{*}P < 0.05$ and $^{**}P < 0.01$.

AlamarBlue assay was performed to evaluate the cellular metabolic activity caused by polyplexes under transfection conditions (4 h) and compared with uncomplexed polymers. Results from the alamarBlue assay revealed that Man-bPEI-HA/*p*DNA complexes showed greater cellular metabolic activity than polymers alone for 4 h of incubation with RAW 264.7 cells at the same concentration (Supporting Information, Figure 4). For polyplexes, alamarBlue reduction was between 23.75 ± 1.99% and 17.37 ± 2.61% and was comparable to control cells that were incubated in complete media (25.21 ± 1.99%).

Further, comprehensive evaluation of metabolic activity was performed using MTT assay in an in vitro transfection experimental setup. Man-bPEI-HA/*p*DNA, bPEI-HA/*p*DNA, and bPEI/*p*DNA of a different ratio (0.1, 1, 2, 5 and 10) were incubated with cells pretreated with Man-BSA and BSA alone. The Man-bPEI-HA/*p*DNA complexes have similar cell viability to those of the control (cell alone) except the ratios 5 and 10, both of which showed lower cell viability than that of cell alone and polymer/*p*DNA ratios 0.1, 1, 2, and 3 (Supporting Information, Figure 5A and B). There was no significant difference in cell viability between Man-bPEI-HA/*p*DNA and bPEI-HA/*p*DNA (Supporting Information, Figure 6A and B), whereas the bPEI/*p*DNA complexes showed lower cell viability than the control, as well as to other ratios of Man-bPEI-HA/*p*DNA and bPEI-HA/*p*DNA (Supporting Information, Figure 6A and B). This trend was found to be similar for both RAW 264.7 and THP1 cells. It can also be seen that pretreatment of cells with Man-BSA and BSA did not cause any adverse effects to cell viability.

Transfection Studies. Transfection studies were performed on RAW 264.7 murine macrophage cells expressing high levels of mannose receptors and on NIH-3T3 mouse fibroblasts lacking this receptor. The transfection efficiency was dependent on cell line and polymer to *p*DNA weight ratios (Supporting Information, Figure 7A). For RAW 264.7 cells, Man-bPEI-HA showed an increased transfection of luciferase reporter gene compared to unmodified bPEI and bPEI-HA for each weight ratio. At weight ratio 2, Man-bPEI-HA showed significantly higher ($P < 0.01$) reporter gene expression compared to *p*DNA alone, bPEI-HA, and unmodified bPEI, while differences between the bPEI-HA and bPEI were not significant. Luciferase levels of expression were increased with increasing weight ratio of Man-bPEI-HA and bPEI-HA conjugates to *p*DNA, and reached the maximum at a weight ratio of 2. Thereafter, increasing the weight ratio clearly decreased the level of expression of luciferase reporter gene, although the difference was not significant.

The target specificity of mannosylated nanohybrids was evaluated in the nonspecific cell types, i.e., NIH3T3 mouse fibroblast cells which lack in mannose receptors. Compared to unmodified bPEI, the transfection efficiency of Man-bPEI-HA polyplexes in NIH-3T3 mouse fibroblasts was decreased for all weight ratios tested. Polyplexes with Man-bPEI-HA, bPEI-HA, and unmodified bPEI were investigated at polymer to DNA weight ratios ranging from 0.5 to 10 (Supporting Information, Figure 7B). At lower weight ratios (≤2), luciferase expression mediated by Man-bPEI-HA conjugates was lower with unmodified bPEI in NIH3T3 cells. At higher weight ratios (≥2), the luciferase expression was not significantly different for all the conjugates when compared with unmodified bPEI. However, it was observed that the higher the polymer to *p*DNA weight ratio, the greater the reduction in luciferase reporter gene expression. When the transfection results in RAW 264.7 and NIH-3T3 for Man-bPEI-HA at weight ratio 2 were compared, no significant differences in transfection level were observed.

The competition studies with cells pretreated with Man-BSA showed a significant reduction (~2 times) in the GLuc expression level of Man-bPEI-HA/*p*CMV-GLuc compared to that of cells pretreated with BSA alone in the case of both RAW 264.7 and THP1 cells (Figure 8A,B). Also, the cells pretreated with BSA alone showed an almost a similar level of expression to that of untreated cells, as previously shown in the case of RAW 264.7 cells. On the other hand, bPEI-HA/*p*CMV-GLuc and bPEI /*p*CMV-GLuc showed no significant difference in the GLuc expression level in between Man-BSA and BSA in the case of both cell types (Supporting Information, Figure 8A and B).

The competitive assay was further carried out using *p*CMV-GFP as a reporter gene and taking Man-bPEI-HA/*p*CMV-GLuc of ratio 2 for this specific study. The FACS analysis showed a reduction (2.5 times) in percentage of cells expressing GFP in the case of cells treated with Man-BSA than that of BSA treated cells. A similar trend was found in both RAW 264.7 and THP1 cells (Figure 9). Imaging of cellular expression of GFP was performed using confocal microscopy (Supporting Information, Figures 9 and 10). The results revealed that the Man-bPEI-HA complex was able to mediate transfection of RAW 264.7 and THP1 cells and more intense green colored cells were observed. The green fluorescence was

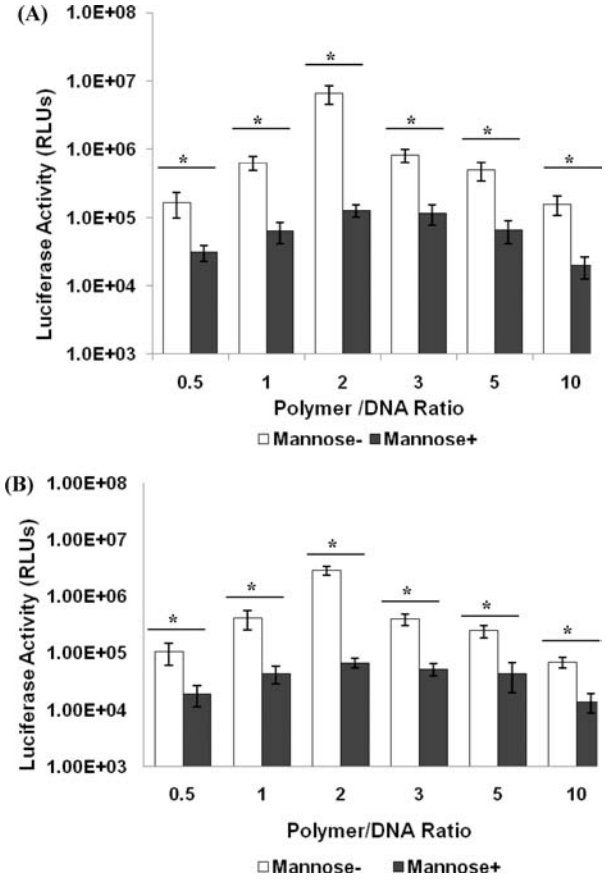

Figure 8. In vitro *gaussia* luciferase gene expression in (A) RAW 264.7 and (B) THP1 cells using reporter plasmid pCMV-GLuc. Cells were pretreated with Man-BSA (a specific competitor) and BSA (a nonspecific competitor) for 30 min followed by incubation with Man-bPEI-HA complexes at different weight ratios, and after 48 h, supernatant was collected and assayed for reporter luciferase activity. Data are shown as mean ± SD (n = 3) and considered significant if *P < 0.05.

seen to be distributed homogenously throughout the cells (Supporting Information, Figures 9 and 10).

Fluorescence Colocalization Studies. The Man-bPEI-HA/*p*DNA complexes can be observed inside RAW 264.7 and THP1 cells (Figure 10A,B). The merged images of polyplex stained with FITC and lysosomes stained with Lysotracker Blue showed colocalization of the polyplexes inside lysosomes in both cells. Man-BSA treated cells showed less fluorescence intensity of FITC labeled polyplexes than that of BSA treated cells. The internalization pattern was found to be similar in both the cell types.

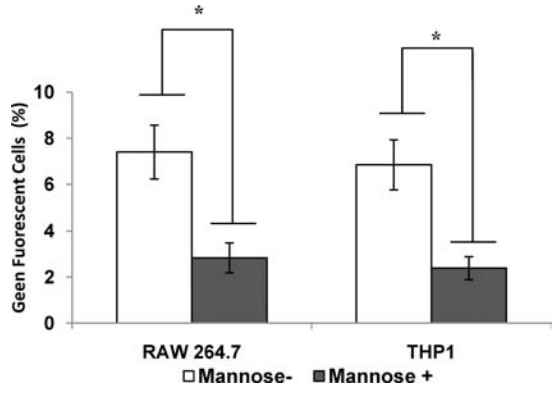

Figure 9. In vitro transfection analysis of in RAW 264.7 and THP1 cells using pCMV-GFP and Man-bPEI-HA at polymer to DNA weight ratio of 2. FACS analysis of GFP expressing RAW 264.7 and THP1 cells preincubated with either Man-BSA or BSA. Data are shown as mean ± SD (n = 3) and considered significant if *P < 0.05.

DISCUSSION

Macrophages play a crucial role in tissue maintenance, immune regulation, and pathogen control and thus are crucial targets for gene therapy.[37] Several attempts to deliver genes have been made using electroporation, lipoplex, or polymer to modulate the function and dysfunction of macrophages.[38−43] However, gene transfection in macrophages has proven difficult.

In the present study, we developed functionalized hyaluronan based nanohybrids, i.e., Man-bPEI-HA, for enhanced gene delivery in both murine and human macrophages in vitro. As mannose receptors are overexpressed in macrophages, and this expression mediates mannose receptor endocytosis, this phenomenon could be used in designing targeted gene therapy applications. Development of an efficient mannosylated nonviral carrier is potentially a powerful approach for macrophage-specific gene delivery.[44] In a previous study, low molecular weight HA coated PEI/*p*DNA polyplexes showed reduced cytotoxicity and enhanced CD44 receptor mediated cellular uptake.[14] Therefore, to obtain both gene transfection activity and macrophage cell specificity Man-bPEI-HA nanohybrids were developed using mannopyranosylphenyl isothiocynate and HA conjugate of bPEI. As shown in Figure 1, N—H and thionyl (C═S) stretching peaks appeared in the regions of 3250−3350 and 1550−1620 cm^{-1}, respectively, indicating that bPEI was coupled to HA and mannose residue was grafted to the bPEI-HA conjugates. ^{1}H NMR spectra further proves the conjugation of Man-bPEI-HA with the final ^{1}H NMR spectrum containing three peaks corresponding to HA (1.9 ppm), PEI (2.5−3.2 ppm), and mannose (7 ppm). Previous studies reported that a lower degree of substitution enhanced gene transfection in a hepatocyte cell culture model (HepG2) expressing the asialoglycoprotein receptors.[45] As shown in Figure 3A, ninhydrin assay revealed that the unmodified bPEI possesses a higher number of primary amines than do bPEI-HA and Man-bPEI-HA nanohybrids. The degree of substitution for mannose residue in Man-bPEI-HA was calculated and found to be approximately 8%. The mechanism of polyethyleneimine-based gene transfection is well-studied.[4,6,7] As shown in (Supporting Information, Figure 1), the Man-bPEI-HA nanohybrids have a buffering ability comparable to bPEI, which might be essential for endosomal escape of *p*DNA to enter the nucleus for good transfection ability. The binding ability of Man-bPEI-HA with *p*DNA was also confirmed using gel retardation and UV spectrophotometry studies (Figure 4 and Supporting Information, Figure 2).

Surface charge is also a key property for a nonviral gene delivery system, as it can influence stability, cell adhesion, and transfection efficiency.[46,47] The presence of a net positive surface charge on the complex could lead to attachment to cell surfaces that have a negative charge at neutral pH.[48] Man-bPEI-HA/*p*DNA complexes were also characterized for size and surface charge distribution, and it was found that the polyplexes were nanometric in size having net positive charge on their surfaces (Figure 5 and Supporting Information, Table 1). The zeta potential analysis of mannosylated nanohybrids/*p*DNA

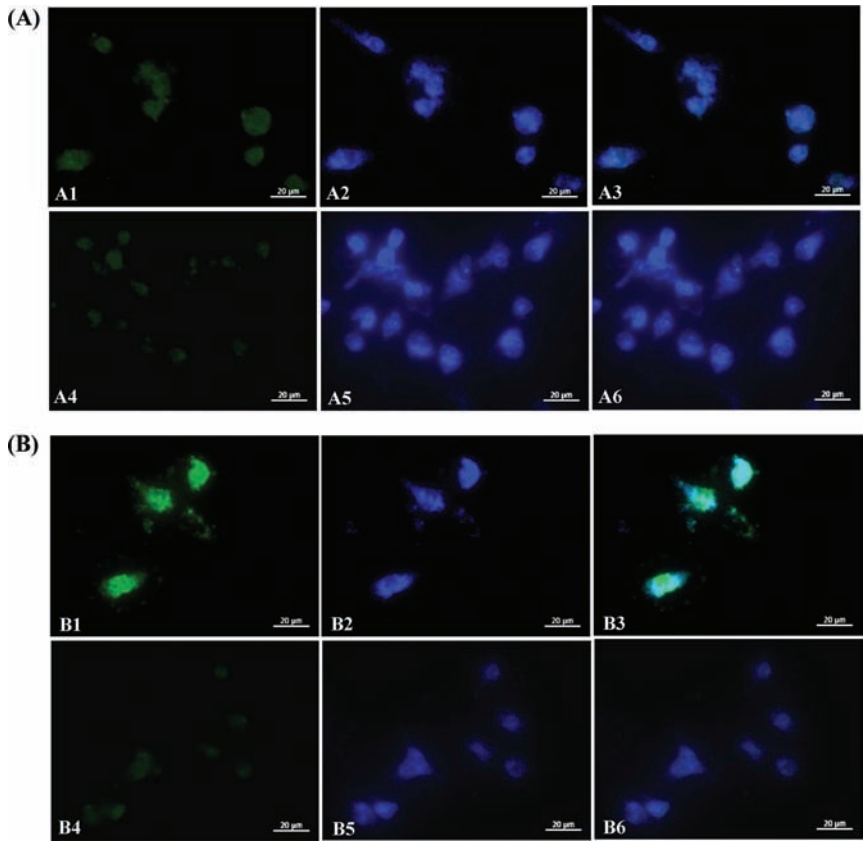

Figure 10. Colocalization study of FITC labeled Man-bPEI-HA/pDNA in (A) THP1 and (B) RAW 264.7 cells. THP1 cells preincubated with (A1-A3) BSA and (A4-A6) Man-BSA. RAW 264.7 cells pretreated with (B1−B3) and (B4−B6) Man-BSA. (A1, A4, B1, B4) FITC labeled polyplex inside the cells tinted as green, (A2, A5, B2, B5) lysosome stained with lysotracker blue, and (A3, A6, B3, B6) composite images of green-tinted polyplexes and blue lysosomes.

complexes at various weight ratios are shown in Figure 5. The Man-bPEI-HA/*p*DNA complexes of weight ratio 0.5 show a negative zeta potential, whereas complexes with a weight ratio from 1 to 10 show increasing positive charges as the weight ratio is increased. The weight ratio of HA to bPEI used in the present study was 1:5, which is the primary cause of the net positive charge of these conjugates. HA is an anionic polymer that has a carboxylic group. The conjugation of HA to PEI using EDC cross-linking chemistry results in the reduction of the primary amino groups (Figure 3) as COOH of HA couples to primary amino groups of bPEI. Figure 5 represents the size and surface charge of polyplexes (polymer-*p*DNA complexes) at different weight ratio of polymer to *p*DNA. As polymer to *p*DNA weight ratio increases, the net surface charge of polyplexes increases. These results indicate that mannosylated nanohybrids are able to facilitate gene transfer due to their advantageous particle sizes and surface charges. In previous studies, protection of plasmid DNA against endonuclease enzyme is a critical parameter for efficient gene transfection.[34] Protection studies revealed that the Man-bPEI-HA/*p*DNA complexes were stable against DNase I attack once they form complexes at each ratio, whereas naked *p*DNA was degraded by DNase I (Figure 6A). Further investigations were carried out using PGA. PGA is highly negatively charged, and incubation of polyplex with a high concentration of PGA leads to destabilization of the polymer/*p*DNA complex by breaking the electrostatic interaction between polymer and *p*DNA. The agarose gel showed a migrated band similar to the native one when treated with PGA (Figure 6B). These results further confirmed the previous assumption that *p*DNA retention in the gel pockets is caused by complexation of Man-bPEI-HA with *p*DNA, which protected the *p*DNA from the enzymatic degradation. These results overall indicate that mannosylated nanohybrids/*p*DNA complexes are sufficiently able to deliver DNA inside the target cells.

In vitro cell viability studies with RAW 264.7 cells revealed that Man-bPEI-HA showed comparable cell viability with bPEI-HA and significantly improved when HA was conjugated with bPEI at both time points, i.e., 4 and 24 h (Figure 7 and Supporting Information, Figure 3). The in vitro cytotoxicity results were consistent with the previous findings that demonstrated the protective effect of HA for bPEI/*p*DNA complexes.[14] The cell viability of the polyplexes (Man-bPEI-HA, bPEI-HA, and bPEI) when carried out under in vitro transfection conditions showed better cell viability than that of polymer alone (Supporting Information, Figures 5 and 6). The Man-bPEI-HA and bPEI-HA polyplexes showed comparable viability, more than that of bPEI-based polyplexes. It can also been seen that pretreatment of Man-BSA and BSA did not cause any adverse effect on cell viability and thus did not influence the interpretation of cell viability data of the polyplexes. The cell-specificity for mannosylated nanohybrids was also studied using specific cells (RAW 264.7) and nonspecific cells (NIH 3T3) for mannose receptor. The gene transfection studies showed that mannosylated nanohybrids enhanced the gene transfection of reporter gene in RAW 264.7 cells significantly more than the nonmannosylated nanohybrids (Supporting Information, Figure 7). Also, the competitive

transfection study performed on RAW 264.7 and THP1 cells using Man-BSA and BSA showed lower levels of GLuc in the case Man-BSA pretreated cell than those of BSA pretreated cells and proves that the higher transfection efficiency of Man-bPEI-HA is attributable to mannose specific targeting of the nanohybrids (Figure 8). This was further proven in the FACS analysis of *p*CMV-GFP reporter expression analysis, where a smaller percentage of green fluorescent cells was found in the case of Man-BSA pretreated cells than that of BSA treated cells (Figure 9).

To further prove the concept of mannose targeting and understand the mechanism, an internalization study was performed with Man-bPEI-HA/*p*CMV-GLuc complex tethered with FITC and lysosome with lysotracker blue. Both RAW 264.7 and THP1 cells showed higher levels of colocalization of the complexes inside the lysosome (Figure 10A,B). The higher level of colocalization of polyplexes in the case of BSA pretreated cells can be attributed to mannose-specific targeting, whereas the lower level of colocalization of the polyplexes in the case Man-BSA-treated cells can be ascribed to nonspecific phagocytic internalization by the macrophages. Lysosome was chosen for this study because both the mannose receptor mediated endocytosis and nonspecific phagocytosis involve lysosome. The nanohybrid/*p*DNA complex protects the *p*DNA inside the endolysosomal vesicles during the endocytosis process by rupturing the membrane. Our understanding regarding this escape of endolysosomal escape by polyplex is that a relatively cationic polymer becomes protonated inside the endolysosome due to the low pH. The charged form of this molecule cannot cross the membrane. This accumulation of charge causes an osmotic imbalance between different sides of the membrane, thereby inducing swelling of the endolysosome and, consequently, destabilization of the membrane.[49]

CONCLUSIONS

Hyaluronan conjugation with bPEI and subsequent mannosylation influenced the physicochemical properties of nanohybrids as well as that of polyplexes formed with *p*DNA. Man-bPEI-HA conjugates showed DNA binding capability, and thus polyplexes formed are nanometric in size range, having net positive charge. In addition, Man-bPEI-HA/*p*DNA complexes were seen to be stable against DNase I and intracellular degradation. Furthermore, in vitro cytotoxicity of Man-bPEI-HA conjugates was reduced in comparison to bPEI. As a consequence, transfection efficiency was increased in mannose receptor positive murine macrophages and decreased in mannose receptor negative fibroblasts, and a similar pattern was found when the transfection efficiency was characterized using BSA and Man-BSA, where mannose acts as a competitive inhibitor for the mannose receptor and thus gives a reduced transfection efficiency for the Man-BSA than that of BSA pretreated RAW 264.7 and THP1 cells. This enhanced transfection is most likely because of the improved uptake of polyplexes facilitated by a receptor-mediated phenomenon functionalized with mannose, as shown by the competitive internalization studies. Further in vivo studies, cellular interaction, and other blood compatibility studies are needed to show that these mannosylated hyaluronan-based nanohybrids offer potential as macrophage-targeted gene delivery vectors.

ASSOCIATED CONTENT

Supporting Information

Experimental methods involving cell viability and confocal microscopy and results related to physicochemical characterization of the nanohybrid, cell viability, and transfection assays.This material is available free of charge via the Internet at http://pubs.acs.org.

AUTHOR INFORMATION

Corresponding Author

*E-mail: abhay.pandit@nuigalway.ie. Phone: + 353-(0)91-492758. Fax: + 353-(0)91-485585.

Author Contributions

#Authors contributed equally

Notes

The authors declare no competing financial interest.

ACKNOWLEDGMENTS

The authors are grateful to Dr. Christophe Helary for his assistance while working on THP1 and Anthony Sloan for his help in editing this manuscript. This work is supported by the fund provided by Science Foundation Ireland under Research Grant No. 07/SRC/B1163 and 07/RFP/ENMF482.

REFERENCES

(1) Crystal, R. G. (1995) The gene as the drug. *Nat. Med. 1*, 15−17.
(2) Friedmann, T. (1996) Human gene therapy--an immature genie, but certainly out of the bottle. *Nat. Med. 2*, 144−147.
(3) Han, S., Mahato, R. I., Sung, Y. K., and Kim, S. W. (2000) Development of biomaterials for gene therapy. *Mol. Ther. 2*, 302−317.
(4) Boussif, O., Lezoualc'h, F., Zanta, M. A., Mergny, M. D., Scherman, D., Demeneix, B., and Behr, J. P. (1995) A versatile vector for gene and oligonucleotide transfer into cells in culture and in vivo: polyethylenimine. *Proc. Natl. Acad. Sci. U. S. A. 92*, 7297−7301.
(5) Schatzlein, A. G. (2001) Non-viral vectors in cancer gene therapy: principles and progress. *Anticancer Drugs 12*, 275−304.
(6) Yamazaki, Y., Nango, M., Matsuura, M., Hasegawa, Y., Hasegawa, M., and Oku, N. (2000) Polycation liposomes, a novel nonviral gene transfer system, constructed from cetylated polyethylenimine. *Gene Ther. 7*, 1148−1155.
(7) Kircheis, R., Wightman, L., and Wagner, E. (2001) Design and gene delivery activity of modified polyethylenimines. *Adv. Drug Delivery Rev. 53*, 341−358.
(8) Cho, K. C., Choi, S. H., and Park, T. G. (2006) Low molecular weight PEI conjugated pluronic copolymer: Useful additive for enhancing gene Transfection efficiency. *Macromol. Res. 14*, 348−353.
(9) Fischer, D., Bieber, T., Li, Y., Elsasser, H. P., and Kissel, T. (1999) A novel non-viral vector for DNA delivery based on low molecular weight, branched polyethylenimine: effect of molecular weight on transfection efficiency and cytotoxicity. *Pharm. Res. 16*, 1273−1279.
(10) Godbey, W. T., Wu, K. K., Hirasaki, G. J., and Mikos, A. G. (1999) Improved packing of poly(ethylenimine)/DNA complexes increases transfection efficiency. *Gene Ther. 6*, 1380−1388.
(11) Kainthan, R. K., Gnanamani, M., Ganguli, M., Ghosh, T., Brooks, D. E., Maiti, S., and Kizhakkedathu, J. N. (2006) Blood compatibility of novel water soluble hyperbranched polyglycerol-based multivalent cationic polymers and their interaction with DNA. *Biomaterials 27*, 5377−5390.
(12) Erbacher, P., Bettinger, T., Belguise-Valladier, P., Zou, S., Coll, J. L., Behr, J. P., and Remy, J. S. (1999) Transfection and physical properties of various saccharide, poly(ethylene glycol), and antibody-derivatized polyethylenimines (PEI). *J. Gene Med. 1*, 210−222.
(13) Meyer, M., and Wagner, E. (2006) pH-responsive shielding of non-viral gene vectors. *Expert Opin. Drug Delivery 3*, 563−571.

(14) Hornof, M., de la Fuente, M., Hallikainen, M., Tammi, R. H., and Urtti, A. (2008) Low molecular weight hyaluronan shielding of DNA/PEI polyplexes facilitates CD44 receptor mediated uptake in human corneal epithelial cells. *J. Gene Med. 10*, 70−80.
(15) Kim, A., Checkla, D. M., Dehazya, P., and Chen, W. (2003) Characterization of DNA-hyaluronan matrix for sustained gene transfer. *J. Controlled Release 90*, 81−95.
(16) Yun, Y. H., Goetz, D. J., Yellen, P., and Chen, W. (2004) Hyaluronan microspheres for sustained gene delivery and site-specific targeting. *Biomaterials 25*, 147−157.
(17) Jiang, G., Park, K., Kim, J., Kim, K. S., and Hahn, S. K. (2009) Target specific intracellular delivery of siRNA/PEI-HA complex by receptor mediated endocytosis. *Mol. Pharmaceutics 6*, 727−737.
(18) Porgador, A., Irvine, K. R., Iwasaki, A., Barber, B. H., Restifo, N. P., and Germain, R. N. (1998) Predominant role for directly transfected dendritic cells in antigen presentation to CD8+ T cells after gene gun immunization. *J. Exp. Med. 188*, 1075−1082.
(19) Paliwal, R., Rai, S., Vaidya, B., Mahor, S., Gupta, P. N., Rawat, A., and Vyas, S. P. (2007) Cell-selective mitochondrial targeting: progress in mitochondrial medicine. *Curr. Drug Delivery 4*, 211−224.
(20) Martinez-Pomares, L., Linehan, S. A., Taylor, P. R., and Gordon, S. (2001) Binding properties of the mannose receptor. *Immunobiology 204*, 527−535.
(21) Park, K. H., Sung, W. J., Kim, S., Kim, D. H., Akaike, T., and Chung, H. M. (2005) Specific interaction of mannosylated glycopolymers with macrophage cells mediated by mannose receptor. *J. Biosci. Bioeng. 99*, 285−289.
(22) Vyas, S. P., Singh, A., and Sihorkar, V. (2001) Ligand-receptor-mediated drug delivery: an emerging paradigm in cellular drug targeting. *Crit. Rev. Ther. Drug Carrier Syst. 18*, 1−76.
(23) Ferkol, T., Perales, J. C., Mularo, F., and Hanson, R. W. (1996) Receptor-mediated gene transfer into macrophages. *Proc. Natl. Acad. Sci. U. S. A. 93*, 101−105.
(24) Billiet, L., Furman, C., Larigauderie, G., Copin, C., Brand, K., Fruchart, J. C., and Rouis, M. (2005) Extracellular human thioredoxin-1 inhibits lipopolysaccharide-induced interleukin-1beta expression in human monocyte-derived macrophages. *J. Biol. Chem. 280*, 40310−40318.
(25) Hashimoto, M., Morimoto, M., Saimoto, H., Shigemasa, Y., Yanagie, H., Eriguchi, M., and Sato, T. (2006) Gene transfer by DNA/mannosylated chitosan complexes into mouse peritoneal macrophages. *Biotechnol. Lett. 28*, 815−821.
(26) Jiang, H. L., Kim, Y. K., Arote, R., Jere, D., Quan, J. S., Yu, J. H., Choi, Y. J., Nah, J. W., Cho, M. H., and Cho, C. S. (2009) Mannosylated chitosan-graft-polyethylenimine as a gene carrier for Raw 264.7 cell targeting. *Int. J. Pharm. 375*, 133−139.
(27) Jiang, G., Park, K., Kim, J., Kim, K. S., Oh, E. J., Kang, H., Han, S. E., Oh, Y. K., Park, T. G., and Kwang Hahn, S. (2008) Hyaluronic acid-polyethyleneimine conjugate for target specific intracellular delivery of siRNA. *Biopolymers 89*, 635−642.
(28) Dash, B. C., Rethore, G., Monaghan, M., Fitzgerald, K., Gallagher, W., and Pandit, A. (2010) The influence of size and charge of chitosan/polyglutamic acid hollow spheres on cellular internalization, viability and blood compatibility. *Biomaterials 31*, 8188−8197.
(29) Xu, Z. H., Xu, T. W., Cheng, Y. Y., Ma, M. L., Xu, P., Qu, H. O., and Wen, L. P. (2008) Colorimetric determination of polyamidoamine dendrimers and their derivates using a simple and rapid ninhydrin assay. *Anal. Lett. 41*, 444−455.
(30) Mahor, S., Rawat, A., Dubey, P. K., Gupta, P. N., Khatri, K., Goyal, A. K., and Vyas, S. P. (2007) Cationic transfersomes based topical genetic vaccine against hepatitis B. *Int. J. Pharm. 340*, 13−19.
(31) Dash, B. C., Mahor, S., Carroll, O., Mathew, A., Wang, W., Woodhouse, K. A., and Pandit, A. (2011) Tunable elastin-like polypeptide hollow sphere as a high payload and controlled delivery gene depot. *J. Controlled Release 152*, 382−392.
(32) Banka, C. L., Black, A. S., Dyer, C. A., and Curtiss, L. K. (1991) THP-1 cells form foam cells in response to coculture with lipoproteins but not platelets. *J. Lipid Res. 32*, 35−43.
(33) Mosmann, T. (1983) Rapid colorimetric assay for cellular growth and survival: application to proliferation and cytotoxicity assays. *J. Immunol. Methods 65*, 55−63.
(34) Liang, W. W., Shi, X., Deshpande, D., Malanga, C. J., and Rojanasakul, Y. (1996) Oligonucleotide targeting to alveolar macrophages by mannose receptor-mediated endocytosis. *Biochim. Biophys. Acta 1279*, 227−234.
(35) Largent, B. L., Walton, K. M., Hoppe, C. A., Lee, Y. C., and Schnaar, R. L. (1984) Carbohydrate-specific adhesion of alveolar macrophages to mannose-derivatized surfaces. *J. Biol. Chem. 259*, 1764−1769.
(36) Kasturi, S. P., Sachaphibulkij, K., and Roy, K. (2005) Covalent conjugation of polyethyleneimine on biodegradable microparticles for delivery of plasmid DNA vaccines. *Biomaterials 26*, 6375−6385.
(37) Pierce, G. F. (1990) Macrophages: important physiologic and pathologic sources of polypeptide growth factors. *Am. J. Respir. Cell Mol. Biol. 2*, 233−234.
(38) Ohashi, T., Boggs, S., Robbins, P., Bahnson, A., Patrene, K., Wei, F. S., Wei, J. F., Li, J., Lucht, L., Fei, Y., et al. (1992) Efficient transfer and sustained high expression of the human glucocerebrosidase gene in mice and their functional macrophages following transplantation of bone marrow transduced by a retroviral vector. *Proc. Natl. Acad. Sci. U. S. A. 89*, 11332−11336.
(39) Burke, B., Sumner, S., Maitland, N., and Lewis, C. E. (2002) Macrophages in gene therapy: cellular delivery vehicles and in vivo targets. *J. Leukoc. Biol. 72*, 417−428.
(40) Freas, D. L., Correll, P. H., Dougherty, S. F., Karlsson, S., and Pluznik, D. H. (1993) Evaluation of expression of transferred genes in differentiating myeloid cells: expression of human glucocerebrosidase in murine macrophages. *Hum. Gene Ther. 4*, 283−290.
(41) Bartholeyns, J., and Lopez, M. (1994) Immune control of neoplasia by adoptive transfer of macrophages: potentiality for antigen presentation and gene transfer. *Anticancer Res. 14*, 2673−2676.
(42) Parrish, E. P., Cifuentes-Diaz, C., Li, Z. L., Vicart, P., Paulin, D., Dreyfus, P. A., Peschanski, M., Harris, A. J., and Garcia, L. (1996) Targeting widespread sites of damage in dystrophic muscle: engrafted macrophages as potential shuttles. *Gene Ther. 3*, 13−20.
(43) Stacey, K. J., Ross, I. L., and Hume, D. A. (1993) Electroporation and DNA-dependent cell death in murine macrophages. *Immunol. Cell Biol. 71* (Pt 2), 75−85.
(44) Diebold, S. S., Kursa, M., Wagner, E., Cotten, M., and Zenke, M. (1999) Mannose polyethylenimine conjugates for targeted DNA delivery into dendritic cells. *J. Biol. Chem. 274*, 19087−19094.
(45) Kunath, K., von Harpe, A., Fischer, D., and Kissel, T. (2003) Galactose-PEI-DNA complexes for targeted gene delivery: degree of substitution affects complex size and transfection efficiency. *J. Controlled Release 88*, 159−172.
(46) Mahato, R. I., Takakura, Y., and Hashida, M. (1997) Nonviral vectors for in vivo gene delivery: physicochemical and pharmacokinetic considerations. *Crit. Rev. Ther. Drug Carrier Syst. 14*, 133−172.
(47) Nomura, T., Nakajima, S., Kawabata, K., Yamashita, F., Takakura, Y., and Hashida, M. (1997) Intratumoral pharmacokinetics and in vivo gene expression of naked plasmid DNA and its cationic liposome complexes after direct gene transfer. *Cancer Res. 57*, 2681−2686.
(48) Mislick, K. A., and Baldeschwieler, J. D. (1996) Evidence for the role of proteoglycans in cation-mediated gene transfer. *Proc. Natl. Acad. Sci. U. S. A. 93*, 12349−12354.
(49) Varkouhi, A. K., Scholte, M., Storm, G., and Haisma, H. J. (2011) Endosomal escape pathways for delivery of biologicals. *J. Controlled Release 151*, 220−228.

Bioconjugate Chemistry

Article

pubs.acs.org/bc

Evaluation of Four Affibody-Based Near-Infrared Fluorescent Probes for Optical Imaging of Epidermal Growth Factor Receptor Positive Tumors

Shibo Qi,[†,‡] Zheng Miao,[†] Hongguang Liu,[†] Yingding Xu,[†] Yaqing Feng,[‡] and Zhen Cheng*[,†]

[†]Molecular Imaging Program at Stanford (MIPS), Department of Radiology, and Bio-X Program, Canary Center at Stanford for Cancer Early Detection, Stanford University, Stanford, California, 94305-5344

[‡]School of Chemical Engineering and Technology, Tianjin University, Tianjin 300072, China

ABSTRACT: The epidermal growth factor receptor 1 (EGFR) has become an attractive target for cancer molecular imaging and therapy. An Affibody protein with strong binding affinity for EGFR, $Z_{EGFR:1907}$, has been reported. We are interested in translating Affibody molecules to potential clinical optical imaging of EGFR positive cancers. In this study, four anti-EGFR Affibody based near-infrared (NIR) fluorescent probes were thus prepared, and their *in vivo* performance was evaluated in the mice bearing EGFR positive subcutaneous A431 tumors. Methods: The Affibody analogue, Ac-Cys-$Z_{EGFR:1907}$, was synthesized using solid-phase peptide synthesis method. The purified small protein was then site-specifically conjugated with four NIR fluorescent dyes, Cy5.5-monomaleimide, Alex-Fluor-680-maleimide, SRfluor680-maleimide, or IRDye-800CW-maleimide, to produce four optical probes—Cy5.5-$Z_{EGFR:1907}$, Alexa680-$Z_{EGFR:1907}$, SR680-$Z_{EGFR:1907}$, and 800CW-$Z_{EGFR:1907}$. The EGFR binding property and specificity of the four NIR fluorescent Affibody probes were studied by fluorescence microscopy using high EGFR expressing A431 cells and low expressing MCF7 cells. The binding affinities of the probes (K_D) to EGFR were further determined by flow cytometry. *In vivo* optical imaging of the four probes was performed in the mice bearing subcutaneous A431 tumors. Results: The four NIR optical probes were prepared in high purity. *In vitro* cell imaging studies demonstrated that all of them could specifically bind to EGFR positive A431 cells while showing minimum uptake in low EGFR expressing MCF7 cells. Flow cytometry showed that Cy5.5-$Z_{EGFR:1907}$ and Alexa680-$Z_{EGFR:1907}$ possessed high binding affinity in low nanomolar range (43.6 ± 8.4 and 28.3 ± 4.9, respectively). *In vivo* optical imaging of the four probes revealed that they all showed fast tumor targeting ability and good tumor-to-normal tissue contrast as early as 0.5 h postinjection (p.i.). The tumor-to-normal tissue ratio reached a peak at 2 to 4 h p.i. by regional of interest (ROI) analysis of images. *Ex vivo* studies further demonstrated that the four probes had high tumor uptakes. Particularly, Cy5.5-$Z_{EGFR:1907}$ and Alex680-$Z_{EGFR:1907}$ displayed higher tumor-to-normal tissue ratios than those of the other two probes. Conclusion: This work demonstrates that Affibody proteins can be modified with different NIR fluorescent dyes and used for imaging of EGFR expressing tumors. Different NIR fluorescent dyes have variable impact on the *in vitro* binding and *in vivo* performance of the resulting Affibody based probes. Therefore, selection of an appropriate NIRF label is important for optical probe development. The probes developed are promising for further tumor imaging applications and clinical translation. Particularly, Alex680-$Z_{EGFR:1907}$ and Cy5.5-$Z_{EGFR:1907}$ are excellent candidates as EGFR-targeted probes for optical imaging.

INTRODUCTION

Epidermal growth factor receptor (EGFR) is a very important tumor target and has been found to be overexpressed in a wide range of human tumors such as nonsmall cell lung cancer, small cell carcinoma of head and neck, colon cancer, breast cancer, ovary cancer, prostate cancer, and so forth.[1] Many biopharmaceuticals and drugs including Cetuximab, Lapatinib, Gefitinib, and Erlotinib have been developed and extensively studied for EGFR targeted therapies.[2−5] Novel molecular probes for EGFR imaging have also been under active investigation.[6,7] The EGFR specific molecular probes are expected to be very useful in many applications including early detection of EGFR positive tumors and metastases, surgical guidance, and prediction of EGFR targeted therapy efficacy.

Small protein scaffolds have recently shown great potential for molecular recognition.[8,9] The Affibody protein scaffold is a great example that is based on the Z-domain scaffold derived from one of the IgG-binding domains of staphylococcal protein A (SPA) and has been demonstrated to be a generalizable platform for developing imaging and therapeutic agents.[10] Affibody molecules are composed of 58-amino-acid residues and form a three-helix bundle scaffold structure. High-affinity Affibody proteins against different targets could be readily constructed through randomization of the 13 amino acid residues in helices 1 and 2.[11−13] Because of the small size and high affinities, Affibody proteins have the advantages of fast tumor targeting, high tumor uptake, and quick clearance from normal tissues. With reasonable yield, Affibody proteins can be obtained using conventional solid-phase peptide synthesis; importantly, high binding affinity and specificity are retained

Received: November 10, 2011
Revised: April 20, 2012
Published: May 23, 2012

through the synthetic process. In the past few years, Affibody molecules with high affinities and specificities against a variety of targets including EGFR, human epidermal growth factor receptor 2 (HER2), platelet derived growth factor receptor (PDGFR), and others have been constructed. Additionally, Affibody proteins have been labeled with various radionuclides, organic dyes, and nanoparticles for imaging applications.[14−17] These studies have demonstrated that Affibody molecules are a promising platform for tumor targeting and therapy.

An anti-EGFR Affibody protein, $Z_{EGFR:1907}$, has shown strong binding affinity to EGFR with good specificity.[18] ^{64}Cu and ^{111}In labeled $Z_{EGFR:1907}$ display fast tumor targeting and excellent imaging contrast.[19,20] Of note, this Affibody molecule possesses a good binding affinity to human EGFR expressed in A431 cells and a good tumor uptake in murine liver, spleen, and colon, all of which express a high level of EGFR.[18] Additionally, binding of the native ligand EGF to the murine organs can be saturated, and thus, both pieces of evidence suggest that $Z_{EGFR:1907}$ possesses cross-reactivity with both human and murine EGFR.[21] We thus hypothesized that this Affibody protein could be utilized to develop probes for near-infrared (NIR) fluorescent (NIRF) imaging of EGFR positive tumors using murine models. In this research, a cysteine residue was first added to the N-terminus of Ac-Cys-$Z_{EGFR:1907}$. The resulting chemically synthesized protein, Ac-CVDNKFNKEMWAA-WEEIRNLPNLNGWQMTAFIASLV DDPSQSANL-LAEAKKLNDAQAPK-NH_2, was then site specifically labeled with four different NIR dyes, Cy5.5-monomaleimide, Alexa-Fluor-680-maleimide, SRfluor680-maleimide (SR-1004, a far-red emitting dye which belongs to the squaraine rotaxane family of dyes),[22−24] or IRDye-800CW-malelimide, to generate optical probe, Cy5.5-$Z_{EGFR:1907}$, Alexa680-$Z_{EGFR:1907}$, SR680-$Z_{EGFR:1907}$, 800CW-$Z_{EGFR:1907}$, respectively (Figure 1). All of the four NIR

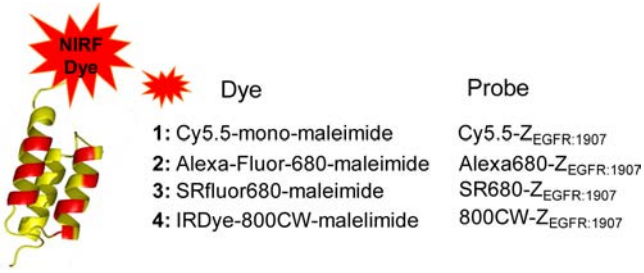

Figure 1. Schematic structure of anti-EGFR Affibody protein based NIR fluorescent probes.

dyes are commercially available and have demonstrated both chemical and photochemical stabilities. The four Affibody-based NIR fluorescent probes were further evaluated in EGFR positive human epithelial carcinoma A431 cell culture and tumor bearing mice with the goal to systematically compare *in vitro* and *in vivo* characteristics of the four NIR dyes in the context of $Z_{EGFR:1907}$ analogues, and with the additional goal of discovering a good Affibody based optical imaging probe for EGFR positive tumors.

MATERIALS AND METHODS

General. All commercially available chemical reagents were used without further purification. Cy5.5-monomaleimide was purchased from GE Healthcare (Piscataway, NJ). Alexa-Fluor-680-C2 maleimide was purchased from Invitrogen Co. (Carlsbad, CA), SRfluor680-maleimide (SR-1004, molecular weight = 1231) was purchased from Molecular Targeting Technologies Inc. (West Chester, PA), and IRDye-800CW-malelimide was purchased from LI-COR Biosciences (Lincoln, NE). Dichloromethane, triethylamine, *N*-hydroxybenzotriazole hydrate (HOBT), and ethyl acetate were purchased from Sigma-Aldrich Chemical Co. (St. Louis, MO). Dimethyl sulfoxide (DMSO) was purchased from Fisher Scientific (Pittsburgh, PA). All the other standard reagents were obtained from Sigma-Aldrich Chemical Co. (St. Louis, MO). The purification of the crude product was carried out on a semipreparative reversed-phase high-performance liquid chromatography (HPLC) system equipped with a 170U 5-Channel UV−vis absorbance detector (Dionex Summit HPLC systme, Dionex Corporation, Sunnyvale, CA) using a Vydac protein and peptide column (218TP510, 5 μm 250 × 10 mm). The mobile phase was solvent A, 0.1% trifluoroacetic acid (TFA)/H_2O, and solvent B, 0.1% TFA/acetonitrile. The flow rate was 1 mL/min, with the mobile phase starting from 65% solvent A and 35% solvent B (0−2 min) to 55% solvent A and 45% solvent B at 32 min for Cy5.5-$Z_{EGFR:1907}$, Alexa680-$Z_{EGFR:1907}$, and 800CW-$Z_{EGFR:1907}$. While for SR680-$Z_{EGFR:1907}$, the mobile phase started from 60% solvent A and 40% solvent B (0−2 min) to 50% solvent A and 50% solvent B at 32 min. Matrix-assisted laser desorption/ionization time-of-flight mass spectrometry (MALDI-TOF-MS, model: Perspective Voyager-DE RP Biospectrometer) (Framingham, MA) was performed by the Stanford Protein and Nucleic Acid Biotechnology Facility. The human epithelial carcinoma cancer cell line A431 was obtained from the American Type Tissue Culture Collection (Manassas, VA). Female athymic nude mice (nu/nu) were purchased from Charles River Laboratories (Boston, MA).

Synthesis of Ac-Cys-$Z_{EGFR:1907}$ and Conjugation of NIRF Dyes with Ac-Cys-$Z_{EGFR:1907}$. The Affibody analogue, Ac-Cys-$Z_{EGFR:1907}$, was prepared by a solid-phase peptide synthesis method as previously described.[19,25] The peptide was purified by a RP-HPLC on a C-4 column. The target product was collected and lyophilized. Characterization of the Affibody analogue was confirmed using MALDI-TOF-MS. The purity of the product was confirmed by the analytical HPLC.

The general procedure for the conjugation of each of the four monomaleimide-NIRF dye with Ac-Cys-$Z_{EGFR:1907}$ is as follows. The Affibody molecule was dissolved in freshly degassed phosphate buffer (0.1 M, pH 7.4) at concentration of approximately 1 mg/mL. The NIRF dye in DMSO was then irrespectively added (2.5 equiv of the Affibody). After vortexing for 3 h at room temperature, the crude product was purified by a RP-HPLC on a C-4 column. The fractions containing the probes were collected and lyophilized. Characterization of the four probes was also carried out using MALDI-TOF-MS. The purities of the four probes were confirmed by the analytical HPLC.

Fluorescence emission of the four probes was measured on the Fluomax-3 fluorophotometer (HORIBA, Jobin Yvon, Edison, NJ), and the spectrum was scanned from 700 to 850 nm (for Cy5.5-$Z_{EGFR:1907}$, Alexa680-$Z_{EGFR:1907}$, and SR680-$Z_{EGFR:1907}$) or 780 to 850 nm (for 800CW-$Z_{EGFR:1907}$) with increments of 5 nm. The absorption spectra of the four probes were recorded on an Agilent 8453 UV−visible ChemStation (Agilent Technologies, Wilmington, DE). The spectrum was scanned from 450 to 850 nm with increments of 1 nm.

Fluorescence Microcopy Studies. The A431 cells and MCF7 cells were cultured in high-glucose Dulbecco modified Eagle's medium (DMEM) and modified Eagle's medium

(MEM) supplemented with 10% fetal bovine serum (FBS) and 1% penicillin−streptomycin (Invitrogen Life Technologies, Carlsbad, CA). The cell line was maintained in humidified atmosphere of 5% CO_2 at 37 °C, with medium changed every other day. A confluent monolayer was detached with trypsin and dissociated into a single cell suspension for further cell culture.

For fluorescence microscopy study, A431 or MCF7 cells (1×10^5) were cultured in 35 mm MatTek glass-bottom cultures dishes (Ashland, MA). After 24 h, the cells were washed with phosphate-buffered saline (PBS) and then incubated with the probes (100 nM) for 1 h in dark. The EGFR-binding specificity of the four probes in the cell culture was verified by incubating the A431 and MCF7 cells with or without large amounts (blocking dose) of nonfluorescent Ac-Cys-$Z_{EGFR:1907}$ (10 μM). After the incubation period, cells were washed three times with ice-cold PBS. The fluorescence signal of the cells was observed and measured using an Axiovert 2000 M fluorescence microscope (Carl Zeiss MicroImaging, Inc., Thornwood, New Jersey) equipped with a Cy5.5 filter set (exciter, HQ 650/20 nm; emitter, HQ 695/35 nm). An AttoArcHBO 100-W microscopic illuminator was used as a light source for fluorescence excitation. Images were taken using a thermo-electrically cooled charge-coupled device (CCD) (Micromax, model RTE/CCD-576, Princeton Instruments Inc., Trenton, NJ) and analyzed using *MetaMorph* software v 6.2r4 (Molecular Devices Corporation, Downingtown, PA).

Binding Affinity Measurement with Flow Cytometry. The flow cytometric analysis was performed as described in the literature with minor modifications.[19,20,25] Samples were illuminated with a sapphire laser at 488 nm and a red laser at 635 nm on a BD FACSCalibur. The fluorescence of the forward-scattered and side-scattered light from 10 000 cells was detected at rate of 150 events/second. Flow cytometric data were analyzed with *FACSDiva* software (BD Biosciences, San Jose, CA). Prior to the flow cytometric analysis, A431 cells seeded in 75 cm^2 flasks approximately 3 days before the experiment were trypsinized (0.05% trypsin to 0.02% ethyl-enediaminetetraacetic acid (EDTA), 2.5 mL, ∼10 min, 37 °C) followed by a centrifugation (1000 *g*, 3 min). The pellet was subsequently resuspended in the binding buffer (PBS containing 1% bovine serum albumin (BSA) and 0.1% sodium azide (NaAz)). A431 cells (0.2 M each, expressing $\sim 2 \times 10^6$ receptors/cells) were then distributed in Falcon tubes (15 mL). After centrifugation, the cells were incubated with 5 mL of each of the three probes (Cy5.5-$Z_{EGFR:1907}$, Alexa680-$Z_{EGFR:1907}$, and SR680-$Z_{EGFR:1907}$) at different concentrations (ranging from 0.1 to 100 nM) for 1 h at room temperature in the dark, with continuous rocking. The cells were then centrifuged (178 g, 4 min, 4 °C), washed with binding buffer twice, resuspended in 500 μL of binding buffer, and subjected to flow cytometric analysis. All procedures after the incubation with the probe were performed in the ice with ice-cold buffers. A triplicate of the flow cytometric data was analyzed with *GraphPad Prism 5* (GraphPad Software, San Diego, CA), and a nonlinear regression one-site-specific model was used to calculate the K_D of each probe.

Optical Imaging of A431 Tumors in Mice. All animal studies were carried out according to a protocol approved by the Stanford University Administrative Panels on Laboratory Animal Care (APLAC). Female athymic nude mice (nu/nu) at 4 to 6 weeks of age were injected subcutaneously in the shoulder with 3×10^6 A431 cells suspended in 100 μL of PBS. The tumor-bearing mice were subjected to *in vivo* optical imaging studies 3 weeks after inoculation.

In vivo fluorescence imaging was performed with an IVIS 200 small animal imaging system (Caliper, Alameda, CA). A Cy5.5 filter set (excitation 615 to 655 nm; emission 695 to 770 nm) was used for acquiring Cy5.5-$Z_{EGFR:1907}$ fluorescence *in vivo*. Identical illumination settings (lamp voltage, filters, f/stop, fields of view, binning) were used to acquire all images, and fluorescence emission was normalized to photons per second per centimeter squared per steradian (p/s/cm^2/sr). Images were acquired and analyzed using *Living Image 3.0* software (Caliper, Alameda, CA). For the experiment, mice ($n = 5$) were injected via tail vein with 0.5 nmol of each probe (20 nmol/kg) and subjected to optical imaging at various time points postinjection (p.i.). IVIS-200 NIRF images were acquired using 1 s exposure time (f/stop = 4, binning = 4). The mice in the experiment were then euthanized at 24 h p.i. The tumor and major tissues and organs were dissected, wet weighted, and placed on black paper. The *ex vivo* fluorescence images were acquired, and mean fluorescence flux (p/s/cm^2/sr) for each sample was obtained, and the tumor to normal tissue ratios were then calculated.

Statistical Analysis. All the data are given as mean ± SD (standard deviation) of independent measurements. Statistical analysis was performed using a Student's *t* test. Statistical significance was assigned for *p* values <0.05. To determined tumor contrast, mean fluorescence intensities of the tumor area (*T*) of the shoulder of the animal and of the right flank (*N*, normal tissue) were calculated by the region-of-interest (ROI) function of *Living Image* software integrated with Igor (Wavemetrics, Lake Oswego, OR). Dividing *T* by *N* yielded the contrast between tumor and normal tissue.

RESULTS

Synthesis and Characterization of the Four NIRF Probes. The Affibody protein Ac-Cys-$Z_{EGFR:1907}$ with a cysteine at the N terminal was successfully synthesized using a peptide synthesizer and purified by semipreparative HPLC. The peptide was generally obtained in 2% yield with over 95% purity. The purified Ac-Cys-$Z_{EGFR:1907}$ was characterized by MALDI-TOF-MS, and the measured molecular weight (MW) was consistent with the expected value as previously reported by us.[19,20] Ac-Cys-$Z_{EGFR:1907}$ was then site specifically conjugated with the four dyes with maleimide functionality in PBS buffer and purified by HPLC. MS analysis verified the successful preparation of the final products (Table 1, expected MW for Alexa680-$Z_{EGFR:1907}$ was not provided in Table 1 because the structure and MW have not been released by the vendor). The purities for the final products were all over 95% (Figure 2A) and the recovery yields of the probe were over 45%. Spectral analysis showed that the four probes had similar

Table 1. K_D Values of the anti-EGFR Affibody-Based NIRF Probes and Their Expected and Measured Molecular Weight (M.W.) for $[M+H]^+$ by MALDI-TOF-MS[a]

NIRF probe	expected M.W.	measured M.W.	K_D (nM)
Cy5.5-$Z_{EGFR:1907}$	7727.4	7729.4	43.6 ± 8.4
Alexa680-$Z_{EGFR:1907}$	Unknown	7683.5	28.3 ± 4.9
SR680-$Z_{EGFR:1907}$	7920.1	7923.7	388 ± 20.7
800CW-$Z_{EGFR:1907}$	7875.8	7879.4	N.D.

[a]N.D. = not determined.

dx.doi.org/10.1021/bc200596a | *Bioconjugate Chem.* 2012, 23, 1149−1156

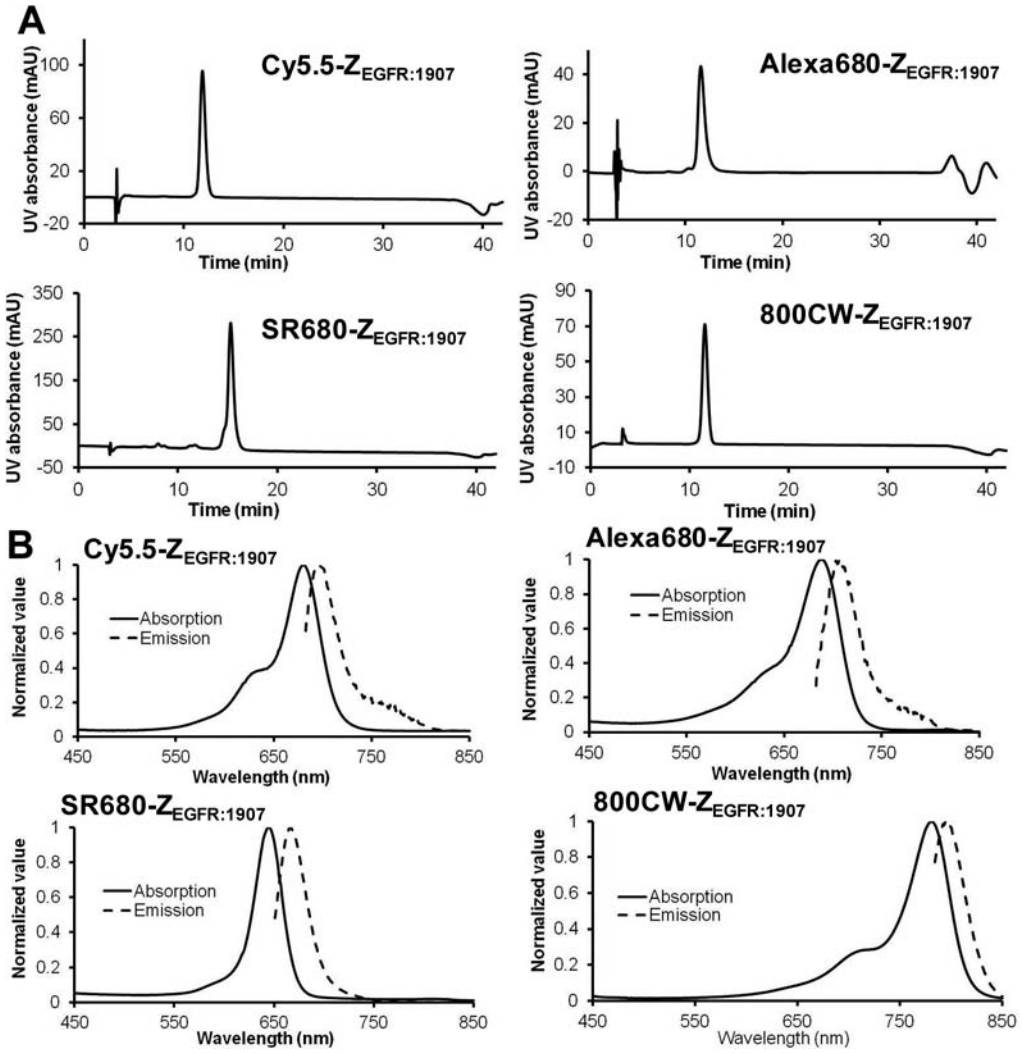

Figure 2. (A) HPLC chromatogram of purified NIRF probes and (B) absorption and emission fluorescence spectra of the four probes.

absorption and fluorescence emission characteristics as the corresponding free dyes (Figure 2B).

Binding Affinity and Specificity of the Four Probes. Flow cytometry study was performed to measure binding affinity of Cy5.5-$Z_{EGFR:1907}$, Alexa680-$Z_{EGFR:1907}$, and SR680-$Z_{EGFR:1907}$, while binding affinity of 800CW-$Z_{EGFR:1907}$ was not determined by this method because the instrument was not able to monitor IRDye-800CW. The equilibrium dissociation constant K_D was calculated using a nonlinear regression one-site-specific model (Table 1). It was found that both Alexa680-$Z_{EGFR:1907}$ and Cy5.5-$Z_{EGFR:1907}$ showed good binding affinity, while modification of the SRfluor680-maleimide dye with the Affibody protein dramatically reduced its binding affinity (Table 1). To demonstrate EGFR specificity and subcellular localization of the four probes, the probes were incubated with A431 tumor cells and fluorescent microscopic imaging was performed. With 1 h incubation at 37 °C, intensive fluorescent signal was observed from the A431 cell membrane; some intracellular signals were also visible (Figure 3). Furthermore, the fluorescent signal from the cells was significantly reduced by incubation of cells with large excess of Ac-Cys-$Z_{EGFR:1907}$ (10 μM), thus demonstrating the binding specificity of the four probes (Figure 3). Notably, staining of low EGFR expression MCF7 is barely visible.

***In Vivo* and *Ex Vivo* Optical Imaging.** Figure 4A shows typical NIR fluorescent images of nude mice bearing subcutaneous A431 tumor after intravenous injection of 0.5 nmol of four different probes. For all the probes, the A431 tumor could be clearly visualized and differentiated from the background tissue from 0.25 to 12 h p.i.. For Cy5.5-$Z_{EGFR:1907}$, prominent signals were observed from kidneys at early time points (0.25 to 1 h), while some uptakes from abdomen region were seen at later time (4 and 12 h). In contrast, Alexa680-$Z_{EGFR:1907}$ and SR680-$Z_{EGFR:1907}$ displayed quite high uptakes in abdomen even at 0.5 and 1 h p.i., while 800CW-$Z_{EGFR:1907}$ mainly showed high uptakes in kidneys and tumor at later time. Quantification analysis of ROIs was performed and the tumor-to-normal tissue ratio (T/N) as function of time is depicted in Figure 4B. All four probes exhibited fast tumor targeting *in vivo*. The tumor-to-normal tissue ratio reached a peak at 2 to 4 h p.i., and then the ratio decreased slightly, while there is no significant difference for the T/N ratios for different probes at the same time points p.i. Notably, at 4 h p.i., Cy5.5-$Z_{EGFR:1907}$ and Alexa680-$Z_{EGFR:1907}$ showed higher T/N values than that of SR680-$Z_{EGFR:1907}$ and 800CW-$Z_{EGFR:1907}$ (3.28 ± 0.68, 3.43 ± 0.82, 2.87 ± 0.57, 2.80 ± 0.61, respectively).

The result for *ex vivo* tumor mice imaging at 24 h p.i. is shown in Figure 5A. High uptake in tumor was clearly seen for

dx.doi.org/10.1021/bc200596a | *Bioconjugate Chem.* 2012, 23, 1149–1156

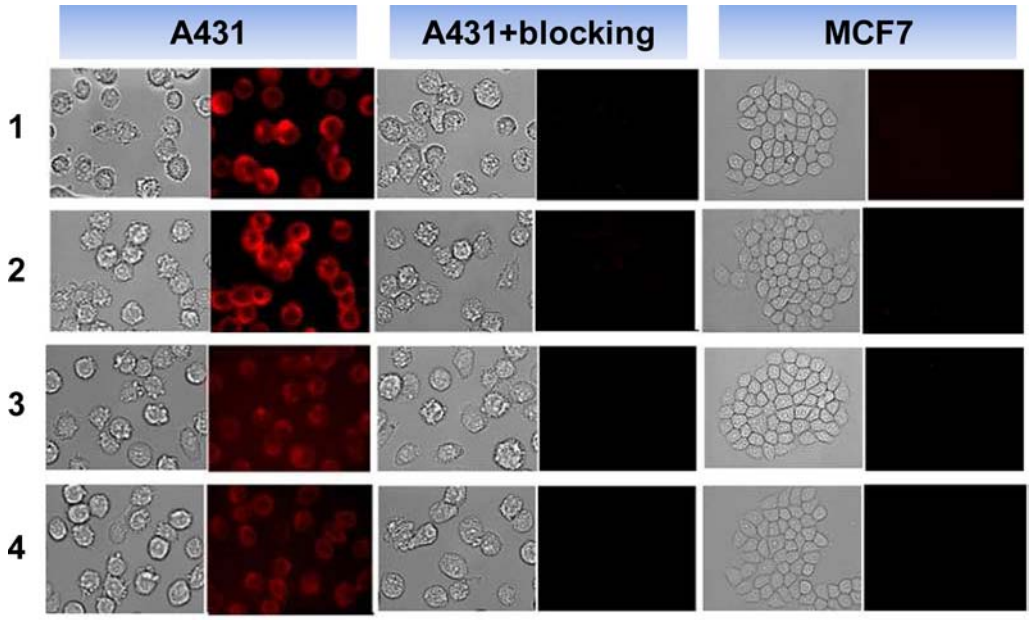

Figure 3. Cell uptake of the Cy5.5-$Z_{EGFR:1907}$ (**1**), Alexa680-$Z_{EGFR:1907}$ (**2**), SR680-$Z_{EGFR:1907}$ (**3**), and 800CW-$Z_{EGFR:1907}$ (**4**) (100 nM) in A431 and MCF7 cells at 37 °C incubated with (blocking) or without the presence of the Affibody molecule Ac-Cys-$Z_{EGFR:1907}$ (10 μM). NIR fluorescent and light images are shown at right and left column in each group, respectively.

all the probes. Interestingly, it was found that Cy5.5-$Z_{EGFR:1907}$ and 800CW-$Z_{EGFR:1907}$ showed high uptakes in kidneys, while Alexa680-$Z_{EGFR:1907}$ and SR680-$Z_{EGFR:1907}$ displayed much lower uptakes in kidneys, which is consistent with the *in vivo* imaging data (Figure 4A). Quantitative analysis further revealed that Cy5.5-$Z_{EGFR:1907}$, Alexa680-$Z_{EGFR:1907}$, and SR680-$Z_{EGFR:1907}$ had similar tumor to blood, tumor to muscle, and tumor to lung ratios ($p > 0.05$). In contrast, 800CW-$Z_{EGFR:1907}$ exhibited much lower tumor to normal organ ratios in general (Figure 5B, $p < 0.05$).

DISCUSSION

NIRF imaging is emerging as a powerful tool for noninvasively imaging diseases in preclinical studies, and it also has a great potential in clinical applications such as providing real-time surgical information, as well as functional/molecular information of the disease process. Optical molecular probes with high sensitivity, stability, fast targeting, and rapid clearance can usually be readily prepared.[15,26] EGFR is an important tumor biomarker. *In vivo* optical imaging of EGFR has been extensively investigated using monoclonal antibody such as cetuximab (Erbitux) labeled with NIR dyes.[27,28] However, Cy5.5-labeled cetuximab suffered from slow localization and clearance. NIR dye labeled EGF protein has also been studied for *in vivo* imaging.[29] However, EGF as a native ligand has significant side effects such as vomiting and diarrhea, as consequences of stimulation of EGFR.[30] Furthermore, NIR nanoparticles such as quantum dots have also been used to conjugate with reduced EGF(r-Egf) for imaging. However, this method was reported to suffer from poor imaging quality and significant toxicity.[31] Therefore, new strategies for development of optical probes for EGFR are highly desired.

Affibody proteins have been demonstrated to be great platforms for molecular probe development.[13,14] HER2 and EGFR specific Affibody molecule based optical probes have been studied and successfully used for cell imaging and *in vivo* tumor imaging.[19,20,29,30,32,33] In one of our recent studies, the anti-EGFR Affibody molecule, Ac-Cys-$Z_{EGFR:1907}$, was radiolabeled with ^{64}Cu and displayed fast tumor targeting, good tumor uptake, and long retention.[19] Furthermore, in an accompanying study we also site-specifically conjugated Ac-Cys-$Z_{EGFR:1907}$ with Cy5.5-monomaleimide and demonstrated that this optical probe rapidly achieved good tumor-to-normal tissue contrasts.[20] It should also be noted here that one important advantage of this particular anti-EGFR Affibody molecule over the native ligand EGF in molecular imaging lies in its inability to stimulate the EGFR signaling pathway.[33] As a consequence, unlike EGF this Affibody protein will not cause side effects such as vomiting and diarrhea if it is used for clinical purposes. With this proof-of-principle study, we are confident of the potential that the Affibody-based optical imaging probes possess for EGFR-targeted cancer molecular imaging. However, to take one step forward in translating Affibody molecules to clinical optical imaging of EGFR positive cancers we feel that it is of much importance that a systematic approach be taken to evaluate NIR dyes that are currently available. Beyond the commonly used dyes such as Cy5.5, the optical EGFR probe that has the best performance after the systematic evaluation would in theory give the highest sensitivity, which is crucial in clinical applications such as surgical guidance. Thus, in this study four anti-EGFR Affibody based probes were prepared with promising NIR fluorescence dyes, and their *in vivo* performance was systematically evaluated both in cell culture and in tumor bearing mice.

To prepare the proposed probes, the Affibody analogue, Ac-Cys-$Z_{EGFR:1907}$, was synthesized using the solid-phase peptide synthesis method. The purified protein was site-specifically conjugated with NIR fluorescent dyes including Cy5.5-monomaleimide, Alexa-Fluor-680-maleimide, IRDye-800CW-maleimide, and SRfluor680-maleimide to prepare Cy5.5-$Z_{EGFR:1907}$, Alexa680-$Z_{EGFR:1907}$, SR680-$Z_{EGFR:1907}$, and 800CW-$Z_{EGFR:1907}$. Conjugation of the small protein with four monomaleimide fluorescent dyes was straightforward and could be successfully completed in PBS. As expected, the

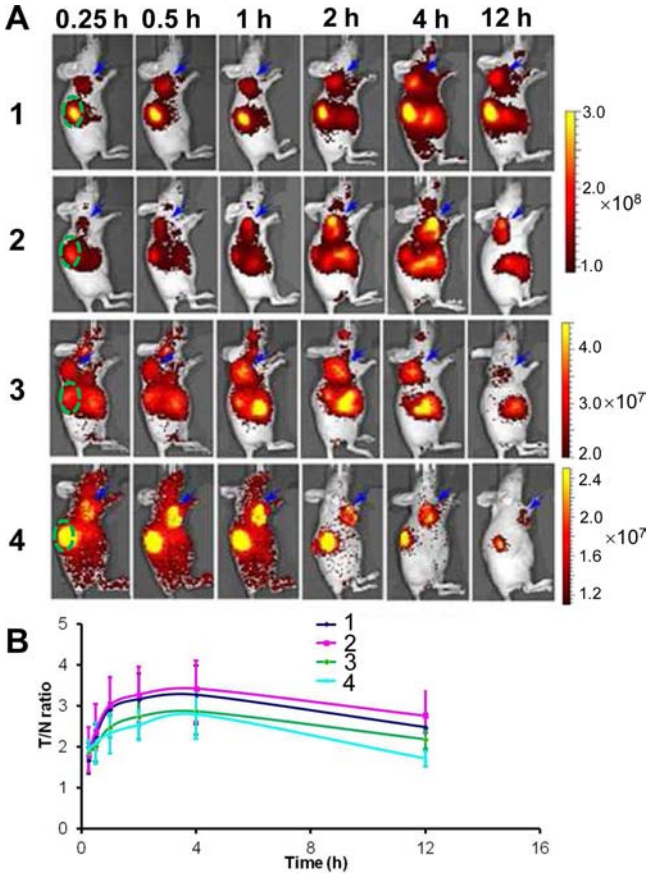

Figure 4. (A) In vivo fluorescence imaging of subcutaneous A431 tumor-bearing nude mice at 0.25, 0.5, 1, 2, 4, and 12 h after injection of 0.5 nmol Cy5.5-$Z_{EGFR:1907}$ (**1**), Alexa680-$Z_{EGFR:1907}$ (**2**), SR680-$Z_{EGFR:1907}$ (**3**), or 800CW-$Z_{EGFR:1907}$ (**4**). Arrows in blue color and ovals in green color indicate the location of tumors and kidneys, respectively. (B) ROI analysis of tumor-to-normal tissue ratios of the four probes in mice bearing A431 tumor at different time points p.i. (n = 5).

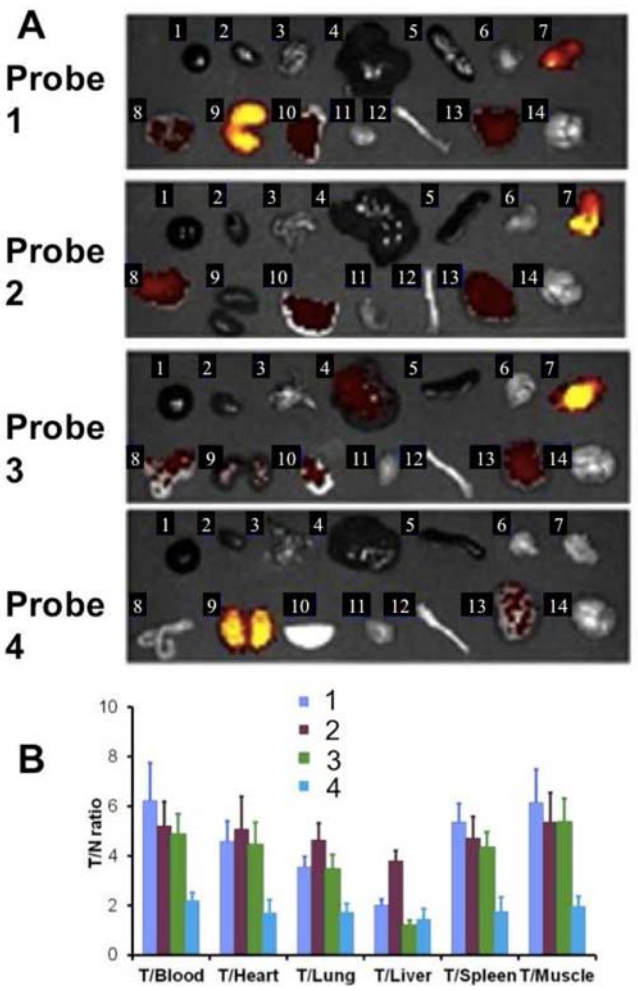

Figure 5. (A) Representative *ex vivo* NIRF images of dissected organs of mice bearing A431 tumor sacrificed 24 h after intravenous injection of Cy5.5-$Z_{EGFR:1907}$ (Probe 1), Alexa680-$Z_{EGFR:1907}$ (Probe 2), SR680-$Z_{EGFR:1907}$ (Probe 3), or 800CW-$Z_{EGFR:1907}$ (Probe 4) at a dose of 0.5 nmol per mouse. The numeric label for each organ is as follows: 1: Blood; 2: Heart; 3: Lung; 4: Liver; 5: Spleen; 6: Pancreas; 7: Stomach; 8: Intestines; 9: Kidneys; 10: Skin; 11: Muscle; 12: Bone; 13: Tumor; 14: Brain. (B) Fluorescence intensity ratios of tumor-to-normal tissues based on the ROI analysis. Error bar was calculated as the standard deviation (n = 5).

absorption and emission fluorescence properties of the probes remained very close to the unconjugated dyes (Figure 2B). Using FACS analysis, it was found that Cy5.5-$Z_{EGFR:1907}$ and Alexa680-$Z_{EGFR:1907}$ exhibited high binding affinity, while SR680-$Z_{EGFR:1907}$ had much lower binding affinity (Table 1), suggesting that different fluorescent dyes could affect the bioactivity of the resulting probes. The cell uptake and binding specificity of the four NIR fluorescent Affibody probes were studied with high-EGFR-expressing A431 cells as well as low-EGFR-expressing MCF7 cells using fluorescence microscopy. The results showed that with all four fluorescent Affibody analogues the majority of the probes bound to cell surface receptors at 1 h incubation, indicating slow internalization of the Affibody molecules. Importantly, the specificity of all the probes was verified by both blocking with unlabeled Affibody and their low uptakes in low EGFR expressing MCF7 cells (Figure 3). Interestingly, it was also found that SR680-$Z_{EGFR:1907}$ displayed low signals in A431 cells with a high background. This could be caused by its relatively low binding affinity than that of Cy5.5-$Z_{EGFR:1907}$ and Alexa680-$Z_{EGFR:1907}$. In general, the reasonable tumor cell binding affinity and high specificity warranted further evaluations and characterizations of the four probes with *in vivo* tumor imaging study, particularly Cy5.5-$Z_{EGFR:1907}$ and Alexa680-$Z_{EGFR:1907}$, given their high binding affinity.

Whole-body optical imaging of subcutaneous tumor xenograft mice was then performed by the IVIS-200 system. As shown in Figure 4A, the subcutaneous A431 tumor could be clearly distinguished from the surrounding tissue from 0.25 h up to 12 h p.i. of 0.5 nmol of each probe. It was found that all probes showed fast tumor targeting and good T/N contrast as early as 0.25 h p.i.; the T/N ratio reached the peak at 2 to 4 h p.i. by ROI analysis of images (Figure 4B) before the probes were slowly washed out over time. The favorable *in vivo* imaging results of these probes are attributable at least partially to fast tumor targeting and rapid blood clearance abilities of Affibody molecules.

Although all four probes displayed favorable *in vitro* and *in vivo* characteristics, there did exist some significant differences. In particular, Cy5.5-$Z_{EGFR:1907}$ and Alexa680-$Z_{EGFR:1907}$ showed higher T/N ratios than other two, though it is not significant,

dx.doi.org/10.1021/bc200596a | *Bioconjugate Chem.* 2012, 23, 1149–1156

which is consistent with the fact that these two probes possess high binding affinity (Figure 4B). More importantly, compared to Cy5.5-$Z_{EGFR:1907}$ and 800CW-$Z_{EGFR:1907}$, both Alexa680-$Z_{EGFR:1907}$ and SR680-$Z_{EGFR:1907}$ were found to show much lower uptakes in kidneys especially at later time points (Figure 4A and Figure 5A). Their distribution patterns in liver, which is characterized by EGFR overexpression, were also variable. While Cy5.5-$Z_{EGFR:1907}$, Alexa680-$Z_{EGFR:1907}$, and SR680-$Z_{EGFR:1907}$ all showed expectedly high liver uptakes that were comparable to corresponding tumor uptakes from 0.25 to 12 h p.i., 800CW-$Z_{EGFR:1907}$ showed significantly lower liver uptake than its tumor uptake during the same time period (Figure 4A, $p < 0.05$). At 24 h p.i., however, Figure 5 showed that for all probes except 800CW-$Z_{EGFR:1907}$ tumor-to-liver ratios reached upward of 3-to-1, which indicated a more rapid washout from liver when compared with that of tumor for these 3 probes. The only exception is 800CW-$Z_{EGFR:1907}$, for which tumor-to-liver ratio approximated 1-to-1 at 24 h p.i.. This can be explained by a high washout rate from tumor and a relatively low washout rate from liver. Unfortunately, we were not able to characterize 800CW-$Z_{EGFR:1907}$ further regarding its binding affinity, but from *in vitro* fluorescent microscopy, we know that this probe displays inferior cell uptake, particularly when compared with Cy5.5-$Z_{EGFR:1907}$ and Alexa680-$Z_{EGFR:1907}$. The *ex vivo* imaging results also demonstrated that 800CW-$Z_{EGFR:1907}$ had the lowest tumor-to-normal organ ratio. It should also be noted here that there is one caveat when using OI to image liver. Liver, similar to spleen and kidneys, is notable for the dark color as well as a high concentration of hemoglobin, both of which can lead to a significant absorption of luminescent signals. Therefore, special considerations should be taken when interpreting liver uptake results from OI studies, particularly when one would like to compare these with nuclear imaging studies. Collectively, these data suggest that different NIRF dyes have variable impact on the *in vivo* behavior of the resulting Affibody-based probes. It is highly important to investigate the effects of different dyes on the *in vivo* profile of a biomolecule. Because of the high affinity and contrast, for further applications, Cy5.5-$Z_{EGFR:1907}$ and Alexa680-$Z_{EGFR:1907}$ are the most promising among all the probes tested in this research.

CONCLUSION

All anti-EGFR Affibody based NIRF probes studied in this research show good tumor imaging quality, tumor-to-normal tissue ratios, and fast tumor targeting ability, which demonstrates that the Affibody molecule Ac-Cys-$Z_{EGFR:1907}$ can be used for tumor EGFR optical imaging. Especially, Cy5.5-$Z_{EGFR:1907}$ and Alexa680-$Z_{EGFR:1907}$ are shown to be the most promising probes for further tumor imaging applications and clinical translations. Furthermore, it also demonstrates that different NIRF dyes have different impact on the *in vitro* binding and *in vivo* performance of the resulting Affibody based probes. Therefore, selection of an appropriate NIRF label is important for optical probe development.

AUTHOR INFORMATION

Corresponding Author

*650-723-7866 (Voice), 650-736-7925 (Fax), E-mail: zcheng@stanford.edu.

Notes

The authors declare no competing financial interest.

ACKNOWLEDGMENTS

This work was supported, in part, by a Startup fund from Department of Radiology, Stanford University (to Z.C.), and a fellowship from China Scholarship Council (to S. Q.).

ABBREVIATIONS:

EGFR, Epidermal growth factor receptor 1; NIR, near-infrared; PET, positron emission tomography; HPLC, high-performance liquid chromatography; p.i., postinjection

REFERENCES

(1) Jemal, A., Siegel, R., Xu, J., and Ward, E. (2010) Cancer statistics, 2010. *CA Cancer J. Clin. 60*, 277−300.

(2) Burris, H. A., 3rd. (2004) Dual kinase inhibition in the treatment of breast cancer: initial experience with the EGFR/ErbB-2 inhibitor lapatinib. *Oncologist 9* (Suppl 3), 10−5.

(3) Geyer, C. E., Forster, J., Lindquist, D., Chan, S., Romieu, C. G., Pienkowski, T., Jagiello-Gruszfeld, A., Crown, J., Chan, A., Kaufman, B., Skarlos, D., Campone, M., Davidson, N., Berger, M., Oliva, C., Rubin, S. D., Stein, S., and Cameron, D. (2006) Lapatinib plus capecitabine for HER2-positive advanced breast cancer. *N. Engl. J. Med. 355*, 2733−43.

(4) Jones, H. E., Goddard, L., Gee, J. M., Hiscox, S., Rubini, M., Barrow, D., Knowlden, J. M., Williams, S., Wakeling, A. E., and Nicholson, R. I. (2004) Insulin-like growth factor-I receptor signalling and acquired resistance to gefitinib (ZD1839; Iressa) in human breast and prostate cancer cells. *Endocr. Relat. Cancer 11*, 793−814.

(5) Van Cutsem, E., Kohne, C. H., Hitre, E., Zaluski, J., Chang Chien, C. R., Makhson, A., D'Haens, G., Pinter, T., Lim, R., Bodoky, G., Roh, J. K., Folprecht, G., Ruff, P., Stroh, C., Tejpar, S., Schlichting, M., Nippgen, J., and Rougier, P. (2009) Cetuximab and chemotherapy as initial treatment for metastatic colorectal cancer. *N. Engl. J. Med. 360*, 1408−17.

(6) Wang, H., Yu, J., Yang, G., Song, X., Sun, X., Zhao, S., and Mu, D. (2007) Assessment of 11C-labeled-4-N-(3-bromoanilino)-6,7-dimethoxyquinazoline as a positron emission tomography agent to monitor epidermal growth factor receptor expression. *Cancer Sci. 98*, 1413−6.

(7) Su, H., Seimbille, Y., Ferl, G. Z., Bodenstein, C., Fueger, B., Kim, K. J., Hsu, Y. T., Dubinett, S. M., Phelps, M. E., Czernin, J., and Weber, W. A. (2008) Evaluation of [(18)F]gefitinib as a molecular imaging probe for the assessment of the epidermal growth factor receptor status in malignant tumors. *Eur. J. Nucl. Med. Mol. Imaging 35*, 1089−99.

(8) Hosse, R. J., Rothe, A., and Power, B. E. (2006) A new generation of protein display scaffolds for molecular recognition. *Protein Sci. 15*, 14−27.

(9) Binz, H. K., Amstutz, P., and Pluckthun, A. (2005) Engineering novel binding proteins from nonimmunoglobulin domains. *Nat. Biotechnol. 23*, 1257−68.

(10) Lofblom, J., Feldwisch, J., Tolmachev, V., Carlsson, J., Stahl, S., and Frejd, F. Y. (2010) Affibody molecules: engineered proteins for therapeutic, diagnostic and biotechnological applications. *FEBS Lett. 584*, 2670−80.

(11) Nilsson, F. Y., and Tolmachev, V. (2007) Affibody molecules: new protein domains for molecular imaging and targeted tumor therapy. *Curr. Opin. Drug Discovery Dev. 10*, 167−75.

(12) Tolmachev, V., Orlova, A., Nilsson, F. Y., Feldwisch, J., Wennborg, A., and Abrahmsen, L. (2007) Affibody molecules: potential for in vivo imaging of molecular targets for cancer therapy. *Expert Opin. Biol. Ther. 7*, 555−68.

(13) Miao, Z., Levi, J., and Cheng, Z. (2010) Protein scaffold-based molecular probes for cancer molecular imaging. *Amino Acids,*.

(14) Cheng, Z., De Jesus, O. P., Namavari, M., De, A., Levi, J., Webster, J. M., Zhang, R., Lee, B., Syud, F. A., and Gambhir, S. S. (2008) Small-animal PET imaging of human epidermal growth factor receptor type 2 expression with site-specific 18F-labeled protein scaffold molecules. *J. Nucl. Med. 49*, 804−13.

(15) Lee, S. B., Hassan, M., Fisher, R., Chertov, O., Chernomordik, V., Kramer-Marek, G., Gandjbakhche, A., and Capala, J. (2008) Affibody molecules for in vivo characterization of HER2-positive tumors by near-infrared imaging. *Clin. Cancer Res. 14*, 3840−9.
(16) Miao, Z., Levi, J., and Cheng, Z. (2011) Protein scaffold-based molecular probes for cancer molecular imaging. *Amino Acids 41*, 1037−47.
(17) Lindborg, M., Cortez, E., Hoiden-Guthenberg, I., Gunneriusson, E., von Hage, E., Syud, F., Morrison, M., Abrahmsen, L., Herne, N., Pietras, K., and Frejd, F. Y. (2011) Engineered high-affinity affibody molecules targeting platelet-derived growth factor receptor beta in vivo. *J. Mol. Biol. 407*, 298−315.
(18) Friedman, M., Orlova, A., Johansson, E., Eriksson, T. L., Hoiden-Guthenberg, I., Tolmachev, V., Nilsson, F. Y., and Stahl, S. (2008) Directed evolution to low nanomolar affinity of a tumor-targeting epidermal growth factor receptor-binding affibody molecule. *J. Mol. Biol. 376*, 1388−402.
(19) Miao, Z., Ren, G., Liu, H., Jiang, L., and Cheng, Z. (2010) Small-animal PET imaging of human epidermal growth factor receptor positive tumor with a 64Cu labeled affibody protein. *Bioconjugate Chem. 21*, 947−54.
(20) Miao, Z., Ren, G., Liu, H., Jiang, L., and Cheng, Z. (2010) Cy5.5-labeled Affibody molecule for near-infrared fluorescent optical imaging of epidermal growth factor receptor positive tumors. *J. Biomed. Opt. 15*, 036007.
(21) Tolmachev, V., Orlova, A., Wei, Q., Bruskin, A., Carlsson, J., and Gedda, L. (2004) Comparative biodistribution of potential anti-glioblastoma conjugates [111In]DTPA-hEGF and [111In]Bz-DTPA-hEGF in normal mice. *Cancer Biother. Radiopharm. 19*, 491−501.
(22) Johnson, J. R., Fu, N., Arunkumar, E., Leevy, W. M., Gammon, S. T., Piwnica-Worms, D., and Smith, B. D. (2007) Squaraine rotaxanes: superior substitutes for Cy-5 in molecular probes for near-infrared fluorescence cell imaging. *Angew. Chem., Int. Ed. Engl. 46*, 5528−31.
(23) Arunkumar, E., Fu, N., and Smith, B. D. (2006) Squaraine-derived rotaxanes: highly stable, fluorescent near-IR dyes. *Chemistry 12*, 4684−90.
(24) Arunkumar, E., Forbes, C. C., Noll, B. C., and Smith, B. D. (2005) Squaraine-derived rotaxanes: sterically protected fluorescent near-IR dyes. *J. Am. Chem. Soc. 127*, 3288−9.
(25) Troy, T., Jekic-McMullen, D., Sambucetti, L., and Rice, B. (2004) Quantitative comparison of the sensitivity of detection of fluorescent and bioluminescent reporters in animal models. *Mol. Imaging 3*, 9−23.
(26) Cheng, Z., Wu, Y., Xiong, Z., Gambhir, S. S., and Chen, X. (2005) Near-infrared fluorescent RGD peptides for optical imaging of integrin alphavbeta3 expression in living mice. *Bioconjugate Chem. 16*, 1433−41.
(27) Withrow, K. P., Newman, J. R., Skipper, J. B., Gleysteen, J. P., Magnuson, J. S., Zinn, K., and Rosenthal, E. L. (2008) Assessment of bevacizumab conjugated to Cy5.5 for detection of head and neck cancer xenografts. *Technol. Cancer Res. Treat. 7*, 61−6.
(28) Wang, K., Li, W., Huang, T., Li, R., Wang, D., Shen, B., and Chen, X. (2009) Characterizing breast cancer xenograft epidermal growth factor receptor expression by using near-infrared optical imaging. *Acta Radiol. 50*, 1095−103.
(29) Adams, K. E., Ke, S., Kwon, S., Liang, F., Fan, Z., Lu, Y., Hirschi, K., Mawad, M. E., Barry, M. A., and Sevick-Muraca, E. M. (2007) Comparison of visible and near-infrared wavelength-excitable fluorescent dyes for molecular imaging of cancer. *J. Biomed. Opt. 12*, 024017.
(30) Cuartero-Plaza, A., Martinez-Miralles, E., Rosell, R., Vadell-Nadal, C., Farre, M., and Real, F. X. (1996) Radiolocalization of squamous lung carcinoma with 131I-labeled epidermal growth factor. *Clin. Cancer Res. 2*, 13−20.
(31) Diagaradjane, P., Orenstein-Cardona, J. M., Colon-Casasnovas, N. E., Deorukhkar, A., Shentu, S., Kuno, N., Schwartz, D. L., Gelovani, J. G., and Krishnan, S. (2008) Imaging epidermal growth factor receptor expression in vivo: pharmacokinetic and biodistribution characterization of a bioconjugated quantum dot nanoprobe. *Clin. Cancer Res. 14*, 731−41.
(32) Lyakhov, I., Zielinski, R., Kuban, M., Kramer-Marek, G., Fisher, R., Chertov, O., Bindu, L., and Capala, J. (2010) HER2- and EGFR-specific affiprobes: novel recombinant optical probes for cell imaging. *ChemBioChem 11*, 345−50.
(33) Gong, H., Kovar, J., Little, G., Chen, H., and Olive, D. M. (2010) In vivo imaging of xenograft tumors using an epidermal growth factor receptor-specific affibody molecule labeled with a near-infrared fluorophore. *Neoplasia 12*, 139−49.

Bioconjugate Chemistry

Article

pubs.acs.org/bc

New Sequence-Defined Polyaminoamides with Tailored Endosomolytic Properties for Plasmid DNA Delivery

David Schaffert,*[,†,#] Christina Troiber,[†] and Ernst Wagner*[,†]

[†]Pharmaceutical Biotechnology, Department of Pharmacy, Center for Drug Research, and [‡]Center for NanoScience (CeNS), Ludwig-Maximilians-Universität Munich, Germany

Supporting Information

ABSTRACT: Heterogeneity of polymeric carriers is one of the most elusive obstacles in the development of nonviral gene delivery systems, concealing interaction mechanisms and limiting the use of structure–activity relationship studies. In this report, novel sequence-defined polyaminoamides, prepared by solid-phase assisted synthesis, were used to establish first structure–activity relationships for polymer-based plasmid DNA delivery. By combining a cationic building block with hydrophobic modifications and bioreversible disulfide cross-linking sites, transfection polymers with tailored lytic and DNA binding properties were designed. These polymers demonstrated clear correlation between structure and performance in lysis and DNA binding assays. In vitro studies showed negligible toxicity and highly efficient gene transfer, demonstrating the potential of this platform in the fast, combinatorial development of new transfection polymers.

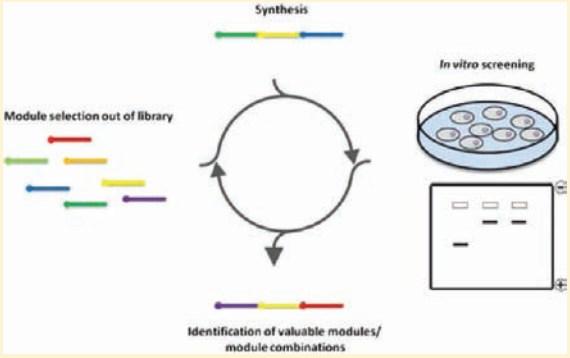

INTRODUCTION

Gene therapy is a promising therapeutic strategy based on the concept of treating a disease at its molecular point of origin.[1] By introducing new genetic material into target cells, deficient genes can be replaced by functional copies, new genes can be introduced into the cell, or existing expression patterns can be altered. These properties make gene therapy a potentially useful tool for treating diseases, which cannot be remedied by more conventional means.[2−4] Broad clinical use has not been achieved so far, due to the specific hurdles of delivering nucleic acids (NA) to the target cells. While recombinant viral delivery vectors are quite effectively used in clinical studies and demonstrate unequaled delivery efficiency, there are major concerns about their clinical safety with special emphasis on risks like insertional mutagenesis, immunogenicity, and inflammatory potential.[5,6] Polymeric delivery systems as alternatives allow faster development circles, easy modification, and increased loading capacity, and are in general better tolerated by the immune system. However, despite significant progress in the development of polymeric carriers, they are still characterized by a rather low efficiency and their potential is far from being fully exploited.

The low efficiency of nonviral vectors stems from the numerous extracellular and intracellular barriers entrapping or destroying significant amounts of the payload before entering the cell.[7] As most of the carrier systems enter cells by endosomal uptake routes, one of the biggest barriers is the successful escape out of the endosome. Viral delivery systems use a sophisticated protein machinery to interact with the endosomal microenvironment with the aim to escape the endosome.[8] The hemagglutinin, a glycoprotein of influenza virus A, for example, is triggered by the acidification of the endosome, causing a conformational change, which results in the fusion between viral and host cell membranes and penetration of the viral genome into the cytosol.[9] Polymeric systems employing complex structural changes like this have not been constructed up to now, but the described systems exploit similar endosomal escape characteristics. Polymeric carriers like polyethylenimine (PEI) or polyamidoamine (PAMAM) dendrimers utilize their high intrinsic buffer capacity to cause an osmotic burst of the endosome.[10] The required high endosomal concentration of these polymers necessitates the use of a large excess or a high M_w species to achieve an acceptable rate of success. To further improve their efficiencies, different strategies were introduced, e.g., the incorporation of membrane disrupting peptides[11,12] into the delivery system, or the use of hydrophobic modifications. These modifications increase the interactions with cellular membranes[13,14] and have also been used for stabilization and modulation of polymer nanoaggregate formation *in vitro* and *in vitro*.[15,16] Although all of these approaches have their advantages, they are still limited by the inherent heterogeneity of the polymeric carriers, which conceals precise structure–activity relationships. This is especially important for programmed, bioresponsive delivery systems, which consist of multiple domains including elements for targeting, shielding,

Received: November 14, 2011
Revised: April 16, 2012
Published: May 2, 2012

and release of the payload.[17] Increased molecular precision in the assembly of these systems would allow the design of even more complex systems. Hartman et al.[18] demonstrated recently the synthesis of linear polyaminoamides (PAAs) using solid-phase assisted synthesis. Adopting this approach for combinatorial polymer development, although with a different chemical strategy, gave access to highly defined and functionalized polymers. We recently described the synthesis of protected polyamino acid building blocks for fmoc solid-phase assisted polymer synthesis,[19] and their application in the construction of a modular polymeric platform for plasmid DNA (pDNA) and siRNA delivery was reported in a short communication.[20] The current paper describes in more detail the design and evaluation of 26 modular constructed PAAs for pDNA delivery. Polymers with tailored complexation capabilities and lytic activity were constructed by combining different elements for DNA binding, pH-triggered endosomal escape, and bioresponsive stabilization. Correlation of the results of pDNA complexation and pH-dependent lytic activity assays with their *in vitro* pDNA transfection potential allowed establishment of first structure–activity relationships for this new class of transfection reagents.

MATERIALS AND METHODS

Materials. Fmoc-amino acids and resins (base resins and preloaded resins) were purchased from IRIS Biotech, Marktredwitz, and Novabiochem GmbH, Darmstadt. PyBOP was bought from MultiSynTech GmbH, Witten. DCM, DMF, MeOH, and THF were obtained from Merck and distilled before use. Water was used as purified, deionized water. LPEI and fmoc-Stp(boc)$_3$-OH were synthesized as described.[19,21] DMSO, EtOH, ACN, deuterated solvents, and MTT bromide were obtained from Sigma-Aldrich (Munich, Germany). Plasmid pEGFPLuc (encoding a fusion of enhanced green fluorescent protein (EGFP) and *Photinus pyralis* luciferase under control of the CMV promoter) was produced with the Qiagen Plasmid Giga Kit (Qiagen, Hilden, Germany) according to the manufacturer recommendations. Cell culture media, antibiotics, and fetal calf serum were purchased from Invitrogen (Karlsruhe, Germany). Luciferase cell culture lysis buffer and D-luciferin sodium salt were obtained from Promega (Mannheim, Germany). All polymer characterization data can be found in the Supporting Information.

Synthesis of i-Shapes with two FAs: HO-K-Stp$_1$-K-FA$_2$. After swelling of fmoc-Lys(boc)-Wang resin (0.05–0.20 mmol) in DCM (30 min) and cleavage of the fmoc protecting group (20% piperidine in DMF, twice), 4 equiv of a solution of fmoc-Stp(boc)$_3$-OH in DMF, DIPEA (8 equiv), and PyBOP/HOBt (4 equiv) were added to the resin, and the vessel was agitated until Kaiser test indicated complete conversion (30 min). The reaction solvent was drained, and the resin was washed five times with DMF. To couple two fatty acids to the N-terminus of the PAA, fmoc-Lys(fmoc)-OH was incorporated before the coupling of the fatty acid. To cap residual, unreacted primary amino groups before introduction of the fatty acid, the resin was acetylated using 5 equiv of acetic anhydride and 10 equiv of DIPEA, before subsequent removal of the fmoc protecting group. The resin was washed three times with DMF followed by three DCM washes after removal of the fmoc protecting group. Ten equivalents of the fatty acid were dissolved in DCM and were added to the resin together with 10 equiv of PyBOP/HOBt and 20 equiv of DIPEA in the smallest possible amount of DMF. The mixture was agitated until Kaiser test indicated complete conversion (normally 30 min). After completion of the reaction, the resin was washed with DMF, DCM, and *n*-hexane and dried for 12 h over KOH *in vacuo*.

Synthesis of i-Shapes with Two Coupling Domains: HO-C-Stp$_3$-C-K-FA$_2$. After swelling 0.035 mmol of a fmoc-Cys(trt)-Wang resin in DCM and cleavage of the fmoc protecting group (20% piperidine in DMF, twice), 4 equiv of a solution of fmoc-Stp(boc)$_3$-OH in DMF, DIPEA (8 equiv), and PyBOP/HOBt (4 equiv) were added to the resin, and the vessel was agitated until Kaiser test indicated complete conversion (normally 30 min). The reaction solvent was drained and the resin was washed five times with DMF. This cycle was repeated twice. Afterward, the amino acid fmoc-Cys(trt)-OH was coupled. Then, in order to couple two fatty acids to the linear PAA, fmoc-Lys(fmoc)-OH was incorporated at the N-terminus before coupling the fatty acid. To cap unreacted primary amino groups, the resin was acetylated using 5 equiv of acetic anhydride and 10 equiv of DIPEA, before the subsequent removal of the fmoc protecting group. To couple the fatty acid, the solvent was changed to DCM after fmoc cleavage. Therefore, after removal of the fmoc protecting group, the resin was washed three times with DMF and DCM. Ten equivalents of the fatty acid were dissolved in DCM; 20 equiv of DIPEA, and 10 equiv of PyBOP/HOBt in DMF were added to the resin; and the mixture was agitated for 30 min. After completion of the reaction, the resin was washed with DMF, DCM, and *n*-hexanes and dried over KOH *in vacuo*.

Synthesis of T-Shapes with Two FAs: HO-C-Stp$_1$-K(K-FA$_2$)-Stp$_1$-C. After swelling 0.05–0.20 mmol of fmoc-Cys(trt)-Wang resin in DCM for 30 min, the fmoc protection group was cleaved (20% piperidine in DMF, twice). After washing the resin, 4 equiv of fmoc-Stp(boc)$_3$-OH, DIPEA (8 equiv) and PyBOP/HOBt (4 equiv) was added for 30 min. The reaction solvent was drained and the resin was washed five times with DMF. Reaction progress was monitored by Kaiser test. To introduce a branching point, dde-Lys(fmoc)-OH was used in the next coupling step. Dde-Lys(fmoc)-OH (4 equiv), DIPEA (8 equiv), and PyBOP/HOBt (4 equiv) dissolved in DMF were added, and the synthesis vessel was agitated for 30 min. After a negative Kaiser test, the resin was washed with DMF. After treatment with 20% piperidine in DMF and washing the resin with DMF, fmoc-Lys(fmoc)-OH (4 equiv), DIPEA (8 equiv), and PyBOP)/HOBt (4 equiv) were added. In order to cap unreacted primary amino groups, the resin was acetylated using 5 equiv of acetic anhydride and 10 equiv of DIPEA, before the subsequent removal of the fmoc protecting group. To couple the fatty acid, the solvent was changed to DCM after fmoc-cleavage. Therefore, the resin was washed three times with DMF and DCM after removal of the fmoc protecting group. Ten equivalents of the fatty acid dissolved in the minimal amount of DCM, 20 equiv of DIPEA and 10 equiv of PyBOP/HOBt were added to the resin for 30 min. After completion of the reaction, the resin was washed five times with DCM and three times with DMF. The dde protecting group was cleaved using 2% hydrazine monohydrate in DMF (10–15 times for 5 min) until no significant A_{300} was measurable in the deprotection mixture. After washing the resin 5 times with DMF, fmoc-Stp(boc)$_3$-OH, DIPEA (8 equiv) and PyBOP/HOBt (4 equiv) in DMF were added for 30 min. After successful reaction, the resin was treated twice with 20% piperidine in DMF. After washing the resin, boc-Cys(trt)-OH (4 equiv) dissolved in DMF, DIPEA (8 equiv), and PyBOP/HOBt (4 equiv) were added for 30 min. Afterward, the resin was washed and dried over KOH in vacuo.

Cleavage Conditions. For cleavage, the resin was treated with 10 mL/$g_{(resin)}$ of cleavage solution: PAAs without cysteines were treated with a TFA/water (95:5) mixture, whereas cysteine-containing PAAs were treated with a TFA/Water/TIS (95:2.5:2.5) mixture for 1−2 h. The resin was filtered off and washed twice using pure TFA followed by one DCM wash. The combined filtrates were concentrated and either precipitated by dropwise addition into ice-cold MTBE or other suitable mixtures. The precipitate was collected by centrifugation. The precipitate/film was dissolved in 5% acetic acid, snap-frozen, and lyophilized to obtain the PAA.

DNA Polyplex Formation Using PAA-Based Carriers. Polyplex formulations for pDNA delivery were prepared as follows: 200 ng of pDNA/well and the calculated amount of PAA were diluted in separate tubes in HBG pH 7.4. The pDNA solution was added to the polymer solution, mixed by pipetting, and incubated for 30−40 min at RT in order to form the polyplexes.

Electrophoretic Mobility Shift Assay. A 1% agarose gel was prepared by dissolving 1.2 g agarose in 120 mL TBE buffer and heating the mixture to 100 °C. After cooling down to approximately 50 °C, 120 μL Gel-Red (1 mg/mL) were added and the gel was poured in a casting unit. Polyplex-samples containing 200 ng pDNA, polymer, HBG-buffer, and loading buffer were placed into the pockets after an incubation time of 30 min at RT. Electrophoresis was performed at 120 V for 80 min.

Erythrocyte Leakage Assay. Murine erythrocytes were isolated from fresh, citrate buffered blood and washed with phosphate-buffered saline (PBS) several times. The erythrocyte pellet was diluted to 5×10^7 erythrocytes per mL with PBS (pH 7.4, 6.5, and 5.5). The polymers were diluted in 75 μL of PBS in a V-bottom 96-well plate (NUNC, Denmark). For 100% lysis, control wells contained buffer with 1% Triton X-100. A volume of 75 μL of erythrocyte suspension was added to each well, and the plates were incubated at 37 °C under constant shaking for 1 h. After centrifugation, 80 μL of the supernatant was analyzed for hemoglobin release at 405 nm using a microplate plate reader (Spectrafluor Plus, Tecan Austria GmbH, Grödig, Austria). PBS-buffers with pH values of 7.4, 6.5, and 5.5 were used as negative control. Relative hemolysis was defined as hemolysis (%) = (A_{405}(PAA treated) − A_{405}(buffer treated))/(A_{405}(TritonX treated − (A_{405}(Buffer treated)) × 100.

Measurement of Particle Size via Dynamic Light Scattering. DNA polyplexes were formed as follows: 10 μg of pEGFPLuc and 100 μg or 200 μg polymer, resulting in a weight to weight of 10 or 20, respectively, were diluted in separate tubes in buffer (20 mM HEPES pH 7.4) to a total volume of 25 μL. The pDNA solution was added to the polymer solution and mixed by rapidly pipetting up and down at least 5 times, resulting in a final pDNA concentration of 200 μg/mL. The incubation time was 30−40 min, in order to complete polyplex formation. The polyplex solution was then diluted 1:20 with buffer and measured in a folded capillary cell (DTS1061) with laser light scattering using a Zetasizer Nano ZS with backscatter detection (Malvern Instruments, Worcestershire, UK).

Luciferase Reporter Gene Expression. Cells were plated in 96-well plates at a density of 10 000 cells/well 24 h prior to transfection. The polyplexes, formed using 200 ng of pDNA/well, were added to the cells in 100 μL culture medium containing 10% serum, 100 U/mL penicillin, and 100 μg/mL streptomycin. Twenty-four hours after initial transfection, medium was removed and cells were lysed in 50 μL 0.5× Promega cell lysis solution to measure the gene expression. Luciferase activity was measured using a Lumat LB9507 instrument (Berthold, Bad Wildbad, Germany). Luciferase light units were recorded from a 20 μL aliquot of the cell lysate with 10 s integration time after automatic injection of freshly prepared luciferin using the luciferase assay system (LAR, Promega, Mannheim, Germany). Transfection efficiency was evaluated as relative light units (RLU) per number of seeded cells. Two nanograms of recombinant luciferase (Promega, Mannheim, Germany) corresponded to 10^7 light units.

Cell Viability Assay. The metabolic activity of polyplex-treated cells was determined in parallel to the transfection studies using a methylthiazole tetrazolium (MTT)[22] assay. Twenty-two hours after initiation of transfection, 10 μL per 100 μL of medium of a 5 mg/mL solution of MTT in sterile PBS-buffer was added per well. After incubation for 1−2 h at 37 °C, the medium was removed and the cells were frozen at −80 °C for at least 1 h. 200 μL DMSO were added and the samples were incubated under constant shaking at 37 °C for 30 min to dissolve the crystals completely. The optical absorbance was measured at 590 nm with a reference wavelength of 630 nm using a microplate reader (Spectrafluor Plus,Tecan Autstria GmbH, Grödig, Austria). The relative cell viability was defined as viability (%) = A_{590}(polyplex treated)/A_{590}(Buffer treated control) × 100.

RESULTS AND DISCUSSION

Design and Synthesis of Sequence-Defined Transfection Polymers. A small library of sequence-defined PAAs was designed with the aim of identifying a set of minimal prerequisites for efficient pDNA delivery. The design was limited to three structural motifs: compaction domain, lipophilic element, and dimerizing/cross-linking anchors. The compaction domain was introduced by variable repeats of Stp, an artificial polyamino acid mimicking the diaminoethane motif of PEI.[19] Lipophilic chains of varying length (C_4, C_8, C_{14}, C_{18}), anchored to the polymers either via their N-terminus or by acylation of both amines of a lysine, were used to control the lipophilicity. Cysteines were introduced to compensate for the rather small size of the synthesized polymers ($M_w \leq 3100$ Da) and to limit possible polyplex destabilization in serum. The disulfide bonds formed by oxidation of cysteine thiols have been reported to stabilize polyplexes in the rather low extracellular reductive potential and can be reduced in the cytosol to facilitate pDNA release.[23]

Figure 1 shows the general structures of the synthesized polymer families. The exact configuration of the modules was varied in the different families to allow impact analysis of the different modules. The simplest structural family is the PAA chain (**structure I**), constructed by linear chain elongation using Stp and/or amino acid units. These polymers, comparable to OEI800 in M_w and number of protonable amines, were included as negative controls. The PAA chain (**structure II**) contains two cysteine residues, introducing the ability to form disulfide bridges. Both families were hydrophobically modified using fatty acids (FA) at their N-terminus, resulting in the i-shape families (**structures III + IV**). The dimerizing i-shapes (**structure V**) were synthesized to test polyplex stabilization using dimerization anchors, whereas the symmetrical T-shape family (**structure VI**) was used to examine the influence of a changed polymer topology on

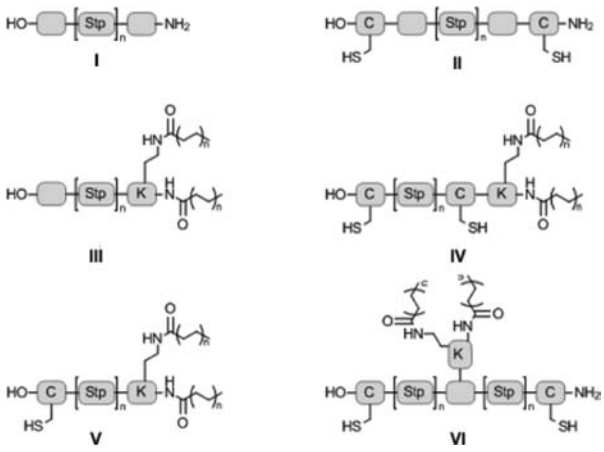

Figure 1. Structural overview over the different polymer families in the library. PAA chain (I), PAA chain with cross-linking cysteines (II), PAA with acylation at N-terminal lysine (i-shape type) without (III), with one dimerizing (V), or with two cross-linking cysteines (IV); PAA with acylation in the center (T-shape type) and cross-linking cysteines (VI).

transfection efficacy. Scheme 1 shows the general synthetic procedure using standard fmoc-synthesis conditions. A branching point was incorporated by using dde-Lys(fmoc)-OH to introduce a bis-fatty acid modified lysine at the center of the molecule. After successful side chain deprotection and introduction of the fatty acid residues, the dde protective group on the α-amino function was removed by hydrazine treatment and the synthesis continued. All polymers were cleaved from the support using a mixture of TFA/H_2O or TFA/H_2O/TIS and characterized by ^{1}H NMR. The sequences of all used polymers can be found in Table 1.

Evaluation of pH-Dependent Lytic Activity. To escape endosomal entrapment, an effective lytic activity of the carrier is a desirable prerequisite for successful delivery of nucleic acids into the cytosol. Potential cytotoxic interactions with cell membranes in the beginning of the transfection process should be reduced by using pH-specific lytic delivery systems, thereby lowering the overall cytotoxic potential of the carrier. The different polymer families were screened in a mouse erythrocyte leakage assay system to identify structural motifs, resulting in lytic activity. All measured values were buffer-corrected and lysis caused by 1% Triton X-100 was set as 100%. By testing the polymers at different pH values, comparable to the pH of different stages of the endosome,[24] highly pH-specific lytic polymers were identified. Figure 2a shows the lytic activity

Table 1

polymer	sequence[a]
1	K-Stp_1-K
6	K-Stp_2-K
23	K-Stp_5-K
34	K-Stp_2-ButA
35	K-Stp_2-CapA
36	K-Stp_2-MyrA
37	K-Stp_2-OleA
8	K-Stp_2-K-$CapA_2$
9	K-Stp_2-K-$MyrA_2$
10	K-Stp_2-K-$OleA_2$
21	K-Stp_4-K-$MyrA_2$
22	K-Stp_4-K-$OleA_2$
69	C-Stp_2-K-$MyrA_2$
70	C-K-Stp_2-K-$MyrA_2$
72	C-Stp_2-K-$OleA_2$
71	C-K-Stp2-K-$OleA_2$
51	C-Stp_3-C-K
45	C-Stp_3-C-K-$MyrA_2$
46	C-Stp_3-C-K-$OleA_2$
76	C-Stp_1-K(K-OleA2)-Stp_1-C
49	C-Stp_2-K-(K-OleA2)-Stp_2-C
80	C-Stp_3-K(K-OleA2)-Stp_3-C
84	C-Stp_4-K(K-OleA2)-Stp_4-C
74	C-Stp_1-K(K)-Stp_1-C
78	C-Stp_3-K(K)-Stp_3-C
82	C-Stp_4-K(K)-Stp_4-C

[a]ButA, Butyric acid; CapA, Caprylic acid; MyrA, Myristic acid; OleA, Oleic acid.

Scheme 1. Solid-Phase Synthesis Procedure Exemplified by T-Shape Synthesis

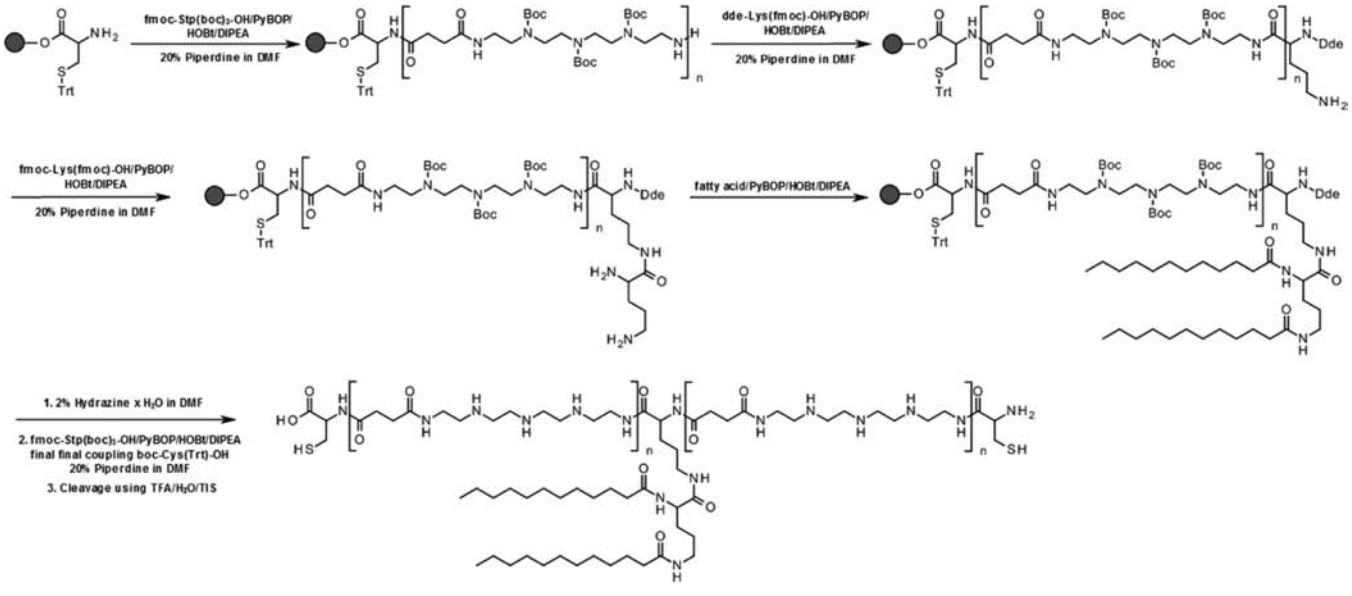

dx.doi.org/10.1021/bc200614x | *Bioconjugate Chem.* 2012, 23, 1157–1165

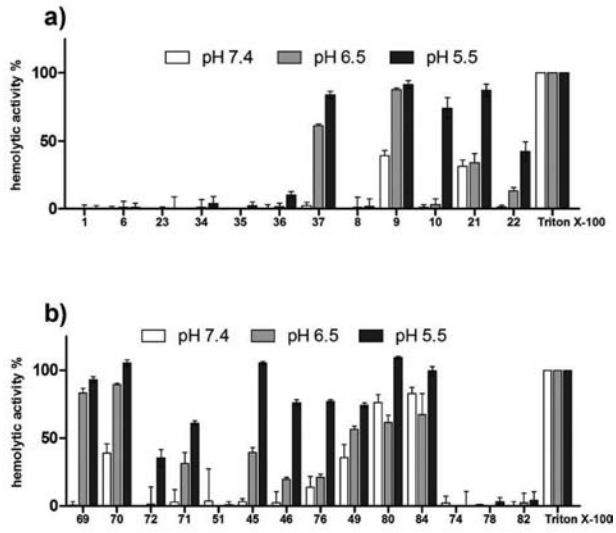

Figure 2. Relative pH-dependent lytic activity of the polymer library (5 μM). All values are buffer corrected; 1% Triton-X 100 was used as positive control. (a) Non-thiol-containing polymers. (b) Thiol-containing polymers.

of a subset of the library at pH 5.5, pH 6.5, and pH 7.4 in PBS. Lytic activity of the unmodified PAA backbone was assessed by the model sequences K-Stp$_1$-K (**1**), K-Stp$_2$-K (**6**); K-Stp$_5$-K (**23**). These plain PAA sequences did not demonstrate any lytic activity even at concentrations >5 μM (data not shown). Introduction of a single N-terminal fatty acid into a K-Stp$_2$ sequence (**34**–**37**) showed a slight increase in activity with oleic (**37**) and myristic acid (**36**) as the most effective modifications. In contrast, polymers modified with fatty acids < C_{14} (**34**, **35**) were not lytic.

Lytic potency of the polymers was further increased by using a N-terminal lysine as branching point for two fatty acids (double fatty acid motif). The increased lytic activity can be attributed to the close vicinity of the fatty acids resembling the general structure of amphipathic lipids.[25] Acylation of the N-terminal lysine, using caprylic acid (**8**), did not result in strong lytic activity, due to the rather short alkyl chain. Incorporation of myristyl residues (**9**), however, resulted in strong, unspecific lysis already causing up to 40% of erythrocyte rupture at neutral pH. Oleic acid modification (**10**) led to moderate, highly pH-specific lytic activity, rendering this modification the most valuable. A generally advantageous trend of an increased activity at lower pH was observed for all PAAs double-modified with fatty acid. This pH-specificity might be caused by the increased protonation of the polyamine backbone at the slightly acidic pH and, thus, increased interaction with negatively charged domains of the cell membranes. The size of the nucleic acid binding domain had only moderate effects on lytic activity (**21** vs **9**, **10** vs **22**) and did not influence the pH-dependency. A plausible explanation is the reduced molar proportion of the hydrophobic domain in the polymer, indicating that 2–3 Stp units may be the optimal chain length for specific and high lytic activity, using polymers with one hydrophobic module. The introduction of cysteines into the sequence as dimerization/cross-linking handle did not significantly alter the extent and pH-specificity of erythrocyte lysis (**9**, **10** vs **70**, **71** and **45**, **46**).

The position of the hydrophobic element had no significant influence on the specificity of lytic activity, when comparing oleic acid modified i-shapes and T-shapes (**45** vs **76**). However, with increasing molecular weight of the T-shapes (**76**, **49**, **80**, **84**) an increase in general lytic potency was observed. This is probably connected to a stronger interaction of the polymers with the negatively charged cell membrane. The corresponding control polymers (**74**, **78**, **82**) without fatty acid modification demonstrated no lytic activity, confirming the need of hydrophobic modification for lytic cell membrane interaction.

The results clearly demonstrate that the lytic activity of the polymers can be controlled by their molecular structure, especially by the substitution pattern and type of fatty acids used. Whereas unmodified PAAs demonstrated no lytic activity, introduction of fatty acids with a chain length of > C_8 resulted in significant lytic activity. This was amplified by the use of a double fatty acid motif. The pH-specificity of the lytic activity was controlled by the type of fatty acid used. Oleic acid modification resulted in the most specific lytic activity of the tested polymers.

DNA Binding. The interaction of the polymers with pDNA was evaluated using an agarose gel shift assay (Figure 3), in

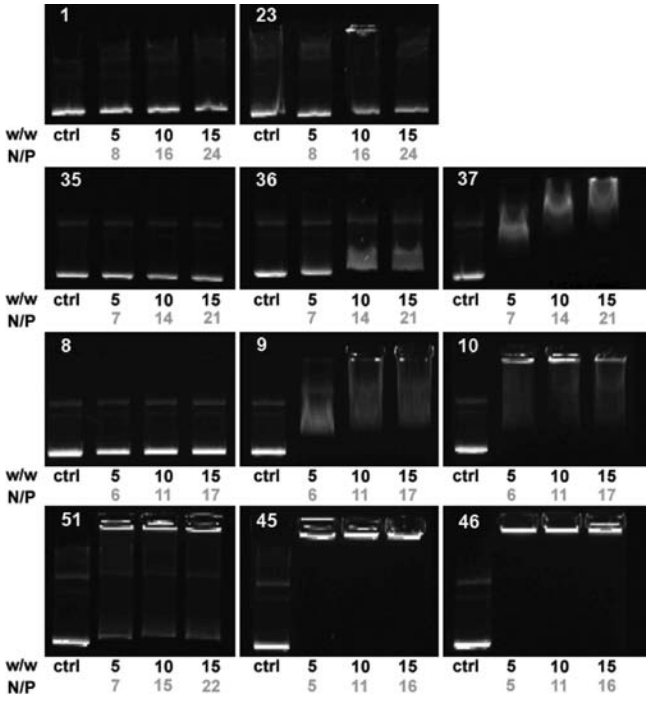

Figure 3. Electrophoretic mobility shift assay of different PAA/pDNA complexes in HBG at different w/w ratios.

which binding strength correlates to the amount of polymer needed for complete pDNA retardation. Polymers with only Stp and terminal lysines were not able to inhibit pDNA migration at the tested concentrations (**1**, **23**). To identify a minimal binding motif, the short K-Stp$_2$ sequence was modified either with a single N-terminal fatty acid (**35**–**37**) or the double fatty acid modified lysine motif (**8**–**10**), which were already used to increase the lytic activity. Single N-terminal fatty acid modification of the polymers resulted only in the case of oleic acid (**37**) in some, however, weak pDNA interaction at w/w 15 (N/P = 21). Introduction of a second fatty acid via a lysine branching point significantly improved interaction with pDNA. The dual fatty acid motif displayed strong pDNA/polymer interactions with almost complete pDNA retardation at a w/w of 10 (**8**–**10**, N/P = 11) if the fatty acid was either C_{14} (**9**) or C_{18} (**10**). Use of a C_8 (**8**) modification did not result

dx.doi.org/10.1021/bc200614x | *Bioconjugate Chem.* 2012, 23, 1157–1165

in pDNA retardation at the tested concentrations. These results were reflected by DLS-measurements (Figure 4). Thus, neither

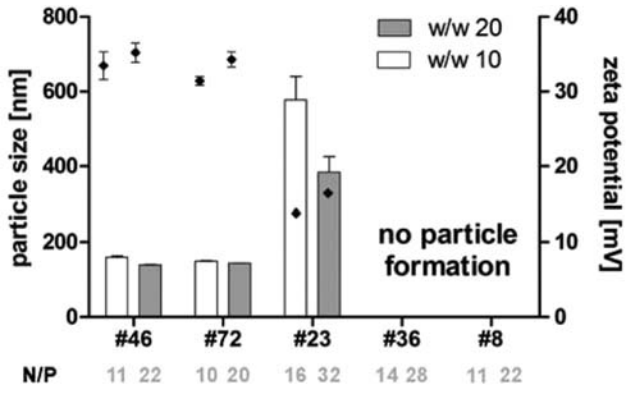

Figure 4. Particle size and zeta potential of selected examples out of the different PAA families, formed in HEPES buffer at different w/w ratios (bars represent the measured particle size, rhombi the measured zeta potential).

the double C_8 (**8**) modified nor the single C_{14} (**36**) modified polymer were able to form stable polyplexes. However, particle formation was observed with unmodified polymer **23** (17 protonable nitrogens). These polyplexes were characterized by a size of more than 400 nm and a zeta potential of +15 mV, supporting the hypothesis of rather weak interactions between polymer and pDNA, as observed in the gel-shift assay. The introduction of two cysteines into the polymers (**45**, **46**, **51**) showed only a moderate effect on polyplex stabilization in the gel shift assay. Polymer **51** containing 3 Stp units and 2 cysteines displayed incomplete pDNA retardation, whereas the fatty acid modified dimerizing polymers (**45**, **46**) were able to efficiently complex the pDNA at w/w ratios of 5 (N/P = 5). Only polymers containing 6 or more Stp units and cysteine modifications (**78**, **82**, Supporting Information) showed comparable interaction with pDNA. The stabilizing effect of cysteine incorporation could also be observed in DLS measurements (Figure 4; **46**, **72**). The resulting polyplexes had a size below 200 nm and a zeta potential around +30 mV, irrespective of modification with one (**72**) or two cysteines (**46**).

Taken together, these results showed that polyplex stabilization was controlled by all three used motifs. Hydrophobic modification played a key role in lytic activity, but it had only supporting function in stabilizing the polyplex. By contrast, size of compaction domain (number of charges) and stabilization by disulfide bridging or cross-linking had a more pronounced influence on particle formation. This allowed tailoring of polymer/DNA interaction strength, which supported the formation of stable particles in the extracellular environment and their efficient disassembly in the cytosol.

Transfection Efficiency and Cytotoxicity. The transfection efficiency of the different polymers was assessed in vitro, using Neuro2A cells and employing a pEGFPLuc reporter gene system. Linear polyethylenimine 22 kDa (LPEI 22 kDa) was used as control at its optimal w/w ratio of 0.8 (N/P = 6) to allow comparison of the different polymers. Due to the small size (1−3 kDa) of the screened polymers, property changes due to an altered polymer sequence were reflected in transfection efficiency and cytotoxicity, allowing quick assessment of the potential benefit of a modification.

To assess their delivery capability and toxicity, plain PAA chains and fatty acid modified sequences (i-shapes) were compared to K-Stp_5-K (**23**). This sequence resembles OEI_{800}, a rather weak performing member of the PEI family, in terms of M_w and number of protonable amines. As shown in Figure 5a, even the use of relatively high polymer concentrations (w/w 20, N/P = 32) displayed no significant increase of luciferase expression compared to untreated cells. One reason might be the inferior condensation properties of plain PAA sequences compared to the fatty acid modified PAAs (Figure 4, **23**), as well as the absence of lytic activity in the leakage assay (activity <10% at all pH values). The synergistic effect of polyplex stabilization and lytic activity was reflected in the reporter gene expression profiles of all fatty acid modified polymers. Modification of a K-Stp_2-K sequence with either myristic (**9**) or oleic acid (**10**) increased the transfection compared to K-Stp_5-K (**23**) 10-fold at w/w 10 (N/P = 11). Elongation of the chain by two additional Stp units (**21** and **22**) resulted in an up to 100-fold increase of reporter gene expression. This was accompanied by a moderate increase in cytotoxicity for the myristic acid derivatives in all tested concentrations (**9** and **21**). Oleic acid modification had a comparable effect on transfection efficiency, whereas the toxicity of the polymers in the tested concentration range was negligible (**10** and **22**). Compared to the LPEI control, all polymers showed a 1000-fold lower transfection activity, but demonstrated the beneficial influence of hydrophobic modifications on polyplex stability and gene delivery.

To study the influence of a dimerization handle on transfection efficiency, a single C-terminal cysteine was introduced into i-shape sequences (**69**−**72**). The introduction of the C-terminal cysteine into fatty acid bearing polymers showed no significant impact on pDNA complexation, as a w/w of 10 (N/P = 10−11) was still sufficient for complete retardation (see Supporting Information). However, using these dimerizable, fatty acid modified PAAs for pDNA delivery had a significant effect on reporter gene expression. In comparison to their analogous sequences K-Stp_2-K-$MyrA_2$ (**9**) and K-Stp_2-K-$OleA_2$ (**10**), the cysteine containing polymers (**69** and **71**) demonstrated a 100-fold increased reporter gene expression at a w/w of 10 (N/P = 10−11). To evaluate the possible influence of the primary amine of the lysine residue on pDNA delivery, sequences without the lysine were screened. Whereas the lysine had no significant effect on the oleic acid modified PAAs (**72** vs **71**), the delivery efficiency of **69** compared to **70** was increased 100-fold. Oleic acid modification had no pronounced effect on cell viability, regardless of sequence composition. C-terminal cysteine modification seemed to be a viable option to increase the delivery capability of short-chain PAAs, a theory which was additionally supported by the results of DLS-measurements (Figure 4), demonstrating the increased stability of cysteine containing polyplexes. These results supported the hypothesis that PAA polymers without the ability of disulfide bridge formation suffer from inadequate stabilization of the resulting polyplexes.

By insertion of a second cysteine into the sequence, the polymers gained the ability of in situ polymerization, allowing the formation of larger polymeric structures. Gel retardation assay (see Supporting Information) showed that in comparison with single cysteine modified PAAs the pDNA complexation was improved, but still heavily dependent on hydrophobic modifications. Figure 5b (**45**, **46**, **51**) showed the reporter gene expression of the cross-linking i-shape formulations with

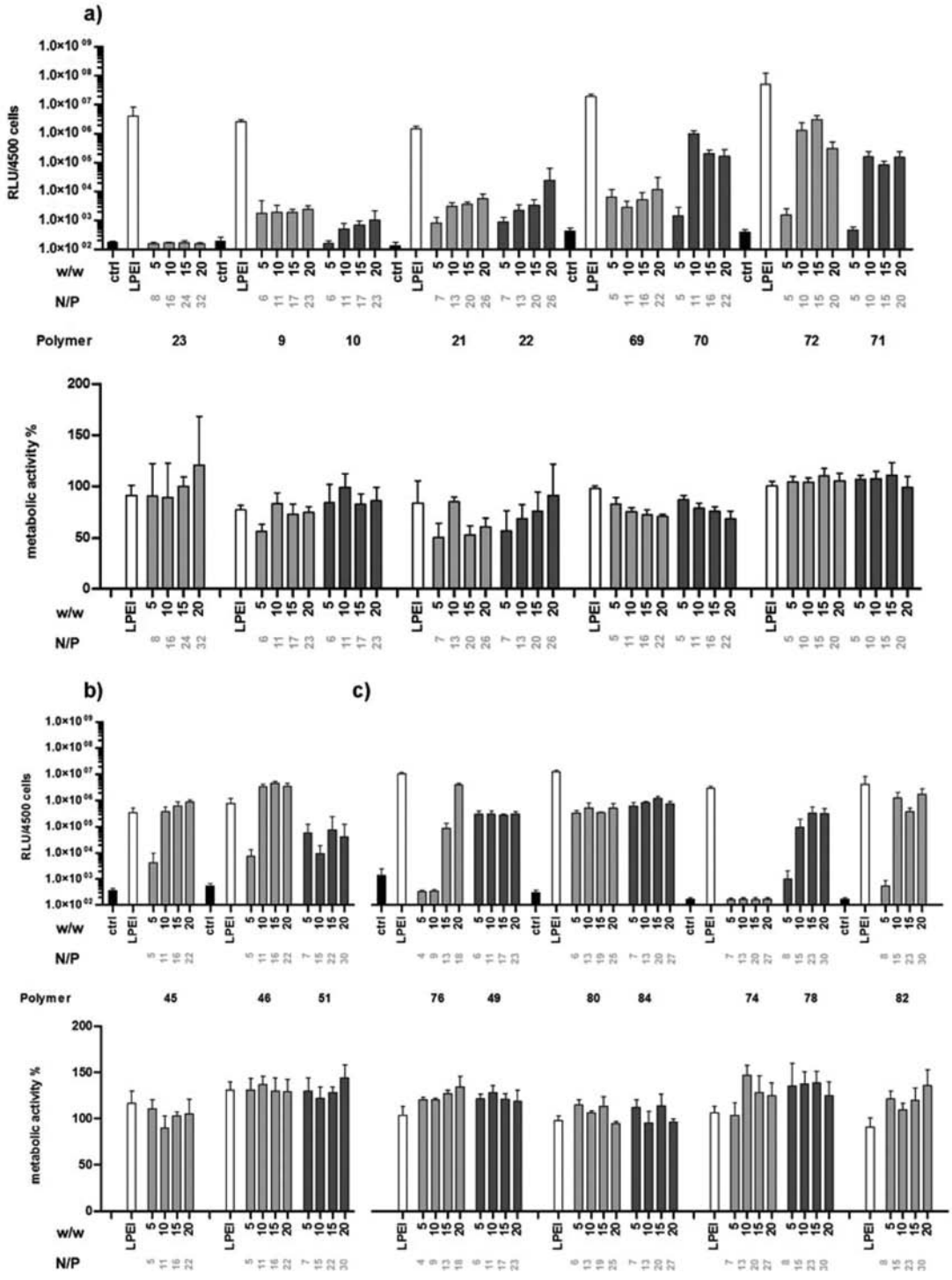

Figure 5. Luciferase reporter gene expression and metabolic activity in Neuro2a cells 24 h after transfection. Polyplexes were formed at different w/w ratios (polymer/DNA); the LPEI control was always used at its optimal w/w of 0.8 (N/P = 6).

different fatty acid modifications on a C-Stp$_3$-C-K backbone. The polymers were able to effectively transfer pDNA into target cells and showed a transgene expression profile characterized by a plateau phase beginning at w/w 10 (N/P = 11−15). As soon as this concentration was reached, reporter gene expression was not increased by higher polymer concentrations. For other polymeric delivery systems, this effect was normally connected to increased cytotoxicity at higher polymer concentrations, resulting in reduced transfection levels. In the case of the PAA systems, the MTT assay did not show toxic side effects, indicating additional intracellular delivery bottlenecks. The myristic and oleic acid modified i-shapes were able to compete with the LPEI control in terms of luciferase expression, demonstrating the delivery potential of these structures. The use of the backbone control polymer (**51**) resulted in a 10- to 50-fold lower efficiency, highlighting the importance of the hydrophobic modification.

By synthesizing a set of symmetrical polymers with a fixed, central hydrophobic domain (T-shapes), the influence of parameters, like the amount of protonable groups per molecule

dx.doi.org/10.1021/bc200614x | *Bioconjugate Chem.* 2012, 23, 1157−1165

and hydrophilic−lipophilic ratio, were studied. All tested polymers were modified with a dual oleic acid motif at the central lysine, as oleic acid modification was the most effective modification in terms of toxicity and efficiency in previous experiments. Figure 5c (compounds **49**−**84**) shows a comparison between dioleoyl modified T-shapes (**76**, **49**, **80**, **84**) and not hydrophobically modified linear chains with terminal cysteines (**74**, **78**, **82**). The oleoyl T-shape/pDNA complexes were strong enough to prevent migration in the gel at a w/w of 10 (N/P = 9−13), whereas the interaction of the unmodified chains at the same w/w (N/P = 13−15) was not strong enough to prevent NA migration (see Supporting Information). Figure 5c shows the transfection efficiency and cytotoxic potential of oleoyl T-shapes with different numbers of Stp building blocks per molecule. The balance between hydrophobic and cationic domain had a significant impact on efficacy, as seen by comparing the transfection efficiency of **49** and **76**. Whereas increasing concentrations of **76** led to reporter gene expression almost comparable with the LPEI control, the use of a polymer containing two additional Stp units resulted in an early, only moderate, plateau of activity. The introduction of additional Stp units did not improve their overall performance, regardless of tested concentrations. The reporter gene expression was always 10-fold lower than the LPEI control. These results indicated a fine balance between hydrophobicity and hydrophilicity as exemplified by **76**. Compound **76** had the highest molar proportion of fatty acid substitution in the screen and exhibited the strongest activity in terms of expression level. All other T-shape derivatives could not compete in terms of expression level and reached their maximum level at lower concentrations of w/w 5 (N/P = 6−7).

To verify the importance of the hydrophobic domain and to study the influence of polymer chain length on the efficiency of the T-shape polymers in more detail, a second set of polymers with increasing number of monomer units and without hydrophobic modification (but with cross-linking cysteines) was synthesized and screened (**74**, **78**, **82**). Here, the trend of chain length influence was reversed. Compound **74**, a structural analogue of **76**, did not show any reporter gene expression, whereas an increase in Stp-building blocks per molecule did result in an increasing gene expression (**78**, **82**). Compared to the gene expression levels of the oleoyl T-shapes, these polymers had the disadvantage of requiring rather high polymer concentrations to achieve comparable transfection efficiency. The dual fatty acid motif could increase the delivery efficiency, but the influence of the modification diminished with an increasing number of Stp units in the backbone. This supports earlier findings that the hydrophobic modification was more effective on smaller PAAs and could increase their efficiency dramatically, whereas an increasing amount of Stp units in a fatty acid-free polymer also resulted in an improved, but still less efficient delivery.

CONCLUSIONS

In this study, we successfully designed and synthesized a small library of sequence-defined polymers with optimized pH-dependent lytic activity, pDNA binding, and bioresponsive cargo release. Using a solid-phase assisted synthesis approach and a small set of different modules, we were able to construct sequence-defined, multifunctional polymers. Despite the small size (M_w 500−3100 Da) of the polymers, the library screen identified several polymers with a pDNA transfection efficiency comparable to LPEI. The polymers and the synthetic approach could be seen as model systems to increase the knowledge about the rational design of polymeric nonviral vectors and will ultimately lead to even more sophisticated, programmable polymeric vectors.

ASSOCIATED CONTENT

Supporting Information

Additional gel shift data for polymers (**49**, **69**, **70**, **71**, **72**, **74**, **76**, **78**, **80**, **82**, **84**) and analytical data of all polymers. This material is available free of charge via the Internet at http://pubs.acs.org.

AUTHOR INFORMATION

Corresponding Author

*Phone: ++49-89-2180-77840. Fax: ++49-89-2180-77798. E-mail: davidsch@mb.au.dk, ernst.wagner@cup.uni-muenchen.de.

Present Address

[#]Department of Molecular Biology, Århus University, C.F. Møllers Allé, Building 1130, DK-8000 Århus C, Denmark

Notes

The authors declare no competing financial interest.

Abbreviations:

ButA, Butyric Acid; CapA, Caprylic Acid; DCM, Dichloromethane; DMF, Dimethylformamide; DMSO, Diemethylsulfoxide; DLS, Dynamic Light Scattering; EtOH, Ethanol; FA, Fatty acid; HBG, HEPES-buffered glucose; HOBt, Hydroxybenzotriazol; LAR, Luciferase assay reagent; MeOH, Methanol; MTT, (3-(4,5-Dimethylthiazol-2-yl)-2,5-diphenyltetrazolium; MyrA, Myristic acid; NA, Nucleic acid; N/P, Nitrogen to Phosphate ratio; OleA, Oleic acid; PAA, Polyaminoamide; PAMAM, Polyamidoamine; PBS, Phosphate-buffered saline; pDNA, plasmid DNA; PEI, Polyethylenimine; RLU, relative light units; siRNA, Small interfering RNA; TBE, Tris-Borate-EDTA buffer; TFA, Trifluoroacetic acid; THF, Tetrahydrofurane

ACKNOWLEDGMENTS

This work was supported by the DFG Cluster "Nanosystems Initiative Munich", a grant from Roche, and the Biotech Cluster m4 project T12. We want to thank Matthias Wassenberg and Verena Brand for their technical assistance with the in vitro assays and Dr. Lars Allmendinger for helpful discussions about NMR techniques.

REFERENCES

(1) Friedmann, T., and Roblin, R. (1972) Gene therapy for human genetic disease? *Science 175*, 949−955.

(2) Ashtari, M., Cyckowski, L. L., Monroe, J. F., Marshall, K. A., Chung, D. C., Auricchio, A., Simonelli, F., Leroy, B. P., Maguire, A. M., Shindler, K. S., and Bennett, J. (2011) The human visual cortex responds to gene therapy-mediated recovery of retinal function. *J. Clin. Invest. 121*, 2160−8.

(3) Edelstein, M. L., Abedi, M. R., and Wixon, J. (2007) Gene therapy clinical trials worldwide to 2007--an update. *J.Gene Med. 9*, 833−842.

(4) Cavazzana-Calvo, M., and Fischer, A. (2007) Gene therapy for severe combined immunodeficiency: are we there yet? *J. Clin. Invest. 117*, 1456−1465.

(5) Escors, D., and Breckpot, K. (2010) Lentiviral vectors in gene therapy: their current status and future potential. *Arch. Immunol. Ther. Exp. (Warsz.) 58*, 107−19.

(6) Nair, V. (2008) Retrovirus-induced oncogenesis and safety of retroviral vectors. *Curr. Opin. Mol. Ther. 10*, 431−8.

(7) Wiethoff, C. M., and Middaugh, C. R. (2003) Barriers to nonviral gene delivery. *J. Pharm. Sci. 92*, 203−217.
(8) Mercer, J., Schelhaas, M., and Helenius, A. (2010) Virus entry by endocytosis. *Annu. Rev. Biochem. 79*, 803−33.
(9) Doms, R. W., Helenius, A., and White, J. (1985) Membrane fusion activity of the influenza virus hemagglutinin. The low pH-induced conformational change. *J. Biol. Chem. 260*, 2973−81.
(10) Behr, J. P. (1997) The proton sponge: A trick to enter cells the viruses did not exploit. *Chimia 51*, 34−36.
(11) Ogris, M., Carlisle, R. C., Bettinger, T., and Seymour, L. W. (2001) Melittin enables efficient vesicular escape and enhanced nuclear access of nonviral gene delivery vectors. *J. Biol. Chem. 276*, 47550−47555.
(12) Subbarao, N. K., Parente, R. A., Szoka, F. C., Jr., Nadasdi, L., and Pongracz, K. (1987) pH-dependent bilayer destabilization by an amphipathic peptide. *Biochemistry 26*, 2964−2972.
(13) Oskuee, R. K., Dehshahri, A., Shier, W. T., and Ramezani, M. (2009) Alkylcarboxylate grafting to polyethylenimine: a simple approach to producing a DNA nanocarrier with low toxicity. *J. Gene Med. 11*, 921−32.
(14) Philipp, A., Zhao, X., Tarcha, P., Wagner, E., and Zintchenko, A. (2009) Hydrophobically modified oligoethylenimines as highly efficient transfection agents for siRNA delivery. *Bioconjugate Chem. 20*, 2055−61.
(15) Barz, M., Tarantola, M., Fischer, K., Schmidt, M., Luxenhofer, R., Janshoff, A., Theato, P., and Zentel, R. (2008) From defined reactive diblock copolymers to functional HPMA-based self-assembled nanoaggregates. *Biomacromolecules 9*, 3114−8.
(16) Allmeroth, M., Moderegger, D., Biesalski, B., Koynov, K., Rosch, F., Thews, O., and Zentel, R. (2011) Modifying the body distribution of HPMA-based copolymers by molecular weight and aggregate formation. *Biomacromolecules 12*, 2841−9.
(17) Rozema, D. B., Lewis, D. L., Wakefield, D. H., Wong, S. C., Klein, J. J., Roesch, P. L., Bertin, S. L., Reppen, T. W., Chu, Q., Blokhin, A. V., Hagstrom, J. E., and Wolff, J. A. (2007) Dynamic PolyConjugates for targeted in vivo delivery of siRNA to hepatocytes. *Proc. Natl. Acad. Sci. U. S. A. 104*, 12982−12987.
(18) Hartmann, L., Krause, E., Antonietti, M., and Borner, H. G. (2006) Solid-phase supported polymer synthesis of sequence-defined, multifunctional poly(amidoamines). *Biomacromolecules 7*, 1239−1244.
(19) Schaffert, D., Badgujar, N., and Wagner, E. (2011) Novel Fmoc-polyamino acids for solid-phase synthesis of defined polyamidoamines. *Org. Lett. 13*, 1586−9.
(20) Schaffert, D., Troiber, C., Salcher, E. E., Frohlich, T., Martin, I., Badgujar, N., Dohmen, C., Edinger, D., Klager, R., Maiwald, G., Farkasova, K., Seeber, S., Jahn-Hofmann, K., Hadwiger, P., and Wagner, E. (2011) Solid-Phase Synthesis of Sequence-Defined T-, i-, and U-Shape Polymers for pDNA and siRNA Delivery. *Angew. Chem., Int. Ed. Engl. 50*, 8986−8989.
(21) Schaffert, D., Kiss, M., Rodl, W., Shir, A., Levitzki, A., Ogris, M., and Wagner, E. (2011) Poly(I:C)-mediated tumor growth suppression in EGF-receptor overexpressing tumors using EGF-polyethylene glycol-linear polyethylenimine as carrier. *Pharm. Res. 28*, 731−41.
(22) Mosmann, T. (1983) Rapid colorimetric assay for cellular growth and survival: Application to proliferation and cytotoxicity assays. *J. Immunol. Methods 65*, 55−63.
(23) Wang, Y., Chen, P., and Shen, J. (2006) The development and characterization of a glutathione-sensitive cross-linked polyethylenimine gene vector. *Biomaterials 27*, 5292−5298.
(24) Lee, R. J., Wang, S., and Low, P. S. (1996) Measurement of endosome pH following folate receptor-mediated endocytosis. *Biochim. Biophys. Acta 1312*, 237−242.
(25) Felgner, P. L., Gadek, T. R., Holm, M., Roman, R., Chan, H. W., Wenz, M., Northrop, J. P., Ringold, G. M., and Danielsen, M. (1987) Lipofection: A highly efficient, lipid mediated DNA-transfection procedure. *Proc. Natl. Acad. Sci. U. S. A. 84*, 7413−7417.

Bioconjugate Chemistry

Article

pubs.acs.org/bc

Carbohydrate-Coated Fluorescent Silica Nanoparticles as Probes for the Galactose/3-Sulfogalactose Carbohydrate−Carbohydrate Interaction Using Model Systems and Cellular Binding Studies

Jingsha Zhao,[†] Yuanfang Liu,[‡] Hyun-Joo Park,[‡] Joan M. Boggs,[‡,§] and Amit Basu*[,†]

[†]Department of Chemistry, Brown University, Providence, Rhode Island 02912, United States

[‡]Molecular Structure and Function Program, Research Institute, Hospital for Sick Children, Toronto, Ontario, Canada M5G 1X8

[§]Department of Laboratory Medicine and Pathobiology, University of Toronto, Toronto, Ontario, Canada M5G 1L5

Supporting Information

ABSTRACT: The carbohydrates galactose and 3-sulfogalactose, found on sphingolipids in myelin, interact with each other via a carbohydrate−carbohydrate interaction (CCI). In oligodendrocytes, this interaction triggers a signaling cascade resulting in cytoskeletal rearrangements and reorganization of glycolipids and proteins at the cellular surface. These rearrangements can also be triggered by synthetic multivalent glycoconjugates. In this report, we describe the synthesis of glycan-coated silica nanoparticles and their subsequent binding to cultured oligodendrocytes and purified myelin. Fluorescent silica nanoparticles with an azidosiloxane-derived outer shell were functionalized with carbohydrates using the copper-promoted azide−alkyne cycloaddition reaction. The carbohydrate−carbohydrate interaction between galactose and 3-sulfogalactose was examined by measuring the binding of 3-sulfogalactose-containing nanoparticles to galactolipids that had been immobilized in a multiwell plate. Particle aggregation mediated by CCI was observed by TEM. The interaction of the particles with oligodendrocytes and purified myelin was examined using fluorescence microscopy, providing direct evidence for binding of galactose and 3-sulfogalactose-coated nanoparticles to oligodendrocytes and myelin fragments.

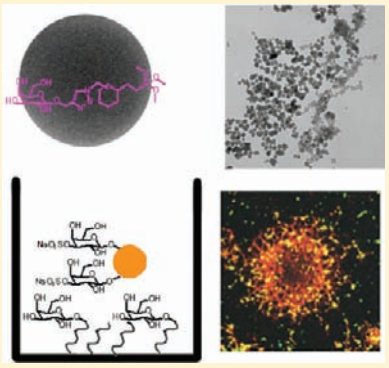

INTRODUCTION

Carbohydrate−carbohydrate interactions (CCIs) are molecular recognition events that involve the binding or association of one glycan with another.[1,2] CCIs between polysaccharides mediate processes such as cellulose fibril formation and their subsequent cross-linking by xyloglucan,[3] as well as proteoglycan-mediated self-association of sponge cells.[4,5] Other CCIs engage cell surface glycolipids for the proper compaction of developing embryos and mediate melanoma cell adhesion to endothelia.[6,7] As with much of carbohydrate recognition, CCIs are weak interactions and involve multivalent presentations of glycans.

Studies of CCI in their native context are complicated by the heterogeneous environment of the cell surface, and the use of multivalent glycoconjugates as model systems have been invaluable in establishing the occurrence of several CCIs. We and others have examined the interaction between Langmuir monolayers of glycolipids and glycoconjugates such as micelles,[8] glycodendrimers,[9] and glycopolymers.[10] Quantitative measurements of CCI-mediated binding and adhesion have been provided by surface plasmon resonance (SPR), quartz crystal microbalance, and giant vesicle micropipet experiments.[11−13] Carbohydrate-coated gold nanoparticles are a versatile platform for studies of CCI, and have been used to investigate the interaction using TEM, SPR, and calorimetry.[14−17]

Fluorescent nanoparticles are an attractive platform for presenting carbohydrates, as they can be used for diagnostics, sensors, and cellular imaging applications.[18−23] In particular, silica nanoparticles with encapsulated fluorescent dyes offer several attractive features—(i) they are readily and cheaply synthesized; (ii) silica is biocompatible; and (iii) encapsulation of fluorescent dyes by the silica matrix enhances photostability of the chromophore.[24] A fourth benefit is the ability to readily modify the nanoparticle surface with ligands for subsequent studies.

A variety of different methods for the functionalization of silica nanoparticles have been reported. A large number of these methods involve coating nanoparticles with an amino-terminated silane, followed by subsequent coupling to the amino group.[25−27] The thiol exchange reaction of a disulfide has been used to attach oligonucleotides onto silica nanoparticles coated with a mercaptosilane.[28] Pentafluorophenylazide coated silica nanoparticles can be covalently modified via photochemical generation of a nitrene.[29,30] Surface chlorination with thionyl chloride has also been reported.[31] Nickel nitrilotriacetic acid modified particles have been used to capture His6-tagged proteins.[32]

Received: November 15, 2011
Revised: April 24, 2012
Published: May 3, 2012

   dx.doi.org/10.1021/bc2006169 | *Bioconjugate Chem.* 2012, 23, 1166−1173

The copper(I) promoted azide−alkyne cycloaddition reaction[33,34] is a "click" reaction[35] which provides a facile and mild method for nanoparticle functionalization.[36−41] The reaction is regioselective, high-yielding, compatible with a large number of functional groups, and has recently been used to attach polymers, peptides, and fluorophores to silica nanoparticles.[42−46] These features make this a useful reaction for attaching carbohydrates to fluorescent silica nanoparticles. In this paper, we report the synthesis of fluorescent carbohydrate-coated nanoparticles and their use in probing a CCI found in myelin.

The myelin sheath is a multilayered membrane in the nervous system which encircles axons and facilitates the propagation of action potentials down the axon. Myelin membranes are formed by oligodendrocytes in the central nervous system and by Schwann cells in the peripheral nervous system. The lipid bilayer of myelin is highly enriched in glycolipids—it has been estimated that up to 40% of the outer leaflet is composed of two glycolipids, galactosylceramide (GalCer), and its 3-sulfo derivative, sulfatide (SGalCer).[47] These lipids are important for proper myelination, and knockout mice that lack one or both of these exhibit abnormal myelination and various other molecular and physiological defects.[48]

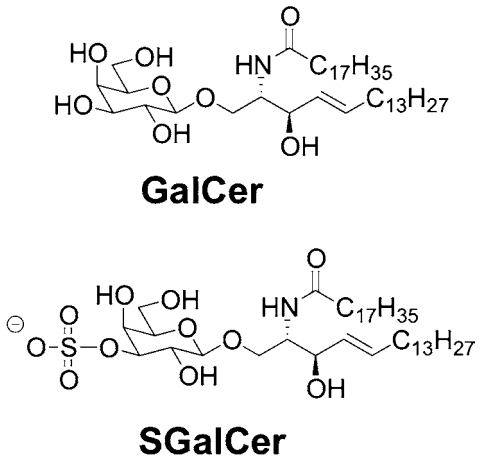

Figure 1. Myelin glycolipids.

Model systems have been valuable in establishing the CCI between GalCer and SGalCer. In a study of the aggregation of various glycolipid-containing liposomes in the presence of various divalent cations, the highest amount of aggregation was observed between vesicles containing GalCer and vesicles containing SGalCer.[49] This interaction was studied using fluorescent and spin label probes, as well as antiglycolipid antibodies, all of which indicated a preferential trans-bilayer interaction between the glycolipids.[50] If the GalCer and SGalCer were embedded in PC/cholesterol bilayers, divalent cations were required for the CCI to occur.[49] However, if bilayers of only GalCer and SGalCer were used, the interaction occurred in the absence of divalent cations.[50] Ternary complexes of GalCer, SGalCer, and calcium have been detected using electrospray mass spectrometry.[51]

More recent studies have shown that the Gal•SGal CCI is involved in signal transduction in oligodendrocytes. Addition of GalCer and SGalCer-containing liposomes to oligodendrocytes resulted in redistribution of GalCer and proteins on the oligodendrocyte cell surface.[52,55] Consistent with the hypothesis that the liposomal GalCer and SGalCer bind to GalCer and SGalCer in the cell membrane, Fab fragments of anti-GalCer antibodies and fumonisin B1, which inhibits glycosphingolipid synthesis, prevented liposome-induced glycolipid redistribution on the cell surface.[53] Subsequent studies using galactose-coated bovine serum albumin (Gal-BSA), a commercially available glycoconjugate, as well as glycosylated nanoparticles, yielded results similar to those observed with the liposomes.[54,55] It is believed that the "receptor" for SGal and Gal on the oligodendrocyte are GalCer and SGalCer, respectively, and that the glycan-presenting liposomes and BSA engage in a CCI on the cell surface that triggers transmembrane signaling and a cytoskeletal rearrangement. We envisioned that glycosylated fluorescent silica nanoparticles would provide a powerful tool for studying the CCI between Gal and SGal, since they can both be used to examine CCI with a well-defined model system, and can also be used to examine the CCI in a cellular context by directly visualizing the binding of glycoconjugates on the oligodendrocyte surface.

EXPERIMENTAL METHODS

General experimental procedures are provided in the Supporting Information.

Synthesis of Azide Linker-Coated Fluorescent Silica Nanoparticles (FITC-doped Si NPs, 4). 3-Aminopropyltriethoxysilane (APTS) (8 mg, 0.039 mmol) and fluorescein isothiocyanate (FITC) (15 mg, 0.039 mmol) were combined together in anhydrous DMF (1 mL) under a dry nitrogen atmosphere and stirred for 12 h. The solution was wrapped with aluminum foil during the reaction. The solution of the FITC-APTS conjugate **3** was used directly in the next step. Igepal CO-520 (240 μL) was dissolved in cyclohexane (4.5 mL) in a 20 mL vial. After stirring the solution for 10 min, NH_4OH solution (120 μL) was added, and the mixture was stirred for 10 min to provide a homogeneous suspension. FITC-APTS conjugate (20 μL) was added, followed by TEOS (60 μL, 0.27 mmol) another 5 min later. In order to get a pure silica surface, TEOS (20 μL) was added after 24 h, and stirring was continued for another 24 h. To this solution was added siloxane **2** (4 mg, 0.015 mmol) and stirring was continued for another 24 h. Acetone (10 mL) was added. The mixture containing silica nanoparticles was distributed in a 20 mL centrifuge tube, and the suspension was centrifuged for 15 min. The silica nanoparticles were precipitated on the bottom, and the supernatant was discarded. The centrifuge tube was refilled with acetone (15 mL) and centrifuged to recover silica nanoparticles. The precipitation and redistribution process was repeated four times to wash the nanoparticles. Finally, the nanoparticles were dried under a gentle stream of nitrogen to obtain an orange powder (45 mg).

Elemental Analysis of Azide-Coated Nanoparticles (4-dark). The weight fraction of nitrogen in the "dark" nanoparticles is given by eq 1[29]

$$\frac{x \times 3 \times \mathrm{MW}_N}{\frac{4}{3}\pi r^3 \times d + x \times \mathrm{MW}_{\mathrm{coating}}} = N\% \quad (1)$$

where r is the radius of the silica nanoparticles (17 nm as determined by TEM; see Supporting Information), d is the density of silica (2.0×10^{-21} g/nm^3), MW_N and $\mathrm{MW}_{\mathrm{coating}}$ are the formula weights of nitrogen and the silane on the nanoparticle surface, respectively. x stands for the moles of azidosiloxane **2** on the surface of each nanoparticle.

dx.doi.org/10.1021/bc2006169 | Bioconjugate Chem. 2012, 23, 1166−1173

According to eq 1

$$\{x[\text{mol/particle}] \times 3 \times 14.01[\text{g/mol}]\} / \left\{\frac{4}{3}\pi \times 17^3[\text{nm}^3/\text{particle}] \times 2.0 \times 10^{-21}[\text{g/nm}^3] + x[\text{mol/particle}] \times 457.71[\text{g/mol}]\right\} = 2.84\% \quad (2)$$

$$x = 3.3 \times 10^{-20}[\text{mol/particle}]$$

The functional groups/particle is given by

$$3.3 \times 10^{-20}[\text{mol/particle}] \times 6.02 \times 10^{23}[\text{groups/mol}] = 19866[\text{groups/particle}] \quad (3)$$

The functional groups/nm^2 is given by

$$19866[\text{groups/particle}]/4\pi \times 17^2[\text{nm}^2/\text{particle}] = 5.5[\text{groups/nm}^2]$$

The mol/mg of linker on the surface of nanoparticles is calculated as follows:

$$\frac{2.84\%}{3 \times 14.01[\text{g/mol}]} = 0.68[\mu\text{mol/mg}] \quad (4)$$

General Reaction Protocol for Copper-Promoted Azide Alkyne Cycloadditions on 4 to Provide 5a–c. Azide-coated fluorescent Si NPs (10 mg, 6.8 μmol) were suspended in THF (2 mL) in a 3 mL microwave reactor vessel. An aqueous solution of propargyl pyranoside (34 μL, 1 M, 5 equiv) was added, followed by an aqueous solution of $CuSO_4$ (34 μL, 0.1 M, 0.5 equiv) and an aqueous solution of sodium ascorbate (34 μL, 0.2 M, 1 equiv). The reactor vessel was put into the microwave reactor and heated at 70 °C for 10 min. After the reaction, methanol (10 mL) was added to precipitate the nanoparticles and the suspension was centrifuged for 5 min. The supernatant was discarded, and the precipitation and redispersion steps were repeated with 0.1 M EDTA solution (3×), nanopure water, and acetone. A gentle stream of nitrogen was used to dry the nanoparticles to provide an orange powder (11 mg).

Synthesis of 3-Sulfogalactose-Coated Fluorescent Si NPs—5d. Azide-coated fluorescent Si NPs (10 mg, 6.8 μmol) were dissolved in THF (2 mL) in a 3 mL microwave reactor vessel. A methanolic solution of sodium propargyl 3-sulfonato-β-D-galactopyranoside (100 μL, 1 M, 5 equiv) was added. After that, CuI (19 mg, 0.1 mmol, 15 equiv) and diisopropylethylamine (20 μL, 0.1 mmol, 15 equiv) were added. The reactor vessel was put into the microwave reactor and heated at 70 °C for 3 h. The nanoparticles were precipitated, washed, and dried as above to provide an orange powder (12 mg).

Determination of Carbohydrate Loading of 5a Using Phenol/Sulfuric Acid. Galactose-coated silica nanoparticles **5a** (1 mg) were dissolved in nanopure water (2 mL). This solution (200 μL) was added to a glass vial. To this vial was added an aqueous solution of phenol (0.5 M, 200 μL), followed rapidly by concentrated sulfuric acid (1000 μL). After 30 min, the absorbance was measured at 490 nm (A = 0.479). Blank absorbance measurements contained an aqueous solution of nonfunctionalized silica nanoparticles (0.5 mg/mL 200 μL), phenol solution (200 μL), and concentrated sulfuric acid (1000 μL). A control experiment was carried out with **4-dark** that had been functionalized with propargyl alcohol (A = 0.001). The absorbance of galactose-coated nanoparticles is fitted to the calibration curve (Supporting Information) to calculate the concentration of carbohydrate on the surface of silica nanoparticles.

CCI-Induced Aggregation of Carbohydrate Coated Silica Nanoparticles. 0.1 mg/mL solution of 3-sulfogalactose coated fluorescent silica nanoparticles and 0.1 mg/mL solution of different carbohydrate-coated dark silica nanoparticles were prepared in HEPES buffer (0.05 M HEPES buffer with 0.15 M NaCl, pH = 7.11). The 3-sulfogalactose-coated fluorescent silica nanoparticles solution (1 mL) and the other carbohydrate-coated dark silica nanoparticles solution (1 mL) were combined. After 30 min, samples for TEM analyses were prepared by drying solutions of the particles on amorphous carbon-coated copper grids.

Measurement of CCI Using High-Binding Microtiter Plates. A methanolic solution of glycolipid **7a** or **7b** (50 μL, 0.1 M) was loaded in each well. The microtiter plate was placed in a fume hood, and the solvent was evaporated at room temperature in the hood; the wells were incubated with a 1% BSA in PBS buffer solution (120 μL, PBS buffer solution (pH = 7.1)) overnight. The wells were then incubated with fluorescent nanoparticles (100 μL, 1 mg/mL) in a 1% BSA in PBS buffer solution (pH = 7.1) for 1 h. The binding buffer solution was removed, and the wells were washed with 1% BSA in PBS buffer solution twice. Each wash consisted of three agitations of the solution using an automatic pipettor. The fluorescence was measured at λ_{ex} 480 nm and λ_{em} 519 nm when buffer solution was added to the wells for the third time.

Measurement of Binding of Carbohydrate-Coated Silica Nanoparticles to Cultured Oligodendrocytes and Myelin. Oligodendrocytes were cultured as described previously.[55] The medium was replaced on day 8 in culture with phenol red-free medium (Invitrogen Canada, Inc.), and the live cells were treated with 40 μg/mL glycoparticles in medium for 1 h. They were then washed three times with PBS, fixed with 4% paraformaldehyde for 10 min at room temperature, and stained with anti-MAG to visualize oligodendrocytes or antiglial fibrillary acidic protein (GFAP) to detect astrocytes, plus fluorescent Cy3-conjugated second antibodies, as described. For some experiments, cells were fixed first before addition of glycoparticles. If O1 Ab was added to block binding, it (1 μg per well) was added to live or fixed cells for 15 min, followed by washing three times. Glycoparticles were then added as above.

Prepared slides were viewed in a Zeiss confocal laser scanning microscope with LSM 510 program. The green (FITC) and red (Cy3) data sets were acquired separately at 488 and 553 nm, respectively. Each optical section was 0.45 μm thick, and the sections showing the most intense staining are presented. A Reichert-Jung fluorescence microscope was used for initial viewing of the cells. The percent of MAG$^+$ cells with a number of bound particles (sufficient to reveal the cell shape and different from random background particles) was determined by counting cells starting in one corner of the coverslip and proceeding through the coverslip until 300 cells were counted. This was usually one-half to two-thirds of the cells on the coverslip.

CM-DiI-labeled myelin (10 μL containing 170 μg of protein) was combined with 20 μL (20 μg) FITC-Gal/SGal particles **5e** or FITC–OH particles **5f**. For blocking experiments, 10 μL

Scheme 1. Synthesis of Carbohydrate-Functionalized Silica Nanoparticles and Glycolipids

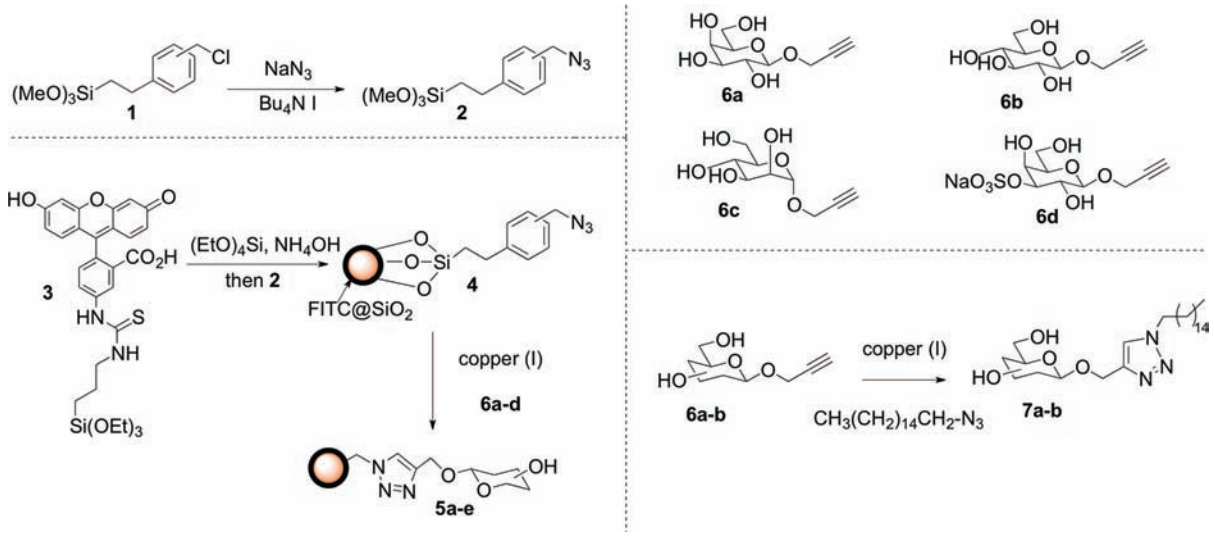

myelin was combined with a 4-fold excess of dark Gal/SGal particles (80 μL containing 80 μg particles) or 20 μL (20 μg) mouse monoclonal anti-GalCer O1 IgM antibody or 20 μL (76 μg) rabbit anti-GalCer IgG Fab for 1.5 h. The final volume was adjusted to 90 μL with distilled water, and then 20 μL (20 μg) FITC-Gal/SGal particles **5e** were added. An aliquot (5.5 μL) of 200 mM $CaCl_2$ solution was added to give a final concentration of 10 mM $CaCl_2$. The samples were incubated for 2 h at room temperature. They were mounted on slides and examined using a confocal microscope.

RESULTS AND DISCUSSION

Nanoparticle Synthesis and Characterization. Fluorescein isothiocyanate (FITC) doped silica nanoparticles were synthesized following an adaptation of reported procedures (Scheme 1).[56,57] The surface of these nanoparticles was subsequently coated with the azide-containing siloxane **2**, which was synthesized from the commercially available chlorosiloxane **1**. The diameter of the azide-modified nanoparticles (**4**), measured using TEM, was 54 ± 4 nm. The IR spectrum of these nanoparticles exhibited a strong peak at 2100 cm^{-1} corresponding to the azide antisymmetric stretch (Figure 2). The fluorescence spectrum of **4** exhibited the characteristic emission curve of fluorescein (Supporting Information) with a maximum at 514 nm (λ_{ex} 480 nm).

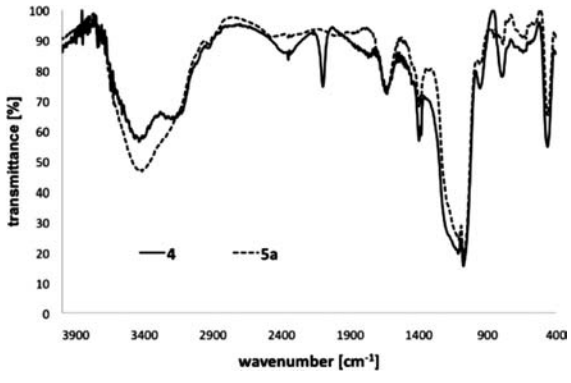

Figure 2. IR spectra of (a) azide-functionalized particles **4**, solid line; (b) fully functionalized particles **5a**, dashed line.

Quantification of azide incorporation into the nanoparticles was carried out using elemental analysis for carbon, hydrogen, and nitrogen (Table 1). Bare nanoparticles lacking both fluorophore and azide contain a trace amount of nitrogen along with low amounts of carbon and hydrogen. The latter components are presumably derived from residual ethoxy groups within the silica matrix. In order to simplify interpretation of the elemental analysis data, azide-functionalized nanoparticles lacking the fluorescent dye were prepared. These "dark" analogues of **4** contain carbon, hydrogen, and nitrogen in ratios that reflect their composition in the silanol derived from the linker **2** (Table 1). The 2.84% nitrogen content in these nanoparticles is derived solely from the azide and translates to an azide loading of 0.68 μmol/mg and a density of 5.5 azides/nm^2.

Functionalization of the particles using alkyne-terminated glycosides was subsequently conducted. Reaction progress was monitored by following the loss of the azide peak in the IR spectrum. The reaction of **4** with propargyl β-D-galactopyranoside **6a** to give **5a** was carried out under microwave irradiation using 2.5 equiv of the alkyne, 50 mol % copper sulfate, and 100 mol % sodium ascorbate in a THF/water mixture. Under these conditions, complete conversion, as determined by IR, was achieved in 10 min at 70 °C. Purification was straightforward, as the nanoparticles could be recovered after several washing and precipitation cycles. TEM analysis of the nanoparticles before and after reaction showed that the shape and size distribution of the particles remained largely unchanged, indicating that the nanoparticles were stable under the reaction conditions.

The azide-terminated nanoparticles were functionalized with propargyl β-D-glucopyranoside **6b** and α-D-mannopyranoside **6c** to provide particles **5b** and **5c**. The reaction of propargyl 3-sulfo β-D-galactopyranoside **6d** with the azide-terminated nanoparticles was carried out using copper(I) iodide as catalyst with complete conversion obtained under microwave irradiation at 70 °C for 3 h. Nanoparticles **5e**, functionalized with both **6a** and **6d** in approximately equal ratios, were prepared by functionalization with the sulfo sugar **6d** for 1.5 h followed by subsequent capping with **6a**. Carbohydrate functionalization of the nanoparticles **5a**–**e** was quantitated using elemental analysis (Table 1, entries 3–6). As before, these analyses

dx.doi.org/10.1021/bc2006169 | Bioconjugate Chem. 2012, 23, 1166–1173

Table 1. Elemental Analysis of Silica Nanoparticles

entry	nanoparticle (coating)	wt % C	wt % N	wt % H	wt % S	mole ratio C:N	coverage μmol/mg	functional groups per nm^2
1	bare silica	2.27	0.15	1.05				
2	**4** (N_3)	11.92	2.84	1.25		4.9:1	0.68	5.5
3	**5a** (Gal)	15.39	2.56	1.86		7.0:1	0.61	5.6
4	**5b** (Glc)	15.94	2.66	1.97		7.0:1	0.63	5.9
5	**5c** (Man)	15.04	2.51	1.90		7.0:1	0.60	5.6
6	**5d** (SGal)	14.35	2.37	1.79	1.81	7.0:1	0.56	5.6
7	**5e** (SGal+Gal[a])	19.94	2.47	1.91	0.95	7.0:1	0.59	5.7[a]

[a]SGal:Gal = 2.9:2.8.

were carried out with the "dark" analogues of **5** lacking fluorescein in order to simplify data analysis. Functionalization of **4** with carbohydrates resulted in an increase in carbon and hydrogen weight percentages and a decrease in the nitrogen percentage. The surface coverage remains fairly constant for all three sugars, at approximately 0.6 μmol/mg. The lower molar loading value (0.68 vs 0.61 μmol/mg) reflects the increase in the molecular weight of the coating on the silica nanoparticles (42 for the azide vs 457 for the glycosyl triazoles). These correspond to 90 000 and 78 000 azide and carbohydrate groups per particle, respectively, translating to an 87% conversion based on elemental analysis.

The presence and concentration of carbohydrates on the nanoparticles were also confirmed by treating the nanoparticles with phenol in sulfuric acid.[58] This colorimetric assay indicated that the concentration of galactose on **5a** is 0.58 μmol/mg, results that are consistent with those derived from elemental analysis. To provide additional confirmation of triazole formation, HF•pyridine was used to dissolve the silica nanoparticles, providing a triazole-containing glycoside, which was characterized using ^{1}H NMR and mass spectrometry.[59]

Nanoparticle CCIs. To study the CCI of the carbohydrate-coated nanoparticles, we examined their binding to glycolipid-coated microtiter plates, a glycan presentation that has been used previously for screening both CCI as well as carbohydrate–protein interactions.[60,61] Glycolipids **7a,b** containing a single hydrocarbon chain were prepared by the reaction of propargyl glycosides **6a,b** with azidohexadecane. The lipids were subsequently immobilized in a 96-well polystyrene microtiter plate. The loading of the glycolipid in the wells was quantitated using phenol/sulfuric acid. Previous experiments with a similar glycolipid indicated that a hexadecyl chain was retained most effectively after multiple washing steps, and we find that this holds true with our glycosyl triazole lipids as well.[61,62]

We examined the binding of SGal-coated nanoparticles **5d** to wells coated with galactolipid **7a**. Variation of the incubation conditions identified a 60 min incubation of nanoparticles in PBS buffer at a 500 μg/mL concentration as being optimal for providing the maximal signal. We observed almost no difference in fluorescence signal when the binding was carried out in the presence or absence of 100 mM calcium ions, as observed for binding of pure GalCer to pure SGalCer.[49]

The CCI between the nanoparticles and the glycolipid is extremely specific for galactose and SGal, as seen in Table 2. When the wells are loaded with galactolipid, significant fluorescence is only observed when nanoparticles coated with SGal (**5d**) or a mixture of SGal and Gal (**5e**) are used. Only background levels of fluorescence are observed with the Gal and Glc nanoparticles **5a** and **5b**. A nanoparticle functionalized with propargyl alcohol (**5f**) was used as a control to evaluate

Table 2. Fluorescence Measurements of Nanoparticle Binding to Glycolipids in Multiwell Plate

	glycolipid coating in well	
nanoparticle (sugar coating)	**7a** (Gal)	**7b** (Glc)
5d (SGal)	3163 ± 80	467 ± 58
5e (Gal + SGal)	2780 ± 70	523 ± 65
5a (Gal)	498 ± 59	499 ± 47
5b (Glc)	465 ± 64	434 ± 62
5f[a] (OH)	465 ± 61	550 ± 50

[a]**5f** was prepared by capping **4** with propargyl alcohol using the standard click conditions.

the role of nonspecific binding of the nanoparticles. In contrast, when the glucolipid **7b** was immobilized in the wells, no binding was observed with any of the nanoparticles. These results demonstrate that the carbohydrate coated nanoparticles can be used as a platform for studying the CCI between SGal and Gal.

Additional corroboration of the ability of the glyconanoparticles to engage in CCI was provided by TEM images of various nanoparticle combinations. Mixtures of fluorescent and dark nanoparticles could be distinguished in the TEM by virtue of their differences in size and contrast. The dye-loaded nanoparticles appear darker than nanoparticles lacking the dye and the former are larger in diameter. Examination of TEM images of fluorescent SGal nanoparticles mixed with non-fluorescent Gal nanoparticles shows large aggregates containing both types of nanoparticles within the aggregate (Figure 3A). In contrast, when a combination of the fluorescent SGal nanoparticles **5d** mixed with nonfluorescent Glc nanoparticles **5b** is examined, very few mixed aggregates are seen, and each type of particle is most likely to be found in an aggregate of like particles (Figure 3B).

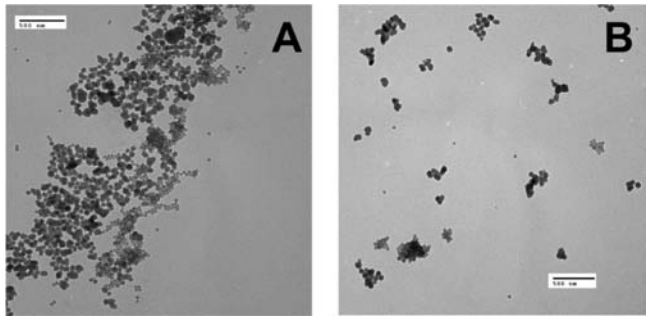

Figure 3. TEM images of (A) a mixture of dark Gal nanoparticles (0.1 mg/mL) and fluorescent SGal nanoparticles (0.1 mg/mL); (B) a mixture of dark Glc nanoparticles (0.1 mg/mL) and fluorescent SGal nanoparticles (0.1 mg/mL).

dx.doi.org/10.1021/bc2006169 | *Bioconjugate Chem.* 2012, 23, 1166–1173

We have previously shown that nonfluorescent "dark" Gal, SGal, and Gal/SGal coated particles induce the same redistribution of cell surface GalCer that is seen with liposomes and Gal-BSA.[54] However, those studies did not detect glycoconjugate binding directly; instead, carbohydrate binding was inferred from the cellular effects of the glycoconjugates, inhibition using anti-GalCer antibodies, and additional experiment using glycolipid biosynthesis inhibitors.[53] Using fluorescent silica nanoparticles, we sought to directly visualize the interaction of Gal and SGal-containing nanoparticles with oligodendrocytes. Oligodendrocytes were isolated from rat pup spinal cords and cultured and were identified by staining with an antibody to myelin-associated glycoprotein (MAG; red/yellow stains in Figure 4A–D). Particle binding to oligodendrocytes was determined directly using the fluorescein emission (green/yellow stains in Figure 4). Both the Gal/SGal and Gal particles **5e** and **5a** bound to live oligodendrocytes (Figure 4A,B), and weak binding of the SGal particles **5d** was also observed (SI). Glucose and mannose functionalized particles **5b** and **5c** did not bind significantly to oligodendrocytes, and **5e** did not bind to astrocytes present in the culture, which lack GalCer and SGalCer (SI).

If cell surface GalCer is indeed the target for SGal on the Gal/SGal particles, the binding should be reduced if a competing ligand is present. Indeed, incubation of oligodendrocytes with the O1 anti-GalCer monoclonal antibody for 15 min before addition of **5e** greatly reduced binding of the particles to the oligodendrocytes but had no effect on the binding of **5a** (Figure 4C,D and Table 3). The antibody completely prevented the weak binding of **5d** (SI) These results are consistent with the conclusions that (a) the ligand for SGal particles is galactosylceramide (GalCer) in the oligodendrocyte membranes and (b) the ligand for Gal particles in the oligodendrocyte membrane is SGal, which would not be blocked by anti-GalCer.

CONCLUSIONS

In conclusion, we have developed a multivalent platform for presenting carbohydrates and studying their CCI. Fluorescent silica nanoparticles were efficiently functionalized with carbohydrates via a copper-promoted click reaction. Attaching the azide coupling partner on the nanoparticle facilitates reaction monitoring by tracking the disappearance of the diagnostic azide IR band. High levels of functionalization can be obtained and the functionalization conditions are mild and general, which should permit the attachment of a wide variety of additional ligands on nanoparticles.

Particles coated with SGal as well as a mixture of Gal and SGal adhered to multiwell plates coated with a galactolipid and preferentially formed mixed aggregates with their binding partner on a TEM grid. These experiments indicate that the Gal•SGal CCI is also extremely specific for those two sugars, as glucose-coated nanoparticles did not interact with SGal. Additionally, these findings indicate that the Gal•SGal CCI does not require the sphingolipid chain, and that monosaccharides are necessary and sufficient for the CCI, similar to other glycolipid CCIs that have been studied using model systems.

The use of a fluorescent multivalent glycoconjugate allowed us to probe CCI both using model systems, as well as in a more complex and heterogeneous cellular environment. Particle binding to oligodendrocytes was examined using fluorescence microscopy, and enabled the direct visualization of the binding

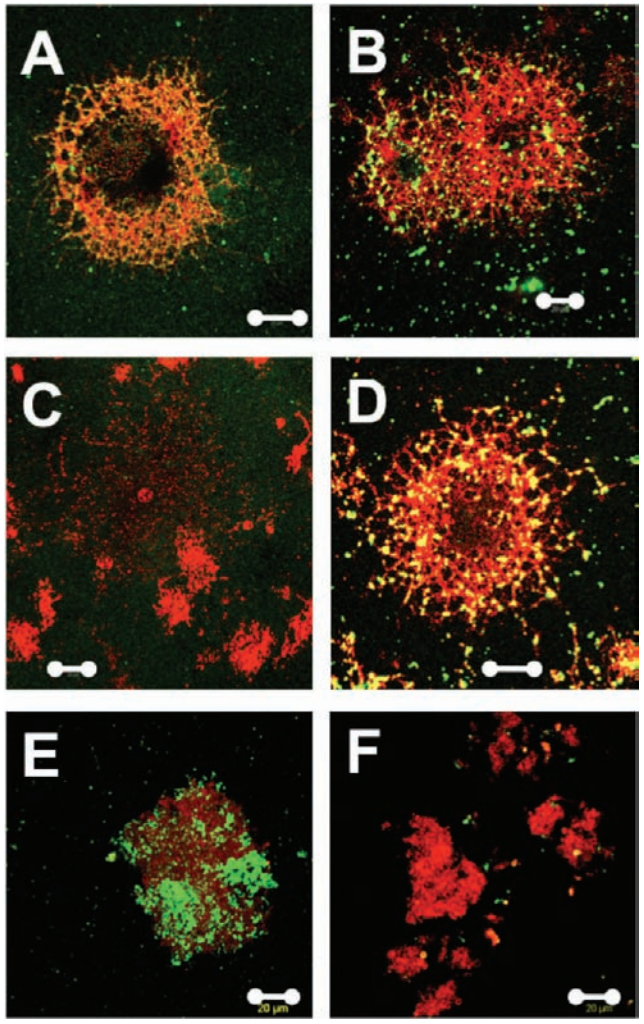

Figure 4. (A–D) Fluorescence microscope images of nanoparticles (green) bound to live oligodendrocytes followed by fixation and staining with anti-MAG Ab (red); yellow indicates overlap. (A) Gal/SGal nanoparticles **5e**; (B) Gal nanoparticles **5a**; (C) *Cells were incubated with Anti GalCer O1 Ab added for 15 min prior to binding of **5e**; (D) Cells were incubated with anti-GalCer O1 Ab added for 15 min prior to binding of **5a**. (E,F) Fluorescence microscope images of nanoparticles (green) bound to myelin fragments labeled with CD-DiI (red). (E) Gal/SGal nanoparticles **5e**; (F) 76 μg anti-GalCer IgG Fab fragments followed by **5e**. Scale bars = 20 μm. Representative pictures are shown. [*Anti-GalCer Ab added to live cells for 15 min causes some damage to the cells, resulting in a number of small MAG$^+$ condensed cells. One large cell remaining has greatly reduced MAG staining. Results for binding to fixed cells are provided in the SI.]

Table 3. FITC-Containing Nanoparticle Binding to Oligodendrocytes and in Presence and Absence of anti-GalCer O1 Antibody[a]

	% of MAG$^+$ oligodendrocytes with bound particles	
nanoparticles	no Ab	with O1 Ab
5e	74	29.4
5a	92.1	95.5

[a]The Gal/SGal nanoparticles **5e** also bound to purified myelin fragments (Figure 4E). The binding was inhibited by an excess of the "dark" nonfluorescent version of **5e** (SI) and also by a monovalent anti-GalCer IgG Fab fragment (Figure 4F).

dx.doi.org/10.1021/bc2006169 | *Bioconjugate Chem.* 2012, 23, 1166–1173

of Gal and SGal glycoconjugates to these cells. These results provide a new tool for studying the Gal•SGal and other CCIs. The fluorescence readout allows for the rapid evaluation of the effect of carbohydrate structural modifications to CCI and can be used to screen for compounds that can inhibit the interaction, particularly in a cellular context.

■ ASSOCIATED CONTENT

Supporting Information

Additional experimental procedures, microscopy images, and characterization data. This material is available free of charge via the Internet at http://pubs.acs.org.

■ AUTHOR INFORMATION

Corresponding Author

*abasu@brown.edu.

Notes

The authors declare no competing financial interest.

■ ACKNOWLEDGMENTS

This work was funded by the National Science Foundation (A.B.), the Multiple Sclerosis Society of Canada (J.M.B.), and in part by a Research Seed Fund from Brown University (A.B.).

■ REFERENCES

(1) Begley, T. P., Seah, N., and Basu, A. (2008) *Wiley Encyclopedia of Chemical Biology*, 1−7.

(2) Bucior, I., and Burger, M. (2004) Carbohydrate-carbohydrate interactions in cell recognition. *Curr. Opin. Struct. Biol. 14*, 631−637.

(3) Gorshkova, T. A., Mikshina, P. V., Gurjanov, O. P., and Chemikosova, S. B. (2010) Formation of plant cell wall supramolecular structure. *Biochemistry Moscow 75*, 159−172.

(4) Bucior, I. (2004) Carbohydrate-carbohydrate interaction provides adhesion force and specificity for cellular recognition. *J. Cell Biol. 165*, 529−537.

(5) Bucior, I., and Burger, M. M. (2004) Carbohydrate-carbohydrate interaction as a major force initiating cell-cell recognition. *Glycoconj. J. 21*, 111−123.

(6) Eggens, I., Fenderson, B., Toyokuni, T., Dean, B., Stroud, M., and Hakomori, S. (1989) Specific interaction between Lex and Lex determinants. A possible basis for cell recognition in preimplantation embryos and in embryonal carcinoma cells. *J. Biol. Chem. 264*, 9476−9484.

(7) Naoya Kojima, M. S., Sadahira, Y., and Hakomori, S.-I. (1992) Cell adhesion in a dynamic flow system as compared to static system. *J. Biol. Chem. 267*, 17264−17270.

(8) Santacroce, P. V., and Basu, A. (2003) Probing specificity in carbohydrate-carbohydrate interactions with micelles and Langmuir monolayers. *Angew. Chem., Int. Ed. 42*, 95−98.

(9) Seah, N., Santacroce, P. V., and Basu, A. (2009) Probing the lactose•GM3 carbohydrate-carbohydrate interaction with glycodendrimers. *Org. Lett. 11*, 559−562.

(10) Matsuura, K., Kitakouji, H., Oda, R., Morimoto, Y., Asano, H., Ishida, H., Kiso, M., Kitajima, K., and Kobayashi, K. (2002) Selective expansion of the GM3 glycolipid monolayer induced by carbohydrate - Carbohydrate interaction with Gg3 trisaccharide-bearing glycoconjugate polystyrene at the air-water interface. *Langmuir 18*, 6940−6945.

(11) Matsuura, K., Oda, R., Kitakouji, H., Kiso, M., Kitajima, K., and Kobayashi, K. (2004) Surface plasmon resonance study of carbohydrate-carbohydrate interaction between various gangliosides and Gg3-carrying polystyrene. *Biomacromolecules 5*, 937−941.

(12) Matsuura, K., Tsuchida, A., Okahata, Y., Akaike, T., and Kobayashi, K. (1998) A quartz-crystal microbalance study of adsorption behaviors of artificial glycoconjugate polymers onto chemically modified gold surfaces and their interactions with lectins. *Bull. Chem. Soc. Jpn. 71*, 2973−2977.

(13) Pincet, F., Le Bouar, T., Zhang, Y., Esnault, J., Mallet, J., Perez, E., and Sinay, P. (2001) Ultraweak sugar-sugar interactions for transient cell adhesion. *Biophys. J. 80*, 1354−1358.

(14) Carvalho De Souza, A., Halkes, K. M., Meeldijk, J. D., Verkleij, A. J., Vliegenthart, J. F. G., and Kamerling, J. P. (2005) Gold glyconanoparticles as probes to explore the carbohydrate-mediated self-recognition of marine sponge cells. *ChemBioChem 6*, 828−831.

(15) de la Fuente, J., Barrientos, A., Rojas, T., Rojo, J., Canada, J., Fernandez, A., and Penades, S. (2001) Gold glyconanoparticles as water-soluble polyvalent models to study carbohydrate interactions. *Angew. Chem., Int. Ed. 40*, 2257−2261.

(16) De La Fuente, J. M., Eaton, P., Barrientos, A. G., Menéndez, M., and Penadés, S. (2005) Thermodynamic evidence for Ca^{2+}-mediated self-aggregation of Lewis X gold glyconanoparticles. A model for cell adhesion via carbohydrate-carbohydrate interaction. *J. Am. Chem. Soc. 127*, 6192−6197.

(17) Hernaiz, M., de la Fuente, J., Barrientos, A., and Penades, S. (2002) A model system mimicking glycosphingolipid clusters to quantify carbohydrate self-interactions by surface plasmon resonance. *Angew. Chem., Int. Ed. 41*, 1554−1557.

(18) Babu, P., Sinha, S., and Surolia, A. (2007) Sugar-quantum dot conjugates for a selective and sensitive detection of lectins. *Bioconjugate Chem. 18*, 146−151.

(19) Chen, C.-T., Munot, Y. S., Salunke, S. B., Wang, Y.-C., Lin, R.-K., Lin, C.-C., Chen, C.-C., and Liu, Y.-H. (2008) A triantennary dendritic galactoside-capped nanohybrid with a ZnS/CdSe nanoparticle core as a hydrophilic, fluorescent, multivalent probe for metastatic lung cancer cells. *Adv. Funct. Mater. 18*, 527−540.

(20) de la Fuente, J., and Penades, S. (2005) Glyco-quantum dots: a new luminescent system with multivalent carbohydrate display. *Tetrahedron-Asymmetry 16*, 387−391.

(21) Earhart, C., Jana, N. R., Erathodiyil, N., and Ying, J. Y. (2008) Synthesis of carbohydrate-conjugated nanoparticles and quantum dots. *Langmuir 24*, 6215−6219.

(22) Higuchi, Y., Oka, M., Kawakami, S., and Hashida, M. (2008) Mannosylated semiconductor quantum dots for the labeling of macrophages. *J. Controlled Release 125*, 131−136.

(23) Robinson, A., Fang, J.-M., Chou, P.-T., Liao, K.-W., Chu, R.-M., and Lee, S.-J. (2005) Probing lectin and sperm with carbohydrate-modified quantum dots. *ChemBioChem 6*, 1899−1905.

(24) Bonacchi, S., Genovese, D., Juris, R., Montalti, M., Prodi, L., Rampazzo, E., and Zaccheroni, N. (2011) Luminescent silica nanoparticles: extending the frontiers of brightness. *Angew. Chem., Int. Ed. 50*, 4056−4066.

(25) Wang, L., Zhao, W., O'Donoghue, M. B., and Tan, W. (2007) Fluorescent nanoparticles for multiplexed bacteria monitoring. *Bioconjugate Chem. 18*, 297−301.

(26) Peng, J., Wang, K., Tan, W., He, X., He, C., Wu, P., and Liu, F. (2007) Identification of live liver cancer cells in a mixed cell system using galactose-conjugated fluorescent nanoparticles. *Talanta 71*, 833−840.

(27) Ling, X. Y., Reinhoudt, D. N., and Huskens, J. (2006) Ferrocenyl-functionalized silica nanoparticles: preparation, characterization, and molecular recognition at interfaces. *Langmuir 22*, 8777−8783.

(28) Hilliard, L., Zhao, X., and Tan, W. (2002) Immobilization of oligonucleotides onto silica nanoparticles for DNA hybridization studies. *Anal. Chim. Acta 470*, 51−56.

(29) Gann, J. P., and Yan, M. (2008) A versatile method for grafting polymers on nanoparticles. *Langmuir 24*, 5319−5323.

(30) Wang, X., Ramström, O., and Yan, M. (2011) Dye-doped silica nanoparticles as efficient labels for glycans. *Chem. Commun. 47*, 4261.

(31) Wang, Y., Pei, X., He, X., and Yuan, K. (2005) Synthesis of well-defined, polymer-grafted silica nanoparticles via reverse ATRP. *Eur. Polym. J. 41*, 1326−1332.

(32) Kim, S. H., Jeyakumar, M., and Katzenellenbogen, J. A. (2007) Dual-mode fluorophore-doped nickel nitrilotriacetic acid-modified silica nanoparticles combine histidine-tagged protein purification

with site-specific fluorophore labeling. *J. Am. Chem. Soc. 129*, 13254−13264.
(33) Binder, W. H., and Sachsenhofer, R. (2007) 'Click' chemistry in polymer and materials science. *Macromol. Rapid Commun. 28*, 15−54.
(34) Nandivada, H., Jiang, X., and Lahann, J. (2007) Click chemistry: versatility and control in the hands of materials scientists. *Adv. Mater. 19*, 2197−2208.
(35) Kolb, H. C., Finn, M. G., and Sharpless, K. B. (2001) Click chemistry: Diverse chemical function from a few good reactions. *Angew. Chem., Int. Ed. 40*, 2004−2021.
(36) Polito, L., Monti, D., Caneva, E., Delnevo, E., Russo, G., and Prosperi, D. (2008) One-step bioengineering of magnetic nanoparticles via a surface diazo transfer/azide-alkyne click reaction sequence. *Chem. Commun.*, 621−623.
(37) Binder, W. H., Lomoschitz, M., Sachsenhofer, R., and Friedbacher, G. (2009) Reversible and irreversible binding of nanoparticles to polymeric surfaces. *J. Nanomaterials 2009*, 1−15.
(38) He, H., Zhang, Y., Gao, C., and Wu, J. (2009) 'Clicked' magnetic nanohybrids with a soft polymer interlayer. *Chem. Commun.*, 1655.
(39) Lin, P.-C., Ueng, S.-H., Yu, S.-C., Jan, M.-D., Adak, A. K., Yu, C.-C., and Lin, C.-C. (2007) Surface modification of magnetic nanoparticle via Cu(I)-Catalyzed alkyne-azide [2 + 3] cycloaddition. *Org. Lett. 9*, 2131−2134.
(40) White, M. A., Johnson, J. A., Koberstein, J. T., and Turro, N. J. (2006) Toward the syntheses of universal ligands for metal oxide surfaces: Controlling surface functionality through click chemistry. *J. Am. Chem. Soc. 128*, 11356−11357.
(41) Sommer, W. J., and Weck, M. (2007) Facile functionalization of gold nanoparticles via microwave-assisted 1,3 dipolar cycloaddition. *Langmuir 23*, 11991−11995.
(42) Achatz, D. E., Mezo, G., Kele, P., and Wolfbeis, O. S. (2009) Probing the activity of matrix metalloproteinase II with a sequentially click-labeled silica nanoparticle FRET probe. *ChemBioChem 10*, 2316−2320.
(43) Balamurugan, S. S., Soto-Cantu, E., Cueto, R., and Russo, P. S. (2010) Preparation of organosoluble silica−polypeptide particles by "click" chemistry. *Macromolecules 43*, 62−70.
(44) Chandran, S. P., Hotha, S., and Prasad, B. L. V. (2008) Tunable surface modification of silica nanoparticles through 'click' chemistry. *Curr. Sci. India 95*, 1327−1333.
(45) Ranjan, R., and Brittain, W. J. (2007) Combination of living radical polymerization and click chemistry for surface modification. *Macromolecules 40*, 6217−6223.
(46) Kar, M., Vijayakumar, P. S., Prasad, B. L. V., and Gupta, S. S. (2010) Synthesis and characterization of poly-l-lysine-grafted silica nanoparticles synthesized via NCA polymerization and click chemistry. *Langmuir 26*, 5772−5781.
(47) Boggs, J. M., Gao, W., and Hirahara, Y. (2008) Myelin glycosphingolipids, galactosylceramide and sulfatide, participate in carbohydrate-carbohydrate interactions between apposed membranes and may form glycosynapses between oligodendrocyte and/or myelin membranes. *Biochim. Biophys. Acta 1780*, 445−455.
(48) Coetzee, T., Suzuki, K., and Popko, B. (1998) New perspectives on the function of myelin galactolipids. *Trends Neurosci. 21*, 126−130.
(49) Stewart, R. J., and Boggs, J. M. (1993) A carbohydrate-carbohydrate interaction between galactosylceramide-containing liposomes and cerebroside sulfate-containing liposomes: dependence on the glycolipid ceramide composition. *Biochemistry 32*, 10666−10674.
(50) Boggs, J. M., Menikh, A., and Rangaraj, G. (2000) Trans interactions between galactosylceramide and cerebroside sulfate across apposed bilayers. *Biophys. J. 78*, 874−885.
(51) Koshy, K. M., and Boggs, J. M. (1996) Investigation of the calcium-mediated association between the carbohydrate head groups of galactosylceramide and galactosylceramide I3 sulfate by electrospray ionization mass spectrometry. *J. Biol. Chem. 271*, 3496−3499.
(52) Boggs, J. M., and Wang, H. (2001) Effect of liposomes containing cerebroside and cerebroside sulfate on cytoskeleton of cultured oligodendrocytes. *J. Neurosci. Res. 66*, 242−253.
(53) Boggs, J. M., Gao, W., and Hirahara, Y. (2008) Signal transduction pathways involved in interaction of galactosylceramide/sulfatide-containing liposomes with cultured oligodendrocytes and requirement for myelin basic protein and glycosphingolipids. *J. Neurosci. Res. 86*, 1448−1458.
(54) Boggs, J. M., Gao, W., Zhao, J., Park, H.-J., Liu, Y., and Basu, A. (2010) Participation of galactosylceramide and sulfatide in glycosynapses between oligodendrocyte or myelin membranes. *FEBS Lett. 584*, 1771−1778.
(55) Boggs, J. M., and Wang, H. (2004) Co-clustering of galactosylceramide and membrane proteins in oligodendrocyte membranes on interaction with polyvalent carbohydrate and prevention by an intact cytoskeleton. *J. Neurosci. Res. 76*, 342−355.
(56) Bagwe, R. P., Yang, C., Hilliard, L. R., and Tan, W. (2004) Optimization of dye-doped silica nanoparticles prepared using a reverse microemulsion method. *Langmuir 20*, 8336−8342.
(57) Santra, S., Liesenfeld, B., Bertolino, C., Dutta, D., Cao, Z. H., Tan, W. H., Moudgil, B. M., and Mericle, R. A. (2006) Fluorescence lifetime measurements to determine the core-shell nanostructure of FITC-doped silica nanoparticles: An optical approach to evaluate nanoparticle photostability. *J. Lumin. 117*, 75−82.
(58) Saha, S. K., and Brewer, C. F. (1994) Determination of the concentrations of oligosaccharides, complex type carbohydrates, and glycoproteins using the phenol sulfuric-acid method. *Carb. Res. 254*, 157−167.
(59) In order to obtain a sufficient amount of glycosyl triazole upon cleavage, we used particles that had a thicker azide coating. These were prepared by increasing the amount of azidosiloxane **2** by 8-fold during nanoparticle synthesis.
(60) Hakomori, S. (1991) Carbohydrate-carbohydrate interaction as an initial step in cell recognition. *Pure Appl. Chem. 63*, 473−482.
(61) Bryan, M. C., Plettenburg, O., Sears, P., Rabuka, D., Wacowich-Sgarbi, S., and Wong, C.-H. (2002) Saccharide display on microtiter plates. *Chem. Biol. 9*, 713−720.
(62) We examined the immobilization of C14 and C18 lipids as well, and found that 70% and 59%, respectively, were lost after three washes.

Bioconjugate Chemistry

Article

pubs.acs.org/bc

T Cell-Specific siRNA Delivery Using Antibody-Conjugated Chitosan Nanoparticles

Jangwook Lee,[†] Kyoung-Soo Yun,[†] Chang Seon Choi, Seung-Hwa Shin, Hong-Seok Ban, Taiyoun Rhim, Sang Kyung Lee,* and Kuen Yong Lee*

Department of Bioengineering and Institute for Bioengineering and Biopharmaceutical Research, Hanyang University, Seoul 133-791, Republic of Korea

Supporting Information

ABSTRACT: The intracellular delivery of small interfering RNA (siRNA) plays a key role in RNA interference (RNAi) and provides an emerging technique to treat various diseases, including infectious diseases. Chitosan has frequently been used in gene delivery applications, including siRNA delivery. However, studies regarding the modification of chitosan with antibodies specifically targeting T cells are lacking. We hypothesized that chitosan nanoparticles modified with T cell-specific antibodies would be useful for delivering siRNA to T cells. CD7-specific single-chain antibody (scFvCD7) was chemically conjugated to chitosan by carbodiimide chemistry, and nanoparticles were prepared by a complex coacervation method in the presence of siRNA. The mean diameter and zeta potential of the scFvCD7-chitosan/siRNA nanoparticles were approximately 320 nm and +17 mV, respectively, and were not significantly influenced by the coupling of antibody to chitosan. The cellular association of antibody-conjugated nanoparticles to CD4+ T cell lines as well as gene silencing efficiency in the cells was significantly improved compared to nonmodified chitosan nanoparticles. This approach to introducing T cell-specific antibody to chitosan nanoparticles may find useful applications for the treatment of various infectious diseases.

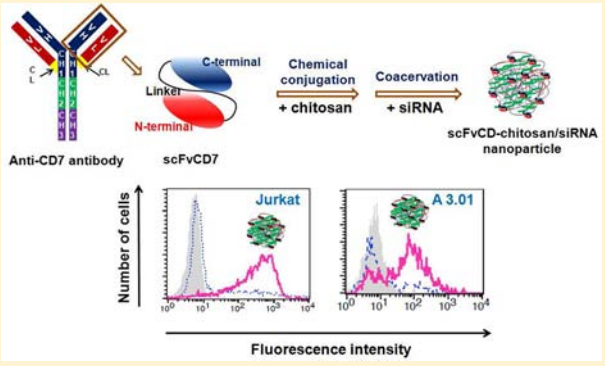

INTRODUCTION

RNA interference (RNAi) facilitates the development of new therapeutics for the treatment of various diseases, including infectious diseases.[1,2] Small interfering RNA (siRNA), consisting of double-stranded RNA molecules of 20−25 nucleotides, catalyzes target mRNA cleavage by forming an RNA-induced silencing complex (RISC) and interferes with the expression of specific proteins encoded by mRNA.[3] Despite promising features of RNAi that may be clinically useful, the use of siRNA has several limitations, such as rapid degradation by nucleases, limited stability in the bloodstream, low delivery efficiency to target cells, and nonspecific gene suppression (off-target effects). Thus, many researchers have developed delivery systems to overcome these limitations and to enhance intracellular uptake and stability against nucleases.[4]

Both viral and nonviral systems have been widely exploited for gene delivery. Viral systems include adenovirus, adeno-associated virus, and retrovirus, all of which are very efficient for gene transfection both *in vitro* and *in vivo*.[5] However, these viruses may induce oncogenic effects, immune responses, and endogenous recombination, leading to potential complications. The risks of inducing immune responses and off-target effects have raised significant concern over viral systems in clinical trials. Nonviral systems have many potential advantages, including no risk of infection, low toxicity, relatively low immunogenicity, and low probability of oncogenicity in comparison with viral systems, and can be prepared and modified relatively easily.[6,7] Cationic liposome, polyethylenimine, poly(L-lysine), and their various derivatives are frequently exploited as nonviral delivery systems.[8,9] However, low transfection efficiency has limited their use in therapeutic applications compared with viral systems.[10,11] In addition, several lipid-based systems and cationic polymers may induce significant toxicity in both *in vitro* and *in vivo* applications.

Chitosan has found potential applications in gene delivery, including siRNA delivery. Chitosan is derived from chitin by partial deacetylation, which is the second most abundant natural polysaccharide and is composed of glucosamine and *N*-acetylglucosamine residues.[12] Chitosan is biocompatible, minimally toxic, minimally immunogenic, and degradable by enzymes.[13] Chitosan has frequently been used in biomedical applications, including gene delivery, due to its ability to form stable complexes with genes via electrostatic interactions between positively charged amino groups in chitosan and negatively charged nucleic acids.[14] There have been many reports describing attempts to use chitosan-based nanoparticles for gene delivery.[15,16] A complex of chitosan and DNA was prepared and used to deliver plasmid DNA into various cell

Received: November 17, 2011
Revised: May 3, 2012
Published: May 20, 2012

dx.doi.org/10.1021/bc2006219 | *Bioconjugate Chem.* 2012, 23, 1174−1180

types, including mesenchymal stem cells.[17] The complex formation between chitosan and siRNA was controlled by varying the molecular weight and degree of deacetylation of chitosan,[18] and freeze−dried chitosan/siRNA complexes were able to be stored for 2 months without the loss of siRNA transfection activity.[19] Chitosan/sodium tripolyphosphate nanoparticles significantly enhanced the loading efficiency siRNA and resultant transfection efficiency.[20] Chitosan/siRNA nanoparticles were also formed in the presence of polyguluronate, a derivative of sodium alginate, which enhanced the stability of the nanoparticles and increased transfection efficiency.[21] In addition, chitosan-based nanoparticles were found to be effective in the RNA-mediated therapy of systemic and mucosal disease *in vivo*.[22]

In this study, we hypothesized that antibody-conjugated chitosan nanoparticles could be useful for siRNA delivery, specifically targeting T cells. CD7-specific single-chain antibody (scFvCD7) was chemically conjugated to the chitosan backbone and used to prepare nanoparticles entrapping siRNA. CD7 is a surface antigen present on human T cells[23] and has been exploited for antibody-based targeted delivery in both preclinical and clinical studies due to rapid internalization after antibody binding.[24] Nanoparticles were prepared from scFvCD7-chitosan and siRNA by a coacervation method, and their various physicochemical characteristics such as size, zeta potential, morphology, and stability in serum-containing media were investigated. The cytotoxicity, cellular association, and gene silencing efficiency of antibody-conjugated chitosan nanoparticles were evaluated using CD4+ T cell lines.

EXPERIMENTAL PROCEDURES

Materials. Chitosan glutamate (MW = 470 kDa, DD = 86%) was purchased from FMC Biopolymer (Norway). Sodium acetate and 1-ethyl-3-(dimethylaminopropyl) carbodiimide (EDC) were purchased from Sigma-Aldrich (USA) and *N*-hydroxysulfosuccinimide (sulfo-NHS) was purchased from Thermo (USA). Synthetic siRNA targeting human T cell receptor CD4 (siCD4), fluorescein isothiocyanate (FITC)-conjugated siCD4, and diethylpyrocarbonate (DEPC)-treated water were purchased from Samchulli Pharmaceutical (Korea). FITC-mouse antihuman CD4 antibody was purchased from BD Bioscience (USA), and FITC-IgG antibody was used as an isotype control (Santa Cruz Biotechnology, USA). Dulbecco's modified Eagle's medium (DMEM), RPMI medium 1640, phosphate buffered saline (PBS), penicillin−streptomycin, trypsin−EDTA, and fetal bovine serum (FBS) were purchased from Gibco (USA). Lipofectamine 2000 reagent was purchased from Invitrogen (USA). Water was distilled and deionized using the Milli-Q System (USA). Other reagents were also commercially available and used without further purification.

Purification of Single-Chain Antibody and Conjugation to Chitosan. CD7-specific single-chain antibody (scFvCD7) was expressed and purified from bacterial lysates.[25] In brief, the scFvCD7 coding sequence was PCR amplified from the VL-VH region of CD7 antibody plasmid, and the amplified scFvCD7 was cloned into the pET 26b(+) vector (Novagen, USA). The extracted protein from the bacteria was purified by affinity chromatography using an Ni-NTA column, dialyzed against PBS overnight at 4 °C, and concentrated using Amicon Ultra-15 centrifugal filter units (Millipore) ([protein] = 1.5 mg/mL). The antibody solution was mixed with a chitosan solution dissolved in 0.1 M sodium acetate buffer (pH 5.5) at the molar ratio of 1:1 for preparation of antibody-conjugated chitosan (scFvCD7-chitosan). EDC (0.5 mM) and sulfo-NHS (0.25 mM) as activation agents were added to the mixture, which was gently stirred for 24 h at 4 °C and dialyzed using a membrane with MWCO of 14 000 for three days at 4 °C to avoid denaturation of the antibody used. Conjugation between antibody and chitosan was confirmed by polyacrylamide gel electrophoresis (PAGE). A 12% (w/v) separating gel and a 4% (w/v) stacking gel were used, and the gels were stained with Coomassie Blue to identify the antibody. FITC-labeled scFvCD7 was used to determine the conjugation efficiency by measuring the amount of unreacted scFvCD7 after the conjugation reaction.

Preparation and Characterization of Nanoparticles. Antibody-conjugated chitosan was dissolved in a sodium acetate buffer solution (0.1 M sodium acetate, pH 5.5) and mixed with a solution of nonmodified chitosan at various mixing ratios, leading to molar ratios of antibody per total chitosan in resultant nanoparticles in the range 0−33% (mol %). The chitosan solution was then added to a solution containing both polyguluronate (PG) and siRNA dissolved in a 0.05 M sodium sulfate buffer solution. Polyguluronate (PG) was isolated from sodium alginate by acid hydrolysis and used to form stable chitosan-based nanoparticles as previously reported.[21] The weight ratio of chitosan to PG was fixed at 20. The nanoparticle suspension was then incubated at room temperature for 30 min before use or further analysis. The mean diameter and surface charge of nanoparticles were measured at 25 °C using a Nano ZS Zetasizer (Malvern Instruments, UK). Four different samples were prepared, measured, and averaged (n = 4).

Gel Retardation Assay. Complex formation between antibody-conjugated chitosan and siRNA was confirmed by gel electrophoresis using a 3% agarose gel. Nanoparticles with different antibody contents were loaded into the gel ([siCD4] = 1 μM), and electrophoresis was carried out at 55 mV for 80 min in a TBE buffer (4.45 mM Tris-base, 1 mM sodium EDTA, 4.45 mM boric acid, pH 8.3). Ethidium bromide was used to visualize siRNA bands using a UV transilluminator at 365 nm. Naked siRNA was used as a control.

Serum Stability of siRNA-Loaded Nanoparticles. Naked siRNA and 20% scFVCD7-chitosan/siRNA nanoparticles ([siCD4] = 0.1 μM) were incubated at 37 °C in RPMI media (1 mL) supplemented with various amounts of FBS (20%, 50%, and 90%). At each predetermined time point, the media (0.1 mL) were withdrawn and stored at −20 °C. To detach siRNA from the nanoparticles, a phenol/chloroform extraction method was used. The integrity of the siRNA was then analyzed by gel electrophoresis using a 3% agarose gel.

Cytotoxicity Assay. Jurkat and A3.01 cells were cultured in RPMI with 10% FBS and 1% penicillin and used to assess the toxicity of chitosan-based nanoparticles. Briefly, cells were plated in 96-well tissue culture plates at a cell density of 1×10^5 per well and incubated at 37 °C under a 5% CO_2 atmosphere overnight. After 24 h postincubation with nanoparticles at 37 °C ([siCD4] = 200 pmol/well), 10 μL of Alamar Blue reagent (Invitrogen, USA) was added to each well and then incubated for 4 h. The fluorescence intensity was measured using a spectrophotometer (λ_{ex} = 570 nm, λ_{em} = 585 nm). The toxicity of both siRNA only and siRNA-loaded Lipofectamine 2000, a widely used commercial transfection agent, was also tested as control ([siCD4] = 200 pmol/well).

Cellular Association of Nanoparticles. Jurkat and A3.01 cells were placed on 24-well culture plates (1×10^5 cells/well)

dx.doi.org/10.1021/bc2006219 | *Bioconjugate Chem.* 2012, 23, 1174−1180

and treated with nanoparticles containing FITC-conjugated siRNA in RPMI media without serum ([FITC-siRNA] = 200 pmol/well). After 4 h, the media were replaced with fresh media containing serum and incubated at 37 °C under a 5% CO_2 atmosphere for 18 h. Cells were then fixed with 2% formaldehyde and analyzed by a flow cytometer (Beckton Dickenson FACS Caliber, USA) to determine the efficiency of cellular association of the antibody-conjugated chitosan nanoparticles. The cellular uptake of nanoparticles was also confirmed by fluorescence microscopy. In brief, cells were placed on 8-well chamber slides (1×10^4 cells/well) and treated with the nanoparticles as described above, and then images were taken by fluorescence microscopy (TE2000-E, Nikon, Japan). Cells pretreated with free scFvCD7 antibody before treatment with 20% scFvCD7-chitosan/siRNA nanoparticles were used as a control. HEK 293FT and HeLa cells were also used as a negative control to confirm specific binding of antibody-conjugated chitosan nanoparticles to T cells.

Gene Silencing. Jurkat and A3.01 cells were seeded on 24-well tissue culture plates at a density of 1×10^5 cells/well and incubated overnight in RPMI media. On the day of transfection, the media were removed and replaced with fresh media without serum. A volume of 100 μL of chitosan-based nanoparticles containing siCD4 was added dropwise to each well, and cells were treated with the nanoparticles for 4 h. The media were then removed and cells were washed with PBS, followed by replenishment with fresh media containing serum. Cells were incubated at 37 °C under a 5% CO_2 atmosphere for an additional 48 h, treated with FITC-conjugated anti-CD4 antibody, fixed with 2% formaldehyde, and subjected to flow cytometry. Cells treated with 20% scFvCD7-chitosan nanoparticles containing siRNA targeting luciferase (mismatch siRNA) were used as a control to test off-targeting effect. Cells pretreated with free scFvCD7 antibody before treatment with 20% scFvCD7-chitosan/siCD4 nanoparticles were also used as a control. The final concentration of siRNA was kept constant for all gene silencing experiments ([siRNA] = 200 pmol/well). Gene expression levels of CD4 mRNA were also determined by quantitative real-time PCR (qRT-PCR). RNA was isolated from cells using an RNAiso plus kit (TaKaRa, Japan), and the RNA samples were reverse-transcribed to cDNA using a Maxime RT Premix kit (iNtRON Biotechnology, Korea). The mRNA expression of siCD4 was quantitatively evaluated by applying real-time SYBR Green PCR technology with an ABI PRISM 7500 Real-Time PCR System (Applied Biosystems, USA). The relative level of gene expression was determined by comparison with that of the reference gene GAPDH. The sequences of the primers used were as follows: CD4, 5′-AACATCAAGGTTCTGCCCACAT-3′ (forward) and 5′-AGCACAATCAGGGCCATTG-3′ (reverse); GAPDH, 5′-GCACCGTCAAGGCTGAGAAC-3′ (forward) and 5′-ATGGTGGTGAAGACGCCAGT-3′ (reverse).

Statistical Analysis. All data are presented as mean ± standard deviation ($n = 4$). Statistical analyses were performed using Student's t test. Values of $^{**}P < 0.01$ and $^{***}P < 0.001$ were considered statistically significant.

RESULTS AND DISCUSSION

Conjugation of scFvCD7 to Chitosan. Single-chain antibody (scFvCD7) was expressed and purified from bacterial lysates, and then conjugated to the chitosan backbone for T-cell-targeting siRNA delivery. Pretreatment of T cells with scFvCD7 completely blocked the binding of phycoerythrin-labeled anti-CD7 antibody (data not shown),[25] indicating the targeting capability of scFvCD7 to T cells. scFvCD7 was chemically conjugated to the amino group of chitosan by a carbodiimide reaction, and a gel electrophoresis method was used to confirm the conjugation (Figure 1). Separate bands of

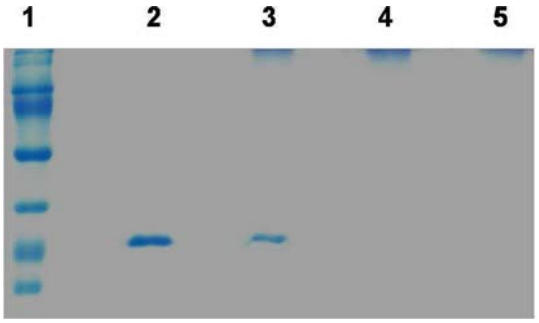

Figure 1. Conjugation of scFvCD7-chitosan confirmed by PAGE (lane 1, protein markers; 2, scFvCD7; 3, physical mixture of scFvCD7 and chitosan; 4, scFvCD7-conjugated chitosan; 5, chitosan).

chitosan and antibody were observed when a physical mixture of chitosan and antibody was tested. On the other hand, free antibody was not observed after the conjugation reaction, indicating efficient conjugation of scFvCD7 to chitosan (conjugation efficiency = 89.4%).

Preparation of scFvCD7-Chitosan/siRNA Nanoparticles. We next evaluated the ability of scFvCD7-chitosan to form complexes with siRNA. A scFvCD7-chitosan solution was mixed with a nonmodified chitosan solution at various volume ratios, followed by the addition of a solution containing both siRNA and PG. The content of the antibody-conjugated chitosan in the chitosan-based nanoparticles was varied from 0% to 33% (antibody/total chitosan in nanoparticles, mol %). The weight ratio of chitosan to siRNA was fixed at 40, as complete complex formation was observed over the weight ratio of 40. Complex formation was confirmed by gel electrophoresis (Figure 2). The mobility of siRNA was significantly retarded when complexed with chitosan, and the content of scFvCD7 in the nanoparticles did not significantly alter the complex forming ability of chitosan within the range of antibody concentrations used in this study.

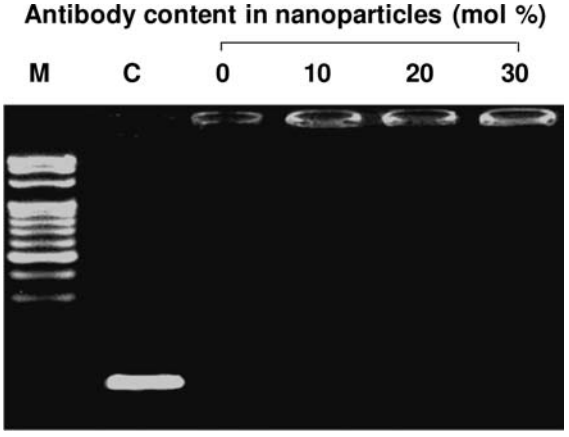

Figure 2. Gel retardation assay of scFvCD7-chitosan/siRNA nanoparticles at various antibody contents (M, DNA markers; C, naked siRNA). The weight ratio of chitosan to siRNA was fixed at 40 ([siCD4] = 1 μM).

dx.doi.org/10.1021/bc2006219 | Bioconjugate Chem. 2012, 23, 1174–1180

Various parameters, such as degree of deacetylation, concentration, molecular weight, salt form, and charge ratio between chitosan and nucleotide have been extensively exploited in order to enhance the capabilities of chitosan nanoparticles in gene delivery applications.[26] In addition, proper additives to chitosan nanoparticles enable improved transfection efficiency of siRNA.[27,28] We previously reported that stable chitosan/siRNA nanoparticles could be formed using polyguluronate (PG), derived from sodium alginate, and that these nanoparticles were useful for the delivery of siRNA to HeLa and HEK 293FT cells.[21] Direct complex formation between chitosan and nucleotide is rapid and often uncontrollable, resulting in the formation of precipitates. The inclusion of PG did not alter the complex-forming ability of scFvCD7-chitosan and siRNA and provided stable nanoparticles. The weight ratio of chitosan to PG was fixed at 20, since the use of large amounts of anionic molecules may interfere with complex formation of chitosan with siRNA.[21]

Size and Surface Charge of Nanoparticles. The size and/or surface charge of gene delivery vehicles greatly influence their cellular uptake and resultant transfection efficiency. We next tested whether the size and zeta potential of scFvCD7-chitosan/siRNA nanoparticles could be influenced by the introduction of an antibody to chitosan. The mean diameter of nonmodified chitosan nanoparticles was 319 nm, and no significant difference was found when antibody-conjugated chitosan was used, except for nanoparticles prepared with 33% scFvCD7-chitosan (Table 1). The zeta potential of chitosan-based nanoparticles was not significantly affected by the use of scFvCD7-chitosan in the preparation of the nanoparticles (approximately +17 mV).

Table 1. Size and Zeta Potential of Antibody-Conjugated Chitosan/siRNA Nanoparticles

sample	scFvCD7/chitosan in nanoparticles[a] (mol/mol)	size (nm)	ζ-potential (mV)
Chitosan NPs	0[b]	319.2 ± 10.4	16.1 ± 0.8
5% scFvCD7-chitosan NPs	0.05	305.1 ± 8.4	17.5 ± 1.2
10% scFvCD7-chitosan NPs	0.1	332.8 ± 5.9	15.2 ± 3.0
20% scFvCD7-chitosan NPs	0.2	311.9 ± 4.4	17.4 ± 2.7
33% scFvCD7-chitosan NPs	0.33	345.9 ± 3.8	17.1 ± 1.8

[a]An antibody-conjugated chitosan solution was mixed with a nonmodified chitosan solution to prepare chitosan-based nanoparticles in the presence of siRNA containing various antibody concentrations ([siRNA] = 1 μM). [b]Nonmodified chitosan nanoparticles (no antibody used).

Serum Stability of Nanoparticles. The serum stability of siRNA loaded in chitosan-based nanoparticles was tested in RPMI media containing 20%, 50%, and 90% serum at 37 °C (Figure 3). Complete degradation of naked siRNA was observed after 30 min in 20% serum-containing media. However, the degradation of siRNA in nanoparticles was much slower than that of naked siRNA. A substantial amount of siRNA was still intact after 30 min of incubation, even in 90% serum containing media. One critical hurdle for RNAi using siRNA is rapid degradation in the bloodstream by endo- and exonucleases; chitosan-based nanoparticles effectively protect siRNA from degradation, which may lead to improved cellular association and enhanced transfection efficiency *in vivo*.

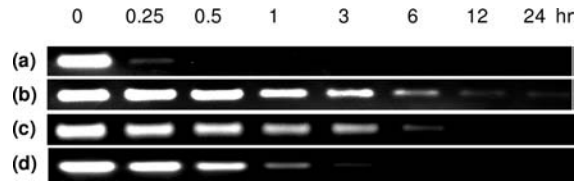

Figure 3. Stability of (a) naked siRNA incubated in 20% serum-containing media and siRNA entrapped in 20% scFvCD7-chitosan nanoparticles incubated in (b) 20%, (c) 50%, and (d) 90% serum-containing media over time ([siCD4] = 0.1 μM).

Cytotoxicity. The toxicity of chitosan-based nanoparticles was evaluated using Jurkat and A3.01 cells. More than 90% of cells initially seeded maintained their viability after treatment with scFvCD7-chitosan nanoparticles, while the viability of cells treated with Lipofectamine 2000 was significantly decreased (Figure 4). Even though Lipofectamine 2000 is commercially available and widely used as a nonviral gene delivery system, its *in vivo* application has been limited by severe toxicity.[29] Our findings indicate that chitosan has minimal toxicity and the conjugation of scFvCD7 to chitosan does not influence cytotoxicity when treating Jurkat and A3.01 cells.

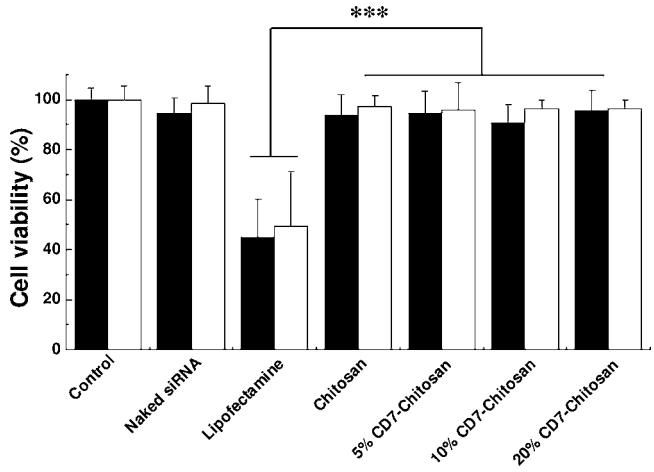

Figure 4. Cytotoxicity of nanoparticles tested with Jurkat (filled bars) and A3.01 (empty bars) cells (***P < 0.001).

Cellular Association. The effect of scFvCD7 conjugated to chitosan-based nanoparticles on cellular association with targeting cells with abundant CD7 receptor as model T cells were next investigated. Cellular uptake of antibody-conjugated chitosan nanoparticles and their translocation to the cytoplasm were clearly observed, compared with nonmodified chitosan nanoparticles (SI Figure S1). The introduction of scFvCD7 significantly enhanced the cellular association of chitosan-based nanoparticles with T cells, as demonstrated by flow cytometry analysis (Figure 5a,b). The targeting efficiency was dependent upon the amount of scFvCD7 in the nanoparticles. An equal amount of model siRNA (200 pmol/mL) was used to form nanoparticles in the presence of various antibody concentrations, and the percentage of cellular association dramatically increased when the antibody concentration in the nanoparticles increased up to 10% (Figure 5c). No significant increase in cellular association was observed over the antibody concentration, and this might be attributed to steric effect of the large

dx.doi.org/10.1021/bc2006219 | *Bioconjugate Chem.* 2012, 23, 1174–1180

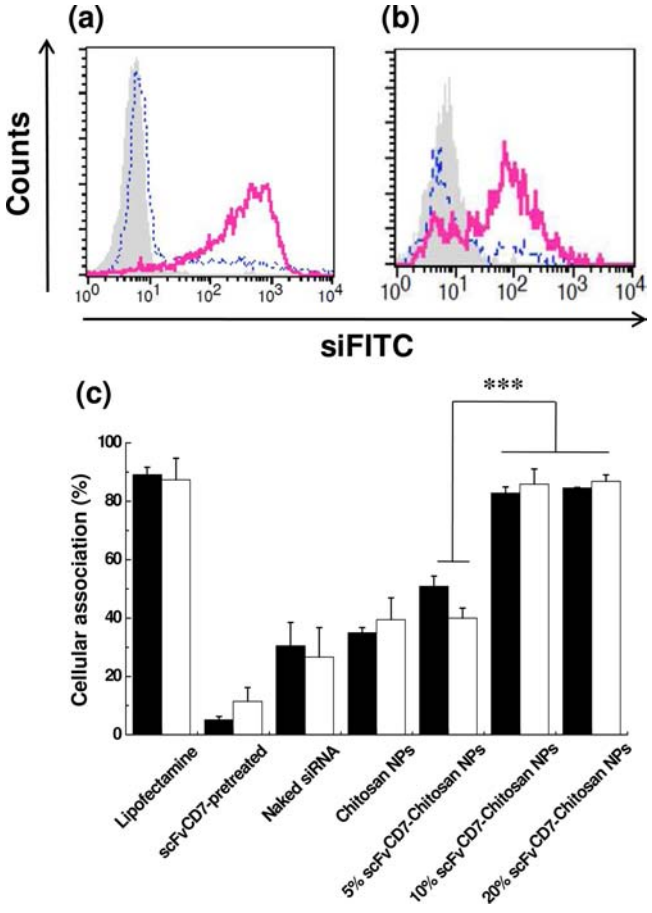

Figure 5. Cellular association of chitosan (blue dashed line) and 20% scFvCD7-chitosan (red solid line) nanoparticles with (a) Jurkat and (b) A3.01 cells was monitored by flow cytometry. Filled histogram indicates untreated cells as a control. (c) Quantitative analysis of the cellular association with Jurkat (filled bars) and A3.01 (empty bars) cells ([FITC-siRNA] = 200 pmol/well, ***$P < 0.001$).

antibody. The cellular association of scFvCD7-chitosan nanoparticles was dramatically reduced after pretreatment of cells with soluble anti-CD7 antibody, indicating specific binding of antibody-conjugated chitosan nanoparticles to the T cell lines (Figures S1d and 5c). We also confirmed that cellular association of chitosan-based nanoparticles was not significantly influenced by the introduction of scFvCD7 to chitosan-based nanoparticles for both HEK 293FT and HeLa cells (SI Figure S2), likely due to the lack of CD7 receptors on the cells (SI Figure S3). This finding also clearly supports that scFvCD7-chitosan/siRNA nanoparticles are promising as a T cell-targeting delivery vehicle. Surface-modified chitosan nanoparticles using lactobionic acid were attempted to increase the cellular uptake efficiency as a gene carrier.[30] In addition, many antibody-conjugated nanoparticles for selective targeting effect have been reported.[31,32] However, few studies regarding antibody-conjugated chitosan nanoparticles for T cell delivery have been reported.

Gene Silencing. We next investigated the gene silencing efficacy of scFvCD7-chitosan nanoparticles containing siCD4 by the detection of CD4 receptors on Jurkat and A3.01 cells. About 80% of the population of Jurkat and A3.01 cells was stained with FITC-anti CD4 antibody, and the expression level of CD4 for cells treated with either nonmodified chitosan nanoparticles (no scFvCD7 used) or naked siCD4 was not significantly changed (Figure 6). However, the expression level was dramatically reduced when scFvCD7-chitosan nanoparticles were used to deliver siCD4 to the cells. The gene silencing efficiency for both cell types was about 40% when treated with scFvCD7-chitosan/siCD4 nanoparticles, similar to that of Lipofectamine/siCD4 complexes (Figure 7). The improved gene silencing may be attributed to the increased cellular association of antibody-conjugated chitosan nanoparticles, as demonstrated in Figure 5. Negligible reduction in the CD4 expression level was observed when the cells were treated with either scFvCD7-chitosan/siLuc nanoparticles (mismatch siRNA) or anti CD7 antibody before treatment with nanoparticles in order to block receptors (CD7-pretreated), indicating knockdown specificity of the siRNA used in this study.

We further investigated the CD4 mRNA expression level of Jurkat and A3.01 cells treated with chitosan-based nanoparticles

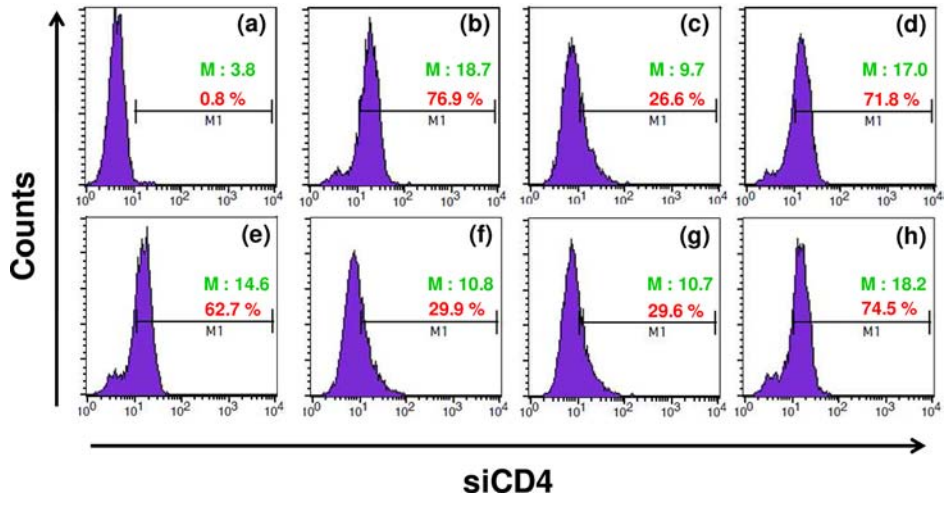

Figure 6. Jurkat cells treated with (c) Lipofectamine/siCD4 nanoparticles, (d) naked siCD4, (e) chitosan/siCD4 nanoparticles, (f) 10% scFvCD7-chitosan/siCD4 nanoparticles, and (g) 20% scFvCD7-chitosan/siCD4 nanoparticles were analyzed by flow cytometry. (h) 20% scFvCD7-chitosan nanoparticles entrapping siLuc (mismatch) was also tested. (a) Nontreated and (b) FITC-anti CD4 antibody-treated cells were used as controls (M, mean fluorescence intensity; [siCD4] = 200 pmol/well).

dx.doi.org/10.1021/bc2006219 | *Bioconjugate Chem.* 2012, 23, 1174–1180

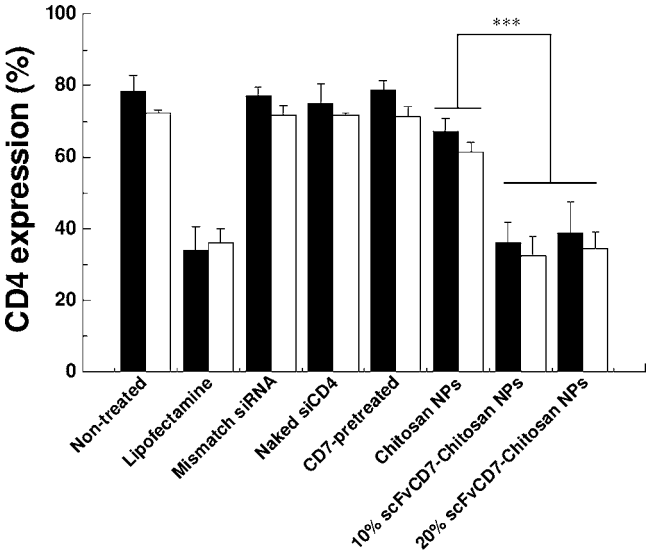

Figure 7. CD4 expression levels of Jurkat (filled bars) and A3.01 (empty bars) cells treated with antibody-conjugated chitosan/siCD4 nanoparticles determined by flow cytometry. Cells treated with 20% scFvCD7-chitosan nanoparticles entrapping siLuc (mismatch siRNA) were used as a control. Cells pretreated with free scFvCD7 antibody before treatment with 20% scFvCD7-chitosan/siCD4 nanoparticles were also tested as a control (***$P < 0.001$).

using qRT-PCR. Figure 8 demonstrates significant inhibition of mRNA expression in cells treated with scFvCD7-chitosan nanoparticles compared to those treated with chitosan nanoparticles, indicating their specificity and efficacy as a T cell-targeting delivery system. The gene silencing efficiency was not significantly affected by difference in antibody concentrations in the nanoparticles tested, which was consistent with results obtained from cellular association experiments (Figure 5c).

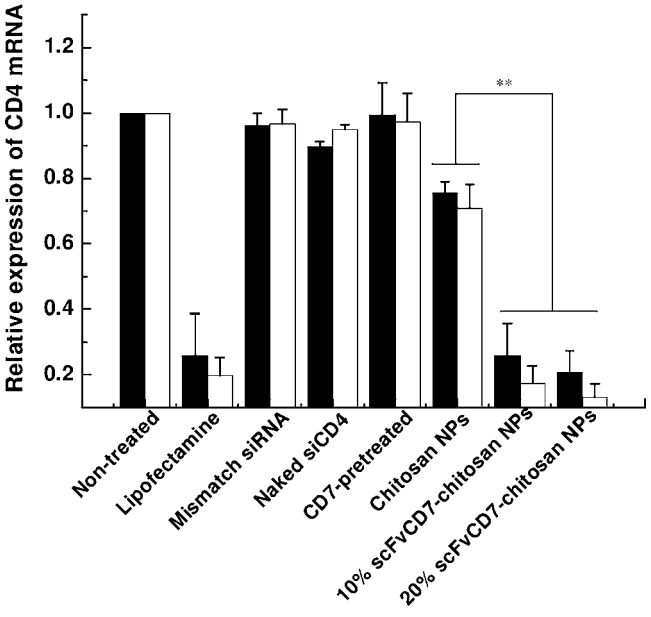

Figure 8. Quantification of CD4 mRNA expression levels of Jurkat (filled bars) and A3.01 (empty bars) cells treated with antibody-conjugated chitosan/siCD4 nanoparticles determined by qRT-PCR. Cells treated with 20% scFvCD7-chitosan nanoparticles entrapping siLuc (mismatch siRNA) were used as a control. Cells pretreated with free scFvCD7 antibody before treatment with 20% scFvCD7-chitosan/siCD4 nanoparticles were also tested as a control (**$P < 0.01$).

The CD4 receptor is mainly activated on T cells and often targeted for the treatment of infectious diseases, including HIV.[33] The reduction of CD4 receptors on the cell surface does not allow for virus attachment and production.[34] Thus, the effective suppression of CD4 receptors on the surface of T cells using T cell-specific chitosan nanoparticles may play a crucial role in the treatment of HIV infection, as both the entry of HIV-1 into cells and virus production are greatly suppressed by the silencing of the CD4 receptor. Recent studies have implicated antibody-complexed siRNA in the enhancement of targeting efficiency to T cells and association into cells.[35,36]

CONCLUSION

We demonstrated that antibody-conjugated chitosan nanoparticles were useful for the delivery of siRNA into CD4+ T cell lines. CD7-specific single-chain antibody (scFvCD7) was successfully conjugated to a chitosan backbone by carbodiimide chemistry. Introduction of the antibody to chitosan did not interfere with complex formation, and scFvCD7-chitosan formed stable nanoparticles with siRNA. The cellular association of scFvCD7-chitosan/siRNA nanoparticles with T cells significantly increased compared with nonconjugated chitosan nanoparticles. The expression levels of CD4 receptors on T cells were greatly reduced by the delivery of CD4 siRNA using antibody-conjugated chitosan nanoparticles. This finding clearly suggests that scFvCD7-chitosan is useful for the delivery of siRNA specifically to T cells. Although an RNAi technique has been increasingly applied to clinical trials as a new therapeutic tool, systemic siRNA delivery into target cells is still challenging. Introduction of peptide and antibody to polymer-based nanoparticles for tissue-specific targeting could be promising, and our approach reported here may find potential applications in the design and tailoring of novel delivery vehicles for many therapeutic purposes.

ASSOCIATED CONTENT

Supporting Information

Additional figures as described. This material is available free of charge via the Internet at http://pubs.acs.org.

AUTHOR INFORMATION

Corresponding Author

*Kuen Yong Lee, Ph.D.: Tel +82-2-2220-0482, Fax +82-2-2293-2642, E-mail leeky@hanyang.ac.kr. Sang Kyung Lee, Ph.D.: Tel +82-2-2220-2344, Fax +82-2-2220-1998, E-mail sangkyunglee@hanyang.ac.kr.

Author Contributions

†These authors contributed equally to this work.

Notes

The authors declare no competing financial interest.

ACKNOWLEDGMENTS

This work was supported by the National Research Foundation of Korea (NRF) grant funded by the Korea government (MEST) (No. 20110017959).

REFERENCES

(1) Manjunath, N., Kumar, P., Lee, S. K., and Shankar, P. (2006) Interfering antiviral immunity: application, subversion, hope? *Trends Immunol. 27*, 328−335.

(2) Shankar, P., Manjunath, N., and Lieberman, J. (2005) The prospect of silencing disease using RNA interference. *JAMA 293*, 1367−1373.

(3) Plasterk, R. H. A. (2002) RNA silencing: the genome's immune system. *Science 296*, 1263−1265.

(4) Schaffert, D., and Wagner, E. (2008) Gene therapy progress and prospects: synthetic polymer-based systems. *Gene Ther. 15*, 1131−1138.

(5) Somia, N., and Verma, I. M. (2000) Gene therapy: trials and tribulations. *Nat. Rev. Genet. 1*, 91−99.

(6) Li, S.-D., and Huang, L. (2007) Non-viral is superior to viral gene delivery. *J. Controlled Release 123*, 181−183.

(7) Park, T. G., Jeong, J. H., and Kim, S. W. (2006) Current status of polymeric gene delivery systems. *Adv. Drug Delivery Rev. 58*, 467−486.

(8) Christensen, L. V., Chang, C.-W., Kim, W. J., Kim, S. W., Zhong, Z., Lin, C., Enqbersen, J. E., and Fellen, J. (2006) Reducible poly(amido ethylenimine)s designed for triggered intracellular gene delivery. *Bioconjugate Chem. 17*, 1233−1240.

(9) Hashida, M., Takemura, S., Nishikawa, M., and Takakura, Y. (1998) Targeted delivery of plasmid DNA complexed with galactosylated poly(L-lysine). *J. Controlled Release 53*, 301−310.

(10) Lungwitz, U., Breunig, M., Blunk, T., and Göpferich, A. (2005) Polyethylenimine-based non-viral gene delivery systems. *Eur. J. Pharm. Biopharm. 60*, 247−266.

(11) Davis, M. E. (2002) Non-viral gene delivery systems. *Curr. Opin. Biotechnol. 13*, 128−131.

(12) Ilium, L. (1998) Chitosan and its use as a pharmaceutical excipient. *Pharm. Res. 15*, 1326−1331.

(13) Kumar, M. N. V. R., Muzzarelli, R. A. A., Muzzarelli, C., Sashiwa., H., and Domb, A. J. (2004) Chitosan chemistry and pharmaceutical perspectives. *Chem. Rev. 104*, 6017−6084.

(14) Mao, H.-Q., Roy, K., Troung-Le, V., Janes, K. A., Lin, K. Y., Wang, Y., August, J. T., and Leong, W. K. (2001) Chitosan-DNA nanoparticles as gene carriers: synthesis, characterization and transfection efficiency. *J. Controlled Release 70*, 399−421.

(15) Leong, K. W., Mao, H. Q., Truong-Le, V. L., Roy, K., Walsh, S. M., and August, J. T. (1998) DNA-polycation nanospheres as non-viral gene delivery vehicles. *J. Controlled Release 53*, 183−193.

(16) Lee, K. Y., Kwon, I. C., Kim, Y. H., Jo, W. H., and Jeong, S. Y. (1998) Preparation of chitosan self-aggregates as a gene delivery system. *J. Controlled Release 51*, 213−220.

(17) Corsi, K., Chellat, F., Yahia, L., and Fernandes, J. C. (2003) Mesenchymal stem cells, MG63 and HEK293 transfection using chitosan-DNA nanoparticles. *Biomaterials 24*, 1255−1264.

(18) Liu, X., Howard, K. A., Dong, M., Andersen, M. O., Rahbek, U. L., Johnsen, M. G., Hansen, O. C., Besenbacher, F., and Kjems, J. (2007) The influence of polymeric properties on chitosan/siRNA nanoparticle formulation and gene silencing. *Biomaterials 28*, 1280−1288.

(19) Andersen, M. O., Howard, K. A., Paludan, S. R., Besenbacher, F., and Kjems, J. (2008) Delivery of siRNA from lyophilized polymeric surfaces. *Biomaterials 29*, 506−512.

(20) Katas, H., and Alpar, H. O. (2006) Development and characterisation of chitosan nanoparticles for siRNA delivery. *J. Controlled Release 115*, 216−225.

(21) Lee, D. W., Yun, K.-S., Ban, H.-S., Choe, W., Lee, S. K., and Lee, K. Y. (2009) Preparation and characterization of chitosan/polyguluronate nanoparticles for siRNA delivery. *J. Controlled Release 139*, 146−152.

(22) Howard, K. A., Rahbek, U. L., Liu, X., Damgaard, C. K., Glud, S. Z., Andersen, M. O., Hovgaard, M. B., Schmitz, A., Nyengaard, J. R., Besenbacher, F., and Kjems, J. (2006) RNA interference in vitro and in vivo using a novel chitosan/siRNA nanoparticle system. *Mol. Ther. 14*, 476−484.

(23) Peipp, M., Kupers, H., Saul, D., Schlierf, B., Greil, J., Zunino, S. J., Gramatzki, M., and Fey, G. H. (2002) A recombinant CD7-specific single-chain immunotoxin is a potent inducer of apoptosis in acute leukemic T cells. *Cancer Res. 62*, 2848−2855.

(24) Bremer, E., Samplonius, D. F., Peipp, M., van Genne, L., Kroesen, B.-J., Fey, G. H., Gramatzki, M., de Leij, L. F. M. H., and Helfrich, W. (2005) Target cell-restricted apoptosis induction of acute leukemic T cells by a recombinant tumor necrosis factor-related apoptosis-inducing ligand fusion protein with specificity for human CD7. *Cancer Res. 65*, 3380−3388.

(25) Kumar, P., Ban, H.-S., Kim, S.-S., Wu, H., Pearson, T., Greiner, D. L., Laouar, A., Yao, J., Haridas, V., Habiro, K., Yang, Y.-G., Jeong, J. H., Lee, K.-Y., Kim, Y.-H., Kim, S. W., Peipp, M., Fey, G. H., Manjunath, N., Shultz, D. L., Lee, S.-K., and Shankar, P. (2008) T cell-specific siRNA delivery suppresses HIV-1 infection in humanized mice. *Cell 134*, 577−586.

(26) Mao, S., Sun, W., and Kissel, T. (2010) Chitosan-based formulations for delivery of DNA and siRNA. *Adv. Drug Delivery Rev. 62*, 12−27.

(27) Tan, M. L., Choong, P. F., and Dass, C. R. (2009) Cancer, chitosan nanoparticles and catalytic nucleic acids. *J. Pharm. Pharmacol. 61*, 3−12.

(28) Rojanarata, T., Opanasopit, P., Techaarpornkul, S., Ngawhirunpat, T., and Ruktanonchai, U. (2008) Chitosan-thiamine pyrophosphate as a novel carrier for siRNA delivery. *Pharm. Res. 25*, 2807−2814.

(29) Lv, H., Zhang, S., Wang, B., Cui, S., and Yan, J. (2006) Toxicity of cationic lipids and cationic polymers in gene delivery. *J. Controlled Release 114*, 100−109.

(30) Park, I. K., Park, Y. H., Shin, B. A., Choi, E. S., Park, Y. R., Akaike, T., and Cho, C. S. (2000) Galactosylated chitosan-graft-dextran as hepatocyte-targeting DNA carrier. *J. Controlled Release 69*, 97−108.

(31) Ackerson, C. J., Jadzinsky, P. D., Jensen, G. J., and Kornberg, R. D. (2006) Rigid, specific, and discrete gold nanoparticle/antibody conjugates. *J. Am. Chem. Soc. 128*, 2635−2640.

(32) Dinauera, N., Balthasarb, S., Weberb, C., Kreuterb, J., Langerb, K., and von Briesen, H. (2005) Selective targeting of antibody-conjugated nanoparticles to leukemic cells and primary T-lymphocytes. *Biomaterials 26*, 5898−5906.

(33) Martínez, M. A., Clotet, B., and Esté, J. A. (2002) RNA interference of HIV replication. *Trends Immunol. 23*, 559−561.

(34) Novina, C. D., Murray, M. F., Dykxhoorn, D. M., Beresford, P. J., Riess, J., Lee, S.-K., Collman, R. G., Lieberman, J., Shankar, P., and Sharp, P. A. (2002) siRNA-directed inhibition of HIV-1 infection. *Nat. Med. 8*, 681−686.

(35) Anderson, J., Banerjea, A., Planelles, V., and Akkina, R. (2003) Potent suppression of HIV type 1 infection by a short hairpin anti-CXCR4 siRNA. *AIDS Res. Hum. Retrov. 19*, 699−706.

(36) Song, E., Zhu, P., Lee, S.-K., Chowdhury, D., Kussman, S., Dykxhoorn, S. M., Feng, Y., Palliser, D., Weiner, D. B., Shankar, P., Marasco, W. A., and Lieberman, J. (2005) Antibody mediated in vivo delivery of small interfering RNAs via cell-surface receptors. *Nat. Biotechnol. 23*, 709−717.

Bioconjugate Chemistry

Article

pubs.acs.org/bc

DOTAGA-Trastuzumab. A New Antibody Conjugate Targeting HER2/*Neu* Antigen for Diagnostic Purposes

Mathieu Moreau,[†] Olivier Raguin,[‡] Jean-Marc Vrigneaud,[§] Bertrand Collin,[§] Claire Bernhard,[†] Xavier Tizon,[‡] Frédéric Boschetti,[∥] Olivier Duchamp,[‡] François Brunotte,[§] and Franck Denat*[,†]

[†]Institut de Chimie Moléculaire de l'Université de Bourgogne, UMR CNRS 6302, 21078 Dijon Cedex, France

[‡]Oncodesign, 21076 Dijon Cedex, France

[§]Service de médecine nucléaire, Centre Georges-François Leclerc, 21000 Dijon, France

[∥]Chematech, 21000 Dijon, France

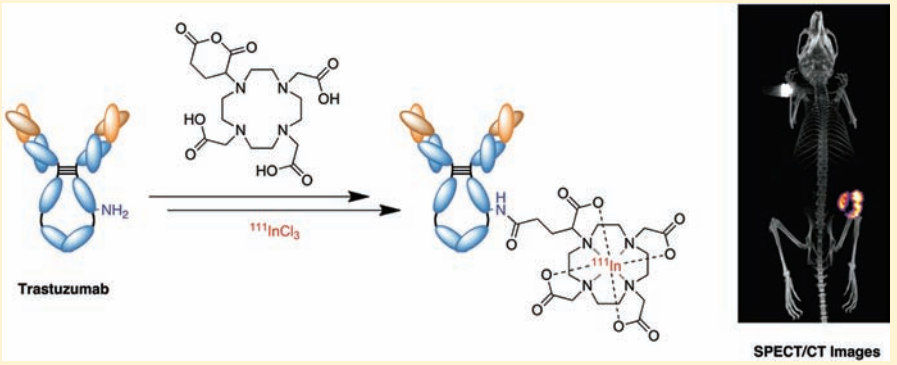

ABSTRACT: Improved bifunctional chelating agents (BFC) are required for indium-111 radiolabeling of monoclonal antibodies (mAbs) under mild conditions to yield stable, target-specific agents. 2,2′,2″-(10-(2,6-Dioxotetrahydro-2*H*-pyran-3-yl)-1,4,7,10-tetraazacyclododecane-1,4,7-triyl)triacetic acid (DOTAGA-anhydride) was evaluated for mAb conjugation and labeling with indium-111. The DOTA analogue was synthesized and conjugated to trastuzumab—which targets the HER2/*neu* receptor—in mild conditions (PBS pH 7.4, 25 °C, 30 min) and gave a mean degree of conjugation of 2.6 macrocycle per antibody. Labeling of this immunoconjugate with indium-111 was performed in 75% yield after 1 h at 37 °C, and the proportion of ^{111}In-DOTAGA-trastuzumab reached 97% after purification. The affinity of DOTAGA-trastuzumab was 5.5 ± 0.6 nM as evaluated by *in vitro* saturation assays using HCC1954 breast cancer cell line. SPECT/CT imaging and biodistribution studies were performed in mice bearing breast cancer BT-474 xenografts. BT-474 tumors were clearly visualized on SPECT images at 24, 48, and 72 h postinjection. The tumor uptake of [^{111}In-DOTAGA]-trastuzumab reached 65%ID/g 72 h postinjection. These results show that the DOTAGA BFC appears to be a valuable tool for biologics conjugation.

INTRODUCTION

Monoclonal antibodies (mAb) are attractive molecules in the field of molecular imaging agent development, partly because of the development of personalized medicine.[1,2] Indeed, tumor-specific antibodies have been widely used as delivery vectors to transport radiometal ions for cancer therapy.[1,3] They have also been used for cancer imaging to determine antigen expression in the whole body, to evaluate therapeutic response, or to classify patients for specific treatments.[4] Nevertheless, this field of research is in constant evolution in order to develop and improve labeling technique suitable to antibodies' half-life, for both preclinical biodistribution studies and further possible applications in diagnosis and treatments.

Although the specificity of mAbs makes them attractive targeting vectors, their large size (150 kDa) is sterically hindering: the slow accumulation rate limits their accretion in tumors. Besides, mAbs have a slow blood and hepatic clearance. Consequently, image acquisitions are usually done 24−72 h postinjection when the optimal target to background ratio is reached (this requires the use of long half-life radioisotopes). To overcome these drawbacks, two options can be considered. The first one is to improve the specific activity of the radiolabeled mAb by increasing the radiolabeling yield. Such an improvement can be obtained by raising the incubation temperature, but this is not always a viable option as it can alter the mAb. Moreover, increasing the specific activity may lead to an increase of radiolysis. The second option is to use mAb fragments or smaller targeting agents such as affibodies or peptides, which are designed to clear more rapidly from blood and allow early image acquisition, but these moieties frequently show lower target accumulation and higher kidney uptake.[5,6] Finally, it is still very difficult to determine if a small fragment

Received: December 22, 2011
Revised: March 2, 2012
Published: April 23, 2012

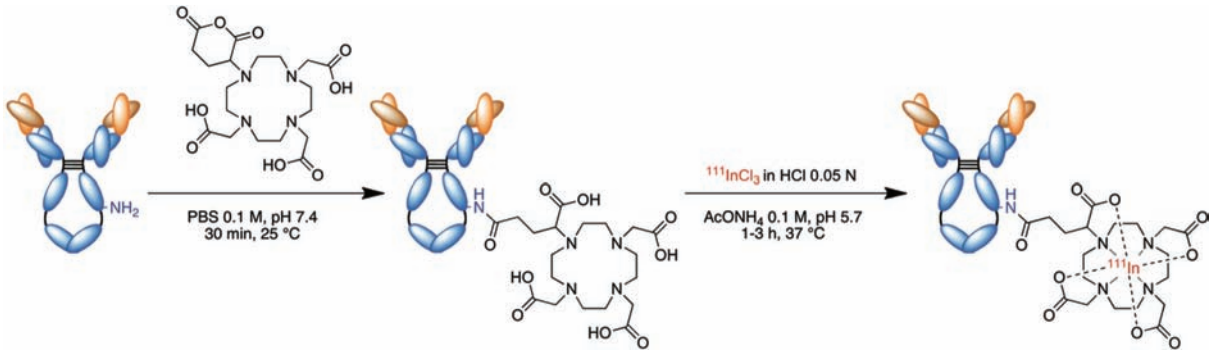

Figure 1. Strategy for the construction of ^{111}In-modified trastuzumab bioconjugate using DOTAGA-anhydride.

will be more efficient than a "native" mAb for molecular imaging, because each species shows benefits and disadvantages.[7] As a consequence, and despite their drawbacks, mAbs are still highly valuable vectors in targeted radiopharmaceutical development, providing that stable complexes with long half-life radiometals are used for their labeling.

The humanized mAb trastuzumab (Herceptin) is directed against the human epithelial growth factor receptor 2 (HER2/*neu*), which is overexpressed in a variety of epithelial tumors, especially breast cancer.[8,9] HER2/*neu* amplification is normally assessed *ex vivo* in a primary tumor biopsy by immunohistochemical staining for HER2 protein or by fluorescence *in situ* hybridization (FISH) to detect increased HER2/*neu* gene copy number.[10] However, this invasive technique has shown discordance in HER2/*neu* expression between primary and metastatic breast cancer,[11,12] and thus, it would be useful to have a more reliable imaging technique to assess HER2/*neu* phenotype *in vivo* in breast cancer lesions. Trastuzumab has been radiolabeled for preclinical studies and clinical trials, using a large variety of BFCs to chelate metallic radioisotopes such as indium-111, zirconium-89, or lutetium-177,[13−20] whose half-lives fit perfectly with the clearance of the antibody. During past years, polyamine carboxylate ligands such as diethylenetriaminepentaacetic acid (DTPA) and 1,4,7,10-tetraazacyclododecane-*N*,*N*′,*N*″,*N*‴-tetraacetic acid (DOTA) have been the BFCs of choice for trivalent radiometals.[14,16] Conjugation of these chelates to the biomolecule can be accomplished by introduction of a primary amine targeting grafting function such as *N*-hydroxysuccinimidyl (NHS), isothiocyanate (NCS), or cyclic anhydride. One should note that the number of chelating agents conjugated to the antibody has to be controlled, since too high a degree of conjugation could induce modifications in the protein (such as chelating agent linked to an amino acid located at the binding site, modification of the structure) that reduce or inhibit its ability to bind its target. The DOTA analogues result generally in more stable radiometal bioconjugates than the DTPA, due to the so-called macrocyclic effect, coupled with the hepta- or octadenticity of these chelates.[21−23] Among these BFCs, *p*-SCN-Bn-DOTA is the most commonly used, because of the high *in vivo* stability of the resulting radiometal complexes. If the isothiocyanate grafting function shows good stability in water, several hours are needed to get good yields when reacting with proteins. Besides, the synthesis of such molecules remains difficult and costly, and results in low yields.[24,25]

2-(4,7,10-Tris(carboxymethyl)-1,4,7,10-tetraazacyclododecan-1-yl)pentanedioic acid (DOTAGA) is a DOTA derivative that leaves four acetate pendant arms intact and can be easily synthesized in good yield.[26,27] This macrocycle has shown good chelation properties with trivalent metallic cations such as Gd^{3+} or Y^{3+},[28] and has been attached to biologic vectors for therapy and nuclear imaging.[29]

In this work, we describe the synthesis and the conjugation of the BFC 2,2′,2″-(10-(2,6-dioxotetrahydro-2*H*-pyran-3-yl)-1,4,7,10-tetraazacyclododecane-1,4,7-triyl)triacetic acid (DOTAGA-anhydride), bearing a cyclic anhydride grafting function (Figure 1). This BFC, which has been very recently grafted on gadolinium nanoparticles,[30] was conjugated to trastuzumab. The yield of the conjugation reaction was determined by MALDI-TOF mass spectrometry. The DOTAGA-trastuzumab conjugate was then radiolabeled with indium-111, and its biological activity was evaluated by *in vitro* assays on HER2/*neu*-expressing cell lines and *in vivo* in a model of human breast tumor-bearing mouse model.

EXPERIMENTAL PROCEDURES

Instrument and Methods. Matrix-assisted laser desorption ionization/time of flight (MALDI/TOF) mass spectra were obtained on a Bruker DALTONICS Ultraflex II (Bruker Daltonics, Bremen, Germany) mass spectrometer using sinapinic acid as matrix (Sigma-Aldrich, St. Quentin Falavier, France), at the "Plateforme d'Analyse Chimique et de Synthèse Moléculaire de l'Université de Bourgogne" (PACSMUB, Dijon, France). Radiochromatograms were carried out with a Raytest miniGITA-Star γ radiochromatograph (Raytest, Straubenhardt, Germany) or with a Bioscan AR-2000 radio-TLC Imaging Scanner (Bioscan Inc., Washington, DC).

Reagents. Pure water (18.2 MΩ.cm^{-1}, PURELAB Ultra, ELGA) was used throughout. When metal-free conditions were needed, glassware and plasticware were washed with 3 N HCl and thoroughly rinsed with deionized distilled water. Ammonium acetate buffer was prepared under metal-free conditions using *Trace select* ammonium acetate and acetic acid (Sigma-Aldrich, St. Quentin Falavier, France). Pyridine and acetic anhydride were purchased from Acros Organics (Illkirch, France) and used without further purification. DOTAGA was provided by CheMatech (Dijon, France), and trastuzumab (Herceptin; Roche, Welwyn Garden City, U.K.) was obtained through the "Centre de lutte contre le cancer G.-F. Leclerc" (Dijon, France). [^{111}In]indium chloride ($^{111}InCl_3$, 370 MBq.mL^{-1} in 0.05 N HCl) was purchased from Covidien (Petten, The Netherlands) for *in vitro* studies and the first *in vivo* biodistribution study. For the second *in vivo* biodistribution study, [^{111}In]indium chloride ($^{111}InCl_3$, 370 MBq.mL^{-1} in 0.05 N HCl) was purchased from Perkin-Elmer (Boston, MA, USA). The radiolabeling yield and the absence of free indium-111 in

the labeled antibody were determined using ITLC-SG strips from Pall Gelman Sciences (Ann Arbor, MI, USA).

Synthesis of DOTAGA-Anhydride. Two milliliters of acetic anhydride under nitrogen were added to a suspension of DOTAGA, 2HCl (1 g, 1.85 mmol) in pyridine (0.85 mL, 0.01 mol, 6 equiv), and the mixture was stirred at 65 °C for 18 h. After cooling down, the suspension was filtered and washed with acetic anhydride (10 mL), acetonitrile (15 mL), and diethyl ether (20 mL). The precipitate was dried under vacuum to afford DOTAGA-anhyride as a gray powder (0.95 g, 96%). The BFC was used without further purification. Mp: 108 ± 2 °C. HRMS (ESI): m/z calculated for $C_{19}H_{30}N_4O_9$ + Na^+: 481.19050; found 481.18922.

Conjugation of DOTAGA-Anhydride to Trastuzumab. Following the instructions of the manufacturer, trastuzumab was reconstituted in water for injection to obtain a 21 mg.mL^{-1} solution which was purified from other excipients (histidine, polysorbate, and α,α-trehalose) by ultrafiltration (Vivaspin 20 filter 10 kDa, Sartorius; 1 h at 2684 g).

Conjugation was performed at a 20:1 DOTAGA-anhydride/trastuzumab molar ratio. 36.2 μL of a 5 mg.mL^{-1} suspension of DOTAGA-anhydride (181.6 μg, 0.39 μmol, 20 equiv) in dry chloroform (Carlo Erba, Val de Reuil, France) were pipetted under ultrasonication and transferred to a polypropylene microtube. The chloroform was evaporated under a gentle stream of air. 88.4 μL of a solution of purified trastuzumab (33.92 mg.mL^{-1}, 3 mg, 19.8 nmol, 1 equiv) in PBS 0.1 M, pH 7.4, (Fisher Scientific, Illkirch, France) was subsequently added. The solution was completed to 750 μL with PBS 0.1 M, pH 7.4, and gently mixed at 25 °C for 30 min. Unbound DOTAGA was then removed by ultrafiltration (Nanosep filter 30 kDa, Pall, 12 min at 8100 g, 4 °C). Conjugated trastuzumab was washed twice with 500 μL of PBS 0.1 M, pH 7.4, and the concentrated solution was diluted in 500 μL of ammonium acetate buffer 0.1 M pH 5.7. The purified immunoconjugate DOTAGA-trastuzumab was stored at 4 °C. Concentration of the antibody was determined by UV spectrophotometry at 280 nm. The molar extinction coefficient $\varepsilon 280_{Trastuzumab}$ (218 500 M^{-1}.cm^{-1}) was calculated using ExPASy ProtParam tool (http://web.expasy.org/protparam).

Radiolabeling. *Radiolabeling for in Vitro Studies.* 6 MBq of $^{111}InCl_3$ was added to 40 μg of the immunoconjugate in 0.1 M ammonium acetate buffer, pH 5.7, to reach a buffer/HCl (from $^{111}InCl_3$ solution) ratio of 1.5:1 resulting in a pH 5 solution. The solution was stirred in a thermomixer at 37 °C during 1 h. After incubation, 50 mM EDTA in 0.1 M ammonium acetate was added in order to chelate free indium-111. The resulting ^{111}In-EDTA was then removed by ultrafiltration, and the product was diluted in PBS 0.1 M, pH 7.4. Instant thin layer chromatographies (ITLC) were performed before and after ultrafiltration to determine the radiolabeling yield and to assess the absence of free indium-111. 1 μL of each solution was deposited on ITLC-SG strips at 2 cm of the bottom. The solvent (sodium citrate 0.1 M, pH 5) was allowed to rise to 10 cm from the bottom of the strips. Radiolabeled antibody remained at the application point while free indium-111 or ^{111}In-chelates migrated with solvent front. The strips were then analyzed using a γ radiochromatograph.

Radiolabeling for in Vivo Studies. The radiolabeling was performed as described for *in vitro* studies, using 125 MBq of $^{111}InCl_3$ and 125 μg of trastuzumab, and the solution was stirred for 3 h at 37 °C. After purification, the radiolabeled antibody was diluted in PBS 0.1 M, pH 7.4, for injection.

Stability Testing of the Radiolabeled Conjugate. A DTPA-challenge test was performed to evaluate the labeling stability of ^{111}In-DOTAGA-trastuzumab. Two samples were diluted with a 2000-fold molar excess of a DTPA solution in PBS 0.1 M, pH 7.4, and were incubated for several days. Radio-ITLC controls were performed every day for 5 consecutive days.

***In Vitro* Studies.** *Tumor Cells.* HCC1954 and BT-474 cells (ATCC, Rockville, MD) are human breast adenocarcinoma cells[31,32] that express the HER2/*neu* antigen at their surface. These cells were grown as adherent monolayer in RPMI1640 medium (Lonza, Belgium) supplemented with 10% fetal calf serum (Lonza).

Tumor cells were harvested just prior to experiments. For *in vitro* experiments, cells were washed twice with PBS 0.1 M pH 7.4 (Lonza) and resuspended in PBS 0.1 M pH 7.4 containing 0.2% bovine serum albumin (BSA) and 0.02% azide (Sigma, France). For *in vivo* experiments, cells were washed twice with RPMI1640 medium and resuspended in a mixture of RPMI1640 and matrigel (BD Biosciences) (1/1, v/v). Before all experiments, the viability of the cells was assessed by trypan blue exclusion assay. In all cases, viability was greater than 90%.

Quality Control. The fraction of ^{111}In-DOTAGA-trastuzumab able to bind to HER2/*neu* (i.e., immunoreactivity) was determined by incubating trace amounts of ^{111}In-DOTAGA-trastuzumab (7.0×10^{-9} M) with increasing concentrations of HCC1954 tumor cells (0.4 to 24 × 10^6 cells.mL^{-1}) in a total volume of 0.2 mL for 1 h at 4 °C. At the end of the incubation period, cells were centrifuged, rinsed twice with ice-cold PBS 0.1 M pH 7.4, and then dissolved in 0.1 N NaOH. The radioactivity associated to cells (bound radioactivity, B) and an aliquot of the supernatant (total radioactivity, T) were counted with a scintillation γ counter (Cobra 4180, Perkin-Elmer Inc.) in order to calculate the bound-to-total ratios (B/T, expressed in %). Nonspecific binding was evaluated in the presence of a >100-fold excess unlabeled trastuzumab. Immunoreactivity was defined as the highest B/T% ratio that could be reached.

Determination of DOTAGA-Trastuzumab Binding Affinity. The HER2/*neu* antigen density and the affinity constant (K_d) of the ^{111}In-DOTAGA-trastuzumab were determined in radioligand binding saturation assays.

Approximately 3 × 10^5 HCC1954 tumor cells were incubated with increasing concentrations of ^{111}In-DOTAGA-trastuzumab (5.8×10^{-11} to 6.0×10^{-8} M, 100 MBq.mg^{-1}) in a total volume of 0.2 mL for 1 h at 4 °C. At the end of the incubation period, cells were centrifuged, rinsed twice with ice-cold PBS 0.1 M pH 7.4, and then dissolved in 0.1 N NaOH. Radioactivity associated to cells was counted with a scintillation γ-counter. Nonspecific binding was evaluated in the presence of a >100-fold excess unlabeled trastuzumab.

The dissociation constant and the number of binding sites were determined from experimental results by curve-fitting using *GraphPad Prism* v 5.04 for Windows (GraphPad Software, San Diego, California, USA, www.graphpad.com).

Biodistribution and Tumor Imaging. All animal experiments were performed in compliance with guidelines governing such work and according to the ethical committee protocols.[33]

Female Balb/c nu/nu mice (6−8 weeks old, purchased from Charles River, France) were grafted by subcutaneous injection in the flank with 2 × 10^7 BT-474 human breast carcinoma cells.

Three or five weeks after tumor cells injection, BT-474 tumor bearing-mice were given 25 μg ^{111}In-DOTAGA-trastuzumab (13−15 [first experiment] or 3−3.5 MBq [second experiment]) by intravenous injection. In the second experi-

dx.doi.org/10.1021/bc200680x | *Bioconjugate Chem.* 2012, 23, 1181−1188

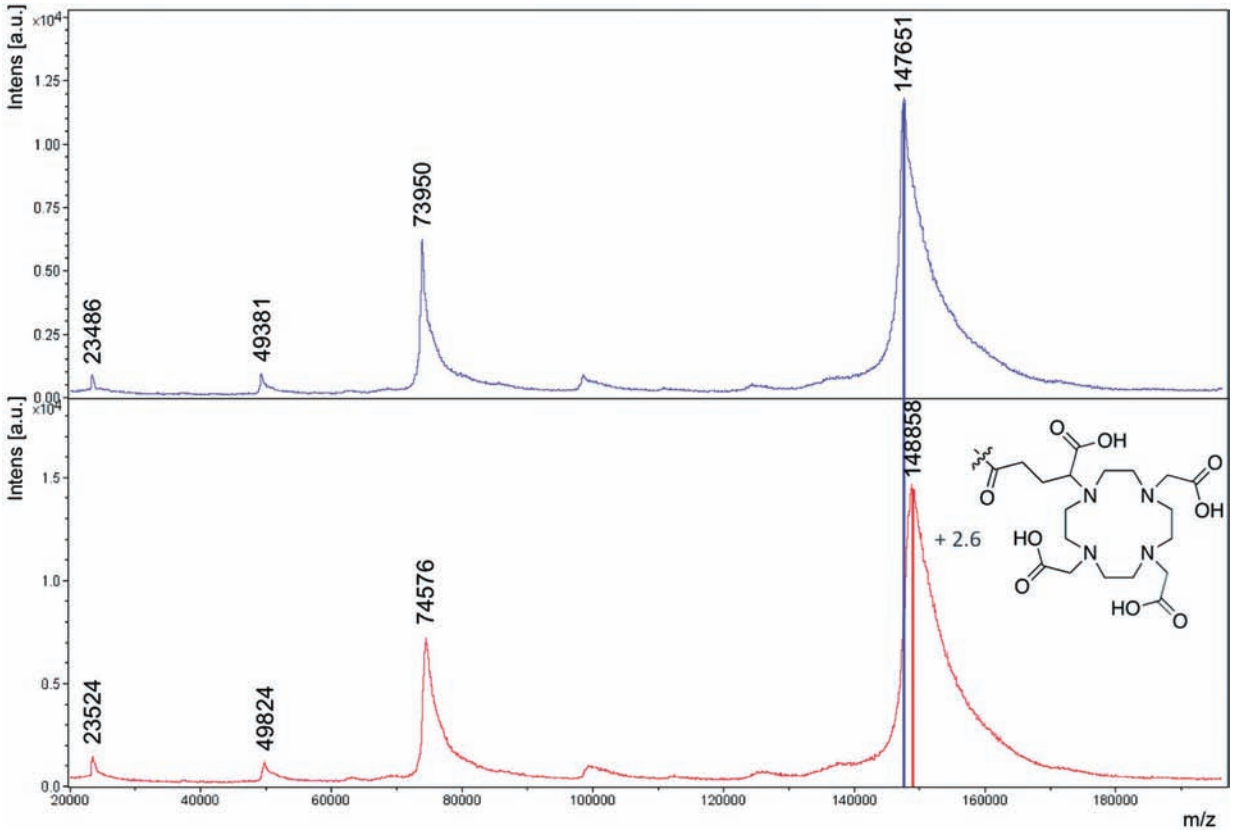

Figure 2. MALDI-TOF MS characterization of unmodified trastuzumab (blue) vs DOTAGA-trastuzumab (red). The difference of mass (δ = 1207) between the molecular peaks gives a degree of conjugation of 2.6 macrocycles per antibody.

ment, to assess the specificity of the targeting *in vivo*, a group of mice received the ^{111}In-DOTA-trastuzumab in coinjection with excess (2500 μg) trastuzumab.

SPECT/CT dual imaging was performed 24, 48, and 72 h after the injection of the radiolabeled conjugate using a NanoSPECT/CT small animal imaging tomographic γ-camera (Bioscan Inc., Washington, DC). Mice were anaesthetized with isoflurane (1.5−3% in air) and positioned in a dedicated cradle. CT and SPECT acquisitions were performed in immediate sequence. CT acquisitions (55 kVp, 34 mAs) were first acquired during 15−20 min, followed by helical SPECT acquisitions with 90−120 s per projection frame resulting in acquisition times of 45−60 min. Both indium-111 photopeaks (171 and 245 keV) were used with 10% wide energy windows. After the last image acquisition, animals were terminated. Blood, tumor, and organs were collected, and radioactivity in these samples was measured with a scintillation γ-counter. Data were then converted to percentage of injected dose and to percentage of injected dose per gram of tissue (the injected doses being corrected for subcutaneously injected material remaining in the animal tail).

The CT and SPECT reconstructions were performed using image processing softwares provided by Bioscan Inc. Eventually, the SPECT/CT fusion image was obtained using the *InVivoScope* software (Bioscan Inc.). Each scan was then visually interpreted, and 3D regions of interest corresponding to the tumor and whole body were manually drawn in order to determine their radioactivity content. *In vivo* quantification was obtained by accurate calibration of the NanoSPECT/CT γ-camera. Radioactivity contents from image analysis were expressed in Bq, converted to percentage of injected dose, and compared to those determined by *ex vivo* counting.

RESULTS AND DISCUSSION

The aim of the study was to radiolabel trastuzumab (a humanized mAb) with indium-111 using DOTAGA-anhydride and to characterize this conjugate *in vivo* and *in vitro* in human breast cancer models expressing high levels of HER-2/*neu* antigen.

Indium-111 was chosen because of its suitable physical characteristics. Its physical half-life (2.8 days) is highly compatible with the labeling procedures using macrocyclic chelating agent and with *in vivo* experiments with antibodies known to have long biological half lifes (several days). Besides, indium-111 emits two photons (171 and 245 keV) that are both detected for SPECT imaging.

The coupling of DOTAGA-anhydride on trastuzumab was performed at a 20:1 molar excess of chelate to protein, using slight modifications of previous methods.[14,34,35] Concentration of the immunoconjugate solution was deduced from absorbance at 280 nm, assuming that conjugation of DOTAGA on trastuzumab did not change significantly $\epsilon 280_{\text{Trastuzumab}}$. The number of DOTAGA moieties on trastuzumab was determined by MALDI-TOF mass spectrometry. As shown in Figure 2, a difference of 1207 mass units was observed, which corresponds to an average of 2.6 DOTAGAs per antibody. Conjugation with an equimolar amount of anhydride chelate and antibody was not satisfactory probably due to an excessively fast hydrolysis of the anhydride function, resulting in a poor degree of conjugation. The large excess of macrocycle used for conjugation did not result in major modifications of the

dx.doi.org/10.1021/bc200680x | *Bioconjugate Chem.* 2012, 23, 1181−1188

binding capabilities. Despite the rapid hydrolysis of the anhydride function, cyclic anhydride remains a powerful tool for bioconjugation. Indeed, conjugation of DOTAGA-anhydride is achieved in only 30 min at room temperature and in PBS, while conjugation of molecules containing isothiocyanate or succinimidyl functions needs several hours and/or requires heating to reach a satisfactory yield.[36,37] Moreover, the ring-opening of the cyclic anhydride leads to a DOTA moiety bearing four acetate arms, which is a key point for transposition to yttrium-90 radioimmunotherapy.[38−40]

Radiolabeling was performed using two different procedures based on a previous protocol,[41] depending on whether the radioimmunoconjugate was used for *in vitro* or *in vivo* studies.

For *in vitro* studies, radiolabeling was carried out with a specific activity of 150 MBq.mg^{-1} of protein. The reaction was achieved in 1 h at 37 °C and gave a radiolabeling yield of 90% (ITLC) before purification. Reaction was quenched with excess EDTA, followed by another radio-ITLC quality control, and radiolabeling yield fell to 75%. This experiment demonstrated the crucial importance of quenching by EDTA to prevent nonspecific chelation of indium-111 on the antibody or incomplete coordination of the metal. Crude product was then purified by ultrafiltration to reach a proportion of ^{111}In-DOTAGA-trastuzumab >97% and was used immediately for *in vitro* experiments after dilution in PBS 0.1 M pH 7.4 containing 0.2% BSA and 0.02% azide.

For *in vivo* studies, radiolabeling was carried out with a specific activity of 1 GBq.mg^{-1} of protein. The reaction was achieved in 3 h at 37 °C and gave a radiolabeling yield of 80%. In the same manner as for *in vitro* studies, radiolabeling yield fell down to 66% after quenching by EDTA. After purification by ultracentrifugation, the proportion of ^{111}In-DOTAGA-trastuzumab was >97% and the product was diluted in PBS 0.1 M pH 7.4 and injected to animals within 30 min.

The stability of ^{111}In-DOTAGA-trastuzumab was evaluated by competition with 2000-fold molar excess of DTPA over 5 consecutive days as described in a previous study.[6] The complex showed good stability with no significant trans-chelation observed. The proportion of ^{111}In-DOTAGA-trastuzumab in the treated sample was >97% after 24 h and did not vary significantly during the following days, which was comparable to results obtained for *p*-SCN-Bn-DOTA or DOTA-NHS radiolabeling.[23,42]

The HCC1954 cell line was used for *in vitro* assays because it was easier to handle than the BT-474 cell line. For *in vivo* experiments, we chose the BT-474 model, as the growth of BT-474 tumors is more homogeneous than HCC1954 tumors. Besides, the BT-474 tumor model is the gold standard for evaluation of molecules that target HER2/*neu*.

The immunoreactivity was determined from a binding experiment of the ^{111}In-DOTAGA-trastuzumab to increasing concentrations of HCC1954 tumor cells and was found to be 65% (Figure 3). The immunoreactivity of our DOTAGA trastuzumab conjugate appeared to be slightly lower than values reported for DOTA/DTPA trastuzumab conjugates bearing the chelating agent on lysine residues.[14,18] The binding affinity constant was 5.5 ± 0.6 nM as determined in a saturation experiment (Figure 4), being similar to values published for DOTA/DTPA trastuzumab conjugates.[43,44] The biological characteristics of our DOTAGA-trastuzumab conjugate are suitable for *in vivo* targeting applications.

The ability of the ^{111}In-DOTAGA-trastuzumab to target HER2/*neu* expressing tumors was evaluated in nude mice

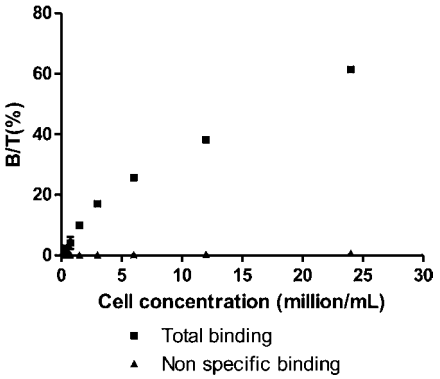

Figure 3. Determination of the immunoreactivity of ^{111}In-DOTAGA-trastuzumab (■, total binding; ▲, nonspecific binding). Trace amounts of ^{111}In-DOTAGA-trastuzumab were incubated with increasing concentration of HCC1954 tumor cells. Nonspecific binding was evaluated with excess unlabeled trastuzumab. The fraction of radioactivity bound to cells (*B*/*T*%) was counted. The means of duplicate samples are plotted ± standard deviation (unless smaller than the point as plotted).

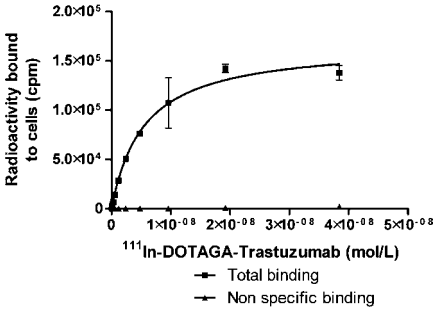

Figure 4. Dissociation constant of the ^{111}In-DOTAGA-trastuzumab was determined in *in vitro* binding saturation assays (■, total binding; ▲, nonspecific binding; solid line, curve-fitting). Briefly, HCC1954 tumor cells were incubated with increasing concentration of the radiolabeled conjugate. Nonspecific binding was evaluated with excess unlabeled trastuzumab. The radioactivity associated to cells (expressed in counts per minute, cpm) was counted. The means of duplicate samples are plotted ± standard deviation (unless smaller than the point as plotted).

bearing subcutaneous human breast tumors. For the first experiment, mice were given 25 μg of the ^{111}In-DOTAGA-trastuzumab (13−15 MBq). Tomographic SPECT/CT images were recorded 24, 48, and 72 h postinjection (Figure 5). Image analysis showed that tumor uptake reached 11.0 ± 5.6, 13.1 ± 7.6, and 14.0 ± 8.1%ID at 24, 48, and 72 h postinjection, respectively, demonstrating that the accretion of the ^{111}In-DOTAGA-trastuzumab had reached a plateau within 24 h. The ^{111}In-DOTAGA-trastuzumab was located mainly in the rim of the tumor, while a lower accumulation was seen inside, which may be due to necrosis in the center of the tumor. The effective half-life of the ^{111}In-DOTAGA-trastuzumab was 53.5 ± 4.0 h from image analysis. The biological half-life was then found to be 268 ± 92 h, which appeared higher than that of a trastuzumab conjugate labeled with yttrium-86 (160 h).[13] The observed difference could be related to the higher accretion in tumors of our conjugate (66.9 ± 0.9%ID/g at 72 h vs 7.4 ± 1.2%ID/g at 144 h). Also, the study from Palm et al.[13] was conducted in mice bearing ovarian disseminated tumors with DTPA as chelating agent, whereas our own study involved mice

dx.doi.org/10.1021/bc200680x | *Bioconjugate Chem.* 2012, 23, 1181−1188

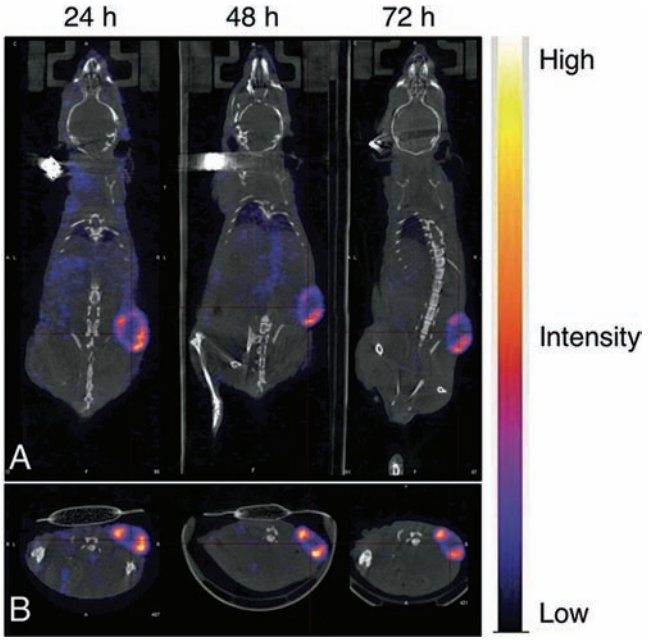

Figure 5. First *in vivo* experiment. SPECT/CT reconstructed images of a mouse bearing subcutaneous BT-474 breast human tumors (A, coronal slice; B, transverse slice). Mice received a single IV injection of ^{111}In-DOTAGA-trastuzumab (25 μg, 13−15 MBq) and images were recorded 24, 48, and 72 h later. All images have the same color scale. Image analysis showed that tumor uptake reached 11.0 ± 5.6%ID, 13.1 ± 7.6%ID, and 14.0 ± 8.1%ID at 24, 48, and 72 h postinjection.

bearing breast human tumors with a macrocyclic chelating agent. To our knowledge, no other publication describes the determination of the pharmacokinetic parameters of a trastuzumab conjugate in rodent obtained from image analysis. Extrapolation of these data to humans was not performed because assessment of organ-absorbed radiation doses was beyond the scope of this study.

After the last imaging time point (i.e., 72 h postinjection), tumor, blood, and organs were collected and radioactivity in these samples was determined. Tumor uptake was 13.2 ± 8.2% ID, confirming image analysis (14.0 ± 8.1%ID). Radioactivity uptakes were 66.9 ± 0.9 and 10.0 ± 3.5%ID/g in tumor and blood, respectively, leading to a tumor-to-blood uptake ratio of 7.8 ± 4.3 (Table 1). For the liver and the spleen, involved in the catabolism of antibodies, radioactivity uptakes were 4.3 ± 0.5 and 6.9 ± 1.2%ID/g, respectively, and tumor-to-organ ratios were over 10. Radioactivity in kidneys (6.3 ± 0.2%ID/g) could result from a partial degradation of the ^{111}In-DOTAGA-trastuzumab into small fragments excreted via the urinary pathway. Nevertheless, the fate of the ^{111}In-DOTAGA-trastuzumab after injection in mice remains to be elucidated. Radioactivity uptakes in blood, liver, and kidneys were similar to those of other radiolabeled trastuzumab analogues,[14,18,44] while an increased uptake (by a factor 3 to 4) was observed in tumors. This could be related to a high expression of HER2/*neu* antigen *in vivo* in our tumor model or to tumor physiologic parameters such as vascular density or interstitial pressure.

The specificity of ^{111}In-DOTAGA-trastuzumab was assessed in the second experiment. Mice were given 25 μg of the ^{111}In-DOTAGA-trastuzumab (3−3.5 MBq) alone or coinjected with a 100-fold excess unlabeled trastuzumab. Animals were terminated 72 h postinjection, and blood and tumors were collected for radioactivity uptake determination. Radioactivity

Table 1. Biodistribution Study of ^{111}In-DOTAGA-Trastuzumab in balb/c Nude Mice Bearing Subcutaneous BT-474 Breast Human Tumors[a]

Tissue	%ID/g	tumor-to-organ ratio
Tumor	66.9 ± 0.9	-
Blood	10.0 ± 3.5	7.8 ± 4.3
Heart	3.6 ± 0.5	18.8 ± 2.6
Lungs	5.6 ± 0.5	11.9 ± 1.0
Liver	4.3 ± 0.5	15.7 ± 1.8
Spleen	6.9 ± 1.2	10.0 ± 1.9
Kidneys	6.3 ± 0.2	10.6 ± 0.2
Ovaries	8.0 ± 3.7	9.6 ± 3.4
Gastrointestinal tract	1.8 ± 0.2	38.1 ± 3.5

[a]Mice were grafted subcutaneously by injection of BT-474 tumor cells. Mice received a single IV injection of ^{111}In-DOTAGA-trastuzumab and were terminated 72 h later. Blood, tumor, and organs were collected, and the radioactivity in these samples was determined. Tissue radioactivity is expressed as percentage injected dose/g tissue (%ID/g). Data are expressed as mean ± standard deviation (n = 4).

uptake in tumors was reduced from 65.2 ± 2.1 to 17.6 ± 2.4% ID/g, showing the specificity of HER2/*neu* targeting (Figure 6). Radioactivity persistence of the ^{111}In-DOTAGA-trastuzumab in blood was not affected by the injection of the unlabeled trastuzumab (10.0 ± 2.7 vs 11.9 ± 0.7%ID/g). These results suggest that the coinjection of the excess of trastuzumab may

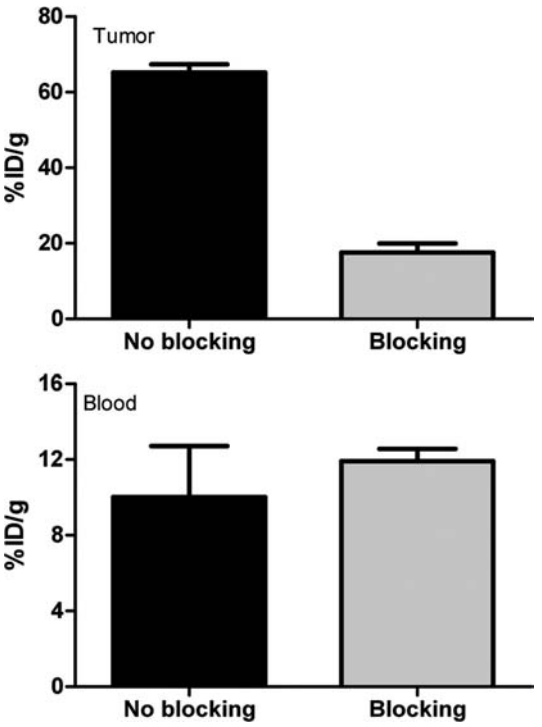

Figure 6. Second *in vivo* experiment. Biodistribution study of the ^{111}In-DOTAGA-trastuzumab in Balb/c nude mice bearing subcutaneous BT-474 breast human tumors. Mice received a single IV injection of ^{111}In-DOTAGA-trastuzumab (25 μg, 3−3.5 MBq) with (blocking) or without (no blocking) excess unlabeled trastuzumab (2500 μg). Animals were terminated 72 h later just after SPECT/CT dual imaging. Blood and tumor were collected and the radioactivity in these samples was determined. Tissue radioactivity is expressed as percentage injected dose/g tissue (%ID/g). Data are expressed as mean ± standard deviation (n = 3).

dx.doi.org/10.1021/bc200680x | *Bioconjugate Chem.* 2012, 23, 1181−1188

have no influence on the kinetic parameters of the ^{111}In-DOTAGA-trastuzumab in blood. Similar data were obtained when the 100-fold excess unlabeled trastuzumab was administered 24 h before the injection of the ^{111}In-DOTAGA-trastuzumab (data not shown).

CONCLUSION

The bifunctional chelating agent DOTAGA-anhydride was successfully linked to a humanized mAb. The DOTAGA conjugation and the labeling procedure with indium-111 did not alter the binding properties of the mAb. A high specific tumor targeting was shown in a model of human breast tumors overexpressing HER2/*neu* antigen. The DOTAGA-anhydride appears to be a valuable tool for biologic conjugation in the development of new radiolabeled tumor targeting agents suitable for diagnostic and/or therapeutic applications. The scope of use of this BFC is currently being extended to the labeling of peptides and bioengineered molecules such as antibody fragments, for both imaging and therapeutic purposes.

AUTHOR INFORMATION

Corresponding Author

*Phone: +33 (0)3 80 39 61 15; E-mail: franck.denat@u-bourgogne.fr.

Notes

The authors declare no competing financial interest.

ACKNOWLEDGMENTS

This study is a part of Pharm'image® project. Support was provided by OSEO, the CNRS, the "Université de Bourgogne" and the "Conseil Régional de Bourgogne" through the 3MIM integrated project ("Marquage de Molécules par les Métaux pour l'Imagerie Médicale").

REFERENCES

(1) Barbet, J., Kraeber-Bodere, F., and Chatal, J.-F. (2008) Review: what can be expected from nuclear medicine tomorrow? *Cancer Biother. Radiopharm. 23*, 483−504.

(2) Wu, A. M. (2009) Antibodies and antimatter: the resurgence of immuno-PET. *J. Nucl. Med. 50*, 2−5.

(3) Verel, I., Visser, G. W. M., and Van Dongen, G. A. (2005) The promise of immuno-PET in radioimmunotherapy. *J. Nucl. Med. 46* (Suppl 1), 164S−71S.

(4) Niu, G., Li, Z., Cao, Q., and Chen, X. (2009) Monitoring therapeutic response of human ovarian cancer to 17-DMAG by noninvasive PET imaging with 64Cu-DOTA-trastuzumab. *Eur. J. Nucl. Med. Mol. Imaging 36*, 1510−1519.

(5) Ahlgren, S., Waallberg, H., Tran, T. A., Widstroem, C., Hjertman, M., Abrahmsen, L., Berndorff, D., Dinkelborg, L. M., Cyr, J. E., Feldwisch, J., Orlova, A., and Tolmachev, V. (2009) Targeting of HER2-expressing tumors with a site-specifically 99mTc-labeled recombinant affibody molecule, ZHER2:2395, with C-terminally engineered cysteine. *J. Nucl. Med. 50*, 781−789.

(6) Tolmachev, V., Altai, M., Sandstrom, M., Perols, A., Karlstrom, A. E., Boschetti, F., and Orlova, A. (2011) Evaluation of a maleimido derivative of NOTA for site-specific labeling of affibody molecules. *Bioconjugate Chem. 22*, 894−902.

(7) Olafsen, T., and Wu, A. M. (2010) Antibody vectors for imaging. *Semin. Nucl. Med. 40*, 167−181.

(8) Bange, J., Zwick, E., and Ullrich, A. (2001) Molecular targets for breast cancer therapy and prevention. *Nat. Med. 7*, 548−552.

(9) Smith, I., Procter, M., Gelber, R. D., Guillaume, S., Feyereislova, A., Dowsett, M., Goldhirsch, A., Untch, M., Mariani, G., Baselga, J., Kaufmann, M., Cameron, D., Bell, R., Bergh, J., Coleman, R., Wardley, A., Harbeck, N., Lopez, R. I., Mallmann, P., Gelmon, K., Wilcken, N., Wist, E., S·nchez Rovira, P., and Piccart-Gebhart, M. J. (2007) 2-year follow-up of trastuzumab after adjuvant chemotherapy in HER2-positive breast cancer: a randomised controlled trial. *The Lancet 369*, 29−36.

(10) Owens, M., Horten, B., and Da Silva, M. (2004) HER2 amplification ratios by fluorescence in situ hybridization and correlation with immunohistochemistry in a cohort of 6556 breast cancer tissues. *Clin. Breast Cancer 5*, 63−69.

(11) Pestrin, M., Bessi, S., Galardi, F., Truglia, M., Biggeri, A., Biagioni, C., Cappadona, S., Biganzoli, L., Giannini, A., and Di Leo, A. (2009) Correlation of HER2 status between primary tumors and corresponding circulating tumor cells in advanced breast cancer patients. *Breast Cancer Res. Treat. 118*, 523−530.

(12) Munzone, E., Nolé, F., Goldhirsch, A., Botteri, E., Esposito, A., Zorzino, L., Curigliano, G., Minchella, I., Adamoli, L., Cassatella, M. C., Casadio, C., and Sandri, M. T. (2010) Changes of HER2 status in circulating tumor cells compared with the primary tumor during treatment for advanced breast cancer. *Clin. Breast Cancer 10*, 392−397.

(13) Palm, S., Enmon, R. M., Jr., Matei, C., Kolbert, K. S., Xu, S., Zanzonico, P. B., Finn, R. L., Koutcher, J. A., Larson, S. M., and Sgouros, G. (2003) Pharmacokinetics and biodistribution of 86Y-trastuzumab for 90Y dosimetry in an ovarian carcinoma model: Correlative microPET and MRI. *J. Nucl. Med. 44*, 1148−1155.

(14) Lub-de Hooge, M. N., Kosterink, J. G., Perik, P. J., Nijnuis, H., Tran, L., Bart, J., Suurmeijer, A. J., De Jong, S., Jager, P. L., and De Vries, E. G. (2004) Preclinical characterisation of 111In-DTPA-trastuzumab. *Br. J. Pharmacol. 143*, 99−106.

(15) Perik, P. J., Lub-de Hooge, M. N., Gietema, J. A., Van der Graaf, W. T. A., De Korte, M. A., Jonkman, S., Kosterink, J. G. W., Van Veldhuisen, D. J., Sleijfer, D. T., Jager, P. L., and De Vries, E. G. E. (2006) Indium-111-labeled trastuzumab scintigraphy in patients with human epidermal growth factor receptor 2-positive metastatic breast cancer. *J. Clin. Oncol. 24*, 2276−2282.

(16) Dennis, M. S., Jin, H. K., Dugger, D., Yang, R. H., McFarland, L., Ogasawara, A., Williams, S., Cole, M. J., Ross, S., and Schwall, R. (2007) Imaging tumors with an albumin-binding Fab, a novel tumor-targeting agent. *Cancer Res. 67*, 254−261.

(17) Dijkers, E. C. F., Kosterink, J. G. W., Rademaker, A. P., Perk, L. R., Van Dongen, G. A. M. S., Bart, J., De Jong, J. R., De Vries, E. G. E., and Lub-de Hooge, M. N. (2009) Development and characterization of clinical-grade 89Zr-trastuzumab for HER2/neu immunolPET imaging. *J. Nucl. Med. 50*, 974−981.

(18) Rasaneh, S., Rajabi, H., Babaei, M. H., Daha, F. J., and Salouti, M. (2009) Radiolabeling of trastuzumab with (177)Lu via DOTA, a new radiopharmaceutical for radioimmunotherapy of breast cancer. *Nucl. Med. Biol. 36*, 363−369.

(19) Oude Munnink, T. H., De Korte, M. A., Nagengast, W. B., Timmer-Bosscha, H., Schroeder, C. P., De Jong, J. R., Van Dongen, G. A. M. S., Jensen, M. R., Quadt, C., Lub-de Hooge, M. N., and De Vries, E. G. E. (2010) 89Zr-trastuzumab PET visualises HER2 down-regulation by the HSP90 inhibitor NVP-AUY922 in a human tumour xenograft. *Eur. J. Cancer 46*, 678−684.

(20) Zeglis, B. M., Mohindra, P., Weissmann, G. I., Divilov, V., Hilderbrand, S. A., Weissleder, R., and Lewis, J. S. (2011) A modular strategy for the construction of radiometallated antibodies for positron emission tomography based on inverse electron demand Diels-Alder click chemistry. *Bioconjugate Chem.*, 2048−2059.

(21) Camera, L., Kinuya, S., Garmestani, K., Wu, C. C., Brechbiel, M. W., Pai, L. H., McMurry, T. J., Gansow, O. A., Pastan, I., Paik, C. H., and Carrasquillo, J. A. (1994) Evaluation of the serum stability and in-vivo biodistribution of Chx-Dtpa and other ligands for yttrium labeling of monoclonal-antibodies. *J. Nucl. Med. 35*, 882−889.

(22) Cutler, C. S., Smith, C. J., Ehrhardt, G. J., Tyler, T. T., Jurisson, S. S., and Deutsch, E. (2000) Current and potential therapeutic uses of lanthanide radioisotopes. *Cancer Biother. Radiopharm. 15*, 531−545.

(23) Smith-Jones, P. M., Vallabahajosula, S., Goldsmith, S. J., Navarro, V., Hunter, C. J., Bastidas, D., and Bander, N. H. (2000) In vitro characterization of radiolabeled monoclonal antibodies specific

for the extracellular domain of prostate-specific membrane antigen. *Cancer Res. 60*, 5237−5243.
(24) McMurry, T. J., Brechbiel, M., Kumar, K., and Gansow, O. A. (1992) Convenient synthesis of bifunctional tetraaza macrocycles. *Bioconjugate Chem. 3*, 108−17.
(25) Mishra, A. K., Gestin, J. F., Benoist, E., FaivreChauvet, A., and Chatal, J. F. (1996) Simplified synthesis of the bifunctional chelating agent 2-(4-aminobenzyl)-1,4,7,10-tetraazacyclododecane-N,N′,N″,N‴-tetraacetic acid. *New J. Chem. 20*, 585−588.
(26) Maecke, H. R., Eisenwiener, K. P., and Powell, P. (2000) A convenient synthesis of novel bifunctional prochelators for coupling to bioactive peptides for radiometal labelling. *Bioorg. Med. Chem. Lett. 10*, 2133−2135.
(27) Botta, M., Kielar, F., Tei, L., and Terreno, E. (2010) Large relaxivity enhancement of paramagnetic lipid nanoparticles by restricting the local motions of the Gd(III) chelates. *J. Am. Chem. Soc. 132*, 7836.
(28) Mayer, H. A., Henig, J., Toth, E., Engelmann, J., and Gottschalk, S. (2010) Macrocyclic Gd(3+) chelates attached to a silsesquioxane core as potential magnetic resonance imaging contrast agents: synthesis, physicochemical characterization, and stability studies. *Inorg. Chem. 49*, 6124−6138.
(29) Cordier, D., Forrer, F., Kneifel, S., Sailer, M., Mariani, L., Maecke, H., Muller-Brand, J., and Merlo, A. (2010) Neoadjuvant targeting of glioblastoma multiforme with radiolabeled DOTAGA-substance P-results from a phase I study. *J. Neurooncol. 100*, 129−136.
(30) Lux, F., Mignot, A., Mowat, P., Louis, C., Dufort, S., Bernhard, C., Denat, F., Boschetti, F., Brunet, C., Antoine, R., Dugourd, P., Laurent, S., Elst, L. V., Muller, R., Sancey, L., Josserand, V., Coll, J.-L., Stupar, V., Barbier, E., Remy, C., Broisat, A., Ghezzi, C., Le, D. G., Roux, S., Perriat, P., and Tillement, O. (2011) Ultrasmall rigid particles as multimodal probes for medical applications. *Angew. Chem., Int. Ed. 50*, 12299−12303.
(31) Lasfargues, E. Y., Coutinho, W. G., and Redfield, E. S. (1978) Isolation of two human tumor epithelial cell lines from solid breast carcinomas. *J. Natl. Cancer Inst. 61*, 967−78.
(32) Gazdar, A. F., Kurvari, V., Virmani, A., Gollahon, L., Sakaguchi, M., Westerfield, M., Kodagoda, D., Stasny, V., Cunningham, H. T., Wistuba, I. I., Tomlinson, G., Tonk, V., Ashfaq, R., Leitch, A. M., Minna, J. D., and Shay, J. W. (1998) Characterization of paired tumor and non-tumor cell lines established from patients with breast cancer. *Int. J. Cancer 78*, 766−74.
(33) Workman, P., Aboagye, E. O., Balkwill, F., Balmain, A., Bruder, G., Chaplin, D. J., Double, J. A., Everitt, J., Farningham, D. A. H., Glennie, M. J., Kelland, L. R., Robinson, V., Stratford, I. J., Tozer, G. M., Watson, S., Wedge, S. R., and Eccles, S. A. (2010) Guidelines for the welfare and use of animals in cancer research. *Br. J. Cancer 102*, 1555−77.
(34) Hnatowich, D. J., Childs, R. L., Lanteigne, D., and Najafi, A. (1983) The preparation of DTPA-coupled antibodies radiolabeled with metallic radionuclides: an improved method. *J. Immunol. Methods 65*, 147−57.
(35) Hnatowich, D. J., Layne, W. W., Childs, R. L., Lanteigne, D., Davis, M. A., Griffin, T. W., and Doherty, P. W. (1983) Radioactive labeling of antibody: a simple and efficient method. *Science 220*, 613−5.
(36) Ferreira, C. L., Yapp, D. T. T., Crisp, S., Sutherland, B. W., Ng, S. S. W., Gleave, M., Bensimon, C., Jurek, P., and Kiefer, G. E. (2010) Comparison of bifunctional chelates for (64)Cu antibody imaging. *Eur. J. Nucl. Med. Mol. Imaging 37*, 2117−2126.
(37) Chong, H. S., Song, H. A., Kang, C. S., Baidoo, K. E., Milenic, D. E., Chen, Y. W., Dai, A. Z., and Brechbiel, M. W. (2011) Efficient bifunctional decadentate ligand 3p-C-DEPA for targeted alpha-radioimmunotherapy applications. *Bioconjugate Chem. 22*, 1128−1135.
(38) Liu, S., He, Z., Hsieh, W.-Y., and Fanwick, P. E. (2003) Synthesis, characterization, and X-ray crystal structure of In(DOTA-AA) (AA = p-Aminoanilide): a model for 111In-labeled DOTA-biomolecule conjugates. *Inorg. Chem. 42*, 8831−8837.
(39) Colvin, M. E., Lau, E. Y., and Lightstone, F. C. (2006) Environmental effects on the structure of metal ion-DOTA complexes: An ab initio study of radiopharmaceutical metals. *Inorg. Chem. 45*, 9225−9232.
(40) Wadas, T. J., Wong, E. H., Weisman, G. R., and Anderson, C. J. (2010) Coordinating radiometals of copper, gallium, indium, yttrium, and zirconium for PET and SPECT imaging of disease. *Chem. Rev. 110*, 2858−2902.
(41) Mather, S. J., Cooper, M. S., and Sabbah, E. (2006) Conjugation of chelating agents to proteins and radiolabeling with trivalent metallic isotopes. *Nat. Protoc. 1*, 314−317.
(42) Jurisson, S. S., Mohsin, H., Fitzsimmons, J., Shelton, T., Hoffman, T. J., Cutlerc, C. S., Lewis, M. R., Atheye, P. S., Gulyas, G., Kiefer, G. E., Frank, R. K., Simon, J., and Lever, S. Z. (2007) Preparation and biological evaluation of In-111-, Lu-177- and Y-90-labeled DOTA analogues conjugated to B72.3. *Nucl. Med. Biol. 34*, 493−502.
(43) Luo, T.-Y., Tang, I. C., Wu, Y.-L., Hsu, K.-L., Liu, S.-W., Kung, H.-C., Lai, P.-S., and Lin, W.-J. (2009) Evaluating the potential of 188Re-SOCTA-trastuzumab as a new radioimmunoagent for breast cancer treatment. *Nucl. Med. Biol. 36*, 81−88.
(44) McLarty, K., Cornelissen, B., Scollard, D. A., Done, S. J., Chun, K., and Reilly, R. M. (2009) Associations between the uptake of 111In-DTPA-trastuzumab, HER2 density and response to trastuzumab (Herceptin) in athymic mice bearing subcutaneous human tumour xenografts. *Eur. J. Nucl. Med. Mol. Imaging 36*, 81−93.

Bioconjugate Chemistry

Article

pubs.acs.org/bc

Multifunctional Hyperbranched Glycoconjugated Polymers Based on Natural Aminoglycosides

Mingsheng Chen,[#,†,‡] Mei Hu,[#,§] Dali Wang,[†] Guojian Wang,[†] Xinyuan Zhu,*[,†] Deyue Yan,*[,†] and Jian Sun*[,§]

[†]School of Chemistry and Chemical Engineering, State Key Laboratory of Metal Matrix Composites, Shanghai Jiao Tong University, 800 Dongchuan Road, Shanghai 200240, P. R. China

[‡]The Sericultural Research Institute, Chinese Academy of Agricultural Sciences, Zhenjiang 212018, P. R. China

[§]Department of Oral and Maxillofacial Surgery, Ninth People's Hospital, School of Stomatology, Shanghai Jiao Tong University School of Medicine, 639 Zhizaoju Road, Shanghai 200011, P. R. China

Supporting Information

ABSTRACT: Multifunctional gene vectors with high transfection, low cytotoxicity, and good antitumor and antibacterial activities were prepared from natural aminoglycosides. Through the Michael-addition polymerization of gentamycin and *N*,*N*′-methylenebisacrylamide, cationic hyperbranched glycoconjugated polymers were synthesized, and their physical and chemical properties were analyzed by FTIR, ^{1}H NMR, ^{13}C NMR, GPC, ζ-potential, and acid−base titration techniques. The cytotoxicity of these hyperbranched glycoconjugated polycations was low because of the hydrolysis of degradable glycosidic and amide linkages in acid conditions. Owing to the presence of various primary, secondary, and tertiary amines in the polymers, hyperbranched glycoconjugated polymers showed high buffering capacity and strong DNA condensation ability, resulting in the high transfection efficiency. In the meantime, due to the introduction of natural aminoglycosides into the polymeric backbone, the resultant hyperbranched glycoconjugated polymers inhibited the growth of cancer cells and bacteria efficiently. Combining the gene transfection, antitumor, and antibacterial abilities together, the multifunctional hyperbranched glycoconjugated polymers based on natural aminoglycosides may play an important role in protecting cancer patients from bacterial infections.

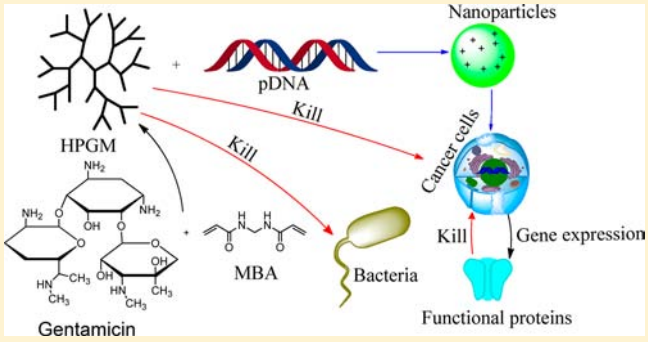

INTRODUCTION

Combining several useful properties together, multifunctional nanocarriers in gene therapy have drawn much attention.[1] Among various multifunctional gene nanocarriers, the combination of biotherapy and chemotherapy is dominant, in which chemical drugs are conjugated or complexed into the gene vectors.[2,3] Through the synergism of gene and drugs, the therapeutic efficacy can be significantly enhanced. However, the introduction of antitumor drugs usually weakens the immunity of patients dramatically, which frequently induces serious bacterial infections and thus results in treatment failure. Therefore, the multifunctional gene vectors with antitumor and antibacterial activities are urgently needed in clinical practice.

As an abundance of renewable biological resources, natural polysaccharides with aminoglycosides have attracted great attention in recent years.[4] Benefiting from the existence of many amino and glycosyl groups, these natural cationic polysaccharides with good biodegradability and low cytotoxicity have been widely used as gene vectors. Moreover, natural cationic polysaccharides exhibit exciting biological activity, such as antitumor, antibacterial, and antiviral activity.[5−8] Unfortunately, the transfection efficiency of natural cationic polysaccharides is usually disappointing. Even worse, natural cationic polysaccharides are insoluble in physiological conditions, which greatly restricts their applications in disease treatment.[9−16] It can be imagined that, if the natural aminoglycosides could be incorporated into the water-soluble polymers, multifunctional gene vectors with high transfection efficiency, antitumor ability, and antibacterial activity might be obtained.

By introduction of a branching structure into the polymer backbone, the cationic polymers exhibit compact and globular structures in combination with a great number of various amine groups, which facilitates DNA condensation, gene delivery, and transfection improvement. Very recently, we proposed the construction of highly branched polycations from natural small molecules with plenty of amines such as aminoglycosides.[17]

Received: January 13, 2012
Revised: April 4, 2012
Published: May 17, 2012

Table 1. Reaction Conditions and Results of Michael-Addition Polymerization of MBA and Gentamicin[a]

sample	gentamicin (mol)	MBA (mol)	M_n ($\times 10^3$)	M_w ($\times 10^3$)	M_w/M_n	yield (%)	ζ-potential (mV)	D (%)	T (%)	L (%)	DB
HPGM1	0.01	0.015	5.4	12.4	2.7	28	4.7 ± 0.5	22	23	55	0.45
HPGM2[b]	0.01	0.02	5.8	15.0	2.6	35	9.0 ± 0.5	21	25	54	0.46
HPGM3[b]	0.01	0.025	6.1	15.3	2.5	39	10.1 ± 0.9	23	24	53	0.47

[a] D, T, and L represent the fractions of the dendritic, terminal, and linear units, respectively. [b] The yield and DB of HPGM2 and HPGM3 were obtained from HPGM2-V and HPGM3-V separately.

Based on this new strategy, hyperbranched glycoconjugated polycations with high transfection efficiency, negligible cytotoxicity, and excellent solubility in physiological conditions were prepared, suggesting a possibility for the development of multifunctional gene vectors. In the present work, low toxicity and highly efficient gene vectors were prepared by Michael-addition polymerization of natural aminoglycoside gentamycin and *N*,*N*′-methylenebisacrylamide. Thanks to the incorporation of natural aminoglycoside into the polymer backbone, the resultant hyperbranched glycoconjugated polymers could efficiently inhibit the growth of cancer cells and bacteria. These results indicate that the natural small molecules with biological activity can be linked together to construct versatile nanocarriers for gene therapy. Considering that many useful natural small molecules can be used for the biomedical field, our work provides a new perspective in development of renewable biological resources.

MATERIALS AND METHODS

Materials. Gentamycin sulfate was purchased from Aladdin. *N*,*N*′-Methylenebisacrylamide (MBA, 98%) was purchased from J&K China Chemical Ltd.. Branched polyethylenimine (PEI, M_w = 25 kDa, M_n = 10 kDa), 3-(4,5-dimethyl-thiazol-2-yl)-2,5-diphenyl tetrazolium bromide (MTT) were purchased from Sigma-Aldrich. Dialysis bag (MWCO = 3.5 kDa, soaked and boiled for 10 min separately before use) was purchased from Shanghai Green Bird Development Co. Ltd., China. BCA protein assay kit was purchased from Beyotime (China). Luciferase assay kit was purchased from Promega. All reagents were used as received.

Synthesis of Hyperbranched Poly(Gentamicin-MBA)s by Michael-Addition Polymerization. Typically, gentamicin sulfate (5.76 g, 0.01 mol) was dissolved into three round-bottomed flasks with 150 mL saturated N_aHCO_3 aqueous solution, and then different amounts of MBA (2.36 g, 0.015 mol; 3.1 g, 0.020 mol; 3.93 g, 0.025 mol) were added separately. The reaction solution was stirred at 60, 60, and 45 °C for 3 days, respectively. Crude products were concentrated by evaporation. After dialysis against distilled water for 48 h (MWCO = 3.5 kDa), the residues without or with vinyl groups (HPGM and HPGM-V) were evaporated and dried in a vacuum oven overnight. Yields of HPGM1, HPGM2-V, and HPGM3-V: 1.96 g, 28%; 2.76 g, 35%; and 3.34 g, 39%. Considering that the terminal vinyl groups might induce high cytotoxicity, diethylamine was used to end-cap the excess vinyl groups of HPGM2-V and HPGM3-V. Briefly, HPGM2-V (2.75 g) or HPGM3-V (3.30 g) was dissolved in 100 mL distilled water, and then excessive diethylamine was added. After the reaction solution was stirred at 45 °C for 3 days, the rotary evaporation was carried out to remove the solvent and excess diethylamine. The residues were evaporated and dried in vacuum oven overnight. The final products hyperbranched poly(gentamicin-MBA)s (HPGM2 and HPGM3) were obtained.

For gel permeation chromatography (GPC) measurements, the amino groups of HPGMs were end-capped by benzoyl chloride. Briefly, 0.3 g HPGM (HPGM1, HPGM2, or HPGM3) was dispersed in 30 mL dichloromethane (DCM) with 6 mL triethylamine. Then, 5 mL benzoyl chloride was added slowly, and the solution was stirred at room temperature for 24 h. Subsequently, the liquid was collected. Sufficient hydrochloric acid was added, and the upper aqueous solution was discarded. After addition of a large number of diluted sodium hydroxide aqueous solutions, the upper aqueous solution was discarded. Distilled water was added to wash the remaining solution several times. The DCM solution was added in anhydrous magnesium sulfate, which was filtered and washed with DCM until the color faded. The solution was concentrated by rotary evaporation, and the product was precipitated three times by diethyl ether and dried in vacuum oven overnight. GPC measurements gave the number-average molecular weight (M_n) and molecular weight distribution, which were summarized in Table 1.

^{1}H NMR (400 MHz, D_2O, 298 K) δ: 0.80−1.12 (C***H***$_3$CHCHO-, CC***H***$_3$); 1.12−2.08 (CHC***H***$_2$CH); 2.08−2.34 (O═CC***H2***CH2); 2.34−2.48 (CC***H***); 2.60 (C***H***CH$_2$-CH$_2$CHO−); 2.80 (C***H***CH2C***H***, -OC***H***CHOHCHO−); 3.08−3.28 (O═CCH2C***H2***); 3.28−3.64 (CHNC***H***$_3$, CHN-HC***H***$_3$); 4.44 (NHC***H***$_2$NH); 4.84 (OC***H***OCHOH). ^{13}C NMR (400 MHz, D_2O, 298 K) δ: 28.0−30.0 (NH$_2$CH***C***H$_2$CHNH-, -NHCH***C***H$_2$CHNH$_2$, -NHCH***C***H$_2$CHNH-); 30.0−32.8 (NH$_2$-CH***C***H$_2$CHNH$_2$); 34−34.8 (O═C***C***H$_2$CH$_2$N-); 34.8−37.2 (O═C***C***H$_2$CH$_2$NH); 43.6−45.6 (NH***C***H$_2$NH); 48.8−50.0 (NH$_2$***C***HCH$_2$CH$_2$); 51.2−53.2 (−NH***C***HCH$_2$CH$_2$, -N***C***H-CH$_2$CH$_2$); 64.0−66.0 (HOCH***C***HNHCH$_3$); 66.0−67.2 (HOCH***C***HNCH$_3$); 71.2−72.8 (-NCH(CH$_3$)***C***HCH$_2$CH$_2$-CHNH-, -NCH(CH$_3$)***C***HCH$_2$CH$_2$CHN); 74.0−75.4 (−NH-CH(CH$_3$)***C***HCH$_2$CH$_2$CHNH$_2$); 75.4−77.2((-NCH(CH$_3$)-***C***HCH$_2$CH$_2$CHNH$_2$, NHCH(CH$_3$)***C***HCH$_2$CH$_2$CHNH-, NHCH(CH$_3$)***C***HCH$_2$CH$_2$CHN) 128.0−129.0 (O═CCH$_2$-***C***H$_2$); 129.0−130.0 (O═C***C***H$_2$CH$_2$); 168.0−169, 174−177 (C═O). IR (cm^{-1}): 3435 ($\nu_{as\ NH2}$, $\nu_{as\ OH}$), 2946 ($\nu_{as\ CH3}$), 2865 ($\nu_{s\ CH2}$), 1665 ($\nu_{as\ carbonyl}$), 1533 ($\nu_{\ C-N}$, δ_{NH}, δ_{NH2}), 1045 (ν_{C-O-C}).

Polymer Characterization. ^{1}H NMR and ^{13}C NMR spectra were recorded using Bruker Avance III 400 spectrometer in D_2O at 298 K. Quantitative ^{13}C NMR spectra were measured to determine the degree of branching with inverse gated ^{1}H decoupling method. Fourier transform infrared (FTIR) spectra were measured by Bruker Equinox-55 FTIR spectrometer with KBr pellets in the range 3600−400 cm^{-1}. The ζ-potential values were measured with Zetasizer 2000 (Malvern, U.K.) at 25 °C. HPGMs were dissolved in neutral phosphate buffered saline solution (PBS, pH 7.4) with a concentration of 1.0 mg/mL, and the ζ-potential was assessed three times. The molecular weight and molecular weight distribution of HPGMs were determined by a TSK guadcolumn AW-H (R0064) GPC system (TSKgel SuperAWM-H*2

column, R0091+R0093 Column lot, PMMA calibration) equipped with a refractive index (RI) detector. Dimethylfomamide (DMF) containing 10 mM LiBr was used as the mobile phase at a flow rate of 0.6 mL/min at 40 °C.

Evaluation of Buffering Capacity. The buffering capacity of HPGMs was determined by acid−base titration.[18] Specifically, HPGMs were dissolved in 0.15 M NaCl solution to get 1 mg/mL polymer aqueous solution. At the same time, control was set with 0.15 M NaCl solution. The pH value of solutions was adjusted to about 2 with 0.1 M HCl aqueous solution. 50 μL 0.1 M NaOH aqueous solution was dropped into 10 mL assessed solution every time, and the bottle was shaken frequently until a stable reading could be obtained. The pH values were recorded.

Cell Culture. Briefly, COS-7 (a kidney cell line of the African green monkey) and HeLa cells (a cell line derived from cervical cancer cells from Henrietta Lacks) were grown at 37 °C with 5% CO_2 environment. DMEM (Dulbecco's modified Eagle's medium) with 10% fetal bovine serum (FBS), penicillin (100 units/mL), and streptomycin (100 units/mL) were used. Cells were subcultured every 2−3 days.

Cell Viability Assay. The relative cytotoxicity of HPGMs was estimated by standard MTT method. COS-7 cells were seeded in 96-well plates at a density of 9000 cells/well. The cells were cultured for 24 h, and then DMEM was replaced with fresh 200 μL medium. 50 μL of phosphate buffered saline (PBS) containing serial concentrations of HPGM solutions was added in corresponding wells to get final concentrations of 0.1, 0.2, 0.5, 1, and 2 mg/mL. Branched PEI was set as controls. After the cells were incubated for 24 h, stock reagents of 25 μL MTT (5 mg/mL) were added into every well. Four hours later, the medium was removed carefully. 200 μL DMSO was used in every well to dissolve formazan crystals, and the OD_{490} (optical density at the wavelength of 490 nm) was recorded by BioTech System. The cell survival ratios were converted by the formula as follows:

$$\text{cell viability} = ([OD_{490}]\text{sample}/[OD_{490}]\text{control}) \times 100\%$$

In Vitro Degradation of HPGM. In vitro degradation of HPGM was analyzed by NMR technique. Briefly, HPGM was dissolved in different PBS buffer (pH = 7.4, 5.5) to get 10 mg/mL HPGM aqueous solutions. The solutions were added into tubes and oscillated at 37 °C. At some intervals, 1 mL HPGM aqueous solutions were sucked out, freeze−dried, and analyzed via ^1H NMR in D_2O.

Biophysical Properties of HPGM/pDNA Complexes. A certain amount of pGL3-control vector as a model plasmid DNA (pDNA) was dissolved in PBS (pH = 7.4) solution. To prepare the complex solution of different molar ratios of polymer nitrogen to pDNA phosphorus (N/P ratios), the various concentrations of HPGM aqueous solutions were added separately. The HPGM/pDNA complex solutions of N/P ratios with 0, 1, 5, 10, 20, 30, 40, and 50 were mixed with appropriate amounts of 6× loading buffer, which were applied in the slots of a 1% agarose gel in sequence. Ethidium bromide (EB) was used to label pDNA. Then, electrophoresis was performed at 100 V for about 1 h. The profile was analyzed with a UV transilluminator (Bio-RAD gel-phase system).

HPGM was dissolved in PBS buffer (pH 7.4). A certain amount of pDNA was added to get the aqueous solution of HPGM/pDNA complexes with N/P = 30. After incubation at room temperature for 30 min, a droplet was dropped onto carbon-coated copper grids, dried in the air with natural way. Morphology of HPGM/pDNA complexes was observed by transmission electron microscopy (TEM) with a JEOL 2010 instrument operated at 200 kV.

In Vitro Transfection Assay. HPGM was dissolved in PBS (pH 7.4) and filtered through a Millipore filter (pore size: 0.22 μm). HPGM and pDNA were mixed according to the N/P ratios of 0, 5, 10, 20, 30, 40, and 50. Branched PEI was set as controls and N/P ratio was 20 according to the optimized performance. The dosage of pDNA was 0.2 μg in every well. COS-7 cells were seeded at a density of 10 000 cells/well in 100 μL medium (96-well plates), and cells were cultivated for 24 h. The medium was replaced with 50 μL serum-free medium or in the presence of 10% FBS. Then, 50 μL complex solution was added. Cells were incubated for 4 h, and fresh medium with 10% serum replaced the previous. Then, cells were lysed. The transfection activity was evaluated by luciferase assay according to the protocol of Promega. Protein concentration was evaluated according to BCA protein assay kit. Relative light units (RLU) and corresponding protein concentrations were measured by microplate reader system (Biotech).

In Vitro Antitumor Evaluation. The 96-well plates were used and HeLa cells were seeded at a density of 9000 cells/well. The cells were cultured for 24 h, and then various concentrations of HPGM solution (HPGM1, HPGM2, and HPGM3) with DMEM were prepared and filtered through a Millipore filter (pore size: 0.22 μm). Appropriate solution was added to get HPGM solution at different concentrations (0.1, 0.2, 0.5, 1, and 2 mg/mL) and cells were incubated for 24 h. The subsequent procedures were the same as those described in the cell viability assay. The cell inhibition efficiency was calculated by the formula as follows:

$$\text{inhibition efficiency} = (1 - [OD_{490}]\text{sample}/[OD_{490}]\text{control}) \times 100\%$$

Antibacterial Activity Assay. The antibacterial activity was evaluated by the LB broth method.[19] The inhibition ratio based on the optical density (OD_{600}) of bacterial suspension was presented as the antibacterial efficiency. Briefly, HPGM aqueous solution was prepared with sterilized LB broth and filtered through a Millipore filter (pore size: 0.22 μm). Then, 5 mL sterilized LB broth was added into a sterile tube with various concentrations of HPGM. The activated *Escherichia coli* (*E. coli*) was inoculated into the buret containing the LB solution and incubated with shaking at 37 °C for 12 h. Then, the OD_{600} values of the bacterial medium were measured by a UV−vis spectrophotometer. The culture with pure LB medium served as the negative control and the bacteria-free solution served as the positive control. The inhibition ratios for HPGM were calculated as follows:

$$\text{inhibition efficiency}(\%) = 100 - 100 \times (A_t - A_0)/(A_c - A_0)$$

Here, A_0 corresponded to the OD_{600} values for positive control; A_t and A_c were OD_{600} values for HPGM sample and negative control after incubation for 12 h, respectively.

RESULTS AND DISCUSSION

Synthesis and Characterization of HPGMs. As mentioned in previous parts, gentamycin sulfate is a kind of natural aminoglycosides. Unfortunately, cationic small molecule is hard to compress pDNA. To improve its pDNA condensation

Scheme 1. Preparation and Application of Multifunctional Hyperbranched Glycoconjugated Polymers

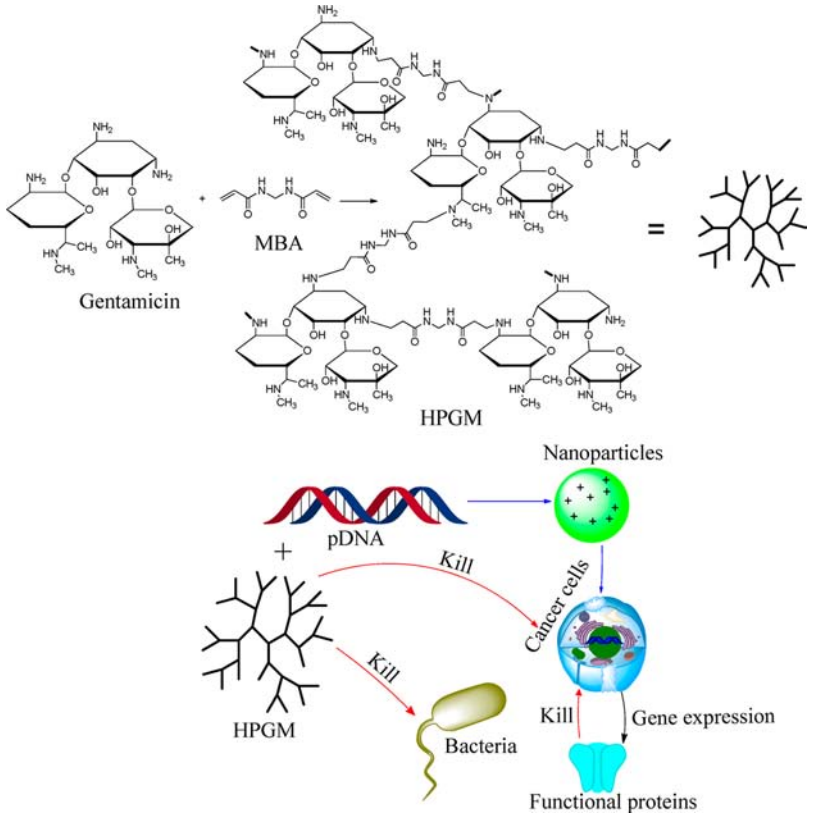

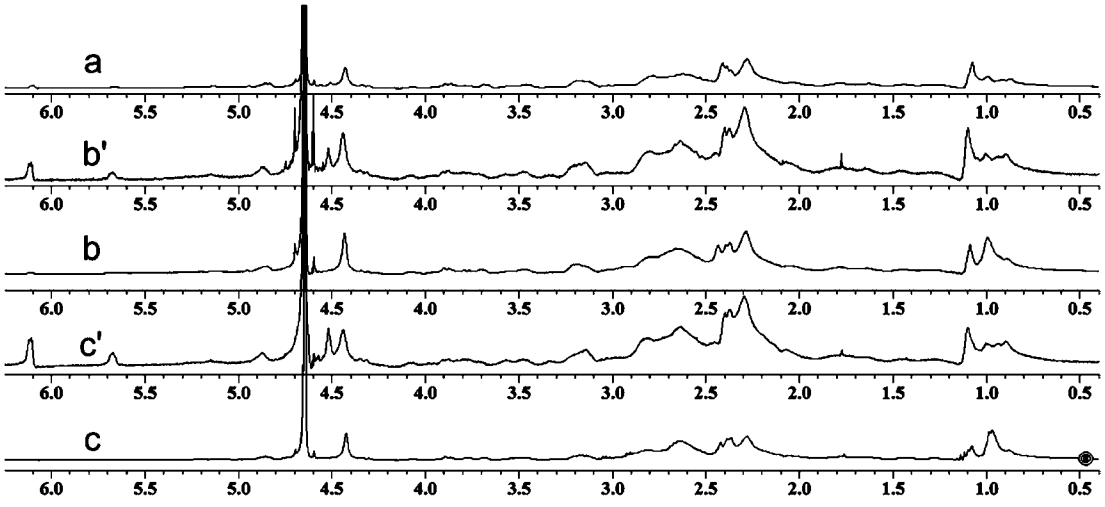

Figure 1. ^{1}H NMR spectra of HPGMs (400 MHz, in D_2O, 298 K): (a) HPGM1, (b′) HPGM2-V, (b) HPGM2, (c′) HPGM3-V, and (c) HPGM3.

ability, we prepare hyperbranched glycoconjugated polymers by Michael addition between *N*,*N*′-methylenebisacrylamide (A_2 monomer) and gentamycin sulfate (B_8 monomer). The synthetic route to the gentamycin-based hyperbranched polycations and their application is shown in Scheme 1. To promote rapid proton transfer and stabilize charged intermediates, protic solvent (aqueous solution) was chosen to generate branched architecture. Since gentamycin sulfate was used, the base environment was needed to stabilize the resulting negative charges. Therefore, saturated $NaHCO_3$ aqueous solution was adopted as catalyst to increase the reaction activity and then form the highly branched polymers.[20]

The resulting hyperbranched poly(gentamicin-MBA)s (HPGMs) were characterized by NMR, FTIR, GPC, and ζ-potential measurements. Typical ^{1}H NMR spectra of HPGMs are shown in Figure 1. After Michael-addition polymerization, all proton signals become broad in HPGMs. The proton at 4.44 ppm corresponds to $-CH_2-$ of the MBA unit ($NHCH_2NH$). Signals of vinyl terminals in HPGM2-V and HPGM3-V are located at 5.68 and 6.12 ppm, which increase with the feeding ratio of the MBA unit. Since the oxidation−reduction potential of vinyl groups induces high toxicity, the terminal double bonds were end-capped by diethylamine. After end-capping, the signals of vinyl groups disappear in HPGM2 and HPGM3 and the methyl signals at 0.95 ppm increase dramatically. Figure 2

dx.doi.org/10.1021/bc300016b | *Bioconjugate Chem.* 2012, 23, 1189−1199

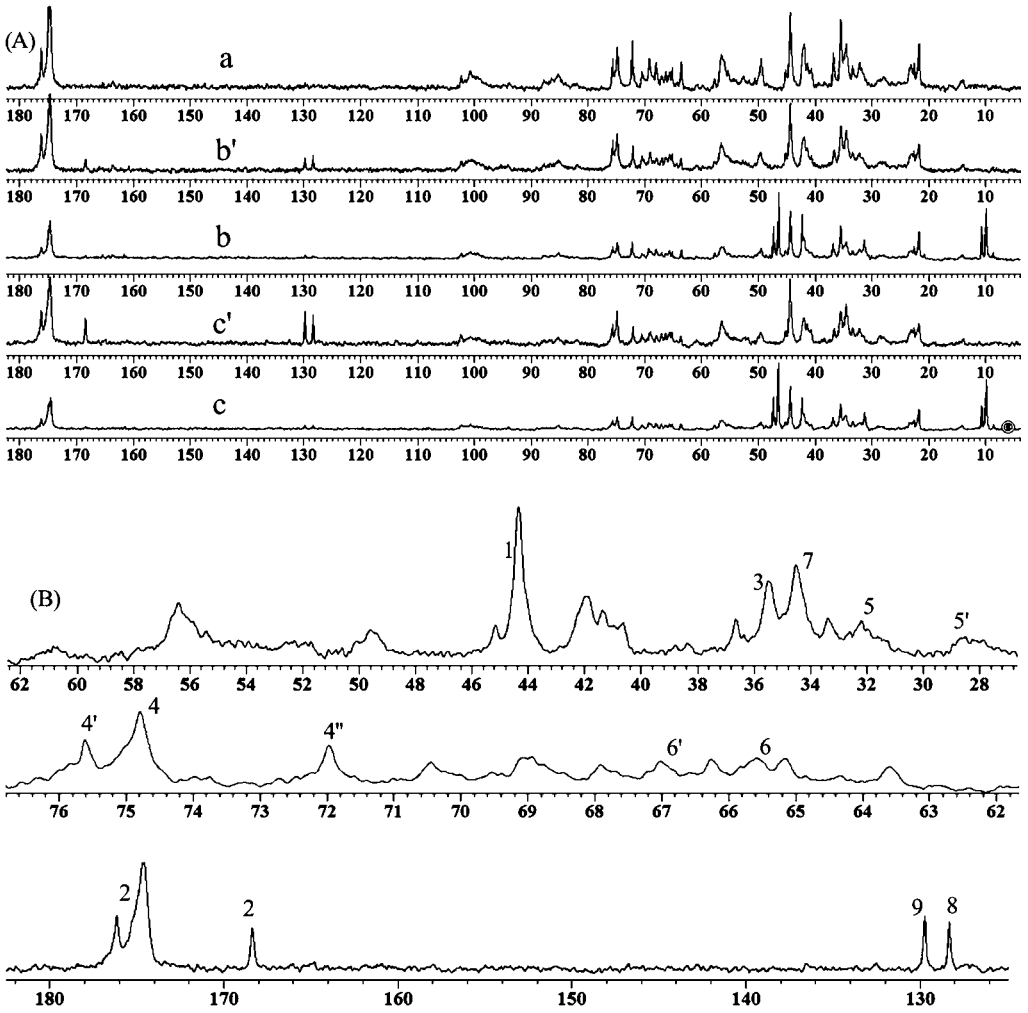

Figure 2. (A) ^{13}C NMR spectra of HPGMs (400 MHz, in D_2O, 298 K): (a) HPGM1, (b′) HPGM2-V, (b) HPGM2, (c′) HPGM3-V, and (c) HPGM3; (B) Enlarged and assigned ^{13}C NMR spectra of HPGM3-V.

gives the correspondent ^{13}C NMR spectra. The signals at 128.5/130.0 and 168.5 ppm come from the double-bond and carbonyl groups of acrylamide terminals, which disappear completely after end-capping with diethylamine. As expected, new strong signals at 10.0 ppm assigned to the methyl groups from the diethylamine unit appear.

In order to calculate the degree of branching (DB), all structural units of HPGMs including linear, terminal, and dendritic units are listed in Scheme 2. On the basis of quantitative ^{13}C NMR analysis, the DB values of HPGMs could be determined from the following equation:[21]

$$DB = (D + T)/(D + T + L)$$

where L, T, and D represent the fractions of the linear, terminal and dendritic units, respectively. As listed in Table 1, the DBs of these HPGMs are 0.45, 0.46, and 0.47, suggesting the formation of hyperbranched glycoconjugated polymers.

FTIR results provide the additional chemical structure information of polymerization products. As displayed in Figure 3, the absorption peaks at 1045 and 1533 cm are assigned to the C−O−C stretching vibration and amino bending vibration, which originate from the gentamycin unit. A strong carbonyl band at 1655 cm^{-1} confirms the presence of amide bond from MBA unit. The bands at 2865 and 2946 cm^{-1} are attributed to the symmetric $-CH_2-$ and asymmetric $-CH_3$ stretching vibrations, respectively. The broad stretching vibration around 3435 cm^{-1} suggests the existence of many hydroxyl and amino groups in HPGMs. The FTIR data suggest that HPGMs are polymerized from gentamycin and MBA monomers.

The molecular weights and molecular weight distributions of HPGMs were measured by GPC, and the data are summarized in Table 1. In detail, the number average molecular weights of HPGM1, HPGM2, and HPGM3 are 5400, 5800, and 6100 g/mol, with the PDI values of 2.7, 2.6, and 2.5, respectively. The real molecular weights of HPGMs should be larger than the values estimated by GPC analysis, because many tertiary amines are present in end-capped polymers and the cationic polymers tend to interact with columns. ζ-Potential analysis demonstrates that HPGMs are positively charged and the charge density is low, giving a chance to further study gene transfer.

Buffering Capacity of HPGMs. Through the proton sponge effect, the strong buffering capacity of cationic polymers could enhance the endosomal escape of polyplexes and facilitate their gene transfection.[22,23] Therefore, the buffering capacity of HPGMs was assessed by acid−base titration before in vitro transfection. As shown in Figure 4, the pH of NaCl solution changes rapidly with addition of NaOH solution, while all HPGMs show a good pH-buffering capacity. HPGMs are highly branched polymers with some primary, secondary, and tertiary amines, which makes a great contribution to their

dx.doi.org/10.1021/bc300016b | Bioconjugate Chem. 2012, 23, 1189−1199

Scheme 2. Schematic Illustration of the Molecular Structure of HPGMs

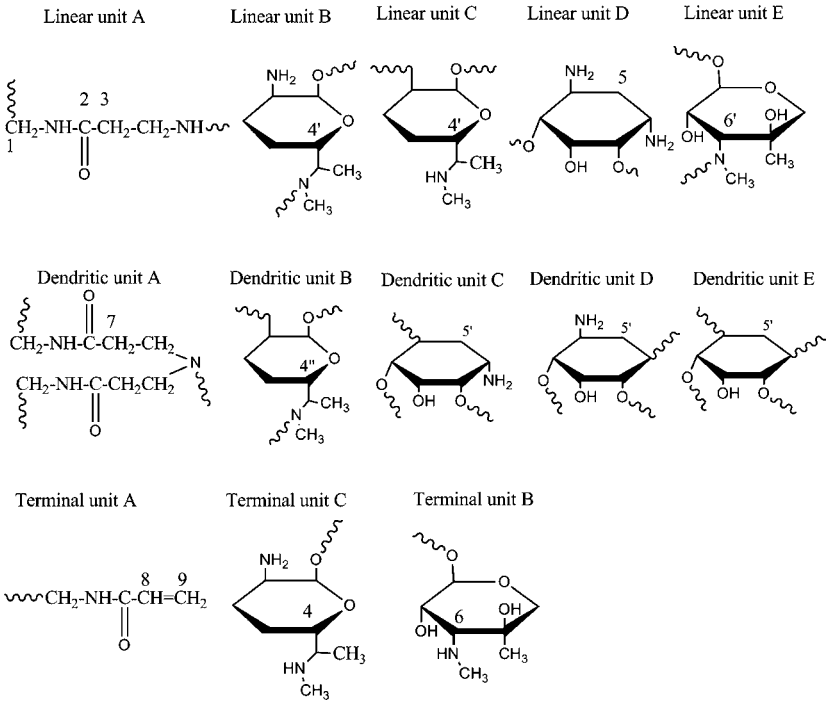

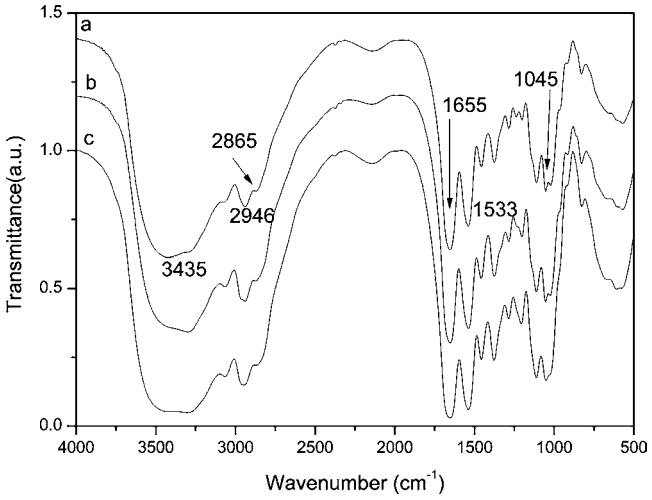

Figure 3. FTIR spectra of (a) HPGM1, (b) HPGM2, and (c) HPGM3.

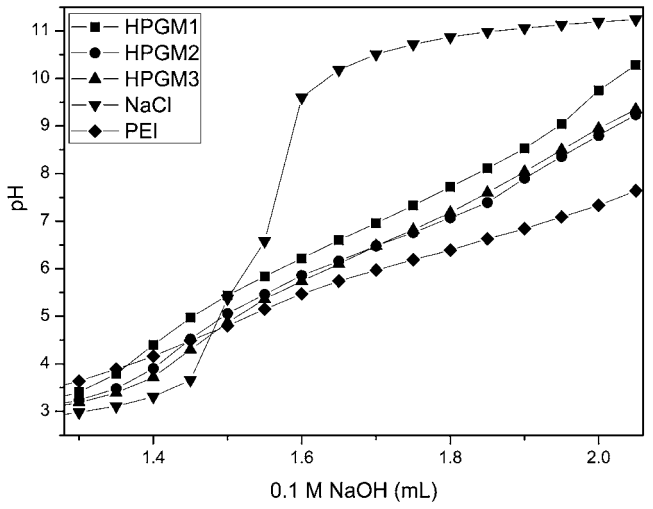

Figure 4. Acid−base titration curves of HPGMs, NaCl, and PEI.

buffering capacity. On the other hand, the nitrogen atoms in HPGMs are limited, so the buffering capacity of HPGMs is lower than that of PEI. Considering that the high nitrogen content of polycations frequently results in serious cytotoxicity, the low nitrogen content of HPGMs might reduce the cytotoxicity of materials greatly.

Cytotoxicity of HPGMs. Low toxicity is very important for the biomedical application of polymeric materials. Based on the MTT assay, the cell viability of HPGMs was evaluated against COS-7 cells with PEI (M_w = 25 kDa) as a control. Figure 5 demonstrates that HPGM1 has low cytotoxicity, while both HPGM2 and HPGM3 exhibit some cytotoxicity. Compared to the PEI control, all HPGMs show much lower cytotoxicity. As we know, high charge density is one factor that contributes to their cytotoxicity.[24,25] Different from the high charge density of PEI, the nitrogen content of HPGMs is low, resulting in the low cytotoxicity. On the other hand, some terminal vinyl groups appear after the Michael addition of gentamicin and MBA monomers. After end-capping of vinyl groups by diethylamine, the amount of terminal amine increases with the feeding ratio of MBA monomer. Correspondingly, the ζ-potential increases from 4.7 ± 0.5 (HPGM1) to 10.1 ± 0.9 (HPGM3), inducing the improved cytotoxicity. Therefore, only HPGM1 with the lowest toxicity was used to evaluate the gene transfection behavior.

In Vitro Degradation. As we all know, the degradation of macromolecules decreases the harm and makes them easy to eliminate through the excretion pathway in vivo.[26,27] HPGM1 contains many glycosidic and amide linkages, which could be hydrolyzed in acidic, glycosidase, or lactamase environment in vivo.[28−30] Figure 6A gives the ^{1}H NMR spectra of the original HPGM1 and the incubated products at pH 7.4 condition for

dx.doi.org/10.1021/bc300016b | Bioconjugate Chem. 2012, 23, 1189−1199

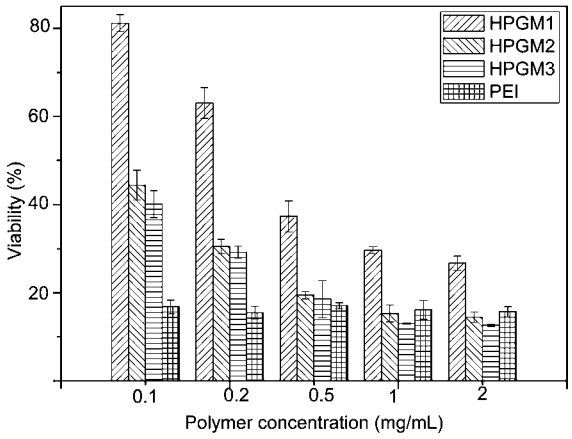

Figure 5. In vitro cytotoxicity of HPGMs with different concentrations to COS-7 cells after 24 h incubation (mean ± SD, n = 3).

different time. It can be found that the ^{1}H NMR spectra are almost unchanged in 51 days, indicating the high stability of HPGM1 at physiological condition. At an acidic environment, the degradation of HPGM1 is accelerated dramatically. Figure 6B gives the variation of chemical shift at 3.84, 2.60, and 2.33 ppm at pH 5.5, which reflects the degradation of glycosidic (3.84 ppm) and amide (2.60 and 2.33 ppm) linkages. It can be observed that both glycosidic and amide linkages degrade obviously in 5 days. As a multifunctional carrier, the polymer should accumulate an appropriate concentration to the target position during its long blood circulation, which facilitates the inhibition of tumors and bacteria. In the meantime, the polymer carrier should be biodegradable after the stimulus of specific triggers for security reasons. According to these requirements, the pH-sensitive HPGM1 seems to be a good candidate.

Biophysical Properties of HPGM/pDNA Complexes. HPGM1 is a kind of hyperbranched polycation, which could complex with the negatively charged pDNA through the electrostatic interaction. To realize the efficient cell uptake and gene transfection, proper particle size and stability of polycation/pDNA complexes are required. The DNA condensation capability of HPGM1 was studied by agarose gel electrophoresis. Figure 7A shows that pDNA is completely blocked at N/P = 1, suggesting an excellent pDNA condensation capability of HPGM1. To further confirm the gel electrophoresis observation, the TEM measurement was employed to analyze the size and distribution of the HPGM1/pDNA complexes. It can be observed from Figure 7B that many homogeneous nanoparticles with a diameter smaller than 100

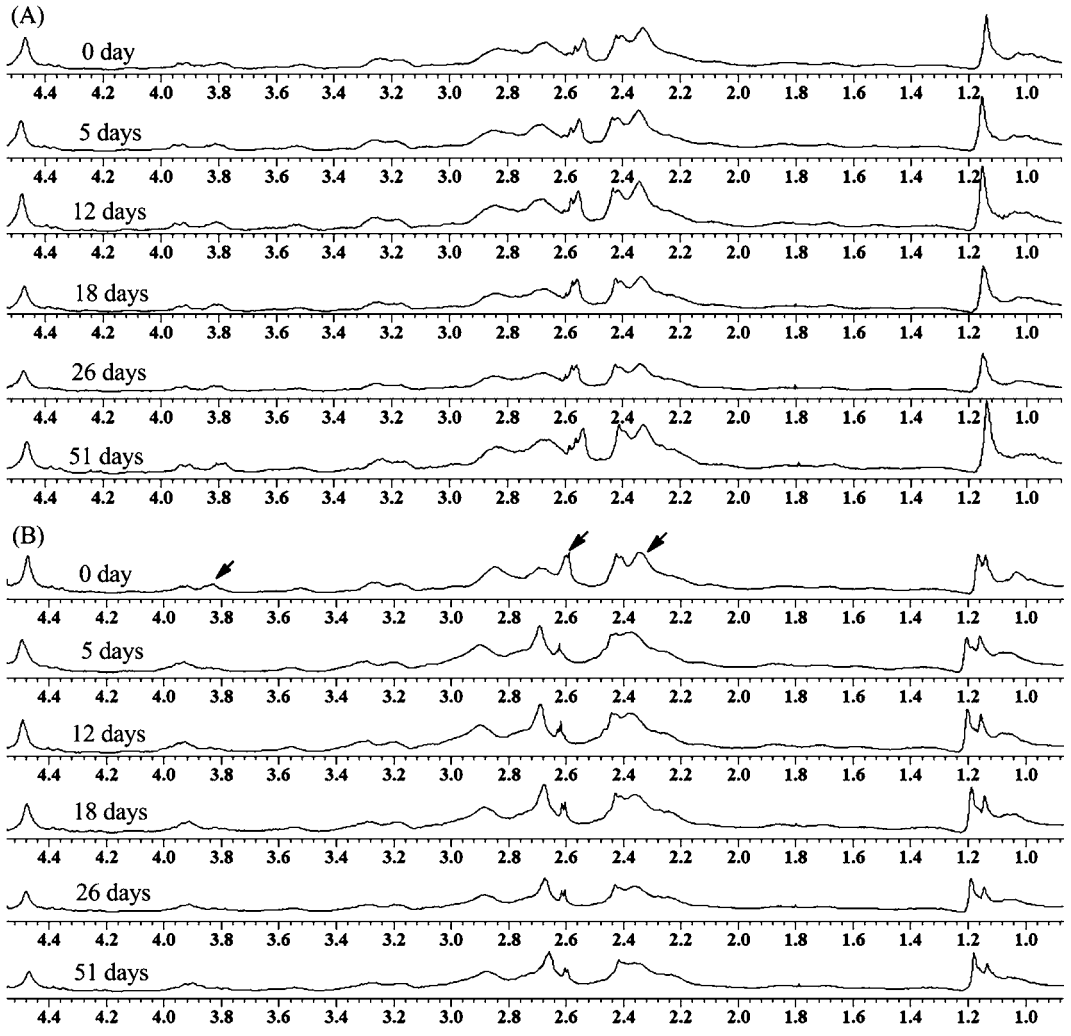

Figure 6. (A) ^{1}H NMR spectra of HPGM1 in D_2O at different degradation time cultured at 37 °C under neutral condition (pH 7.4). (B) ^{1}H NMR spectra of HPGM1 in D_2O at different degradation time cultured at 37 °C under acidic condition (pH 5.5).

dx.doi.org/10.1021/bc300016b | *Bioconjugate Chem.* 2012, 23, 1189–1199

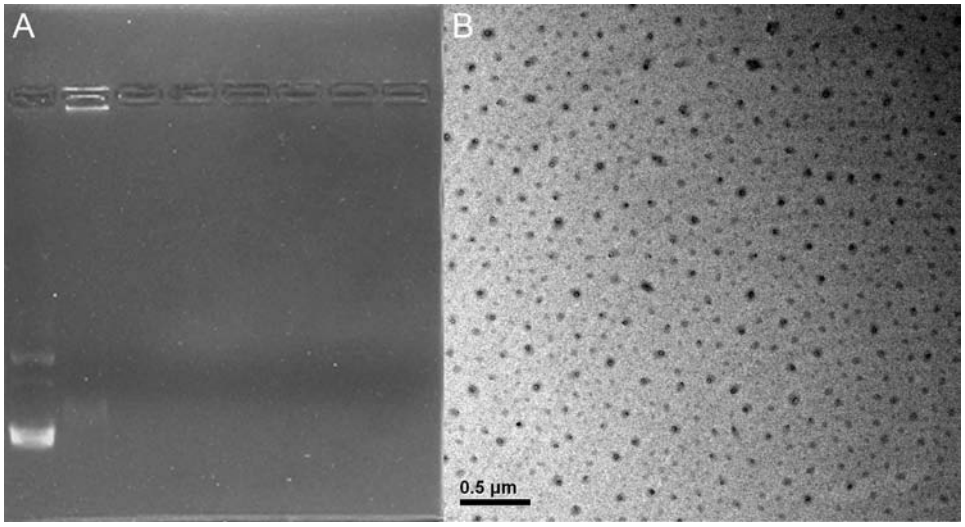

Figure 7. Biophysical properties of the HPGM1/pDNA complexes. (A) Agarose gel electrophoretic images of the HPGM1/pDNA complexes: N/P ratios of 0, 1, 5, 10, 20, 30, 40, and 50 from left to right in each well; (B) the TEM image of HPGM1/pDNA complexes at N/P = 30.

nm appear after the complexation of HPGM1 and pDNA. Both gel electrophoresis and TEM results demonstrate that HPGM1 can condense pDNA very well, although the charge density of hyperbranched glycoconjugated polymer is low.

In Vitro Transfection Assay. The transfection efficiency was assessed with a luciferase reporter system. Due to its strong proton sponge effect and high charge density, branched PEI containing primary, second, and tertiary amines leads to high transfection efficiency. Therefore, it has been frequently used as a gold standard in polycationic transfection materials.[31,32] As shown in Figure 8, the transfection efficiency of HPGM1 in

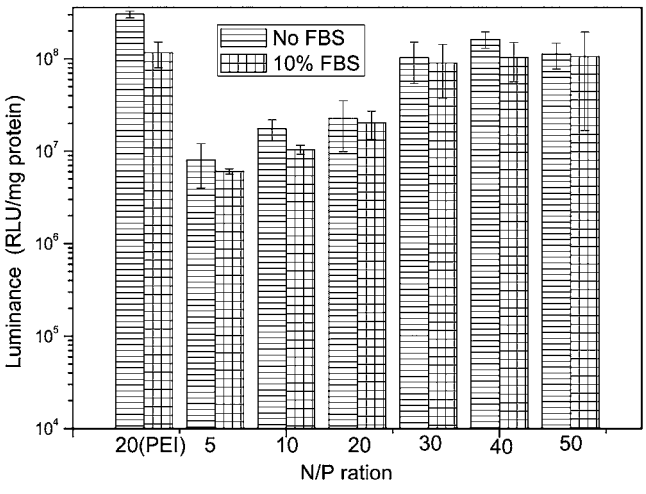

Figure 8. Luciferase expression of the HPGM1/pDNA at various N/P ratios in COS-7 cells (the expression levels were measured 48 h later, mean ± SD, n = 4).

COS-7 is similar to that of PEI, reflecting the excellent transfection performance of HPGM1. High transfection efficiency in cell lines involves multiple factors of polycations, such as the charge density, the ability to penetrate the cell membrane, and the buffering capacity.[33,34] As mentioned above, the buffering capacity of HPGM1 is lower than that of PEI, so the high transfection activity of HPGM1 not only results from the buffering capacity. One possible explanation is that glycosylation of polycations plays an important role in the delivery of HPGM1/pDNA complexes. As we know, glycosyl units are frequently used as signal molecules to interact with the glycoproteins or glycolipids on the cell membranes.[35−37] The glycosylation of polycations might facilitate the recognition of HPGM/pDNA complexes to the cells, which makes a contribution of gene transfer and expression.

For potential in vivo applications, it is important to evaluate the influence of serum on the transfection capacity. Therefore, the transfection ability of the HPGM1/pDNA complexes in the presence of serum (10% FBS) was also investigated using COS-7 cells. Generally speaking, the transfection efficiency in the presence of serum reduces dramatically due to the nonspecific interactions between polycation/pDNA complexes and negatively charged proteins.[38−41] However, Figure 8 shows that no significant reduction in transfection efficiency occurs in the presence of serum. Compared to highly positively charged PEI, the low nitrogen content of HPGM1 results in the small zeta-potential, which avoids the nonspecific combination of negatively charged proteins. Moreover, the existence of many hydrophilic hydroxyl groups in HPGM1 further improves the stability of polycation/pDNA complexes.[42] The high serum-tolerant ability of HPGM1 makes it a promising gene delivery vector.

In Vitro Antitumor Activity Evaluation. The combination of biotherapy with chemotherapy suppresses tumor growth more effectively than conventional biotherapy alone. Of all the currently employed combination of biotherapy with chemotherapy modalities, the assembly or modification of drugs with macromolecules to prepare the cationic polymer prodrug/plasmid nanocomplexes is common.[2] However, the preparation of such nanocomplexes is usually tedious, which raises the cost of preparation and provides opportunities for chemical pollution. It can be imagined that if the gene vector owns inherent anticancer function, the combination of biotherapy with chemotherapy will become much effective. Considering that many natural cationic polysaccharides exhibit good biological activities, the antitumor ability of HPGM1 was evaluated by MTT assay against HeLa cancer cells. Figure 9 shows that HPGM1 can inhibit the growth of cancer cells. When the final concentration of HPGM1 increases to 0.2 mg/mL, more than 50% cancer cells die. The inhibitory effect of

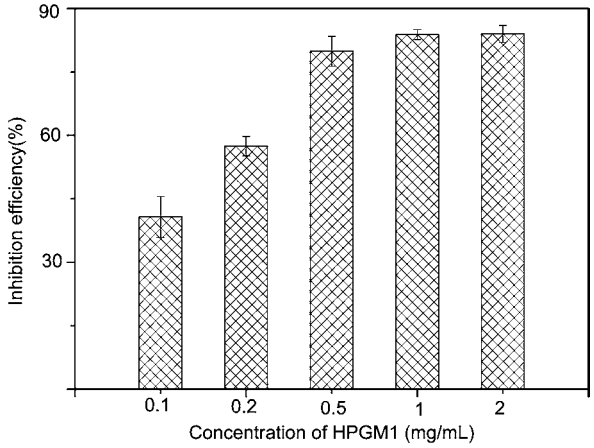

Figure 9. Activity of HPGM1 against HeLa cells after incubation for 24 h.

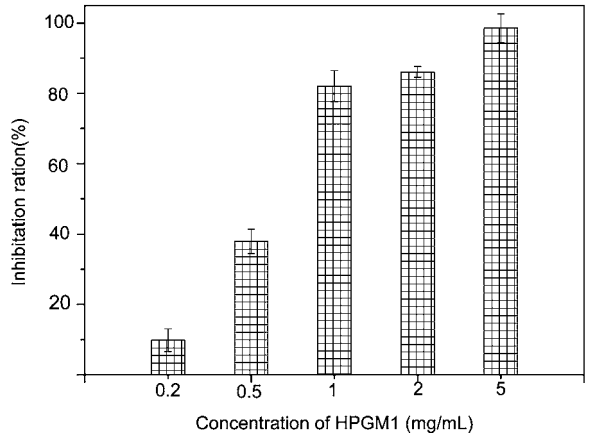

Figure 10. Antibacterial evaluation of HPGM1 against *E. coli* after culture for 12 h.

HPGM1 against the HeLa cell is better than that of chitosan (1 mg/mL) from the larvae of the housefly.[43] Both HPGM2 and HPGM3 show similar growth inhibition for cancer cells, and the results are given in Figure S3 in the Supporting Information. Despite cationic polysaccharides showing a lower antitumor ability comparing to efficient antineoplastic agents such as doxorubicin, cisplatin, and paclitaxel, there are rarely reports about their side effect and drug resistance, while highly effective antineoplastic agents usually arouse side effect and drug resistance.[44] The synergism of gene transfection and antitumor activity of HPGM1 might play an important contribution for the therapeutic efficacy.

Antibacterial Activity Assay. Cancer treatments such as chemotherapy and radiation therapy usually result in the low immunity, which frequently induces the bacterial infections. Therefore, the introduction of antibacterial and antitumor properties into the gene vectors becomes very attractive. Considering that the cationic polysaccharides can usually inhibit the growth of bacteria, the antibacterial activities of HPGM1 were evaluated at different concentrations by using the LB broth method. Here, the culture with pure LB medium served as a negative control and the bacteria-free solution served as a positive control. After adding 5 mg/mL HPGM1 into the *E. coli* LB medium for 12 h, transparent aqueous solution was obtained and no precipitate was observed. Obviously, the growth of the bacteria had been inhibited effectively by HPGM1. The broth absorbance OD_{600} gives us a more accurate assessment of antibacterial activity, and the result is shown in Figure 10. With the concentration of HPGM1 at 2 mg/mL, 86.1% of *E. coli* is suppressed. Further increasing the HPGM1 concentration to 5 mg/mL, *E. coli* is almost completely suppressed. Although many chemical antiseptics such as penicillin exhibit low inhibitory concentration, they usually induce drug resistance and/or serious side effects.[45,46] For cationic polysaccharides, both drug resistance and side effects can be avoided. The minimum bactericidal concentrations of many biologically active substances against to *E. coli* are close to that of HPGM1. For example, minimum bactericidal concentration of scleraldehyde is about 7 mg/mL.[47,48] Therefore, HPGM1 seems to be in the same good antibacterial category as those conventional biologically active substances/polysaccharides. Combining the antibacterial, antitumor, and gene transfection abilities together, the multifunctional hyperbranched glycoconjugated polymer based on natural aminoglycosides may play an important role in protecting cancer patients from bacterial infections.

CONCLUSIONS

Natural aminoglycosides with biological activity were used as a building block to construct multifunctional hyperbranched glycoconjugated polymers. After polymerization, the antitumor and antibacterial abilities of natural aminoglycosides were endowed into the resultant glycoconjugated polymers. On the other hand, benefiting from their highly branched architecture and degradable polymeric backbone, these cationic glycoconjugated polymers exhibited low cytotoxicity and high gene transfection efficiency. Therefore, multifunctional glycoconjugated gene vectors with high transfection, low cytotoxicity, and good antitumor and antibacterial activities were successfully prepared. The construction of multifunctional gene vectors from natural functional small molecules provides a new opportunity for gene therapy.

ASSOCIATED CONTENT

Supporting Information

Supplementary figures including ^{1}H NMR and ^{13}C NMR spectra of gentamycin sulfate. This material is available free of charge via the Internet at http://pubs.acs.org.

AUTHOR INFORMATION

Corresponding Author

*E-mail: xyzhu@sjtu.edu.cn (X. Z.); dyyan@sjtu.edu.cn (D. Y.); jianjian60@yahoo.com (J. S.). Tel.: +86-21-34205699. Fax: +86-21-34205722.

Author Contributions

#These authors are joint first authors.

Notes

The authors declare no competing financial interest.

ACKNOWLEDGMENTS

This work is sponsored by the National Natural Science Foundation of China (20974062) and National Basic Research Program 2009CB930400, the Fok Ying Tung Education Foundation (111048), and China National Funds for Distinguished Young Scientists (21025417).

REFERENCES

(1) Torchilin, V. P. (2006) Multifunctional nanocarriers. *Adv. Drug Delivery Rev. 58*, 1532−1555.

(2) Lu, X., Wang, Q., Xu, F., Tang, G., and Yang, W. (2011) A cationic prodrug/therapeutic gene nanocomplex for the synergistic treatment of tumors. *Biomaterials 32*, 4849−4856.

(3) Singh, A., Boldin-Adamsky, S., Thimmulappa, R. K., Rath, S. K., Ashush, H., Coulter, J., Blackford, A., Goodman, S. N., Bunz, F., Watson, W. H., Gabrielson, E., Feinstein, E., and Biswal, S. (2008) RNAi-mediated silencing of nuclear factor erythroid-2-related factor 2 gene expression in non-small cell lung cancer inhibits tumor growth and increases efficacy of chemotherapy. *Cancer Res. 68*, 7975−7984.

(4) Ravi Kumar, M. N. V., Muzzarelli, R. A. A., Muzzarelli, C., Sashiwa, H., and Domb, A. J. (2004) Chitosan chemistry and pharmaceutical perspectives. *Chem. Rev. 104*, 6017−6084.

(5) Qin, C., Du, Y., Xiao, L., Li, Z., and Gao, X. (2002) Enzymic preparation of water-soluble chitosan and their antitumor activity. *Int. J. Biol. Macromol. 31*, 111−117.

(6) Liang, T., Chen, Y., Yen, Y., and Wang, S. (2007) The antitumor activity of the hydrolysates of chitinous materials hydrolyzed by crude enzyme from Bacillus amyloliquefaciens V656. *Process Biochem. 42*, 527−534.

(7) Felt, O., Carrel, A., Baehni, P., Buri, P., and Gurny, R. (2000) Chitosan as tear substitute: a wetting agent endowed with antimicrobial efficacy. *J. Ocular Pharmacol. Ther. 16*, 261−270.

(8) Vo, T., and Kim, S. (2010) Potential anti-HIV agents from marine resources: an overview. *Mar. Drugs 8*, 2871−2892.

(9) Bhattarai, N., Ramay, H. R., Gunn, J., Matsen, F. A., and Zhang, M. (2005) PEG-grafted chitosan as an injectable thermosensitive hydrogel for sustained protein release. *J. Controlled Release 103*, 609−624.

(10) Ruel-Gariépy, E., Chenite, A., Chaput, C., Guirguis, S, and Leroux, J. C. (2000) Characterization of thermosensitive chitosan gels for the sustained delivery of drugs. *Int. J. Pharm. 203*, 89−98.

(11) Kushwaha, S. K. S., Rai, A. K., and Singh, S. (2010) Chitosan: a platform for targeted drug delivery. *Int. J. Pharm. Technol. Res. 2*, 2271−2282.

(12) MacLaughlin, F. C., Mumper, R. J., Wang, J., Tagliaferri, J. M., Gill, I., Hinchcliffe, M., and Rolland, A. P. (1998) Chitosan and depolymerized chitosan oligomers as condensing carriers for in vivo plasmid delivery. *J. Controlled Release 56*, 259−272.

(13) Erbacher, P., Zou, S., Bettinger, T., Steffan, A. M., and Remy, J. S. (1998) Chitosanbased vector/DNA complexes for gene delivery: biophysical characteristics and transfection ability. *Pharm. Res. 15*, 1332−1339.

(14) Venkatesh, S., and Smith, T. J. (1997) Chitosan-mediated transfection of HeLa cells. *Pharm. Dev. Technol. 2*, 417−418.

(15) Lin, C., and Lin, J. (2003) Characterization and blood coagulation evaluation of the water-soluble chitooligosaccharides prepared by a facile fractionation method. *Biomacromolecules 4*, 1691−1697.

(16) Cole, C. L., and Jayson, G. C. (2008) Oligosaccharides as anti-angiogenic agents. *Expert Opin. Biol. Ther. 8*, 351−362.

(17) Chen, M., Wu, J., Zhou, L., Jin, C., Tu, C., Zhu, B., Wu, F., Zhu, Q., Zhu, X., and Yan, D. (2011) Hyperbranched glycoconjugated polymer from natural small molecule kanamycin as a safe and efficient gene vector. *Polym. Chem. 2*, 2674−2682.

(18) Benns, J. M., Mahato, R. I., and Kim, S. W. (2002) Optimization of factors influencing the transfection efficiency of folate-PEG-folate-graft-polyethylenimine. *J. Controlled Release 79*, 255−269.

(19) Zhang, Y., Peng, H., Huang, W., Zhou, Y., Zhang, X., and Yan, D. (2008) Hyperbranched poly(amidoamine) as the stabilizer and reductant to prepare colloid silver nanoparticles in situ and their antibacterial activity. *J. Phys. Chem. C 112*, 2330−2336.

(20) Mather, B. D., Viswanathan, K., Miller, K. M., and Long, T. E. (2006) Michael addition reactions in macromolecular design for emerging technologies. *Prog. Polym. Sci. 31*, 487−531.

(21) Hawker, C. J., Lee, R., and Fréchet, J. M. J. (1991) One-step synthesis of hyperbranched dendritic polyesters. *J. Am. Chem. Soc. 113*, 4583−4588.

(22) Moore, N. M., Sheppard, C. L., and Sakiyama-Elbert, S. E. (2009) Characterization of a multifunctional PEG-based gene delivery system containing nuclear localization signals and endosomal escape peptides. *Acta Biomater. 5*, 854−864.

(23) Moore, N. M., Sheppard, C. L., Barbour, T. R., and Sakiyama-Elbert, S. E. (2008) The effect of endosomal escape peptides on in vitro gene delivery of polyethylene glycol-based vehicles. *J. Gene Med. 10*, 1134−1149.

(24) Wang, Y., Robertson, J. L., Spillman, W. B., Jr., and Claus, R. O. (2004) Effects of the chemical structure and the surface properties of polymeric biomaterials on their biocompatibility. *Pharm. Res. 21*, 1362−1373.

(25) Putnam, D., Gentry, C. A., Pack, D. W., and Langer, R. (2001) Polymer-based gene delivery with low cytotoxicity by a unique balance of side-chain termini. *Proc. Natl. Acad. Sci. U. S. A. 98*, 1200−1205.

(26) Kima, T. H., Cook, S. E., Arote, R. B., Cho, M. H., Nah, J. W., Choi, Y. J., and Cho, C. S. (2007) A degradable hyperbranched poly(ester amine) based on poloxamer diacrylate and polyethylenimine as a gene carrier. *Macromol. Biosci. 7*, 611−619.

(27) Arote, R. B., Lee, E. S., Jiang, H. L., Kim, Y. K., Choi, Y. J., Cho, M. H., and Cho, C. S. (2009) Efficient gene delivery with osmotically active and hyperbranched poly(ester amine)s. *Bioconjugate Chem. 20*, 2231−2241.

(28) Poole, R. A., Kasper, P. T., and Jiskoot, W. (2011) Formation of amide- and imide-linked degradation products between the peptide drug oxytocin and citrate in citrate-buffered formulations. *J. Pharm. Sci. 100*, 3018−3022.

(29) Guay, D. F., Cole, B. J. W., Fort, R. C., Jr., Hausman, M. C., Genco, J. M., and Elder, T. J. (2002) Mechanisms of oxidative degradation of carbohydrates during oxygen delignification. Part III: reaction of photochemically generated hydroxyl radicals with 1,5-anhydrocellobitol and cellulose. *J. Pulp Paper Sci. 28*, 217−221.

(30) Holtan, S., Zhang, Q., Strand, W. I., and Skjåk-Bræk, G. (2006) Characterization of the hydrolysis mechanism of polyalternating alginate in weak acid and assignment of the resulting Mgoligosaccharides by NMR spectroscopy and ESI-mass spectrometry. *Biomacromolecules 7*, 2108−2121.

(31) Kunath, K., Harpe, A., Fischer, D., and Kissel, T. (2003) Galactose-PEI−DNA complexes for targeted gene delivery: degree of substitution affects complex size and transfection efficiency. *J. Controlled Release 88*, 159−172.

(32) Godbey, W. T., Wu, K. K., and Mikos, A. G. (1999) Poly(ethylenimine) and its role in gene delivery. *J. Controlled Release 60*, 149−160.

(33) Chong, K. W. Y., Lee, A. Y., Koay, E. S. C., Seet, S. J., and Cheung, N. S. (2006) pH dependent high transfection efficiency of mouse neuroblastomas using TransFectin. *J. Neurosci. Methods 15*, 856−863.

(34) Mintzer, M. A., and Simanek, E. E. (2009) Nonviral vectors for gene delivery. *Chem. Rev. 109*, 259−302.

(35) Tu, Y., and Kim, J. (2008) A fusogenic segment of glycoprotein H from herpes simplex virus enhances transfection efficiency of cationic liposomes. *J. Gene Med. 10*, 646−654.

(36) Mukthavaram, R., Marepally, S., Venkata, M. Y., Vegi, G. N., Sistla, R., and Chaudhuri, A. (2009) Cationic glycolipids with cyclic and open galactose head groups for the selective targeting of genes to mouse liver. *Biomaterials 30*, 2369−2384.

(37) Banerjee, R., Mahidhar, Y. V., and Chaudhuri, A. (2001) Design, synthesis, and transfection biology of novel cationic glycolipids for use in liposomal gene delivery. *J. Med. Chem. 44*, 4176−4185.

(38) Funhoff, A. M., Van Nostrum, C. F., Lok, M. C., Fretz, M. M., Crommelin, D. J. A., and Hennink, W. E. (2004) Poly(3-guanidinopropyl methacrylate): a novel cationic polymer for gene delivery. *Bioconjugate Chem. 15*, 1212−1220.

(39) Son, S., and Kim, W. J. (2010) Biodegradable nanoparticles modified by branched polyethylenimine for plasmid DNA delivery. *Biomaterials 31*, 133−143.
(40) Abe, A., Miyanohara, A., and Friedmann, T. (1998) Polybrene increases the efficiency of gene transfer by lipofection. *Gene Ther. 5*, 708−711.
(41) Yang, J., and Huang, L. (1997) Overcoming the inhibitory effect of serum on lipofection by increasing the charge ratio of cationic liposome to DNA. *Gene Ther. 4*, 950−960.
(42) Luo, X., Huang, F., Qin, S., Wang, H., Feng, J., Zhang, X., and Zhuo, R. (2011) A strategy to improve serum-tolerant transfection activity of polycation vectors by surface hydroxylation. *Biomaterials 32*, 9925−9939.
(43) Ai, H., Wang, F., Yang, Q., Zhu, F., and Lei, C. (2008) Preparation and biological activities of chitosan from the larvae of housefly Musca Domestica. *Carbohydr. Polym. 72*, 419−423.
(44) Humber, C. E., Tierney, J. F., Symonds, R. P., Collingwood, M., Kirwan, J., Williams, C., and Green, J. A. (2007) Chemotherapy for advanced, recurrent or metastatic endometrial cancer: a systematic review of Cochrane collaboration. *Ann. Oncol. 18*, 409−420.
(45) Busha, K., and Pucci, M. J. (2011) New antimicrobial agents on the horizon. *Biochem. Pharmacol. 82*, 1528−1539.
(46) Vermeulen, H., Westerbos, S. J., and Ubbink, D. T. (2010) Benefit and harm of iodine in wound care: a systematic review. *J. Hosp. Infect. 76*, 191−199.
(47) Jayakumar, G. C., Kanth, S. V., Chandrasekaran, B., Rao, J. R., and Nair, B. U. (2010) Preparation and antimicrobial activity of scleraldehyde from Schizophyllum commune. *Carbohydr. Res. 345*, 2213−2219.
(48) Qin, C., Du, Y., Xiao, L., Liu, Y., and Yu, H. (2002) Moisture retention and antibacterial activity of modified chitosan by hydrogen peroxide. *J. Appl. Polym. Sci. 86*, 1724−1730.

Bioconjugate Chemistry

Article

pubs.acs.org/bc

Peptide–Drug Conjugate Linked via a Disulfide Bond for Kidney Targeted Drug Delivery

Qian Geng, Xun Sun, Tao Gong, and Zhi-Rong Zhang*

Key Laboratory of Drug Targeting and Drug Delivery Systems, Ministry of Education, West China School of Pharmacy, Sichuan University, Southern Renmin Road, No. 17, Section 3, Chengdu 610041, P. R. China

ABSTRACT: Chronic kidney disease (CKD) is a worldwide public health problem, and unfortunately, the therapeutic index of clinically available drugs is limited. Thus, there is a great need to exploit effective treatment strategies, and the carrier-drug approach is an attractive method to improve the kidney specificity of the therapeutic agents. The aim of this present study is to develop a peptide–drug conjugate for the kidney targeted delivery of angiotensin-converting enzyme (ACE) inhibitor captopril (CAP), since G3-C12 peptide (ANTPCGPYTHDCPVKR) could specifically accumulate in the kidney after intravenous injection. Therefore, FITC labeled G3-C12 peptide (G3-C12-FITC) and peptide–drug conjugate (G3-C12-CAP) with a disulfide bond which can be cleaved by reduced glutathione in the kidney were prepared by solid-phase peptide synthesis. The fluorescence imaging of G3-C12-FITC revealed that the labeled peptide specifically accumulated in the kidney soon after i.v. injection to mice, and the accumulation is due largely to the reabsorption of the peptide by the proximal renal tubule cells. Furthermore, in comparison with the corresponding nonconjugated form, a 2.7-fold increase in renal area under concentration–time curve produced by the conjugate was observed in mice. Interestingly, the CAP entirely released in the kidney even at 0.05 h postinjection through disulfide reduction. As a consequence, the *in vivo* renal ACE inhibition was significantly increased. In conclusion, these findings suggest the potential of G3-C12 peptide serving as a suitable candidate carrier for kidney-targeted drug delivery.

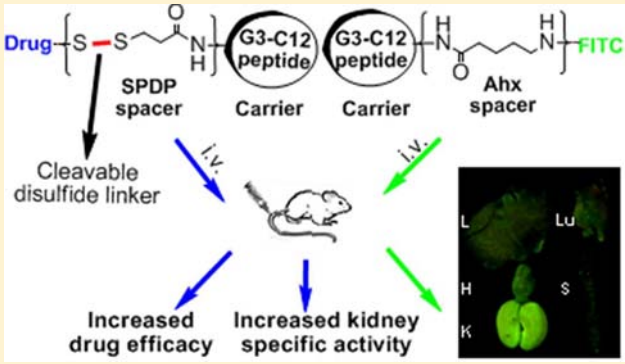

INTRODUCTION

Chronic kidney disease (CKD) is increasingly recognized as a major public health issue.[1−4] It affects 7% of people aged 30 years or older and up to 30% in persons aged 64 years or older.[5] Furthermore, CKD will progress relentlessly to end-stage renal disease, in which renal dialysis and kidney transplantation are then the only possibilities to maintain patients' long-term survival, and the costs are extremely high and may be prohibitive. In addition, facilities for dialysis are extremely scarce or altogether nonexistent in low-income countries, and patients with CKD face ominous fate.[6,7] Therefore, there is a great need to prevent or delay CKD from progressing to end-stage renal disease through early treatment.[8−10]

Treatments for CKD most commonly involve dietary protein restriction[11] and renin-angiotensin system blockade[12] using angiotensin-converting enzyme (ACE) inhibitors or angiotensin receptor blockers. Among them, ACE inhibitors are the classical regimen and have been proven to retard the progression of CKD. In patients and animal models with nephropathies,[13−20] ACE inhibitors are highly effective in slowing the progression of renal disease by reducing glomerular pressures and proteinuria. Compared with a non-ACE-inhibitor regimen, captopril (CAP), a representative ACE inhibitor, was better in reducing glomerular hypertension and renal injury.[21] Moreover, to improve the kidney-specific activity of CAP, a prodrug of CAP was developed by coupling the drug to lysozyme.[22] This CAP–lysozyme conjugate resulted in optimal inhibition of ACE in the kidney, and therefore increased the renoprotective effect of CAP. The results indicated that improved therapeutic index of CAP for treatment of CKD can be achieved by renal targeting.

Drug-targeting delivery to the kidney is an attractive method to increase the drug efficacy, as this approach will generate higher renal drug concentration.[23] In recent years, our research group has successfully developed several strategies to selectively deliver therapeutic agents to the kidney using macromolecules as carriers, such as lysozyme[24] and chitosan,[25,26] and the carrier–drug conjugates have resulted in higher intrarenal drug concentration compared to the free drug.

Encouraged by these achievements, we hope to utilize peptide as a renal-targeting tool, to be used as a carrier when conjugated with therapeutic agents. As such, the possible disadvantages associated with macromolecular conjugates, including low drug loading capability, low purity, and cardiovascular side effects,[27,28] could be avoided. It is shown that peptides have been extensively used as vehicles of radioactive substance for targeted imaging and radiotherapy, and usually caused high and persistent localization of

Received: January 16, 2012
Revised: May 18, 2012
Published: June 5, 2012

dx.doi.org/10.1021/bc300020f | *Bioconjugate Chem.* 2012, 23, 1200–1210

radioactivity in the kidney, such as octreotide and its analogues.[29] Moreover, it is well-known that peptides usually undergo reabsorption in the proximal renal tubules after filtration by glomerulars, which will benefit the renal accumulation of therapeutic agents after coupling to the peptide carrier. Furthermore, peptides possess many advantages, such as small size, high drug loading capability, control over routes of biodegradation, convenience in modification at the amino terminus, and good biocompatibility. Therefore, a proper peptide serving as carrier is needed.

In an effort to improve the kidney-specific activity, therapeutic agents are often attached to drug carrier that selectively accumulated in the kidney. G3-C12 (ANTPCGPYTHDCPVKR), a galectin-3 targeting peptide identified by phage display, could be a suitable candidate carrier. Because it was reported[30−32] that, in spite of its tumor targeting properties after intravenous injection, the radiolabeled G3-C12 specifically accumulated in the kidneys (uptake of radiolabeled G3-C12 in tumor and kidney were 1.27 ± 0.10%ID/g and 30.6 ± 4.48% ID/g at 30 min, respectively). In this study, a G3-C12 based conjugate was developed to promote the intrarenal delivery of CAP. G3-C12 peptide containing the Gly-Ser-Gly (GSG) sequence (G3-C12(GSG)), fluorescein isothiocyannate (FITC) labeled G3-C12 conjugate (G3-C12-FITC), and peptide−drug conjugate (G3-C12-CAP) were prepared in solid phase. The tissue localization and possible renal uptake mechanism of G3-C12-FITC after intravenous injection in mice were investigated using fluorescence imaging. Then, the distribution of the G3-C12-CAP conjugate in mice was studied using LC-MS/MS analysis. Finally, the inhibition effects of the conjugate on ACE activity in plasma and kidney were examined and compared with the unconjugated CAP in mice.

EXPERIMENTAL PROCEDURES

Materials. All starting reagents listed below were obtained from commercial sources and used without further purification. Amino acids and aminomethyl resin were purchased from Sichuan Sangao Biochemical Co., LTD (China). Fluorescein isothiocyannate (FITC), captopril (CAP), 2,4′-dibromoacetophenone, and N-Hippuryl-His-Leu were purchased from Sigma Chemical Co. (St Louis, MO). N-Succinimidyl 3-(2-pyridyldithio) propionate (SPDP) was obtained from Pierce Chemical Co. Ltd. (Rockford, IL). Watsons distilled water was used as water phase in LC-MS/MS system. All other chemicals and solvents were reagent grade or better.

Animal experiments were performed on Kunming mice (25−30 g, male), provided by West China Experimental Animal Center of Sichuan University (China). All *in vivo* protocols were approved by the Institutional Animal Care and Use Committee of Sichuan University and Project of Sichuan Animal Experiment Committee, license 045, China.

Synthesis and Characterization of G3-C12(GSG) Peptide. *Synthesis of G3-C12(GSG) Peptide.* Peptide was synthesized using standard fluorenylmethyloxycarbonyl procedure on a CSBio (CS536) peptide synthesizer. Aminomethyl resin was used for the solid-phase synthesis. After cleavage and removal of the resin by filtration, the reaction mixture was concentrated under vacuum at room temperature. The crude product was purified to homogeneity using preparative reverse-phase HPLC on a C18 column (100A, YMC), [Varian SD1, λ = 215 nm; t_R = 10.8 min; solvent gradient: 14% B to 27% B in 15 min, 27% B to 14% B in 21 min; A = 100% water with 0.1% trifluoroacetic acid (TFA); B = 100% acetonitrile with 0.1% TFA.], and the purity was rechecked by HPLC. Identity of the peptide was confirmed by electrospray ionization mass spectrometry and amino acid analysis.

Synthesis and Characterization of G3-C12-FITC Conjugate. *Synthesis of G3-C12-FITC Conjugate.* Solid-phase synthesis of G3-C12-FITC with 6-aminohexanoic acid (Ahx) between FITC and the NH_2 terminus glycine was carried out using CSBio (CS536) peptide synthesizer. G3-C12-Ahx-resin was washed with *N*,*N*-dimethylformamide (DMF) (3 × 70 mL), then a solution of FITC (2 equiv) and diisopropylamine (3 equiv) in 50 mL DMF was added. After stirred for 6 h, the G3-C12-FITC was cleaved from the resin by treatment with TFA/H_2O (v/v, 95/5). After removal of the resin by filtration, the residue was concentrated under vacuum at room temperature. Then, the crude product was purified to homogeneity using preparative reverse-phase HPLC on a C18 column (100A, YMC), [Varian SD1, λ = 215 nm; t_R = 12.7 min; solvent gradient: 23% B to 36% B in 15 min, 36% B to 23% B in 21 min; A = 100% water with 0.1% TFA; B = 100% acetonitrile with 0.1% TFA.], and the purity was rechecked by HPLC. Identity of the conjugate was confirmed by electrospray ionization mass spectrometry.

Synthesis and Characterization of G3-C12-CAP Conjugate. *Synthesis of G3-C12-CAP Conjugate.* CAP was coupled to the NH_2 terminus of G3-C12(GSG) with SPDP spacer between CAP and the NH_2 terminus glycine. G3-C12(GSG)-resin was washed with DMF (3 × 70 mL), the coupling reagent SPDP (2 equiv) dissolved in 50 mL DMF was added. After stirring for 3 h, the resin was washed with DMF (3 × 50 mL), dichloromethane (3 × 50 mL), and DMF (3 × 50 mL). Then, CAP (3 equiv) dissolved in 25% TEA/DMF (300 mL) was added to the G3-C12 -SPDP-resin mixture. The reaction mixture was stirred for another 1.5 h, and the resin was washed with DMF (3 × 50 mL), dichloromethane (3 × 50 mL), and CH_3OH (3 × 50 mL). The G3-C12-CAP was cleaved from the resin by treatment with TFA/H_2O (v/v, 95/5); after removal of the resin by filtration, the reaction was concentrated under vacuum at room temperature. Then, the final compound was purified to homogeneity by preparative reverse-phase HPLC on a C18 column (100A, YMC), [Varian SD1, λ = 215 nm; t_R = 10.7 min; solvent gradient: 19% B to 32% B in 15 min, 32% B to 19% B in 21 min; A = 100% water with 0.1% TFA; B = 100% acetonitrile with 0.1% TFA], and the purity was rechecked by HPLC. The molecular weight was confirmed by electrospray ionization mass spectrometry.

Fluorescence Imaging of G3-C12-FITC Conjugate. 46 $\mu M \cdot kg^{-1}$ of G3-C12-FITC was given to mice intravenously, and then, the mice were sacrificed at 0.05, 0.25, 0.5, 1, 2, 4, 6, and 12 h after injection. The tissues were collected, and fluorescence imaging was performed on a 470 nm light source of the LT-99D2 Illumatool Dual Light System (Lightools Research, Encinitas, CA). The images were recorded with a built-in CCD camera. In the blocking experiment, the lysine coinfusion experiment was performed, and the effects of an amino acid blocking on the renal uptake of free FITC and G3-C12-FITC conjugate were evaluated. Briefly, two groups of mice received a tail vein bolus of free FITC (46 $\mu M \cdot kg^{-1}$) or equimolar dose of G3-C12-FITC conjugate only, respectively. The blocking experiment was performed using 100 μg of lysine administered 20 min before injecting the free FITC or G3-C12-FITC conjugate. The fluorescence imaging was performed at 2 h after injection to assess the difference in the accumulation of fluorescent probe in the kidneys. Meanwhile, another mouse

served as the blank control was processed following the same procedure, but normal saline (NS) was given intravenously.

Drug Biodistribution Study of G3-C12-CAP Conjugate. Since CAP contains a thiol group, it usually forms mixed disulfides with endogenous thiol-containing compounds (CAP itself, cysteine, and proteins). So, the free CAP and its mixed disulfides in blood and tissues were measured collectively as total CAP (CAP-SH plus CAP-disulfides). Mixed CAP-disulfides were reduced with tributyl phosphate to form CAP for detection. Thus, both free CAP and total CAP were measured.

Male Kunming strain mice (25−30 g) were divided into CAP group and G3-C12-CAP group at random, and each group had 25 mice (n = 5 for each time point). 46 μM·kg^{-1} of CAP or G3-C12-CAP conjugate dissolved in NS were given to mice through tail vein injection. Five mice of each group were sacrificed at 0.05, 0.25, 1, 2, and 6 h after administration. Blood samples were collected from the ocular artery directly from the mice after eyeball removal and placed immediately in heparinized tubes. These samples were immediately centrifuged at 4000 rpm for 10 min at 4 °C to obtain plasma. Then, the mice were sacrificed and the selected tissues including heart, liver, lung, kidney, and spleen were dissected. Tissue samples were washed with NS, and the redundant liquid was blotted using absorbent paper. Tissues were snap-frozen in liquid nitrogen and stored at −80 °C until use. Before use, the plasma was diluted with 2-fold of phosphate buffer (pH 7.4) and the tissues were homogenized in an ice-bath with a volume of ice-cold phosphate buffer (pH 7.4) that resulted in a 6-fold dilution (g/mL).

Sample Preparation for Free CAP. 200 μL aliquots of plasma or the tissue homogenates were added to tubes containing 20 μL 0.1 M EDTA and 0.1 M ascorbic acid (1:1) as stabilizer. Then, the plasma or the tissue homogenates were mixed with 100 μL phosphate buffer (pH 7.0) and 50 μL of 29 nM/mL 2,4′-dibromoacetophenone acetonitrile solution. This mixture was carefully vortex-mixed and left protected from the light at room temperature for 30 min to complete the process of derivatization. After that, 0.4 mL methanol was added and vortex-mixed for 5 min. The mixtures were centrifuged at 13 500 rpm for 15 min. Then, the supernatants were filtered over 0.2 μm membranes and analyzed by LC-MS/MS analysis.

Sample Preparation for Total CAP. After addition of 100 μL phosphate buffer (pH 7.4) and 100 μL of 1% tributyl phosphate methanol solution to 200 μL of the plasma or tissue homogenate in tubes containing 20 μL 0.1 M EDTA and 0.1 M ascorbic acid (1:1) as stabilizer, the mixture was vortex-mixed for 15 s and allowed to stand at room temperature for 30 min. Then, 50 μL of 29 nM/mL 2,4′-dibromoacetophenone acetonitrile solution was added, and this mixture was carefully vortex-mixed and left protected from the light at room temperature for 30 min to complete the process of derivatization. Proteins were precipitated by addition of 0.4 mL of methanol and vortex-mixed for 5 min. After centrifugation at 13 500 rpm for 15 min, the supernatants were filtered over 0.2 μm membranes and analyzed by LC-MS/MS analysis.

LC-MS/MS Analysis. *Apparatus.* The LC-MS/MS system consisted of an Agilent 1200 series RRLC system, which including an SL autosampler, degasser, and SL binary pump and an Agilent triple-quadrupole MS. The system was controlled with B01.03 software for qualitative analysis and B01.04 software for quantification.

Chromatographic Conditions. Separation was performed on a diamonsil column (50 × 4.6 mm, ODS, 1.8 μm) with the corresponding guard column (ODS, 5 μm). The column was maintained at 30 °C and a 1 μL aliquot was injected into the LC-MS/MS system. The mobile phase consisted of methanol and water including 0.23% formic acid (v/v, 70:30) at a flow rate of 0.3 mL/min.

Mass Spectrometry Condition. The mass spectrometer was operated using an electrospray source and configured to positive ion mode, and quantification was performed using multiple reaction monitoring (MRM). Selected reaction monitoring mode with transitions of m/z 416.0→216.1 was adopted to quantify the CAP derivate. The corresponding optimized collision-induced dissociation (CID) voltages of the analyte were 110 eV and 15 eV for the fragmentor and collision energy, respectively. Instrumental parameters were as follows: gas temperature, 350 °C; gas flow, 8 mL/min; nebulizer, 30 psi; capillary, 4000 v. The calibration curves for CAP derivate were measured over a range of 0.115−5.76 nM/mL in plasma and tissue homogenates (0.115−73 nM/mL for the kidney homogenate) and were proven to be linear with a correlation coefficient (r) of 0.99 of all the calibration curves. The limit of detection (LOD) was 0.0046 nM/mL.

Measurement of ACE Activity. Five groups of animals were studied after intravenous bolus injection as follows: (1) blank group (NS; n = 5 for each time points); (2) G3-C12(GSG) group (46 μM·kg^{-1}; n = 5 for each time point); (3) G3-C12-CAP group (46 μM·kg^{-1}; n = 5 for each time point); (4) CAP group (46 μM·kg^{-1}; n = 5 for each time points); (5) CAP plus G3-C12(GSG) group (46 μM·kg^{-1} G3-C12(GSG) plus equimolar dose of CAP; n = 5 for each time point). The analysis method was used according to the reported procedure with some modification.[33,34] At the indicated time point, blood samples were collected from the ocular artery directly after eyeball removal and placed in heparinized test tubes. Plasma was immediately separated by centrifugation (4000 rpm) for 10 min at 4 °C. The mice were sacrificed and the kidneys were dissected. Kidney samples were washed with NS and the redundant liquid was blotted using an absorbent paper. Plasma and kidney samples were snap-frozen in liquid nitrogen and stored at −80 °C until the assay was performed.

ACE activity was measured by the conversion of the ACE substrate N-Hippuryl-His-Leu to hippuric acid according to the reported procedure[34] with some modifications. In short, the tissues were homogenized in an ice-bath with a volume of ice-cold phosphate buffer (pH 7.4) that resulted in a 6-fold dilution (g/mL). 100 μL of plasma or kidney homogenate and 50 μL water were mixed. The assay was performed by incubation of the mixture at 37 °C with 100 μL of the substrate in 0.4 M sodium borate buffer containing 0.9 M NaC1 (pH 8.3, 5 mM) for 15 min. The generation of hippuric acid was stopped by adding 250 μL 1 M HCl. Each sample was vortexed with 1.4 mL of acetic ether (AcOEt) for 5 min. After 10 min of centrifugation (4000 rpm), 1 mL of the AcOEt layer was transferred to a 1.5 mL tube and dried at 60 °C under air. The residue was reconstituted with 200 μL of mobile phase of HPLC. The samples were assayed by a Agilent 1260 Infinity LC system (G1329B autosampler, G1311C pump, and G1314C detector) on a Kromasil C18 reverse-phase column (4.6 × 150 mm, 5 μm) with the corresponding guard column (ODS, 5 μm). The mobile phase consisted of sodium acetate buffer (10

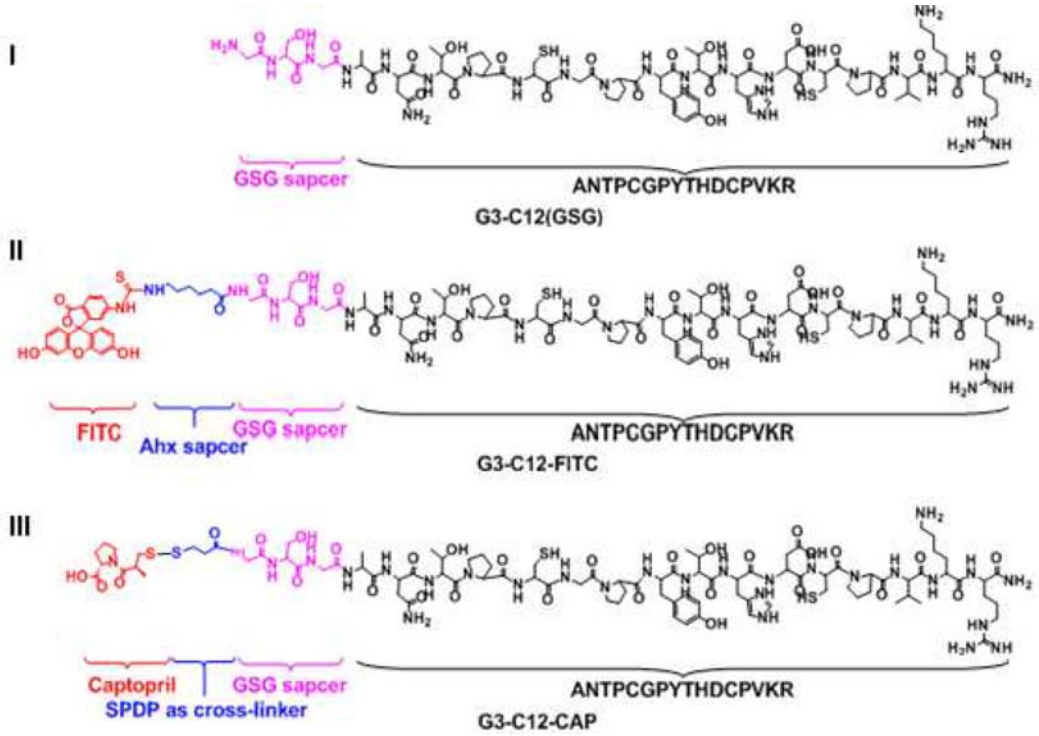

Figure 1. (A) Structure of G3-C12(GSG) peptide, contains a G3-C12 peptide and a GSG spacer. (B) Structure of G3-C12-FITC conjugate, Ahx was used as spacer between FITC and the peptide. (C) Structure of G3-C12-CAP conjugate, which contains a G3-C12(GSG) peptide, a cross-linker SPDP, and a CAP.

Scheme 1. Synthesis of G3-C12-FITC Conjugate and G3-C12-CAP Conjugate[a]

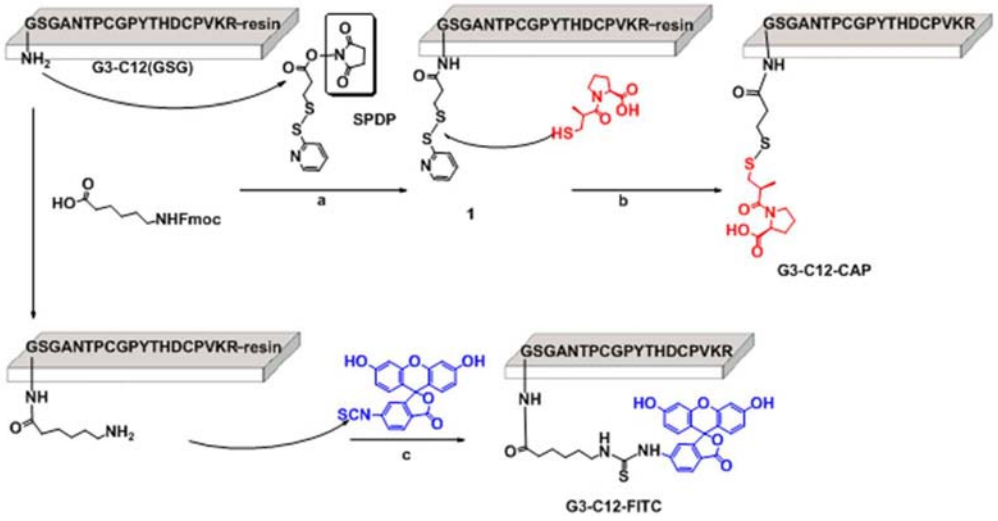

[a]Reagents and conditions: (a) 2 equiv SPDP, DMF, rt, 3 h; (b) (I) 3 equiv CAP, DMF, rt, 1.5 h; (II) TFA/H_2O (v/v, 95/5); (c) (I) 2 equiv FITC, 3 equiv DIPEA, rt, 6 h; (II) TFA/H_2O (v/v, 95/5).

mM, pH 4.0) with 10% methanol and 7.5% acetonitrile, and the flow rate was set at 1.0 mL/min. Samples were tested as 50 μL injections, and the hippuric acid concentration was monitored by UV detector at 228 nm (elution time 4.8 min). ACE activity was defined as the formation of nM hippuric acid per minute per milliliter of plasma or nM of hippuric acid per minute per gram of kidney.

Calculation and Statistics. The ACE inhibition at selected time points was calculated by dividing the inhibited ACE activities by the ACE activity found in the control group. Data are expressed as mean ± SD. Differences were considered statistically significant $P < 0.05$.

RESULTS

Synthesis. G3-C12(GSG), G3-C12-FITC conjugate, and G3-C12-CAP conjugate (Figure 1) have been prepared by solid-phase peptide synthesis using standard fluorenylmethyloxycarbonyl procedure. The experimental procedures were given in detail and illustrated in Scheme 1. To enhance the conformational freedom and avoid any potential steric

dx.doi.org/10.1021/bc300020f | Bioconjugate Chem. 2012, 23, 1200−1210

hindrance, a GSG was used as a spacer at the amino-terminus of the peptide in these three compounds according to the published literature.[32] In the case of G3-C12-FITC conjugate, Ahx was used as spacer to avoid the cyclization side reaction which resulted in the formation of a fluorescein with subsequent removal of the last amino acid in acidic conditions on solid support. Later on, for the G3-C12-CAP conjugate, SPDP was used as heterobifunctional cross-linker between the peptide and CAP. Characterization and purity of the three compounds were reported in Table 1. Amino acid analyses (Table 2) revealed the expected composition of the carrier peptide.

Table 1. Characterization and Purity of G3-C12(GSG) Peptide, G3-C12-FITC, and G3-C12-CAP Conjugate

compound	formula	MW calc.	ions detected (ESI+)	purity[a] (%)
G3-C12(GSG)	$C_{81}H_{127}N_{27}O_{26}S_2$	1959.2	$[M+2H]^{2+}$ m/z = 980.8	98.7
G3-C12-FITC	$C_{108}H_{149}N_{29}O_{32}S_3$	2461.7	$[M+2H]^{2+}$ m/z = 1231.4	95.3
			$[M+3H]^{3+}$ m/z = 820.7	
G3-C12-CAP	$C_{93}H_{144}N_{28}O_{30}S_4$	2262.6	$[M+H]^{+}$ m/z = 2261.8	97.5

[a]Purity percentage was estimated by integration of peak area in HPLC chromatogram recorded at 215 nm.

Fluorescence Imaging. To examine the tissue-specific localization of G3-C12 peptide, fluorescence imaging was used to visualize the biodistribution of FITC labeled G3-C12 peptide in the kidneys in mice (Figure 2). The image revealed good renal uptake of G3-C12-FITC even at 0.05 h postinjection, while it was scarcely observed in other tissues (Figure 2B). Figure 2C exhibited the accumulation of labeled peptide in the kidney at different time points.

In addition, the blocking study was studied by coinfusion with lysine to study the possible uptake mechanism of G3-C12 peptide. This cationic amino acid generally interferes with the proximal tubule cell peptide reabsorption system and therefore reduces the renal accumulation of peptides.[29] As shown in Figure 2D, following infusion of lysine via intravenous injection, the renal uptake of G3-C12-FITC was extremely reduced. However, in the control group, there was no difference between the free FITC group and the FITC plus lysine group. These results revealed that the renal uptake was mainly attributed to the peptide carrier rather than the free FITC. Therefore, the visual images indicated that G3-C12 peptide specifically accumulated in the kidney due largely to its reabsorption by proximal tubule cells.

Biodistribution of G3-C12-CAP Conjugate. In order to evaluate the influence of conjugation on the localization of the CAP, we studied the tissue distribution of G3-C12-CAP conjugate and free CAP. The concentration of CAP and total CAP (CAP-SH plus CAP-disulfides that represent G3-C12-CAP conjugate and a fraction of CAP covalently binding to thiol compounds such as CAP itself, cysteine, and proteins) were measured.

The plasma and renal time courses of CAP and total CAP after the intravenous administration of free CAP and G3-C12-CAP conjugate were shown in Figure 3. Increased intrarenal CAP concentration was successfully achieved at all time points (Figure 3B), and was consistent with the results indicated by

Table 2. Amino Acid Analysis of the Carrier Peptide after Acidic Hydrolysis

	Asp	Asn	Thr	Ser	Gly	Ala	Cys	Val	Tyr	Lys	His	Arg	Pro
Peptide	1 × 1.01	1 × 1.01	2 × 0.96	1 × 0.96	3 × 1.01	1 × 1.02	2 × 0.97	1 × 1.02	1 × 0.96	1 × 1.02	1 × 1.02	1 × 1.00	3 × 1.05

dx.doi.org/10.1021/bc300020f | Bioconjugate Chem. 2012, 23, 1200−1210

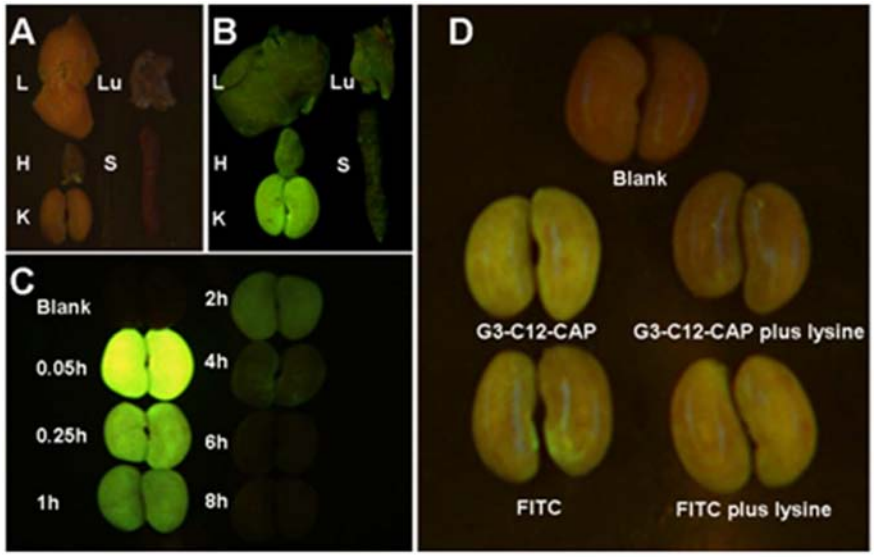

Figure 2. Fluorescence imaging of tissues after intravenous administration of 46 μM·kg^{-1} of FITC or equimolar dose of G3-C12-FITC conjugate in mice. (A) Blank group, mouse received NS only; (B) The mouse received i.v. injection of G3-C12-FITC conjugate. The tissues of the mouse sacrificed at 0.05 h. L, liver; H, heart; K, kidney; Lu, lung; S, spleen. (C) The mouse received intravenous administration of G3-C12-FITC conjugate. The kidneys of mice sacrificed at various time points. (D) Effects of lysine coinfusion on the kidney uptake of G3-C12-FITC conjugate. Mice were injected with G3-C12-FITC conjugate or FITC alone or co-infused with lysine (100 μg). In the blank group, mice received NS only. Two hours after injection, mice were sacrificed.

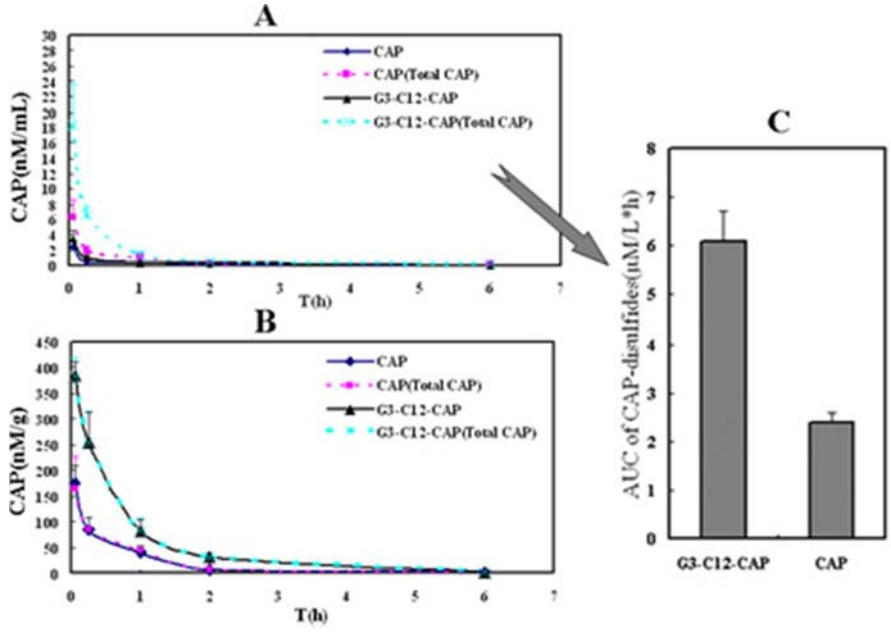

Figure 3. (1) Plasma (panel A) and renal (panel B) time courses of CAP concentration and total CAP (CAP-SH plus CAP-disulfides) concentration after intravenous injection of 46 μM·kg^{-1} of parent drug or G3-C12-CAP conjugate. (2) The plasma area under the concentration−time curve ($AUC_{0\rightarrow t}$) of CAP disulfides (panel C) was calculated ($AUC_{CAP\ disulfides} = AUC_{total\ CAP}$ minus $AUC_{free\ CAP}$). **, significant difference between G3-C12-CAP conjugate group and free CAP group ($P < 0.001$). Values are given as mean ± SD ($n = 5$).

fluorescence imaging (Figure 2B). Furthermore, no significant difference was observed between the amounts of total CAP and free CAP in the conjugate group at all time points. This result revealed that the G3-C12-CAP conjugate could immediately be cleaved in the kidney, which led to the release of free CAP. The figure also showed that at 0.05 h after intravenous injection, in the G3-C12-CAP conjugate group, the plasma concentration of total CAP was 5.3-fold higher than the concentration of CAP (Figure 3A). Consequently, the plasma area under concentration−time curve ($AUC_{0\rightarrow t}$) of CAP disulfides ($AUC_{CAP\ disulfides} = AUC_{total\ CAP} - AUC_{free\ CAP}$) of the G3-C12-CAP conjugate group was 2.5-fold higher than the CAP group (Figure 3C), indicating that the amount of CAP disulfides significantly increased after conjugation to the peptide carrier in the plasma.

Furthermore, the pharmacological benefit of the peptide−drug conjugate was estimated by $AUC_{0\rightarrow t}$ values of the total CAP in the plasma and tissues (Figure 4A). Free CAP and CAP-disulfides were measured collectively as total CAP to evaluate the targeting efficiency of the conjugate. The renal area

dx.doi.org/10.1021/bc300020f | *Bioconjugate Chem.* 2012, 23, 1200−1210

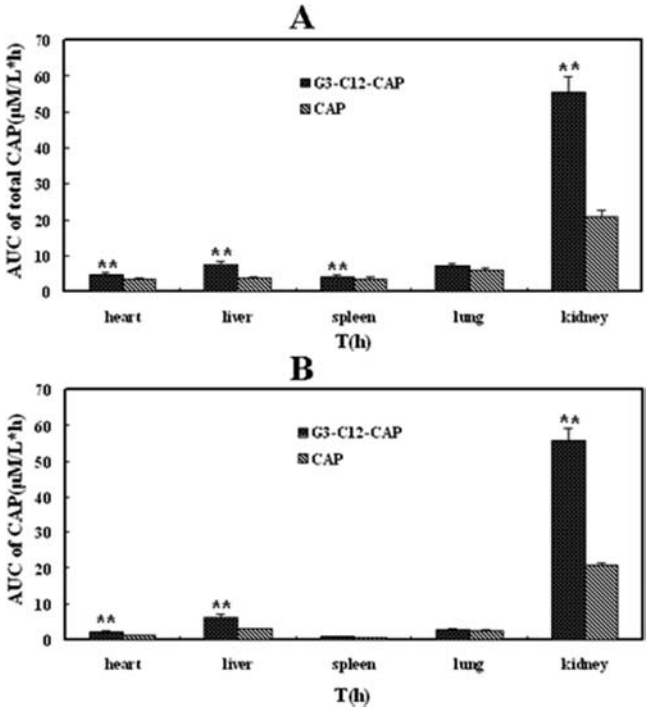

Figure 4. Biodistribution of the G3-C12-CAP conjugate and free CAP after intravenous injection (46 μM·kg^{-1} of CAP or G3-C12-CAP conjugate). (A) CAP concentrations were determined as total CAP (CAP-SH plus CAP-disulfides). (B) Free CAP (CAP-SH) in plasma and tissues were measured. Values are given as mean ± SD (n = 5). **, significant difference between G3-C12-CAP conjugate group and free CAP group (**, P < 0.01).

under concentration−time curve ($AUC_{0\rightarrow t}$) of G3-C12-CAP group was 55.6 μM/L·h, which was 2.7 times the controlled CAP group. Moreover, the mean retention time (MRT) of G3-C12-CAP (1.3 h) showed no significant difference compared to the control CAP group (1.2 h).

As shown in Figure 4B, the concentration of free CAP (CAP-SH) was also examined. After intravenous administration of the G3-C12-CAP conjugate, the $AUC_{0\rightarrow t}$ was substantially higher in kidney (55.8 μM/L·h) compared to liver (6.4 μM/L·h), lung (2.9 μM/L·h), heart (2.1 μM/L·h), and spleen (0.9 μM/L·h). Moreover, the $AUC_{0\rightarrow t}$ of G3-C12-CAP conjugate in kidney was 2.7-fold higher than that of CAP. These results indicated that the G3-C12-CAP conjugate generated higher intrarenal drug concentration and increased the kidney-specific activity.

Measurement of ACE Activity. We studied the plasma and renal ACE activity in the NS-treated control mice and the mice that had been injected with G3-C12(GSG) in advance to investigate a possible effect of the carrier on ACE activity. Figure 5A,B showed that plasma and renal ACE activity remained rather constant in time, and not influenced by administration of G3-C12(GSG). Then, to examine the effects of coinfusion carrier on the ACE activity of CAP, we determined the ACE-inhibitory effects of G3-C12(GSG) plus CAP or free CAP in time by measuring the ACE activity in the plasma and kidney. Similarly, there was no significant difference between the two groups in ACE activity (Figure 5C,D) and indicated that the carrier had no effects on the ACE inhibition capacity of the CAP.

Subsequently, the plasma and renal ACE activity were measured after intravenous bolus administration of G3-C12-CAP or G3-C12(GSG) plus CAP and the effects were shown in Figure 6. The plasma and renal ACE inhibition of both treatments were significant versus the NS group at all time points, and the G3-C12-CAP conjugate significantly exhibited increased the plasma and kidney ACE activity inhibition compared with G3-C12(GSG) plus CAP group. Compared to the mixed group, G3-C12-CAP decreased the renal ACE activity about 1.7-fold at 4 h. A longer-lasting plasma ACE inhibition was also observed.

DISCUSSION

Drug−carrier conjugates have been widely used to increase the accumulation of therapeutic agents in kidney. In this paper, disulfide-bridged G3-C12-CAP conjugate was prepared in solid phase, and the CAP was specifically delivered to the kidney after conjugation. Thus, the renal ACE inhibition of CAP was significantly increased with the use of cleavable disulfide linker that immediately released the free CAP via disulfide reduction in the kidney after i.v. administration. Moreover, the fluorescence imaging of G3-C12-FITC revealed that the renal uptake of this peptide carrier was due largely to its reabsorption by proximal tubule cells.

For a carrier−drug conjugate, drug release is very important. It is reported that the thiol group of the CAP is essential for the capacity of ACE inhibition,[35] and therefore, the G3-C12-CAP conjugate is an inactive prodrug due to the formation of disulfide bond. Yet, this disulfide bond may be cleaved by the reduced glutathione, which is abundant in the kidney. Thus, we studied the approach using disulfide bond as linking group for the renal drug delivery. SPDP, one of the heterobifunctional cross-linking reagents, has a NHS (activated ester) group and a 2-pyridyldithio group which reacts with an amine group (NH_2) and sulfhydryl group (SH), respectively.

In recent years, an amine-reactive derivative of fluorescein dye called FITC has been extensively used to label peptides and proteins. However, in solid-phase peptide synthesis, N-termini of the FITC-labeled peptides undergo a cyclization leading to the formation of a fluorescein with subsequent removal of the last amino acid in acidic conditions required for linker cleavage; thus, its application is restricted. However, this side reaction can be avoided by the introduction of a non-α-amino acid spacer such as Ahx between the thiourea bond and the peptide or by using basic conditions for final deprotection of the FITC peptide from the resin.[36] In our study, therefore, G3-C12 peptide was labeled by FITC using Ahx as a spacer, and G3-C12-FITC conjugate was successfully synthesized with high purity.

In this paper, we focused on developing a carrier−drug system that could generate higher intrarenal drug concentration. In theory, this can be tackled with tubular cell-targeted drug delivery. This targeting strategy requires a carrier system that can reach the target cells and subsequently internalized by this cell type. It is well-known that peptides with molecular weight of less than 25 kDa can be filtered in the glomerulus, and reabsorbed in the proximal tubules facilitated by various receptors and transporters on the tubular cell surface, and then transported to and metabolized in the lysosomal compartment.[37,38]

In the present study, the possible uptake mechanism of G3-C12 peptide was studied using fluorescence imaging, and lysine was utilized as the blocking agent to inhibit proximal tubular reabsorption. It is reported that lysine treatment could reduce renal accumulation of radiolabeled antibody fragments and peptides.[39−45] Similarly, the renal uptake of G3-C12-FITC was

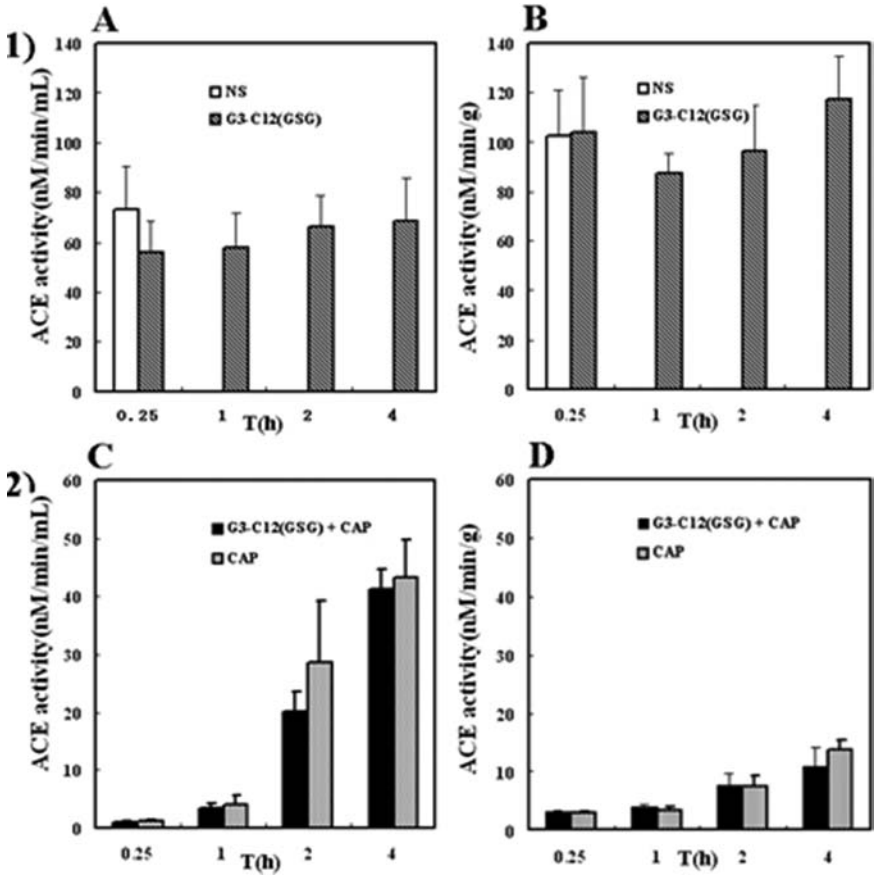

Figure 5. (1) ACE activity in control experiments after i.v. injection of NS or 46 μM·kg^{-1} G3-C12(GSG). Panel A, plasma ACE activity; panel B, renal ACE activity. (2) ACE activity after i.v. injection of CAP (46 μM·kg^{-1}) only or equimolar dose of G3-C12(GSG) plus CAP. Panel C, plasma ACE activity; panel D, renal ACE activity. The results are expressed as the mean ± SD (n = 5). ACE activities are presented as nanomolars of hippurate per minute per milliliter of plasma or nanomolars of hippurate per minute per gram of kidney.

extremely inhibited by lysine coinjection in our studies. Since co-infusion injection of lysine showed no influence on the renal uptake of free FITC, we conclude that the renal retention of G3-C12-FITC was due to the reabsorption of G3-C12 peptide in the proximal renal tubules rather than FITC. In general, renal uptake of peptide depends on size, structure, net charge,[46] and the number of positively charged amino acids which can bind to the negatively charged surface of tubule cell via electrostatic interaction.[46,47] It is plausible that the higher kidney distribution of G3-C12 peptide may correlated with the positively charged amino acids (3 out of 16 total amino acids), the chemical nature of the charged species, and the charge interactions within the kidneys. In addition, peptide and protein were reabsorbed in the proximal tubule mostly via endocytosis. Renal proximal tubule cells which are known as the most active cells in kidney may play a role in this process. A possible receptor responsible for reabsorption is megalin, a negatively charged and multiligand (predominantly proteins and peptides) scavenger receptor, intensively expressed in the renal proximal tubules.[48] A complete disclosure of the uptake mechanism of G3-C12 peptide in kidney needs further study.

In the biodistribution study, free CAP and total CAP (CAP-SH plus CAP-disulfides) in the plasma and tissues were determined. The amount of free CAP and total CAP accumulated in the kidney were significantly increased by administering CAP as G3-C12-CAP conjugate, suggesting that more CAP was successfully delivered to the kidney (Figure 4). Interestingly, the amount of CAP-disulfides in the plasma was significantly increased but could hardly be detected in the kidney after administration. In addition, the amounts of free CAP and total CAP in the kidney showed no difference even at 0.05 h postinjection of the conjugate. These phenomena suggested that free CAP was rapidly released from G3-C12-CAP in the kidney, probably due to the presence of reduced glutathione in the proximal tubular cells in a large amount.[49] Because kidney is the primary organ for the uptake of circulating glutathione, glutathione in plasma can be transported across the basal-lateral membrane into the renal proximal tubular cells[50,51] and exists in the cytosol and mitochondria.[52] Therefore, it was postulated that the conjugate was transported into the renal proximal tubular cells. Further experiments are warranted to support this hypothesis. Nevertheless, free CAP was also detected in the plasma after injection of G3-C12-CAP. It was assumed that the thiol−disulfide exchange between G3-C12-CAP and endogenous thiols caused the release of CAP from the conjugate in the circulation.

Although the *in vivo* studies in mice showed only little accumulation of CAP in other tissues, the CAP concentration of the conjugate group in liver and heart was relatively higher compared to that the CAP group. This is perhaps due to several reasons. First, CAP and total CAP were quickly excreted to urine (29.0% and 62.6% of the dose for 24 h, respectively) after the administration of free CAP.[53] Second, the conjugate was reabsorbed in the kidney, which may act intracellularly and partly released back into the circulation after degradation in the lysosomes. Finally, the mixed disulfides in the plasma of the

dx.doi.org/10.1021/bc300020f | *Bioconjugate Chem.* 2012, 23, 1200−1210

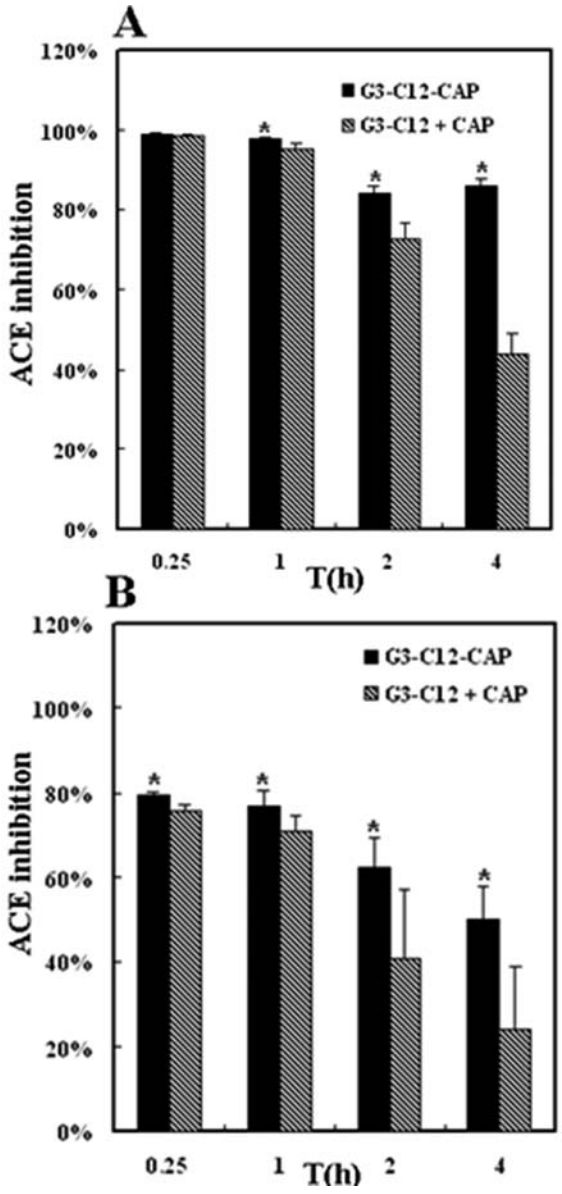

Figure 6. ACE inhibition after intravenous bolus administration. Solid bars, G3-C12-CAP conjugate (46 μM·kg^{-1} CAP); striped bars, G3-C12(GSG) plus CAP (46 μM·kg^{-1} G3-C12(GSG) plus equimolar dose of CAP). Panel A, plasma ACE inhibition; panel B, renal plasma ACE inhibition. The results are expressed as the mean ± SD (n = 5). *, significant difference between G3-C12-CAP conjugate and G3-C12(GSG) plus CAP (*, P < 0.05).

conjugate were significantly increased compared to the unconjugated CAP. These reversible inactive disulfides contribute to the longer action than free CAP, as the conjugate can serve as a reservoir for CAP. This may also be the reason for the longer-lasting plasma ACE inhibition (Figure 6A); its contribution to the beneficial effect of the ACE inhibitors remains an object of study.

Owing to the higher intrarenal drug concentration, the ACE inhibition in the kidney was increased significantly by G3-C12-CAP conjugate compared to free CAP. The ACE inhibition was beneficial to the treatment of renal disease, as the increased ACE activity inhibition would result in an increasing antiproteinuric effect in the kidney[54] and antiproteinuria could decrease the risk of progression to end-stage renal disease presumably by interfering with glomerular injury.[55−57] Future studies regarding the antiproteinuric effects of the conjugate and potential renoprotective effects after long-term treatment will be evaluated.

In a word, the coupling of CAP to G3-C12 peptide resulted in increased CAP concentrations and ACE inhibition in the kidney. These results are in accordance with those reported by Kok and colleagues,[33] who used lysozyme as the carrier. In their work, lysozyme-CAP exhibited enhanced kidney accumulation efficiency by 6-fold compared to free CAP. This enhancement was more dramatic than that of G3-C12-CAP (2.7-fold) reported in our study. However, lysozyme−CAP was synthesized by coupling lysine residues with CAP. Because there are several lysine residues in lysozyme providing more than one reaction sites, the resulting conjugate is a mixture. Hence, the reproducibility of such a conjugate is hard to control, which limits its further clinical application. In contrast, CAP is site-selectively attached to the amino terminus of G3-C12 peptide by solid-phase synthesis in the present study, leading to a conjugate with high purity. The novel chemical entity with clarified structure is more promising for clinical use.

■ CONCLUSIONS

Our achievement represents a peptide carrier toward targeting delivery of renal drugs. We examined the utility of G3-C12 peptide used as a renal drug targeting carrier by covalently coupling the drug to the peptide carrier by solid-phase peptide synthesis. This G3-C12-CAP conjugate displayed targeting competence toward the kidney, containing the increased intrarenal drug concentration in the kidney and renal ACE inhibition produced by the conjugation of the drug to the peptide carrier. The results led us to the conclusion that G3-C12 peptide is therefore a suitable candidate as a carrier for renal drug targeted delivery.

■ AUTHOR INFORMATION

Corresponding Author

*Tel.: +86-28-85501566. Fax: +86-28-85501615. E-mail address: zrzzl@vip.sina.com.

Notes

The authors declare no competing financial interest.

■ ACKNOWLEDGMENTS

The authors thank the financial support from the National Natural Science Foundation of China (No. 30873167 and No.81130060).

■ ABBREVIATIONS

CKD, Chronic kidney disease; ACE, Angiotensin-converting enzyme; CAP, Captopril; GSG, Gly-Ser-Gly; FITC, Fluorescein isothiocyannate; SPDP, *N*-succinimidyl 3-(2-pyridyldithio) propionate; HPLC, High-pressure liquid chromatography; TFA, Trifluoroacetic acid; Ahx, 6-Aminohexanoic acid; DMF, *N*,*N*-Dimethylformamide; NS, Normal saline

■ REFERENCES

(1) Levey, A. S., Eckardt, K. U., Tsukamoto, Y., Levin, A., Coresh, J., Rossert, J., De Zeeuw, D., Hostetter, T. H., Lameire, N., and Eknoyan, G. (2005)) Definition and classification of chronic kidney disease: a position statement from Kidney Disease: Improving Global Outcomes (KDIGO). *Kidney Int. 67*, 2089−2100.

(2) Stenvinkel, P. (2010) Chronic kidney disease: a public health priority and harbinger of premature cardiovascular disease. *J. Intern. Med. 268*, 456−467.
(3) Chen, J., Wildman, R. P., Gu, D., Kusek, J. W., Spruill, M., Reynolds, K., Liu, D., Hamm, L. L., Whelton, P. K., and He, J. (2005) Prevalence of decreased kidney function in Chinese adults aged 35 to 74 years. *Kidney Int. 68*, 2837−2845.
(4) Vassalotti, J. A., Stevens, L. A., and Levey, A. S. (2007) Testing for chronic kidney disease: a position statement from the National Kidney Foundation. *Am. J. Kidney Dis. 50*, 169−180.
(5) Zhang, Q. L., and Rothenbacher, D. (2008) Prevalence of chronic kidney disease in population-based studies: systematic review. *BMC Public Health. 8*, 117.
(6) Remuzzi, G., Ruggenenti, P., and Perico, N. (2002) Chronic renal diseases: renoprotective benefits of renin-angiotensin system inhibition. *Ann. Intern. Med. 136*, 604−615.
(7) Remuzzi, G., Benigni, A., and Remuzzi, A. (2006) Mechanisms of progression and regression of renal lesions of chronic nephropathies and diabetes. *J. Clin. Invest. 116*, 288−296.
(8) Locatelli, F., Vecchio, L. D., and Pozzoni, P. (2002) The importance of early detection of chronic kidney disease. *Nephrol. Dial. Transplant. 17* (Suppl 11), S2−S7.
(9) Ruggenenti, P., Schieppati, A., and Remuzzi, G. (2001) Progression, remission, regression of chronic renal diseases. *Lancet. 357*, 1601−1608.
(10) Perico, N., Codreanu, I., Schieppati, A., and Remuzzi, G. (2005) Prevention of progression and remission/regression strategies for chronic renal diseases: can we do better now than five years ago? *Kidney Int. 68* (Suppl 98), S21−S24.
(11) Mitch, W. E. (2000) Dietary therapy in uremia: the impact on nutrition and progressive renal disease. *Kidney Int. 57* (Suppl 75), S38−S43.
(12) Taal, M. W., and Brenner, B. M. (2000) Renoprotective benefits of RAS inhibition: from ACEI to angiotensin II antagonists. *Kidney Int. 57*, 1803−1817.
(13) Viberti, G., Mogensen, C. E., Groop, L. C., Pauls, J. F., Boner, G., van Dyk, D. J., Lucas, A., Romero, R., Salinas, I., Sanmarti, A., Blomqvist, A. C., Ekstrand, A., Kirsi, V. L., Koivisto, V. A., Groop, L. C., Groop, P. H., Escobar, F., Jimenez, F. E., Campos-Pastor, M. M., Muñoz, M., Gomez, M., Mangili, R., Pozza, G., Spotti, D., Wurgler Hansen, K., Sandahl Christiansen, J., Klein, F., Mogensen, C. E., van Doorn, L. G., Spooren, P. F. M. J., Cruickshank, J. K., Jervell, J., Paus, P. N., Collins, A., Viberti, G., Williams, G., and Nelstrop, G. A. (1994) Effect of captopril on progression to clinical proteinuria in patients with insulin-dependent diabetes mellitus and microalbuminuria. *J. Am. Med. Assoc. 271*, 275−279.
(14) Remuzzi, G., Perico, N., Macia, M., and Ruggenenti, P. (2005) The role of renin-angiotensin-aldosterone system in the progression of chronic kidney disease. *Kidney Int. 68* (Suppl 99), S57−S65.
(15) Jafar, T. H., Schmid, C. H., Landa, M., Giatras, I., Toto, R., Remuzzi, G., Maschio, G., Brenner, B. M., Kamper, A., Zucchelli, P., Becker, G., Himmelmann, A., Bannister, K., Landais, P., Shahinfar, S., de Jong, P. E., de Zeeuw, D., Lau, J., and Levey, A. S. (2001) Angiotensin-converting enzyme inhibitors and progression of non-diabetic renal disease. A meta-analysis of patient-level data. *Ann. Intern. Med. 135*, 73−87.
(16) Remuzzi, G., Ruggenenti, P., and Perico, N. (2002) Chronic renal diseases: renoprotective benefits of rennin-angiotensin system inhibition. *Ann. Intern. Med. 136*, 604−615.
(17) Anderson, S., Rennke, H. G., and Brenner, B. M. (1986) Therapeutic advantage of converting enzyme inhibitors in arresting progressive renal disease associated with systemic hypertension in the rat. *J. Clin. Invest. 77*, 1993−2000.
(18) Björck, S., Nyberg, G., Mulec, H., Granerus, G., Herlitz, H., and Aurell, M. (1986) Beneficial effects of angiotensin converting enzyme inhibition on renal function in patients with diabetic nephropathy. *Br. Med. J. 293*, 471−474.
(19) Keane, W. F., Anderson, S., Aurell, M., de Zeeuw, D., Narins, R. G., and Povar, G. (1989) Angiotensin converting enzyme inhibitors and progressive renal insufficiency. Current experience and future directions. *Ann. Intern. Med. 111*, 503−516.
(20) Ruilope, L. M., Miranda, B., Morales, J. M., Rodicio, J. L., Romero, J. C., and Raij, L. (1989) Converting enzyme inhibition in chronic renal failure. *Am. J. Kidney Dis. 13*, 120−126.
(21) Campbell, R. C., Ruggenenti, P., and Remuzzi, G. (2002) Halting the progression of chronic nephropathy. *J. Am. Soc. Nephrol. 13* (Suppl 3), S190−S195.
(22) Haas, M., Moolenaar, F., Meijer, D. K., and de Zeeuw, D. (2002) Specific drug delivery to the kidney. *Cardiovasc. Drugs Ther. 16*, 489−496.
(23) Dolman, M. E., Harmsen, S., Storm, G., Hennink, W. E., and Kok, R. J. (2010) Drug targeting to the kidney: advances in the active targeting of therapeutics to proximal tubular cells. *Adv. Drug Delivery Rev. 62*, 1344−1357.
(24) Zhang, Z. R., Zheng, Q., Han, J., Gao, G. P., Liu, J., Gong, T., Gu, Z. W., Huang, Y., Sun, X., and He, Q. (2009) The targeting of 14-succinate triptolide-lysozyme conjugate to proximal renal tubular epithelial cells. *Biomaterials. 30*, 1372−1381.
(25) Yuan, Z. X., Sun, X., Gong, T., Ding, H., Fu, Y., and Zhang, Z. R. (2007) Randomly 50% N-acetylated low molecular weight chitosan as a novel renal targeting carrier. *J. Drug Targeting 15*, 269−278.
(26) Yuan, Z. X., Zhang, Z. R., Zhu, D., Sun, X., Gong, T., Liu, J., and Luan, C. T. (2008) Specific renal uptake of randomly 50% N-acetylated low molecular weight chitosan. *Mol. Pharmaceutics 6*, 305−314.
(27) Haverdings, R. F., Haas, M., Greupink, A. R., de Vries, P. A., Moolenaar, F., de Zeeuw, D., and Meijer, D. K. (2001) Potentials and limitations of the low-molecular-weight protein lysozyme as a carrier for renal drug targeting. *Ren. Fail. 23*, 397−409.
(28) Schechter, B., Arnon, R., Colas, C., Burakova, T., and Wilchek, M. (1995) Renal accumulation of streptavidin: potential use for targeted therapy to the kidney. *Kidney Int. 47*, 1327−1335.
(29) Akizawa, H., Uehara, T., and Arano, Y. (2008) Renal uptake and metabolism of radiopharmaceuticals derived from peptide and proteins. *Adv. Drug Delivery Rev. 60*, 1319−1328.
(30) Zou, J., Glinsky, V. V., Landon, L. A., Matthews, L., and Deutscher, S. L. (2005) Peptides specific to the galectin-3 carbohydrate recognition domain inhibit metastasis-associated cancer cell adhesion. *Carcinogenesis 26*, 309−318.
(31) Kumar, S. R., and Deutscher, S. L. (2008) ^{111}In-Labeled galectin-3−targeting peptide as a SPECT agent for imaging breast tumors. *J. Nucl. Med. 49*, 796−803.
(32) Deutscher, S. L., Figueroa, S. D., and Kumar, S. R. (2009) Tumor targeting and SPECT imaging properties of an ^{111}In-labeled galectin-3 binding peptide in prostate carcinoma. *Nucl. Med. Biol. 36*, 137−146.
(33) Kok, R. J., Haverdings, R. F., Grijpstra, F., Koiter, J., Moolenaar, F., de Zeeuw, D., and Meijer, D. K. (2002) Targeting of captopril to the kidney reduces renal angiotensin-converting enzyme activity without affecting systemic blood pressure. *J. Pharmacol. Exp.Ther. 301*, 1139−1143.
(34) Koiter, J., Navis, G., de Jong, P. E., van Gilst, W. H., and de Zeeuw, D. (1998) Sample dilution: a methodological pitfall in the measurement of tissue but not serum ace-activity. *J. Pharmacol. Toxicol. Methods. 39*, 45−49.
(35) Ondetti, M. A., and Cushman, D. W. (1981) Inhibition of the renin-angiotensin system. A new approach to the therapy of the hypertension. *J. Med. Chem. 24*, 355−361.
(36) Jullian, M., Hernandez, A., Maurras, A., Puget, K., Amblard, M., Martinez, J., and Subra, G. (2009) N-terminus FITC labeling of peptides on solid support: the truth behind the spacer. *Tetrahedron Lett. 50*, 260−263.
(37) Christensen, E. I., and Nielsen, S. (1991) Structural and functional features of protein handling in the kidney proximal tubule. *Semin. Nephrol. 11*, 414−439.
(38) Nielsen, S. (1993) Endocytosis in proximal tubule cells involves a two-phase membrane-recycling pathway. *Am. J. Physiol. 264*, C823−C835.

(39) Behr, T. M., Sharkey, R. M., Juweid, M. E., Blumenthal, R. D., Dunn, R. M., Griffiths, G. L., Bair, H. J., Wolf, F. G., Becker, W. S., and Goldenberg, D. M. (1995) Reduction of the renal uptake of radiolabeled monoclonal antibody fragments by cationic amino acids and their derivatives. *Cancer Res. 55*, 3825−3834.
(40) DePalatis, L. R., Frazier, K. A., Cheng, R. C., and Kotite, N. J. (1995) Lysine reduces renal accumulation of radioactivity associated with injection of the [^{177}Lu]alpha-[2-(4-aminophenyl) ethyl]-1,4,7,10-tetraaza-cyclodecane-1,4,7,10-tetraacetic acid-CC49 Fab radioimmunoconjugate. *Cancer Res. 55*, 5288−5295.
(41) Pimm, M. V., and Gribben, S. J. (1994) Prevention of renal tubule re-absorption of radiometal(indium-111) labelled Fab fragment of a monoclonal antibody in mice by systemic administration of lysine. *Eur. J. Nucl. Med. 21*, 663−665.
(42) Morgenson, C. E., and Sölling, K. (1997) Studies on renal tubular protein reabsorption: partial and near complete inhibition by certain amino acids. *Scand. J. Clin. Lab. Invest. 37*, 477−486.
(43) Hammond, P. J., Wade, A. F., Gwilliam, M. E., Peters, A. M., Myers, M. J., Gilbey, S. G., Bloom, S. R., and Calam, J. (1993) Amino acid infusion blocks renal tubular uptake of an indium-labelled somatostatin analogue. *Br. J. Cancer. 67*, 1437−1439.
(44) Kobayashi, H., Yoo, T. M., Kim, I. S., Kim, M. K., Le, N., Webber, K. O., Pastan, I., Paik, C. H., Eckelman, W. C., and Carrasquillo, J. A. (1996) L-lysine effectively blocks renal uptake of ^{125}I- or ^{99m}Tc-labeled anti-Tac difulide-stabilized Fv fragment. *Cancer Res. 56*, 3788−3795.
(45) Behr, T. M., Becker, W. S., Bair, H. J., Klein, M. W., Stühler, C. M., Cidlinsky, K. P., Wittekind, C. W., Scheele, J. R., and Wolf, F. G. (1995) Comparison of complete versus fragmented technetium-99m-labeled anti-CEA monoclonal antibodies for immunoscintigraphy in colorectal cancer. *J. Nucl. Med. 36*, 430−441.
(46) Akizawa, H., Arano, Y., Mifune, M., Iwado, A., Saito, Y., Mukai, T., Uehara, T., Ono, M., Fujioka, Y., Ogawa, K., Kiso, Y., and Saji, H. (2001) Effect of molecular charges on renal uptake of ^{111}In-DTPA-conjugated peptides. *Nucl. Med. Biol. 28*, 761−768.
(47) Chen, J., Cheng, Z., Hoffman, T. J., Jurisson, S. S., and Quinn, T. P. (2000) Melanoma-targeting properties of ^{99m}technetium-labeled cyclic α-melanocyte-stimulating hormone peptide analogues. *Cancer Res. 60*, 5649−5658.
(48) Christensen, E. I., Verroust, P. J., and Nielsen, R. (2009) Receptor-mediated endocytosis in renal proximal tubule. *Pflugers Arch. 458*, 1039−1048.
(49) Commandeur, J. N., and Vermeulen, N. P. (1990) Molecular and biochemical mechanisms of chemically induced nephrotoxicity:a review. *Chem. Res. Toxicol. 3*, 171−194.
(50) Lash, L. H., and Jones, D. P. (1984) Renal glutathione transport. Characteristics of the sodium-dependent system in the basal-lateral membrane. *J. Biol. Chem. 259*, 14508−14514.
(51) Meister, A., and Anderson, M. E. (1983) Glutathione. *Annu. Rev. Biochem. 52*, 711−760.
(52) Schnellmann, R. G., Gilchrist, S. M., and Mandel, L. J. (1988) Intracellular distribution and depletion of glutathione in rabbit renal proximal tubules. *Kidney Int. 34*, 229−233.
(53) Hayashi, K., Miyamoto, M., and Sekine, Y. (1985) Determination of captopril and its mixed disulphides in plasma and urine by high-performance liquid chromatography. *J. Chromatogr. 338*, 161−169.
(54) Windt, W. A., Prakash, J., Kok, R. J., Moolenaar, F., Kluppel, C. A., de Zeeuw, D., van Dokkum, R. P., and Henning, R. H. (2004) Renal targeting of captopril using captopril-lysozyme conjugate enhances its antiproteinuric effect in adriamycin-induced nephrosis. *J. Renin Angiotensin Aldosterone Syst. 5*, 197−202.
(55) Remuzzi, G., and Bertani, T. (1998) Pathophysiology of progressive nephropathies. *N. Engl. J. Med. 339*, 1448−1456.
(56) Ritz, E., Schömig, M., and Wagner, J. (2000) Counteracting progression of renal disease: a look into the future. *Kidney Int. 57* (Suppl 75), 71−76.
(57) Hausberg, M., Barenbrock, M., Hohage, H., MÜller, S., Heidenreich, S., and Rahn, K. H. (1999) ACE inhibitor versus beta-blocker for the treatment of hypertension in renal allograft recipients. *Hypertension 33*, 862−868.

Bioconjugate Chemistry

Article

pubs.acs.org/bc

Modular Synthesis of Folate Conjugated Ternary Copolymers: Polyethylenimine-*graft*-Polycaprolactone-*block*-Poly(ethylene glycol)-Folate for Targeted Gene Delivery

Li Liu,[†,‡,§] Mengyao Zheng,[†,‡] Thomas Renette,[‡] and Thomas Kissel*[,‡]

[‡]Department of Pharmaceutics and Biopharmacy, Philipps-University Marburg, Ketzerbach 63, D-35032 Marburg, Germany

[§]School of Pharmacy, Shanghai Jiao Tong University, 200240 Shanghai, China

Supporting Information

ABSTRACT: Folate receptor (FR) is overexpressed in a variety of human cancers. Gene delivery vectors conjugated with folate as a ligand could possibly deliver gene materials into target tumor cells via FR-mediated endocytosis. This study addresses novel folate-conjugated ternary copolymers based on polyethylenimine-graft-polycaprolactone-block-poly(ethylene glycol) (PEI-*g*-PCL-*b*-PEG-Fol) as targeted gene delivery system using a modular synthesis approach including "click" conjugation of folate moieties with heterobifunctional PEG-*b*-PCL at PEG terminus and subsequently the introduction of PEI by a Michael addition between folate-PEG-*b*-PCL and PEI via active PCL terminus. This well-controlled synthetic procedure avoids tedious separation of byproduct. The structure of PEI-*g*-PCL-*b*-PEG-Fol was confirmed by ^{1}H NMR and UV spectra. DNA condensation of PEI-*g*-PCL-*b*-PEG-Fol was tested using a SYBR Gold quenching assay and agarose gel electrophoresis upon heparin competition assay. Although PEI-*g*-PCL-*b*-PEG-Fol could condense DNA completely at N/P ratio >2, polyplexes of N/P ratio 10 with sizes of about 120 nm and positive zeta potentials were selected for further biological evaluations due to polyplex stability. An enhancement of cellular uptake of PEI-*g*-PCL-*b*-PEG-Fol/pDNA polyplexes was observed in FR overexpressing KB cells in comparison to unmodified PEI-*g*-PCL-*b*-PEG, through flow cytometry analysis and confocal laser scanning imaging. Importantly, this enhanced cellular uptake could be inhibited by free folic acid and did not occur in FR-negative A549 cells, demonstrating specific cell uptake by FR-mediated endocytosis. Furthermore, the transfection efficiency of PEI-*g*-PCL-*b*-PEG-Fol/pDNA polyplexes was increased approximately 14-fold in comparison to folate-negative polyplexes. Therefore, the PEI-*g*-PCL-*b*-PEG-Fol merits further investigation under in vivo conditions for targeting FR overexpressing tumors.

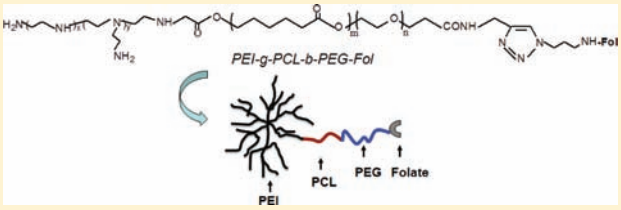

INTRODUCTION

Gene therapy has received increasing attention over the past two decades as a promising method for treating various inherited and acquired human diseases.[1−3] An efficient and safe delivery system that delivers the therapeutic genes into target cells is regarded as a prerequisite for successful gene therapy. Recently, a large number of studies focused on the development of polymer-based nonviral gene delivery vectors due to their non-immunogenicity, low cost, physiochemical versatility, and ease of manipulation.[4,5] Among them, polyethylenimine (PEI)-based delivery systems have emerged as one of the most successful and efficient candidates for gene delivery both in vitro and in vivo.[6] PEI is a cationic polymer with a high density of amines, which condense nucleic acids via electrostatic interaction into nanoscaled polyplexes. Importantly, the protonable amine group endowed PEI-containing polyplexes with efficient endosomal escape property through the proton-sponge mechanism, which was believed to be the main reason for the relatively high gene-transfer activity of PEI.[6,7] Nevertheless, the PEI-based gene delivery systems have suffered from relatively high toxicity, especially at high molecular weights, affecting their potential applications under in vivo conditions.

To decrease cytotoxicity and enhance gene transfection efficiency, many efforts have relied on the modification of PEI with either hydrophilic segments such as poly(ethylene glycol) (PEG)[8,9] or hydrophobic segments such as poly(L-lactide-*co*-glycolide),[10] or other biocompatible compositions such as cyclodextrin.[11] Moreover, PEI derivates have also been decorated with a variety of targeting ligands[12] to generate gene delivery systems with targeting functionality for specific tissues/cells. For example, the folate receptor (FR) is known to be overexpressed in many types of carcinoma cells.[13−15] By conjugation with folate, the PEI-containing polyplexes were expected to target the folate receptor on cell surface and transfect specific cells by receptor-mediated endocytosis.[16−23]

In previous studies by our group, a series of ternary copolymers based on PEI-*g*-PCL-*b*-PEG were synthesized and investigated as potential gene delivery vectors.[24−27] The PEI-*g*-

Received: January 18, 2012
Revised: March 27, 2012
Published: May 2, 2012

   dx.doi.org/10.1021/bc300025d | *Bioconjugate Chem.* 2012, 23, 1211−1220

PCL-*b*-PEG copolymers were shown to be biodegradable and amphiphilic in character, hypothetically generating micelle-like polyplexes with excellent colloidal stability. Structure−function relationships suggested that higher graft densities of PCL-PEG led to decreased cytotoxicity and copolymers with short PCL segment displayed higher transfection efficiency in vitro compared with PEI 25 kDa.[25,27]

In this study, folate conjugated PEI-*g*-PCL-*b*-PEG was synthesized and examined for targeted gene delivery. It should be noted that the folate moiety was designed to be conjugated at the distal PEG end, instead of direct linkage to PEI.[22] This strategy provides more flexibility for the folate ligands via PEG spacers possibly improving their target binding efficacy. Therefore, to achieve the well-structured PEI-*g*-PCL-*b*-PEG-Folate copolymer, a modular synthesis procedure was designed, which involved the conjugation of folate moiety with heterobifunctional PEG-*b*-PCL by click chemistry followed by a Michael addition between folate-PEG-*b*-PCL and PEI. The mild reaction conditions of click chemistry and Michael addition were beneficial to maintain the biological activity of folate and to avoid tedious cleaning procedures. The resulting copolymers were investigated regarding biophysical properties, DNA condensation, and cytotoxicity. Furthermore, cell-uptake and transfection efficiency of PEI-*g*-PCL-*b*-PEG-Fol/pDNA complexes were evaluated in vitro in FR-positive KB cells to determine their potential as targeted gene delivery vehicles.

EXPERIMENTAL SECTION

Materials. Heterobifunctional poly(ethylene glycol) (HO-PEG-COOH, 3 kDa) was purchased from Rapp Polymere GmbH (Germany). ε-Caprolactone from Fluka was distilled before use under vacuum over CaH_2. Branched polyethylenimine (*hy*-PEI, 25 kDa) was obtained from BASF. Folic acid, *N*-hydroxysuccinimide, dicyclohexylcarbodiimide, and solvents were purchased from Acros. Propargylamine and acryloyl chloride were from Sigma-Aldrich. 1-Azido-3-aminopropane was synthesized from 3-bromopropylamine hydrobromide and sodium azide (details in Supplement information). All other reagents for synthesis were obtained from Sigma-Aldrich and used as received without further purification. Endotoxin-free luciferase-encoding plasmid DNA (pCMV-luc) was provided by Plasmid Factory (Bielefeld, Germany). SYBR Gold and YOYO-1 were obtained from Invitrogen.

Synthesis of Azido-Functionalized Folate. Azido-functionalized folate was prepared by a method modified from the literature.[28] Folic acid (0.5 g, 1.135 mmol) was dissolved in DMSO (20 mL) containing triethylamine (0.25 mL). After addition of *N*-hydroxysuccinimide (NHS) (0.26 g, 2.2 equiv), and dicyclohexylcarbodiimide (DCC) (0.25 g, 1.1 equiv), the mixture was stirred at room temperature in the dark for 24 h. Then, 1-azido-3-aminopropane (0.24 g, 2 equiv) was added into the mixture under stirring. The reaction was continued for another 24 h. After the precipitated side-product dicyclohexylurea (DCU) was removed by filtration, the product was precipitated in ethyl acetate and dried under vacuum. The crude product was purified by dissolving in 1 M NaOH and precipitation by addition of 1 M HCl. The precipitates were collected by centrifugation, washed with EtOH/H_2O (1:1), and dried under vacuum to give an orange−yellow product in 86% yield.

FT-IR (ν, cm^{-1}): 2800−3200, 2095 ($-N_3$), 1682, 1602, 1506, 1297, 1236, 1174, 1126. ^{1}H NMR (d_6-DMSO, 400M): δ (ppm) = 11.37 (s, 1H, −CONHCHCO**OH**), 8.62 (s, 1H, PtC7H), 7.93−7.95 (d, 1H, PtC6-CH2**NH**-Ph), 7.79−7.80 (d, 1H, −CO**NH**CHCOOH), 7.63−7.60 (d, 2H, Ph−C2H and Ph−C6H), 6.87 (br s, 2H, NH_2), 6.62−6.59 (d, 2H, Ph−C3H and Ph−C5H), 4.46−4.44 (d, 2H, PtC6-**CH_2**NH-Ph), 4.30−4.26 (m, 1H, −CONH**CH**COOH), 3.44−3.39 (m, 2H, −**CH_2**N_3), 3.29 (br s, OH), 3.10−3.02 (m, 2H, −CONH**CH_2**$CH_2CH_2N_3$), 2.30−2.15 (m, 2H, −CH_2**CH_2**CONH), 2.05−1.85 (m, 2H, -**CH_2**CH_2CONH-), 1.60−1.56 (m, 2H, −CONHCH$_2$**CH_2**CH_2N_3). Pt = pteridine.

Synthesis of PCL-*b*-PEG with Heterobifunctional Terminal Group (acrylate-PCL-*b*-PEG-alkyne). PCL-*b*-PEG was first synthesized by ring-opening polymerization of ε-caprolactone initiated from the hydroxyl end group of HO-PEG-COOH. Defined amounts of HO-PEG-COOH and caprolactone monomers were sealed in dry argon and stirred at 120 °C for 24 h with $Sn(Oct)_2$ (about 0.1% molar ratio of caprolactone) as catalyst.[29] The product was dissolved in chloroform and precipitated with cold methanol/ether (1/1, v/v). The precipitate obtained as HO-PCL-*b*-PEG-COOH was dried under vacuum for 24 h for the following modification. (Yield: 88%).

HO-PCL-*b*-PEG-COOH (0.3 mmol) was dissolved in dry dichloromethane (DCM) with NHS (0.6 mmol) and DCC (1.2 mmol). The mixture was stirred at 0 °C for 1 h and then at room temperature for 24 h, during which time the mixture became turbid due to DCU. Propargylamine (0.6 mmol) and triethylamine were added into the above mixture, and stirred at room temperature for another 24 h. The mixture was filtered to remove the precipitated DCU, and then precipitated in cold ether. The precipitates were dried under vacuum for 24 h to obtain HO-PCL-*b*-PEG-alkyne (yield: 79%).

Next, the terminal hydroxyl group of HO-PCL-*b*-PEG-alkyne (0.1 mmol) was coupled with acryloyl chloride (0.2 mmol) in dry toluene containing triethylamine (0.2 mmol). The reaction mixture was stirred at 80 °C for 10 h, and then cooled to room temperature, filtered to remove triethylamine hydrochloride, and precipitated in cold *n*-hexane. The precipitates were collected and dried under vacuum overnight to produce heterobifunctional acrylate-PCL-*b*-PEG-alkyne (yield: 78%).

^{1}H NMR ($CDCl_3$, 400M): δ (ppm) = 5.7−6.5 (m, −CH═CH_2), 4.25−4.20 (m, NHCO**CH_2**CH_2CO), 4.07−4.01 (t, CO**CH_2**$CH_2CH_2CH_2$O), 3.82−3.80 (m, weak), 3.67−3.60 (s, OCH_2CH_2O), 3.46−3.43 (m,weak), 2.32−2.28 (t, $COCH_2CH_2CH_2$**CH_2**O), 2.23−2.21 (m, -C≡CH), 1.68−1.60 (m, $COCH_2$**CH_2**CH_2**CH_2**CH_2O), 1.42−1.33 (m, $COCH_2CH_2$**CH_2**CH_2CH_2O).

"Click" Conjugation of Azido-Folate with PCL-*b*-PEG at PEG Terminal Alkyne. Azido-folate (0.12 mmol) and acrylate-PCL-*b*-PEG-alkyne (0.1 mmol) were dissolved in 15 mL aq. NH_4HCO_3 (10 mM). $CuSO_4$ (20 mol % to the azido group) and fresh sodium ascorbate solution (50 mol % to the azido group) were added, respectively. The mixture was stirred at room temperature for 24 h. Afterward, the mixture was filtered through a 0.45 μm filter. The clear solution was diluted with equal volume of saturated NaCl aqueous solution, and then extracted five times by DCM. The clear yellow DCM solution was concentrated by rotary evaporation and then precipitated in cold ether. The yellow product (acrylate-PCL-*b*-PEG-Fol) was dried under vacuum overnight (yield: 85%).

^{1}H NMR (d_6-DMSO, 400M): δ (ppm) = 8.6, 7.8, 6.9, 6.6 (weak multiplets, folate terminus), 7.9 (s, weak, 1H, triazoles), 6.5−5.9 (m, −CH═CH_2), 4.0−3.9 (t, CO**CH_2**$CH_2CH_2CH_2$O), 3.5−3.4 (s, OCH_2CH_2O), 2.3−

dx.doi.org/10.1021/bc300025d | *Bioconjugate Chem.* 2012, 23, 1211−1220

2.2 (t, $COCH_2CH_2CH_2CH_2\mathbf{CH_2}O$), 1.6−1.4 (m, $COCH_2\mathbf{CH_2}CH_2\mathbf{CH_2}CH_2O$), 1.3−1.2 (m, $COCH_2CH_2\mathbf{CH_2}CH_2CH_2O$).

Synthesis of PEI-*g*-PCL-*b*-PEG-Fol. *Hy*-PEI (10 μmol) and acrylate-PCL-*b*-PEG-Fol (10 μmol or 30 μmol) were dissolved in 3 mL of chloroform, respectively. The chloroform solution of folate-conjugated diblock copolymer was added dropwise into PEI solution at 40−45 °C and stirred for 24 h. Afterward, the product was collected by solvent replacement (via methanol and water), dialyzed against water (M_w cut off 10 000) at 4 °C for 24 h and lyophilized to generate PEI-*g*-PCL-*b*-PEG-Fol (yield: 85%). ^{1}H NMR (D_2O, 400M): δ (ppm) = 8.6, 8.0, 7.6, 6.8 (weak, folate terminus), 3.6 (s, strong, OCH_2CH_2O), 1.6−1.2 (weak and broad, $COCH_2\mathbf{CH_2}\mathbf{CH_2}\mathbf{CH_2}CH_2O$).

The corresponding copolymers with nonfolate conjugation were prepared from *hy*-PEI and acrylate-PCL-b-mPEG by a synthesis route reported previously.[25]

Polymer Characterization. FTIR was performed on a Nicolet FT-IR 510 P spectrometer (Thermo Fischer Scientific Inc., Waltham, MA, USA) in a range between 4000 and 400 cm^{-1}. NMR analysis was carried out using a JEOL ECX-400 spectrometer (Japan) in ppm relative to solvent signals.

Folate Content in Copolymers determined by UV−vis Spectroscopy. Folic acid and copolymers were dissolved in DMSO, respectively, and measured by a UV−vis spectrometer (Pharmacia Biotech Ultrospec 3000, GE Healthcare) from 200 to 600 nm. Folic acid showed two typical absorbance peaks at 280 and 360 nm, respectively. The absorbance intensity at 360 nm was determined as a function of folic acid concentration, which showed a linear relation to folate concentration during $(0.025-2.14) \times 10^{-7}$ mol/mL (Supporting Information). The concentration of folate in PEI-*g*-PCL-*b*-PEG-Fol was calculated from the copolymer/DMSO solution with predetermined polymer concentration, according to the calibration curve made from free folic acid.

Preparation of the Copolymer/DNA Complexes. PEI-*g*-PCL-*b*-PEG-Fol was dissolved in water to prepare a stock copolymer solution of 1 mg/mL (based on *hy*-PEI 25 kDa). All polymer stock solutions were filtered using disposable 0.22 μm filters and then diluted with 5% glucose solution. The DNA solution of 0.04 mg/mL was obtained by diluting 1 mg/mL stock solution with 5% glucose solution. To prepare polyplexes, 50 μL of DNA solution was taken and mixed with equal volume of copolymer solution at the appropriate concentration depending on the required N/P ratio by pipetting. Then, the complexes were incubated at 25 °C for 20 min, followed by the corresponding characterizations.

SYBR Gold Assay. The complexation between copolymer and DNA was determined by the SYBR Gold quenching assay as previously reported.[30] Briefly, 100 μL of polyplexes containing 2 μg DNA were prepared at different N/P ratios in 96-well plate. After 20 min of incubation at room temperature, 20 μL diluted 4× SYBR Gold solution was added and incubated for another 10 min in the dark. The fluorescence was directly detected with a fluorescence plate reader (BMG Labtech, Offenburg) at 495 nm excitation and 537 nm emission. Triplicate samples were investigated, and the results were transformed into relative fluorescent intensity values ($F_{sample}/F_{free\ DNA}$).

Heparin Competition Assay. The stability of polyplexes against heparin (a model molecule of competing polyanion) was assessed by agarose gel electrophoresis in TAE buffer (0.04 M Tris−acetate, 0.001 M EDTA, pH 7.4) containing 0.5 mg/mL ethidium bromide (EtBr). Heparin (150 000 IU/g, Serva, Pharm., USPXV2, Merck, Darmstadt, Germany) solution was added to reach a final heparin concentration of 0.5 mg/mL into the polyplex solution at different N/P-ratios. After 15 min of incubation with heparin, 25 μL of polyplex solution containing 1.5 μg DNA was loaded into the agarose gel wells, and the agarose gels were run in TAE buffer for 45 min at 80 V using an Electro-4 electrophoresis unit (Thermo Electron, Waltham, MA, USA). The gels were recorded after irradiation with UV-light using a gel documentation system (BioDocAnalyze, Biometra, Göttingen, Germany).

Size and Zeta-Potential Analysis. The size and zeta potential of the polyplexes were monitored by a dynamic light scattering (DLS) instrument (Zetasizer 3000HS, Malvern, Worcestershire, UK). Polyplexes were measured in a low volume cuvette (100 μL) first, and then zeta-potential measurements were performed on the samples prepared by diluting 100 μL of polyplexes solution with additional 600 μL of 5% glucose solution to a final volume of 700 μL in a transparent zeta cuvette. The samples were carried out in the standard clear capillary electrophoresis cell at 25 °C. Three measurements were performed on each sample.

Cell Culture. Human epithelial nasopharyngeal carcinoma (KB) cells were gifts from Prof. P. S. Low's group (Purdue University) and continuously cultured in folate-free RPMI-1640 medium supplemented with 10% fetal calf serum (FCS) at 37 °C in a humidified atmosphere containing 5% CO_2. FR negative human lung epithelial carcinoma (A549) cells were obtained from DSMZ (Braunschweig, Germany) and cultured in DMEM medium supplemented with 10% FCS at 37 °C in a humidified atmosphere containing 5% CO_2.

Cytotoxicity Assay. KB cells were seeded into 96-well plates at a density of 8×10^3 cells/well. After 24 h, cell culture medium was aspirated and replaced by 200 μL of serial dilutions of polymer stock solution in cell culture medium with FCS. The cells were then incubated for 24 h at 37 °C. Afterward, medium was replaced by medium without serum containing 0.5 mg/mL 3-(4,5-dimethylthiazol-2-yl)-2,5-diphenyl tetrazolium bromide (MTT). After 4 h incubation at 37 °C in the dark, medium was removed and then 200 μL of DMSO was added to dissolve the formazan crystals formed by proliferating cells. After 15 min incubation with DMSO, measurement was performed using an ELISA reader (Titertek Plus MS 212, ICN, Eschwege, Germany) at wavelengths of 570 and 690 nm. Relative viability was calculated using wells with untreated cells as 100% controls. Data are presented as mean values (±SD) of four experiments. The IC_{50} values were calculated with *Original 8* using Logistic fit.

Cellular Uptake by Flow Cytometry. KB cells and A549 cells were seeded at a density of 6×10^4 cells/well in 24 well plates 24 h prior to the experiment. Polymers including PEI 25 kDa, PEI-*g*-PCL-*b*-mPEG (PCE3), and PEI-*g*-PCL-*b*-PEG-Fol (PCE3-F) were labeled with FITC in parallel assay. Polyplexes were prepared at N/P = 10 using pCMV-Luc as described above. Cells were incubated with polyplexes containing 4 μg DNA per well for 4 h at 37 °C. In free folate competition studies, the normal RPMI-1640 medium (containing 1 mg/L folic acid) was replaced as incubation medium 1 h before polyplexes added. Afterward, cells were washed with PBS once and incubated with 0.4% trypan blue solution for 5 min to quench extracellular fluorescence. Cells were washed again, detached using 100 μL of trypsin, and treated with 900 μL of

Scheme 1. Synthesis Strategy of PEI-*g*-PCL-*b*-PEG-Fol

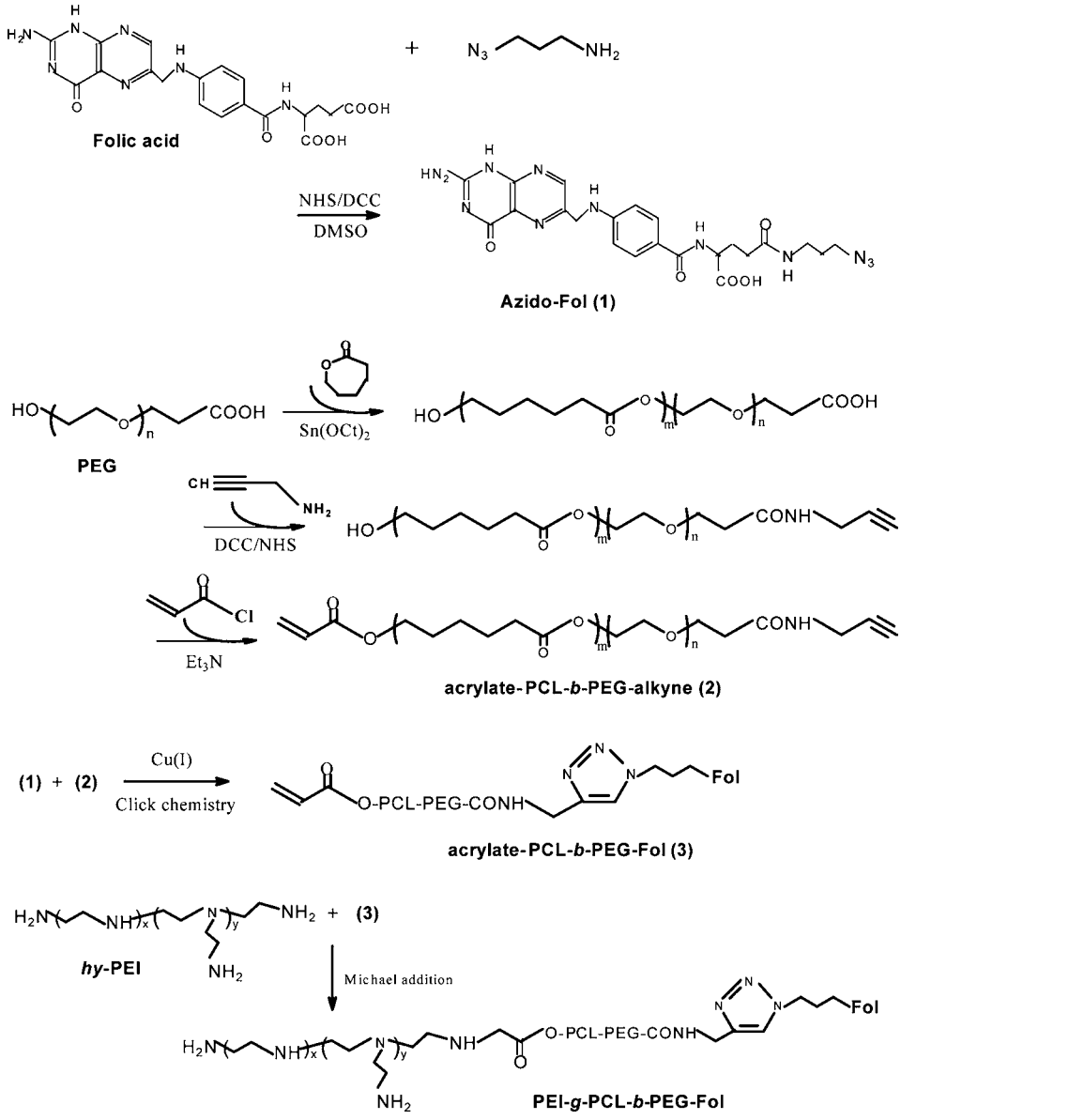

PBS solution containing 10% FCS. Cells were then collected by centrifugation and resuspended in 300 μL of Cellfix solution (BD Biosciences, San Jose, CA) for cell fixation. Cell suspensions were measured on a FACS CantoTM Π (BD Biosciences, San Jose, CA) with excitation at 488 nm and emission filter set to 530/30 bandpass. Ten thousand viable cells were evaluated in each experiment, and results are the mean of three independent measurements.

Confocal Laser Scanning Microscopy. KB cells were seeded at a density of 2×10^4 cells per well in 8 well chamber slides (Nunc, Wiesbaden, Germany) and allowed to grow for 24 h. Polyplexes were prepared at N/P = 10 as described above using YOYO-1 labeled pCMV-Luc. Cells were incubated with polyplexes containing 1 μg DNA per well in medium with FCS for 4 h at 37 °C. Subsequently, cells were washed with PBS, quenched with 0.4% trypan blue solution, washed again with PBS, fixed using 4% paraformaldehyde in PBS, DAPI stained, and washed again with PBS. Finally, cells were embedded using FluorSave Reagent (Calbiochem, San Diego, CA). A Zeiss Axiovert 100 M microscope coupled to a Zeiss LSM 510 scanning device (Zeiss, Oberkochen, Germany) was used for confocal microscopy. For excitation of YOYO-1 fluorescence, an argon laser with an excitation wavelength of 488 nm was used. Fluorescence emission was detected using a 505−530 nm bandpass filter. Transmission images were obtained in the same scan.

In Vitro Gene Transfection. KB cells were seeded in 48 well plates (1.5×10^4 cells/well) 24 h prior to the experiment. Polyplexes were prepared at N/P = 10 as described above using plasmid pCMV-luc. Medium was replaced by 200 μL of fresh cell culture medium with 10% FCS, then 50 μL of polyplexes (containing 1 μg pDNA) were added in each well. For folate competition assay, normal RPMI1640 medium (containing 1 mg/L folic acid) was replaced 1 h before polyplexes addition. After incubation for 4 h, the medium was exchanged and cells were cultured for another 44 h. Then, cells were washed with PBS twice and lysed in 100 μL cell culture lysis buffer for 15 min. Luciferase activity was quantified by injection of 50 μL luciferase assay buffer, containing 10 mM luciferin, to 25 μL of the cell lysate. The relative light units (RLU) were measured

dx.doi.org/10.1021/bc300025d | *Bioconjugate Chem.* 2012, 23, 1211−1220

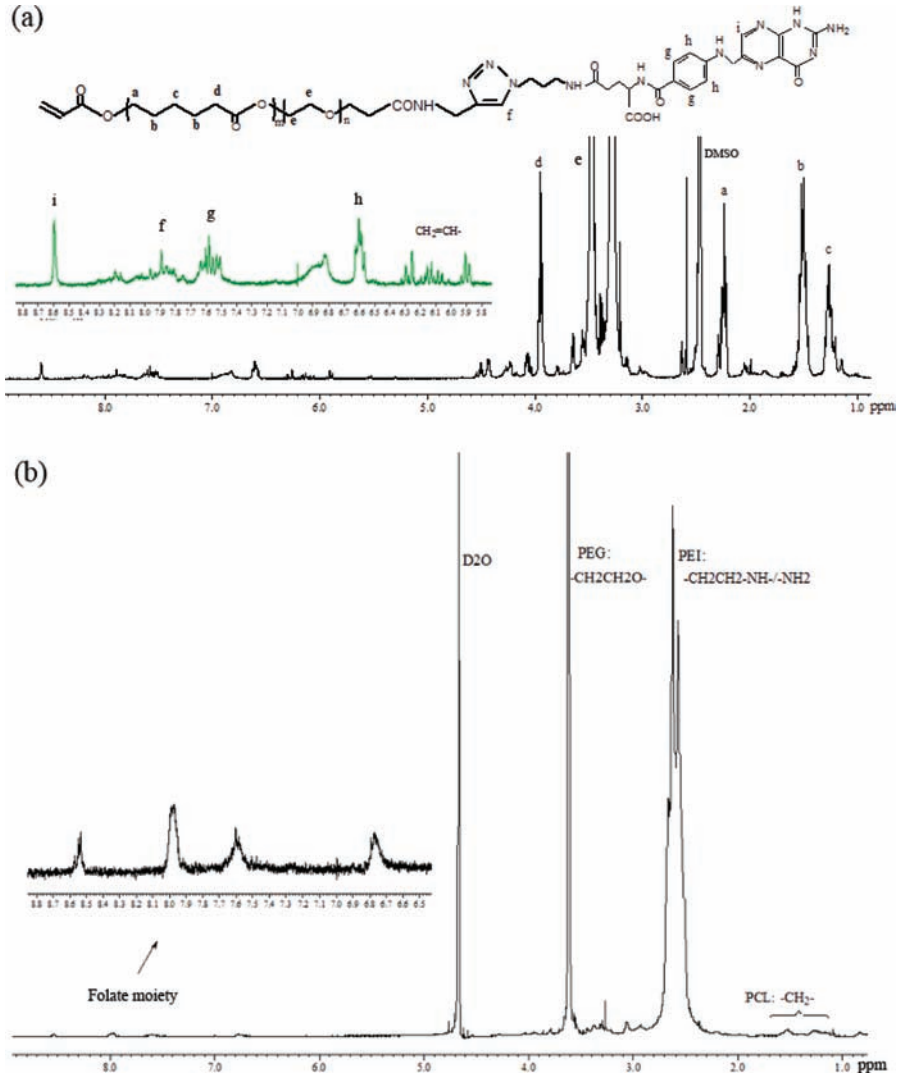

Figure 1. ^{1}H NMR spectra of (a) Fol-PEG-*b*-PCL with terminal acrylate in d_6-DMSO and (b) PEI-*g*-PCL-*b*-PEG-Fol in D_2O.

with a plate luminometer (LumiSTAR Optima, BMG Labtech GMBH, Offenburg, Germany). Protein concentration was determined using a Pierce BCA protein assay Kit (Thermo Scientific). All experiments were performed in triplicate, and data were expressed in RLU per milligram protein (±SD).

Statistics. Significance between the means was tested by two-way ANOVA and statistical evaluations using *GraphPad Prism 4.03* (Graph Pad Software, La Jolla, USA).

RESULTS AND DISCUSSION

Synthesis and Characterization of PEI-*g*-PCL-*b*-PEG-Fol. In most of the previously reported synthesis routes of folate-receptor targeted polycations, folate moieties were conjugated with polycation either directly[22,23,31] or via heterobifunctional PEG linker like HOOC-PEG-NH_2 through the amine-carboxyl reaction using NHS chemistry.[18,19] NHS reactions are widely used in bioconjugations due to their mild reaction conditions, but purification of the final product from excess NHS, byproduct, and solvent may present considerable challenges. On the other hand, it was postulated that the rigid folate moiety attached at the distal end of flexible PEG chains would allow more efficient interaction and binding to folate receptor on the cell surface. However, in the conventional HOOC-PEG-NH_2/NHS strategy, random coupling between different PEG chains coexisted inevitably with PEG-Fol. The coupled PEG chains were difficult to separate and may also generate byproducts.

In this study, the folate-conjugated ternary copolymer of PEI-*g*-PCL-*b*-PEG-Fol was synthesized through a modular procedure as shown in Scheme1, which involved click conjugation of folate moiety with alkyne-terminated PCL-*b*-PEG, followed by the Michael addition between acrylate-terminated folate-PEG-*b*-PCL and PEI.

First, the diblock copolymer of PCL-*b*-PEG was synthesized from heterobifunctional HO-PEG-COOH initiated from the hydroxyl group. The molecular weight of the PCL block could be predetermined by the molar ratio of monomers to hydroxyl groups, which were confirmed by ^{1}H NMR analysis through the calculation of the integral intensity at 1.3−1.4 ppm ($-COCH_2CH_2\mathbf{CH_2}CH_2CH_2O-$, PCL) and 3.4−3.5 ppm ($-CH_2CH_2O-$, PEG) based on the known molecular weight of PEG. The obtained diblock copolymer HO-PCL-*b*-PEG-COOH was then converted into alkyne end group at the PEG terminus and acrylate end group at the PCL terminus, respectively. The structures of intermediates in different steps were characterized by ^{1}H NMR analysis (Figure S-3), where the appearance of signals belonging to alkyne and double bond was

dx.doi.org/10.1021/bc300025d | *Bioconjugate Chem.* 2012, 23, 1211−1220

verified accordingly. Here, the heterobifunctional acrylate-PCL-*b*-PEG-alkyne was a key element for obtaining regioselectivity during synthesis. On one hand, the PEG-terminal alkyne was specific for conjugation with azido-folate through the copper-(I)-catalyzed azide−alkyne click reaction. This cycloaddition reaction is well-known for its high efficiency and selectivity under mild conditions, which has been applied in many bioconjugations of ligands or drugs to polymers.[28,32−34] On the other hand, the PCL-terminal acrylate group was reactive to couple with the amino group of PEI according to a Michael addition under mild conditions afterward. This strategy avoided the risk of intersectional reactions between diblock copolymers. Importantly, both click conjugation and Michael addition were carried through under the mild conditions, which were advantageous to maintain the activity of folate in the objective material since folate is sensitive to light and heat.

Thereafter, the heterobifunctional acrylate-PCL-*b*-PEG-alkyne was transformed into folate-terminated PCL-*b*-PEG-Fol via "click" cyclo-addition with azido-modified folate in weak basic aqueous solution (for water-soluble copolymer with short PCL block). The ^{1}H NMR spectra in Figure 1a verified the structure of acrylate-PCL-*b*-PEG-Fol with signal assignment. The successful conjugation of folate moiety onto PCL-*b*-PEG was further confirmed by UV spectra as shown in Figure 2.

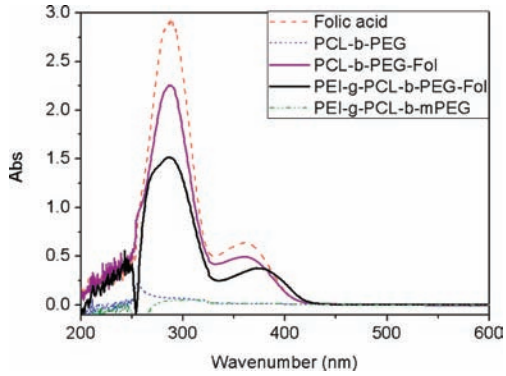

Figure 2. UV absorbance of folic acid solution, folate-conjugated copolymer solutions, and control copolymer (without folate-conjugating) solutions in DMSO.

Two absorbance peaks appeared at 280 and 360 nm, respectively, for PCL-*b*-PEG-Fol, while its precursor PCL-*b*-PEG had no characteristic absorbance in this range. The content of folate conjugated in PCL-*b*-PEG-Fol was about 2.1 × 10^{-7} mol/mg, obtained on the basis of the standard curve using the UV absorbance at 360 nm as reference. This value is equivalent to the conjugation percent of folate onto PCL-*b*-PEG as about 95 mol %.

Finally, the acrylate-PCL-*b*-PEG-Fol was linked to *hy*-PEI via Michael addition between the active double bond and the amine group. Graft density of folate-conjugated branches could be predetermined by the feed ratio of acrylate-PCL-*b*-PEG-Fol to PEI. Figure 1b shows the ^{1}H NMR spectrum of the resulting copolymer PEI-*g*-PCL-*b*-PEG-Fol in D_2O, where the proton signals could be related to the PEI, PCL, PEG, and folate moiety, respectively. Nevertheless, the peaks belonging to PCL segments were rather weak due to its hydrophobicity. The ratio of integral −C$\underline{H_2}$C$\underline{H_2}$O− to integral −C$\underline{H_2}$C$\underline{H_2}$NH− was calculated to give the graft density, which coincided with the predetermined value. The compositions of synthesized PEI-*g*-PCL-*b*-PEG-Fol copolymers were summarized in Table 1. The

Table 1. Copolymer Composition

sample name	composition[a]	folate content[b] (mol/mg)
PCE3-F	PEI25k-(PCL570-PEG3k-Fol)$_3$	1.53 × 10^{-8}
PCE3	PEI25k-(PCL570-mPEG2k)$_3$	

[a]Calculated from ^{1}H NMR spectra. [b]Calculated from the UV absorbance at 360 nm.

folate content was obtained by the UV absorbance. On the basis of the previous investigations of PEI-*g*-PCL-*b*-PEG, those ternary copolymers with short PCL segment and low graft density showed potential as efficient gene delivery carriers, like *hy*PEI25k-(PCL570-mPEG5k)$_3$.[27] Therefore, PEI-*g*-PCL-*b*-PEG-Fol copolymers with molecular weight of PCL at 570 and graft density of 3 were designed and synthesized successfully here for targeting purposes.

Complexation of PEI-*g*-PCL-*b*-PEG-Fol with DNA. The DNA condensing capabilities of folate-conjugated copolymer (PCE3-F), non-folate-conjugated polymer (PCE3), and unmodified PEI 25 kDa were investigated and compared by SYBR Gold quenching assay, as shown in Figure 3a. Generally, all the copolymers showed significant fluorescence quenching above N/P ratio of 2. This demonstrated that the copolymers could condense DNA efficiently above N/P ratio of 2. However, folate-conjugated copolymers exhibited less efficient nucleic acid-binding efficiency than the corresponding non-folate-conjugated PEI-*g*-PCL-*b*-PEG regarding the fluorescence

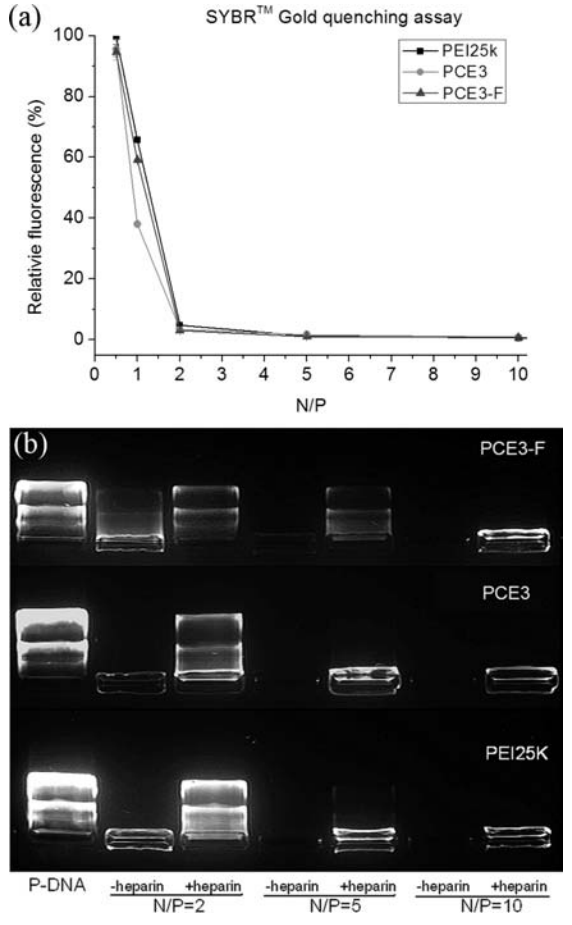

Figure 3. (a) Complexation of copolymers with pDNA measured by SYBR Gold quenching assay. (b) Agarose gel electrophoresis images of polyplexes at different N/P ratios treated with heparin.

dx.doi.org/10.1021/bc300025d | *Bioconjugate Chem.* 2012, 23, 1211−1220

quenching of polyplexes at N/P ratio of 1, indicating the weakening effect of folate ligands on the DNA-binding ability of copolymers to some extent. The binding affinity of copolymers with DNA originated from the electrostatic interaction between negatively charged phosphates along nucleic acid and cationic PEI segments in copolymers. A sufficient condensation of DNA into polyplexes is a prerequisite to protect DNA from competing polyions, serum, and enzyme. To further investigate the stability of polyplexes, the heparin competition assay was performed by agarose gel electrophoresis. Figure 3b shows that the polyplexes formed at N/P 2 could be dissociated to release DNA if treated with heparin (0.5 mg/mL). Stable polyplexes against heparin could be obtained when N/P ratio increased up to 5 for PCE3 and unmodified PEI 25 kDa and 10 for the folate-conjugated PCE3-F copolymer. These results confirm the similar trends as the SYBR Gold quenching assay above, that the binding affinity between folate-conjugated copolymers and DNA is lower. An explanation could be that some folate ligands were buried inside the polyplexes during complexation due to the hydrophobic interaction between folate and PCL[35] or/and the hydrogen bonding interaction between folate and PEI. The interactions of buried folate ligands with positive PEI weakened electrostatic interactions between DNA and copolymers.

Sizes and Zeta-Potential of the Resulting Polyplexes. The hydrodynamic diameters and zeta potentials of the polyplexes at different N/P ratios were shown in Figure 4. It

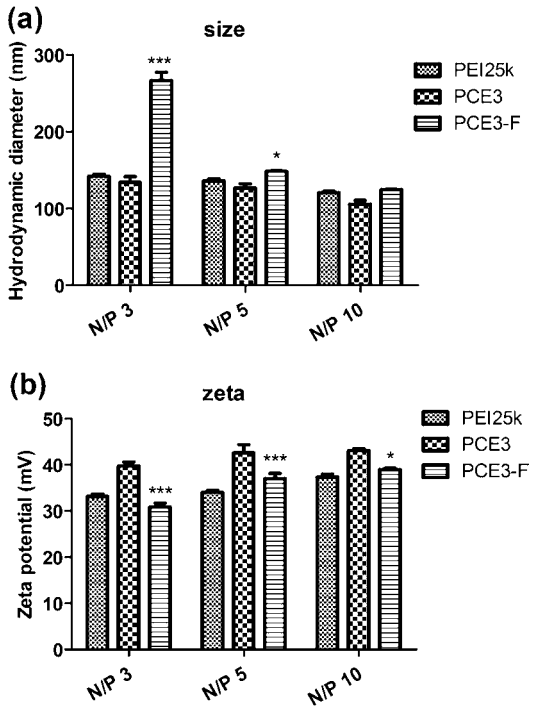

Figure 4. Hydrodynamic diameters and zeta-potentials of copolymer/pDNA polyplexes at different N/P ratio. (* $p < 0.05$, *** $p < 0.001$).

presented a decreasing tendency of the hydrodynamic diameters with the increasing N/P ratio and an increasing one on the zeta-potentials. The size distribution was narrow (0.23 > PDI > 0.15) for all polyplexes, except for PCE3-F at N/P 3 (PDI > 0.3). At certain N/P ratio, the PCE3-F/DNA polyplexes were found to have somewhat larger sizes and lower zeta potentials than folate negative polyplexes (PCE3). This confirms the previous hypothesis that a few of folate ligands buried inside polyplexes would weaken the carrier−DNA interaction, resulting in looser and larger polyplexes. Generally, all polyplexes at N/P 10 were within the size range of 100−120 nm with no significant differences, which were selected for in vitro biological evaluations. Their zeta-potentials were positive in 35−40 mV.

Biological Evaluations of PEI-*g*-PCL-*b*-PEG-Fol. *Cytotoxicity.* The cytotoxicity of the ternary PEI-*g*-PCL-*b*-PEG copolymers with varying PCL/PEG segment length and graft density was investigated in A549 cells and L929 cells previously.[25,27] Reduction of the cytotoxicity was found to be a function of longer PCL and PEG block lengths as well as higher graft density due to the shielding of grafted neutral PCL-PEG segments to cationic PEI. This study focused on the folate-conjugated PEI-*g*-PCL-*b*-PEG copolymers for targeting purposes. The cytotoxicity of PCE3-F copolymer was examined using FR-positive KB cells as shown in Figure 5, where the

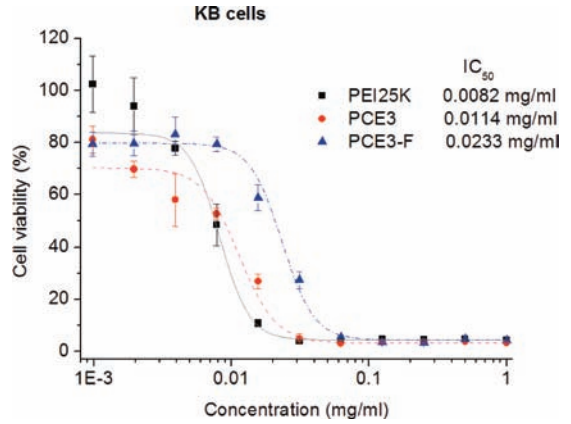

Figure 5. Cell viability of PEI-*g*-PCL-*b*-PEG-Fol and PEI-*g*-PCL-*b*-PEG copolymers in comparison with PEI 25 kDa in KB cells.

corresponding non-folate-conjugated copolymer PCE3 and unmodified PEI 25 kDa were studied for comparison. Interestingly, the folate conjugates PCE3-F exhibited less cytotoxicity than the non-folate conjugates PCE3. The IC_{50} value of PCE3-F was found to be 0.0233 mg/mL, about 2-fold to PCE3 and 3-fold to PEI 25 kDa ($p < 0.001$). The cytotoxicity of polycations like PEI was believed to result from their positive charge density. Some literature reported that FR-mediated targeting may increase the cytotoxicity of folate conjugates due to greater interaction of materials with cells.[36] On the other hand, folate ligands could shield the positive charge of PEI, leading to a decreasing cytotoxicity of folate-conjugated copolymer. Then, the cytotoxicity of folate-conjugated PEI copolymer would rely on the competition of these two effects mentioned above. In this study, PCE3-F/DNA polyplexes were demonstrated with significantly lower zeta potential than PCE3. Therefore, the shielding effect of the folate moiety was predominating, resulting in decreased cytotoxicity of PCE3-F than PCE3. There are also some reports in the literature demonstrating no significant difference of the cytotoxicity between the folate-conjugated PEI-based copolymers and the nonfolate ones.[19,22]

Cellular Uptake of PEI-g-PCL-b-PEG-Fol/pDNA Polyplexes. To evaluate folate receptor targeting efficiency, uptake of polyplexes was determined by flow cytometry. A panel of carrier materials (PCE3-F, PCE3, and *hy*-PEI 25 kDa) were

dx.doi.org/10.1021/bc300025d | *Bioconjugate Chem.* 2012, 23, 1211−1220

fluorescently labeled using FITC and then used to prepare fluorescent polyplexes with pCMV-Luc and incubated with KB cells and A549 cells, respectively. As shown in Figure 6a, almost

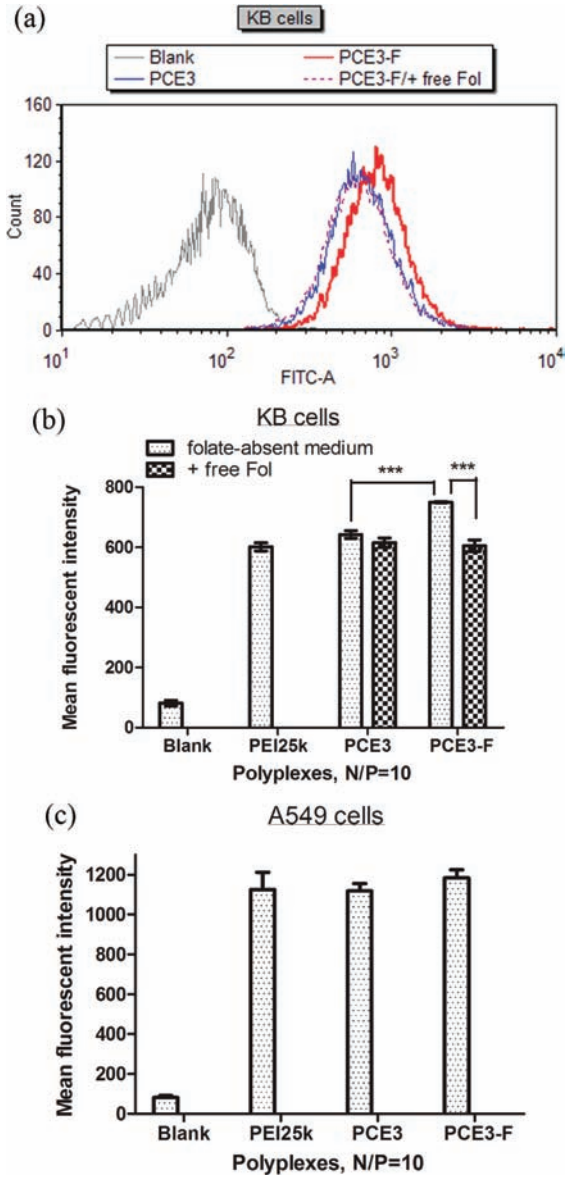

Figure 6. Quantitative determination of cellular uptake of polyplexes by flow cytometry in KB cells (a,b) and A549 cells (c), expressed as the mean fluorescence intensity of FITC-positive cells. (n = 3, ***p < 0.001, using FITC-labeled polymer).

all the cells internalized fluorescent polyplexes after 4 h of incubation with FR-positive KB cells. Nevertheless, the amount of the internalized polyplexes, as determinate from the mean fluorescent intensity (Figure 6b), exhibited increased values for the folate-conjugated polyplexes (PCE3-F) of approximately 117% in comparison to folate-negative PCE3 polyplexes (p < 0.001). Importantly, the competition experiments in the presence of free folate decreased the amount of internalized PCE3-F/pDNA polyplexes down to 80% in KB cells (p < 0.001). The control experiments performed in FR-negative A549 cells presented no distinct difference of the internalized polyplex amount between PCE3-F and PCE3 (Figure 6c). Taken together, these results indicated significantly enhanced cell uptake of folate-conjugated polyplexes via FR-mediated endocytosis. Generally, reduction of cytotoxicity or zeta potential is usually linked to reduced cell uptake. Here, PEI-*g*-PCL-*b*-PEG-Fol copolymers with graft density 3 showed optimized cell uptake of pDNA polyplexes into cytosol and reduced cytotoxicity at the same time.

Furthermore, the FR-targeted gene delivery via PEI-*g*-PCL-*b*-PEG-Fol was confirmed using YOYO-1 labeled pDNA in KB cells. The results from flow cytometry (SI Figure S-5) were consistent, showing that the cell uptake of PCE3-F/pDNA polyplexes was higher than that of PCE3/pDNA polyplexes. The uptake and subcellular localization of polyplexes inside KB cells were also examined by confocal laser scanning microscopy. In Figure 7, it could be visualized that the YOYO-1 labeled pDNA (green) was distributed not only in the cytoplasm, but also in the nuclei. The KB cells treated with PCE3-F/pDNA polyplexes showed brighter green fluorescence than those with PCE3/pDNA polyplexes, which again demonstrated increased uptake of polyplexes via PEI-*g*-PCL-*b*-PEG-Fol due to a specific FR interaction.

In Vitro Gene Transfection. To further address targeted gene delivery effect of PEI-*g*-PCL-*b*-PEG-Fol, transfection efficiency of the PCE3-F/pDNA polyplexes at N/P ratio of 10 was tested in KB cells and compared to the corresponding PCE3/pDNA polyplexes. As shown in Figure 8, PEI-*g*-PCL-*b*-PEG-Fol (PCE3-F) displayed significantly higher transfection efficiency by approximately 14-fold than PCE3 (p < 0.05) in the folate-absent medium. Previous study has demonstrated that PEI25k-(PCL570-PEG5k)$_3$ is efficient with high transfection activity due to high buffer capacity and zeta-potential.[27] Here, PCE3-F/pDNA polyplexes also exhibit high positive zeta potential. Though it is a little lower than PCE3, the specific binding of folate-conjugated polyplexes due to folate/FR recognition enhanced cell uptake in KB cells as mentioned previously. More importantly, the transfection efficiency of PCE3-F/pDNA polyplexes decreased to about 12% in the folate-enriched regular medium when the folate receptors on KB cell surface were occupied with free folate molecules. Consistently, the improvement of transfection efficiency for PEI-*g*-PCL-*b*-PEG-Fol could be attributed to the enhanced uptake of polyplexes by folate-mediated targeting to folate receptors on the cell surface. These results are consistent with the previous reports showing a similar increase of transfection efficiency for folate-conjugated PEI-polyplexes in FR-positive cells, including Hela cells,[22] B16 cells,[23] and KB cells.[19] Their transfection efficiency could additionally be blocked by excess free folic acid. Although cell type as well as copolymer structure account for difference in absolute values of transfection efficiency, here PCE3-F polyplexes exhibited enhanced gene transfection than PCE3 in KB cells, which was comparable to PEI 25 kDa. Hence, the conjugation of folate molecules indeed endowed PEI-*g*-PCL-*b*-PEG-Fol to be a targeted gene vector for FR-positive cells.

CONCLUSIONS

Folate-conjugated ternary copolymer PEI-*g*-PCL-*b*-PEG-Fol was successfully synthesized by click cyclo-addition of azido-folate with heterobifunctional acrylate-PCL-*b*-PEG-alkyne, followed by Michael addition with PEI, for targeted gene delivery. Lower cytotoxicity was observed for PEI-*g*-PCL-*b*-PEG-Fol than PEI-*g*-PCL-*b*-PEG, which was much lower than that of unmodified PEI 25 kDa. The cellular uptake of polyplexes was enhanced by PEI-*g*-PCL-*b*-PEG-Fol in FR

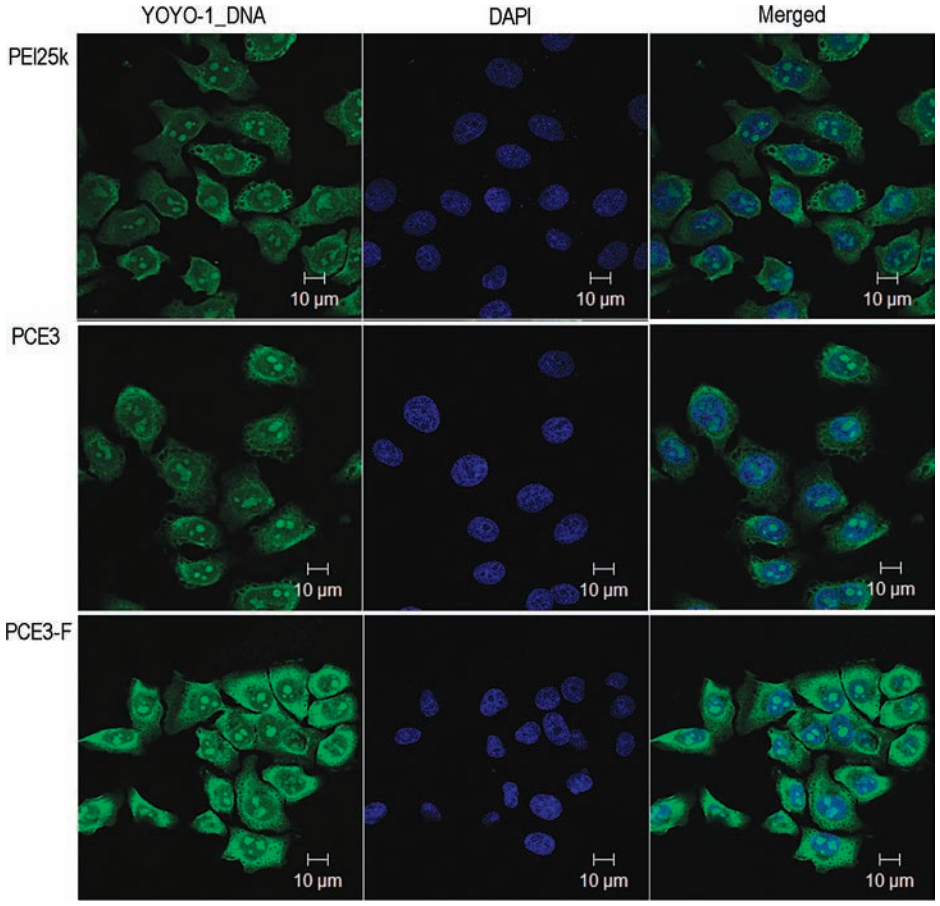

Figure 7. Confocal laser scanning microscopy of KB cells treated with polyplexes of PEI 25k, PEI-*g*-PCL-*b*-PEG, and PEI-*g*-PCL-*b*-PEG-Fol. Cell nuclei were stained with DAPI (blue), and pDNA was labeled with YOYO-1 (green).

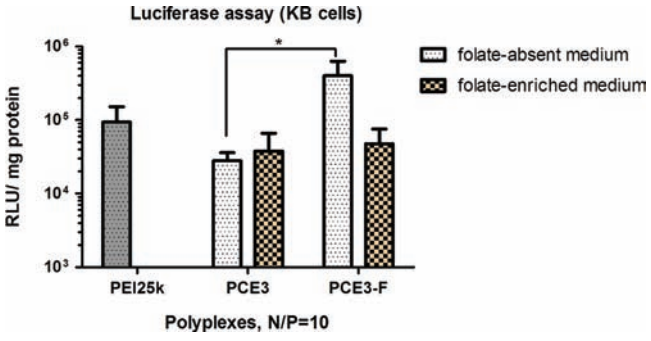

Figure 8. Transfection efficiency of PEI-*g*-PCL-*b*-PEG-Fol/pDNA polyplexes in comparison to PEI-*g*-PCL-*b*-PEG/pDNA polyplexes in KB cells at N/P ratio of 10, where PEI 25 kDa/pDNA polyplexes are the control (n = 3, *p < 0.05).

overexpressing KB cells compared with those by PEI-*g*-PCL-*b*-PEG. Importantly, this enhancement was inhibited by free folic acid, which did not appear in FR-negative A549 cells. All these suggested specific cell uptake of PEI-*g*-PCL-*b*-PEG-Fol/pDNA polyplexes via folate receptor-mediated endocytosis. Consequently, PEI-*g*-PCL-*b*-PEG-Fol/pDNA polyplexes revealed higher transfection than PEI-*g*-PCL-*b*-PEG/pDNA. Here, PEI-*g*-PCL-*b*-PEG-Fol is a novel kind of ternary copolymer with amphiphilicity, cationic property, and folate ligands, which endows them with multifunctional prospects for codelivery of both gene and hydrophobic chemotherapeutic drug to target tumor tissue. Nevertheless, continued efforts still need to be considered to reduce nonspecific uptake and increase transfection efficiency further. Additional studies on gene transfection in vivo and utilizing these described folate-conjugated copolymers for targeted siRNA delivery are in process.

■ ASSOCIATED CONTENT

Supporting Information

Details of characterization of intermediate products, standard line of UV absorbance of folate solution, and FACS data of polyplexes with YOYO-1 labeled pDNA in KB cells. This material is available free of charge via the Internet at http://pubs.acs.org.

■ AUTHOR INFORMATION

Corresponding Author

*TEL: +49-6421-282 5881. FAX: +49-6421-282 7016. E-mail: kissel@staff.uni-marburg.de (T. Kissel).

Author Contributions

†Both authors contributed equally to this work.

Notes

The authors declare no competing financial interest.

■ ACKNOWLEDGMENTS

Financial support of Dr. Liu, L., by the Alexander von Humboldt Foundation is gratefully acknowledged. We thank Ms. E. Mohr for her support in the cell culture laboratory and Dr. Yu Liu for fruitful discussion on copolymer synthesis.

REFERENCES

(1) Olefsky, J. M. (2000) Diabetes: Gene therapy for rats and mice. *Nature 408*, 420−421.

(2) Merdan, T., Kopecek, J., and Kissel, T. (2002) Prospects for cationic polymers in gene and oligonucleotide therapy against cancer. *Adv. Drug Delivery Rev. 54*, 715−758.

(3) Wagner, A. M., Schoeberlein, A., and Surbek, D. (2009) Fetal gene therapy: Opportunities and risks. *Adv. Drug Delivery Rev. 61*, 813−821.

(4) Mintzer, M. A., and Simanek, E. E. (2008) Nonviral vectors for gene delivery. *Chem. Rev. 109*, 259−302.

(5) Pack, D. W., Hoffman, A. S., Pun, S., and Stayton, P. S. (2005) Design and development of polymers for gene delivery. *Nat. Rev. Drug Discovery 4*, 581−593.

(6) Boussif, O., Lezoualc'h, F., Zanta, M. A., Mergny, M. D., Scherman, D., Demeneix, B., and Behr, J. P. (1995) A versatile vector for gene and oligonucleotide transfer into cells in culture and in vivo: polyethylenimine. *Proc. Natl. Acad. Sci. U.S.A. 92*, 7297−7301.

(7) Behr, J.-P. (1997) The proton sponge: a trick to enter cells the viruses did not exploit. *CHIMIA Int. J. Chem. 51*, 34−36.

(8) Petersen, H., Fechner, P. M., Fischer, D., and Kissel, T. (2002) Synthesis, characterization, and biocompatibility of polyethylenimine-graft-poly(ethylene glycol) block copolymers. *Macromolecules 35*, 6867−6874.

(9) Petersen, H., Fechner, P. M., Martin, A. L., Kunath, K., Stolnik, S., Roberts, C. J., Fischer, D., Davies, M. C., and Kissel, T. (2002) Polyethylenimine-graft-poly(ethylene glycol) copolymers:influence of copolymer block structure on dna complexation and biological activities as gene delivery system. *Bioconjugate Chem. 13*, 845−854.

(10) Lee, M., Kim, M., Jang, Y., Lee, K., Kim, T., Kim, S., Park, T., Kim, H., and Jeong, J. (2011) Polyethylenimine-g-poly(lactic-co-glycolic acid) as non-toxic micelle-type carrier for gene delivery. *Macromol. Res. 19*, 688−693.

(11) Pun, S. H., Bellocq, N. C., Liu, A., Jensen, G., Machemer, T., Quijano, E., Schluep, T., Wen, S., Engler, H., Heidel, J., and Davis, M. E. (2004) Cyclodextrin-modified polyethylenimine polymers for gene delivery. *Bioconjugate Chem. 15*, 831−840.

(12) Dachs, G., Dougherty, G., Stratford, I., and Chaplin, D. (1997) Targeting gene therapy to cancer: a review. *Oncol. Res. 9*, 313−25.

(13) Salazar, M., and Ratnam, M. (2007) The folate receptor: What does it promise in tissue-targeted therapeutics? *Cancer Metast. Rev. 26*, 141−152.

(14) Low, P. S., and Kularatne, S. A. (2009) Folate-targeted therapeutic and imaging agents for cancer. *Curr. Opin. Chem. Biol. 13*, 256−262.

(15) Xia, W., and Low, P. S. (2010) Folate-targeted therapies for cancer. *J. Med. Chem. 53*, 6811−6824.

(16) Benns, J. M., Maheshwari, A., Furgeson, D. Y., Mahato, R. I., and Kim, S. W. (2001) Folate-PEG-folate-graft-polyethylenimine-based gene delivery. *J. Drug Targeting 9*, 123−139.

(17) Liang, B., He, M. L., Xiao, Z. P., Li, Y., Chan, C. Y., Kung, H. F., Shuai, X. T., and Peng, Y. (2008) Synthesis and characterization of folate-PEG-grafted-hyperbranched-PEI for tumor-targeted gene delivery. *Biochem. Biophys. Res. Commun. 367*, 874−880.

(18) Liang, B., He, M.-L., Chan, C.-y., Chen, Y.-c., Li, X.-P., Li, Y., Zheng, D., Lin, M. C., Kung, H.-F., Shuai, X.-T., and Peng, Y. (2009) The use of folate-PEG-grafted-hybranched-PEI nonviral vector for the inhibition of glioma growth in the rat. *Biomaterials 30*, 4014−4020.

(19) Arote, R. B., Hwang, S. K., Lim, H. T., Kim, T. H., Jere, D., Jiang, H. L., Kim, Y. K., Cho, M. H., and Cho, C. S. (2010) The therapeutic efficiency of FP-PEA/TAM67 gene complexes via folate receptor-mediated endocytosis in a xenograft mice model. *Biomaterials 31*, 2435−2445.

(20) He, M. L. (2009) The use of folate-PEG-grafted-hybranched-PEI nonviral vector for the inhibition of glioma growth in the rat. *Int. J. Mol. Med. 24*, 168.

(21) Hwa Kim, S., Hoon Jeong, J., Chul Cho, K., Wan Kim, S., and Gwan Park, T. (2005) Target-specific gene silencing by siRNA plasmid DNA complexed with folate-modified poly(ethylenimine). *J. Controlled Release 104*, 223−232.

(22) Cheng, H., Zhu, J. L., Zeng, X., Jing, Y., Zhang, X. Z., and Zhuo, R. X. (2009) Targeted gene delivery mediated by folate-polyethylenimine-block-poly(ethylene glycol) with receptor selectivity. *Bioconjugate Chem. 20*, 481−487.

(23) Yao, H., Ng, S. S., Tucker, W. O., Tsang, Y. K. T., Man, K., Wang, X. M., Chow, B. K. C., Kung, H. F., Tang, G. P., and Lin, M. C. (2009) The gene transfection efficiency of a folate-PEI600-cyclodextrin nanopolymer. *Biomaterials 30*, 5793−5803.

(24) Shuai, X., Merdan, T., Unger, F., Wittmar, M., and Kissel, T. (2003) Novel biodegradable ternary copolymers hy-PEI-g-PCL-b-PEG: synthesis, characterization, and potential as efficient nonviral gene delivery vectors. *Macromolecules 36*, 5751−5759.

(25) Liu, Y., Nguyen, J., Steele, T., Merkel, O., and Kissel, T. (2009) A new synthesis method and degradation of hyper-branched polyethylenimine grafted polycaprolactone block mono-methoxyl poly (ethylene glycol) copolymers (hy-PEI-g-PCL-b-mPEG) as potential DNA delivery vectors. *Polymer 50*, 3895−3904.

(26) Liu, Y., Samsonova, O., Sproat, B., Merkel, O., and Kissel, T. (2011) Biophysical characterization of hyper-branched polyethylenimine-graft-polycaprolactone-block-mono-methoxyl-poly(ethylene glycol) copolymers (hy-PEI-PCL-mPEG) for siRNA delivery. *J. Controlled Release 153*, 262−8.

(27) Zheng, M., Liu, Y., Samsonova, O., Endres, T., Merkel, O., and Kissel, T. (2012) Amphiphilic and biodegradable hy-PEI-g-PCL-b-PEG copolymers efficiently mediate transgene expression depending on their graft density. *Int. J. Pharm. 427*, 80−87.

(28) Lee, S. M., Chen, H. M., O'Halloran, T. V., and Nguyen, S. T. (2009) "Clickable" polymer-caged nanobins as a modular drug delivery platform. *J. Am. Chem. Soc. 131*, 9311−9320.

(29) Storey, R. F., and Sherman, J. W. (2002) Kinetics and mechanism of the stannous octoate-catalyzed bulk polymerization of caprolactone. *Macromolecules 35*, 1504−1512.

(30) Merkel, O. M., Mintzer, M. A., Librizzi, D., Samsonova, O., Dicke, T., Sproat, B., Garn, H., Barth, P. J., Simanek, E. E., and Kissel, T. (2010) Triazine dendrimers as nonviral vectors for in vitro and in vivo RNAi: the effects of peripheral groups and core structure on biological activity. *Mol. Pharmaceutics 7*, 969−983.

(31) Jiang, H. L., Xu, C. X., Kim, Y. K., Arote, R., Jere, D., Lim, H. T., Cho, M. H., and Cho, C. S. (2009) The suppression of lung tumorigenesis by aerosol-delivered folate-chitosan-graft-polyethylenimine/Akt1 shRNA complexes through the Akt signaling pathway. *Biomaterials 30*, 5844−5852.

(32) Parrish, B., and Emrick, T. (2006) Soluble camptothecin derivatives prepared by click cycloaddition chemistry on functional aliphatic polyesters. *Bioconjugate Chem. 18*, 263−267.

(33) Mindt, T. L., Muller, C., Stuker, F., Salazar, J. F., Hohn, A., Mueggler, T., Rudin, M., and Schibli, R. (2009) A "click chemistry" approach to the efficient synthesis of multiple imaging probes derived from a single precursor. *Bioconjugate Chem. 20*, 1940−1949.

(34) van Dijk, M., Rijkers, D. T. S., Liskamp, R. M. J., van Nostrum, C. F., and Hennink, W. E. (2009) Synthesis and applications of biomedical and pharmaceutical polymers via click chemistry methodologies. *Bioconjugate Chem. 20*, 2001−2016.

(35) Valencia, P. M., Hanewich-Hollatz, M. H., Gao, W., Karim, F., Langer, R., Karnik, R., and Farokhzad, O. C. (2011) Effects of ligands with different water solubilities on self-assembly and properties of targeted nanoparticles. *Biomaterials 32*, 6226−6233.

(36) Zheng, Y., Cai, Z., Song, X., Yu, B., Bi, Y., Chen, Q., Zhao, D., Xu, J., and Hou, S. (2009) Receptor mediated gene delivery by folate conjugated N-trimethyl chitosan in vitro. *Int. J. Pharm. 382*, 262−269.

Bioconjugate Chemistry

Article

pubs.acs.org/bc

Development of a Novel Long-Lived ImmunoPET Tracer for Monitoring Lymphoma Therapy in a Humanized Transgenic Mouse Model

Arutselvan Natarajan, Frezghi Habte, and Sanjiv S. Gambhir*,§

Molecular Imaging Program at Stanford (MIPS), Department of Radiology and

§Bioengineering, Department of Materials Science and Engineering, Bio-X Program, Stanford University, Stanford, California, United States

Supporting Information

ABSTRACT: Positron emission tomography (PET) is an attractive imaging tool to localize and quantify tracer biodistribution. ImmunoPET with an intact mAb typically requires two to four days to achieve optimized tumor-to-normal ratios. Thus, a positron emitter with a half-life of two to four days such as zirconium-89 [^{89}Zr] ($t_{1/2}$: 78.4 h) is ideal. We have developed an antibody-based, long-lived immunoPET tracer ^{89}Zr-Desferrioxamine-p-SCN (Df-Bz-NCS)-rituximab (Zr-iPET) to image tumor for longer durations in a humanized CD20-expressing transgenic mouse model. To optimize the radiolabeling efficiency of ^{89}Zr with Df-Bz-rituximab, multiple radiolabelings were performed. Radiochemical yield, purity, immunoreactivity, and stability assays were carried out to characterize the Zr-iPET for chemical and biological integrity. This tracer was used to image transgenic mice that express the human CD20 on their B cells (huCD20TM). Each huCD20TM mouse received a 7.4 MBq/dose. One group (n = 3) received a 2 mg/kg predose (blocking) of cold rituximab 2 h prior to ^{89}Zr-iPET; the other group (n = 3) had no predose (nonblocking). Small animal PET/CT was used to image mice at 1, 4, 24, 48, 72, and 120 h. Quality assurance of the ^{89}Zr-iPET demonstrated NCS-Bz-Df: antibody ratio (c/a: 1.5 ± 0.31), specific activity (0.44−1.64 TBq/mol), radiochemical yield (>70%), and purity (>98%). The Zr-iPET immunoreactivity was >80%. At 120 h, Zr-iPET uptake (% ID/g) as mean ± STD for blocking and nonblocking groups in spleen was 3.2 ± 0.1% and 83.3 ± 2.0% (p value <0.0013.). Liver uptake was 1.32 ± 0.05% and 0.61 ± 0.001% (p value <0.0128) for blocking and nonblocking, respectively. The small animal PET/CT image shows the spleen specific uptake of Zr-iPET in mice at 120 h after tracer injection. Compared to the liver, the spleen specific uptake of Zr-iPET is very high due to the expression of huCD20. We optimized the radiolabeling efficiency of ^{89}Zr with Df-Bz-rituximab. These radioimmunoconjugate lots were stable up to 5 days in serum *in vitro*. The present study showed that ^{89}Zr is well-suited for mAbs to image cancer over an extended period of time (up to 5 days).

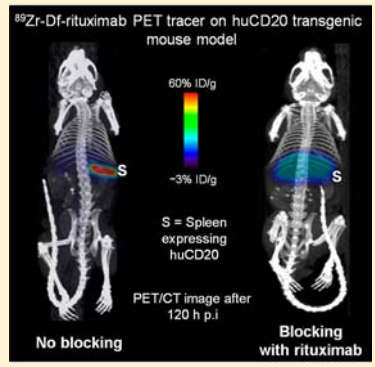

INTRODUCTION

Many monoclonal antibodies (mAbs) and mAb fragments are currently under clinical investigation due to their excellent potential for cancer diagnosis, therapy, and other pathological conditions.[1,2] The Food and Drug Administration (FDA) has approved several of these mAbs for cancer therapy including rituximab, panitumumab, bevacizumab, cetuximab, ^{90}Y-ibritumomab tiuxetan, and ^{131}I-tositumomab. The annual sales of these mAbs were estimated approximately $20 billion.[3,4] However, very few mAbs have been applied for positron emission tomography (PET) imaging. PET is an attractive molecular imaging tool to visualize and quantify tumor using targeting molecules.[2,5,6] Compared to SPECT imaging, PET has many advantages including increased sensitivity. MAbs labeled with positron radionuclides (immunoPET) are a powerful molecular imaging strategy to track, visualize, and measure the tumor gene expression, since immunoPET can characterize and quantify antigen expression specific to a tumor type, whereas FDG measures glucose metabolism.

To develop immunoPET agent(s) using intact mAbs or mAb-fragments, an appropriate positron emitter with a half-life of 2−4 days would be ideal. ^{89}Zirconium (^{89}Zr) is one of the most promising radionuclides with which to develop immunoPET agents with intact antibodies for *in vivo* imaging of cancer.[1−4] The physical properties of ^{89}Zr ($t_{1/2}$ = 78.4 h, $E\gamma$ = 908.97 keV) are well-suited for use in a monoclonal antibody-based imaging agent. The relatively low translational energy (distance traveled by the positron before annihilation with an electron) of the emitted positron from ^{89}Zr ($R_{ave}(\beta+)$ = 1.18 mm) results in high-resolution ^{89}Zr images comparable to those observed with the ^{18}F and ^{64}Cu radionuclides $R_{ave}(\beta+)$ = 0.69 and 0.70 mm, respectively.[5−7] Furthermore, routine commercial availability of ^{89}Zr worldwide makes this radionuclide broadly available for research and clinical applications.

Received: January 26, 2012
Revised: May 21, 2012
Published: May 23, 2012

To prepare a systemically stable immunoPET agent the choice of chelator to load the radionuclide is an important criterion. For ^{89}Zr labeling, desferrioxamine (Df) is a well-known chelator that provides stable complexes with zirconium and has been safely used in clinical studies for many years.[8−11] ImmunoPET images and quantification results of ^{89}Zr−mAb have been reported in both preclinical[12−16] and clinical studies.[8−10,17,18] In these studies, results indicated neither pharmacokinetic changes nor a specific accumulation of ^{89}Zr−mAb in nontarget organs, except liver and kidneys. The only potential concern is the high radiation dose administered to the patient, which is inherent to the use of long-lived positron emitters like ^{89}Zr and ^{124}I. This might preclude repeated application of ^{89}Zr−immunoPET.[9]

The purpose of the current study was to develop and evaluate an antibody-based PET imaging agent for Non-Hodgkin's lymphoma (NHL) to monitor lymphoma therapy. NHL is the fifth most common cancer in the United States with 60 000 new cases and approximately 20 000 deaths each year. There are several known associations and genetic disorders that may play a role in the etiology of NHL. These include genetic abnormalities, environmental factors, viruses, immunodeficiency states, and connective tissue disorders.[19] Most (80−85%) NHLs arise from B cells; the remainder arises from T cells or natural killer cells. Either precursor or mature cells may be involved. Overlap exists between leukemia and NHL because both involve proliferation of lymphocytes or their precursors. Although substantial progress has been made in understanding the molecular pathogenesis of several forms of NHL, prognostic information is based on morphology and histology.

To overcome these limitations, we developed, optimized, and evaluated a novel PET radiopharmaceutical, of an antibody-based (rituximab) tracer using ^{89}Zr radionuclide chelated to *p*-isothiocyanatobenzyl-desferrioxamine B (Df-Bz-NCS). This tracer was evaluted using a humanized transgenic B-cell lymphoma mouse (huCD20TM) model. In this model, the spleen is one of the key sites for B cell sequestration. These splenic B cells overexpress CD20 antigens, and thus in our study, the imaging agent accumulates in the spleen. The CD20 antigen is a 32 kDa nonglycosylated phosphoprotein, which is commonly expressed by human lymphoma cells, a target in radioimmunotherapy, and overexpressed on the surface of mature B cells.[20,21] The huCD20TM model is thus an excellent model for predicting the targeting capacity of the ^{89}Zr-rituximab tracers. The rationale for this study is the fact that Rituxan, Bexxar, and Zevalin are all antibodies known to target the CD20 antigen in B-cell NHL. Several research groups including our own have attempted to develop rituximab-based immunoPET agents to target the CD20 antigen in both preclinical and clinical models.[22−24] For example, Olafsen et al. developed immunoPET agents for imaging CD20-positive lymphomas in preclinical models using ^{64}Cu-DOTA-minibody and ^{124}I-scFv-Fc fragment; these immunoPET agents produced high-contrast images in vivo.[23] In another study, Tran et al. performed a clinical trial to target human CD20 using ^{124}I-rituximab in five patients for detection of inflamed joints in rheumatoid arthritis.[24] Although these are only pilot studies, they show encouraging results.

In this report, we describe the preparation, quality assurance (QA) methods, and results of a preclinical study to evaluate the novel ^{89}Zr-immunoPET (ZriPET) radiopharmaceutical against human CD20 antigen expressed in humanized transgenic mice prior to clinical translation into NHL patients.

MATERIALS AND METHODS

Reagents, Antibodies, and Radiochemicals. All reagents were obtained from Sigma-Aldrich (St. Louis, MO) unless otherwise stated. *p*-Isothiocyanatobenzyl-desferrioxamine (Df-Bz-NCS) was purchased from Macrocyclics (Dallas, TX, USA). The mAb rituximab (Rituxan; 10 mg/mL) directed against the human CD20 was purchased from Stanford hospital pharmacy (Stanford University, Stanford). Rituximab is a high-affinity chimeric monoclonal antibody of the IgG1 subtype (human κ light chain and human γ1 heavy chain), which recognizes humanized B cell CD20. ^{89}Zr ($t_{1/2}$ = 78.4 h, β+ = 22.6%; ∼2.7 GBq/mL in 1 M oxalic acid) was obtained from the University of Wisconsin.

Cell Lines and Instruments. The CD20+ B-cell lymphoma cell line Ramos was obtained from the American Type Culture Collection (ATCC number: CRL-1555). The CD20- Jurkat cells were obtained from ATCC (TIB-152) as well. Ramos cells were maintained in Dulbecco's modified Eagle's medium (DMEM) (4.5 g/L glucose), Jurkat cells in MEM/Ham's F-12 (1:1), and 1% nonessential amino acids. All media were supplemented with 10% fetal calf serum (FCS), 2 mmol/L glutamine, 100 units/mL penicillin, 100 μg streptomycin, and 0.25 μg/mL fungizone. All media and additives were obtained from Invitrogen Corporation (Carlsbad, CA USA).

High-performance liquid chromatography (HPLC) was performed on HPLC-Ultimate 3000 with an ultraviolet detector and an online radioactivity detector. The system used a SEC 3000 LC column (300 × 7.8 mm) with 5 μm hydrophilic bonded silica support and 400 Å pore size (Phenomenex, Torrance, CA 90501−1430, USA) Mass spectrometry (AB SCIEX TOF/TOF 5800) was performed at Stanford University and operated in linear mode with sinapinic acid as matrix.

Preparation of Immunoconjugate. *Optimization of Chelate Conjugation to Antibody.* To optimize the Df-Bz-NCS conjugation with rituximab and bind 1−2 chelates per antibody, the conjugation reaction was performed under 9 different conditions. These experiments used 3 different pH conditions, and 3 sets of chelate concentrations were tested. Briefly, 20 μL of a 50 μM solution of rituximab (7.5 mg/mL) was added to each reaction vial followed by addition of 2−10 μL of 0.1 M Na_2CO_3 at pH 8, 8.5, and 9.0 in triplicate. Three separate reaction vials from each pH condition received 20 μL of Df-Bz-NCS of 250, 375, and 500 μM concentrations in DMSO. At each pH condition, the final chelate concentrations of Df-Bz-NCS was 5-fold, 7.5-fold, and 10-fold molar excess over rituximab concentrations. Finally, all reaction tubes were brought to 50 μL total volume using 0.1 mol/L sodium phosphate buffer (pH 8). Excess Df-Bz-NCS was then removed by 30 kDa membrane dialysis using slide-A-lyzer of 0.2 mL volume (Pierce, USA) with 0.1 M sodium acetate buffer (pH 7.0) as dialysis buffer. The conjugation experiments were repeated twice.

For the preclinical study, the Df-Bz-rituximab was prepared as a separate lot. An aqueous solution of rituximab (0.1 mM; 350 μL) was buffer exchanged with 0.1 M Na_2CO_3 (pH 9.0) and then mixed with 5-fold molar excess of Df-Bz-NCS (5 mM; 35 μL of DMSO) in a 1 mL Eppendorf vial. The final reaction mixture was diluted to 0.5 mL (pH = 8.5) using 0.1 mol/L sodium phosphate buffer. The reaction was kept for 1 h at

room temperature. Excess Df-Bz-NCS was then removed by 30 kDa membrane dialysis using Slide-A-lyzer (Pierce, USA) and buffer exchanged into 0.1 M sodium acetate buffer (pH 7.0) for ^{89}Zr labeling. The immunoconjugates were concentrated by centrifugation-dialysis to 0.1 to 0.2 mg/mL and stored at −80 °C. The number of chelators (c) coupled per antibody (a), i.e., c/a molecule, was estimated with MALDI-TOF MS by comparison of rituximab and Df-Bz-rituximab.[15]

Optimization of Radiolabeling. On the basis of previous reports,[25] we further refined the radiolabeling conditions to create immunoconjugates with high specific activity and radiochemical yields. Labeling of Df-Bz-rituximab (c/a = 1.5) using ^{89}Zr was optimized for two variables: (a) pH conditions (pH = 6.5, 7.0, and 7.5) and (b) labeling reaction time (45 and 60 min) at 37 °C. The reaction was performed in a 1.5 mL Eppendorf tube in the following sequence: First, ^{89}Zr (37 MBq; 250 μL) and 2.5 M Na_2CO_3 (50 μL) were added. After 3 min, 10 mM ammonium acetate buffer (150 μL, pH 7.0), Df-Bz-rituximab (150 μL, 10 μg), and 10 mM ammonium acetate buffer (150 μL, pH 7.0) were added. After incubation (45 min), 0.1 M diethylenetriaminepentaacetic acid (DTPA, pH 7.0) was added to a final concentration of 5 mmol/L for 15 min to scavenge unchelated ^{89}Zr in the reaction mixture. On the basis of the labeling optimization for preclinical study, the reaction mixture was kept at pH 7. 0 for 60 min. The Df-Bz-NCS-mAb (20−50 μg; 100 μL) and ^{89}Zr (74−190 MBq; 500 μL) and the other reagents were added as mentioned above. Purification of the radioimmunoconjugate (25 μg in 500 μL volume) was achieved by size exclusion chromatography on a Phenomenex SEC 3000 column (Torrance, CA, USA) in PBS buffer [0.1 mol/L NaCl, 0.05 mol/L sodium phosphate (pH 7.4)] at a flow rate of 1.0 mL/min. The radioimmunoconjugate peak (retention time at 8.5 min) corresponding to antibody was collected and concentrated using Amicon Ultra-15 (Millipore, USA) device and centrifuged at 3000g for 15 min. The final product was filtered through a 0.2 μm filter into a sterile vial.

Immunoreactivity and Stability of the Radiolabeled Immunoconjugates. Each lot of the radioimmunoconjugate was evaluated for the immunoreactive fraction and immunoreactivity by cell-binding assays as described in previous publications.[5,26] Briefly, Ramos (CD20 +) cells were suspended in microcentrifuge tubes at concentrations of 5.0, 4.0, 3.0, 2.5, 2.0, 1.5, and 0.5 × 10^6 cells/mL in 500 μL PBS (pH 7.4). Aliquots of ^{89}Zr-Df-rituximab (50 μL of a stock solution of 0.37 kBq, [0.01 mCi] in 10 mL of 1% bovine serum albumin [BSA]; 0.37 kBq [1 μCi], 0.01 μg of mAb) were added to each tube (n = 3; final volume 550 mL). After addition of tracer, the solutions were gently vortexed and incubated at 37 °C. Two hours later, the solutions were centrifuged (300g for 3 min.), resuspended, and washed twice with ice-cold PBS before removing the supernatant. Cells were then pelleted by centrifugation, and the ^{89}Zr-activity associated with the cell pellet was measured with a gamma counter (1470 WIZARD Automatic Gamma Counter; Perkin-Elmer, Walthem, MA). The count data were background corrected and compared with the total number of counts in control samples. Competitive inhibition (blocking) assays were conducted by using the same procedure but with the addition of unmodified rituximab (50 μL, 0.2 mg/mL in 1% BSA, [1000-fold excess mAb; 10 μg]) to the ^{89}Zr-Df-rituximab solutions.

Immunoreactive fractions were determined by linear regression analysis of a plot of (total/bound) activity versus (1/[normalized cell concentration]), and calculated as 1/y-intercept. Stability of the labeled antibodies after incubation in human serum at 37 °C was analyzed by cellulose acetate electrophoresis (CAE) at 45 min and tested at 1, 4, 24, 48, 72, and 120 h.[27,28]

Animal Studies. Animal studies were performed in compliance with approval from the Administrative Panel on Laboratory Animal Care (APLAC) at Stanford University. Nude mice (CD1-nu) from Charles River, Inc., and huCD20 transgenic mice (Genentech, South San Francisco) were purchased for the experiments.[22,29] Prior to the animal study, huCD20 transgenic mice were screened to confirm the expression of CD20 positive targets by RT-PCR. The average weight of the mice was 25.0 ± 2.0 g. Nude mice and two other groups of human CD20 positive transgenic mice (3 animals for each group) were imaged at 1, 4, 24, 48, 72, 96, and 120 h using small animal PET. All experimental mice received ^{89}Zr-labeled radiopharmaceutical [200 μL, corresponding to 7.4 MBq, 2 μg of Df-Bz-rituximab] via tail vein injection. After radiotracer administration, the animals were scanned at the time points indicated above. Results are reported as % injected dose per gram of tissue (%ID/g). Statistical analysis was done with Student's t test (two-tailed, unequal variance).

Small Animal PET Imaging. Prior to the imaging experiments, the animals (nude and huCD20 transgenic mice) were lightly restrained and administered the dose of ^{89}Zr-Df-Bz-rituximab (7.4 MBq/2 μg Df-Bz-rituximab) via a lateral tail vein. At each time point (1, 4, 24, 48, 72, 96, and 120 h), the animals were anesthetized and scanned as described before. PET was performed on a Siemens Inveon small-animal multimodality PET/CT system (Preclinical Solutions; Siemens Healthcare Molecular Imaging, Knoxville, TN). This PET/CT system combines two independently operating PET and CT scanners with excellent radial, tangential, and axial resolutions higher than 1.5 mm at the center of the field of view of the PET module. The CT raw images were acquired at 80 kVp at 500 μA, two bed position, half-scan 220° of rotation, and 120 projections per bed position with a cone beam micro-X-ray source (50-μm focal spot size) and a 2048 × 3072 pixel X-ray detector. CT raw data sets were reconstructed using Shepp-Logan filter and cone-beam filtered back-projection. On the basis of attenuation correction from the CT measurements, static PET scan was acquired with default settings of coincidence timing window of 3.4 ns and energy window of 350 to 650 keV. The first acquisition was started 60 min after the tracer injection and acquired for 5 min. We then performed 10 min acquisitions after 4 h, 24 h, 48 h, and 20 min scans after 72, 96, and 120 h after the tracer injection. The images were reconstructed with two-dimensional ordered-subset expectation maximization (OSEM 2D) algorithm.[30] Image files were analyzed using open source software, a Medical Image Data Examiner (AMIDE).[31] For each small animal PET scan, three-dimensional regions of interest (ROIs) were drawn over the heart, liver, spleen, and whole body on decay-corrected whole-body images. The average radioactivity concentration in the ROI was obtained from the mean pixel values within the ROI volume. These data was converted to counts per milliliter per minute by using a predetermined conversion factor. The results were then divided by the injected dose to obtain an image region of interest-derived percentage injected dose per gram of tissue (%ID/g).

Scheme 1. Schematic Representation of Immuno-PET Tracer Synthesis

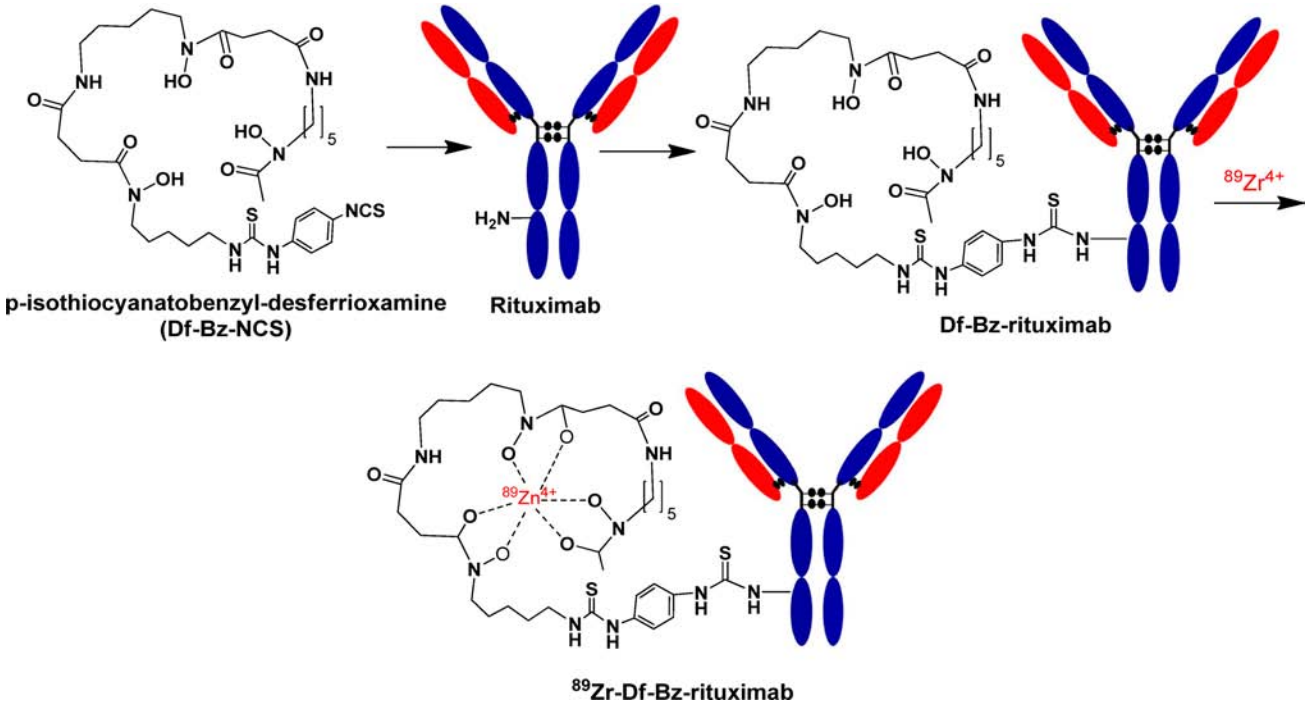

RESULTS

Preparation of Df-Bz-rituximab. The Df-Bz-rituximab immunoconjugate was prepared by coupling Df-Bz-NCS to the lysine groups of rituximab mAb (Scheme 1). Table 1A shows the various conditions of the immunoconjugation; various pH and molar concentrations of the chelates are listed in the table to optimize the immunoconjugation to achieve best chelates per Ab. The best immunoconjugation was achieved by the addition of a 5-fold molar excess of Df-Bz-NCS over rituximab at pH of 8.5, incubated at 25 °C for 45 min. These conditions resulted in a reproducible chelate/rituximab of 1.5 as assessed by MALDI-TOF. Although high concentrations of chelate (10-fold excess over mAb) provided maximum 2.6 *c*/*a*, we prefer to retain 5-fold molar excess to retain biological properties of the mAb as close to unmodified mAb.

Table 1. Optimization of Reaction Conditions for Df Chelate Conjugation and Radiochemistry to Prepare ^{89}Zr-Df-Bz-rituximab

A: Df-Bz Chelate Conjugation to Antibody[a]				
pH	time (min)	mAb (nmol)	Df-bz chelates (excess nm fold)	chelates/mAb (*c*/*a*)
8	45	0.5	5	1.30 ± 0.14
8	45	0.5	7.5	1.55 ± 0.07
8	45	0.5	10	2.20 ± 0.14
8.5	45	0.5	5	1.55 ± 0.07
8.5	45	0.5	7.5	2.30 ± 0.14
8.5	45	0.5	10	2.35 ± 0.07
9	45	0.5	5	1.65 ± 0.21
9	45	0.5	7.5	2.30 ± 0.14
9	45	0.5	10	2.60 ± 0.57
B: Radiochemical Yield Optimization[b]				
pH		time (min)	radiochemical yield (%)	
6.5		45	74.06 ± 3.51	
7		45	76.25 ± 0.86	
7.5		45	76.49 ± 0.54	
6.5		60	76.16 ± 1.05	
7		60	77.01 ± 2.16	
7.5		60	76.78 ± 1.24	

[a]25° C. [b]37° C.

Radiolabeling of Df-Bz-rituximab. Table 1B shows the optimization of the ^{89}Zr radiochemistry with Df-Bz-rituximab to achieve high radiochemical yield. Radiolabeling of Df-Bz-rituximab with ^{89}Zr in $NaHCO_3$ buffer (pH 7.0) yielded greater than 75% (Mean ± STD: 77.0 ± 2.1%). The highest radiochemical yield achieved was 77% at 37 °C, of pH 7.0, at incubation for 60 min. Table 2 shows the quality assurance of the ^{89}Zr-Df-Bz-rituximab PET tracer. Figure 1A shows the radiochemical purity was >95% (Mean ± STD: 98.0 ± 0.7%) determined by SEC.

Serum Stability Assay. Figure 1B shows the stability of the radiotracer in human serum over 5 days, tested by CAE at 45 min. The radio peaks in Figure 1B correspond to radiotracer at each time point. These results show that the tracer was stable in

Table 2. Quality Assurance of the ^{89}Zr-Df-Bz-rituximab PET Tracer

Characterization of ^{89}Zr-Df-Bz-rituximab		
test #	test specification	results (mean ± STD)
1	chelate/mAb	1.5 ± 0.3
2	radiochemical yield (%)	77.1 ± 2.1
3	final product yield (%)	70 ± 2.8
4	specific activity (TBq/mmol)	(5.1–6.0) × 10^2
5	purity by radio HPLC (%)	98 ± 0.7
6	purity by ITLC (%)	>95
7	purity by CAE 45 min (%)	>95
8	immunoreactivity (%)	84.2 ± 2.8

dx.doi.org/10.1021/bc300039r | *Bioconjugate Chem.* 2012, 23, 1221–1229

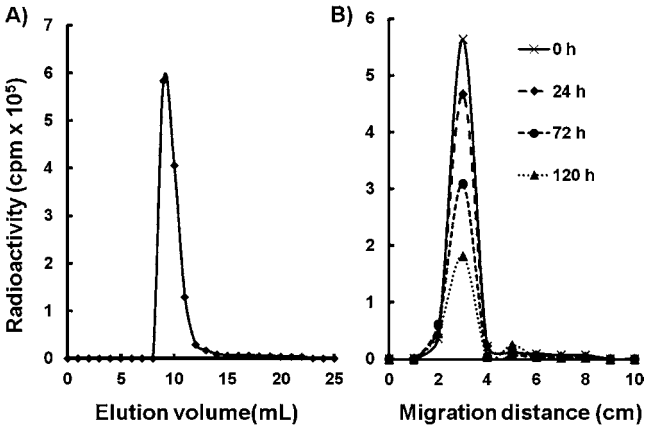

Figure 1. Purity and serum stability of the ^{89}Zr-Df-rituximab. (A) Radio-HPLC chromatogram PET tracer shows the purity of the tracer. The PET tracer was eluted by SEC 3000 column at a flow rate of 1 mL/min using PBS. Radioactivity of each of the 1 mL fractions was measured by a gamma counter and the data was used to plot the chromatogram. (B) Serum stability of ^{89}Zr-Df-rituximab assayed by cellulose acetate electrophoresis (CAE) at 45 min: The results of serum stability study of PET tracer tested by CAE are shown. CAE was performed for 45 min with barbital buffer (0.05 M, pH 8.6) at room temperature. Radioconjugate (50 μg) was mixed per mL of human serum and kept at 37 °C for 3 days. At various time points (0, 24, 72, and 120 h), 2−10 μL samples were drawn and tested for stability on CAE. Radioactivity peaks in the figure correspond to radioconjugate in the serum at days 1−5, demonstrating that radioconjugates are at identical migration distance.

serum and greater than 98% of the immunoconjugate was intact for up to 5 days.

Cell Binding Study. Figure 2 shows the binding fraction of the ^{89}Zr-Df-Bz-rituximab tested with CD20 positive Ramos cells. The average immunoreactive fraction of ^{89}Zr-Df-Bz-rituximab from each lot was 0.85 ± 0.07 (n = 6). The control experiment was performed with CD20 negative Jurkat cells, and CD20 positive Ramos cells preblocked with 100-fold excess of cold rituximab over ^{89}Zr-rituximab. The immunoreactivity of the tracer was 84.2 ± 2.8% (Mean ± STD) compared to the binding effect on same cells but preblocked with cold rituximab and Jurkat cells were 5 ± 1.6% (Mean ± STD) and 4 ± 2.1% (Mean ± STD) respectively, indicating the specific reactivity of the tracer.

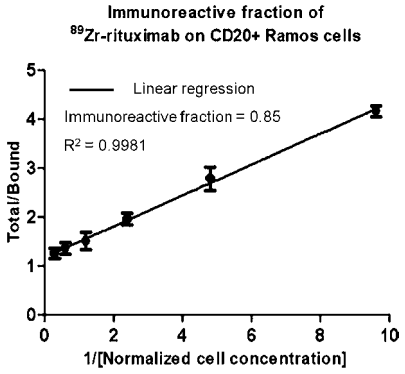

Figure 2. Live cell binding assay for the determination of the immunoreactive fraction of an ^{89}Zr-rituximab tracer using Ramos cells. The assay was set up using six concentrations of Ramos cells in 1:2 dilutions from 3.3 to 0.1 million cells/mL, and the final concentrations of tracer was 10 ng/mL. Cells were used at various concentrations to infinite antigen excess (1/y-intercept). A plot of (X axis) total/bound activity against (Y axis) 1/normalized cell concentration (mL/million) provided immunoreactive fraction (0.85 ± 0.07). X axis of graph represents cell concentrations (mL/million) 0.3, 0.6, 1.2, 2.4, 4.8, and 9.62, the corresponding immunoreactive fractions (mean ± SD) represent Y axis are 1.25 ± 0.11, 1.35 ± 0.12, 1.5 ± 0.18, 1.95 ± 0.12, 2.78 ± 0.24, and 4.16 ± 0.11, respectively. The data represented in the graph are corrected with subtraction of immunoreactive fractions on preblocked cells [nonspecific binding (mean ± SD) = 0.008 ± 0.001] with cold rituximab prior to tracer application.

Small Animal PET and CT Imaging. To evaluate antibody-based PET tracer targeting anti-CD20 B-cell lymphoma, we used a huCD20TM model that mimics a human B-cell lymphoma tumor and provides a clearance pattern such that rituximab recognizes CD-20 antigens on B-cells in human lymphoma patients. The *in vivo* targeting ability of ^{89}Zr-Df-Bz-rituximab in huCD20TM was demonstrated at various time points post tail-vein injection of radiopharmaceutical, with and without blocking of CD20 antigens by cold rituximab. Each mouse was imaged at various time points (1, 4, 24, 48, 72, 96, and 120 h) after tracer injection of 7−8 MBq of ^{89}Zr-Df-Bz-rituximab (2−3 μg of rituximab).

Figures 3 and 4 show the immunoPET images of huCD20TM using the ^{89}Zr-Df-Bz-rituximab tracer. Figure 3A PET images were obtained at 4, 24, 48, 72, 96, and 120 h after injection of tracer. At each time point, PET/CT images were obtained from the control huCD20TM (Figure 3 top row: blocking = preblocked with 100-fold excess cold rituximab over tracer mass 2 h prior to tracer injection) and experimental huCD20TM (Figure 3 bottom row: nonblocking = tracer alone). Figure 3B images shown are huCD20 images of just CT and co-registered with PET/CT for organ delineation. Organs marked as follows: H = heart, L = liver, and the spleen is marked with a yellow arrow. From these images, it is evident that ^{89}Zr-Df-Bz-rituximab had uptake primarily in the spleen, a major site for B cells, which express CD20 antigen. Figure 4 shows immunoPET images of huCD20TM at the maximum intensity projection of ^{89}Zr-Df-Bz-rituximab after 5 days post injection of the tracer. The spleen and liver uptake (%ID/g) is shown in Figure 5 at 120 h post injection compared with the predose group (human CD20 antigens were preblocked with cold rituximab). The radiopharmaceutical uptake (%ID/g) in the preblocked (n = 3) and unblocked (n = 3) groups is 3.19 ± 0.14, and 83.3 ± 1.99 for spleen; 1.32 ± 0.05, and 0.61 ± 0.01 for liver, respectively.

■ DISCUSSION

To monitor NHL therapy, we have developed a novel immunoPET tracer using ^{89}Zr radionuclide that chelated to desferrioxamine (Df) linked to rituximab. This work was conducted in an effort to eventually translate the methods developed here for human lymphoma patient management through PET imaging. In this report, we present *in vitro* characterization and preclinical evaluation of ^{89}Zr-Df-rituximab tracer in a huCD20TM mouse model, which expresses the human CD20. Previously, we developed a ^{64}Cu-DOTA-rituximab immunoPET tracer[22] that received FDA approval for a physician-sponsored IND (#104995) for safety and clearance and is currently being tested in a clinical trial. We are also interested in developing immunoPET tracers for radioimmunotherapy monitoring with longer half-life radionuclides for comparable half-life of antibody (2−5 days). To match the half-life of antibody, currently very few long half-life PET

dx.doi.org/10.1021/bc300039r | Bioconjugate Chem. 2012, 23, 1221−1229

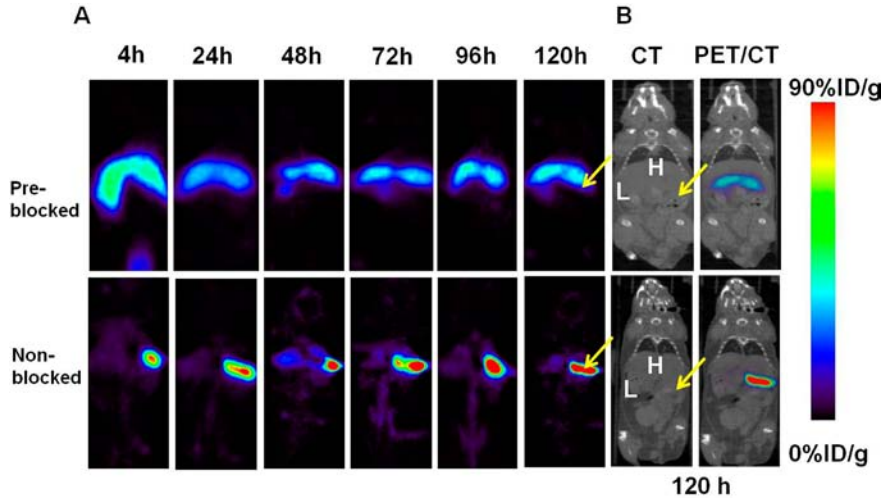

Figure 3. ImmunoPET images of ^{89}Zr-Df-rituximab on huCD20TM model. The representative images were scanned (5−20 min) at 4−120 h after tracer injection (7.4 MBq/2−3 μg of rituximab). Panels A,B: top (blocked = Predose; control) and bottom (nonblocked = no predose; experiment) rows are huCD20TM coronal images of preblocked and unblocked, respectively. Panel A represents a mouse that received 4 mg/kg cold rituximab 2 h prior to tracer injection and panel B represents a mouse that received the PET tracer only. Panel C shows the CT and PET/CT images at 120 h after tracer injection for organ identification. Spleen is indicated by the yellow arrow. The other major organs are as marked (H = heart and L = liver). The color bar shows tracer %ID/g.

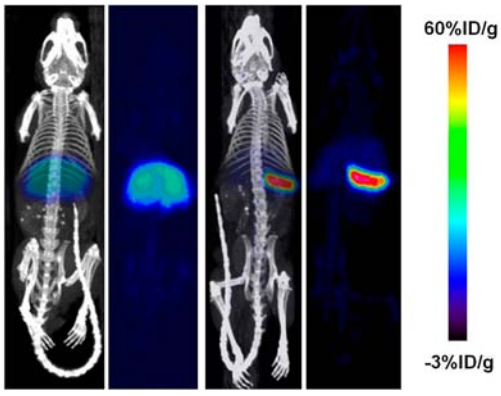

Figure 4. ImmunoPET images of huCD20TM at 120 h post injection with maximum intensity projections(MIP) shows mouse with and without predose of rituximab. The ^{89}Zr-Df-rituximab uptake by spleen is very high compared to preblocked mouse by cold rituximab. ImmunoPET tracer was stable even after 120 h, and no PET signals were observed in bone marrow.

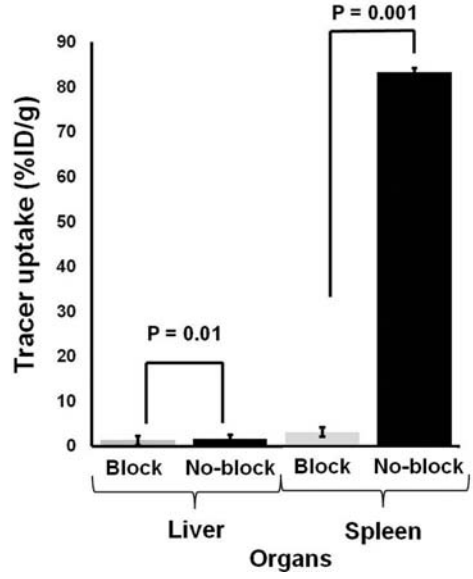

Figure 5. Quantitative analysis of organ uptake estimated from the ROI of the images. Data shown are tracer uptake values at 120 h post injection by liver (gray bar) and spleen (black bar) of huCD20 mice with and without predose groups. *Y* axis is %ID/gram and *X* axis shows comparison of control and experiment groups. Tracer uptake by the liver is similar for both study groups, and the spleen uptake for the group without predose is >50 times higher than that with the predose group, confirming the specificity of the tracer. The data represent the mean ± STD of 3 mice per group.

radionuclides are available for use in clinical studies; i.e., ^{124}I and ^{89}Zr. Although iodination (^{124}I) of antibodies for PET is simple, it has widespread limitations of lower resolution and enzymatic deiodination.[32,33]

Recently, ^{89}Zr-immunoPET tracers are being increasingly used in clinical studies.[34,35] This is because the low production cost, purity, stability, and extended half-life period of the ^{89}Zr radionuclides make it a perfect choice to link to an antibody for targetable PET tracers. On the other hand, GMP-grade Df-Bz-NCS bifunctional chelator is also commercially available for ^{89}Zr labeling for clinical studies. The Df-Bz-NCS ligand has already shown good biological performance when used in protein conjugation of radionuclides such as ^{68}Ga, ^{66}Ga, ^{225}Ac, ^{177}Lu, and lead radionuclides.[36,37] Furthermore, currently both Df-Bz-NCS conjugated antibodies and ^{89}Zr-labeled antibodies are in clinical trials after FDA approval. Although few studies have shown that DTPA can be used for the chelation of ^{89}Zr ions, it shows demetalation *in vivo* and hence Df continues to remain the best chelator for ^{89}Zr.[38−40] Thus, in our study, Df-Bz-NCS was utilized to prepare Df-Bz-rituximab according to published procedures.[25,41]

In the present report, we optimized the reaction conditions for conjugation of Df and radiolabeling of ^{89}Zr to chelate for high radiochemical yield and specific activity specifically for the rituximab antibody. The conjugation optimization yielded maximum 2.6 chelates per antibody (Table 1) at pH 9.0, with 10-fold molar excess ratio after 45 min; although chelate

dx.doi.org/10.1021/bc300039r | *Bioconjugate Chem.* 2012, 23, 1221−1229

ratio per antibody was dictated by the number of lysine molecules per antibody, in our case the c/a is comparable to the results reported elsewhere using different antibody.[41] Although we have achieved 2.6 c/a, we realize that too many lysine group modifications may alter the biodistribution from the parent molecule.[42,43] Hence, we restrict our chelate conjugation to not more than 2.0 per antibody for the use of preclinical studies. Similarly, the radiolabeling optimization yielded maximum 77.0 ± 2.16 (mean ± STD) at pH 7, and after purification, the final product purity was >98% monomeric (Figure 1A and Table 2).

The ^{89}Zr-Df-Bz-rituximab conjugate showed good *in vitro* stability for up to 5 days at 37 °C in 0.9% saline, 50 mM DTPA, and human serum (Figure 1B). Our results confirmed with previous reports elsewhere that the Df-Bz-SCN linked immunoconjugates were stable over a 6 day period in serum at 37 °C.[36,41] After 5 days, less than 1.5% activity appeared at 5 cm in CAE at 45 min, which may correspond to ^{89}Zr-transchelated protein in serum, possibly due to demetalation from the ^{89}Zr-Df-rituximab (Figure 1B). Figure 2 shows the estimation of immunoreactive fraction of ^{89}Zr-Df-Bz-rituximab used in the preclinical studies. The immunoreactive fraction of the ^{89}Zr-Df-rituximab was measured by specific *in vitro* cellular association assays using CD20-positive Ramos cells prior to each preclinical study. The average immunoreactive fraction of ^{89}Zr-Df-rituximab (Figure 2) was found to be 0.85 (n = 6). Control experiments were performed using the CD20-negative Jurkat cells (no CD20 expression), and Ramos cells preblocked with 100-fold excess of cold unmodified rituximab 1 h prior to tracer application showed <4% binding. These data clearly demonstrated that the ^{89}Zr-Df-rituximab tracer preparation was highly immunoreactive with specific binding effect on huCD20 expressing live cells.

ImmunoPET images of ^{89}Zr-Df-rituximab were acquired on huCD20TM using the Inveon small animal CT-PET scanner at 0−120 h post injection presented in Figures 3 and 4. Figure 3A,B bottom row (nonblocking-huCD20TM) shows clearly that the tracer uptake in spleen is very high compared to the liver and other organs. In the same figure, the top row PET images pertaining to blocking-huCD20TM (control group) show that the tracer uptake was very low at all time points due to preblocking by cold rituximab. Figure 5 shows %ID/g of tracer uptake by organs of huCD20TM: (a) liver and (b) spleen from both nonblocked and blocked huCD20TM PET images (calculated from the region-of-interest), respectively. ROI quantification of these images showed that at 120 h post injection the absolute uptake of ^{89}Zr-rituximab by spleen was 83.0 and 3.2%ID/g in nonblocked and blocked huCD20TM mice, respectively. These data show that ^{89}Zr-Df-rituximab immuno-PET imaging provides a very high contrast image at CD20 expressing marker compared to the liver. The huCD20TM model we used in this study will mimic human patients with respect to targeting protein, which is identical to human CD20. Thus, the outcome of this study would be more favorable for clinical translation.

To see a high-contrast image, we prepared tracer with high specific activity by using a very low mass of antibody (2−3 μg/dose; 80−120 μg/kg) compared to studies carried out by others (0.2 mg/dose; 8 mg/kg).[36] This is because high mass rituximab may induce apoptosis, by complement-mediated lysis and antibody-dependent cellular toxicity which will lead to eradication of B cells. To visualize optimal high-contrast images over extended periods, the tracer affinity for CD20 target should be high and the tracer should be intact over longer times. Thus, compared to other published studies our tracer with high specific activity showed very high contrast images over extended period of time. This was reflected in Figures 3B and 4 at 120 h where the immunoPET demonstrated very high contrast images for spleen of nonblocked-huCD20TM, compared to blocked-huCD20TM. ROI quantitative analysis of ^{89}Zr-Df-rituximab uptake in spleen (Figure 5), of non-blocked-huCD20TM, was approximately 25-fold higher %ID/g than blocked-huCD20TM. Thus, our study data observed from the high specific activity tracer may be useful for other mAbs and mAb-fragments for high imaging contrast and for imaging for extended periods of time.

Zirconium is known to bind plasma proteins[44] and is later deposited in mineral bone.[45,46] However, in our study we did not see bone uptake of the radionuclide originating from the breakdown of the ^{89}Zr-antibody or any nonspecific association of ^{89}Zr to antibody, which could then easily transchelate to plasma proteins compared to ^{89}Zr bound to Df. The results reported here are consistent with previous investigations and confirm that ^{89}Zr is a suitable radionuclide for labeling full, intact antibodies (150 kDa).[36] The ^{89}Zr has the potential to solve many problems associated with various PET isotopes such as (a) PET isotopes of ^{64}Cu and ^{86}Y having short half-life, (b) ^{64}Cu, ^{68}Ga, and ^{124}I demonstrated to have high uptake in background tissue, (c) ^{124}I are known for low *in vivo* stability (for any internalizing antibody−antigen constructs) and poor dosimetry. Contrary to the above-mentioned isotopes, ^{89}Zr-labeled mAbs can be used for both localizing tumors and measuring the long-term effects (5 days) of drug treatment from a single radiotracer injection. Such measurements cannot be achieved by using ^{64}Cu,^{124}I, and ^{99m}Tc radiolabeled rituximab.[23,24,47] The image quality and chelate chemistry of ^{89}Zr-Df-mab immunoPET tracers were well-demonstrated by various PET images.[36,41,48] For example, studies pertaining to ^{89}Zr-Df-trastuzumab represent one of the most promising radiotracers for noninvasive immunoPET measurements of HER2/neu expression *in vivo*.[48]

CONCLUSIONS

We have prepared ^{89}Zr-Df-rituximab with high specific activity, purity, stability, and immunoreactivity. The ^{89}Zr-immuoPET tracer was shown to be stable for up to five days in human serum. The desferrioxamine chelate conjugation to antibody and radiolabeling of immunoconjugates were optimized in such a way that the biological activity of the antibody was intact. The preclinical studies of ^{89}Zr-Df-rituximab with the huCD20TM model clearly indicated that this tracer is specifically targeted to huCD20 antigen and has the potential to translate to patients. Compared to our previous immunoPET tracer (^{64}Cu-DOTA-rituximab), ^{89}Zr-Df-rituximab could be used to monitor and measure therapeutic effects over extended periods of time in both preclinical and clinical studies. Further, using ^{89}Zr-Df-rituximab the pharmacodynamic effects of any novel drugs can potentially be studied along with patient response to drug treatment. Currently, optimization toward GMP preparation for an IND application to FDA and eventual clinical translation of ^{89}Zr-Df-rituxiab are underway.

ASSOCIATED CONTENT

Supporting Information

Additional information is available, such as method of ^{89}Zr production and ex vivo biodistribution study; biodistribution

data of ^{89}Zr-Df-rituximab from ROI of PET images and from ex vivo organ uptake; and movie of immuno-PET tracer on huCD20TM. This material is available free of charge via the Internet at http://pubs.acs.org.

AUTHOR INFORMATION

Corresponding Author

*Phone: 650-725-2309, Fax: 650-724-4948, E-mail: sgambhir@stanford.edu.

Notes

The authors declare no competing financial interest.

ACKNOWLEDGMENTS

We thank Ataya Sathirachinda, Drs. Fred Chin, David Dick, Mark Stolowitz, and the staff in the radiochemistry and cyclotron facilities, the small animal imaging center, image analysis and quantitation core and Canary Center at Stanford for Cancer Early Detection for instrumentation support and analysis. This work was supported by grants NCI ICMIC P50-CA114747 (SSG).

REFERENCES

(1) Carter, P. J. (2006) Potent antibody therapeutics by design. *Nat. Rev. Immunol. 6*, 343−57.

(2) Wu, A. M. (2009) Antibodies and antimatter: the resurgence of immuno-PET. *J. Nucl. Med. 50*, 2−5.

(3) Lawrence, S. (2007) Billion dollar babies--biotech drugs as blockbusters. *Nat. Biotechnol. 25*, 380−2.

(4) Maggon, K. (2007) Monoclonal antibody "gold rush". *Curr. Med. Chem. 14*, 1978−87.

(5) Nayak, T. K., and Brechbiel, M. W. (2009) Radioimmunoimaging with longer-lived positron-emitting radionuclides: potentials and challenges. *Bioconjugate Chem. 20*, 825−41.

(6) van Dongen, G. A., Visser, G. W., Lub-de Hooge, M. N., de Vries, E. G., and Perk, L. R. (2007) Immuno-PET: a navigator in monoclonal antibody development and applications. *Oncologist 12*, 1379−89.

(7) Boswell, C. A., and Brechbiel, M. W. (2007) Development of radioimmunotherapeutic and diagnostic antibodies: an inside-out view. *Nucl. Med. Biol. 34*, 757−78.

(8) Borjesson, P. K., Jauw, Y. W., Boellaard, R., de Bree, R., Comans, E. F., Roos, J. C., Castelijns, J. A., Vosjan, M. J., Kummer, J. A., Leemans, C. R., Lammertsma, A. A., and van Dongen, G. A. (2006) Performance of immuno-positron emission tomography with zirconium-89-labeled chimeric monoclonal antibody U36 in the detection of lymph node metastases in head and neck cancer patients. *Clin. Cancer Res. 12*, 2133−2140.

(9) Borjesson, P. K. E., Jauw, Y. W. S., de Bree, R., Roos, J. C., Castelijns, J. A., Leemans, C. R., van Dongen, G. A. M. S., and Boellaard, R. (2009) Radiation dosimetry of zirconium-89-labeled chimeric monoclonal antibody U36 as used for immuno-PET in head and neck cancer patients. *J. Nucl. Med. 50*, 1828−1836.

(10) Dijkers, E., Kosterink, J. G., Rademaker, A. P., Perk, L. R., van Dongen, G. A., Bart, J., de Jong, J. R., de Vries, E. G., and Lub-de Hooge, M. N. (2009) Development and characterization of clinical-grade 89Zr-trastuzumab for HER2/neu immunoPET imaging. *J. Nucl. Med. 50*, 974−981.

(11) Perk, L. R., Vosjan, M. J., Visser, G. W., Budde, M., Jurek, P., Kiefer, G. E., and van Dongen, G. A. (2010) p-Isothiocyanatobenzyl-deferrioxamine: a new bifunctional chelate for facile radiolabeling of monoclonal antibodies with zirconium-89 for immuno-PET imaging. *Eur. J. Nucl. Med. Mol. Imaging 37*, 250−259.

(12) Aerts, H. J., Dubois, L., Perk, L., Vermaelen, P., van Dongen, G. A., Wouters, B. G., and Lambin, P. (2008) Disparity between in vivo EGFR expression and zirconium-89-labeled cetuximab uptake assessed by PET. *J. Nucl. Med. 50*, 123−131.

(13) Brouwers, A., Verel, I., Van Eerd, J., Visser, G., Steffens, M., Oosterwijk, E., Corstens, F., Oyen, W., Van Dongen, G., and Boerman, O. (2004) PET radioimmunoscintigraphy of renal cell cancer using 89Zr-labeled cG250 monoclonal antibody in nude rats. *Cancer Biother. Radiopharm. 19*, 155−163.

(14) Nagengast, W. B., de Vries, E. G., Hospers, G. A., Mulder, N. H., de Jong, J. R., Hollema, H., Brouwers, A. H., van Dongen, G. A., Perk, L. R., and Lub-de Hooge, M. N. (2007) In vivo VEGF imaging with radiolabeled bevacizumab in a human ovarian tumor xenograft. *J. Nucl. Med. 48*, 1313−1319.

(15) Verel, I., Visser, G. W., Boellaard, R., Stigter-van Walsum, M., Snow, G. B., and van Dongen, G. A. (2003) 89Zr immuno-PET: comprehensive procedures for the production of 89Zr-labeled monoclonal antibodies. *J. Nucl. Med. 44*, 1271−1281.

(16) Verel, I., Visser, G. W., Boerman, O. C., van Eerd, J. E., Finn, R., Boellaard, R., Vosjan, M. J., Stigter-van Walsum, M., Snow, G. B., and van Dongen, G. A. (2003) Long-lived positron emitters zirconium-89 and iodine-124 for scouting of therapeutic radioimmunoconjugates with PET. *Cancer Biother. Radiopharm. 18*, 655−661.

(17) Perk, L. R., Visser, O. J., Stigter-van Walsum, M., Vosjan, M. J., Visser, G. W., Zijlstra, J. M., Huijgens, P. C., and van Dongen, G. A. (2006) Preparation and evaluation of 89Zr-Zevalin for monitoring of 90Y-Zevalin biodistribution with positron emission tomography. *Eur. J. Nucl. Med. Mol. Imaging 33*, 1337−1345.

(18) Zalutsky, M. R. (2006) Potential of immuno-positron emission tomography for tumor imaging and immunotherapy planning. *Clin. Cancer Res. 12*, 1958−1960.

(19) Fisher, S. G., and Fisher, R. I. (2004) The epidemiology of non-Hodgkin's lymphoma. *Oncogene 23*, 6524−6534.

(20) Zhou, X., Hu, W., and Qin, X. (2008) The role of complement in the mechanism of action of rituximab for B-cell lymphoma: implications for therapy. *Oncologist 13*, 954−66.

(21) Glennie, M. J., French, R. R., Cragg, M. S., and Taylor, R. P. (2007) Mechanisms of killing by anti-CD20 monoclonal antibodies. *Mol. Immunol. 44*, 3823−3837.

(22) Natarajan, A., Gowrishankar, G., Nielsen, C. H., Wang, S., Iagaru, A., Goris, M. L., and Gambhir, S. S. (2012) Positron emission tomography of (64)Cu-DOTA-Rituximab in a transgenic mouse model expressing human CD20 for clinical translation to image NHL. *Mol. Imaging Biol.*, DOI: 10.1007/s11307-011-0537-8.

(23) Olafsen, T., Betting, D., Kenanova, V. E., Salazar, F. B., Clarke, P., Said, J., Raubitschek, A. A., Timmerman, J. M., and Wu, A. M. (2009) Recombinant anti-CD20 antibody fragments for small-animal PET imaging of B-cell lymphomas. *J. Nucl. Med. 50*, 1500−8.

(24) Tran, L., Huitema, A. D., van Rijswijk, M. H., Dinant, H. J., Baars, J. W., Beijnen, J. H., and Vogel, W. V. (2011) CD20 antigen imaging with ^{124}I-rituximab PET/CT in patients with rheumatoid arthritis. *Hum. Antibodies 20*, 29−35.

(25) Vosjan, M. J., Perk, L. R., Visser, G. W. M., Budde, M., Jurek, P., Kiefer, G. E., and van Dongen, G. A. M. S. (2010) Conjugation and radiolabeling of monoclonal antibodies with zirconium-89 for PET imaging using the bifunctional chelate p-isothiocyanatobenzyl-desferrioxamine. *Nat. Protoc. 5*, 739−743.

(26) Lindmo, T., Boven, E., Cuttitta, F., Fedorko, J., and Bunn, P. A., Jr. (1984) Determination of the immunoreactive fraction of radiolabeled monoclonal antibodies by linear extrapolation to binding at infinite antigen excess. *J. Immunol. Methods 72*, 77−89.

(27) Adams, G. P., DeNardo, S. J., Deshpande, S. V., DeNardo, G. L., Meares, C. F., McCall, M. J., and Epstein, A. L. (1989) Effect of mass of ^{111}In-benzyl-EDTA monoclonal antibody on hepatic uptake and processing in mice. *Cancer Res. 49*, 1707−11.

(28) Saludes, J. P., Natarajan, A., DeNardo, S. J., and Gervay-Hague, J. (2010) The remarkable stability of chimeric, sialic acid-derived alpha/delta-peptides in human blood plasma. *Chem. Biol. Drug Design 75*, 455−460.

(29) Gong, Q., Ou, Q., Ye, S., Lee, W. P., Cornelius, J., Diehl, L., Lin, W. Y., Hu, Z., Lu, Y., Chen, Y., Wu, Y., Meng, Y. G., Gribling, P., Lin, Z., Nguyen, K., Tran, T., Zhang, Y., Rosen, H., Martin, F., and Chan,

A. C. (2005) Importance of cellular microenvironment and circulatory dynamics in B cell immunotherapy. *J. Immunol. 174*, 817−26.
(30) Irmler, I. M., Opfermann, T., Gebhardt, P., Gajda, M., Brauer, R., Saluz, H. P., and Kamradt, T. (2010) In vivo molecular imaging of experimental joint inflammation by combined(18)F-FDG positron emission tomography and computed tomography. *Arthritis Res. Ther. 12*, R203.
(31) Loening, A. M., and Gambhir, S. S. (2003) AMIDE: a free software tool for multimodality medical image analysis. *Mol. Imaging 2*, 131−7.
(32) Geissler, F., Anderson, S. K., and Press, O. (1991) Intracellular catabolism of radiolabeled anti-CD3 antibodies by leukemic T cells. *Cell Immunol. 137*, 96−110.
(33) Shih, L. B., Thorpe, S. R., Griffiths, G. L., Diril, H., Ong, G. L., Hansen, H. J., Goldenberg, D. M., and Mattes, M. J. (1994) The processing and fate of antibodies and their radiolabels bound to the surface of tumor cells in vitro: a comparison of nine radiolabels. *J. Nucl. Med. 35*, 899−908.
(34) Dijkers, E. C., Oude Munnink, T. H., Kosterink, J. G., Brouwers, A. H., Jager, P. L., de Jong, J. R., van Dongen, G. A., Schroder, C. P., Lub-de Hooge, M. N., and de Vries, E. G. (2010) Biodistribution of ^{89}Zr-trastuzumab and PET imaging of HER2-positive lesions in patients with metastatic breast cancer. *Clin. Pharmacol. Ther. 87*, 586−92.
(35) Dijkers, E. C., Kosterink, J. G., Rademaker, A. P., Perk, L. R., van Dongen, G. A., Bart, J., de Jong, J. R., de Vries, E. G., and Lub-de Hooge, M. N. (2009) Development and characterization of clinical-grade ^{89}Zr-trastuzumab for HER2/neu immunoPET imaging. *J. Nucl. Med. 50*, 974−81.
(36) Perk, L. R., Vosjan, M. J., Visser, G. W., Budde, M., Jurek, P., Kiefer, G. E., and van Dongen, G. A. (2010) p-Isothiocyanatobenzyl-desferrioxamine: a new bifunctional chelate for facile radiolabeling of monoclonal antibodies with zirconium-89 for immuno-PET imaging. *Eur. J. Nucl. Med. Mol. Imaging 37*, 250−9.
(37) Mathias, C. J., Lewis, M. R., Reichert, D. E., Laforest, R., Sharp, T. L., Lewis, J. S., Yang, Z. F., Waters, D. J., Snyder, P. W., Low, P. S., Welch, M. J., and Green, M. A. (2003) Preparation of 66Ga- and 68Ga-labeled Ga(III)-deferoxamine-folate as potential folate-receptor-targeted PET radiopharmaceuticals. *Nucl. Med. Biol. 30*, 725−31.
(38) Holland, J. P., Sheh, Y., and Lewis, J. S. (2009) Standardized methods for the production of high specific-activity zirconium-89. *Nucl. Med. Biol. 36*, 729−39.
(39) Meijs, W. E., Haisma, H. J., Klok, R. P., van Gog, F. B., Kievit, E., Pinedo, H. M., and Herscheid, J. D. (1997) Zirconium-labeled monoclonal antibodies and their distribution in tumor-bearing nude mice. *J. Nucl. Med. 38*, 112−8.
(40) Meijs, W. E., Herscheid, J. D., Haisma, H. J., and Pinedo, H. M. (1992) Evaluation of desferal as a bifunctional chelating agent for labeling antibodies with Zr-89. *Int. J. Rad. Appl. Instrum. A 43*, 1443−7.
(41) Tinianow, J. N., Gill, H. S., Ogasawara, A., Flores, J. E., Vanderbilt, A. N., Luis, E., Vandlen, R., Darwish, M., Junutula, J. R., Williams, S.-P., and Marik, J. (2010) Site-specifically 89Zr-labeled monoclonal antibodies for ImmunoPET. *Nucl. Med. Biol. 37*, 289−297.
(42) van Gog, F. B., Visser, G. W., Klok, R., van der Schors, R., Snow, G. B., and van Dongen, G. A. (1996) Monoclonal antibodies labeled with rhenium-186 using the MAG3 chelate: relationship between the number of chelated groups and biodistribution characteristics. *J. Nucl. Med. 37*, 352−62.
(43) van Gog, F. B., Visser, G. W., Stroomer, J. W., Roos, J. C., Snow, G. B., and van Dongen, G. A. (1997) High dose rhenium-186-labeling of monoclonal antibodies for clinical application: pitfalls and solutions. *Cancer 80*, 2360−70.
(44) Mealey, J., Jr. (1957) Turn-over of carrier-free zirconium-89 in man. *Nature 179*, 673−4.
(45) Fletcher, C. R. (1969) The radiological hazards of zirconium-95 and niobium-95. *Health Phys. 16*, 209−20.
(46) Shiraishi, Y., and Ichikawa, R. (1972) Absorption and retention of 144 Ce and 95 Zr- 95 Nb in newborn, juvenile and adult rats. *Health Phys. 22*, 373−8.
(47) Stopar, T. G., Mlinaric-Rascan, I., Fettich, J., Hojker, S., and Mather, S. J. (2006) (99m)Tc-rituximab radiolabelled by photo-activation: a new non-Hodgkin's lymphoma imaging agent. *Eur. J. Nucl. Med. Mol. Imaging 33*, 53−9.
(48) Holland, J. P., Caldas-Lopes, E., Divilov, V., Longo, V. A., Taldone, T., Zatorska, D., Chiosis, G., and Lewis, J. S. (2010) Measuring the pharmacodynamic effects of a novel Hsp90 Inhibitor on HER2/*neu* expression in mice using ^{89}Zr-DFO-Trastuzumab. *PLoS ONE 5*, e8859.

Bioconjugate Chemistry

Article

pubs.acs.org/bc

Cross-Linked DNA: Site-Selective "Click" Ligation in Duplexes with Bis-Azides and Stability Changes Caused by Internal Cross-Links

Hai Xiong and Frank Seela*

Laboratory of Bioorganic Chemistry and Chemical Biology, Center for Nanotechnology, Heisenbergstraße 11, 48149 Münster, Germany

Laboratorium für Organische und Bioorganische Chemie, Institut für Chemie, Universität Osnabrück, Barbarastraße 7, 49069 Osnabrück, Germany

Supporting Information

ABSTRACT: Heterodimeric interstrand cross-linked DNA was constructed by the "bis-click" reaction carried out on preformed oligonucleotide duplexes with the bis-azide **1**. For this, alkynylated 8-aza-7-deazapurine or corresponding 5-substituted pyrimidine nucleosides were synthesized. Cross-linking resulted in chemoselective formation of heterodimeric duplexes while homodimers were suppressed. For product identification, heterodimeric DNA was prepared by the "stepwise click" reaction, while noncomplementary homodimers were accessible by "bis-click" chemistry, unequivocally. Studies on duplex melting of complementary cross-linked duplexes (heterodimers) revealed significantly increased T_m values compared to the non-cross-linked congeners. The stability of this cross-linked DNA depends on the linker length and the site of modification. Cross-linked homodimers hybridized with single-stranded complementary oligonucleotides show much lower stability.

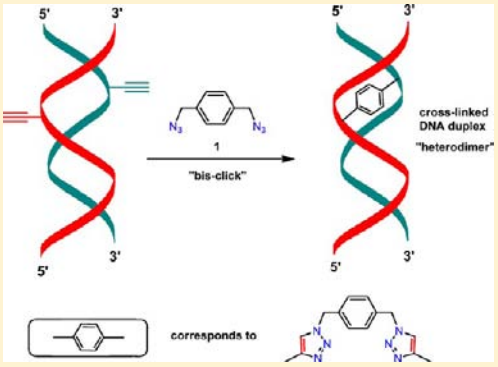

INTRODUCTION

Currently, our laboratory has reported on the cross-linking of oligonucleotide strands[1,2] using the Huisgen-Meldal-Sharpless "click" chemistry.[3−13] The reaction was performed on single-stranded oligonucleotides by two methods: (i) the "bis-click" reaction, which was limited to the cross-linking of identical oligonucleotide strands (homodimers) and (ii) the "stepwise click" protocol to cross-link nonidentical DNA strands (heterodimers) in a two-step method with a large excess of cross-linking agent.[1,2] Both methods made use of DNA modified at the nucleobases with alkynyl side chains and bis-azides like **1**, functioning as cross-linking reagents.[14−16] As a result, internal cross-links were generated at various positions and with linkers of different lengths.[17−35]

Now, the cross-linking of cDNA strands in duplex DNA will be investigated, thereby using duplex formation as a tool ("template") for the selective generation of heterodimeric DNA duplexes by the "bis-click" reaction, while the "stepwise click" protocol will be used for heterodimer assignment. We show that a diversity of alkynylated nucleosides related to the four canonical DNA bases can provide terminal triple bonds to construct cross-linked DNA within a duplex.[2,36−42]

In our study, cross-linking is performed by the "bis-click" protocol using a duplex with triple bonds in each of the complementary strands and the bis-azide **1**.[16] The "stepwise click" protocol was used for the unambiguous assignment of the heterodimers and was performed with one strand bearing the triple bond and the other one carrying the azido function. The latter was previously used to cross-link nonidentical strands selectively. We show now that under optimal conditions side chain triple bonds can be connected in a chemoselective way by "bis- click" chemistry or for comparison by the "stepwise click" protocol (Figure 1). For this, it is a prerequisite that the size of the cross-linker and the distance between the triple bonds have to be of comparable length. Then, the linker is well-accommodated in the duplex structure and the formation of heterodimers is favored while homodimers are suppressed. It will be shown that DNA cross-links induce additional stability to duplex DNA as displayed by strongly increased T_m values of cross-linked species. In this context, the impact of a variety of modified alkynylated nucleobases and the influence of the side chain length and distance of triple bonds regarding duplex stability is evaluated. The cross-linking reaction using "bis-click" or "stepwise click" chemistry is applicable for duplex DNA and might be exerted to cross-link other DNA assemblies such as triplexes or quartets.

EXPERIMENTAL PROCEDURES

General Methods and Materials. All chemicals were purchased from Acros, Fluka, or Sigma-Aldrich (Sigma-Aldrich Chemie GmbH, Deisenhofen, Germany). Standard phosphoramidites were purchased from Sigma (Sigma-Aldrich Chemie

Received: February 13, 2012
Revised: April 13, 2012
Published: May 4, 2012

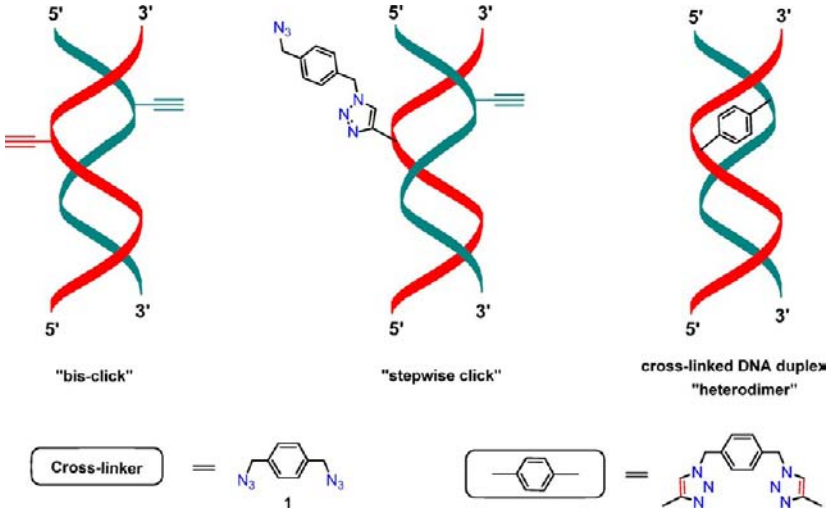

Figure 1. Cross-linked DNA formed by the "bis-click" or "stepwise click" reaction performed on duplex DNA. Red and green display complementary oligonucleotide strands.

Scheme 1. Synthesis of the Azido-Functionalized Conjugate 10

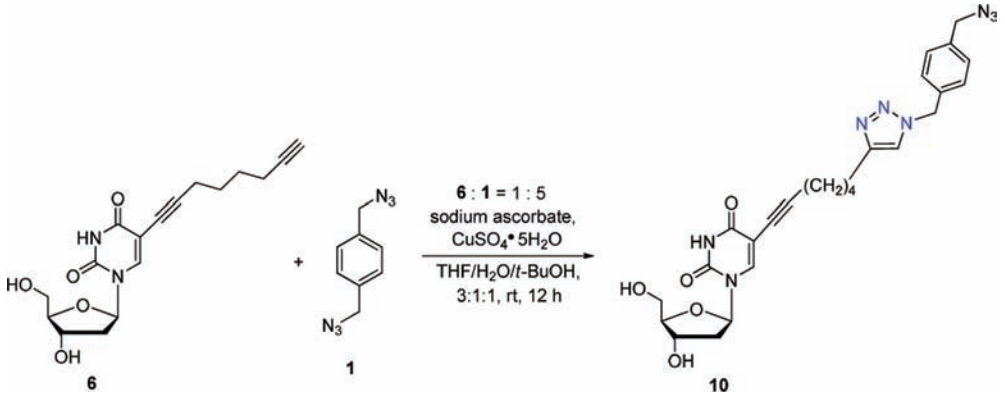

GmbH, Deisenhofen, Germany). Solvents were of laboratory grade. Thin layer chromatography (TLC) was performed on TLC aluminum sheets covered with silica gel 60 F254 (0.2 mm, VWR International, Germany). Flash column chromatography (FC): silica gel 60 (40−60 μM, VWR International, Germany) at 0.4 bar. UV spectra: U-3000 spectrophotometer (Hitachi, Japan); λ_{max} (ε) in nm, ε in dm^3 mol^{-1} cm^{-1}. NMR spectra: DPX 300 spectrometer (Bruker, Germany) at 300.15 MHz for ^{1}H and 75.48 MHz for ^{13}C. The J values are given in Hz; δ values in ppm relative to Me_4Si as internal standard. For NMR spectra recorded in DMSO, the chemical shift of the solvent peak was set to 2.50 ppm for ^{1}H NMR and 39.50 ppm for ^{13}C NMR. Elemental analysis was performed by the Mikroanalytisches Laboratorium Beller, Göttingen, Germany. Reversed-phase HPLC was carried out on a 250 × 4 mm RP-18 LiChrospher 100 column (Merck, Darmstadt, Germany) with a Merck-Hitachi HPLC pump connected with a variable wavelength monitor, a controller, and an integrator. Gradients used for HPLC chromatography (A = MeCN, B = 0.1 M (Et_3NH)OAc (pH 7.0)/MeCN, 95: 5): (*I*) 3 min 15% A in B, 12 min 15 −50% A in B, and 5 min 50−10% A in B, flow rate 0.7 mL min^{-1}; (*II*) 0−25 min 0−20% A in B, flow rate 0.7 mL min^{-1}; (*III*) 0−15 min 0−20% A in B, 15−18 min 20−40% A in B, flow rate 0.7 mL min^{-1}; (*IV*) 0−30 min 20−80% D in C with a flow rate of 0.75 mL min^{-1}. C = 25 mM Tris-HCl, 10% MeCN, pH 7.0; D = 25 mM Tris-HCl, 1.0 M NaCl, and 10% MeCN, pH 7.0. The ion-exchange chromatography was performed on a 4 × 250 mm DNA PAC PA-100 column (P/N 043011; Dionex, USA) connected with a 50 mm NucleoPac PA-100 Guard (P/N 43018; Dionex, USA) precolumn using a Merck-Hitachi HPLC apparatus with a pump (model L-6200A) and a UV detector (model L-4000) connected with an integrator (model D-2000). Elution profiles were recorded at 260 nm. The molecular masses of oligonucleotides were determined by LC-ESI-TOF (Agilent 1200 Series, Bruker Micro-TOF Q2) or MALDI-TOF (MS Autoflex, Bruker and Voyager-DE PRO spectrometer, Applied Biosystems) in the linear negative or positive mode with 3-hydroxypicolinic acid (3-HPA) as a matrix. Melting curves were measured with a Cary-100 Bio UV−vis spectrophotometer (Varian, Australia) equipped with a Cary thermoelectrical controller with a heating rate of 1 °C/min. Nanopure water (resistance <0.055 μS/cm) from MembraPure water system (Astacus) was used for all experiments.

1-(2-Deoxy-β-D-*erythro*-pentofuranosyl)-5-{1-(4-azidomethylbenzyl)-1*H*-[1,2,3-triazol-4-yl]}hexylidene uracil (10) (Scheme 1). To a solution of compound **6**[38,39] (99.4 mg, 0.3 mmol) and **1**[16] (282 mg, 1.5 mmol) in THF/H_2O/*t*-BuOH, 3:1:1 (4.5 mL), was added a freshly prepared 1 M solution of sodium ascorbate (239 μL, 0.24 mmol) in water, followed by the addition of copper(II) sulfate pentahydrate 7.5% in water (192 μL, 0.057 mmol). The reaction mixture was stirred in the dark at room temperature for 12 h. After completion of the

dx.doi.org/10.1021/bc300074k | *Bioconjugate Chem.* 2012, 23, 1230−1243

reaction (monitored by TLC), the solvent was evaporated, and the residue was applied to FC (silica gel, column 8 × 3 cm, eluted with CH_2Cl_2/MeOH, 95:5 → 90:10). Evaporation of the main zone gave **10** as a pale yellow solid (80 mg, 51%). TLC (CH_2Cl_2/MeOH, 90:10): R_f 0.58; UV λ_{max} (MeOH)/nm 230 (ε/dm^3 mol^{-1} cm^{-1} 17 800), 260 (3700), 292 (11 400). Anal. ($C_{26}H_{29}N_{11}O_4$) C, H, N. ^{1}H NMR (300 MHz, DMSO-d_6): δ = 1.47−1.56 (m, 2H, CH_2), 1.68−1.75 (m, 2H, CH_2), 2.09−2.12 (m, 2H, 2′-H_α + 2′-H_β), 2.38 (t, J = 7.2 Hz, 2H, CH_2), 2.64 (t, J = 7.2 Hz, 2H, CH_2), 3.50−3.63 (m, 2H, 5′-H), 3.77−3.79 (m, 1H, 4′-H), 4.22−4.23 (m, 1H, 3′-H), 4.43 (s, 2H, PhCH_2), 5.15 (br s, 1H, 5′-OH), 5.25 (br s, 1H, 3′-OH), 5.55 (s, 2H, PhCH_2), 6.11 (t, J = 6.6 Hz, 1H, 1′-H), 7.28−7.38 (m, 4H, H-phenylene), 7.92 (s, 1H, H-triazole), 8.13 (s, 1H, C6-H), 11.56 (s, 1H, HN).

Synthesis, Purification, and Characterization of Oligonucleotides. The syntheses of oligonucleotides was performed on a DNA synthesizer, model 392−08 (Applied Biosystems, Weiterstadt, Gemany) on a 1 μmol scale using the phosphoramidites **67**−**72**[2,37,39−43] (Figure S2, Supporting Information) and the standard phosphoramidite building blocks following the synthesis protocol for 3′-*O*-(2-cyanoethyl)-phosphoramidites.[44] After cleavage from the solid support, the oligonucleotides were deprotected in 25% aqueous ammonia solution for 12−16 h at 60 °C. The purification of the "trityl-on" oligonucleotides was carried out on reversed-phase HPLC (Merck-Hitachi-HPLC; RP-18 column; LiChrospher 250 × 5 mm, gradient system (*I*)). The purified "trityl-on" oligonucleotides were treated with 2.5% $Cl_2CHCOOH$/CH_2Cl_2 for 5 min at 0 °C to remove the 4,4′-dimethoxytrityl residues. The detritylated oligomers were purified by reversed-phase HPLC (gradient *II*). The oligomers were desalted by reversed-phase HPLC (RP-18, LiChrospher, 125 × 5 mm) using nanopure water for elution of salt, while the oligonucleotides were eluted with H_2O/MeOH (2:3). Then, they were lyophilized on a Speed Vac evaporator to yield colorless solids which were frozen at −24 °C. The molecular masses of the oligonucleotides were determined by LC-ESI-TOF or MALDI-TOF mass spectrometry in the linear negative or linear positive mode (see Tables 2, 3, and 5; and Tables S3 and S4, Supporting Information). Extinction coefficients ε_{260} (MeOH) of nucleosides: dA, 15400; dG, 11700; dT, 8800; dC, 7300; **2**, 10900;[2] **3**, 11500;[41] **4**, 8500;[42] **5**, 10500;[45] **6**, 3800,[39] **7**, 4900.[40]

Ion-Exchange HPLC Analysis of Interstrand Cross-Linked Oligonucleotides. The ion-exchange chromatography was performed on a 4 × 250 mm DNA PA 100 column (P/N 043011; Dionex, USA) connected with a 50 mm NucleoPac PA-100 Guard (P/N 43018; Dionex, USA) precolumn using a Merck-Hitachi HPLC apparatus with a pump (model L-6200A), and a UV detector (model L-4000) connected with an integrator (model D-2000). Elution profiles were recorded at 260 nm. An artificial mixture of oligonucleotides was prepared as follows: 0.1−0.2 A_{260} units of the oligonucleotides were dissolved in 20 μL of distilled water. Crude reaction mixtures were treated as follows before injection: the crude reaction mixture was concentrated in a Speed Vac, dissolved in 300 μL of bidistilled water, and centrifuged for 20 min at 12 000 rpm. Thirty microliters of the supernatant solution was then injected into the system, and gradient *IV* was used for elution: 0−30 min with 20−80% D in C with a flow rate of 0.75 mL min^{-1} (C: 25 mM Tris-HCl, 10% MeCN, pH 7.0; D: 25 mM Tris-HCl, 1.0 M NaCl, 10% MeCN, pH 7.0).

T_m Measurements. For the T_m measurements, the oligonucleotides were dissolved in 1 M NaCl, 100 mM $MgCl_2$, and 60 mM Na cacodylate buffer, pH 7.0. For non-cross-linked oligonucleotide duplexes 5 μM + 5 μM single-strand concentration was used. Hybridization experiments on cross-linked duplexes were carried out with 5 μM of the cross-linked oligonucleotide. The melting curves were measured with a UV−vis spectrophotometer equipped with a thermoelectrical controller. The temperature was measured continuously in the reference cell with a Pt-100 resistor with a heating rate of 1 °C min^{-1}, and the absorbance at 260 nm was recorded as a function of the temperature. The thermodynamic data of duplex formation were calculated by the *MeltWin* (v 3.0) program using the curve fitting of the melting profiles according to a two-state model.[46]

The thermal hypochromicity ($h\%$ = $[(\varepsilon_{monomer} - \varepsilon_{polymer})\cdot(\varepsilon_{monomer})^{-1})] \times 100\%$) of the oligonucleotides was determined from the melting curves. The extinction coefficients of the oligonucleotides were calculated from the sum of the extinction coefficients of the monomeric 2′-deoxyribonucleosides divided by the hyperchromicity.[47]

T_m Measurements under the Reaction Conditions used for the "Bis-click" and the "Stepwise Click" reaction: For the T_m measurements under "click" reaction conditions, the oligonucleotides were dissolved in 0.4 M NaCl, 40 mM $NaHCO_3$ containing 6 vol % *t*-BuOH ("bis-click"). In the case of the "stepwise click" reaction conditions, the measurements were performed without adding NaCl (40 mM $NaHCO_3$ containing 6 vol% *t*-BuOH). These measurements were performed with 5 μM + 5 μM oligonucleotide single-strand concentration.

Denaturing Polyacrylamide Gel Electrophoresis (PAGE) of Oligonucleotides. Analysis of oligonucleotides was carried out by polyacrylamide gel electrophoresis (17% polyacrylamide gel, 19:1, acrylamide: bisacrylamide, containing 7 M urea (8.4 g in 8.5 mL bisacrylamide/acrylamide (1:19) solution). In order to catalyze polymerization, 20 μL of TEMEDA (*N,N,N′,N′*-tetramethylethylendiamine) and 60 μL of 10% ammonium persulfate (APS) were added. After complete polymerization (1 h), the gel (10 × 10 cm) was prerun for 30 min at r.t using 1 × tris-borate-EDTA (TBE) buffer containing 20 mM $MgCl_2$ (pH 8.4). The individual oligonucleotides (0.15−0.30 A_{260} units) were dissolved in 2−5 μL of distilled water at r.t. Ten microliters of gel loading buffer containing formamide was added, and the oligonucleotide solution was loaded onto the gel. Electrophoresis was run at r.t. for 6 h using 1 × TBE buffer containing 20 mM $MgCl_2$ (pH 8.4) at a constant field strength of 12 V/cm. The gel was stained with 0.02% methylene blue for 20 min and was then incubated in water for 1 h to remove excess dye from the background.

General Procedure for the Cross-Linking of Complementary Oligonucleotides (Heterodimers) using the "Bis-Click" Cycloaddition. A solution of the alkynylated complementary oligonucleotide strands (2.0 A_{260} units each) in aq. NaCl (100 μL of a 1 M stock solution) was heated at 80 °C for 5 min, then slowly cooled down to 20 °C using a water-bath. Then, $CuSO_4$-TBTA (tris[(1-benzyl-1*H*-1,2,3-triazol-4-yl)methyl]amine) ligand complex (25 μL of a 20 mM stock solution in H_2O/DMSO/*t*-BuOH 4:3:1 for TBTA; 25 μL of a 20 mM stock solution in H_2O/DMSO/*t*-BuOH 4:3:1 for $CuSO_4$) was added to the solution. Next, TCEP (tris(2-carboxyethyl)phosphine, 25 μL of a 20 mM stock solution in water), sodium bicarbonate (20 μL of a 200 mM aq. solution), bis-azide **1**[16] (1.5 μL of a 20 mM stock solution in dioxane/H_2O 1:1),

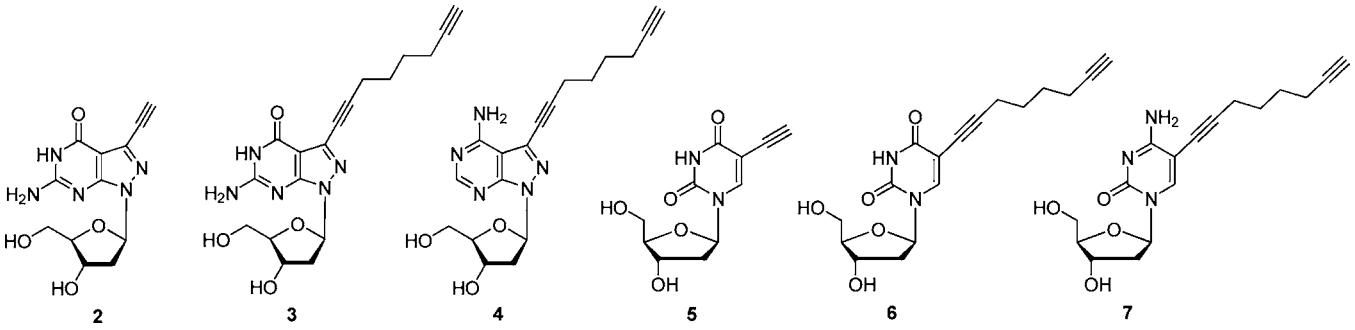

Figure 2. Alkynylated nucleosides **2**–**7** incorporated into oligonucleotides.

Table 1. T_m Values of Duplexes Containing the Alkynylated Nucleosides 2–7 as well as Azido-Functionalized Nucleoside Derivatives 8–12

Duplexes	T_m[a] [°C]	ΔT_m[b] [°C]	% h[c]	$\Delta G°_{310}$[d] [kcal/mol]	Duplexes	T_m[a] [°C]	ΔT_m[b] [°C]	% h[c]	$\Delta G°_{310}$[d] [kcal/mol]
5'-d(TAG GTC AAT ACT) (**13**) 3'-d(ATC CAG TTA TGA) (**14**)	51.0 (49.0)	---	18 15	-11.4 -10.8					
5'-d(TAG 2TC AAT ACT) (**16**) 3'-d(ATC CA2 TTA TGA) (**24**)	57.0	+6	18	-12.8	5'-d(TAG G6C AAT ACT) (**22**) 3'-d(AT7 CAG TTA TGA) (**27**)	53.0	+2	17	-12.2
5'-d(TAG 2TC AAT ACT) (**16**) 3'-d(ATC CA3 TTA TGA) (**25**)	54.5	+3.5	18	-12.2	5'-d(6AG GTC AAT ACT) (**21**) 3'-d(AT7 CAG TTA TGA) (**27**)	53.5	+2.5	18	-12.2
5'-d(TAG 3TC AAT ACT) (**18**) 3'-d(ATC CA3 TTA TGA) (**25**)	55.5	+4.5	19	-13.0	5'-d(TAG GT7 AAT ACT) (**23**) 3'-d(ATC 7AG TTA TGA) (**28**)	52.5	+1.5	18	-11.8
5'-d(TA2 GTC AAT ACT) (**15**) 3'-d(ATC CA2 TTA TGA) (**24**)	55.0	+4	19	-12.8	5'-d(TAG GT7 AAT ACT) (**23**) 3'-d(AT7 CAG TTA TGA) (**27**)	54.0	+3	17	-12.2
5'-d(TAG GT7 AAT ACT) (**23**) 3'-d(ATC CA2 TTA TGA) (**24**)	55.5	+4.5	18	-13.0	5'-d(TAG 2TC AAT ACT) (**16**) 3'-d(ATC CA8 TTA TGA) (**35**)	54.5	+3.5	19	-12.3
5'-d(TA2 GTC AAT ACT) (**15**) 3'-d(AT7 CAG TTA TGA) (**27**)	54.5	+3.5	18	-12.4	5'-d(TAG 2TC AAT ACT) (**16**) 3'-d(ATC CA9 TTA TGA) (**36**)	52.0	+1.0	17	-11.8
5'-d(TAG 2TC AAT ACT) (**16**) 3'-d(AT7 CAG TTA TGA) (**27**)	55.0	+4	19	-12.7	5'-d(TAG 9TC AAT ACT) (**31**) 3'-d(ATC CA3 TTA TGA) (**25**)	53.5 (52.0)	+2.5 +3.0	18 17	-11.8 -11.5
5'-d(TAG 3TC AAT ACT) (**18**) 3'-d(AT7 CAG TTA TGA) (**27**)	53.5	+2.5	19	-12.3	5'-d(10AG GTC AAT ACT) (**37**) 3'-d(ATC CA2 TTA TGA) (**24**)	55.5	+4.5	19	-12.8
5'-d(TAG G6C AAT ACT) (**22**) 3'-d(ATC CA2 TTA TGA) (**24**)	54.5	+3.5	18	-12.8	5'-d(TAG G10C AAT ACT) (**32**) 3'-d(ATC CA3 TTA TGA) (**25**)	50.0 (48.5)	-1.0 -0.5	15 14	-11.2 -10.9
5'-d(TAG G6C AAT ACT) (**22**) 3'-d(ATC CA3 TTA TGA) (**25**)	52.0	+1	18	-11.8	5'-d(5AG GTC AAT ACT) (**20**) 3'-d(A10C CAG TTA TGA) (**38**)	49.5	-1.5	18	-11.2
5'-d(5AG GTC AAT ACT) (**20**) 3'-d(A6C CAG TTA TGA) (**26**)	50.0 (49.0)	-1.0 0	18 18	-11.0 -10.9	5'-d(TAG GT11 AAT ACT) (**33**) 3'-d(ATC CA3 TTA TGA) (**25**)	50.0 (48.0)	-1.0 -1.0	17 17	-11.1 -10.5
5'-d(TAG GTC 2AT ACT) (**17**) 3'-d(ATC CA2 TTA TGA) (**24**)	47.0	-4	17	-10.4	5'-d(TAG GTC 12AT ACT) (**34**) 3'-d(ATC CA3 TTA TGA) (**25**)	49.5 (47.5)	-1.5 -1.5	15 14	-11.0 -10.5
5'-d(TAG2TCAATACT) (**16**) 3'-d(A_6ATCCA3TTATGAT$_6$) (**30**)	55.5	+4.5	14	-12.4	5'-d(TAG2TCAATACT) (**16**) 3'-d(T_6ATCCA3TTATGAT$_6$) (**29**)	55.0	+4	15	-12.6

[a]Measured at 260 nm in a 1 M NaCl solution containing 100 mM $MgCl_2$ and 60 mM Na cacodylate (pH 7.0) with 5 μM + 5 μM single-strand concentration. Data in parentheses were measured at a 2 μM + 2 μM single-strand concentration. [b]Refers to the contribution of the modified residues. [c]%h refers to the percentage of hypochromicity. [d]$\Delta G°_{310}$ were determined from the melting curves by using the software *MELTWIN* v 3.0 (J. A. Mc Dowell, **1996**). The $\Delta G°_{310}$ values are given within an error of 15%.

and 30 μL of DMSO were introduced, and the reaction mixture was kept at room temperature for 12 h. The reaction mixture was concentrated in a Speed Vac, and dissolved in 300 μL bidistilled water and centrifuged for 20 min at 12 000 rpm. The supernatant was collected and further purified by reversed-phase HPLC using gradient *III*. Using this procedure, the cross-linked oligonucleotides ICL-**39**, ICL-**40**, ICL-**43**, ICL-**44**, ICL-**46**, and ICL-**47** to ICL-**59** were obtained in 40–50% yield. The reversed-phase HPLC profiles of the crude and purified reaction mixtures for selected cross-linked oligonucleotides obtained after the "bis-click" reaction are shown in Figure S7–S9 (Supporting Information). The molecular masses of the cross-linked oligonucleotides were determined by MALDI-TOF or LC-ESI-TOF mass spectrometry (Tables 2 and 3; and Table S4 and Figures S21–S43, Supporting Information).

General Procedure for the Cross-Linking of Identical Oligonucleotides (Homodimers ICL-60 to ICL-65) Using the "Bis-Click" Huisgen-Sharpless-Meldal [3 + 2] Cycloaddition. To a solution of the alkynylated oligonucleotide (5.0 A_{260} units) in 20 μL of water were added $CuSO_4$-TBTA ligand complex (50 μL of a 20 mM stock solution in H_2O/DMSO/*t*-BuOH 4:3:1 for TBTA; 50 μL of a 20 mM stock solution in H_2O/DMSO/*t*-BuOH 4:3:1 for $CuSO_4$). Next, TCEP (50 μL of a 20 mM stock solution in water), sodium bicarbonate (20 μL of a 200 mM aq. solution), bis-azide **1** (1.5 μL of a 20 mM stock solution in dioxane/H_2O 1:1), and 30 μL of DMSO were introduced, and the reaction mixture was kept at room temperature for 12 h. The reaction mixture was concentrated in a Speed Vac, and dissolved in 300 μL bidistilled water and centrifuged for 20 min at 12 000 rpm. The supernatant was collected and further purified by reversed-phase HPLC using

dx.doi.org/10.1021/bc300074k | *Bioconjugate Chem.* 2012, 23, 1230–1243

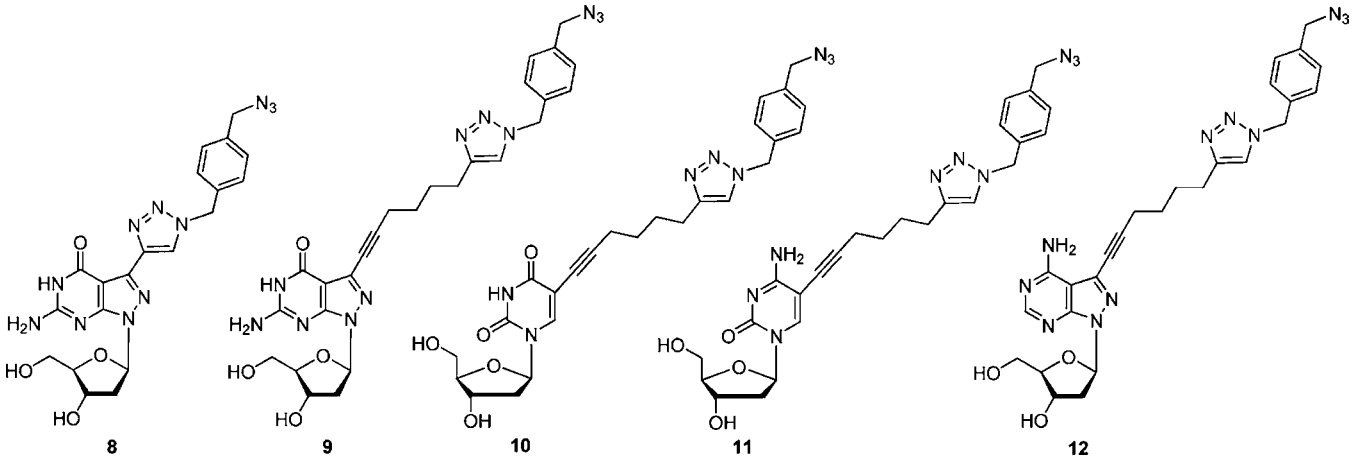

Figure 3. Azidomethylbenzyl-labeled nucleosides **8**−**12** obtained after the "first click" of the "stepwise click" reaction performed on oligonucleotides.

Scheme 2. Typical Example for the Synthesis of Mono-Functionalized Azido-Oligonucleotides Synthesized by the "Stepwise Click" Chemistry

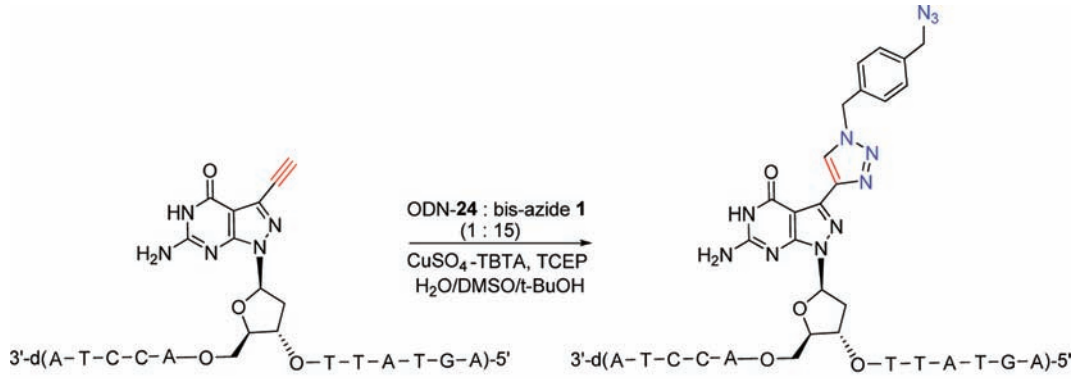

gradient *III*. Using this procedure, the cross-linked oligonucleotides ICL-**60** to ICL-**65** were obtained. Their molecular masses were determined by MALDI-TOF or LC-ESI-TOF mass spectrometry (Tables 3 and 5).

General Procedure for the "Stepwise Click" Cycloaddition. Synthesis of the Azidomethylbenzyl-Labeled Oligonucleotides ODN-31 to ODN-38 Using Oligonucleotides ODN-18, ODN-19, and ODN-21 to ODN-26 and Bis-Azide 1 ("First Click"). To the single-stranded oligonucleotide (5 A_{260} units), a mixture of the $CuSO_4$-TBTA ligand complex (50 μL of a 20 mM stock solution in H_2O/DMSO/*t*-BuOH, 4:3:1 for TBTA; 50 μL of a 20 mM stock solution in H_2O/DMSO/*t*-BuOH, 4:3:1 for $CuSO_4$), tris(carboxyethyl)-phosphine (TCEP; 50 μL of a 20 mM stock solution in water), 1,4-bis-azidomethylbenzene **1**[16] (37.5 μL of a 20 mM stock solution in dioxane/H_2O, 1:1), sodium bicarbonate (50 μL of a 20 mM aq. solution) and 30 μL of DMSO were added, and the reaction proceeded at room temperature for 2 h. The reaction mixture was concentrated in a Speed Vac, and dissolved in 300 μL bidistilled water and centrifuged for 20 min at 12 000 rpm. The supernatant solution was collected and further purified by reversed-phase HPLC (gradient *III*) to give about 80% isolated yield of the azidomethylbenzyl oligonucleotide. The reversed-phase HPLC profiles of the crude and purified reaction mixtures for monofunctionalized intermediates ODN-**31** to ODN-**38** obtained after the "first click" reaction are shown in Figure S5−S6 (Supporting Information). Their molecular masses were determined by MALDI-TOF or LC-ESI-TOF mass spectrometry (Table S3, Supporting Information).

Scheme 3. Principle of Duplex DNA Assisted Cross-Linking Using the "Bis-Click" Reaction[a]

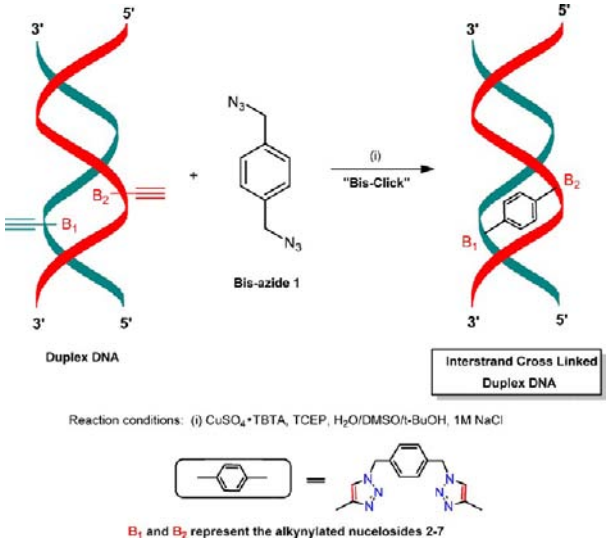

[a]Red and green display complementary oligonucleotide strands both bearing terminal triple bonds.

dx.doi.org/10.1021/bc300074k | *Bioconjugate Chem.* 2012, 23, 1230−1243

Scheme 4. "Bis-Click" Cross-Linking on Duplex DNA Using the Complementary Ethynylated Oligonucleotides ODN-16 and ODN-24 as Starting Materials

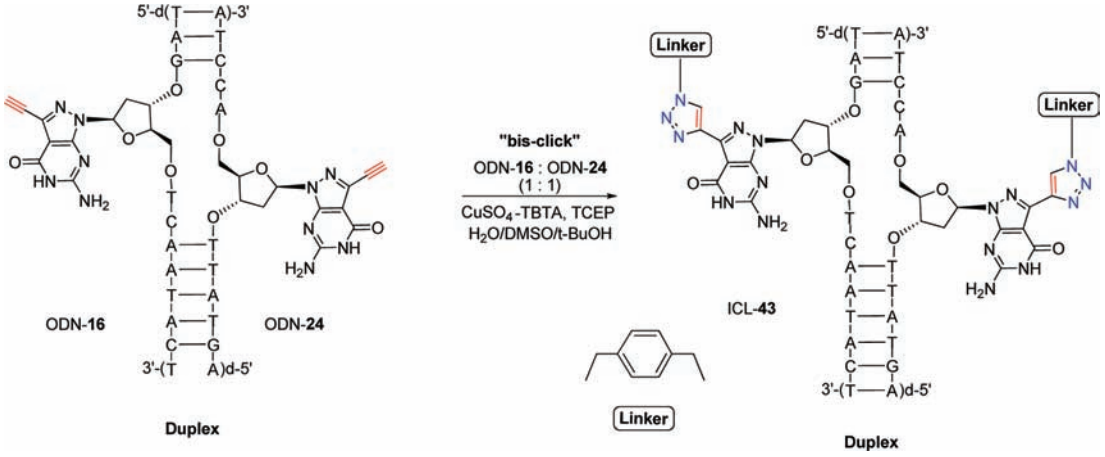

Table 2. Structure and Mass Spectrometric Data of Interstrand Cross-Linked Oligonucleotides (ICL 39 to 59) Prepared by "Bis-Click" or "Stepwise Click" Chemistry on Duplexes

Duplex DNA (ICL)	MS (calc.) found	Duplex DNA (ICL)	MS (calc.) found
5'-d(TAG 3TC AAT ACT) (39)* 3'-d(ATC CA3 TTA TGA)	[7681.5][c] 7685.5[d]	5'-d(TAG 2TC AAT ACT) (50)* 3'-d(A_6 ATCCA3TTATGA T_6)	[11308.6][c] 11309.0[d]
5'-d(TAG G6C AAT ACT) (40)* 3'-d(ATC CA3 TTA TGA)	[7667.5][c] 7669.4[d]	5'-d(TAG GT7 AAT ACT) (51)* 3'-d(ATC CA2 TTA TGA)	[7604.2][e] 7604.2[f]
5'-d(TAG GT7 AAT ACT) (41)# 3'-d(ATC CA3 TTA TGA)	[7685.3][a] 7688.3[b]	5'-d(TA2 GTC AAT ACT) (52)* 3'-d(AT7 CAG TTA TGA)	[7601.5][e] 7605.4[d]
5'-d(TAG GTC 4AT ACT) (42)# 3'-d(ATC CA3 TTA TGA)	[7686.3][a] 7689.2[b]	5'-d(TAG 2TC AAT ACT) (53)* 3'-d(AT7 CAG TTA TGA)	[7601.5][e] 7603.5[d]
5'-d(TAG 2TC AAT ACT) (43)* 3'-d(ATC CA2 TTA TGA)	[7521.4][c] 7524.5[d]	5'-d(TAG 3TC AAT ACT) (54)* 3'-d(AT7 CAG TTA TGA)	[7680.5][e] 7685.5[d]
5'-d(TAG 2TC AAT ACT) (44)* 3'-d(ATC CA3 TTA TGA)	[7601.5][c] 7604.5[d]	5'-d(TAG G6C AAT ACT) (55)* 3'-d(ATC CA2 TTA TGA)	[7587.5][e] 7589.5[d]
5'-d(6AG GTC AAT ACT) (45)# 3'-d(ATC CA2 TTA TGA)	[7594.2][a] 7599.7[b]	5'-d(TAG G6C AAT ACT) (56)* 3'-d(AT7 CAG TTA TGA)	[7667.5][e] 7673.5[d]
5'-d(5AG GTC AAT ACT) (46)* 3'-d(A6C CAG TTA TGA)	[7578.1][a] 7575.0[b]	5'-d(6AG GTC AAT ACT) (57)* 3'-d(AT7 CAG TTA TGA)	[7667.5][e] 7670.3[d]
5'-d(TA2G TC AAT ACT) (47)* 3'-d(ATC CA2TTA TGA)	[7521.4][c] 7523.3[d]	5'-d(TAG G T7 AAT ACT) (58)* 3'-d(AT7 CAG TTA TGA)	[7681.5][e] 7682.3[d]
5'-d(TAG GTC 2AT ACT) (48)* 3'-d(ATC CA2 TTA TGA)	[7537.4][c] 7539.3[d]	5'-d(TAG GT7 AAT ACT) (59)* 3'-d(ATC 7AG TTA TGA)	[7681.5][e] 7682.5[d]
5'-d(TAG 2TC AAT ACT) (49)* 3'-d(T_6 ATCCA3TTATGA T_6)	[11250.0][c] 11250.9[d]		

[a]Calculated on the basis of molecular weight as $[M+1]^+$. [b]Determined by MALDI-TOF mass spectrometry as $[M+1]^+$ in the linear positive mode. [c]Calculated on the basis of exact mass. [d]Determined by LC-ESI-TOF mass spectrometry. [e]Calculated on the basis of molecular weight as $[M-1]^-$. [f]Determined by MALDI-TOF mass spectrometry as $[M-1]^-$ in the linear negative mode. *Refers to interstrand cross-linked oligonucleotides prepared by the "bis-click" reaction. #Refers to interstrand cross-linked oligonucleotides prepared by the "stepwise click" reaction. The particular cross-linked nucleobases, e.g., **2-2**, are shown in the Supporting Information (Figure S3 and Figure S4).

Cross-Linked Complementary Oligonucleotides Using Azidomethylbenzyl Oligonucleotides ODN-31 to ODN-38 and Alkynylated Oligonucleotides ("Second Click"). To the azidomethylbenzyl oligonucleotides ODN-**31** to ODN-**38** (2.0 A_{260} units) and complementary alkynylated oligonucleotides (1.5 A_{260} units), a mixture of the $CuSO_4$-TBTA ligand complex (50 μL of a 20 mM stock solution in H_2O/DMSO/*t*-BuOH, 4:3:1 for TBTA; 25 μL of a 20 mM stock solution in H_2O/DMSO/*t*-BuOH, 4:3:1 for $CuSO_4$), TCEP (30 μL of a 20 mM stock solution in water), sodium bicarbonate (10 μL of a 200 mM aq. solution), and 20 μL of DMSO were added, and the reaction proceeded at room temperature for 12 h. The reaction mixture was concentrated in a Speed Vac, dissolved in 300 μL bidistilled water, and centrifuged for 20 min at 12 000 rpm. The supernatant solution was collected and further purified by reversed-phase HPLC (gradient *III*) to give

dx.doi.org/10.1021/bc300074k | *Bioconjugate Chem.* 2012, 23, 1230−1243

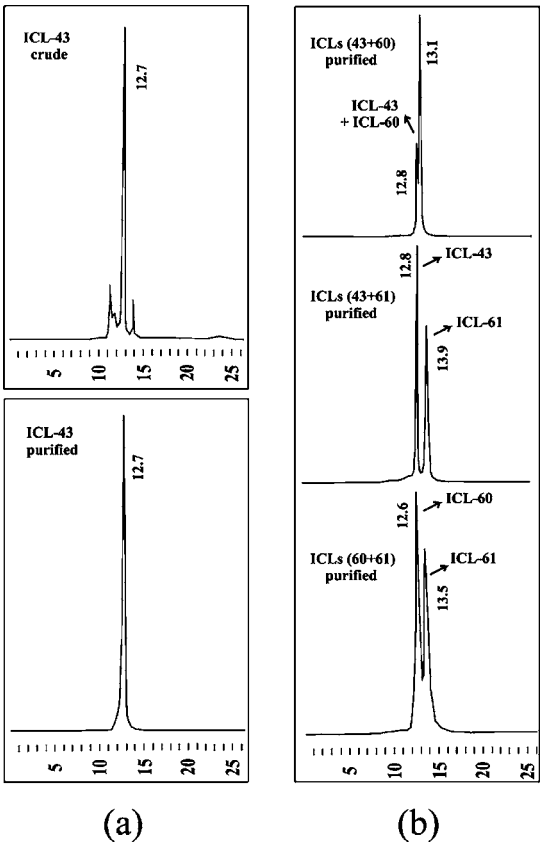

Figure 4. Reversed-phase HPLC profiles of (a) crude ICL-**43** obtained after the "bis-click" reaction; (b) artificial mixtures of purified ICL-**43** (heterodimer), ICL-**60**, and ICL-**61** (homodimers) measured at 260 nm. The following gradient system was used: MeCN (A) and 0.1 M (Et_3NH)OAc (pH 7.0) (B). Gradient *III*: 0−15 min 0−20% A, 15−18 min 20−40% A in B, 20−25 min 40−0% A in B with a flow rate of 0.7 mL min^{-1}.

about 40−50% isolated yield of the cross-linked oligonucleotide. ICL-**43** and ICL-**45** were prepared according to a procedure published earlier.[2] SI Figures S5 and S6 depict the reversed-phase HPLC profiles of the crude and purified reaction mixtures of cross-linked oligonucleotides ICL-**39** to ICL-**46** obtained after the "second click" reaction. Their molecular masses were determined by MALDI-TOF or ESI-TOF mass spectrometry (Table 2).

RESULTS AND DISCUSSION

Synthesis of Oligonucleotide Cross-Link Precursors with Modified Nucleobases and Side Chains of Different Length and Their Duplex Stability. The alkynylated nucleosides **2**−**7** (Figure 2) are representing analogues of the canonical nucleosides 2′-deoxyguanosine, 2′-deoxyadenosine, 2′-deoxythymidine, and 2′-deoxycytidine and are bearing ethynyl or octadiynyl side chains at the 7-position of 8-aza-7-deazapurines or the 5-position of pyrimidine nucleosides (purine numbering is used throughout the discussion part).[2,36−42] They have been incorporated into the 12-mer oligonucleotides 5′-d(TAG GTC AAT ACT) (**13**) and 3′-d(ATC CAG TTA TGA) (**14**) which served as reference duplex. For this, phosphoramidites of the monomeric building blocks were synthesized by existing procedures[2,37,39−43] and oligonucleotides have been prepared using modified as well as standard phosphoramidites (Table 1 and Table S3, Supporting Information).

Additionally, monofunctionalized oligonucleotides (ODN-**31** to ODN-**38**) incorporating nucleosides **8**−**12** (Figure 3) were prepared. They were obtained by the "stepwise click" reaction from the alkynylated oligonucleotides ODN-**18**, ODN-**19**, and ODN-**21** to ODN-**26** by using an excess of the bis-azide **1**[16] (15:1) (Scheme 2, Table 1, and Table S3, Supporting Information). The reaction was performed at room temperature in aqueous solution (H_2O/DMSO/*t*-BuOH) employing a premixed 1:1 complex of $CuSO_4$−TBTA (tris(benzyltriazoylmethyl)amine), TCEP (tris(carboxyethyl)phosphine), and $NaHCO_3$ leading to the azido oligonucleotides ODN-**31** to ODN-**38** (Table 1). The use of excess of bis-azide **1** guarantees that only one azido group is employed in the cycloaddition, thereby yielding almost exclusively the monofunctionalized "click" intermediates ODN-**31** to ODN-**38** with a terminal azido group in the side chain as shown in Figure 3. Compound **10** was newly synthesized (experimental part) while **8**[2] and **9**[2] were reported earlier. Compounds **11** and **12** are solely components of oligonucleotides (Table 1, SI Table S3, and Figure 3).

All oligonucleotides have been characterized by LC-ESI-TOF or MALDI-TOF mass spectrometry (for details, see Supporting Information). Hybridization experiments were performed on the non-cross-linked functionalized oligonucleotides ODN-**15** to ODN-**18** and ODN-**20** to ODN-**38**, which served as starting materials for cross-linking using "stepwise" or "bis-click" chemistry (Table 1). It will be shown later that particular duplexes can be cross-linked in a chemoselective way. The T_m values, hypochromicities, as well as thermodynamic data of duplexes used for cross-linking experiments are presented in Table 1 (for additional T_m values see Table S3, Supporting Information).

From the T_m values displayed in Table 1 (see also SI Table S3), it was concluded that duplexes incorporating the alkynylated nucleosides **2**−**7** in one strand at central positions show similar T_m values as the reference duplex, while azido-functionalized nucleosides **8**−**12** (Figure 3) at the same positions slightly decreased the duplex stability. The destabilizing effect is less pronounced when the monofunctionalized nucleosides are located at a terminal position. Duplexes modified in both strands with alkynylated nucleosides showed increased T_m values. These findings coincide with earlier observations made on side chain modifications in DNA duplexes.[2,38−41,48]

Cross-Linking Performed on Oligonucleotide Duplexes with a Diversity of Nucleobases Bearing Short and Long Linkers at Proximal and Distant Positions. DNA cross-linking with bis-azides was already reported and was performed on oligonucleotides with identical strands by the "bis-click" reaction and on nonidentical strands by the "stepwise click" protocol. The work was carried out exclusively on DNA single strands.[1,2] Now, cross-linking was performed on duplex DNA by the "bis-click" reaction and the identity of the compounds was unambiguously confirmed by the "stepwise click" reaction. We assumed that the cross-linking reaction can be controlled by a possible template effect of a preformed duplex and thus resulting in the chemoselective formation of heterodimers, while homodimers are suppressed. Until now, the efficiency of internal cross-linking in duplex DNA employing bis-azides is unexplored. However, it has been shown that template-assisted "click" reactions at the terminus of an oligonucleotide duplex are accelerated compared to single strand reactions.[25,26] In this case, the "clickable" residues are flexible, and by duplex formation, their local concentration is

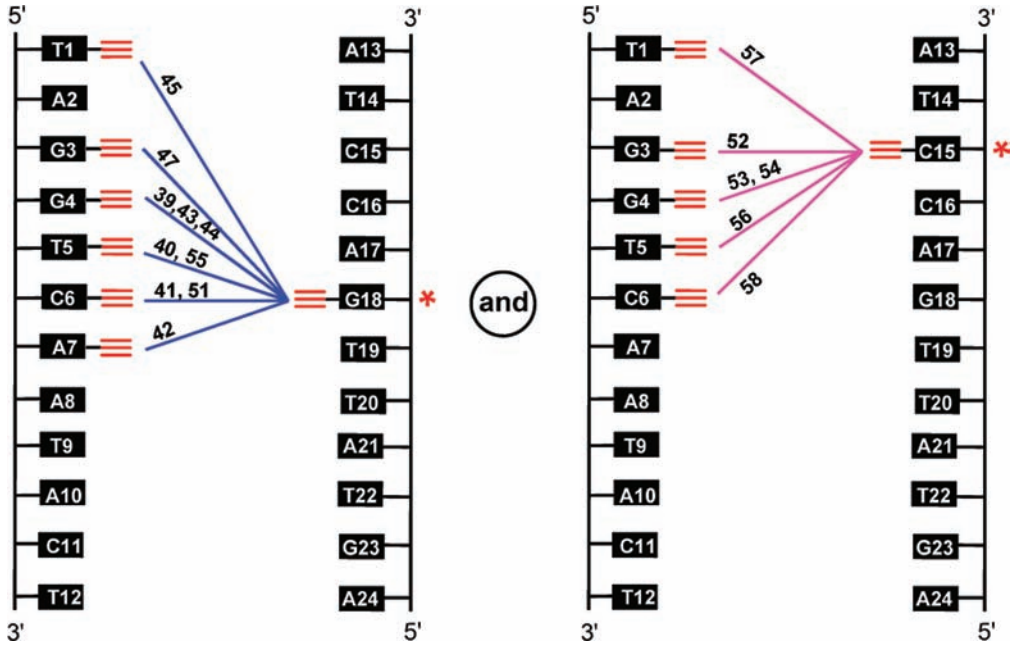

Figure 5. Linking positions of the cross-linked duplexes ICL **39** to **45** (left side) and ICL **52** to **58** (right side) prepared by "bis-click" or "stepwise click" chemistry. The cross-link is located between a central 7-(octa-1,7-diynylated) or 7-ethynylated 8-aza-7-deaza-2′-deoxyguanosine (G18)* or an octa-(1,7-diynylated) dC (C15*) residue in one oligonucleotide chain and a dG, dU, dC, or dA derivative in the complementary strand. The numbers on the arrows represent the individual ICLs.

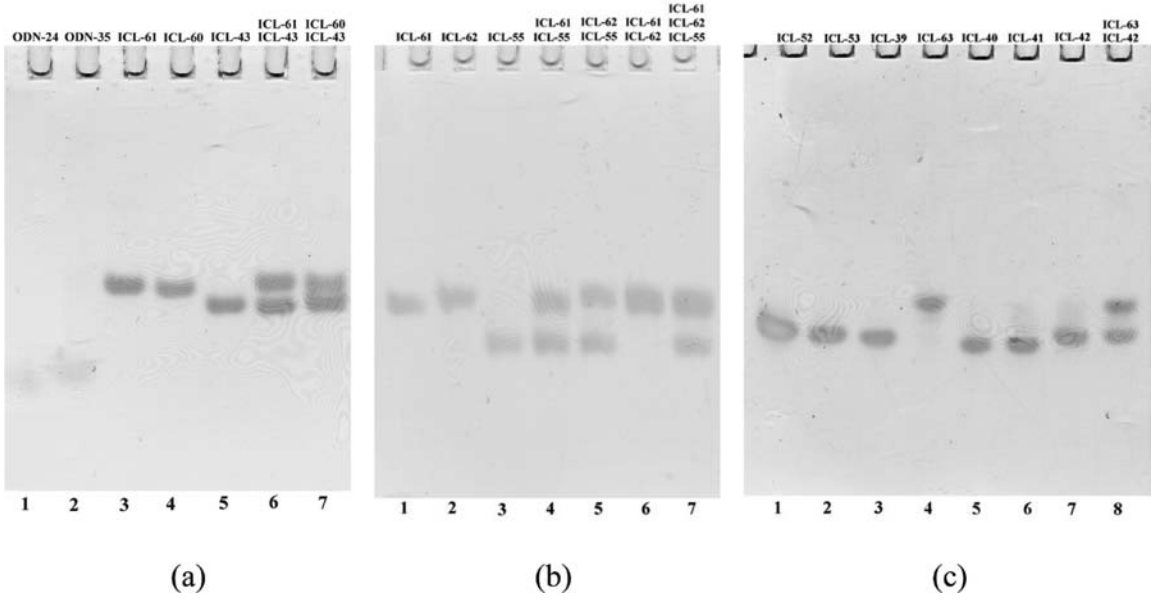

Figure 6. Denaturing PAGE analysis of oligonucleotides on a 17% polyacrylamide/7 M urea gel. (a) Lane 1: 12-mer ODN-**24**; lane 2: 12-mer ODN-**35**; lane 3: 24-mer homodimer ICL-**61**;[2] lane 4: 24-mer homodimer ICL-**60**;[2] lane 5: 24-mer heterodimer ICL-**43**; lane 6: artificial mixture of ICL-**61** + ICL-**43**; lane 7: artificial mixture of ICL-**60** + ICL-**43**. (b) Lane 1: 24-mer homodimer ICL-**61**; lane 2: 24-mer homodimer ICL-**62**; lane 3: 24-mer heterodimer ICL-**55**; lane 4: artificial mixture of ICL-**61** + ICL-**55**; lane 5: artificial mixture of ICL-**62** + ICL-**55**; lane 6: artificial mixture of ICL-**61** + ICL-**62**; lane 7: artificial mixture of ICL-**61** + ICL-**62** + ICL-**55**. (c) Lane 1 → lane 3: 24-mer heterodimers (ICL-**52**, ICL-**53**, ICL-**39**); lane 4: 24-mer homodimer ICL-**63**;[1,2] lane 5 → lane 7: 24-mer heterodimers (ICL-**40**, ICL-**41**, ICL-**42**); lane 8: artificial mixture of ICL-**63** + ICL-**42**.

increased. On the contrary, when "click" cross-linking is performed on an internal side chain of the duplex the terminal triple bonds are located in the major groove of DNA duplexes. Consequently, their accessibility and reactivity might be different. A positive template effect can be expected, when the triple bonds are freely accessible by the bis-azide **1**, and the final linker fits perfectly into the gap of the two alkyne functionalities. In order to study the outcome of cross-linking reactions performed on duplex DNA using "click" chemistry, the nucleobases, the linker length, and the linking positions were altered, and the stability of the various cross-linked duplexes was compared.

Oligonucleotide Cross-Linking Performed on Duplex DNA Using "Bis-Click"Chemistry. Cross-linking of complementary strands by the "bis-click" reaction was performed using DNA duplexes as a tool ("template"). Standard reaction conditions

dx.doi.org/10.1021/bc300074k | *Bioconjugate Chem.* 2012, 23, 1230−1243

Scheme 5. Cross-Linking on DNA Duplexes by the "Stepwise Click" Reaction Using the Complementary Oligonucleotides ODN-16 (ethynylated) and azido-ODN-35 as Starting Materials

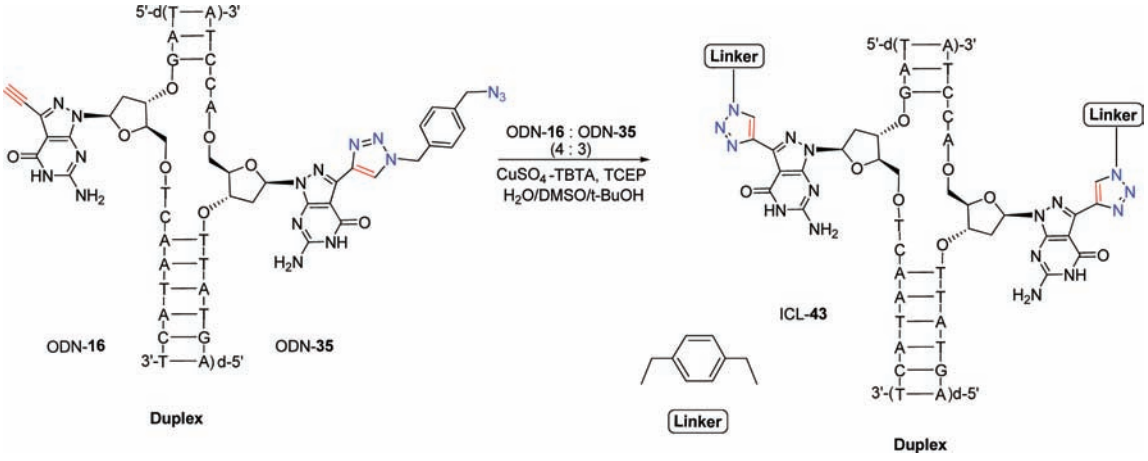

Table 3. Structure of Interstrand Cross-Linked Complementary Oligonucleotides (ICL) Synthesized by "Bis-Click" or "Stepwise Click" Reaction

Duplexes	MS [calc.] found	ICL Duplex	MS [calc.] found
5'-d(TAG G6C AAT ACT) (**22**) 3'-d(ATC CA3 TTA TGA) (**25**)	[3735.5][a] 3733.0[b] (ODN-**22**) [3747.6][e] 3746.9[f] (ODN-**25**)	5'-d(TAG G6C AAT ACT) (**40**)* 3'-d(ATC CA3 TTA TGA) (heterodimer)	[7670.3][e] 7669.4[d]
		5'-d(TAG G6C AAT ACT) (**62**)* 5'-d(TAG G6C AAT ACT) (homodimer)	[7658.3][a] 7658.0[b]
		3'-d(ATC CA3 TTA TGA) (**63**)*1,2 3'-d(ATC CA3 TTA TGA) (homodimer)	[7681.5][c] 7685.3[d]
5'-d(TAG G10C AAT ACT) (**32**) 3'-d(ATC CA3 TTA TGA) (**25**)	[3923.7][a] 3922.2[b] (ODN-**32**)	5'-d(TAG G6C AAT ACT) (**40**)# 3'-d(ATC CA3 TTA TGA) (control heterodimer)	[7670.3][e] 7670.2[f]
5'-d(TAG 2TC AAT ACT) (**16**) 3'-d(ATC CA2 TTA TGA) (**24**)	[3666.7][c] 3668.6[d] (ODN-**16**) [3667.4][e] 3667.2[f] (ODN-**24**)	5'-d(TAG 2TC AAT ACT) (**43**)* 3'-d(ATC CA2 TTA TGA) (heterodimer)	[7521.4][c] 7524.5[d]
		5'-d(TAG 2TC AAT ACT) (**60**)*2 5'-d(TAG 2TC AAT ACT) (homodimer)	[7521.4][c] 7521.3[d]
		3'-d(ATC CA2 TTA TGA) (**61**)*2 3'-d(ATC CA2 TTA TGA) (homodimer)	[7521.4][c] 7524.3[d]
5'-d(TAG 2TC AAT ACT) (**16**) 3'-d(ATC CA8 TTA TGA) (**35**)	[3855.6][e] 3855.1[f] (ODN-**35**)	5'-d(TAG 2TC AAT ACT) (**43**)# 3'-d(ATC CA2 TTA TGA) (control heterodimer)	[7521.4][c] 7525.5[d]

[a]Calculated on the basis of molecular weight as $[M+1]^+$. [b]Determined by MALDI-TOF mass spectrometry as $[M+1]^+$ in the linear positive mode. [c]Calculated on the basis of exact mass. [d]Determined by LC-ESI-TOF mass spectrometry. [e]Calculated on the basis of molecular weight as $[M-1]^-$. [f]Determined by MALDI-TOF mass spectrometry as $[M-1]^-$ in the linear negative mode. *Refers to interstrand cross-linked oligonucleotides prepared by the "bis-click" reaction. #Refers to interstrand cross-linked oligonucleotides prepared by the "stepwise click" reaction. The particular cross-linked nucleobases, e.g., **2**-**2**, are shown in the Supporting Information Figure S3 and Figure S4.

were used for the "bis-click" reaction except that the solution contains 1 M NaCl (see Experimental Procedures). Under these conditions, stable duplexes were formed in all cases with T_m values 10−15 °C lower than those reported in Table 1, but all above 40 °C (Supporting Information, Figure S19) which guarantees that the "bis-click" reaction occurs on duplex DNA. A schematic illustration of the reaction is outlined in Scheme 3.

For the synthesis of the cross-linked oligonucleotides, equimolar amounts of two complementary oligonucleotide strands were dissolved in 1 M NaCl solution. Then, $CuSO_4$-TBTA complex in H_2O/DMSO/*t*-BuOH was added, followed by TCEP, aq. $NaHCO_3$, the bis-azide **1**, as well as DMSO (Scheme 4). As a typical example, the cross-linking reaction of two complementary oligonucleotide strands (ODN-**16** and

Table 4. T_m Values of Interstrand Cross-Linked Oligonucleotide Duplexes Prepared by the "Bis-Click" or "Stepwise Click" Reaction

Cross-linked Duplexes	T_m[a] [°C]	ΔT_m[b] [°C]	% h[c]	Cross-linked Duplexes	T_m[a] [°C]	ΔT_m[b] [°C]	% h[c]	Cross-linked Duplexes	T_m[a] [°C]	ΔT_m[b] [°C]	% h[c]
5'-d(TAG2TC AAT ACT) (43)*#	> 80.0 (>80.0)	> 29 > 29	- -	5'-d(TA2 G TC AAT ACT) (47)*	> 80.0	> 29	-	5'-d(TAG GT7 AAT ACT) (51)*	> 80.0	> 29	-
3'-d(ATC CA2 TTA TGA)	56.0*	+5	11	3'-d(ATC CA2 TTA TGA)				3'-d(ATC CA2 TTA TGA)			
5'-d(TAG 2TC AAT ACT) (44)*#	75.5 (75.5)	+24.5 +24.5	19 18	5'-d(TAG 3TC AAT ACT) (39)*#	75.5 (75.0)	+24.5 +26	18 19	5'-d(TAG G6C AAT ACT) (40)*#	75.5 (75.0)	+24.5 +26	17 17
3'-d(ATC CA3 TTA TGA)	50.0*	-1.0	19	3'-d(ATC CA3 TTA TGA)				3'-d(ATC CA3 TTA TGA)			
5'-d(TAG 2TC AAT ACT) (53)*	74.0	+23	17	5'-d(TA2 GTC AAT ACT) (52)*	73.0	+22	16	5'-d(TAG GT7 AAT ACT) (41)#	73.5 (73.5)	+22.5 +24.5	17 17
3'-d(AT7 CAG TTA TGA)				3'-d(AT7 CAG TTA TGA)				3'-d(ATC CA3 TTA TGA)			
5'-d(TAG G6C AAT ACT) (55)*	73.0	+22	16	5'-d(6AG GTC AAT ACT) (45)#	72.5	+21.5	16	5'-d(TAG 3TC AAT ACT) (54)*	72.0	+21	16
3'-d(ATC CA2 TTA TGA)				3'-d(ATC CA2 TTA TGA)				3'-d(AT7 CAG TTA TGA)			
5'-d(6AG GTC AAT ACT) (57)*	75.5	+24.5	15	5'-d(5AG GTC AAT ACT) (46)*#	76.5 (76.5)	+25.5 +27.5	19 19				
3'-d(AT 7CAG TTA TGA)				3'-d(A6C CAG TTA TGA)							
5'-d(TAG2TCAATACT) (49)*	76.5	+25.5	14	5'-d(TAG2TCAATACT) (50)*	75.0	+24	17				
3'-d(T_6 ATCCA3TTATGA T_6)				3'-d(A_6ATCCA3TTATGAT_6)							
5'-d(TAG GT7 AAT ACT) (59)*	67.0	+16	16	5'-d(TAG G6C AAT ACT) (56)*	68.0	+17	16	5'-d(TAG G T 7AAT ACT) (58)*	62.5	+11.5	15
3'-d(ATC 7AG TTA TGA)				3'-d(AT7CAG TTA TGA)				3'-d(AT 7CAG TTA TGA)			
5'-d(TAG GTC 4AT ACT) (42)#	68.5 (68.5)	+17.5 +19.5	16 15					5'-d(TAG GTC 2AT ACT) (48)*	61.0	+10	16
3'-d(ATC CA3 TTA TGA)								3'-d(ATC CA2 TTA TGA)			

[a]Measured at 260 nm in a 1 M NaCl solution containing 100 mM $MgCl_2$ and 60 mM Na cacodylate (pH 7.0) with 5 μM cross-linked DNA concentration. Data in parentheses were measured with 2 μM cross-linked DNA concentration. T_m values marked with an asterisk were measured in 1:1 (v/v) mixture of the above salt buffer and formamide with the identical ICL duplex concentration (5 μM). [b]ΔT_m refers to the increase/decrease of the T_m value compared to the reference duplex **13•14** (see Table 1). [c]% h refers to percentage hypochromicity. *Refers to interstrand cross-linked oligonucleotides prepared by the "bis-click" reaction. #Refers to interstrand cross-linked oligonucleotides prepared by the "stepwise click" reaction. The particular cross-linked nucleobases, e.g., **2**-**2**, are shown in the Supporting Information Figure S3 and Figure S4.

ODN-**24**) both bearing a 7-ethynyl-7-deaza-8-azapurine residue is depicted in Scheme 4.

The reaction proceeded to completion in 12 h, and the cross-linked oligonucleotides were purified by reversed-phase HPLC. This protocol was applied to cross-link a whole series of oligonucleotides. The interstrand cross-linked duplexes obtained by this method are summarized in Table 2. The reaction yield was in the range 40−50% yield; in a typical example, 4 OD of starting material gave 2 OD of cross-linked duplex. The products were characterized by LC-ESI-TOF or MALDI-TOF mass spectrometry, ion-exchange HPLC, as well as gel-electrophoresis (Figures 4 and 6 and Supporting Information).

Comparing the "bis-click" reaction performed earlier on identical single strands and the cross-linking of complementary strands in duplex DNA described now, we found that the reaction is significantly faster for single-stranded DNA than for duplex DNA. Steric reasons might account for these differences. Compared to DNA single strands, duplex DNA is compact and inflexible, so that the cross-linker has to overcome these limitations, when the cross-link is introduced in an internal stable region of the duplex (central position).

Analytical Characterization of Heterodimers and Homodimers. Theoretically, cross-linking of complementary oligonucleotide strands by the "bis-click" reaction can lead to a mixture of three different compounds. One species is the desired heterodimer connecting two complementary strands (duplex); the others are homodimers composed from identical single strands. The statistic ratio of heterodimer to homodimer formation in the crude reaction mixture would be 50% heterodimer to 25% of each homodimer. However, by comparing the reversed-phase HPLC profiles (Figure 4a,b) of the crude reaction mixtures it is obvious that the dominating product is the hetereodimer and the corresponding homodimers are suppressed. The formation of homodimers might occur with remaining free single strands in solution or by reactions among two duplexes in close proximity. For example, almost exclusive formation of cross-linked heterodimers was observed for the cross-linked ICL-**43** as well as for the duplexes ICL-**44** and ICL-**49** (Figure 4a and Figures S7b and S8a, Supporting Information).

In other cases, small amounts of side products were observed in the reaction mixture, which were identified as homodimers. These observations were exemplarily confirmed by ion-exchange HPLC and gel electrophoresis (Figures 4 and 6). Following the approach of "bis-click" cross-linking on duplexes, we were able to cross-link duplexes using different connectivities which varied in linker length, position in the duplex, and type of nucleobase. Figure 5 displays the various connectivities formed by the "click" cross-linking with G18* (8-aza-7-deazapurine analogue) or C15* (cytosine analogue) as central anchoring sites. The cross-link is formed between an 7-(octa-1,7-diynylated) or 7-ethynylated 8-aza-7-deaza-2′-deoxyguanosine (G18)*, as well as an octa-(1,7-diynylated) dC (C15*) residue in one oligonucleotide chain and a dG, dU, dC, or dA derivative in the complementary strand.

In order to confirm the structure of heterodimers prepared by the "bis-click" protocol on duplexes, they were also synthesized by the "stepwise click" reaction. For this, corresponding oligonucleotides shown in Table 1 were used. The "stepwise click" reaction carried out to form heterodimers (complementary sequences) differs from that performed to generate homodimers. As oligonucleotides are now complementary, they form duplexes in the reaction medium which was

dx.doi.org/10.1021/bc300074k | Bioconjugate Chem. 2012, 23, 1230−1243

Table 5. T_m Values of Interstrand Cross-Linked Oligonucleotides ICL-60 to ICL-65 (Homodimers)

Duplexes	T_m[a] [°C]	ΔT_m[b] [°C]	MS [calc.] found	Duplexes	T_m[a] [°C]	ΔT_m[b] [°C]	MS [calc.] found
5'-d(TAG GTC AAT ACT) (**13**) 3'-d(ATC CAG TTA TGA) (**14**)	51.0 (49.0)	- -					
3'-d(ATC CAG TTA TGA) (**14**) 5'-d(TAG 2TC AAT ACT) (**60**)^2 5'-d(TAG 2TC AAT ACT) 3'-d(ATC CAG TTA TGA) (**14**)	41.0 (39.0)	-10 -10	[7521.4][e] 7521.3[f]	3'-d(ATC CAG TTA TGA) (**14**) 5'-d(TAG GT7 AAT ACT) (**64**) 5'-d(TAG GT7 AAT ACT) 3'-d(ATC CAG TTA TGA) (**14**)	46.0 (43.5)	-5.0 -5.5	[7683.3][c] 7688.0[d]
5'-d(TAG GTC AAT ACT) (**13**) 3'-d(ATC CA2 TTA TGA) (**61**)^2 3'-d(ATC CA2 TTA TGA) 5'-d(TAG GTC AAT ACT) (**13**)	34.0 (31.0)	-17 -18	[7521.4][e] 7524.3[f]	5'-d(TAG GTC AAT ACT) (**13**) 3'-d(ATC 7AG TTA TGA) (**65**) 3'-d(ATC 7AG TTA TGA) 5'-d(TAG GTC AAT ACT) (**13**)	48.5 (45.5)	-2.5 -3.5	[7683.3][c] 7688.0[d]
5'-d(TAG GTC AAT ACT) (**13**) 3'-d(ATC CA3TTA TGA) (**63**)^{1,2} 3'-d(ATC CA3 TTA TGA) 5'-d(TAG GTC AAT ACT) (**13**)	45.0 (43.5)	-6.0 -5.5	[7681.5][e] 7685.3[f]	3'-d(ATC CAG TTA TGA) (**14**) 5'-d(TAG G6C AAT ACT) (**62**) 5'-d(TAG G6C AAT ACT) 3'-d(ATC CAG TTA TGA) (**14**)	46.5 (45.0)	-4.5 -4.0	[7658.3][c] 7658.0[d]
5'-d(TAG2 TC AAT ACT) 3'-d(ATC CA2 TTA TGA) (**60+61**)^2 3'-d(ATC CA2 TTA TGA) 5'-d(TAG2 TC AAT ACT)	56.0	+5.0		5'-d(TAGG6C AAT ACT) 3'-d(ATC C:A2 TTA TGA) (**62+61**) 3'-d(ATC C:A2 TTA TGA) 5'-d(TAGG6C AAT ACT)	49.0 (47.0)	-2.0 -2.0	
5'-d(TAG2 TC AAT ACT) 3'-d(ATC CA3 TTA TGA) (**60+63**)^2 3'-d(ATC CA3 TTA TGA) 5'-d(TAG2 TC AAT ACT)	57.0 (56.0)	+6.0 +7.0		5'-d(TAGG6C AAT ACT) 3'-d(ATC C:A3 TTA TGA) (**62+63**) 3'-d(ATC C:A3TTA TGA) 5'-d(TAGG6C AAT ACT)	62.0 (60.0)	+11.0 +11.0	
5'-d(TAG GT7 AAT ACT) 3'-d(ATC 7A GTTA TGA) (**64+65**) 3'-d(ATC 7A GTTA TGA) 5'-d(TAG GT7 AAT ACT)	47.0 (45.5)	-4.0 -3.5					

[a]Measured at 260 nm in a 1 M NaCl solution containing 100 mM $MgCl_2$ and 60 mM Na cacodylate (pH 7.0) with 2.5 μM of cross-linked DNA and 5 μM of the single-stranded complementary oligonucleotides. Data in parentheses were measured at a 1 μM of cross-linked DNA and 2 μM of the single-stranded complementary oligonucleotides. [b]ΔT_m refers to the increase/decrease of the T_m value compared to the reference duplex **13**•**14** (see Table 1). [c]Calculated on the basis of molecular weight as $[M+1]^+$. [d]Determined by MALDI-TOF mass spectrometry as $[M+1]^+$ in the linear positive mode. [e]Calculated on the basis of exact mass. [f]Determined by LC-ESI-TOF mass spectrometry. The particular cross-linked nucleobases, e.g., **2**-**2**, are shown in the Supporting Information Figure S3 and Figure S4.

proven by T_m measurements. For example, for ODN-**16** and ODN-**35** duplex melting was observed under the conditions of the "click" reaction. This does not interfere with the exclusive formation of heterodimers but increases the reaction time significantly. A typical example for the "stepwise click" reaction is shown in Scheme 5. Similar to the "bis-click" reaction the cross-link is formed internally within a DNA duplex (→ ICL-**43**, Scheme 5). The cross-linked duplexes ICl-**39** to ICL-**46** were synthesized as proofs according to the "stepwise click" protocol (Table 2).[2]

A central feature for the identification of heterodimers and homodimers results from their unambiguous characterization. In principle, two methods were used to identify the various cross-linked oligonucleotides, mass spectrometry and gel-electrophoresis. Mass spectroscopy was used in cases when the masses of homodimers and heterodimers are different. This is exemplified for selected compounds shown in Table 3. A complementary cross-linked duplex (ICL-**40***, heterodimer) is formed from ODN-**22** and ODN-**25** as well as the cross-linked homodimers ICL-**62** and ICL-**63**. The heterodimer ICL-**40*** and the two homodimers have different molecular masses. Thus, they can be distinguished. As a control, the heterodimer was also synthesized by the "stepwise click" reaction. On the contrary, in the second example homodimers ICL-**60** and ICL-**61** and heterodimer ICL-**43*** cannot be distinguished due to identical masses.

Unexpectedly, we found that cross-linked homodimers and heterodimers of identical molecular weight can be easily distinguished by denaturating polyacrylamide gel electrophoresis (PAGE) as depicted in Figure 6a–c (for further examples and experimental details, see Supporting Information as well as Experimental Procedures). Cross-linked heterodimers migrate significantly more rapidly than cross-linked homodimers. Although it is not possible to distinguish between two different homodimers, the desired heterodimers can be nicely characterized and/or separated by this method. A final proof results from the comparison of T_m values of cross-linked homomeric and heteromeric duplexes, which will be discussed in the next section.

Stability of Cross-Linked Duplexes. Next, the influence of cross-links on the duplex stability was investigated. For this, T_m values of cross-linked duplexes were measured and were compared to those of nonligated duplexes. T_m values marked with an asterisk were measured in a 1:1 (v/v) mixture of 1 M NaCl buffer (pH 7.0)/formamide mixture, when the T_m value was too high. When canonical nucleosides were replaced by those providing the linker, the Watson–Crick base pairing was always kept intact, indicated by the T_m values of Table 1

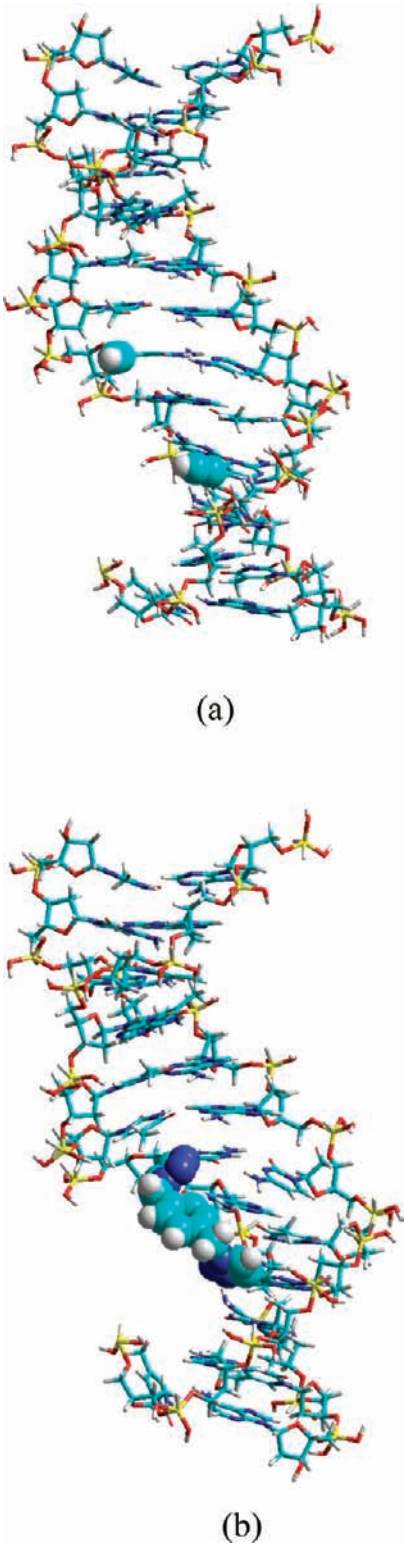

Figure 7. Comparison of cross-linked and non-cross-linked duplexes. Molecular models of (a) duplex **16•24** and (b) ICL-**43**. The modification sites are presented as colored space-filling overlapping spheres. The models were constructed using *Hyperchem 7.0/8.0* and energy-minimized by using *AMBER* calculations.

(Table S3, Supporting Information). Hypochromicities (% h) are similar for cross-linked and non-cross-linked duplexes.

It can be seen that the T_m values of the cross-linked duplexes are significantly (20−29 °C) increased compared to those of the non-cross-linked ones. This results from the different stoichiometries of duplex melting. From the identical number of base pairs, one can expect that all cross-linked duplexes should show similar T_m values. However, the cross-link generates steric stress on the duplex, which depends on the linker length and the linking position. These phenomena are reflected by the T_m changes shown in Table 4. Regarding duplex stability, the cross-linked oligonucleotides can be divided into three groups displaying the following various influences by the cross-links.

(1) The highest duplex stabilization (T_m > 80 °C) is obtained when the ethynylated compound **2** was cross-linked with another compound **2** residue (ICL-**43** and ICL-**47**) or with the 5-octa-(1,7-diynylated)-dC (**7**) (ICL-**51**). The latter consists of a modified dG-dC base pair which is cross-linked and stabilized. In these cases, the duplex structure of the cross-linked species does not seem to be significantly perturbed and the cross-link is nicely integrated in the duplex structure. For these duplexes, the cross-linked nucleobases are in close proximity separated by at least one base pair.

(2) Most of the duplexes are represented by the second group. They are covered by cross-links which are different in linker length, type of alkyne, nucleobase, and position in the duplex. The T_m values for these duplexes are all in the range 72−76 °C. A partial disruption of base pairs is most likely induced by a cross-link not having the ideal spatial demands to be well accommodated in the DNA duplex.

(3) The duplexes with the lowest T_m values (62−68 °C) are represented by the third group. Here, a certain disorder of the duplex is present, in which at least one or more base pairs are disturbed. This is proved by comparison of ICL-**58** (T_m = 61 °C) with ICL-**48** (T_m = 61 °C) bearing a **2**-dT mismatch, both showing similar duplex stability.

Contrary to the heterodimers, homodimers with identical strands do not form duplexes. Nevertheless, duplexes can be generated when they are hybridized with individual single strands complementary to the homodimers. Examples for cross-linked homodimers with two complementary strands are shown in Table 5. The duplex stabilization of heterodimeric cross-linked duplexes was significantly higher as observed for cross-linked heterodimeric duplexes when paired with complementary strands. This is also true when double duplexes of homodimers were generated by introducing two cross-links between two helices (Table 5).

■ CONCLUSION AND OUTLOOK

A diversity of complementary oligonucleotides incorporating alkynylated 8-aza-7-deazapurine or corresponding 5-alkynylated pyrimidine nucleosides (**2**−**7**) which are related to the four canonical DNA bases were synthesized. The "bis-click" reaction was performed on oligonucleotide duplexes with the bis-azide **1** which resulted in the chemoselective formation of interstrand cross-linked DNA. Preformed DNA duplexes served as a tool ("template") for the selective generation of heterodimers, while homodimer formation was suppressed. The chemoselective formation of heterodimers is likely when the linker length and the linking positions are optimal as shown during the formation of cross-linked DNA ICL-**43**. The formation of homodimers increases under nonoptimal conditions. Internal "bis-click" cross-linking was always slower on duplex DNA compared to reactions performed on noncomplementary strands due to the rigid duplex structure. This is different from cross-linking reactions performed at the terminus of a duplex.[25−27] Due to

the higher flexibility of the strands, these ligation reactions are accelerated.

Studies on interstrand cross-linked heterodimeric duplexes revealed significantly increased T_m values compared to non-cross-linked congeners. It was shown that the increase of duplex stability depends on the nucleobase, the linker length, and the linking positions. As an example, molecular dynamic simulations using Amber MM+ force field (*Hyperchem 7.0/8.0*; Hypercube Inc., Gainesville, FL, USA, 2001) was performed for the duplex **16•24** and the resulting interstrand cross-linked heterodimer ICL-**43** (Figure 7). Obviously, the DNA duplex structure is not perturbed and the cross-link seems to be well accommodated in the major groove of the DNA duplex. This corresponds to the high T_m value of the duplex, while others are more obstructed resulting in lower T_m values. Consequently, the interstrand cross-linking reaction using "bis-click" chemistry is applicable for duplex DNA and can be exerted to the generation of very stable cross-linked DNA. We anticipate that this internal cross-linking protocol will find application in chemical biology and the construction of nanoassemblies.

■ ASSOCIATED CONTENT

Supporting Information

Additional T_m values of alkynylated and azido-functionalized DNA duplexes, structures, and analytical data of cross-linked duplexes, reversed-phase HPLC profiles of cross-linked and non-cross-linked oligonucleotides, ion-exchange HPLC profiles of cross-linked and non-cross-linked oligonucleotides, denaturing PAGE analysis of oligonucleotides, melting profiles, MALDI-TOF and LC-ESI-TOF data of oligonucleotides. This material is available free of charge via the Internet at http://pubs.acs.org.

■ AUTHOR INFORMATION

Corresponding Author

*Tel: +49 (0)251 53406 500. Fax: +49 (0)251 53406 857. E-mail: Frank.Seela@uni-osnabrueck.de.

Notes

The authors declare no competing financial interest.

■ ACKNOWLEDGMENTS

We thank Dr. P. Leonard and Dr. S. Budow for their continuous support throughout the preparation of the manuscript and N. Q. Tran for oligonucleotide synthesis. We appreciate the measurement of ESI mass spectra by Dr. E. Uhlmann, Coley Pharmaceuticals GmbH, and the measurement of MALDI spectra by Dr. R. Thiele from Roche Diagnostics, Penzberg, Germany, and Dr. H. Luftmann, Organisch-chemisches Institut, Universität Münster, Germany. Financial support by ChemBiotech, Münster, Germany, is gratefully acknowledged.

■ REFERENCES

(1) Pujari, S. S., Xiong, H., and Seela, F. (2010) Cross-linked DNA generated by "bis-click" reactions with bis-functional azides: Site independent ligation of oligonucleotides via nucleobase alkynyl chains. *J. Org. Chem. 75*, 8693−8696.

(2) Xiong, H., and Seela, F. (2011) Stepwise "click" chemistry for the template independent construction of a broad variety of cross-linked oligonucleotides: Influence of linker length, position, and linking number on DNA duplex stability. *J. Org. Chem. 76*, 5584−5597.

(3) Huisgen, R., Szeimies, G., and Möbius, L. (1967) Kinetik der Additionen organischer Azide an CC-Mehrfachbindungen. *Chem. Ber. 100*, 2494−2507.

(4) Huisgen, R. (1989) Kinetics and reaction mechanisms: Selected examples from the experience of forty years. *Pure Appl. Chem. 61*, 613−628.

(5) Kolb, H. C., Finn, M. G., and Sharpless, K. B. (2001) Click chemistry: Diverse chemical function from a few good reactions. *Angew. Chem., Int. Ed. 40*, 2004−2021.

(6) Rostovtsev, V. V., Green, L. G., Fokin, V. V., and Sharpless, K. B. (2002) A stepwise Huisgen cycloaddition process: Copper(I)-catalyzed regioselective "ligation" of azides and terminal alkynes. *Angew. Chem., Int. Ed. 41*, 2596−2599.

(7) Kolb, H. C., and Sharpless, K. B. (2003) The growing impact of click chemistry on drug discovery. *Drug Discovery Today 8*, 1128−1137.

(8) Meldal, M., and Tornøe, C. W. (2008) Cu-catalyzed azide-alkyne cycloaddition. *Chem. Rev. 108*, 2952−3015.

(9) van Dijk, M., Rijkers, D. T. S., Liskamp, R. M. J., van Nostrum, C. F., and Hennink, W. E. (2009) Synthesis and applications of biomedical and pharmaceutical polymers via click chemistry methodologies. *Bioconjugate Chem. 20*, 2001−2016.

(10) Gramlich, P. M. E., Wirges, C. T., Manetto, A., and Carell, T. (2008) Postsynthetic DNA modification through the copper-catalyzed azide−alkyne cycloaddition reaction. *Angew. Chem., Int. Ed. 47*, 8350−8358.

(11) El-Sagheer, A. H., and Brown, T. (2010) Click chemistry with DNA. *Chem. Soc. Rev. 39*, 1388−1405.

(12) Amblard, F., Cho, J. H., and Schinazi, R. F. (2009) Cu(I)-catalyzed Huisgen azide-alkyne 1,3-dipolar cycloaddition reaction in nucleoside, nucleotide, and oligonucleotide chemistry. *Chem. Rev. 109*, 4207−4220.

(13) Tron, G. C., Pirali, T., Billington, R. A., Canonico, P. L., Sorba, G., and Genazzani, A. A. (2008) Click chemistry reactions in medicinal chemistry: Applications of the 1,3-dipolar cycloaddition between azides and alkynes. *Med. Res. Rev. 28*, 278−308.

(14) Bräse, S., and Banert, K. (2010) *Organic Azides*, John Wiley & Sons, Chichester, U.K.

(15) Scriven, E. F. V., and Turnbull, K. (1988) Azides: Their preparation and synthetic uses. *Chem. Rev. 88*, 297−368.

(16) Thomas, J. R., Liu, X., and Hergenrother, P. J. (2005) Size-specific ligands for RNA hairpin loops. *J. Am. Chem. Soc. 127*, 12434−12435.

(17) Wilds, C. J., Noronha, A. M., Robidoux, S., and Miller, P. S. (2004) Mispair-aligned N^3T-alkyl-N^3T interstrand cross-linked DNA: Synthesis and characterization of duplexes with interstrand cross-links of variable lengths. *J. Am. Chem. Soc. 126*, 9257−9265.

(18) Noll, D. M., McGregor Mason, T., and Miller, P. S. (2006) Formation and repair of interstrand cross-links in DNA. *Chem. Rev. 106*, 277−301.

(19) Kiviniemi, A., Virta, P., and Lönnberg, H. (2008) Utilization of intrachain 4′-*C*-Azidomethylthymidine for preparation of oligodeoxyribonucleotide conjugates by click chemistry in solution and on a solid support. *Bioconjugate Chem. 19*, 1726−1734.

(20) Sczepanski, J. T., Jacobs, A. C., and Greenberg, M. M. (2008) Self-promoted DNA interstrand cross-link formation by an abasic site. *J. Am. Chem. Soc. 130*, 9646−9647.

(21) Ding, H., and Greenberg, M. M. (2010) DNA damage and interstrand cross-link formation upon irradiation of aryl iodide C-nucleotide analogues. *J. Org. Chem. 75*, 535−544.

(22) Chaudhuri, N. C., and Kool, E. T. (1995) Very high affinity DNA recognition by bicyclic and cross-linked oligonucleotides. *J. Am. Chem. Soc. 117*, 10434−10442.

(23) Endo, M., and Majima, T. (2005) Structural arrangement of DNA constrained by a cross-linker. *Org. Biomol. Chem. 3*, 3476−3478.

(24) Czlapinski, J. L., and Sheppard, T. L. (2005) Template-directed assembly and characterization of metallosalen-DNA conjugates. *Bioconjugate Chem. 16*, 169−177.

(25) El-Sagheer, A. H., and Brown, T. (2009) Synthesis and polymerase chain reaction amplification of DNA strands containing an unnatural triazole linkage. *J. Am. Chem. Soc. 131*, 3958−3964.
(26) Kočalka, P., El-Sagheer, A. H., and Brown, T. (2008) Rapid and efficient DNA strand cross-linking by click chemistry. *ChemBioChem 9*, 1280−1285.
(27) Peng, X., Li, H., and Seidman, M. (2010) A template-mediated click−click reaction: PNA−DNA, PNA−PNA (or peptide) ligation, and single nucleotide discrimination. *Eur. J. Org. Chem. 2010*, 4194−4197.
(28) Nakane, M., Ichikawa, S., and Matsuda, A. (2008) Triazole-linked dumbbell oligodeoxynucleotides with NF-κB binding ability as potential decoy molecules. *J. Org. Chem. 73*, 1842−1851.
(29) Li, X., and Liu, D. R. (2004) DNA-templated organic synthesis: Nature's strategy for controlling chemical reactivity applied to synthetic molecules. *Angew. Chem., Int. Ed. 43*, 4848−4870.
(30) Streeper, R. T., Cotter, R. J., Colvin, M. E., Hilton, J., and Colvin, O. M. (1995) Molecular pharmacology of hepsulfam, NSC 3296801: Identification of alkylated nucleosides, alkylation site, and site of DNA cross-linking. *Cancer Res. 55*, 1491−1498.
(31) Angelov, T., Guainazzi, A., and Schärer, O. D. (2009) Generation of DNA interstrand cross-links by post-synthetic reductive amination. *Org. Lett. 11*, 661−664.
(32) Ho, T. V., Guainazzi, A., Derkunt, S. B., Enoiu, M., and Schärer, O. D. (2011) Structure-dependent bypass of DNA interstrand crosslinks by translesion synthesis polymerases. *Nucleic Acids Res. 39*, 7455−7464.
(33) Jawalekar, A. M., Op de Beeck, M., van Delft, F. L., and Madder, A. (2011) Synthesis and incorporation of a furan-modified adenosine building block for DNA interstrand crosslinking. *Chem. Commun. 47*, 2796−2798.
(34) Stevens, K., Claeys, D. D., Catak, S., Figaroli, S., Hocek, M., Tromp, J. M., Schürch, S., Van Speybroeck, V., and Madder, A. (2011) Furan-oxidation-triggered inducible DNA cross-linking: Acyclic versus cyclic furan-containing building blocks − on the benefit of restoring the cyclic sugar backbone. *Chem.—Eur. J. 17*, 6940−6953.
(35) Op de Beeck, M., and Madder, A. (2011) Unprecedented C-selective interstrand cross-linking through *in situ* oxidation of furan-modified oligodeoxynucleotides. *J. Am. Chem. Soc. 133*, 796−807.
(36) Barr, P. J., Jones, A. S., Serafinowski, P., and Walker, R. T. (1978) The synthesis of nucleosides derived from 5-ethynyluracil and 5-ethynylcytosine. *J. Chem. Soc., Perkin Trans. 1*, 1263−1267.
(37) Gramlich, P. M. E., Warncke, S., Gierlich, J., and Carell, T. (2008) Click−click−click: Single to triple modification of DNA. *Angew. Chem., Int. Ed. 47*, 3442−3444.
(38) Seela, F., and Sirivolu, V. R. (2006) DNA containing side chains with terminal triple bonds: Base-pair stability and functionalization of alkynylated pyrimidines and 7-deazapurines. *Chem. Biodivers. 3*, 509−514.
(39) Seela, F., and Sirivolu, V. R. (2007) Nucleosides and oligonucleotides with diynyl side chains: Base pairing and functionalization of 2′-deoxyuridine derivatives by the copper(I)-catalyzed alkyne−azide 'click' cycloaddition. *Helv. Chim. Acta 90*, 535−552.
(40) Seela, F., Sirivolu, V. R., and Chittepu, P. (2008) Modification of DNA with octadiynyl side chains: Synthesis, base pairing, and formation of fluorescent coumarin dye conjugates of four nucleobases by the alkyne-azide "click" reaction. *Bioconjugate Chem. 19*, 211−224.
(41) Seela, F., Xiong, H., Leonard, P., and Budow, S. (2009) 8-Aza-7-deazaguanine nucleosides and oligonucleotides with octadiynyl side chains: Synthesis, functionalization by the azide-alkyne 'click' reaction and nucleobase specific fluorescence quenching of coumarin dye conjugates. *Org. Biomol. Chem. 7*, 1374−1387.
(42) Seela, F., and Pujari, S. S. (2010) Azide-alkyne "click" conjugation of 8-aza-7-deazaadenine-DNA: Synthesis, duplex stability, and fluorogenic dye labeling. *Bioconjugate Chem. 21*, 1629−1641.
(43) Graham, D., Parkinson, J. A., and Brown, T. (1998) DNA duplexes stabilized by modified monomer residues: Synthesis and stability. *J. Chem. Soc., Perkin Trans. 1*, 1131−1138.
(44) *User's Manual of the DNA Synthesizer*, Applied Biosystems, Weiterstadt, Germany.
(45) Ding, P., Wunnicke, D., Steinhoff, H.-J., and Seela, F. (2010) Site-directed spin-labeling of DNA by the azide-alkyne 'click' reaction: Nanometer distance measurements on 7-deaza-2′-deoxyadenosine and 2′-deoxyuridine nitroxide conjugates spatially separated or linked to a 'dA-dT' base pair. *Chem.—Eur. J. 16*, 14385−14396.
(46) Petersheim, M., and Turner, D. H. (1983) Base-stacking and base-pairing contributions to helix stability: Thermodynamics of double-helix formation with CCGG, CCGGp, CCGGAp, ACCGGp, CCGGUp, and ACCGGUp. *Biochemistry 22*, 256−263.
(47) Seela, F., and Wenzel, T. (1992) 1,7-Dideaza-2′-deoxyadenosine: Building blocks for solid-phase synthesis and secondary structure of base-modified oligodeoxyribonucleotides. *Helv. Chim. Acta 75*, 1111−1122.
(48) Seela, F., He, Y., He, J., Becher, G., Kröschel, R., Zulauf, M., and Leonard, P. (2004) Base-modified oligonucleotides with increased duplex stability: Pyrazolo[3,4-*d*]pyrimidines replacing purines, Methods in Molecular Biology, in *Oligonucleotide Synthesis: Methods and Applications* (Herdewijn, P., Ed.) pp 165−186, Vol. *288*, Humana Press Inc., Totowa, NJ.

Bioconjugate Chemistry

Article

pubs.acs.org/bc

New Class of Tetradentate β-Diketonate-Europium Complexes That Can Be Covalently Bound to Proteins for Time-Gated Fluorometric Application

Lin Zhang,[†] Yanjiao Wang,[†] Zhiqiang Ye,*[,†] Dayong Jin,[‡] and Jingli Yuan*[,†]

[†]State Key Laboratory of Fine Chemicals, School of Chemistry, Dalian University of Technology, Dalian 116024, P. R. China

[‡]MQ Photonics Centre, Faculty of Science, Macquarie University, NSW 2109, Sydney, Australia

Supporting Information

ABSTRACT: Luminescent lanthanide complexes that can be covalently bound to proteins have shown great utility as biolabels for highly sensitive time-gated luminescence bioassays in clinical diagnostics and biotechnology discoveries. In this work, three new tetradentate β-diketonate−europium complexes that can be covalently bound to proteins to display strong and long-lived Eu^{3+} luminescence, 1,2-bis[4′-(1″,1″,1″,2″,2″,3″,3″-heptafluoro-4″,6″-hexanedion-6″-yl)-benzyl]-4-chlorosulfobenzene-Eu^{3+} (BHHBCB-Eu^{3+}), 1,2-bis-[4′-(1″,1″,1″,2″,2″-pentafluoro-3″,5″-pentanedion-5″-yl)-benzyl]-4-chlorosulfo-benzene-Eu^{3+} (BPPBCB-Eu^{3+}), and 1,2-bis[4′-(1″,1″,1″-trifluoro-2″,4″-butanedion-4″-yl)-benzyl]-4-chlorosulfobenzene-Eu^{3+} (BTBBCB-Eu^{3+}), have been designed and synthesized as biolabels for time-gated luminescence bioassay applications. The luminescence spectroscopy characterizations of the aqueous solutions of three complex-bound bovine serum albumin reveal that BHHBCB-Eu^{3+} has the strongest luminescence with the largest quantum yield (40%) and longest luminescence lifetime (0.52 ms) among the complexes, which is superior to the other currently available europium biolabels. The BHHBCB-Eu^{3+}-labeled streptavidin was prepared and used for both the time-gated luminescence immunoassay of human prostate specific antigen and the time-gated luminescence microscopy imaging of a pathogenic microorganism *Cryptosporidium muris*. The results demonstrated the practical utility of the new Eu^{3+} complex-based biolabel for time-gated luminescence bioassay applications.

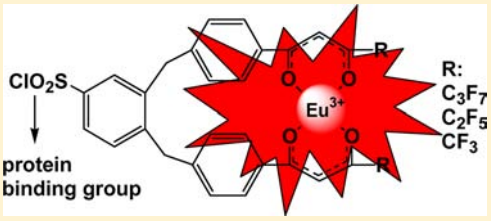

INTRODUCTION

As one of the most highly sensitive bioassay methods, time-gated (or time-resolved) luminescence bioassay technique using lanthanide complexes as labels has been comprehensively studied and widely used for clinical diagnostics and biotechnology discoveries over the past two decades.[1−9] The most important advantage of this technique is that the strong autofluorescence from complicated biological samples and scattering light from nearby optics can be easily eliminated by the time-gated detection mode, since the specific luminescence signal from the lanthanide complex label is super long-lived compared to the background fluorescence. On the basis of this feature, several powerful time-gated luminescence bioassay methods, such as time-gated luminescence immunoassay (TR-FIA), DNA hybridization assay, microscopy imaging assay, and high-speed cytometry assay, have been successfully developed for the highly sensitive detection of various analytes in complicated biological and environmental samples.[10−13]

The main luminescent lanthanide complex-based biolabels used in the current time-gated luminescence bioassay technique are the Eu^{3+} and Tb^{3+} complexes with various β-diketone and aromatic amine derivative ligands.[1−7,14,15] Although several classic bidentate β-diketonate-Eu^{3+} complexes, such as 2-naphthoyltrifluoroacetonate-Eu^{3+} (β-NTA-Eu^{3+}) and 2-thenoyltrifluoroacetonate-Eu^{3+} (TTA-Eu^{3+}), have been successfully used in the dissociation enhanced lanthanide fluoroimmunoassay system (DELFIA system),[1−3,16] this kind of complex is unsuitable for direct use as a biolabel due to the relatively low stability in aqueous solution (dissociation of the complexes at lower concentration will quench their luminescence) and the lack of a reactive group in the complexes for covalent binding to biomolecules. For this reason, several chlorosulfonylated tetradentate β-diketone ligands that can form stable and highly luminescent complexes with Eu^{3+} ions in aqueous solutions for labeling biomolecules, 4,4′-bis(1″,1″,1″,2″,2″,3″,3″-heptafluoro-4″,6″-hexanedion-6″-yl)-chlorosulfo-*o*-terphenyl (BHHCT),[17] 4,4′-bis(1″,1″,1″,2″,2″-pentafluoro-3″,5″-pentanedion-5″-yl)-chlorosulfo-*o*-terphenyl (BPPCT),[18] 4,4′-bis(1″,1″,1″-trifluoro-2″,4″-butanedion-4″-yl)-chlorosulfo-*o*-terphenyl (BTBCT),[19] 1,10-bis(4″-chlorosulfo-1′,1″-diphenyl-4′-yl)-4,4,5,5,6,6,7,7-octafluorodecane-1,3,8,10-tetraone (BCDOT),[20] 1,10-bis(8′-chlorosulfo-dibenzothiophene-2′-yl)-4,4,5,5,6,6,7,7-octafluorodecane- 1,3,8,10-tetraone (BCOT),[21] and 1,10-bis(5′-chlorosulfothiophene-2′-yl)-4,4,5,5,6,6,7,7- octafluorodecane-1,3,8,10-tetraone (BCTOT),[22] have been developed for time-gated luminescence bioassay applications in recent years.

It is worth noting that, among the above β-diketones, BPPCT and BTBCT are the simple analogues of BHHCT

Received: February 14, 2012
Revised: May 5, 2012
Published: May 31, 2012

without significant improvement, while BCDOT, BCOT, and BCTOT have the problem of protein−protein cross-linking owing to their two chlorosulfonyl groups; only the Eu^{3+} complex of BHHCT has shown good utility for a variety of time-gated luminescence bioassays, such as TR-FIAs of various antibodies and antigens,[5,7] hybridization assays of DNAs,[23,24] and microscopy imaging assays of environmental pathogens.[25−27] This complex was also found to be useful for preparing highly luminescent europium nanobiolabels,[28−31] and biosensors.[32,33] As a biolabel, BHHCT-Eu^{3+} has advantages including being easy to conjugate to proteins through the formation of sulfonamide (protein-NH-SO_2-label) without the protein cross-linking and strong luminescence with a larger quantum yield (~27%) and longer luminescence lifetime (~380 μs) in an aqueous buffer (bound to BSA).[4,17] However, because BHHCT is a 1,2-diphenylbenzene derivative, the angle between the three benzene rings is hard to change, which makes the two bidentate β-diketone groups in BHHCT short of flexibility to simultaneously coordinate to a Eu^{3+} ion, to reduce the emission efficiency of its Eu^{3+} complex.

To further improve the luminescence properties of β-diketonate-Eu^{3+} biolabels, especially those of BHHCT-Eu^{3+} analogues, in this work, three new chlorosulfonylated tetradentate β-diketonate-Eu^{3+} complexes that can display strong and long-lived Eu^{3+} luminescence, 1,2-bis[4′-(1″,1″,1″,2″,2″,3″,3″-heptafluoro-4″,6″-hexanedion-6″-yl)-benzyl]-4-chlorosulfobenzene-Eu^{3+} (BHHBCB-Eu^{3+}), 1,2-bis[4′-(1″,1″,1″,2″,2″-pentafluoro-3″,5″-pentanedion-5″-yl)-benzyl]-4-chlorosulfobenzene-Eu^{3+} (BPPBCB-Eu^{3+}), and 1,2-bis[4′-(1″,1″,1″-trifluoro-2″,4″-butanedion-4″-yl)-benzyl]-4-chlorosulfobenzene-Eu^{3+} (BTBBCB-Eu^{3+}), were designed and synthesized as biolabels for the time-gated luminescence bioassay application. Since there are two freely rotatable methylene groups introduced into the three benzene rings to enable the two bidentate β-diketone groups to simultaneously coordinate a Eu^{3+} ion easier, three such Eu^{3+} complexes can be expected to have higher emission efficiency and longer luminescence lifetime than those of BHHCT-Eu^{3+} analogues. To examine the practical utility of the new Eu^{3+} complexes as biolabels for time-gated luminescence bioassays, the BHHBCB-Eu^{3+}-labeled streptavidin (SA) was prepared and used for the TR-FIA of human prostate specific antigen (PSA) and time-gated luminescence microscopy imaging of an environmental pathogen *Cryptosporidium muris*. Figure 1 shows the structures of three BHHCT analogues and the newly synthesized β-diketones.

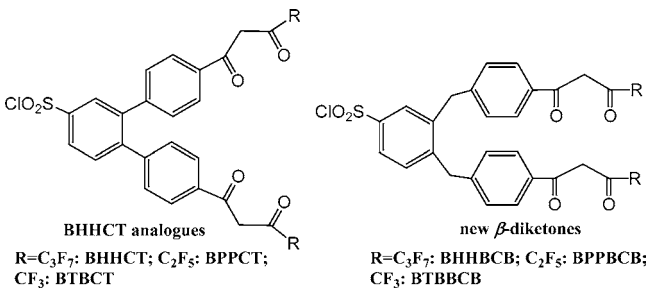

Figure 1. Structures of BHHCT analogues and new β-diketones BHHBCB, BPPBCB, and BTBBCB.

RESULTS AND DISCUSSION

Design, Synthesis, and Characterization of the New β-Diketonate-Eu^{3+} Complexes. It has been known for a while that some β-diketones can form strongly luminescent complexes with lanthanide ions (mainly Eu^{3+}, Sm^{3+}, Tb^{3+}, and Dy^{3+}). The early application of these complexes to bioassays was pioneered by the successful establishment of highly sensitive TR-FIA technique in 1980s,[1,3,34] in which isothiocyanatophenyl-ethylenediamine tetraacetate-Eu^{3+} or N^1-(*p*-isothiocyanatobenzyl)-diethylenetriamine-N^1,N^2,N^3,N^4-tetraacetate-Eu^{3+} was employed for labeling antibodies or antigens. After the immune reaction, the immunocomplexes were reacted with a luminescence enhancement solution consisting of Triton X-100, β-diketone (2-naphthoyltrifluoroacetone, 2-thenoyltrifluoroacetone, or pivaloyltrifluoroacetone), and tri-*n*-octylphosphine oxide (TOPO) at pH 3.2 to transform Eu^{3+} from the nonluminescent Eu^{3+} label into a highly luminescent β-diketonate-Eu^{3+}-TOPO ternary complex, so that the time-gated luminescence measurement could be carried out. Because this method suffers from the problem that the luminescence enhancement solution could be easily contaminated by the Eu(III)-containing experimental materials and environments (e.g., solvents, reagents, house dust, etc.), many efforts have been initiated to develop highly luminescent lanthanide complexes that can be directly used for biolabeling to avoid the use of luminescence enhancement solutions. However, the current status is still that there are only a few of luminescent lanthanide complexes, such as BHHCT-Eu^{3+} analogues and some lanthanide complexes with aromatic amine derivatives,[35−47] suitable for direct biolabeling due to the strict requirements of strong luminescence and high stability in aqueous buffers and an appropriate biomolecule-coupling group for a lanthanide complex biolabel.

To develop a better luminescent Eu^{3+} complex biolabel, we identify a new strategy of increasing the flexibility in the structure of BHHCT-type β-diketone, so that the two bidentate β-diketone groups can simultaneously coordinate to a Eu^{3+} ion easier, to improve the emission efficiency of its Eu^{3+} complex. In this work, by introducing two freely rotatable methylene groups into the three benzene rings of the 1,2-diphenylbenzene skeleton, a new class of chlorosulfonylated tetradentate β-diketones that can form strongly luminescent complexes with Eu^{3+} ions in aqueous solutions, BHHBCB, BPPBCB, and BTBBCB, were synthesized for improving the luminescence properties of BHHCT-Eu^{3+} analogues. The molecular modeling results of BHHCT-Eu^{3+} and BHHBCB-Eu^{3+} calculated using a *Gaussian 09* software reveal that the four oxygen atoms in BHHBCB are more equally coordinated to the central Eu^{3+} ion than those in BHHCT (Figure 2), and the atomic population charges of Eu^{3+} in BHHCT-Eu^{3+} and BHHBCB-Eu^{3+} are 2.790 and 2.924, respectively.

Three new chlorosulfonylated tetradentate β-diketones were synthesized according to the procedure shown in Scheme 1. After 1,2-bis(4′-acetyl-benzyl)-benzene was synthesized by using the Suzuki cross-coupling reaction between 1,2-dibromomethyl-benzene and 4-acetyl-phenylboronic acid,[48] three tetradentate β-diketones, 1,2-bis[4′-(1″,1″,1″,2″,2″,3″,3″-heptafluoro-4″,6″-hexanedion-6″-yl)-benzyl]-benzene, 1,2-bis-[4′-(1″,1″,1″,2″,2″-pentafluoro-3″,5″-pentanedion-5″-yl)-benzyl]-benzene, and 1,2-bis[4′-(1″,1″,1″-trifluoro-2″,4″-butanedion-4″-yl)-benzyl]-benzene were synthesized by the Claisen condensation reaction between 1,2-bis(4′-acetyl-benzyl)-benzene

dx.doi.org/10.1021/bc300075t | *Bioconjugate Chem.* 2012, 23, 1244−1251

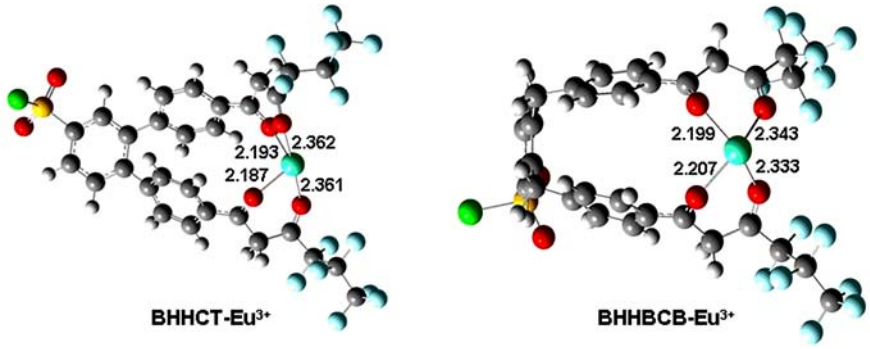

Figure 2. Molecular modeling results of BHHCT-Eu^{3+} and BHHBCB-Eu^{3+} calculated using *Gaussian 09* software.

Scheme 1. Synthesis Procedure of Three New Chlorosulfonylated Tetradentate β-Diketones

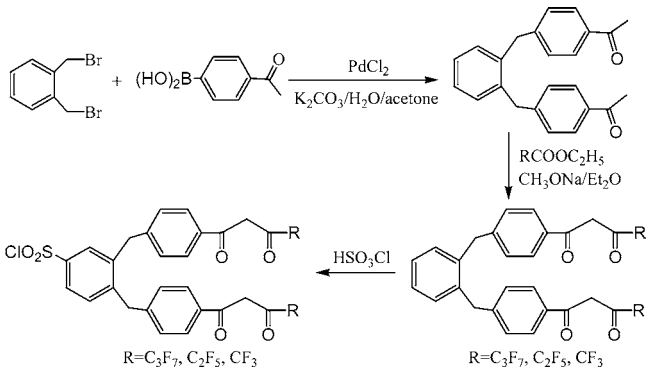

and $C_nF_{2n+1}CO_2Et$ (n = 1−3) in dry diethyl ether in the presence of $NaOCH_3$.[49] Finally, the chlorosulfonylated β-diketones were obtained with high yields by reacting the β-diketones with HSO_3Cl.[17] The three compounds were well-characterized by the NMR, MS, and elementary analyses.

The water-soluble conjugates of three Eu^{3+} complex-labeled bovine serum albumins (BSA), BSA-BHHBCB-Eu^{3+}, BSA-BPPBCB-Eu^{3+}, and BSA-BTBBCB-Eu^{3+}, were prepared for characterizing the luminescence properties of the Eu^{3+} complexes in aqueous buffers. Figure 3 shows the time-gated excitation and emission spectra of the conjugates of Eu^{3+} complexes (1.0×10^{-6} M) in 0.05 M Tris-HCl buffer of pH 7.8. Three Eu^{3+} complexes displayed similar excitation and emission patterns with the maximum excitations at 327, 328, and 324 nm, and a sharp main emission peak at 608 nm ($^5D_0 \rightarrow {}^7F_2$ transition of Eu^{3+}) for BHHBCB-Eu^{3+}, BPPBCB-Eu^{3+}, and BTBBCB-Eu^{3+}, respectively. The luminescence properties of three Eu^{3+} complexes in 0.05 M borate buffer of pH 9.1 were measured, and the results were summarized in Table 1. It can

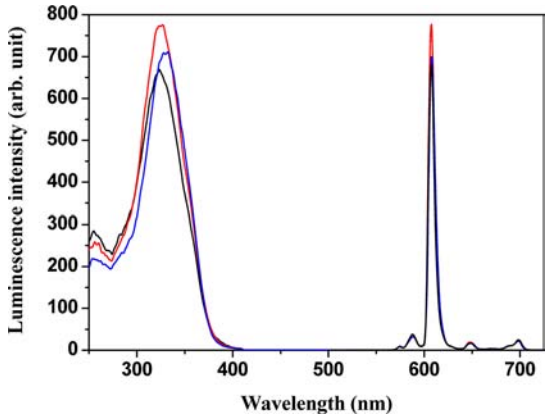

Figure 3. Time-gated excitation and emission spectra of the BSA conjugates of three Eu^{3+} complexes (1.0×10^{-6} M; red, BHHBCB-Eu^{3+}; blue, BPPBCB-Eu^{3+}; black, BTBBCB-Eu^{3+}) in 0.05 M Tris-HCl buffer of pH 7.8.

Table 1. Luminescence Properties of BHHBCB-Eu^{3+}, BPPBCB-Eu^{3+}, and BTBBCB-Eu^{3+} (bound to BSA) in 0.05 M Borate Buffer of pH 9.1

complex (bound to BSA)	$\lambda_{ex,max}$ (nm)	$\lambda_{em,max}$ (nm)	ϕ (%)	τ (ms)
BHHBCB-Eu^{3+}	327	608	40	0.52
BPPBCB-Eu^{3+}	328	608	36	0.49
BTBBCB-Eu^{3+}	324	608	34	0.48

be observed that, among three Eu^{3+} complexes, BHHBCB-Eu^{3+} has both the highest quantum yield and the longest luminescence lifetime than those of BPPBCB-Eu^{3+} and BTBBCB-Eu^{3+}, which indicates that BHHBCB-Eu^{3+} is the most suitable biolabel for highly sensitive time-gated luminescence bioassays. Furthermore, compared to BHHCT-Eu^{3+}, the emissions of all three new Eu^{3+} complexes showed higher efficiency and longer lifetimes, which demonstrated the validity of our molecular structure design in this work.

The new Eu^{3+} complexes also exhibited excellent stabilities in the biological buffer. As shown in Figure S1, the luminescence intensities of BHHBCB-Eu^{3+} at low concentrations (1−10 nM) are stable in 0.05 M Tris-HCl buffer of pH 7.8. To further compare the stability of BHHBCB-Eu^{3+} with that of BHHCT-Eu^{3+}, the luminescence intensity changes of the BSA conjugated BHHBCB-Eu^{3+} (1.0×10^{-6} M) and BHHCT-Eu^{3+} (1.0×10^{-6} M) in the presence of different concentrations of EDTA in 0.05 M Tris-HCl buffer of pH 7.8 were investigated. As shown in Figure S2, the luminescence intensity of BHHCT-Eu^{3+} is decreased in the presence of 1.0×10^{-4} M of EDTA, whereas that of BHHBCB-Eu^{3+} remains stable even in the presence of 1.0×10^{-2} M of EDTA. These results clearly indicate that the stability of BHHBCB-Eu^{3+} is much higher than that of BHHCT-Eu^{3+} in aqueous buffers.

The time-gated luminescence detection sensitivities of three Eu^{3+} complexes (bound to BSA) in 0.05 M Tris-HCl buffer of pH 7.8 were further measured on a more sensitive time-gated luminescence counter, Perkin-Elmer Victor 1420 multilabel counter, using 96-well microtiter plates as the cuvettes. As shown in Figure 4, the luminescence intensities displayed good linear relationships to the Eu^{3+} complex concentrations with

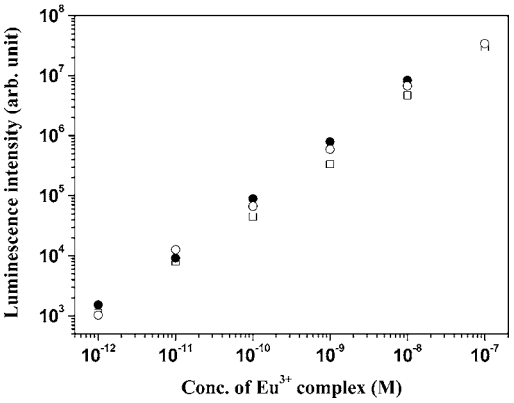

Figure 4. Time-gated luminescence measurements of different concentrations of BHHBCB-Eu^{3+} (●), BPPBCB-Eu^{3+} (○), and BTBBCB-Eu^{3+} (□) in 0.05 M Tris-HCl buffer of pH 7.8 (the BSA bound complexes were used for the measurements).

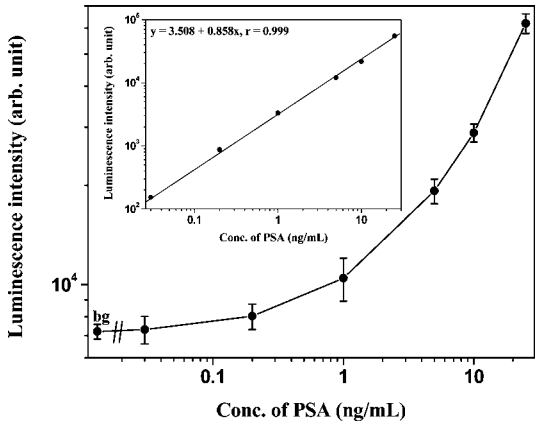

Figure 5. Calibration curve of TR-FIA for human PSA using the BHHBCB-Eu^{3+}-labeled SA (bg: background). The inset shows the plot of background-subtracted signal against human PSA concentration.

wide dynamic ranges. The detection limits, calculated as the concentrations corresponding to three standard deviations of the background signals, are 2.5×10^{-13} M, 2.8×10^{-13} M, and 4.6×10^{-13} M for BHHBCB-Eu^{3+}, BPPBCB-Eu^{3+}, and BTBBCB-Eu^{3+}, respectively. These results indicate that the time-gated luminescence measurements using the new Eu^{3+} complexes as labels are more sensitive than that using BHHCT-Eu^{3+} as a label (the detection limit of BHHCT-Eu^{3+} under the same condition is 8.4×10^{-13} M).[4,17]

TR-FIA of Human PSA Using BHHBCB-Eu^{3+} as a Label. As an important tumor marker, the human PSA measurement with various immunoassay methods, i.e., enzyme immunoassay,[50] radioimmunoassay,[51] chemiluminescence immunoassay,[52] and TR-FIA,[53,54] has been widely used for the clinical diagnoses of malignant tumors, such as prostatic cancer[55] and breast cancer.[56] To evaluate the utility of the new Eu^{3+} complexes as labels for quantitative TR-FIA, the BHHBCB-Eu^{3+}-labeled SA was prepared and used for the solid-phase TR-FIA of human PSA.

The BHHBCB-Eu^{3+}-labeled SA was prepared by using a previously reported indirect method established for conjugating BHHCT-Eu^{3+} to SA.[57] In the method, SA was first conjugated to BSA by cross-linking SA and BSA with glutaraldehyde, and then, the SA-BSA conjugate was labeled with BHHBCB-Eu^{3+}. Because this method enables much more BHHBCB-Eu^{3+} molecules to be labeled to a SA molecule, as a result, an average of ~47 BHHBCB-Eu^{3+} molecules were conjugated to each SA-BSA conjugate to yield the Eu^{3+} complex-labeled SA with an approximate composition of SA-BSA(BHHBCB-Eu^{3+})$_{47}$.

The TR-FIA of human PSA was carried out using a 96-well microtiter plate as the solid-phase carrier. After the wells were coated with antihuman PSA monoclonal antibody, the standard human PSA solutions with different concentrations and biotinylated antihuman PSA polyclonal antibody were successively added into the wells for reacting with the PSA antibody to form the sandwich-type immunocomplex, (anti-PSA antibody)-PSA-(biotinylated anti-PSA antibody), on the surface of the wells. Finally, the BHHBCB-Eu^{3+}-labeled SA was added into each well of the plate to react with the biotinylated antibody. After washing, the plate was directly used for the solid-phase time-gated luminescence measurement on the Perkin-Elmer Victor 1420 multilabel counter. Figure 5 shows the calibration curve of TR-FIA for human PSA using the BHHBCB-Eu^{3+}-labeled SA. When background-subtracted signal vs antigen concentration was plotted (the inset in Figure 5), the calibration curve showed a good linearity that could be expressed as log (signal) = 0.858 log[PSA] + 3.508 (r = 0.999). The detection limit, calculated as the concentration corresponding to three standard deviations of the background signal, is 57 pg/mL, which is low enough for the detection of PSA in human sera,[50−54] and indicates that BHHBCB-Eu^{3+} can be used as a label for highly sensitive TR-FIA applications.

Time-Gated Luminescence Microscopy Imaging of *Cryptosporidium muris* Using BHHBCB-Eu^{3+} as a Label. The waterborne pathogen *cryptosporidium* is an intestinal parasite in humans and animals that can cause a number of diarrheal disease outbreaks worldwide.[58] In general, its detection can be carried out by using the immunofluorescence microscopy imaging technique.[59,60] However, the food or environmental water samples of *cryptosporidium* are usually complicated, containing large amounts of strongly autofluorescent algae, organic debris, and mineral particles, which would obscure the immunofluorescence microscopy imaging result. It is noteworthy that the recent advances in time-gated luminescence microscopy imaging have demonstrated the background-suppression power for detecting pathogens in complicated environmental samples.[25−27,29,30] To further confirm the utility of the new Eu^{3+} complexes as labels for time-gated luminescence bioassays, the BHHBCB-Eu^{3+}-labeled SA was used for the immunoluminescence microscopy imaging of *Cryptosporidium muris* in both the steady-state and time-gated modes.

Figure 6 shows the bright-field, steady-state luminescence and time-gated luminescence images of *Cryptosporidium muris* oocysts that have been immunostained by anti-*cryptosporidium* antibody, biotinylated secondary antibody, and the BHHBCB-Eu^{3+}-labeled SA in water and fruit juice samples. It should be mentioned that the strong red luminescence signals could be clearly observed from the BHHBCB-Eu^{3+}-stained pathogen oocysts in a water sample in both steady-state and time-gated modes, but for the autofluorescence-rich juice sample, the steady-state luminescence imaging suffered the effect of autofluorescence from the coexisting substances within the sample, while the time-gated luminescence imaging provided highly specific background-free images of the oocysts. These results demonstrated that BHHBCB-Eu^{3+} is a favorably useful

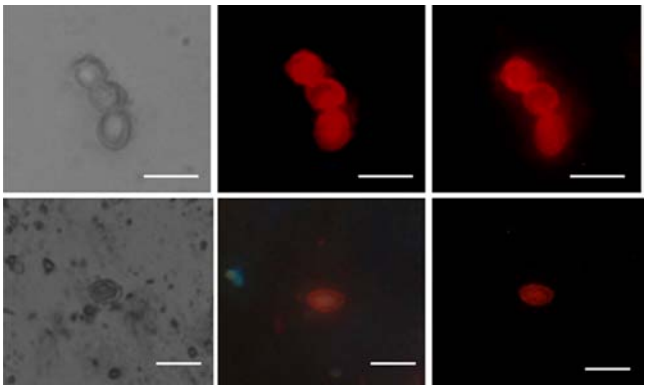

Figure 6. Bright-field (left), steady-state (middle), and time-gated (right) luminescence images of *Cryptosporidium muris* oocysts immunostained by the BHHBCB-Eu^{3+}-labeled SA in water (top) and fruit juice (bottom) samples. Scale bar: 10 μm.

biolabel for time-gated immuno-luminescence microscopy imaging to effectively eliminate the interference from short-lived background fluorescence.

■ CONCLUSIONS

In summary, a new class of chlorosulfonylated tetradentate β-diketonate-Eu^{3+} complexes, BHHBCB-Eu^{3+}, BPPBCB-Eu^{3+}, and BTBBCB-Eu^{3+}, has been successfully designed, synthesized, and characterized as biolabels for time-gated luminescence bioassay applications. Our demonstrations of TR-FIA for human PSA and luminescence microscopy imaging for pathogen *Cryptosporidium muris* using the BHHBCB-Eu^{3+}-labeled SA approved the practical utility of the label for time-gated luminescence bioassays. Compared to the Eu^{3+} complex biolabel BHHCT-Eu^{3+}, the new biolabels show the further improved luminescence properties with higher emission efficiency and longer luminescence lifetimes, which reveals a new underpinning theory in the structure design of tetradentate β-dikatonate-Eu^{3+} complex biolabels. Our new class of chlorosulfonylated tetradentate β-diketonate-Eu^{3+} complexes should enhance various time-gated luminescence bioassay applications piloted by BHHCT-Eu^{3+} or the other lanthanide complex biolabels. Furthermore, the successful development of the new Eu^{3+} complex biolabels suggests that the lanthanide complex-based biolabels could be improved through the rational design of ligands, which would be a useful strategy for developing new lanthanide biolabels with better luminescence properties.

■ EXPERIMENTAL SECTION

Materials and Physical Measurements. Mouse monoclonal and goat polyclonal antihuman PSA antibodies were purchased from OEM Concepts Co. Biotinylated goat antihuman PSA antibody was prepared and used according to a previous method.[61] The standard solutions of human PSA were prepared by diluting human PSA antigen (Biogenesis Ltd.) with 0.05 M Tris-HCl buffer of pH 7.8 containing 5% BSA, 0.9% NaCl, and 0.1% NaN_3. BSA and SA were purchased from Sigma. *Cryptosporidium muris* and its monoclonal antibody (IgM) were purchased from Anapure Bioscientific Co. Ltd. Rabbit antimouse IgM antibody was purchased from Beijing Biosynthesis Biotechnology Co. Ltd. Biotinylated rabbit antimouse IgM antibody was prepared and used according to a previous method.[61] Diethyl ether was used after appropriate distillation and purification. Unless otherwise stated, all chemical materials were purchased from commercial sources and used without further purification.

^{1}H NMR spectra were measured on a Bruker Avance spectrometer (400 MHz). Mass spectra were measured on a HP1100LC/MSD electrospray ionization mass spectrometry (ESI-MS). Elemental analysis was carried out on a Vario-EL analyzer. Absorption spectra were measured on a Perkin-Elmer Lambda 35 UV−vis spectrometer. Time-gated luminescence spectra were measured on a Perkin-Elmer LS 50B luminescence spectrometer with the conditions of delay time, 0.2 ms; gate time, 1.0 ms; cycle time, 20 ms; excitation slit, 10 nm; and emission slit, 5 nm. The luminescence quantum yields (ϕ_1) of the Eu^{3+} complexes were measured with a previous method.[62] The TR-FIA of human PSA was carried out with 96-well microtiter plate (PerkinElmer Life Sciences) as the solid-phase carrier and measured on a Perkin-Elmer Victor 1420 multilabel counter. All bright-field, steady-state, and time-gated luminescence imaging measurements were carried out on a laboratory-use luminescence microscope.[62]

Synthesis of 1,2-Bis(4′-acetyl-benzyl)-benzene. In an ice−water bath, 2.46 g (10 mmol) of 1,2-bis(bromomethyl)-benzene, 5.91 g (36 mmol) of 4-acetyl-phenylboronic acid and 6.90 g (50 mmol) of K_2CO_3 were dissolved in the mixture of acetone (60 mL) and water (20 mL) in a flask. After 70.9 mg (0.4 mmol) of $PdCl_2$ was added, the solution was heated to 50 °C with stirring, and then the reaction was allowed to continue for 12 h under an argon atmosphere. The solvents were evaporated, and the residue was extracted with 2 × 100 mL chloroform, and then the organic phase was dried with Na_2SO_4. After evaporation of the solvent, the crude product was purified by silica gel column chromatography with petroleum ether/ethyl acetate (2/1, v/v) as eluent to afford the target compound 1,2-bis(4′-acetyl-benzyl)-benzene as a white powder (1.58 g, 49% yield). ^{1}H NMR (400 MHz, $CDCl_3$): δ = 7.83 (d, J = 8.0 Hz,4H), 7.24−7.27 (m, 2H), 7.11−7.15 (m, 6H), 3.96 (s, 4H), 2.57 (s, 6H).

Syntheses of Three 1,2-Bis[4′-(fluoroalkyl-β-diketonyl)-benzyl]-benzenes. To 30 mL of dry diethyl ether solution containing 2.92 mmol (1.0 g) of 1,2-bis(4′-acetyl-benzyl)-benzene and 8.75 mmol of $C_nF_{2n+1}CO_2Et$ (2.04 g $C_3F_7CO_2Et$, 1.68 g $C_2F_5CO_2Et$, or 1.25 g CF_3CO_2Et) was added 8.75 mmol (0.47 g) of $NaOCH_3$ with stirring. After the solution was stirred for 42 h at room temperature, 20 mL of 15% H_2SO_4 was added, and the mixture was further stirred for 20 min. Diethyl ether was evaporated, and the precipitate was collected and washed with distilled water. The crude product was recrystallized from ethanol to afford the target compound as yellow crystals (50−60% yields for the three compounds). ^{1}H NMR (400 MHz, $CDCl_3$) for 1,2-bis[4′-(1″,1″,1″,2″,2″,3″,3″-heptafluoro-4″,6″-hexanedion-6″-yl)-benzyl]-benzene: δ = 8.00 (d, J = 8.0 Hz, 4H), 7.29 (d, J = 5.6 Hz, 4H), 7.27 (d, J = 8.4 Hz, 4H), 6.92 (s, 2H), 4.14 (s, 4H); for 1,2-bis[4′-(1″,1″,1″,2″,2″-pentafluoro-3″,5″-pentanedion-5″-yl)-benzyl]-benzene: δ = 8.00 (d, J = 8.0 Hz, 4H), 7.25−7.30 (m, 8H), 6.92 (s, 2H), 4.14 (s, 4H); for 1,2-bis[4′-(1″,1″,1″-trifluoro-2″,4″-butanedion-4″-yl)-benzyl]-benzene: δ = 7.96 (d, J = 8.0 Hz, 4H), 7. 23−7.30 (m, 8H), 6.84 (s, 2H), 4.14 (s, 4H).

Syntheses of BHHBCB, BPPBCB, and BTBBCB. To 4.0 mL of HSO_3Cl was gradually added 1.0 g of the above 1,2-bis[4′-(fluoroalkyl-β-diketonyl)-benzyl]-benzene with stirring. After stirring for 5 h at room temperature, the solution was added dropwise to 200 mL of ice−water with stirring. The

precipitate was filtered, washed with cold water, and then dried under vacuum for more than 48 h to afford the target compound as a yellow powder (80−90% yields for the three compounds). ^{1}H NMR (400 MHz, $CDCl_3$) for BHHBCB: δ = 8.02−8.06 (m, 6H), 7.66 (d, J = 8.0 Hz, 1H), 7.33 (t, J = 8.8 Hz, 2H), 6.92 (s, 2H), 4.41 (s, 2H), 4.36 (s, 2H); for BPPBCB: δ = 7.92−7.96 (m, 6H), 7.57 (d, J = 8.0 Hz, 1H), 7.25 (t, J = 8.8 Hz, 4H), 6.83 (s, 2H), 4.32 (s, 2H), 4.26 (s, 2H); for BTBBCB: δ = 8.01−8.06 (m, 6H), 7.67 (d, J = 8.0 Hz, 1H), 7.35 (t, J = 8.8 Hz, 4H), 6.85 (s, 2H), 4.41 (s, 2H), 4.35 (s, 2H). ^{13}C NMR (100 MHz, acetone-d_6) for BHHBCB: δ = 39.27, 39.51, 93.28, 126.56, 129.16, 129.55, 129.67, 130.44, 130.49, 130.56, 130.62, 131.90, 133.48, 142.08, 143.60, 146.90, 147.14, 148.50, 176.72, 177.08; for BPPBCB: δ = 38.35, 38.59, 93.81, 125.65, 128.34, 128.36, 128.37, 129.59, 129.73, 130.77, 132.53, 141.17, 142.71, 146.17, 146.39, 147.60, 185.00; for BTBBCB: δ = 39.26, 39.51, 94.56, 126.56, 129.27, 129.64, 130.48, 130.61, 131.79, 133.44, 142.07, 143.61, 147.06, 147.29, 148.50. Elemental analysis results: calcd. (%) for BHHBCB ($C_{32}H_{19}ClF_{14}O_6S\cdot 2.5H_2O$), C 43.78, H 2.16; found (%), C 43.53, H 2.38; calcd. (%) for BPPBCB ($C_{30}H_{19}ClF_{10}O_6S\cdot H_2O$), C 47.98, H 2.80; found (%), C 47.54, H 2.43; calcd. (%) for BTBBCB ($C_{28}H_{19}ClF_6O_6S\cdot H_2O$), C 51.67, H 3.23; found (%), C 51.46, H 2.90. API-ES-MS (negative mode) results: for BHHBCB, m/z 833.0 (45%), $[M\text{-}H]^-$; for BPPBCB, m/z 733.0 (100%), $[M\text{-}H]^-$; for BTBBCB, m/z 633.0 (100%), $[M\text{-}H]^-$.

Preparation of the Eu^{3+} Complex-Labeled BSA. To the solution of 10.0 mg BSA dissolved in 2.0 mL of 0.05 M carbonate buffer at pH 9.3 was added dropwise 9.0 μmol of the chlorosulfonylated tetradentate β-diketone (7.9, 6.8, and 5.9 mg for BHHBCB, BTBBCB, and BTBBCB, respectively) dissolved in 400 μL of ethanol with stirring. After 2 h of stirring at room temperature, the β-diketone-labeled BSA was separated from the unreacted β-diketone (the hydrolyzed product) by Sephadex G-50 column chromatography with 0.05 M NH_4HCO_3 of pH 8.0 as eluent. To estimate the labeling ratio (the bound β-diketone numbers per BSA molecule), the molar extinction coefficient of the β-diketone at its maximum absorption wavelength (328, 326, and 324 nm for BHHBCB, BTBBCB, and BTBBCB, respectively) was measured by using the unchromatographed solution appropriately diluted with 0.05 M NH_4HCO_3 of pH 8.0 (3.08×10^4, 2.65×10^4, and 1.60×10^4 cm^{-1} M^{-1} for BHHBCB, BTBBCB, and BTBBCB, respectively). Assuming that the molar extinction coefficient of the β-diketone did not change before and after the BSA binding, the labeling ratio was calculated (~34, ~18, and ~17 for BHHBCB-BSA, BTBBCB-BSA, and BTBBCB-BSA, respectively).

After $EuCl_3$ (1.5-fold concentrations of the β-diketone) and NaN_3 (0.1%) were added into the labeled BSA solution, the Eu^{3+} complex-labeled BSA solution was obtained, and then stored at 4 °C before use.

Preparation of the BHHBCB-Eu^{3+}-Labeled SA. To 0.6 mL of 0.1 M phosphate buffer at pH 7.1 containing 0.4 mg SA and 0.4 mg BSA was added 0.1 mL of 1% glutaraldehyde. After the solution was stirred for 24 h at 4 °C, 0.4 mg of $NaBH_4$ was added, and then the solution was further incubated for 2 h at room temperature. The solution was dialyzed twice each for 24 h against 3 L of 0.9% NaCl solution at 4 °C. After 10 mg $NaHCO_3$ was added, the solution's pH was adjusted to 9.1 with 1.0 M of NaOH. To the solution was added dropwise 1.0 mg of BHHBCB dissolved in 40 μL of dimethyl sulfoxide (DMSO), and then the solution was stirred for 1 h at room temperature. The solution was dialyzed twice each for 24 h against 3 L of 0.9% NaCl solution at 4 °C to delete the unreacted BHHBCB. After 0.63 mg of $EuCl_3\cdot 6H_2O$ was added, the solution was 50-fold diluted with 0.05 M Tris-HCl buffer of pH 7.8 containing 0.2% BSA, 0.9% NaCl, and 0.1% NaN_3, and then stored at −20 °C before use. Because the actual species of the SA−BSA conjugate cross-linked by glutaraldehyde were rather complicated, the composition of the BHHBCB-Eu^{3+}-labeled SA−BSA conjugate prepared by the above method was approximately determined to be SA-BSA(BHHBCB-Eu^{3+})$_{47}$.

TR-FIA of Human PSA. After antihuman PSA monoclonal antibody (diluted to 10 μg/mL with 0.1 M carbonate buffer of pH 9.6) was coated on the wells (45 μL per well) of a 96-well microtiter plate by physical adsorption,[63] 45 μL of human PSA standard solutions with different concentrations were added to the wells. The plate was incubated at 37 °C for 1 h and washed twice with 0.05 M Tris-HCl buffer of pH 7.8 containing 0.05% Tween 20 and once with 0.05 M Tris-HCl buffer of pH 7.8. Then, 45 μL aliquots of the biotinylated antibody (~1.1 μg/mL) were added to each well, and the plate was incubated at 37 °C for 1 h. After washing, 45 μL aliquots of the BHHBCB-Eu^{3+}-labeled SA were added to each well, and the plate was incubated at 37 °C for 1 h. The plate was washed four times with 0.05 M Tris-HCl buffer of pH 7.8 containing 0.05% Tween 20, and then subjected to the solid-phase time-gated luminescence measurement on Perkin-Elmer Victor 1420 multilabel counter under the conditions of excitation wavelength, 340 nm; emission wavelength, 615 nm; delay time, 0.2 ms; and window time (counting time), 0.4 ms.

Time-Gated Luminescence Microscopy Imaging of *Cryptosporidium muris*. A suspension of 10 μL *Cryptosporidium muris* (2.5×10^5 oocysts/mL in water) was mixed with 8 μL of anti-*cryptosporidium* monoclonal antibody (mouse IgM, ~50 μg/mL), 8 μL of biotinylated rabbit antimouse IgM antibody (~44 μg/mL), and 8 μL of the BHHBCB-Eu^{3+}-labeled SA in a tube. After incubation for 10 h at room temperature, the oocysts were separated by centrifugation at 500 rpm, and washed three times each with 50 μL of distilled water. The oocysts were resuspended in 20 μL of water or an autofluorescence-rich fruit juice sample, and then spotted on a glass slide for the luminescence microscopy imaging measurement.

The luminescence microscope, equipped with a 100 W Hg lamp, UV-2A filters (excitation filter, 330−380 nm; dichroic mirror, 400 nm; emission filter, >420 nm), V-2A filters (excitation filter, 380−420 nm; dichroic mirror, 430 nm; emission filter, >450 nm) and a cooled color CCD camera system (RET-2000R-F-CLR-12-C, Qimaging Ltd.), was used for the steady-state luminescence imaging measurement with an exposure time of 5 s. The microscope, equipped with a 30 W xenon flashlamp, UV-2A and V-2A filters, and a time-resolved digital black-and-white CCD camera system (Imagex-TGi, Photonic Research Systems Ltd.), was used for the time-gated luminescence imaging measurement with the conditions of delay time, 100 μs; gate time, 1 ms; lamp pulse width, 6 μs; and exposure time, 180 s. The time-gated luminescence images are shown in pseudocolor treated by a *SimplePCI* software.[62]

■ ASSOCIATED CONTENT

Ⓢ Supporting Information

Two supplementary figures. This material is available free of charge via the Internet at http://pubs.acs.org.

AUTHOR INFORMATION

Corresponding Author

*Tel/Fax: +86-411-84986041. E-mail addresses: zhiqiangye2001@yahoo.com.cn (Z.Ye); jingliyuan@yahoo.com.cn (J.Yuan).

Notes

The authors declare no competing financial interest.

ACKNOWLEDGMENTS

Financial supports from the National Natural Science Foundation of China (Grant No. 20835001) and the Specialized Research Fund for the Doctoral Program of Higher Education of China (Grant No. 200801410003) are gratefully acknowledged.

ABBREVIATIONS USED:

BHHBCB, 1,2-bis[4′-(1″,1″,1″,2″,2″,3″,3″-heptafluoro-4″,6″-hexanedion-6″- yl)benzyl]-4-chlorosulfobenzene; BPPBCB, 1,2-bis-[4′-(1″,1″,1″,2″,2″-pentafluoro-3″,5″- pentanedion-5″-yl)benzyl]-4-chlorosulfobenzene; BTBBCB, 1,2-bis[4′-(1″,1″,1″-trifluoro-2″,4″- butanedion-4″-yl)benzyl]-4-chlorosulfobenzene; BHHCT, 4,4′-bis(1″,1″,1″,2″,2″,3″,3″- heptafluoro-4″,6″-hexanedion-6″-yl)-chlorosulfo-*o*-terphenyl; BPPCT, 4,4′-bis-(1″,1″,1″,2″,2″- pentafluoro-3″,5″-pentanedion-5″-yl)-chlorosulfo-*o*-terphenyl; BTBCT, 4,4′-bis(1″,1″,1″-trifluoro- 2″,4″-butanedion-4″-yl)-chlorosulfo-*o*-terphenyl; BCDOT, 1,10-bis(4″-chlorosulfo-1′,1″-diphenyl- 4′-yl)-4,4,5,5,6,6,7,7-octafluorodecane-1,3,8,10-tetraone; BCOT, 1,10-bis(8′-chlorosulfo- dibenzothiophene-2′-yl)-4,4,5,5,6,6,7,7-octafluorodecane-1,3,8,10-tetraone; BCTOT, 1,10-bis(5′- chlorosulfothiophene-2′-yl)-4,4,5,5,6,6,7,7-octafluorodecane-1,3,8,10-tetraone; TR-FIA, time-gated luminescence immunoassay; BSA, bovine serum albumin; SA, streptavidin; PSA, prostate specific antigen; TOPO, tri-*n*-octylphosphine oxide; EDTA, ethylenediamine tetraacetic acid.

REFERENCES

(1) Soini, E., and Lövgren, T. (1987) Time-resolved fluorescence of lanthanide probes and applications in biotechnology. *CRC Crit. Rev. Anal. Chem. 18*, 105−154.

(2) Dickson, E. F. G., Pollak, A., and Diamandis, E. P. (1995) Ultrasensitive bioanalytical assays using time-resolved fluorescence detection. *Pharmac. Ther. 66*, 207−235.

(3) Hemmilä, I., and Mukkala, V. M. (2001) Time-resolution in fluorometry: technologies, labels, and applications in bioanalytical assays. *Crit. Rev. Clin. Lab. Sci. 38*, 441−519.

(4) Matsumoto, K., and Yuan, J. L. (2003) Lanthanide chelates as fluorescence labels for diagnostics and biotechnology, in *Metal Ions in Biological Systems* (Sigel, A., and Sigel, H., Eds.) pp 191−232, Vol. *40*, Marcel Dekker, Inc., New York and Basel.

(5) Yuan, J. L., and Wang, G. L. (2005) Lanthanide complex-based fluorescence label for time-resolved fluorescence bioassay. *J. Fluoresc. 15*, 559−568.

(6) Bünzli, J. C. G., and Piguet, C. (2005) Taking advantage of luminescent lanthanide ions. *Chem. Soc. Rev. 34*, 1048−1077.

(7) Yuan, J. L., and Wang, G. L. (2006) Lanthanide-based luminescence probes and time-resolved luminescence bioassays. *Trends Anal. Chem. 25*, 490−500.

(8) Eliseeva, S. V., and Bünzli, J. C. G. (2010) Lanthanide luminescence for functional materials and bio-sciences. *Chem. Soc. Rev. 39*, 189−227.

(9) Hagan, A. K., and Zuchner, T. (2011) Lanthanide-based time-resolved luminescence immunoassay. *Anal. Bioanal. Chem. 400*, 2847−2864.

(10) Montgomery, C. P., Murray, B. S., New, E. J., Pal, R., and Parker, D. (2009) Cell-penetrating metal complex optical probes: targeted and responsive systems based on lanthanide luminescence. *Acc. Chem. Res. 42*, 925−937.

(11) Thibon, A., and Pierre, V. C. (2009) Principle of responsive lanthanide-based luminescent probes for cellular imaging. *Anal. Bioanal. Chem. 394*, 107−120.

(12) Bünzli, J. C. G. (2010) Lanthanide luminescence for biomedical analyses and imaging. *Chem. Rev. 110*, 2729−2755.

(13) Jin, D. Y., Piper, J., Leif, R., Yang, S., Ferrari, B., Yuan, J. L., Wang, G. L., Vallarino, L., and Williams, J. W. (2009) Time-gated flow cytometry: an ultra-high selectivity method to recover ultra-rare-event μ-target in high-background biosamples. *J. Biomed. Opt. 14*, 024023.

(14) Hovinen, J., and Guy, P. M. (2009) Bioconjugation with stable luminescent lanthanide(III) chelates comprising pyridine subunits. *Bioconjugate Chem. 20*, 404−421.

(15) Moore, E. G., Samuel, A. P. S., and Raymond, K. N. (2009) From antenna to assay: lessons learned in lanthanide luminescence. *Acc. Chem. Res. 42*, 542−552.

(16) Xu, Y. Y., and Hemmilä, I. (1992) Co-fluorescence enhancement system based on pivaloyltrifluoroacetone and yttrium for the simultaneous detection of europium, terbium, samarium and dysprosium. *Anal. Chim. Acta 256*, 9−16.

(17) Yuan, J. L., Matsumoto, K., and Kimura, H. (1998) A new tetradentate β-diketonate-europium chelate that can be covalently bound to proteins for time-resolved fluoroimmunoassay. *Anal. Chem. 70*, 596−601.

(18) Connally, R., Veal, D., and Piper, J. (2002) High resolution detection of fluorescently labeled microorganisms in environmental samples using time-resolved fluorescence microscopy. *FEMS Microbiol. Ecol. 41*, 239−245.

(19) Wu, F. B., and Zhang, C. (2002) A new europium β-diketone chelate for ultrasensitive time-resolved fluorescence immunoassays. *Anal. Biochem. 311*, 57−67.

(20) Yuan, J. L., and Matsumoto, K. (1996) Synthesis of a new tetradentate β-diketonate-europium chelate that can be covalently bound to protein in time-resolved fluorometry. *Anal. Sci. 12*, 695−699.

(21) Yuan, J. L., and Matsumoto, K. (1997) Synthesis of a new tetradentate β-diketonate-europium chelate and its application for time-resolved fluorimetry of albumin. *J. Pharm. Biomed. Anal. 15*, 1397−1403.

(22) Wu, F. B., Han, S. Q., Zhang, C., and He, Y. F. (2002) Synthesis of a highly fluorescent β-diketone-europium chelate and its utility in time-resolved fluoroimmunoassay of serum total thyroxine. *Anal. Chem. 74*, 5882−5889.

(23) Sueda, S., Yuan, J. L., and Matsumoto, K. (2000) Homogeneous DNA hybridization assay by using europium luminescence energy transfer. *Bioconjugate Chem. 11*, 827−831.

(24) Li, J. S., Zhou, W. Y., Ouyang, X. Y., Yu, H., Ronghua Yang, R. H., Tan, W. H., and Yuan, J. L. (2011) Design of a room temperature phosphorescence-based molecular beacon for highly sensitive detection of nucleic acids in biological fluids. *Anal. Chem. 83*, 1356−1362.

(25) Connally, R., Veal, D., and Piper, J. (2004) Flash lamp-excited time-resolved fluorescence microscope suppresses autofluorescence in water concentrates to deliver an 11-fold increase in signal-to-noise ratio. *J. Biomed. Opt. 9*, 725−734.

(26) Jin, D. Y., and Piper, J. A. (2011) Time-gated luminescence microscopy allowing direct visual inspection of lanthanide-stained microorganisms in background-free condition. *Anal. Chem. 83*, 2294−2300.

(27) Lu, Y. Q., Jin, D. Y., Leif, R. C., Deng, W., Piper, J. A., Yuan, J. L., Duan, Y. S., and Huo, Y. J. (2011) Automated detection of rare-event pathogens through time-gated luminescence scanning microscopy. *Cytometry Part A 79A*, 349−355.

(28) Tan, M. Q., Wang, G. L., Hai, X. D., Ye, Z. Q., and Yuan, J. L. (2004) Development of functionalized fluorescent europium nanoparticles for biolabeling and time-resolved fluorometric application. *J. Mater. Chem. 14*, 2896−2901.

(29) Wu, J., Ye, Z. Q., Wang, G. L., Jin, D. Y., Yuan, J. L., Yafeng Guan, Y. F., and Piper, J. (2009) Visible-light-sensitized highly luminescent europium nanoparticles: preparation and application for time-gated luminescence bioimaging. *J. Mater. Chem. 19*, 1258−1264.
(30) Deng, W., Jin, D. Y., Drozdowicz-Tomsia, K., Yuan, J. L., and Goldys, E. M. (2010) Europium chelate (BHHCT-Eu^{3+}) and its metal nanostructure enhanced luminescence applied to bioassays and time-gated bioimaging. *Langmuir 26*, 10036−10043.
(31) Deng, W., Jin, D. Y., Drozdowicz-Tomsia, K., Yuan, J. L., Wu, J., and Goldys, E. M. (2011) Ultrabright Eu-doped plasmonic Ag@SiO_2 nanostructures: time-gated bioprobes with single particle sensitivity and negligible background. *Adv. Mater. 23*, 4649−4654.
(32) Shao, N., Jin, J. Y., Wang, G. L., Zhang, Y., Yang, R. H., and Yuan, J. L. (2008) Europium(III) complex-based luminescent sensing probes for multi-phosphate anions: modulating selectivity by ligand choice. *Chem. Commun.*, 1127−1129.
(33) Ouyang, X. Y., Yu, R. Q., Jin, J. Y., Li, J. S., Yang, R. H., Tan, W. H., and Yuan, J. L. (2011) New strategy for label-free and time-resolved luminescent assay of protein: conjugate Eu^{3+} complex and aptamer-wrapped carbon nanotubes. *Anal. Chem. 83*, 782−789.
(34) Siitari, H., Hemmilä, I., Soini, E., Lövgren, T., and Koistinen, V. (1983) Detection of hepatitis B surface antigen using time-resolved fluoroimmunoassay. *Nature 301*, 258−260.
(35) Evangelista, R. A., Pollak, A., Allore, B., Templeton, E. F., Morton, R. C., and Diamandis, E. P. (1988) A new europium chelate for protein labelling and time-resolved fluorometric applications. *Clin. Biochem. 21*, 173−177.
(36) Mathis, G. (1993) Rare earth cryptates and homogeneous fluoroimmunoassays with human sera. *Clin Chem. 39*, 1953−1959.
(37) Saha, A. K., Kross, K., Kloszewski, E. D., Upson, D. A., Toner, J. L., Snow, R. A., Black, C. D. V., and Desai, V. C. (1993) Time-resolved fluorescence of a new europium-chelate complex: demonstration of highly sensitive detection of protein and DNA samples. *J. Am. Chem. Soc. 115*, 11032−11033.
(38) Mukkala, V.-M., Helenius, M., Hemmilä, I., Kankare, J., and Takalo, H. (1993) Development of luminescent europium(III) and terbium(III) chelates of 2,2′:6′,2″-terpyridine derivatives for protein labeling. *Helv. Chim. Acta 76*, 1361−1378.
(39) Takalo, H., Mukkala, V. M., Mikola, H., Liitti, P., and Hemmilä, I. (1994) Synthesis of europium(III) chelates suitable for labeling of bioactive molecules. *Bioconjugate Chem. 5*, 278−282.
(40) Takalo, H., Mukkala, V. M., Meriö, L., Rodríguez-Ubis, J. C., Sedano, R., Juanes, O., and Brunet, E. (1997) Development of luminescent terbium(III) chelates for protein labeling: effect of triplet-state energy level. *Helv. Chim. Acta 80*, 372−387.
(41) Karsilayan, H., Hemmilä, I., Takalo, H., Toivonen, A., Pettersson, K., Lövgren, T., and Mukkala, V. M. (1997) Influence of coupling method on the luminescence properties, coupling efficiency, and binding affinity of antibodies labeled with europium(III) chelates. *Bioconjugate Chem. 8*, 71−75.
(42) Weibel, N., Charbonniere, L. J., Guardigli, M., Roda, A., and Ziessel, R. (2004) Engineering of highly luminescent lanthanide tags suitable for protein labeling and time-resolved luminescence imaging. *J. Am. Chem. Soc. 126*, 4888−4896.
(43) Li, M., and Selvin, P. R. (1997) Amine-reactive forms of a luminescent diethylenetriaminepentaacetic acid chelate of terbium and europium: attachment to DNA and energy transfer measurements. *Bioconjugate Chem. 8*, 127−132.
(44) Chen, J., and Selvin, P. R. (1999) Thiol-reactive luminescent chelates of terbium and europium. *Bioconjugate Chem. 10*, 311−315.
(45) Nishioka, T., Yuan, J. L., Yamamoto, Y., Sumitomo, K., Wang, Z., Hashino, K., Hosoya, C., Ikawa, K., Wang, G. L., and Matsumoto, K. (2006) New luminescent europium(III) chelates for DNA labeling. *Inorg. Chem. 45*, 4088−4096.
(46) Ge, P. H., and Selvin, P. R. (2008) New 9- or 10-dentate luminescent lanthanide chelates. *Bioconjugate Chem. 19*, 1105−1111.
(47) Krasnoperov, L. N., Marras, S. A. E., Kozlov, M., Wirpsza, L., and Mustaev, A. (2010) Luminescent probes for ultrasensitive detection of nucleic acids. *Bioconjugate Chem. 21*, 319−327.
(48) Miyaura, N., and Suzuki, A. (1995) Palladium-catalyzed cross-coupling reactions of organoboron compounds. *Chem. Rev. 95*, 2457−2483.
(49) Yuan, J. L., and Matsumoto, K. (1996) Fluorescence enhancement by electron-withdrawing groups on β-diketones in Eu(III)-β-diketonato-topo ternary complexes. *Anal. Sci. 12*, 31−36.
(50) Vessella, R. L., Noteboom, J., and Lange, P. H. (1992) Evaluation of the abbott IMx automated immunoassay of prostate-specific antigen. *Clin. Chem. 38*, 2044−2054.
(51) Ooi, D. S., and Escares, E. (1991) High-dose hook effect" in IRMA-count PSA assay of prostate-specific antigen. *Clin. Chem. 37*, 771−772.
(52) Dudley, R. F. (1990) Chemiluminescence immunoassay-an alternative to RIA. *Lab. Med. 21*, 216−222.
(53) Yu, H., Diamandis, E. P., Prestigiacomo, A. F., and Stamey, T. A. (1995) Ultrasensitive assay of prostate-specific antigen used for early detection of prestate-cancer relapse and estimation of tumor-doubling time after radical prostatectomy. *Clin. Chem. 41*, 430−434.
(54) Qin, Q. P., Lövgren, T., and Pettersson, K. (2001) Development of highly fluorescent detection reagents for the construction of ultrasensitive immunoassays. *Anal. Chem. 73*, 1521−1529.
(55) Armbruster, D. A. (1993) Prostate-specific antigen-biochemistry, analytical methods, and clinical-application. *Clin. Chem. 39*, 181−195.
(56) Ferguson, R. A., Yu, H., Kalyvas, M., Zammit, S., and Diamandis, E. P. (1996) Ultrasensitive detection of prostate-specific antigen by a time-resolved immunofluorometric assay and the immulite immuno-chemiluminescent third-generation assay: potential applications in prostate and breast cancers. *Clin. Chem. 42*, 675−684.
(57) Yuan, J. L., Wang, G. L., Kimura, H., and Matsumoto, K. (1997) Highly sensitive time- resolved fluoroimmunoassay of human immunoglobulin E by using a new europium fluorescent chelate as a label. *Anal. Biochem. 254*, 283−287.
(58) Fayer, R., Morgan, U., and Upton, S. J. (2000) Epidemiology of cryptosporidium: transmission, detection and identification. *Int. J. Parasitol. 30*, 1305−1322.
(59) Quintero-Betancourt, W., Peele, E. R., and Rose, J. B. (2002) Cryptosporidium parvum and cyclospora cayetanensis: a review of laboratory methods for detection of these waterborne parasites. *J. Microbiol. Methods 49*, 209−224.
(60) Zhu, L., Ang, S., and Liu, W. T. (2004) Quantum dots as a novel immunofluorescent detection system for cryptosporidium parvum and giardia lamblia. *Appl. Environ. Microbiol. 70*, 597−598.
(61) Jiang, L. N., Wu, J., Wang, G. L., Ye, Z. Q., Zhang, W. Z., Jin, D. Y., Yuan, J. L., and Piper, J. (2010) Development of a visible-light-sensitized europium complex for time-resolved fluorometric application. *Anal. Chem. 82*, 2529−2535.
(62) Song, B., Wang, G. L., Tan, M. Q., and Yuan, J. L. (2006) A europium(III) complex as an efficient singlet oxygen luminescence probe. *J. Am. Chem. Soc. 128*, 13442−13450.
(63) Ye, Z. Q., Tan, M. Q., Wang, G. L., and Yuan, J. L. (2004) Preparation, characterization and time-resolved fluorometric application of silica-coated terbium(III) fluorescent nanoparticles. *Anal. Chem. 76*, 513−518.

Bioconjugate Chemistry

Article

pubs.acs.org/bc

Design of a Modular Tetrameric Scaffold for the Synthesis of Membrane-Localized D-Peptide Inhibitors of HIV-1 Entry

J. Nicholas Francis, Joseph S. Redman, Debra M. Eckert, and Michael S. Kay*

Department of Biochemistry, University of Utah School of Medicine, 15 N Medical Drive East Room 4100, Salt Lake City, Utah 84112-5650, United States

ABSTRACT: The highly conserved HIV-1 gp41 "pocket" region is a promising target for inhibiting viral entry. PIE12-trimer is a protease-resistant trimeric D-peptide inhibitor that binds to this pocket and potently blocks HIV entry. PIE12-trimer also possesses a reserve of binding energy that provides it with a strong genetic barrier to resistance ("resistance capacitor"). Here, we report the design of a modular scaffold employing PEGs of discrete lengths for the efficient optimization and synthesis of PIE12-trimer. This scaffold also allows us to conjugate PIE12-trimer to several membrane-localizing cargoes, resulting in dramatically improved potency and retention of PIE12-trimer's ability to absorb the impact of resistance mutations. This scaffold design strategy should be of broad utility for the rapid prototyping of multimeric peptide inhibitors attached to potency- or pharmacokinetics-enhancing groups.

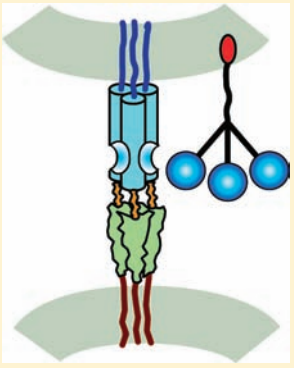

INTRODUCTION

HIV entry is mediated by the trimeric viral envelope glycoprotein (Env), which is cleaved into surface (gp120) and transmembrane (gp41) subunits.[1,2] Viral entry is triggered by binding of gp120 to a primary receptor (CD4) and subsequently a coreceptor (typically CXCR4 or CCR5), which induces large conformation changes in gp120 that activate gp41 for fusion.[3] gp41 then adopts an extended pre-hairpin conformation, embedding its N-terminal hydrophobic fusion peptide into the host cell membrane, bridging the virus and the host cell (Figure 1). In this state, the gp41 N-peptide region forms a trimeric coiled-coil (N-trimer), while the C-peptide region is in a structurally undefined state. This pre-hairpin intermediate then slowly collapses into a hairpin structure, with the C-peptide folding back upon the N-trimer to pack in an antiparallel orientation into the grooves of the N-trimer. The formation of this trimer-of-hairpins structure brings the viral and host membranes into close proximity and drives membrane fusion.[4,5]

In the pre-hairpin intermediate, gp41 is vulnerable to inhibitors that bind to either the N-trimer or C-peptide[2,6] and prevent hairpin formation.[7−9] This vulnerability has been exploited by the C-peptide-derived therapeutic Fuzeon (enfuvirtide). Fuzeon binds to a portion of the N-trimer groove, preventing fusion with nanomolar potency. Though effective, Fuzeon is currently utilized only as "salvage therapy" for patients with multidrug resistance because of its high cost (~$30 000/year/patient), dosing requirements (90 mg twice daily), injection site reactions, and the rapid emergence of resistant strains.[10,11]

The gp41 N-trimer contains a functionally critical and highly conserved deep hydrophobic pocket at its C-terminus.[4,12,13] The genomic region that encodes for the pocket also forms the structured RNA region of the Rev-responsive element (RRE), which is critical for the export of viral mRNA to the cytoplasm,[14] further constraining evolution of this region on

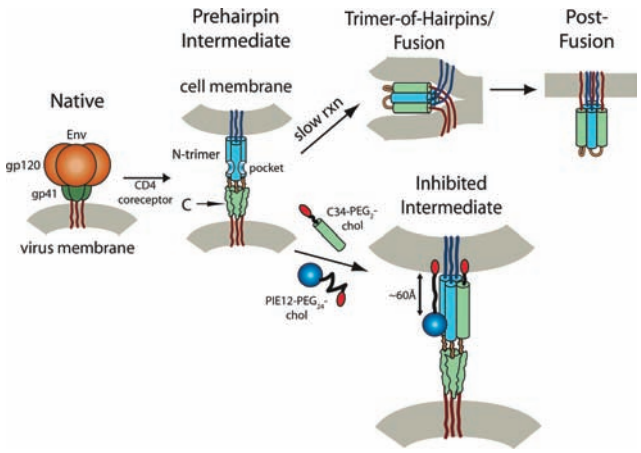

Figure 1. HIV entry pathway. Upon engagement with cellular receptor and coreceptor, gp120 and gp41 undergo a conformational change resulting in extension of gp41 into the pre-hairpin intermediate, exposing the hydrophobic pocket region of the N-trimer. gp41 collapses into the trimer-of-hairpins structure, juxtaposing the viral and host membranes and causing membrane fusion. The hydrophobic pocket targeted by PIE12 is an estimated 60 Å from the cell membrane, which can be bridged by a relaxed PEG24 linker. In contrast, the C-peptide C-terminus is directly adjacent to the membrane. Cholesterol (red) conjugated with PEG spacers (black lines) are shown.

Received: February 15, 2012
Revised: April 25, 2012
Published: May 1, 2012

dx.doi.org/10.1021/bc300076f | *Bioconjugate Chem.* 2012, 23, 1252−1258

the nucleotide level. Fuzeon binds to the N-trimer groove region just outside the pocket, an area that is more tolerant of resistance mutations. Second/third-generation C-peptide inhibitors (e.g, T1249, T2635) bind the groove and pocket and are much less susceptible to resistance.[10,15−20]

We have utilized structure-guided mirror-image phage display to generate D-peptide inhibitors that bind with high affinity to the pocket.[13,21,22] D-Peptides are protease resistant (as proteases have stereochemical specificity and generally only cleave L-substrates),[23] giving them the potential for a much longer lifetime in the body. PIE12, our most potent monomeric D-peptide, is a pocket-specific inhibitor of HIV-1 with high-nM potency against the difficult-to-inhibit primary HIV isolate JRFL. Since the N-trimer contains three symmetric pockets, we designed a trimeric version of PIE12 that uses PEG to link three monomers and greatly improves affinity and potency via avidity. PIE12-trimer inhibits all major HIV clades with high-pM to low-nM potency[21] and is a promising preclinical candidate for the treatment and prevention of HIV-1. Here, we describe a novel modular PEG scaffold used to optimize the production and the potency of PIE12-trimer.

While designing D-peptide inhibitors with progressively greater potency, we encountered a potency limit that could not be overcome by affinity optimization because the target is only available in the short-lived pre-hairpin intermediate. Due to the finite target exposure and the limits of diffusion, the potency of inhibitors with very high affinities (and on-rates) is limited by the diffusion-limited on-rate rather than binding affinity. For such diffusion-limited inhibitors, a potency plateau is reached beyond which further improvements in affinity do not improve potency. Similar potency plateaus have been observed for several inhibitors that target the transient pre-hairpin intermediate.[21,22,24−26] "Over-engineering" our inhibitors with improved affinity, but no corresponding improvement in potency, provides a reserve of binding energy and slows the evolution of resistance mutations. This "resistance capacitor" eliminates the selective advantage conferred by affinity-disrupting resistance mutations, since viruses bearing mutations that reduce affinity are still inhibited with equal potency, depriving HIV of an efficient evolutionary pathway to resistance. A profoundly disruptive mutation could escape the resistance capacitor, but such severe pocket mutations are discouraged due to the high cost to viral fitness. With high pM to low nM potency but sub-fM binding affinity, PIE12-trimer has a very strong resistance capacitor.[21]

We hypothesize that potency could be improved beyond the plateau by pre-positioning inhibitor on the cell surface, the site of viral entry, thus increasing the association rate beyond the diffusion limit. Using our novel modular PEG scaffold, we conjugate PIE12-trimer to membrane-localizing groups (cholesterol and alkyl chains) that improve potency up to ∼160-fold. This approach greatly simplifies trimer synthesis and improves yield. Importantly, our data show that this gain in potency does not disrupt the resistance capacitor, leaving intact PIE12-trimer's strong barrier to resistance mutations. Using a discrete PEG scaffold with orthogonal reactive groups and defined geometry allows for rapid optimization of multimeric inhibitors and scouting of various potency-enhancing cargoes and should be of broad utility for the design of other multimeric peptide inhibitors.

EXPERIMENTAL PROCEDURES

Peptide Synthesis. Peptides were synthesized using a PTI PS3 peptide synthesizer or by RS Synthesis as previously described[21,22] to generate either PIE12-GK or ΔHP-PIE12-GK (lacks two N-terminal residues, D-His and D-Pro). PIE12-dPEG$_{4/5}$-NH$_2$ (the precursor to PIE12-trimer synthesis) was synthesized as follows: PIE12-GK (10 mM in dimethylacetamide, DMAC) was reacted with 250 mM stock solution of Fmoc-N-amido-dPEG$_{4/5}$-NHS ester (Quanta BioDesign 10994 and 10053) in dry DMAC (Acros Organics, septa sealed with molecular sieves) at a 1:1 molar ratio buffered by triethylamine (200 mM, pH 7.5) for 60 min at RT. This reaction was quenched by addition of acetic acid to 5% and purified by reverse-phase HPLC (water/acetonitrile gradient in 0.1% TFA) on a Waters BEH X-Bridge 10 μm, 300 Å C$_{18}$ column (RP-HPLC). Purified product was lyophilized, then resuspended in 20% piperidine in DMAC for 20 min to remove Fmoc and produce PIE12-PEG$_{4/5}$-NH$_2$, which was then purified by RP-HPLC.

Trimer Synthesis. PIE12-PEG$_{4/5}$-NH$_2$ (10 mM) was reacted with 250 mM stock solution trimethylolethane-triNHS ester (Figure 2A, Quanta BioDesign 10674) in DMAC at a 3.3:1 (peptide/scaffold) ratio in DMAC buffered by triethylamine (200 mM, pH 7.5) for 60 min at RT. Product was purified by RP-HPLC. All masses were confirmed by ESI-MS (AB Sciex API-3000).

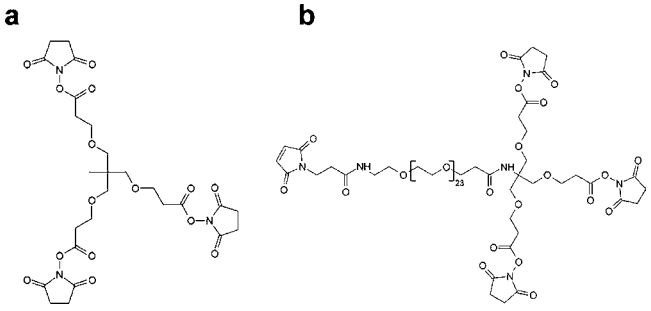

Figure 2. Trimeric and heterotetrameric PEG scaffolds and cargoes. A. Trimethoylethane-triNHS ester. B. Heterotetrameric PEG scaffold. The fourth maleimide arm is available for reaction with thiol-containing cargoes, such as 1-octadecanethiol (C18-SH) and thiocholesterol.

Cholesterol-PIE12-trimer and alkyl-PIE12-trimer were synthesized as follows: PIE12-PEG$_4$-NH$_2$ (10 mM) was reacted with Maleimide-PEG$_{12}$-triNHS ester (Quanta BioDesign 10676, 250 mM in DMAC) or Maleimide-PEG$_{24}$-triNHS ester (Figure 2B, Quanta BioDesign 10680, 250 mM in DMAC) at a 3.3:1 (peptide/scaffold) ratio in DMAC buffered by triethylamine (200 mM, pH 7.5) for 45 min at RT. Thiocholesterol (Sigma Aldrich, 136115, 250 mM in chloroform), 1-octanethiol (Sigma-Aldrich 471836), 1-hexadecanethiol (Sigma-Aldrich 52270), or 1-octadecanethiol (Sigma Aldrich 01858) were then added to a final concentration of 4.5 mM and reacted for an additional 60 min. For PEG$_{16}$, PIE12-PEG$_4$-NH$_2$ was first reacted with Mal-PEG$_{12}$-triNHS ester, followed by reaction with D-Cysteine (5 mM) to yield (PIE12-PEG$_4$)$_3$-PEG$_{12}$-Cys. This product was then purified by RP-HPLC before sequential reaction with Maleimide-PEG$_4$-NHS and thiocholesterol under conditions identical to those used to generate chol-PEG$_{24}$-PIE12-trimer. PEG$_{36}$, PEG$_{57}$, and PEG$_{132}$-trimer were produced through conjugation of PIE12-

dx.doi.org/10.1021/bc300076f | Bioconjugate Chem. 2012, 23, 1252−1258

PEG_4-NH_2 to Maleimide-PEG_{24}-triNHS ester, followed by addition of D-cysteine. This intermediate was then conjugated to Mal-PEG_{12}-NHS ester (Quanta Biodesign, 10284), Mal-PEG_{2K}-NHS ester (Creative PEGWorks, PHB-950, ~45 PEG units), or Mal-PEG_{5K}-NHS ester (Creative PEGWorks, PHB-952, ~120 PEG units) to yield Chol-PEG_{36}-PIE12-Trimer, Chol-PEG_{57}-PIE12-trimer, and Chol-PEG_{132}-PIE12-trimer, respectively. The reaction was quenched by addition of acetic acid to 5% before purification by RP-HPLC.

Viral Infectivity Assays. Pseudovirion infectivity assays were carried out as previously described[21,22] using HXB2 and JRFL luciferase reporter pseudovirions (NL4−3 strain) and HOS-CD4-CXCR4 (for HXB2) or HOS-CD4-CCR5 (for JRFL) target cells. Inhibitor curves were generated using six concentration points measured in quadruplicate, and luciferase counts were normalized to an uninhibited control. Inhibition curves were fit using a standard IC_{50} eq $[1 - c/(IC_{50} + c)]$ weighting each concentration point by its standard error in KaleidaGraph (*Synergy* software). Reported IC_{50} values are the average of at least 2 independent assays.

RESULTS

Our first goal was to simplify the synthesis of PIE12-trimer while also optimizing the linkages between PIE12 monomers. In our previous work, we synthesized PIE12-trimer by attaching bis-NHS ester PEG_5 spacers to PIE12-GK. After purification, two of these PEGylated monomers were reacted with a central PIE12-GKK monomer (two primary amines) to produce PIE12-trimer.[21] This method is cumbersome for large-scale production, because it requires the synthesis of two distinct D-peptides and a series of HPLC purifications to assemble the trimer, resulting in low yields. In addition, our PIE12 crystal structure suggested that shorter PEG linkers might adequately bridge the neighboring pockets and improve avidity. To address these goals, we redesigned the PIE12-trimer using a scaffold strategy. We designed a homotrimeric scaffold containing three NHS ester arms for conjugation to PIE12-GK (Figure 2a) in a single-pot reaction. PEG linkers of various lengths can be appended to the PIE12-GK peptide, allowing for the simple production of PIE12-trimers with varying PEG lengths.

PIE12-trimer's estimated sub-fM affinity for the N-trimer makes direct comparative K_D measurements (e.g., by surface plasmon resonance) very challenging. Although antiviral potency can be used as a surrogate for affinity, PIE12-trimer's potency plateau can mask even large changes in affinity. To overcome this problem, we designed a PIE12 variant with weakened affinity to allow comparative evaluation of different trimer geometries by measuring inhibitor potency. We previously observed that PIE12's two N-terminal residues make important contacts with the N-trimer and reasoned that deletion of these residues (D-His and D-Pro) would significantly reduce binding affinity without disrupting the overall orientation of PIE12 binding to the gp41 pocket or the local structure at the C-terminal PEG linkage site. ΔHP-PIE12 is 84-fold less potent than PIE12 (Table 1). In the context of the homotrimeric scaffold, ΔHP-PIE12 connected via our standard PEG_5 linkers has an IC_{50} of 380 nM against HXB2 (a standard lab-adapted strain) and is therefore well outside of the potency plateau (~500 pM for HXB2). Using ΔHP-PIE12-trimer, we can now detect changes in potency due to linker changes that subtly alter affinity.

Our initial exploration of PEG linker lengths in PIE12-trimer showed that PEG_2 and PEG_3 were slightly less potent than the original PEG_5. To determine whether PEG_4 or PEG_5 was the optimal arm length, both PEG_5 and PEG_4 ΔHP-PIE12 conjugates were attached to the homotrimeric scaffold, and we observed that a PEG_4 linker was slightly more optimal (Table 1). Therefore, PEG_4 was selected as the new standard linker for conjugating PIE12 to the scaffold. The scaffold synthesis strategy is dramatically simpler than our previous method for generating trimer since it requires only one peptide and a single purification. Additionally, the yields are considerably higher due to the reduced number of purification and lyophilization steps that led to loss of active NHS esters in the previous strategy. Finally, the high activity of the scaffold and single-pot reaction allow for near-stoichiometric concentrations of peptide and scaffold, further improving yield.

Table 1. D-Peptide Inhibition Data[a]

inhibitor	IC_{50} (nM) HXB2	JRFL
PIE12[b]	37 ± 2.3	580 ± 21.4
ΔHP-PIE12	3100 ± 783	nd
Chol-PEG_2-PIE12	69 ± 11	nd
Chol-PEG_{12}-PIE12	12 ± 3.6	nd
Chol-PEG_{24}-PIE12	0.64 ± 0.25	nd
C34	1.4 ± 0.3	13.4 ± 0.1
C34-PEG_2-Chol	0.044 ± 0.0004	0.05 ± 0.01
C34-PEG_{11}-Chol	0.021 ± 0.0014	0.024 ± 0.005
C34-PEG_{80}-Chol	0.022 ± 0.0004	0.1 ± 0.045
PEG_4-ΔHP-PIE12-trimer	300 ± 7.2	nd
PEG_5-ΔHP-PIE12-trimer	380 ± 13	nd
PEG_4-PIE12-trimer	0.72 ± 0.04	2.1 ± 0.28
Chol-PEG_{12}-PIE12-trimer	0.052 ± 0.02	0.06 ± 0.004
Chol-PEG_{16}-PIE12-trimer	0.02 ± 0.002	0.017 ± 0.0002
Chol-PEG_{24}-PIE12-trimer	0.013 ± 0.0013	0.019 ± 0.003
Chol-PEG_{36}-PIE12-trimer	0.011 ± 0.0015	0.015 ± 0.005
Chol-PEG_{57}-PIE12-trimer	0.007 ± 0.0013	0.013 ± 0.003
Chol-PEG_{132}-PIE12-trimer	0.012 ± 0.0015	0.025 ± 0.002
C8-PIE12-trimer	0.42 ± 0.01	nd
C16-PIE12-trimer	0.09 ± 0.014	0.11 ± 0.012
C18-PIE12-trimer	0.054 ± 0.018	0.087 ± 0.012

[a]Antiviral potency against HXB2 and JRFL HIV-1 strains. [b]From ref 21.

Heterotetrameric Scaffold. With the optimal PEG linker length in place, we next turned our attention to improving PIE12-trimer's potency via localization to sites of viral entry (the cell surface). To enable the conjugation of membrane-localizing groups to PIE12-trimer, we designed a heterotetrameric scaffold containing three short arms with NHS ester groups (for addition of PIE12-PEG_4-NH_2) and a fourth PEG arm of variable length functionalized with maleimide (an orthogonal reactive group for the addition of thiol-containing cargoes) (Figure 2b).

Our first cargo for the heterotetrameric scaffold was cholesterol. Several recent studies have shown that cholesterol conjugation improves both the potency and the circulating half-life of C-peptide inhibitors of HIV[27] and paramyxoviruses.[28,29] Cholesterol conjugation has also been shown to specifically localize dyes to the membrane surface.[30,31] A challenge of applying this approach to PIE12 is that, while the N-terminus of the C-peptide lies immediately adjacent to the membrane, PIE12 targets a pocket that we estimate is ~60 Å from the membrane (Figure 1). We used flexible PEG linkers of varying lengths to span this distance. PEG_{12} is sufficiently long if

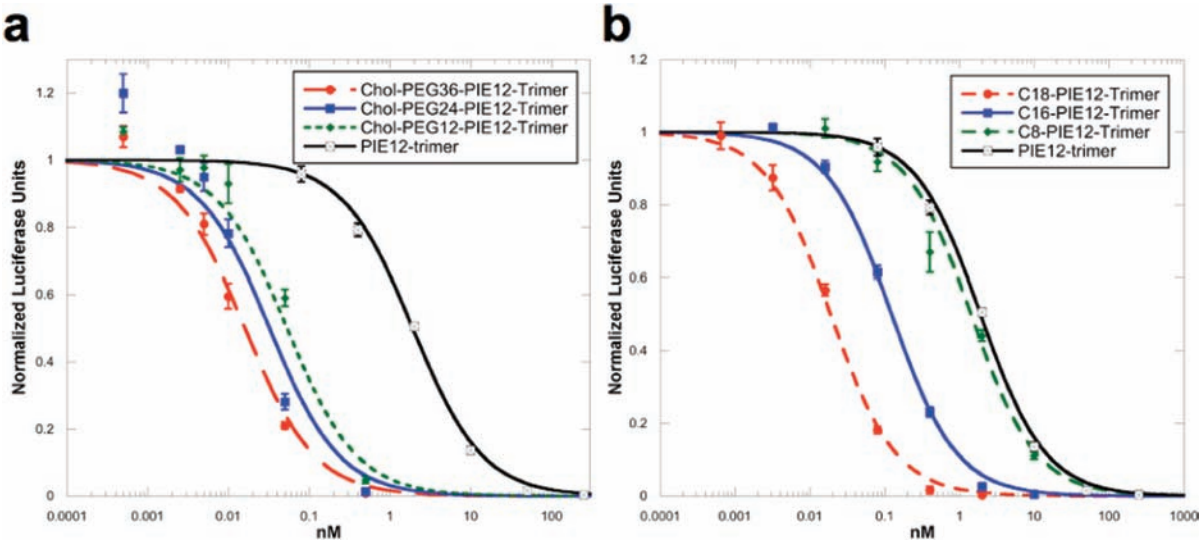

Figure 3. JRFL pseudovirion infectivity assay. A. Dependence of linker length on chol-PIE12-trimer potency. B. Thio-alkane-conjugated PIE12-trimer series with differing alkane lengths. Representative curves shown.

stretched taut, but PEG typically assumes an average length approximately half of its fully stretched distance.[32]

To study the potency effects of cholesterol (chol) conjugation to PIE12 and the length of the linker between chol and PIE12, we used monomeric PIE12, which is not in a potency plateau and therefore should be a sensitive reporter for optimal linker length. We began by generating chol-PIE12 conjugates using heterobifunctional PEG_2, PEG_{12}, and PEG_{24} NHS ester/maleimide cross-linkers to conjugate thiocholesterol (cholesterol with a thiol replacing its hydroxyl group) to PIE12's C-terminal Lys (its only primary amine). We observed that the PEG_2 conjugate, much too short to bridge the membrane to pocket distance, causes a 2-fold loss of potency (HXB2 strain) compared to unconjugated PIE12. In contrast, chol-PEG_{12}-PIE12 shows 3-fold improved potency, while PEG_{24} provides an even greater 58-fold increase in potency compared to PIE12. For comparison, we also synthesized C-peptide (C34) cholesterol conjugates of varying lengths (Table 1). We reproduce Ingalinella's finding of ~40-fold improved potency[27] using a short PEG_2 linker, but surprisingly, a longer linker (PEG_{11}) provides an additional 2-fold improvement in potency, and a much longer linker (PEG_{80}) maintains the same potency (HXB2 strain). A similar pattern is seen with the JRFL strain, but with significant attenuation at very long PEG linker lengths (4-fold worse than the optimal PEG length).

On the basis of these dramatic potency gains, we next conjugated cholesterol to PIE12-trimer using the heterotetrameric scaffold. Using the optimal PEG_4 linker determined earlier for the three NHS ester (PIE12) arms, we synthesized chol-PIE12-trimers with a variety of fourth arm (maleimide) lengths to confirm the relationship between PEG length and potency observed with the monomer. In the context of chol-PIE12-trimer, we did not need to utilize ΔHP-PIE12, as the cholesterol-mediated improvement in potency was discernible using PIE12. This sensitivity was expected because membrane localization affects the association rate rather than changing affinity (masked by the resistance capacitor). We varied the fourth arm from 12 to 132 PEG units, covering a distance range of ~60 to 480 Å (fully extended).

Cholesterol conjugation dramatically improves PEG_4-PIE12-trimer potency against both HXB2 and JRFL entry (up to 160-fold, Table 1 and Figure 3). Comparison of varying fourth arm lengths in chol-PIE12-trimer shows that inhibitor potency varies modestly in an optimal range between PEG_{24} and PEG_{57}. A shorter PEG_{12} linker is suboptimal, though it performs better than seen in the monomer series, likely due to the additional length provided by the PEG_4 arms. Only a slight decrease in potency is observed with the longest (PEG_{132}) linker. Despite being slightly less potent than Chol-PEG_{57}-PIE12-trimer, we have chosen Chol-PEG_{24}-PIE12-trimer as our lead candidate due to its ease of synthesis and the availability of monodisperse PEG_{24}. A monodisperse PEG scaffold will ease future preclinical studies of chol-PIE12-trimer purity, metabolism, pharmacokinetics, and stability. Importantly, cholesterol conjugates retain high (mM) aqueous solubility.

Another established strategy for localizing inhibitors to membranes is fatty acid conjugation.[33−37] Using the same heterotetramer scaffold strategy described above with cholesterol, we synthesized PIE12-trimers conjugated to aliphatic chains of 8, 16, and 18 carbons (C8/C16/C18-PIE12-trimer). While C8 conjugation has little effect on PIE12-trimer potency, C16 and C18 both provide substantial gains in potency, though to a lesser degree than seen with cholesterol (Table 1). C18-PIE12-trimer was slightly more potent than C16-PIE12-trimer.

Effect of Membrane Localization on the Resistance Capacitor. Drug resistance is a constant threat to the effectiveness of HIV inhibitors. PIE12-trimer is an attractive drug candidate in part because of its strong resistance capacitor, which provides a high genetic barrier to resistance.[21] The resistance capacitor depends on the diffusion-limited association rate for PIE12-trimer binding to gp41. The cholesterol and C16/18 conjugation strategies described here break through this kinetic barrier via inhibitor localization to viral entry sites (i.e., increasing effective inhibitor concentration and overcoming the diffusion rate limitation). In theory, this improvement in potency could come at the cost of weakening the resistance capacitor. To test for this possibility, we measured the potency of chol- and C16/C18-conjugated PIE12-trimer against resistance mutations we have previously identified.[21]

Previous selection for resistance to PIE7-dimer (an earlier-generation D-peptide inhibitor)[22] generated E560K/V570I, which minimally affects the potency of PIE12-trimer, but

dx.doi.org/10.1021/bc300076f | Bioconjugate Chem. 2012, 23, 1252−1258

dramatically reduces PIE7-dimer potency.[21] Selection of resistance to PIE12-trimer required more than a year of viral passaging, but ultimately resulted in the Q577R mutation, which decreases PIE12-trimer potency by >1000-fold.[21] The effect of these resistance mutations on chol- and C16/18-PIE12-trimer potency is shown in Table 2. The relative effects

Table 2. Antiviral Potency against Resistant Strains[a]

	IC_{50} (nM)		
inhibitor	WT HXB2	E560K/V570I	Q577R
PEG_4-PIE12-trimer	0.72	0.89	>3 μM
Chol-PEG_{24}-PIE12-trimer	0.013	0.01	10.1
C8-PIE12-trimer	0.42	0.86	452
C16-PIE12-trimer	0.09	0.045	39
C18-PIE12-trimer	0.054	0.035	32.5

[a]Antiviral potency against identified resistant strains (HXB2 background). The IC_{50} standard error of the mean values are <35% for all samples.

of both resistance mutations are similar for PIE12-trimer and the cholesterol/alkane-conjugated PIE12-trimers. However, because of the greatly improved potency of the conjugated PIE12-trimers, these inhibitors maintain nanomolar potency even against the severe Q577R resistance mutation. The impact of the less severe E560K/V570I resistance mutation is absorbed by all of the conjugated PIE12-trimers, as well as plain PIE12-trimer. These data suggest that the improvement in potency through C16/C18 and cholesterol conjugation retains enough excess binding energy to maintain an effective resistance capacitor.

DISCUSSION

PIE12-trimer, our previously described D-peptide inhibitor, is a promising preclinical candidate for the treatment and prevention of HIV-1 due to its strong potency, wide breadth, and highly charged resistance capacitor that slows the emergence of resistance mutations. However, the transient nature of PIE12-trimer's target means that its potency is restricted by its diffusion-limited association rate with the gp41 pocket. In an attempt to break through this potency barrier, we designed a heterotetrameric scaffold to allow us to conjugate various membrane-localizing cargoes to PIE12-trimer. This scaffold also allows us to produce PIE12-trimer variants much more efficiently than previously reported. As hoped, conjugation of PIE12-trimer to cholesterol or C16/C18 reduces the kinetic limitation and greatly improves potency up to 160-fold.

We hypothesize that this increased potency is due to local concentration of inhibitor at membrane sites of viral entry. Cholesterol is specifically enriched at sites of viral entry (lipid rafts, where CD4 and coreceptor are localized).[38,39] The mechanism by which cholesterol improves potency is the focus of ongoing work. Preliminary evidence suggests that the interaction between cholesterol and the membrane is readily reversible, which may explain why there is a broad range of compatible linker lengths. It may also be the case that cholesterol-conjugated inhibitors interact directly with Env, as a cholesterol recognition/interaction amino acid consensus sequence (CRAC) has been identified in the membrane proximal region of gp41.[40]

By comparison, C16 and C18 conjugates are less potent than the cholesterol conjugate. Saturated fatty acids C16:0 (palmitate) and C18:0 (stearate) are also enriched in lipid rafts,[41] but are abundant in the general plasma membrane as well.[42] The reduced potency of alkylated PIE12-trimer compared to cholesterol may therefore be explained by a relatively lower affinity of alkyl chains for lipid rafts. Another possible explanation is fatty-acid sequestration by albumin, which is known to bind fatty acids with high affinity (compared to cholesterol),[43] though it is not known how loss of the acid group (leaving an alkane chain) affects this binding.

GPI anchors in lipid rafts contain C16 and C18 alkyl chains as well as acylated C16 and C18 fatty acids.[44] Originally, we synthesized alkyl conjugates, and noted that they improved potency through membrane association (overcoming the potency plateau). For completeness, we also synthesized an acylated C16 (fatty acid) conjugate. Surprisingly, the C16 acyl conjugate was much less potent than the C16 alkyl conjugate (data not shown), presumably because it does not associate as effectively with plasma membranes. This finding may explain why a recent study did not observe a potency enhancement with C16 acylation of C34.[27]

Importantly, we show that membrane localization does not impair the resistance capacitor. Both chol- and C16/C18-conjugated PIE12-trimer are able to absorb the affinity-disrupting impact of PIE7-dimer resistance mutations (E560K/V570I). For the more severe PIE12-trimer resistance mutation Q577R, the relative loss of potency for both conjugates is comparable to that seen with PIE12-trimer. The full resistance profile of these conjugates will be determined by ongoing viral passaging studies starting from both wild-type and PIE12-trimer resistant virus.

Although PIE12-trimer has ideal antiviral properties, its relatively small size (~8 kD) will likely lead to a short serum half-life due to renal filtration. In addition to their potency-boosting effects, we hypothesize that both cholesterol and alkyl conjugation will also lead to improvements in the pharmacokinetic (PK) properties of these inhibitors via interaction with cell membranes and albumin that slow renal clearance. Albumin serves as a carrier for both cholesterol[45] and fatty acids,[46] reducing the rate of renal filtration. Adherence to membrane surfaces may also slow the absorption of inhibitor from the subcutaneous space, enabling prolonged dosing via a slow-release depot effect. This type of depot would be especially attractive for nondegradable D-peptides.

This work demonstrates the successful application of modular PEG scaffold-based design to peptide drug optimization (both peptide geometry and localization to the site of action via conjugated localizing cargoes). This approach allows for alterations in the scaffold to accommodate a variety of cargoes and chemistries (e.g., "click" chemistry), as well as rapid optimization of PEG arm lengths. For viruses that undergo membrane fusion within the endosome, such as Ebola, this strategy could be employed to attach an endosome-targeting moiety to localize inhibitor to the site of entry and increase potency. Additionally, the scaffold allows for conjugation to a variety of cargoes to modulate PK properties (e.g., large branched PEGs, albumin, or albumin-binding peptides).[47,48] The scaffold itself is inexpensive to produce and can be used directly for cost-effective large-scale production.

PK and animal toxicity studies for chol- and C16/C18-PIE12-trimer are underway to determine how conjugation alters serum half-life and to determine if any specific toxicity arises as a result of conjugation. Fatty acid conjugation has been used to prolong serum half-life of a GLP-1 peptide (liraglutide,

C16) and insulin (detemir, C14). Alkane toxicity in the context of peptide conjugates has not been studied.

The *in vivo* efficacy of these conjugates will be determined in future studies of systemic treatment via subcutaneous injection or as a vaginally/rectally applied preventative (microbicide) in human tissue and animal models. Our D-peptide scaffold is especially advantageous for application as a microbicide due to its protease resistance, which should enable it to persist for extended periods in the vaginal/rectal mucosa's harsh protease-rich environment. The addition of membrane-binding groups may also improve microbicide tissue penetration and retention.

AUTHOR INFORMATION

Corresponding Author

*E-mail: kay@biochem.utah.edu. Phone: (801) 585-5021. Fax: (801) 581-7959.

Notes

The authors declare the following competing financial interest(s): DME and MSK are consultants and equity holders in Navigen, which is commercializing D-peptide inhibitors of HIV entry.

ACKNOWLEDGMENTS

We thank Paul Davis, James Guyo, and Robert Woodman of Quanta BioDesign for custom synthesis of the PEG scaffolds. This research was funded by an NIH grant AI076168 to M.S.K. J.N.F. is supported by an NIH Microbial Pathogenesis Predoctoral Training Grant (AI055434). Special thanks to Michael Root for providing cloned resistant strains and Brett Welch for critical review of the manuscript.

REFERENCES

(1) Freed, E. O., and Martin, M. A. (1995) The role of human immunodeficiency virus type 1 envelope glycoproteins in virus infection. *J. Biol. Chem. 270*, 23883−6.

(2) Eckert, D. M., and Kim, P. S. (2001) Mechanisms of viral membrane fusion and its inhibition. *Annu. Rev. Biochem. 70*, 777−810.

(3) Jones, P. L., Korte, T., and Blumenthal, R. (1998) Conformational changes in cell surface HIV-1 envelope glycoproteins are triggered by cooperation between cell surface CD4 and co-receptors. *J. Biol. Chem. 273*, 404−9.

(4) Chan, D. C., Fass, D., Berger, J. M., and Kim, P. S. (1997) Core structure of gp41 from the HIV envelope glycoprotein. *Cell 89*, 263−73.

(5) Weissenhorn, W., Dessen, A., Harrison, S. C., Skehel, J. J., and Wiley, D. C. (1997) Atomic structure of the ectodomain from HIV-1 gp41. *Nature 387*, 426−30.

(6) Root, M. J., Kay, M. S., and Kim, P. S. (2001) Protein design of an HIV-1 entry inhibitor. *Science 291*, 884−8.

(7) Jiang, S., Lin, K., Strick, N., and Neurath, A. R. (1993) HIV-1 inhibition by a peptide. *Nature 365*, 113.

(8) Wild, C., Oas, T., McDanal, C., Bolognesi, D., and Matthews, T. (1992) A synthetic peptide inhibitor of human immunodeficiency virus replication: correlation between solution structure and viral inhibition. *Proc. Natl. Acad. Sci. U. S. A. 89*, 10537−41.

(9) Wild, C. T., Shugars, D. C., Greenwell, T. K., McDanal, C. B., and Matthews, T. J. (1994) Peptides corresponding to a predictive alpha-helical domain of human immunodeficiency virus type 1 gp41 are potent inhibitors of virus infection. *Proc. Natl. Acad. Sci. U. S. A. 91*, 9770−4.

(10) Rimsky, L. T., Shugars, D. C., and Matthews, T. J. (1998) Determinants of human immunodeficiency virus type 1 resistance to gp41-derived inhibitory peptides. *J. Virol. 72*, 986−93.

(11) Golding, H., Zaitseva, M., de Rosny, E., King, L. R., Manischewitz, J., Sidorov, I., Gorny, M. K., Zolla-Pazner, S., Dimitrov, D. S., and Weiss, C. D. (2002) Dissection of human immunodeficiency virus type 1 entry with neutralizing antibodies to gp41 fusion intermediates. *J. Virol. 76*, 6780−90.

(12) Chan, D. C., Chutkowski, C. T., and Kim, P. S. (1998) Evidence that a prominent cavity in the coiled coil of HIV type 1 gp41 is an attractive drug target. *Proc. Natl. Acad. Sci. U. S. A. 95*, 15613−7.

(13) Eckert, D. M., Malashkevich, V. N., Hong, L. H., Carr, P. A., and Kim, P. S. (1999) Inhibiting HIV-1 entry: discovery of D-peptide inhibitors that target the gp41 coiled-coil pocket. *Cell 99*, 103−15.

(14) Pollard, V. W., and Malim, M. H. (1998) The HIV-1 Rev protein. *Annu. Rev. Microbiol. 52*, 491−532.

(15) Derdeyn, C. A., Decker, J. M., Sfakianos, J. N., Zhang, Z., O'Brien, W. A., Ratner, L., Shaw, G. M., and Hunter, E. (2001) Sensitivity of human immunodeficiency virus type 1 to fusion inhibitors targeted to the gp41 first heptad repeat involves distinct regions of gp41 and is consistently modulated by gp120 interactions with the coreceptor. *J. Virol. 75*, 8605−14.

(16) Eggink, D., Baldwin, C. E., Deng, Y., Langedijk, J. P., Lu, M., Sanders, R. W., and Berkhout, B. (2008) Selection of T1249-resistant human immunodeficiency virus type 1 variants. *J. Virol. 82*, 6678−88.

(17) Eggink, D., Bontjer, I., Langedijk, J. P., Berkhout, B., and Sanders, R. W. (2011) Resistance of human immunodeficiency virus type 1 to a third-generation fusion inhibitor requires multiple mutations in gp41 and is accompanied by a dramatic loss of gp41 function. *J. Virol. 85*, 10785−97.

(18) Ray, N., Harrison, J. E., Blackburn, L. A., Martin, J. N., Deeks, S. G., and Doms, R. W. (2007) Clinical resistance to enfuvirtide does not affect susceptibility of human immunodeficiency virus type 1 to other classes of entry inhibitors. *J. Virol. 81*, 3240−50.

(19) Reeves, J. D., Lee, F. H., Miamidian, J. L., Jabara, C. B., Juntilla, M. M., and Doms, R. W. (2005) Enfuvirtide resistance mutations: impact on human immunodeficiency virus envelope function, entry inhibitor sensitivity, and virus neutralization. *J. Virol. 79*, 4991−9.

(20) Lalezari, J. P., Bellos, N. C., Sathasivam, K., Richmond, G. J., Cohen, C. J., Myers, R. A., Jr., Henry, D. H., Raskino, C., Melby, T., Murchison, H., Zhang, Y., Spence, R., Greenberg, M. L., Demasi, R. A., and Miralles, G. D. (2005) T-1249 retains potent antiretroviral activity in patients who had experienced virological failure while on an enfuvirtide-containing treatment regimen. *J. Infect. Dis. 191*, 1155−63.

(21) Welch, B. D., Francis, J. N., Redman, J. S., Paul, S., Weinstock, M. T., Reeves, J. D., Lie, Y. S., Whitby, F. G., Eckert, D. M., Hill, C. P., Root, M. J., and Kay, M. S. (2010) Design of a potent D-peptide HIV-1 entry inhibitor with a strong barrier to resistance. *J. Virol. 84*, 11235−44.

(22) Welch, B. D., VanDemark, A. P., Heroux, A., Hill, C. P., and Kay, M. S. (2007) Potent D-peptide inhibitors of HIV-1 entry. *Proc. Natl. Acad. Sci. U. S. A. 104*, 16828−33.

(23) Milton, R. C., Milton, S. C., and Kent, S. B. (1992) Total chemical synthesis of a D-enzyme: the enantiomers of HIV-1 protease show reciprocal chiral substrate specificity. *Science 256*, 1445−8.

(24) Kahle, K. M., Steger, H. K., and Root, M. J. (2009) Asymmetric deactivation of HIV-1 gp41 following fusion inhibitor binding. *PLoS Pathog. 5*, e1000674.

(25) Platt, E. J., Durnin, J. P., and Kabat, D. (2005) Kinetic factors control efficiencies of cell entry, efficacies of entry inhibitors, and mechanisms of adaptation of human immunodeficiency virus. *J. Virol. 79*, 4347−56.

(26) Steger, H. K., and Root, M. J. (2006) Kinetic dependence to HIV-1 entry inhibition. *J. Biol. Chem. 281*, 25813−21.

(27) Ingallinella, P., Bianchi, E., Ladwa, N. A., Wang, Y. J., Hrin, R., Veneziano, M., Bonelli, F., Ketas, T. J., Moore, J. P., Miller, M. D., and Pessi, A. (2009) Addition of a cholesterol group to an HIV-1 peptide fusion inhibitor dramatically increases its antiviral potency. *Proc. Natl. Acad. Sci. U. S. A. 106*, 5801−6.

(28) Porotto, M., Rockx, B., Yokoyama, C. C., Talekar, A., Devito, I., Palermo, L. M., Liu, J., Cortese, R., Lu, M., Feldmann, H., Pessi, A., and Moscona, A. (2010) Inhibition of Nipah virus infection in vivo: targeting an early stage of paramyxovirus fusion activation during viral entry. *PLoS Pathog. 6*, e1001168.

(29) Porotto, M., Yokoyama, C. C., Palermo, L. M., Mungall, B., Aljofan, M., Cortese, R., Pessi, A., and Moscona, A. (2010) Viral entry inhibitors targeted to the membrane site of action. *J. Virol. 84*, 6760−8.
(30) Rajendran, L., Schneider, A., Schlechtingen, G., Weidlich, S., Ries, J., Braxmeier, T., Schwille, P., Schulz, J. B., Schroeder, C., Simons, M., Jennings, G., Knolker, H. J., and Simons, K. (2008) Efficient inhibition of the Alzheimer's disease beta-secretase by membrane targeting. *Science 320*, 520−3.
(31) Teruya, K., Nishizawa, K., and Doh-ura, K. (2010) Semisynthesis of a protein with cholesterol at the C-terminal, targeted to the cell membrane of live cells. *Protein J. 29*, 493−500.
(32) Lee, H., Venable, R. M., Mackerell, A. D., Jr., and Pastor, R. W. (2008) Molecular dynamics studies of polyethylene oxide and polyethylene glycol: hydrodynamic radius and shape anisotropy. *Biophys. J. 95*, 1590−9.
(33) Wexler-Cohen, Y., Ashkenazi, A., Viard, M., Blumenthal, R., and Shai, Y. (2010) Virus-cell and cell-cell fusion mediated by the HIV-1 envelope glycoprotein is inhibited by short gp41 N-terminal membrane-anchored peptides lacking the critical pocket domain. *FASEB J. 24*, 4196−202.
(34) Wexler-Cohen, Y., and Shai, Y. (2007) Demonstrating the C-terminal boundary of the HIV 1 fusion conformation in a dynamic ongoing fusion process and implication for fusion inhibition. *FASEB J. 21*, 3677−84.
(35) Wexler-Cohen, Y., and Shai, Y. (2009) Membrane-anchored HIV-1 N-heptad repeat peptides are highly potent cell fusion inhibitors via an altered mode of action. *PLoS Pathog. 5*, e1000509.
(36) Bader, B., Kuhn, K., Owen, D. J., Waldmann, H., Wittinghofer, A., and Kuhlmann, J. (2000) Bioorganic synthesis of lipid-modified proteins for the study of signal transduction. *Nature 403*, 223−6.
(37) Peisajovich, S. G., Gallo, S. A., Blumenthal, R., and Shai, Y. (2003) C-terminal octylation rescues an inactive T20 mutant: implications for the mechanism of HIV/SIMIAN immunodeficiency virus-induced membrane fusion. *J. Biol. Chem. 278*, 21012−7.
(38) Luo, C., Wang, K., Liu de, Q., Li, Y., and Zhao, Q. S. (2008) The functional roles of lipid rafts in T cell activation, immune diseases and HIV infection and prevention. *Cell Mol. Immunol. 5*, 1−7.
(39) Waheed, A. A., and Freed, E. O. (2010) The Role of Lipids in Retrovirus Replication. *Viruses 2*, 1146−1180.
(40) Vincent, N., Genin, C., and Malvoisin, E. (2002) Identification of a conserved domain of the HIV-1 transmembrane protein gp41 which interacts with cholesteryl groups. *Biochim. Biophys. Acta 1567*, 157−64.
(41) Van Laethem, F., Liang, X., Andris, F., Urbain, J., Vandenbranden, M., Ruysschaert, J. M., Resh, M. D., Stulnig, T. M., and Leo, O. (2003) Glucocorticoids alter the lipid and protein composition of membrane rafts of a murine T cell hybridoma. *J. Immunol. 170*, 2932−9.
(42) Schumann, J., Leichtle, A., Thiery, J., and Fuhrmann, H. (2011) Fatty acid and peptide profiles in plasma membrane and membrane rafts of PUFA supplemented RAW264.7 macrophages. *PLoS One 6*, e24066.
(43) Spector, A. A. (1975) Fatty acid binding to plasma albumin. *J. Lipid Res. 16*, 165−79.
(44) Benting, J., Rietveld, A., Ansorge, I., and Simons, K. (1999) Acyl and alkyl chain length of GPI-anchors is critical for raft association in vitro. *FEBS Lett. 462*, 47−50.
(45) Peng, L., Minbo, H., Fang, C., Xi, L., and Chaocan, Z. (2008) The interaction between cholesterol and human serum albumin. *Protein Pept. Lett. 15*, 360−4.
(46) Charbonneau, D. M., and Tajmir-Riahi, H. A. (2010) Study on the interaction of cationic lipids with bovine serum albumin. *J. Phys. Chem. B 114*, 1148−55.
(47) Fishburn, C. S. (2008) The pharmacology of PEGylation: balancing PD with PK to generate novel therapeutics. *J. Pharm. Sci. 97*, 4167−83.
(48) Dennis, M. S., Zhang, M., Meng, Y. G., Kadkhodayan, M., Kirchhofer, D., Combs, D., and Damico, L. A. (2002) Albumin binding as a general strategy for improving the pharmacokinetics of proteins. *J. Biol. Chem. 277*, 35035−43.

Bioconjugate Chemistry

Article

pubs.acs.org/bc

Paradoxical Downregulation of CXC Chemokine Receptor 4 Induced by Polyphemusin II-Derived Antagonists

Ryo Masuda,[†] Shinya Oishi,*[,†] Noriko Tanahara,[†] Hiroaki Ohno,[†] Akira Hirasawa,[†] Gozoh Tsujimoto,[†] Yoshiaki Yano,[†] Katsumi Matsuzaki,[†] Jean-Marc Navenot,[‡] Stephen C. Peiper,[‡] and Nobutaka Fujii*[,†]

[†]Graduate School of Pharmaceutical Sciences, Kyoto University, Sakyo-ku, Kyoto 606-8501, Japan

[‡]Department of Pathology, Anatomy and Cell Biology, Thomas Jefferson University, Philadelphia, Pennsylvania 19107, United States

Supporting Information

ABSTRACT: CXC chemokine receptor 4 (CXCR4) is a G protein-coupled receptor implicated in cell entry of T-cell line-tropic HIV-1 strains. CXCR4 and its ligand stromal cell derived factor-1 (SDF-1)/CXCL12 play pivotal parts in many physiological processes and pathogenetic conditions (e.g., immune cell-homing and cancer metastasis). We previously developed the potent CXCR4 antagonist T140 from structure−activity relationship studies of the antimicrobial peptide polyphemusin II. T140 and its derivatives have been exploited in biological and biomedical studies for the SDF-1/CXCR4 axis. We investigated receptor localization upon ligand stimulation using fluorescent SDF-1 and T140 derivatives as well as a specific labeling technique for cellular-membrane CXCR4. Fluorescent T140 derivatives induced translocation of CXCR4 into the perinuclear region as observed by treatment with fluorescent SDF-1. T140 derivative-mediated internalization of CXCR4 was also monitored by the coiled-coil tag-probe system. These findings demonstrated that the CXCR4 antagonistic activity and anti-HIV activity of T140 derivatives were derived (at least in part) from antagonist-mediated receptor internalization.

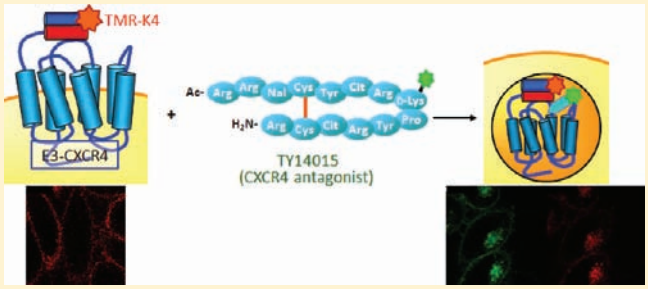

INTRODUCTION

CXC chemokine receptor 4 (CXCR4) is a G-protein-coupled receptor. It is widely expressed in leukocytes such as T-cells, B-cells, and monocytes.[1,2] Under physiological conditions, the endogenous ligand, stromal cell-derived factor-1 (SDF-1)/CXCL12, is secreted by bone marrow stromal cells for expansion and development of precursor B-cells.[3] High concentrations of SDF-1 are present at inflammatory sites, so the migration of CXCR4-expressing stem cells toward an SDF-1 gradient promotes repair of injured tissues.[4] There have been many reports on the pathology of CXCR4-related cancer, including CXCR4 overexpression and organ-specific metastasis among various types of cancer cells.[5,6] During metastasis, SDF-1 from secondary lesions functions as a chemoattractant for directional migration of CXCR4-expressing malignant cells.[5,6]

The activation process of CXCR4 by SDF-1 has been well documented.[7] Upon SDF-1 binding, CXCR4 evokes downstream signaling via dissociation of heterotrimeric G proteins, followed by decrease in intracellular cyclic adenosine monophosphate (cAMP) concentrations, upregulation of Ca^{2+} release, and increase in extracellular-signal-regulated kinase (ERK) 1/2 phosphorylations.[8−10] Furthermore, CXCR4 internalization in response to SDF-1 occurs in early endosomes through β-arrestin recruitment, just like other GPCRs,[11] in which phosphorylated serine residues and a dileucine motif at the CXCR4 C-terminus have critical roles.[12,13] The complex is sorted into late endosomes/lysosomes for the degradation pathway or for recycling endosomes.[11,14] In addition, CXCR4 is used as a major co-receptor for the entry of T-cell line tropic human immunodeficiency virus type 1 (HIV-1) into target host cells.[15,16] The inhibitory effect of SDF-1 on HIV infection is thought to be by competitive binding to CXCR4 as well as CXCR4 downregulation.[17,18] CXCR4 is a promising molecular target for potential anti-metastatic agents and anti-HIV agents, so several CXCR4 ligands have been developed.[5,19−22]

We previously developed the potent anti-HIV peptide T140. This was designed from the structure−activity relationship studies of a self-defense peptide of horseshoe crabs, polyphemusin II (Figure 1).[19] Inhibition of HIV-induced cytopathogenicity by T140 and its derivatives was derived from selective CXCR4 antagonistic and/or inverse agonistic activity (in which the basal signal levels were decreased in the guanosine triphosphate (GTP) binding and intracellular calcium flux assay using a constitutively active mutant).[23] A recent report on the crystal structure of CXCR4 in complex with the T140 derivative CVX15 revealed that arginine residues in CVX15 made polar interactions with Asp171 and Asp187 in CXCR4.[24] Point-mutation experiments of CXCR4 revealed that additional residues on the extracellular domain (Arg188, Gly207, and Asp262) are necessary for the interaction of

Received: February 18, 2012
Revised: April 7, 2012
Published: April 10, 2012

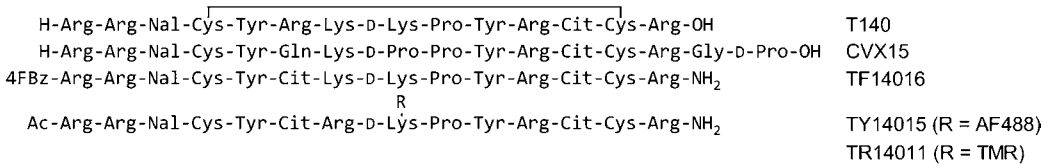

Figure 1. Amino acid sequences of CXCR4 antagonist peptides. The disulfide bonds between cysteine residues are shown by solid lines. D-Amino acids are not first-letter capitalized. Abbreviations: Nal, L-3-(2-naphthyl)alanine; Cit, L-citrulline; 4FBz, 4-fluorobenzoyl; AF488, AlexaFluor 488; TMR, tetramethylrhodamine.

T140, which is independent of the interaction with SDF-1.[25,26] These residues contribute to stabilization of the CXCR4 structure via formation of hydrogen bonds with adjacent residues, so T140 binding to these residues may impair SDF-1 binding via conformational changes of CXCR4. ALX-40C is an alternative CXCR4 antagonist that inhibits HIV-1 infection into T-cells.[27] The anti-HIV activity of ALX-40C with a sequence of nine D-Arg is also reported to be derived from binding to acidic residues in the second extracellular loop of CXCR4.[27]

It was demonstrated that highly basic peptides such as ALX-40C and HIV-1 Tat translocate into the intracellular compartment through endocytosis.[28−31] On the basis of the biological properties of these highly basic peptides, we assumed that polyphemusin II-derived CXCR4 antagonists could induce the internalization and/or translocation of receptors into the intracellular compartment, resulting in the apparent antagonistic or inverse agonistic activity for CXCR4.

In the present study, we investigated the mechanism of action of T140 derivatives using novel fluorescent probes. The uptake and localization of CXCR4 was monitored by analyses of flow cytometry and confocal microscopy using the coiled-coil tag-probe system[32] for the labeling of cell-surface CXCR4.

EXPERIMENTAL SECTION

Quantitative Analyses of Cell-Surface E3-CXCR4 Using a Fluorescent K4-Peptide by Flow Cytometry. E3-CXCR4 CHO cells were detached using versene and incubated with 100 nM FL-K4 in F-12 medium (500 μL) at 0 °C for 15 min in the absence or presence of unlabeled K4-peptide or SDF-1. The intensity of cell staining was analyzed using a FACScalibur system (BD Biosciences, San Jose, CA, USA). Ten thousand events per sample were analyzed, and the data collected from FL1 in log mode. Fluorescent intensity was calculated as a geometric mean of cellular fluorescence. Data were analyzed using *CellQuest Pro* software (BD Biosciences). Data were analyzed using a two-tailed Student's *t* test with significance set at $p \leq 0.05$.

Quantitative Analyses of Ligand-Mediated CXCR4 Internalization by Flow Cytometry. E3-CXCR4 CHO cells were detached using versene and resuspended in F-12 medium (100 μL) containing each ligand. After incubation at 37 °C for 30 min, ice-cold F-12 medium (400 μL) was added to the mixture, and cells centrifuged at 500 × *g* for 5 min at 4 °C. Cell pellets were then incubated with 100 nM FL-K4 in F-12 (100 μL) at 0 °C for 15 min. The mixture was diluted with ice-cold F-12 medium (400 μL), and analyzed using a FACScalibur flow cytometer.

Binding and Displacement of [^{125}I]-SDF-1. A membrane fraction of cells expressing CXCR4 was incubated with 0.5 nM of [^{125}I]-SDF-1 and FL-K4 in binding buffer [50 mM HEPES (pH 7.4), 5 mM $MgCl_2$, 1 mM $CaCl_2$, and 0.1% bovine serum albumin (BSA) in H_2O] for 1 h at room temperature. Reaction mixtures were filtered through GF/B filters (PerkinElmer, Waltham, MA, USA) pretreated with 0.1% polyethyleneimine. The filter plate was washed with wash buffer [50 mM HEPES (pH 7.4), 500 mM NaCl, and 0.1% BSA in H_2O] and bound radioactivity measured by TopCount (PerkinElmer).

Confocal Microscopy Analyses of Ligand and CXCR4 Internalization. E3-CXCR4 CHO cells were plated on 35 mm glass-bottomed dishes and cultured in F-12 medium containing 10% heat-inactivated fetal bovine serum supplemented with penicillin/streptomycin and hygromycin. Cells were washed once with cold F-12 medium, and incubated with fluorescent ligands [SDF-1^{AF488} (100 nM) or TY14015 (1 μM)] in F-12 medium (100 μL) at 30 °C for 30 min. After rinsing once with cold F-12 medium, cells were observed by confocal microscopy (Eclipse Ti-E: Nikon, Tokyo, Japan). To monitor CXCR4 localization, E3-CXCR4 CHO cells were pretreated with 100 nM fluorescent K4-peptide in F-12 medium (100 μL) at 0 °C for 15 min before treatment with CXCR4 ligands.

For staining of cellular compartments, after incubation with fluorescent ligands or K4-peptide, cells were rinsed once with cold F-12 medium and treated with the marker (FM 4−64 for the cell membrane; LysoTracker Red DND-99 for lysosomes; ER-tracker Red for the endoplasmic reticulum; or AlexaFluor 568-conjugated transferrin for endosomes) according to the manufacturer (Invitrogen, Carlsbad, CA, USA, for all markers) protocol. The green (AlexaFluor 488 and ATTO488) channel was excited by a 488 nm laser and detected through a BP 500−550 nm emission filter. The red (TMR and AlexaFluor 568) channel was excited by a 568 nm laser, and detected through a BP 575−605 nm emission filter. The blue (FM 4−64) channel was excited by a 568 nm laser, and detected through a LP 665 nm emission filter. Data were analyzed using *EZ-C1 Viewer* software (Nikon).

RESULTS

Labeling of Cell-Membrane CXCR4 by the Coiled-Coil Tag-Probe System. A stable CXCR4-expressing cell line was established to monitor the internalization of CXCR4. The surface-exposed tag sequence E3 $(EIAALEK)_3$ was appended at the N-terminus of CXCR4 for detection using the peptide probe K4 $(KIAALKE)_4$ with an appropriate tracer group.[32] This coiled-coil tag-probe system provides several distinct advantages to visualize cell-surface CXCR4. For example, K4-peptide is much smaller than anti-epitope antibodies, so ligand binding to the receptor is hardly disturbed. In addition, specific labeling of E3-tagged receptors on cell membranes with fluorescent K4-peptides can distinguish the internalized receptor from the receptor that is originally present in the cytosolic compartment. This is in contrast to receptors fused with fluorescent proteins, which have usually been employed for monitoring receptor localization.[14,33]

CHO cells stably expressing E3-tagged CXCR4 (E3-CXCR4) were generated by the Flp-In expression system, and were studied by flow cytometric analyses. E3-CXCR4

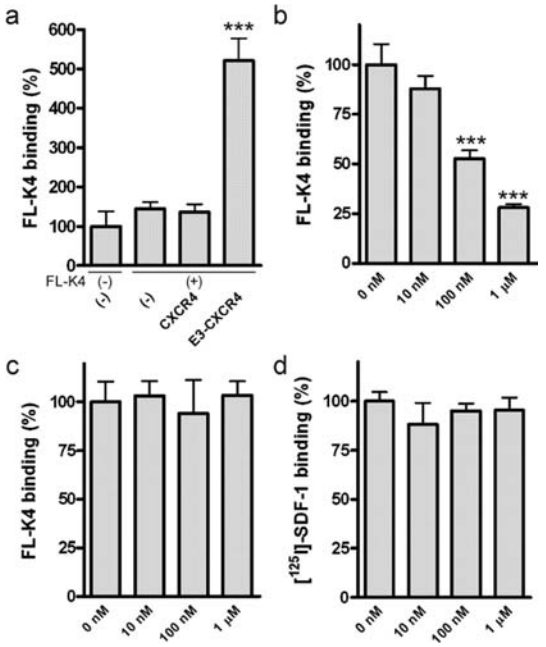

Figure 2. Labeling of E3-CXCR4 cells with fluorescein-K4-peptide (FL-K4). (a) FL-K4 binding to CXCR4 cell lines. After cells were treated with FL-K4 (100 nM) at 0 °C for 15 min, bound FL-K4 was measured by flow cytometry. (b) Inhibition of FL-K4 binding to E3-CXCR4 by unlabeled K4-peptide. After E3-CXCR4 CHO cells were labeled with FL-K4 (100 nM) in the presence of various concentrations of unlabeled K4-peptide at 0 °C for 15 min, bound FL-K4 was measured by flow cytometry. (c) Effect of SDF-1 on FL-K4 binding to E3-CXCR4. After E3-CXCR4 CHO cells were labeled with FL-K4 (100 nM) in the presence of various concentrations of SDF-1 at 0 °C for 15 min, bound various concentrations of FL-K4 was measured by flow cytometry. (d) Effect of K4-peptide on SDF-1 binding to E3-CXCR4. [^{125}I]-SDF-1 (0.5 nM) binding to E3-CXCR4. (±S.D., n = 3; *** $p \leq 0.005$).

CHO cells were clearly seen to be stained by fluorescein-conjugated K4-peptide (FL-K4) (Figure 2a). This staining was inhibited by unlabeled K4-peptide in a dose-dependent manner, suggesting specific labeling of E3-CXCR4 by interaction between E3-tag and K4-peptide (Figure 2b). FL-K4 binding to E3-CXCR4 was not disturbed by SDF-1 even at 1 μM, which demonstrated that FL-K4-mediated staining was independent of SDF-1 binding to CXCR4 (Figure 2c). SDF-1 binding to E3-CXCR4 was also unaffected by K4-peptide, which was verified by the binding inhibition assay using [^{125}I]-SDF-1 (Figure 2d). Taken together, specific fluorescent labeling of CXCR4 was accomplished by the coiled-coil tag-probe system without mutual competitive inhibition of SDF-1 and K4-peptide binding to the receptor.

Monitoring and Quantitative Analyses of SDF-1-Induced CXCR4 Internalization. The level of residual CXCR4 on the cell membrane after SDF-1 stimulation has been measured by flow cytometry using a CXCR4-specific antibody.[34,35] For example, Honczarenko et al. assessed SDF-1-induced internalization of CXCR4 by staining cell-surface CXCR4 by the monoclonal antibody 12G5.[34] However, the possible competitive binding of SDF-1 and antibody to cell-surface CXCR4 may impair receptor detection. To overcome this potential disadvantage, the coiled-coil tag-probe pair system could be an alternative to quantify cell-surface CXCR4.

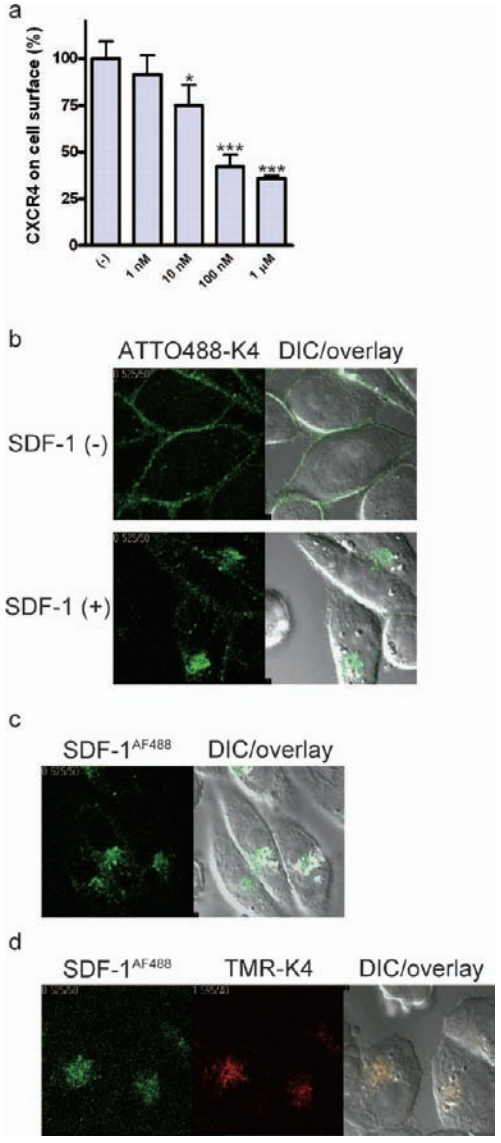

Figure 3. CXCR4 internalization induced by SDF-1 derivatives. (a) Quantitative analyses of E3-CXCR4 internalization by flow cytometry. After E3-CXCR4 CHO cells were treated with various concentrations of SDF-1 at 37 °C for 30 min, cells were labeled by FL-K4 (100 nM) at 0 °C for 15 min (±S.D., n = 3; * $p \leq 0.05$; *** $p \leq 0.005$). (b) Confocal microscopy images of SDF-1-mediated CXCR4 internalization. After E3-CXCR4-expressing cells were labeled with ATTO488-K4 (100 nM) at 0 °C for 15 min, cells were treated with SDF-1 (100 nM) at 30 °C for 30 min. (c) Confocal microscopy images of internalized fluorescent SDF-1. E3-CXCR4-expressing cells were treated with SDF-1^{AF488} (100 nM) for 30 min. (d) Confocal microscopy images of internalized SDF-1 (green) and CXCR4 (red). After E3-CXCR4-expressing cells were labeled with TMR-K4 (100 nM) at 0 °C for 15 min, and cells were treated with SDF-1^{AF488} (100 nM) at 30 °C for 30 min. Representative z-slice confocal microscopy images are shown.

SDF-1-mediated CXCR4 internalization was investigated using the established system. Initially, quantitative analyses of residual cell-surface E3-CXCR4 after SDF-1 stimulation were undertaken by flow cytometry. Cells were stained with FL-K4 after E3-CXCR4 CHO cells were treated with SDF-1 over a range of concentrations. The fluorescent intensity of FL-K4 was significantly decreased in a dose-dependent manner (Figure 3a). Confocal microscopy studies using ATTO488-conjugated

dx.doi.org/10.1021/bc300084h | Bioconjugate Chem. 2012, 23, 1259−1265

K4-peptide (ATTO488-K4) confirmed the translocation of E3-CXCR4 to the intracellular compartment by treatment with SDF-1, whereas ATTO488-K4/E3-CXCR4 remained on the cell surface without SDF-1 treatment (Figure 3b). Both results suggested that SDF-1 stimulation induced FL-K4 labeled E3-CXCR4 internalization, and that the E3 sequence on the N-terminus of CXCR4 could work as a functional tag to detect receptor localization without disturbing receptor internalization.

CXCR4 internalization was also monitored by confocal microscopy using a fluorescent SDF-1 derivative.[36] Translocation of SDF-1^{AF488} into the intracellular compartment was observed by treatment of E3-CXCR4 cells (without labeling by fluorescent K4-peptide) (Figure 3c). This was consistent with the SDF-1-mediated internalization of FL-K4-labeled E3-CXCR4 (Figure 3b). The intracellular localization of SDF-1^{AF488} was not observed in CHO cells without CXCR4 expression (see Supporting Information, Supplementary Figure 1). Hence, it could be concluded that this translocation was mediated by the interaction with CXCR4. To confirm the colocalization of SDF-1 and CXCR4, the same experiment was conducted using E3-CXCR4-expressing cells labeled with TMR-conjugated K4-peptide (TMR-K4). Incubation of cells with SDF-1^{AF488} induced translocation of TMR-K4/E3-CXCR4 complexes into the intracellular compartment, which was verified by colocalization of SDF-1^{AF488} and TMR-K4/E3-CXCR4 (Figure 3d). An identical phenotype was observed in an experiment using SDF-1^{TMR} and ATTO488-K4/E3-CXCR4, indicating that the fluorophore functional groups on the ligand and receptor did not influence the translocation (see Supporting Information, Supplementary Figure 2).

Polyphemusin-Derived CXCR4 Antagonists Induce Receptor Internalization. Next, we investigated receptor internalization by CXCR4 antagonists using the coiled-coil tag-probe system. E3-CXCR4 CHO cells were treated with polyphemusin II and CXCR4 antagonists (TF14016[37] or FC131[38]) at 37 °C. The proportion of residual receptors on the cell membrane was subsequently determined by flow cytometry in the presence of FL-K4 (Figure 4a). The fluorescence intensity of FL-K4 was reduced by 20−25% by the antagonists.[39] In contrast, a decrease in FL-K4 fluorescence was not observed in the same experiment at 0 °C, in which receptor internalization does not occur,[40] suggesting that the E3-tag/K4-peptide interaction was not inhibited by the antagonists. Antagonist-induced internalization was also confirmed by fluorescence microscopy analyses of ATTO488-K4/E3-CXCR4 CHO cells. TF14016 induced the translocation of ATTO488-K4/E3-CXCR4 into the perinuclear region, just like that seen in SDF-1 stimulation (Figure 4b). As such, it was demonstrated that CXCR4 antagonists partially induced receptor internalization.

The fluorescent CXCR4 antagonist TY14015 was similarly accumulated in the cytosolic perinuclear domain in E3-CXCR4 CHO cells after 30 min incubation at 30 °C (Figure 4c). TY14015-mediated translocation was not observed in the same experiments using nontransfected CHO cells,[41] nor by incubation of E3-CXCR4 CHO cells with TY14015 at 0 °C (see Supporting Information, Supplementary Figure 1). These findings indicated that CXCR4 serves as an essential receptor for the translocation of CXCR4 antagonists by an active pathway such as endocytosis. In contrast to the experiment using SDF-1^{AF488} (Figure 3c), staining of the cell membrane by TY14015 was also observed (Figure 4c).

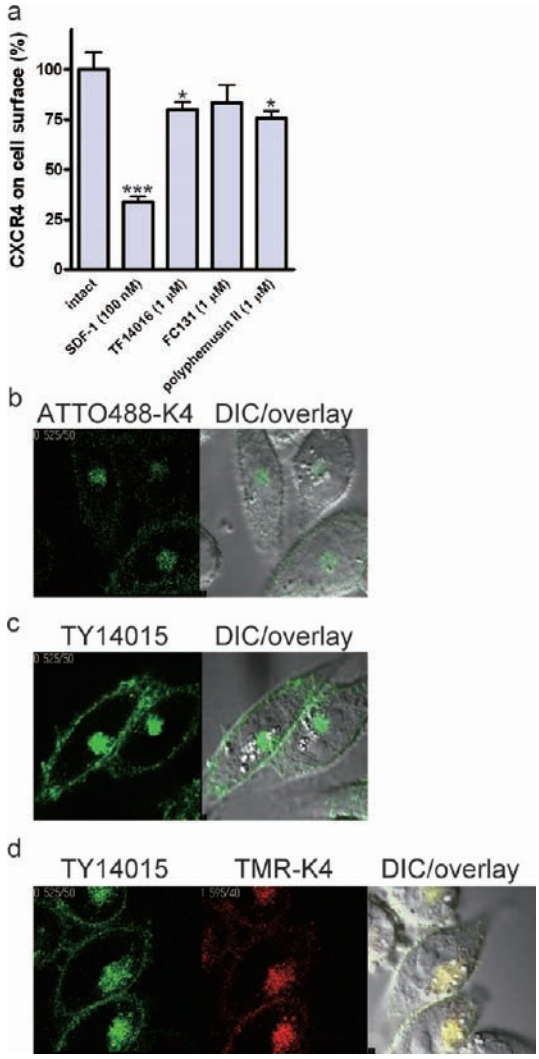

Figure 4. CXCR4 internalization upon stimulation by CXCR4 antagonists. (a) Quantitative analyses of E3-CXCR4 internalization by flow cytometry. After E3-CXCR4 CHO cells were treated with each antagonist (1 μM) at 37 °C for 30 min, and cells were labeled by FL-K4 (100 nM) at 0 °C for 15 min (±S.D., n = 3; * $p \leq 0.05$; *** $p \leq 0.005$). (b) Confocal microscopy images of TF14016-mediated CXCR4 internalization. After E3-CXCR4 CHO cells were labeled with ATTO488-K4 (100 nM) at 0 °C for 15 min, cells were treated with TF14016 (1 μM) at 30 °C for 30 min. (c) Confocal microscopy images of internalized TY14015. E3-CXCR4 CHO cells were treated with TY14015 (1 μM) at 30 °C for 30 min. (d) Confocal microscopy images of internalized TY14015 (green) and CXCR4 (red). After E3-CXCR4 CHO cells were labeled with TMR-K4 (100 nM) at 0 °C for 15 min, cells were treated with TY14015 (1 μM) at 30 °C for 30 min. Representative z-slice confocal microscopy images are shown.

The localization of fluorescent T140 derivatives and CXCR4 was simultaneously monitored by confocal microscopy using the coiled-coil tag-probe system. After preincubation with TMR-K4, E3-CXCR4 CHO cells were stimulated by TY14015. Merged confocal microscopy images revealed that TY14015 colocalized with TMR-K4/E3-CXCR4 (Figure 4d). This colocalization was not affected by the fluorophores, which was verified by experiments using ATTO488-K4/E3-CXCR4 and TR14011 (Figure 1, see also Supporting Information, Supplementary Figure 2). CXCR4-Venus CHO cells (in which a fluorescent Venus protein was fused at the C-terminus of CXCR4) showed an identical phenotype upon stimulation with

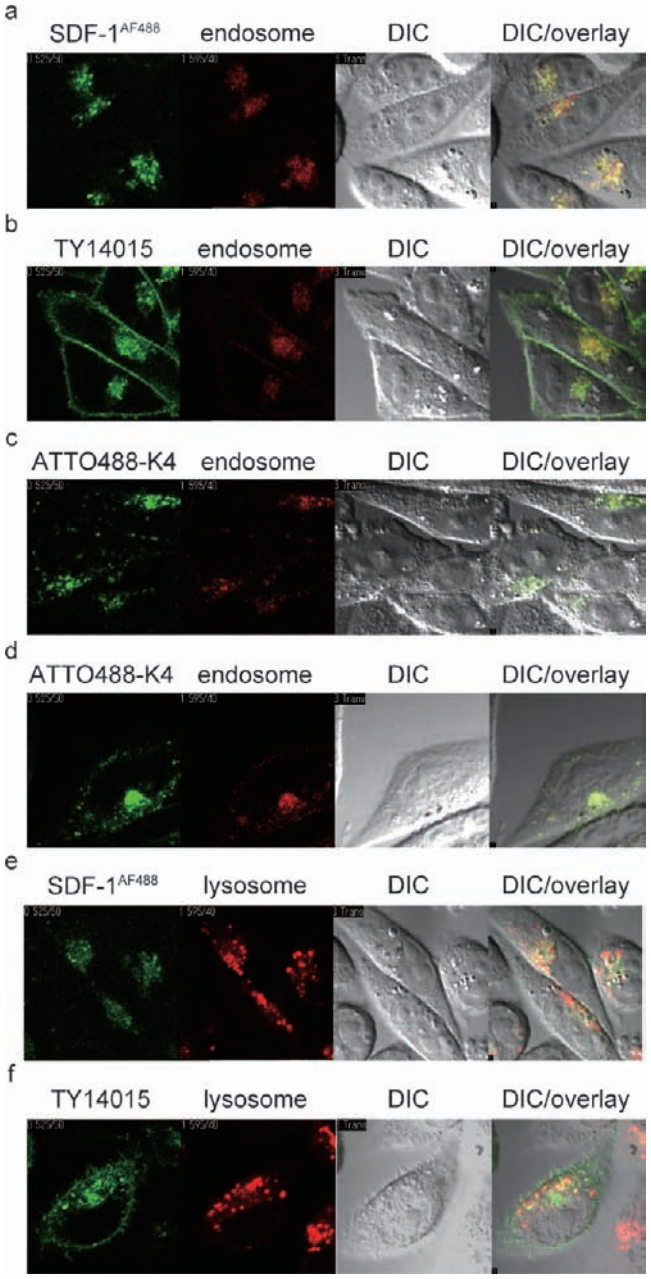

Figure 5. Translocation of fluorescent CXCR4 ligands and the receptor. (a,b) Confocal microscopy images of SDF-1^{AF488} (a) or TY14015 (b) and endosome. After E3-CXCR4 CHO cells were treated with fluorescent ligands at 30 °C for 30 min, cells were stained with AlexaFluor 568-transferrin (50 μg/mL) for 60 min. (c,d) Confocal microscopy images of internalized CXCR4 and endosome after stimulation with SDF-1 (c) or TF14016 (d). After E3-CXCR4 CHO cells were labeled with ATTO488-K4 (100 nM) at 0 °C for 15 min, cells were treated with ligand at 30 °C for 30 min and stained with AlexaFluor 568-transferrin (50 μg/mL) for 60 min. (e,f) Confocal microscopy images of SDF-1^{AF488} (e) or TY14015 (f) and lysosome. After E3-CXCR4 CHO cells were treated with fluorescent ligands at 30 °C for 30 min, cells were stained with LysoTracker (1 μM) for 30 min. Representative *z*-slice confocal microscopy images are shown.

SDF-1^{TMR} or TR14011 (see Supporting Information, Supplementary Figure 2). These data suggested that T140 derivatives translocated into the intracellular compartment with formation of ligand–receptor complexes.

Intracellular Translocation of CXCR4 Ligands and Receptor. The intracellular destination of CXCR4 ligand–receptor complexes after the binding of CXCR4 antagonists was investigated by confocal microscopy (Figure 5; see also Supporting Information, Supplementary Figure 3). After E3-CXCR4 CHO cells were treated with CXCR4 ligands, cells were stained with several organelle-specific fluorescent markers. SDF-1^{AF488} translocated to endosomal compartments in 30 min, which were stained by AlexaFluor 568-conjugated transferrin (Figure 5a). This result was in agreement with another report on SDF-1-mediated CXCR4 internalization.[17] Similarly, TY14015 accumulated in the same intracellular compartment (Figure 5b). Localization of ATTO-K4/E3-CXCR4 after treatment with SDF-1 and TF14016 was also similar to the distribution of transferrin, indicating that internalized CXCR4 ligand–receptor complexes translocate into endosomal compartments (Figure 5c,d). Meanwhile, localization of the fluorescent CXCR4 ligands in lysosomes was partial (Figure 5e,f). Agonists and antagonists of CXCR4 may indirectly affect the distributions of lysosomes. Staining with FM 4–64 or ER-trackers suggested that SDF-1^{AF488} existed neither on the cell membrane nor in the endoplasmic reticulum, whereas partial staining with TY14015 on cell membranes was observed (see Supporting Information, Supplementary Figure 3).

■ DISCUSSION

Agonist-mediated internalization of GPCRs induces the transduction of downstream signaling and desensitization to regulate cell homeostasis. In contrast, reports on antagonist-induced receptor internalization (e.g., cholecystokinin A, 5-HT_{2A}, and neuropeptide Y_1 receptors) are limited.[42−44] This is the first report on the antagonist-mediated internalization of CXCR4. A series of polyphemusin II-derived and other CXCR4 antagonists contain basic functional groups such as arginine and lysine residues, which are involved in the interactions with the extracellular domain of CXCR4-bearing negative charges. In the present study, using the coiled-coil tag-probe system to visualize cell-surface CXCR4, CXCR4-mediated translocation of T140 derivatives into intracellular compartments was demonstrated. Although the internalization effect of surface CXCR4 by T140 derivatives was partial (only 25%, much less than the agonist SDF-1), this CXCR4 internalization supports the apparent antagonistic activity of T140 derivatives against SDF-1 binding to CXCR4 as well as the induction of inverse agonistic activity signaling.[23] It was reported that treatment of CXCR4-expressing cells with HIV-1 gp120 peptide induces similar CXCR4 internalization without agonistic activity, which is closely related to HIV infection.[14] Although T140 derivatives have been thought to be competitive inhibitors against gp120 binding to CXCR4,[19] antagonist-mediated internalization of cell-surface CXCR4 could be an alternative mode of action for anti-HIV activity.[17,18] Further investigation of the mechanisms of this paradoxical antagonist-mediated down-regulation of CXCR4 could facilitate development of novel anti-metastatic and anti-HIV agents.

■ ASSOCIATED CONTENT

Ⓢ Supporting Information

Experimental procedures as well as confocal microscopy images of ligand and receptor internalization in the control experiments. This material is available free of charge via the Internet at http://pubs.acs.org.

AUTHOR INFORMATION

Corresponding Author

*Tel: +81-75-753-4551, Fax: +81-75-753-4570, E-mail: soishi@pharm.kyoto-u.ac.jp (S.O.), nfujii@pharm.kyoto-u.ac.jp (N.F.).

Notes

The authors declare no competing financial interest.

ACKNOWLEDGMENTS

We thank Prof. Shiroh Futaki and Dr. Ikuhiko Nakase (Institute for Chemical Research, Kyoto University) for excellent technical advices. This work was supported by Grants-in-Aid for Scientific Research and Targeted Proteins Research Program from the Ministry of Education, Culture, Sports, Science, and Technology of Japan; and by a grant for Promotion of AIDS Research from the Ministry of Health and Welfare of Japan. R.M. is grateful for Research Fellowships from the JSPS for Young Scientists.

REFERENCES

(1) Viola, A., and Luster, A. D. (2008) Chemokines and their receptors: drug targets in immunity and inflammation. *Annu. Rev. Pharmacol. Toxicol. 48*, 171−197.

(2) Bleul, C. C., Farzan, M., Choe, H., Parolin, C., Clark-Lewis, I., Sodroski, J., and Springer, T. A. (1996) The lymphocyte chemoattractant SDF-1 is a ligand for LESTR/fusin and blocks HIV-1 entry. *Nature 382*, 829−833.

(3) Egawa, T., Kawabata, K., Kawamoto, H., Amada, K., Okamoto, R., Fujii, N., Kishimoto, T., Katsura, Y., and Nagasawa, T. (2001) The earliest stages of B cell development require a chemokine stromal cell-derived factor/pre-B cell growth-stimulating factor. *Immunity 15*, 323−334.

(4) Ratajczak, M. Z., Majka, M., Kucia, M., Drukala, J., Pietrzkowski, Z., Peiper, S., and Janowska-Wieczorek, A. (2003) Expression of functional CXCR4 by muscle satellite cells and secretion of SDF-1 by muscle-derived fibroblasts is associated with the presence of both muscle progenitors in bone marrow and hematopoietic stem/progenitor cells in muscles. *Stem Cells 21*, 363−371.

(5) Rubin, J. B., Kung, A. L., Klein, R. S., Chan, J. A., Sun, Y., Schmidt, K., Kieran, M. W., Luster, A. D., and Segal, R. A. (2003) A small-molecule antagonist of CXCR4 inhibits intracranial growth of primary brain tumors. *Proc. Natl. Acad. Sci. U. S. A. 100*, 13513−13518.

(6) Monaco, G., Belmont, J. W., Konopleva, M., Andreeff, M., Tavor, S., Petit, I., Kollet, O., and Lapidot, T. (2004) Correlation between CXCR4 and homing or engraftment of acute myelogenous leukemia. *Cancer Res. 64*, 6832−6833.

(7) Busillo, J. M., and Benovic, J. L. (2007) Regulation of CXCR4 signaling. *Biochim. Biophys. Acta 1768*, 952−963.

(8) Rollins, B. J. (1997) Chemokines. *Blood 90*, 909−928.

(9) Dwinell, M. B., Ogawa, H., Barrett, K. E., and Kagnoff, M. F. (2004) SDF-1/CXCL12 regulates cAMP production and ion transport in intestinal epithelial cells via CXCR4. *Am. J. Physiol. Gastrointest. Liver Physiol. 286*, 844−850.

(10) Busillo, J. M., Armando, S., Sengupta, R., Meucci, O., Bouvier, M., and Benovic, J. L. (2010) Site-specific phosphorylation of CXCR4 is dynamically regulated by multiple kinases and results in differential modulation of CXCR4 signaling. *J. Biol. Chem. 285*, 7805−7817.

(11) Kumar, A., Kremer, K. N., Dominguez, D., Tadi, M., and Hedin, K. E. (2011) Gα13 and Rho mediate endosomal trafficking of CXCR4 into Rab11+ vesicles upon stromal cell-derived factor-1 stimulation. *J. Immunol. 186*, 951−958.

(12) Marchese, A., and Benovic, J. L. (2001) Agonist-promoted ubiquitination of the G protein-coupled receptor CXCR4 mediates lysosomal sorting. *J. Biol. Chem. 276*, 45509−45512.

(13) Orsini, M. J., Parent, J. L., Mundell, S. J., Marchese, A., and Benovic, J. L. (1999) Trafficking of the HIV coreceptor CXCR4. Role of arrestins and identification of residues in the C-terminal tail that mediate receptor internalization. *J. Biol. Chem. 274*, 31076−31086.

(14) Tarasova, N. I., Stauber, R. H., and Michejda, C. J. (1998) Spontaneous and ligand-induced trafficking of CXC-chemokine receptor 4. *J. Biol. Chem. 273*, 15883−15886.

(15) Feng, Y., Broder, C. C., Kennedy, P. E., and Berger, E. A. (1996) HIV-1 entry cofactor: functional cDNA cloning of a seven-transmembrane, G protein-coupled receptor. *Science 272*, 872−877.

(16) Berson, J. F., Long, D., Doranz, B. J., Rucker, J., Jirik, F. R., and Doms, R. W. (1996) A seven-transmembrane domain receptor involved in fusion and entry of T-cell-tropic human immunodeficiency virus type 1 strains. *J. Virol. 70*, 6288−6295.

(17) Amara, A., Gall, S. L., Schwartz, O., Salamero, J., Montes, M., Loetscher, P., Baggiolini, M., Virelizier, J. L., and Arenzana-Seisdedos, F. (1997) HIV coreceptor downregulation as antiviral principle: SDF-1alpha-dependent internalization of the chemokine receptor CXCR4 contributes to inhibition of HIV replication. *J. Exp. Med. 186*, 139−146.

(18) Altenburg, J. D., Jin, Q., Alkhatib, B., and Alkhatib, G.. (2010) The potent anti-HIV activity of CXCL12γ correlates with efficient CXCR4 binding and internalization. *J. Virol. 84*, 2563−2572.

(19) Tamamura, H., Xu, Y., Hattori, T., Zhang, X., Arakaki, R., Kanbara., K., Omagari, A., Otaka, A., Ibuka, T., Yamamoto, N., Nakashima, H., and Fujii, N. (1998) A low-molecular-weight inhibitor against the chemokine receptor CXCR4: a strong anti-HIV peptide T140. *Biochem. Biophys. Res. Commun. 253*, 877−882.

(20) Gerlach, L. O., Skerlj, R. T., Bridger, G. J., and Schwartz, T. W. (2001) Molecular interactions of cyclam and bicyclam non-peptide antagonists with the CXCR4 chemokine receptor. *J. Biol. Chem. 276*, 14153−14160.

(21) Oishi, S., Masuda, R., Evans, B., Ueda, S., Goto, Y., Ohno, H., Hirasawa, A., Tsujimoto, G., Wang, Z., Peiper, S. C., Naito, T., Kodama, E., Matsuoka, M., and Fujii, N. (2008) Synthesis and application of fluorescein- and biotin-labeled molecular probes for the chemokine receptor CXCR4. *ChemBioChem 9*, 1154−1158.

(22) Masuda, R., Oishi, S., Ohno, H., Kimura, H., Saji, H., and Fujii, N. (2011) Concise site-specific synthesis of DTPA-peptide conjugates: application to imaging probes for the chemokine receptor CXCR4. *Bioorg. Med. Chem. 19*, 3216−3220.

(23) Zhang, W. B., Navenot, J. M., Haribabu, B., Tamamura, H., Hiramatu, K., Omagari, A., Pei, G., Manfredi, J. P., Fujii, N., Broach, J. R., and Peiper, S. C. (2002) A point mutation that confers constitutive activity to CXCR4 reveals that T140 is an inverse agonist and that AMD3100 and ALX40−4C are weak partial agonists. *J. Biol. Chem. 277*, 24515−24521.

(24) Wu, B., Chien, E. Y., Mol, C. D., Fenalti, G., Liu, W., Katritch, V., Abagyan, R., Brooun, A., Wells, P., Bi, F. C., Hamel, D. J., Kuhn, P., Handel, T. M., Cherezov, V., and Stevens, R. C. (2010) Structures of the CXCR4 chemokine GPCR with small-molecule and cyclic peptide antagonists. *Science 330*, 1066−1071.

(25) Crump, M. P., Gong, J. H., Loetscher, P., Rajarathnam, K., Amara, A., Arenzana-Seisdedos, F., Virelizier, J. L., Baggiolini, M., Sykes, B. D., and Clark-Lewis, I. (1997) Solution structure and basis for functional activity of stromal cell-derived factor-1; dissociation of CXCR4 activation from binding and inhibition of HIV-1. *EMBO J. 16*, 6996−7007.

(26) Trent, J. O., Wang, Z. X., Murray, J. L., Shao, W., Tamamura, H., Fujii, N., and Peiper, S. C. (2003) Lipid bilayer simulations of CXCR4 with inverse agonists and weak partial agonists. *J. Biol. Chem. 278*, 47136−47144.

(27) Doranz, B. J., Grovit-Ferbas, K., Sharron, M. P., Mao, S. H., Goetz, M. B., Daar, E. S., Doms, R. W., and O'Brien, W. A. (1997) A small-molecule inhibitor directed against the chemokine receptor CXCR4 prevents its use as an HIV-1 coreceptor. *J. Exp. Med. 186*, 1395−1400.

(28) Futaki, S., Nakase, I., Tadokoro, A., Takeuchi, T., and Jones, A. T. (2007) Arginine-rich peptides and their internalization mechanisms. *Biochem. Soc. Trans. 35*, 784−787.

(29) Nakase, I., Tadokoro, A., Kawabata, N., Takeuchi, T., Katoh, H., Hiramoto, K., Negishi, M., Nomizu, M., Sugiura, Y., and Futaki, S. (2007) Interaction of arginine-rich peptides with membrane-associated proteoglycans is crucial for induction of actin organization and macropinocytosis. *Biochemistry 46*, 492−501.
(30) Fuchs, S. M., and Raines, R. T. (2004) Pathway for polyarginine entry into mammalian cells. *Biochemistry 9*, 2438−2444.
(31) Jones, S. W., Christison, R., Bundell, K., Voyce, C. J., Brockbank, S. M., Newham, P., and Lindsay, M. A. (2005) Characterisation of cell-penetrating peptide-mediated peptide delivery. *Br. J. Pharmacol. 145*, 1093−1102.
(32) Yano, Y., Yano, A., Oishi, S., Sugimoto, Y., Tsujimoto, G., Fujii, N., and Matsuzaki, K. (2008) Coiled-coil tag--probe system for quick labeling of membrane receptors in living cell. *ACS Chem. Biol. 3*, 341−345.
(33) Zhang, Y., Foudi, A., Geay, J. F., Berthebaud, M., Buet, D., Jarrier, P., Jalil, A., Vainchenker, W., and Louache, F. (2004) Intracellular localization and constitutive endocytosis of CXCR4 in human CD34+ hematopoietic progenitor cells. *Stem Cells 22*, 1015−1029.
(34) Hesselgesser, J., Liang, M., Hoxie, J., Greenberg, M., Brass, L. F., Orsini, M. J., Taub, D., and Horuk, R. (1998) Identification and characterization of the CXCR4 chemokine receptor in human T cell lines: ligand binding, biological activity, and HIV-1 infectivity. *J. Immunol. 160*, 877−883.
(35) Honczarenko, M., Douglas, R. S., Mathias, C., Lee, B., Ratajczak, M. Z., and Silberstein, L. E. (1999) SDF-1 responsiveness does not correlate with CXCR4 expression levels of developing human bone marrow B cells. *Blood 94*, 2990−2998.
(36) Masuda, R.; Oishi, S.; Tanahara, N.; Ohno, H.; Hirasawa, A.; Tsujimoto, G.; Kodama, E.; Matsuoka, M.; Fujii, N. Development and application of fluorescent SDF-1 derivatives. *Future Med. Chem.* **2012**, in press.
(37) Tamamura, H., Hiramatsu, K., Mizumoto, M., Ueda, S., Kusano, S., Terakubo, S., Akamatsu, M., Yamamoto, N., Trent, J. O., Wang, Z., Peiper, S. C., Nakashima, H., Otaka, A., and Fujii, N. (2003) Enhancement of the T140-based pharmacophores leads to the development of more potent and bio-stable CXCR4 antagonists. *Org. Biomol. Chem. 1*, 3663−3669.
(38) Fujii, N., Oishi, S., Hiramatsu, K., Araki, T., Ueda, S., Tamamura, H., Otaka, A., Kusano, S., Terakubo, S., Nakashima, H., Broach, J. A., Trent, J. O., Wang, Z. X., and Peiper, S. C. (2003) Molecular-size reduction of a potent CXCR4-chemokine antagonist using orthogonal combination of conformation- and sequence-based libraries. *Angew. Chem., Int. Ed. 42*, 3251−3253.
(39) Partial CXCR4 internalization was induced even by 1 nM TF14016, which was consistent with the potent bioactivity for CXCR4 as reported.[37]
(40) Vida, T. A, and Emr, S. D. (1995) A new vital stain for visualizing vacuolar membrane dynamics and endocytosis in yeast. *J. Cell. Biol. 128*, 779−792.
(41) Harvey, J. R., Mellor, P., Eldaly, H., Lennard, T. W., Kirby, J. A., and Ali, S. (2007) Inhibition of CXCR4-mediated breast cancer metastasis: a potential role for heparinoids? *Clin. Cancer Res. 13*, 1562−1570.
(42) Roettger, B. F., Ghanekar, D., Rao, R., Toledo, C., Yingling, J., Pinon, D., and Miller, L. J. (1997) Antagonist-stimulated internalization of the G protein-coupled cholecystokinin receptor. *Mol. Pharmacol. 51*, 357−362.
(43) Gray, J. A., and Roth, B. L. (2001) Paradoxical trafficking and regulation of 5-HT(2A) receptors by agonists and antagonists. *Brain Res. Bull. 56*, 441−451.
(44) Pheng, L. H., Dumont, Y., Fournier, A., Chabot, J. G., Beaudet, A., and Quirion, R. (2003) Agonist- and antagonist-induced sequestration/internalization of neuropeptide Y Y1 receptors in HEK293 cells. *Br. J. Pharmacol. 139*, 695−704.

Bioconjugate Chemistry

Article

pubs.acs.org/bc

Mimicking Adhesive Functionalities of Blood Platelets using Ligand-Decorated Liposomes

Madhumitha Ravikumar, Christa L. Modery, Timothy L. Wong, Michael Dzuricky, and Anirban Sen Gupta, Ph.D.*

Department of Biomedical Engineering, Case Western Reserve University, Cleveland, Ohio 44106, United States

Supporting Information

ABSTRACT: Platelet transfusion is used for treating a variety of bleeding complications. Natural platelet-based transfusion products have very short storage life (3−7 days) and high risks of biological contamination and side effects. Consequently, there is significant clinical interest in synthetic platelet-mimetic constructs that can promote hemostasis, while allowing convenient large-scale production, easy portability, long storage life, and minimal biological risks. To this end, research efforts are being directed toward particles that can amplify aggregation of activated platelets or can mimic platelet's ability to undergo adhesion to various vascular matrix proteins. Here, we report on a synthetic construct design that combines the mimicry of platelet's shear-dependent adhesion to vWF and shear-independent adhesion to collagen under flow, on a single particle. For this, we have used 150-nm-diameter liposomes as model particles and have decorated their surface simultaneously with vWF-binding and collagen-binding recombinant protein fragments or synthetic peptide motifs. We demonstrate *in vitro* that these surface-modified liposomes are able to adhere onto vWF surfaces in a shear-dependent fashion and onto collagen surfaces in a shear-independent fashion under flow. Moreover, when the vWF-binding and the collagen-binding were integrated on a single liposomal platform, the resultant heteromultivalent liposomes showed significantly enhanced adhesion to a vWF/collagen mixed surface compared to liposomes bearing vWF-binding or collagen-binding ligands only, as long as the ligand motifs did not spatially interfere with each other. Altogether, our results establish the feasibility of efficiently mimicking platelet's dual adhesion mechanisms on synthetic particles.

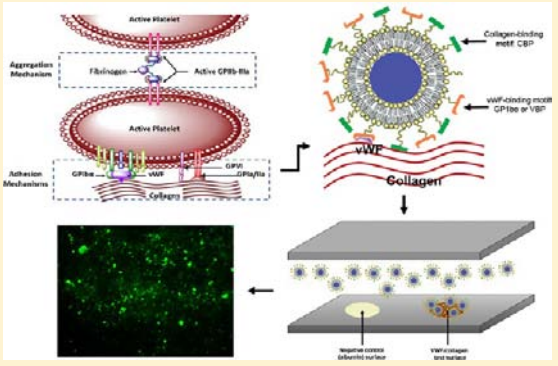

INTRODUCTION

Platelet transfusion plays a major role in the treatment of bleeding complications in patients with various hematologic or oncologic platelet disorders.[1−6] Additionally, platelet transfusion is often applied in presurgical settings and in traumatic injury for rapid staunching of heavy bleeding.[5,6] The current clinical platelet transfusions consist of allogeneic platelet concentrates resuspended in autologous plasma stored at ∼22 °C, which have a shelf life of only 3−7 days.[7−10] Other products based on natural platelets under clinical investigation are frozen platelets (−80 °C), cold-stored platelets (4 °C), photochemically treated platelets, lyophilized platelets, platelet-derived microparticles, and infusible platelet membranes (IPM).[7−10] Since all of these products are derived from pooled platelets of multiple donors, there is high risk of biologic (viral, protozoal, and bacterial) infections. The infection risk can be partly reduced by excluding high-risk individuals from the donor pool, serological testing of donor blood, and prestorage leukoreduction processes.[9−14] However, these further increase costs of platelet concentrate preparation. In addition, natural platelet-based products present risks of febrile nonhemolytic reactions, alloimmunization-induced refractoriness, graft-versus-host disease, acute lung injury risks, and immunosuppression.[15−18] Altogether, these factors severely limit the efficacy of natural platelet-based transfusion products. Consequently, there is significant clinical interest in synthetic constructs that can mimic or amplify platelet's hemostatic functionalities, while allowing large-scale preparation, reproducible quality, long storage life, and absence of biologic infections.[19]

Past approaches on mimicking platelet's hemostasis-relevant functions on synthetic platforms have mainly focused on amplifying platelet's "aggregation" functionality by decorating synthetic particle surfaces with aggregation-promoting biomolecules like Fibrinogen (Fg) or Fg-derived peptide sequences. For example, synthetic particle platforms like liposomes, albumin spheres, and synthetic polymeric particles have been surface-decorated with platelet membrane-derived glycoproteins,[20,21] Fg,[22,23] Fg-derived Arginine-Glycine-Aspartic Acid (RGD) peptides,[24] and Fg-derived H12 dodecapeptides.[25,26] All of these are essentially various designs of "superfibrinogen" particles that can amplify the aggregation of active platelets due to the increased surface-valency of their platelet-bridging motifs (i.e., Fg or Fg-derived peptides), compared to hexavalent Fg itself. However, in natural primary hemostasis, *platelet aggregation* is

Received: February 20, 2012
Revised: May 3, 2012
Published: May 20, 2012

dx.doi.org/10.1021/bc300086d | *Bioconjugate Chem.* 2012, 23, 1266−1275

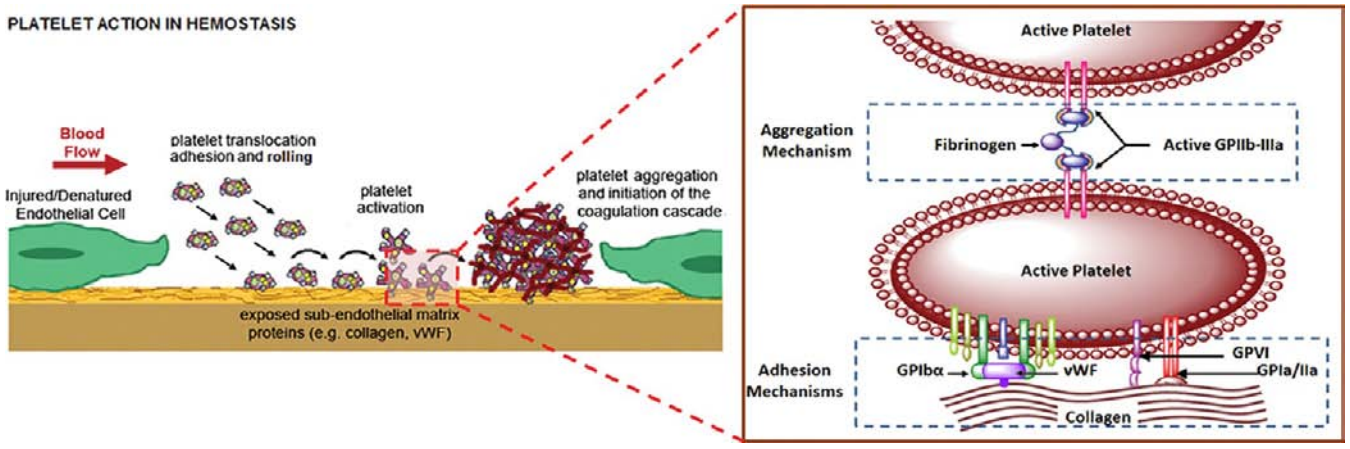

Figure 1. Schematic representation of molecular mechanisms showing adhesion and aggregation of blood platelets in primary hemostasis. Adhesion is mediated by binding of the extracellular domain of GPIbα of the platelet surface receptor GPIb/IX/V to vWF and binding of the platelet surface receptors GPIa/IIa and GPVI to collagen.

preceded by stable *platelet adhesion* at the injury site under blood flow[27,28] as shown in Figure 1.[27,28]

Platelet adhesion is mediated by shear-dependent binding of the GPIbα extracellular domain of the platelet surface glycoprotein GPIb/IX/V complex with von Willebrand Factor (vWF) secreted from the injured endothelium,[29,30] augmented by binding of platelet surface glycoproteins GPIa/IIa and GPVI[31,32] to sub-endothelial collagen. The vWF-binding helps in the initial arrest and rolling of platelets at the injury site, while collagen-binding stabilizes the adhered platelets under the hemodynamic flow environment. These adhesion mechanisms result in platelet activation signaling, ultimately leading to a ligand-binding conformational change of the platelet surface integrin GPIIb-IIIa, which then binds to Fg to promote aggregation of the activated platelets to form the primary hemostatic plug.[33,34] A few research approaches have investigated the mimicry of platelet's adhesion mechanisms by decoration of liposomes, albumin particles, or latex particles with adhesion-promoting motifs like recombinant GPIbα (vWF-binding) or GPIa/IIa (collagen-binding) fragments.[35−38] However, these designs have not demonstrated the integration of the dual adhesion mechanisms (simultaneous vWF-binding and collagen-binding). In addition, recombinant protein fragments are quite expensive for large-scale production, purification, and scale-up. Furthermore, they can also potentially present immunogenic risks.

Rationalizing from these attributes of past research, here we report on bioengineering of synthetic constructs where vWF-binding and collagen-binding ligand motifs are integrated on the same particle (Figure 2), and investigate their platelet-mimetic adhesive capabilities under physiologically relevant flow environment (wall shear stresses) *in vitro*, using a parallel plate flow chamber (PPFC). For vWF-binding, we have investigated a small synthetic peptide with amino acid sequence, **TRYLRIHPQSWVHQI**, that is derived from the C2 domain (residues 2303−2332) of the coagulation factor FVIII, which is known to form a complex with vWF prior to thrombin or factor Xa catalyzed activation in the coagulation cascade.[39] We have compared the vWF-binding of liposomes surface-decorated with this vWF-binding peptide (**VBP**) to liposomes surface-decorated with the previously reported recombinant GPIbα fragment. For collagen-binding, we have investigated a short 7-repeat of the Glycine(G)-Proline(P)-Hydroxyproline(O) tripeptide

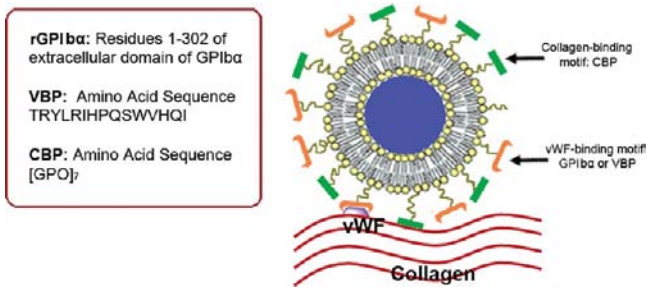

Figure 2. Design of heteromultivalent liposomes, surface-modified with vWF-binding, and collagen-binding ligand motifs that can mimic the adhesion mechanisms of platelets under flow.

(−[GPO]$_7$-), with helicogenic affinity to fibrillar collagen.[40−42] This small collagen-binding peptide (**CBP**) can promote adhesion to fibrillar collagen, but cannot activate quiescent platelets due to the absence of long triple-helical conformation. We have demonstrated that the vWF-binding constructs undergo enhanced adhesion under increasing wall shear, while the collagen-binding constructs undergo stable adhesion in an apparent shear-independent fashion. Furthermore, we have integrated simultaneous vWF-binding and collagen-binding motifs on the same liposome platform and have investigated their adhesion capability to a vWF/collagen mixed surface under flow, *in vitro*. In such heteromultivalent liposome surface-decoration, we have demonstrated that the platelet-mimetic dual adhesion mechanisms (simultaneous vWF-binding and collagen-binding) can be successfully achieved provided that the vWF-binding and the collagen-binding ligand motifs do not spatially interfere with each other while conjugated onto the liposome surface. Altogether, by surface engineering of liposomes via decoration of specific ligands, we demonstrate efficient molecular mimicry of platelet's dual adhesion mechanisms. This approach can be potentially adapted to various particle platforms to optimize the design of a platelet-mimetic synthetic bioconjugate construct.

EXPERIMENTAL PROCEDURES

Materials. Cholesterol, dimethyl sulfoxide (DMSO), and collagen were purchased from Sigma Aldrich (Saint Louis, MO, USA). The lipids distearyl phosphatidyl choline (DSPC), 2000 MW polyethylene glycol-modified distearyl phosphatidyl

dx.doi.org/10.1021/bc300086d | *Bioconjugate Chem.* 2012, 23, 1266−1275

ethanolamine (DSPE-PEG_{2000}), and carboxy-terminated polyethylene glycol-modified DSPE (DSPE-PEG_{2000}-COOH) were purchased from Avanti Polar Lipids (Alabaster, AL, USA). *N*-Hydroxysuccinimide-modified fluorescein (NHS-Fluorescein) was purchased from Invitrogen Corporation (Carlsbad, CA, USA). Human vWF (FXIII free) was purchased from Hematologic Technologies Incorporation (Essex Jn, VT, USA). The Parallel Plate Flow Chamber (PPFC) system was purchased from Glycotech (Gaithersburg, MD, USA).

Ligand Motifs. *vWF-Binding Motifs.* For vWF binding, a recombinant GPIbα fragment (**rGPIbα**) containing the vWF binding sites (residues 1 to 302) or a short-chain vWF-binding peptide (**VBP**) was used. The GPIbα fragment was expressed in CHO cells and isolated, adapting methods described by Murata et al.[43] The VBP, **TRYLRIHPQSWVHQI**, was synthesized using fluorenylmethyloxycarbonyl chloride (FMoc)-based solid-phase chemistry on a Knorr resin, and characterized using mass spectroscopy. Each vWF molecule has only one binding region for this peptide. Hence, we rationalized that a vWF-precoated surface or shear-enhanced multimerization of vWF on a collagen-coated surface will present multiple binding sites for multiple copies of this peptide decorated on the liposome surface, thereby providing a mechanism for enhanced adhesion of the liposomes with increasing shear.

Collagen-Binding Motifs. The CBP, $[\mathbf{GPO}]_7$, was also synthesized using FMoc-based solid-phase chemistry on Knorr resin and characterized using mass spectroscopy. The GPO trimer is based on amino acid repeats found in the native collagen structure. It has been reported that the activation of platelets usually caused by interaction with collagen through GPVI and GPIa/IIa can also potentially occur when platelets interact with collagen-derived peptides.[41,42] This can be a potential problem regarding decorating synthetic particle surfaces with collagen-derived peptides for binding of collagen, because *in vivo*, the constructs can potentially interact with quiescent blood platelets and systemically activate them, posing thromboembolic risks. However, Farndale et al. have reported that interaction of platelet receptors with collagen and the subsequent platelet activation mechanisms are dependent upon receptor clustering induced by multimeric long chain triple-helical fibrillar collagen and not by short collagen-mimetic peptide repeats.[44] In fact, it has been shown that GPO-trimer repeats as high as a 30-mer (10 repeats) only partially interact with platelet GPIa/IIa and GPVI integrins and are incapable of activating platelets, yet they can effectively bind to fibrillar collagen via helicogenic interaction.[45,46] Hence, we rationalized that our 7-mer short chain monomeric CBP will not activate quiescent platelets in circulation but can still allow binding of CBP-decorated liposomes to collagen-covered surface, under flow. The mass spectrometric characterization data of the peptides are available in the Supporting Information. Additionally, aggregometry data confirming the inability of both VBP and CBP to activate platelets is also available in the Supporting Information.

Ligand-Modified Liposomal Construct Fabrication. The rGPIbα, VBP, or CBP were conjugated to DSPE-PEG-COOH using carbodiimide-mediated amidation chemistry to form DSPE-PEG-ligand molecules, utilizing previously reported methods.[47,48] For lipid−peptide conjugation, the N-terminal amine of the peptide sequence was reacted with DSPE-PEG-COOH while all amino acid side-chains remained protected and the peptide itself still remained conjugated onto the solid-phase resin bead through its C-terminus. Hence, the carbodiimide-mediated conjugation reaction was selective to the N-terminus of the VBP and CBP peptides. Deprotection of the side-chain groups and the cleavage of the lipid−peptide conjugate from the resin was carried out only after this selective conjugation. Hence, it was not necessary to confirm that the conjugation reaction occurred only at the N-termini and not at the side chain amine groups. We have utilized this method extensively in preparing ligand-modified liposomes, as reported previously.[49,50] In the current studies, we followed exactly the same methods for the lipid−peptide conjugation reactions and assessed reaction efficiency using a ninhydrin assay. The assay showed peptide conjugation to have occurred at 95.7% ± 4.9% conjugation efficiency. To fluorescently label the liposomes, DSPE-Fluorescein (green fluorescence, $\lambda_{max} \approx 530$ nm) was synthesized by reacting the free amine ($-NH_2$) termini of DSPE with NHS-Fluorescein at basic pH. Specific proportions of the DSPE-PEG-rGPIbα, DSPE-PEG-VBP, or DSPE-PEG-CBP were combined with unmodified DSPE-PEG, DSPC, cholesterol, and DSPE-Fluorescein to fabricate peptide-decorated green fluorescent liposomal constructs, using the standard reverse-phase evaporation and extrusion technique.[51] The liposome size distribution, characterized by dynamic light scattering (DLS), was found to be ~150 nm diameter (Supporting Information).

Parallel Plate Flow Chamber (PPFC). The PPFC setup is appropriate for biomolecular interaction analysis under a dynamic shear flow environment.[52,53] In the PPFC, by maintaining Renyold's number in the "laminar" range ($\sim 10^5$), the wall shear stress (τ_w) can be modulated as a function of flow rate (Q) by

$$\tau_w = \frac{6\mu Q}{bh^2} \quad (1)$$

where μ = fluid viscosity, b = width of the chamber, and h = distance between plates. For our experiments, b/h was >20 and Q was maintained to provide τ_w in the range 5−55 dyn/cm^2, which covers a substantial range of physiological shear in blood flow.[54] Distinct circular areas on glass slides were coated with collagen, vWF, or 50:50 mixture of vWF/collagen (test surfaces) and bovine serum albumin (BSA, negative control surface with no adhesion specificity). The coated slides were vacuum-sealed into the PPFC for subsequent experiments.

Platelet-Mimetic Adhesion Studies under Flow *in Vitro*. For studying platelet-mimetic vWF-adhesive functionality, 2.5 mol % DSPE-PEG-rGPIbα or DSPE-PEG-VBP was combined with DSPC (49 mol %), cholesterol (45 mol %), DSPE-PEG (2.5 mol %), and DSPE-Fluorescein (1 mol %) to form the final liposomal construct. The fluorescein-labeled (green fluorescent, $\lambda_{max} = 530$ nm) liposomes, at a concentration of 10 μM total lipid, were allowed to flow through the PPFC in a closed loop over the vWF-coated and BSA-coated surface under various flow rates to produce wall shear stresses from 5 to 55 dyn/cm^2 for 30 min. After 30 min, flow of just PBS was maintained in an open loop for an additional 15 min in order to remove any loosely bound constructs and gain insight on the adhesion stability and retention of the constructs on the test and control surfaces. The slides were imaged at various time points (5, 15, 30, 35, and 45 min) of flow in the PPFC using an inverted epifluorescence microscope (Carl Zeiss Axio Observer D1) with a photometrics chilled CCD camera (Axiocam MRM) and a 63× objective. Images were collected using *Axiovision* software with fixed exposure times of 400 ms. From each image, extent of adhesion and retention was quantified by measuring surface-averaged fluorescence intensity using *Adobe Photoshop CS5* software. Statistical analysis of fluorescence intensity was performed using

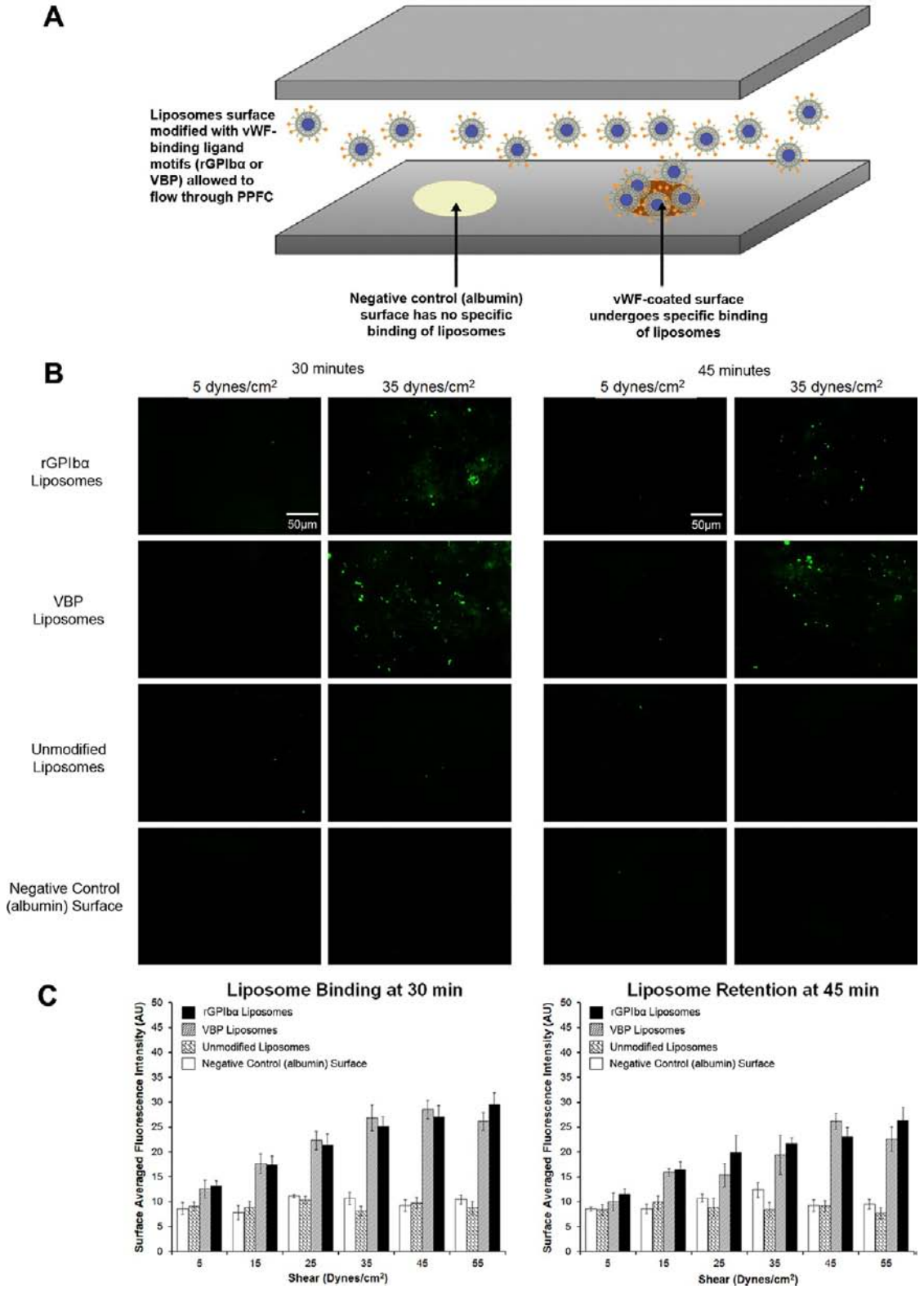

Figure 3. Representative results from PPFC studies using rGPIbα- or VBP-decorated liposomal constructs allowed flow over the vWF-coated surface versus the albumin surface. (**A**) Schematic of experimental setup. (**B**) Ligand-modified liposomes showed minimal adhesion and retention on the albumin surface and unmodified liposomes showed minimal adhesion and retention on the vWF surface. On the other hand, rGPIbα-modified and the VBP-modified liposomes both showed significant adhesion and retention on the vWF surface under flow. (**C**) Quantitative analysis of the adhesion (at 30 min) and retention (at 45 min) using surface-averaged fluorescence intensity shows that both rGPIbα-modified and VBP-modified liposomes undergo increasing adhesion and retention on vWF surface with increasing shear, mimicking the vWF-binding of platelets.

ANOVA and significance was considered as $p < 0.05$. Figure 3A shows a schematic view of the PPFC experimental setup and the expected interaction of the vWF-binding liposomal constructs with the test and control surface regions. In an additional

dx.doi.org/10.1021/bc300086d | *Bioconjugate Chem.* 2012, 23, 1266−1275

experimental design, we aimed to investigate if soluble vWF could adhere to collagen and multimerize under high shear stress, and then induce adhesion of VBP-decorated liposomes. This was inspired by the natural physiological mechanism where soluble vWF adheres to exposed subendothelial collagen, multimerizes under shear, and subsequently allows adhesion of platelets via interaction with platelet surface GPIbα. For this, green fluorescent VBP-modified liposomes and soluble FVIII-free human vWF were introduced into the PPFC and allowed to flow over collagen-coated surface or albumin-coated surface under high shear stress of 55 dyn/cm^2 for 5−30 min and the adhesion of the liposomes over time was imaged with epifluorescence microscopy using the PPFC setup described previously.

For studying platelet-mimetic collagen-adhesive functionality, 2.5 mol % DSPE-PEG-CBP was combined with DSPC (49 mol %), cholesterol (45 mol %), DSPE-PEG (2.5 mol %), and DSPE-Fluorescein (1 mol %) to form the final liposomal construct. These fluorescently labeled liposomes were allowed to flow through the PPFC over collagen-coated and BSA-coated surfaces in the same way as VBP-decorated liposomes (30 min in closed loop followed by 15 min open loop circulation of just PBS). Imaging at various time points and image analysis were carried out as before. Figure 5A shows a schematic view of the PPFC experimental setup and the expected interaction of the CBP-decorated liposomes with the test and control surfaces.

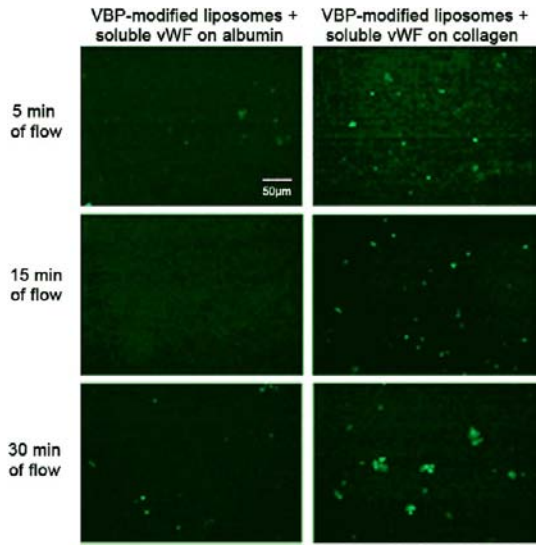

Figure 4. Representative fluorescent micrographs from PPFC experiments where VBP-modified liposomes were allowed to flow with soluble vWF over the collagen surface versus the albumin surface under high shear (55 dyn/cm^2). Soluble vWF cannot adhere and multimerize on the albumin surface, but can adhere and multimerize on the collagen surface. Consequently, with time (5 to 30 min of flow), soluble vWF formed larger multimerized areas on the collagen surface, allowing higher extent of adhesion of green fluorescent VBP-modified liposomes. Adhesion of VBP-modified liposomes on the albumin surface was minimal since vWF did not multimerize on the albumin surface.

For studying cumulative effects of simultaneous vWF and collagen-binding, 2.5 mol % DSPE-PEG-rGPIbα or DSPE-PEG-VBP and 2.5 mol % of DSPE-PEG-CBP were combined with DSPC (49 mol %), cholesterol (45 mol %), and DSPE-Fluorescein (1 mol %) to form the final heteromultivalently decorated liposomal constructs. These fluorescently labeled liposomes were allowed to flow in the PPFC over a surface coated with 50:50 vWF/collagen (mixed coating) under 5−55 dyn/cm^2 shear stress, and the imaging and analysis were carried out as before. For all adhesion studies, besides testing the interaction of ligand-modified liposomes on negative control albumin surfaces, additional control studies were also carried out by testing unmodified (no surface decoration) liposomes on vWF-coated, collagen-coated, or mixed-coated surfaces.

RESULTS

Platelet-Mimetic vWF Adhesion of Ligand-Decorated Liposomes under Flow *in Vitro*. Figure 3B shows a representative set of fluorescence images from PPFC experiments using rGPIbα-decorated liposomes and VBP-decorated liposomes on vWF-coated surfaces versus albumin-coated surfaces under flow. Although images were taken at six shear values between 5 and 55 dyn/cm^2 and at five time points during flow between 5 and 45 min for each of the liposomal constructs, representative fluorescent images are shown at only two shear values (5 and 35 dyn/cm^2) and two time points (30 and 45 min) for convenience. Figure 3C shows the quantitative analysis of surface-averaged fluorescence intensity values from the adhesion of the various liposomal constructs on vWF-coated surfaces over the entire shear stress range at 30 and 45 min. Statistical analysis of fluorescence intensity values shows that rGPIbα-decorated liposomal constructs undergo increased adhesion on the vWF-coated surfaces with increasing shear, while on albumin-coated surfaces, these constructs showed only minimal adhesion irrespective of shear stress values. VBP-decorated constructs also showed similar trends of increased adhesion with increasing shear. However, beyond 45 dyn/cm^2 shear stress values, the level of adhesion of the VBP-modified constructs was not found to increase further statistically. The unmodified liposomes showed minimal adhesion to vWF at all shear stresses.

Figure 4 shows representative fluorescent images from the additional experimental design involving flow of soluble vWF and VBP-modified liposomes over collagen or albumin surface under high shear stress. Representative results are shown for the highest shear stress value of 55 dyn/cm^2 for three time-points of 5, 15, and 30 min of flow. As evident from the results, green fluorescent VBP-modified liposomes are able to adhere when introduced in flow along with soluble vWF, to a collagen-coated surface, but not to an albumin-coated surface. Furthermore, the VBP-modified liposomes seemed to undergo enhanced amount of adhesion (larger fluorescent "patch" areas) with time, under the high shear value.

Platelet-Mimetic Collagen Adhesion of Ligand-Decorated Liposomes under Flow *in Vitro*. Figure 5B shows a representative set of fluorescence images from PPFC experiments using CBP-decorated liposomes on collagen-coated surfaces versus albumin-coated surfaces under flow. As before, the representative images are shown at only two shear values (5 and 35 dyn/cm^2) and two time points (30 and 45 min) for convenience. Figure 5C shows quantitative analysis of the surface-averaged fluorescence intensity values from the adhesion of the various liposomal constructs on collagen-coated surfaces over the entire shear stress range at 30 and 45 min. Statistical analysis of fluorescence intensity measurements shows the CBP-decorated liposomal constructs undergoing significant adhesion to collagen-coated surfaces under flow with no apparent shear-dependent effect, but minimal adhesion to albumin surfaces. In addition, the unmodified constructs showed minimal adhesion on collagen surfaces.

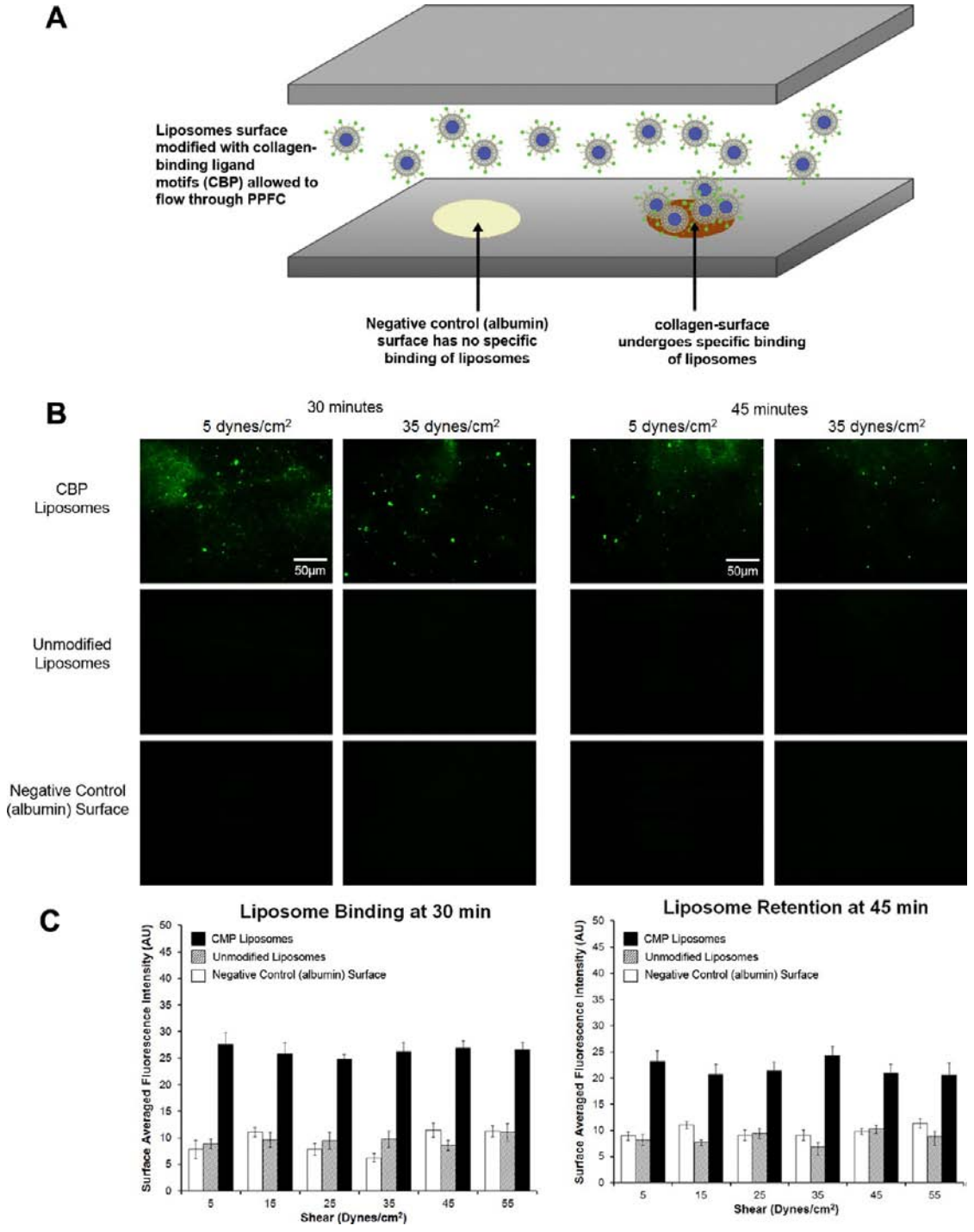

Figure 5. Representative results from PPFC studies using CBP-decorated liposomal constructs allowing flow over the collagen-coated surface versus the albumin surface. (**A**) Schematic of experimental setup. (**B**) Ligand-modified liposomes showed minimal adhesion and retention on the albumin surface, and the unmodified liposomes showed minimal adhesion and retention on the collagen surface. On the other hand, CBP-modified liposomes showed significant adhesion and retention on collagen surface under flow. (**C**) Quantitative analysis of the adhesion (at 30 min) and retention (at 45 min) using surface-averaged fluorescence intensity shows that the CBP-modified liposomes undergo enhanced adhesion and retention on the collagen surface in a shear-independent fashion.

Combining vWF-Adhesion and Collagen Adhesion on the Surface of Liposomes *in Vitro*. Figure 6A shows representative set of fluorescence images for adhesion of liposomes surface-decorated with both rGPIbα and CBP (2.5 mol % each), or both VBP and CBP (2.5 mol % each), onto a mixed coated (vWF/collagen 50:50) surface under flow in the PPFC. The adhesion of unmodified liposomes on these mixed coated surfaces and the adhesion of the ligand-modified liposomes on the negative control (albumin) surfaces are also shown in the figure for comparison. As before, the representative images are shown at only two shear values (5 and 35 dyn/cm^2) and two time points (30 and 45 min) for convenience. Figure 6B shows the quantitative analyses of the fluorescence intensity data from the adhesion of the various heteromultivalent liposomal

dx.doi.org/10.1021/bc300086d | *Bioconjugate Chem.* 2012, 23, 1266−1275

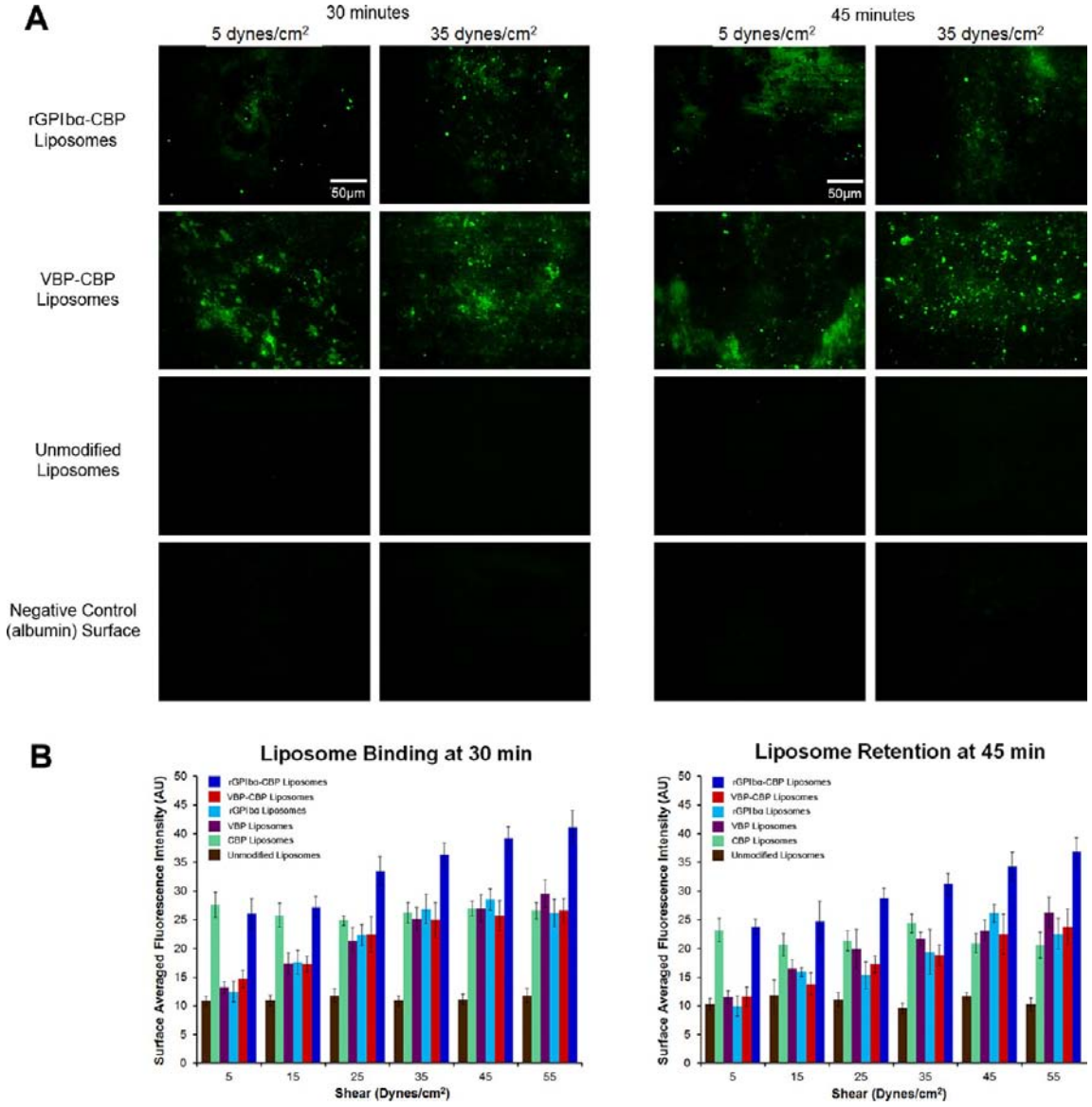

Figure 6. Representative results from PPFC studies using heteromultivalent liposomal constructs surface-modified with both vWF-binding (rGPIbα or VBP) and collagen-binding (CBP) ligand motifs allowed to flow over the vWF/collagen mixed (50:50) surface versus the albumin surface. (**A**) Heteromultivalent ligand-modified liposomes showed minimal adhesion and retention on the albumin surface and unmodified liposomes showed minimal adhesion and retention on the vWF/collagen mixed surface. On the other hand, liposomes modified simultaneously with both vWF-binding and collagen-binding ligand motifs showed significant adhesion and retention on the vWF/collagen mixed surface. (**B**) Quantitative analysis of the adhesion (at 30 min) and retention (at 45 min) using surface-averaged fluorescence intensity shows that the liposomes surface-modified simultaneously with rGPIbα and CBP (red bars) do not undergo statistically different adhesion and retention on the vWF/collagen surface compared to liposomes surface-modified with rGPIbα alone. However, liposomes modified with VBP and CBP (purple bars) undergo significantly enhanced adhesion and retention on the vWF/collagen surface with increasing shear, compared to liposomes surface-modified with VBP alone or CBP alone.

constructs over the entire shear stress range, compared with the adhesion data for liposomes bearing rGPIbα-decorations only, VBP-decorations only, and CBP-decorations only, all on mixed coated (vWF/collagen 50:50) surfaces. As evident from the fluorescent images as well as the quantitative data, liposomes bearing both rGPIbα and CMP showed enhanced adhesion on the mixed coated surface with increasing shear, but this was not statistically different from liposomes bearing rGPIbα modification alone. In comparison, liposomes bearing both VBP and CBP not only showed enhanced adhesion to the mixed coated surface under increasing shear, but the levels of adhesion were significantly higher than liposomes bearing VBP decoration or CBP decoration alone.

DISCUSSION

In the current research, we have investigated the mimicry of platelet's dual adhesion mechanisms on a model synthetic particle platform (liposome). Our results suggest that the shear-dependent enhancement in adhesion of the rGPIbα-decorated or VBP-decorated liposomal constructs were due to specific interactions of the ligands to the vWF surface, since the same liposomes showed only minimum adhesion on albumin surfaces. Furthermore, the results from experiments with VBP-decorated liposomes and soluble vWF under flow on collagen surfaces, indicate that possible multimerization of the soluble vWF with time on the collagen surface under high shear allows increased adhesion of VBP-decorated liposomes on the vWF-rich areas, as

dx.doi.org/10.1021/bc300086d | *Bioconjugate Chem.* 2012, 23, 1266–1275

evident from the formation of larger fluorescent patches of liposomes binding to vWF with time. Altogether, these results demonstrate successful mimicry of shear-dependent platelet adhesion to vWF using surface-engineered liposomes. The results from interaction of CBP-decorated liposomes on collagen-coated surface indicate that the adhesion is mostly shear-independent and is due to specific helicogenic interaction of the CBP with collagen. Hence, these data establish successful mimicry of the collagen-binding property of platelets with CBP-decorated liposomes. Here, it is also interesting to note that our CBP-decorated constructs showed higher adhesion capabilities under shear flow compared to GPIaIIa-modified liposomes reported previously.[55] We rationalize this observation by the fact that, because GPIaIIa is a big protein fragment, there are only a limited number of copies of it that can be decorated on a nanoscale particle surface (e.g., liposome), which would lead to a limited extent of binding interactions with a collagen substrate. On the other hand, since CBP is a small peptide, a lot more copies of it can be decorated on the liposome surface, leading to a higher extent of helicogenic interactions with collagen and hence a higher extent of adhesive property of the CBP-decorated constructs.

We would like to point out that, in all the *in vitro* experiments carried out in the current studies, the constructs were tested in the shear stress ranges of 5−55 dyn/cm^2 since this range covers the physiological shear conditions in most vasculature. The fluorescent images of construct adhesion are shown only for 5 dyn/cm^2 and 35 dyn/cm^2 as representative physiological low shear and high shear scenarios,[54] although image data was collected over the whole shear range of 5−55 dyn/cm^2. This collective data over the entire range is shown in the histogram plots of Figures 3, 5, and 6. Also, in these figures the histogram plots are shown only for the 30 min and 45 min time points as representative scenarios for convenience, although the analyses were carried out at multiple time points of 5, 15, 30, 35, and 45 min. The rationale for showing the 30 min time point was that it was the last time point up until which the constructs were allowed to "bind" to their target substrate in a recirculating loop flow. The rationale for showing the 45 min time point was that it was the last time point up until which the bound constructs were exposed to open loop flow of PBS to test binding strength and retention in a hemodynamically relevant shear environment. Beyond the 45 min time point, no further statistical variation in retention of constructs was observed in our experiments. We also point out that all the *in vitro* experiments had durations of ≤60 min, because in longer time periods, human blood tends to gradually clot *in vitro* and becomes unsuitable for experiments.

Analysis of the results from experiments with liposomes simultaneously bearing vWF-binding and collagen-binding motifs suggest that, when decorated simultaneously on the liposomal surface, the larger rGPIbα motif (∼300 amino acid residues) possibly masks the much smaller CBP motif (∼21 residues), thereby preventing the synergistic effect of simultaneous vWF-binding and collagen-binding by the liposomes. The resultant adhesion seems to happen primarily due to only rGPIbα−vWF interaction in a shear-dependent fashion. This observation is similar to the results demonstrated by Okamura et al.[56] where simultaneous decoration of a particle surface with rGPIbα motifs and Fg-mimetic H12 peptide motifs showed apparent masking of the peptide by the bigger protein fragment. In contrast, when VBP (∼15 amino acid residues) is used in conjunction with CBP for liposome surface decoration, these two small peptides possibly do not mask each other's specific interactions, and therefore, a combined effect of vWF binding and collagen binding becomes evident in the enhanced adhesion of the heteromultivalent liposomal constructs on the mixed coated surfaces under flow. Hence, we demonstrate that, by decorating a synthetic particle (liposome) surface with ligands binding simultaneously to vWF and collagen, and ensuring that the decorated ligands do not spatially mask each other, we can successfully mimic the hemostatically relevant dual adhesion mechanisms of platelets. Furthermore, simultaneous mimicry of these dual mechanisms of adhesion significantly enhanced the retention of the heteromultivalently modified liposomal constructs on vWF/collagen-coated surface, compared to liposomes bearing only one adhesion mechanism functionality (homomultivalent) or no functionality (unmodified). This is indicative of a much enhanced mimicry of natural platelet adhesion where the initial adhesion through vWF interaction is stabilized by subsequent supplemental binding interactions with collagen. In the current studies, we have used a 50:50 mixture of vWF/collagen as a representative test surface for demonstrating feasibility of our platelet adhesion-mimetic design. In addition, we have also tested surfaces of 100% collagen with vWF in the soluble form under flow. Our ongoing and future studies are directed at modulating the relative peptide densities on the particle surface and the relative substrate ratios on the test surface, to optimize our design. Results from these studies will become part of a future research publications.

We rationalize that the functional biomimetic design of a platelet-mimetic synthetic construct should incorporate both the "adhesion" functionalities and the "aggregation" functionalities of natural platelets. In fact, a recent report by Okamura et al. has demonstrated that synthetic particles surface-modified by "platelet aggregation" promoting H12 peptides and those surface-modified by "adhesion" promoting vWF-binding recombinant rGPIbα motifs, when introduced together in a thrombocytopenic bleeding model in a rabbits, showed a higher hemostatic efficacy via cumulative (adhesion plus aggregation) effects, compared to either of these particles alone.[56] Building on this rationale, we envision that platelet-mimetic hemostatic efficacy of synthetic constructs can be further enhanced if the "aggregation"-promoting component and "adhesion"-promoting component can be combined on the same particle. Therefore, in subsequent studies, we will combine the adhesion-promoting VBP and CBP motifs along with aggregation-promoting Fg-mimetic RGD peptide motifs on the same liposome, and investigate whether these functionally integrated constructs can themselves adhere to vWF/collagen surfaces under flow and promote recruitment and aggregation of platelets at the sites of liposome adhesion.

It is to be noted that the model particle used in our studies were spherical unilamellar liposomes about 150 nm in diameter. Several recent mathematical modeling, as well as experimental, studies have demonstrated that there exist significant correlations between the shape and size of particles to their location in hemodynamically relevant flow patterns.[57−59] For natural platelets, their hemostatic functions at the vessel wall depend upon their ability of "margination" to the wall injury site through RBCs and other blood components. This hemodynamic migration is significantly influenced by platelet's shape and size.[60] On the basis of such observations, we rationalize that an additional critical component of synthetic platelet design will be identification of the optimum particle geometry (size and shape) that can facilitate enhanced wall-margination of the particles. We envision that, by integration of margination-favoring optimal

physical parameters (size and shape) with adhesion- and aggregation-promoting optimal biological parameters (chemistry and density of ligand modifications), an ideal biomimetic design of synthetic platelet can be achieved. Also, these design components and resultant insight can provide novel avenues to target such particles as efficient drug delivery vehicles to vascular disease sites with exposed vWF or collagen.

■ ASSOCIATED CONTENT

Supporting Information

The peptides used for decorating liposomes were characterized by MALDI-TOF mass spectrometry. The GPIbα fragment raised by recombinant technology in CHO cells was characterized by Western Blot. The risk of platelet activation and resultant aggregation by VBP and CBP peptides was assessed by aggregometry. The liposome size distribution was characterized by dynamic light scattering. Representative results from these characterization studies are shown. This material is available free of charge via the Internet at http://pubs.acs.org.

■ AUTHOR INFORMATION

Corresponding Author

*E-mail: axs262@case.edu.

Notes

The authors declare no competing financial interest.

■ ACKNOWLEDGMENTS

The research was partly supported by American Heart Association Beginning-Grant-in-Aid #0765371B and Case Coulter Translational Research Partnership pilot funding. The authors would also like to acknowledge the facilities provided by the Center for Cardiovascular Biomaterials (CCB) in the department of Biomedical Engineering at Case Western Reserve University. MALDI-TOF support was funded by NSF Grant No. MRI-0821515 (PI: Rowan).

■ REFERENCES

(1) Mohanty, D. (2009) Current concepts in platelet transfusion. *Asian J. Transfus. Sci. 3*, 18−21.
(2) Pisciotto, P. T., Benson, K., Hume, H., Glassman, A. B., Oberman, H., Popovsky, M., Hines, D., and Anderson, K. (1995) Prophylactic versus therapeutic platelet transfusion practices in hematology and/or oncology patients. *Transfusion 35*, 498−502.
(3) Stroncek, D. F., and Rebulla, P. (2007) Platelet transfusions. *Lancet 370*, 427−38.
(4) Wallace, E. L., Surgenor, D. M., Hao, H. S., An, J., Chapman, R. H., and Churchill, W. H. (1993) Collection and transfusion of blood and blood components in the United States, 1989. *Transfusion 33*, 139−44.
(5) Heal, J. M., and Blumberg, N. (2004) Optimizing platelet transfusion therapy. *Blood Rev. 18*, 149−65.
(6) Krug, E. G., Sharma, G. K., and Lozano, R. (2000) The global burden of injuries. *Am. J. Public Health 90*, 523−6.
(7) Lee, D. H., and Blajchman, M. A. (2000) Platelet substitutes and novel platelet products. *Expert Opin. Invest. Drugs 9*, 457−69.
(8) Lee, D. H., and Blajchman, M. A. (2001) Novel treatment modalities: new platelet preparations and substitutes. *Br. J. Hamaetol. 114*, 496−505.
(9) Moroff, G., and Holme, S. (1991) Concepts about current conditions for the preparation and storage of platelets. *Transfus. Med. Rev. 5*, 48−59.
(10) Murphy, S. (1985) Platelet storage for transfusion. *Semin. Hematol. 22*, 165−77.
(11) Bordin, J. O., Heddle, N. M., and Blajchman, M. A. (1994) Biologic effects of leukocytes present in transfused cellular blood products. *Blood 84*, 1703−21.
(12) Corash, L. (1998) Inactivation of viruses, bacteria, protozoa, and leukocytes in platelet concentrates. *Vox Sang. 74* (Suppl 2), 173−6.
(13) Heddle, N. M., Klama, L. N., Griffith, L., Roberts, R., Shukla, G., and Kelton, J. G. (1993) A prospective study to identify the risk factors associated with acute reactions to platelet and red cell transfusions. *Transfusion 33*, 794−7.
(14) Schreiber, G. B., Busch, M. P., Kleinman, S. H., and Korelitz, J. J. (1996) The risk of transfusion-transmitted viral infections. The Retrovirus Epidemiology Donor Study. *N. Engl. J. Med. 334*, 1685−90.
(15) Blajchman, M. A. (1998) Immunomodulatory effects of allogeneic blood transfusions: clinical manifestations and mechanisms. *Vox Sang. 74* (Suppl 2), 315−9.
(16) Novotny, V. M., Doxiadis, II, and Brand, A. (1999) The reduction of HLA class I expression on platelets: a potential approach in the management of HLA-alloimmunized refractory patients. *Transfus. Med. Rev. 13*, 95−105.
(17) Orlin, J. B., and Ellis, M. H. (1997) Transfusion-associated graft-versus-host disease. *Curr. Opin. Hematol. 4*, 442−8.
(18) Slichter, S. J. (1998) Platelet refractoriness and alloimmunization. *Leukemia 12* (Suppl 1), S51−3.
(19) Blajchman, M. A. (1999) Substitutes for success. *Nat. Med. 5*, 17−8.
(20) Baldassare, J. J., Tarver, A. P., Henderson, P. A., Mackin, W. M., Sahagan, B., and Fisher, G. J. (1993) Reconstitution of thromboxane A2 receptor-stimulated phosphoinositide hydrolysis in isolated platelet membranes: involvement of phosphoinositide-specific phospholipase C-beta and GTP-binding protein Gq. *Biochem. J. 291* (Pt 1), 235−40.
(21) Rybak, M. E., and Renzulli, L. A. (1993) A liposome based platelet substitute, the plateletsome, with hemostatic efficacy. *Biomater. Artif. Cells Immobilization Biotechnol. 21*, 101−18.
(22) Davies, A. R., Judge, H. M., May, J. A., Glenn, J. R., and Heptinstall, S. (2002) Interactions of platelets with Synthocytes, a novel platelet substitute. *Platelets 13*, 197−205.
(23) Levi, M., Friederich, P. W., Middleton, S., de Groot, P. G., Wu, Y. P., Harris, R., Biemond, B. J., Heijnen, H. F., Levin, J., and ten Cate, J. W. (1999) Fibrinogen-coated albumin microcapsules reduce bleeding in severely thrombocytopenic rabbits. *Nat. Med. 5*, 107−11.
(24) Bertram, J. P., Williams, C. A., Robinson, R., Segal, S. S., Flynn, N. T., and Lavik, E. B. (2009) Intravenous hemostat: nanotechnology to halt bleeding. *Sci. Transl. Med. 1*, 11ra22.
(25) Okamura, Y., Fujie, T., Nogawa, M., Maruyama, H., Handa, M., Ikeda, Y., and Takeoka, S. (2008) Haemostatic effects of polymerized albumin particles carrying fibrinogen gamma-chain dodecapeptide as platelet substitutes in severely thrombocytopenic rabbits. *Transfus. Med. 18*, 158−66.
(26) Okamura, Y., Takeoka, S., Eto, K., Maekawa, I., Fujie, T., Maruyama, H., Ikeda, Y., and Handa, M. (2009) Development of fibrinogen gamma-chain peptide-coated, adenosine diphosphate-encapsulated liposomes as a synthetic platelet substitute. *J. Thromb. Haemost. 7*, 470−7.
(27) Michelson, A. D., and Newburger, P. E. (2007) Platelets and leukocytes: aggregate knowledge. *Blood 110*, 794−795.
(28) Spencer, F. A., and Becker, R. C. (1997) Platelets: Structure, Function, and Their Fundamental Contribution to Hemostasis and Pathologic Thrombosis, in *Textbook of Coronary Thrombosis and Thrombolysis* (Becker, R. C., Ed.) pp 31−49, Springer US, New York.
(29) Berndt, M. C., Shen, Y., Dopheide, S. M., Gardiner, E. E., and Andrews, R. K. (2001) The vascular biology of the glycoprotein Ib-IX-V complex. *Thromb. Haemost. 86*, 178−88.
(30) Ruggeri, Z. M., and Mendolicchio, G. L. (2007) Adhesion mechanisms in platelet function. *Circ. Res. 100*, 1673−85.
(31) Clemetson, K. J., and Clemetson, J. M. (2001) Platelet collagen receptors. *Thromb. Haemost. 86*, 189−97.
(32) Nieswandt, B., and Watson, S. P. (2003) Platelet-collagen interaction: is GPVI the central receptor? *Blood 102*, 449−61.
(33) D'Souza, S. E., Ginsberg, M. H., Matsueda, G. R., and Plow, E. F. (1991) A discrete sequence in a platelet integrin is involved in ligand recognition. *Nature 350*, 66−8.

(34) Pytela, R., Pierschbacher, M. D., Ginsberg, M. H., Plow, E. F., and Ruoslahti, E. (1986) Platelet membrane glycoprotein IIb/IIIa: member of a family of Arg-Gly-Asp--specific adhesion receptors. *Science 231*, 1559−62.
(35) Nishiya, T., Kainoh, M., Murata, M., Handa, M., and Ikeda, Y. (2002) Reconstitution of adhesive properties of human platelets in liposomes carrying both recombinant glycoproteins Ia/IIa and Ib alpha under flow conditions: specific synergy of receptor-ligand interactions. *Blood 100*, 136−142.
(36) Nishiya, T., Murata, M., Handa, M., and Ikeda, Y. (2000) Targeting of liposomes carrying recombinant fragments of platelet membrane glycoprotein Ib alpha to immobilized von Willebrand factor under flow conditions. *Biochem. Biophys. Res. Commun. 270*, 755−760.
(37) Takeoka, S., Teramura, Y., Ohkawa, H., Ikeda, Y., and Tsuchida, E. (2000) Conjugation of von Willebrand factor-binding domain of platelet glycoprotein IB alpha to size-controlled albumin microspheres. *Biomacromolecules 1*, 290−295.
(38) Teramura, Y., Okamura, Y., Takeoka, S., Tsuchiyama, H., Narumi, H., Kainoh, M., Handa, M., Ikeda, Y., and Tsuchida, E. (2003) Hemostatic effects of polymerized albumin particles bearing rGPIa/IIa in thrombocytopenic mice. *Biochem. Biophys. Res. Commun. 306*, 256−60.
(39) Nogami, K., Shirria, M., Giddings, J. C., Takeyama, M., Tanaka, I., and Yoshioka, A. (2007) Relationship between the binding sites for von Willebrand factor, phospholipid, and human factor VIII c2 inhibitor Alloantibodies within the factor VIII c2 domain. *Int. J. Hematol. 85*, 317−322.
(40) Rao, G. H. R., Fields, C. G., White, J. G., and Fields, G. B. (1994) Promotion of human platelet-adhesion and aggregation by a synthetic, triple-helical mini-collagen. *J. Biol. Chem. 269*, 13899−13903.
(41) Cejas, M. A., Chen, C., Kinney, W. A., and Maryanoff, B. E. (2007) Nanoparticles that display short collagen-related peptides. Potent stimulation of human platelet aggregation by triple helical motifs. *Bioconjugate Chem. 18*, 1025−1027.
(42) Cejas, M. A., Kinnney, W. A., Chen, C., Vinter, J. G., Almond, H. R., Balss, K. M., Maryanoff, C. A., Schmidt, U., Breslav, M., Mahan, A., Lacy, E., and Maryanoff, B. E. (2008) Thrombogenic collagen-mimetic peptides: Self-assembly of triple helix-based fibrils driven by hydrophobic interactions. *Proc. Natl. Acad. Sci. U.S.A. 105*, 8513−8518.
(43) Murata, M., Ware, J., and Ruggeri, Z. M. (1991) Site-directed mutagenesis of a soluble recombinant fragment of platelet glycoprotein Ib-alpha-demonstrating negatively charged residues involved in vonwillebrand-factor binding. *J. Biol. Chem. 266*, 15474−15480.
(44) Farndale, R. W. (2006) Collagen-induced platelet activation. *Blood Cells, Mol. Dis. 36*, 162−165.
(45) Mo, X., An, Y. J., Yun, C. S., and Yu, S. M. (2006) Nanoparticle-assisted visualization of binding interactions between collagen mimetic peptide and collagen fibers. *Angew. Chem., Int. Ed. 45*, 2267−2270.
(46) Wang, A. Y., Foss, C. A., Leong, S., Mo, X., Pomper, M. G., and Yu, S. M. (2008) Spatio-temporal modification of collagen scaffolds mediated by triple helical propensity. *Biomacromolecules 9*, 1755−1763.
(47) Nobs, L., Buchegger, F., Gurny, R., and Allemann, E. (2004) Current methods for attaching targeting ligands to liposomes and nanoparticles. *J. Pharm. Sci. 93*, 1980−1992.
(48) Simpura, I. (2007) CTT Cancer Targeting Technologies OY, United States.
(49) Sen Gupta, A., Huang, G., Lestini, B. J., Sagnella, S., Kottke-Marchant, K., and Marchant, R. E. (2005) RGD-modified liposomes targeted to activated platelets as a potential vascular drug delivery system. *Thrombosis Haemostasis 93*, 106−114.
(50) Huang, G., Zhou, Z., Srinivasan, R., Penn, M. S., Kottke-Marchant, K., Marchant, R. E., and Gupta, A. S. (2008) Affinity manipulation of surface-conjugated RGD peptide to modulate binding of liposomes to activated platelets. *Biomaterials 29*, 1676−85.
(51) Szoka, F., Olson, F., Heath, T., Vail, W., Mayhew, E., and Papahadjopoulos, D. (1980) Preparation of unilamellar liposomes of intermediate size (0.1−0.2-Mumm) by a combination of reverse phase evaporation and extrusion through polycarbonate membranes. *Biochim. Biophys. Acta 601*, 559−571.
(52) Bacabac, R. G., Smit, T. H., Cowin, S. C., Van Loon, J. J., Nieuwstadt, F. T., Heethaar, R., and Klein-Nulend, J. (2005) Dynamic shear stress in parallel-plate flow chambers. *J. Biomech. 38*, 159−67.
(53) Sakhalkar, H. S., Dalal, M. K., Salem, A. K., Ansari, R., Fu, J., Kiani, M. F., Kurjiaka, D. T., Hanes, J., Shakesheff, K. M., and Goetz, D. J. (2003) Leukocyte-inspired biodegradable particles that selectively and avidly adhere to inflamed endothelium in vitro and in vivo. *Proc. Natl. Acad. Sci. U. S. A. 100*, 15895−900.
(54) Kroll, M. H., Hellums, J. D., McIntire, L. V., Schafer, A. I., and Moake, J. L. (1996) Platelets and shear stress. *Blood 88*, 1525−41.
(55) Kainoh, M, and Tanaka, T (2002) Production of soluble integrin $\alpha 2\beta 1$ heterodimer complex functionally in vitro and in vivo. *Biochem. Biophys. Res. Commun. 290*, 305−310.
(56) Okamura, Y., Handa, M., Suzuki, H., Ikeda, Y., and Takeoka, S. (2006) New strategy of platelet substitutes for enhancing platelet aggregation at high shear rates: cooperative effects of a mixed system of fibrinogen gamma-chain dodecapeptide- or glycoprotein Ibalpha-conjugated latex beads under flow conditions. *J. Artif. Organs 9*, 251−8.
(57) AlMomani, T., Udaykumar, H. S., Marshall, J. S., and Chandran, K. B. (2008) Micro-scale dynamic simulation of erythrocyte-platelet interaction in blood flow. *Ann. Biomed. Eng. 36*, 905−20.
(58) Charoenphol, P., Mocherla, S., Bouis, D., Namdee, K., Pinsky, D. J., and Eniola-Adefeso, O. (2011) Targeting therapeutics to the vascular wall in atherosclerosis--carrier size matters. *Atherosclerosis 217*, 364−70.
(59) Decuzzi, P., Lee, S., Bhushan, B., and Ferrari, M. (2005) A theoretical model for the margination of particles within blood vessels. *Ann. Biomed. Eng. 33*, 179−90.
(60) Aarts, P. A., van den Broek, S. A., Prins, G. W., Kuiken, G. D., Sixma, J. J., and Heethaar, R. M. (1988) Blood platelets are concentrated near the wall and red blood cells, in the center in flowing blood. *Arteriosclerosis 8*, 819−24.

Bioconjugate Chemistry

Article

pubs.acs.org/bc

Efficient Transfection of Hepatocytes Mediated by mRNA Complexed to Galactosylated Cyclodextrins

Nathalie Symens,[†] Alejandro Méndez-Ardoy,[‡] Alejandro Díaz-Moscoso,[§,#] Elena Sánchez-Fernández,[§,⊥] Katrien Remaut,[†] Joseph Demeester,[†] José M. García Fernández,[§] Stefaan C. De Smedt,[†] and Joanna Rejman*[,†]

[†]Laboratory of General Biochemistry and Physical Pharmacy, Ghent University, Harelbekestraat 72, B-9000 Ghent, Belgium

[‡]Departamento de Química Organica, Universidad de Sevilla, c/ Profesor Garcia Gonzalez 1, E-41012 Sevilla, Spain

[§]Instituto de Investigaciones Químicas (IIQ), CSIC-Universidad de Sevilla, Américo 49, Isla de Cartuja, E-41092 Sevilla, Spain

Supporting Information

ABSTRACT: In this study, we aimed at specific targeting of polycationic amphiphilic cyclodextrins (paCDs) to HepG2 cells via the asialoglycoprotein receptor (ASGPr). The transfection efficiencies of paCDs modified with galactose moieties were evaluated. In preliminary experiments, attempts to transfect HepG2 cells with pDNA complexed with different modified paCDs resulted in very low transfection levels. In additional series of experiments, we found out that nucleic acid/cyclodextrin complexes (CDplexes) were efficiently taken up by the cells and that photochemical internalization, which facilitates release from endosomes, did not improve transfection. Further experiments showed that pDNA can be readily released from the CDplexes when exposed to negatively charged vesicles. These observations imply that the lack of transfection cannot be attributed to a lack of internalization, release of CDplexes from the endosomal compartment, or release of free pDNA from the CDplexes. This in turn suggests that the nuclear entry of the pDNA represents the main limiting factor in the transfection process. To verify that HepG2 cells were transfected with targeted CDplexes containing mRNA, which does not require entry into the nucleus for being translated. With mRNA encoding the green fluorescent protein, fractions of GFP-positive cells of up to 31% were obtained. The results confirmed that the galactosylated complexes are specifically internalized via the ASGPr.

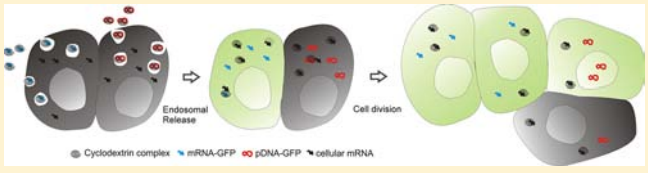

INTRODUCTION

Although the liver has unique features which make it attractive for *in vivo* and *ex vivo* gene delivery, no effective treatment of any liver-associated genetic disease has been obtained thus far despite many years of research on viral and nonviral vectors.[1,2] Several problems still have to be overcome before gene-therapeutic treatment of liver disease might become a reality. The formation of aggregates of vectors and blood components, which may occur upon systemic administration, should be prevented.[3] The induction of host immune responses against the transgene product and/or the vector[4] is another major hurdle which needs to be overcome, possibly by the use of liver-specific promoters,[5,6] hepatocyte-specific targeting,[7] and/or the use of poly(ethylene glycol) (PEG) moieties.[8] Gene delivery by means of nonviral vectors meets with additional obstacles at the intracellular level, which mostly do not present a problem for viral vectors.[9−11] The major ones are the escape of the delivered genetic material from the endosomal compartment, and its translocation into the nucleus.[12]

Recently, a new family of polycationic amphiphilic cyclodextrins (paCDs) has been developed. These paCDs are equipped with thiourea segments, polycationic clusters, and lipophilic tails. They were shown to efficiently complex polyanionic nucleic acids using thiourea segments together with polycationic clusters.[13−16] In the present work, a paCD derivative bearing 14 hexanoyl chains at the secondary hydroxyl face and 21 protonable amino groups at the primary face (Figure 1, Hex-CD-N_{21}) will be used as a reference compound. The resulting positively charged nucleic acid/cyclodextrin complexes (CDplexes) (Figure 2) can interact with the negatively charged proteoglycans at the cell surface and be taken up by endocytosis.[17−19] Involvement of the lipophilic tails in the internalization and endosomal release process is probably of minor importance, because it is conceivable that the hydrocarbon chains are oriented toward the inner core of the CDplex, which will limit their interaction with plasma and endosomal membrane lipids.[15]

The general scheme for the synthesis of paCDs allows the introduction of additional functional elements allowing visualization or targeting.[15,20] We hypothesized that this approach could be exploited to design paCD-systems for hepatocyte-specific cell uptake by the incorporation of multivalent D-galactose ligands which could interact with the asiologlycoprotein receptor (ASGPr).[21] The ASGPr is predominantly

Received: February 28, 2012
Revised: May 3, 2012
Published: June 5, 2012

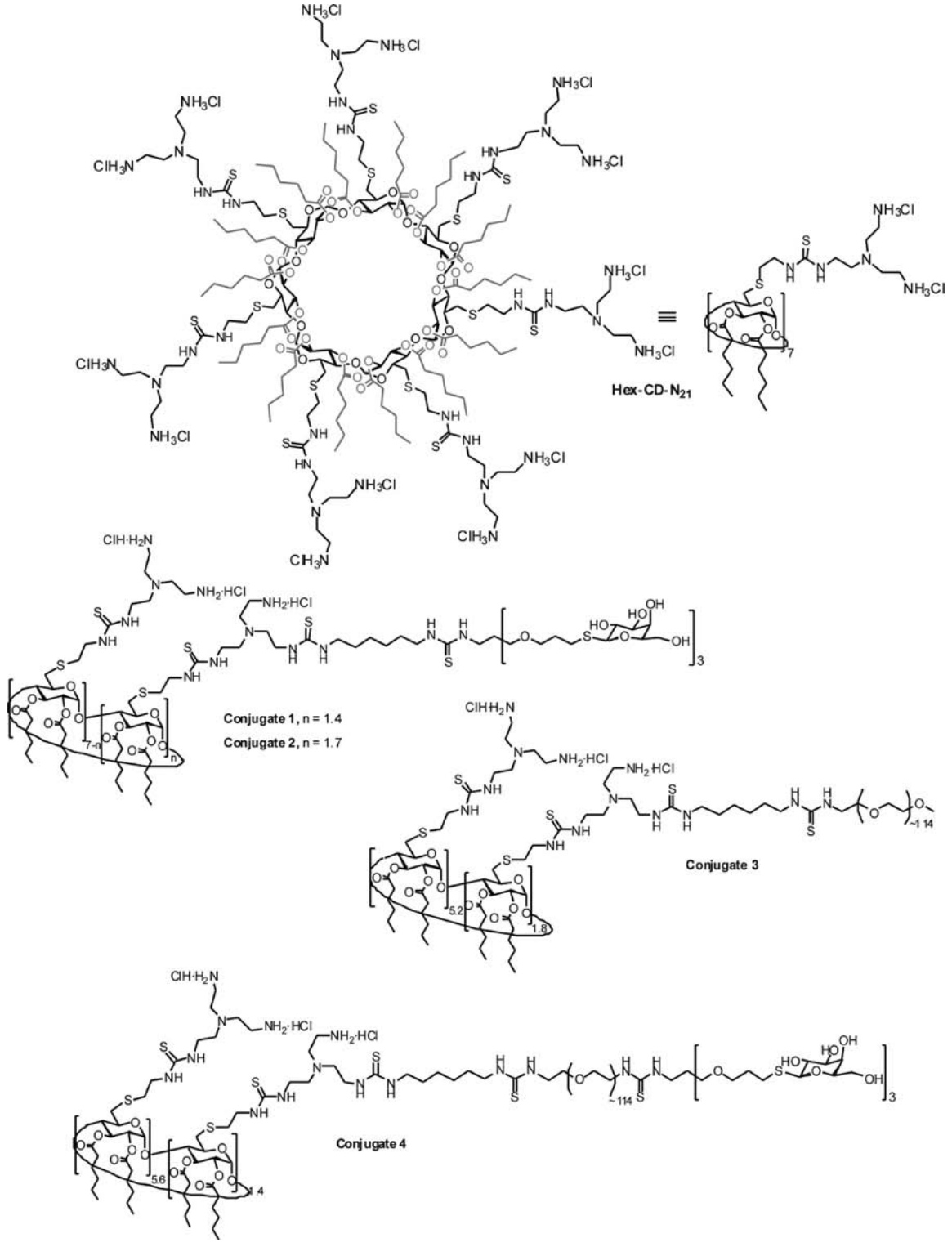

Figure 1. Chemical structures of modified polycationic amphiphilic cyclodextrins: reference hexanoylated CD with 21 potentially protonable nitrogens (**Hex-CD-N_{21}**; only the primary amino groups are represented as the corresponding hydrochlorides according to the microanalytical data of the synthesized compound), 10% triantennary-galactose-bearing reference CD (**conjugate 1**; Gal10CDs), 12% triantennary-galactose-bearing reference CD (**conjugate 2**; Gal12CDs), 13% thio-PEG5000-bearing reference CD (**conjugate 3**; PEGCDs) and 10% thio-PEG5000-triantennary-galactose-bearing reference CD (**conjugate 4**; GalPEGCDs). These abbreviations are used throughout the text.

expressed on the basolateral surface of mammalian hepatocytes and is responsible for the clearance of glyco- and lipoproteins.[22] The extracellular domain of the receptor specifically recognizes and binds ligands with terminal galactose (Gal) or *N*-acetyl-galactosamine (Gal*N*Ac) residues upon which clathrin-mediated internalization of the receptor−ligand complex occurs, which provides a unique means for the development of liver-specific carriers, for drug and gene delivery to the hepatic parenchymal cells.[23] Then, ASGPr-ligand containing endosomes are captured by microtubules just below the actin

dx.doi.org/10.1021/bc3001003 | *Bioconjugate Chem.* 2012, 23, 1276−1289

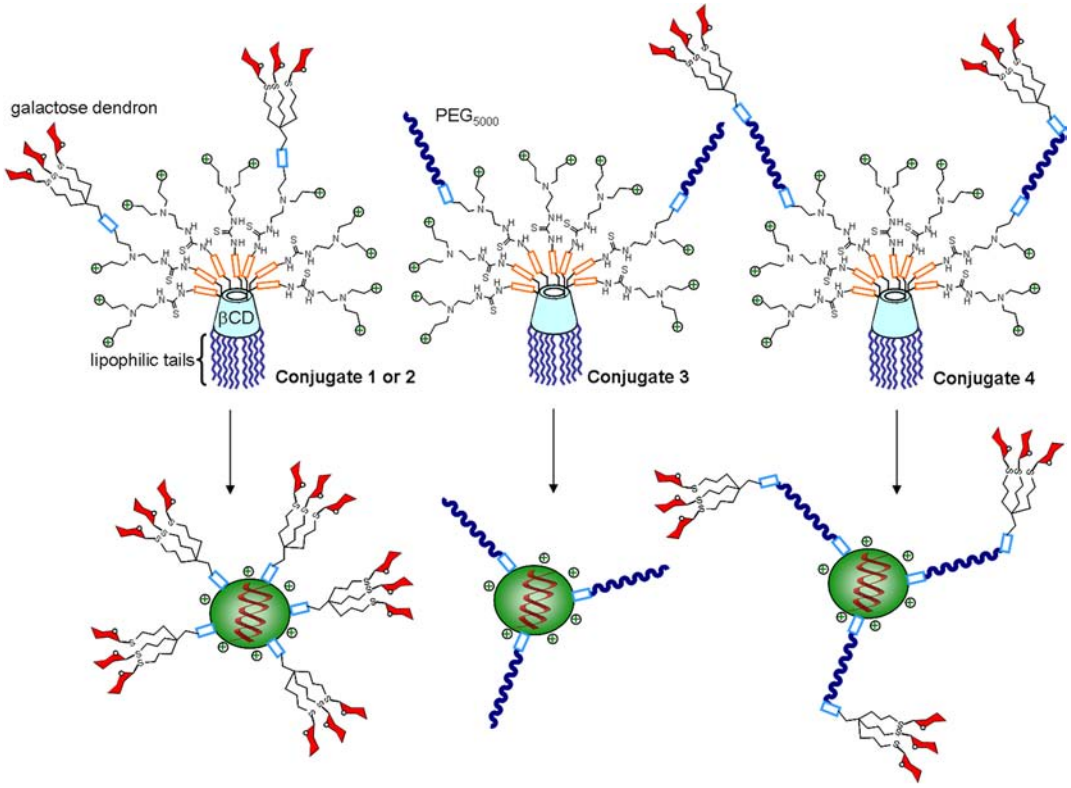

Figure 2. Schematic representation of the polycationic amphiphilic cyclodextrin derivatives prepared in this work (top) and of the different CDplexes which are generated after complexation with nucleic acids (down). The positive charges represent protonated amino groups.

Scheme 1. Synthesis of Modified paCDs[a]

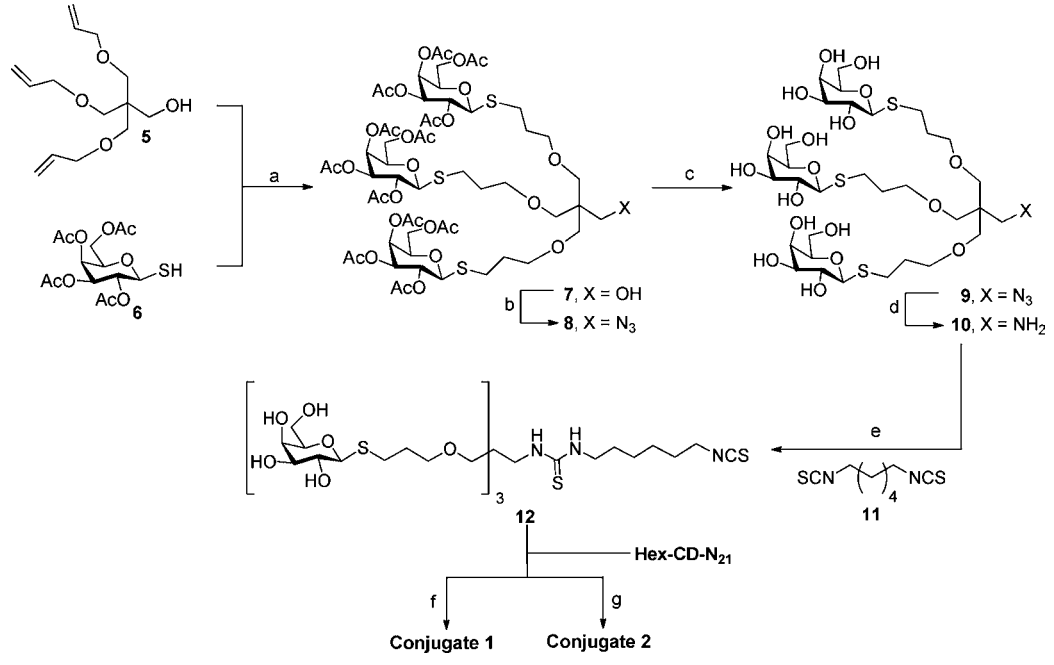

[a]Reaction scheme of 10% tri-antennary-galactose-bearing reference CDs (**conjugate 1**; Gal10CDs) or 12% tri-antennary-galactose-bearing reference CDs (**conjugate 2**; Gal12CDs). Reagents and conditions: (a) AIBN, dioxane, 75 °C, 9 h, 64%. (b) i. Tf_2O, DCM, py, −25 °C, 30 min. ii. NaN_3, DMF, RT, 17 h, 87%. (c) NaOMe, MeOH, RT, 3h, Amberlite 120 (H^+), 99%. (d) TPP, 1:3 water-dioxane; then NH_4OH, RT, 24 h, 99%. (e) acetone-water, $NaHCO_3$, RT, 20 h, 99%. (f) DMF, Et_3N, RT, 4 days, 75%. (g) DMF, Et_3N, RT, 4 days, 78%.

layer at the cell periphery and they are actively transported to the center of the cell along microtubules by cytoplasmic dynein.[24] Early endosomes interact then with vesicles in which the uncoupling of receptors and ligands occurs.[25] It is generally believed that the acidification within this compartment leads to dissociation of ligand from the receptor, while receptor

dx.doi.org/10.1021/bc3001003 | Bioconjugate Chem. 2012, 23, 1276−1289

molecules are recycled back to the plasma membrane.[26] However, several groups have reported that the efficient dissociation of intracellular ASGPr-ligand complexes is independent of pH changes [27] and may require inactivation of the receptors.[28] There is also strong evidence that a large fraction of the receptor recycles back to the cell surface still associated with ligand.[29] Ligand−ASGPr interaction is based on the sugar preference (*N*-acetylgalactosamine ≫ galactose[30]), the antennary structure (tetra- > tri- ≫ di- ≫ monoantennary[31]), and sugar spacing (20 ≫ 10 ≫ 4 Å).[32,33]

In our present study, we aimed at specific targeting of HepG2 cells via the ASGPr. HepG2 cells derive from human hepatoblastoma. They are able to form bile canalicular structures (apical) between two neighboring cells which means they can exhibit a certain degree of polarity. The basolateral membrane domains of hepatocytes in the intact liver face the sinusoidal blood and adjacent cells. Apical and basolateral membrane domains are separated by tight junctions which prevent intermixing of membrane components between both domains.[34] These properties make us believe that HepG2 cells bear sufficient resemblance to the human hepatocyte *in vivo* and present a useful model to study the uptake and transfection potential of modified paCDs by the human liver cells.[35]

To evaluate the possibility to specifically target HepG2 cells, the transfection efficiencies of reference CDs modified with galactose moieties were investigated in a series of preliminary experiments. Attempts to transfect HepG2 cells with pDNA complexed with different modified reference CDs resulted in hardly any transfection. To determine the cause of this failure, we performed a set of additional experiments. They strongly pointed to the nuclear envelope as the major barrier toward successful transfection of HepG2 cells with the pDNA-CDplexes. To verify this hypothesis, we transfected HepG2 cells with mRNA instead of pDNA. We were able to show remarkable transfection efficiencies with mRNA-CDplexes. With mRNA encoding GFP, fractions of GFP-positive cells up to 31% were obtained. Furthermore, the mRNA galactosylated CDplexes were shown to be specifically taken up via the ASGPr. These results lead us to believe that properly modified paCDs complexed with mRNA may represent a promising system to transfect hepatocytes *in vivo*.

EXPERIMENTAL PROCEDURES

Cyclodextrin Synthesis and Conjugation. The chemical structures of the five different paCDs (abbreviations between brackets): reference CDs (Hex-CD-N_{21} in Figure 1), 10% triantennary-galactose-bearing reference CDs (Gal10CDs; conjugate 1 in Figure 1), 12% triantennary-galactose-bearing reference CDs (Gal12CDs; conjugate 2 in Figure 1), 13% thio-PEG5000-bearing reference CDs (PEGCDs; conjugate 3 in Figure 1), and 10% thio-PEG5000-triantennary-galactose-bearing reference CDs (GalPEGCDs, conjugate 4 in Figure 1) are shown in Figure 1, their schematic representations before and after complexation with nucleic acids in Figure 2, and their synthesis in Schemes 1−3.

Common reagents and materials were purchased from commercial sources. Optical rotations were measured at room temperature in 1-dm tubes on a Perkin-Elmer 141 MC polarimeter. Infrared (IR) spectra were recorded on a Bomen Michelson MB-120 FTIR spectrophotometer. ^{1}H (and ^{13}C NMR) spectra were recorded at 300 (75.5 for ^{13}C) and 500 (125.7 for ^{13}C) MHz with Bruker 300 and 500 DRX instruments. 1D ^{1}H TOCSY, 2D ^{1}H TOCSY, COSY, ^{1}H−^{13}C HMQC, and

Scheme 2. Synthesis of Modified paCDs[a]

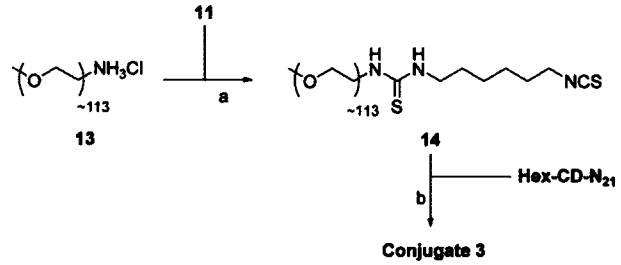

[a]Reaction scheme of 13% thio-PEG5000-bearing reference CDs (**conjugate 3**; PEGCDs). Reagents and conditions: (a) DCM, Et_3N, RT, 16h, 84%. (b) DMF, Et_3N, RT, 6 days. 86%.

Scheme 3. Synthesis of Modified paCDs[a]

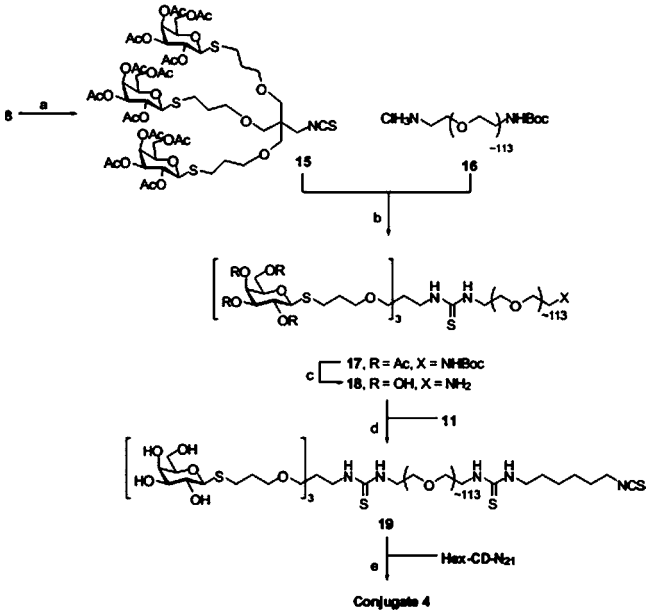

[a]Reaction scheme of 10% thio-PEG5000-tri-antennary-galactose-bearing reference CDs (**conjugate 4**; GalPEGCDs). Reagents and conditions: (a) CS_2, TPP, dioxane, RT, 16 h, 68%. (b) $NaHCO_3$, acetone-water, RT, overnight, 63%. (c) i. MeONa, MeOH, RT, 3h. ii. H_2O:TFA, RT, 1 h, 99%. (d) NaHCO3, water-acetone, RT, 16 h, 90%. (e) DMF, Et_3N, 40 °C, 2 days. 70%.

HSQC experiments were used to assist NMR assignments. Thin-layer chromatography (TLC) was carried out on aluminum sheets coated with Kieselgel 60 F254 (Merck), with visualization by UV light, and by charring with 10% H_2SO_4 or 0.2% ninhydrin. Column chromatography was carried out on Silica Gel 60 (Merck, 230−400 mesh). Gel permeation chromatography (GPC) of the fully unprotected βCD adducts was carried out on a Sephadex G-25 (eluent H_2O) column (Pharmacia Amersham) attached to a Gradifrac system using a UV detector set at 248 nm. Electrospray mass spectra (ESIMS) were obtained with a Bruker Esquire6000 instrument. Heptakis [6-(2-(*N*′-(2-(*N*,*N*-bis-(2-aminoethyl)amino)ethyl)thioureido)ethylthio)-2,3-di-*O*-hexanoyl]-cyclomaltoheptose (Hex-CD-N_{21}) was synthesized following the procedure previously reported.[15] 2,3,4,6-Tetra-*O*-acetyl-1-thio-α-D-galactopyranose (**6**) was prepared from D-galactose pentaacetate in three steps by transformation into the corresponding glycosyl bromide, reaction with thiourea, and subsequent hydrolysis of the resulting isothiouronium salt with potassium metabisulfite ($K_2S_2O_5$).[36] Elemental analyses were performed at the Instituto

dx.doi.org/10.1021/bc3001003 | *Bioconjugate Chem.* 2012, 23, 1276−1289

de Investigaciones Químicas (Sevilla, Spain). Triphenylphosphine, trifluoromethanesulfonic anhydride, and *N*,*N*-dimethylformamide are indicated by the acronyms TPP, Tf_2O, and DMF, respectively (Scheme 1).

2,2,2-Tris[5-(2,3,4,6-tetra-*O*-acetyl-β-D-galactopyranosylthio)-2-oxapentyl]ethanol (7). A solution of the tri-*O*-allylated pentaerythritol derivative **5**[37] (745 mg, 2.91 mmol), 2,3,4,6-tetra-*O*-acetyl-1-thio-β-D-galactopyranose[36] (**6**, 3.18 g, 8.74 mmol), and AIBN (477 mg, 2.91 mmol) in dry and degassed dioxane (21 mL), was stirred at 75 °C under Ar atmosphere for 3 h. Then, a solution of **6** (3.18 g) and AIBN (477 mg) in dioxane (21 mL) was added, and the reaction mixture was stirred at 75 °C for 6 h (TLC monitoring). The solvent was removed under reduced pressure and the residue was purified by column chromatography (1:1 EtOAc−petroleum ether). Yield: 2.48 g (64%); R_f = 0.22 (2:1 EtOAc-petroleum ether); $[\alpha]_D$ = −8.5 (c 1.0 in $CHCl_3$); ^{1}H NMR (500 MHz, $CDCl_3$) δ 5.44 (d, 3 H, $J_{3,4}$ = 3.0 Hz, H-4), 5.23 (t, 3 H, $J_{1,2}$ = $J_{2,3}$ = 10.0 Hz, H-2), 5.07 (dd, 3 H, H-3), 4.51 (d, 3 H, H-1), 4.17 (dd, 3 H, $J_{6a,6b}$ = 11.3 Hz, $J_{5,6a}$ = 6.6 Hz, H-6a), 4.11 (dd, 3 H, $J_{5,6b}$ = 6.9 Hz, H-6b), 3.96 (t, 3 H, H-5), 3.67 (bs, 2 H, CH_2OH), 3.49 (t, 6 H, $^3J_{H,H}$ = 6.1 Hz, H-3_{Pent}), 3.43 (s, 6 H, H-1_{Pent}), 2.81, 2.74 (2 dt, 6 H, $^2J_{H,H}$ = 13.0 Hz, $^3J_{H,H}$ = 7.2 Hz, H-5_{Pent}), 2.17−1.99 (4 s, 36 H, *Me*CO), 1.93−1.85 (m, 6 H, H-4_{Pent}); ^{13}C NMR (125.7 MHz, $CDCl_3$) δ 170.4−169.6 (Me*C*O), 84.4 (C-1), 74.4 (C-5), 71.9 (C-3), 71.2 (C-1_{Pent}), 69.7 (C-3_{Pent}), 67.2 (C-2, C-4), 65.4 (*C*H_2OH), 61.4 (C-6), 45.0 (Cq), 29.9 (C-4_{Pent}), 27.2 (C-5_{Pent}), 21.0−20.6 (*Me*CO). ESIMS: *m*/*z* 1371.2 $[M + Na]^+$. Anal. Calcd for $C_{56}H_{84}O_{31}S_3$: C 49.84, H 6.27, S 7.13. Found: C 49.89, H 6.12, S 6.89 (Scheme 1; SI Figure S1).

2,2,2-Tris[5-(2,3,4,6-tetra-*O*-acetyl-β-D-galactopyranosylthio)-2-oxapentyl]ethyl azide (8). To a solution of **7** (204 mg, 0.15 mmol) in dry DCM (1 mL), pyridine (60 μL) and Tf_2O (30 μL, 0.19 mmol) were added at −25 °C under Ar atmosphere. The solution was stirred for 15 min at −25 °C (TLC monitoring), diluted with CH_2Cl_2, washed with cold aq saturated $NaHCO_3$, dried (Na_2SO_4), and concentrated. The residue was dissolved in DMF (1 mL) and NaN_3 (30 mg, 0.45 mmol) was added. The mixture was stirred at RT for 17 h and concentrated. The resulting residue was dissolved in DCM, washed with water, dried (Na_2SO_4), concentrated, and purified by column chromatography (3:2 EtOAc−petroleum ether). Yield: 179 mg (87%); R_f = 0.54 (2:1 EtOAc-petroleum ether); $[\alpha]_D$ = −12.4 (c 1.6 in $CHCl_3$); ^{1}H NMR (500 MHz, $CDCl_3$) δ 5.41 (d, 3 H, $J_{3,4}$ = 3.0 Hz, H-4), 5.19 (t, 3 H, $J_{1,2}$ = $J_{2,3}$ = 10.0 Hz, H-2), 5.03 (dd, 3 H, H-3), 4.48 (d, 3 H, H-1), 4.06−4.17 (m, 6 H, H-6), 3.92 (t, 3 H, $J_{5,6}$ = 6.5 Hz, H-5), 3.44 (t, 6 H, $^3J_{H,H}$ = 6.0 Hz, H-3_{Pent}), 3.31 (s, 2 H, CH_2N_3), 3.30 (s, 6 H, H-1_{Pent}), 2.77, 2.70 (2 dt, 6 H, $^2J_{H,H}$ = 12.5 Hz, $^3J_{H,H}$ = 5.5 Hz, H-5_{Pent}), 2.13−1.96 (4 s, 36 H, *Me*CO), 1.90−1.80 (m, 6 H, H-4_{Pent}); ^{13}C NMR (125.7 MHz, $CDCl_3$) δ 170.3−169.5 (Me*C*O), 84.4 (C-1), 74.3 (C-5), 71.8 (C-3), 69.6 (C-1_{Pent}, C-3_{Pent}), 67.5 (C-2), 67.2 (C-4), 61.3 (C-6), 52.0 (CH_2N_3), 45.4 (Cq), 29.9 (C-4_{Pent}), 27.3 (C-5_{Pent}), 21.0−20.5 (*Me*CO). ESIMS: *m*/*z* 1396.4 $[M + Na]^+$. Anal. Calcd for $C_{56}H_{83}O_{30}S_3N_3$: C 48.94, H 6.09, N 3.06, S 7.00. Found: C 48.85, H 5.92, N 2.86, S 6.81 (Scheme 1, SI Figure S2).

CAUTION! Sodium azide (NaN_3) is extremely toxic and potentially explosive under certain conditions. The use of dichloromethane as reaction medium may result in the formation of highly explosive-unstable diazidomethane. Even though the risk is mitigated in the presence of water, dichloromethane should be replaced for the liquid−liquid extraction by a non-chlorinated solvent such as ethyl acetate (EtOAc) if the synthesis is scaled up over 1 g.

Tris[5-β-D-galactopyranosylthio)-2-oxapentyl]-ethylazide (9). A solution of **8** (50 mg, 36.4 μmol) in MeOH (5 mL) was treated with MeONa (2.4 mg, 43.7 μmol, 0.1 equiv) at RT for 3 h. Then, the mixture was neutralized with acid resin (Amberlite IR-120 H^+), filtered, and concentrated. Yield: 31.4 mg (99%). R_f = 0.7 (MeOH). $[\alpha]_D$ = −24.8 (c 0.99, MeOH), IR (NaCl): υ_{max} = 2106 cm^{-1}; ^{1}H NMR (500 MHz, CD_3OD, 313 K): δ 4.34 (d, 3 H, $J_{1,2}$ = 9.6 Hz, H-1), 3.92 (d, 3 H, $J_{3,4}$ = 3.0 Hz, H-4), 3.77 (dd, 3 H, $J_{5,6a}$ = 6.7 Hz, $J_{6a,6b}$ = 11.4 Hz, H-6a), 3.72 (dd, 3 H, $J_{5,6b}$ = 5.5 Hz, H-6b), 3.58 (t, 3 H, $J_{2,3}$ = 9.6 Hz, H-2), 3.56 (m, 9 H, H-5, H-3_{Pent}), 3.50 (dd, 3 H, H-3), 3.39 (m, 8 H, CH_2N_3, H-1_{Pent}), 2.85, 2.79 (2 dt, 6 H, $^2J_{H,H}$ = 13.0 Hz, $^3J_{H,H}$ = 7.3 Hz, H-5_{Pent}), 1.92 (m, 6 H, $^3J_{H,H}$ = 6.6 Hz, H-4_{Pent}); ^{13}C NMR (125.7 MHz, CD_3OD, 313 K): δ 87.9 (C-1), 80.6 (C-2), 76.3 (C-3), 71.6 (C-3_{Pent}), 71.0 (C-5), 70.7 (C-1_{Pent}), 70.6 (C-4), 62.7 (C-6), 53.3 (CH_2N_3), 46.7 (Cq), 31.4 (C-4_{Pent}), 28.0 (C-5_{Pent}). ESIMS: *m*/*z* 891.8 $[M + Na]^+$, 867.7 $[M - H]^-$, 903.6 $[M + Cl]^-$. Anal. Calcd for $C_{32}H_{59}N_3O_{18}S_3$: C, 44.18; H, 6.84; N, 4.83; S, 11.06. Found: C, 43.81; H, 6.69; N, 4.60; S, 10.83 (Scheme 1, SI Figure S3).

Tris[5-β-D-galactopyranosylthio)-2-oxapentyl]-ethylamine (10). To a solution of **9** (60 mg, 69 μmol) and TPP (63 mg, 0.24 mmol, 3.5 equiv) in a 1:3 mixture of water:dioxane (4 mL) was added a solution of 25% NH_4OH in water (1 mL), and the mixture was stirred at RT for 24 h. Solvents were removed under reduced pressure and the residue was washed with DCM (10 mL) and water (10 mL). The aqueous layer was washed twice with DCM (10 mL) and once with AcOEt (10 mL) and finally freeze-dried. Yield: 58.1 mg (99%). R_f = 0.1 (MeOH). $[\alpha]_D$ = −15.2 (c 1.05, H_2O); ^{1}H NMR (500 MHz, D_2O, 313 K): δ 4.58 (d, 3 H, $J_{1,2}$ = 9.7 Hz, H-1), 4.11 (d, 3 H, $J_{3,4}$ = 2.7 Hz, H-4), 3.85 (m, 12 H, H-6a, H-6b, H-1_{Pent}), 3.77 (dd, 3 H, $J_{2,3}$ = 8.7 Hz, H-3), 3.70 (m, 12 H, H-2, H-5, H-3_{Pent}), 3.58 (s, 2 H, CH_2NH_2), 2.95 (m, 6 H, H-5_{Pent}), 2.06 (m, 6 H, $^3J_{H,H}$ = 6.6 Hz, H-4_{Pent}); ^{13}C NMR (125.7 MHz, D_2O, 313 K): δ 86.2 (C-1), 79.1 (C-2), 74.2 (C-3), 70.5, 70.3 (C-1,3_{Pent}), 69.9 (C-5), 69.1 (C-4), 61.3 (C-6), 43.9 (CH_2NH_2), 42.4 (Cq), 29.4 (C-4_{Pent}), 27.0 (C-5_{Pent}). ESIMS: *m*/*z* 843.9 $[M + H]^+$, 865.8 $[M + Na]^+$, 841.7 $[M - H]^-$, 877.6 $[M + Cl]^-$. Anal. Calcd for $C_{32}H_{61}NO_{18}S_3$: C, 45.54; H, 7.28; N, 1.66. Found: C, 45.15; H, 6.978; N, 1.31 (Scheme 1; SI Figure S4).

***N*-(6-isothiocyanate)hexyl-*N*′-2,2,2-tris[5-β-D-galactopyranosylthio-2-oxapentyl]ethylthiourea (12).** To a solution of 1,6-hexamethylenediisothiocyanate[38] (**11**, 36 mg, 178 μmol, 5 equiv) in acetone (3 mL), a solution of **10** (30 mg, 35 μmol) and saturated aqueous $NaHCO_3$ (35 μL) in water (2 mL) was added dropwise under and vigorously stirring. The mixture was stirred at RT during 20 h. Then, solvents were eliminated under vacuum and the residue was purified by column chromatography (5:1 MeCN−H_2O). Yield: 37 mg (99%). R_f = 0.81 (MeCN-H_2O 3:1). $[\alpha]_D$ = −12.8 (c 0.78, MeOH); IR (NaCl): υ_{max} = 2110 cm^{-1}, ^{1}H NMR (500 MHz, D_2O, 298 K): δ 4.58 (d, 3 H, $J_{1,2}$ = 9.5 Hz, H-1), 4.10 (d, 3 H, $J_{3,4}$ = 3.2 Hz, H-4), 3.84 (m, 12 H, H-6a, H-6b, H-1_{Pent}), 3.77 (dd, 3 H, $J_{2,3}$ = 9.5 Hz, H-3), 3.74 (t, 2 H, $^3J_{H,H}$ = 6.8 Hz, CH_2NCS), 3.71 (m, 9 H, H-5, H-3_{Pent}), 3.69 (t, 3 H, H-2), 3.59 (m, 4 H, CH_2NH), 2.96 (2 dt, 6 H, $^2J_{H,H}$ = 13.7 Hz, $^3J_{H,H}$ = 7.0 Hz, H-5_{Pent}), 2.06 (m, 6 H, $^3J_{H,H}$ = 6.5 Hz, H-4_{Pent}), 1.86, 1.75, 1.59, 1.53 (4 m, 8 H, $^3J_{H,H}$ = 6.8 Hz, $CH_2CH_2CH_2$); ^{13}C NMR (125.7 MHz, D_2O, 298 K): δ 181.3 (CS), 127.4 (NCS), 86.3

dx.doi.org/10.1021/bc3001003 | *Bioconjugate Chem.* 2012, 23, 1276−1289

(C-1), 79.0 (C-2), 74.2 (C-3), 70.4, 70.0 (C-1,3$_{Pent}$, C-5), 69.0 (C-4), 61.2 (C-6), 45.1 (CH_2NCS), 44.3 (Cq, CH_2NH), 29.6 (C-4$_{Pent}$), 27.2 (C-5$_{Pent}$), 29.1, 28.4, 28.8, 27.5 ($CH_2CH_2CH_2$). ESIMS: m/z 1065.8 $[M + Na]^+$, 1082.8 $[M + K]^+$, 1041.7 $[M - H]^-$, 1077.6 $[M + Cl]^-$. Anal. Calcd for $C_{40}H_{73}N_3O_{18}S_5$: C, 46.00; H, 7.05; N, 4.02; S, 15.02. Found: C, 45.87; H, 6.804; N, 3.93; S, 15.02 (Scheme 1; SI Figure S5).

***O*-Methyl-*O*′-[3-(6-isothiocyanatohexyl)thioureidoethyl]-polyethylenglycol 5000 (14).** To a solution of *O*-methyl-*O*′-(2-aminoethyl) polyethylenglycol 5000 hydrochloride (**13**, 50 mg, 10 μmol) in freshly distilled DCM (2.5 mL), Et_3N (5 μL, 40 μmol, 4 equiv) was added. Then, a solution of 1,6-hexamethylenediisothiocyanate (**11**, 40 mg, 0.2 mmol, 20 equiv) in DCM (2.5 mL) was added and the reaction mixture was stirred for 16 h at RT. The solvent was evaporated down to 1 mL, and the crude was precipitated by addition of Et_2O (20 mL). The solid was filtered and washed with Et_2O until complete removal of unreacted 1,6-diisothiocyanatohexane (TLC). Yield: 42 mg (84%). R_f = 0.60 (5:1 DCM-MeOH). IR (ATR): υ_{max} = 2881, 1341, 1103, 960, 842 cm^{-1}; UV (CH_2Cl_2): 248 nm (ε_{mM} 3.7). ^{1}H NMR (500 MHz, $CDCl_3$): δ 3.76−3.45 (m, 506 H, CH_2OCH_2, S═CNHCH_2, CH_2NCS, CH_2OCH_3), 3.35 (s, 3 H, OCH_3), 1.68 (m, 1 H, $^3J_{H,H}$ = 6.6 Hz, CH_2), 1.58 (m, 1 H, $^3J_{H,H}$ = 7.5 Hz, CH_2), 1.45, 1.36 (m, 2 H, 2 × CH_2). ESIMS: m/z 2693.1 ± 22 $[M \pm 44\ n + 2\ Na]^{2+}$ (Scheme 2; SI Figure S6).

2,2,2-Tris[5-(2,3,4,6-tetra-*O*-acetyl-β-D-galactopyranosylthio)-2-oxapentyl]ethyl isothiocyanate (15). To a solution of the corresponding azide derivative **8** (892 mg, 0.65 mmol) in dioxane (30 mL), TPP (190 mg, 0.71 mmol) and CS_2 (0.4 mL, 6.5 mmol) were added. The reaction mixture was stirred at RT for 16 h under Ar atmosphere, then concentrated, and the residue was purified by column chromatography using 1:1 EtOAc−petroleum ether as an eluent. Yield: 618 mg (68%); R_f = 0.54 (2:1 EtOAc−petroleum ether); $[\alpha]_D$ = −10.7 (c 1.0 in $CHCl_3$); ^{1}H NMR (400 MHz, $CDCl_3$) δ 5.43 (d, 3 H, $J_{3,4}$ = 3.0 Hz, H-4), 5.21 (t, 3 H, $J_{1,2}$ = $J_{2,3}$ = 10.0 Hz, H-2), 5.05 (dd, 3 H, H-3), 4.50 (d, 3 H, H-1), 4.15 (dd, 3 H, $J_{6a,6b}$ = 12.0 Hz, $J_{5,6a}$ = 6.8 Hz, H-6a), 4.09 (dd, 3 H, $J_{5,6b}$ = 6.8 Hz, H-6b), 3.94 (t, 3 H, H-5), 3.57 (s, 2 H, CH_2NCS), 3.47 (t, 6 H, $^3J_{H,H}$ = 6.0 Hz, H-3$_{Pent}$), 3.35 (bs, 6 H, H-1$_{Pent}$), 2.79, 2.71 (2 dt, 6 H, $^2J_{H,H}$ = 12.8 Hz, $^3J_{H,H}$ = 7.2 Hz, H-5$_{Pent}$), 2.15−1.98 (4 s, 36 H, *Me*CO), 1.91−1.83 (6 H, m, H-4$_{Pent}$); ^{13}C NMR (125.7 MHz, $CDCl_3$) δ 170.3−169.5 (Me*C*O), 84.4 (C-1), 74.3 (C-5), 71.8 (C-3), 69.7 (C-3$_{Pent}$), 69.5 (C-1$_{Pent}$), 67.2 (C-2, C-4), 61.3 (C-6), 45.9 (CH_2NCS), 45.6 (Cq), 29.8 (C-4$_{Pent}$), 27.3 (C-5$_{Pent}$), 21.0−20.6 (*Me*CO). ESIMS: m/z 1412.3 $[M + Na]^+$. Anal. Calcd for $C_{57}H_{83}O_{30}S_4N$: C 49.23, H 6.02, N 1.01, S 9.22. Found: C 49.24, H 6.03, N 1.15, S 9.22 (Scheme 3; SI Figure S7).

***O*-[2-(2-(Tris(5-(2,3,4,6-tetra-*O*-acetyl-β-D-galactopyranosylthio))-2-oxapentyl)ethylthioureido)ethyl]-*O*′-2-[(*N*-(*tert*-butoxycarbonyl)amino)ethyl]polyethylene glycol 5000 (17).** To a solution of *O*-(2-aminoethyl)-*O*′-[2-(Boc-amino)ethyl] PEG_{5000} hydrochloride (**16**, 30 mg, 6 μmol) and $NaHCO_3$ (1 mg, 12 μmol, 2 equiv) in water (80 μL), a solution of **15** (41 mg, 30 μmol, 5 equiv) in acetone (5 mL) was added. The reaction mixture was stirred overnight at RT. The acetone was evaporated and the solution was diluted with water (1 mL) and extracted with CH_2Cl_2 (6 × 5 mL). The organic layer was dried, filtered and concentrated up to 1 mL. Then the crude was precipitated by addition of Et_2O (15 mL). The solid was filtered and washed with Et_2O until removal of unreacted **15** (TLC). Yield: 24.1 mg (63%). R_f = 0.65 (5:1 DCM−MeOH). $[\alpha]_D$ = −1.6 (c 0.82, DCM). IR (ATR): υ_{max} = 2882, 1712, 1343, 1240, 1109 cm^{-1}. UV (CH_2Cl_2): 246 nm (ε_{mM} 7.8); ^{1}H NMR (500 MHz, CD_3OD): δ 5.46 (bs, 1 H, H-4), 5.18 (m, 1 H, H-2), 4.95 (t, 1 H, $J_{2,3}$ = $J_{3,4}$ = 10.0 Hz, H-3), 4.78 (d, 1 H, $J_{1,2}$ = 9.8 Hz, H-1), 4.30 (dd, 1 H, $J_{6a,6b}$ = 11.5 Hz, $J_{5,6a}$ = 7.5 Hz, H-6a), 4.19 (dd, 1 H, $J_{5,6a}$ = 4.6 Hz, H-6b), 3.80−3.50 (m, 554 H, CH_2NHC=S, CH_2OCH_2, H-5, H-3$_{Pent}$, H-5$_{Pent}$), 3.45 (s, 2 H, H-1$_{Pent}$), 3.24 (t, 2 H, $^3J_{H,H}$ = 5.3 Hz, CH_2NHBoc), 2.84 (2 m, 2 H, H-5$_{Pent}$), 2.18, 2 × 2.09, 1.98 (4 s, 12 H, MeCO), 1.93 (m, 2 H, H-4$_{Pent}$), 1.48 (s, 9 H, CMe_3). ESIMS: m/z 3197.5 ± 22 $[M \pm 44n + 2\ K]^{2+}$ (Scheme 3; SI Figure S8).

***O*-[2-(2-(Tris(5-β-D-galactopyranosylthio)-2-oxapentyl)-ethylthioureido) ethyl]-*O*′-2-(aminoethyl)polyethylene glycol 5000 (18).** To a solution of **17** (12.3 mg, 2 μmol) in MeOH (1 mL), MeONa 1 M (2.3 μL) was added and the reaction mixture was stirred for 3 h at RT. The solution was neutralized (Amberlite IRA-120), filtered, and concentrated. The residue was treated with TFA−H_2O (1:1, 0.4 mL) for 1 h, the solvent was coevaporated several times with water. Yield: 12 mg (99%). R_f = 0.59 (5:1 DCM−MeOH). $[\alpha]_D$ = −1.3 (c 0.66, MeOH). IR (ATR): υ_{max} = 3373, 2881, 1465, 1342, 1104 cm^{-1}. UV (CH_2Cl_2): 244 nm (ε_{mM} 7.6). ^{1}H NMR (500 MHz, CD_3OD): δ 4.36 (d, 2 H, $J_{1,2}$ = 8.7 Hz, H-1), 3.92 (d, 2 H, $J_{3,4}$ = 8.6 Hz, H-4), 3.80−3.40 (m, 628 H, $CH_2CH_2NH_2$, CH_2OCH_2, S═CNHCH_2, H-5, H-6a, H-6b, H-1$_{Pent}$, H-3$_{Pent}$), 3.58 (t, 2 H, $J_{2,3}$ = 9.7 Hz, H-2), 3.50 (dd, 2 H, H-3), 3.23 (t, 2 H, $^3J_{H,H}$ = 4.5 Hz, CH_2NH_2), 2.84 (m, 4 H, H-5$_{Pent}$), 1.93 (m, 4 H, $^3J_{H,H}$ = 6.3 Hz, H-4$_{Pent}$). ESIMS: m/z 2759.4 ± 22 $[M \pm 44n + Na + K]^{2+}$ (Scheme 3; SI Figure S9).

***O*-[2-(Tris(5-β-D-galactopyranosylthio)-2-oxapentyl)-ethylthioureido]ethyl]-*O*′-2-(3-(6-isothiocyanatohexyl)-thioureidoethyl)polyethylene glycol 5000 (19).** To a solution of **18** (39.5 mg, 7 μmol) and $NaHCO_3$ (1 mg, 13 μmol, 2 equiv) in water (500 μL), a solution of 1,6-diisothiocyanatohexane (12 mg, 34 μmol, 5 equiv) in acetone (1 mL) was added and the reaction mixture was stirred overnight at RT. The acetone was evaporated and the solution was diluted in water (1 mL) and extracted with DCM (6 × 5 mL). The solvent was evaporated to 1 mL and the crude was precipitated by addition of Et_2O (30 mL). The solid was filtered and washed with Et_2O until ermoval of unreacted 1,6-diisothiocyanatohexane (TLC). Yield: 35 mg (90%). R_f = 0.59 (5:1 DCM−MeOH). $[\alpha]_D$ = −0.4 (c 0.8, DMSO). IR (ATR): υ_{max} = 3333, 2881, 1467, 1342, 1101, 961, 842 cm^{-1}. ^{1}H NMR (500 MHz, 5:1 $CDCl_3$−CD_3OD): δ 4.18 (d, 3 H, $J_{1,2}$ = 10.0 Hz, H-1), 3.82 (d, 3 H, $J_{3,4}$ = 5.3 Hz, H-4), 3.70−3.00 (m, 568 H, H-1$_{Pent}$, CH_2OCH_2, H-5, H-6a, H-6b, H-3$_{Pent}$, H-2, H-3, 4 × S═CNHCH_2, CH_2NCS), 2.67 (m, 6 H, H-5$_{Pent}$), 1.77 (m, 6 H, $^3J_{H,H}$ = 5.1 Hz, H-4$_{Pent}$), 1.59 (m, 2 H, $^3J_{H,H}$ = 5.1 Hz, CH_2), 1.50 (m, 2 H, $^3J_{H,H}$ = 7.6 Hz, CH_2), 1.33 (m, 4 H, 2 × CH_2) (Scheme 3; SI Figure S10).

Conjugates 1 and 2 (Gal10CDs and Gal12CDs). To a solution of Hex-CD-N_{21} (25 mg, 5.25 μmol) and Et_3N (20 μL, 0.147 mmol, 2 equiv) in DMF (1 mL), a solution of **12** (11.5 or 23 mg, 11 or 22 μmol, 0.15 or 0.3 equiv) in DMF (2 mL) was dropwise added. The mixture was stirred at RT for 4 days. The solvent was removed under reduced pressure and the residue was purified by gel exclusion chromatography (Sephadex G-25, H_2O) and freeze−dried from diluted HCl. Yield: 24 and 26 mg, respectively (75% and 78%). ^{1}H NMR (500 MHz, CD_3OD, 313 K): δ 5.36 (bt, 7 H, H-3), 5.18 (bd, 7 H, H-1), 4.84 (m, 7 H, H-2), 4.38 (m, 4.2 or 5.1, H-1$_{Gal}$), 4.21 (m, 11.2 or 12.1 H, H-5, H-4$_{Gal}$), 3.96 (7 H, H-4), 3.80−3.40 (m, 43 H, CH_2-NHCS, H-2$_{Gal}$, H-3$_{Gal}$,H-5$_{Gal}$, H-1$_{Pent}$, H-3$_{Pent}$, H-6a$_{Gal}$, H-6b$_{Gal}$,

dx.doi.org/10.1021/bc3001003 | *Bioconjugate Chem.* 2012, 23, 1276−1289

$CH_2CH_2S_{cyst}$), 3.03 (m, 28 H, CH_2NH_2), 2.79 (m, 45 H, CH_2N, H-6a, H-6b, H-5_{Pent}), 2.46 (m, 17.6 H, $CH_2S_{Cyst,}$), 2.37, 2.29 (2 m, 28 H, CH_2CO), 1.90 (m, 8.4 or 10.2 H, H-4_{Pent}), 1.66, 1.42−1.31 (2 m, 89 H, $CH_2CH_2CH_3$, CH_2CH_3), 0.86 (m, 42 H, CH_3) (Scheme 1; SI Figure S11).

Conjugate 3 (PEGCDs). To a solution of Hex-CD-N_{21} (14,7 mg, 3 μmol) and Et_3N (22 μL, 80 μmol, 4 equiv) in dry DMF (1 mL) under Ar atmosphere, a solution of **14** (22,6 mg, 4.3 μmol, 1.4 equiv) in DMF (1 mL) was added, and the reaction mixture was stirred for 6 days at RT. The solvents were removed under reduced pressure and the residue was diluted with water (60 mL) and dialyzed against a 3 kDa membrane. The solution was acidified with HCl 1 M and freeze−dried to give a white powder. Yield 32 mg (86%). $[\alpha]_D$ = +17.6 (c 1.1, MeOH). IR υ_{max} = 2883, 1749, 1341, 1101, 961, 841 cm^{-1}. UV (DCM): λ_{max} 246 nm (ε_{mM} 86). ^1H NMR (500 MHz, CD_3OD): δ 5.39 (bs, 7 H, H-3), 5.19 (bs, 7 H, H-1), 4.85 (m, 7 H, H-2), 4.20 (bs, 7 H, H-5), 3.97 (bs, 7 H, H-4), 3.85−3.40 (m, 898 H, OCH_2CH_2, 4 × S═$CNHCH_2$, $NHCH_2CH_2O$, $CH_2CH_2S_{Cyst}$), 3.37 (s, 7.2 H, OCH_3), 3.24 (m, 70 H, $CH_2CH_2NH_2$, H-6a, H-6b), 2.89 (m, 28 H, CH_2CH_2NHCS, $CH_2CH_2S_{Cyst}$), 2.50−2.20 (m, 28 H, CH_2CO), 1.65 (m, 28 H, CH_2CH_2CO), 1.60−1.40 (m, 8 H, 4 × CH_2), 1.37 (m, 56 H, CH_3CH_2, $CH_3CH_2CH_2$), 0.95, 0.94 (2 t, 42 H, $^3J_{H,H}$ = 7.0 Hz, CH_3) (Scheme 2; SI Figure S12).

Conjugate 4 (GalPEGCDs). A solution of Hex-CD-N_{21} (10.7 mg, 2.2 μmol), **19** (19.4 mg, 3.1 μmol, 1.4 equiv) and Et_3N (8 μL, 61 μmol, 2 equiv) in dry DMF (1 mL) was stirred at RT overnight and at 40 °C for 24 h. The solvent was evaporated under reduced pressure and the residue was diluted with water (60 mL) and dialyzed using a 3 kDa membrane. The solution was acidified with 1 M HCl and freeze−dried. Yield 21 mg (70%). $[\alpha]_D$ = +17.3 (c 0.3, MeOH). IR υ_{max} = 2881, 1750, 1342, 1105, 962, 841 cm^{-1}. UV (MeOH): λ_{max} 242 nm (ε_{mM} 56). ^1H NMR (500 MHz, CD_3OD): δ 5.37 (bs, 7 H, H-3), 5.19 (bs, 7 H, H-1), 4.85 (m, 7 H, H-2), 4.36 (d, 3.4 H, $J_{1,2}$ = 9.4 Hz, H-1_{Gal}), 4.20 (bs, 7 H, H-5), 3.92 (bs, 10.4 H, H-4, H-4_{Gal}), 3.85−3.40 (m, 1013 H, OCH_2CH_2, CH_2-6, $NHCH_2CH_2O$, 6 × S═$CCNHH_2$, $CH_2CH_2S_{Cyst}$, H-1_{Pent}, H-3_{Pent}, H-3_{Gal}, H-5_{Gal}, H-$6a_{Gal}$, H-$6b_{Gal}$, H-2), 3.15 (m, 70 H, $CH_2CH_2NH_2$, H-6a, H-6b), 2.89 (m, 34 H, CH_2CH_2NHCS, $CH_2CH_2S_{Cyst}$, H-5_{Pent}), 2.50−2.20 (m, 28 H, CH_2CO), 1.94 (m, 0.6.8 H, $^3J_{H,H}$ = 6.5 Hz, H-4_{Pent}), 1.64 (m, 28 H, CH_2CH_2CO), 1.60−1.40 (m, 9 H, 4 × CH_2), 1.37 (m, 56 H, CH_3CH_2, $CH_3CH_2CH_2$), 0.95, 0.94 (2 t, 42 H, $^3J_{H,H}$ = 7.2 Hz, CH_3) (Scheme 3; SI Figure S13).

pDNA Production. Heat-competent *E. coli* transformed with the gWIZ-GFP plasmid (GeneTherapy Systems, San Diego, California), pGEM4Z-EGFP-A64 plasmid (previously described by Rejman et al.[46]) or pBlue-Luc-A50 plasmid (previously described by Rejman et al.[46]) were grown in LB medium with, respectively, kanamycin and ampicillin at 37 °C for 20 h. pDNA was isolated and purified with the Qiafilter Plasmid Giga Kit (Qiagen, Venlo, The Netherlands) according to the manufacturer's instructions.

pDNA Labeling. For fluorescence microscopy, the pDNA was labeled with YOYO-1 (Molecular Probes, Merelbeke, Belgium) according to the manufacturer's instructions. Briefly, for a 10:1 base pair to dye ratio, 150 μL of 10 μM of YOYO-1 was mixed with 50 μL of 0.2 μg/μL pDNA. This was incubated in the dark for 1 h at RT and afterward the labeled pDNA was precipitated by salt/ethanol precipitation which was followed by a 70% ethanol wash to remove free YOYO-1.

mRNA Production. To produce mRNA by *in vitro* transcription, pGEM4Z-EGFP-A64 or pBlue-Luc-A50 plasmids were first purified using a QIAquick PCR purification kit (Qiagen, Venlo, The Netherlands). The plasmids were linearized using Spe I and Dra I restriction enzymes, respectively, and then used as templates for the *in vitro* transcription reaction using a T7 mMessage mMachine kit (Ambion, Merelbeke, Belgium) according to the manufacturer's instructions. mRNAs were purified by DNase I digestion, which was followed by LiCl precipitation and 70% ethanol wash. The produced mGFP and mLuc were both capped and polyadenylated. mRNAs were stored in small aliquots at −80 °C

CDplexes and Transfection. pDNA. Different amounts of modified reference CDs were diluted in HEPES buffer (50 μL) according to the wanted N/P ratio (the ratio of moles of the amine groups of the specific cyclodextrin to those of the phosphate groups of the nucleic acids). They were mixed with pDNA (1 μg) diluted in HEPES buffer (50 μL). After 10 min of incubation, 400 μL OPTIMEM (Gibco, Merelbeke, Belgium) were added and the mixture was added to HepG2 cells. After 4 h, the transfection medium was replaced by fresh culture medium. pDNA transfections were done in 3 separate experiments in duplicate.

mRNA. Different amounts of modified reference CDs were diluted in OPTIMEM (50 μL). They were mixed with mRNA (1 μg) diluted in OPTIMEM (50 μL). After 10 min of incubation, 400 μL OPTIMEM or full culture medium containing serum were added, and the mixture was added to HepG2 cells. After 4 h, the transfection medium was replaced by fresh culture medium. mRNA transfections with Gal10CDs and Gal12CDs were done in 2 separate experiments in duplicate. mRNA transfections with PEGCDs and GalPEGCDs were done in 1 experiment in quadruplicate.

jetPEI-Hepatocyte Polyplexes. jetPEI-Hepatocyte DNA transfection agent (Polyplus Transfection, Leuven, Belgium) was chosen as positive control transfection agent, since it has been developed for specific gene delivery to hepatocytes. PEI-polyplexes with 1 μg pDNA or mRNA were prepared according to the manufacturer's instructions. pDNA transfections were done in 3 experiments in duplicate. mRNA transfections were done in 2 separate experiments in quadruplicate.

Complex Destabilization. The ability of the CDplexes to escape out of the early endosomes was investigated as previously described by Xu and Szoka (1996).[39] CDplexes were made as described earlier and then the free pDNA was labeled by adding PicoGreen (Molecular Probes, Merelbeke, Belgium) (excitation/emission 502/520 nm) to the suspensions. Then, liposomes with the same lipid composition as early endosomal membranes phosphatidylcholine (PC):dioleoyl phosphatidylethanolamine (DOPE):phosphatidylserine (PS) in a molar ratio 6:3:1 (Avanti Polar Lipids, Delfzijl, The Netherlands) were added. The fluorescence of free pDNA was measured over time with a spectrometer (SLM-Aminco Bowman Series 2, Thermo Fisher Scientific, Erembodegem-Aalst, Belgium). To know the maximal release of pDNA out of the CDplexes, 200 μL of 10% zwittergent (3-(*N*,*N*-dimethylmyristylammonio)propanesulfonate; Sigma-Aldrich, Bornem, Belgium) was added and the fluorescence of free pDNA was measured.

Cell Culture Conditions. HepG2 cells (Human Hepatoblastoma, ATCC-HB-8065, Molsheim Cedex, France) were cultured in Dulbecco's modified Eagle's medium (DMEM) (Gibco, Merelbeke, Belgium) containing 2 mM glutamine (Gibco, Merelbeke, Belgium), 10% heat-inactivated fetal bovine

serum (FBS) (Hyclone/Perbio, Thermo Fisher Scientific, Erembodegem-Aalst, Belgium), and 100 U/mL penicillin−streptomycin liquid (Gibco, Merelbeke, Belgium) at 37 °C in a humidified atmosphere containing 5% CO_2. For the expression experiments, HepG2 cells were plated 1 day prior to the experiment onto 12-well plates (2×10^5 cells/well) or 24-well plates (1×10^5 cells/well).

Flow Cytometry. Flow cytometry (BD FACSCalibur, Erembodegem, Belgium) was used to determine the percentage of GFP-positive cells. For expression efficiencies, the fraction of cells expressing GFP (pGFP or mGFP) and the fluorescence intensities per positive cell were assessed. This was done 24 and 48 h after transfection for pDNA and after 24 h after transfection for mRNA.

Luciferase Assay. The culture medium was removed and the cells were washed twice with PBS (Gibco/Invitrogen, Merelbeke, Belgium). This was followed by adding 100 μL of Cell Culture Lysis Reagent (Promega, Leiden, The Netherlands). After 30 min, the samples were centrifuged (12 000 rpm at 4 °C for 5 min). 40 μL of the supernatants were transferred to a 96-well plate. Luciferase activity of each sample was assayed in a GloMax 96 Luminometer (Promega, Leiden, The Netherlands) by adding a 100 μL of the substrate solution in each well. The emitted light was measured over a 10 s period. The protein content of each sample was determined by a standard Bradford assay (Biorad, Nazareth Eke, Belgium). The results are expressed as relative light units per mg of protein (RLU/mg).

Photochemical Internalization (PCI). The night before transfection, the cells were incubated with 250 μL photosensitizer (PhSen) *meso*-tetraphenylporphine disulfonate (TPPS2a) (PCI Biotech, Lysaker, Norway) (0.4 μg/mL in regular culture medium). Fresh culture medium was administered to the cells 1 h before transfection to remove nonassociated PhSen. Following 4 h of incubation, the pDNA-complexes were removed, fresh culture medium was added and the cells were illuminated for 40 s with blue light (375−450 nm) emitted by LumiSource. After another incubation of 24 h, the expression efficiency was measured by flow cytometry. This experiment was done in duplicate.

Inhibition of Uptake through the ASGPr. Preceding transfection, rabbit polyclonal antibodies to ASGPr1 (Abcam, Cambridge, UK) were applied to the HepG2 cells in order to assess to which extent the uptake of CDplexes carrying galactose is accounted for the ASGPrs. The cells were washed once in 2% FBS in PBS and then unspecific binding was blocked by incubation with 2% goat serum (in PBS, 30 min, at 37 °C in cell incubator). Then, the cells were incubated for another 2 h at 37 °C (cell incubator) with 4 μg of ASGPr1-antibodies and washed twice with 2% FBS in PBS followed by transfection. This experiment was done in quadruplicate.

Viability Tests. The viability of the cells at 24 h after transfection with mRNA-CDplexes was assayed with the Cell Proliferation Kit I (MTT) (Roche, Vilvoorde, Belgium) according to the manufacturer's instructions. To that end, HepG2 cells were seeded in 12-well plates (2×10^5 cells/well) one day before transfection. The absorbance was measured at 600 nm with a spectrophotometer (UV-1800, Shimadzu Corporation, Deurne-Antwerpen, Belgium) or Nanodrop 2000c (Thermo Fisher Scientific, Erembodegem-Aalst, Belgium).

Confocal Microscopy. To study the uptake of CDplexes, HepG2 cells (3×10^5 cells) were plated onto sterile glass-bottom culture dishes (MatTek Corporation, Ashland, MA, USA) and allowed to adhere for 1 day. Transfections were performed with reference CDplexes at N/P ratio 10. The pDNA was labeled beforehand with YOYO-1. After 4 h of transfection, pictures were taken with a Nikon EZC1-si (Nikon Belux, Brussels, Belgium).

RESULTS

Synthesis. *Design Criteria.* Previous attempts to formulate glycosylated CDplexes using different ratios of a paCD and a neutral glycoamphiphlic CD (GaCD) led to disruption of the complexes even at very low proportion of the GaCD-component. This was probably due to a destabilizing effect of neutral microdomains. Installing the sugar functional elements and the cationic groups as regular arrangements onto the CD-platform restored the capacity to form stable CDplexes, but implied a high synthetic cost.[20] To overcome this limitation, we have now adopted a much more straightforward and flexible approach. It consists of the coupling of the reference CD (Figure 1: Hex-CD-N_{21}), a C_7-symmetrical β-cyclodextrin derivative with isothiocyanate-armed β-D-galactopyranosyl ligands. The incorporation of PEG-chains was considered to prevent aggregation in the presence of serum proteins. The new CD derivatives shown in Figure 1 were thus prepared.

The thiourea-forming reaction was favored as the ligation method because thiourea segments have been shown to contribute to pDNA complexation through hydrogen bonding.[14,40] Nevertheless, we anticipated that extensive functionalization of the reference CD might compromise the pDNA complexing abilities, since an amino group is deactivated at every coupling event. To overcome this problem, trivalent galactose dendrons were used as the basic ligand units. This strategy offers a very convenient manner to control the density of the sugar epitopes at the surface of the resulting CDplexes after interaction with nucleic acids.

Synthetic Strategy. The synthesis of the triantennary galactose ASGPr-recognition element involved the radical addition of the per-*O*-acetylated 1-thio-β-D-galactopyranose **6**[36] to the tri-*O*-allylated pentaerythritol derivative **5**.[37] The hydroxyl group in the resulting conjugate **7** was then replaced by azide **8** via a trifluoromethanesulfonate ester intermediate (87%, 2 steps). After deacetylation (→**9**), the azido group was reduced under Staudinger conditions to amine **10**, which was subsequently coupled with an excess of 1,6-hexamethylenediisothiocyanate **11**[38] to yield the isothiocyanate-armed glycodendron **12** in quantitative yield. Base-catalyzed reaction of variable proportions of **12** with reference CD in DMF using long reaction times yielded Gal10CD and Gal12CD, in which 10% and 12% of the primary amine group incorporate de glycol-dendron, respectively, in 75−78% yields (Scheme 1). Higher proportions of the glycol-dendron resulted in compounds with poor pDNA complexing capacity (data not shown) and were not further considered.

PEGylation of reference CDs also relied in the thiourea-forming ligation strategy (Scheme 2). Incorporation of PEG_{5000} elements were considered in view of its higher stabilization effect against serum proteins in comparison to lower-weighted analogues.[41] The preparation of the nonglycosylated PEGCDs involved the *O*-methyl-PEG_{5000}-NCS derivative **14**, prepared by reaction of commercially available *O*-methyl-PEG_{5000}-NH_2·HCl **13** with an excess of diisothiocyanate **11**. The formation of the thiourea linker was confirmed by MS spectrometry and ^{1}H NMR. Subsequent conjugation of **14** with reference CDs was carried out in DMF to yield PEGCDs having 13% of the primary amino groups substituted with PEG_{5000} chains as determined from the ratio of the ^{1}H NMR signal integration for

the terminal methyl group in *O*-methyl-PEG and the anomeric proton of the D-glucopyranose units in the β-cyclodextrin core.

The synthesis of GalPEGCDs required the isothiocyanate-armed PEG_{5000}-glycodendron **19**. Its preparation was accomplished in five steps from azide **8**. Isothiocyanation by treatment with triphenylphosphine (TPP) and carbon disulfide afforded isothiocyanate **15** (68% yield), which was coupled with commercial H_2N-PEG_{5000}-NHBoc **16** to yield the *N*-Boc-protected PEGylated glycodendron **17**. Deacetylation of **17** with NaOMe/MeOH followed by acid-catalyzed Boc cleavage afforded the unprotected galactopyranose dendron-PEG_{5000}-NH_2 **18** that, after reaction with excess of **11**, provided the key precursor **19**. Final coupling of Hex-CD-N_{21} and **19** was carried out in DMF/Et_3N at 40 °C for two days and the crude was purified by dialysis (Scheme 3). Integration of ^{1}H NMR anomeric signals from βCD and β-D-galactopyranose units evidenced that 10% of the amino groups have been transformed into thiourea segments bearing the PEG-dendron element, meaning 1.4 galactopyranose dendron-PEG_{5000} units per CD.

pDNA. *Transfection Efficiencies of pDNA-CDplexes.* The potential of modified reference CDs to deliver pDNA to HepG2 cells, resulting in reporter gene expression, was determined. pDNA encoding GFP was complexed with reference CDs, Gal10CDs, or Gal12CDs at N/P ratios (the ratio of moles of the amine groups of the specific cyclodextrin to those of the phosphate groups of the nucleic acids) varying from 10 to 30. The gel retardation assay demonstrated that the reference CDs efficiently complex pDNA at N/P $\geq$ 2.5 (SI Figure S14). The same was observed for Gal10CDs and Gal12CDs (data not shown).

The fraction of GFP-positive cells was assessed 24 and 48 h after transfection. As shown in Figure 3, levels of transfection

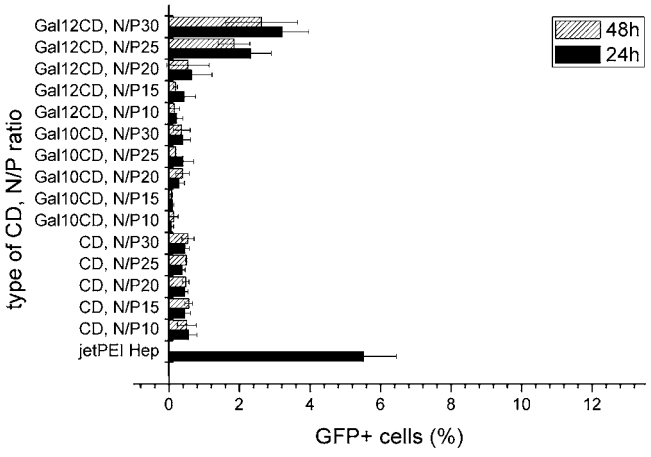

Figure 3. Fractions of GFP-positive HepG2 cells. The complexes were prepared by mixing reference CDs, Gal10CDs, or Gal12CDs with pDNA at different N/P ratios. Transfection efficiency was determined 24 and 48 h after transfection by flow cytometry. The results are compared with the transfection efficiency obtained by jetPEI-Hepatocyte/pDNA-complexes. The cells were seeded in 12-well plates. One microgram of pDNA was added per well. Increase to 2 μg/well did not yield larger fractions of GFP-positive HepG2 cells, nor did the use of OPTIMEM instead of HEPES buffer to prepare the CDplexes. Complexes were incubated with the cells for 4 h. The graphs represent mean values ± SD (n = 6).

obtained by pDNA-CDplexes were very low. The most efficient CDplexes transfected maximally 4% of the cells. Remarkably, transfection efficiencies obtained by jetPEI-Hepatocyte, a cationic polymer specifically designed to transfect hepatocytes, were quite modest. Only a maximum of 6% GFP-positive HepG2 cells was reached. This result is much lower than the expected transfection efficiency given by the provider (30%). By the same token, Candiani et al. reported lower transfection efficiencies with Lipofectamine2000 than those found in the literature.[42]

To ascertain at what stage in the process from uptake to translation the pDNA-CDplexes fail, we focused individually on the different potential intracellular barriers, in the order of their appearance in the process. The results are presented in the following paragraphs.

Uptake of pDNA-CDplexes. First, we verified if the CDplexes attach to the plasma membrane and are subsequently internalized by cells. To that end, fluorescently labeled CDplexes were incubated with HepG2 cells and analyzed by means of confocal microscopy. As shown in Figure 4, HepG2

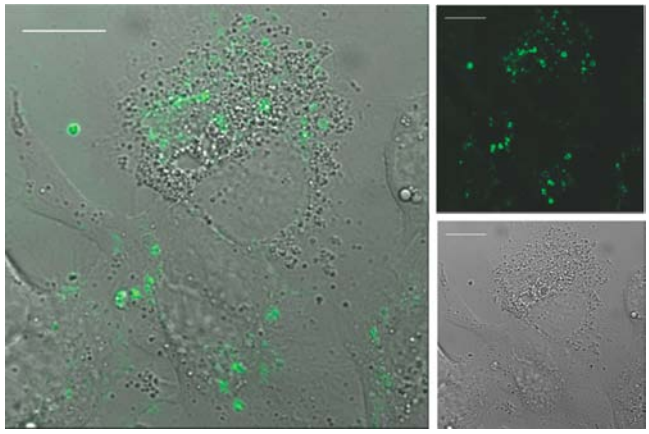

Figure 4. Representative confocal images of HepG2 cells which internalized pDNA-CDplexes. pDNA and reference CDs were mixed at an N/P ratio of 10. Cells were seeded on glass-bottom culture dishes one day before. The pDNA was labeled beforehand with YOYO-1 (green). Scalebars = 15 μm.

cells efficiently internalized fluorescently labeled CDplexes. These results demonstrate that interaction with the plasma membrane and subsequent internalization do not present an obstacle for transfection mediated by CDplexes.

Photochemical Internalization. In order to determine whether the endosomal entrapment limits the transfection potential of CDplexes, a technique called photochemical internalization (PCI) was used. PCI causes disruption of the endosomal membrane and thus facilitates release of material, which is localized in this compartment. If the CDplexes are trapped in the endosomes and degraded further on in the lysosomes, there should be no gene expression. When PCI is applied, the trapped CDplexes should be released from the endosomes, which could result in an elevated gene expression, provided there are no other obstacles on the delivery path to the nucleoplasm. As shown in Figure 5, there is no significant difference between fractions of GFP-positive cells or mean fluorescence intensities per GFP-positive cell for illuminated and non-illuminated HepG2 cells transfected with reference CD-, Gal10CD-, or Gal12CDplexes. This lack of effect of PCI on expression mediated by different CDplexes points out that the escape of the complexes from the endosomes is not responsible for the low level of gene expression.

dx.doi.org/10.1021/bc3001003 | *Bioconjugate Chem.* 2012, 23, 1276–1289

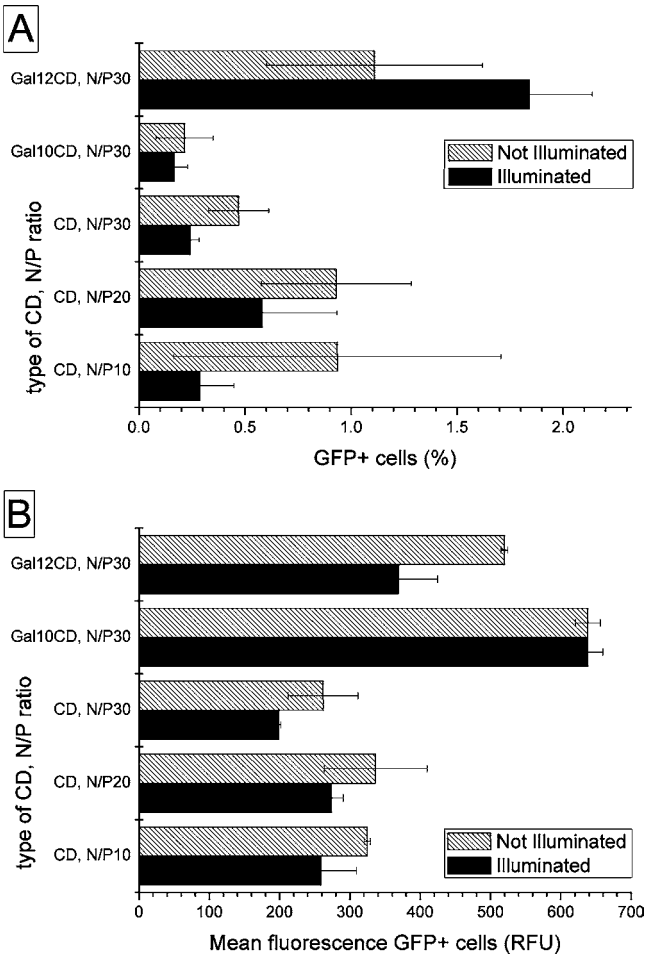

Figure 5. (a) The fraction and (b) mean relative fluorescence of GFP-positive HepG2 cells after exposure to the PCI treatment. The complexes were prepared by mixing reference CDs, Gal10CDs, or Gal12CDs with pDNA at different N/P ratios. Transfection efficiency was determined 24 h after transfection by flow cytometry. The cells were seeded in 12-well plates and incubated overnight with photosensitizer (PhSen). One hour before transfection, the culture medium was removed and fresh culture medium without PhSen was added. One microgram of pDNA was added per well (increase to 2 μg/well did not yield larger fractions of GFP-positive HepG2 cells). Complexes were incubated with the cells for 4 h. The graphs represent mean values ± SD (n = 2).

Release of pDNA from CDplexes. In a subsequent series of experiments, we investigated the possibility that the low expression level is related to insufficient release of the plasmid from the complex. Therefore, we followed the approach first described by Xu and Szoka.[39] pDNA-CDplexes were added to a picogreen solution followed by addition of negatively charged liposomes with the same lipid composition as early endosomal membranes. The changes in fluorescence, indicating an increase in the amount of free pDNA as only free pDNA is accessible for picogreen, were measured with a fluorometer. As demonstrated in Figure 6, the development of the fluorescence signal, which represents release of pDNA, occurs during the first 2−3 min and then reaches plateau values. We can conclude from these experiments that the low levels of transfection achieved by pDNA-CDplexes can neither be attributed to the lack of release of free pDNA from the CDplexes.

Taken together, these results suggest that the translocation of the pDNA into the nucleus represents the main obstacle for

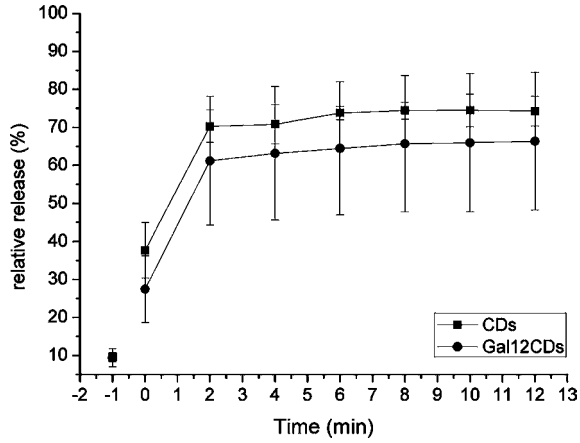

Figure 6. Accessibility of pDNA toward picogreen in pDNA-CDplexes. pDNA was complexed with reference CDs or Gal12CDs at N/P ratio 10 (time point −1). The complexes were mixed with negatively charged liposomes (time point 0) and the release of free pDNA interacting with picogreen was monitored over time. The relative release (mean ± SD) is plotted over a period of 12 min and shown as a fraction of the maximal release which was reached with zwittergent (100%). ($n \geq 2$.)

pDNA-CDplexes to become efficient. To verify that, we transfected HepG2 cells with mRNA-CDplexes. The results are presented in the next section.

mRNA. *Transfection Efficiency of mRNA-CDplexes.* Our experiments strongly pointed out the nuclear envelope as the main obstacle for efficient transfection of HepG2 cells. To verify that, we transfected the cells with mRNA, which only needs to reach the cytoplasm to result in biological activity, instead of pDNA. Different CDs also efficiently complex mRNA as evidenced in SI Figure S15. Figure 7a presents levels

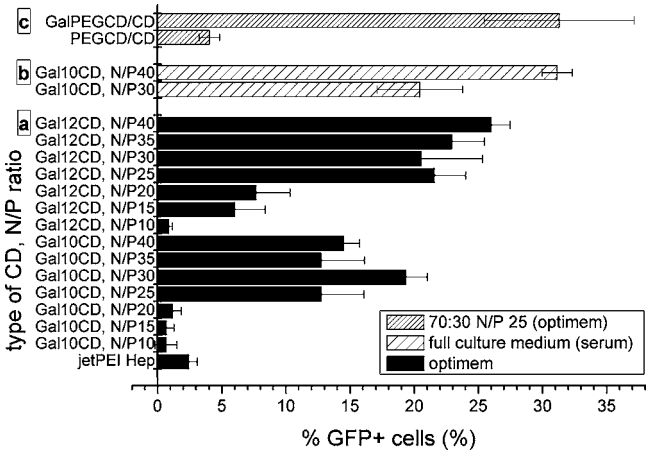

Figure 7. Fraction of GFP-positive HepG2 cells after transfection with mRNA-CDplexes. (a + b) The complexes were prepared by mixing Gal10CDs or Gal12CDs with mRNA at different N/P ratios (n = 4) or (c) they were prepared by mixing PEGCDs or GalPEGCDs and reference CDs at a ratio of 70:30 with mRNA at N/P ratio 25 (n = 4). Transfection efficiencies were determined 24 h after transfection by flow cytometry. The cells were seeded in 24-well plates. One microgram of mRNA was added per well. Complexes were incubated with the cells for 4 h in OPTIMEM (a + c) or full culture medium containing 10% FBS (b). The results are compared with the transfection efficiency obtained by jetPEI-Hepatocyte/mRNA-complexes (n = 8). The graphs represent mean values ± SD.

dx.doi.org/10.1021/bc3001003 | Bioconjugate Chem. 2012, 23, 1276−1289

of transfection obtained for two galactosylated reference CD species (Gal10CDs and Gal12CDs) mixed with mRNA at different N/P ratios, expressed as fractions of GFP-positive cells. The results were compared with those obtained with complexes made of mRNA and jetPEI-Hepatocyte. The results clearly demonstrate that, in contrast to the cationic polymers, modified reference CDs mixed with mRNA at higher N/P ratios (>20) were very efficient in transfecting HepG2 cells. The fractions of GFP-positive cells obtained with Gal12CD-plexes were well above 20%. Moreover, as shown in Figure 7b transfection efficiencies obtained by the Gal10CDplexes incubated with the cells in full culture medium containing serum were equal or even higher than in OPTIMEM.

We further studied transfection capacities of PEGCDs and GalPEGCDs. The expression efficiency was expected to drop for PEGCDplexes, because the PEG was expected to prevent or diminish the interaction with the cellular membrane. The presence of galactose at the tip of PEG-moieties was expected to restore the uptake as a result of specific interaction with the ASGPr. Complexes based on PEGCDs or GalPEGCDs alone were not active. This could be due to the lack of a sufficient number of cationic groups in these derivatives.[14] Therefore, the complexes were made by premixing PEGCDs or GalPEGCDs with reference CDs at a ratio of 7:3, which were then added to mRNA. Figure 7c represents fractions of GFP-positive cells obtained for these complexes. As expected, there was a minimal expression of GFP in HepG2 cells transfected with PEGCDplexes. Interestingly, GalPEGCD-plexes restored levels of transfection to values up to 31%.

ASGPr-Mediated Endocytosis of Galactosylated CDplexes. Since the ideal carrier for mRNA delivery to hepatocytes needs to be specific, we verified whether galactosylated CDplexes are internalized via the mechanism that involves the ASGPrs. To that end, the ASGPrs were blocked with anti-ASGPr1 antibodies prior to transfection with GalCDplexes carrying mRNA encoding luciferase. As shown in Figure 8, relative levels of luciferase activity in HepG2 cells, in which ASGPr-mediated uptake was blocked, decreased significantly compared to the levels in the untreated cells.

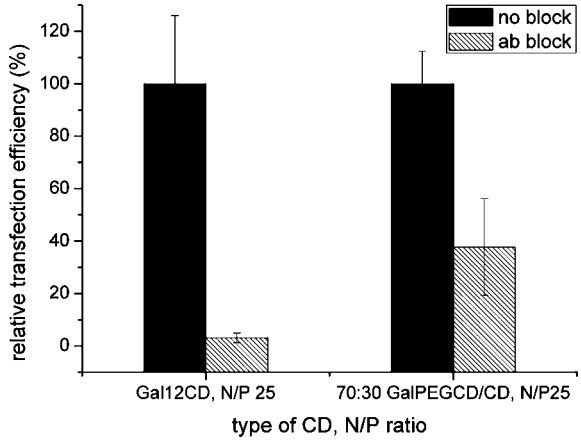

Figure 8. Inhibition of internalization of galactosylated reference CDs complexed with mRNA by blocking ASGPr. ASGPrs were blocked by incubation with rabbit polyclonal antibodies against ASGPr1 (2 h, 37 °C). Gal12CDs or GalPEGCDs/CDs (70:30) were complexed with mRNA encoding luciferase at N/P 25 and incubated with HepG2 cells for 4 h. Luciferase activity was measured 6 h later with a luminometer. Relative light units per mg of protein were calculated for each sample. The data are presented as percentages (mean ± SD) of transfection levels obtained for control cells. (n = 4.)

Viability of HepG2 Cells after mRNA Transfection. The viability of the HepG2 cells was determined 24 h after transfection with mRNA-CDplexes using the MTT cell proliferation assay. The viability of HepG2 cells treated with CDplexes was around 80%, which is comparable with the viability after transfection with jetPEI-Hepatocyte (SI Figure S16).

DISCUSSION

HepG2 cells in culture display a certain polarity and are morphologically and functionally differentiated, which makes them resemble the human hepatocytes in the *in vivo* situation and thus renders them an interesting and relevant model system. HepG2 cells are polarized and divide very slowly. The doubling time of HepG2 cells used in this study was 48 h. It should be noted, however, that the number of cells in culture did not change during the first 24 h (data not shown). For that reason, these cells are difficult to transfect with pDNA-cationic carrier complexes (CDplexes and polyplexes), as shown in the present work. Results reported by Kichler et al.[43] are compatible with this observation. These authors demonstrated that luciferase activity detected in HepG2 cells was significantly lower than in epithelial 293 cells transfected with polyethyleneimine (PEI)-complexes.

To pinpoint the cause of this failure, we performed a set of experiments to detect at what point(s) along the transfection pathway the CDplexes fail. We first determined whether or not the pDNA-CDplexes are internalized by HepG2 cells. Although we confirmed that they are taken up, it is conceivable that this occurs through an unproductive pathway. Díaz-Moscoso et al.[15] have shown that in Vero cells ligand-devoid pDNA-CDplexes were internalized by both clathrin-dependent and clathrin-independent endocytosis. The largest fraction of pDNA-CDplexes was taken up by the transfection-ineffective clathrin-dependent route. The CDplexes taken up this way end up in acidic late endosomes/lysosomes and therefore do not lead to expression of the reporter gene. It is the smaller fraction which is internalized via caveolae-mediated endocytosis that is predominantly responsible for productive transfection in these cells. Also, for pDNA/PEI-polyplexes it has been shown that it is predominantly the fraction which is taken up via caveolae-mediated endocytosis, which leads to gene expression.[44−46] In this context, it is important to stress that HepG2 cells lack endogenous caveolins which causes their inability to carry out caveolae-mediated endocytosis.[47] This implies that complexes carrying pDNA enter HepG2 cells via other pathways. Indeed, it has been reported that histidylated polylysine pDNA-complexes enter these cells via clathrin-mediated endocytosis and a macropinocytosis-like mechanism.[37]

The next step was to investigate if the transfection-limiting factor is the escape of CDplexes out of the endosomes. We provided evidence that this is also not the main problem by showing that the disruption of endosomes by PCI following uptake of CDplexes does not lead to enhanced transfection. Third, we demonstrated the ability of pDNA to be released from the CDplexes by conditions that mimic the endosomal environment. This suggests also that inside the cell the DNA is likely to be released from the complexes. Therefore, the nuclear envelope is remaining as the major barrier standing in the way of successful transfection of HepG2 cells with the pDNA-CDplexes. To obtain experimental evidence in favor of this hypothesis, we transfected HepG2 cells with mRNA instead of pDNA. As mRNA is translated in the cytoplasm, no transport step of the mRNA into the nucleus is required. We found up to

31% of GFP-positive cells upon transfection in OPTIMEM and full culture medium containing serum with mRNA-CDplexes, which is significantly higher even than with the jetPEI-Hepatocyte polymer, which is especially developed for *in vitro* hepatocyte transfections. By showing that mRNA-mediated transfection by the galactosylated CDplexes was effectively blocked by antibodies to ASGPr, we confirmed the involvement of this receptor in the transfection process.

The results obtained for mRNA-CDplexes indicate that even though they are internalized by receptor- mediated endocytosis they lead to efficient transfection. This is likely due to the fact that the translation of mRNA occurs in the cytosol. In contrast to pDNA, its release from the endosomal compartment does not have to coincide with cell division to ensure its translation. In the case of pDNA complexes, the release from the endosomal compartment should occur not long before cell division, in order to prevent the pDNA present in the cytosol from degradation by cytosolic nucleases. As reported by Lechardeur et al.,[48] the half-life of pDNA in the cytosol does not exceed 90 min. This leaves a narrow window for pDNA to enter the nucleus during mitosis.

Ideally, transfection of cells with mRNA complexes should result in 100% positive cells, but this number was not even approached. This might be explained by the occurrence of two distinct populations of ASGP receptors, which operate through two parallel but kinetically distinct endocytic pathways. Interestingly, the rate of ligand degradation is much faster in the State 1 receptor-mediated pathway and starts almost immediately after internalization. Differently, a distinct lag period between internalization and lysosomal localization was observed for ligand taken up via the State 2-dependent mechanism. In addition, recycling of ligand−receptor complex to the cell surface was only observed for the State 1 receptor-subtype.[49,50] These marked differences between the two receptor subpopulations lead us believe that only those mRNA-CDplexes that bind to State 2 receptors lead to successful transfection, basically because there is a larger time window for these complexes to timely escape from the endosomal compartment.

The less impressive performance of jetPEI-Hepatocyte complexed to mRNA could be explained by the fact that the polymer's affinity to mRNA is so strong it does not allow its release from once-formed complexes as demonstrated in our earlier work.[51]

A potential problem that may arise when applying our ASGPr-targeted CDplexes *in vivo* by intravenous administration is severe competition by other cell types, such as macrophages. PEGylation of particles has been shown to be quite effective in preventing or reducing the latter process and coupling of a ligand to the distal end of the PEG-molecule has been reported to improve cell-specific targeting.[52−54] Therefore, we also coupled the galactose-moieties to the distal end of the PEG-chain and showed that interaction with the ASGPr was fully restored after it was nearly abolished by just coupling the unmodified PEG to the CDplexes. We speculate that the distal coupling of galactose moieties to the PEG-chains in our CDplexes will also improve the selective uptake by hepatocytes upon intravenous application.

In conclusion, our results show that the modified paCDs may serve as a valuable mRNA delivery platform for the transient transfection of hepatocytes, further widening the potential of cyclodextrin-based vectors in gene therapy.[55] Using mRNA instead of pDNA would be a solution to the major problem associated with hepatocyte transfection, i.e., their low proliferation state, which is quite unfavorable for effective pDNA-mediated transfection.[1,56] Moreover, the use of mRNA would ensure no danger of introducing irreversible genetic modifications in the genome, often leading to oncogenesis or deactivation of vital genes. This feature defines mRNA-based transfection as a tool to deliver proteins to cells without interfering with their physiology. Therefore, it is expected that mRNA will prove its value in a broad range of therapeutic applications, as well as in basic research.

■ ASSOCIATED CONTENT

Supporting Information

^{1}H and ^{13}C NMR spectra of the different intermediates and conjugates are added as supplementary figures S1 to S13. The ability of the different CDs to complex pDNA and mRNA are shown in the supplementary figures S14 and S15. The viability data after mRNA transfection are added as supplementary figure S16. This material is available free of charge via the Internet at http://pubs.acs.org.

■ AUTHOR INFORMATION

Corresponding Author

*E-mail: j_rejman@hotmail.com, tel +3292648047, fax +3292648189.

Present Addresses

[#]School of Chemistry, University of East Anglia (UK).
[⊥]Department of Chemistry, Oxford University (UK).

Notes

The authors declare no competing financial interest.

■ ACKNOWLEDGMENTS

The Agency for Innovation through Science and Technology in Flanders (IWT) is acknowledged with gratitude for their financial support. Further, the Spanish Ministerio de Ciencia e Innovación (contract numbers SAF2010-15670 and CTQ2010-15848), the Fondo Europeo de Desarrollo Regional (FEDER), the Fondo Social Europeo (FSE), and the Junta de Andalucía are thanked for funding. We also thank the CITIUS (Universidad de Sevilla) for technical support.

■ ABBREVIATIONS

PEG, poly(ethylene glycol); paCDs, polycationic amphiphilic cyclodextrins; Hex-CD-N_{21}, a paCD: hexanoyl cyclodextrin with 21 protonable nitrogens; Reference CD, Hex-CD-N_{21} as a reference to evaluate the effect of galactose; this compound is not a reference for other paCDs; CDplexes, nucleic acid/cyclodextrin complexes; ASGPr, asialoglycoprotein receptor; Gal10CDs, 10% triantennary-galactose-bearing Hex-CD-N_{21}; Gal12CDs, 12% triantennary-galactose-bearing Hex-CD-N_{21}; PEGCDs, 13% thio-PEG5000-bearing Hex-CD-N_{21}; Gal-PEGCDs, 10% thio-PEG5000-triantennary-galactose-bearing Hex-CD-N_{21}; PCI, photochemical internalization; PhSen, photosensitizer; gaCDs, neutral glycoamphiphilic cyclodextrins

■ REFERENCES

(1) Nguyen, T. H., and Ferry, N. (2004) Liver gene therapy: advances and hurdles. *Gene Ther. 11* (Suppl 1), S76−84.

(2) Suda, T., Kamimura, K., Kubota, T., Tamura, Y., Igarashi, M., Kawai, H., Aoyagi, Y., and Liu, D. (2009) Progress toward liver-based gene therapy. *Hepatol. Res. 39*, 325−40.

(3) Braeckmans, K., Buyens, K., Bouquet, W., Vervaet, C., Joye, P., De Vos, F., Plawinski, L., Doeuvre, L., Angles-Cano, E., Sanders, N. N.,

Demeester, J., De Smedt, S. C. (2010) Sizing nanomatter in biological fluids by fluorescence single particle tracking. *Nano Lett. 10* 4435-42.
(4) Jooss, K., Ertl, H. C., and Wilson, J. M. (1998) Cytotoxic T-lymphocyte target proteins and their major histocompatibility complex class I restriction in response to adenovirus vectors delivered to mouse liver. *J. Virol. 72*, 2945−54.
(5) Mingozzi, F., Liu, Y. L., Dobrzynski, E., Kaufhold, A., Liu, J. H., Wang, Y., Arruda, V. R., High, K. A., and Herzog, R. W. (2003) Induction of immune tolerance to coagulation factor IX antigen by in vivo hepatic gene transfer. *J. Clin. Invest. 111*, 1347−56.
(6) Follenzi, A., Battaglia, M., Lombardo, A., Annoni, A., Roncarolo, M. G., and Naldini, L. (2004) Targeting lentiviral vector expression to hepatocytes limits transgene-specific immune response and establishes long-term expression of human antihemophilic factor IX in mice. *Blood 103*, 3700−9.
(7) Wu, G. Y., and Wu, C. H. (1988) Receptor-mediated gene delivery and expression in vivo. *J. Biol. Chem. 263*, 14621−4.
(8) Ryan, S. M., Mantovani, G., Wang, X., Haddleton, D. M., and Brayden, D. J. (2008) Advances in PEGylation of important biotech molecules: delivery aspects. *Expert Opin. Drug Delivery 5*, 371−83.
(9) Mintzer, M. A., and Simanek, E. E. (2009) Nonviral vectors for gene delivery. *Chem. Rev. 109*, 259−302.
(10) Kay, M. A., Glorioso, J. C., and Naldini, L. (2001) Viral vectors for gene therapy: the art of turning infectious agents into vehicles of therapeutics. *Nat. Med. 7*, 33−40.
(11) Nayak, S., and Herzog, R. W. (2010) Progress and prospects: immune responses to viral vectors. *Gene Ther. 17*, 295−304.
(12) Kasuya, T., and Kuroda, S. (2009) Nanoparticles for human liver-specific drug and gene delivery systems: in vitro and in vivo advances. *Expert Opin. Drug Delivery 6*, 39−52.
(13) Diaz-Moscoso, A., Balbuena, P., Gomez-Garcia, M., Ortiz Mellet, C., Benito, J. M., Le Gourrierec, L., Di Giorgio, C., Vierling, P., Mazzaglia, A., Micali, N., Defaye, J., and Garcia Fernandez, J. M. (2008) Rational design of cationic cyclooligosaccharides as efficient gene delivery systems. *Chem. Commun.*, 2001−3.
(14) Diaz-Moscoso, A., Le Gourrierec, L., Gomez-Garcia, M., Benito, J. M., Balbuena, P., Ortega-Caballero, F., Guilloteau, N., Di Giorgio, C., Vierling, P., Defaye, J., Ortiz Mellet, C., and Garcia Fernandez, J. M. (2009) Polycationic amphiphilic cyclodextrins for gene delivery: synthesis and effect of structural modifications on plasmid DNA complex stability, cytotoxicity, and gene expression. *Chem.—Eur. J. 15*, 12871−88.
(15) Diaz-Moscoso, A., Vercauteren, D., Rejman, J., Benito, J. M., Ortiz Mellet, C., De Smedt, S. C., and Garcia Fernandez, J. M. (2010) Insights in cellular uptake mechanisms of pDNA-polycationic amphiphilic cyclodextrin nanoparticles (CDplexes). *J. Controlled Release 143*, 318−25.
(16) Mendez-Ardoy, A., Urbiola, K., Aranda, C., Ortiz-Mellet, C., Garcia Fernandez, J. M., and Tros de Ilarduya, C. (2011) Polycationic amphiphilic cyclodextrin-based nanoparticles for therapeutic gene delivery. *Nanomedicine 6*, 1697−707.
(17) Mislick, K. A., and Baldeschwieler, J. D. (1996) Evidence for the role of proteoglycans in cation-mediated gene transfer. *Proc. Natl. Acad. Sci. U. S. A. 93*, 12349−54.
(18) Baeuerle, P. A., and Huttner, W. B. (1986) Chlorate--a potent inhibitor of protein sulfation in intact cells. *Biochem. Biophys. Res. Commun. 141*, 870−7.
(19) Mounkes, L. C., Zhong, W., Cipres-Palacin, G., Heath, T. D., and Debs, R. J. (1998) Proteoglycans mediate cationic liposome-DNA complex-based gene delivery in vitro and in vivo. *J. Biol. Chem. 273*, 26164−70.
(20) Diaz-Moscoso, A., Guilloteau, N., Bienvenu, C., Mendez-Ardoy, A., Blanco, J. L., Benito, J. M., Le Gourrierec, L., Di Giorgio, C., Vierling, P., Defaye, J., Ortiz Mellet, C., and Garcia Fernandez, J. M. (2011) Mannosyl-coated nanocomplexes from amphiphilic cyclodextrins and pDNA for site-specific gene delivery. *Biomaterials 32*, 7263−73.
(21) Bernardes, G. J., Kikkeri, R., Maglinao, M., Laurino, P., Collot, M., Hong, S. Y., Lepenies, B., and Seeberger, P. H. (2010) Design, synthesis and biological evaluation of carbohydrate-functionalized cyclodextrins and liposomes for hepatocyte-specific targeting. *Org. Biomol. Chem. 8*, 4987−96.
(22) Bianucci, A. M., and Chiellini, F. (2000) A 3D model for the human hepatic asialoglycoprotein receptor (ASGP-R). *J. Biomol. Struct. Dyn. 18*, 435−51.
(23) Wragg, S., and Drickamer, K. (1999) Identification of amino acid residues that determine pH dependence of ligand binding to the asialoglycoprotein receptor during endocytosis. *J. Biol. Chem. 274*, 35400−6.
(24) Novikoff, P. M., Cammer, M., Tao, L., Oda, H., Stockert, R. J., Wolkoff, A. W., and Satir, P. (1996) Three-dimensional organization of rat hepatocyte cytoskeleton: relation to the asialoglycoprotein endocytosis pathway. *J. Cell Sci. 109* (Pt 1), 21−32.
(25) Geuze, H. J., Slot, J. W., Strous, G. J., Lodish, H. F., and Schwartz, A. L. (1983) Intracellular site of asialoglycoprotein receptor-ligand uncoupling: double-label immunoelectron microscopy during receptor-mediated endocytosis. *Cell 32*, 277−87.
(26) Schwartz, A. L. (1991) Trafficking of asialoglycoproteins and the asialoglycoprotein receptor. *Targeted Diagn. Ther. 4*, 3−39.
(27) Signoret, N., Christophe, T., Oppermann, M., and Marsh, M. (2004) pH-independent endocytic cycling of the chemokine receptor CCR5. *Traffic (Copenhagen, Denmark) 5*, 529−43.
(28) DiPaola, M., and Maxfield, F. R. (1984) Conformational changes in the receptors for epidermal growth factor and asialoglycoproteins induced by the mildly acidic pH found in endocytic vesicles. *J. Biol. Chem. 259*, 9163−71.
(29) Clarke, B. L., Oka, J. A., and Weigel, P. H. (1987) Degradation of asialoglycoproteins mediated by the galactosyl receptor system in isolated hepatocytes. Evidence for two parallel pathways. *J. Biol. Chem. 262*, 17384−92.
(30) Sarkar, M., Liao, J., Kabat, E. A., Tanabe, T., and Ashwell, G. (1979) The binding site of rabbit hepatic lectin. *J. Biol. Chem. 254*, 3170−4.
(31) Rice, K. G., and Lee, Y. C. (1993) Oligosaccharide valency and conformation in determining binding to the asialoglycoprotein receptor of rat hepatocytes. *Adv. Enzymol. Relat. Areas Mol. Biol. 66*, 41−83.
(32) Khorev, O., Stokmaier, D., Schwardt, O., Cutting, B., and Ernst, B. (2008) Trivalent, Gal/GalNAc-containing ligands designed for the asialoglycoprotein receptor. *Bioorg. Med. Chem. 16*, 5216−31.
(33) Biessen, E. A., Bakkeren, H. F., Beuting, D. M., Kuiper, J., and Van Berkel, T. J. (1994) Ligand size is a major determinant of high-affinity binding of fucose- and galactose-exposing (lipo)proteins by the hepatic fucose receptor. *Biochem. J. 299* (Pt 1), 291−6.
(34) Zegers, M. M., and Hoekstra, D. (1998) Mechanisms and functional features of polarized membrane traffic in epithelial and hepatic cells. *Biochem. J. 336* (Pt 2), 257−69.
(35) Knowles, B. B., Howe, C. C., and Aden, D. P. (1980) Human hepatocellular carcinoma cell lines secrete the major plasma proteins and hepatitis B surface antigen. *Science 209*, 497−9.
(36) Haque, M. B., Roberts, B. P., and Tocher, D. A. (1998) Enantioselective radical-chain hydrosilylation of alkenes using homochiral thiols as polarity-reversal catalysts. *J. Chem. Soc., Perkin Trans. 1*, 2881−2889.
(37) Lubineau, A., Malleron, A., and Le Narvor, C. (2000) Chemo-enzymatic synthesis of oligosaccharides using a dendritic soluble support. *Tetrahedron Lett. 41*, 8887−8891.
(38) Li, G., Tajima, H., and Ohtani, T. (1997) An improved procedure for the preparation of isothiocyanates from primary amines by using hydrogen peroxide as the dehydrosulfurization reagent. *J. Org. Chem. 62*, 4539−4540.
(39) Xu, Y., and Szoka, F. C., Jr. (1996) Mechanism of DNA release from cationic liposome/DNA complexes used in cell transfection. *Biochemistry 35*, 5616−23.
(40) Breton, M., Leblond, J., Seguin, J., Midoux, P., Scherman, D., Herscovici, J., Pichon, C., and Mignet, N. (2010) Comparative gene transfer between cationic and thiourea lipoplexes. *J. Gene Med. 12*, 45−54.

(41) Gref, R., Luck, M., Quellec, P., Marchand, M., Dellacherie, E., Harnisch, S., Blunk, T., and Muller, R. H. (2000) 'Stealth' corona-core nanoparticles surface modified by polyethylene glycol (PEG): influences of the corona (PEG chain length and surface density) and of the core composition on phagocytic uptake and plasma protein adsorption. *Colloids Surf., B: Biointerfaces 18*, 301−313.
(42) Candiani, G., Pezzoli, D., Ciani, L., Chiesa, R., and Ristori, S. (2010) Bioreducible liposomes for gene delivery: from the formulation to the mechanism of action. *PLoS One 5*, e13430.
(43) Kichler, A., Leborgne, C., Coeytaux, E., and Danos, O. (2001) Polyethylenimine-mediated gene delivery: a mechanistic study. *J. Gene Med. 3*, 135−44.
(44) Rejman, J., Bragonzi, A., and Conese, M. (2005) Role of clathrin- and caveolae-mediated endocytosis in gene transfer mediated by lipo- and polyplexes. *Mol. Ther. 12*, 468−74.
(45) Rejman, J., Conese, M., and Hoekstra, D. (2006) Gene transfer by means of lipo- and polyplexes: role of clathrin and caveolae-mediated endocytosis. *J. Liposome Res. 16*, 237−47.
(46) Goncalves, C., Mennesson, E., Fuchs, R., Gorvel, J. P., Midoux, P., and Pichon, C. (2004) Macropinocytosis of polyplexes and recycling of plasmid via the clathrin-dependent pathway impair the transfection efficiency of human hepatocarcinoma cells. *Mol. Ther. 10*, 373−85.
(47) Fujimoto, T., Kogo, H., Nomura, R., and Une, T. (2000) Isoforms of caveolin-1 and caveolar structure. *J. Cell Sci. 113* (Pt 19), 3509−17.
(48) Lechardeur, D., Sohn, K. J., Haardt, M., Joshi, P. B., Monck, M., Graham, R. W., Beatty, B., Squire, J., O'Brodovich, H., and Lukacs, G. L. (1999) Metabolic instability of plasmid DNA in the cytosol: a potential barrier to gene transfer. *Gene Ther. 6*, 482−497.
(49) Oka, J. A., and Weigel, P. H. (1983) Recycling of the asialoglycoprotein receptor in isolated rat hepatocytes. Dissociation of internalized ligand from receptor occurs in two kinetically and thermally distinguishable compartments. *J. Biol. Chem. 258*, 10253−62.
(50) Weigel, P. H., Clarke, B. L., and Oka, J. A. (1986) The hepatic galactosyl receptor system: two different ligand dissociation pathways are mediated by distinct receptor populations. *Biochem. Biophys. Res. Commun. 140*, 43−50.
(51) Rejman, J., Tavernier, G., Bavarsad, N., Demeester, J., and De Smedt, S. C. (2010) mRNA transfection of cervical carcinoma and mesenchymal stem cells mediated by cationic carriers. *J. Controlled Release 147*, 385−91.
(52) Guo, W., and Lee, R. L. (1999) Receptor-targeted gene delivery via folate-conjugated polyethylenimine. *AAPS PharmSci 1*, E19.
(53) Brown, M. D., Gray, A. I., Tetley, L., Santovena, A., Rene, J., Schatzlein, A. G., and Uchegbu, I. F. (2003) In vitro and in vivo gene transfer with poly(amino acid) vesicles. *J. Controlled Release 93*, 193−211.
(54) Frisch, B., Carriere, M., Largeau, C., Mathey, F., Masson, C., Schuber, F., Scherman, D., and Escriou, V. (2004) A new triantennary galactose-targeted PEGylated gene carrier, characterization of its complex with DNA, and transfection of hepatoma cells. *Bioconjugate Chem. 15*, 754−64.
(55) Ortiz Mellet, C., García Fernández, J. M., and Benito, J. M. (2011) Cyclodextrin-based gene delivery systems. *Chem. Soc. Rev. 40*, 1586−1608.
(56) Nguyen, T. H., Pages, J. C., Farge, D., Briand, P., and Weber, A. (1998) Amphotropic retroviral vectors displaying hepatocyte growth factor-envelope fusion proteins improve transduction efficiency of primary hepatocytes. *Hum. Gene Ther. 9*, 2469−79.

Bioconjugate Chemistry

Article

pubs.acs.org/bc

Disulfide-Containing Brushed Polyethylenimine Derivative Synthesized by Click Chemistry for Nonviral Gene Delivery

Guangyan Zhang, Jia Liu, Qizhi Yang, Renxi Zhuo, and Xulin Jiang*

Key Laboratory of Biomedical Polymers of Ministry of Education and Department of Chemistry, Wuhan University, Wuhan 430072, P.R. China

Supporting Information

ABSTRACT: Polyaspartamide-based disulfide-containing brushed polyethylenimine derivatives P(Asp-Az)$_X$-SS-PEIs were synthesized via click chemistry and evaluated as nonviral gene delivery carrier. First, azide-functional poly(aspartic acid) derivatives with various azide-group densities and monoalkyne-terminated PEI with disulfide linkages were synthesized. Then, click reaction between the azide-functional poly(aspartic acid) derivative as main chain and the monoalkyne-terminated PEI as branched chain resulted in high-molecular-weight disulfide-containing brushed PEI derivative. The structure of obtained polymers was confirmed by ^{1}H NMR and FTIR. It was shown that the disulfide-containing P(Asp-Az)$_X$-SS-PEIs were able to bind plasmid DNA and condense DNA into small positive nanoparticles. The reduction-sensitivity of the P(Asp-Az)$_X$-SS-PEI/DNA polyplexes was confirmed by gel retardation assay and dynamic light scattering (DLS) in the presence of DTT. In vitro experiments revealed that the reducible P(Asp-Az)$_X$-SS-PEI not only had much lower cytotoxicity, but also posed high transfection activity (both in the presence and absence of serum) as compared to the control nondegradable 25 kDa PEI. This study indicates that a reducibly degradable brushed polymer P(Asp-Az)$_X$-SS-PEI composed of low-molecular-weight (LMW) PEI via a disulfide-containing linkage can be a promising gene delivery carrier.

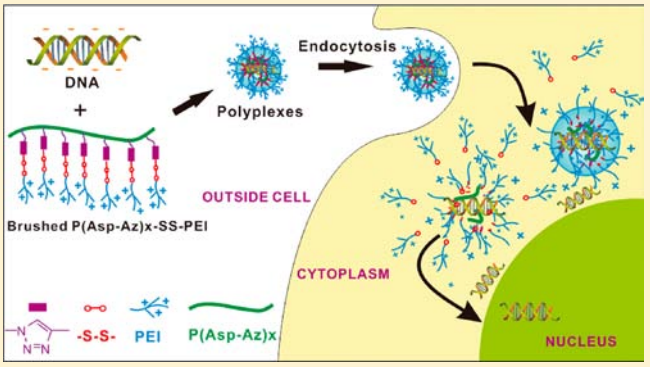

INTRODUCTION

Gene therapy was viewed as an approach for treating hereditary diseases and acquired diseases such as cancer.[1] Cationic nonviral vectors, which interact with negatively charged DNA through electrostatic interactions leading to polyplexes, can enhance cellular uptake efficiency and improve transfection efficiency compared with naked DNA.[2] Polyethylenimine (PEI) has a privileged place in nonviral polymeric gene delivery systems due to the superior transfection efficiency of PEI-based polyplexes, probably caused by its proton sponge effect.[3,4] However, the high amount of positive charges and their non-biodegradability result in fairly high cytotoxicity of PEIs, especially for high-molecular-weight (HMW) PEIs, such as 25 kDa PEI.[5] Low-molecular-weight (LMW) PEIs such as 1.8 kDa PEI are reported to be less cytotoxic but less effective in gene transfection.[6]

In order to enhance the transfection efficiency and reduce the cytotoxicity, hydrolytically degradable[7−9] and reductively degradable[10−13] cationic polymers have been designed for gene delivery. Göpferich et al.[14] have published a good review on the reducible disulfide-containing polymers for gene delivery. Reductively degradable polymers with disulfide linkage are usually stable in blood circulation[15] and can degrade rapidly (minutes to hours) and release DNA in the presence of reductive 1,4-dithio-DL-threitol (DTT) or glutathione (GSH) mimicking the reductive intracellular environment.[16,17] Therefore, the introduction of disulfide bridges in the main chain,[18−21] in side chains,[22] or in the cross-links[23−25] of polymers has been widely investigated for the design of polymeric gene delivery carriers.

Brushed polymers have recently received much attention due to their unique chemical and physical properties, as well as their potential applications in gene delivery.[26−29] Huang et al.[30] reported polyaspartamide-based oligo-ethylenimine brushes from poly(L-succinimide) (PSI) via the ring-opening reaction with linear PEI (Mn = 423) as gene delivery vector. Cho et al.[31] synthesized brushed PEI for gene delivery by the ring-opening reaction of PSI with branched LMW PEI (with molecular weight of 0.6 kDa or 1.2 kDa). However, there are many active amino groups in one PEI molecule; the ring-opening reactions between PSI and PEI had poor selectivity and should be carefully controlled to avoid cross-linking.[30]

Because of the high selectivity and high fidelity, "click" chemistry has rapidly become a very popular method for polymer synthesis and modification.[32,33] However, no report has been published on reducible brushed PEI via click

Received: March 16, 2012
Revised: May 8, 2012
Published: May 23, 2012

Scheme 1. Synthesis Route towards P(Asp-Az)$_X$-SS-PEI

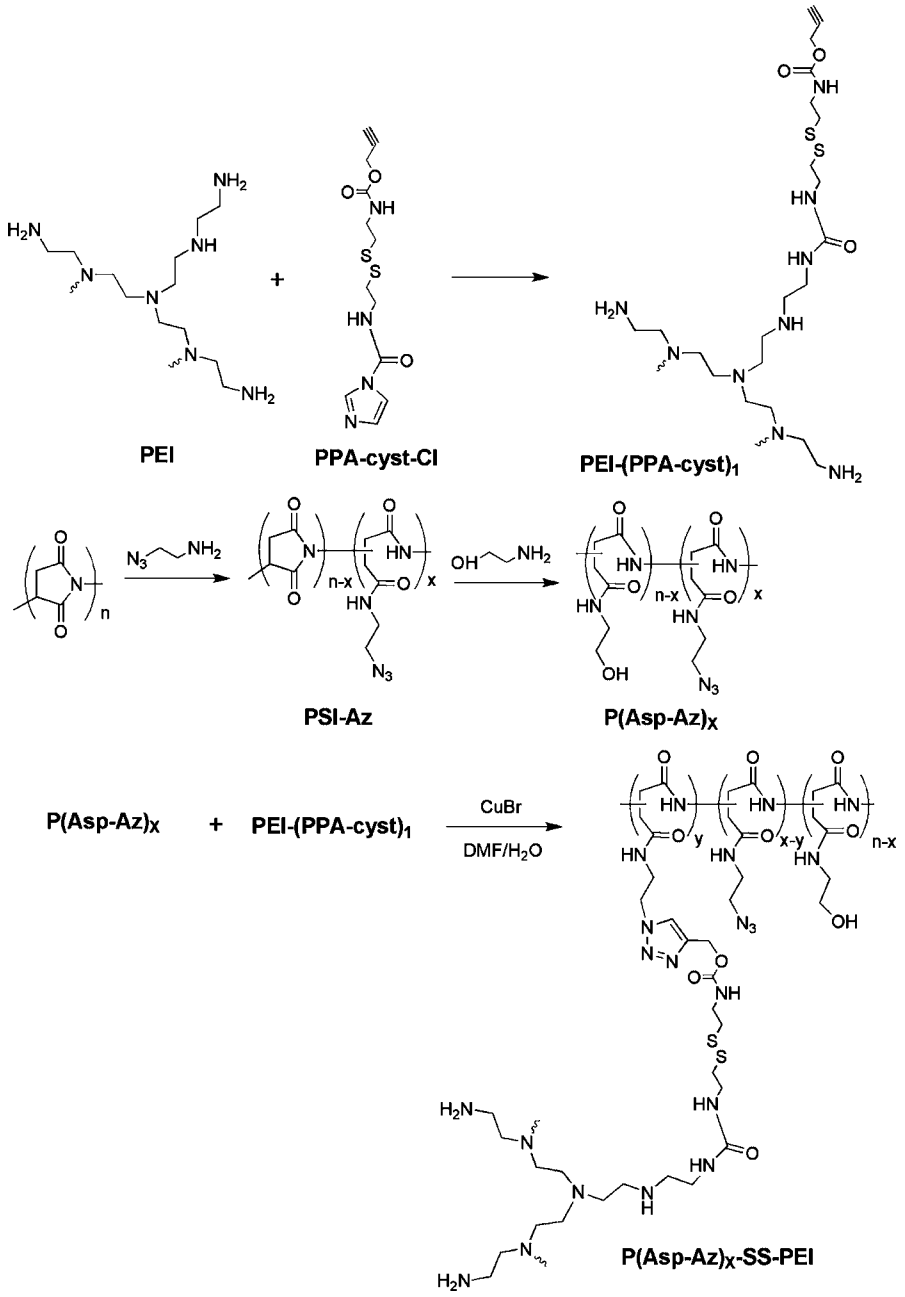

chemistry for gene delivery so far. In our previous work, hydrolytically degradable brushed pHEMA–pDMAEMA,[9] reduction-responsive cross-linked,[25] and hyperbranched[34] polyethylenimine derivatives containing disulfide bridges synthesized via click reaction were investigated as gene delivery carriers. In this study, a new strategy for synthesis of disulfide-containing polyaspartamide-based brushed polyethylenimine derivatives P(Asp-Az)$_X$-SS-PEIs via click reaction is explored, as depicted in Scheme 1. This paper describes the synthesis of the disulfide-containing brushed polyethylenimine derivative and the reduction sensitivity and gene transfection activities of the corresponding polyplexes.

EXPERIMENTAL PROCEDURES

Materials. Branched polyethylenimine (PEI) with molecular weight of 1.8 kDa was purchased from Alfa Aesar, and branched PEI with molecular weight of 25 kDa was from Sigma-Aldrich. 2-Bromoethylamine hydrobromide (Shanghai Nanxiang Reagent Co., Ltd., China), 1,1′-carbonyldiimidazole (CDI) (Shanghai Medpep Co., Ltd., China), propargyl alcohol (Wuhan FengFan Chemical Co., Ltd., China), cystamine dihydrochloride (Jiangsu Jintan Medicine Chemical Factory, Jiangsu, China), and 1,4-dithio-DL-threitol (DTT) (Sigma-Aldrich) were used as received. Plasmid pcDNA3-Luc in TE buffer with concentration of 5.0 mg/mL was from Plasmid-Factory (Germany). The purified plasmids were diluted with TE buffer solution and stored at −20 °C. All other chemicals were analytical grade and used as received.

Synthesis of Monoalkyne-Functionalized PEI Derivative. A general procedure for the synthesis of monoalkyne-functionalized PEI derivative [PEI$_{1800}$-(PPA-Cyst)$_1$] has been described in our previous work.[34] Here, a slightly modified

dx.doi.org/10.1021/bc300133r | Bioconjugate Chem. 2012, 23, 1290−1299

version has been used: (propargylcarbamate)ethyldisulfide ethyl-1-carbamide-imidazole (PPA-cyst-CI, 0.33 g, 1 mmol) dissolved in chloroform (30 mL) was slowly dropped (around 2 h) into a solution of 1.8 kDa PEI (5.40 g, 3 mmol, 30.75 mmol of primary amine groups, assuming that the primary amine content of the 1.8 kDa PEI is 25% of the total amines) in chloroform (80 mL). Next, the reaction mixture was refluxed using an oil bath (60 °C) for 24 h. The chloroform was removed yielding a yellow liquid (5.61 g, containing imidazole) with a yield of 98%. The structure of the obtained PEI_{1800}-$(PPA\text{-}Cyst)_1$ was confirmed by ^1H NMR and FTIR spectra (Figure S1 and Figure S2).

Synthesis of Azide-Functional Poly(aspartic acid). Poly(L-succinimide) (PSI) was synthesized according to the literature[35] and characterized by ^1H NMR in d_6-DMSO (Figure 1D). The molecular weight and the molecular weight

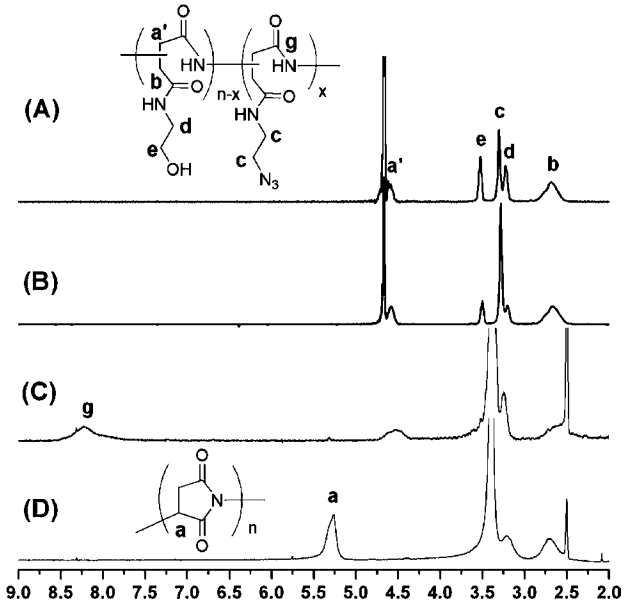

Figure 1. ^1H NMR spectra of (A) $P(Asp\text{-}Az)_{33}$ and (B) $P(Asp\text{-}Az)_{65}$ in D_2O, (C) $P(Asp\text{-}Az)_{100}$, and (D) Poly(L-succinimide) in d_6-DMSO.

distribution (MWD) of the PSI were evaluated by size-exclusion chromatography-multiangle light scattering (SEC-MALLS) using DMF as eluent. The weight-average molecular weight and MWD of PSI are 18.0 kDa and 1.29, respectively.

2-Azidoethylamine was synthesized according to the literature.[36] The details describing synthesis and characterization of 2-azidoethylamine are provided in the Supporting Information (Figure S3 and Figure S4). PSI (0.28 g, 2.89 mmol) and varying amounts of 2-azidoethylamine were dissolved in 3 mL DMF. The mixture was left to react at room temperature for 4 days. The resulting solution was added to ether slowly and the formed white precipitate was collected and dried in vacuum to obtain azide-functional poly(L-succinimide) (PSI-Az). The reaction efficiency of 2-azidoethylamine with PSI determined by ^1H NMR analysis was about 80% (Table 1). The remaining succinimide rings of PSI-Az were further reacted at room temperature for 4 days in DMF with excess ethanolamine. The azide group content for the obtained azide-functional poly(aspartic acid)s was determined by ^1H NMR analysis (Figure 1). The polymers are denoted as $P(Asp\text{-}Az)_X$, where X represents the average number of azide groups per 100 polymer units. The molecular weights and

Table 1. Synthesis and Characterization of Azide-Functional Poly(aspartic acid)s

sample	molar feed ratio of 2-azidoethylamine to the polymer unit of PSI	average number of azide groups per 100 polymer units[a]	M_w[b] (kDa)	PDI[b]
$P(Asp\text{-}Az)_{33}$	0.4	33	26	1.40
$P(Asp\text{-}Az)_{65}$	0.8	65	26	1.41
$P(Asp\text{-}Az)_{100}$	2	100	27	1.47

[a]Calculated from ^1H NMR spectra. [b]Estimated by SEC-MALLS in DMF.

MWDs of $P(Asp\text{-}Az)_X$ were evaluated by SEC-MALLS using DMF as eluent. The results were summarized in Table 1. FTIR analysis of the resulting product showed an absorption peak at 2100 cm^{-1} corresponding to the azide group (Figure 2A).

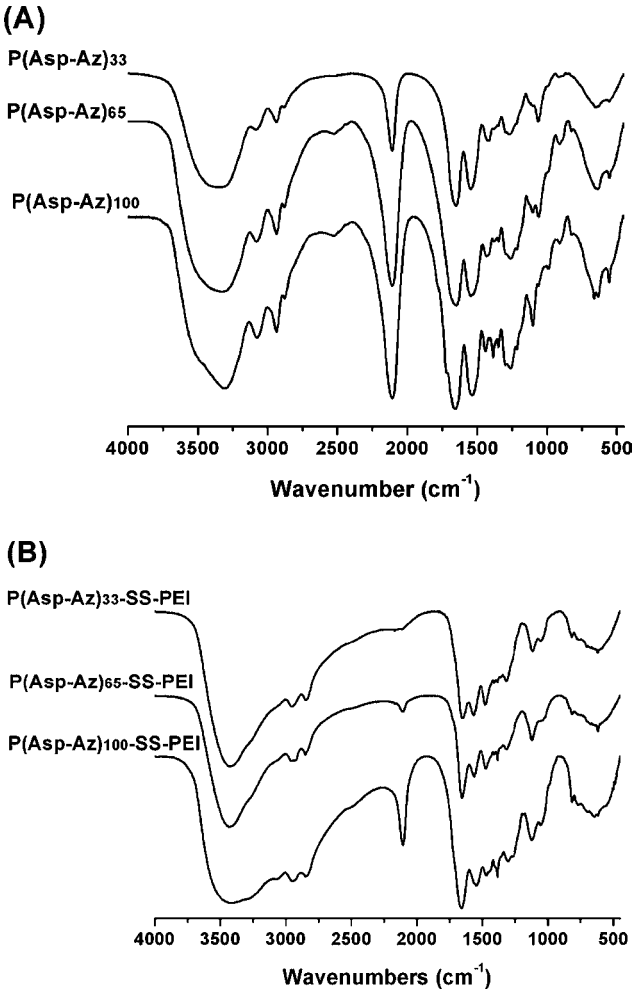

Figure 2. FTIR spectra of (A) $P(Asp\text{-}Az)_X$ and (B) $P(Asp\text{-}Az)_X$-SS-PEI.

Synthesis of Disulfide-Containing Brushed PEI Derivative via Click Reaction. Azide-functional $P(Asp\text{-}Az)_X$ (50 mg, 1 equiv azide groups) and monoalkyne-functionalized PEI_{1800}-$(PPA\text{-}Cyst)_1$ (2 equiv alkyne groups) were dissolved in 10 mL solvent (water, DMF, or the mixture of water and DMF; see Table 2). CuBr (20 mg) was added as catalyst under a nitrogen atmosphere. The reaction mixture was stirred at 50 °C

dx.doi.org/10.1021/bc300133r | Bioconjugate Chem. 2012, 23, 1290−1299

Table 2. Synthesis and Characterization of Disulfide-Containing P(Asp-Az)$_X$-SS-PEIs

sample	solvent (the mixture of water and DMF) (v%)	percentage of reacted azide group[a]	percentage of grafted PEI$_{1800}$-(PPA-Cyst)$_1$ to the polymer unit of P(Asp-Az)$_X$[a]	W_{PEI}(%)[a]	M_w[b] (kDa)	PDI[b]
P(Asp-Az)$_{33}$-SS-PEI	100% water	33.9%	11.2%	51	140	1.92
P(Asp-Az)$_{65}$-SS-PEI	50% water	9.5%	6.2%	37	63	2.15
P(Asp-Az)$_{100}$-SS-PEI	100% DMF	3.6%	3.6%	25	-	-

[a]Calculated from ^{1}H NMR spectra (see the calculation method of the percentage of grafted PEI$_{1800}$-(PPA-Cyst)$_1$ to the polymer unit of P(Asp-Az)$_X$ in Supporting Information). [b]Estimated by aqueous SEC-MALLS.

for 2 days. The resulting solution was purified by dialysis against water for 1 week (dialysis tube, MWCO 3.5 kDa) to remove unreacted PEI$_{1800}$-(PPA-Cyst)$_1$ and unmodified PEI, and the formed disulfide-containing brushed PEI derivative P(Asp-Az)$_X$-SS-PEI was collected after freeze−drying.

The structure of the P(Asp-Az)$_X$-SS-PEI was analyzed by ^{1}H NMR (Figure 3) and FTIR (Figure 2B). The molecular weights were obtained by aqueous SEC-MALLS as described below.

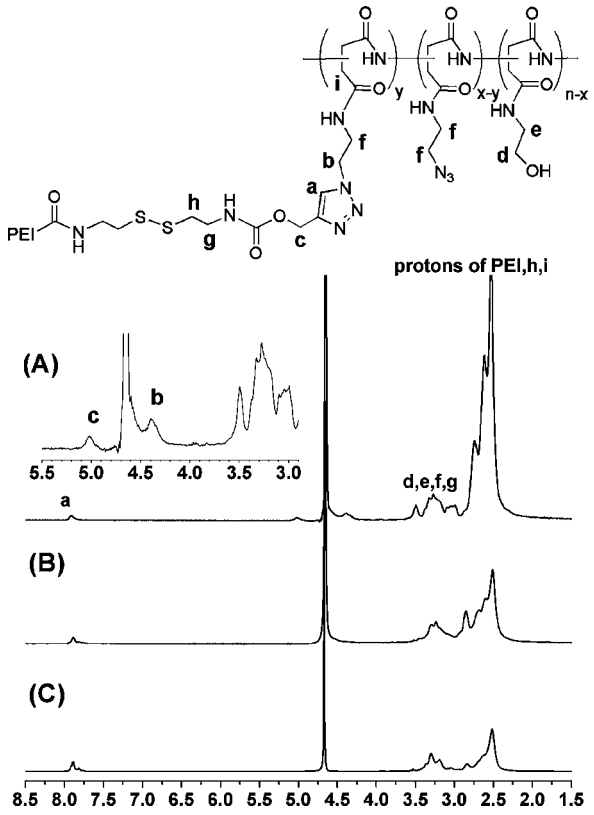

Figure 3. ^{1}H NMR spectra of (A) P(Asp-Az)$_{33}$-SS-PEI, (B) P(Asp-Az)$_{65}$-SS-PEI, and (C) P(Asp-Az)$_{100}$-SS-PEI in D_2O.

Characterizations. ^{1}H nuclear magnetic resonance (^{1}H NMR) spectra were determined with Mercury VX-300 spectrometer (300 MHz, Varian, USA). Fourier transformed infrared (FTIR) spectra were recorded on a Spectrum one spectrometer (Perkin-Elmer). The molecular weights and the molecular weight distributions of the polymers were evaluated by SEC-MALLS system consisting of a Waters 2690D separations module, a Waters 2414 refractive index detector (RI), and a Wyatt DAWN EOS MALLS detector. For aqueous SEC, two chromatographic columns (Shodex OHpak SB-803 and SB-802.5, Showa Denko, Japan) with a precolumn (Shodex SB-G) were used in series. Sodium acetate (NaAc) solution was prepared by dissolving a calculated amount of sodium acetate in reverse osmosis water (0.3 M), and the pH was adjusted to 4.4 with acetic acid.[37] A mixture of 70% 0.3 M NaAc solution, pH 4.4, and 30% acetonitrile was used as the eluent at a flow rate of 0.3 mL/min. For SEC in DMF, two chromatographic columns (Styragel HR3, HR4) with a precolumn were used in series. DMF containing 10 mM LiBr was used as the mobile phase at a flow rate of 0.3 mL/min at 30 °C. The eluent was filtrated through a 0.22 μm HPLC filter and degassed prior to use by ultrasound. The data were processed with *Astra* software (Wyatt Technology).

Cell Culture. Human embryonic kidney transformed (293T) cells were incubated in Dulbecco's Modified Eagle's Medium (DMEM) containing 10% fetal bovine serum (FBS), 100 units/mL penicillin, and 100 mg/L streptomycin at 37 °C under a humidified atmosphere of 95% air and 5% CO_2.

Cytotoxicity Assay. The cytotoxicity of the different polymers was studied using the MTT assay on 293T cells. The cells were seeded into 96-well plates at a density of 3000 cells/well and 100 μL DMEM containing 10% FBS was added. The cells were allowed to grow at 37 °C under a humidified atmosphere of 95% air and 5% CO_2 for 48 h. Thereafter, the medium was replaced with 100 μL of fresh medium, and 100 μL solution of P(Asp-Az)$_X$-SS-PEI or 25 kDa PEI were added (final polymer concentrations ranging from 0.01 to 0.20 mg/mL). The cells were incubated for 24 h and the medium containing polymer solution was replaced with 200 μL fresh medium. Next, the MTT reagent (20 μL in PBS, 5 mg/mL) was added to each well for further 4 h incubation at 37 °C. Then, the medium was removed and 100 μL of DMSO was added to dissolve the formed formazan crystals. The absorbance at 570 nm was recorded using Multiskan GO microplate spectrophotometer (Thermo Scientific, USA). The relative cell viability (mean ± SD, n = 4) was calculated as cell viability = $(OD_{sample} - OD_{blank})/(OD_{control} - OD_{blank}) \times 100\%$, where OD_{sample} is the absorbance of solution with cells treated by polymers, $OD_{control}$ is the absorbance for untreated cells (without polymer), and OD_{blank} is the absorbance without cells.

Formation of P(Asp-Az)$_X$-SS-PEI/DNA Polyplexes and Agarose Gel Retardation Assay. P(Asp-Az)$_X$-SS-PEI based complexes were prepared by addition of 5 μL polymer solution with designed concentrations in HBS (20 mM HEPES, 130 mM NaCl, pH 7.4) to 1 μL of pcDNA3-Luc plasmid DNA (100 ng/μL in TE buffer). The resulting polyplexes dispersions were incubated at 37 °C for 30 min and were then analyzed by electrophoresis in a 0.7% (w/v) agarose gel containing GelRed and in Tris-acetate (TAE) running buffer at 80 V for 60 min. DNA bands were visualized with a UV (254 nm) illuminator and photographed with a Vilber Lourmat imaging system.

Particle Size and Zeta Potential Measurements. Particle size of the polyplexes was examined in HBS by DLS (dynamic light scattering). The desired amounts of cationic polymers were diluted in 800 μL HBS and mixed with 200 μL HBS containing DNA. The amount of polymer used was calculated on the basis of chosen w/w ratios (weight of polymer to DNA). Zeta potentials of polyplexes were examined in HBG (20 mM HEPES, 5% glucose, pH 7.4). The polyplexes of various w/w ratios prepared as described above were incubated at 37 °C for 30 min. Particle size and ζ-potential were measured by Nano-ZS ZEN3600 (Malvern Instruments) at 25 °C.

Reduction Sensitivity of Polyplexes. To 1 mL of dispersions of P(Asp-Az)$_X$-SS-PEI/DNA polyplexes prepared at w/w ratios ranging from 0.2 to 1.4, 100 μL of 100 mM DTT in HBS was added The polyplexes were incubated at 37 °C for 30 min and were then analyzed by electrophoresis in a 0.7% (w/v) agarose gel containing GelRed and in Tris-acetate (TAE) running buffer at 80 V for 60 min.

The reduction sensitivity of P(Asp-Az)$_X$-SS-PEI/DNA polyplexes in response to DTT in HBS was also monitored by DLS measurement. Briefly, to a glass cell containing 1 mL P(Asp-Az)$_X$-SS-PEI/DNA polyplexes (w/w ratio of 2.5) in HBS incubated at 37 °C for 30 min, 10 μL of 1.0 M DTT was added. After mixing, the particle size of the polyplexes was monitored at constant time intervals by DLS. The polyplex solution in HBS without DTT was also measured as control.

Luciferase Transfection Assay. Transfection activity of polyplexes based on pcDNA3-Luc plasmid, complexed with P(Asp-Az)$_X$-SS-PEI or 25 kDa PEI, was evaluated in 293T cells. The cells were seeded at a density of 70 000 cells/well in a 24-well plate. Subsequently, 1 mL of DMEM containing of 10% FBS was added and the cells were incubated at 37 °C in a humidified atmosphere of 95% air and 5% CO_2 for 24 h. Next, the medium in each well was replaced by 0.9 mL of serum-free DMEM. The polymer/DNA polyplexes (100 μL, w/w ratios ranging from 2.5 to 30) were then added and incubated with cells for 4 h at 37 °C. The medium was replaced by fresh DMEM containing 10% FBS, and the cells were incubated for 48 h. Thereafter, the medium was removed and the luciferase assay was performed according to manufacture's protocols. Relative light units (RLUs) were measured with chemiluminometer (Lumat LB9507, EG&G Berthold, Germany). The total protein was measured according to a BCA protein assay kit (Pierce). Luciferase activity was expressed as RLU/mg protein.

Transfection experiments in 293T cells in the presence of serum were also carried out. The protocol was the same as described above, except that the cell medium of DMEM with 10% FBS was used instead of the serum-free DMEM medium. All the transfection assays were carried out in triplicate.

RESULTS AND DISCUSSION

Synthesis and Characterization of Disulfide-Containing Brushed PEI Derivative. The three-step synthetic route of disulfide-containing brushed polyethylenimine derivative P(Asp-Az)$_X$-SS-PEI via click reaction is illustrated in Scheme 1. First, one alkyne pendant group was introduced into a low-molecular-weight (LMW) PEI (1.8 kDa) to obtain monoalkyne-terminated disulfide-containing PEI derivative [PEI$_{1800}$-(PPA-Cyst)$_1$]. Second, azide groups were introduced into the side chains of poly(amino acid) by the aminolysis reaction to poly(L-succinimide) (PSI) to obtain azide-functional poly(aspartic acid) [P(Asp-Az)$_X$]. Then, click reaction between azide-functional poly(aspartic acid) as main chain and monoalkyne-terminated PEI derivative as branched chain was carried out with CuBr as catalyst, resulting in reducible brushed PEI derivatives with high molecular weight.

Monoalkyne-functionalized LMW PEI was synthesized by coupling of (propargylcarbamate)ethy disulfide ethyl 1-carbamide-imidazole (PPA-cyst-CI) to PEI following our previous work.[34] The structure of the obtained monoalkyne-functionalized PEI derivative PEI$_{1800}$-(PPA-Cyst)$_1$ was confirmed by ^{1}H NMR and FTIR spectra (SI Figure S1 and Figure S2). It can be seen from the ^{1}H NMR spectrum in Figure S1 that reagent PPA-cyst-CI had reacted quantitatively with PEI. Therefore, no further purification was required for the next click reaction after evaporation removal of the solvent, chloroform. The use of excess PEI was to prevent the formation of the multialkyne-functionalized PEI.

In order to investigate the effect of azide group density on the next click reaction, various azide-functional poly(aspartic acid)s were synthesized using different molar feed ratio of 2-azidoethylamine to the polymer unit of PSI (Table 1). It can be seen from Table 1 that the azide group content for the obtained azide-functional poly(aspartic acid)s increased with increasing molar feed ratio of 2-azidoethylamine to the polymer unit of PSI. All the reaction efficiencies of 2-azidoethylamine with PSI determined by ^{1}H NMR analysis were close to 80%. It is worth noting that the remaining succinimide rings in azide-functional poly(L-succinimide) (PSI-Az) can react with the amino group of monoalkyne-functionalized LMW PEI, which will cause cross-linking for the next click reaction. Therefore, excessive ethanolamine was used to further react with PSI-Az. The obtained azide-functional poly(aspartic acid)s are denoted as P(Asp-Az)$_X$, where X represents the average number of azide groups per 100 polymer units determined by ^{1}H NMR analysis. It can been seen from Figure 1 that no peak around 5.3 ppm is observed for all the obtained azide-functional poly(aspartic acid)s, which indicates that no unreacted succinimide rings existed in all resulting P(Asp-Az)$_X$ polymers. Because the chemical shifts of the methene protons for the coupled 2-azidoethylamine overlap with HDO signal at 3.3 ppm in d_6-DMSO, ^{1}H NMR spectra for both P(Asp-Az)$_{33}$ and P(Asp-Az)$_{65}$ in D_2O are shown in Figure 1 and used to calculate the average number of azide groups per 100 polymer units, based on the ratio of the integral between 3.4 and 3.7 ppm (peak *e*) to the integral from 3.1 to 3.4 ppm (peaks *c* and *d*) in Figure 1A,B. However, P(Asp-Az)$_{100}$ is barely soluble in water; the ^{1}H NMR spectrum of P(Asp-Az)$_{100}$ was determined only in d_6-DMSO (Figure 1C). An absorption peak at 2100 cm^{-1} corresponding to the azide group is observed for all the FTIR spectra of P(Asp-Az)$_X$ polymers (Figure 2A). Thus, the azide-functional poly(aspartic acid)s with various azide group contents has been synthesized successfully.

The disulfide-containing brushed PEI derivative was synthesized via click reaction between azide-functional P(Asp-Az)$_X$ as main chain and monoalkyne-terminated PEI$_{1800}$-(PPA-Cyst)$_1$ as branched chain. The click reaction media were DMF, water, or the mixture of water and DMF (Table 2), because P(Asp-Az)$_{100}$ is soluble in DMF and not soluble in water. The structure of the obtained disulfide-containing brushed PEI derivative, denoted as P(Asp-Az)$_X$-SS-PEI, was confirmed by ^{1}H NMR and FTIR analysis. The ^{1}H NMR spectra of P(Asp-Az)$_X$-SS-PEIs are shown in Figure 3. It can be seen clearly from Figure 3A that three new peaks appear at δ = 7.9 (*a*, H of the triazole ring), 5.0 (*c*), and 4.4 (*b*), indicating the formation of triazole groups by click reaction. The percentage of grafted

PEI_{1800}-$(PPA\text{-}Cyst)_1$ to the polymer unit of $P(Asp\text{-}Az)_X$ was calculated based on the ^1H NMR spectra (see the calculation method of the percentage of grafted PEI_{1800}-$(PPA\text{-}Cyst)_1$ to the polymer unit of $P(Asp\text{-}Az)_X$ in Supporting Information). The absorption peaks at 2100 and 2120 cm^{-1} for $P(Asp\text{-}Az)_X$-SS-PEIs become weak (Figure 2B), which implies that the azide groups reacted with the alkyne groups. The molecular weights and MWDs of the $P(Asp\text{-}Az)_X$-SS-PEIs were determined by aqueous SEC-MALLS. The SEC traces of the $P(Asp\text{-}Az)_{33}$-SS-PEI, $P(Asp\text{-}Az)_{65}$-SS-PEI, and 1.8 kDa PEI were supplied in SI Figure S5, which indicates that the starting LMW PEI is negligible in the obtained brushed PEI derivatives $P(Asp\text{-}Az)_X$-SS-PEIs. The results were summarized in Table 2. The weight-average molecular weights of $P(Asp\text{-}Az)_{33}$-SS-PEI and $P(Asp\text{-}Az)_{65}$-SS-PEI are 140 kDa and 63 kDa, respectively, much higher than that of starting polymer $P(Asp\text{-}Az)_X$, 26 kDa, which also indicates that PEI grafted into poly(aspartic acid)s. With all ^1H NMR, FTIR, and SEC-MALLS analysis results taken together, it can be concluded that the click reactions between $P(Asp\text{-}Az)_X$ and PEI_{1800}-$(PPA\text{-}Cyst)_1$ were successful.

Interestingly, the PEI-grafted percentage decreased with increasing the average number of azide groups per 100 polymer units in azide-functional poly(aspartic acid), as shown in Table 2. For example, the percentage of grafted PEI_{1800}-$(PPA\text{-}Cyst)_1$ to the polymer unit of $P(Asp\text{-}Az)_{100}$ was very low (about 3.6%). A possible reason is the solvent DMF used in this click reaction, because DMF is not a good solvent for high-molecular-weight PEI polymer, and a gel-like substance in DMF was observed in this click reaction. In order to investigate the solvent effect on the click reaction, a series of $P(Asp\text{-}Az)_{33}$-SS-PEIs were synthesized under the same click reaction conditions (50 °C, 48 h, using CuBr as catalyst), but in pure DMF, pure water, or mixtures of different DMF/water ratios as solvent, respectively (Table 3). The ^1H NMR spectra and the percentage of grafted

Table 3. Solvent Effect on the Synthesis of Disulfide-Containing $P(Asp\text{-}Az)_{33}$-SS-PEI

solvent (the mixture of water and DMF) (v%)	percentage of reacted azide group[a]	percentage of grafted PEI_{1800}-$(PPA\text{-}Cyst)_1$ to the polymer unit of $P(Asp\text{-}Az)_X$[a]	W_{PEI}(%)[a]
100% DMF	11.5%	3.8%	28
50% water	17.9%	5.9%	37
75% water	20.0%	6.6%	39
87.5% water	26.1%	8.6%	45
100% water	33.9%	11.2%	51

[a]Calculated from ^1H NMR spectra.

PEI to the polymer unit of $P(Asp\text{-}Az)_{33}$ for such $P(Asp\text{-}Az)_{33}$-SS-PEIs were shown in Figure 4 and Table 3, respectively. It can be seen from Figure 4 that the signal intensities from *b* (δ = 4.4), *c* (δ = 5.0), and the protons of PEI-grafted branches increase with the increase of water content in click reaction solvent. The percentage of grafted PEI to the polymer unit of $P(Asp\text{-}Az)_{33}$ increases from 3.8% to 11.2% with the increase of water content in click reaction solvent, as seen in Table 3. By comparison in Tables 2 and 3, very low influence of azide-group density of $P(Asp\text{-}Az)_X$ on the PEI-grafted number of $P(Asp\text{-}Az)_X$-SS-PEI is observed for both pure DMF and DMF/water (50/50, v/v) as click reaction solvents, whereas the solvent effect on the click reaction between azide-functional poly(aspartic acid) and the monoalkyne-terminated PEI derivative is obvious. Because of low PEI-grafted number in

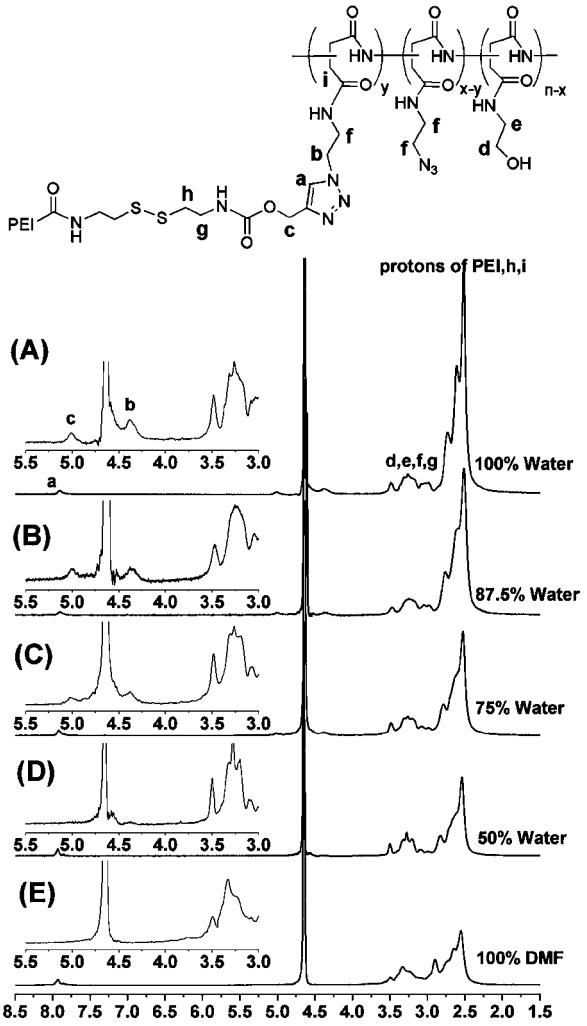

Figure 4. ^1H NMR spectra of $P(Asp\text{-}Az)_{33}$-SS-PEI in D_2O synthesized with pure water, mixtures of different DMF/water ratios (v%), or pure DMF as click reaction solvent.

$P(Asp\text{-}Az)_{100}$-SS-PEI, samples $P(Asp\text{-}Az)_{33}$-SS-PEI and $P(Asp\text{-}Az)_{65}$-SS-PEI were used in the later investigation.

Characterization of $P(Asp\text{-}Az)_X$-SS-PEI-Based Polyplexes. To be effective as gene vectors, cationic polymer must be able to bind and condense plasmid DNA into nanoparticles. As shown in Figure 5A, when the cationic polymer/DNA weight ratio increased, the mobility of the DNA pcDNA3-Luc was reduced. When the w/w ratio was above 0.8 for $P(Asp\text{-}Az)_{33}$-SS-PEI based polyplexes, the DNA migration

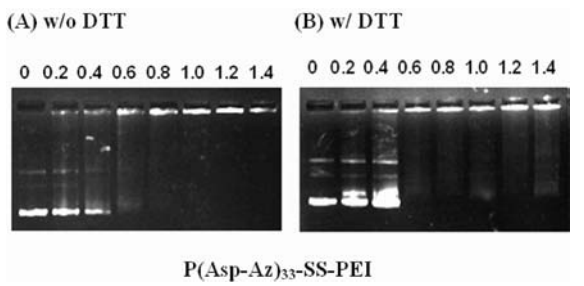

Figure 5. Agarose gel electrophoresis retardation assay of $P(Asp\text{-}Az)_{33}$-SS-PEI/DNA polyplexes at different w/w ratios (A) without DTT and (B) with 10 mM DTT.

dx.doi.org/10.1021/bc300133r | *Bioconjugate Chem.* 2012, 23, 1290−1299

was almost retarded. According to our previous work, 1.8 kDa PEI was unable to bind DNA even at an N/P ratio of 30 (corresponding to w/w ratio of 3.9).[34] This indicates that the obtained brushed PEI derivatives show better DNA binding capability than the starting polymer 1.8 kDa PEI.

The particle sizes of P(Asp-Az)$_X$-SS-PEIs/DNA polyplexes were also investigated by DLS as shown in Figure 6A. The

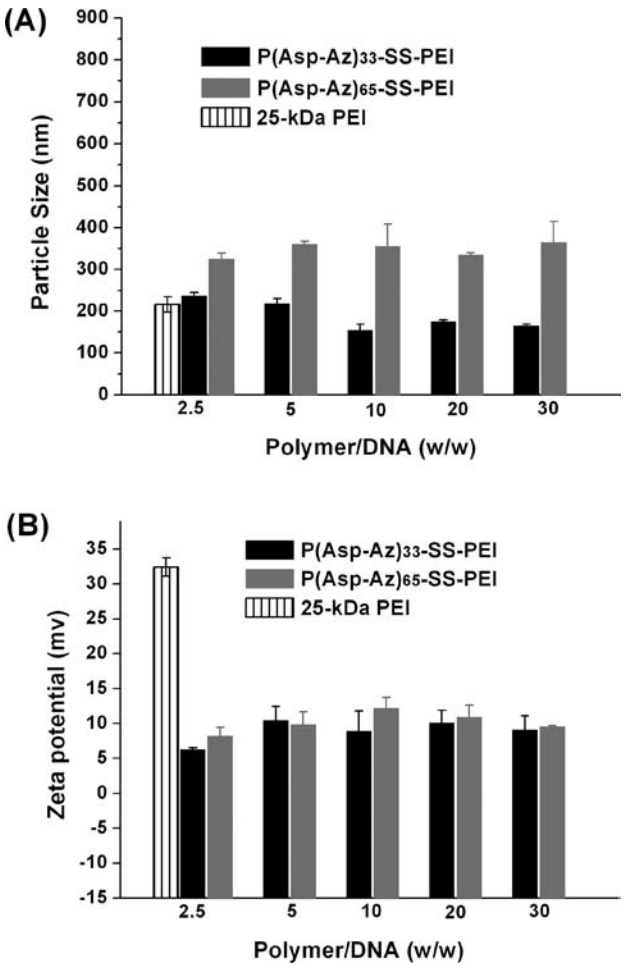

Figure 6. (A) Particle size by DLS in HBS and (B) zeta potential in HBG of the P(Asp-Az)$_X$-SS-PEI/DNA polyplexes at various w/w ratios. Error bars are standard deviations of 3 measurements.

disulfide-containing P(Asp-Az)$_X$-SS-PEIs prepared from the 1.8 kDa PEI were able to condense DNA into small particles (less than 370 nm). The polyplexes based on P(Asp-Az)$_{33}$-SS-PEI (with a size of about 150 nm at w/w ratios above 10 in HBS) were much smaller than those based on P(Asp-Az)$_{65}$-SS-PEI, because the molecular weight of P(Asp-Az)$_{33}$-SS-PEI was higher than that of P(Asp-Az)$_{33}$-SS-PEI (Table 2). Zeta potentials of the P(Asp-Az)$_X$-SS-PEI based polyplexes were measured in HBG and shown in Figure 6B. Positive zeta potentials of about 10 mV were observed at w/w ratios above 2.5 for all the P(Asp-Az)$_X$-SS-PEI based polyplexes, whereas polyplexes based on 25 kDa PEI showed higher zeta potential around +32 mV, which indicates that the positive charge density of the P(Asp-Az)$_X$-SS-PEI is lower than that of pure PEI. The reason is that only the grafted PEI part can provide cationic groups and the weight percentages of grafted PEI in P(Asp-Az)$_X$-SS-PEIs are below 51%, as shown in Table 2.

Reduction Sensitivity of the P(Asp-Az)$_X$-SS-PEI/DNA Polyplexes. The DTT-triggered reduction sensitivity of P(Asp-Az)$_X$-SS-PEI based polyplexes was investigated by agarose gel retardation assay (Figure 5B) and DLS (Figure 7). Free DNA in P(Asp-Az)$_{33}$-SS-PEI/DNA polyplexes

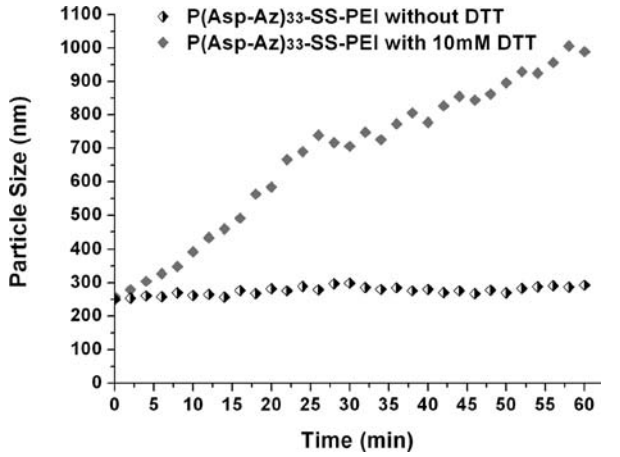

Figure 7. Particle size by DLS of the P(Asp-Az)$_{33}$-SS-PEI/DNA polyplexes at w/w ratio of 2.5 in the presence and absence of 10 mM DTT in HBS.

incubated with 10 mM DTT (30 min) was visible in Figure 5B (see the difference of Figure 5A and B when the w/w ratios are above 0.8), which indicates that P(Asp-Az)$_{33}$-SS-PEI based polyplexes released DNA in a reductive environment. The similar results were obtained with 1 h incubation in the presence of 10 mM DTT (SI Figure S6). It can be seen from Figure 7 that the size of P(Asp-Az)$_{33}$-SS-PEI based polyplexes was stable in HBS without addition of DTT, while it increased rapidly from 250 to 1000 nm over 1 h in the presence of 10 mM DTT, which also confirms the reduction sensitivity of the P(Asp-Az)$_X$-SS-PEI/DNA polyplexes.

In Vitro Cytotoxicity. Cytotoxicity of disulfide-containing P(Asp-Az)$_X$-SS-PEIs was determined using MTT assay with 293T cells. Branched PEI (25 kDa) was used as control. As shown in Figure 8, the cytotoxicity of P(Asp-Az)$_{65}$-SS-PEI was lower than that of P(Asp-Az)$_{33}$-SS-PEI, because the molecular weight of P(Asp-Az)$_{65}$-SS-PEI was lower than that of P(Asp-

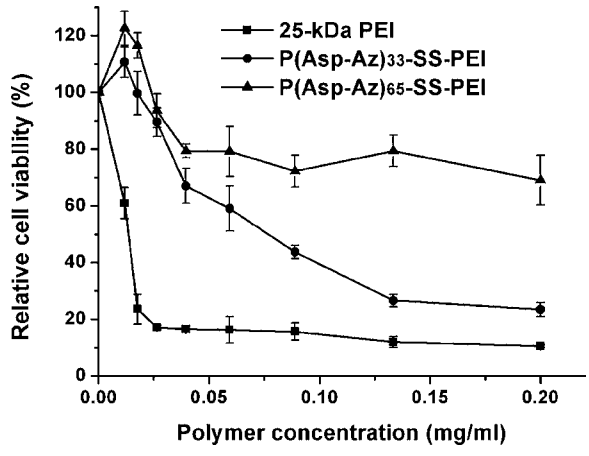

Figure 8. Cytotoxicity of disulfide-containing brushed cationic polymer P(Asp-Az)$_X$-SS-PEI and control 25 kDa PEI to 293T cells after 24 h incubation (mean ± SD, n = 4).

Az)$_{33}$-SS-PEI (Table 2). It can also be seen from Figure 8 that both of disulfide-containing P(Asp-Az)$_X$-SS-PEIs had a lower cytotoxicity than 25 kDa PEI, although both the molecular weights were higher than that of 25 kDa PEI. One reason may be that disulfide-containing brushed P(Asp-Az)$_X$-SS-PEIs can be intracellularly degraded, triggered by glutathione after cellular binding and internalization, into relatively low toxicity products, which is in agreement with our previous reports.[25,34] Another reason for the low cytotoxicity of disulfide-containing P(Asp-Az)$_X$-SS-PEIs may be their low charge density.[38]

In Vitro Transfection. The transfection activity of P(Asp-Az)$_X$-SS-PEI based polyplexes was evaluated in 293T cell using the plasmid pcDNA3-Luc (expressing luciferase) as reporter genes. Branched 25 kDa PEI was used as control. It can be seen from Figure 9 that both P(Asp-Az)$_X$-SS-PEI/DNA polyplexes were able to transfect cells. The transfection efficiency of P(Asp-Az)$_{33}$-SS-PEI/DNA polyplexes was higher than that of P(Asp-Az)$_{65}$-SS-PEI/DNA polyplexes in most case. This is due to higher PEI-grafted density of P(Asp-Az)$_{33}$-SS-PEI than that of P(Asp-Az)$_{65}$-SS-PEI (Table 2). The transfection efficiency of P(Asp-Az)$_{33}$-SS-PEI/DNA polyplexes was similar to that based on branched 25 kDa PEI under optimized conditions at N/P ratio of 10 (corresponding to w/w ratio of 1.3) in the absence of serum. More importantly, the transfection efficiency of P(Asp-Az)$_{33}$-SS-PEI/DNA polyplexes at w/w ratio of 10 was even higher than that based on branched 25 kDa PEI in the presence of serum. This may be ascribed to its degradability through cleavage of disulfide bonds inside the cells. Thus, the obtained disulfide-containing brushed P(Asp-Az)$_{33}$-SS-PEI might be suitable for further in vivo gene transfection study.

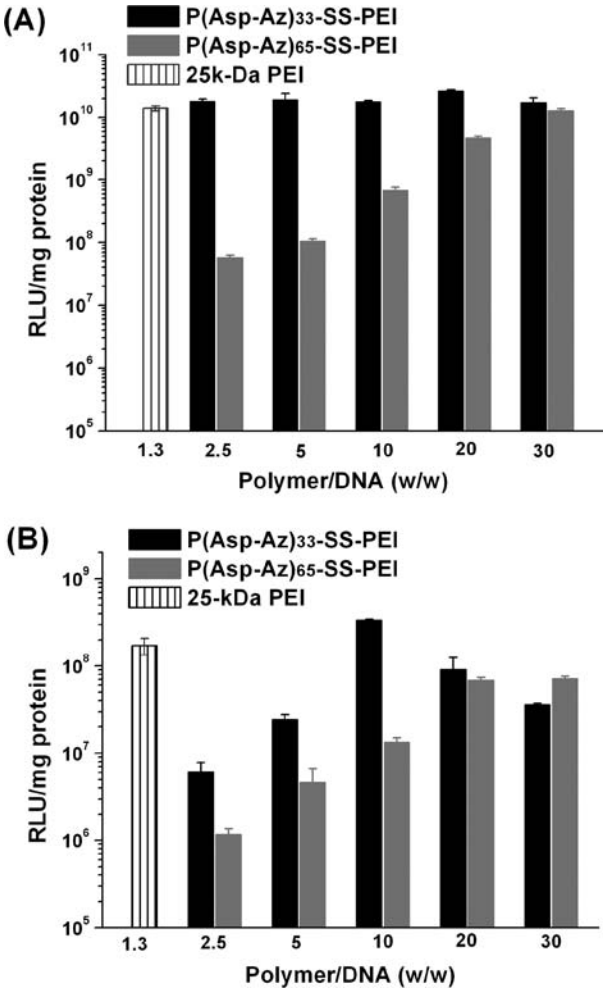

Figure 9. Luciferase expression of the P(Asp-Az)$_X$-SS-PEI/DNA polyplexes at different w/w ratios with control 25 kDa PEI in serum-free DMEM (A) and in DMEM medium with 10% FBS (B) in 293T cells.

CONCLUSIONS

Designed amounts of azide groups were introduced to poly(L-succinimide) to obtain azide-functionalized P(Asp-Az)$_X$. Then, the click reaction between the azide-functionalized P(Asp-Az)$_X$ as main chain and the monoalkyne-terminated PEI [PEI$_{1800}$-(PPA-cyst)$_1$] was carried out to synthesize disulfide-containing brushed PEI derivatives P(Asp-Az)$_X$-SS-PEIs. The obtained polymer was characterized by ^{1}H NMR, FTIR, and SEC-MALLS. Very low influence of azide-group density of P(Asp-Az)$_X$ on the PEI-grafted number of P(Asp-Az)$_X$-SS-PEI was observed for both pure DMF and DMF/water (50/50 v/v) as click reaction solvents, whereas the solvent (water content) effect on the click reaction between azide-functional poly(aspartic acid) and monoalkyne-terminated PEI derivative was obvious. It was demonstrated that the disulfide-containing P(Asp-Az)$_X$-SS-PEIs were able to bind plasmid DNA efficiently and condense DNA into small positive nanoparticles. The reduction-sensitivity of the P(Asp-Az)$_X$-SS-PEIs was confirmed by gel retardation assay and DLS in the presence of DTT. In vitro experiments showed that the reducible P(Asp-Az)$_X$-SS-PEIs were less cytotoxic, and more effective in gene transfection (both in the presence and in the absence of serum) as compared to the control nondegradable 25 kDa PEI. These results indicate that the obtained disulfide-containing brushed P(Asp-Az)$_{33}$-SS-PEI might be a promising gene delivery carrier for further in vivo gene transfection.

ASSOCIATED CONTENT

Supporting Information

Synthesis and characterization of monoalkyne-functionalized PEI derivative [PEI$_{1800}$-(PPA-Cyst)$_1$] and 2-azidoethylamine; Calculation method of the percentage of grafted PEI$_{1800}$-(PPA-Cyst)$_1$ to the structure unit of P(Asp-Az)$_X$. This material is available free of charge via the Internet at http://pubs.acs.org.

AUTHOR INFORMATION

Corresponding Author

*Tel. +86-27-68755200; fax +86-27-68754509; E-mail address: xljiang@whu.edu.cn.

Notes

The authors declare no competing financial interest.

ACKNOWLEDGMENTS

This research was financially supported by the National Natural Science Foundation of China (21174109, 21074100, 20774068), the National Key Basic Research Program of China (2011CB606202, 2009CB930300), and Program for Changjiang Scholars and Innovative Research Team in University (IRT1030).

REFERENCES

(1) Guo, X., and Huang, L. (2012) Recent advances in nonviral vectors for gene delivery. *Acc. Chem. Res.*, DOI: 10.1021/ar200151m.

(2) Morille, M., Passirani, C., Vonarbourg, A., Clavreul, A., and Benoit, J. P. (2008) Progress in developing cationic vectors for non-viral systemic gene therapy against cancer. *Biomaterials 29*, 3477−3496.
(3) Akinc, A., Thomas, M., Klibanov, A. M., and Langer, R. (2005) Exploring polyethylenimine- mediated DNA transfection and the proton sponge hypothesis. *J. Gene Med. 7*, 657−663.
(4) Godbey, W. T., Wu, K. K., and Mikos, A. G. (1999) Poly(ethylenimine) and its role in gene delivery. *J. Controlled Release 60*, 149−160.
(5) Godbey, W. T., Wu, K. K., and Mikos, A. G. (1999) Size matters: Molecular weight affects the efficiency of poly(ethylenimine) as a gene delivery vehicle. *J. Biomed. Mater. Res. 45*, 268−275.
(6) Fischer, D., Bieber, T., Li, Y. X., Elsasser, H. P., and Kissel, T. (1999) A novel non-viral vector for DNA delivery based on low molecular weight, branched polyethylenimine: Effect of molecular weight on transfection efficiency and cytotoxicity. *Pharm. Res. 16*, 1273−1279.
(7) Luten, J., van Nostruin, C. F., De Smedt, S. C., and Hennink, W. E. (2008) Biodegradable polymers as non-viral carriers for plasmid DNA delivery. *J. Controlled Release 126*, 97−110.
(8) Liu, Z. Z., Zheng, M., Meng, F. H., and Zhong, Z. Y. (2011) Non-viral gene transfection in vitro using endosomal pH-sensitive reversibly hydrophobilized polyethylenimine. *Biomaterials 32*, 9109−9119.
(9) Jiang, X. L., Lok, M. C., and Hennink, W. E. (2007) Degradable-brushed pHEMA−pDMAEMA synthesized via ATRP and click chemistry for gene delivery. *Bioconjugate Chem. 18*, 2077−2084.
(10) Brumbach, J. H., Lin, C., Yockman, J., Kim, W. J., Blevins, K. S., Engbersen, J. F. J., Feijen, J., and Kim, S. W. (2010) Mixtures of poly(triethylenetetramine/cystamine bisacrylamide) and poly-(triethylenetetramine/cystamine bisacrylamide)-g-poly(ethylene glycol) for improved gene delivery. *Bioconjugate Chem. 21*, 1753−1761.
(11) Wang, Y. H., Zheng, M., Meng, F. H., Zhang, J., Peng, R., and Zhong, Z. Y. (2011) Branched polyethylenimine derivatives with reductively cleavable periphery for safe and efficient in vitro gene transfer. *Biomacromolecules 12*, 1032−1040.
(12) Zhu, C. H., Zheng, M., Meng, F. H., Mickler, F. M., Ruthardt, N., Zhu, X. L., and Zhong, Z. Y. (2012) Reversibly shielded DNA polyplexes based on bioreducible PDMAEMA-SS-PEG-SS-PDMAEMA triblock copolymers mediate markedly enhanced nonviral gene transfection. *Biomacromolecules 13*, 769−778.
(13) Dai, F. Y., Sun, P., Liu, Y. J., and Liu, W. G. (2010) Redox-cleavable star cationic PDMAEMA by arm-first approach of ATRP as a nonviral vector for gene delivery. *Biomaterials 31*, 559−569.
(14) Bauhuber, S., Hozsa, C., Breunig, M., and Göpferich, A. (2009) Delivery of nucleic acids via disulfide-based carrier systems. *Adv. Mater. 21*, 3286−3306.
(15) Saito, G., Swanson, J. A., and Lee, K. D. (2003) Drug delivery strategy utilizing conjugation via reversible disulfide linkages: role and site of cellular reducing activities. *Adv. Drug Delivery Rev. 55*, 199−215.
(16) Schafer, F. Q., and Buettner, G. R. (2001) Redox environment of the cell as viewed through the redox state of the glutathione disulfide/glutathione couple. *Free Radical Biol. Med. 30*, 1191−1212.
(17) Wu, C. L., Belenda, C., Leroux, J. C., and Gauthier, M. A. (2011) Interplay of chemical microenvironment and redox environment on thiol−disulfide exchange kinetics. *Chem.−Eur. J. 17*, 10064−10070.
(18) Piest, M., Lin, C., Mateos-Timoneda, M. A., Lok, M. C., Hennink, W. E., Feijen, J., and Engbersen, J. F. J. (2008) Novel poly(amido amine)s with bioreducible disulfide linkages in their diamino-units: Structure effects and in vitro gene transfer properties. *J. Controlled Release 130*, 38−45.
(19) Lee, Y., Mo, H., Koo, H., Park, J. Y., Cho, M. Y., Jin, G. W., and Park, J. S. (2007) Visualization of the degradation of a disulfide polymer, linear poly(ethylenimine sulfide), for gene delivery. *Bioconjugate Chem. 18*, 13−18.
(20) Manickam, D. S., Li, J., Putt, D. A., Zhou, Q. H., Wu, C., Lash, L. H., and Oupicky, D. (2010) Effect of innate glutathione levels on activity of redox-responsive gene delivery vectors. *J. Controlled Release 141*, 77−84.
(21) Xue, Y. N., Liu, M., Peng, L., Huang, S. W., and Zhuo, R. X. (2010) Improving gene delivery efficiency of bioreducible poly-(amidoamine)s via grafting with dendritic poly(amidoamine)s. *Macromol. Biosci. 10*, 404−414.
(22) Zugates, G. T., Anderson, D. G., Little, S. R., Lawhorn, I. E. B., and Langer, R. (2006) Synthesis of poly(β-amino ester)s with thiol-reactive side chains for DNA delivery. *J. Am. Chem. Soc. 128*, 12726−12734.
(23) Deng, J. Z., Sun, Y. X., Wang, H. Y., Li, C., Huang, F. W., Cheng, S. X., Zhuo, R. X., and Zhang, X. Z. (2011) Poly(β-amino amine) cross-linked PEIs as highly efficient gene vectors. *Acta Biomater. 7*, 2200−2208.
(24) Berthold, P. R., Shiraishi, T., and Nielsen, P. E. (2010) Cellular delivery and antisense effects of peptide nucleic acid conjugated to polyethyleneimine via disulfide linkers. *Bioconjugate Chem. 21*, 1933−1938.
(25) Liu, J., Jiang, X. L., Xu, L., Wang, X. M., Hennink, W. E., and Zhuo, R. X. (2010) Novel reduction-responsive cross-linked polyethylenimine derivatives by click chemistry for nonviral gene delivery. *Bioconjugate Chem. 21*, 1827−1835.
(26) Yang, X. C., Chai, M. Y., Zhu, Y., Yang, W. T., and Xu, F. J. (2012) Facilitation of gene transfection with well-defined degradable comb-shaped poly(glycidyl methacrylate) derivative vectors. *Bioconjugate Chem. 23*, 618−626.
(27) Liu, X. Q., Du, J. Z., Zhang, C. P., Zhao, F., Yang, X. Z., and Wang, J. (2010) Brush-shaped polycation with poly(ethylenimine)-b-poly(ethylene glycol) side chains as highly efficient gene delivery vector. *Int. J. Pharm. 392*, 118−126.
(28) Dai, J., Zou, S. Y., Pei, Y. Y., Cheng, D., Ai, H., and Shuai, X. T. (2011) Polyethylenimine-grafted copolymer of poly(l-lysine) and poly(ethylene glycol) for gene delivery. *Biomaterials 32*, 1694−1705.
(29) Khan, M., Beniah, G., Wiradharma, N., Guo, X., and Yang, Y. Y. (2010) Brush-Like Amphoteric Poly[isobutylene-alt-(maleic acid)-graft-oligoethyleneamine)]/DNA Complexes for Efficient Gene Transfection. *Macromol. Rapid Commun. 31*, 1142−1147.
(30) Zhang, M., Liu, M., Xue, Y. N., Huang, S. W., and Zhuo, R. X. (2009) Polyaspartamide-based oligo-ethylenimine brushes with high buffer capacity and low cytotoxicity for highly efficient gene delivery. *Bioconjugate Chem. 20*, 440−446.
(31) Yu, J. H., Quan, J. S., Huang, J., Wang, C. Y., Sun, B., Nah, J. W., Cho, M. H., and Cho, C. S. (2009) Alpha,beta-poly(L-aspartate-graft-PEI): a pseudo-branched PEI as a gene carrier with low toxicity and high transfection efficiency. *Acta Biomater. 5*, 2485−2494.
(32) van Dijk, M., Rijkers, D. T. S., Liskamp, R. M. J., van Nostrum, C. F., and Hennink, W. E. (2009) Synthesis and applications of biomedical and pharmaceutical polymers via click chemistry methodologies. *Bioconjugate Chem. 20*, 2001−2016.
(33) Narumi, A., Fuchise, K., Kakuchi, R., Toda, A., Satoh, T., Kawaguchi, S., Sugiyama, K., Hirao, A., and Kakuchi, T. (2008) A versatile method for adjusting thermoresponsivity: synthesis and 'click' reaction of an azido end-functionalized poly(N-isopropylacrylamide). *Macromol. Rapid Commun. 29*, 1126−1133.
(34) Jiang, X. L., Liu, J., Xu, L., and Zhuo, R. X. (2011) Disulfide-containing hyperbranched polyethylenimine derivatives via click chemistry for nonviral gene delivery. *Macromol. Chem. Phys. 212*, 64−71.
(35) Cheng, H., Li, Y. Y., Zeng, X., Sun, Y. X., Zhang, X. Z., and Zhuo, R. X. (2009) Protamine sulfate/poly(L-aspartic acid) polyionic complexes self-assembled via electrostatic attractions for combined delivery of drug and gene. *Biomaterials 30*, 1246−1253.
(36) Angelos, S., Yang, Y. W., Patel, K., Stoddart, J. F., and Zink, J. I. (2008) pH-responsive supramolecular nanovalves based on cucurbit 6 uril pseudorotaxanes. *Angew. Chem., Int. Ed. 47*, 2222−2226.
(37) Jiang, X. L., Chu, Y. F., Liu, J., Zhang, G. Y., and Zhuo, R. X. (2011) Aqueous sec analysis of cationic polymers as gene carriers. *Chin. J. Polym. Sci. 29*, 421−426.

(38) Mastrobattista, E., and Hennink, W. E. (2012) Polymer for gene delivery charged for success. *Nat. Mater. 11*, 10−12.

Bioconjugate Chemistry

Article

pubs.acs.org/bc

Elegant Chemistry to Directly Anchor Intact Saccharides on Solid Surfaces Used for the Fabrication of Bioactivity-Conserved Saccharide Microarrays

Kai Liang[†] and Yi Chen*[,†,‡]

[†]Key Laboratory of Analytical Chemistry for Living Biosystems, Institute of Chemistry, Chinese Academy of Sciences, Beijing 100190, China

[‡]Beijing National Laboratory for Molecular Science, Beijing 100190, China

Supporting Information

ABSTRACT: An easy chemical strategy was proposed and used to establish a method for direct anchoring of intact saccharides on solid surfaces with well conserved bioaffinity. The anchoring was achieved by temperature-modulated stepwise reactions with cyanuric chloride as a key linker, and was successfully applied to the fabrication of saccharide chips. To demonstrate, 15 intact reducing and nonreducing saccharides with various molecular sizes were dotted on a cyanuric-chloride-modified chip (1.0 × 1.0 cm^2) and made to react with lectins. As expected, the anchored saccharides were capable of recognizing their target lectins, and more exciting were the perfect conservation of the specific recognizing ability of the anchored monosaccharides such as mannose, glucose, and even fructose (interacting only weakly with concanavalin A). This conservation was ascribed to the maintenance of the original structure (especially the anomeric configuration) of saccharides after immobilization and to the allowance of the anchored saccharides to rotate with and/or on the scaffold of cyanuric chloride, which makes them easily adapt to the recognition-preferred spatial position. The expected linkage of saccharides on cyanuric chloride and the maintenance of their anomeric configuration were characterized by mass spectrometry and nuclear magnetic resonance, respectively. The new method can be highlighted not only by its conservation of saccharide bioaffinity and universal applicability but also by its merits of easy manipulation or facile control of the reactions and cost-effectiveness due to the use of extremely cheap cyanuric chloride.

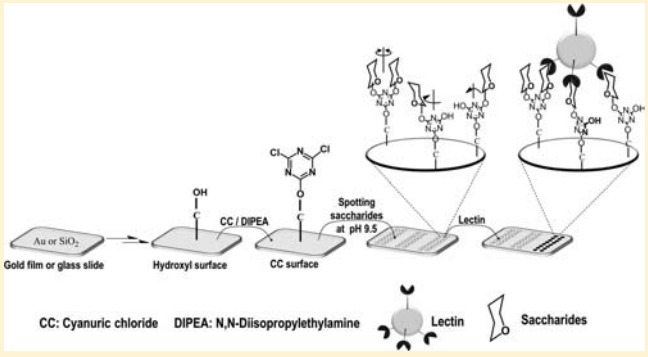

INTRODUCTION

It is widely recognized that saccharides and their associated complexes can play crucial roles in a series of specific physiological processes,[1] but they are also one class of the most complicated substances hard to detect and analyze, which has made glycomic research full of challenges.[2−4] To attack the challenges, microarray method or chip technology has been tried and is drawing great attention[5−9] because it offers a new high throughput and low consumption way to simultaneously observe the behaviors of various saccharides, even capable of simulating some functions of saccharides on cell surfaces.[10] It has since been expected to be one of the most powerful potential tools for the future study of glycomics.

However, a prerequisite to use such a chip is to anchor the saccharides on the chip with their bioaffinity conserved. This has activated correlative researchers to find the anchoring strategies.[11−15] Physical adsorption was first tried for its ease of manipulation. This strategy is applicable to the fixing of polysaccharides on some absorptive surfaces such as nitrocellulose-[16] or black polystyrene-coated[17] glass slides but commonly not applicable to less or not adsorptive substances such as mono- and oligo-saccharides unless their adsorbability is largely increased by some special ways such as the fluorous-targeting technique.[18] It may also have the problem of gradual loss of the adsorbed polysaccharides during a continuous wash or reaction in solutions. Chemical reactions were then explored to stably immobilize the saccharides on solid surfaces by the formation of covalent bounds through Schiff's base[19,20] or amidation.[21,22] This strategy is easily widened by the exploration of more reactions such as click chemistry,[23] Staudinger ligation,[24] Diels−Alder reaction,[25] Michael addition,[26] and even streptavidin- and biotin-based immunoreactions.[27] In general, chemical strategy is flexible and applicable to the firm immobilization of saccharides on various surfaces,[28−37] but at present, its manipulation is generally not as easy as the physical adsorption.

Chemical strategy is in many aspects favorable, but it may not be applicable to the direct immobilization of intact or

Received: March 20, 2012
Revised: April 29, 2012
Published: May 6, 2012

dx.doi.org/10.1021/bc300142s | Bioconjugate Chem. 2012, 23, 1300−1308

natural saccharides without a loss of their bioactivity.[29,36] For example, reducing saccharides can directly be immobilized on hydrazide-, aminooxy-[33,34] or aminooxyacetyl-modified[35] substrates, but their delicate structure is changed after reactions: the aminooxy-based reaction preferentially generated acyclic products,[33,38] while the hydrazide-based reaction predominantly yields β-anomeric configuration adducts.[33,34] The immobilized saccharides, especially the small saccharides, will change or adjust their bioaffinity accordingly.

A further question is that many of the chemical approaches are not universally applicable or only applicable to the immobilization of reducing saccharides.[33−35] In order to establish a universal method, we have explored a photochemical approach by use of perfluorophenyl azide (PFPA) as a critical linker.[37] It was demonstrated that, on a PFPA-functioned chip surface, all intact reducing and nonreducing saccharides, and even sugar alcohols, could firmly be immobilized through a solid phase photochemical reaction. Nevertheless, the loss of the bioaffinity of the anchored saccharides remains a problem and an interspacing arm of polylysine was used to recover and enhance the recognition of small saccharides.[37] The interspacing arm could make the small saccharides work collaboratively or in a way of cluster(s).[37,39] This implies that the saccharides were seemingly anchored too firmly to adjust their spatial position to favor the recognition. A better immobilizing way should thus be capable of allowing the saccharides to turn around a bond on the surface, which must lie greatly in the finding of a better linker.

Some new chemical reactions were thus tried, and cyanuric chloride (CC) was shown to be at the top of the selection. CC is a heterocyclic trifunctional compound, manufactured on the scale of several millions of tons per year and is among the reagents of lowest price.[40] Its most known feature is that the three chlorines on the triazine ring can be replaced stepwise by hydroxyls and/or amino groups through the regulation of reaction temperature. The additional attracting feature for us is that, after immobilization on a solid surface, it has the potential to turn around its immobilization bond and thus endow some extra possibility to the molecules linked on it to adjust their spatial position. Surprisingly, although the stepwise substitution of the chlorines on CC with nucleophiles has been documented well[41−43] and has been applied extensively to organic synthesis[44] and material surface modifications,[45−47] there were only limited examples focused on microarray fabrications.[48−52] To the best of our knowledge, no attempt has been made to directly immobilize various intact saccharides on solid surfaces aiming at the preparation of saccharide chips.

In this article, we will demonstrate that the CC-based chemistry is indeed favorable as a new, bioaffinity-conserved strategy to covalently immobilize intact saccharides on solid surfaces. A model reaction was designed to conjugate saccharides with an alkoxyl group through CC in solution, studied to simulate the reaction of saccharides with a CC-functionalized surface, and characterized by liquid chromatography−mass spectrometry (LC-MS) and nuclear magnetic resonance (NMR) spectroscopy. On the basis of the study, an easy method was established to fabricate saccharide chips. To demonstrate, 15 mono-, oligo-, and polysaccharides were successfully dotted on 1.0 × 1.0 cm^2 glass slides with or without a gold film and characterized by various techniques such as X-ray photoelectron spectra (XPS), vapor condensation imaging (VCi), surface plasmon resonance sensing and imaging (SPR and SPRi), and laser-induced fluorescence imaging (LIFi). The immobilized saccharides, especially the monosaccharides, could all display their inherent recognizing ability with their target lectins such as concanavalin A (Con A) and peanut agglutinin (PNA). The new method can thus be highlighted not only by its conservation of saccharide bioaffinity and universal applicability but also by its merits of easy manipulation or facile control of reaction, and cost-effectiveness due to the use of extremely cheap CC.

EXPERIMENTAL PROCEDURES

Materials and Reagents. Concanavalin A (Con A), peanut agglutinin (PNA), fluorescein isothiocyanate (FITC), 3-aminopropyltrimethoxysilane (APTMS), and 1-ethyl-3-(3-dimethyllaminopropyl)carbodiimide (EDC) hydrochloride were purchased from Sigma (St. Louis, Mo, USA). Cyanuric chloride (CC) and 11-mercaptoundecanoic acid (MUA) were obtained from Aldrich (Milwaukee, WI, USA). *N*-Hydroxysuccinimide (NHS) was purchased from Acros (New Jersey, USA). *N*,*N*-Diisopropylethylamine (DIPEA) was purchased from Aladdin Chemistry Co. Ltd. (Shanghai, China), and 4-hydroxyphenylacetic acid (HPA) was from Fluka (Switzerland). NaOH, NaCl, $CaCl_2$, $MnCl_2$, absolute ethanol, ethanolamine (EOA), ethanediamine (EDA), and tris(hydroxylmethyl)aminomethane (Tris) were of analytical reagent grade from Beijing Chemical Works (Beijing, China). All saccharides were of biochemical reagent grade from Beijing Reagent Work (Beijing, China). All reagents and solvents were used as received. Triply distilled water was used for the preparation of all solutions and rinsing.

Preparation of Hydroxyl-Terminated Gold Film. Glass slides (1.0 cm ×1.0 cm, Shitai Co. Ltd., China) were deposited with 50-nm-thick gold films by vapor-deposition in a JEE-4X vacuum evaporator (JEOL Ltd., Tokyo, Japan). The cleaned gold chips were immersed in a solution of MUA in ethanol (1 mM) for at least 8 h, rinsed with ethanol and distilled water sequentially, and were then immersed for 25 min in an aqueous solution of EDC (75 mM) and NHS (15 mM). The resulting chips were treated with an aqueous solution of EOA (1 M, adjusted with 5 M HCl to pH 8.6) for 1.5 h. Finally, the substrates were flushed thoroughly with water and dried under N_2 stream.

Preparation of Hydroxyl-Terminated Glass Slides. First, glass slides (1.0 cm ×1.0 cm, Shitai Co. Ltd., China) were exposed to oxygen plasma for 5 min (PDC-MG, Chengdu Mingheng S&T CO. Ltd., China). Then they were immediately immersed in a freshly prepared APTMS solution (3% in methanol) for 2.5 h. The silanized glass slides were sonicated in methanol three times and dried under N_2 stream. The resulted chips were treated with a 1:1 mixed solution of HPA in ethanol (113 mM) and EDC in water (219 mM) for 3 h. At last, the substrates were flushed thoroughly with ethanol and dried under N_2 stream.

Preparation of Saccharide Microarray Chips. First, the hydroxyl-terminated substrates (on gold film or glass slide) were incubated with a mixed solution of CC (100 mM) and DIPEA (100 mM) in acetone at 4 °C for 6 h. Then the substrates were flushed thoroughly with acetone and dried under N_2 stream. An aqueous saccharide solution (30 mM for small saccharides or 3 mg/mL for polysaccharides, adjusted to pH 9.0 with 1 M NaOH) was spotted on the CC-functionalized chips by a laboratory-fabricated microprinting system, which allows the delivery of 15 nL solution onto the substrate to form a spot of 250 μm in diameter. After all the samples were

Scheme 1. Process to Immobilize Saccharides on a Gold Film and/or a Glass Slide and Their Interaction with Lectins

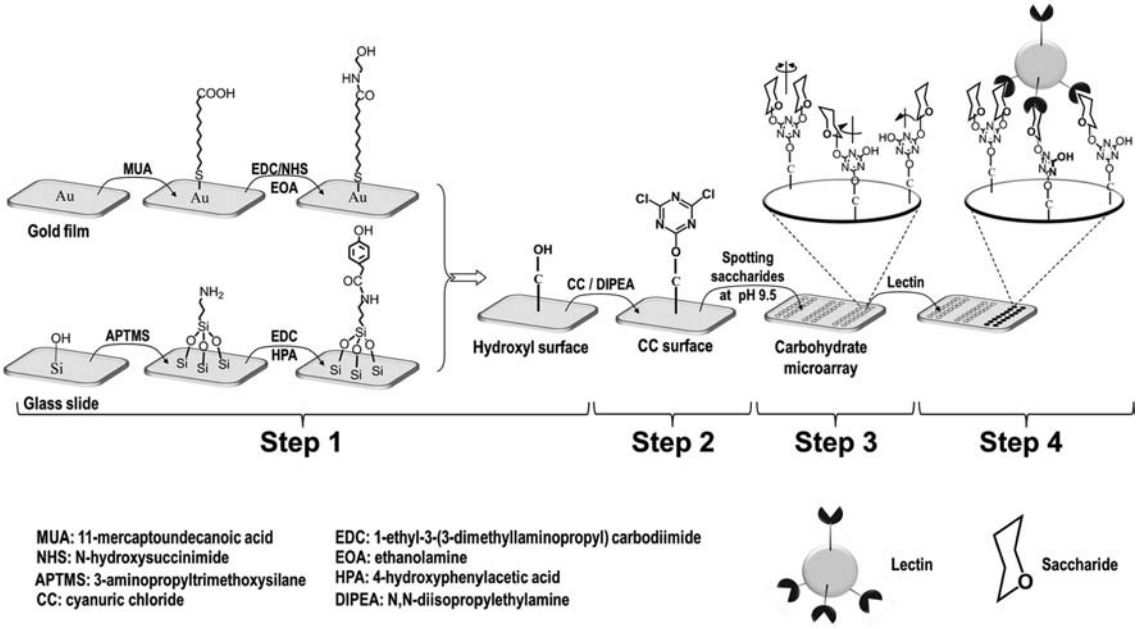

spotted, the chips were put in a sealed humid bottle (humidified by a paper filter wetted with 1 μL water per milliliter volume) at room temperature for 10 h to allow the completion of the coupling reaction. They were then washed by sonication in water at least three times to remove the unbound saccharides and dried under N_2 stream. These saccharide chips were used directly or stored at −20 °C before use. For biological tests, the chips were further blocked in 1 M EOA aqueous solution (adjusted to pH 9.0 with HCl) for 3 h.

Synthesis of 2,4-Dichloro-6-methoxy-triazine (MeO−CC). A 3-mL solution of 1.7 mmol CC (310 mg in acetone) was mixed with 5 mL of methanol and 0.593 mL of DIPEA (3.4 mmol). After 30 min of stirring in an ice bath, the mixed solution was concentrated by vacuum rotary evaporation, and the residue was purified through silica column chromatography (homemade with silica gel of 45−75 μm) eluted with petroleum ether/acetone (v/v = 25:1). The first eluted peak was collected and dried by vacuum rotary evaporation to give the targeted compound (MeO−CC) as white powder, with data of ^{1}H NMR (400 MHz, DMSO, δ) at 3.9 (s, 3H, −O−CH_3) and EI-MS at m/z 179 for both of calcd $[C_3H_3N_3Cl_2O]^-$ and found.

Synthesis of MeO−CC-mannose. A 74-mM mannose aqueous solution (80 mg in 6 mL) was mixed with 26.4 mg of solid NaOH (equal to 0.66 mmol), 80 mg of MeO−CC (0.45 mmol), and 1 mL of acetone. After stirring at 25 °C for 8 h, the mixed solution was freeze-dried, and the crude product was purified by preparative thin layer chromatography (HP-TLC from Merck KGaA, Darmstadt, Germany) developed by 12:1:0.4 (v/v/v) isopropanal/methanol/water to remove the unreacted MeO−CC and free mannose. The product was collected from the original points, and after isolation with methanol and drying by vacuum rotary evaporation, the resulting white powder was characterized by ESI-MS, giving m/z at 306 ($[M+H]^+$) for MeO−CC-mannose. Some MeO−CC-$(mannose)_2$ was also found at m/z 468 ($[M+H]^+$). This procedure is applicable to other saccharides.

XPS Characterization of Surfaces. X-ray photoelectron spectra were obtained by AlKα radiation at 300 W and base pressure of about 3×10^{-9} mbar with an ESCALab220i-XL electron spectrometer from VG Scientific (VG Scientific Ltd., East Grinstead, Sussex, U.K.). The binding energies were calculated with the C1s line at 284.8 eV from adventitious carbon as a reference.

In Figure S2 (Supporting Information), the hydroxyl surface (step 1) and the CC modified surface (step 2) were prepared based on the procedure introduced above. The chip of step 3 was prepared through immersing the chip of step 2 directly into the mannose solution (pH 9.0, 30 mM) for 10 h followed by washing carefully with distilled water and drying with a N_2 stream.

Vapor Condensation Imaging (VCi). VCi was conducted under a stereo microscope model XTL-500 from Guilin Optical Instrument Factory (Guilin, China) with a charge-coupled device (CCD) camera. Images were recorded after a gentle breath from the operator. The recorded images were subsequently saved and analyzed.

Surface Plasmon Resonance Imaging (SPRi). Saccharide microarray chips prepared on gold slides were studied using our laboratory-built SPR imager, SPRi-TX7100. Briefly, a collimated beam of p-polarized light was directed, at a fixed angle, toward a prism on which a microarray chip was assembled via a thin layer of index matching fluid and sealed in a flow cell. The reflected light beam filtered through a narrow bandpass filter (λ 645 nm) was collected by a CCD camera (WAT-902B, Watec Co., Ltd., Japan), and the images were saved and analyzed with a laboratory-edited imaging workstation, v 1.0.

The general process to monitor the immune reaction of lectins to the saccharides on the microarray using SPRi is presented next. A Tris-HCl buffer (pH 7.6, 25 mM) containing 1 mM $CaCl_2$, 1 mM $MnCl_2$, and 0.1% Tween 20 was pneumatically pumped through the flow cell (located in the SPRi instrument) at a flow rate of 60 μL/min until the SPR signal reached equilibrium. Then a Con A solution (50 μg/mL, in the aforementioned Tris-HCl buffer) was introduced into the

cell and incubated for 10−20 min. After that, the Tris-HCl buffer was pumped into the cell again to wash the unbound ConA molecules away. The experiments were carried out at 25 °C, and if needed, an aqueous solution of phosphoric acid (0.1 M) could be introduced into the cell to remove the ConA molecules bound on the saccharide microarray, and then the Tris-HCl buffer was utilized to regenerate the chip surface.

LC-MS of MeO−CC-Saccharide. All LC-MS characterizations were conducted on the LC-MS-2010EV from Shimadzu (Hong Kong) LTD., mounted with a Waters Sunfire C18 column (particle diameter 3.5 μm; length 50 mm, internal diameter 2.1 mm). The separation was conducted by elution, at a flow rate of 0.2 mL/min, with 0.1% formic acid in water (solution A) and acetonitrile (solution B) at a volume ratio of A/B changed continuously from 95/5 to 0/100 in 1.2 min. The eluted peaks were detected by a UV detector and evaporative light-scattering detector.

Preparation of FITC-Labeled Con A. FITC-labeled Con A was synthesized according to a previously reported procedure.[37] Briefly, 1.12 mL of Con A solution (5 mg/mL) in Tris-HCl buffer (pH 9.5) was mixed with 56 μL of FITC solution in acetone (1 mg/mL) at 20 °C and stirred for 20 h. The resulting product was dialyzed against Tris-HCl buffer (0.1 M, pH 7.0) 3 times (8 h for each). The dialyzed ConA solution was diluted with the Tris-HCl buffer (25 mM, pH 7.6, containing 1 mM $CaCl_2$ and 1 mM $MnCl_2$) to 0.05 mg/mL and used immediately for the subsequent experiments with microarray chips.

Laser-Induced Fluorescence Imaging (LIFi). A saccharide microarray chip prepared on a glass slide was allowed to react with a solution of FITC-labeled Con A in pH 7.6 Tris-HCl buffer (20 μg/mL) for 1 h. Fluorescent images were recorded using a Typhoon Trio Variable Mode Imager (Amersham, Biosciences/GE Healthcare) at a pixel size of 25 μm. The fluorescence was excited by a 488 nm laser and collected through a 520 nm filter (40 nm band-pass).

RESULTS AND DISCUSSION

Strategy and Mechanism to Anchor Intact Saccharides via CC Chemistry. A universal strategy was designed to immobilize any an intact saccharide on a solid surface by CC-based chemistry as illustrated in Scheme 1. The chemistry includes three key steps: formation of hydroxyl-terminated surfaces; modification of the hydroxyl terminal with CC; and spotting of saccharide solution on the CC-terminated surfaces. The hydroxyl-terminated surfaces can be prepared by different reactions dependent on the nature of solid materials used. For example, a glass slide can be hydroxyl-terminated by silanization with a reagent containing hydroxyl groups. In this article, it was achieved by treating the glass slides first with APTMS and then with EDC/HPA to have biocompatibility. The hydroxyl groups can be introduced onto a gold surface by direct treatment with a hydroxyl alkyl mercaptan or by more steps of reactions, such as, treatment first with MUA and then with EDC/NHS/EOA. The latter one needs more reaction steps but is also more cost-effective and was adopted in this work.

On the hydroxyl-terminated surfaces, a layer of CC was easily formed, followed a layer of saccharides, in basic conditions. Figure 1 shows that neutral and acidic conditions (lines 2 and 5 in Figure 1) cannot produce visible images by the vapor-condensed imaging (VCi) method[37,53,54] (useful to quickly reveal the hydrophilic position from the hydrophobic). Only at pH above 8.0 can the immobilization be successful (lines 3 and 4 in Figure 1). The improper pH values will also influence later recognition experiments (Figure 1 C and D), which will be discussed in the next section. By basic conditions, the anchoring of a saccharide could be achieved through temperature-modulated stepwise replacement of the three chlorines on CC. Although this stepwise replacement is mild, applicable to both of hydroxyl or amino groups,[41−43] and has been explored to derivatize and/or synthesize various molecules,[44−47] the direct reaction of CC with saccharide's hydroxyls has not yet been studied in depth. To the best of our knowledge, this is the first attempt, especially with respect to the direct construction of saccharide microarray chips.[55]

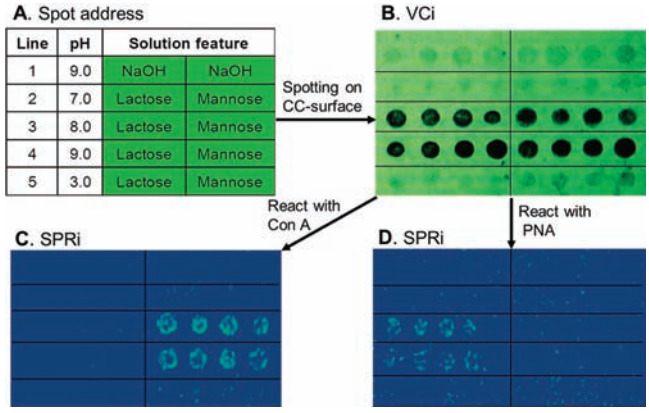

Figure 1. pH value of spotting solutions (A) controls the reaction of saccharides and even OH^- from NaOH (the first line in A) with the CC-terminated surface as viewed by vapor condensed imaging (VCi) (B) and in turn their recognition abilities with Con A (C) and PNA (D) as viewed by SPRi (C and D, with pseudocolor). The spots of NaOH at pH 9.0 were used as blanks.

By using CC as a linker, hydroxyl surfaces were shown to be better than amino ones. We have tried to use an amino-terminated surface to anchor intact saccharides via CC, but the spot quality and signals were poor or even undetectable (Figure S1, Supporting Information). Only when a hydroxyl surface was used and reacted with the CC through replacement of its first chlorine could the remaining chlorines keep high reactivity with the saccharide's hydroxyls, which also agrees with the literature.[42] Hydroxyls on a solid surface are also preferred to suppress nonspecific adsorptions, which is in generel a big issue in surface-related recognition reactions.

To exclude possible nonchemical adsorptions, saccharides were purposely spotted on a hydroxyl-terminated surface (before CC modification) (Figure 2B and E) and on a NaOH (pH 9.0)-hydrolyzed CC-surface (Figure 2C and F). No recognizable or only negligible signals were verified by VCi. These results effectively foreclosed the possibility of physical or nonspecific adsorption from the designed strategy.

The stepwise reaction was verified by XPS measurement using mannose as a testing sample. The immobilization of CC on a hydroxyl-terminated surface (step 1 in Figure S2, Supporting Information) was found to cause an increase of nitrogen peak at ca. 400 eV and an appearance of a new binding energy peak at 200.8 eV corresponding to chlorine (step 2 in Figure S2, Supporting Information). The chlorine signal disappeared (step 3 in Figure S2, Supporting Information) after the CC-immobilized surface was further treated with a mannose solution in basic conditions (required to make the reaction happen and to hydrolyze all the unreplaced chlorine). An evident decrease of the nitrogen signal was also observed

dx.doi.org/10.1021/bc300142s | Bioconjugate Chem. 2012, 23, 1300−1308

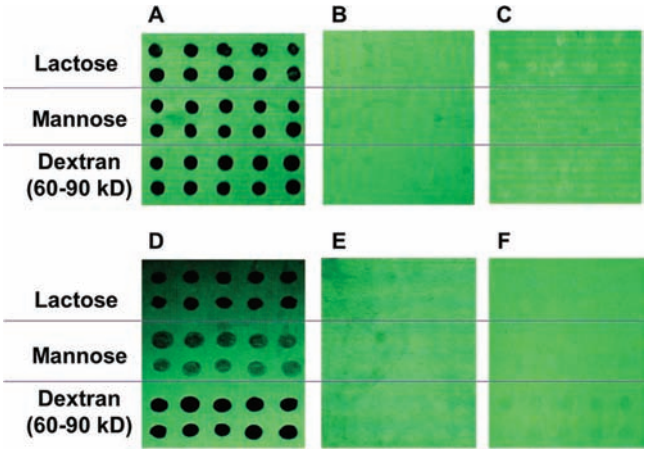

Figure 2. VCi images of saccharide microarray prepared on (A) gold/hydroxyl/CC surface, (B) gold/hydroxyl surface (free of CC), (C) gold/hydroxyl/hydrolyzed CC surface (treated by NaOH beforehand), (D) glass/hydroxyl/CC surface, (E) glass/hydroxyl surface (free of CC), and (F) glass/hydroxyl/hydrolyzed CC surface (treated by NaOH beforehand).

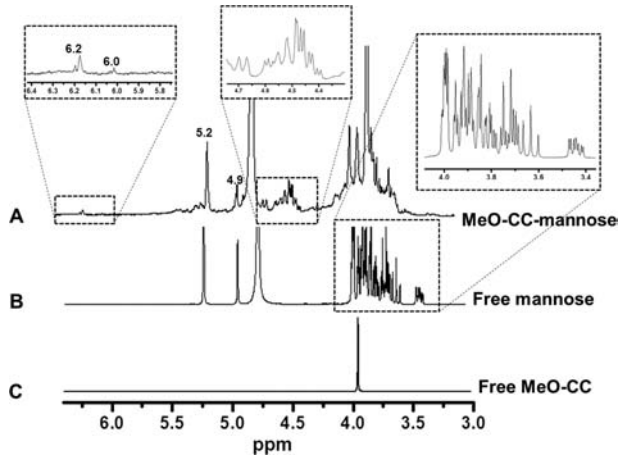

Figure 3. Comparison of 1H NMR spectra between MeO−CC-mannose (A), free mannose (B), and free MeO−CC (C).

due to the embedment of its atoms under the newly immobilized mannose. These clear evidences revealed not only the ascertained route of step-by-step reactions during the deposition of mannose but also the substitution sites on CC.

However, the XPS data revealed no information about the linking site(s) on a mannose molecule, which contains at least 5 different hydroxyl reaction positions. More importantly, we need to know if the anomeric configuration can be conserved after the reaction, which is critical to determine the binding affinity toward lectins.[56]

To have insight into the issues, the mannose-CC-deposited slides were inspected by solid state ^{1}H NMR but failed; the sensitivity was too poor to yield any useable information. Instead, mannose-CC-gold nanoparticles were synthesized and subjected to ^{1}H NMR, and the signals remained under recognition (Figure S3, Supporting Information). In order to increase the detection sensitivity, soluble methoxy-CC-sugars were then synthesized by making the CC react first with methanol (MeOH, Scheme S1A, Supporting Information), instead of the solid slides or particles, to give MeO−CC, and then with target saccharides (Scheme S1B, Supporting Information). By liquid chromatography−mass spectrometry (LC-MS) (Figure S4, Supporting Information), MeO−CC was confirmed to be capable of reaction with both of aldoses (Figure S4A, Supporting Information) and ketoses (Figure S4B, Supporting Information), as in the case of solid surface-CC, while its third chlorine could be replaced by either a second saccharide or −OH (Figure S4A, Supporting Information). These MeO−CC-saccharides were thus considered to be capable of simulating the case of saccharides immobilized on CC-modified slides and subjected to ^{1}H NMR. As expected and also to our surprise, the most preferred α-anomer was well maintained after the saccharides reacted with MeO−CC. For example, the ratio of α-/β-anomers was 2.0:1 for MeO−CC-mannose measured by peak areas at 6.2/6.0 (Figure 3A), similar to 2.1:1 measured at 5.2/4.9 ppm for free mannose (Figure 1B). The immobilization reaction did not change the critical ratio or did not damage the original cyclic structure of saccharides. This foretells that the new method can well conserve the recognition function.

Except for the maintenance of the anomeric configuration, the CC did not actually selectively link a special site on the saccharide molecules. The linking reaction happened stochastically along all the hydroxyl groups on a saccharide. Figure 3A shows that, after the mannose reacted with the MeO−CC, a series of new peaks appeared at 4.4−5.5 ppm and 6.0−6.2 ppm, accompanied by a large reduction of peaks at 3.4−4.1 ppm for C2−C6 and 4.9−5.2 for C1. Clearly, the former peaks could be assigned to the protons on C2−C6 of the reacted mannose and the latter to the proton on C1.[57] They shifted for about 1 ppm away the original position due to the attachment of CC. Unfortunately, calculation of an exact ratio on each reacted ^{1}H-site was not possible because the resonant ^{1}H peaks overlapped each other seriously and with other signals. Fortunately, these overlapped peaks are enough to deduce that MeO−CC has roughly a similar reactivity toward the saccharide's hydroxyls. This was further validated in the reaction of MeO−CC with fructose (Figure S5, Supporting Information). The proton signals on C1−C5 moved from 3.5−4.2 ppm for free fructose (Figure S5B, Supporting Information) to 4.2−4.5 ppm and 5.1−5.4 ppm, for MeO−CC-fructose (Figure S5A, Supporting Information), indicating again the nonselective linking of CC with the hydroxyls on fructose. Considering that the recognition ability of the immobilized saccharides can be well conserved (to be discussed in the next section), it can interestingly be concluded that which site is linked on a saccharide is not as important as what we expected if the original cyclic structure and configuration of a saccharide can be well conserved.

Preparation of Bioaffinity-Conserved Saccharide Microarrays. On the basis of the proposed chemical strategy (Scheme 1), 15 different saccharides, including mono-, oligo-, and polysaccharides, were successfully immobilized on the same hydroxyl-terminated chip by spotting them in an addressable way (Figure 4A and B). Different from most of the currently used immobilizing strategies which may require complicated synthetic steps, intensive modification of saccharides, or expensive coupling reagents, this CC-based chemistry needs just to drop or spot the basic aqueous saccharide solutions on the chip surface and then leave it at room temperature to react for a certain time. Both reducing and nonreducing (such as sucrose and trehalose, spot (4,iii) and (3,i) in Figure 4B) saccharides can directly be spotted on a CC-terminated surface. Further modification of the saccharides is allowed but not

dx.doi.org/10.1021/bc300142s | Bioconjugate Chem. 2012, 23, 1300−1308

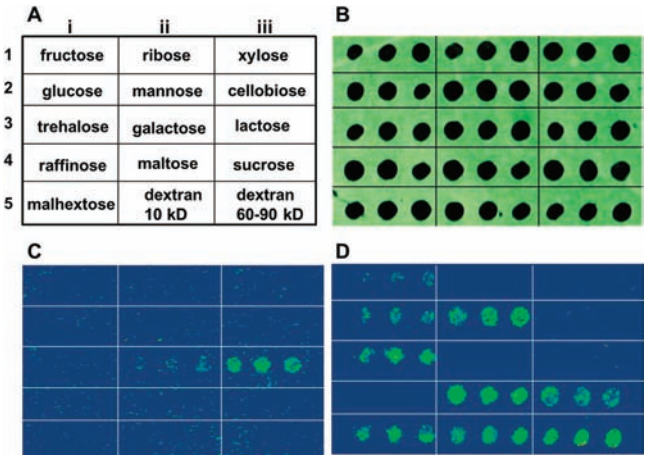

Figure 4. VCi (B) and SPRi (C and D) images of 15 intact saccharides (A) spotted on a CC-modified gold surface. VCi was conducted just after immobilization (B) and the pseudocolored SPRi after incubation with PNA (C) or ConA (D).

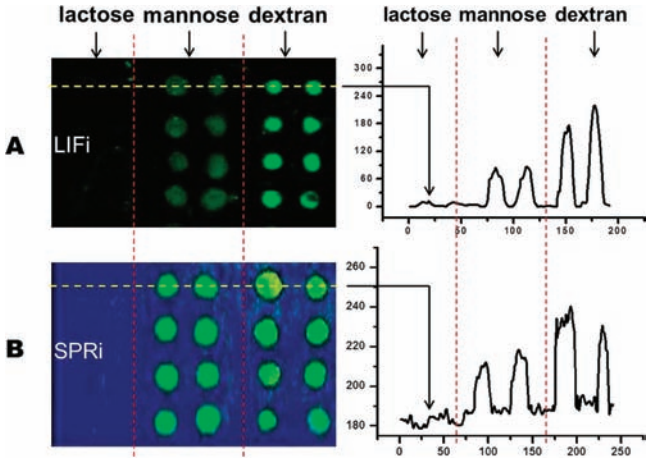

Figure 5. LIFi (A) and SPRi (B, pseudo colored) images of saccharide microarrays measured after reaction with FITC-labeled ConA (A) or intact ConA (B). The chip for LIFi was prepared on a glass slide and for SPRi on gold film. The linear profiles represent the relative signal intensities across the dashed line on the images.

required, suggesting that the new strategy is universally applicable. Anchoring becomes now much simple and easy to manipulate. The experimental cost is greatly reduced due to the use of very cheap CC.

The bioaffinity of saccharides spotted this way was shown to be well preserved. To demonstrate, the chip with 15 different saccharides was made to react with two lectins, concanavalin A (ConA) and peanut agglutinin (PNA). According to the literature,[56] ConA will specifically recognize terminal α-D-glucose and α-D-mannose in an affinity order of mannose > glucose, and PNA specifically recognizes terminal β-D-galactose. The expected results were observed by surface plasmon resonance imaging (SPRi): Figure 4 shows clearly that the galβ1-structured saccharides, such as lactose and galactose, exhibit recognition signals with PNA (Figure 4C); all the gluα1- or manα1-structured saccharides, including glucose, mannose, trehalose, maltose, sucrose, malhextose, and dextran, have strong binding signals with ConA (Figure 4D); and all the nonlectin targets do not show any visible signal. Unexpectedly, fructose was measured to have a weak but visible interaction with ConA in our measurement (spots (1,i) in Figure 4D). After some search of the literature, this weak affinity was found to have been documented,[58−60] but it is generally too weak to be visible by many existing methods. The visibility of this weak recognition further highlights the merit of our new method.

These SPRi results were experimentally compared with laser-induced fluorescence imaging (LIFi) by using FITC-labled Con A, which is frequently used in bioassays. Figure 5 shows a parallel illustration of both LIFi and SPRi images. The recognition behaviors of the immobilized saccharides agree well with each other, demonstrating that the newly proposed strategy is reliable and applicable to also LIFi assays if labeled samples are available.

It is until now satisfactory that all the tried saccharides, small and large or reducing and nonreducing, can be well immobilized by the new method and can play their expected recognition roles with the selected lectins. A special highlight is that the new strategy can well conserve the recognition ability of small saccharides, including even monosaccharides. According to the above-elucidated chemical mechanism, there are two reasons responsible for the conservation of bioaffinity of the immobilized saccharides: first, the CC-based coupling reaction is mild and gentle. Different from the direct coupling of intact saccharides by reductive amination of the aldehyde groups, the CC-reaction does not directly touch the atoms of the cyclic scaffold of saccharides but reacts only at room temperature with the far and nonring atoms on hydroxyls having the original cyclic structure and with the anomeric configuration easily maintained (Figure 3). Second, CC offers three rotation axes with a theoretical angle of 120°. It can rotate on a surface even after anchoring, and similarly, the saccharides anchored on the CC ring can also revolve freely round the linking bond, making them more easily adjust or adapt their orientation to favor their collaborative recognition for a better "cluster effect"[39] (steps 3 and 4 in Scheme 1). In recognition, the hydroxyl groups should be important because they contribute to the formation of the hydrogen bond,[56] but in this test, the use of one hydroxyl for saccharide immobilization (Figure 3 and Figure S4, Supporting Information) did not show detectable impact on the recognition behavior of saccharides. This can also be explained by the free rotation offered by CC. In short, the CC-based chemistry opens an ideal way to prepare bioaffinity-preserved saccharide chips through chemical immobilization, which coincides with our original intention to design this strategy.

Recognition Features of the Immobilized Saccharides. By the chip in combination with imaging techniques, the recognition behaviors were inspected to validate the real applicability of the proposed method. Both LIFi (Figure 5A) and SPRi (Figures 5B and 4C,D) showed that the recognition signals were dependent on the type of saccharides immobilized and lectins used, which agrees with the theoretical expectation. By closer inspection of Figure 5A or B, it could be found that the signals increased also with the molecular weight or residue number of saccharides. Figure 4D shows that the larger dextran (spots (5, iii) in Figure 4D) gives stronger signals than the smaller one (spots (5, i) or (5, ii) in Figure 4D). This is reasonable because a molecule with more binding sites must link more targets and produce stronger signals than a molecule with less binding sites. There are also differences in the recognition dynamics as revealed by the SPR observation shown in Figure 6. Mannose recognized Con A as the fastest, glucose as the second, and dextran as the slowest. This implies that the large molecules need a longer time than small ones to

dx.doi.org/10.1021/bc300142s | Bioconjugate Chem. 2012, 23, 1300−1308

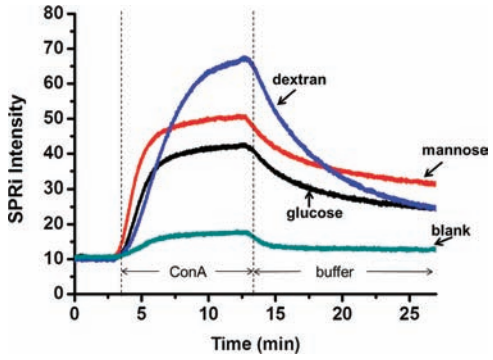

Figure 6. SPR sensorgram of ConA binding to the different saccharides immobilized by CC-based chemistry. The dynamic experiment includes 2 steps: (a) incubation of the saccharide chip with ConA solution (50 μg/mL, in the pH 7.6 Tris-HCl buffer); and (b) washing of the chip surface with Tris-HCl buffer at pH 7.6.

adjust their structure and/or position for recognition or that the dextran has less affinity than mannose toward ConA. Nevertheless, the recognition process took several minutes, not surpassing 15 min. These are fast recognition reactions. In contrast, the large dextran showed the fastest washing-off dynamic among the tested saccharides (Figure 6), which agrees with the suspicion that its binding affinity is weaker than that of mannose with ConA. This is also highly consistent with the reported results.[37,56] It can thus be concluded that the CC-based chemistry can preserve not only the recognition ability of the immobilized saccharides but also a way to study the relative strength of the binding affinity.

Stability of the Microarrayed Saccharide Chips. By stability, we mean two events here: the first is with respect to their shelf life or storage time; and the second is concerning their reusable times in a continuous recognition experiment. The reusable times were checked by SPR sensing of the ConA-based recognition−regeneration cycle. In a typical experiment, a chip could be reused for more than 10 cycles or for 48 h in acidic washing conditions without an evident loss of SPR sensitivity. Figure 7 shows an example where the highly reproducible SPR signals were measured during 4 successive

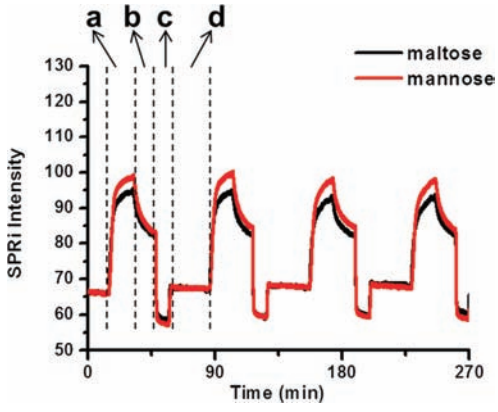

Figure 7. SPR sensorgram of successive binding-regenerating cycles measured from the recognitions of ConA with maltose and mannose immobilized on the same CC surface. Each cycle includes 4 steps: (a) incubation of the saccharide chip with ConA solution; (b) wash of the chip surface with Tris-HCl buffer at pH 7.6; (c) removal of the ConA molecules by flashing the chip surface with 0.1 M phosphoric acid; and (d) regeneration of the chip surface with Tris-HCl buffer at pH 7.6.

binding−regenerating cycles. On shelf life, more experimental checks were conducted, and it was found that the fabricated microarray chips could maintain their binding performance after they were stored at −20 °C for at least 2 months. These results demonstrate that the immobilization strategy is robust and can benefit its practical application in the future.

CONCLUSIONS

A new strategy was proposed to chemically immobilize various intact saccharides on a solid surface using CC as a key linking agent. An easy, cost-effective, and universal method was then established for the preparation of saccharide-dotted chips with well-preserved bioaffinity and enough stability. The key innovation present was the use of CC as a linker, which is very economical, abundant, and easily available. It is due to the use of CC that all the intact saccharides could directly be immobilized on hydroxyl-terminated solid surfaces which are biocompatible and can largely suppress the nonspecific adsorption effect. The highly attractive features are that the recognition affinity of the covalently anchored small (monosaccharides) and large (polysaccharides) saccharides could be well conserved as was proved by the recognition with lectins. This conservation was ascribed to the rotable structure of CC that offers three rotary axes, allowing the anchored saccharides to adapt their spatial position to favor their recognition in a cluster format, and to the mild and gentle reaction of CC with the nonring-determining atoms of hydroxyls, allowing maintenance of the original structure and configuration of the saccharides after immobilization. The CC was shown to react stochastically with each hydroxyl on a saccharide. This phenomenon suggests that replacement of one of the hydroxyl protons on a saccharides may not necessarily impact its bioaffinity if its ring structure is not disturbed, which opens a new trace to anchor saccharides. Furthermore, the CC-based chemistry is in theory extendable to the immobilization of other biological molecules having hydroxyl group(s) or amino groups (better on amino-terminated surfaces). In short, the new strategy offers a favorable toolbox with various means for exploration of better methods, not only the discussed one.

ASSOCIATED CONTENT

Supporting Information

VCi images of saccharide microarray spotted on CC-amino-functioned surfaces; the XPS N 1s and Cl 2p spectra of the surface in different preparing steps; ^{1}H NMR spectra of gold nanoparticle modified with mannose through CC-chemistry; LC-MS characterization of products from the reaction of MeO−CC with saccharides; comparison of ^{1}H NMR spectra among MeO−CC-fructose, free fructose, and free MeO−CC; and scheme of model reaction of CC with saccharides. This material is available free of charge via the Internet at http://pubs.acs.org.

AUTHOR INFORMATION

Corresponding Author

*Institute of Chemistry, Chinese Academy of Sciences, Zhongguancun North First Street 2, 100190 Beijing, PR China. Tel: +86-10-62618240. Fax: +86-10-62559373. E-mail: chenyi@iccas.ac.cn.

Notes

The authors declare no competing financial interest.

■ ACKNOWLEDGMENTS

We acknowledge the financial support from NSFC (No. 21027003 & 91117010), MOST, and CAS.

■ ABBREVIATIONS

Con A, concanavalin A; PNA, peanut agglutinin; FITC, fluorescein isothiocyanate; APTMS, 3-aminopropyltrimethoxysilane; EDC, 1-ethyl-3-(3-dimethyllaminopropyl)-carbodiimide; CC, cyanuric chloride; MUA, 11-mercaptoundecanoic acid; NHS, *N*-hydroxysuccinimide; DIPEA, *N*,*N*-diisopropylethylamine; HPA, 4-hydroxyphenylacetic acid; EOA, ethanolamine; EDA, ethanediamine

■ REFERENCES

(1) Varki, A. (1993) Biological roles of oligosaccharides — all of the theories are correct. *Glycobiology 3*, 97−130.
(2) Paulson, J. C., Blixt, O., and Collins, B. E. (2006) Sweet spots in functional glycomics. *Nat. Chem. Biol. 2*, 238−248.
(3) Lonardi, E., Balog, C. I., Deelder, A. M., and Wuhrer, M. (2010) Natural glycan microarrays. *Expert Rev. Proteomics 7*, 761−774.
(4) Campbell, C. T., and Yarema, K. J. (2005) Large-scale approaches for glycobiology. *Geno. Biol. 6*, 236.
(5) Horlacher, T., and Seeberger, P. H. (2008) Carbohydrate arrays as tools for research and diagnostics. *Chem. Soc. Rev. 37*, 1414−1422.
(6) Krishnamoorthy, L., and Mahal, L. K. (2009) Glycomic analysis: an array of technologies. *ACS Chem. Biol. 4*, 715−732.
(7) Zhang, Y., Li, Q., Rodriguez, L. G., and Gildersleeve, J. C. (2010) An array-based method to identify multivalent inhibitors. *J. Am. Chem. Soc. 132*, 9653−9662.
(8) Manimala, J. C., Li, Z., Jain, A., Vedbrat, S., and Gildersleeve, J. C. (2005) Carbohydrate array analysis of anti-Tn antibodies and lectins reveals unexpected specificities: implications for diagnostic and vaccine development. *ChemBioChem 6*, 2229−2241.
(9) Oyelaran, O., Li, Q., Farnsworth, D., and Gildersleeve, J. C. (2009) Microarrays with varying carbohydrate density reveal distinct subpopulations of serum antibodies. *J. Proteome Res. 8*, 3529−3538.
(10) Liang, C. H., and Wu, C. Y. (2009) Microarrays with varying carbohydrate density reveal distinct subpopulations of serum antibodies. *Expert Rev. Proteomics 6*, 631−645.
(11) Shin, I., Park, S., and Lee, M. R. (2005) Carbohydrate microarrays: an advanced technology for functional studies of glycans. *Chem.—Eur. J. 11*, 2894−2901.
(12) Park, S., Lee, M. R., and Shin, I. (2008) Chemical tools for functional studies of glycans. *Chem. Soc. Rev. 37*, 1579−1591.
(13) Park, S., Lee, M. R., and Shin, I. (2008) Carbohydrate microarrays as powerful tools in studies of carbohydrate-mediated biological processes. *Chem. Commun.*, 4389−4399.
(14) Laurent, N., Voglmeir, J., and Flitsch, S. L. (2008) Glycoarrays — tools for determining protein−carbohydrate interactions and glycoenzyme specificity. *Chem. Commun.*, 4400−4412.
(15) Ban, L., and Mrksich, M. (2008) On-chip synthesis and label-free assays of oligosaccharide arrays. *Angew. Chem., Int. Ed. 47*, 3396−3399.
(16) Wang, D., Liu, S., Trummer, B. J., Deng, C., and Wang, A. (2002) Carbohydrate microarrays for the recognition of cross-reactive molecular markers of microbes and host cells. *Nat. Biotechnol. 20*, 275−281.
(17) Willats, W. G., Rasmussen, S. E., Kristensen, T., Mikkelsen, J. D., and Knox, J. P. (2002) Sugar-coated microarrays: A novel slide surface for the high-throughput analysis of glycans. *Proteomics 2*, 1666−1671.
(18) Ko, K. S., Jaipuri, F. A., and Pohl, N. L. (2005) Fluorous-based carbohydrate microarrays. *J. Am. Chem. Soc. 127*, 13162−13163.
(19) Paz, J. L. D., Spillmann, D., and Seeberger, P. H. (2006) Microarrays of heparin oligosaccharides obtained by nitrous acid depolymerization of isolated heparin. *Chem. Commun.*, 3116−3118.
(20) Tully, S. E., Rawat, M., and Hsieh-Wilson, L. C. (2006) Discovery of a TNF-α antagonist using chondroitin sulfate microarrays. *J. Am. Chem. Soc. 128*, 7740−7741.
(21) Blixt, O., Head, S., Mondala, T., Scanlan, C., Huflejt, M. E., Alvarez, R., Bryan, M. C., Fazio, F., Calarese, D., Stevens, J., Razi, N., Stevens, D. J., Skehel, J. J., Van Die, I., Burton, D. R., Wilson, I. A., Cummings, R. D., Bovin, N., Wong, C. H., and Paulson, J. C. (2004) Printed covalent glycan array for ligand profiling of diverse glycan binding proteins. *Proc. Natl. Acad. Sci. U.S.A. 101*, 17033−17038.
(22) Paz, J. L. D., Noti, C., and Seeberger, P. H. (2006) Microarrays of synthetic heparin oligosaccharides. *J. Am. Chem. Soc. 128*, 2766−2767.
(23) Bryan, M. C., Fazio, F., Lee, H. K., Huang, C. Y., Chang, A., Best, M. D., Calarese, D. A., Blixt, O., Paulson, J. C., Burton, D., Wilson, I. A., and Wong, C. H. (2004) Covalent display of oligosaccharide arrays in microtiter plates. *J. Am. Chem. Soc. 126*, 8640−8641.
(24) Köhn, M., Wacker, R., Peters, C., Schröder, H., Soulère, L., Breinbauer, R., Niemeyer, C. M., and Waldmann, H. (2003) Staudinger ligation: a new immobilization strategy for the preparation of small-molecule arrays. *Angew. Chem., Int. Ed. 42*, 5830−5834.
(25) Houseman, B. T., and Mrksich, M. (2002) Carbohydrate arrays for the evaluation of protein binding and enzymatic modification. *Chem. Biol. 9*, 443−454.
(26) Park, S., Lee, M. R., Pyo, S. J., and Shin, I. (2004) Carbohydrate chips for studying high-throughput carbohydrate-protein interactions. *J. Am. Chem. Soc. 126*, 4812−4819.
(27) Karamanska, R., Clarke, J., Blixt, O., Macrae, J. I., Zhang, J. Q., Crocker, P. R., Laurent, N., Wright, A., Flitsch, S. L., Russell, D. A., and Field, R. A. (2008) Surface plasmon resonance imaging for real-time, label-free analysis of protein interactions with carbohydrate microarrays. *Glycoconjugate J. 25*, 69−74.
(28) Angeloni, S., Ridet, J. L., Kusy, N., Gao, H., Crevoisier, F., Guinchard, S., Kochhar, S., Sigrist, H., and Sprenger, N. (2005) Glycoprofiling with micro-arrays of glycoconjugates and lectins. *Glycobiology 15*, 31−41.
(29) Carroll, G. T., Wang, D., Turro, N. J., and Koberstein, J. T. (2008) Photons to illuminate the universe of sugar diversity through bioarrays. *Glycoconjugate J. 25*, 5−10.
(30) Tyagi, A., Wang, X., Deng, L., Ramström, O., and Yan, M. (2010) Photogenerated carbohydrate microarrays to study carbohydrate−protein interactions using surface plasmon resonance imaging. *Biosens. Bioelectron. 26*, 344−350.
(31) Cheng, F., Shang, J., and Ratner, D. M. (2011) A versatile method for functionalizing surfaces with bioactive glycans. *Bioconjugate Chem. 22*, 50−57.
(32) Hsiao, H. Y., Chen, M. L., Wu, H. T., Huang, L. D., Chien, W. T., Yu, C. C., Jan, F. D., Sahabuddin, S., Chang, T. C., and Lin, C. C. (2011) Fabrication of carbohydrate microarrays through boronate formation. *Chem. Commun. 47*, 1187−1189.
(33) Lee, M. R., and Shin, I. (2005) Facile preparation of carbohydrate microarrays by site-specific, covalent immobilization of unmodified carbohydrates on hydrazide-coated glass slides. *Org. Lett. 7*, 4269−4272.
(34) Park, S., Lee, M. R., and Shin, I. (2009) Construction of carbohydrate microarrays by using one-step, direct immobilizations of diverse unmodified glycans on solid surfaces. *Bioconjugate Chem. 20*, 155−162.
(35) Zhou, X., and Zhou, J. (2006) Oligosaccharide microarrays fabricated on aminooxyacetyl functionalized glass surface for characterization of carbohydrate−protein interaction. *Biosens. Bioelectron. 21*, 1451−1458.
(36) Carroll, G. T., Wang, D., Turro, N. J., and Koberstein, J. T. (2006) Photochemical micropatterning of carbohydrates on a surface. *Langmuir 22*, 2899−2905.
(37) Wang, H., Zhang, Y., Yuan, X., Chen, Y., and Yan, M. (2011) A universal protocol for photochemical covalent immobilization of intact carbohydrates for the preparation of carbohydrate microarrays. *Bioconjugate Chem. 22*, 26−32.

(38) Hatanaka, Y., Kempin, U., and Jong-Jip, P. (2000) One-step synthesis of biotinyl photoprobes from unprotected carbohydrates. *J. Org. Chem. 65*, 5639−5643.
(39) Jayaraman, N. (2009) Multivalent ligand presentation as a central concept to study intricate carbohydrate−protein interactions. *Chem. Soc. Rev. 38*, 3463−3483.
(40) Kamiński, Z. J. (2000) Triazine-based condensing reagents. *Biopolymers 55*, 140−164.
(41) Thurston, J. T., Dudley, J. R., Kaiser, D. W., Hechenbleikner, I., Schaefer, F. C., and Holm-Hansen, D. (1951) Cyanuric chloride derivatives. I. aminochloro-s-triazines. *J. Am. Chem. Soc. 73*, 2981−2983.
(42) Dudley, J. R., Thurston, J. T., Schaefer, F. C., Holm-Hansen, D., Hull, C. J., and Adams, P. (1951) Cyanuric chloride derivatives. III. alkoxy-s-triazines. *J. Am. Chem. Soc. 73*, 2986−2990.
(43) Schaefer, F. C., Thurston, J. T., and Dudley, J. R. (1951) Cyanuric chloride derivatives. IV. aryloxy-s-triazines. *J. Am. Chem. Soc. 73*, 2990−2992.
(44) Blotny, G. (2006) Recent applications of 2,4,6-trichloro-1,3,5-triazine and its derivatives in organic synthesis. *Tetrahedron 62*, 9507−9522.
(45) Li, Y., Neoh, K. G., Cen, L., and Kang, E.-T. (2003) Physicochemical and blood compatibility characterization of polypyrrole surface functionalized with heparin. *Biotechnol. Bioeng. 84*, 305−313.
(46) Sateesh, A., Vogel, J., Dayss, E., Fricke, B., Dölling, K., and Rothe, U. J. (2007) Surface modification of medical-grade polyurethane by cyanurchloride-activated tetraether lipid (a new approach for bacterial antiadhesion). *Biomed. Mater. Res. Part A*, 672−681.
(47) Vepari, C., Matheson, D., Drummy, L., Naik, R., and Kaplan, D. L. J. (2009) Surface modification of silk fibroin with poly(ethylene glycol) for antiadhesion and antithrombotic applications. *Biomed. Mater. Res. Part A*, 595−606.
(48) Lee, P. H., Sawan, S. P., Modrusan, Z., Arnold., L. J., Jr., and Reynolds, M. A. (2002) An efficient binding chemistry for glass polynucleotide microarrays. *Bioconjugate Chem. 13*, 97−103.
(49) Wildeboera, D., Jiangb, P., Pricea, R. G., Yub, S., Jeganathana, F., and Abuknesha, R. A. (2010) Use of antibody−hapten complexes attached to optical sensor surfaces as a substrate for proteases: Real-time biosensing of protease activity. *Talanta 81*, 68−75.
(50) Walter, J. G., Kökpinar, Ö., Friehs, K., Stahl, F., and Scheper, T. (2008) Systematic investigation of optimal aptamer immobilization for protein-microarray applications. *Anal. Chem. 80*, 7372−7378.
(51) Uttamchandani, M., Walsh, D. P., Khersonsky, S. M., Huang, X., Yao, S. Q., and Chang, Y. T. (2004) Microarrays of tagged combinatorial triazine libraries in the discovery of small-molecule ligands of human IgG. *J. Comb. Chem. 6*, 862−868.
(52) Schwarz, M., Spector, L., Gargir, A., Shtevi, A., Gortler, M., Altstock, R. T., Dukler, A. A., and Dotan, N. (2003) A new kind of carbohydrate array, its use for profiling antiglycan antibodies, and the discovery of a novel human cellulose-binding antibody. *Glycobiology 13*, 749−754.
(53) Holmgren, J., Svennerholm, L., Elwing, H., Fredman, P., and Strannegård, O. (1980) Sendai virus receptor: proposed recognition structure based on binding to plastic-adsorbed gangliosides. *Proc. Natl. Acad. Sci. U.S.A. 77*, 1947−1950.
(54) Elwing, H., Nilsson, L. A., and Ouchterlony, O. J. (1977) A simple spot technique for thin layer immunoassays (TIA) on plastic surfaces. *Immunol. Methods 17*, 131−145.
(55) Blais, B. W., and Yamazaki, H. (1990) Activation of polyester cloth for the immobilization of a polysaccharide antigen. *Biotechnology Techniques 4*, 11−14.
(56) Lis, H., and Sharon, N. (1998) Lectins: carbohydrate-specific proteins that mediate cellular recognition. *Chem. Rev. 98*, 637−674.
(57) Agrawal, P. K. (1992) NMR spectroscopy in the structural elucidation of oligosaccharides and glycosides. *Phytochemistry 31*, 3307−3330.
(58) Bernhard, W., and Avrameas, S. (1971) Ultrastructural visualization of cellular carbohydrate components by means of concanavalin A. *Exp. Cell Res. 64*, 232−235.
(59) Villafranca, J. J., and Viola, R. E. (1974) Proton nuclear magnetic resonance studies of the manganese (II) binding site of concanavalin A: Effect of saccharides on the solvent relaxation rates. *Arch. Biochem. Biophys. 165*, 51−59.
(60) Moothoo, D. N., and Naismith, J. H. (1999) A general method for co-crystallization of concanavalin A with carbohydrates. *Acta Crystallogr., Sect. D 55*, 353−355.

Bioconjugate Chemistry

Article

pubs.acs.org/bc

Labeling Lysosomes and Tracking Lysosome-Dependent Apoptosis with a Cell-Permeable Activity-Based Probe

Fengkai Fan,[†,‡] Si Nie,[†,‡] Dongmei Yang,[†,‡] Meijie Luo,[†,‡] Hua Shi,[†,‡] and Yu-Hui Zhang*[,†,‡]

[†]Britton Chance Center for Biomedical Photonics, Wuhan National Laboratory for Optoelectronics-Huazhong University of Science and Technology, and [‡]Key Laboratory of Biomedical Photonics of Ministry of Education, Department of Biomedical Engineering, Huazhong University of Science and Technology (HUST), 1037 Luoyu Road, Wuhan 430074, P. R. China

Supporting Information

ABSTRACT: In this study, we describe a new strategy for labeling and tracking lysosomes with a cell-permeable fluorescent activity-based probe (CpFABP) that is covalently bound to select lysosomal proteins. Colocalization studies that utilized LysoTracker probes as standard lysosomal markers demonstrated that our novel probe is effective in specifically labeling lysosomes in various kinds of live cells. Furthermore, our studies revealed that this probe has the ability to label fixed cells, permeabilized cells, and NH_4Cl-treated cells, unlike LysoTracker probes, which show ineffective labeling under the same conditions. Remarkably, when applied to monitor the process of lysosome-dependent apoptosis, our probe not only displayed the expected release of lysosomal cathepsins from lysosomes into the cytosol but also revealed additional information about the location of the cathepsins during apoptosis, which is undetectable by other chemical lysosome markers. These results suggest a wide array of promising applications for our probe and provide useful guidelines for its use as a lysosome marker in lysosome-related studies.

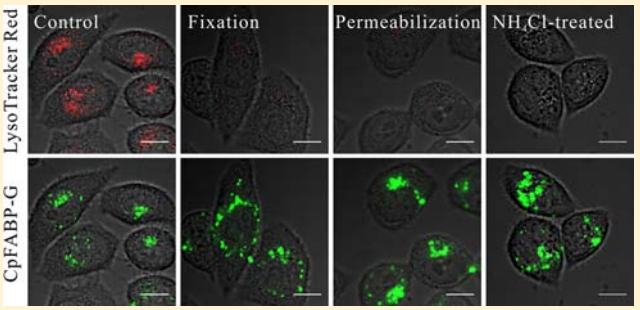

INTRODUCTION

Lysosomes are dynamic, membrane-bound organelles that contain more than 50 acid hydrolases and a high proton concentration (pH ≤ 5).[1] The primary function of lysosomes is to degrade endocytosed and intracellular material. However, increasing evidence has shown that lysosomes are also involved in other complex and layered activities, such as intracellular transport, cell antigen processing, and the initiation of apoptosis.[1−4] Lysosomal dysfunction has been implicated in diverse diseases, including inflammation, tumor formation, and several neurodegenerative diseases.[5−7] The ability to visualize lysosomes is critical for understanding intracellular metabolism[8] and cell membrane recycling,[9] and for evaluating drug and gene delivery systems.[10,11] A variety of chemical markers for labeling lysosomes have been developed, and their labeling strategies can be divided into two main types. The first type of label exploits the acidic property of lysosomes and the tendency for weak basic amines to selectively accumulate in acidic organelles. Small-molecule markers, including DAMP,[12] neutral red,[13] acridine orange,[14] and the LysoTracker probes,[15] are examples of this labeling strategy. The other strategy utilizes large molecules, such as dextran labeled with a fluorophore,[16,17] modified quantum dots,[18] and nanoparticles (DSiNPs),[19] and their ability to enter living cells through endocytosis.[18−20] This ultimately leads to localization within the lysosome, as it is the final compartment of the degradative endocytotic pathway.[21]

Activity-based probes (ABPs) are small synthetic molecules that can profile the enzymatic activity in proteomes.[22] ABPs contain two key elements: a reactive "warhead", which covalently binds the active site of the targeted enzymes, and a reporter tag, such as a fluorophore or biotin, which allows the labeled enzymes to be identified, purified, and/or visualized. Recently, ABPs have been used widely for functional proteomic studies of various enzymes, such as metalloproteases, serine, and cysteine proteases.[22] However, ABPs have not yet been utilized as markers for labeling and tracking intracellular organelles. In this study, we describe a novel strategy that employs cell-permeable fluorescent ABPs (CpFABPs) to label and track lysosomes. The CpFABPs have three components: (a) an epoxysuccinyl scaffold that has been reported to selectively form covalent bonds with cysteine cathepsins,[23−25] (b) a fluorophore for visualizing the covalently bound enzymes, and (c) an arginine-rich cell-penetrating peptide (CPP) to engender the cellular permeability of the probe.[26] We demonstrate that the CpFABPs may be used as highly selective and biocompatible lysosomal markers not only in various kinds of live cells but also in fixed cells, permeabilized cells, and NH_4Cl-treated cells. In addition, the CpFABP was also shown to track lysosome-dependent apoptosis in real-time in live cells.

Received: March 20, 2012
Revised: May 7, 2012
Published: May 31, 2012

EXPERIMENTAL PROCEDURES

Materials. Dulbecco's modified Eagle's medium (DMEM), fetal bovine serum (FBS), horse serum (hyclone), glutamax, CO_2-independent medium, and Opti-MEM I Reduced Serum Medium (Opti-MEM) were purchased from Gibco BRL. 3-(4,5-Dimethylthiazol-2-yl)-2,5-diphenyltetrazolium bromide (MTT) was obtained from Sigma-Aldrich. Lipofectamine 2000 and LysoTracker DND 26 were purchased from Invitrogen. LysoTracker Red was obtained from Beyotime. Ammonium chloride (NH_4Cl) and hydrogen peroxide (H_2O_2) were supplied by the Sinopharm Chemical Reagent Beijing Co. Ltd. Fmoc-amino acids and all other chemical reagents were obtained from GL Biochem. All starting materials were used without additional purification.

Synthesis of the Probes. Probes CpFABP-G, CpFABP-R, **1**, and **2** were synthesized using 9-fluorenylmethoxycarbonyl (Fmoc) solid-phase peptide synthesis (SPPS) on 2-chlorotrityl chloride resin, with standard deprotection and coupling procedures. The probes were purified by preparative high-performance liquid chromatography (HPLC) to reach a purity greater than 90%, and the mass was confirmed by electrospray ionization (ESI) mass spectrometry (Figure S1 of the Supporting Information).

Cell Culture. HeLa cells (human epitheloid cervix carcinoma cell line), MCF-7 cells (human breast adenocarcinoma cell line), Cos-7 cells (African Green Monkey fibroblast-like kidney cell line), and RAW 264.7 cells (mouse leukemic monocyte macrophage cell line) were cultured in DMEM supplemented with 10% (v/v) FBS. Cells were grown at 37 °C under CO_2 (5%, v/v) for 2−3 days. Peritoneal macrophage cells were collected from C57 black mice 3 days after intraperitoneal injection of 1.5 mL 6% starch broth and suspended in RPMI-1640 medium containing 10% FBS, penicillin (100 IU/mL), and streptomycin (50 μg/mL). The cell suspensions were plated onto eight-well Lab-Tek chamber slides (Nunc). After incubation for 3 h at 37 °C under an atmosphere of 5% CO_2, the cells were then washed gently twice to remove the nonadherent cells. Primary hippocampal neurons were obtained from embryos (E18) of pregnant mice. Hippocampi was dissected and treated with 0.125% trypsin at 37 °C for 10 min. The cells were dissociated by trituration and then suspended in DMEM containing 10% heat-inactivated horse serum and 2 mM glutamax. Then, the cells were seeded onto eight-well Lab-Tek chamber slides at a density of 2.0×10^4 cells/well. The chamber slides were precoated via a 12 h incubation in poly(L-lysine) followed by washing and an 8 h incubation with laminin. The cells were cultured at 37 °C under CO_2 (5%, v/v) for 3 days.

Confocal Laser Scanning Microscopy. HeLa cells, MCF-7 cells, Cos-7 cells, or RAW 264.7 cells were seeded onto eight-well Lab-Tek chamber slides (Nunc) at a density of 1.0×10^4 cells/well in DMEM (300 μL) containing 10% FBS. The cells were then grown at 37 °C in CO_2 (5%, v/v) overnight. They were washed with phosphate-buffered saline (PBS, pH 7.4) and were incubated with the indicated probes (10 μM, 300 μL) in PBS for 30 min. The medium was discarded, and the cells were rinsed with PBS. After a postincubation in DMEM (300 μL) containing 10% FBS for 0, 2, 4, 8, 12, or 23 h, the cells were analyzed with a confocal laser scanning microscope. To stain lysosomes, the cells were incubated with the indicated concentrations of LysoTracker Red or DND 26 (300 μL) for 30 min before imaging.

Cells were also stained with the indicated probes and LysoTracker Red or DND 26 (as mentioned previously) before NH_4Cl treatment or fixation and permeabilization. The labeled cells were washed with PBS and exposed to 10 mM NH_4Cl in PBS (300 μL) for 1 h at 37 °C with 5% CO_2, or fixed by 4% paraformaldehyde in PBS (300 μL) at room temperature for 20 min, or fixed (4% paraformaldehyde) and then permeabilized by 0.2% Triton-X 100 in PBS (300 μL) at room temperature for 5 min.

To track lysosome-dependent apoptosis, HeLa cells were either transfected or not transfected with cathepsin B-mLumin. They were then incubated with CpFABP-G (10 μM, 300 μL) in PBS for 30 min followed by a 4 h postincubation in DMEM (300 μL) containing 10% FBS, or they were labeled with LysoTracker Red or DND 26 (300 μL, 1 μM in PBS) for 30 min. The stained cells were either left untreated or treated with 1 mM H_2O_2 in a CO_2-independent medium at 37 °C under 5% CO_2 for 1.5 h and were analyzed using a confocal laser scanning microscope. Images were obtained every 5 min.

To detect the probes, the fluorescence signals were detected using a Fluoview FV1000 (Olympus, Japan) confocal laser scanning microscope equipped with a 60× oil-immersion objective lens (NA 1.4) and a HeNe-G laser (Green CpFABP-G channel: excitation (EX) 488 nm, emission (EM) 505−555 nm; LysoTracker DND 26 channel: EX 488 nm, EM 505−535 nm; Red CpFABP-R, LysoTracker Red, and cathepsin B-mLumin channel: EX 543 nm, EM 570−680 nm). All fluorescence images were analyzed and the background subtracted with *Image J* software. Pearson's coefficient was quantified using the JACOP plugin from *Image J*.[27]

Direct Labeling of Proteins in Living Cells. RAW 264.7 cells were seeded onto 100 mm culture dishes (Corning) at a density of 1.0×10^7 cells/well in DMEM (8 mL) containing 10% FBS and grown at 37 °C in CO_2 (5%) overnight. The cells were then incubated with CpFABP-G or probe **2** in PBS (5 mL, 10 μM) for 30 min. Subsequently, all media were replaced by DMEM containing 10% FBS. After a 5 h postincubation, the cells were harvested by trypsin digestion and washed with cold PBS. The cell pellets were incubated in RIPA buffer (Beyotime Inst. Biotech) containing 1× complete Mini Protease Inhibitor Cocktail (Roche Applied Science) and were sonicated with 100 × 1 s pulses (with a 2 s pause between pulses) in an ice-cold water bath. Subsequently, the cell lysates were centrifuged at 40 000 *g* for 20 min at 4 °C to remove cellular debris. The protein concentration of the supernatant was determined using Pierce's Coomassie (Bradford) Assay.

The supernatants (20 μg/lane) were added to 5× SDS sample buffer, denatured by boiling for 5 min, and resolved on a 13.5% SDS-PAGE gel. The gels were visualized using a Typhoon 9410 laser scanning system (Amersham Biosciences). In addition, some samples on the gel were transferred onto a polyvinylidenedifluoride membrane, and the membrane was then divided into several pieces. The membrane containing proteins between 26 kD and 43 kD was analyzed by Western blot with anticathepsin B polyclonal antibody (1:1000). The membrane was incubated with horseradish peroxidase (HRP)-conjugated goat antirabbit secondary antibody (1:4000). The HRP activity was visualized using the enhanced chemiluminescence (ECL) system. The images were collected using a ChemiDoc XRS system (Bio-Rad).

Competitive Labeling Study. RAW 264.7 cells were seeded onto 100 mm culture dishes (Corning) at a density of 1.0×10^7 cells/well in DMEM (8 mL) containing 10% FBS and

grown at 37 °C under CO_2 (5%, v/v) overnight. The cells were harvested by trypsin digestion. Then, they were washed with cold PBS, and the cell pellets were lysed with 50 mM citrate phosphate buffer (pH 4.5) containing 1% CHAPS, 0.5% Triton X-100, and 5 mM DTT for 30 min on ice. Subsequently, the cell lysates were centrifuged at 17 000 *g* for 15 min at 4 °C to remove cellular debris. The supernatants were diluted in the lysis buffer to reach a final concentration of 10 μg/μL, and they were aliquoted and stored at −80 °C.

The supernatants (8 μL, 10 μg/μL) were treated with the indicated concentrations of E-64 for 1 h and were incubated with CpFABP-G (final concentration of 10 μM) for an additional hour. Subsequently, the lysates were added to the 5× SDS sample buffer, denatured by boiling for 5 min, and resolved on a 13.5% SDS-PAGE gel. The results were visualized and recorded by the Typhoon 9410 laser scanning system (Amersham Biosciences).

Cell Toxicity Analysis. The cytotoxicity of CpFABP-G was evaluated using a 3-(4,5-dimethylthiazol-2-yl)-2,5-diphenyltetrazolium bromide (MTT) assay. HeLa cells were seeded into a 96-well plate at a density of 5000 cells/well in DMEM (150 μL) containing 10% FBS. The cells were then grown at 37 °C under CO_2 (5%, v/v) overnight. The cells were incubated with 150 μL of CpFABP-G (5, 10, or 20 μM) in DMEM containing 10% FBS for 12 h. Then, 15 μL of the MTT solution (5 mg/mL in PBS) was added to each well. After 4 h, the medium was gently removed, and the formazan products were solubilized with 200 μL of dimethyl sulfoxide (DMSO) for 30 min. Absorbance was measured at 570 nm using the ELISA Reader GeniosPlus (Tecan). Cell viability was expressed as a ratio of the A_{570} of probe-treated cells to the untreated controls. All measurements were performed in triplicate.

Plasmid Construction. Using the pDsRed-N1-cathepsin B template (a generous gift from Prof. Jianping Liu, Inst. of Genetics, Fudan University), a DNA fragment encoding cathepsin B with restriction sites for *BamH*I and *Xho*I was amplified by PCR. The primers used for the cathepsin B amplification were as follows: forward 5′-ACGCGGATCCCACCATGCTGCCTGCAAGCTTCGAT-3′ and reverse 5′-CGGTCGGAATTCCTCGAGATCGGTGCGTGGAATGCCAGCCACCACTTCTGATTCGA-3′. The coding sequence of mLumin was amplified according to methods recently reported[28] and contained restriction sites for *Xho*I and *Eco*RI. The mLumin forward primer was 5′-CGCACCGATCTAGAGCCGGTCGCCACCATGGTGTCTAAGGGCGAAGAGC-3′, and the reverse was 5′-ACCGGAATTCTTACTTGTACAGCTCGTCCATGCCATTAA-3′. After the products were purified on an agarose gel (1%), the cathepsin B sequence was digested with *BamH*I and *Xho*I. The mLumin DNA fragment was cut by *Xho*I and *Eco*RI. The resulting DNA fragments were inserted into the pCDNA 3.1 vector (Invitrogen) that had been digested by *BamH*I and *Eco*RI. The sequence of the pCDNA 3.1-cathersin B-mLumin construct was confirmed by sequencing.

Transfection. HeLa cells were seeded onto eight-well Lab-Tek chamber slides at a density of 2×10^4 cells/well in DMEM (300 μL) containing 10% FBS. The cells were then grown at 37 °C with CO_2 (5%, v/v) for 24 h. Then, all medium was replaced by fresh Opti-MEM (150 μL). Transient transfections were performed using the Lipofectamine 2000 reagent following the manufacturer's instructions. After 24 h, the transfected cells were used for the labeling experiments.

RESULTS

Synthesis of CpFABPs. We synthesized the CpFABPs using standard solid-phase peptide synthesis (Figure 1).[29,30]

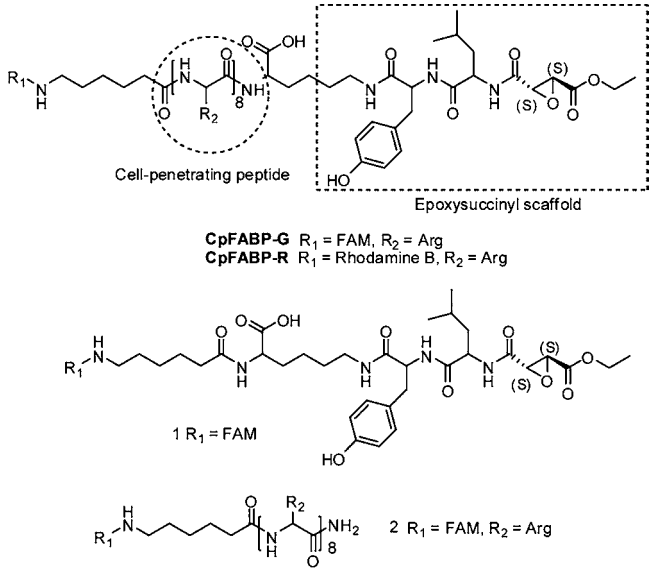

Figure 1. Structures of probes CpFABP-G, CpFABP-R, **1**, and **2**, FAM, 5(6)-carboxyfluorescein.

CpFABP-G and CpFABP-R contain different fluorophores (5(6)-carboxyfluorescein (FAM) in CpFABP-G and rhodamine B in CpFABP-R). The epoxysuccinyl scaffold (Figure 1) is generated from the commonly used cysteine cathepsin ABP DCG-04 and has been shown to selectively label numerous cysteine cathepsins in cell and tissue lysates, including cathepsins B, F, C, H, K, L, S, and Z, which are typically localized to lysosomal compartments.[24,31] We employed a cell-penetrating octa-arginine peptide (rRrRrRRR, r: D-Arg, R: L-Arg) to enhance the cellular permeability of CpFABPs, which contain cell-impermeable fluorophore (e.g., FAM). We also generated probe **1**, which does not contain a cell-penetrating peptide, and probe **2**, which does not contain the reactive scaffold, as controls for CpFABP-G (Figure 1b).

Characterization of CpFABPs for Labeling Lysosomes. The LysoTracker probes are the most popular fluorescent acidotropic probes for lysosome labeling and tracking due to their high selectivity and effective labeling of living cells.[15] Therefore, we investigated the feasibility of using CpFABP-G and CpFABP-R as lysosome markers by performing a colocalization study employing the LysoTracker probes as the standard lysosome markers. After incubation with LysoTracker Red for 30 min or 2 h at 75 nM (a recommended working concentration in the manufacturer's instructions), the cells could not be sufficiently stained; therefore, we increased the labeling concentration of the dye, as shown in previous studies (Figure S2 of the Supporting Information).[19] Figure 2a indicates that, after incubation with living cells for 30 min, CpFABP-G entered the cells efficiently and exhibited a diffuse pattern with a small amount of vesicle staining. In contrast, no obvious fluorescent signal was detected for probe **1**, the probe that lacked a cell-penetrating peptide (Figure 2b). These results suggest that the introduction of the cell-penetrating peptide significantly increases the cell permeability of CpFABP-G. An increase in postincubation time from 0 to 4 h (Figure 2a) revealed that the diffuse green fluorescence staining of

dx.doi.org/10.1021/bc300143p | *Bioconjugate Chem.* 2012, 23, 1309−1317

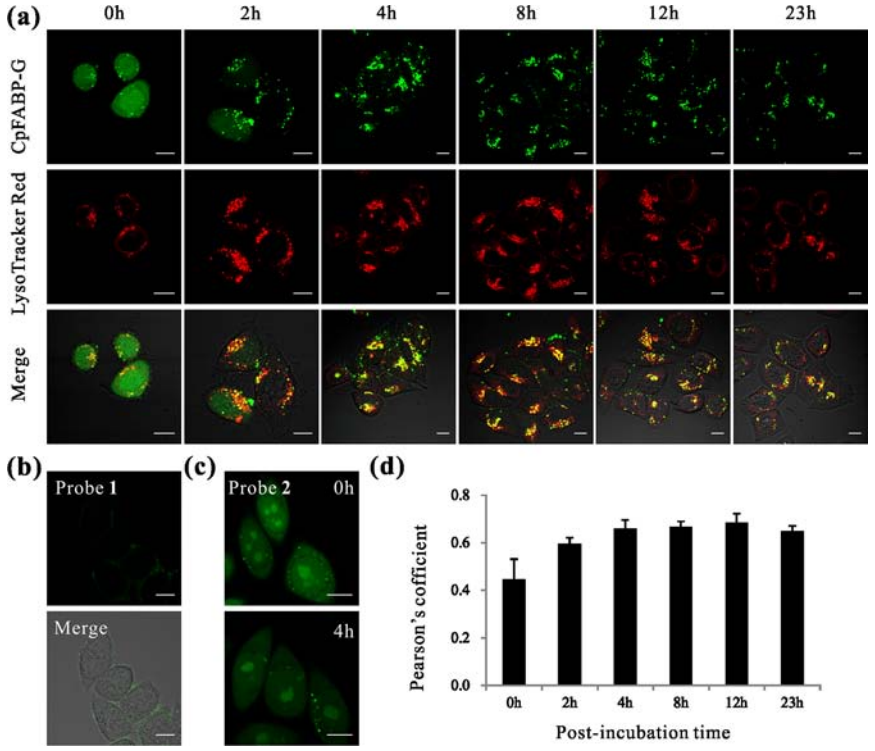

Figure 2. Feasibility of CpFABP-G as a lysosome marker. (a) Confocal microscopy of living HeLa cells that were incubated with CpFABP-G (green, 10 μM) for 30 min and postincubated in DMEM containing 10% FBS for 0, 2, 4, 8, 12, and 23 h, respectively. Lysosomes were labeled with LysoTracker Red (500 nM) for 30 min before imaging. (b) Confocal microscopy of living HeLa cells that were incubated with probe **1** (10 μM) for 30 min. (c) Confocal microscopy of living HeLa cells that were incubated with probe **2** (10 μM) for 30 min and postincubated in DMEM containing 10% FBS for 0 and 4 h, respectively. Scale bar: 10 μm. (d) Quantitative fluorescence colocalization analysis. The colocalization of CpFABP-G with LysoTracker Red was quantified by Pearson's coefficients[35] (mean ± SD, n = 6) that were obtained with *Image J*.

CpFABP-G throughout the cytosol gradually gave way to increased staining in punctate vesicles. After 4 h postincubation, CpFABP-G colocalized with the LysoTracker Red (200 or 500 nM) probe extremely well (Figure 2d and Figure S2 of the Supporting Information),[27] indicating that it may be used as a highly specific lysosomal marker in living cells. In contrast, probe **2**, which lacked the reactive warhead (Figure 2c), maintained a diffuse staining pattern throughout the cytoplasm and nucleus during the postincubation from 0 to 4 h, suggesting that cellular clearance of the probe is not obvious within 4 h. The results also imply that the disappearance of the cytosolic diffuse staining of CpFABP-G is likely due to accumulation of the probe into lysosomes from the cytosol rather than due to exclusion from the cells. Moreover, prolonging the postincubation time to 8 and 12 h did not significantly increase the colocalization efficiency of CpFABP-G (Figure 2d). Therefore, the postincubation time of 4 h was utilized in further experiments. Increasing the concentration of CpFABP-G from 2.5 to 10 μM increased its colocalization efficiency, and no further obvious increment was observed at 15 μM (Figure S3 of the Supporting Information). It is worth noting that, even after 23 h postincubation, CpFABP-G maintained excellent colocalization with the LysoTracker Red (freshly applied to the cells before imaging) with a Pearson's coefficient of 0.648 ± 0.022 (Figure 2a and d), indicating that it was retained in lysosomes for a long time (>23 h).

We also tested the ability of CpFABP-G to label lysosomes in various kinds of cells. As shown in Figure 3a, excellent staining patterns of lysosomes have been achieved in all live cells that were tested, with Pearson's coefficients of 0.804 ± 0.030, 0.746 ± 0.053, 0.841 ± 0.007, 0.834 ± 0.098, and 0.832 ± 0.013 for Cos-7 cells, MCF-7 cells, Raw 264.7 cells, primary peritoneal macrophage cells, and primary neurons, respectively. The results indicate that CpFABP-G is an effective lysosomal marker in many cell types.

We also measured cell viability using the MTT assay to test the cellular toxicity of CpFABP-G (Figure S4 of the Supporting Information). HeLa cells were incubated with CpFABP-G for 12 h at concentrations up to 20 μM, and no obvious cytotoxicity was observed, indicating that the probe is very biocompatible.

As shown in Figure 3b, CpFABP-R, with the red fluorophore (rhodamine B), also colocalized well with the green LysoTracker DND 26 probe (Pearson's coefficient = 0.749 ± 0.025), suggesting that altering the fluorophore that is attached to the probe does not influence its ability to label lysosomes. We used fluorescein and rhodamine B because they are the most commonly used and relatively inexpensive. Considering that various small-molecule fluorophores with pH-insensitivity, high photostability, and different fluorescent colors, such as Alexa Fluor dyes,[32] are commercially available and that CpFABP-G exhibited a long retention time (>23 h) in lysosomes (Figure 2a and d), a variety of the probes with an array of fluorophores are promising for multicolor labeling applications and long-term lysosomal tracking.

Living cells were labeled with CpFABP-G or probe **2**, lysed, and analyzed by SDS-PAGE and in-gel fluorescence scanning or Western blotting. Figure 4a shows that there was no obvious fluorescent staining on the SDS-PAGE gel for probe **2**, the probe lacking a reactive warhead. In contrast, multiple proteases were labeled by CpFABP-G, and Western blot analysis using

dx.doi.org/10.1021/bc300143p | *Bioconjugate Chem.* 2012, 23, 1309−1317

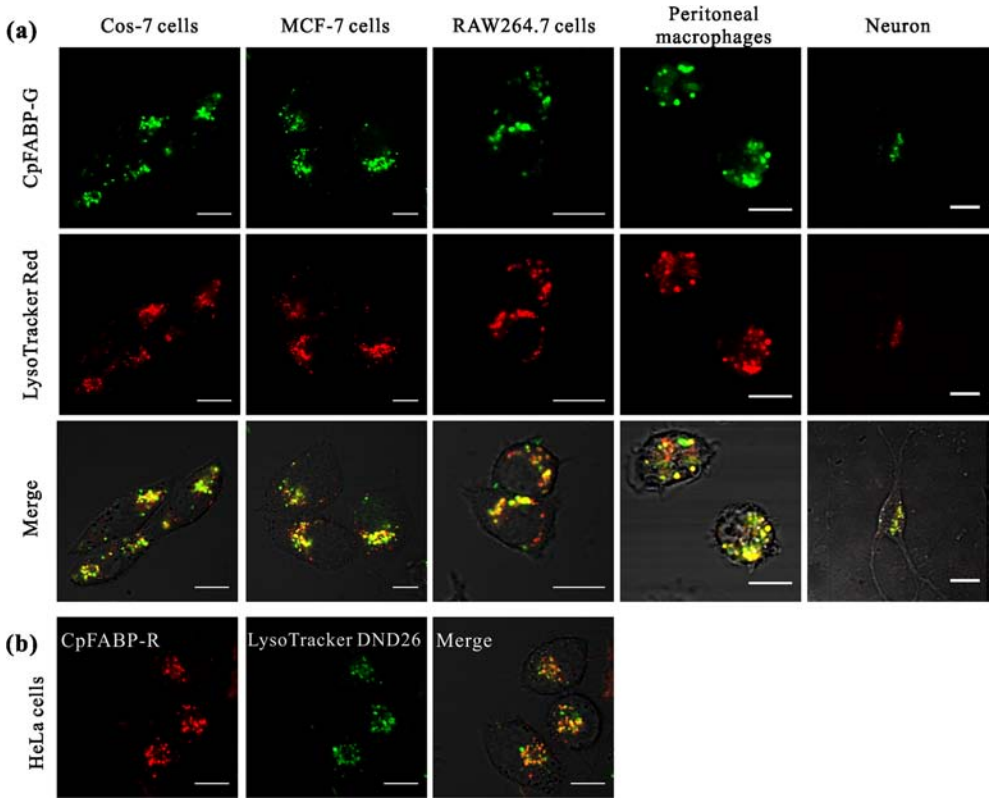

Figure 3. Confocal microscopy images of (a) living Cos-7 cells, MCF-7 cells, Raw 264.7 cells, primary peritoneal macrophage cells, and primary neurons that were incubated with CpFABP-G (10 μM) for 30 min and postincubated in DMEM containing 10% FBS for 4 h and (b) living HeLa cells that were incubated with CpFABP-R (10 μM) for 30 min and postincubated in DMEM containing 10% FBS for 4 h. Lysosomes were labeled with LysoTracker Red or DND 26 (500 nM) for 30 min before imaging. Scale bar: 10 μm. Pearson's coefficients (mean ± SD, n = 6) for Cos-7 cells, MCF-7 cells, Raw 264.7 cells, primary peritoneal macrophage cells, primary neurons, and HeLa cells 0.804 ± 0.030, 0.746 ± 0.053, 0.841 ± 0.007, 0.834 ± 0.098, 0.832 ± 0.013, and 0.749 ± 0.025, respectively.

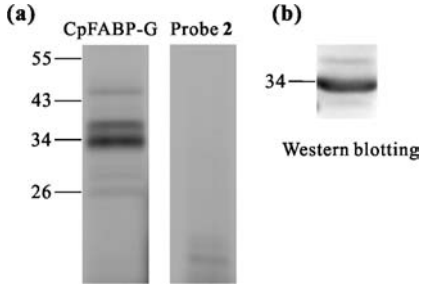

Figure 4. Analysis of labeled proteins by SDS-PAGE followed by in-gel fluorescence scanning or Western blotting. RAW 264.7 cells were incubated with CpFABP-G or probe **2** (10 μM) for 30 min. After 5 h postincubation in DMEM with 10% FBS, the cells were lysed. Samples were separated on a 13.5% SDS-PAGE gel and visualized by in-gel fluorescence scanning (a) or by Western blotting using anticathepsin B polyclonal antibody (b).

anticathepsin B polyclonal antibody indicated that one of the labeled proteins is possibly cathepsin B (Figure 4a and b). Pretreatment with E-64, a natural, potent, and irreversible inhibitor of cysteine cathepsins,[33] competes specifically with the labeling by CpFABP-G in the lysates, suggesting that CpFABP-G is specific for cysteine cathepsins, in good agreement with previous studies (Figure S5 of the Supporting Information).[34] At this time, we are unable to identify each of the proteases labeled by CpFABP-G in living cells; however, the results indicate that the ability of CpFABP-G to label cysteine cathepsins, such as cathepsin B, is through the reactive warhead.

Application of CpFABPs to Fixed Cells, Permeabilized Cells, and NH_4Cl-Treated Cells. Cell fixation and permeabilization are often required to probe intracellular structures using immunocytochemistry or are used for better morphological preservation.[35] Therefore, we investigated the ability of CpFABPs to label lysosomes following fixation and permeabilization. After fixation by 4% paraformaldehyde or fixation following permeabilization with 0.2% Triton X-100, the fluorescence of both LysoTracker Red (red, Figure 5a–c) and DND 26 (green, Figure S6 of the Supporting Information) completely disappeared within the cells. In contrast, fixation and permeabilization had little effect on the lysosome labeling pattern of CpFABP-G (Figure 5a–c) and CpFABP-R (Figure S6 of the Supporting Information). The absence of the fluorescence of the LysoTracker probes may be a result of cellular fixation and permeabilization-mediated destruction of the acidic environment of lysosomes, which prevents these weak basic probes from accumulating in the lysosomes. In contrast, CpFABP-G, which is pH-independent and labels lysosomes by binding the proteins inside them, maintained its ability to label lysosomes under the same conditions.

Ammonium chloride (NH_4Cl), a lysosomal inhibitor, is often employed in lysosome-related studies. It can neutralize the acidic environment in lysosomes and thus decrease normal lysosomal protease activities.[36,37] Figure 5d shows that, after the cells were treated with NH_4Cl, the red fluorescence of LysoTracker Red completely disappeared due to the neutralization of the acidic environment in lysosomes with NH_4Cl. In contrast,

dx.doi.org/10.1021/bc300143p | Bioconjugate Chem. 2012, 23, 1309–1317

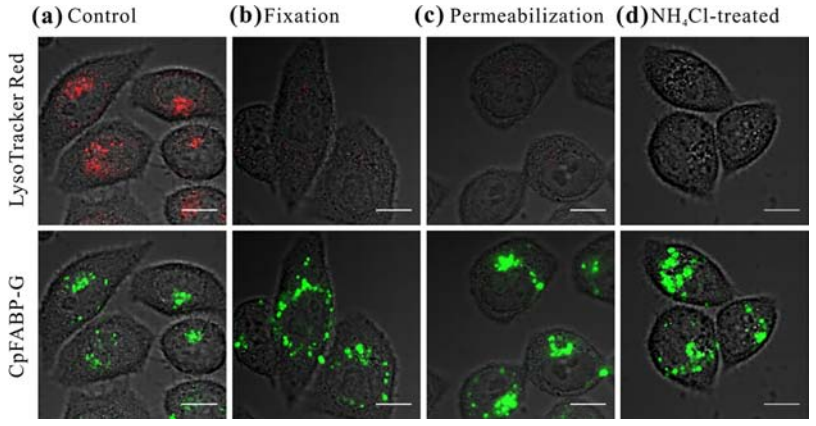

Figure 5. Confocal microscopy images of living HeLa cells (a) stained with CpFABP-G and LysoTracker Red, (b) stained with CpFABP-G and LysoTracker Red and then fixed with 4% paraformaldehyde, (c) stained with CpFABP-G and LysoTracker Red and then fixed with 4% paraformaldehyde following permeabilization with 0.2% Triton X-100, and (d) stained with CpFABP-G and LysoTracker Red and then treated with 50 mM NH_4Cl for 1 h. Scale bar: 10 μm.

the treatment with NH_4Cl had little effect on the lysosome labeling pattern of CpFABP-G. Taken together, these results suggest that CpFABPs may be employed for lysosome labeling in living cells, fixed cells, permeabilized cells, and NH_4Cl-treated cells, demonstrating their potential for use in a wide array of applications.

Application of CpFABP-G for Tracking Lysosome-Dependent Apoptosis. Apoptosis is a tightly regulated process of programmed cell death. Improper regulation of apoptosis has been implicated in various cancers, autoimmune diseases, and neurodegenerative disorders.[7,38,39] Throughout the past decade, accumulating evidence has suggested that lysosomes play an important role in the regulation of cell death and that the release of lysosomal cathepsins, such as cathepsins D, B, and L, into the cytosol, is often involved in the initiation of apoptosis.[1,3,40] Lysosomal markers, such as the LysoTracker probes, acridine orange, and fluorescence-labeled dextran, have been used to monitor lysosome-dependent apoptosis.[17,40] They monitor apoptosis indirectly by tracking diffusion of the probe upon lysosomal membrane breakdown, rather than by visualizing the release of lysosomal cathepsins. A pepstatin A–BODIPY FL conjugate can directly track cathepsin release by binding with cathepsin D through pepstatin A; however, after pepstatin A–BODIPY FL–cathepsin D complexes are released into the cytosol, their green fluorescence disappears.[41] Probes that are designed based on the substrates of cathepsins, such as the Magic Red cathepsin reagent, have also been employed to detect apoptosis.[42] However, these substrate-based probes provide a readout of enzyme activity but is not linked to the target of the protease; hence, the signals observed in living cells cannot be directly correlated with the localization of cathepsins.

Because the epoxysuccinyl scaffold of CpFABP-G can selectively form a covalent bond with cysteine cathepsins, we investigated the feasibility of using CpFABP-G as a marker to track lysosome-dependent apoptosis. Although we have not currently identified all of the proteases labeled by CpFABP-G in living cells, Figure 4 reveals that CpFABP-G was indeed able to label cathepsin B. We used a cathepsin B-mLumin[28] (a red fluorescent protein) fusion protein as a standard for cathepsin release because cathepsin B has been shown to be translocated from lysosomes into the cytosol during apoptosis.[42,43] Figure 6a indicates that CpFABP-G colocalized extremely well with

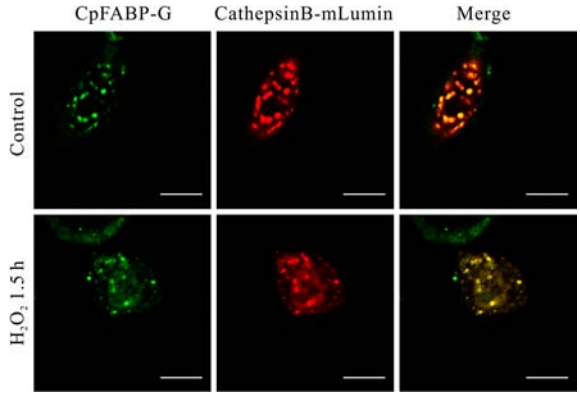

Figure 6. Treatment with 1 mM H_2O_2 results in the partial release of cathepsin B from lysosomes. HeLa cells transiently transfected by cathepsin B-mLumin were stained with CpFABP-G (green, 10 μM) for 30 min and were postincubated for 4 h. The cells were then either left untreated (control) or treated with 1 mM H_2O_2 for 1.5 h. The cells were imaged with confocal laser scanning microscopy. Scale bar: 10 μm.

cathepsin B-mLumin in living cells, which further confirmed the high selectivity of CpFABP-G as a lysosomal marker. After H_2O_2-mediated induction of apoptosis,[4,30,44] CpFABP-G and cathepsin B-mLumin were partially released from lysosomes into the cytosol and the high degree of colocalization was maintained. In contrast, the punctate labeling pattern of LysoTracker DND 26 showed no obvious change before and after the induction of apoptosis, and its colocalization with cathepsin B-mLumin in the cytosol was poor after the activation of apoptosis (Figure S7 of the Supporting Information). These results suggest that CpFABP-G may be used an excellent marker to track lysosome-dependent apoptosis.

We applied CpFABP-G to monitor the entire process of lysosome-dependent apoptosis in real-time in living cells without transfection with cathepsin B-mLumin. Figure 7 shows that the CpFABP-G–protein complexes were released significantly into the cytosol with a portion remaining in lysosomes after the activation of apoptosis, consistent with previous reports.[35,38,43] The stronger fluorescence from some of the lysosomes after the H_2O_2 treatment might be because these lysosomes slightly moved along the z axis during the successive imaging process in living cells. Quantitative analysis reveals that, after a significant increase, the

dx.doi.org/10.1021/bc300143p | Bioconjugate Chem. 2012, 23, 1309–1317

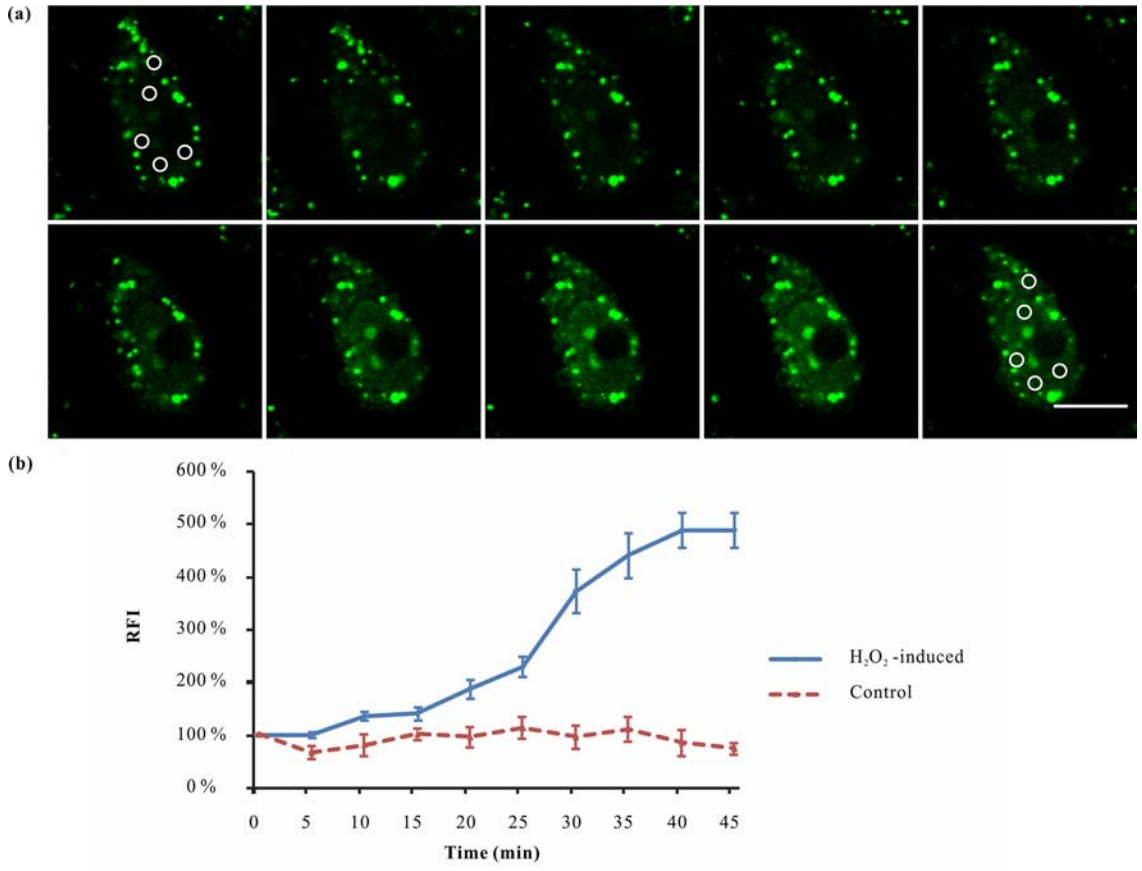

Figure 7. Process of the release of lysosomal cathepsins into the cytosol after H_2O_2-mediated induction of apoptosis. (a) Time-lapse confocal microscopy images and (b) increase of mean fluorescence intensities from the areas of the circles [chosen at random in (a) or Figure S8 of the Supporting Information] over time. The fluorescence intensity values (means ± standard error of the mean, $n = 5$) are expressed in fold increase in comparison with the intracellular signal at the beginning (RFI: relative fluorescence intensity). The images were obtained every 5 min. HeLa cells were labeled with CpFABP-G (green, 10 μM) for 30 min. After 4 h postincubation, the cells were then either left untreated (control) or treated with 1 mM H_2O_2 for 1.5 h. Scale bar: 10 μm.

fluorescence in the cytosol reached a plateau (Figure 7b). In the control group (without adding H_2O_2), no obvious changes of the fluorescence intensity were observed in the cytosol (Figures 7b and S8 of the Supporting Information). In contrast, LysoTracker Red was unable to track the induction of apoptosis and showed extensive punctate labeling before and after induction of apoptosis (Figure S9 of the Supporting Information).

■ DISCUSSION

Although several cell-permeable ABPs containing the epoxysuccinyl scaffold have been developed for *in vivo* application, most of them are employed to profile and identify cysteine cathepsins through SDS-PAGE and/or MS analysis.[2,23−25] DCG-04 labeled with membrane-permeable boron-dipyrromethene (BODIPY) was capable of penetrating cell membranes and visualizing proteases in live cells. However, a long incubation time (~12 h) was needed for its efficient cellular uptake.[31] Moreover, the requirement of using cell-permeable dyes, such as BODIPY and cyanine, would prevent large-scale production of the ABP because the commercially available activated ester forms of these cell-permeable fluorophores are extremely expensive. ABPs relying on the "click" chemistry are able to label proteins in intact cells. However, the visualization of target proteins with the reporter tag needs to be carried out in cell lysates or fixed cells; thus, these ABPs are not suitable for imaging intracellular proteins directly in live cells.[25] ABPs equipped with a mannose cluster could enter live cells via receptor-mediated endocytosis but are limited to several specialized cell types, such as dendritic cells and macrophage cells.[24] To the best of our knowledge, no cathepsin-targeted ABPs as well as other ABPs have been evaluated as markers for labeling and tracking intracellular organelles in living cells.

By exploiting the properties that cysteine cathepsins are typically localized to lysosomal compartments, we have developed a new approach to label lysosomes via novel cathepsin-targeted CpFABPs, which contain a cell-penetrating peptide (CPP) to enhance their cellular permeability and an epoxysuccinyl scaffold to selectively form covalent bonds with cysteine cathepsins. The fluorophores attached to our probes are rhodamine B and 5(6)-carboxyfluorescein, which are cheap and commercially available, thus facilitating their large-scale production and potential applications. Although CPPs have been widely used to deliver various membrane-impermeable molecules into living cells, very few ABPs containing CPPs have been reported.[2,45,46] Our CpFABPs entered live cells not only efficiently but also quickly (Figure 2), possibly due to the ability of CPPs to efficiently carry molecules into cells.[26] The extremely good colocalization of CpFABPs with both LysoTracker probes (Figures 2 and 3) and cathepsin B-mLumin (Figure 6) in living cells as well as the competitive studies with E-64

dx.doi.org/10.1021/bc300143p | *Bioconjugate Chem.* 2012, 23, 1309−1317

in vitro (Figure S5 of the Supporting Information) suggests that CpFABPs are effective in specifically labeling lysosomes.

Compared with previous small-molecule markers, such as LysoTracker probes (30 min), the incubation time of CpFABPs was longer (4 h). However, our CpFABPs were capable of labeling lysosomes in fixed cells, permeabilized cells, and NH_4Cl-treated cells, unlike these small-molecule markers, which show ineffective labeling under the same conditions. Although a relatively high incubation concentration was required (10 μM), CpFABP-G showed low cytotoxicity even at a concentration of 20 μM. When applied to monitor the process of lysosome-dependent apoptosis, CpFABP-G (Figure 7) not only displayed the expected release of lysosomal cathepsins from lysosomes into the cytosol, but also revealed additional information about the location of the cathepsins during apoptosis, which is undetectable by other chemical lysosome markers.

CONCLUSIONS

In summary, we have developed a new strategy for labeling and tracking lysosomes via a cell-permeable fluorescent activity-based probe containing a reactive warhead that covalently binds to select lysosomal proteins. We have demonstrated that CpFABP-G enters living cells efficiently and specifically labels lysosomes in different kinds of live cells. Moreover, we showed that the probe maintains its labeling ability in fixed cells, permeabilized cells, and NH_4Cl-treated cells. In addition, CpFABP-G possesses low cytotoxicity. Perhaps most remarkably, CpFABP-G can track lysosome-dependent apoptosis in real-time in living cells. These results provide useful guidelines for the use of CpFABP-G as a lysosomal marker in lysosome-related studies and expand the application ranges of activity-based probes.

ASSOCIATED CONTENT

Supporting Information

Characterization data of probes CpFABP-G, CpFABP-R, **1**, and **2**, supplemental confocal microscopy images, and cell viability data. This material is available free of charge via the Internet at http://pubs.acs.org.

AUTHOR INFORMATION

Corresponding Author

*Tel. (+86) 27 87792033; fax (+86) 27 87792034. E-mail address: zhangyh@mail.hust.edu.cn.

Notes

The authors declare no competing financial interest.

ACKNOWLEDGMENTS

We thank the Analytical and Testing Center (Huazhong University of Science and Technology) for spectral measurements. This study was supported by the National Major Scientific Research Program of China (Grant No. 2011CB910401), Science Fund for Creative Research Group of China (Grant No.61121004), the National High-Tech Research and Development Program of China (863 Program: 2008AA02Z107), and the National Natural Science Foundation of China (Grant No. 30800183).

REFERENCES

(1) Repnik, U., and Turk, B. (2010) Lysosomal-mitochondrial cross-talk during cell death. *Mitochondrion 10*, 662−669.

(2) Reich, M., van Swieten, P. F., Sommandas, V., Kraus, M., Fischer, R., Weber, E., Kalbacher, H., Overkleeft, H. S., and Driessen, C. (2007) Endocytosis targets exogenous material selectively to cathepsin S in live human dendritic cells, while cell-penetrating peptides mediate nonselective transport to cysteine cathepsins. *J. Leukocyte Biol. 81*, 990−1001.

(3) Guicciardi, M. E., Leist, M., and Gores, G. J. (2004) Lysosomes in cell death. *Oncogene 23*, 2881−2890.

(4) Ghosh, M., Carlsson, F., Laskar, A., Yuan, X. M., and Li, W. (2011) Lysosomal membrane permeabilization causes oxidative stress and ferritin induction in macrophages. *FEBS Lett. 585*, 623−629.

(5) Mizukami, H., Mi, Y., Wada, R., Kono, M., Yamashita, T., Liu, Y., Werth, N., Sandhoff, R., Sandhoff, K., and Proia, R. L. (2002) Systemic inflammation in glucocerebrosidase-deficient mice with minimal glucosylceramide storage. *J. Clin. Invest. 109*, 1215−1221.

(6) Mohamed, M. M., and Sloane, B. F. (2006) Cysteine cathepsins: multifunctional enzymes in cancer. *Nat. Rev. Cancer 6*, 764−775.

(7) Soreghan, B., Thomas, S. N., and Yang, A. J. (2003) Aberrant sphingomyelin/ceramide metabolic-induced neuronal endosomal/lysosomal dysfunction: potential pathological consequences in age-related neurodegeneration. *Adv. Drug Delivery Rev. 55*, 1515−1524.

(8) Berthiaume, E. P., Medina, C., and Swanson, J. A. (1995) Molecular size-fractionation during endocytosis in macrophages. *J. Cell Biol. 129*, 989−998.

(9) Teter, K., Chandy, G., Quinones, B., Pereyra, K., Machen, T., and Moore, H. P. (1998) Cellubrevin-targeted fluorescence uncovers heterogeneity in the recycling endosomes. *J. Biol. Chem. 273*, 19625−19633.

(10) Hu, Q., Bally, M. B., and Madden, T. D. (2002) Subcellular trafficking of antisense oligonucleotides and down-regulation of bcl-2 gene expression in human melanoma cells using a fusogenic liposome delivery system. *Nucleic Acids Res. 30*, 3632−3641.

(11) Hanaki, K., Momo, A., Oku, T., Komoto, A., Maenosono, S., Yamaguchi, Y., and Yamamoto, K. (2003) Semiconductor quantum dot/albumin complex is a long-life and highly photostable endosome marker. *Biochem. Biophys. Res. Commun. 302*, 496−501.

(12) Anderson, R. G., Falck, J. R., Goldstein, J. L., and Brown, M. S. (1984) Visualization of acidic organelles in intact cells by electron microscopy. *Proc. Natl. Acad. Sci. U. S. A. 81*, 4838−4842.

(13) Svendsen, C., Spurgeon, D. J., Hankard, P. K., and Weeks, J. M. (2004) A review of lysosomal membrane stability measured by neutral red retention: is it a workable earthworm biomarker? *Ecotoxicol. Environ. Saf. 57*, 20−29.

(14) Anderson, R. G., and Orci, L. (1988) A view of acidic intracellular compartments. *J. Cell Biol. 106*, 539−543.

(15) Freundt, E. C., Czapiga, M., and Lenardo, M. J. (2007) Photoconversion of Lysotracker Red to a green fluorescent molecule. *Cell Res. 17*, 956−958.

(16) Ohkuma, S., and Poole, B. (1978) Fluorescence probe measurement of the intralysosomal pH in living cells and the perturbation of pH by various agents. *Proc. Natl. Acad. Sci. U. S. A. 75*, 3327−3331.

(17) Bidere, N., Lorenzo, H. K., Carmona, S., Laforge, M., Harper, F., Dumont, C., and Senik, A. (2003) Cathepsin D triggers Bax activation, resulting in selective apoptosis-inducing factor (AIF) relocation in T lymphocytes entering the early commitment phase to apoptosis. *J. Biol. Chem. 278*, 31401−31411.

(18) Xiao, Y., Forry, S. P., Gao, X., Holbrook, R. D., Telford, W. G., and Tona, A. (2010) Dynamics and mechanisms of quantum dot nanoparticle cellular uptake. *J. Nanobiotechnol. 8*, 13−22.

(19) Shi, H., He, X., Yuan, Y., Wang, K., and Liu, D. (2010) Nanoparticle-based biocompatible and long-life marker for lysosome labeling and tracking. *Anal. Chem. 82*, 2213−2220.

(20) Rejman, J., Oberle, V., Zuhorn, I. S., and Hoekstra, D. (2004) Size-dependent internalization of particles via the pathways of clathrin- and caveolae-mediated endocytosis. *Biochem. J. 377*, 159−169.

(21) Pryor, P. R., and Luzio, J. P. (2009) Delivery of endocytosed membrane proteins to the lysosome. *Biochim. Biophys. Acta 1793*, 615−624.

(22) Cravatt, B. F., Wright, A. T., and Kozarich, J. W. (2008) Activity-based protein profiling: from enzyme chemistry to proteomic chemistry. *Annu. Rev. Biochem. 77*, 383−414.
(23) Greenbaum, D., Medzihradszky, K. F., Burlingame, A., and Bogyo, M. (2000) Epoxide electrophiles as activity-dependent cysteine protease profiling and discovery tools. *Chem. Biol. 7*, 569−581.
(24) Hillaert, U., Verdoes, M., Florea, B. I., Saragliadis, A., Habets, K. L., Kuiper, J., Van Calenbergh, S., Ossendorp, F., van der Marel, G. A., Driessen, C., and Overkleeft, H. S. (2009) Receptor-mediated targeting of cathepsins in professional antigen presenting cells. *Angew. Chem., Int. Ed. Engl. 48*, 1629−1632.
(25) Kaschani, F., Verhelst, S. H., van Swieten, P. F., Verdoes, M., Wong, C. S., Wang, Z., Kaiser, M., Overkleeft, H. S., Bogyo, M., and van der Hoorn, R. A. (2009) Minitags for small molecules: detecting targets of reactive small molecules in living plant tissues using 'click chemistry'. *Plant J. 57*, 373−385.
(26) Mizuno, T., Miyashita, M., and Miyagawa, H. (2009) Cellular internalization of arginine-rich peptides into tobacco suspension cells: a structure-activity relationship study. *J. Pept. Sci. 15*, 259−263.
(27) Bolte, S., and Cordelieres, F. P. (2006) A guided tour into subcellular colocalization analysis in light microscopy. *J. Microsc. 224*, 213−232.
(28) Chu, J., Zhang, Z., Zheng, Y., Yang, J., Qin, L., Lu, J., Huang, Z. L., Zeng, S., and Luo, Q. (2009) A novel far-red bimolecular fluorescence complementation system that allows for efficient visualization of protein interactions under physiological conditions. *Biosens. Bioelectron. 25*, 234−239.
(29) Kato, D., Verhelst, S. H., Sexton, K. B., and Bogyo, M. (2005) A general solid phase method for the preparation of diverse azapeptide probes directed against cysteine proteases. *Org. Lett. 7*, 5649−5652.
(30) Verhelst, S. H., and Bogyo, M. (2005) Solid-phase synthesis of double-headed epoxysuccinyl activity-based probes for selective targeting of papain family cysteine proteases. *ChemBioChem 6*, 824−827.
(31) Greenbaum, D., Baruch, A., Hayrapetian, L., Darula, Z., Burlingame, A., Medzihradszky, K. F., and Bogyo, M. (2002) Chemical approaches for functionally probing the proteome. *Mol. Cell Proteomics 1*, 60−68.
(32) Berlier, J. E., Rothe, A., Buller, G., Bradford, J., Gray, D. R., Filanoski, B. J., Telford, W. G., Yue, S., Liu, J., Cheung, C. Y., Chang, W., Hirsch, J. D., Beechem, J. M., Haugland, R. P., and Haugland, R. P. (2003) Quantitative comparison of long-wavelength Alexa Fluor dyes to Cy dyes: fluorescence of the dyes and their bioconjugates. *J. Histochem. Cytochem. 51*, 1699−1712.
(33) Barrett, A. J., Kembhavi, A. A., Brown, M. A., Kirschke, H., Knight, C. G., Tamai, M., and Hanada, K. (1982) L-trans-Epoxysuccinyl-leucylamido(4-guanidino)butane (E-64) and its analogues as inhibitors of cysteine proteinases including cathepsins B, H and L. *Biochem. J. 201*, 189−198.
(34) Fonovic, M., Verhelst, S. H., Sorum, M. T., and Bogyo, M. (2007) Proteomics evaluation of chemically cleavable activity-based probes. *Mol. Cell Proteomics 6*, 1761−1770.
(35) Ramos-Vara, J. A. (2011) Principles and methods of immunohistochemistry. *Methods Mol. Biol. 691*, 83−96.
(36) Yang, Q., She, H., Gearing, M., Colla, E., Lee, M., Shacka, J. J., and Mao, Z. (2009) Regulation of neuronal survival factor MEF2D by chaperone-mediated autophagy. *Science 323*, 124−127.
(37) Koh, Y. H., von Arnim, C. A., Hyman, B. T., Tanzi, R. E., and Tesco, G. (2005) BACE is degraded via the lysosomal pathway. *J. Biol. Chem. 280*, 32499−32504.
(38) Vaux, D. L., and Flavell, R. A. (2000) Apoptosis genes and autoimmunity. *Curr. Opin. Immunol. 12*, 719−724.
(39) Yuan, J., and Yankner, B. A. (2000) Apoptosis in the nervous system. *Nature 407*, 802−809.
(40) Boya, P., and Kroemer, G. (2008) Lysosomal membrane permeabilization in cell death. *Oncogene 27*, 6434−6451.
(41) Yin, L., Stearns, R., and Gonzalez-Flecha, B. (2005) Lysosomal and mitochondrial pathways in H2O2-induced apoptosis of alveolar type II cells. *J. Cell Biochem. 94*, 433−445.
(42) Lamparska-Przybysz, M., Gajkowska, B., and Motyl, T. (2005) Cathepsins and BID are involved in the molecular switch between apoptosis and autophagy in breast cancer MCF-7 cells exposed to camptothecin. *J. Physiol. Pharmacol. 56* (Suppl3), 159−179.
(43) Werneburg, N. W., Guicciardi, M. E., Bronk, S. F., and Gores, G. J. (2002) Tumor necrosis factor-alpha-associated lysosomal permeabilization is cathepsin B dependent. *Am. J. Physiol. Gastrointest. Liver Physiol. 283*, G947−G956.
(44) Jiang, B., Liang, P., Deng, G., Tu, Z., Liu, M., and Xiao, X. (2011) Increased stability of Bcl-2 in HSP70-mediated protection against apoptosis induced by oxidative stress. *Cell Stress Chaperones 16*, 143−152.
(45) Edgington, L. E., Berger, A. B., Blum, G., Albrow, V. E., Paulick, M. G., Lineberry, N., and Bogyo, M. (2009) Noninvasive optical imaging of apoptosis by caspase-targeted activity-based probes. *Nat. Med. 15*, 967−973.
(46) Lee, J., and Bogyo, M. (2010) Development of near-infrared fluorophore (NIRF)-labeled activity-based probes for in vivo imaging of legumain. *ACS Chem. Biol. 5*, 233−543.

Bioconjugate Chemistry

Article

pubs.acs.org/bc

Imaging Amyloid Plaque in Alzheimer's Disease Brain with a Biotinylated Aβ Peptide Radiopharmaceutical Conjugated to an IgG-Avidin Fusion Protein

Rachita K. Sumbria,[†] Ruben J. Boado,[†,‡] and William M. Pardridge*[,†]

[†]Department of Medicine, University of Califonia Los Angeles, Los Angeles, California 90024, United States

[‡]ArmaGen Technologies, Inc., Santa Monica, California 90401, United States

ABSTRACT: The Aβ amyloid peptide of Alzheimer's disease (AD) is a potentially large molecule radiopharmaceutical for imaging the brain amyloid burden, should the peptide be made transportable across the blood-brain barrier (BBB). Peptides can be made BBB-penetrating with the combined use of Trojan horse and avidin−biotin technologies. The peptide is monobiotinylated and attached to a fusion protein of avidin (AV) and a genetically engineered monoclonal antibody (mAb) against the human insulin receptor (HIR). The fusion protein is designated HIRMAb-AV, and is produced by stably transfected mammalian host cells grown in biotin free medium. The HIRMAb domain of the fusion protein acts as a molecular Trojan horse, which crosses the BBB via transport on the endogenous insulin receptor. The avidin domain of the fusion protein creates a high-affinity linker between the HIRMAb and the biotinylated peptide radiopharmaceutical. The 4 kDa Aβ(1−40) amyloid peptide of AD was N-biotinylated and radiolabeled with ^{125}I. The amyloid plaque binding of the [^{125}I]-N-biotinyl-Aβ(1−40) peptide, either without or with conjugation to the HIRMAb-AV fusion protein, was tested with film autoradiography and tissue sections of autopsy AD brain. The study shows the biotinyl-Aβ(1−40) peptide still binds to amyloid plaque in AD brain to the same extent when the peptide radiopharmaceutical is either free or conjugated to the HIRMAb-AV fusion protein. The study supports further evaluation of antibody-targeted peptide radiopharmaceuticals as large molecule neuro-imaging agents that penetrate the BBB.

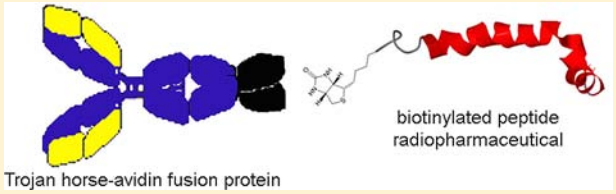

INTRODUCTION

The dementia of Alzheimer's disease (AD) correlates with the accumulation in the brain of amyloid plaque formed by the Aβ$^{1-42/43}$ amyloid peptide.[1,2] Amyloid forms via a process of nucleation-dependent polymerization,[3] and radiolabeled forms of the amyloid peptide, such as Aβ$^{1-40}$, image amyloid plaque in tissue sections of AD brain with film autoradiography.[4] Aβ peptide radiopharmaceuticals have not been developed as *in vivo* neuro-imaging agents, because the water-soluble Aβ peptide does not cross the blood-brain barrier (BBB).[5,6] Peptide radiopharmaceuticals, such as the Aβ peptide, can be reformulated for transport across the BBB with the combined use of molecular Trojan horse and avidin−biotin technologies. The Aβ$^{1-40}$ peptide was mono-biotinylated and coupled to a fusion protein of avidin (AV), and a genetically engineered chimeric monoclonal antibody (mAb) against the mouse transferrin receptor (TfR), designated the cTfRMAb-AV fusion protein.[6] The cTfRMAb binds the BBB TfR, and this triggers receptor-mediated transport across the BBB of the cTfRMAb and the Aβ$^{1-40}$ peptide radiopharmaceutical, which is joined to the mAb via a biotin-AV linker. Following intravenous (IV) injection in the mouse, the brain uptake of the [^{125}I]-N-biotinyl]Aβ$^{1-40}$ peptide was very low, 0.1% injected dose (ID)/gram brain.[6] Conversely, following conjugation to the cTfRMAb-AV fusion protein, the brain uptake of the peptide radiopharmaceutical was 2.1% ID/g.[6] This level of brain uptake is high, and comparable to the brain uptake of lipid soluble small molecule brain amyloid imaging agents.[7]

The cTfRMAb Trojan horse is specific for the mouse, and cannot be developed as a neuro-imaging agent for humans with AD. A human-specific BBB Trojan horse is the genetically engineered mAb against the human insulin receptor (HIR), and both chimeric and humanized forms of the HIRMAb have been produced.[8] A fusion protein of the engineered HIRMAb and AV was produced in stably transfected Chinese hamster ovary (CHO) cells grown in biotin depleted serum-free medium.[9] The HIRMAb-AV fusion protein is a 200 kDa bifunctional molecule, which both binds the HIR on the human BBB to trigger receptor-mediated penetration of the brain from blood and binds biotinylated peptides, such as the 4 kDa Aβ$^{1-40}$ peptide. Once in brain, the complex of the Aβ$^{1-40}$/HIRMAb has dual binding targets: the Aβ amyloid plaque and the endogenous HIR on brain cells. The objectives of the present study were twofold. First, the binding of the free Aβ$^{1-40}$ peptide vs the Aβ$^{1-40}$/HIRMAb complex to amyloid plaque was evaluated with film autoradiography and frozen sections of AD autopsy brain. Second, the relative binding of the Aβ$^{1-40}$/HIRMAb complex to the amyloid plaque vs binding to the

Received: March 30, 2012
Revised: April 22, 2012
Published: May 24, 2012

endogenous insulin receptor on human brain cells was examined.

EXPERIMENTAL PROCEDURES

Materials. Human Aβ^{1-40} was purchased from Bachem Inc. (Torrance, CA). Biotin-LC-β-Amyloid (1 - 40) (*N*-biotinyl Aβ^{1-40}) was obtained from Anaspec Inc. (Fremont, CA) and Iodine-125 [^{125}I] was purchased from Perkin-Elmer (Waltham, MA). Chloramine T, sodium metabisulfite, and other reagents were purchased from Sigma Aldrich (St. Louis, MO). Snap-frozen human autopsy Alzheimer's disease brain, used for the film autoradiography experiments, was provided by Prof. Harry Vinters (UCLA Department of Pathology, Neuropathology). The HIRMAb-AV fusion protein was produced in stably transfected CHO cells as described previously.[9] The CHO cells were grown for 4 weeks in biotin depleted serum-free medium, and the harvested condition medium was clarified by depth filtration, and the fusion protein was purified by protein A affinity chromatography.[9] The fusion protein was formulated in 0.01 M Tris buffered saline, pH = 5.5, and was stored either sterile filtered at 4 °C or at −70 °C. The murine HIRMAb was produced from the hybridoma with the ascites method and purified by protein G affinity chromatography, as described previously.[10]

Iodination of *N*-biotinyl-Aβ^{1-40}. *N*-biotinyl Aβ^{1-40} (10 ug, 2.1 nmol) was iodinated with ^{125}I (2 mCi; 1.1 nmol) and chloramine T (42 nmol) at room temperature. The reaction was quenched by the addition of sodium metabisulfite (126 nmol), and 100 μL of 0.01 M PBS (0.01 M Na_2HPO_4, 0.15 M NaCl, pH 7.4) containing 1% Tween-20 (PBST) was added to the reaction solution. [^{125}I]-*N*-Biotinyl-Aβ^{1-40} was purified by Sephadex G25 size-exclusion chromatography using PBST as elution buffer. [^{125}I]-*N*-Biotinyl-Aβ^{1-40} had a trichloroacetic acid (TCA) precipitability of >99% and a specific activity of 173 μCi/μg.

Film Autoradiography. Snap-frozen AD brain specimens were embedded in Tissue-Tek OCT Compound (Sakura Finetek, Torrance, CA), and 20 μm frozen sections were prepared with a Mikron cryostat at −20 °C, thaw-mounted onto glass slides and preserved at −70 °C until use. The slides were warmed to room temperature and briefly air-dried. Slides were then incubated in duplicates with 250 μL of PBSB buffer (0.01 M Na_2HPO_4, 0.15 M NaCl, pH 7.4, 0.1% bovine serum albumin) containing one of several solutions: (a) 1 nM [^{125}I]-*N*-biotinyl-Aβ^{1-40} alone; (b) 1 nM [^{125}I]-*N*-biotinyl-Aβ^{1-40} conjugated with 5 nM HIRMAb-AV; (c) 1 nM [^{125}I]-*N*-biotinyl-Aβ^{1-40} coincubated with 10 μM of unlabeled Aβ^{1-40}; (d) 1 nM [^{125}I]-*N*-biotinyl-Aβ^{1-40} conjugated with 5 nM HIRMAb-AV and coincubated with 10 μM of unlabeled Aβ^{1-40}; (e) 1 nM [^{125}I]-*N*-biotinyl-Aβ^{1-40} conjugated with 5 nM HIRMAb-AV and coincubated with 100 ug/mL murine HIRMAb; and (f) 1 nM [^{125}I]-*N*-biotinyl-Aβ^{1-40} conjugated with 5 nM HIRMAb-AV and coincubated with 100 ug/mL murine HIRMAb and 10 μM of unlabeled Aβ^{1-40}. The slides were incubated at room temperature for 2 h and washed four times with 2 min washes in PBSB at 4 °C followed by two 5 s washes in H_2O at 4 °C. After air-drying, the slides were placed in opposition to the Kodak Biomax MR X-ray film (Carestream Health, Rochester, MN), and exposed for up to 24 h at −70 °C. The films were then developed, fixed, and washed. Autoradiography images were digitized using a UMAX PowerLook III flatbed scanner and Adobe Photoshop, and quantified by estimating the mean gray matter integrated optical density of 5 randomly selected areas, using NIH *Image* v 1.62.

RESULTS

The [^{125}I]-*N*-biotinyl-Aβ^{1-40} peptide radiopharmaceutical was avidly bound by sections of AD brain (Figure 1A), and this

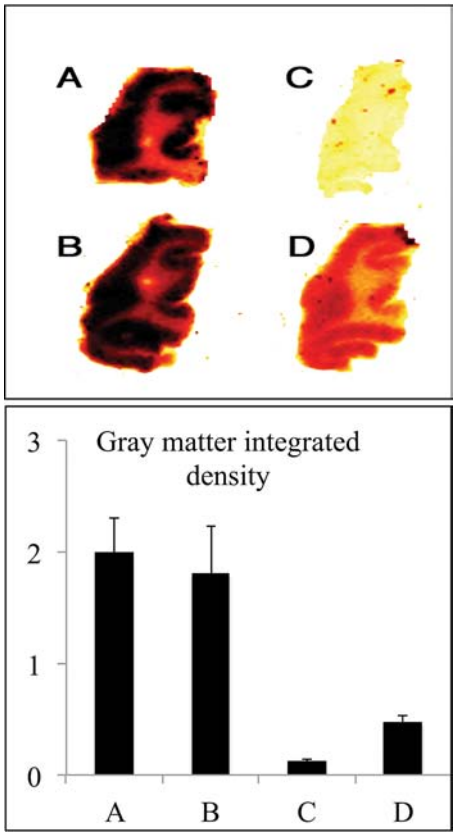

Figure 1. Labeling amyloid plaque in Alzheimer's disease brain with [^{125}I]-*N*-biotinyl Aβ^{1-40} conjugated to HIRMAb-AV fusion protein. (Top panel) Film autoradiograms of human AD brain sections showing the binding of 1 nM [^{125}I]-*N*-biotinyl Aβ^{1-40} coincubated with no additive (A); coincubated with a 5-fold molar excess of the HIRMAb-AV fusion protein (B); coincubated with 10 μM unlabeled Aβ^{1-40} (C); and coincubated with both a 5-fold molar excess of the HIRMAb-AV fusion protein and 10 μM unlabeled Aβ^{1-40} (D). (Bottom panel) Integrated density of radiolabeling over gray matter corresponding to autoradiograms in panels A, B, C, and D. Mean ± SD (n = 5 fields each section).

binding was not altered when the Aβ peptide was first conjugated to the HIRMAb-AV fusion protein (Figure 1B). The binding of the Aβ peptide alone to AD brain was displaced by coincubation of the Aβ with 10 μM unlabeled Aβ^{1-40} (Figure 1C); scanning densitometry shows that the binding of free Aβ peptide is decreased 94% by 10 μM unlabeled Aβ^{1-40} (Figure 1, bottom panel) . There was residual binding of the Aβ/HIRMAb complex to brain in the presence of 10 μM unlabeled Aβ^{1-40} (Figure 1D); scanning densitometry shows the binding of the Aβ/HIRMAb complex is decreased 76% by 10 μM unlabeled Aβ^{1-40} (Figure 1, bottom panel). Therefore, 76% of the Aβ/HIRMAb complex is bound by amyloid plaque in AD brain, and 24% is either bound to the HIR or bound nonspecifically.

dx.doi.org/10.1021/bc3001744 | *Bioconjugate Chem.* 2012, 23, 1318−1321

The selective binding of the Aβ/HIRMAb complex to amyloid plaque in AD brain was observed when the Aβ/HIRMAb complex was coincubated with 100 ug/mL HIRMAb (Figure 2A). The HIRMAb alone, without a fused AV domain, preferentially binds the Aβ amyloid plaque of AD brain as compared to the endogenous HIR on brain cells (Figures 1 and 2).

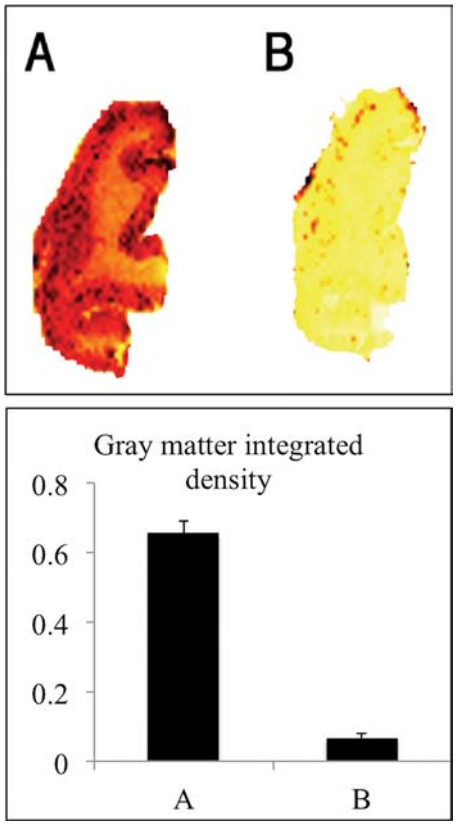

Figure 2. Labeling amyloid plaque in Alzheimer's disease brain with [^{125}I]-*N*-biotinyl Aβ^{1-40} conjugated to HIRMAb-AV fusion protein. (Top panel) Film autoradiograms of human AD brain sections showing the binding of 1 nM [^{125}I]-*N*-biotinyl Aβ^{1-40} coincubated with a 5-fold molar excess of the HIRMAb-AV fusion protein and 100 ug/mL murine HIRMAb (A); coincubated with a 5-fold molar excess of the HIRMAb-AV fusion protein, 100 ug/mL murine HIRMAb, and 10 μM unlabeled Aβ^{1-40} (B). (Bottom panel) Integrated density of radiolabeling over gray matter corresponding to autoradiograms in panels A and B. Mean ± SD (n = 5 fields each section).

suppresses binding to the endogenous HIR on brain cells. Under these conditions, the amyloid plaques in gray matter of AD brain are clearly visible (Figure 2A). The coincubation of the Aβ/HIRMAb complex with both 100 ug/mL HIRMAb and 10 uM unlabeled Aβ^{1-40} causes a 90% reduction in the binding of the Aβ/HIRMAb complex to AD brain (Figure 2B).

DISCUSSION

The results of the present studies are consistent with the following conclusions. First, a new form of Aβ peptide radiopharmaceutical is described, wherein the monobiotinylated Aβ^{1-40} is conjugated to a novel fusion protein of the genetically engineered HIRMAb and avidin. This fusion protein is designated the HIRMAb-AV fusion protein and the complex of biotinylated Aβ^{1-40} to the HIRMAb-AV fusion protein is designated the Aβ/HIRMAb complex. Second, autoradiography of AD brain shows that the Aβ peptide still binds the amyloid plaque of AD brain following conjugation to the HIRMAb-AV fusion protein (Figure 1). Third, the Aβ/HIRMAb complex

Radiolabeled forms of the Aβ peptide are potent agents for detection of amyloid plaque in autopsy sections of AD brain, and the sensitivity of detection of amyloid plaques with the radiolabeled Aβ^{1-40} and autoradiography is far greater than that with an anti-Aβ antibody and immunocytochemistry.[4] The binding of Aβ^{1-40} to amyloid plaques in AD brain is 50% saturated at 30 nM,[4] the binding follows first-order kinetics,[11] and the active binding species is the monomer/dimer, not the oligomer of the Aβ^{1-40} peptide.[12] All of these properties make the Aβ^{1-40} peptide an ideal candidate for drug development as a peptide radiopharmaceutical for imaging the amyloid plaque in AD. However, the IV injection of Aβ peptide radiopharmaceuticals in AD transgenic mice does not image amyloid plaque in brain,[13] because the Aβ peptide does not cross the BBB.[5,6] What is needed is a reformulation of the Aβ peptide radiopharmaceutical as a BBB-penetrating molecule. The Aβ/HIRMAb complex is a new brain-penetrating form of the Aβ peptide radiopharmaceutical. In order for the Aβ/HIRMAb complex to enable effective imaging of the amyloid plaque burden in AD, the imaging agent must have several properties. First, the Aβ/HIRMAb complex must penetrate the brain from blood via receptor-mediated transport on an endogenous BBB receptor. Early studies with the murine HIRMAb showed that Aβ alone did not cross the BBB, but that a complex of Aβ and the murine HIRMAb rapidly penetrated the Rhesus monkey brain *in vivo*.[10] Transport into brain via the BBB insulin receptor allows the imaging agent to penetrate the entire brain volume, including both regions of interest (ROI) bearing amyloid plaque and non-ROI areas with no amyloid plaque. Second, the amyloid binding properties of the Aβ peptide must be retained following reformulation as the Aβ/HIRMAb complex, so that the imaging agent is sequestered within the ROI following penetration into the brain. This is demonstrated by the autoradiography results of the present study (Figures 1 and 2). Third, the Aβ/HIRMAb complex must undergo efflux from brain back to blood, so that the radioactivity is selectively sequestered within the ROI of brain. Prior work in primates shows that the Aβ/HIRMAβ complex does efflux from brain with a half-time of 16 h.[10] The efflux from brain to blood of IgG molecules is mediated by a BBB Fc receptor,[14] and confocal microscopy of brain shows the principal Fc receptor on the BBB is the neonatal Fc receptor, or FcRn.[15] These 3 properties contribute to the successful imaging of amyloid plaque in brain with either large-molecule peptide radiopharmaceuticals, such as Aβ, or lipid-soluble small-molecule amyloid binding agents.[7]

In the absence of BBB drug delivery technology, the brain uptake of Aβ peptide radiopharmaceuticals is very low compared to the brain uptake of small-molecule imaging agents.[7] The brain uptake and biodistribution of the Aβ/HIRMAb complex cannot be assessed in lower animals such as rodents, because the HIRMAb does not cross react with the insulin receptor of lower animals, including New World primates such as squirrel monkeys.[16] However, brain uptake can be assessed in the mouse using a surrogate Trojan horse, the cTfRMAb-AV fusion protein.[6] The brain uptake in the mouse of [^{125}I]-*N*-biotinyl Aβ alone is very low following IV injection, 0.10 ± 0.06% of ID/gram brain.[6] However, following conjugation of [^{125}I]-*N*-biotinyl Aβ to the cTfRMAb-AV fusion protein, the brain uptake in the mouse is high, 2.1% ± 0.2% of ID/gram brain after IV administration,[6] which is comparable to

dx.doi.org/10.1021/bc3001744 | *Bioconjugate Chem.* 2012, 23, 1318–1321

the brain uptake of lipid-soluble small-molecule amyloid imaging agents.[7]

The Aβ/HIRMAb complex can be developed as a radiopharmaceutical for either positron emission tomography (PET) or single photon emission computed tomography (SPECT). The 124-iodine nuclide, which has a half-time of 4.2 days, could be incorporated for PET imaging. Alternatively, the 111-indium nuclide, which has a half-time of 2.8 days, could be incorporated for SPECT imaging. Prior work has shown that *N*-biotinyl Aβ^{1-40} can be conjugated with an ^{111}In-chelator moiety, and this modification does not alter peptide binding to amyloid plaque in AD brain.[17]

AUTHOR INFORMATION

Corresponding Author

*Ph: +1 310 825 8858. Fax: +1 310 206 5163. E-mail Address: wpardridge@mednet.ucla.edu.

Notes

The authors declare the following competing financial interest(s): Dr. Boado is an employee and Dr. Pardridge is a consultant to ArmaGen Technologies.

REFERENCES

(1) Cummings, B. J., and Cotman, C. W. (1995) Image analysis of beta-amyloid load in Alzheimer's disease and relation to dementia severity. *Lancet 346*, 1524−1528.

(2) Naslund, J., Haroutunian, V., Mohs, R., Davis, K. L., Davies, P., Greengard, P., and Buxbaum, J. D. (2000) Correlation between elevated levels of amyloid beta-peptide in the brain and cognitive decline. *J. Am. Med. Assoc. 283*, 1571−1577.

(3) Harper, J. D., Lieber, C. M., and Lansbury, P. T. (1997) Atomic force microscopic imaging of seeded fibril formation and fibril branching by the Alzheimer's disease amyloid-beta protein. *Chem. Biol. 4*, 951−959.

(4) Maggio, J. E., Stimson, E. R., Ghilardi, J. R., Allen, C. J., Dahl, C. E., Whitcomb, D. C., Vigna, S. R., Vinters, H. V., Labenski, M. E., and Mantyh, P. W. (1992) Reversible in vitro growth of Alzheimer disease beta-amyloid plaques by deposition of labeled amyloid peptide. *Proc. Natl. Acad. Sci. U. S. A. 89*, 5462−5466.

(5) Saito., Y., Buciak, J., Yang, J., and Pardridge, W. M. (1995) Vector-mediated delivery of 125I-labeled beta-amyloid peptide A beta 1−40 through the blood-brain barrier and binding to Alzheimer disease amyloid of the A beta 1−40/vector complex. *Proc. Natl. Acad. Sci. U. S. A 92*, 10227−10231.

(6) Zhou, Q. H., Lu, J. Z., Hui, E. K., Boado, R. J., and Pardridge, W. M. (2011) Delivery of a peptide radiopharmaceutical to brain with an IgG-avidin fusion protein. *Bioconjugate Chem 22*, 1611−1618.

(7) Ono, M., Cheng, Y., Kimura, H., Cui, M., Kagawa, S., Nishii, R., and Saji, H. (2011) Novel (18)F-labeled benzofuran derivatives with improved properties for positron emission tomography (PET) imaging of beta-amyloid plaques in Alzheimer's brains. *J. Med. Chem. 54*, 2971−2979.

(8) Boado, R. J., Zhang, Y., Zhang, Y., and Pardridge, W. M. (2007) Humanization of anti-human insulin receptor antibody for drug targeting across the human blood-brain barrier. *Biotechnol. Bioeng. 96*, 381−391.

(9) Boado, R. J., Zhang, Y., Xia, C. F., Wang, Y., and Pardridge, W. M. (2008) Genetic engineering, expression, and activity of a chimeric monoclonal antibody-avidin fusion protein for receptor-mediated delivery of biotinylated drugs in humans. *Bioconjugate Chem. 19*, 731−739.

(10) Wu, D., Yang, J., and Pardridge, W. M. (1997) Drug targeting of a peptide radiopharmaceutical through the primate blood-brain barrier in vivo with a monoclonal antibody to the human insulin receptor. *J. Clin. Invest. 100*, 1804−1812.

(11) Esler, W. P., Stimson, E. R., Ghilardi, J. R., Vinters, H. V., Lee, J. P., Mantyh, P. W., and Maggio, J. E. (1996) In vitro growth of Alzheimer's disease β-amyloid plaques displays first-order kinetics. *Biochemistry 35*, 749−757.

(12) Tseng, B. P., Esler, W. P., Clish, C. B., Stimson, E. R., Ghilardi, J. R., Vinters, H. V., Mantyh, P. W., Lee, J. P., and Maggio, J. E. (1999) Deposition of monomeric, not oligomeric, Aβ mediates growth of Alzheimer's disease amyloid plaques in human brain preparations. *Biochemistry 38*, 10424−10431.

(13) Wengenack, T. M., Curran, G. L., and Poduslo, J. F. (2000) Targeting Alzheimer amyloid plaques in vivo. *Nat. Biotechnol. 18*, 868−872.

(14) Zhang, Y., and Pardridge, W. M. (2001) Mediated efflux of IgG molecules from brain to blood across the blood-brain barrier. *J. Neuroimmunol. 114*, 168−172.

(15) Schlachetzki, F., Zhu, C., and Pardridge, W. M. (2002) Expression of the neonatal Fc receptor (FcRn) at the blood-brain barrier. *J. Neurochem. 81*, 203−206.

(16) Pardridge, W. M., Kang, Y.-S., Buciak, J. L., and Yang, J. (1995) Human insulin receptor monoclonal antibody undergoes high affinity binding to human brain capillaries in vitro and rapid transcytosis through the blood-brain barrier in vivo in the primate. *Pharm. Res. 12*, 807−816.

(17) Kurihara, A., and Pardridge, W. M. (2000) Aβ^{1-40} peptide radiopharmaceuticals for brain amyloid imaging; ^{111}In chelation, conjugation to polyethyleneglycol-biotin linkers, and autoradiography with Alzheimer's disease brain sections. *Bioconjugate Chem. 11*, 380−386.

Bioconjugate Chemistry

Article

pubs.acs.org/bc

Novel Multifunctional Theranostic Liposome Drug Delivery System: Construction, Characterization, and Multimodality MR, Near-Infrared Fluorescent, and Nuclear Imaging

Shihong Li,[†] Beth Goins,[†] Lujun Zhang,[‡] and Ande Bao*[,†,‡]

[†]Department of Radiology and [‡]Department of Otolaryngology − Head and Neck Surgery, University of Texas Health Science Center at San Antonio, San Antonio, Texas

ABSTRACT: Liposomes are effective lipid nanoparticle drug delivery systems, which can also be functionalized with noninvasive multimodality imaging agents with each modality providing distinct information and having synergistic advantages in diagnosis, monitoring of disease treatment, and evaluation of liposomal drug pharmacokinetics. We designed and constructed a multifunctional theranostic liposomal drug delivery system, which integrated multimodality magnetic resonance (MR), near-infrared (NIR) fluorescent and nuclear imaging of liposomal drug delivery, and therapy monitoring and prediction. The premanufactured liposomes were composed of DSPC/cholesterol/Gd-DOTA-DSPE/DOTA-DSPE with the molar ratio of 39:35:25:1 and having ammonium sulfate/pH gradient. A lipidized NIR fluorescent tracer, IRDye-DSPE, was effectively postinserted into the premanufactured liposomes. Doxorubicin could be effectively postloaded into the multifunctional liposomes. The multifunctional doxorubicin-liposomes could also be stably radiolabeled with ^{99m}Tc or ^{64}Cu for single-photon emission computed tomography (SPECT) or positron emission tomography (PET) imaging, respectively. MR images displayed the high-resolution micro-intratumoral distribution of the liposomes in squamous cell carcinoma of head and neck (SCCHN) tumor xenografts in nude rats after intratumoral injection. NIR fluorescent, SPECT, and PET images also clearly showed either the high intratumoral retention or distribution of the multifunctional liposomes. This multifunctional drug carrying liposome system is promising for disease theranostics allowing noninvasive multimodality NIR fluorescent, MR, SPECT, and PET imaging of their in vivo behavior and capitalizing on the inherent advantages of each modality.

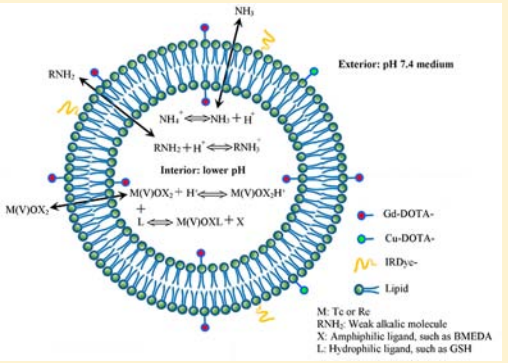

INTRODUCTION

Noninvasive imaging modalities, such as computed tomography (CT), magnetic resonance (MR), single photon emission computed tomography (SPECT), positron emission tomography (PET), and ultrasound (US) imaging, play key roles in clinical diagnosis, monitoring of disease status, and evaluation of treatment. The optical imaging technology, especially suitable for small animals, provides a cheaper and convenient alternative to the more complicated nuclear and MR imaging modalities. Near-infrared (NIR) fluorescent probes and in vivo imaging have drawn particular interest, due to their low optical absorption and scattering by the tissue, and there is minimal tissue autofluorescence in the NIR window (wavelengths from 700 to 900 nm).[1] A recent clinical trial has shown that in vivo NIR fluorescent imaging could be used in lymph node mapping for surgical excision of lymph nodes in breast cancer.[2]

Each imaging modality, based on its individual mechanism of tissue contrast or function, has a specific sensitivity, spatial and temporal resolution in relationship to diseases, and physiological or molecular biological procedures.[3−6] Noninvasive multimodality imaging can synergize their advantages and compensate the shortcomings of individual imaging modalities.[7−9] The use of multimodality imaging for improved disease diagnosis and therapy evaluation represents an optimal direction in radiology. In addition to the instrument innovation, new imaging tracers and probes are necessary for the development of multimodality imaging techniques. The introduction of a single platform, which integrates multiple probes to enable multimodality imaging of diseases and/or therapy response, will have advantages over a single functional probe, as each probe in the platform can afford complementary information for the other modalities. Accordingly, nanoparticle systems have shown the excellence of achieving this goal, while being used for drug delivery to advance disease treatment.[7,10−12]

The use of drug delivery systems can improve the stability, pharmacokinetics, and biodistribution of a wide variety of therapeutic agents, leading to more convenient drug administration or improved treatment efficacy with decreased side effects.[7,11,12] A multifunctional drug delivery system, containing both therapeutic and imaging agents, will contribute to a more personalized cancer therapy approach by facilitating efficient delivery through image guidance and therapy response monitoring.[7] Liposomes, unilamellar lipid bilayer nanoparticles

Received: March 30, 2012
Revised: May 2, 2012
Published: May 13, 2012

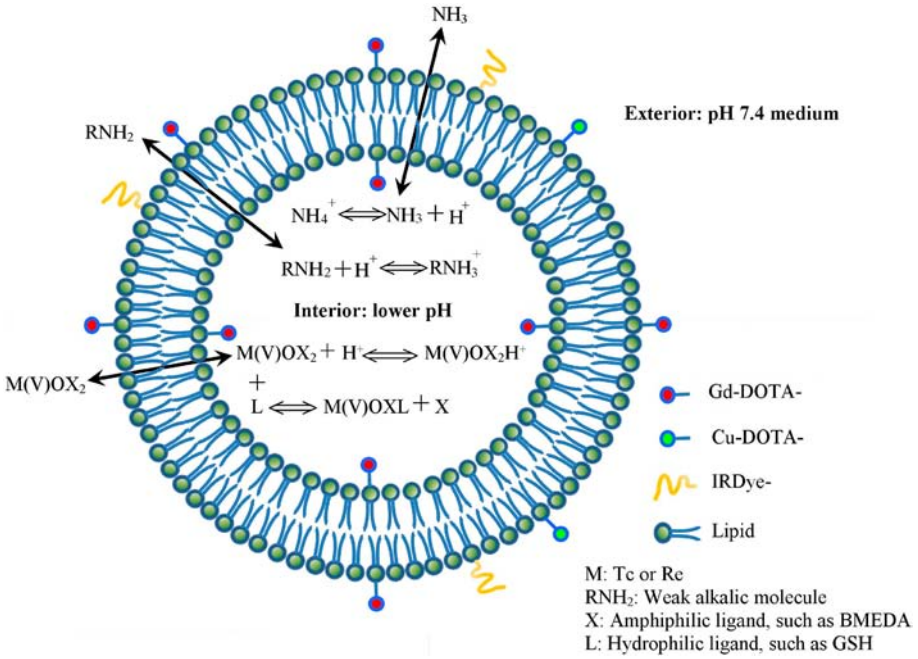

Figure 1. Schematic diagram of multifunctional liposomes.

enclosing an aqueous compartment that can accommodate lipophilic or hydrophilic drug molecules, are effective drug delivery systems with an ideal construction of biocompatible, nontoxic, and biodegradable materials. Liposomes can passively accumulate in tumor by extravasation through abnormal leaky tumor vasculature known as the enhanced permeability and retention effect, or actively accumulate in tumor by tumor cell specific targeting or tumor angiogenic marker targeting.[13,14] Various liposome formulations have been approved by the FDA for clinical cancer treatment or are under trials.[15,16] Liposomes have versatile modifiability by allowing functional molecules to be encapsulated in the interior, inserted in the bilayer, or attached on the bilayer membrane surface. Thus, liposomes may be constructed to provide an ideal multiprobe platform with the capability of multimodality theranostics. The multimodality imaging functionalization of therapeutic drug carrying liposomes is an important and necessary theranostic component for personalized monitoring of the in vivo tumor targeting and pharmacokinetics of liposomal therapeutic agents, predicting therapy outcome and gaining a better understanding of the prognosis-associated disease status by combining the advantageous information from each imaging modality.[7] For example, higher spatial resolution and better tissue contrast from MR imaging plus better quantification from nuclear imaging will provide a better understanding of the relationship of liposome formulation to associated drug effect information. Further incorporation of NIR fluorescent imaging in the liposome platform for superficial lymph node mapping will provide identification of the metastatic lymph nodes for focused lymph node treatment or guiding surgical excision.[1,2]

Herein, we have constructed a multifunctional liposomal drug delivery system comprising DSPC/cholesterol/Gd-DOTA-DSPE/DOTA-DSPE/IRDye-DSPE with ammonium/pH gradient (Figure 1). By using the ammonium/pH gradient, this system can also be postloaded with the most widely used gamma imaging radionuclide, technetium-99m (^{99m}Tc) ($T_{1/2}$ = 6.0 h, 141 keV γ-ray),[17] the therapeutic radionuclides, rhenium-186/188 (^{186}Re/^{188}Re)[18] and weak alkalic chemotherapeutic agents, such as doxorubicin.[19] The inclusion of DOTA-DSPE in the lipid formulation enables the liposome membrane labeling of radionuclides, such as copper-64 (^{64}Cu) ($T_{1/2}$ = 12.7 h, β^+ decay (17.4%))[20] for PET imaging. The Gd-DOTA-DSPE component, a chelate of gadolinium(III) (Gd (III)) with lipidized macrocyclic DOTA ligand provides the liposome MR imaging capability.[21−24] The NIR fluorescent molecule, IRDye-DSPE inserted in the liposome bilayer allows NIR fluorescent imaging of tumors or tumor-associated lymph node mapping.[1,2]

Recent studies have suggested a promising regimen by direct intratumoral infusion of nanoparticle carried therapeutic agents to treat solid tumors.[25−32] To assess the multimodality imaging functions of our liposomal drug delivery system following intratumoral infusion in a squamous cell carcinoma of head and neck (SCCHN) xenograft model in nude rats, in vivo MR, NIR fluorescent, SPECT, or PET images of the multifunctional liposomes with/without radiolabeling with ^{99m}Tc or ^{64}Cu, respectively, were acquired for multimodality monitoring of their in vivo behaviors including intratumoral distribution, retention, and systemic distribution.

MATERIALS AND METHODS

Materials. 1,2-Distearoyl-*sn*-glycero-3-phosphocholine (DSPC) and 1,2-distearoyl-*sn*-glycero-3-phosphoethanolamine (DSPE) were purchased from Avanti Polar Lipids (Alabaster, AL). Cholesterol was from Calbiochem (San Diego, CA). 1,4,7,10-Tetraazacyclododecane-1,4,7-tris(acetic acid)-10-acetic acid mono(*N*-hydroxysuccinimidyl ester) (DOTA-NHS ester) was from Macrocyclics (Dallas, TX). IRDye 800CW NHS ester was from LI-COR Biosciences (Lincoln, NE). Doxorubicin hydrochloride was from LC Laboratories (Woburn, MA). *N,N*-Bis(2-mercaptoethyl)-*N′,N′*-diethyl-ethylenediamine (BMEDA) was from ABX GmbH (Radeberg, Germany). Sodium ^{99m}Tc-pertechnetate was from GE Healthcare (San Antonio, Texas). Carrier-free $^{153}GdCl_3$ was from PerkinElmer Life Science (Boston, MA). Carrier-free $^{64}CuCl_2$ was from University of Wisconsin−Madison (Madison, WI). GFC-04−500 gel (4% agarose cross-linked, 50−150 μm beads) was from Sooner

dx.doi.org/10.1021/bc300175d | *Bioconjugate Chem.* 2012, 23, 1322−1332

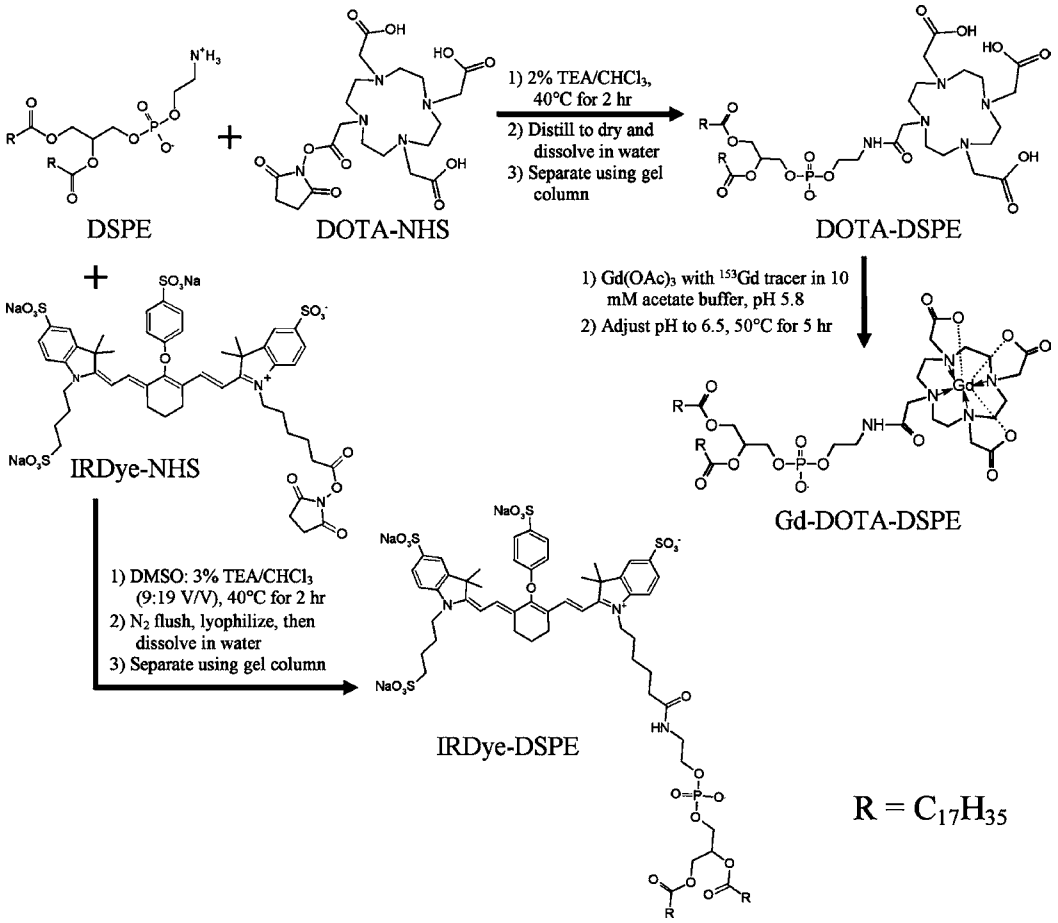

Figure 2. Synthesis of DOTA-DSPE, Gd-DOTA-DSPE, and IRDye-DSPE.[21,22,33]

Scientific (Garvin, OK). The HiPrep and PD-10 desalting columns were products of GE Healthcare (Piscataway, New Jersey). Ultrapure water was prepared by a Nanopure Infinity ultrapure water system (Barnstead Int., Dubuque, IA). All other chemicals were obtained from Sigma-Aldrich (St. Louis, MO).

Synthesis of DOTA-DSPE and Gd-DOTA-DSPE. A schematic diagram of the syntheses of DOTA-DSPE, Gd-DOTA-DSPE, and IRDye-DSPE is shown in Figure 2.[21,22,33] For the preparation of DOTA-DSPE, 2.0 g of DSPE was mixed with 2.3 g of DOTA-NHS ester (molar ratio, 1: 1) in a round flask, followed by the addition of 260 mL of 2% (v/v) triethylamine (TEA) in $CHCl_3$, incubation of the mixture until dissolved thoroughly and heated at 40 °C for 2 h. The obtained clear solution was concentrated by distillation under reduced pressure and dried in vacuo. Then, 130 mL of ultrapure water was added to dissolve the resulted product. The suspension was transferred into several 50 mL conical centrifugation tubes (Corning, Corning, NY). Each tube was exposed to 5 cycles of freezing in liquid nitrogen followed by thawing in 60 °C water bath and then centrifuged at 4500 *g* for 10 min. The DOTA-DSPE containing supernatant was filtered with a 0.45 μm membrane filter, and then purified with an AKTADesign FPLC system equipped with a HiPrep desalting column, a 280 nm UV detector, and an automatic fraction collector (Amersham Biosciences). Ten millilter samples were loaded for each run and ultrapure water was used as mobile phase. The elution velocity was 8 mL/min. Two milliliter aliquots of eluate fractions were collected. Fractions 3−18 containing DOTA-DSPE, verified by UV absorption detection and thin layer chromatography with Silica gel 60 F254 plastic plate (EM Science, Gibbstown, NJ) using 64:25:4 $CHCl_3$/MeOH/water as mobile phase (DOTA-DSPE: blue spot with molybdemum spraying, Rf at 0.15, also stained by iodine exposure but negative to UV light and ninhydrin staining), were combined and lyophilized. The obtained white product was 2.80 g (93% yield).

To prepare Gd-DOTA-DSPE, DOTA-DSPE (0.384 g, 0.339 mmol) was dissolved in 38 mL of 10 mM sodium acetate buffer, pH 5.8, followed by the addition of 0.337 mmol of $Gd(OAc)_3$ in 3.1 mL water containing 3 kBq (0.081 μCi) $^{153}GdCl_3$ radioactive tracer.[20] The pH of solution was adjusted to 6.5 with 1 M NaOH. The opaque solution was heated at 50 °C for 5 h. Then, the resulting product was centrifuged at 4500 *g* for 10 min. The obtained precipitate was washed sequentially 2 times with 10 mL 50 mM sodium acetate buffer, pH 5.8, followed by 10 mL water. The precipitate was then lyophilized and measured for ^{153}Gd radioactivity with an automatic Minaxi γ A5550 gamma counter (Packard, Downers Grove, Illinois). The final white product was 0.40 g, corresponding to 92% yield, which also matched the yield calculated from ^{153}Gd tracer measurement.

The DOTA-DSPE and Gd-DOTA-DSPE products were also verified by MALDI-TOF MS assay using 2,5-dihydroxybenzoic acid (DHB) matrix (Applied Biosystems Voyager DE PRO MALDI-TOF mass spectrometer). (DOTA-DSPE: *m/z* in positive mode. $[M\text{-}C_{17}H_{35}CO+H]^+$: 868.0; $[M+H]^+$: 1134.1; Gd-DOTA-DSPE: *m/z* in negative mode. $[868.0+Gd\text{-}5H]^-$: 1020.9; $[1134.1+Gd\text{-}5H]^-$: 1287.1).

dx.doi.org/10.1021/bc300175d | *Bioconjugate Chem.* 2012, 23, 1322−1332

Synthesis of IRDye-DSPE. IRDye-DSPE was synthesized by conjugating IRDye 800CW NHS ester to DSPE.[33] IRDye 800CW NHS ester powder (2.6 mg) in a glass vial was dissolved with 0.9 mL DMSO on ice and mixed with 1.92 mL of 3% TEA/$CHCl_3$ containing 1.9 mg DSPE (molar ratio, 1:1.15). The vial was kept in the dark at 35 °C for 20 h with constant shaking. Then, the mixture was flushed with nitrogen gas to near dryness and then freeze−dried. The dried product was dissolved with 1 mL water, centrifuged at 5000 *g* for 1 min. The residual pellets were washed with another 1 mL water and centrifuged again. Each 1 mL of the combined supernatants was loaded on a FPLC HiTrap column and eluted with water. The 0.4 mL eluent fractions with color were analyzed by thin layer chromatography (Silica gel 60 F254, plastic sheet, EM Science, NJ) with a mobile phase of MeOH and the absorbance at 778 nm was measured for determination of the dye content. Then, the fractions were freeze−dried and stored in the dark at −20 °C until needed. The yield of IRDye-DSPE in the first 4 fractions was approximately 42% of IRDye, assuming the same molar absorption coefficient with IRDye and IRDye-DSPE.

The IRDye-DSPE product was also verified by MALDI-TOF MS assay using DHB matrix (IRDye 800CW: *m*/*z* in positive mode. M^+: 1002.2; IRDye-DSPE: *m*/*z* in positive mode. $[1002.2+DSPE\text{-}H_2O\text{-}C_{17}H_{35}CO]^+$: 1467.1).

Preparation of Gd-Liposomes. Gadolinium-liposomes (Gd-liposomes), composed of DSPC/cholesterol/Gd-DOTA-DSPE/DOTA-DSPE (molar ratio: 39:35:25:1) containing trace amount of ^{153}Gd and having ammonium sulfate/pH gradient, were prepared by lipid film hydration and extrusion.[18] Briefly, the lipid components were mixed and dissolved with chloroform in a round flask and dried by rotary evaporation under reduced pressure. The formed lipid film was hydrated with 300 mM ammonium sulfate, pH 5.1, to give a concentration of 60 mM total lipids, incubated at 56 °C, and vortexed vigorously. The formed milky suspension was sequentially extruded through Whatman Nuclepore polycarbonate membrane filters with different pore sizes (two passes for 2 μm, 1 μm, 400 nm, and 200 nm pore sizes; and six passes for 100 nm pore size) at 56 °C (Lipex Extruder; Northern Lipids, Vancouver, British Columbia, Canada). Radioactivity of ^{153}Gd in the extruded liposomes was measured for calculation of lipid recovery. Particle sizes of the liposomes were measured with a DynaPro dynamic light scattering system (Wyatt Technology, CA). Endotoxin levels assayed with limulus amebocyte lysate (LAL) Pyrotell (Associates of Cape Cod Inc., E. Falmouth, MA) were <12.5 EU/mL. There were no bacteria or fungus growth during 14-day culture.

Postinsertion of IRDye-DSPE into Premanufactured Gd-Liposomes. The synthesized IRDye-DSPE was incorporated into premanufactured Gd-liposomes using the reported postinsertion method of phospholipid conjugates.[34−36] The premanufactured Gd-liposomes (0.16 mL) were mixed with 0.8 mL of IRDye-DSPE in water (molar ratio of IRDye-DSPE to total lipids: 0.05%) and incubated at 60 °C in dark with intermittent vortexing for 1 h. The mixture was cooled to room temperature and centrifuged at 244 000 *g* for 45 min at 4 °C. After the supernatant was aspirated, the pellets were resuspended in 100 mM ammonium sulfate and centrifuged again. The pellets were resuspended in 300 mM ammonium sulfate and stored at 4 °C. The absorbance of supernatants at 780 nm was measured to obtain the efficiency of IRDye-DSPE insertion to liposomes.

Postloading of ^{99m}Tc into Liposomes and in Vitro Stability of ^{99m}Tc-Liposomes. The prepared liposomes were labeled with ^{99m}Tc using the method developed in our laboratory with slight modification.[17,37] In brief, 3.5 μL BMEDA and 50 mg sodium glucoheptonate were dissolved with 5 mL nitrogen gas flushed saline, and added with 60 μL of 15 mg/mL $SnCl_2$ in 0.12 M HCl/saline. Then, 50 mM NaOH was added to adjust the pH to 7−8. A 1 mL aliquot of the mixture was mixed with 0.2 mL (740 MBq (20 mCi)) of sodium ^{99m}Tc-pertechnetate (GE Healthcare) and incubated at 25 °C for 20 min to form ^{99m}Tc(V)-BMEDA complex. Then, 0.5 mL of liposomes (total lipids: 60 mM for Gd-liposomes, 30 mM for IRDye-Gd-liposomes) was buffer-exchanged by loading on a PD-10 desalting column and elution with phosphate buffered saline (PBS), pH 7.4, then mixed with the ^{99m}Tc(V)-BMEDA complex and incubated at 39 °C for 1 h. The ^{99m}Tc labeled liposomes were purified using the desalting column chromatography. Radiolabeling efficiency was calculated as the ratio of radioactivities of ^{99m}Tc-liposomes post- and prepurification measured with a dose calibrator (Atomlab 100; Biodex Medical Systems, Shirley, New York).

An aliquot of purified ^{99m}Tc-liposomes was 1:1 v/v diluted with fetal bovine serum (FBS) and incubated at 37 °C, and the remaining ^{99m}Tc-liposomes were stored at 25 °C. The ^{99m}Tc-labeling stability of ^{99m}Tc-liposomes at different times in these two conditions was measured by a GFC-04−500 gel spin microcolumn separation method as described previously.[17,38]

Radiolabeling of Gd-Liposomes with ^{64}Cu. Sixty microliters of $^{64}CuCl_2$ stock solution (~78 MBq (2.11 mCi)) was diluted with 200 μL 100 mM sodium acetate buffer, pH 6.5. Gd-liposomes (0.5 mL) were loaded on a PD-10 column and eluted with 100 mM acetate buffer, pH 6.5. The collected liposome fraction (1.7 mL) was mixed with the ^{64}Cu radiotracer and incubated at 43 °C for 2 h. Then, the mixture was purified using another PD-10 column pre-equilibrated with saline. The percentage of ^{64}Cu associated with Gd-liposomes was determined as the ratio of radioactivities of liposomes post- and prepurification. For stability evaluation, an aliquot of purified ^{64}Cu-liposomes was 1:1 (v/v) diluted with FBS and incubated at 37 °C. Another aliquot of the purified ^{64}Cu-liposomes was stored at room temperature (25 °C). Twenty-four hours later, the ^{64}Cu-liposomes were purified using the above-mentioned column separation method for in vitro stability evaluation of ^{99m}Tc-liposomes.

Postloading of Doxorubicin into Gd-Liposomes. One milliliter of premanufactured Gd-liposomes was loaded on a PD-10 column and eluted with saline. The liposomes in saline and doxorubicin hydrochloride in saline were preheated at 43, 50, 56, or 60 °C, respectively, then mixed together at different drug/lipid ratios and final liposome concentrations. After 30 min, 1 h, 1.5 h, and 2 h of incubation with intermittent shaking, a 100 μL aliquot of the mixture was purified by loading on a pre-equilibrated 1 mL Sephadex microcolumn and eluted with saline. The collected liposome fractions, together with the unpurified samples as standards, were digested by 1:2 (v/v) dilution with 2-propanol containing 100 mM HCl (120/1 (v/v) of 2-propanol/12 M HCl). The absorbance at 480 nm was measured for quantification of doxorubicin. Doxorubicin loading efficiency was calculated as the ratio of doxorubicin in doxorubicin-liposomes to the unpurified mixture. The stability of purified doxorubicin-liposomes in saline or in 50% FBS/saline following incubation was also determined by a

GFC-04-500 gel spin microcolumn separation method as described previously.[17,38]

Animal Model. Animal experiments were preformed in accordance with the NIH Animal Use Guidelines and with approval of local Institutional Animal Care Committee. A human SCCHN xenograft model in nude rats previously established[39] was used for all the imaging experiments. All the animal handling procedures, including cell inoculation, drug injection, and in vivo imaging, were conducted while the animals were anesthetized with 1−3% isoflurane (Vedco, St. Joseph, MO) in 100% oxygen using an anesthesia inhalation unit (Bickford, Wales Center, NY). SCC-4 cell line (ATCC, Manassas, VA) was cultured in DMEM supplemented with 10% FBS, 100 U/mL penicillin, 100 mg/mL streptomycin, and 10 mM HEPES buffer solution (Invitrogen, Grand Island, NY) at 37 °C with 5% CO_2. The cells at 80−90% confluence were collected and made into a cell suspension in saline. Male *rnu/rnu* athymic nude rats (Harlan, Indianapolis, IN) at age 4−5 weeks (75−100 g) were inoculated subcutaneously with 5 million of SCC-4 tumor cells in 0.20 mL of saline on the dorsum at the level of the scapulae. The tumor was usually palpable 7 days post tumor cell inoculation. The tumor volume (V) was determined by measuring the length (l), width (w), and depth (d) of each tumor with a digital caliper and using an ellipsoid volume formula, $V = (\pi/6)lwd$. Animals were used for the study at 15 to 25 days after tumor cell inoculation, with an average tumor volume of 1.9 ± 1.1 cm^3.

MR Imaging. The Gd-liposomes (0.6 mL with 52 mM total lipids) were purified by PD10 column separation using PBS, pH 7.4, as eluant and diluted to 7 mM of total lipids. Eight nude rats bearing SCCHN tumors were each intratumorally infused with the Gd-liposomes at a volume of 15% of tumor volume and a rate of 0.5 mL/min using a microinfusion pump (KD Scientific, Holliston, Massachusetts). Pre- and post-infusion of the Gd-liposomes, MR images were acquired with a 7T Bruker PharmaScan MR scanner (Bruker BioSpin, Ettlingen, Germany) with 7-T/16-cm horizontal bore and a 37 gauss/cm gradient insert (Billerica, MA). Each rat was positioned so that the entire tumor could fit into the surface coil, and covered with a warm water blanket to maintain the body temperature. Prior to Gd-liposome infusion, high-resolution T2- and T1-weighted MR imaging of the tumor was performed. T2-weighted MR images were acquired using rapid acquisition with relaxation enhancement (RARE) pulse sequence with 2D acquisition mode (matrix size, 128 × 128; voxel size, 0.20 × 0.20 mm^2 with 0.52 mm slice thickness; TE = 33.2 ms; TR = 3500 ms; ETL = 8; number of average = 12). T1-weighted MR images were acquired using fast low angle shot (FLASH) pulse sequence with 3D acquisition mode (matrix size, 256 × 256; voxel size, 0.088 × 0.088 × 0.088 mm^3; TE = 3.14 ms; TR = 22.17 ms; flip angle = 45°; number of average = 6). The number of slices of each MR image acquisition was selected to ensure that the entire tumor had been included with each MR image acquisition. Repeated T1-weighted MR imaging with the same imaging parameters and field of view was performed postinfusion of Gd-liposomes to obtain liposome intratumoral microdistribution.

NIR Fluorescent Imaging. The freshly prepared IRDye-Gd-liposomes were diluted to 7 mM of total lipids. Four nude rats bearing the SCCHN tumor were each intratumorally infused with the liposomes using the same infusion conditions described above. For comparison, the free IRDye dissolved in PBS, pH 7.4, at the same dye concentration as the IRDye-Gd-liposomes was intratumorally infused into another 4 SCCHN tumor bearing rats. In vivo NIR images of the animals in the supine position during the infusion, and at 2 and 24 h postinfusion, were obtained with a Xenogen IVIS Spectrum system using *Living Imaging* software (Caliper, Xenogen, Alameda, CA). The NIR images (subject size, 3.5; emission filter, 800 nm; excitation filter, 745 nm; exposure time, 1 s; F number, 2; binning factor, 8) were fused with corresponding photographic images (FOV, 13.1 cm; exposure time, 0.2 s; binning factor, 4) for display. At 24 h after image acquisition, the rats were euthanized by cervical dislocation under deep anesthesia sedation. The NIR images of dissected tumor and other major organs in the body cavity were also acquired.

Gamma Camera Imaging. ^{99m}Tc labeled Gd-liposomes (222 MBq/mL (6.0 mCi/mL), 7 mM total lipids) were intratumorally infused into 4 SCCHN tumor bearing nude rats. Planar gamma camera images were acquired at various time points with each rat in prone position using a micro-SPECT/CT scanner (XSPECT, Gamma Medica, CA) equipped with parallel hole collimators. A vial of known amount of ^{99m}Tc was located in the image field of view as a reference standard. The acquisition time was 1 min at baseline, 2 and 4 h postinfusion, 5 min at 24 h, and 10 min at 44 h. The percent of injected dose (%ID) of ^{99m}Tc associated with the tumor was quantified by drawing regions of interest and comparing with the ^{99m}Tc standard measured together with the rat.

Micro-PET Imaging. Two SCCHN tumor-bearing nude rats were intratumorally infused with 15% tumor volume of freshly purified ^{64}Cu-labeled liposomes described above. PET images were acquired immediately and 24 h postinjection of ^{64}Cu-liposomes with a microPET R4 scanner (Siemens Medical Systems), while the rat was positioned to align the tumor in the center of the field of view in both axial and longitudinal directions.

The PET images were reconstructed using 2D ordered-subset expectation maximization (OSEM) into single-frame images and 10 s/frame dynamic images with small-animal PET manager software (Concorde MicroSystems) (matrix size, 128 × 128 × 63; voxel size, 0.85 × 0.85 mm^2; slice thickness, 1.20 mm). The PET images were displayed and analyzed with IDL-based *ASIPro* software (Concorde MicroSystems).

RESULTS

Preparation of Liposomes Containing Synthesized Functional Components. DOTA-DSPE and Gd-DOTA-DSPE were prepared by one-step syntheses and purified with high yields (>90%) using more simple and convenient procedures than previously reported.[21,22] IRDye-DSPE was also effectively synthesized. Some of the IRDye-DSPE was not recovered due to the incomplete separation from free dye during the gel filtration chromatography, leading to the yield of pure IRDye-DSPE being about 40%.

The particle sizes of prepared Gd-liposomes were 112.9 ± 1.5 nm^2 of diameter with 18.2% polydispersity. The Gd-liposome preparation described herein also had a high recovery of Gd-DOTA-DSPE as obtained by ^{153}Gd radioactivity measurement (nearly 90%) and the particle sizes did not vary during 6 months storage at 4 °C, indicating the effective integration of Gd-DOTA-DSPE with other lipid components to form stable liposomes. Cautious extrusion through a series of filters with decreasing pore sizes should be preformed to avoid the loss of lipids retained on filters, which may contribute to the reported low recovery of Gd-DOTA-DSPE.[21] IRDye-DSPE

(0.05% of total lipids) could be postinserted into preformed liposomes at high efficiencies (>95%) without a significant change in liposome particle size.

Radiolabeling of Preformed Gd-Liposomes. The ^{99m}Tc labeling efficiencies of Gd-liposomes and IRDye-Gd-liposomes were in the range 58−89%, similar to that of liposomes comprising DSPC and cholesterol only.[38] The ^{99m}Tc−Gd-liposomes were stable both in PBS, pH 7.4, and in 50% FBS/PBS; more than 79% of ^{99m}Tc still associated with liposomes at 72 h postincubation (Figure 3). The presence of DOTA-DSPE

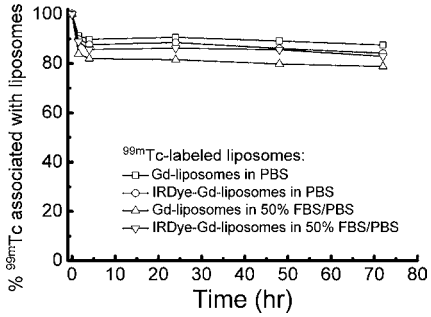

Figure 3. Percentage of ^{99m}Tc associated with liposomes at different times following incubation in phosphate buffered saline (PBS) and PBS containing 50% fetal bovine serum (FBS).

in the liposome formulation slightly decreased the ^{99m}Tc labeling stability in PBS, pH 7.4, as compared with DSPC/cholesterol liposomes.[38] However, the ^{99m}Tc labeling stabilities of liposomes with or without DOTA-DSPE component were similar in 50% FBS/PBS.

The labeling efficiency of Gd-liposomes containing 1 mol % DOTA-DSPE with ^{64}Cu tracer was 96.4 ± 2.9% (n = 2). After 24 h in PBS, pH 7.4, at 25 °C or in 50% FBS/PBS at 37 °C, the percentage of ^{64}Cu associated with liposomes were 96.6% and 94.4%, respectively, indicating that the addition of only 1% of the DOTA-DSPE component was reliable for conjugating and anchoring ^{64}Cu stably on the liposome surface.

Doxorubicin Loading of Preformed Gd-Liposomes. Doxorubicin is a well-established weak alkalic anticancer agent for the treatment of a broad range of solid tumors. The remote loading of doxorubicin into liposomes has remarkable advantages of high drug to lipid ratio, as well as improved drug cancer targeting for enhanced cancer therapy and reduced toxicity.[40,41] In our study, highly efficient encapsulation of doxorubicin into ammonium/pH gradient DSPC/cholesterol liposomes was achieved. Under conditions of changing the liposome medium to saline and heating the mixture of doxorubicin and liposomes (drug/lipid ratio, w/w 1:5, 16 mM of total lipids) at 60 °C for 40 min, a drug loading of >90% was achieved. However, the remote loading of doxorubicin into the ammonium sulfate/pH-gradient Gd-liposomes was relatively more difficult. After incubation at 43 °C for 2 h, the loading of doxorubicin into Gd-liposomes was insignificant. Incubation at 56−60 °C tended to cause the aggregation of liposomes at drug/lipid ratios (w/w) of 1/10−1/4 and total lipid concentrations of 5−9 mM, a low doxorubicin loading efficiency (<32% after 1 h incubation); whereas when the drug/lipid ratio was reduced to 1/15 and the mixture was diluted to 2.5 mM of total lipids, the loading efficiency could be improved to 56%, but the absolute drug loading amount was lower. The optimized loading conditions were 1/10 of a drug/lipid ratio, 5 mM of total lipids in saline, and incubation at 50 °C for 1.5 h, which led to a 65% loading efficiency, corresponding to 6.5/100 of doxorubicin/lipids in purified liposomes. Simply increasing the drug/lipid ratio and liposome concentration or extending the incubation time could not improve the drug loading amount.

The particle sizes of purified doxorubicin-Gd-liposomes were 131.1 ± 3.8 nm. The particle sizes of initial Gd-liposomes were 112.9 ± 1.5 nm. The purified doxorubicin-liposomes were stable at 4 °C for weeks without significant drug leakage observed by desalting column separation. The concentration of doxorubicin-Gd-liposomes can be adjusted with centrifugation and resuspension. Although the doxorubicin drug/lipid ratio was lower than that of current doxorubicin-liposome formulations, it is expected that the doxorubicin dose would be high enough for cancer therapy, especially in the situation of direct intratumoral administration.

MR Imaging of SCCHN Tumor Xenografts in Nude Rats with Intratumoral Infusion of Gd-Liposomes. The typical T2- and T1-weighted MR images of SCCHN tumor pre- and post-Gd-liposome infusion are shown in Figure 4. The

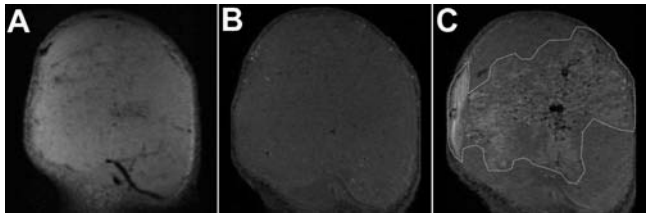

Figure 4. T2- (A) and T1- (B,C) weighted 7T MR images of SCCHN tumor pre- (A,B) and post- (C) intratumoral infusion of Gd-liposomes using a surface coil. Intratumoral distribution of Gd-liposomes has been circumscribed with dashed white line (C).

heterogeneous microstructure of tumor could be visualized by both the T2- and T1-weighted MR images. Post-intratumoral infusion, the T1-weighted MR images clearly showed the region of Gd-liposome distribution in the tumor (Figure 4). Thus, contrast-enhanced MR imaging could enable the noninvasive evaluation of Gd-liposome distribution in the tumor, guide the treatment planning for local drug administration, and predict the cancer therapy response.

Contrast-enhanced MR imaging has advantages of providing anatomic function and affording high resolution of intratumoral microdistribution of liposomes compared to nuclear imaging. The disadvantage of contrast-enhanced MR imaging is that a relatively high concentration of Gd has to be present in the liposome formulation to surmount its low intrinsic sensitivity. Accordingly, nuclear imaging provides high sensitivity and better quantification.

NIR Fluorescent Imaging of SCCHN Tumor Xenografted Nude Rats with Intratumoral Infusion of IRDye-Gd-Liposomes. The series of NIR fluorescent images acquired in a dynamic mode showed the gradual dispersion of IRDye-Gd-liposomes or free IRDye inside the tumor during the intratumoral infusion. The fluorescent intensities (radiant efficiency, p/s/cm^2/sr/(μW/cm^2)) of the IRDye-liposome group measured at 24 h postinfusion were lower than that measured at 1 min, whereas those measured at 2 h postinfusion were significantly stronger, which is projected to be caused by the local diffusion and stable intratumoral retention of IRDye-liposomes. On the contrary, the fluorescent intensities at the tumor site of the free IRDye group were decreased significantly

dx.doi.org/10.1021/bc300175d | Bioconjugate Chem. 2012, 23, 1322−1332

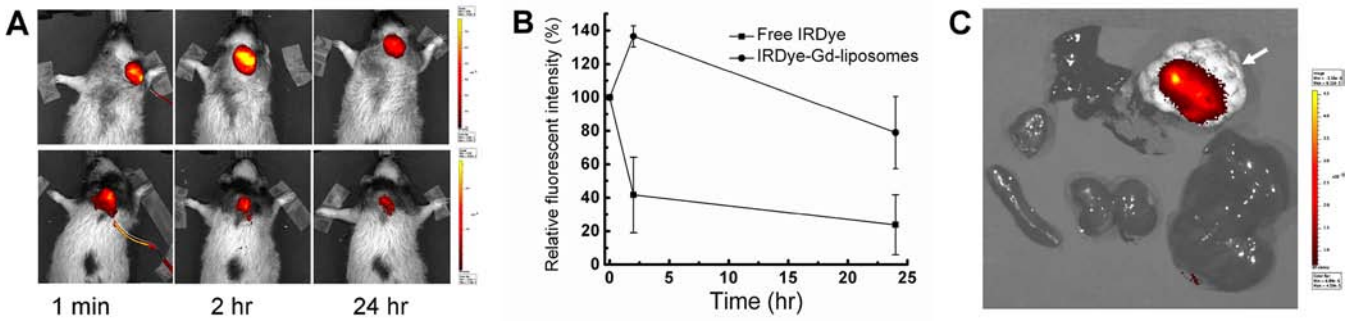

Figure 5. NIR images and intratumoral fluorescent intensity change of SCCHN xenografted nude rats intratumorally infused with NIR agents. (A) NIR images at 1 min, 2 h, and 24 h post intratumoral infusion of IRDye-Gd-liposomes (upper panel) and free IRDye (lower panel); (B) NIR fluorescent intensity change with time in the tumor area normalized to 1 min post infusion; (C) NIR images of dissected tumor (white arrow) and normal organs from the rats euthanized 24 h post intratumoral infusion of IRDye-Gd-liposomes.

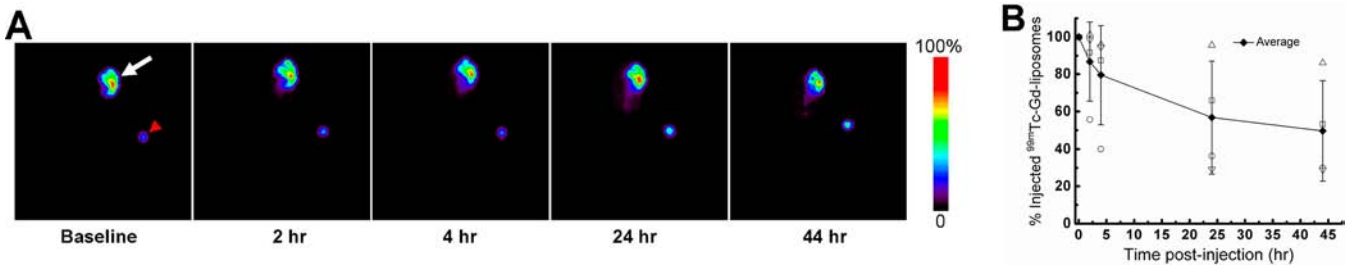

Figure 6. Planar gamma camera images of SCCHN xenografted nude rats intratumorally infused with ^{99m}Tc-Gd-liposomes (white arrow, tumor; red arrowhead, reference standard outside the animal body) (A) and the intratumoral retention of injected ^{99m}Tc radioactivity with time (B).

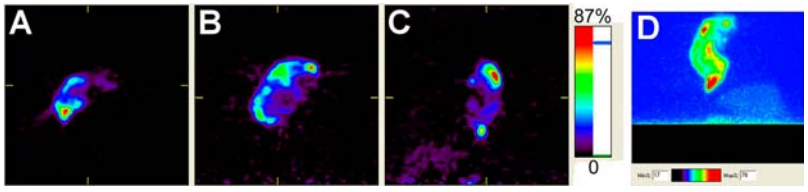

Figure 7. Micro-PET images depicting the locoregional retention of the ^{64}Cu-Gd-liposomes 24 h after intratumoral infusion (A, B, C, and D show the axial, coronal, sagittal, and projection images, respectively).

at 2 h postinjection (Figure 5A), which is coincident with the rapid clearance of IDye 800CW in the circulation system (half-life in Sprague−Dawley rats: 35.7 min post-intravenous injection, 235.6 min post-intradermal injection).[42] The average relative fluorescent intensities normalized to that at 1 min postinjection are shown in Figure 5B. These results reflected the high sensitivity of IRDye-DSPE tracer to identify the local spatial and temporal distribution and retention of the liposomes, indicating it is feasible for the monitoring of IRDye-liposomes with NIR fluorescence tomography technique.

The NIR images of dissected tumor and normal organs revealed that the liposomes injected at 15% of tumor volume might not cover the entire tumor, and the cleared liposomes showed insignificant accumulation of trace dye component in liver, spleen, kidneys, lung, and heart (Figure 5C). Multiple injection locations and higher injection volume of liposomes will be necessary for more effective delivery of drug inside the tumor.

Gamma Camera Imaging of SCCHN Xenografted Nude Rats with Intratumoral Infusion of ^{99m}Tc-Gd-Liposomes. Planar gamma camera images were acquired at different times for monitoring the in vivo distribution of ^{99m}Tc-Gd-liposomes post-intratumoral injection in the SCCHN xenografted nude rats. These images revealed that a high percentage of injected dose (ID) was retained inside the tumor during the 44 h experimental period. The cleared radioactivity from tumor was excreted rapidly and had no significant accumulation in any vital organ (Figure 6), similar to our previous observations with liposomes comprising DSPC/cholesterol and having ammonium sulfate/pH gradient but without functional lipid derivative.[27] The quantification of ^{99m}Tc-Gd-liposomes retained in the tumor at various times postinjection was derived from region of interest analysis of these gamma camera images and indicated their high intratumoral retention.

Micro-PET Imaging of SCCHN Xenografts with Intratumoral Infusion of ^{64}Cu-Gd-Liposomes. Micro-PET images were acquired at 24 h postintratumoral infusion of ^{64}Cu-Gd-liposomes (Figure 7). The 3D tomographic and projection images clearly showed the local retention and microdistribution of radioactivity in the tumor.

DISCUSSION

Liposomal drug delivery systems have shown promising applications for cancer treatment with chemotherapeutic drugs, genetic agents, and therapeutic radionuclides.[14] The

dx.doi.org/10.1021/bc300175d | Bioconjugate Chem. 2012, 23, 1322−1332

noninvasive multimodality imaging of theranostics will enable optimal real-time monitoring of both the systemic and microdistribution of delivered therapeutic agents, taking advantage of their synergistic effect to guide the adjustable personalized scheme of drug administration and therapy with an accurate prediction of treatment response. To achieve this goal, we designed and investigated a liposomal drug delivery system, which integrated MR, NIR fluorescent, and SPECT or PET multimodality imaging, as well as with the carriage of chemotherapeutic drug and/or therapeutic radionuclides for personalized cancer theranostics.

As shown in Figure 1, liposomes are lipid nanoparticles comprising various kinds of lipids, including cholesterol or its similar chemicals, which form a lipid double membrane spherical structure, while enclosing a segregated aqueous space. This unique structural feature possessed by liposomes has long been recognized as an ideal drug delivery vehicle for in vivo controlled drug release, improved efficacy, or lower toxicity. The drug molecules can be encapsulated in the inner aqueous space, or if lipophilic drug molecules, they can be embedded in the lipid double membrane. Meanwhile, through conjugation to a lipid chain, various drug molecules can also be linked to the membrane surface either during liposome manufacture or via postinsertion. Correspondingly, a broad spectrum of imaging or targeting groups can also be added to liposomes based on the same mechanisms. As with liposomes, other nanoparticles may also be modified to be multifunctional.[10] Comparably, liposomes excel over other nanoparticle systems in efficient and high-concentration drug loading, universally applicable methods of imaging and targeting modifications, as well as the proven clinical success in human disease treatment.[11−17]

The liposomes, composed of Gd-DOTA-DSPE/DOTA-DSPE/DSPC/cholesterol (molar ratio: 25:1:39:35) and having ammonium sulfate/pH gradient, were prepared by lipid film hydration and extrusion. IRDye-DSPE tracer can be effectively incorporated into liposomes by the postinsertion method. By using the ammonium sulfate/pH gradient between liposome interior and exterior, the premanufactured liposomes can also be radiolabeled with the most widely used diagnostic radionuclide, ^{99m}Tc, as well as its chemical mimic, therapeutic radionuclides, ^{186}Re/^{188}Re.[18,20] The introduction of a low percentage of DOTA-DSPE allows for the liposome surface labeling with PET imaging radionuclide, ^{64}Cu, or other appropriate radionuclides with high labeling stabilities. The chemotherapeutic agent, doxorubicin, could be effectively postloaded into the premanufactured liposomes. A weight ratio of doxorubicin to total lipids, 6.1/100, corresponding to 1.9 mg of doxorubicin in a liposome suspension of 40 mM of total lipids, was achieved under the optimized conditions. The doxorubicin-liposomes were stable when stored at 4 °C. These results indicated the successful establishment of a noninvasive in vivo multimodality functional imaging and therapeutic liposomal drug delivery system for cancer theranostics.

In the preliminary in vivo multimodality imaging evaluation of the multifunctional liposomal drug delivery system, we investigated the locoregional retention and biodistribution of the Gd-liposomes, IRDye-liposomes, ^{99m}Tc-labeled liposomes, or ^{64}Cu-labeled liposomes after intratumoral infusion into SCCHN xenografts in nude rats using MR, NIR fluorescent, planar gamma, and PET imaging modalities, respectively. MR imaging provided a 3D high-resolution intratumoral microdistribution of the liposomes, which will be important for the prediction of cancer therapy response. Both the in vivo NIR fluorescent and nuclear images clearly showed the retention and distribution of liposomes inside the tumor. The NIR fluorescent signal emitted by the trace IRDye moiety had high sensitivity and was convenient for detecting the locoregional retention and systemic distribution at superficial areas of the body. Nuclear images can accurately measure the quantitative biodistribution of administrated radioactivity in vivo. Our radiolabeling of liposomes with ^{99m}Tc and ^{64}Cu used distinct mechanisms. ^{99m}Tc was encapsulated into the inner aqueous space, whereas ^{64}Cu was chelated with the DOTA group on the bilayer membrane surface. Their stabilities represented the specific transmembrane permeability shown by ^{99m}Tc and lipid bilayer integrity by ^{64}Cu. The in vivo imaging results of ^{99m}Tc- and ^{64}Cu-labeled Gd-liposomes verified the effectiveness of delivery of radionuclides by liposome carriers, which could be highly retained inside the tumor with a microheterogeneous intratumoral distribution. The resolution of nuclear images was lower than MR images; however, nuclear imaging possesses better quantification features.

The biological behavior of the liposomes obtained by each imaging modality may be interfered with by others in the same multifunctional nanoparticle. Investigation of the pharmacokinetics with noninvasive imaging techniques has great potential for the optimal design and application of multifunctional nanoparticles. In this study, we integrated noninterfering mechanisms for constructing the multifunctional liposomes with different biocompatible functional constitutes, avoiding the pitfalls of low yield and low stability typically observed with multistep constructions of multifunctional nanoparticles.

Some other methods of enabling MR contrast have been demonstrated for monitoring of liposomal drug delivery.[43−46] For MR imaging, lipidized or lipophilic Gd agent can be incorporated in the lipid bilayers.[45,47−49] Hydrophilic manganese (Mn) ions or Gd-DTPA complexes have been encapsulated in the liposome internal aqueous space to study the release of drug molecules from liposomes by a triggering mechanism, such as hyperthermia, and imaged by T1-weighted MR.[32,43,44,50−52] However, the toxicity of Mn ions limits its clinical application.[53] The chelation of Gd with macrocyclic ligand, DOTA, has higher thermodynamic and kinetic stability than with the linear ligand, DTPA.[54] Passive encapsulation of Gd-DTPA into liposomes results in a low concentration of Gd in the liposome suspension and, consequently, a relatively low MR signal sensitivity. The use of Gd-DOTA-DSPE can avoid these shortcomings. The high percentage of Gd-DOTA-DSPE component presented in our liposome formulation produced strong T1-weighted MR signal indicating the microdistribution of liposomes following intratumoral infusion, which can lead to accurate prediction of the tumor response of local liposomal chemotherapy or radiotherapy.

The lipidized macrocyclic ligand, DOTA-DSPE, was incorporated in liposomes for chelation of ^{64}Cu. Although radiolabeling of liposomes with ^{64}Cu can be realized via a postloading method[55] or conjugation with maleimide lipid of ^{64}Cu prelabeled bifunctional chelators with thiol group,[56,57] our method represents an option for convenient and stable ^{64}Cu-liposome radiolabeling. Notably, our liposome drug delivery system has the capability of being radiolabeled with therapeutic radionuclides for radionuclide therapy, which when compared with most chemotherapy and gene therapy agents has the advantages of not requiring so close a proximity of the liposomes to the cell surface and intracellular uptake of the

radionuclides. In spite of the therapeutic potential of ^{186}Re/^{188}Re-encapsulated Gd-liposomes, the DOTA-DSPE component is also potentially suitable for the labeling of liposomes with other beta-emitting therapeutic radionuclides of rare earth elements as they share similar chemical properties, such as samarium-153(^{153}Sm) and lutetium-177 (^{177}Lu),[58] and also copper-67 (^{67}Cu) ($T_{1/2}$ = 61.8 h).[59,60]

Other approaches have been used to construct multifunctional and theranostic liposomes.[7−9] Some of these approaches can be combined with ours to further improve the function and application potential of liposomes. For example, our radiolabeling method could be useful for investigating the systemic pharmacokinetics of other types of liposomes. We will investigate the possibility of extended functionalization, such as active targeting modification and the image guided therapeutic potential of our multifunctional liposome drug delivery system in future studies.

CONCLUSION

We developed a multifunctional liposome drug delivery system containing Gd-DOTA-DSPE and DOTA-DSPE and having ammonium sulfate/pH gradient. These multifunctional liposomes can be labeled with NIR fluorescent tracer, IRDye-DSPE, by postinsertion method and radiolabeled with radioisotopes for nuclear imaging, such as ^{99m}Tc by postloading, or ^{64}Cu by conjugation to DOTA moiety on the liposome surface. The representative chemotherapeutic agent, doxorubicin, can also be effectively remotely loaded into the multifunctional liposomes. The local retention and systemic biodistribution data with a tumor xenograft model of SCCHN demonstrated that these multifunctional liposomes are promising drug carriers, enabling noninvasive multimodality imaging of their in vivo behavior with MR, NIR fluorescence, SPECT, or PET imaging techniques. In addition, these multifunctional liposomes have the potential for accurate monitoring and guidance of the in vivo delivery of liposomal chemotherapeutic drugs or therapeutic radionuclides by taking advantage of various available noninvasive imaging modalities.

AUTHOR INFORMATION

Corresponding Author

*Tel: 210-567-5657; Fax: 210-567-5549; E-mail: bao@uthscsa.edu.

Notes

The authors declare no competing financial interest.

ACKNOWLEDGMENTS

This study was financially supported by NIH/NCI grant, R01 CA131039. The MR and PET imaging study cost was supported by CTSA grant, UL1 RR025767. In vivo near-infrared fluorescent images were generated in the Core Optical Imaging Facility, University of Texas Health Science Center at San Antonio.

REFERENCES

(1) Khullar, O., Frangioni, J. V., Grinstaff, M., and Colson, Y. L. (2009) Image-guided sentinel lymph node mapping and nanotechnology-based nodal treatment in lung cancer using invisible near-infrared fluorescent light. *Semin. Thorac. Cardiovasc. Surg. 21*, 309−315.

(2) Troyan, S. L., Kianzad, V., Gibbs-Strauss, S. L., Gioux, S., Matsui, A., Oketokoun, R., Ngo, L., Khamene, A., Azar, F., and Frangioni, J. V. (2009) The FLARE intraoperative near-infrared fluorescence imaging system: a first-in-human clinical trial in breast cancer sentinel lymph node mapping. *Ann. Surg. Oncol. 16*, 2943−2952.

(3) Moser, E., Stadlbauer, A., Windischberger, C., Quick, H. H., and Ladd, M. E. (2009) Magnetic resonance imaging methodology. *Eur. J. Nucl. Med. Mol. Imaging 36* (Suppl 1), S30−S41.

(4) Lanza, G. M., Winter, P. M., Caruthers, S. D., Morawski, A. M., Schmieder, A. H., Crowder, K. C., and Wickline, S. A. (2004) Magnetic resonance molecular imaging with nanoparticles. *J. Nucl. Cardiol. 11*, 733−743.

(5) Blasberg, R. G., and Gelovani, J. (2002) Molecular-genetic imaging: A nuclear medicine−based perspective. *Mol. Imaging 1*, 280−300.

(6) Margolis, D. J. A., Hoffman, J. M., Herfkens, R. J., Jeffrey, R. B., Quon, A., and Gambhir, S. S. (2007) Molecular imaging techniques in body imaging. *Radiology 245*, 333−356.

(7) Koning, G. A., and Krijger, G. C. (2007) Targeted multifunctional lipid-based nanocarriers for image-guided drug delivery. *Anticancer Agents Med. Chem. 7*, 425−440.

(8) Jennings, L. E., and Long, N. J. (2009) 'Two is better than one' — probes for dual-modality molecular imaging. *Chem. Commun. (Camb.) 24*, 3511−3524.

(9) Martí-Bonmatí, L., Sopena, R., Bartumeus, P., and Sopena, P. (2010) Multimodality imaging techniques. *Contrast Media Mol. Imaging 5*, 180−189.

(10) Louie, A. (2010) Multimodality imaging probes: design and challenges. *Chem. Rev. 110*, 3146−3195.

(11) Buse, J., and El-Aneed, A. (2010) Properties, engineering and applications of lipid-based nanoparticle drug-delivery systems: current research and advances. *Nanomedicine 5*, 1237−1260.

(12) Lammers, T., Kiessling, F., Hennink, W. E., and Storm, G. (2010) Nanotheranostics and image-guided drug delivery: current concepts and future directions. *Mol. Pharmaceutics 7*, 1899−1912.

(13) Gabizon, A. (2007) Applications of liposomal drug delivery systems to cancer therapy. In *Nanotechnology for Cancer Therapy* (Amiji, M. M., Ed.) pp 595−611, CRC Press, Boca Raton.

(14) Elbayoumi, T. A., and Torchilin, V. P. (2010) Current trends in liposome research. *Methods Mol. Biol. 605*, 1−27.

(15) Farokhzad, O., and Langer, R. (2006) Nanomedicine: developing smarter therapeutic and diagnostic modalities. *Adv. Drug Delivery Rev. 58*, 1456−1459.

(16) Puri, A., Loomis, K., Smith, B., Lee, J. H., Yavlovich, A., Heldman, E., and Blumenthal, R. (2009) Lipid-based nanoparticles as pharmaceutical drug carriers: from concepts to clinic. *Crit. Rev. Ther. Drug Carrier Syst. 26*, 523−580.

(17) Bao, A., Goins, B., Klipper, R., Negrete, G., and Phillips, W. T. (2004) Direct ^{99m}Tc labeling of pegylated liposomal doxorubicin (Doxil) for pharmacokinetic and non-invasive imaging studies. *J. Pharmacol. Exp. Ther. 308*, 419−425.

(18) Bao, A., Goins, B., Klipper, R., Negrete, G., and Phillips, W. T. (2003) ^{186}Re-liposome labeling using ^{186}Re-SNS/S complexes: in vitro stability, imaging, and biodistribution in rats. *J. Nucl. Med. 44*, 1992−1999.

(19) Cullis, P. R., Hope, M. J., Bally, M. B., Madden, T. D., Mayer, L. D., and Fenske, D. B. (1997) Influence of pH gradients on the transbilayer transport of drugs, lipids, peptides and metal ions into large unilamellar vesicles. *Biochim. Biophys. Acta 1331*, 187−211.

(20) Eckerman, K. F., and Endo, A. (2008) MIRD: Radionuclide Data and Decay Schemes, 2nd ed., p 103, Society of Nuclear Medicine, Reston, VA; (^{64}Cu); 232−233 (^{99m}Tc); 392−393 (^{153}Sm); 415−417 (^{153}Gd); 460−461 (^{177}Lu); 485−486 (^{188}W); 487−488 (^{186}Re); 489−490 (^{188}Re).

(21) Hak, S., Sanders, H. M., Agrawal, P., Langereis, S., Grüll, H., Keizer, H. M., Arena, F., Terreno, E., Strijkers, G. J., and Nicolay, K. (2009) A high relaxivity Gd(III)DOTA-DSPE-based liposomal contrast agent for magnetic resonance imaging. *Eur. J. Pharm. Biopharm. 72*, 397−404.

(22) Oliver, M., Ahmed, A., Kamaly, N., Perouzel, E., Caussin, A., Keller, M., Herlihy, A., Bell, J., Miller, A. D., and Jorgensen, M. R.

(2006) MAGfect: a novel liposome formulation for MRI labeling and visualization of cells. *Org. Biomol. Chem. 4*, 3489−3497.
(23) Mulder, W. J. M., Strijkers, G. J., van Tilborg, G. A. F., Griffioen, A. W., and Nicolay, K. (2006) Lipid-based nanoparticles for contrast-enhanced MRI and molecular imaging. *NMR Biomed. 19*, 142−164.
(24) Mulder, W. J., van der Schaft, D. W., Hautvast, P. A., Strijkers, G. J., Koning, G. A., Storm, G., Mayo, K. H., Griffioen, A. W., and Nicolay, K. (2007) Early in vivo assessment of angiostatic therapy efficacy by molecular MRI. *FASEB J. 21*, 378−383.
(25) Harrington, K. J., Rowlinson-Busza, G., Syrigos, K. N., Uster, P. S., Vile, R. G., and Stewart, J. S. (2000) Pegylated liposomes have potential as vehicles for intratumoral and subcutaneous drug delivery. *Clin. Cancer Res. 6*, 2528−2537.
(26) Bao, A., Phillips, W. T., Goins, B., Zheng, X., Sabour, S., Natarajan, M., Woolley, F. R., Zavaleta, C., and Otto, R. A. (2006) Potential use of drug carried-liposomes for cancer therapy via direct intratumoral injection. *Int. J. Pharm. 316*, 162−169.
(27) French, J. T., Goins, B., Phillips, W. T., Saenz, M., Li, S., Garcia-Rojas, X., Otto, R. A., and Bao, A. (2010) Interventional therapy of head and neck cancer with lipid nanoparticle-carried rhenium-186 radionuclide. *J. Vasc. Interven. Radiology 21*, 1271−1279.
(28) Wang, S. X., Bao, A., Herrera, S. J., Phillips, W. T., Goins, B., Santoyo, C., Miller, F. R., and Otto, R. A. (2008) Intraoperative ^{186}Re-liposome radionuclide therapy in a head and neck squamous cell carcinoma xenograft positive surgical margin model. *Clin. Cancer Res. 14*, 3975−3983.
(29) Hrycushko, B. A., Ware, S., Li, S., and Bao, A. (2011) Improved tumour response prediction with equivalent uniform dose in pre-clinical study using direct intratumoural infusion of liposome-encapsulated ^{186}Re radionuclides. *Phys. Med. Biol. 56*, 5721−5734.
(30) Luboldt, W., Pinkert, J., Matzky, C., Wunderlich, G., and Kotzerke, J. (2009) Radiopharmaceutical tracking of particles injected into tumors: a model to study clearance kinetics. *Curr. Drug Delivery 6*, 255−260.
(31) Allard, E., Passirani, C., and Benoit, J. P. (2009) Convection-enhanced delivery of nanocarriers for the treatment of brain tumors. *Biomaterials 30*, 2302−2318.
(32) Tagami, T., Foltz, W. D., Ernsting, M. J., Lee, C. M., Tannock, I. F., May, J. P., and Li, S. D. (2011) MRI monitoring of intratumoral drug delivery and prediction of the therapeutic effect with a multifunctional thermosensitive liposome. *Biomaterials 32*, 6570−6578.
(33) Hermanson, G. T. (1996) Bioconjugate Techniques, pp 139−140 and 173−176, Academic Press − An Imprint of Elsevier, San Diego, CA.
(34) Uster, P. S., Allen, T. M., Daniel, B. E., Mendez, C. J., Newman, M. S., and Zhu, G. Z. (1996) Insertion of poly(ethylene glycol) derivatized phospholipid into pre-formed liposomes results in prolonged in vivo circulation time. *FEBS Lett. 386*, 243−246.
(35) Allen, T. M., Sapra, P., and Moase, E. (2002) Use of the post-insertion method for the formation of ligand-coupled liposomes. *Cell. Mol. Biol. Lett. 7*, 889−894.
(36) Moreira, J. N., Ishida, T., Gaspar, R., and Allen, T. M. (2002) Use of the post-insertion technique to insert peptide ligands into pre-formed stealth liposomes with retention of binding activity and cytotoxicity. *Pharm. Res. 19*, 265−269.
(37) Goins, B., Bao, A., and Phillips, W. T. (2010) Techniques for loading technetium-99m and rhenium-186/188 radionuclides into pre-formed liposomes for diagnostic imaging and radionuclide therapy. *Methods Mol. Biol. 606*, 469−491.
(38) Li, S., Goins, B., Phillips, W. T., and Bao, A. (2011) Remote-loading labeling of liposomes with ^{99m}Tc-BMEDA and its stability evaluation: effects of lipid formulation and pH/chemical gradient. *J. Liposome Res. 21*, 17−27.
(39) Bao, A., Phillips, W. T., Goins, B., McGuff, H. S., Zheng, X., Woolley, F. R., Natarajan, M., Santoyo, C., Miller, F. R., and Otto, R. A. (2006) Setup and characterization of a human head and neck squamous cell carcinoma xenograft model in nude rats. *Otolaryngol. Head Neck Surg. 135*, 583−587.
(40) Gabizon, A., Shmeeda, H., and Barenholz, Y. (2003) Pharmacokinetics of pegylated liposomal doxorubicin: Review of animal and human studies. *Clin. Pharmacokinet. 42*, 419−436.
(41) Fenske, D. B., and Cullis, P. R. (2005) Entrapment of small molecules and nucleic acid-based drugs in liposomes. *Methods Enzymol. 391*, 7−40.
(42) Marshall, M. V., Draney, D., Sevick-Muraca, E. M., and Olive, D. M. (2010) Single-dose intravenous toxicity study of IRDye 800CW in Sprague-Dawley rats. *Mol. Imaging Biol. 12*, 583−594.
(43) Krauze, M. T., Forsayeth, J., Park, J. W., and Bankiewicz, K. S. (2006) Real-time imaging and quantification of brain delivery of liposomes. *Pharm. Res. 23*, 2493−2504.
(44) Hossann, M., Wang, T., Wiggenhorn, M., Schmidt, R., Zengerle, A., Winter, G., Eibl, H., Peller, M., Reiser, M., Issels, R. D., and Lindner, L. H. (2010) Size of thermosensitive liposomes influences content release. *J. Controlled Release 147*, 436−443.
(45) Grange, C., Geninatti-Crich, S., Esposito, G., Alberti, D., Tei, L., Bussolati, B., Aime, S., and Camussi, G. (2010) Combined delivery and magnetic resonance imaging of neural cell adhesion molecule-targeted doxorubicin-containing liposomes in experimentally induced Kaposi's sarcoma. *Cancer Res. 70*, 2180−2190.
(46) De Smet, M., Heijman, E., Langereis, S., Hijnen, N. M., and Grüll, H. (2011) Magnetic resonance imaging of high intensity focused ultrasound mediated drug delivery from temperature-sensitive liposomes: an in vivo proof-of-concept study. *J. Controlled Release 150*, 102−110.
(47) Trubetskoy, V. S., Cannillo, J. A., Milshtein, A., Wolf, G. L., and Torchilin, V. P. (1995) Controlled delivery of Gd-containing liposomes to lymph nodes: surface modification may enhance MRI contrast properties. *Magn. Reson. Imaging 13*, 31−37.
(48) Weissig, V. V., Babich, J., and Torchilin, V. V. (2000) Long-circulating gadolinium-loaded liposomes: potential use for magnetic resonance imaging of the blood pool. *Colloids Surf., B: Biointerfaces 18*, 293−299.
(49) Bui, T., Stevenson, J., Hoekman, J., Zhang, S., Maravilla, K., and Ho, R. J. (2010) Novel Gd nanoparticles enhance vascular contrast for high-resolution magnetic resonance imaging. *PLoS One 5*, pii: e13082.
(50) Viglianti, B. L., Abraham, S. A., Michelich, C. R., Yarmolenko, P. S., MacFall, J. R., Bally, M. B., and Dewhirst, M. W. (2004) In vivo monitoring of tissue pharmacokinetics of liposome/drug using MRI: illustration of targeted delivery. *Magn. Reson. Med. 51*, 1153−1162.
(51) Viglianti, B. L., Ponce, A. M., Michelich, C. R., Yu, D., Abraham, S. A., Sanders, L., Yarmolenko, P. S., Schroeder, T., MacFall, J. R., Barboriak, D. P., Colvin, O. M., Bally, M. B., and Dewhirst, M. W. (2006) Chemodosimetry of in vivo tumor liposomal drug concentration using MRI. *Magn. Reson. Med. 56*, 1011−1018.
(52) Ponce, A. M., Viglianti, B. L., Yu, D., Yarmolenko, P. S., Michelich, C. R., Woo, J., Bally, M. B., and Dewhirst, M. W. (2007) Magnetic resonance imaging of temperature-sensitive liposome release: drug dose painting and antitumor effects. *J. Natl. Cancer Inst. 99*, 53−63.
(53) Silva, A. C., Lee, J. H., Aoki, I., and Koretsky, A. P. (2004) Manganese-enhanced magnetic resonance imaging (MEMRI): methodological and practical considerations. *NMR Biomed. 17*, 532−543.
(54) Morcos, S. K. (2008) Extracellular gadolinium contrast agents: differences in stability. *Eur. J. Radiol. 66*, 175−179.
(55) Petersen, A. L., Binderup, T., Rasmussen, P., Henriksen, J. R., Elema, D. R., Kjær, A., and Andresen, T. L. (2011) ^{64}Cu loaded liposomes as positron emission tomography imaging agents. *Biomaterials 32*, 2334−2341.
(56) Seo, J. W., Zhang, H., Kukis, D. L., Meares, C. F., and Ferrara, K. W. (2008) A novel method to label preformed liposomes with ^{64}Cu for positron emission tomography (PET) imaging. *Bioconjugate Chem. 19*, 2577−2584.
(57) Andreozzi, E., Seo, J. W., Ferrara, K., and Louie, A. (2011) Novel method to label solid lipid nanoparticles with ^{64}Cu for positron emission tomography imaging. *Bioconjugate Chem. 22*, 808−818.
(58) Uusijärvi, H., Bernhardt, P., Rösch, F., Maecke, H. R., and Forssell-Aronsson, E. (2006) Electron- and positron-emitting radio-

lanthanides for therapy: aspects of dosimetry and production. *J. Nucl. Med. 47*, 807−814.
(59) Howell, R. W., Rao, D. V., and Sastry, K. S. (1989) Macroscopic dosimetry for radioimmunotherapy: nonuniform activity distributions in solid tumours. *Med. Phys. 16*, 66−74.
(60) Novak-Hofer, I., and Schubiger, P. A. (2002) Copper-67 as a therapeutic nuclide for radioimmunotherapy. *Eur. J. Nucl. Med. Mol. Imaging 29*, 821−830.

Bioconjugate Chemistry

Article

pubs.acs.org/bc

Derivatization of a Bioorthogonal Protected Trisaccharide Linker—Toward Multimodal Tools for Chemical Biology

Timmy Fyrner,[†] Karin Magnusson,[†] K. Peter R. Nilsson,[†] Per Hammarström,[†] Daniel Aili,[‡] and Peter Konradsson*,[†]

[†]Division of Chemistry and [‡]Division of Molecular Physics, IFM, Linköping University, SE-581 83 Linköping, Sweden

Supporting Information

ABSTRACT: When cross-linking biomolecules to surfaces or to other biomolecules, the use of appropriate spacer molecules is of great importance. Mimicking the naturally occurring spacer molecules will give further insight into their role and function, possibly unveil important issues regarding the importance of the specificity of carbohydrate-based anchor moieties, in e.g., glycoproteins and glycosylphosphatidylinositols. Herein, we present the synthesis of a lactoside-based trisaccharide, potentially suitable as a heterobifunctional bioorthogonal linker molecule whereon valuable chemical handles have been conjugated. An amino-derivative having thiol functionality shows promise as novel SPR-surfaces. Furthermore, the trisaccharide has been conjugated to a cholesterol moiety in combination with a fluorophore which successfully assemble on the cell surface in lipid microdomains, possibly lipid-rafts. Finally, a Cu^{I}-catalyzed azide−alkyne cycloaddition reaction (CuAAC) confirms the potential use of oligosaccharides as bioorthogonal linkers in chemical biology.

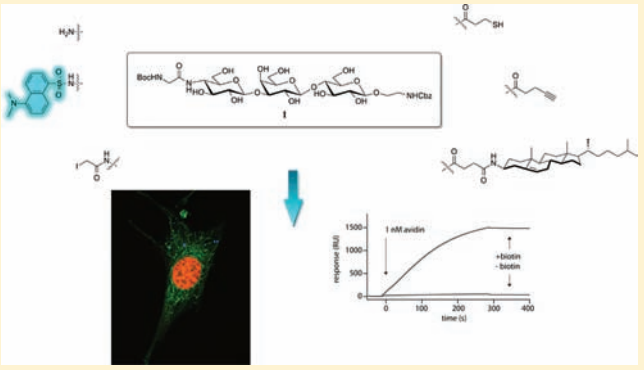

INTRODUCTION

To investigate biomolecules *in situ*, their functionality and possible applications, the choice of linker molecule is often focused on availability,[1,2] (i.e., commercially available or easily accessible via chemical synthesis) and bioorthogonality.[3] The understanding of the specific role of spacers, as well as the excavation of suitable bioavailable spacers have been an intensive area of research.[4−9] The use of oligo(ethylene) glycols (OEGs) as linker molecules have been shown to be fruitful in many fields.[10−13] However, OEGs have a rather high degree of variability in comparison to the naturally occurring oligosaccharides as glycosylphosphatidylinositols or lipopolysaccharides. Our interest is to investigate how a more rigid, rod-like[14] carbohydrate-based linker can be adequate as a cross-linking derivative. In spite of carbohydrates' abundance and biological significance, their use as biofunctional molecules in nanotechnology lags behind those of protein and nucleic acids,[15] mainly due to their complexity and challenging availability.[16] In surface plasmon resonace (SPR), however, a caboxymethylated polysaccharide (dextran) is often used to form a three-dimensional matrix on the sensor surface, enabled for conjugation.[17] The synthesized trisaccharide **1** (Figure 1)[18] has been utilized to generate a variety of cross-linking derivatives presenting reactive groups, e.g., (i) amino group for biotinylation,[19] (ii) thiol group for assembly upon gold surfaces,[20−22] (iii) alkyne residue for "click-chemistry" conjugation,[23−25] (iv) Dansyl for fluorescence microscopy, and (iv) *N*-cholesterol moiety as a lipid anchor.[26] Employing a orthogonally protected molecule enables conjugation and elongation in a great variety of sequences, independent of each other, thereby serving as an ideal framework for heterobifunctional cross-linking. In this work, we report such a heterobifunctional rod-like trisaccharide cross-linking molecule for applications in chemical biology. We foresee that future applications of these derivatives will entail, e.g., glyco-lipid−protein or glyco-lipid−fluorophore conjugates with variable linker lengths (tri-, penta-, and heptasaccharide moieties) to probe, e.g., for protein stability as a function of spacer length in relation to the cell membrane, biomembrane organization, and/or glyco-lipid distribution dependence.

RESULTS AND DISCUSSION

Synthesis. Starting from the known 3-β-Azido-5-cholestene **2**,[27] (Scheme 1) lipid-anchor derivative **5** was synthesized by reducing the azido-group to the corresponding amine using standard $NaBH_4/NiCl_2$ condition. The crude aminosteroid was further coupled to the mono-*tert*-butyl-succinate **3**[28] to give compound **4**. The *tert*-butyl was deprotected by refluxing with formic acid in diethyl ether giving the lipid anchor **5**.

The synthesis of the different conjugates commences from trisaccharide **1**, previously synthesized.[18] The thioacetylated derivative **7** (Scheme 2) was synthesized from **1** using catalytic hydrogenolysis followed by coupling with 3-acetylthio-

Received: April 5, 2012
Published: May 9, 2012

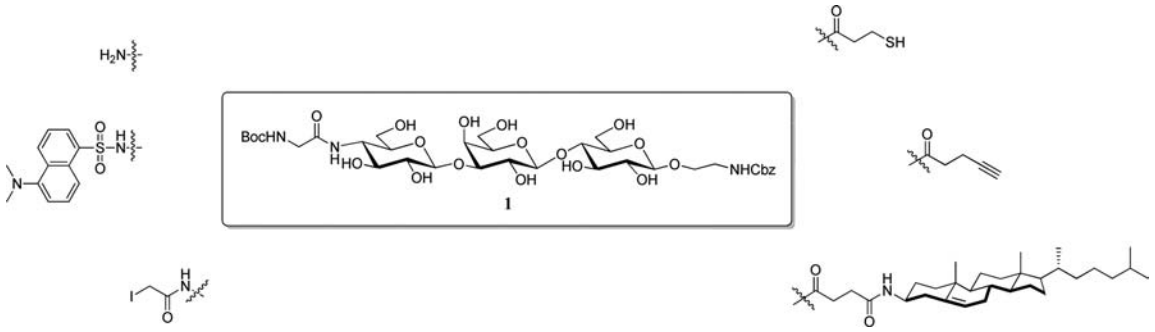

Figure 1. Target cross-linking trisaccharide, having chemically tailored properties to address a diversity of biophysical applications or biological systems.

Scheme 1[a]

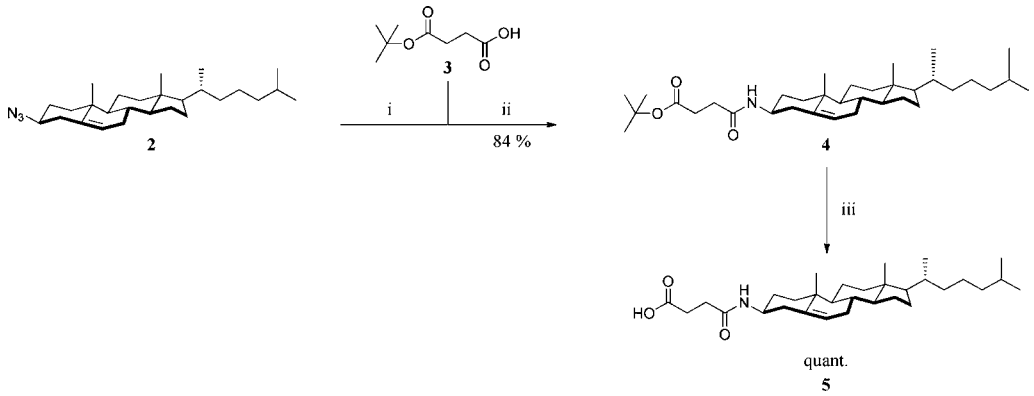

[a]Reagents and conditions: (i) $NaBH_4$, $NiCl_2{\cdot}6H_2O$ (cat.), $EtOH/CH_2Cl_2$; (ii) **3**,[28] DIPEA TBTU, DMF; (iii) HCOOH, Et_2O, reflux.

Scheme 2[a]

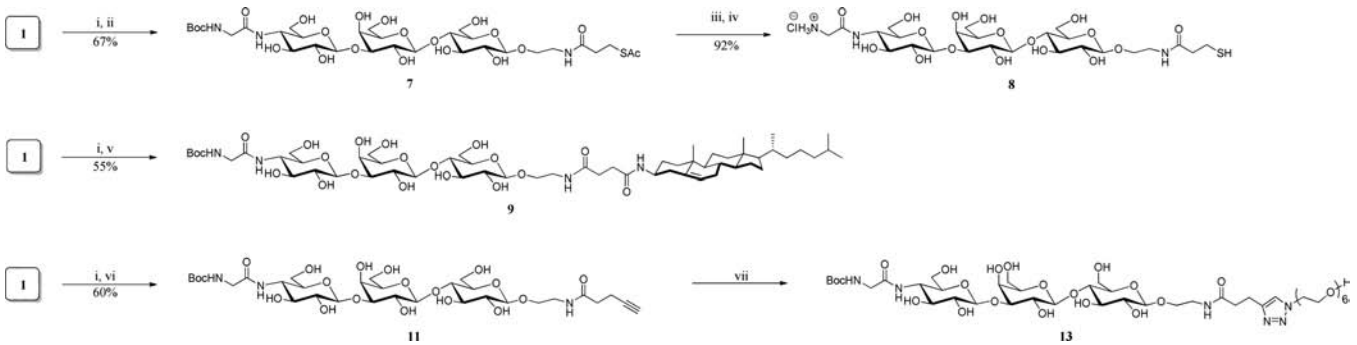

[a]Reagents and conditions: (i) Pd/C (10%), H_2 (g), MeOH; (ii) **6**,[29] $NaHCO_3$ (s), $MeOH/H_2O$ (1:1); (iii) NaOMe, MeOH; (iv) HCl 1 M (aq.); (v) **5**, 0.5 M HOAt (DMF), *N*-methylmorpholine, EDC·HCl, MeOH; (vi) **10**,[30] $NaHCO_3$ (s), $MeOH/H_2O$ (1:1); (vii) **12**, $CuSO_4{\cdot}5H_2O$, sodium ascorbate.

propionic acid *N*-hydroxysuccinimide ester **6**.[29] A two-step deprotection procedure comprising a Zemplén deacetylation followed by an acid deprotection of the *N*-Boc using 1 M HCl (aq.) yielded the target compound **8**. The lipid-anchoring derivative **9** was synthesized by hydrogenolysis and subsequent coupling with steroid derivative **5** using the same method as optimized earlier.[18] It should be noted that the amphiphilic character of compound **9** is reflected by its low solubility in solvents for standard purifications. In our experience, a highly concentrated solution can only be acquired using either MeOH or a combination of solvent, i.e., chloroform/MeOH/H_2O (7:4:1).

The alkyne derivative **11** was synthesized using protocols in accordance as for the earlier mentioned compounds by hydrogenolysis followed by coupling with 4-pentynoic acid *N*-hydroxysuccinimide ester **10**.[30] In comparison, yields for compound **7** and **11** were improved using the preactivated N-hydroxysuccinimide ester rather than the corresponding carboxylic acids.

A Cu^I-catalyzed azide−alkyne cycloaddition (CuAAC) with azidohexa(ethylene) glycol **12**,[32] was performed on a 2 mg scale; hence, characterization data are incomplete. The following compounds **14** and **16** have been synthesized on a 1−2 mg scale (Scheme 3), i.e., full characterization data not available, as a possible lipid raft dye or for protein conjugation

dx.doi.org/10.1021/bc300160a | *Bioconjugate Chem.* 2012, 23, 1333−1340

Scheme 3[a]

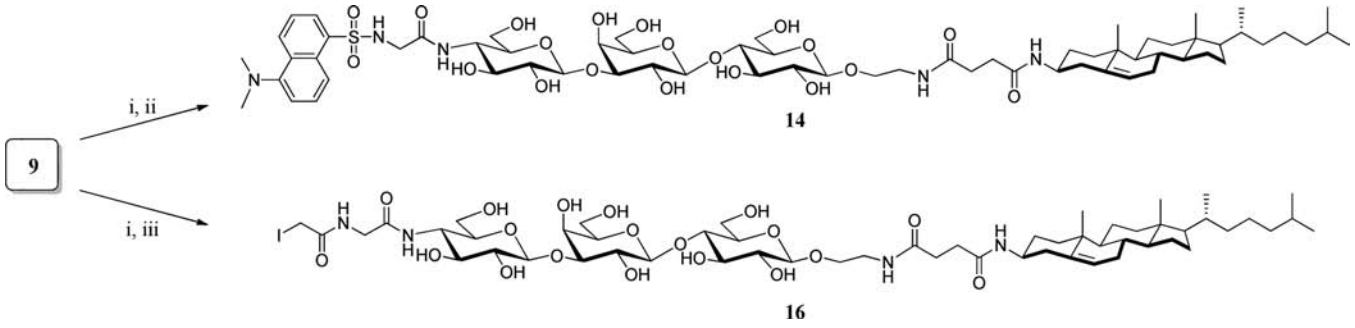

[a]Reagents and conditions: (i) 1 M HCl (aq.), MeOH; (ii) Dansyl chloride, $NaHCO_3$ (s), $MeOH/H_2O$ (1:1); (iii) **15**,[31] $NaHCO_3$ (s), $MeOH/H_2O$ (1:1).

studies, respectively. From intermediate **9**, the dansyl structure **14**, as well as the 2-iodoacetamido derivative **16**, was synthesized. The two-step conversion was commenced by a deprotection of **9** followed by subsequent coupling with dansyl chloride (→**14**) or iodoacetic acid *N*-hydroxysuccinimide ester **15**[31] to give target compound **16**.

Application of 8 for Surface Plasmon Resonance. The intention to improve and refine biosensors is of great interests. We set out to synthesize a bifunctional trisaccharide having both amine as well as thiol functionality **8** (Scheme 2). This derivative was successfully assembled onto gold surfaces and able to perform as a novel biosensor surface. The thiol moiety in compound **8** enabled formation of self-assembled monolayers (SAMs) on gold surfaces. Biotin-NHS was coupled to the terminal amine group in order to render a flexible biosensor surface. Infrared reflection absorption spectroscopy (IRAS) was employed to confirm the derivatization of the SAMs with biotin. No significant changes were observed in the fingerprint region after biotinylation, but a slight increase in the amide I band (1657 cm^{-1}) and the appearance of a new vibrational mode at 1711 cm^{-1} originating from the biotin C═O stretch indicate successful coupling (Figure 2). The ellipsometric thickness of SAMs of compound **8** was 15.6 ± 0.5 Å. After biotinylation, the thickness increased to 16.7 ± 0.2 Å.

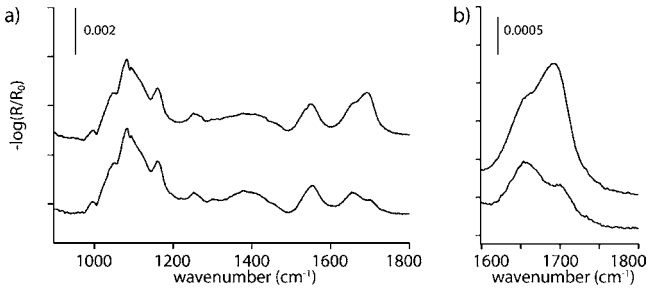

Figure 2. (a) IRAS spectra of the fingerprint and amide regions before (bottom) and after (top) biotinylation. (b) Magnified view of the amide I region.

Compound **8** was subsequently immobilized on SPR-gold substrates. After biotinylation, a 5 min injection of 1 nM avidin at a flow rate of 20 μL/min resulted in the binding of 1500 RU (Figure 3) corresponding to 1.5 ng/mm^2 (+biotin). No binding was observed in the reference channel pretreated with acetic acid *N*-hydroxysuccinimide[33] (−biotin). The surface was saturated with avidin after a second 5 min injection of 10 nM

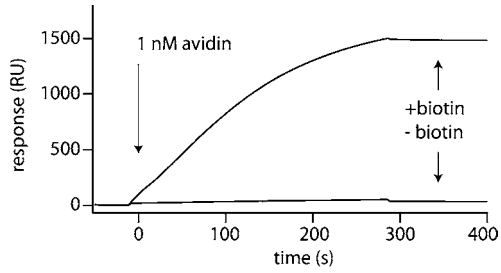

Figure 3. Sensorgram showing the binding of avidin to the biotinylated SAM.

avidin, resulting in an additional increase of 500 RU in the biotinylated channel (not shown).

Application of 14 for Selective Binding to Lipid Microdomains in Living Cells. To generate a molecular tool for studies of glyco-conjugated lipids and for understanding their molecular distributions, we have synthesized a cholesterol containing glycoside **9** (Scheme 2).[34] It was further derivatized with either a fluorophore (Dansyl) containing derivative **14**, for the monitoring of lipid-microdomains (lipid rafts) or an iodoacetamide derivative **16** (Scheme 3), for site-specific conjugation to cysteine residues in proteins.[35,36] It was shown by Peterson and co-workers that having an amide bond compared to a secondary amine on the *N*-cholesterol residue essentially abolished the internalization.[26] Hence, derivatives **14** and **16** should be predicted to accumulate on the cell surface.

To investigate the binding and distribution of **14** in live cells, we stained human fibroblasts with the probe. When adding **14** to living cells for 18 h of incubation, the probe clearly binds to a compartment of the cell (Figure 4a). Comparing with different compartments of the cell, such as the nucleus, mitochondria, and α-tubulin, the probe seems to attach exclusively to the cell membrane. The staining was uneven and punctuated, likely reflecting binding to lipid-microdomains (lipid-rafts). The staining pattern was very similar to that reported previously for lipid-rafts on fibroblasts.[37] An analogous staining procedure was also performed using free Dansyl (5-dimethylamino)-1-naphthalenesulfonamide (DNSA) instead of **14**. No cellular staining was observed from DNSA even though a 15-fold higher staining concentration than that used for **14** was employed (not presented herein). It is most plausible that the cholesterol tag of **14** interacts through hydrophobic partitioning with the target and hence shows specificity toward the membrane lipid bilayer. Lipid rafts are compartments on the cell surface enriched in monosialotetrahexosylganglioside

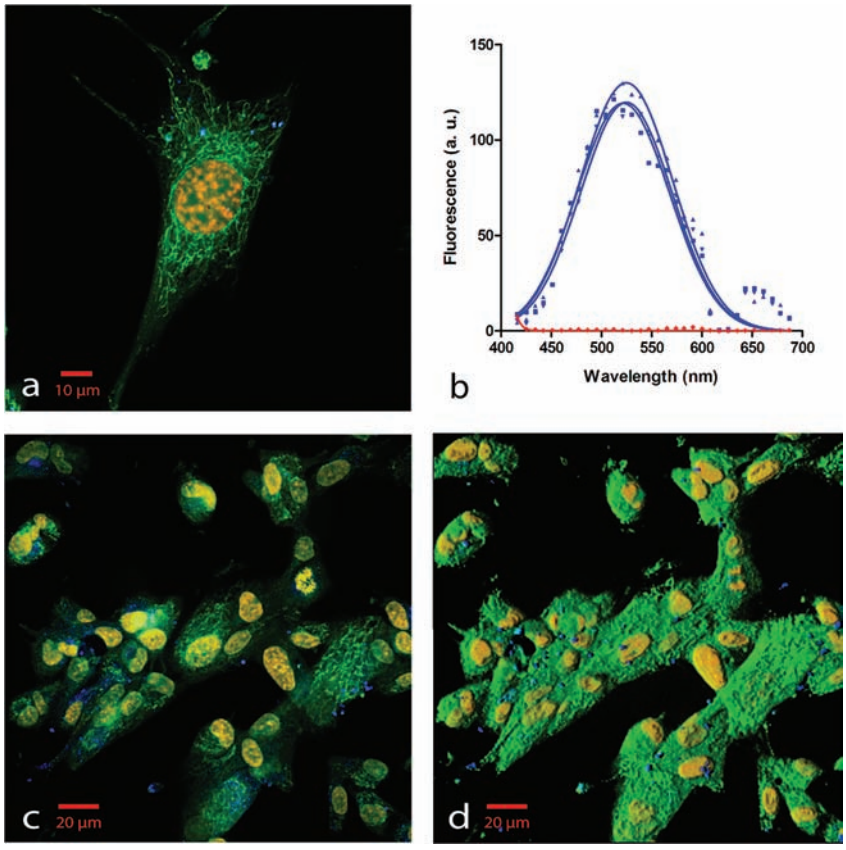

Figure 4. Compound **14** stains lipid-microdomains in living cells. Cultured lung fibroblasts were incubated with 0.3 μM of **14** for 18 h. (a) Single fibroblast with small punctuate microdomains visible at the top of the cell (blue), counterstaining of cells were performed using Mitotracker (green) and ToPro3 (red). (b) Fluorescence emission spectra of punctuate microdomains from three regions of interest showing emission peaks at 521.6–524.8 nm (blue). Background emission was very low (red). (c) Confocal microscope image showing clustered fibroblasts stained as in (a). (d) Computer-generated surface enhanced (3D) image of (c).

(GM1), cholesterol, and GPI-anchored proteins.[38] Hence, specificity of **14** toward lipid-rafts can be assumed and is possibly also reinforced through glycolic interactions with GM1. The cell staining of **14** was weaker in the antitubulin antibody staining protocol (not presented herein), which could be a result of the probe being washed away during several incubation steps which were performed in the presence of the detergent Triton-X.

With fluorescence microspectroscopy, the emission spectrum of the punctuate microdomains where **14** was accumulated showed typical Dansyl emission spectra with emission peaks at 523.7 ± 1.5 nm (Figure 4b). This emission peak distribution of compound **14** reflects a Stokes shift of the probe to reflect a slightly hydrophobic environment.[39] This shows that the probe, when enriched within lipid microdomains on the cell surface, is partially shielded from water. Using confocal scanning fluorescence microscopy, we found that the fluorescently tagged compound **14** showed prevalent labeling of microdomains in clustered fibroblasts (Figure 4c,d), which was more pronounced than for solitary cells (c.f., Figure 4a and Figure 4c,d). This could indicate that lipid rafts are up-regulated during cell–cell interactions.

Application of 11 for Click Chemistry. Finally, to ensure the possible usefulness of derivative **11** (Scheme 2), bearing an alkyne functionality for further "click chemistry" conjugations, a test reaction (2 mg) was performed with hexa(ethylene) glycol **12** having an azido-functionality.[32] The result displayed complete consumption of the alkyne derivative **11** (according to MALDI-TOF) which establishes the potential use of oligosaccharides as spacer molecules as an alternative to the commonly used oligo(ethylene) glycols.

■ CONCLUSION

In conclusion, an orthogonally protected trisaccharide has been demonstrated as a general spacer/linker molecule by conjugation with different chemical functionalities. It has been illustrated that defined carbohydrate-based compounds have potential use in biosensing applications, i.e., novel SPR surfaces. The result from live cell incubation experiments indicates that the trisaccharide-based linker incorporates into cell surfaces, and was specifically enriched in microdomains. These findings also show promise for conjugating biomolecules onto cell surfaces, thereby mimicking glycoproteins. Using compound **14** as an example of lipid-raft specificity, this opens up the possibility of using compound **16** as either a "fishing hook" for protein conjugation in living cells or a tool for directed interaction of a recombinant protein toward these cellular structures. Furthermore, a successful "click chemistry" cycloaddition confirms the potential of using oligosaccharides as unique bioorthogonal cross-linking derivatives.

■ EXPERIMENTAL SECTION

Synthesis. *General.* CH_2Cl_2 and toluene was distilled over calcium hydride and collected onto predried 4 Å MS. Thin layer chromatography (TLC) was carried out on Merck 60 F_{254}

plates and visualized by UV light and/or developed with PAA [EtOH (95%, 744 mL), H_2SO_4 (conc., 27.6 mL), AcOH (100%, 8.4 mL), *p*-anisaldehyde (20.4 mL)]. Flash column chromatography (FC) was carried out on silica gel Merck 60 (40−63 μm). Reverse-phase chromatography (RP) was carried out on Merck LiChroprep (RP-18). Gel permeation was performed using Sephadex LH-20. Dialysis was performed using Spectra/Por MWCO = 500 or MWCO = 1000. Proton nuclear magnetic resonance (^{1}H) and carbon nuclear magnetic resonance (^{13}C) was recorded on a Varian 300 MHz spectrometer; multiplicities are quoted as singlet (s), doublet (d), doublet of doublets (dd), triplet (t), apparent doublet (ad), apparent triplet (at). ESI-MS (recorded at Medivir AB, Huddinge, Sweden) was performed on a Water Synapt HDMS instrument equipped with electrospray interface. Matrix-assisted laser desorption ionization − time of flight (MALDI-TOF) mass spectroscopy was recorded on a Voyager-DE STR Biochemistry Workstation in a positive mode using using α-cyano-4-hydroxycinnamic acid (CHCA) as matrix. Optical measurements were recorded at 20 °C with a Perkin-Elmer 141 polarimeter. FT-IR was recorded on a Perkin-Elmer Spectrum 1000 using KBr pellets; appearances are quoted as strong (s), medium (m), and weak (w). Melting points were recorded on a Stuart melting point apparatus.

***tert*-Butyl-*N*-succinyl-3β-amino-5-cholestene (4).** The 3-β-Azido-5-cholestene[27] **2** (1.00 g, 2.43 mmol) was dissolved in EtOH/CH_2Cl_2 (20 mL, 3:1) whereupon $NaBH_4$ (180 mg, 4.86 mmol) and $NiCl_2{\cdot}6H_2O$ (cat.) were added. After 1 h, the solution was diluted with CH_2Cl_2 and washed with NaCl (sat. aq.), dried, and concentrated. Without further purification, the amine was dissolved in DMF (10 mL) whereupon mono-*tert*-butyl-succinate **3**[28] (850 mg, 4.86 mmol), DIPEA (1.70 mL, 9.72 mmol), and TBTU (1.56 g, 4.86 mmol) were added. After 1 h, the solution was diluted with toluene and washed sequentially with NaCl (sat. aq.), $NaHCO_3$ (sat. aq.), dried, and concentrated. FC (toluene/EtOAc 4:1) followed by crystallization from MeOH afforded **4** (1.11 g, 2.04 mmol, 84%) as white needles. R_f = 0.57 (toluene/EtOAc 2:1); mp = 146−148 °C (MeOH); $[\alpha]_D$ − 35 (c 1, $CHCl_3$); IR (KBr) $\nu_{max}cm^{-1}$: 2934 (s), 1732 (s), 1644 (s), 1547 (s), 1366 (m), 1153 (s); NMR: ^{13}C (75.4 MHz, $CDCl_3$) δ 11.9, 18.8, 19.4, 22.6, 22.9, 28.1, 28.2, 28.3, 29.2, 31.1, 31.6, 31.9, 31.9, 35.9, 39.6, 42.4, 49.7, 50.2, 56.2, 56.8, 80.7, 121.9, 140.4, 170.8, 172.4 (overlaps occur in spectra); ^{1}H (300 MHz, $CDCl_3$): δ 0.67 (s, 3H), 0.85 (d, 3H, *J* = 0.6 Hz), 0.87 (d, 3H, *J* = 0.6 Hz), 0.91 (d, 3H, *J* = 6.3 Hz), 0.94−1.58 (m, 33H), 1.76−1.86 (m, 3H), 1.90−2.11 (m, 3H), 2.25−2.31 (m, 1H), 2.38 (t, 2H, *J* = 6.7 Hz), 2.56 (t, 2H, *J* = 6.7 Hz), 3.60−3.74 (m, 1H), 5.33−5.35 (m, 1H), 5.54 (d, 1H, *J* = 8.1 Hz); ESI-MS: $[M+H]^+$ calcd for $C_{35}H_{60}NO_3$, 542.4495; found 542.4505.

***N*-Succinyl-3β-amino-5-cholestene (5).** The *tert*-butyl-succinyl-3β-amino-5-cholestene **4** (0.50 g, 0.92 mmol) was added to a solution of formic acid/Et_2O (1:1, 20 mL) and heated to reflux. After 1 h, the reaction mixture was evaporated and coconcentrated subsequently with toluene affording **5** (0.44 g, 0.92 mmol, quant.) as a white solid. R_f = 0.66 (EtOAc/MeOH 4:1); $[\alpha]_D$ − 20 (c 0.1, chloroform/MeOH/H_2O 7:4:1); IR (KBr) $\nu_{max}cm^{-1}$: 2963 (m), 2936 (s), 1731 (s), 1625 (s), 1555 (s), 1187 (m), 1158 (s), 822 (w); NMR: ^{13}C (75.4 MHz, $CDCl_3$/CD_3OD 9:1) δ 11.9, 18.8, 19.4, 21.0, 22.6, 22.8, 23.9, 24.3, 28.1, 28.3, 28.9, 29.9, 31.1, 31.9, 31.9, 35.9, 36.3, 36.6, 37.9, 39.0, 39.6, 39.8, 42.4, 49.9, 50.2, 56.2, 56.8, 122.0, 140.3, 171.7, 175.3; ^{1}H (300 MHz, $CDCl_3$/CD_3OD 9:1): δ 0.68 (s, 3H), 0.86 (d, 3H, *J* = 1.3 Hz), 0.88 (d, 3H, *J* = 1.3 Hz), 0.92 (d, 3H, *J* = 6.4 Hz), 0.95−1.63 (m, 24H), 1.78−1.88 (m, 3H), 1.92−2.06 (m, 2H), 2.10−2.15 (m, 1H), 2.23−2.30 (m, 1H), 2.44 (d, 2H, *J* = 6.8 Hz), 2.63 (d, 2H, *J* = 6.8 Hz), 3.58−3.68 (m, 1H), 5.34−5.37 (m, 1H); ESI-MS: $[M+H]^+$ calcd for $C_{31}H_{52}NO_3$, 486.3869; found 486.3844.

***N*-(3-Acetylthio-propanoyl)-2-aminoethyl (4-Deoxy-4-*N*-tert-butyloxycarbonyl-glycyl-glucopyranosyl)-(1→3)-(β-D-galactopyranosyl)-(1→4)-β-D-glucopyranoside (7).** To a solution of **1** (0.15 g, 0.18 mmol) in MeOH (5 mL), 10% Pd/C was added and stirred for 4 h under H_2(g) atomsphere (1 atm) followed by filtration though Celite and evaporation. The residue was dissolved in MeOH/H_2O (10 mL) whereupon $NaHCO_3$ (s) (0.15 g, 0.18 mmol) and 3-acetylthio-propionic acid *N*-hydroxysuccinimide ester **6**[29] (46 mg, 0.19 mmol) were added and stirred overnight. The solution was neutralized with Dowex-H^+, filtered, and evaporated. RP (H_2O → H_2O/MeOH 1:1) gave **7** (0.10 g, 0.12 mmol, 67%) as a white solid. R_f = 0.69 (chloroform/MeOH/H_2O 7:4:1); $[\alpha]_D$ - 10 (c 0.1, H_2O); IR (KBr) $\nu_{max}cm^{-1}$: 2933 (w), 1693 (s), 1546 (m), 1368 (w), 1160 (w), 1072 (s); NMR: ^{13}C (75.4 MHz, CD_3OD): δ 25.9, 28.7, 30.5, 36.6, 40.6, 44.8, 53.2, 62.0, 62.5, 62.6, 69.6, 69.6, 71.6, 74.6, 74.8, 75.9, 76.3, 76.4, 76.7, 80.8, 84.5, 104.3, 104.7, 105.6, 158.5, 173.5, 173.7, 197.2, (several overlaps occur in spectra); ^{1}H (300 MHz, CD_3OD): δ 1.46 (s, 9H), 2.32 (s, 3H), 2.50 (t, 2H, *J* = 7.0 Hz), 3.11 (t, 2H, *J* = 7.0 Hz), 3.25−3.90 (m, 23H), 4.10 (ad, 1H, *J* = 3.0 Hz), 4.33 (d, 1H, *J* = 8.0 Hz), 4.43 (d, 1H, *J* = 7.6 Hz), 4.56 (d, 1H, *J* = 7.8 Hz); ESI-MS: $[M+H]^+$ calcd for $C_{32}H_{56}N_3O_{20}S$, 834.3100; found 834.3096.

***N*-(3-Thio-propanoyl)-2-aminoethyl (4-deoxy-4-*N*-glycyl-glucopyranosyl)-(1→3)-(β-D-galactopyranosyl)-(1→4)-β-D-glucopyranosyl-ammonium hydrochloride (8).** To a solution of **7** (50 mg, 60 μmol) in MeOH (5 mL), NaOMe (7 mg, 0.12 mmol) was added. After 1.5 h, the mixture was neutralized with Dowex-H^+, filtered, and evaporated. RP (H_2O → H_2O/MeOH (1:1)) gave the thiol which was used subsequently in the following step. The deacetylated compound was dissolved in H_2O (5 mL) whereupon 1 M HCl (0.1 mL) was added. After 1 h, the solution was evaporated and coconcentrated repeatedly with MeOH giving the title compound **8** (40 mg, 55 mmol, 92%) as an off-white solid. R_f = not available; $[\alpha]_D$ + 6 (c 0.1, H_2O); IR (KBr) $\nu_{max}cm^{-1}$: 2882 (w), 1692 (s), 1643 (s), 1648 (s), 1566 (m), 1434 (m), 1158 (w), 1071 (s), 1021 (s), 950 (s); NMR: ^{13}C (75.4 MHz, CD_3OD): δ 19.8, 39.2, 39.6, 40.4, 51.8, 60.3, 60.9, 61.0, 68.3, 68.4, 70.2, 73.2, 73.4, 74.2, 74.7, 75.0, 75.2, 79.0, 82.7, 102.7, 103.0, 103.9, 167.0, 173.2 (overlap occur in spectra); ^{1}H (300 MHz, CD_3OD): δ 2.54 (t, 2H, *J* = 6.7 Hz), 2.76 (t, 2H, *J* = 6.7 Hz), 3.33−3.98 (m, 23H), 4.12−4.13 (m, 1H), 4.39 (d, 1H, *J* = 7.8 Hz), 4.46 (d, 1H, *J* = 7.6 Hz), 4.63 (d, 1H, *J* = 7.7 Hz); ESI-MS: $[M+H]^+$ calcd for $C_{25}H_{46}N_3O_{17}S$, 692.2470; found 692.2491.

3β-Amino-5-cholestene-*N*,*N*-succinyl-2-*N*-aminoethyl (4-Deoxy-4-*N*-tert-butyloxycarbonyl-glycyl-glucopyranosyl)-(1→3)-(β-D-galactopyranosyl)-(1→4)-(β-D-glucopyranoside (9). Compound **1** (42 mg, 50 μmol) was dissolved in MeOH (10 mL) followed by the addition of Pd/C (10%, cat.). The mixture was stirred under H_2 pressure (1 atm) for 2 h, then filtered through Celite and evaporated. The residue was dissolved in MeOH (10 mL), followed by the addition of **5** (26 mg, 53 μmol), 0.5 M (DMF) HOAt (10 μL, 5 μmol), *N*-methylmorpholine (6 μL, 53 μmol), and stirred for 10 min

whereupon EDC·HCl (10 mg, 53 μmol) were added and stirred overnight. The mixture was evaporated and the obtained residue was purified on a sephadex LH-20 column using MeOH to give **9** (32 mg, 27 μmol, 55%) as a white solid. R_f = 0.14 (EtOAc/MeOH/H_2O 7:1:0.5); $[\alpha]_D$ − 31 (c 0.1, chloroform/MeOH/H_2O 7:4:1); IR (KBr) $\nu_{max}cm^{-1}$: 2933 (s), 1643 (s), 1547 (s), 1367 (m), 1160 (m), 1074 (s); NMR: ^{13}C (75.4 MHz, $CDCl_3/CD_3OD/D_2O$ 7:4:1): δ 11.4, 18.2, 18.7, 20.6, 22.0, 22.2, 23.4, 23.9, 27.6, 27.8, 28.1, 29.3, 31.1, 31.2, 31.4, 31.5, 35.4, 35.8, 36.2, 37.6, 38.3, 39.0, 39.1, 39.4, 42.0, 43.3, 49.5, 49.9, 51.3, 55.8, 56.4, 60.2, 60.7, 60.8, 68.0, 68.2, 69.8, 72.7, 72.8, 73.8, 74.3, 74.6, 74.8, 74.9, 77.4, 78.8, 80.0, 82.6, 102.4, 102.7, 103.7, 121.3, 140.2, 156.8, 172.1, 173.4 (overlaps occur in spectra); ^1H (300 MHz, $CDCl_3/CD_3OD/D_2O$ 7:4:1): δ 0.41 (m, 3H), 0.57−1.35 (m, 40H), 1.46−1.76 (m, 6H), 1.82−1.97 (m, 3H), 2.12−2.22 (m, 4H), 2.34−2.49 (m, 1H), 2.96−3.72 (m, 23H), 3.81 (ad, 1H, *J* = 2.9 Hz), 4.05−4.1 (m, 2H), 4.29 (d, 1H, *J* = 7.8 Hz), 5.06 (m, 1H); ESI-MS: $[M+H]^+$ calcd for $C_{58}H_{99}N_4O_{20}$, 1171.6775; found 1171.6777.

***N*-(4-Pentynoyl)-2-aminoethyl (4-Deoxy-4-*N*-*tert*-butyloxycarbonyl-glycyl-glucopyranosyl)-(1→3)-(β-D-galactopyranosyl)-(1→4)-β-D-glucopyranoside (11).** Compound **1** (38 mg, 45 μmol) was dissolved in MeOH (2 mL) whereupon 10% Pd/C (cat.) was added. The solution was stirred for 3 h under H_2 (g) pressure (1 atm) followed by filtration though Celite and evaporation. The residue was dissolved in MeOH/H_2O (2 mL, 1:1) whereupon $NaHCO_3$(s) (10 mg, 0.12 mmol) and 4-pentynoic acid *N*-hydroxysuccinimide ester **10**[30] (10 mg, 47 μmol) were added and stirred overnight followed by concentration. RP (H_2O → H_2O/MeOH 1:1) gave **11** (21 mg, 26 μmol, 60%) as a white solid. R_f = 0.73 (Chloroform/MeOH/H_2O 7:4:1); $[\alpha]_D$ + 3 (c 0.1, H_2O); IR (KBr) $\nu_{max}cm^{-1}$: 2933 (w), 1702 (s), 1692 (s), 1660 (s), 1552 (s), 1369 (m), 1159 (m), 1073 (s); NMR: ^{13}C (75.4 MHz, CD_3OD): δ 15.7, 28.7, 36.0, 40.6, 44.8, 53.2, 61.9, 62.5, 62.6, 69.6, 69.7, 71.6, 74.6, 74.7, 75.8, 76.2, 76.4, 76.7, 76.8, 80.7, 81.0 84.4, 104.3, 104.6, 105.5, 158.6, 173.6, 174.2 (overlaps occur in spectra); ^1H (300 MHz, CD_3OD): δ 1.45 (s, 9H), 2.37−2.49 (m, 4H), 3.24−3.94 (m, 24H), 4.09 (ad, 1H, *J* = 2.9 Hz), 4.32 (d, 1H, *J* = 7.7 Hz), 4.42 (d, 1H, *J* = 7.6 Hz), 4.55 (d, 1H, *J* = 7.8 Hz); ESI-MS: $[M+H]^+$ calcd for $C_{32}H_{54}N_3O_{19}$, 784.3274; found 784.3236.

***N*-[(4-Propanoyl)-2-aminoethyl [(4-deoxy-4-*N*-*tert*-butyloxycarbonyl-glycyl-glucopyranosyl)-(1→3)-(β-D-galactopyranosyl)-(1→4)-β-D-glucopyranosyl]-1*H*-1,2,3-triazol-1-yl-hexa(ethylene) glycol (13).** The alkyne-derivative **11** (2 mg, 3 μmol) was dissolved in H_2O/MeOH (1.5 mL, 2:1) whereupon azidohexa(ethylene) glycol **12**[32] (1 mg, 3 μmol), $CuSO_4·5H_2O$ (6 mg, 0.02 mmol), and sodium ascorbate (2 mg, 0.01 mmol) were added and stirred overnight. According to MALDI-TOF, complete consumption of alkyne **11** was detected to give compound **13**. MALDI-TOF (CHCA): $[M + Na]^+$ calcd for $C_{44}H_{78}NaO_{25}$, 1113.50; found 1113.32.

3β-Amino-5-cholestene-*N*,*N*-succinyl-2-*N*-aminoethyl [4-Deoxy-4-*N*-(5-(dimethylamino)naphthalene-1-sulfonyl)-glycyl-glucopyranosyl]-(1→3)-(β-D-galactopyranosyl)-(1→4)-(β-D-glucopyranoside (14). To a solution of **9** (1 mg, 0.9 μmol) in MeOH (2 mL), 1 M HCl (aq.) (10 μL) was added. After 15 min, the solution was evaporated and co-concentrated repeatedly with MeOH. Without further purification the amine was dissolved in H_2O/MeOH (2 mL, 1:1) whereupon $NaHCO_3$ (s) (2 mg, 0.02 mmol) and Dansylchloride (3 mg, 0.01 mmol) were added and stirred overnight. The mixture was diluted in H_2O (15 mL) and purified with dialysis (MWCO = 1000) over 3 days in the dark (4 × 2 L, H_2O) followed by evaporation. R_f = 0.80 (chloroform/MeOH/H_2O 7:4:1); ESI-MS: $[M+H]^+$ calcd for $C_{65}H_{102}N_5O_{20}S$, 1304.6761; found 1304.6731.

3β-Amino-5-cholestene-*N*,*N*-succinyl-2-*N*-aminoethyl [4-deoxy-4-*N*-(2-iodoacetyl)-glycyl-glucopyranosyl]-(1→3)-(β-D-galactopyranosyl)-(1→4)-(β-D-glucopyranoside (16). To a solution of **9** (1 mg, 1 μmol) in MeOH (2 mL), 1 M HCl (aq.) (10 μL) was added. After 15 min the solution was evaporated and co-concentrated repeatedly with MeOH. Without further purification the amine was dissolved in H_2O/MeOH (2 mL, 1:1) whereupon $NaHCO_3$ (s) (2 mg, 0.02 mmol) and iodoacetic acid *N*-hydroxysuccinimide ester **15**[31] (3 mg, 0.01 mmol) were added and stirred overnight. The mixture was diluted in H_2O (4 mL) and purified with dialysis (MWCO = 500) over 3 days in the dark (4 × 2 L, H_2O) followed by evaporation. R_f = 0.74 (chloroform/MeOH/H_2O 7:4:1); ESI-MS: $[M+H]^+$ calcd for $C_{55}H_{92}IN_4O_{19}$, 1239.532; found 1239.5408.

Gold Surface Preparation and Characterization. SAMs for IRAS and ellipsometry were prepared on gold-coated pieces of silicon wafers. A wafer was cut into 40 × 20 mm^2 pieces, cleaned in a mixture of H_2O, 30% H_2O_2, and 25% NH_3 in a 5:1:1 volume ratio, at 80 C for 10 min (TL1-cleaning), rinsed with Milli-Q (MQ) water, and then blown dry with nitrogen gas. The pieces were mounted in a custom-built electron-beam evaporation system with a base pressure of about 10^{-9} Torr, where a 25 Å Ti layer was deposited immediately before a 2000 Å gold layer. Gold-coated glass slides for SPR were obtained from GE Healthcare. Gold surfaces were TL1-cleaned before 24 h incubation in 100 μM aqueous solutions of the oligosaccharide. After incubation, the SAMs were rinsed with water, sonicated for 2 min, rinsed again, and finally dried before characterization.

IRAS spectra were recorded using a Bruker IFS 66 system, equipped with a liquid nitrogen cooled mercury cadmium telluride (MCT) detector unit and a grazing angle (85°) infrared reflection accessory. The measurement chamber was continuously purged with nitrogen gas during the measurements to reduce the amount of interfering water. 3000 scans were collected at a resolution of 2 cm^{-1}. Before Fourier transformation a three-term Blackmann-Harris apodization function was applied to the interferrograms. Deuterated hexadecanthiol ($HS(CD_2)_{15}CD_3$) immobilized on gold was used as a reference to record the background spectrum.

Null-ellipsometric measurements were conducted on an automatic Rudolph Research AutoEL III ellipsometer with a He−Ne laser light source operating at 632.8 nm at an angle of incidence of 70°. An optical model based on isotropic optical constants for the peptide layer $N_{pep} = n + ik = 1.50$, with *n* = refractive index and *k* = extinction coefficient, was used for the evaluation of the film thickness. Results from at least five measurement spots for each sample were averaged.

Sensorgrams were recorded by a Biacore 3000 instrument (GE Healthcare, Sweden) operating at a wavelength of 760 nm and equipped with four flow channels. The temperature was 25 °C and HBS-EP (10 mM hepes, 0.15 M NaCl, 3 mM EDTA, 0.005% surfactant P20, pH 7.4, from GE Healthcare) was used as a running buffer. Avidin from hen egg white (Thermo Scientific) and (+)-Biotin *N*-hydroxysuccinimide ester (Sigma Aldrich) were used.

Cell Biology. *Cell Culture.* MRC-5 cells (human lung fibroblast, ATCC CCL-171) were maintained in BIOAMF 2, complete medium, (Biological Industries; Beit Haemek, Israel) at 37 °C in humidified air with 5% CO_2 (g). These cells were seeded in a 12 well plate on round glass coverslips with a diameter of 18 mm.

Reagents. MitoTracker Orange CMTMRos, Alexa Fluor 488 antirabbit IgG (H+L) and ToPro3 were purchased from Invitrogen. Rabbit polyclonal antibody for alpha Tubulin (ab18251) was purchased from Abcam and Fluorescence Mounting Medium was from DAKO.

*Staining of Cells with **14** and Mitotracker.* Derivative **14** (96 μM, 50% DMSO in deionized water) was diluted with cell culture medium to 0.3 μM and added to the cells for 18 h. MitoTracker Orange CMTMRos (1 mM in DMSO) was diluted with cell culture medium to 150 nM. The diluted solution with compound **14** was discarded and the mitochondria were stained with the mitotracker solution for 30 min. After three washings with PBS (pH 7.3, Dubecco without Ca/Mg), the cells were fixed in 4% formaldehyde in 37 °C. The fixed cells were washed three times in PBS. ToPro3 (1 mM in DMSO) was diluted with PBS to a final concentration of 15 μM. The nucleus was stained with this solution for 15 min. After washing two times with deionized water, the coverslips were mounted on glass slides with Fluorescence Mounting Medium and dried overnight. The coverslips were sealed with nail polish before further analysis. An analogous staining procedure was also performed using 5 μM free Dansyl (5-Dimethylamino)-1-naphthalenesulfonamide (SigmaAldrich CAS: 1431−39−6) instead of **14**.

*Staining of Cells with **14** and Antialpha-Tubulin.* The staining with derivative **14** was performed equivalent to the procedure with the mitochondria staining, except that the staining concentration of **14** was 0.6 μM. The cells were washed three times in PBS and fixed in 4% formaldehyde at 37 °C. After washing two times in PBS, the cells were permeabilized for 30 min in 0.2% Triton X-100 in PBS. Three washings in PBS for five minutes were performed followed by incubation in blocking solution containing 10% normal goat serum in PBS. The diluted primary antibody, alpha Tubulin, (1:5000 in blocking solution) was added and incubated for one hour. After three washings in PBS for five minutes, the secondary antibody, Alexa Fluor 488 antirabbit IgG (H+L) (1:1000 in blocking buffer), was added and incubated for one hour. The cells were washed three times in PBS for five minutes. The nucleus was stained with ToPro3 and the cells were mounted as previously described in the mitotracker staining procedure.

Cellular Imaging. The fluorescence from the cell preparations was recorded with a confocal laser scanning microscope, LSM 780. The lasers used were at 405 nm (**14**), 550 nm (mitotracker), and 633 nm (ToPro3). Filters were set up at 375−539 nm, 543−630 nm, and 638−735 nm.

■ ASSOCIATED CONTENT

Ⓢ Supporting Information

Figure 4 and NMR spectra of synthesized compounds. This material is available free of charge via the Internet at http://pubs.acs.org.

■ AUTHOR INFORMATION

Corresponding Author

*E-mail: petko@ifm.liu.se.

Notes

The authors declare no competing financial interest.

■ ACKNOWLEDGMENTS

Financial support from the Swedish Research Council (VR), the Swedish Foundation for Strategic Research (SSF) and Knut and Alice Wallenbergs Stiftelse (KAW) is gratefully acknowledged.

■ REFERENCES

(1) Derda, R., Wherritt, D. J., and Kiessling, L. L. (2007) Solid-phase synthesis of alkanethiols for the preparation of self-assembled monolayers. *Langmuir 23*, 11164−11167.

(2) Houseman, B. T., and Mrksich, M. (1998) Efficient solid-phase synthesis of peptide-substituted alkanethiols for the preparation of substrates that support the adhesion of cells. *J. Org. Chem. 63*, 7552−7555.

(3) Sletten, E. M., and Bertozzi, C. R. (2011) From Mechanism to Mouse: A Tale of Two Bioorthogonal Reactions. *Acc. Chem. Res. 44*, 666−676.

(4) Degennes, P. G. (1992) Soft Matter. *Science 256*, 495−497.

(5) Polyak, S. W., Forsberg, G., Forbes, B. E., McNeil, K. A., Aplin, S. E., and Wallace, J. C. (1997) Introduction of spacer peptides N-terminal to a cleavage recognition motif in recombinant fusion proteins can improve site-specific cleavage. *Protein Eng. 10*, 615−619.

(6) Matsuyama, A., and Kato, T. (1998) Weakly nematic-highly nematic phase transitions in main-chain liquid-crystalline polymers. *Phys. Rev. E 58*, 585−594.

(7) Wong, J. Y., Kuhl, T. L., Israelachvili, J. N., Mullah, N., and Zalipsky, S. (1997) Direct measurement of a tethered ligand-receptor interaction potential. *Science 275*, 820−822.

(8) Moreira, A. G., and Marques, C. M. (2004) The role of polymer spacers in specific adhesion. *J. Chem. Phys. 120*, 6229−6237.

(9) Zalipsky, S. (1995) Chemistry of polyethylene-glycol conjugates with biologically-active molecules. *Adv. Drug Delivery Rev. 16*, 157−182.

(10) Harris, J. M. (1992) *Poly(ethylene glycol) chemistry: biotechnical and biomedical applications*, Plenum, New York.

(11) Andersson, M., Oscarson, S., and Oberg, L. (1993) Synthesis of oligosaccharides with oligoethylene glycol spacers and their conversion into glycoconjugates using N,N,N′,N″-tetramethyl(succinimido)-uronium tetrafluoroborate as coupling reagent. *Glycoconjugate Journal 10*, 197−201.

(12) Dziadek, S., Jacques, S., and Bundle, D. R. (2008) A novel linker methodology for the synthesis of tailored conjugate vaccines composed of complex carbohydrate antigens and specific T(H)-cell peptide epitopes. *Chem.—Eur. J. 14*, 5908−5917.

(13) Moreau, J., and Marchand-Brynaert, J. (2011) Modular synthesis of bifunctional linkers for materials science. *Eur. J. Org. Chem.*, 1641−1644.

(14) Schneider, M. F., Mathe, G., Tanaka, M., Gege, C., and Schmidt, R. R. (2001) Thermodynamic properties and swelling behavior of glycolipid monolayers at interfaces. *J. Phys. Chem. B 105*, 5178−5185.

(15) Narain, R. (2011) *Engineered carbohydrate-based materials for biomedical applications: polymers, surfaces, dendrimers, nanoparticles, and hydrogels*, Wiley, Hoboken, NJ.

(16) Hederos, M., and Konradsson, P. (2006) Synthesis of the Trypanosoma cruzi LPPG heptasaccharyl myo-inositol. *J. Am. Chem. Soc. 128*, 3414−3419.

(17) Löfås, S. (1995) Dextran modified self-assembled monolayer surfaces for use in biointeraction analysis with surface-plasmon resonance. *Pure Appl. Chem. 67*, 829−834.

(18) Fyrner, T., Svensson, S. C. T., Konradsson, P. Synthesis of tri-, penta-, and hepta-saccharides, functionalized with orthogonally N-protected amino residues at the reducing and non-reducing ends. *Tetrahedron*, DOI: 10.1016/j.tet.2012.05.118.

(19) Huang, N. P., Voros, J., De Paul, S. M., Textor, M., and Spencer, N. D. (2002) Biotin-derivatized poly(L-lysine)-g-poly(ethylene

glycol): A novel polymeric interface for bioaffinity sensing. *Langmuir 18*, 220−230.
(20) Fyrner, T., Lee, H. H., Mangone, A., Ekblad, T., Pettitt, M. E., Callow, M. E., Callow, J. A., Conlan, S. L., Mutton, R., Clare, A. S., Konradsson, P., Liedberg, B., and Ederth, T. (2011) Saccharide-functionalized alkanethiols for fouling-resistant self-assembled monolayers: synthesis, monolayer properties, and antifouling behavior. *Langmuir 27*, 15034−15047.
(21) Hederos, M., Konradsson, P., and Liedberg, B. (2005) Synthesis and self-assembly of galactose-terminated alkanethiols and their ability to resist proteins. *Langmuir 21*, 2971−2980.
(22) Ekeroth, J., Borgh, A., Konradsson, P., and Liedberg, B. (2002) Synthesis and monolayer characterization of phosphorylated amino acid analogs. *J. Colloid Interface Sci. 254*, 322−330.
(23) Lallana, E., Riguera, R., and Fernandez-Megia, E. (2011) Reliable and efficient procedures for the conjugation of biomolecules through Huisgen azide-alkyne cycloadditions. *Angew. Chem., Int. Ed. 50*, 8794−8804.
(24) Grabosch, C., Kleinert, M., and Lindhorst, T. K. (2010) Glyco-SAMs by 'dual click': thiourea-bridged Glyco-OEG azides for cycloaddition on surfaces. *Synthesis-Stuttgart*, 828−836.
(25) Bryan, M. C., Fazio, F., Lee, H. K., Huang, C. Y., Chang, A., Best, M. D., Calarese, D. A., Blixt, C., Paulson, J. C., Burton, D., Wilson, I. A., and Wong, C. H. (2004) Covalent display of oligosaccharide arrays in microtiter plates. *J. Am. Chem. Soc. 126*, 8640−8641.
(26) Boonyarattanakalin, S., Martin, S. E., Dykstra, S. A., and Peterson, B. R. (2004) Synthetic mimics of small mammalian cell surface receptors. *J. Am. Chem. Soc. 126*, 16379−16386.
(27) Sun, Q., Cai, S., and Peterson, B. R. (2009) Practical synthesis of 3 beta-amino-5-cholestene and related 3 beta-halides involving i-steroid and retro-i-steroid rearrangements. *Org. Lett. 11*, 567−570.
(28) Guzzo, P. R., and Miller, M. J. (1994) Catalytic, asymmetric-synthesis of the carbacephem framework. *J. Org. Chem. 59*, 4862−4867.
(29) Liu, L., Rozenman, M., and Breslow, R. (2002) Hydrophobic effects on rates and substrate selectivities in polymeric transaminase mimics. *J. Am. Chem. Soc. 124*, 12660−12661.
(30) Galibert, M., Dumy, P., and Boturyn, D. (2009) One-pot approach to well-defined biomolecular assemblies by orthogonal chemoselective ligations. *Angew. Chem., Int. Ed. 48*, 2576−2579.
(31) Schechter, I., Clerici, E., and Zakepitzki, E. (1971) Distinct antigenic specificities of alanine peptide determinants attached to protein carriers via terminal amino or carboxyl groups. *Eur. J. Biochem./FEBS 18*, 561−72.
(32) Svedhem, S., Hollander, C. A., Shi, J., Konradsson, P., Liedberg, B., and Svensson, S. C. T. (2001) Synthesis of a series of oligo(ethylene glycol)-terminated alkanethiol amides designed to address structure and stability of biosensing interfaces. *J. Org. Chem. 66*, 4494−4503.
(33) Jacobson, K. A., Kirk, K. L., Padgett, W. L., and Daly, J. W. (1985) Functionalized congeners of adenosine - preparation of analogs with high-affinity for A1-adenosine receptors. *J. Med. Chem. 28*, 1341−1346.
(34) Seeberger, P. H., and Werz, D. B. (2007) Synthesis and medical applications of oligosaccharides. *Nature 446*, 1046−1051.
(35) Davis, N. J., and Flitsch, S. L. (1991) A novel method for the specific glycosylation of proteins. *Tetrahedron Lett. 32*, 6793−6796.
(36) Hammarström, P., Owenius, R., Mårtensson, L. G., Carlsson, U., and Lindgren, M. (2001) High-resolution probing of local conformational changes in proteins by the use of multiple labeling: Unfolding and self-assembly of human carbonic anhydrase II monitored by spin, fluorescent, and chemical reactivity probes. *Biophys. J. 80*, 2867−2885.
(37) Ishitsuka, R., Sato, S. B., and Kobayashi, T. (2005) Imaging lipid rafts. *J. Biochem. 137*, 249−254.
(38) Simons, K., and Gerl, M. J. (2010) Revitalizing membrane rafts: new tools and insights. *Nat. Rev. Mol. Cell Biol. 11*, 688−699.
(39) Ren, B. Y., Gao, F., Tong, Z., and Yan, Y. (1999) Solvent polarity scale on the fluorescence spectra of a dansyl monomer copolymerizable in aqueous media. *Chem. Phys. Lett. 307*, 55−61.

Bioconjugate Chemistry

Article

pubs.acs.org/bc

Gallium-67-Labeled Lactam Bridge-Cyclized Alpha-MSH Peptides with Enhanced Melanoma Uptake and Reduced Renal Uptake

Haixun Guo,[†] Fabio Gallazzi,[‖] and Yubin Miao*[,†,‡,§]

[†]College of Pharmacy, [‡]Cancer Research and Treatment Center, [§]Department of Dermatology, University of New Mexico, Albuquerque, New Mexico 87131, United States

[‖]Department of Biochemistry, University of Missouri, Columbia, Missouri 65211, United States

ABSTRACT: The purpose of this study was to examine the melanoma targeting and pharmacokinetic properties of ^{67}Ga-DOTA-GGNle-CycMSH$_{hex}$ {^{67}Ga-1,4,7,10-tetraazacyclononane-1,4,7,10-tetraacetic acid-Gly-Gly-Nle-c[Asp-His-DPhe-Arg-Trp-Lys]-CONH$_2$} and ^{67}Ga-NOTA-GGNle-CycMSH$_{hex}$ {^{67}Ga-1,4,7-triazacyclononane-1,4,7-triacetic acid-Gly-Gly-Nle-c-[Asp-His-DPhe-Arg-Trp-Lys]-CONH$_2$} and compare with ^{67}Ga-DOTA-GlyGlu-CycMSH {^{67}Ga-DOTA-Gly-Glu-c[Lys-Nle-Glu-His-DPhe-Arg-Trp-Gly-Arg-Pro-Val-Asp]} we previously reported. DOTA-GGNle-CycMSH$_{hex}$ and NOTA-GGNle-CycMSH$_{hex}$ were synthesized using fluorenylmethyloxy carbonyl (Fmoc) chemistry. The melanocortin-1 (MC1) receptor binding affinity of NOTA-GGNle-CycMSH$_{hex}$ was determined in B16/F1 melanoma cells and compared with DOTA-GGNle-CycMSH$_{hex}$. The melanoma targeting and pharmacokinetic properties of ^{67}Ga-NOTA-GGNle-CycMSH$_{hex}$ and ^{67}Ga-DOTA-GGNle-CycMSH$_{hex}$ were determined in B16/F1 melanoma-bearing C57 mice. NOTA-GGNle-CycMSH$_{hex}$ and DOTA-GGNle-CycMSH$_{hex}$ displayed comparable MC1 receptor binding affinities (1.6 vs 2.1 nM) in B16/F1 melanoma cells. Both ^{67}Ga-NOTA-GGNle-CycMSH$_{hex}$ and ^{67}Ga-DOTA-GGNle-CycMSH$_{hex}$ exhibited dramatically enhanced melanoma uptake and reduced renal uptake than ^{67}Ga-DOTA-GlyGlu-CycMSH in B16/F1 melanoma-bearing C57 mice. Furthermore, ^{67}Ga-NOTA-GGNle-CycMSH$_{hex}$ exhibited more favorable radiolabeling conditions (>85% radiolabeling yields started at 37 °C), as well as higher tumor/kidney uptake ratios than ^{67}Ga-DOTA-GGNle-CycMSH$_{hex}$ at 0.5, 2, and 24 h postinjection. High melanoma uptake coupled with low renal uptake highlighted the potential of ^{67}Ga-NOTA-GGNle-CycMSH$_{hex}$ for melanoma imaging and therapy.

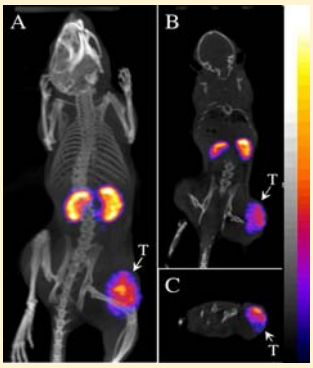

INTRODUCTION

It is highly desirable to develop novel melanoma-specific diagnostic and therapeutic agents[1−18] for melanoma, since no curative treatment is available for patients with metastatic melanoma. Over the past several years, we and others have been interested in developing lactam bridge-cyclized alpha-melanocyte stimulating hormone (α-MSH) peptide radiopharmaceuticals targeting melanocortin-1 (MC1) receptors for melanoma imaging.[19−26] Specifically, we have developed two generations of ^{111}In-labeled novel lactam bridge-cyclized α-MSH peptides for melanoma targeting.[19−24] The first-generation peptides were designed based on the construct of CycMSH peptide {c[Lys-Nle-Glu-His-DPhe-Arg-Trp-Gly-Arg-Pro-Val-Asp}], which was a 12-amino-acid peptide cyclized by a Lys-Asp lactam bridge. The second-generation peptides built upon the backbone of CycMSH$_{hex}$ peptide {c[Asp-His-DPhe-Arg-Trp-Lys]-CONH$_2$}, which was a 6-amino-acid peptide cyclized by an Asp-Lys lactam bridge. The structural modifications from the first-generation peptides to the second-generation peptides enhanced melanoma uptake and reduced renal uptake of ^{111}In-labeled CycMSH$_{hex}$ peptides.[19−24] For instance, ^{111}In-DOTA-Nle-CycMSH$_{hex}$ displayed higher melanoma uptake (19.39 ± 1.65% ID/g at 2 h postinjection) and lower renal uptake (9.52 ± 0.44% ID/g at 2 h postinjection) than ^{111}In-DOTA-GlyGlu-CycMSH in B16/F1 melanoma-bearing C57 mice.[19,23]

In 2009, we reported ^{67}Ga-DOTA-GlyGlu-CycMSH[22] as a potential melanoma imaging agent taking advantage of the diagnostic properties of ^{67}Ga ($T_{1/2}$ = 78.3 h; 93, 185, and 300 keV γ-emissions). Both flank primary B16/F1 melanoma and B16/F10 pulmonary melanoma metastases were clearly visualized by SPECT/CT using ^{67}Ga-DOTA-GlyGlu-CycMSH as an imaging probe 2 h postinjection.[22] However, despite the substantial tumor uptake (12.93 ± 1.63% ID/g at 2 h postinjection), ^{67}Ga-DOTA-GlyGlu-CycMSH also exhibited relatively high renal uptake (27.55 ± 7.87% ID/g at 2 h postinjection) in B16/F1 melanoma-bearing C57 mice.[22] It is important to note that ^{67}Ga is also a potential therapeutic radionuclide because of its emissions of Auger and conversion electrons.[27] Hence, we managed to reduce the renal uptake of ^{67}Ga-DOTA-GlyGlu-CycMSH via L-lysine coinjection to facilitate its potential therapeutic application. L-Lysine coinjection successfully decreased the renal uptake of ^{67}Ga-DOTA-GlyGlu-CycMSH by 69.8% without affecting the melanoma uptake at 2 h postinjection.[22]

Received: April 6, 2012
Revised: May 7, 2012
Published: May 23, 2012

Structural modification on peptide sequence is another way to reduce the renal uptake of radiolabeled α-MSH peptides.[22−24] Recently, we found that ^{111}In-DOTA-GGNle-CycMSH$_{hex}$ displayed higher B16/F1 melanoma uptake (19.05 ± 5.04% ID/g at 2 h postinjection) and reduced renal uptake (6.84 ± 0.92% ID/g at 2 h postinjection) compared to ^{111}In-DOTA-GlyGlu-CycMSH.[22−24] Therefore, we hypothesized that ^{67}Ga-DOTA-GGNle-CycMSH$_{hex}$ would exhibit enhanced melanoma uptake and reduced renal uptake than ^{67}Ga-DOTA-GlyGlu-CycMSH. To examine our hypothesis, we determined the biodistribution of ^{67}Ga-DOTA-GGNle-CycMSH$_{hex}$ in B16/F1 melanoma-bearing C57 mice in this study. Despite the fact that DOTA can form stable complexes with a variety of radionuclides including ^{67}Ga, NOTA can also form a stable complex with ^{67}Ga at lower reaction temperature.[28,29] Thus, we also determined the melanoma targeting and pharmacokinetic properties of ^{67}Ga-NOTA-GGNle-CycMSH$_{hex}$ in B16/F1 melanoma-bearing C57 mice in this study.

EXPERIMENTAL PROCEDURES

Chemicals and Reagents. Amino acid and resin were purchased from Advanced ChemTech Inc. (Louisville, KY) and Novabiochem (San Diego, CA). NO2AtBu was purchased from CheMatech Inc. (Dijon, France) for peptide synthesis. ^{125}I-Tyr^2-[Nle^4, D-Phe^7]-α-MSH {^{125}I-(Tyr^2)-NDP-MSH} was obtained from PerkinElmer, Inc. (Waltham, MA) for receptor binding assay. $^{67}GaCl_3$ was purchased from MDS Nordion, Inc. (Vancouver, Canada) for radiolabeling. All other chemicals used in this study were purchased from Thermo Fischer Scientific (Waltham, MA) and used without further purification. B16/F1 murine melanoma cells were obtained from American Type Culture Collection (Manassas, VA).

Peptide Synthesis and Receptor Binding Assay. DOTA-GGNle-CycMSH$_{hex}$ was synthesized, purified by RP-HPLC, and characterized by liquid chromatography−mass spectrometry (LC-MS) according to our published procedure.[24] New NOTA-GGNle-CycMSH$_{hex}$ was synthesized using Fmoc chemistry. Briefly, the intermediate scaffold of Fmoc-Asp(O-2-PhiPr)-His(Trt)-DPhe-Arg(Pbf)-Trp(Boc)-Lys(Mtt) was synthesized on H_2N-Novagel resin by an Advanced ChemTech multiple-peptide synthesizer (Louisville, KY). Generally, 70 μmol of resin, 210 μmol of each Fmoc-protected amino acid and NO2AtBu were used for the synthesis. The protecting groups of Mtt and 2-phenylisopropyl were removed by 2.5% of trifluoroacetic acid (TFA) for peptide cyclization. The cyclization reaction was achieved on the resin by an overnight reaction in dimethylformamide (DMF) using benzotriazole-1-yl-oxy-tris-pyrrolidino-phosphonium-hexafluorophosphate (PyBOP) as a coupling agent in the presence of *N*,*N*-diisopropylethylamine (DIEA). After the cyclization, the moiety of NO2AtBu-CH_2-Gly-Gly-Nle was coupled to the cyclic intermediate scaffold to yield NO2AtBu-CH_2-Gly-Gly-Nle-Cyclic[Asp-His(Trt)-DPhe-Arg(Pbf)-Trp(Boc)-Lys] on the resin. All protecting groups were totally removed and the peptide was cleaved from the resin by treating with a mixture of trifluoroacetic acid (TFA), thioanisole, phenol, water, ethanedithiol, and triisopropylsilane (87.5:2.5:2.5:2.5:2.5:2.5) for 2 h at 25 °C. The peptide was precipitated and washed with ice-cold ether four times, purified by RP-HPLC on a Grace Vydac C-18 reverse phase analytical column (Vydac 218TP54: 5 μm, 4.6 mm i.d. × 250 mm), and characterized by LC-MS. The MC1 receptor binding affinity (IC_{50} value) of NOTA-GGNle-CycMSH$_{hex}$ was determined in B16/F1 melanoma cells by *in vitro* competitive receptor binding assay according to our published procedure[24] and compared with DOTA-GGNle-CycMSH$_{hex}$.

Effects of Reaction Time and Temperature on ^{67}Ga Radiolabeling Yield. NOTA can form stable complex with ^{67}Ga at lower temperature than DOTA.[28,29] To examine the effects of reaction time and temperature on radiolabeling yield, DOTA-GGNle-CycMSH$_{hex}$ and NOTA-GGNle-CycMSH$_{hex}$ were radiolabeled with ^{67}Ga in a 0.5 M NH_4OAc-buffered solution (pH 3.5) at different temperatures for different reaction time points, respectively. Briefly, 10 μL of $^{67}GaCl_3$ (18.5−37.0 MBq in 0.05 M HCl), 10 μL of 1 mg/mL DOTA-GGNle-CycMSH$_{hex}$ or NOTA-GGNle-CycMSH$_{hex}$ aqueous solution and 100 μL of 0.5 M NH_4OAc (pH 3.5) were added into a reaction vial and incubated at 25, 37, 45, and 75 °C for 5, 15, 30, and 45 min, respectively. After the incubation, 10 μL of 0.5% EDTA aqueous solution was added into each reaction vial to bind unbound $^{67}Ga^{3+}$. The radiolabeling yield of each peptide was determined by Waters RP-HPLC (Milford, MA) on a Grace Vadyc C-18 reverse phase analytical column (Deerfield, IL) using the following gradient at a flow rate of 1 mL/min. The mobile phase consisted of solvent A (20 mM HCl aqueous solution) and solvent B (100% CH_3CN). The gradient was initiated and kept at 82:18 A/B for 3 min followed by a linear gradient of 82:18 A/B to 72:28 A/B over 20 min. Then, the gradient was changed from 72:28 A/B to 10:90 A/B over 3 min followed by an additional 5 min at 10:90 A/B. Thereafter, the gradient was changed from 10:90 A/B to 82:18 A/B over 3 min.

Biodistribution Studies. All animal studies were conducted in compliance with Institutional Animal Care and Use Committee approval. The melanoma targeting and pharmacokinetic properties of ^{67}Ga-DOTA-GGNle-CycMSH$_{hex}$ and ^{67}Ga-NOTA-GGNle-CycMSH$_{hex}$ were determined in B16/F1 melanoma-bearing C57 female mice (Harlan, Indianapolis, IN). The C57 mice were subcutaneously inoculated with 1×10^6 B16/F1 cells on the right flank for each mouse to generate B16/F1 tumors. The weights of tumors reached approximately 0.2 g at 10 days post cell inoculation. Each melanoma-bearing mouse was injected with 0.037 MBq of ^{67}Ga-DOTA-GGNle-CycMSH$_{hex}$ or ^{67}Ga-NOTA-GGNle-CycMSH$_{hex}$ via the tail vein. Groups of 5 mice were sacrificed at 0.5, 2, 4, and 24 h postinjection, and tumors and organs of interest were harvested, weighed, and counted. Blood values were taken as 6.5% of the whole-body weight. The specificity of tumor uptake of ^{67}Ga-DOTA-GGNle-CycMSH$_{hex}$ or ^{67}Ga-NOTA-GGNle-CycMSH$_{hex}$ was determined by coinjecting 10 μg (6.07 nmol) of unlabeled NDP-MSH peptide at 2 h postinjection.

Melanoma Imaging with ^{67}Ga-NOTA-GGNle-CycMSH$_{hex}$. ^{67}Ga-NOTA-GGNle-CycMSH$_{hex}$ exhibited more favorable radiolabeling conditions (>85% radiolabeling yields at 37 °C for 30 min), as well as higher tumor/kidney uptake ratio than ^{67}Ga-DOTA-GGNle-CycMSH$_{hex}$ at 2 h postinjection. Thus, we further evaluated the melanoma imaging property of ^{67}Ga-NOTA-GGNle-CycMSH$_{hex}$. Approximately 11.1 MBq of ^{67}Ga-NOTA-GGNle-CycMSH$_{hex}$ was injected into a B16/F1 melanoma-bearing mouse via the tail vein. The mouse was euthanized for small animal SPECT/CT (Nano-SPECT/CT, Bioscan) imaging at 2 h postinjection. The CT imaging was immediately followed by single photon emission computed tomography (SPECT) imaging of whole-body. The SPECT

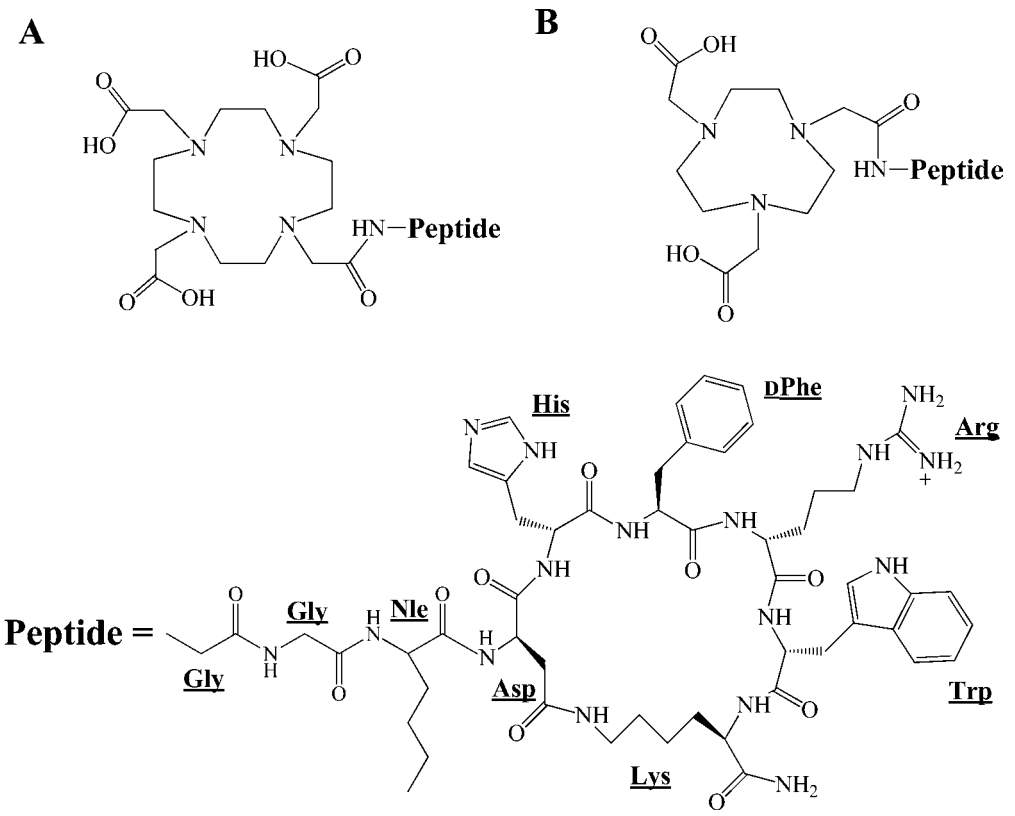

Figure 1. Schematic structures of DOTA-GGNle-CycMSH$_{hex}$ (A) and NOTA-GGNle-CycMSH$_{hex}$ (B).

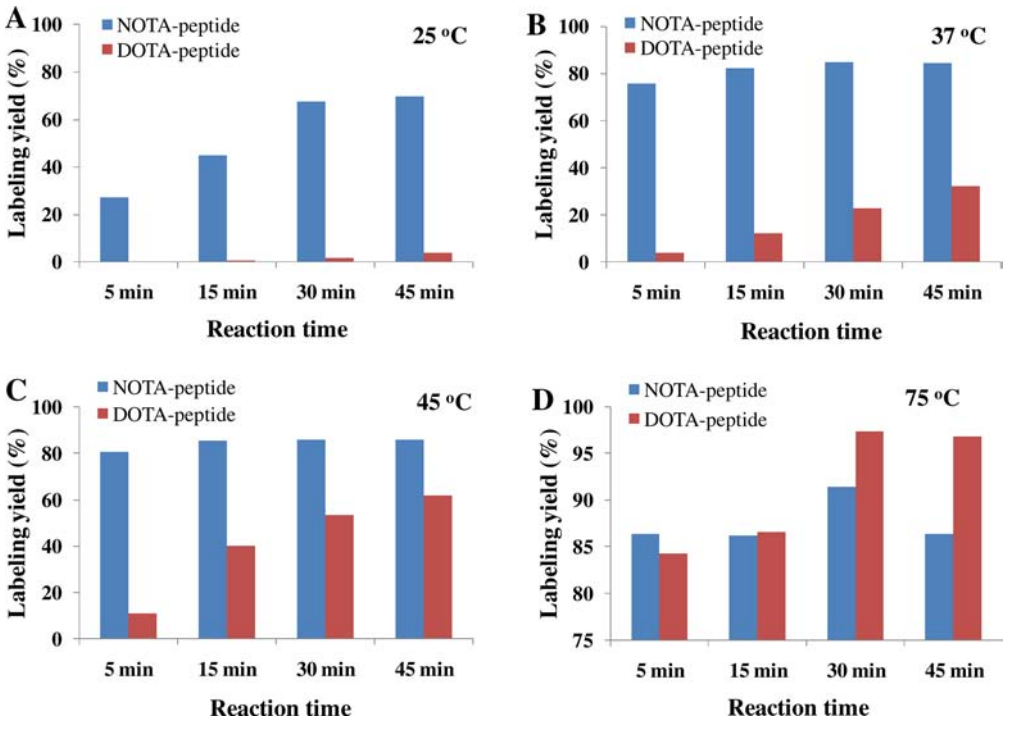

Figure 2. Effects of reaction time and temperature on radiolabeling yields of ^{67}Ga-DOTA-GGNle-CycMSH$_{hex}$ and ^{67}Ga-NOTA-GGNle-CycMSH$_{hex}$.

scans of 24 projections were acquired. Reconstructed SPECT and CT data were visualized and coregistered using InVivoScope (Bioscan, Washington, DC).

Statistical Analysis. Statistical analysis was performed using the Student's *t* test for unpaired data. A 95% confidence level was chosen to determine the significance of the difference in tumor and renal uptake between ^{67}Ga-NOTA-GGNle-CycMSH$_{hex}$ and ^{67}Ga-DOTA-GGNle-CycMSH$_{hex}$, as well as the significance of the difference in tumor uptake between ^{67}Ga-NOTA-GGNle-CycMSH$_{hex}$ with/without NDP-MSH co-injection, and between ^{67}Ga-DOTA-GGNle-CycMSH$_{hex}$ with/

dx.doi.org/10.1021/bc300191z | *Bioconjugate Chem.* 2012, 23, 1341−1348

Table 1. Biodistribution of ^{67}Ga-DOTA-GGNle-CycMSH$_{hex}$ and ^{67}Ga-NOTA-GGNle-CycMSH$_{hex}$ in B16/F1 Melanoma-Bearing C57 Mice[a]

Tissues	^{67}Ga-DOTA-GGNle-CycMSH$_{hex}$				^{67}Ga-NOTA-GGNle-CycMSH$_{hex}$			
	0.5 h	2 h	4 h	24 h	0.5 h	2 h	4 h	24 h
	percent injected dose/gram (%ID/g)							
Tumor	26.96 ± 3.82	25.53 ± 2.22	25.13 ± 4.13	7.54 ± 1.19	20.59 ± 1.97[b]	25.12 ± 1.03	18.17 ± 4.89	7.95 ± 2.58
Brain	0.25 ± 0.07	0.15 ± 0.12	0.08 ± 0.03	0.06 ± 0.03	0.21 ± 0.01	0.11 ± 0.07	0.08 ± 0.03	0.08 ± 0.02
Blood	3.33 ± 1.08	0.97 ± 0.91	0.53 ± 0.25	0.29 ± 0.05	2.25 ± 0.09	0.40 ± 0.19	1.02 ± 0.06	0.55 ± 0.12
Heart	1.64 ± 0.18	0.23 ± 0.09	0.24 ± 0.04	0.37 ± 0.08	1.52 ± 0.28	0.45 ± 0.09	0.39 ± 0.17	0.96 ± 0.39
Lung	3.23 ± 0.07	0.40 ± 0.15	0.36 ± 0.08	0.32 ± 0.19	3.71 ± 0.25	0.54 ± 0.04	0.30 ± 0.10	0.35 ± 0.08
Liver	1.82 ± 0.13	0.86 ± 0.19	0.85 ± 0.02	0.54 ± 0.14	1.28 ± 0.14	0.59 ± 0.09	0.54 ± 0.05	0.50 ± 0.12
Spleen	1.39 ± 0.13	0.44 ± 0.09	0.64 ± 0.06	0.52 ± 0.16	1.25 ± 0.11	0.67 ± 0.19	0.57 ± 0.14	0.85 ± 0.23
Stomach	2.51 ± 0.50	1.68 ± 0.50	1.26 ± 0.11	0.62 ± 0.23	1.79 ± 0.22	1.62 ± 0.63	1.45 ± 0.23	1.21 ± 0.40
Kidneys	16.42 ± 2.99	8.90 ± 1.81	8.44 ± 0.11	5.60 ± 1.24	11.67 ± 0.06[b]	8.34 ± 3.25	7.58 ± 2.70	2.74 ± 0.64[b]
Muscle	0.75 ± 0.20	0.34 ± 0.10	0.32 ± 0.07	0.30 ± 0.18	0.73 ± 0.26	0.34 ± 0.12	0.33 ± 0.11	0.99 ± 0.56
Pancreas	0.83 ± 0.26	0.34 ± 0.07	0.23 ± 0.06	0.37 ± 0.06	1.03 ± 0.16	0.54 ± 0.13	0.36 ± 0.04	0.88 ± 0.31
Bone	1.44 ± 0.63	1.04 ± 0.24	0.87 ± 0.09	0.72 ± 0.70	1.95 ± 0.08	0.91 ± 0.56	0.96 ± 0.87	0.71 ± 0.24
Skin	5.31 ± 2.35	0.84 ± 0.25	0.81 ± 0.22	0.76 ± 0.21	4.00 ± 0.32	0.54 ± 0.35	0.65 ± 0.24	0.96 ± 0.24
	percent injected dose (%ID)							
Intestines	1.60 ± 0.30	1.52 ± 1.14	0.98 ± 0.18	0.46 ± 0.06	1.86 ± 0.24	1.22 ± 0.97	0.91 ± 0.05	1.23 ± 0.35
Urine	59.37 ± 5.31	84.91 ± 2.81	87.75 ± 1.44	92.72 ± 1.09	54.16 ± 13.08	84.02 ± 5.71	86.39 ± 3.94	94.57 ± 0.25
	uptake ratio of tumor/normal tissue							
Tumor/liver	14.84	29.73	29.66	13.86	16.09	42.39	33.40	15.75
Tumor/kidney	1.64	2.87	2.98	1.35	1.76	3.01	2.40	2.90
Tumor/lung	8.35	63.55	69.97	23.35	5.54	46.37	60.24	22.52
Tumor/muscle	35.77	76.04	78.34	25.47	28.19	74.55	54.71	8.05
Tumor/blood	8.10	26.21	47.74	25.56	9.14	62.93	17.75	14.46
Tumor/skin	5.08	30.44	31.10	9.95	5.15	46.35	28.10	8.27

[a]Data were presented as percent injected dose/gram or as percent injected dose (Mean ± SD, n = 5). [b]$P < 0.05$ for determining significance of differences in tumor and kidney uptake between ^{67}Ga-DOTA-GGNle-CycMSH$_{hex}$ and ^{67}Ga-NOTA-GGNle-CycMSH$_{hex}$ at the same time point.

without NDP-MSH coinjection. The differences at the 95% confidence level ($p < 0.05$) were considered significant.

RESULTS

New NOTA-GGNle-CycMSH$_{hex}$ was synthesized and purified by RP-HPLC. NOTA-GGNle-CycMSH$_{hex}$ displayed greater than 90% chemical purity after HPLC purification with 30% synthetic yield. The identity of NOTA-GGNle-CycMSH$_{hex}$ was confirmed by electrospray ionization mass spectrometry. The calculated and found molecular weights of NOTA-GGNle-CycMSH$_{hex}$ were 1381 and 1381, respectively. Meanwhile, DOTA-GGNle-CycMSH$_{hex}$ was synthesized and characterized according to our published procedure[24] for comparison. The calculated and found molecular weights of DOTA-GGNle-CycMSH$_{hex}$ were 1482 and 1482, respectively. The schematic structures of NOTA-GGNle-CycMSH$_{hex}$ and DOTA-GGNle-CycMSH$_{hex}$ are shown in Figure 1. The IC_{50} value of NOTA-GGNle-CycMSH$_{hex}$ was 1.6 nM in B16/F1 melanoma cells, which was comparable to that of DOTA-GGNle-CycMSH$_{hex}$ (2.1 nM).[24]

The effects of reaction time and temperature on radiolabeling yields are presented in Figure 2. The radiolabeling yield of ^{67}Ga-DOTA-GGNle-CycMSH$_{hex}$ or ^{67}Ga-NOTA-GGNle-CycMSH$_{hex}$ was reaction time-dependent at 25, 37, 45, and 75 °C, respectively. The radiolabeling yield improved when the reaction time prolonged from 5 to 45 min. For instance, as shown in Figure 2 at 25 °C, the radiolabeling yield of ^{67}Ga-NOTA-GGNle-CycMSH$_{hex}$ was 27% after 5 min incubation, and 70% after 45 min incubation. Meanwhile, the time-dependent fashion was observed for ^{67}Ga-DOTA-GGNle-CycMSH$_{hex}$ as well despite the fact that the radiolabeling yield of ^{67}Ga-DOTA-GGNle-CycMSH$_{hex}$ was lower than 5% at 25 °C even after 45 min incubation. The radiolabeling yield of ^{67}Ga-DOTA-GGNle-CycMSH$_{hex}$ or ^{67}Ga-NOTA-GGNle-CycMSH$_{hex}$ was reaction temperature dependent after 5, 15, 30, and 45 min incubation, respectively. The radiolabeling yield increased when the reaction temperature was elevated from 25 to 75 °C. For example, as showed in Figure 2 after 30 min incubation, the radiolabeling yield of ^{67}Ga-NOTA-GGNle-CycMSH$_{hex}$ was 67% at 25 °C and 91% at 75 °C. Similarly, the radiolabeling yield of ^{67}Ga-DOTA-GGNle-CycMSH$_{hex}$ was less than 5% at 25 °C and was 97% at 75 °C. Overall, the radiolabeling yield of ^{67}Ga-NOTA-GGNle-CycMSH$_{hex}$ could reach greater than 85% starting from 37 °C, whereas the radiolabeling yield of ^{67}Ga-DOTA-GGNle-CycMSH$_{hex}$ could achieve greater than 84% only at 75 °C. After we examined the effects of reaction time and temperature on radiolabeling yield, we performed peptide radiolabeling at 75 °C for 30 min for biodistribution and imaging studies. DOTA-GGNle-CycMSH$_{hex}$ and NOTA-GGNle-CycMSH$_{hex}$ were readily labeled with ^{67}Ga in a 0.5 M NH_4OAc-buffered solution (pH 3.5) with greater than 90% radiolabeling yields. ^{67}Ga-DOTA-GGNle-CycMSH$_{hex}$ and ^{67}Ga-NOTA-GGNle-CycMSH$_{hex}$ were completely separated from their excess nonlabeled peptides by RP-HPLC. The retention times of ^{67}Ga-DOTA-GGNle-CycMSH$_{hex}$ and ^{67}Ga-NOTA-GGNle-CycMSH$_{hex}$ were 16.3 and 16.4 min, respectively.

The melanoma targeting and pharmacokinetic properties of ^{67}Ga-DOTA-GGNle-CycMSH$_{hex}$ and ^{67}Ga-NOTA-GGNle-CycMSH$_{hex}$ were determined in B16/F1 melanoma-bearing C57 mice. The biodistribution results of ^{67}Ga-DOTA-GGNle-CycMSH$_{hex}$ and ^{67}Ga-NOTA-GGNle-CycMSH$_{hex}$ are pre-

dx.doi.org/10.1021/bc300191z | Bioconjugate Chem. 2012, 23, 1341−1348

sented in Table 1. ^{67}Ga-DOTA-GGNle-CycMSH$_{hex}$ exhibited rapid high melanoma uptake and prolonged tumor retention. The tumor uptake of ^{67}Ga-DOTA-GGNle-CycMSH$_{hex}$ was 26.96 ± 3.82% ID/g at 0.5 h postinjection. ^{67}Ga-DOTA-GGNle-CycMSH$_{hex}$ displayed similar high tumor uptake (25.53 ± 2.22% and 25.13 ± 4.13% ID/g) at 2 and 4 h postinjection. Even at 24 h postinjection, there was 7.54 ± 1.19% ID/g of ^{67}Ga-DOTA-GGNle-CycMSH$_{hex}$ activity remained in the tumor. Approximately 96.3% of the tumor uptake of ^{67}Ga-DOTA-GGNle-CycMSH$_{hex}$ was blocked by 10 μg (6.07 nmol) of non-radiolabeled NDP-MSH ($p < 0.05$) (Figure 3),

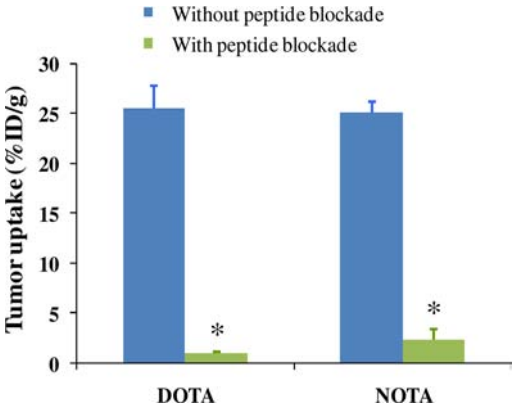

Figure 3. Tumor uptake of ^{67}Ga-DOTA-GGNle-CycMSH$_{hex}$ (DOTA) and ^{67}Ga-NOTA-GGNle-CycMSH$_{hex}$ (NOTA) with (green) or without (blue) 10 μg of NDP-MSH blockade at 2 h postinjection. *$p < 0.05$.

demonstrating that the tumor uptake was specific and MC1 receptor-mediated. Whole-body clearance of ^{67}Ga-DOTA-GGNle-CycMSH$_{hex}$ was rapid, with 84.9% of the injected radioactivity cleared through the urinary system by 2 h postinjection. Normal organ uptake of ^{67}Ga-DOTA-GGNle-CycMSH$_{hex}$ was lower than 1.68% ID/g except for the kidneys at 2, 4, and 24 h postinjection. The kidney uptake was 8.90 ± 1.81% ID/g at 2 h postinjection and decreased to 5.60 ± 1.24% ID/g at 24 h postinjection. High tumor uptake and prolonged retention coupled with rapid whole-body clearance resulted in high tumor/blood and high tumor/normal organ uptake ratios achieved as early as 0.5 h postinjection. The tumor/kidney uptake ratio of ^{67}Ga-DOTA-GGNle-CycMSH$_{hex}$ was 1.64, 2.87, 2.98, and 1.35 at 0.5, 2, 4, and 24 h postinjection, respectively.

^{67}Ga-NOTA-GGNle-CycMSH$_{hex}$ showed comparably high melanoma uptake with ^{67}Ga-DOTA-GGNle-CycMSH$_{hex}$ at 2 and 24 h postinjection. The tumor uptake of ^{67}Ga-NOTA-GGNle-CycMSH$_{hex}$ was 20.59 ± 1.57% ID/g at 0.5 h postinjection. ^{67}Ga-NOTA-GGNle-CycMSH$_{hex}$ reached its peak tumor uptake of 25.12 ± 1.03% ID/g at 2 h postinjection. The tumor uptake of ^{67}Ga-NOTA-GGNle-CycMSH$_{hex}$ was 18.17 ± 4.89% and 7.95 ± 2.58% ID/g at 4 and 24 h postinjection. Approximately 90.8% of the tumor uptake of ^{67}Ga-NOTA-GGNle-CycMSH$_{hex}$ was blocked by 10 μg (6.07 nmol) of nonradiolabeled NDP-MSH ($p < 0.05$) (Figure 3), demonstrating that the tumor uptake was specific and MC1 receptor-mediated. Whole-body clearance of ^{67}Ga-NOTA-GGNle-CycMSH$_{hex}$ was rapid, with 84.1% of the injected radioactivity cleared through the urinary system by 2 h postinjection. Normal organ uptakes of ^{67}Ga-NOTA-GGNle-CycMSH$_{hex}$ were lower than 1.62% ID/g except for the kidneys at 2, 4, and 24 h postinjection. The kidney uptake was 8.34 ± 3.25% ID/g at 2 h postinjection and decreased to 2.74 ± 0.64% ID/g at 24 h postinjection. High tumor uptake and prolonged retention coupled with rapid whole-body clearance resulted in high tumor/blood and high tumor/normal organ uptake ratios achieved as early as 0.5 h postinjection. The tumor/kidney uptake ratio of ^{67}Ga-DOTA-GGNle-CycMSH$_{hex}$ was 1.76, 3.01, 2.40, and 2.90 at 0.5, 2, 4, and 24 h postinjection, respectively.

^{67}Ga-NOTA-GGNle-CycMSH$_{hex}$ exhibited more favorable radiolabeling conditions (>85% radiolabeling yields started at 37 °C), as well as higher tumor/kidney uptake ratio than ^{67}Ga-DOTA-GGNle-CycMSH$_{hex}$ at 2 h postinjection. Therefore, we further evaluated the melanoma imaging properties of ^{67}Ga-NOTA-GGNle-CycMSH$_{hex}$ at 2 h postinjection. The whole-body, coronal, and transverse SPECT/CT images are presented in Figure 5. The melanoma tumors were clearly visualized by SPECT/CT using ^{67}Ga-NOTA-GGNle-CycMSH$_{hex}$ as an

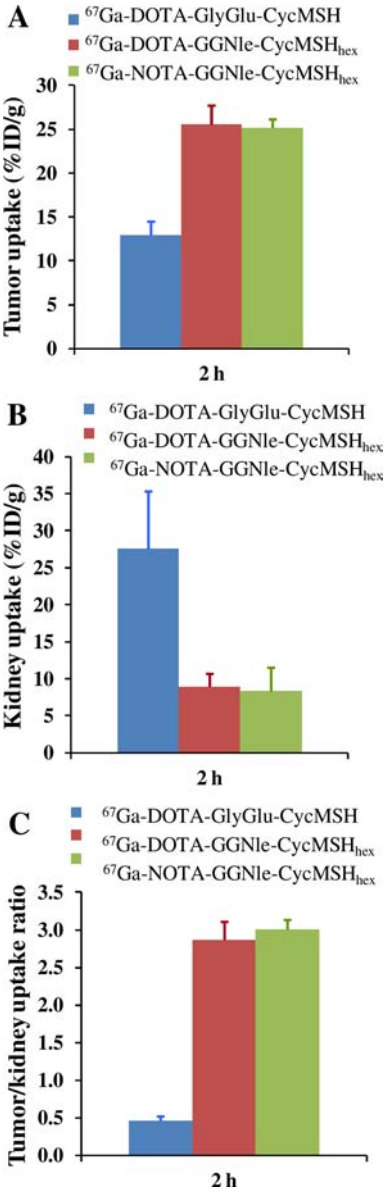

Figure 4. The comparisons of tumor (A) and kidney (B) uptake, and tumor/kidney uptake ratios (C) at 2 h postinjection among ^{67}Ga-DOTA-GlyGlu-CycMSH (blue), ^{67}Ga-DOTA-GGNle-CycMSH$_{hex}$ (red), and ^{67}Ga-NOTA-GGNle-CycMSH$_{hex}$ (green).

dx.doi.org/10.1021/bc300191z | Bioconjugate Chem. 2012, 23, 1341−1348

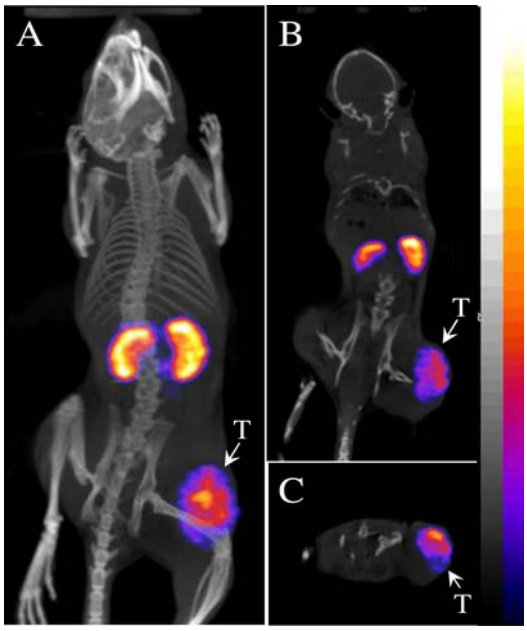

Figure 5. Representative whole-body (A), coronal (B), and transversal (C) SPECT/CT images of a B16/F1 melanoma-bearing C57 mouse at 2 h postinjection of ^{67}Ga-NOTA-GGNle-CycMSH$_{hex}$. The tumor lesions (T) were highlighted with arrows on the images.

imaging probe. ^{67}Ga-NOTA-GGNle-CycMSH$_{hex}$ exhibited high tumor to normal organ uptake ratios except for the kidneys, which was consistent with the biodistribution results.

DISCUSSION

Gallium-67 is an attractive SPECT radionuclide with a half-life of 78.3 h and three γ-emissions (38% 93 keV, 24% 185 keV, and 16% 300 keV).[30−33] Meanwhile, ^{67}Ga is also a potential therapeutic radionuclide due to its emissions of Auger and conversion electrons.[27] Both linear and cyclic ^{67}Ga-labeled α-MSH peptides[8,22] have been reported for melanoma imaging over the past several years. Initially, Froidevaux et al. reported the linear ^{67}Ga-DOTA-NAPamide, which exhibited 9.43 ± 1.06% and 3.10 ± 0.36% ID/g of B16/F1 melanoma uptake at 4 and 24 postinjection, respectively.[8] Thereafter, we reported the lactam bridge-cyclized ^{67}Ga-DOTA-GlyGlu-CycMSH.[22] The B16/F1 melanoma uptake of ^{67}Ga-DOTA-GlyGlu-CycMSH was 14% less than that of ^{67}Ga-DOTA-NAPamide at 4 h postinjection, whereas the B16/F1 melanoma uptake of ^{67}Ga-DOTA-GlyGlu-CycMSH was 1.6 times the melanoma uptake of ^{67}Ga-DOTA-NAPamide at 24 h postinjection. Surprisingly, the renal uptake of ^{67}Ga-DOTA-GlyGlu-CycMSH was 5.7 and 10.3 times the renal uptake of ^{67}Ga-DOTA-NAPamide at 4 and 24 h postinjection, respectively. Dramatic difference in renal uptake between ^{67}Ga-DOTA-GlyGlu-CycMSH and ^{67}Ga-DOTA-NAPamide was likely due to their structural differences.

Recently, we have identified a novel class of lactam bridge cyclized α-MSH peptides with enhanced melanoma uptake and reduced renal uptake.[23,24] Specifically, ^{111}In-DOTA-GGNle-CycMSH$_{hex}$ exhibited the highest tumor/kidney uptake ratios (2.8 and 2.7 at 2 and 4 h postinjection, respectively) among all reported ^{111}In-labeled cyclic peptides.[23,24] Thus, we were interested in determining whether or not ^{67}Ga-DOTA-GGNle-CycMSH$_{hex}$ could display higher melanoma uptake and lower renal uptake compared to ^{67}Ga-DOTA-GlyGlu-CycMSH in this study. Meanwhile, we also evaluated ^{67}Ga-NOTA-GGNle-CycMSH$_{hex}$ because NOTA can also form a stable complex with ^{67}Ga even at lower reaction temperature than DOTA.[28,29] As we anticipated, NOTA-GGNle-CycMSH$_{hex}$ showed comparable MC1 receptor binding affinity with DOTA-GGNle-CycMSH$_{hex}$ (1.6 vs 2.1 nM). In terms of radiolabeling yield, ^{67}Ga-NOTA-GGNle-CycMSH$_{hex}$ could reach 70% and 85% radiolabeling yields even at 25 and 37 °C, respectively. Meanwhile, the radiolabeling yield of ^{67}Ga-DOTA-GGNle-CycMSH$_{hex}$ could be greater than 85% only at 75 °C. At 75 °C, both ^{67}Ga-NOTA-GGNle-CycMSH$_{hex}$ and ^{67}Ga-DOTA-GGNle-CycMSH$_{hex}$ could achieve greater than 90% radiolabeling yield after 30 min incubation. It was important to note that high radiolabeling yield of ^{67}Ga-NOTA-GGNle-CycMSH$_{hex}$ at 37 °C represented a distinct practical advantage compared to ^{67}Ga-DOTA-GGNle-CycMSH$_{hex}$.

The biodistribution results supported our hypothesis. ^{67}Ga-DOTA-GGNle-CycMSH$_{hex}$ exhibited higher melanoma uptake and lower renal uptake compared to ^{67}Ga-DOTA-GlyGlu-CycMSH. The tumor uptake of ^{67}Ga-DOTA-GGNle-CycMSH$_{hex}$ was 3.1, 2.0, and 3.1 times the tumor uptake of ^{67}Ga-DOTA-GlyGlu-CycMSH at 0.5, 2, and 4 h postinjection, respectively. Meanwhile, the renal uptake of ^{67}Ga-DOTA-GGNle-CycMSH$_{hex}$ was only 69%, 32%, 37%, and 27% of the renal uptake of ^{67}Ga-DOTA-GlyGlu-CycMSH at 0.5, 2, 4, and 24 h postinjection, respectively. The increased tumor uptake and decreased renal uptake dramatically improved the tumor to kidney uptake ratios of ^{67}Ga-DOTA-GGNle-CycMSH$_{hex}$ at all time points investigated in this study (Table 1). The tumor to kidney uptake ratio of ^{67}Ga-DOTA-GGNle-CycMSH$_{hex}$ was 4.6, 6.2, 8.3, and 5.6 times those of ^{67}Ga-DOTA-GlyGlu-CycMSH at 0.5, 2, 4, and 24 h postinjection, respectively.

^{67}Ga-NOTA-GGNle-CycMSH$_{hex}$ displayed comparable high melanoma uptake with ^{67}Ga-DOTA-GGNle-CycMSH$_{hex}$ at 2 and 24 h postinjection. Meanwhile, ^{67}Ga-NOTA-GGNle-CycMSH$_{hex}$ exhibited comparable renal uptake with ^{67}Ga-DOTA-GGNle-CycMSH$_{hex}$ at 2 and 4 h postinjection. Interestingly, the renal uptake of with ^{67}Ga-NOTA-GGNle-CycMSH$_{hex}$ was only 71% and 49% of that of ^{67}Ga-DOTA-GGNle-CycMSH$_{hex}$ at 0.5 and 24 h postinjection. The further reduced renal uptake resulted in higher tumor/kidney uptake ratios of ^{67}Ga-NOTA-GGNle-CycMSH$_{hex}$ than ^{67}Ga-DOTA-GGNle-CycMSH$_{hex}$ at 0.5 and 24 h postinjection. Moreover, ^{67}Ga-NOTA-GGNle-CycMSH$_{hex}$ showed slightly higher tumor/kidney uptake ratio than ^{67}Ga-DOTA-GGNle-CycMSH$_{hex}$ at 2 h postinjection (Figure 4). We have demonstrated that *L*-lysine coinjection decreased the renal uptake of ^{67}Ga-DOTA-GlyGlu-CycMSH by 69.8% at 2 h postinjection in our previous report.[22] In this study, the renal uptake of ^{67}Ga-NOTA-GGNle-CycMSH$_{hex}$ and ^{67}Ga-DOTA-GGNle-CycMSH$_{hex}$ was only 30% and 32% of the renal uptake of ^{67}Ga-DOTA-GlyGlu-CycMSH at 2 h postinjection (Figure 4). The dramatic difference in renal uptake among ^{67}Ga-DOTA-GlyGlu-CycMSH, ^{67}Ga-NOTA-GGNle-CycMSH$_{hex}$ and ^{67}Ga-DOTA-GGNle-CycMSH$_{hex}$ was likely due to their structural differences.

Despite the fact that the melanoma lesions could be visualized by SPECT/CT using ^{67}Ga-DOTA-GlyGlu-CycMSH as an imaging probe,[22] ^{67}Ga-NOTA-GGNle-CycMSH$_{hex}$ exhibited higher tumor imaging contrast (Figure 5) than ^{67}Ga-DOTA-GlyGlu-CycMSH. Higher melanoma uptake

coupled with lower renal uptake underscored the potential therapeutic application of ^{67}Ga-NOTA-GGNle-CycMSH$_{hex}$. It will be interesting to examine the therapeutic efficacy of ^{67}Ga-NOTA-GGNle-CycMSH$_{hex}$ in melanoma-bearing mouse model taking advantage of the therapeutic properties of ^{67}Ga in the future. Another potential application of NOTA-GGNle-CycMSH$_{hex}$ peptide is to develop ^{68}Ga-NOTA-GGNle-CycMSH$_{hex}$ for positron emission tomography (PET) imaging of melanoma. Gallium-68 is an attractive PET radionuclide with a half-life of 68 min and can be easily obtained via an in-house commercial ^{68}Ge−^{68}Ga generator. The combination of ^{68}Ga-NOTA-GGNle-CycMSH$_{hex}$ with PET, taking advantage of the outstanding imaging properties of PET and receptor-targeting properties of ^{68}Ga-NOTA-GGNle-CycMSH$_{hex}$, will offer an exciting opportunity for sensitive tumor-specific imaging of melanoma metastases.

In conclusion, both ^{67}Ga-NOTA-GGNle-CycMSH$_{hex}$ and ^{67}Ga-DOTA-GGNle-CycMSH$_{hex}$ exhibited dramatically enhanced melanoma uptake and reduced renal uptake than ^{67}Ga-DOTA-GlyGlu-CycMSH in B16/F1 melanoma bearing C57 mice. ^{67}Ga-NOTA-GGNle-CycMSH$_{hex}$ exhibited more favorable radiolabeling conditions (>85% radiolabeling yields started at 37 °C), as well as higher tumor/kidney uptake ratio than ^{67}Ga-DOTA-GGNle-CycMSH$_{hex}$ at 0.5, 2, and 24 h postinjection. High melanoma uptake coupled with low renal uptake highlighted the potential of ^{67}Ga-NOTA-GGNle-CycMSH$_{hex}$ for melanoma imaging and therapy.

AUTHOR INFORMATION

Corresponding Author

*Phone: (505) 925-4437; Fax: (505) 272-6749; E-mail: ymiao@salud.unm.edu.

Notes

The authors declare no competing financial interest.

ACKNOWLEDGMENTS

We thank Dr. Jianquan Yang for his technical assistance. This work was supported in part by the NIH grant NM-INBRE P20RR016480/P20GM103451 and University of New Mexico HSC RAC Award. The image in this article was generated by the Keck-UNM Small Animal Imaging Resource established with funding from the W.M. Keck Foundation and the University of New Mexico Cancer Research and Treatment Center (NIH P30 CA118100).

REFERENCES

(1) Giblin, M. F., Wang, N. N., Hoffman, T. J., Jurisson, S. S., and Quinn, T. P. (1998) Design and characterization of α-melanotropin peptide analogs cyclized through rhenium and technetium metal coordination. *Proc. Natl. Acad. Sci. U.S.A. 95*, 12814−12818.

(2) Chen, J., Cheng, Z., Hoffman, T. J., Jurisson, S. S., and Quinn, T. P. (2000) Melanoma-targeting properties of ^{99m}technetium-labeled cyclic alpha-melanocyte-stimulating hormone peptide analogues. *Cancer Res. 60*, 5649−5658.

(3) Chen, J., Cheng, Z., Owen, N. K., Hoffman, T. J., Miao, Y., Jurisson, S. S., and Quinn, T. P. (2001) Evaluation of an ^{111}In-DOTA-rhenium cyclized alpha-MSH analog: a novel cyclic-peptide analog with improved tumor-targeting properties. *J. Nucl. Med. 42*, 1847−1855.

(4) Miao, Y., Owen, N. K., Whitener, D., Gallazzi, F., Hoffman, T. J., and Quinn, T. P. (2002) In vivo evaluation of ^{188}Re-labeled alpha-melanocyte stimulating hormone peptide analogs for melanoma therapy. *Int. J. Cancer 101*, 480−487.

(5) Froidevaux, S., Calame-Christe, M., Tanner, H., Sumanovski, L., and Eberle, A. N. (2002) A novel DOTA-alpha-melanocyte-stimulating hormone analog for metastatic melanoma diagnosis. *J. Nucl. Med. 43*, 1699−1706.

(6) Cheng, Z., Chen, J., Miao, Y., Owen, N. K., Quinn, T. P., and Jurisson, S. S. (2002) Modification of the structure of a metallopeptide: synthesis and biological evaluation of ^{111}In-labeled DOTA-conjugated rhenium-cyclized alpha-MSH analogues. *J. Med. Chem. 45*, 3048−3056.

(7) Miao, Y., Whitener, D., Feng, W., Owen, N. K., Chen, J., and Quinn, T. P. (2003) Evaluation of the human melanoma targeting properties of radiolabeled alpha-melanocyte stimulating hormone peptide analogues. *Bioconjugate Chem. 14*, 1177−1184.

(8) Froidevaux, S., Calame-Christe, M., Schuhmacher, J., Tanner, H., Saffrich, R., Henze, M., and Eberle, A. N. (2004) A gallium-labeled DOTA-alpha-melanocyte-stimulating hormone analog for PET imaging of melanoma metastases. *J. Nucl. Med. 45*, 116−123.

(9) Miao, Y., Owen, N. K., Fisher, D. R., Hoffman, T. J., and Quinn, T. P. (2005) Therapeutic efficacy of a ^{188}Re-labeled alpha-melanocyte-stimulating hormone peptide analog in murine and human melanoma-bearing mouse models. *J. Nucl. Med. 46*, 121−129.

(10) Froidevaux, S., Calame-Christe, M., Tanner, H., and Eberle, A. N. (2005) Melanoma targeting with DOTA-alpha-melanocyte-stimulating hormone analogs: structural parameters affecting tumor uptake and kidney uptake. *J. Nucl. Med. 46*, 887−895.

(11) Miao, Y., Hylarides, M., Fisher, D. R., Shelton, T., Moore, H., Wester, D. W., Fritzberg, A. R., Winkelmann, C. T., Hoffman, T. J., and Quinn, T. P. (2005) Melanoma therapy via peptide-targeted alpha-radiation. *Clin. Cancer Res. 11*, 5616−5621.

(12) McQuade, P., Miao, Y., Yoo, J., Quinn, T. P., Welch, M. J., and Lewis, J. S. (2005) Imaging of melanoma using ^{64}Cu- and ^{86}Y-DOTA-ReCCMSH(Arg11), a cyclized peptide analogue of alpha-MSH. *J. Med. Chem. 48*, 2985−2992.

(13) Miao, Y., Hoffman, T. J., and Quinn, T. P. (2005) Tumor-targeting properties of ^{90}Y- and ^{177}Lu-labeled α-melanocyte stimulating hormone peptide analogues in a murine melanoma model. *Nucl. Med. Biol. 32*, 485−493.

(14) Miao, Y., Fisher, D. R., and Quinn, T. P. (2006) Reducing renal uptake of ^{90}Y and ^{177}Lu labeled alpha-melanocyte stimulating hormone peptide analogues. *Nucl. Med. Biol. 33*, 723−733.

(15) Wei, L., Butcher, C., Miao, Y., Gallazzi, F., Quinn, T. P., Welch, M. J., and Lewis, J. S. (2007) Synthesis and biologic evaluation of ^{64}Cu-labeled rhenium-cyclized alpha-MSH peptide analog using a cross-bridged cyclam chelator. *J. Nucl. Med. 48*, 64−72.

(16) Cheng, Z., Xiong, Z., Subbarayan, M., Chen, X., and Gambhir, S. S. (2007) ^{64}Cu-labeled alpha-melanocyte-stimulating hormone analog for MicroPET imaging of melanocortin 1 receptor expression. *Bioconjugate Chem. 18*, 765−772.

(17) Miao, Y., Benwell, K., and Quinn, T. P. (2007) ^{99m}Tc- and ^{111}In-labeled alpha-melanocyte-stimulating hormone peptides as imaging probes for primary and pulmonary metastatic melanoma detection. *J. Nucl. Med. 48*, 73−80.

(18) Miao, Y., Shelton, T., and Quinn, T. P. (2007) Therapeutic efficacy of a ^{177}Lu-labeled DOTA conjugated alpha-melanocyte-stimulating hormone peptide in a murine melanoma-bearing mouse model. *Cancer Biother. Radiopharm. 22*, 333−341.

(19) Miao, Y., Gallazzi, F., Guo, H., and Quinn, T. P. (2008) ^{111}In-labeled lactam bridge-cyclized alpha-melanocyte stimulating hormone peptide analogues for melanoma imaging. *Bioconjugate Chem. 19*, 539−547.

(20) Guo, H., Shenoy, N., Gershman, B. M., Yang, J., Sklar, L. A., and Miao, Y. (2009) Metastatic melanoma imaging with an ^{111}In-labeled lactam bridge-cyclized alpha-melanocyte-stimulating hormone peptide. *Nucl. Med. Biol. 36*, 267−276.

(21) Guo, H., Yang, J., Gallazzi, F., Prossnitz, E. R., Sklar, L. A., and Miao, Y. (2009) Effect of DOTA position on melanoma targeting and pharmacokinetic properties of ^{111}In-labeled lactam bridge-cyclized α-melanocyte stimulating hormone peptide. *Bioconjugate Chem. 20*, 2162−2168.

(22) Guo, H., Yang, J., Shenoy, N., and Miao, Y. (2009) Gallium-67-labeled lactam bridge-cyclized alpha-melanocyte stimulating hormone peptide for primary and metastatic melanoma imaging. *Bioconjugate Chem. 20*, 2356−2363.
(23) Guo, H., Yang, J., Gallazzi, F., and Miao, Y. (2010) Reduction of the ring size of radiolabeled lactam bridge-cyclized alpha-MSH peptide resulting in enhanced melanoma uptake. *J. Nucl. Med. 51*, 418−426.
(24) Guo, H., Yang, J., Gallazzi, F., and Miao, Y. (2011) Effects of the amino acid linkers on melanoma-targeting and pharmacokinetic properties of Indium-111-labeled lactam bridge-cyclized α-MSH peptides. *J. Nucl. Med. 52*, 608−616.
(25) Raposinho, P. D., Xavier, C., Correia, J. D., Falcao, S., Gomes, P., and Santos, I. (2008) Melanoma targeting with alpha-melanocyte stimulating hormone analogs labeled with fac-$[^{99m}Tc(CO)_3]^+$: effect of cyclization on tumor-seeking properties. *J. Biol. Inorg. Chem. 13*, 449−459.
(26) Raposinho, P. D., Correia, J. D., Alves, S., Botelho, M. F., Santos, A. C., and Santos, I. (2008) A $^{99m}Tc(CO)_3$-labeled pyrazolyl−α-melanocyte-stimulating hormone analog conjugate for melanoma targeting. *Nucl. Med. Biol. 35*, 91−99.
(27) Mariani, G., Bodei, L., Adelstein, S. J., and Kassis, A. I. (2000) Emerging roles for radiometabolic therapy of tumors based on auger electron emission. *J. Nucl. Med. 41*, 1519−1521.
(28) Clarke, E. T., and Martell, A. E. (1991) Stabilities of trivalent metal ion complexes of the tetraacetate derivatives of 12-, 13-, and 14-membered tetraazamacrocycles. *Inorg. Chim. Acta 190*, 37−46.
(29) Clarke, E. T., and Martell, A. E. (1991) Stabilities of the Fe(III), Ga(III) and In(III) chelators of N,N′,N″-triazacyclononanetriacetic acid. *Inorg. Chim. Acta 181*, 273−280.
(30) Green, M. A., and Welch, M. J. (1989) Gallium radiopharmaceutical chemistry. *Int. J. Rad. Appl. Instrum. B 16*, 435−448.
(31) Anderson, C. J., and Welch, M. J. (1999) Radiometal-labeled agents (non-technetium) for diagnostic imaging. *Chem. Rev. 99*, 2219−2234.
(32) Eisenwiener, K., Prata, M. I., Buschmann, I., Zhang, H. W., Santos, A. C., Wenger, S., Reubi, J. C., and Mäecke, H. R. (2002) NODAGATOC, a new chelator-coupled somatostatin analogue labeled with $[^{67/68}Ga]$ and $[^{111}In]$ for SPECT, PET, and targeted therapeutic applications of somatostatin receptor (hsst2) expression tumors. *Bioconjugate Chem. 13*, 530−541.
(33) Zhernosekov, K., Aschoff, P., Filosofov, D., Jahn, M., Jennewein, M., Adrian, H. J., Bihl, H., and Rösch, F. (2005) Visualisation of a somatostatin receptor-expressing tumour with ^{67}Ga-DOTATOC SPECT. *Eur. J. Nucl. Med. Mol. Imaging 32*, 1129.

Bioconjugate Chemistry

Technical Note

pubs.acs.org/bc

Construction of Semisynthetic DNA–Protein Conjugates with Phi X174 Gene-A* Protein

Yasumasa Mashimo, Hitomi Maeda, Masayasu Mie, and Eiry Kobatake*

Department of Biological Information, Graduate School of Bioscience and Biotechnology, Tokyo Institute of Technology, 4259, Nagatsuta, Midori-ku, Yokohama-shi, 226-8501, Japan

Supporting Information

ABSTRACT: DNA–protein conjugates have frequently been used as versatile molecular tools for a variety of applications in biotechnology to harness synergistic effects of DNA and protein functions. With applications for DNA–protein conjugates growing, easy-to-use and economical methods for the synthesis of DNA–protein conjugates are required. In this study, we developed a method for site-specific labeling of single-stranded DNA (ssDNA) to a recombinant protein of interest (POI) through the Gene-A* protein (Gene-A*) from bacteriophage phi X174, without any chemical modifications of ssDNA. Gene-A* protein is an enzyme that site-selectively cleaves an oligodeoxyribonucleotide (ODN) containing a Gene-A* recognition sequence, at which point a tyrosine residue of Gene-A* is bonded to the 5′-phosphoryl group of the cleavage site via a stable phosphotyrosine linkage. Here, we constructed three kinds of recombinant proteins fused to Gene-A*: N-terminally Gene-A*-fused enhanced green fluorescent protein (EGFP), C-terminally Gene-A*-fused EGFP, and N-terminally Gene-A*-fused firefly luciferase (FLuc). The reaction yields of DNA–protein conjugation catalyzed by the Gene-A* moiety reached 80–90% in the three proteins, and kinetic study revealed that the reaction achieved a steady state after 10 min. Moreover, dot blot analyses were performed to evaluate the hybridization and aptamer-forming ability of ssDNA conjugated to the Gene-A* moiety of a recombinant Gene-A*-FLuc protein. This study demonstrated that a strategy using recombinant proteins fused to Gene-A* could offer a versatile, rapid, easy-to-use, and economical platform for producing DNA–protein conjugates.

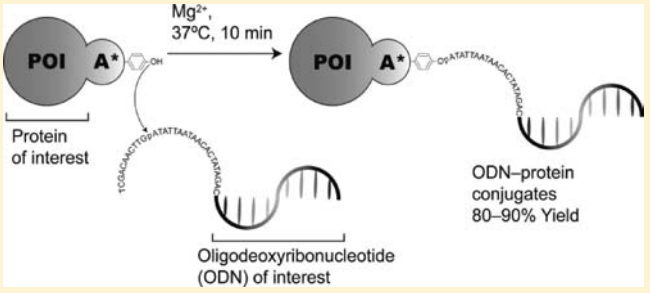

INTRODUCTION

In recent years, semisynthetic DNA–protein conjugates have been used as versatile molecular tools for a variety of applications in biotechnology and materials science.[1,2] In particular, the utility of DNA–protein conjugates has emerged in ultrasensitive detection methods to quantify target biomolecules,[3,4] and DNA-directed immobilization techniques for the fabrication of protein microarrays.[5] Moreover, some potential applications of DNA–protein conjugates are being developed in cutting-edge biotechnologies, such as kinetic analysis of complementation of split-proteins,[6,7] biomolecular delivery systems,[8,9] and programmable extracellular matrices.[10]

Despite the potential applicability of DNA–protein conjugates, synthetic methods remain challenging. Total chemical synthesis of DNA–protein conjugates has been successful over the past years,[11−13] although the incorporation of oligonucleotides into larger recombinant proteins, such as antibodies, is still poorly developed, and it is not possible, in many cases, to engineer a single chemically accessible cysteine into the protein of interest (POI). Furthermore, the methods require extensive purification of the conjugates to remove excessive protein and oligonucleotides after each coupling step.[14] As alternatives, expressed protein ligation reactions[15] and enzyme-mediated (e.g., sortase and transglutaminase)[16−18] conjugation reactions have been reported. They are advantageous because one can achieve a relatively high yield (50–75%) of the reaction product stoichiometrically conjugated to single-stranded DNA (ssDNA). Another approach to generate DNA–protein conjugates harnesses a tag-protein with specific self-labeling activity (e.g., methyltransferase and O^6-alkylguanine-DNA-alkyl-transferase),[19,20] possessing the marked features of a high yield (~85%) and few preparation steps. In these methods, however, it is indispensable to prepare DNA substrates modified with a specific functional moiety, which is cumbersome and not economical.

In the present study, we developed an easy-to-use and economical method for site-selective conjugation of a recombinant POI with nonmodified ssDNA. This approach made use of phi X174 Gene-A* (Gene-A*) of coliphage phi X174 (Figure 1). The A-gene of phage phi X174 encodes two polypeptides:[21] the Gene-A protein (55 kDa) and the Gene-A* protein (37 kDa), which results from internal translation of the gene-A message beginning at the 173rd codon. The Gene-A protein cleaves the double-stranded phi X174 DNA between

Received: March 12, 2012
Revised: May 19, 2012
Published: May 23, 2012

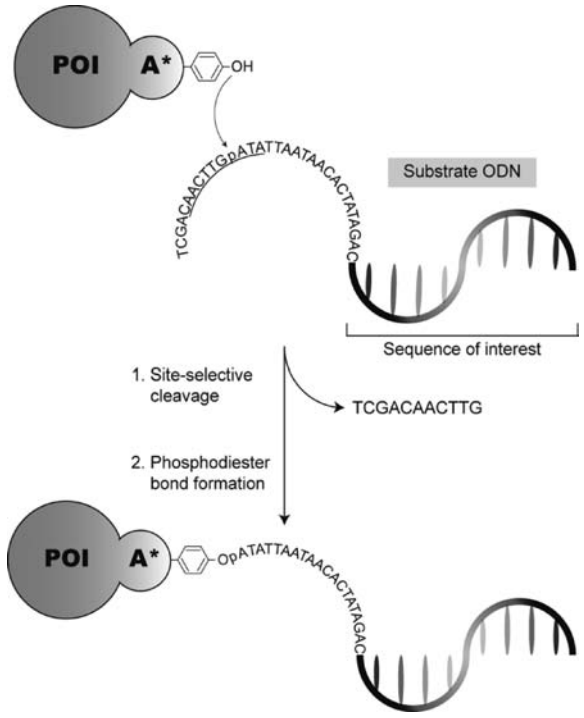

Figure 1. Schematic representation of strategy for conjugation of a recombinant protein of interest (POI) with ssDNA through the fused Gene-A* moiety (A*). The recombinant protein cleaves the recognition sequence, and a phosphodiester bond is formed between the 5′-phosphoryl group of the cleavage site and the tyrosine residue of the Gene-A* moiety. An underline in the substrate oligodeoxyribonucleotide (ODN) shows the Gene-A* recognition sequence. The GpA in the recognition sequence denotes the cleavage site.

nucleotides G-4305 and A-4306 at the replication origin of the viral strand and binds covalently to the 5′-phosphoryl group of A-4306 via a stable phosphotyrosine link. In the presence of *E. coli* rep DNA helicase and DNA polymerase III, elongation of of phi X174 DNA is initiated at the 3′-OH of G-4305 generated by Gene-A. Gene-A* also has the property of cleaving and binding covalently to ssDNA as well as Gene-A.[22,23]

Remarkably, Gene-A* can link to ssDNA *in vitro* in the presence of only divalent metal ions (e.g., Mg^{2+}) and does not require other proteins or biomolecules.[24] Specifically, Gene-A* can couple itself to ssDNA containing the conserved nucleotide sequence present in the replication origin of phi X174 DNA, without any chemical modification.[24,25] In this paper, we describe the synthesis of novel DNA−protein conjugates using three recombinant proteins with the autolabeling activity: N-terminally Gene-A*-fused enhanced green fluorescent protein (EGFP), C-terminal Gene-A*-fused EGFP, and N-terminally Gene-A*-fused firefly luciferase (FLuc). The recombinant proteins cleave the recognition sequence, and a phosphodiester bond is formed between the 5′-phosphoryl group of the cleavage site and the tyrosine residue of the Gene-A* moiety. We demonstrated that the robust autolabeling activity of Gene-A* could be maintained with any proteins. Moreover, the Gene-A* moiety did not interfere with the functions of the fusion partner protein or conjugated ssDNA.

EXPERIMENTAL PROCEDURES

Materials. All substrate oligodeoxyribonucleotide (S-ODN) sequences (Table 1), containing the conserved Gene-A* recognition sequence,[25] and all other oligonucleotide sequences were purchased from Greiner Bio-One. Reagents for a bioluminescent assay were obtained from PicaGene kit (TOYO B-Net). All other chemicals and proteins were of analytical grade.

Table 1. Sequences of Gene-A* Substrate Oligodeoxyribonucleotides (S-ODN)

name	sequence
S-ODN-31-FITC	5′-TCG ACA ACT TGA[a] TAT TAA TAA CAC TAT AGA C-FITC-3′
S-ODN-51	5′-TCG ACA ACT TGA *TAT TAA TAA CAC TAT AGA CCA CCG CCC CGA AGG GGA CGA*[b]-3′
S-ODN-TBA	5′-TCG ACA ACT TGA TAT TAA TAA CAC TAT AGA **CGG TTG GTG TGG TTG G**[c]-3′

[a]The underline shows the Gene-A* cleavage site. [b]The italic characters show the hybridization site. [c]The bold characters show the trombin binding aptamer sequence.

Plasmid Construction. The phi X174 Gene-A* protein gene fragment was amplified by the polymerase chain reaction (PCR) from ϕX174 DNA (Takara Bio), and inserted into the pBSII(SK+) (Cosmo Bio) plasmid. The expression plasmid pET28b-Gene-A* with the N-terminal His-tag sequence was constructed from the pBSII(SK+) plasmid encoding Gene-A* (pBS-A*). It turns out that the Y303H mutation is necessary for overexpression of the Gene-A* protein in *E. coli*.[24] Therefore, Y303H mutation was introduced into pET28b-Gene-A* as described in the instruction of QuikChange II Site-Directed Mutagenesis Kits (Agilent Technologies). In all of the following plasmid construction procedures, the plasmids encoding the Gene-A* gene with the Y303H mutation were used. Enhanced green fluorescent protein (EGFP) and firefly luciferase (FLuc) gene fragments were amplified by PCR from pEGFP-N3 (BD Biosciences) and pBS-FLuc encoding a FLuc gene, which was constructed previously, respectively. The plasmid pET28b-NHis-EGFP-A* was generated by inserting the EGFP gene fragment into the N-terminal of the Gene-A* gene of pET28b-A*. The plasmid pET28b-NHis-A*-EGFP and pET28b-NHis-A*-FLuc were constructed by inserting EGFP and FLuc gene fragments into the C-terminal of Gene-A* gene of pET28b-A*.

Protein Expression and Purification. *E. coli* BL21(DE3) transformed with each of the three pET28b-NHis-(A*-EGFP, EGFP-A*, A*-FLuc) plasmids was grown in 50 mL of Luria broth supplemented with 0.5% glucose at 37 °C to an apparent optical density of 0.3 at 600 nm. Expression of the Gene-A* fusion protein was induced by the addition of isopropyl-β-D-thiogalactopyranoside (IPTG) to 0.5 mM. After the incubation at 19 °C for 16 h, cells were pelleted, resuspended in 5 mL/g_{pellet} of sucrose buffer (50 mM HEPES, 20% sucrose, 1 mM EDTA pH 7.9) before repelleting by centrifugation at 7000*g* for 30 min at 4 °C. The supernatant was discarded and the pellet resuspended in 5 mL/g_{pellet} of 5 mM $MgCl_2$ and incubated on ice for 10 min. Cells were pelleted by centrifugation at 4500*g* for 20 min, the supernatant was discarded, and the pellet was resuspended in 1.5 mL/g_{pellet} lysis buffer (50 mM sodium phosphate, 300 mM NaCl, 10 mM $MgCl_2$, 10% glycerol, 10% sucrose, 10 mM β-mercaptoethanol, 50 mM L-arginine hydrochloride, pH 8.0). Cell lysis was carried out by adding BugBuster (Merck Chemicals), incubation for 30 min at 4 °C, and then sonication for 5 min in 5 s pulses. The lysates were centrifuged at 15 000 rpm for 15 min. All steps were performed on ice or at 4 °C. Then, the collected supernatants were applied

to TALON Metal Affinity Resins (Takara Bio), and the fusion proteins were purified by metal-ion affinity chromatography using the His-tag. The fusion proteins were concentrated by the use of Amicon Ultra-15 10K (Merck), and dialyzed against the storage buffer (50% glycerol, 1 M NaCl, 50 mM Tris-HCl, 1 mM EDTA, 5 mM β-mercaptoethanol, pH 7.5), and stored at −20 °C. All fusion proteins were analyzed by SDS-PAGE (8% acrylamide gels). Each concentration of the purified proteins was determined with the bicinchoninic acid protein assay reagent kit (Pierce).

Synthesis of DNA−Protein Conjugates. The appropriate concentration of each Gene-A* fusion protein was mixed with a 2× concentration of S-ODN in the reaction buffer (150 mM NaCl, 50 mM Tris-HCl, pH 7.5, 5 mM dithiothreitol (DTT), and 5 mM $MgCl_2$), and then, the DNA cleavage and joining reaction was carried out at 30 °C for 30 min, resulting in the tyrosyl residue (Tyr-343 or Tyr-347) of Gene-A* being condensed in a phosphodiester bond formation. To remove unreacted S-ODNs, the fusion proteins reacted with S-ODNs were dialyzed against the storage buffer using 20 000 MWCO Slide-A-Lyzer (Thermo Scientific), and stored at −20 °C until use.

Dot Blot Analysis. Dot blot analysis was performed on a synthetic complementary oligodeoxyribonucleotide (C-ODN) and a human α-thrombin. The C-ODN and α-thrombin were dissolved in formaldehyde/SSC buffer (1.8 M NaCl, 0.1 M sodium phosphate, 0.01 M EDTA, 6.15 M formaldehyde, pH 7.7) and selection buffer (20 mM Tris-acetate, 140 mM NaCl, 50 mM KCl, 10 mM $CaCl_2$, pH 7.4),[26] respectively. Before spotting, the C-ODN in the buffer was heated at 95 °C for 3 min, and then chilled on ice for at least 3 min. Then, the C-ODN and α-thrombin were spotted onto the Hybond-C nitrocellulose membranes (Amersham Life Science) prewetted in 10× standard saline citrate (SSC) and selection buffer, respectively. Subsequently, the membranes were dried, and the membranes spotted with the C-ODN were baked at 80 °C for 2 h. The sample spotted membranes were incubated in prebinding buffer for C-ODN (5× sodium chloride/sodium potassium/EDTA (SSPE), 500 μg/mL sonicated salmon sperm DNA, 0.2× Blocking One (Nacalai Tesque), 5 mM DTT, 0.05% (v/v) Tween 20, pH 7.7), and for α-thrombin (1× selection buffer, 500 μg/mL sonicated salmon sperm DNA, 0.2× Blocking One (Nacalai Tesque), 0.05% (v/v) Tween 20, pH 7.4) at 37 °C for 3 h. Then, DNA−protein conjugates were added to the prebinding solution, and incubated at 37 °C for 3 h. Following the binding assay, the filters were washed by incubating themselves in the wash buffer (C-ODN: 2 × SSPE, 0.05% Tween 20, 1 mM DTT, pH 7.7; α-thrombin: 1 × selection buffer, 0.05% Tween 20, 1 mM DTT, pH 7.4) for 15 min, repeatedly, and then the wash buffer was replaced with the second wash buffer (C-ODN: 1 × SSPE, 0.05% Tween 20, 1 mM DTT, pH 7.7; α-thrombin: 1 × selection buffer, 0.05% Tween 20, 1 mM DTT, pH 7.4), and washed for 15 min. After two washes with the second wash buffer, the membranes were immersed in a 1 mL PicaGene solution as a substrate for luciferase and monitored for a fixed amount of time by LumiCube (Liponics) to measure the luminescence of each spot.

RESULTS AND DISCUSSION

Characterization of Gene-A* Fused to POI. Gene-A* from coliphage phi X174 has not been analyzed for its activity as a fusion protein. To determine whether Gene-A* fused to another protein has the capacity to form a complex with a substrate oligodeoxyribonucleotide (ODN), sodium dodecyl sulfate polyacrylamide gel electrophoresis (SDS-PAGE) analysis of the conjugates of the Gene-A* fusion protein with the substrate ODN in a cell lysate was performed. A cell lysate of an *E. coli* BL21(DE3) expressing the N-terminally thioredoxin-His_6-tagged Gene-A* (Trx-Gene-A*) protein was mixed with the 3′-FITC-labeled substrate ODN (S-ODN-31-FITC). The substrate ODN sequence is the 31 nucleotide derived from the replication origin of phi X174 DNA, including the conserved Gene-A* recognition sequence (CAA CTT GATA). The ODN-Trx-Gene-A* conjugates in the cell lysate were electrophoretically separated, imaged with FITC labeled via the conjugated ODN, and verified as a single band (Figure S1A in the Supporting Information). It has been reported that both of two tyrosine residues, Tyr-343 and Tyr-347, of the Gene-A* protein are directly involved in Gene-A*-mediated cleavage and joining.[27] Therefore, we constructed Y343F, Y347F, and Y343F/Y347F Gene-A* mutants fused to Trx to examine the stoichiometrically DNA binding activity of wild-type (WT) Gene-A* fusions by SDS-PAGE (Figure S1B in the Supporting Information). It was found that the fusion proteins with WT, Y343F, and Y347F Gene-A* could cleave the single-stranded substrate ODN and join the cleavage site to itself stoichiometrically, while the Y343F/Y347F mutant could not. Since no differences in the binding abilities to the substrate ODN were observed among the proteins, we used Gene-A* WT for the following experiments.

To ensure whether Gene-A* could form a complex with DNA without affecting the DNA binding activity and the activity of the accompanied fused protein, plasmids coding N-terminally EGFP-fused Gene-A* (N-EA*) and C-terminally EGFP-fused Gene-A* (A*E-C) proteins were constructed. The proteins with His_6-tag were overexpressed in *E. coli* BL21(DE3) and purified in a single step using a TALON metal affinity gel. First, the fluorescence of N-EA* and A*E-C proteins was confirmed by spectrofluorometric analysis (FP-6500, Jasco) (data not shown). The expected sizes from their amino acid sequences of the N-EA* and A*E-C proteins were 67.9 kDa and 67.2 kDa, respectively. The estimated molecular weights of the proteins from SDS-PAGE were a little smaller than the expected sizes. The bands of both N-EA* and A*E-C were shifted to higher molecular weights, after the reaction with S-ODN-31-FITC (Figure 2A,B). Thus, it was shown as with the case of Trx that the Gene-A* moiety of Gene-A* and EGFP fusion proteins had the DNA binding activity. The single-shifted bands of FITC-labeled substrate ODN after the reaction with N-EA* and A*E-C were confirmed by fluorescence imaging. Those results indicated that each product contained a single molecular species, with only slight impurities of the unconjugated protein (SI Figure S2). Subsequently, we examined the yield of the DNA−protein conjugation reaction. On the basis of the protein bands in SDS-PAGE analysis, both the reaction yields of N-EA* and A*E-C were estimated to be approximately 80−90% when the conjugation reaction was conducted with a 2-fold molar excess of S-ODN-31-FITC to fusion proteins (Figure 2B). The yield of present method is comparable to that of previously reported conjugation methods advantageous in yield.[16,20] We speculate as one reason of the high yields of DNA−N-EA* and DNA−A*E-C conjugates that the reaction efficiency is increased because the substrate ODN includes the Gene-A* interacting sequence (CAC TAT AGA C) as well as the recognition sequence.[25]

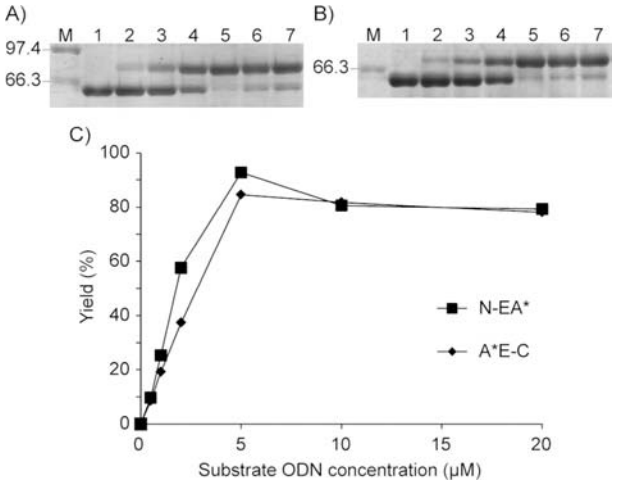

Figure 2. Gel electrophoretic analysis of the ODN−EGFP conjugates. (A,B) 10% SDS-PAGE analysis of 2.5 μM N-EA* (A) and A*E-C (B) in the reactions with different concentrations of single-stranded substrate ODN: lane M, SDS Broadrange Marker (Bio-Rad); lane 1, no substrate ODN; lane 2, 0.5 μM S-ODN-31-FITC; lane 3, 1 μM S-ODN-31-FITC; lane 4, 2 μM S-ODN-31-FITC; lane 5, 5 μM S-ODN-31-FITC; lane 6, 10 μM S-ODN-31-FITC; lane 7, 20 μM S-ODN-31-FITC. (C) The fractions of the ODN−EGFP conjugates were quantified using *ImageJ* software. The yield was calculated as a ratio by value of a band intensity of the ODN−protein conjugates and a total band intensity of the proteins reacted and nonreacted with S-ODN.

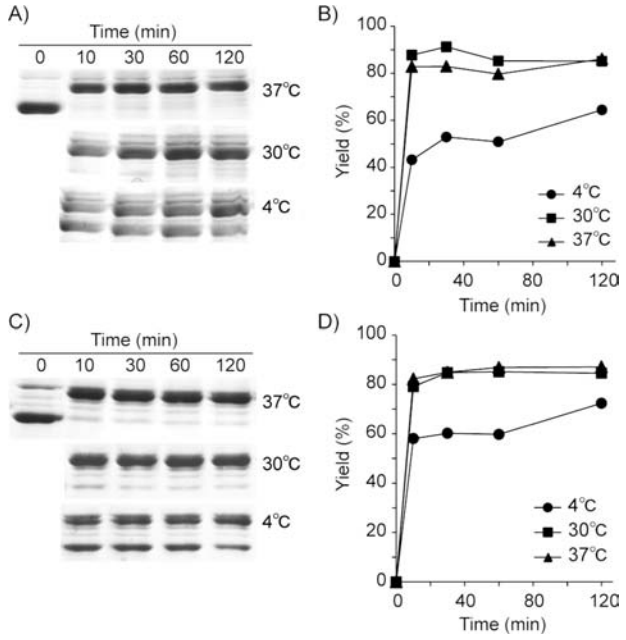

Figure 3. Reaction kinetics of ODN−Gene-A*-EGFP conjugation. (A,C) N-EA* proteins (2.5 μM) (A) and A*E-C proteins (2.5 μM) (C) were mixed with S-ODN-31-FITC (5 μM) for the times indicated at different temperatures. The proteins were separated by SDS-PAGE and visualized by Coomassie blue staining. The retarded bands correspond to the ODN−Gene-A*-EGFP conjugates. (B,D) The fractions of conjugates of N-EA* (B) and A*E-C (D) with S-ODN were quantified using *ImageJ* software. The yield was calculated as a ratio by value of a band intensity of the ODN−protein conjugate and a total band intensity of the proteins reacted and nonreacted with S-ODN.

The reaction kinetics were investigated with preformed DNA−A*E-C and DNA−N-EA* conjugates. The yield of conjugates was assessed by SDS-PAGE followed by Coomassie blue staining (Figure 3A,C). The upper band, appearing over time at various temperatures, corresponds to the conjugated DNA−protein complex. The DNA−protein conjugation reactions mediated by the Gene-A* moiety reached a plateau after 10 min at 30 and 37 °C (Figure 3B,D). These results indicated that there was little differences between DNA binding kinetics of the Gene-A* moiety of recombinant fusion proteins and natural Gene-A*.[23] Given that there are few methods which could complete the reaction for synthesis of DNA−protein conjugates within 10 min, the present strategy allowed the extremely rapid reaction. Moreover, the yields of DNA−A*E-C and DNA−EA* conjugates were similar at 4, 30, and 37 °C at each time point. Thus, these data showed that Gene-A* could be fused to both the N-terminus and the C-terminus of a POI without significant reduction in DNA binding activity of Gene-A* or decline in the fused protein function.

In the next stage, we investigated the versatility of the Gene-A* fusion strategy and the function of ssDNA conjugated to the Gene-A* fusion protein. It has been reported that there are some problems in processing of the genetically engineered firefly luciferase (FLuc) fusion protein when the C-terminus of FLuc is fused to other proteins.[28] Therefore, we constructed the plasmids coding for a C-terminally FLuc-fused Gene-A* (A*L) protein with His_6-tag, and a protein was overexpressed and purified in the same procedures as in the preparation of N-EA* and A*E-C. To evaluate the activity of the A*L protein, three μM A*L protein and different concentrations of S-ODN-31-FITC were mixed, separated by SDS-PAGE and visualized by Coomassie blue staining and fluorescence (SI Figure S3). The expected size of the A*L protein was 100.2 kDa, and the estimated molecular weight from SDS-PAGE was a little smaller than the expected one. The bands of the A*L proteins mixed with various concentrations of S-ODN-31-FITC were shifted in a manner similar to that of both N-EA* and A*E-C proteins (SI Figure S3A), and the single-shifted band of S-ODN-31-FITC was observed in samples mixed with the A*L protein (SI Figure S3B). The reaction efficiency of the Gene-A* moiety of the A*L protein was similar to that of the N-EA* and A*E-C proteins (SI Figure S3C). Thus, the Gene-A* protein fusion strategy for fabricating DNA−protein conjugates could be applied to the FLuc protein. One reason for the versatility of our strategy would be that the Gene-A* moiety is not susceptible to steric hindrance by the fused protein of interest because the Gene-A* protein has the relatively large molecular weight, unlike a small reactive group (e.g., cysteine residue).[13]

Dot Blot Analysis of DNA−Protein Conjugates Immobilized by Hybridization. To evaluate the function of the fused ssDNA, we fabricated the A*L protein conjugated to the S-ODN-51 substrate oligodeoxyribonucleotide. The conjugation reaction was conducted with a 2-fold molar excess of S-ODN-51 to the A*L protein, and unreacted oligonucleotides were removed by dialysis. The presence of some unconjugated fusion protein did not affect the efficiency of binding to the membrane, because that process was exclusively dependent on the presence of the conjugated oligonucleotide. First, we investigated whether the ODN conjugated to the A*L protein could hybridize to a complementary oligonucleotide sequence. Thus, ODN−A*L conjugates were immobilized on a nitrocellulose membrane through hybridization with a complementary oligodeoxyribonucleotide (C-ODN: 5′-AAA ACC

dx.doi.org/10.1021/bc300118m | *Bioconjugate Chem.* 2012, 23, 1349−1355

ATT TTT CGT CCC CTT CGG GGC GGT GGT CTA TAG TGT TAT TAA TAT-3′). The bioluminescent signals were observed in membranes spotted with different amounts of C-ODN and a noncomplementary oligodeoxyribonucleotide (NC-ODN: 5′-TTT ATC GTG GAT CGT GAT AAG TCT TTA ATC-3′) after hybridization with the ODN−A*L conjugates (Figure 4). The bioluminescence from the ODN−A*L conjugates immobilized on the spots was directly proportional to the amount of C-ODN, not NC-ODN. Thus, the results demonstrated that ssDNA conjugated to the Gene-A* moiety could hybridize selectively to the complementary sequence.

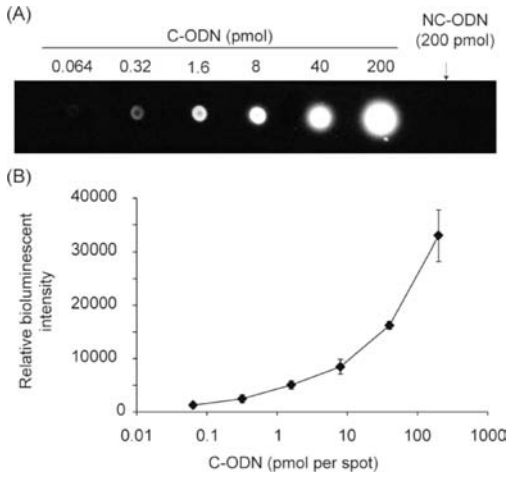

Figure 4. Dot blot analysis of DNA-directed immobilization of S-ODN-51−A*L conjugates. (A) The bioluminescent image of the spots of various concentrations of C-ODN (0.064, 0.32, 1.6, 8, 40, and 200 pmol) and NC-ODN (200 pmol) visualized by the bioluminescence of immobilized S-ODN-51−A*L conjugates. (B) The bioluminescent intensity of the respective spots was quantified using *ImageJ* software. Error bars represent the mean ± s.d., n = 3.

Dot Blot Analysis of TBA−Protein Conjugates binding to Thrombin. We then investigated whether a ssDNA aptamer conjugated to A*L could bind targets depending upon the folding and three-dimensional structure. In this study, a thorombin binding aptamer (TBA) was used as a model. The A*L protein conjugated to a S-ODN-TBA substrate oligodeoxyribonucleotide, containing a Gene-A* recognition sequence and a TBA sequence, was obtained in the same manner as the S-ODN-51−A*L conjugates. The functional analysis was conducted by using a dot blot method with a nitrocellulose membrane spotted with thrombin and other proteins (Figure 5). The different amounts (μg per spot) of thrombin or lysozyme were spotted on a nitrocellulose membrane, and the membrane was incubated in the binding buffer containing 50 nM TBA−A*L conjugates at 37 °C for three hours. After washout of nonbinding conjugates, the bioluminescence on the respective spots was visualized (Figure 5A). We observed that the bioluminescence signal increased significantly over 0.125−1 μg of thrombin. Furthermore, using a membrane spotted with 1 μg of thrombin, BSA, lysozyme, or myoglobin, thrombin-specific binding of TBA−A*L conjugates was examined. The strong bioluminescence signal was detected specifically from the spot of thrombin (Figure 5B). Thus, the results showed that the TBA conjugated to the Gene-A* moiety maintained its aptamer forming ability. Although 1 μg of thrombin corresponds approximately to 27 pmol, the signal intensity

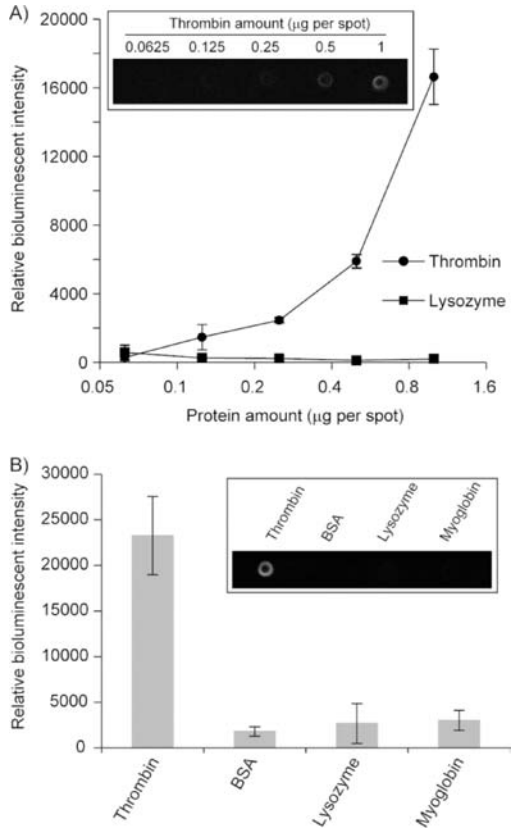

Figure 5. Dot blot analysis of the S-ODN-TBA−A*L conjugates specifically binding to thrombin. The respective bioluminescent intensities of the S-ODN-TBA−A*L conjugates immobilized on spots of indicated amounts of thrombin and lysozyme (A) and 1 μg of thrombin, BSA, lysozyme, and myoglobin (B) on a nitrocellulose membrane were quantified using *ImageJ* software. The insets in A and B show the bioluminescent image of spots of the respective proteins visualized by the bioluminescence of immobilized S-ODN-TBA−A*L conjugates. Error bars represent the mean ± s.d., n = 3.

was much weaker than that of conjugates immobilized through hybridization. A possible explanation for this outcome is that the aptamer structure is susceptible to the incubation conditions and buffer composition. Alternatively, the instability of the TBA might have increased due to the addition of 20 nucleotides and large protein moiety to its 5′-end.[29] To improve the performance of the assay, optimization of assay conditions should be pursued. Parameters should include incubation temperature and time, the concentration of TBA−protein conjugates, the pore size and affinity of the membrane, and buffer composition. Moreover, utilization of chemical ligation methods, or the fusion protein strategy with other DNA binding proteins that could covalently bond themselves to 3′-terminus of substrate ODN,[30] instead of the Gene-A* protein, could be beneficial.

CONCLUSION

We have described an easy-to-use and economical method for conjugating recombinant proteins site-specifically to the 5′-end of ssDNA, using the Gene-A* protein. The method consists of the breakage and joining of DNA strands via stable trans-esterification reactions, without any chemical modification of the substrate ODN. Once the recombinant protein fused to either N-terminus or C-terminus of Gene-A* is constructed using genetic engineering methods, the present method should

dx.doi.org/10.1021/bc300118m | *Bioconjugate Chem.* 2012, 23, 1349−1355

be applicable for the attachment of proteins to DNA in fewer steps than currently available methods. Furthermore, the yield of DNA−protein conjugates in the present method reached approximately 80−90% in all three proteins for only 10 min. For the functional assessment of conjugated ssDNA, we developed two kinds of biomolecular detection systems to evaluate the hybridization ability toward cDNA and the thrombin binding ability of TBA. It has been demonstrated that S-ODN-51 and S-ODN-TBA conjugated to recombinant protein can selectively hybridize to the complementary oligonucleotide sequence and bind to thrombin.

Recently, notable advances have been made in DNA-based nanotechnology such as DNA origami, DNA architecture, and DNA-fueled molecular machines.[31−34] In combination with the technology, DNA−protein conjugates could become a platform for the construction of nanometer-sized functional biomaterials. To accelerate the research, development and diffusion of the functionalized nanostructures, therefore, an easy-to-use and economical method to conjugate proteins site-selectively and stoichiometrically to DNA is necessary. It is hoped that the present method for the synthesis of DNA−protein conjugates using the Gene-A* protein will serve as a valuable tool for DNA-based nanotechnology, or offer important implications for development of better conjugation strategies.

■ ASSOCIATED CONTENT

Supporting Information

Confirmation of the stoichiometrically DNA binding activity of wild-type and mutant Gene-A* proteins, SDS-PAGE analysis by fluorescence imaging, characterization of the DNA binding activity of A*L. This material is available free of charge via the Internet at http://pubs.acs.org.

■ AUTHOR INFORMATION

Corresponding Author

*E-mail: ekobatak@bio.titech.ac.jp. Tel.: +81-45-924-5760. Fax: +81-45-924-5779.

Notes

The authors declare no competing financial interest.

■ ACKNOWLEDGMENTS

This work was financially supported in part by the JSPS Global Centers of Excellence (COE) Program.

■ REFERENCES

(1) Saccà, B., and Niemeyer, C. M. (2011) Functionalization of DNA nanostructures with proteins. *Chem. Soc. Rev. 40*, 5910−5921.

(2) Röglin, L., and Seitz, O. (2008) Controlling the activity of peptides and proteins with smart nucleic acid-protein hybrids. *Org. Biomol. Chem. 6*, 3881−3887.

(3) Burbulis, I., Yamaguchi, K., Gordon, A., Carlson, R., and Brent, R. (2005) Using protein-DNA chimeras to detect and count small numbers of molecules. *Nat. Methods 2*, 31−37.

(4) Morin, I., Dixon, N. E., and Schaeffer, P. M. (2010) Ultrasensitive detection of antibodies using a new Tus-Ter-lock immunoPCR system. *Mol. Biosyst. 6*, 1173−1175.

(5) Tang, Y. C., Wan, G., Ng, J. K., Ajikumar, P. K., and Too, H. P. (2008) DNA-directed assembly of protein microarrays. *Front. Biosci. 13*, 5755−5771.

(6) Demidov, V. V., Dokholyan, N. V., Witte-Hoffmann, C., Chalasani, P., Yiu, H. W., Ding, F., Yu, Y., Cantor, C. R., and Broude, N. E. (2006) Fast complementation of split fluorescent protein triggered by DNA hybridization. *Proc. Natl. Acad. Sci. U.S.A. 103*, 2052−2056.

(7) Takeda, S., Tsukiji, S., Ueda, H., and Nagamune, T. (2008) Covalent split protein fragment-DNA hybrids generated through N-terminus-specific modification of proteins by oligonucleotides. *Org. Biomol. Chem. 6*, 2187−2194.

(8) Chen, C. H., Dellamaggiore, K. R., Ouellette, C. P., Sedano, C. D., Lizadjohry, M., Chernis, G. A., Gonzales, M., Baltasar, F. E., Fan, A. L., Myerowitz, R., and Neufeld, E. F. (2008) Aptamer-based endocytosis of a lysosomal enzyme. *Proc. Natl. Acad. Sci. U.S.A. 105*, 15908−15913.

(9) Tong, G. J., Hsiao, S. C., Carrico, Z. M., and Francis, M. B. (2009) Viral capsid DNA aptamer conjugates as multivalent cell-targeting vehicles. *J. Am. Chem. Soc. 131*, 11174−11178.

(10) Aldaye, F. A., Senapedis, W. T., Silver, P. A., and Way, J. C. (2010) A structurally tunable DNA-based extracellular matrix. *J. Am. Chem. Soc. 132*, 14727−14729.

(11) Niemeyer, C. M., Sano, T., Smith, C. L., and Cantor, C. R. (1994) Oligonucleotide-directed self-assembly of proteins: semi-synthetic DNA−streptavidin hybrid molecules as connectors for the generation of macroscopic arrays and the construction of supra-molecular bioconjugates. *Nucleic Acids Res. 22*, 5530−5539.

(12) Kukolka, F., and Niemeyer, C. M. (2004) Synthesis of fluorescent oligonucleotide−EYFP conjugate: towards supramolecular construction of semisynthetic biomolecular antennae. *Org. Biomol. Chem. 2*, 2203−2206.

(13) Lapiene, V., Kukolka, F., Kiko, K., Arndt, A., and Niemeyer, C. M. (2010) Conjugation of fluorescent proteins with DNA oligonucleotides. *Bioconjugate Chem. 21*, 921−927.

(14) Niemeyer, C. M. (2010) Semisynthetic DNA-protein conjugates for biosensing and nanofabrication. *Angew. Chem., Int. Ed. Engl. 49*, 1200−1216.

(15) Lovrinovic, M., Seidel, R., Wacker, R., Schroeder, H., Seitz, O., Engelhard, M., Goody, R. S., and Niemeyer, C. M. (2003) Synthesis of protein-nucleic acid conjugates by expressed protein ligation. *Chem. Commun.*, 822−823.

(16) Pritz, S., Wolf, Y., Kraetke, O., Klose, J., Bienert, M., and Beyermann, M. (2007) Synthesis of biologically active peptide nucleic acid-peptide conjugates by sortase-mediated ligation. *J. Org. Chem. 72*, 3909−3912.

(17) Tominaga, J., Kemori, Y., Tanaka, Y., Maruyama, T., Kamiya, N., and Goto, M. (2007) An enzymatic method for site-specific labeling of recombinant proteins with oligonucleotides. *Chem. Commun.*, 401−403.

(18) Kitaoka, M., Tsuruda, Y., Tanaka, Y., Goto, M., Mitsumori, M., Hayashi, K., Hiraishi, Y., Miyawaki, K., Noji, S., and Kamiya, N. (2011) Transglutaminase-mediated synthesis of a DNA-(enzyme)n probe for highly sensitive DNA detection. *Chemistry 17*, 5387−5392.

(19) Smith, S. S., Niu, L., Baker, D. J., Wendel, J. A., Kane, S. E., and Joy, D. S. (1997) Nucleoprotein-based nanoscale assembly. *Proc. Natl. Acad. Sci. U.S.A. 94*, 2162−2167.

(20) Jongsma, M. A., and Litjens, R. H. (2006) Self-assembling protein arrays on DNA chips by auto-labeling fusion proteins with a single DNA address. *Proteomics 6*, 2650−2655.

(21) Linney, E., and Hayashi, M. (1973) Two proteins of Gene A of ϕX174. *Nat. New Biol. 245*, 6−8.

(22) Langeveld, S. A., van Mansfeld, A. D., Baas, P. D., Jansz, H. S., van Arkel, G. A., and Weisbeek, P. J. (1978) Nucleotide sequence of the origin of replication in bacteriophage ϕX174 RF DNA. *Nature 271*, 417−420.

(23) Sanhueza, S., and Eisenberg, S. (1984) Cleavage of single-stranded DNA by the ϕX174 A* protein: The A*-single-stranded DNA covalent linkage. *Proc. Natl. Acad. Sci. U.S.A. 81*, 4285−4289.

(24) Hanai, R., and Wang, J. C. (1993) The mechanism of sequence-specific DNA cleavage and strand transfer by phi X174 gene A* protein. *J. Biol. Chem. 268*, 23830−23836.

(25) Heidekamp, F., Baas, P. D., and Jansz, H. S. (1982) Nucleotide sequences at the ϕX gene A protein cleavage site in replicative form I DNAs of bacteriophages U3, G14, and α3. *J. Virol. 42*, 91−99.

(26) Bock, L. C., Griffin, L. C., Latham, J. A., Vermaas, E. H., and Toole, J. J. (1992) Selection of single-stranded DNA molecules that bind and inhibit human thrombin. *Nature 355*, 564−566.
(27) van Mansfeld, A. D., van Teeffelen, H. A., Baas, P. D., and Jansz, H. S. (1986) Two juxtaposed tyrosyl-OH groups participate in phi X174 gene A protein catalysed cleavage and ligation of DNA. *Nucleic Acids Res. 14*, 4229−4238.
(28) Venkatesh, B., Arifuzzaman, M., Mori, H., Suzuki, S., Taguchi, T., and Ohmiya, Y. (2005) Use of GFP tags to monitor localization of different luciferases in E. coli. *Photochem. Photobiol. Sci. 4*, 740−743.
(29) Baldrich, E., Restrepo, A., and O'Sullivan, C. K. (2004) Aptasensor development: elucidation of critical parameters for optimal aptamer performance. *Anal. Chem. 76*, 7053−7063.
(30) Sekiguchi, J., and Shuman, S. (1994) Requirements for noncovalent binding of vaccinia topoisomerase I to duplex DNA. *Nucleic Acids Res. 22*, 5360−5365.
(31) Nangreave, J., Han, D., Liu, Y., and Yan, H. (2010) DNA origami: a history and current perspective. *Curr. Opin. Chem. Biol. 14*, 608−615.
(32) Rajendran, A., Endo, M., and Sugiyama, H. (2012) Single-molecule analysis using DNA origami. *Angew. Chem., Int. Ed. Engl. 51*, 874−890.
(33) Lin, C., Liu, Y., and Yan, H. (2009) Designer DNA nanoarchitectures. *Biochemistry 48*, 1663−1674.
(34) Zhang, D. Y., and Seelig, G. (2011) Dynamic DNA nanotechnology using strand-displacement reactions. *Nat. Chem. 3*, 103−113.